

Conference Proceedings

Engineering Science and Technology

Volume 1 (2019)

The 4th International Symposium on Fluid Mechanics and Thermal Sciences

14 December 2019

Palm Garden Hotel, IOI Resort City, Putrajaya, Malaysia

Copyright Page

Proceeding of the Fourth International Symposium on Fluid Mechanics and Thermal Sciences (4th IS-FMTS 2019)
Palm Garden Hotel IOI Resort City, Putrajaya, Malaysia December 14, 2019
Assoc. Prof. Dr. Nor Azwadi Che Sidik (Editor)

Copyright © 2019 the 4th International Symposium on Fluid Mechanics and Thermal Sciences
Personal use of this material is permitted. However, permission to reprint/republish this material for advertising or promotional purposes or for creating new collective works for resale or redistribution to servers or lists, or to reuse any copyrighted component of this work in other works must be obtained from 4th IS-FMTS 2019. Authors' rights are stated in the 4th IS-FMTS 2019 Copyright Transfer Agreement.

For copyright issues, please contact:

4th IS-FMTS 2019
c/o AKADEMIA BARU PUBLISHING (M) SDN BHD
NO. 22, Jalan Puteri 5A/3, Bandar Puteri Bangi,
43000 Kajang, Selangor, MALAYSIA
+60177541097

PREFACE

The Fourth International Symposium on Fluid Mechanics and Thermal Sciences (4th IS-FMTS 2019) was held in Malaysia on 14 December 2019 at Palm Garden Hotel IOI Resort City, Putrajaya. The conference was organized by AKADEMIA BARU PUBLISHING (M) SDN BHD. The goal of is to gather scholars, researchers, and scientists from all over the world to present advances in the fields of transport phenomena and to foster an environment conducive to exchanging ideas and information.

One keynote speaker was invited from TAKASAGO THERMAL ENGINEERING CO, LTD. His area of expertise is BEMS (Building and Energy Management System) and automatic control of air conditioning system. The conference provided a setting for discussing recent development in a wide variety of topics including Engineering Flow, Drops and Bubbles, Computational Heat Transfer, Compressible Flows, Heat Exchangers, Electrohydrodynamic, Condensation, Biological Flows, Geophysical Flows, Heat Transfer in Combustion and Engines, Multiphase Flows, Nanofluids, Turbulence and so on. The conference has been a good opportunity for participants coming from Japan, Algeria, Nigeria, so many ASEAN countries and European countries to present and discuss topics in their respective areas. Over one hundred and twenty-eight well-qualified papers were presented. Because of the rapid progress in the fluid mechanics and thermal sciences, a large number of papers was submitted. For the first time in these conferences, several parallel sessions were held. Even so, many goods papers had been rejected.

We would like to thank all participants for their contributions to the Conference program and for their contributions to these Proceedings. Our special thanks go to our colleagues for their devoted assistance in the overall organization of the conference. We also express our sincere thanks to Professor Dr Yutaka Asako for his help in chairing the keynote session. Special thanks go to Dr Rozanti A. Hamid for her invaluable organizing efforts. Without her skills the conference could not have been such a technical success and a very pleasant experience.

It is our pleasant duty to acknowledge the financial support from AKADEMIA BARU PUBLISHING (M) SDN BHD.

We are looking forward to the FIFTH International Symposium on Fluid Mechanics and Thermal Sciences that will be held on June 2020. We hope that it will be interesting and enjoying at least as all of its ten predecessors.

Assoc. Prof. Dr. Nor Azwadi Che Sidik
Conference chair- 4th IS-FMTS 2019

TABLE OF CONTENT

	Page
Preface	i
Evaluation on the Performance of Cross-Matrix Absorber Double-Pass Solar Air Heater (CMA-DPSAH) With and Without Thermal Energy Storage Material	1-10
Numerical Studies of In-Cylinder Combustion and Soot Emission Characteristics of Biodiesel Fuels from Different Feedstock	11-25
Second Grade Nanofluid Flow Over A Vertical Plate With Wall Transpiration	26-35
Statistical Relationship of Drilled Solid Concentration on Drilling Mud Rheology	36-49
Using Solar Energy for Irrigation in Kirkuk City and Outskirt	50-57
Two-Phase Region Effect on Film Condensation on an Inclined Plate Embedded in a Porous Medium	58-74
Performance Analysis of Vortex Cooler	75-84
A Simple Stabilization and Calibration Method for K-Type Thermocouple and MAX6675 Module with Reference DS18B20 Thermistor Based on Low-cost Arduino Microprocessor at Ambient Conditions	85-93
Transport Phenomena in Organic Solvent Nanofiltration: A Review	94-102
Photo degradation of Biobased Oils Polymer blended with High Density Polyethylene upon Ultra Violet Irradiation Exposure	103-109
Effectiveness of Stern Foil Application on High Speed Vessel To Reduce Total Resistance Using Computational Fluid Dynamics (CFD) Method	110-116
CFD Study on Impeller Effect on Mixing in Miniature Stirred Tank Reactor	116-128
The Magnetohydrodynamics Casson Fluid Flow, Heat and Mass Transfer Due to the Presence of Assisting Flow and Buoyancy Ratio Parameters	129-139
Soret and Dufour Effects on Magneto-hydrodynamics Newtonian Fluid Flow beyond a Stretching/Shrinking Sheet	140-151
Dual Numerical Solutions on Mixed Convection Casson Fluid Flow Due to the Effect of The Rate of Extending and Compressing Sheet – Stability Analysis	152-160
CFD Simulation of Steam Condensation in Nozzle using Different Turbulence Models	161-177
Heat Transfer Properties of Biobased Polymer Coating for Mortar Cement Filled Aggregate from Recycled Materials	178-188
MHD Squeezing Flow of Casson Nanofluid with Chemical Reaction, Thermal Radiation and Heat Generation/Absorption	189-206
Study on Shape Geometry of Floating Oscillating Water Column Wave Energy Converter for Low Heave Wave Condition	207-217
Application of Computational Fluid Dynamic Method (CFD) on Solar Still: A Review	218-225
Quantifying Heat Losses in Micro Combustor with Wire Mesh Using Numerical Simulation	226-234
The Effect Of Sedimentation To The Pump Sump System By Using Computational Fluid Dynamics	235-244

TABLE OF CONTENT

(CFD) Model

Combination of Dehumidifier, Heat Pump and Air Heater: Influence of Temperature, Specific Humidity, and mass flow rate of Air on Specific Energy Consumption 245-254

Enhancement of Syngas Production Via Co-Gasification Experimental of Renewable Densified Fuels (RDF) in A Open- Top Downdraft Fixed Bed Gasifier 255-265

Experiments on Measurement of Heat Transfer Rate Of Gas Flow Through Microchannel With Constant Wall Temperature 266-274

Prediction of Water Saturation Using Fuzzy Logic 275-285

Torrefaction of Densified Palm Kernel Shell with Mixture of Starch and Water as Binder 286-299

Production of Volatile and Char During Pyrolysis and Combustion in Domestic Wastewater Sludge By Using Thermogravimetric Analysis 300-305

Effect of Internal Diameter and Working Fluids on Thermal Performance of a Vertical Closed-Loop Oscillating Heat Pipe with Double Heat Sources 306-311

Simulation of Internal Undular Bores of Depression Propagating over a Slowly Varying Region 312-324

Numerical Analysis of Aluminium Oxide and Silicon Dioxide Nanofluids in Serpentine Cooling Plate of PEMFC 325-336

Heat Transfer Characteristic for Premixed Flame Jet from Swirl Chamber 337-349

Drag Reduction and Degradation Characteristics of Nata de Coco Suspension in Spiral Pipe 350-358

Chaotic Mixing of Microdroplets Using Surface Acoustic Waves Device 359-369

An Investigation of Heat Transfer on the Downstream Surface and an Experimental Study on Flow Structure of Continuous Jet of the Single Row Circular Orifice Injecting nto Mainstream 370-378

Effects of using Different Coal on Combustion Characteristics in Coal-fired Boiler 379-386

Numerical Approach Used To Evaluate The Damage Structural Capacity Of a Composite Concrete Slab Under Fire By Confirming Its Behaviour 387-402

Review of Fluid-Structure Interaction Model for the Wave Current Behaviour With the Offshore Structures 403-416

The Effect Of Varying Tube Diameters on Enhancement Heat Transfer by Forced Convection Through A Horizontal Tube 417-426

The Role of Coherent Vortices in The Mixing Process Of a Coaxial Jet 427-439

An Overview of Different Indirect and Semi-Indirect Evaporative Cooling System for Study Potency of Nanopore Skinless Bamboo as An Evaporative Cooling New Porous Material 440-447

Evaluation on the Performance of Cross-Matrix Absorber Double-Pass Solar Air Heater (CMA-DPSAH) With and Without Thermal Energy Storage Material 448-457

Plasma Temperature Profiles Modelling and Experimental Validation Using Graphene Electrode for Steel Wire Surface Cleaning 458-470

Stability Analysis on Stagnation-Point Flow and Heat Transfer Towards a Permeable Shrinking Sheet 471-484

TABLE OF CONTENT

with Heat Source in a Casson Fluid

Unsteady Three-Dimensional Free Convection Flow near the Stagnation Point over a General Curved Isothermal Surface in a Nanofluid 485-498

Application of Flywheel Energy Storage on Generator-set 499-508

Comparative Assessment of Closed Loop Heat Pump Dryer and Direct Solar Dryer System for Banana Drying 509-517

The Effect of Downcomer Depth Variation with Air Entrainment Process on Vertical Plunging Water Jet with a Height of 28 Cm on the Water Surface 518-524

Meshless Fluid Structural Interaction (FSI) Simulation of Deformation of Flexible Structure due to Water Dam Break 525-530

Experimental Investigation In Improving Thermal Performance Of Passive Heat Removal System Of VVERs Using Mist Assisted Evaporative Cooling 531-540

Study on the Performance Analysis on Dual Fuel Diesel Main Engine of Passenger Ship 3200 DWT 541-551

Oil Reclamation of In-Service Power Transformer using Fuller's Earth: An Experience 552-560

Evaluation of The Prediction of Wave Pattern And Hull Performance of MTC 092 Hull Form Using Commercial Software 561-568

Preliminary Study of Occupants' Thermal Sensation with Different Set-point temperature of Postgraduate Office with Cooling Mode in University Campus 569-578

Indirect Evaporative Cooler Using Solar Energy 579-592

Evaluation of Atmospheric Boundary Layer in Open Loop Boundary Layer Wind Tunnel Experiment 593-605

Characterization of Raw Materials and Manufactured Binderless Particleboard from Spent Mushroom Substrate and Open Rubberwood Sawdust 606-615

A Recent Review of Energy Recovery Ventilator on Low and High-Rise Buildings 616-621

Characterisation of Calcium Carbonate and Its Polymorphs from Molluscan Shells of *Anadara Granosa* (Blood Cockle), Open *Paphia Undulata* (Surf Clam), *Dosinia Exesperata* (Venus Access Clam) and Marble 622-629

Mechanical Properties of Palm Composites: Date, Bertam, Coconut and Oil Palm – A Review 630-633

Hall Effect on Mixed Convection Casson Fluid Flow over an Exponentially Extending Sheet in Porous Media 634-643

Enhancement of Tribological Behaviour and Thermal Properties of Hybrid Nanocellulose/Copper (II) Oxide Nanolubricant 644-652

Potential Augmentation of the Ampacity of a Medium Voltage Underground Cable in Power Distribution Networks by CHT Thermal Modelling 653-665

Aerodynamic Drag Study of Time-Trial Cycling Helmets Using CFD Analysis 666-675

Large-Eddy Simulation on Pedestrian Wind Environment in Urban Buildings of Random Staggered Arrays 676-684

TABLE OF CONTENT

CFD Investigation on The Jet-Engine Inspired Wind Turbine	685-692
Feasibility Study of using Oil Palm Trunk Waste Fiber as Fluid Loss Control Agent and Lost Circulation Material in Drilling Mud	693-702
Thermal Conductivity and Viscosity of TiO2/CNTs-ethylene glycol based Nanofluids for Different Ratio of Nanoparticle	703-714
Thermal Conductivity and Dynamic Viscosity of Nanofluids: A Comprehensive Review	715-731
Experimental Assessment of a Novel Eutectic Binary Molten Salt-based Hexagonal Boron Nitride nanocomposite as a Promising PCM with Enhanced Specific Heat Capacity	732-741
Investigation of Newtonian and Power-Law Blood Flow Models in a 180o Curved Pipe at Low to Medium Shear Rate	742-755
Influence of Double Entry Volute on Incidence Angle Variation Under Steady Flow: Numerical Investigation	756-767
Experimental Investigation of the Effect of a Downstream Square Plate on Vortex-induced Vibration and Galloping of a Square Cylinder in Uniform Flow	768-780
Experimental Investigation of Mixed Convection Heat Transfer Within a Cavity Containing a Rotating Cylinder	781-790
Magnetohydrodynamic Flow of Maxwell Nanofluid Over a Vertical Plate in a Porous Medium	791-800
Intelligent Control Based Estimation of Heat Transfer Coefficient from Four Flat Tubes with Different Air Inlet Angles	801-813
Experimental Investigation on the Stability of 40% Ethylene Glycol Based TiO_2-Al_2O_3 Hybrid Nanofluids	814-823
Application Of Magneto Rheological Damper System In Warren Truss Bridge Structure	824-834
On-Design Operation and Performance Characteristic of Custom Engine	835-844
Ferroconvection in an Anisotropic Porous Medium with Variable Gravity	845-854
Unsteady MHD Mixed Convective Flow of Buongiorno's Nanofluid in a Lid-Driven Cavity with Heat Generation and Chemical Reaction Effects	855-866
Subsurface Vortex Control Parametric Study at Submersible Pump Intake Using Plate-Type Floor Splitters	867-873
Application of Computational Fluid Dynamic Simulation for the Study of Heat Stress and Heat Strain- A Review	874-879
Rheological Behaviour of Purified Acid-extracted Pectin from 'Saba' Banana [*Musa* BBB 'saba' (*Musa acuminata x Musa balbisiana*)] Peel Applied to Beverage	880-888
Waste Heat Recovery from Automotive Exhaust Using Thermoelectric Cell for Electrical Power Generation	889-897
Preparation methods and challenges of hybrid nanofluids: A Review	898-910
Drying Droplets : A Review on Its Numerical and Experimental Studies To Remove Coffee Ring Effect	911-927

TABLE OF CONTENT

Synthesis, Characterization and Modelling of Nickel Nanowires Synthesized Via Template-Assisted Electrodeposition	928-941
Numerical Simulation of Fluid Flow and Heat transfer Through Porous Media	942-951
Aerodynamic Performances of Paper Planes	952-959
Experimental Study on Two-Phase Flow of Gas-Liquid with High Viscosity in Capillary with The Slope of 5o Against Horizontal Position	960-968
Investigation Of Thermal Hydraulic Performance Of Microchannel Heat Sink With Hourglass Profile	969-979
Visualization of Heat Transfer via Heatlines and Entropy Generation for Marangoni Convection in an Open Top Rectangular Cavity	980-986
Flow and Heat Transfer Characteristics of Impinging Bubbly Jet	987-998
CFD Investigation of The Effect of Heave Plate on Vertical Motion Responses of A Floating Jetty	999-1009
Flame Structure and Heat Transfer Characteristic of Premixed Flame Jet With Pulsating Effect	1010-1024
Effect of Channel Rotation Speed on Heat Transfer Characteristics of Impinging Jets	1025-1034
Temperature Profile Assessment of Sub-Bituminous Coal using a Single Burner Combustion Test Facility	1035-1042
The Effect of Liquid Viscosity on The Gas-Liquid Two-Phase Flow Pattern In 45o Inclined Capillary Pipe	1043-1051
Nanofluid as an Alternative Coolant in Machining: A Review	1052-1061
Groundwater Analysis for Unconfined and Clayey Layer by using Response Surface Methodology	1062-1070
Engineering Science and Technology Conference Proceedings	1071-1080
Analysis of Absorber Material Effect on Optimization of Heat Absorption in Solar Collectors	1081-1088
Study of Ability Level of the Sun Absorption Intensity by Building Yard Materials on Environmental Thermal Comfort	1089-1095
Index	1096

Penerbit Akademia Baru

Engineering Science and Technology Conference Proceedings

Journal homepage: www.akademiabaru.com/EST.html
ISSN: XXXX-XXXX

Evaluation on the Performance of Cross-Matrix Absorber Double-Pass Solar Air Heater (CMA-DPSAH) With and Without Thermal Energy Storage Material

Open Access

Ahmad Fadzil Sharol[1], Amir Abdul Razak[1*], Zafri Azran Abdul Majid[2], Muhammad Amirul Azwan Azmi[1], Muhammad Amir Syahiran Muhammad Tarminzi[1]

[1] Department of Energy and Environmental, Faculty of Engineering Technology, Universiti Malaysia Pahang, 26300 Gambang, Pahang, Malaysia
[2] Department of Radiography, Kuliyyah of Allied Health and Sciences, International Ismalic University of Malaysia, 25200 Kuantan, Pahang, Malaysia

ABSTRACT

Solar engineering technology was going through a great technological advancement in terms of the design of the solar collector in the past decades. However, due to the intermittent nature of solar energy, it is very difficult to achieve a better performance of the solar heater especially in the application of air as the heat transfer fluid. The utilization of thermal storage materials demonstrate an effective way in order to improve an overall performance of solar air heater. In the present study, the performance of cross-matrix absorber double-pass solar air heater (CMA-DPSAH) integrated with the phase change material (PCM) as thermal energy storage was conducted. The PCM material was inserted inside the rectangular aluminium tube used as the thermal absorber. The air mass flow rate of 0.007 kg/s was used during the entire experimental period. The experiment was conducted on several phase; Phase 1 (CMA-DPSAH with PCM) and Phase 2 (CMA-DPSAH without PCM) in order to compare and evaluate the effectiveness of the PCM utilization. Based on the result, CMA-DPSAH with PCM performed better than the CMA-DPSAH without PCM with maximum of heat gain and temperature output were 127 W and 53 °C, respectively. The instantaneous efficiency of CMA-DPSAH with PCM consistently higher than the CMA-DPSAH without PCM for about 17 – 19% with the maximum was 64 % during the low radiation flux. This feature offer a great potential of solar air heater application in the intermittent solar radiation condition, especially for drying of the agriculture products.

Keywords:
Cross-Matrix absorber (CMA); Double-pass solar air heater (DPSAH); phase change material (PCM); instantaneous efficiency

Copyright © 2019 PENERBIT AKADEMIA BARU - All rights reserved

1. Introduction

Solar engineering technology was going through a great technological advancement in terms of the design configuration of the solar collector in the past decades. In the application of solar air heater (SAH), there were a lot of innovative design of the solar energy harvesting devices have been highlighted in the literature in order to maximize the rate of heat transfer from the surface of thermal absorber to the flowing heat transfer fluid [1]. These advancement including the utilization of finned thermal absorber surfaces [2–4], insertion of porous structure [5–7] and the

* *Corresponding author.*
E-mail address: amirrazak@ump.edu.my (Amir Abdul Razak)

implementation of artificial roughness on the thermal absorber surface [8–10]. However with the intermittent nature of solar energy source [11,12], making the SAH difficult to achieve a better overall efficiency and limit their operating time. The incorporation of thermal energy storage material into the solar energy system has been seen as a suitable and practical solution in order to maximize the utilization of solar thermal devices in the situation of intermittent solar radiation and/or during off-sunshine period.

From literature, there have been increasing trends on the study related to the integrated SAH with the thermal energy storage system. Bouadilla et al. [13] has conducted an experimental investigation about the SAH integrated with packed-bed of spherical capsules of SN27 material as the thermal energy storage materials. The spherical capsules were built from a blend of polyolefin and was painted with flat black in order to act as the thermal absorber component of the SAH. Based on their study, it was concluded that the SAH system managed to supply an amount of useful heat of 200 W/m^2 for an extended period of time after the off-sunshine period. Double-pass solar air heater (DPSAH) integrated with rectangular capsules of paraffin wax was investigated by Salih et al. [14]. The experimental work was conducted to evaluate the DPSAH thermal efficiency with the variation of solar radiation and mass flow rate. The numerical study was also conducted with the result from the developed mathematical model agreed well with the experimental result. W. Baig and M.H. Ali [15] investigated the effect of using the aluminum foam embedded in the PCM duct located on the top of the thermal absorber of DPSAH. The configuration was compared with the DPSAH having a similar arrangement but with no aluminum foam insertion. They concluded that the insertion of aluminum foam material was increase the PCM conductivity but reduce its thermal storage capability with useful heat gain time was 30 minutes faster than the one without aluminum foam insertion.

Comparison between rectangular and cylindrical shape of PCM encapsulation was conducted experimentally by A.K. Raj et al. [16]. The PCM encapsulations were located on the top side of thermal absorber in order to investigate the thermal efficiency of both DPSAH configurations. According to the studies, they concluded that the rectangular encapsulation provides thermal storage efficiency of 67 % as compared to the cylindrical encapsulation of 47.2 %. This was due to the fact that during the rectangular encapsulation mode, the temperature different between the thermal absorber and the bottom plate is higher, which mean that the absorption of radiation flux was higher than the cylindrical encapsulation mode. The indoor experimental investigation of integrated zig-zag configuration of cross-matrix absorber in single-pass solar air heater (SPSAH) has been conducted by A.F. Sharol et al. [17] by varying the input parameters of mass flow rate and solar radiation. Based on the result, it is concluded that the output temperature and heat gain were directly and indirectly proportional to the mass flow rate, respectively. Based on author knowledge, there was no study conducted on the integration of thermal storage material into the rectangular aluminum tube of cross-matrix absorber with staging configuration in the DPSAH. In this study, the effect of incorporation of thermal storage material into cross-matrix absorber of DPSAH was investigated experimentally.

2. Description of CMA-DPSAH

The schematic diagram of the CMA-DPSAH as shown in Fig. 1 was constructed using the locally available materials. The device consists of a set of collector made of polypropylene having a dimension of 525 mm length, 400 mm width and 180 mm height. The CMA-DPSAH was built from polycarbonate transparent cover, intermediate polycarbonate transparent cover, and set of rectangular aluminium tubes act as an absorber. The rectangular aluminium tube comprises of two

types of aluminium tube namely; type A (326 mm Length, 19.1 mm width, 19.1 height and 1 mm thickness) which was positioned perpendicular to the air flow and type B (427 mm Length, 19.1 mm width, 19.1 height and 1 mm thickness) which was positioned parallel with the air flow. The spacers were located at the bottom absorber of each pass in order to avoid direct contact to the bottom wall of the absorber and surface of the intermediate glazing plate. The tubes were sprayed with flat black coating and arranged in a staging manner in order to increase the heat absorption and to optimize the aperture area of the tubes [18], respectively. The total aperture area of the thermal absorber was calculated to be 0.3786 m^2. The 6 mm thickness of insulation sheet was applied at the edge and bottom side of the collector in order to reduce the heat losses. Three units of brushless 24 V DC fan were installed at the outlet chamber of the collector in order to force the outdoor air into the air passage of the collector. The incoming air entered to the first pass of the collector through the three identical circle shape inlet duct before went to the second pass through 3.3 cm diameter flexible hose. Fig. 2 shows the experimental setup used in this work.

Additionally, paraffin wax in the form of granulated particle was inserted in the tube type B and was sealed with rubber cap to prevent from leaking. The thermophysical properties of the paraffin wax is shown in Table 1.

Table 1
Thermophysical properties of paraffin wax used in this study [19]

Properties	Value
Melting temperature, T_m (°C)	58 - 60
Specific heat (solid), $C_{P,s}$ (J/kg.K)	900
Enthalpy of fusion, H_f (kJ/kg)	214.4
Total weight (g)	624

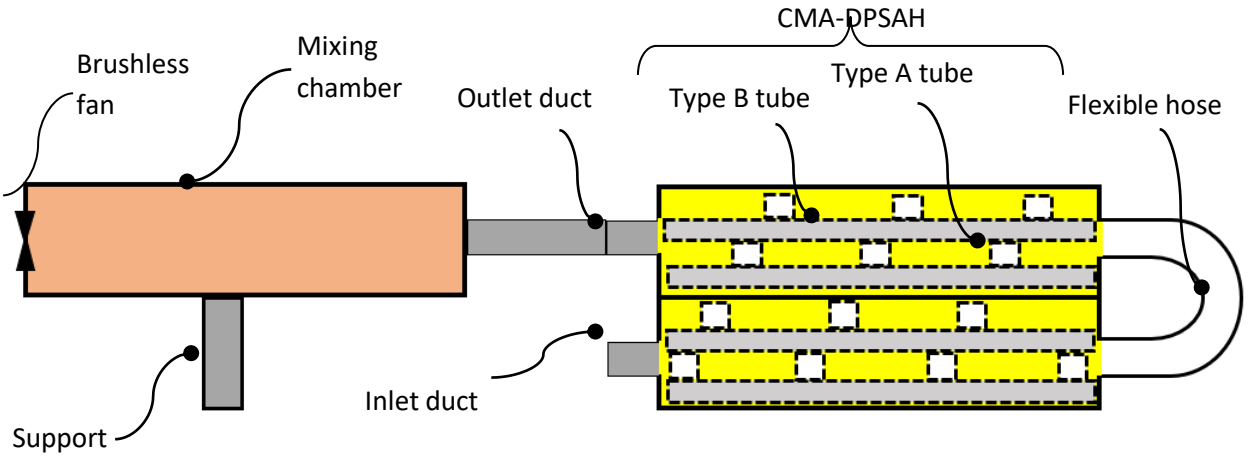


Fig. 1. Schematic diagram of the CMA-DPSAH system

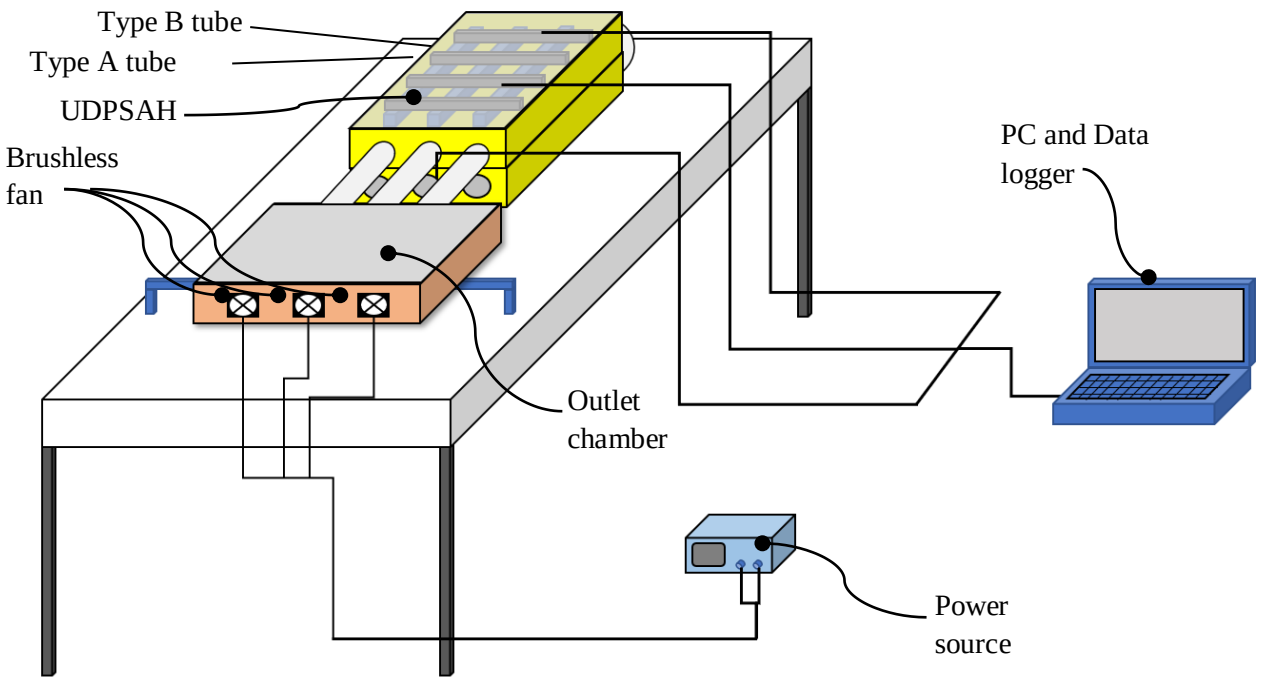


Fig. 2. Experimental setup used in this work

2.1 Description of Experimental Method and Apparatus

The outdoor experiment was conducted at Islamic International University of Malaysia (IIUM) located in Kuantan, Pahang (latitude N 3°50'42.47'' (3.84513°) and longitude of E 103°18'11.76'' (103.30327°)). The temperature data was recorded by using Advantech ADAMview data logger system at every 1-minute time span from 9:00 a.m. until 7:00 p.m. The K-type thermocouple with reading tolerance of ± 1.5 ^{o}C used to measure the temperature data was installed at multiple location across the system as shown in the Fig. 3. The solar radiation and wind speed were measured using Apogee pyranometer (calibration uncertainty of 5 %) and hot wire anemometer, respectively. The air mass flowrate was set to be flowing through the collector at 0.007 kg/s for the entire experimental period. The thermal performance of CMA-DPSAH (Phase 1) was compared with the CMA-DPSAH without thermal energy storage (Phase 2) material inserted.

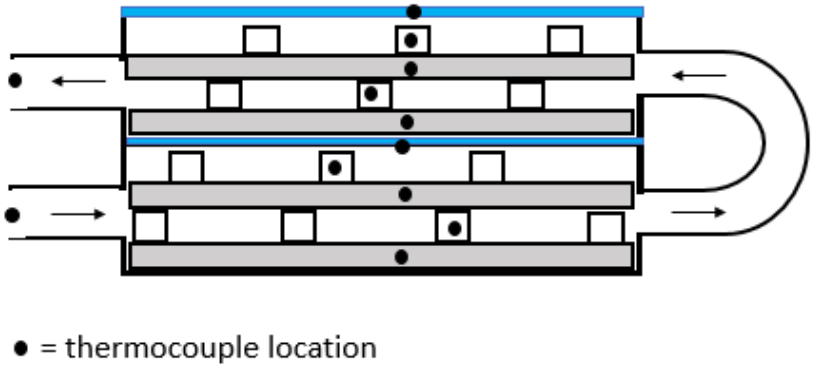


Fig. 3. Thermocouple positioning on respective tube and glazing

The thermal efficiency of the collector during charging and discharging process was calculated based on the Eq. (1) and (2), respectively [20]:

$$\eta_{Charging} = \frac{Q_U + Q_S}{A_T I} \quad (1)$$

$$\eta_{Discharging} = \frac{Q_U}{Q_S} \quad (2)$$

where Q_U and Q_S are useful heat gained and heat stored which were given by equation (3) and (4), as follows:

$$Q_U = \dot{m} c_p (T_{out} - T_{in}) \quad (3)$$

$$\begin{aligned} Q_s &= \frac{m_{pcm}}{\Delta t} c_{p,s} \Delta T_{pcm} && T_{avg,pcm} < T_m \\ Q_s &= \left(\frac{m_{pcm} L_{pcm}}{\Delta t}\right) && T_{avg,pcm} = T_m \\ Q_s &= \frac{m_{pcm}}{\Delta t} c_{p,l} \Delta T_{pcm} && T_{avg,pcm} > T_m \end{aligned} \quad (4)$$

where T_{pcm}, $T_{avg,pcm}$, T_m, $c_{p,s}$, $c_{p,l}$ and m_{pcm} are PCM temperature rise, average PCM temperature, solid phase, liquid phase specific heat of PCM and PCM mass, respectively. As for latent heat calculation, in which for the case of stored heat by the PCM, the sensible heat mode will be take placed when the average PCM temperature, $T_{avg,pcm}$ is below or exceeding the melting temperature, T_m, otherwise the method will be latent heat [20,21].

2.2 Uncertainty Analysis

It is imperative to ensure the measurement of the parameters taken using the correct tool in order to produce the reliable data and to avoid error. This error might come from a various source such as human, measurement apparatus and environment of an experimental work. In this work, uncertainty analysis was conducted using the method available in the literature [22, 23] based on the following expression:

$$W_R = \left[\left(\frac{\partial R}{\partial x_1} w_1\right)^2 + \left(\frac{\partial R}{\partial x_2} w_2\right)^2 + \cdots + \left(\frac{\partial R}{\partial x_n} w_n\right)^2\right] \quad (5)$$

In which the average percentage value of an uncertainty of each measured and calculated parameter were 1.52 % and 7.85 %; respectively.

3. Results and Discussion

The experimental work was conducted in between the month of April and May 2019 under the cloudy sunny day condition. Figure 4 show the solar radiation profile as a function of time starting from 9:00 a.m. until 7:00 p.m. for each phase of an experiment. As can be seen in the Figure the solar radiation distribution for phase 1 having a stable profile with the weather slightly in better shape as compared to the condition of phase 2. During the phase 2, the weather condition in the morning was slightly cloudy with the condition becomes better as the day passes by. As expected, the highest solar radiation was recorded during the middle of the day for both cases with maximum value of 1017 W/m^2 and 944 W/m^2 for phase 1 and phase 2, respectively. At the end of the experiment period which was at around 6:30 p.m., solar radiation for both phases approached zero.

In order to further enlighten this occasion, inlet and outlet temperature of each phase were plotted as a function of time as shown in Figure 5. The output temperature profile was increased

gradually with the increase of inlet temperature and also solar radiation as previously explained from the Fig. 4. It is expected that the inlet and outlet temperature of phase 1 experiment was higher than the one of phase 2 experiment due to the slightly higher solar radiation. During this period, the temperature increases due to the sensible heat of the absorber material for each CMA-DPSAH used in the experiment. In the middle of the day, which was around 12:30 p.m. to 1:30 p.m., the latent heat of fusion started to take over for the CMA-DPSAH used in phase 1 (with PCM). As can be seen in the purple dotted box region shown in Figure 5, the output temperature profile slightly shows a flat profile even though the radiation flux already started to descend. This shows that albeit part of the PCM was melted, it gave the significant improvement in terms of maintaining the output temperature stability of the CMA-DPSAH. As compared to the one of without PCM from phase 2, the output temperature profile was fluctuated with the fluctuation of the solar radiation.

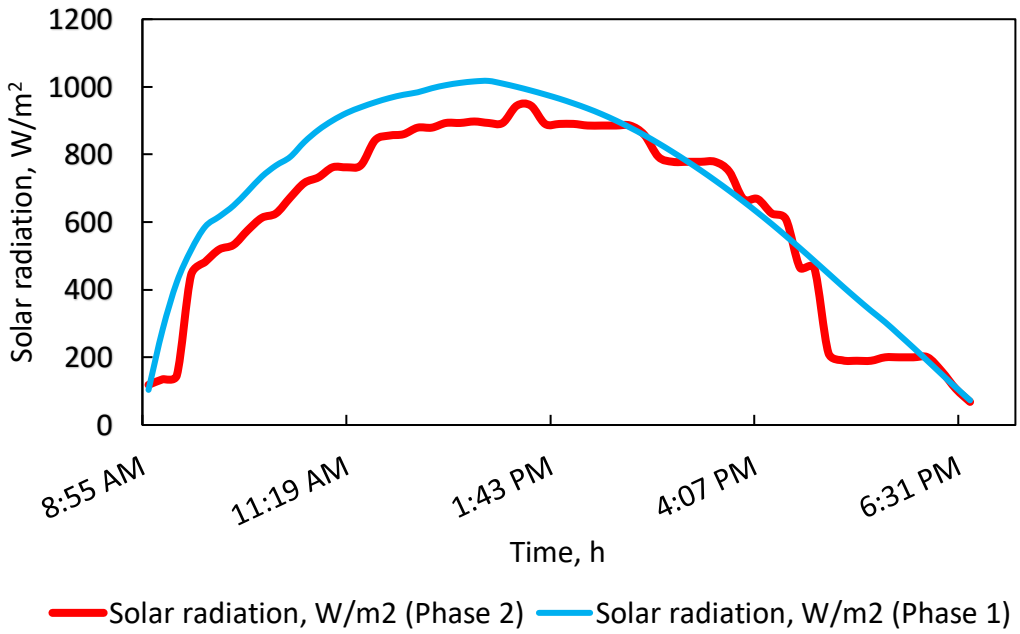


Fig. 4. Solar radiation distribution during phase 1 (CMA-DPSAH with PCM) and phase 2 (CMA-DPSAH without PCM) of the experiments

In order to evaluate the effectiveness of using PCM inside the absorber tube, the heat gain and temperature different for each phase was presented in Fig. 6. Heat gained by each collector was calculated using equation (3) and (4) with the latent heat effect was take into consideration for the phase 1 collector. The maximum energy gain by each collector was at a maximum value at the middle of the day as expected with CMA-DPSAH with PCM and CMA-DPSAH without PCM maximum heat gain is 127 W and 89 W, respectively at around 1:40 p.m. The temperature difference profile for each collector is in according to the heat gain profile, with the CMA-DPSAH with PCM achieved better performance as compare to the one of without PCM. This is expected, because the total heat gained by the collector with PCM was not only in the form of sensible heat from the absorber tube material itself, but also from the sensible heat (before the melting of the paraffin wax) and latent heat (during the freezing of the melted paraffin wax due to the fluctuation of the radiation flux) of the paraffin wax.

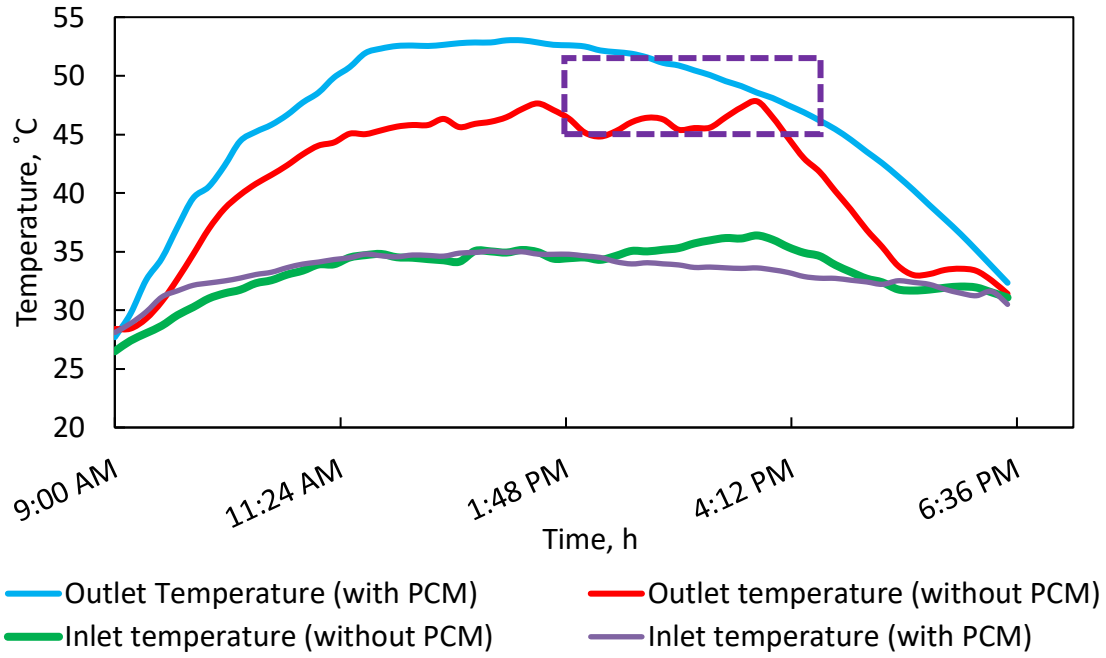


Fig. 5. Inlet and outlet temperature profile for configuration with PCM (Phase 1) and without PCM (Phase 2)

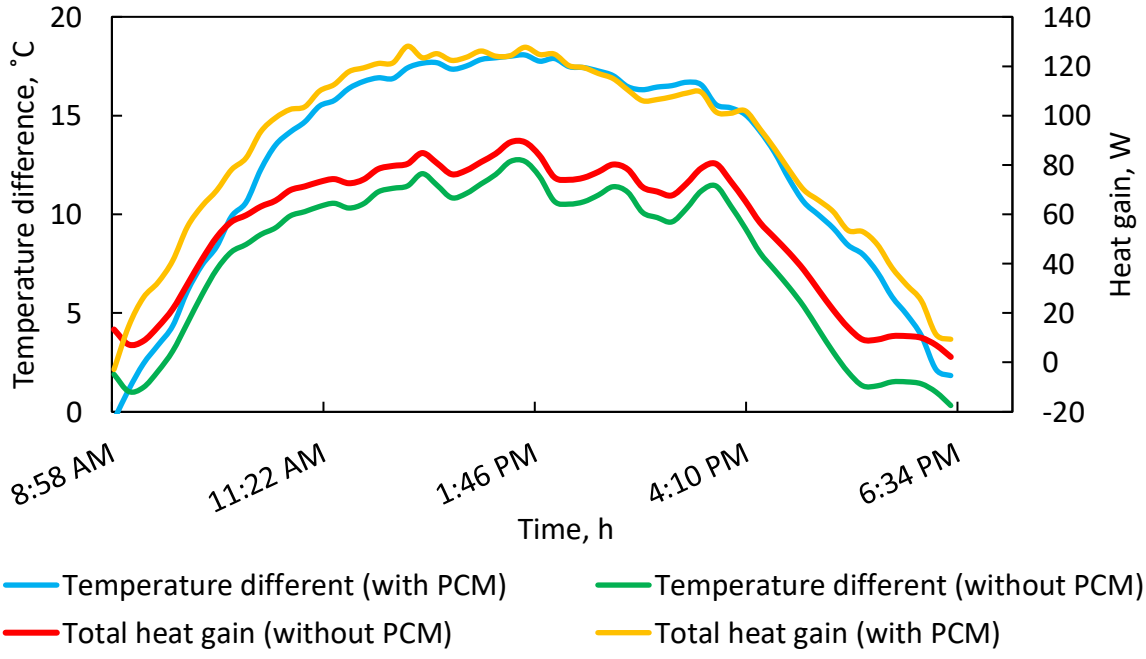


Fig. 6. Temperature difference and heat gain profile for each collector

This is proven with the instantaneous efficiency value of CMA-DPSAH with PCM which is consistently higher than the one without PCM as presented by Figure 7. From the Figure 7, the instantaneous efficiency of CMA-DPSAH with PCM varies with the maximum value was achieved during the condition of low radiation flux, which is about 64 %. This was due to the fact that during the low radiation flux, the air flowing through the collector still be heated by the heat that released from the paraffin wax during the freezing process. The instantaneous efficiency for CMA-DPSAH with PCM during the dropping of the radiation flux, which was significantly started at 3:00 p.m., was

varied between 40 – 64 % whereas for CMA-DPSAH without PCM, the instantaneous efficiency was consistently lower by 17- 19 %. This result was due to the fact that the only heat source for the air going through the collector was a sensible heat of absorber tube material, which was aluminium. The higher value of thermal diffusivity of Aluminium making the temperature of the absorber tube drop much faster with the dropping of radiation flux [24, 25].

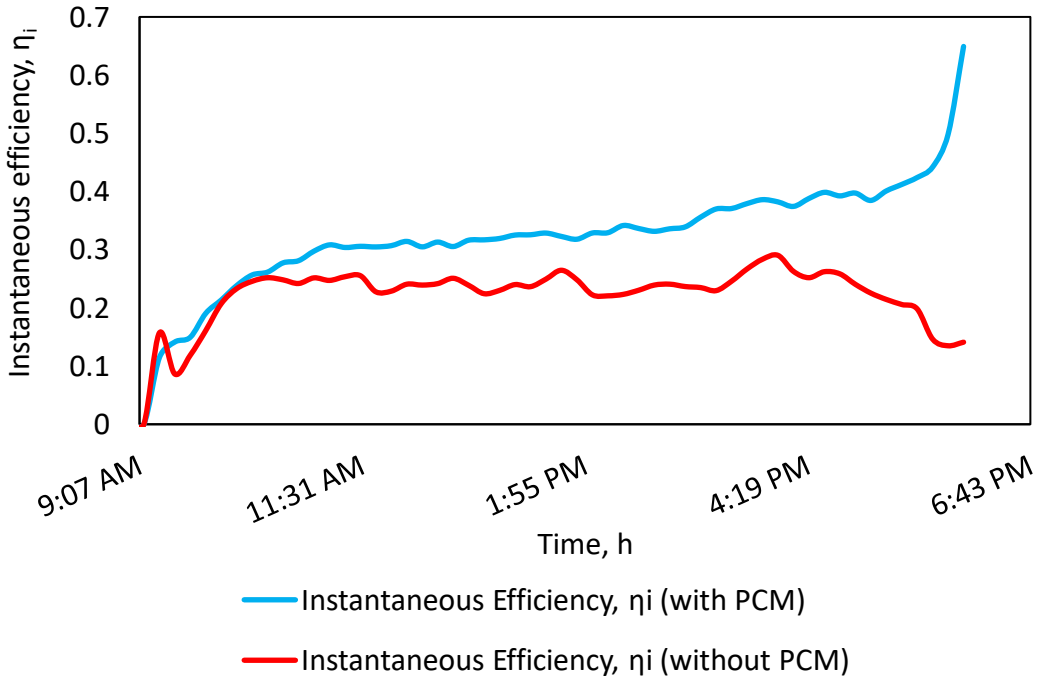


Fig. 7. Instantaneous efficiency of each collector as a function of time

4. Conclusions

The performance of DPSAH with PCM and without PCM were evaluated experimentally in the outdoor condition. Based on the result, several conclusions can be drawn as follows:

i) With the incorporation of PCM, the performance of CMA-DPAH can be improved significantly especially in the condition where there is a fluctuation of solar radiation or during the off-sunshine period.

ii) The ability of the PCM to store the energy is depend on the mass of the PCM used. The total weight of the PCM used in this study was 0.624 kg. With the value of latent heat of fusion, the energy can be stored by the PCM will be higher if the total weight of the PCM increased.

iii) The instantaneous efficiency of the CMA-DPSAH with the PCM was consistently higher than the one without PCM by 17- 19 % with the CMA-DPSAH with PCM gaining more energy that can be transferred to the flowing air. This condition was significant after the solar radiation flux started to drop (from 3:00 p.m. onwards).

iv) The features demonstrated by the CMA-DPSAH with PCM is suitable to be used in the drying application, especially for the agriculture products as that is the main focus by the Malaysian government in order to increase the production of drying products for Small and Medium-sized Industries.

Acknowledgment

The authors would like to thank University Malaysia Pahang (UMP) for the financial support under project grant RDU1703137 and International Islamic University of Malaysia (IIUM) for providing testing facilities.

References

[1] N. Kannan, D. Vakeesan. "Solar energy for future world: A review." *Renew. Sustain. Energy Rev.* 62 (2016) 1092–1105.
[2] A.J. Mahmood, L.B.Y. Aldabbagh, F. Egelioglu. "Investigation of single and double pass solar air heater with transverse fins and a package wire mesh layer." *Energy Convers. Manag*. 89 (2015) 599–607.
[3] A.J. Mahmood, L.B.Y. Aldabbagh. "Double pass solar air heater with transvers fins and without absorber plate." *Int. J. Mech. Aerospace, Ind. Mechatron. Manuf. Eng.* 7 (2013) 1293–1298.
[4] S. Ebadi, R.J.D. Wong, S. Mahmud, M. Al-Jethelah, A. Singh. "Investigation of phase change materials integrated with fin-tube baseboard convector for space heating." *Energy Build.* 187 (2019) 241–256.
[5] M.T. Jamal-Abad, S. Saedodin, M. Aminy. "Heat transfer in concentrated solar air-heaters filled with a porous medium with radiation effects: A perturbation solution." *Renew. Energy.* 91 (2016) 147–154.
[6] D. Zhou, C.Y. Zhao. "Experimental investigations on heat transfer in phase change materials (PCMs) embedded in porous materials." *Appl. Therm. Eng.* 31 (2011) 970–977.
[7] M. Dehghan, Y. Rahmani, D. Domiri, S. Saedodin. "Convection - radiation heat transfer in solar heat exchangers filled with a porous medium: Homotopy perturbation method versus numerical analysis." *Renew. Energy.* 74 (2015) 448–455.
[8] S. Hans, Gill. "Heat transfer and friction factor correlations for a solar air heater duct roughened artificially with broken arc ribs." *Exp. Therm. Fluid Sci*. 80 (2017) 77–89.
[9] R.K. Ravi, R.P. Saini. "Experimental investigation on performance of a double pass artificial roughened solar air heater duct having roughness elements of the combination of discrete multi V shaped and staggered ribs." *Energy.* 116 (2016) 507–516.
[10] R.K. Ravi, R.P. Saini. "Effect of roughness elements on thermal and thermohydraulic performance of double pass solar air heater duct having discrete multi V-shaped and staggered rib roughness on both sides of the absorber plate." *Exp. Heat Transf.* 31 (2018) 47–67.
[11] G. Kalaiarasi, R. Velraj, M. V. Swami. "Experimental energy and exergy analysis of a flat plate solar air heater with a new design of integrated sensible heat storage." *Energy* 111 (2016) 609–619.
[12] S.K. Singh."Performance analysis of solar air heater with phase change material." *National Institute of Technology Jamshedpur,* Jharkhand, 2017.
[13] S. Bouadila, S. Kooli, M. Lazaar, S. Skouri, A. Farhat. "Performance of a new solar air heater with packed-bed latent storage energy for nocturnal use." *Appl. Energy.* 110 (2013) 267–275.
[14] S.M. Salih, J.M. Jalil, S.E. Najim. "Experimental and numerical analysis of double-pass solar air heater utilizing multiple capsules PCM." *Renew. Energy.* (2019).
[15] W. Baig, H.M. Ali. "An experimental investigation of performance of a double pass solar air heater with foam aluminum thermal storage medium." *Case Stud. Therm. Eng.* 14 (2019) 100440.
[16] A.K. Raj, M. Srinivas, S. Jayaraj. "A cost-effective method to improve the performance of solar air heaters using discrete macro-encapsulated PCM capsules for drying applications." *Appl. Therm. Eng.* 146 (2019) 910–920.
[17] A.F. Sharol, A.A. Razak, Z.A.A. Majid, M.A.A. Azmi, M.A.S.M. Tarminzi. "Performance of force circulation cross-matrix absorber solar heater integrated with latent heat energy storage material." *IOP Conf. Ser. Mater. Sci. Eng.*, 2019.
[18] A.A. Razak, Z.A.A. Majid, F. Basrawi, A.F. Sharol, M.H. Ruslan, K. Sopian. "A performance and technoeconomic study of different geometrical designs of compact single-pass cross-matrix solar air collector with square-tube absorbers." *Sol. Energy.* 178 (2019) 314–330.
[19] S.O. Enibe. "Thermal analysis of a natural circulation solar air heater with phase change material energy storage." *Renew. Energy.* (2003).
[20] A.E. Kabeel, A. Khalil, S.M. Shalaby, M.E. Zayed. "Improvement of thermal performance of the finned plate solar air heater by using latent heat thermal storage." *Appl. Therm. Eng.* 123 (2017) 546–553.
[21] A.A. El-Sebaii, A.A. Al-Ghamdi, F.S. Al-Hazmi, A.S. Faidah. "Thermal performance of a single basin solar still with PCM as a storage medium." *Appl. Energy.* 86 (2009) 1187–1195.
[22] M. Yahya, A. Fudholi, K. Sopian. "Energy and exergy analyses of solar-assisted fl uidized bed drying integrated with biomass furnace." *Renew. Energy.* 105 (2017) 22–29.
[23] S. Şevik. "Experimental investigation of a new design solar-heat pump dryer under the different climatic

conditions and drying behavior of selected products." *Sol. Energy.* 105 (2014) 190–205.
[24] Z.A.A. Majid, A.A. Razak, M.H. Ruslan, K. Sopian. "Characteristics of solar thermal absorber materials for cross absorber design in solar air collector." *Int. J. Automot. Mech. Eng.* 11 (2015) 2582–2590.
[25] M.B. Y. Cengel. "Thermodynamics-An engineering approaches." *5th ed., Mc Graw-Hill*, 2010.

Penerbit Akademia Baru

Engineering Science and Technology Conference Proceedings

Journal homepage: www.akademiabaru.com/EST.html

Numerical Studies of In-Cylinder Combustion and Soot Emission Characteristics of Biodiesel Fuels from Different Feedstock

Open

Shin Mei Tan[1], Hoon Kiat Ng[1,*], Suyin Gan[2]

[1] Department of Mechanical, Materials and Manufacturing Engineering, University of Nottingham Malaysia, Jalan Broga, 43500 Semenyih, Selangor, Malaysia
[2] Department of Chemical and Environmental Engineering, University of Nottingham Malaysia, Jalan Broga, 43500 Semenyih, Selangor, Malaysia

ABSTRACT

Multi-dimensional computation of in-cylinder biodiesel combustion and soot emission characteristics is performed using a commercial Computational Fluid Dynamics (CFD) software, ANSYS FLUENT 13, which is coupled to a chemical kinetic model via a plug-in chemistry solver, CHEMKIN-CFD. To represent the oxygenated straight chain hydrocarbon (HC) of biodiesel, a combined mechanism is utilised by employing the reduced mechanisms of two surrogate fuels, namely methyl butanoate (MB) and n-heptane. The biodiesel fuel types considered in this study include the methyl esters of soy (SME), palm (PME) and coconut (CME), which are modelled by employing the respective thermophysical properties of the fuel and through variation of ratio between MB and n-heptane for accurate representation of its oxygen content. Diesel combustion is also simulated to serve as a benchmark for the study. The computational results indicate that diesel has better combustion efficiency at low engine power with the highest peak of premixed combustion (PMC) and the earliest end of combustion (EOC). As engine power increases, the heat released during PMC is lowered by 30% and the combustion duration are lengthened comparatively. In contrast, biodiesel combustion improves at high power, with CME having the most significant effect whereby the peak heat released rate during PMC improves and the EOC advances to be the earliest among all test fuels. The short HC chain length of CME exerts a more significant effect on the combustion. Comparisons between SME and PME which have similar ignition delays highlight that a high level of unsaturation improves the combustion at low engine power. This effect lessens with increased engine power. At high engine power, the end of PMC and the EOC for SME and PME are similar. The highest level of soot emission is observed for diesel at all levels of engine power followed by SME, PME and CME accordingly.

Keywords:
Biodiesel; Computational Fluid Dynamics; diesel combustion; soot emission

Copyright © 2019 PENERBIT AKADEMIA BARU - All rights reserved

1. Introduction

Biodiesel has been gaining popularity as a renewable substitute to fossil diesel fuel due to its compatibility with the existing engine technology and generally lower pollutant emissions. The commonly used vegetable oils for biodiesel production includes soybean oil, rapeseed oil, coconut oil and palm oil [1]. Biodiesel fuels from different feedstock have different effects on the combustion and emission characteristics due to the different fatty acids methyl ester (FAME)

* *Corresponding author.*
E-mail address: hoonkiat.ng@nottingham.edu.my (H.K. Ng)

compositions. Saturation of the biodiesel fuel components is also a factor influencing the emissions level. Apart from the saturation level, variations in biodiesel emissions are also associated with its oxygen content and physical properties such as viscosity and density which are dictated by the hydrocarbon (HC) chain length [2-5].

The literature has reported that the use of biodiesel in diesel engines is generally linked to reductions in HCs and carbon monoxide (CO) emissions, with trade-offs in power loss and increased fuel consumption [1, 6]. Whilst some researchers claim that biodiesel combustion reduces soot or particulate matter (PM) formation, others report contrarily. For instance, certain studies [7-8] found that replacing diesel with biodiesel blends reduced carbon deposition in the combustion chamber. The reduction was attributed to the oxygen content in biodiesel. In contrast, it has also been reported that the use of biodiesel increased the emissions of PM, CO and HC over the New European Driving Cycle (NEDC) as a result of the different physicochemical properties of biodiesel which affected the fuel spray characteristics under varying engine operating conditions [9]. Furthermore, the higher viscosity and lower volatility of biodiesel give rise to problems in spray atomisation and mixture formation leading to higher smoke and gummy deposits in the combustion chamber [10].

As such, this study aims to carry out numerical studies of in-cylinder combustion and soot emission characteristics of biodiesel fuels from different feedstock to enhance understanding of biodiesel combustion in compression ignition engines. The motivation behind the selection of biodiesel from different feedstock is to understand the effects of different biodiesel fuel characteristics, specifically saturation level and straight HC chain length, on the combustion and soot emission processes.

2. Methodology

2.1 Computational Mesh and Model Formulations

In this study, numerical computation of a test engine with the specifications shown in Table 1 is conducted using ANSYS FLUENT 12, a commercial CFD software coupled with CHEMKIN-CFD as the chemistry solver. The simulation focuses only on the closed part of the engine cycle, from the intake valve closure (IVC) at -140 crank angle degree (CAD) after top dead centre (ATDC) to the exhaust valve opening time (EVO) at +140 CAD ATDC. As shown in Figure 1, the computational mesh represents 90° sector of the combustion chamber due to the symmetry imposed by the four equally spaced injector nozzle holes. The mesh is created with a cell size of 1.5 mm. Grid independent results were achieved with this setting and further refinement in the resolution was found to give insignificant improvement in the predicted results.

The fuel spray breakup is modelled using the Kelvin-Helmholtz/Rayleigh-Taylor (KH-RT) breakup model. The wall-jet model is applied as the discrete phase boundary condition for the combustion chamber surfaces. Turbulence is solved using the Renormalisation Group (RNG) k-ε turbulence model, and the Standard Wall Function is implemented for the near wall treatment. The chemistry of the surrogate fuel as described later in the Section 2.2 is integrated with the CFD solver through CHEMKIN-CFD. The Eddy-Dissipation Concept (EDC) model is implemented to incorporate the finite-rate chemistry with turbulent mixing, where the chemical reactions are assumed to occur in fine scales of the small turbulent structure. Predictions of soot formation and oxidation processes are made through the Moss-Brookes soot formation model and the Fenimore-Jones soot oxidation model, respectively. In the Moss-Brookes model, the nucleation of soot precursor, coagulation and surface growth are the variables for the solutions of soot particle concentration and soot mass fraction. Acetylene is considered the most important species for soot formation in diesel

combustion [11] and is used to represent the soot precursor species as well as the surface growth species [12]. As proposed by [13], the mass density of soot and the mass of incipient soot particle are fixed at 2000 kg/m^3 and 1200 kg/kmol, respectively for applications involving higher HC fuels. The model constants for the rates of soot inception, coagulation, surface growth and oxidation are set at the values given by [14].

Table 1
Test engine, injector and fuel specifications

Parameter	Specification
Engine type	Light-duty diesel engine
Piston type	Bowl-in-piston
Cylinder head type	Flat cylinder head
Displacement per cylinder (L)	0.347
Compression ratio	19.1
Stroke (cm)	6.9
Bore (cm)	8.0
Piston bowl volume (cm^3)	11.6
Connecting rod length (cm)	11.45
Number of injector holes	4
Nozzle diameter (mm)	0.128
Nozzle nap angle (°)	152
Fuel temperature (K)	312

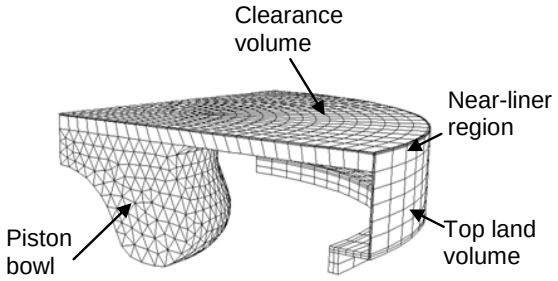


Fig. 1. Computational domain of the combustion chamber

2.2 Operating Conditions and Fuel Injection Parameters

The effects of the fuel types on the combustion processes are examined for a range of engine operating conditions, from low engine power of 0.5 kW to mid and high engine power of 1.5 kW and 2.5 kW, respectively. The engine is maintained at a medium speed of 2000 rpm which is the typical operating range of on-road vehicles and lies within the engine's drivability limits. The test fuels include diesel and three types of biodiesel namely the methyl esters of soy (SME), palm (PME) and coconut (CME), which are the commonly used biodiesels [1]. These fuels are chosen to represent different biodiesel characteristics, namely the saturation level and the straight HC chain length. SME and PME with similar chain length are used to compare the effects of saturation level since SME is 90% unsaturated while PME is only 50% unsaturated. Meanwhile, CME is studied for its representation of short HC chain length.

The fuel injection system operates with a pressure of 210 bar and a coefficient of discharge value of 0.75. The injection specifications and the operating conditions for each case are summarised in Table 2. The SOI timings marginally vary for different fuel types due to the differences in the bulk modulus, density, viscosity and speed of sound of the fuel. Apart from this,

the initial conditions at IVC also vary with different engine powers due to the differences in the temperature of the residual gas in the combustion chamber at the end of each cycle.

Table 2
Injection parameters and operating conditions for varying fuel types at different engine powers

Engine power (kW)	Injection parameter	Diesel	SME	PME	CME
0.5	SOI (CAD ATDC)	-13.5	-15	-15	-16
	EOI (CAD ATDC)	-5.79	-6.29	-6.37	-6.29
	Fuel consumption (kg/h)	0.236	0.274	0.270	0.303
	Total injection quantity (mg/cycle)	3.93	4.57	4.49	5.04
	Initial pressure (bar)	1.23	1.23	1.23	1.23
	Initial Temperature (K)	313	313	313	313
1.5	SOI (CAD ATDC)	-13.5	-15	-15	-16
	EOI (CAD ATDC)	-0.37	1.14	0.42	0.68
	Fuel consumption (kg/h)	0.402	0.508	0.482	0.520
	Total injection quantity (mg/cycle)	6.70	8.46	8.03	8.67
	Initial pressure (bar)	1.27	1.27	1.27	1.27
	Initial Temperature (K)	323	323	323	323
2.5	SOI (CAD ATDC)	-13.5	-15	-15	-16
	EOI (CAD ATDC)	5.74	7.34	7.41	8.49
	Fuel consumption (kg/h)	0.589	0.703	0.700	0.764
	Total injection quantity (mg/cycle)	9.81	11.71	11.67	12.73
	Initial pressure (bar)	1.38	1.38	1.38	1.38
	Initial Temperature (K)	353	353	353	353

2.3 Chemistry and Liquid Properties of Surrogate Fuel Parameters

A combination of methyl butanoate (MB) and n-heptane reaction mechanisms by [15] is utilised as a surrogate fuel model to represent the chemical kinetics of the biodiesel fuel, which is henceforth referred to as the Combined Biodiesel Surrogate (CBS). MB is used to represent the oxygenated content of the FAME while n-heptane represents the straight chain HC. With adjustment to the Arrhenius rate constants, the CBS was successfully validated against both the baseline mechanism in a constant volume adiabatic system at 24 operating conditions relevant to the ignition point of diesel engine. The resulting mechanism consists of 50 species and 201 reactions.

Prior to setting the composition of the simulated fuel, the fatty acids compositions of SME, PME and CME biodiesels are compiled [16-19]. The properties of the biodiesel fuels such as the oxygen content, chemical composition and molecular mass are then determined [15]. In the computation, the chemistry of the biodiesel fuel is represented by the combination of the MB and n-heptane mechanisms while maintaining the oxygen content in the fuel composition. Using the molecular mass, the proportions of MB to n-heptane for each fuel type are calculated. The properties of the experimental biodiesel feedstock and the simulated surrogate fuels are given in Table 3. By preserving the oxygen content of the surrogate fuel to represent the biodiesel fuel, the ratio of carbon to hydrogen as observed from the chemical composition and the molecular mass are also found to be represented effectively.

Defining the physical properties of the liquid fuel is another important aspect in the setup of the computational modelling of diesel/biodiesel combustion. Due to the differences in the fuel structures such as the saturation level and HC chain length, there are variations in fuel properties. The key properties include density, vapour pressure, heat of vaporisation, liquid heat capacity,

liquid dynamic viscosity, liquid thermal conductivity, surface tension and binary diffusivity. The fuel properties of SME, PME and CME utilised in this study have been developed and validated in a constant volume combustion chamber with operating conditions of a compression ignition (CI) engine [20].

Table 3
Properties of simulated surrogate fuels

Type	Properties	SME	PME	CME
Experimental	Chemical composition	$C_{18.8}H_{34.6}O_2$	$C_{18.1}H_{34.9}O_2$	$C_{14.5}H_{29.8}O_2$
	Molecular mass (kg/kmol)	292.5	284.1	234.6
	Oxygen content (wt%)	10.7	11.7	13.5
Simulated	Proportion of MB (wt%)	34.1	35.3	43.0
	Proportion of n-heptane (wt%)	65.9	64.7	57.0
	Chemical composition	$C_{18.8}H_{41.5}O_2$	$C_{18.1}H_{39.9}O_2$	$C_{14.5}H_{31.6}O_2$
	Molecular mass (kg/kmol)	299.5	289.1	237.5

3. Results

3.1 Validation

Validation study is first carried out at three different levels of engine power for every fuel type, i.e. pure diesel, SME, PME and CME. The results of the simulated test cases for variations in engine power are validated against the experimental data, which include the pressure trace, heat released rate (HRR) and tailpipe soot emission as shown in Figure 2 and Figure 3. The comparison between the experimental and simulated results shows that the percentage error in the predicted peak pressure is less than 5.5 %. The over-prediction in the ignition delay (ID) of the main combustion event is maintained to within 18%, which is approximately 2 CAD. Similar HRR curves are also observed between the simulation and experimental data for all cases. With the small offset in the predicted ID, the predictions of the timings of the peak HRR of premixed combustion (PMC) phase are advanced by up to 2 CAD. A possible reason for this observation is that the experimental HRR data itself is often smoothened as reported [21], which increases the width of experimental peak HRR for the PMC phase.

The simulation and experimental exhaust soot concentration are normalised (Figure 3) to the same order of magnitude, by setting the soot amount produced by the case with diesel fuel as the baseline for each engine power. This provides a clear comparison of the trend of soot emission when the fuel type is changed. Although there is discrepancy of up to 21%, the effects of the fuel types on the soot emission are similar in trends for both experimental and simulated results. At the three investigated engine powers, all types of biodiesel produce lower soot levels as compared to diesel. CME produces the least amount of soot followed by PME and SME.

Generally, across all the test cases, the simulated combustion processes and soot emissions agree well with the experimental data, showing that the selected models have been appropriately calibrated for the simulation of this combustion system. Therefore, the combustion and emission characteristics of the three types of biodiesel fuels are well represented by the discrete phase modelling of the fuel liquid properties as well as the reaction mechanism of the surrogate fuel, MB and n-heptane. The above validation exercise indicates the reliability of the model in predicting the relative progression and development of the in-cylinder processes, including the fuel spray penetration and soot cloud formation.

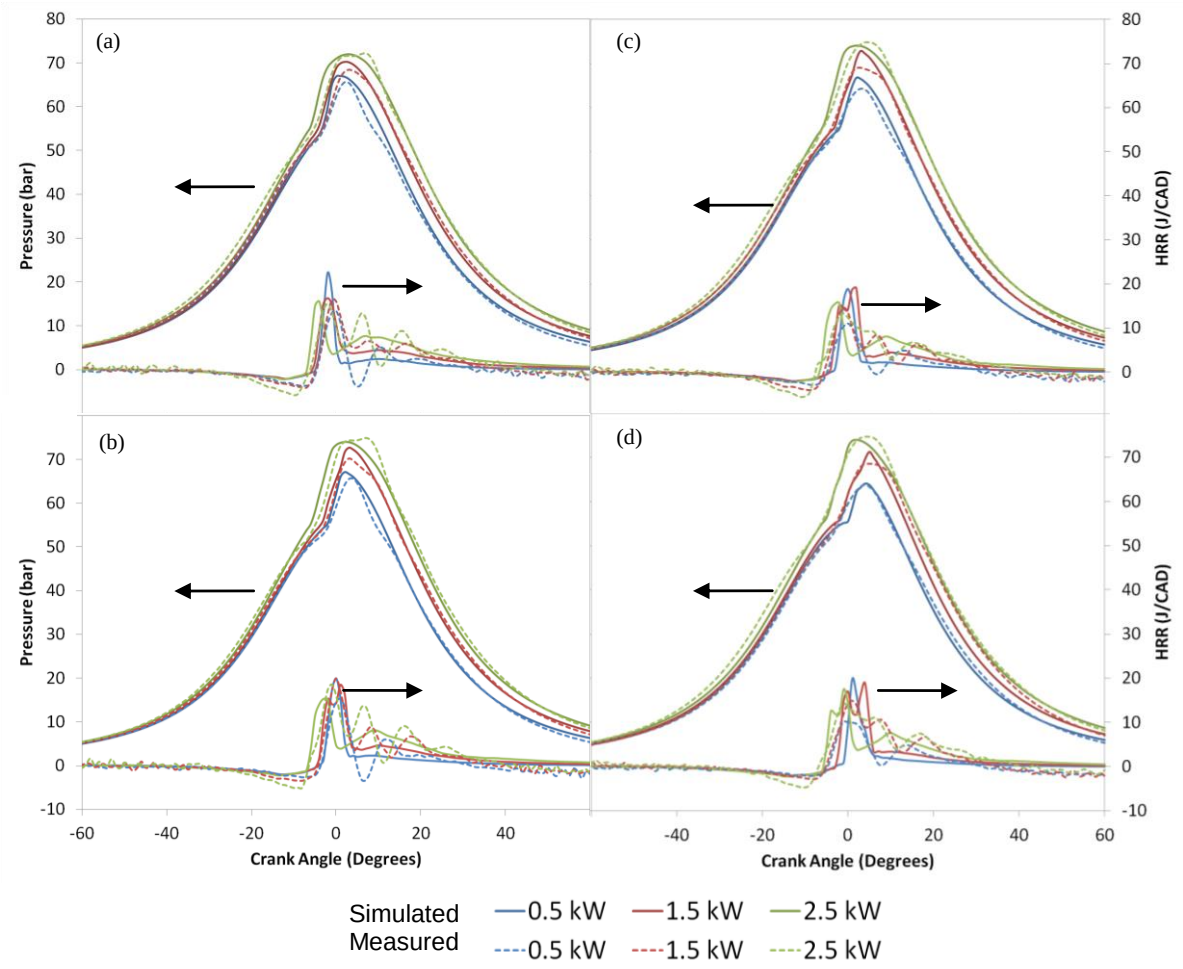


Fig. 2. Measured and simulated pressure and HRR profiles at varying engine power for (a) diesel, (b) SME, (c) PME and (d) CME

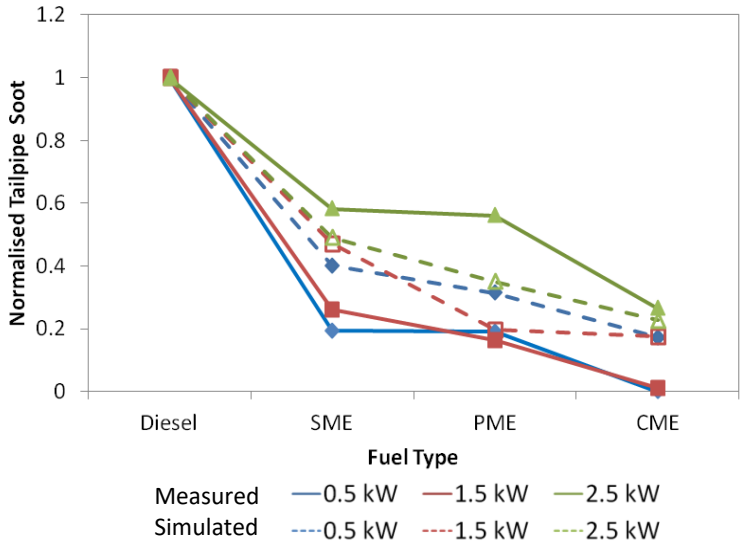


Fig. 3. Normalised tailpipe soot at varying engine power for different fuel types

3.2 Combustion Characteristics

Comparisons of the combustion characteristics are carried out with the data extracted from the simulated pressure and HRR, which includes the ID and the combustion stages of PMC and mixing-controlled combustion (MCC). To obtain the ID, the timing at the onset of positive HRR value is considered to be the start of combustion (SOC). The end of premixed combustion (EOPMC) takes place where the HRR drops to a minimum after the peak of PMC before MCC occurs. The EOC is taken at the point where 90% of the injected fuel is burned. These data are selected for investigation based on the nature of diesel engine combustion, where the thermal efficiency is higher if it approaches the constant volume process, in which combustion takes place instantaneously ATDC [22]. The analysis includes descriptions of the associations between the results with the fuel evaporation rate and the equivalence ratio (ER) of the air-fuel mixture. ER in the combustion chamber at SOC and EOPMC are utilised to illustrate the development of the combustible mixture. Iso-contours of ER value at 0.8 and 1.8 are marked to aid in visualisation as combustion can occur within this region [23].

3.2.1 Overall trends

The results pertaining to the combustion characteristics of different fuel types are presented in Figure 4 and Figure 5. It is observed that the IDs of all fuel types lower as engine power increases. This is attributed to the initial conditions at IVC where the gas temperature and pressure are higher due to the high temperature of the residual gas from the previous cycle produced by a larger amount of fuel burned. Diesel has the shortest ID among all fuels. EOPMC of diesel is advanced compared to biodiesel for all cases, although the peak HRR during PMC and end of combustion (EOC) differ from biodiesel cases at different levels of engine power. Diesel fuel appears to have the best combustion efficiency at low engine power, where it has the highest peak HRR during PMC and the earliest EOC. However, as engine power increases to medium and high level, the heat released during PMC is lower and combustion duration is lengthened comparatively.

SME and PME demonstrate different combustion characteristics at different engine powers, although their IDs are similar. At low power, using SME fuel results in a higher peak HRR during PMC as well as earlier EOPMC and EOC. This remains similar at medium power with earlier EOPMC, but prolonged EOC for SME. The peak HRR during PMC produced by SME drops lower than PME at high engine power. Additionally, high engine power reveals a convergence of the EOPMC and EOC for both the SME and PME cases demonstrating similar combustion characteristics.

The largest ID and the latest EOPMC are observed in the test case of CME combustion. The EOC is retarded when the engine power is low. However, CME shows the best combustion efficiency at high engine power whereby the peak HRR during PMC improves and the EOC advances to be the earliest among all test fuels.

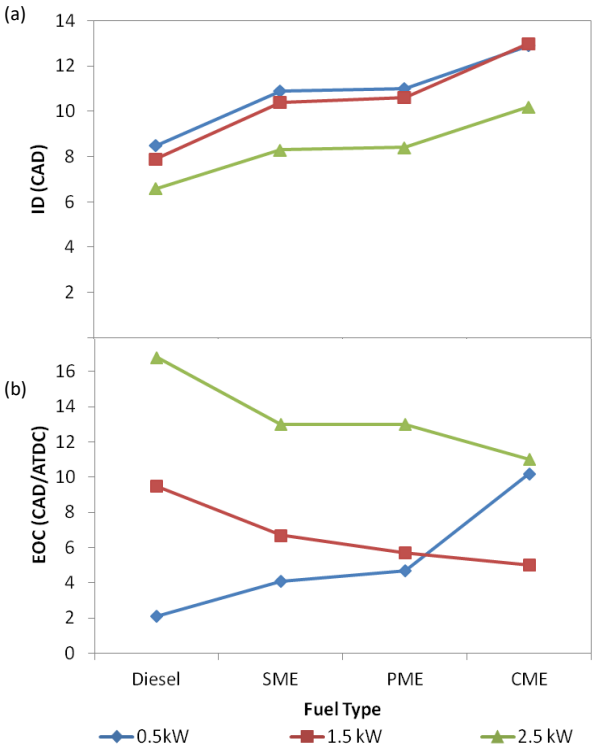


Fig. 4. Combustion characteristics at varying engine power for different fuel types: (a) ID and (b) EOC

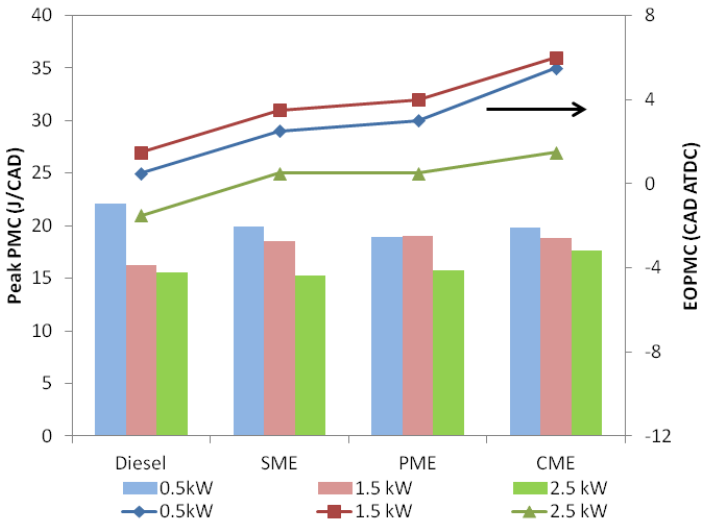


Fig. 5. Combustion characteristics at varying engine power for different fuel types: Peak HRR during PMC and EOPMC

3.2.2 Diesel

The combustion characteristics of diesel fuel are first compared to all biodiesel fuels. Figure 6 shows the evaporation rate of the liquid fuels at all engine powers. The initial evaporation rates are of concern here as they directly affect the IDs. It is observed that within 4 CAD from the SOI, diesel fuel demonstrates the highest evaporation rate which can be attributed to its physical properties of diesel [20]. The surface tension, vapour pressure and density of diesel are at values favourable to

high evaporation rate. Consequently, the combustible mixture prepared by the rapid evaporation of diesel fuel enables it to attain the shortest ID. This deduction is supported by observing the local ER in the combustion chamber in Figure 7. The rich air-fuel mixture of diesel at SOC shows that the ER reaches the optimum level for ignition more rapidly during the ID.

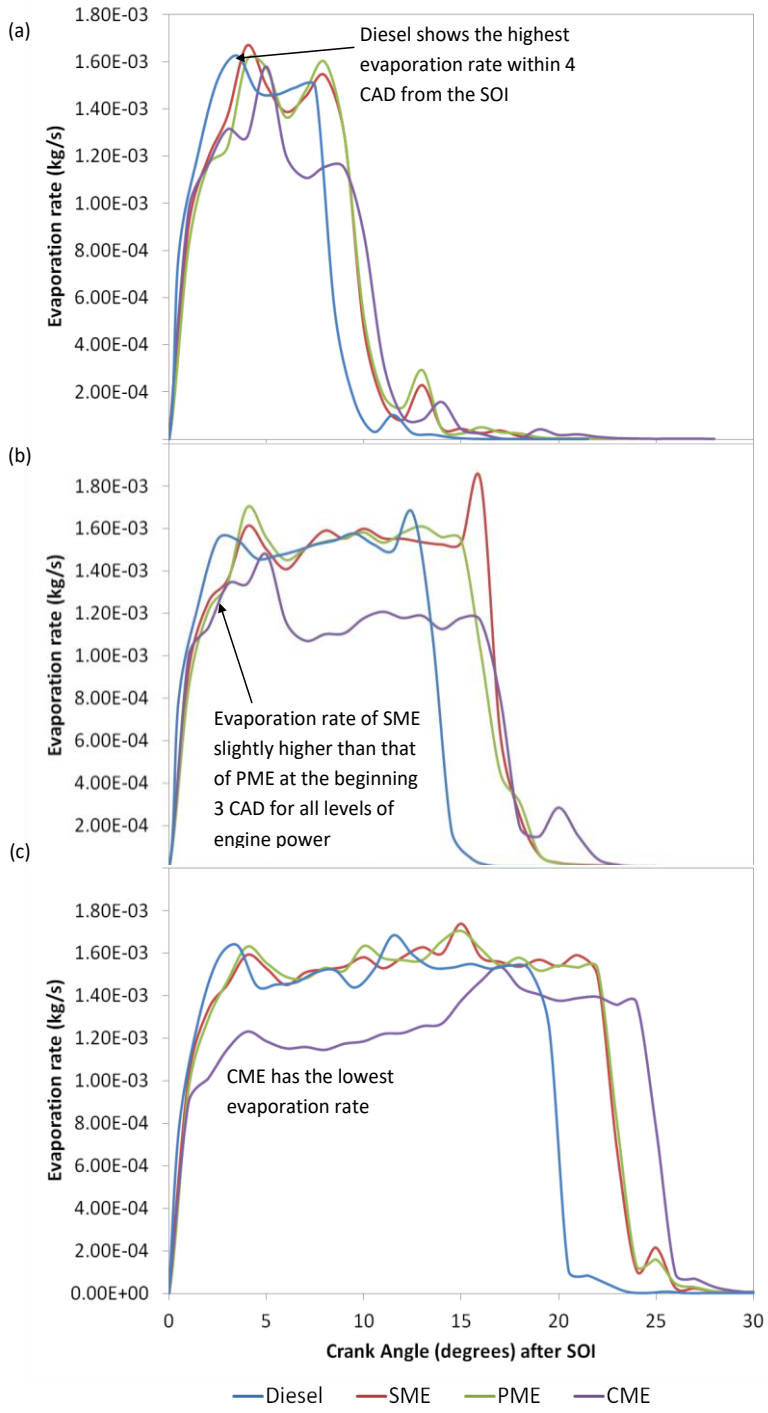


Fig. 6. Fuel evaporation rates for different fuel types at engine power of (a) 0.5 kW, (b) 1.5 kW and (c) 2.5 kW

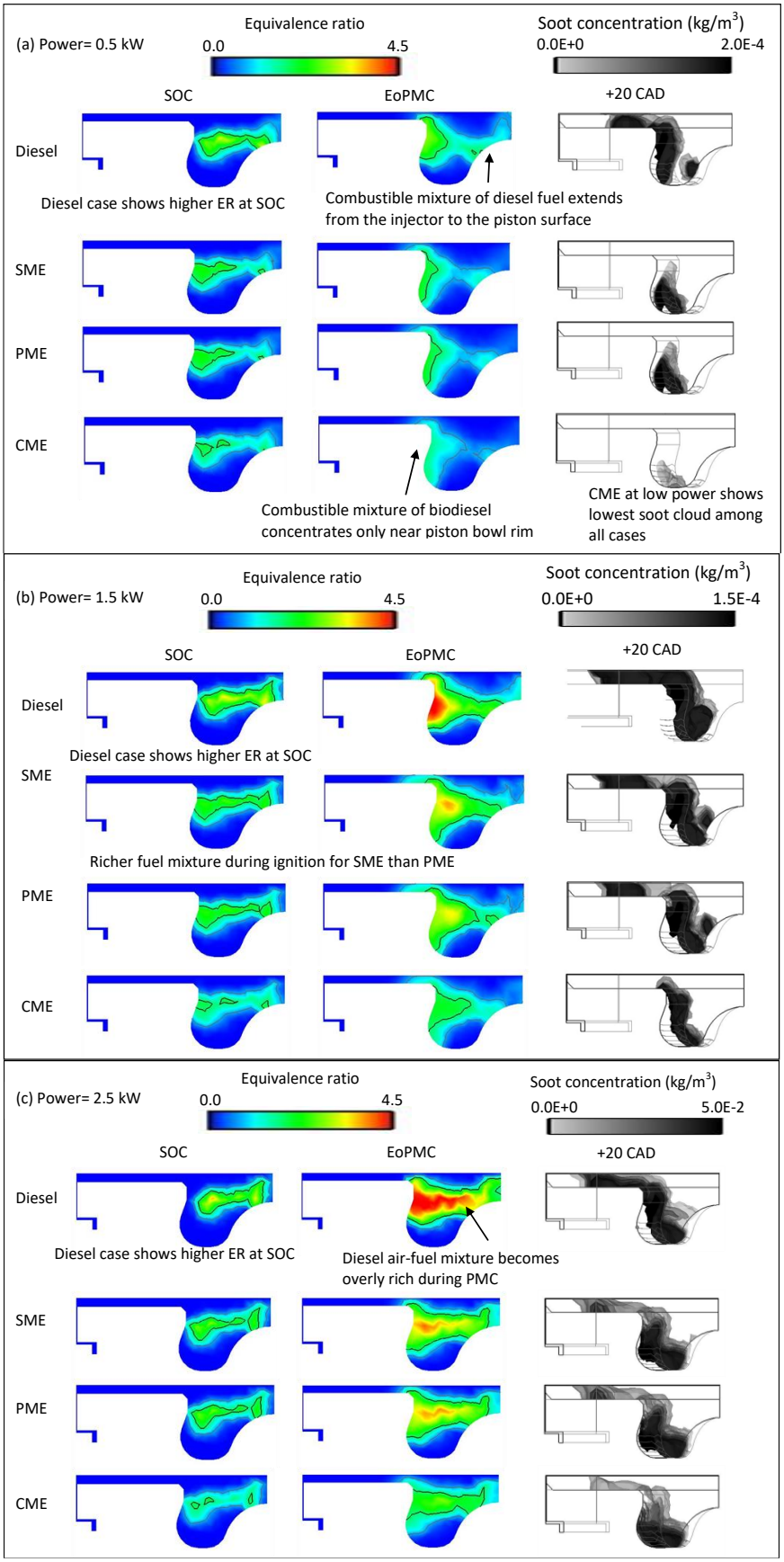


Fig. 7. Contour of ER (left) and soot concentration distributions (right) for different fuel types at SOC and EOPMC: (a) 0.5 kW, (b) 1.5 kW and (c) 2.5 kW

Due to the shortened ID, the heat released is limited by the amount of vaporised fuel at SOC as well as the volume of combustible mixture which is constrained by the undeveloped fuel penetration length. This results in early EOPMC for diesel combustion as compared to other fuels. Conversely, the peak HRR during PMC and EOC of diesel shows variations at different engine powers. At low engine power, the peak of PMC of diesel fuel is the highest as its high evaporation rate results in a volume increase of the combustion region. The combustible mixture of diesel fuel extends from the injector to the piston surface while the mixture of biodiesel fuel at EOPMC concentrates only near the piston bowl rim. Consequently, MCC is improved due to the combined effect of high HRR during the PMC and the early ignition occurring close to TDC. This results in the earliest EOC, where the duration of MCC only sustains for 1.5 CAD.

As engine power increases, the heat released during the MCC stage becomes more prominent. In contrast to low engine power, the peak HRR during PMC of diesel fuel combustion is the lowest among all types of fuels. Subject to the prolonged injection duration, the air-fuel mixture becomes overly rich and suppresses the combustion efficiency. This is illustrated in Figure 7 from the contour of ER at EOPMC. Apart from the high evaporation rate, the rich mixture is also a result of the absence of oxygen content in the diesel fuel as compared to biodiesel. With the short EOPMC and low peak HRR during PMC, the mixing strength of the fuel injected during MCC stage is subsequently deteriorated, therefore delaying the EOC.

3.2.3 Biodiesel

The effects of biodiesel saturation level on combustion characteristics are compared using the cases of SME and PME. Owing to the similarity of oxygen content between these two fuels, the differences in their combustion characteristics are mainly attributed to liquid properties. Although fuel density plays an important role in the atomisation of fuel droplets, the variations between the two biodiesel fuels are less than 2%, which can be considered insignificant as compared to the difference to diesel fuel. The evaporation rate of SME shown in Figure 6 is slightly higher than that of PME at the beginning 3 CAD for all levels of engine power, which is then followed by slight fluctuations at similar magnitudes between the two fuels. At low temperatures, SME has similar vapour pressure as compared to PME, but lower surface tension leading to a higher initial evaporation rate [20].

SME and PME demonstrate different combustion characteristics at different engine powers although their IDs are similar. It is observed from Figure 4 that the MCC phase is not prominent at low engine power. The higher evaporation rate of SME proves to be an advantage when the engine power is low as the maximum local ER of 2 limited by short injection duration promotes complete combustion during the PMC stage. This advances both the EOPMC and EOC. When engine power is increased to 1.5 kW, the duration of combustion is extended during the MCC phase. With increased injection duration, the richer fuel mixture during ignition for SME causes deterioration of PMC as reflected by the lower peak HRR during PMC of 18.5 J/CAD as recorded in Figure 5. In order to compensate for the power loss during PMC, fuel consumption is increased as shown in Table 2. The associated MCC duration is extended, which consecutively delays the EOC.

Both SME and PME show similar combustion characteristics at high engine power. At higher temperatures, the surface tension of PME is lower than that of SME [20]. The initially low evaporation rate of PME is overcome as the fuel injection progresses and the difference between evaporation rates of SME and PME fuel become less evident. As the injection duration increases with engine power, the effects of the initial difference between the fuel evaporation rates on the development of fuel combustion become less significant.

CME is compared against other biodiesel fuels to represent the effects of its short HC chain length on the combustion characteristics. The largest ID and a delayed EOPMC are observed in the combustion of CME. However, CME shows the highest combustion efficiency at high engine power. The evaporation rate of CME is the lowest among the tested fuels as shown in Figure 6, which can be related to its large ID. As CME has the highest oxygen content of 14%, the air-fuel mixture prepared for combustion are leaner as compared to those of other fuels thus delaying the ignition process. This also reduces the amount of chemical heat release within the ID period, causing a lower in-cylinder temperature. Heat transfer to the injected fuel is impeded leading to a low evaporation rate. The low evaporation rate of CME results in an overly lean air-fuel mixture which deteriorates the quality of the combustion and delays both the EOPMC and EOC.

However, as engine power increases, the peak HRR during PMC of CME is improved. The ER of other fuel mixtures becomes too rich for complete combustion while this phenomenon does not occur with CME with its high oxygen content. The EOC of CME also advances to be the earliest among all test fuels. The increasing injection duration extends the fuel delivery to the MCC stage. With less fuel being burned during PMC due to large ID and early EOPMC, the evaporated fuel is carried onto the later stage and creates a more complete combustion in the MCC stage.

In summary, diesel demonstrates better combustion efficiency at low engine power whereas the combustion efficiency of biodiesel fuels improves at high power with CME being the highest. Comparisons between SME and PME demonstrate that a high level of unsaturation improves the combustion at low engine power. The difference in the combustion characteristics between biodiesels of different saturation levels diminishes as the engine power increases. The significant influence of HC chain length on the combustion process is highlighted through the case of CME combustion.

3.3 Tailpipe Soot Emission Characteristics

Figure 3 depicts the normalised tailpipe soot emission produced by different fuel types. The highest level of soot emission is observed for the use of diesel fuel at all levels of engine power. SME produces slightly higher soot level than PME while the combustion of CME results the least amount of soot emission. The ratio between the highest and lowest level of soot produced between the test cases of diesel and CME at the same engine power increases as the engine power decreases. To analyse the soot emission in association with the combustion characteristics in further detail, the net soot level and the soot oxidant, OH radical, are monitored. In addition, the images of predicted soot concentration are shown as side view projections of the 3-D soot iso-surfaces, where the soot cloud layers are featured as semi-transparent. The in-cylinder event at +20 CAD ATDC is chosen for illustration when the combustion processes for all test cases are complete.

3.3.1 Diesel

The results of soot emission are first evaluated for diesel fuel. Figure 8 highlights that diesel combustion produces the highest soot formation rate in all the cases as a result of the high ER in the combustion chamber. With the wide region of rich combustible mixture that extends towards the injector as shown in Figure 7, the combustion region has limited contact area with oxygen which slows down the oxidation process. It is verified by the OH mole fraction illustrated in Figure 8, where the lowest OH concentration is observed in the diesel test case, although the corresponding timespan is longer. The peak of soot oxidation rate in the diesel case appears to be

the highest due to the large amount of soot produced, however, it is insufficient to off-set the high soot formation rate.

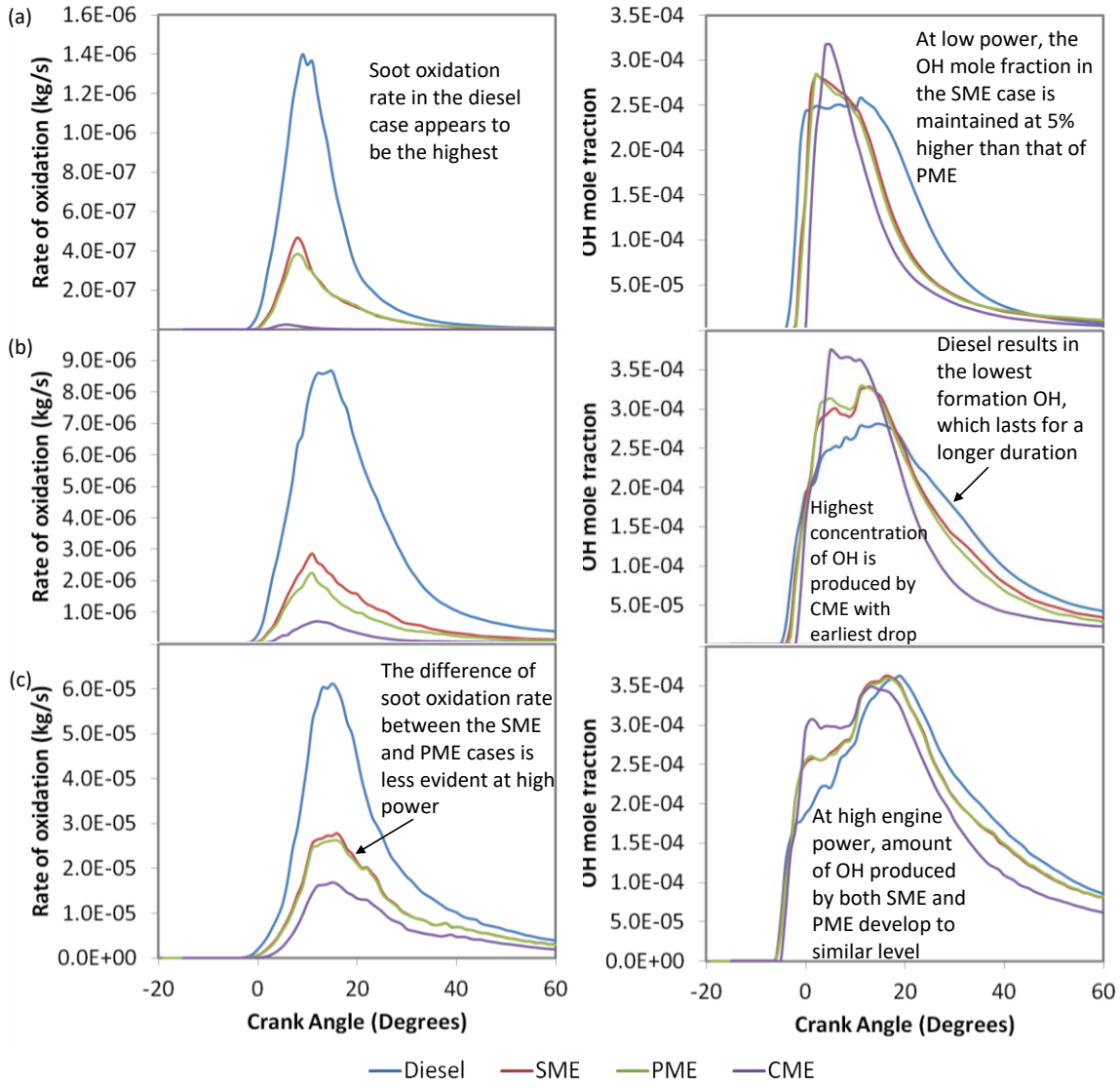


Fig. 8. Rate of oxidation (left) and OH mole fraction (right) for different fuel types at engine power of a) 0.5 kW, (b) 1.5 kW and (c) 2.5 kW

3.3.2 Biodiesel

A comparison of the tailpipe soot emission indicates that SME produces slightly higher soot level than PME. Since both fuel types have similar oxygen content, the difference is mainly attributed to the liquid fuel properties. The rich air-fuel mixture prepared in the event of high evaporation rate of SME fuel droplets provides a higher ER at the point of ignition thus favouring soot formation. In contrast, rapid combustion promotes soot oxidation, ultimately producing a minor difference in the soot level produced by both fuel types. At low power, the OH mole fraction in the SME case is maintained at 5% higher than that of PME during the window of soot oxidation process between +0 and +40 CAD ATDC. At high engine power of 2.5 kW, the amount of OH radicals produced in both SME and PME cases develop to similar levels. Similarly, the difference in soot oxidation rates between the two cases is less evident as observed in Figure 8. This development

matches the combustion characteristics of both the fuel types which converge as engine power increases. Therefore, the difference in the soot emission level of the two fuel types is minimal.

Implementation of CME fuel in the diesel engine results in the least amount of soot emission. This is attributed to the high oxygen content of the fuel due to the short HC chain length which results in an air-fuel mixture with low ER for combustion. With oxygen being available in the fuel, the production of the oxidant is increased as seen in Figure 8. The highest concentration of OH after the onset of combustion is produced by CME in all cases. It is also observed that OH level produced by CME has an earlier drop as compared to the other fuel types. As described in Section 4.1.4, owing to the large ID and high oxygen content of CME, a large region of lean air-fuel mixture is created resulting in a wider lean flame region with lower local temperatures. This results in an earlier drop of temperature as well as soot and OH levels.

It is noted that at low engine power, the reduction of tailpipe soot level by replacing diesel fuel with CME is much larger than that of high engine power. This is attributed to the size of the soot cloud produced by CME combustion in the low engine power case, which is much smaller in comparison to the other fuel types. The surface area-to-volume ratio is reduced significantly and this increases the availability of oxidants for soot oxidation.

Acknowledgment
The Ministry of Higher Education (MOHE) Malaysia is acknowledged for its financial support towards this work under the Fundamental Research Grant Scheme (FRGS) FRGS/1/2014/TK01/UNIM/01/1.

References

[1] Demirbaş, Ayhan. "Progress and recent trends in biodiesel fuels." *Energy Conversion and Management* 50, no. 1 (2009): 14-34.

[2] Cardone, Massimo, Maria Vittoria Prati, Vittorio Rocco, Maurizia Seggiani, Adolfo Senatore, and Sandra Vitolo. "*Brassica carinata* as an alternative oil crop for the production of biodiesel in Italy: engine performance and regulated and unregulated exhaust emissions." *Environmental Science and Technology* 36, no. 21 (2002): 4656-4662.

[3] Di, Yague, C.S. Cheung, and Zuohua Huang. "Experimental investigation on regulated and unregulated emissions of a diesel engine fueled with ultra-low sulfur diesel fuel blended with biodiesel from waste cooking oil." *Science of the Total Environment* 407, no. 2 (2009): 835-846.

[4] Hossain, Abul Kalam and Philip A. Davies. "Plant oils as fuels for compression ignition engines: a technical review and life-cycle analysis." *Renewable Energy* 35, no. 1 (2010): 1-13.

[5] Janaun, Jidon and Naoko Ellis. "Perspectives on biodiesel as a sustainable fuel." *Renewable and Sustainable Energy Reviews* 14, no. 4 (2010): 1312-1320.

[6] Xue, Jinlin, Tony E. Grift, and Alan C. Hansen. "Effect of biodiesel on engine performances and emissions." *Renewable and Sustainable Energy Reviews* 15, no. 2 (2011): 1098-1116.

[7] Agarwal, Avinash Kumar, Jayashree Bijwe, and L.M. Das. "Effect of biodiesel utilization of wear of vital parts in compression ignition engine." *Journal of Engineering for Gas Turbines and Power* 125, no. 2 (2003): 604-611.

[8] Reksowardojo, Iman K., Ngoc Dung Nguyen, Q.T. Tran, R. Sopheak, Tirto P. Brodjonegoro, Tatang H. Soerawidjaja, H. Ogawa, and W. Arismunandar. "The comparison the effect of biodiesel fuel from palm oil and physic nut oil (*Jatropha curcas*) on an direct injection (DI) diesel engine." *Proceedings of the FISITA 2006 World Automotive Congress, Yokohama, October 2006* (2006).

[9] Fontaras, Georgios, Georgios Karavalakis, Marina Kousoulidou, Theodoros Tzamkiozis, Leonidas Ntziachristos, Evangelos Bakeas, Stamoulis Stournas, and Zissis Samaras. "Effects of biodiesel on passenger car fuel consumption, regulated and non-regulated pollutant emissions over legislated and real-world driving cycles." *Fuel* 88, no. 9 (2009): 1608-1617.

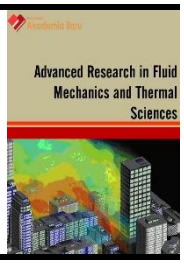
[10] Ng, Jo-Han, Hoon Kiat Ng, and Suyin Gan. "Advances in biodiesel fuel for application in compression ignition engines." *Clean Technologies and Environmental Policy* 12, no. 5 (2010): 459–493.

[11] Kong, Songcharng, Yong Sun, and Rolf D. Reitz. "Modeling diesel spray flame liftoff, sooting tendency, and NO_x emissions using detailed chemistry with phenomenological soot model." *Journal of Engineering for Gas Turbines and Power* 129, no. 1 (2007): 245-251.
[12] Pang, Kar Mun, Hoon Kiat Ng, and Suyin Gan. "Simulation of temporal and spatial soot evolution in an automotive diesel engine using the Moss-Brookes soot model." *Energy Conversion and Management* 58, (2012): 171-184.
[13] Hall, R.J., M.D. Smooke, and M.B. Colket. "Predictions of Soot Dynamics in Opposed Jet Diffusion Flames." In *Physical and Chemical Aspects of Combustion: A Tribute to Irvin Glassman*, Gordon and Breach, p. 189. 1997.
[14] Moss, J.B., S.A.L. Perera, C.D. Stewart, and M. Makida. "Radiation heat transfer in gas turbine combustors." *Proceedings of the 16th International Symposium on Air Breathing Engines, Cleveland, 2003* (2003).
[15] Tan, Shin Mei. (2015). *CFD Modelling of Soot Entrainment via Thermophoretic Deposition and Crevice Flow in CI Engines Fuelled with Diesel-Biodiesel Fuel Blends*. PhD Thesis, University of Nottingham Malaysia.
[16] Demirbaş, Ayhan. "Biodiesel fuels from vegetable oils via catalytic and non-catalytic supercritical alcohol transesterifications and other methods: a survey." *Energy Conversion and Management* 44, no. 13 (2003): 2093-2109.
[17] Demirbaş, Ayhan. "Biodiesel production from vegetable oils via catalytic and non-catalytic supercritical methanol transesterification methods." *Progress in Energy and Combustion Science* 31, no. 5-6 (2005): 466-487.
[18] Graboski, Michael S. and Robert L. McCormick. "Combustion of fat and vegetable oil derived fuels in diesel engines." *Progress in Energy and Combustion Science* 24, no. 2 (1998): 125-164.
[19] Ng, J.-H., Hoon Kiat Ng, and S. Gan. "Recent trends in policies, socioeconomy and future directions of the biodiesel industry." *Clean Technologies and Environmental Policy* 12, no. 3 (2010): 213-238.
[20] Mohamed Ismail, Harun, Hoon Kiat Ng, Xinwei Cheng, Suyin Gan, Tommaso Lucchini, and Gianluca D'Errico. "Development of thermophysical and transport properties for the CFD simulations of in-cylinder biodiesel spray combustion." *Energy and Fuels* 26, no. 8 (2012): 4857-4870.
[21] Brakora, Jessica L., Youngchul Ra, Rolf D. Reitz, Joanna McFarlane, and C. Stuart Daw. "Development and validation of a reduced reaction mechanism for biodiesel-fueled engine simulations." *SAE International Journal of Fuels and Lubricants* 1, no. 1 (2009): 675-702.
[22] Gupta, H.N. *Fundamentals of Internal Combustion Engines*. Prentice-Hall Of India Pvt. Limited. 2006.
[23] Pulkrabek, Willard W. Engineering Fundamentals of the Internal Combustion Engine. Pearson Prentice Hall. 2004.

Penerbit Akademia Baru

Engineering Science and Technology Conference Proceedings

Journal homepage: www.akademiabaru.com/EST.html



Second Grade Nanofluid Flow Over A Vertical Plate With Wall Transpiration

Open

Sidra Aman[1], Zulkhibri Ismail[1,*], Mohd Zuki Salleh[1]

[1] Centre for Mathematical Sciences, Faculty of Computing and Applied Sciences, Universiti Malaysia Pahang, 26300 UMP Kuantan, Pahang, Malaysia

ABSTRACT

Flow of second grade nanofluid over a vertical plate with wall transpiration is inspected in this paper. Carboxymethyl cellulose (CMC) is taken as carrier fluid with copper nanoparticles. Some appropriate variables are introduced for the reduction of partial differential equations to ordinary differential equations. Analytical solution for momentum, heat and concentration has established using a combination of Laplace transform, the perturbation technique and numerical inversion of Laplace transform. Numerical inverse Laplace was acquired and coding for plotting results were done using Tzou's algorithm in MathCAD software. Graphical illustration was carried out for the ingrained parameters to shed light on the physical insight of the flow, heat and mass transfer of the nanofluid. Velocity of the fluid maximizes with increasing values of injection parameter while decreases with suction values.

Keywords:
Second grade fluid; Nano-fluid; Laplace transform technique

Copyright © 2019 PENERBIT AKADEMIA BARU - All rights reserved

1. Introduction

Non-Newtonian fluid is a huge class of fluids in which the relation between shear stress and shear rate is non-linear, hence they are much complicated and impossible to have a single constitutive relation. A number of non-Newtonian fluids can be found in the literature such as Micropolar fluid, Maxwell fluid, Casson fluid, Jeffrey fluid and second grade fluid. The second grade fluid has been examined widely by the researchers and scientists due to its simplicity. Bazhlekova et al. [1] analyzed the Rayleigh-Stokes problem for second grade fluid. Flow of second grade fluid through a microtube with wall slip was investigated by Chen et al. [2]. They evaluate five cases for volume inlet flow which are (i) constant acceleration (ii) trapezoidal piston motion (iii) impulsively started flow (iv) impulsively blocked and (v) oscillatory flow. They tack-led the problem using Laplace transform technique.

Analytical and numerical solutions were established for second grade fluid modeled in terms of fractional derivatives by Wang *et al.,* [3]. Numerical solution for flow of second grade fluid Rayleigh-Stokes problem was exam-ined via finite element method Dehghan and Abbaszadeh [4]. VeeraKrishna *et al.,* [5] studied Hall effects on second grade fluid driven by oscillating pressure gradient between two vertical plates. Khan *et al.,* [6] explored the influences of thermophoresis and

* *Corresponding author.*
E-mail address: zulkhibri@ump.edu.my (Zulkhibri Ismail)

thermal radiation second grade fluid with heat and mass transfer flow. Some recent and relevant literature can be found in [7-9] and the references in there.

Scientists use several kinds of nanoparticles for enormous purposes in industrial disciplines such as medical sciences, drug delivery, cooling process, cancer therapeutics and many more. A very interesting use of Ginger-derived nanoparticles (GDN) was executed by Zhuang *et al.,* [10] in a Cancer center Kentucky, United States of America. They provided the GDN orally to a mouse model which protected the mice against alcohol-induced liver damage. Some theoretical based researches in this area of nanoparticles and their implementations can be found in the literature [11-13]. Copper nanoparticles due to its importance in industry and engineering applications has been used in the research areas either experimental or theoretical (Hayat *et al.,* [14]). Khan *et al.,* [15] investigated MHD flow of copper nanofluids with water as base fluid between parallel plates for various shapes of nanoparticles.

Recently, Toghraie *et al.,* [16] examined molecular dynamics simulation of Couette and Poiseuille nanofluid flows for copper nanoparticles. The flow was investigated in rough and smooth nanochannels with different rough-ness configurations. Some recent studies on copper nanoparticles and heat transfer flow can be found in [17-19] and the references cited in them

The problem of second grade nanofluid with CMC base fluid and copper nanoparticles has not been reported yet (Please see Figure 1 for the structure of copper nanoparticles). Laplace transform technique and Inverse Laplace transform has been employed to solve the present model for the flow of second grade fluid over a vertical plate (Following Tzou's algorithm [20]).

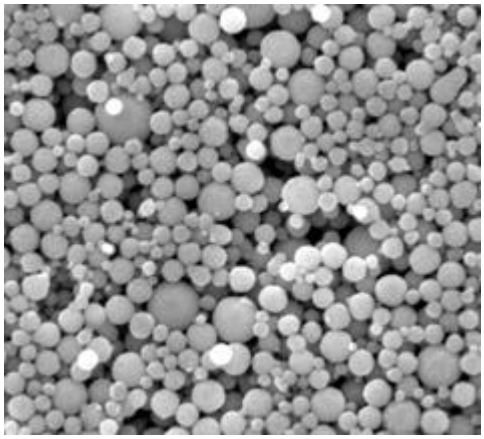


Fig. 1. Copper nanoparticles (Cu, 500 nm)

2. Mathematical Formulation

The problem of an unsteady, incompressible second grade nanofluid flow over a flat plate with wall transpiration is contemplated here. The plate is static at time $t=0$ with the nanofluid embedded in the region $y>0$. It starts vibrating movement at time $t>0$. The plate is considered to be placed vertically in $x-$ direction and flow is also assumed to be in $x-$ direction. The flow geometry has been shown in Figure 2. The governing equations in dimensionless form are as follows:

$$\left((1-\phi)+\phi\frac{\rho_s}{\rho_f}\right)\left(\frac{\partial u}{\partial t}-V_0\frac{\partial u}{\partial y}\right)=\frac{1}{(1-\phi)^{2.5}}\frac{\partial^2 u}{\partial y^2}+\alpha\frac{\partial^3 u}{\partial y^2\partial t}-\alpha V_0\frac{\partial^3 u}{\partial y^3}$$
$$+Gr\left((1-\phi)+\phi\frac{(\rho\beta_T)_s}{(\rho\beta_T)_f}\right)\theta+Gm\left((1-\phi)+\phi\frac{(\rho\beta_C)_s}{(\rho\beta_C)_f}\right)C,\quad y>0,\ t>0, \tag{1}$$

$$\left(\frac{\partial\theta}{\partial t}-V_0\frac{\partial\theta}{\partial y}\right)=\frac{1}{\Pr}\frac{k_s+2k_f-2\phi(k_f-k_s)}{\left(k_s+2k_f+\phi(k_f-k_s)\right)\left((1-\phi)+\phi\dfrac{(\rho c_p)_s}{(\rho c_p)_f}\right)}\frac{\partial^2\theta}{\partial y^2}, \tag{2}$$

$$\left(\frac{\partial C}{\partial t}-V_0\frac{\partial C}{\partial y}\right)=\frac{(1-\phi)}{Sc}\frac{\partial^2 C}{\partial y^2}, \tag{3}$$

with the dimensionless boundary conditions:

$$\begin{aligned}&u(y,0)=0,\ \ u(0,t)=H(t)e^{iwt},\ \ u(\infty,t)=0,\\ &\theta(y,0)=1,\ \ \frac{\partial\theta(0,t)}{\partial y}=-\frac{Br}{\mathrm{Re}}\left[1-\theta(0,t)\right],\ \ \theta(\infty,t)=0,\\ &C(y,0)=0,\quad C(0,t)=1,\quad C(\infty,t)=0,\end{aligned} \tag{4}$$

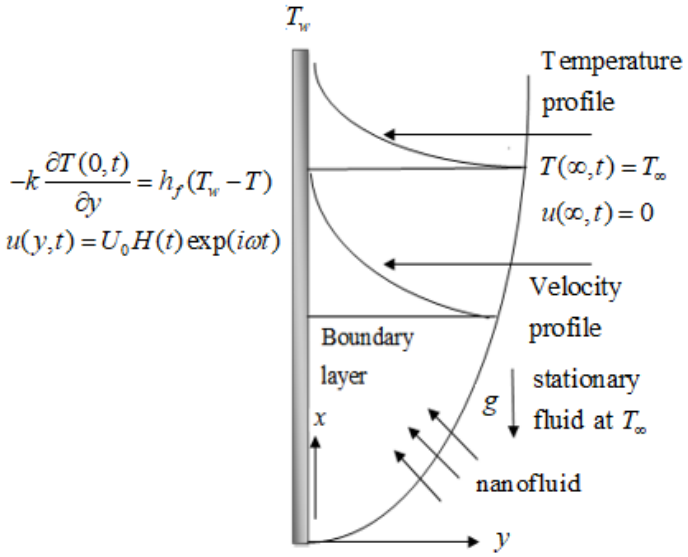


Fig. 2. Flow geometry

where ω is the oscillating frequency, $H(t)$ is the unit step function, $V_0, \alpha, Gr, Gm, \Pr, Sc, Br$ and Re represents wall transpiration, Second grade fluid parameter, Grashof number, Solutal Grashof number, Prandtl number, Schmidt number, Brinkman number and Reynolds number.

Table 1
The values of CMC base fluid and nanoparticles

Thermophysical properties	CMC	Nanoparticles (Cu)

$\rho(Kgm^{-3})$	997.1	8933
$k(Wm^{-1}K^{-1})$	0.613	401
$\beta\times10^{5}(K^{-1})$	21	1.67
$c_p(JKg^{-1}K^{-1})$	4179	385

Laplace transform is employed to Eqs. (1)-(4), we get:

$$\xi_1\left(q\bar{u}-V_0\frac{\partial\bar{u}}{\partial y}\right)=\xi_2\frac{\partial^2\bar{u}}{\partial y^2}+\alpha q\frac{\partial^2\bar{u}}{\partial y^2}-\alpha V_0\frac{\partial^3\bar{u}}{\partial y^3}+\xi_3\bar{\theta}+\xi_4\bar{C}, \tag{5}$$

$$q\bar{\theta}-V_0\frac{\partial\bar{\theta}}{\partial y}=\frac{1}{\xi_5}\frac{\partial^2\bar{\theta}}{\partial y^2}, \tag{6}$$

$$q\bar{C}-V_0\frac{\partial\bar{C}}{\partial y}=\frac{1}{\xi_6}\frac{\partial^2\bar{C}}{\partial y^2}, \tag{7}$$

with the transformed boundary conditions:

$$\begin{aligned}&\bar{u}(y,0)=0,\ \bar{u}(\infty,q)=0,\ \bar{u}(0,q)=\frac{1}{q-i\omega},\\&\bar{\theta}(y,0)=0,\ \bar{\theta}(\infty,q)=0,\ \frac{\partial\bar{\theta}(0,q)}{\partial y}=-\gamma\left[1-\theta(0)\right],\\&\bar{C}(y,0)=0,\ \bar{C}(0,q)=\frac{1}{q},\ \bar{C}(\infty,q)=0.\end{aligned} \tag{8}$$

The following thermophysical properties are introduced:

$$\xi_1=(1-\phi)+\phi\frac{\rho_s}{\rho_f},\ \xi_2=\frac{1}{(1-\phi)^{2.5}},\ \xi_3=Gr\left((1-\phi)+\phi\frac{(\rho\beta_T)_s}{(\rho\beta_T)_f}\right),\ \xi_4=Gm\left((1-\phi)+\phi\frac{(\rho\beta_C)_s}{(\rho\beta_C)_f}\right),$$

$$\xi_5=\mathrm{Pr}\frac{\left(k_s+2k_f+\phi(k_f-k_s)\right)\left((1-\phi)+\phi\left.(\rho c_p)_s\right/(\rho c_p)_f\right)}{k_s+2k_f-2\phi(k_f-k_s)},\ \xi_6=\frac{Sc}{(1-\phi)},\ \gamma=\frac{Br}{\mathrm{Re}}.$$

Here $\rho_f,\rho_s,k_s,k_f,c_p,\beta_T,\beta_C$ represent density, thermal conductivity, specific heat capacity, volumetric thermal and mass expansion of the fluid and nanoparticles. These properties have been listed in Table. 1 for CMC fluid and copper nanoparticles used in this research work. The transformed solutions for Eqs. (5)-(7)are obtained for these equations using Eq. (8):

$$\begin{aligned}\bar{u}(y,q)=&\left[B_0(q)-\beta\left(Q(q)+R(q)\right)\right]\exp\left(-zW_0(q)\right)+\left[B_1(q)+\beta Q(q)\right]\exp\left(-zW_1(q)\right)\\&+\left[B_2(q)+\beta R(q)\right]\exp\left(-zW_2(q)\right),\end{aligned} \tag{9}$$

$$\bar{\theta}(y,q)=\frac{\gamma}{\sqrt{\xi_5}}\exp\left(-\frac{y}{2}V_0\xi_5\right)\frac{1}{q}\frac{\exp\left(-y\sqrt{\xi_5}\sqrt{q+m_2}\right)}{\left(\sqrt{q+m_2}+m_1\right)}, \tag{10}$$

$$\bar{C}(z,q)=\exp\left(-\frac{z}{2}V_0\xi_6\right)\frac{1}{q}\exp\left(-z\sqrt{\xi_6}\sqrt{q+m_3}\right), \tag{11}$$

where

$$B_0(q)=\frac{1}{q-\omega i}+B_1(q)+B_2(q),\qquad B_2(q)=-\frac{\xi_4}{q}\frac{1}{\left[\left(\xi_6-1\right)q+\xi_6 m_3-V_0\sqrt{\xi_6}\sqrt{q+m_3}\right]},$$

$$B_1(q)=-\frac{\xi_3\gamma}{q\sqrt{\xi_5}\left(\sqrt{q+m_2}+m_1\right)}\frac{1}{\left[\left(\xi_5-1\right)q+\xi_5 m_2-V_0\sqrt{\xi_5}\sqrt{q+m_2}\right]},$$

$$Q(q)=\frac{A_1(q)}{W_1^2(q)-V_0W_1(q)-q},\ R(q)=\frac{A_2(q)}{\left(W_2^2(q)-V_0W_2(q)-q\right)},$$

$$A_1(q)=B_1(q)W_1(q)\left[1-V_0W_1^2(q)\right],A_2(q)=B_2(q)W_2(q)\left[1-V_0W_2^2(q)\right],$$

$$W_0(q)=\left(\frac{V_0}{2}+\frac{1}{2}\sqrt{V_0^2+4q}\right),\ W_1(q)=\left(\frac{V_0\xi_5}{2}+\sqrt{\xi_5}\sqrt{q+m_2}\right),$$

$$W_2(q)=\left(\frac{V_0\xi_6}{2}+\sqrt{\xi_6}\sqrt{q+m_3}\right),\ m_2=\frac{V_0^2\xi_5}{4},m_1=\frac{V_0\sqrt{\xi_5}}{2}+\frac{\gamma}{\sqrt{\xi_5}},\quad m_3=\frac{V_0^2\xi_6}{4}.$$

Applying Laplace Inverse to Eqs. (10)-(11) and using Appendix (A1)-(A3), we acquire the solutions as:

$$\theta(y,t)=\frac{\gamma}{\sqrt{\xi_5}}\exp\left(-\frac{y}{2}V_0\xi_5\right)\int_0^t\left\{\frac{1}{\sqrt{\pi\tau}}\exp\left(-\frac{y^2\xi_5^2}{4\tau}-m_2\tau\right)-m_1\exp\left(ym_1\sqrt{\xi_5}+m_1^2\tau\right)erfc\left(\frac{y\sqrt{\xi_5}}{2\sqrt{\tau}}+m_1\tau\right)\right\}d\tau, \tag{12}$$

$$C(z,t)=\frac{1}{2}erfc\left(\frac{y\sqrt{\xi_6}}{2\sqrt{t}}+\frac{V_0}{2}\sqrt{\xi_6 t}\right)+\frac{1}{2}\exp\left(-V_0\xi_6 y\right)erfc\left(\frac{y\sqrt{\xi_6}}{2\sqrt{t}}-\frac{V_0}{2}\sqrt{\xi_6 t}\right). \tag{13}$$

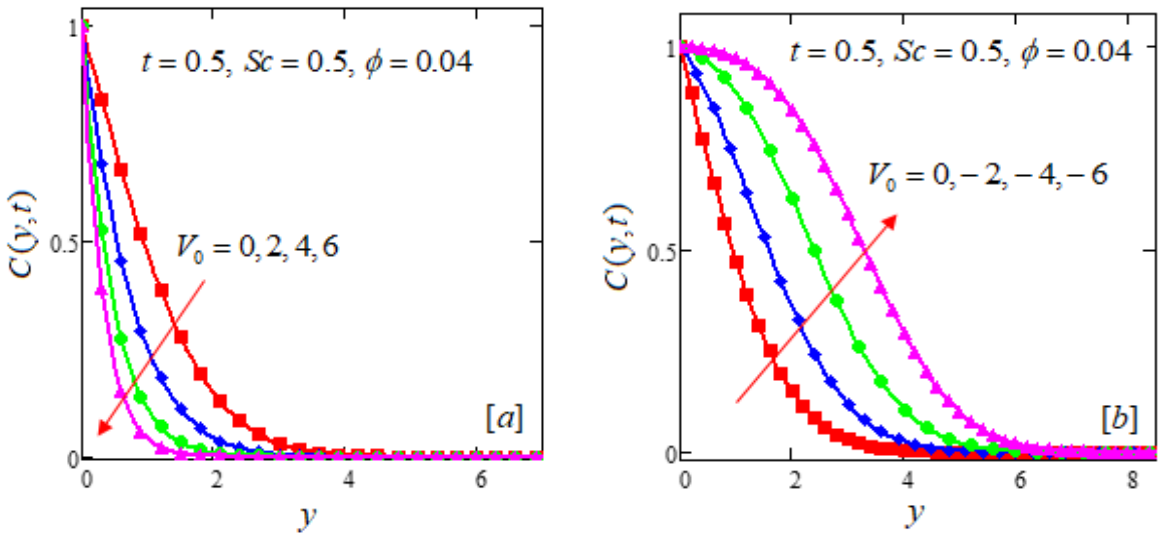


Fig. 3. Concentration profile variation with a) suction b) injection parameter, V_0.

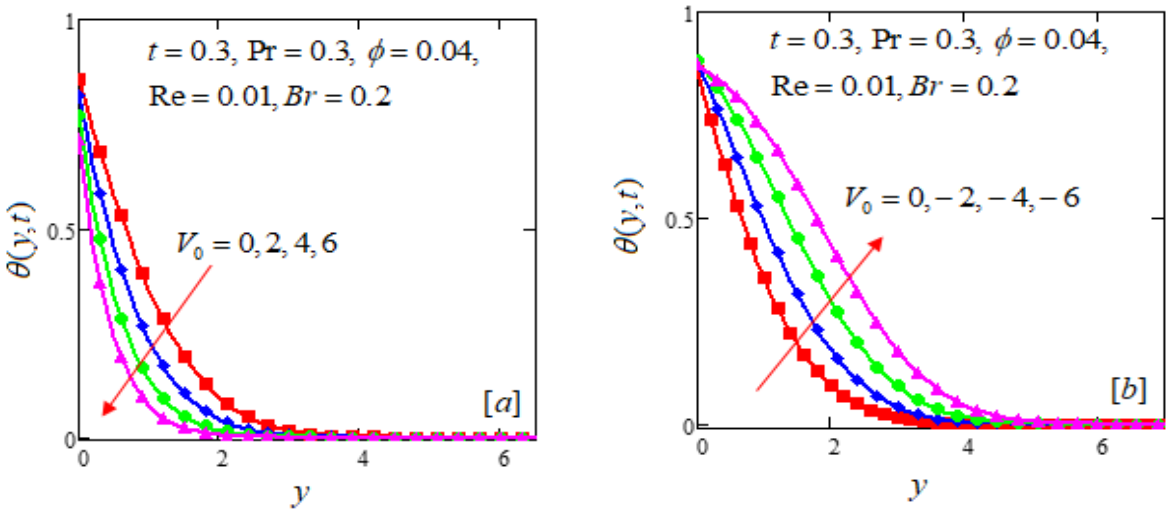


Fig. 4. Temperature profile variation with a) suction b) injection parameter, V_0.

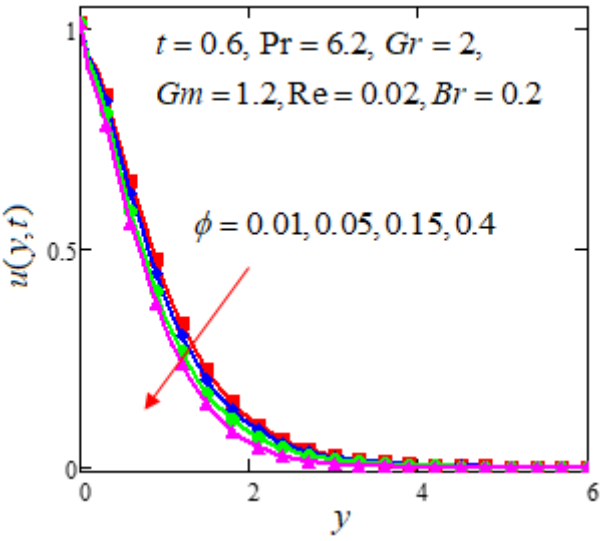


Fig. 5. Velocity profile variation with volume fraction of nanoparticles, ϕ.

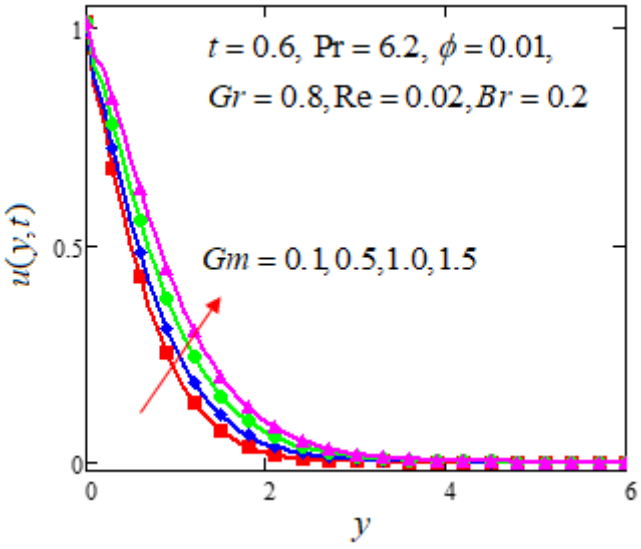


Fig. 6. Velocity profile variation with Solutal Grashof number, Gm.

The solutions are acquired via Inverse Laplace transform given by Tzou and Puri [18] for momentum Eq. (9). We used numerical Inverse Laplace here due to complexity of the resulting equations. The solution for Tzou's algorithm is given as:

$$u(z,t)=\frac{e^{4.7}}{2}\left(\frac{\bar{u}\left(z,\frac{4.7}{t}\right)}{2}+\mathrm{Re}\left(\sum_{q=1}^{N1}(-1)^q\bar{u}\left(z,\frac{4.7+n\pi i}{t}\right)\right)\right), \tag{14}$$

where i is the imaginary unit, $N_1 >> 1$ is a natural number [18].

3. Results

The problem of second grade nanofluid flow over a plate has been investigated for CMC as base fluid with copper nanoparticles. The thermophysical properties of CMC and copper has been listed in the Table 1. Results are established using numerical inversion of Laplace transform technique for some specific circumstances and discussed below.

Besides heat transfer, this study also involves mass transfer. For which, the concentration of the nanofluid is totally effected by the parameters embedded in the equation (3). Figure 3(a) and 3(b) portrays that concentration profile of the fluid is a decreasing function of suction parameter for $V_0 = 0, 2, 4, 6$ while increasing function of suction parameter, $V_0 = 0, -2, -4, -6$. Other parameters Sc and t are kept constant as $Sc = 0.5,\ t = 0.5, \phi = 0.04$. The fluid becomes hot due to injection through the wall. Near the plate, the fluid is hotter and becomes cool gradually for $y > 0$. Maximum variation occurs in the area $0.5 \le y \le 1.5$ above the plate. The flow is induced due to buoyancy forces which is clear from the equation one which contains solutal and thermal Grashof terms. Thus the results for velocity profile must be effected significantly by these parameters.

Figure 4(a) and 4(b) depict that temperature of the fluid is a decreasing function of suction for $V_0 = 0, 2, 4, 6$ while increasing function of injection parameter for $V_0 = 0, -2, -4, -6$. The fluid becomes hot due to injection through the wall. Near the plate, the fluid is hotter and becomes cool gradually for $y > 0$. Maximum variation occurs in the area $0.5 \le y \le 1.5$ above the plate for the constant parameters $\mathrm{Pr} = 0.3,\ t = 0.5, \phi = 0.04, \mathrm{Re} = 0.01$.

Figure 5 portrays that velocity profile of the fluid is an decreasing function of volume fraction ϕ of copper nanoparticles under the conditions considered. The flow velocity profile is decreasing for increasing values of ϕ . Increasing values of this parameter causes a variation in the viscosity of the resulting fluid and it becomes denser compared to the initial fluid. These results are acquired for $\phi = 0.01, 0.05, 0.15, 0.4$ while other involved parameters are kept constant as $\mathrm{Pr} = 6.2,\ t = 0.6,$ $Gr = 2, \mathrm{Re} = 0.02, Br = 0.2, Gm = 1.2$. The nanofluid gets denser due to addition of solid nanoparticles, thus it flows with lower velocity. Maximum variation in the velocity profile can be observed in the range $0 \le y \le 2.5$ over the plate.

The nanofluid encounters a significant and unique variation above the plate with the variation of Solutal Grashof number, Gm in Figure 6. It is due to dominant buoyancy forces enhanced by the heat transfer. Therefore, the nanofluid flows with higher velocity which is clear from Figure 6. The CMC based nanofluid have lowest fluid profile for the lowest considered value $Gm = 0.1$ while highest at greatest value of Gm . Maximum variation in the velocity profile can be observed in the range $0 \le y \le 2$ over the plate. These results were plotted for the range $Gm = 0.1, 0.5, 1.0, 1.5$ and $Gr = 0.8, \mathrm{Re} = 0.02,\ Br = 0.2,\ \phi = 0.01, \mathrm{Pr} = 6.2$.

The flow of the tackled problem for second grade nanofluid was greatly influenced and powered by the embedded parameters which can be refer as the physical circumstances for the flow of a fluid or nanofluid under consideration.

4. Conclusions

The second grade fluid problem is investigated for nanofluids with suction and injection effects in this attempt. The problem was tackled using semi analytical method i.e. a combination of Laplace transform technique and Tzou's algorithm. This problem has not been reported yet in the literature for nanofluids. The outcomes achieved in this investigation are as:

- The suction effect tends to decrease the temperature and concentration profile of the CMC based nanofluid while the injection values enhances these profiles.
- The profile is opposed by increasing volume fraction of nanoparticles values, ϕ.
- The flow is totally favoured by solutal Grashof number Gm, hence buoyancy forces induced the flow at a great extent.

Acknowledgement
This research was funded by a grant from Universiti Malaysia Pahang (RDU190376).

References

[1] Bazhlekova, Emilia, Bangti Jin, Raytcho Lazarov, and Zhi Zhou. "An analysis of the Rayleigh–Stokes problem for a generalized second-grade fluid." Numerische mathematik 131, no. 1 (2015): 1-31.
[2] Chen, Cha'o-Kuang, Hsin-Yi Lai, and Wei-Fan Chen. "Unsteady unidirectional flow of second-grade fluid through a microtube with wall slip and different given volume flow rate." Mathematical Problems in Engineering 2010 (2010).
[3] Wang, Xiaoping, Haitao Qi, Bo Yu, Zhen Xiong, and Huanying Xu. "Analytical and numerical study of electroosmotic slip flows of fractional second grade fluids." Communications in Nonlinear Science and Numerical Simulation 50 (2017): 77-87.
[4] Dehghan, Mehdi, and Mostafa Abbaszadeh. "A finite element method for the numerical solution of Rayleigh–Stokes problem for a heated generalized second grade fluid with fractional derivatives." Engineering with Computers 33, no. 3 (2017): 587-605.
[5] VeeraKrishna, M., G. Subba Reddy, and A. J. Chamkha. "Hall effects on unsteady MHD oscillatory free convective flow of second grade fluid through porous medium between two vertical plates." Physics of Fluids 30, no. 2 (2018): 023106..
[6] Khan, Noor Saeed, Taza Gul, Saeed Islam, and Waris Khan. "Thermophoresis and thermal radiation with heat and mass transfer in a magnetohydrodynamic thin-film second-grade fluid of variable properties past a stretching sheet." The European Physical Journal Plus 132, no. 1 (2017): 11.
[7] Rawi, Noraihan Afiqah, Mohd Rijal Ilias, Zaiton Mat Isa, and Sharidan Shafie. "Effect of gravity modulation on mixed convection flow of second grade fluid with different shapes of nanoparticles." Malaysian Journal of Fundamental and Applied Sciences 13, no. 2 (2017).
[8] Kataria, H. R., & Patel, H. R. *Effect of thermo-diffusion and parabolic motion on MHD second grade fluid flow with ramped wall temperature and ramped surface concentration*. Alexandria engineering journal, 2018. **57**(1): 73-85.
[9] Aman, S., Ismail, Z., Salleh, M. Z., & Khan, I. *Flow analysis of second grade fluid with wall suction/injection and convective boundary condition*. Journal of Advanced Research in Fluid Mechanics and Thermal Sciences, 2019 (1): 135-143.
[10] Zhuang, X., Deng, Z. B., Mu, J., Zhang, L., Yan, J., Miller, D., Feng, W., McClain, C. J., & Zhang H. G. *Ginger-derived nanoparticles protect against alcohol-induced liver damage*. Journal of extracellular vesicles, 2015. **4**(1): 28713.
[11] Xuan, Y., &. Li, Q. *Heat transfer enhancement of nanofluids*. International Journal of heat and fluid flow, 2000. **21**(1): 58-64.
[12] Hussanan, A., Salleh, M. Z., Khan, I., & Shafie, S. *Convection heat transfer in micropolar nanofluids with oxide nanoparticles in water, kerosene and engine oil*. Journal of Molecular Liquids, 2017. 229:. 482-488.
[13] Haq, R., & Aman, S. *Water functionalized CuO nanoparticles filled in a partially heated trapezoidal cavity with inner heated obstacle: FEM approach*. International Journal of Heat and Mass Transfer, 2019. 128: 401-417.
[14] Hayat, T., Khan, M. I., Qayyum, S., & Alsaedi, A. *Entropy generation in flow with silver and copper nanoparticles*. Colloids and Surfaces A: Physicochemical and Engineering Aspects, 2018. 539: 335-346.

[15] Khan, U., Ahmed, N., & Mohyud-Din, S. T. *Analysis of magneto hydrodynamic flow and heat transfer of Cu–water nanofluid between parallel plates for different shapes of nanoparticles*. Neural Computing and Applications, 2018. **29**(10): 695-703.
[16] Toghraie, D., Hekmatifar, M., Salehipour, Y., & Afrand, M. *Molecular dynamics simulation of Couette and Poiseuille Water-Copper nanofluid flows in rough and smooth nanochannels with different roughness configurations*. Chemical Physics, 2019: 110505.
[17] Aman, S., Zokri, M. S., Ismail, Z., Salleh, M. Z., & Khan, I. *Effect of MHD and porosity on exact solutions and flow of a hybrid Casson-Nanofluid*. Journal of Advanced Research in Fluid Mechanics and Thermal Sciences, 2018 (44): 131-139.
[18] Mehryan, S. A. M., Izadpanahi, E., Ghalambaz, M., & Chamkha, A. J. *Mixed convection flow caused by an oscillating cylinder in a square cavity filled with Cu–Al 2 O 3/water hybrid nanofluid.* Journal of Thermal Analysis and Calorimetry, 2019: 1-18.
[19] Dzulkifli, N. F., Bachok, N., Pop, I., Yacob, N. A., Arifin, N. M., & Rosali, H. *Soret and Dufour Effects on Unsteady Boundary Layer Flow and Heat Transfer in Copper-Water Nanofluid Over a Shrinking Sheet with Partial Slip and Stability Analysis*. Journal of Nanofluids, 2019. **8**(7), 1601-1608.
[20] Tzou, D. and P. Puri, *Macro-to microscale heat transfer: the lagging behavior*. Applied Mechanics Reviews, 1997. 50: B82-B82.

Penerbit Akademia Baru

Engineering Science and Technology Conference Proceedings

Journal homepage: www.akademiabaru.com/EST.html

Statistical Relationship of Drilled Solid Concentration on Drilling Mud Rheology

Open

Arina Sauki[1,*], Putri Nadzrul Faizura Megat Khamaruddin[1,*], Sonny Irawan[2], Imros Kinif[3], Syahrir Ridha[4]

[1] Department of Oil and Gas, Faculty of Chemical Engineering, Universiti Teknologi MARA, 40450 Shah Alam, Malaysia
[2] Department of Petroleum Engineering, School of Mining and Geosciences, Nazarbayev University, Kazakhstan
[3] Kuwait Oil Company, Kuwait
[4] Institute of Hydrocarbon Recovery, Universiti Teknologi PETRONAS, Malaysia

ABSTRACT

Drilled solid is a continuous contaminant in drilling mud during drilling operation. The purpose of this study is to evaluate the statistical correlation of drilled solid concentration on mud rheology. A Spearman's correlation was used to determine the relationship between 31 mud rheology data and the drilled solid concentration data from North Kuwait Field. Five rheological models were used to compare the rheological behaviour of the drilled solid-laden drilling fluid which were Bingham Plastic, Power Law, Herschel-Bulkley, Casson and Robertson-Stiff Model. Results showed that a positive monotonic relationship was observed between all drilled solid concentration and mud rheology parameters. An excessive relationship was observed between drilled solid concentration and mud density with a Spearman coefficient (ρ) of 0.942. Other mud rheology parameters such as plastic viscosity, yield point and gel strength show a significant (high) relationship with a spearman coefficient (ρ) in between 0.833 and 0.704. Flow curves of the drilled solid-laden drilling fluids used in this study can be well depicted by the Herschel-Bulkley and Robertson-Stiff Model. These results are not only support the justifiable attention given to address drilled solid impact to the mud rheology, but they also proposed a statistically approach in preparing data for analysis.

Keywords:
Drilled solid; Mud rheology; Rheological Model

Copyright © 2019 PENERBIT AKADEMIA BARU - All rights reserved

1. Introduction

Drilling fluid or drilling mud is characterized as shear-thinning and time dependent fluid whereby it can promote the transportation of cuttings to the surface during drilling and remain suspend when the circulation stops. Suitable rheology of the drilling fluid is important to avoid solids sedimentation during stops and prevent damages such as stuck pipe, loss of circulation, high overpull margin, drill bit jamming and increase in bit torque when the system restart operation [1], [2]. The cuttings generated during drilling are dispersed in the mud and being removed from the fluid using solids-control equipment at the drill site and return the valuable drilling fluid back to the active system [3]. However, small amounts of drilled solids are occasionally unavoidable gets to be re-circulated back to the active system due to insufficient settling time, inefficient mechanical separation equipment, the type of formation being drilled, and the type of drilling fluid being used.

* *Corresponding author.*
E-mail address: arina_sauki@uitm.edu.my (Arina Sauki); putrinadzrul@uitm.edu.my (Dr. Putri Nadzrul Faizura)

Serious problems can develop if these small percentages of drilled solids are continually re-circulated and acted as contaminants. According to Kosun (2015), the solid particle size that is less than 5 microns could not be removed by mechanical methods, and they will stay in the mud forever and may deteriorate the mud properties over time. The degree of contaminating effect exhibited by these drilled solids depends largely on their size, shape and concentration [4], [5]. A study by Du et al. (2018) showed that the concentration and size of the drilled solid gave combined effects to the rheology of cuttings-laden mud and the Herschel Buckley model is suitable to describe its rheological behavior [6]. Nevertheless, the shape and size of the drilled solid generated is a function of the bit types used [7]. Hence, these parameters cannot be controlled and are not being covered in this study except for the concentration of the drilled solid.

Effects of drilled solid on rheology has been studied experimentally by the previous researchers over the last decade [4], [6], [8]. However, there is no statistically proven that their relationship is existed. There are many statistical correlation methods that can justify the relationship between data such as Pearson product-moment correlation coefficient method for normal distribution data and Spearman rank correlation coefficient method for non-normal distribution data [9]–[12]. The decision of which method to be used for analysis was made based on the normality of the data. Spearman rank correlation coefficient method was initially proposed by Charles Spearman as a measure of the quality of a relationship between two factors and is a measure of a monotone affiliation that is utilized when the seizure of data makes Pearson's relationship coefficient undesirable or misleading [10]. It is also less sensitive to the influence of outliers [13]. Unlike Pearson's product-moment correlation coefficient, Spearman's correlation coefficient is not a measure of the linear relationship between two variables, but it assesses how well an arbitrary monotonic function can describe the relationship between two variables, without making any assumption about the frequency distribution of the variables and there is no requirement for normality [14]. A monotonic relationship is a relationship that does one of the following: (1) as the value of one variable increases, so does the value of the other variable; or (2) as the value of one variable increases, the other variable value decreases. Examples of monotonic and non-monotonic relationships are presented in Fig. 1 [15]. This research will focus on the statistical correlation between drilled solid concentration on mud rheology. The findings are noteworthy because of the limited data in the literature looking at the strength of relationship between all those parameters and this outcome is significant to provide better rheological modelling on the drilled solid-laden drilling fluid.

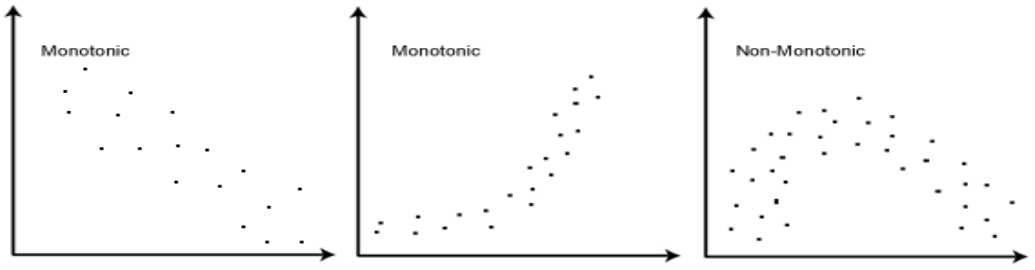


Fig. 1. Monotonic and Non-monotonic Data relationships for Spearman correlation [15]

2. Methodology

2.1 Received Data

Mud properties data of a well drilled in North Kuwait field were gathered from daily drilling report and daily mud report. The data were taken at different hole sections from the depth of 1,215 ft until 8,952 ft and are summarized in Appendices (Table A1 and A2).

2.2 Data Preparation

The data was prepared for analysis to investigate (1) the relationship between drilled solid and mud rheology such as density, plastic viscosity (PV), yield point (YP), gel strength-10 seconds (GS-10s), gel strength-10 minutes (GS-10m) and gel strength-30 minutes (GS-30m) and (2) their rheological model property [11]. A boxplot graph was initiated to test for any data outliers. Then, the normal probability plot and the Anderson Darling Normality Test were used as a basic descriptive statistic test to check the normality of the data. Probability plot provides graphical method to assess normality while the Anderson Darling method provides a hypothesis test for normality. The Anderson Darling method is differed than other hypothesis tests because it is used to prove the null hypothesis rather than disprove it [16]. The Null Hypothesis (H_0) is that the data is normally distributed. The Alternative Hypothesis (Ha) is that the data is not normally distributed. If the p-value is less than the 0.05, the null hypothesis was rejected in agreement with an alternative hypothesis that the data is not normal [17]. But if the p-value is greater than 0.05, there is a reasonable chance that the data could be normally distributed. Non-normally distributed data need to be transformed into a normal distribution depending on the skewness of the data. However, if the data cannot be transferred into a normal data, a non-parametric statistical tool can be utilized [9]. This work suggests the used of Spearman Correlation method for non-normal data.

2.3 Statistical Data Correlation Analysis

Statistical correlation analysis was conducted using Spearman rank correlation coefficient method for non-normal distribution data [9], [10], [12]–[15], [18]–[26]. This analysis was conducted using Minitab 18 Software. Spearman correlation coefficient (ρ) produces a correlation coefficient that ranges from –1 to +1. The ρ values close to either +1 or –1 constitute strong correlation whereas values that near to zero are likely to prove non-significant and no relationship between the variables. A negative value indicates that the relationship is negative. In other words, as one variable increases, the other variable decreases and vice versa. However, a positive value indicates a positive relationship between the variables. In other words, as one variable increases, the other variable increases as well [9]. The strength of the correlation can be categorized using the following guide in Table 1.

Table 1.
Spearman's correlation coefficient: Strength indicator [22], [27]

Correlation Coefficient	Strength indicator
0.90 – 1.00 (-0.90 to -1.00)	Very high positive (negative) correlation
0.70 – 0.90 (-0.70 to -0.90)	High positive (negative) correlation
0.50 – 0.70 (-0.50 to -0.70)	Moderate positive (negative) correlation
0.30 – 0.50 (-0.30 to -0.50)	Low positive (negative) correlation
0.00 – 0.30 (-0.00 to -0.30)	Negligible correlation

A scatterplot was used to represent the correlation coefficient that exists between two factors. However, it is possible for a scatter plot to suggest a correlation between two factors when in fact none exists especially when a random and small sample size data are taken [16]. As such, it is needed to evaluate its statistically significance whether the data is real or not. The statistical significance was determined based on Null hypothesis where a correlation exists when p-value is less than 0.05. If the p-value is more than 0.05, it indicates that no correlation exists [16]. Spearman correlation was done using the rank of data. The original data must be converted into rank prior to Spearman correlation analysis [10]. The data with the highest value was ranked as "1" and the lowest data value was ranked according to the number of cases that we have.

2.4 Determination of Rheological Model Parameters

There are five established rheological models were used to describe the rheological behaviors of the field measured data parameters which are Bingham plastic model, Power law Model, Hershel-Buckley model, Casson model and Robertson-Stiff model. The summary of the rheology models is shown in Table 2.

Table 2
Summary of rheological models used [22], [27]

Rheological model	Equation	Legend
Bingham plastic	$\tau = \tau_0 + \mu_p$ $\tau_0 = \theta_{300} - \mu_p$ $\mu_p = \theta_{600} - \theta_{300}$	τ_o = yield point (lb/100ft^2); μ_p = plastic viscosity (cP)
Power Law	$\tau = k\gamma^n$ $n = 3.32log\left(\frac{\theta_{600}}{\theta_{300}}\right)$ $k = \frac{\tau}{\gamma^n} = \frac{\theta_{600}}{1022^n}$	n = fluid flow behaviour index and dimensionless; k = consistency coefficient (lb/100ft^2) which can be converted to Pa by multiplying with a factor of 0.51 [30].
Herschel-Bulkley	$\tau = \tau_{0H} + k_H\gamma^{n_H}$	γ = shear rate (s^{-1}); τ= shear stress (Pa); n_H = flow behaviour index (dimensionless); k_H= Herschel-Bulkley consistency index (Pa.s^n); τ_{oH} = Herschel-Bulkley yield stress (Pa). The parameters of k_H and n_H can be determined by linearizing the equation with a plot of log ($\tau - \tau_{oH}$) versus log (γ). This plot will result in a straight line with intercept (log k_H) and slope (n_H) respectively.
Casson	$\tau^{\frac{1}{2}} = k_{oc}^{\frac{1}{2}} + k_c^{\frac{1}{2}}\gamma^{\frac{1}{2}}$	k_{oc} = Casson yield stress (Pa.s); k_c = Casson plastic viscosity (mPa.s). k_{oc} and k_c parameters can be obtained from the straight line that is drawn when the square root of shear stress ($\tau^{0.5}$) is plotted against the square root of shear rate ($\gamma^{0.5}$) with the slope k_c and intercept k_{oc}. The Casson yield stress is calculated as the square of the intercept, $\tau_{oc} = (k_{oc})^2$ and the Casson plastic viscosity is the square of the slope $\eta_{ca} = (k_c)^2$.
Robertson-Stiff	$\tau = A(\gamma + C)^B$ $C = \frac{\gamma_{min}\gamma_{max} - \gamma^{*2}}{2\gamma^* - \gamma_{min} - \gamma_{max}}$	A, B, and C are model parameters. A and B can be considered similar to the parameters k and n of the Power-law model. The third parameter C is a correction factor to the shear rate, and the term (γ+C) is considered

$\tau^* = (\tau_{min} \times \tau_{max})^{\frac{1}{2}}$	effective shear rate. γ* is the shear rate value corresponding to the geometric mean of the shear stress, τ*.

All these models are categorized under non-Newtonian fluid model whereby the fluid viscosity is not constant but a function of the shear stress and/or the dominant shear rate [28], [29]. Prior to this analysis, the viscometry data from Table A2 was converted into shear stress-shear rate data. Conversion was made based on geometry of the rotor and bob of the viscometer. For Fann 35A six speed model, the conversion of rpm to shear rate (sec-1) is given by the Eq. 1. The shear stress from this instrument is taken from the dial reading (R) and converted into Eq. 2. For selecting the suitable rheological model for the field measured data, the Absolute Average Percentage Error (ϵ_{AAP}) was determined and compared using Eq. 3.

$$Shear\ rate\ (sec\text{-}1) = rpm\ x\ 1.703 \quad (1)$$

$$Shear\ stress\ (Pa) = R\ x\ 0.51 \quad (2)$$

$$\epsilon_{AAP} = \left[\frac{1}{N}\sum\left|\frac{\tau_{measured}-\tau_{calculated}}{\tau_{measured}}\right|\right] \times 100 \quad (3)$$

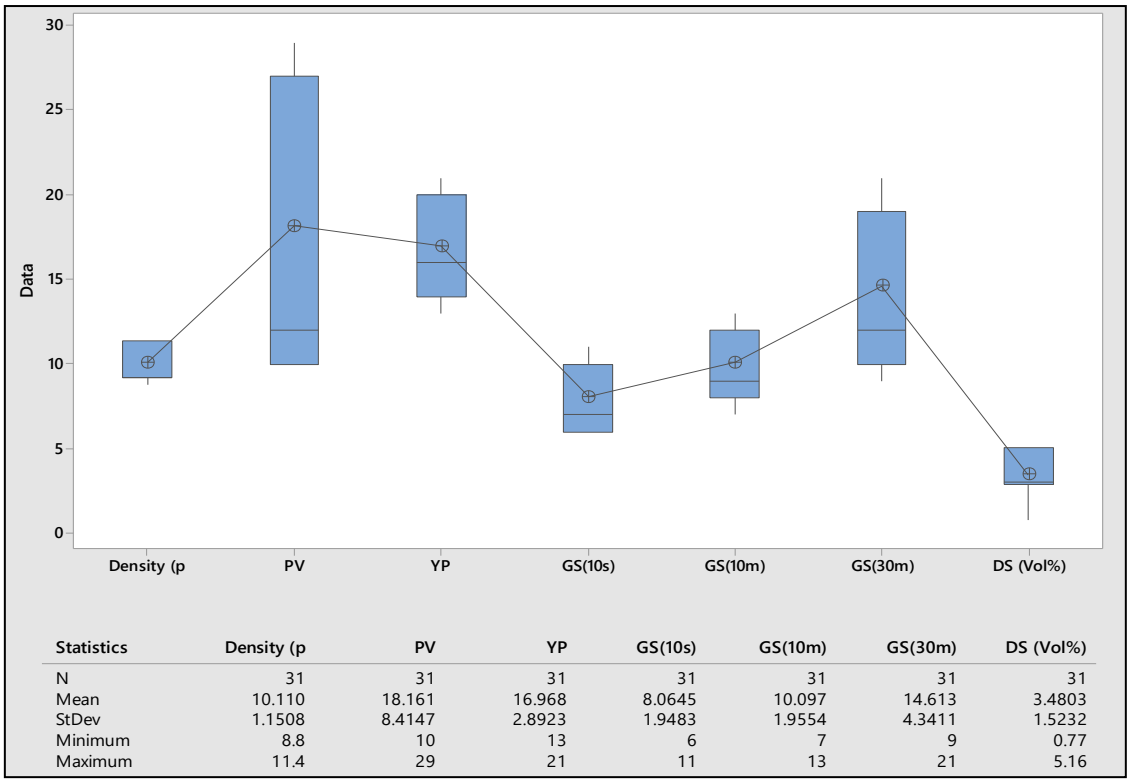
3. Results

3.1 Relationship Between Drilled Solid and Mud Rheology

Thirty-one samples of mud rheology data such as density, plastic viscosity (PV), yield point (YP), gel strength (GS for 10 seconds, 10 minutes and 30 minutes) and drilled solid concentration data (DS) were utilized in these analyses. The drilled solid concentrations of the received data were in between 0.5 to 5.1 percent in volume (vol%). A boxplot graph was used to test for any outliers in the data where any data points falling outside the boxplot minimum and maximum limits are outliers [9]. The minimum and maximum values can be observed through the vertical line (whiskers) attached to the box while the horizontal line in the box indicates the median. The dotted-circle mark in the box indicates the mean value and the box itself represents 50% of the data [16]. Based on Fig. 2, it was observed that there were no outliers shown in the graph. PV appears to have lower median data than YP while GS (10s) appears to have lower median data than those from GS (10m) and GS (30m). Among all these parameters, PV indicates a wider range in values while density shows a more condensed value. In overall, all the boxes show a skewed right data where the longer part of the box is to the above of the median. This indicates that the data were possibly not normal. A normal probability plot was used to confirm the normality of the data.

From the normal probability plot (Fig. 3), it was obvious that the normality assumption was not fulfilled by the response variables. The structure of the plot in Fig. 2 displays the deflections in point whereby the curvature evinces bimodality. In addition, Table 3 shows the Anderson Darling Normality test results and it was observed that all the measurements demonstrated the p-value of less than 0.05. Thus, there is enough evidence to say that the normality assumption was contravened in this case. The data were also failed to be transformed into a normal distribution data. As such, a non-parametric test (Spearman rank correlation method) was used to assess the relationship between drilled solid and mud rheology. Hence, the first step was to convert the

original data in Table A1 into ranks before calculating the Spearman correlation coefficient and this is summarized in Table 4.



Statistics	Density (p	PV	YP	GS(10s)	GS(10m)	GS(30m)	DS (Vol%)
N	31	31	31	31	31	31	31
Mean	10.110	18.161	16.968	8.0645	10.097	14.613	3.4803
StDev	1.1508	8.4147	2.8923	1.9483	1.9554	4.3411	1.5232
Minimum	8.8	10	13	6	7	9	0.77
Maximum	11.4	29	21	11	13	21	5.16

Fig. 2. Boxplots graph for Mud Rheology and Drilled Solid Concentration Data

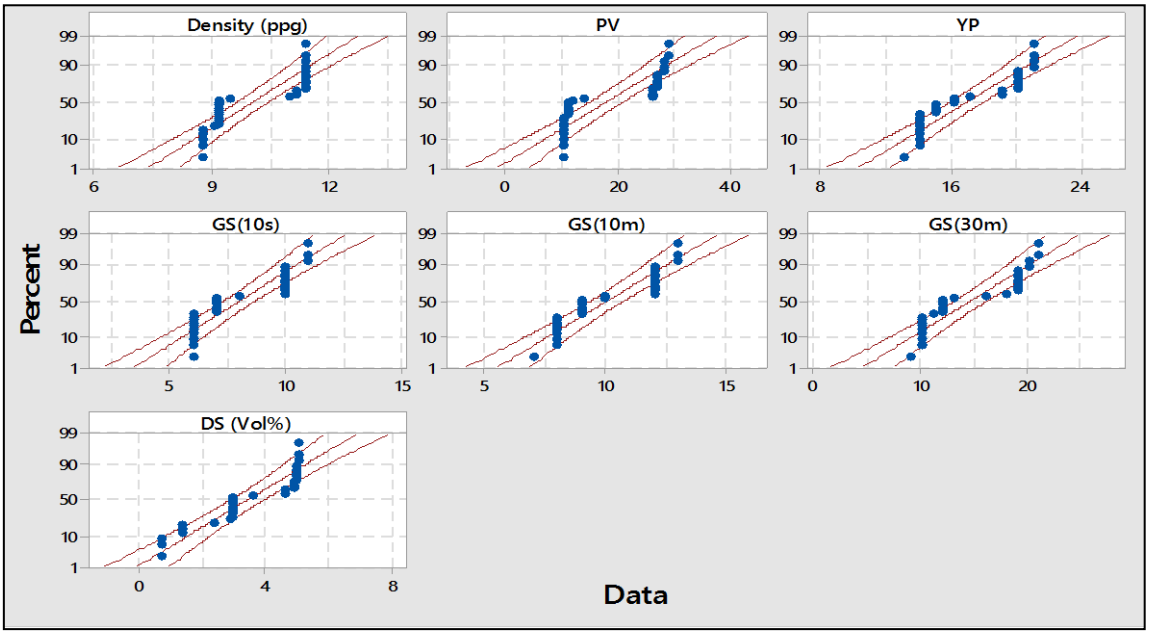


Fig. 3. Normal Probability Plot of Original Mud Rheology and Drilled Solid Concentration Data

Table 3
Anderson Darling Normality Test Results

Sample	Sample size	Mean	Std. Dev	Anderson Darling Normality Test	
				P-value	*Decision*
Density	31	10.11	1.15	<0.005	Fail
PV	31	18.16	8.41	<0.005	Fail
YP	31	16.97	2.89	<0.005	Fail
GS (10s)	31	8.06	1.94	<0.005	Fail
GS (10m)	31	10.10	1.96	<0.005	Fail
GS (30m)	31	14.61	4.34	<0.005	Fail
Drilled Solid	31	3.48	1.52	<0.005	Fail

Table 4
Rank data for Spearman correlation analysis

Data entry	Hole Section	MD (ft)	Rank Density	Rank PV	Rank YP	Rank GS 10sec	Rank GS 10min	Rank GS 30min	Rank DS
1	22.00	1,215	4	5	5	4	4	8	11
2	16.00	1,500	7	6	5	4	4	7	13
3		2,270	7	8	6	4	4	7	13
4		3,300	7	8	6	4	4	7	13
5		3,500	7	8	7	4	4	7	12
6		3,630	7	8	7	4	4	7	12
7		4,145	6	7	5	4	3	6	9
8		4,680	5	7	6	5	4	7	10
9		4,680	5	7	7	5	5	9	8
10		4,680	5	7	7	5	5	9	8
11		5,445	5	7	7	5	5	9	8
12		6,006	5	8	7	5	5	9	8
13		6,150	5	7	7	5	5	9	8
14		6,150	5	8	7	5	5	9	8
15		6,150	5	8	7	5	5	9	8
16		6,150	5	8	8	5	6	10	8
17		6,150	5	8	6	5	5	9	8
18	12.25	6,720	3	4	4	3	3	5	7
19		7,100	2	3	2	2	2	4	5
20		7,530	2	3	1	2	2	3	6
21		7,610	1	2	1	2	1	2	1
22		7,990	1	1	2	1	1	1	2
23		8,395	1	1	2	1	1	1	2
24		8,952	1	3	2	2	2	3	3
25		8,952	1	2	1	1	2	2	3
26		8,952	1	2	1	2	2	3	3
27		8,952	1	3	3	2	2	3	3
28		8,952	1	3	3	2	2	3	3
29		8,952	1	4	2	2	2	3	4
30		8,952	1	4	2	2	2	3	4
31		8,952	1	4	2	2	2	3	4

Spearman coefficient analysis revealed statistically significant evidence that the drilled solid concentration is positively influenced by the mud rheology parameters with the P-value of less than 0.05 as shown in Table 5. Fig. 4 also shows that all the variables are positively monotonic correlated. There was a very strong positive correlation between drilled solid concentration and density with a Spearman coefficient (ρ) of 0.942, followed with PV, GS-30m, GS-10m, GS-10s and YP with a positive Spearman coefficient (ρ) of 0.833, 0.716, 0.715, 0.711 and 0.704 respectively. The drilled solid concentration positively influenced the mud rheology be theoretically, as the volume percent of drilled solids increases, the density increases. Typically, drilled solids have a specific gravity (SG) in the range of 2.1 to 2.8 [31]. Since the SG of mud used for drilling this well is in between 1.05 to 1.37, the addition of higher SG of drilled solid will dramatically increase the fluid's density.

Plastic viscosity (PV) is another parameter that demonstrates a strong relationship with drilled solid concentration. However, its effectiveness was not as great as density because it depends on the reactivity scale or swelling ability of the solid into the mud. Swelling solid like clay can increase the PV of the mud while low-swelling clay or inactive solid may not really affect the PV [32]. Furthermore, it also depends on the type of the base mud used. Theoretically, when the free water in water-based mud is chemically attached to the solids, it will gradually increase the internal friction between particle and fluid and also increase the fluid's viscosity. However, excessive and insufficient PV is unfavorable as it will reduce the ability to bring the cuttings to the surface and allow the cuttings to be re-grinded into a smaller size. In practical field application, PV is generally used as a guide for solid control where the removal of drilled solid from drilling fluid will decrease PV [33,34].

Moreover, Gel strength (GS) is a rheological measurement taken after varying the length of static condition such as 10 seconds, 10 minutes and 30 minutes. It relates to the suspension capacity of drilling fluid at rest [35]. The suspension capacity of the drilling fluid is important as it helps in hole cleaning as it prevents the differential sticking as well as accumulation of cuttings that causes the pressure build up and frac out. Severe increase in GS can exert excessive subsurface pressure when flow is re-established making them more problematic. High GS is not desired for removing cutting through gravity settling at surface. Based on Table IV, DS concentration has also affected the GS significantly. The correlation is greater for GS-30m as compared with GS-10s and GS-10m. This suggests that close monitoring of GS-30m should be more vigorous for drilled solid build-up. In a condition where the mud has high GS and the mud is static for a long period, the subsequent build-up of pressure in the pump is required to break circulation. Hence, further treatment is needed to reduce the progressive gel build-up such as addition of chemicals or perform dilution. Many drilling fluids have thixotropic properties where it becomes gel in static condition and will flow over time when sheared or stressed [33].

In addition, DS concentration was also a strong contributor to the positive association of YP (ρ = 0.704). This is consistent with previous work which showed that YP rises while DS concentration increases [4]. Yield point (YP) is the initial resistance to flow caused by the electrochemical forces between the particles. Increase in solid content decreases the interparticle distance and consequently increases the forces between the drilled solid and other mud particles. This would result in difficulty for solid removal at the shale shaker as it cannot handle the smaller mesh screen size [34].

Table 5
Spearman Rho of the relation between drilled solid concentration and mud rheology parameters

CONTENT	DENSITY	PV	YP	GS (10s)	GS (10m)	GS (30m)
Spearman ρ	0.942	0.833	0.704	0.711	0.715	0.716
P-Value	0.000	0.000	0.000	0.000	0.000	0.000
Strength	Very strong	Strong	Strong	Strong	Strong	Strong

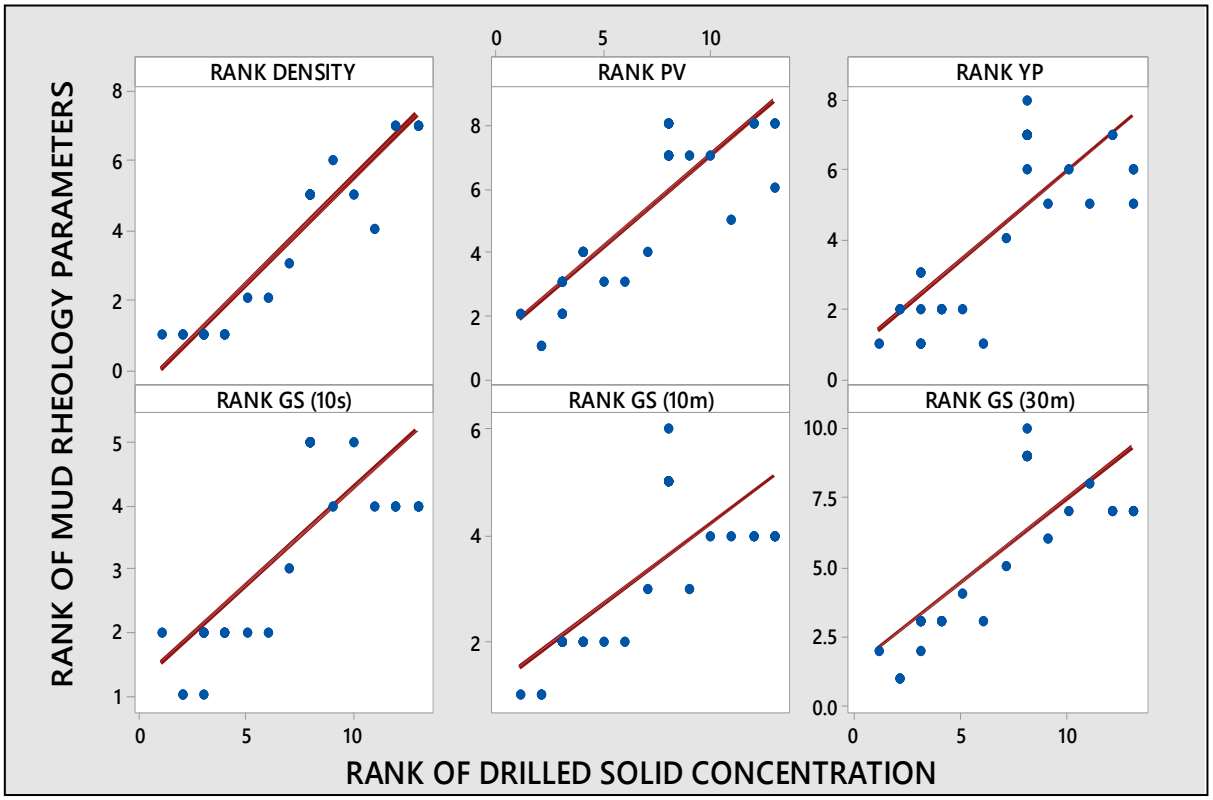


Fig. 4. Scatterplot of Mud Rheology Parameters Rank vs Drilled Solid Concentration Rank

3.2 Rheological Model Property

Table 6 shows the summary of two different mud systems used for drilling the well which are Water based mud (WBM) and Oil-based Mud (OBM). As such, it is noteworthy to identify their rheological models in order to predict the shear stress-shear rate behaviour of both systems. Five models were compared which are Bingham Plastic, Power Law, Herschel-Bulkley, Casson and Robertson-Stiff using the flow curve of the shear stress vs. shear rate plots. The results are shown in Fig. 5 (WBM) and Fig. 6 (OBM). According to these two plots, the flow curve is curvilinear and an intercept of flow curve at the vertical axis shows a yield stress value of the samples. WBM appears to have a lower shear stress values than the OBM due to a smaller amount of drilled solid presence in this mud. An abrupt increase in shear stress was observed for OBM at low shear rate due to the higher density of this region than the WBM. Selection of the best goodness-of-fit model was done based on its Absolute Average Percentage Error (ϵAAP) between the models and field data in which the closer the error to zero, the better the fit is [28]. Table 7 shows that Bingham Plastic model was not suitable for the systems due to the straight flow curve especially for high shear stress mud (OBM) with the absolute percentage error of 32.11%. It was also observed that the poor performance of Bingham model was due to the large deviation of predicted shear stress at high shear rates for both systems. The Power Law and Casson model showed poor fitted to the both

systems due to the lack of the yield stress in these models as compared to the field measured data. The best fitting model would be Herschel-Bulkley model followed by Robertson & Stiff model with the absolute average percentage errors of less than 5% for both systems. These models used non-linear shear-stress rate behavior along with a yield stress that could cater a high yield stress mud [36]. This finding is consistent with previous published work that used KCL-polymer mud in their analysis and had selected Herschel-Bulkley model for that system [6]. However, Du et al. (2018) studied the effects of mudstone cuttings addition into KCl-polymer mud whilst this study generally focused on the effects of drilled solid mainly from limestone cuttings (based on major limestone formation in North Kuwait field) into water-based mud and oil-based mud. Similar with our case, J. Sadigov (2016) conducted rheology model prediction using field measured data [37]. They proposed the least error model was Robertson-Stiff (1.93% error) followed by Hershel Buckley (4.25% error), power law (6.55% error) and the highest error was Bingham Law model (26.79%). However, the type of mud system used was not being mentioned in their study, thus, these results are not directly comparable to theirs. In contrast, Adewale et al. (2017) found that Casson was the best fitted model to their experimental works using synthetic based mud [28]. Nevertheless, this type of mud system is totally different than this study. As such, it is noteworthy to mention that different application of rheological model is required for different mud system and selection of proper rheological model is important for further analysis on the frictional pressure losses associated with the flow of the drilling fluids in the wellbore.

Table 6
Summary of Shear Stress Values of drilled solid-laden water-based mud (DS_{conc} =2.91 vol%) and oil-based mud (DS_{conc} =5.13 vol%) using Different Rheological Models

Speed (RPM)	Dial Reading (lb/100ft^2)	Shear Rate (S^{-1})	Shear Stress Values of drilled solid-laden Water-based mud (DS_{conc} =2.91 vol%)					
			Measured (Pa)	Bingham Plastic (Pa)	Power Law (Pa)	Herschel-Bulkley (Pa)	Casson (Pa)	Robertson-Stiff (Pa)
600	38	1022	19.38	13.28	19.09	20.00	29.87	19.40
300	27	511	13.77	9.19	13.59	13.34	16.49	14.04
200	22	340.6	11.22	7.82	11.14	10.78	11.82	11.68
100	16	170.3	8.16	6.46	7.93	7.86	6.90	8.69
6	8	10.22	4.08	5.18	2.00	4.09	1.32	4.13
3	7	5.11	3.57	5.14	1.42	3.88	1.02	3.89
Speed (RPM)	Dial Reading (lb/100ft^2)	Shear Rate (S^{-1})	Shear Stress Values of drilled solid-laden Oil-based mud (DS_{conc} =5.13 vol%)					
			Measured (Pa)	Bingham Plastic (Pa)	Power Law (Pa)	Herschel-Bulkley (Pa)	Casson (Pa)	Robertson-Stiff (Pa)
600	78	1022	39.78	19.89	39.46	47.82	46.02	40.35
300	49	511	24.99	12.50	24.80	27.28	25.05	25.91
200	42	340.6	21.42	10.03	18.90	20.15	17.78	20.16
100	33	170.3	16.83	7.56	11.88	12.76	10.17	13.45
6	10	10.22	5.1	5.25	1.80	5.19	1.74	4.86
3	9	5.11	4.59	5.17	1.13	4.90	1.30	4.48

Table 7
Summary of Absolute Average Percentage Error, ϵAAP of drilled solid-laden water-based mud (DSconc =2.91 vol%) and oil-based mud (DSconc =5.13 vol%) using Different Rheological Models

Mud system	Absolute Average Percentage Error, ϵ_{AAP}				
	Bingham Plastic (Pa)	Power Law (Pa)	Herschel-Bulkley (Pa)	Casson (Pa)	Robertson & Stiff (Pa)
WBM	7.49	19.59	0.23	12.54	3.81
OBM	32.11	30.47	1.30	29.72	4.66

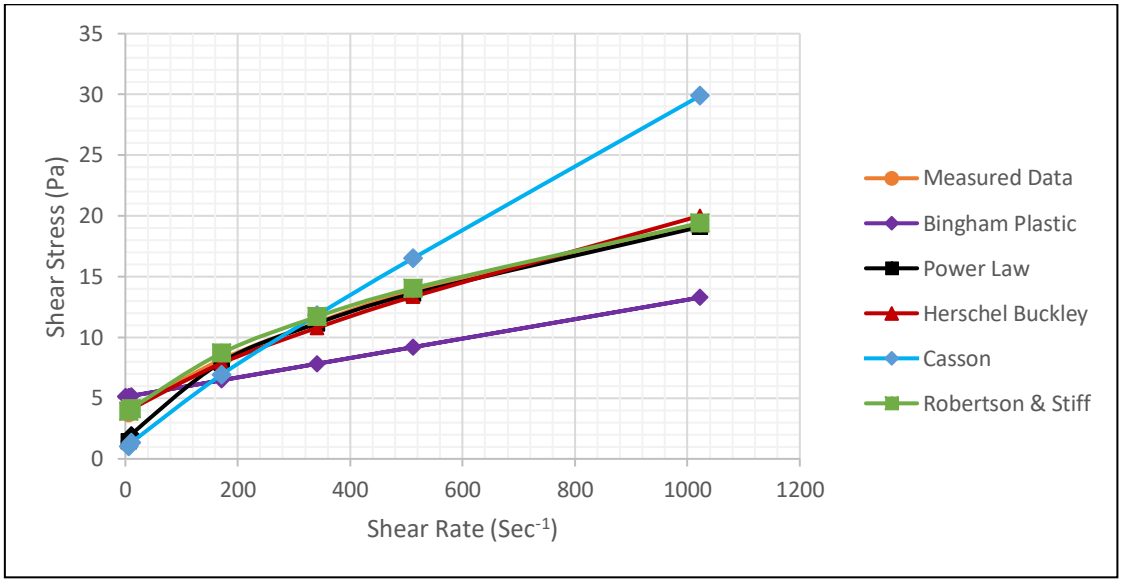


Fig. 5. Shear Stress-Shear Rate Graph of drilled solid-laden water-based mud (DSconc =2.91 vol%) using Different Rheological Models

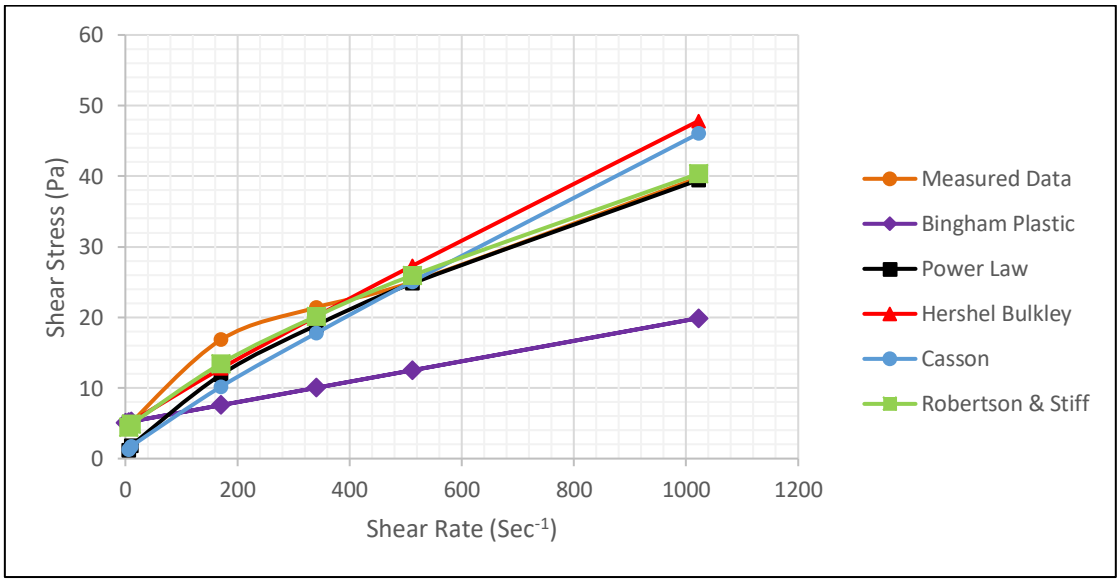


Fig. 6. Shear Stress-Shear Rate Graph of drilled solid-laden oil-based mud (DSconc =5.13 vol%) using Different Rheological Models

4. Conclusions

Based on the field data collected from North Kuwait field, it can be concluded that the effects of drilled solid concentration on mud rheology is significant. The highest correlation was found between drilled solid concentration and density followed by plastic viscosity, gel strength (30 min), gel strength (10min), gel strength (10 sec) and yield point. The rheology behaviours for the mud used in this field i.e. water-based mud and oil-based mud are both well depicted by Herschel Buckley and followed by Robertson-stiff model. It is hope that these findings would stimulate further study on the application of the selected models for determining frictional pressure losses and flow regime and their impact towards drilling rate.

Acknowledgement
The authors would like to thank Faculty of Chemical Engineering, Universiti Teknologi MARA for the support and facilities on this research.

References

[1] Santos, Nara Brandão Costa, Flávia Marques Fagundes, Fábio de Oliveira Arouca, and João Jorge Ribeiro Damasceno. "Sedimentation of solids in drilling fluids used in oil well drilling operations." Journal of Petroleum Science and Engineering 162 (2018): 137-142.

[2] Werner, Benjamin, Velaug Myrseth, and Arild Saasen. "Viscoelastic properties of drilling fluids and their influence on cuttings transport." Journal of Petroleum Science and Engineering 156 (2017): 845-851.

[3] McCosh, K., and J. Getliff. Effect of drilling fluid components on composting and consequences for mud formulation. AADE Drilling Fluid Conference, Radisson Astrodome, Houston, Texas. AADE-04-DF-HO-25. Posted Jan 23 rd 2005, Retrieved April 6-2007 from http://www. aade. org/TechPapers/2004Papers/Environmental% 20Assurance/A, 2004.

[4] Njobuenwu, Derrick O., and Chimeka A. Wobo. "Effect of drilled solids on drilling rate and performance." Journal of Petroleum Science and Engineering 55, no. 3-4 (2007): 271-276.

[5] Hemphill, Terry, B. Murphy, and K. Mix. "Optimization of Rates of Penetration in Deepwater Drilling: Identifying the Limits." In SPE Annual Technical Conference and Exhibition. Society of Petroleum Engineers, 2001.

[6] Du, Hui, Gui Wang, Guicai Deng, and Cheng Cao. "Modelling the effect of mudstone cuttings on rheological properties of KCl/Polymer water-based drilling fluid." Journal of Petroleum Science and Engineering 170 (2018): 422-429.

[7] Girmaa Jimaa, “Cutting transport parametric sensitivity simulation studies in vertical and deviated wells,” (2013).

[8] Robinson, Leon. "Economic Consequences of Poor Solids Control." American Association of Drilling Engineer (AADE) (2006).

[9] Alkinani, Husam H., Abo Taleb T. Al-Hameedi, Shari Dunn-Norman, Ralph E. Flori, Steven A. Hilgedick, Madhi A. Al-Maliki, Yousif Q. Alshawi, Mortadha T. Alsaba, and Ahmed S. Amer. "Examination of the relationship between rate of penetration and mud weight based on unconfined compressive strength of the rock." Journal of King Saud University-Science (2018).

[10] Thirumalai, Chandrasegar, Swapna Anupriya Chandhini, and M. Vaishnavi. "Analysing the concrete compressive strength using Pearson and Spearman." In 2017 International conference of Electronics, Communication and Aerospace Technology (ICECA), vol. 2, pp. 215-218. IEEE, 2017.

[11] C. Spearman, “The Proof and Measurement of Association between Two Things,” Am. J. Psychol., vol. 15, no. 1, pp. 72–101, 1904.

[12] Mackridge, Adam, and Philip Rowe. A Practical Approach to Using Statistics in Health Research: From Planning to Reporting. John Wiley & Sons, 2018.

[13] Quek, June, Yong-Hao Pua, Ross A. Clark, and Adam L. Bryant. "Effects of thoracic kyphosis and forward head posture on cervical range of motion in older adults." Manual therapy 18, no. 1 (2013): 65-71.

[14] Hauke, Jan, and Tomasz Kossowski. "Comparison of values of Pearson's and Spearman's correlation coefficients

on the same sets of data." Quaestiones geographicae 30, no. 2 (2011): 87-93.
[15] A. W. S. Of, “Spearman’s correlation,” pp. 1–36, 2015.
[16] Brook, Quentin Stephen. Six Sigma and Minitab: A complete toolbox guide for all Six Sigma practitioners. QSB consulting, 2006.
[17] Ahad, Nor Aishah, Teh Sin Yin, Abdul Rahman Othman, and Che Rohani Yaacob. "Sensitivity of normality tests to non-normal data." Sains Malaysiana 40, no. 6 (2011): 637-641.
[18] Rebekić, Andrijana, Zdenko Lončarić, Sonja Petrović, and Sonja Marić. "Pearson's or Spearman's correlation coefficient-which one to use?." Poljoprivreda (Osijek) 21, no. 2 (2015): 47-54.
[19] Bishara, Anthony J., and James B. Hittner. "Testing the significance of a correlation with nonnormal data: comparison of Pearson, Spearman, transformation, and resampling approaches." Psychological methods 17, no. 3 (2012): 399.
[20] Fields, David A., and Ellen W. Demerath. "Relationship of insulin, glucose, leptin, IL-6 and TNF-α in human breast milk with infant growth and body composition." Pediatric obesity 7, no. 4 (2012): 304-312.
[21] Datta, Vivek, Avril Chang, Sean Mackay, and Ara Darzi. "The relationship between motion analysis and surgical technical assessments." The American journal of surgery 184, no. 1 (2002): 70-73.
[22] Mukaka, Mavuto M. "A guide to appropriate use of correlation coefficient in medical research." Malawi Medical Journal 24, no. 3 (2012): 69-71.
[23] Strom, Alexander, Kirti Kaul, Jutta Brüggemann, Iris Ziegler, Ilka Rokitta, Sonja Püttgen, Julia Szendroedi, Karsten Müssig, Michael Roden, and Dan Ziegler. "Lower serum extracellular superoxide dismutase levels are associated with polyneuropathy in recent-onset diabetes." Experimental & molecular medicine 49, no. 11 (2017): e394.
[24] Evans, James D. Straightforward statistics for the behavioral sciences. Thomson Brooks/Cole Publishing Co, 1996.
[25] DordiNejad, Farhad Ghorban, Hamideh Hakimi, Maryam Ashouri, Maryam Dehghani, Zhaleh Zeinali, Maryam Sadegh Daghighi, and Naghmeh Bahrami. "On the relationship between test anxiety and academic performance." Procedia-Social and Behavioral Sciences 15 (2011): 3774-3778.
[26] Uysal, Tancan, Sabri Ilhan Ramoglu, Faruk Ayhan Basciftci, and Zafer Sari. "Chronologic age and skeletal maturation of the cervical vertebrae and hand-wrist: is there a relationship?." American Journal of Orthodontics and Dentofacial Orthopedics 130, no. 5 (2006): 622-628.
[27] Hinkle, Dennis E., William Wiersma, and Stephen G. Jurs. Applied statistics for the behavioral sciences. Vol. 663. Houghton Mifflin College Division, 2003.
[28] Folayan, J. Adewale, Paul Apeye Lucky Anawe, P. Oluwabunmi Abioye, and F. Boluwaji Elehinafe. "Selecting the most appropriate model for rheological characterization of synthetic based drilling mud." International Journal of Applied Engineering Research 12, no. 18 (2017): 7614-7649.
[29] Mitchell, Rober, and Stefan Miska. Fundamentals of drilling engineering. Society of Petroleum Engineers, 2011.
[30] M. Reiner, “About the flow of an elastic fluid through a capillary,” *Colloid J.*, vol. 39, no. 1, pp. 80–87, 1926.
[31] Eritia, “Drilling Fluids,” *Drilling fluid org*, 2017. .
[32] G. Altun and U. Serpen, “Investigating Improved Rheological and Fluid Loss Performance of Sepiolite Muds under Elevated Temperatures,” *Stress Int. J. Biol. Stress*, no. April, pp. 24–29, 2005.
[33] Alum, Moses A., and F. Egbon. "Semi-analytical models on the effect of drilling fluid properties on rate of penetration (ROP)." In Nigeria Annual International Conference and Exhibition. Society of Petroleum Engineers, 2011.
[34] Kinif, Imros, Sonny Irawan, and Abhilash M. Bharadwaj. "DEVELOPMENT AND EVALUATION OF SOLID CONTROL SYSTEM TO OPTIMIZE DRILLING PERFORMANCE." Jurnal Teknologi 78, no. 6-7 (2016).
[35] Ryen Caenn HCH Darley George R. Gray, *Composition and Properties of Drilling and Completion Fluids*. Gulf Professional Publishing, 2016.
[36] Khataniar, Santanu, Godwin A. Chukwu, and Hua Xu. "Evaluation of rheological models and application to flow regime determination." Journal of petroleum science and engineering 11, no. 2 (1994): 155-164.
[37] M. B. J. Sadigov, “Analyses of Field Measured Data With Rheology and Hydraulics Models,” *Int. J. Fluids Eng.*, vol. 8, no. 1, pp. 1–12, 2016.

[38] Paiaman, Abouzar Mirzaei, M. K. Al-Askari, Barat Salmani, Bandar Duraya Alanazi, and Mohsen Masihi. "Effect of drilling fluid properties on rate of Penetration." Nafta 60, no. 3 (2009): 129-134.

[39] Kosun Solids Control Lily, "The Impact on Drilling Fluid by Solid Content," 2015. [Online]. Available: https://www.linkedin.com/pulse/impact-drilling-fluid-solid-content-lily-z-/?fbclid=IwAR0XWi_dlf6TlEnsS30lQI19ok9kZqB1IUH-OjgPfQl6ABz2N2KCFnDpUh4. [Accessed: 06-Jan-2015].

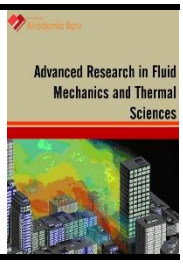
[40] Machado, J. C., and P. F. Castilho. "Solids control and low-solids: important binary to drill deep wells." In SPE Latin America Petroleum Engineering Conference. Society of Petroleum Engineers, 1992.

[41] Agwu, Okorie E., Julius U. Akpabio, Sunday B. Alabi, and Adewale Dosunmu. "Artificial intelligence techniques and their applications in drilling fluid engineering: A review." Journal of Petroleum Science and Engineering 167 (2018): 300-315. drilling fluid engineering: A review," *J. Pet. Sci. Eng.*, vol. 167, no. April, pp. 300–315, 2018.

Penerbit Akademia Baru

Engineering Science and Technology Conference Proceedings

Journal homepage: www.akademiabaru.com/EST.html



Using Solar Energy for Irrigation in Kirkuk City and Outskirt

Open

Ayad Fouad Hameed[1,*], Bilal Mohammed Qasim[1]

[1] Mechanical Engineering Department, College of Engineering, University of Kirkuk, Kirkuk, Iraq

ABSTRACT

In this study, the possibility of using the produced energy from solar energy system for irrigation in Kirkuk city and outskirt is studied. The power from the photovoltaic PV panel is (300 W). Three values for the well depth (h) which are (60,70, and 80 m) are used respectively. Depending on the data from Iraqi Meteorological Organization and Seismology, the relations between the angle of solar radiation along the year, the solar radiation, and the actual and theoretical solar brightness in each month showed in graphical diagrams. The volume flow rate was represented graphically for each value of well depth. It was found that the volume flow rate increase with increasing PV panel power and the solar system is more efficient in mid-day and at mid-year (summer season). However, flow rate was inversely proportional and affected by the well depth. The solar power from the PV panel can be used in irrigation since the volume flow rate from the system fulfil water requirements for most crops that cultivated in Kirkuk city.

Keywords:
Solar System; PV panel; irrigation;
volume flow rate; well depth

Copyright © 2019 PENERBIT AKADEMIA BARU - All rights reserved

1. Introduction

Solar energy is the most abundant source of energy in the world, it is not only an answer to today's energy crisis but also an environmentally friendly form of energy [1]. One of the most important renewable energy is the energy from the sun or what we called solar radiation because it is free, pollution free, and distributed throughout the earth.

There are many studies concern the possibility of using solar energy in both domestic and industrial applications, among these are the following:

Basheer N. *et al.,* [2] design a program in the field of PV which differ from other programs in terms of suitability with the atmosphere of Iraq. The program using Visual Basic program which contains all the calculations needed, A comparing between the theoretical results and the experimental results showed an acceptable accuracy in the program design.

Maya Su Kyi, *et al.,* [3] designed and analyzed the calculation of the efficiency of the solar panels system to pump water by the solar PV pumps. The study area is located at (21°-58 '-30 "N) Latitude and (96°-5'-0" E) Longitude from Mandalay. The PV system is designed to irrigate one acre of asparagus with an estimated daily water of (25 m^3/ day).

R. C. Srivastava and Harsha Pandey [4] used Angstrom-Prescott model for some cities in India to estimate the solar radiation depending on the sunshine's hours with solar radiation as a

* *Corresponding author.*
E-mail address: mscfd2001@gmail.com (Ayad Fouad Hameed)

relationship and that presented in a model from Angstrom-Prescott ($H/H_c = a+b\ (n/m)$). Where H, is average daily global radiation ($W.hr/m^2/day$), and Hc, is monthly global radiation, n, is a sunshine hour. The models supported to find a new method for programming models to develop depending on Angstrom-Prescott model.

A.M. Muzathik, *et al.,* [5] studied the global radiation based on sunshine hours depending on Angstrom-Prescott model. The study computed monthly mean values from (2004 -2007) in Terengganu state (Malaysia), models are estimating on a horizontal surface and found out a good source from those models in case lost the data of radiation in that period, a new linear model which used was (H/Ho= 0.2207 + 0.5249) based on Angstrom model.

M. Dursun and S. Ozden [6] had been used an automatic irrigation system to irrigate an area of the plants with cherry trees by two motors, the first was placed inside a deep well to transfer a water in the tank. The second motor has a task to transfer the water from the tank to the drip irrigation system. In this study, a high-efficiency solar panels were used by calculate the maximum power consumed by the motors. Solar panels equipped the power needed to operate motors. The tracking system was also used to increase the efficiency of the system. As well as sensors to calculate soil moisture. The system contains (48) solar panels and a power of (3.84 kW).

M. A. Murtaza. *et al.,* [7] design an experimental model of automatic irrigation arrangement which is based on microcontroller and solar power. Many sensors are placed if the paddy field to measure soil moisture and temperature, and then by using software application developed for the system, the farmer can control the pumps water to the field. It is found that using the automatic irrigation system can lead to massive water saving if applied in the right way.

J. A. Jervase, H. Bourdoucen, and A. Al-lawati [8] used a technique to improve extracted precision of variables such as resistance, current, electric charge, and temperature, as well as other variables in a model of solar cells using mathematical algorithm. The mathematical relationship used is to reduce the error ratio of variables of solar cells.

Widiastuti and D S Wijayanto [9] used a hybrid system to irrigate the dragon fruit fields using wind and solar power in some Indonesian cities. The irrigation system used a drip irrigation system with a 120-watt pump and a 5-blade turbine. The electric power generated to operate the water pump is sufficient to fill the irrigation tank with 3000 m2 of cultivated fruit. Cost / benefit analysis was used to estimate the economic feasibility of using such a system.

Ali M. Al-Salihi. *et al.,* [10] studied solar radiation on a horizontal surface of various sites in Iraq. The maximum temperature, the duration of the sunrise and the relative humidity of the cities (Baghdad, Mosul and Rutbah) were studied. The results showed a reasonable estimate of global solar radiation on the horizontal surface and expected behavior of solar radiation. The correction coefficient which is a factor that varies from 89% for the city of Rutbah to (97%) for the city of Baghdad and the error rate was 0.035 and 0.063 for Baghdad and Rutbah.

S. K. Mohammed and E. H. Jasem [11] calculated the cost of setting up a solar-powered farm in remote areas. The system is used to generate solar energy capacity (1000 W) (equivalent to 5 amps), sufficient to meet the needs of the rural home, and the agricultural pump is feasible Economically, compared with the conventional fuel generator and with the same capacity above, the system needs of (10 m^2) and at (18000 $) to works for three cloudy days. Heating of the house and poultry hall costed about (2535 $) and heating for the house protected costed is about (3040 $).

All above studies are concern with calculation of the amount of solar radiation depending on mathematical relations and the design conditions of the solar panel needed to enhance the collected solar radiation. This paper deals with the possibility of using the solar energy in irrigation in Kirkuk city and outskirt. The flow rate from the solar system calculated in two steps. First, the

current and voltage are calculated from the sun radiation depending on the equations from literatures, then using another set of equations, the volume flow rate is calculated from the value of current and voltage.

2. Methodology

Mathematical equations used to convert solar energy into electrical energy:
There are many mathematical methods and equations used in which solar energy is converted to electrical energy, the following equation is used to calculate the current-voltage (I-V) characteristic of the photovoltaic (PV) cells [12]:

$$I=I_{pv}-I_s\left[\exp\left(\left(\frac{q}{k\,T_c\,a}\right)V+R_s\,I\right)-1\right]-\left(\frac{V+R_s\,I}{R_p}\right) \quad (1)$$

where:
I = total DC current generated
I_{pv} = photovoltaic current
I_s = cell saturation of dark current
q = charge of the electron= (1.60217×10^{-19} C)
k = Constant Boltz Man= (1.38×10^{-23} J/K)
T_c = Operating temperature of the solar cell
a = diode ideality constant
V = voltage
R_s = Series resistance
R_p = Shunt resistance

Now, the output DC power (P) can be determined simply from [12]:

$$P = V.I \quad (2)$$

Calculating the volume flow rate**:**
The volume flow rate can be calculated as follows [13]:

$$Q = 367\ \frac{\eta_p\,P}{h} \quad (3)$$

where:
Q = volume flow rate in (L/hr)
η_p = selected pump efficiency
P = power developed from the PV
h = the well depth in (m)

The power developed from the PV panel is a function of the solar radiation, which is in turn a function of the angle of solar radiation fall, the following figures 1 shows the change of the angle of solar radiation along the year, the solar radiation, the actual and theoretical solar brightness, and the optimum solar panel tilt angle respectively [14, 15, 16].

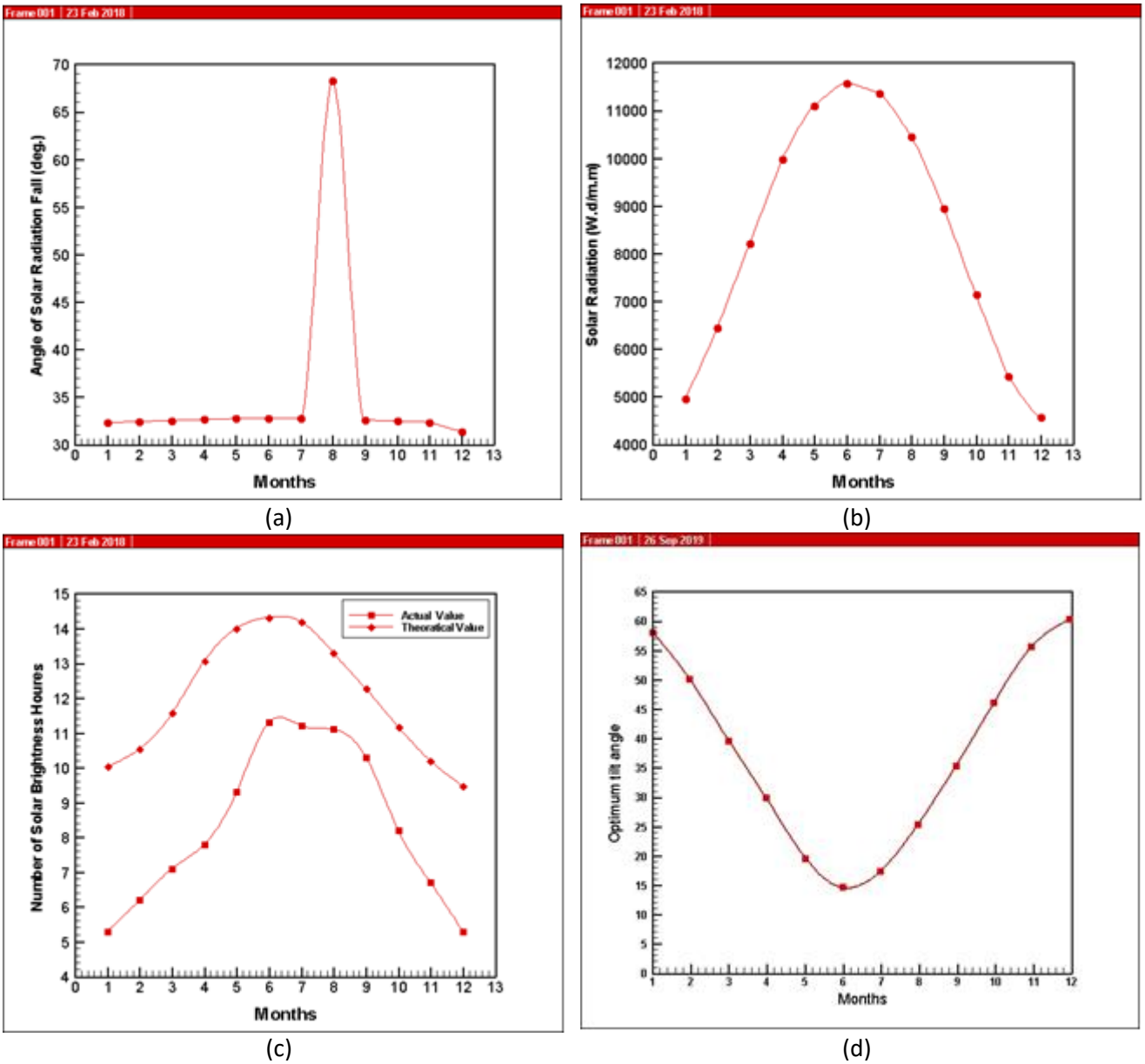


Fig. 1. (a) angle of radiation falls change (b) solar radiation change (c) number of solar brightness hours (d) PV panel optimum tilt angle over twelve months of the year for Kirkuk city

Table 1
Monthly current and voltage /m2 of PV panel for Kirkuk city [17]

	Jan	Feb	Mar	Apr	May	June	July	Aug	Sept	Oct	Nov	Dec
Current (A)	359.6	336	542.5	600	635.7	639	660.3	705.25	354	461.9	297	254.2
Voltage (V)	6014	5376	6153.5	6000	6293	6105	6308.5	6370.5	5910	6076	5745	5859

The results obtained assuming that the power developed in the PV panel is (100 W), the pump efficiency (η_p = 70%), and for three well depth (h= 60,70, and 80 m).

3. Results and Discussion

In this paper, study and analysis of the data from a solar energy-based system was done to use for irrigation system in Kirkuk city. Figure 2 depicts the variation of PV panel power with time from (7 am to 5 pm). The hole time duration is (10 hr) in each day, also the results are for a (300 W) power generated from the PV panel. It is obvious that the trend of change of power is similar with increasing rate from early morning (sunshine) to the (12 pm), after that the power decrease with time. The figure shows that the PV panel power is increase with increasing the solar radiation (or time) during each day along the year. The maximum value of the PV panel power obtained between (12 and 1 pm). After that, the solar radiation will drop, so the value of the power from the system will also decrease. Though the trend of power generation is similar, summer months shows higher power generation compared to the other seasons. The water volume flow rate is the output from the system and considered as the factor that assess their efficiency.

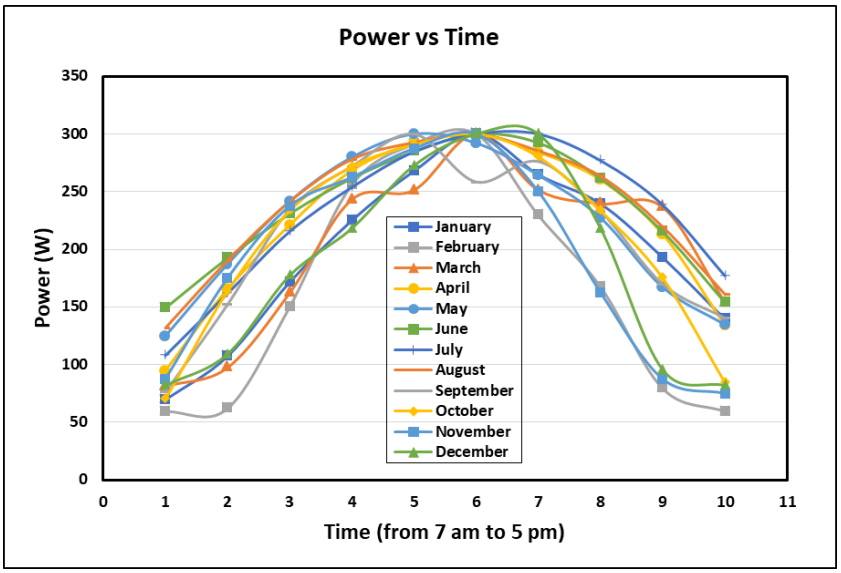


Fig. 2. Variation of PV panel power with time for (h=60 m)

In this study the results were taken for ten hours daily in each month along the year. Depending on the estimation of the water depth in Kirkuk city, the water depths in the wells were measured to be (60, 70, and 80 m).

The relation between the volume flow rate (Q) in (L/hr) for (h = 60 m) with time is done as shown in figure (5), the time changed from (7 am) (labelled 1 in the horizontal axis of the figures) to (5 pm) (labelled 10 in the horizontal axis of the figures). So, the hole time duration is (10 hr) in each day, also the results are for a (300 W) power generated from the PV panel. The figure shows that the volume flow rate is increase with increasing the solar radiation (or time) during each day along the year. The maximum value of the volume flow rate is (1284 L/hr) between (12 and 1 pm). After that, the solar radiation will drop, so the value of the flow rate from the system will also decrease.

Increasing the depth of water level from (h = 60 m) to (h = 70 m) will affect the maximum value of the flow rate. The maximum value of (Q) in this case is (1100 L/hr) as shown in figure (6) which is decreased by about (14 %) compared to that of (60 m) well depth. The same relation between the volume flow rate and time is obtained, were the value of the volume flow rate is increased with increasing the time until (1 pm) after that its value decreases.

If the depth increased furthermore, the maximum volume flow rate will decrease more. This have seen in figure (7) were (Q = 923 L/hr) which is decreased by about (16 %) compared to that of

(70 m) well depth. The behaviour mentioned in the above is repeated here but with lower values in each month over the year.

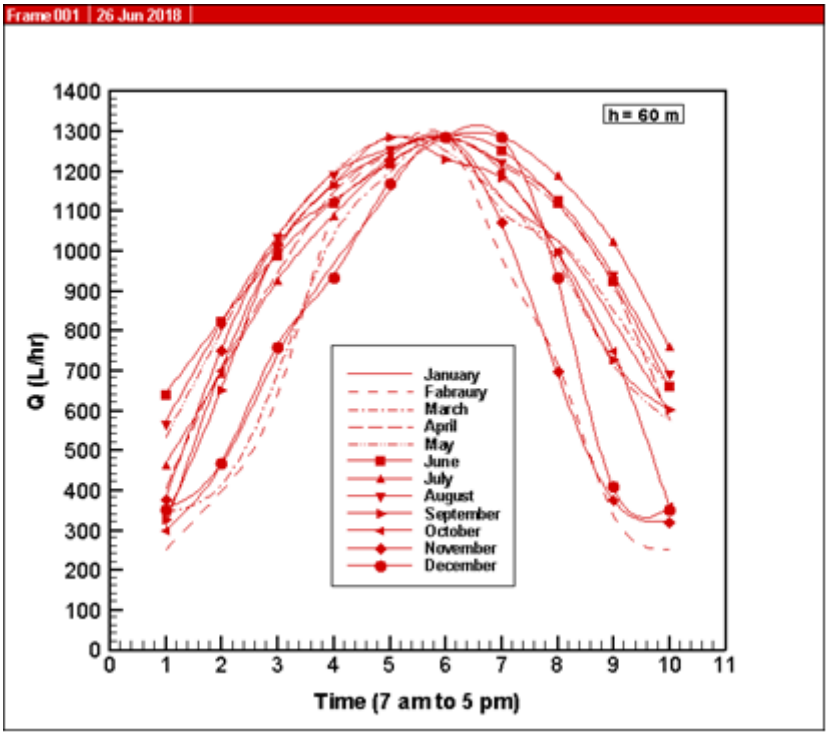


Fig. 3. Variation of volume flow rate with time for (h=60 m)

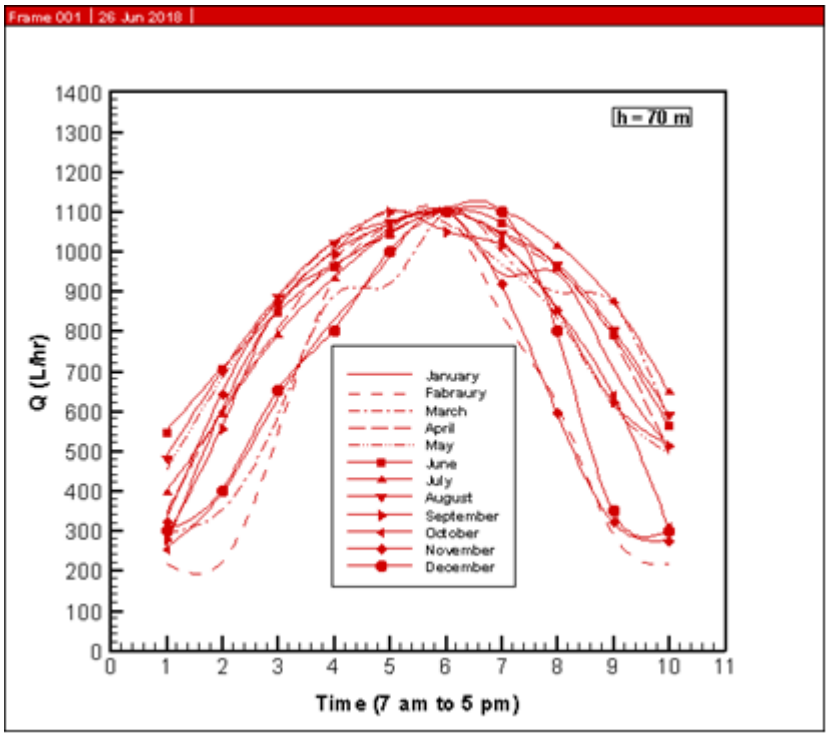


Fig. 4. Variation of volume flow rate with time for (h=70 m)

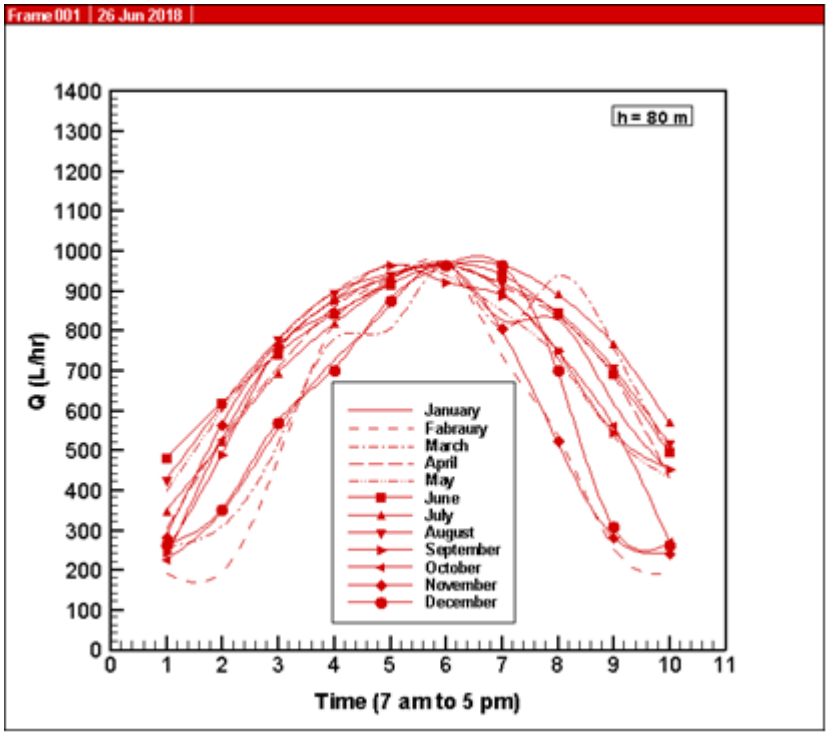


Fig. 5. Variation of volume flow rate with time for (h=80 m)

4. Conclusions

Through the analysis of the data obtained in the study, the following conclusions are to be considered:

1- The solar water pumping system provide a good quantity of water even in winter season.
2- The volume flow rate increase with increasing PV panel power and the solar system is more efficient in mid-day and at mid-year (summer season).
3- The volume flow rate proportional inversely with the well depth. Water flow rate decrease by (14 %) for (h = 70 m) compared to that of (60 m) and decrease by (16 %) for (h = 80 m) compared to that of (70 m).
4- Field crops water needs determine the possibility of using the system for irrigations, increasing the assumed power generated from the PV panels will increase the volume flow rate from the system which fulfil the requirements of water needs for crops.

References

[1] V. B. Shinde and S. S. Wandre “Solar photovoltaic water pumping system for irrigation: A review”, African Journal of Agricultural Research, vol. 10 (2015): pp. 2267–2273.
[2] Hussein, Basheer Noaman, Imad Abdulkareem Essa, and Dhia Jalil Hussein. "Introducing a PV design program compatible with Iraq conditions." Energy Procedia 36 (2013): 852-861.
[3] M. S. Kyi, L. Maw, and H. M. Tun, “Study of Solar PV Sizing of Water Pumping System For Irrigation Of Asparagus”, Ijstr, vol. 5 (2016): no. 6, pp. 71–75.
[4] R. C. Srivastava and H. Pandey, “Estimating Angstrom-Prescott Coefficients for India and Developing a Correlation between Sunshine Hours and Global Solar Radiation for India”, ISRN Renew. Energy, vol. 2013, no. 1 (2013): pp. 1–7.
[5] Muzathik, A. M., W. B. W. Nik, M. Z. Ibrahim, K. B. Samo, Kamaruzzaman Sopian, and M. A. Alghoul. "Daily Global Solar Radiation Estimate Based on Sunshine Hours." International journal of mechanical and materials engineering 6, no. 1 (2011): 75-80.
[6] Dursun, Mahir, and Semih Ozden. "Application of solar powered automatic water pumping in Turkey." International Journal of Computer and Electrical Engineering 4, no. 2 (2012): 161.

[7] M. A. Murtaza. "Solar powered automatic irrigation system" International Journal of Engineering Science and Computing, Vol. 7, No. 4 (2017): pp. 10719-10722.
[8] Jervase, Joseph A., Hadj Bourdoucen, and Ali Al-Lawati. "Solar cell parameter extraction using genetic algorithms." Measurement science and technology 12, no. 11 (2001): 1922.
[9] Widiastuti, I., and D. S. Wijayanto. "Developing a Hybrid Solar/Wind Powered Drip Irrigation System for Dragon Fruit Yield." In IOP Conference Series: Materials Science and Engineering, vol. 180, no. 1, p. 012034. IOP Publishing, 2017.
[10] Al-Salihi, Ali M., Maylaa M. Kadum, and Ali J. Mohammed. "Estimation of global solar radiation on horizontal surface using routine meteorological measurements for different cities in Iraq." Asian Journal of Scientific Research 3, no. 4 (2010): 240-248.
[11] S. K. Mohammed and E. H. Jasem. "Calculating the cost of solar-powered farm establishment of in Remote areas". DjAS, Vol 2-431-413, 2010.
[12] Tsai, Huan-Liang, Ci-Siang Tu, and Yi-Jie Su. "Development of generalized photovoltaic model using MATLAB/SIMULINK." In Proceedings of the world congress on Engineering and computer science, vol. 2008, pp. 1-6. 2008.
[13] Azab, Mohamed & Salem, Fawzan & Mossad, Mohamed I. "PV parameter estimation using different evolutionary algorithms". Journal of Electrical Engineering. 13 (2013): 187-196.
[14] Iraqi Meteorological Organization and Seismology, info@meteoseism.gov.iq
[15] Ali, Firas Aziz. "Computation of solar radiation on horizontal surface over some Iraqi cities." Engineering and Technology Journal 29, no. 10 (2011): 2026-2043.
[16] Ahmad, I., N. Al-Hamadani, and K. Ibrahim. "Solar radiation maps for Iraq." Solar Energy 31, no. 1 (1983): 29-44.
[17] Ali, Firas Aziz. "Optimum Tilt Angle of Photovoltaic Panels for Some Iraq Cities." Journal of University of Babylon 26, no. 1 (2018): 155-163.
[18] H Darweesh, Shaima, and Waleed I Al-Rijabo. "Study of Spatial Variation of Total Solar Radiation Falling on Horizontal Surface in Iraq." Rafidain Journal of Science 22, no. 8 (2011): 119-134.

Penerbit Akademia Baru

Engineering Science and Technology Conference Proceedings

Journal homepage: www.akademiabaru.com/EST.html

Two-Phase Region Effect on Film Condensation on an Inclined Plate Embedded in a Porous Medium

Open

Y.L. Yeu[1], A. Gorin[1*]

[1] School of Chemical Engineering and Science, Faculty of Engineering, Computing and Science, Swinburne University of Technology (Sarawak Campus), Kuching, Sarawak, Malaysia.

ABSTRACT

Film condensation in a porous medium has been receiving increasing attention due to its wide range of heat transfer applications. Some examples of these practical applications are distillation, drying technology, geothermal energy, cooling towers, heat exchangers and air conditioning. One of the characteristic features of film condensation in porous media is the formation of two-phase zone separating the liquid film and the vapour zone due to capillary pressure. In this paper, a physico-mathematical model of liquid film condensation on a surface embedded in a porous medium with a two-phase region effect is developed and presented. The model is based on momentum and continuity equations as applied to the liquid film and the two-phase flow region supplemented with the Darcy flow assumption and assumptions on the Leverette J-function and the saturation behavior near the edge of the liquid film. The developed model allows a simple analytical solution to the problem in distinction to semi-analytical and numerical solutions published by different authors. Accounting for the capillary effects results in higher heat transfer and condensation rate due to the decrease in the liquid film thickness. The presented model yields good agreement when compared to the theoretical results and experimental data by other authors. The developed model addresses the fundamental concepts of phase transition in porous media which can effectively find applications in many areas.

Keywords:
Film condensation; two-phase region; porous medium; porous media; heat pipe; capillary effect; surface tension

Copyright © 2019 PENERBIT AKADEMIA BARU - All rights reserved

1. Introduction

Film condensation in the absence of porous medium has been extensively studied and well understood [1-7]. Nakoryakov and Gorin [8] represented a simple model for a film condensation on an inclined plate embedded in a porous medium assuming a distinct interface, constant transport properties, the Darcy regime for condensate film flow, and uniform porous structure across the film, which resulted in the correlation for the average heat transfer coefficient,

$$\overline{Nu} = \frac{\bar{\alpha}_L L}{\lambda_e} = (2\, Ar^* \mathrm{Pr}\, \mathrm{K_u})^{1/2} \tag{1}$$

where Ar^* is the modified Archimedes number, $\mathrm{K_u}$ is the phase conversion criterion or known as Kutateladze condensation number and Pr is the Prandtl number.

* *Corresponding author.*
E-mail address: yyeu@swinburne.edu.my (Elaine Yeu)

The Nakoryakov and Gorin's [8] model showed good agreement with the Cheng's [9] model, which required numerical solution of ordinary differential equation. It agreed well with experimental data by different authors too.

It should be emphasized that thermodynamics governing film condensation in the presence of porous medium differs noticeably from that in the absence of porous medium. In the past decade there has been an increased interest in research on film condensation in porous media [8-23], due to its wide range of heat transfer applications. Some examples on these practical applications are design of heat pipes, heat exchangers, food drying, and many other applications.

Until today, there are limited numbers of experimental studies carried out to support, refute, or validate hypothesis in physical models. The Dvorovenko's [18] comprehensive experimental study of heat transfer in film condensation on a plate embedded in a packed bed is deserving of more attention. Porous media were modelled by using glass beads of various sizes placed on a plate length changing from 250 mm to 1000 mm. The temperature profiles across the liquid film thickness of condensate of refrigerant-12 were measured by seven precise thermocouples placed across the porous layer. The heat flux was also measured and recorded. The results could be considered of the highest quality of data possible.

Despite the long list of the study of condensation in porous media, the understanding of condensation in porous media with two-phase region effect remains incomplete. Two-phase zone or two-phase region is where the liquid and vapour coexist at a condition of local equilibrium. The existence of the two-phase region is due to the surface tension and capillary effect which can result in liquid being sucked into fine pores. In the two-phase region, the liquid phase and vapour phase are flowing in a counter-current direction. Capillary pressure and relative permeability are the key parameters governing the fluid flow in a porous medium. Although many researchers did not consider the surface tension effect in their theoretical investigation [9, 14, 15, 24-26], many experimental studies have reported that a two-phase zone is formed when a confined water-saturated porous medium is heated [27-30].

Udell [31] conducted an experiment to study heat and mass transfer characteristics in porous media. The porous media were formed using coarse and fine sand with a grain size of 833-589 µm and 208-149 µm respectively. The porous test sample was heated at the top and cooled at the bottom. From the experimental result, the author identified three distinct regions at steady-state conditions. These three distinct zones were the vapour at the upper region, liquid at the lower region and the region separating the upper vapour zone and the lower liquid zone is a two-phase zone. It was found that the length of the two-phase zone of the fine grain sand porous sample was longer than the coarse grain sand porous sample at comparable heat fluxes.

Udell [31] developed as well a theoretical model for one-dimensional, steady-state heat and mass transfer in porous media saturated with the liquid and vapour phases of a single component fluid with various gravitational orientations and medium permeability to predict the length of the two-phase zone as a function of the heat flux, fluid properties and porous medium characteristic. Udell [32] extended his study by including the effects of the capillary, gravity forces and phase change. He found that the two-phase zone was nearly isothermal and convection dominated. The temperature, pressure, and saturation profiles were obtained corresponding to various gravitational orientations in the two-phase zone. The conditions in which the gravitational effects can be neglected and the criteria to determine the dry-out heat flux were identified. Apparent thermal conductivities of the two-phase zone for various gravitational orientations and permeability were evaluated as well [32].

As the effective pore radii are small in many porous media applications, many researchers have drawn attention to the capillary pressure effects in porous media. Plumb [33] examined the effect

of the capillary action on film condensation in porous materials theoretically. A two-phase capillary fringe that separated the liquid film from the vapour was presented in his model. He found the capillary transport plays an important role in increasing the heat transfer and condensation rates on a vertical isothermal surface as the liquid film thickness decreases due to the capillary effects. The results for both a constant temperature capillary fringe model and a constant pressure capillary fringe model are well predicted in many practical applications. Majumdar and Tien [34] studied the effects of surface tension on film condensation in a porous medium and validated the three-zone model that developed by Plumb [33]. They presented that the existence of a two-phase zone lying between the liquid and the vapour regions is required to achieve the thermodynamics of phase equilibria for film condensation in a porous medium. Three models with different assumptions were suggested by Majumdar and Tien [34]. They refined the liquid film and two-phase zone by neglecting the effect of vapour flow in isothermal two-phase zone. It is due to the no-slip condition at the wall and no-shear condition at the interface with the two-phase zone.

Chung *et al.,* [35] then continued with the development of three-zone model and developed a unified model combining the three models of Majumdar and Tien [34]. In their numerical solutions to the mathematical model, they include the assumption of the existence of a two-phase region between the liquid film and the vapour phase. The effect of vapour flow is included in the two-phase zone. They also investigated the problem of condensation in a porous medium near a cold vertical surface experimentally. Their numerical results are compared with experimental data and show satisfactory agreement between the numerical and experimental results.

In one of the recent paper, a new formulation for one-dimensional, steady-state heat and mass transfer in a porous medium with two-phase zone was presented [36]. The problem of steady filmwise condensation on a finite size horizontal plate embedded in a porous medium with the effect of surface tension, was studied by Chang [37]. A non-dimensionless parameter Bo_c was introduced. It gives the ratio of capillary force to gravitational force, which is actually the reciprocal of the Bond number, Bo. If the Bo number is small, the surface tension force would be dominant and hence the two-phase zone would contribute to the total liquid flow. It was observed that, a porous medium with higher Bo_c has better heat transfer performance. It induced a greater average Nusselt number and lower liquid film thickness. The dimensionless liquid film thickness was obtained by using the Runge-Kutta shooting method.

Although many researchers had discovered and proved that the two-phase zone exists during condensation in porous media, the problem remains complex to solve. Hence, a simple solution to this complex problem is presented. This paper is aimed to study the steady heat transfer in a two-phase region of a water-saturated porous medium. A theoretical model of film condensation in a porous medium with a two-phase region effect is herein developed and presented.

2. Mathematical Formulation

To develop the mathematical formulation for film condensation on an inclined plate embedded in a porous medium with two-phase region effect, and with the liquid film of condensate adjacent to the cold plate surface, the (x, y) coordinate system shown in **Error! Reference source not found.** is introduced.

The cold plate temperature is uniform and maintained at temperature T_w. Far away from the plate is a pure vapour region. The vapour temperature is uniform and maintained at the saturation temperature, T_{sat}. The condensation takes place on the cold plate wall embedded in a porous

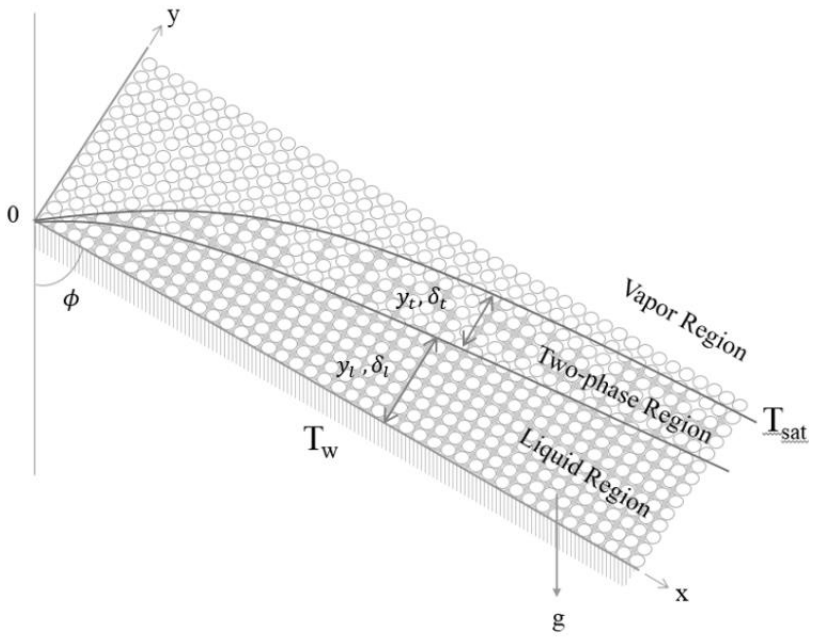


Fig. 1. Schematic diagram of film condensation with a two-phase region on an inclined plate embedded in a porous medium

medium. In between the liquid and vapour regions there is a two-phase zone where liquid and vapour co-exist at conditions of local equilibrium. The liquid film thickness δ_l and two-phase region film thickness $\delta_t$grow continuously with increasing x by reasons of liquid film flow downwards due to gravitational effect and newly condensing vapour in the downward direction.

Additional assumptions are as follows:

(a) Steady-state condensation.
(b) The film thickness exceeds much the pore size, $\delta \gg d$.
(c) Darcy's flow in both liquid zone and two-phase zone.
(d) Change in kinetic energy and potential energy within the film flow is negligible.
(e) Convection heat transfer and conduction heat transfer along the film (in the x-direction) is negligible.
(f) The transport properties of condensate are constant.
(g) No impurities in the vapour zone and condensate film.
(h) The temperature in the two-phase zone is uniform and maintained at T_{sat}.
(i) Condensation occurs only at the interface between the two-phase region and the saturated liquid region, $y = \delta_l$.
(j) Liquid phase pressure change in the x-direction is negligible, $\frac{\partial P_l}{\partial x} = 0$.
(k) The change in capillary pressure is mainly due to the change in liquid pressure.

The governing equations for film condensation on an inclined plate embedded in a porous medium with the two-phase region effect are written in the following form.

At the interface of a two-phase zone with the liquid film, $y_t = 0$ or $y_l = \delta_l$, the mass conservation equations can be written as

$$\frac{\partial U_{lt}}{\partial x} + \frac{\partial V_{lt}}{\partial y_t} = 0 \tag{2}$$

The density of the liquid is higher than vapour, $\rho_l \gg \rho_v$. Therefore, the assumption of a change in capillary pressure due to a change in liquid pressure is valid. Hence, the vapour pressure P_v is approaching saturation P_{sat} according to the Clausius-Clapeyron equation.

Darcy's law gives relations between the velocity and the pressure gradient for film flow in a two-phase region by using the concepts of capillary pressure. Hence the liquid velocity in the two-phase region can be written as follows.

For the x-component velocity,

$$U_{lt} = -\frac{K_l}{\mu_l}\frac{\partial P_c}{\partial x} + \frac{K_l(\rho_l - \rho_v)g}{\mu_l}\cos\phi \tag{3}$$

For the y-component velocity,

$$V_{lt} = -\frac{K_l}{\mu_l}\frac{\partial P_c}{\partial y} \tag{4}$$

where P_c is the capillary pressure, defined as [31]

$$P_c = \frac{\sigma}{\sqrt{K/\epsilon}} j_s \tag{5}$$

and j_s is a non-dimensional function of non-dimensional saturation. It is used to normalize capillary pressure data to take into account variations in porosity and permeability.

The capillary pressure represented in the form of $P_g - P_l = P_c(S, etc.)$ can be reduced to $P_c = P_c(S)$. If the capillary pressure is a function only of the non-dimensional saturation, s which defined as [34]

$$S = \frac{S_l - S_{li}}{1 - S_{li}} \tag{6}$$

The capillary pressure can be obtained by correlating the Leverett's [38] cubic polynomial of equation [34, 35, 39, 40]

$$j_S = 1.417(1-S) - 2.120(1-S)^2 + 1.263(1-S)^3 \tag{7}$$

with the boundary condition of $S = 1$ at liquid film thickness $\delta = 0$.

Eq. (7) shows how the Leverett J-function (known as well as the dimensionless function of saturation) varies with y from $S = 0$ (at the interface of a two-phase zone with vapour zone $y = \delta_t$) to $S = 1$ (at the interface of a two-phase zone with liquid film $y = \delta_l$). Since the liquid film in a two-phase region that near to the interface $y_t \cong 0$ (or $y \cong \delta_l$) is almost fully saturated, one can say that the saturation is approaching unity $(S \to 1)$. Hence the liquid saturation correlation at $y_t \cong 0$ (or $y \cong \delta_l$) could be approximated with a linear function expressed as

$$S = \frac{y}{\delta_t} \tag{8}$$

The liquid phase permeability is given as

$$K_l = KK_{rl} \tag{9}$$

where K is the absolute permeability or the permeability of the porous medium in single-phase flow and K_{rl} is the relative permeability of the liquid phase.

If S close to 1 ($S \to 1$), the liquid relative permeability could be approximated as the following.

$$K_{rl} = \xi S \tag{10}$$

$$K_l = \xi SK \tag{11}$$

where ξ is the constant of proportionality.

Since the two-phase zone is isothermal, and condensation occurs only at the interface between the two-phase region and the liquid saturated region $y_t \cong 0$ (or $y \cong \delta_l$), the mass balance equation for the mass of condensate at the interface of the liquid film with the two-phase zone $y = \delta_l$ can then be obtained as:

$$\frac{\partial}{\partial x}\int_0^{\delta_l} \rho_l U_l dy = \dot{m}''_{condensate} - \dot{m}''_{capillary} \tag{12}$$

The energy balance which states that the rate of energy release due to condensation at the interface of a liquid film with the two-phase zone $y = \delta_l$ is equal to the heat conducted through the liquid film. Hence, the mass flux of condensate can be represented as

$$\dot{m}''_{condensate} = \frac{q''}{h_{fg}} \tag{13}$$

Fourier's law is adequately described the conduction heat transfer in a liquid film,

$$q'' = \frac{\lambda}{\delta_l}(T_{sat} - T_w) \tag{14}$$

However, not all the condensate flows down the plane by gravitational force. Due to capillary pressure, some portion of the condensate flows along the y-direction, which is perpendicular to the plate and causes the presence of a two-phase zone.

At the interface of a liquid film with a two-phase zone ($y = \delta_l$), the velocity in the y-direction could be represented as,

$$V_{lt\left\{\substack{S=1\\ y=\delta_l}\right\}} = -\frac{K_l}{\mu_l}\left(\frac{\partial P_c}{\partial S}\right)_{S=1}\left(\frac{\partial S}{\partial y}\right)_{y=\delta_l} \tag{15}$$

Since both j_s and K_{rl} are functions of S, one can get

$$\left(\frac{\partial P_c}{\partial S}\right)_{S=1} = \frac{\sigma}{\sqrt{K_l/\varepsilon}}\frac{\partial j_S}{\partial S} + j_S\frac{\varepsilon^{1/2}}{K_l^{3/2}}\frac{\partial K_l}{\partial S}\sigma \tag{16}$$

In the neighbourhood of the film surface S is close to 1 ($S \to 1$), so that Eq. (7) can be simplified by taking [8]

$$j_s = \gamma(1-S) \tag{17}$$

where γ is the constant of proportionality that relates the Leverette J-function and the saturation.

Substituting Eq. (10)-(11) and (16)-(17) into Eq. (15), a simplified form of liquid velocity at the interface of a liquid film with two-phase zone $y = \delta_l$ due to the capillary force is re-written as

$$V_{lt\left\{\substack{S=1\\ y=\delta_l}\right\}} = \frac{\gamma\sigma}{\mu}\sqrt{\xi K\varepsilon}\left(\frac{\partial S}{\partial y}\right)_{y=\delta_l} \tag{18}$$

The film thickness is small compared to the plate length, $\delta \ll L$. The liquid pressure in the x-direction is negligible as suggested by many previous researchers [34, 35, 39]. The change in capillary pressure is mainly due to the change in liquid pressure. Hence the capillary effect in the x-direction is negligible $\partial P_c/\partial x = 0$. Also, $K_l = \xi SK$ and $S = 1$ at the interface of the liquid film with a two-phase zone, $y = \delta_l$, the liquid film velocity can be represented as

$$U_l \approx (\rho_l - \rho_v)g\frac{\xi K}{\mu}\cos\phi \tag{19}$$

By substituting Eq. (14), (18), (19) into Eq.(12) and integrating over y, the mass balance equation for the mass of condensate at the interface of a liquid film with two-phase zone $y = \delta_t$ can be re-written as

$$\frac{\partial \delta_l}{\partial x} = \frac{B}{\delta_l} - \frac{A}{\delta_t} \tag{20}$$

where

$$A = \frac{\gamma\sigma}{(\rho_l - \rho_v) g \cos\phi} \sqrt{\frac{\varepsilon}{\xi K}} \tag{21}$$

$$B = \frac{\mu\lambda}{\rho_l(\rho_l - \rho_v) g \cos\phi \, K\xi h_{fg}} (T_{sat} - T_w) \tag{22}$$

Eq. (20) represents the liquid film thickness change along the plate.

Since liquid is sucked from the liquid film across the interface of the liquid film with a two-phase zone and flows due to capillary force in the y-direction only the mass flow rate of condensate at the interface of a two-phase zone with the liquid film, $y_t = 0$ is represented as

$$\frac{\partial}{\partial x} \int_{y_t=0}^{y_t=\delta_t} U_l dy = -\frac{K_l}{\mu_l} \left(\frac{\partial P_c}{\partial S}\right)_{S=1} \left(\frac{\partial S}{\partial y}\right)_{y_t=0} \tag{23}$$

where $y_t = 0$ is at the interface of a liquid film with a two-phase zone, $y = \delta_l$.

The liquid saturation is unity, $S = 1$ at the interface of the two-phase zone with liquid film $y_t = 0$. Substituting Eq. (8)**Error! Reference source not found.**, (18) and (19) into Eq.(23), the resulting expression is rearranged to get

$$\frac{\partial}{\partial x} \int_{y_t=0}^{y_t=\delta_t} \frac{y}{\delta_t} dy = \frac{A}{\delta_t} \tag{24}$$

Solve Eq. (24) and substitute into (20), the film thickness varying in the x-direction at liquid film could be rewritten in the following form

$$\frac{d\delta_l}{dx} = \frac{B}{\delta_l} - \frac{\sqrt{A}}{2\sqrt{x}} \tag{25}$$

Based on the structure of Eq. (25) one shall seek the solution of Eq. (25) in the form

$$\delta_l = c\sqrt{x} \tag{26}$$

Substituting Eq. (26) into (25) find c as follows

$$c = \frac{-\sqrt{A} + \sqrt{A + 8B}}{2} \tag{27}$$

Substitute Eq. (21), (22) into (27) and solve for Eq. (26) yields

$$\delta_l = \frac{\sqrt{x}}{2}\left\{-\left[\frac{\gamma\sigma}{(\rho_l-\rho_v)g\cos\phi}\left(\frac{\varepsilon}{\xi K}\right)^{\frac{1}{2}}\right]^{\frac{1}{2}} + \left[\frac{\gamma\sigma}{(\rho_l-\rho_v)g\cos\phi}\left(\frac{\varepsilon}{\xi K}\right)^{\frac{1}{2}} + \frac{8\mu\lambda}{\rho_l(\rho_l-\rho_v)g\cos\phi\, K\xi h_{fg}}(T_{sat}-T_w)\right]^{\frac{1}{2}}\right\} \quad (28)$$

From the heat balance equation,

$$\alpha = \frac{\lambda}{\mathrm{c}\sqrt{x}} \quad (29)$$

one obtains

$$Nu = \frac{\sqrt{x}}{c} \quad (30)$$

Consequently, the local Nusselt number is

$$Nu = 2\sqrt{x}\left\{-\left[\frac{\gamma\sigma}{(\rho_l-\rho_v)g\cos\phi}\left(\frac{\varepsilon}{\xi K}\right)^{\frac{1}{2}}\right]^{\frac{1}{2}} + \left[\frac{\gamma\sigma}{(\rho_l-\rho_v)g\cos\phi}\left(\frac{\varepsilon}{\xi K}\right)^{\frac{1}{2}} + \frac{8\mu\lambda}{\rho_l(\rho_l-\rho_v)g\cos\phi\, K\xi h_{fg}}(T_{sat}-T_w)\right]\right\}^{-1} \quad (31)$$

In the criterion form, the average Nusselt number for steady-state heat transfer within the two-phase zone of a porous layer on an inclined plate can be represented as

$$\overline{Nu} = \frac{1}{-\sqrt{\frac{\gamma}{16\xi}\frac{\sqrt{K}}{L}\frac{1}{Bo}} + \sqrt{\frac{\gamma}{16\xi}\frac{\sqrt{K}}{L}\frac{1}{Bo} + \frac{1}{2\xi Ar^{*}Pr\mathrm{K_u}}}} \quad (32)$$

The parameters ξ and γ are estimated from experimental data. ξ is taken to be 1. γ estimated from the Leverett J-function. The constant γ is determined by using trial and error analysis method. It is found that γ = 0.025 best matches to the experimental data.

3. Results

Without the two-phase region effect, $Bo \gg 1$, the term $\frac{\gamma}{16\xi}\frac{\sqrt{K}}{L}\frac{1}{Bo}$ in Eq. (32) is negligible. By substituting $\xi = 1$, the Eq. (32) could be reduced to the classical solution (1) of film condensation in porous media, $\overline{Nu} = (2Ar^*Pr\mathrm{K_u})^{\frac{1}{2}}$. The Nusselt number as a function of $Ar^*Pr\mathrm{K_u}$ for different Bo number is shown in **Error! Reference source not found.**. **Error! Reference source not found.** and 4 show how capillary force affects the condensation heat transfer by Kutateladze number $\mathrm{K_u}$. The larger the Kutateladze number, the higher the heat transfer rate. In terms of thermal resistance, the temperature drops across any film layer is proportional to the thermal resistance of that layer if the heat flux is remaining constant. When heat is transferred through a low resistance film layer, the temperature drop is lesser. Consequently, the Kutateladze number is high and causes a high heat transfer rate. It can also be seen from **Error! Reference source not found.** that the smaller the Bond number, the higher the heat transfer rate.

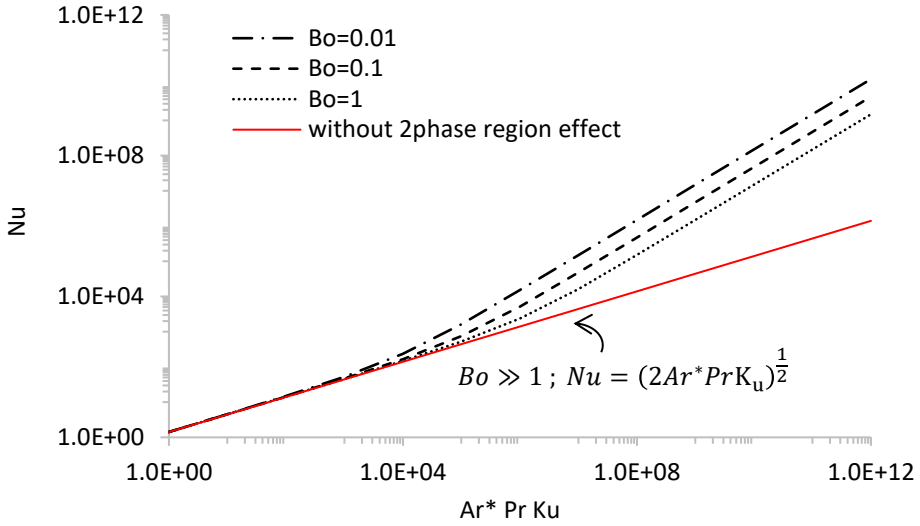


Fig. 2. Nusselt number as function of $\boldsymbol{Ar^*PrK_u}$ for $\boldsymbol{\varepsilon}$ = 0.38, K = 0.0005075 mm^2, γ = 0.025 and $\boldsymbol{\xi}$= 1

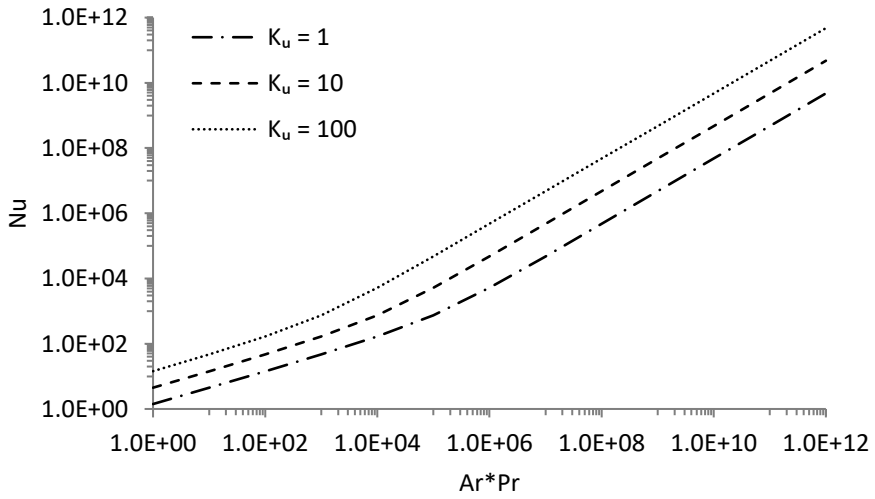


Fig. 3. The effect of Kutateladze number, $\boldsymbol{K_u}$.

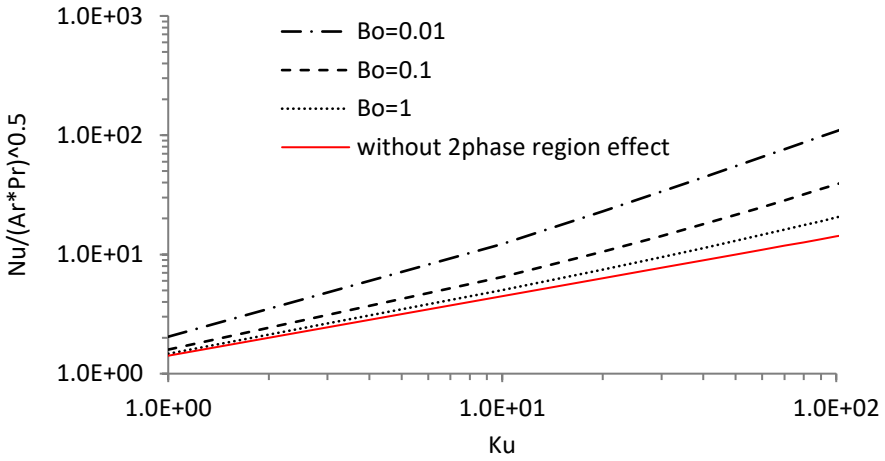


Fig. 4. The condensation heat transfer results for porosity ε = 0.38, permeability K = 0.0005075 mm^2, γ = 0.025 and ξ = 1

The smaller the Bond number, the stronger the surface tension force. Hence, more liquid will be sucked up to the two-phase region making liquid film thinner and causing a steeper temperature gradient in the liquid zone resulting in the higher heat transfer rate for the smaller Bond number.

The comparison between the predictions of Majumdar and Tien's [34] model, Plumb's [33] model, present model and experimental results of Dvorovenko [18] with no two-phase region effect is shown in **Error! Reference source not found.** below. The results show that there is a good agreement between the predictions of the present model to the experimental data, whereas the model developed by Plumb [33], and Majumdar and Tien [34] underpredicts the heat transfer coefficient of this zone and hence shows a lower heat transfer rate.

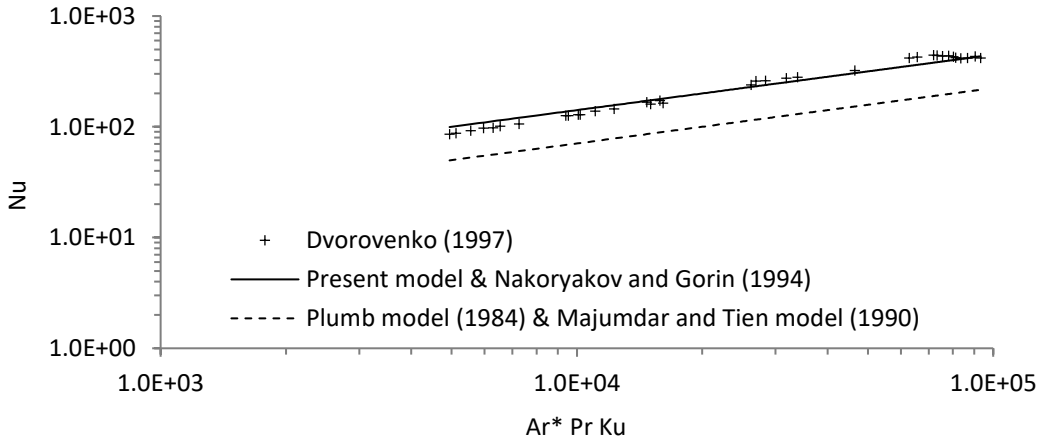


Fig. 5. Comparison of the predicted model developed by Majumdar and Tien [34], Plumb [33] to the present model (with $\xi = 1$) and experimental data with no two-phase region effect ($Bo \gg 1$) for film condensation on an inclined plate with a length of 500 mm embedded in porous media with a grain size of 800 m.

Error! Reference source not found. shows the comparison of experimental results with the present model and theoretical model developed by Nakoryakov and Gorin [8]. Among the numerous data of Dvorovenko [18], the sample of d = 0.8 mm, L = 250 mm, cos ϕ = 0.10343 was selected for further investigation as it deviates far above the solution by Nakoryakov and Gorin [8]. It means this sample has a higher heat transfer rate compared to other samples and this might be due to the presence of two-phase region effect.

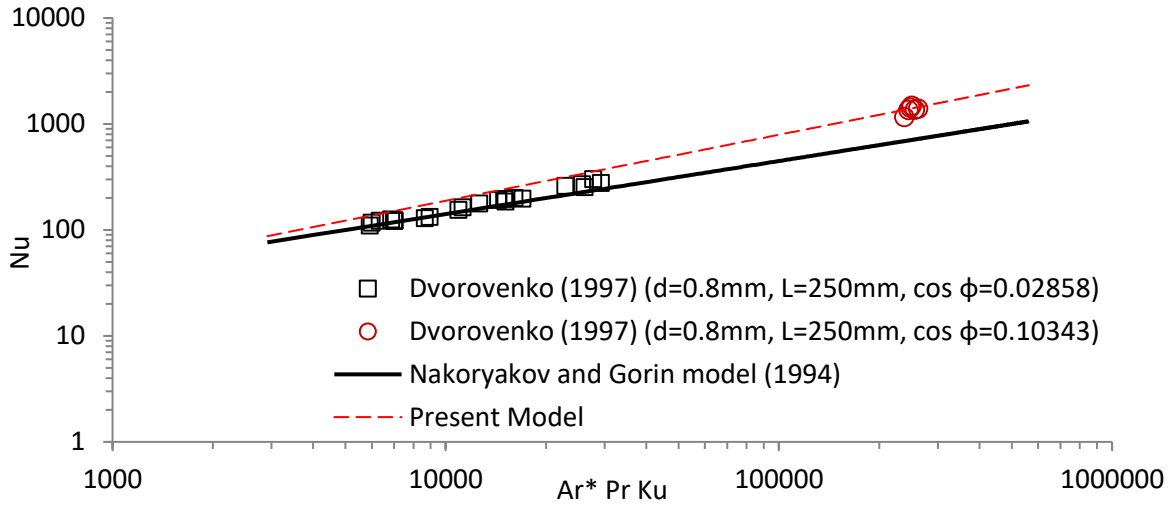


Fig. 6. Comparison of experimental results with the theoretical model for film condensation on an inclined plate embedded in porous media with a grain size of 800 μm and plate length of 250 mm

From the experimental data collected by Dvorovenko [18], it was found that this sample has relatively small temperature difference between the plate wall temperature T_w and saturation temperature T_{sat}, which is less than 4℃ if compared to other samples. In addition, the gradient of the slope (or the thermal resistance) is the smallest and has the thinnest liquid film thickness. The liquid film thickness is approximately $\delta = 0.45\ \mathrm{mm}$. It is about half the grain size. While for other samples, the liquid film thickness is thicker than the grain size. This finding helps to clarify Chang's research finding in which the heat transfer rate is higher for the sample with two-phase region effect. It is due to more liquid condensate into the two-phase region causing the thinning of liquid film thickness and gives a sharper temperature gradient in the liquid zone [37].

Therefore, the experimental results [18] were then compared to the present two-phase model and some other two-phase models developed by Cheng [9], Plumb [33], and Majumdar and Tien [34].

The two-phase model developed by Majumdar and Tien [34] and Plumb [33] were rearranged to ease the comparison. Both models employed the same parameters used in the current study and represented as

Majumdar and Tien's model:

$$Nu_L = \left[-\sqrt{0.373^2 \frac{\sqrt{K}}{L}\frac{1}{Bo}} + \sqrt{0.373^2 \frac{\sqrt{K}}{L}\frac{1}{Bo} + \frac{2}{Ar^* Pr \mathrm{K_u}}} \right]^{-1} \tag{33}$$

Plumb's model:

$$Nu_L = \left[-\sqrt{\frac{j_s}{6(1+2\Lambda)}\frac{\sqrt{K}}{L}\frac{1}{Bo}} + \sqrt{\frac{j_s}{6(1+2\Lambda)}\frac{\sqrt{K}}{L}\frac{1}{Bo} + \frac{2}{Ar^* Pr \mathrm{K_u}}} \right]^{-1} \tag{34}$$

where Λ is the parameter relating the saturation and capillary pressure. According to Brooks and Corey [41], Λ will be in the range of $2 \leq \Lambda \leq 8$ for a variety of unconsolidated porous materials. If the boundary condition is $S_e = 1$ at $y = \delta_T$, P_b is assumed to be equals to P_c.

The graph of both numerical and experimental results are presented in terms of the dimensionless parameters $(Nu, Ar^*, Pr, \mathrm{K_u})$ for film condensation on an inclined plate embedded in porous media with the grain size of 800 µm and plate length of 250 mm was plotted as shown in **Error! Reference source not found.**. The experimental result does show a good agreement with the present model. The parameter of γ in the present model was adjusted. It has found that the present model would obtain the best match with experimental data by substituting $\gamma = 0.025$ and ξ would always equal to 1 as mentioned above.

The present model, Plumb's [33] model, and Majumdar & Tien [34]'s model all have a higher heat transfer coefficient than the model developed by Nakoryakov and Gorin [8]. In the Nakoryakov and Gorin's [8] model, the two-phase region effect was not taken into consideration. The pure vapour is assumed to be in direct contact with the liquid film. However, Chang's [37] model is very much lower than the model developed by Nakoryakov and Gorin [8]. The Chang's [37] model could be improved by adjusting the constant coefficient of 1.23 to a higher value.

Furthermore, the present model is compared with the model developed by Cheng [9], Plumb [33], Majumdar and Tien [34], Chung *et al.,* [35] and Nakoryakov and Gorin [8]. The experimental results presented by Chung *et al.,* [35] were also included for comparison. The condensation heat transfer rate represented by $\frac{Nu}{\sqrt{Ar^* Pr}}$ versus Kutateladze number for film condensation embedded in porous media with glass beads size of 900μm is shown in **Error! Reference source not found.**. The model developed by Cheng [9] and Nakoryakov and Gorin [8] did not include the two-phase region effect. It can be seen that the line is less steep and is far below the models account for the two-phase region effect.

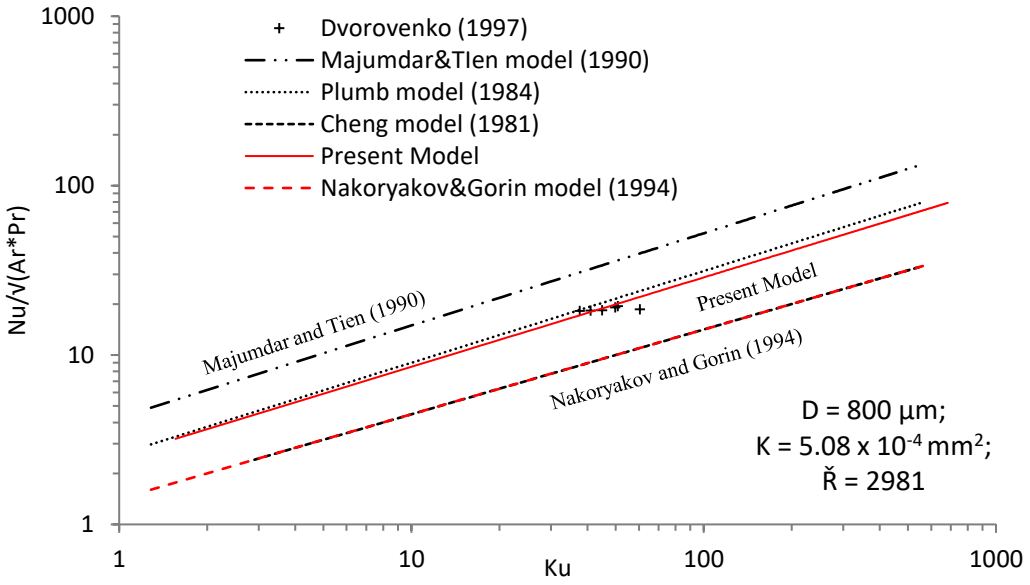


Fig. 7. Film condensation on an inclined plate with inclination angle of $\boldsymbol{cos\,\varphi = 0.10343}$ and length of 250 mm embedded in porous media with grain size of 800 $\boldsymbol{\mu}$m

The local Nusselt equation for Cheng's model [9] used by Chung et al. [35] to plot the comparison graph is expressed in the following equation. It gives the heat transfer coefficient at a particular point on the heat-transfer surface.

$$Nu_x = \left[\frac{(2n+1)Ra_{x,L}}{2Ja}\right]^{\frac{1}{2}} \tag{35}$$

where, $Ra_{x,L}$ is the local Rayleigh number, Ja is the Jakob number, and $n = 0$ for wedge; $n = 1$ for cone.

By substituting $n = 0$, represent $Ra_{x,L}$ as Ar^*Pr, and Ja as $1/\mathrm{K_u}$, the Eq. (35) becomes

$$Nu_x = \left[\frac{Ar^*Pr\mathrm{K_u}}{2}\right]^{\frac{1}{2}} \tag{36}$$

From Eq. (36), the average Nusselt number is $\overline{Nu} = (2Ar^*Pr\mathrm{K_u})^{\frac{1}{2}}$, which completely coincides with the solution by Nakoryakov & Gorin [8].

The experimental results by Chung *et al.,* [35] are far below the two-phase model developed by Majumdar and Tien [34], Plumb [33], and present model. The experimental results have a better agreement with the solution of film condensation developed by Nakoryakov & Gorin [8] and Cheng [9]. The heat transfer rate from the Majumdar and Tien's model are higher than the Plumb's model for all three glass beads size. According to Majumdar and Tien [34], this is because of the Plumb's model under-predicts the size and liquid flux in the two-phase zone.

Chung *et al.,* [35] account for the Non-Darcian and the capillary effects in their model. Although their results were shown to match with experimental results, the results did not show a good representation of liquid film condensation in a porous medium with the two-phase region effect. The experimental results by Chung *et al.,* [35] were much closer to the models developed by Nakoryakov & Gorin [8] and Cheng [9]. Their models had well-predicted liquid film condensation in porous media. Plumb [42] also indicated that the physical models by Chung *et al.,* [35] and Cheng [9] get very similar results for the condensation heat transfer rate.

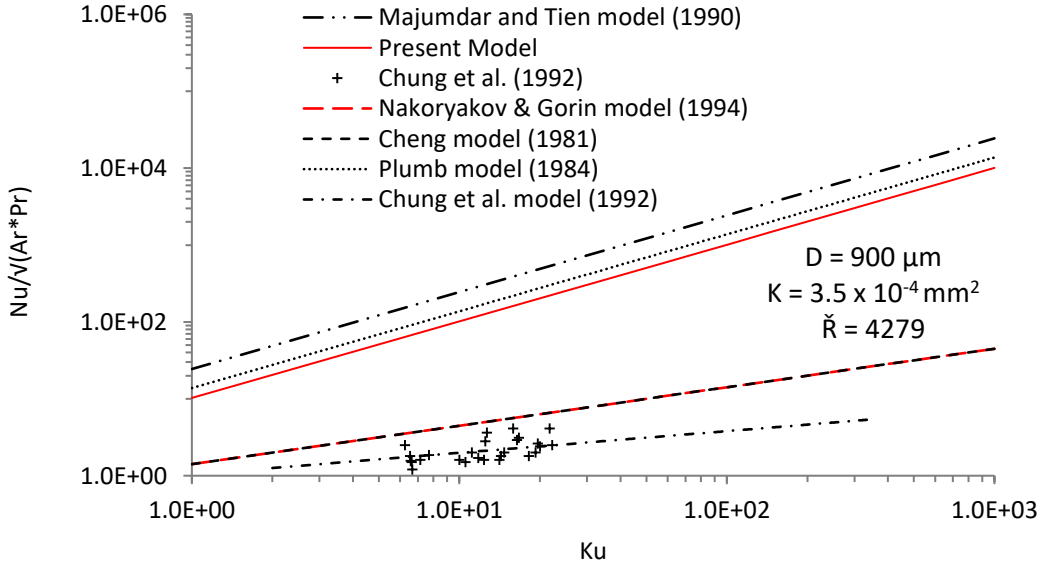


Fig. 8. Film condensation embedded in porous media with glass beads size of 900 μm

Other than that, Wang & Beckermann [40] said it was inappropriate to use the experimental results of Chung *et al.,* [35] for two-phase models validation because the local film thickness in their experiments was about of the same order as the glass bead diameters. Kaviany [23] also stated that for local film thickness that comparable to particle size, the local volume averaged treatments is no longer valid as it breaks the continuum treatment. From the experimental results by White and Tien [16], they also could not conclude that the two-phase zone was present. This is because the porous sample used by White and Tien [16] had a dimension of 1.6 cm x 1.6 cm only. This small area might not sufficient for a two-phase zone to be fully developed. Moreover, no temperature profile along the porous layer thickness was presented by White and Tien [16] and Chung et al. [35]. In their experiment, the temperature distribution across the porous layer thickness had not been measured. Hence the results could not prove that the isothermal two-phase region did exist.

As seen in **Error! Reference source not found.**, both the experimental results and model by Chung et al. [35] are similar to the model by Nakoryakov & Gorin [8] and Cheng [9]. It provides additional evidences the experimental results by Chung *et al.,* [35] might not have the two-phase region effect. Therefore, we can then examine the validity of the developed model with the experimental results of Dvorovenko [18] based on the present two-phase solution as shown in Eq. (32).

4. Conclusions

In the two-phase region, the capillary pressure and relative permeability are the key parameters governing the fluid flow in a porous medium. The simple physico-mathematical model for two-phase region effect on film condensation on an inclined plate embedded in a porous medium has been developed. Accounting for the capillary effects into consideration results in higher heat transfer and condensation rate. The presence of the two-phase region causes the liquid film thickness to become thin. Therefore, the smaller the Bo number, the stronger the surface tension force, the higher the heat transfer rate. Generally, numerical and experimental results are in similar trends. The Nusselt number increases when $Ar^{*}Pr\mathrm{K_u}$ increases. The present model is proved to give comparable results with the experimental data. The parameter of γ in the present model was adjusted. It was found that the present model would obtain the best match with experimental data by substituting $\gamma = 0.025$ and ξ would always equal to 1 as mentioned above.

The model developed for film condensation on an inclined plate embedded in a porous medium with two-phase region enables the engineers and designers to obtain the condensation heat transfer coefficient easily. It also allows them to evaluate the rates of condensation heat transfer to allow control of “flooding” in the condensation section of heat pipes.

References

[1] W. Nusselt, *Die Oberflächenkondesation des Wasserdampfes (The Surface Condensation of the Water Vapor)*. Z. Ver. Dt. Ing., 60(27), 1916.

[2] E. M. Sparrow and J. L. Gregg, "A boundary layer treatment of laminar film condensation," *Journal of Heat Transfer* 81, no. 1 (1959): 13-18.

[3] M. M. Chen, "An analytical study of laminar film condensation: Part 1 - Flat plates," *Journal of Heat Transfer,* vol. 83, no. 48, pp. 48-54, 1961.

[4] J. C. Y. Koh, E. M. Sparrow, and J. P. Hartnett, "The two phase boundary layer in laminar film condensation," *International Journal of Heat and Mass Transfer,* vol. 2, no. 1, pp. 69-82, 1961/03/01/ 1961.

[5] V. Dhir and J. Lienhard, "Laminar Film Condensation on Plane and Axisymmetric Bodies in Nonuniform Gravity," *Journal of Heat Transfer,* vol. 93, no. 1, pp. 97-100, 1971.

[6] H. Merte, "Condensation Heat Transfer," in *Advances in Heat Transfer*, vol. 9, T. F. Irvine and J. P. Hartnett, Eds.: Elsevier, 1973, pp. 181-272.
[7] J. Rose, "Fundamentals of condensation heat transfer: laminar film condensation," *JSME international journal. Ser. 2, Fluids engineering, heat transfer, power, combustion, thermophysical properties,* vol. 31, no. 3, pp. 357-375, 1988.
[8] V. E. Nakoryakov and A. V. Gorin, *Heat and mass transfer in two-phase systems*. Institute of Thermophysics, Siberian Branch of Russian Academy of Sciences, Novosibirsk, 1994.
[9] P. Cheng, "Film condensation along an inclined surface in a porous medium," *International Journal of Heat and Mass Transfer,* vol. 24, no. 6, pp. 983-990, 1981/06/01/ 1981.
[10] E. M. Sparrow and R. D. Cess, "Free Convection With Blowing or Suction," *Journal of Heat Transfer,* vol. 83, no. 3, pp. 387-389, 1961.
[11] E. Parmentier, "Two phase natural convection adjacent to a vertical heated surface in a permeable medium," *International Journal of Heat and Mass Transfer,* vol. 22, no. 6, pp. 849-855, 1979.
[12] J. T. Hong, C. L. Tien, and M. Kaviany, "Non-Darcian effects on vertical-plate natural convection in porous media with high porosities," *International Journal of Heat and Mass Transfer,* vol. 28, no. 11, pp. 2149-2157, 1985/11/01/ 1985.
[13] T. W. Tong and E. Subramanian, "A boundary-layer analysis for natural convection in vertical porous enclosures—use of the Brinkman-extended Darcy model," *International Journal of Heat and Mass Transfer,* vol. 28, no. 3, pp. 563-571, 1985/03/01/ 1985.
[14] M. Kaviany, "Boundary-layer treatment of film condensation in the presence of a solid matrix," *International Journal of Heat and Mass Transfer,* vol. 29, no. 6, pp. 951-954, 1986/06/01/ 1986.
[15] S. White and C. Tien, "Analysis of laminar film condensation in a porous medium," in *ASME, AIChE, and ANS, 24th National Heat Transfer Conference and Exhibition*, 1987.
[16] S. White and C. Tien, "An experimental investigation of film condensation in porous structures," in *International Heat Pipe Conference, 6th, Grenoble, France, 1987, 6 p.*, 1987.
[17] K. J. Renken, M. Aboye, M. Carneiro, and K. Meechan, "Effect of vapor velocity on film condensation along a surface embedded in a porous medium," *International Communications in Heat and Mass Transfer,* vol. 20, no. 1, pp. 1-13, 1993/01/01/ 1993.
[18] I. V. Dvorovenko, "Heat Transfer in Film Condensation on a Plate Embedded in a Packed Bed," PhD, Kuzbass State Technical University, Kemerovo, Russia, 1997.
[19] A. R. Dorokhov, V. S. Loginov, I. P. Ozerova, P. T. Petrik, A. R. Bogomolov, and I. V. Dvorovenko, "Transient Heat Transfer during Steam Film Condensation on a Horizontal Tube," *Thermal Engineering,* Article vol. 44, no. 3, pp. 244-246, 1997.
[20] M. A. Al-Nimr and M. K. AlKam, "Film condensation on a vertical plate imbedded in a porous medium," *Applied Energy,* vol. 56, no. 1, pp. 47-57, 1997/01/01/ 1997.
[21] S. Masoud, M. Al-Nimr, and M. Alkam, *Transient Film Condensation on a Vertical Plate Imbedded in Porous Medium*. 2000, pp. 345-354.
[22] D. K. Todd and L. W. Mays, *Groundwater Hydrology*. Wiley, 2005.
[23] M. Kaviany, *Principles of Heat Transfer in Porous Media*. Springer New York, 2012.
[24] R. H. Nilson and L. A. Romero, "Self-Similar Condensing Films in Porous Media," *International Journal of Heat and Mass Transfer,* vol. 23, pp. 1461-1470, 1980.
[25] P. Cheng and D. K. Chui, "Transient film condensation on a vertical surface in a porous medium," *International Journal of Heat and Mass Transfer,* vol. 27, no. 5, pp. 795-798, 1984/05/01/ 1984.
[26] D. Poulikakos and J. Orozco, "A Study of Condensation on a Vertical Internally Cooled Pipe Embedded in a Porous Medium," *International Communications in Heat and Mass Transfer,* vol. 13, pp. 181-192, 1986.
[27] H. H. Bau and K. E. Torrance, "Boiling in low permeability porous materials," *International Journal Heat and Mass Transfer,* vol. 25, No. 1, pp. 45-55, 1982.
[28] C. H. Sondergeld and D. L. Turcotte, "An experimental study of two-phase convection in a porous medium with applications to geological problems," *Journal of Geophysical Research,* vol. 82, no. 14, pp. 2045-2053, 1977.

[29] T. Abe, E. R. G. Eckert, and R. J. Goldstein, "A parametric study of boiling in a porous bed," *Wärme - und Stoffübertragung,* journal article vol. 16, no. 2, pp. 119-126, June 01 1982.
[30] V. Dhir and I. Catton, "Dryout heat fluxes for inductively heated particulate beds," *Journal of Heat Transfer,* vol. 99, no. 2, pp. 250-256, 1977.
[31] K. S. Udell, "Heat transfer in porous media heated from above with evaporation, condensation, and capillary effects," *ASME J. Heat Transfer,* vol. 105, no. 2, pp. 485-492, 1983.
[32] K. S. Udell, "Heat transfer in porous media considering phase change and capillarity—the heat pipe effect," *International Journal of Heat and Mass Transfer,* vol. 28, no. 2, pp. 485-495, 1985.
[33] O. Plumb, "Capillary effects on film condensation in porous media," in *19th Thermophysics Conference*(Fluid Dynamics and Co-located Conferences: American Institute of Aeronautics and Astronautics, 1984.
[34] A. Majumdar and C. L. Tien, "Effects of Surface Tension on Film Condensation in a Porous Medium," *Journal of Heat Transfer,* vol. 112, no. 3, pp. 751-757, 1990.
[35] J. N. Chung, O. A. Plumb, and W. C. Lee, "Condensation in a Porous Region Bounded by a Cold Vertical Surface," *Journal of Heat Transfer,* vol. 114, no. 4, pp. 1011-1018, 1992.
[36] L. Bridge, R. Bradean, M. J. Ward, and B. R. Wetton, "The analysis of a two-phase zone with condensation in a porous medium," *Journal of Engineering Mathematics,* journal article vol. 45, no. 3, pp. 247-268, 2003.
[37] T.-B. Chang, "Laminar Film Condensation on a Horizontal Plate in a Porous Medium with Surface Tension Effects," (in 英文), *Journal of Marine Science and Technology,* vol. 13, no. 4, pp. 257-264, 2005.
[38] M. C. Leverett, "Capillary Behavior in Porous Solids," *Transaction of AIME,* vol. 142, no. No. 1, pp. 341-358, 1941/12/1 1941.
[39] A. Shekarriz and O. Plumb, "A theoretical study of the enhancement of filmwise condensation using porous fins," in *AIAA-ASME 4th Joint Conference, Boston, June*, 1986, pp. 1-4.
[40] C. Y. Wang and C. Beckermann, "Boundary Layer Analysis of Buoyancy-Driven Two-Phase Flow in Capillary Porous Media," *Journal of Heat Transfer,* vol. 117, no. 4, pp. 1082-1087, 1995.
[41] R. H. Brooks and A. T. Corey, "Properties of porous media affecting fluid flow," *Journal of the Irrigation and Drainage Division,* vol. 92, no. 2, pp. 61-90, 1966.
[42] O. A. Plumb, "Heat Transfer During Unsaturated Flow in Porous Media," in *Convective Heat and Mass Transfer in Porous Media*, S. Kakaç, B. Kilkiş, F. A. Kulacki, and F. Arinç, Eds. Dordrecht: Springer Netherlands, 1991, pp. 435-464.

Penerbit Akademia Baru

Engineering Science and Technology Conference Proceedings

Journal homepage: www.akademiabaru.com/EST.html

Performance Analysis of Vortex Cooler

Open Access

Waritsa Intratep A/P Phon Thip[1,*]

[1] Universiti Malaysia Pahang, 26600 Pekan, Pahang

ABSTRACT

Vortex tube is a type of mechanical device where it releases out hot and cold temperature at different ends by applying air from a compressor. Since the invention of this device, many researches were done in order to explain the working principle of the vortex tube and its properties. The analysis was divided into two part where the main part is to find the energy separation and the second part is to find the Coefficient of Performance (COP) of cooling. Both of these analyses were completed by using Computational Fluid Dynamic (CFD). The pressure inlets data varies ranging from 100 kPa to 400 kPa. The energy separation focused on the cold mass fraction of the vortex tube where it is the ratio of temperature rise to temperature drop of the vortex tube, while COP of cooling is basically the efficiency of the vortex tube at the cold end orifice that focused on the work done by the compressor and the cooling load. The results obtained shows that energy separation have a maximum cold mass fraction at -0.1301 and the COP or efficiency of the cooling zone calculated at range of 0.1604 to 1.7944. In conclusion, this study also shows that higher cold mass fraction results in better energy separation of the vortex tube. In addition, the higher the compressor power and cooling load, the higher the COP of cooling of the vortex tube.

Keywords:

Meshless; Smoothed Particle Hydrodynamics (SPH); Lattice-Spring Model (LSM); Fluid Structural Interaction (FSI); particle method

Copyright © 2019 PENERBIT AKADEMIA BARU - All rights reserved

1. Introduction

Vortex tube is a tool that generates warm air at one end and cold air at the other end, at the same time as pressure air flows through the inlet nozzles tangentially into the vortex chamber. Ranque first discovered it in 1933, the metallurgist and physicist, and Rudolf Hilsch, the German physicist, then improved the design. The vortex tube is therefore also known as the Ranque Vortex Tube, Hilsch Vortex Tube, or Ranque-Hilsch Vortex Tube (RHVT). The parts consist of a vortex tube consisting of one or more inlet nozzles, a vortex chamber, a cold end orifice, a hot end valve and a pipe [1].

Energy separation is also known as temperature separation. It is basically the phenomenon where there is one stream with higher temperature and the other streams with lower temperature than that of the inlet [2]. Another researcher said that this temperature separation has two types which is temperature drop and temperature rise. The pressure gradient in the front part in the vortex tube causes the temperature to drop. Meanwhile, at the same time the partial stagnation and mixture due to the multi-circulation flow structure in the rear part causes the temperature to rise [3]. Meanwhile, another study stated that the primary variables influencing the energy separation efficiency are the cold mass fraction. They researched the impact of distinct external settings on the flow structure based on a 3D computational simulation. In order to provide a better energy separation, they must improve the cold mass fraction according to their research [4].

Vortex tube had been used in various applications especially for cooling and heating applications. For instance, of cooling applications are spot cooling, cooling of cutting tools in manufacturing processes. Meanwhile, for heating applications are such as melting glues, softening plastics and humidifying ambient air [5]. Vortex tube is very useful in many applications as it is non-complex, light, compact and does not need a refrigerant [6]. Other than that, vortex cooler was used in the mining area due to the uncomfortable working area and inappropriate to build a conventional system [7].

2. Vortex Tube Computational Model

2.1 Numerical Methodology

Airflow inside the vortex tube is assumed compressible, followed by the strong swirling, three-dimensional. Hence, it is in a steady state which developed the governing equations. The continuity, momentum conservation and energy conservation equations are included in the governing equations which is given by Eq. (2.1), Eq. (2.2) and Eq. (2.3) respectively. This was indicated in the description of the physical model of the vortex tube [8].

Continuity equation

$$\nabla \cdot (\rho \vec{v}) = 0 \tag{2.1}$$

Momentum conservation equation

$$\nabla \cdot (\rho \vec{v} \vec{v}) = -\nabla p + \rho \vec{g} + \nabla \cdot \bar{\bar{\tau}} + \vec{F} \tag{2.2}$$

Energy conservation equation

$$\nabla \cdot [\vec{v}(\rho E + p)] = \nabla \cdot (k_e \nabla T + \bar{\bar{\tau}} \cdot \vec{v}) + S_h \tag{2.3}$$

Where,

ρ = Air density, kg/m^3
E = Volumetric total energy, J
$\vec{v}$ = Velocity vector static pressure, Pa
T = Static temperature, K
$\rho \vec{g}$ = Gravitational body force, N
$\vec{F}$ = External body forces, N
k_e = Effective conductivity, W/m.K
S_h = Volumetric heat sources, kW/h

The total energy and stress tensor can be expressed by Eq. (2.4) and Eq. (2.5) respectively.

$$\rho E = \rho e + \frac{1}{2}\rho(\vec{v} \cdot \vec{v}), \quad e = c_v T \tag{2.4}$$

$$\bar{\bar{\tau}} = \mu \left[(\nabla \vec{v} + \vec{v}^T) - \frac{2}{3} \nabla \cdot \vec{v} I \right] \tag{2.5}$$

Where,

ρE = Total energy, J
e = Internal energy, J
$\bar{\bar{\tau}}$ = Stress tensor, N/m^2

μ = Air molecular viscosity, m^2/s
I = Unit tensor

2.2 Turbulence Modelling

It is important to choose a suitable turbulence model by considering the strong swirling motion of the flow inside the vortex tube. This is for the reason that the turbulence concentration is significant to identify the flow pattern with the high-speed flows [8]. There is a research which compared the standard k-ε, RNG k-ε, standard k-ω and SST k-ω turbulence models and come up with a conclusion that standard k-ε turbulence model predict better temperature separation compared to the others. Hence, the standard k-ε turbulence model is used for the spinning and swirling flows inside the vortex tube for all the simulations [9].

2.3 Energy Separation Analysis

The cold mass fraction, ξ is defined as Eq. (2.6) [8]. Cold mass fraction can be controlled by the conical valve inside the vortex tube [5]. In addition, the total mass flow rate of air, $\dot{m}$ (kg/s) is given by the Eq. (2.7) [6].

$$\xi = \frac{\dot{m}_c}{\dot{m}_\iota} \tag{2.6}$$

$$\dot{m} = \dot{m}_c + \dot{m}_h \tag{2.7}$$

Where,
$\dot{m}_c$ = mass flow rate of cold air, kg/s
$\dot{m}_\iota$ = total inlet mass flow rate of the working fluid, kg/s

The performance of the vortex tube is related to the cooling and heating effect which derived as Eqs. (2.8) and (2.9) respectively [10]. Hence, temperature difference can be obtained by solving Eqs. (2.8) and (2.9) which is given by the Eq. (2.10).

$$\Delta T_c = T_i - T_c \tag{2.8}$$

$$\Delta T_h = T_h - T_i \tag{2.9}$$

$$\Delta T = \Delta T_h - \Delta T_c \tag{2.10}$$

Where,
ΔT_c = Cooling effect, K
ΔT_h = Heating effect, K
T_i = Temperature inlet, (K)
T_c = Cold stream temperature, (K)
T_h = Hot stream temperature, (K)
ΔT = Energy separation of the hot and cold stream, (K)

2.4 Experimental Setup

An experiment is conducted to determine the temperature difference at varies pressure and temperature inlet. The experiment setup is shown in Figure 1.

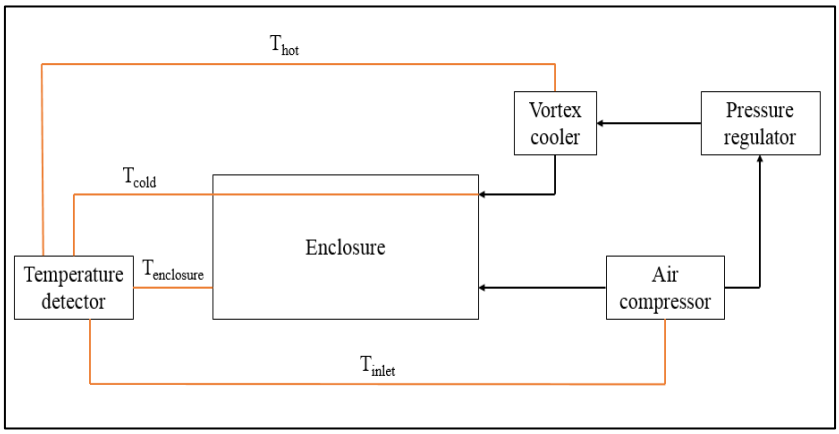


Fig. 1. Schematic diagram of the experiment setup

These data are the input data for CFD simulation. The vortex cooler is connected to the pressure regulator as well as to the enclosure as shown in Figure 1. The air compressor supplies the air into the vortex cooler (enter through the six nozzles) as well as the enclosure. Hence, the cold stream temperature from the vortex tube will be supplied into the enclosure to cool down the equipment inside the enclosure. Meanwhile, the hot stream temperature will be release to the surrounding.

The temperature detector function as to detect the cold temperature from inside of the enclosure and the hot temperature is measured from the wall of the vortex tube. Therefore, the temperature inlet will be detected at the inlet of the enclosure. In addition, the pressure inlet will be varies ranging by 1 to 4 bar by controlling the pressure regulator. The maximum reachable pressure by the compressor is 7 bar.

Next, the computational simulation in this study uses the software of ANSYS Fluent to run simulations by simulating the results of a mathematical model related with system. The computational simulation includes the mesh convergence test, finding of the energy separations and the COP of cooling of the vortex tube.

2.5 Geometry Model of Vortex Tube

Basically, the main part consisting in a vortex tube is the vortex generator and control valve. The vortex generator function as to control the air consumption. This generator has a total of six nozzles which acts as the inlet. Meanwhile, the control valve is where the hot temperature exit from the vortex tube. The geometry of the vortex tube as shown in Figure 2 while the detail dimensions of the vortex tube are as shown in Figure 3.

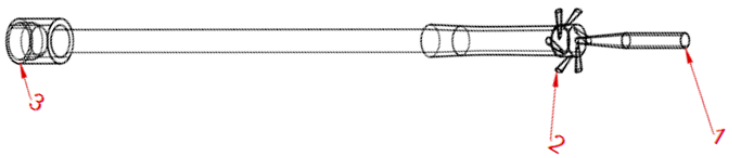


Fig. 2. Geometry of vortex tube (1) cold end outlet, (2) inlet (6 nozzles), (3) hot end outlet

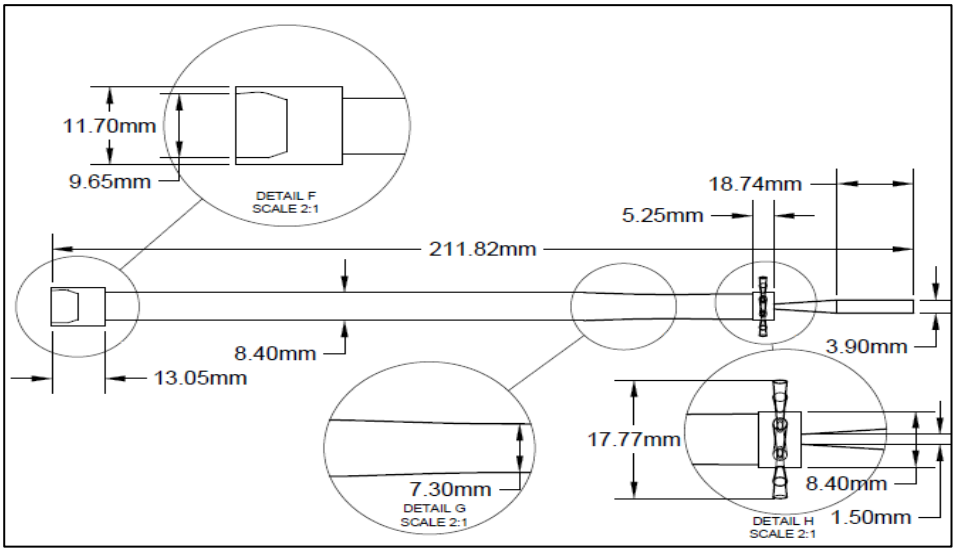


Fig. 3. Detail dimensions of the vortex tube

2.6 Computational Simulation

Table 1 lists the boundary conditions and the primary operation parameters used for simulations. The implicit stress solver will be used to solve the governing equations. The convective relationships in the equality of momentum, energy and turbulence uses the second order up-winding scheme. Besides that, pressure-based solver is used with absolute velocity formulation. SIMPLE algorithm with the pressure-velocity coupling alteration is used.

Table 1
Boundary conditions [8]

	Condition type	Pressure	Temperature	Mass flow rate
Inlet	Mass flow inlet	0.35-0.7 MPa	298.15 K	0.11 kg/s
Cold end outlet	Pressure outlet	0.12-0.25 MPa	-	0-0.11 kg/s
Hot end outlet	Pressure outlet	0.12-0.25 MPa	-	0-0.11 kg/s

3. Results and Discussions

Mesh convergence test will include the mesh generation on the vortex tube and the test analysis. The generation of mesh is basically to get better and faster solution of the computational domain. For this test, four different total number of cells are analysed and the results is as shown in Table 2 and Figure 4. The parameter involved are the hot and cold temperature. It is concluded that the grid of 424,463 cells ensured a better result. Therefore, cell number of 424,463 will be used in further simulation to study the energy separation and the coefficient of performance of cooling of the vortex tube.

Table 2
Results of the mesh convergence test

Number of cells	286,522	424,463	629,163	819,569
Temperature Difference, ΔT	236.075	248.48	248.48	248.48

(K)

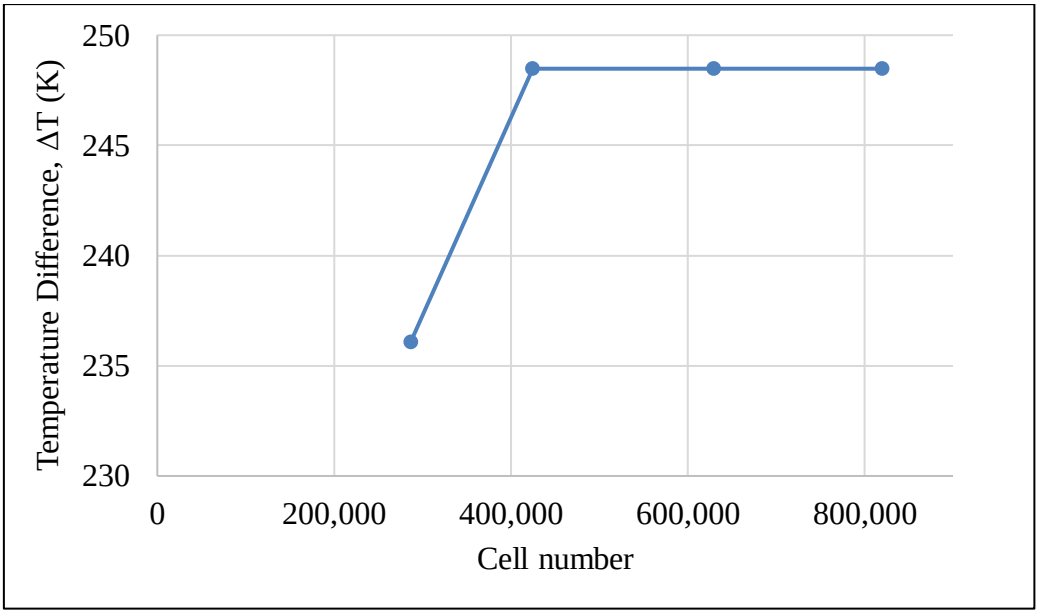


Fig. 4. Graph of temperature difference against cell number

Next, the experiment was done with varies of inlet pressure which ranging from 100 to 400 kPa. The temperature inlet was recorded by the temperature detector as well as the temperature at hot and cold end of the vortex tube. The time taken to run each test at different pressure was 10 minutes. However, the results will not be the same as in the field due to there are many different sizes of the enclosure used. The size of the enclosure used in this experiment was 400mm x 400mm.

According to the experimental data, a CFD simulation is performed to compare the results of the obtained temperature differences. The value of pressure and temperature inlet are similar to the value from experiment. Hence, Table 3 and Figure 5 shows the result obtained by CFD simulation compared with the experimental data.

Table 3
Results from experiment

Experiment			CFD simulation	Percentage error (%)
Inlet		Outlet		
Pressure (kPa)	Temperature (K)	ΔT (K)	ΔT (K)	
100	296.95	291.75	247.53	17.86
200	299.65	291.15	249.76	16.57
300	303.85	297.85	253.29	17.59
400	305.55	297.85	254.72	16.93

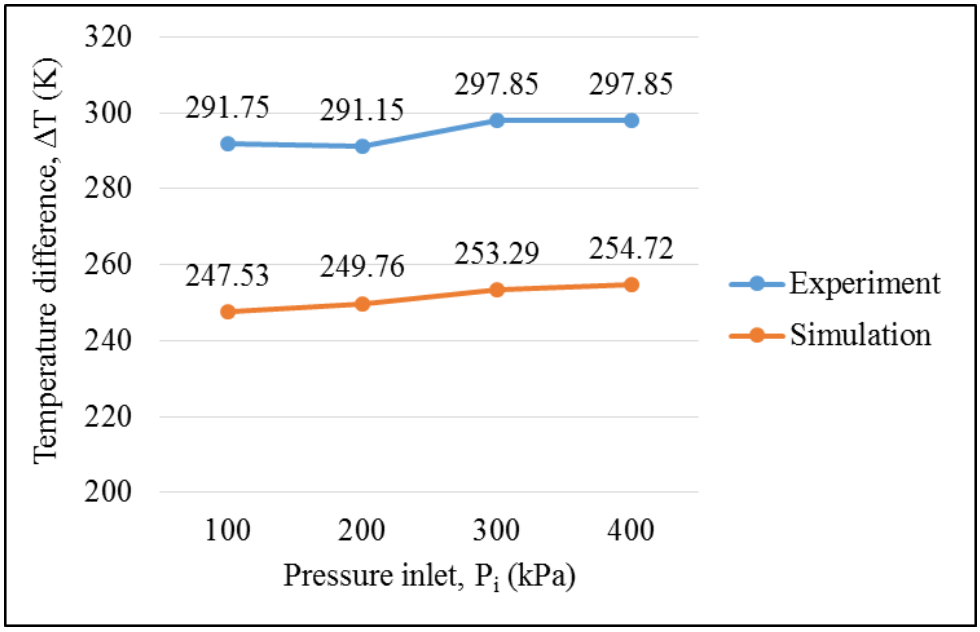


Fig. 5. Graph of temperature difference against pressure inlet for experiment and simulation

There are several factors which may contribute to the difference in data between the experiment and simulation. Firstly, the hot temperature obtained by simulation is taken directly at the surface of the hot end of the vortex tube. However, the hot temperature measured during the experiment is taken at the wall of the cabinet cooler which is the body of the vortex tube. Hence, the hot temperature is mixed with the surrounding temperature. Next, there is no filter placed after the air compressor to filter the air before entering the vortex tube. Thus, the air entered might not be clean and its affect the pressure distribution inside the vortex tube. Furthermore, the dimension of the vortex tube used in simulation is not exactly the same as the vortex tube used in experiment. The dimension and the length might be slightly different. Though these factors occurred, the results is still as expected where the temperature difference should be increase when the inlet pressure increase. In brief, the CFD simulation is considered as valid.

The first objective of this study is to analyse the energy separation of the vortex tube. Thus, the energy separation is concluded by comparing the experimental and simulation data above. Another way of analysing the energy separation is by finding the cold mass fraction which is related to the mass flow rate of the inlet and cold air. The cold mass fraction in this study is based on the temperature rise and temperature drop at the hot end and cold end respectively. Table 4 shows the result of the cold mass fraction calculated. It can be seen that the temperature rise increases alongside with the increase of inlet pressure. Thus, more air is flow out from the vortex tube through the cold end outlet.

Table 4
Results from experiment

Pressure inlet, P_i (kPa)	100	200	300	400
Inlet temperature, T_i (K)	296.95	299.65	303.85	305.55
Hot stream temperature, T_h (K)	259.90	262.25	265.95	267.45
Cold stream temperature, T_c (K)	12.38	12.49	12.67	12.74
Temperature difference, ΔT (K)	247.53	249.76	253.29	254.72
Temperature drop, T_C (K)	284.57	287.16	291.18	292.79
Temperature rise, T_H (K)	-37.05	-37.40	-37.90	-38.10
Cold mass fraction, μ	-0.1302	-0.1302	-0.1302	-0.1301

Figure 6 shows the graph of temperature difference against the cold fraction calculated. It shows that when the cold mass fraction increases, the temperature difference between the hot and cold stream increases as well. This is due to greater temperature drop at the cold end of the vortex tube. In addition, the rise in cold mass fraction will result in greater separation flow inside the vortex tube.

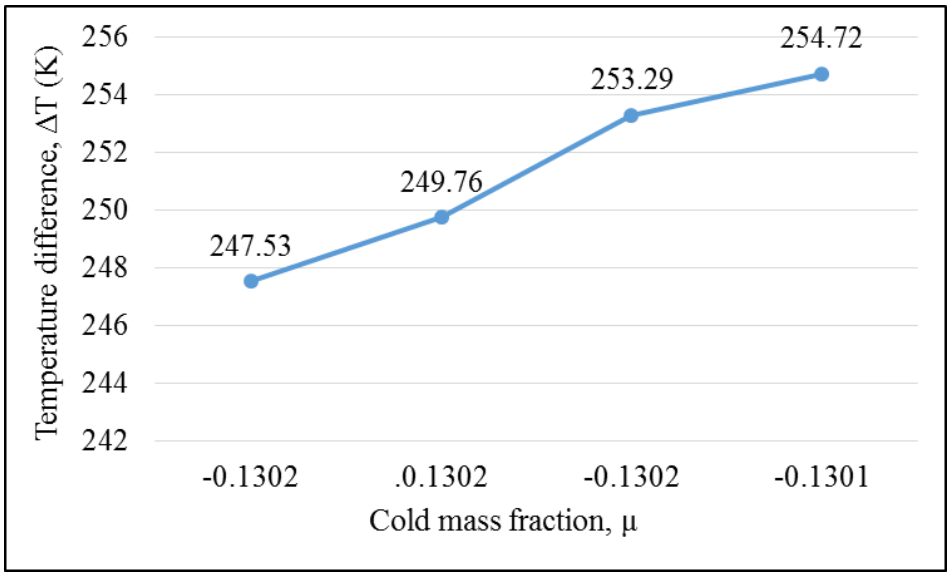


Fig. 6. Graph of temperature difference against the cold mass fraction by simulation

The negative value of the cold mass fraction is due to numerical dispersion related with the numerical scheme. Numerical dispersion is a form of error in CFD where it causes unphysical value. Besides that, it is related to the type of material used on the model of the vortex tube in ANSYS. The material used is fluid, however, the simulated medium might have a greater diffusivity than the true medium. Thus, the simulated system acts otherwise from the intended physical system and the negative value can be ignored.

COP cooling is the ratio of the cooling load, $\dot{Q}$ to the work done by the compressor, $\dot{W}$. Hence, the results of the simulation consisting of the value of pressure, mass flow rate and temperature inlet, and cold end temperature are shown in Table 5.

Table 5
Results of COP calculated by simulation data

Pressure inlet, P_i (kPa)	100	200	300	400
Temperature difference, ΔT (K)	247.53	249.76	253.29	254.72
Mass flow rate of cold air, $\dot{m}_c$ (kg/s)	-0.01432	-0.01432	-0.01432	-0.0131
Compression power, $\dot{W}$ (W)	-18242.35	-11851.08	-8127.74	-5398.15
Cooling load, $\dot{Q}$ (W)	-2925.88	-2952.51	-2993.84	-3008.29
Coefficient of performance cooling, COP_c	0.1604	0.2491	0.3683	1.7944

From the results calculated, it can be seen that the coefficient of performance for cooling increases when the inlet pressure increases. These results are the expected result as it is known when the higher the pressure inlet, the higher the velocity of the airflow inside the vortex tube. In addition, this high speed of airflow is basically the vortex angular momentum which is the main driving force for the temperature difference. Thus, it will be produced higher cold stream temperature at the cold end of the vortex tube.

4. Conclusion

An experiment and CFD simulation were conducted to test the performance of the vortex tube which varies the parameters of inlet pressure and temperature. The following results were obtained;

1. The number of cells obtained was 424,463 from mesh convergence test.
2. The energy separation can be improved by increasing the cold mass fraction. The range of the temperature rise is in between -37.05 K to -38.10 K while the range for temperature drop is 284.57 K to 292.79 K. Hence, the cold mass fraction calculated is between -0.3102 to -0.3101.
3. The coefficient of performance of cooling can be calculated when the cooling load is divided by the work done on compressor. The COP of cooling calculated was in range of 0.1604 to 1.7944.
4. The temperature difference of the hot and cold stream is the crucial results which used to study the performance of the vortex tube as it can be related to the pressure inlet, cold mass fraction, COP of cooling and etc.

References

[1] Pinar, A. M., Uluer, O., & Kirmaci, V. (2009). Optimization of counter floe Ranque-Hilsch Vortex Tube performance using Taguchi method. International Journal of Refrigeration, 32, 1487-1494.
[2] Zhang, B., & Guo, X. (2018). Prospective applications of Ranque–Hilsch vortex tubes to sustainable energy utilization and energy efficiency improvement with energy and mass separation. Renewable and Sustainable Energy Reviews, 89, 135-150.
[3] Xue, Y., Arjomandi, M., & Kelso, R. (2014). Energy analysis within a vortex tube. Experimental Thermal and Fluid Science, 52, 139-145.
[4] Guo, X., & Zhang, B. (2018). Computational investigation of precessing vortex breakdown and energy separation in a Ranque–Hilsch vortex tube. International Journal of Refrigeration, 85, 42-57.
[5] Kirmaci, V. (2009). Exergy analysis and performance of a counter flow Ranque-Hilsch vortex tube nozzle numbers at different inlet pressures of oxygen and air. International Journal of Refrigeration, 32(7), 1626-1633.
[6] Attalla, M., Ahmed, H., Ahmed, M. S., & Wafa, A. A. (2017). An experimental study of nozzle number on Ranque Hilsch counter-flow vortex tube. Experimental Thermal and Fluid Science, 82, 381-389.
[7] Rattanongphisat, W., & Thungthong, K. (2014). Improvement Vortex Cooling Capacity by Reducing Hot Tube Surface Temperature: Experiment. Energy Procedia, 52, 1-9.
[8] Liu, X., & Liu, Z. (2014). Investigation of the energy separation effect and flow mechanism inside a vortex tube. Applied Thermal Engineering, 67, 494-506.
[9] Dutta, T., Sinhamahapatra, K. P., & Bandyopdhyay, S. S. (2010). Comparison of different turbulence models in predicting the temperature separation in a Ranque-Hilsch vortex tube. International Journal of Refrigeration, 33, 783-792.
[10] Wu, Y. T., Ding, Y., Ji, Y. B., Ma, C. F., & Ge, m. C. (2007). Modification and experimental research on vortex tube. International Journal of Refrigeration, 30, 1042-1049.

Penerbit Akademia Baru

Engineering Science and Technology Conference Proceedings

Journal homepage: www.akademiabaru.com/EST.html
ISSN: XXXX-XXXX

A Simple Stabilization and Calibration Method for K-Type Thermocouple and MAX6675 Module with Reference DS18B20 Thermistor Based on Low-cost Arduino Microprocessor at Ambient Conditions

Open

Reski Septiana[1], Ibnu Roihan[1], Raldi A. Koestoer[1,*]

[1] Department of Mechanical Engineering, Faculty of Engineering, Universitas Indonesia, Depok, Indonesia

ABSTRACT

Temperature is one of the crucial parameters in every aspect of life, so an accurate temperature measurement is needed. Temperature data acquisition utilizing a K - type thermocouple and MAX6675 module as cold junction compensation is becoming more common to be used by researchers because of its availability and relatively easy to use. K-type thermocouple and MAX6675 can be used as a valid data acquisition if the sensor is properly calibrated. This research proposes a calibration method for K-type thermocouple and MAX6675 sensors based on Arduino microprocessor with DS18B20 thermistor as the reference which has been previously calibrated with the ASTM-117C thermometer. Calibration is performed at ambient conditions utilizing the energy from the environment where four K-type thermocouple and MAX6675 sensors will be calibrated alongside two DS18B20 sensors in ambient water for 24 hours, so the test illustrates the general characteristics of the sensors under the same conditions. To increase the accuracy of the K-type thermocouple and MAX6675 sensors, a simple mathematical method will be used in Arduino coding so the results are automatically calibrated values. The result of this study is a simple method to improve the accuracy of K-type thermocouples and MAX6675 sensors in reading temperature values using Arduino Data Acquisition (DAQ). The error value before calibration is 4.9% compared to 0.42% and 0.61% after calibration in ambient-water and ambient-air respectively.

Keywords:
Arduino; calibration; MAX6675; K-type thermocouple; low-cost data acquisition

Copyright © 2019 PENERBIT AKADEMIA BARU - All rights reserved

1. Introduction

Temperature is an important parameter in every system. Because of its crucial role, the temperature measurement is needed either in the academic field or industrial field [1, 2]. K-type thermocouple has widely used to measure the temperature because of its wide range of measurement, relatively low-price, self-powered, and can be applied to complex systems [2, 3]. To ease the measurement nowadays, people use data acquisition. But commercial instruments expense is a significant obstacle to setting up important monitoring networks such as data acquisition [4]. Arduino, a highly customizable open-platform electronics prototyping system [5], can be a valid data acquisition if the sensors are well-calibrated [6].

To make a temperature data acquisition using Arduino and K-type thermocouple, a module to compensate for thermocouple cold junction is needed. MAX6675 is one of many modules compatible with Arduino to compensate for K-type thermocouple cold junction. The use of K-type

* *Corresponding author.*
E-mail address: koestoer@eng.ui.ac.id (Raldi A. Koestoer)

thermocouple mounted on MAX6675 module is becoming more common to be used by researchers [3, 7-9], but not many have tried to calibrate the sensor especially at ambient conditions. At ambient conditions, where there is almost no temperature difference between cold junction and hot junction thermocouple, the reading from K-type thermocouple and MAX6675 is erratic and not so accurate compared to DS18B20 sensor [10]. The purpose of this study is to stabilize and calibrate the measurement value resulted from K-type thermocouple and MAX6675 sensor.

2. Methodology

The sensors used in this experiment are two DS18B20 waterproof thermistors as the calibrator and four K-type thermocouples which each is mounted on MAX6675 module. DS18B20 sensors were only used as the calibrator because of two reasons. First, the sensors have a limited range of measurements from -55°C to 125°C [11, 12], and their relatively big body only good for measuring bulk temperature, not for specific purposes. DS18B20 sensors have been previously calibrated using an ASTM-117C thermometer [13] and have a great resolution of 0.0625°C [12]. K-type thermocouple has a wide range of measurement starting from -250°C to 1100°C [14], but while mounting on MAX6675 as cold junction compensation module, the measurement range is limited from 0°C to 1024°C with resolution 0.25°C [15].

The calibration was taken advantage of Arduino microprocessor. Although Arduino is mostly used as a controller [16, 17], it can also be used as data acquisition [4, 11, 18, 19]. The output of Arduino can be engineered, which is beneficial for calibration [20]. The engineered output then will be saved to SD Card [11, 21], which is very practical. SD Card and Arduino compatibility reduce power consumption for computers, but the data can barely be monitored directly without the help of the LCD.

All sensors are connected to Arduino which is connected to the computer to input the commands for measuring temperature. Temperature data retrieval from six sensors is done every 100 milliseconds. The measured temperatures then were engineered in Arduino to be saved in SD Card as a .txt file.

The stabilization and calibration process were carried out in ambient conditions, utilizing the environment's energy and environmental heat-transfer. Ambient conditions were made as a reference because of thermocouple's working principle. If in these conditions, where there is almost no temperature difference between thermocouple junction, the K-thermocouple mounted on MAX6675 can measure the temperature accurately then the sensor can be applied to measure greater temperature differences.

To test whether K-type thermocouples mounted on MAX6675 can be calibrated with DS18B20 sensors, first have to see their rhythms in reading the water-ambient temperature. Four K-type thermocouples which each is mounted on MAX6675 (TC_i) will be immersed in an open vessel contains ambient water for 24 hours with two DS18B20 thermistors (DS_i), as shown in Figure 1. Ambient water medium is chosen to see the initial characteristics of the sensors because water has a high specific heat capacity, so even the change in the environment's temperature will not much affect the water's temperature.

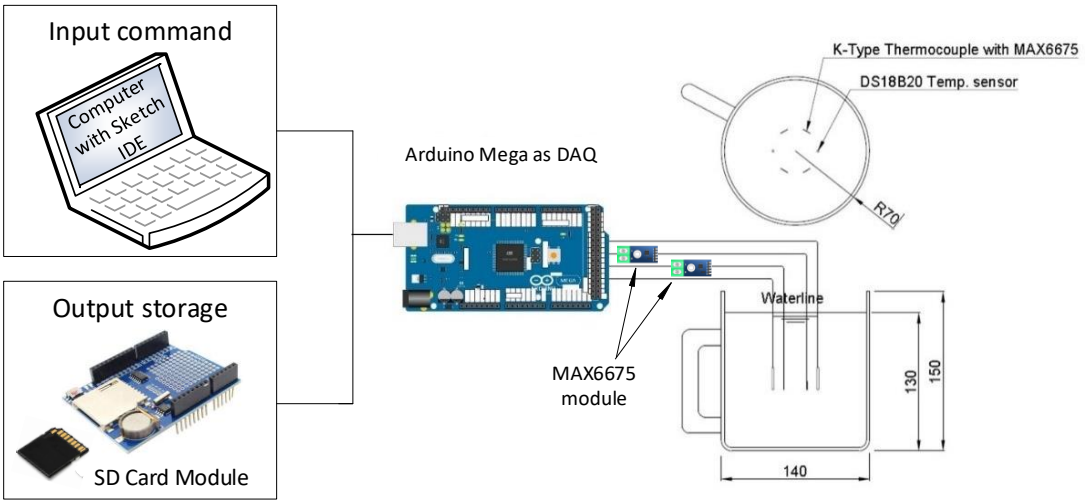


Fig. 1. Experimental set-up

If the rhythms of both sensors in reading water-ambient temperature are the same, then the next question is how to calibrate the sensors. Simple mathematics methods are chosen to calibrate the K-type thermocouple mounted on MAX6675 sensors, such as averaging, filtering, and fitting. Averaging four data of each K-type thermocouple and MAX6675's measurement using Eq. 1 can reduce the fluctuation of the sensors. Filtering process using Eq. 2, based on MAX6675 resolution, 0.25°C, can further reduce the noise of the measurement. While fitting process using Eq. 4, can boost the accuracy of K-type thermocouple in reading temperature values. Fitting process or so-called line translation is an important process to reduce the systematic error of the sensors. Factor of translation or later will be described as fitting value (FV) is calculated by averaging the delta of measurements taken from DS18B20 sensors and K-type thermocouple mounted on MAX6675's sensors at steady condition.

$$\overline{TC_{\iota}} = \frac{\sum_{n=1}^{4} TC_{i,n}}{4} \tag{1}$$

$$TC_i = \left|\overline{TC_{\iota,n+1}} - \overline{TC_{\iota,n}}\right| < 0.25℃\ ;\ "\overline{TC_{\iota,n}}" \tag{2}$$

$$TC = \frac{\sum_{i=1}^{4} TC_i}{4} \tag{3}$$

$$TC^* = TC - FV \tag{4}$$

Between 08 PM and 11 PM; $08PM \leq t \leq 11PM$

$$FV = \frac{TC_t - DS_{AV_t}}{n_t} \tag{5}$$

$$DS_{AV_t} = \frac{\sum_{i=1}^{2} DS_i}{2} \tag{6}$$

The above methods are written as coding and uploaded in Arduino's Sketch so the results are automatically calibrated values. The above methods will be used in reading not only water-ambient temperature but also air-ambient temperature. The results from reading water-ambient and air-

ambient temperature with the proposed methods then will be compared. The standard deviation (°C) and error value (%) before and after calibration will be calculated using Equation 7 and 8.

$$\text{Standard deviation} = \sqrt{\frac{\sum(TC_i - DS_{AV})^2}{n-1}} \quad (7)$$

$$\text{Error} = \left|\frac{TC_i - DS_{AV}}{DS_{AV}}\right| \times 100\% \quad (8)$$

3. Results

3.1 Before Calibration

The initial characteristics of K-type thermocouple sensors mounted on MAX6675 (TC) compared to the average of DS18B20 sensors (DSAv) in reading the water ambient temperature value are shown in Figure 2. Since each K-type thermocouple sensor has the same rhythm with the average of DS18B20 sensors, the calibration of K-type thermocouple to DS18B20 sensor can be done.

Based on Figure 2 and Table 1, K-type thermocouple mounted on MAX6675 relatively precise in reading the ambient temperature but not so accurate. The range of ambient temperature on that day (24 hours) as shown by the average of DS18B20 sensors starts from 27.7°C to 28.7°C, different readings were produced from the K-type thermocouple and MAX6675 sensors. The temperature measured by K-type thermocouples and MAX6675 sensors were not the same even though they have the same specifications and were purchased from the same manufacturer. The deviation between sensors varies from 0.23°C to 0.26°C. The systematic error of each sensor respectively is 1.72°C, 0.86°C, 1.46°C, and 1.49°C compared to the average of DS18B20 sensor as the true value. The average error value (%) before calibration is 4.9%.

Table 1
Uncertainties of the measurement before calibration

K-type Thermocouple mounted on MAX6675 (pair -)	Initial Characteristic	
	Deviation (°C)	Error (%)
1st	0.26	6.1
2nd	0.25	3.0
3rd	0.23	5.2
4th	0.24	5.3

3.2 After Calibration

With 100ms delay of data retrieval, only four readings are produced by Arduino in one second. This is most likely because Arduino needs time to convert and save the printed date, time, and measurement values into text in SD Card. By averaging four data of each measurement taken by K-type thermocouple and MAX6675, the deviation becomes smaller, which varies from 0.12°C to 0.14°C. While filtering the data by ±0.25°C, reduce the noise of measurement as shown in Figure 3. The deviation after averaging and filtering the data varies from 0.11°C to 0.13°C as summarized in Table 2.

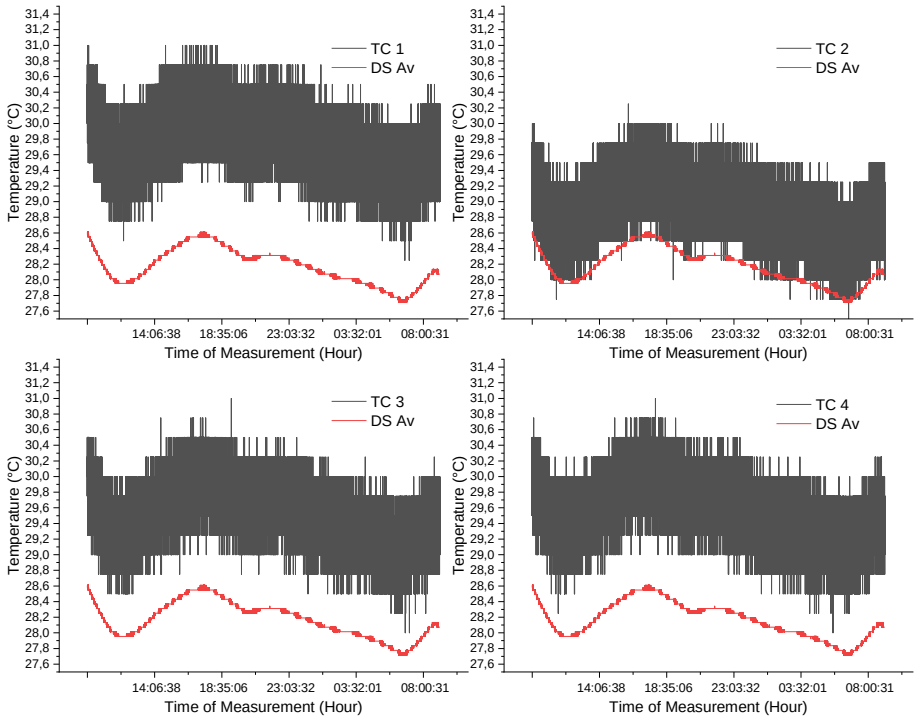


Fig. 2. Initial characteristics of K-type thermocouples (TC) in reading ambient water temperature before calibration compared to the average of two DS18B20 sensors (DSAv)

To ease the data-fitting of four K-type thermocouple and MAX6675 sensors to DS18B20, the averaging of those four pairs was conducted using Eq. 3. The measurement values taken by either four pairs of K-type thermocouple mounted on MAX6675 and two DS18B20 sensors should have shown the same result because they were placed under the same condition with distance relatively near to each other. But according to Figure 2, they showed different results in reading temperature value, so the averaging process was done to make the four pairs shown only one value that represents the four of them. After all the four values become one as shown in Figure 4, the delta between that one value and the average of DS18B20 were calculated. The delta of measurements between the sensors at ambient-steady conditions, from 08 PM to 11 PM, were then being averaged to calculate one constant value or fitting value to fit the uncalibrated sensors, which in this case are K-type thermocouple and MAX6675 sensors, to the DS18B20 sensors. The fitting value for this experiment is 1.31°C.

Table 2
Uncertainties of the measurement after calibration

K-type Thermocouple mounted on MAX6675 (pair -)	Averaging		Filtering		Fitting – Water		Fitting - Air	
	Deviation (°C)	Error (%)	Deviation (°C)	Error (%)	Deviation (°C)	Error (%)	Deviation (°C)	Error (%)
1st	0.13	6.1	0.12	6.1	0.087	0.42	0.112	0.61
2nd	0.14	3.0	0.13	3.0	0.087	0.42	0.112	0.61
3rd	0.12	5.2	0.11	5.2	0.087	0.42	0.112	0.61
4th	0.13	5.3	0.12	5.3	0.087	0.42	0.112	0.61

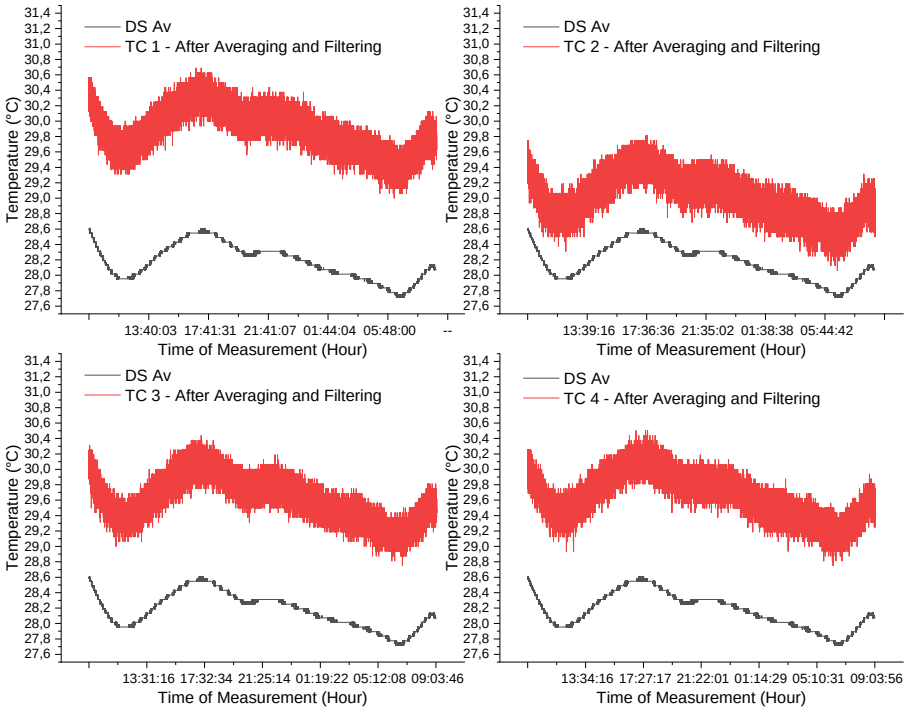


Fig. 3. Results after filtering and averaging four data measured by each K-type thermocouple mounted on MAX6675

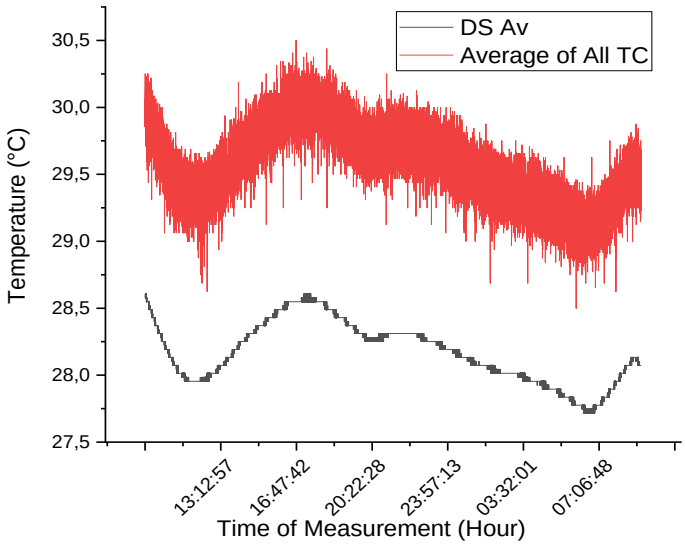


Fig. 4. Average of All K-type thermocouple and MAX6675 to ease the fitting process

As shown in Figure 5, the measurement taken after inserting the fitting value based on Eq. 4 in the Arduino's coding has proven that K-type thermocouple and MAX6675 already measure the same temperature as DS18B20 sensors in water-ambient medium but with bigger fluctuation due to the resolution of the sensors. The deviation and error (%) after calibration in ambient water respectively are 0.087°C and 0.42%.

The same coding was used to measure air ambient conditions for 24 hours so both hot junction and cold junction thermocouple were in ambient air. Based on Figure 6, the proposed methods with fitting value of 1.31°C still can be used even though the fitting value was a result of hot junction

thermocouple in the water medium. The deviation and error (%) after calibration in ambient air as summarized in Table 2 respectively, are 0.112°C and 0.61%.

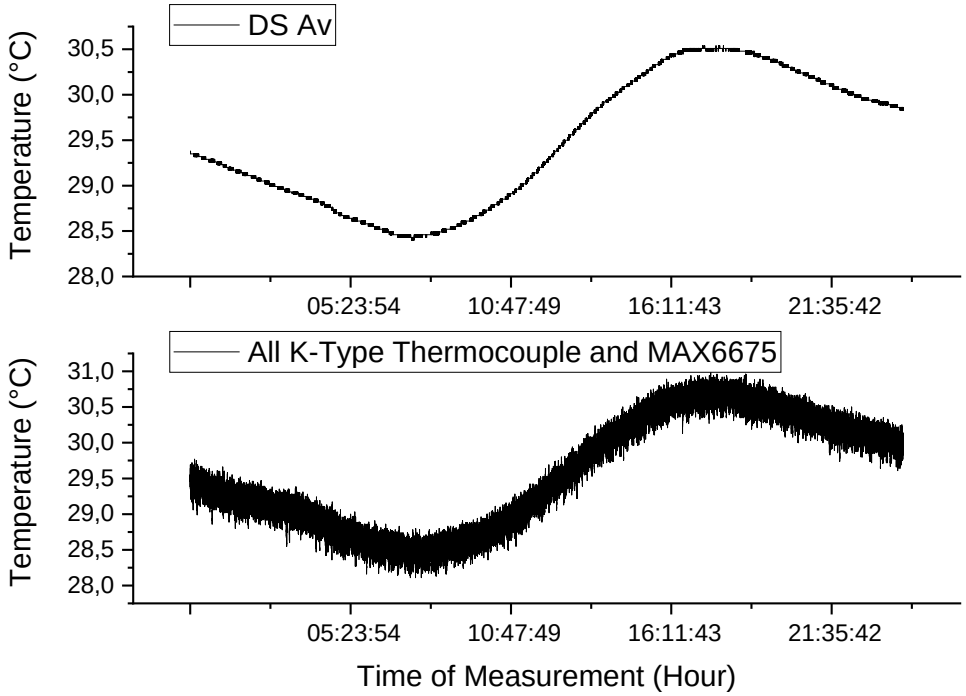


Fig. 5. K-type thermocouple and MAX6675 in reading water ambient temperature values after calibration

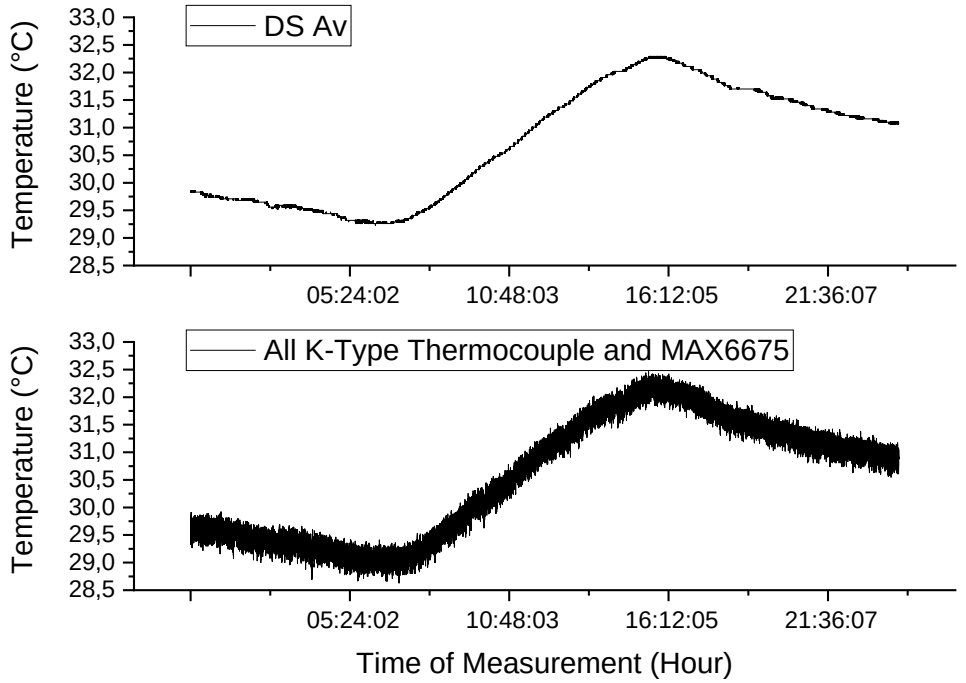


Fig. 6. K-type thermocouple and MAX6675 in reading air ambient temperature values after calibration

4. Conclusions

The stabilization and calibration of MAX6675 and K-type thermocouple in reading ambient temperatures are needed because of the working principle of thermocouple. In ambient conditions, the thermocouple junctions almost have no temperature difference, so the values measured should be stabilized as the basis of zero offset. Ambient conditions that close to the natural-steady state can be used as the basis to calibrate the K-type thermocouple mounted on MAX6675 sensors because in this condition the temperature only varies very slightly.

Calibration process utilizing simple mathematic processing such as averaging, filtering, and fitting can be used as the methods to stabilize and calibrate the sensors. Averaging and filtering process increased the precision of the measured values, while fitting process reduces the systematic error. Using the proposed methods, $TC^* = TC - 1.31$, and natural steady-state condition to calibrate the sensors increase the accuracy of the sensors from 4.9% to 0.42% in reading ambient water temperature and to 0.61% in reading ambient air temperature with the average of deviations is 0.12°C. It is proven that the proposed method utilizing Arduino microprocessor can be used to increase the precision and the accuracy of K-type thermocouple and MAX6675 in reading temperature values.

Acknowledgement
This work was supported by the Ministry of Research, Technology and Higher Education of the Republic of Indonesia (PMDSU Grant NKB-3044/UN2.R3.1/HKP.05.00/2019).

References

[1] Zeeshan, Mohammad, Kashif Javed, Bharat Bhushan Sharma, and Shahzad Ahsan. "Signal Conditioning of Thermocouple Using Intelligent Technique." *Materials Today: Proceedings* 4, no. 9 (2017): 10627–31.
[2] Sarma, Utpal, and P.k. Boruah. "Design and Development of a High Precision Thermocouple Based Smart Industrial Thermometer with on Line Linearisation and Data Logging Feature." *Measurement* 43, no. 10 (2010): 1589–94.
[3] Han, Yanhui, Yue Feng, Haozhe Lou, and Xinzhao Zhang. "Thermocouple-Based Temperature Sensing System for Chemical Cell Inside Micro UAV Device." *Journal of Physics: Conference Series* 986 (2018): 012012.
[4] Beddows, Patricia A., and Edward K. Mallon. "Cave Pearl Data Logger: A Flexible Arduino-Based Logging Platform for Long-Term Monitoring in Harsh Environments." Sensors 18, no. 2 (September 2018): 530.
[5] Gandra, Miguel, Rui Seabra, and Fernando P. Lima. "A Low-Cost, Versatile Data Logging System for Ecological Applications." *Limnology and Oceanography: Methods* 13, no. 3 (2015).
[6] D'Ausilio, Alessandro. "Arduino: A Low-Cost Multipurpose Lab Equipment." Behavior Research Methods 44, no. 2 (2011): 305–13.
[7] Zambaldi, Edimilson, Ricardo R. Magalhães, Bruno H.g. Barbosa, Sandro P. Da Silva, and Danton D. Ferreira. "Lowcost Automated Control for Steel Heat Treatments." Applied Thermal Engineering 114 (2017): 163–69.
[8] Xiao, Chengdi, Hailong Liao, Yan Wang, Junhui Li, and Wenhui Zhu. "A Novel Automated Heat-Pipe Cooling Device for High-Power LEDs." Applied Thermal Engineering 111 (2017): 1320–29.
[9] Li, Bin, and Jinhui Lei. "Design of Industrial Temperature Monitoring System Based on Single Chip Microcontroller." 2011 International Conference on Computer Science and Service System (CSSS), 2011.
[10] MAX6675 Type K Thermocouple Huge Fluctuation. Accessed October 28, 2019.
[11] Lopez-Vargas, Ascension, Manuel Fuentes, Marta Vivar Garcia, and Francisco J. Munoz-Rodriguez. "Low-Cost Datalogger Intended for Remote Monitoring of Solar Photovoltaic Standalone Systems Based on Arduino™." IEEE Sensors Journal 19, no. 11 (January 2019): 4308–20.
[12] "DS18B20 Programmable Resolution 1-Wire Digital Thermometer." Maxim. Accessed October 28, 2019.
[13] Koestoer, R. A., Y. A. Saleh, I. Roihan, and Harinaldi. "A Simple Method for Calibration of Temperature Sensor DS18B20 Waterproof in Oil Bath Based on Arduino Data Acquisition System," 2019.
[14] Childs, Peter R. N. Practical Temperature Measurement. Boston: Butterworth-Heinemann, 2001.
[15] "MAX6675 Cold-Junction-Compensated K-Thermocouple-to-Digital Converter (0°C to 1024°C)." Maxim. Accessed October 28, 2019.

[16] Candelas, F.a., G.j. García, S. Puente, J. Pomares, C.a. Jara, J. Pérez, D. Mira, and F. Torres. "Experiences on Using Arduino for Laboratory Experiments of Automatic Control and Robotics." IFAC-PapersOnLine 48, no. 29 (2015): 105–10.
[17] Costa, Eric Tavares Da, Maria F. Mora, Peter A. Willis, Claudimir L. Do Lago, Hong Jiao, and Carlos D. Garcia. "Getting Started with Open-Hardware: Development and Control of Microfluidic Devices." Electrophoresis 35, no. 16 (2014): 2370–77.
[18] Fuentes, M., M. Vivar, J.m. Burgos, J. Aguilera, and J.a. Vacas. "Design of an Accurate, Low-Cost Autonomous Data Logger for PV System Monitoring Using Arduino™ That Complies with IEC Standards." Solar Energy Materials and Solar Cells 130 (2014): 529–43.
[19] Cvjetkovic, Vladimir M, and Milan Matijevic. "Overview of Architectures with Arduino Boards as Building Blocks for Data Acquisition and Control Systems." International Journal of Online Engineering (IJOE) 12, no. 07 (2016): 10.
[20] Koestoer, R. A., N. Pancasaputra, I. Roihan, and Harinaldi. "A Simple Calibration Methods of Relative Humidity Sensor DHT22 for Tropical Climates Based on Arduino Data Acquisition System," 2019.
[21] Zainal, Nur Izzati, Khairul Azami Sidek, Teddy Surya Gunawan, Hasmah Manser, and Mira Kartiwi. "Design and Development of Portable Classroom Attendance System Based on Arduino and Fingerprint Biometric." The 5th International Conference on Information and Communication Technology for The Muslim World (ICT4M), 2014.

Penerbit Akademia Baru

Journal of Advanced Research in Fluid Mechanics and Thermal Sciences

Journal homepage: www.akademiabaru.com/EST.html

Transport Phenomena in Organic Solvent Nanofiltration: A Review

Open Access

Nazlee Faisal Ghazali[1,*], Ki Min Lim[2]

[1] Department of Bioprocess and Polymer Engineering, School of Chemical and Energy Engineering, Faculty of Engineering, Faculty of Engineering, Universiti Teknologi Malaysia, 81310 Skudai, Johor, Malaysia
[2] Malaysia-Japan International Institute of Technology (MJIIT), Universiti Teknologi Malaysia, Jalan Sultan Yahya Petra, 54100 Kuala Lumpur, Malaysia

ABSTRACT

Membrane technology has been gradually used as an alternative to the conventional separation and purification method in various industries. In recent years, solvent-stable nanofiltration or organic solvent nanofiltration has becoming practicable through the development of solvent-stable commercial polymeric membranes. Organic solvent nanofiltration has a great potential to replace the conventional energy-demanding process such as distillation due to its ability of separating organic solvents and solutes on a molecular level without phase change and operation at relatively mild temperature. Predicting the performance of such membrane separations is crucial in the process design. Important performance indicator such as the permeate flux and the rejections are strongly related to the fluid dynamics, mass transfer and solute-solvent-membrane interactions. The aim of this paper is to review and assess the transport models of solute and solvent transport relevant to organic solvent nanofiltration. The link between concentration polarization and the hydrodynamics in various configurations are discussed. The effects of process variables on membrane performance and solute-solvent membrane interactions are also reviewed.

Keywords:
Organic solvent nanofiltration; parameter estimation, concentration polarization; transport model

Copyright © 2019 PENERBIT AKADEMIA BARU - All rights reserved

1. Introduction

Towards the efforts of purifying and separating chemical mixtures, various methods have been investigated and discovered. As of current, the techniques employed in the industries to refine chemicals are by extraction, distillation, chromatographic, electrophoresis and crystallization techniques [1]. Although these methods of refining are considered feasible in the current chemical industry, the methods require a significant amount of energy, for example, during distillation process as well as other processes [1]. As the conventional refining method has been found decades ago, membrane separation methods have been proposed in the literatures, which were found to be a viable solution to address the problem of energy expenditure [2]. Membrane purification method is currently actively used in purifying water and air[3, 4]. Despite the early discovery of this method, membrane purification technique is currently still in its development stage for the separation of organic chemicals [5]. The use of membranes for organic solvents is

* *Corresponding author.*
E-mail address: nazlee@utm.my (Nazlee Faisal Ghazali)

commonly known as organic solvent nanofiltration (OSN) or solvent resistant nanofiltration (SRNF) in the field of membrane separation research. In the course of enabling membrane purification method in refining chemicals, various factors which impede its implementation in the industry have been thoroughly considered. Some of the factors are the volumetric flux of permeate, the stability of membranes towards organic chemicals, and the selectivity of the membrane towards chemical compounds[2]. In order to provide solutions to the problems, the prediction of the membrane separation performances is essential [2, 6]. The prediction and quantification of the membrane separation performance will enlighten the researchers on the approaches that should be taken to improve the membranes. In this paper, the current researches on the use of different transport models to predict mass transfer in organic solvent systems were reviewed. Besides that, the effects of concentration polarization on the transport processes were also briefly discussed.

2. Transport Model

The transport models that are currently being actively applied in the prediction of membrane performance are irreversible thermodynamics models, solution-diffusion models, and pore-flow models [2, 6]. From the literatures, the irreversible thermodynamics transport models can be used for the description of solute and solvent transport of nanofiltration membranes. The irreversible thermodynamics models are namely Kedem-Katchalsky model [7]:

$$J_V = L_p\left(\Delta P - \sigma_i \Delta\pi\right) \tag{1.}$$

$$J_S = P_i \Delta c_i + \left(1-\sigma_i\right) J_V \bar{c}_i \tag{2.}$$

where J_V is the volumetric flux of solvent, J_S is the volumetric flux of solute, P_i is the permeability coefficient of the solute *i*, σ is reflective coefficient, L_p is the mechanical filtration coefficient and $\bar{c}$ is the average solute concentration in the membrane, and Spiegler-Kedem model [8]

$$J_v = L_p\left(\Delta P - \sigma_i \Delta\pi\right) \tag{3.}$$

$$J_S = -P_i \Delta x \frac{d}{dx} c_i + \left(1-\sigma_i\right) J_V \bar{c}_i \tag{4.}$$

However, the models do not consider the transport processes within the membranes[2]. On the other hand, solution-diffusion models are suitable to describe the solute and solvent transport when the mechanism of transport processes within the membrane is known[9, 10]. Eq. 5 and Eq. 6 shows the solution diffusion model:

Solvent flux

$$J_i = \frac{D_i K_i}{l}\left(c_{io} - c_{il} e^{\left(\frac{-v_i\left(p_o - p_l\right)}{RT}\right)}\right) \tag{5.}$$

Solute flux

$$J_j = \frac{D_j K_j}{l}\left(c_{jo} - c_{jl}\right) \tag{6.}$$

By including the effect of viscous flow, solution-diffusion with imperfections model was formed:

$$J_i = \frac{D_i K_i c_{io} v_i}{l R_g T}(\Delta p - \Delta \pi) + \frac{c_{io} B_0}{\eta l}\Delta p \quad (7.)$$

where B_0 is the specific permeability of the membrane (m^2)

Meanwhile, pore-flow model (Eq. 8) is suitable for the description of transport processes in porous membranes such as microfiltration membranes and ultrafiltration membranes[2, 6].

$$J = \frac{k(p_o - p_l)}{l}, k = Lv \quad (8.)$$

where *k* is the Darcy's law coefficient.

From Eq. 8, a more popular derivative of pore-flow model, Hagen-Pouseuille model was derived:

$$J = \frac{\varepsilon r^2}{8\mu\tau}\frac{\Delta P}{\Delta x} \quad (9.)$$

where r, ε, τ and Δx represents pore size, membrane porosity, membrane tortuosity and membrane thickness respectively.

3. Membrane Performance Prediction by Transport Models

In the development of membrane processes, several stages of modeling were involved starting from lab scale till the implementation in the actual industrial scale [2]. Parameter estimation is performed in the membrane scale, through non-linear regression of transport models against the experimental data in solute and solvent system. The regression is performed by a certain selected algorithm which minimizes the error between the expected data and the model output, which results in the estimation of model parameters[6]. When the model parameters are available, modeling can be performed to predict the performance of the membrane, as shown in the process flow in Fig.1. The selection of models for the estimation and prediction depends on the type of membrane as well as the operating conditions[11]. Some researchers compare different types of models for a selected solute-solvent system, in order to obtain the best model to describe the separation process [6, 12].

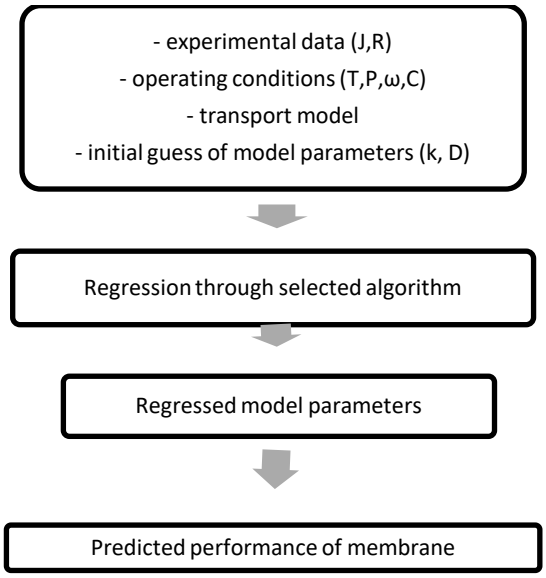


Fig. 1. A typical process flow for a modeling process [2, 6, 11]

Table 1
Some of the current application of transport models to experimental data

Model	Membrane	Solute/solvent	Reference
Generalized Maxwell-Stefan model	Polyimide	Toluene, isopropanol, methanol, decane, dodecane, tetradecane, hexadecane, octadecane, docosane, tetracosane	[13]
Nernst-Planck pore flow equation	Polyimide	Acetone toluene	[14]
Classical solution-diffusion with film theory	Polyimide	Ethyl acetate, sucrose octaacetate	[15]
Nernst-Planck equation with Hagen-Poiseuille model	TiO_2/ZrO_2	Polystyrene, THF	[16]
Solution-diffusion, pore-flow, reduced solution-diffusion imperfection models	Polyimide, composite PDMS	n-hexane, ethanol, rapeseed oil, olive oil, babassu oil, oleic acid, lauric acid	[12]
Solution-diffusion	Composite PDMS	Dodecene, polyethylene glycol ether	[17]
Maxwell-Stefan with Flory-Huggins model	Composite PDMS/PAN	ρ-cymene, d-limonene, α-pinene, canola oil, n-hexane, n-heptane	[18]

Postel *et al.,* had found that the changes in the solvent properties resulted from the mixture of different solvents had affected the interactions between membrane, solvent and solute. The interaction causes a different flux and retention trends. In their study, Maxwell-Stefan model which includes effect from the interactions was able to describe the solvent and solute fluxes successfully [13]. Campbell *et al.,* [14], on the other hand, had emphasized on the effect of pore size on the separation process due to the use of hybrid metal organic/ polyimide ultrafiltration membranes in their experiments. In order to include the effect of pore size in the calculations, Nernst-Planck equation was described as a function of pore size to estimate the rejection of solutes. In another study by Shi *et al.,* [15], classical solution-diffusion model and film theory were used to describe the effect of mass transfer. Based on the model implementation by using OSN Designer software tool, the necessary parameters such as pressure drops and mass transfer were successfully obtained through experimental data regression[15].

In attempt to implement an existing nanofiltration model to OSN, a model which was developed by Bowen and Welfoot [19] to describe the transport of uncharged solute in aqueous application was studied by Blumenschein *et al.,* [16]. Various effects of organic solvents and interactions of solutes were included for the model adaptation to OSN. From the results obtained from their study [16], it was found the transport model based on the model of Bowen and Welfoot [19] was able to predict the rejections of ceramic OSN membranes.

In the recent paper by Werth *et al.,* [12], they had investigated the applicability of different models to describe the mass transfer in oil and solvent mixtures. From their investigation, a reduced form of solution-diffusion imperfection model was able to describe the mass transfer most accurately, as compared to the solution-diffusion model and pore-flow model. They had concluded that the small compounds (free fatty acid and solvent) contributes to mass transfer by convection and alternatively, triglycerides can be described by diffusion [12]. In a different study, the feasibility of OSN for the recovery of organic compound (terpenes) from oil was investigated [18]. Another equation, Flory-Huggins model were used to describe the interactions between polymer, solvent and oil [18]. From the ternary Flory-Huggins model, volume fractions of oil and solvent were obtained, which were then used to simulate mass transfer by a linearized Maxwell-Stefan model [18]. They had found that sorption level of oil and solvents can be predicted by Flory-Huggins model, and both the fluxes of solvent and oil can be calculated by a linearized Maxwell-Stefan model [18].

4. Concentration Polarization

When a membrane is subjected to a filtration process of fluids with impurities or mixtures, a phenomenon known as concentration polarization will occur. Concentration polarization can be simply explained by the formation of a composition gradient at the feed-membrane interface (as shown in Fig.2). It is crucial to decrease the effect of concentration polarization, as it will increase the possibility of membrane fouling [20].

The effect of concentration polarization can be described by several ways. Some of the earlier publication on the effect of concentration polarization were presented in the late 80's in the case of protein ultrafiltration [21, 22]. Years afterward, Peeva *et al.* published the first work to consider concentration polarization in OSN [23]. Peeva *et al.* [23] had listed seven non-linear algebraic equations (Eq.10 to Eq.16) which allows the prediction of permeate flux and solute rejection.

$$\frac{J}{k_1} = \ln\left(\frac{c_{1,A2} - c_{1,A3}}{c_{1,A1} - c_{1,A3}}\right) \tag{10.}$$

$$\frac{J}{k_2} = \ln\left(\frac{c_{2,A3} - c_{2,A2}}{c_{2,A3} - c_{2,A1}}\right) \tag{11.}$$

$$J = J_1 v_1 + J_2 v_2 \tag{12.}$$

$$J_1 = P_{1,M}\left(x_{1,A2} - \frac{\gamma_{1,A3}}{\gamma_{1,A2}}\frac{J_1}{J_1 + J_2}\exp\left(-\frac{v_1 p}{RT}\right)\right) \tag{13.}$$

$$J_2 = P_{2,M}\left(x_{2,A2} - \frac{\gamma_{2,A3}}{\gamma_{2,A2}}\frac{J_2}{J_2 + J_1}\exp\left(-\frac{v_2 p}{RT}\right)\right) \tag{14.}$$

$$\gamma_1 = f(x_1), \quad \gamma_2 = f(x_2) \quad \text{or} \quad \gamma_1 = \gamma_2 = 1 \tag{15.}$$

$$\text{Rej}_{\text{calc}} = 1 - \frac{J_1}{J_{C_1,A1}} \tag{16.}$$

Baker [4] proposed another equation (Eq. 17) to estimate concentration polarization which is based on Peclet number. In comparison with the equations proposed by Peeva *et al.* [23], the equation by Baker [4] only requires the estimation of mass transfer coefficient, and the experimental data of flux, permeate and retentate concentration. Zwijnenberg *et al.*[24] had published an article on the application of the equation by Baker [4] for the nanofiltration of organic solvents. For the equation by Baker [4], concentration polarization is described by concentration polarization modulus which is written as E_0/E.

$$\frac{E_0}{E} = \frac{C_{A2}}{C_{A1}} = \frac{\exp(J_V / k)}{1 + E_0[\exp(J_V / k) - 1)]} \tag{17.}$$

whereby E_0 is enrichment factor, which can be defined as C_{A3} / C_{A1}; E is true enrichment factor, also written as C_{A3} / C_{A2}. The ratio of the convective transport, J_v, and diffusive transport, k, is known as Peclet number [25].

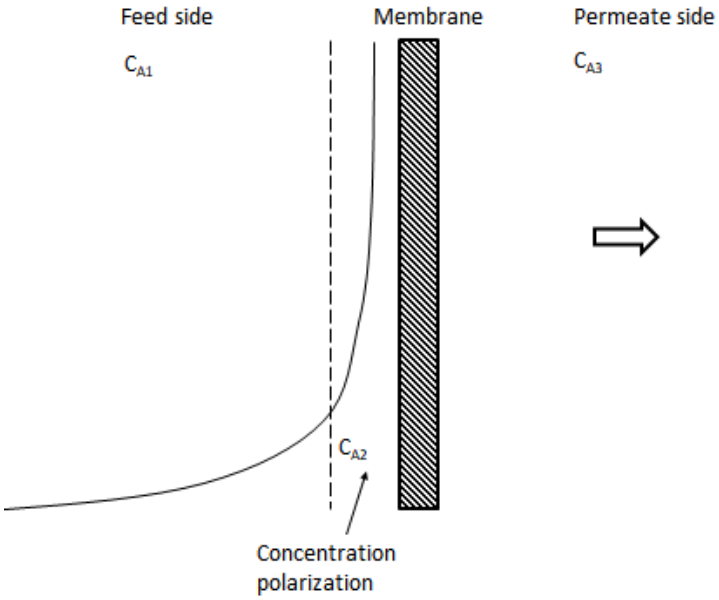


Fig. 2. A schematic showing the concentration polarization effect [20, 25]

The mass transfer coefficient can be determined by several ways. Peeva *et al.,* [23] had proposed the use of Eq (18), paired with Chilton-Colburn correlation (Eq. 19) to obtain the mass transfer coefficient. Equation 18 was used for the calculation of mass transfer coefficient, which can be determined from the independent measurements of dissolution of benzoic acid plate in water at two cross-flow rates.

$$\ln\left(\frac{c_b^*}{c_b^* - c_b}\right) = \frac{kA}{V}t \tag{18.}$$

where c_b is the molar concentration of benzoic acid (mol/m^3), c_b^* is the solubility of benzoic acid in water at 30°C (mol/m^3), *A* is the active membrane area (m^2), volume of water (m^3), *t* is the time duration for the dissolution of benzoic acid and k is the mass transfer coefficient (m/s).

The mass transfer coefficient of benzoic acid obtained from Eq.(18) can then be used to obtain the mass transfer coefficient of selected solute through the correlation with the following empirical formula:

$$Sh = \frac{kd_h}{D} = a\,\mathrm{Re}^{\,b}\,Sc^{c}\left(\frac{d_h}{L}\right)^{d} \tag{19.}$$

where k is the mass transfer coefficient (m/s), d_h is the hydraulic diameter (m), D is the diffusivity (m^2/s), L is the channel length (m) and constants a, b, c, d which depends on the system geometry, flow, and type of fluid.

Equation 19 can then be simplified to equation 20 where the system conditions are assumed to be constant.

$$k \propto \eta^{(c-b)} D^{(1-c)} \tag{20.}$$

Equation 21 can then be obtained from equation 20.

$$\frac{k_{solute}}{k_{benzoicacid}} \propto \left(\frac{\eta_{solute}}{\eta_{benzoicacid}}\right)^{(c-b)} \left(\frac{D_{solute}}{D_{benzoicacid}}\right)^{(1-c)} \tag{21.}$$

Besides that, mass transfer coefficient can also be obtained through non-linear parameter estimation method. This method is usually performed through the use of computer equipped with software such as MATLAB, CAPE OPEN and Aspen One as suggested by Peshev et al. [11]. The procedure of the parameter estimation is as shown in Figure 1, whereby, a set of experimental data of permeation flux and rejection is required, coupled with a selected membrane transport model.

In the paper by Murthy and Gupta [26], they have suggested a simplified graphical method for the estimation of mass transfer coefficient. A combined equation of solution diffusion and film theory was employed in their study:

$$\ln\left[\frac{(1-R_0)\times J_V}{R_0}\right]=\ln\left(\frac{D_{AM}}{K\delta}\right)+\frac{J_V}{k} \quad (22.)$$

whereby through the plot of $\ln\left[(1-R_0)\times J_V / R_0\right]$ against J_V will yield a straight line, and the gradient of the plot will be $(1/k)$ and the y-intercept will be $\ln(D_{AM} / K\delta)$ [26].

Table 2
Comparison between concentration polarization equation by Peeva *et al.,* [23] and Baker [4]

	Peeva et al. [23]	Baker [4]
Equation parameters	J_i , k_i , v_i, γ_i, c_i	J_i, k, c_i
Parameters which requires estimation	k_i, γ_i, v_i	k
Methods of estimation	k_i - Chilton-Colburn correlation [27] v_i - Fedors method [28] γ_i - modified UNIFAC method [29]	k - nonlinear parameter estimation by using regression method [25]
Number of components	Two	Not stated
Description of concentration polarization	Rejection and permeate flux which includes the effect of concentration polarization	By the term concentration polarization modulus
Membrane module	Cross-flow	Cross-flow

As concentration polarization will definitely occur during membrane filtration process, steps need to be taken to reduce its effects. One of the steps is by using a higher feed velocity for cross-flow module. The high velocity of feed will obstruct the formation of stagnant layer on the membrane. As for dead-end module, a stirrer should be employed to prevent the settling of fluid mixtures, as well as to create turbulence for an improved mass transfer[4, 20].

5. Conclusions

The use of transport model to predict the performance of a transport process is undeniably important, considering its ability to forecast the flux and mass transfer in a membrane separation process. As there can be various systems of organic solvents, the model to best describe each system can be different. The model which is suitable to describe the transport process is greatly dependent on the interaction between solute, solvent and membrane. From the brief review, solution-diffusion imperfection model is a good model to describe the mass transport of both small and large solutes in an organic solvent system, as it considers the effects of both convection and diffusion. However, the description of solute and solvent fluxes can be best described by the Flory-Huggins model paired with linearized Maxwell-Stefan model, where the ternary interactions between solute, solvent and membrane polymer can be taken into account. As for the pore-flow

model, it is best to be used when a membrane having large pores, such as ultrafiltration membrane is involved.

For the investigation of the effect of concentration polarization, there are various ways to describe its effects. The variation in the description of concentration polarization is mostly due to the method of mass transfer coefficient estimation. From the review, the selection of concentration polarization model is based on the assumption made for the organic solvent system. The description of concentration polarization can be solely based on the diffusion or convection depending on the type of transport model selected for the mass transfer estimation.

Acknowledgement
This research was funded by a grant from trans-disciplinary research grant UTM-TDR 31.2 (T2) (Vot no. 06G42) and UTM Zamalah Scholarship.

References

[1] Chai, C. and Armarego, W.L.F. (2003). *Purification of Laboratory Chemicals,* Elsevier Science, Great Britain.
[2] Marchetti, P., Jimenez Solomon, M.F., Szekely, G. and Livingston, A.G. "Molecular separation with organic solvent nanofiltration: a critical review." *Chemical reviews* 114 (2014): 10735-10806.
[3] Bodzek, M. "Membrane techniques in air cleaning." *Polish Journal of Environmental Studies* 9 (2000): 1-12.
[4] Baker, R.W. (2007). *Membrane Technology and Applications,* John Wiley and Sons, England.
[5] Priske, M., Lazar, M., Schnitzer, C. and Baumgarten, G. "Recent applications of organic solvent nanofiltration." *Chemie Ingenieur Technik* 88 (2016): 39-49.
[6] Marchetti, P. and Livingston, A.G. "Predictive membrane transport models for Organic Solvent Nanofiltration: How complex do we need to be?" *Journal of Membrane Science* 476 (2015): 530-553.
[7] Kedem, O. and Katchalsky, A. "A physical interpretation of the phenomenological coefficients of membrane permeability." *The Journal of general physiology* 45 (1961): 143-179.
[8] Spiegler, K. and Kedem, O. "Thermodynamics of hyperfiltration (reverse osmosis): criteria for efficient membranes." *Desalination* 1 (1966): 311-326.
[9] Wijmans, J.G. and Baker, R.W. "The solution-diffusion model: a review." *Journal of Membrane Science* 107 (1995): 1-21.
[10] Lonsdale, H., Merten, U. and Riley, R. "Transport properties of cellulose acetate osmotic membranes." *Journal of Applied Polymer Science* 9 (1965): 1341-1362.
[11] Peshev, D. and Livingston, A.G. "OSN Designer, a tool for predicting organic solvent nanofiltration technology performance using Aspen One, MATLAB and CAPE OPEN." *Chemical engineering science* 104 (2013): 975-987.
[12] Werth, K., Kaupenjohann, P., Knierbein, M. and Skiborowski, M. "Solvent recovery and deacidification by organic solvent nanofiltration: Experimental investigation and mass transfer modeling." *Journal of Membrane Science* 528 (2017): 369-380.
[13] Postel, S., Wessel, S., Keil, T., Eiselt, P. and Wessling, M. "Multicomponent mass transport in organic solvent nanofiltration with solvent mixtures." *Journal of Membrane Science* 466 (2014): 361-369.
[14] Campbell, J., Burgal, J.D.S., Szekely, G., Davies, R., Braddock, D.C. and Livingston, A. "Hybrid polymer/MOF membranes for Organic Solvent Nanofiltration (OSN): Chemical modification and the quest for perfection." *Journal of Membrane Science* 503 (2016): 166-176.
[15] Shi, B., Peshev, D., Marchetti, P., Zhang, S. and Livingston, A.G. "Multi-scale modelling of OSN batch concentration with spiral-wound membrane modules using OSN Designer." *Chemical Engineering Research and Design* 109 (2016): 385-396.
[16] Blumenschein, S., Böcking, A., Kätzel, U., Postel, S. and Wessling, M. "Rejection modeling of ceramic membranes in organic solvent nanofiltration." *Journal of Membrane Science* 510 (2016): 191-200.
[17] Zedel, D., Kraume, M. and Drews, A. "Modelling and prediction of organic solvent flux and retention of surfactants by organic solvent nanofiltration." *Journal of Membrane Science* 544 (2017): 323-332.
[18] Abdellah, M., Liu, L., Scholes, C., Freeman, B. and Kentish, S. "Organic solvent nanofiltration of binary vegetable oil/terpene mixtures: Experiments and modelling." *Journal of Membrane Science* 573 (2019): 694-703.
[19] Bowen, W.R. and Welfoot, J.S. "Modelling the performance of membrane nanofiltration—critical assessment and model development." *Chemical engineering science* 57 (2002): 1121-1137.
[20] Wijmans, H. (2000). "Concentration polarization" *Encyclopaedia of Separation Sciences*, Academic Press, San Diego, USA, pp. 1682.

[21] Nakao, S., Wijmans, J. and Smolders, C. "Resistance to the permeate flux in unstirred ultrafiltration of dissolved macromolecular solutions." *Journal of Membrane Science* 26 (1986): 165-178.
[22] Van den Berg, G. and Smolders, C. "The boundary-layer resistance model for unstirred ultrafiltration. A new approach." *Journal of Membrane Science* 40 (1989): 149-172.
[23] Peeva, L.G., Gibbins, E., Luthra, S.S., White, L.S., Stateva, R.P. and Livingston, A.G. "Effect of concentration polarisation and osmotic pressure on flux in organic solvent nanofiltration." *Journal of Membrane Science* 236 (2004): 121-136.
[24] Zwijnenberg, H.J., Dutczak, S., Boerrigter, M., Hempenius, M.A., Luiten-Olieman, M.W., Benes, N.E., Wessling, M. and Stamatialis, D. "Important factors influencing molecular weight cut-off determination of membranes in organic solvents." *Journal of Membrane Science* 390 (2012): 211-217.
[25] Murthy, Z. and Chaudhari, L.B. "Application of nanofiltration for the rejection of nickel ions from aqueous solutions and estimation of membrane transport parameters." *Journal of Hazardous Materials* 160 (2008): 70-77.
[26] Murthy, Z. and Gupta, S.K. "Simple graphical method to estimate membrane transport parameters and mass transfer coefficient in a membrane cell." *Separation Science and Technology* 31 (1996): 77-94.
[27] Gekas, V. and Hallström, B. "Mass transfer in the membrane concentration polarization layer under turbulent cross flow: I. Critical literature review and adaptation of existing sherwood correlations to membrane operations." *Journal of Membrane Science* 30 (1987): 153-170.
[28] Fedors, R.F. "A method for estimating both the solubility parameters and molar volumes of liquids." *Polymer Engineering & Science* 14 (1974): 147-154.
[29] Fredenslund, A., Gmehling, J. and Rasmussen, P. (1977). *Vapor-liquid Equilibria Using UNIFAC: A Group-contribution Methods,* Elsevier Scientific, The Netherlands.

Penerbit Akademia Baru

Engineering Science and Technology Conference Proceedings

Journal homepage: www.akademiabaru.com/EST.html

Photo degradation of Biobased Oils Polymer blended with High Density Polyethylene upon Ultra Violet Irradiation Exposure

Open

Nurul Syamimi Mohd Salim[1], Anika Zafiah Mohd Rus[1,*], Nursaidatulsyida Sulong[1,2]

[1] Sustainable Polymer Engineering (SPEN-AMMC), Fakulti Kejuruteraan Mekanikal dan Pembuatan, Universiti Tun Hussein Onn Malaysia (UTHM), 86400 Parit Raja, Batu Pahat, Johor,Malaysia

[2] Fakulti Kejuruteraan Mekanikal, Universiti Teknologi MARA (UiTM), Cawangan Johor, Kampus Pasir Gudang, Jalan Purnama, 81750 Masai, Johor

ABSTRACT

Abstract. In the present study, bio based oils polymer which is ideal for high-heat applications due to its high cross-link and thermoplastic of High Density Polyethylene (HDPE) that is easily remolded and recycled was blended together. This is in advantage to eliminate the risk of the bio based polymer to re-melt when heat is applied and creating a new polymer blend. The blended polymer of HDPE with 30% bio based oils polymer via melt mixing technique using Brabender (B) and manually mixed (M) namely as HB and HM respectively. The injected samples in the form of dumbbell shape were then exposed to Ultra Violet (UV) irradiation at constant temperature of 50°C to characterize its photochemical stability. The FTIR spectroscopy were identify that both HB and HM have same functional group of C-H group at 2915 cm^{-1} and 2848 cm^{-1} attributed to the stretching vibration of the main backbone of blended structure. Both HB and HM shows similar peak at 1697 cm^{-1}- 1714 cm^{-1} which were contribute to C=O group in amide region as well as CH_3 bending peaks at 1472 cm^{-1} - 1462 cm^{-1}. The carbonyl Index (CI) for HB is the highest at 1000 hours UV irradiation exposure which is 1.1035 and the lowest at 500 hours with 0.77119. Meanwhile for HM at 500 hours UV irradiation exposure is 0.926 while the lowest is at 3000 hours with 0.5566. The CI values for HB and HM shows fluctuated trend due to degradation occurring under photo-oxidation circumstances is the chain scission accompanying with the cross-linking and the formation of the carbonyl group.

Keywords:
Biopolymers; high density polyethylene; thermal degradation; ultra-violet irradiation; Carbonyl Index (CI); fourier transformation infrared spectroscopy

Copyright © 2019 PENERBIT AKADEMIA BARU - All rights reserved

1.Introduction

Polyethylene (PE) is a semi crystalline thermoplastic and is the most widely produced polymer in the world, making it an important commercial polymer material nowadays [1-2]. It also serves as a model thermoplastic system due to its simple structure based on ethylene (CH_2-CH_2) repeat units with varying degrees of crosslinking and branching. One of the various types of PE, high-density PE (HDPE) is a linear form with low levels of branching, and consequently a higher density and degree of crystallinity. HDPE is commonly utilized due to its high ductility, toughness, and chemical resistance, for instance in geomembranes, pipelines, and plastic lumber [2]. According to [3], plastic bags are produced from one of three basic polymers: polyethylene, high density

* *Corresponding author.*
E-mail address: zafiah@uthm.edu.my (Anika Zafiah Mohd Rus)

polyethylene (HDPE), low density polyethylene (LDPE), or linear low-density polyethylene (LLDPE). Plastics are not toxic or harmful, however, plastic bags are manufactured using organic and inorganic additives such as colorants and pigments, plasticizers, antioxidants, stabilizers and metals make them against thermal decomposition then contributed to a great source of atmospheric pollution and ozone destruction [3].

In current scenario, renewable materials derived from vegetable oils are now widely developed for obtaining green polymers. Palm oil is one of the vegetable oils which contain unsaturated fatty acids such as oleic acid. The content of oleic acid in palm oil is about 30-40%. Oleochemical industries use oleic acid as the starting material for many important chemical reactions such as olefin metathesis, ozonolysis and epoxidation [4]. When compared to their petroleum-based counterparts, renewable materials can be degradable, sustainable, more environmentally friendly (lower greenhouse gas emission and fossil fuel usage) and/ or should be a renewable option to plastic product production. Despite certain limitations, bioplastics remain a front runner as a suitable replacement for petroleum-based plastic [5].

The important of renewable polymer is comes with its' degradation pathways. These could be started by heat (thermal degradation), light (photo degradation), ionizing radiation (radio degradation), mechanical action, or by fungi, bacteria, yeasts, algae, and their enzymes (bio degradation). Photo degradation is degradation of a photo degradable molecule caused by the absorption of photons, particularly those wavelengths found in sunlight, such as infrared radiation, visible light, and ultraviolet light. However, other forms of electromagnetic radiation can cause photo degradation. Photo degradation includes photodissociation, the breakup of molecules into smaller pieces by photons. A common photo degradation reaction is oxidation. Photo degradation also destroys paintings and other artefacts. Light is an induced polymer degradation, or photo degradation, includes the physical and chemical changes caused by irradiation of polymers with ultraviolet or visible light. In order to be effective, light must be absorbed by the substrate (polymeric system) [6].

Accelerating the degradation process of the blended biopolymer and petroleum based polymer by exposing it under UV irradiation exposure in Weatherometer is conducted. In this research, HDPE was blended with 30% of biobased polymer were prepared by two types of blending technique of melt mixing by using Brabender machine named as HB and secondly by manually mixing named as HM. Unexposed and exposed HB and HM to UV irradiation at constant temperature of 50°C for 500H, 1000H, 2000H and 3000 hours were prepared. Photostability by means of Fourier Transmittance Infrared (FTIR) spectroscopy is to observe the stability properties of HB and HB as well as the quantitative analysis of calculated carbonyl index (CI). This is also used to study the changes in surface chemistry of PE after weathering exposure as well as to monitor the carbonyl group formation, vinyl group formation, and changes in crystallinity of weathered polyethylene [7].

2. Materials & Instruments

2.1 High Density Polyethylene (HDPE) for HB

HDPE (HI1600) injection moulding grade with a density of 0.94 to 0.965 g / cm^3 and the HDPE melting point is 120 ° was supplied by Titan Petchem (M) Sdn. Bhd.

2.2 High Density Polyethylene (HDPE) for HM

High density polyethylene (HB0972) with density of 0.957 g/cm^3, melt index of 4 g/10 min and vicat softening point of 124°C was supplied by Lotte Chemical Titan Sdn. Bhd.

2.3 Bio-monomer

VeSawit Palm oil was used as the original palm oil to produce the virgin biomonomer (VM) for HB while waste palm oil is used as waste oil to produce waste monomer (WM) for HM. The conversion of the monomer starts with the catalyst preparation to generate the epoxies from the unsaturated fatty compound, and the second reaction is the opening of the acid catalyst ring of the epoxies to form polyols or bio-monomer [8-17].

2.4 Blended Biopolymer

Bio-monomer was mixed with cross linking agent that was 4, 4'-Methylene Diphenyl Diisocyanate (MDI). The mixture was vigorous stirred resulting viscous compound and left to cure at room temperature. The solid virgin oil biopolymer (VB) was cut into smaller size and then crushed using Pulverisette14 (Brand Fritch from Germany). 6 mm sieved at 14 000 rpm for 1 minute while the second cycle is using 0.75 mm sieve ring at 10 000 rpm for 2 minutes to collect VB in particle form. Then, by using BrabenderPlastograph® EC machine (from Germany), HDPE were added with VP at 30% loading (wt /wt of biopolymer) at 130°C and 25 rpm speed rate for 20 minutes. The blended biopolymer produced was crushes using Plastic Granulator SLM 50FY to produce smaller particle for HB production by using injection moulding.

2.5 Blended Biopolymer

The monomer was heated in an oven at 80°C until liquidized. Bio-monomer was mixed with flexible Polymethane Polyphenyl Isocyanate (Modified polymeric-MDI) with a viscosity at 25°C of 120-160 cps, specific gravity of 1.18-1.20 g/ml, NCO content and % wt of 26.3-27.3.The liquid bio-monomer and MDI was stirred together at 1:0.5 ratio to solidify at room temperature and namely as waste oil biopolymer (WP). Then, HDPE and 30% WP were mixed manually until homogenous. HDPE and WP blended is left for 30 minutes to solidify and ready for injection moulding.

2.6 Injection Moulding

The dog-bone tensile specimens namely as HB and HM respectively produce from brabender and manual mixed process were then fed to injection moulding machine (Nissei Horizontal Screw Type NP7 Real Mini, Japan). The barrel temperature set points from nozzle zone which is 170°C, 170°C for front zone, 165°C for middle zone, 160°C for rear 1 zone, 155°C for rear 2 zone and 70°C for feed zone.

2.7 Fourier Transform Infrared Spectroscopy (FTIR)

FTIR spectroscopy was conducted using Perkin–Elmer (UK) Spectrum One FT-IR spectrometer (in the range 4000–400 cm^{-1}, absorbance units) to provide detailed information of the functional groups present at the surface of samples. The scans were executed at 32 times scanning at resolution 4 cm^{-1}. The spectra were acquired using the spectrometer of Attenuated Total Reflection

(ATR). HB and HM were placed flat on the crystal plate for infrared spectroscopy analysis. The generated spectrum or fingerprint is used to identify the molecular composition of the materials. The Carbonyl Index (CI) was evaluated by following equation to obtain a quantitative comparison of the functional groups formed during the UV irradiation [18] [19].

$CI = A_{1715}/A_{2850}$

Where A_{1715} is the absorbance of carbonyl stretching vibration at 1715 cm^{-1}, and A_{2850} is the symmetrical stretching vibration of methylene at 2850 cm^{-1}.

3. Results & Discussion

Figure 1 show the overlay of FTIR spectra for HB and HM at 30% loading of bio-based polymer at different ultra-violet irradiation exposure hours. The C-H group, C=O group, CH_3 and C-O group (esters group) were assigned in Table 1 and Table 2. The 2914 cm^{-1} and 2848 cm^{-1} functional group are referring to C-H structure. Previous researcher was identifying that the frequency of C-H group is at 3000 cm^{-1} - 2850 cm^{-1} [25-26]. Another peaks of 1698 cm^{-1} to 1701 cm^{-1} is contributing to C=O group in amide region while 1472 cm^{-1} - 1310 cm^{-1} is assigned to the CH_3 bending peaks. Meanwhile a strong intensity absorptions near 1000 cm^{-1} - 1300 cm^{-1} indicating the esters group (C-O). FTIR spectra verified that nearly all the diisocyanate groups was reacted during polymerization and urethane linkages and amide groups due to disappearance of 2254 cm^{-1}- 2310 cm^{-1} peak. This is a characteristic of isocyanate (-N=C=O) group of the MDI [20,21].

As refer to Figure 1, the intensity of the absorbance for HB peaks gradually increased with the increasing of UV irradiation exposure hours. The highest intensity for HB is at 2000H exposure while the lowest intensity is at 500H exposure for all peaks. The absorbance intensity of C-H group and C=O group for HB at 2000H are 0.45A and 0.30A respectively. Meanwhile, at 500H exposure, the absorbance intensity for C-H and C=O is 0.32A and 0.18A respectively. By increasing the exposure time, the carbonyl and ester groups increased at approximately the same rate for all exposure time. This is to suggest that the carbonyl and ester group formation after weathering is known to be proportional to the number of chain scissions in the polymer. According to [22], polyolefin is well known to mainly undergo two chain fracture reactions, Norrish I and Norrish II, under UV irradiation, affording a carbonyl group and a vinyl group, respectively. The short chain undergoes a cross-linking reaction. In the Norrish I reaction, the resulting free radicals can attack the polyolefin, which may lead to chain scission or crosslinking. In the Norrish II reaction, vinyl groups and terminal carbonyl groups are produced, and a chain scission occurs.

The intensity of HM absorbance peaks shows decreasing with increasing in UV irradiation exposure hours. The highest intensity absorbance is at 500H exposure with 0.44A for C-H peak and 0.29A for C=O peak while the lowest intensity is at 3000H exposure with the intensity for C-H is 0.26A and for C=O is 0.12A. This decreases in intensity of C-H bond absorption after UV irradiation exposure indicated that a large number of C-H bonds were consumed during the photooxidation reaction by converted them into free radicals and removing the hydrogen atom during the initiation step. It is also could be due to the reaction with a peroxy radical to form hydroperoxide and another free radical during the propagation step [23].

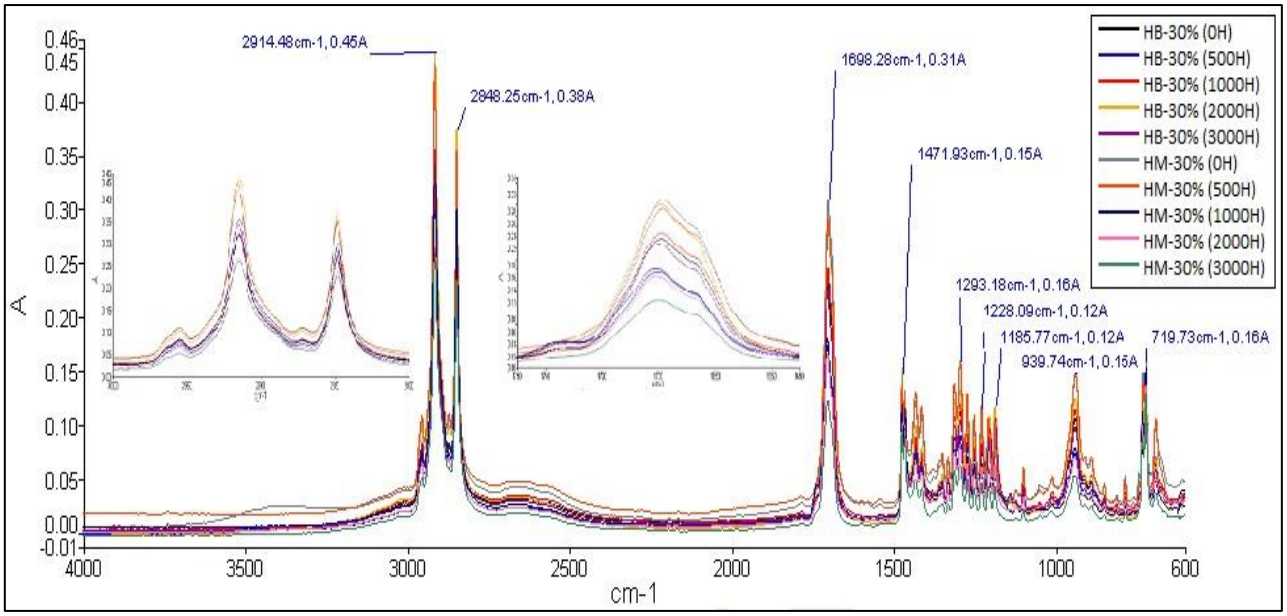


Fig. 1. Overlay of FTIR spectra for HB and HM at 30% loading of BP at different UV irradiation exposure (H)

Table 1
Wavenumbers (cm^{-1}) assigns to IR bands of HB at different UV irradiation (H)

Wavenumbers (cm1) / Assignments of IR bands	0 hours	500 hours	1000 hours	2000 hours	3000 hours
C-H (stretching)	2914/ 2848	2914/ 2848	2914/ 2848	2914/ 2848	2914/ 2848
C=O	1698	1701	1698	1698	1699
CH_3 bending	1471	1472	1471	1471	1472
C-O (Esters Group)	1293-1186	1290-1184	1293-1186	1293-1185	1292-1099

Table 2
Wavenumbers (cm^{-1}) assigns to IR bands of HM at different UV irradiation (H)

Wavenumbers (cm1) / Assignments of IR bands	0 hours	500 hours	1000 hours	2000 hours	3000 hours
C-H (stretching)	2915/ 2848	2915/ 2848	2915/ 2848	2914/ 2848	2914/ 2848
C=O	1698	1698	1700	1700	1699
CH3 bending	1471	1471	1472	1472	1472
C-O (Esters Group)	1293-1185	1293-1186	1293-1185	1293-1185	1293-1185

Figure 2 illustrates the formation of carbonyl group (CI value) as the function of UV irradiation exposure (H). The carbonyl index (CI) is the most commonly used indicator to measure the chemical oxidation of polyolefins such as polyethylene and polypropylene which reflect the degradation of the mechanical properties of these polymers [24]. In Figure 2, CI value for HB decrease at 500H exposure then increases at 1000H then gradually decrease at 2000H and 3000H. Meanwhile for HM the CI value decreases at 500H and 1000H then was increased back at 2000H. Increasing in CI value implying easy oxidation reaction occur due to increases aging time. According to [25], this indicates that photo-oxidative aging and cross-linking between molecular chains are in pair with rivalry reactions in the UV aging process that contributed to the increasing of CI value. Furthermore, CI

value for HB shows slight decreases at 2000H until 3000H while for HM the decreases up to 2000H and eventually increases again at 3000H. The decreases of CI value due to carbonyl groups formation were assumed to form macromolecular radicals that further combine to form new double bonds during the UV irradiation process of polyolefins. During the UV irradiation, the cross-linking structures are produced, which is the reason that the CI of HB and HM were decreases. The carbonyl group is interrupted by high-energy ultraviolet light to form free radicals during the degradation process, and the molecular chains with free radicals react with each other to form a new cross-linking structure.

The intensity absorbing and CI value for HB shows parallel to each other, which is at 500H shows lowest intensity with lowest CI value that is 0.7712. Meanwhile, the highest intensity absorption is at 2000H with the CI value is 0.9828. For HM, intensity absorbing, and CI value also shows parallel to each other at the lowest absorbing intensity with lowest CI value that is at 3000H with 0.5566 CI value respectively. For the highest intensity absorbance is at 500H with the highest CI value that is 0.925 also at 500H exposure. This shows a correlation agreement of the increment value between the intensity absorbance and CI during the oxidation process. The HB and HM shows different oxidation process occurs at different UV irradiation exposure (H) due to different starting bio oils being used for HB and HM which is VP and WP respectively as well as the blended technique and different crosslinking agent.

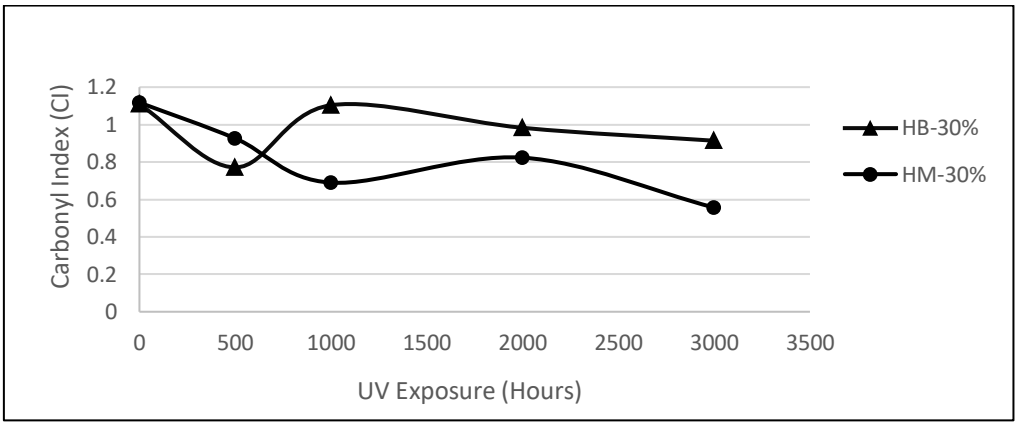


Fig. 2. Carbonyl index value of HB and HM

4. Conclusions

In this study, HB and HM was blended by using different technique with different origin biopolymer which is VP and WP also using different crosslinking agent. HB and HM were exposed to different exposure hour to identify the photodegradation process. HB shows the maximum oxidation process occur at 2000H while HM shows at 500H. UV exposure may cause photooxidative degradation which results in breaking of the polymer chains, produces free radical and reduces the molecular weight, causing deterioration of mechanical properties and leading to useless materials, after some period of time exposure.

Acknowledgement
The authors would like to thank the Ministry of Education Malaysia, University Tun Hussein Onn Malaysia (UTHM), Johor for supporting this research study under research grant GPPS Vot H359.

References

[1] Peng Zou, Hanguo Xiong and Shangwen Tang. “Natural weathering of rape straw flour (RSF)/HDPE and nano-SiO2/RSF/HDPE composites.” Carbohydrate Polymers. 73. (2008):378–383.
[2] Andrew Fairbrother, Hsiang-Chun Hsueh, Jae Hyun Kim, Deborah Jacobs, Lakesha Perry, David Goodwin, Christopher White, Stephanie Watson and Li-Piin Sung. “Temperature and light intensity effects on photodegradation of high-density polyethylene.” Polymer Degradation and Stability. 165. (2019):153-160.
[3] Jonathan-David Morales-Mendez and Ramon Silva-Rodríguez. “Environmental assessment of ozone layer depletion due to the manufacture of plastic bags.” Heliyon. 4. (2018).
[4] Desnellia, B., Mujahidina , D. Y., Permanaa and Radimana, C.L. “The Olefin Reaction between Crude Palm Oil Fatty Acid Methyl Ester (CPO FAME) and Ethylene Using Grubbs II Catalyst.” (2015).
[5] Harding, K. G., Gounden, T., and Pretorius. S. ‘“Biodegradable” Plastics: A myth of Marketing.” Procedia Manufacturing 7. (2017):106-110.
[6] Emad Yousif* and Raghad Haddad. “Photodegradation and photostabilization of polymers, especially polystyrene:Review.” (2013).
[7] Peng Zou, HanguoXiong and Shangwen Tang. “Natural weathering of rape straw flour (RSF)/HDPE and nano-SiO2/RSF/HDPE composites.” Carbohydrate Polymers. 73. (2008):378–383.
[8] Nurulsaidatulsyida Sulong and Anika Zafiah Mohd Rus. "Influence of TiO2 on Selfclean Bio Coating.” Applied Mechanics and Materials. 315. (2013): 399-403.
[9] Anika Zafiah Mohd Rus , Nur Abdullah and Mohammad Faiz Liew Abdullah, “Interconnected Interface Enhanced Electrical Properties of Graphite in Bio-based Epoxy from Insulating to Conductor Composites.” Indian Journal of Science and Technology. 8. (2015).
[10] Rahimah Abd Rahim , Anika Zafiah Mohd Rus and Anis Suraya Ahmad Bakhtiar. "Preliminary Fabrication of Polymer Membranes from Renewable Resources". Applied Mechanics and Materials. 315. (2013): 428-432.
[11] Anika Zafiah Mohd Rus. “ Polymers from renewable materials.” Science Progress. 93. (2010):285-300.
[12] Najibah Ab Latif and Anika Zafiah Mohd Rus. “Vibration Transmissibility Study Of High Density Solid Waste Biopolymer Foam.” Journal of mechanical engineering and science. 6. (2014):772-781.
[13] Anika Zafiah Mohd Rus and Nik Normunira Mat Hassan. “Thermal Degradation and Damping Characteristic of UV Irradiated Biopolymer.” International Journal of Polymer Science, vol. 2015, Article ID 615284, 11 pages, 2015.
[14] Mohd Khairul Zaimy Abd Ghani and Anika Zafiah Mohd Rus. "Influence of Hot Compression Moulding of Biopolymer Filled Waste Granulate Biopolymer.” Applied Mechanics and Materials. 315. (2013): 448-452, 2013
[15] Nik Normunira Mat Hassan, Anika Zafiah Mohd Rus, Nurulsaidatulsyida Sulong and Siti Rahmah Mohid. “Acoustic study based on sustainable green polymer treated with H2O.” Advance Materials Research. 74. (2013):281-285.
[16] Anika Zafiah Mohd Rus, Siti Rahmah Mohid, Nurulsaidatulsyida Sulong and Noraini Marsi. “Biopolymer doped with Titanium Dioxide Superhydrophobic Photocatalysis as Self-clean Coating for Lightweight Composite.” Advances in Materials Science and Engineering. (2013).
[17] Siti Rahmah Mohid, Anika Zafiah Mohd Rus and Nurul Hamizah Harun. “Influence of bio polymer composites as heat absorption coating.” Applied Mechanics and Materials. 315. (2013):404-407.
[18] Shichao Wang, Jun Zhang, Li Liu, Fan Yang, Yuhao Zhang. “Evaluation of cooling property of high-density polyethylene (HDPE)/ Titanium Dioxide (TiO2) composites after accelerated ultraviolet (UV) irradiation.” Solar Energy Materials & Solar Cells. 143. (2015): 120–127.
[19] L. Barbes, C. Radulescu, C. Stihi. “ATR-FTIR Spectrometry Characterisation of Polymeric Materials.” Romanian Reports in Physics. 66 (3). (2014): 765-777.
[20] Yongshang Lu, Richard C. Larock. “Soybean Oil-based, Aqueous Cationic Polyurethane Dispersions: Synthesis and Properties.” Progress in Organic Coatings. 69(1) (2010): 31-37.
[21] AD Macalino, VA Salen, LQ Reyes. “Castor Oil Based Polyurethanes: Synthesis and Characterization.” IOP Conference Series: Materials Science and Engineering. (2017): 229.
[22] Van Dinh Nguyen, Jianxiu Hao, Weihong Wang. “Ultraviolet Weathering Performance of High-Density Polyethylene/Wood-Flour Composites with a Basalt-Fiber-Included Shell.” Polymers. 10. (2018): 831
[23] Hongyu Cui, Riley Hanus, Michael R. Kessler. “Degradation of ROMP-based bio-renewable polymers by UV radiation.” Polymer Degradation and Stability. 98. (2013) 2357- 2365.
[24] C. Rouillon, P.-O. Bussiere, E. Desnoux, S. Collin, C. Vial, S. Therias, J.-L. Gardette. “Is carbonyl index a quantitative probe to monitor polypropylene photodegradation?.” Polymer Degradation and Stability. 128 (2016): 200- 208.
[25] Tiankai Jiang, Yanli Qi, Yuchen Wu, Jun Zhang. “ Application of antioxidant and ultraviolet absorber into HDPE: Enhanced resistance to UV irradiation.” e-Polymers. 19. (2019) : 499–510.

Penerbit Akademia Baru

Engineering Science and Technology Conference Proceedings

Journal homepage: www.akademiabaru.com/EST.html

Effectiveness of Stern Foil Application on High Speed Vessel To Reduce Total Resistance Using Computational Fluid Dynamics (CFD) Method

Open Access

Muhammad Arif Budiyanto [1,*], Hadi Tresno Wibowo [1], Muhammad Aziz Murdianto[1], Muhamad Fuad Syahrudin[1]

[1] Department of Mechanical Engineering, Universitas Indonesia, Kampus Baru UI Depok, Jawa Barat, Indonesia. 16424

ABSTRACT

Stern Foil is an innovation that can be used on patrol boats. This innovation uses the same principles as Ductile and Interceptor but by using Hydrofoil. Ductile and Interceptor are used to reduce the Wetted Surface Area (WSA) of the transom by making vortex under the transom, this kind of change will increase speed and reduce the total resistance of the ship. And Hydrofoil is a tool like wings on a plane that will be used on ships. This study aims to analyze the effect of Stern Foil mounted on patrol boats with hydrodynamic parameters using 3˚ and 0˚ Stern Foil, Froude Number 0.6 - 1.3 with service load at 2 kg. This research was conducted using the Computational Fluid Dynamics program. From the simulation results concludes that the optimal work for stern foil is at service load (2 kg), with a reduction in resistance of about 23,26% and 26,70% respectively with Stern Foil 3˚ and 0˚ in Froude Number 1.1 and Froude Number 0.9.

Keywords:
Patrol Boat; hydrofoil; stern foil; ship resistance

Copyright © 2019 PENERBIT AKADEMIA BARU - All rights reserved

1. Introduction

Fuel efficiency is the main problem in terms of vehicle design, both land, air, and even sea vehicles. In the efficiency of marine vehicles, specifically the ship, is affected by ship resistance where the way to minimize the resistance is to optimize the form of the hull [1]–[3]. Reducing ship resistance could be achieved in various ways such as reducing wave or friction resistance with the use of stern flaps [4], and / or tshe use of hydrofoils that can lift the hull above the water surface thereby reducing resistance and increasing efficiency more than planning hulls [5]. There is also an interceptor that produces lift such as hydrofoil but with a different principle [6], called vortex, and the use of stern foil under transom hull. This technology was invented by Van Oossanen and was named Hull Vane. In a study with 64m Holland Class OPV yachts and 108m Holland Class OPV, Hull Vane succeeded in reducing ship barriers by 26.5% and 15.3% respectively [7], [8]. In the study also stated that there was a fuel reduction of 15.3% with a speed of 17.5 knots in the Holland Class 108m OPV.

In addition to reducing the resistance, Hull Vane also affects the ship's pitch motion and wave resistance [9]. This was demonstrated in research using a 167m Ropax Vessel Norbank and 167m

* *Corresponding author.*
E-mail address: arif@eng.ui.ac.id (Muhammad Arif Budiyanto)

Container Vessel Rijinborg vessel with simulation and experimentation method stated that the pitch motion decreased by 9.7% and 4.9% respectively, with 2m wave height, reducing wave resistance by 17.3% and 4.46%.

With the same boat as Andrews, et al., (2015), which is AMERC Series # 13 Patrol Vessel [10], a comparative study between the use of Hull Vane, trim wedges, interceptors, and ballasting is done by Uithof, et al., (2016) showing that the Hull Vane has the greatest reduction in resistance on Fn 0.35 specifically 32.4% [11]. In other studies with different series, namely # 3, # 4, # 8, # 11, and # 13 at Fn 0.5-0.7 by Avala, (2017) using Hull Vane, indicating that there was a 4% reduction in resistance, - 10%, 18.3%, 21.3%, and 12.3% [12].

Objective of this research is to calculate application of stern foil on patrol boat using asymmetry NACA foil to generate lift force. Displacement were specified as a different service load. Researchers set the stern foil parallels to the keel at the angle of 3° counter clockwise towards x-axis to prove additional translation force on x-axis. Furthermore, this research carried out simulation with Froude number range between 0.6 - 1.3 and validated with experimental data. This Froude number value based on high speed vessel category which was above 0.5.

2. Design of Ship Model and Simulation Method

2.1 Particular dimension of ship model with stern foil

The ship model used in this study is the Mark VI Patrol Vessel which has a high speed and unique slender body model [13], [14]. The simulation was conducted with ANSYS (Fluent) Student Version on Froude Number 0.6-1.3 which is different to another researches before that used Froude Number below 1. The model used uses a ratio of 1: 25.8, where the dimensions and plan of the ship are being illustrated on Table 1 and Fig. 1:

Table 1. Scaled ship's dimension

Model	
L (m)	1
B (m)	0.2403
T (m)	0.0465
Cb	0.3751

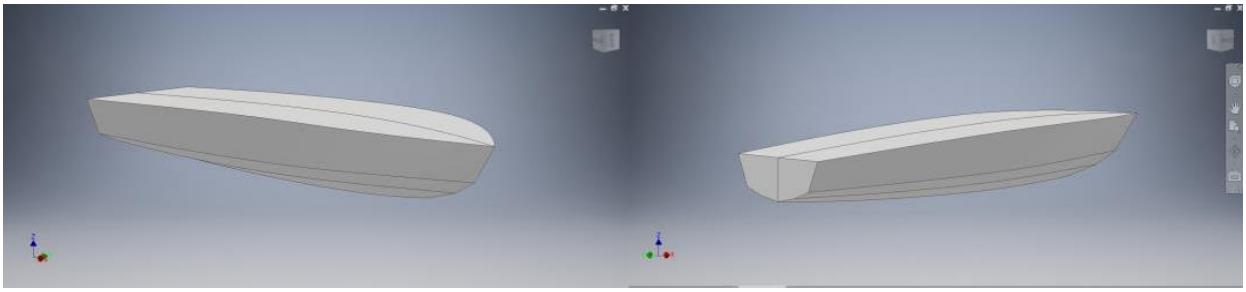


Fig. 1. Patrol hull design without stern foil

Stern foil used was asymmetrical NACA 4412[15] because of this type of NACA is most often used and researched by researchers, besides that, the lifts produced at NACA were designed to reach 80% of ship load. With this provision, the NACA 4412 chord line was obtained by 4 cm and with a span of 20 cm as shown in Fig. 2. This study also uses symmetrical NACA 0010 as a strut which is connected the stern foil and ship.

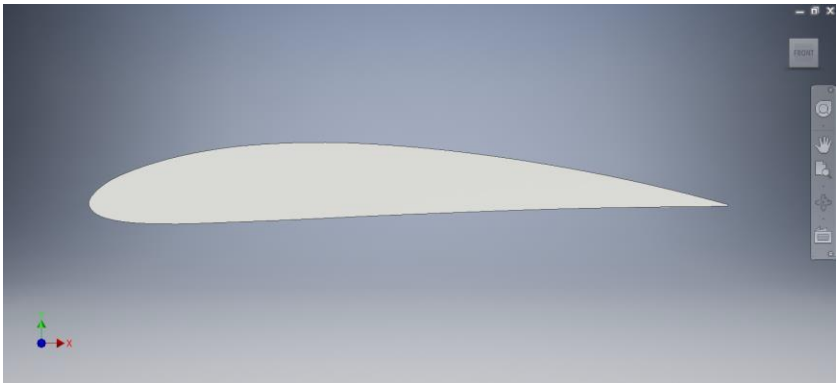


Fig. 2. *Side view hydrofoil* NACA 4412

The stern foil was below the keel with trailing edge equal to transom equally. In addition, the depth of the stern foil is 1.5 c (6 cm) from the water surface based on Velingga, (2009) with an angle of attack 3˚ and also 0 ˚ towards the x-axis. The configuration described is illustrated on Fig. 3.

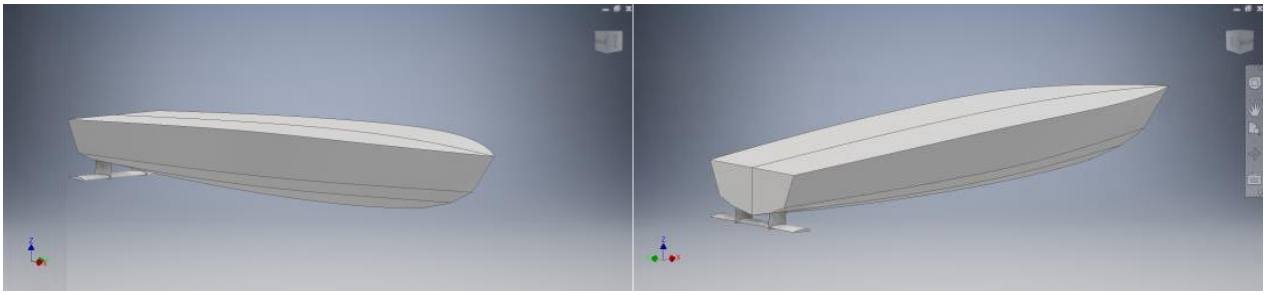


Fig. 3. Configuration of stern foil on the transom of Patrol hull

2.2. Simulation Method

In this study, researchers used Ansys Fluent as a computational fluid dynamics media for multi-fluid [16]. Reynold's Averaged Navier Stokes (RANS) equation became the basis of this simulation, using k-ω SST as tubulent and incompressible flow media, the equation will go down to equation (2) and (3) [17] :

$$\frac{\partial_{(\rho k)}}{\partial_t} + \frac{\partial_{(\rho u_j k)}}{\partial x_j} = P - \beta^* \rho \omega k + \frac{\partial}{\partial x_j}\left[\left(\mu + \sigma_k \frac{\rho k}{\omega}\right)\frac{\partial k}{\partial x_j}\right] \quad (1)$$

$$\frac{\partial_{(\rho k)}}{\partial_t} + \frac{\partial_{(\rho u_j \omega)}}{\partial x_j} = \frac{\gamma \omega}{k} P - \beta \rho \omega^2 + \frac{\partial}{\partial x_j}\left[\left(\mu + \sigma_\omega \frac{\rho k}{\omega}\right)\frac{\partial k}{\partial x_j}\right] + \frac{\rho \sigma_d}{\omega}\frac{\partial k}{\partial x_j}\frac{\partial \omega}{\partial x_j} \quad (2)$$

Where β, β*, γ, σk, and σd are closure constant coefficient and $P = \tau_{ij}\frac{\partial U_i}{\partial x_j}$, this simulation was incompressible flow, so P = 0. Boundary conditions for models in Fig. 4 were following ITTC[18], [19], as follows, Inlet is 1-L from the bow of the model ship (where L is LWL), with input fluid velocity equal to ship speed (because the ship is stationary and fluid moves towards the ship) . The outlet is 2-L from the ship's transom with incompressible flow option. The top and bottom of the

wall are respectively at 0.25 L from the deck and 1-L from the keel. And the side of the wall is 1-L from the longitudinal axis. The model and wall are defined as no-slip conditions but with the addition of the numerical beach option to damp wave near the outlet [20]. The ship model is free to moves pitch and heave, but the other 4 DOF are prohibited by using UDF, where moment of inertia (IYY) and product of inertia (IXZ) are specified [21]. In addition, the weight of the ship is also specified according to the draft (2 kg).

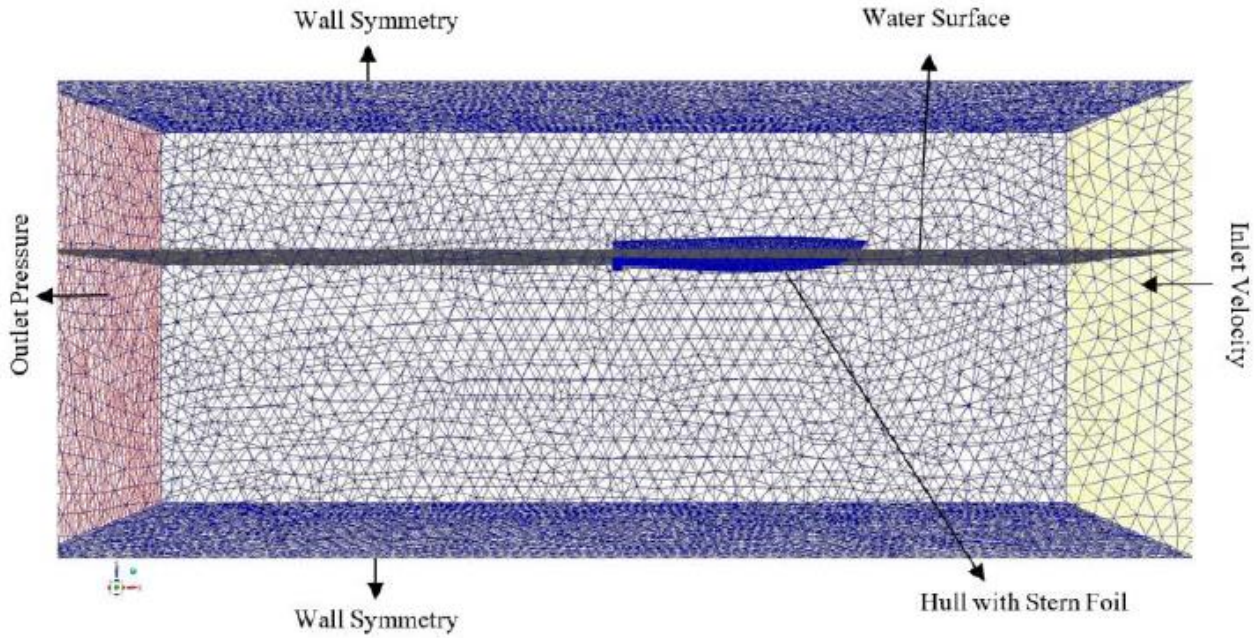


Fig. 4. Boundary condition of simulation model

3. Result and Discussion

3.1. Turbulent Intensity

Figure 5 shows the turbulent intensity at the same Froude Number that is 0.9 with half-full loading, which in this Froude Number has the greatest reduction of resistance among other Froude Numbers with stern foil 0˚. As shown in the red circle, the greatest turbulent intensity when not using stern foil 0˚ based on the scale in the figure ranged from 34.5% -37.7% and when using stern foil 0˚ ranged from 30% -40%. However, the turbulent intensity far behind the transom when using stern foil 0˚ is in the range of 20% -30%, this certainly affects the magnitude of the ship resistance. Figure 6 illustrates the difference when using and not using stern foil 3˚ during Froude Number 1.1 with a loading of 2 kg which in this condition stern foil can reduce resistance by 23.268%. The greatest turbulent intensity shown by the red circle according to the color and scale that exists when not using and using stern foil respectively around 39.3-42.9% and 33.8-39.4%, and also the flow far behind the transom has a intensity of turbulence that is smaller is around 22.6-28.2%. This difference also affects the wetted surface area where there are differences in the waves created by hull when using and not using stern foil 3˚. This is illustrated in Figure 7 which shows that the conditions under the back of the transom are very dry and uniform when using stern foil 3˚.

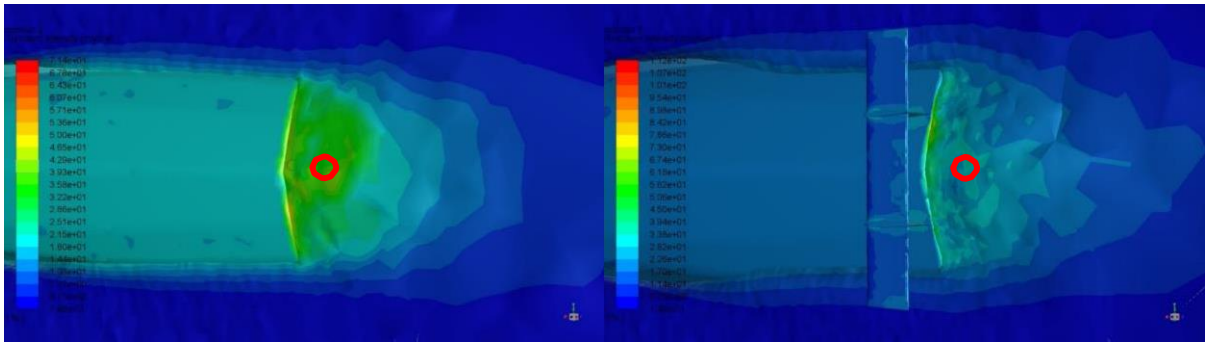


Fig. 5. Turbulent intensity stern foil 0˚ with 2 kg loading condition on Froude Number 0.9

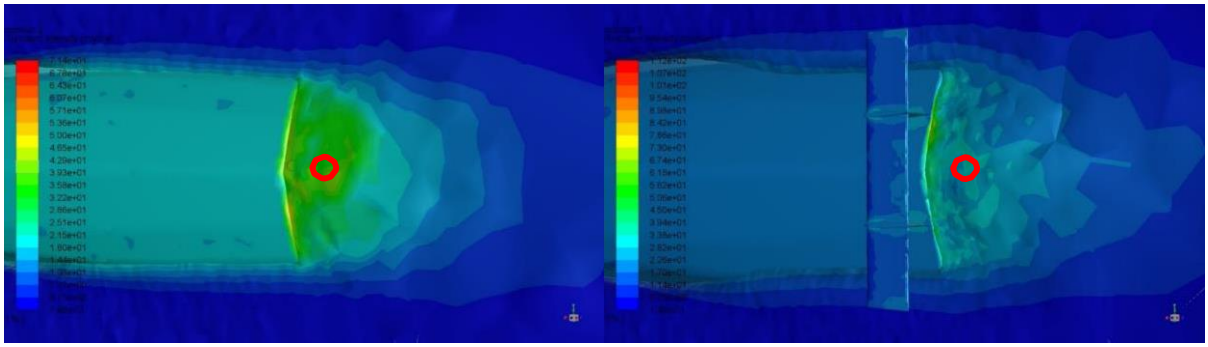


Fig. 6. Turbulent intensity stern foil 3˚ with 2 kg loading on Froude Number 1.1

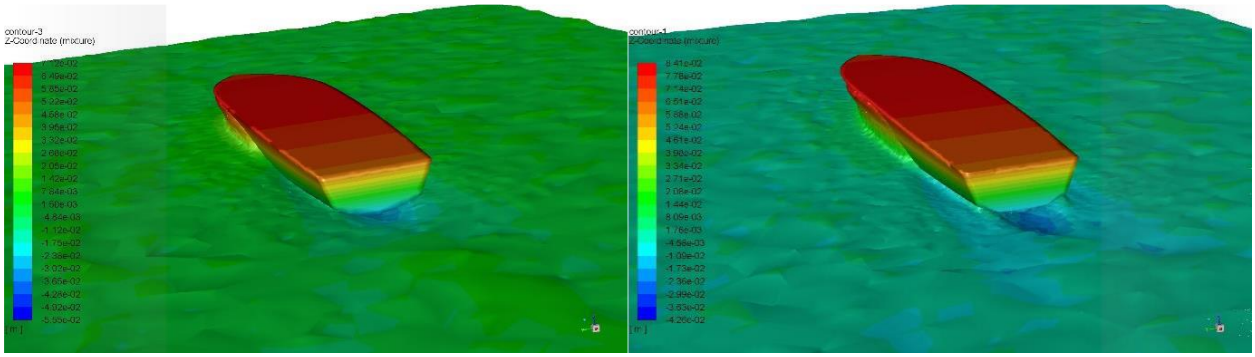


Fig. 7. Volume of Fraction comparison without and using stern foil 3˚ (stern view)

3.2. Effective to Reduce Total Resistance

Figures 7 and 8 show that the stern foil 0˚ and 3˚ are quite optimal in a half-full vessel condition or with a load of 2 kg. Seen in the trend line referred to starting Froude Number 0.7 shows a significant difference from when not using stern foil 3˚. Reduction of total resistance occurred around 3.218% - 23.268% compared to the model of the ship without a 3˚ stern foil. The total reduction occurred at Fn 1.1 around 23.268% which is in accordance with the experimental results. Furthermore, a total decrease of 20% occurred in the compilation of Froude Numbers above 1, 23.268%, 21.86%, and 21.455% in Froude Numbers 1.1, 1.2, and 1.3, which showed that stern foil 3 ˚ works more effectively on Froude Figures above 1. This proves about which increases the power produced in the stern foil Compared to the effective stern foil 3˚ at Fn> 1, with an angle of attack 0˚, the effectiveness of the total resistance reduction occurs at around Fn < 1, Further Froude Number 0.7 - 0.9 when related to corresponding reductions reached 7.795%, 18.865%, and 26.705%. In addition, the reduction of total resistance is less effective at Fn≥1 compared to stern foil 3˚. And also, the reduction of total resistance occurs around 7.795% - 26.705% with the highest

reduction value occurring at Froude Number 0.9, then increasing due to the increase in Froude Number respectively about 17.338%, 16.554%, 13.305%, and 14.743% at Fn 1, 1.1, 1.2 and 1.3. The difference is that due to the ship planning or trimming the rear the greater the angle, the thing that affects the angle of attack on the stern of the foil becomes greater with respect to the x axis which causes obstacles to be higher by 3˚.

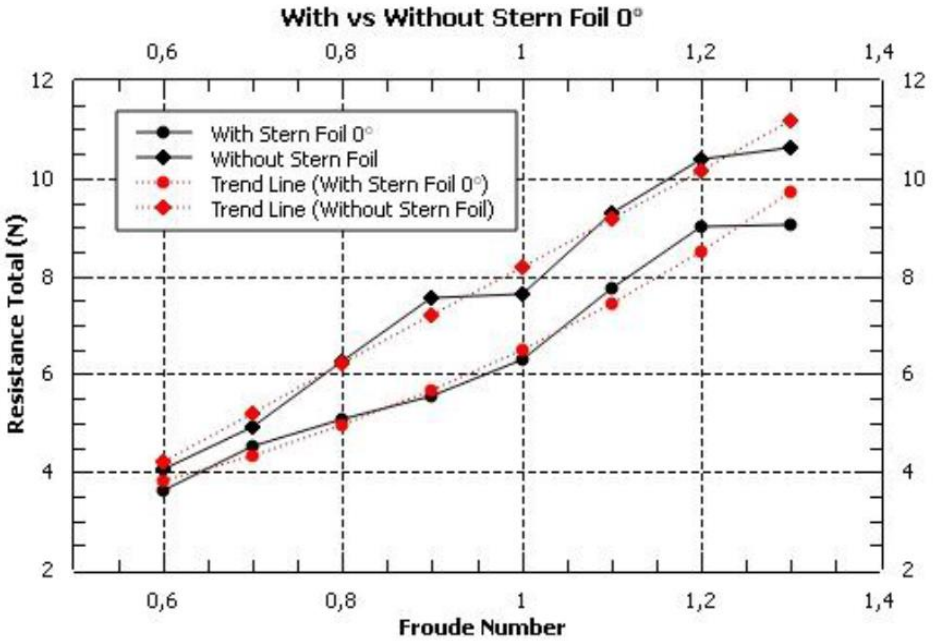


Fig. 8. Comparison application of stern foil using 0 ˚ angle

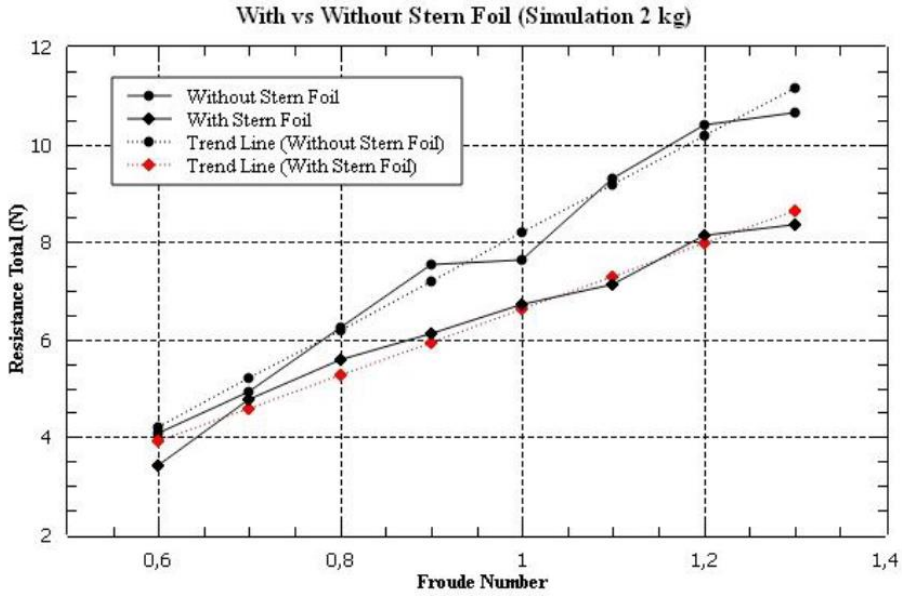


Fig. 8. Comparison application of stern foil using 3 ˚ angles

4. Conclusion

Simulations with the CFD method have been carried out on patrol vessels using stern foil. Based on the data and analysis of the research, the following conclusions can be concluded from the

model simulated with different loading, stern foil works optimally at a load of 2 kg, either by using 3 ern stern foil or 0 ˚ stern foil. In 3˚ stern foil, the optimum resistance reduction occurred in Froude Number 1.1 - 1.3 with the reduction of successively 23.268%, 21.86%, and 21.455% where in Froude Number 1.1 had the largest reduction reduction. Whereas at 0˚ stern foil, the reduction of optimal resistance occurs in Froude Number 0.7 - 0.9 with the reduction of successively 7,795%, 18,865%, and 26,705% where in Froude Number 0.9 has the largest resistance reduction.

Acknowledgements

Authors would like to thanks to Directorate of Research and Community Engagements (DRPM) Universitas Indonesia for providing grant PITTA B contract number NKB-0761/UN2.R3.1/HKP.05.00/2019. Authors also thanks to Department of Mechanical Engineering, Faculty of Engineering, Universitas Indonesia for supporting facility equipment.

References

[1] E. F. Campana et al., “A multi-objective DIRECT algorithm for ship hull optimization,” Comput. Optim. Appl., vol. 71, no. 1, pp. 53–72, 2018.
[2] M. Diez, A. Serani, and E. F. Campana, “CFD-based Stochastic Optimization of a Destroyer Hull Form for Realistic Ocean Operations,” 14th Int. Conf. Fast Sea Transp. - FAST 2017, pp. 1–9, 2017.
[3] K. Suastika, A. Hidayat, and S. Riyadi, “Effects of the Application of a Stern Foil on Ship Resistance: A Case Study of an Orela Crew Boat,” Int. J. Technol., vol. 8, no. 7, p. 1266, 2017.
[4] K. wei Song, C. yu Guo, J. Gong, P. Li, and L. zhou Wang, “Influence of interceptors, stern flaps, and their combinations on the hydrodynamic performance of a deep-vee ship,” Ocean Eng., vol. 170, no. January, pp. 306–320, 2018.
[5] R. Vellinga, “Hydrofoils Design Built Fly” 1st Edition, January, 2009.
[6] G. Avci and B. Barlas, “An experimental investigation of interceptors for a high speed hull,” Int. J. Nav. Archit. Ocean Eng., vol. 11, no. 1, pp. 256–273, 2019.
[7] Bouckaert, K. Uithof, P. van Oossanen, N. Moerke, B. Nienhuis, and an van Bergen, “A Life-cycle Cost Analysis of the Application of a Hull Vane ® to an Offshore Patrol Vessel,” vol. 1, no. V, p. 10, 2015.
[8] K. Uithof, P. Van Oossanen, N. Moerke, P. G. Van Oossanen, and K. S. Zaaijer, “an Update on the Development of the Hull Vane ®,” 2015.
[9] K. Uithof, N. Hagemeister, B. Bouckaert, P. G. van Oossanen, and N. Moerke, “the Effects of the Hull Vane on Ship Motions of Ferries and Ropax Vessels,” Warsh. 2016 Adv. Technol. Nav. Des. Constr. Oper., no. May, p. 7, 2016.
[10] Andrews, V. K. Avala, P. Sahoo, and S. Ramakrishnan, “Resistance Characteristics For High-Speed Hull Forms with Vanes,” no. October, pp. 5–10, 2015.
[11] Uithof et al., “a Systematic Comparison of the Influence of the Hull Vane ® , Inter- Ceptors , Trim Wedges , and Ballasting on the Performace of the 50M Amecrc Series # 13 Patrol Vessel,” no. June, pp. 15–16, 2016.
[12] V. K. Avala, “CFD Analysis of Resistance Characteristics of High-Speed Displacement Hull Forms fitted with Hull Vane,” no. May, 2017.
[13] HamiltonJet, “‘MK VI Coastal Riverine Force’ JetBrief,”. 467, p. 651.
[14] U. S. N. E. C. Command, “MK V a t r o l o a t a c t h e e t a t r o l o a t a c t h e e t.”
[15] AirfoilTools.com, “NACA 4412.” [Online]
[16] ANSYS Inc., “Tutorial : Heave and Pitch Simulation of Ship hull moving through head sea waves Introduction Setup and Solution Preparation,” pp. 1–27, 2011.
[17] W. Zuo, “Introduction of Computational Fluids Dynamics,” 2015.
[18] ITTC - Recommended Procedures and Guidelines, “Practical Guidelines for Ship CFD,” 26th Int. Towing Tank Conf., 2011.
[19] ITTC, “Practical Guidelines for Ship Resistance CFD,” ITTC – Recomm. Proced. Guidel. 27th, pp. 1–9, 2014.
[20] Dorozhko, V. M., Bugaev, V. G., & Kitaev, M. V. (2015, July 27). CFD Simulation of an Extreme Wave Impact on a Ship. International Society of Offshore and Polar Engineers.
[21] Reza Yousefi, Rouzbeh Shafaghat, Mostafa Shakeri, Hydrodynamic analysis techniques for high-speed planing hulls, Applied Ocean Research, Volume 42, 2013, Pages 105-113, ISSN 0141-1187, https://doi.org/10.1016/j.apor.2013.05.004.

Penerbit Akademia Baru

Engineering Science and Technology Conference Proceedings

Journal homepage: www.akademiabaru.com/xx.html
ISSN: XXXX-XXXX

CFD Study on Impeller Effect on Mixing in Miniature Stirred Tank Reactor

Open Access

Adnan Ghulam Mustafa[1], Mohd Fadhil Majnis[1,*], Nor Azyati Abdul Muttalib[2]

[1] Department of Chemical and Petroleum Engineering, Faculty of Engineering, Technology & Built Environment, UCSI University Kuala Lumpur, Malaysia
[2] Department of Bioprocess Engineering, Faculty of Engineering, Universiti Teknologi Malaysia, Malaysia

ABSTRACT

This paper describes the effect of various designs of impeller in miniature stirred tank reactor towards the mixing of the calcium alginate beads with the milk using Computational Fluid Dynamics (CFD) software, ANSYS Fluent 19.2. The four different type of impellers are edge beater, 5-turbine blade, t-shape, and paddle. The impeller was simulated at different speeds of 150 rpm, 250 rpm, and 300 rpm. K-epsilon turbulence model was employed to simulate the flow distribution pattern of calcium alginate beads and the Multiple Reference Frame approach was used for the impeller rotation's simulation. The simulation results obtained have a good agreement with the experimental results in term of vortex formation. The simulation results obtained for contour plots were fitted well with the experimental results as well as with pattern of impeller flow which was also studied. As a result, an optimal design of the impeller that is able to produce good mixing can be achieved using CFD analysis. The obtained results are good relevant to choose the impeller design that can be used for mixing in miniature vessels. The result obtained can conclude that the edge beater blade took 10s to distribute the calcium alginate beads over the tank at 250 rpm compared to the other impellers and the times the impeller was run in the tank was even lesser than the other impeller. It can also conclude that the impeller which produce mixed flow pattern is better for the mixing of two-phase fluid mixing. The obtained results from CFD can also be used to scale up the mixing process in larger systems.

Keywords:
ANSYS fluent; computational fluid dynamics; multiple reference frame; turbulent mixing; two-phase mixing.

Copyright © 2019 PENERBIT AKADEMIA BARU - All rights reserved

1. Introduction

Various process industries such as chemicals, bio-chemicals, polymer, crystallization, mineral, food and pharmaceutical industries use fluid mixing to mix a phase of the fluid system (homogeneous mixing) or liquid with solid (heterogeneous mixing). Homogeneous mixing happens when the fluid is the same phase whereby heterogeneous mixing happens when the fluid is in different phase. Regarding the widespread of these processes in industries, mixing of the fluid is done in various ways and in many kinds of equipment such as stirred vessels, rotor-stator mixers, and static mixers. Stirred vessels among all the other mixers equipment are the most recorded common devices in mixing of fluid in the area of process application used. The reason of mixing

* *Corresponding author.*
Email address: fadhil@ucsiuniversity.edu.my (Mohd Fadhil Majnis)

fluids two or more phases in stirred vessels is to decrease the dead zone, which is inhomogeneity, in order to accomplish a required process result, for instance the decrease of heterogeneity in the liquid-solid system of the solid distribution. This would increase the yield of the product without the raw material wasting. In CFD, modelling of mixing of numerous fluids in single-phase system in impeller vessel of various configuration and design has been broadly validated. However, because of the deficiency in experimental information and limitations in the technique establishment has led to the method of the computational domain.

In this study, a different type of four impellers were used to find the effect of different impeller on the mixing of two-phase system which is solid as calcium alginate beads and liquid as milk. Types of impeller studied in this research were T-shape, edge beater blade, paddle blade and 5-turbine blade and studied the effect of impeller on the flow pattern of the milk. Computational Fluid Dynamic (CFD) was used to simulate and investigate all these effects and the result obtained were compared with experimental result to investigate the validity of experiment with the simulation result. Simulations were done using commercial software, ANSYS Fluent 19.2 solver and meshing was achieved by the hyper-mesh software. The standard k-epsilon (ε) model was used to set up the turbulent flow process and the multiple reference frames (MRF) approach used to model the impeller motion in a tank.

2. Methodology

A preliminary study is the step of data collection for the data input of the different impeller modelling. Therefore, the data input for this study was obtained from the research work by Muttalib [1] on the distribution of calcium alginate beads in the miniature stirred tank reactor associated with complete experiment validation and the result of the different impeller at different speed and whether vortex was formed. The distance from bottom of the tank to the impeller and diameter of each impeller is shown in Table 1 whereby C(cm) is the distance from the bottom of the tank; D(cm) is the diameter of the impeller; W(cm) is the width of the impeller.

Table 1
Dimension of impellers

Impeller Type	C(cm)	D(cm)	W(cm)
T-shape	0.4	1.8	0.5
5-Blade Turbine	0.1	1.8	0.8
Paddle	1.6	1.4	1.2
Edge Beater blade	0.1	1.9	2.1

The computational domain, as a consequence of using multiple reference frame (MRF) methods, the MRF frame was chosen in such a dimension so that all the impeller have the same size and dimension of it and it is necessary to be divided into two regions, as shown in Figure 1 inner domain containing all of the rotating elements (hub, blades and shaft), and the other containing the stationary parts (tank wall, base and other parts of shaft which is out of the inner domain) which is outer domain separated by three interfaces. MRF is chosen as it takes much less computational domain compared to the SG [2].

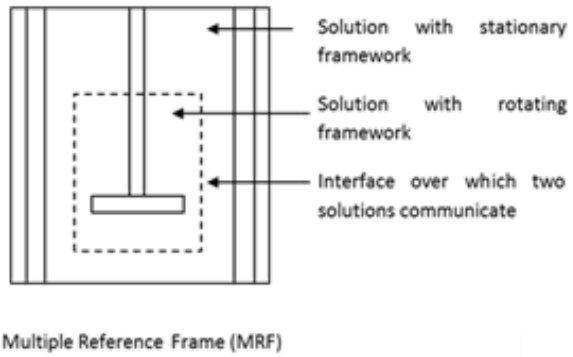


Fig. 1. Display show stationary and rotational zone

The design of each model was done using ANSYS 19.2 built-in software called Design-Modeler. After designing each part, Boolean (subtract section) was selected to make three section inner domain as MRF, impeller and outer domain the tank.

2.1 Meshing

The geometry of each design was imported to Hyper-mesh software to be meshed, the mesh size for this study for all the design was set to 0.1 cm. later the file was imported to mesh mode to generate in the mesh file for ANSYS Fluent solver.

2.3 Setup (Ansys Fluent)

After the mesh was generated and done naming on the boundaries in hyper mesh, it was then imported to ANSYS Workbench and imported into the solver, Fluent. The setup stage was divided into general, model, materials, cell zone conditions, boundary conditions and mesh interfaces. For this study, a pressure-based solver is chosen due to its suitability for this case whereby there are no density changes in the incompressible flow of milk. Then, the transient state was chosen instead of steady-state for this study because of the lab work which conducted certain impeller for to run for different time frame. For this study only two models are used for solving the algorithm which is viscous model and multiphase model. Multiphase model because of two phases of fluid was chosen whereby viscous model is the model for fluid flow in the system and in this case, k-epsilon is selected for the viscous model.

There are two fluid streams in this study, Calcium Alginate beads (solid) and milk which was chosen as water and some of the properties for both the fluid were changed accordingly to the experimental work. The properties of air were initially built-in in the Fluent Database where it only requires selecting it from the Fluent database and apply it to the material panel and then the air properties were changed to calcium alginate bead as shown in Table 2.

Table 2
Physical properties of calcium alginate

Fluid	Calcium Alginate	Milk
Density	2117.3 kg/m^3	1030 kg/m^3
Molecular weight	1170.93	18.01528
Viscosity	-	0.002127
Diameter size	300 µm	-

In the boundary condition, impeller rotation speed was set up in rpm in z-axis and the simulation was run at three different speed as stated earlier. Time step size for all the design was specified as 0.05 for run of calculation for each computational design, different number of time step was specified as shown in Table 3. Maximum iteration for each time step was specified as 10 iteration/time step. The calculations were performed for all computational design and each of the design solutions converged after different time step for all of them.

Table 3
Number of iterations for different impeller

Impeller	Time Step Size(s)	Number of iterations	Time for impeller
T-shape	0.05	600	30
Edge Beater Blade	0.05	200	10
Paddle Blade	0.05	420	21
5-Turbine Blade	0.05	260	13

2.4 Post-Processing

This stage covers an important step which view/show the result analysis for the different shape and configuration of the impeller. Mixing of the fluid can be checked from the result of the volume fraction of milk and calcium alginate beads. The pressure drop should be low as possible for the good mixing and for high-efficiency impeller.

Contour plot was the function applicable in CFD-Post whereby it displayed the graphical results according to the data generated in Fluent. This function is significant because it allows the user to view the trend of the process happening in the domain and able to identify the exact location of the reaction happened during the simulation. In this study, the variables of contour plot that applied were velocity, pressure and volume fraction

3. Results

Result obtained were from the contour plot and different parameter which were observed were compared with the experimental work and discussion were done to validate for both data obtained.

3.1 Comparison Between Different Impeller Flow Pattern

Different impeller shows different flow for the calcium alginate bead which is important for the fluid mixing to identify the impeller flow pattern for the fluid. As can be observed from Figure 2 that the impeller pushes the fluid downwards producing one single loop in one direction that is along the axis of the miniature tank which is the indication for the axial flow pattern and single loop is due to the smaller gap between the impeller and bottom of the tank.

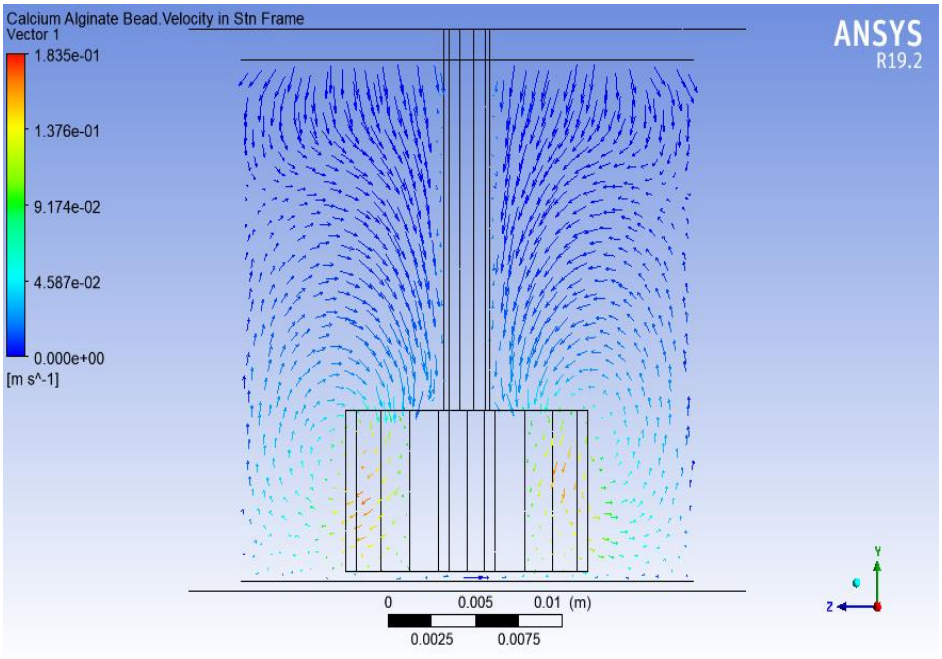


Fig. 2. Flow pattern for cross-section view of the 5-Turbine blade at 250 rpm

In Figure 3 can be observed that the t-shape blade produces the same flow pattern as for 5-turbine blade except it produces to two loops, it is also a radial impeller due to this flow pattern.

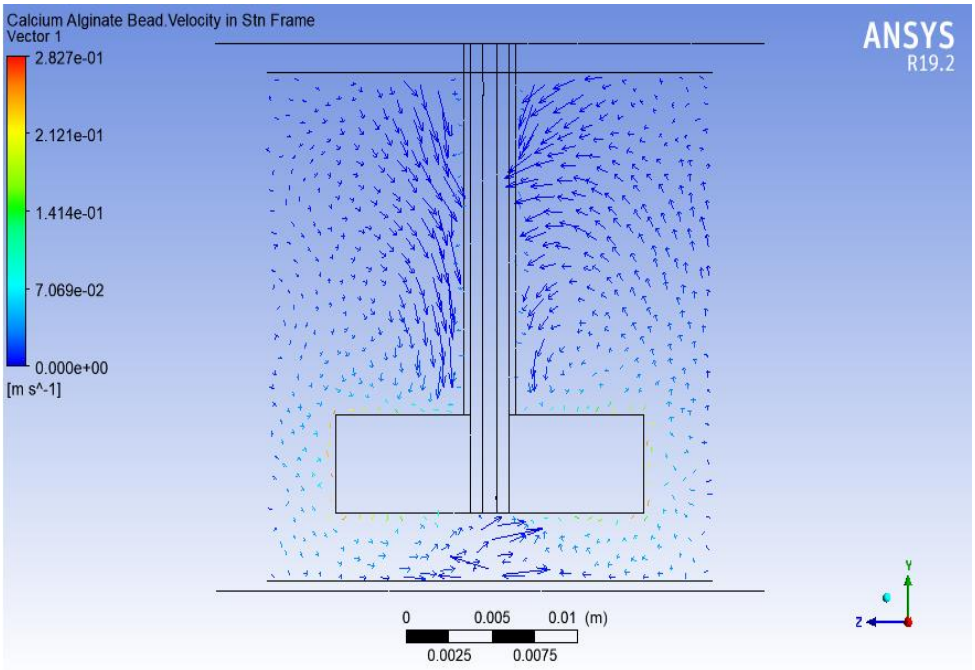
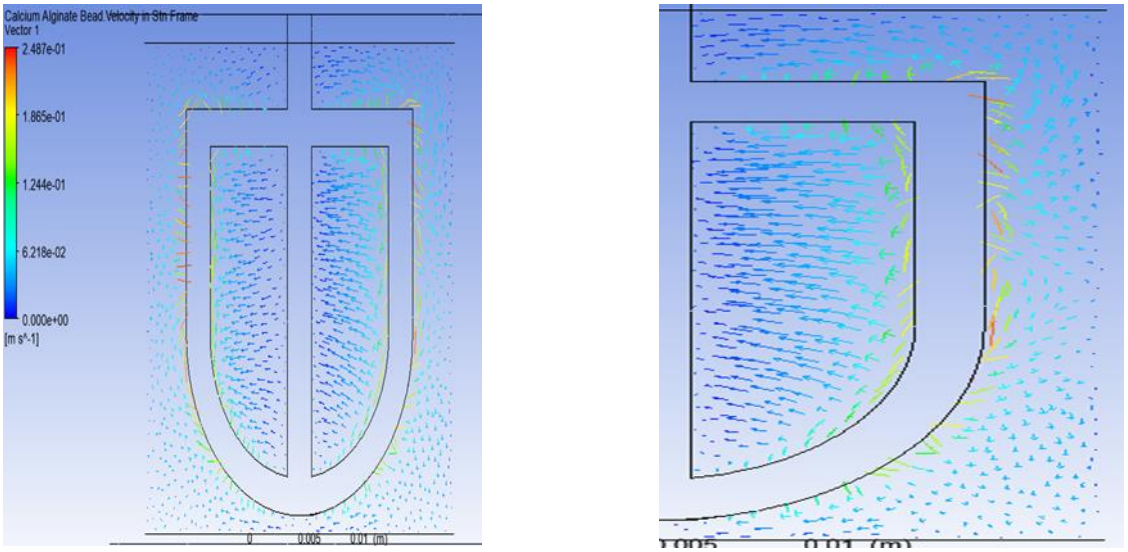


Fig. 3. Flow pattern for cross-section view of the 5-Turbine blade at 250 rpm

Edge beater blade is a radial flow impeller because of its large diameter and long height and its cover 90-95% of the tank diameter and are also known as clearance impeller [3] but in this study the diameter of impeller is 1.8 cm and the tank diameter is 3.2 cm so the ratio of impeller diameter to tank diameter is 59.4% which produces radial flow pattern, produces two loops flow pattern in opposite direction furthermore small rotational flow is produced as well in the between the impeller as it can be seen in Figure 4. So, can be concluded that this impeller flow pattern is mixed.



(a) b

Fig. 4. Edge beater blade flow pattern at 250 rpm a) front view b) half bade zoom-in

Lastly for the last impeller in Figure 5 the flow could not able to recognize the impeller flow from the front view so had to analyze it from the top view, whether it is radial or axial or mixed impeller. In Figure 6 shows that the impeller makes axial flow as all the vector plane was placed in the centre of the blade make the arrow in same direction.

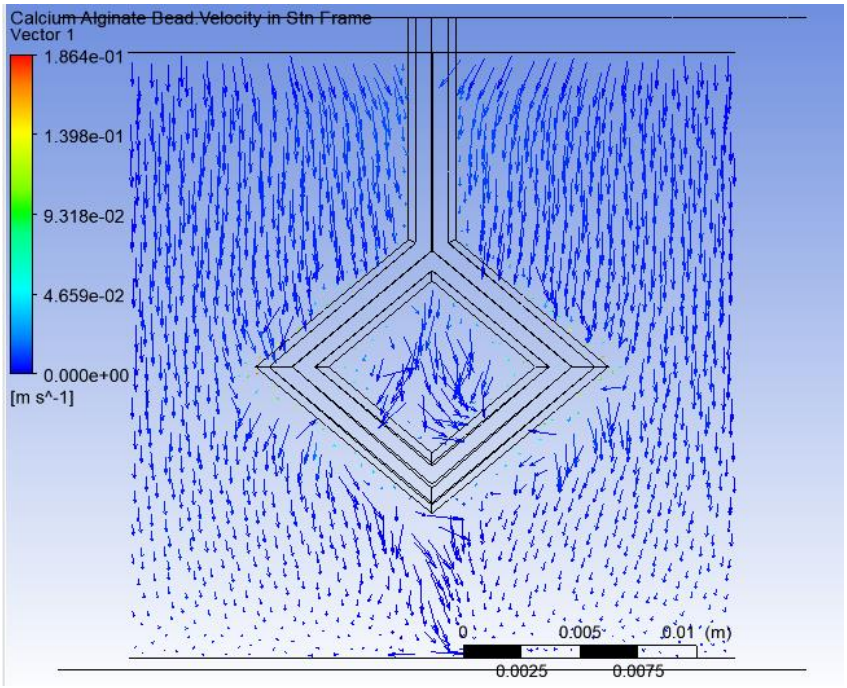


Fig. 5. Front view for paddle blade impeller flow pattern at 250 rpm

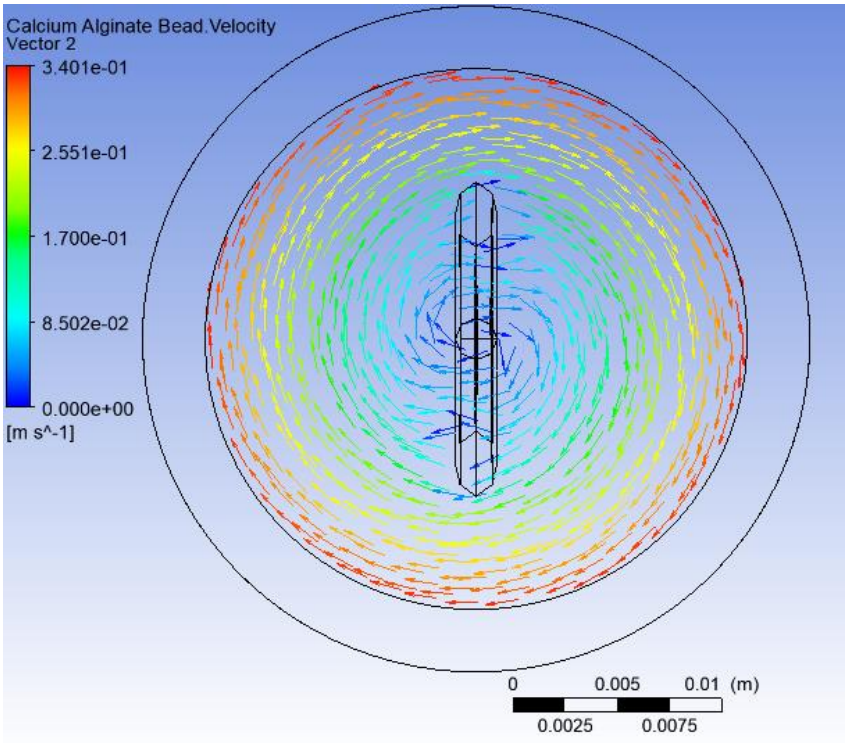


Fig. 6. Top mid-plane view for paddle blade impeller flow pattern at 250 rpm.

3.3 Impeller Speed Effect On The Fluid

The impeller speed rotation has great influence effect on the process of mixing as well as on the fluid motion. Subsequently, it also affects the efficiency of settling solid beads (calcium alginate) by the small change in the impeller speed of rotation. To achieve homogeneous mixing throughout the stirred vessel, the impeller must be run with optimum speed to accomplish the homogenous mixing and to avoid any vortex formation.

Figure 7 illustrates the volume fraction of the calcium alginate bead at 150, 250 and 300 rpm for the paddle blade impeller. At z-axis mid plane, all the simulation was run according to the time frame that was initially set for the experiment for each impeller as mentioned in Table 3. As it can see that for 150 rpm and 250 rpm there is only slightly changes and it is almost the same whereby for the 300 rpm the beads are all over the tank which indicates that at 300 rpm there is homogenous mixing which also indicates that 300 rpm is optimum impeller rotation speed for homogeneous mixing.

As mentioned above that it makes axial pattern flow by the impeller which pushes the beads downwards in the centre this is the reason for the accumulation of the solid beads at the centre at 150 rpm and 250 rpm. Y. Zhang et al. [4] also reported the phenomena when studied the effect of impeller on behaviour of suspending particle materials in stirred tank.

In Figure 8 can be observed that all three speed produces a different result and the running time for this simulation was 10s. At impeller speed of 150 rpm all the calcium alginate bead was half of the tank diameter without any formation of the vortex as it was mentioned earlier that such impeller is clearance impeller which means it will make radial flow pattern instead of axial flow.

At 250rpm a magnificent change can be observed for Figure 8. the axial flow produces two loops in opposite direction and the downward loop is more dominating which pushes the calcium alginate bead towards the bottom of the tank and also some fraction of beads is now above the impeller compared to the 150 rpm speed of impeller. At 300 rpm as compared to 250 rpm most of the beads are at the bottom of the tank which indicates that vortex is formed. Vortex is undesired because some of the portions do not mix very well, reduces the contact portion of milk and beads at the above of the impeller less compared the 250rpm.

T-shape simulation was run for 30s, as this blade also makes axial flow at 150 rpm 75% of the tank is occupied with beads and this speed makes slightly vortex formation near to the shaft. As the speed is changed to 250 rpm the axial flow pattern becomes bigger and the volume fraction makes the vortex formation more the shaft.

At 300 rpm the beads are distributed throughout the tank is can be observed through the Figure 9. No vortex formation of the calcium alginate beads can be observed at this speed. Figure 10 shows that at 250 rpm and 300 rpm it shows almost the same result which means increasing 50rpm of the speed of the impeller there will not show significant effect on the distribution of the beads whereby compared to 150 rpm it is a massive change in the volume fraction of the beads. At 150 rpm there is a slight vortex formation near to the shaft of the impeller, this simulation was run 13 s for all the speed.

It was quite hard to do a comparison between the impeller as each impeller was run for a different period and even the distance from the bottom of the vessel wasn’t consistent. Table 4 shows the time for each impeller to run and the formation of the vortex. And the summary of all the impeller data.

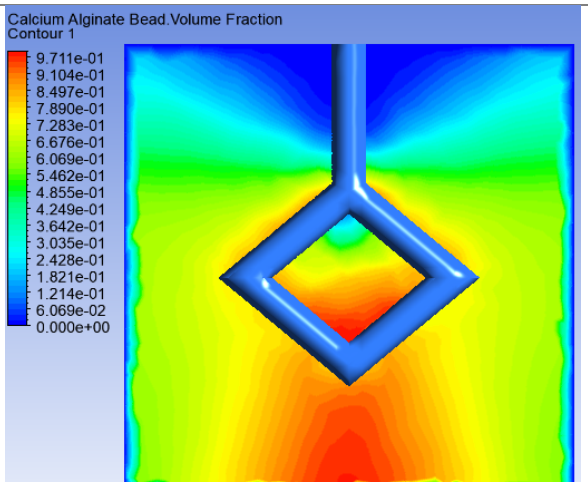
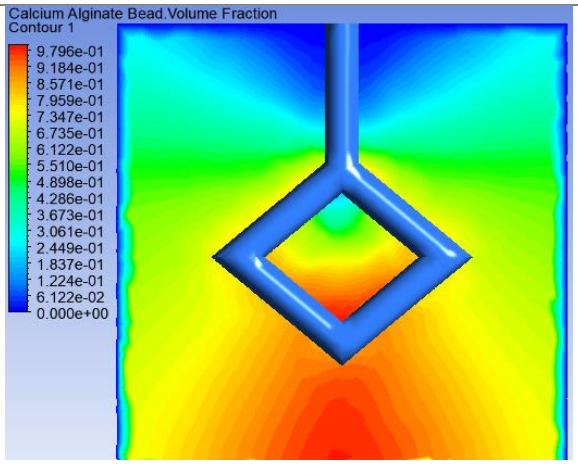
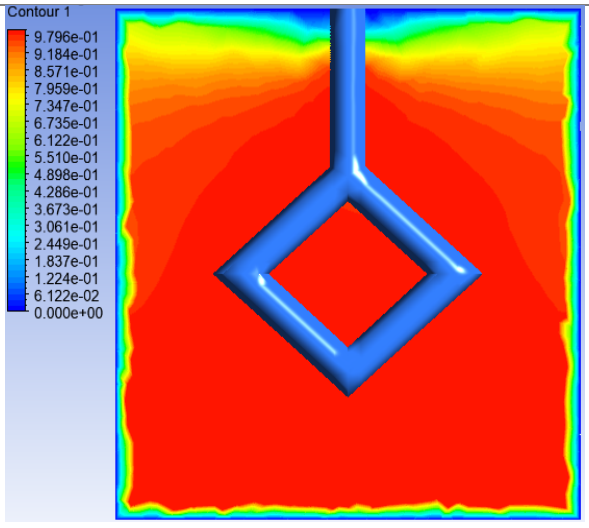
Mid-plane	
150 rpm	
250 rpm	
300 rpm	

Fig. 7. Volume fraction of calcium alginate bead at 150, 250 and 300 rpm for the paddle blade impeller

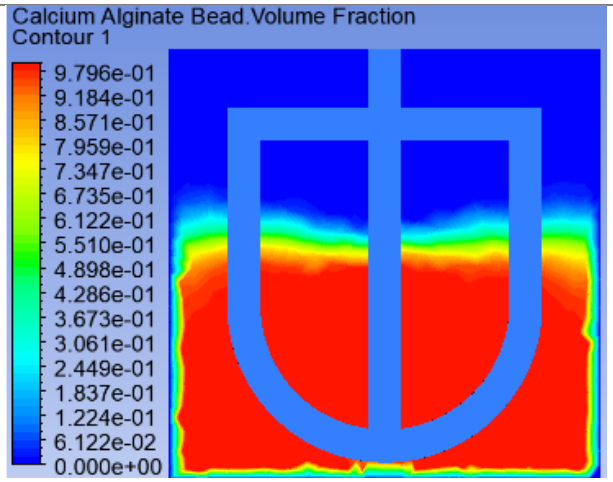
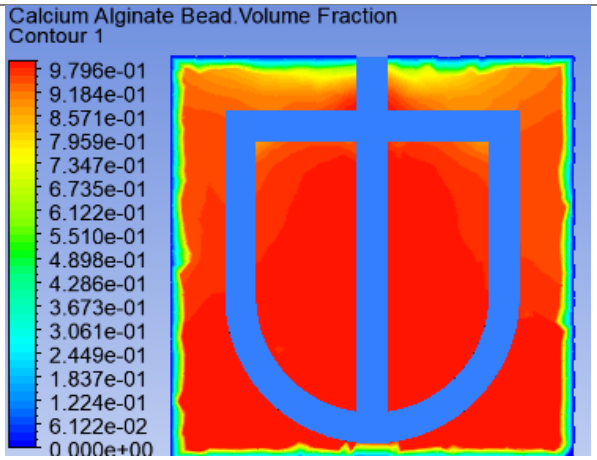
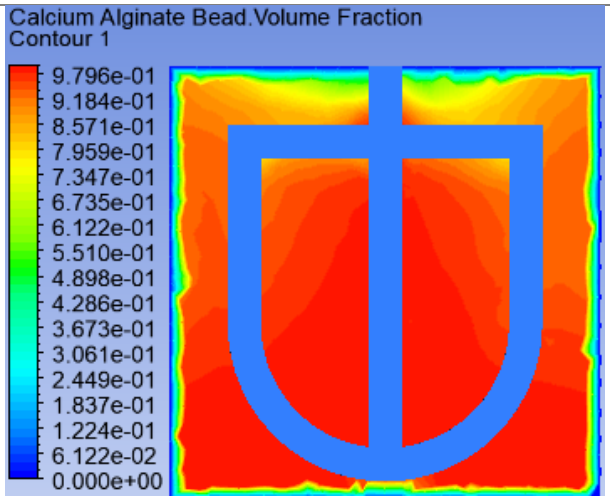
Mid-plane	
150 rpm	
250 rpm	
300 rpm	

Fig. 8. Volume fraction of calcium alginate bead at 150, 250 and 300 rpm for the EB blade impeller

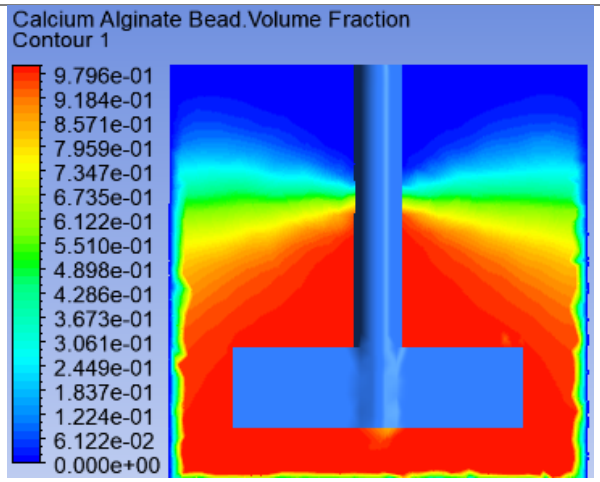
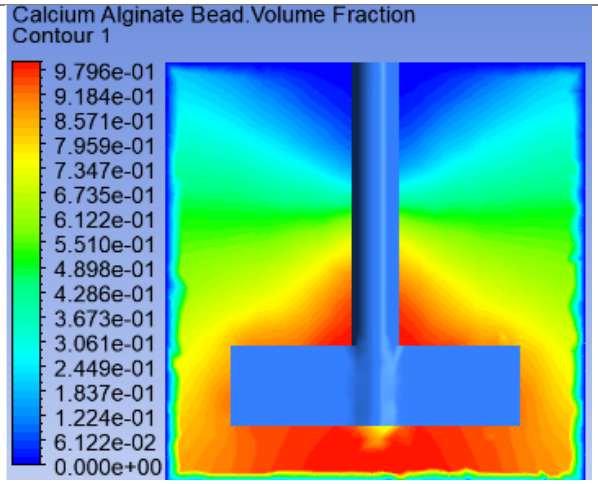
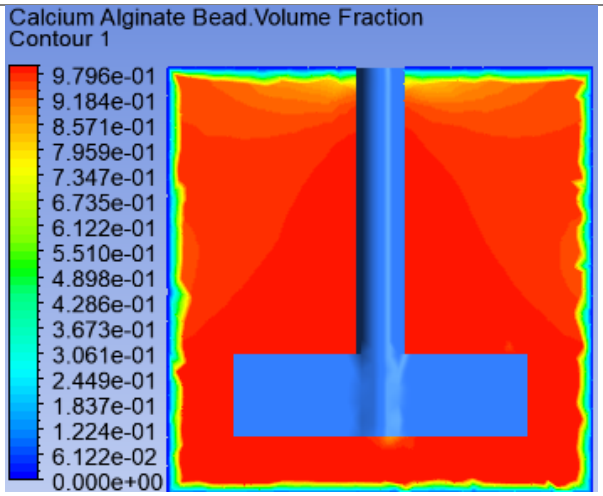
Mid-plane	
150 rpm	
250 rpm	
300 rpm	

Fig. 9. Volume fraction of calcium alginate bead at 150, 250 and 300 rpm for the T-shape blade impeller

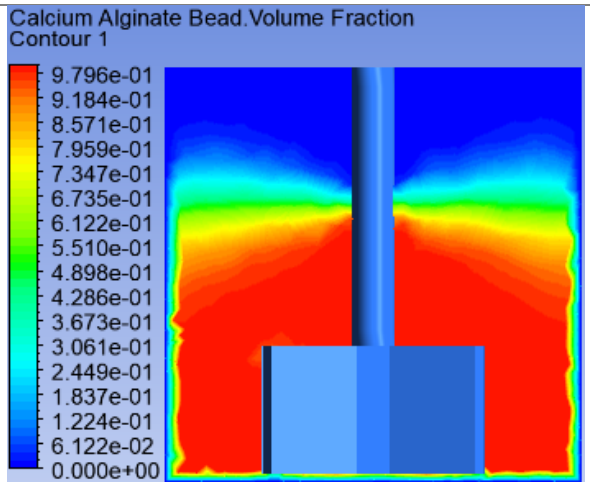
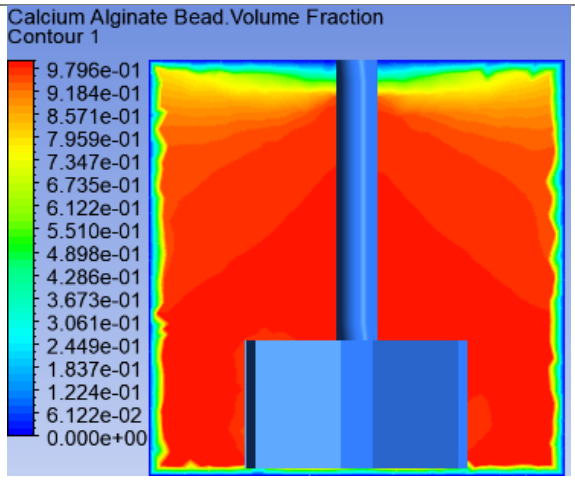
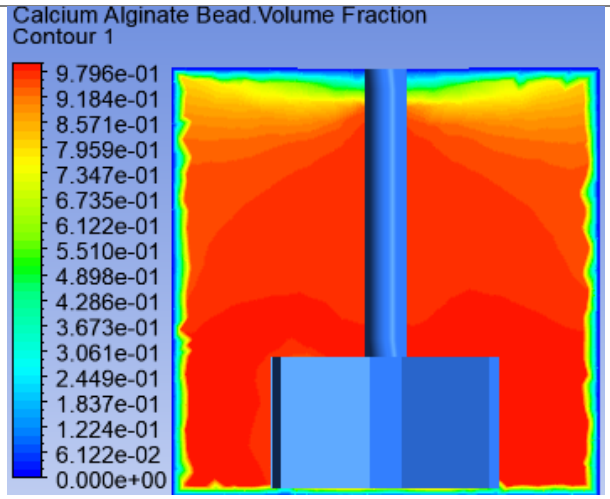
Mid-plane	
150 rpm	
250 rpm	
300 rpm	

Fig. 10. Volume fraction of calcium alginate bead at 150, 250 and 300 rpm for the 5-turbine blade impeller

Table 4
Comparison between experimental and simulation result

Impeller Type	Impeller rotation speed (rpm)	Simulation time (s)	Vortex Formation (Simulation)	Vortex Formation (Experimental)
T-shape blade	150	30	No	No
	250	30	No	No
	300	30	No	No
Paddle blade	150	21	No	No
	250	21	No	No
	300	21	No	No
5-Turbine blade	150	13	No	No
	250	13	No	No
	300	13	Yes	Yes
Edge Beater Blade	150	10	No	No
	250	10	No	Yes
	300	10	Yes	Yes

As the result was compared with the experimental and simulation data of the vortex, it can be observed from the data that T-shape blade, paddle blade and 5-turbine blade shows that there was no formation of the vortex whereby for the edge beater blade result for simulation shows that there was vortex formation at 300 rpm only and for the experimental at 250 and 300 rpm which makes a little conflict. Edge beater blade took 10s for the distribution the calcium alginate beads over the tank at 250 rpm compared to the others and the times the impeller was run in the tank was even lesser than the other impeller. It can also conclude that the impeller which produces mixed flow pattern is better for the mixing of two-phase fluid mixing.

4. Conclusions

It can be concluded that the edge beater blade took 10s to distribute the calcium alginate beads over the tank at 250 rpm compared to the others and the times the impeller was run in the tank was even lesser than the other impeller. It can also conclude that the impeller which produces mixed flow pattern is better for the mixing of two-phase fluid mixing. In this study, the position of the impeller wasn't kept constant from the bottom of the tank and the time to run each of the design wasn't the same so it was quite hard to compare between the impeller effectiveness in mixing. this study was a continuous study for the researched done by Muttalib [1].

Acknowledgement
The authors gratefully acknowledge the financial support from Centre of Excellence for Research, Value Innovative and Entrepreneurship (CERVIE), UCSI University.

References
[1] Muttalib. (2019). Design and performance of millilitre range bioreactor prototype for bioprocess operation, PhD, university teknologi malaysia, Malaysia
[2] Santos-Moreau, Vania, Lena Brunet-Errard, and Matthieu Rolland. "Numerical CFD simulation of a batch stirred tank reactor with stationary catalytic basket." *Chemical Engineering Journal* 207 (2012): 596-606.
[3] Tekchandaney, J. (2019). Mixing expert. Retrieved from http://mixing-expert.com/
[4] Zhang, Yulong, Zhengming Gao, Zhipeng Li, and J. J. Derksen. "Transitional flow in a Rushton turbine stirred tank." *AIChE Journal* 63, no. 8 (2017): 3610-3623.

Penerbit Akademia Baru

Engineering Science and Technology Conference Proceedings

Journal homepage: www.akademiabaru.com/EST.html

The Magnetohydrodynamics Casson Fluid Flow, Heat and Mass Transfer Due to the Presence of Assisting Flow and Buoyancy Ratio Parameters

Open Access

Siti Suzilliana Putri Mohamed Isa[1,2,*], Shahanaz Parvin[1], Norihan Md. Arifin[1,3], Fadzilah Md Ali[1,3]

[1] Institute for Mathematical Research, Universiti Putra Malaysia, 43400 UPM Serdang, Selangor Darul Ehsan, Malaysia
[2] Centre of Foundation Studies for Agricultural Science, Universiti Putra Malaysia, 43400 UPM Serdang, Selangor Darul Ehsan, Malaysia
[3] Department of Mathematics, Faculty of Science, Universiti Putra Malaysia, 43400 UPM Serdang, Selangor Darul Ehsan, Malaysia

ABSTRACT

A The mathematical modelling and numerical solutions of boundary layer flow, heat and mass transfer on magneto-hydrodynamics Casson fluid are reported in this paper. The model problem is subjected to the presence of mixed convection with assisting flow, together with the buoyant feature. The Casson fluid is assumed to flow over an exponentially stretching sheet, together with the exponential variations of fluid temperature and fluid concentration. The momentum, energy and concentration equations are formed as the controlling equations and written as partial differential equations (PDE). Subsequently, these equations were transformed into the ordinary differential equations (ODE) by using the similarity transformation. Finally, the ODE are solved numerically by bvp4c program in Matlab software. The graphs of velocity, temperature and concentration profiles and the numerical values of skin friction coefficient, local Nusselt number and local Sherwood number are presented. These results are obtained due to the controlling parameter, namely as magnetic field, assisting
flow and buoyancy ratio parameters.

Keywords:
Casson fluid; stretching sheet; magneto-hydrodynamics; assisting flow; buoyancy ratio

Copyright © 2019 PENERBIT AKADEMIA BARU - All rights reserved

1. Introduction:

Double-diffusive convection occurs in the fluid due to the combination of temperature and concentration gradients, and both of these components diffuse at different rates. This type of convection is affected by gravity. The existence of double-diffusive convection can be observed in the field of oceanography, astrophysics and geology. Both of these gradients are under the impact of gravitational acceleration of the earth. Therefore, the significant developments of double diffusive convection has been described in details [1-2]. Some of researchers considered the fluid bounded by square cavity [3-5] to explain the double diffusive natural convection. Beside this, Chen and Liu [6] dealed with heated cylinder submerged in a salt-stratified fluid and Kalla et al [7] considered the case of shallow porous cavity with vertical fluxes of heat and mass in their study. Double diffusive convection in Newtonian fluid [8-11] and various types of non-Newtonian fluid [12-21] are reported with different conditions. These types of non-Newtonian include viscoelastic [12,

* *Corresponding author.*
E-mail address: ctsuzilliana@upm.edu.my (Siti Suzilliana Putri Mohamed Isa)

17], power-law fluid [13, 19], nanofluid [14, 20], viscoelastic nanofluid [15], Maxwell fluid [16] and Casson fluid [18, 21].

There are various contributions of boundary layer flow and heat transfer induced by a stretching sheet, to the engineering processes. One of the application is the production of glass fibre, paper and polymer sheet. Therefore, the study of the boundary layer flow, heat and mass transfer bounded by stretching/shrinking sheet are conducted [8-12, 15, 17, 20]. Moreover, Soret and Dufour effects must not be neglected in the process of boundary layer fluid flow with the occurrence of coupled heat and mass transfer. Mass transfer induced by temperature differences is known as Soret effect, whereas Dufour effect refers to the heat transfer caused by concentration gradient in the fluid. The research works that include the impacts of Soret-Dufour parameters were reported by the following references [8-13, 17]. Besides, magnetohydrodynamics related to the occurrence of magnetic properties on electrically conducting fluids. The industrial applications of magnetohydrodynamics are for the production of solar energy by fusion process and cooling of nuclear fission reactors. The significant role of magnetohydrodynamics in the properties of fluid flow, heat and mass transfer contributes to the development of the double-diffusive convection model [17-18, 20].

The central focus of the study is to examine the Casson fluid flow, heat and mass transfer in the presence of magnetic field, assisting flow and buoyancy ratio parameters, which is subjected to the exponential variation of stretching sheet. To our best of knowledge, no report has far been published in the literature with this investigation. MatLab bvp4c programme are used to calculate the numerical data and graph. Velocity, temperature and concentration profiles for different values of mixed convection parameter, magnetic field parameter and buoyancy parameter are shown graphically for both shrinking and stretching cases. Also, effect of skin friction coefficient, local Nusselt number and local Sherwood number for the above parameter are presented by table. This study is chronologically structured as Methodology, Results and Discussion, and finally Conclusion.

2. Methodology:

Consider the mathematical formulation for two-dimensional incompressible, viscous and electrically conducting fluid over an exponentially permeable stretching sheet with the effect of magnetic field. The *x*-axis runs along the stretching surface and the *y*-axis is perpendicular to it. The subscripts w and ∞ at parameters T and C represent the situation at the stretching sheet and at the point far from the sheet. A transverse magnetic field is assumed to be applied in the *y*-axis and constant magnetic field is denoted by B_0. As we can see, the temperature and concentration gradients between the point at stretching sheet and at the point out from the fluid region are placed in Eq. 2. These components denoted the existence of double-diffusion convection, in magnetohydrodynamics Casson fluid (since the Casson parameter ω and magnetic field B_0 also placed in the same equation. The mathematical model of this problem are governed by continuity, momentum, energy and concentration equations (Eqs. 1-4). These controlling equations are listed as below:

$$\frac{\partial u}{\partial x}+\frac{\partial v}{\partial y}=0 \tag{1}$$

$$\frac{\partial u}{\partial t}+u\frac{\partial u}{\partial x}+v\frac{\partial u}{\partial y}=\upsilon\left(1+\frac{1}{\omega}\right)\frac{\partial^2 u}{\partial y^2}+g\beta_T\left(T-T_\infty\right)+g\beta_C\left(C-C_\infty\right)+\frac{\sigma B_0^2}{\rho}u \tag{2}$$

$$u\frac{\partial T}{\partial x}+v\frac{\partial T}{\partial y}=\alpha\frac{\partial^2 T}{\partial y^2}+\frac{DK_T}{C_sC_P}\frac{\partial^2 C}{\partial y^2} \tag{3}$$

$$u\frac{\partial C}{\partial x}+v\frac{\partial C}{\partial y}=D\frac{\partial^2 C}{\partial y^2}+\frac{DK_T}{T_m}\frac{\partial^2 T}{\partial y^2} \tag{4}$$

where u and v are the components of velocity in the x and y directions, $\upsilon=\mu/\rho$ is the kinematic viscosity, μ denotes the viscosity, ρ is the fluid density, g is the gravitational acceleration, β_T is the coefficient of thermal expansion, β_C is the coefficient of solutal expansions, T is the temperature of the fluid, C is concentration of the fluid, σ is the electrical conductivity, α is the thermal diffusivity, D is the solutal diffusivity of the medium, K_T is the thermal diffusion ratio, C_S is the concentration susceptibility, C_P is the specific heat at constant pressure and T_m is the mean fluid temperature.

The appropriate boundary conditions are:

$$\begin{aligned} &u=u_w(x)=\lambda U_0\exp(x/L),\quad v=v_w(x),\quad T_w(x)=T_\infty+T_0\exp(x/2L),\\ &C_w(x)=C_\infty+C_0\exp(x/2L), && \text{at } y=0,\\ &u\to 0,\quad T\to T_\infty,\quad C\to C_\infty && \text{as } y\to\infty. \end{aligned} \tag{5}$$

where $\lambda>0$ is the stretching parameter and the wall mass suction velocity is represented by $v_w(x)<0$. The term $\exp(x/2L)$ in temperature T_w and concentration distribution C_w are taken from [8-11], so that the numerical results will satisfy final boundary condition after substituting similarity variables.

Introducing new similarity variables:

$$\begin{aligned} &\theta(\eta)=\frac{T-T_\infty}{T_w-T_\infty},\qquad \phi(\eta)=\frac{C-C_\infty}{C_w-C_\infty},\qquad \eta=y\left(\frac{U_0}{2\upsilon L}\right)^{1/2}\exp(x/2L),\\ &u=U_0\exp(x/L)\,f'(\eta),\\ &v=-\left(\frac{\upsilon U_0}{2L}\right)^{1/2}\exp(x/2L)\left[f(\eta)+\eta f'(\eta)\right], \end{aligned} \tag{6}$$

where prime indicates the differentiation with respect to η.

Substituting Eq. 6 into Eqs. 2 – 5, the new ordinary differential equations and boundary conditions are obtained as below:

$$\left(1+\frac{1}{\omega}\right)f'''+ff''-2(f')^2+2Ri\left[\exp\left(\frac{-3X}{2}\right)\right](\theta+N\phi)-2H\left[\exp(-X)\right]f'=0. \tag{7}$$

$$\frac{1}{\mathrm{Pr}}\theta''+f\theta'-f'\theta+Db\phi''=0. \tag{8}$$

$$\frac{1}{Sc}\phi''+f\phi'-f'\phi+Sr\,\theta''=0. \tag{9}$$

$$\begin{aligned} &f'(\eta)=\lambda,\ f(\eta)=S,\ \theta(\eta)=1,\ \phi(\eta)=1\ \ at\ \eta=0\\ &f'(\eta)\to 0,\ \theta(\eta)\to 0,\ \phi(\eta)\to 0,\ as\ \eta\to\infty \end{aligned} \tag{10}$$

The parameters involved in this problem are mixed convection parameter $Ri=Gr/\mathrm{Re}^2$, magnetic field parameter $H=2\sigma LB_0^{\,2}/\rho U_0$, thermal Grashof number $Gr=g\beta_T(T_0-T_\infty)L^3/\nu^2$,

Reynolds number $\mathrm{Re} = u_0 L/\nu$, dimensionless coordinate along the plate parameter $X = x/L$, length of the extended/compressed sheet L, buoyancy ratio $N = \beta_C (C_0 - C_\infty)/\beta_T (T_0 - T_\infty)$, Prandtl number $\mathrm{Pr} = \upsilon/\alpha$, Schmidt number $Sc = \upsilon/D$, Soret number $Sr = DK_T (T_0 - T_\infty)/T_m \upsilon (C_0 - C_\infty)$, Dufour number $Db = DK_T (C_0 - C_\infty)/C_s C_p \upsilon (T_0 - T_\infty)$, and suction parameter is defined as $S = (v_w(x)/\exp(x/2L)) \times \sqrt{2L/\upsilon U_0} > 0$. The opposing flow is when $Ri < 0$. Otherwise, the positive Ri indicates the case of aiding flow.

The physical parameters of skin friction coefficient C_f, local Nusselt number Nu_x and local Sherwood number Sh_x are presented as follow:

$$C_f = \left(\frac{\mu}{\rho U_0^{\,2}}\right)\left(\frac{\partial u}{\partial y}\right), \quad Nu_x = \left(\frac{L}{T_w - T_\infty}\right)\left(-\frac{\partial T}{\partial y}\right)_{y=0}, \quad Sh_x = \left(\frac{L}{C_w - C_\infty}\right)\left(-\frac{\partial C}{\partial y}\right)_{y=0}. \tag{11}$$

Substituting (6) into (11), then we get

$$C_f \sqrt{2\,\mathrm{Re}_x}\exp\left(\frac{-3X}{2}\right) = f''(0), \quad Nu_x \sqrt{\frac{2}{\mathrm{Re}_x}}\exp\left(\frac{-X}{2}\right) = -\theta'(0), \quad Sh_x \sqrt{\frac{2}{\mathrm{Re}_x}}\exp\left(\frac{-X}{2}\right) = -\phi'(0). \tag{12}$$

The final stage of methodology is by performing numerical calculation on the system of exponentially ordinary differential equation together with the boundary conditions (Eqs. -10) using MatLab programming. The results are represented in the form of graphs and tables, showing the effect of the controlling parameters namely as magnetic field, assisting flow and buoyancy ratio.

3. Results and Discussion:

The system of exponentially ordinary differential equations (7)-(9), together with the boundary conditions (10) are solved numerically using Matlab programming (namel as Matlab bvp4c). The accuracy of our numerical method is reached by comparing numerical data obtained (a), with another numerical method (b) showed in Table 1. Table 1 shows the comparison of skin friction coefficient $C_f \sqrt{2\,\mathrm{Re}_x}\exp(-3X/2)$, local Nusselt number $Nu_x \sqrt{2/\mathrm{Re}_x}\exp(-X/2)$ and local Sherwood number $Sh_x \sqrt{2/\mathrm{Re}_x}\exp(-X/2)$ between current data and with shooting method. This technique is developed in Maple software, by converting the Equations (7)-(9) into an initial value problem. The fourth-order Runge–Kutta integration scheme is applied to solve the initial value problem. The values for $f''(0)$, $-\theta'(0)$ and $-\phi'(0)$ are required to perform the shooting technique, together with the predicted highest boundary layer thickness η. Generally, both of the methods (Maple and MatLab) have to produce numerical results which satisfy final boundary conditions (10). As a conclusion, the present values are in good agreement with the different numerical technique. Therefore, the good comparison proves that our bvp4c MATLAB is applicable to use for providing subsequent findings in this paper.

The numerical solutions obtained from this article are dual. They are labelled by the first solution (solid line), and the second solution (second line). However, there is only one solution which is that is stable and physically reliable. Besides, another solution is unstable and not physically occur in actual state in fluid. Therefore, stability analysis is used to select the most stable solution among multiple solutions. However, we did not perform the calculations of stability due to the restrictions of paper pages. In this article, the stable solution is recognized by the pattern of

velocity, temperature and concentration variations against boundary layer thickness. The stable solution always following the conditions at the boundary (Equation 10), with minimal existence of minimum or maximum peaks. In this article, the stable solution is declared as the first one. The MatLab program declares the uniform variation as first solution, otherwise it will labeled as the second one. Besides, second solution is denoted as unstable, not physically reliable and rejected.

The velocity, temperature and concentration profiles for different values of H are depicted in Figures 1-3. The values of the fluid velocity at a point near the stretching sheet for the both solutions show that the velocity is the lowest when the value of $H=1$. Velocity profile reduces due to the increment of magnetic parameter. The effect of magnetic parameter is to increase the Lorentz force. Consequently, an augmentation of the Lorentz force opposes the flow and the velocity of the fluid is decreased. The temperature profile for the first solution when the sheet is stretched (Figure 2) presents the improvement by addition rate of magnetic parameter H. The rate of the fluid temperature for the first solution in Figure 2 are continuously decrease until they reach the zero value. The rate of concentration for the first solution in Figure 3 is the highest, for the highest H. It is clear from Figures 2-3 that an increase in the magnetic field increases the thickness of thermal and concentration boundary layer. This means that as the magnetic parameter increases, the temperature and concentration profile also increases. The decrement of the magnitude of velocity rate in the boundary layer, due to the effect of magnetic field induces the increment of the fluid temperature and concentration.

The velocity, temperature and concentration profiles for different values of Ri are depicted in Figures 4, 5 and 6, respectively. The values of the fluid velocity in Figure 4 at a point near the stretching sheet for the both solutions show that the velocity is the lowest when the value of $Ri=0.5$. From Figure 5 when the value of $Ri=0.5,$ the value of temperature is the highest for the first solution while in second solution the value of temperature is the lowest. When the point near the stretching sheet for the value of $Ri=0.5,$ the maximum peaks exist for the first solution shown in Figure 6. The variation of concentration profile against η for the second solution (in Figure 6) shows a decrement, to reach minimum peak. Further, it increases continuously.

The graph of velocity, temperature and concentration profiles are shown in Figures 7-9. These graphs are drawn for various values of N. When $N=4,$ the momentum boundary layer thickness is the highest for the both solutions at a point near the stretching sheet (Figure 7). This figure presented the addition in velocity in the first solution, due to the addition of N and for small η. The variation of temperature profile (Figure 8) are continuously decreased until they reach the limit point. The values of the fluid temperature for the second solution show that the temperature is the highest for the lowest value of N. The concentration is decreased (Figure 9) by the increment of N and for the first solution. Figure 9 shows that the existences of the positive peaks for the first solution at point near the stretching sheet and the negative peaks exist for the second solution. These negative peaks are increased as the value of N increases.

It is clear from Figures 4 and 7 that velocity distribution is increased for the increment of mixed convection parameter Ri and buoyancy ratio parameter N. This is due to the fact that higher rate of mixed convection parameter is caused by a greater buoyancy effects. Therefore, the fluid flow is accelerated and the instantaneous velocity increases. Figures 5-6 and 8-9 show that the temperature and concentration decrease with increasing values of mixed convection parameter Ri and buoyancy ratio parameter N. When parameter Ri (i.e. buoyancy effects) increase, it contributes to the increment of the convection cooling effect. As a result, the temperature and concentration reduce.

The tabulation of skin friction coefficient, local Nusselt number and local Sherwood number for the impact of parameters H, Ri and N is presented in Table 2. It can be seen from Table 2 that the increment values of H cause the values of skin friction coefficient number, local Nusselt

number and Sherwood number become decrease for the first solution. Second solution shows that the values of skin friction coefficient number and local Nusselt number decrease but the values of local Sherwood number increase due to increasing value of H. Table 2 also shows that the first solution always had an increment for the skin friction coefficient, the local Nusselt number and the local Sherwood number caused by the effect of increasing parameter Ri. Moreover, second solution only had an increment in skin friction coefficient and the local Sherwood number which are affected by the same parameter. The effect of parameter N is to increase the values of skin friction coefficient number, local Nusselt number and local Sherwood number for the first solution. However, the impact of parameter N for the second solution is to enhance the values of the skin friction coefficient number and the local Nusselt number. A decrement in the values of the Sherwood number observed in second solution due to an increment in the values of N.

Table 1
The comparison with shooting method for various values of ω and H when ω = 100, Ri = 0.5, Sr = 2.0, Db = 0.03, X = 0.1, λ = 1, Sc = 1, N = 0.5, Pr = 1 and S = 2.5

Solution	H	$C_f\sqrt{2\mathrm{Re}_x}\times\exp(-3X/2)$		$Nu_x\sqrt{2/\mathrm{Re}_x}\times\exp(-X/2)$		$Sh_x\sqrt{2/\mathrm{Re}_x}\times\exp(-X/2)$	
		(a)	(b)	(a)	(b)	(a)	(b)
First	0.5	-2.68915	-2.68916	2.94868	2.94869	-2.64919	-2.64918
	1	-2.94117	-2.94117	2.93502	2.93501	-2.66278	-2.66278
	1.5	-3.16702	-3.16701	2.92340	2.92340	-2.67369	-2.67368
Second	0.5	-4.18403	-4.18403	3.10758	3.10757	-2.99277	-2.99277
	1	-4.44169	-4.44168	3.14122	3.14122	0.93555	0.93554
	1.5	-4.64893	-4.64893	3.44751	3.44750	3.40391	3.40391

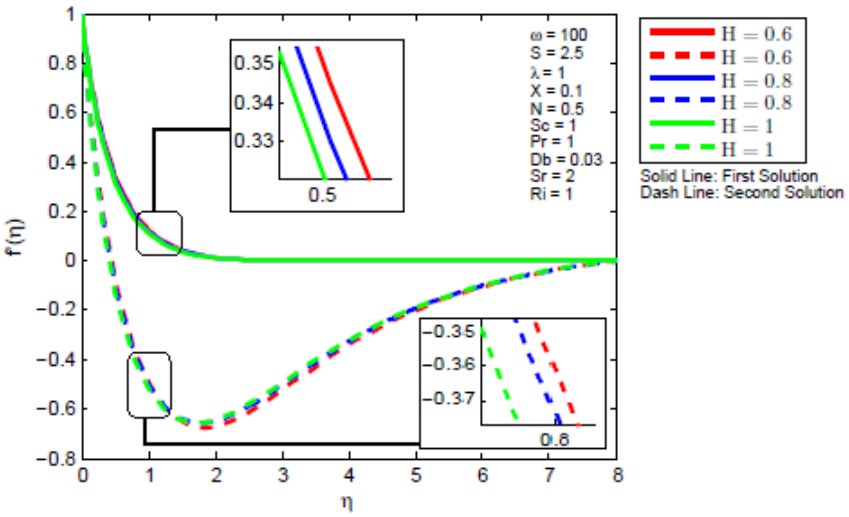


Fig. 1. Velocity profile for different values of H.

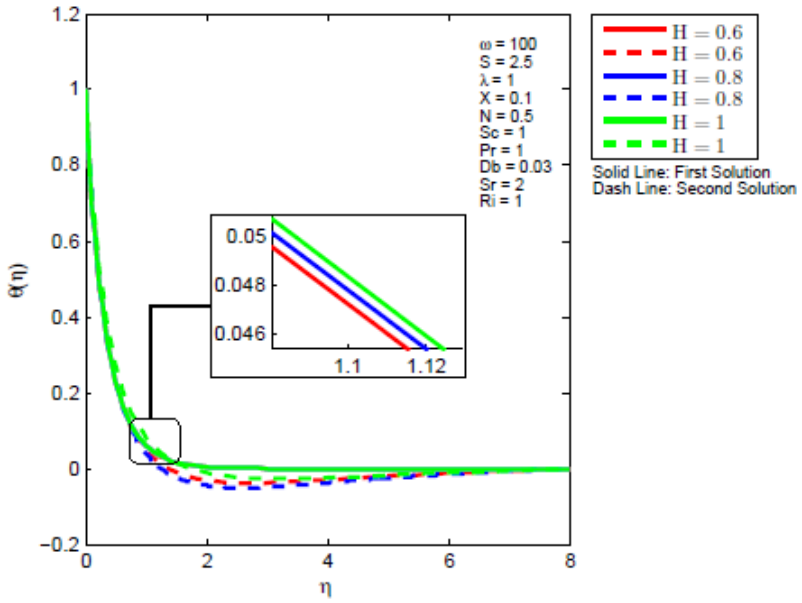


Fig. 2. Temperature profiles for different value of H.

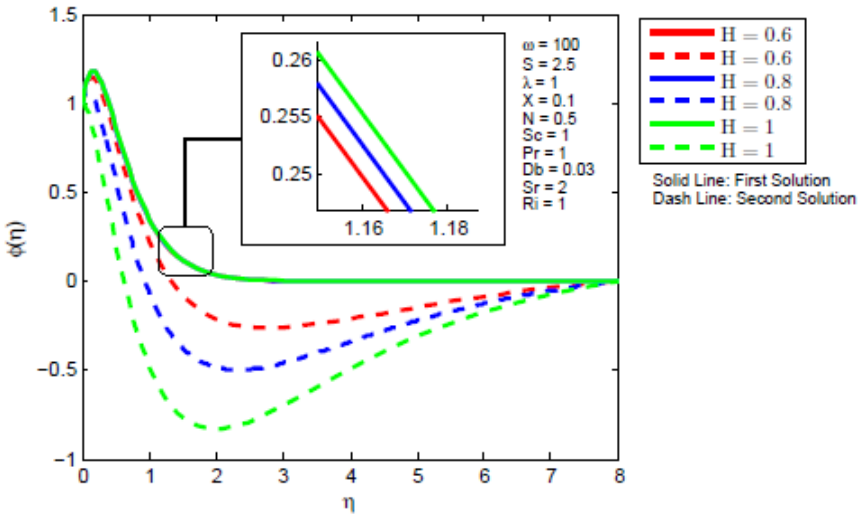


Fig. 3. Concentration profiles for different value of H.

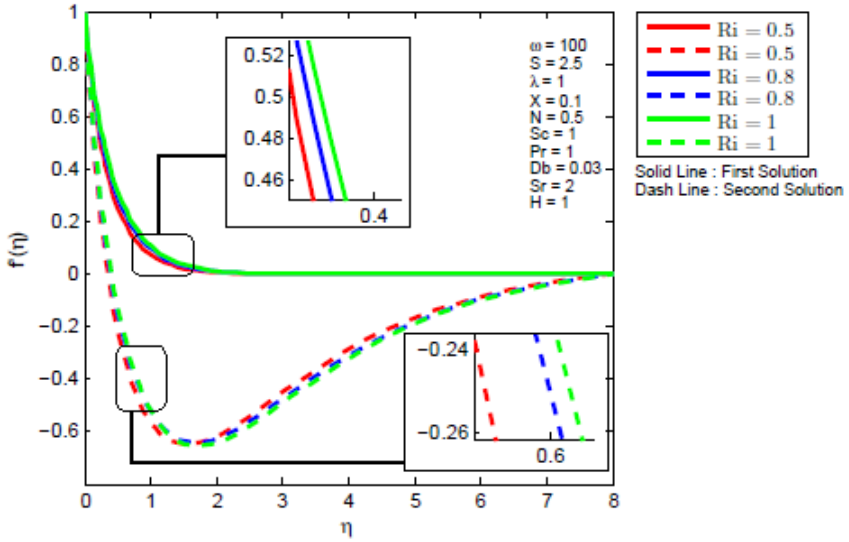


Fig. 4. Velocity profile for different values of Ri.

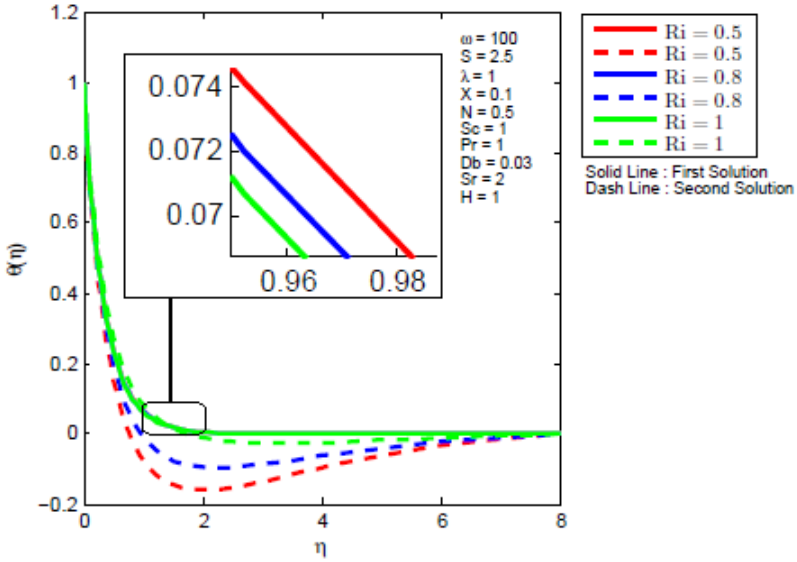


Fig. 5. Temperature profile for different value of Ri.

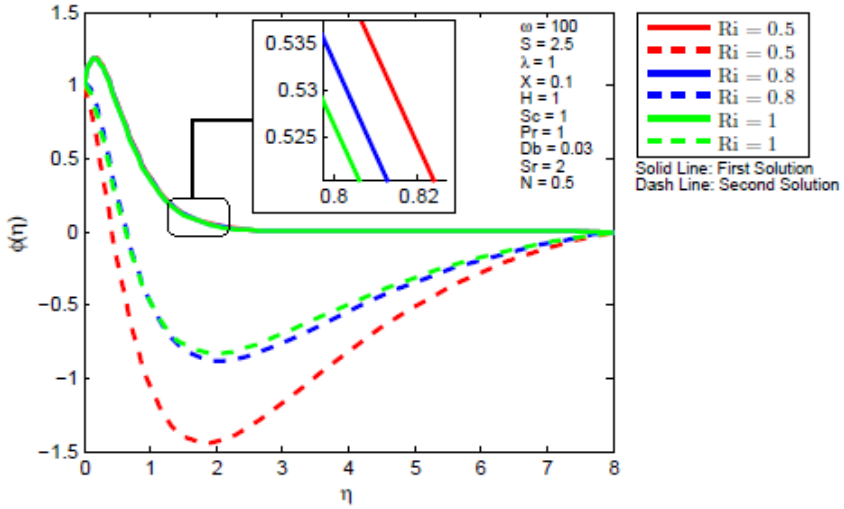


Fig. 6. Concentration profile for different value of Ri.

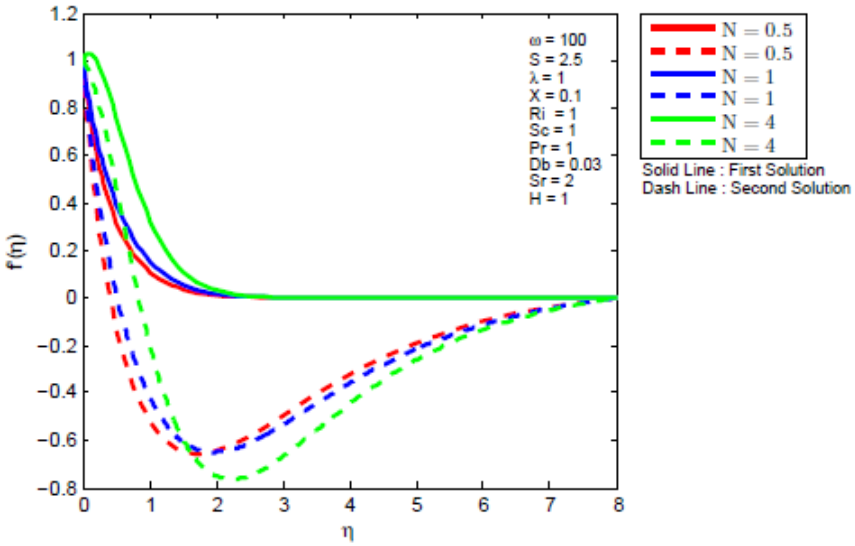


Fig. 7. Velocity profiles for different value of N.

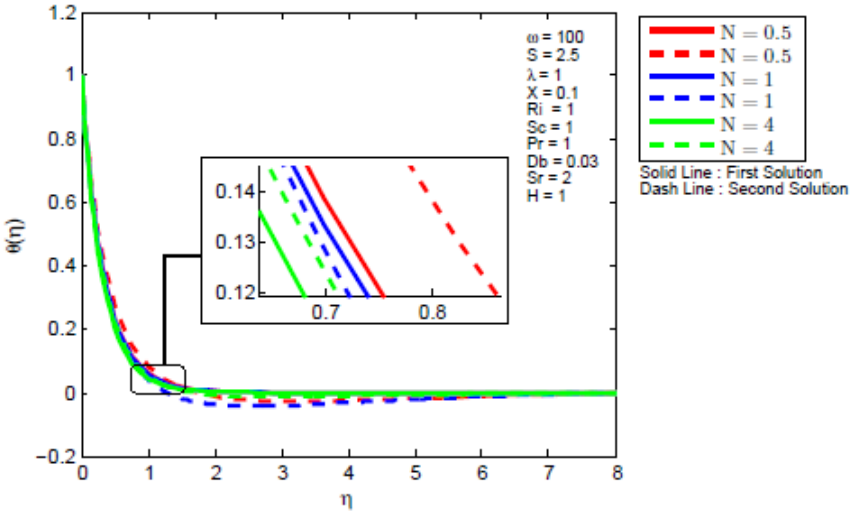


Fig. 8. Temperature profiles for different value of N.

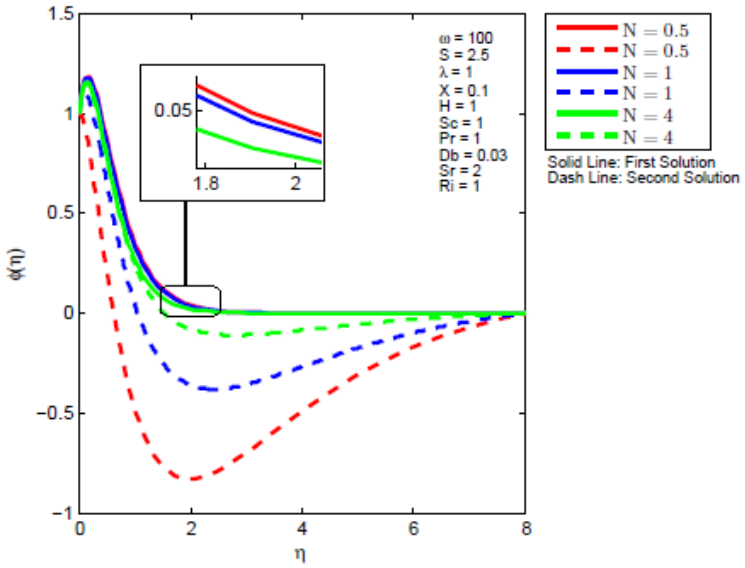


Fig. 9. Concentration profiles for different value of N

Table 2
The values of skin friction coefficient, local Nusselt number and local Sherwood number due to the effect of parameters *H*, *Ri* and *N*

Parameters	Values	$C_f\sqrt{2\mathrm{Re}_x}\exp(-3X/2)$		$Nu_x\sqrt{2/\mathrm{Re}_x}\exp(-X/2)$		$Sh_x\sqrt{2/\mathrm{Re}_x}\exp(-X/2)$	
		First solution	Second solution	First solution	Second solution	First solution	Second solution
H	0.6	-2.24482	-3.55708	2.97580	2.89334	-2.61965	-2.31887
	0.8	-2.35792	-3.70017	2.96950	2.90050	-2.62615	-1.48953
	1	-2.46571	-3.88426	2.96361	2.73122	-2.63212	-0.04634
Ri	0.5	-2.94117	-4.44169	2.93502	3.14122	-2.66278	0.93555
	0.8	-2.65316	-4.05712	2.95254	3.00205	-2.64382	-0.49706
	1	-2.46571	-3.88426	2.96361	2.73122	-2.63212	-0.04634
N	0.5	-2.46571	-3.88426	2.96361	2.73122	-2.63212	-0.04634
	1	-1.97500	-3.17300	2.99533	2.93917	-2.59654	-1.83899
	4	0.56325	-0.28188	3.13401	3.05900	-2.45916	-2.38784

4. Conclusions

The magnetohydrodynamics casson fluid flow, heat and mass transfer in the presence of assisting flow and buoyancy ratio parameters are reported. From the graphs and tables, following conclusion are listed as below:

a) Fluid velocity of the first solution is enhanced due to the increment of mixed convection and buoyancy ratio parameters. In addition, minimum peak arise in the velocity graphs for the small η on the second solution.
b) The impact of magnetic field parameter is to increase the rate of fluid temperature and concentration of the first solution. The temperature and concentration is the highest at the wall ($\eta = 0$).
c) The increment values of skin friction coefficient, local Nusselt number and local Sherwood number on the first solution are influenced by the augmentation of parameters *Ri* and *N*.

Acknowledgement
This research was funded by a grant from Universiti Putra Malaysia (Project code: GP-IPM/2018/9596900).

References

[1] Huppert, H. E., and D. R. Moore. "Nonlinear double-diffusive convection." *Journal of Fluid Mechanics* 78, no. 4 (1976): 821-854.
[2] Huppert, H. E., and J. S. Turner. "Double-diffusive convection." *Journal of Fluid Mechanics* 106 (1981): 299-329.
[3] Beghein, C., F. Haghighat, and F. Allard. "Numerical study of double-diffusive natural convection in a square cavity." *International Journal of Heat and Mass Transfer* 35, no. 4 (1992): 833-846.
[4] Costa, V. A. F. "Double diffusive natural convection in a square enclosure with heat and mass diffusive walls. *International Journal of Heat and Mass Transfer* 40, no. 17 (1997): 4061-4071.
[5] Badruddin, I. A., T. M. Y. Khan, N. J. S. Ahmed, and S. Kamangar. "Effect of variable heating on double diffusive flow in a square porous cavity." In *AIP Conference Proceedings*, vol. 1728, no. 1, p. 020689. AIP Publishing, 2016.
[6] Chen, Y. M., and C. K. Liu. "Double-diffusive convection for a heated cylinder submerged in a salt-stratified fluid layer." *Heat and mass transfer* 33, no. 1-2 (1997): 17-26.
[7] Kalla, L., M. Mamou, P. Vasseur, and L. Robillard. "Multiple solutions for double diffusive convection in a shallow porous cavity with vertical fluxes of heat and mass." *International journal of heat and mass transfer* 44, no. 23 (2001): 4493-4504.
[8] Isa, S. S. P. M., N. M. Arifin, and U. Farooq. "Effect of Soret and Dufour numbers on double diffusive mixed convection boundary layer flow induced by a shrinking sheet." Journal of Physics: Conference Series 1298, (2019): 012024.
[9] Srinivasacharya, D., and Ch RamReddy. "Soret and Dufour effects on mixed convection from an exponentially stretching surface." *International Journal of Nonlinear Science* 12, no. 1 (2011): 60-68.
[10] Sreenivasulu, P., and N. Bhaskar Reddy. "Thermo-diffusion and diffusion-thermo effects on MHD boundary layer flow past an exponential stretching sheet with thermal radiation and viscous dissipation." *Advances in Applied Science Research* 3, no. 6 (2012): 3890-3901.
[11] Hayat, T., T. Muhammad, S. A. Shehzad, and A. Alsaedi, "Soret and Dufour effects in three-dimensional flow over an exponentially stretching surface with porous medium, chemical reaction and heat source/sink." *International Journal of Numerical Methods for Heat & Fluid Flow* 25, no. (2015): 762-781.
[12] Gbadeyan, J. A., A. S. Idowu, A. W. Ogunsola, O. O. Agboola, and P. O. Olanrewaju. "Heat and mass transfer for Soret and Dufour's effect on mixed convection boundary layer flow over a stretching vertical surface in a porous medium filled with a viscoelastic fluid in the presence of magnetic field." Global Journal of Science Frontier Research 11, no. 8 (2011): 97-114.
[13] Srinivasacharya, D., and S. Reddy. "Double diffusive natural convection in power-law fluid saturated porous medium with Soret and Dufour effects." *Journal of the Brazilian Society of Mechanical Sciences and Engineering* 34, no.4 (2012): 525-530
[14] Murthy, P. V. S. N., A. Sutradhar, and Ch RamReddy. "Double-diffusive free convection flow past an inclined plate embedded in a non-Darcy porous medium saturated with a nanofluid. "*Transport in Porous Media* 98, no.3 (2013):553-564.

[15] Goyal, M., and R. Bhargava. "Finite element solution of double-diffusive boundary layer flow of viscoelastic nanofluids over a stretching sheet." *Computational Mathematics and Mathematical Physics* 54, no. 5 (2014): 848-863.
[16] Hayat, T., M. Farooq, and A. Alsaedi. "Melting heat transfer in the stagnation-point flow of Maxwell fluid with double-diffusive convection." *International Journal of Numerical Methods for Heat and Fluid Flow* 24, no. 3 (2014): 760-774.
[17] Rashidi, M. M., M. Ali, B. Rostami, P. Rostami, and G. N. Xie. "Heat and mass transfer for MHD viscoelastic fluid flow over a vertical stretching sheet with considering Soret and Dufour effects." *Mathematical Problems in Engineering* 2015 (2015): 861065.
[18] Raju, C. S. K., and N. Sandeep. "Heat and mass transfer in MHD non-Newtonian bio-convection flow over a rotating cone/plate with cross diffusion." *Journal of Molecular Liquids* 215 (2016): 115-126.
[19] Zhuang, Y. J., H. Z. Yu, Q. Y. Zhu. "A thermal non-equilibrium model for 3D double diffusive convection of power-law fluids with chemical reaction in the porous medium." *International Journal of Heat and Mass Transfer* 115, Part B, (2017): 670-694
[20] Pal, D., and G. Mandal. "Double diffusive magnetohydrodynamic heat and mass transfer of nanofluids over a nonlinear stretching/shrinking sheet with viscous-Ohmic dissipation and thermal radiation." *Propulsion and Power Research* 6, no. 1 (2017): 58-69.
[21] Prasad, D.V. K., G. S. K. Chaitanya, R. S. Raju. "Double diffusive effects on mixed convection Casson fluid flow past a wavy inclined plate in presence of Darcian porous medium." *Results in Engineering* 3, (2019): 100019

Penerbit Akademia Baru

Engineering Science and Technology
Conference Proceedings

Journal homepage: www.akademiabaru.com/EST.html

Soret and Dufour Effects on Magneto-hydrodynamics Newtonian Fluid Flow beyond a Stretching/Shrinking Sheet

Open Access

Siti Suzilliana Putri Mohamed Isa[1,2,*], Shahanaz Parvin[1], Norihan Md. Arifin[1,3], Fadzilah Md Ali[1,3]

[1] Institute for Mathematical Research, Universiti Putra Malaysia, 43400 UPM Serdang, Selangor Darul Ehsan, Malaysia.
[2] Centre of Foundation Studies for Agricultural Science, Universiti Putra Malaysia, 43400 UPM Serdang, Selangor Darul Ehsan, Malaysia.
[3] Department of Mathematics, Faculty of Science, Universiti Putra Malaysia, 43400 UPM Serdang, Selangor Darul Ehsan, Malaysia.

ABSTRACT

The numerical reports of magneto- hydrodynamics Newtonian fluid flow, which is induced by a stretching/shrinking sheet is developed. This model is subjected to the impact of Soret and Dufour parameters. The velocity, temperature and concentration of the Newtonian fluid are assumed to have exponential function forms. The governing equations are in the form of partial differential equations (PDE), and contain the features of momentum, energy and concentrations. Subsequently, non-similarity transformation is applied on the governing basic equations. As a result, these PDE will converted to the ordinary differential equations (ODE). These ODE are then solved numerically using the shooting method. The numerical results of skin friction coefficient, local Nusselt number and local Sherwood number are obtained for several sets of values of the parameters. In addition, the profiles of velocity, temperature and concentration are presented due to the effect of controlling parameters. The characteristics of the flow, heat and mass transfer on the Newtonian fluid are described in detail in this study.

Keywords:
Magneto-hydrodynamics; stretching surface; suction; Soret number; Dufour number

Copyright © 2019 PENERBIT AKADEMIA BARU - All rights reserved

1. Introduction

In the process in fluid flow induced by coupled heat and mass transfer, Soret and Dufour effects must not be neglected. The boundary layer fluid flow with the occurrence of coupled heat and mass transfer have significant contributions in heat insulation, compact heat exchangers, paper production, drying technology and catalytic reactors [1]. The mass transfer created by the temperature gradient is called the Soret effect (thermo-diffusion), whilst the heat transfer generated by the concentration gradient is called the Dufour effects (diffusion-thermo). From experimental reports, the diffusion of matter and heat due to Soret and Dufour effects become effective when the gradients of these two elements are very large. When the gradient of the temperature and the concentration are large, the coupled interaction between Soret and Dufour effects are sufficiently great [2]. As a result, the boundary layer layer fluid flow in the presence of heat and mass transfer considering Soret and Dufour effects are being explored due to the stretching or shrinking surface. The published reports are taking into account the various function of stretching/shrinking velocity, temperature and concentration distributions. Therefore, the linear function Soret-Dufour fluid flow model are being explored due to the additional impacts and

* *Corresponding author.*
E-mail address: ctsuzilliana@upm.edu.my (Siti Suzilliana Putri Mohamed Isa)

various types of fluid [3-8]. The impact of magnetic field on the Soret-Dufour fluid flow model are developed by Bég et al. [3] and Hayat et al. [4]. The Soret Dufour fluid flow model on the following fluid: Casson [4], Oldroyd-B [5, 7], hyperbolic tangent [6], and Carreau–Yasuda [8] are reported respectively. These reports [3-8] show different characteristics on the aspects of flow, heat and mass transfer due to the various types of fluid model. However, the velocity of the stretching/shrinking layer may not essentially be linear. The magnetohydrodynamics fluid flow beyond a nonlinear stretching/shrinking sheet are studied by Rashidi et al. [9] and Pal et al. [10]. Besides, the fluid flow model that applied the velocity, temperature and concentration functions in exponential forms were solved theoretically [11-16]. Two-dimensional Soret-Dufour exponential model [11-12, 14, 16] and three-dimensional fluid flow exponential function model [13, 15] are formed on the stretching or shrinking sheet. The various numerical techniques are applied to determine the numerical results from governing equations (which form the equations of momentum, energy and concentration). The methods are namely as Keller-box method [11, 14], Homotopy analysis method [13, 15], shooting method [12] and bvp4c program under Matlab software [16].

Recently, the problem of convection in the fluid bounded/beyond the shape other than flat stretching/shrinking sheet with the addition of Soret-Dufour parameters has been solved. The mixed convection magnetohydrodynamics fluid flow over a rotating vertical cone is studied by Chamkha and Rashad [17]. Ali et al. [18] solved the model problem of Soret-Dufour fluid flow with the occurrence of natural convection in porous trapezoidal enclosures. Meanwhile, Hayat et al. [19] reported the incompressible couple stress fluid in an inclined asymmetric channel, subjected to the effect of magnetic field and chemical reaction. The second grade fluid flow along a cylindrical coordinate system due to the effect of thermal radiation is analysed by Shojaei et al. [20].

This paper applies the problem formulation developed by Srinivasacharya and RamReddy [11], and the fluid model is extended to the permeable shrinking case. The exponential functions of velocity, temperature and concentration is applied in the Soret-Dufour fluid model [11-12, 14, 16]. In addition, previous finding solved the case of mixed convection opposing flow [16]. Besides, this paper changes the previous model [16] to the assisting convective fluid flow. The main purpose of this paper is to explore the Soret and Dufour effects on magneto-hydrodynamics Newtonian fluid flow beyond a stretching/shrinking sheet. The numerical and graphical findings are obtained by using shooting method. Skin friction coefficient, local Nusselt number and local Sherwood number are tabulated for different values of Soret and Dufour number. The graphical results of velocity, temperature and concentration profiles for various values of Soret and Dufour number are explained in details. The main findings are mentioned in the conclusions.

2. Methodology

The two-dimensional of an incompressible, viscous and electrically conducting Newtonian fluid bounded by a stretching/shrinking sheet is considered to develop the mathematical formulation. The exponential variation of the stretching/shrinking sheet is expressed as $u_w(x) = \lambda U_0 \exp(x/L)$. The stretching parameter is denoted as $\lambda > 0$, whereas shrinking parameter is measured when $\lambda < 0$. The stretching/shrinking sheet is placed on the *x*-axis and the uniform magnetic field B_0 is applied on the *y*-axis. Therefore, the model problem are expressed by the governing equations (1-4). These governing equations are continuity, momentum, energy and concentrations. In addition, these governing equations are under the boundary conditions (as shown in Equation 5). The governing equations, together with the boundary conditions are shown, as below:

$$\frac{\partial u}{\partial x}+\frac{\partial v}{\partial y}=0 \tag{1}$$

$$\frac{\partial u}{\partial t}+u\frac{\partial u}{\partial x}+v\frac{\partial u}{\partial y}=\upsilon\frac{\partial^2 u}{\partial y^2}+g\beta_T\left(T-T_\infty\right)+g\beta_C\left(C-C_\infty\right)+\frac{\sigma B_0^2}{\rho}u \tag{2}$$

$$u\frac{\partial T}{\partial x}+v\frac{\partial T}{\partial y}=\alpha\frac{\partial^2 T}{\partial y^2}+\frac{DK_T}{C_sC_P}\frac{\partial^2 C}{\partial y^2} \tag{3}$$

$$u\frac{\partial C}{\partial x}+v\frac{\partial C}{\partial y}=D\frac{\partial^2 C}{\partial y^2}+\frac{DK_T}{T_m}\frac{\partial^2 T}{\partial y^2} \tag{4}$$

$$\begin{aligned} &u=u_w(x)=\lambda U_0\exp(x/L),\quad v=v_w(x),\quad T_w(x)=T_\infty+T_0\exp(x/2L),\\ &C_w(x)=C_\infty+C_0\exp(x/2L), \qquad \text{at } y=0,\\ &u\to 0,\quad T\to T_\infty,\quad C\to C_\infty \qquad \text{as } y\to\infty. \end{aligned} \tag{5}$$

where u and v are the components of velocity in the x and y directions, $\upsilon=\mu/\rho$ is the kinematic viscosity, μ denotes the viscosity, ρ is the fluid density, g is the gravitational acceleration, β_T is the coefficient of thermal expansion, β_C is the coefficient of solutal expansions, T is the temperature of the fluid, C is concentration of the fluid, σ is the electrical conductivity, α is the thermal diffusivity, D is the solutal diffusivity of the medium, K_T is the thermal diffusion ratio, C_S is the concentration susceptibility, C_P is the specific heat at constant pressure, T_m is the mean fluid temperature. and the wall mass suction velocity is represented by $v_w(x)<0$. The term $\exp(x/2L)$ in temperature T_w and concentration distribution C_w are used [11-12, 14, 16] in this problem for the case of two-dimensional flow exponential variation with the presence of Soret-Dufour effects and when concentration equation included in governing equations. The assumption of temperature and concentration functions are to make sure the numerical results will satisfy final boundary condition after substituting similarity variables (Equation 6).

The purpose of using Equation 6 is to convert the governing equations (in the form of partial differential equations PDE) into ordinary differential equations ODE. The list of ODE are presented by Equations (7-9). Besides, the new boundary conditions (Equation 10) will be obtained due to the assistance of similarity variables. Finally, the new ordinary differential equations and boundary conditions are obtained as below:

$$\begin{aligned} &\theta(\eta)=\frac{T-T_\infty}{T_w-T_\infty},\qquad \phi(\eta)=\frac{C-C_\infty}{C_w-C_\infty},\qquad \eta=y\left(\frac{U_0}{2\upsilon L}\right)^{1/2}\exp(x/2L),\\ &u=U_0\exp(x/L)\ f'(\eta), \end{aligned} \tag{6}$$

$$v=-\left(\frac{\upsilon U_0}{2L}\right)^{1/2}\exp(x/2L)\left[f(\eta)+\eta f'(\eta)\right],$$

$$f'''+ff''-2(f')^2+2Ri\left[\exp\left(\frac{-3X}{2}\right)\right](\theta+N\phi)-2H\left[\exp(-X)\right]f'=0. \tag{7}$$

$$\frac{1}{\Pr}\theta''+f\theta'-f'\theta+Db\phi''=0. \tag{8}$$

$$\frac{1}{Sc}\phi''+f\phi'-f'\phi+Sr\,\theta''=0. \tag{9}$$

$$f'(\eta)=\lambda,\ \ f(\eta)=S,\ \theta(\eta)=1,\ \ \phi(\eta)=1\ \ at\ \eta=0$$
$$f'(\eta)\to 0,\ \theta(\eta)\to 0,\ \phi(\eta)\to 0,\ as\ \eta\to\infty \tag{10}$$

where prime indicates the differentiation with respect to η, where η is the boundary layer thickness. The parameters involved in this problem are formulated in Table 1. From this table, negative Ri indicates opposing flow, otherwise it indicates the case of aiding flow. Besides, the profiles of velocity, temperature and concentration are denoted by $f'(\eta), \theta(\eta)$ and $\phi(\eta)$.

Table 1
List of parameters and profiles.

Parameter/Profiles Name	Formula/Denotation
Mixed convection parameter	$Ri = Gr/\mathrm{Re}^2$
Magnetic field parameter	$H = 2\sigma LB_0{}^2/\rho U_0$
Thermal Grashof number	$Gr = g\beta_T (T_0 - T_\infty) L^3/\nu^2$
Reynolds number	$\mathrm{Re} = u_0 L/\nu$
Buoyancy ratio	$N = [\beta_C (C_0 - C_\infty)]/[\beta_T (T_0 - T_\infty)]$
Dimensionless coordinate along the plate parameter, where *L* is the length of the sheet	$X = x/L$
Prandtl number	$\mathrm{Pr} = \upsilon/\alpha$
Schmidt number	$Sc = \upsilon/D$
Soret number	$Sr = [DK_T (T_0 - T_\infty)]/[T_m \upsilon (C_0 - C_\infty)]$
Dufour number	$Db = [DK_T (C_0 - C_\infty)]/[C_s C_p \upsilon (T_0 - T_\infty)]$
Suction parameter	$S = [v_w(x)/\exp(x/2L)] \times \sqrt{2L/\upsilon U_0} > 0$

The physical parameters of skin friction coefficient C_f, local Nusselt number Nu_x and local Sherwood number Sh_x are presented as follow:

$$C_f = \left(\frac{\mu}{\rho U_0{}^2}\right)\left(\frac{\partial u}{\partial y}\right),\quad Nu_x = \left(\frac{L}{T_w - T_\infty}\right)\left(-\frac{\partial T}{\partial y}\right)_{y=0},\quad Sh_x = \left(\frac{L}{C_w - C_\infty}\right)\left(-\frac{\partial C}{\partial y}\right)_{y=0}. \tag{11}$$

Substituting (6) into (11), then we get

$$C_f\sqrt{2\,\mathrm{Re}_x}\exp\left(\frac{-3X}{2}\right) = f''(0),\qquad Nu_x\sqrt{\frac{2}{\mathrm{Re}_x}}\exp\left(\frac{-X}{2}\right) = -\theta'(0),$$
$$Sh_x\sqrt{\frac{2}{\mathrm{Re}_x}}\exp\left(\frac{-X}{2}\right) = -\phi'(0). \tag{12}$$

The numerical solutions are obtained by applying shooting method, which developed in Maple software. The shooting technique gives the solutions for the boundary value problems by changing Equations (7-10) into an initial value problem. The fourth-order of Runge-Kutta integration scheme is applied to solve the initial value problem. We set:

$$f' = fp,$$
$$fp' = fpp,$$
$$fpp' = -\frac{f\ fpp - 2(fp)^2 + 2Ri\left[\exp(-3X/2)\right](\theta + N\phi) - 2H\left[\exp(-X)\right] fp}{1+(1/\omega)} \quad (13)$$

$$\theta' = \theta p,$$
$$\theta p' = -\Pr\left(f\theta p - fp\theta + Db\phi p'\right), \quad (14)$$

$$\phi' = \phi p,$$
$$\phi p' = -Sc\left(f\phi p - fp\phi + Sr\,\theta p'\right), \quad (15)$$

$$fp(\eta) = \lambda,\ f(\eta) = S,\ \theta(\eta) = 1,\ \phi(\eta) = 1 \quad at\ \eta = 0$$
$$fp(\eta) \to 0,\ \theta(\eta) \to 0,\ \phi(\eta) \to 0, \quad as\ \eta \to \infty \quad (16)$$

The guess value for $f''(0), -\theta'(0)$ and $-\phi'(0)$ have to be predicted in this method, together with the guess value of highest boundary layer thickness η_∞. The final numerical results are obtained when the most appropriate value of η_∞ is selected and until two consecutive values of $f''(0),\ \theta'(0)$ and $\phi'(0)$ vary significantly by a specified values.

3. Results and Discussion

Dual numerical solutions are obtained in this article in the graphs of velocity, temperature and concentration profiles. Dual solutions also appeared in the calculations of skin friction coefficient, local Nusselt number and local Sherwood number. However, only one solution is linearly stable and physically realizable. Stable solution shows the satisfaction of boundary conditions (Equation 10) without or with the minimal existence of minimum and maximum peak. This solution can be determined, by performing stability analysis [21]. In this paper, the stability analysis is not calculated due to the limitations of number pages. Therefore, the stable solution is labelled as the first solution and it is selected due to its pattern which follows continuously the boundary conditions. Besides, another solution is labelled as second solution and it is unstable. As a conclusion, second solution is not physically reliable in the actual state of fluid.

Numerical graphics have been performed for the velocity profile $f'(\eta)$, temperature profile $\theta(\eta)$ and concentration profile $\phi(\eta)$ for various values of physical parameters as Soret *Sr* and Dufour parameters *Db*. First and second solutions are drawn by solid and dashed line, respectively. In the present study, the following values are fixed for the entire MatLab programme unless otherwise mentioned: $S = 2.5,\ H = 1,\ Sc = 1,\ \Pr = 1,\ Ri = 1,\ N = 0.5,\ X = 0.1,\ Sr = 2$ and $Db = 0.03$. Moreover, the largest of fluid thickness $\eta = 8$ is constantly used for numerical computations.

The validation of our numerical results obtained from MatLab is performed, by presenting the comparison with the pioneer investigators [11, 22] in the case of exponentially stretching sheet $\lambda > 0$. Magyari and Keller [22] were the original pioneers who studied the flow and thermal boundary layers on a stretching sheet that has temperature and velocity in exponential forms. Besides, Srinivasacharya and RamReddy [11] were the pioneers who explored the model of Soret-Dufour fluid flow, beyond an exponentially stretching sheet. This comparison is reported for the numerical values of wall-temperature gradient $-\theta'(0)$ for various values of Prandtl number $\Pr$ and

stretching parameter λ, as shown in Table 2. As a conclusion, the present values of $-\theta'(0)$ are in good agreement with those reported by the previous investigators. Therefore, the good comparison proves that our shooting method is applicable to use for providing subsequent findings in this paper.

Table 2
The comparison on wall-temperature gradient $\theta'(0)$ for various values of *Sr* and *Db* when *S* = *H* = *Ri* = *Sc* = *N* = *X* = *Sr* = *Db* = 0

λ	Pr	Magyari and Keller [22]	Srinivasacharya and RamReddy [11]	Present
1	1	-0.95478	-0.95478	-0.95478
	3	-1.86908	-1.86908	-1.86907
	5	-2.50014	-2.50015	-2.50013
0.9	1	-	-	0.90579
	3			1.77316
	5			0.07692
0.8	1	-	-	-0.85399
	3			-1.67175
	5			-2.23618

Figure 1 shows the influence of Soret number Sr on velocity (a), temperature (b) and concentration (c) respectively in the flow induced by stretching sheet $\lambda = 1$. The first solution shows the uniform decrement of instantaneous velocity due to the distance from the stretching sheet η, until the velocity reaches constant zero value. Therefore, it is proved that the zero velocity at the point far from stretching sheet denoted that there is no fluid movement at this point. Velocity profiles for second solution decreases for small η and reach minimum point, then it increases until it achieve zero value. The rate of velocity in the first solution increases as the value of Soret number Sr increases. On the other hand, the velocity pattern of second solution due to the impact of Sr shows the same result as the first solution for the small value of η. However, the values of velocity for the second solution influenced by the same parameter is decrease for large value of η. Furthermore, the first solution of temperature distribution decreases with the increasing value of Sr for the small η. However, the effect of Sr is to enhance the rate of $\theta(\eta)$ for the first solution, at the large η. In addition, the effect of Sr is to reduce the temperature profile of the second solution. The concentration profile of the fluid for the first solution has an increment due to impact of Sr at a very small value of η. As the value of Sr and η increase, the value of first solution concentration remain constant. In second solution, the impact of Sr is significant near the stretching sheet, and this point shows the augmentation of concentration.

Figure 2 shows the effect of Dufour number Db on velocity (a), temperature (b) and concentration (c) profiles respectively in the flow induced by stretching sheet $\lambda = 1$. In this figure, as the value of Dufour number increases, the line graph of first solution is clearly shows that the values of velocity as well as the boundary layer thickness increase. However, for second solution, it is observed that the result is same as the first solution for the small value of η. For the thicker fluid, the value of velocity for second solution is decrease. Furthermore, Figure 2 shows the first solution of temperature distribution increases with the increasing value of Db. However, the second solution of temperature distribution decreases for larger η. The concentration profile of the fluid for first solution has a significant increase for a thinner fluid. However, the reversible pattern is observed for a thicker fluid and influenced by the same parameter. This means that the

concentration profile increases for the first solution due to the impact of Db for the very small and very large η. In second solution, the concentration profile is raise up as the value of Dufour number is enhanced.

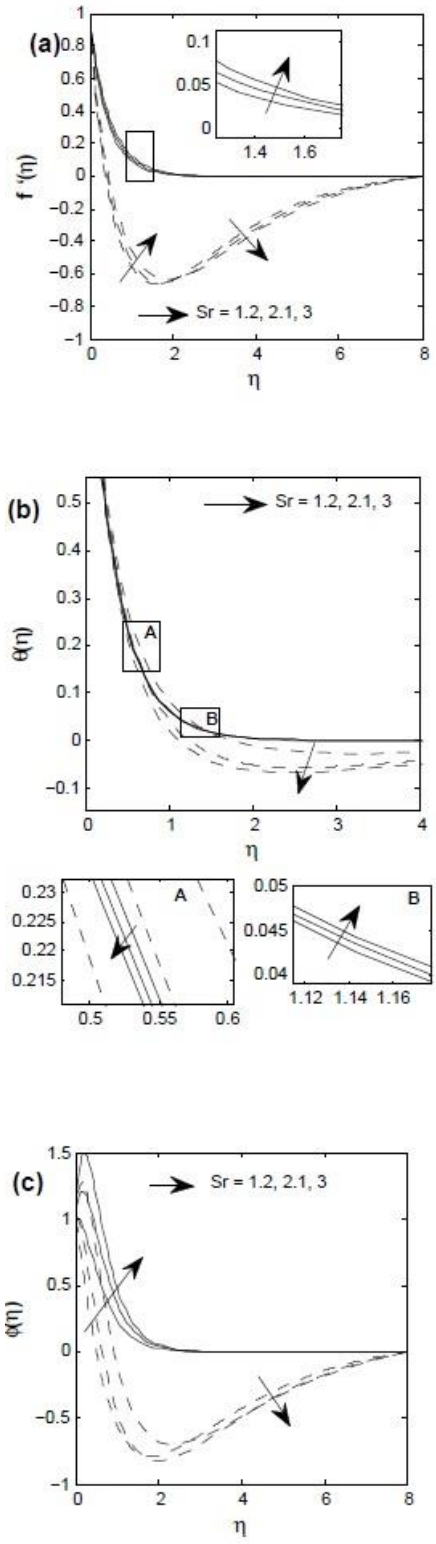


Fig. 1. The effect of Sr on velocity (a), temperature (b) and concentration (c) profiles for the stretching case

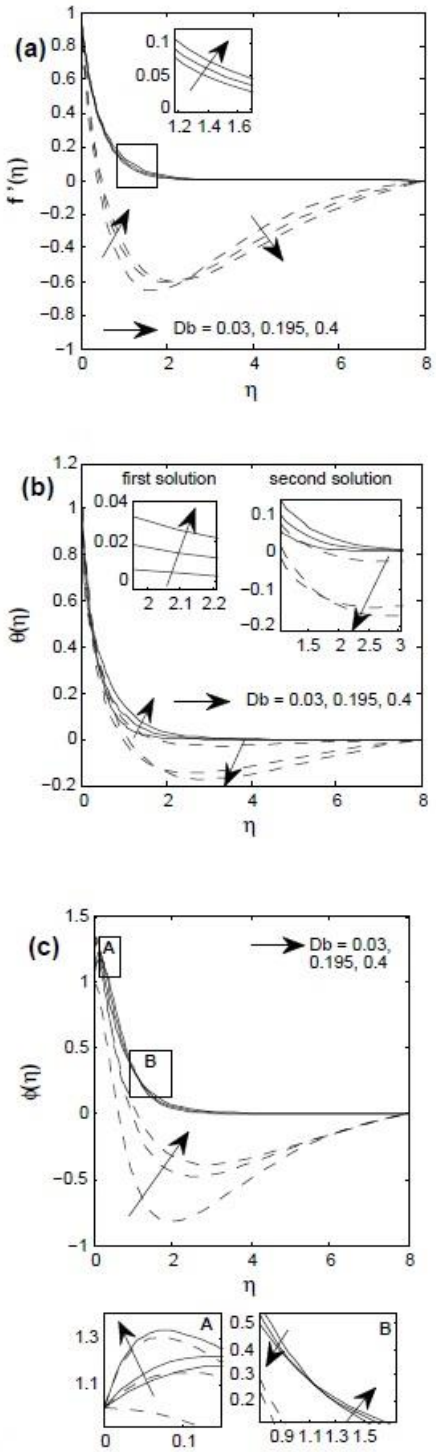


Fig. 2. The effect of Db on velocity (a), temperature (b) and concentration (c) profiles for the stretching case

Figure 3 shows the impact of Soret number Sr on velocity (a), temperature (b) and concentration (c) respectively in the flow due to the shrinking case $\lambda = -1$. It is observed that the velocity profile for the first solutions increases due to the addition of Sr. Besides, the parameter Sr reduces the variation of velocity of the second solution. This figure shows that the first solution temperature profile decreases as the value of Sr increases. This decrement can be seen at the small η for the first solution. The increment of temperature profile for the thicker fluid is observed, by the impact of Sr and for the first solution. The temperature rate is increased for the second solution, due to the parameter Sr. Moreover, this graphic representations show the existence of maximum peak of concentration profile at small η. The first solution concentration reaches certain maximum point and then it continuously reduces, and finally the concentration vanishes. In addition, it is found that the increase of Sr causes an increment of the concentration profile variation for the first solution. The existence of minimum peak can be observed for the second solution concentration variation. When the Soret parameter is incremented, the concentration profile for the second solution decreases.

The impact of Dufour number Db on velocity (a), temperature (b) and concentration profiles (c) are depicted respectively in Figure 4 for the shrinking case $\lambda = -1$. The effectiveness of Db on second solution velocity variation showing that the velocity is increased when the fluid is thin and reduced at the thicker fluid. On the other hand, the velocity profile increases for the first solution. From Figure 4, the temperature profile for the first solution is increased with the increasing value of Db. On the other hand, the decrement of temperature profile can be seen for the second solution. Figure 4 shows that the concentration distribution increases with the increasing Dufour parameter Db, for the first solution. This pattern can be seen at the distance close and far from the shrinking sheet. The impact of Db is significant on second solution concentration profile, showing that the concentration in enhanced due to the same parameter.

From all the figures, they can be seen that Sr and Db have opposite characteristics on the temperature and concentration profiles. These characteristics are described on the first solution only, since this solution is stable and physically reliable. Mass transfer from the lower to the higher rate of concentration due to temperature gradient is recognized by Soret effect. Therefore, concentration is enhanced due to the increment of Soret number (Figure 1 and 3). Concentration gradient induces heat transfer from the lower to the higher temperature profile, which labeled by Dufour effect. As a result, Figure 2 and 4 show that large Db increases temperature and thickness of thermal layer at the distance close to the stretching/shrinking sheet.

The distribution of skin friction coefficient $C_f\sqrt{2\mathrm{Re}_x}\exp(-3X/2)$, local Nusselt number $Nu_x(2/\mathrm{Re}_x)^{1/2}\exp(-X/2)$ and local Sherwood number $Sh_x(2/\mathrm{Re}_x)^{1/2}\exp(-X/2)$ for various values of Soret and Dufour parameters and for stretching and shrinking cases are presented in Tables 3 and 4, respectively. Table 3 shows that both $C_f\sqrt{2\mathrm{Re}_x}\exp(-3X/2)$ and $Nu_x(2/\mathrm{Re}_x)^{1/2}\exp(-X/2)$ are increasing for the first solution when the values of Soret and Dufour number rise, while $Sh_x(2/\mathrm{Re}_x)^{1/2}\exp(-X/2)$ is decreasing due to the same parameters and for the both solutions. From Table 4, it is clear that there are increasing values for $C_f\sqrt{2\mathrm{Re}_x}\exp(-3X/2)$ and decreasing values for $Sh_x(2/\mathrm{Re}_x)^{1/2}\exp(-X/2)$ as the values of Soret and Dufour number is increased for both solutions. The local Nusselt number rate increases with the augmentation of Sr and Db for the second solution and for the shrinking case, as shown in Table 4.

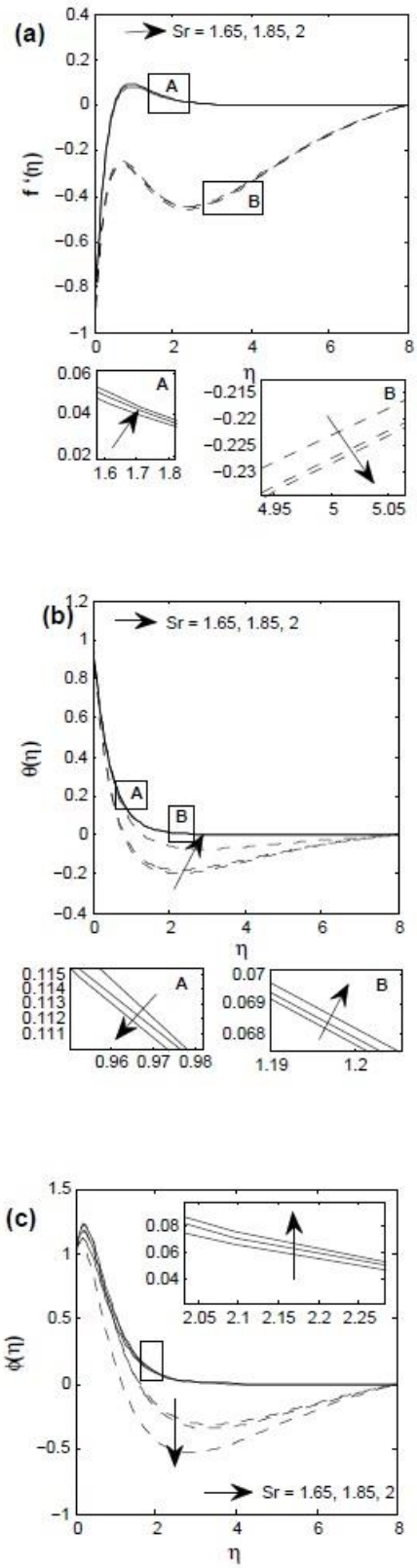


Fig. 3. The effect of Sr on velocity (a), temperature (b) and concentration (c) profiles for the shrinking case

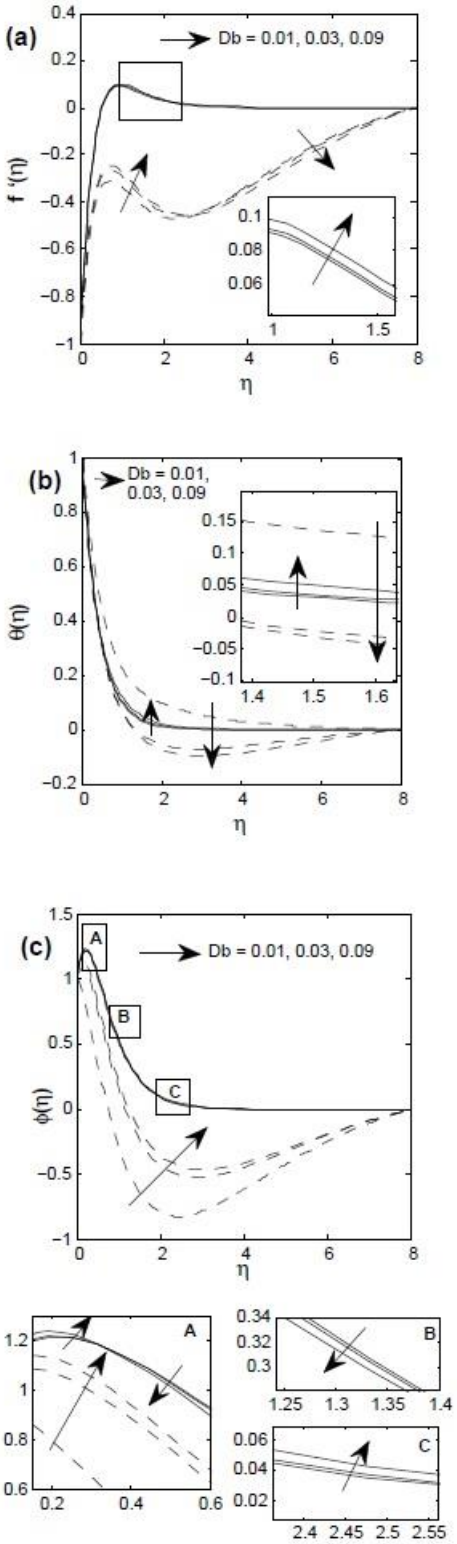


Fig. 4. The effect of Db on velocity (a), temperature (b) and concentration (c) profiles for the shrinking case

Table 3
The values of skin friction coefficient, local Nusselt number and local Sherwood number due to the effect of parameters *Sr* and *Db* for the stretching case (λ = 1)

Parameters	Values	$C_f\sqrt{2\mathrm{Re}_x}\exp(-3X/2)$		$Nu_x\sqrt{2/\mathrm{Re}_x}\exp(-X/2)$		$Sh_x\sqrt{2/\mathrm{Re}_x}\exp(-X/2)$	
		First solution	Second solution	First solution	Second solution	First solution	Second solution
	1.3	-2.58789	-4.07059	2.89582	2.75452	-0.63794	1.67585
Sr	2.1	-2.46788	-3.88627	2.97252	2.74340	-2.92478	-0.36510
	3.0	-2.33589	-3.59395	3.06222	3.05994	-5.63404	-4.17941
Db	0.030	-2.48273	-3.90949	2.96279	2.73702	-2.63288	-0.08310
	0.195	-2.45895	-3.62822	3.68698	3.84603	-4.06988	-3.37517
	0.400	-2.43029	-3.50409	7.89786	8.07367	-12.47691	-12.04820

Table 4
The values of skin friction coefficient, local Nusselt number and local Sherwood number due to the effect of parameters *Sr* and *Db* for the shrinking case (λ = -1)

Parameters	Values	$C_f\sqrt{2\mathrm{Re}_x}\exp(-3X/2)$		$Nu_x\sqrt{2/\mathrm{Re}_x}\exp(-X/2)$		$Sh_x\sqrt{2/\mathrm{Re}_x}\exp(-X/2)$	
		First solution	Second solution	First solution	Second solution	First solution	Second solution
	0.5	2.57800	3.79400	2.37344	2.16731	1.73509	1.07689
Sr	1.0	2.77988	3.91108	2.29725	2.21874	0.76163	-0.06763
	1.9	3.19806	4.11190	2.68274	2.31146	-2.73267	-2.22744
Db	0.03	3.11325	4.13354	2.30703	2.32182	-1.51473	-2.47570
	0.09	3.17325	4.14262	2.54168	2.51275	-2.15800	-2.85551
	0.16	3.94684	4.15310	2.75938	2.82199	-3.62853	-3.47250

4. Conclusions

The effect of increasing Soret number (and a simultaneous decrease in Dufour number) and Dufour number (and a simultaneous decrease in Soret number) on magnetohydrodynamics Newtonian fluid flow beyond a stretching/shrinking sheet are investigated. In this section, only the first solution is described because it is physically possible in actual fluid flow, heat and mass transfer. As a result, the following conclusions have been made:

a) The velocity and concentration profiles for both cases (stretching and shrinking sheet) are increased by increasing the Soret and Dufour numbers. The increment functions of velocity and concentration are significant at the distance close to the stretching sheet. At the same distance, the temperature field is increased when Dufour number increases, and shows reverse pattern due to the impact of Soret number.
b) Skin-friction coefficient increases whereas local Sherwood number decreases with the increasing Sr and Db, for both stretching and shrinking sheets. Local Nusselt number increases for stretching sheet due to the both parameters, whereas it will be increased with the increasing Db.

Acknowledgement

This research was funded by a grant from Universiti Putra Malaysia (Project code: GP-IPM/2018/9596900).

References:

[1] Bhattacharyya, K., G. C. Layek, and G. S. Seth. "Soret and Dufour Effects on Convective Heat and Mass Transfer in Stagnation-Point Flow towards a Shrinking Surface." *Physica Scripta* **89**, 2014: 095203.

[2] Pal, D., Mondal, H, 2013, Influence of Soret and Dufour on MHD Buoyancy-Driven Heat and Mass Transfer over a Stretching Sheet in Porous Media with Temperature-Dependent Viscosity, Nucl Eng Des**, 256**, pp. 350–357.

[3] Bég, O. A., A. Y. Bakier, and V. R. Prasad. "Numerical study of free convection magnetohydrodynamic heat and mass transfer from a stretching surface to a saturated porous medium with Soret and Dufour effects." *Computational Materials Science* 46, no. 1 (2009): 57-65.

[4] Hayat, T., S. A. Shehzad, and A. Alsaedi. "Soret and Dufour effects on magnetohydrodynamic (MHD) flow of Casson fluid." *Applied Mathematics and Mechanics* 33, no. 10 (2012): 1301-1312.

[5] Ashraf, M. B., T. Hayat, A. Alsaedi, and S.A. Shehzad. "Soret and Dufour effects on the mixed convection flow of an Oldroyd-B fluid with convective boundary conditions." *Results in Physics* 6, (2016): 917–924

[6] Hayat, T., M. I. Khan, M. Waqas, and A. Alsaedi. "Stagnation point flow of hyperbolic tangent fluid with Soret-Dufour effects." *Results in Physics* 7, (2017): 2711–2717

[7] Farooq, A., R. Ali, and A. C. Benim. "Soret and Dufour effects on three dimensional Oldroyd-B fluid." *Physica A: Statistical Mechanics and its Applications* 503, (2018): 345-354.

[8] Khan, M. I., T. Hayat, S. Afzal, M. I. Khan, and A. Alsaedi. "Theoretical and numerical investigation of Carreau–Yasuda fluid flow subject to Soret and Dufour effects." *Computer Methods and Programs in Biomedicine* 186, (2020): 105145

[9] Rashidi, M. M., M. Ali, B. Rostami, P. Rostami, and G-N. Xie. "Heat and mass transfer for MHD viscoelastic fluid flow over a vertical stretching sheet with considering Soret and Dufour effects." *Mathematical Problems in Engineering* 2015, (2015): 861065.

[10] Pal, D., G. Mandal, and K. Vajravalu. "Soret and Dufour effects on MHD convective–radiative heat and mass transfer of nanofluids over a vertical non-linear stretching/shrinking sheet." *Applied Mathematics and Computation* 287 (2016): 184-200.

[11] Srinivasacharya, D., and Ch. RamReddy. "Soret and Dufour effects on mixed convection from an exponentially stretching surface." *International Journal of Nonlinear Science* 12, no. 1 (2011): 60–68.

[12] Sreenivasulu, P., and N. B. Redddy. "Soret and Dufour effects on boundary layer flow past an exponential stretching sheet with thermal radiation and viscous dissipation." *Elixir Applied Mathematics* 51, (2012): 10809–10816.

[13] Hayat, T., T. Muhammad, S. A. Shehzad, and A. Alsaedi. "Soret and Dufour effects in three-dimensional flow over an exponentially stretching surface with porous medium, chemical reaction and heat source/sink." *International Journal of Numerical Methods for Heat & Fluid Flow* 25, no. 4 (2015): 762-781.

[14] Sharada, K., and B. Shankar. "MHD mixed convection flow of a Casson fluid over an exponentially stretching surface with the effects of Soret, Dufour, thermal radiation and chemical reaction." World Journal of Mechanics 5, no. 9 (2015): 165–177.

[15] Hayat, T., I. Ullah, T. Muhammad, and A. Alsaedi. "Radiative three-dimensional flow with Soret and Dufour effects." *International Journal of Mechanical Sciences* 133, (2017): 829–837.

[16] Isa, S. S. P. M., N. M. Arifin, and U. Farooq. "Effect of Soret and Dufour numbers on double diffusive mixed convection boundary layer flow induced by a shrinking sheet." Journal of Physics: Conference Series 1298, (2019): 012024.

[17] Chamkha, Ali J., and A. M. Rashad. "Unsteady heat and mass transfer by MHD mixed convection flow from a rotating vertical cone with chemical reaction and Soret and Dufour effects." *The Canadian Journal of Chemical Engineering* 92, no. 4 (2014): 758-767.

[18] Al-Mudhaf, A. F., A.M. Rashad, Sameh E. Ahmed, A. J. Chamkha, and S.M.M. EL-Kabeir. "Soret and Dufour effects on unsteady double diffusive natural convection in porous trapezoidal enclosures." *International Journal of Mechanical Sciences* 140, (2018): 172–178.

[19] Hayat, T., S. Asghar, A. Tanveer, and A. Alsaedi. "Chemical reaction in peristaltic motion of MHD couple stress fluid in channel with Soret and Dufour effects." Results in Physics 10, (2018) 69–80.

[20] Shojaei, A., A. J. Amiri, S. S. Ardahaie, Kh. Hosseinzadeh, and D.D. Ganji. "Hydrothermal analysis of Non-Newtonian second grade fluid flow on radiative stretching cylinder with Soret and Dufour effects. *Case Studies in Thermal Engineering* 13, (2019): 100384.

[21] Ishak, A. "Flow and heat transfer over a shrinking sheet: A stability Analysis." *International Journal of Mechanical, Aerospace, Industrial and Mechatronics Engineering* 8, no. 5 (2014): 902-906.
[22] Magyari, E., Keller, B. “Heat and mass transfer in the boundary layers on an exponentially stretching continuous surface. “ *Journal of Physics D: Applied Physics* 32, (1999): 577–585.

Penerbit Akademia Baru

Engineering Science and Technology Conference Proceedings

Journal homepage: www.akademiabaru.com/EST.html

Dual Numerical Solutions on Mixed Convection Casson Fluid Flow Due to the Effect of The Rate of Extending and Compressing Sheet – Stability Analysis

Open Access

Siti Suzilliana Putri Mohamed Isa[1,2,*], Shahanaz Parvin[1], Norihan Md. Arifin[1,3], Fadzilah Md **Ali**[1,3]

[1] Institute for Mathematical Research, Universiti Putra Malaysia, 43400 UPM Serdang, Selangor Darul Ehsan, Malaysia
[2] Centre of Foundation Studies for Agricultural Science, Universiti Putra Malaysia, 43400 UPM Serdang, Selangor Darul Ehsan, Malaysia
[3] Department of Mathematics, Faculty of Science, Universiti Putra Malaysia, 43400 UPM Serdang, Selangor Darul Ehsan, Malaysia

ABSTRACT

The dual numerical solutions of mixed convection Casson fluid flow, which is subjected to the rate of extending and compressing sheet is reported in this paper. The extending rate is denoted as positive values, otherwise it is declared as compression of the sheet. The usage of similarity variables is to perform the conversion from partial differential equations (PDE) to ordinary differential equations (ODE). The PDE are formed from the equations of momentum, energy and concentration. Finally, ODE are solved numerically by bvp4c program in Matlab software. Stability analysis is performed to deal with dual numerical solutions, which select the most stable solution and physically reliable. The numerical results of velocity, temperature and concentration are presented, subjected to the governed parameters in the modelled problem

Keywords:
Casson fluid; extending/compressing sheet; dual solutions; stability analysis

Copyright © 2019 PENERBIT AKADEMIA BARU - All rights reserved

1. Introduction

Research on non-Newtonian fluid is becoming more important and interesting topics because of its flow characteristics which has variety of industrial applications such as polymer processing, abstraction of crude oil from petroleum products, optical fibers, paper production and hot rolling [1-2]. Among them, Casson fluid has noticeable features because it will deform when the rate of shear stress is higher than yield stress and in reverse condition it will become a solid. The most familiar Casson fluid are namely as jelly, honey, tomato sauce, concentrated fruit juice and chocolate [3]. On the other hand, the usual implementation of fluid flow over stretching/shrinking surface (extending/compressing surface) are as follow: polymer transforming industries, controlling environmental pollution and biological process. As a result, the effect of extending/compressing sheet on casson fluid flow have been explored by many researchers as it is widely using in the sector of science and engineering [1-12]. Mixed convection, which is defined as the combination of forced and natural convection exists when both of these convection mechanisms act together to transfer heat. The numerical results of mixed convection fluid flow bounded by

* *Corresponding author.*
E-mail address: ctsuzilliana@upm.edu.my (Siti Suzilliana Putri Mohamed Isa)

extending/compressing sheet were published, due to their applications in science and engineering [8-11, 15, 17, 21, 25].

In the presence of mixed convection with extending and compressing sheet, there is high possibility to achieve multiple numerical solutions. The occurrence of multiple solutions in the related cases (stretching/shrinking sheet) have been done by some researchers [5, 9, 13-17]. Thus, to verify the excepted solution stability analysis is used, and the rest is decided as unstable. This investigation can be operated by using the bvp4c programme from MATLAB and processed numerically for dual solutions. The solution with initial decay of disturbance labelled as stable solution (first solution). Besides, unstable solution which is mentioned as second solution owns initial growth of disturbance. The application of stability analysis in the related cases (stretching/shrinking sheet) have been done by some researchers [17-20].

The main priority of the study is to examine the dual numerical solutions of mixed convection Casson fluid flow in the presence of extending and compressing sheet. To the best of the researchers' observation, the stability analysis of the current experimentation is not published yet in the literature. This study is chronologically structured as followings: Section 2 is Methodology, Section 3 is Results and Discussion, and final section is Conclusion.

2. Methodology

2.1 Mathematical Formulation

Consider the two-dimensional incompressible, viscous and electrically conducting magneto-hydrodynamics Casson fluid over a permeable extending and compressing surface. The horizontal x-axis is a shrinking/stretching sheet and transverse magnetic field is placed at vertical y-axis. The parameter of Casson fluid ω in Eq. 2 has been derived by the previous report [9]. The mathematical formula are governed by the following equations:

$$\frac{\partial u}{\partial x}+\frac{\partial v}{\partial y}=0 \tag{1}$$

$$\frac{\partial u}{\partial t}+u\frac{\partial u}{\partial x}+v\frac{\partial u}{\partial y}=\upsilon\left(1+\frac{1}{\omega}\right)\frac{\partial^2 u}{\partial y^2}+g\beta_T\left(T-T_\infty\right)+g\beta_C\left(C-C_\infty\right)+\frac{\sigma B_0^2}{\rho}u \tag{2}$$

$$u\frac{\partial T}{\partial x}+v\frac{\partial T}{\partial y}=\alpha\frac{\partial^2 T}{\partial y^2}+\frac{DK_T}{C_sC_P}\frac{\partial^2 C}{\partial y^2} \tag{3}$$

$$u\frac{\partial C}{\partial x}+v\frac{\partial C}{\partial y}=D\frac{\partial^2 C}{\partial y^2}+\frac{DK_T}{T_m}\frac{\partial^2 T}{\partial y^2} \tag{4}$$

where u and v are the components of velocity in the x and y directions, $\upsilon=\mu/\rho$ is the kinematic viscosity, μ denotes the viscosity, ρ is the fluid density, g is the gravitational acceleration, β_T is the coefficient of thermal expansion, β_C is the coefficient of solutal expansions, T is the temperature of the fluid, C is concentration of the fluid, β_0 is the constant strength of magnetic field, σ is the electrical conductivity, α is the thermal diffusivity, D is the solutal diffusivity of the medium, K_T is the thermal diffusion ratio, C_S is the concentration susceptibility, C_P is the specific heat at constant pressure and T_m is the mean fluid temperature. The subscripts w and ∞ at parameters T and C represent the situation at the wall and at the outer region of the boundary layer.

The appropriate boundary conditions are:

$$\begin{aligned} &u = u_w(x) = \lambda U_0 \exp(x/L), \quad v = v_w(x), \quad T_w(x) = T_\infty + T_0 \exp(x/2L), \\ &C_w(x) = C_\infty + C_0 \exp(x/2L), \qquad \text{at } y = 0, \\ &u \to 0, \quad T \to T_\infty, \quad C \to C_\infty \qquad \text{as } y \to \infty. \end{aligned} \tag{5}$$

where $\lambda < 0$ is the compressing parameter whereas positive λ represent the extending parameter. Besides, the wall mass suction velocity is represented by $v_w(x) < 0$. The term $\exp(x/2L)$ in temperature T_w and concentration distribution C_w are taken from [17, 21-23] in the problem for two-dimensional fluid flow with the presence of Soret Dufour effects and when concentration equation is included in governing equations. The assumption of temperature and concentration functions are to make sure the numerical results will satisfy final boundary condition after substituting similarity variables.

The stream function is stated as:

$$\psi(x,y) = (2\upsilon L U_0)^{1/2} \exp(x/2L)\ f(\eta), \qquad u = \frac{\partial \psi}{\partial y}, \qquad v = -\frac{\partial \psi}{\partial x}, \tag{6}$$

Introducing new similarity variables:

$$\begin{aligned} &\theta(\eta) = \frac{T - T_\infty}{T_w - T_\infty}, \qquad \phi(\eta) = \frac{C - C_\infty}{C_w - C_\infty}, \qquad \eta = y\left(\frac{U_0}{2\upsilon L}\right)^{1/2} \exp(x/2L), \\ &u = U_0 \exp(x/L)\ f'(\eta), \\ &v = -\left(\frac{\upsilon U_0}{2L}\right)^{1/2} \exp(x/2L)\left[f(\eta) + \eta f'(\eta)\right], \end{aligned} \tag{7}$$

where prime indicates the differentiation with respect to η.

Substituting Eq. 7 into Eqs. 2 – 5, transformed ordinary differential equations occur in the following form:

$$\left(1+\frac{1}{\omega}\right) f''' + ff'' - 2(f')^2 + 2Ri\left[\exp\left(\frac{-3X}{2}\right)\right](\theta + N\phi) - 2H\left[\exp(-X)\right] f' = 0. \tag{8}$$

$$\frac{1}{\Pr}\theta'' + f\theta' - f'\theta + Db\phi'' = 0. \tag{9}$$

$$\frac{1}{Sc}\phi'' + f\phi' - f'\phi + Sr\theta'' = 0. \tag{10}$$

The new boundary conditions are

$$\begin{aligned} &f'(\eta) = \lambda, \ f(\eta) = S, \ \theta(\eta) = 1, \ \phi(\eta) = 1 \ \ at\ \eta = 0 \\ &f'(\eta) \to 0, \ \theta(\eta) \to 0, \ \phi(\eta) \to 0, \ as\ \eta \to \infty \end{aligned} \tag{11}$$

The parameters involved in this problem are mixed convection parameter $Ri = Gr/\mathrm{Re}^2$, magnetic field parameter $H = 2\sigma L B_0^{\,2}/\rho U_0$, thermal Grashof number $Gr = g\beta_T (T_0 - T_\infty) L^3/\nu^2$, Reynolds number $\mathrm{Re} = u_0 L/\nu$, dimensionless coordinate along the plate parameter $X = x/L$,

length of the extended/compressed sheet L, buoyancy ratio $N=\beta_C\left(C_0-C_\infty\right)/\beta_T\left(T_0-T_\infty\right)$, Prandtl number $\Pr=\upsilon/\alpha$, Schmidt number $Sc=\upsilon/D$, Soret number $Sr=DK_T\left(T_0-T_\infty\right)/T_m\,\upsilon\left(C_0-C_\infty\right)$, Dufour number $Db=DK_T\left(C_0-C_\infty\right)/C_s\,C_p\upsilon\left(T_0-T_\infty\right)$, and suction parameter is defined as $S=\left(v_w\left(x\right)/\exp\left(x/2L\right)\right)\times\sqrt{2L/\upsilon U_0}>0$. The opposing flow is when $Ri<0$. Otherwise, the positive Ri indicates the case of aiding flow.

2.2 Stability Analysis

The initial step of stability analysis is to write down the governing equations in the state of unsteady. Then, the dimensionless variable τ is introduced [24] in similarity variables.

$$\frac{\partial u}{\partial t}+u\frac{\partial u}{\partial x}+v\frac{\partial u}{\partial y}=\upsilon\left(1+\frac{1}{\omega}\right)\frac{\partial^2 u}{\partial y^2}+g\beta_T\left(T-T_\infty\right)+g\beta_C\left(C-C_\infty\right)+\frac{\sigma\beta_0^2}{\rho}u \tag{12}$$

$$\frac{\partial T}{\partial t}+u\frac{\partial T}{\partial x}+v\frac{\partial T}{\partial y}=\alpha\frac{\partial^2 T}{\partial y^2}+\frac{DK_T}{C_sC_P}\frac{\partial^2 C}{\partial y^2} \tag{13}$$

$$\frac{\partial C}{\partial t}+u\frac{\partial C}{\partial x}+v\frac{\partial C}{\partial y}=D\frac{\partial^2 C}{\partial y^2}+\frac{DK_T}{T_m}\frac{\partial^2 T}{\partial y^2} \tag{14}$$

New similarity variables are

$$\begin{aligned}&\theta\left(\eta,\tau\right)=\frac{T-T_\infty}{T_w-T_\infty},\quad \phi\left(\eta,\tau\right)=\frac{C-C_\infty}{C_w-C_\infty},\quad \tau=\frac{U_0}{2L}\left(\exp\left(x/L\right)\right)t,\quad \eta=y\left(\frac{U_0}{2\upsilon L}\right)^{1/2}\exp\left(x/2L\right),\\ &u=U_0\exp\left(x/L\right)\frac{\partial}{\partial\eta}f\left(\eta,\tau\right),\\ &v=-\frac{\eta}{2L}\sqrt{2\upsilon LU_0}\exp\left(x/2L\right)\frac{\partial}{\partial\eta}f\left(\eta,\tau\right)-\frac{U_0}{2L^2}\exp\left(3x/L\right)t\sqrt{2\upsilon LU_0}\frac{\partial}{\partial\tau}f\left(\eta,\tau\right)\\ &\quad-\frac{1}{2L}\sqrt{2\upsilon LU_0}\exp\left(x/2L\right)f\left(\eta,\tau\right)\end{aligned} \tag{15}$$

The analysis introduced by previous investigators in stability field [24] are stated as below:

$$\begin{aligned}&f\left(\eta,\tau\right)=f_0\left(\eta\right)+\left(\exp\left(-\gamma\tau\right)\right)F\left(\eta,\tau\right),\quad \theta\left(\eta,\tau\right)=\theta_0\left(\eta\right)+\left(\exp\left(-\gamma\tau\right)\right)G\left(\eta,\tau\right),\\ &\phi\left(\eta,\tau\right)=\phi_0\left(\eta\right)+\left(\exp\left(-\gamma\tau\right)\right)H\left(\eta,\tau\right),\end{aligned} \tag{16}$$

where γ denotes an unknown eigenvalue while $F\left(\eta,\tau\right)$, $G\left(\eta,\tau\right)$ and $H\left(\eta,\tau\right)$ are small relative to $f_0\left(\eta\right)$, $\theta_0\left(\eta\right)$ and $\phi_0\left(\eta\right)$. Eq. 16 is substituted into governing equations (Eqs. 12 -14) and boundary conditions (Eq. 11) and set $\tau=0$. As a result, the following equations are obtained:

$$\begin{aligned}&\left(1+\frac{1}{\omega}\right)F_0'''+f_0F_0''+f_0''F_0-4f_0'F_0'\\ &+2Ri\left(\exp\left(\frac{-3X}{2}\right)\right)\left(G_0+NH_0\right)+\left[\gamma-2H\left(\exp\left(-X\right)\right)\right]F_0'=0\end{aligned} \tag{17}$$

$$\frac{1}{\mathrm{Pr}}G_0'' + f_0G_0' + \theta_0'F_0 - \theta_0F_0' - G_0f_0' + Db\,H_0'' + \gamma G_0' = 0 \quad (18)$$

$$\frac{1}{Sc}H_0'' + f_0H_0' + \phi_0'F_0 - \phi_0F_0' - H_0f_0' + Sr\,G_0'' + \gamma H_0' = 0 \quad (19)$$

with the boundary conditions

$$\begin{aligned} &F_0'(\eta)=0, \quad F_0(\eta)=0, \quad G_0(\eta)=0, H_0(\eta)=0 \qquad \text{at } \eta=0, \\ &F_0'(\eta)\to 0, \quad G_0(\eta)\to 0, \quad H_0(\eta)\to 0 \qquad \text{as } \eta\to\infty. \end{aligned} \quad (20)$$

For the present problem, the first boundary condition as $\eta\to\infty$ is relaxed. The relaxation technique of boundary condition has been described by the previous investigators [25]. Finally, the Eqs. 17 – 19 along with the new boundary condition $F_0''(0)=1$ is solved in Matlab software.

3. Results and Discussion:

Numerical computations are generated by using bvp4c MATLAB programming method and the resulting data are presented graphically by velocity profiles, temperature profiles and concentration profiles for different values of extending and compressing parameter. Negative λ denotes the shrinking parameter, where as positive one for stretching parameter. The calculation is performed by using the fixed values of the following parameters unless otherwise mentioned:, ω = 1800, *Pr* = 1, *Sc* = 0.5, *Ri* = -0.01, *N* = 0.5, *Db* = 0.1, *Sr* = 1.8, *S* = 3.1, *X* = -0.5 and *H* = 0.02. Since we got dual solutions, first solution is identified as solid line and the dashed line indicates the second solution.

The authentication of numerical results occurred from MATLAB programming is performed. The current numerical data is compared with the result by previous investigators [21] for the case of exponentially extending sheet (λ > 0) and for various values of Prandtl number *Pr*. This table is tabulated for the following fixed values: *Ri* = 1.0, *Sr* = 2.0, *Db* = 0.03, *X* = 0.5, ω = 100000000, *Sc* = 0.22, *N* = 0.5 and *H* = *S* = 0.The comparison values of skin friction coefficient, local Nusselt number and local Sherwood number are presented in Table 1. The formulation of skin friction coefficient, local Nusselt number and local Sherwood number are reported as $C_f\sqrt{2\mathrm{Re}_x}\exp(-3X/2)$, $Nu_x\sqrt{2/\mathrm{Re}_x}\exp(-X/2)$ and $Sh_x\sqrt{2/\mathrm{Re}_x}\exp(-X/2)$, respectively [21]. As a conclusion, these values are in good agreement compared with previous researchers.

The function of stability analysis is to select the solution which is stable and physically reliable. The declaration of the stable solution is obtained when the values of smallest eigenvalue γ is positive, otherwise it is unstable and not physically occur in actual state in fluid. Table 2 represents the stability analysis for several values of compressing parameter at *S* =1.7 and 1.72. For the smallest eigenvalue, γ first solution are positive whereas opposite for second solution. Positive value represents the acceptance of first solution and the second solution is unstable and rejected. Moreover, the stable solution always following the conditions at the boundary (Equation 11), with minimal existence of minimum or maximum peaks (see Figures 1-9). Therefore, all of the results in this articles (only for the first solution) are stable, accepted and really occur in the actual mechanism in fluid flow.

From the first solution in Figure 1, the velocity value for the compressing sheet is negative at the wall and the value is increasing until it reaches zero velocity for large η. However, for the case of extending sheet the velocity value for the first solution is positive for the small η, and it decreases until velocity is zero. Negative velocity when $\lambda < 0$ indicates the opposite direction of instantaneous fluid flow, compared to the case of fluid flow affected by extending sheet $\lambda > 0$. Moreover, the highest velocity is obtained at the sheet ($\eta = 0$) for the extending sheet (highest λ). However, minimum peak arises for the second solution in velocity profile. For the temperature and concentration profiles (Figure 2 and 3) these values go down with the raising of η and λ. The effect of λ on temperature and concentration profiles are significant at the point close to the sheet (small η). The occurrence of maximum peak is observed at concentration profile, near to the sheet. Therefore, the concentration level is the highest at that point.

Table 1
The comparison with the previous researchers [21] for a) skin friction coefficient, b) local Nusselt number and c) local Sherwood number

λ	Pr	a)		b)		c)	
		[21]	Present	[21]	Present	[21]	Present
1	1.0	-0.63185	-0.63185	1.11260	1.11260	0.07884	0.07884
	3.0	-0.70730	-0.70730	2.03606	2.03605	-0.13554	-0.31553
	5.0	-0.73931	-0.73931	2.70661	2.70657	-0.60416	-0.60414
1.02	1.0		-0.52867		1.09382		0.08111
	3.0	-	-0.60440	-	1.99450	-	-0.30392
	5.0		-0.63670		2.64803		-0.58536

Table 2
The smallest eigenvalues for various values of compressing parameter

S	λ	Solutions	
		First solution	Second solution
1.70	-0.4000	0.19877	-0.20665
	-0.4002	0.19785	-0.20566
	-0.4004	0.19693	-0.20466
1.72	-0.4000	0.26728	-0.28206
	-0.4002	0.26661	-0.28131
	-0.4004	0.26594	-0.28055

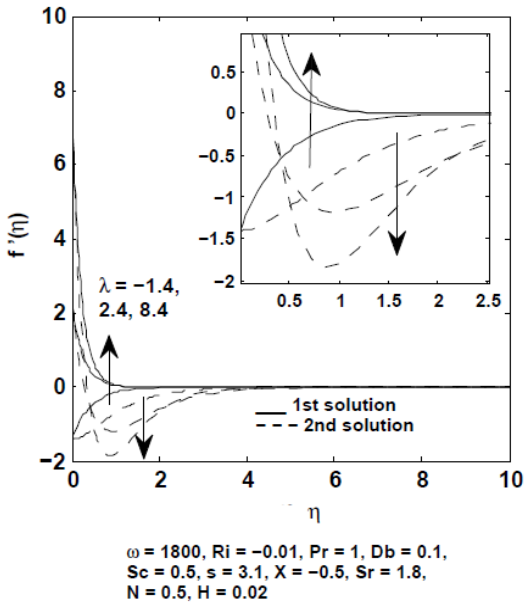


Fig. 1. Velocity profile for different values of λ

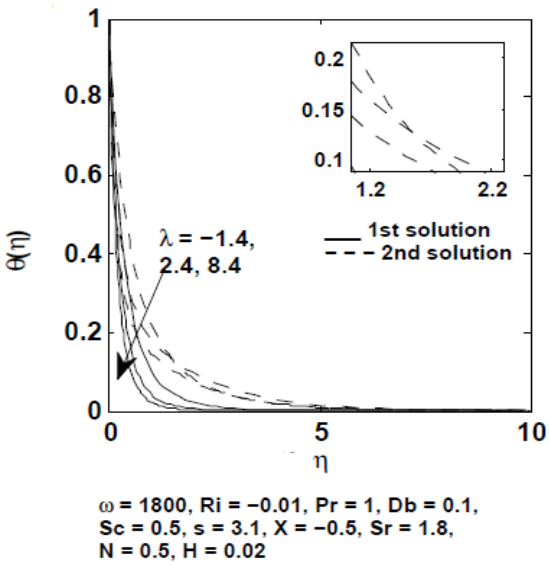


Fig. 2. Temperature profile for different values of λ

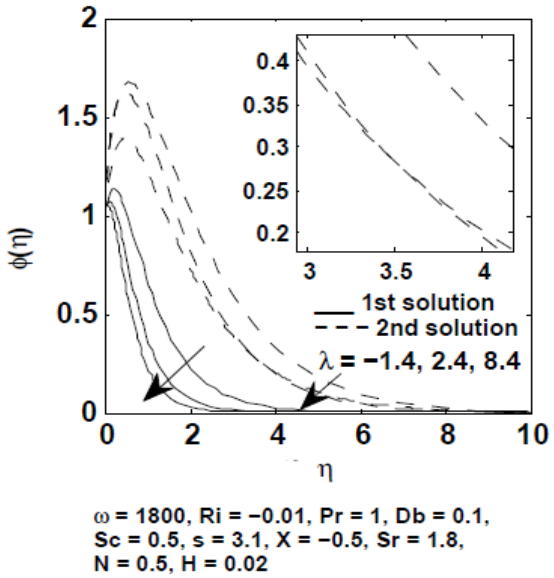


Fig. 3. Concentration profile for different values of λ

4. Conclusions

The dual numerical solutions of mixed convection Casson fluid flow, which is subjected to the rate of extending and compressing sheet are investigated. Observing the findings from figures and tables following conclusions are noted:

a) Results comparing with the previous work it is clear that Matlab programming are acceptable to obtain the numerical calculation.
b) Velocity is negative near the wall for shrinking sheet, whereas it is positive for extending case and coincides as it goes far from the wall.
c) Temperature and concentration profiles, both are declined with the increment of λ and η for both solutions and if the distance from the wall increased (η become larger), effects of temperature and concentration becomes negligible.

Acknowledgement

This research was funded by a grant from Universiti Putra Malaysia (Project code: GP-IPM/2018/9596900).

References

[1] Nadeem, S., R. U. Haq, N. S. Akbar, and Z. H. Khan. "MHD three-dimensional Casson fluid flow past a porous linearly stretching sheet." *Alexandria Engineering Journal* 52, no. 4 (2013): 577-582.
[2] Haq, R. U., S. Nadeem, Z. Khan, and T. G. Okedayo. "Convective heat transfer and MHD effects on Casson nanofluid flow over a shrinking sheet." *Open Physics* 12, no. 12 (2014): 862-871.
[3] Ibrahim, S. M., G. Lorenzini, P. V. Kumar, and C. S. K. Raju. "Influence of chemical reaction and heat source on dissipative MHD mixed convection flow of a Casson nanofluid over a nonlinear permeable stretching sheet." *International Journal of Heat and Mass Transfer* 111 (2017): 346-355.
[4] Nadeem, S., R. U. Haq, and C. Lee. "MHD flow of a Casson fluid over an exponentially shrinking sheet." *Scientia Iranica* 19, no. 6 (2012): 1550-1553.
[5] S. P. M. Isa, N. M. Arifin, R. Nazar, N. Bachok, F. M. Ali, and I. Pop. "Forced Convection in a Casson Fluid Flow due to a Flat Sheet in Motion." *Indian Journal of Science and Technology* 8 no. 32 (2015): 1-7.
[6] Abbas, Z., M. Sheikh, and S. S. Motsa. "Numerical solution of binary chemical reaction on stagnation point flow of Casson fluid over a stretching/shrinking sheet with thermal radiation." *Energy* 95 (2016): 12-20.

[7] Qing, J., M. M. Bhatti, M. A. Abbas, M. M. Rashidi, and M E. Hassan. "Entropy generation on MHD Casson nanofluid flow over a porous stretching/shrinking surface." *Entropy* 18, no. 4 (2016): 123.
[8] Ullah, I., K. Bhattacharyya, S. Shafie, and I. Khan. "Unsteady MHD mixed convection slip flow of Casson fluid over nonlinearly stretching sheet embedded in a porous medium with chemical reaction, thermal radiation, geat generation/absorption and convective boundary conditions. *PLoS ONE* 11, no. 10 (2016): e0165348.
[9] Isa, S. S. P. M., N. M. Arifin, R. Nazar, N. Bachok, F. M. Ali, and I. Pop. "MHD Mixed Convection Boundary Layer Flow of a Casson Fluid Bounded by Permeable Shrinking Sheet with Exponential Variation." *Sciencia Iranica* 24, no. 2 (2017): 637–647.
[10] Rawi, N. A., M. R. Ilias, Y. J. Lim, Z. M. Isa, and S. Shafie. "Unsteady mixed convection flow of Casson fluid past an inclined stretching sheet in the presence of nanoparticles." *Journal of Physics: Conference Series* 890, (2017): 012048.
[11] Bilal Ashraf, M., T. Hayat, and A. Alsaedi. "Mixed convection flow of Casson fluid over a stretching sheet with convective boundary conditions and Hall effect." *Boundary Value Problems* 2017, (2017): 137.
[12] Eswaramoorthi, S., S. Sivasankaran, and A. S. Alshomrani. "Effect of thermal radiation and heat absorption of MHD Casson nanofluid over a stretching surface in a porous medium with convective heat and mass conditions." In *Journal of Physics: Conference Series*, vol. 1139, no. 1, p. 012017. IOP Publishing, 2018.
[13] Zaib, A., K. Bhattacharyya, M. Uddin, and S. Shafie. "Dual solutions of non-Newtonian Casson fluid flow and heat transfer over an exponentially permeable shrinking sheet with viscous dissipation." *Modelling and Simulation in Engineering* 2016, (2016): 6968371.
[14] Vajravelu, K., G. Sarojamma, K. Sreelakshmi, and Ch Kalyani. "Dual solutions of an unsteady flow, heat and mass transfer of an electrically conducting fluid over a shrinking sheet in the presence of radiation and viscous dissipation." *International Journal of Mechanical Sciences* 130 (2017): 119-132.
[15] Isa, S. S. P. M., N. M. Arifin, R. Nazar, N. Bachok, and F. M. Ali. "The effect of convective boundary condition on MHD mixed convection boundary layer flow over an exponentially stretching vertical sheet." *Journal of Physics: Conference Series* 949, (2017): 012016.
[16] Isa, S. S. P. M., N. M. Arifin, and U. Farooq. "The impact of slip conditions on magnetohydrodynamics radiating fluid beyond an exponentially extended sheet." *Journal of Physics: Conference Series* 1039, (2018): 012015.
[17] Isa, S. S. P. M., N. M. Arifin, and U. Farooq. "Effect of Soret and Dufour numbers on double diffusive mixed convection boundary layer flow induced by a shrinking sheet." *Journal of Physics: Conference Series* 1298, (2019): 012024.
[18] Ishak, A. "Flow and heat transfer over a shrinking sheet: A stability Analysis." *International Journal of Mechanical, Aerospace, Industrial and Mechatronics Engineering* 8, no. 5 (2014): 902-906.
[19] Adnan, N. S. M., and N. M. Arifin. "Stability analysis of boundary layer flow and heat transfer over a permeable exponentially shrinking sheet in the presence of thermal radiation and partial slip." In *Journal of Physics: Conference Series*, vol. 890, no. 1, p. 012046. IOP Publishing, 2017.
[20] Najib, N., N. Bachok, N. M. Arifin and F. M. Ali. "Stability analysis of stagnation-point flow in a nanofluid over a stretching/shrinking Sheet with second-order slip, Soret and Dufour effects: A revised model. " *Applied Sciences* 2018, 8, 642.
[21] Srinivasacharya, D., and Ch RamReddy. "Soret and Dufour effects on mixed convection from an exponentially stretching surface." *International Journal of Nonlinear Science* 12, no. 1 (2011): 60-68.
[22] Sreenivasulu, P., and N. Bhaskar Reddy. "Thermo-diffusion and diffusion-thermo effects on MHD boundary layer flow past an exponential stretching sheet with thermal radiation and viscous dissipation." *Advances in Applied Science Research* 3, no. 6 (2012): 3890-3901.
[23] Hayat, T., T. Muhammad, S. A. Shehzad, and A. Alsaedi, "Soret and Dufour effects in three-dimensional flow over an exponentially stretching surface with porous medium, chemical reaction and heat source/sink." *International Journal of Numerical Methods for Heat & Fluid Flow* 25, no. (2015): 762-781.
[24] Weidman, P. D., D. G. Kubitschek, and A. M. J. Davis. "The effect of transpiration on self-similar boundary layer flow over moving surfaces." *International Journal of Engineering Science* 44, no. 11-12 (2006): 730-737.
[25] Harris, S. D., D. B. Ingham, and I. Pop. "Mixed convection boundary-layer flow near the stagnation point on a vertical
surface in a porous medium: Brinkman model with slip." *Transport in Porous Media* 77, no. 2 (2009): 267-285.

Penerbit Akademia Baru

Engineering Science and Technology Conference Proceedings

Journal homepage: www.akademiabaru.com/EST.html

Open Access

CFD Simulation of Steam Condensation in Nozzle using Different Turbulence Models

Norhazwani Abd Malek[1,*], Muhammad Hydil Arief Md Razip[2]

[1] Centre for Fluid Dynamics, Department of Mechanical Engineering, College of Engineerging, Universiti Tenaga Nasional, Jalan IKRAM-UNITEN,
[2] Tenaga Nasional Berhad

ABSTRACT

In this study, the computational fluid dynamic (CFD) simulations in a nozzle and the validation of the numerical approach using the geometry and experimental data reported by Moore et al. [1] have been done. The purpose of this research is to study the behavior of wet steam in a converging-diverging nozzle as well as to understand the steam spontaneous condensation for the interpretation of droplet size, velocity and pressure measurement, etc. There are three turbulence models that have been utilized in this work namely the realizable k-ε, standard k-ω and Spalart-Allmaras. These methods are economical compared to Direct Numerical Simulation (DNS) or Large Eddy Simulation (LES) which require a high computation power and longer time to solve. For the pressure profile, the general trend of the graph is decreasing with the axial distance of the nozzle but there is a sudden pressure increase downstream of the nozzle throat which indicates the onset of spontaneous condensation. Subsequently, the velocity profile of the flow can be deducted from the Mach number, where the trend of the graph is the inverse to the pressure graph. At the spontaneous condensation location, the supercooling increases due to the increment of water droplets in that area. This in turn leads to the drop of the flow temperature at the affected area due to the water droplet is absorbing the surrounding heat in that particular area. In addition to that, the comparison between the three different turbulence models show that the realizable k-ε and Spalart-Allmaras models display the closest results to the experimental values and numerical simulations done by Sharifi et al. [23]. This may be due to the models that are suitable for the round jet flow. As for the standard k-ω model, the results obtained using this model deviates quiet noticeably from the results obtained from the other models as this model is not modified to cater for the round jet type of flow. All in all, the behavior of wet steam in a convergent-divergent nozzle can be understood and predicted. This will help in understanding a similar but more complex phenomenon occurred in the turbine cascades as the behavior is quite similar. In the future, it is recommended to include more turbulence models as comparisons, user-defined function (UDF) in the Fluent
simulations and turbine cascades are used as the geometry.

Keywords:
Nozzle; wet steam; turbulence model

Copyright © 2019 PENERBIT AKADEMIA BARU - All rights reserved

1. Introduction

Despite many promising advancements in the field of green energy or renewable energy, steam turbine still remains the primary source of production of electricity. Steam turbine utilizes high pressure, superheated steam in order to turn the rotor that is coupled to the generator. This is achieved by converting the high potential energy in the superheated steam to kinetic energy by means of nozzles (fixed blades). Steam expands in the nozzles due to the pressure drop, forming a high-speed jet flow. As with any other mechanical equipment, the main concern of a steam turbine is its efficiency. However, the efficiency of steam turbine is decreased due to the spontaneous

* *Corresponding author.*
E-mail address: norhazwani@uniten.edu.my (Norhazwani Abd Malek)

condensation. The condensing steam, which is also known as wet steam is mostly formed at the low pressure (LP) steam turbine as the pressure drops rapidly at this stage. Transformation of steam which is in gaseous state into its liquid form is an undesired occurrence in a steam turbine because not only it causes thermodynamic losses but it also damages the turbine blades over the time. Hence, more cost is needed to repair or replace the affected blades. With that being said, it is of the utmost importance to understand the behavior of the wet steam in a steam turbine specifically at the nozzle section where steam expansion takes place, so that the occurrence can be predicted and the effects can be reduced.

Condensation of steam is not a new topic to the field of engineering especially when involving a flow in a converging-diverging nozzle. In fact, it has been studied vigorously for over five decades and was initially concentrated on one-dimensional (1D) and two-dimensional (2D) flow calculations and experiments in Laval nozzles by some pioneers like Moore et al. [1], Gyamarthy [2-3], Skillings et al. [4], Moses and Stein [5], and Hill [6]. Developing mathematical models for the theoretical investigations of wet steam have also been done by many researchers and discussed by them in the literature [7-14]. Nowadays, the commercial Computational Fluid Dynamics (CFD) packages facilitate many things and save time. However, to make use of the CFD packages, numerical methodology underlying the packages must first be understood.

In the past decades, many researchers have used the wet steam model adopted in the commercial CFD packages to simulate the wet steam flows with different geometries and conditions [15-19]. However, it was reported by Giacomelli et al. [20] and Mazelli et al. [21] that the wet steam built-in models in the commercial codes generally have some limitations in the change of the physical parameters and settings. In their work, they developed their own customized model via the user defined function (UDF) within a commercial code, ANSYS Fluent. There were also some other researchers who employed UDF in their work [22-23]. Although the results show very good agreement with the well-known experimental data, the works require skills in translating the related equations to the programming language, hence giving more complexity to flow analysis. In this study, the basic fundamental knowledge underlying the wet steam model used in ANSYS Fluent is discussed. All of the simulations done in this work is done on one of the nozzles by Moore et al. [1], which is Nozzle B. The geometry of the nozzle is taken from Sharifi et al. [23] and chosen among all the four nozzles done by Moore et al. as it shows better agreement between the experimental values and numerical values by both researchers respectively, compared to the other nozzle geometries. Realizing the importance of turbulence that influences the wet steam flow as discussed in [24], this study will also employ a few turbulence models available in ANSYS Fluent.

2. Methodology

2.1 The Governing Equations and Limitations

ANSYS Fluent has employed the Eulerian-Eulerian approach for modeling wet steam flow by using the general compressible Navier-Stokes equations, coupled with the two transport equations for the liquid mass fraction and the number of liquid droplets per unit volume. The primary transport variables are the velocity vector $u_i(\mathbf{x}, t)$, the fluid pressure $p(\mathbf{x}, t)$, the fluid density $\rho(\mathbf{x}, t)$ and the energy $e(\mathbf{x}, t)$, where $\mathbf{x}$ denotes the spatial coordinates. These variables are obtained via the conservation of mass, momentum and energy:

$$\frac{\partial \rho}{\partial t} + \frac{\partial}{\partial x_i}\left[\rho u_j\right] = 0 \tag{1}$$

$$\frac{\partial \rho}{\partial t}[\rho u_i] + \frac{\partial}{\partial x_j}\left[\rho u_i u_j + p\partial_{ij} - \tau_{ij}\right] = 0 \quad (2)$$

$$\frac{\partial \rho}{\partial t}[\rho e_0] + \frac{\partial}{\partial x_j}\left[\rho u_j e_0 + u_j p + q_j - u_i \tau_{ij}\right] = 0 \quad (3)$$

where τ_{ij} is the stress tensor. The solution of the governing equations is achieved through its built-in steam property functions that uses a density-based solver.

When using the wet steam model in ANSYS Fluent, it is to be assumed that the velocity slip between the droplets and gaseous-phase is negligible, the interactions between droplets are neglected, the mass fraction of the condensed liquid phase, β is small which is less than 0.2. Since droplet sizes are typically very small, it is assumed that the volume of the condensed liquid phase is negligible. Following that, the mixture density ρ can be related to the vapor density ρ_v by the following equation:

$$\rho = \frac{\rho_v}{1-\beta} \quad (4)$$

The mixture flow is governed by the compressible Navier-Stokes equations given in vector form by the equation:

$$\frac{\partial \boldsymbol{W}}{\partial \boldsymbol{Q}} = \frac{\partial}{\partial \boldsymbol{t}}\int_V \boldsymbol{Q}\, dV + \oint[\boldsymbol{F} - \boldsymbol{G}]\,.\,d\boldsymbol{A} = \int_V \boldsymbol{H}\, dV \quad (5)$$

where **Q** = (P,u,v,w,T) are mixture quantities.

The transport equation governs the mass fraction of the condensed liquid phase, β is given by:

$$\frac{\partial \rho\beta}{\partial t} + \nabla.(\rho\vec{v}\beta) = \Gamma \quad (6)$$

where Γ is the mass generation rate due to condensation and evaporation (kg per unit volume per second). The other transport equation calculates the number density of the droplets per unit volume:

$$\frac{\partial \rho\eta}{\partial t} + \nabla.(\rho\vec{v}\eta) = \rho I \quad (7)$$

where I is the nucleation rate (number of new droplets per unit volume per second). To determine the number of droplets per unit volume, the equation below is used:

$$\eta = \frac{\beta}{(1-\beta)V_d\left(\frac{\rho_l}{\rho_v}\right)} \quad (8)$$

where ρ_l is the liquid density and the average droplet volume is obtained from:

$$V_d = \frac{4}{3}\pi \bar{r}_d{}^3 \quad (9)$$

$\bar{r}_d$ is the droplet radius. Equation (5), (6) and (7) form a closed system of equations which when combined with Equation (4) allows the calculation of the wet steam flow field.

The phase change model, which involves the formation of liquid droplets in a homogeneous non-equilibrium condensation process, is based on the classical non-isothermal nucleation theory. Some assumptions are made, in which the condensation is homogeneous, meaning that no impurities present to form nuclei, the droplet growth is based on average mean radii, while the droplet is spherical and surrounded by infinite vapor space. Other than that, the heat capacity of the fine droplet is negligible compared with the latent heat released in condensation. The

spontaneous condensation occurs in non-equilibrium manner. Based on classical nucleation theory, the mass generation rate is given by:

$$\Gamma = \frac{4}{3}\pi\rho_l I r^{*3} + 4\pi\rho_l \eta \bar{r}_d{}^2 \frac{\partial \bar{r}}{\partial t} \quad (10)$$

$\bar{r}$ is the average radius of the droplet and $r^*$is the Kelvin-Helmholtz critical droplet radius, above which the droplet will grow and below which the droplet will evaporate. Equation (11) shows the equation to calculate r^*:

$$r^* = \frac{2\sigma}{\rho_l RT lnS} \quad (11)$$

where σ and ρ_l is the liquid surface tension and the condensed liquid density, respectively, evaluated at temperature *T*, and *S* is the supersaturation ratio defined as the ratio of vapor pressure to the equilibrium saturation pressure.

The nucleation rate described by the steady-state classical homogeneous nucleation theory and corrected for non-isothermal effects, is given by:

$$I = \frac{q_c}{(1+\theta)}\left(\frac{\rho_v{}^2}{\rho_l}\right)\sqrt{\frac{2\sigma}{M_m{}^3\pi}}\, e^{-\left(\frac{4\pi r^{*2}\sigma}{3K_b T}\right)} \quad (12)$$

where q_c is evaporation coefficient, K_b is the Boltzmann constant, M_m is mass of one molecule, σ is the liquid surface tension, and ρ_l is the liquid density at temperature. A non-isothermal correction factor, θ, is given by:

$$\theta = \frac{2(\gamma-1)}{(\gamma+1)}\left(\frac{h_{lv}}{RT}\right)\left(\frac{h_{lv}}{RT} - 0.5\right) \quad (13)$$

where h_{lv} is the specific enthalpy of evaporation at pressure *p* and γ is the ratio of specific heat capacities.

2.3 Turbulence Model

In CFD, there are three approaches to solve a turbulent flow problem, namely Direct Numerical Simulation (DNS), Large Eddy Simulation (LES) and Reynolds Averaged Navier-Stokes Simulation (RANS). DNS is computationally very expensive, but undeniably highly accurate. Since no turbulence model for the flow is used, hence the grid spacing must be small enough to capture the smallest of the eddies in the turbulent flow. Therefore, it requires a very high computing cost and takes the longest time to achieve convergence. Moreover, DNS only works on small Reynolds number flow. LES is more accurate than RANS approach but requires a longer computing time. An advantage of LES over the DNS approach is that it is able to compute flows with higher Reynolds number and more complicated flows. RANS approach solves the time-averaged Navier-Stokes equations for all turbulent motion. Many different turbulence models are available in RANS and it helps the calculation by allowing it to achieve a solution without having to calculate in advance the full time-dependant flow field. Only the effect of the turbulence flow has to be taken into consideration.

For a turbulence model to be chosen, it needs to have a wide applicability, robust, accurate, simple as well as it has to be economical to run. ANSYS Fluent offers the choice of many turbulence models such as Spalart-Allmaras, standard k-ε, realizable k-ε, RNG k-ε, standard k-ω, SST k-ω and Reynold-Stress Model (RSM). However, due to some limitations on the computing time and

capability, only a few turbulence models are chosen in this study and discussed in the following subsections:

2.3.1 Spalart-Allmaras model (one-equation model)

The Spallart-Allmaras turbulence model is a one equation model applicable to aerospace applications developed by [25]. It solves a modelled transport equation given in Equation (14) for kinematic eddy viscosity without calculating the length scale related to the shear layer thickness. The transported variable in the Spalart-Allmaras model is $\tilde{v}$ which is assimilated, in the regions which are not affected by strong viscous effects such as the near wall region, to the turbulent kinematic viscosity.

$$\frac{\partial}{\partial t}(\rho\tilde{v}) + \frac{\partial}{\partial x_i}(\rho\tilde{v}u_i) = G_v + \frac{1}{\sigma_{\tilde{v}}}\left[\frac{\partial}{\partial x_j}\left\{(\mu + \rho\tilde{v})\frac{\partial\tilde{v}}{\partial x_j}\right\} + C_{b2}\rho\left(\frac{\partial\tilde{v}}{\partial x_j}\right)^2\right] - \gamma_v + S_{\tilde{v}} \tag{14}$$

G_v is the production of turbulent viscosity, γ_v is the destruction of turbulent viscosity that occurs in the near-wall region due to wall blocking and viscous damping, $\sigma_{\tilde{v}}$ and C_{b2} are the constants and v is the molecular kinematic viscosity. $S_{\tilde{v}}$ is a user-defined source term. The turbulence kinetic energy, *k* is not calculated in the Spalart-Allmaras model.

2.3.2 Realizable k-ε model (two-equation model)

The standard k-ε models consist of two variables *k* and *ε* together with the eddy-viscosity stress-strain relationship, where *ε* is the dissipation rate of k. The results imply all normal stresses being equal which is not accurate. However, this model performs poorly for complex flows involving severe pressure gradient, separation and strong streamline curvature. There are few improved models that are based on the standard k-ε turbulent model, which includes k-ε Re-Normalization Group (RNG) model and k-ε realizable model. The realizable k-ε model developed by [26], shares the same turbulent kinetic energy equation as the standard k-ε turbulent model but with an improved equation for the rate of dissipation, *ε*. Its performance has been improved for a numerous types of flow problems that includes planar and round jet flows, boundary layers under strong adverse pressure gradients or separation, rotation, recirculation as well as flows that have excessive streamline curvature. This is the main reason that this model is chosen in the current study as the wet steam flow inside the nozzle is a round jet flow.

The transport equations for realizable k-ε model are given below:

$$\frac{\partial}{\partial t}(\rho k) + \frac{\partial}{\partial x_j}(\rho k u_j) = \frac{\partial}{\partial x_j}\left[(\mu + \frac{\mu_t}{\sigma_k})\frac{\partial k}{\partial x_j}\right] + G_k + G_b - \rho\epsilon - \gamma_M + S_k \tag{15}$$

$$\frac{\partial}{\partial t}(\rho\epsilon) + \frac{\partial}{\partial x_j}(\rho\epsilon u_j) = \frac{\partial}{\partial x_j}\left[(\mu + \frac{\mu_t}{\sigma_\epsilon})\frac{\partial\epsilon}{\partial x_j}\right] + \rho C_1 S_\epsilon - \rho C_2 \frac{\epsilon^2}{k+\sqrt{v\epsilon}} + C_{1\epsilon}\frac{\epsilon}{k}C_{3\epsilon}G_b + S_\epsilon \tag{16}$$

where,

$$C_1 = max\left[0.43, \frac{\eta}{\eta+5}\right], \quad \eta = S\frac{k}{\epsilon}, \quad S = \sqrt{2S_{ij}S_{ij}}$$

In these equations, G_k represents the generation of turbulence kinetic energy due to the mean velocity gradients, G_b is the generation of turbulence kinetic energy due to buoyancy, γ_M represents the contribution of the fluctuating dilatation in compressible turbulence to the

overall dissipation rate, C_2 and $C_{1\epsilon}$ are constants. σ_k and σ_ϵ are the turbulent Prandtl numbers for *k* and *ε*, respectively. S_k and S_ϵ are user-defined source terms.

2.3.3 The standard k-ω model (two-equation model)

In this model, the *ω* term is introduced which represent an inverse time scale that is linked with the turbulence. The k-ω model developed by [27], is an empirical model based on model transport equations for the turbulence kinetic energy *k* and the specific dissipation rate *ω*, which can also be thought of as the ratio of *ε* to *k*. This model is suitable for complex boundary layer flows under adverse pressure gradient and separation (external aerodynamics and turbomachinery). Separation can be predicted to be excessive and early.

The transport equations for realizable k-*ω* model are given below:

$$\frac{\partial}{\partial t}(\rho k) + \frac{\partial}{\partial x_i}(\rho k u_i) = \frac{\partial}{\partial x_j}\left(\Gamma_k \frac{\partial k}{\partial x_j}\right) + G_k - \gamma_k + S_k \tag{17}$$

$$\frac{\partial}{\partial t}(\rho \omega) + \frac{\partial}{\partial x_i}(\rho \omega u_i) = \frac{\partial}{\partial x_j}\left(\Gamma_\omega \frac{\partial \omega}{\partial x_j}\right) + G_\omega - \gamma_\omega + S_\omega \tag{18}$$

In these equations, G_k represents the generation of turbulence kinetic energy due to mean velocity gradients. G_ω represents the generation of *ω*. γ_k and γ_ω represent the effective diffusivity of *k* and *ω*, respectively. γ_k and γ_ω represent the dissipation of *k* and *ω* due to turbulence. S_k and S_ω are user-defined source terms.

2.4 Geometry of the Nozzle and Boundary Condition

Figure 1 illustrates the top half of the whole nozzle and the geometry is mirrored when used in the simulation to create a full 2D nozzle. It consists of a converging section at -0.2 < x < 0 m, a throat at x = 0 m and a diverging section at 0 < x < 0.5 m. It should also be noted that the line connecting point (-0.25, 0) and point (0.5, 0) act as the mirroring plane and also it is the centreline of the whole nozzle. The Cartesian coordinates for the nozzle geometry are listed in Table 1.

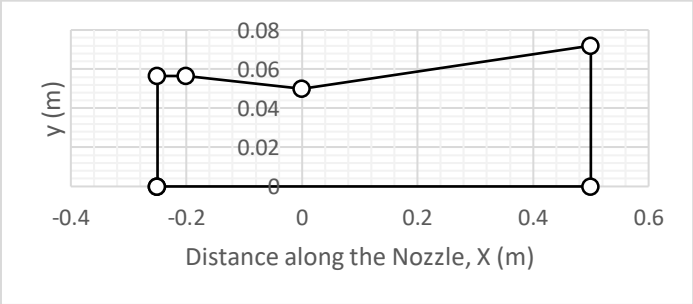


Fig. 1. Nozzle B geometry by Moore et al. [1]

Table 1
Cartesian coordinate of Nozzle B geometry

X (m)	-0.25	-0.25	-0.2	0	0.5	0.5
Y (m)	0	0.05635	0.05635	0.05	0.072	0

Supposing that the flow is symmetrical around the longitudinal pivot of the nozzle, symmetry conditions are used for all flow variables along the centreline. The accompanying pressure and temperature conditions in Table 2 were considered for the inlet pressure and temperature, and the outlet pressure.

Table 2
Boundary conditions of the flow

Boundary	Value
Inlet temperature	354.6 K
Inlet pressure	25 kPa
Outlet pressure	5.3 kPa

It is ought to known that the expressed pressure value for the exiting flow was assumed to be as sufficiently low so as to ensure the occurrence of supersonic condition in the nozzle. In this manner, the pressure and temperature values are induced from the inside of computational area.

3. Results

3.1 Validation of the CFD Fluent Software

To make sure that the CFD Fluent software is apt to use for this study, a validation has to be made. In this case, the results obtained from the simulation of the study is compared to the experiment done by Moore et al. [1] and the result of the work that is the most similar to this study which is done by Sharifi et al [23]. The following observation is made based on Figure 2.

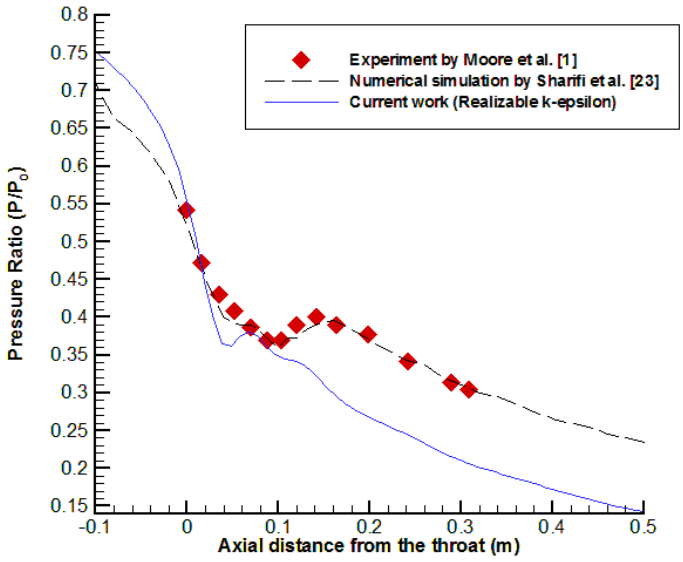


Fig. 2. Pressure ratio versus axial distance from the throat (m)

It can be seen that the trend of the graph in Figure 2 is almost similar compared to the numerical result of Sharifi et al. [23] and also the experimental values of Moore et al. [1]. In the converging section, the results are close to that of both the experimental and numerical values but at the throat and also downstream of the flow towards the diverging section, the results obtained from the current work differ significantly despite its similar trend. This may be due to the reason that the default wet steam model is chosen in the current work and hence, supporting the statement that

the built-in wet steam model in ANSYS Fluent that has some limitations, especially when the temperature is low. In the study conducted by Sharifi et al. [23], they coupled the default solver with UDF to their numerical solution which enabled them to obtain a result fairly close to the experimental result.

3.2 Behavior of Wet Steam in a Converging Diverging Nozzle

Based on Figure 3, it can be seen that the overall trend of the pressure ratio is decreasing starting from the inlet of the nozzle up to the position just after the throat. After this position, there is a sudden increase in the pressure ratio, which indicates the occurrence of condensation process as the steam reaches its metastable state and passes over the supersaturation line. Regardless of inviscid or flow with turbulence, the lines show similar trend as this is a typical occurrence in the wet steam supersonic expansion. The lines then continue to decrease downstream of the throat.

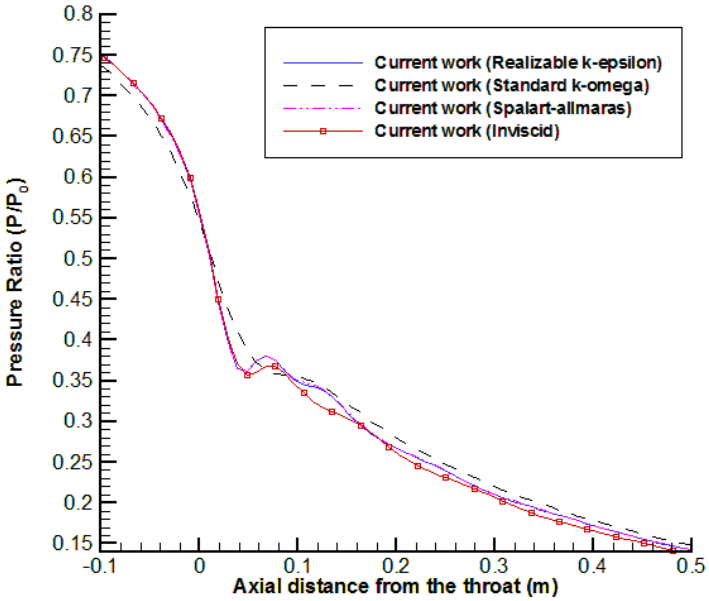


Fig. 3. Comparison of pressure ratio for inviscid and turbulence models

In contrast to the pressure ratio, the Mach number profile illustrated in Figure 4 shows an increasing trend as the steam enters the nozzle. This is true due to the reduction in the cross-sectional flow area causing the velocity to increase. The trend continues to increase downstream of the throat as the steam reaches supersonic velocity. Similar to pressure ratio profile, there is one location after the throat where condensation starts to occur and can be seen by a sudden drop in the Mach profile along the nozzle. The results do not show significant deviations between each turbulence model.

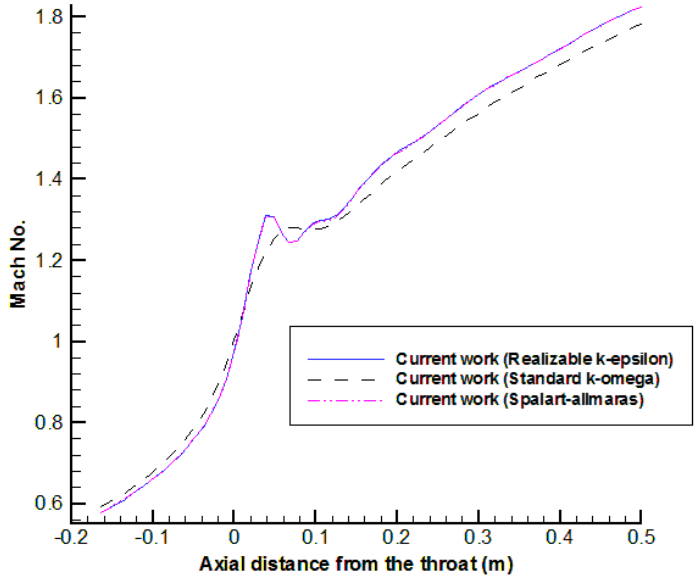


Fig. 4. Mach number versus axial distance from the throat (m)

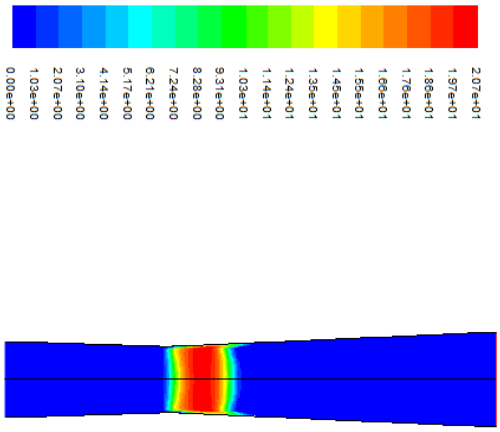
3.3 Various Wet Steam Properties in The Nozzle

In order to further understand the behavior of the wet steam flow inside the nozzle, a number of wet steam properties have been illustrated in the graphs and discussed. Before the spontaneous condensation occurs, the nucleation has to occur initially, in which the molecule cluster size must be greater than the critical nucleus size. If this does not happen, the molecules will just be evaporated. To ensure this phenomenon, the nucleation rate is analysed. The contours of the $\log_{10}$ of the nucleation rate can be observed in Figure 5a, 5b and 5c. The highest nucleation rate for both the realizable k-ε and Spalart-Allmaras model is 21.1 particle/m^3.s, while for the standard k-ω model, the value is 20.7 particle/m^3.s



a. Realizable k-ε model

b. Spalart-Allmaras



c. Standard k-ω model

Fig. 5. Log_{10} Nucleation rate

The condensation process involves two mechanisms, namely the transfer of mass from the vapor to the droplets and the transfer of heat from the droplets to the vapor in the form of latent heat. As in Figure 6, it can be observed that following the condensation process, the supercooling or subcooled temperature increases until it reaches approximately 40 K. Following this phenomenon, the steam static temperature also drops rapidly as can be observed in Figure 7. Supercooling can be defined as the rate of which the static temperature of the wet steam decrease as the name suggested “cooling”. When this happens, water molecules absorb the surrounding heat, resulting in the reduced static temperature. Supercooled steam state is unstable and it will disappear if equilibrium is achieved. This also means that it only exists during a dynamic process. Both supercooling and the wet steam static temperature go hand in hand i.e. as supercooling increases, the temperature of the steam decreases and vice versa.

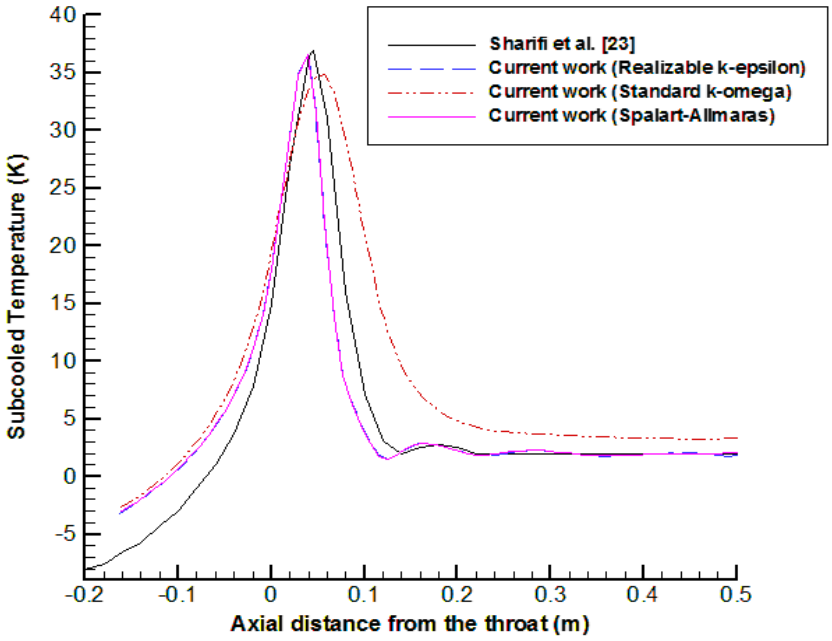


Fig. 6. Supercooling versus axial distance from the throat (m)

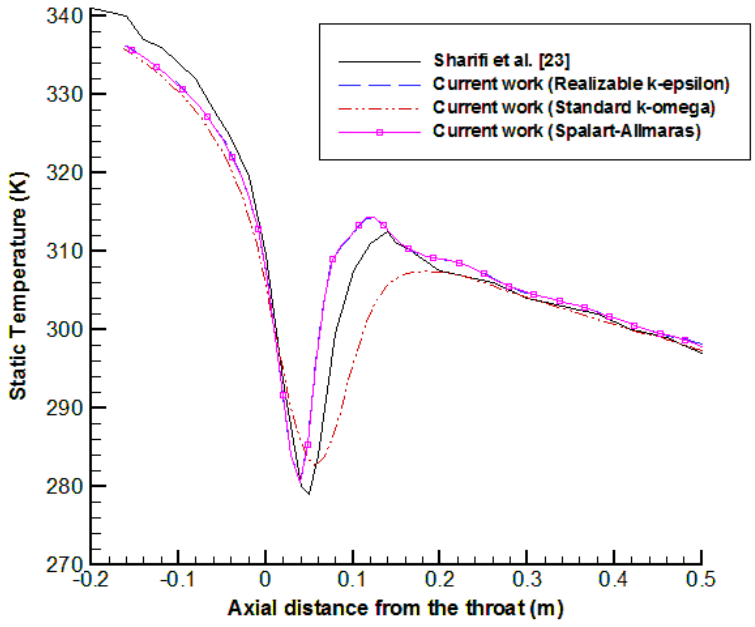


Fig. 7. Static temperature versus axial distance from the throat (m)

The expansion process is usually very rapid. Once the saturated vapor line has been crossed by the molecules, the process will depart from equilibrium, and the supersaturation ratio can take on values greater than one. Based on Figure 8, it can be observed that the supersaturation ratio is at its peak right after the nozzle throat where condensation occurs and the water molecules is the most abundant which leads to saturated amount of water droplets at this area. This data corresponds in agreement with the data that can be observed in Figure 9. In the figure, the droplet radius increase significantly at the throat region (x = 0 m), where it can be noted that before the throat, there is absolutely no traces of water droplet and the water droplet grow rapidly from the size of 10^{-10} m to 10^{-2} m where it remains constant towards the exit of the nozzle.

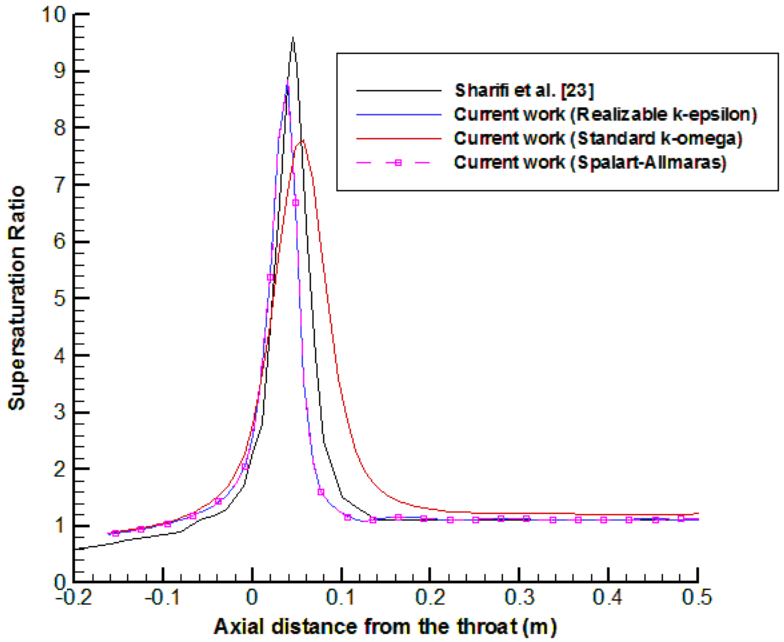


Fig. 8. Supersaturation ratio versus axial distance from the throat (m)

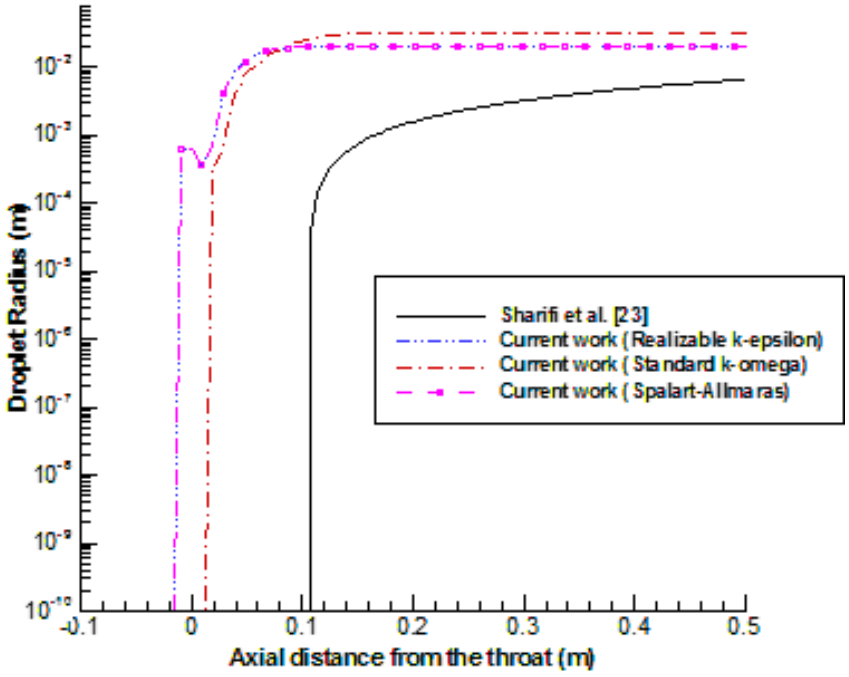


Fig. 9. Droplet radius versus axial distance from the throat (m)

The total amount of wetness in the flow is typically represented by the wetness fraction or liquid mass fraction. Based on Figure 10, the wetness fraction increases downstream of the wet steam flow in the nozzle. This is due to the fact that following the condensation process immediately after the throat, the water droplet formed will be carried by the flow towards the diverging section of the nozzle which causes the wetness fraction to increase. This is then verified by the contours of the liquid generation rate that is measured in kg/m^3 in Figure 11a, 11b and 11c and the number of droplet per unit volume in Figure 12a, 12b and 12c.

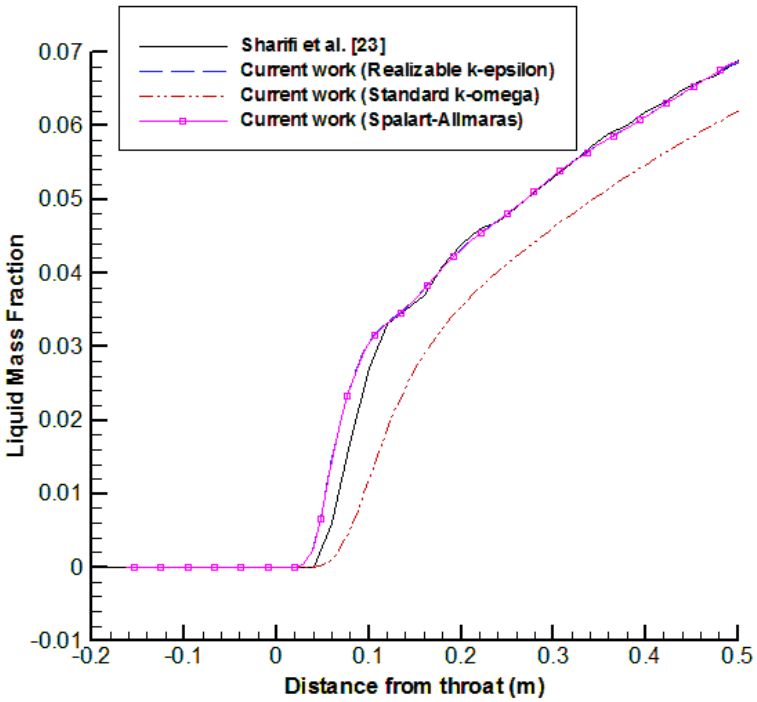
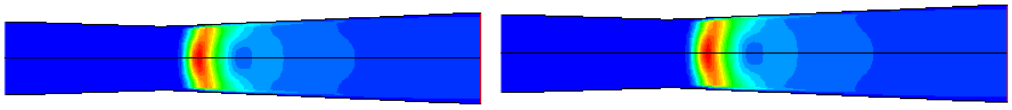
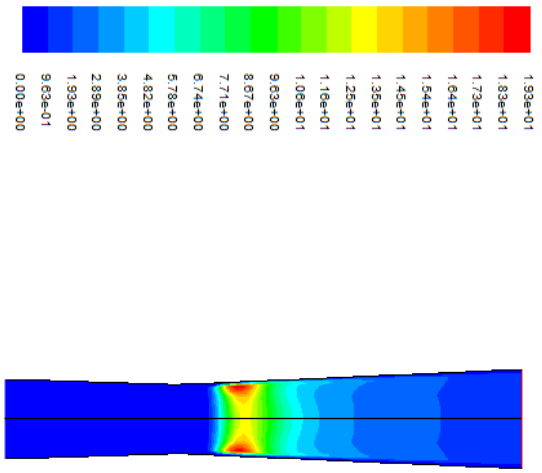


Fig. 10. Liquid mass fraction versus axial distance from the throat (m)



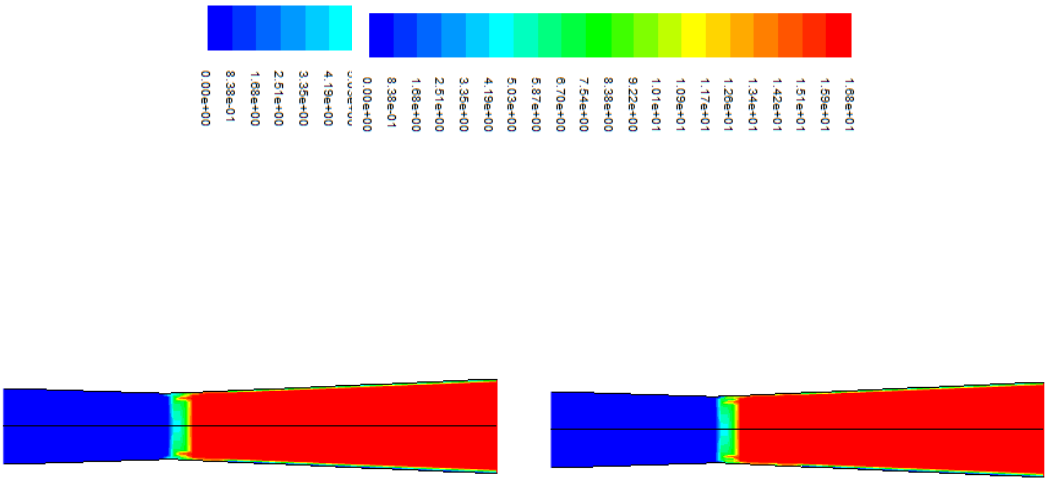
a. Realizable *k-ε model*

b. Spalart-Allmaras



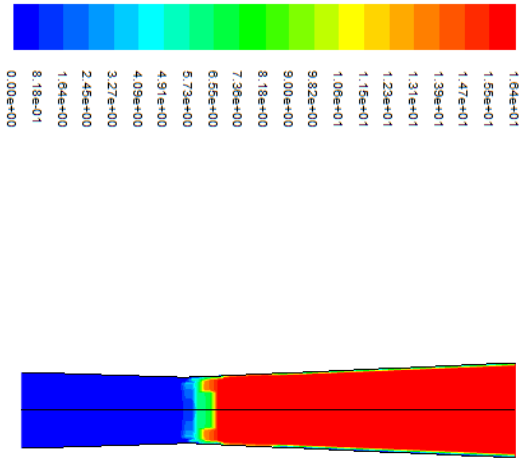
c. Standard k-ω model

Fig. 11. Liquid mass generation rate



a. Realizable *k-ε model*

b. Spalart-Allmaras



c. Standard k-ω model

Fig. 12. Number of droplets per unit volume

Based on graphs and contours shown, the performance of each turbulent model can be observed and compared. Both the realizable k-ε and Spalart-Allmaras models depict the closest trend and flow behavior as with Sharifi et al. [23]. It is to be noted in most graphs, the line representing the current works show similar trend with a significant difference shown when using standard k-ω model especially on the wet steam properties. This deviation occurs especially downstream the throat as compared to the other lines. The reason to this trend may be due to both the realizable k-ε and Spalart-Allmaras models that are suitable to be used for this type of flows which is a round jet flow type, while the standard k-ω is not.

4. Conclusions

From the data and results obtained, it can be seen that the graphs and contours presented clearly describe in detail the behavior of the flow of wet steam in a converging-diverging nozzle. For the pressure profile, the general trend of the graph is decreasing with the axial distance of the nozzle but there is a sudden jump of pressure downstream the throat of the nozzle. This occurrence indicates the spontaneous condensation process. Subsequently, the velocity profile of the flow can be deducted from the Mach number, where the trend of the graph is the inverse to the pressure graph. Other than that, it can be observed that at the spontaneous condensation location, the supercooling increases due to the increment of water droplet in that area. This in turn leads to the drop of the flow temperature at the affected area due to the water droplet is absorbing the surrounding heat in that particular area.

In addition to that, the comparison between the three different turbulence models show that the realizable k-ε and also Spalart-Allmaras model display the closest results to the experimental values and numerical simulations done by another researcher. This may be due to the realizable k-ε and also the Spalart-Allmaras model that are suitable for the round jet flow. As for the standard k-ω model, it shows that the results obtained using this model deviates quiet noticeably especially

when comparing the values to the other models for the wet steam properties. The reason to this is that the standard k-ω model is not modified to cater for round jet type of flow and it displays some deviation in the results. All in all, the behavior of wet steam in a convergent-divergent nozzle can be understood and predicted. This will help in understanding a similar but more complex phenomenon occurred in the turbine cascades as the behavior is quite similar. In the future, it is recommended that more turbulence models to be included as comparisons, UDF functions to be employed in some of the equations and boundary conditions and turbine cascades are used as the geometry. However, wet-steam flow remains still difficult to predict accurately because it includes non-equilibrium phase transition phenomena of which the physics are not fully understood. Also, high computational cost is one of the difficulties in simulating multiphase flow. Therefore, existing results should be refined and further studies are required to obtain results that agree well with experimental data at a lower computational cost.

Acknowledgement
This research was funded by the Innovation and Research Management Centre (iRMC) of Universiti Tenaga Nasional under its Publication Fund, RJO10436494.

References

[1] Moore M.J., Walters P.T., Crane R.I. "Predicting the Fog-Drop Size in Wet-Steam Turbines." *In: Proc IMECHE Conf Wet Steam 4*. Coventry, UK, 1982.
[2] Gyarmathy, G., Lesch, F. "Fog Droplet Observation in Laval Nozzles and in an Experimental Turbine." *Proc. Inst. Mech. Eng*. 1969, 184, 29–36.
[3] Gyarmathy, G. "Condensation in Flowing Steam." *In A von Karman Institute Book on Two-Phase Steam Flow in Turbines and Separators; Moore, M.J., Sieverding, C.H., Eds.; Hemisphere: London, UK*, 1976; pp. 127–189.
[4] Skillings, S., Walters, P., Moore, M.J. "A Study of Supercritical Heat Addition as Potential Loss Mechanism in Condensing Steam Turbines." *in: Int. Mech. Engrs., Intl. Conf. on Turbomachinery, Cambridge*. C259/87, 1987, pp. 125–134.
[5] Moses, C.A., Stein, G.D. "On the Growth of Steam Droplets Formed in a Laval Nozzle Using Both Static Pressure and Light Scattering Measurements." *J. Fluids Eng.* 1978, 100, 311–322.
[6] Hill, P.G. "Condensation of Water Vapour during Supersonic Expansion in Nozzles." *J Fluid Mech* 1966; 25: 593–620.
[7] Bakhtar, F., Zidi, K. "Nucleation Phenomena in Flowing High-Pressure Steam, Part 1: Experimental Results." *Proc. Inst. Mech. Eng.* 1989, 203, 195–200.
[8] Bakhtar, F., Zidi, K. "Nucleation Phenomena in Flowing High-Pressure Steam, Part 2: Theoretical Analysis." *Proc. Inst. Mech. Eng*. 1990, 204, 233–242.
[9] Guha, A. and Young, J.B. "Time-Marching Prediction of Unsteady Condensation Phenomena due to Supercritical Heat Addition." *In: Turbomachinery: latest developments in a changing scene. Proc. IMECHE*, 1991, paper C423/057, pp.167–177.
[10] Young, J.B. "Two-dimensional, Nonequilibrium, Wet-Steam Calculations for Nozzles and Turbine Cascades." *J. Turbomach.* 1992, 114, 569–579.
[11] Young, J.B. "The Spontaneous Condensation of Steam in Supersonic Nozzles." *Phys. Chem. Hydrodyn*. 1982, 3, 57–82.
[12] White, A.J., Young, J.B. "Time-Marching Method for the Prediction of Two-Dimensional, Unsteady Flows of Condensing Steam." *J. Propuls. Power* 1993, 9, 579–587.
[13] White, A.J., Young, J.B., Walters, P.T. "Experimental Validation of Condensing Flow Theory for a Stationary Cascade of Steam Turbine Blades." *Philos. Trans. R. Soc. A* 1996, 354, 59–88.
[14] Kermani, M.J., Gerber, A.G. "A General Formula for the Evaluation of Thermodynamic and Aerodynamic Losses in Nucleating Steam Flow." *Int. J. Heat Mass Trans.* 2003, 46, 3265–3278.
[15] Schnerr, G.H. "Unsteadiness in Condensing Flow: Dynamics of Internal Flows with Phase Transition and Application to Turbomachinery." *Proc IMechE, Part C: J Mech Eng Sci* 2005; 219: 1369–1410.
[16] Y. Yang and S. Shen. "Numerical Simulation on Nonequilibrium Spontaneous Condensation in Supersonic Steam Flow." *International Communications in Heat and Mass Transfer*. 2009, 36 (9), 902–907.

[17] Hasini, H., M. Zamri Yusoff and N. A. Malek. "Numerical Modelling of Wet Steam Flow in Steam Turbine Channel." *Intech Book Chapter: Mechanical Engineering, Dr. Murat Gokcek (Ed.)*, 2012.
[18] Norhazwani Abd Malek, Syarir Akram Jamaluddin, Mohd Zamri Yusoff, Hasril Hasini. "CFD Analysis of Unsteady Flows due to Supercritical Heat Addition in High Speed Condensing Steam." *Jurnal Teknologi (Sciences & Engineering)*, 76:10 (2015): 37–42.
[19] Chang Hyun Kima, Jae Hyeon Parka, Dong Il Kimb and Je Hyun Baeka. "Numerical Analysis of Non-Equilibrium Steam Condensing Flows in Various Laval Nozzles and Cascades." *Engineering Applications of Computational Fluid Mechanics*, 2017, Vol. 11, No. 1, 172–183.
[20] F. Giacomelli, G. Biferi, F. Mazzelli and A. Milazzo. "CFD Modeling of Supersonic Condensation inside a Steam Ejector." *Energy Procedia*, n. 101, pp. 1224-1231, 2016.
[21] Mazzelli Federicoa, Giacomelli Francescoa, Milazzo Adrianoa. "CFD Modelling of the Condensation inside a Supersonic Nozzle: Implementing Customized Wet-Steam Model in Commercial Codes. *Energy Procedia*, 126 (201709) 34–41.
[22] Miah Md Ashraful Alam, Manabu Takao and Toshiaki Setoguchi. "Numerical Simulation of Non-Equilibrium Two-Phase Wet Steam Flow through an Asymmetric Nozzle". *Fluids*, 2(4):63, 2017.
[23] N. Sharifi, M. Sharifi. "Numerical Investigation of Heat Transfer in Wet Steam Flow in Convergent-Divergent Nozzles." *Proceedings of the ASME 2013 International Mechanical Engineering Congress and Exposition*, 2013.
[24] Yogini Patel, Giteshkumar Patel, Teemu Turunen-Saaresti. "Influence of Turbulence Modelling on Non-Equilibrium Condensing Flows in Nozzle and Turbine Cascade." *International Journal of Heat and Mass Transfer* 88 (2015) 165–180.
[25] P. Spalart and S. Allmaras. "A One-Equation Turbulence Model for Aerodynamic Flows." Technical Report AIAA-92-0439, American Institute of Aeronautics and Astronautics, 1992.
[26] T.H. Shih, W. W. Liou, A. Shabbir, Z. Yang, and J. Zhu. "A New k-epsilon Eddy-Viscosity Model for High Reynolds Number Turbulent Flows - Model Development and Validation." Computers Fluids, 24(3):227-238, 1995.
[27] D. C. Wilcox. "Turbulence Modeling for CFD." DCW Industries, Inc., La Canada, California, 1998

Penerbit Akademia Baru

Engineering Science and Technology Conference Proceedings

Journal homepage: www. akademiabaru.com/EST.html
ISSN: XXXX-XXXX

Heat Transfer Properties of Biobased Polymer Coating for Mortar Cement Filled Aggregate from Recycled Materials

Open Access

Mahmud Junoh[1] , Anika Zafiah M. Rus[1,*], Nur Afiqah S.[1], Nurulsaidatulsyida S.[1], N. Syamimi M. Salim[1], Hanani Wahab[1] , Noraini Marsi[1] , Nik AlNur Auli[1] , Siti Aida I.[1]

[1] Sustainable Polymer Engineering (SPEN-AMMC), Fakulti Kejuruteraan Mekanikal dan Pembuatan, Universiti Tun Hussein Onn Malaysia (UTHM), 86400 Parit Raja, Batu Pahat, Johor,Malaysia.

ABSTRACT

The thermal insulation material is used to solve environmental problem with a relevant initiative by recycling industrial and domestic waste. It is also benefited to reduce energy consumption in construction which comes together with an alternative study on heat transfer properties of mortar cement or plaster filled with recycled materials. The work is started by mixing plaster solution (cement, sand and water) with recycled aggregate materials such as coconut shell, kenaf fibre, wood fibre, glass, waste polypropylene (PP) and recycled rubber solid wastes with various composition (100m^3, 200m^3, and 300m^3). Then the dried mortar cement filled recycled aggregate samples were coated with biobased polymer solutions. The heat transfer properties on the sunlight exposed mortar cement composites were calculated. The measurement is recorded for each sample in one hour interval time using Fourier's equation to determine the heat transfer rate. The sample with kenaf fibre composition of 100m^3 (K100) has the lowest heat transfer rate, 0.078 W while the highest is the sample with 300m^3 of glass mixture (G300), 3.9 W. The high rate of heat transfer material is suitable for inner plastering while low rate of heat transfer material can be used for outer plastering which is glass and kenaf fiber respectively. This is to give an examples of materials which suitable for maintaining and control the building's thermal comfort and also revealed that different mixture ratios is an affecting factor on thermal conductivity of mortar cement.

Keywords:
Heat Transfer, Composite, Plaster, Waste Material, Polymer

Copyright © 2019 PENERBIT AKADEMIA BARU - All rights reserved

1. Introduction

Global warming and energy shortages have put a lot of research into addressing this problem and finding the best way to deal with it [1]. The issue of today's hot climate, interior and exterior design especially for residential construction in urban areas should been studied in terms of thermal comfort [2]. Improving energy efficiency and reducing environmental effects are the main challenges faced by the construction industry today [3]. Generally, human and physical capital are externality assets owned by a country which are obtained from the transformation of subsoil assets such as minerals and hydrocarbons. These assets are developed to promote job opportunities and coherently generate a country's income [4].

In addition, the natural resources used today will face deficiency if they are not managed carefully [5]. These include all the elements of nature that humans use especially for economic and building purposes such as palm oils industry specifically from Malaysian palm mills. At the moment, Indonesia and Malaysia are the two countries produce over 80% of the world's palm oil supply [6]. The palm oil industry is competing on a global scale with producers of other vegetable oils made from olives, rape seeds, maize, coconut and soy [7]. With many of these sources, it is became the

main concern of the adverse effects from waste disposal. Instead, the use of materials, especially bio-polymers from wastes such as cooking oil residues can benefit humans by creating and expanding them into new and different things, while at the same time can protect the environment from further pollution [8]. Towards sustainability of materials, as well as to reduce our dependability of natural resources, waste materials can be studied as sustainable insulation materials as composite fillers.

2. Theoretical Analysis

2.1 Heat Conduction

When particles interact with each other and energy is transferred, this process is known as heat conduction. Almost similar to the concept of heat transfer, energy is transferred adjacently from particles of higher energy to the lower ones. This process takes place in solid, liquid and gas state. For gasses and liquid, heat conduction occurs during the random movement caused by collisions and molecular diffusion whereas a combination of molecular vibrations in lattice and free electrons causes heat conduction in solids [9].

There are several aspects that effect the rate of heat conduction through a medium and these include the geometry of medium, thickness, material and the temperature difference across a medium. A simple example can be seen when a cold canned drink turns warm equivalent to the surrounding temperature when left in a room. The process of heat conduction occurs from the surrounding temperature of room to the drink through aluminum can. Increase in insulation layer will lead to smaller heat loss. Hence, it can be presumed that rate of heat conductivity through a plane is directly proportional to the temperature difference across the layer and area of heat transfer but inversely proportional to the thickness of the layer[10].

Figure 2.1 shows how describes the heat conduction that takes place across the surface area of a solid slab during a steady state based on Fourier's Law (1).

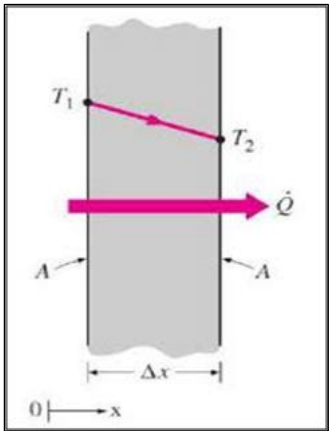


Fig. 1. Heat conduction through a large plane wall of thickness, Δx and area, A[10]

$$\dot{Q}_{cond} = kA\frac{T_1 - T_2}{\Delta x} = -kA\frac{\Delta T}{\Delta x} \quad \text{(W)} \tag{1}$$

Based on equation (1), $\dot{Q}$ is the rate of heat transfer by conduction, k as thermal conductivity of material, A is the area of sample, ΔT or $T_1 - T_2$ is the difference of temperature across the sample, and Δx is the thickness of the sample. A body or a medium with high temperature possess a higher kinetic energy compared to cold ones.

2.2 Heat Convection

An energy transfer mode known as convection occurs between surface of a solid and liquid or gas with adjacent movement. It comprises a combination effect of conduction and movement of fluid [11]. Higher rate of convection is caused by faster moving fluid. Pure conduction minus the bulk fluid movement leads to the transfer of heat between surface of a solid and fluid in adjacent. When there is presence of fluid's bulk movement, the rate of heat transfer is enhanced. However, this process makes it difficult to determine the rate of heat transfer. In altering the thermal conductivity of concrete and mortar, their constituent(s) can be substitute with either thermally insulating or thermally conductive materials [12].

Figure 2 illustrates how a hot block is cooled down by blowing air over its top surface. Firstly, energy is transmitted to the layer of air in adjacent to the block through the process of conduction. Later, convection causes the energy to be carried away from the surface. This process consists of combination of conduction effects where heated air near the surface is removed or replaced with cooler ones by random motion of bulk air molecules. Newton's Law of Cooling (2) can be used to explain the heat transfer of convection.

$$\dot{Q} = hAs(T_s - T_\infty) \quad \text{(W)} \tag{2}$$

Where $\dot{Q}$ is the rate of heat transfer by convection, h is the convection heat transfer coefficient, A_s is the surface area through which convection heat transfer takes place, T_s is the surface temperature, and T_∞ is the temperature of the fluid sufficiently far from the surface [10]. $(T_s - T_\infty)$ denotes the temperature difference between the surface and surrounding. The temperature of fluid in contact with the surface is equivalent to the surface temperature of the solid. The coefficient of convection heat transfer, h is not part of the fluid's property but a parameter determined experimentally. Its value is dependent on all the variables that influence the process of convection which includes geometry of the surface, characteristic of fluid motion, fluid properties and velocity of bulk fluid.

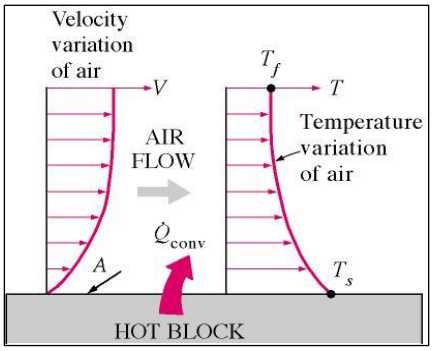


Fig. 2. Heat transfer from hot surface to air by convection [10]

2.3 Heat Radiation

Changes in electronic arrangements in atoms or molecules cause energy discharged by matter in the form of electromagnetic waves known as radiation. The difference between radiation and the previously mentioned processes (conduction and convection) is that no presence of medium is required. As a matter of fact, energy is transferred by means of radiations and it is the fastest process of energy transfer. Apart from that, energy transfer in radiation does not diminished in vacuum [9]. Heat from the sun reaching earth is the simplest way to describe how radiation works.

Most intriguing aspect in the studies of heat transfer is the thermal radiation emitted by a medium due to its temperature unlike other forms of electromagnetic radiations such as gamma rays, x-rays, microwaves, radio waves, and television waves. Every medium with a temperature greater than absolute zero is capable to emit thermal radiation. Radiation occurs in all volumetric substances and variously through emission, absorption, transmission and radiation. However, for solids that are fuliginous to thermal radiation such as wood, metals and rocks radiation is generally considered to be a surface phenomenon considering the radiation released by the inner regions of those materials are unable to reach the surface. Radiation released by these materials is usually absorbed within a few microns when it reached the surface.

3. Methodology

3.1 Materials Selection

Thermal insulation can be provided to a building by means of thermal insulating plaster when alteration of thermal performance is needed. Due to highly cost raw materials and the depletion of natural resources, application of recycled waste material or by-products is beginning to caught the attention of big industries as an alternative[13]. Six (6) different types of waste materials were tested and the best material has been selected for thermal insulator plaster based on several criteria of insulation.

In terms of construction sustainability, there are three types organic and inorganic waste material are selected. The first organic material is coconut shell (Cs) from the Palmae family. Thermal conductivity, k of Cs is 0.143 W/mK. The second waste material collected is kenaf fibre (K). Kenaf has mechanical properties of 890-960 strength (MPa) [14]. The K, Hibiscus Cannabicus are found in the bark and core wood, where the bark constitutes 40% of the plant. Kenaf can be mostly found in countries such as South Africa, Bangladesh, United State of America, India, Indonesia, Vietnam, Thailand and even in Malaysia [10]. The last organic waste material is wood fibre (Wf). Wf have high roughness of fibre content [15]. Wf are usually have large amount of cellulose that extracted from trees and used to make materials including paper.

The first inorganic waste material collected was glass (G). Known as a non-crystalline amorphous solid which is often transparent in colour and has various practical, technological, and decorative application such as window panes and tableware [16]. Usually, the shiny surface of material will produce reflection to the surface. Rubber (R) is known as an elastic polymeric substance made from or synthetically made from the latex of a tropical plant. Usually rubber produces products like boots, shoe soles, tents, containers of water, etc. Therefore, rubber is suitable for insulation [10]. The last inorganic waste material selected is Polypropylene (PP) waste. The fibre density is 0.91 g/cm3 [17] with high flexibility in applications, both in industry and in consumer goods. PP can function as both fiber and structural plastic. Often used in the food industries, the high melting point of PP which is 160°C (320°F) is one of its desired attributes compared to other plastics especially when it comes to high temperature application for warping prevention.

Table 1
List of recycled materials and its thermal conductivity

Name	Material	Thermal conductivity, k (W/m.K)
Cs	Coconut shell	0.143
K	Kenaf fibre	0.0208
Wf	Wood fibre	0.130
G	Glass	1.050
R	Rubber	0.130
Pp	PP waste	0.110

3.2 Experimental Apparatus and Instrumentation

3.2.1 Fabrication of mortar cement filled aggregate from recycled materials

The samples were made from crushed or fine grain of recycled waste materials mixed as in Figure 3 with various sand compositions (100m^3, 200m^3, and 300m^3) in a mould of 10cm x 10cm x 5cm size as shown in Table 2 and Figure 3 respectively. A clear and transparent container was selected as the mould for mortar sample. After the materials were mixed and dried, they were taken out from the mould before further testing.

Table 2
Mixture proportions and consistency of mortar's mixture

Mixture	Volume of mixture (m^3)			
	REF	C_{100}	C_{200}	C_{300}
Cement	200	200	200	200
Sand	400	300	200	100
Filler	-	100	200	300



Fig. 3. Organic and inorganic waste material

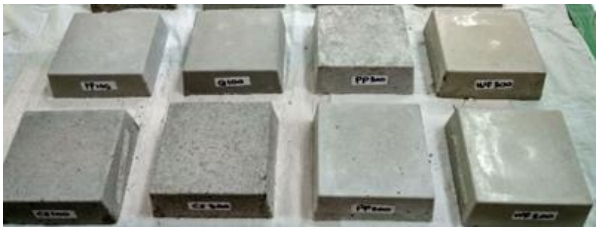


Fig. 4. Mortar cement filled from recycled aggregate materials

3.2.2 Average Thickness

Thickness of samples plays an important role for calculating the rate of heat transfer property. Each samples were measured on four different sides to obtain average thickness. The thickness of each corner of the specimen was measured using a Vernier caliper. Table 3 shows the measured thickness of each sample. The fixed thickness selected is 42 mm.

Table 3
Measured thickness of each Mortar Cement Filled Aggregate samples

Surface / Side	1	2	3	4	Average thickness (mm)
REF	45.72	44.64	44.59	44.9	44.96
CS100	40.73	40.42	39.30	40.28	40.18
CS200	40.09	41.8	41.7	40.02	40.90
CS300	41.68	41.58	41.0	40.29	41.14
K100	40.80	40.74	40.95	41.65	41.04
K200	39.65	39.84	39.76	39.10	39.59
K300	43.53	43.13	43.22	44.31	43.55
WF100	43.60	44.63	43.42	43.19	43.71
WF200	44.33	44.34	44.00	43.74	44.10
WF300	41.26	40.82	43.60	42.88	42.14
G100	41.00	41.47	40.94	40.9	41.08
G200	40.16	40.37	41.73	41.60	40.97
G300	42.19	40.98	42.69	43.43	42.32
R100	49.43	49.05	48.78	49.89	49.29
R200	38.16	37.61	37.58	38.53	37.97
R300	39.48	39.90	39.46	39.94	39.70
PP100	40.90	40.79	41.83	42.21	41.43
PP200	41.50	42.60	43.00	41.07	42.04
PP300	45.67	43.78	42.54	43.46	43.86

3.2.3 Preparation of coating solution

Waste Palm oil was used as the original palm oil to produce the origin bio-polymer (B). The conversion of the monomer starts with the catalyst preparation to generate the epoxies from the unsaturated fatty compound, and the second reaction is the opening of the acid catalyst ring of the epoxies to form polyols or bio monomer [18-24]. Biobased coating solution was prepared by mixing bio monomer with cross linking agent. Mixing process are handled with mechanical stirrer to allow complete dissolution. Biobased polymer coating is then ready to be coated on mortar cement samples.

3.2.4 The Instrument and measuring procedures of heat transfer analysis

Temperature readings from the top and bottom surfaces of the mortar samples were taken for 5 days straight from 9am to 5pm. All the samples were exposed to sunlight on the rack sample. The temperature were recorded at 1 hour interval using Laser Infrared Thermometer. Figure 5 shows the all samples during exposure to UV sunlight.



Fig. 5. The sunlight exposure setup for temperature measurement for heat transfer analysis

4. Results and Discussion

4.1 Experimental Results

4.1.1 Average temperature for top surface

Material with high rate of heat transfer or also known as heat absorbing materials can absorb most of the heat from sunlight before heat is transferred further into a house or a room. As refer to Figure 6 and Figure 7 show the graphs of recorded temperature for top surface for the mortar cement filled waste aggregate samples; average temperature for samples with organic and inorganic fillers.

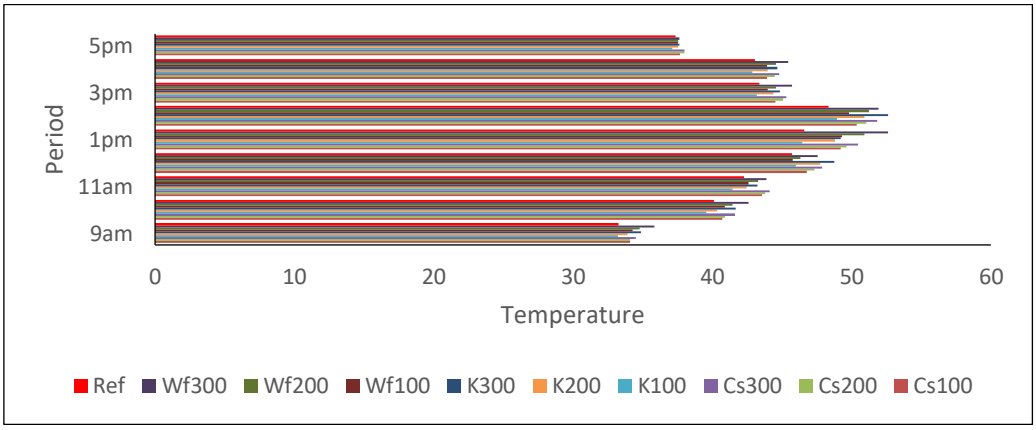


Fig. 6. Period versus temperature,°C for mortar cement filled waste organic aggregate

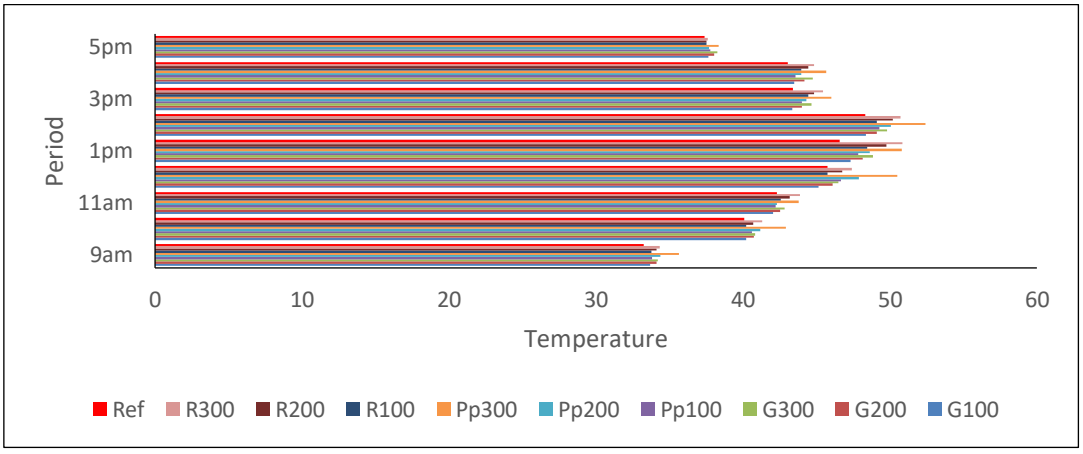


Fig. 7. Period versus temperature, °C for mortar cement filled Inorganic waste aggregate

4.1.2 Average temperature for bottom surface

Figure 8 and Figure 9 below are the graphs of data collection for bottom surface average temperature for organic and inorganic fillers for mortar cement filled aggregate.

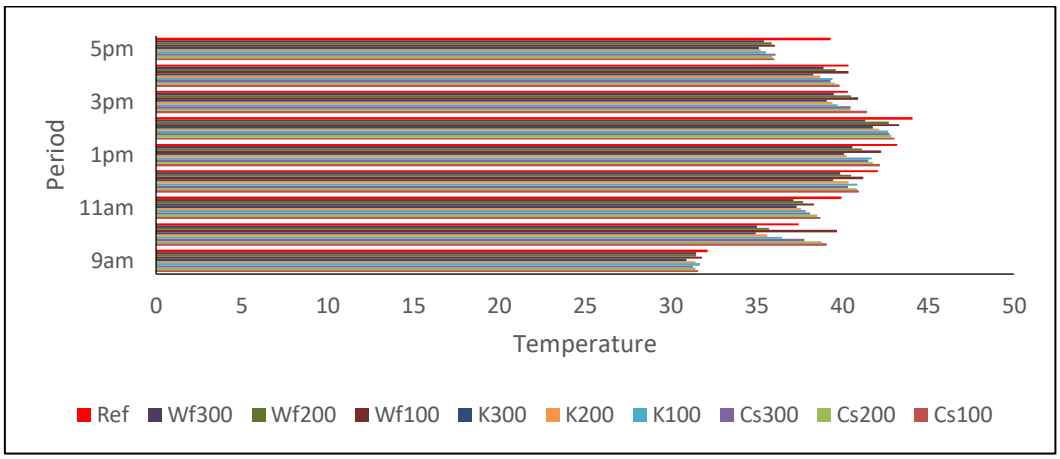


Fig. 8. Period versus temperature, °C for mortar cement filled organic waste aggregate

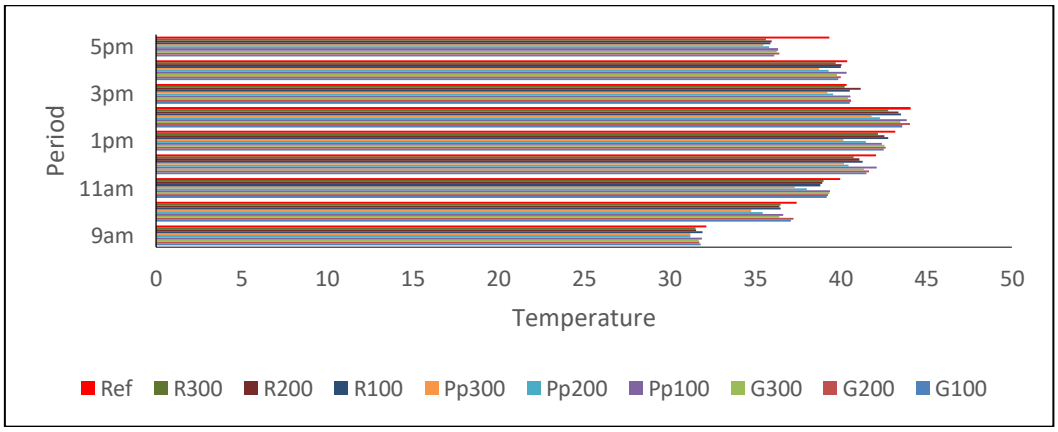


Fig. 9. Period versus temperature,°C for mortar cement filled Inorganic waste aggregate

4.2 Heat Transfer Rate

Figure 10 shows the comparison of the rate of heat transfer for glass, G and kenaf, K which both is opaque insulation. The mixture of 300m^3 and 100m^3 of G and K had been chosen due to G300 and K100 has the highest and lowest temperature detected using Laser Infrared Thermometer respectively. The plotted graph is from the calculated data which use the equation of Fourier's law of heat conduction. The mortar sample with G of 300m^3 represented by the red line while blue line represented sample with 100m^3 of K. The rate of heat transfer, $\dot{Q}_{max}$ for G300 is 3.9 W while for K100 is 0.078 W. $\dot{Q}_{max}$ for each material were recorded at the same time, which was during fifth period (at 1pm).

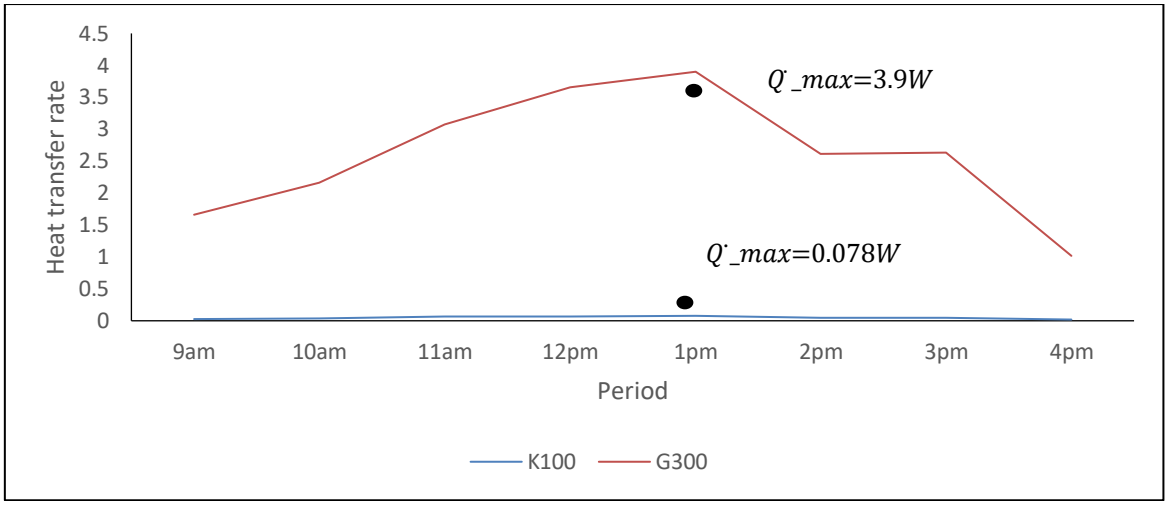


Fig. 10. Comparison rate of heat transfer (Watt) versus period of measuring time (top surface)

Figure 11 shows the comparison of heat transfer rate at the bottom surface for mixture of 200m^3 and 200m^3 of G and K respectively. This samples had been chosen because G200 has the highest temperature while K200 has the lowest temperature recorded. The rate of heat transfer, $\dot{Q}_{max}$for G200 is 3.07 W while for K200 is 0.053 W, where $\dot{Q}_{max}$ also occurred at the same time, but during the fourth period (at 1pm).

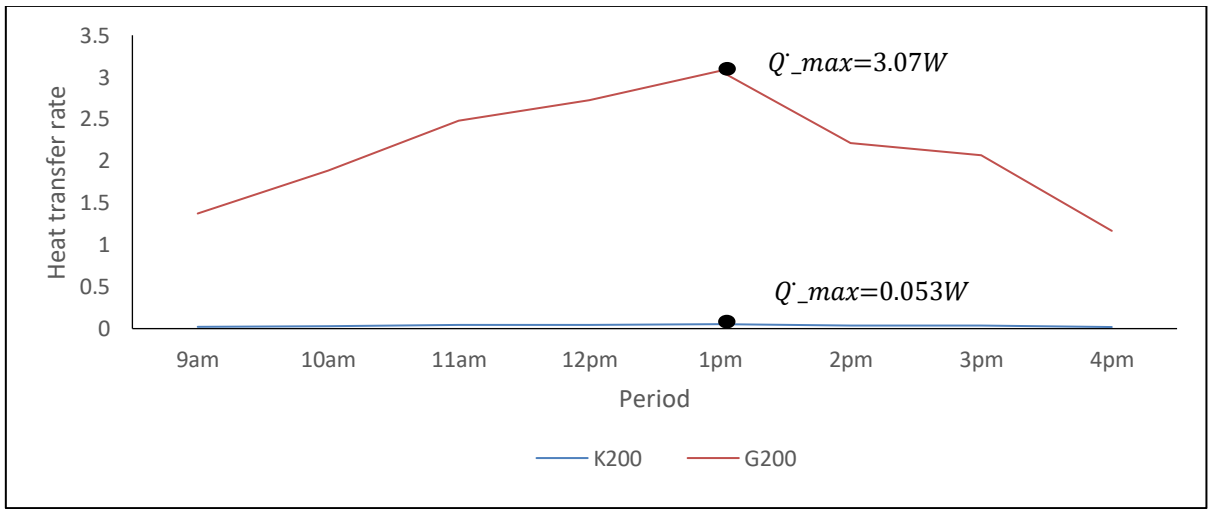


Fig. 11. Comparison rate of heat transfer (Watt) versus period of measuring time (bottom surface)

According to equation (1), the rate of heat transfer,$\dot{Q}_{cond}$ for all recorded data can be find. For example; maximum heat transfer rate, $\dot{Q}_{max}$for G300 as refer to Figure 10.

$$\dot{Q}_{cond} = kA\frac{T_1 - T_2}{\Delta x}, \Delta x = 0.042m, (T_1 - T_2) = 15.6℃$$
$$= (1.050)(0.01)(15.6)/(0.042)$$
$$= 3.9\ W$$

5. Conclusions

Based on previous work, which is on uncoated result, G100 shows higher rate of heat transfer at the bottom surface compared to G300 due to the mixtures with high portion of fine aggregate

possessed higher thermal conductivity compared to those with high portion of course aggregate. Sand itself as fine aggregate possesses good thermal conductivity. However, the capability of sand to transfer heat is reduced when it is replaced with glass as fine aggregate. Hence, G300 has lower heat transfer rate recorded at the bottom surface of specimen because the ability of the material to transfer heat is reduced with the increase of glass portion in the mixture.

The study conducted has shown that out of all the fine aggregate materials used, specimen with glass in its constituent possessed better heat transfer rate. However, the volume of proportion used in the specimen could also affect its heat transfer rate. Thus, better replacement of basic constituents in the construction industry from solid waste with lowest and highest rate of heat transfer is suggested from this study to be used as plaster for building applications. In other hand, the use of domestic waste such as kenaf and wood fibre is alternative functional filler with lowest heat transfer rate for building materials.

Acknowledgement
The authors would like to thank the Ministry of Education Malaysia, University Tun Hussein Onn Malaysia (UTHM), Johor for supporting this research study under research grant GPPS Vot H359.

References

[1] S. Gou, Z. Li, Q. Zhao, V. Nik, and J. Scartezzini, "Climate Responsive Strategies of Traditional Dwellings located in an Ancient Village in Hot Summer and Cold Winter Region of China," *Build. Environ.*, 2015.
[2] A. Qaid, H. Bin Lamit, D. R. Ossen, and R. N. Raja Shahminan, "Urban heat island and thermal comfort conditions at micro-climate scale in a tropical planned city," *Energy Build.*, vol. 133, pp. 577–595, 2016.
[3] L. Qin, X. Gao, and T. Chen, "SC," *J. Clean. Prod.*, 2018.
[4] A. J. Venables, "Using Natural Resources for Development: Why Has It Proven So Difficult?," vol. 30, no. 1, pp. 161–184, 2016.
[5] S. Yang and H. Lee, "Mechanical properties of recycled aggregate concrete proportioned with modified equivalent mortar volume method for paving applications," *Constr. Build. Mater.*, vol. 136, pp. 9–17, 2017.
[6] W. Is and P. Oil, "Palm Oil: Good or Bad? | IPOM," pp. 1–15, 2019.
[7] M. Ancrenaz, E. Meijaard, S. Wich, and J. Simery, *Palm Oil Paradox*. 2016.
[8] K. Z. A. Ghani and A. Z. M. Rus, "Influence of hot compression moulding of biopolymer filled waste Granulate Biopolymer," *Appl. Mech. Mater.*, vol. 315, no. April 2013, pp. 448–452, 2013.
[9] J. Meseguer, I. Pérez-Grande, and A. Sanz-Andrés, *Thermal radiation heat transfer*. 2012.
[10] A. T. Din, N. M. Hafiz, and A. Z. M. Rus, "Akademia Baru Exploration to Find Green Building Materials from Recycled Solid Wastes Akademia Baru," vol. 12, no. 1, pp. 12–23, 2015.
[11] E. M. Dede *et al.*, "Heat flux cloaking , focusing , and reversal in ultra-thin composites considering conduction-convection effects Heat flux cloaking , focusing , and reversal in ultra-thin composites considering conduction-convection effects," vol. 063501, 2013.
[12] K. Liu, Z. Wang, C. Jin, F. Wang, and X. Lu, "An experimental study on thermal conductivity of iron ore sand cement mortar," *Constr. Build. Mater.*, vol. 101, pp. 932–941, 2015.
[13] Z. Pavlík, M. Záleská, M. Pavlíková, and R. Č, "The thermal and mechanical performance of cement-based composites with enhanced thermal insulation properties," no. July 2014, pp. 250–260, 2016.
[14] A. Alavudeen, N. Rajini, S. Karthikeyan, M. Thiruchitrambalam, and N. Venkateshwaren, "Mechanical properties of banana/kenaf fiber-reinforced hybrid polyester composites: Effect of woven fabric and random orientation," *Mater. Des.*, vol. 66, no. PA, pp. 246–257, 2015.
[15] A. Feng, G. Wu, Y. Wang, and C. Pan, "Synthesis, Preparation and Mechanical Property of Wood Fiber-Reinforced Poly(vinyl chloride) Composites," *J. Nanosci. Nanotechnol.*, vol. 17, no. 6, pp. 3859–3863, 2017.
[16] J. Kim, C. Yi, and G. Zi, "Waste glass sludge as a partial cement replacement in mortar," *Constr. Build. Mater.*, vol. 75, pp. 242–246, 2015.
[17] G. Di Bella, V. Fiore, G. Galtieri, C. Borsellino, and A. Valenza, "Effects of natural fibres reinforcement in lime plasters (kenaf and sisal vs . Polypropylene)," *Constr. Build. Mater.*, vol. 58, pp. 159–165, 2014.
[18] R. A. Rahim, A. Z. M. Rus, and A. S. A. Bakhtiar, "Preliminary fabrication of polymer membranes from renewable resources," *Appl. Mech. Mater.*, vol. 315, pp. 428–432, 2013.
[19] S. M. Rus, N. A. Latif, M. I. Ghazali, and A. Z. M. Rus, "Characteristics of UV irradiated waste biopolymer from

renewable resources (Part 1)," *Adv. Mater. Res.*, vol. 974, no. June, pp. 252–256, 2014.
[20] A. Z. M. Rus, "Polymers from renewable materials," *Sci. Prog.*, vol. 93, no. 3, pp. 285–300, 2010.
[21] N. Ab Latif and A. Z. M. Rus, "Vibration transmissibility study of high density solid waste biopolymer foam," *J. Mech. Eng. Sci.*, vol. 6, no. June 2014, pp. 772–781, 2014.
[22] A. Z. M. Rus, N. Normunira, and M. Hassan, "UV Irradiated Biopolymer," *Int. J. Polym. Sci.*, vol. 2015, 2015.
[23] A. Z. M. Rus, N. M. Abdullah, and M. F. L. Abdullah, "Interconnected interface enhanced electrical properties of graphite in bio-based epoxy from insulating to conductor composites," *Indian J. Sci. Technol.*, vol. 8, no. 17, pp. 8–12, 2015.
[24] N. Sulong and A. Z. M. Rus, "Influence of TiO2 on selfclean bio coating," *Appl. Mech. Mater.*, vol. 315, pp. 399–403, 2013.

Penerbit Akademia Baru

Engineering Science and Technology Conference Proceedings

Journal homepage: www.akademiabaru.com/EST.html

MHD Squeezing Flow of Casson Nanofluid with Chemical Reaction, Thermal Radiation and Heat Generation/Absorption

Open Access

Nur Azlina Mat Noor[1], Sharidan Shafie[1], Mohd Ariff Admon[1,*]

[1] Department of Mathematical Sciences, Faculty of Science, Universiti Teknologi Malaysia, 81310 Johor Bahru, Johor, Malaysia

ABSTRACT

The heat and mass transfer characteristics on unsteady squeezing flow of magnetohydrodynamic (MHD) Casson nanofluid with chemical reaction, thermal radiation and heat generation/absorption effects is investigated in this study. The influences of viscous and joule dissipation are also examined. The flow is caused by squeezing between two parallel plates embedded in a porous medium. The highly coupled nonlinear partial differential equations are reduced to a system of nonlinear ordinary differential equations via similarity transformations. The transformed equations are solved using numerical scheme of Keller-box method. The accuracy of present method is validated through comparison of skin friction coefficient, Nusselt and Sherwood numbers with previously published results. Comparisons reveal that good agreements are achieved. Graphical results for velocity, temperature and nanoparticles concentration are analysed with various parameters. Findings demonstrate that the fluid velocity and temperature enhance when the plates move closer. Besides, increase in Hartmann number suppressed the fluid velocity and concentration due to the presence of strong Lorentz forces. The Brownian motion boosts the fluid temperature and concentration. Moreover, nanoparticles concentration is found to be higher in constructive chemical reaction and opposite effect is observed in destructive chemical reaction.

Keywords:
Squeezing flow; Casson nanofluid;
chemical reaction; thermal radiation;
heat generation/absorption

Copyright © 2019 PENERBIT AKADEMIA BARU - All rights reserved

1. Introduction

Recent advancement in nanotechnology has led to the development of a new innovative class of heat transfer fluids known as nanofluid. Choi and Eastman (1995) were the first to introduce the nanofluids engineered by colloidal suspensions of nanometer-sized particles in a base fluid. Conventional heat transfer fluids or base fluids such as water, ethylene glycol or kerosene oil have limited heat transfer capability due to their low thermal conductivity. Thus, the concept of nanofluid was discovered to improve the heat transfer performance by dispersing metallic or non-metallic nanoparticles in the conventional fluids. Eastman *et al*. (2001) reported that the addition of copper (10 nm) particles in ethylene glycol increases the thermal conductivity up to 40%. Several researchers reported that suspending 1–5% volume of nanoparticles in base fluids can enhance the thermal conductivity by more than 20% (Xuan and Li, 2003; Xue, 2003; Maiga *et al*., 2005). Later, Buongiorno (2006) examined seven slip mechanisms that generate a relative velocity between nanoparticles and base fluids. He concluded that among all the mechanisms, only Brownian diffusion and thermophoresis are found to be important factors in convective flow of nanofluid.

* *Corresponding author.*
E-mail address: ariffadmon@utm.my (Mohd Ariff Admon)

Brownian motion and thermophoresis of nanoparticles effectively boost the thermal conductivity of base fluid. Nowadays, Buongiorno's model has been adopted by many researchers in their study (Sheikholeslami *et al*., 2015; Azimi and Riazi, 2016; Muhammmad *et al*., 2018).

The study of boundary layer flow caused by squeezing between two parallel plates has increased tremendously due to its applications in chemical engineering and food industry. Some practical examples of squeeze flow include compression, polymer processing and injection molding. Stefan (1874) initiated the investigation on behavior of a lubricant confined between approaching horizontal surfaces. Later, the study of squeeze film lubrication between two infinitely long parallel plates was introduced by Cameron (1981). The squeeze film phenomenon occurs when two surfaces are separated by a lubricant and moved towards each other with a normal stress. Commonly, the lubricant is a viscous fluid. Wang (1976) studied unsteady squeezing flow of an incompressible viscous fluid between two parallel plates. The similar problem was solved by Bujurke *et al*. (1995), Rashidi *et al*. (2008) and Khan *et al*. (2014a) via semi-analytical methods.

Casson fluid is a non-Newtonian fluid classified as shear thinning fluid because it exhibits an infinite viscosity at zero velocity gradient, no flow occurs when force is applied below the yield stress, and zero viscosity at infinite velocity gradient. The Casson model was originally invented by Casson (1959) for printing inks and silicon suspension. The model is ideal for studying the flow characteristics of blood. Common examples of Casson fluid are honey, jelly, tomato sauce and concentrated fruit juices (Sobamowo, 2018). Researches done by Khan *et al.* (2014b) and Sampath *et al.* (2018) are among the pioneering works to investigate the unsteady squeezing flow of Casson fluid between two parallel plates.

The squeeze flow of electrically conducting fluids between parallel plates under the influence of magnetic field has been studied extensively in recent years. The unsteady two-dimensional flow of a viscous MHD fluid between two parallel plates was solved by Siddiqui *et al.* (2008) using homotopy perturbation method (HPM). Sweet *et al*. (2010) extended the work of Siddiqui *et al*. (2008) by varying the fluid density to be a model parameter. In non-Newtonian fluid, Ahmed *et al*. (2015) presented the analytical solutions of unsteady MHD squeezing flow of Casson fluid between two parallel plates. A novel algorithm was developed by Al-Saif and Jasim (2019) to solve the similar problem of Ahmed *et al*. (2015). The research of fluid flow through a porous medium in the presence of MHD effect is important in the applications of geothermal energy recovery, oil extraction, nuclear reactors and thermal energy storage. A porous medium is a material that contains fluid-filled pores. Khan *et al*. (2016) analysed MHD flow of Casson fluid squeezing between two parallel plates embedded in porous medium.

The impact of viscous dissipation on heat transfer of nanofluid flow has received great attention due to its engineering applications such as temperature rises in polymer processing, injection molding and high rates extrusion. The viscous dissipation effect is only significant for the fluids with high velocity and viscosity. It is worth mentioning that Tiwari and Das model was recently used by Sheikholeslami and Ganji (2012), Pourmehran *et al*. (2014) and Mittal and Pandit (2017). All of them investigated the problem of unsteady flow and heat transfer of a nanofluid squeezing between two parallel plates in the presence of viscous dissipation. They implemented different types of methods in obtaining the solution. The squeezing flow of Copper-water and Copper-kerosene with magnetic field and viscous dissipation effects using Tiwari and Das model was discussed by Acharya *et al*. (2016) and Celik (2019). A series of studies on the similar problem had been investigated by Sheikholeslami *et al*. (2015), Hedayati and Ramiar (2015) and Azimi and Riazi (2016). They employed Buongiorno's model on their study. Muhammad *et al*. (2018) analysed the effects of MHD and thermal radiation on squeezing nanofluid flow between two parallel plates. Heat and mass transfer characteristics were examined by considering Brownian motion and thermophoresis.

The unsteady squeezing flow and heat transfer of nanofluid under the influence of MHD, viscous dissipation and thermal radiation was reported by Dogonchi *et al*. (2016) and Sheikholeslami *et al*. (2016) using Tiwari and Das model and Buongiorno's model, respectively. Madaki *et al*. (2016) studied the unsteady squeezing nanofluid flow with viscous dissipation and thermal radiation effects using Tiwari and Das model. Madaki *et al*. (2017) extended their works by including heat generation or absorption on the flow field. In non-Newtonian fluid, the influence of magnetic field on unsteady squeezing flow of Casson nanofluid between parallel plates in a porous medium was presented by Sobamowo (2018). The analytical solution was obtained via method of matched asymptotic expansion. Later, Sobamowo *et al*. (2019) performed the similar problem by applying two different techniques, differential transformation method and variation of parameters method.

The literature survey discussed above reveals that most of the existing studies on unsteady squeezing flow between two parallel plates are done for viscous fluid. The study involving non-Newtonian fluids, especially Casson nanofluid, has not been given much consideration. Motivated by the limitation of the above references, this study concentrates on the unsteady MHD flow of Casson nanofluid with the effects of chemical reaction, thermal radiation and heat generation or absorption. The fluid flow is generated by squeezing between two parallel plates through a porous medium in the presence of viscous and Joule dissipation. The governing equations are reduced to ordinary differential equations using non dimensional variables. The transformed equations are solved numerically via Keller box method. An algorithm is developed in MATLAB software to compute the numerical solutions and plot the associated graphs. The results for wall shear stress, heat and mass transfer rate are compared with existing literature results to check the accuracy of the present algorithm. The effects of various parameters on the behavior of fluid velocity, temperature and nanoparticles concentration are examined.

2. Mathematical Formulation

Consider an unsteady, two dimensional, incompressible MHD flow of Casson nanofluid squeezing between two parallel plates through a porous medium under the influence of chemical reaction, thermal radiation and heat generation/absorption. The viscous and Joule dissipation effects is retained. The physical behavior of this model is studied using the Cartesian coordinate system. The x-axis is measured along the horizontal direction of the plates and y-axis is taken normal to the plates. The two plates are separated by a time-dependent distance $y = \pm l(1-\alpha t)^{1/2} = \pm h(t)$. The fluid flow occurs due to the motion of the upper plate at a distance $h(t) = +l(1-\alpha t)^{1/2}$ with the velocity of the form $v_w(t) = \frac{-\alpha l}{2\sqrt{1-\alpha t}}$ towards or away from the stationary lower plate located at $h(t) = -l(1-\alpha t)^{1/2}$. Both plates are squeezed when $\alpha > 0$ until they reach $t = 1/\alpha$ and they are separated for $\alpha < 0$. The parameter α is correlated to the dimensions of $(\text{time})^{-1}$ and $\alpha t < 1$. Here, α is a constant, l denotes the initial position of the plate (at $t = 0$) and t is the time throughout the flow. A uniform magnetic field of strength $B(t) = B_0(1-\alpha t)^{-1/2}$ is applied perpendicular to the plates with constant B_0. The flow configurations and coordinate system are presented in Figure 1.

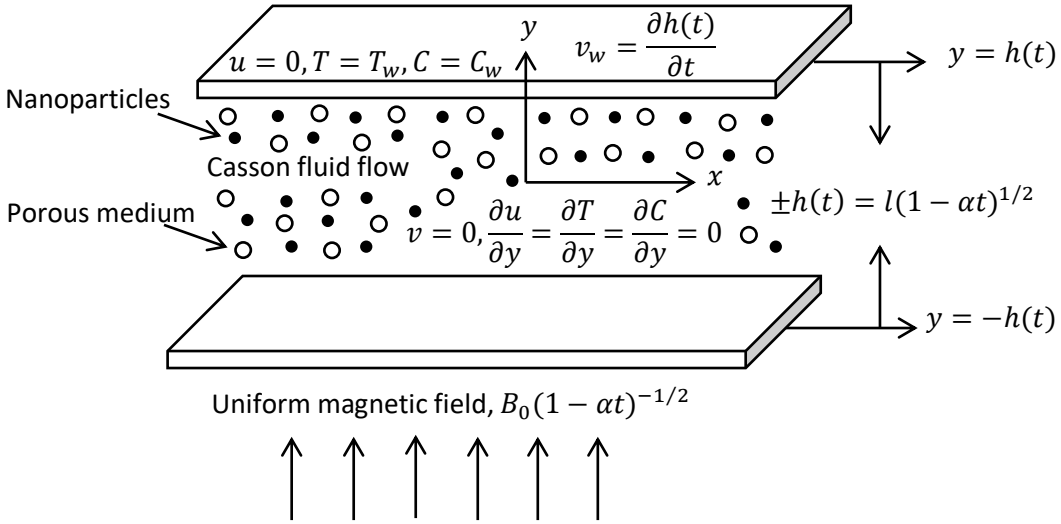


Fig. 1. Physical model and coordinate system

The governing equations of continuity, momentum, energy and concentration for Casson nanofluid using above-mentioned assumptions with boundary layer approximations are given as

$$\frac{\partial u}{\partial x} + \frac{\partial v}{\partial y} = 0, \tag{1}$$

$$\frac{\partial u}{\partial t} + u\frac{\partial u}{\partial x} + v\frac{\partial u}{\partial y} = \nu_f\left(1 + \frac{1}{\beta}\right)\frac{\partial^2 u}{\partial y^2} - \frac{\sigma B^2(t)}{\rho_f}u - \nu_f\left(1 + \frac{1}{\beta}\right)\frac{\varphi}{k_1}u, \tag{2}$$

$$\frac{\partial T}{\partial t} + u\frac{\partial T}{\partial x} + v\frac{\partial T}{\partial y} = \alpha_f\frac{\partial^2 T}{\partial y^2} + \tau\left[D_B\frac{\partial C}{\partial y}\frac{\partial T}{\partial y} + \frac{D_T}{T_\infty}\left(\frac{\partial T}{\partial y}\right)^2\right] + \frac{\nu_f}{c_f}\left(1 + \frac{1}{\beta}\right)\left[4\left(\frac{\partial u}{\partial x}\right)^2 + \left(\frac{\partial u}{\partial y}\right)^2\right] + \frac{\sigma B^2(t)}{(\rho c)_f}u^2 - \frac{1}{(\rho c)_f}\frac{\partial q_r}{\partial y} + \frac{Q(t)}{(\rho c)_f}(T - T_\infty), \tag{3}$$

$$\frac{\partial C}{\partial t} + u\frac{\partial C}{\partial x} + v\frac{\partial C}{\partial y} = D_B\frac{\partial^2 C}{\partial y^2} + \frac{D_T}{T_\infty}\frac{\partial^2 T}{\partial y^2} - k_c(C - C_\infty), \tag{4}$$

where u and v are the velocity components along the x and y directions, respectively, ν_f is kinematic viscosity, ρ_f is the fluid density, σ is the electrical conductivity, β is the Casson parameter, φ is the porosity, $k_1(t) = k_0(1 - \alpha t)$ is the time dependent permeability of porous medium, k_0 is the permeability constant, T is the fluid temperature, C is the nanoparticles concentration, $\alpha_f = \frac{k}{(\rho c)_f}$ is the thermal diffusivity of the Casson fluid, k is the thermal conductivity of the Casson fluid, c_f is the specific heat of fluid, $\tau = \frac{(\rho c)_p}{(\rho c)_f}$ is the ratio between the heat capacity of the nanoparticles material and heat capacity of the fluid, ρ_p is the density of nanoparticles, c_p is the specific heat of nanoparticles, D_B is the Brownian diffusion coefficient, D_T is the thermophoretic diffusion coefficient, q_r is the radiative heat flux, $Q(t) = \frac{Q_0}{1 - \alpha t}$ is heat generation or absorption coefficient, $k_c(t) = ak_2(1 - \alpha t)^{-1}$ is the variable rate of chemical reaction, k_2 is the

constant reaction rate and a is the reference length along the fluid flow. The temperature and nanoparticles concentration at free stream are T_∞ and C_∞, respectively.

The corresponding boundary conditions are written as follows

$$u = 0, v = v_w = \frac{\partial h(t)}{\partial t}, T = T_w, C = C_w, \text{ at } y = h(t), \tag{5}$$

$$\frac{\partial u}{\partial y} = 0, v = 0, \frac{\partial T}{\partial y} = 0, \frac{\partial C}{\partial y} = 0, \quad \text{at } y = 0, \tag{6}$$

where the wall of plates is indicated by temperature T_w and concentration C_w. Following Roseland approximation, the radiative heat flux is defined as (Ullah *et al*., 2016)

$$q_r = \frac{-4\sigma^*}{3k_1^*}\frac{\partial T^4}{\partial y}, \tag{7}$$

where σ^* is the Stefan-Boltzmann constant and ${k_1}^*$ is the mean absorption coefficient. It is assumed that the temperature differences within the flow are sufficiently small such that T^4 can be expressed as linear function of temperature. Hence, expanding T^4 in Taylor series about T_∞ and ignoring higher order terms lead to the following relation

$$T^4 \cong 4T_\infty^3\, T - 3T_\infty^4. \tag{8}$$

Thus, substituting equations (7) and (8) into equation (3) yields

$$\begin{aligned}\frac{\partial T}{\partial t} + u\frac{\partial T}{\partial x} + v\frac{\partial T}{\partial y} = \alpha_f\left(1 + \frac{16\sigma^* T_\infty^3}{3k_f k_1^*}\right)\frac{\partial^2 T}{\partial y^2} + \tau\left[D_B\frac{\partial C}{\partial y}\frac{\partial T}{\partial y} + \frac{D_T}{T_\infty}\left(\frac{\partial T}{\partial y}\right)^2\right] \\ + \frac{\nu_f}{c_f}\left(1 + \frac{1}{\beta}\right)\left[4\left(\frac{\partial u}{\partial x}\right)^2 + \left(\frac{\partial u}{\partial y}\right)^2\right] + \frac{\sigma B^2(t)}{(\rho c)_f}u^2 + \frac{Q(t)}{(\rho c)_f}(T - T_\infty).\end{aligned} \tag{9}$$

The following similarity transformations adopted from Mustafa *et al.* (2012) and Ahmed *et al.* (2015) are introduced to reduce the nonlinear partial differential equations into the system of ordinary differential equations;

$$\begin{aligned}u = \frac{\alpha x}{2(1-\alpha t)}f'(\eta), \quad v = -\frac{\alpha l}{2\sqrt{(1-\alpha t)}}f(\eta), \quad \eta = \frac{y}{l\sqrt{(1-\alpha t)}}, \\ \theta = \frac{T - T_\infty}{T_w - T_\infty}, \quad \phi = \frac{C - C_\infty}{C_w - C_\infty},\end{aligned} \tag{10}$$

where η is the local similarity variable, $f(\eta)$, $\theta(\eta)$ and $\phi(\eta)$ are the dimensionless velocity, temperature and concentration of the fluid in the boundary layer region, respectively.

Using equation (10), the governing equations (2), (4) and (9) are converted to the following non-dimensional ordinary differential equations form

$$\left(1+\frac{1}{\beta}\right)f'''' - S(\eta f''' + 3f'' + f'f'' - ff''') - Ha^2 f'' - \left(1+\frac{1}{\beta}\right)\frac{1}{Da}f'' = 0, \tag{11}$$

$$\frac{1}{Pr}\left(1+\frac{4}{3}R_d\right)\theta'' + S(f\theta' - \eta\theta' + \gamma\theta) + Ec\left[\left(1+\frac{1}{\beta}\right)[(f'')^2 + 4\delta^2(f')^2] + Ha^2(f')^2\right] + N_b\phi'\theta' + N_t(\theta')^2 = 0, \tag{12}$$

$$\frac{1}{Le}\phi'' + S(f\phi' - \eta\phi') + \frac{1}{Le}\frac{N_t}{N_b}\theta'' - R\phi = 0, \tag{13}$$

subject to the boundary conditions

$$f(\eta) = 0,\ f''(\eta) = 0,\ \theta'(\eta) = 0,\ \phi'(\eta) = 0, \quad \text{at } \eta = 0, \tag{14}$$

$$f(\eta) = 1,\ f'(\eta) = 0,\ \theta(\eta) = 1,\ \phi(\eta) = 0, \quad \text{at } \eta = 1. \tag{15}$$

The physical parameters involved in the above expressions, S, Ha, Da, δ, Pr, Ec, R_d, γ, N_b, N_t, Le and R are the squeeze number, Hartmann number, Darcy number, dimensionless length, Prandtl number, Eckert number, radiation parameter, heat generation/absorption parameter, Brownian motion parameter, thermophoresis parameter, Lewis number and chemical reaction parameter, respectively, and are defined as

$$S = \frac{\alpha l^2}{2\nu_f},\ Ha = lB_0\sqrt{\frac{\sigma}{\rho_f\nu_f}},\ Da = \frac{k_0}{\varphi l^2},\ \delta = \frac{l}{x}(1-\alpha t)^{1/2},$$
$$Pr = \frac{\nu_f}{\alpha_f},\ Ec = \frac{\alpha^2 x^2}{4c_f(T_H - T_\infty)(1-\alpha t)^2},\ R_d = \frac{4\sigma^* T_\infty^3}{k_f k_1^*},\ \gamma = \frac{2Q_0}{\alpha(\rho c)_f},$$
$$N_b = \frac{\tau D_B(C_H - C_\infty)}{\nu_f},\ N_t = \frac{\tau D_T(T_H - T_\infty)}{\nu_f T_\infty},\ Le = \frac{\nu_f}{D_B},\ R = \frac{ak_2 l^2}{\nu_f}.$$

The physical quantities of interest which govern the flow such as local skin friction coefficient Cf_x, local Nusselt number Nu_x and local Sherwood number Sh_x are defined by Naduvinamani and Shanka (2019) as follows

$$Cf_x = \frac{\tau_w}{\rho_f v_w^2},\ Nu_x = \frac{lq_w}{\alpha_f(T_H - T_\infty)},\ Sh_x = \frac{lq_s}{D_B(C_H - C_\infty)},$$

where τ_w, q_w and q_s are the wall skin friction, wall heat flux and wall mass flux, respectively, and are given by

$$\tau_w = \mu_B\left(1+\frac{1}{\beta}\right)\left[\frac{\partial u}{\partial y}\right]_{y=h(t)},\ q_w = -\left(\left(\alpha_f + \frac{16\sigma^* T_\infty^3}{3(\rho c)_f k_1^*}\right)\frac{\partial T}{\partial y}\right)_{y=h(t)},\ q_s = -D_B\left(\frac{\partial C}{\partial y}\right)_{y=h(t)}.$$

The non dimensional forms of the skin friction coefficient, Nusselt number and Sherwood number in terms of similarity variable are

$$\frac{l^2}{x^2}(1-\alpha t)Re_x Cf_x = \left(1+\frac{1}{\beta}\right)f''(1),$$

$$\sqrt{(1-\alpha t)}Nu_x = -\left(1+\frac{4}{3}R_d\right)\theta'(1),$$

$$\sqrt{(1-\alpha t)}Sh_x = -\phi'(1),$$

where $Re_x = \frac{xv_w}{\nu_f}$ is the local Reynolds number based on the squeezing velocity v_w.

3. Results and Discussion

The nonlinear ordinary differential equations (11) to (13) subject to boundary conditions (14) and (15) are solved numerically via Keller-box method. An algorithm is developed in MATLAB software in order to generate numerical and graphical solutions. Moreover, it is necessary to choose suitable guess for the step size $\Delta\eta$ and boundary layer thickness η_∞. In the present study, $\Delta\eta = 0.01$ and $\eta_\infty = 1$ are considered. The convergence criteria mainly refer to the relative difference between current and previous iterative values of velocity, temperature and concentration. The iteration process is terminated when all the values in η direction satisfy the convergence criteria 10^{-5} (Naduvinamani and Shanka, 2019).

In order to examine the physical behavior of velocity, temperature and concentration profiles, numerical computations are carried out for various values of squeeze number S, Casson fluid parameter β, Hartmann number Ha, radiation parameter R_d, heat generation or absorption parameter γ, Brownian motion parameter N_b, thermophoresis parameter N_t and chemical reaction parameter R. The present algorithm developed in MATLAB software are validated by comparing the numerical results with previous published works as limiting cases and presented in Table 1.

Table 1 displays the comparison of skin friction coefficient, Nusselt and Sherwood numbers for different values of S with the results of Mustafa *et al*. (2012) and Naduvinamani and Shanka (2019). The results showed an excellent agreement.

Table 1
Comparison of $-f''(1)$, $-\theta'(1)$ and $-\phi'(1)$ for different values of S when $\beta \to \infty$, $Da \to \infty$ and $Ha = R_d = \gamma = N_b = N_t = 0$.

	Mustafa *et al*. (2012)			Naduvinamani and Shanka (2019)			Present results		
S	$-f''(1)$	$-\theta'(1)$	$-\phi'(1)$	$-f''(1)$	$-\theta'(1)$	$-\phi'(1)$	$-f''(1)$	$-\theta'(1)$	$-\phi'(1)$
-1.0	2.170090	3.319899	0.804558	2.170091	3.319899	0.804559	2.170255	3.319904	0.804558
-0.5	2.614038	3.129491	0.781402	2.617404	3.129491	0.781402	2.617512	3.129556	0.781404
0.01	3.007134	3.047092	0.761225	3.007134	3.047092	0.761225	3.007208	3.047166	0.761229
0.5	3.336449	3.026324	0.744224	3.336449	3.026324	0.744224	3.336504	3.026389	0.744229
2.0	4.167389	3.118551	0.701813	4.167389	3.118551	0.701813	4.167412	3.118564	0.701819

Figures 2 to 5 are plotted to analyse the dimensionless velocity, temperature and nanoparticles concentration profiles for effect of S. It is noteworthy here that $S > 0$ represents the plates move away from each other and $S < 0$ corresponds to the plates move towards each other. Figure 2 reveals that the component of normal velocity declines for increasing values of $S > 0$ and the velocity increases for $S < 0$ case. The increment in fluid velocity is due to the reason that the fluid pass through the channel at a faster rate when the plates move closer. Meanwhile, the velocity slow down as the fluid encounters more resistance when flowing in a wide channel (the plates move apart). The variation of S on axial velocity is displayed in Figure 3. It is found that fluid

velocity reduces in the region $0 \leq \eta < 0.45$ and it increases in the region $0.45 < \eta \leq 1$ for $S > 0$. Also, the velocity rises in the region $0 \leq \eta < 0.45$ and it decreases in the region $0.45 < \eta \leq 1$ for $S < 0$. The cross-behavior of fluid flow is noticed on the centre of the channel. There is no significant effect of squeeze number on the velocity field at the critical point $\eta_c = 0.45$.

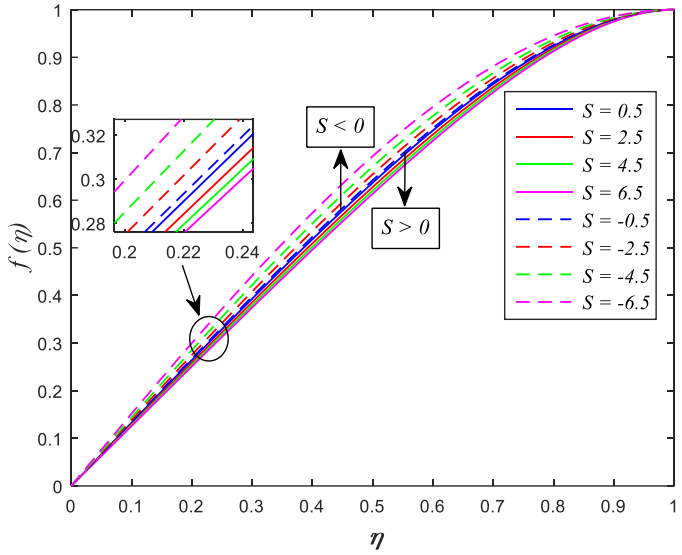


Fig.2. Effect of S on radial velocity.

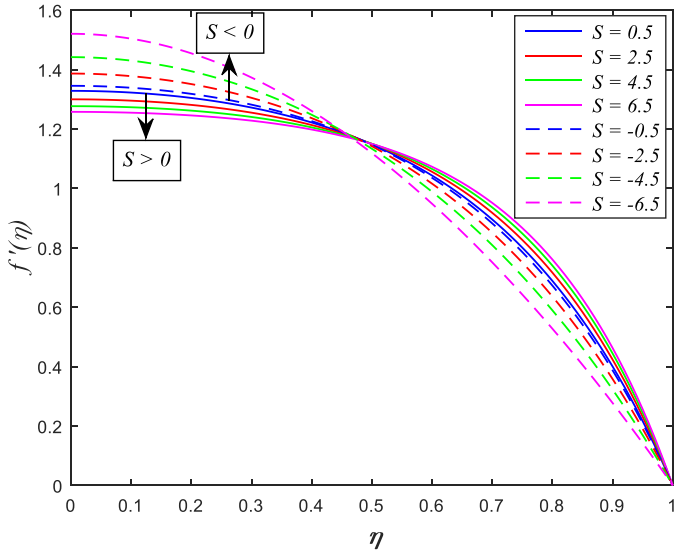


Fig.3. Effect of S on axial velocity.

The influence of S on temperature profile for both $S > 0$ and $S < 0$ cases is plotted in Figure 4. The fluid temperature drops for $S > 0$ and rises for $S < 0$. The speed of fluid flow declines when the plates moves further, which cause the kinetic energy of fluid particles become weaker and consequently decreasing the temperature. It is stated that the kinetic energy is directly proportional to the temperature. Figure 5 depicts that increasing values of positive S enhance the nanoparticles concentration and it reduces for decreasing values of negative S. The squeeze number did not affect the concentration near the upper plate $\eta = 1$.

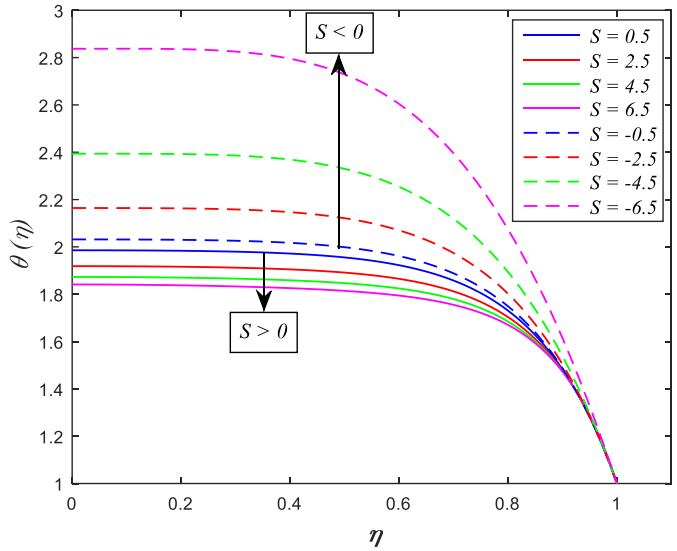


Fig.4. Effect of S on temperature.

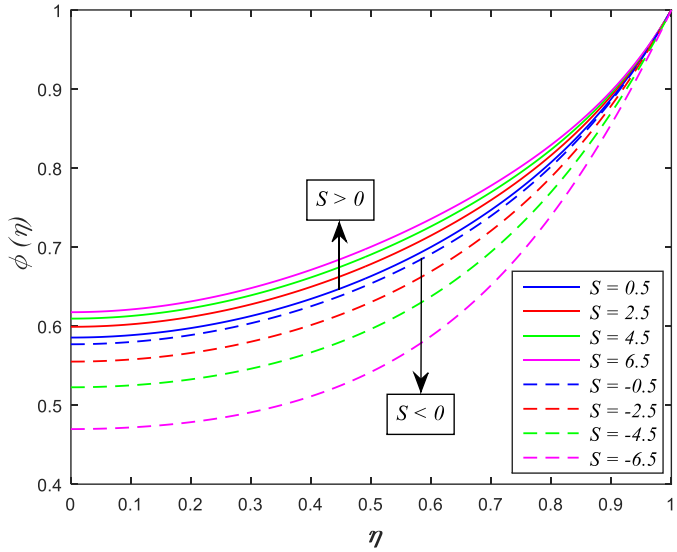


Fig.5. Effect of S on nanoparticles concentration.

The effect of β on the velocity, temperature and nanoparticles concentration profiles is presented in Figures 6 to 9. It is noticed from Figure 6 that the normal velocity decelerates with increase in β. The reason behind this behavior is that higher values of β increase the viscosity of fluid, which offers more resistance to the fluid flow inside the channel. Figure 7 demonstrates that the axial velocity reduces in the region $\eta < 0.5$ and it rises in the remaining region $\eta > 0.5$ for increasing values of β. There is cross-behavior of fluid flow occurs at the centre region of the channel. The variation of temperature profile for different values of β is illustrated in Figure 8. It is observed that fluid temperature drops when β increases. This phenomenon indicates that increasing β cause enhancement in the modulus of elasticity of fluid. The reduction in the temperature is caused by larger modulus of elasticity, which results in thermal boundary layer becoming thinner. Figure 9 portrays that nanoparticles concentration is a decreasing function of β.

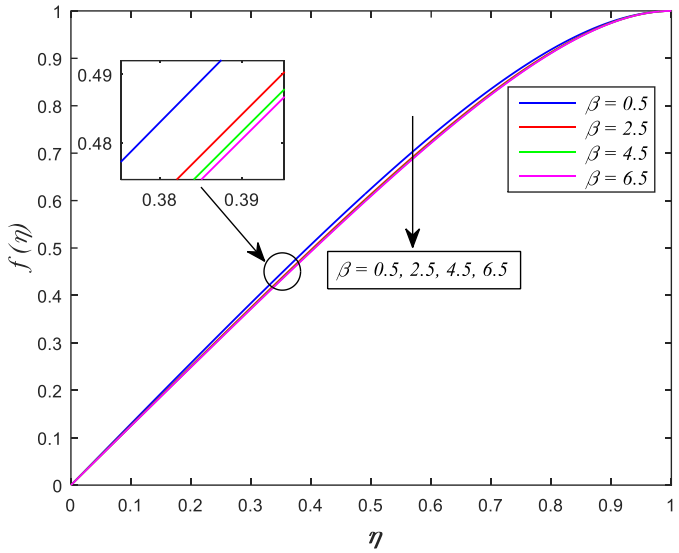


Fig.6. Effect of β on radial velocity.

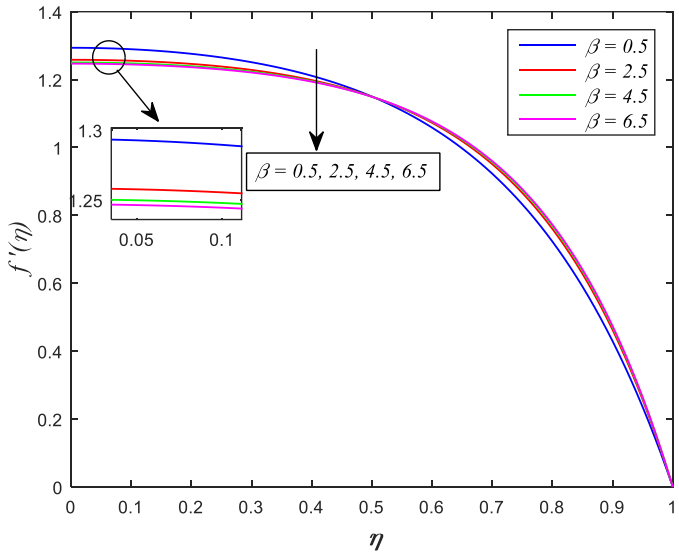


Fig.7. Effect of β on axial velocity.

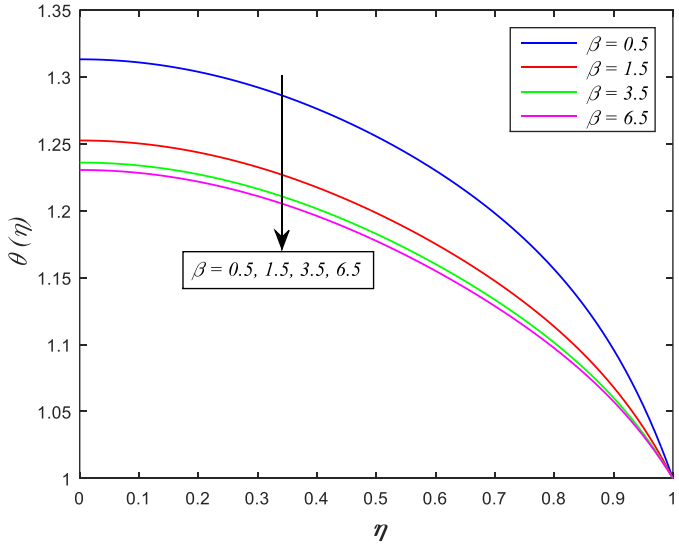


Fig.8. Effect of β on temperature.

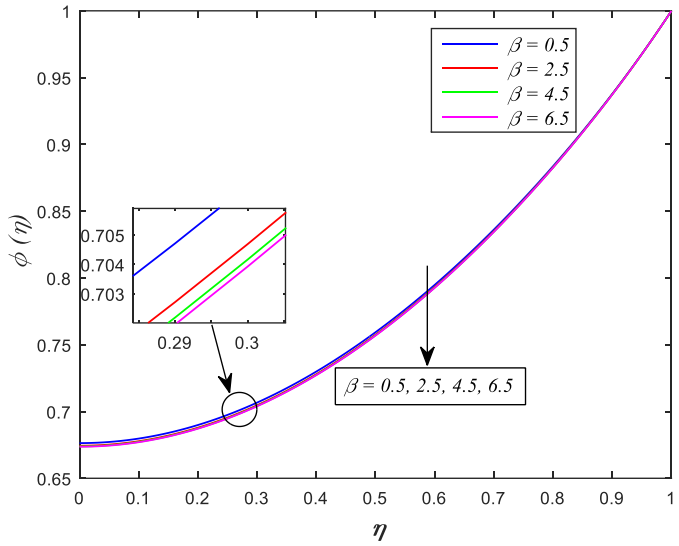


Fig.9. Effect of β on nanoparticles concentration.

Figures 10 to 13 exhibit the influence of Ha on the velocity, temperature and nanoparticles concentration profiles. Figure 10 shows that increasing values of Ha reduce the normal velocity of fluid. A resistive-type force known as Lorentz force is generated due to an application of magnetic field in the electrically conducting fluid. This force presents resistance to the flow, which cause the fluid flow in the channel to slow down. It is clear from Figure 11 that the axial velocity declines in the region $\eta < 0.5$ and rises in the other region $\eta > 0.5$ when Ha increases. The midpoint of the channel is the centre of cross flow behavior. The variation of temperature profile for various values of Ha is portrayed in Figure 12. It is found that fluid temperature rises with increase in Ha. The presence of Joule and viscous dissipation in the energy equation also boosts the temperature. Figure 13 reveals that nanoparticles concentration decreases for increasing values of Ha.

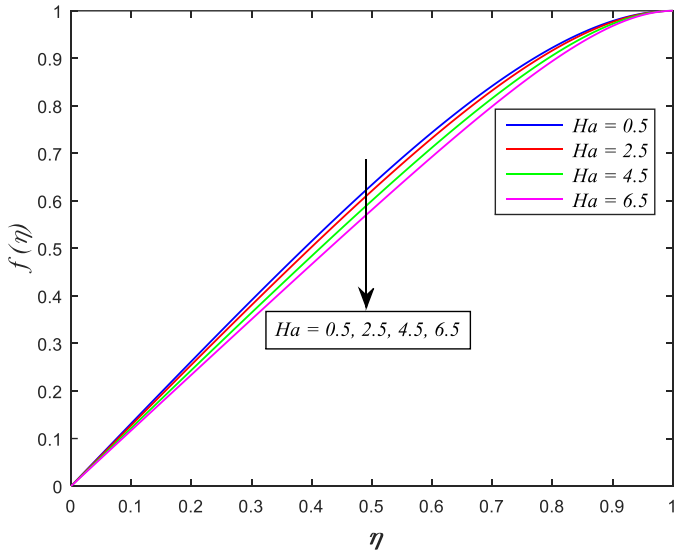


Fig.10. Effect of Ha on radial velocity.

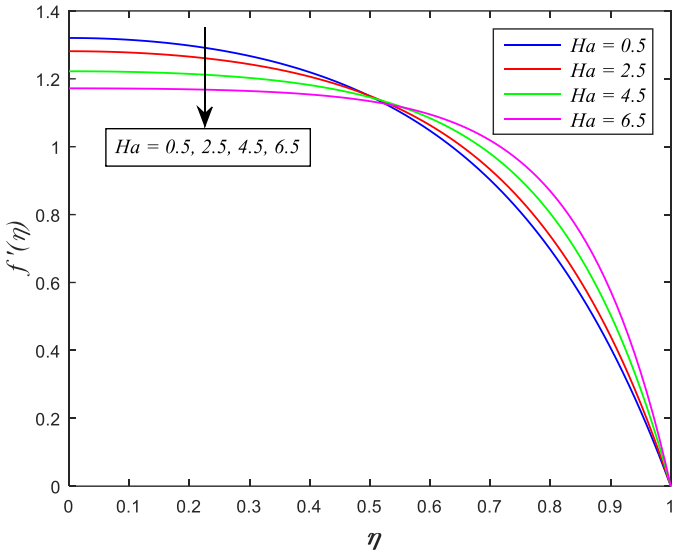


Fig.11. Effect of Ha on axial velocity.

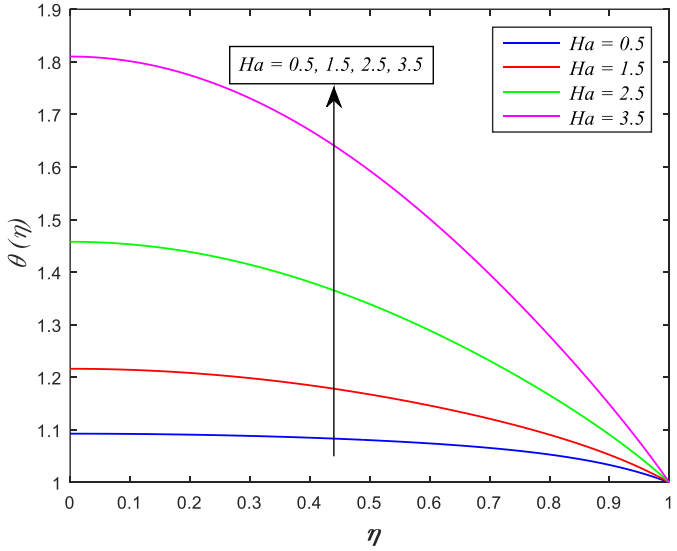


Fig.12. Effect of Ha on temperature.

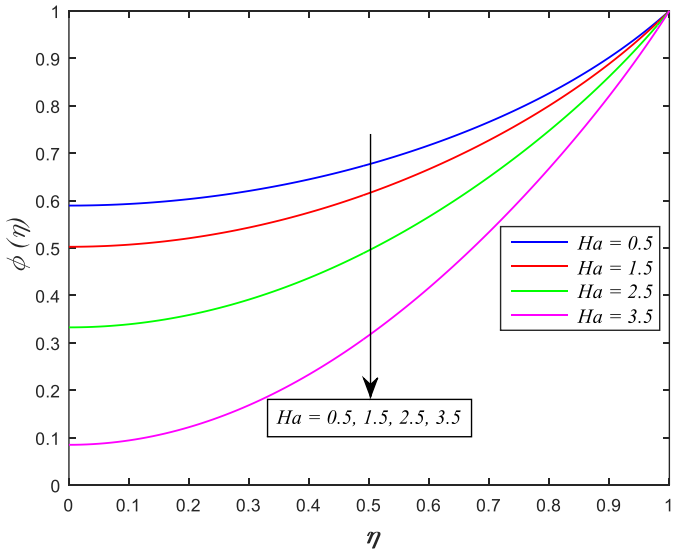


Fig.13. Effect of Ha on nanoparticles concentration.

The effect of R_d on temperature profile is depicted in Figure 14. It is noticed that the temperature of fluid drops as R_d increases. Figure 15 describes the influence of γ on temperature profile. It is noteworthy here that $\gamma > 0$ and $\gamma < 0$ represent heat generation and heat absorption case. It is observed that the temperature increases when $\gamma > 0$ and decreases when $\gamma < 0$. The existence of heat source enhances the thermal energy of fluid and consequently raises the fluid temperature. The impact of N_b on temperature profile is shown in Figure 16. It is noticed that the temperature is an increasing function of N_b. It is due to the fact that Brownian motion of nanoparticles that occurs in nanofluid systems promotes the thermal conductivity of fluid. Therefore, increasing N_b elevates the heat transfer properties of nanofluid which results in enhancing fluid temperature. Figure 17 portrays the effect of N_t on temperature profile. It is found that the temperature rises slightly with increase in N_t. The reason is higher values of N_t indicates larger temperature gradient between fluid flow and hot plates. The presence of temperature difference induces the thermophoretic force on nanoparticles. The force boosts the disperse of nanoparticles from the hot plates to the fluid inside the channel which cause temperature increases in the flow region.

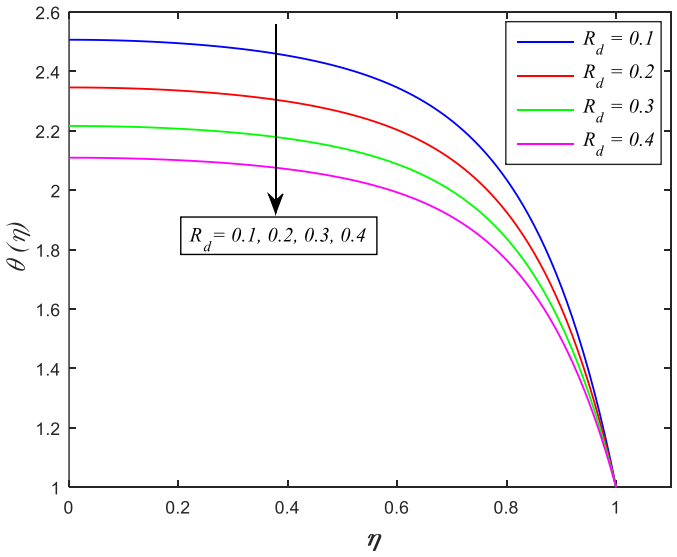


Fig.14. Effect of R_d on temperature.

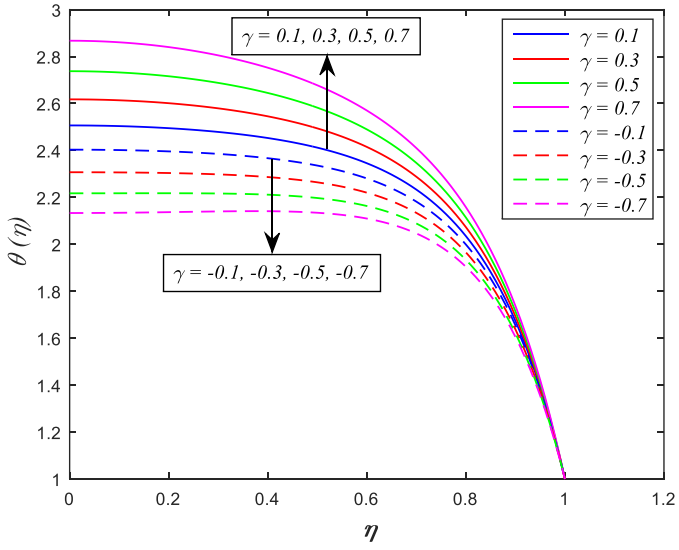


Fig.15. Effect of γ on temperature.

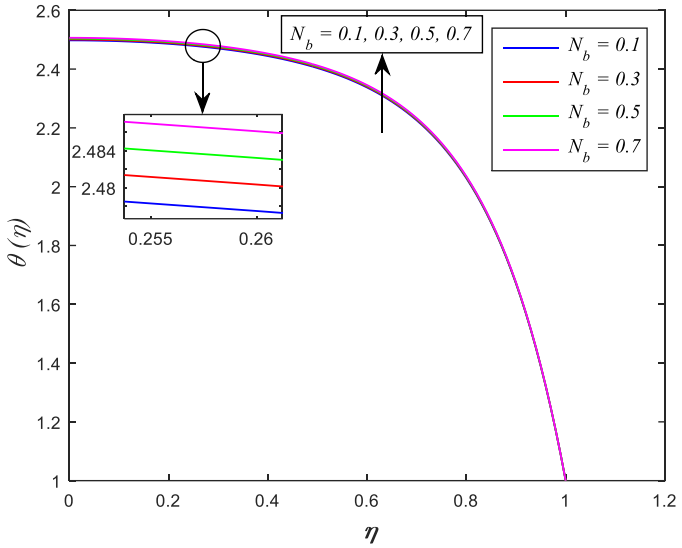


Fig.16. Effect of N_b on temperature.

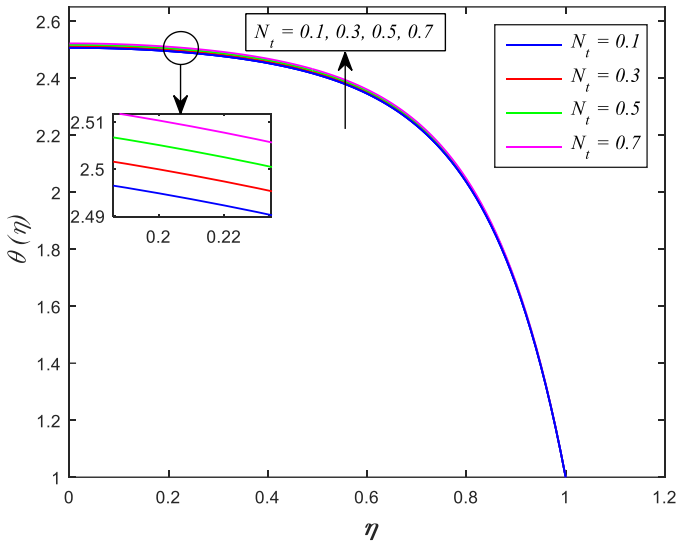


Fig.17. Effect of N_t on temperature.

The influence of N_b on concentration profile is exhibited in Figure 18. Clearly, nanoparticles concentration rises when values of N_b increases. It is important to note that the increment of random motion raise the kinetic energy of nanoparticles. The effective movement of nanoparticles from the plates to the moving fluid lead to enhancement in nanoparticles concentration. Figure 19 displays the impact of N_t on concentration profile. The larger values of N_t reduce the nanoparticles concentration. The thermophoretic force imposed on nanoparticles elevates the mass transfer from the moving fluid to the plates which results in decreasing nanoparticles concentration. The effect of R on concentration profile is demonstrated in Figure 20. It is observed that nanoparticles concentration declines in the case of destructive chemical reaction $(R > 0)$ and increases in the case of constructive chemical reaction $(R < 0)$. It is true with the fact that the mass transfer rate rises when $R > 0$, which cause reduction in nanoparticles concentration (Mustafa *et al.*, 2012).

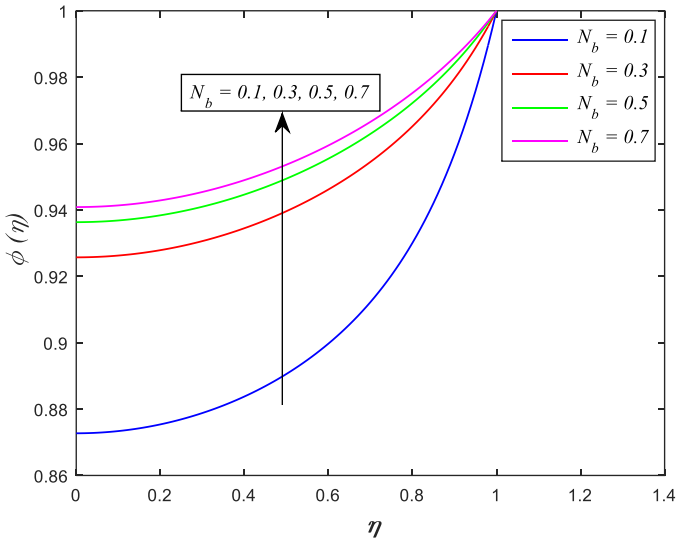


Fig.18. Effect of N_b on nanoparticles concentration.

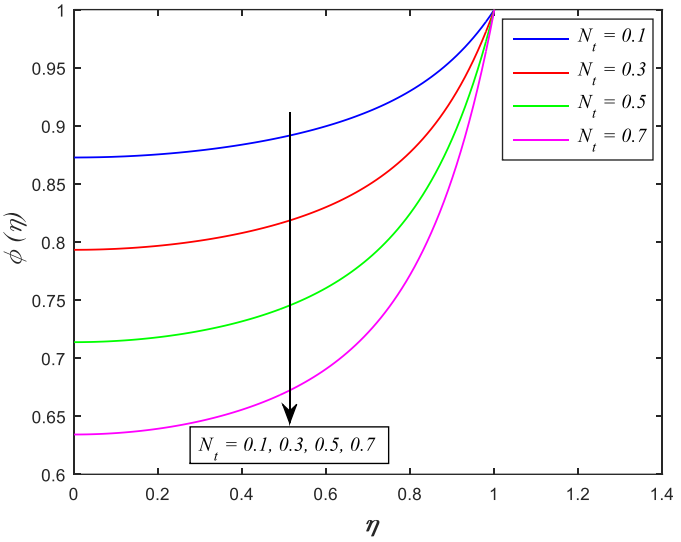


Fig.19. Effect of N_t on nanoparticles concentration.

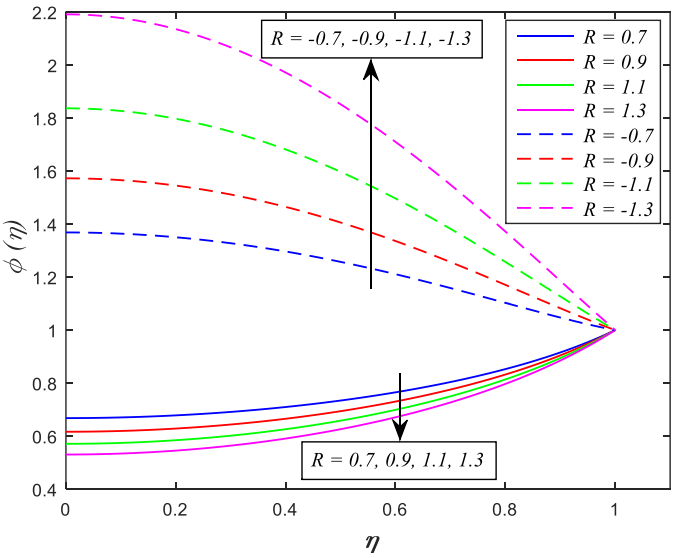


Fig.20. Effect of R on nanoparticles concentration.

4. Conclusions

The heat and mass transfer characteristics of unsteady MHD flow of Casson nanofluid squeezing between two parallel plates saturated in a porous medium under the influence of chemical reaction, thermal radiation and heat generation or absorption was investigated numerically. The effects of viscous and Joule dissipation were also considered. The flow is induced by the motion of the upper plate towards or away from lower plate with an external velocity. The transformed governing equations are solved through Keller box method. The numerical solutions for skin friction coefficient, Nusselt and Sherwood numbers are validated with the previous works and excellent agreement is observed from both results. The effects of physical parameters, namely, squeeze number S, Casson fluid parameter β, Hartmann number Ha, radiation parameter R_d, heat generation/absorption parameter γ, Brownian motion parameter N_b, thermophoresis parameter N_t and chemical reaction parameter R on fluid velocity, temperature and concentration are analysed graphically. The main findings of this study can be summarized as follows:

1. The fluid velocity decelerates when the plates move apart $(S > 0)$ and it accelerates when the plates move closer $(S < 0)$.
2. The fluid velocity and nanoparticles concentration decrease with increase in Ha.
3. The fluid temperature drops for increasing values of R_d.
4. The fluid temperature enhances in the case of heat generation $(\gamma > 0)$ and it reduces in the case of heat absorption $(\gamma < 0)$.
5. The increment of N_b boosts the fluid temperature and nanoparticles concentration.
6. The fluid temperature rises and nanoparticles concentration decreases when N_t increases.
7. The nanoparticles concentration declines for destructive chemical reaction $(R > 0)$ and it enhances for constructive chemical reaction $(R < 0)$.

Acknowledgement
The authors would like to acknowledge Ministry of Education (MOE) and Research Management Centre, Universiti Teknologi Malaysia (UTM) for financial support through vote number 07G77 for this research.

References

[1] Acharya, N., Das, K., and Kundu, P. K. (2016). The squeezing flow of Cu-water and Cu-kerosene nanofluids between two parallel plates. *Alexandria Engineering Journal*, 55, 1177-1186.
[2] Ahmed, N., Khan, U., Khan, S. I., Bano, S., and Mohyud-Din S. T. (2015). Effects on magnetic field in squeezing flow of a Casson fluid between parallel plates. *Journal of King Saud University-Science*, 29, 119-125.
[3] Al-Saif, A-S. A., and Jasim, A. M. (2019). A novel algorithm for studying the effects of squeezing flow of a Casson fluid between parallel plates on magnetic field. *Journal of Applied Mathematics*.
[4] Azimi, M., and Riazi, R. (2016). MHD unsteady GO-water squeezing nanofluid flow heat and mass transfer between two infinite parallel moving plates: analytical investigation. *Sadhana*.
[5] Bujurke, N. M., Achar, P. K., and Pai, N. P. (1995). Computer extended series for squeezing flow between plates. *Fluid Dynamics Research*, 16, 173-187.
[6] Buongiorno, J. (2006). Convective Transport in Nanofluids. *ASME Journal of Heat Transfer*, 128(3), 240-250.
[7] Cameron, A. (1981). *Basic Lubrication Theory*. Prentice Hall Europe.
[8] Casson, N. (1959). *A flow equation for the pigment oil suspensions of the printing ink type, in rheology of disperse systems*. Pergamon, New York.
[9] Celik, I. (2019). Squeezing flow of nanofuids of Cu-water and kerosene between two parallel plates by Gegenbauer wavelet collocation method. *Engineering with Computers*.
[10] Choi, S. and Eastman, J. A. (1995). Enhancing thermal conductivity of fluids with nanoparticles. *ASME-Publications Fed*, 231, 99-106.

[11] Dogonchi, A., Divsalar, S. K., and Ganji, D. D. (2016). Flow and heat transfer of MHD nanofluid between parallel plates in the presence of thermal radiation. *Computer Methods in Applied Mechanics and Engineering*. 310, 58-76.
[12] Eastman, J. A., Choi S. U. S., Li, S., Yu, W., and Thompson, L. J. (2001). Anomalously increased effective thermal conductivities of ethylene glycol-based nanofluids containing copper nanoparticles. *Applied Physics Letters*, 78(6), 718-720.
[13] Hedayati, N., and Ramiar, A. (2015). Investigation of two phase unsteady nanofluid flow and heat transfer between moving parallel plates in the presence of the magnetic field using GM. *Trans. Phenom. Nano Micro Scales*, 4(2), 47-53.
[14] Khan, U., Ahmed, N., Khan, S. I., Zaidi, Z. A., Xiao-Jun, Y., and Mohyud-Din, S. T. (2014a). On unsteady two-dimensional and axisymmetric squeezing flow between parallel plates. *Alexandria Engineering Journal*, 53, 463-468.
[15] Khan, U., Ahmed, N., Khan, S. I., Bano, S., and Mohyud-Din, S. T. (2014b). Unsteady squeezing flow of a Casson fluid between parallel plates. *World Journal of Modelling and Simulation*, 10, 308-319.
[16] Khan, H., Qayyum, M., Khan, O., and Ali, M. (2016). Unsteady squeezing flow of Casson fluid with magnetohydrodynamic effect and passing through porous medium. *Mathematical Problems in Engineering*.
[17] Madaki, A. G., Roslan, R., Mohamad, M., and Kamardan, M. G. (2016). Analytical solution of squeezing unsteady nanofluid flow in the presence of thermal radiation. *Journal of Computer Science & Computational Mathematics*, 6(4).
[18] Madaki, A. G., Roslan, R., Rusiman, M. S., and Raju, C. S. K. (2017). Analytical and numerical solutions of squeezing unsteady Cu and TiO2-nanofluid flow in the presence of thermal radiation and heat generation/absorption. *Alexandria Engineering Journal*, 57(2), 1033-1040.
[19] Maiga, S. E. B., Palm, S. J., Nguyen, C. T., Roy, G., and Galanis, N. (2005) Heat transfer enhancement by using nanofluids in forced convection flows. *International Journal of Heat and Fluid Flow*, 26(4), 530-546.
[20] Mittal, R. C. and Pandit, S. (2017). Numerical simulation of unsteady squeezing nanofluid and heat flow between two parallel plates using wavelets. *International Journal of Thermal Sciences*, 118, 410-422.
[21] Muhammad, S., Shah, S. I. A., Ali, G., Ishaq, M., Hussain, S. A., and Ullah, H. (2018). Squeezing nanofluid flow between two parallel plates under the influence of MHD and thermal radiation. *Asian Research Journal of Mathematics*, 10(1), 1-20.
[22] Mustafa, M., Hayat, T., and Obaidat, S. (2012). On heat and mass transfer in the unsteady squeezing flow between parallel plates. *Meccanica*, 47, 1581-1589.
[23] Naduvinamani, N. B., and Shankar, U. (2019). Radiative squeezing flow of unsteady magnetohydrodynamic Casson fluid between two parallel plates. *Journal of Central South University*, 26(5), 1184-1204.
[24] Pourmehran, O., Rahimi-Gorji, M., Gorji-Bandpy, and M. Ganji, D. D. (2014). Analytical investigation of squeezing unsteady nanofluid flow between parallel plates by LSM and CM. *Alexandria Engineering Journal*, 54, 17-26.
[25] Rashidi, M., Shahmohamadi, H., and Dinarvand, S. (2008). Analytic approximate solutions for unsteady two-dimensional and axisymmetric squeezing flows between parallel plates. *Mathematical Problems in Engineering*.
[26] Sampath, K. V. S., Pai, N. P., and Jacub, K. (2018). A semi-numerical approach to unsteady squeezing flow of Casson fluid between two parallel plates. *Malaysian Journal of Mathematical Science*, 12(1), 35-47.
[27] Sheikholeslami, M., and Ganji, D. D. (2012). Heat transfer of Cu-water nanofluid flow between parallel plates. Powder Technology, 235, 873-879.
[28] Sheikholeslami, M., Hatami, M., and Domairry, G. (2015). Numerical simulation of two phase unsteady nanofluid flow and heat transfer between parallel plates in presence of time dependent magnetic field. *Journal of the Taiwan Institute of Chemical Engineers*, 46, 43-50.
[29] Sheikholeslami, M., Ganji, D. D., and Rashidi, M. M. (2016). Magnetic field effect on unsteady nanofluid flow and heat transfer using Buongiorno model. *Journal of Magnetism and Magnetic Materials*, 416, 164-173.
[30] Siddiqui, A. M., Irum, S., and Ansari, A. R. (2008). Unsteady squeezing flow of a viscous MHD fluid between parallel plates, a solution using the homotopy perturbation method. *Mathematical Modelling and Analysis*, 13(4), 565-576.
[31] Sobamowo, G. (2018). Magnetohydrodynamic squeezing flow of Casson nanofluid between two parallel plates in a porous medium using method of matched asymptotic expansion. *Research on Engineering Structures and Materials*, 4(4), 257-277.
[32] Sobamowo, G., Jayesimi, L., Oke, D., Yinusa, A., and Adedibu, O. (2019). Unsteady Casson nanofluid squeezing flow between two parallel plates embedded in a porous medium under the influence of magnetic field, *Open Journal of Mathematical Sciences*, 3, 59-73.
[33] Stefan, M. (1874). Experiments on apparent adhesion. *The London, Edinburgh, and Dublin Philosophical Magazine and Journal of Science*, 47(314), 465-466.

[34] Sweet, E., Vajravelu, K., Gorder R. A. V., and Pop, I. (2010). Analytical solution for the unsteady MHD flow of a viscous fluid between moving parallel plates. *Communications in Nonlinear Science and Numerical Simulation*, 16(1), 266-273.
[35] Ullah, I., Shafie, S., and Khan, I. (2016). MHD natural convection flow of Casson Nanofluid over nonlinearly stretching sheet through porous medium with chemical reaction and thermal radiation. *Nanoscale Research Letters*, 11, 527.
[36] Wang, C. Y. (1976). The squeezing of a fluid between two plates. *Journal of Applied Mechanics*, 43(4), 579-583.
[37] Xuan Y, and Li, Q. (2003). Investigation on convective heat transfer and flow features of nanofluids. *Journal of Heat Transfer*, 125(1), 151-155.
[38] Xue, Q-Z. (2003). Model for effective thermal conductivity of nanofluids. *Applied Physics Letters*, 307(5), 313-317.

Penerbit Akademia Baru

Engineering Science and Technology Conference Proceedings

Journal homepage: www.akademiabaru.com/EST.html

Study on Shape Geometry of Floating Oscillating Water Column Wave Energy Converter for Low Heave Wave Condition

Open Access

Muhamad Jalani Aiman[1], Nur Izzati Ismail[1], Mohd Rashdan Saad[1], Yasutaka Imai[2], Shuichi Nagata[2], Mohd Kamarul Huda Samion[3], Ernie Abd Manan[3], Mohd Rosdzimin Abdul Rahman[1,*]

[1] Department of Mechanical Engineering, Faculty of Engineering, Universiti Pertahanan Nasional Malaysia, Kem Sg. Besi, 57000, Kuala Lumpur
[2] Institute of Ocean Energy, Saga University, Japan
[3] Hydraulic and Instrumentation Laboratory, National Hydraulic Research Institute of Malaysia (NAHRIM), Malaysia

ABSTRACT

The Oscillating Water Column (OWC) is one of the most promising Wave Energy Converter (WEC) concepts in terms of practicality, survivability, and efficiency. One of the potential OWC types is the Backward Bent Duct Buoy (BBDB). The objective of this research is to investigate the performance of different BBDB shapes in low heave wave conditions. Three different bottom corner shapes were chosen for the experiments in a 3D wave basin. Wave height of 0.15m with period of 1s to 5s were used in regular wave conditions. Results show that different BBDB bottom corner shapes produces different pneumatic output characteristics. It was found that the highest primary conversion efficiency of the BBDB was produced by the BBDB with a round bottom corner shape with an efficiency of 1.47 follow by BBDB with a square bottom corner shape with an efficiency of 1.24 and BBDB with 45° bottom corner shape with the efficiency of 0.86. Thus, the round bottom corner shape is proposed to be the most efficient shape in low wave heave wave conditions.

Keywords:
Wave energy converter; shape optimization; floating OWC; BBDB; primary conversion efficiency

Copyright © 2019 PENERBIT AKADEMIA BARU - All rights reserved

1. Introduction

To tackle important global climate change issues and rising CO2 levels, we need to reduce the dependence on fossil fuels and the focus on generating renewable energy. There are many types of renewable energy, such as wind, solar, wave and hydro [1]. Wave energy is one of the renewable energies that can be widely explored [2]. Ocean wave energy has the second-largest potential of all ocean renewable energy sources [3].

Wave Energy Converter (WEC) is a device that converts wave energy into useful energy such as electricity. It can operate in any harsh environment, constraints in wave power inputs and massive loads experienced in extreme weather conditions [4]. There are more than a thousand different WEC in literatures from floating, oscillating, and bottom-standing to submerged types [5].

* *Corresponding author.*
E-mail address: rosdzimin@gmail.com (Mohd Rosdzimin Abdul Rahman)

An oscillating WEC type such as Wavebob, Wavestar, OPT Powerbuoy, Archimedes Wave Swing, Pelamis, Aquamarine Power's Oyster and Oscillating Water Column (OWC) are being used according to the geometric suitability, environmental conditions, and the amount of output power required to accommodate local loads [6]. In addition, the buoyancy and economic costs of the buoys also become one of the considering factors for the selection of wave energy converter types.

The OWC type is a well-established wave energy device concept, which will continue to contribute greatly to the progression of wave energy [7]. An OWC device is an energy converting device that does not produce CO_2 as a by-product thus is deemed as a great alternative for “green” electricity power. In an OWC device, power is produced by the incoming plane surface waves that give rise to water-air column designed within the device [8].

The OWC device consists of a partially submerged chamber with open water bottom and duct that allows movement of air internally and externally from the environment into the chamber. The wave behaviour constantly changes the water elevation in the chamber, hence enabling the volume of air inside the column to be constantly being pushed and sucked through the orifice. Attached to an air turbine, the generator is being driven from the air movements in both directions [9].

Currently, four types of FOWCs have been developed, namely Forward Bent Ducted Buoy (FBDB), Backward Bent Ducted Buoy (BBDB), Centre Buoy Pipe and Sloped Buoy. In 3D wave tanks, the WEC Model BBDB were found to reach a peak of primary conversion efficiency of 1.72 under a regular wave and 0.52 under an irregular wave [10]. Due to the design of BBDB devices which typically have shallow drafts, they can be easily transported and installed. Centre Buoy Pipe and Sloped Buoy have in-depth drafts that require special equipment for transportation. These adjustments are also complicated and more time will be spent for installation purposes.

The oscillating water column (OWC) Backward Bent Duct Buoy (BBDB) was created following the most successful OWC navigation buoys in wave energy converter, with the target of building a large and efficient OWC wave energy converter for large-wave power production [11]. Compared to other WECs, BBDB has a simple single floating structure, low cost, and high conversion efficiency. Since Yoshio Masuda [12] first introduced the concept of BBDB converters in 1986, there have been many researchers from various countries who have conducted various types of experimental studies on this concept in 2D and 3D wave tanks. The previous studies about the conversion performance of the wave power to pneumatic power are summarised and listed in Table 1.

In addition, there have been several studies on the geometric shape changes made to these BBDB models by previous researchers. For the front buoy, three different shape geometries have been tested in a 2D and 3D wave tanks and a semi-cylindrical buoyancy module was found to give the best performance [13]. As for the length of the duct, the increase in the length of the duct decreases the primary conversion efficiency [14].

However, the authors found that the effect of different geometry of bottom corner shape of BBDB towards the performance has not been studied. The authors also believed that the design of the bottom corner shape contributes significantly towards the oscillation motion of the BBDB device and eventually affecting the performance output. Thus, the purpose of this study is to investigate the characteristics and performance of BBDB with different bottom corner shape designs at low heave wave conditions.

Table 1
Experimental studies on BBDB conversion efficiency

Year	Authors	Maximum Efficiency				References
		2D Regular waves	3D Regular waves	2D Irregular wave	3D Irregular wave	
1995	Liang et al.	0.41				[15]
1997	Liang et al.	0.73				[16]
1998	Liang et al.		2.04		0.37	[17]
1999	Pathak et al.		1.73	0.52		[18]
2000	Liang et al.	0.79				[19]
2001	Liang et al.		1.50			[20]
2008	Toyota et al.	0.35				[21]
2011	Imai et al.	0.70	0.78		0.49	[14]
2017	Wu et al.	1.19	1.46		0.87	[22]

2. Description of Models

As BBDB technology relies on the movement of oscillating bodies to convert wave energy, it is essential to enhance the oscillation of the device to improve conversion efficiency. In this study, the shape of the BBDB model was changed from the initial flat bottom corner to different bottom corner shapes and from one buoy to two buoy system, similar to the study conducted by Bailey et al. [23]. The purpose of incorporating both the front and rear buoys together is to reduce hydrodynamic resistance and consequently increasing the amplitude of the BBDB oscillation as shown in Figure 1.

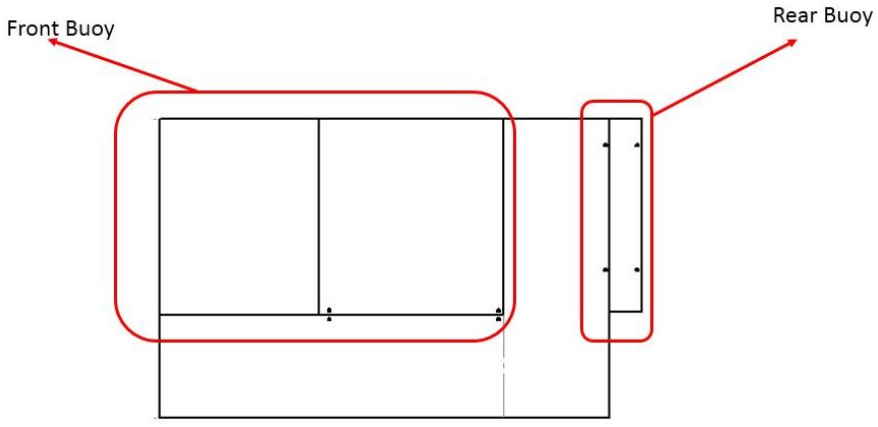


Figure 1: Illustration of front and rear buoy (side view)

Three BBDB devices with different bottom corner shapes (Model A, B and C) were fabricated and tested in the experiments. All models have the same basic dimensions; horizontal water column of 0.85 m length, 0.565 m height and 0.6 m width, with a vertical water column of 0.6 m × 0.2 m size. The material used for the fabrication of all models are transparent acrylic boards with thickness 5mm. The diameter of orifice to allow airflow in the both directions is 40mm, located on top of the air column.

For Model A, a curved bottom corner with radius of 0.2m replaced the initial shape. The detail design of model A can be seen in Figure 2. Model B is similar to basic (baseline) model of the BBDB,

with a rectangular shape of the bottom corner. However, the difference between Model B with the basic model previously tested by other researchers is the addition of the rear buoy. A detail design of model B can be seen in Figure 3. For Model C, the bottom corner of the model was designed to have an inclined edge at an angle of 45^0 as depicted in Figure 4.

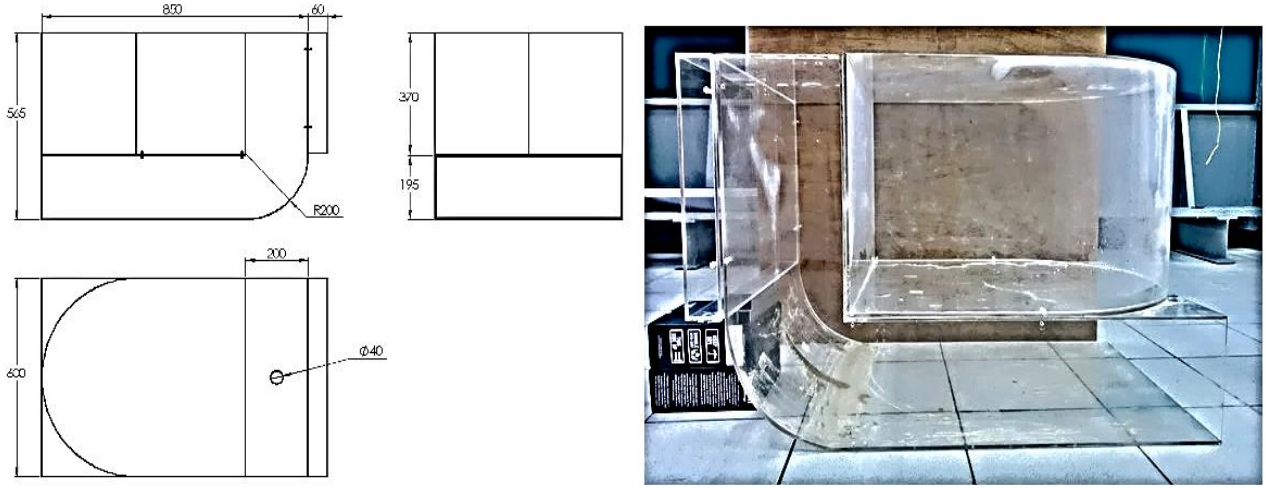


Figure 2. Drawing (left) and picture (right) of Model A with a rounded corner

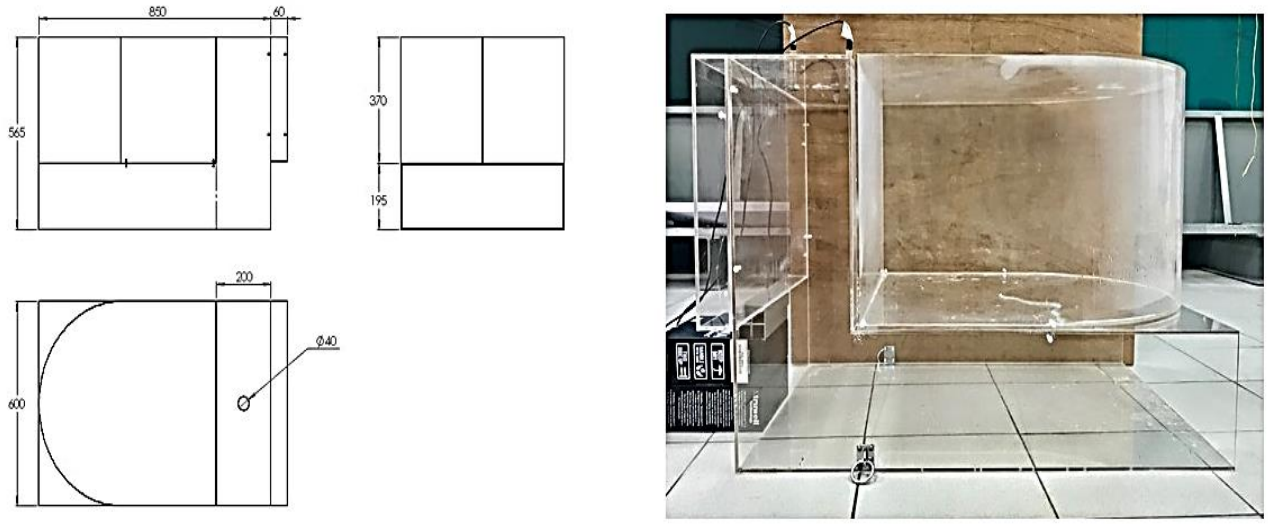


Figure 3. Drawing (left) and picture (right) of Model B with a rectangular corner

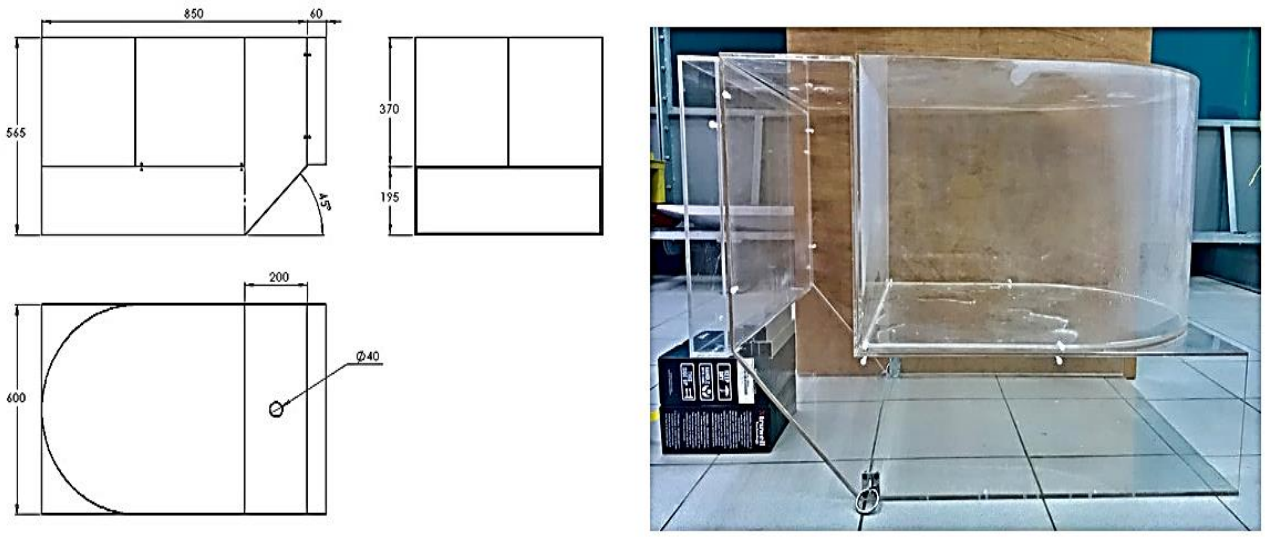


Figure 4. Drawing (left) and picture (right) of Model C with a 45° edge

3. Experimental Set-Up

3.1 3D Wave Tank Test

The primary conversion efficiency of small scale BBDB models in regular waves was measured in a 3D wave basin. Experiments were carried out in the wave basin at the National Hydraulic Research Institute of Malaysia (NAHRIM) shown in Figure 5. The basin is 30 m long, 30 m wide and 1.2 m deep. Active absorbing wavemakers are located at the upstream of the basin. For this experiment, 0.05 - 0.15 m of wave height and 1 – 5 s of wave period were selected to match low heave wave condition.

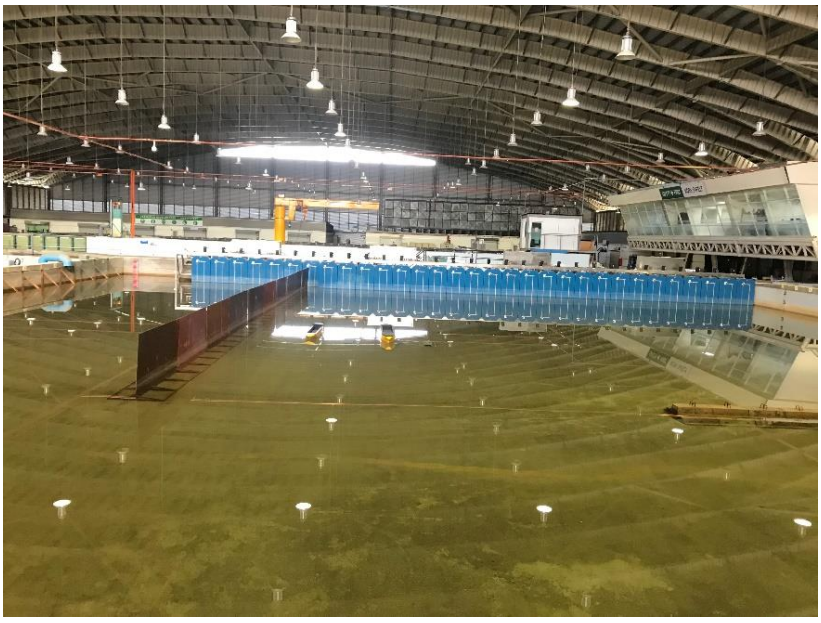


Figure 5. 3D wave basin at NAHRIM

3.2 The Primary Performance of OWC

The primary conversion efficiency η_1 is defined as the ratio of the energy of air to the energy of incident waves from Elhanafi et al. [24].

$$\eta_1 = \frac{E_{air}}{E_{wave}} \tag{1}$$

$$E_{wave} = \frac{1}{2}\rho g \zeta_i^2 C_g B \tag{2}$$

$$E_{air} = \frac{1}{T}\int_0^T \Delta P(t)\, Q(t)\, \mathrm{dt} \tag{3}$$

$$C_g = \frac{\omega}{2k}\left(1 + \frac{2kh}{sinh(2kh)}\right) \tag{4}$$

$$\frac{\omega^2}{g} = k tanh(kh) \tag{5}$$

$$k = \frac{2\pi}{L} \tag{6}$$

3.3 Instrumentations

The complete setup of instrumentations is shown in Figure 6, consisting two digital ultrasonic water level sensors KEYENCE FW-H07 (±0.001 m accuracy) to measure the water level inside the water column, a pitot tube anemometer EXTECH HD-350 (0.0001 m^3/min accuracy) to measure the flow rate at the orifice and KEYENCE AP-10S (0.01 kPa accuracy) air pressure sensor to measure the air pressure inside the chamber. KEYENCE NR-500 was used as the data acquisition system connecting all sensors to the workstations.

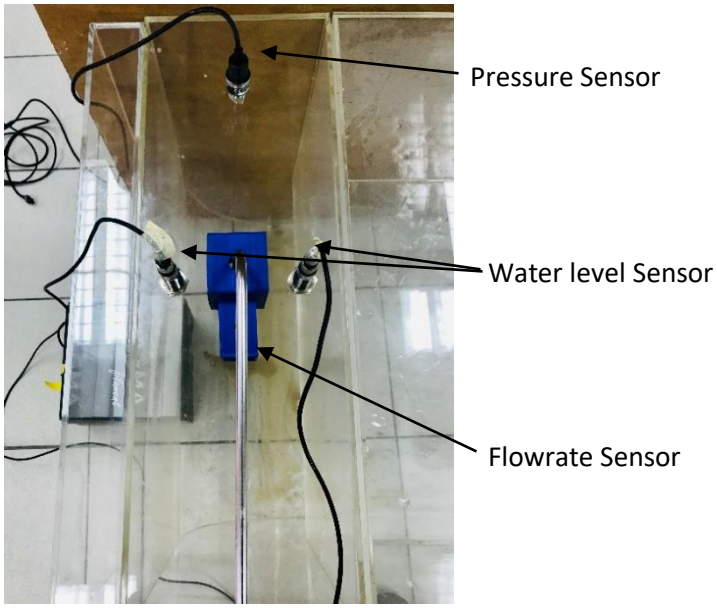


Figure 6. Instrumentation setup onboard the BBDB models

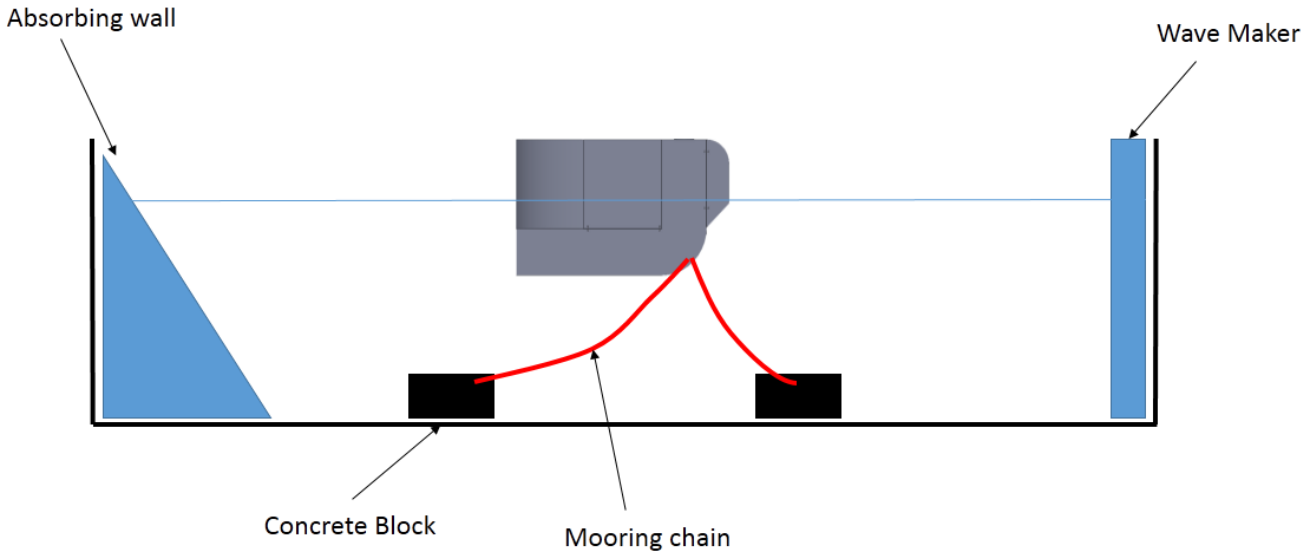


Figure 7. Schematic diagram of the experiment setup

The schematic diagram of the experimental setup is shown in Figure 7. The BBDB was attached to two mooring nylon lines at the bottom section. At the other end, the nylon lines were tied to 4 heavy concrete blocks at the bottom of the wave basin to prevent the device from moving during the experiments as shown in Figure 8.

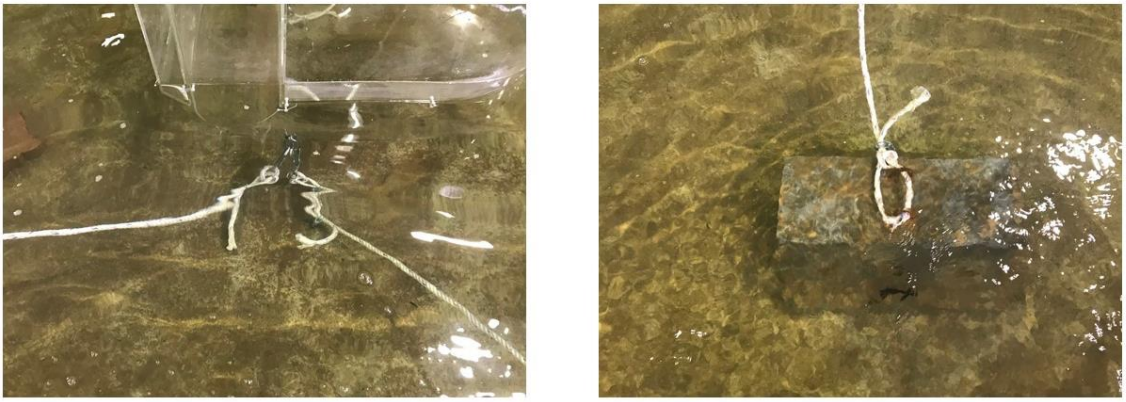


Figure 8. Mooring connection for model (left) and concrete block (right)

4. Results & Discussion

The results of water elevation, pressure and flow rate inside the water column chamber are shown in Figure 9 - 11, respectively. Figure 9 shows the water elevation in the water column chamber for all models A, B and C. The horizontal axis is the ratio of the wavelength (λ) of the incident wave and the characteristic length of the BBDB (L) while the vertical axis represents the water elevation, ζ divided by the incident wave amplitude ζ_i. It was found that the trends of all models are slightly similar. Furthermore, at λ/L = 3.0, all model reaches a maximum value and model A gives the highest value compared to other models with a value of ζ/ζ_i = 1.98 at 0.15m wave height.

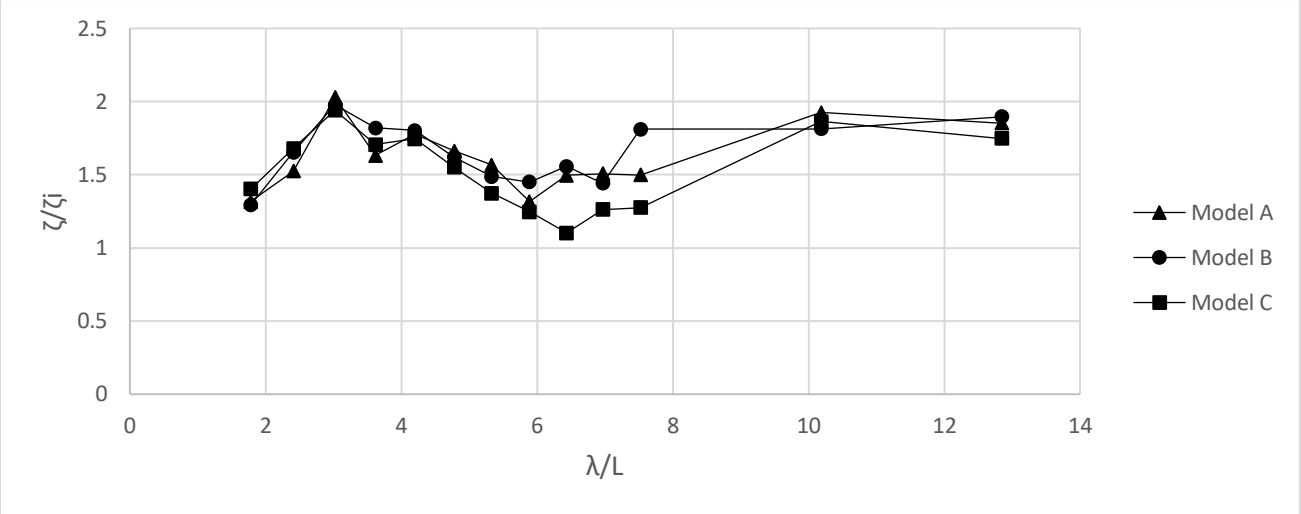


Figure 9. Amplitude of wave inside water column chamber for all three models

The pressure inside the water column during the test we acquired and plotted in Figure 10. The pressure is made dimensionless using ρ, g, and ζ_i. The pressure measurements for the three models shows similar trends. The pressure increases from λ/L = 2.0 to 3.0 and later it decreases to λ/L = 7.0. At λ/L = 8.0 to λ/L = 13.0 the pressure reaches a plateau. It was found that maximum pressure was given by Model A followed by Model B and C. Overall, by increasing the wavelength (by varying the wave period), the water column chamber pressure increases until reaches a peak. After the peak pressure, the chamber pressure drop sharply and later continue to increase at point λ/L = 6.0. After the point λ/L = 7.0, increasing the wavelength causes insignificant changes towards the pressure.

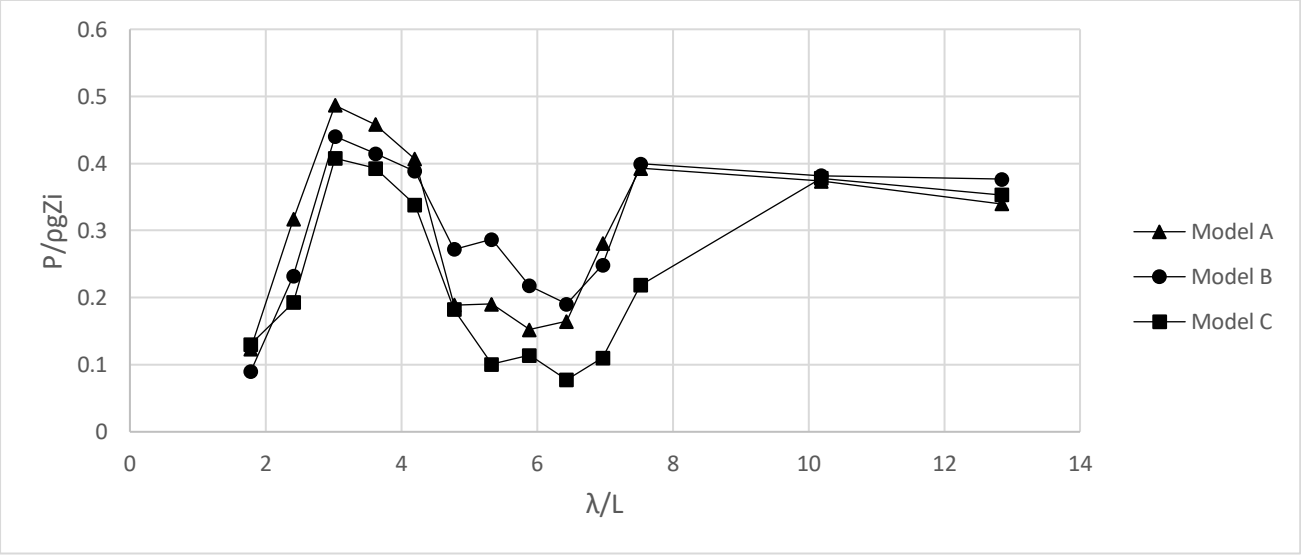


Figure 10. Pressure inside water column for all models.

It was observed at Figure 11 that the air flow rate at the orifice of the air column increased up to a peak point and decreases after that at low λ/L between 1.9 and 5.0. At higher λ/L, the air flow rate is not significant. In all models, model A produces a higher airflow rate compared to other models. It also seen that the airflow rate of the model B and C is typical at low λ/L. A high air flow rate is favourable at the orifice in order to run the turbine system attached to the orifice in real case.

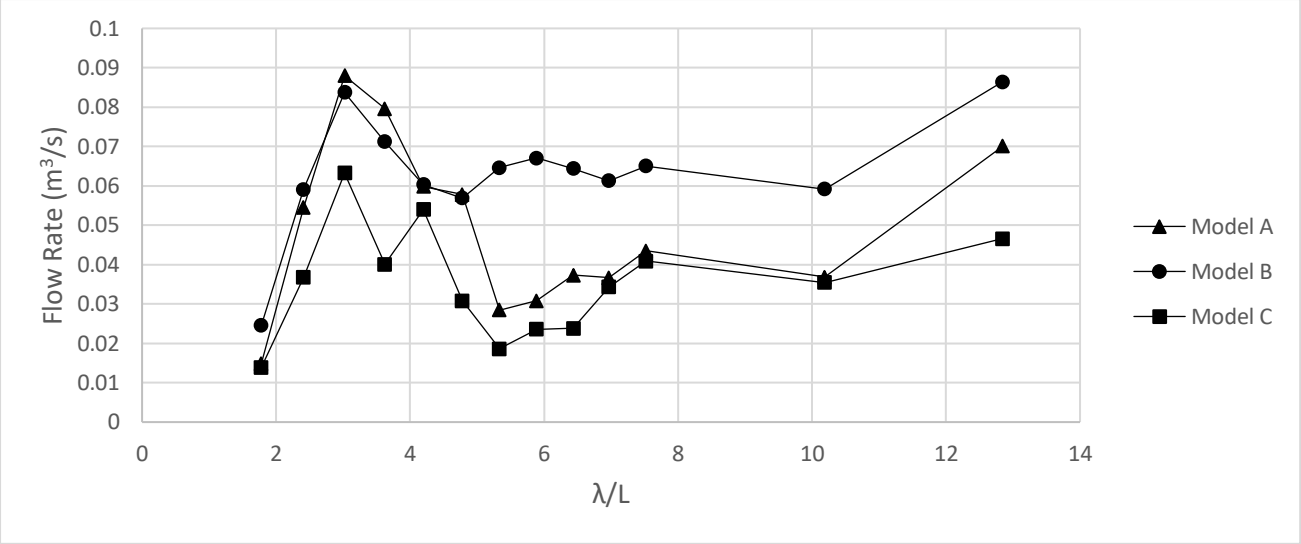


Figure 11. Air flow rate at the nozzle outlet for all Model

Figure 12 shows the incident wave energy (E_{wave}) and pneumatic energy from the water column chamber for all three models. It appears that the wave energy increases significantly following the increase in λ/L. This is because the wave energy is affected by the wavelength (λ), which is one of the components in calculation of group velocity (C_g) in the wave energy formula. Based on Figure 12, Model A reaches maximum pneumatic energy at 22.5 kgm^2/s^2. For all models, the pneumatic energy is not significant at λ/L = 4.0 and onwards. Therefore, all model produces higher air energy at low λ/L, which shows the suitability of the BBDB for low heave wave conditions.

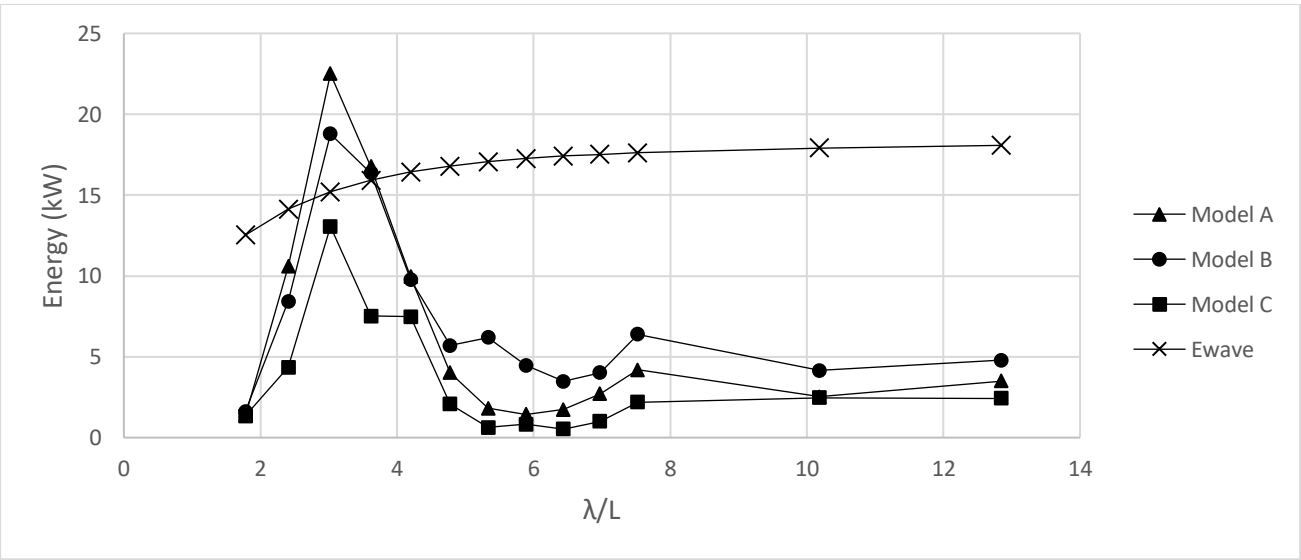


Figure 12. Wave energy and air energy from the water column

Results in Figure 13 shows the primary conversion efficiency of all three BBDB models tested. Model A performed the best by exhibiting the highest efficiency compared to all three models, at 1.47. This was followed by Model B is at 1.23 and Model C producing below 1.0. Overall, it can be seen that all models produced higher primary conversion efficiency at low λ/L conditions. The worst

wave conditions were found to be between λ/L 5.0 until 7.0, which clearly shows the design region that needs to be avoided for BBDB.

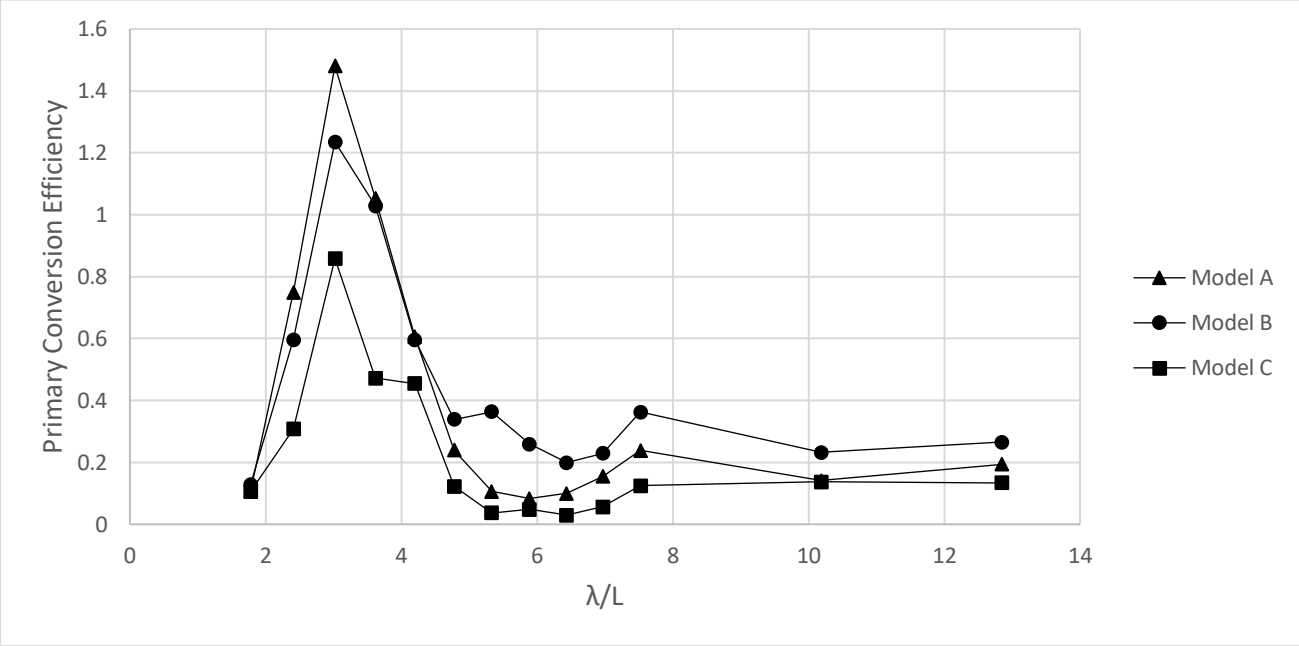


Figure 13. Primary Conversion Efficiency

5. Conclusion

This study investigates the characteristics and performance of different shape backward bent-duct buoys. The three models of BBDB having different bottom corner shapes were tested in a 3D wave tank by applying regular waves. The finding of this study can be summarized as follow;

- Water column chamber pressure and elevation are significantly influenced by the wave period at the low value of λ/L.
- The effect of the variation in water column chamber pressure and elevation produces a higher airflow rate at the nozzle outlet.
- Model A gives higher performance compared to other models with primary conversion efficiency higher than 1.0 at a low value of λ/L.
- Overall the BBDB produces higher primary conversion efficiency at low λ/L regardless of different bottom corner shapes.

Acknowledgments

The authors would like to thank Ain Latif and Asyraf Abdullah, from the Civil Engineering Team for the assistance in setting up the mooring connections during the experiments. A big appreciation also to KEYENCE Malaysia for providing technical support on the instrumentation system. This study was performed under Cooperative Research Program of IOES, Institute of Ocean Energy, Saga University, Japan (#2019-B-10). This project is made possible by the funding assistance from Akaun Amanah Industri Bekalan Elektrik (AAIBE) - UPNM/2018/AAIBE-KETTHA/TK/1/P4.

References

[1] C. Cargo, "Design and Control of Hydraulic Power Take-Offs for Wave Energy Converters," p. 185, 2012.
[2] T. W. Thorpe, "A Brief Review of Wave Energy," *Tech. Rep. ETSU-R120*, no. May, p. 200, 1999.
[3] P. Meisen and A. Loiseau, "Ocean Energy Technology for Renewable Energy Generation," *Dev. Renew. Energy*, no. August, pp. 56–80, 2009.
[4] G. Nolan and J. Ringwood, "Design and control considerations for a wave energy converter," *Proceedings, Irish Signals Syst. Conf. ISSC 2004, Belfast*, vol. 2004, pp. 475–480, 2004.
[5] A. Ilyas, S. A. R. Kashif, M. A. Saqib, and M. M. Asad, "Wave electrical energy systems: Implementation, challenges and environmental issues," *Renew. Sustain. Energy Rev.*, vol. 40, pp. 260–268, 2014.
[6] C. N. Dtmc, R. E. Q. No, S. Street, and K. Ave, "WAVE ENERGY SYSTEMS – FINAL REPORT," no. January, 2006.
[7] S. Doyle and G. A. Aggidis, "Development of multi-oscillating water columns as wave energy converters," *Renew. Sustain. Energy Rev.*, vol. 107, no. February, pp. 75–86, 2019.
[8] C. Chang, F. N. Chou, Y. Chen, and Y. Hsieh, "Analytical and experimental investigation of hydrodynamic performance and chamber optimization of oscillating water column system," *Energy*, vol. 113, pp. 597–614, 2016.
[9] A. El Barakaz and A. El Marjani, "The oscillatory free water surface motion inside OWC chamber for wave energy conversion," *Proc. 2016 Int. Renew. Sustain. Energy Conf. IRSEC 2016*, pp. 686–691, 2017.
[10] B. Wu, M. Li, R. Wu, T. Chen, Y. Zhang, and Y. Ye, "BBDB wave energy conversion technology and perspective in China," *Ocean Eng.*, vol. 169, no. August, pp. 281–291, 2018.
[11] W. Sheng, "Motion and performance of BBDB OWC wave energy converters: I, hydrodynamics," *Renew. Energy*, vol. 138, pp. 106–120, 2019.
[12] Y. Masuda, "Experience in pneumatic wave energy conversion in Japan," in *ASCE Specialty Conference on Utilization of Ocean Waves-wave Energy Conversion*, 1986.
[13] K. Toyota, S. Nagata, Y. Imai, J. Oda, and T. Setoguchi, "Primary Energy Conversion Characteristics of a Floating OWC ' Backward Bent Duct Buoy ,'" vol. 7, pp. 850–855, 2010.
[14] Y. Imai, K. Toyota, S. Nagata, T. Setoguchi, and M. Takao, "An Experimental Study on Generating Efficiency of a Wave Energy Converter 'Backward Bent Duct Buoy,'" *EWTEC 2011 Proc.*, 2011.
[15] J. N. Liang Xianguang, Wang Wei, "An experimental research on performance of the 5kW BBDB model," *New Energy*, vol. 17, no. 6, pp. 5–10, 1995.
[16] D. Bin Liang Xianguang, Wang Wei, "Experimental research on performance of BBDB wave-activated generation device model," *Ocean Eng.*, vol. 15, no. 3, pp. 77–86, 1997.
[17] W. W. Liang Xianguang, Sun Peiya, "Performance test on the SWBF2. 86× 2.2 BBDB wave power navigation buoy," *New Energy*, vol. 20, no. 9, pp. 4–10, 1998.
[18] A. G. Pathak, V. A. Subramanian, and Y. Masuda, "Performance studies on a scaled model of Backward Bent Ducted Buoy (BBDB) type wave energy converter in regular and random waves," *Proc. 1999 Ninth Int. Offshore Polar Eng. Conf. (Volume 1), Brest, Fr. 30 May - 4 June 1999*, vol. I, pp. 139–141, 1999.
[19] W. W. Liang Xianguang, Sun Peiya, "The experiment study of BBDB generating body model," *New Energy*, vol. 22, no. 2, pp. 10–18, 2000.
[20] W. W. Liang Xianguang, Sun Peiya, "Experimental study of BBDB model with multi-points mooring," *Ocean Eng.*, vol. 19, no. 1, pp. 70–78, 2001.
[21] K. TOYOTA, S. NAGATA, Y. IMAI, and T. SETOGUCHI, "Effects of Hull Shape on Primary Conversion Characteristics of a Floating OWC "Backward Bent Duct Buoy"," *J. Fluid Sci. Technol.*, vol. 3, no. 3, pp. 458–465, 2008.
[22] B. jun Wu, M. Li, R. kang Wu, Y. qiu Zhang, and W. Peng, "Experimental study on primary efficiency of a new pentagonal backward bent duct buoy and assessment of prototypes," *Renew. Energy*, vol. 113, pp. 774–783, 2017.
[23] H. Bailey, B. R. D. Robertson, and B. J. Buckham, "Wave-to-wire simulation of a fl oating oscillating water column wave energy converter," *Ocean Eng.*, vol. 125, pp. 248–260, 2016.
[24] A. Elhanafi, G. Macfarlane, A. Fleming, and Z. Leong, "Experimental and numerical investigations on the hydrodynamic performance of a floating–moored oscillating water column wave energy converter," *Appl. Energy*, vol. 205, no. July, pp. 369–390, 2017.

Penerbit Akademia Baru

Engineering Science and Technology Conference Proceedings

Journal homepage: www.akademiabaru.com/EST.html

Application of Computational Fluid Dynamic Method (CFD) on Solar Still: A Review

Open Access

Muhammad Muzzammil Shahabudin[1], Sabariah Musa[2], Al Emran Ismail [3,*]

[1] Faculty of Civil and Environmental Engineering, University Tun Hussein Onn Malaysia, 86400, Parit Raja, Batu Pahat, Johor, Malaysia
[2] Senior Lecturer, Department of Water and Environmental Engineering Faculty of Civil and Environmental Engineering, University Tun Hussein Onn Malaysia, 86400, Parit Raja, Batu Pahat, Johor,Malaysia
[3] Senior Lecturer, Department of Mechanical Engineering, Faculty of Mechanical Engineering and Manufacturing, University Tun Hussein Onn Malaysia, 86400, Parit Raja, Batu Pahat, Johor,Malaysia

ABSTRACT

Freshwater is a key of living things around us. There are many applications used to produce freshwater and one of them is solar still. It is important of solar still to produce as much as can for distilled water but matters on cost issues have make the researchers goes into alternatives options for designing. One of the options tools for designing the solar still is computational fluid dynamic (CFD). CFD method providing the low cost, fast and reliable results compared to the experimentation which taking too long time and cost. Previous studies has shown that simulation and experimental provides good agreement, but lack in highlighting the ability of CFD on designing process either on complex or simple design which applied the CFD process. This paper is reviewing the of CFD method on solar still designing process both on simple and complex structures which has been applied.

Keywords:
CFD; CFD simulation; solar still;
optimization

Copyright © 2019 PENERBIT AKADEMIA BARU - All rights reserved

1. Introduction

Access on drinking water is one of the important things in our life as water also widely used in our life routine for domestics, industrial and agriculture purposes [1]. As our world is covered in 75% of water, only about 0.014% of global water can be directly used for drinking and industry sectors [2]. Freshwater is a key of live for living things such animals, plants and also human being [3].

Some technologies are used to produce the freshwater from the salty and raw water such reverse osmosis (RO) and electro-dialysis. But, the issues on cost also the availability has turn into another alternatives to use another types of energy resources to produce fresh water [1]. Since solar energy are available everywhere, it can be used for the domestic or alternative energy resources on freshwater production [4].

Solar radiation is available everywhere, abundance, and free can be used on solar still to produce freshwater as the solar energy can reduce the use of non-renewable fuels also the pollutants [1]. Solar stills have a lot of advantages as they are low in maintenance, cheap and easy to fabricate to meet any conditions [4].

Solar stills have been done both in experimental and numerical procedures when searching for better design or performance of the stills. Certain limitation has restricted the researchers to run the test such due to cost and time. In addition, some researchers has going further in modeling the still through the computational fluid dynamic (CFD)[1]. Computational fluid dynamic (CFD) are

helping the researchers with low cost and high of processing data on simulating a real or an ideal condition. This benefits has provides on data processing or examining a large number of state of parameters [5].

CFD method applied by Papanicolaou and Belessiotis [6] in his study on unsteady behavior of laminar and turbulent flow regime in an asymmetric trapezoidal enclosure has resulting on numbers of multicellular flow fields are depending on the Rayleigh numbers for a fix Lewis number and geometry. A study by Omri et. al. [7] used a control volume finite element method on the sensitivity of flow structure to Rayleigh number and tilting angle. By applying the finite difference method, Rheinlànder [8] has studied on heat and mass transfer occurrences to solve the principal equation in solar still. The results have shown that there is a close agreement with the numerical and experimental data. A CFD method can be useful for solar still simulation also as a tool to act out the flow structure inside a still [4][7][9].

It is important to design the solar still with optimum functions in order to estimate the productivity of the still. CFD simulation can be applied on solar still on designing process for the economic aspects and performance at certain cost given. As CFD study on solar still was less attention, this paper aiming to put on review on CFD method which has been done by various researchers on various design of solar still improving the efficiencies of the still. Also this paper is trying to provide future research on CFD to be applied on solar still for the designing stages with more complex conditions.

2. Theoretical Formulation

a) Theoretical Formulation

Theoretically, the principal equation happened in the devices consist of conservation of mass, momentum; energy and concentration are described as follow [10-15]:

$$\frac{\partial U}{\partial x}+\frac{\partial V}{\partial y}=0 \tag{1}$$

$$U\frac{\partial U}{\partial x}+V\frac{\partial U}{\partial y}=-\frac{\partial P}{\partial x}+Pr\left(\frac{\partial^2 U}{\partial x^2}+\frac{\partial^2 U}{\partial y^2}\right) \tag{2}$$

$$U\frac{\partial V}{\partial x}+V\frac{\partial V}{\partial y}=-\frac{\partial P}{\partial y}+Pr\left(\frac{\partial^2 V}{\partial x^2}+\frac{\partial^2 V}{\partial y^2}\right)+Ra\,.Pr.(\theta+Br.C) \tag{3}$$

$$U\frac{\partial \theta}{\partial x}+V\frac{\partial \theta}{\partial y}=\left(\frac{\partial^2 \theta}{\partial x^2}+\frac{\partial^2 \theta}{\partial y^2}\right) \tag{4}$$

$$U\frac{\partial C}{\partial x}+V\frac{\partial C}{\partial y}=\frac{1}{Le}\left(\frac{\partial^2 C}{\partial x^2}+\frac{\partial^2 C}{\partial y^2}\right) \tag{5}$$

Where

$$\beta_T=-\frac{1}{\rho_0}\left(\frac{\partial \rho_0}{\partial T}\right)_P,\ \beta_S=-\frac{1}{\rho_0}\left(\frac{\partial \rho_0}{\partial C}\right)_P \tag{6}$$

$$X=\frac{x}{R},\ Y=\frac{y}{R},\qquad U=\frac{uR}{\alpha},\qquad V=\frac{vR}{\alpha},$$
$$\theta=\frac{T-T_g}{T_w-T_g},\ C=\frac{C-C_g}{C_w-C_g},\qquad P=\frac{(p+\rho g y)R^2}{\alpha^2} \tag{7}$$
$$Pr=\frac{v}{\alpha},\ Ra=\frac{g\beta_T(T_w-T_g)R^3}{v\alpha},\qquad Le=\frac{\alpha}{D_{AB}}=\frac{Sc}{Pr}$$

$$Sc=\frac{v}{D_{AB}}\quad,Br=\frac{\beta_s(c_w-c_g)}{\beta_T(T_w-T_g)} \tag{8}$$

The boundary conditions is dimensionless corresponding to the applied problem are:

Glass cover: $U = 0,\ V = 0,\ \vartheta = 0,\ C = 0,$

Water surface: $U = 0,\ V = 0,\ \vartheta = 1,\ C = 1,$

Through wall: $U = 0,\ V = 0, \frac{\partial \theta}{\partial m} = 0, \quad \frac{\partial C}{\partial m} = 0,$

Symmetry: $U = 0, \frac{\partial \theta}{\partial X} = 0, \quad \frac{\partial C}{\partial X} = 0,$ (9)

For the local heat and mass transfer on the surface of heat and contaminant sources are described as follows:

$$Nu_x = \frac{h_x R}{k} = -\frac{\partial \theta}{\partial Y}\Big|_{water}, \quad Sh_x = \frac{h_{m,x} R}{D_{AB}} = -\frac{\partial C}{\partial Y}\Big|_{water} \tag{10}$$

An average heat and mass transfer rates on the surfaces of heat and contaminant sources can be evaluated by the average Nusselt (*Nu*) and Sherwood (*Sh*) numbers, which are described as follows:

$$Nu = -\frac{R}{W}\int_0^{\frac{W}{R}} \frac{\partial \theta}{\partial Y}\Big|_{water} dX,$$

$$Sh = -\frac{R}{W}\int_0^{\frac{W}{R}} \frac{\partial C}{\partial Y}\Big|_{water} dX \tag{11}$$

In addition, the function of stream is calculated by:

$$U = \frac{\partial \psi}{\partial Y}, \qquad V = -\frac{\partial \psi}{\partial X} \tag{12}$$

b) Principal Equation

Sampathkumar et al. [16] has written that the hourly yield of a solar still, $\dot{m}_{hourly}$, can be calculated as follow:

$$\dot{m}_{hourly} = 3600\ x\ h_m(\rho_w - \rho_g) = \frac{Q_{ev}^{\eta}}{h_{fg}}\ x\ A_w\ x\ 3600 \tag{13}$$

Where

$$Q_{ev}^{\eta} = h_{ev,w-g}(T_w - T_g) \tag{14}$$

The most well-known and used relationship for the estimation on single slope solar still for the heat transfer coefficient is Dunkle's model where the principal are described as follow (Dunkle, 1961)[17]:

$$h_{ev,w-g} = 0.016273\ x\ h_{c,w-g}\ x\ \frac{P_w - P_g}{T_w - T_g} \tag{15}$$

Where

$$h_{c,w-g} = 0.884(\Delta T)^{\frac{1}{3}} \tag{16}$$

$$\Delta T' = \left[(T_w - T_g) + \frac{(P_w - P_g)(T_w + 273)}{268.9\ x\ 10^3 - P_w}\right] \tag{17}$$

$$P_w = \exp\left(25.317 - \frac{5144}{T_w + 273}\right) \tag{18}$$

$$P_g = \exp\left(25.317 - \frac{5144}{T_g + 273}\right) \tag{19}$$

Estimation on water production of a single slope solar still, Rahbar and Esfahani [1] has proposed a governing equation for the process. The equation showed that the ratio of evaporative to convective heat transfer coefficients was a function of mean temperature is described as follow:

$$\frac{h_{ev,w-g}}{h_{c,w-g}} = f(T_i),\ where\ T_i = \frac{T_w+T_g}{2} \quad (20)$$

Also, based on the Eqn. 20, the evaporative mass is described as follows:

$$\dot{m}_{ev} = \frac{h_{ev,w-g}}{h_{c,w-g}}\ x\ \frac{(T_w-T_g)}{h_{fg}}\ x\ h_{c,w-g} \quad (21)$$

3. Review of Previous Studies Applying the Computation Fluid Dynamics (CFD) on Solar Still

Previous studies on computational fluid dynamic (CFD) have shown that it has been applied on the solar still designing process. The simulation process of the still including the fluid flow, heat transfer, mass transfer and other related process through the mathematical equations which direct the process of numerical methods. Also the CFD can act out on water flows, pressure and velocity which occurred in the still. CFD process is a process of problem solving on fluid flows through computers applications [18].

a) Murugesan, R., Selvaraju, S., and Dhanasekaran, S. (2018) [19] studies upon latent heat storage

This study puts an experimental and CFD simulation on latent heat storage in different materials. This system on latent heat storage materials in varies capsules in the area of experimentation flows. With analysis of stratification between packed storage and sensible heated recovery, it is considered as enhancement of performance achieved in the system.

b) Ambarita, H., Ronowikarto, A. D., Siregar, R. E. T., and Setyawan, E. Y. (2018) [20] comparisons of available data with CFD upon evaporation-condensation

Comparisons between CFD simulations with available data are on incident of evaporation-condensation in evaporation chamber. Through the simulations process, yield production of fresh water is 2.21 liter compared to experimental at 2.1 liter. With error on simulations at magnitude 0.4%, the CFD results show the degradation of saturation of temperature of sea water due to vacuum pressure.

c) Rashidi, S., Bovand, M., Rahbar, N., and Esfahani, J. A (2018) [21] studies on steps cascade with nanofluids on productivity of solar still

A study of steps cascade on the effects of nanofluids on productivity of solar still. Enhancement observed on the solar still shows that 22% of productivity is produced with nanoparticle concentration from 0% to 5%. Also with CFD simulation, maximum errors between RSM (respond surface method) data and CFD simulations was 2.4%.

d) Rashidi, S., Akar, S., Bovand, M., and Ellahi, R. (2018) [22] studies on productivity of single slope still with Al_2O_3

Investigations of Al_2O_3 – water nanofluid to improve the water production in the single slope solar still. Increased the productivity are due to the solid volume fractions on nanoparticles which resulting in 05 to 5% as the solid volume fraction at 25%.

e) Rai Khare, V., Singh, A. P., Kumar, H., Khatri, R., (2017) [23] studies on simulatiomg the single slope solar still with ANSYS FLUENT

Simulating the single slope solar still using ANSYS FLUENT with some parametric analysis. Simulation and experimental data are compared and shown that efficiencies of still varied with 32%, 29% and 27% for5L, 10L and 15L of water quantity respectively. CFD is a powerful tool for design, parametric analysis difficulties removal on design stages.

f) Rashidi, S and Esfahani, J. A. (2017) [24] studies on entropy generation using CFD

Entropy generation are calculated with CFD and each different of entropy generation comprise of frictional, diffusive, thermal entropy generations were studied. The most dominant is thermal entropy generation to all cases.

g) Kumar Thakur, A and Kumar Pathak, S (2017) [25] studies on optimization of solar still using CFD

Simulation using CFD and experimental was evaluated. Optimization of solar still conducted using CFD through the fabrication before the experimental work has turned into increased of the solar still productivity.

h) Taamneh, Y (2016) [26] studies on CFD simulations upon pyramid shape solar still

CFD simulations has been put on the experimental and simulation both on pyramid shape solar still which has been filled with Jordanian zeolite - seawater and sweater only. Volume of Fluid (VOF) has been used in simulating the process inside the still itself upon evaporation-condensation process. Through the investigation, there is good agreement between simulation and experiment data with effect of volume fraction of zeolite particles on heat and distillate water was $0 \leq .\Phi \leq 0.05$.

i) Shehabuddeen, K., Al Katyiem, H. H., and Mazhanash, H., (2015) [27] studies on determination of highest rate fresh water production by solar still

CFD simulations conducted in this study are to determine the highest rate of fresh water production by the solar still. Test are done both in simulations and experimental. Simulations estimates and the experimental results are agreeable with percentage deviation between 7.8% - 15.7% between the rate of fresh water production from both analysis which is single slope cascade solar still and an inclined solar still.

j) **Malaeb, L., Ayoub, G. M., Al-Hindi, M., (2014) [28] studies simulations through three different approaches on simulation**

Studies are done using three different approaches on simulation to estimate the heat transfer coefficients. The model are calibrated and validated upon experimental data and error upon analysis also shown. The model used factors such wind speed, solar radiation, brine water level, and temperature also speed on the drum which in variety. Results show that there is good agreement on experimental and simulations upon design adjustments and optimization for the still to function on the challenges of severe water needs.

k) Hamadou, O. A., Abdellatif, K. (2014)[29] modelling the solar still using MATLAB

Modeling of a solar still for this study was using MATLAB environment. Broad parametric studies are done after that which shown that investigated ranges of parameters, the water depth, controlling the yield of distilled water. For the heat transfer, fluid rate and the simulations resulting that the wind speeds also affects the distilled water production. As the yield production is not

proportional to the heat transfer fluid rate, with this computational method, cost optimization can be performed in order to determine the optimal design parameters on active solar still

l) Panchal, H. N., Shah, P. K. (2013)[30] studies on hemispherical solar still using ANSYS CFD

In this study, author has put its investigation upon hemispherical solar still through three phase model oh simulations. The phase simulating the evaporation-condensation process where results such water temperature, vapor temperature, distillate output are compared with actual data. The results between the simulations and the actual data are good and shown that computational method using ANSYS CFD are capable for designing, comparison purposes on hemispherical solar still.

m) Setoodeh, N., Rahimi, R., Ameri, A. (2011) [31] studies on simulating the evaporation-condensation process through CFD process

This study used CFD to simulate the evaporation-condensation process through three dimensional, two-phase model of solar still. The results show that there is a good agreement both in experimental and simulation on fresh water productivity and water temperature. Convective and evaporative heat transfer coefficients on CFD and experimental are calculated and compared. Shown that the ability of CFD on design, parameter analysis and indicative purposes of solar still.

n) Panchal, H. N., Shah, P. K. (2011)[32] studies on modelling of the still using ANSYS CFX

Modeling process in this study using ANSYS CFX also a computational method combined with three dimensional models made for the evaporation and condensation process in the still. Resulting in good agreement upon experimental and simulation results of distillate water output, water temperature, and heat transfer coefficients. It's shown that the ANSYS CFX also a powerful tools which can be used as well as analysis of the still.

4. Conclusions

A computational method is also as a solution method on investigating the process in the solar still which has proven with variety design and also by different researchers. Computational method gives a lot of advantages to the researchers compared with experimentation methods as it can reduce the cost of fabrications at early stages, can work fast, data can be analyzed in parallel and together in overall stages. It also functions as multi-purpose technique which can be applied together during the analysis process. In future, as computational fluid dynamics is a powerful tools for design, parameter analysis also the removals of difficulties in solar still construction, hoping with this paper will attract more researchers to do research upon solar still by applying the computational fluid dynamic method (CFD)

Acknowledgement

The authors would like to acknowledge this research has been funded under Postgraduate Research Grant (GPPS), Universiti Tun Hussein Onn Malaysia (VOT U942).

References

[1] N. Rahbar and J. A. Esfahani, 2013, Productivity estimation of a single-slope solar still: Theoretical and numerical analysis, Energy 49 (2013) 289-297.
[2] Kaushal A and Varun, 2010, Solar still: A review, Renewable and Sustainable Energy Reviews 14 (2010) 446–453,
[3] Hitesh N. Panchal and P. K. Shah, 2013, Modeling and verification of hemispherical solar still using ANSYS CFD, INTERNATIONAL JOURNAL OF ENERGY AND ENVIRONMENT, Vol. 4, Issue 3, 2013 pp.427-440.
[4] Nader Rahbar, Javad Abolfazli Esfahani, Ehsan Fotouh-Bafghi, 2015, Estimation of convective heat transfer coefficient and water productivity in a tubular solar still- CFD simulation and theoretical analysis.
[5] FLUENT 6.3 User's Guide, Fluent Inc., 2006.
[6] Papanicolaou E, Belessiotis V, 2005, Double diffusive natural convection in an asymmetric trapezoidal enclosure: unsteady behavior in the laminar and the turbulent flow regime. International Journal of Heat and Mass Transfer 48 (2005) 191–209.
[7] Omri A, Orfi J, Nasrallah SB, 2005, Natural convection effects in solar still. Desalination 183, 173-178
[8] Rheinlȁnder J, 1982, Numerical calculation of heat and mass transfer in solar still. Solar Energy 28, 173-179.
[9] Omri A, 2007, Numerical investigation on optimization of a solar distiller dimensions. Desalination 206 (1- 3), 373-9.
[10] Kays, W M., Crawford, M. E., Weigand, B., 2005, Convective heat and mass transfer, 4th Ed., McGraw-Hill.
[11] Talukdar, P., Iskra, C. R., Simonson, C. J., 2008, Combined heat and mass transfer for laminar flow of moist air in a 3d rectangular duct: CFD simulation and validation with experimental data. Int. Journal Heat Mass Transfer 51, 3091-3102.
[12] Bejan, A., 1985, Mass and heat transfer by natural convection in a vertical cavity. Int. Journal Heat Fluid Flow 6, 149-159.
[13] Nithyadevi, N., Yang, R. J., 2009, Double diffusive natural convection in a partially heated enclosure with Soret and Dufour effects. Int. Journal Heat Fluid Flow 30, 902-910
[14] Esfahani, J. A., Bordbar, V., 2011, Double diffusive natural convection heat transfer in a square enclosure using nanofluids. Journal Nanotechnology Engineering Med. 22,021002-021009.,
[15] Nikbakhti, R., Rahimi, A. B., 2012, Double diffusive natural convection in a rectangular cavity with partially thermally active side walls. Journal of Taiwan Institutional Chemical Engineering 43, 535-41.
[16] Sampathkumar, K., Arjunan, T.V., Pitchandi, P., Senthilkumar, P., 2010, Active solar distillation- a detailed review. Renewable, Sustainable Energy Revised 14, 1503-1526.
[17] Dunkle. R., 1961, Solar water distillation: The roof type still and a multiple effect diffusion still. Internet. In: developments in heat transfer, ASME, proceedia international heat transfer, part V, Boulder, Colorado, USA: University of Colorado; 1961. P. 895.
[18] Zawawi, M. H., Saleha, A., Salwa, A., Hassan, N. H., Zahari, N. M., Ramli, M. Z., and Muda, Z. C., 2018, A Review: Fundamentals of Computational Fluid Dynamics (CFD), Green Design and Manufacturer: Advanced and Emerging Applications, AIP Conference Proceedings 2030, 020252 (2018);
[19] Murugesan, R., Selvaraju, S., Dhanasekaran, C., 2018, Computational fluid dynamic analysis and experimentation on solar desalination system used different latent heat materials.
[20] Ambarita, H., Ronowikarto, A. D., Siregar, R. E. T., and Setyawan, E. Y., 2018, CFD Analysis of evaporation-condensation phenomenon in an evaporation chamber of natural vaccum solar desalination.
[21] Rashidi, S., Bovand, M., Rahbar, N., and Esfahani, J. A., 2018, Steps optimization and productivity enhancement in a nanofluid cascade solar still.
[22] Rashidi, S., Akar, S., Bovand, M., and Ellahi, R., 2018, Volume of fluid to simulate the nanofluid flow and entropy generation in a single slope solar still.
[23] Rai Khare, V., Singh, A. P., Kumar, H., Khatri, R., 2017, Modeling and performance enhancement of single slope solar still using CFD.
[24] Rashidi, S., and Esfahani, J. A., 2017, Spatial entropy generation analysis for the design improvement of a single slope solar still.
[25] Kumar Thakur, A., and Kumar Pathak, S., 2017, Single basin solar still with varying depth of water: optimization by computational method.
[26] Taamneh, Y., 2016, Influence of Jordanian zeolite on the performance of a solar still: experiments and CFD simulation studies.
[27] Shehabuddeen, K., Al Katyiem, H. H., Mazhanash, H., 2015, Efficient water recycling through solar distillation, Journal of Adv. Res. In Fluid Mechanics and Thermal Sciences, ISSN (online): 2289-7879, Vol. 15, No. 1, Pages 17-27.

[28] Malaeb, L., Ayoub, G. M., Al-Hindi, M., 2014, The Effect of cover geometry on the productivity of a modified solar still desalination unit, The International Conference on Technologies and Materials for Renewable Energy, Environment and Sustainability, TMREES14, Energy Procedia 50 (2014) 406 – 413

[29] Hamadou, O. A., Abdellatif, K., 2014, Modeling an active solar still for sea water desalination process optimization, Desalination 354 (2014) 1–8.

[30] Panchal, H. N., Shah, P. K., 2013, Modeling and verification of hemispherical solar still using ANSYS CFD, INTERNATIONAL JOURNAL OF ENERGY AND ENVIRONMENT, Volume 4, Issue 3, pp.427-440

[31] Setoodeh, N., Rahimi, R., Ameri, A., 2011, Modeling and determination of heat transfer coefficient in a basin solar still using CFD, Desalination 268 (2011) 103–110.

[32] Panchal, H. N., Shah, P. K., 2011, Modeling and verification of single slope solar still using ANSYS-CFX, INTERNATIONAL JOURNAL OF ENERGY AND ENVIRONMENT, Vol.- 2, Issue 6, 2011 pp.985-998

[33] Kumar Kanti, P., Chandran, S., 2016, A review paper on basics of CFD and its applications, National conference on advances in mechanical engineering science (NCAMES-2016), ISSN: 2231-5381.

Penerbit Akademia Baru

Engineering Science and Technology Conference Proceedings

Journal homepage: www.akademiabaru.com/EST.html

Quantifying Heat Losses in Micro Combustor with Wire Mesh Using Numerical Simulation

Open Access

Fudhail Abdul Munir[1,2], Nurfarah Diana Mohd Ridzuan Tan[2,*], Masato Mikami[3]

[1] Centre for Advanced Research on Energy (CARe), Universiti Teknikal Melaka Malaysia, 76100 Durian Tunggal Melaka, Malaysia
[2] Faculty of Mechanical Engineering, Universiti Teknikal Melaka Malaysia, 76100 Durian Tunggal, Melaka
[3] Faculty of Mechanical Engineering, Yamaguchi University, 755-0053 Ube Yamaguchi, Japan

ABSTRACT

Micro power generation system is a field of study that has come into interest by many researchers due to the strong demands for low weight and long-life power sources of electronic devices. These has led to the increasement of meso and micro-scale combustion investigations. In order to fully understand more on this field of study, a numerical stimulation is utilized to investigate the effect of heat recirculation on the blowout limit for micro combustion. Four different combination of tube combustors is used to investigate their blowout limit such as quartz-brass tube combustion combination for unburned-burned region of micro combustor tube. The combination of tube combustors is then investigated using three-dimensional (3D) numerical simulation. The results suggested that by utilizing brass tube on either region of unburned or burned tube is able to improve the value of heat conducted on inner wall of via inner wall of the tube greatly. Due to the conductivity of brass tube is much larger than quartz tube, the improvement is expected.

Keywords:
Heat recirculation; blowout limit; micro combustion

Copyright © 2019 PENERBIT AKADEMIA BARU - All rights reserved

1. Introduction

Micro power generation for the field of micro-scale combustion has attracted many researchers in increasing the effort of studying the possible usage of such power source. To focus on the potential of using micro combustion as power sources, there must be studies on analyzing the effects of many different variables on the micro combustion. Flame stabilization had been proven to be achievable in narrow spaces [1] yet the sustainability of such flame are extremely difficult due to the large surface to volume ratio of the micro-scale combustor [2]. This results to flame instability as smaller combustion channels suffers from thermal quenching which then influences the blowout limit of the combustion [3, 4].

Flame stabilization is essential in meso and micro channel combustors. The experiments on micro combustion has revealed several characteristics of flames that are of importance in accordance to variables and to overcome these weaknesses, several strategies such as the flame stabilization in micro-scale combustors with wire mesh [5, 6], flame stabilization with flame holder [7-9] and the studies of different fuel-air mixture [10, 11] were conducted. Not only gaseous fuels were used, liquid fuels were also introduced and utilized in search for better fuel consumption.

* *Corresponding author.*
E-mail address: ndianatan96@gmail.com (Nurfarah Diana Mohd Ridzuan Tan)

Heat recirculation in combustion is a method that is widely recognized as a way to enhance the stability of flame and can distribute temperature effectively. According to the paper Tang, et al. [12] and [13], the presence of heat recirculation gives a large impact on stabilization of flame and temperature distribution. Besides, the study of inner and outer heat recirculation done by Bagheri and Hosseini [14] has concluded that while inner heat recirculation (IHR) distinctly improve flame characteristics and flame stabilization, outer heat recirculation (OHR) presents greater range emitter efficiencies. Although heat recirculation gives positive effect on combustion, the combustion experiment itself is not easy to be examined and experimental items may not be able to be obtained easily.

Thus, simulation approach is performed to substitute the actual experimentation. Numerical simulation approach is recently gaining more popularity to explore on the feasibility of combustion in meso and micro-scale combustion chamber. With numerical simulation, any new design of micro combustors can be reproduced and optimized after analyzing the simulation results. Computational Fluid Dynamics (CFD) has been used in the last two decades for numerical investigation on flame propagation and heat characteristics of combustion. Commercial software was utilized to study combustion fundamentals of gaseous fuels like propane and methane in micro combustors. For example, the characteristics of burner dimensions, external heat losses and effect of wall conductivity in meso-scale burners were employed using FLUENT software [15]. Recent numerical works has also given new ideas of blowout limits in different condition like in high pressure conditions [16], in preheating channels [17] and on the planar combustors [18]. Concerning the dimension of numerical simulation, two-dimensional (2-D) numerical simulation is unable to present the conductive heat transfer from a flame holder to the outer wall of combustor.

In this research, a three-dimensional (3D) numerical simulation of the effect of heat recirculation on blowout limit in micro-scale combustion is presented. Since conductive heat transfer from the wire mesh to the outer wall of combustor is needed to be presented, a 3D numerical simulation is performed instead of 2D simulation. The effect of heat recirculation on blowout limit is investigated. The blowout limit for each combination of quartz-brass tube for unburned-burned region are determined and comparisons are made based on the results of simulation. The main purpose of this study is to study the effect of heat recirculation on blowout limit for micro combustion.

2. Numerical Setup

A 3-D steady-state numerical simulation model of micro combustor with wire mesh was executed using the software ANSYS Release 14.0 with Fluent 6.3 [19]. The 3-D numerical model was developed primarily to analyze the heat recirculation flow within the combustor channel. The size of combustor is replicated based on the paper by Munir and Mikami [20] where the length of tube combustor is 40.2 mm. The combustor has an inner diameter of 3.5 mm and wall thickness of 0.7 mm.

The model has two different region that is separated by a stainless-steel wire mesh which is called the unburned and burned gas region. The wire mesh is set to 10 mm apart from the outlet burned region tube and is 30 mm from the center of combustor inlet. The distance is set to 30 mm for the flow to fully developed before going through the wire mesh. Based on Karagiannidis, et al. [21], the typical value of k for stainless-steel is 20 W/m/K which is set in this research for the wall thermal conductivity (k) value on the wire mesh for conductive heat transfer. A set amount 0.28 mm square holes were drawn onto the wire mesh to allow fluids to pass through it. Propane-air

mixture is utilized as the fuel for this research. Figure 1 illustrates the working model for the micro-scale combustor.

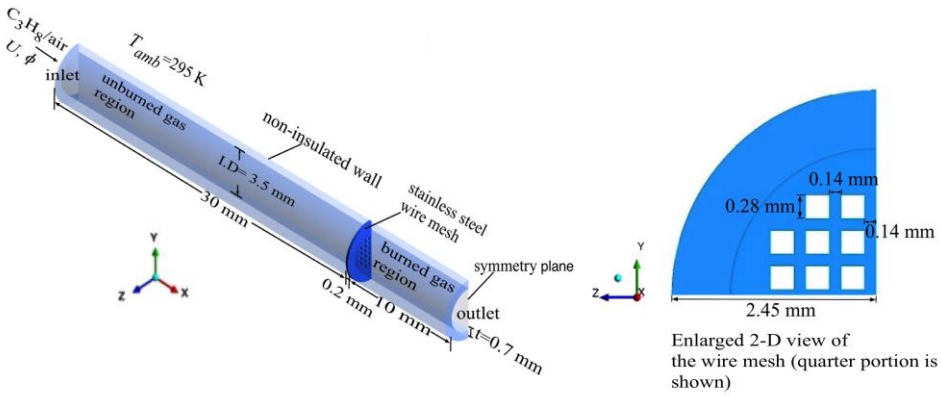


Fig. 1. 3-D numerical model of micro-scale combustor (Figure size is not to scale)[20]

For this research, Dufour, effects of gas radiation and work done by viscous and pressure force are assumed to be negligible. This is because the research done by Norton and Vlachos [22] shows that the gas phase radiation does not give much impact on the combustion reactions. For the gas density, ideal gas law is assumed. Besides, a piecewise-polynomial fit of temperature is used to calculate the specific heat for all the species. Whereas mixing law and kinetic theory are used to calculate the specific heat and thermal diffusion coefficient of the gas-fuel mixture. A reduced one-step propane combustion with five species is utilized as the combustion chemistry [23], where the affected species are C_3H_8, O_2, N_2, CO_2 and H_2O. the utilized combustion chemistry is as followed;

$$C_3H_8 + 5O_2 \rightarrow 3CO_2 + 4H_2O \quad (1)$$

In order to perform simulations, a comprehensive kinetic mechanism is necessary to study the stabilization of flame mechanism in micro-scale combustor, where the single step mechanism is sufficient. The employment of high grid concentrations is done using non-uniform grid element size in the area surrounding the wire mesh. The elements are totaled to a number of 42548 and applied for all cases. The execution of grid dependent test was done, and the results are such that larger number of elements has no significant numerical advantage.

In this work, boundary conditions are employed using similar conditions that was done by Li, et al. [24] and applying no-slip boundary type condition between the interface of fluid and solid wall. Fourier's law is utilized to calculate the heat flux of this interface. Given that the heat transfer per unit area by means of convection at the outer surface of the tube combustor such that;

$$q_{loss} = h_{conc}(T_{wall} - T_{amb}) + \varepsilon\sigma(T_{wall}^4 - T_{amb}^4) \quad (2)$$

Where convective heat transfer coefficient is represented by h, wall temperature of combustor is T_{wall} and ambient temperature is T_{amb}. Initially, the value of ambient temperature (T_{amb}) is 296 K. the convective heat transfer coefficient (h) is set to a constant $4\ W/m^2K$, representing weak natural convection [24]. For the outer wall and wire mesh external emissivity (ε), it is fixed at 0.90 and 0.70, correspondingly. Meanwhile, the value $5.67 \times 10^{-8} W/m^2K^4$ is set for Stefan-Boltzman constant (σ). The right and left wall edge of the micro combustor is equipped with thermal insulation (zero heat flux boundary) whereas for a typical value of *k* for quartz tube, the *k* value is fixed to 1.6 W/m/K. A fixed pressure inlet is applied to the outlet boundary condition. At z-plane of origin, a symmetrical boundary condition is determined in order for the half domain to be

calculated. By utilizing data from Kutz [23] and ANSYS® Academic Research [19], the thermodynamic properties and gas transport data can be replicated.

At the combustor's inlet, a flat velocity profile with laminar flow of *U* is applied. The feed temperature at the inlet is initially set to 295 K while no application of swirl flow velocity is done. At first, the *U* value is fixed at 0.20 m/s and equivalent ratio (ϕ) is set to 1 in order start combustion of the propane-air mixture. In step one, "cold flow" technique is applied where momentum and continuity equation is first solved. Energy and species equations are calculated and solved after the first step by defining an area of high temperature as patch zone. The location of the patch zone is 2.5 mm distance to the outlet and cannot be set too near to the outlet as ignition process can be affected negatively due to reverse gas flow. In the patch zone, 1500 K temperature is employed which is highly sufficient in ensuring that the propane-air mixture is able to be ignited. During ignition, the flame will propagate upstream and slowly stabilized close to the wire mesh. The value of U steadily increases to find the blowout limit range with an interval of 0.05 m/s. The process will start all over again by applying the previous value of *U* if the new *U* value causes propagation of flame to the outlet. The interval will decrease to 0.01 m/s until blowout phenomena occurs. Once the blowout phenomena happen, the blowout limit for the experiment will consider the maximum value of *U* before the occurrence of the blowout phenomena.

Figure 2 demonstrates the supply of heat in the micro combustor for a near blowout phenomena. The designation of terms in the figure are as below:

Q_{C1}=heat conducted via the inner wall of the burned gas region
Q_{C2}=heat conducted via the inner wall of the unburned gas region
Q_{RU}= heat recirculated to the unburned gas region
Q_{RM}=heat recirculated to the wire mesh
Q_{LB}=heat loss from the outer wall of the burned gas region to the ambient
Q_{LM}=heat loss from the outer wall of the wire mesh to the ambient
Q_{LU}=heat loss from the outer wall of the unburned gas region to the ambient

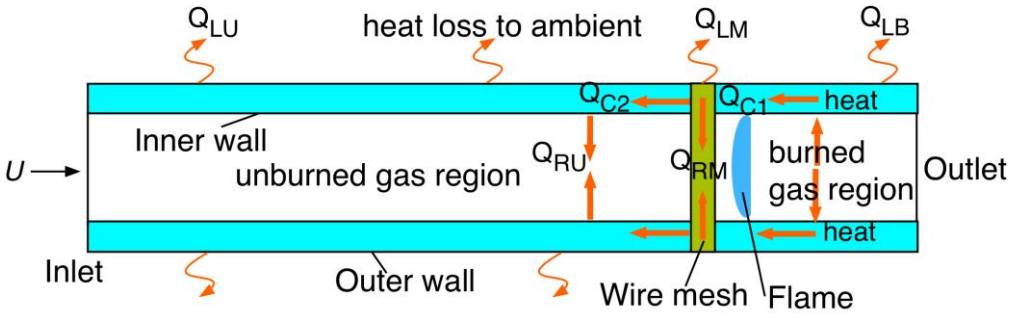


Fig. 2. Heat recirculated in the combustor near blowout conditions

3. Results and Discussion

Higher flow velocity (*U*) causes the behaviour of wire mesh thermal path to be reversed. This is due to flame position varies according to *U*. the lower the value of *U*, the nearer the flame is to the wire mesh. However, the higher the value of *U*, the more displaced the flame is from the wire mesh. The flame position is likely to be determined via numerical simulation as shown in Figure 3 where at *U*=30 cm/s, the position of flame is at 0.43 mm away from the wire mesh. Heat recirculation happens when the heat from burned gas region is circulating through inner wall of the

burned region towards the wire mesh. While Table 1 depicts the values of blowout limit range for four different tube combustor combination. The numerical simulation results show that with the use of brass tube at the burned gas region, the overall blowout limit value increases significantly.

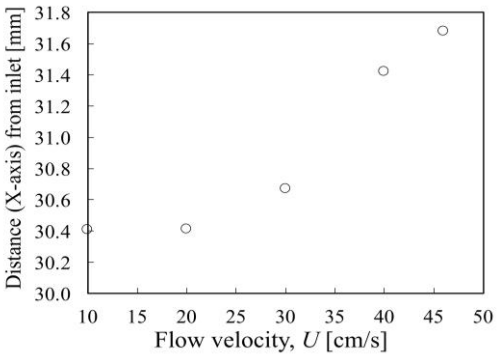


Fig. 3. Flame displacement for varies value of flow velocity U at ϕ=1.0 for quartz-quartz tube combustor

Table 1
Blowout limits for different tube combustors (from 3-D simulation)

Type of combustor	Blowout limits [cm/s]
Quartz-quartz tube	46
Quartz-brass tube	79
Brass-quartz tube	37
Brass-brass tube	69

Firstly, once the unburned gas enters the inlet, the heat from burned region circulates to the unburned gas region (Q_{RU}) which then allows the unburned gas to be pre heated by recirculated heat. Further into the chamber, the gas is again heated by the recirculated heat through the wire mesh (Q_{RM}). So, Q_{RU} and Q_{RM} values plays a significant role to signify the amount of heat recirculated to pre-heat unburned gas. These values cause the increment of gas temperature prior to combustion. The energy balance for every boundary is calculated using the FLUENT software. Figure 4 shows the results produced for Q_{RU} and Q_{RM} for four different combustor tube combinations. Q_{RM} in negative value only occurs when there is a low flow velocity which illustrates the flow of heat from the wire mesh center to the outer wall. At this point, the wire mesh functions as a flame inhibitor. When quartz tube is used in the unburned region as depicted in Figure 4 (a) and (b), the blowout limit is affected by the significant role played by the wire mesh as heat is recirculated to the unburned gas (Q_{RM}) during the near blowout conditions. Thus, at higher flow velocity, the wire mesh functions as flame enhancer. However, when brass tube is used in the unburned region as shown in Figure 4 (c) and (d), the wire mesh is less likely to play an important role in recirculating the heat. In this condition, the inner wall of combustor has a more essential role in recirculating heat to the unburned gas (Q_{RU}).

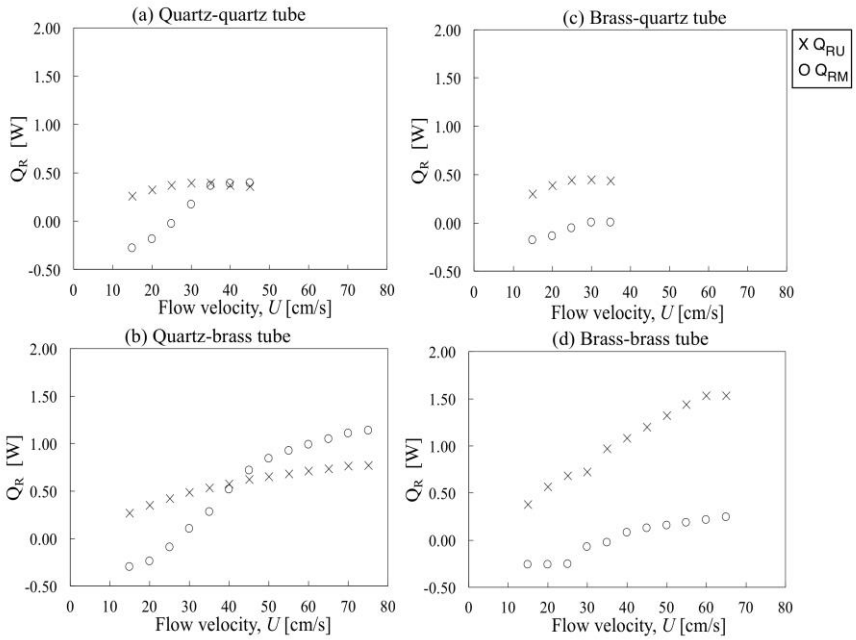


Fig. 4. Values of Q_{RU} and Q_{RM} with different flow velocities for each of combustor

Q_{RU} and Q_{RM} values were then plotted on together on a graph for the four different tube combustor combination. The comparisons are shown clearly in Figure 5. It can be seen that the usage of brass tube in burned gas region drastically increases the value of recirculated heat (Q_{RU}+Q_{RM}) to the unburned gas. In Figure 5 (d), the percentage of heat release rate (HRR) that is being recirculated to the unburned gas region is up to 19% for the tube combustor combination of brass-brass and quartz-brass tube combustor. It is considered a high value for combustors with wire mesh.

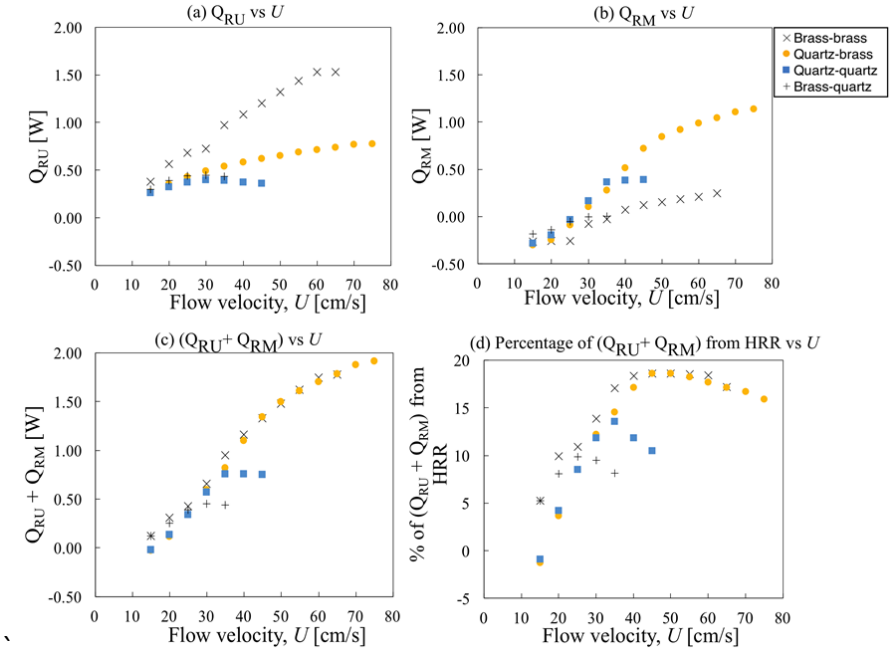


Fig. 5. Q_{RU} and Q_{RM} values for different flow velocities for the four different tube combustor combination

Primarily, the solid walls of the tube combustor conduct heat from the burned gas region when the flow velocity (U) is high. The heat conducted is represented as Q_{C1} and Q_{C2} which their values are directly proportional to the wall thermal conductivity (k) of the tube. Two equations were formed to define Q_{C1} and Q_{C2} values. The following are the equations;

$$Q_{C1}=Q_{C2}+Q_{RM}+Q_{LM} \quad (3)$$

$$Q_{C2}=Q_{RU}+Q_{LU} \quad (4)$$

Q_{C1} and Q_{C2} can be calculated using the created equation as the values of Q_{RM}, Q_{LM}, Q_{RU} and Q_{LU} were collected from the simulation using FLUENT software. Figure 6 shows the result of Q_{C1} and Q_{C2} values with varied flow velocities for the four different combustors. The result proves that when brass tube is utilized in either unburned or burned gas region, the values of Q_{C1} and Q_{C2} enhances significantly. This improvement in values are expected due to brass tube is known to have better wall thermal conductivity compared to quartz tube.

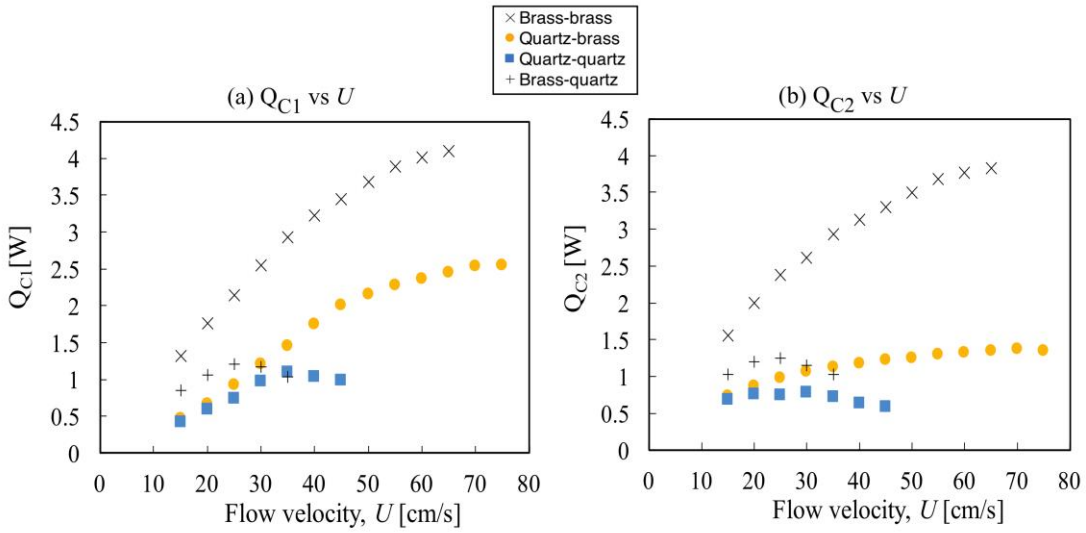


Fig. 6. Values of Q_{C1} and Q_{C2} with different flow velocities for each of combustor

4. Conclusions

The simulation of three-dimensional (3D) model for micro scale combustion of propane-air fuel with stainless steel wire-mesh has been successfully accomplished. The simulation demonstrated clearly that at low flow velocity, the flames are much nearer towards the wire mesh whereas at higher flow velocity, there are flame displacement causing the flame to be further away from the wire mesh while keeping the flame relatively stable. At low flow velocity where flame is much nearer to the wire mesh. The heat flows from wire mesh to the outer wall causing the wire mesh to act as inhibitor. Meanwhile, at high flow velocity, the wire mesh does not play a significant role as the flame is further away from the wire mesh, which then causing the wire mesh to act as flame enhancer. Through the numerical simulations, it is proven that by utilizing brass tube at either unburned or burned gas region, the blowout limit of the flame in micro combustors dramatically increases.

Acknowledgement

This study was funded by a grant from Ministry of Higher Education of Malaysia (FRGS Grant FRGS/2018/FKM-CARE/F00370). Authors are thankful to Universiti Teknikal Malaysia Melaka (UTeM) and Yamaguchi University for sponsoring this research activity.

References

[1] C. M. Miesse, R. I. Masel, C. D. Jensen, M. A. Shannon, and M. Short, "Submillimeter-scale combustion," *AIChE Journal,* vol. 50, no. 12, pp. 3206-3214, 2004, doi: 10.1002/aic.10271.

[2] K. Maruta, "Micro and mesoscale combustion," *Proceedings of the Combustion Institute,* vol. 33, no. 1, pp. 125-150, 2011, doi: 10.1016/j.proci.2010.09.005.

[3] S. K. Chou, W. M. Yang, K. J. Chua, J. Li, and K. L. Zhang, "Development of micro power generators – A review," *Applied Energy,* vol. 88, no. 1, pp. 1-16, 2011, doi: 10.1016/j.apenergy.2010.07.010.

[4] N. S. Kaisare and D. G. Vlachos, "A review on microcombustion: Fundamentals, devices and applications," *Progress in Energy and Combustion Science,* vol. 38, no. 3, pp. 321-359, 2012, doi: 10.1016/j.pecs.2012.01.001.

[5] F. A. Munir, M. Mikami, M. Z. Hassan, and M. A. Salim, "Flame Stabilization In Multiple Inlet Channel Meso-Scale Tube Combustors With Wire Mesh," *Journal of Advanced Vehicle System 4,* no. Issue 1, pp. 20-27, 2017.

[6] F. Munir, T. Seo, and M. Mikami, "Optimization of Flame Stabilization Limits In Meso-Scale Tube Combustors with Wire Mesh," *International Journal of Mechanical & Mechatronics Engineering,* vol. 17, 12/01 2017.

[7] L. Yuliati, "Flame stability and behavior inside meso-scale combustor with different flame holder," *MATEC Web of Conferences,* vol. 159, p. 01021, 01/01 2018, doi: 10.1051/matecconf/201815901021.

[8] J. Wan and A. Fan, "Effect of solid material on the blow-off limit of CH4/air flames in a micro combustor with a plate flame holder and preheating channels," *Energy Conversion and Management,* vol. 101, pp. 552-560, 2015, doi: 10.1016/j.enconman.2015.06.010.

[9] L. Ma, H. Xu, X. Wang, Q. Fang, C. Zhang, and G. Chen, "A novel flame-anchorage micro-combustor: Effects of flame holder shape and height on premixed CH4/air flame blow-off limit," *Applied Thermal Engineering,* vol. 158, p. 113836, 2019/07/25/ 2019.

[10] A. Tang, Y. Xu, J. Pan, W. Yang, D. Jiang, and Q. Lu, "Combustion characteristics and performance evaluation of premixed methane/air with hydrogen addition in a micro planar combustor," *Chemical Engineering Science,* 2015, doi: 10.1016/j.ces.2015.03.030.

[11] A. Tang, Y. Xu, C. Shan, J. Pan, and Y. Liu, "A comparative study on combustion characteristics of methane, propane and hydrogen fuels in a micro-combustor," *International Journal of Hydrogen Energy,* 2015, doi: 10.1016/j.ijhydene.2015.09.101.

[12] A. Tang, T. Cai, J. Deng, Y. Xu, and J. Pan, "Experimental investigation on combustion characteristics of premixed propane/air in a micro-planar heat recirculation combustor," *Energy Conversion and Management,* vol. 152, pp. 65-71, 2017/11/15/ 2017.

[13] A. Tang, T. Cai, Q. Huang, J. Deng, and J. Pan, "Numerical study on energy conversion performance of micro-thermophotovoltaic system adopting a heat recirculation micro-combustor," *Fuel Processing Technology,* vol. 180, pp. 23-31, 2018/11/01/ 2018.

[14] G. Bagheri and S. E. Hosseini, "Impacts of inner/outer reactor heat recirculation on the characteristic of micro-scale combustion system," *Energy Conversion and Management,* vol. 105, pp. 45-53, 2015, doi: 10.1016/j.enconman.2015.07.056.

[15] D. G. Norton and D. G. Vlachos, "A CFD study of propane/air microflame stability," *Combustion and Flame,* vol. 138, no. 1-2, pp. 97-107, 2004.

[16] S. Akhtar, S. Piffaretti, and T. Shamim, "Numerical investigation of flame structure and blowout limit for lean premixed turbulent methane-air flames under high pressure conditions," *Applied Energy,* vol. 228, pp. 21-32, 2018/10/15/ 2018.

[17] J. Wan, A. Fan, and H. Yao, "Effect of the length of a plate flame holder on flame blowout limit in a micro-combustor with preheating channels," *Combustion and Flame,* vol. 170, pp. 53-62, 2016/08/01/ 2016, doi:

[18] T. Cai, A. Tang, D. Zhao, C. Zhou, and Q. Huang, "Experimental observation and numerical study on flame structures, blowout limit and radiant efficiency of premixed methane/air in micro-scale planar combustors," *Applied Thermal Engineering,* vol. 158, p. 113810, 2019/07/25/ 2019.

[19] R. ANSYS® Academic Research. A. Inc. (2012). ANSYS® Academic Research, Release 14.0.

[20] F. A. Munir and M. Mikami, "Modeling of Propane-air Combustion in Meso-scale Tubes with Wire Mesh," presented at the 10th Asia Pacific Conference on Combustion (ASPACC 2015), Beijing China, 2015.

[21] S. Karagiannidis, J. Mantzaras, G. Jackson, and K. Boulouchos, "Hetero-/homogeneous combustion and stability maps in methane-fueled catalytic microreactors," *Proceedings of the Combustion Institute,* vol. 31, no. 2, pp. 3309-3317, 2007.
[22] D. G. Norton and D. G. Vlachos, "Combustion characteristics and flame stability at the microscale: a CFD study of premixed methane/air mixtures," *Chemical Engineering Science,* vol. 58, no. 21, pp. 4871-4882, 2003.
[23] M. Kutz, *Mechanical Engineers Handbook*. USA: John Wiley & Sons, 1998.
[24] J. Li, S. K. Chou, W. M. Yang, and Z. W. Li, "A numerical study on premixed micro-combustion of CH4–air mixture: Effects of combustor size, geometry and boundary conditions on flame temperature," *Chemical Engineering Journal,* vol. 150, no. 1, pp. 213-222, 2009.

Penerbit Akademia Baru

Engineering Science and Technology Conference Proceedings

Journal homepage: www.akademiabaru.com/EST.html

The Effect Of Sedimentation To The Pump Sump System By Using Computational Fluid Dynamics (CFD) Model

Open Access

Norsyazliana Syamira Saiful Anuar[1], Siti Hidayah Abu Talib[1,*], Nur Fatin Izureen Radzaly[1], Syarifah Intan Najla Syed Hashim[1], and Muhammad Salleh Abustan[1]

[1] Faculty of Civil and Environmental Engineering, Universiti Tun Hussein Onn Malaysia, 86400 Parit Raja, Batu Pahat, Johor, Malaysia

ABSTRACT

Pump sump plays an important role in water supply which it's a hydraulic machine that have been designed to transmitted water. Therefore, effectiveness of pump sump is important to make sure the storage capacity of reservoir is maintained and prevent water shortage at reservoir so that reservoir has enough water to supply. However, water from river or lake contains sediment and it will disturb the entering flow at water intake. Sediment also will cause erosion and abrasion to the pump sump which it will affect the effectiveness of the pump sump. This will lead to economic losses due to maintenance work and lack of pump sump operational. Therefore, study is conducted to determine the efficiency of pump sump due to sedimentation using CFD model which is ANSYS Fluent. Model simulation is conducted using different size of sediment and different water flow velocity to observed how it will effect on pump sump. The CFD model are well computed the sediment deposition in pump sump. Percentage of particle deposited increased with increased of particle size but at lower velocity. Higher water level in pump sump give lower percentage of particle deposited in pump sump.

Keywords:
Sedimentation; pump sump; CFD

Copyright © 2019 PENERBIT AKADEMIA BARU - All rights reserved

1. Introduction

Pump sump intake plays an important role in water supply. There are many usage of pump. For example, in water resources, pump is used to transfer raw water (from river, lakes, etc.) to the intake. Pump is selected based on system requirements, discharge pressure required, flow capacity required and availability of space [1]. Nowadays, there are many development has been implemented resulting many new land clearing. Some of development has been carried out near the river and this kind of development will produce sediment loads in the river which it will transport to the reservoir. Besides, the most sediment releases come from land development activities where it may cause sedimentation problem in watercourse.

Sedimentation is the build-up (aggradation) of sediment on the land surface or the bed of a watercourse and cause particles to depart from flow lines [2-3]. Therefore, it allowing particles in water to settle out of the suspension under the effect of gravity. Sedimentation will give an effect to the pump sump system especially to its efficiency. The smaller particle or the suspended particle will flow to the intake and this may cause an erosion and abrasion to the expensive hydraulic machinery [4]. The erosion and abrasion to the hydraulic machinery will reduce the efficiency of the pump system and increasing the maintenance cost. Besides, the excessive of the sedimentation in

* *Corresponding author.*
E-mail address: hidayaht@uthm.edu.my (Siti Hidayah Binti Abu Talib)

the waterway will cause sediment entrainment and reduction of pump efficiency in delivering because of clogged or locked at the outlet of the structure and it may lead to damage of the system because the pump system is not designed for sediment passage. [5-6]. Furthermore, sedimentation problems can lead to pump operational difficulties due to it being either conveyed with the diverted flow or deposited in the intake and interferes with the flow [7]. In addition, sedimentation will reduce the water storage and eliminate the capacity of water flow regulation which it will cause economic losses due to maintenance work and operational lack.

Therefore, effectiveness of pump is the most important thing and have to takes it into a consideration to prevent any losses. This is because installation of pump sump is expensive because it need a lot of construction material, electricity and maintenance. Physical model is commonly used to investigated the effect of sedimentation to the pump sump system. However, usage of physical model will require high cost due to construction and transportation of the physical model itself besides it also required long time period.

Computational Fluid Dynamics (CFD) is one of the tool that can be used to investigate the problem which it is can save cost and time. However, it requires a skill and quite difficult to understand how to use the software which it need a lot of studies. CFD is now become one of an important tool to study the flow either the flow of gas, solid or liquid and it also can analyze single phase and multiphase flow [8]. Since CFD has been choose as a method to analyse the problem. Therefore, more research has to be done to decide the most appropriate CFD model that suitable to use where other similar research works is studied to understand the different model and theories are used in CFD as following.

Wingstedt. and Reif [9] conducted a numerical simulation of particle dispersion in urban area using Euler-Lagrange model. Realizable k-ε model was used for turbulence modelling and Discrete Phase model (DPM) was used for particle transport model. The results obtained shows that ANSYS Fluent is capable to predict the dispersion and deposition of the particle.

Kaushal et al., [10] have used multiphase flow ANSYS Fluent modelling to study about CFD modelling for pipeline flow of fine particles at high concentration. Two types of model are used such as mixture model and Eulerian model to modelled three-dimensional concentration distributions, pressure drops and velocity distributions. Mixture model fails to predict pressure drops correctly. Eulerian model gives fairly accurate predictions for pressure drop at all the efflux concentrations and flow velocities.

Yan [11] conducted CFD model to investigate the 3D modelling of hydrodynamics, sediment transport, settling and resuspension under unsteady conditions in an urban storm water detention basin. Discrete Phase Model (DPM) is been used to observed the sediment transport. RNG k-ε model is used to represent turbulent phenomenon. For the results, the simulated flow pattern showed a good level of agreement with the measured spatial distribution of particle size.

Gopaliya and Kaushal [12] has conducted modelling of sand-water slurry flow through horizontal pipe using CFD using Eulerian model. The turbulence model that have been used is RNG k-ε model. As the results, local volumetric concentration of solid phase across pipe outlet is very well simulated for all three particles sizes under consideration. However, scatter in data of various flow parameters especially in case of slurry flows with bigger particle sizes indicates that the model used in the present study needs further development.

Tarpagkou and Pantokratoras [13] has conducted CFD methodology to investigate the 3D hydrodynamics and flow behaviour of a sedimentation tank using Discrete Phase Model (DPM). RNG k-ε model is used for turbulence model.

Next study has been done by Bikmukhametov [14] which to study the capabilities of CFD software ANSYS Fluent in modelling of particle flows. Eulerian granular model has been used to

stimulate particle plug propagation in bent pipes and DPM model was used to determine the critical velocity. Realizable k-ε model is used for turbulence modelling. As the results, Eulerian granular model are capable to reproduce the particle plug movement in pipes and the results fit the experimental results. While for the DPM, it gives reasonably good performance in predicting critical velocity in slurry flows, but the value of the velocity is underestimated.

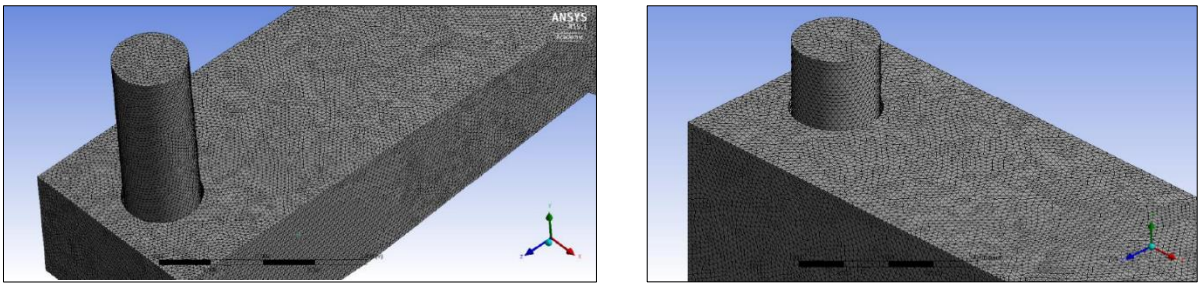
Dufresne et al., [15] studied the use of CFD and particle tracking in other and various hydraulic conditions. k-ε model is used for turbulence model and DPM is used for particle tracking. As a results, CFD shows seems a good way to model the sediment transport in the pilot tank.

Mohsin and Kaushal [16] used Volume on fluid (VOF) model to validate the invert trap efficiency for sewer solid management. VOF model is used because it is suitable for free surface flow and it coupled with DPM model which it used to determine the sediment trapped. Realizable k-ε is used as turbulence model. As a results, CFD model closely fit the experiment data.

The aim of this study is to determine the sediment deposition area and accumulation in pump sump. Most of the researchers are conducted the sediment transport in the pipeline. However, the most appropriate models will be choosing based on the similar research about sediment transport or particle tracking in fluid flow.

2. Methodology

Parameters that used in the simulation has been identified first such as velocity, flow rate, particle diameter and particle density. The model has been made based on the real physical model and 3D modelling have been developed by using Solidworks 2017. There are two water level that has been used in this study which is minimum water level and normal water level. Unstructured grids and tetrahedral mesh was used as shown in Figure 1. The mesh has 1.13 million and 2.5 million elements for minimum and normal water level respectively.



(a) (b)

Fig 1. (a) Meshing for minimum water level. (b) Meshing for normal water level

For boundary condition, no slip boundary condition was applied at walls and pressure-outlet at the outlet. At the inlet, velocity-inlet with velocity of 0.007m/s, 0.037m/s and 0.071m/s was used for both water level. Initial studies show that realizable k-ε model perform better compare to standard k-ε and RNG k-ε model especially in complex flow [8, 17]. Therefore, realizable k-ε model is used for turbulence model. After that, Discrete Phase Model (DPM) is activated and particle are released at the inlet surface of the pump model. Three particle sizes is used which is 800µm, 425µm and 150µm with density of 1450 kg/m3.

3. Results

Simulation has been analysed by using two different water level which is normal water level and minimum water level. Furthermore, each of water level is divided into three cases where there are three value of inlet velocity which is 0.007 m/s, 0.037 m/s and 0.071 m/s. Three different particle sizes was injected for each velocity which is 150µm, 425µm and 800µm. The pump sump is divided into several zone as shown at Figure 2.

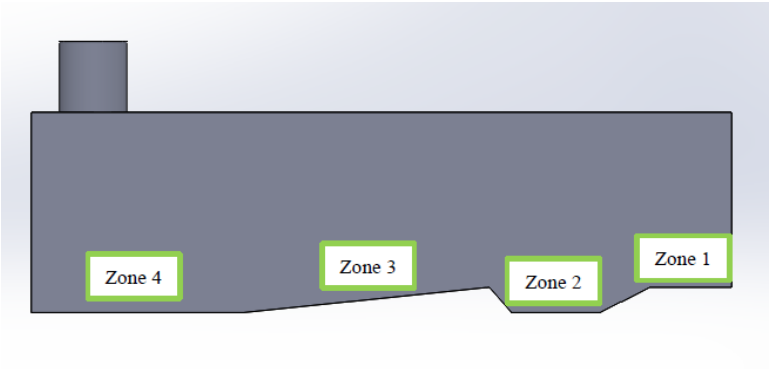


Fig 2. Zone area in pump sump

3.1 Sediment Deposition Area for Minimum Water Level

3.1.1 Case 1 – Velocity 0.007 m/s with difference particle sizes

The most of the particles are deposited at zone 1 for particle size 800µm. For particle 425µm, the deposition area still at the zone 1 but there is some of the particle are deposited at the zone 2. While for the particle size of 150µm, the deposition area started scattered from zone 1 to 3.

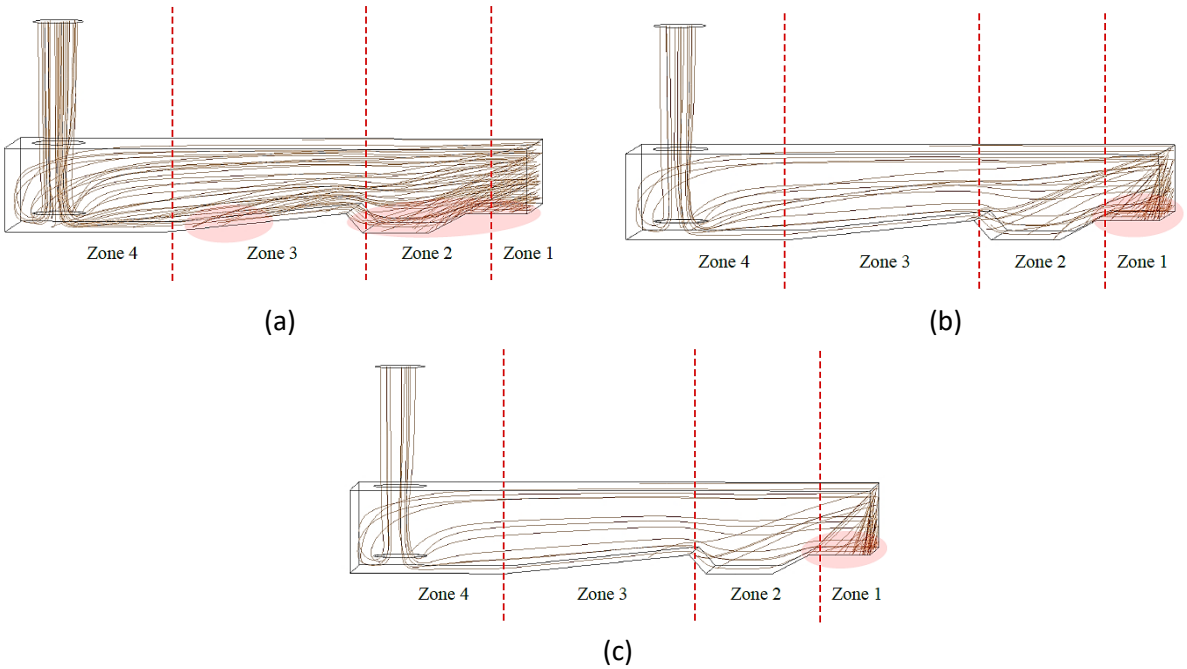


Fig 3. (a) Velocity 0.007 m/s with particle size 150µm. (b) Velocity 0.007 m/s with particle size 425µm. (c) Velocity 0.007 m/s with particle size 800µm

3.1.2 Case 2 – Velocity 0.037 m/s with difference particle sizes

Compared to case 1, the deposition area of particle for particle size 800µm more dispersed from zone 1 to 2 and particle that transported to the suction pipe are slightly increased. For particle size 425µm, the deposition area of the particle same as 800µm but the particle transported for 425µm is more compared to size 800µm. Contrast to 150µm size, most of the particle are transported into suction pipe but there still have a few amount of particle deposited at zone 2, 3 and 4.

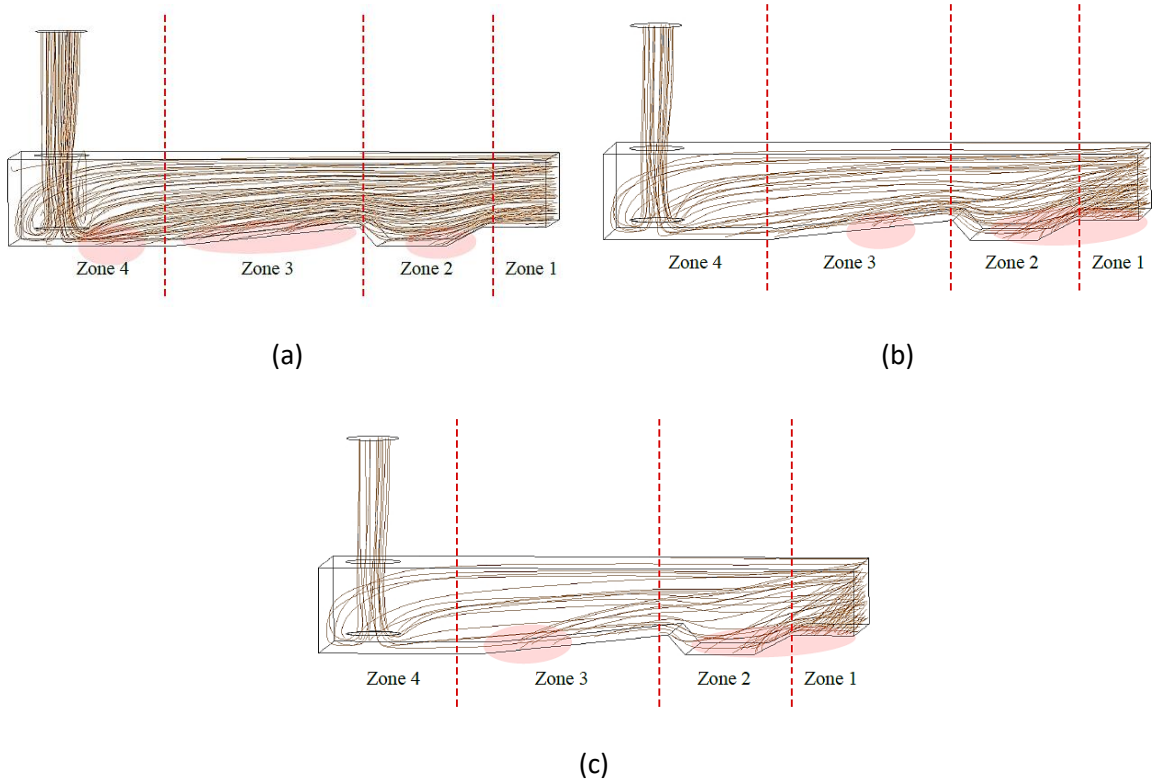
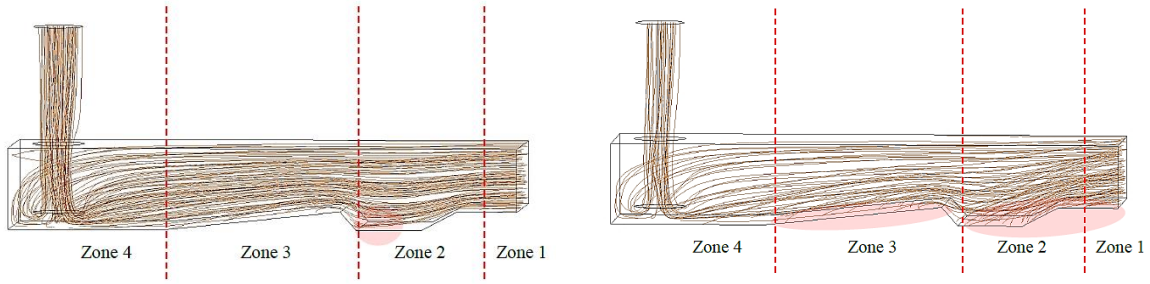


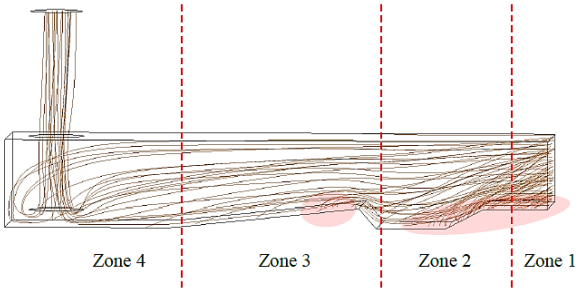
Fig 4. (a) Velocity 0.037 m/s with particle size 150µm. (b) Velocity 0.037 m/s with particle size 425µm. (c) Velocity 0.037 m/s with particle size 800µm

3.1.3 Case 3 – Velocity 0.071 m/s with difference particle sizes

The particle transported and deposition area for 800µm for this cases are almost same as cases 2 but the particle is more dispersed compared to case 2. For particle size 425µm, most of particle deposited at zone 2 and 3. Furthermore, the particle transported to the suction pipe is higher and there are only a few particles deposited at zone 2.



(a) (b)



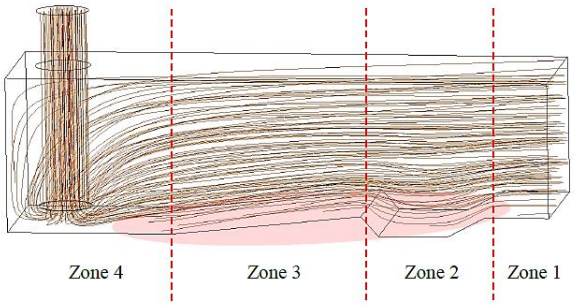
(c)

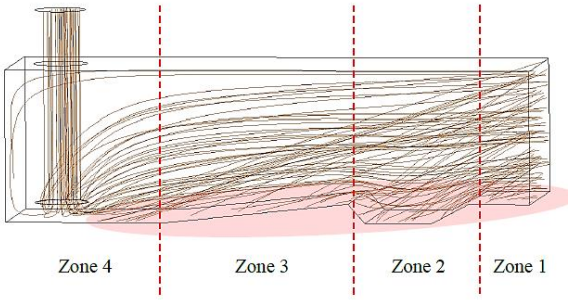
Fig 5. (a) Velocity 0.071 m/s with particle size 150µm. (b) Velocity 0.071 m/s with particle size 425µm. (c) Velocity 0.071 m/s with particle size 800µm

3.2 Sediment Deposition Area for Minimum Water Level

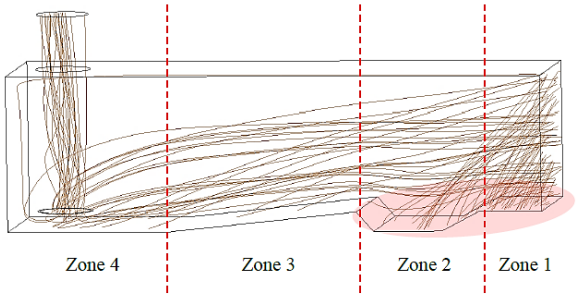
3.2.1 Case 1 – Velocity 0.007 m/s with difference particle sizes

Particle with size 800µm shows that most of particle deposited at zone 1 and 2. When smaller particle injected to the pump sump with size 425µm, the particle start moves and deposited forward to zone 3 and 4. The particle that transported into suction pipe is increased. For particle sizes 150µm is injected, particle that transported to the suction pipe is increased and particle that deposited is reduced. There are some of the particle deposited at zone 3 and 4.





(a) (b)



(c)

Fig 6. (a) Velocity 0.007 m/s with particle size 150µm. (b) Velocity 0.007 m/s with particle size 425µm. (c) Velocity 0.007 m/s with particle size 800µm

3.2.2 Case 2 – Velocity 0.037 m/s with difference particle sizes

In this case, the inlet velocity has been increased to 0.037 m/s. Particle with size 800µm shows that the particle is deposited more scattered from zone 1 to 4 compared to case 1. When particle size of 425µm is injected, most of the particle deposited at zone 3 and 4. For particle size 150µm, there are only few particles deposited along the zone 1 to zone 3 and most of the particle are transported into the suction pipe.

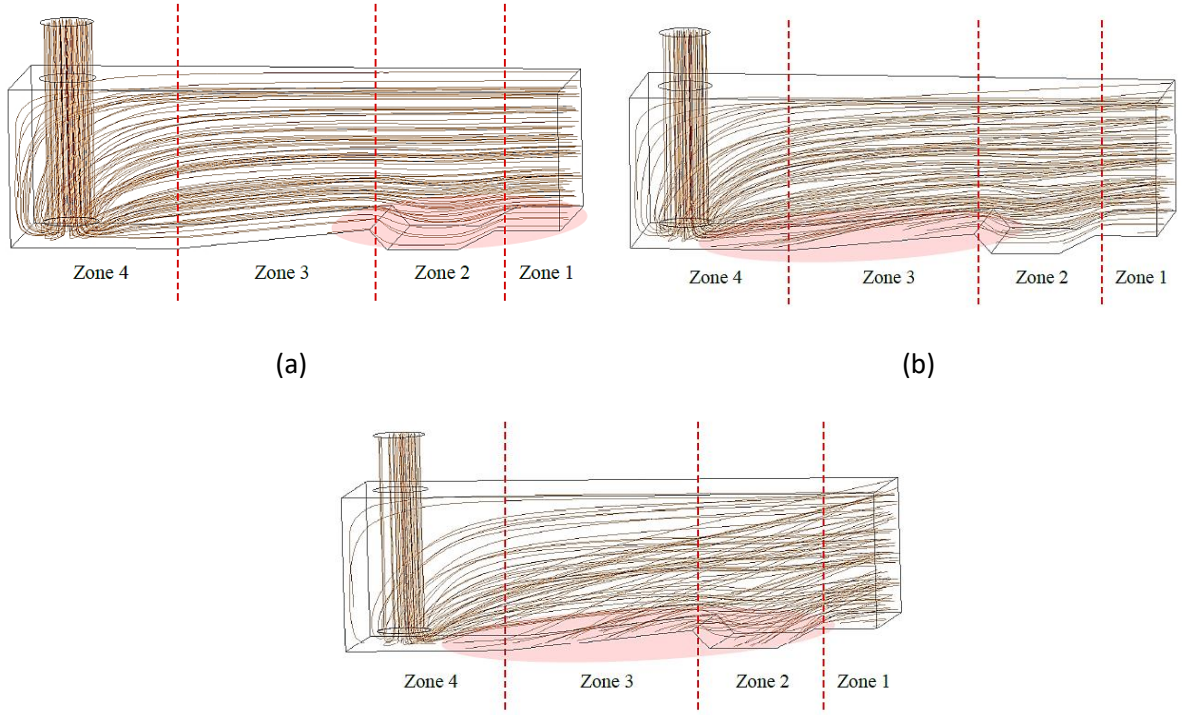


Fig 7. (a)Velocity 0.037 m/s with particle size 150µm. (b) Velocity 0.037 m/s with particle size 425µm. (c) Velocity 0.037 m/s with particle size 800µm

3.2.3 Case 3 – Velocity 0.071 m/s with difference particle sizes

In this case, higher velocity is used which is 0.071 m/s. The particle deposited in the pump sump decreased more compared to case 1 and 2. The deposition area for particle size 800µm have moving forward to zone 2, 3 and 4. For particle size 425µm, there's a few particles deposited at zone 2, 3 and 4. Besides, for smallest particle size 150µm, particle deposited at zone 3 but in small amount.

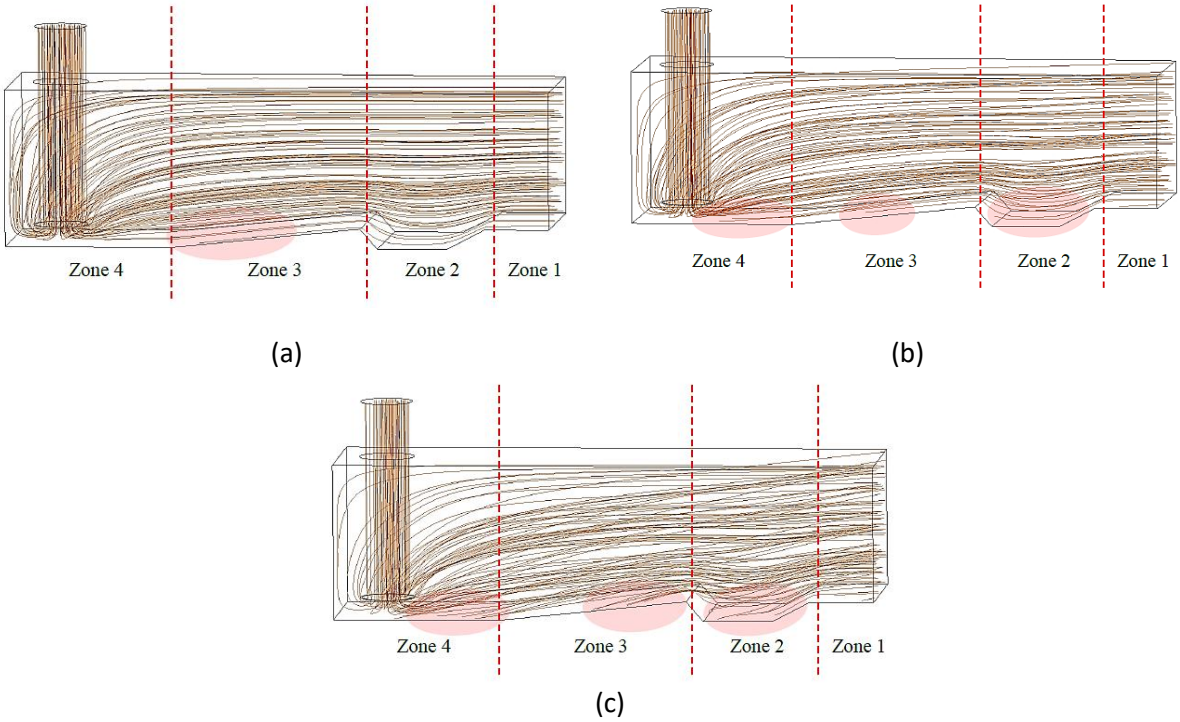


Fig 8. (a) Velocity 0.071 m/s with particle size 150µm. (b) Velocity 0.071 m/s with particle size 425µm. (c) Velocity 0.071 m/s with particle size 800µm

The deposition area for minimum water level is the same as normal water level where when the velocity is slower, the deposition area of the sediment is located at the zone 1 and 2 but more at the zone 1 especially for particle size 800µm. For smallest particle size which is 150µm, the particle deposited is more and dispersed compared to normal water level. In addition, as can been seen, minimum water level has lower particle transported into the suction pipe. This is because the lower water depth, the water velocity also decreased [18]. Therefore, the particle is easier to deposited in the pump sump.

3.3 Sediment Accumulation

Sediment accumulation is interpreted in percentage in Figure 9 for normal water level and Figure 10 for minimum water level. For normal water level, particle size 80µm shows higher percentage of particle trapped in the pump sump especially in velocity 0.007 m/s where the value is 76%. When particle size 425µm is injected into the pump sump, it only gives slightly less percentage than 800µm at slowest velocity 0.007 m/s. When higher velocity applied which is 0.037 m/s, the particle trapped in pump sump reduce from 61% to 23%. While for the smallest particle size 150µm, there is a huge difference amount of percentage of particle trapped in pump sump compared to other particle sizes where there is only 18% particle trapped in pump sump for velocity 0.007 m/s. Even in the slowest velocity, the amount of particle that trapped in very small.

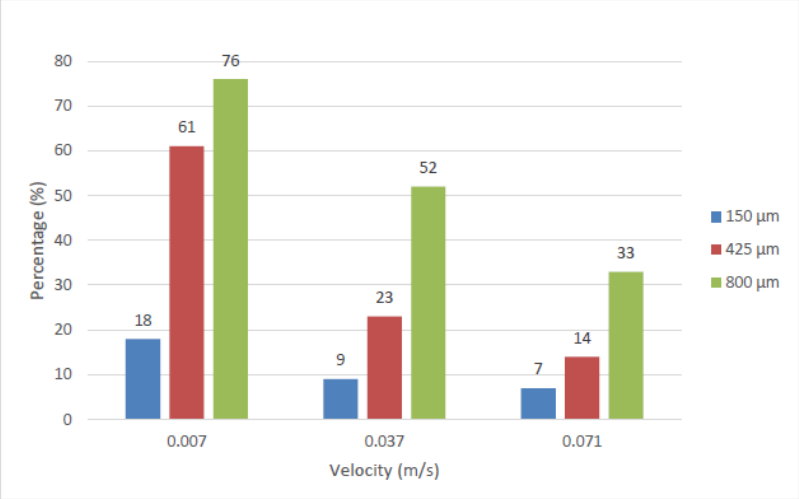


Fig 9. Percentage of sediment accumulation for normal water level

Contrast to minimum water level, the percentage of particle accumulate is higher especially for 800µm and 425µ. At velocity 0.007 m/s, percentage of particle trapped for particle size 800µm, 425µm and 150µm is 90%, 87% and 72% respectively. For particle size 800µm, there are only 5% difference for all velocity which is 90% for 0.007 m/s, 85% for 0.037 m/s and 80% for 0.071 m/s. Besides, for particle size 425µm, there are 87%, 76% and 67% of particle trapped for velocity 0.007 m/s, 0.037 m/s and 0.071 m/s respectively. Hence, there are only 11% and 9% differences. In addition, for smallest particle injected in pump sump which is 150µm, the percentage drop 33% from 72% to 39% for 0.007 m/s and 0.037 m/s.

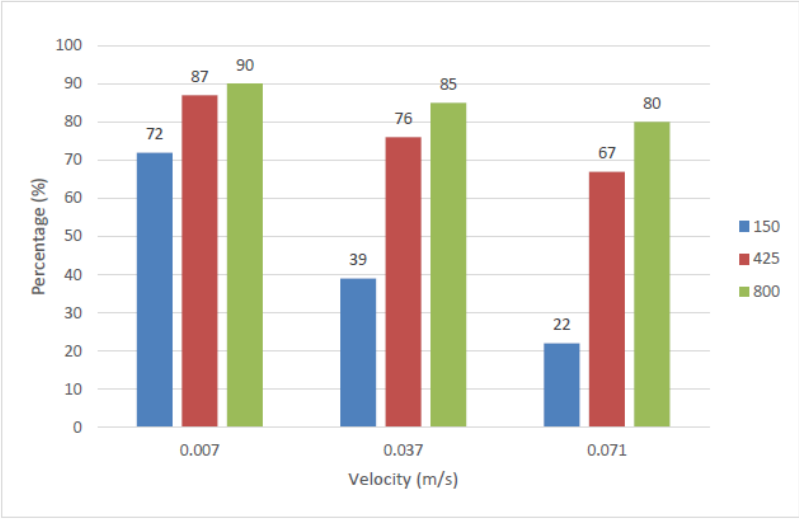


Fig 10. Percentage of sediment accumulation for minimum water level

4. Conclusions

From the study, the percentage of trapped particle in pump sump is decreased with increased of velocity. Besides, the particle sizes also influence the particle deposition in pump sump. Bigger size of particle give higher percentage of particle deposited in pump sump. The smaller particle size which is 150µm shows give higher percentage of particle transported to the suction pipe. This may lead to the sediment erosion to the pump sump or pump blade [19]. However, larger particle size give higher percentage of particle deposited especially in lower velocity and the deposited area

located near to the inlet and slope section of pump sump. Higher number of particle deposited will cause shortage capacity in reservoir [20]. Furthermore, height of water level also will affect the percentage of particle transported into the suction pipe. Percentage of particle deposited in pump sump decreased with increased of water level in pump sump.

Acknowledgement
The authors would like to thank Universiti Tun Hussein Onn and Research Management Centre (RMC) for funding this project under Postgraduate Research Grant (GPPS) phase 2/2019.

References

[1] Bhardwaj, Vipin, and Bethany Reed. "Pumps." *Water Encyclopedia 1* (2005): 391-395.
[2] DID. "Urban Stormwater Management Manual for Malaysia." Department of Irrigation and Drainage. Percetakan Nasional Berhad. (2001)
[3] Gregory, John. "Particles in water: properties and processes." CRC Press, 2005.
[4] Hillebrand, G., I. Klassen, and N. R. B. Olsen. "3D CFD modelling of velocities and sediment transport in the Iffezheim hydropower reservoir." *Hydrology Research 48*, no. 1 (2016): 147-159.
[5] Faghihirad, Shervin, Binliang Lin, and Roger Falconer. "Application of a 3D layer integrated numerical model of flow and sediment transport processes to a reservoir." *Water 7*, no. 10 (2015): 5239-5257.
[6] Shahidan, Noor FN, Zorkeflee A. Hasan, Mohd Z. Abdullah, and Aminuddin A. Ghani. "Mathematical modelling of flow and sediment pattern at Ijok Intake, Ijok River, Perak, Malaysia." *International Journal of Modelling and Simulation 32*, no. 3 (2012): 165-170.
[7] Samsudin, M. L., K. M. Munisamy, and Savithry K. Thangaraju. "Application of multiphase modelling for vortex occurrence in vertical pump intake-a review." In *IOP Conference Series: Materials Science and Engineering*, vol. 88, no. 1, p. 012024. IOP Publishing, 2015.
[8] Andersson, Bengt, Ronnie Andersson, Love Håkansson, Mikael Mortensen, Rahman Sudiyo, and Berend Van Wachem."Computational fluid dynamics for engineers." *Cambridge University Press*, 2011.
[9] Wingstedt, Emma, and Bjørn Anders P. Reif. "Numerical simulations of particle dispersion in an urban area." *Norwegian Defence Research Establishment*, FFI Rapprt 2012/00266 (2012).
[10] Kaushal, D. R., T. Thinglas, Yuji Tomita, Shigeru Kuchii, and Hiroshi Tsukamoto. "CFD modeling for pipeline flow of fine particles at high concentration." *International Journal of Multiphase Flow* 43 (2012): 85-100.
[11] Yan, Hexiang. "Experiments and 3D modelling of hydrodynamics, sediment transport, settling and resuspension under unsteady conditions in an urban stormwater detention basin." PhD diss., 2013.
[12] Gopaliya, Manoj Kumar, and D. R. Kaushal. "Modeling of sand-water slurry flow through horizontal pipe using CFD." *Journal of Hydrology and Hydromechanics 64*, no. 3 (2016): 261-272.
[13] Tarpagkou, Roza, and Asterios Pantokratoras. "CFD methodology for sedimentation tanks: The effect of secondary phase on fluid phase using DPM coupled calculations." *Applied Mathematical Modelling 37*, no. 5 (2013): 3478-3494.
[14] Bikmukhametov, Timur. "CFD Simulations of multiphase flows with particles." Master's thesis, NTNU, 2016.
[15] Dufresne, Matthieu, José Vazquez, Abdelali Terfous, Abdellah Ghenaim, and Jean-Bernard Poulet. "Experimental investigation and CFD modelling of flow, sedimentation, and solids separation in a combined sewer detention tank." *Computers & Fluids 38*, no. 5 (2009): 1042-1049.
[16] Mohsin, Mohammad, and Deo Raj Kaushal. "3D CFD validation of invert trap efficiency for sewer solid management using VOF model." *Water Science and Engineering 9*, no. 2 (2016): 106-114.
[17] Ansys Inc. "ANSYS FLUENT theory guide." *Canonsburg, PA, Release 15.0* (2013).
[18] Dorfmann, Clemens. "Flow Phenomena in a Reservoir investigated by Field Measurements and Numerical Modelling" Doctoral thesis, Graz University of Technology, 2017.
[19] Thapa, Biraj Singh, Ole Gunnar Dahlhaug, and Bhola Thapa. "Sediment erosion in hydro turbines and its effect on the flow around guide vanes of Francis turbine." *Renewable and Sustainable Energy Reviews* 49 (2015): 1100-1113
[20] Teh, Soo Huey. "Soil erosion modeling using RUSLE and GIS on Cameron highlands, Malaysia for hydropower development." PhD diss., 2011.

Penerbit Akademia Baru

Engineering Science and Technology Conference Proceedings

Journal homepage: www.akademiabaru.com/EST.html

Combination of Dehumidifier, Heat Pump and Air Heater: Influence of Temperature, Specific Humidity, and mass flow rate of Air on Specific Energy Consumption

Open Access

Engkos Achmad Kosasih[1,*], Muhammad Irfan Dzaky[1], Ahmad Zikri[1], Firdaus[1]

[1] Department of Mechanical Engineering, Faculty of Engineering, Universitas Indonesia, Kampus Baru UI Depok 16424, West Java, Indonesia

ABSTRACT

Drying is the process of transferring heat and mass to remove water by heat application, from solid or liquid food, to decrease water content. The temperature and drying conditions imposed on a product have an essential influence on it. Drying in high temperatures can cause damage the sensitive materials. To overcome this problem, in this paper, to show the effect of temperature, specific humidity, mass flow content of water on the specific energy consumption on the use of air heaters, and the combination refrigeration system. In this study, we use an experimental method by using temperature variations of 60°C, 90°C, 120°C, and 150°C. Air mass flow rates using 100 lpm, 150 lpm, 200 lpm, and 250 lpm variation. The air from the environment is sucked up by the blower and then enters the evaporator. In hot air, the evaporator undergoes a dehumidification process caused by condensation of water vapor contained in the air. Hot air in the condenser is used as preheating before entering the heater. Then the dry air heater from condenser 1 is given additional heat so that the desired dry air outlet temperature is obtained then air flows into the drying chamber. SEC (specific energy coefficient) ratio system using a dehumidifier at 250 lpm air flow has a value of less than one. The use of dehumidifier systems is not always beneficial as seen in the air discharge of 100 lpm, 150 lpm, and 200 lpm SEC ratio of more than one so that the use of a dehumidifier system is inefficient.

Keywords:
Drying; specific energy consumption; relative humidity; refrigeration; heat pump

Copyright © 2019 PENERBIT AKADEMIA BARU - All rights reserved

1. Introduction

In recent years, many fruits have been processed to facilitate the process of consumption, one example is in the form of fruit juice or fruit juice. However, this has the disadvantage of being able to change color to brown because it requires a longer and heavier time for the distribution process related to the water reserves needed in the juice or fruit juice. Another form of processing to solve the existing problem with the form of powder with the process of drying [1]. Drying is the process of transferring heat and mass to remove water by heat application, from solid or liquid food, with the aim of obtaining solid products that are low enough in water content [2].

The main objective of any drying process is to produce a dried product of desired quality at a minimum cost and maximum through put by optimizing the design and operating conditions. Spray Drying is a type of dryer used to evaporate and dry the solution and slurry in order to obtain the

* *Corresponding author.*
E-mail address: kosri@eng.ui.ac.id (Engkos Achmad Kosasih)

results of a dry solid [3]. This technology uses drying temperatures above 100°C [4]. High-temperature air dryers reduce the moisture content in the material. The higher the air temperature in the drying chamber, the faster the material dries [5]. The temperature and drying conditions imposed on a product have an important influence on it. Drying temperatures in spray drying are a common problem during the drying process. Drying in high temperatures can cause damage the sensitive materials [6].

The more heat exposed to the material, the faster the material dries[7]. Drying materials using high drying air temperatures can damage products in heat sensitive materials, such as vitamins, proteins and β-carotene [8]. Food that is sensitive to heat cannot accept physical, chemical, microbiological and mechanical treatment, when it is dried using high degrees of temperature, such as drying in a spray dryer [9]. Because of the high operating temperature, this spray drying technology cannot be used on heat sensitive materials [10].

The ideal drying air temperature for heat-sensitive material is in the temperature range of 50-60°C. However, this method has shortcomings in terms of performance resulting from increased temperatures which can cause damage to vitamins, proteins, and β-carotene. on the type of material to be dried, as well as the sugar content that can be determined the reduction in glass temperature. In addition, the drawback is the low efficiency of large energy consumption [11]. The process of drying a material occurs through two processes, namely the heating process and the drying process. Drying is done to reduce the amount of hot water by mechanical conditions of temperature, RH and air flow control, without damaging the structure of the product.

Heat pump is a device that can generate heat besides coal-fired boilers and heater. The heat pump system includes an air source heat pump and solar heat pump [12]. Currently, the use of Waste Heat Recovery (WHR) in applied technology to process food is increasingly being investigated, especially for the drying process. For instance, In soy protein powder factories, an effective heat recovery system is needed to reduce energy consumption. For spray drying and space heating during the heating season, a circular water with a heat pump is used to recover waste heat from the exhaust air to preheat the air around the inlet. Drosou C. G. has found that the heat recovery system could reach 21.3% energy-saving amount compared to the traditional spray drying system. And the static payback period of the heat recovery system is around 2.4 years [13]. In general, there are several types of drying technology used in food processing. Extra energy is needed to encourage an efficient drying process to reduce system energy consumption. To improve the performance of the heat pump system, research on modifying heat pump system and combining to other mechanism has been done widely. Heat pump dryer is proven as drying system that ensure the product's quality especially food and agriculture products, able to control drying temperature, relative humidity, moisture contain extraction, drying air velocity, drying period and etc [14].

Applications for heat pump systems are widely used in space heating and cooling, desalination and drying. For instance in tomato flavor from a heat pump dehumidifier dryer was characterized and compared to fresh and freeze-dried tomato samples for the retention of fresh flavor compounds [15]. Nonvolatile, volatile, and odor intensity are quality parameters that will be monitored. In the non-volatile profile there is no difference but there is a significant change in the volatile impact of the main odor observed. In other hand, commercial spray dried tomatoes are also evaluated to check thermally induced volatile changes. The volatile and sensory profiles of heat pump dried tomato were comparable to freeze-dried tomato, with good retention of fresh aroma.

Operation energy consumption of heat pump systems is one of the key problems for system design [16]. The main advantages of using HP technology are the energy saving potential and the ability to control drying temperature and air humidity. This creates the possibility of a wide range of

drying conditions [17]. Using a heat pump dryer, which is a combination of heat pump and drying unit, both the latent heat and sensible heat can be recovered from the exhaust air, thus improving the overall thermal performance and yielding effective control of air conditions at the inlet of the dryer. The combination of spray dryers with electric air heaters and cooling systems has proven to be efficient in terms of energy consumption [18]. The combination of spray dryer and cooling system with double condenser using R134a cooler. The cooling system is supported by the amount of heat energy that is wasted from the refrigerant condensation step which can increase engine efficiency and increase productivity [19].

Experiments on the combination of spray dryers and refrigeration systems have been carried out at an air flow rate of 450 lpm and drying air temperature at 60°C with a refrigeration system at a humidity ratio of 0.005 (kg H_2O/kg dry air), resulting in a drying capacity equal to the capacity drying at a drying air temperature of 120°C without a refrigeration system at a humidity ratio of 0.021 (kg H_2O/kg dry air). For an air flow rate of 450 lpm, drying capacity at 90°C with a refrigeration system at a humidity ratio of 0.005 (kg H_2O/kg dry air) produces a drying capacity of 1.5 times the drying capacity at 120°C drying air temperature C without a refrigeration system at a moisture ratio of 0.021 (kg H_2O/kg dry air) [20]. This shows that the system can reduce the temperature of the drying air without reducing productivity capacity. By regulating the temperature of air that passes through the evaporator at 10°C, the drying temperature at 140°C, and the air flow rate at 450 lpm, the productivity of drying with a cooling system is even 3 times greater than the yield of drying productivity with conventional methods [21].

In other studies, the energy analysis of a cooling system with multistage evaporative coolers using liquid desiccant dehumidifier between the stages [22]. The researched evaporative cooling system utilizes the air humidity for cooling in humid areas and requires no additional water supply. In this cooling system, energy to regenerate a weak drying fluid is the main energy needed. In this study, the heat input for regeneration is supplied from the conventional energy sources such as a simple line heater. For the results show that the energy consumption is about 25% less for the mechanical regeneration system with 3 % recovery than the thermal energy regeneration system to increase the desiccant solution temperature of 22°C. The COP of the proposed cooling system is defined as the cooling effect by the mass rate of water evaporated in the system divided by the amount of energy supplied to the system, that is the COP is independent of the energy source.

The condenser produces waste heat reaches 90°C and the heat is accumulated into a space heater up to 140°C. That means: the heater works only up to 50°C, so the temperature of the air is high and dry but has a very low RCES (Ratio of Specific Energy Consumption) in dew point 20°C, which is indicate that the system is very significant [23]. In a study conducted by E.A. Kosasih, combining spray dryers with a dehumidifier system based on a refrigeration system with an air heater to increase the humidity of the air by increasing the level of air condensation so as to reduce the water content will be reduced. The refrigeration system is composed of an evaporator that functions as a dehumidifier, a hermetic compressor works to increase the pressure, then turns on two condensers arranged in parallel as preheaters and economizers. By utilizing the heat coming out of the condenser which will be used to increase the temperature of the air before entering the air dryer and expansion valve. Condensers that function as economizers can prevent the exergy of the system so that it can increase system efficiency. The combination of this system is able to reduce the use of energy/specific energy released from the whole system 39%, combination with a spray dryer system with a cooler 39%, compared to a spray dryer system without a dehumidifier [20].

The drying productivity with the refrigeration system is even 3 times larger than the result of the drying productivity with conventional methode. These results indicate that the combination of

spray drying and refrigeration systems with low evaporator temperatures can have a significant positive impact [24]. In a study conducted by Bagaswara, the dehumidifier system based on a refrigeration system uses two condensers arranged in series and uses a hratic compressor that has a power of 0.5 PK, specific energy consumption at a flow rate of 450 lpm at a dew point of 100°C over a low dehumidifier energy consumption However, this refrigeration system has a low coefficient of performance (COP).

Today, conventional drying processes are often carried out when pre-harvesting, postharvest handling, and thermal processing. But it significantly affects the typical fresh fruit color, aroma, and overall taste due to high temperatures or prolonged exposure to heat and oxygen. Technologies such as freeze drying, where low temperatures are used, may preserve quality better than other techniques but are prohibitively expensive and time consuming [25]. Hence, there is a significant opportunity for developing economically viable technologies to produce high quality flavor ingredients.

2. Methodology

In this research, we measure the dry bulb temperatures and relative humidity in environmental air and the air coming out of the evaporator. In the air has a specific humidity value from the magnitude of the relative humidity value. This can be formulated into the equation as follows:

$$\dot{m}_a = \dot{m}_{da} + \dot{m}_v \quad (1)$$

Then the equation is divided by the mass flow rate of dry air :

$$\frac{\dot{m}_a}{\dot{m}_{da}} = 1 + \frac{\dot{m}_v}{\dot{m}_{da}} \quad (2)$$

ω is the ratio between the mass flow rate of vapor and the mass flow rate of dry air. Then,

$$\dot{m}_{da} = \frac{\dot{m}_a}{1+\omega} \quad (3)$$

To calculate the heat released on the evaporator, you can use the following equation:

$$(\dot{m}_{da}\ x\ h_{a1}) = Q_{evap} + (\dot{m}_w\ x\ h_w) + (\dot{m}_{da}\ x\ h_{a2}) \quad (4)$$

Where h_{a1} is the environmental enthalpy of air, h_{a2} the evaporator air enthalpy, $\dot{m}_w$ is the mass of evaporating water dan h_w is the evaporating enthalpy.

$$\dot{m}_w = \dot{m}_{v1} - \dot{m}_{v2} \quad (5)$$

$$\dot{m}_v = \dot{m}_{da}\ \omega_a \quad (6)$$

To calculate the refrigerant mass flow rate can use the following formula:

$$\eta_m\ x\ \eta_e\ x\ P = \dot{m}_r\ (h_3 - h_4) \quad (7)$$

Which:

$$P = V\ x\ I\ x\ cos\varphi \quad (8)$$

From the equation of the mass flow rate of the refrigerant to the heat released in the evaporator, it can be seen the enthalpy value of the refrigerant entering the evaporator through the equation below:

$$Q_{evap} = \dot{m}_r\ (h_2 - h_1) \quad (9)$$

To calculate the heat released in condenser 1, can use the following equation:

$$Q_{c1} = \dot{m}_{da}\ (h_{a3} - h_{a2}) \quad (10)$$

To calculate the amount of enthalpy coming out of condenser 1, can use the following equation:

$$Q_{c1} = \dot{m}_r\ (h_3 - h_4) \quad (11)$$

To calculate the heat released in condenser 2, can use the following equation:

$$Q_{c2} = \dot{m}_r\ (h_4 - h_5) \quad (12)$$

To calculate energy consumption using a dehumdifier, can use the following equation:

$$SEC = \frac{P_{comp} + P_{fan} + P_h + P_{blower}}{\dot{m}_{da}} \quad (13)$$

To calculate the power in a heater using the following equation:

$$P_h = \dot{m}_{da}\ x\ C_p\ x\ (T_{heater} - T_{ac1}) \quad (14)$$

To calculate the specific energy consumption without using a dehumidifier can use the following equation:

$$SEC = (h_{a4\,wet} - h_{a1}) \quad (15)$$

Then to calculate the ratio of specific energy consumption using the following equation:

$$R_{SEC} = \frac{SEC_{Dehumidifier}}{SEC_{Tanpa\ Dehumidifeir}} \quad (16)$$

To get the value of COP the refrigeration system uses the equation:

$$COP = \frac{Q_{Evaporator}}{P_{Compresor}} \quad (17)$$

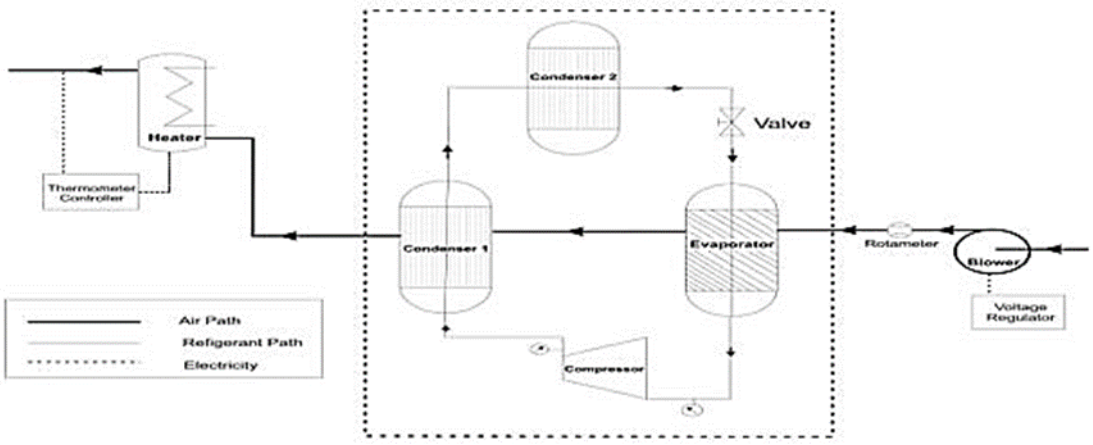


Fig. 1. Illustration of experiment

In this experiment, the tools to be assembled so that it can be done data retrieval. The data was collected at Heat Transfer Laboratory, 6th floor MRC Building, Faculty of Engineering, University of Indonesia. Here is a picture captured image shown in Fig. 1.

The air from the environment is first sucked by the blower then enters the evaporator. In the hot air evaporator undergoes a dehumidification process caused by condensation of water vapor contained in the air, then the air enters condenser 1, where the hot air in the condenser is used as a preheater before entering the heater. then the dry air heater from condenser 1 is given additional heat so that the desired dry air outlet temperature is obtained. Then the air is flowed into the drying chamber.

3. Results

In this experiment, we get the measurement graphs of evaporator outlet air temperature which can be seen in the picture below:

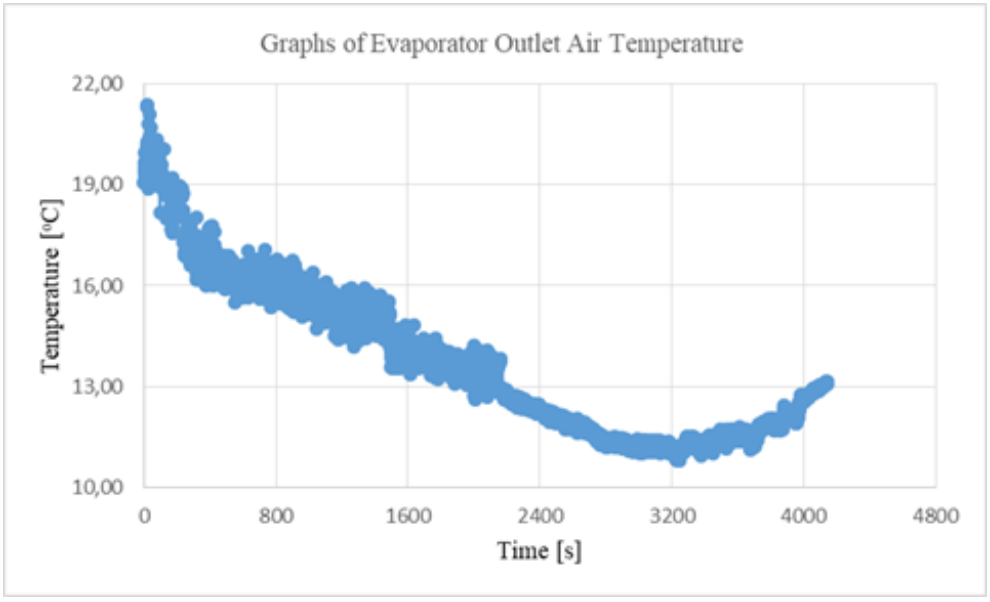
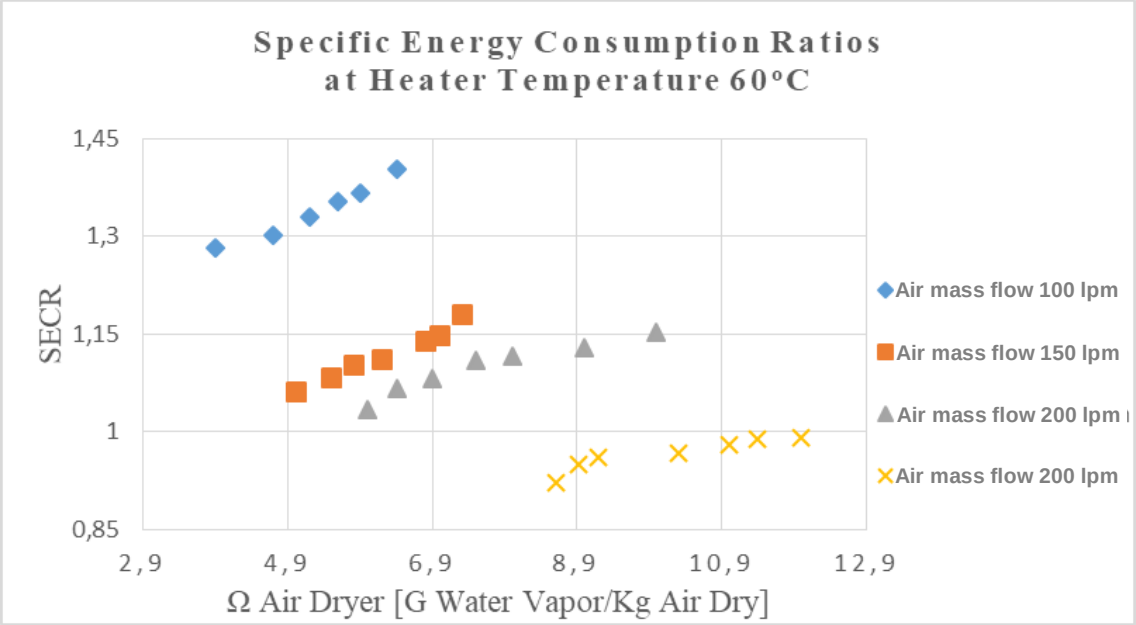


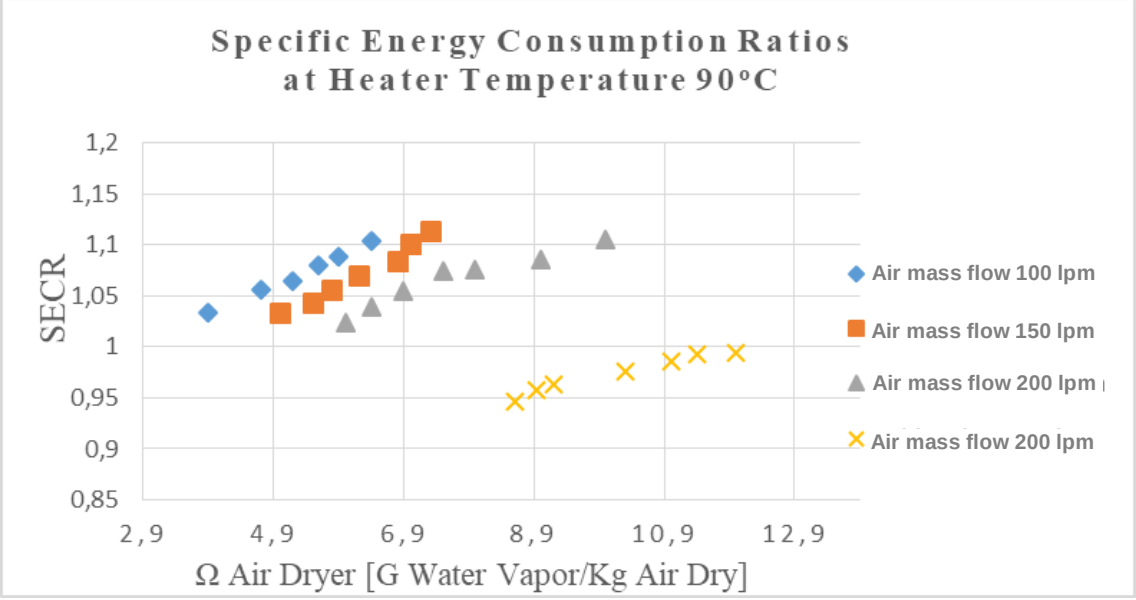
Fig. 2. Graphs of Evaporator outlet air temperature

Air temperature is still in a transient condition where the air temperature conditions will continue to rise and fall until it reaches a steady state. The variation of the refrigerant pressure entering the evaporator is done by turning the expansion valve, the lower the refrigerant pressure, the lower the refrigerant temperature. The minimum air temperature conditions can be achieved before the air temperature rises even though the refrigerant inlet pressure to the evaporator is getting lower. Most likely, in a tube sleeve (tube) formed a layer of ice. The layer is water vapor contained in the air and freezes on the wall of the tube sleeve because the temperature of the tube wall sleeve is less than zero. So that the layer makes the heat energy contained in the air cannot be given to the refrigerant.

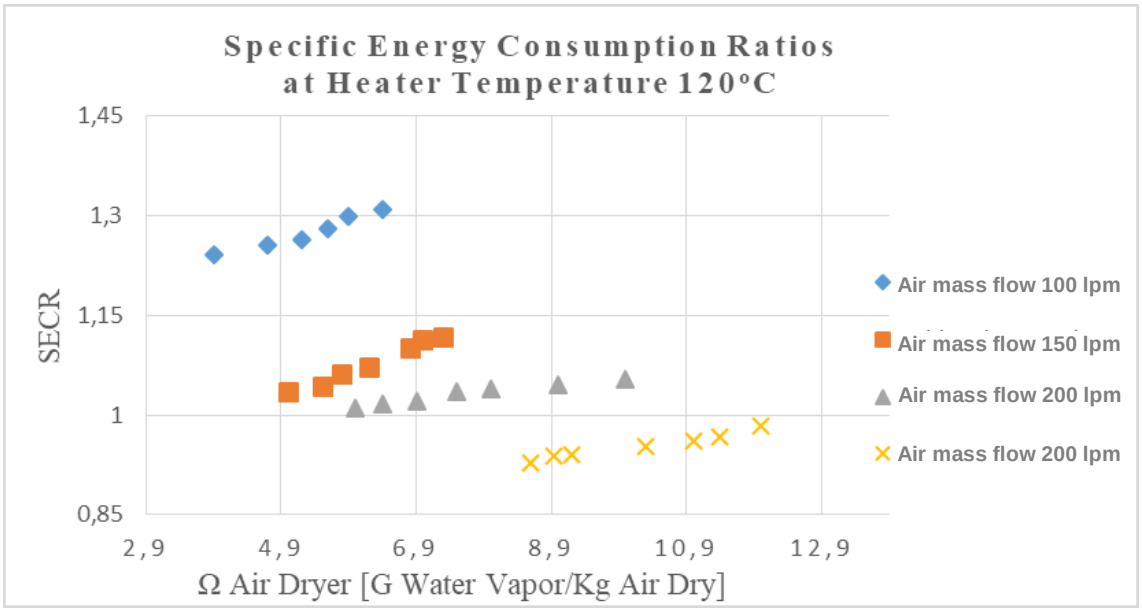
For the relationship of the specific energy consumption ratio (SECR) in the spray dryer system with a heater temperature of 60°C, 90°C, 120°C, and 150°C can be seen in the following figure.



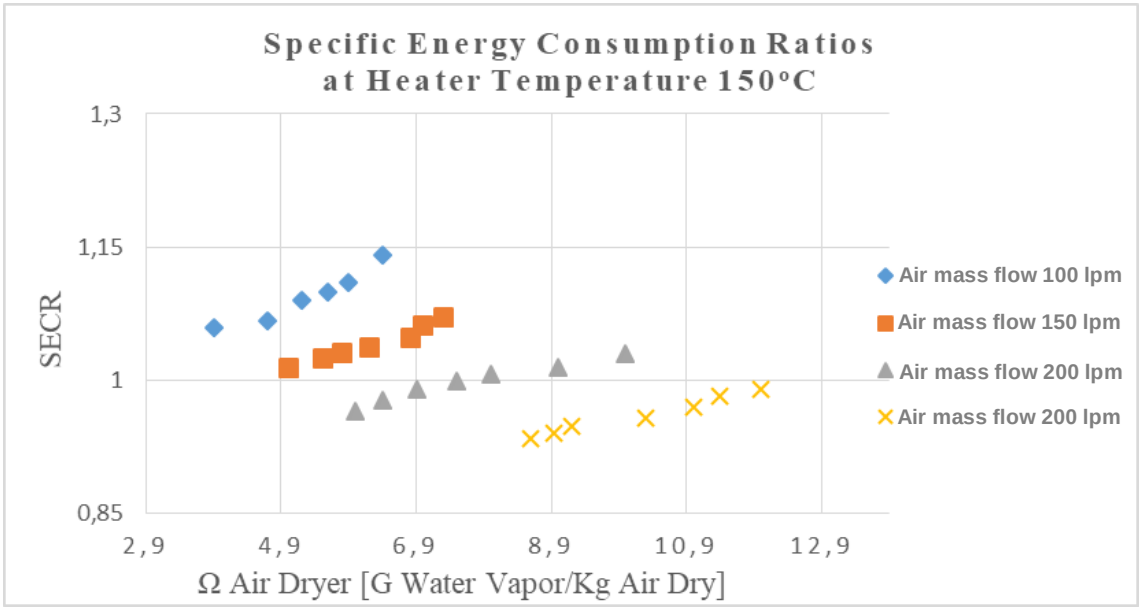
(a)



(b)



(c)



(d)

Fig. 3. Graph SECR at Heater Temperature (a) 60°C (b) 90°C (c) 120°C, and (d)150°C

Specific Energy Consumption Ratios (SECR) is a comparison between the specific energy consumption of a spray dryer system using a dehumidifier and without a dehumidifier. So in the calculation presented in the graph has two possibilities, namely SECR less than one or more than one. When SECR is less than one means using a dehumidifier system, where the specific energy consumption is more efficient than without using a dehumidifier.

Based on the picture above, namely in Figure 3.2, Figure 3.3, Figure 3.4 and Figure 3.5 it can be concluded that the relationship of the specific energy consumption ratio at each heater temperature is affected by the given air discharge. Where when the air discharge is 250 lpm, the value of the specific energy consumption ratio is the lowest compared to other air discharges. So by using a dehumidifier system, when the air discharge is 250 lpm, a SEC is more efficient than using a dehumidifier system.

And in certain conditions when the air discharge used is 200 lpm and 250 lpm at a heater temperature of 150^{o}C the value of the specific energy consumption ratio is lower than other air discharges. This means that energy consumption using a dehumidifier system is still more efficient than not using a dehumidifier system.

Briefly, the graph can be concluded; at the same air discharge, the lower the humidity ratio value, the SEC value will be lower. This is because the lower the value of the humidity ratio, the moisture content contained in the air is less, so that when the air is heated using a heater, the heater power consumption will be lower than without using a dehumidifier system. On the other hand, at the same humidity ratio value, the greater the air discharge, the SEC ratio value will decrease. This is because the greater the air discharge, the more air that can condense on the evaporator, so that the condensed air will contribute more latent heat to the air which will be heated by the heater. This condition causes the heater power consumption to heat the air to be lower.

4. Conclusions

Based on the results of these experiments, it can be concluded that the coefficient of performance (COP) value of the refrigeration system is influenced by air discharge and refrigerant inlet pressure into the evaporator. The value of the COP maximum is obtained at an air flow mass rate of 250 lpm which is 1.14 and a minimum value of 0.54 at an air mass flow rate of 100 lpm. The SEC (specific energy coefficient) ratio of the system using a dehumidifier at 250 lpm air flow has a value of less than one. So that the system in terms of SEC is more efficient and profitable compared to without using a dehumidifier system. The use of a dehumidifier system is not always beneficial as seen in the air discharge of 100 lpm, 150 lpm, and 200 lpm SEC ratio is more than one so that the use of a dehumidifier system is inefficient. Increasing the evaporator's ability to absorb heat from the environment can increase the COP value of the refrigeration system, so this will reduce the humidity of the air taken from the environment for use as a spray dryer.

Acknowledgement

This research was sponsored by PITTA A funding (NKB-0461/UN2.R3.1/HKP.05.00/2019) from the Directorate of Research and Community Service (DRPM) University of Indonesia. In addition, the authors are also grateful for University of Indonesia for facilities and management support.

References

[1] Sousa, A. S. D., Soraia Vilela Borges, S. V., Magalhães, N. F., Ricardo. H. V., Aline Damico Azevedo, A. D. (2008). “Spray-Dried Tomato Powder: Reconstitution Properties and Colour”. Brazilian Archives of Biology and Technology, Vol. 51 (4), pp 807-814.

[2] Yashwant Kumar, Soumitra Tiwari and Seema A. Belorkar. (2015). “Drying: An Excellent Method for Food Preservation”. International Journal of Engineering Studies and Technical Approach, Volume 01, No.8, August, ISSN No. 2395-0900.

[3] Sun L, Islam MR, Ho JC, Mujumdar AS. (2005). “ A Diffusion Model for Drying of A Heat Sensitive Solid Under Multiple Heat Input Modes. Bioresource Technology 2005; 96:1551–60.

[4] Liu, Fengxia, Xiamin Cao, Houyin Wang, and Xiaojun Liao. (2010). "Changes of Tomato Powder Qualities During Storage". Powder Technology 204, no. 1 (2010): 159-166.

[5] Langrish, T. A. G., & Fletcher, D. F. (2001). Spray drying of food ingredients and applications of CFD in spray drying. Chemical Engineering & Processing: Process Intensification, 40(4), 345-354.

[6] Kosasih,EA., Rafdi, Muhammad, and Firdaus. (2018). "Experimental investigation of vitamin c yield of tomatoes and vitamin C essence by spray drying and dehumidifying the dring air: Product quality and energy consumption". AIP Conference Proceedings. 2001, 040008, doi: 10.1063/1.5049990.

[7] Fletcher, D. F., Guo, B., Harvie, D. J. E., Langrish, T. A. G., Nijdam, J. J., & Williams, J. (2006). What is important in the simulation of spray dryer performance and how do current CFD models perform? Applied Mathematical Modelling, 30(11), 1281-1292.

[8] Solval, K. M., Sundararajan, S., Alfaro, L., & Sathivel, S. (2012). Development of cantaloupe (cucumis melo) juice powders using spray drying technology. LWT - Food Science and Technology, 46(1), 287-293.

[9] Rattes, A.L.R. and W.P. Oliveira. (2007). "Spray Drying Conditions and Encapsulating Composition Effects on Formation and Properties of Sodium Diclofenac Microparticles". Powder Technology. 171(1): p. 7-14.

[10] Fang, Zhongxiang, and Bhesh Bhandari. (2012). "Encapsulation Techniques For Food Ingredient Systems". Food Materials Science and Engineering (2012): 320-348.

[11] Goula, Athanasia M., & Adamopoulos, Konstantinos G. (2010). "A New Technique for Spray Drying Orange Juice Concentrate". Innovative Food Science and Emerging Technologies, Vol. 11, pp 342–351.

[12] C. Bai, Z. Han, H. Wei, X. Ju, X. Meng, and Q. Fu, "Simulation Study on Performance of a Dual-Source Hybrid Heat Pump Unit with Alternative Refrigerants," Energy and Built Environment, 2019, doi: 10.1016/j.enbenv.2019.08.004.

[13] Drosou, C. G., Krokida, M. K., & Biliaderis, C. G. (2017). Encapsulation of bioactive compounds through electrospinning/electrospraying and spray drying: A comparative assessment of food-related applications. Drying Technology, 35(2), 139-162. doi:10.1080/07373937.2016.1162797.

[14] Li Jin Goh, Mohd Yusof Othman, Sohif Mat, Hafidz Ruslan and Kamaruzzaman Sopian. (2012). " Review of Heat Pump Systems for Drying Application". Renewable and Sustainable Energy Reviews, 2011, vol. 15, issue 9, 4788-479.

[15] Jeyaprakash, S., Frank, D. C., & Driscoll, R. H. (2016). Influence of heat pump drying on tomato flavor. Drying Technology, 34(14), 1709-1718. doi:10.1080/07373937.2016.1174937.

[16] X. Zheng, R. Z. Wang, and Y. D. Tu, "Investigation on energy consumption of desiccant coated heat exchanger based heat pump: Limitation of adsorption heat of desiccant," Energy Conversion and Management, vol. 188, pp. 473-479, 2019, doi: 10.1016/j.enconman.2019.03.077.

[17] Claussen IC, Ustad TS, Strommen I, Walde PM. (2007). " Atmospheric Freeze Drying Review". Drying Technology 2007;25:957–67.

[18] Sarkar J, Bhattacharyya S, Gopal R. (2006). "Transcritical M. CO_2 Heat Pump Dryer: Part 1 Mathematical Model and Simulation". Drying Technology 2006; 24:1583–91.

[19] Kosasih, E.A. and N. Ruhyat. (2017). "Combination of Electric Air Heater and Refrigeration System to Reduce Energy Consumption: A Simulation of Thermodynamic System". A simulation of thermodynamic system. International Journal of Technology, 7(2), 288-295.

[20] Kosasih, EA., Warjito, Imansyah I. H., and N. Ruhyat. (2017). "Use of A Double Condenser in A Dehumidifier with A Spray Dryer for Vitamin A Extraction in Tomato as A Heat-Sensitive Material". AIP Conference Proceedings. 1855, 020008, doi: 10.1063/1.4985453.

[21] Nanang Ruhyat and Engkos Achmad Kosasih. (2019). "Low Energy-Specific Consumption of Refrigerants for Combination of Electric Air Heater and Refrigeration System Using Double Condensers: A Simulation of Thermodynamic System". AIP Conference Proceedings 2062, 020063.

[22] Al-Sulaiman, Faleh A., and Gandhidasan, P. "Energy Analysis of Liquid Desiccant Based Evaporative Cooling System." Proceedings of the ASME 2005 International Mechanical Engineering Congress and Exposition. Advanced Energy Systems. Orlando, Florida, USA. November 5–11, 2005. pp. 3-12. ASME.

[23] Kosasih, E. A., Harinaldi, & Trisno, R. (2016). Characteristics of vortex ring formation by synthetic jet actuators in different cavities. International Journal of Technology, 7(2), 296-305.

[24] Nanang Ruhyat, Engkos Achmad Kosasih, Warjito, Imansyah I. H. (2019). "Low Combination System of Spray Dryer and Low Evaporator Temperature Refrigeration for Drying Vitamine B1". Journal of Advanced Research in Fluid Mechanics and Thermal Sciences, 55(1), 102-110.

[25] Abano, E.E.; Ma, H.; Qu, W. Influence of air temperature on the drying kinetics and quality of tomato slices. Journal of Food Processing and Technology 2011, 2(5), 2–9.

Penerbit Akademia Baru

Engineering Science and Technology Conference Proceedings

Journal homepage: www.akademiabaru.com/EST.html

Enhancement of Syngas Production Via Co-Gasification Experimental of Renewable Densified Fuels (RDF) in A Open-Top Downdraft Fixed Bed Gasifier

Open Access

Apri Wiyono[1], Dedi Rohendi[1], Yusep Sukrawan[1], Ega Taqwali Berman[1], Indra Mamad Gandidi[1], Nugroho Agung Pambudi[2]

[1] Department of Mechanical Engineering Education, Faculty of Technology and Vocational Education, Universitas Pendidikan Indonesia
[2] Departement of Mechanical Engineering Education, Teacher Training and Education Faculty, Sebelas Maret University

ABSTRACT

The increase in world population is always followed by the rate of waste generation and energy needs in various sectors. Where the largest contribution comes from organic waste, it can be utilized as a mixed raw material, biomass to help save on the conversion of fuel from waste energy.The main objective of this paper is to study the enhancement of syngas production from co-gasification with renewable densifief fuels (RDF), especially gasification temperature, lower heating value and gas emission, on the performance of the biomass belnding co-gasification process in a open-top downdraft fixed bed gasifier. In this study, organic waste used woods, coconut fibers and rice husks in the pelletization as blending compositions of raw materials on co-gasification process. Methods were carried out by co-gasification techniques between WCF (wood- coconut fiber) pellets and RH (rice husk) pellets on 100% WCF pellets composition, 75:25, 50:50, 25:75 and 100% RH pellets. Where syngas testing is done direct measurement on burner with TCD type Shimadzu 8A gas chromatography. The highest reactor temperature in the pyrolysis zone is 700 C - 900 C which significantly stability at 800 C and the temperature in the oxidation zone is 1000 C - 1100 C. The result of the syntetic gas testing obtained the highest lower heating value in 100% WCF pellet composition at 3.582 kJ/Nm^3. Lower heating value of the blending of RDF composition (75:25) of 3.392 kJ/Nm^3, where the increase of pellet fuels will increase the LHV syngas value. This results in visually low tar content and low ash particles in all compositions of approximately 30-35% of the initial mass of each composition, with the lowest ash in 100% WCF pellets composition at 0.25 g.

Keywords:
Syngas production; co- gasification; renewable densified fuels; open-top downdraft gasifier

Copyright © 2019 PENERBIT AKADEMIA BARU - All rights reserved

1. Introduction

Almost 80% of the world's energy consumption comes from fossil fuels which disrupt the environment and health are associated with increased emissions of CO2, NOx and SO2. Alternative energy is needed to overcome the scarcity of energy resources is increasing. Biomass is organic waste is a renewable energy source applied to the production of clean energy to zero greenhouse, carbon dioxide (CO2) emissions and NOx levels are relatively low [1]. Biomass supply approximately 11-12% of primary energy consumption of the world. In developing countries, biomass is the most primary energy by the amount of approximately 38% of total primary energy consumption in rural areas and approximately 90% of the total energy supply. With an estimated 90% of world population are in the developing regions in 2050, the biomass energy will remain a source of substantial energy reserves [2, 3, 4]. After fossil fuels, biomass is the fourth largest energy source in the world.

Energy diversification through the use of renewable energy sources in accordance with Indonesian of Presidential Regulation No.5 of 2006, is very possible to answer the discussion of electricity in the displaced areas and islands, both with microhidro power plant and PV power plant. But in its realization, this program relies heavily on local resources that are available at the location. However, the continuity of operations is not

guaranteed because it depends on the availability of large water discharge and not all remote villages have water sources for microhidro power plant [5]. Similarly to PV power plant, this alternative technology is very well known to answer the procurement of electricity without the problems of local resources around the site. However, procurement of these technologies, consuming a huge budget for the small energy generation capacity [6].

Waste in Indonesia is one of the biggest environmental problems because as the population increases, the correlation with the more waste generated. In 2015 Indonesia produces 175.000 tonnes of waste/day or 64 million tons/year equivalent [7]. Indonesia produced landfill waste by 64 million tons/day garbage will cause problems such as environmental pollution and health problems, if not done properly waste management. It would be excellent if it can be recovered by processing the fuel conversion of waste energy. In the scope of the smaller volume of waste Depok residents reached 1200 tons/day The largest percentage of waste derived from organic waste components with a percentage up to 32%. Therefore, the organic waste can be used as a raw material mixture of biomass for efforts to increase the calorific value of the fuel conversion.

They utilize one or more of the three main thermochemical conversion processes of combustion, pyrolysis and gasification [9]. Gasification has several potential benefits over traditional combustion of solid wastes, mainly related to the possibility of combining the operating conditions (in particular, temperature and equivalent ratio) and the features of the specific reactor (fixed bed, fluidized bed, entrained bed, vertical shaft, moving grate furnace, rotary kiln, plasma reactor) to obtain a syngas suited for use in different applications [10, 11, 12]. The gasification process (exotermic) releasing energy to be gas products such as carbon monoxide, hygrogen and carbondioxide (CO2) as well as moisture in which turn is reduced to carbon monoxide, methane and hydrogen with hot bed charcoal raised during the gasification process [13]. Fuel Gas Product CO, H2, CH4 will be used as fuel motor drive generator to generate energy [13, 14].

In India nowadays, rural electrification programs, with small-scale gasification technology, are growing in extension with aim to increase the energy services in the country. The most used reactor technology here is the open-top model because of the easy access to the reactor core and to manually feed the reactor [15]. Therefore this investigation choose downdraft fixed bed as the gasifier. Other studies of downdraft gasifier show that the feeding rate regulation affects the performance of the reactor and the quality of the gas produced. That the higher the feeding rate, the calorific value of producer gas and tar content will decrease [16, 28].

In addition, it is important to study the impact of fuel particle size and composition on the gasification process in one and the same gasifier in order to draw conclusions regarding performance differences in between different fuels. Various studies show that pressure plays an important role in increasing the density of solid fuels like briquetting, pelletizatition, solid torrefaction and other [17, 29]. The densification process gives a briquette / pellet density value greater than 1 gr/cm3 [18]. By pelletizing wood and EFB residues, it is possible to introduce them in fixed-bed gasification [19]. Transforming these biomass resources in pellets would bring along several advantages, both for the industry and for the people living in villages nearby the mills [20]. Kjellström et al. [21] defined that one problem with downdraft gasification is the fuel inflexibility, another the need of active staff during operation of the gasifier. Introducing pellets as fuel would enable a variety of fuels to be used in one and the same gasifier, less need of service during operation is needed since a commercial automatic pellet feeder is not costly to introduce about 300 Euro [22, 30]. Since pellets have very high density, the common problem of bridging in the bed will be reduced, and thus manual dispersion of bed during operation will not be needed [31, 32]. By simplifying the feeding and remove maintenance need during operation, there is no reason to work with open parts in the gasifier system, thus the health risks for the operators would significantly become reduced. State of [23], the co-gasification of wood and straw pellet can be additionally controlled by varying the air supply rate into the gasifier, while the additional heat energy supply being constant. Under these conditions the increase of CO and H2 production with the limited production of ash and tars can be obtained. Other research of co-gasification conducted [24] comparison of pellets fuels of wood and coconut fibers shows the most optimal LHV value and composition of CO and H2 gas greatest was 4.07 MJ / Nm. The effect of more WCF pellets increase, the larger the LHV value and the resulting combustible gas levels will be.

In this work, will be displayed in how to optimize the result of high producer gas and environmentally friendly with CO2 levels and low tar the stage of co-gasification process. By applying renewable densified fuels (RDF) in the open-top fixed bed downdraft gasifier lab scale, carried out the data comparison gasification of raw materials and co-gasification of rice husk (RH) pellets and wood coconut-fiber (WCF) pellets, then varying the co-gasification of various compositions WCF and rice husk pellets.

2. Materials and Methods

2.1 Renewable Densified Fuels Characterization



Fig. 1. Bulk of material (a) Woods (b) Coconut fibers (c) Rice husks

Biomass used in this study is wood, coconut fiber, rice husk. Rice husk is the largest agricultural waste with the potential of 13,662 MWe per year [25]. Based on previous research, the best comparison retrieved wood and coconut fibers is 75:25 to yield the highest blending of composition which the calorific value is 4142.96 cal/g [24]. However, there needs to be a mixture of rice hulls to increase the calorific value in the gasification process. Mix some experiments done on wood and coconut fibers (WCF pellets) with rice husk which aims to determine the optimum composition in generating energy burning tar best with the lowest. All three samples obtained from the environment around Depok, Indonesia. Before the test, three samples dried in an oven (Memmert UL 30) at a temperature of 80 C. The proximate analysis of ASTM method D5142 using the automatic proximate analyzer (TGA 701 LECO). The ultimate analysis ASTM method D5373 using a CHN Analyzer (LECO CHN 628). Analysis of syngas using Shimadzu GC TCD 8A. Table 1 shows the characteristics of the pellets and raw materials used in this research.

Table 1
Properties of WCF Pellet

	WCF pellet	RH pellets	Wood	Coconut Fiber	Rice Husk
Bomb Calorimeter					
Caloric value (cal/g)	4142.96	3986.17	3860.23	3693.78	3300
Ultimate Analysis					
Nitrogen, %	0.74	0.73	0.87	0.42	0.29
Carbon, %	40.91	41.03	42.43	40.96	35.03
Hydrogen, %	6.06	6.06	5.49	5.23	5.46
Sulfur, %	0.12	0.12	0.11	0.11	0.21
Proximate Analysis					
Moisture	11.53	11.57	9.36	8.45	7.82
Volatile	65.9	65.28	63.46	59.60	65.55
Fixed Carbon	13.92	14.55	16.43	17.37	13.91
Ash	8.64	8.61	10.76	14.58	25.61

2.2 Multiple Pellet Press

Part of the problem of agricultural waste can be solved with the densification process which is a method for treating loose material, turning it into a briquette / solid fuel [26]. In this way, the characteristics of material handling such as transportation, storage, etc. also increase [27]. One of the method to densified of fuels is pelletization, it was performed with a pellet printer and durability test conducted on the product pellets produced from the molding tool to determine the strength and toughness of the characteristics of the pellet fuels. The type of dies used consists of many round holes which aim to obtain a fuel pellet that is denser, not easily destroyed and has a high density.

2.3 *Experimental Prodecure*

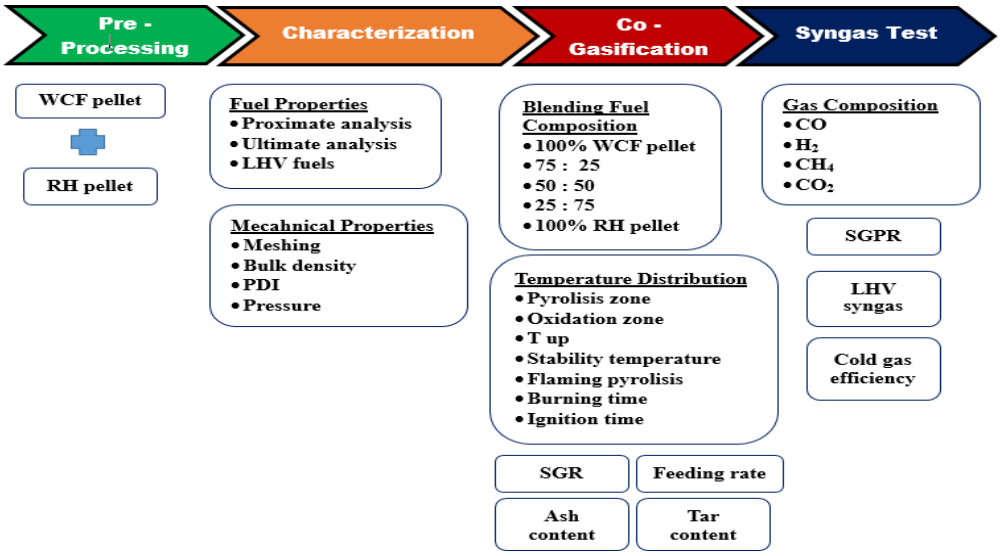


Fig. 3. Schematic of research

For each composition of feedstock sort a primary char bed was first created in the gasifier in order to enable quick start in the subsequent gasification runs. All fuels have been mixed with one another and each run was done solely with char of the same, except composition of 100% WCF pelets and 100% RH pellets. When changing the fuel, the gasifier was scraped inside and filter materials were changed. Before each run, both the char bed and fresh compositions of feedstocks were weighed carefully before added in the gasifier. The char bed reached up to the constriction, while feedstocks were added from air-inlets to the top of the gasifier. All experiments started with a cold fuel bed, no external heating has been used. For security reasons, the system was checked for being air-tight before each run. After this check and possible adjustments in system, the gasifier could be started. Different aspects of gasification will be investigate of this research experimental, such as : investigation of co-gasification characteristics of variations in WCF pellets and RH pellets to get optimum composition (pre-gasification); impact variation composition of WCF pellets and RH pellets to temperature distribution of reactor and ash particle (gasification processes); impact variation composition of WCF pellets and RH pellets to gas compotition and lower heating value producer gas results (post-gasification) and the effect and efficiency of all variation blending composition.

2.4 *Experimental Apparatus*



Fig. 4. Schematic of co-gasification experimental apparatus

In this test set some conditions to facilitate the data collection and testing. The samples used are WCF pellets (Wood-Coconut fiber) and rice husk (RH) pellets. Fuel is inserted into the reactor is 4 kg in one running. The density of the air 1.2 kg / m3. Trial [31] showed that the selection of the ER value (air supply) must match the needs. If the goal is to lower the tar production of selected ER value of 0:32 to 0:52 tar content g / Nm3. Whereas, if desired is cold gas efficiency and the highest LHV, the ER is selected is located on the value of 0:25 to 0:27. Thus, ER variation used in the study was 0:25, 0:29 and 0:32. Fuel flowrate adjusted to the volume of the gasifier with a height of 18 cm from the grate. Which were obtained by the pellet mass of 4 kg and 0.8 kg of rice husk transform and reaches a height of the volume. Based downdraft gasification capacity of the medium (± 1 meter altitude reactor) and the type of fuel used. The process used is the technique of co-gasification. Co- gasification technique chosen because it can increase the calorific value of the gas producer and lower levels of CO2 and tar by combining two materials calorific value or more. This study used a different composition of renewable densified fuels (RDF) to obtain the best composition. The ratio used is 100% compositions of WCF and RH pellets s a control, then another composition pellets WC: rice husk 75:25, 50:50 and 25:75.

3. Results and discussion

3.1 Impact of Blending Fuel Composition

Changing the contents and types of coal and/or biomass in co-gasification has a significant effect on different output parameters such as gas production, carbon conversion, gas yield, cold gas efficiency, tar yield, caloric value and release of H2S and NH3. In the co-gasification research conducted between renewable densified fuels (RDF) on the variation of raw material compositions, their some type of blending fuel compositions are 100% pellets, WCF pellets : RH pellets (75:25), (50:50) and (25:75) which shows that the increase of the volume ratio of the pellets resulting in encroachment on the calorific value of syngas (lower heating value). And increase the value of the gas composition of CO and H2.

Table 2

Average composition of WCF pellet : RH pellet and lower heating value of product gas (this research)

Blending composition	Gas Composition (%)					Energy Content
	N_2	H_2	CO	CH_4	CO_2	LHV (MJ/kg)
100% WCF pellet	11.65	13.15	1.85	8.21	11.65	3.58
(75:25)	10.25	12.65	1.92	10.5	10.25	3.39
(50:50)	9.25	12.11	2.01	10.9	9.25	3.25
(25:75)	8.24	11.02	2.22	12.1	8.24	3.08
100% RH pellet	7.37	9.11	2.41	12.4	7.37	2.81

3.2 Blending Fuel Composition Effect on Temperature Profile of RDF Co-Gasification

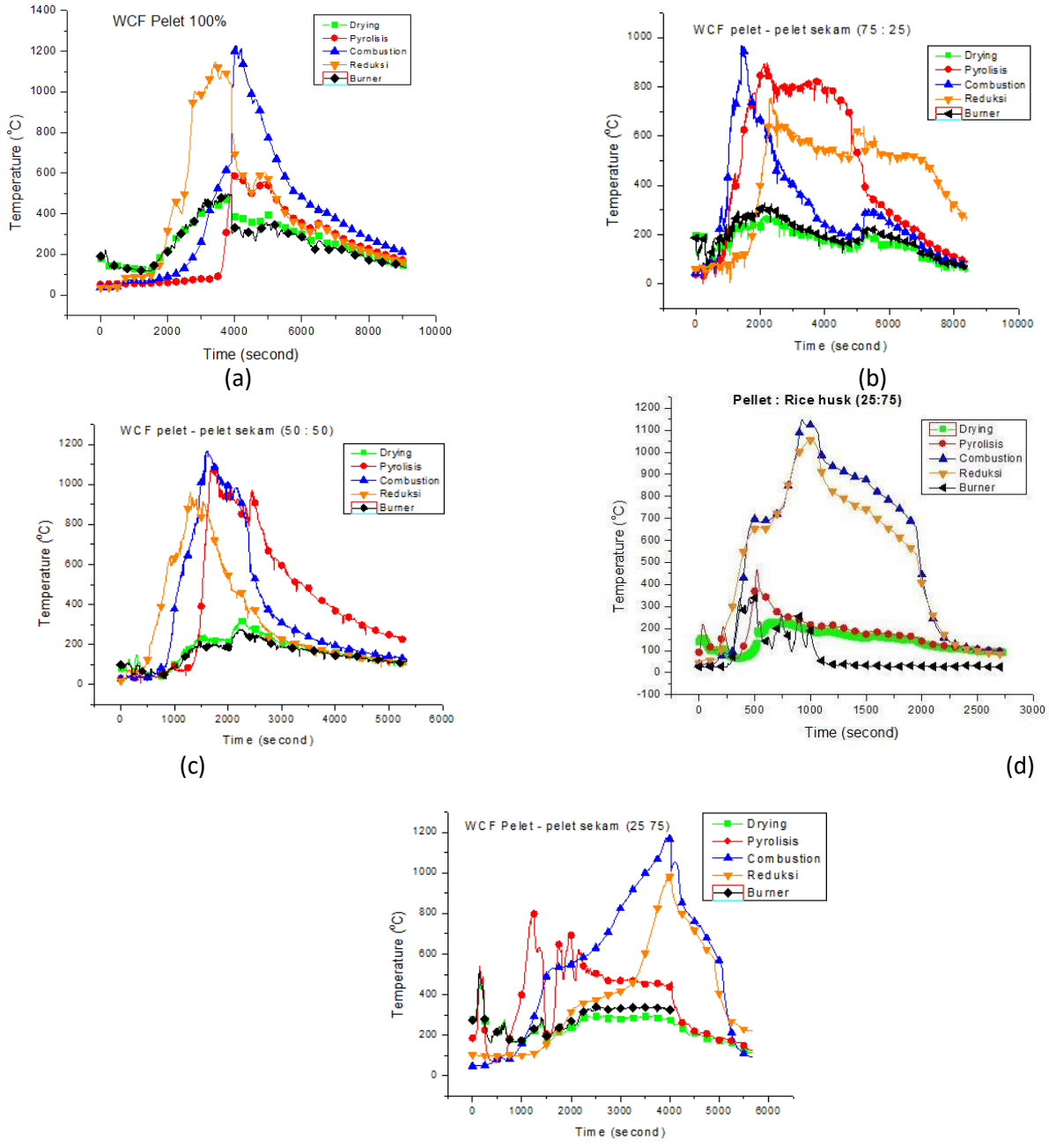


Fig. 5. Temperature distribution on the gasifier and burner (a) Composition WCF pellet 100% (b) WCF : RH 75:25 (c) WCF : RH 50:50 (d) WCF : RH 25:75 (e) RH pellet 100%

Temperature drying and pyrolisis at 100% pellet composition and composition of 75:25 obtained from the low temperature is gradually increased, due to both the composition is dominated by raw materials pellets that its density is greater than the chaff. Thus, the composition of which is dominated by the husk has a tendency to be on the drying and pyrolisis zone will cause the temperature in this zone is both higher and more stable. However, it looks a 75:25 composition shows a temperature drying and pyrolisis which starts higher than 200 C indicates the initial DEX ignition from burning more reactive mixture composition of WCF and RH pellets are 75:25. On the graph shows that the temperature pyrolisis zone on the third chart happens to 500-900 C. The highest temperature is obtained on the composition of 50:50, this indicates that the combination of this composition provides advantages in the process of burning a mixture of rice husk raw materials have characteristics suitable for ignition and pellets provide stable combustion and stable flame. In the graph shown composition 50:50 has a stable temperature at 500-900 C indicates the occurrence of flaming pyrolisis. By [26] at a temperature of 500-800 C in the area will result in the phenomenon falming pyrolysis pyrolisis are events where most of the products pyrolisis got a little supply of oxygen from the oxidation zone to produce a flame burning fuel-rich (fuel-rich flame).

The figure 5 shows the composition of 75:25 composition has a temperature of oxidation and reduction of the most high and stable at a temperature of 1187 C. Meanwhile, the composition of the pellets 100% obtained lower temperatures closer to the temperature 75:25 In the graph of oxidation (red) shows that the temperature rise on the third composition to the range 1112 - 1180^{o}C. Wherein the composition of 75:25 and 50:50 on the second rise in temperature climax to 900 ^{o}C and the second the temperature reached 1800 ^{o}C and then dropped with increasing operating time. This indicates that oxidation of pyrolysis products produces a high energy up one time and then the energy is transferred to the reduction zone for the purposes of an endothermic reaction so that its oxidation temperature down. Meanwhile, the rise in temperature on the composition of 100% pellets tend to be stable at temperatures of 800-118 ^{o}C.

3.3 Flaming pyrolisis effects on blending fuels of renewable densified fuels (RDF)

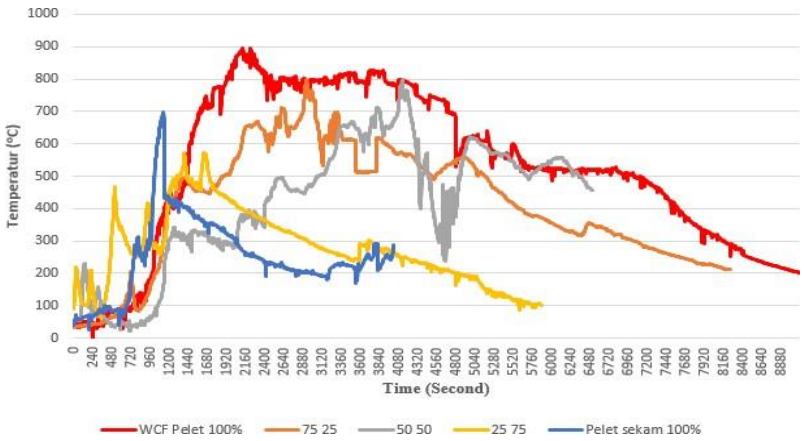


Fig. 5. Flaming pyrolisis of WCF pellets and RH pellets

Figure 5 describes the temperature distribution of the pyrolysis zone with respect to time on the blending fuel of the WCF pellet: husk with a variation of the composition of the full WCF pellet and 100% husk as a control variable and the variation of the WCF pellet blending: husk (75 25, 50 50 and 25 75). In the figure it can be seen that the pyrolysis temperature of the five variations in composition is high at 500-800 ^{0}C. This indicates that CO and H2 production is also quite high. Which is also directly proportional to the value of the LHV calculation. Besides that, another factor that also affects producer gas output is tar content. This can be seen from the pyrolysis temperature of the composition of the 100% pellet WCF (red color), the graph of the WCF pyrolysis zone temperature graph

shows the reach of 1100^{0}C and stable at 600^{0}C.

Energy (heating value) of producer gas

In the test carried out, the energy from combustion of producer gas is quite high based on the LHV calculation results obtained the best composition in pellet WCF 100% reaches 3582.23KJ / Nm3 at 1814 seconds duration and the blending composition in pellet WCF: husk pellets (75: 25) reaches 3392.95KJ / Nm3. The combustion energy of the producer gas is influenced by the composition of the gases that form it. In gasification generally producer gas consists of CO, H2, CH4, and CO2 which is often called combustible gas. CO and H2 gas are gases that contribute the greatest energy to producer gas while CO2 is a gas that does not burn. In short, the higher the CO and H2 then the higher the energy of producer gas and vice versa the higher the CO2 of producer gas energy will be lower. This is evidenced by [33] that an increase in the amount of air in the blower causes a significant increase in the LHV value, where the gas composition results show that the composition of CO and H2 compositions is inversely proportional to the CO2 production trend. In other words, when CO and H2 production are up, CO2 production decreases. Likewise with the CH4 gas composition levels have been proven by [34] that with an indication of low CH4 content, it can be concluded that the process of decomposition (decomposition) of biomass in the pyrolysis zone is going well. With good pyrolysis, light components such as (CO, H2, CH4, and CO2) will be more easily decomposed in the oxidation zone so that the gas composition reduced.

Tar content

To predict the tar content can be seen from the temperature of the reactor pyrolysis zone. From the graph it can be seen that the pyrolysis temperature produced is in the range of 500-800oC in quite a long time. This indicates that the pyrolysis zone temperature is quite stable at this value. Based on [13] at a temperature of 500-800 oC in the pyrolysis region will produce the phenomenon of flaming pyrolysis. Where flaming pyrolysis is an event where a portion of pyrolysis product gets a little supply of oxygen from the oxidation zone so that it burns to produce a fuel rich flame. In this phenomenon, tar produced from combustion of raw material composition will experience tar cracking in accordance with [13,33] so that the amount will decrease. In other words, the longer the duration of the temperature withstands (its stability) in the range of the range, the more tar will be split. The low tar content in producer gas makes syngas combustion in the burner better. This can be seen from the burner temperature curve in each of the compositions above (black) will have a fairly high and stable temperature.

3.4 Oxidation process effects on blending fuels of renewable densified fuels (RDF)

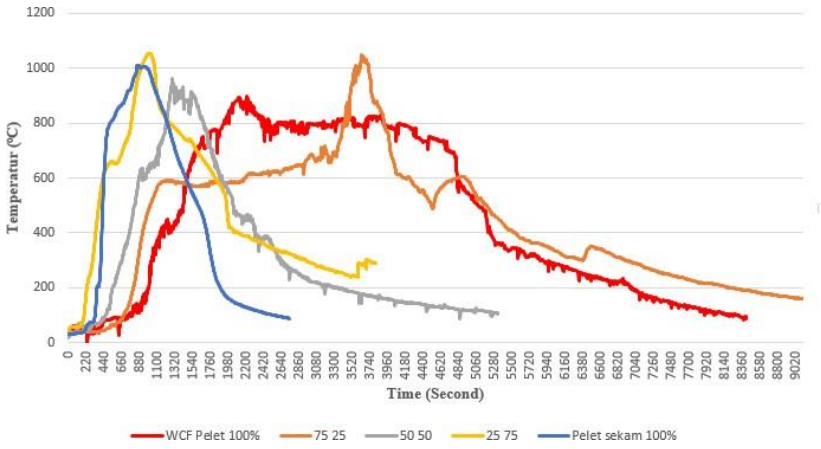


Fig. 6. Oxidation process of WCF pellets and RH pellets

Figure 6 shows the temperature distribution of oxidation zones with respect to the time of blending fuel WCF pellets: husks with a variation of the composition of full WCF pellets and 100% husks as control variables and the variation of WCF pellets : RH pellets (75 25, 50 50 and 25 75). In the figure it can be seen that the oxidation temperature of the five variations in composition is quite high at 650-850 0C. This indicates that CO and H2 production is also quite high. Which is also directly proportional to the energy output of the LHV calculation value. Besides that, another factor that also affects producer gas output is tar content. This can be seen from the oxidation temperature of the composition of 100% pellet WCF (red color), it is seen that the oxidation zone temperature graph reaches the range of 1100 0C and stable at 8000^0 C. The above statement in the explanation of the pyrolysis zone is reinforced by [33] that the trend of CO2 production is inversely proportional to the composition of CO and H2 gases because in the oxidation zone a reaction occurs between pyrolysis products (CO, H2, CH4) with oxygen producing CO2 and H2O and releasing energy in the form of heat (exothermic). On the fifth oxidation graph the composition of WCF pellets: husk pellets above, that the temperature rises to 900^o C at 441 seconds and then decreases steadily and steadily at 800^o C for a duration of 549 seconds with increasing operating time. Reaction of pyrolysis products produces high energy until one time and then the energy is transferred to the reduction region. In this reaction, CO2 and carbon (C) gas will react to form CO gas. The heat energy obtained from oxidation is used for energy sources in this reaction so that the temperature increases [34]. In accordance with the chemical equilibrium law, if the temperature rises, the equilibrium reaction will shift towards the endotherm. As a result, more CO gas is produced as a product. This also applies to water-gas reactions where a portion of the oxidized H2O will react with carbon in the reduction region to form CO and H2. It can be seen that the oxidation temperature in pellet WCF is 100% highest among other compositions. It can be concluded that the energy that can be transferred for the reduction reaction (boudouard and water-gas) is large. The result is CO and H2 gas produced in the composition of 100% pellet WCF so that producer gas has high energy. This is consistent with experiments conducted by [20,33] that the composition of CO and H2 is directly proportional to the LHV (energy) of producer gas.

3.5 Producer Gas(syngas)

Gasification output product comprises a mixture of carbon monoxide (CO), hydrogen (H2) and methane (CH4) called syngas and inorganic impurities such as NH3, HCN, H2S, fine dust, as well as organic impurities are tar. This research will be tested characteristics of co-gasification of variations in composition of WCF pellets and RH pellets including temperature, LHV and syngas produced.

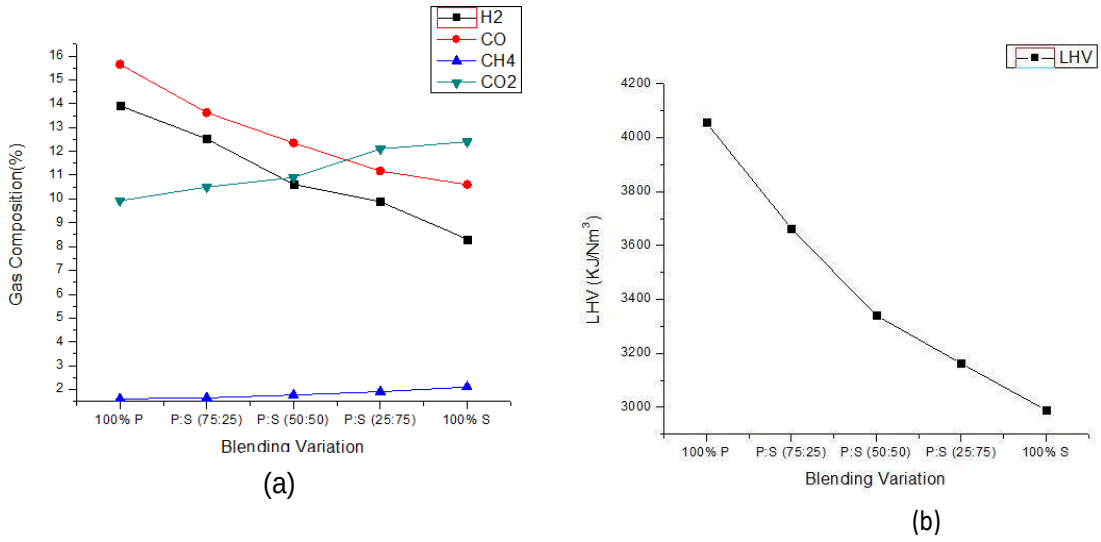


Fig. 7. Gas composisition and LHV all blending variation (a) Gas composisition (b) LHV syngas

GC analysis of the results can be calculated calorific value contained in the syngas by the formula [3.1]. Which the value smaller hydrocarbons then not taken into account. Lower heating value obtained highest gasification pellet composition WCF : RH (75%: 25%) was 7840.37 kJ / Nm3. It was influenced by

the levels of CO in biomass gasification process, where the higher levels of CO, the greater the lower heating value. Gasification composition pellet WC: rice husks (50%: 50%) have the highest H2, where the three variations range from 8.31 to 11.98%. Gasification composition pellet WC: rice husks (75%: 50%) have the highest CH4, where the three variations range from 0.89 to 1.18%.

Conclusion

The result of the syntetic gas testing obtained the highest lower heating value in 100% WCF pellet composition at 3.582 kJ/Nm^3. Lower heating value of the blending of RDF composition (75:25) of 3.392 kJ/Nm^3, where the increase of pellet fuels will increase the LHV syngas value. This results in visually low tar content and low ash particles in all compositions of approximately 30-35% of the initial mass of each composition, with the lowest ash in 100% WCF pellets composition at 0.25 g. Comparative advantage of WCF pellets and RH pellets: WCF pellets (gas composition, LHV fuel, LHV syngas, burning time, pyrolysis & oxidation temperature, moisture, durability); RH pellets (low ash content, fast ignition time). Effects of the densification (pelletization) process of RDF on rice husk and RH pellets; RH pellets (density, fuel homogeneity, gas composition, LHV fuel, LHV syngas, burning time, pyrolysis & oxidation temperature, moisture, durability); rice husk (low ash content, faster ignition time, simple processing). This proves that the pelletization process is able to increase the calorific value of the fuel and increase syngas production in the RDF co-gasification process. In this case the blending composition of WCF pellets and RH pellets (75:25) is able to replace rice husk fuel with higher syngas production performance.

Acknowledgements

This work was supported by LPPM, Universitas Pendidikan Indonesia [Grant Number 293/UN40.D/PP/2019]. Authors are also grateful to Department of Mechanical Engineering Education, Faculty of Technology and Vocational Education for refrigeration & air conditioning laboratory and facilities during this research process.

References

[1] Balat, M. “Mechanism of Thermochemical Biomass Conversion Processes”. Part 2 : Reactions of Gasification, Taylor & Francis Group, (2008) : 636-648.
[2] Surjosatyo, Adi., Wicaksono, Ryan. “Gasification application study on pottery industry: Effect of fuel mixture persentage coconut shell and rice husk on flame stability in downdraft gasification system”. IMAT (2013).
[3] Ariyaratne et al. *Determination of fossil fraction of refuse derived fuel by selective dissolution method in caloric value basic:development of simpied method*. Fuel 98, (2012) : 41-47.
[4] Agus Sunjariano Pamitran, Nandy Putra, Bambang Sugiarto. “Thermal Evolution Profile Analysis for Pyrolisis of Coal – Acacia Mangium Wood Blends”. 2016.
[5] Hasan MH, Muzammil WK, Mahlia TMI, Jannifar A, Hasanuddin I. “A review on the pattern of electricity generation and emission in Indonesia from 1987 to 2009”. Renewable and Sustainable Energy Reviews 2012 ;16 (5):3206–19.
[6] Van Ruijven BJ, Schers J, van Vuuren DP. *Model-based scenarios for rural electrification in developing countries.* Energy 2012 ;38(1) : 386–97.
[7] MENLHKRI. “String of HLH 2015 - Dialogue For Plastic Waste Management”. http://www.menlh.go.id/rangkaian-hlh-2015-dialog-penanganan-sampah-plastik/, 2015.
[8] Depok, D.K. “Switzerland Learns Waste Management to Depok City”. http://www.depok.go.id/22/02/2017/01-berita-depok/swiss-belajar-pengolahan-sampah-ke-kota-depok, 2017.
[9] Heermann C., Schawager F.J., Whiting K.J. Pyrolisis & Gasification of Waste. “A Worldwide Wechnology & Business Review”. 2 nd Edition. Juniper Consultancy Services Ltd. 2001.
[10] Young, G. “Municipal solid waste to energy conversion processes : economic, technical and renewable comparisons”, J. Wiley and Sons, Inc. 2010.
[11] Van de steene L, Tagutchou JP, Mermoud F, Martin E, Salvador S. “A new experimental continous fixed bed reactor to characterise wood char gasification”. Fuel 2010 ; 89 :3320 – 9.
[12] Sheth PN, Babu BV. “Production of hydrogen energy through biomass (waste wood) gasification”. Int J Hydrogen Energy (2010); 35 :10803 – 10.
[13] Basu, Prabir. *Biomass Gasification and Pyrolisis Practical Design*, Elsevier.Inc, USA. 2010.
[14] Salam, Abdul.P., dkk. *Report OnThe Status of Biomass GasificationInThailand And Cambodia*, Prepared for: Energy Environment Partnership (EEP), Mekong Region, Asian Institute of Technology. 2010.

[15] Erlich, C. "Comparative study of residue pellets from cane sugar and palm-oil industries with commercial wood pellets, applied in downdraft gasification". Doctoral Thesis, Royal Institute of Technology, Stockholm, Sweden. ISBN: 978-91-7415-455-9; 2009.
[16] Puig-Arnavat, Maria, Carles Bruno, Joan, Coranas. Alberto. Review and analysis of biomass gasification models. Renewable and sustainable energy reviews ;14, (2010) : pp 2841 – 2851.
[17] Tumuluru., J.S, Hess., J.R and Wright., C.T. "A Review on Biomass Densification for Energy Applications". INL U.S Department of Energy National Laboratory operated by Batelle Energy Alliance. 2011.
[18] Li., Y, Liu., H. "High-pressure densification of wood residues to form an upgraded fuel". Biomass and Bioenergy 19(3), (2000) pp:177-186
[19] Maria Puig Arnavat, Lei Shang, Zsuzsa Sarossy, Jesper Ahrendiet, Ulrik B Henriksen.. "From a single pellet press to a bench scale pellet mill – Pelletizing six different biomass feedstocks", Fuel Processing Technology 142; (2016) : pp 27-33.
[20] Guo, Feiqiang; Dong, Yuping; Dong, Lei; Guo, Chenlong. Effect of design and operating parameters on the gasification process of biomass in a downdraft fixed bed: An experimental study. International Journal of Hydrogen Energy; 39; (2014) : pp 5625-5633.
[21] Kjellström B., Arvidsson A., Forslund H. and Martinac I. "Renewable energy technologies for decentralised rural electricity services". SEI climate and energy programme, Swedish Environment Institute (SEI), Stockholm, Sweden; 2005.
[22] Erlich C. "Downdraft gasification of pellets made of wood, palm-oil residues respective bagasse : Experimental study". Applied Energy 88 (2011) 899–908.
[23] Suzdalenko V., Barmina I., Lickrastina A and Zake M. "The Effect of Co-gasification of the Biomass Pellets with Gas on the Thermal Degradation of Biomass". Chemical Engineering Transaction, 24, (2011) pp : 7-12.
[24] Wiyono., A et.al. "Investigation of Co-gasification Characteristics of Wood-coconut Fibers Pellet and Rice Husk Mixtures in a Downdraft Fixed Bed Gasifier". International Journal of Technology 8(7), (2017) :1207.
[25] CDIEMR. "Handbook of Energy and Economic Statistics of Indonesia 2012". Center for Data and Information on Energy and Mineral Resources, Ministry of Energy and Mineral Resources, Jakarta. 2012.
[26] FAO,1986, *Wood Gas as Engine Fuel*, Publications Division, Food and Agriculture Organization of the United Nations, Rome, Italy.
[27] Lakshmi., V.Vijaya. "Briquetting an alternate method for recycling agrowaste". International Journal of Management Information Technology and Engineering, (2017) : pp 9 - 16.
[28] Tapas Kumar Patra, Pratik N. Sheth. "Biomass gassification models for downdraft gasifier : a state of the art review". Renewable and Sustainable Energy Reviews 50, (2015) pp : 583.
[29] Psomopoulos, C.S., Bourka, A., Themelis, N.J. Waste-to-energy : a review of the status and benefits in USA. Waste Management 29, (2009) : 1718 – 1724.
[30] U. Arena. A review : Process and technological aspects of muicipal solid waste gasification. Waste Management 32 (2012) 625-639. 15
[31] Young, G. Municipal solid waste to energy conversion processes : economic, technical and renewable comparisons, J. Wiley and Sons, Inc. 2010.
[32] Erlich C. Comparative study of residue pellets from cane sugar and palm-oil industries with commercial wood pellets, applied in downdraft gasification. Doctoral Thesis, Royal Institute of Technology, Stockholm, Sweden. ISBN: 978-91-7415-455-9; 2009.
[33] Singh., V.ChristusJeya, Sekhar., S.Joseph. "Performance studies on a downdraft biomass gasifier with blends of coconut shell and rubber seed shell as feedstock". Applied Thermal Engineering 97, (2015) : pp 22-27.
[34] Zainal., et al. "Experimental investigation of a downdraft biomass gasifier". Biomass and Bioenergy 23(4), (2002) pp : 283-289.

Penerbit Akademia Baru

Engineering Science and Technology Conference Proceedings

Journal homepage: www.akademiabaru.com/EST.html

Experiments on Measurement of Heat Transfer Rate Of Gas Flow Through Microchannel With Constant Wall Temperature

Open

Chungpyo Hong[1,*], Yutaka Asako[2], Mohammad Faghri[3], Danish Rehman[4], Gian Luca Morini[4]

[1] Department of Mechanical Engineering, Kagoshima University, Kagoshima 890-8580, Japan
[2] Department of Mechanical Precision Engineering, Malaysia-Japan International Institute of Technology, Universiti Teknologi Malaysia, Kuala Lumpur, 54100 Kuala Lumpur, Malaysia
[3] Department of Mechanical, Industrial and System Engineering, University of Rhode Island Kingston, RI 02881, USA
[4] Department of Industrial Engineering, University of Bologna, Via del Lazzaretto 15/5, 40131 Bologna, Italy

ABSTRACT

Experimental results for the measurement of heat transfer rates in microchannel gas flow is crucial for gas to gas micro heat exchangers. A critical overview of the main factors that play an important role in the determination of heat transfer rate is presented. The experimental and numerical data obtained from authors' previous studies are used in order to highlight characteristics of convective heat transfer of gas through microchannels with constant wall temperature. It is suggested to obtain heat transfer rates by determining the difference in gas enthalpies through measuring temperature and pressure at the inlet and outlet. The heat transfer rate obtained in the present study were compared with those determined by the difference in only total temperatures and the Nusselt number of incompressible flow.

Keywords:
Heat transfer rate; gas flow; convective heat transfer; total enthalpy and temperature; microtube

Copyright © 2019 PENERBIT AKADEMIA BARU - All rights reserved

1. Introduction

Recently, an understanding of heat transfer characteristics of microchannel is becoming more important in the miniaturization of the electronic devices. Since the pioneer work of Tuckerman and Pease [1], numerous experimental and numerical investigations on convective heat transfer of microchannel flow have been undertaken.

In the case of microchannel liquid flow, flow and heat transfer characteristics can be predicted well by conventional correlations [2 and 3], with minor deviations caused by experimental errors [4].

However, in the case of microchannel gas flow, it is well known that the rarefaction, the surface roughness and the compressibility significantly affect the flow and heat transfer characteristics separately or simultaneously [5]. And the effect of compressibility is more dominant on flow and

* *Corresponding author.*

E-mail address: hong@mech.kagoshima-u.ac.jp (Chungpyo Hong)

heat transfer characteristics than those of surface roughness and rarefaction for the microchannels with $10\,\mu m$ or more in hydraulic diameter. The compressibility effect leads flow acceleration along the length and large gas expansion near the outlet. This results in decrease in gas temperature and additional heat transfer from the wall to the gas near the outlet [6]. Therefore, conventional correlations for the prediction of Nusselt number to obtain heat transfer fail in the presence of compressibility [7].

Experimental Investigations on heat transfer characteristics of gas flow in microchannels have been performed with most common thermal boundary conditions, namely constant heat flux (CHF) and constant wall temperature (CWT). Most of them have been studied with the thermal boundary of CHF [7-10]. The literature is well surveyed and critically reviewed by Lin et al. [8] and Morini et al., [9]. It is reported that the thermal behavior at microscale of gas and liquid flows through microchannel in terms of convective heat transfer coefficients can be strongly affected by scaling and micro-effects but also by practical issues linked to the geometry of the testing, the real thermal boundary conditions, the presence of fittings, position and type of the sensors, and so on [9]. All these aspects have to be taken into account during the data post processing in order to obtain a correct evaluation of heat transfer characteristics. One of them except Authors' studies, Choi et al. [11] has been studied with CWT. They obtained using nitrogen gas flow in micro-tubes with inner diameters ranged from $3\,\mu m$ to $81\,\mu m$ very low values of Nusselt number compared to the prediction of the conventional correlation. However, it is not clear to describe the detail measurement of gas temperature. This is the motivation of the present study to measure the total temperature to quantitively determine the heat transfer rate through a micro-tube with constant wall temperature with critical overview on authors' previous studies.

2. Convective heat transfer of gas flow through microchannels with CWT

The pressure distributions along the channel length obtained numerically for gas flow through a parallel plate microchannel of h=10μm and L=0.002mm is plotted Fig. 1

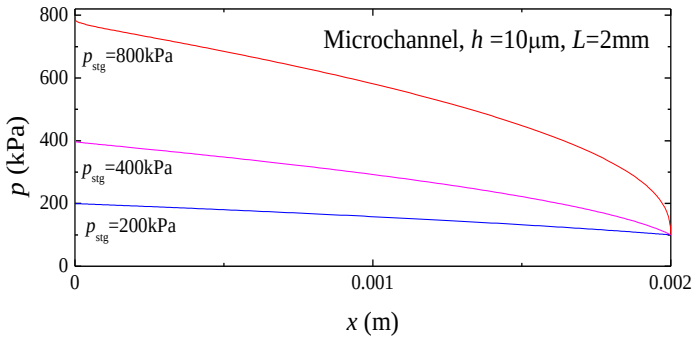


Fig. 1 Pressure distributions as a function of x

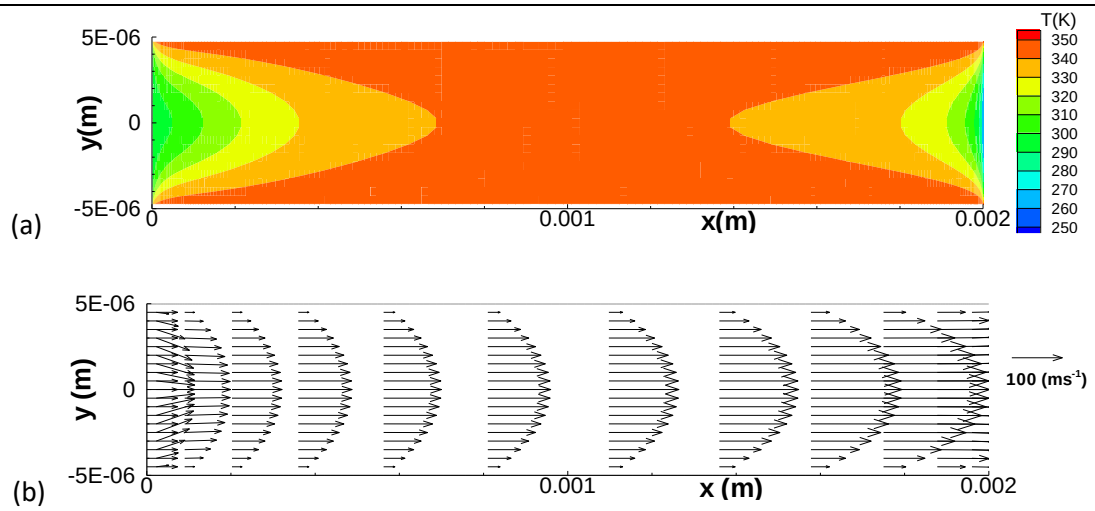


Fig. 2. (a) Velocity vector and (b) contour plot of temperature

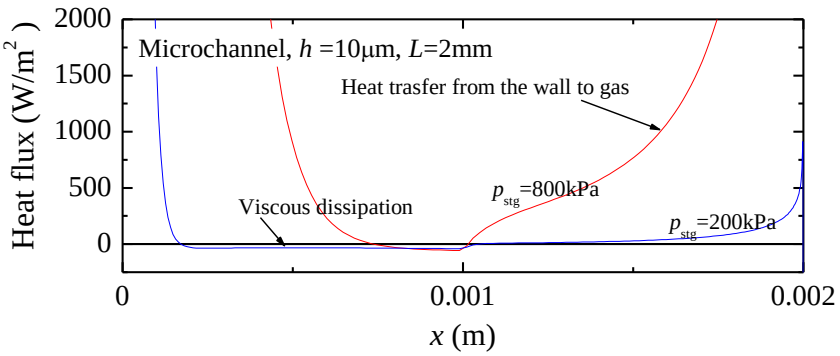


Fig. 3 Heat flux from the wall

[12]. This results in T_w=350 K and T_{stg}=300 K. The pressure gradient becomes steep due to flow acceleration near the outlet as the stagnation pressure increases. Namely, the pressure distribution is almost linear for the flow conditions at p_{stg}=200 kPa, and the compressibility effect was negligible. But with increasing inlet pressure, the pressure distribution becomes more and more nonlinear due to the compressibility effects. For the stagnation pressure, p_{stg}= 800 kPa in the figure, velocity vectors and the contour plots of the temperature are presented in Figs. 2 (a) and (b), respectively. The reference arrow in the figure represents a velocity of 100 m/s. Fig. 2(a) shows that because of the viscosity, the velocity profile becomes nearly parabolic. After the inlet region, however, the flow in the channel is accelerated and the average velocity increases. This is due to the volume expansion of the gas caused by large pressure drop. Fig. 2(b) represents the temperature contours in the channel. The temperature in the core region of the channel decreases as a result of energy conversion into kinetic energy. And the additional hear transfers from the wall to gas. Therefore, the heat flux from the wall in Fig. 2 (b) is plotted in Fig. 3 along the length. Note that the heat flux has a positive value when the gas temperature is lower than the wall temperature. In the case of slow flow (p_{stg}= 200 kPa) represented by the blue line, the heat flux from the wall converges to zero asymptotically. This is a similar heat flux to that of the

incompressible flow. On the other hand, in the case of fast flow (p_{stg}= 800 kPa) represented by the solid lines, part of the thermal energy converts into kinetic energy near the outlet. This results in a decrease in temperature and additional heat transfer from the wall near the outlet. That is the heat flux increases near the outlet. Therefore, the total temperature is higher than the wall temperature. This is numerically and numerically demonstrated for our previous study [6, 12-16].

3. Heat Transfer rate

The heat transfer rate of gas flow is expressed as [17]

$$\dot{Q}_{\mathrm{h}} = \dot{m}\ (h_{\mathrm{T,out}} - h_{\mathrm{stg}}) \tag{1}$$

If the gas is an ideal gas, the enthalpy is a function of temperature as

$$dh = c_{\mathrm{p,ave}} dT \tag{2}$$

And the heat transfer rate of an ideal gas is

$$\dot{Q}_{\mathrm{T}} = \dot{m}\ c_{\mathrm{p}} (T_{\mathrm{T,\ out}} - T_{\mathrm{stg}}) \tag{3}$$

For the case of slow flow of an ideal gas, the heat transfer rate can be obtained with the bulk temperature at the outlet as

$$\dot{Q}_{\mathrm{slow}} = \dot{m}\ c_{\mathrm{p}} (T_{\mathrm{b,incomp}} - T_{\mathrm{in}}) \tag{4}$$

where the bulk temperature of incompressible flow is expressed as a function of mean Nusselt number and location as (e.g., Burmeister [18])

$$T_{\mathrm{b,incomp}} = T_{\mathrm{w}} - \left(T_{\mathrm{w}} - T_{\mathrm{stg}}\right) e^{-4 Nu_{\mathrm{m}} X^*} \tag{5}$$

The mean Nusselt number of a turbulent fully developed flow in a duct, defined by [19]

$$Nu_m = 0.022 Re^{0.8} Pr^{0.5} \tag{6}$$

and X^* is the inverse of Graetz number, defined by

$$X^* = \frac{x}{D\ Re\ Pr} \tag{7}$$

Many researchers have investigated the turbulent heat transfer characteristics of duct flows and Nusselt numbers are reported in the literature (e.g., Kays and Crawford [19] and Shah and London [20]). In the present study the Nusselt number obtained by Kays and Crawford [19] with the range of $0.5 < Pr \leq 1.0$ for a fully developed flow in tubes was used for the calculation of the bulk temperature for incompressible flow.

In order to obtain heat transfer rates, the total enthalpy difference between the inlet and outlet is needed as show in Eq. (1). The enthalpy of a gas is determined from the pressure and the temperature, $h = h\ (p, T)$. Therefore, to obtain the total enthalpy at the microtube outlet, the total temperature measuring device was fabricated with a similar structure to that proposed by

Yamada et al. [21] for our recent studies [22-24] as shown in Fig. 4. The test section of heat transfer in the figure consists of three components: an inlet tube, a microtube and a temperature measuring device. The inlet tube made of copper is placed inside the upper water jacket to control the gas temperature in the inlet tube. The pressure transducer and the thermocouple are inserted in the inlet tube and the gas temperature and pressure in the inlet tube are measured. The measured gas temperature and pressure are considered to the stagnation temperature, T_{stg} and the stagnation pressure, p_{stg}, since the gas is rest. The microtube is tested using different material (stainless steel, copper and fused silica) and diameter ($D \cong 150 \sim 530 \mu\mathrm{m}$) microtubes in our recent studies [22-24]. The microtube is placed inside the lower water jacket to keep the wall temperature constant. Water is circulated between the water jacket and a thermostatic bath. A thermally insulated exterior foamed polystyrene tube with six baffle plates fabricated where the gas velocity reduces and the kinetic energy is converted into the thermal energy, was attached to the outlet of the microtube as a total temperature measuring device. More details of the total temperature measuring device are documented in Yamada et al. [21] and our recent studies [22-24].

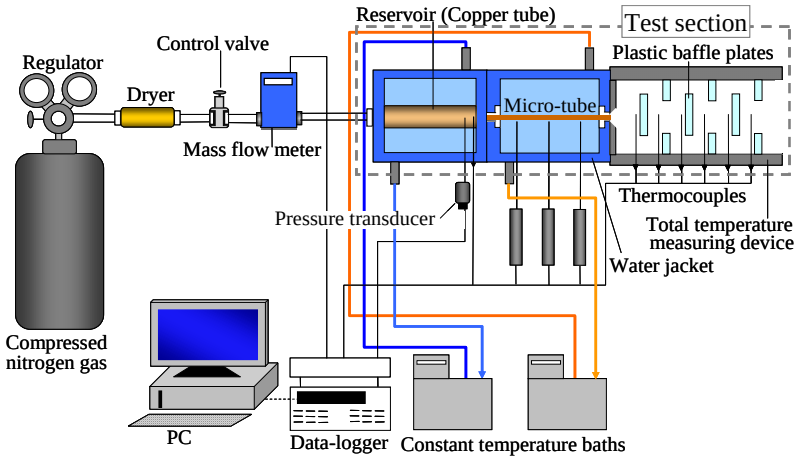


Fig. 4. A schematic diagram of experimental setup

Here, Fig. 5 shows the measured total temperature difference between the outlet and the stagnation temperature, $T_{\mathrm{T,out}} - T_{\mathrm{stg}}$ as a function of the stagnation pressure. The temperature difference between the wall and the stagnation temperature, $T_{\mathrm{wall}} - T_{\mathrm{stg}}$ is also plotted in the figure with a dotted line. The total enthalpy difference between the micro-tube outlet and the stagnation enthalpy, $h_{\mathrm{T,out}} - h_{\mathrm{stg}}$ is plotted in the figure with the values of the mass flow rate and the inlet Mach number. The enthalpy was obtained as a function of pressure and temperature. The figure is the results for the case of $T_{\mathrm{w}} \cong 294\mathrm{K}$ and $T_{\mathrm{stg}} \cong 297\mathrm{K}$ ($T_{\mathrm{w}} - T_{\mathrm{stg}} \cong 3\mathrm{K}$). This flow is turbulent flow since $3629 \le Re \le 19905$. The measured total temperature at the microtube outlet is higher than wall temperature since additional heat transfer from the wall to gas due to thermal energy conversion into kinetic energy. The similar results were obtained in the previous numerical study [14]. Inlet Mach number increases as the stagnation pressure increase, and nearly levels off in the range of

$p_{stg} \geq 300$kPa. This reflects that the flow becomes choked under higher stagnation pressure. The value of $T_{T,out} - T_{stg}$ increases with increase in the stagnation pressure and slightly decrease in the range of $p_{stg} \geq 300$kPa due to gas expansion from a large pressure difference between the stagnation and the outlet pressure. However, the value of $h_{T,out} - h_{stg}$ increases with increased stagnation pressure and maintains a specific value in the range of $p_{stg} \geq 300$kPa. Note that the value of $h_{T,out}$ - h_{stg} remains almost constant in the range when the flow is choked even though the stagnation pressure increases. The enthalpy difference between the inlet and the outlet of the tube corresponds to the heat transfer rate from the wall. From this fact, the heat transfer rate remains unchanged even if the flow becomes a choked flow.

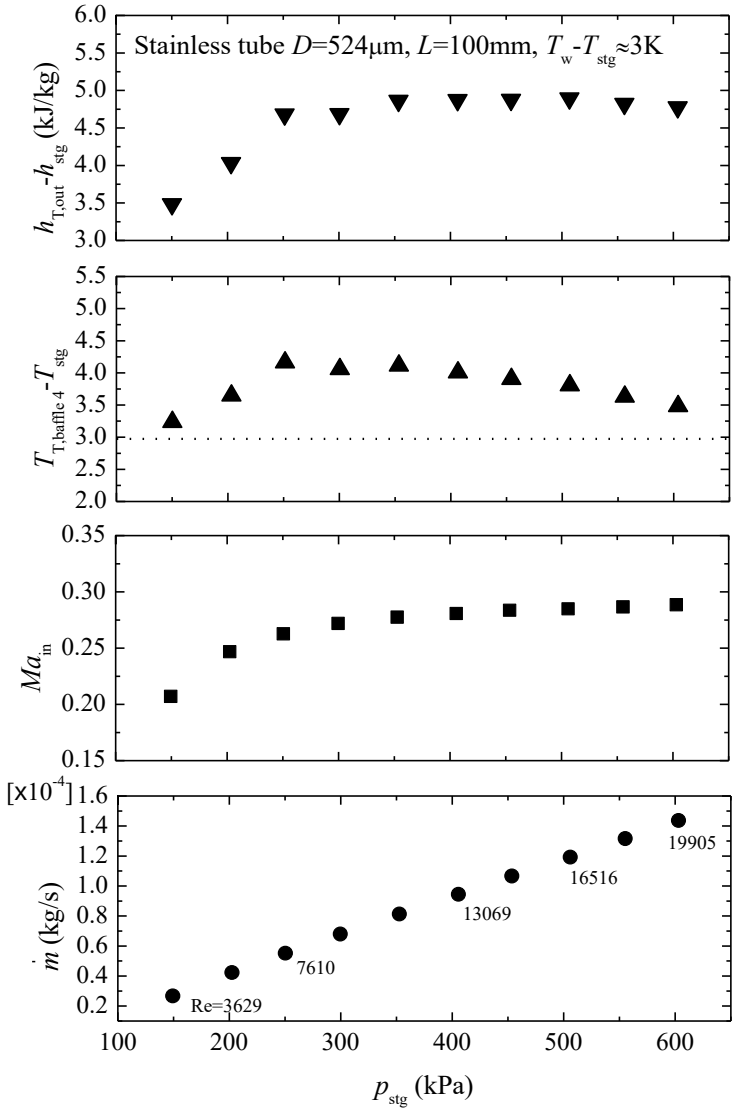


Fig. 5. Total temperature, total enthalpy, inlet Mach number and mass flow rate as function of p_{stg}

The heat transfer rates were obtained by Eqs. (1), (3) and (4) with measured data. The heat transfer rates normalized by $\dot{Q}_{slow}$, $\dot{Q}_h/\dot{Q}_{slow}$ and $\dot{Q}_T/\dot{Q}_{slow}$ is plotted as a function of the stagnation pressure in Fig. 6. A part of the thermal energy converts into kinetic energy near the outlet when

the flow is fast. This results in a bulk temperature decreases and additional heat transfer from the wall to gas. As results of this both values of $\dot{Q}_{\mathrm{h}}/\dot{Q}_{\mathrm{slow}}$ and $\dot{Q}_{\mathrm{T}}/\dot{Q}_{\mathrm{slow}}$ are more than unity. In the case of $T_{\mathrm{w}}-T_{\mathrm{stg}}\cong 10\mathrm{K}$, the maximum increment of both values due to addition heat transfer is less than 20 %. However, in the cases of $T_{\mathrm{w}}-T_{\mathrm{stg}}\cong 3\mathrm{K}$ and $T_{\mathrm{w}}-T_{\mathrm{stg}}\cong 5\mathrm{K}$, the maximum increment in them is more than 80% and 40 %, respectively. The value of $\dot{Q}_{\mathrm{T}}/\dot{Q}_{\mathrm{slow}}$ with the stagnation pressure increases and levels off in the range of choked flow ($p_{\mathrm{stg}}\geq 300\ \mathrm{kPa}$). In the range, the measured $T_{\mathrm{T,\ out}}$ slightly decreases with the stagnation pressure increasing as shown in Fig. 5. Therefore, $\dot{Q}_{\mathrm{T}}/\dot{Q}_{\mathrm{slow}}$ obtained by temperature difference, $T_{\mathrm{T,out}}-T_{\mathrm{stg}}$, remains almost constant with the stagnation pressure increasing. However, the value of $\dot{Q}_{\mathrm{h}}/\dot{Q}_{\mathrm{slow}}$ increase with the stagnation pressure increase since $\dot{Q}_{\mathrm{h}}$ was obtained by the enthalpy difference determined from a pressure and a temperature, $h_{\mathrm{T,out}}-h_{\mathrm{stg}}$. Therefore, the value of $\dot{Q}_{\mathrm{h}}/\dot{Q}_{\mathrm{slow}}$ is higher than that of $\dot{Q}_{\mathrm{T}}/\dot{Q}_{\mathrm{slow}}$. And the difference between $\dot{Q}_{\mathrm{h}}$ and $\dot{Q}_{\mathrm{T}}$ is large with the stagnation pressure increasing since the Joule-Thomson effect present in a real gas. As a result of that, in the case of presence in large gas expansion between the inlet and outlet a heat transfer rate should be obtained with the enthalpy differences determined from a pressure and a temperature.

4. Conclusions

In this study, experiments on measurement of heat transfer rate of gas flow through microchannel with constant wall temperature were described with authors' recent studies. The following conclusions were obtained.

(1) For convective Heat transfer of gas flow through microchannel with constant wall temperature, the total temperature is higher than the wall temperature since due to an additional heat transfer from the wall to gas since gas static temperature decreases because of conversion of thermal energy into kinetic energy.

(2) The value of $T_{\mathrm{T,out}}-T_{\mathrm{stg}}$ increases with the stagnation pressure increasing and slightly decrease in the range where the flow is under-expanded (choked). However, the value of $h_{\mathrm{T,out}}-h_{\mathrm{stg}}$ increases with the stagnation pressure increasing and maintains a specific value.

(3) Both $\dot{Q}_{\mathrm{h}}$ and $\dot{Q}_{\mathrm{T}}$ are higher than $\dot{Q}_{\mathrm{slow}}$ obtained from the bulk temperature of incompressible flow because of the additional heat transfer. And the difference between

$\dot{Q}_h$ and $\dot{Q}_T$ is large with the stagnation increasing since the Joule-Thomson effect present in gas.

References

[1] Tuckerman, D.B. and Pease, R.F.W., "High-performance heat sinking for VLSI." IEEE Electron Device Lett. EDL-2 (5) (1981): 126–129.

[2] Yang, C.Y. and Lin, T.Y., "Heat Transfer Characteristics of Water Flow in Mcrotubes." Exp. Therm. Fluid Sci., 32 (2) (2007): 432-439.

[3] Lin, T.Y. and Yang, C.Y., "An Experimental Investigation on Forced Convection Heat Trnsfer Perfoormance in Micro Tube by the Method of Liquid Crystal Thermography." Int. J. Heat Mass Transfer., 50 (23-24) (2007): 4736-3742.

[4] Lelea, D., Nishhio, S., and Takano, K., "The Experimental Research on Microtube Heat Transfer and Fluid Flow of Distilled Water." Int. J. Heat Mass Transfer., 47 (12-13) (2004): 2812-2830.

[5] Hong, C., Asako, Y., and Lee, J-H., "Poiseuille number correlation for high speed microflows." J. Phys. D Appl. Phys. 41 (2008): p. 105111(1-10).

[6] Hong, C., and Asako, Y., "Heat Transfer Characteristics of Gaseous Flows in a Microchannel and a Microtube with Constant Wall Temperature." Numerical Heat Transfer, Part A 52 (2007): 219-238.

[7] Yang, Y., Hong, C., Morini, G.L., and Asako, Y., "Experimental and numerical investigation of forced convection of subsonic gas flows in microtubes." Int. J. Heat Mass Transfer., 78 (2014): 732-740.

[8] Lin, T-Y., and Kandlikar, S.G., "Heat Transfer Investigation of Air Flow in Microtubes-Part I: Effects of Heat Loss, Viscous Heating, and Axial Conduction." Journal of Heat Transfer 135 (2013): p. 031703 (1-9).

[9] Morini, G.L., and Yang, Y., "Guidelines for the Determination of Single-Phase Forced Convection Coefficients in Microchannesl." Journal of Heat Transfer 135 (2013): p. 101004 (1-10).

[10] Yang, C.Y., Chen, C.W, Lin, T.Y, and Kandlikar, S.G., "Heat Transfer and Friction Characteristics of Air Flow in Microtubes." Experimental Thermal and Fluid Science 37 (3) (2012): 12-18.

[11] Choi, S.B., Barron, R.F., and Warrington, R.O., "Fluid Flow and Heat Transfer in Micro Tubes." Micro Mechanical Sensors, Actuators and Systems, ASME DSC 32 (1991): 123-134.

[12] Hong, C., Yamamoto, T., Asako, Y., and Suzuki, K., "Heat Transfer Characteristics of Compressible Laminar Flow Through Microtubes." Journal of Heat Transfer 134 (2012): p. 011602 (1-8).

[13] Hong, C, Uchida, Y., Yamamoto, T., Asako, Y., and Suzuki, K., "Heat Transfer Characteristics of Turbulent Gas Flow through Micro-Tubes." Proc. Of the International Heat Transfer Conference (2010): IHTC2014-36965.

[14] Isobe, K., Hong, C., Asako, Y., and Ueno, I., "Numerical Simulation on Heat Transfer Characteristics of Turbulent Gas Flow in Micro-Tubes." Proc. of the ASME 2011 International Mechanical Engineering Congress & Exposition (2011): IMECE2011-64513.

[15] Isobe, K., Hong, C., Asako, Y., and Ueno, I., "Heat transfer characteristics of gas flow in micro-tubes with constant wall temperature." Proc. of the 4th International Conference on Heat Transfer and Fluid Flow in microscale (2011): HTFFM-IV-068.

[16] Hong, C., Isobe, K., Asako, Y., and Ueno, I., "Total Temperature Measurement of Turbulent Gas Flow at Microtube Exit." Proc. of the ASME 11th International Conference on Nanochannels, Microchannels, and Minichannels (2013): ICNMM2013-73180.

[17] Cengel, Y., and Boles, M.A., Thermodynamics, McGraw-Hill, Inc., 1994.

[18] Burmeister, L. C., Convection Heat Transfer, 2nd ed. John Wiley & Sons, 1983.

[19] Kays, W.M., and Crawford, M.E., Convection heat and Mass Transfer, 2nd ed. New York McGraw-Hill, 1980

[20] Shah, R.K., and London, A.L., Laminar flow forced convection in ducts, advances in heat transfer supplement 1, Academic Press, New York, 1978.

[21] Yamada, M., Hong, C., and Asako, Y., "Total Temperature measurement of micro-gas jet." Proc. of the ASME 2014 International Mechanical Engineering Congress & Exposition (2014): IMECE2014-36965.

[22] Matsushita, S., Nakamura, T., Hong, C., and Asako, Y., "Total Temperature Measurement of Gas Flow in Micro-tube with Constant Wall Temperature." Proc. of the ASME 2014 International Mechanical Engineering Congress & Exposition (2014): IMECE2014-36660.

[23] Sakashita, T., Hong, C., and Asako Y., "Total Temperature Measurement of Gas at Microtube Outlet." Proc. of the ASME 2017 International Mechanical Engineering Congress & Exposition (2017): IMECE2017-71146.

[24] Sakashita, T., Hong, C., and Asako Y., "Heat Transfer Rate of Gas Flow through a Stainless Steel Micro-tube with Constant Wall Temperature." Proc. of the 29th International Symposium on Transport Phenomena (2018): ISTP29-171.

Penerbit Akademia Baru

Engineering Science and Technology Conference Proceedings

Journal homepage: www.akademiabaru.com/EST.html

Open Access

Prediction of Water Saturation Using Fuzzy Logic

Agus Maman Abadi[1,*], Allen Haryanto Lukmana[2], Aditya Wisnugraha Sugiyarto[1], Hihin Vita Amalia[1]

[1] Department of Mathematics, Universitas Negeri Yogyakarta, Jalan Colombo No. 1, Yogyakarta, Indonesia 55281
[2] Department of Petroleum Engineering, University of National Development of Yogyakarta, Jalan SWK No. 104, Condongcatur, Yogyakarta, Indonesia, 55283

ABSTRACT

Indonesia has many sources of oil. According to CBNC Indonesia, oil reserves in Indonesia are still around 3.15 billion barrels, which is predicted to be sufficient for the next ten years. Petroleum extraction has a long process from drilling to refining. The process of finding an oil source requires accurate predictions and calculations. Hydrocarbons are a major component of compounds in petroleum. Water saturation is one important factor in determining the hydrocarbon content in a rock where the less water content in the rock affects the greater the number of hydrocarbons. The purpose of this study is to determine water saturation at various depths in drilling using fuzzy logic. Input variables used are depth, effective porosity, effective porosity of log neutron density, total porosity, total porosity of log neutron density. Furthermore, the fuzzy C-Mean Clustering (FCM) method is used to determine the optimal number of rules. The results showed that the prediction of water saturation with zero order Sugeno fuzzy logic gives better accuracy compared to Mamdani fuzzy logic, BPNN, and LSTM-RNN.

Keywords:
Water saturation, fuzzy logic, fuzzy c-mean clustering

Copyright © 2019 PENERBIT AKADEMIA BARU - All rights reserved

1. Introduction

Petroleum is the main energy source for industry, transportation, and households in Indonesia. Based on data from [1], it is said that the energy sector contributes around 7.6% to 8% annually to Indonesia's Gross Domestic Product (GDP). Among this 8%, 3.3% is contributed by the petroleum mining sector. In 2014, Indonesia had around 15 oil refineries that were actively producing [2]. Indonesia has oil reserves of around 3.15 billion barrels, which is estimated to be sufficient for the next ten years [3].

Petroleum processing requires a long process from drilling to refining [4]. In the process of finding suitable oil sources, precise calculations and predictions need to be conducted. Petroleum is principally found in oil reserves stored in rock deposits in the bowels of the earth [5]. Although the formation of petroleum is not precisely known, generally petroleum is formed from marine animals and plant debris that experienced high pressure and temperature. Petroleum contains a number of mixtures of hydrocarbons, non-hydrocarbons, and organometallic compounds [6]. Hydrocarbon compounds are the main components in petroleum because all hydrocarbon classes are present in petroleum, except for alkenes and alkynes [7].

* *Corresponding author.*
E-mail address: agusmaman@uny.ac.id (Agus Maman Abadi)

Water saturation is one of the important factors in determining the hydrocarbon content in a rock layer where the less water content in the rocks, the greater the hydrocarbon content [8]. It is the amount of pore volume in the water-filled rocks [9]. The method for estimating the volume of hydrocarbons in ground surface formation is determined based on the vertical and horizontal resistivity values. These values are calculated based on the saturation of bound water, total porosity for each layer, and the estimated volume of bulk water that cannot be reduced in each layer [10]. Therefore, to determine the volume of hydrocarbons contained in the soil layer, it is necessary to conduct a prediction process of the water saturation in the layer.

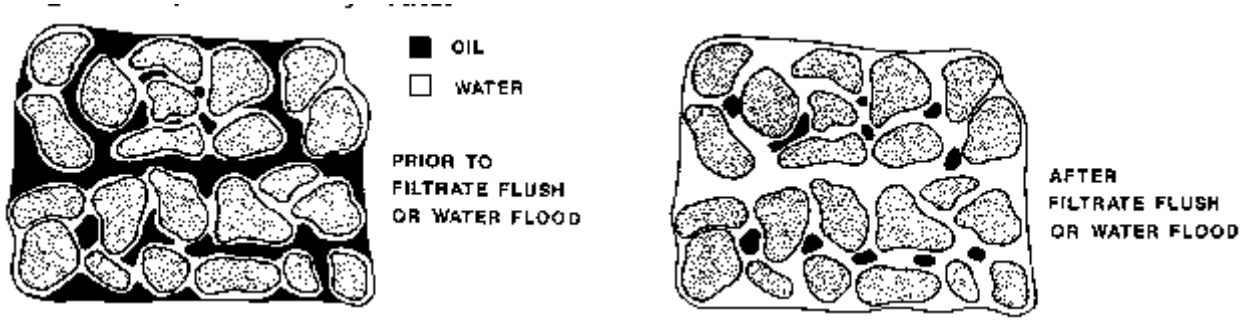
At present, there is a method called machine learning, which is a collection of methods that allow computers for automatization of modeling and programming, supported by data through systematic discovery and statistically significant patterns in available data [11]. Prediction of water saturation has been carried out by utilizing several machine learning methods such as using robust committee machine [12] and neural networks [13-16]. In addition, the prediction of water saturation has also been done by equation modeling [17]. Fuzzy system is one of the techniques of soft computing and part of artificial intelligence with machine learning [18-21].

The purpose of this study is to predict water saturation at various depths in drilling using a fuzzy system. In this study, the prediction process of water saturation is based on the depth variable input, effective porosity, effective porosity of neutron log density, total porosity, and total porosity of neutron log density. Fuzzy rule formation uses fuzzy c-means clustering (FCM) and zero-order Sugeno fuzzy logic. The FCM method is used to determine the most optimal number of rules used in the formation of fuzzy rules. Furthermore, the kind of fuzzy rules of the fuzzy system is the zero-order Sugeno.

2. Theoretical Review

2.1 Water Saturation

All petroleum, whichever its origin has a main component which is hydrocarbons mixture. The mixture of hydrocarbons contained in the petroleum has several variations, namely sulfur compounds, nitrogen, and oxygen [22]. Hydrocarbon saturation can be determined by water saturation, which is 1 minus the value of water saturation. Water saturation is the ratio of water volume to pore volume. In a wet water reservoir, water is held by surface tension and surface water does not move when oil or gas is produced. This situation can be shown by Figure 1.



(a) (b)

Fig. 1. Water wet formation with hydrocarbons before the invasion (a) and after the invasion (b) [23]

When the reservoir is drilled, fluids near the wellbore are pushed away and the zone is attacked by the drilling fluid. If hydrocarbons exist, the value of water saturation after the invasion will be higher than the original reservoir conditions. Shallow log resistivity will indicate the water

saturation of the invasion zone whereas the deep resistivity log will indicate the water saturation of the original formation if only the invasion is not too deep.

Almost all water saturation calculations are carried out by using the Archie's Laws approach in which the depth resistivity, porosity, water resistivity, and electronic property variables are used. However, in the calculation, water saturation can be calculated from the effective porosity and resistivity log [23]. Since porosity is the capacity of a rock to hold a liquid, it can be used to calculate water saturation that occurs.

2.2 Fuzzy Logic of Zero-Order Sugeno

There are several types of fuzzy logic such as Mamdani, Sugeno, and Tsukamoto. In this study, zero-order Sugeno fuzzy logic is used. Sugeno fuzzy logic model, also known as Takagi-Sugeno-Kang (TSK) fuzzy logic model, is a systematic approach to produce fuzzy rules from the applied input-output data [24, 25]. Sugeno fuzzy logic of zero-order is stated in the following form.

$$IF\ x_1\ is\ A_1, \dots, and\ x_n\ is\ A_n, then\ z = b$$

where $(x_1, \dots, x_n)$ is the input of fuzzy logic, A_i is the fuzzy set on the ith input, and consequent b is a real constant.

2.3 Fuzzy C-Means Clustering

Fuzzy clustering is a powerful non-supervised method for data analysis and model construction. In many situations, fuzzy clustering is more natural than hard clustering. The data that are located on the boundary between several classes are not forced to be part of one class but the data are rather represented in a degree of membership between 0 and 1, indicating the partial membership of the data. Fuzzy c-means (FCM) algorithm is the most widely used. This algorithm was first reported in the literature for special cases (*m* = 2) by Joe Dunn in 1974. The general case (for every *m* greater than 1) was developed by Jim Bezdek in his Ph.D. thesis at Cornell University in 1973. The algorithm was then improved by Bezdek in 1981 [26]. The FCM method uses fuzzy partitions so that data points can belong to all groups with varying membership values between 0 and 1 with the following algorithm [26].

1. The initialization of matrix $U = [u_{ij}]$, U^0
2. In the kth step calculate the center of vector $C^{(k)} = [c_j]$ with U^k
$$C_i = \frac{\sum_{j=1}^{n} u_{ij}^m x_j}{\sum_{j=1}^{n} u_{ij}^m}$$
3. Update U^k, $U^{(k+1)}$
4. $d_{ij} = \sqrt{\sum_{i=1}^{n}(x_i - c_i)}$
$$u_{ij} = \frac{1}{\sum_{k=1}^{c}\left(\frac{d_{ij}}{d_{kj}}\right)^{\frac{2}{m-1}}}$$
5. If $|\mathrm{U(k+1)} - \mathrm{U(k)}| < \varepsilon$ then, stop. If not, then return to step 2.

Where m is a random real number greater than 1, u_{ij} is the degree of membership of x_i in cluster j, x_i is the measurement of the ith *d*-dimension, and c_j is the center of the *d*-dimension of the cluster.

3. Research Method

In this study, 2252 data were used. The data is divided into 75% for training data and 25% for testing data. The data was obtained from PT. Geotama Energi, Yogyakarta, Indonesia. PT. Geotama Energy is a service-oriented business providing specialized oilfield general equipment, mechanical electrical, and engineering that was established since 2006. The Input variables used in this study are depth, effective porosity, effective porosity of neutron log density, total porosity, and total porosity of neutron log density. The output variable of the fuzzy system is water saturation. The next step was the clustering process using FCM, which was followed by the fuzzification and processing of the fuzzification results data using the zero-order Sugeno fuzzy system. The accuracy of the predicted results is measured by the mean absolute percentage error (MAPE) value with the following formula.

$$MAPE = \frac{\sum_{i=1}^{n} \frac{|X_i - F_i|}{X_i} x100\%}{n}$$

where X_i is the original data, F_i is predictive data, and n is the amount of data. The determination of the model accuracy is measured separately based on the type of data, so two MAPE values were obtained, namely for training data and testing data. In general, the research flow diagram can be seen in Figure 2.

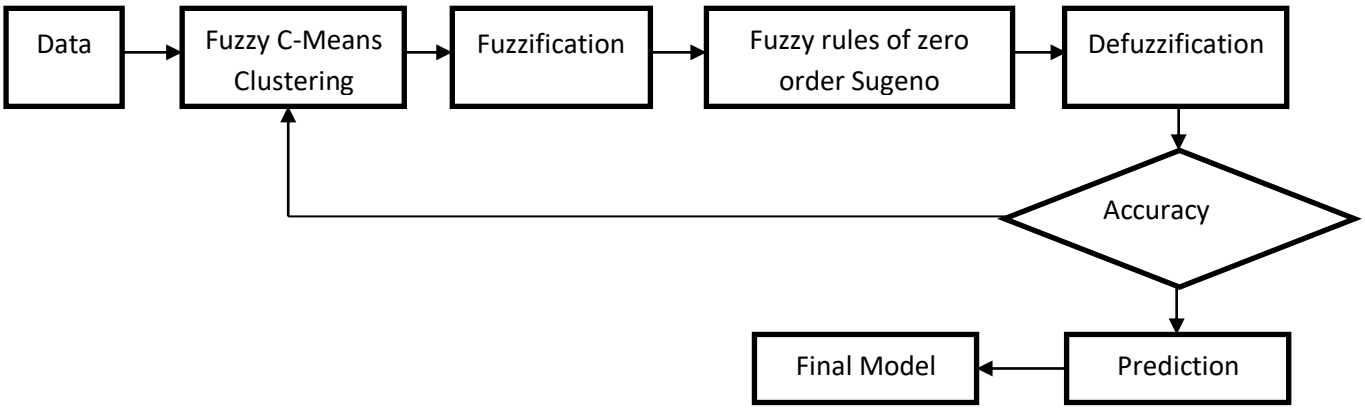


Fig. 2. Research Flow Chart

4. Result and Discussion

4.1 Fuzzy C-Means Clustering

The determination of the optimal cluster is conducted through a try and error method to get the lowest MAPE value for training and testing data. The results are illustrated in Table 1.

Table 1
The results of the try and error method

Cluster Number	MAPE (%)		Mean MAPE (%)
	Training	Testing	
10	28.71424	29.12068	28.91746
11	28.94677	28.84113	28.89395
12	27.48908	27.6391	27.56409
..	...	...	...
150	15.55787	15.26276	15.41031
151	14.16582	13.64534	13.90558
152	14.22539	14.17532	14.20036
...	...	...	...
481	10.98571	10.83086	10.90829
482	10.72528	10.53904	10.63216
483	10.93887	10.49228	10.71557
484	9.939734	9.343554	9.641644

Based on Table 1, it is found that the lowest MAPE value was achieved in the 484th cluster so that the center matrix of 484 x 6 was obtained. After that, the obtained center was then used to create a zero-order Sugeno fuzzy rules with 484 fuzzy rules. The obtained center matrix can be seen in Table 2.

Table 2
The center of optimal cluster

Cluster	Depth	PHIE	PHIE_DN	PHIT	PHIT_DN	SWE
1	1570.634471	0.157510931	0.157511004	0.157511554	0.157511627	0.20790815
2	1665.302142	0.175397492	0.175398214	0.17540327	0.175403992	0.176808947
3	1456.999665	0.200987456	0.20098793	0.201035045	0.201035518	0.189031043
...	...	...	...	...	...	...
...	...	...	...	...	...	...
484	1465.251391	0.212678851	0.212679213	0.212692605	0.212692967	0.18424892

4.2 Prediction Using Zero-order Sugeno Fuzzy Logic

The process of water saturation prediction using zero-order Sugeno fuzzy logic was carried out with the following steps:

4.2.1 Fuzzy Set Formation for each input variable

a) Variable of Depth

Based on the data, the depth variable has a minimum value of 1393,393 and a maximum value of 1720,748. Therefore, the universal set of this variable is $U_{depth} = [1393.393,1720.748]$. After that, the 484 fuzzy sets are defined based on the centers that have been obtained from FCM, namely $DEP_1, DEP_2, DEP_3, \dots, DEP_{484}$ with the membership function as follows.

$$\mu_{DEP_1}(x) = e^{-\frac{(x-1570.634471)^2}{2(17.38)^2}}$$

$$\mu_{DEP_2}(x) = e^{-\frac{(x-1665.302142)^2}{2(17.38)^2}}$$

$$\mu_{DEP_3}(x) = e^{-\frac{(x-1457)^2}{2(17.38)^2}}$$

...

$$\mu_{DEP_{484}}(x) = e^{-\frac{(x-1465.251391)^2}{2(17.38)^2}}$$

The membership functions of the fuzzy sets are presented in Figure 3.

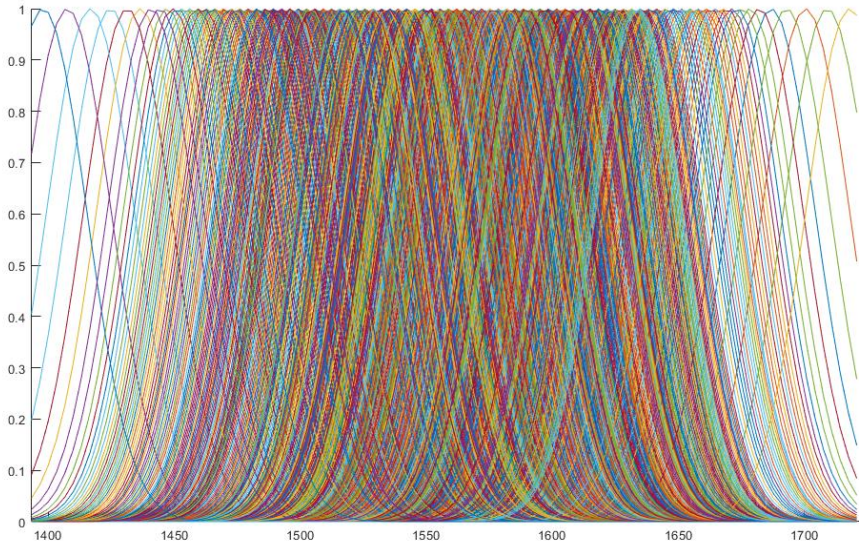


Fig. 3. Membership Function of fuzzy sets in the variable of depth

b) Variable of Effective Porosity (PHIE)

Based on the data, the effective porosity variable has a minimum value of 0 and a maximum value of 0.3. Therefore, the universal set of this variable is $U_{PHIE} = [0,0.3]$. After that, the 484 fuzzy sets are defined based on the centers that have been obtained from FCM, which are $PHIE_1, PHIE_2, PHIE_3, \dots, PHIE_{484}$ with the membership function as follows.

$$\mu_{PHIE_1}(x) = e^{-\frac{(x-0.157510931)^2}{2(0.01593)^2}}$$

$$\mu_{PHIE_2}(x) = e^{-\frac{(x-0.175397492)^2}{2(0.01593)^2}}$$

$$\mu_{PHIE_3}(x) = e^{-\frac{(x-0.200987456)^2}{2(0.01593)^2}}$$

...

$$\mu_{PHIE_{484}}(x) = e^{-\frac{(x-0.212678851)^2}{2(0.01593)^2}}$$

The membership functions of the fuzzy sets are presented in Figure 4.

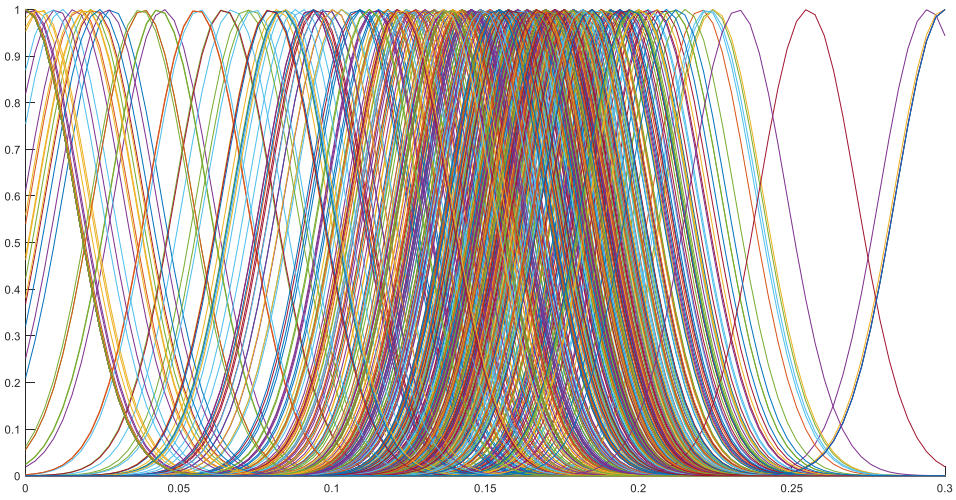


Fig. 4. Membership Function of fuzzy sets in PHIE variable

c) Variable of Effective Porosity of Log Neutron Density (PHIE_DN)

Based on the data, the minimum and maximum values of the effective porosity of log neutron density variable are -0.0021 and 0.467655, respectively, and so the universal set for this variable is $U_{PHIE_DN} = [-0.0021, 0.467655]$. After that, the 484 fuzzy sets are defined based on the centers that have been obtained from FCM, namely $PHIE_DN_1, PHIE_DN_2, PHIE_DN_3, \dots, PHIE_DN_{484}$ with the membership function as follows.

$$\mu_{PHIE_DN_1}(x) = e^{-\frac{(x-0.157511004)^2}{2(0.02462)^2}}$$

$$\mu_{PHIE_DN_2}(x) = e^{-\frac{(x-0.175398214)^2}{2(0.02462)^2}}$$

$$\mu_{PHIE_DN_3}(x) = e^{-\frac{(x-0.20098793)^2}{2(0.02462)^2}}$$

$$\dots$$

$$\mu_{PHIE_DN484}(x) = e^{-\frac{(x-0.212679213)^2}{2(0.02462)^2}}$$

The membership functions of the fuzzy sets are presented in Figure 5.

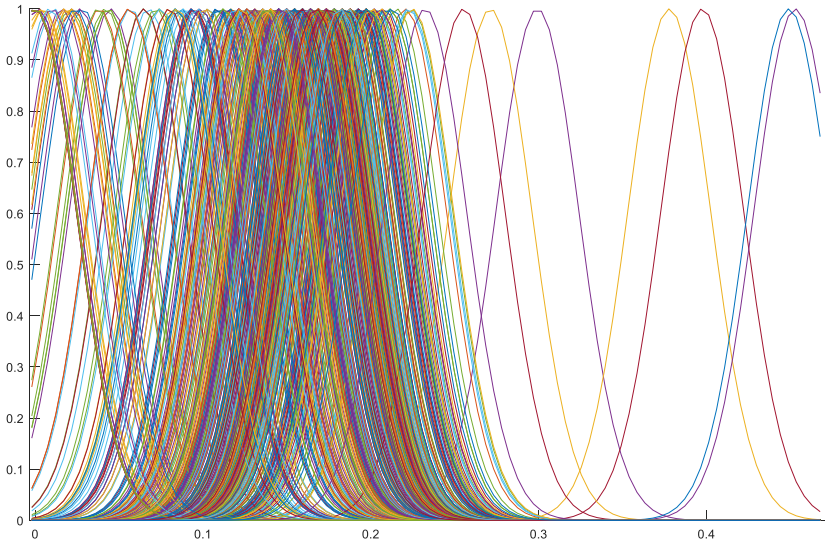


Fig. 5. Membership Function of fuzzy sets in PHIE_DN variable

d) Variable of Total Porosity (PHIT)

Based on the data, the minimum and maximum values of the total effective porosity are 0.077538 and 0.3, respectively, therefore the universal set of this variable is $U_{PHIE} = [0.077538,0.3]$. Thereafter, the 484 fuzzy sets are defined based on the centers that have been obtained from FCM, namely $PHIT_1, PHIT_2, PHIT_3, \dots, PHIT_{484}$ with the membership function as follows.

$$\mu_{PHIT_1}(x) = e^{-\frac{(x-0.157511554)^2}{2(0.01182)^2}}$$
$$\mu_{PHIT_2}(x) = e^{-\frac{(x-0.17540327)^2}{2(0.01182)^2}}$$
$$\mu_{PHIT_3}(x) = e^{-\frac{(x-0.201035045)^2}{2(0.01182)^2}}$$
$$\dots$$
$$\mu_{PHIT_{484}}(x) = e^{-\frac{(x-0.212692605)^2}{2(0.01182)^2}}$$

The membership functions of the fuzzy sets are presented in Figure 6.

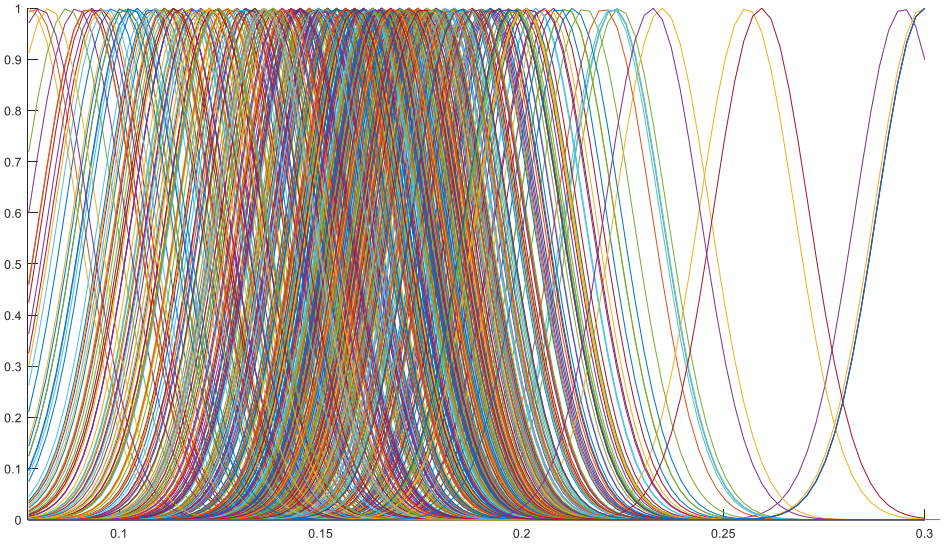


Fig. 6. Membership Function of fuzzy sets in PHIT variable

e) Variable of Total Porosity of Log Neutron Density (PHIT_DN)

Based on the data, the minimum and maximum values of the total porosity of log neutron density variable are 0.077538 and 0.467655, consecutively. Therefore, the universal set of this variable is $U_{PHIT_DN} = [0.077538,0.467655]$. After that, the 484 fuzzy sets are defined, which are $PHIT_DN_1, PHIT_DN_2, PHIT_DN_3, \dots, PHIT_DN_{484}$ with the membership function as follows.

$$\mu_{PHIT_DN_1}(x) = e^{-\frac{(x-0.157511627)^2}{2(0.0204)^2}}$$
$$\mu_{PHIT_DN_2}(x) = e^{-\frac{(x-0.175403992)^2}{2(0.0204)^2}}$$
$$\mu_{PHIT_DN_3}(x) = e^{-\frac{(x-0.201035518)^2}{2(0.0204)^2}}$$
$$\dots$$
$$\mu_{PHIT_DN484}(x) = e^{-\frac{(x-0.212692967)^2}{2(0.0204)^2}}$$

The membership functions of the fuzzy sets are presented in Figure 7.

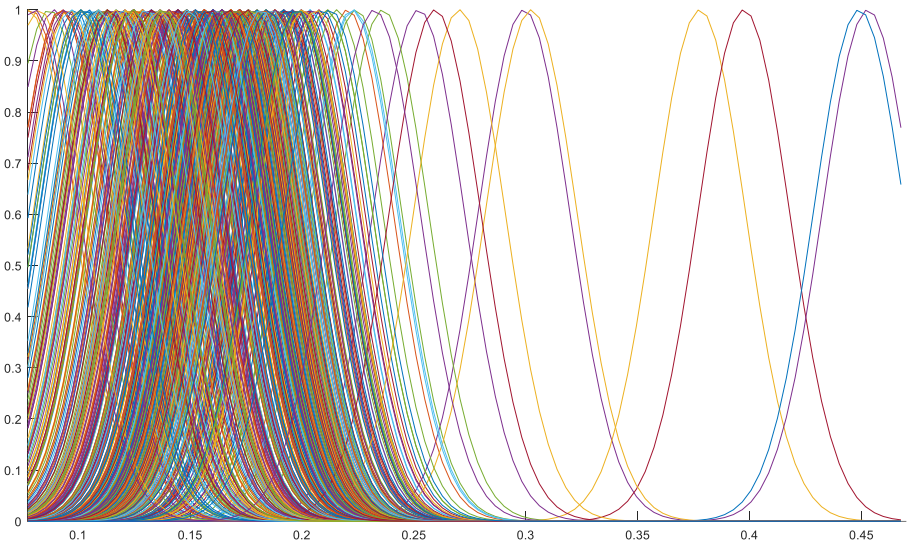


Fig. 7. Membership Function of fuzzy sets in PHIT_DN variable

4.2.2 The Determination of fuzzy rules

Based on Table 1, 484 optimal clusters are obtained and therefore there are 484 zero-order Sugeno fuzzy rules which can be expressed in the following form:

Rule (1) "IF x_1 = DEP_1 and x_2 = $PHIE_1$ and x_3 = $PHIE_DN_1$ and x_4 = $PHIT_1$ and x_5 = $PHIT_DN_1$, THEN y = b_1"
Rule (2) "IF x_1 = DEP_2 and x_2 = $PHIE_2$ and x_3 = $PHIE_DN_2$ and x_4 = $PHIT_2$ and x_5 = $PHIT_DN_2$, THEN y = b_2"
Rule (3) "IF x_1 = DEP_3 and x_2 = $PHIE_3$ and x_3 = $PHIE_DN_3$ and x_4 = $PHIT_3$ and x_5 = $PHIT_DN_3$, THEN y = b_3"

…

Rule (484) "IF x_1 = DEP_{484} and x_2 = $PHIE_{484}$ and x_3 = $PHIE_DN_{484}$ and x_4 = $PHIT_{484}$ and x_5 = $PHIT_DN_{484}$, THEN y = b_{484}"
where b is the value of the 6th column in the matrix center presented in Table 2.

4.2.3 Defuzzification

Furthermore, the defuzzification, which is a process of changing a fuzzy set into a real number [27], was carried out. In this study, the weight average is used in the defuzzification process using the following equation [28]:

$$y = \frac{\sum_{i=1}^{484} y_i(\mu_{A_{i1}}(x_1)\mu_{A_{i2}}(x_2) \dots \mu_{A_{in}}(x_n))}{\sum_{i=1}^{484}(\mu_{A_{i1}}(x_1)\mu_{A_{i2}}(x_2) \dots \mu_{A_{in}}(x_n)}$$

where $\mu_{A_{ij}}$ is a membership function of fuzzy set of the j^{th} input and i^{th} rule, and y_i is a consequent part of the i^{th} rule.

4.3 Model Testing For Prediction

Model testing was carried out by comparing the MAPE values of each model. The model that has the smallest MAPE will be used as the final model. In this study, the smallest obtained value of MAPE for training data and testing data are:

$$MAPE_{Training} = \frac{\sum_{i=1}^{1689} \frac{|X_i - F_i|}{X_i} x100\%}{1689} = 9.9397\ \%$$

$$MAPE_{Testing} = \frac{\sum_{i=1}^{563} \frac{|X_i - F_i|}{X_i} x100\%}{563} = 9.3436\ \%$$

Furthermore, the prediction of water saturation by using several other methods was also performed such as fuzzy Mamdani, Back-Propagation Neural Network (BPNN), and Long Short Term Memory Recurrent Neural Network (LSTM-RNN). A comparison of the results of prediction accuracy with various methods can be seen in Table 3.

Table 3
The comparison of prediction using several methods

Method	MAPE (%)	
	Training	Testing
Zero-order Sugeno	9.9397	9.3436
Fuzzy Mamdani	17.0139	16.3307
BPNN	10.9144	10.2579
LSTM-RNN	41.5080	36.6248

Based on Table 3, prediction accuracy with the zero-order Sugeno fuzzy method gives better results compared to other methods, with MAPE values for training and testing data 9.9397% and 9.3436%, respectively.

4. Conclusions

This research resulted the zero-order Sugeno fuzzy models to predict water saturation. The FCM method was used to reduce the number of rules in the zero-order Sugeno fuzzy model. The results of this study indicate that the prediction of water saturation using the zero-order Sugeno fuzzy method provides accuracy for training and testing data which are 90.0603% and 90.6564%, respectively. These prediction results are much better compared to the Mamdani fuzzy model, BPNN, and LSTM-RNN. This shows that the zero-order Sugeno fuzzy model has advantages for the prediction of water saturation compared to other methods. The results of this study will be used for future research development, namely, the prediction of hydrocarbon content in various layers of soil and rock using a fuzzy model of first-order Sugeno and deep learning.

Acknowledgement
We would like to thank PT. Geotama Energi, Yogyakarta, Indonesia for the supporting data of water saturation.

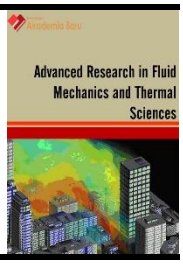
References
[1] Badan Pusat Statistika Indonesia. (2019). *Produk Domestik Bruto Indonesia Triwulanan 2015-2019*. Page 65 – 68.
[2] Finance Detik.com. (2014). *Ini dia daftar kilang minyak milik Indonesia*. https://finance.detik.com/energi/d-2576861/ini-dia-daftar-kilang-minyak-milik-indonesia. Accessed at October 13, 2019.

[3] CNBC Indonesia. (2019). Cadangan Minyak RI Turun: Sisa 10 Tahun Lagi. https://www.cnbcindonesia.com/news/20190116111811-4-50891/waduh-cadangan-minyak-ri-turun-sisa-10-tahun-lagi. Accessed at October 13, 2019.
[4] Speight, J.G. (2011). *An Introduction to Petroleum Technology, Economics, and Politics*. Scrivener Publishing: Masachussets, USA.
[5] Younes, M.A.A. (2012). *Crude oil exploration in the world*. InTech: Rijeka, Croatia.
[6] Han, Y., Zhang, Y., Xu, C. and Hsu, C.S. "Molecular characterization of sulfur-containing compounds in petroleum." *Fuel 221,* (2018): 144-158.
[7] Bayona, J.M., Dominguez, C. and Albaiges, J. "Analytical developments for oil spill fingerprint." *Trends in Environmental Analytical Chemistry 5*, (2015): 26-34.
[8] Goodwin, A.R.H., Pirolli, L., May, E.F. and Marsh, K.N. (2014). *Future Energy*. Elseiver: Amsterdam, The Netherlands. Page 19-52.
[9] Lyons, W.C. (2010). *Working Guide to Reservoir Engineering*. Elseiver: Amsterdam, The Netherlands. Page 97-232.
[10] Afizu, M. "Determining the Relationship between Resistivity, Water and Hydrocarbon Saturation of Rock Formation Using Composite Well Logs."*Academic Journal of Interdisciplinary Studies 2,* no. 13 (2013): 119-123.
[11] Bhavsar, P., Safro, I., Bouaynaya, N., Polikar, R., and Dera, D. (2017). *Data Analytics for Intelligent Transportation System*. Elseiver: Amsterdam, The Netherlands. Page 283-307.
[12] Kenari, S.A.J. and Mashohor, S. "Robust committee machine for water saturation prediction."*Journal of Petroleum Science and Engineering 104,* (2013): 1-10.
[13] Alrumah, M. and Ertekin, T. "Prediction of the water saturation around wells with bottom water drive using artificial neural networks." *Journal of Petroleum and Gas Engineering 10,* no. 2 (2019): 14-22.
[14] Mohamed, I.A., Hemdan, M., Hosny, A. and Rashidy, M. "High-resolution water-saturation prediction using geostatistical inversion and neural network methods." *Interpretation 7,* no. 2 (2019): 455-465.
[15] Mardi, M., Nurozi, H. and Edalatkhah, S. "A water saturation prediction using artificial neural networks and an investigation on cementation factors and saturation exponent variations in an iranian oil well." *Journal Petroleum Science and Technology 30,* (2011): 425-434.
[16] Hamada M, G., Ahmed, E. and Chaw Y, N. "Artificial neural network (ANN) prediction of porosity and water saturation of shaly sandstone reservoirs." *Advances in Applied Science Research 9,* (2018): 26-31.
[17] Marcus, J.S., Enaworu, E., Rotimi, O.J., and Seteyeobot, I. "A proposed solution to the determination of water saturation: using a modelled equation." *Journal of Petroleum Exploration and Production Technology 8,* (2018): 1009-1015.
[18] Ibrahim, D. "An overview of soft computing." *Procedia Computer Science 102,* (2016): 34-38.
[19] Thampi, S.M. and El-Alfy, E.S.M. "Soft computing and intelligent systems: techniques and applications." *Journal of Intelligence and Fuzzy Systems 36,* (2019): 1939-1944.
[20] Potey, M. and Sinha, P.K. "Review and analysis of machine learning and soft computing approaches for user modeling." *International Journal of Web & Semantic Technology 6,* no. 1 (2015): 39-55.
[21] Dutta, A.K. "A fuzzy based soft computing technique to predict the movement of the price of stock." *International Journal of Advanced Computer Science and Applications 9,* no. 1 (2018): 39-55.
[22] Matar, S. and Hatch, L.F. (2000). *Ilmu Kimia: Proses Petrokimia*. Gulf Publishing Company: Houston, Texas, USA.
[23] Crain, E.R. (2018). *Crain's Petrophysical Handbook*. https://spec2000.net. Accessed at October 19, 2019.
[24] Takagi, T. and Sugeno, M. "Fuzzy identification of systems and its application to modelling and control." *IEEE Trans Syst Man Cybern 15,* (1985): 116-132.
[25] Sugeno, M. and Yasukawa, T. "A fuzzy logic based approach to qualitative modelling." *IEEE Trans Fuzzy Syst 1,* (1993): 7-31.
[26] Suganya, R. and Shanthi, R. "Fuzzy C-Means algorithm- a review." *International Journal of Scientific and Research Publications 2,* (2012): 1-3.
[27] Uzga-Rebrovs, O. and Kulesova, G. "Comparative analysis of fuzzy set defuzzification methods in the context of ecological risk assessment." *Information Technology and Management Science 20,* (2017): 25-29.
[28] Wang, L.X. (1997). *A course in fuzzy system and control.* Prentice Hall: Princeton.

Penerbit Akademia Baru

Engineering Science and Technology Conference Proceedings

Journal homepage: www.akademiabaru.com/EST.html



Torrefaction of Densified Palm Kernel Shell with Mixture of Starch and Water as Binder

Open Access

Muhammad Ariff Hanaffi Mohd Fuada[1], Mohamad Muslihuddin Razali[1], Zaitul Nadiah Mohamad Izal[1], Hasan Mohd Faizal[1, 2, *], Norhayati Ahmad[1, 3], Mohd Rosdzimin Abdul Rahman[4], Md. Mizanur Rahman[1]

[1] School of Mechanical Engineering, Faculty of Engineering, Universiti Teknologi Malaysia, 81310 UTM Johor Bahru, Johor, Malaysia.
[2] Automotive Development Centre (ADC), Institute for Vehicle System and Engineering, School of Mechanical Engineering, Faculty of Engineering, Universiti Teknologi Malaysia, 81310 UTM Johor Bahru, Johor, Malaysia
[3] Department of Material Engineering, Faculty of Engineering, Universiti Teknologi Malaysia, 81310 UTM Johor Bahru, Johor, Malaysia
[4] Department of Mechanical Engineering, Faculty of Engineering, Universiti Pertahanan Nasional Malaysia, Kem Sg. Besi, 57000, Kuala Lumpur, Malaysia

ABSTRACT

This study presents physical and fuel properties of mixture of palm kernel shell (PKS) and starch binder (weight ratio of 60:40) briquette torrefied at various temperatures (225-275℃) and nitrogen flow rates (1000-3000 mL/min). The physical appearance, compressive strength, density and mass yield as well as fuel properties such as high heating value (HHV), energy yield and proximate analysis of untorrefied and torrefied briquettes were determined in the present study. The properties of torrefied briquettes were also compared with the case of untorrefied briquettes as well as international benchmark. Torrefaction temperature significantly influenced the properties of torrefied briquette rather than flow rate of nitrogen. At severe torrefaction condition (temperature of 275℃), HHV of 22.16±0.23 MJ/kg was obtained, that is considered highest if compared to HHV of briquette torrefied at other temperatures. It was found that properties of the torrefied briquettes do not really affected when nitrogen flow rate is varied. Overall, with the presence of starch binder, briquettes with considerably high compressive strength were obtained if compared to the previously developed binderless PKS briquettes.

Keywords:
Palm kernel shell; starch binder; torrefaction; briquette; temperature effect; flow rate effect

Copyright © 2019 PENERBIT AKADEMIA BARU - All rights reserved

1. Introduction

Depletion of global coal sources, environmental and health issues are major limitations for the energy industries to cope with the needs of large energy demand. According to National Emission Inventory (2014) [1], coal combustion alone can contribute up to 2862 tonnes of toxicity gases per year, thus leading to the environmental and health issues globally. Therefore, global coal depletion sources that being used since 1973 [2] can be substituted by shifting to alternative fuel (cleaner-fuel).

Biomass based cleaner-fuel offers promising benefits due to "clean", energy potentiality, marketable and availability. Biomass-based fuel covers wide range of sources; from agricultural

* *Corresponding author.*
E-mail address: mfaizal@mail.fkm.utm.my (Hasan Mohd Faizal)

waste to municipal solid waste. Malaysia, being a world's dominant oil palm producer, oil palm wastes are among the highest commodity produced throughout the year with accounted 56.45 million tonnes of waste from different types [3]. The wastes majorly consist of 18.88 million tonnes of empty fruit bunch (EFB), 11.59 million tonnes of mesocarp fibre (MSF), 4.72 million tonnes of palm kernel shell (PKS), 17.10 million tonnes of trunk and 4.16 million tonnes of frond [3]. Due to the large volume of wastes, it is currently being used in multiple applications; manufacturing, agricultural, and energy production [4,5]. In the energy perspective, oil palm wastes are considered as carbon-based waste and potentially to be used in energy production due to the presence of considerable amount of carbon content and energy content with approximately 46 to 58% and 16 to 20MJ/kg, respectively [6]. Among the oil palm wastes, raw PKS has the highest amount of carbon content and energy content, that are 58% and 20 MJ/kg, respectively [6]. However, the performances of raw PKS are uncompetitive and unreadily used commercially if compared to coal. Therefore, combined pre-treatments; densification and torrefaction can convert raw PKS into a solid fuel with a high energy density [7]. Here, energy density is known as the amount of energy that contained in a unit volume of the densified products.

Densification (or compaction) is a conversion process of any loose materials into highly dense and durable products through compaction at high pressure [8,9]. In addition, densification allows proper utilization of loose materials or wastes and beneficial to the logistic purposes. Due to the flexibility, densification process is implemented for wide range of applications; energy productions [10], building industry[11], pharmaceutical [12], and electrical [13]. In the case of energy production, generally, biomass is densified in prior to the end-use purposes. However, the physical quality of densified biomass especially made of PKS is still unsatisfactory, thus adding supplemental binder is expected could address the issue.

Torrefaction is known for its capability to enhance the properties of raw biomass, to some extent become superior properties than that of coal [14]. Interestingly, torrefaction offers improvement at mild reaction; temperature range of 200 to 300℃ with heating rate of ≤50℃/min [15]. Torrefaction is typically performed in an inert environment with mild (200-250℃) or severe (250-300℃) reactions [16]. In both torrefaction reactions, degradation of lignocellulose components of biomass occurs [17], resulting the formation of various energy sources; bio-char, bio-oils and non-condensable gases. In addition, sufficiently high amount of energy obtained from severe reaction has been reported suitable for energy productions [18]. Interestingly, the syngas obtained from gasification of torrefied biomass has considerably higher quality if compared to the syngas obtained from direct-gasification of biomass [19]. Based on the advantages as mentioned above, solid products obtained from torrefaction have potential to be used as coal replacement. Development of oil palm biomass based briquette has been initiated by Husain, Zainac and Abdullah [10], by using mixture of palm fibre and palm kernel shell. In general, the use of excessively high compaction pressures that range from 150-800 MPa have been used for studies of densification of biomass as well as for commercialization [20,21] for obtaining high quality products. Thus, the scenarios, in turn making the densification process as an uneconomical process due large energy consumption; for example, a biomass pellet produced from 158 MPa had consumed energy of about 56.8 MJ/t [21]. Due to that, considerable amount of efforts in producing oil palm briquette with high quality have been performed until now.

The effect of various parameters such as compaction pressure, composition, type of binder as well as size of particles on the performance of briquettes have been studied in making a durable briquette [22,23]. Briquette made of PKS has drawn attentions from a few parties such as industries and researchers due to the substantial amount of energy obtained during combustion. Besides, the presence of high composition of lignin [23] in PKS can be a source of binder for high

quality briquette development. A study revealed that the thermally heated lignin during briquetting can produce physically strong oil palm briquettes with average of 7.9MPa of compressive strength, showing that the potential of lignin to become as a binder, and adding additional binder might enhance the physical strength of the briquettes [24]. Meanwhile, in a recent study, briquettes made of PKS have been developed at a controlled condition (operating pressure of 7 MPa, temperature of 150℃ and holding time of 30 minutes), nevertheless the strength was found to be poor after torrefaction even though sufficiently high amount of lignin contained in PKS [7].

On the other hand, to eliminate the thermally heated process during briquetting, the use of additional binder could be a potential alternative. Interestingly, the additional binder could be made of readily available sources derived from organic (i.e natural sources) and inorganic (synthetic sources) by-products [23]. Generally, natural sources are environmentally friendly [12] rather than synthetic sources which are more hazardous [25]. Both sources of binder have been used and tested by many researchers and the results demonstrated the possibility of producing durable and high density briquette, ranging from 1 to 14 MPa of compressive strength and 820 to 1137kg/m^3 of mass density [21,23,25–31]. For the case of the natural binder, the mixture of PKS bio-char and starch briquette has been developed [29]. Interestingly, the study has shown the presence of starch binder played an important role in making a durable PKS briquette [29]. Based on their study, they obtained 821±26 kN/m^2 of tensile crushing strength and 167 of impact resistance index (IRI) [29]. However, the study had reported that the briquette has achieved a considerably low water resistance index of less than 50%, revealing that the briquette with starch binder is more hygroscopic, and this phenomena could degrade the combustibility performance as well as inconvenience for logistic activities (handling, storage and transportation) [29]. Interestingly, by torrefaction, the aforementioned problem could be potentially addressed so that the products have potential to become more hydrophobic nature [14,32].

Combined pretreatments of biomass densification (with additional binder) followed by torrefaction can become the state-of-the-art effort to be studied. The study on combined pretreatments has not been performed yet for the case of PKS with starch binder, even though numerous studies on the combined densification and torrefaction are widely published. The previous studies on combined densification and followed by torrefaction or vice versa have shown a significant improvement in terms of the quality of biomass pellets or briquettes due to the torrefaction effect [7,14,32–34]. As recorded previously, combined torrefaction and followed by densification could produce the physically strong and dense biomass pellets, however, large energy consumption used during densification have been reported [33,34]. A recent study has shown that binderless PKS briquette suffered a severe physical destruction at severe torrefaction reaction [7]. Nevertheless, there is no study used PKS briquette with starch as binder for the combined pretreatments of densification and torrefaction.

The present study is performed to understand fundamentally the physical and combustion properties of PKS briquette that containing starch binder (with weight ratio of 60:40) after torrefaction. The parameters involved were torrefaction temperature (225-275℃) and nitrogen flow rate (1000-3000 mL/min). Physical and combustibility performances of briquette were evaluated in terms of physical appearance, density, compressive strength, density yield and mass yield as well as energy yield, heating value, and proximate analysis. Furthermore, the produced briquettes in the present study are also compared with international benchmarks as well as previously produced binderless PKS briquette [7].

2. Materials preparation and methodology

2.1 Materials

The PKS was collected from a local oil palm mill and was pulverized by using crushing machine (RETSCH BB50). The pulverized PKS was then sieved to obtain particles with size of less than 500µm by using a sieve shaker machine (RETSCH type AS200 digit). Meanwhile, corn starch was purchased from a local supplier. The properties of materials are shown in Table 1. In this study, the moisture content and volatile matter of raw PKS were found to be lower than that of corn starch binder. Meanwhile, ash content, fixed carbon and high heating value of raw PKS are higher if compared to corn starch binder.

Table 1
Properties of raw PKS and corn starch binder

	Raw PKS	Corn starch binder
Proximate analysis		
Moisture content (wt %)	6.75±3.23	77.35±0.56
Volatile matter (db %)[a]	74.77±0.79	96.98±0.36
Ash content (db%)[a]	4.66±0.92	0.22±0.22
Fixed carbon (db %) [a, b]	20.57±0.54	2.79±0.58
High heating value (MJ/kg)	17.88±0.02	1.31±0.33

[a] dry basis
[b] Calculated by difference

2.2 Gelatinization of starch binder and briquetting

For preparation of starch binder , the corn starch and distilled water with weight ratio of 80:20 [35] were mixed and continuously stirred at stirring speed of 200 rpm for 10 minutes at room temperature to ensure the homogeneity of the mixture [35]. The mixture of starch and water were then gelatinized and continuously stirred at the same rated speed of 200rpm in warm water with temperature of 75℃ for 30 minutes [12,36]. The gelatinized starch binder was left to cool inside a desiccator for a day in prior to mixing with pulverized PKS.

Then, the PKS and starch binder with weight ratio of 60:40 were mixed homogeneously by using a stand mixer (Model PM-215) at low speed (at level 1) for 30 minutes [37]. The mixing ratio of 60:40 was employed due to the promising abrasive resistance, in which higher than 95% obtained from previously developed briquette made of rice husk and sugarcane bagasse [38]. Based on that statement, 50g of the mixture of PKS and starch binder were loaded into a 50mm diameter of cylindrical stainless-steel die set and the mixture was compressed at constant conditions (compaction pressure of 7 MPa and holding time of 30 minutes) by using INSTRON 600 DX Universal Testing Machine. The produced PKS and starch binder briquette was left at an ambient condition for a week to achieve stability

2.3 Torrefaction of PKS and starch binder briquette

In the present study, a single-process torrefaction was performed in a vertical reactor with internal diameter of 100mm. The reactor was equipped with heater clamp on the outer surface of reactor as well as K-type thermocouple sensor. The K-type thermocouple sensor was set 3 mm above the briquette in the reactor. In this study, the briquette was torrefied for various torrefaction temperatures and nitrogen flow rates of 225 to 275℃ and 1000 to 3000 mL/min, respectively. Initially, the briquette was settled on the mesh holder and was placed inside the reactor. The lid of reactor was sealed tightly. Later, the reactor was purged by designated nitrogen flow rates for one hour and subsequently the briquette was heated according to the desired

torrefaction temperature for 30 minutes. Upon completion, the heater was set to 30℃ and the briquette was cooled under continuous flow of nitrogen. Finally, the briquette was taken out from the reactor and was left at an ambient condition for a week to ensure the stability and rigidity.

2.4 Characterization

Proximate analysis of the untorrefied and torrefied briquettes were performed in accordance to the ISO standards; moisture contents (EN ISO 18134-2:2015) [39], volatile matter content (EN ISO 18123:2015) [40], and ash content (EN ISO 18122:2015) [41]. Meanwhile, high heating value was determined in accordance to ISO standards EN ISO 14918:2010 [42]. The heating values for the untorrefied and torrefied briquettes were determined by using IKA calorimeter system (model C2000).

In the present study, the relaxed density was also determined by measuring the mass and volume of the untorrefied and torrefied briquette [43] while mass and energy yields were determined by following method introduced by Bridgeman et al. [44] and Huang et al. [45], respectively. The equation for determining density, mass and energy yield of briquettes are shown in Equation 1 to 4.

$$\text{Relaxed density (kg/m}^3\text{)} = \text{mass (kg)} / \text{volume (m}^3\text{)} \quad (1)$$

$$\text{Mass yield (\%)} = [(\text{mass of torrefied briquette})/ (\text{mass of untorrefied briquette})] \text{ X } 100 \quad (2)$$

$$\text{Density yield (\%)} = [(\text{density of torrefied briquette})/(\text{density of untorrefied briquette}) \text{ X } 100 \quad (3)$$

$$\text{Energy yield (\%)} = \text{mass yield (\%) X (heating value of torrefied biomass/heating value of untorrefied biomass)} \times 100 \quad (4)$$

2.5 Compressive testing

In the present study, the compressive strength of the untorrefied and torrefied briquettes were tested by using INSTRON 100 kN Universal Testing Machine. The produced briquette was put on the centre of bottom plate of the compression machine. The top plate of the compression machine was then moved downward with a speed of 0.05 mm/sec to compress the briquette. The test was completed when the sudden drop of force (that representing the crack) was observed.

3. Results and discussion

3.1 Effect of torrefaction temperature on physical and combustion properties of briquettes

Generally, temperature plays an important role in affecting physically and combustibility of torrefied products. The reaction becomes more severe as the temperature is increased. For investigation on the effect of temperature, the briquettes were torrefied under various torrefaction temperatures (225, 250 and 275℃) at a constant flow rate of nitrogen (1000 mL/min).

3.1.1 Physical appearance of torrefied briquettes

Figure 1 shows the physical appearance of briquettes that contained mixture of PKS and starch binder torrefied under various torrefaction temperatures (225, 250 and 275℃) at a constant flow

rate of nitrogen (1000 mL/min). Here, the image of the untorrefied briquette is also enclosed. With an increase in torrefaction temperature, the physical condition of the torrefied briquettes was found to be slowly degraded (mild crack surface). This is mainly due to the intense reaction of torrefaction as the temperature is increased. Interestingly, the physical condition of the torrefied briquettes in this study was considerably improved and sustained even after intensively torrefied at severe torrefaction condition if compared to the previous study, in which the briquettes suffered a mild and severe deterioration at 250℃ and 275℃, respectively [7]. These findings revealed that the starch binder is hardened as it is thermally heated [23]. Meanwhile, the colour of the torrefied briquettes changed from light brownish to darker as torrefaction temperature is increased, indicating the increase of carbon content after torrefaction [14].

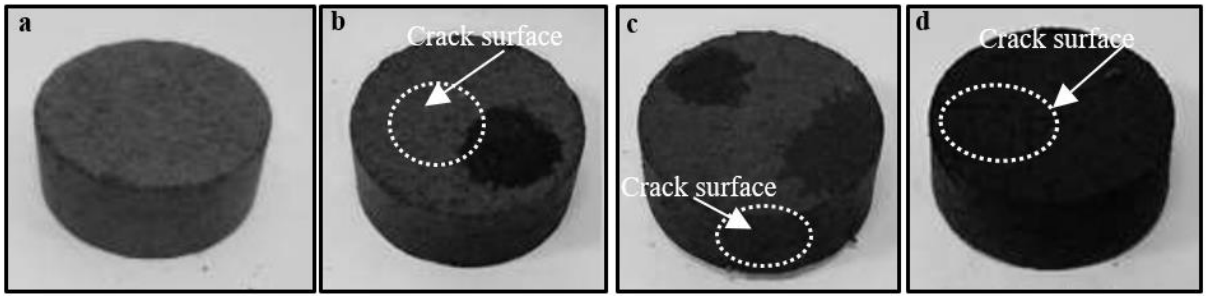


Fig. 1. Physical appearance of (a) untorrefied briquette, (b) briquette torrefied at 225℃, (c) briquette torrefied at 250℃ and (d) briquette torrefied at 275℃

3.1.2 Physical properties of torrefied briquette

Figure 2 shows the compressive strength of torrefied briquettes produced under various torrefaction temperatures. It was found that the compressive strength decreases, ranging from around 9.61±1.20 to around 3.41±0.01 MPa when the torrefaction temperature is increased from 225 to 275℃. This phenomenon is mainly due to the more intense reaction during torrefaction as temperature is increased, resulting in more severe physical degradation. This phenomenon is also well agreed by few studies on torrefied briquette [7,26,46]. Interestingly, in the present study, strengths of the produced torrefied briquettes regardless of torrefaction temperature were considerably higher if compared to the strength of the untorrefied briquette (2.59±0.07 MPa) and the strength of the previously developed torrefied binderless PKS briquettes (0.8 to 2.5 MPa) [7], thus revealing the importance of starch binder in producing highly durable briquette [23]. Meanwhile, the densities of the torrefied briquettes (Figure 3) in the present study were recorded a slight lower if compared to the untorrefied briquette, with the range of around 846 to 753 kg/m^3.

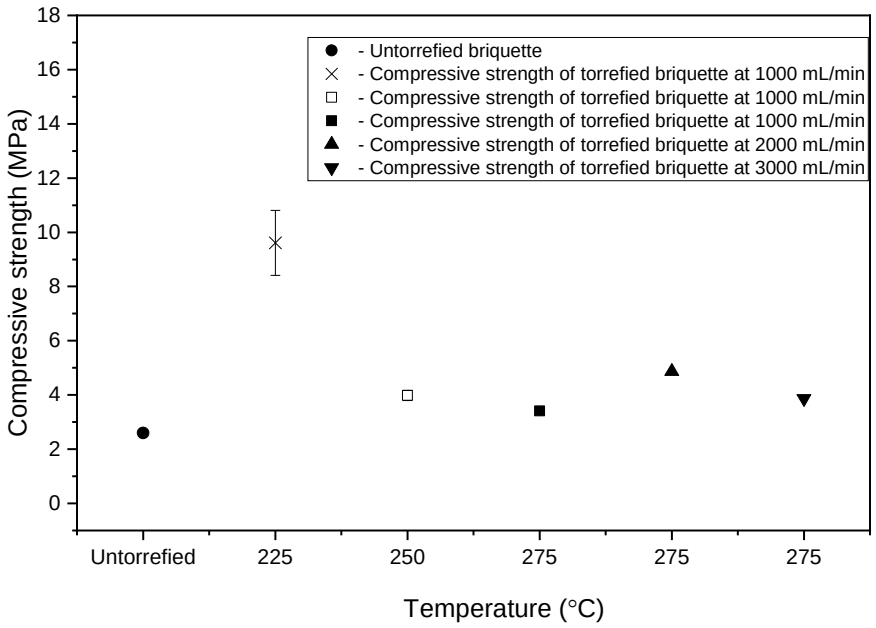


Fig. 2. Compressive strength of briquettes torrefied under various temperatures and flow rates of nitrogen

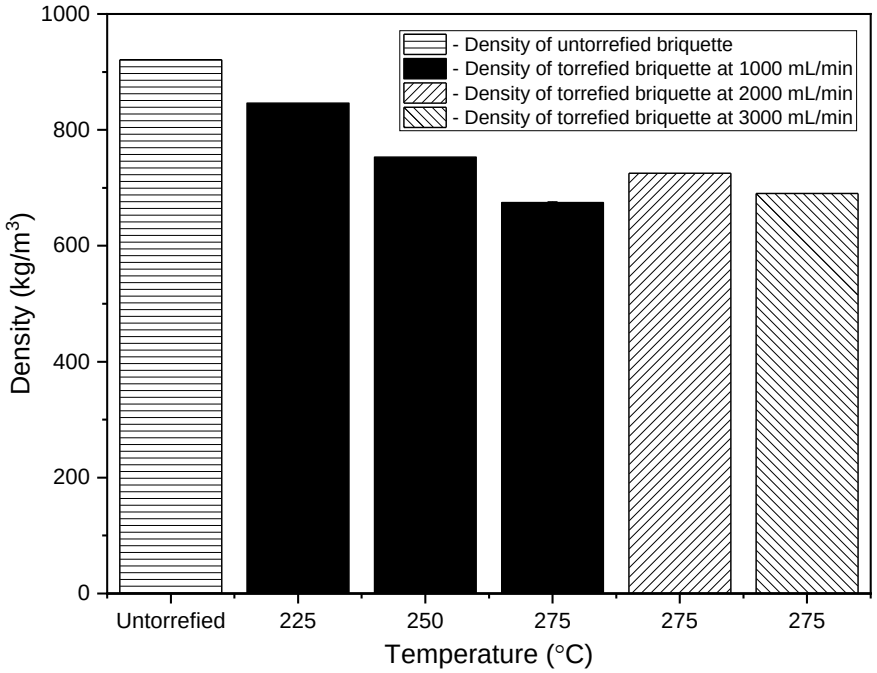


Fig. 3. Density of briquettes torrefied at various temperatures and flow rates of nitrogen

3.1.3 Combustion properties of torrefied briquette

Figure 4 illustrates the mass and energy yields of briquettes torrefied under various torrefaction temperatures. In the present study, the mass and energy yields of the torrefied briquettes decrease from 84 to 59 % and 89 to 73%, respectively as the torrefaction temperature is increased from 225 to 275℃. The decreasing trend of mass and energy yields of the torrefied briquettes revealed that the rapid devolatilization takes place during torrefaction [14,34].

The high heating value (HHV) of the briquettes torrefied at various torrefaction temperatures are shown in Table 2. It could be observed that as the torrefaction temperature is increased, the HHV of the torrefied briquettes increased from 17.88±0.01 to 22.16±0.23 MJ/kg, thus implying the increase of carbon and fixed carbon contents. However, the HHV of the briquettes torrefied at 225℃ showed a slight increase of about only 6% from HHV of the untorrefied briquette due to mild decomposition phase. Generally, the HHV of the torrefied briquettes produced in the present study are higher if compared to the HHV of the untorrefied briquettes. However, the HHV of the torrefied briquettes in the present study were slightly lower than that of the previously developed torrefied binderless PKS briquette [7]. In addition, it was found that the performance still fulfills the requirement stated by international benchmarks. As comparison, at the same torrefaction temperature (i.e 275℃), HHV of the torrefied binderless PKS briquette [7] was recorded as 24.12 MJ/kg while torrefied PKS briquette with starch binder in the present study has HHV of 22.16±0.23 MJ/kg. This phenomenon is supposed due to the high composition of starch binder, thus causing the produced torrefied briquettes in the present study tend to be more hygroscopic.

The proximate analysis of the untorrefied briquettes and briquettes torrefied at various temperatures is shown in Table 2. Generally, fixed carbon of the torrefied briquettes in the present study increased from 19.15±0.68 to 35.73±2.27 db% when the torrefaction temperature is increased. Meanwhile, it was found that the volatile matter of the torrefied briquettes slightly increases after torrefied at 225℃ and subsequently decreases from 69.95±1.00 to 58.27±2.45 db% when the torrefaction temperature is increased. On the other hand, the ash content of the torrefied briquettes produced under various torrefaction temperatures were found to be significantly higher (within the range of 4.42±0.48 to 6.00±0.18 db%) if compared to the ash content of the untorrefied briquette (only 4.66±0.91 db%). However, it can be said that the ash content of the torrefied briquettes in the present study is still competitive if compared to the international benchmarks. The occurrence of this phenomena is due to the lower torrefaction temperatures employed in the present study than the temperature of vaporization phase of alkali salts in ash [47,48]. In the present study, moisture content of the torrefied briquettes were recorded within the range of 3.53±1.13 to 4.28±0.15%. Generally, it can be said that the moisture content of the briquettes decreases when the torrefaction reaction is applied due to the drying and vaporization process. Overall, it was found that the moisture content of the torrefied briquettes in the present study fulfill the requirement as stated by EN ISO 18134-2:2015 (<10%) [39] while the ash content was recorded to be competitive if compared to the requirement as stated by EN ISO 18122:2015 (<3%) [41].

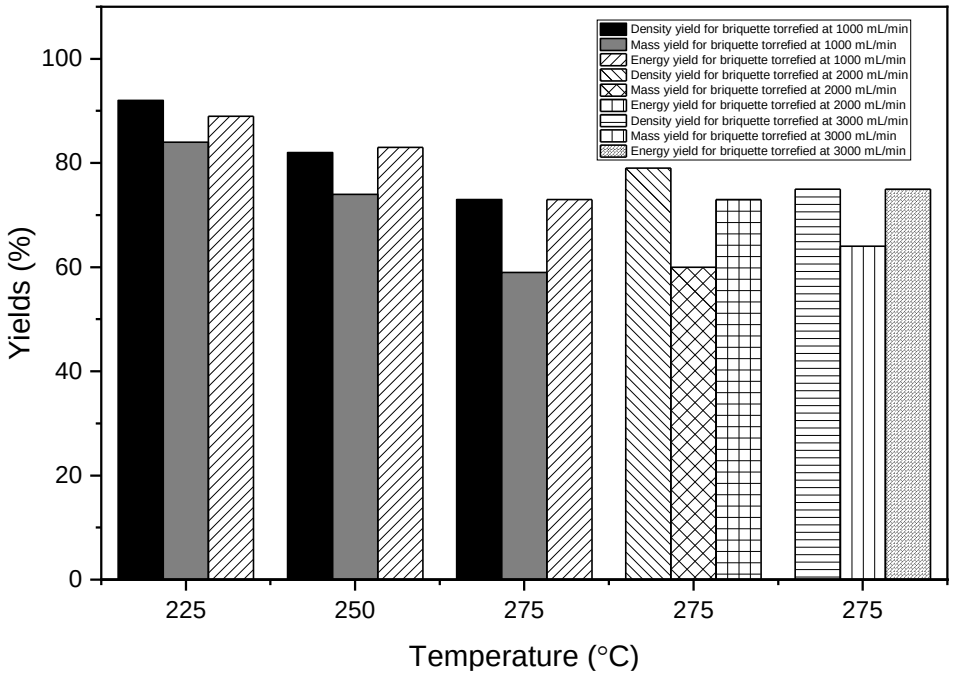


Fig. 4. Yields of briquettes torrefied under various temperatures and flow rates of nitrogen

Table 2
Summary of fuel properties of untorrefied briquettes and briquettes torrefied under various torrefaction temperatures and nitrogen flow rates

Analysis	**Conditions**						**International benchmark**
	Untorrefied	225[a]	250[a]	275[a]	275[b]	275[c]	
Proximate analysis							
Moisture content (%)	6.75±3.22	3.53±1.13	3.82±1.20	4.28±0.15	4.71±0.19	5.23±0.28	<10[d]
Volatile matter (db %)	74.77±0.78	76.42±0.36	69.95±1.00	58.27±2.45	58.31±1.00	61.33±1.65	
Ash content (db %)	4.66±0.91	4.42±0.48	4.97±0.64	6.00±0.18	7.41±0.31	7.28±0.29	<5[e]
Fixed carbon (db %)	20.57±0.54	19.15±0.68	25.08±1.63	35.73±2.27	34.28±1.32	31.39±1.36	
High heating value (MJ/kg)	17.88±0.01	18.96±0.33	20.07±0.38	22.16±0.23	21.82±0.58	20.85±0.26	>20[f]

[a] Briquette torrefied with flow rate of 1000 mL/min
[b] Briquette torrefied with flow rate of 2000 mL/min
[c] Briquette torrefied with flow rate of 3000 mL/min
[d] EN ISO 18134-2:2015[39]
[e] EN ISO 18122:2015 [41]
[f] EN ISO18125 [53]

3.2 Effect of nitrogen flow rate on physical and combustion properties of briquettes

In the present study, the investigation on the effect of nitrogen flow rate on the physical and combustion properties of briquette was performed at torrefaction temperature of 275℃ and nitrogen flow rates of 1000 to 3000 mL/min.

3.2.1 Physical appearance of briquettes torrefied under various nitrogen flow rates

Figure 5 shows the physical appearance of the briquettes torrefied at 275℃ under various nitrogen flow rates. It was found that the colour of briquettes torrefied at various nitrogen flow rates change to dark colour after being torrefied. However, the colour level was recorded to become mild once nitrogen flow rate is increased, thus revealing that the briquette may not fully carbonized. This is mainly due to the increasing volume of nitrogen gas that in turn leading to more unreactive atmosphere during torrefaction. This phenomenon is also consistent with previously studied torrefaction of oil palm frond for various flow rates of 50 to 150 mL/min [49]. Meanwhile, the physical appearance of the briquettes torrefied at various flow rates (Figure 5) was considerably sturdy as with only mild crack could be observed on the surface of the torrefied briquette, thus revealing the hardening of binder takes place when the briquette is thermally heated [23].

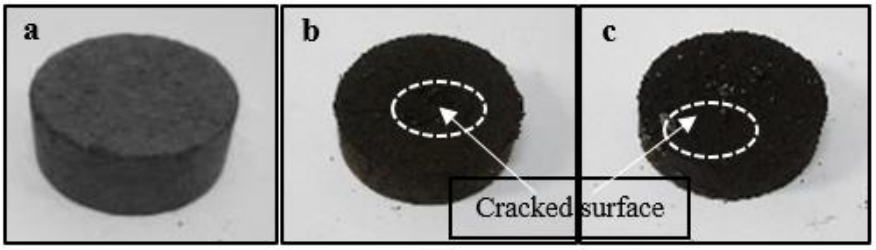


Fig. 5. Physical appearance of briquettes torrefied under various flow rates of nitrogen: a) untorrefied briquette, b) briquette torrefied at 2000 mL/min and c) briquette torrefied at 3000 mL/min

3.2.2 Physical properties of torrefied briquettes for various flow rates

The compressive strength of the torrefied briquettes produced at various flow rates is illustrated in Figure 2. In the present study, the values of compressive strength of the produced briquettes torrefied at various flow rates were recorded up to 4.87 MPa. If compared to the compressive strength of the untorrefied briquettes and briquettes torrefied at 275 ℃ under flow rate of 1000 mL/min, the strength of the briquette after torrefaction under flow rate of 2000 mL/min was relatively higher. It can be said that the strength of the torrrefied briquette slightly increases when the flow rate is increased, showing that the briquettes experience milder degradation due to more unreactive atmosphere. Meanwhile, density of the briquettes ranged from 725.42to 690.50 kg/m^3 when torrefied at various flow rates, showing that briquette is intensively volatilized during torrefaction.

3.3.3 Combustion properties of torrefied briquette for various nitrogen flow rates

The mass and energy yields of the produced briquettes torrefied at different flow rates are illustrated in Figure 4. In the present study, the mass yield of the torrefied briquettes increased from 60 to 64% with an increase in flow rate, proving that an increase in flow rate leads to more

unreactive atmosphere during torrefaction. Meanwhile, the energy yield of the torrefied briquettes in the present study was recorded within the range of 73 to 75%. If comparison is performed between the briquettes torrefied at nitrogen flow rate of 1000 mL/min and 2000 mL/min, it can be said that the changes of the yields (Figure 4) and density (Figure 3) are insignificant. Similar findings on the insignificant changes of yields of torrefied biomass under various nitrogen flow rates have also been reported by several studies [50–52].

Table 2 shows the high heating value for the untorrefied briquettes and briquettes torrefied under various flow rates. It could be observed that the heating value of the torrefied briquettes increases if compared to the untorrefied briquette. In the present study, the highest HHV was recorded about 21.82±0.58 MJ/kg for the briquette torrefied at 2000 mL/min. However, after the flow rate was increased to 3000 mL/min, the HHV of the torrefied briquettes slightly declined to 20.85 MJ/kg, thus proving that the environment for torrefaction becomes less reactive as the flow rate is increased. This phenomenon has been also reported in several studies[49,51]. Based on the proximate analysis of the torrefied briquette, it could be observed that the fixed carbon content of the torrefied briquettes slightly decreases from 34.28±1.32 to 31.39±1.36 db% when the flow rate is increased from 2000 to 3000 mL/min. Meanwhile, the ash content for briquettes torrefied at flow rates of 2000 and 3000 mL/min were recorded 7.41±0.31 and 7.28±0.29 db%, respectively, in which higher than that of the untorrefied briquettes, briquettes torrefied at flow rate of 1000 mL/min and international benchmarks. On the other hand, it was found that the volatile matter and moisture contents of the torrefied briquettes increase slightly from 58.31±1.00 to 61.33±1.65 db% and 4.71±0.19 to 5.23±0.28%, respectively with an increase in flow rate. Based on the comparison between briquettes torrefied at flow rate of 1000 mL/min and 2000 mL/min, it can be said that the changes of fuel properties are insignificant.

4. Conclusions

Briquettes made of mixture of PKS and starch binder were developed and an investigation was performed to study the effect of torrefaction temperature and nitrogen flow rate on the physical and combustion properties of the torrefied products. In terms of the effect of temperature, it can be said that torrefaction temperature is a dominant factor for the changes in physical and combustion properties. When temperature was increased, the compressive strength, density and density yield of the torrefied briquettes decreased. In terms of combustion properties of the torrefied briquettes produced under various temperatures, the mass and energy yields decreased while moisture content, HHV, fixed carbon and ash content increased with increasing temperature. In this study, combustion properties of the briquettes torrefied under various temperatures can be considerably improved than that of the untorrefied briquettes.

For the case of briquettes torrefied under various flow rates of nitrogen, compressive strength of up to 4.87MPa was achieved while density and density yield decreased with an increase in flow rate of nitrogen. When flow rate of nitrogen is increased, the ash content, fixed carbon and HHV of the produced briquettes decreased. However, mass and energy yields as well as moisture content and volatile matter increased with increasing flow rate of nitrogen. Overall, in most cases, due to the presence of starch binder, durable torrefied briquettes with competitive combustion properties could be obtained.

Acknowledgement

The authors acknowledge the Ministry of Higher Education Malaysia, Malaysia and Universiti Teknologi Malaysia, Malaysia for giving cooperation and full support in this research activity. The

authors wish to thank Research Management Center (RMC) for Tier 2 grant (VOT No.: Q.J130000.2651.16J28) from Ministry of Higher Education Malaysia and Universiti Teknologi Malaysia.

References

[1] US Environmental Protection Agency. "2014 national emissions inventory, version 2, technical support document." (2018).
[2] Conti, John, Paul Holtberg, Jim Diefenderfer, Angelina LaRose, James T. Turnure, and Lynn Westfall. International energy outlook 2016 with projections to 2040. No. DOE/EIA-0484 (2016). USDOE Energy Information Administration (EIA), Washington, DC (United States). Office of Energy Analysis, 2016.
[3] Malaysian Palm Oil Board (MPOB). Malaysian oil palm statistics 2016. 36th ed. M. MPOB, ministry of plantation industries and commodities; 2016.
[4] Sukiran, Mohamad Azri, Faisal Abnisa, Wan Mohd Ashri Wan Daud, Nasrin Abu Bakar, and Soh Kheang Loh. "A review of torrefaction of oil palm solid wastes for biofuel production." Energy Conversion and Management 149 (2017): 101-120.
[5] Sulaiman, Fauziah, Nurhayati Abdullah, Heiko Gerhauser, and Adilah Shariff. "A perspective of oil palm and its wastes." Journal of Physical Science 21, no. 1 (2010): 67-77.
[6] Loh, Soh Kheang. "The potential of the Malaysian oil palm biomass as a renewable energy source." Energy conversion and management 141 (2017): 285-298.
[7] Faizal, Hasan Mohd, Hielfarith Suffri Shamsuddin, M. Harif M. Heiree, Mohd Fuad Muhammad Ariff Hanaffi, Mohd Rosdzimin Abdul Rahman, Md Mizanur Rahman, and Z. A. Latiff. "Torrefaction of densified mesocarp fibre and palm kernel shell." Renewable energy 122 (2018): 419-428.
[8] Mitchual, Stephen J., Kwasi Frimpong-Mensah, and Nicholas A. Darkwa. "Effect of species, particle size and compacting pressure on relaxed density and compressive strength of fuel briquettes." International Journal of Energy and Environmental Engineering 4, no. 1 (2013): 30.
[9] Cavallo, Eugenio, and Niccolò Pampuro. "Effects of compressing pressure on briquettes made from woody biomass." Chemical Engineering Transactions 58 (2017): 517-522.
[10] Husain, Z., Z. Zainac, and Z. Abdullah. "Briquetting of palm fibre and shell from the processing of palm nuts to palm oil." Biomass and Bioenergy 22, no. 6 (2002): 505-509.
[11] Chen, Yongliang, Yimin Zhang, Tiejun Chen, Yunliang Zhao, and Shenxu Bao. "Preparation of eco-friendly construction bricks from hematite tailings." Construction and Building Materials 25, no. 4 (2011): 2107-2111.
[12] Chitedze, Judith, Maurice Monjerezi, JD Kalenga Saka, and Jan Steenkamp. "Binding effect of cassava starches on the compression and mechanical properties of Ibuprofen tablets." Journal of Applied Pharmaceutical Science 2, no. 4 (2012): 31.
[13] Li, Huan, Ying Tao, Xiaoyu Zheng, Jiayan Luo, Feiyu Kang, Hui-Ming Cheng, and Quan-Hong Yang. "Ultra-thick graphene bulk supercapacitor electrodes for compact energy storage." Energy & Environmental Science 9, no. 10 (2016): 3135-3142.
[14] Nyakuma, Bemgba Bevan, Arshad Ahmad, Anwar Johari, Tuan Amran Tuan Abdullah, and Olagoke Oladokun. "Torrefaction of pelletized oil palm empty fruit bunches." arXiv preprint arXiv:1505.05469 (2015).
[15] Chen, Wei-Hsin, Yi-Qing Zhuang, Shih-Hsien Liu, Tarng-Tzuen Juang, and Chi-Ming Tsai. "Product characteristics from the torrefaction of oil palm fiber pellets in inert and oxidative atmospheres." Bioresource technology 199 (2016): 367-374.
[16] Chen, Wei-Hsin, Jianghong Peng, and Xiaotao T. Bi. "A state-of-the-art review of biomass torrefaction, densification and applications." Renewable and Sustainable Energy Reviews 44 (2015): 847-866.
[17] Yang, Zixu, Madhura Sarkar, Ajay Kumar, Jaya Shankar Tumuluru, and Raymond L. Huhnke. "Effects of torrefaction and densification on switchgrass pyrolysis products." Bioresource technology 174 (2014): 266-273.
[18] Bergman, Patrick CA, A. R. Boersma, R. W. R. Zwart, and J. H. A. Kiel. "Torrefaction for biomass co-firing in existing coal-fired power stations." Energy Centre of Netherlands, Report No. ECN-C-05-013 (2005).
[19] Prins, Mark J., Krzysztof J. Ptasinski, and Frans JJG Janssen. "Torrefaction of wood: Part 1. Weight loss kinetics." Journal of analytical and applied pyrolysis 77, no. 1 (2006): 28-34.
[20] Demirbaş, A. "Physical properties of briquettes from waste paper and wheat straw mixtures." Energy Conversion and Management 40, no. 4 (1999): 437-445.
[21] Peng, Jianghong, Xiaotao T. Bi, C. Jim Lim, Hanchao Peng, Chang Soo Kim, Dening Jia, and Haibin Zuo. "Sawdust as an effective binder for making torrefied pellets." Applied energy 157 (2015): 491-498.
[22] Faizal, Hasan Mohd, Z. A. Latiff, and Muhammad Amin Mohd Iskandar. "Characteristics of binderless palm biomass briquettes with various particle sizes." Jurnal Teknologi 77, no. 8 (2015).

[23] Kaliyan, Nalladurai, and R. Vance Morey. "Factors affecting strength and durability of densified biomass products." Biomass and bioenergy 33, no. 3 (2009): 337-359.
[24] Nasrin, A. B., A. N. Ma, Y. M. Choo, S. Mohamad, M. H. Rohaya, A. Azali, and Z. Zainal. "Oil palm biomass as potential substitution raw materials for commercial biomass briquettes production." American Journal of Applied Sciences 5, no. 3 (2008): 179-183.
[25] Zannikos, F., S. Kalligeros, G. Anastopoulos, and E. Lois. "Converting biomass and waste plastic to solid fuel briquettes." Journal of Renewable Energy 2013 (2013).
[26] Hanaffi Mohd Fuad, Muhammad Ariff, Hasan Mohd Faizal, Mohd Rosdzimin Abdul Rahman, and Z. A. Latiff. "Torrefaction of densified empty fruit bunches with addition of plastics waste." Biofuels (2018): 1-11.
[27] Faizal, Hasan Mohd, M. Shafiq M. Nazri, Md Mizanur Rahman, S. Syahrullail, and Z. A. Latiff. "Development of palm biomass briquettes with polyethylene plastic waste addition." Jurnal Teknologi 78, no. 9-2 (2016).
[28] Garrido, Maria, Juan Conesa, and Maria Garcia. "Characterization and production of fuel briquettes made from biomass and plastic wastes." Energies 10, no. 7 (2017): 850.
[29] Bazargan, Alireza, Sarah L. Rough, and Gordon McKay. "Compaction of palm kernel shell biochars for application as solid fuel." biomass and bioenergy 70 (2014): 489-497.
[30] Bazargan, Alireza, Sarah L. Rough, and Gordon McKay. "Fine tuning of process parameters for improving briquette production from palm kernel shell gasification waste." Environmental technology 39, no. 7 (2018): 931-938.
[31] Si, Yaohui, Junhao Hu, Xianhua Wang, Haiping Yang, Yingquan Chen, Jingai Shao, and Hanping Chen. "Effect of carboxymethyl cellulose binder on the quality of biomass pellets." Energy & Fuels 30, no. 7 (2016): 5799-5808.
[32] Peng, J. H., H. T. Bi, C. J. Lim, and S. Sokhansanj. "Study on density, hardness, and moisture uptake of torrefied wood pellets." Energy & Fuels 27, no. 2 (2013): 967-974.
[33] Li, Hui, Xinhua Liu, Robert Legros, Xiaotao T. Bi, C. Jim Lim, and Shahab Sokhansanj. "Pelletization of torrefied sawdust and properties of torrefied pellets." Applied Energy 93 (2012): 680-685.
[34] Na, Byeong-Ill, Young-Hun Kim, Woo-Seok Lim, Soo-Min Lee, Hyoung-Woo Lee, and Jae-Won Lee. "Torrefaction of oil palm mesocarp fiber and their effect on pelletizing." Biomass and bioenergy 52 (2013): 159-165.
[35] Amini, Mohd Hazim Mohamad, Rokiah Hashim, Salim Hiziroglu, Nurul Syuhada Sulaiman, and Othman Sulaiman. "Properties of particleboard made from rubberwood using modified starch as binder." Composites Part B: Engineering 50 (2013): 259-264.
[36] Yu, Wenbin, Hong He, Nanpu Cheng, Bingtai Gan, and Xuelian Li. "Preparation and experiments for a novel kind of foundry core binder made from modified potato starch." Materials & Design 30, no. 1 (2009): 210-213.
[37] Dhanalakshmi, K., and Suvendu Bhattacharya. "Compaction agglomeration of corn starch in presence of different binders." Journal of food engineering 104, no. 3 (2011): 348-355.
[38] Law, H. C., L. M. Gan, and H. L. Gan. "Experimental Study on the Mechanical Properties of Biomass Briquettes from Different Agricultural Residues Combination." In MATEC Web of Conferences, vol. 225, p. 04026. EDP Sciences, 2018.
[39] EN ISO 18134-2:2015. Solid biofuels–Determination of moisture content–Oven dry method–Part 2, 2015.
[40] EN ISO 18123:2015. Solid biofuels – Determination of the content of volatile matter., 2015.
[41] EN ISO 18122:2015. Solid Biofuels. Determination of Ash Content, 2015.
[42] EN ISO 14918:2010. Solid Biofuels-Method for the determination of calorific value, 2010.
[43] Rabier, Fabienne, Michaël Temmerman, Thorsten Böhm, Hans Hartmann, Peter Daugbjerg Jensen, Josef Rathbauer, Juan Carrasco, and Miguel Fernández. "Particle density determination of pellets and briquettes." Biomass and Bioenergy 30, no. 11 (2006): 954-963.
[44] Bridgeman, T. G., J. M. Jones, I. Shield, and P. T. Williams. "Torrefaction of reed canary grass, wheat straw and willow to enhance solid fuel qualities and combustion properties." Fuel 87, no. 6 (2008): 844-856.
[45] Huang, Yu-Fong, Pei-Hsin Cheng, Pei-Te Chiueh, and Shang-Lien Lo. "Leucaena biochar produced by microwave torrefaction: Fuel properties and energy efficiency." Applied energy 204 (2017): 1018-1025.
[46] Faizal, Hasan Mohd, M. Amin M. Jusoh, Mohd Rosdzimin Abdul Rahman, S. Syahrullail, and Z. A. Latiff. "Torrefaction of palm biomass briquettes at different temperature." Jurnal Teknologi 78, no. 9-2 (2016).
[47] Uemura, Yoshimitsu, Wissam N. Omar, Toshio Tsutsui, and Suzana Bt Yusup. "Torrefaction of oil palm wastes." Fuel 90, no. 8 (2011): 2585-2591.
[48] Noda, R., Y. Matsuhisa, T. Ito, and M. Horio. "Alkali metal evolution characteristics of wood biomass during pyrolysis and gasification." In Proceedings for the Annual Meeting of the Japan Institute of Energy, Japan, pp. 196-7. 2003.
[49] Susanty, W., and Z. Helwani. "Torrefaction of oil palm frond: The effect of process condition to calorific value and proximate analysis." In IOP Conference Series: Materials Science and Engineering, vol. 345, no. 1, p. 012016. IOP Publishing, 2018.

[50] Ahmad, R., K. Ismail, M. A. M. Ishak, N. N. Kasim, and C. Z. A. Abidin. "Pretreatment of palm kernel shell by torrefaction for co-gasification." (2016): 70-6.
[51] Nyakuma, Bemgba B., Arshad Ahmad, Anwar Johari, Tuan Amran T. Abdullah, Olagoke Oladokun, Ali H. Al-Shatri, Adnan Ripin, and Afizah Alir. "Preliminary torrefaction of oil palm empty fruit bunch pellets." In E3S Web of Conferences, vol. 90, p. 01014. EDP Sciences, 2019.
[52] Asadullah, Mohammad, Ag Mohammad Adi, Nurul Suhada, Nur Hanina Malek, Muhammad Ilmam Saringat, and Amin Azdarpour. "Optimization of palm kernel shell torrefaction to produce energy densified bio-coal." Energy conversion and management 88 (2014): 1086-1093.
[53] ISO, EN. "18125." Solid Biofuels—Determination of Calorific Value (2017).

Penerbit Akademia Baru

Engineering Science and Technology Conference Proceedings

Journal homepage: www.akademiabaru.com/EST.html

Production of Volatile and Char During Pyrolysis and Combustion in Domestic Wastewater Sludge By Using Thermogravimetric Analysis.

Open Access

Zakaria. M. S.[1], S.Hassan[*], M.Faizairi[2]

[1] Department of Mechanical Engineering, Universiti Teknologi PETRONAS, 32610 Seri Iskandar, Perak Darul Ridzuan, Malaysia

ABSTRACT

The rapid increase in world population and economic growth, improvements in living standards after the industrialization of the world brought about high demand of energy. In the last two decades, extensive work has been done for alternative and sustainable sources and technologies to meet up current and future energy demand such as solar energy, wind energy, hydro and biofuels energy. One of the viable biomass sources available in Malaysia is Domestic wastewater sludge. Further study on this biomass is required to promote as the biomass fuel. This study focused on the production of volatile and char yield during pyrolysis and combustion with particle size range between 0.4mm to 2.0mm and heating rate (5,10,15,20,30,50 and 100K/min) by using thermogravimetric analysis. Based on the finding, the total volatile shows a tendency to decrease when the heating rate increase with the highest value was 84.51%. However, the highest char was produced at the highest heating rate was 23.80%. The lowest heating rate is favourable since produce high volatile matter content and low char content.

Keywords:
Volatile; char, sludge; thermogravimetric analysis

Copyright © 2019 PENERBIT AKADEMIA BARU - All rights reserved

1. Introduction

Energy demands in Malaysia are increasing sharply due to the growth of population and economy. Malaysia's population in 2007 hit 27.4 million and expected to reach 33.4 million and 37.4 million by the year of 2020 and 2030, respectively [1]. Until today, fossil fuel has been the main source for electricity generation and is heavily utilized over the past few decades. The overdependence on this single fuel source creates a huge challenge in the energy and power sector in this country. It is known that non-renewable energy such as fossil fuel is not sustainable. In Malaysia, the oil reserve is expected to deplete in around 20 years' time while natural gas may still be sustainable for the next 36 years [3]. The impact to the environment, climate change and pollution due to fossil fuel burning have also become serious issues that caught the attention of the government and authorities. The combustion of petroleum, coal and natural gas produce substantial amount of gaseous emissions such as Carbon Dioxide (CO_2), Nitrogen Oxide (NO_x), and Sulphur Dioxide (SO_2). The increase of CO_2 gas emission based on data recorded from 1980 until 2006, reveals the impact of fossil fuel consumption to the environment, which has reached a worrying state [4].

[*] *Corresponding author.*
E-mail address: mohd_16005855@utp.edu.my (Mohd Safuan Zakaria)

Domestic Wastewater Sludge (DWS), as one of renewable energy has a large potential as an alternative fuel due to its economic viability and benefits to the environment. One of the viable options to solve these problems is by converting this waste material into a source of energy through Thermochemical Conversion (TCC) technologies. In the earlier works, the feasibility of DWS to become an alternative solid fuel for power generation application has been investigated and its potential has been proven [5-10].

In order to recover energy from biomass waste material through TCC process, an in-depth understanding of the thermal conversion involving the decomposition process of DWS during the elevation of temperature is essential. The knowledge of kinetic parameters such as ash, volatile matter and char content should be properly studied. In order to investigate the kinetic analysis of DWS, thermogravimetric kinetic studies are important. Different operational condition and properties of materials are the most important variables that can influence the result of the experiment. Variation of experimental condition can give clues for optimization and reaction mechanism of sample in the thermal decomposition process.

2. Methodology

Proximate analysis is important to determine the relative percentage of the combustible and non-combustible components of the solid fuel. These components are measured when the samples are heated under controlled conditions of temperature using thermogravimetric method. The proximate analysis involves the use of a Thermogravimetric Analyzer (TGA-Perkin Elmer PYRIS1TGA). The TGA test procedures were carried out in accordance to the ASTM E1131-98 Standard, where the changes in sample weight is used as a basis to determine the sample's response to changes in temperature. TGA procedure is used to measure the weight changes in a biomass sample as a function of temperature or time in controlled oxygen and nitrogen environment, and these measurements not only improve the production but also simplify the interpretation of the result [11-14]. A heating procedure as listed in Table 1was then administered in the TGA to remove the moisture content and volatile matter and measure the remaining fixed carbon and ash in the samples .In this study, there are 7 heating rates were studied which are 5, 10, 15, 20, 30, 50 and 100K/min.

Table 1. Heating procedure for TGA analysis.

Temperature (°C)	Time (min)	Heating rate (K/min)	Gas
100 – 600	……	5	N_2
600 – 600	10	……..	N_2
600 – 600	10	……..	N_2
600 – 850	……	5	N_2

3. Results

3.1 Derivative Thermogravimetric (DTG)

Table 2 lists the DTG profiles of DWS at different heating rates. In devolatilization stage, temperature range of DTG is broader as heating rate was increased. DTG curve start at temperature 110˚C for heating rate 5-20 K/min. However, devolatilization stage for heating rate 30, 50 and 100 K/min start at 120 ˚C, 145 ˚C and 150˚C, respectively. The final temperature shows an increment from 430˚C to 550˚C on rising from 5 K/min to 100 K/min heating rate. Peak DTG (DTG_{max}) and the corresponding temperature (T_p) also tends to increase to the higher value.

Based on Table 2, DTG_{max} for 5 K/min is -3.26 %/min. DTG_{max} rises sharply to -59.83 %/min (in absolute value) when 100 K/min heating rate is used. The increment is approximately 20 times higher, corresponding to the increasing of heating rate. The relation of DTG_{max} and heating rate can be clearly seen from linear fit plotted in Figure 4.10, where the heating rate is directly proportional to DTG_{max}. The increasing value of DTG_{max} attributed to the increasing value of maximum decomposition rate of DWS. This reveals that greater thermal energy is provided to improve heat transferred from ambient to DWS material during pyrolysis.

Table 2. DTG profiles of DWS pyrolysis at different heating rates

Heating Rates [K/min]	T_{range} [°C]	DTG_{max} [%/min]	T_p [°C]	Total volatile [%]	Char [%]
5	110-430	-3.26	276.75	84.51	15.49
10	110-450	-6.29	294.52	83.97	17.87
15	110-480	-9.36	306.35	82.13	18.02
20	110-500	-12.69	312.10	80.72	19.28
30	120-510	-17.77	334.12	78.58	21.42
50	145-530	-29.19	341.78	77.90	21.46
100	150-550	-59.83	341.84	76.20	23.80

The relation of T_p to the heating rate is also shown in Figure 1. Based on Figure 1,it can be observed that T_p slightly increase when heating rate is increased. As a result, the curvature of curve shifted to the higher temperature. The maximum rate of decomposition took place at temperature 276.75˚C for 5 K/min and 341.84˚C for 100 K/min respectively. The reason is due to the short retention time when higher heating rate is applied. Decomposition process is delayed, thus higher temperature is required for DWS to decompose. Despite this, at lower heating rate, DWS starts to decompose at maximum rate once reaching low temperature. This indicates that DWS is easier to decompose in lower heating rate than that in the higher heating rate [15-18].

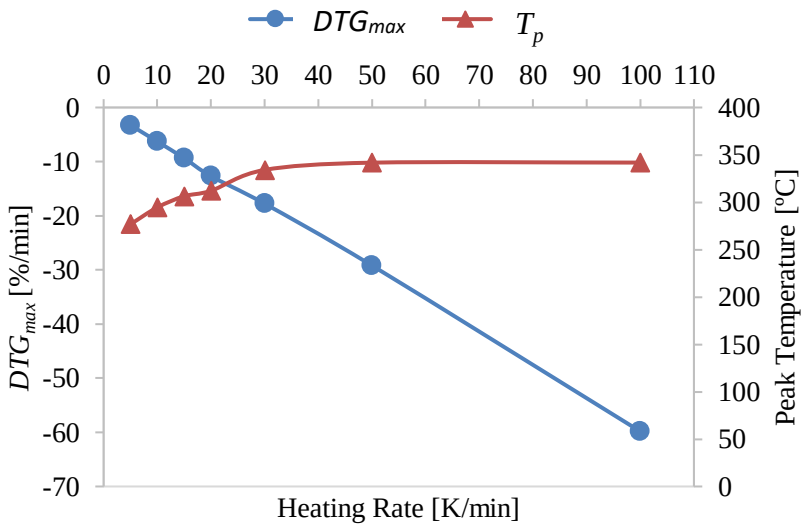


Fig. 1. Maximum decomposition rate, DTG_{max} and the corresponding temperature, T_p as a function of heating rate

Similarly, Mohammed et al. [19] claimed that increasing heating rate implies high thermal energy was equipped to the system instantaneously. Significantly, this is the factor that is hindering the system to obtain equilibrium temperature within the furnace and material. Additionally, at higher heating rate, limitation of heat transfer caused the equilibrium between temperature in furnace and sample takes longer time to be attained [20-23]. Besides, materials react in a short time when higher heating rate is practiced. This causes the shifting of temperature to the higher value in order to complete the decomposition process.

3.2 Total Volatile and Char

Volatile and char are the two important substances that should be taken into consideration in order to examine the influence of heating rate to DWS decomposition process. Apparently, total volatile reduces as a result of increased heating rate. Conversely, char formation increase is influenced by the increasing of heating rate. The reduction of total volatile is from 84.51% to 76.2% is in accordance to the heating rate increment. On the other hand, char production increase from 15.59% to 23.8%. Despite the increment of char production is very little especially when changing the heating rate from 10 K/min to 15 K/min (0.15% difference) and 30 K/min to 50 K/min (0.04% difference), it can be seen that heating rate has significant influence to the total char formation. The relation of heating rate to the total volatile and char can be clearly interpreted as presented in Figure 2.

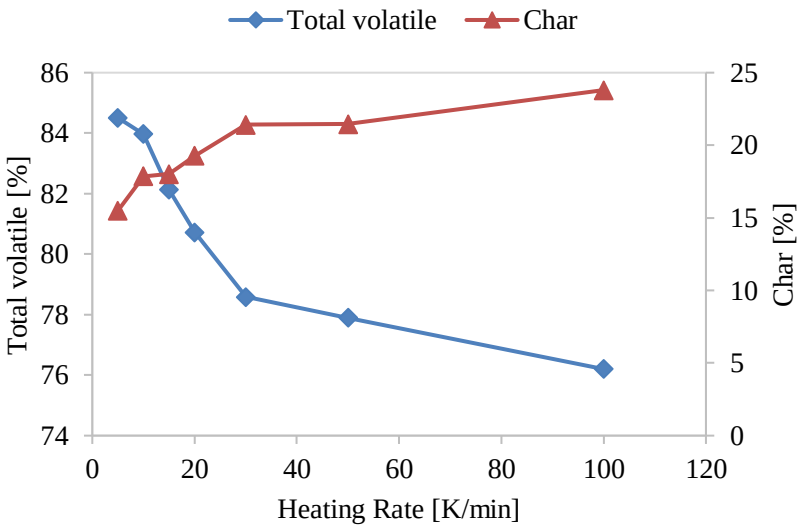


Fig. 2. Total volatile and char yields at every heating rate

Lower heating rate leads to an efficient heat transfer because the process is gradually progressed. As a result, the effectiveness of decomposition process is enhanced, thus increase the liberation of volatile product. In contrast, when carrying out the experiment using higher heating rate, shorter time is given for the material to acquire the heat at a certain temperature. Heat

transfer occurs poorly, hence release less amount of volatile product and oppositely form large amount of char residue at the end of the decomposition process. Studies carried out by Altun et al. [14] on the pyrolysis of Silopi Asphaltite by using TGA also agreed that the reason for volatile increase when lower heating rate was used is due to the effectiveness of heat transfer which occurred when temperature is elevated. The material's particle cracked efficiently resulted more volatile release when weight loss took place.

Ounas et al. [18] defined that the reason for small amount of volatile release during higher heating rate can be related to the heat transfer limitation, where the temperature gap between ambient in furnace and sample's particle is large. Other than the presence of non-equilibrium state, the existence of temperature gradient may also differ the temperature of particle's surface and between its inner parts. Therefore, the decomposition and release of volatile process might be affected, where the decomposition rate is found to occur rapidly than the volatile released. This result is in line with the study conducted by Mani et al. [10] for pyrolysis of wheat straw and Idris et al. [17] for oil palm biomass respectively. However, studies done by Ceylan et al. [11] for hazelnut husk found that heating rate seems not much affected by the yielding of volatile matter.

4. Conclusions

The findings in this study proved that the thermal decomposition process of DWS is thoroughly influenced on experimental conditions such as heating rate and particle size of sample in pyrolysis and combustion environment. The selection of the appropriate heating rate together with the most representative particle size is crucial to be taken into consideration in order to ensure the efficiency of thermal degradation process for later application in TCC technology. According to the finding, it is suggested that the selection of small particle size together with relatively low heating rate is required to meet the optimum outcome of decomposition process.

Acknowledgement

This research was funded by a grant from Yayasan Universiti Teknologi PETRONAS (FRGS Grant).

References

[1] Pang, Yunji, Shengqiang Shen, and Yisheng Chen. "High Temperature Steam Gasification of Corn Straw Pellets in Downdraft Gasifier: Preparation of Hydrogen-Rich Gas." Waste and Biomass Valorization 10, no. 5 (2019): 1333-1341.

[2] Subarmono, Subarmono, Harwin Saptoadi, Musabbikhah Musabbikhah, and Muhammad Arif Wibisono. "Modelling and Optimisation of Coconut Shell Drying and Carbonisation Using Multi-response Taguchi Method with Multi-response Signal-to-noise Procedure." International Journal of Engineering 31, no. 3 (2018): 464-472.

[3] Asadullah, Mohammad. "Barriers of commercial power generation using biomass gasification gas: A review." Renewable and Sustainable Energy Reviews 29 (2014): 201-215.

[4] Bidabadi, M., and M. J. Noroozi. "Effect of Heat Recirculation in Biomass Flame Stability within a Cylindrical Micro-Combustor." International Journal of Engineering-Transactions C: Aspects 28, no. 3 (2015): 454-459.

[5] Manaf, Latifah Abd, Mohd Armi Abu Samah, and Nur Ilyana Mohd Zukki. "Municipal solid waste management in Malaysia: Practices and challenges." Waste management 29, no. 11 (2009): 2902-2906.

[6] Muyibi, Suleyman A., Abdul Raufu Ambali, and Garoot Suleiman Eissa. "The impact of economic development on water pollution: Trends and policy actions in Malaysia." Water resources management 22, no. 4 (2008): 485-508.

[7] Ahmad, Salsabila, Mohd Zainal Abidin Ab Kadir, and Suhaidi Shafie. "Current perspective of the renewable energy development in Malaysia." Renewable and sustainable energy reviews 15, no. 2 (2011): 897-904.

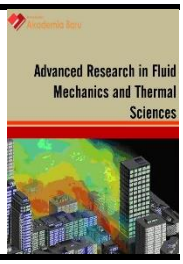
[8] Shamsul, N. S., Siti Kartom Kamarudin, Norliza Abd Rahman, and Noorhisham Tan Kofli. "An overview on the production of bio-methanol as potential renewable energy." Renewable and Sustainable Energy Reviews 33

(2014): 578-588.
[9] Supatata, N., J. Buates, and P. Hariyanont. "Characterization of fuel briquettes made from sewage sludge mixed with water hyacinth and sewage sludge mixed with sedge." International Journal of Environmental Science and Development 4, no. 2 (2013): 179.
[10] Faizal, Muhammad, Tiara Tiara, and Tuty Agustina. "The Effect of Air Fuel Ratio and Temperature on Syngas Composition and Calorific Value Produced from Downdraft Gasifier of Rubber Wood-Coal Mixture." International Journal of Engineering 31, no. 9 (2018): 1480-1486.
[11] Wojciechowska, Ewa. "Application of microwaves for sewage sludge conditioning." Water research 39, no. 19 (2005): 4749-4754.
[12] Jaafar, Mohd Zamzam, Wong Hwee Kheng, and Norhayati Kamaruddin. "Greener energy solutions for a sustainable future: issues and challenges for Malaysia." Energy policy 31, no. 11 (2003): 1061-1072.
[13] Molla, A. H., A. Fakhru'l-Razi, S. Abd-Aziz, M. M. Hanafi, P. K. Roychoudhury, and M. Z. Alam. "A potential resource for bioconversion of domestic wastewater sludge." Bioresource Technology 85, no. 3 (2002): 263-272.
[14] Planquart, P., G. Bonin, A. Prone, and C. Massiani. "Distribution, movement and plant availability of trace metals in soils amended with sewage sludge composts: application to low metal loadings." Science of the total environment 241, no. 1-3 (1999): 161-179.
[15] Manara, P., and A. Zabaniotou. "Towards sewage sludge based biofuels via thermochemical conversion–a review." Renewable and Sustainable Energy Reviews 16, no. 5 (2012): 2566-2582.
[16] Domínguez, A., J. A. Menéndez, M. Inguanzo, and J. J. Pis. "Production of bio-fuels by high temperature pyrolysis of sewage sludge using conventional and microwave heating." Bioresource technology 97, no. 10 (2006): 1185-1193.
[17] Aniza, N., Suhaimi Hassan, M. F. M. Nor, and H. A. M. Fadhil. "Thermogravimetric Kinetic Behavior of Malaysian Poultry Processing Dewatered Sludge (PPDS) During Combustion." In Applied Mechanics and Materials, vol. 695, pp. 433-437. Trans Tech Publications, 2015.
[18] Cheng, Kun, William T. Winter, and Arthur J. Stipanovic. "A modulated-TGA approach to the kinetics of lignocellulosic biomass pyrolysis/combustion." Polymer Degradation and Stability 97, no. 9 (2012): 1606-1615.
[19] Gil, María Victoria, D. Casal, C. Pevida, J. J. Pis, and F. Rubiera. "Thermal behaviour and kinetics of coal/biomass blends during co-combustion." Bioresource Technology 101, no. 14 (2010): 5601-5608.
[20] Mekhilef, Saad, Rahman Saidur, Azadeh Safari, and W. E. S. B. Mustaffa. "Biomass energy in Malaysia: current state and prospects." Renewable and Sustainable Energy Reviews 15, no. 7 (2011): 3360-3370.
[21] A. Abdalla, "Development of Fuel Briquettes From Biomass Residue," Universiti Teknologi Petronas, 2013.
[22] Alam, Md Zahangir, Suleyman A. Muyibi, and Rosmaziah Wahid. "Statistical optimization of process conditions for cellulase production by liquid state bioconversion of domestic wastewater sludge." Bioresource Technology 99, no. 11 (2008): 4709-4716.
[23] Ibrahim, A. B. A., M. S. Aris, and Yee Sing Chin. "Development of fuel briquettes from dewatered poultry sludge." (2012).

Penerbit Akademia Baru

Engineering Science and Technology Conference Proceedings

Journal homepage: www.akademiabaru.com/EST.html



Effect of Internal Diameter and Working Fluids on Thermal Performance of a Vertical Closed-Loop Oscillating Heat Pipe with Double Heat Sources

Open Access

Poomin Krisangsri, Teerasak Hudakorn, Noppong Sritrakul

[1] Department of Mechanical Engineering, Faculty of Engineering and Industrial Technology, Silpakorn University, Nakhon Pathom, 73000, Thailand.

ABSTRACT

Effects of internal diameter and working fluids on the thermal performance of a vertical closed-loop oscillating heat pipe with double heat sources (VCLOHP w/DHS) were investigated. The CLOHP was made of a copper capillary tube with inner diameters of 1.0, 1.5 and 2.0 mm and bent into a meandering turn with 16 turns. Two evaporator sections were located at the outer end of the bundle, while one condenser section was positioned on the middle of the CLOHP with no adiabatic section. Evaporator and condenser section lengths were the same at 50 mm. R123, ethanol, and water were used as working fluids with a filling ratio of 50% by volume. Evaporator temperature was controlled at 90 ± 5°C. Results indicated that pipe inner diameter and thermos-physical properties of working fluids affect thermal performance of a CLOHPw/DHS in a vertical orientation.

Keywords:
Thermal performance; vertical closed-loop oscillating heat pipe; double heat sources

Copyright © 2019 PENERBIT AKADEMIA BARU - All rights reserved

1. Introduction

A heat pipe is a heat transfer device that relocates thermal energy through cycles of vaporization and condensation. Heat pipes are popularly used in laptops, mobile phones, and tablets. Oscillating heat pipes (OHPs) were first introduced by Akachi et al. in 1996 [1]. They differ from conventional heat pipes in design and working principle. An OHP is made of a long capillary tube bent into an undulating bundle. The inner diameter of the OHP must be smaller than the critical inner diameter to allow the working fluid to arrange in slug-train units, forming vapor plugs and liquid slugs along the entire length of the tube due to the effect of surface tension [2-3]. Generally, OHPs can be divided into three groups as (i) closed-end oscillating heat pipe (CEOHP), (ii) closed-loop oscillating heat pipe (CLOHP), and (iii) closed-loop oscillating heat pipe with check valve (CLOHP/CV). This study focuses on a CLOHP because it has higher thermal performance than a CEOHP, and is easier to construct than a CLOHP/CV. Structure of the ordinary CLOHP is shown in Figure 1(a). Nowadays, designs and applications of CLOHP to transfer heat from various heat sources are simple, following knowledge gained from many previous studies on the effects of various parameters on CLOHP thermal performance. For example, studies on inner diameter [4-5, 11], evaporator section lengths [5, 10], working fluid properties [4-10], number of turns [4-5], and orientation of operation [4-7].

A CLOHP is used with one heat source and releases heat to the heat sink. To eliminate more than one heat source of electronic equipment, the CLOHP was redesigned. The new design of CLOHP can simultaneously receive heat from two heat sources at the outer ends and release that heat to the middle section. Here, this new design was named 'a closed-loop oscillating heat pipe with double heat sources' (CLOHP w/DHS) as shown in Figure 1(b).

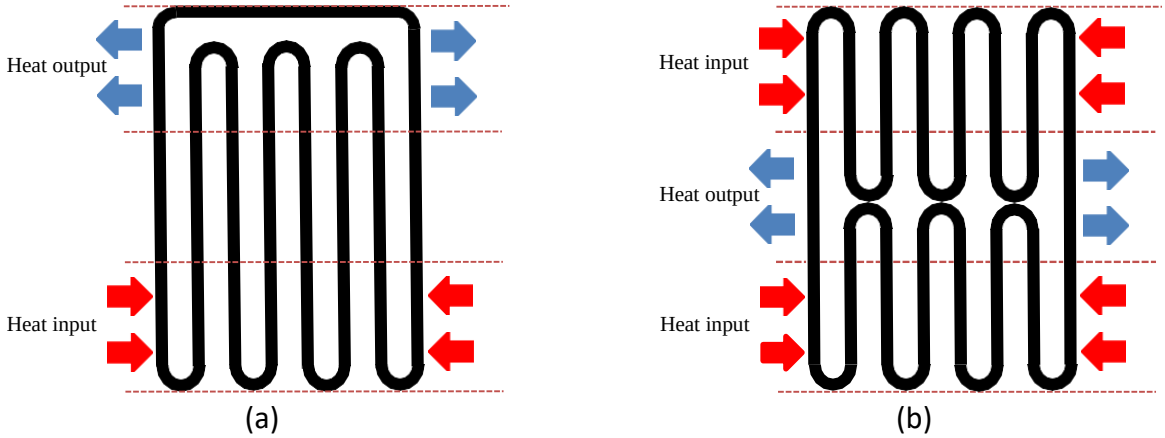


Fig 1. (a) Closed-loop oscillating heat pipe; (b) Closed-loop oscillating heat pipe with double heat sources

This is the first study concerning the effects of various parameters on the performance of a CLOHP w/DHS. Parameters included evaporator section lengths, internal diameters, number of meandering turns, working fluids, and inclination angles which can be used for future designs of CLOHP w/DHS. The main objective was to investigate the effect of inner diameter and the properties of working fluids on the thermal performance of a vertical closed-loop oscillating heat pipe with double heat sources (VCLOHP w/DHS).

2. Methodology

The experimental setup, as shown in Figure 2, consisted of VCLOHPs made of long copper capillary tubes with inner diameters (Di) of 1.0, 1.5, and 2.0 mm, bent into 16 turns along a meandering length. Both ends were connected to form a loop. Two evaporator sections were located at the outer end of the bundle, while one condenser section was placed on the middle of the VCLOHP with no adiabatic section. Evaporator and condenser section length was the same at 50 mm. R123, ethanol, and water were used as working fluids with a filling ratio of 50% by volume. Two heat sources were installed along the longitudinal axis of the evaporator section. Each heat source generated heat using two Ni-Cr alloy resistance wire heaters with a diameter of 0.5 mm. Evaporator temperature was controlled at 90 ± 5℃. Heat was removed from the condenser sections by forced convective heat transfer of in blown ambient air. Airflow velocity was controlled by an AC motor (Mitsumi, F1209) and maintained at 0.3 m/s, while room temperature was kept at 25℃. Twenty chromel-alumel thermocouples (Omega, Type K with ± 0.5 ℃ accuracy) were used to measure the temperature of the evaporator and condenser sections of the VCLOHPs and ambient air temperature at the inlet and outlet of the condenser parts. All temperature data were monitored by a temperature recorder (Graphtec, GL820 with ± 0.1 ℃ accuracy). Air velocity and relative humidity were measured by a Testo 435 (±0.01 m/s and ±0.1 %RH accuracy).

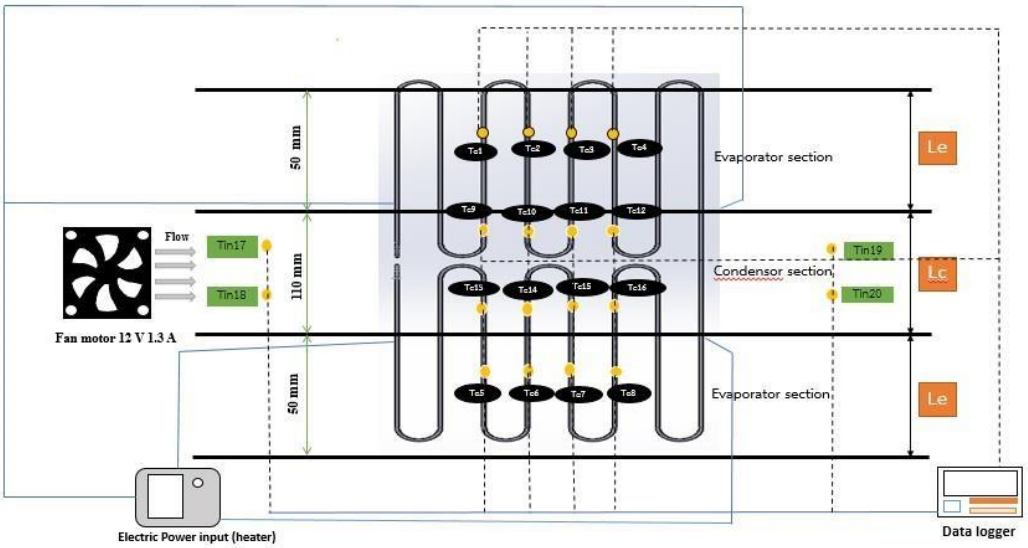


Fig 2. Detail of experimental setup.

The experiment procedure was as follows: Power controllers were started. Heat input of each heat source was supplied by Ni-Cr alloy resistance wire heaters. Evaporator section temperature was controlled at 90 ± 5 oC and ambient air at 25 oC and 0.3 m/s velocity was blown through the condenser section. After a quasi-steady-state was reached, all temperatures and relative humidity were recorded. The experiment was completed after the test was repeatedly conducted three times.

Thermal performance of the VCLOHP was evaluated by calculating the rate of heat transfer to ambient air at the condenser part and applying the conservation of energy equation for a heating process at constant specific humidity as shown by Equation 1.

$$\dot{q} = \frac{\dot{m}_{air}(h_{out} - h_{in})}{A_c} \quad (1)$$

where $\dot{q}$ is the heat transfer rate of a VCLOHP, $\dot{m}$ air is the mass flow rate of dry air, AC is the inner surface area of the tube in the condenser section, and h_{out} and h_{in} are the enthalpies per unit mass of dry air at the exit and inlet of the condenser section, respectively.

This is the first study concerning CLOHP/ wDHS. To more easily understand and analyze the obtained results, thermal resistance per unit area was defined as 'thermal resistance per unit area between the whole evaporator and condenser section' and calculated from Equation 2.

$$R = \frac{(T_{ave} - h_{in})}{\dot{q}} \quad (2)$$

where R is the thermal resistance per unit area, $T_{e,ave}$ is the average evaporator section temperature in every heat source and $T_{c,ave}$ is the condenser section temperature.

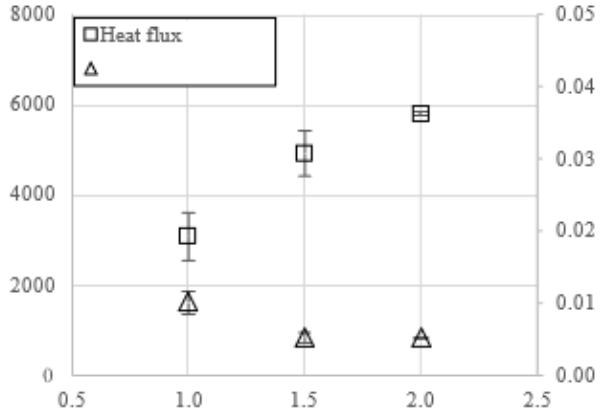
3. Results

3.1 Effects of internal diameter on thermal performance

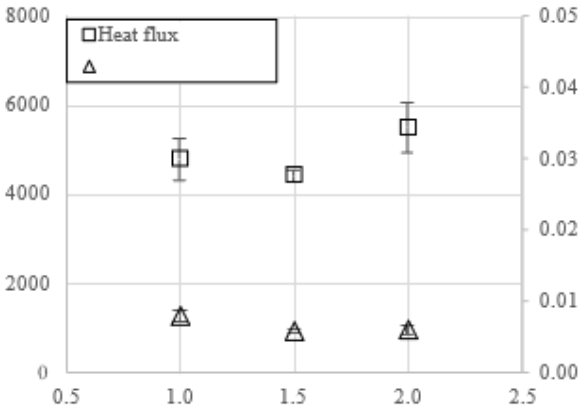
The inner diameter of the tube and type of working fluid used affected the thermal performance of a VCLOHP/wDHS as shown in Figure 3(a), (b) and (c). An inner diameter of up to 2 mm was used

for all the working fluids experiments. This was smaller than the maximum inner diameter proposed in previous research [1-2]. Figure 3(a) shows the relationship of the various inner diameters, heat flux, and thermal resistance of the VCLOHP/wDHS using water, ethanol, and R123 as the working fluids. Heat flux increased and thermal resistance decreased with increase in size of inner diameter.

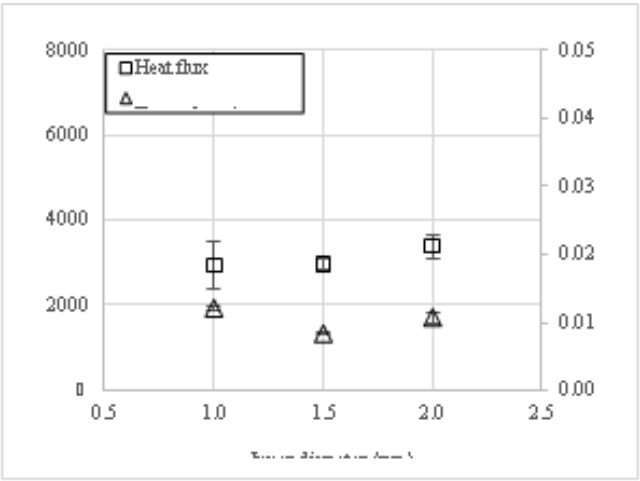
Highest performance was attained at maximum inner diameter of 2 mm. This trend was also seen for all VCLOHPs filled with water, ethanol, and R123. With a larger internal diameter or a wider cross-sectional area of flow passage, the vapor plugs evaporate in the evaporator section and, consequently, flow toward the condenser section more continuously with a higher quantity of working fluid. Thus, the CLOHP can transfer more heat; heat flux subsequently increases and thermal resistance decreases [12]. This result concurred with Charoensawan et al. [5] and Kammuang-lue et al. [12] who indicated that performance increased with larger inner tube diameter.



(a) Water as working fluid.



(b) Ethanol as working fluid.



(c) R123 as working fluid.

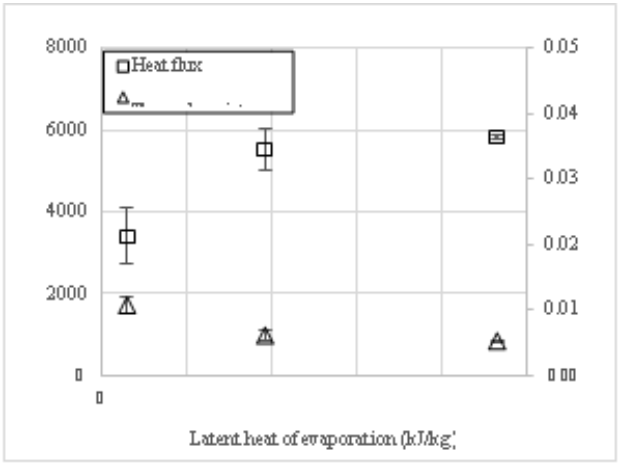
Fig. 3. Effect of internal diameter

3.2 Effects of working fluid on thermal performance

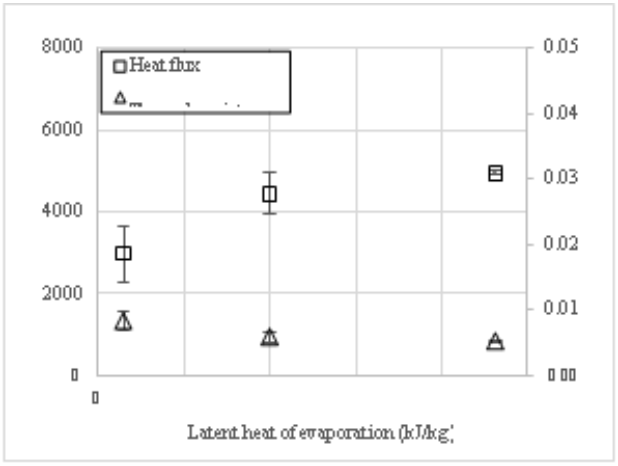
Thermodynamic properties of working fluids include latent heat of evaporation, specific heat, surface tension, viscosity, and thermal conductivity. Latent heat of evaporation was selected as the most suitable parameter to identify differences between the working fluids because the CLOHP

transfers heat by evaporation and condensation mechanisms. Results showed that when the working fluid changed from R123 to ethanol and water, or when the latent heat of evaporation increased, heat flux increased and thermal resistance decreased for inner diameters of 2.0 and 1.5 mm, as shown in Figure 4(a) and (b).

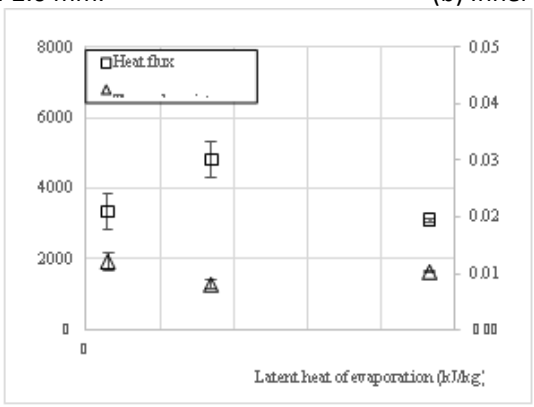
Previous study results indicated that internal flow pattern in VCLOHP consists of slug flow mixing with churn flow inside the evaporator section [13, 14], with the working fluid circulating in one direction [3, 15]. Churn flow has a vapor portion greater than the liquid, and the CLOHP transfers heat mainly by latent heat rather than sensible heat. Heat transfer was higher compared to only single-phase forced convection [3]. From this evidence, the reason that describes why heat flux increases as latent heat of evaporation increases with the same trend in inner diameter of 2.0 and 1.5 mm can be analysed.



(a) Inner diameter of 2.0 mm.



(b) Inner diameter of 1.5 mm.



(c) Inner diameter of 1.0 mm.

Fig. 4. Effect of latent heat of evaporation.

By contrast, ethanol and R123 showed higher heat flux than water for the 1.0 mm inner diameter, as shown in Figure 4(c). Water has high surface tension and a small inner diameter leads to increased frictional pressure flow resistance. Thus, the VCLOHP with water as working fluid needs more heat than R123 and ethanol to move the fluid from the hot region to the cold region of the heat pipe.

4. Conclusions

Effects of diameter and working fluids on the thermal performance of a VCLOHPw/ DHS were investigated. Itemized conclusions are as follows:

- The greater the internal diameter, the higher the thermal performance. With a larger internal diameter, vapor plugs evaporate in the evaporator section and, consequently, flow toward the condenser section more continuously with a higher quantity of working fluid. Thus, the VCLOHP w/DHS can transfer more heat, and thermal performance increases.
- When the latent heat of evaporation increases, thermal performance also increases since a working fluid with higher latent heat can transfer more heat from the hot region to the cold region of the heat pipe.

Acknowledgement
This research was funded by a grant from Ministry of Higher Education of Malaysia (FRGS Grant R.J130000.7824.4X172).

References

[1] Akachi, H, Polasek, F, and Stulc. “Experimental study of flow patterns and improved configurations for pulsating heat pipes.”Proc. of the 5th International Heat Pipe Symposium (Melbourne Australia), (1996): 208-217.
[2] Maezawa, S, Gi K.Y, Minamisawa A, and Akachi, H. “Thermal performance of capillary tube thermosiphon.”Proc. of the 9th International Heat Pipe Conference (Albuquerque USA), (1995): 791-795.
[3] Verma, Bhawna, Vijay Lakshmi Yadav, and Kaushal Kumar Srivastava. "Experimental studies on thermal performance of a pulsating heat pipe with methanol/DI water." Journal of Electronics Cooling and Thermal Control 3.1 (2013): 27-34.
[4] Charoensawan, Piyanun, et al. "Closed loop pulsating heat pipes: Part A: parametric experimental investigations." Applied thermal engineering 23.16 (2003): 2009-2020. [5] Charoensawan, Piyanun, and Pradit Terdtoon. "Thermal performance of horizontal closed-loop oscillating heat pipes." Applied Thermal Engineering 28.5-6 (2008): 460-466.
[6] Li, Jia, and Li Yan. "Experimental research on heat transfer of pulsating heat pipe." Journal of thermal Science 17.2 (2008): 181-185.
[7] Jahan, Suchana Akter, Mohammad Ali, and Md Quamrul Islam. "Effect of inclination angles on heat transfer characteristics of a closed loop pulsating heat pipe (CLPHP)." Procedia Engineering 56 (2013): 82-87.
[8] Pachghare, Pramod R., and Ashish M. Mahalle. "Effect of pure and binary fluids on closed loop pulsating heat pipe thermal performance." Procedia engineering 51 (2013): 624-629.
[9] Qu, Jian, and Qian Wang. "Experimental study on the thermal performance of vertical closed-loop oscillating heat pipes and correlation modeling." Applied energy 112 (2013): 1154-1160.
[10] Babu, E.R., and GV Gnanendra Reddy. "Effect of working fluid and filling ratio on performance of a closed loop pulsating heat pipe." Journal of Engineering Science and Technology 11.6 (2016): 872-880.
[11] Islam, F., Akhter, F., Haider, S.B., and Ali M. “Proceedings of 102nd The IIER International Conference (Singapore,) (2017): 5-8.
[12] Kammuang-Lue, Niti, Phrut Sakulchangsatjatai, and Pradit Terdtoon. "Effect of working fluids and internal diameters on thermal performance of vertical and horizontal closed-loop pulsating heat pipes with multiple heat sources." Thermal Science 20.1 (2016).
[13] Khandekar, Sameer, et al. "Closed loop pulsating heat pipes Part B: visualization and semi-empirical modeling." Applied thermal engineering 23.16 (2003): 2021-2033.
[14] Kammuang-Lue, Niti, et al. "Correlation to predict the maximum heat flux of a vertical closed-loop pulsating heat pipe." Heat Transfer Engineering 30.12 (2009): 961-972.
[15] Karthikeyan, V.K., et al. "Infrared thermography of a pulsating heat pipe: Flow regimes and multiple steady states." Applied thermal engineering 62.2 (2014): 470-480.

Penerbit Akademia Baru

Engineering Science and Technology Conference Proceedings

Journal homepage: www.akademiabaru.com/EST.html

Simulation of Internal Undular Bores of Depression Propagating over a Slowly Varying Region

Open Access

Mun Hoe Hooi[1], Wei King Tiong[1*], Kim Gaik Tay[2], San Nah Sze[1], Kang Leng Chiew[1]

[1] Faculty of Computer Science and Information Technology, Universiti Malaysia Sarawak, 94300 Kota Samarahan, Sarawak, Malaysia
[2] Department of Postgraduate Studies, Faculty of Electrical and Electronic, Universiti Tun Hussein Onn Malaysia, 86400 Parit Raja, Johor, Malaysia

ABSTRACT

Internal undular bores have been observed in many parts of the world. This paper intends to look at the variable topographic effects on the evolution of the internal undular bores of depression. Here, the internal undular bores is considered to be propagating in a two-layer fluid system. The topography is assumed to be slowly varying. Therefore, the appropriate mathematical model is the variable-coefficient extended Korteweg-de Vries equation. The governing equation is solved numerically using the method of lines. We are especially interested in looking at the transformation of two types of internal undular bore of depression, which are Korteweg de Vries-type and table-top internal undular bore. Our numerical results show that the internal undular bore of depression transformed into a positive undular bore as it propagates over a slowly increasing slope and when it involves polarity change. In front of the transformed internal bore, a series of isolated solitary waves or a solitary wavetrain is generated as a non-adiabatic response to the interaction between the internal undular bore with the changing bottom surface. The solitary wavetrain is observed to be climbing the negative pedestal. As time increases, the amplitude of the individual solitary wavetrain is decreasing and finally the solitary wavetrain will die out due to the pedestal. However, if there is no polarity change, the internal undular bores deforms adiabatically and its amplitude decreases slowly until it reaches new limiting amplitude value due the increasing bottom surface. On the other hand, when the slope is decreasing slowly, the internal undular bore deforms adiabatically where its amplitude increases slowly. There is a multi-phase behaviour is observed during the evolution as the results of the interaction between the internal bore and the varying slope. In this case, there is no polarity change. The transformation of internal undular bores of depression depends on the nature of the topographic change.

Keywords:
Internal undular bore of depression; two-layer fluid system; method of lines; solitary wavetrain; multi-phase behaviour

Copyright © 2019 PENERBIT AKADEMIA BARU - All rights reserved

1. Introduction

The study of the internal wave can be traced back to the observation of internal gravity wave at the interface between oil and water in a glass tumbler [1]. The first observation of internal waves in nature have been attributed by Nansen during his expedition in the Arctic ocean in 1893 when his boat was sailing on the surface of water but his boat experienced a great resistance to against it moving forward [2]. Later, Ekman studied Nansen's observation to prove that there is an existence of internal wave hidden entirely in the layer of dead water [3]. Until the 1960s, the interest of internal wave grew up after World War 2 when the United States navy suffered difficulty in

* *Corresponding author.*
E-mail address:wktiong@unimas.my (Wei King Tiong)

controlling their depth detection inside submarine [4]. Until now, internal wave often attracts the attention of the scientific community due to it is important in influencing the ocean environment and human activities.

The existence of internal wave can affect the propagation of the acoustic wave in the deep ocean such that causing interference with the acoustic field [5]. Meanwhile, it can reduce the acoustic signal when internal waves make the temporal and spatial changes of medium density [6]. It is also a major danger to marine activities, submarine navigation and fishery activities due to large amplitude during propagation implying that a large amount of kinetic energy can be transferred in between the ocean layers [7]. When the high energy hits on the physical structures, e.g. deep-sea drilling station [8], [9] and blockwork structures near the coastal areas [10], the great power has sufficient energy to scrape away the surface of them. Besides, it can affect the sea ice evolution in the frozen sea [11] and the growth of corals due to the occurrence of temperature fluctuations between the ocean layers [12-13].

Large internal waves in the ocean usually have a negative polarity which has been proved by the observation of internal wave packets in the deep ocean [14-16]. In nature, the general structure of large-amplitude internal wave in the interior of coastal ocean commonly presents in the form of unsteady undular bores [17] and it has been observed in some part of the coastal regions, i.e. Australian North West Shelf [18], Japan/East Sea shelf-coastal region [19] and Peter the Great Bay [20]. In nature, internal waves are always propagating across an uneven sea-bottom in the ocean region. Therefore, we would like to study the evolution of internal undular of negative polarity or depression propagating over slowly varying region topography.

In the following section, we will present the problem formulation and followed by the numerical methods adopted in our problem in section 3. The numerical results are presented and discussed in section 4 and the conclusion is in the final section.

2. Problem formulation

The Korteweg-de Vries (KdV) equation has been widely used to solve nonlinear long wave problems. It was first used to describe the shallow water waves by Benney [21] and Benjamin [22], and subsequently by many others [23-25]. However, the KdV equation is not appropriate for describing the behaviour of internal wave due to nearly vanishing nonlinear effect under certain condition. Therefore, the extended KdV (eKdV) equation is obtained from the KdV equation by including a cubic nonlinear term to increase the nonlinearity effect for dynamic balancing with the dispersion effect [25].

In this study, we consider the internal wave is propagating in a two-layer fluid system. Thus, the appropriate mathematical model is the variable-coefficient eKdV (veKdV) equation,

$$A_t + cA_x - \frac{cQ_x}{Q}A + \mu AA_x + \mu_1 A^2 A_x + \delta A_{xxx} = 0, \tag{1}$$

where $A(x, t)$ refers to the amplitude of the wave, x and t represent the spatial and temporal variables respectively. The coefficient $c(x)$ denotes the relevant linear long wave speed and $Q(x)$ is the linear modification factor, so that $Q^{-2}A^2$ becomes the wave action flux for linear long waves [26]. The coefficients $\mu(x)$, $\mu_1(x)$, and $\delta(x)$ are the coefficients of the nonlinear and the dispersive terms which are determined by the properties of the basic state of the fluid. All these coefficients are slowly varying functions of x.

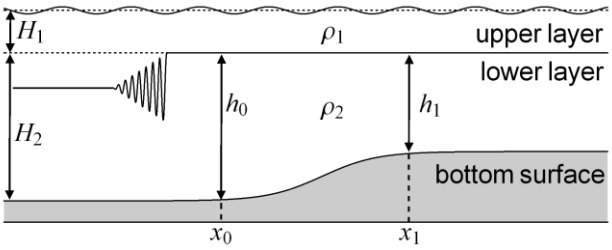


Fig. 1. Schematic illustration of internal undular bore of depression propagating in a two-layer fluid of different density over a slowly decreasing slope region

The schematic of our problem is illustrated in Fig. **1**. Here, we let the depths of upper and lower layers are represented by H_1 and H_2 respectively. Also, we consider the densities of the fluid for both layers are constants and denoted by ρ_1 and ρ_2 respectively. Thus, the coefficients of nonlinear and dispersion terms, i.e. μ, μ_1, and δ in the veKdV equation (1) are given by

$$\mu = \frac{3c\left(\rho_2 H_1^{\,2} - \rho_1 H_2^{\,2}\right)}{2H_1 H_2\left(\rho_2 H_1 + \rho_1 H_2\right)},$$

$$\mu_1 = \frac{-3c}{8\left(H_1^{\,2} H_2^{\,2}\right)\left(\rho_2 H_1 + \rho_1 H_2\right)^2}\left[\left(\rho_1 H_2^{\,2} - \rho_2 H_1^{\,2}\right)^2 + 8\rho_1\rho_2 H_1 H_2\left(H_1 + H_2\right)^2\right],$$

$$\delta = \frac{cH_1 H_2\left(\rho_1 H_1 + \rho_2 H_2\right)}{6\left(\rho_2 H_1 + \rho_1 H_2\right)},$$

where

$$c = \sqrt{\frac{g\left(\rho_2 - \rho_1\right)H_1 H_2}{2\rho_1 H_2}}, \quad \text{and} \quad Q = \sqrt{\frac{1}{2g\left(\rho_2 - \rho_1\right)c}}. \tag{2}$$

By following the usual oceanic condition, the density difference between upper and lower layers to be very small so that $\rho_2 - \rho_1 \ll \rho_2$ [27]. In this paper, we consider initially $H_1 > H_2$ so that we have an internal undular bore of depression. We also consider that the upper layer has a constant depth for all x and the depth of lower layer varies monotonically from h_0 to h_1 in the interval $x_0 \le x \le x_1$ where $x_1 - x_0 \gg 1$.

The first two terms in veKdV equation (1) are the dominant terms. Thus, the veKdV equation (1) can be transformed by introducing new variables [26],

$$A = QU, \qquad T = \int^x \frac{dx}{c}, \qquad X = c(T - t). \tag{3}$$

By substituting the new variables (3) into veKdV equation (1) gives the following equation, to the same leading order of approximation where veKdV equation (1) holds

$$U_T + \alpha U U_X + \beta U^2 U_X + \lambda U_{XXX} = 0 \,, \tag{4}$$

where

$$\alpha = Q\mu \,, \qquad \beta = Q^2 \mu_1 \,, \qquad \lambda = \delta \,. \tag{5}$$

In terms of the new variables $U(X, T)$, $H_1(T)$ is constant for all T and $H_2(T)$ varies monotonically through a monotonic function, $f(T)$ from h_0 to h_1 in the interval $T_0 \le T \le T_1$. In this study, we consider two types of variable topography, i.e. slowly increasing slope and slowly decreasing slope regions.

The structure of undular bore is an oscillatory transition between two different basic states. It can be generated from a simple unit step using the Heaviside function [28]. Hence, we consider the initial condition for the veKdV equation (4) to be in the form of a sharp step,

$$U = U_0 P(-X) \,,$$

where $U_0 < 0$ and P is a Heaviside function (6) to generate a hydraulic jump that connects two different constant depths.

$$P(X) = \begin{cases} 1, & \text{if } X > 0, \\ 0, & \text{if } X < 0. \end{cases} \tag{6}$$

3. Numerical method

To solve the veKdV equation (4) numerically, we apply the method of lines (MOL). In previous studies, the MOL is widely used in solving many KdV-type equations, e.g. constant-coefficient eKdV equation [29], variable-coefficient eKdV equation [30], forced KdV equation [31], and forced KdV-Burgers equation [32]. First, the veKdV equation (4) is rewritten as follows

$$U_T = -\alpha U U_X - \beta U^2 U_X - \lambda U_{XXX} \,.$$

Then, the spatial derivatives are discretized using central finite difference formulae as follows

$$U_X \approx \frac{U_{j+1} - U_{j-1}}{2\Delta X} \text{ , and } U_{XXX} \approx \frac{U_{j+2} - 2U_{j+1} + 2U_{j-1} - U_{j-2}}{2(\Delta X)^3} \,,$$

where j indicates the position along spatial axis and ΔX represents the increment value of the spatial axis. Therefore, the MOL approximation of the veKdV equation (4) is given by

$$\frac{\partial U_j}{\partial T} = -(\alpha U_j + \beta U_j{}^2) \frac{U_{j+1} - U_{j-1}}{2\Delta X} - \lambda \frac{U_{j+2} - 2U_{j+1} + 2U_{j-1} - U_{j-2}}{2(\Delta X)^3} = f(U_j) \,.$$

To solve for the time integration, we adopt the classical fourth-order Runge-Kutta method.

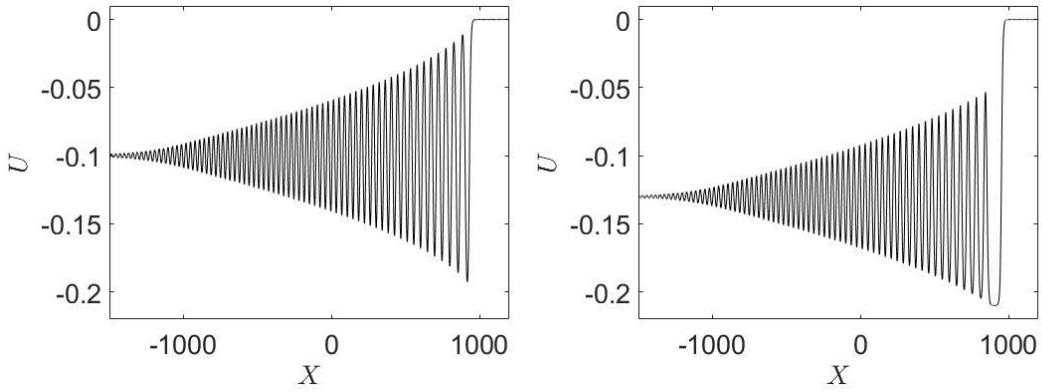


Fig. 2. The structure of internal undular bore of depression: (a) KdV-type internal undular bore where b = –0.10; (b) Table-top internal undular bore where b = –0.13

The initial condition of veKdV equation (4) is taken as

$$U(X) = \frac{b}{2}\left(1 - \tanh\left(\frac{X}{20}\right)\right),$$

where b denotes the height of the sharp step. Here, we consider two values for b, i.e. b = –0.10 and b = –0.13 so that we would have a KdV-type solitary wave and a table-top solitary wave as the leading wave of the internal undular bore of depression (refer to Fig. **2**(a) and Fig. **2**(b)). The values for H_1 and H_2 are chosen to be 1.0 and 1.5 respectively. The amplitude of leading solitary wave of KdV-type internal undular bore is $U_{lim0} \approx 2b$ = –0.20 and the leading solitary wave of table-top internal undular bore has a limiting amplitude, i.e.

$$U_{\lim 0} = \frac{-\alpha}{\beta} = -0.21,$$

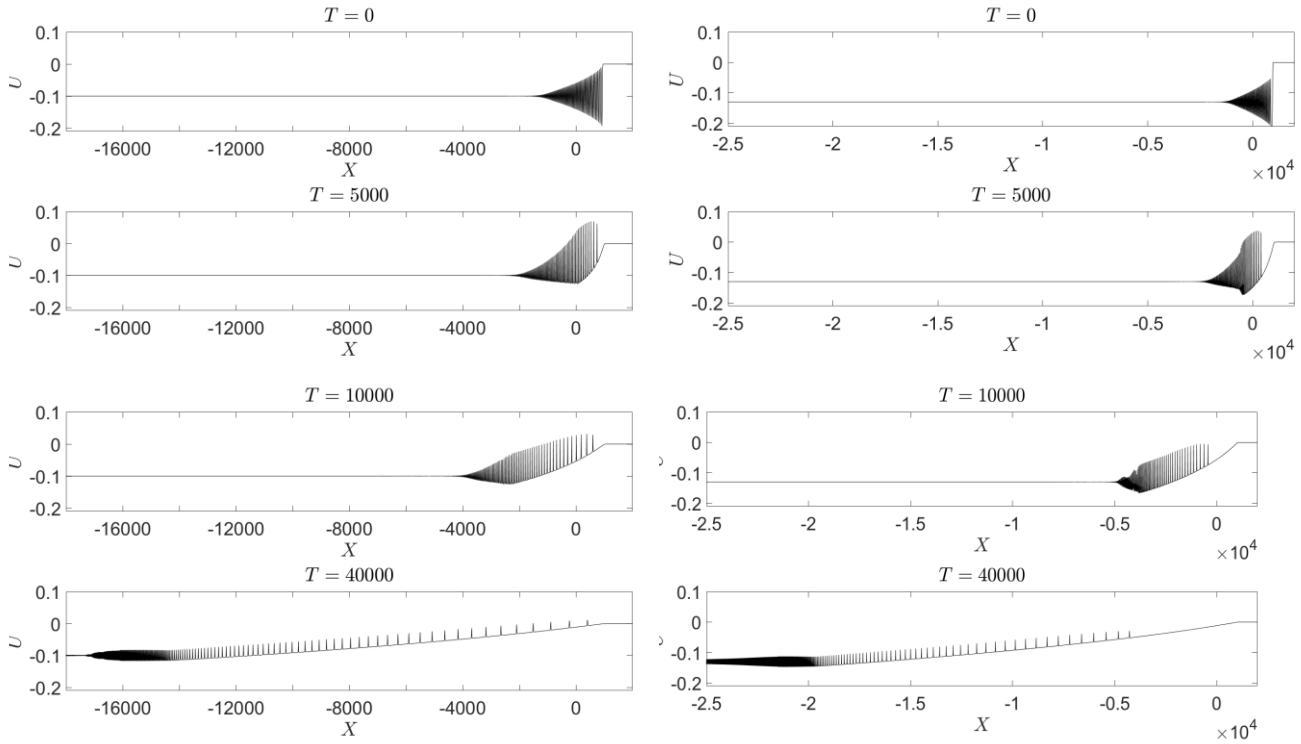
We would like to observe how the varying depth would affect the transformation of the internal undular bore especially the leading solitary wave when it propagates over the slowly varying slope.

3. Numerical results

The numerical results are divided into two categories, i.e. one that involves polarity change and one that without polarity change.

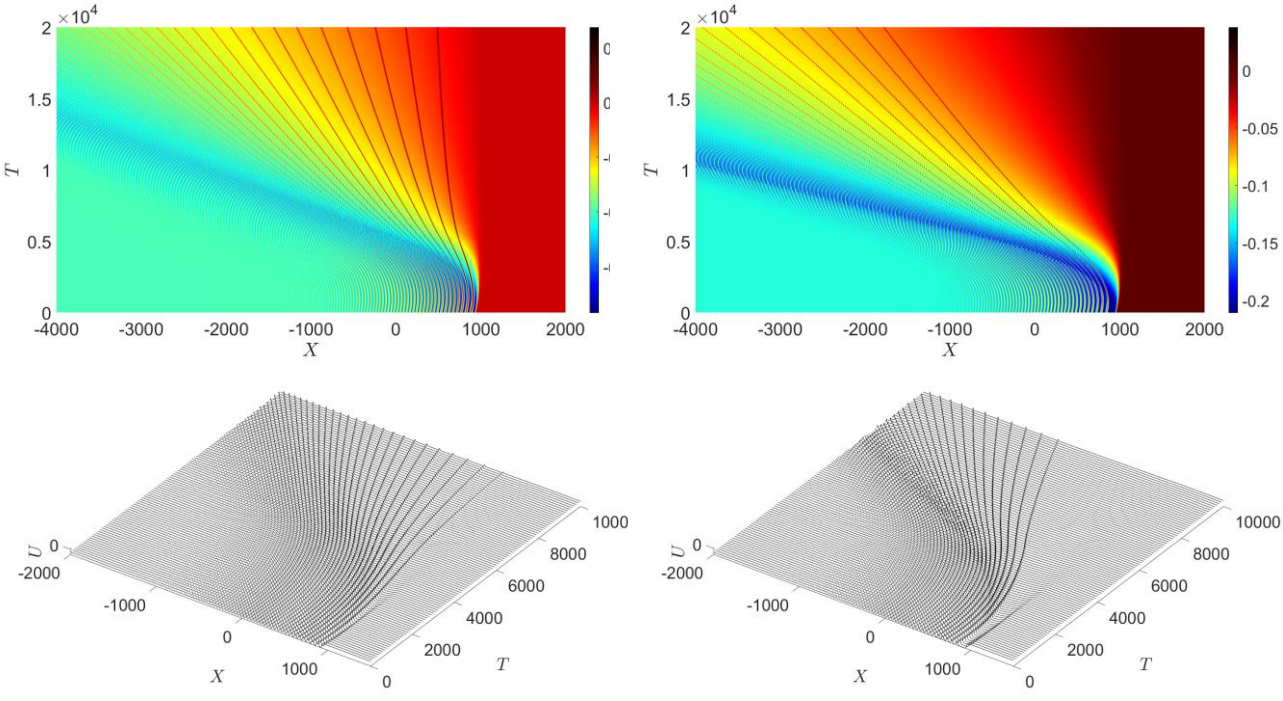
3.1 Transformation of internal undular bore involves polarity change

We observed that the polarity of the internal undular bore changes from negative to polarity when it propagates over a slowly increasing slope where the depth of the lower layer after the slope is less than or equal to the depth of the upper layer, i.e. $h_1 \leq H_1$.



(a) (b)

Fig. 3. 2D plots for the propagation of internal undular bores of depression over a slowly increasing slope where $h_1 < H_1$: (a) KdV-type internal undular bore where $b = -0.10$ and (b) Table-top internal undular bore where $b = -0.13$

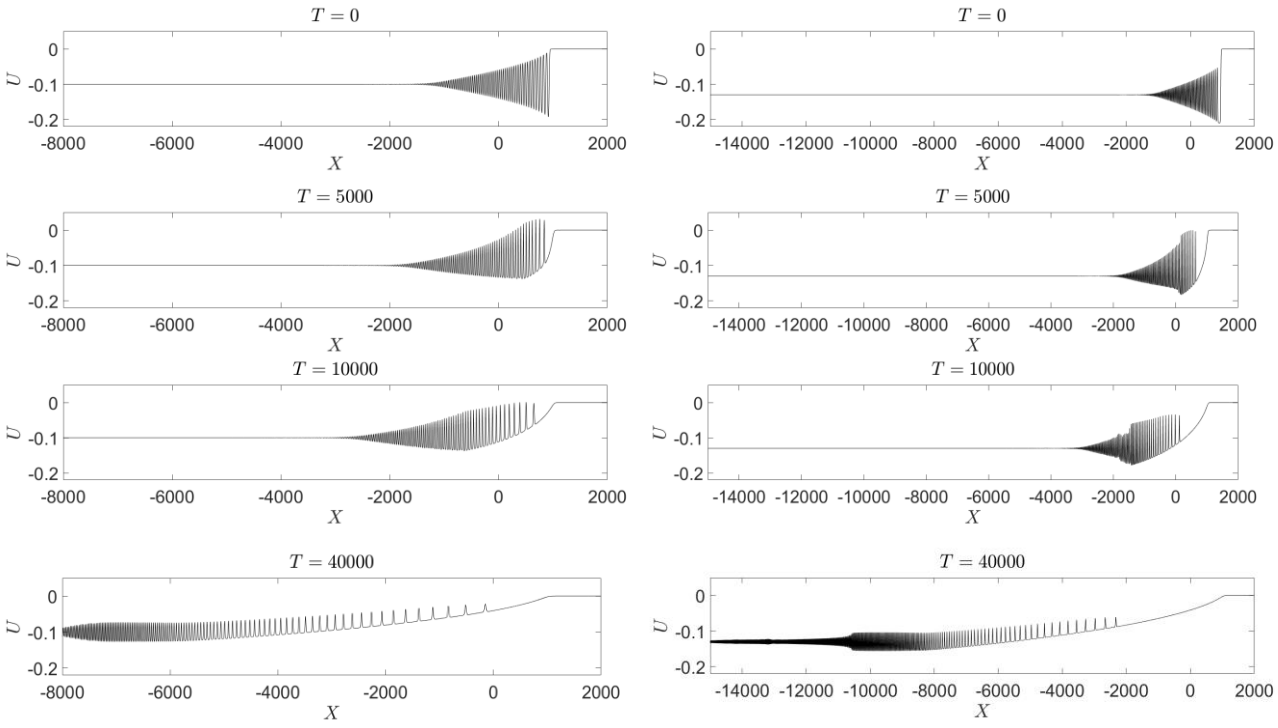


(a) (b)

Fig. 4. Contour plot (upper panel) and 3D plot (lower panel) for the propagation of internal undular bores of depression over a slowly increasing slope where $h_1 < H_1$: (a) KdV-type internal undular bore where $b = -0.10$ and (b) Table-top internal undular bore where $b = -0.13$

During the shoaling process, the internal wave of depression normally involves polarity change when it propagates from the deep sea region to the coastal area [33-35]. This polarity conversion can be well-explained by the KdV theory which stated that the polarity changes for the wave solutions is based on the change of sign of coefficient in the quadratic nonlinear term, α [36-37]. When the internal undular bore of depression is propagating on the slowly increasing slope region, the negative coefficient of quadratic nonlinear term, α in equation (4) is slowly increasing toward positive value. Once the polarity of the internal undular bore has changed to a positive value, the leading solitary wave deforms adiabatically so that the amplitude of the leading solitary wave increases slowly. At the same time, there is a non-adiabatic respond where there is a generation of a set of isolated solitary waves with different amplitude or a solitary wavetrain in front of the transformed bore as the result of the interaction of the undular bore with the slowly varying bottom surface. The solitary wavetrain is seen to be riding on negative pedestal due to the rarefaction wave propagating in the background caused by the polarity change. As the result, the isolated solitary wave is diminishing as it climbs the pedestal and the amplitude of each isolated solitary wave in the wavetrain is slowly decreasing on the negative pedestal. Figure 3 shows the transformation of the internal undular bore over the slope where $h_1 < H_1$ after the slope. Figure 4 shows the contour and 3D plots of the evolution of the internal undular bore. The depth profile of lower layer is given by

$$H_2(T) = \begin{cases} 1.5 & : 0 \le T < 100, \\ -0.00016T + 1.516 & : 100 \le T < 5100, \\ 0.7 & : T \ge 5100, \end{cases}$$



(a) (b)

Fig. 5. 2D plots for the propagation of internal undular bores of depression over a slowly increasing slope where $h_1 = H_1$: (a) KdV-type internal undular bore where b = –0.10 and (b) Table-top internal undular bore where b = –0.13

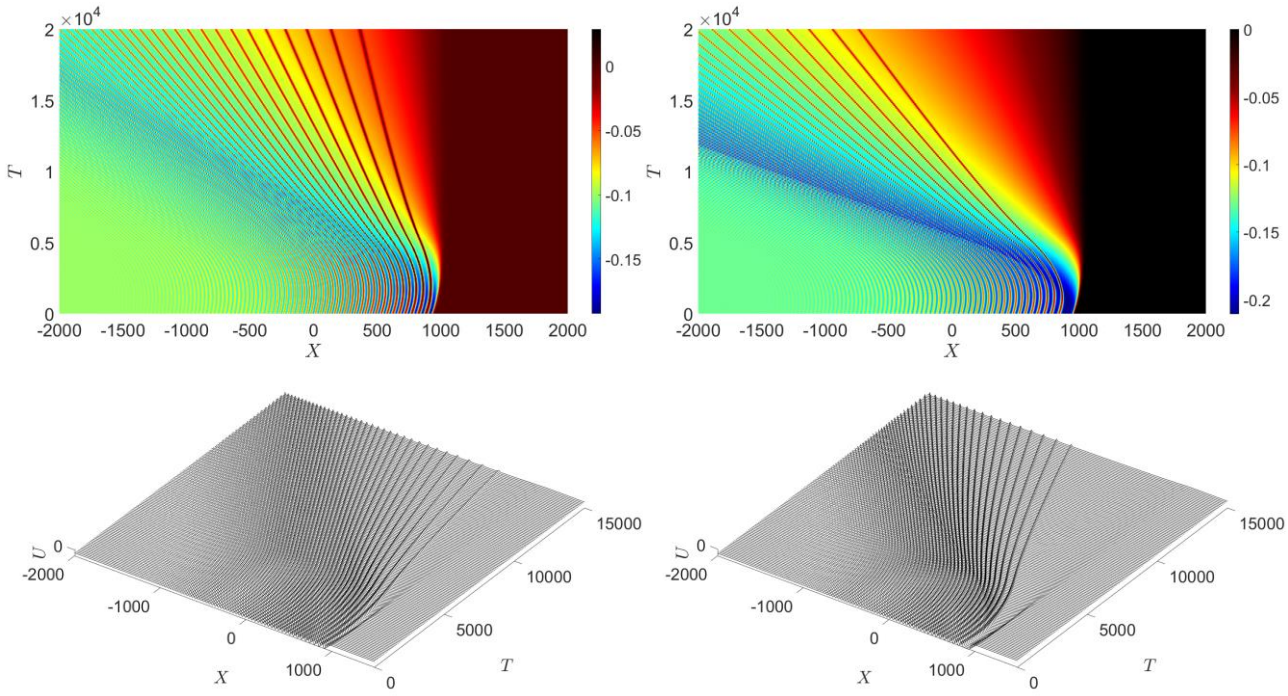


Fig. 6. Contour plot (upper panel) and 3D plot (lower panel) for the propagation of internal undular bores of depression over a slowly increasing slope where $h_1 = H_1$: (a) KdV-type internal undular bore where $b = -0.10$ and (b) Table-top internal undular bore where $b = -0.13$

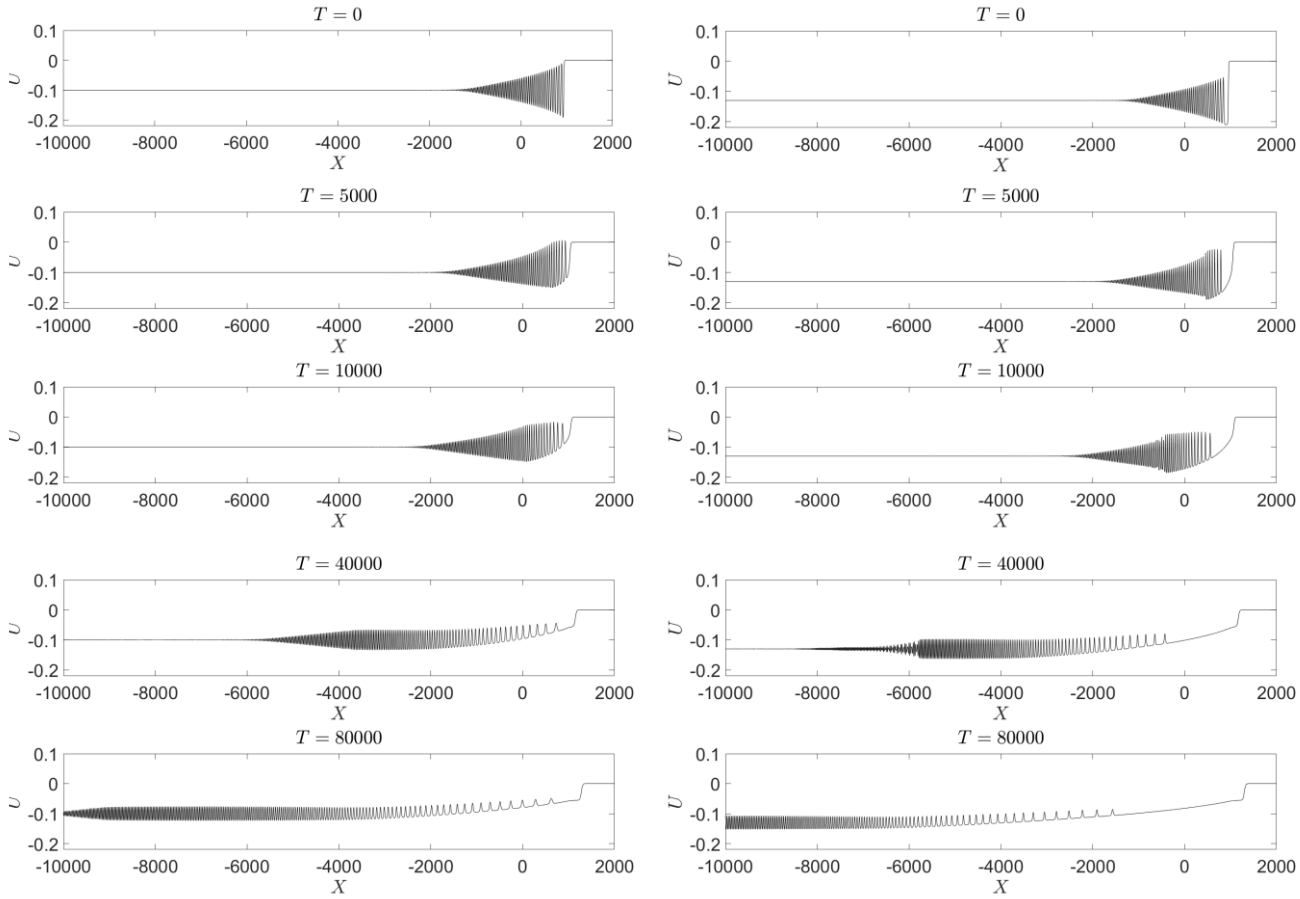
Figure 5 shows the transformation of the internal undular bore over the slope where $h_1 = H_1$ after the slope. Figure 6 shows the contour and 3D plots of the evolution of the internal undular bore. The depth profile of lower layer is

$$H_2(T) = \begin{cases} 1.5 & : \ 0 \le T < 100, \\ -0.0001T \ + \ 1.51 & : \ 100 \le T < 5100, \\ 1.0 & : \ T \ge 5100. \end{cases}$$

3.2 Transformation of internal undular bore without polarity change

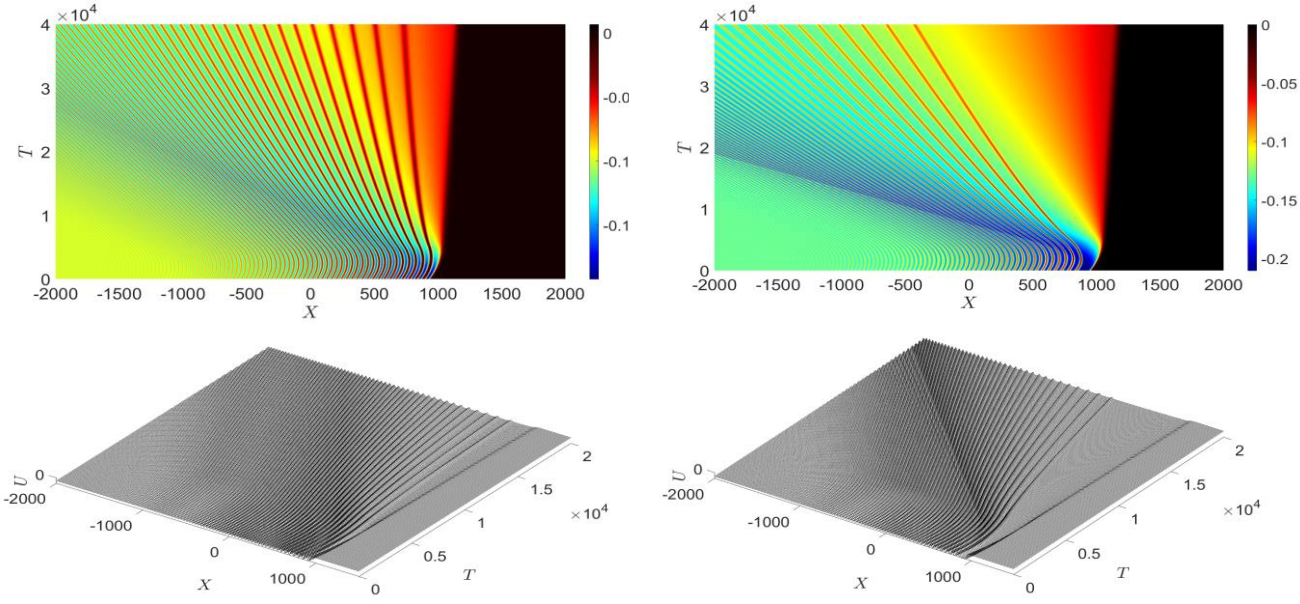
When the depth after the increasing slope is still greater than the depth of the upper layer, i.e. $h_1 > H_1$, the polarity of the internal undular bore remains unchanged throughout the entire propagation. The leading solitary wave deforms adiabatically and its amplitude decreases as it propagates over the slope. However, the value of the limiting amplitude changes to a new value, i.e. $U_{\text{lim1}} = -0.0557$, which is a smaller value compared to the limiting amplitude value before the slope. Therefore, we observe the formation of a step-like wave of negative polarity. Figure 7 shows the transformation of the internal undular bore over the slope where $h_1 > H_1$ after the slope. Figure 8 shows the contour and 3D plots of the evolution of the internal undular bore. The depth profile of lower layer is given by

$$H_2(T)=\begin{cases}1.5 & : 0\le T<100,\\ -0.00006T\ +\ 1.506 & : 100\le T<5100,\\ 1.2 & : T\ge 5100.\end{cases}$$



(a) (b)

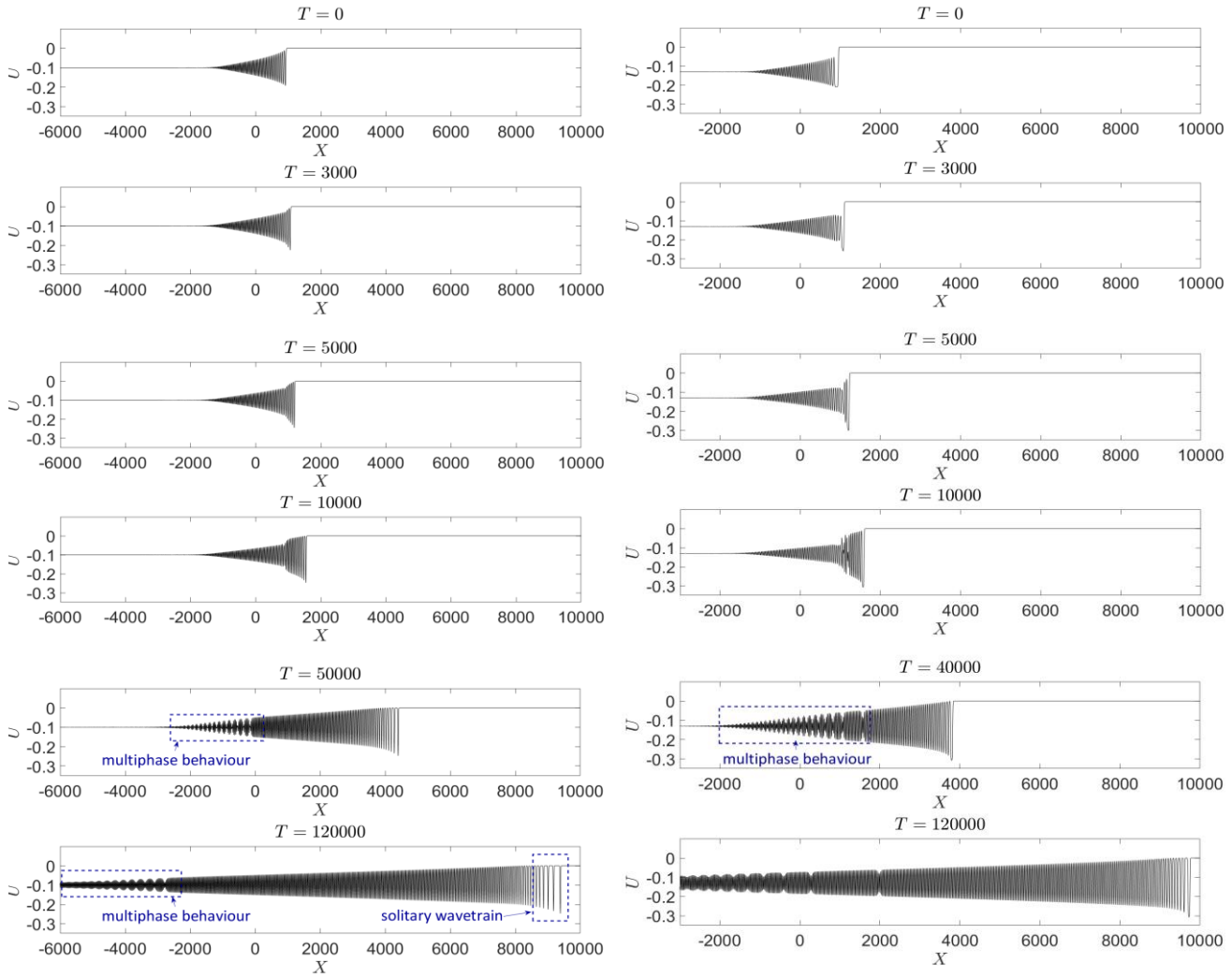
Fig. 7. 2D plots for the propagation of internal undular bores of depression over a slowly increasing slope where $h_1 > H_1$: (a) KdV-type internal undular bore where b = –0.10 and (b) Table-top internal undular bore where b = –0.13



(a) (b)

Fig. 8. Contour plot (upper panel) and 3D plot (lower panel) for the propagation of internal undular bores of depression over a slowly increasing slope where $h_1 > H_1$: (a) KdV-type internal undular bore where b = –0.10 and (b) Table-top internal undular bore where b = –0.13

Now, we look at the case where the bottom slope is decreasing slowly. For the KdV-type internal undular bore, i.e. when b = –0.10, the leading solitary wave of the internal undular bore behaves as an isolated solitary wave and it deforms adiabatically. Its amplitude increases as it enters the varying depth region. Once it reaches new constant depth region, the amplitude stops increasing and remains constant throughout the propagation. It also has a non-adiabatic respond where a solitary wavetrain is generated. This phenomenon has been observed as well when a surface undular bore evolves over a slowly varying region [38]. Also, a multi-phase interaction is observed during the evolution. The multi-phase interaction carries on for quite some time and it diminishes after the transformed bore has settled down on the new constant region.



(a) (b)

Fig. 9. 2D plots for the propagation of internal undular bores of depression over a slowly decreasing slope: (a) KdV-type internal undular bore where b = –0.10 and (b) Table-top internal undular bore where b = –0.13

Fig. **9**(a) shows the evolution of the KdV-type internal undular bore over the slowly decreasing slope region. The depth of lower layer varies according to the following

$$H_2(T)=\begin{cases}1.5 & : 0\le T<100,\\ 0.00004T+1.496 & : 100\le T<5100,\\ 1.7 & : T\ge 5100.\end{cases}$$

Figure 10(a) shows the contour and 3D plots of the evolution of the internal undular bore.

However, we do not observe the generation of solitary wavetrain for the table-top internal undular bore, i.e. when b = –0.13. The leading table-top solitary wave also behaves as an isolated solitary wave such that it deforms adiabatically and reach a new limiting amplitude, i.e. U_{lim2} = –0.3077. We also observe that the occurrence of multi-phase behaviour due (see Fig. **9**(b)). The contour plot and 3D plots of the transformation of internal undular bore over a slowly decreasing slope are shown in Fig. **10**(b).

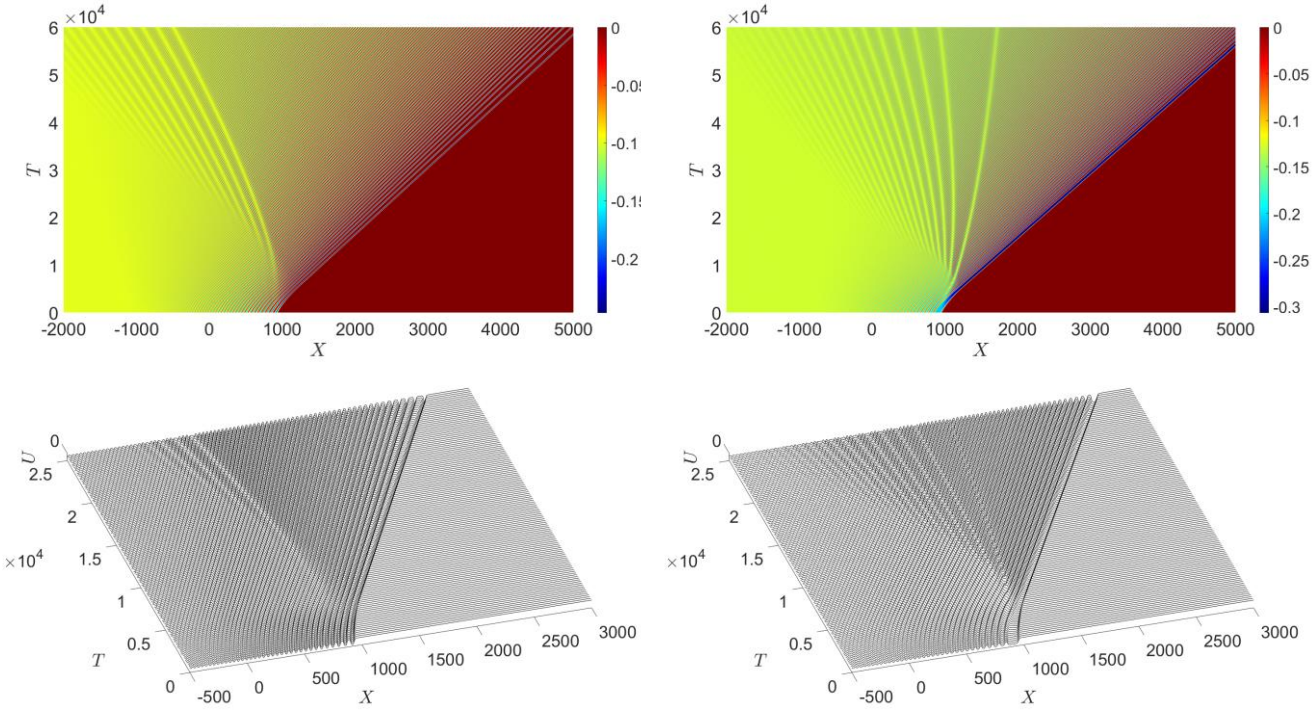


Fig. 10. Contour plot (upper panel) and 3D plot (lower panel) for the propagation of internal undular bores of depression over a slowly decreasing slope: (a) KdV-type internal undular bore where b = –0.10 and (b) Table-top internal undular bore where b = –0.13

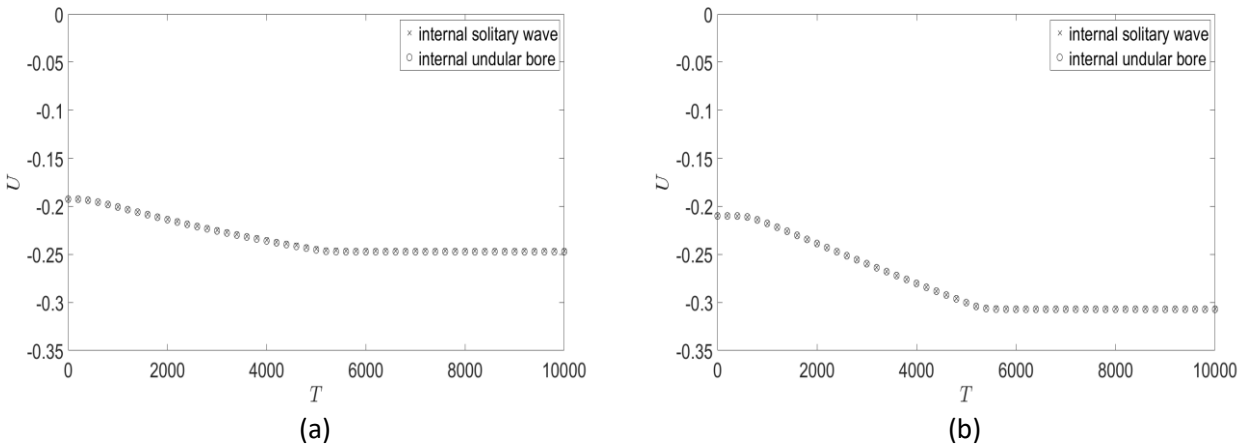


Fig. 11. Comparison of the amplitude variation between the leading solitary wave of internal undular bore and an isolated solitary wave: (a) $b = -0.10$ (b) $b = -0.13$

Fig. **11** shows the comparison of the amplitude variation between the leading solitary wave of the internal undular bore and an isolated solitary wave propagating over a slowly decreasing region. This shows that the leading solitary wave is indeed behaving as an isolated solitary wave during the evolution.

4. Conclusions

In this paper, we have simulated the propagation of internal undular bore of negative polarity with two types of leading wave, i.e. KdV-type and table-top over different types of slowly varying topography in a two-layer fluid system. When the internal undular bores propagates over a slowly increasing region, the polarity of the internal undular bore may change depending on the depth of the constant region after the slope. If the depth after the slope is less than or equal to the depth of the upper layer, then the polarity of the internal undular bore changes from negative polarity to a positive polarity. In this case, we notice that there is a generation of solitary wavetrain riding on a negative pedestal. At larger time-scale, the amplitude of the solitary waves in the solitary wavetrain decreases and diminishes due to the pedestal. However, if there is no polarity change during transformation, the internal undular bore deforms adiabatically until the amplitude of leading wave reaches the new limiting amplitude. This leads to the formation of a step-like wave at the front of the transformed bore. When the internal undular bore propagates over a slowly decreasing slope, the leading wave of the KdV-type internal undular bore behaves as an isolated solitary wave and deforms adiabatically. A non-adiabatically respond in the form of a solitary wavetrain is observed at the front of the transformed bore. However, no solitary wavetrain is generated during the transformation of table-top internal undular bore even though the leading wave also behaves as an isolated solitary wave. These simulation results can be used to provide a useful insight to understand the evolution of internal undular bore of depression propagating in ocean layers for the prevention of oceanic disasters.

References

[1] Franklin, B. *The Works of Benjamin Franklin*. Campe, 1835.
[2] Nansen, F. *Farthest North: The epic adventure of a visionary explorer*. Skyhorse Publishing Inc., 2008.
[3] Ekman, V. W. "On dead water, Norw. N. Polar Exped. 1893–1896: Sci. Results, XV, Christiana." PhD diss., Ph. D. thesis, 1904.
[4] Sonar, A. *Internal wave and their influence upon naval operation*. Cambridge Massachusetts: Arthur D. Little, 1966.
[5] Apel, J.R., Ostrovsky, L.A., Stepanyants, Y.A. and Lynch, J.F. "Internal Solitons in the Ocean and Their Effect on Underwater Sound." *The Journal of the Acoustical Society of America* 121, no. 2 (2007): 695.
[6] Deldar, H., Bidokhti, A.A. and Chegini, V. "An Investigation of the Effects of Internal Waves on Sound Propagation in a Stratified Medium with a Sloping Bed." *Acoustical Physics* 64, no. 1 (January 1, 2018): 58–63.
[7] Huang, X., Chen, Z., Zhao, W., Zhang, Z., Zhou, C., Yang, Q. and Tian, J. "An Extreme Internal Solitary Wave Event Observed in the Northern South China Sea." *Scientific Reports* 6, no. 1 (2016): 30041.
[8] Kurup, N.V., Shi, S., Shi, Z., Miao, W. and Jiang, L. "Study of Nonlinear Internal Waves and Impact on Offshore Drilling Units," 2011.
[9] Osborne, A.R., Burch, T.L. and Scarlet, R.I. "The Influence of Internal Waves on Deep-Water Drilling." *Journal of Petroleum Technology* 30, no. 10 (October 1, 1978): 1497–1504.
[10] Marth, R., Müller, G. and Wolters, G. "Damages of Blockwork Coastal Structures Due to Internal Wave Impact Induced Pressures." In *WIT Transactions on the Built Environment*, 2005.
[11] Morozov, E.G., Marchenko, A.V., Filchuk, K.V., Kowalik, Z., Marchenko, N.A. and Ryzhov, I.V. "Sea Ice Evolution and Internal Wave Generation Due to a Tidal Jet in a Frozen Sea." *Applied Ocean Research*, 2019.

[12] Wall, M., Putchim, L., Schmidt, G.M., Jantzen, C., Khokiattiwong, S. and Richter, C. "Large-Amplitude Internal Waves Benefit Corals during Thermal Stress." *Proceedings of the Royal Society B: Biological Sciences*, 2015.
[13] Schmidt, G.M., Wall, M., Taylor, M., Jantzen, C. and Richter, C. "Large-Amplitude Internal Waves Sustain Coral Health during Thermal Stress." *Coral Reefs*, 2016.
[14] Bai, X., Liu, Z., Li, X., Chen, Z., Hu, J., Sun, Z. and Zhu, J. "Observations of High-Frequency Internal Waves in the Southern Taiwan Strait." *Journal of Coastal Research*, 2013.
[15] Fu, K.H., Wang, Y.H., Lee, C.P. and Lee, I.H. "The Deformation of Shoaling Internal Waves Observed at the Dongsha Atoll in the Northern South China Sea." *Coastal Engineering Journal*, 2016.
[16] Woodson, C.B., Barth, J.A., Cheriton, O.M., McManus, M.A., Ryan, J.P., Washburn, L., Carden, K.N., Cheng, B.S., Fernandes, J., Garske, L.E. and Gouhier, T.C. "Observations of Internal Wave Packets Propagating Along-Shelf in Northern Monterey Bay." *Geophysical Research Letters* 38, no. 1 (2011): 1–6.
[17] Yuan, C., Grimshaw, R. and Johnson, E. "The Evolution of Internal Undular Bores over a Slope in the Presence of Rotation." *Studies in Applied Mathematics* 140, no. 4 (May 2018): 465–82.
[18] Holloway, P. E. "Observations of Shock and Undular Bore Formation in Internal at a Shelf Break." In *Breaking Waves*, 1992.
[19] Novotryasov, V.V., Stepanov, D.V. and Yaroshchuk, I.O. "Observations of Internal Undular Bores on the Japan/East Sea Shelf-Coastal Region." *Ocean Dynamics* 66, no. 1 (January 28, 2016): 19–25.
[20] Dolgikh, G.I., Novotryasov, V.V., Yaroshchuk, I.O. and Permyakov, M.S. "Intense Undular Bores on the Autumn Pycnocline of Shelf Waters of the Peter the Great Bay (Sea of Japan)." *Doklady Earth Sciences*, 2018.
[21] Benney, D.J. "Long Non-Linear Waves in Fluid Flows." *Journal of Mathematics and Physics* 45, no. 1–4 (April 1966): 52–63.
[22] Benjamin, T. B. "Internal Waves of Finite Amplitude and Permanent Form." *Journal of Fluid Mechanics* 25, no. 2 (1966): 241–70.
[23] Helfrich, K.R. and Melville, W.K. "Long Nonlinear Internal Waves." *Annual Review of Fluid Mechanics* 38, no. 1 (January 2006): 395–425.
[24] Holloway, P., Pelinovsky, E. and Talipova, T. "Internal Tide Transformation and Oceanic Internal Solitary Waves." *Environmental Stratified Flows*, no. Springer US (2003): 29–60.
[25] Grimshaw, R. "Internal Solitary Waves." In *Environmental Stratified Flows*, 1–27. Boston: Kluwer Academic Publishers, 2003.
[26] Grimshaw, R., Pelinovsky, E., Talipova, T. and Kurkina, O. "Internal Solitary Waves: Propagation, Deformation and Disintegration." *Nonlinear Processes in Geophysics* 17, no. 6 (November 17, 2010): 633–49.
[27] Weigand, J. G.. "A Model Study of Internal Waves." University of Washington, 1962.
[28] Grimshaw, R. "Transcritical Flow Over a Step," no. 1984 (2007): 27–31.
[29] Tiong, W.K., Tay, K.G., Ong, C.T. and Sze, S.N. "Numerical Solution of the Gardner Equation." In *Proceedings of the International Conference on Computing, Mathematics and Statistics (ICMS 2015)*, 243–51. Singapore: Springer Singapore, 2017.
[30] Hooi, M.H., Tiong, W.K., Tay, K.G., Sze, S.N. and Chiew, K.L. "Simulation of Internal Solitary Waves with Negative Polarity in Slowly Varying Medium," 2018, 020006.
[31] Yazid, N.M., Tay, K.G., Choy, Y.Y., Sudin, A.M., Tiong, W.K. and Ong, C.T. "Numerical Solution of the Forced Korteweg-de Vries (FKDV) Equation." *ARPN Journal of Engineering and Applied Sciences* 11, no. 18 (February 9, 2016): 10757–60.
[32] Yazid, N.M., Tay, K.G., Tiong, W.K., Choy, Y.Y., Sudin, A.M. and Ong, C.T. "The Method of Lines Solution of the Forced Korteweg-de Vries-Burgers Equation." *MATEMATIKA* 33, no. 1 (September 20, 2017): 35.
[33] Bai, Y., Song, H., Guan, Y. and Yang, S. "Estimating Depth of Polarity Conversion of Shoaling Internal Solitary Waves in the Northeastern South China Sea." *Continental Shelf Research*, 2017.
[34] Li, L., Wang, C. and Grimshaw, R. "Observation of Internal Wave Polarity Conversion Generated by a Rising Tide." *Geophysical Research Letters* 42, no. 10 (May 28, 2015): 4007–13.
[35] Orr, M.H. and Mignerey, P.C. "Nonlinear Internal Waves in the South China Sea: Observation of the Conversion of Depression Internal Waves to Elevation Internal Waves." *Journal of Geophysical Research*, 2003.
[36] Grimshaw, R, E Pelinovsky, and T Talipova. "Modelling Internal Solitary Waves in the Coastal Ocean." *Surveys in Geophysics* 28, no. 4 (2007): 273–98.
[37] Grimshaw, R., Pelinovsky, E. and Talipova, T. "Solitary Wave Transformation Due to a Change in Polarity." *Studies in Applied Mathematics*, 1998.
[38] El, G.A., Grimshaw, R.H.J. and Tiong, W.K. "Transformation of a shoaling undular bore." *Journal of Fluid Mechanics*, 2012.

Penerbit Akademia Baru

Engineering Science and Technology Conference Proceedings

Journal homepage: www.akademiabaru.com/EST.html

Numerical Analysis of Aluminium Oxide and Silicon Dioxide Nanofluids in Serpentine Cooling Plate of PEMFC

Open Access

Amira Shahirah Malek Amir Azmin[1], Irnie Azlin Zakaria[1*], Saifuddin Khalid[1], Wan Azmi Wan Hamzah[2], Wan Ahmad Najmi Wan Mohamed[1]

[1] Faculty of Mechanical Engineering, Universiti Teknologi MARA (UiTM), 40450 Shah Alam, Selangor, Malaysia.
[2] Faculty of Mechanical Engineering, Universiti Malaysia Pahang, 26600 Pekan, Pahang, Malaysia.

ABSTRACT

Proton Exchange Membrane Fuel Cell (PEMFC) is an alternative energy application for vehicular power sources and is a strong contender for clean and efficient power generation. However, the heat generated by the PEMFC need to be taken care efficiently to avoid damage to fuel cell component especially membrane due to overheat. Excessive heat can also lead to performance deterioration of PEMFC. Therefore, nanofluids adoption as cooling medium study on combination of nanofluids as cooling medium for PEMFC is explored. In this study, the heat transfer performance of Aluminium Oxide (Al2O3) and Silicon Dioxide (SiO2) in water with different value of low concentration of 0.1%, 0.3% and 0.5% volume are analysed. The nanofluids is adopted as cooling medium in a serpentine cooling plate of PEMFC which is subjected to a constant heat flux of 300W. The result shows that there is 2.04 % improvement in a Al2O3 while 0.9 % improvement in SiO2 in heat transfer coefficient of 0.5% volume concentration as compared to water is recorded. However, the improvement also accompanied by pressure drop increment of 68% in Al2O3 and 189% SiO2 nanofluids as compared to base fluid water.

Keywords:
Aluminium Oxide (Al_2O_3); nanofluids;
PEMFC; Serpentine; Silicon Dioxide (SiO_2)

Copyright © 2019 PENERBIT AKADEMIA BARU - All rights reserved

1. Introduction

The earth's atmosphere produce greenhouse gases (GHGs) which are in the form of water vapor containing small amount of methane (CH4), carbon dioxide (CO2) and nitrous oxide (N2O). The greenhouse gases (GHGs) work as a thermal blanket for the planet by absorbing heat from the sun and keeping the surface warm on average 15℃ to support life [1]. This is natural causes of global warming and it also enable life. The global warming is an important environmental issue that may affect humans and other living organisms. In order to overcome the problems, renewable energy resources are being implemented to minimize demand for fossil fuel even though the power plants are still based on fossil fuel. Therefore, there are alternatives for the energy sources discovered to reduce pollution and depletion of the natural fuel resources. The hydrogen energy has been investigated and the device which use hydrogen as fuel is called fuel cell. Hydrogen has a significant role in future low-carbon economies [2-4] with the versatility to produce or provide power system,

* *Corresponding author.*
E-mail address: irnieazlin@gmail.com (Irnie Azlin Zakaria)

mobility, heat, industrial services and electricity. Therefore, hydrogen can be one of future solution to world's energy needs [5].

One of the power generation technologies that rapidly and quickly developed for greater energy sustainability is the Proton Exchange Membrane Fuel Cell (PEMFC). PEMFC uses hydrogen as fuel which reacts with oxygen to change hydrogen-bound chemical energy into electricity [6]. PEMFC have been chosen for the study due to its rapid start-up with low operating temperature between 60℃ and 80℃ while high operating temperature between 100℃ and 200℃ [6] mainly focusing on the membrane design and the capability. Heat will be generated during the chemical reaction between oxygen and hydrogen. However, the heat generated by the PEMFC need to be removed efficiently to avoid the fuel cell component from causing damage because of overheating. The damage or breakdown of fuel cell component could decrease the stack performance.

Effective cooling is crucial for a safer and more efficient operation of PEMFC especially when handling with higher power of fuel cell stack that has been reported by Zakaria *et al.,* [7]. A better performance PEMFC is produced from the effective thermal management of fuel cell as high temperature can result in membrane degradation while the kinetic reaction will become lower because of the low temperatures and it will cause flooding issues sometimes [8-10]. Therefore, a cooling system and fuel cell needs to be installed together by using the cooling plates. Cooling plate function is to remove the reaction heat by circulating the coolant. In a cooling system of fuel cell, the cooling plate is placed between several unit cells in the fuel cell stack. In industries, the cooling medium that commonly used are liquid and air coolant. Liquid cooling is more efficient than air cooling and enables major reductions in the volume and weight of power electronics.

A new technology is discovered to improve the thermal properties of fluids and it is called nanofluids. The fundamental heat transfer and fluid flow characteristic of nanofluids in mini channel is need to be further investigated. Sohel *et al.,* [11] and Khaleduzzaman *et al.,* [12] have investigated nanofluids in mini channel for electronic heat sink and automotive exchangers. Based on the report, the materials of mini channel normally constructed from highly conductive material such as copper and aluminium. Sohel *et al.,* [11] also investigated the effect of volume fractions of thermal performance Al2O3 towards water. From his investigation, 18% increment of heat transfer for 0.25% volume concentration at 1000 Reynolds number as compared to base fluid. The base fluid in fuel cell mixed with nanofluids coolant which is studied by using Computational Fluid Dynamic (CFD) software to understand the thermal behaviour of nanofluids coolant in fuel cell cooling plates. The addition of nanofluids coolant to the base fluid can increase and augment the thermal conductivity of the base fluid since the thermal conductivity of a metal is many orders of magnitude higher than the base fluid [13]. Aluminium Oxide (Al2O3) and Silicon Dioxide (SiO2) have been used as nanofluids coolant for this study. Therefore, the best properties of coolant will result in higher value of heat transfer as it releases more heat when it flows through the cooling plate. The best cooling system for the fuel cell also depends on design cooling plate pattern flow. Thus, Islam *et al.,* [14] has reported the thermal conductivity increases with the increase of concentration while decrease with increasing temperature.

Serpentine is a conventional design. Ramos-Alvarado *et al.,* [15] has discussed and reviewed a few options for cooling plate design including parallel, distributor and serpentine type. Uniformity of flow distribution was discussed and reported to be in average region and does not change with a big different with the increased of Reynolds number. Regarded as industry standard, the most commonly used flow channel for PEMFC is the serpentine design [16]. The design has long reactant flow path which causes substantial pressure drop and also has significant concentration gradient from the outlet and inlet [17]. Therefore, serpentine cooling plate is investigated in this study.

2. Methodology

2.1 Properties of fluid used in analysis

The properties of Aluminium Oxide (Al2O3) were taken from actual experimental values has been reported by Zakaria *et al.,* [7] has established an experimental investigation of Al2O3 for PEM fuel cell application while properties of Silicon Dioxide (SiO2) has been reported by Talib *et al.,* [18] has established a thermo-physical properties of SiO2 for PEM fuel cell cooling application. In this study, the Al2O3 nanoparticle was chosen because this particle commercially available, stable, cost advantage and has high thermal conductivity while SiO2 nanoparticle has less chance sedimentation. Table 1 shows the thermos-physical properties of nanoparticles and based fluid used in the analysis.

Table 1
Properties of nanoparticles and based fluid used in the analysis.

Nanofluid/ Base Fluid	Density ρ, kg/m^3	Thermal conductivity K, W/m.K	Specific Heat Cp, J/kg.K	Viscosity μ, Kg/m.s	Reference
Distilled Water	999	0.615	4180.0	0.00085	[7]
Al2O3	4000	36	765.0	-	[7]
SiO2	2220	1.38	745.0	-	[18]

2.2 Mathematical formula and governing equations

A few assumptions were made in order simplify the analysis. Assumption of simulation as below:

1. The flow is laminar, steady state and incompressible
2. Viscous dissipation is neglected and remain constant the fluid properties.
3. Zero relative velocity in thermal equilibrium for fluid phase and nanofluids. The resultant mixture is considered as a conventional single phase
4. Free convection heat transfer and radiation is negligible
5. Heat transfer and fluid flow characteristic for all mini channels are identical.

Below are the governing equations for the above assumption simulation.
Continuity equation:

$$\nabla.(\rho_{nf}.V_m) = 0 \quad (1)$$

The above equation is principle of mass conservation for a steady, one dimensional flow with one inlet and outlet. In this study A1= A2 because mass comes in A1 are same goes out to A2 since there is no flow go through the side walls of duct. Where, A = Area of duct

Momentum conservation equation:

$$\nabla.(\rho_{nf}.V_m.V_M) = -\nabla P + \nabla.(\mu_{nf}.\nabla V_m) \quad (2)$$

Energy equation for coolant:

$$\nabla.(\rho_{nf}.C.V_m.T) = \nabla.(k_{nf}.\nabla T) \quad (3)$$

The heat conduction through the solid wall:

$$\mathbf{0} = \boldsymbol{\nabla}.(\mathbf{k_s}.\boldsymbol{\nabla}\mathbf{T_s}) \quad (4)$$

At the wall no slip boundary:

$$\vec{V} = 0 \text{ (at Walls)} \quad (5)$$

At channel inlet the boundary conditions were assumed as:

$$\vec{V} = V_m \text{(at channel inlet)} \quad (6)$$

$$P = \text{atmospheric pressure (at channel outlet)} \quad (7)$$

The thermal energy with constant heat flux was generated from the fuel cell. In the simulation, the energy was applied uniformly at the bottom of cooling plate. Heat was transferred from the wall surface to the fluid via conduction and dispersed through the fluid by forced convection mechanism.

$$-k_{nf}.\nabla T = q \text{ (at bottom of plate or channel)} \quad (8)$$

$$-k_{nf}.\nabla T = 0 \text{ (at top of plate or channel)} \quad (9)$$

2.3 Mathematical Model

In boundary condition, heat flux and heat generation need to be calculated by using Equation 10 and 11. Where, W = Thermal Energy, W
Heat Flux:

$$\frac{W}{m^2} = \frac{300}{0.0462} = 6493.5065\ \mathrm{W}/m^2 \quad (10)$$

Heat Generation Rate:

$$\frac{W}{m^3} = \frac{300}{0.000184} = 1630434.783\ \mathrm{W}/m^3 \quad (11)$$

The coolant temperature differences were determined by calculating the differences between the inlet and outlet temperature of the coolant channel.

Hydraulic diameter, D_h need to be calculated before calculating the inlet velocity. Equation 12 was an equation that used to calculate hydraulic diameter.





$$D_h = \frac{2ab}{a+b} = \frac{(2)(0.0488)(0.001)}{0.0488+0.001} = 0.00196 \text{ m} \quad (12)$$

The value of inlet velocity was calculated by using Equation 13.

$$\mathrm{V} = \frac{\mathrm{R_e}\mu}{\rho \mathrm{D}} \quad (13)$$

Where,
V = Inlet velocity, m/s
R_e = Reynolds Number
μ = Viscosity, Kg/m.s
ρ = Density, kg/m^3
D = Diameter for a rectangle, m

Heat transfer was analyzed based on heat transfer coefficient and Nusselt Number. Heat transfer coefficient and Nusselt Number were calculated using Equation 14 and 15.

$$\mathrm{h} = \frac{\dot{\mathrm{q}}}{(\mathrm{T_{avgplate}} - \mathrm{T_{avgfluid}})} \quad (14)$$

Where,
h = Heat transfer coefficient, W/m^2.K
$\dot{q}$ = Heat Flux, W/m^2
$T_{avgplate}$ = Average Plate Temperature, K
$T_{avgfluid}$ = Average Fluid Temperature, K

$$\mathrm{Nu} = \frac{\mathrm{hD_h}}{\mathrm{k_{nf}}} \quad (15)$$

Where,
Nu = Nusselt Number
D_h = Hydraulic Diameter
k_{nf} = Thermal Conductivity Nanofluids, W/m.K

Meanwhile, fluid flow was analysed on pressure drop between IN and OUT flow. The pressure drops then used to calculate pumping power. Equation 16 used to calculate pumping power.

$$\mathrm{W_{pump}} = \dot{\mathrm{V}} \times \Delta\, \mathrm{P} \quad (16)$$

Where,
W_{pump} = Pumping Power
$\dot{V}$ = inlet velocity × inlet area
$\Delta\, P$ = Pressure drop

2.4 Grid Independent Test

One of the important steps in the Computational Fluid Dynamics (CFD) simulation process was meshing. The meshing process breaks the geometry or domain in small elements that develop mesh [19]. In this study, the grid independent test was set up. The process of mesh was repeated and refined more until the solution was converge. Once it become converge, the elements and nodes already stable to run the simulation. The best way to check the grid independent test was plotted a graph by using the monitor value vs the number of elements. It is shown that element of 335995 is the optimum meshing size for the study.

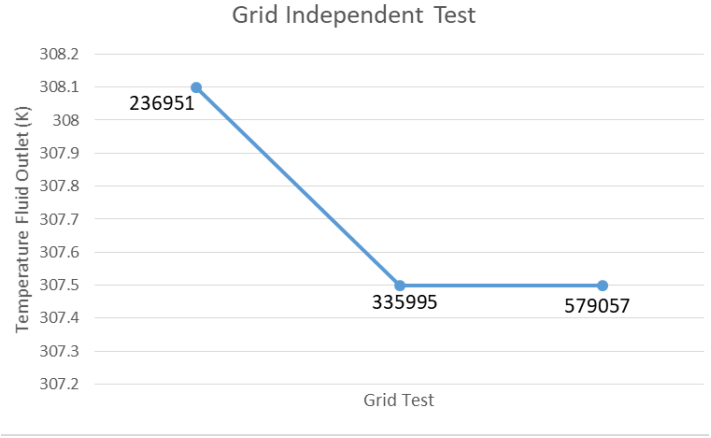


Fig. 1. Graph of Grid Independent Test

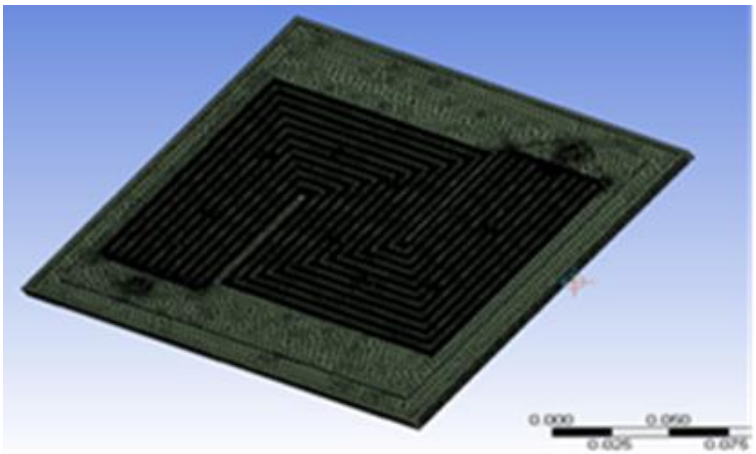


Fig. 2. Geometry of the Mesh for Serpentine Cooling Plate

3. Results and Discussion

3.1 Average Plate Temperature

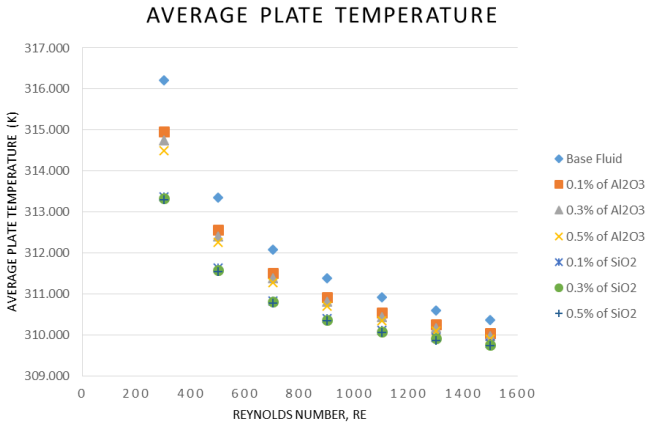


Fig. 3. Graph of Average Plate Temperature vs Reynolds Number

Figure 3 shows the average plate temperature for base fluid, Al2O3 and SiO2 nanofluids. Based on graph, the highest average plate temperature is base fluid in Reynolds number of 300. Meanwhile, the lowest average plate temperature is SiO2 nanofluids. From the observation between Al2O3 and SiO2, the nanofluids SiO2 has a lower average plate temperature as compared to Al2O3 nanofluids. The average plate temperature for Al2O3 is lower by 0.54% while SiO2 is 0.92% for both at 0.5% volume concentration in Reynolds number 300 as compared to base fluid. When the volume concentration and Reynolds number are increased, the value of average plate temperature will be decreased. This is due to improve thermal conductivity property of nanofluids as compared to base fluid. Therefore, the better coolant is at the lower value of average plate temperature. The finding agreed based on graph pattern according to publication [20].

3.2 Heat Transfer Coefficient

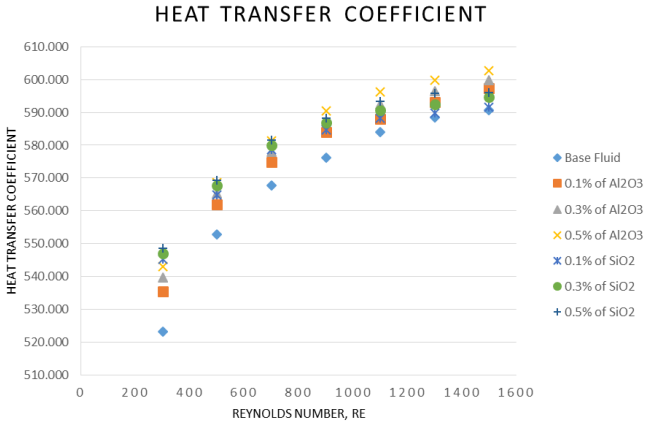


Fig. 4. Graph of Heat Transfer Coefficient

Figure 4 shows the heat transfer coefficient for base fluid, Al2O3 and SiO2. The heat transfer coefficient of Al2O3 at 0.5% volume concentration in 1500 Reynolds number has the highest heat transfer coefficient value. The Al2O3 has highest heat transfer coefficient compare with SiO2 and base fluid due to the highest thermal conductivity characteristic. Nanofluid addition has improved the heat transfer characteristic due to the improved Brownian motion. The highest increment for Al2O3 and SiO2 at 0.5% volume concentration with 2.04% and 0.9% enhancement compared to the base fluid. It is observed that, as the Reynolds Number and volume concentration is increased, the

heat transfer coefficient is also increased. The finding agreed based on graph pattern according to publication [20].

3.3 Nusselt Number

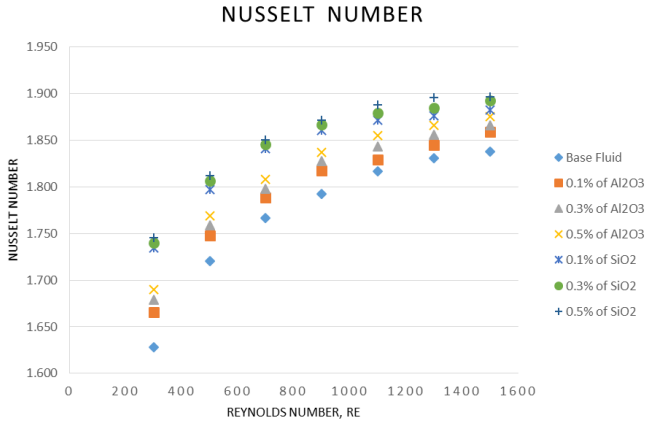


Fig. 5. Graph of Nusselt Number

Figure 5 shows the Nusselt number for base fluid, Al2O3 and SiO2. The Nusselt number was applied from the convection heat transfer coefficient. Based on the graph, the highest Nusselt number is SiO2 at 0.5% volume concentration in Reynolds number 1500. Meanwhile, the lowest Nusselt number is base fluid with the difference of 0.059. The increment for Al2O3 is 2.01% while SiO2 is 3.21% compared to the base fluid at 0.5% volume concentration and 1500 Reynolds number. When the volume of concentration and Reynolds number are increase, the ratio of Nusselt number will increase. Furthermore, Nusselt number is a dimensionless presentation of heat transfer coefficient. The finding agreed based on graph pattern according to publication [20].

3.4 Pressure Drop

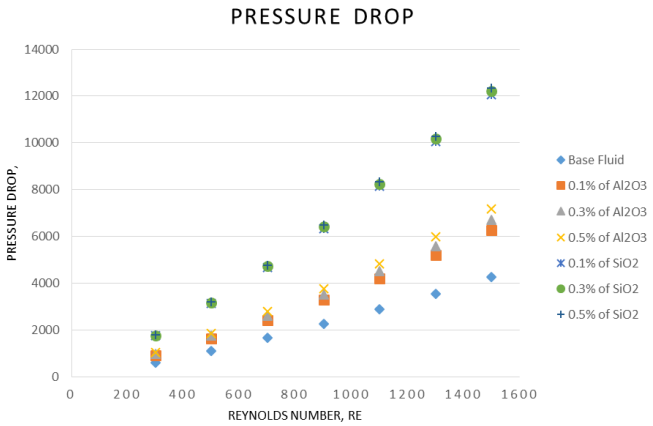


Fig. 6. Graph of Pressure Drop

Figure 6 shows the pressure drop for base fluid, Al2O3 and SiO2. The fluid flow of nanofluids in cooling plate is evaluated by pressure difference. Pressure drop is measured between inlet and outlet fluid. The highest-pressure drop is shown at Reynolds number 1500 for 0.5% volume concentration of SiO2. The lowest pressure drop at 1500 Reynolds number is base fluid. The highest increment for Al2O3 and SiO2 at 0.5% volume concentration with 68% and 189% enhancement

compared to the base fluid. From the observation, when the volume concentration and Reynolds number are increased, the pressure drop increased. Therefore, high pressure drop is already expected and known as the coolant has been forced to go through a narrow channel of cooling plate PEM fuel cell. The pressure drop increase because as the coolant mass flux increase has mention by Kim *et al.,* [21].

3.5 Pumping Power

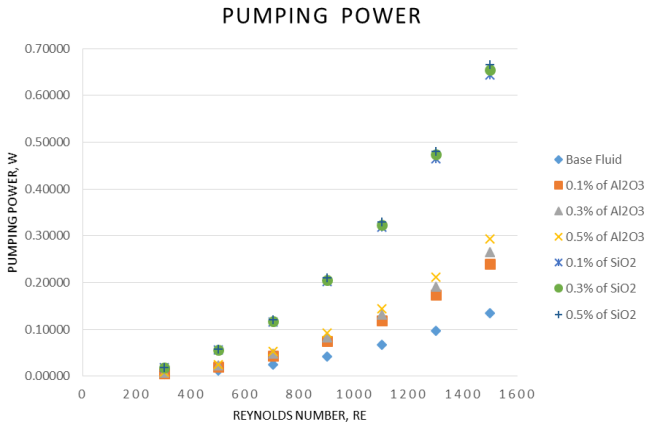
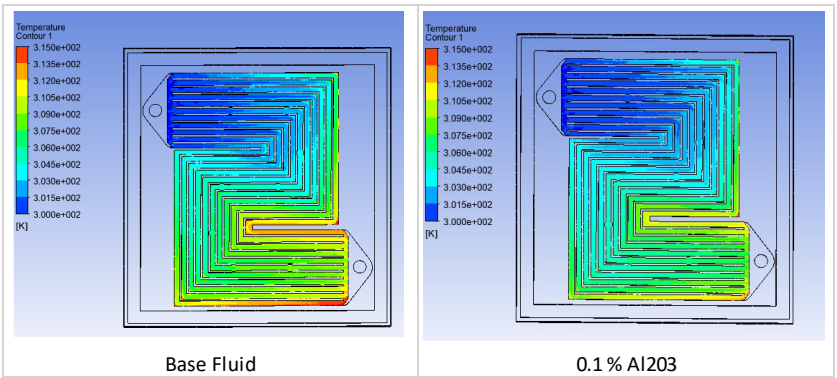


Fig. 7. Graph of Pumping Power

Figure 7 shows the pumping power for base fluid, Al2O3 and SiO2. The highest pumping power is shown at Reynolds number 1500 for 0.5% volume concentration of SiO2. The lowest pressure pumping at base fluid Reynolds number of 300. The highest increment for Al2O3 and SiO2 at 0.5% volume concentration with 116% and 390% enhancement compared to the base fluid. The pumping power value increases when the volume of concentration and Reynolds number increase. In a conclusion, the pumping power also increase when the pressure drop increase in order to move around or circulate more viscous nanofluids through the cooling system. High pumping power is desirable as it is a parasitic loss.

3.6 Cooling Plate Contour Analysis

The pattern flow of the coolant is depending on the design of the flow field. The Serpentine Channel Cooling Plate is used in the analysis. The heat distribution and coolant flow can be observed and analysed through the contour Figure 8 and Figure 9.



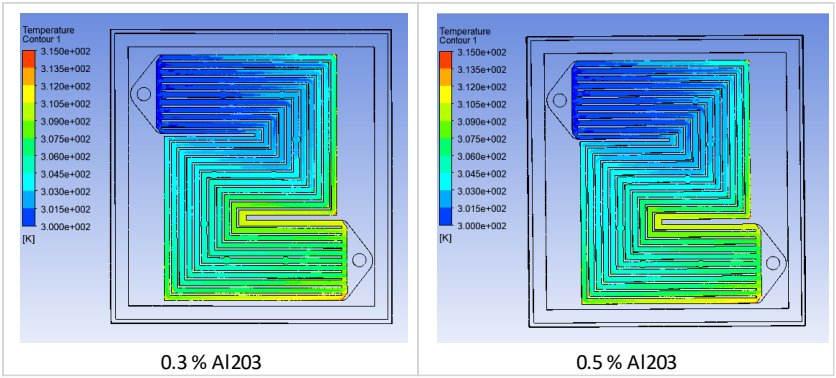


Fig. 8. Coolant Temperature Contour at 300 Reynolds Number for Al2O3 nanofluids

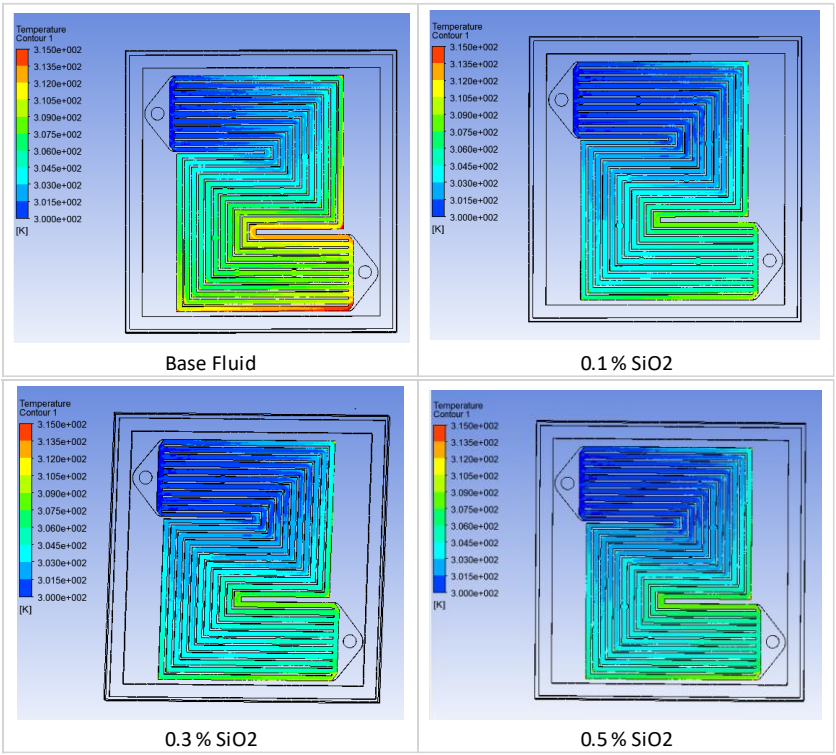


Fig. 9. Coolant Temperature Contour at 300 Reynolds Number for SiO2 nanofluids

In Figure 8 and Figure 9 is showed the example of fluid coolant at similar 300 Reynolds Number in various volume concentration of Al2O3 and SiO2. The temperature contour is compared in order to analyse and observe which fluid coolant that dissipated more heat. The minimum values temperature contour is set up to 300 K while the maximum values is 315 K. Based on coolant contour, the base fluid contain more heat followed by Al2O3 and continued by SiO2. Besides that, the result is showed the heat has been released efficiently after addition of nanofluids. SiO2 is showed the coldest coolant especially at 0.5% volume concentration. Therefore, proven that the heat dissipated increases as the volume concentration increases in the base fluid.

4. Conclusions

As a conclusion, thermal conductivity and viscosity of nanofluid is being studied in the simulation that is given by heat transfer and fluid flow behaviour. Based on result of simulation, there is an

enhancement in heat transfer performance of Al2O3 and SiO2 as compared to the base fluid. The enhancement is produced because of the improvement in both convective heat transfer coefficient and Nusselt number. Besides that, the pressure drop and pumping power also analysed in this study. In this study, the best properties of coolant are Al2O3 because it gives higher value of heat transfer compare to SiO2 and base fluid. The study shows that the heat transfer is improved through adoption of Al2O3 and SiO2 but at the expense of increment in pressure drop. Further study needs to be done in order to study the feasibility of the adoption in serpentine cooling plate of PEMFC.

Acknowledgement
The author would like to thank Universiti Teknologi MARA Shah Alam for financial supports given under 600-IRMI/DANA 5/3 BESTARI PERDANA (045/2018)

References

[1] Abdullah, S. M. "Carbon dioxide emissions causing global warming." *New Straits Times*, (2017 December 13).
[2] Hart, D., Howes, J., Madden, B., Boyd, E. "Hydrogen and Fuel Cells: Opportunities for Growth." *A Roadmap for the UK , E4Tech and Element Energy*, 2016.
[3] Hanley, E. S., Deane, J. P., Gallachóir, B. P. Ó. "The Role of Hydrogen in Low Carbon Energy Futures – A Review of Existing Perspectives." *Renewable and Sustainable Energy Reviews* 82, no. 3 (February 2018): 3027 -3045.
[4] Staffell, I., Scamman, D., Abad, A. V., Balcombe, P., Dodds, P. E., Ekins, P., Shah, N., Ward, K. R. "The Role of Hydrogen and Fuel Cells in The Global Energy System." *Energy and Environmental Science*, no. 2 (2019): 463–491.
[5] World Energy Council. "New Hydrogen Economy-Hope or Hype." *Innovation Insights Brief*, 2019.
[6] Mohamed, W. A. N. W., Talib, S. F. A., Zakaria, I. A., Mamat, A. M. I., Daud, W. R. W. "Effect of dynamic load on the temperature profiles and cooling response time of a proton exchange membrane fuel cell." *Journal of Energy Institute* (2017): 1-9.
[7] Zakaria, I., Mohamed, W. A. N. W., Mamat, A. M. I., Saidur, R., Azmi, W. H., Mamat, R., Talib, S. F. A. "Experimental Investigation of Al2O3-Water Ethylene Glycol Mixture Nanofluid Thermal Behaviour in a Single Cooling Plate for PEM Fuel Cell Application." *International Conference on Alternative Energy in Developing Countries and Emerging Economics*, *Energy Procedia* 79 (2015): 252-258.
[8] Zhang, G., Kandlikar, S. G. "A critical review of cooling techniques in proton exchange membrane fuel cell stacks." *International Journal of Hydrogen Energy* 37, (2012): 2412-2429.
[9] Cieslinski, J. T., Dawidiwicz, B., Smolen, S. "Influence of Stack Temperature on PEM Fuel Cell Performance." *The International Conference, Low Temperature and Waste Heat Use in Energy Supply Systems, Bremen*, 2012.
[10] Wang, Y., Chen, K. S., Mishler, J., Choa, S. C., Adroher, X. C. "A review of polymer electrolyte membrane fuel cells: Technology, applications and needs on fundamental research." *Applied Energy* 88 (2011): 981-1007.
[11] Sohel, M. R., Khaleduzzaman, S. S., Saidur, R., Hepbasli, A., Sabri, M. F. M., Mahbubul, I. M. "An experimental investigation of heat transfer enhancement of nini channel heat sink using Al2O3-H2O nanofluid." *International Journal of Heat and Mass Transfer* 74 (2014): 164-172.
[12] Khaleduzzaman, S. S., Saidur, R., Selvaraj, J., Mahbubul, I. M., Sohel, M. R., Shahrul, I. M. "Nanofluids for Thermal Performance Improvement in Cooling of Electronic Device." *Advance Material Research* 832 (2014): 218-223.
[13] Zakaria, I. A., Michael, Z., Mamat, A. M. I., Mohamed, W. A. N. W. "Thermal and Electrical Experimental Characterization of Ethylene Glycol and Water Mixture Nanofluids for a 400w Proton Exchange Membrane Fuel Cell." *IEEE International Conference on Control System, Computing and Engineering*, (2014 November 28-30).
[14] Islam, M. R., Shabani, B., Rosengarten, G. "Electrical and thermal conductivities of 50/50 water-ethylene glycol based TiO2 nanofluids to be used as coolant in PEM fuel cells." *1st International Conference on Energy and Power, ICEPS2016, Energy Procedia* 110 (2016 December 14-16): 101-108.
[15] Ramos-Alvarado, B., Li, P., Liu, H., Hernandez-Guerrero, A. "CFD study of liquid-cooled heat sinks with microchannel flow field configuration for electronics, fuel cell and concentrated solar cells." *Applied Thermal Engineering* 31 (2011): 2494-2507.
[16] Sainan, K. I., Tijani, A. S., Zakaria, I.A., Mohamed, W. A. N. W. "Study of Multiple 2:1 and Single 1:1 Inlet/Outlet Ratio for Serpentine PEMFC Performance." *Journal of Mechanical Engineering* 5, no. 6 (2018): 1-9.
[17] Li, X., Sabir, I. "Review of bipolar plates in PEM fuel cells: Flow field designs." *International Journal of Hydrogen Energy* 30 (2005): 359-371.

[18] Talib, S. F. A., Azmi, W. H., Zakaria, I., Mohamed, W. A. N. W., Mamat, A. M. I., Ismail, H., Daud, W. R. W. "Thermophysical Properties of Silicon Dioxide (SiO2) in Ethylene Glycol/Water Mixture for Proton Exchange Membrane Fuel Cell Cooling Application." *International Conference on Alternative Energy in Developing Countries and Emerging Economies, Energy Procedia* 79 (2015): 366-371.

[19] Wilberforce, T., El-Hassan, Z., Khatib, F. N., Al Makky, A., Mooney, J., Barouaji, A., Carton, J. G., Olabi, A. G. "Development of Bi-polar plate design of PEM fuel cell using CFD techniques." *International Journal of Hydrogen Energy* 42 (2017): 25663-25685.

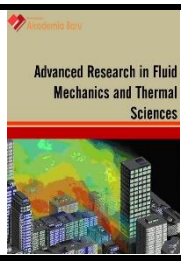
[20] Zakaria, I. A., Mohamed, W. A. N. W., Mamat, A. M. I., Sainan, K. I., Nawi, M. R. M. "Numerical Analysis of Al_2 O_3 nanofluids in serpentine cooling plate of PEM fuel cell." *Journal of Mechanical Engineering* 13, no. 2 (2016): 10-20.

[21] Kim, Y., Kim, M., Ahn, C., Kim, H. U., Kang, S.W., Kim, T. "Numerical study on heat transfer and pressure drop in laminar flow multistage mini-channel heat sink." *International Journal of Heat and Mass Transfer* 108 (2017): 1197-1206.

Penerbit Akademia Baru

Engineering Science and Technology Conference Proceedings

Journal homepage: www.akademiabaru.com/EST.html



Heat Transfer Characteristic for Premixed Flame Jet from Swirl Chamber

Open Access

N. Uppatam[1], W. Boonyopa[1], C. Nuntadusit[1,*]

[1] Department of Mechanical Engineering, Faculty of Engineering, Prince of Songkla University, Hatyai, Songkhla 90110, Thailand

ABSTRACT

This research was to study the structure and heat transfer characteristics of flame jet generated from the swirl chamber. The premixed flame was a mixture of LPG and air which injected to a cylindrical chamber tangentially. In this study, the equivalent ratios between LPG (Propane 70%, Butane 30%) and air were varied at 0.8, 1.0 and 1.2. The height of the swirl chamber was studied at H=2.2D, 4.6D and 7.0D where D is the hydraulic diameter mixture inlet of swirl chamber having 5 mm. The effects of separated jet-to-plate distance were also investigated at L=4D, 6D, 8D and 10D. the structure of swirl flame and impinging flame were recorded with digital camera. For measured, the average heat transfer can be found with the flame impinging on surface. The result showed that H/D at 4.6 with an equivalence ratio at 1.0 from separated jet-to-plate distance L/D at 4 gave the highest average heat flux.

Keywords:
Swirling flame jet; flame structure;
impinging flame jet; heat transfer

Copyright © 2019 PENERBIT AKADEMIA BARU - All rights reserved

1. Introduction

Flame impinging as a high heat transfer technique for heating. The applications of impinging flame jet can be found in industries such as annealing of glass, processing of some metal and glass, including cutting, welding, as well as drying of textiles film and paper will use technology direct the surface [1-4].

The flame combustion is divided into two characteristics which are Diffusion flame and Premixed flame, in a diffusion flame, combustion takes place at the flame surface only, where the fuel meets oxygen in the right concentration - the interior of the flame contains unburnt fuel. This is opposite to combustion in a premixed flame. The impinging flame on a surface gives high heat transfer, lowers fuel consumption and increases productivity [5-8]. For the heat transfer rate using direct flame to the surface, it depends on the flame flow structure from premixed flame or diffusion flame, the separated jet-to-pate distance and heating surface. Fuel and oxidizer depend on

* *Corresponding author.*
E-mail address: chayut.n@psu.ac.th (C.Nuntadusit)

equivalence ratio (ϕ) and Reynolds number (Re) all varied affect to the characteristic and heat transfer distribution on heating surface [9].Chander et al. [10,11] studied the characteristic of heat transfer by three interacting methane-air flame jet impinging normally on a flat surface. The heat transfer characteristic was intimately related to flame shapes. Dong et al. [12-15] has studies performed of heat transfer characteristic of flame jets to impinging on plate. The heat transfer depression effect becomes stronger when S/D and H/D ratios are small.

From the past to the present many studies on the heat transfer rate of flame structure, heat transfer of flame on surface and the emission from combustion of flame. [16,17]

Nowadays, there are many industries foe food processing heating product mainly using flame. This is a problem of rising fuel cost price. From the previously mentioned problem, the concept using impinging flame jet technique to impinging uniformity of heat transfer on a surface using swirling flame

Huang et al. [18] showed that by inducing a swirling flow to a laminar impinging flame jet was able to enhance the thermal performance because the recirculation was enhanced and thus the transport coefficient was decreased by the induced-swirl. Huang et al. [19] the circular flame-holder by a long copper tube, two tangential flow and one axial flow. The swirling flame can produce a higher local heat flux at the stagnation point of impingement plate than the premixed flame jet and the swirling flame jet with induced swirl has the advantage of producing more uniform heat flux distribution on the impingement plate near stagnation point. Boushakia et al. [20] investigated of the dynamic characteristics of non-premixed turbulent swirling flames using the stereo-PIV technique. This indicates a decrease in the size of the recirculation zone because the reaction zone is closer to the burner outlet. Sing et al. [21] studied conducted investigate the heat transfer characteristic of natural gas (CNG)-air swirling flame effect on flat surface. The heat flux distribution on the impingement plate was more uniform with swirl as compared to without swirl effect. In addition, heat flux distribution was observed to be more uniform at moderate separation distance and at a larger helical vane swirl angle. Very few studies are available on heat transfer characteristics of single and multiple impinging swirling flame jets. Huang et al. [22] and Zhao et al. [23] showed that a circular laminar pre-mixed flame jet with induced swirling has more uniform heat flux distribution and higher temperatures compared to without swirling flame jet. Hindasageri et al. [24] Swirling flame jets using twisted tape are found to enhances the heat flux distribution by 40–140% at low Reynolds number. Swirling flame with twisted tapes is also found to give more uniform distribution of heat flux 10-40% at higher Reynolds number.

The research was to study the swirling flame jet structure and characteristic of heat transfer impinging on flat plate from effect varied high of swirl chamber, the mixture which injected into a cylindrical chamber by two tangentially before flowing out to the burner exit.

2. Methodology

2.1 Model and parameter of experiment

The experiment swirl impinging flame was to study free flame structure and characteristic of heat transfer with premixed flame was mixed between LPG (Propane 70%, Butane 30%) and air which injected two channels tangentially in swirl chamber before above to burner exit. In the result swirling flame gave uniform heat flux distribution and higher temperatures Therefore, it was studied on this experiment using swirling flame.

The burner of swirl chamber made by steel plate shows Schematic in Figure 1. cylindrical chamber (swirl chamber) diameter (Do) 20 mm has two channels tangentially for injected mixture

having hydraulic diameter (D) 5 mm. The flame jet impinging on a flat steel plate for study characteristic average heat transfer distribution.

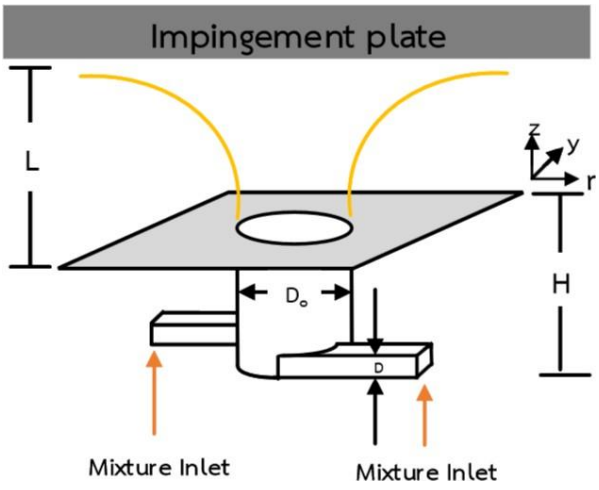


Fig. 1 Schematic swirl burner

The experiment is shown that the parameters in Table 1. The high of swirl chamber (H/D) was varied from 2.2, 4.6 and 7.0, The separated distance burner to plate (L/D) was varied from 4, 6, 8 and 10 with equivalence ratio (□) 0.8, 1.0 and 1.2 and fixed Reynolds number (Re) at 4000.

Table 1.
The parameters for this experiment

Parameters and symbol	Values
Reynolds number of mixtures, Re	4000
Equivalence ratio, ϕ	0.8, 1.0 and 1.2
Hydraulic Diameter of burner, D	5 mm
High of swirl chamber, H	2.2D, 4.6D and 7.0D
Separated distance burner to plate	4D, 6D, 8D and 10D
Diameter of impingement plate	15D

The Reynolds number of mixtures was fixed at 4000 with fuel-lean, stochiometric and fuel-rich, the viscosity and density of mixture can be calculated from Eq. 1-3. and summarize in Table 1.

$$\mu_m = \frac{\sum \mu_j X_j \sqrt{m_j}}{\sum X_j \sqrt{m_j}} \quad (1)$$

$$\rho m = \sum y_i \rho_i \quad (2)$$

$$Re = \frac{\rho_m V_m D}{\mu_m} \quad (3)$$

Here D was hydraulic diameter mixture inlet from swirl chamber, V_m was velocity of mixture before inlet to the swirl chamber, ρ_m was density of mixture mixed between LPG and air and μ_m was viscosity of mixture

2.2 Experiment apparatus

Figure 2 Shows schematic in the experiment set up to studied flame structure for free flame and flame impinging on flat plate. The mixture is mixed between LPG and air. The mixture was filtered humidity by regulator, the volume flow rate controller with a rotameter and pressure of mixture measured by pressure transducer. The fuel and air are thoroughly mixed with the mixing chamber filled with steel ball having diameter 3 mm to reduce flow floatation. The mixture injected in a swirl chamber (cylindrical mixed chamber) two channel tangentially before above the burner exit. the separated burner to plate distance is varied by XY-table. The impinging flame structure recorded with digital camera.

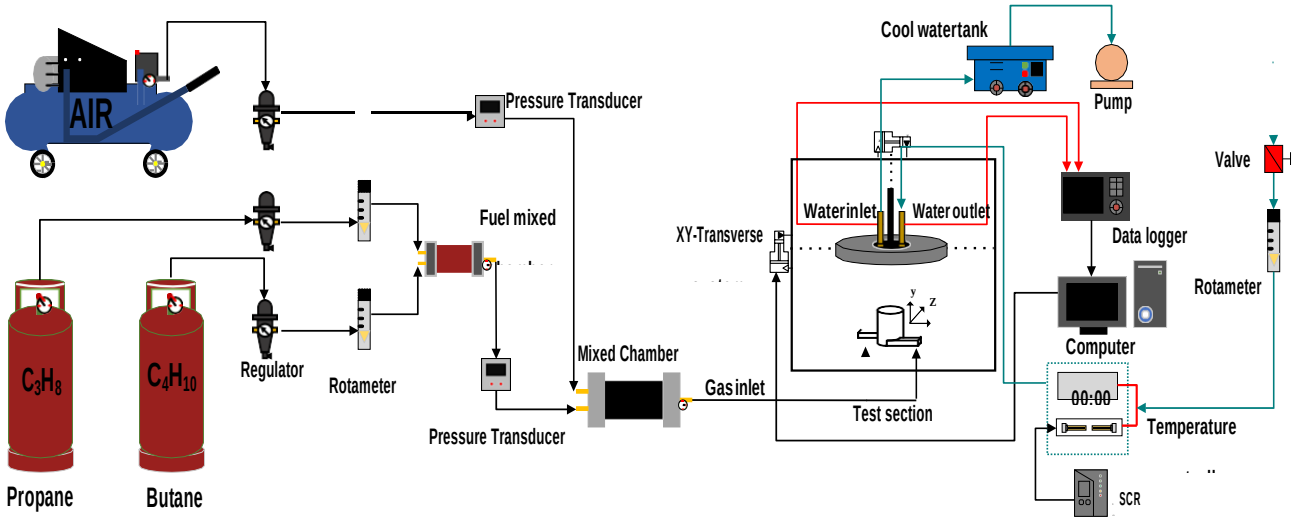


Fig. 2. Schematic in the experiment set up

2.3 Flame temperature measurement

The flame temperature (Tf) mixed fuel between air is measured with type-B thermocouple (70% Pt 30% Rh and 94% Pt 6% Rh) fixed at Reynolds number (Re=4000) and equivalence ratio (⍰). The thermocouple direct exposures to the flame in measurement, when the thermocouple engulfed in a premixed flame jet. The Thermocouple bead fluorescent is red and emissive radiation to the surrounding on a surface area in the bead thermocouple with the measurement that flame temperature by thermocouple is lower than actual flame temperature. This is a result of radiation heat loss with the reduction in the bead surface area.

2.4 Average heat flux

Due to the measurement, the flame jet made to impinge over the circle stainless steel plate having diameter 15D thickness 5 mm and the inside is a hollow cylinder high 25 mm full of water. The flowing into impinge plate from cool water tank with water pump brings water in the system. The volume flow rate of water was controlled by a rotameter. Temperature of water increased with two heaters would be controlled by a temperature controller power adjust by digital indicating before approaching in the impinge plate. The Temperature of water inlet and water outlet were recorded with data logger (midi GL840). The difference of temperature between water inlet and water outlet can be calculated average heat flux ($\dot{q}$) for a case study. The separated distance to plate (L/D) varied with XY-table would be controlled by computer. Due to the different temperature, it can be calculated average heat flux from Eq. 4.

$$\dot{q} = mC_p\Delta T \quad (4)$$

Where m was a mass flow rate of water inlet to plate, Cp was specific heat of water depending on temperature of water inlet, and ΔT was different temperature between water inlet and water outlet.

3. Results

3.1 Flame structure

In the experiment to study structure of swirling flame jet and impinging flame jet using fuel between (propane 70% butane 30%) air mixed in the mixed chamber into mixture inlet having hydraulic diameter 5mm before flowing out to the burner exit for varied height of the swirl chamber H/D at 2.2, 4.6 and 7.0, the experimental structure of impinging flame varied L/D at 4, 6, 8 and 10 from fixed Reynolds number at 4000. For heat transfer characteristic of swirling flame study, it has become imperative to study the flame shapes and structure. Free swirling flame and impinging flame shapes were taken direct photographs with DSLR Canon 1200D in different operating conditions.

3.1.1 Free flame structure

Schematic of free flame in Figure 3. shows the flame shapes are same as the flame shapes obtained by S. Mahesh et al. [25] defined for three flame zones which are anchoring flame, intense blue flame and elongated flame were referenced for clarity in structure of swirling flame. Figure 3. shows the direct photograph of swirling flame H/D at 4.6 and equivalence ratio 1.0, swirling flame at elongated flame was broader at the angle (θf) of 50 and larger intense blue flame from reaction zone in high temperature zone. The different zone of swirling flame consists elongated main flame zone and base zone combined to flame length (Lf) at the burner exit. The reaction zone length was invisible from intense blue flame and the post combustion zone was visible from the elongated flame.

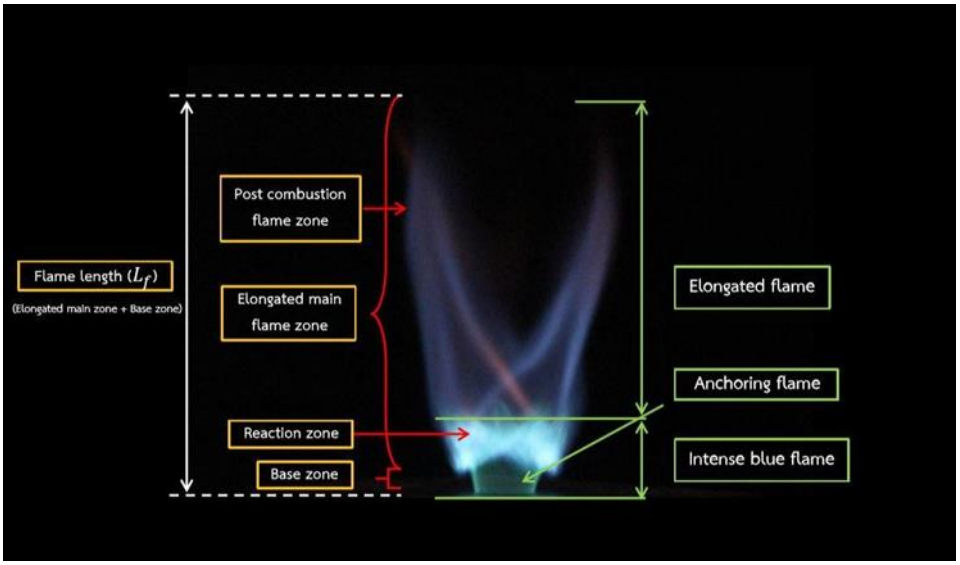


Fig. 3. Shows Schematic of free swirling flame.

Figure 4 Shows direct photographs of swirling flame for different operating conditions varied H/D at 2.2, 4.6 and 7.0 fixed Reynolds number 4000 at equivalence ratios 0.8, 1.0 and 1.2. It has been observed visually from flame image in reaction zone, the intense blue flame was broader and lifting when the equivalence ratio was increased.

The flame length consists of flame zones in Figure 3. it depends on the height of the swirl chamber. At the H/D 2.2, the visible flame was the shortest elongated flame, and the H/D at 7.0 gave the longest elongated flame zone or the increased H/D. The angle formed with elongated flame to widest at 60 at the H/D at 4.6 and became narrower at the H/D 7.0. At large reaction zone with H/D at 4.6 from stochiometric mixture, an intense blue flame zone could be obviously invisible.

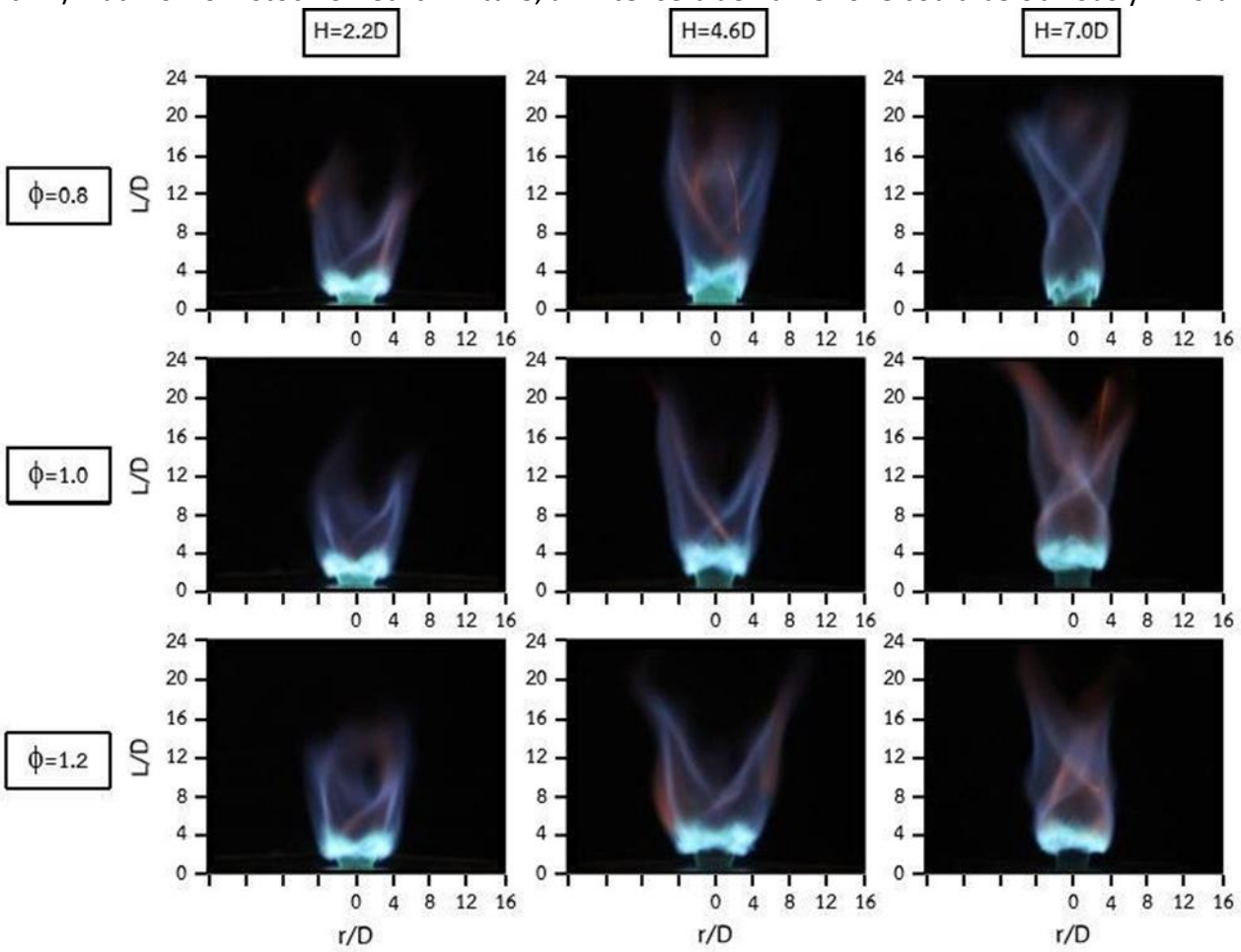


Fig. 4. Shows direct photographs of swirling flame varied for H/D at 2.2, 4.6 and 7.0 fixed Reynolds number 4000 at equivalence ratios 0.8, 1.0 and 1.2

The equivalence ratio has affected to flame length, Fuel-lean gave shortest elongated flame and narrower with increases H/D, stochiometric gave longest reaction zone and can be see anchoring flame from base zone obviously visible and fuel-rich the having orang in elongated flame tip. In the result it can be observed that having orange flame when increased equivalence ratio.

3.1.2 Impinging flame structure

Figure 5-8. Shows the swirl impinging flame shapes at varied dimensionless separation distance to the plate (L/D) was varied from 4, 6, 8, and 10 at a fixed Reynolds number under equivalence

ratios 0.8, 1.0 and 1.2 from H/D at 2.2, 4.6 and 7.0. L/D The direct photograph of swirl impinging flame in Figure 5. At small separated distance L/D at 4 it can be observed that H/D at 2.2 the flame distribution cover on the target surface better more than all H/D for study, the elongated flame impinging a cross- section area on the target surface above the burner exit with increases equivalence ratio. The reaction zone was either closed or intercepted with target plate, for low equivalence ratio it was visible reaction zone with near-field and the reaction zone cloud be obviously invisible when increased equivalence. H/D at 7.0 from equivalence ratio at 0.8 the flame was hold back and flame distribution over burner to plate.

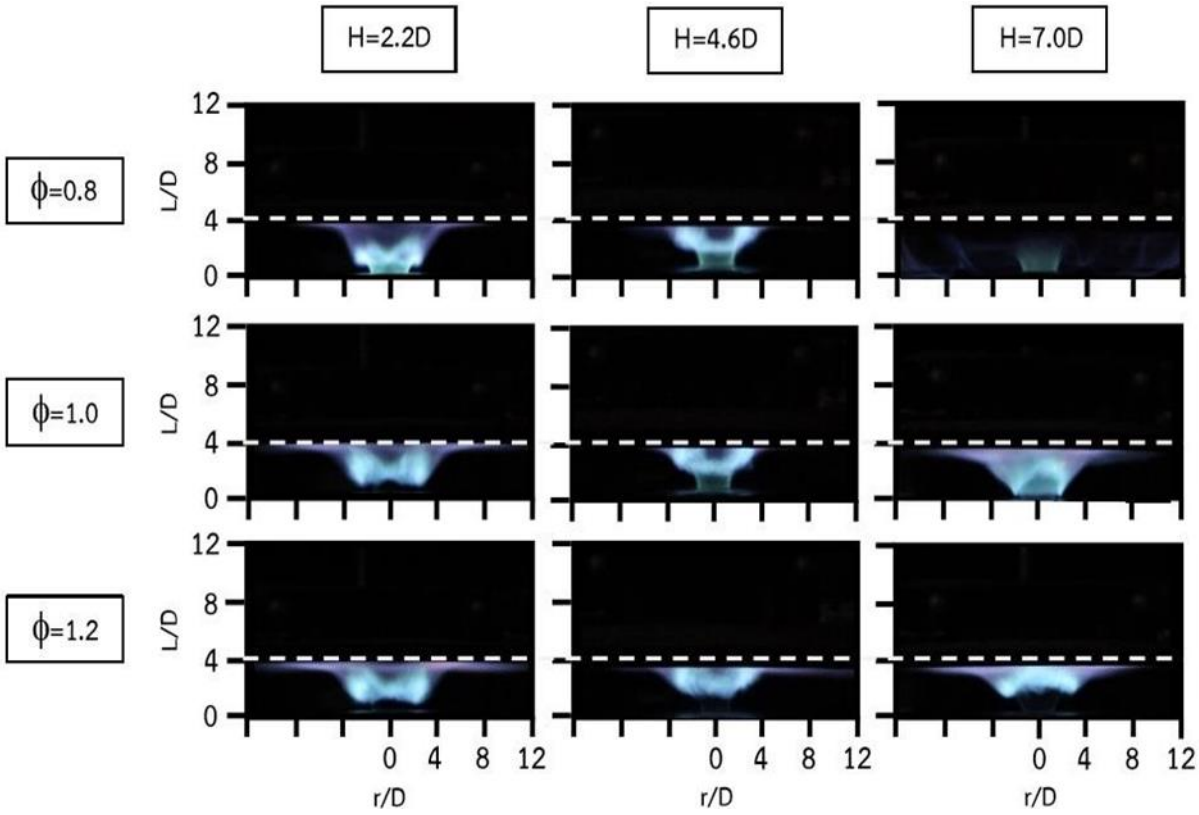


Fig. 5. Swirl impinging flame with separated distance L/D at 4

Figure 6 shows the direct photograph of swirl impinging flame at separated distance L/D at 6 visible flame in the photograph, which is lifted and broader, the elongated flame impinging cross-section area on the target surface above the burner exit to form continuously heating. It has been observed L/D at 6 that the flame at boundary reaction zone will be most visible at the H/D 2.2 and 4.6, at equivalence ratio 0.8 and 1.0 the anchoring flame was visible with near-field and central between burner to plate, and the reaction zone very closed or almost intercepted with the target plate with equivalence ratio 1.0 and 1.2 from equivalence ratio at 0.8 the reaction zone was less visible it can be observed elongated mostly.

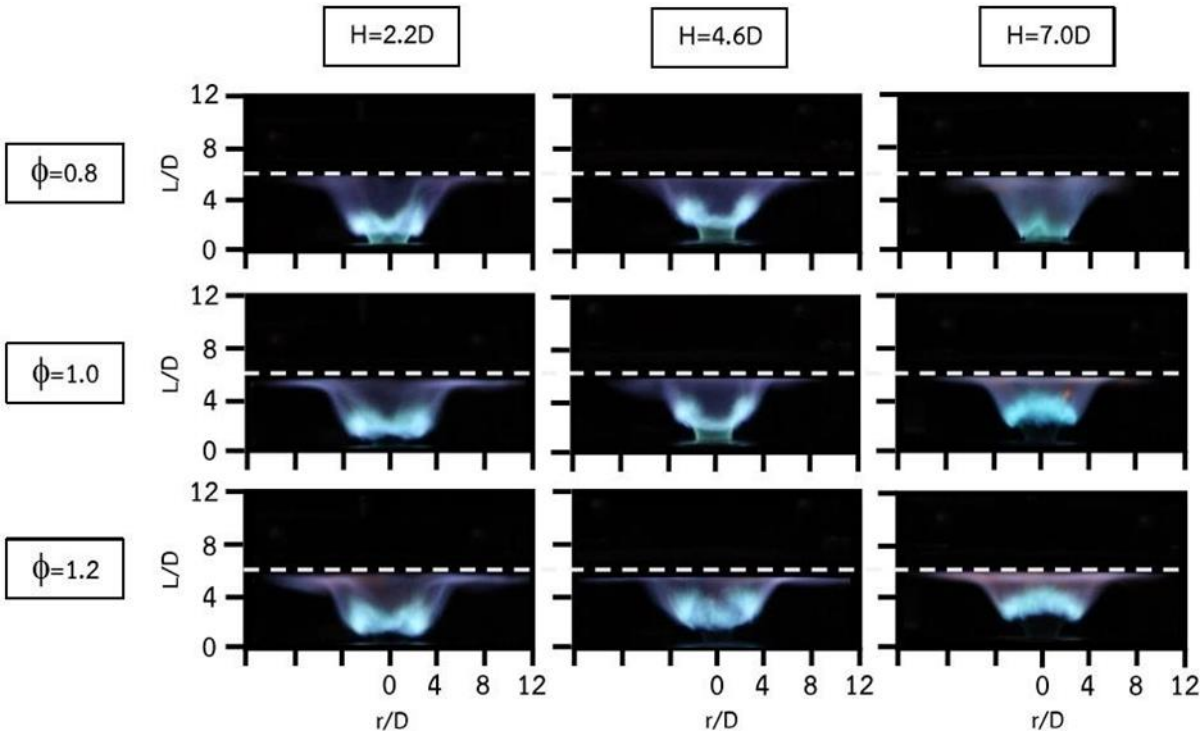


Fig. 6. Swirl impinging flame with separated distance L/D at 6

Figure 7 shows the direct photograph of swirl impinging flame at separated distance L/D at 8 the reaction zone was visible near-filed and the flame impinging on target plate can be observed elongated flame distribution cover on surface by the way, H/D at 2.2 from equivalence ratio 0.8 and 1.0 elongated flame impinging plate was broader and separated, the swirl flame impinging plate the elongated flame to widest H/D at 4.6 at the increases H/D at 7.0 became narrow. The result it can be observed that H/D at 4.6 and 7.0 with equivalence ratio at 1.2 the elongated flame zone had orange combine on the flame.

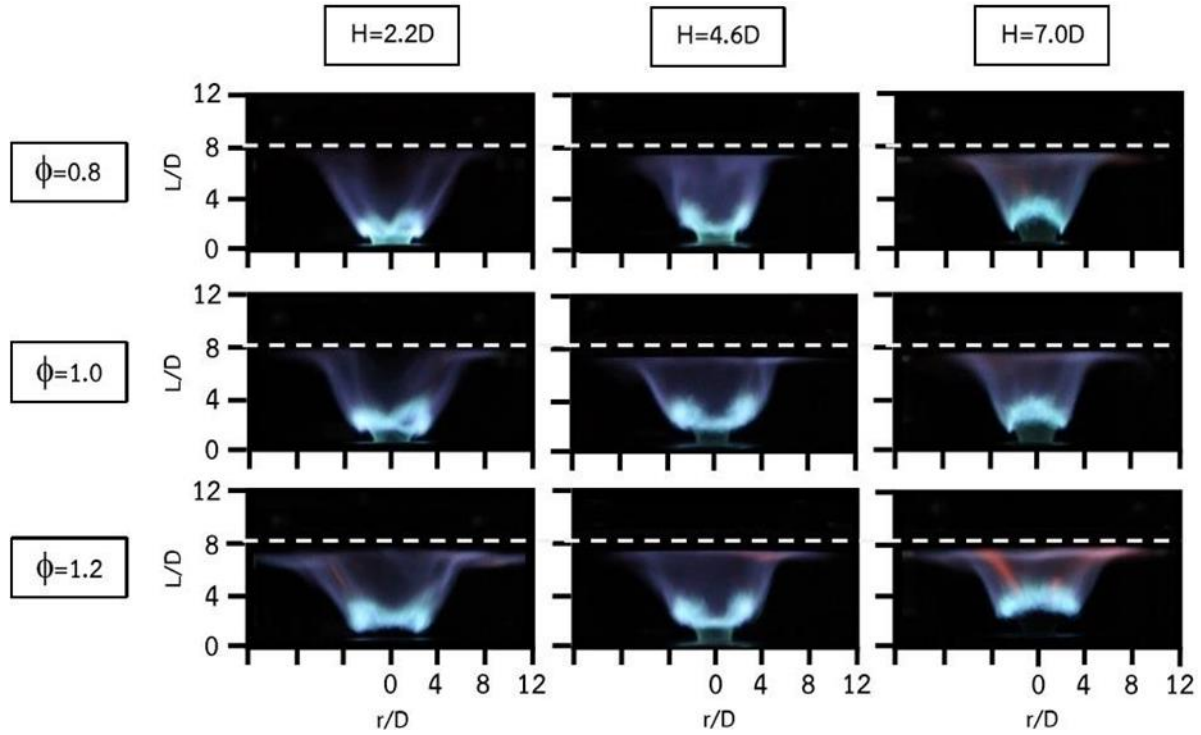


Fig. 7. Swirl impinging flame with separated distance L/D at 8

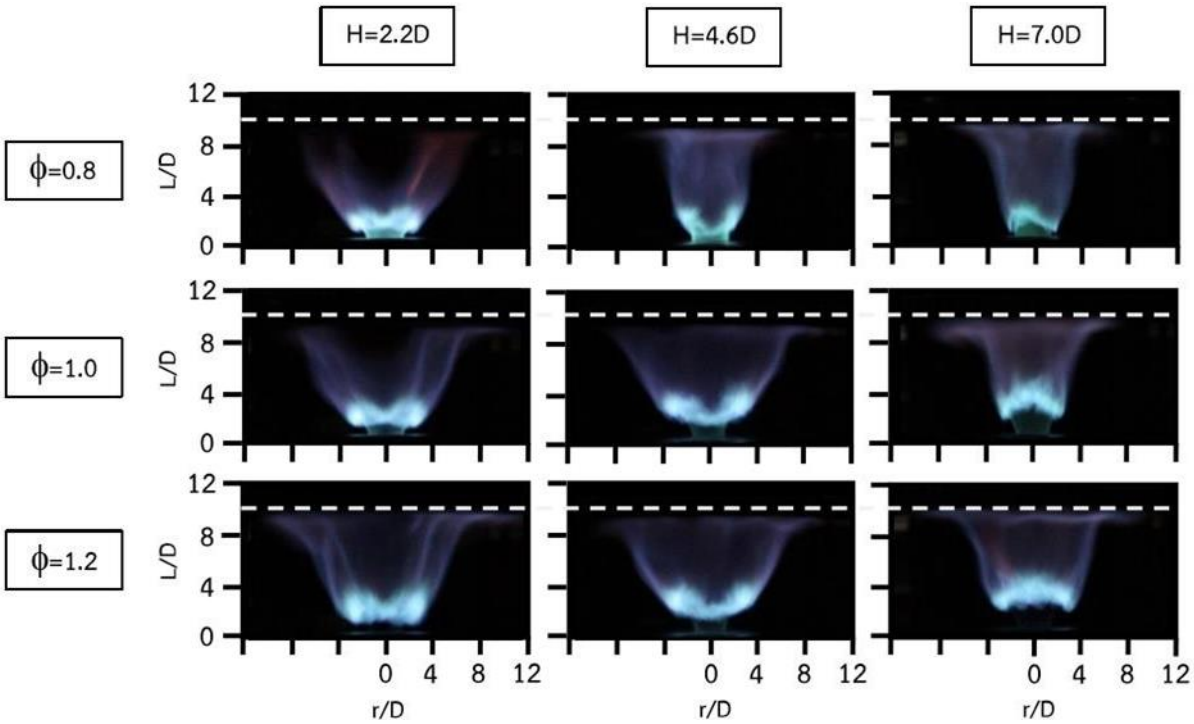


Fig. 8. Swirl impinging flame with separated distance L/D at 10

Figure 8 shows direct photograph of impinging swirl flame L/D at 10, the elongated flame structure was broader and separated at H/D 2.2 causing the flame not cover on target surface resulting for flame temperature non-uniformly in the target surface and some conditions only gave hot combustion products were striking on the target surface. Other than that, it was observed that the elongated flame zone had orange a litter bit on flame tip at in separated distance because air entrainment which causes partially the flame was bluish in colour and shaper at the boundaries showing complete combustion due to better mixing. At large separated distance the visible flame impinging plate can be attributed to high tangential made elongated flame became narrow.

3.2 Flame temperature

Thermocouple radiation correction [26] under the assumption of steady-state temperature, an energy balance abounding in thermocouple bead as some of conductive, convective and radiation, this result of heat loss with the reduction in the bead surface area cloud be calculated Tf.

The measurement of flame temperature is applied for different operating conditions. The hot junction of thermocouple was exposed to the flame tip during measurement. The distance for measurement flame temperature was also investigated flame length (Z/D) at 2,4,6,8,10 and R/D at - 2, 0 and 2

In Figure 9 the result can be shown that at equivalence ratio 0.8, it gave lower flame temperature generally all H/D and at equivalence ratio at 1.0 gave a highest flame temperature on intense blue flame L/D at 6 near stagnation point. In some cases, the result showed equivalence ratio at 1.2 gave highest flame temperature, it was due to difficulty in controlling ambient air entrainment to the flame become to flame-stochiometric immediately. Kuntikana et al [27] shows the flame temperature was found to be pendent of mixture Reynolds number and the maximum flame temperature was observed at the stochiometric mixture condition for all Reynolds numbers. Once it is not stochiometric, the further distance, the more decreased the flame is.

With fuel rich mixture, complete combustion takes place since there is air entrainment which causes partially complete combustion. As the fuel starves of an oxidiser, incomplete combustion takes place. However, the fuel lean mixture has combustion with excess air resulting low flame temperature.

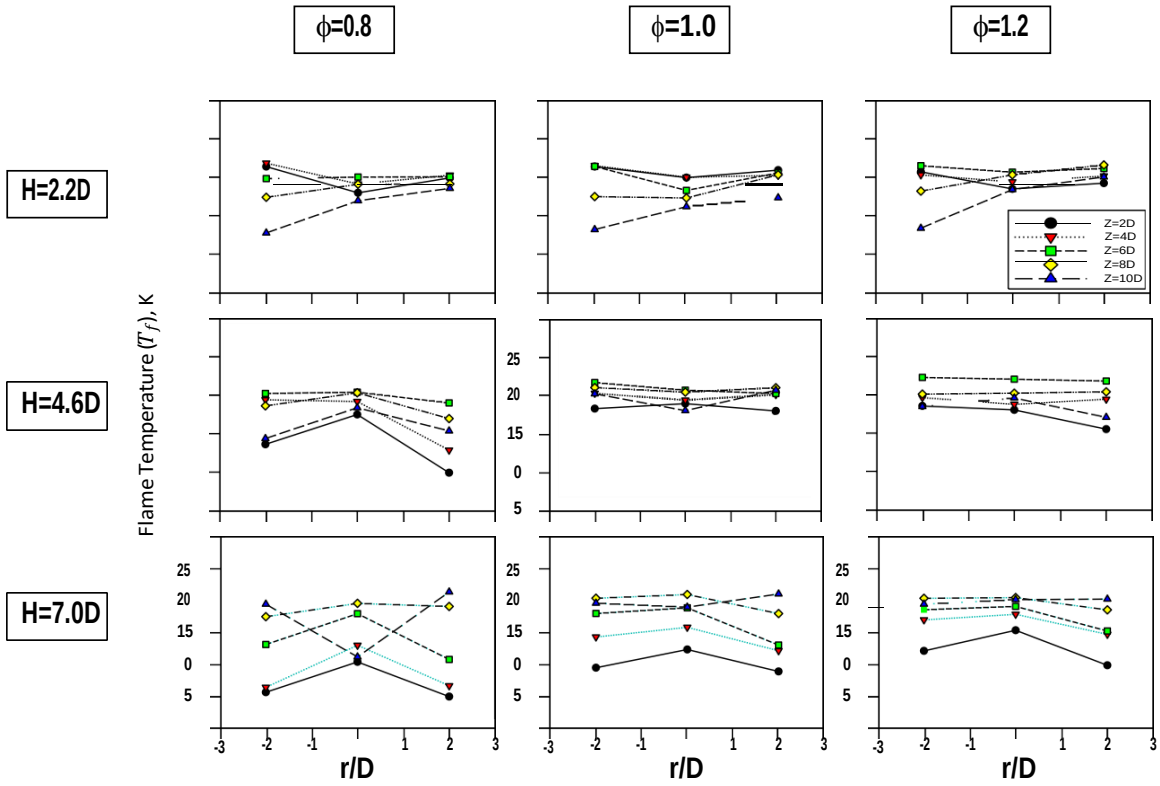


Fig. 9. Flame temperature all in different operating conditions

3.3 Average heat flux

In the experiment for measurement average heat flux different operating condition at equivalence ratio 0.8, 1.0 and 1.2 varied from separated distance (L/D) at 2, 4, 6, 8 and 10, the average heat flux deserves more attention and concerns for practical application impinge plate having dimeter 150 mm, the different temperature of water can be found between water inlet and water outlet that has been recorded in datalogger.

The result shows in Figure 10 average heat flux for all different operating conditions. This observed trend is quite similar to the trend applied for multiple conventional flame. The swirling flame was susceptible to thermal dilution from entrainment of surrounding with the increased L/D, it also caused deteriorating effect on heat transfer as the increase of separated jet to plate distance. As the result in Figure 5-8, this can be explained on the basic of flame impinging theory. The swirling flame gave the highest average heat flux in all H/D and L/D in the reaction zone. The equivalence ratio at 0.8 gave the lowest average heat flux and less than equivalence ratio at 1.0 since the mixture is fuel-lean mixture which made the area from plate flame exposure decreased. Examine the flame impingement plate in Figure 3 which directly affects average heat flux.

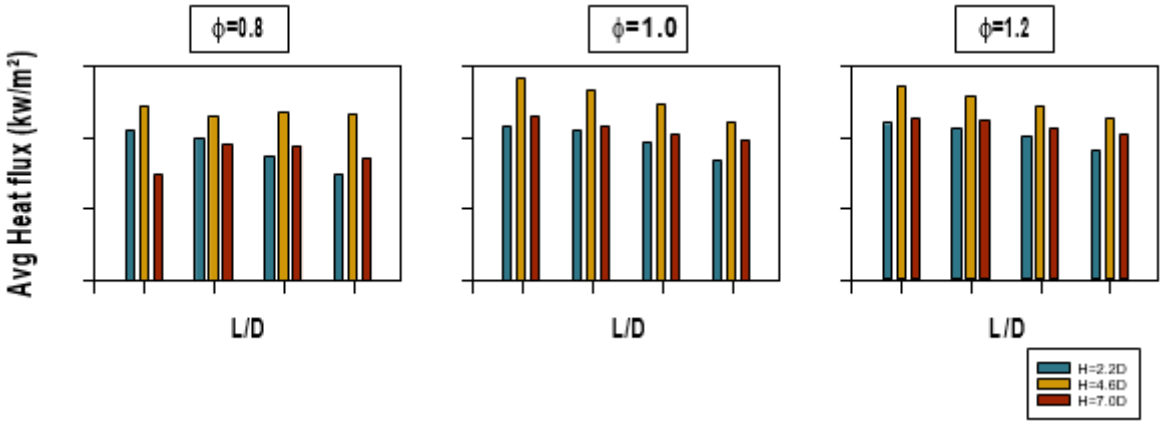


Fig. 10. Average heat flux

The result shows that the equivalence ratios at 1.0 and 1.2 gave similar results in all different operating conditions, L/D at 4 in near-field gave the highest average heat flux causing the flame impinging uniformly heating in cross-section on the target surface and the flame temperature is almost constant. It has been observed that the increased L/D made average heat flux decreased and this depends on of the flame height relative to the burner to plate separating (the locating of the flame tip relative to the target plate and the flame temperature)

For rich mixture, the flame length was longer than stochiometric flame but the flame temperature increased when the mixture was adjusted into the stoichiometric mixture form. For the H/D at 4.6, it has been observed that the highest average heat flux higher than Figure 4 because the angle from elongated flame spared and broader made heating uniformly on the target surface, huge intense blue flame affected flame temperature in the reaction flame zone.

4. Conclusions

It has been observed that the parameter as the height of swirl chamber (H/D), separated jet-to-plate distance (L/D). The equivalence ratios significantly affect the flame shapes, flame structure and average heat flux distribution in the impingement surface for swirl impinging flame. Followings are the major conclusions drown based on the present study:

1. Direct photograph of the free and impinging flame showed that there was a significant change in flame structure with presence and location of separated from jet-to-plate during exiting of the burner. This was ascertained that the reaction zone for free flame and impinging flame will be at H/D 4 to 6 at the same axial height from the exit plane of the burner.
2. The Flame temperature from equivalence ratio at 0.8 gave low temperature, whereas at the equivalence ratio at 1.0 gave higher temperature, but the maximum temperature was given from the equivalence at 1.2 since the flame exposed to ambient the air entrainment which is reason of the flame having complete combustion. However, it has been ascertained that at the R/D at -2 and H/D at 4 to 6 have the peak temperature.
3. The height of swirl chamber (H/D) had effects on flame structure and flame temperature from stochiometric flame produce as a result of heat transfer to impinging plate. The average heat flux increased with decreasing in separated jet-to-plate distance. The result showed that H/D at 4.6 with an equivalence ratio at 1.0 from separated jet-to-plate distance L/D at 4 gave the highest average heat flux.

Acknowledgement

This research was funded by a grant from Department of Mechanical Engineering, Faculty of Engineering, Prince of Songkla University, Thailand

References

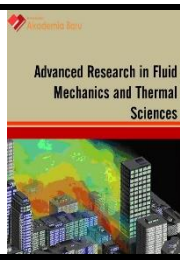
[1] J.N.B. Livingood, P. Hrycak, "Impingement heat transfer from turbulent air stream jets to flat plates-A literature survey", NASA TM X-2778, 1973.
[2] H. Martin., "Heat and mass transfer between impinging gas jets and solid surfaces", Adv. Heat Transf. no.13 (1977): 1–60.
[3] S.J. Downs, E.H. James. "Jet Impingement Heat Transfer-A Literature Survey", ASME, New York, 1987.
[4] Viskanta. R. "Heat transfer to impinging isothermal gas and flame jets", Exp Thermal Fluid Sci no.6(1993):111–134
[5] Lebedev, V. I., and Sokolov, V. A., "Study of Convection Compo- nent of Complex Heat Exchange of a Direct-Heating Furnace", Glass Ceram., no.33(1976): 352-354
[6] Wolf, D. H., Incropera, F. P., and Viskanta, R., "Jet Impinge- ment Boiling", Adv. Heat Transfer, in press.
[7] Button, D. L., and Wilcox, D., "Impingement Heat Transfer A Bibliography 1890-1975", Previews Heat Transfer, no.4(1978): 83-98
[8] Popiel, C. O., van der Meer, T. H., and Hoogendoorn, C. J., "Convective Heat Transfer on a Plate in an Impinging Round Hot Gas Jet of Low Reynolds Number", Int. J. Heat Mass Transfer, no:23(1980): 1055-1068
[9] Viskanta, R., "Enhancement of Heat Transfer in Industrial Com- bustion Sysems: Problems and Future Challenges", Proceedings of the ASME /JSME Thermal Engineering Joint Conference, J. R. Lloyd and Y. Kurosaki, Eds., no. 5(1991): 161-173, ASME/JSME, New York/Tokyo
[10] Chander. S, Ray "A Flame impingement heat transfer", a review. Energy Convers Manag, no.46 (2005):2803– 2837
[11] Chander. S, Ray "Heat transfer characteristics of laminar methane/air flames impinging on flat and cylindrical surfaces", Ph.D Thesis, Indian Institute of Technology, Delhi, New Delhi, India, 2006
[12] L.L. Dong, C.S. Cheung, C.W. Leung, "Heat transfer and wall pressure characteristics of a twin premixed butane/air flame jets", Heat and Mass Transfer, no.47(2004): 489–500
[13] L.L. Dong, C.S. Cheung, C.W. Leung, "Heat transfer of a row of three butane/air flame jets impinging on a flat plate", Heat and Mass Transfer, no.46(2003): 113–125
[14] L.L. Dong, C.S. Cheung, C.W. Leung, "Structure and heat transfer of premixed butane/air flame jets impinging on the flat surface", in:Proceedings of 2001 Technical Meeting, Eastern State Section of TheCombustion Institute,Hilton Head, SouthCalifornia, (2001): 392–395.
[15] L.L. Dong, C.S. Cheung, C.W. Leung, "Heat transfer characteristics of a pair of impinging rectangular flame jets", J. Heat Transfer, no.125(2003)
[16] Zhang, Y. and Bray, K. N. C., "Characterization of impinging jet flame", J. Combustion and flame, no. 116(1999): 671-674.
[17] Foat, T., Yap, K. P. and Zhang, Y.,. "The visualization and mapping of turbulent premixed impinging flame", J. Combustion and Flame, no.125(2001): 839-851
[18] B. Huang, W.J.M. Douglas, A.S. Mujumdar, "Heat transfer under a laminar, swirling impinging jet – a numerical study", in: Proceedings of the Sixth International Heat Transfer Conference, no.5, Washington, DC, (1978): 311–316
[19] X.Q. Huang, C.W. Leung, C.K. Chan, S.D. Probert, "Thermal characteristics of a premixed impinging laminar flame jet with induced swirl", Appl. Energy, no.83(2006): 299–412
[20] Boushakia.b, N. Merloa, S. de Persisa, C. Chauveaua, I. Gökalpa, "Experimental investigation of CH4-air-O2 turbulent swirling flames by Stereo-PIV"
[21] Singh. G, Chander. S, Ray. A, "Heat transfer characteristics of natural gas/air swirling flame impinging on a flat surface" Experimental Thermal and Fluid Science no.41(2012): 165–176
[22] X.Q. Hunag, C.W. Leung, C.K. Chan, S.D. Probert, "Thermal characteristics of a premixed impinging circular laminar-flame jet with induced swirl", Applied Energy no.83(2006): 401–411.
[23] Z. Zhao, D.W. Yuen, C.W. Leung, T.T. Wong, "Thermal performance of a premixed impinging circular flame jet array with induced-swirl", Applied Thermal Engineering no.29(2009): 159–166.
[24] Hindasageri, V., Vedula, P.R., "Heat transfer distribution of swirling flame jet impinging on a flat plate using twisted tapes", International Journal of Heat and Mass Transfer, no.91(2015): 1128–1139
[25] S. Mahesh, D.P. Mishra "Characterization of swirling CNG inverse jet flame in recessed coaxial burner Fuel", no:161(2015): 182–192

[26] Krishnan, S., Benjamin, M., Wendong, W.J.U., Nehorai, A., "An Approach to Thermocouple Measurements that Reduces Uncertainties in High Temperature Environments", Energy & Fuels,(2015)
[27] Kuntikana, P., Prabhu, S. V., "Impinging premixed methane-air flame jet of tube burner: thermal performance analysis for varied equivalence ratios", Heat and Mass Transfer, no.55(2019):1301–1315

Penerbit Akademia Baru

Engineering Science and Technology Conference Proceedings

Journal homepage: www.akademiabaru.com/EST.html



Drag Reduction and Degradation Characteristics of Nata de Coco Suspension in Spiral Pipe

Open Access

S. P. Sari[1,*], Gunawan[2], I. Makmur[3] and A. R. Prayuda[3]

[1] Department of Mechanical Engineering, Faculty of Industrial Technology Gunadarma University, Jakarta, Indonesia
[2] Department of Mechanical Engineering, Universitas Indonesia, Jakarta, 16424, Indonesia
[3] Student at Department of Mechanical Engineering, Faculty of Industrial Technology Gunadarma University, Jakarta, Indonesia

ABSTRACT

Recently, the research of energy efficiency in some areas is the important topic to be developed. In the fluid flow, some techniques are developed in order to decrease the pressure drop. Therefore, some reserchers add several kind of additives in order to obtain the drag reduction. The purpose of this reserch is to investigate the effect of Nata de Coco fiber suspension due to the drag reduction characteristic in the spiral pipe. Experimental was conducted from low to high Reynolds number up to 20,000. The percentage of drag reduction was calculated using the obtained experimental data, in presence of the drag reducing agent. The results showed that the addition of Nata de Coco fiber suspension into water can reduce drag either on circular pipe or spiral pipe. The maximum drag reduction of concentration 60 ppm for spiral pipe is about 24.7% and for circular pipe is about 22.1% at Reynolds number about 19,000. It was observed that the drag reduction tends constant with increasing of concentration after 60 ppm. The Nata de Coco fiber solution tends to spread and flow straightly at the center of the experimental pipe and a water layer develops at the wall. It reduces the wall friction and reaches the maximum drag reduction. Further, the Nata de Coco fiber suspension is good for the mechanical degradation effect. Based on this research, it can be concluded that Nata de Coco can be considered as drag reducing agent.

Keywords:
Energy efficiency; drag reduction; spiral pipe; nata de coco fiber; degradation

Copyright © 2019 PENERBIT AKADEMIA BARU - All rights reserved

1. Introduction

The issue of transportation system in the pipe line continues to be developed due to the energy efficiency. Pipeline is an effective method for transporting the fluids, especially to distribute the fluids to distant places. However, the most important problem is the high of energy consumption. Therefore, the new development method in order to decrease the pressure loss is needed. As is well known, the methods for obtaining drag reduction are divided into two categories: passive control and active control. In the passive control of liquid flow, the most effective drag reduction method is the addition of drag-reducing additives which are high-molecular-weight polymers. The application of drag reduction of polymers or surfactant additives is limited to closed-loop pipeline systems, since the disposal of these solutions has an adverse effect on the environment.

* *Corresponding author.*
E-mail address: sri_ps@staff.gunadarma.ac.id (Sri Poernomo Sari)

Active method and passive method were suggested to reduce drag on the fluid. Passive method is by varying the pipe geometry, such using coated pipe, injecting micro bubble to reduce skin friction as in marine application [1], and utilizing groove on spiral pipe [2, 3]. While the active method is by adding a very small amount of additives into the fluid which can reduce friction factor on turbulent flow [4]. Tom [5] was the first to report this method with addition of small amount of polymethyl methacryaete solution into monochlorobenze to decrease turbulent skin friction drag.

Polymer is not the only kind of drag reducing agents. Surfactant and fiber are also known as the drag reducing agent. Using Surfactant [6-8] as the drag reduction agent had been effectively proven to increase drag reduction on turbulent flow. However, it is not an environmentally friendly. Polymer [9-12] is the most widely used in industry because an inexpensive and showed a good result as surfactants. Yet, its mechanical degradation occurred significantly. Nanoparticles [13] also showed a good results on drag reduction, but it needs higher concentrations and requires a fairly complicated treatment to prevent sedimentation. Like other kind of drag reducing agents, fibers also show a significant effect of drag reduction [14-18]. Coconut fiber [19] as natural fiber has been researched as additive agent and showed a good result in drag reduction.

On the other hand, fibers [20] such as asbestos or nylon are resistant to mechanical degradation but have a disadvantage with regard to environmental load, while pulp, which is a plant-based fiber, requires high concentrations to achieve drag reduction effects. Research on the use of fiber to reduce the loss of pressure drop was made by Ogata, Nukawa and Kubo [16]. They reported that the use of fibers of the material of nata de coco can reduce the pressure drop in turbulent flow. Effect of the addition of nata de coco fiber is a very good impact. Drag reduction that obtained was 11%.

2. Methodology

2.1 Experimental Setup

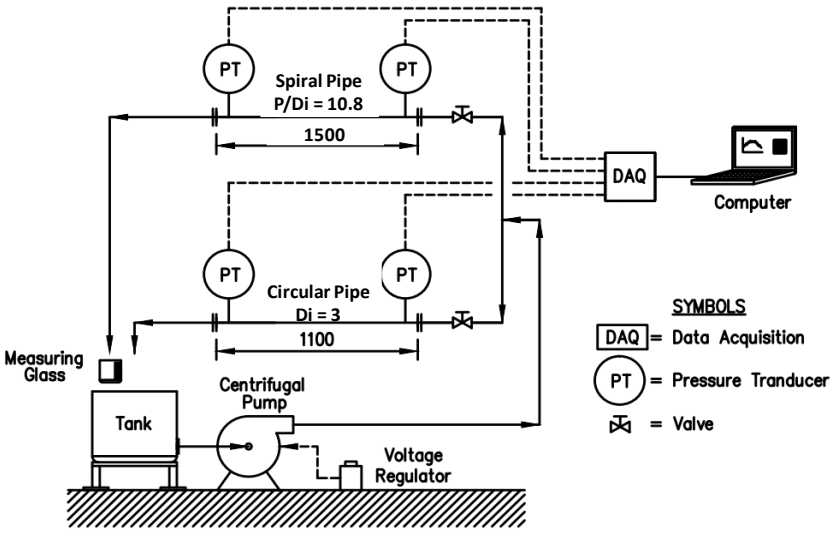


Fig. 1. Experimental setup

Figure 1 is a nata de coco fiber suspension rheology measurement setup. The detail of experimental set up consisted of main tank, centrifugal pump, voltage regulator, spiral pipe P/Di 10.8, circular pipe with inner diameter 3 mm, ball valve, pressure transducer, DAQ, computer, and measuring glass. Horizontal pipe with circular cross section and spiral cross section with five helical lobe were used to determine flows in pipes (Rheology). Flow rate is varied by adjusting the valve

opening. Two manometers mounted on a pipe test connected to the pressure transducer to determine the value of the pressure drop. The outer discharge accommodated with a measuring cup accommodated within a period of time to get the flow capacity.. Relationship shear stress with shear strain will be obtained to make the flow curve.

Table 1 is the data of spiral pipe used in this research where P is pitch, Do is outer diameter, Di is inner diameter, Δd is pipe wall thickness, and P/Di is ratio of pitch to inner diameter.

Table 1.
Dimension of experimental pipes

Pipe	Di (mm)	Do (mm)	Δ d	P (pitch)	P/D i
Circular Pipe	3	4	1	-	-
Spiral Pipe	15	25	10	162	10.8

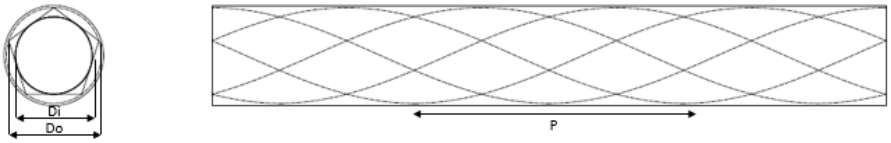


Fig. 2. Schematic diagram of spiral pipe

The nata de coco fiber solution prepared in concentration 20, 60, and 100 ppm. The temperature of the solution was constantly maintained at 27°C. The nata de coco fiber solution mixed in the main tank and then circulated into experimental pipe by using centrifugal pump at various flow rates. The spiral and circular pipe were being tested alternately. The experimental was performed in a closed-loop system, where the output flow from the experimental pipe returns back to the main tank.

2.2 Rheological Model

Experimental data is plotted in the moody chart. The laminar region refers to Hagen-pouiseuille line and the turbulent region refers to Blasius line. Drag reduction is defined by decreasing of the coefficient of friction on the flow. The friction factor caused by shear stress that occurs between each layer of the velocity.

The shear stress, τ is proportional to the velocity gradient, γ (shear rate), can be described by Newtonian model:

$$\tau = \mu \frac{du}{dy} \tag{1}$$

Where μ is constant for the particular fluid that is viscosity. The Newtonian viscosity depends on the temperature and the pressure and is independent of the shear rate. The viscosity is defined as the ratio of shear stress to shear rate. Several rheological models or rheological equations of state have been proposed in order to describe the nonlinear flow curves of non-Newtonian fluids. Non-Newtonian fluids Bingham, pseudo plastics, and dilatants are those for which the flow curve is

not linear. The viscosity of a non-Newtonian fluid is not constant at a given temperature and pressure but depends on other factors such as the rate of shear in the fluids.

Thus, the relationship shear stress and shear rate may be described by measuring the pressure drop gradient and the volumetric flow rate in circular pipe flow is given by:

$$\frac{D\Delta P}{4L} = \mu \frac{8u}{D} \tag{2}$$

Where: D is the inner pipe diameter, ΔP is pressure drop, L is the length of pipe (test section), and u is the average velocity.

Coefficient of friction, f, can be obtained by Darcy Equation:

$$\Delta P = \frac{fLU^2}{2D\rho} \tag{3}$$

Where: f is the coefficient of friction, Δh is the head gradient over the considered pipe length, and g is the gravity acceleration.

The solution concentration, Cw was determined based on the mass ratio of nata de coco fiber to pure water to made test fluid, which is defined by:

$$C_w[\ \%\ ] = \frac{M_n}{M_n + M_w} \text{ x } 100\ \% \tag{4}$$

Mn and Mw denote the masses of nata de coco and pure water, respectively.

Drag reduction can be obtained by using Equation 5 as stated below:

$$DR = \frac{f_{water} - f_{fiber}}{f_{water}} \times 100\% \tag{5}$$

3. Results

The flow behaviour of nata de coco fiber solution can be conducted by comparing the results of water testing on circular pipe. Variations in seaweed fiber solution are divided into three concentrations including 20, 60, and 100 ppm. The test results are displayed on relationship between the shear stress and shear rate.

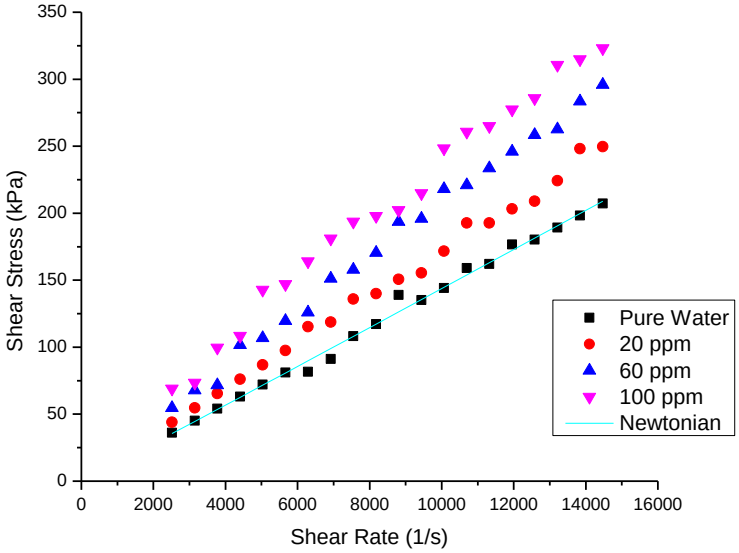


Fig. 3. The relationship of shear stress and shear rate of pure water and nata de coco fiber solution in circular pipe

Figure 3 shows the flow curves of the pure water and nata de coco suspension in circular pipe. The wall stress τ and sheer rate γ were calculated from the experimental data from laminer to turbulent flow regime. The solid line in figure 3 indicates the Newtonian line. The all data are shown linear relationship between wall stress and flow rate. It is incated that all of them are Newtonian behaviour. The slope gradient of pure water seems lower than nata de coco suspension.

The pressure drop is influenced by several factors such as the length of the channel that is flowed by the fluid. Besides that, another factor is the velocity. The pressure drop in fluid is as small as possible to reduce losses in fluid. The pressure on the inlet of the pipe will be higher than the pressure on the outlet of the pipe. The value of pressure drop is an important parameter in fluid flow because it relates to the energy required in the fluid distribution process.

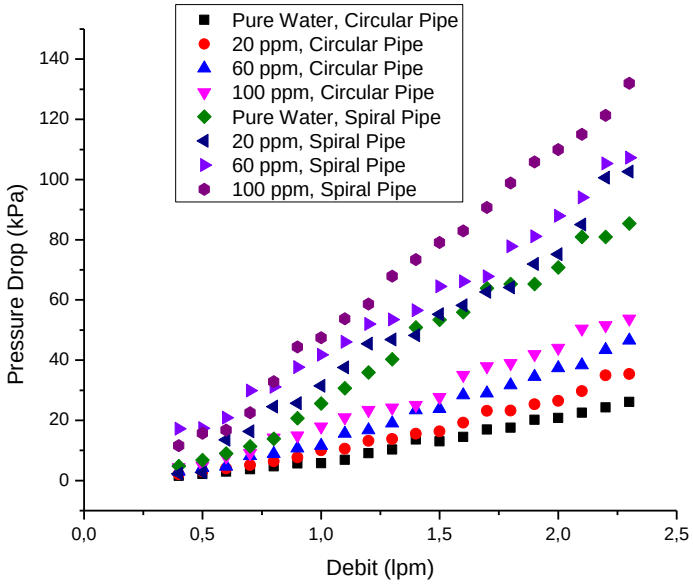


Fig. 4. Pressure drop of nata de coco fiber solution compared to water on circular and spiral pipe

The relationship between the debit and the pressure drop of nata de coco fiber solution with concentration 20, 60, and 100 ppm and water in circular and spiral pipes can be seen in figure 4. It shows that at low velocity (low debit) ranging from about 0.4 lpm to 1 lpm, the pressure drop of nata de coco fiber solution is still relatively similar as water. However, at debit above 1 lpm, the pressure drop of nata decoco fiber solution is higher than water both in the circular and spiral pipe. Based on the figure 4, the pressure drop of spiral pipe is higher than circular pipe.

The higher the concentration of nata de coco fiber solution, the higher the pressure drop when compared to water. This can occur because nata de coco fiber solution has a higher viscosity than water, especially at higher concentration around 100 ppm. Thus, the shear stress that occurs is also higher than water at the same velocity.

In Figure 5, it can be seen that the dashed line shows the Hagen Poiuseulle equation for laminar flow. Whereas the solid line is the Blasius equation for turbulent flow. In the laminar regime, the friction coefficient data is slightly higher than Haegen Pouiselle equation. It can be said that, in the laminar flow there is no drag reduction. However, in the turbulent regime, the data of nata de coco suspension is lower than Blasius equation. This is indicated that in the turbulent flow, the drag reduction is occurred. Different with nata decoco, the data of pure water in the turbulent flow is slightly higher than Blasius equation. The higher the Reynolds number, the lower the friction coefficient. The low friction coefficient results in lower energy use, which can save energy. The maximum drag reduction ratio in the circular pipe is about 22.1% at the 1.9 x 104 Re with 60 ppm concentration. It can be seen that there are two factors that influence the drag reduction ratio, namely Reynolds number and nata de coco solution concentration. The higher the concentration of nata de coco fiber solution, the greater the drag reduction ratio. However, after rise up the 60 ppm, the DR ratio is tent to constant. Thus, it can be concluded that the highest drag reduction ratio in circular pipe is occurred in the 60 ppm of concentration.

The relationship between the Reynolds number compared to the friction factor in the Spiral Pipe P/Di 10.8 is depicted in the Figure 6. The fluid test are the same which is nata de coco fiber solution and water. The dash line shows the Hagen Poiuseulle equation for laminar flow. Whereas the solid line is the Blasius equation for turbulent flow. The test data in this study cover the laminar flow and trubulent flow.

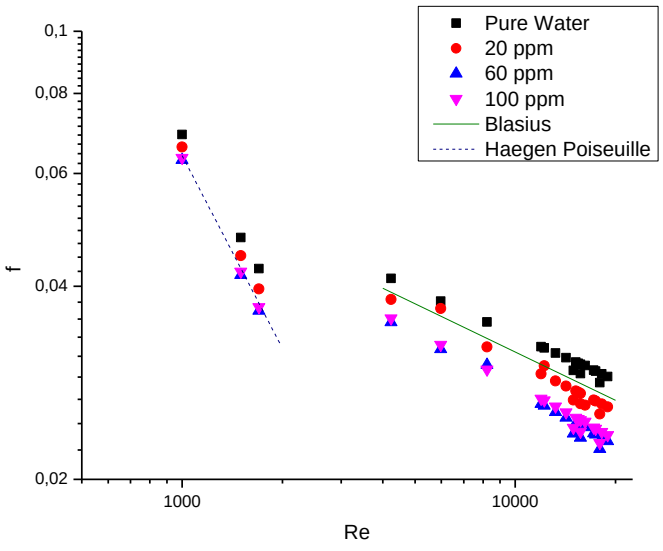


Fig. 5. Friction coefficient of nata de coco fiber solutions in circular pipe

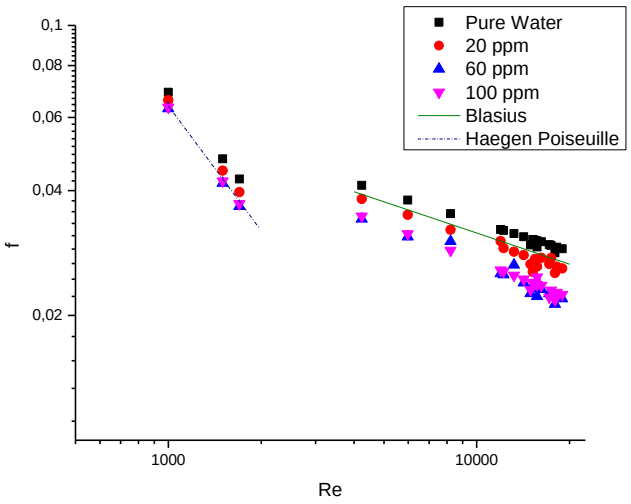


Fig. 6. Friction coefficient of nata de coco fiber solutions in spiral pipe

In the laminar regime, the friction coefficient data is slightly higher than Haegen Pouiselle equation. It can be said that, in the laminar flow there is no drag reduction. However, in the turbulent regime, the data of nata de coco suspension is lower than Blasius equation. This is indicated that in the turbulent flow, the drag reduction is occurred. Different with nata decoco, the data of pure water in the turbulent flow is slightly higher than Blasius equation. The higher the Reynolds number, the lower the friction coefficient. The low friction coefficient results in lower energy use, which can save energy. The maximum drag reduction ratio in the spiral pipe is about 24.7% at the 1.9 x 104 Re with 60 ppm concentration. This is occured due to the presence of fluid flow in the spiral pipe experiencing the swirl flow. The swirl flow cause the flow not only moves horizontally towards the pipe axis, but also flows along the pipe groove at certain distance. Then, the right distance allows the drag reduction occured in the flow in the flow.

The data of drag reduction effectiveness due to the degradation effect is depicted in the Figure 7. This figure shows the DR stability for several hours.

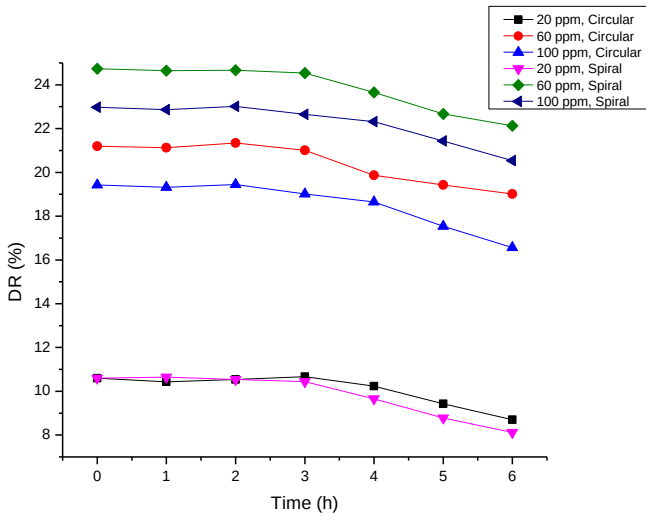


Fig. 7. Drag Reduction Stability of nata de coco suspension

Based on the Figure 7, the stability of drag reduction is seemed very good. Until 6 hours from the start position, the drag reduction tend to same value. This phenomena may be affect of the stability of the robustness of the nata decoco fiber filament. Therefore, the filament is not destruct due to the mechanical equipment.

4. Conclusions

The results of this reseach shown that the nata de coco fiber solution in the circular pipe has an effect on the drag reduction about 22.1% at Reynolds number around 19,000. Whereas the drag reduction in the spiral pipe P/Di 10.8 is about 24.7% at Reynolds number 19,000. The drag reduction is affected by the concentration of fiber solution.The higher the concentration of nata de coco fiber suspension, the greater the drag reduction ratio that occurs. However, the best concentration for this reserch is 60 ppm. After rise up that concentration, the drag reduction tend to constant. In this study, the degradation of drag reduction due to the effect of mechanical equipment is described. The nata de coco fiber suspension resitant to the mechanical degradation up to 6 hours.

Acknowledgement

This research was funded by a grant from Gunadarma University, Indonesia.

References

[1] Jamaluddin, A. "Micro-bubble drag reduction on a high speed vessel model." Journal of Marine Science and Application 11, no. 3 (2012): 301-304.
[2] Koestoer, Raldi A. "Hydraulics conveyances of mud slurry by a spiral pipe." Journal of mechanical science and technology 23, no. 7 (2009): 1835-1839.
[3] Sapjah, Dedih. "Characteristics of silica slurry flow in a spiral pipe." International Journal of Technology 6, no. 6 (2015): 916-923.
[4] Mowla, D., and A. Naderi. "Experimental study of drag reduction by a polymeric additive in slug two-phase flow of crude oil and air in horizontal pipes." Chemical Engineering Science 61, no. 5 (2006): 1549-1554.
[5] Toms, BA. "Some observations on the flow of linear polymer solutions through straight tubes at large Reynolds numbers." In Proc. of the International Congress on Rheology, pp. 135-141. 1949.
[6] Drzazga, Michal, Andrzej Gierczycki, Grzegorz Dzido, and Marcin Lemanowicz. "Influence of nonionic surfactant addition on drag reduction of water based nanofluid in a small diameter pipe." Chinese Journal of Chemical Engineering 21, no. 1 (2013): 104-108.
[7] Huang, Chonghai, Dongjie Liu, and Jinjia Wei. "Experimental study on drag reduction performance of surfactant flow in longitudinal grooved channels." Chemical Engineering Science 152 (2016): 267-279.
[8] Dosunmu, Idowu T., and Subhash N. Shah. "Turbulent flow behavior of surfactant solutions in straight pipes." Journal of Petroleum Science and Engineering 124 (2014): 323-330.
[9] Baqi, M. "Characteristics of drag reduction by guar gum in spiral pipes." Jurnal Teknologi (Sciences and Engineering) 58, no. SUPPL. 2 (2012): 95-99.
[10] Yanuar, Waskito KT, Budiarso Gunawan, André Luiz Salvat Moscato, Santiago del Rio Oliveira, H. Z. Hassan, Marcos Galante Boato, Ezio Castejon Garcia et al. "Drag Reduction and Velocity Profiles Distribution of Crude Oil Flow in Spiral Pipes." International Review of Mechanical Engineering 9, no. 1 (2015): 1-10.

[11] Al-Wahaibi, T., Y. Al-Wahaibi, A. Al-Ajmi, N. Yusuf, A. R. Al-Hashmi, A. S. Olawale, and I. A. Mohammed. "Experimental investigation on the performance of drag reducing polymers through two pipe diameters in horizontal oil–water flows." Experimental Thermal and Fluid Science 50 (2013): 139-146.
[12] Edomwonyi-Otu, L. C., M. Chinaud, and P. Angeli. "Effect of drag reducing polymer on horizontal liquid–liquid flows." Experimental Thermal and Fluid Science 64 (2015): 164-174.
[13] Talahatu, Marcus Alberth, Sealtial Mau, Kurniawan T. Waskito, and Winda Wulandari. "The effect of calcium carbonate (CaCO3) nanoparticles on the flow through a pentagon spiral pipe." International Journal of Technology 8, no. 7 (2017): 1258-1265.
[14] Kazi, S. N., G. G. Duffy, and X. D. Chen. "The Effect of Varying Fiber Characteristics on the Simultaneous Measurement of Heat and Momentum Transfer to Flowing Fiber Suspensions." Journal of Heat Transfer 137, no. 1 (2015): 012601.
[15] Bobkowicz, A. Je, and W. H. Gauvin. "The turbulent flow characteristics of model fibre suspensions." The Canadian Journal of Chemical Engineering 43, no. 2 (1965): 87-91.
[16] Ogata, Satoshi, Tetsuya Numakawa, and Takuya Kubo. "Drag reduction of bacterial cellulose suspensions." Advances in Mechanical Engineering 3 (2011): 528373.
[17] Duffy, G. G., S. N. Kazi, and X. D. Chen. "Heat transfer and pressure drop characteristics of suspensions of synthetic and wood pulp fibres in annular flow." Applied Thermal Engineering 31, no. 14-15 (2011): 2971-2980.
[18] Ogata, Satoshi, Gunawan, Jun Warashina, and Yanuar. "Drag reduction of a pipe flow using nata de coco suspensions." Advances in Mechanical Engineering 6 (2014): 651260.
[19] Wulandari, W., K. T. Waskito, S. Mau, and Marcus A. Talahatu. "Effect of coconut fiber suspensions on drag reduction in circular pipe." In IOP Conference Series: Earth and Environmental Science, vol. 105, no. 1, p. 012050. IOP Publishing, 2018.
[20] Robertson, A. A. "The flow characteristics of dilute fiber suspensions." Tappi 40, no. 5 (1957): 326-334.

Penerbit Akademia Baru

Engineering Science and Technology Conference Proceedings

Journal homepage: www.akademiabaru.com/EST.html

Chaotic mixing of microdroplets using surface acoustic waves device

Open

Nazihah Zainal[1], Norazreen Abd Aziz[1,*],Fatin Afika Abdul Mutalib[1], Muhamad Ramdzan Buyong[2]

[1] Centre of Advance Electronic and Communication Engineering (PAKET), Universiti Kebangsaan Malaysia (UKM), Selangor, Malaysia
[2] Institute of Microengineering and Nanoelectric (IMEN), Universiti Kebangsaan Malaysia (UKM), Selangor, Malaysia

ABSTRACT

Small-scale mixing or actively known as micromixing had an utmost importance in biological and chemical application using micro total analysis systems (TAS) or lab-on-chips. Micromixing is achieved by stirring or agitating liquid or particles. However, in microfluidic technology it is very difficult to do mixing for a very small amount of liquid i.e microliter volume. Chemical reactions often involve in most microfluidic applications hence the fluid diffusivity is very low thus, chaotic advection shall be introduced in this study to shorten the reaction time. Conveniently, a new method has been proposed to actively mix micro volume liquid. In this study, we developed focused-surface acoustic wave (F-SAW) fabricated on a piezoelectric substrate to manipulate or mix two different color dyes with low concentration. Operation frequency of 50 MHz was used to generate acoustic waves along the substrate surface and we vary the droplet volume and input power on the F-SAW mixing. Method comparison between passive and active mixing has been done by studying the time taken for diffusion mixing. Design, fabricate and test a Y-junction channel micromixer in order to compare and examine the mixing performance and time. Experimental results show that mixing by F-SAW device has achieved high efficiency of 91 – 84% in droplet volume of 1 – 5 µL. Therefore, F-SAW mixing is proven more efficient and fast response as compared to diffusion mixing.

Keywords:

Focused-SAW; micromixing

Copyright © 2019 PENERBIT AKADEMIA BARU - All rights reserved

1.Introduction

Mixing has been recognized as one of the most basic and hard-to-reach problems of microfluidic applications. To date, several mixers have been developed and proposed for use in different application areas such as bio-, nano-, and environmental technologies. However, users or designers of microfluidic mixers must be very careful in selecting mixers to use in their particular application because the advantages are stressed more in papers and patents compared to the disadvantages. Microfluidic lab-on-a-chip devices [1], [2] for high-performance drug screening offer the ability to work with small amounts of fluids, which can significantly reduce the costs by reducing the volumes of expensive reagents required.

At microscale level, mixing can be achieved by stirring or agitating fluids. There are a few methods applied in micromixing which widely used in bio-molecular and medical application such as dielectrophoresis (DEP) [3], magnetohydrodynamic (MHD) [4] and acoustic [5]. In depth, dielectrophoresis technique can do

[*] *Corresponding author.*
E-mail address: azreen@vlsi.eng.ukm.my (Norazreen Abd Aziz)

separation, transportation, trapping and sorting of various biological particles by varying the applied electric field frequency [6]. Method of DEP and MHD requires high power to perform mixing process. Mixing of small liquid volume which often referred to as micromixing is crucial in microfluidic application especially for analysis that utilizes rare or valuable sample or high cost reagent. Micromixing in microfluidics can be classified into active and passive mixers [7]. In order to achieve mixing operation, active mixers rely on an external energy source, while passive mixers depend on the phenomenon of mass transport achieved by molecular diffusion and chaotic advection. Passive mixer can be categorized as T- [8] and Y- shaped [9] which recruits lamination mixing and droplet-based mixing [10].

Types of propagating waves at the centre of AIDT depend on the width of electrodes and will produce different types of waves propagation ie. Standing Surface Acoustic Wave (SSAW) and Focused Surface Acoustic Wave (F-SAW). In this study, we propose an active mixing operation of two droplets utilizing focused-surface acoustic waves (F-SAW) device. F-SAW device consist of an annular interdigital transducer (AIDT) that is fabricated on piezoelectric substrate [11]. When a radio frequency (RF) signals is connected to AIDT, surface acoustic waves are generated and propagate constructively by following the shape of AIDT on the substrate's surface [12]. The surface waves will be converged and focused at the center of AIDT. The focused-SAW induced an acoustic streaming or strong internal flow in the liquid thus enhancing the mixing speed of two droplets [13]. We used low concentration dye droplets i.e blue and yellow.

The advantages of F-SAW such as the ability to efficiently induce internal stirring in small liquid volume and the acoustic streaming could be focused at a certain location. It also presents great potential for using F-SAW device to achieve fast response mixing of micro droplet. This mixing technique is proven more reliable and efficient as compared to passive diffusion mixing technique.

2.Operating Principle

When an alternating electrical signal is applied to a piezoelectric medium, a mechanical wave is produced and propagated in the substrate in either a Rayleigh mode or a shear mode wave through the piezoelectric effect. Bulk Acoustic Wave (BAW) and Surface Acoustic Wave (SAW) are two types of acoustic waves. BAW propagates throughout the thickness of the substrate whereas SAW propagates only on the surface of the substrate which defines the differences between the two types of acoustic waves.

SAW is acoustic wave of nm-scale amplitude and oscillating in the MHz range. SAW based microfluidics is one of the most advance technologies. SAW can be exploited to drive actions such as mixing liquid, pumping, jetting and others [14]. Conventional interdigitated transducer (IDT) structure employed in SAW have the arrangement of several electrodes connected in a coupling mode. Formation of IDT on the piezoelectric substrates can be realized through lithography techniques. When an alternating input signal is applied to the electrode, it forms an electric field thus affects the surface acoustic wave due to the impact of piezoelectric coupling. The surface acoustic will propagate away from interdigitated electrode waves act as mechanical actuator to induce mechanical response in the environment. Modification on the electrode design from linear to annular causes the resulting surface acoustic energy to be converged at a point which is at the centre of the device. This will result in a maximum displacement magnitude and cause the high flow of velocity to be induced. The formation of this focused acoustic wave energy on the piezoelectric is important for pumping, particle removal and other applications.

F-SAW device typically consist of an annular interdigital transducer (AIDT) deposited on top of a piezoelectric substrate. When a RF signal is applied to an AIDT, surface acoustic waves are generated and propagate constructively by following the shape of AIDT on the substrate's surface.

F-SAW devices can be operated at high frequencies (25-500 MHz) and high sensitivity (Hz g^{-1}) [15]. Amplitude of wave increases under the influence of focused wave energy and that generates a larger disturbance force. The acoustic streaming or strong internal flow occur when the wave focused into the liquid and enhancing the mixing speed of two droplets. Figure 1 shows the mechanism of focused-surface acoustic wave into liquid.

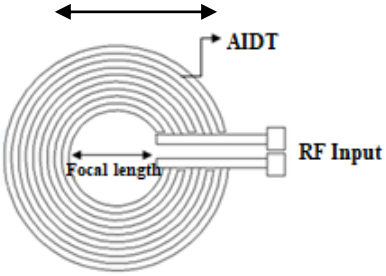


Fig. 1. Mechanism of F-SAW into liquids

Study of the flow characteristics of VFE-2 blunt edged delta wing profiles at high angle of attack [16]. Vortex is formed on the upper surface of the delta wing. The primary vortex is developed at certain chordwise location and progresses upstream with angle of attack; however, there are no data in VFE-2 suggesting that the vortex progressed with increasing angle of attack up to the apex region.

3. Experimental Setup and Method

First experimental setup was conducted using two mixing techniques; diffusion and F-SAW device. Material used to show the mixing performance and efficiency are two different liquid color i.e blue and yellow. Mixing properties has been identified as shown in Table 1.

Table 1. Mixing properties

Mixing method	Power (dBm)	Dye droplet (µl)	
		Yellow	Blue
Diffusion		0.5	0.5
		1.5	1.5
		2.5	2.5
F-SAW	10	0.5	0.5
	15	0.5	0.5
	20	0.5	0.5
		1.5	1.5
		2.5	2.5

3.1.1 Diffusion mixing

A 0.5 µl droplet of yellow and blue dye was injected on a glass plate. The progression of the diffusion mixing was observed with the help of digital microscope. This process was repeated with for every volume tabulated in Table 1. The angle of attack was limited to α = 23° with Reynolds number of 2×10^6.

3.1.2 F-SAW device

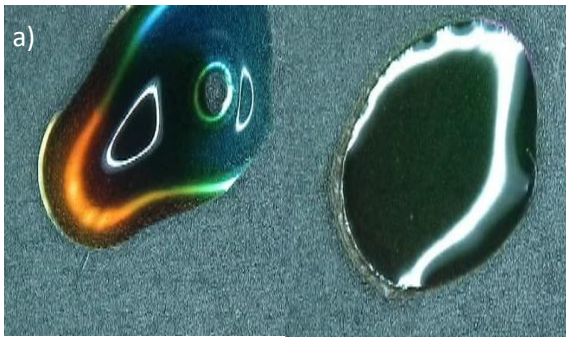
The AIDT have a focal length of 500µm and electrode width of 30µm. The frequency operation of 50MHz and input power of 20dBm was generated by a function generator. The signal was subsequently fed directly to the AIDT to generate F-SAW. A 0.5µl droplet of blue and dye was injected on the substrate. The progression of F-SAW mixing was observed by digital microscope. This process was repeated for every volume tabulated in Table 1. Various powers for total volume of 1µl droplet was conducted.

3.1.3 Y-junction channel

The second experimental setup was carried out to investigate the same type of mixing as in the first experiment i.e active and passive to investigate diffusion and F-SAW mixing but integrating enclosed space. The microfluidic system consists of a Y-channel with two 1mm diameter inlet branches at the same angles to each other merging into a 4mm diameter circular-shaped chamber. Minimum surface area of circular channel exposed to the liquid will reduce the friction between wall surface and liquid hence less energy used to pump the water for a given flow rate.The Y-channel was designed and drew using Coral Draw software and then using photolithography method to PDMS then being poured onto the mold and baked for 1 hour. Tubing was made at both branches by using 1mm inner diameter puncher and PTFE tube connected at both inlets. A syringe pump controller (TS-2A Syringe Pump Controller LongerPump) injected blue and yellow commercial water-diluted food colors into each branch of the Y-branch. From the end of the main channel, the mixing fluid was extracted. The experiments explored the effect of various fluid flow rates pumped at 3µl / min, 5µl / min and 10µl / min by the syringe pump while taking into account the stability of the microfluidic system as a whole. Using a mobile Samsung J7 Pro camera, fluid flow profiles were captured. As vibration can cause small amounts of blurring, care was taken when recording images. While conducting experiments, the microfluidic device was tightly taped to a work desk using a cellophane tape to prevent blurring of the recorded images. Take note that lighting might be varied between various experiments hence has led to different colour contrast in the recorded images.

4. Result and Discussion

Micromixing snapshots by diffusion and F-SAW mixing with different volume as shown in Figure 2 and Figure 3. From the Figure 2 we observed the droplets has spread into liquid. This process utilizing space and require longer time upon completion.



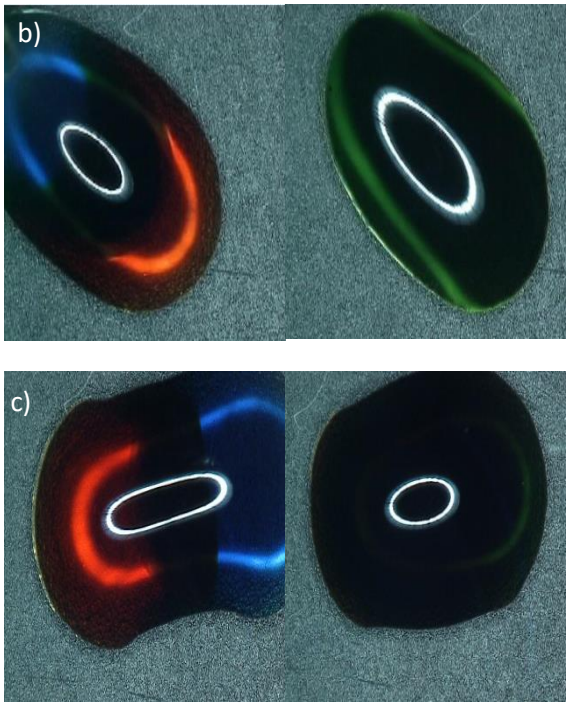
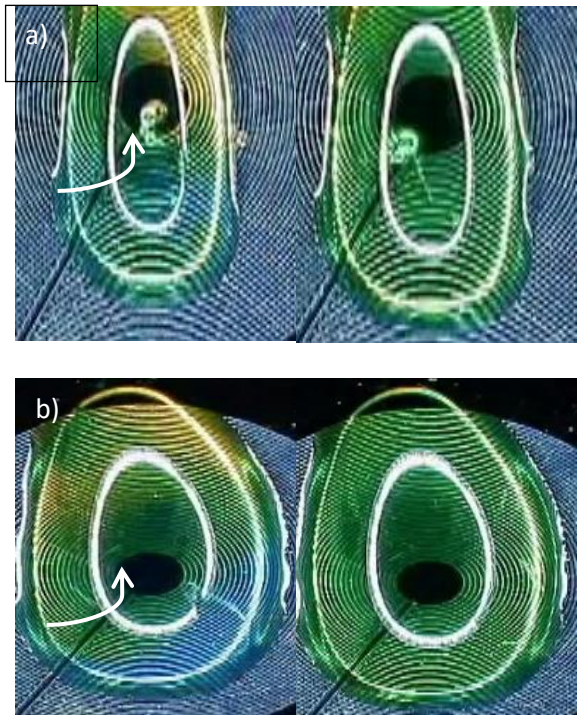


Fig. 2. Complete diffusion mixing a) 1µl at t=240s, b) 3µl at t=300s and c) 5µl at t=420s

In Figure 3, F-SAW show constructive propagation of wave mixing following the shape of AIDT. From the center of droplet area, the internal flow of counter clockwise direction was observed. This process utilizes low power yet produce faster response time for mixing completion as compared to passive mixing



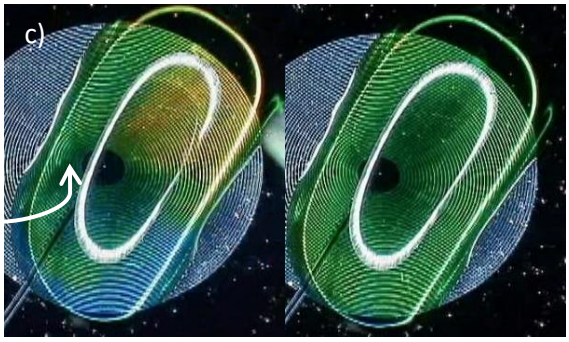


Fig. 3. Complete F-SAW mixing a) 1µl at t=38s b) 3µl at t=45s and c) 5µl at t=56s

From the first set of experiment, F-SAW mixing have shorter period of time than diffusion mixing at various total volume of droplets. F-SAW and diffusion mixing was recorded 38s and 240s of period time for 1 µl droplet. As volume of droplet increases, the time taken to completion mixing also increases for both F-SAW or diffusion mixing.

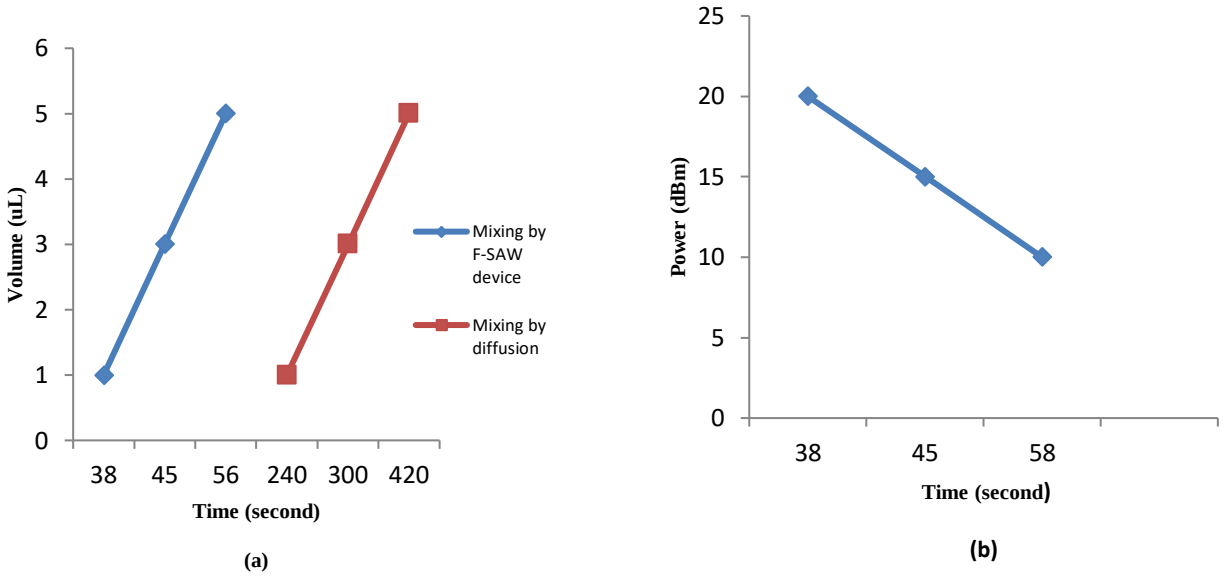


Fig.4. (a) Volume effects on diffusion and F-SAW mixing and (b) Input power effects on F-SAW mixing

Time taken to color changes was decreased with increase in input power on F-SAW mixing as shown in Figure 4 (b). Color changes from yellow and blue to green takes shorter time as input power increases. Input power is more important performance parameter. Results analysis showed that maximum power has higher mixing efficiency of 84% for 1 µl droplet than minimum power. Therefore, the stronger of acoustic energy, the more efficient the mixing.

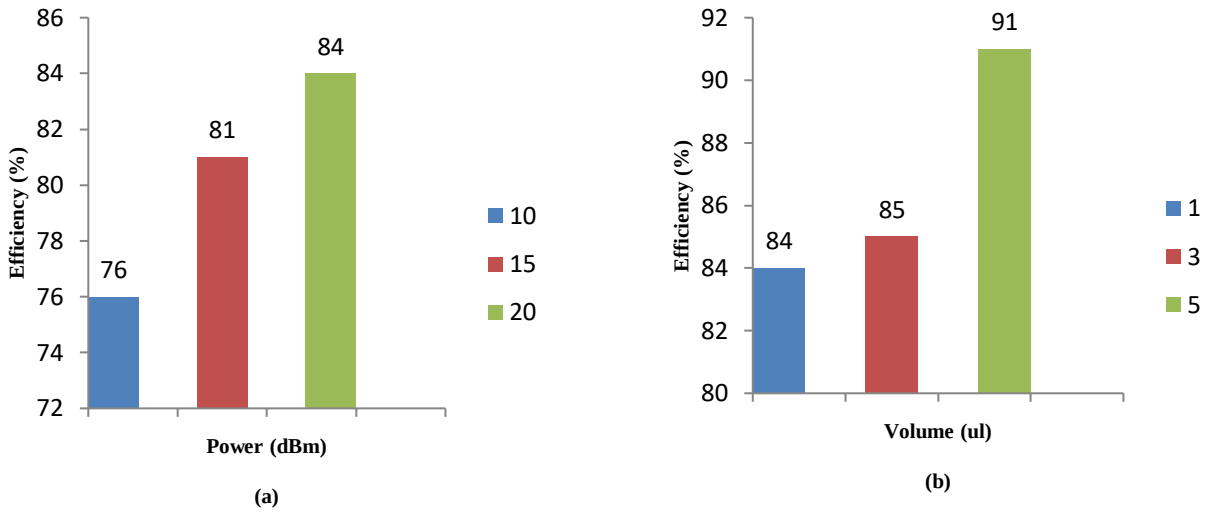
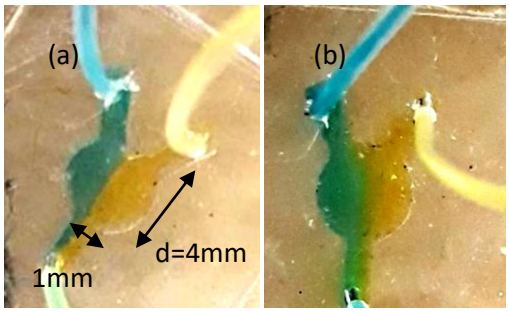


Fig.5 (a) F-SAW device efficiency for 1µl droplet mixing and (b) Mixing efficiency of F-SAW device

From the result as shown in Figure 5, mixing efficiency for F-SAW device also being measured by manipulating the volume of droplets. F-SAW mixing has efficiency of 91-84% for 1-5µl droplets mix. F-SAW mixing is proven more reliable and efficient as compared to passive diffusion mixing technique. Mixing efficiency is higher as volume of droplets increases. Therefore, large volume of droplets can be used in F-SAW mixer.

This work also demonstrates mixing mechanisms for an enclosed microfluidic channel Y-junction. Different fluid flow rates transported through the Y-junction microfluidic channel are studied. We manipulate flow rate for both passive and active mixing in Y-channel microfluidic system are 3µl/min, 5µl/min and 10µl/min. Micrometers dimensions for Y-channel tubing are 80µm in height and 4mm chamber diameter of region of interest. Enclosed Y-channel was used in this experiment to study the concept by integrating F-SAW in active mixing. This will induce shear stress on the interfacial surface that helps the mixing process; adopting an active mixer's structure while maintaining the system as a whole. This experiment also proves that mixing act differently for two condition; open and enclosed channel.

Results of mixing in Y-junction channel (passive and active mixing) show mixing profiles for the different flow rate conditions.



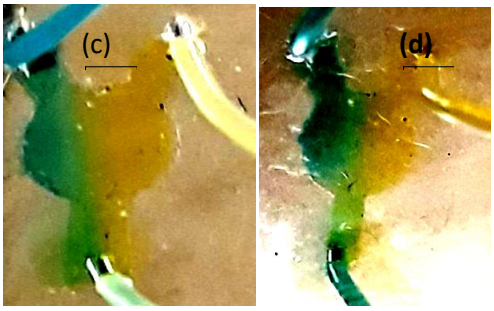


Fig. 6. (a) Flow rate of 3µl/min at time=0s, (b)Flow rate of 3µl/min at time=3.42min, (c) Flow rate of 5µl/min at t=2.26min, (d) Flow rate of 10µl/min at t=1.23min

Mixing profiles in Figure 6 shows different flow rates for passive mixing in Y-junction channel. When the flow rates are lower than 3µl / min at t=0min, little to no mixing is observed because molecular diffusion only was insufficient to promote mixing but after some time at t=3.42min, green colour can already be observed. This differs from the case of higher flow rate of 5µl/min where self-mixing was observed based on the intensity of green colour formed as early as 2.26min. When the flow rate is set higher at 10µl/min, the shorter the time taken for the mixing to occur as we can the yellow and blue dye colour changes to green as early as 1.23min and the intensity of green colour increases when t=3min.

In the first set of experiments, fluid is introduced in the two branches of the Y junction and removed at the base, no external disturbances are imposed. Therefore, any mixing that occurs is in passive nature. Images showed the fluid at a range of different flow rates flowed through the junction. The flow rates used are 3µl / min, 5µl / min and 10µl / min in this series of experiments. Note that the flow across the open junction does not involved any disturbances and is stable during the mixing. Secondly, it can be seen that the yellow and blue streams converge at the junction and continue to flow as separate streams into the chamber for the lower flow rate as shown in Figure 6(a),(b) and (c). Little to no mixing for the higher flow speeds, self-mixing happens as per Figure 6(a) and (b). Mixing was also observed to occur rapidly in (c) and (d) (in space). The mixing at the extraction end is not total, as can be seen from image (d). Slower flow rates may occur at the output channel due to viscous forces since outlet diameter is smaller than the channel width and fluid height at these locations. At these locations unmixed fluid are observed. However the output fluid in the glass was found to be mixed. Colour intensity of fluid was observed in comparing the mixing distribution for different fluid flow rates.

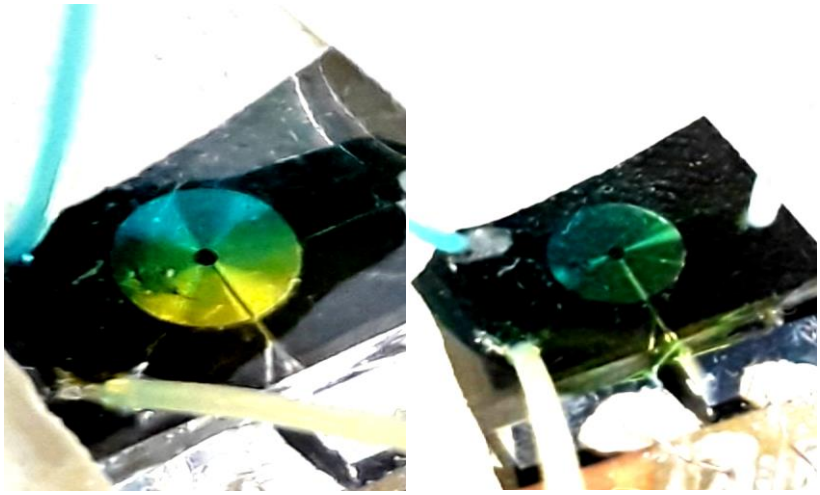


Fig. 7. (a) Flow rate of 3µl/min at t=0min and (b)Flow rate of 3µl/min at time=1.30min

Active mixing in Y-junction channel was carried out by integrating an F-SAW device that was put beneath the Y-junction channel. F-SAW propagate wave and theoretically will perform mixing for the two different colour liquid. As per case Figure 7 (a), even at t=0min, green colour mix can already be observed and mixing efficiency is much higher for Y-channel active mixing compared to Y-channel passive mixing as it took shorter time completion for mixing compared to Y-channel mixing without the introduction of F-SAW device. Higher flow rate was manipulated for the second set of experiment and the results as shown in Figure 8.

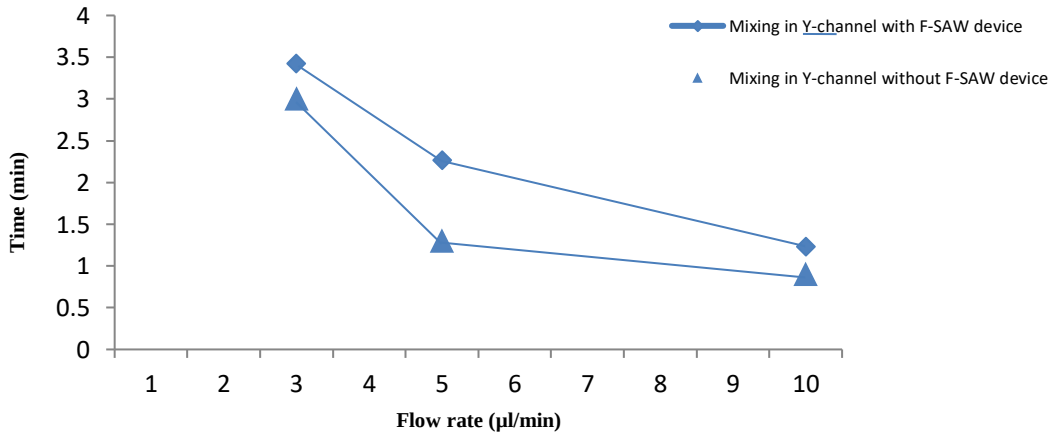


Fig. 8 Different flow rates effects on time for mixing in Y-channel with F-SAW and without F-SAW device

Using the Stokes flow rule, microfluidic systems operate where viscous forces overwhelm inertial effects at low flow rates [13]. Due to the laminar nature of the flow, blue and yellow liquid will flow according to the pressure gradient, so mixing within space will be via molecular diffusion. Liquid color changes in the mixing chamber as a result of manipulating different fluid flow speeds. Mixing

time shorter as the process reaches a higher flow speed. This is due to the different fluid velocity in the mixing region.

To compare both sets of experiment, nature of the channel was discussed where the fluid motion varies according to the nature of the channel. Random motions promote stirring in the flow therefore fluid freedom in the open channel will enhance the effect of perturbations as compared to a closed system ie. Y-channel as we can see in both experiment 1 and 2. As per case of enclosed system, fluid is bounded by solid on one surface and the other surface disturbances by surface acoustic waves which explain Fig. 9 where time taken for mixing in Y-channel with F-SAW is shorter than the mixing in Y-channel without F-SAW.

5. Conclusion

In conclusion, mixing of two droplets utilizing passive diffusion method and F-SAW device has been demonstrated. When fluid flow in a Y-channel, different mixing profiles were observed. In a passive mixing system, fluid flow rates play an important role in the mixing process as higher flow rates influence mixing of the fluids despite of propagation of acoustic wave in active mixing. While high flow rates can cause mixing in open channels, lower flow rates require an active intervention source to achieve this result. This can be provided by surface acoustic wave device which will give the chaotic mixing hence the rapid mixing. Therefore, mixing in open channels with and without interference can be shown as a phase in more complicated open fluidic networks as they are developed. Mixing process performed by F-SAW device produce fast response thus more efficient as compared to passive method despite the condition of mixing in open or enclosed (Y-junction channel) environment. This low powered device has efficiency of 91-84% for mixing 1-5 µl droplets. Mixing process using F-SAW device can be very useful for future biomedical and chemical analysis.

Acknowledgement
Authors would like to gratefully acknowledge this work, which was financially supported by the Universiti Kebangsaan Malaysia (UKM) and Ministry of Education of Malaysia through a grant project (code no: GGPM-2017-035).

References

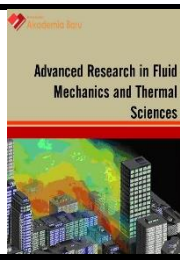
[1] Luo, Jikui, Yong Qing Fu, and William Milne. "Acoustic wave based microfluidic and lab-on-chip." (2013): 515-556.
[2] Aziz, Norazreen Abd, Mimie Asmiera Mohd Zain, and Muhamad Ramdzan Buyong. "Particle Separation using Acoustic Wave Device for Microfluidic Applications." Journal of Advanced Research in Fluid Mechanics and Thermal Sciences 52, no. 1 (2018): 104-114.
[3] Zhang, Haoqing, Honglong Chang, and Pavel Neuzil. "DEP-on-a-chip: Dielectrophoresis applied to microfluidic platforms." Micromachines 10, no. 6 (2019): 423.
[4] Wen, M. M., and C. N. Kim. "Mixing features in an electromagnetic rectangular micromixer for electrolyte solutions." Journal of Hydrodynamics, Ser. B 29, no. 4 (2017): 668-678.
[5] Zeggari, Rabah, Jean-François Manceau, Ece-Neslihan Aybeke, Reda Yahiaoui, Eric Lesniewska, and Wilfrid Boireau. "Design and fabrication of an acoustic micromixer for biological media activation." Procedia Engineering 87 (2014): 935-938.
[6] Buyong, Muhamad Ramdzan, Jumril Yunas, Azrul Azlan Hamzah, B. Yeop Majlis, F. Larki, and N. Abd Aziz. "Design, fabrication and characterization of dielectrophoretic microelectrode array for particle capture." *Microelectronics International 32*, no. 2 (2015): 96-102.
[7] Cai, G., Xue, L., Zhang, H., & Lin, J. A Review on Micromixers. *Micromachines* 8, no. 9 (2017), 274.
[8] Othman, Nur Tantiyani Ali, and An-Najmi Mohd Farid. "Droplets Tracing in a T-junction Microchannel." Jurnal Kejuruteraan 30, no. 1 (2018): 47-53.

[9] Ward, Kevin, and Z. Hugh Fan. "Mixing in microfluidic devices and enhancement methods." *Journal of Micromechanics and Microengineering* 25, no. 9 (2015): 094001.
[10] Ju, Jongil, and Jay Warrick. "Passive micromixer using by convection and surface tension effects with air-liquid interface." *Biochip journal* 7, no. 4 (2013): 361-366.
[11] Mukhtar, Nurul Jannah, Norazreen Abd Aziz, Badariah Bais, and Burhanuddin Yeop Majlis. "Circuit modeling of Surface Acoustic Wave (SAW) resonator with circular geometry." In *2016 IEEE International Conference on Semiconductor Electronics (ICSE)*, pp. 57-60. IEEE, 2016.
[12] Tan, Jue Nee, and Adrian Neild. "Microfluidic mixing in a Y-junction open channel." *Aip Advances* 2, no. 3 (2012): 032160.
[13] Wee, MF Mohd Razip, Muhamad Ramdzan Buyong, and Burhanuddin Yeop Majlis. "Effect of microchannel geometry in fluid flow for PDMS based device." In *RSM 2013 IEEE Regional Symposium on Micro and Nanoelectronics*, pp. 391-393. IEEE, 2013.
[14] Ding, Xiaoyun, Peng Li, Sz-Chin Steven Lin, Zackary S. Stratton, Nitesh Nama, Feng Guo, Daniel Slotcavage et al. "Surface acoustic wave microfluidics." *Lab on a Chip* 13, no. 18 (2013): 3626-3649.
[15] Devkota, Jagannath, Paul R. Ohodnicki, and David W. Greve. "SAW sensors for chemical vapors and gases." *Sensors* 17, no. 4 (2017): 801.
[16] Tajuddin, Nurulhuda, Shabudin Mat, Mazuriah Said, and Shumaimi Mansor. "Flow characteristic of blunt-edged delta wing at high angle of attack." *Journal of Advanced Research in Fluid Mechanics and Thermal Sciences* 39, no. 1 (2017): 17-25.

Penerbit Akademia Baru

Engineering Science and Technology Conference Proceedings

Journal homepage: www.akademiabaru.com/EST.html



An Investigation of Heat Transfer on the Downstream Surface and an Experimental Study on Flow Structure of Continuous Jet of the Single Row Circular Orifice Injecting nto Mainstream

Open Access

P.Juera-ong[1], N.Puzu[1], C.Nuntadusit[1,*]

[1] Department of Mechanical Engineering, Faculty of Engineering, Prince of Songkla University, Hatyai, Songkhla 90110, Thailand

ABSTRACT

This paper presents the study of heat transfer on a flat plate with cross-flow which study is divided into 2 parts. The first parts The effect of continuous jet was investigated by fix the mainstream flow at 10/s and varied the jet velocity corresponding a momentum flux of 0.01, 0.06, 0.25, 1.0, 2.25, 4.0 and 12.25 and this study, the experiment will be divided in 2 parts which are study of temperature distribution on heat transfer surface with constant heat flux is captured by an infrared camera and next this study was show the result of the structural patterns of a single row orifice jet that was perpendicularly injected into the crossflow using laser-induced fluorescence technique. The result reveals that all heat transfer rates on the surface are better than under no-jet conditions.

Keywords:
Orifice jet; ortex generating jet; laser-induced fluorescent; heat transfer enhancement

Copyright © 2019 PENERBIT AKADEMIA BARU - All rights reserved

1. Introduction

The rotation of the fluid while moving on the surface area that requires cooling can increase the rate of heat transfer for example Installation of small wings blocking the flow, embossed surface or pin placement but disadvantages of the above method it increases the pressure drop above the surface and production cost is quite high.

For the design of the heat transfer system cannot accept the pressure drop across. The method to injection using the method of spraying the jet from the surface against the main flow. Compton and Johnson [1] have studied the rotation caused by the jet beam blocking the main flow Found that the rotation can reduce the thickness of the boundary layer. Zhang [2] has studied the rotation characteristics between the main flow and the circle orifice jet maintain the condition and shape well. Dai [3] shown the structure detail of the jet when it clash the mainstream. Ahn [4] has studied the effects of the jet outlet in 4 characteristics and that was found the circulating currents from the downwash side could increase the heat transfer. Lee [5] have shown the experiment about a cooling film by hatch-cut face jet. Kwanmon and Asi [6] has studied about the component of the mainstream and jet that is in the vortex jet at the outlet and the rotation had a contour of the rear

* *Corresponding author.*
E-mail address: chayut.n@psu.ac.th (C.Nuntadusit)

speed close to the jet hole, consisting of almost all jet currents and decreasing along the side. Suzuki [7] has studied by using a pulse jet to develop heat transferability in the mainstream. Qayoum [8] has studied the convection on the back synthetic jet surface from the piezoelectric plate. Rao et al [9] has has compared of optimization between the punched pin group and no drill hole group was conducted. It was found that in the case of drilling holes, the air swirled at the back of the hole which results in better heat transfer rates. Jabbal and Zhong [10] studied the characteristics of flow and heat transfer on the surface using synthetic jet which affects the efficiency of heat transfer.The angle of inclination of the jets is 30 and 45 degrees. There are 2 characteristics of the jet exit which are ellipse shape jet hold and the expansion 10 degree of the jet hole. In a total of 4 cases studies. The little boing jet current will travel to a surface but when the boing ratio increases. The Jet currents will being to divert across and began to lift off the surface. Especially the jet in the first row resulting in reduced maximum cooling efficiency but the cooling area will increase. Jovanovic [11] has studied the characteristics of jet flowing between smooth surface and rough surface. Fric [12] has studied about the swirling close to the jet which can be divided into 4 types: 1. Swirling due to jet sheer stress, 2.Double swirling at the back., Horseshoe rotation on the surface and 4.Group swirling at the back. Yuen and Martinez-Botas [13] has studied about the surface of the heat transfer at the boing ratio at 0.5, 1 and 1.67. The results show that heat transfer more than 10D started to continuously decrease along downstream distance. The heat transfer is similar to all cases, and the blowing ratio does not affect to the heat transfer. For pitched angle of 30 degree, the pitch is equal to 6. The blowing ratio is in the range of 0.33-1.67. The maximum heat transfer will be. Fiebig [14] deployed wing-type vortex generator on a plane surface and compared the efficiency for heat transfer between longitudinal vortices and transverse vortices to show a heat transfer enhancement. Prince [15] has studied the simulation of the use of vortex jet to reduce the isolated flow on the plane wing surface The vortex jet increases the surface area to create momentum into the boundary layer and can significantly reduce separation. Jacobi and Shah [16] has studied about the solid vortex generators could considerably increase heat transfer, again with an increase in friction loss. Sun et al. [17] has studied a film cooling for a fixed coolant mass flow rate and blowing ratio which increase when the cooling effectiveness of fan shaped hole increase. Singh et al. [18] has studied about the investigation of film-cooling over a flat plate and the experimental study is carried out for five values of L/D, the results received from the present study showed that the film-cooling effectiveness is higher for the longest holes (L/D = 5) in the present work in comparison to that for the shorter holes. Aris et al. [19] has improved the thermal performance of fin stacks by changing their attack based on the fin surfaces and that can enhance the heat transfer better than a plain fin stack. Smulsky et al. [20] investigated the effect of rib attachment orientation angle on a heat transfer surface and found that the heat transfer 50-degree angle was the best at approximate 40% higher the perpendicular rib.

From the resulting of reviews found enhancement of the heat transferability of the circle orifice back surface by using the pulse jet were studied in a narrow circle so this research has studied about the enhancement heat transferability and studied the behavior about the distribution of the jet on the surface. In this study case, the characteristic of the orifice is six circle orifices in a single row and these were installed on the surface that needs cooling.

2. Methodology

Fig 1 show the experiment setup details. The open wind tunnel blows a mainstream uniform-velocity-profiled horizontal wind through a square exit over the horizontal flat plate with sharp leading edge and a circular jet is installed perpendicular.

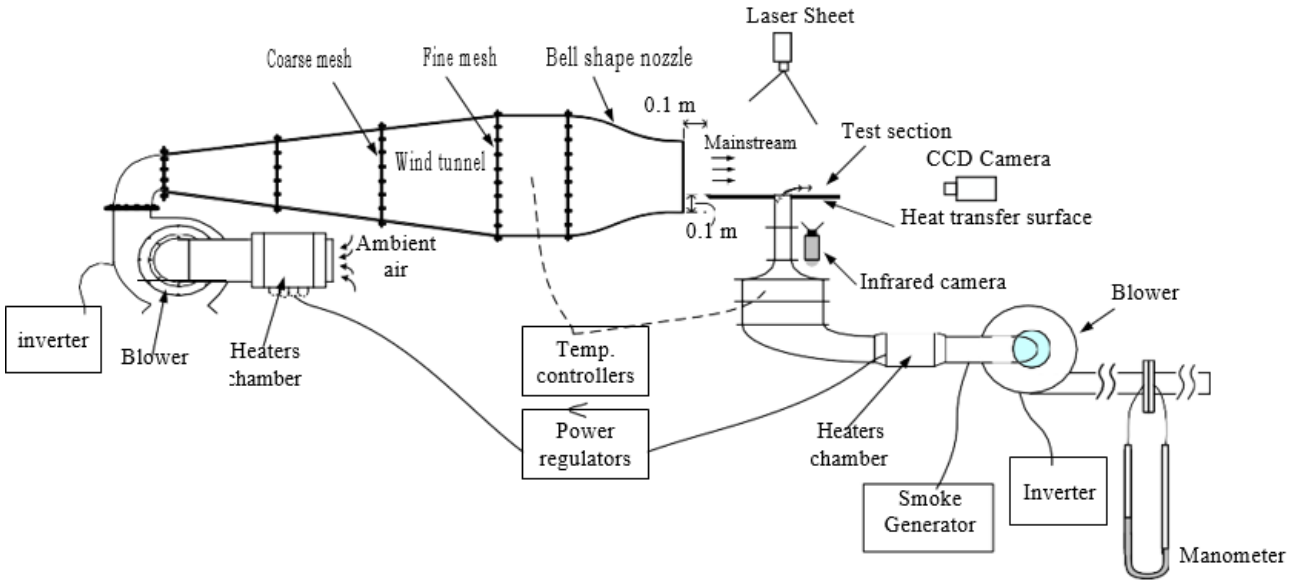


Fig. 1. Experiment setup

2.1 Open flow wind tunnel configuration and characteristics

The open wind tunnel is designed in a bell shape with the size of the outlet a 400 mm x 400 mm square, is as shown in Fig. 1. Air of the room temperature fixed at 24 °C, Air from jet and main stream fixed 26.0 ± 0.2 °C and control by using a PID temperature controller to control the heater installed in the chamber. Before reaching the exit of the jet installed the 7.5 Hp blower inlet. Turbulence inside the tunnel is reduced by using coarse and fine meshes normal to the flow. To remove separation flow on the tunnel wall near the exit, the cross section – The wind tunnel wall is designed with the bell shape which can narrow to re-accelerate the airflow. The uniform-velocity profile of mainstream was controlled at 10.0 m/s via a predetermined blower test speed. Buck velocity were controlled to be salmost constant along own stream direction less than 5% and turbulence intensity less than 0.2% that mean the velocity variation.

2.2. Test section characteristics

The acrylic test section designed to be 20 mm thick and a cross section area of 800 mm long, 480 mm wide and the side adjacent to the outlet has a 15-degree shape edge to keep an initial laminar flow near the leading edge (detail in Fig.2). The single row circle orifice with a diameter D of 14 mm was mounted at grade in front of heat transfer region near the leading edge at a distance 28.6D, and 0.36D from the beginning of the stainless sheet. A 1.5 mm trip wire was at 1.0D from the leading edge to trigger and accelerate a turbulent boundary layer flow. The aluminium jet pipe was designed to be 10D to achieve a fully developed flow at the jet exit.

The boundary layer thickness (δ) at the jet nozzle position was measured to be 1.01D based on distance at X axis from the leading edge and the mainstream Reynolds number, was approximate to be 2.5 x 10^5.

This study, seven value of mainstream to jet momentum flux ratio: J=(ρV2)/(ρV2) of 0.01, 0.06, 0.25,1.0, 2.25, 4.0 and 12.25, were experimented in accordance with jet Reynold number, Rej = Vj

D/υ of 2.2 ⍰ 103, 1.3 ⍰ 104 and 3.1 ⍰ 104, respectively. Since mainstream and jet were the same temperatures and the effect of the density can cancel out in above equation because between mainstream and jet are the same fluid. Downstream of the jet exit was covered by a 0.03 mm thick stainless sheet tightly stretched between two copper bus bars connected with the DC supply that generated uniform heat flux on the stainless sheet to act as the heat transfer surface.

In the second part, The experimental study on flow development of circle orifice jet in crossflow. In this study, the same seven values of the mainstream to jet momentum flux ratio of 0.01, 0.06, 0.25, 1.0, 2.25, 4.0 and 12.25. The flow structure development of the single row circle orifice jet that was perpendicularly injected into the crossflow using the smoke generator (Ate- AEROTECH model: SGS-90) by using oil (SHELL ONDINA 15) to produce the smoke into the jet exit and used laser-induced fluorescence technique and high resolution CCD camera (Sony HP9531PE) to capture the flow structure development and set a distance from behind the 60D jet hole is for avoid the flow disturbance and the camera and the laser generator are placed on the same sliding arm so that the images in each plane are the same size as shown the detail in Figure 2.

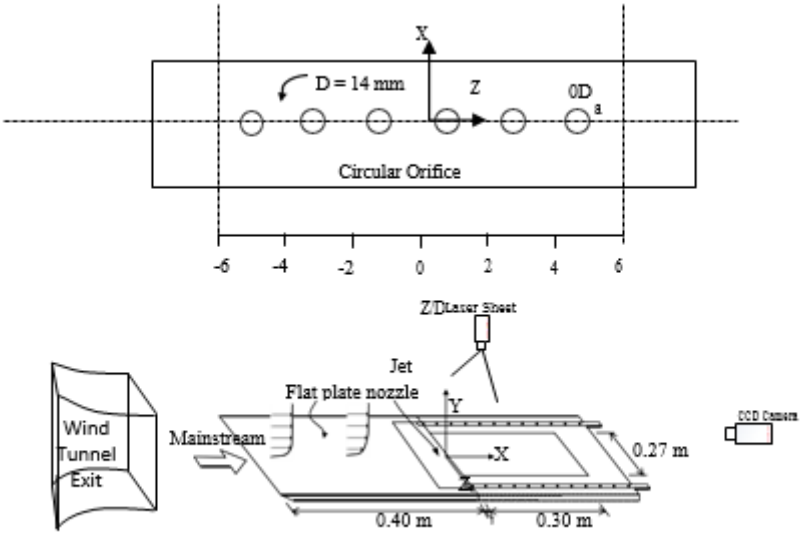


Fig.2. Test Section

2.3 Data measurement and data processing

The temperature distribution on the stainless-steel sheet is measured by the infrared camera (Flir 420) which will be installed at the bottom of the test section, which was sprayed with matt black paint having emissivity of 0.95 at the stainless-steel sheet with a thickness of 0.03 mm. The camera can be captured up to 120 frames/s and the range of -20 to 120 with the accuracy of ± 0.2% Resolutions of the camera is 320 ⍰ 240 pixel to reduce the effect of temperature variation from the measurement.

The Heating on stainless steel plates is done by supplying electricity through the bus bars that are installed on acrylic test section as shown in Fig. 2, the stainless steel sheet is 0.27 x 0.3 mm in size and has a thickness of 0.03 mm. Due to its thinness, the temperature on the heat transfer surface assumed to the identical to the temperature on the measurement surface.

The total heat flux via the adjustable DC power supply could be calculated from Joule heating formula:

⍰ = ⍰⍰ (1)

Where I is the electrical current (A), V is the voltage (V). The total heat loss from the natural convection and the radiation is:

$$Q_{loss}=Q_{conv}+Q_{rad} \quad (2)$$

Where $Qloss$ is the total heat loss, $Qconv$ is the heat loss from free convection, $Qrad$ is the heat loss from radiation. The local convection heat transfer coefficient can be obtained from Newton's law of cooling, thus:

$$h = \frac{Q_{in}-Q_{out}}{(T_w-T_{aw})A} \quad (3)$$

Where
h is the conventive heat transfer surface.
Qin is the total heat loss.
$Qconv$ is the heat loss from free convection.
Tw is the local wall temperature (with wall heat flux).
Taw is the adiabatic wall temperature (without wall heat flux).
A is the area of the heat transfer surface.

The convective heat transfer heat transfer coefficient ratio $h/h0$ is defined in this study to show the heat transfer enhancement, where h is the coefficient for the case with the jet, $h0$ is the coefficient for the case without the jet.

3. Results

3.1 Heat transfer characteristics

Fig. 3 shown the experimental results of a heat transfer coefficient ratio h/h_0 on the down surface according to jet-mainstream momentum flux ratio J was measured with infrared camera. All six J values increased the heat transfer rate from no jet condition. Details are as follow:

For J = 0.01, the effect of jet stream to enhance heat transfer is bounded by -6.0 ? Z/D ? 6.0 along the entire downstream direction, increasing gradually downstream adjacent to the jet exit, and then subsides. At approximate X/D = 2 with h/h0 of 1.1, with a remarkably weak heat transfer region on its sides (the deep blue trails along its lower edges).

For case of J = 0.06. The single high heat transfer region here is in contrast to the 2-tails characteristics exhibited by the former. The effect of jet stream to enhance heat transfer is same with J = 0.01. At approximate X/D = 2.5 with h/h0 of 1.15 is the highest heat transfer rate region.

For case of J = 0.25, at the same enhance heat transfer bounded and the single high heat transfer region in contrast to the 2-tails characteristics exhibited by the former same to the momentum flux ratio equal 0.06. At approximate X/D = 2.5 with h/h0 of 1.26 is the highest heat transfer rate region.

For case of J = 1.0, at the same enhance heat transfer bounded with the momentum flux ratio for all the previous momentum flux ratio. At approximate X/D = 2 with h/h0 of 1.4 is the highest heat transfer rate region for this case.

For case of J = 2.25, At approximate X/D = 1 with h/h0 of 1.45 is the highest heat transfer rate region and for case of J = 4.0 at the same enhance heat transfer bounded with the momentum flux ratio.

For case of J = 12.25, the high heat transfer starts at the immediate downstream area close to the jet exit and reaches a maximum value at approximate X/D = 2.0 with h/h0 of 1.5. The highest heat transfer jet velocity scenario becomes more of a candle flame shape and weak heat transfer region on its sides. However, this highest heat transfer rate exerts greater influence on neighboring regions than the two lower jet scenarios.

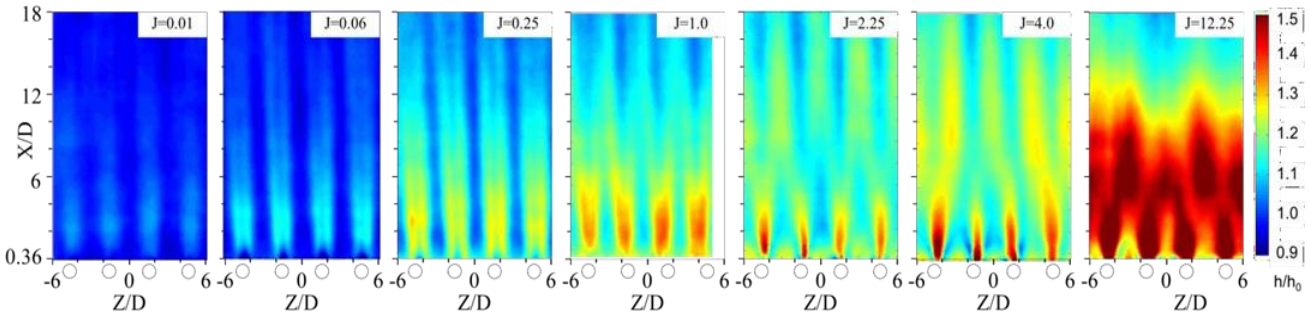


Fig. 3. Contours of heat transfer coefficient ratio

3.2 Flow structure development

Fig.4 shows the development of the structure of the jet stream in the main flow in the case of circular orifices. When moving through a jet hole at various distances and the development of the jet will affect the characteristics of the internal intensity jet structure.

At a position, the center of the circular jet, which is the only plane that passes through the jet at this position will look opaque because the jet is mixed with the main flow. The figure shown only the structure of the jet leaving only half of the round hole, with the development of all injected jet beams starting at X/D = 0 which located at rear jet hold position.

At J = 0.01, which was found that at this position there will be a slight lift by the jet speed at this speed, that will not have much influence and considering the position farther. For example, at position X/D = 8 which is found that the influence of the main flow current will cause the jet current to decrease markedly.

At J = 0.06, it can be observed that the jet current can be seen more clearly compared to J = 0.01. It is found that when the position X/D is far away, the influence of the main current will come in to play a role. The jet stream began to subside.

At J = 0.25, can be observed that jet flows can be seen more clearly, similar to J = 0.06, but jet currents have more influence when compared to J = 0.06.

At J = 1.0 and at J = 2.25, jet will begin to lift away from the surface of the circular jet exit hole but the structure of the jet will become thinner when the distance X/D is away and at the position X/D = 4, they will be about 2D in width.

At J = 4.0, the jet beam will begin to lift itself away from the surface of the circular jet exit hole clearly. But the structure of the jet will become thinner when the distance X/D is away and at the position, X/D = 8, which will be about 2.5D in width. At position X/D = 8, the jet's structure will become thinner until it becomes apparent. However, the jet's structure will remain uneven due to the mixing behavior caused by the jet's swirling flow.

At J = 12.25, it is found that the jet will lift itself away from the surface of the jet hole in a circular motion due to the influence of the main current flowing into the front of the jet and the structure of the jet will become thinner when the distance X /D is away. For example, at the position

X/D = 4, the width is approximately 2D, at the position X/D = 8, the jet will start to look slim until the beginning. Not obvious and the position X/D = 16 will be the lightest until it starts to be consistent with the area around the jet.

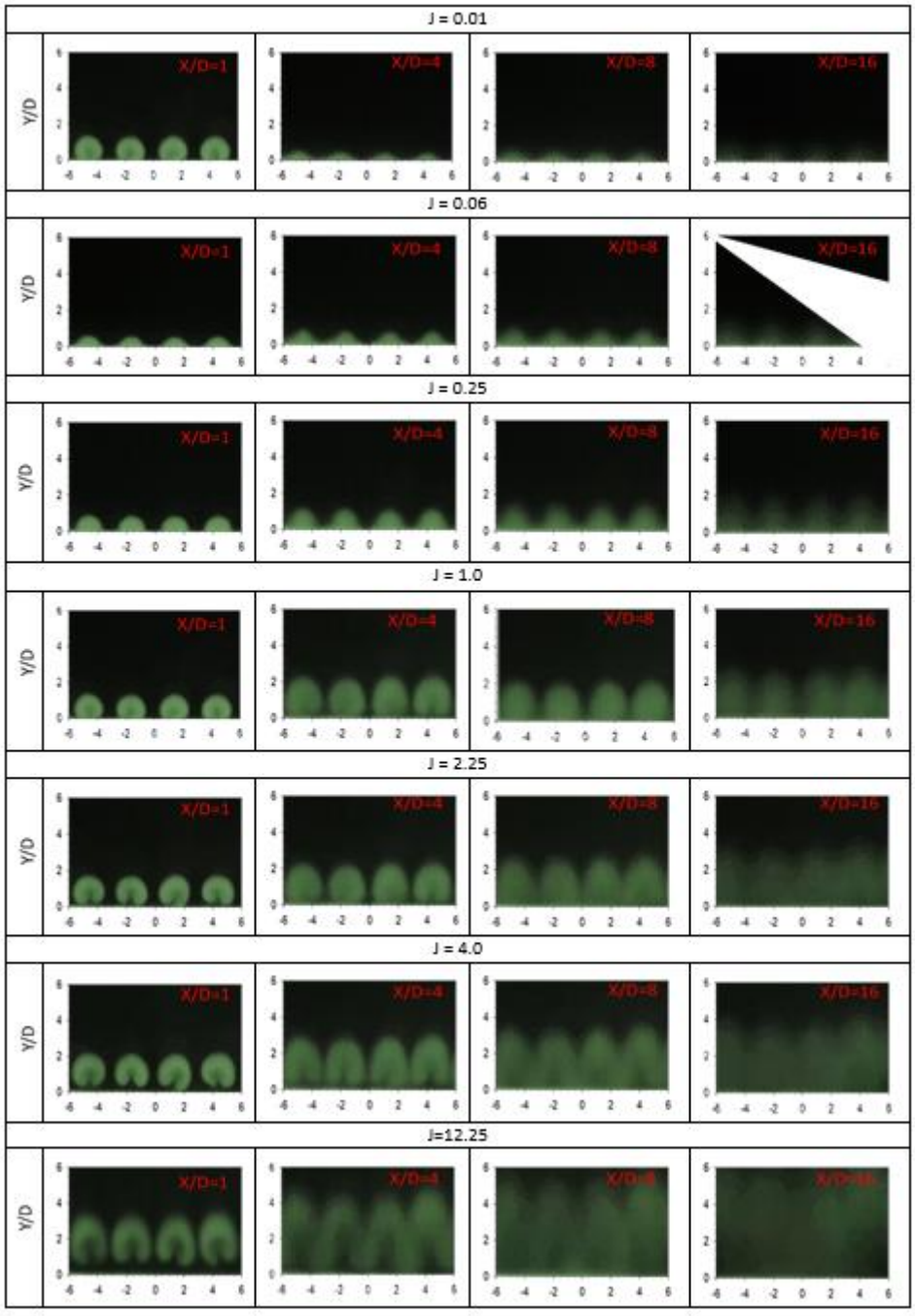


Fig. 4. The Result of Development of The Structure of The Jet Stream

4. Conclusions

An experimental study of an investigation of heat transfer on the downstream surface and an experimental study on flow structure of continuous jet of the single row circular orifice injecting into mainstream, the main result are:

(1) At a low jet velocity, when J = 0.01, there is not much heat transfer capability resulting from jet currents. The heat transfer capability is 1.1 times that of no jet condition. The position with good heat transfer capability will be in the range 1 ≤ X/D ≤ 2.5 and the heat transfer rate will be in the case of the flow structure study, it can be observed that at J = 0.01 there will be a slight lift of velocity which will not have much influence from jet currents.

(2) For J = 0.06, it has better heat transfer capability compared to J = 0.01, with a heat transfer capability of 1.15 times that of no jet conditions. Where the heat transfer capability is in the range of 1 ≤ X / D ≤ 2.5 and the heat transfer rate decreases as far away as for the flow structure study, it can be observed that the jet influence will result in higher speed lifting compared to J = 0.01, which the jet beam will expand and begin to move. Contact with the surface and the formation of the jet in each direction can not be separated when moving away from each other.

(3) For J = 0.25, it has good heat transfer capability, which has a heat transfer capability of 1.26 times that of no jet conditions. Where the heat transfer capability is in the range of 1 ≤ X / D ≤ 3 and the heat transfer rate will decrease as far away as for the flow structure study, it can be observed that the jet influence will result in higher lifting speeds compared to J = 0.01 and J = 0.06. Grew and began to move.

(4) For J = 1.0, it has good heat transfer ability at position 0.5 ≤ X / D ≤ 4, which has a good heat transfer rate of 1.4 times when compared to the no jet condition and from the characterization study The structure of the jet is found to be lifted away from the surface from the edge of the jet hole at the back. And the structure of the jet will be thinner, which shows that in that area there will be an influence of the main currents in and will be more effective when moving away in contact with the surface and formed together until the jet could not be separated in each direction.

(5) For J = 2.25 and 4.0, there is a characteristic of high heat transfer at the position 0.5 ≤ X / D ≤ 4 with a heat transfer capacity of 1.4 and 1.45, respectively, and the result of the flow structure study shows that J = 2.25, jet began to lift itself away from the surface from the rear edge of the jet hole and the structure of the jet beam was reduced, which was the influence of the main flow and for J = 4.0 the structure was similar to J = 2.25. But will have a clearer characteristic.

(6) For case of J=12.25, the high heat starts at the immediate downstream area close to jet exit and reaches a maximum heat transfer of 1.5 times when compared to the no jet condition .The heat transfer area in the highest becomes more of the candle flame shape and the result of the flow it is found that the jet will lift itself away from the surface of the jet hole in a circular motion due to the influence of the main current flowing into the front of the jet and the jet was sparse when the distance is far away, this may be influenced by the mainstream.

Acknowledgement

This research was funded by a grant from Ministry of Higher Education of Malaysia (FRGS Grant R.J130000.7824.4X172).

References

[1] Compton, Debora A., and James P. Johnston. "Streamwise vortex production by pitched and skewed jets in a turbulent boundary layer." AIAA journal 30, no. 3 (1992): 640-647.

[2] Zhang, Xin, and Michael W. Collins. "Flow and heat transfer in a turbulent boundary layer through skewed and pitched jets." AIAA journal 31, no. 9 (1993): 1590-1599.

[3] Dai, C., L. Jia, J. Zhang, Z. Shu, and J. Mi. "On the flow structure of an inclined jet in crossflow at low velocity ratios." International Journal of Heat and Fluid Flow 58 (2016): 11-18.

[4] Ahn, Joon, In Sung Jung, and Joon Sik Lee. "Film cooling from two rows of holes with opposite orientation angles: injectant behavior and adiabatic film cooling effectiveness." International Journal of Heat and Fluid Flow 24, no. 1 (2003): 91-99.
[5] Lee, Ki-Don, and Kwang-Yong Kim. "Shape optimization of a fan-shaped hole to enhance film-cooling effectiveness." International Journal of Heat and Mass Transfer 53, no. 15-16 (2010): 2996-3005.
[6] Kwanmon, S.,and Asi, B., 2016, Structure Jet-and –Crossflow Interactions and Cross-plane Entrainment Mechanism of a jet in crossflow, The 30th Conference of Mechanical Engineering Network of Thailand, Songkhla Thailand. TSF0015
[7] Suzuki, Takayuki, Mitsuhiko Nagata, Takaaki Shizawa, and Shinji Honami. "Optimal injection condition of a single pulsed vortex generator jet to promote the cross-stream mixing." Experimental Thermal and Fluid Science 17, no. 1-2 (1998): 139-146.
[8] Qayoum, Adnan, Vaibhav Gupta, P. K. Panigrahi, and K. Muralidhar. "Perturbation of a laminar boundary layer by a synthetic jet for heat transfer enhancement." International Journal of Heat and Mass Transfer 53, no. 23-24 (2010): 5035-5057.
[9] Rao, Yu, Chaoyi Wan, and Yamin Xu. "An experimental study of pressure loss and heat transfer in the pin fin-dimple channels with various dimple depths." International journal of heat and mass transfer 55, no. 23-24 (2012): 6723-6733.
[10] Jabbal, M., and S. Zhong. "The near wall effect of synthetic jets in a boundary layer." International Journal of Heat and Fluid Flow 29, no. 1 (2008): 119-130.
[11] Jovanović, M. B., H. C. De Lange, and A. A. Van Steenhoven. "Influence of hole imperfection on jet cross flow interaction." International Journal of Heat and fluid flow 27, no. 1 (2006): 42-53.
[12] Fric., 1990, “Structure in the near field of transverse jet., “Thesis of California Institute of Technology.
[13] Yuen, C. H. N., and R. F. Martinez-Botas. "Film cooling characteristics of rows of round holes at various streamwise angles in a crossflow: Part II. Heat transfer coefficients." *International Journal of Heat and Mass Transfer* 48, no. 23-24 (2005): 5017-5035.
[14] Fiebig, M. "Vortices, generators and heat transfer." *Chemical Engineering Research and Design* 76, no. 2 (1998): 108-123.
[15] Prince, Simon A., Vahik Khodagolian, Chrisminder Singh, and T. Kokkalis. "Aerodynamic stall suppression on aerofoil sections using passive air-jet vortex generators." *AIAA journal* 47, no. 9 (2009): 2232-2242.
[16] Jacobi, Anthony M., and R. K. Shah. "Heat transfer surface enhancement through the use of longitudinal vortices: a review of recent progress." *Experimental Thermal and Fluid Science* 11, no. 3 (1995): 295-309.
[17] Sun, Xiaokai, Gang Zhao, Peixue Jiang, Wei Peng, and Jie Wang. "Influence of hole geometry on film cooling effectiveness for a constant exit flow area." *Applied Thermal Engineering* 130 (2018): 1404-1415.
[18] Singh, Kuldeep, B. Premachandran, and M. R. Ravi. "Experimental assessment of film cooling performance of short cylindrical holes on a flat surface." *Heat and Mass Transfer* 52, no. 12 (2016): 2849-2862
[19] Aris, M. S., R. McGlen, I. Owen, and C. J. Sutcliffe. "An experimental investigation into the deployment of 3-D, finned wing and shape memory alloy vortex generators in a forced air convection heat pipe fin stack." *Applied Thermal Engineering* 31, no. 14-15 (2011): 2230-2240.
[20] Smulsky, Ya I., V. I. Terekhov, and N. I. Yarygina. "Heat transfer in turbulent separated flow behind a rib on the surface of square channel at different orientation angles relative to flow direction." *International Journal of Heat and Mass Transfer* 55, no. 4 (2012): 726-733.

Penerbit Akademia Baru

Engineering Science and Technology Conference Proceedings

Journal homepage: www.akademiabaru.com/EST.html

Effects of using Different Coal on Combustion Characteristics in Coal-fired Boiler

Open Access

N.A.W. Mohd Noor[1,*], H. Hasini[2] , M.S.H. Mohd Samsuri[1], M.M.F. Meor Zulkifli[1]

[1] Fuels & Combustion Group, Generation & Environment Unit, TNB Research Sdn. Bhd., 43000 Kajang, Selangor, Malaysia
[2] Department of Mechanical Engineering, Faculty of Engineering, University Tenaga Nasional, 43000, Kajang, Selangor, Malaysia

ABSTRACT

Coal is still expected to be the main source of fuel for power generation in the near future even though renewable energy has undergone rapid deployment. This is due to coal reserve are predicted to last around 150 years. However, global reserves of compliant coal are rapidly being exhausted by burgeoning demand and coal-fired power plants have been receiving coals with wide variations of quality. Even though the coals fall within the acceptable specification range, they tend to give significant problems to boiler, such as slagging. Research on the prediction of Bituminous coal combustion performance by using computer simulation such as Computational Fluid Dynamics (CFD) have been widely performed before. However, the combustion performance of Sub-bituminous coals is not widely explored. Thus, this project has been conducted to predict the effect of sub-bituminous coal towards furnace exit gas temperature (FEGT) using CFD. The results of the study show that the use of different types of coal were found to be able to effect the FEGT in boiler based on several case studies. The problems associated with the slagging can be predicted from the FEGT which influence the deposition in boiler furnace and superheater region.

Keywords:
Boiler; coal blending; combustion; furnace exit gas temperature

Copyright © 2019 PENERBIT AKADEMIA BARU - All rights reserved

1. Introduction

Coal reserve are predicted to last around 150 years and coal is still expected to be the main source of fuel for power generation in Malaysia even though renewable energy such as biomass and solar has undergone rapid deployment [1-2]. However, coal-fired power plants have been receiving coals with wide variations of quality usually known as non-preferred coal by station. Even though the coals fall within the acceptable specification range, they tend to give significant problems to boiler, such as slagging. Thus, the combustion of non-preferred coal needs to be efficient to ensure its consumption at the optimum level to reduce the operational risks.

One way to overcome this problem is by predicting the coal combustion performance by using Computational Fluid Dynamics (CFD) [3-6]. Research on the performance of Bituminous coal combustion have been widely performed before either by using computer simulation or by experimental works [7-13]. Most of the equation derived from experimental works to predict slagging and fouling issue also only works for Bituminous coal [14-18]. Therefore, this paper will focus on the combustion performance of Sub-bituminous coals which is commonly used in Malaysia power plants but not widely explored.

* *Corresponding author.*
E-mail address: noorakma@tnbr.com.my (N.A.W. Mohd Noor)

Many researchers utilized numerical modelling to predict combustion behaviour in boilers. Stopford [19] reviewed some of the recent applications of CFD modelling in the power generation and combustion industries. He identified trends and areas where further work is needed. Similarly, Boyd and Kent [20] conducted Computational Fluid Dynamics (CFD) simulation of a fully three-dimensional computer model of a pulverized fuel, tangentially fired furnace. Their results show agreement between the predictions and data is very satisfactory in terms of furnace measurements of temperatures, O_2 concentrations, wall heat fluxes and carbon burnout.

2. Methodology

The numerical modelling of the boiler combustion process was carried out using an ANSYS-FLUENT 14.5 CFD package assuming steady, turbulent and compressible flow. The research commence with the collection of a boiler design data and configuration. CFD models were built based on the design and validated using operational data from the boiler. The model was then be used to predict the behavior of several coals on combustion characteristics such as flame temperature, O2 & CO species composition and furnace exit gas temperature (FEGT) with the same boiler setting which was mass flow of air & coal and burner tilting angle.

Realizable k-ε model was used as the turbulent model and discrete ordinate method (DOM) was selected for radiation model. The mesh generated for the boiler is shown in Figure 1 below. The model was exactly based on the schematic diagram of the boiler. Table 1 shows the coal properties for three coal types: Coal A, B and C.

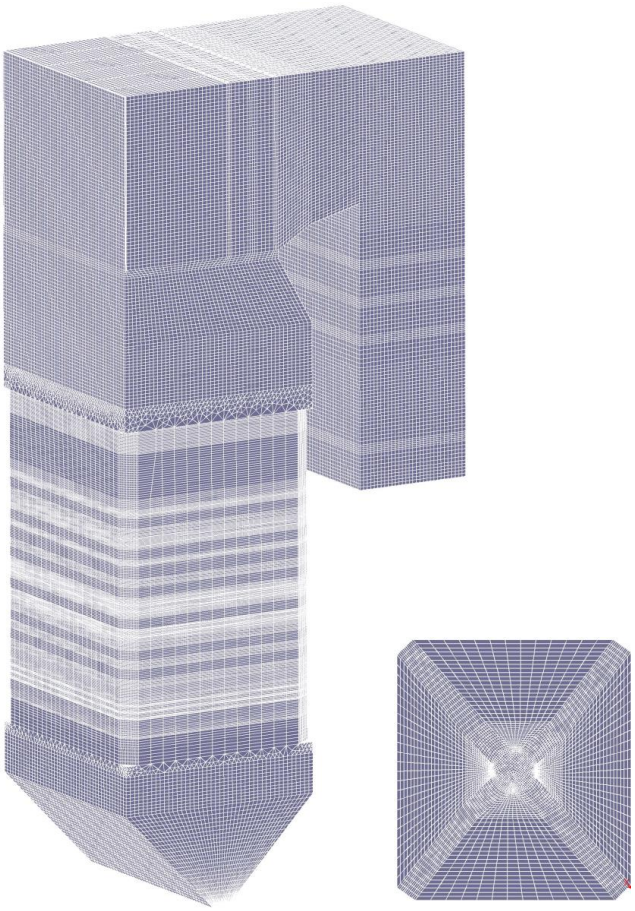


Fig. 1. Mesh generated for the tangential-fired boiler

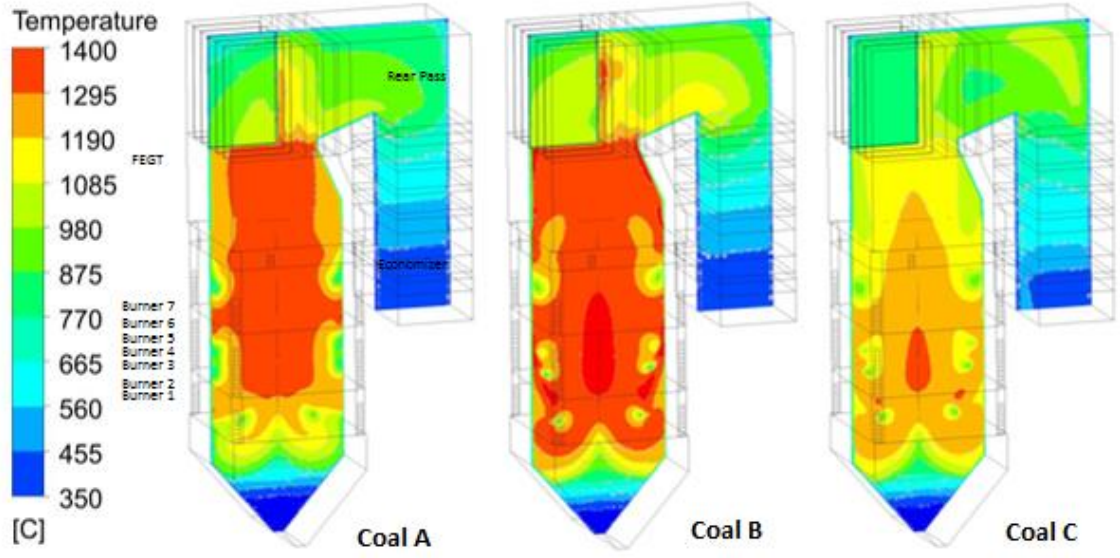
Table 1
The properties of coals

Coal properties	Coal A	Coal B	Coal C
Calorific Value, kJ/kg	5732.57	6122.24	6495.45
Moisture, %	13.30	5.89	6.55
Volatile matter, %	43.80	41.03	40.98
Fixed carbon, %	41.25	43.69	45.32
Ash, %	1.65	9.40	7.16
C, %	61.80	70.80	73.45
H, %	5.63	5.76	5.76
O, %	31.21	21.90	18.81
N, %	1.09	1.34	1.46
S, %	0.27	0.50	0.53

3. Results

3.1 Flame Temperature, Velocity, O_2 and CO Mass Fraction

The flame temperature distribution on the XY plane is shown in Figure 2. The temperature of Coal A case has evenly distributed flame temperature. The fireball develops along the burner zone with peak temperature at the centre of the furnace. For Coal B case, the flame temperature is higher than Coal A case with higher temperature is predicted not only at the centre of the furnace but expanded to the furnace wall. It was found that the flame temperature is much hotter at the upper region of the furnace as compared to Coal A. The flame temperature of Coal C has evenly distributed at the centre of the furnace but has slightly shorter flame length as compared to Coal A and B. The ignition delay of Coal A leads to the development of the high temperature zone in the upper burner levels and above, stretched to the superheater sections. The higher temperature zone may cause severe slagging in the upper level furnace and superheaters. It is also leads to an increase in the flue gas temperature at the rear pass.



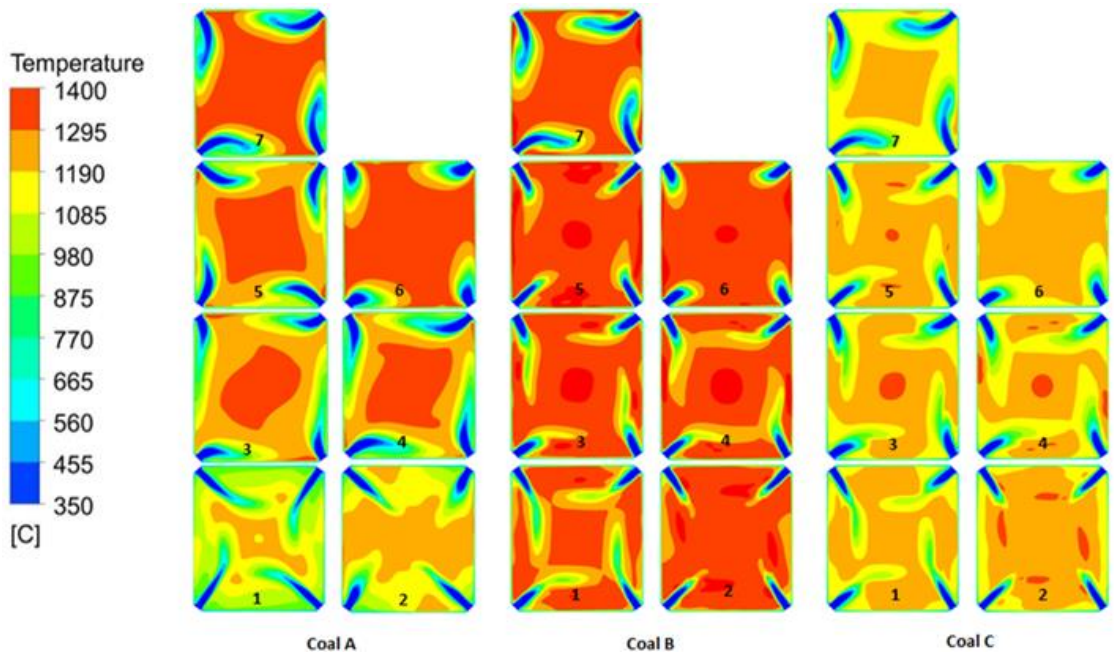


Fig. 2. The flame temperature distribution for Coal A, B and C

As shown in Figure 3, the furnace exit gas temperature (FEGT) for Coal A and B are higher than Coal C case. The FEGT for Coal A and B is below than 1400 °C while for Coal C the FEGT is about 1200 °C. It is expected that Coal A and B have higher chances to have slagging and fouling issue since the temperature at the downstream area are higher.

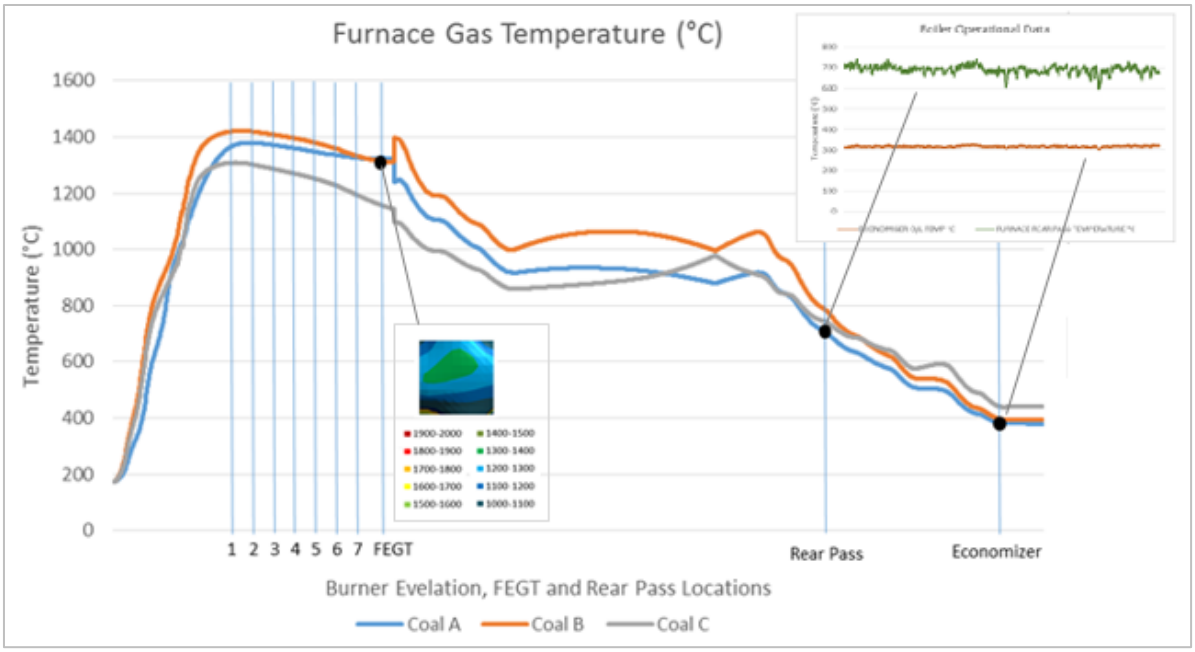


Fig. 3. The predicted furnace exit gas temperature (FEGT) for Coal A, B and C and real operational data for furnace temperature, rear pass temperature and Economizer outlet temperature.

As shown in Figure 4, the fireball develops along the burner zone. The fireball gradually becomes larger from the burner 1 to 7 as more flow is added from the burners. The peak velocity of Coal C started at burner elevation 2 while the peak velocity of Coal A and Coal B are at burner elevation 5 as shown in Figure 5. Adequate vigorous turbulent in the furnace is important for coal

constituents to be exposed to oxygen of the primary and secondary air. When the turbulent is more dominant than the chemical reaction of coal combustion, the optimum combustion would not be achieved and will move to the upper part of the furnace. Inadequate turbulent will cause incomplete combustion in the furnace zone.

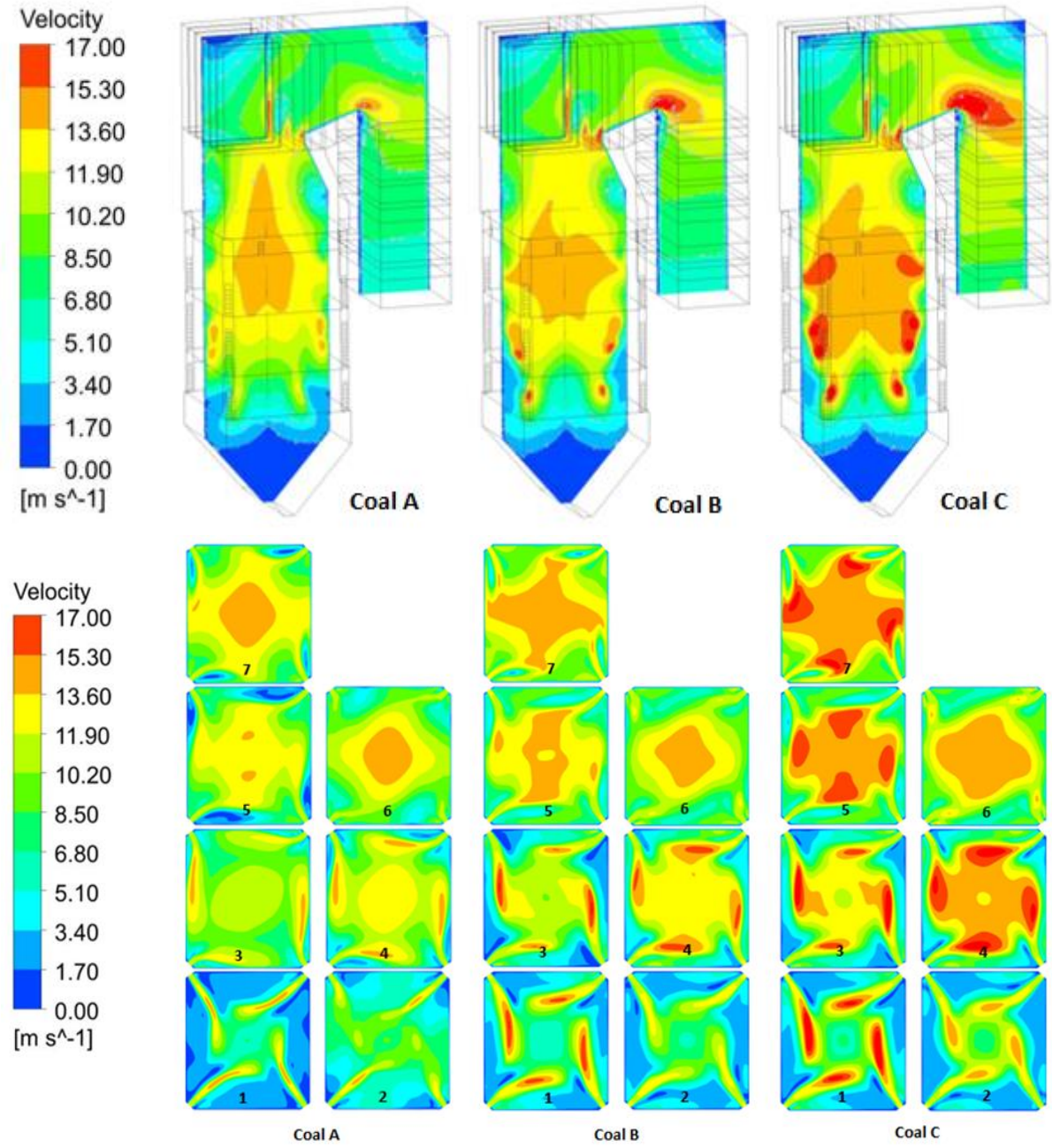


Fig. 4. The velocity magnitude for Coal A, B and C

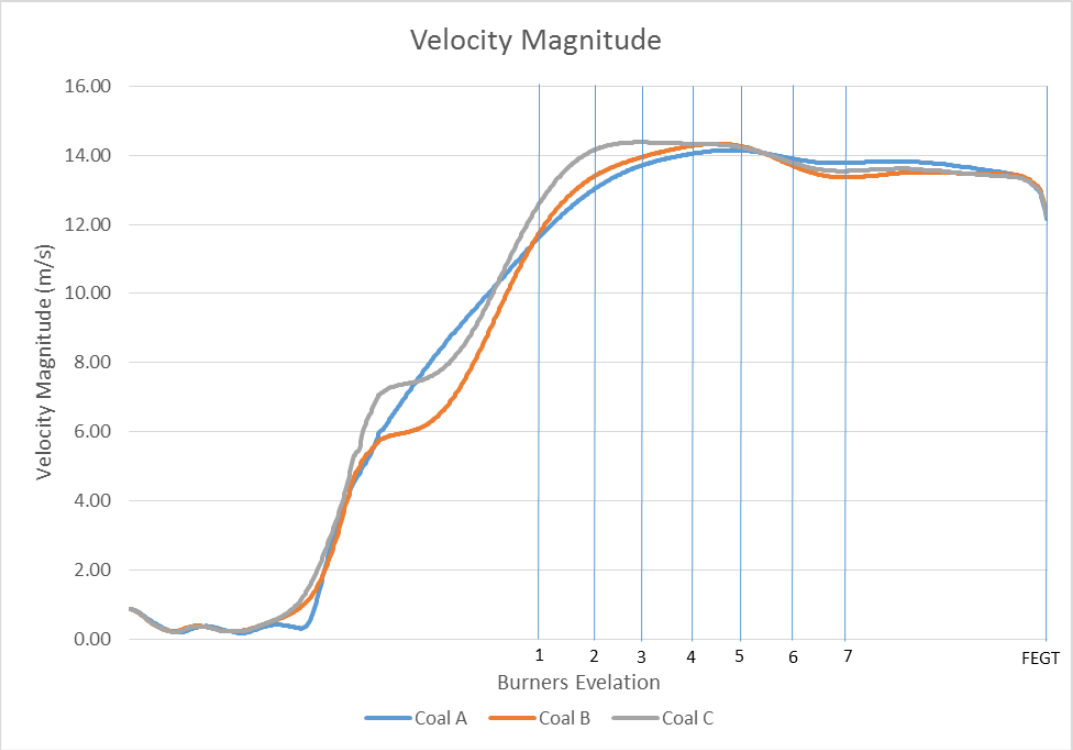


Fig. 5. The peak velocity magnitude for Coal A, B and C

Figure 6 shows the O_2 mass fraction for Coal A, B and C. O_2 is flows from four corners and is available along the wall above the burner zone. It is rapidly consumed by the combustibles released from coal. As a result, O_2 is depleted closer to the wall and completely consumed at the centre of the furnace. For Coal A case, the O_2 distribution is stretched to the top of the furnace and consumed before entering the rear pass. For Coal B and C, there are still remaining O_2 at the rear pass area. The remaining O_2 will flow out as flue gases. It is an indication that the combustion is not optimum or incomplete if too much O_2 in the flue gases.

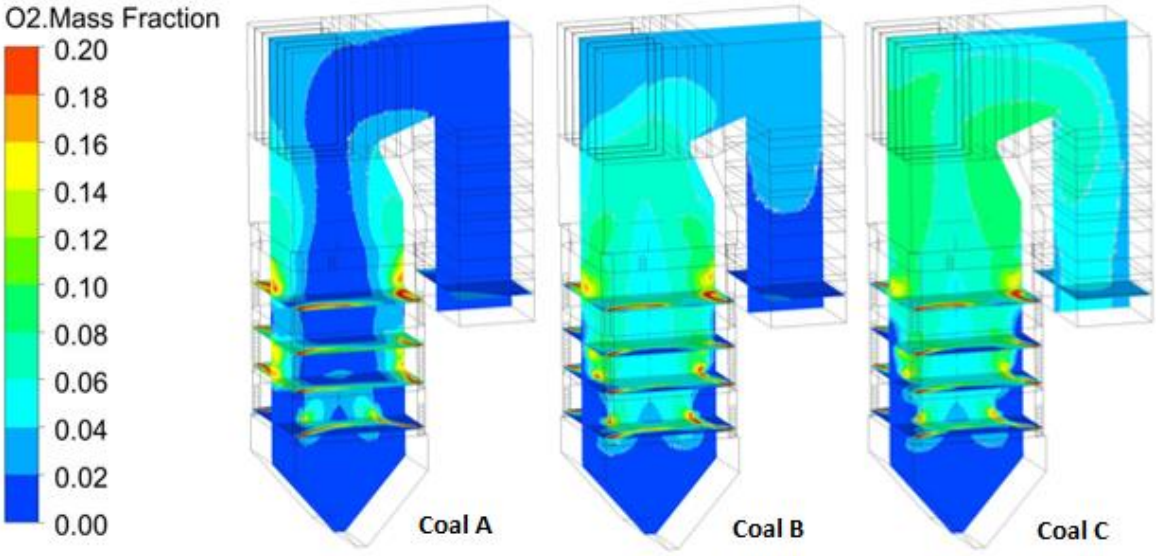


Fig. 6. The O_2 mass fraction for Coal A, B and C

As shown in Figure 7, the mass fraction of CO for the Coal C case is the highest as compared to Coal A and Coal B cases. It is an indication that ignition delay or incomplete combustion in the furnace zone most probably will occur when consuming this type of coal. The completion of gas reactions is prolonged as indicated by several % of CO remaining above the burner zone. The CO concentration above the burner zone is the lowest in the Coal A case which has the maximum flame temperature within the burner zone (refer Figure 2).

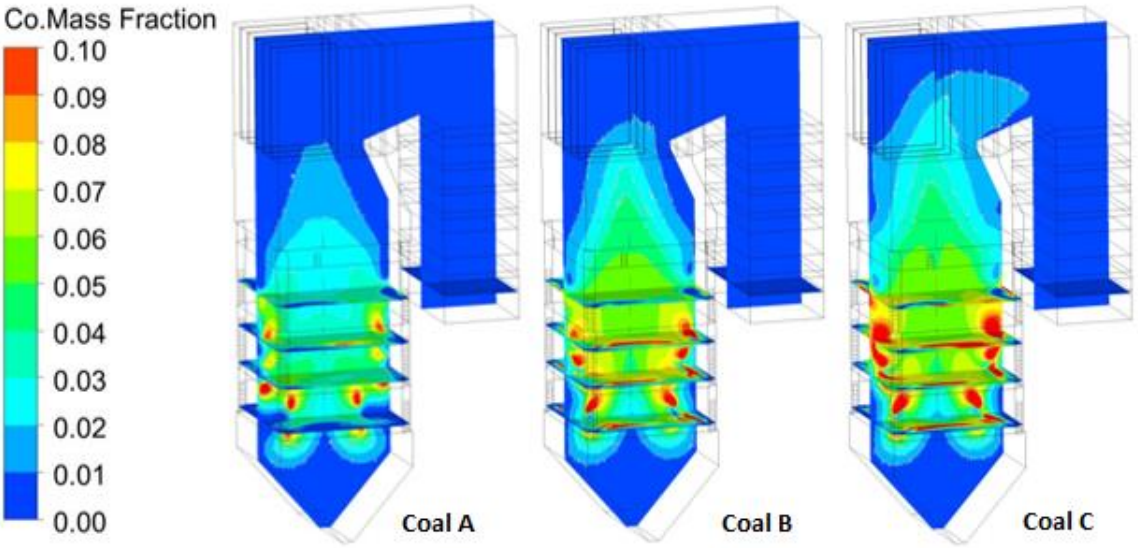


Fig. 7. The CO mass fraction for Coal A, B and C

3.2 The Effect of Operating Parameters

The operating parameters for this simulation is in Table 2. The coal flow rate, stoichiometric ratio, burner tilting angle and flue gas flow rate have a significant influence on the combustion reaction. Too much coal flow will cause incomplete combustion if the amount of air injected to the furnace is unchanged. The burner tilting angle will cause the fireball shift to the upper area of the furnace if the angle is high and the combustion will take place at the upstream of the furnace if the angle is too low. The same combustion situation will be occurred as the burner tilting angle if the flue gas flow rate is too high or too low.

Table 2
The operating parameters

Operating parameters	Coal A, B and C
Coal flow rate, kg/s	60
Stoichiometric ratio	1.2
Burner tilt, °	0
Flue gas flow rate, kg/s	20

4. Conclusions

The flame temperature for Coal B was the highest as compared to Coal A and C, resulting in a higher chances of severe ash deposition to occur. The Coal C case has the shorter flame length and probably required more coal to be consumed. These two condition should be avoided in order to prevent unplanned outage. Inadequate velocity magnitude in the furnace zone will leads to incomplete combustion even though the coal quality is not an issue. As a result, the mass fraction

of O_2 and CO at the rear pass zone is not at the optimum condition. The recommendation to tackle this issue requires adjusting the operating parameters such as coal and air flow and burner tilting angle. Besides that more simulations and combustion testing need to be carried out to verify the combustion reaction which is much more difficult to predict in the real power plant situation.

Acknowledgement
This research was funded by a grant from TNB R&D Fund with collaboration with KEPCO Research Institute (KEPRI).

References

[1] Tillman, David A., Andrew Dobrzanski, and Jason Wong. "Selecting and implementing a fuel blend for scrubbed units at a pulverized coal power plant." *Fuel Processing Technology 141* (2016): 235-242
[2] World coal association, ''Where is coal found'' https://www.worldcoal.org/coal/where-coal-found
[3] Belosevic, Srdjan, et al. "Three-dimensional modeling of utility boiler pulverized coal tangentially fired furnace." *International Journal of Heat and Mass Transfer* 49.19-20 (2006): 3371-3378.
[4] Backreedy, R. I., et al. "Prediction of unburned carbon and NO x in a tangentially fired power station using single coals and blends." Fuel 84.17 (2005): 2196-2203.
[5] Shen, Y. S., et al. "A three-dimensional numerical study of the combustion of coal blends in blast furnace." Fuel 88.2 (2009): 255-263.
[6] Degereji, M. U., et al. "Numerical assessment of coals/blends slagging potential in pulverized coal boilers." Fuel 102 (2012): 345-353.
[7] Asotani, T., et al. "Prediction of ignition behavior in a tangentially fired pulverized coal boiler using CFD." *Fuel* 87.4-5 (2008): 482-490.
[8] Zhou, W., et al. "Two-dimensional computational fluid dynamics simulation of coal combustion in a circulating fluidized bed combustor." Chemical Engineering Journal 166.1 (2011): 306-314.
[9] Sheng, Changdong, et al. "A computational fluid dynamics based study of the combustion characteristics of coal blends in pulverised coal-fired furnace." Fuel 83.11 (2004): 1543-1552.
[10] Choi, Choeng Ryul, and Chang Nyung Kim. "Numerical investigation on the flow, combustion and NOx emission characteristics in a 500 MWe tangentially fired pulverized-coal boiler." *Fuel* 88.9 (2009): 1720-1731.
[11] Himachandra, Jaladi, and L. S. V. Prasad. "CFD Analysis of a 210 MW Tangential Fired Boiler." *International Journal of Scientific Engineering and Technology* 6.1 (2017): 39-44.
[12] Kumar Manish and Santi Gopal Sahu. "Study on the effect of the operating condition on a pulverized coal-fired furnace using computational fluid dynamics commercial code." Energy & Fuels 21.6 (2007): 3189-3193.
[13] Chen, Lei, Sze Zheng Yong, and Ahmed F. Ghoniem. "Modeling the slag behavior in three dimensional CFD simulation of a vertically-oriented oxy-coal combustor." Fuel processing technology 112 (2013): 106-117.
[14] Terry W., Elliot L.., Sanders D. & Conroy A. (2001). A Review of the State-of-Art in Coal Blending for Power Generation.
[15] Couch, Gordon. Understanding slagging and fouling in pf combustion. London: IEA Coal Research, 1994.
[16] McLennan, A. R., et al. "Index for iron-based slagging for pulverized coal firing in oxidizing and reducing conditions." *Energy & fuels* 14.2 (2000): 349-354.
[17] Erickson, T. A., et al. "Modelling of fouling and slagging in coal-fired utility boilers." *Fuel Processing Technology* 44.1-3 (1995): 155-171.
[18] Wall, T. F., et al. "Coal ash fusion temperatures—new characterization techniques, and implications for slagging and fouling." *Progress in energy and combustion science* 24.4 (1998): 345-353.
[19] Stopford, Philip J. "Recent applications of CFD modelling in the power generation and combustion industries." Applied Mathematical Modelling 26.2 (2002): 351-374.
[20] Boyd, R. K., and J. H. Kent. "Three-dimensional furnace computer modelling." Symposium (International) on Combustion. Vol. 21. No. 1. Elsevier, 1988.

Penerbit Akademia Baru

Engineering Science and Technology Conference Proceedings

Journal homepage: www.akademiabaru.com/EST.html

Numerical Approach Used To Evaluate The Damage Structural Capacity Of a Composite Concrete Slab Under Fire By Confirming Its Behaviour

Open Access

Gede Adi Susila[1,*] , Made Sukrawa[1], Rivelino Romario Ximenes Baptista[2]

[1] Department of Civil Engineering, Engineering Faculty, Udayana University, 80361, Bukit Jimbaran, Badung, Bali, Indonesia
[2] Magistes of Civil Engineering School, Faculty of Engineering, Udayana University, 80234, Kampus Sudirman, Denpasar, Bali, Indonesia

ABSTRACT

This paper provides numerical analysis of typical composite structural system which interaction between concrete slab and steel sheet deck under fire has been investigated. An experimental work investigated by Lim-Wad in the year 2002 has been taken into account in order to examine the behaviour of the steel deck plate before collapse. Structural load capacity as well as damage capacity under fire has to be confirmed the previous result of experimental study. Numerical modelling using Abaqus has been calibrated some basic parameters only without pretty much work on plasticity modelling approach. Typical finite element method (FEM): Abaqus package has used to be applied for a certain distribution of heat (changes in temperature gradually) up to 3 (three) hour exposed causes thermal expansion or contraction of composite material, resulting in strain and stress confirmation relates to the deformation of the steel deck. The result of study found significant agreement between experimental and numerical work. Confirmation for both experimental and numerical method was necessarily under control based on the conclusion for both material structures such as reinforcement, sheet deck and the concrete experiences and expansion as well decreasing in its mechanical properties. Certain level of structural damage found to be depends upon the construction experiences (directly exposed) to a fire, the strength of the structure will clearly decrease.

Keywords:
Structural damage capacity; thermal expansion; FEM: Abaqus

Copyright © 2019 PENERBIT AKADEMIA BARU - All rights reserved

1. Introduction

In this study, for a decade a structural component and its material technology along with construction methods used to obtain structural innovations such as the use of a steel deck plates which have a lighter in weight and economically efficient and effective that these innovations can carry the design of working load and did not reduce the strength of the floor deck during the servicibility load working for the ages of the building. These innovation was known as a composite plate with many advantageous in terms of implementation because the plate directly rests on steel beams so that it requires fewer scaffolding. The steel sheet deck has also been functioned as a permanent formwork. Therefore, the construction phase may be reduced and acceleration of whole construction progress can be achieved, because there is no need to install and dismantle scaffolding and no need to dismantle formwork (Anonymous, 2000). That is a typical composite

* *Corresponding author.*
E-mail address: ochakiswara6@gmail.com (Gede Adi Susila)

plate structure which is for high rise structures ideally many floor and high spacing between floors has to be installed which are very difficult to install if the used of scaffolding.

Besides the advantages above, steel also has several disadvantages including being susceptible to corrosion and not being fire resistant. If a steel construction experiences a fire or is directly exposed to a fire, the strength of the structure will decrease (Nwosu & Kodur, 1999). These is a stuctural component made of steel sheet deck combined with concrete added together become a composite material of slab/floor deck which are widely used for buildings or bridges. The used of the composite floor deck was very popular since these structural component was faster and cheaper to construct compared to the conventional concrete slab. For the composite deck, there is no form work has used during the construction phase and typically steel deck plates are used to be put at the bottom of the deck as mainly as taken to be a possitive reinforcement within the bending mechanism of the deck. The steel sheet deck used to provide better performance of the floor deck, even though thickness of the plates may be reduced or thinner which may be produced a lighter in construction due to a high tensile strength of material used. However, what if the vast area of the deck exposed fire during the disaster event such as explosion gas at the kitchen, janitor area, etc. The physical properties under fire will be the major concerned since heat transfer mechanism occurred at the various phase during the expose time of fire.

Steel deck plates are often considered as a substitute for positive reinforcement in a plate planning, so that no additional reinforcement is needed at the positive moment of the plate. The problem is, when the steel deck is exposed to fire (fire), then the steel deck plate which was originally as a substitute for positive reinforcement will not function again as originally planned. Steel deck plates reach the melting point due to fire will not be able to withstand the load above it, so in the initial planning required additional reinforcement as an additional safety factor.

To examine how the structure of reinforced steel and reinforced concrete composite structures, studies related to fire resistance on the structure have been carried out. Especially for experimental research related to fire requires adequate testing facilities, observation with high accuracy when conducting tests, and the cost is quite expensive to obtain a data. Then, if there is an experimental test reviewing more parameters, it also requires a greater cost. An analytical simulation approach can be an alternative in conducting research. Many technological developments and computer programs can now be used as research aids, such as finite element-based programs. In an effort to see the behavior of this steel deck plate structure, the structure modeling was done in the ABAQUS program. The behavior in question is the behavior of the steel deck plate structure with additional and no reinforcement in positive moments when under load temperature or during a fire

To determine the suitability of modeling techniques in ABAQUS with the results of experiments in analyzing stress and strain on composite steel deck plates due to temperature or fire loads

2. To determine the magnitude of deflection that occurs on composite steel deck plates with and without reinforcement in positive moments when subjected to temperature or fire

3. To determine the effect of adding reinforcement to the stiffness of composite steel deck plates when under load temperature or fire

Plates are rigid planar structures typically made of monolith material which are of a small height compared to other dimensions (Schodek, 1998). The plate is a structural element that has a relatively small thickness when compared to the width and length. The load acting on the plate has the property spread out in many directions.

1.1 One-Way Plate

These plates with one-way principal reinforcement will be found if the plates are more dominant to hold the load in the form of a bending moment in a one-way span. Examples of one-way plates are cantilever plates and plates supported by two pedestals. Because the bending moment only works in one direction, that is in the direction of the L span (see Figure 1), the principal reinforcement is also installed in one direction in the direction of the L span. To maintain the position of the principal reinforcement (at the time of concrete casting) does not change from its original place, an additional reinforcement is also installed in the direction perpendicular to the principal reinforcement. This additional reinforcement is called reinforcement. The position of the main reinforcement and reinforcement for always crossing perpendicular, the main reinforcement is placed close to the outer edge of the concrete, while the reinforcement reinforced mounted on the inside and attached to the main reinforcement. Right at the location of the crossing, the two reinforces are fastened with bendrat wire. The reinforcement function for, in addition to strengthening the position of the main reinforcement, is also a reinforcement for anchoring concrete cracks due to shrinkage and concrete temperature differences.

Steel deck plate is a combination plate that uses steel deck instead of positive moment reinforcement (bottom reinforcement), where the steel deck (steel plate) also functions as a formwork plate and work floor, while for negative moment reinforcement can use ordinary steel reinforcement or use wiremash. This wave plate shaped sheet panel is made of structural steel with thickness 0.70 - 1 mm which is evenly galvanized. Steel deck plates when combined with concrete mixes will form a perfect composite floor plate system.

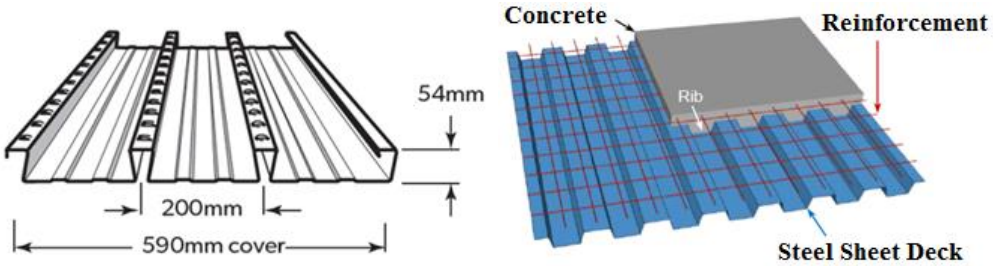


Fig. 1. (a) Steel Sheet Deck [1] and (b) Composite: Sheet Sheet Deck, Steel reinforcement bar and Concrete

Steel deck plates also function as fixed formwork and building ceilings. Can be ordered according to the length needed to facilitate the installation and transportation of the recommended maximum length of 12.00 meters, according to the smartdeck brochure (Lysaght, 2016). The steel deck plate is equipped with a protrude shape system and is a refinement product from steel deck products on the market, manufactured using sophisticated machinery to produce high quality products. Material requirements if following the technical specifications according to [1] namely High-Tensile steel base material, minimum melting stress of steel deck plate 5500 kg / cm^2 or 550 MPa. The thickness of the steel deck plate varies from 0.7 mm - 1.2 mm

Composite plates do have several advantages, but one of the weaknesses of steel deck plates is susceptible to rust and fire. In a fire test using the ISO 834 standard, the temperature of the steel deck plate reaches 750^o C within 30 minutes of combustion. The increased combustion temperature causes the strength of the steel deck plate to decrease and the attachment between the concrete and the steel deck plate has been lost [2]. The nature of concrete when burned is very dependent on the aggregate or mixture of materials used. Andesite, pumice (clinker) and pozolanic materials such as fly ash, red brick powder and the like have properties that are more resistant to high temperatures. While the aggregate of limestone (calcite), obsidian and the like will quickly

change its nature and shape when exposed to heat so that it will expand and eventually it will explode. Concrete strength will decrease significantly starting at temperatures of 200ºC and will be followed by physical damage at temperatures above 450ºC accompanied by changes in physical properties such as cracks, spalling, deflection and other shape changes [3]. In the event of a composite plate fire resulting in a change in shape ie sagging especially in a burdened condition. Based on the fire resistance testing guidelines for building structure components for fire hazard prevention in houses and buildings [4], [5] which regulate deflection requirements for floor components that have fire resistance, as follows:

Table 1
Resistance of plate components relates the duration of combustion

1 hour	2 hour	3 hour
$\delta \leq \frac{L^2}{10000}\ (cm)$	$\delta \leq \frac{L^2}{6000}\ (cm)$	$\delta \leq \frac{L}{20}\ (cm)$

where, δ = deflection (cm); L = span (cm)

1.2 Thermal Effects

Changes in temperature cause the expansion or contraction of material, resulting in thermal strain and thermal stress.

$$\varepsilon_T = \alpha.(\Delta T) = \alpha.\ (t_1 - t_o\ ) \quad (1)$$

where; (ε_T) thermal strain, (α) Coefficient thermal expansion= 1/°C, (ΔT) thermal changes in °C, (t_o) initial set of temperature in °C, (t_1) final set of temperature in °C. The coefficient of thermal expansion or expansion coefficient must be taken according to (SNI-1729, 2015). For steel structures and strengthening one, temperatures calculated at below 150° F (65° C), the thermal expansion coefficient must be 7.8 x 10^{-6}/°F (1.4 x 10^{-5}/°C), for normal concrete calculated temperatures calculations at below 150°F (65°C), the thermal expansion coefficient must be 1.0x 10^{-5} / °F (1.8 x 10^{-5} / °C).

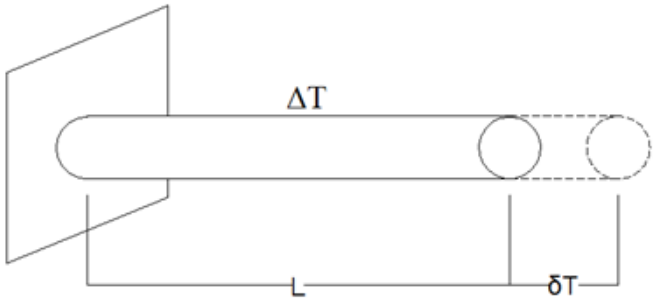


Fig. 2. Length increase due to increased temperature
Sources: [6]

An isotropic and homogeneous material is assumed to experience a uniform temperature increase. From this condition it can be calculated with a formula equation as follows:

$$\delta T = \varepsilon T.L = \alpha.(\Delta T).L \quad (2)$$
$$\sigma = E.\alpha.(\Delta T) \quad (3)$$

where; (ε_T) thermal strain, (α) Coefficient thermal expansion= 1/^oC, (ΔT) thermal changes in ^oC, (δ_T) change in length (m), (L) Length initial set of temperature in oC, (t1) final set of temperature in oC.

The provisions of thermal stress analysis are used in FEM (finite element method) according to (Liu, 2003) are (1). need to determine the values of α (coefficient of thermal expansion) and ΔT on the related element (which changes in temperature), (2). need to determine the values of α (coefficient of thermal expansion) and ΔT on the related elements (which changes in temperature). The difference in temperature during heating a material is a major cause of thermal stress.

There are 4 important stages in the process of fire. These stages can be seen in Figure 3 below. The first stage is the initial ignition phase (incipient ignition), where potential fuel heating occurs. The next stage is the phase of development (growth), in which the flame begins to appear burning.

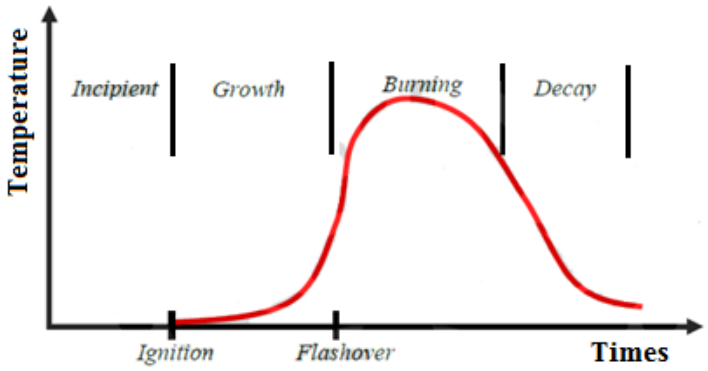


Fig. 3. Stages - stages in the development of fires [7]

During the growth of the fire, so that the fire reaches a high enough temperature (around 600 ° C), the fire will develop perfectly and reach a phase called the ignition condition (flashover), which signifies the arrival of the third phase, the combustion phase (burning). In this phase, the temperature and heat changes that occur are very large, occur on all surfaces exposed to fire, and the availability of ventilation will determine the release of heat that occurs. This section is the most dangerous stage that can be fatal to building elements. After all this time, fuel and fire were happens eventually will decrease, and even the fire will gradually disappear in the next phase, which is called the decay period. This reduction phase usually occurs when 70% of the available fuel is already used. It can be seen that a fire that occurred at a place will automatically disappear or stop (extinguish). However its spread must be prevented as much as possible, because fire can continuously spread in all directions, both vertical and horizontal. This distribution will be followed by a repetition of the fire cycle, namely ignition, growth, combustion, and decay.

Table 2
Relationship of fire load when burning

Average Fire Load (psf)	Average Fire Load (kg/m^2)	Equivalent Fire Endurance (Hour)
5	24,4	0,5
7,5	36,6	0,75
10	48,8	1
15	73,2	1,5
20	97,6	2
30	146,5	3
40	195,3	4,5
50	244,1	6
60	291,9	7,5

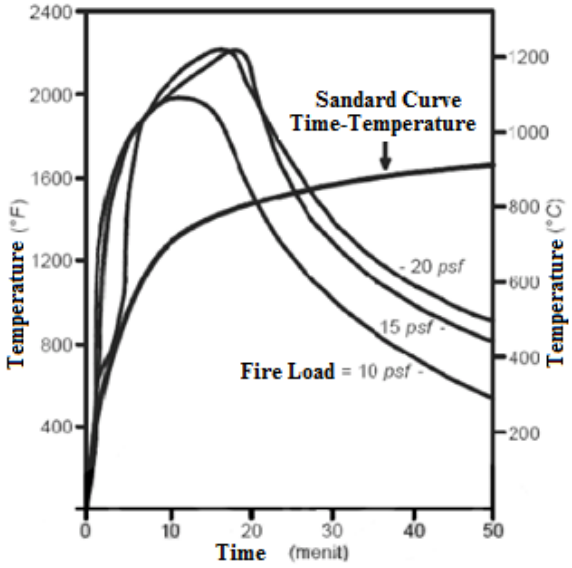


Fig. 4. Curves; relationship between time and temperature due to fire [7]

1.3 Heat Transfer of the Structures

Heat transfer generally involves three processes, namely: conduction, convection and radiation, which can occur separately or together depending on the circumstances.

1. Conduction is a mechanism of heat transfer in solid materials. Good material conducts heat, heat is transferred by involving the interaction of free electrons. In materials that are difficult to transfer heat, heat is channeled through mechanical vibrations from the molecular lattice. Heat conduction is an important factor in channeling heat to solid surfaces. Under strong (stable) conditions, heat transfer by conduction is directly proportional to the temperature change between two points and thermal conductivity.

$$\hbar = \lambda d\vartheta/dx \quad (4)$$

where, heat flow per unit area (W/m^2), ħ, thermal conductivity (W/m.K), λ, Temperature (°C), θ, and distance in heat flow (m), x.
The heat transfer of a dimension by conduction without internal heat release is regulated in the following equation:

$$\delta^2 \vartheta/\delta^2 x = (1/\alpha)(\delta\vartheta/\delta t) \quad (5)$$
$$\alpha = \lambda.\rho.c \quad (6)$$

where, t=time (s), x = Distance in heat flow (m), θ = Temperature (°C), α = thermal diffusivity (m^2/s), λ = thermal conductivity (W/m.K), ρ = density (kg/m^3), c = heat capacity (J/Kg.K)

2. Convection is the transfer of heat through the movement of liquids, either gas or liquid. For certain conditions, heat transfer is proportional to the temperature difference between materials, so the heat flow per unit area can be calculated using:

$$\hbar = \alpha_c \Delta\vartheta \quad (7)$$

where, ħ = heat flow per unit area (W/m^2), α_c = Convection transfer coefficient (Wm^{2}K), Δθ = temperature difference between liquid and solid objects (^{o}C)

3. Radiation is the transfer of energy from electromagnetic waves that can pass through a vacuum. Radiation is the main mechanism for the transfer of heat from a fuel to a surface of an object. The transfer of fire from a burning building to an adjacent building due to hot smoke arising from the burning. The heat flow per unit area can be calculated by:

$$\hbar = \Phi\varepsilon\sigma[(\vartheta_e\ 273)^4 - (\vartheta_r\ 273)^4] \quad (8)$$

$$\varepsilon = 1/(1/\varepsilon_r + 1/\varepsilon_e - 1) \quad (9)$$

where, ħ = Heat flow per unit area (W/m^2), Φ=Configuration factor, ε=Emissivity, σ= Stefan-Boltzmann constant (5.67x10-8 W/m^{2}K^4), εr=Receiver emissivity, εe=Emissivity of the transmitter.

1.4 Effect of Temperature on Steel Performance

Under fire conditions, the temperature in the steel will increase, resulting in both the thermal expansion of the rod and a decrease in its mechanical properties. The level of damage it produces depends on several factors, both from the type of steel used and the protective conditions it has. The duration and natural conditions at the steel touch point with fire will affect the spread of temperature rise on the steel cross section. Steel material does not burn, but its behavior, which absorbs and distributes heat to all parts, needs attention. Look at the strength curve for rising temperatures [8] as follows

From the curve of the strength of the steel against the rise in temperature (Figure.5), it is seen when the temperature rises to exceed 800^o F or 427^o C the strength of the load is reduced. Even when the temperature continues to rise to 1200^o F or 649^o C, the strength seen based on the melting strength parameter (F_y), only 30% compared to the strength at room temperature. At high temperatures, both the flexural and tensile strength of a steel structure will decrease, as does the modulus of elasticity.

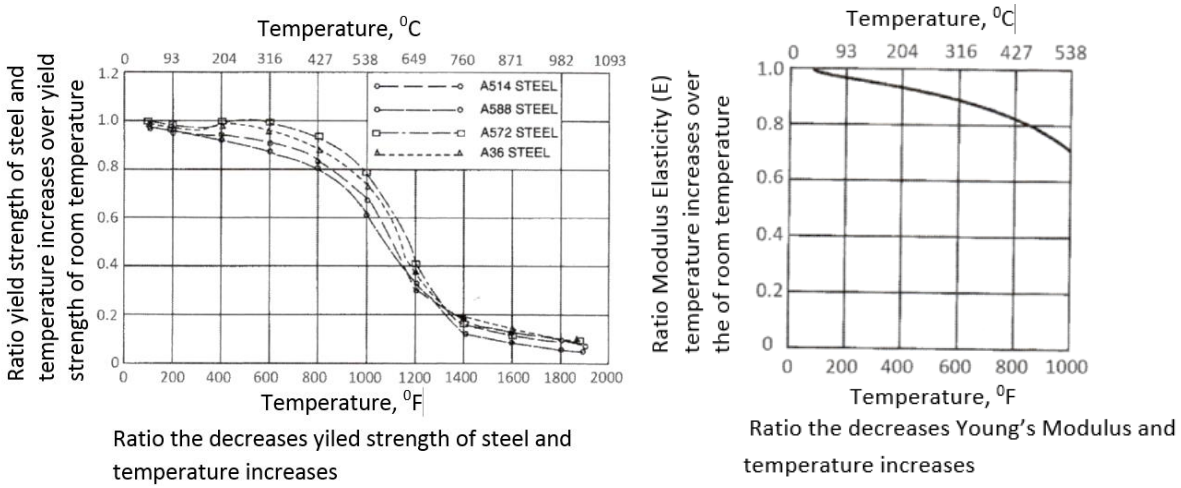


Fig. 5. (a) Effect of temperature on steel and (b) Elastic modulus reduction ratio (E) [8]

Figure 5(b) shows a decrease in the modulus of elasticity at temperature (Brockenbrough & Merritt, 2011). When the temperature reaches 800o F or 427ºC the modulus of elasticity drops

dramatically. When a fire in a steel building and an increase in temperature up to 649o C, the structural system must have experienced a collapse because it is not strong enough to withstand the burden of the weight alone. Steels with high carbon percentages, such as A36 steels, exhibit strain aging at temperatures from 300° F to 700o F (150° C to 370° C). This can be seen from the relative increase in melting point and tensile strength in the temperature region. If the temperature has reached 500° F to 600° F (260° C to 320° C), the tensile strength will increase by approximately 10% above the strength at room temperature and the melting point will return to the melting point at room temperature. Weathering strain that occurs can also result in ductility of the steel material to be decreased. At temperatures of 600° F to 800° F (320° C to 430° C), it will cause brittle formation of the structure. If heating is carried out continuously until past 1000o F (540° C) the carbon compound and its alloying elements will settle, this will cause the microstructure to become more brittle [9].

1.5 Refractory Steel Fireproof Steel Material

Most of steel profiles can perform the same without having to be given a protective layer. The materials contained in a steel material greatly affect the nature, characteristics and behavior. Some materials can change the properties of a steel material such as carbon (C), manganese (Mn) and silicon (Si). According to [10] steel can be classified based on its chemical composition such as carbon content and the alloy used [5], (Amanto & Daryanto, 1999, [11], [12], [13]

2. Methodology (Finite Element Analysis)

A modelling approach to the finite element method (finite element method) is an analysis of approaches based on the assumption of transition or stress assumptions, it can even be based on a combination of the two assumptions earlier in each element [14] In general, the finite element method has several advantages, as follows:

1. The finite element method can be used in various problems, such as heat transfer, voltage analysis, magnetic field analysis and much more.
2. The finite element method does not limit the geometry of objects, so any object can be modeled.
3. Boundary and loading conditions that are carried out are also not restricted.
4. Material data which is defined in the element is also not limited, so that the element of the material data can be changed as needed.
5. Can combine several types of elements, for example reinforced concrete, [14] (Liu, 2003)

2.1 Analysis of Solid 3-Dimensional Elements

In the structural analysis of the finite element method, the element greatly influences the calculation, in this study composite steel deck plates are idealized as 3-Dimensional Solid elements. According (Suhendro, 2000), the types of elements in 3-Dimensional solid that are most widely used are 3 types, namely: Rectangular Solid Element (RS-8) Is a type of Hexahedral element, which forms this element like a brick (brick) which has a nodal point of at least 8 pieces. This element has 3 degrees of freedom at each nodal point, so that overall this element has 24 degrees of freedom. In its application, this element is only used to analyze the regular structure because it resembles a cube. Pictures of these elements can be seen in Figure 6.

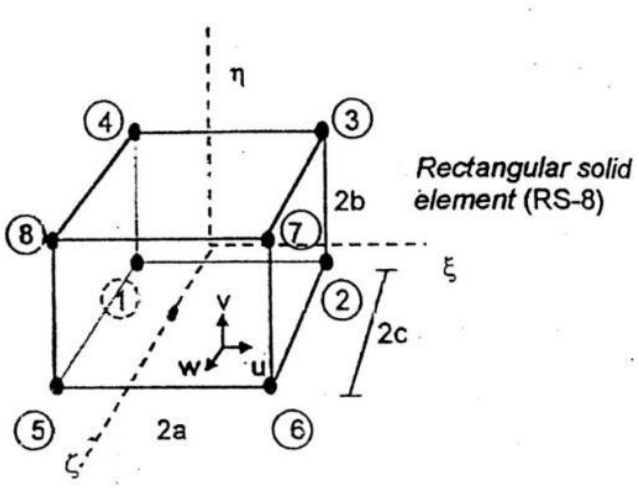


Fig. 6. Element rectangular solid (RS-8) relates to the concrete modelling Suhendro, 2000)

2.2 Shell Element Analysis

The shell element is used in modeling area-shaped objects. This element is usually used in the modeling of floor plates, walls, column details, beam details, and other structural part details. In the ABAQUS [15-17] software, the material in the shell element modeling can be made in homogeneous conditions and layered at any thickness of the element. Homogeneous conditions mean that per unit thickness of the model uses only one type of material, whereas in layered conditions, users can create multiple layers with different material types per unit thickness of the element's plane. Basically, shell elements can be categorized into three, namely membranes, plates, and shells.

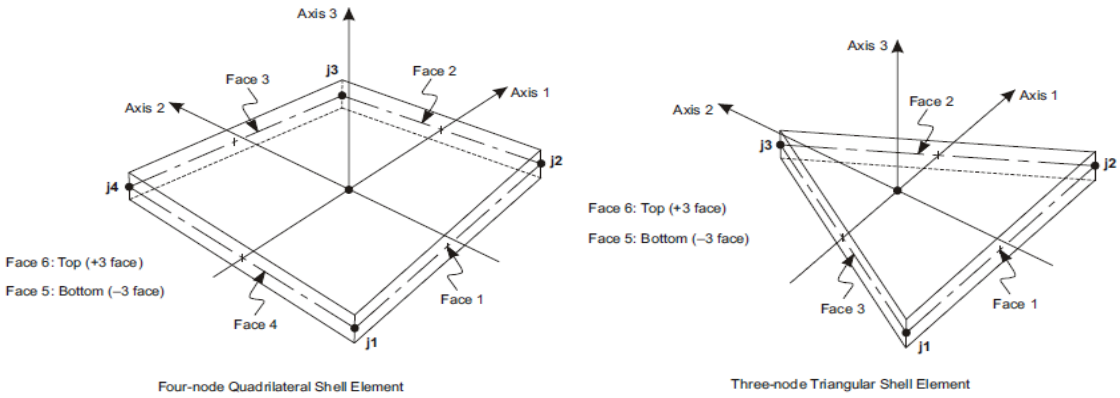


Fig. 7. Shell element relates to the deck modelling [18]

2.3 Experiments Regarding Temperature or Fire Loads

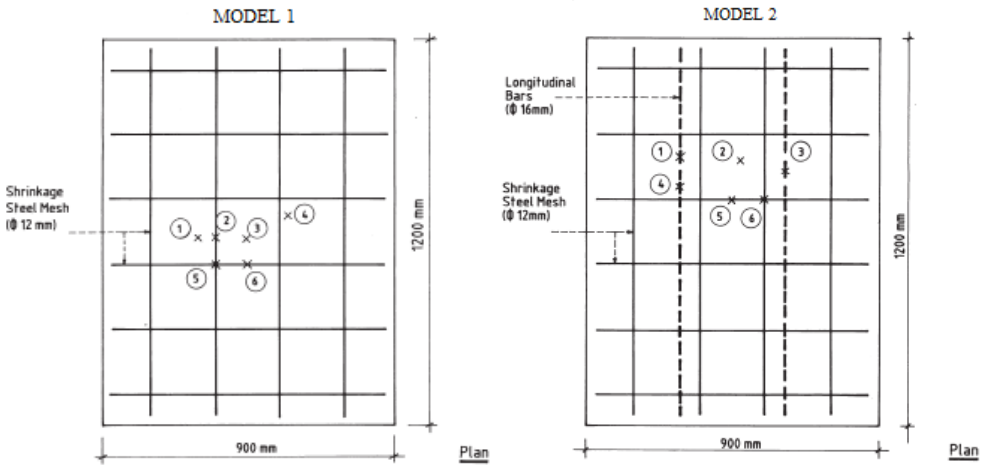


Fig. 8. Composite modelling [19] [20]

This research is about testing to develop basic information about the behavior of composite plates using fire testing. This research was conducted by testing in a laboratory with 2 experimental models. Both models have the same dimensions of 1200x900x110 mm with Ø12 mm wiremash reinforcement as shown in Figure 8 and the thickness of the steel deck plate is 1 mm. In Model 1 without the addition of longitudinal reinforcement and model 2 with the addition of longitudinal reinforcement with Ø16 mm as shown in Figure 8. Coarse aggregate derived from stone [21].

In the burn test conducted at the Department of Civil Engineering, Salford University and the test specimens were placed vertically as shown in Figure 9. After 13 minutes of testing, the furnace temperature averages 710 ° C. Evaporation occurs in the upper corner of the panel and spreads throughout the entire plate. After 20 minutes of combustion, with an average furnace temperature of 770 ° C, a cracking sound was heard, and water began to drip from the cracks of the furnace. Evaporation, the cracking process, and water droplets occur 75 minutes after the start of the test.

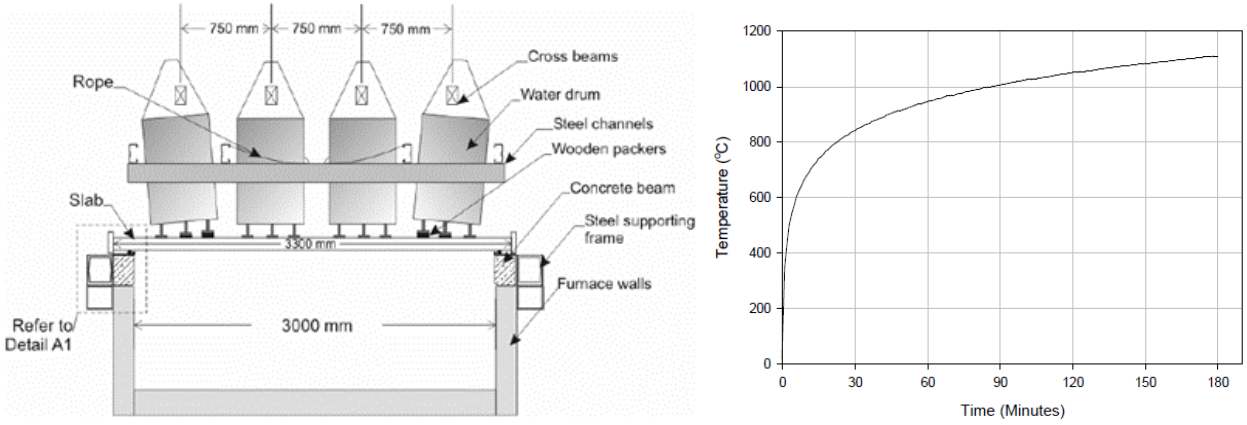


Fig. 9. Composite modelling [19] [20]

Table 3
Experimental data [22]

Steel decking/ joinsts	Steel deck/joist thickness	Yield stress
Dimond Hibond	0.75mm	550 Mpa
Traydec	0.75mm	550 Mpa
Speedfloor	3mm	350 Mpa

In Table 3 are variations of reinforcement used on composite plates when tested for combustion. In this test, the plate specimen used is 3.3 mx 4.3 m and has a thickness ranging from 90 mm to 130 mm. In Figure 10 and Table 3 are the dimensions of the plates used in the burn test.

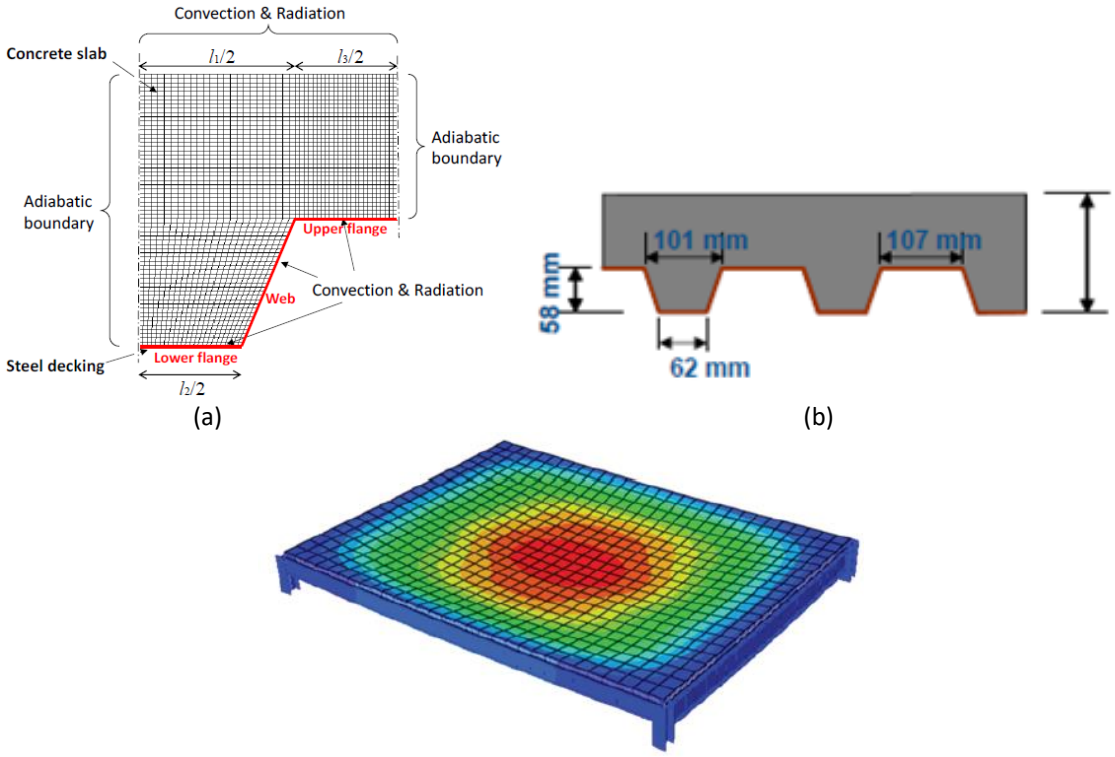


Fig. 10. Composite modelling [19] [20]

2.4 Material Structure Data

Material properties of reinforced concrete used in this study are described as follows: 1. Concrete compressive strength (f'c): 30 Mpa, 2. Concrete elastic modulus (Ec): 25742,96 Mpa, 3. Specific gravity of reinforced concrete (γc): 2400 kg / m34. Concrete Conductivity Coe, fficient: 0.8 W / m K, 5. Heat transfer: 1000 W / (m2.K)

Material properties of steel plates and reinforcement used in this study are using ASTM 615 grade 60: 1. Minimum melting stress (fy) of steel plate: 550 Mpa, 2. Minimum breaking voltage (fu) of steel plate: 620 Mpa, 3. Minimum melting stress (fy) reinforcement: 565 Mpa, 4. Minimum breaking voltage (fu) reinforcement: 635 Mpa, 5. Modulus of elasticity of steel (E): 200,000 Mpa, 6. Steel specific gravity (γs): 7850 kg / m3, 7. Steel Conductivity Coefficient: 50.2 W / (m.K), 8. Heat transfer: 480 W / (m2.K)

The coefficient of thermal expansion used in this study for steel deck plates and reinforcement is 1.4 x 10-5 / ° C (SNI-1729, 2015). The coefficient of thermal expansion for concrete is 1.8 x 10 -5 /

oC (SNI-1729, 2015). The emissivity used for this study was 0.1. In modeling using ABAQUS the steps to enter material data are used as follows: 1. Concrete Plate Material a. Select the Materials - create - Mechanical - Density = 2400 Kg / m3 = 23535.96 N / mm3 feature

3. Results

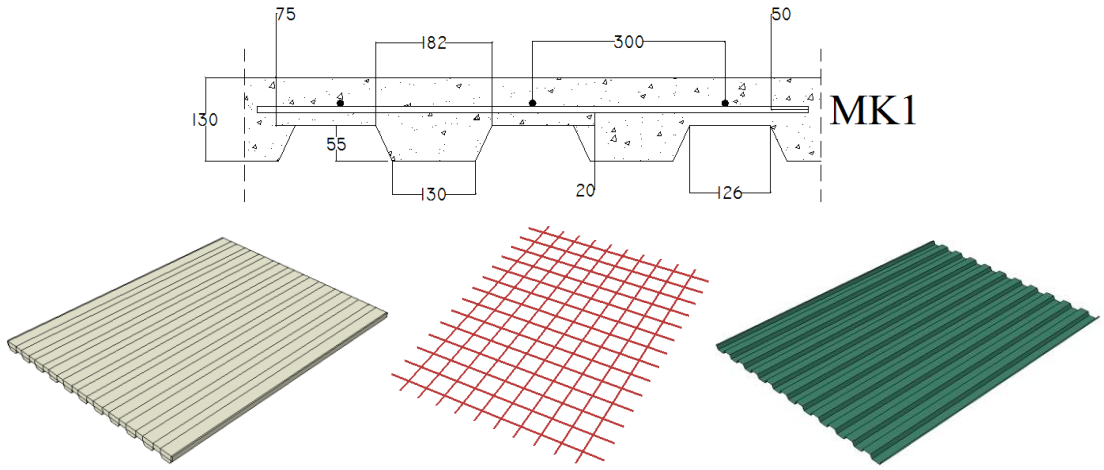
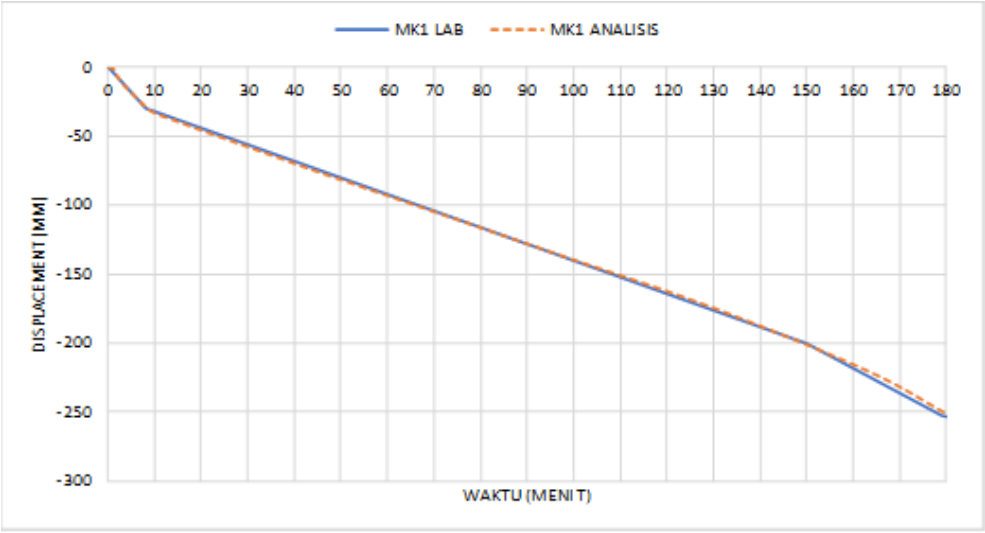


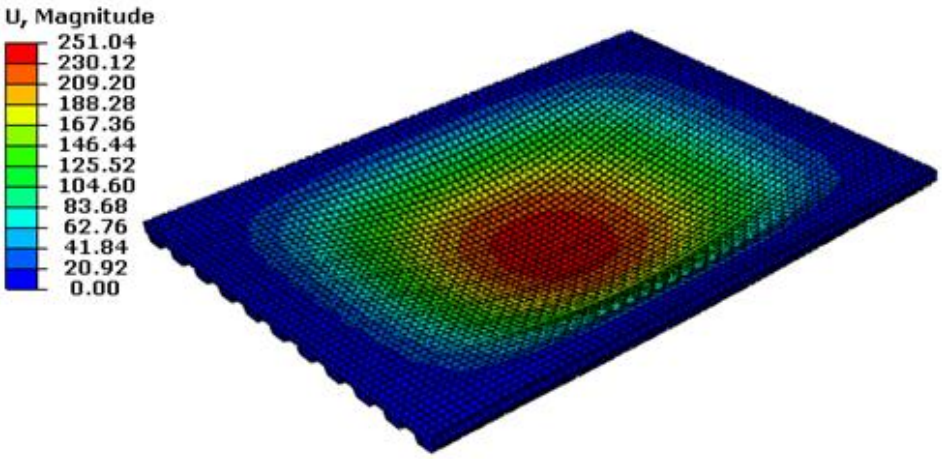
Fig. 11. Composite modelling [19] [20]

3.1 Validation of the Experiment Model

Deflection of Validated Composite Steel Deck Plate; Validated experimental research models refer to research conducted by Lim and Wade (2002), namely research on the behavior of steel deck plates due to temperature loads.



(a)



(b)

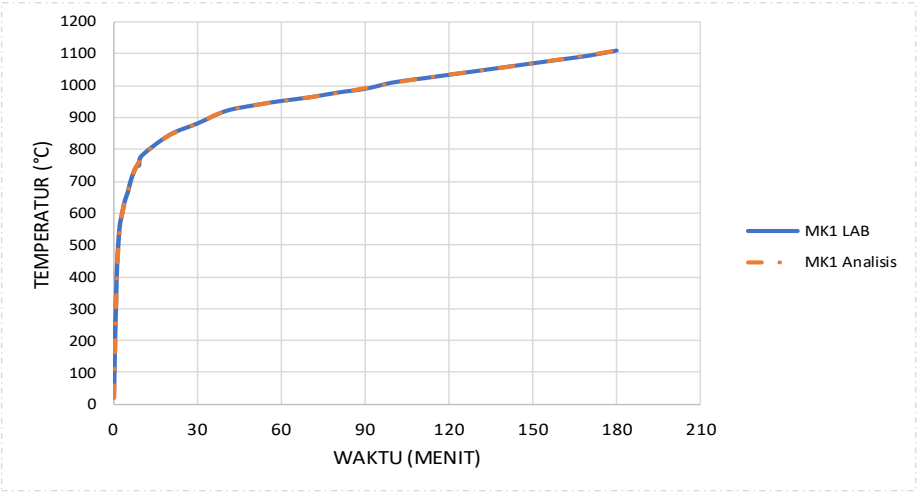
Fig. 12. (a) –(b) Deflection on MK 1 composite steel deck plate analysis

In Figure 12 is the deformation that occurs due to combustion carried out for 3 hours. Deformation of composite steel deck plates is simulated in Abaqus. During the combustion process on the composite steel deck plate, different color contours are seen where maximum deflection occurs in the middle of the composite steel deck plate and is colored red. Based on (SNI 03-1741, 2008) which regulates deflection requirements for floor components that have fire resistance, as follows:

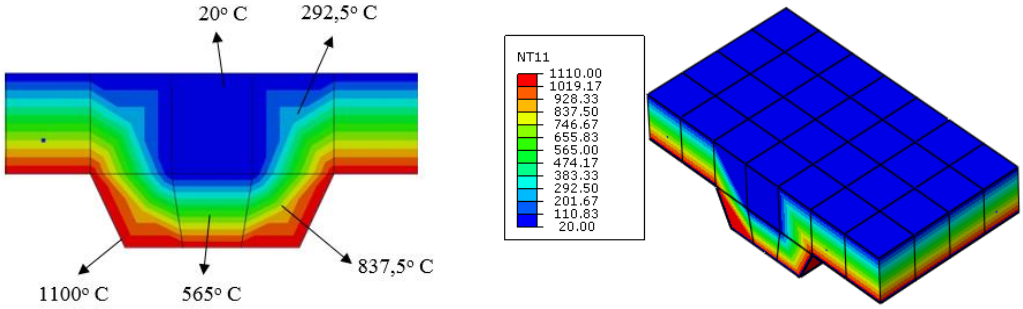
Resistance of composite steel deck plate components in 1, 2 and 3 hours of combustion; $\delta \leq L^2/10000 = 430^2/10000 = 18.49$ cm = 184.9 mm, $\delta \leq L^2/6000 = 430^2/6000 = 30.81$ cm = 308.1 mm, $\delta \leq L / 20 = 430/20 = 21.5$ cm = 215 mm, respectively.

Table 4.
Numerical result meet the Experimental data [22]

Time (menit)	MK1 LAB (mm)	MK1 ANALYSIS (mm)
1	-3.7	-2.34
30	-56	-59.55
60	-92	-94.76
90	-128	-128.88
120	-164	-164.21
150	-200	-202.15
180	-253	-251.04



(a)



(b)

Fig. 13. (a) Comparison graph of temperature and combustion time relationship of composite steel deck plates and (b) Stress distrobution relates to the degradation contours on the MK1; validation plate analysis

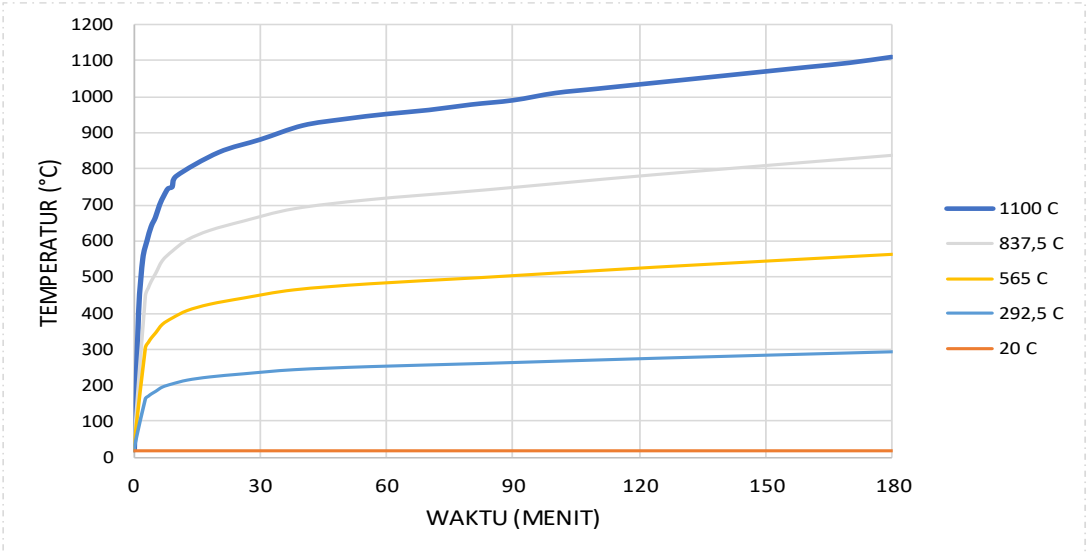


Fig. 14. Graph of relationship between temperature and combustion time of composite steel deck plates

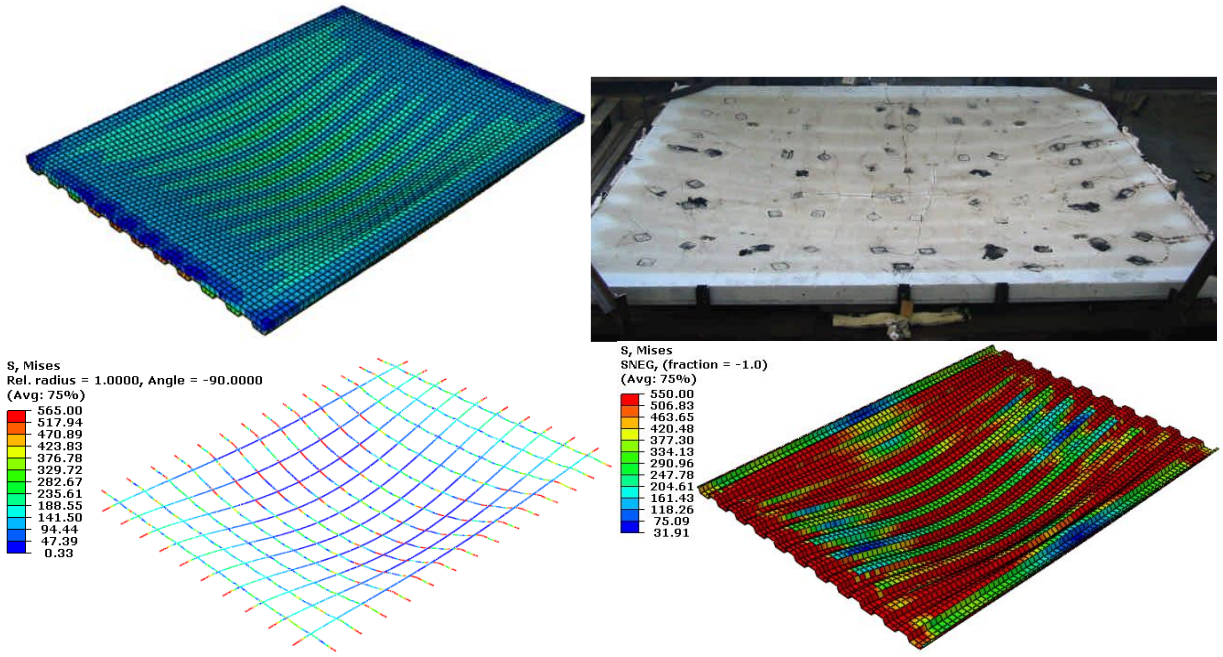


Fig. 15. The stresses at the time step of 65.62 minutes for reinforcement bar and steel sheet deck

4. Conclusions

If the results of validation and modeling with Abaqus are tabulated based on the combustion time and the effect on deflection that occurs on the composite steel deck plate will be seen as in table 4. It is clear that the deformation of the decrease in the model continues to increase along with the increase in temperature value. The stress that occurs on the composite steel deck plate is increasing with increasing combustion temperature. Combustion carried out for 1 hour and 2 hours, causing deflection that occurs in the composite steel deck plate is still in accordance with the deflection permits proclaimed in SNI 03-1741-2008. When burning has occurred for 3 hours, the deflection that occurred has passed the deflection of the required permit

Acknowledgement

This research was funded by a grant from Magistes of Civil Engineering School, Faculty of Engineering, Udayana University

References

[1] (2016). *Bondek Structural Steel Decking*.

[2] G. Li and P. Wang, *Advanced Analysis and Design for Fire Safety of Steel Structures*. Shanghai: Zhejiang University Press, 2012.

[3] L. , D. Cahyadi, and M. N. Fajri, "KETAHANAN PELAT BETON KOMPOSIT ALDECK TERHADAP API DAN KINERJA PELAT BAJA GELOMBANG SEBAGAI PENGGANTI TULANGAN POSITIF," *Jurnal Pemukiman,* vol. 3, 2008.

[4] *Cara Uji Ketahanan Api Komponen Struktur Bangunan untuk Pencegahan Bahaya Kebakaran pada Bangunan Rumah dan Gedung*. Indonesia: BSN, 2008.

[5] H. Wiryosumarto and T. Okumura, *Teknologi Pengelasan Logam*. Jakarta: Pradnya Paramita, 2004.

[6] J. M. Gere and S. P. Timoshenko, *Mekanika Bahan Edisi Ke - 4*. Bandung: Erlangga, 2000.

[7] R. Netriady, *Kajian Keruntuhan Jembatan Krasak Akibat Kebakaran Truk Tangki Bahan Bakar Dengan Memperhitungkan Bentuk Sebenarnya Dari Elemen Diagonal Rangka Utama Dan Pengaku Atas Jembatan*. DEPOK: UNIVERSITAS INDONESIA, 2010.

[8] R. L. Brockenbrough and F. S. Merritt, *Structural Steel Designer's Handbook*. McGraw - Hill: Inc, 2011.

[9] C. G. Salmon and J. E. Jhonson, *Design and Behavior Steel Structure*. Wisconsin: University of Wisconsin, 1980.
[10] *ASM Handbook, Volume 1: Properties and Selection: Irons, Steels, and High-Performance Alloys*: ASM international, 1993.
[11] D. K. Matlock, J. G. Speer, and S. G. Jansto, "Niobium in Fire Resistant," Colorado, 2012.
[12] (1999). *Technical Manual for Pre-Engineered Steel Buildings*.
[13] S. Jones, "INTUMESCENT COATINGS IN THE 21ST CENTURY," Australia, 2017.
[14] R. D. Cook, D. S. Malkus, M. E. Plesha, and R. J. Witt, *Finite Element Modeling For Stress Analysis*. New York: Jhon Wiley and Sons publishers, 2002.
[15] Abaqus-6.12. (2013). *Implicit Dynamic Analysis*. Available: http://abaqus.me.chalmers.se/v6.12/books/stm/default.htm?startat=ch02s04ath19.html
[16] u. s. m. Abaqus 6.10., "Configuring a direct cyclic procedure," 2011.
[17] Abaqus. (2012). *Implicit dynamic analysis*. Available: http://abaqus.civil.uwa.edu.au:2080/v6.10/index.htm http://abaqus.me.chalmers.se/v6.7/books/stm/default.htm?startat=ch02s04ath19.html
[18] C. a. Structures., *CSI Analysis References Manual*: Computers and Structures, 2016.
[19] J. Jiang, J. A. Main, F. Sadik, and J. Weigand, "Numerical Modeling and Analysis of Heat Transfer in Composite Slabs with Profiled Steel Decking," *NIST,* 2017.
[20] L. Both, F. Wald, and R. Zaharia, "Benchmark For Numerical Analysisi of Steel and Composite Floors Exposed to Fire Using A General Purpose FEM Code," *Original Scientific Paper,* 2016.
[21] M. A. H. Abdel Halim, M. R. Hakmi, and D. C. O'Leary, "Fire Resistance Of Composite Floor Slabs Using a Model Fire Test Facility," *Engineering Structures,* pp. 176-182, 1999.
[22] L. Lim and C. Wade, *Experimental Fire Tests of Two-Way Concrete Slabs*. Christchurch, 2002.

Penerbit Akademia Baru

Engineering Science and Technology Conference Proceedings

Journal homepage: www.akademiabaru.com/EST.html

Review of Fluid-Structure Interaction Model for the Wave Current Behaviour With the Offshore Structures

Open Access

Mushtaq Ahmed[1], Zafarullah Nizamani[1,*], Akihiko Nakayama[1], Muntasir Osman[2]

[1] Department of Environmental Engineering, Faculty of Engineering and Green Technology, Universiti Tunku Abdul Rehman, 31900, Kampar, Perak, Malaysia
[2.] Department of Civil Engineering, Faculty of Engineering, Universiti Teknologi PETRONAS, Persiaran UTP, 32610 Seri Iskandar, Perak, Malaysia

ABSTRACT

The effects of the surface waves generated by the wind have a significant effect on the currents. A wave current coupled model plays an important role in the design of offshore structures. The interaction between fluids such as incompressible ocean wave and current and offshore structures is significant with many real-time applications in offshore engineering. These coupled models can be applied to Offshore Floating Production Operating and offloading (FPSO), Wind or current turbines and offshore pipelines. The complex issues related to the design are analyzed by using Computational Fluid Dynamics, which requires an investigation of the multiphase flow between wave and current and the structure which is considered restrictive due to the computational cost. If viscous effects are neglected than the single-phase flow models have been recommended, where wave-current interaction have been modelled successfully. Models have been developed where velocities and pressure are computed and the results can be verified with the experimental results available in the literature. In this study the existing numerical methods, mesh types are reviewed along with their coupling methods. Here single-phase and multiphase models with small and medium movement analysis methods are discussed and their applications are highlighted.

Keywords:
Offshore structures; wave current interactions; governing equations

Copyright © 2019 PENERBIT AKADEMIA BARU - All rights reserved

1. Introduction

The offshore structures serve not only for Oil and gas exploration but they are also used for the development of sustainable energy systems such as offshore windmills, current energy generator. The rapid development of the technology and shallow water oil reserves depletion is pushing engineers to look into deep oceans. The deepwater offshore structures are more vulnerable to environmental loadings such as wind-induced water waves and currents than shallow water. In order to make them operational throughout their design life; it is utmost necessary to ensure the safety of such structures. In past; due to their location and dealing with sensitive material, and environmental hazards associated with the fossil fuels these structures had been designed with conservative loadings. Recently, due to advance in shell technologies the hydrocarbon fuel prices have decreased. Thus it is time to design offshore structures efficiently in order to reduce the extra costs associated with them. For proper structural design, it is necessary to consider the real environmental loads on the structure. The coupled and non-coupled wave-current interaction has

* *Corresponding author.*
E-mail address: zafarullahi@utar.edu.my (Zafarullah Nizamani)

been observed in many cases on the structure. The analysis of such interactions needs different mathematical approaches, observations and experiments. This interaction has been considered as the most complex phenomenon, where current is superimposed with waves.

Initially, studies were performed in laboratory-based wave tanks but after the computational evolution, the experimental tanks have been replaced by Computational Fluid Dynamics (CFD) numerical wave tanks involving computational costs only. The combined wave-current interaction based on Navier-Stokes equations has been studied by various researchers [2, 3, 4, 5, 6, 7, 8]. Most of these studies are done under Numerical wave tank simulations with different CFD solver techniques. Various open-source and commercial codes are available for the simulation of flow dynamics. The accuracy of such simulation depends upon the comparison of model validation results with available experimental works. The experimental works regarding wave and current interaction have not been much studied due to limitations of cost, space and measurements. Under such circumstances, the studies of one CFD techniques could be compared with the results of other CFD technique as done in the study of [7, 9].

The involvement of current with waves make flow characteristics complex. The superimposition of current onto the wave in a numerical wave tank can be achieved either by introducing pressure inlet boundary condition [4, 6] or by velocity inlet boundary condition [3, 11]. The velocity of waves remains the same throughout the depth with velocity wavemaker while waves generated with pressure wavemaker have varying current velocities with the depth. The FLUENT is a CFD commercial software of ANSYS incorporation based on Finite volume method. The software is very effective in modelling the physical phenomenon of flow and turbulence. The world supercomputing record has been set by this software with scaling to 172,000 cores. It is very effective for RANS simulations. It has been successfully used in the studies of [3, 4, 7, 8, 11, 12].

2. Wave Field

The dimensionless quantities are the key to the numerical analysis of flow so non-dimensional parameters are preferred. The most used non-dimensionless parameters are, wave height (H/gT^2), wave steepness (H/L) and water depth (d/gT^2). In a numerical wave tank, the waves are generated at the inlet in order to simulate the wave parameters. Without the presence of current, the free surface displacement and velocity potential equations can be written as Eqs. (1-2);

$$\eta = \frac{H}{2}\sin\left(kx - \omega t\right) \tag{1}$$

$$\emptyset = \frac{g\,H\,\cosh\,k\,(h+z)}{2\,\omega\,\cosh\,k\,h}\cos(kx - \omega t) \tag{2}$$

Where, η is free surface displacement, H is wave height, $(kx - \omega t)$ is wave phase angle, $\emptyset$ is velocity potential, g is acceleration due to gravity, h is water depth, k is wave number, and t is time.

The free surface displacement has two parameters associated with it i.e. Kinematic and dynamic both of which need to be satisfied with velocity potential. If pressure p_η is assumed to be consistent at free surface $z = \eta(x,t)$ than dynamic boundary condition for the free surface can be represented with the Bernoulli equation as Eq. (3):

$$-\frac{\partial\emptyset}{\partial x} + \frac{1}{2}\left|\nabla\emptyset^2\right| + gz = C(t) z = \eta(x,t) \tag{3}$$

The description of water particle in the horizontal direction can be made as:

$$u = -\frac{\partial \emptyset}{\partial x} = Ak\ \cos h\, k(h+\ z)\sin(kx\ -\ \omega t) +\ U \tag{4}$$

$$u^2 =\ U^2 + 2AkU\ \cos h\,(h+\ z)\sin(kx\ -\ \omega t) + (Ak)^2\ \cos h^2\, k(h+z)\ \sin^2\ (kx-\sigma t) \tag{5}$$

Where Ak is the velocity component for the horizontal direction and it is small in magnitude so $(Ak)^2$ is just negligible. So now the Eq. (3) for z=0 can be written as Eq. (6) or Eq. (7):

$$C(t) = \frac{1}{2}[U^2 + 2AkU\ \cos h\,(h+\ z)\sin(kx\ -\ \omega t)] -A\omega\ \cos h\, kh\ sin(kx-\omega t)\ + g\eta \tag{6}$$

Or

$$\eta(x,t) = -\frac{U^2}{2g} + \frac{A\omega}{g}\left(1-\frac{kU}{\omega}\right)\ \cos h\ \ kh\sin(kx\ -\omega t) + C(t) \tag{7}$$

The water particle velocity should be within specified physical conditions in order to satisfy the boundary condition so if satisfied, water particle motion will be considered as the kinematic boundary condition. So under this situation, $z\ -\eta(x,t) = 0$ at any arbitrary moment in the boundary. Now kinematic boundary condition at the free surface will be as shown in Eq. (8);

$$\left(\frac{\partial \eta}{\partial t}\ -\frac{\partial \emptyset}{\partial x}\ \frac{\partial \eta}{\partial x}\right) + \eta\ \frac{\partial}{\partial z}\ \left(\frac{\partial \eta}{\partial t}\ -\frac{\partial \emptyset}{\partial x}\ \frac{\partial \eta}{\partial x}\right) + \cdots = -\frac{\partial \emptyset}{\partial z} - \eta\ \frac{\partial}{\partial z}\ \left(\frac{\partial \emptyset}{\partial z}\right) + \cdots.,\ z = 0 \tag{8}$$

When we arrange Eq. (8) by linear terms, it can be rewritten as Eq. (9):

$$\frac{\partial \eta}{\partial t} + U\ \frac{\partial \eta}{\partial x} = -\frac{\partial \emptyset}{\partial z},\ z = 0 \tag{9}$$

3. Current Field

The currents are directed motions of seawater generated by the action of earth rotation, wind, temperature, water salinity and gravity of sun and moon. They are not like waves and flows at greater distances in the oceans and play a vital role in the earth's climate. They can be divided into deep water currents and surface water currents. The deepwater currents move under the influence of temperature and density of water while the surface currents move under the influence of wind. By assuming a uniform current for the whole depth of the tank, the velocity potential of Eq. (2) can be rewritten as Eq. (10):

$$\emptyset =\ A\ \cos h\ \ k(\ h+z\ )\cos(\ kx\ -\ \omega\ t\ )\ -Ux \tag{10}$$

Where U is current velocity, H is wave height, k is wave number, h is water depth, ω is frequency, and $A = \frac{g\ H}{2\ \omega\ cosh\ k\ h}$.

The amplitude of wave with the consideration of current can be written as Eq. (11):

$$A = \frac{g\ H}{2\ \omega\left(1-\frac{kU}{\omega}\right)cosh\ k\ h} \tag{11}$$

By putting, η and $\emptyset$ in Eq. (6), we can obtain the equation for the dispersion relation with current velocity (U) as shown in Eq. (12);

$$\omega^2 = \frac{g\ k\ \tanh kh}{\left(1-\frac{kU}{\omega}\right)^2} \quad (12)$$

$$\omega = kU + \sqrt{g\ k\ \tanh kh} \quad (13)$$

$$\omega_e = \omega\ - kU \quad (14)$$

Where ω is the absolute frequency and ω_e is encounter frequency.

Table 1
Equations of wave parameters with the involvement and non-involvement of current

Parameters	Without current	With current
Velocity potential	$\emptyset = \frac{g\ H\ \cosh\ k\ (h+z)}{2\ \omega\ cosh\ k\ h} \cos(\ kx\ -\ \omega\ t\ )$	$\emptyset = \frac{g\ H\ \cosh\ k\ (h+z)}{2\ \omega\ cosh\ k\ h} \cos(\ kx\ -\ \omega\ t\ ) + U_x$
Velocity in x-axis	$u = -\frac{\partial \emptyset}{\partial x} = \frac{g\ Hk\ \cosh\ k\ (h+z)}{2\ \omega\ cosh\ k\ h} \sin(\ kx\ -\ \omega\ t\ ) + U$	$u = -\frac{\partial \emptyset}{\partial x} = \frac{g\ Hk\ \cosh\ k\ (h+z)}{2\ \omega_e\ cosh\ k\ h} \sin(\ kx\ -\ \omega_e\ t\ ) + U$
Dispersion relationship	$\omega = \sqrt{gk \tanh kh}$	$\omega_e = kU + \sqrt{gk \tanh kh}$
Wave celerity	$C = \sqrt{\frac{g}{k} \tanh kh}$	$C = U + \sqrt{\frac{g}{k} \tanh kh}$

4. Wave-Current Interaction with Structures

The simultaneous occurrence of wave and current in ocean environments make their interaction as the most prominent factor for the analysis of hydrodynamics of oceans [5]. The major environmental forces for this region are considered to be waves and currents [6]. Every offshore structure before its design requires the analysis of such hydrodynamic forces. Offshore structures have been studied by many authors using frequency domain analysis [13, 14, 15] and Time domain analysis [13, 15, 16, 17]. The forces have been determined by using the Morison equation and linear diffraction wave theory. The main determination of the study involved capturing random wave responses in a surge, heave and pitch [18]. Such a response is called Response Amplitude Operator (RAO). The wave-current interaction with structures involved the numerical approaches in these studies. This numerical approach is based on the potential flow theory, linear waves and small current velocity approximation. The coexisting field of the wave with current involves separation of the velocity potential. This separation is done into the unsteady potential of wave and current. It becomes easier to determine the elevation of water surface around an offshore structure under the coexisting field of wave and current. The unsteady wave potential and current velocity are substituted in first-order dynamic surface boundary condition to obtain the water surface elevation [19]. One of the studies involved the time-domain method [13]. The regular waves diffraction and radiation effects were determined due to current with a 2-D body. The observation proved the Current effects on offshore structures and a non-linear relation with currents was shown with first and second-order results.

Surface wind stress, bottom friction, wave climate, wave field, depth and current refraction and modulation of the absolute and relative wave period are the most common wave-current interaction mechanisms reviewed [16,17,18]. The change is slow drift motions, wave run-up and wave forces have been observed due to the combination of waves and currents [19]. It has been

observed that wave and current occur at the same time in the oceans. A resonance is normally created when wave and current interact with the structures. This resonance causes slow drift motions. The prediction of such motions is also very important from the engineering perspective. The pure wave interaction with the offshore structures has been observed differently as compared to wave current coupled interaction. When time-domain results were compared with the frequency domain, no difference was found in these studies.

The long-crested wave along with current produce more forces as compared to short crested wave involving current. The experimental study of [20] made comparisons between short crested wave with current and long-crested wave with currents. It was found in the study that long-crested wave with the current was able to produce 45% more forces as compared to short crested wave with the current. The author of the study suggested that further study was required to be conducted regarding short crested waves involving six-degree-of-freedom. It has been observed that in intermediate and shallow waters, the short crested wave remain dominant while for the deep waters long-crested waves are dominant. Due to lack of proper data, the offshore structures are designed for the long-crested waves.

The short crested waves along with current produce different results than the long-crested waves with the current. In the analytical study of [2], the effects of the current having uniform velocity were studied on the short crested wave. The wave parameters on which the effect was studied were wave frequency, wave run up, wave force and inertia. The water depth was found be in inverse relation with the short crested wave having uniform current and total wave number was having the direct relation. The wave frequency was influenced by the current velocity and current incident angle. Details of various numerous studies involving wave, current and structure have been briefly described with the purpose, observations and suggestions of the study in Table 2.

Table 2
Some recent studies on Wave-current interaction with structures

Author & Year of Study	Nature of Study			Purpose of the study	Observations and Suggestions	Ref. No
	Exp.	Anal.	Num.			
Wang (2019)	-	Anal.	-	Short crested wave-current interactions with composite bucket foundation for the windmill. Effects of uniform current on wave frequency, wave run-up, wave force and inertia were investigated. Drag coefficients on composite bucket foundation	Total wave number has a direct relation with the short crested wave-current interaction and inverse relation with the water depth. The inertia and drag coefficient increases under increased velocity only if the relative angle is smaller than 90. The current velocity and current incident angle also influence the wave frequency. Main incident forces occur under the condition of current incident forces being parallel to the direction of wave propagation.	[2]
C.Y.Ng (2017)	Exp.	-	-	The dynamic responses of Truss spar were determined under the conditions of short crested wave and long-crested wave with currents. A comparison of both waves with the current was made.	The long-crested waves with current were found to produce (45%) more responses than short crested waves with the current. Suggestion 1: Further study needs to be conducted by considering wind loads also. Suggestion 2: The study should include surge, sway, heave, roll, pitch and yaw (Six degree-of-freedom).	[20]
Kim (2016)	-	-	Num.	To Investigate the combined wave and current loads on a cylinder under the regular wave environment.	Under combined wave and current situations, an increase in current velocity increases the wave height and wavelength. Suggestion 1: numerical simulations for actual jacket structure because complex flow interactions occur at the multiple legs of the platform. Suggestion 2: Vortex induced motion (VIM) and vortex-induced vibrations (VIV) around the structure.	[3]

C.Y.Ng (2016)	Exp.	-	-	Wave-current interaction with truss spar	Dynamic responses of the truss spar model due to wave with current are greater as compared to wave without current. Maybe because current velocity provides additional lateral force in the water body which increased the structure resonance. Dynamic responses were found to be greater under wave with the current. One unit increase in the current velocity was found to increase surge by 24.8%, heave by 31.1% and pitch by 32.2%.	[21]
Persic (2014)	-	-	Num.	Steady flow with a uniform current at subcritical Reynolds number around a smooth circular cylinder	For subcritical flow regime, LES works best because with the increase in Reynolds number (Re) an increase in separation angle while the reduction in recirculation length occurs. Suggestion: For high Re values (Re=13100), if relevant experimental data is not available than same flow regime should be modelled with lower Re values (Re=3900 validated by experimental work) and LES model with high Re should be validated with LES model with low Re values.	[22]

5. Numerical Simulation of Wave-Current Interaction

The wave, current and their interaction can be measured by different technologies currently available. Previously, the ocean environments have been studied on the laboratory basis only. But due to limitations involved with the experimental works, the wave-current interaction has not extensively been studied under field conditions. The advancement in the computational field has created new opportunities for fluid dynamics. The most cost-effective way to study such an environment is by the use of computational fluid dynamics (CFD) techniques. These techniques involve the modelling of ocean waves and currents in open source and commercial computer codes. These studies have been done by various researchers. Some of the CFD techniques provide full details of flow pattern but are computationally very costly. The most common is Direct Numerical Simulations (DNS) technique. The other technique used for the simulation is Large Eddy Simulation (LES) but it involves good knowledge of mathematics and physics to be implemented. It is also computationally costly but not more than DNS.

The numerical simulation with the help of CFD has enabled us to properly create the ocean like environments in numerical wave tanks. The promising results have been obtained to various researchers who simulated ocean flows in numerical wave tanks using Reynold's Average Navier-stokes (RANS) equations. [7, 9, 12]. The numerical wave tank technique using RANS solver has been carried out to study the interaction of waves and currents [3].

6. Numerical Wave Tank Approach

Numerical wave tank flumes are developed in commercial and open source CFD codes. These flumes are mostly based on the finite volume method (FVM). The Stokes and continuity equations are used as the governing equations. Depending on the flow conditions, either Navier-stokes (NS) or Reynolds Average Navier Stokes (RANS) equations are used to model the incompressible flow. The volume of fluid is the most suitable method for tracking the free surface. Table 2 shows some of the recent studies of numerical wave tank simulation with RANS equations. Most of the Numerical tanks mentioned in the Table 3 have applied the turbulent model. All the numerical wave tank use the artificial damping zone to reduce the reflection effects of the waves generated in the tank. Every model involves initial and boundary conditions. The waves and currents are generated at the inlet of the tank while the reflected waves are absorbed at the outlet of the tank. The numerical wave-current flume shown in Figure 1 gives the full details of initials and boundaries.

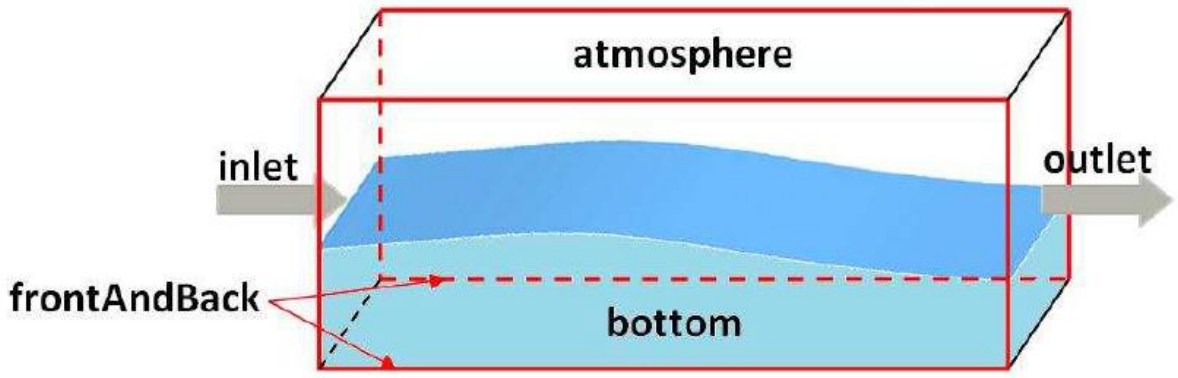


Fig. 1. A numerical wave tank defined with each of its boundary (Jasmine, 2012)

Providing the most favourable initial and boundary conditions is the key to towards the successful simulations. Some of the studies under review involved the pressure based waver maker at the inlet boundary of the wave tank [4, 6]. While on the contrary, the studies of [3, 11] involved velocity based wavemaker. When the authors compared their obtained results with the results of experimental works, the studies involving velocity wavemaker gave the best comparisons. The pressure-based studies provided the best results for the wave condition only. While for current and wave-current interaction, their simulation was not promising enough. The wave tank based on the pressure as a current producing source provided fluctuating current values concerning the depth of the water while in case of velocity, the value of current remained the same throughout the depth. The author of study [6] concluded that the location of the current source in the model should be further studied to get the best results for the current and wave-current interaction cases too.

Table 3
Wave tank simulations with RANS equations

Flow Solver (CFD Solver)	The free surface modelling method	Simulation	Authors
RANS (FLUENT)	VOF (Volume of fluid)	Wave-current interaction	[2]
RANS (FLUENT)	VOF	Wave-current interaction	[3]
RANS (FLUENT)	VOF	Wave current interaction	[4]
RANS (Not mentioned)	VOF	Wave current interaction	[5]
RANS (Not mentioned)	VOF	Wave current interaction	[6]
RANS (Not Mentioned)	VOF	Wave-current interaction	[7]
RANS (REEF3D)	VOF	Wave current interaction	[10]
RANS (FLUENT)	VOF	Waves only	[11]

The RANS equations are most common among the researchers involving less computational costs. The simulations based on RANS equations provide the best simulation results. The accuracy of simulations mainly depends upon the boundary conditions chosen. Most of the studies mentioned in this paper involve the same source region for waves and current except the study of [6] where two separate sources were chosen. This study also involved two separate beaches too, to avoid the reflection effect of these sources. Most of these studies were performed in the two-dimensional domain. Involvement of the Three-dimensional domain consumes a large computer memory and requires some special computers. The accuracy of such simulation depends upon the comparison of model validation results with available experimental works. The experimental works regarding wave and current interaction have not been much studied due to limitations of cost, space and measurements. Under such circumstances, the studies of one CFD techniques could be compared with the results of other CFD technique as done in the study of [7, 9].

Most of the studies mentioned in Table 3 were carried out with commercial CFD solver "FLUENT" which is the most popular tool for the simulations of turbulence. Some studies have involved the use of open source tools too. The most popular CFD opensource software is OpenFOAM. The commercial software is intended to provide ease to the user while open source software involves not many favourable user-friendly interfaces.

Kim [3], studied wave-current interaction and load analysis using a Boundary element method (BEM) based numerical wave tank. CFD studies were done in FLUENT software, where governing equations were discretized by the finite volume method. He used 3rd order Monotone upstream centred scheme (MUSCL) for convection term. The velocity and pressure coupled with Pressure implicit with the splitting of operator (PISO) method. The k-ε model was used for the turbulent stress term in the governing equation. He used Volume of the fluid method with implicit High-resolution interface capturing (HRIC) for the air-water interface.

Zhang *et al.,* [4], developed a numerical wave tank in FLUENT software by using Navier Stokes equations to study the wave and current interaction in the bottom boundary layer. The flow was modelled by RANS equations and the Volume of the fluid method was used to track the free surface. K-ε model was used and at the bottom boundary layer, a low Reynolds number scheme was used instead of high Reynolds's Number scheme. The waves generated were second-order Stokes waves by using velocity inlet boundary. The validation of the wave tank was made by using the experimental data of Kemp, [23]. The implicit high-resolution interface capturing method was used.

Christine *et al.,* [6], studied wave-current interaction without involving any offshore structure by using impulse-based wave-current interaction (WCI) model. Waves and currents were simultaneously generated through the inclusion of source terms, added to the Reynolds Averaged Navier-Stokes (RANS) equations. He used depth varying current velocities but his model was unsuccessful to produce the best results for the wave-current interaction. It gave the best results for the waves only.

Hans *et al.,* [10], used the Boundary element method (BEM) method with Navier-stokes equations. He used the 5th order Finite difference weighted Essentially Non-Oscillatory (WENO) scheme for the field equations. He used the projection method to calculate the pressure in the Navier-stokes equation. The K-ω model was used along with Reynolds Averaged Navier-Stokes (RANS) equations for turbulence closure. Cartesian grid approach was utilized for high order discretization scheme. Ghost cell immersed boundary method (GCIBM) was employed for wave structure analysis.

Markus *et al.,* [24 & 25], also used the same approach as [3] but he used Fenton model [26] to create the depth varying currents The results were found to be more successful but he used nonlinear waves with unsteady flow conditions using URANS (unsteady RANS) equations. He used stream function wave theory to validate his waves generated in the wave tank and compared the results of non-uniform current with uniform currents. His studies mostly involved wave kinematics and no offshore structure was used in the model.

7. Proposed Methodology:

Based on the finite volume method (FVM) a numerical wave-current flume will be developed with the help of ANSYS FLUENT. The simulation with FLUENT involves the following elements [27].

i. A Pre-processor (ANSYS Design Modeller)
ii. A solver (ANSYS FLUENT)
iii. A post-processor (ANSYS CFD Post)

The continuity Eq. (15) and momentum conservation Eq. (16) (also known as Navier-stokes equation) will be used as the governing equation.

$$\frac{\partial \rho}{\partial t} + \nabla . (\rho . \boldsymbol{v}) = 0 \quad (15)$$

$$\rho \frac{Dv}{Dt} = \rho \boldsymbol{g} - \nabla p + \mu \nabla^2 v \quad (16)$$

Where ρ is the density of the fluid, *v* is the kinematic viscosity of the fluid, D*v*/D*t* is called eulerian derivative, *g* is acceleration due to gravity, t is the time.

The flow is considered to be stable (Laminar) at low Reynold number. After a certain limit of Reynolds number, the flow becomes unstable (Turbulent) due to fluctuations in velocity and pressure. These fluctuations cause chaotic motion state known as turbulence in the flow field. The fluid properties based on averaged time are sufficient to resolve these chaotic motions so RANS equations are most popular for computations of turbulent flows. The RANS equations are obtained by decomposing fluid properties into steady mean and fluctuating components. Such a decomposition is called Reynolds's decomposition and is applicable to fluid properties like velocity, pressure and temperature. The governing Eqs. (15) and (16) when decomposed with Reynolds decomposition (x-direction), Eqs. (17-18) are obtained;

$$\nabla . \bar{u} = 0 \quad (17)$$

$$\rho \frac{D\bar{u}}{Dt} = -\frac{\partial p}{\partial x} + \mu \nabla^2 \bar{u} \left[\frac{\partial(-\rho \overline{u\prime^2})}{\partial x} + \frac{\partial(-\rho \overline{u\prime v\prime})}{\partial y} + \frac{\partial(-\rho \overline{u'w\prime})}{\partial z} \right] \quad (18)$$

The above Eqs. (17) and (18) are called RANS equations. The fluctuating terms are inside the bracket while the averaged velocities are outside the bracket. The pressure in the momentum equation doesn't occur in the continuity equation but all the equations contain velocity terms. In other words, the convective term and continuity equations are coupled. Density does not link with the pressure so it is impossible to obtain the pressure of the incompressible fluid from its density. While the determination of pressure is most important for applying velocity to the continuity equation. This problem can be solved by using iterative methods where pressure residuals are monitored for the proper convergence of the process to obtain satisfactory results for the pressure. Pressure and velocity coupling in FLUENT can be done either by the segregation method where governing equations are solved sequentially or by a coupled method where coupled equations are solved. SIMPLE, SIMPLEC and PISO are algorithms for segregation method while the COUPLED algorithm is for coupling. The PISO is recommended by ANSYS inc. [28].

The finite volume method (FVM) will be applied for the discretization of governing equations. The conservation equation of momentum and mass have common characteristics and by introducing a term Ø, we can obtain the Eq. (19).

$$\frac{\partial(\rho \emptyset)}{\partial t} + \nabla . (\rho \emptyset v) = \nabla . (\Gamma \nabla \emptyset) + S_{\emptyset} \quad (19)$$

The Eq. 19 is called the transport equation and it is compared with the Navier-stokes equation too by replacing *v* with Ø. In the left side of the equation, the first terms are called steadiness of the flow while the second term is the convective term. On the right side, the first term is the diffusive term and the second term is source term. The transport equation can be discretized as into Eq. (20) for numerical solution:

$$\frac{d}{dx}\left(\Gamma \frac{d\emptyset}{dx}\right) = 0 \quad (20)$$

The turbulence model (k-ε) will be used for turbulent stress. The K-ϵ is the simplest model requiring only initial and boundary conditions. The model has been most widely used and popular among researchers. Its main disadvantage is that it performs very poor near walls. It is also a poor

performer for unconfined flows. It requires special treatments called enhanced wall treatments to increase accuracy. Due to high gradients near the wall, the turbulent flows are largely influenced by the walls. The modelling of a very thin viscosity layer developed near the wall requires a mesh of very fine size while the minimum 10-20 cells are allowed in FLUENT for boundary coverage. So in such cases when it becomes impossible to meshing up such a tiny region, the wall functions are used for connecting wall and turbulent region. Basically, wall functions are semi-empirical formulae and enhanced wall function is recommended for the k-ε model by ANSYS FLUENT community [29]. The model variants are available for K-ϵ model in FLUENT and the 'realizable model' is the best variant. The air and water interface in the FLUENT is tracked by using the Volume of Fluid method. This method works on the volume fraction principle where each fluid is determined in the form of fraction from each mesh of the computational cell by using the volume fraction Eq. (21).

$$\frac{\partial \alpha}{\partial t} + \nabla . (\alpha U) = 0 \tag{21}$$

Where α is volume fraction (phase fraction) of water and U is the velocity field. Value of α depends on the type of fluid and it is maximum in case of water and minimum in case of air so α=1 if the cell is filled up by water and α=0 if the cell is filled up by air. The volume fraction can also be used to determine the density of fluid inside the mesh cell because density will be required at a later stage to solve the Navier-stokes equation. The density mixture can be written as Eq. (22).

$$\rho = \alpha \rho_{\omega} + (1 - \alpha) \rho_{\alpha} \tag{22}$$

Where ρ_{ω} is the density of water and ρ_{α} is the density of air.

The no-slip boundary conditions will be applied at the top and bottom of the numerical wave. While at the inlet of the numerical wave tank, a wavemaker will be applied for the generation of the wave. In BEM, the wave can be generated at the inlet of the wave tank by applying velocity Eq. (23) at the wavemaker.

$$u(t) = \frac{S}{2}[\left(1 - e^{-\frac{\alpha t}{T}}\right) \omega \cos \omega t + \frac{\alpha}{T}\left(e^{-\frac{\alpha t}{T}}\right) sin\, \omega t \tag{23}$$

Where *T* is the wave period and ω is the angular frequency.

The outlet boundary condition act as a numerical beach where damping zone will be introduced in order to reduce the reflection effect of waves. The Boundary element method (BEM) as used in the studies of [3, 4, and 10] will be used to generate the offshore environments in the wave tank as shown in Figure 2.

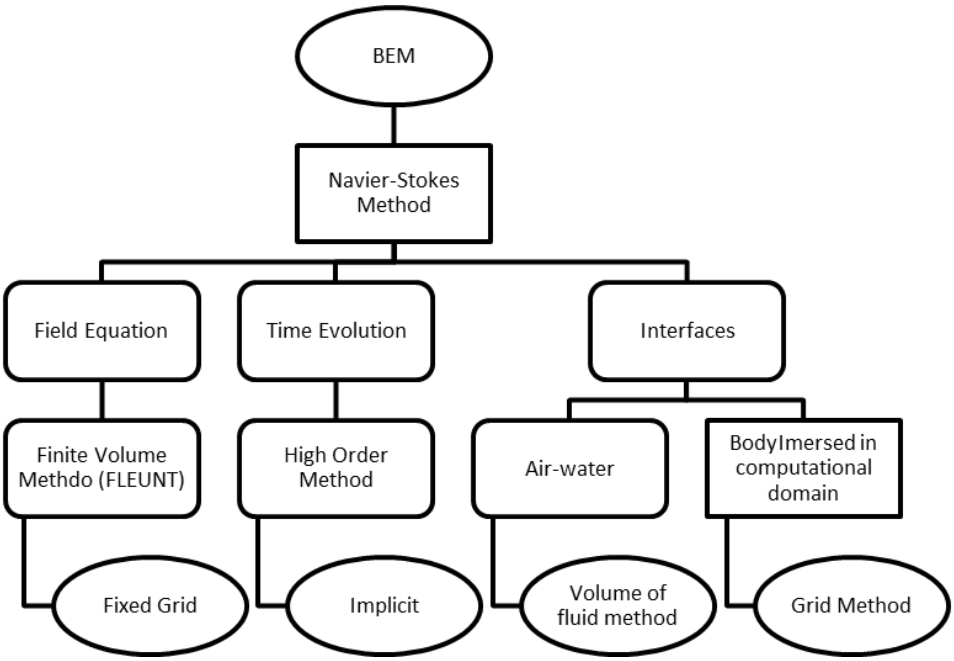


Fig. 2. The flow chart of numerical wave tank

8. Expected Outcomes

The expected results of this study will produce wave and current interaction behaviour modelling. This behaviour modelling will provide the complete details of wave and current parameters and their induced impact on the offshore structure. The simulation of wave generation will investigate the characteristic of the waves generated in the numerical tank and will determine the accuracy of the tank. The grid size will be set accordingly to the results. The reflection effect of the wave generation will be reduced in order to get the best simulation. The results of the computation and damping domain will be depicted in a graphical form in order to know the reflection effect. The result will also provide detail analysis of the wave and current interaction on the elements of the structure.

Acknowledgement

This research is work supported by the Universiti Abdul Rahman (UTAR) under the research funded by an FRGS grant from Ministry of Higher Education of Malaysia (FRGS/1/2018/TK01/UTAR/02/4).

References

[1] Olabarrieta, M., Medina, R., & Castanedo, S. (2010). Effects of Wave- Current Interaction on the Current Profile. *Coastal Engineering*, 643-654.

[2] Wang, C. H., Wai, W. H., Li, Y. S., & Chen, Y. (2006). Modelling of the Wave-Current Interaction in the Pearl River Estuary. *Conference of Global Chinese Scholars on Hydrodynamics*, (pp. 159-165). Hong Kong, China.

[3] Kim, S.Y., (2016). Numerical simulation of wave and current interaction with a fixed offshore substructure.

[4] Zhang, X., Simons, R., & Buldakov, E., (2016). A Numerical Study of wave-current interaction in the bottom boundary layer. *Coastal Engineering*

[5] Zhang, J., S., Zhang, Y., Jeng, D., S., Liu, P., L., & Zhang, C., (2014). Numerical Simulation of wave-current interaction using a RANS solver. *Ocean Engineering,* 157-164.

[6] Christine. W., Pal. S., John. R., Josh. D., (2018). Development of an impulse source-based wave-current interaction (WCI) model.

[7] Anton, K., Olga, S., & Micheal, M., (2014). Numerical Simulation of Droplet impingement and flow around a cylinder using RANS and LES Models. *Journal of fluids and structures.*

[8] Silva, M. C., Vitola, M. A., Esperanca, P.T.T., Sphaier, S.H., Levi, C.A., (2016). Numerical simulations of wave-current flow in an ocean basin. Journal of Applied Ocean Research, vol. 61, pp. 32-41.
[9] Catalano, P., Wang, M., Iaccarino, G., & Moin, P., (2003). Numerical simulation of the flow around a circular cylinder at high Reynold's Number. *International journal of heat and fluid flows* 463-469.
[10] Hans.B., Ankit. A., Shrinov. S., & Dag. M., (2019). Estimation of breaking wave properties and their interaction with a jacket structure.
[11] Sonia, B., H., Sabra, H., & Said, N., M., (2015). Numerical Simulation of wave-structure interaction around an obstacle.
[12] Clauss, G.F., Schmittner, C.E., Stuck, R., (2005). Numerical wave tank Simulation for the investigation of structural responses. 24th Int. conf. offs. Mech. & Arc. Eng. OMAE 2005-67048.
[13] Kurian, V. J., Gasim, M. A., & Narayanan, S. P. (2009). Frequency and Time Domain Analyses for TLP Responses. *7th Asia Pacific Structural Engineering & Construction Conference 2009*, (pp. 555-560). Pulau Langkawi.
[14] Kurian, V. J., Wong, B. S., & Montasir, O. A. (2008). Frequency Domain Analysis of Truss Spar Platform. *International Conference of Construction and Building Technology*, (pp. 235244). Kuala Lumpur.
[15] Roitman, N., Andrade, R. F., & Batista, R. C. (1992). Dynamic Responses Analysis of a small-Scale Model Tension Leg Platform. *Marine Structures*, 491-513.
[16] Isaacson, M., & Cheung, K. F. (1993). Time Domain Solution for Wave-Current Interactions with a Two Dimensional Body. *Applied Ocean Research*, 39-52.
[17] Anam, I., Roesset, J. M., & Niedzwecki, J. M. (2003). Time Domain and Frequency Domain Analysis of Spar Platform. *The Thirteenth International Offshore and Polar Engineering Conference*, (pp. 240-247). Honolulu, Hawaii, USA.
[18] Montasir, O. A., Kurian, V. J., & Shafiq, N. (2009). Numerical and Model Test Results for Truss Spar Platform Subjected to Random Waves. *2nd International Conference on Engineering Technology*, (pp.1-6). Kuala Lumpur.
[19] Lin, M. C., & Hsiao, S. S. (1994). Boundary Element Analysis of Wave-Current Interaction Around A Large Structure. *Engineering Analysis with Boundary Elements*, 14, 325-334.
[20] Ng, C.Y., Sazali, M.S., (2015) Dynamic Response of Truss Spar: A comparison of a long-crested and short-crested wave with the current. Conf. paper.
[21] Ng, C.Y., Kurian, V.J., Tuhaijan, S.N.A, (2016) The Effect of current on the Dynamic Responses of Truss Spar in Malaysia Water. 35th Int. conf. Offs. & Arc. Eng. OMAE2016-54399.
[22] Prsic, M.A., Ong, M.C., Pettersen, B., Myrhaug, D., (2014). Large-eddy simulations of the flow around a smooth circular cylinder in a uniform current in the subcritical flow regime. Ocean Eng. 77, 61-73.
[23] Kemp, P. H., and Simons, R. R. (1982). The interaction between waves and a turbulent current: waves propagating with the current, Journal of Fluid Mechanics, vol. 116, pp. 227-250.
[24] Markus, D., Hojjat, M., Wuchner, R., Bletzinger, K. U. (2013). A CFD approach to modelling wave-current interaction, International journal of offshore and polar engineering.
[25] Markus, D., Hojjat, M., Wuchner, R., Bletzinger, K. U. (2012). A numerical wave channel for the design of offshore structures with consideration of wave-current interaction, International offshore and polar engineering conference.
[26] Fenton, J. D. (1990). Nonlinear wave theories, journal of Ocean engineering science.
[27] ANSYS Inc. (2017, January). ANSYS Fluent Tutorial Guide R 18.0. Canonsburg.
[28] ANSYS Inc. (2014, November). ANSYS Fluent Theory Guide R 15.0. Canonsburg.
[29] ANSYS Inc. (2013, November). ANSYS Fluent User Guide R 15.0. Canonsburg.

Penerbit Akademia Baru

Engineering Science and Technology Conference Proceedings

Journal homepage: www.akademiabaru.com/EST.html

The Effect Of Varying Tube Diameters on Enhancement Heat Transfer by Forced Convection Through A Horizontal Tube

Open Access

Wadhah Hussein Aldoori[1,*], Ahmed Hasan Ahmed[2]

[1] College of Petroleum Process Engineering, Tikrit University, Tikrit, Iraq
[2] Northern Technical University, Technical Institute / Hawija, Iraq

ABSTRACT

In this investigation, experimental work has been led to study the forced convection (FC) through the three cylinders. These tubes have different diameters (D=0.02, 0.035 and 0.045) m, which are fixed horizontally and heated with constant heat flux (CHF). In this study assuming the flow is hydrodynamically fully developed. The experimental covers all the values of the imposed heat flux under investigation of (7.33 ≤ q≤ 107.424 W/m^2) that yields Reynolds numbers range (1252≤ Re ≤ 3032) was investigated. Experimental results show that the effect of varying the diameter is examined and results indicated that the Nusselt number(Nu) increased as the diameter increased which lead to higher surface temperature(SF) distribution along the smallest diameter tube. Results also show that the values of the local Nu (LNu) are always decreased and reached its decrease value at the tube exit section of the imposed HF. For all tubes the result shows that an increase in the tube diameter results increasing in average Nu.

Keywords:
Forced convection; constant heat flux; varying diameter; tubes

Copyright © 2019 PENERBIT AKADEMIA BARU - All rights reserved

1. Introduction

Heat transfer (HT) in forced convection is a significant application in designing. The primary determinant for improving the presentation of steam boilers, heat exchangers, and solar collector, likewise the comparative issue of forced convection has basic applications in geothermal stores where weight slopes are produced because of withdrawal or reinjection of geothermal liquids. Laminar stream in roundabout pipe was evaluated in [1,2,3]. Unfaltering completely created incompressible laminar move through a roundabout conduit is alluded to as Hagen-Poiseuille stream. Laminar convection in roundabout channel was profoundly examined for channels exposed to comparable warming conditions. The authors in [3] explored warmth move of laminar stream in containers of consistent divider temperature. For container of uniform divider temperature, hub conduction was incorporated by [4]. Explored impact of Axial conduction in cylinder divider on warmth move procedure of Fully Developed Laminar Flow (FDLF) in the cylinders under consistent divider temperature, steady warmth motion and convection warmth move limit conditions at the external pipe surface [5,6]. Laminar Flow in cylinders exposed to pivotally fluctuated divider warmth motion was examined in [7,8,9,10,11]. In numerous applications, for example, the water dividers of boilers and sun powered authorities, the Heating surfaces are just halfway warmed along the outline of the pipe while the remainder of cylinder Circumference is thermally protected

* *Corresponding author.*
E-mail address: waddhahhussein@yahoo.com (Wadhah Hussein Aldoori)

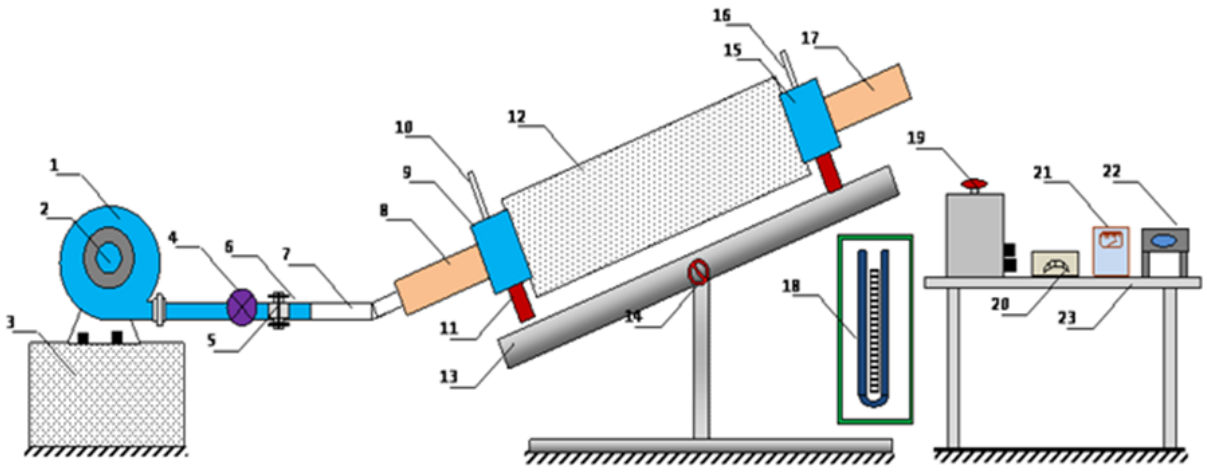
[12,13]. This examination speaks to a numerical investigation of forced convection HT of FDLF in a roundabout cylinder warmed along a fringe point θ of its boundary while the remainder of the circuit is adiabatic. The investigation and tests were done for warming condition; uniform warmth motion along the warmed segment of the cylinder surface. The laminar constrained convection through Newtonian liquids, if there should be an occurrence of pipe streams, was all around examined [14,15]. The speed profile of the completely created laminar stream inside cylinder is outstanding in [16]. The impact of Re and the impact of the heat flow on laminar stream. Their outcomes demonstrated that expansion in the Nu qualities as the HT increments and that free convection impacts would in general decline the HT as proven in [17]. The aim of this study is to change the diameter, fluid velocity and HF to show the effect on heat transfer by mixed convection.

2. Experimental Work

An experimental facility was constructed for laboratory experiments to study the Mixed Convection in a stuffed immersed permeable media warmed with a consistent warmth motion through the three chambers.

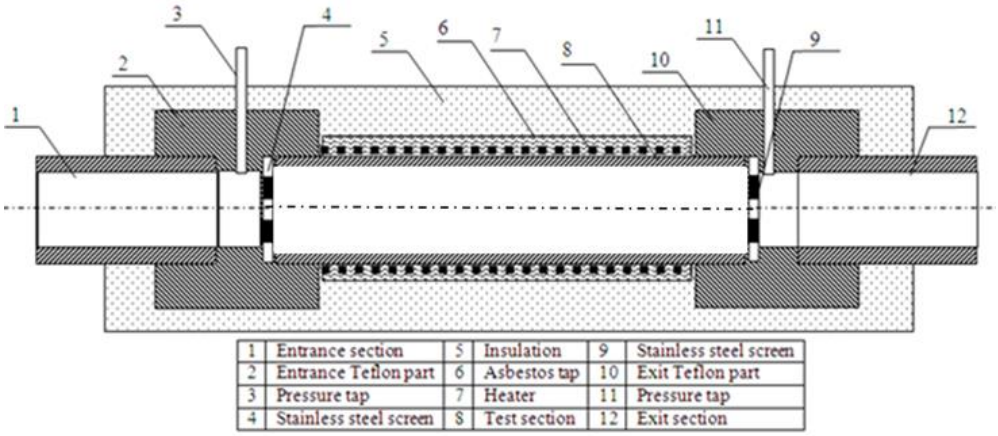
2.1 Test Section and Thermocouples

Three copper cylinder are used, its inside and external separations crosswise over are (0.048, 0.035, 0.02) m and (0.052, 0.038, 0.022) m independently, the length was (0.9 m). 1hp air compressor with a rotational speed of 2500 rpm was used. Thermocouples (T-type) are installed to record the required temperatures along the test section tube. The power supply is used to control the temperature of the Heater. The electrical circuit prepared for this purpose consists of (Ammeter, Voltmeter, Data Koschen, and Variable resistance) to record the required data. An opening plate is used to measure the speed of air. A 1 hp air propeller was used to provide the required flow at the required speed. Figure 1 illustrates all parts of the system. Figure 2 represents the front section of the test section.



1	Centrifugal blower	6	Connection tube	11	Stand	16	Pressure tap	21	Ameter
2	Electrical motor	7	Rubber tube	12	Test section	17	Exit section	22	Digital thermometer
3	Concrete base	8	Entrance section	13	Wooden board	18	U-Tube manometer	23	Stand
4	Flow control valve	9	Entrance teflon part	14	Pointer	19	Variac		
5	Orifice	10	Pressure tap	15	Exit teflon part	20	Voltmeter		

Fig. 1. Schematic of the experimental apparatus



1	Entrance section	5	Insulation	9	Stainless steel screen
2	Entrance Teflon part	6	Asbestos tap	10	Exit Teflon part
3	Pressure tap	7	Heater	11	Pressure tap
4	Stainless steel screen	8	Test section	12	Exit section

Fig. 2. Schematic of test section

2.2 Experimental Procedures

The test method can be recorded as pursue:

1. Turn broadcasting live blower, and the wind stream is controlled.
2. Turn on the power supply.
3. The circuit is closed and held back for three quarters of the hour to reach a steady state condition [19].
4. Logging readings incorporate temperatures, mass flow rate, voltages, and current.

2.3 Data Reduction Analysis

Subsequent to logging the information There are numerous factors have been determined, for example, heat motion, Nu,Re, and Pe Then the nearby warmth move coefficient was determined [19].

$$h_z = \frac{q}{(T_w - T_b)_z} \tag{1}$$

Where (q) is calculated from:

$$q = \frac{Q_i}{A} \tag{2}$$

Where

$$A = \pi DL \tag{3}$$

The bulk temperature was calculated [18].

$$T_b = \frac{(T_o - T_i)}{L} z + T_i \tag{4}$$

The characteristic of the fluid was calculated from equations below [20, 21].

$$\rho_f = 1.21003 + 7.4715 * 10^{-3} T_b - 3.8919 * 10^{-5} * T_b^{\,2} + 4.54786 * 10^{-8} T_b^{\,3} \tag{5}$$

$$\mu_f = 1.577*10^{-4} - 1.285*10^{-6}T_b + 3.836*10^{-9}T_b^{\,2} - 3.662*10^{-12}T_b^{\,3} \quad (6)$$

$$k_f = 0.155 - 1.236*10^{-3}T_b + 3.760*10^{-6}T_b^{\,2} - 3.588*10^{-9}T_b^{\,3} \quad (7)$$

$$\mathrm{Pr}_f = 2.692 - 1.691*10^{-2}T_b - 4.799*10^{-6}T_b^{\,2} - 3.588*10^{-9}T_b^{\,3} \quad (8)$$

$$C_{pf} = 825.885 + 1.627T_b - 4.974*10^{-3}T_b^{\,2} + 5.205*10^{-6}T_b^{\,3} \quad (9)$$

The amount of the heat was determined as pursue..

$$Q = \dot{m}\, C_p(T_o - T_i) \quad (10)$$

Also, the power supply.

$$P = I * V \quad (11)$$

The percentage heat loss.

$$\epsilon = \left(1 - \frac{Q}{P}\right) \quad (12)$$

Also, the LNN was calculated from.

$$Nu_Z = \frac{h_Z\, D}{k} = \frac{q\, D}{k(T_w - T_b)_z} \quad (13)$$

Re was calculated from.

$$Re = \frac{\rho_f u D}{\mu_f} \quad (14)$$

And Pe was calculated as follow.

$$Pe = Re\, Pr \quad (15)$$

Pr was calculated at bulk temperature.

The $Nu_{av}$was calculated from.

$$Nu_{av} = \frac{1}{L}\int_{Z=0}^{Z=L} Nu_Z\, dZ \quad (16)$$

Testes had been curved the following rang ($7.33 \leq q \leq 107.454$) of HF, and Re are used from (1252, 2504, and 3032). Repeat the process at each case or change the diameter of tube (0.02, 0.035 and 0.045) m.

3. Result and Discussion

All tests were performed by changing the following variables HF from $(7.33 - 107.56)\mathrm{W/m^2}$, Re are used from (1252, 2504, and 3032), and the diameter of tube (0.02, 0.035 and 0.045) m.

3.1 Surface Temperature Distribution

Figures 3, 4 and 5 spoke to the connection between the cylinder ST with lenght at deferent estimations of HF pointer as in figs.

For tube diameter of ($D = 0.02m, 0.035m, 0.045m$) and Reynolds numbers are used 3032. The cylinder surface temperature concerning its length proportional to tube length the maximum temperature is occurring at $(\mathrm{z/L} = 0.54,0.6,0.62)$ with temperature differences of (30.44°C and 44.5°C) correspondingly. This conduct because of that limit layer begins from zero at passage of the chamber, and its thickness is expanded to arrive at its greatest incentive at the split.

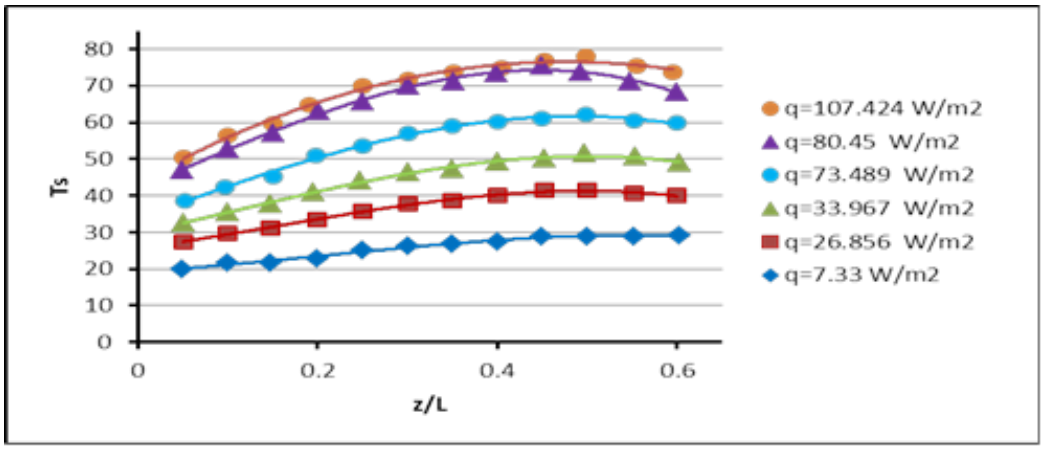


Fig. 3. The cylinder ST with respect to its length for Re = 1252.3 and D = 20mm

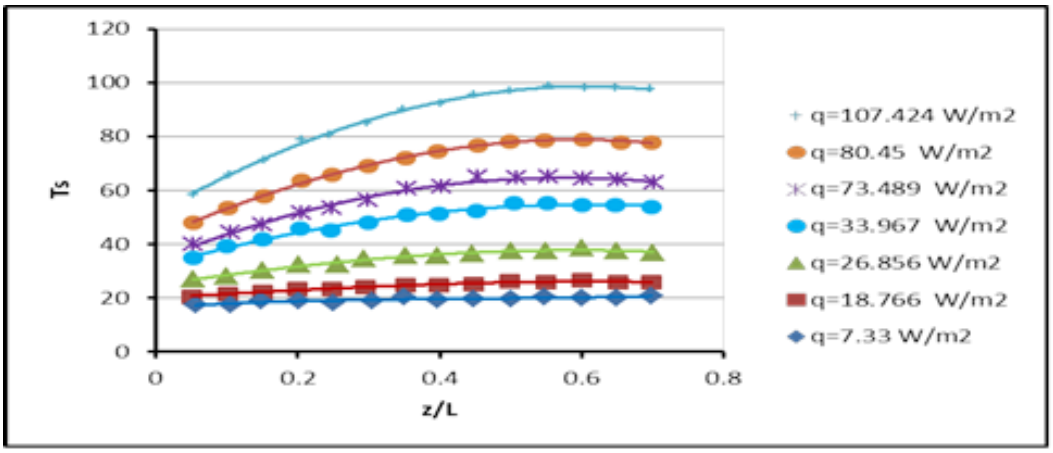


Fig. 4. The cylinder ST with respect to its length for Re = 1252.3 and D = 35mm

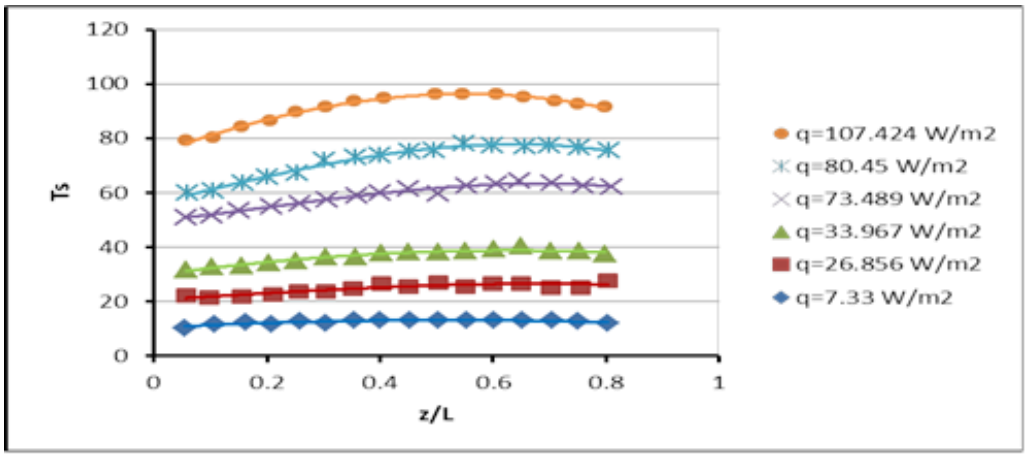


Fig. 5. The cylinder ST with respect to its length for Re = 1252.3 and D = 45mm

3.2 Local Nusselt Distribution (Nu_z)

The variety of (Nu_z for the instance of cylinder distance across (D=0.02m,0.035m,0.045m)and consistent Reynolds number of(Re=1252) regarding tube length is plotted in Figure 6, 7, and 8. As observed from this figures, the nearby Nusselt number abatements with the expansion in the pivotal position in view of the contrast between the mass air and cylinder surface temperature and the thickness of warm limit layer increment to arrive at least an incentive at (z/L=0.4) at that point increment to arrive at beginning worth at(z/L=0.6). The thickness of the limit layer expanding a long way from the bay area, it winds up consistent after warm entrance length. Be that as it may, close to the exit of cylinder warmed locale the Nu_zvalues are slight increments because of the cylinder end misfortunes.

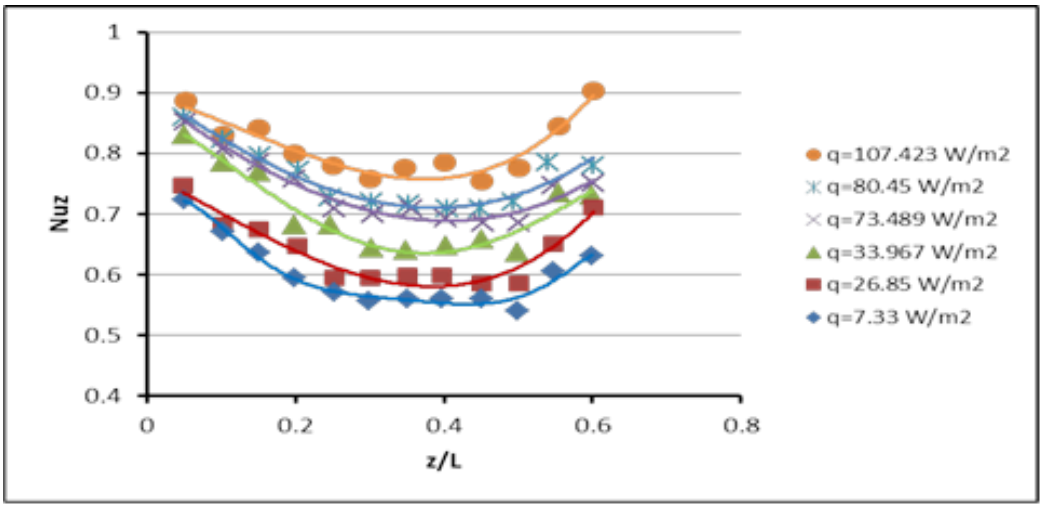


Fig. 6. *Nu$_z$* with respect to tube length for Re = 1252.3 and D = 20mm

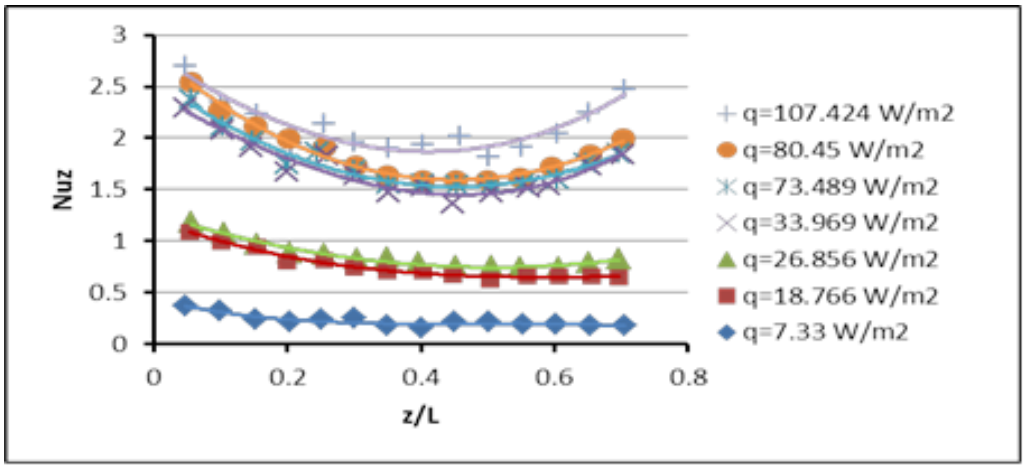


Fig. 7. Nu_z with respect to tube length for Re = 1252.3 and D = 35mm

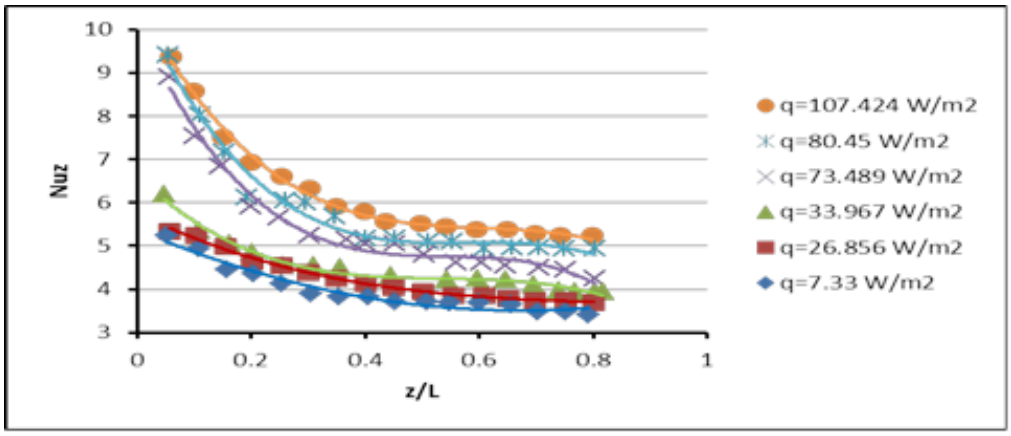


Fig. 8. Nu_z with respect to tube length for Re = 1252.3 and D = 45mm

3.3 Average Nusselt distribution (Nu_{av})

The relationship betweenNu_{av} for the case of tube diameter (D=0.020, 0.035 and 0.045) m at the heat flux $(q = 80.45\ W/m^2)$ for the tube length is plotted in Figure 9. As seen from this figure, at a given heat flux, the LNu increase with the increase in tube diameter. The value of (Nu_{av}) for tube diameter $(D = 0.045m)$ is higher than that for other tubes $(D = 0.035m\ and\ D = 0.02m)$ this is related to the variation of tube diameters. This factor becomes more effective which improves the HT results. Also with increase the tube diameter corresponding higher thermal entrance length for these cases $(at\ D = 0.045\ m, \mathrm{z/L} = 0.5, at\ D = 0.035\ m, \mathrm{z/L} = 0.3, at\ D = 0.02\ m,\ \mathrm{z/L} = 0.23)$ axial position because of the difference between the bulk air and tube ST and the thickness of thermal boundary layer increase.

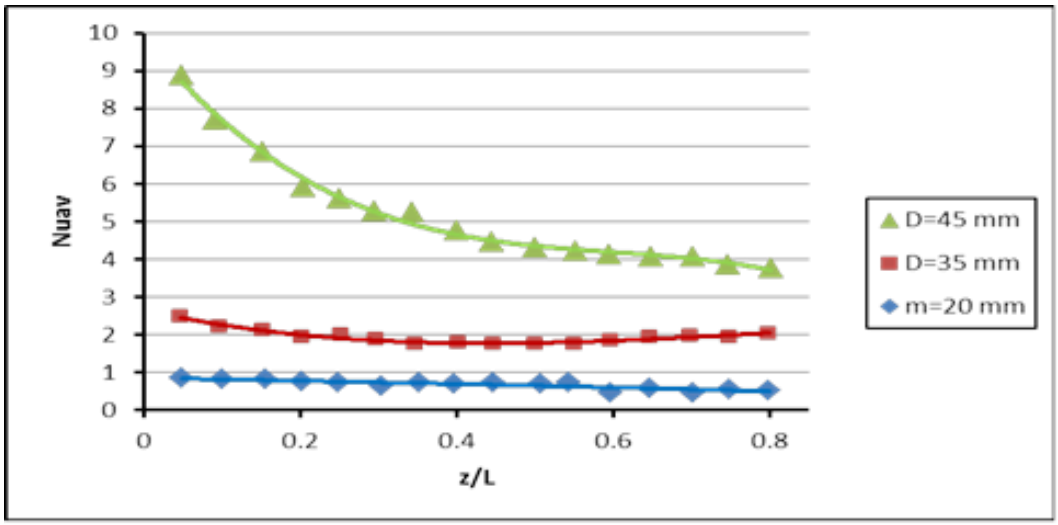


Fig. 9. Nu_{av} with respect to the tube length

The variation of the average Nusselt number (Nu_{av}) with different tubes diameter for different values of heat fluxes which are ranged ($7.33 \le q \le 107.454$) is plotted. The effect of tube diameter on the $Nu_{av}$is illustrated in Figure 10 which indicated that the (Nu_{av}) value increase with the increase in tube diameter. As seen from this figure at tube diameter ($D = 0.02\ m$) the Nussselt has lower value and concentration about average value equal to (0.8). also, with an increase in tube diameter ($D = 0.035\ m$) the value of Nu_{av} increasing at beginning with nonlinear and there is variation these values equal (1.3-2.3). While at ($D = 0.045\ m$) the trend of the curves are nonlinear, and the values of Nu_{av} is ranged for minimum to maximum (4-6.3). So the Nusselt number more variation in this case.

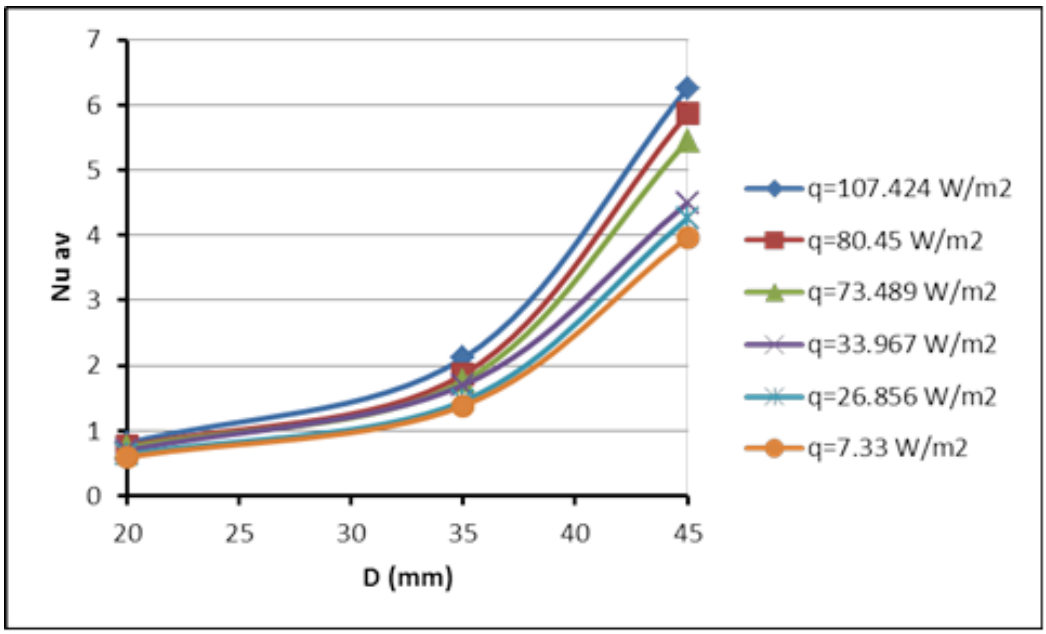


Fig. 10. Nu_{av} with respect to the tube diameter

4. Conclusions

1- Both wall and fluid temperatures increased in a manner that the wall temperatures are higher than the fluid temperatures in the tube center.

2- The surface temperatures decreased as the diameter increased for the same imposed heat flux.
3- At the tube entrance section, the values of the LNu are almost close together, and after the tube entrance section, the values of the local Nusselt number decreased slightly and reached its minimum value at the tube exit section.
4- The LNu increased as the Re, and HF increased for the same tube diameter.
5- The average Nu increased as the tube diameter increased and the variation between then is nonlinear.

Acknowledgement
The authors would like to thank Tikrit University and the Northern Technical University for providing laboratory facilities.

References

[1] J. P. Hartnett, "Single Phase Channel Flow Forced Convection HT," DOE/ER/1331/--T1, (1999). DOI: 10.2172/335180
[2] R. K. Shah and M. S. Bhatti, "Laminar Convective HT in Ducts," Handbook of Single-Phase Convective HT, Edit. S. Kakaç and W. Aung, Chapter 3, (1987).
[3] R. K. Shah and A. L. London, "Laminar Flow Forced Convection in Ducts", Chapter 5, pp.78-152, (1978).
[4] M. L. Michelsen and J. Villadsen, "The Graetz Problem with Axial Heat Conduction", Int. *Journal of Heat Mass Transfer*, Vol. 17, No.11, pp. 1391-1402, (1974). https://doi.org/10.1016/0017-9310(74)90140-9
[5] J. W. Ou and K. C. Cheng, "Viscous Dissipation Effects on Thermal Entrance HT in Laminar and Turbulent Pipe Flows with Uniform Wall Temperature", ASME, 74- HT-50, **(1974).**
[6] M. E Arici, "Analysis of the conjugate effect of wall and flow parameters on pipe flow heat Transfer", Proceedings of the Institution of Mechanical Engineers. Part C, *Journal of Mechanical Engineering Science*, vol. 215 C3 pp. 307, (2001). https://doi.org/10.1243/0954406011520733
[7] V. P. Tyagi, "Laminar Forced Convection of Dissipative Fluid in a Channel", *Journal of HT*, Vol. 88, No.2, pp. 161-169, (1966). https://doi.org/10.1115/1.3691501
[8] L. N. Tao, "On Some Laminar Forced Convection Problems", *Journal of HT*, Vol. 83, No.4, pp. 466-472, (1961). https://doi.org/10.1115/1.3683669
[9] Al Doori, Wadhah. Hussein, "Enhancement of natural convection HT from the rectangular fins by circular perforations", *International Journal of Automotive and Mechanical Engineering*, 2011. 4: p. 428-436, (2011). DOI: http://dx.doi.org/10.15282/ijame.4.2011.5.0035
[10] W. C. Reynolds, "HT to Fully Developed Laminar Flow in a Circular Tube with Arbitrary Circumferential Heat Input", *Journal of HT*, Vol. 82, No.2, pp. 108-112, (1960). https://doi.org/10.1115/1.3679887
[11] Al Doori, Wadhah H., "Numerical estimation of pressure drop and HT characteristics in annular finned channel heat exchangers with different channel configuration", *HT—Asian Research*, vol. 48, issue 4, PP. 1280-1291, (2019). DOI: 10.1002/htj.21432, https://onlinelibrary.wiley.com/journal/15231496
[12] E. M. Sparrow and S. V. Patankar, "Relationships Among Boundary Conditions and Nusselt Numbers for Thermally Developed Duct Flows", *Journal of HT*, Vol. 99, No.3, pp. 483-485,(1977). https://doi.org/10.1115/1.3450722
[13] Al Doori, Wadhah Hussein Abdulrazzaq, "Effect of using various longitudinal fin number in annular finned channel heat exchangers on Heat flow characteristics", *Journal of Advanced Research in Fluid Mechanics and Thermal Sciences* 53, Issue 1, 1-10, (2019). http://www.akademiabaru.com/arfmts.html
[14] J. N. N. Quaresma and R.M. Cotta, "Exact solutions for thermally developing tube flow with variable wall heat flux", *International Communications in Heat and Mass Transfer*, Vol. 21 No. 5, pp. 729-742, (1994). https://doi.org/10.1016/0735-1933(94)90074-4
[15] A. Barletta, E. Zanchini, "Thermal entrance region for laminar forced convection in a circular tube with a power-law wall heat flux", *International Journal Heat Mass Transfer*, Vol. 39, No. 6, pp. 1265-1272, (1996). https://doi.org/10.1016/0017-9310(95)00200-6
[16] Al-Taha, Wadhah Hussein Abdulrazzaq, "Effect of the circular perforations on the HT enhancement by the forced convection from the rectangular fins", *Diyala Journal of Engineering Sciences*, Iraq, Vol.11, No.3, PP. 62-70, Sept. 2018. http://www.enginmag.uodiyala.edu.iq/pages?id=70

[17] Y. K. Salman, Hussein A. Mohammed, "Experimental investigation of mixed convection HT for thermally developing flow in a horizontal circular cylinder", *Applied Thermal Engineering*, Vol. 27, No. 8-9, pp.1522–1533. (2007). https://doi.org/10.1016/j.applthermaleng.2006.09.023
[18] Holman JP. HT, 10th ed., USA: McGrawHill Companies, Inc.; 2010.
[19] Thamir K. Ibrahima, Ahmed T. Al-Sammarraie, Wadhah H. Al-Taha, Mohammad Reza Salimpour, Manar Al-Jethelah, Ahmed N. Abdalla, Hai Tao, "Experimental and numerical investigation of HT augmentation in heat sinks using perforation technique", *Applied Thermal Engineering*, 160,m113974. Publisher: Elsevier (2019). https://doi.org/10.1016/j.applthermaleng.2019.113974
[20] Al Doori, Wadhah.H., "Analysis, Performance, And Optimization Of Perforated And Non-Perforated Fins Under Forced Convection", Ph.D., thesis, Sudan University of Science & Technology, Sudan, (2018). http://repository.sustech.edu/handle/123456789/20703
[21] Nageeb Salman Abtan, Ataalah Hussain Jassim, Mustafa Shakir Marmoos, " Study on the Effects of Rotational and Transverse Speed on Temperature Distribution through Friction Stir Welding of AA2024-T3 Aluminium Alloy", *Journal of Advanced Research in Fluid Mechanics and Thermal Sciences*, Vol.11, No. 1, pp. 55-69, (2019).

Penerbit Akademia Baru

Engineering Science and Technology Conference Proceedings

Journal homepage: www.akademiabaru.com/EST.html

The Role of Coherent Vortices in The Mixing Process Of a Coaxial Jet

Open Access

Safer Nabil Belkacem[1,*]

[1] Department of physics, university of M'hamed Bouguerra Boumerdes, Algeria

ABSTRACT

This paper examines the role of coaxial jet vortex structures in the mixing process, using a numerical approach such as Large Scale Simulation, considering the coaxial jet configuration as a hot primary jet and an unheated secondary jet. This study is based on the implementation of a new Riemann solver for convective flues resolution. Therefore, the contour and profile of the average and instantaneous fraction of the mixture were plotted and analyzed. Two coherent vortices were observed in a coaxial jet after a molecular diffusion phase. The first vortex was the Kelvin-Helmholtz vortices, which play a very important role in the mixing process. These vortices carry the species and promote the radial transfer of the mixing fraction. The second vortex concerns longitudinal vortices, which allow the passive tracer of the annular jet to be ejected into the central jet and into the surrounding fluid.

Keywords:
Coherent vortices; mixing process;
coaxial jet

Copyright © 2019 PENERBIT AKADEMIA BARU - All rights reserved

1. Introduction

Coaxial jets are considered an effective way to mix two different fluids. The coaxial jet configuration is widely used in industrial systems, e. g. in combustion chambers and gas turbines.

Jet flow dynamics are largely defined by the movement of coherent vortices during their first development, it is interesting to understand the dynamics of these vortices and to be able to control them in a second time. Efficient manipulation of the behaviour of these coherent vortices to improve industrial processes related to mixing phenomena.

The prediction of coherent vortices in the mixing process involves in-depth information on the spatial and temporal evolution of the scalar field, which is difficult to obtain in experiments requiring a lot of material resources [1-6], therefore, numerical simulation is the most widely used and least expensive process.

The use of RANS [7-9] turbulence closure models to study the role of coherent vortices in the mixing process cannot be obtained with more precision. However, direct numerical simulation is a more efficient way to predict the behaviour of coherent vortices in the mixing process, but the simulation of unstable flows and Reynolds number is very high and involves a calculation cost too high in memory size and CPU time for current computer resources. Therefore, Large Eddy Simulation remains the best method possible to study these flows.

[*] *safer nabil bellkacem.*
Safer_n@hotmail.com (safer nabil belkacem)

The Large Eddy Simulation is a very effective tool for investigating coherent vortice sand their role in the mixing process in coaxial jet flow [10-13]; this method provides more accurate information on temporal and spatial evolutions of the mixture fraction.

Therefore, the objective of this work is to study the vortex dynamics of the coaxial jet in order to improve its mixing properties. The coaxial jet configuration adopted in this study is a coaxial jet with a hot primary jet and an unheated secondary jet, where the passive scalar is injected at the secondary jet, or this configuration is widely used in industrial applications.

The turbulence model (LES) is used as the investigation tool in this work. This approach allows to solve the largest scales and to apply the Smagorinsky turbulence model on small scales. The mass, Navier stockes, energy and species conservation equations are solved through a new solver of the Riemann problem called the linearization solver of the characteristic equations [14-15], which is a simple to build and quick to use solver compared to other Riemann solvers [16-17].

2. Governing Equations

The equations for conservation of mass, momentum, energy and concentration, in conservative and dimensional form are expressed as follows:

$$\frac{\partial U}{\partial t} + \sum_{i=1}^{3} \frac{\partial \vec{F_i}}{\partial x_i} = 0 \tag{1}$$

Where, U is the conservative variables; and F_i represents the numerical flows on each flow direction x, y and z.

Equation (1) can be expressed using the matrix-vector notation as:

$$U = \begin{bmatrix} \rho \\ \rho u \\ \rho v \\ \rho w \\ \rho E \\ \rho f_l \end{bmatrix} \qquad F_i \begin{bmatrix} \rho u \\ \rho u_i u + \delta_{i1} p - (\frac{\mu}{Re} + \rho \nu_{sgs})\tau_{i1} \\ \rho u_i v + \delta_{i1} p - (\frac{\mu}{Re} + \rho \nu_{sgs})\tau_{i2} \\ \rho u_i w + \delta_{i1} p - (\frac{\mu}{Re} + \rho \nu_{sgs})\tau_{i3} \\ (\rho e + p)u_i - \frac{\gamma M^2 \mu}{Re}(u\tau_{i1} + v\tau_{i2} + w\tau_{i3}) + \frac{\gamma}{\gamma - 1}(\frac{\mu}{RePr} + \frac{\rho \nu_{sgs}}{Pr_{sgs}})\frac{\partial T}{\partial x_i} \\ \rho f_l u_i + \rho \left(\frac{1}{Sc.Re} + \frac{\nu_{sgs}}{Sc_{sgs}}\right)\frac{\partial f_l}{\partial x_i} \end{bmatrix}$$

Where, ρ, u , v, w, e and Y are the density, velocity components on each flow direction x, y and z, the total specific energy, and fraction mixing respectively.

The systems of equations (1) are closed using the equation of state for a perfect gas:

$$P = \rho RT \tag{2}$$

Viscous stress tensorτ_{ij} is defined by:

$$\tau_{ij} = \frac{1}{2}\left(\frac{\partial u_i}{\partial x_j} + \frac{\partial u_j}{\partial x_i} - \frac{2}{3}\delta_{ij}\left(\frac{\partial u_k}{\partial x_k}\right)\right) \tag{4}$$

The turbulence model of large eddy simulation is an alternative for computing flows at higher Reynolds number. In this technique, only larger structures are computed, and smaller scales effects are taken into account via a sub-grid scale model. In this study, the Smagorinsky model [18] was chosen, a turbulent viscosity ν_{sgs} can by calculate as follows:

$$\nu_{sgs} = (C_s\Delta)^2\sqrt{2S_{ij}S_{ij}} \tag{5}$$

Where, C_s is a Smagorinsky constant, and Δ is the filter width and is defined [19]:

$$\Delta = \left(\Delta_x\Delta_y\Delta_z\right)^{1/3} \tag{6}$$

Where,$\Delta_x, \Delta_y, \Delta_z$ are the local mesh spacing in x, y and z directions respectively.

2.1. Initial conditions

Similar to a single jet initial profile, an initial hyperbolic double tangent velocity profile is used to approximate the actual velocity profile of a coaxial jet, as follows:

.

$$u(r) = \begin{cases} U_s - \frac{U_P - U_S}{2}\left[1 - tanh\left[\frac{R_p}{4\theta_p}\left[\frac{r}{R_p} - \frac{R_p}{r}\right]\right]\right] & si \quad r \geq R_m \\ U_\infty - \frac{U_S - U_\infty}{2}\left[1 - tanh\left[\frac{R_S}{4\theta_S}\left[\frac{r}{R_s} - \frac{R_s}{r}\right]\right]\right] & si \quad r \leq R_m \end{cases} \tag{7}$$

Were $\theta_p$and θ_s are the momentum thicknesses of the shear layer of primary and secondary jet respectively.

2.2. Initial condition of passive tracer

Similar to initial profile of velocity, the initial profile of the mixture fraction can by expressed as:

$$f(x=0,r,t) = \begin{cases} \frac{f_1+f_2}{2} + \frac{f_1-f_2}{2}\left[1 - tanh\left[\frac{R_p}{4\theta_p}\left[\frac{r}{R_p} - \frac{R_p}{r}\right]\right]\right] & si \quad r \leq R_m \\ \frac{f_2}{2} + \frac{f_2}{2}\left[1 - tanh\left[\frac{R_S}{4\theta_S}\left[\frac{r}{R_s} - \frac{R_s}{r}\right]\right]\right] & si \quad r > R_m \end{cases} \tag{8}$$

If the passive scalar is injected into annular jet, set: $f_1 = 0$ and $f_2 = 1$ and if the passive scalar is injected into central jet, set: $f_1 = 1$ and$f_2 = 0$.

2.3. Boundaries Conditions

At initial domain, the transverse direction *y* and *z* are zero Velocity components. Randomly generated disturbances are imposed on the transverse direction *y* and *z*. At the Upper and lower boundaries are the sliding conditions. At the front and rear boundaries of the domain are periodic. At the exit of the domain the boundary conditions are convective.

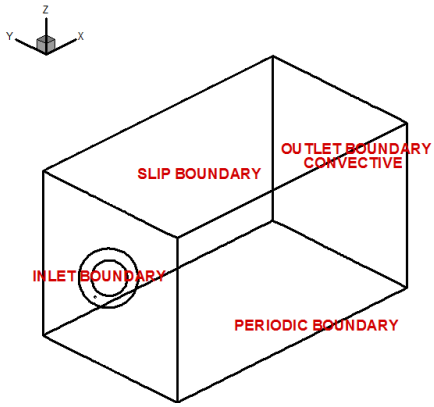


Fig.1. Boundaries conditions

3. Numerical Methods

Spatial derivatives of fluxes in Eq. (1) for Cartesian grid can be expressed by spatial finite differencing operators:

$$L_h\left(\bar{U}_{ijk}^n\right) = \frac{{F_1}_{i-\frac{1}{2},j,k}^{n} - {F_1}_{i+\frac{1}{2},j,k}^{n}}{\Delta x} + \frac{{F_2}_{i,j-\frac{1}{2},k}^{n} - {F_2}_{i,j+\frac{1}{2},k}^{n}}{\Delta y} + \frac{{F_3}_{i,j,k-\frac{1}{2}}^{n} - {F_3}_{i,j,k+\frac{1}{2}}^{n}}{\Delta z} \tag{9}$$

The new linearization solver for the equation's characteristic of the approximate Riemann problem is applied to resolve the one-dimensional hyperbolic equation, the solver is based on the linearization of the differential relations along the characteristic curves of the one-dimensional hyperbolic conservation laws. It involves construction of the parameters at the cell interface such that they are consistent with the system of characteristic relations [20].

In order to evaluate the in-viscid (hyperbolic) fluxes on the cell boundaries, In the first step, the flow vector F_1^{inv} evaluated with as u the normal velocity component, and v and w as tangential components and the tangential components are passively convected by the normal component, but taking into consideration the direction of the information flow in the normal direction. Similarly, flux vector F_2^{inv} in y −direction is evaluated using v as the normal velocity component, and u and w as the tangential components. Finally, flux vector F_3^{inv} in z − direction is evaluated using $w$as the normal velocity component, and u and v as the tangential components Kopchenovet and al. [21]. Riemann invariants$\vartheta_{0_{i+\frac{1}{2}}}$, $\vartheta_{-_{i+\frac{1}{2}}}$ and $\vartheta_{+_{i+\frac{1}{2}}}$ are expressed in terms of the coefficients Lany [22]:

$$\vartheta_{0_{i+\frac{1}{2}}} = p + \alpha_{0_{i+\frac{1}{2}}}\rho \tag{10}$$

$$\vartheta_{-_{i+\frac{1}{2}}} = u + \alpha_{-_{i+\frac{1}{2}}}p \tag{11}$$

$$\vartheta_{+_{i+\frac{1}{2}}} = u + \alpha_{+_{i+\frac{1}{2}}}p \tag{12}$$

A one-step non-iterative method is used to calculate the coefficients and invariants at interface point at $(i+\frac{1}{2})$. Coefficients$\alpha_{+_{i+\frac{1}{2}}}$, $\alpha_{-_{i+\frac{1}{2}}}$and $\alpha_{0_{i+\frac{1}{2}}}$are expressed in terms of the Riemann invariants$\vartheta_{+_{i+\frac{1}{2}}}$, $\vartheta_{-_{i+\frac{1}{2}}}$ and$\vartheta_{0_{i+\frac{1}{2}}}$.

$$\alpha_{+_{i+\frac{1}{2}}} = \begin{cases} \frac{\gamma-1}{2}\frac{(\vartheta^L_{-B}-\vartheta^L_{+A})}{\vartheta^L_0} & if \quad C_+ > 0 \\ \frac{\gamma-1}{2}\frac{(\vartheta^R_{-B}-\vartheta^R_{+A})}{\vartheta^R_0} & if \quad not \end{cases} \tag{13}$$

$$\alpha_{-_{i+\frac{1}{2}}} = \begin{cases} \frac{\gamma-1}{2}\frac{(\vartheta^L_{+A}-\vartheta^L_{-B})}{\vartheta^L_{0C}} & if \quad C_- > 0 \\ \frac{\gamma-1}{2}\frac{(\vartheta^R_{+A}-\vartheta^R_{-B})}{\vartheta^R_{0C}} & if \quad not \end{cases} \tag{14}$$

$$\alpha_{0_{i+\frac{1}{2}}} = \begin{cases} -\left[\frac{\gamma}{2}(\vartheta^L_{-B}-\vartheta^L_{+A})\right]^2 & if \quad C_0 > 0 \\ -\left[\frac{\gamma}{2}(\vartheta^R_{-B}-\vartheta^R_{+A})\right]^2 & if \quad not \end{cases} \tag{15}$$

$$\vartheta_{+_{i+\frac{1}{2}}} = \begin{cases} \vartheta^L_{+A} & if \quad C_+ > 0 \\ \vartheta^R_{+A} & if \quad not \end{cases} \tag{16}$$

$$\vartheta_{-_{i+\frac{1}{2}}} = \begin{cases} \vartheta^L_{-B} & if \quad C_- > 0 \\ \vartheta^R_{-B} & if \quad not \end{cases} \tag{17}$$

$$\vartheta_{0_{i+\frac{1}{2}}} = \begin{cases} \vartheta^L_{0C} & if \quad C_0 > 0 \\ \vartheta^R_{0C} & if \quad not \end{cases} \tag{18}$$

Characteristic speeds $C_+, C_0 \; and \; C_-$ are estimated using the following formulas:

$$C_+ = u + a \tag{19}$$

$$C_0 = u \tag{20}$$

$$C_- = u - a \tag{21}$$

Using these constants for the calculation of the primitive variables, the results obtained are as follows:

$$p = \left(\vartheta_{+_{i+\frac{1}{2}}} - \vartheta_{-_{i+\frac{1}{2}}}\right)\left(\alpha_{+_{i+\frac{1}{2}}} - \alpha_{-_{i+\frac{1}{2}}}\right) \tag{19}$$

$$u = \vartheta_{+_{i+\frac{1}{2}}} - \alpha_{+_{i+\frac{1}{2}}} p \tag{20}$$

$$\rho = \frac{\left(\vartheta_{0_{i+\frac{1}{2}}} - p\right)}{\alpha_{0_{i+\frac{1}{2}}}} \tag{21}$$

Using the values of *p, ρ* and *u*, to calculate the in-viscid flows at the interfaces of cell i.

In order to evaluate the viscous (elliptic) components of the numerical flux, both the solution values and their gradients at the cell boundaries must be known as:

$$F_1^{vis}{}^n_{i+\frac{1}{2},j,k} = F_1^{vis}(W^n_{i+\frac{1}{2},j,k}, \nabla W^n_{i+\frac{1}{2},j,k}) \quad (22)$$

$W^n_{i+\frac{1}{2},j,k}$ is evaluated as an average of the left and right solution states of cell interface *i* :

$$W^n_{i+\frac{1}{2},j,k} = \frac{W^n_L + W^n_R}{2} \quad (23)$$

Gradient at the cell face, $W^n_{i+\frac{1}{2},j,k}$ is evaluated using:

$$\nabla W^n_{i+\frac{1}{2},j,k} = \frac{W^n_{i+1,j,k} - W^n_{i,j,k}}{dx} \quad (24)$$

The time step is determined by the stability analysis of a numerical scheme, which verifies the Friedrichs-Lewy Current criterion [23] and is defined by a classical advective criterion Δt_1, and a diffusive criterion Δt_2 [24].

$$\Delta t_1 = \frac{CFL}{max\left(\frac{|u|+c}{\Delta x}, \frac{|v|+c}{\Delta x}, \frac{|w|+c}{\Delta x}\right)} \quad (25)$$

$$\Delta t_2 = \frac{VNN}{max\left(\frac{4\mu}{3\rho}, \frac{\gamma.\mu}{\rho;Pr}\right)\left(\frac{1}{\Delta x^2}, \frac{1}{\Delta y^2}, \frac{1}{\Delta z^2}\right)} \quad (26)$$

Simulation time step then takes the more restrictive of the two criteria:

$$\Delta t = min(\Delta t_1, \Delta t_2) \quad (27)$$

4. Results and Discussions

Calculation range extends over $30D_p$ in the axial direction and $17D_p$ in the transverse directions *y* and *z*. [L_x x L_y x L_z] = [$30D_p$ x $17D_p$ x $17D_p$]. The main physical characteristics of the simulated jet are given in Table. 1.

Table 1
Physical parameters of coaxial jet simulations

U_s/U_p	D_p/D_s	T_p/Ts	M_p	M_s	Re_p	U_s/U_{amb}	T_s/T_{amb}
0.7	2	2.7	0.5	0.57	$6.25x10^5$	0.1	1

$(\ )_p$, $(\ )_s$ and $(\ )_{amb}$: Index of primary, secondary and ambient environment.

4.1 Mesh size selection

Three Cartesian structured meshes with different mesh densities (3D) were tested to study the mesh sensitivity, when the mesh resolution is sufficiently improved. Mesh 1: used 160×75×75 mesh points along the *x*-, *y*- and *z*-directions, mesh 2: used 215×125×125 mesh points along the *x*-, *y*- and *z*-directions and mesh 3: used 385×125×125 mesh points along the *x*-, *y*- and *z*-directions.

Figure 3 shows the development of the longitudinal velocity fluctuation spectrum on the primary jet axis in x/D_p = 10. Figure 2 show that the solver used in this work properly detects turbulence when the resolution of the mesh is sufficiently improved.

The spectrum has an inertial zone with a power law in *K=-5/3*. This observation indicates that large eddies are well represented with minimal dependence on short waves as the calculation mesh increases. Therefore, this result shows that the solver used is chosen for its stability, convergence robustness and high degree of validation. The mesh used in the rest of the work will be 385x 125x 125 points. This choice is based on the compromise between the available computing materials and the accuracy of the results.

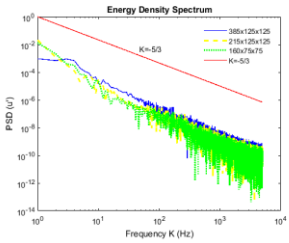


Fig. 2. PSD longitudinal velocity at different grid resolutions

4.2 Validation

A convergence test was performed to demonstrate that the converging calculations satisfying the experimental measurements. The mean development of a coaxial jet with a velocity ratio less than one seems very similar to that of a single jet. To ensure that the procedure that was introduced for the mixing study is valid, we proceed to compare the results of this simulation with those of the experimental results of Mi and al. [25] and Perez-Alvarado [26], for a single jet.

In Figure 3 the transverse profile of the mean of the mixture fraction obtained in the present work is plotted with the average profile obtained by Mi et al. [25] and Perez-Alvarado [26]. A very good agreement is observed between the three profiles, despite different downstream measurement locations, it is observed that the cross-sectional profile of the average mixture fraction had reached its state of self-similarity at x/D_{p}=10.

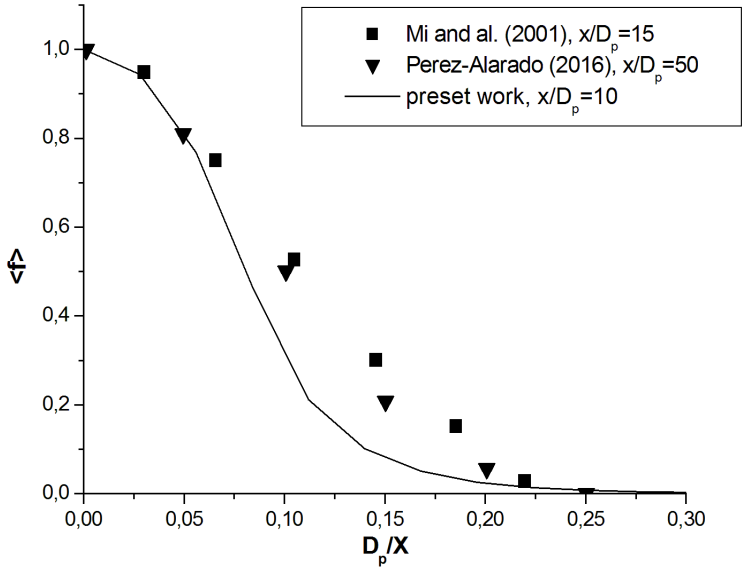


Fig. 3. Transverse profile of the mean of the fraction mixture for the coaxial jet with tracer injected in central jet at x/D=10. Data of authors: Mi et al. [25], Perez-Alvarado [26] included for comparison.

4.3. Inner and outer Kelvin-Helmholtz vortices

The studied jet corresponds to a heated coaxial jet and the passive tracer is introduced at the level of the external jet. The mixing fraction, modelled by a passive scalar, has an initial profile of f=1 in the annular jet and f = 0 in the inner jet and in the co-current.

Figure 4 shows the instantaneous contours of the mixture fraction in the central plane of the jet. In the vicinity of the outlet nozzle up to x/D_p = 7, the disturbances are low; it is observed that the mixture between species of the annular jet and the central jet, and between the annular jet species and the ambient fluid are mainly due to molecular diffusion.

Above x/D_p = 7, the natural development of instabilities occurs in the internal and external shear layers, and the turbulent mixing is initiated by the emergence of the internal and external Kelvin-Helmholtz eddies. Finally, above x/D_p= 20, the development of secondary structures initiates turbulence at small scales of turbulence, resulting in a more intense turbulent mixture.

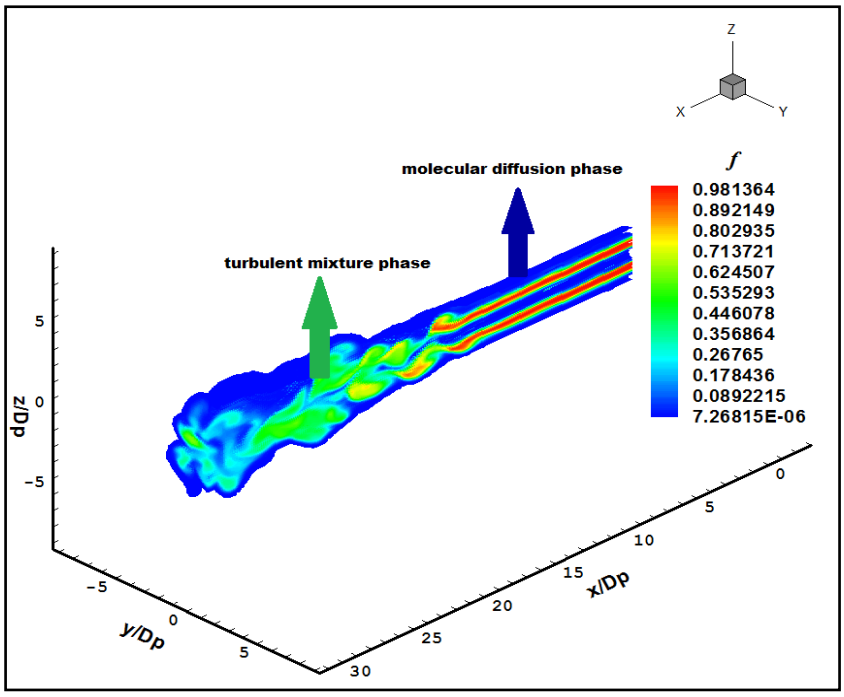


Fig. 4. Cross-section view of the instantaneous contours of the mixing fraction in the central plane

Figure 5 shows the instantaneous contours of the mixture fraction in the transverse plane at several downstream locations; it is observed that in the fully developed turbulence zone, the longitudinal vortices lead the tracer to the mushroom shapes in the transverse planes of the mixture fraction.

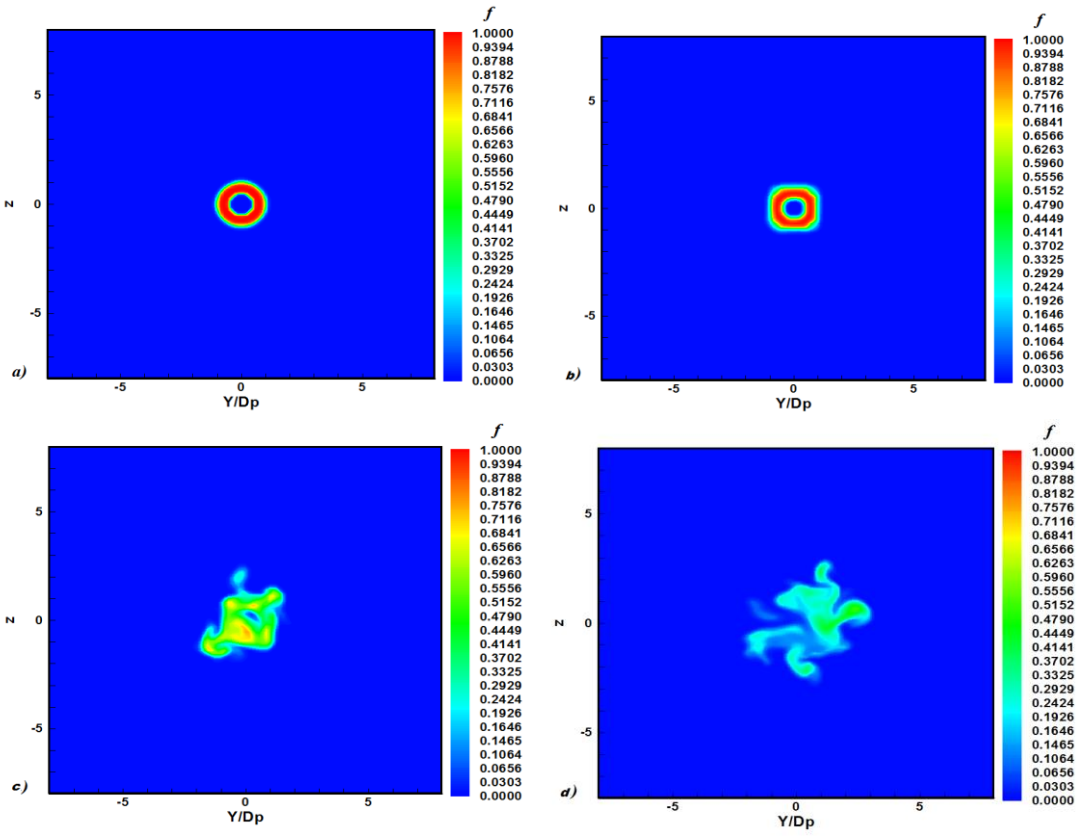


Fig. 5. Instantaneous contours of mixing fraction in the transverse plane and at several downstream locations: a) x/D_p=2, b) x/D_p=5, c) x/D_p=10, d) x/D_p=20

Geometric characterization of surfaces where species are in equal proportions is important for understanding combustion processes. Figure 6 shows the isosurface of the mixing fraction (f = 0.5) with tangential vorticity. The tangential vorticity is cut off in the central plane to observe the mixing layer's (inner and outer). It can be seen that the isosurface of the mixing fraction deforms after the amplification of the jet instabilities. Therefore, this isosurface highlights the presence of the large-scale flow structures (Kelvin-Helmholtz vortices).

The inner and outer Kelvin-Helmholtz vortices increased beyond x/D_p = 7, and they transported the mixture fraction, promoting the radial transfer of the mixing fraction on each side of the sheared layers (inner and outer). As a result, the inner and outer isosurfaces were recorded as having two distinct shapes: up to x/D_p= 15, the two isosurfaces corresponding to the inner and outer sheared layers are completely dissociated. Then, beyond x/D_p = 20, the isosurfaces were fused and only one mixing layer was distinguished. This shows an interpenetration of the species of each jet that result from the emergence of longitudinal vortices. These vortices, allow the tracer of the annular jet to be ejected into the central jet and into the surrounding fluid.

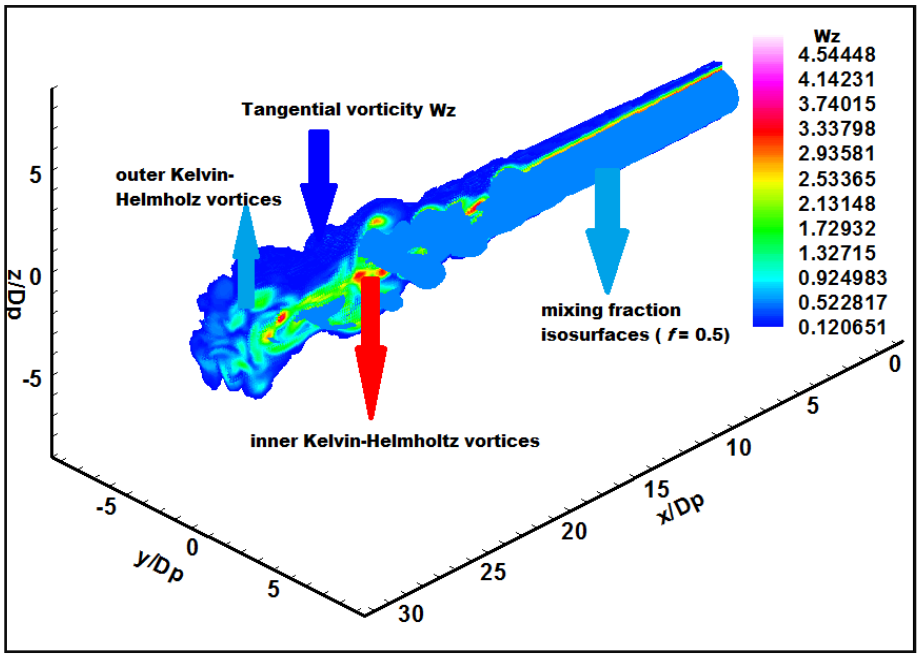


Fig. 6. Cut view of the tangential vorticity with mixing fraction isosurface (f = 0.5)

Figure 7 illustrates the ejection mechanism by the longitudinal vortices. These vortices are illustrated by isosurfaces of positive Q, we recall that Q is the second invariant of the velocity gradient tensor. In Figure 7 the isosurface of the mixing fraction (f = 0.5) with isosurfaces of positive Q are shown. The tracer is pumped from the annular jet to be ejected into the surrounding fluid. This mechanism leads the tracer to mushroom shapes in transverse planes of the mixture fraction as show in figure 5. The tracer in different transverse planes reveals that the intermittent specificity of the turbulent mixture during the transition comes from a combination of radial pulsation due to the Kelvin-Helmholtz rings and these mushroom structures that characterize the ejection phenomenon involved by the longitudinal vortices.

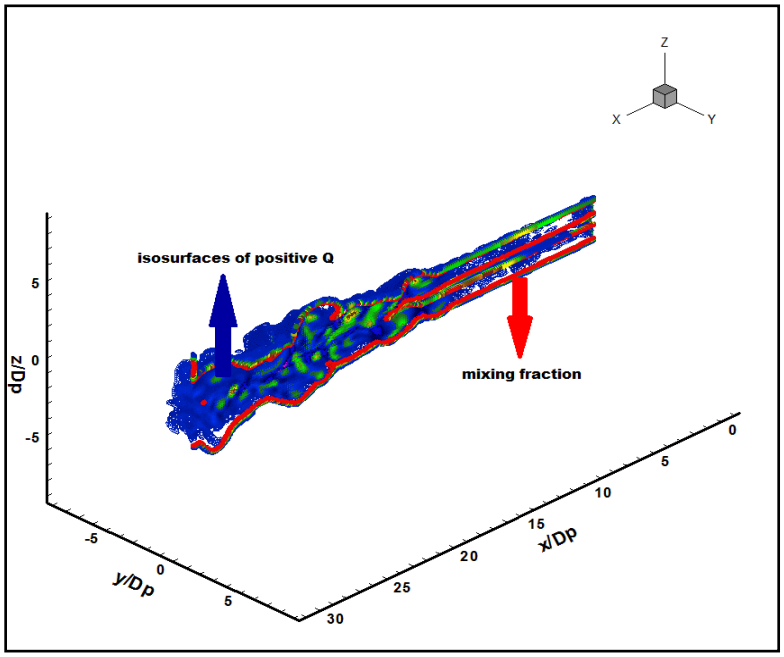


Fig. 7. Isosurfaces of positive Q with mixing fraction isosurface (f = 0.5)

Figure 8 shows the temporal power spectral density (PSD) of the transverse velocity fluctuation at x/D_p = 5 and along the internal and external shear layer. Indeed, the figure 9 shows the predominance of an axisymmetric mode (Kelvin-Holmheltz vortices) on each of the shear layers. This mode is characterized by peaks with Strouhal number St = 0.6 and S t = 0.75 for the inner and outer layers respectively.

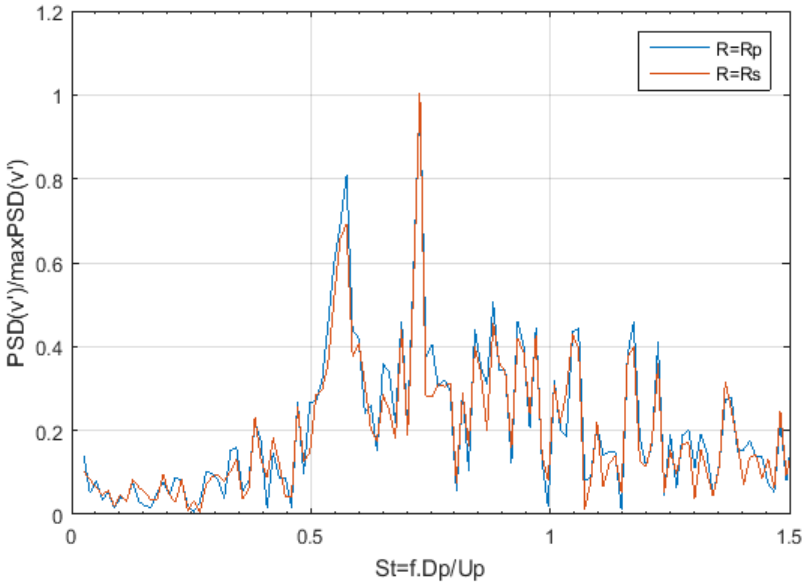


Fig.8. PSD radial velocity profile at x/D_p=5

Figure 9 shows the temporal power spectral density (PSD) of the transverse velocity fluctuation at x/D_p = 15 and along the internal and external shear layer. Indeed the figure 12 shows the frequency of vortex matching St = 0.45 of the external shear layer for x/D_p= 10, this frequency corresponds to the frequency of the most amplified mode of the inner layer (longitudinal vortices),

that means, the vortex pairing of the outer layer is thus linked to the formation of the structures of the inner layer.

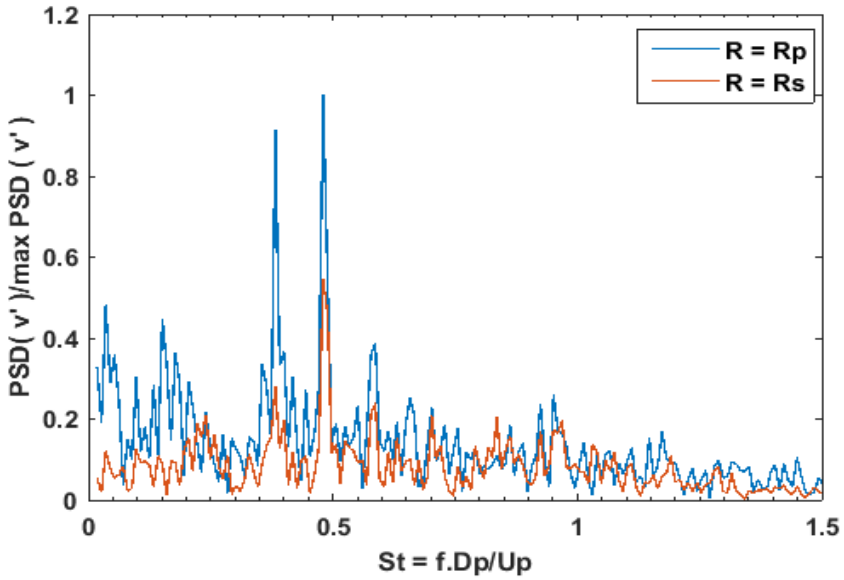


Fig. 10. PSD radial velocity profile at x/D_p=15

5. Conclusions

This paper studied the role of coherent vortices in the mixing process in a turbulent coaxial jet, using a numerical approach such as Smagorinsky Large Scale Simulation. The research approach of this study was based on the implementation of a new Riemann solver, called the linearization solver of the equation's characteristic.

As a result, it can be concluded that two coherent vortices were observed in a coaxial jet flow after a molecular diffusion phase; the first vortices are the Kelvin-Helmholtz vortices and their development during the transition phase. These coherent vortices play a very important role in the mixing process, transporting species by promoting the radial transfer of the mixture fraction on each side of the sheared layers (inner and outer).

In the fully developed turbulence zone, the longitudinal vortices that appear in pairs allow the passive tracer from the annular jet to be ejected into the central jet and into the surrounding fluid. This is caused by the interpenetration of the species of each jet (central and annular) due to the emergence of longitudinal vortices.

The ejection mechanism of the passive tracer by the longitudinal vortices leads it to mushroom-shaped shapes for views in transverse planes of the mixture fraction.

The tracer in different transverse planes reveals that the intermittent specificity of the turbulent mixture during the transition comes from a combination of radial pulsation due to the Kelvin-Helmholtz vortices and these mushroom structures that characterize the ejection phenomenon involved by the longitudinal vortices.

It is necessary to observe the predominance of an axisymmetric mode (Kelvin-Helmholtz vortices) on each of the shear layers. This mode is characterized by peaks with the Strouhal number St = 0.6 and St = 0.75 for the inner and outer layers respectively.

In addition, the vortex adaptation frequency St = 0.45 of the external shear layers to x/D_p= 15, corresponding to the frequency of the most amplified mode of the internal layer (longitudinal

vortices), is also demonstrated. The vortex pairing of the outer layer is therefore related to the formation of the structures of the inner layer.

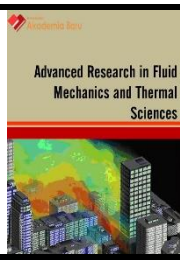
References

[1] de Almeida Areal, Pedro Miguel Rosas. "Study of the Turbulent Mixing of Confined Coaxial Jets." PhD diss., Universidade do Porto (Portugal), 2009.
[2] Mergheni, Mohamed Ali, Zouhair Riahi, Jean-Charles Sautet, and Sassi Ben Nasrallah. "Swirl Effects On Dynamics Characteristics Of A Coaxial Jet." Thermal Science 21, no. 6 (2017).
[3] Çelık, Nevin, Daniel W. Bettenhausen, and Ryan D. Lovik. "Formation of Co-Axial Jets And Their Downstream Development." Isi Bilimi ve Teknigi Dergisi/Journal of Thermal Science & Technology 32, no. 1 (2012).
[4] Alvarado, Alejandro Perez. "Effect of Background Turbulence on the Scalar Field of a Turbulent Jet." PhD diss., McGill University Libraries, 2016.
[5] Li, Wei. "Effects of Mean Shear and Scalar Initial Length Scale on Three-Scalar Mixing in Turbulent Coaxial Jets." (2016).
[6] Gloor, Michael R. "Numerical investigation on hydrodynamic stability and noise radiation of coaxial jet flows." PhD diss., ETH Zurich, 2014.
[7] Pietroniro, Asuka Gabrielle. "Modelling coaxial jets relevat to turbofan jet engines." (2016).
[8] Ku Shaari, Ku Zilati, Afiq Mohd Laziz, Kerstin Heinen, Mokhtar Awang, Suriati Sufian, and Mahadzir Shuhaimi. "CFD Simulation of Coaxial Jet Mixer using RANS Turbulent Models." In Defect and Diffusion Forum, vol. 326, pp. 416-421. Trans Tech Publications, 2012.
[9] Segalini, Antonio. "Experimental analysis of coaxial jets: instability, flow and mixing characterization." PhD diss., alma, 2010.
[10] Segalini, Antonio, and A. Talamelli. "Experimental analysis of dominant instabilities in coaxial jets." Physics of fluids 23, no. 2 (2011): 024103.
[11] Milanovic, Gilbert. "The Developing Region of a Turbulent Coaxial Jet." PhD diss., McGill University Libraries, 2018.
[12] Tiago Filipe Santos Silva "Structure of the Turbulent/non-turbulent interface at high Reynolds numbers: the velocity and scalar fields. " Thesis to obtain the Master of Science Degree in Aerospace Engineering, 2016.
[13] Cai, J., M. J. Dinger, W. Li, C. D. Carter, M. D. Ryan, and C. Tong. "Experimental study of three-scalar mixing in a turbulent coaxial jet." Journal of Fluid Mechanics 685 (2011): 495-531.
[14] Toro, E. F. "A linearized Riemann solver for the time-dependent Euler equations of gas dynamics." Proceedings of the Royal Society of London. Series A: Mathematical and Physical Sciences 434, no. 1892 (1991): 683-693.
[15] Srinivasan, B., A. Jameson, and S. Krishnamoorthy. "An upwinded state approximate Riemann solver." International Journal for Numerical Methods in Fluids 70, no. 5 (2012): 578-602.
[16] Colella, Phillip. "Multidimensional upwind methods for hyperbolic conservation laws." Journal of Computational Physics 87, no. 1 (1990): 171-200.
[17] Brio, Moysey, A. R. Zakharian, and G. M. Webb. "Two-dimensional Riemann solver for Euler equations of gas dynamics." Journal of Computational Physics 167, no. 1 (2001): 177-195.
[18] Smagorinsky, Joseph. "General circulation experiments with the primitive equations: I. The basic experiment." Monthly weather review 91, no. 3 (1963): 99-164.
[19] Kirkil, Gokhan, Jeff Mirocha, Elie Bou-Zeid, Fotini Katopodes Chow, and Branko Kosović. "Implementation and evaluation of dynamic subfilter-scale stress models for large-eddy simulation using WRF." Monthly Weather Review 140, no. 1 (2012): 266-284.
[20] Godunov, Sergei Konstantinovich. "A difference method for numerical calculation of discontinuous solutions of the equations of hydrodynamics." Matematicheskii Sbornik 89, no. 3 (1959): 271-306.
[21] Kopchenov, Valerii Igorevich, and Aleksandr Nikolaevich Kraiko. "A monotonic second-order difference scheme for hyperbolic systems with two independent variables." USSR Computational Mathematics and Mathematical Physics 23, no. 4 (1983): 50-56.
[22] Laney, C.B. (1993): Computational Gas Dynamics. Cambridge University Press.
[23] Lomax, Harvard, Thomas H. Pulliam, and David W. Zingg. Fundamentals of computational fluid dynamics. Springer Science & Business Media, 2013.
[24] P. Wesseling, ed (2001): Principles of Computational Fluid Dynamics. Verlag Berlin Heidelberg: Springer.
[25] Mi, J., D. S. Nobes, and G. J. Nathan. "Influence of jet exit conditions on the passive scalar field of an axisymmetric free jet." Journal of Fluid Mechanics 432 (2001): 91-125.
[26] Alvarado, Alejandro Perez. "Effect of Background Turbulence on the Scalar Field of a Turbulent Jet." PhD diss., McGill University Libraries, 2016.

Penerbit Akademia Baru

Engineering Science and Technology Conference Proceedings

Journal homepage: www.akademiabaru.com/EST.html



An Overview of Different Indirect and Semi-Indirect Evaporative Cooling System for Study Potency of Nanopore Skinless Bamboo as An Evaporative Cooling New Porous Material

Open Access

Hendra Wijaksana[1], I.N.S.Winaya[1,*], Made Sucipta[1], Ainul.Ghurri[1]

[1] 1Department of Mechanical Engineering, Engineering Faculty, Udayana University Kampus Bukit Jimbaran, Denpasar, Bali, Indonesia

ABSTRACT

The high energy consumption of compressor-based cooling system has prompted the researchers to study and develop non-compressor-based cooling system that less energy consumption, less environment damaging but still has high enough cooling performances. Indirect and semi indirect evaporative cooling system is the feasible non-compressor-based cooling systems that can reach the cooling performance required. These two evaporative cooling systems has some different in construction, porous material used, airflow scheme and secondary air-cooling method used for various applications. This paper would report the cooling performances achieved by those two cooling systems in terms of cooling efficiency, cooling capacity, wet bulb effectiveness, dew point effectiveness, and temperature drop. Porous material used in indirect and semi-indirect evaporative cooling would be highlighted in terms of their type, size, thickness and any other feature. The introduction of nanopore skinless bamboo potency as a new porous material for either indirect or semi-indirect evaporative cooling would be described. In the future study of nanopore skinless bamboo, a surface morphology and several hygrothermal test including sorption, water vapor transmission, thermal conductivity test would be applied, before it utilizes as a new porous material for direct or semi indirect evaporative cooling.

Keywords:
Indirect evaporative cooling system; semi-indirect evaporative cooling system; nanopore skinless bamboo potency

Copyright © 2019 PENERBIT AKADEMIA BARU - All rights reserved

1. Introduction

The rapid consumption energy growth for building cooling applications using compressor-based cooling system, has prompted researchers to develop a lower energy consumption cooling system. However, the study on Indirect Evaporative Cooling (IEC) system has been shown that this system would cooling the outdoor air without modifying outdoor air moisture content. In a conventional IEC system, there is no directly contact between water as a cooling medium and outdoor air. It would be applied two air streams for the IEC system, first the primary air stream (outdoor /product air) which is flowing in dry channel and the secondary air stream which is flowing in wet channel. The dry and wet channel is separated by a plate heat exchanger, at which the sensible heat of outdoor air (primary air) in the dry channel would be absorbed by heat surface in dry channel side

* *Corresponding author.*
E-mail address: nswinaya@gmail.com (I.N.S.Winaya)

and aids the evaporation of the secondary air in wet channel, thus the primary air is cooled conductively in the dry channel without adding its moisture content, the product air become cold and dry, meanwhile the secondary (working) air would receive the latent heat of vaporized water and adding the moisture content of the secondary air. It can be stated that using the conventional IEC, the product air resulted is far from its dew point temperature as the cooling of the product air is limited by the wet bulb secondary (working) air temperature in the wet channel, which limiting the amount sensible heat could be absorbed to evaporate water in the wet channel. However, the IEC system was providing more attractive evaporative cooling option than that DEC system, as it worked at constant moisture [1]. This conventional IEC system could provide a 20% of energy saving when it combined with dehumidifier into air retraction and air delivery of radiant cooling system [2]. The integration of direct and indirect evaporative cooling in a single and two stage operation mode could result a 51% energy saving during intermediate seasons but required 36% more energy input during cooling seasons [3]. However, the conventional IEC has provided a low energy consumption evaporative cooling system, a cooling process without modifying outdoor air moisture content, but it required the present of the secondary air to favor the cooling of the primary air and the outdoor air has not been able to cool to its dew point temperature yet. It could be considered that there are three basic energy requirement in the conventional IEC system including input energy to supply the primary (outdoor) air stream into dry channel, to supply the secondary (working) air stream into the wet channel and input energy for spraying water into the wet channel, these input energy would influence the cooling effectiveness of the conventional IEC system. The purpose of cooling the outdoor air into its dew point temperature (DPT) in the conventional IEC system could be improved by employing a Regenerative Indirect Evaporative Cooling (R-IEC) or Dew Point Indirect Evaporative Cooling (DP-IEC) and Maisotsenko Indirect Evaporative Cooling (M-IEC). In the R-IEC system, the primary air would be cooled by a regenerated secondary air stream which is extracting from the primary air stream at outlet. This part of the primary air has already cooled, so then the corresponding wet bulb temperature (WBT) of secondary air in the R-IEC system has become lower than the regular secondary air WBT compare to using outdoor air or returned air as the secondary air. This lower secondary air WBT would lowering the limit at which the primary air can be cooled, then it would decrease the primary air temperature at outlet. [4-9]. The main advantage of the R-IEC is the outdoor air is cooled at a constant moisture below its WBT of the outdoor air, as the cooled primary air was extracting become the secondary air. Then the disadvantage of the R-IEC is the primary air flow rate become decreased due to those air extracting process. In this system, the primary air could only be cooled until obtaining the WBT of the secondary air at inlet, this system was also named as sub wet bulb IEC [10]. It is cooled the primary air not so close to its DPT. The improvement of the R-IEC system is the DP-IEC system, at which it would cool the primary air near to the limit of its DPT at inlet. It consists two stages of R-IEC equipment, at which the outlet primary air would be partly used as the secondary air for first stage and the rest of the primary air would be flowing to the second stage as the primary air. The secondary air of this system would be much cooler than that of the secondary air in classic IEC system and the primary air could be continue cooled to reach near its DPT of the primary air at inlet and this become the advantage of the DP-IEC, the most disadvantage of the DP-IEC is the primary air flow rate become decreased with the number of stage. Due to the primary air behavior, this system was also named as dry bulb IEC [10]. The DP-IEC system has presented a better primary air-cooling process than the R-IEC system, as the primary air could nearly reach its DPT of the primary air at inlet. A super performance of dew point air cooler has been studied by Peng Xu et.al [11] It established of using a super performance wet material layer, better heat and mass exchanger and an intermittent water supply scheme at which could produce a higher cooling

performance. It consists of a complex exchanging sheets which contain many dry and wet channel, and works as the IEC system with primary and secondary air stream scheme, so then the outdoor air (primary air) could be cooled into nearly its DPT. The research results showed that this system have obtained wet-bulb cooling effectiveness of 114%, dew point cooling effectiveness of 75% and a significant higher COP of 52.5, at standard condition dry bulb temperature (TDB) of 37.8oC and wet bulb temperature (WBT) of 21.1oC. It also indicated that the lower the inlet air relative humidity would lead to a higher cooling efficiency. These results indicated that this system has a 100 – 160% higher COP and reduce the electricity used by 50-70% compared to the existing dew point cooler. Furthermore, the improved performance in terms of cooling the primary air into its dew point temperature at constant moisture content for the DP-IEC has been provided by the M-IEC system. This M-IEC system representing an alternative dew point evaporative cooling system at which the primary air can be cooled more closer to its DPT at constant moisture content. It consists of two dry channels, one for the primary stream and the other one for the secondary air. The secondary air stream has multiple passages from its dry channel into wet channel at which in each passage of the equipment, the secondary air moisture content would be increased until it reached the saturation condition, as the evaporated water would be diffused into the secondary air as moisture [10]. The uses of many passages for the secondary air would result a better sensible cooling for the primary air, at which the final DBT of the primary (product) air at outlet could reach near the DPT of the primary air at inlet, it very close to its DPT. The main merit of the M-IEC is the outdoor air can be cooled near its DPT in constant moisture content, but it required most complex construction and air flow scheme.

On the other hand, there is a Semi-Indirect Evaporative Cooling (SIEC) system which could work as direct evaporative cooling or indirect evaporative cooling depend on the outdoor air and return air stream relative humidity [12]. It usually consists of porous material tube, at which its external surface would act as the heat exchange surface which has directly contact to the outdoor air, while water would be sprayed into the inside of porous tube to cool the secondary air and capillarity transported into the external surface to absorb the sensible heat of the primary air. When the vapor pressure of the outdoor air lower than the vapor pressure of the water in the heat exchange surface (low relative humidity ambient air), the SIEC would act as direct evaporative cooling, at which the water would evaporate and adding the moisture content of the outdoor air. In contrary, when the vapor pressure of the outdoor air higher than the vapor pressure of water in the heat exchange surface (high relative humidity ambient air), the SIEC would work as indirect evaporative cooling (sensible cooling), at which the cooled heat exchange surface would absorb only the sensible heat of the outdoor air conductively into the wet channel without modifying outdoor air moisture content. Further study has investigated two types of the SIEC system which were named Semi-Indirect Evaporative Recuperator made with Ceramic Pipe (SIERCP) and Semi- Indirect Evaporative Cooling made with Hollow Bricks (SIECHB) [12]. The SIERCP consists of porous ceramic pipe with the secondary air flowing inside the pipe and has a counter flow contact manner with the water sprayed, then allowing the evaporative cooling phenomena occurred. The secondary air in the inside of the pipe could be the outdoor air or any return air which associated to an energy recovery system. The water from inside the pipe would be capillarity transported to the external surface of pipe and absorbed the sensible heat of the outdoor air. So, then the outdoor air would be cooled sensibly without modifying its moisture content. If the outdoor air vapor pressure lower than that of water present in the external surface of pipe, the SIERCP would act as direct evaporative cooling at which allowing the humidification of the outdoor air. In reverse, it would act as indirect evaporative cooling and the porous pipe would work as a heat exchange that sensibly cooling the outdoor air without modifying its moisture content. While the SIECHB consists of

hollow bricks which filled with stagnant cold water. The water is previously cooled in a cooling tower that utilized return air from conditioned air chamber and in such way the water would capillarity transported into the external hollow brick surface. When the vapor pressure of the outdoor air higher than the water in the external surface, the SIECHB would act as indirect evaporative cooling and conversely it would work as direct evaporative cooling [13]. The experiment test on both semi-indirect evaporative cooling system in various outdoor air velocity, various humidity level, various outside dry bulb temperature has been resulting an evaporative cooling system that can cool the outdoor air close to its dew point temperature as that in indirect and dew point evaporative cooling system. This system can be used for cooling system in hot-arid or hot-humid area.

Other supply air cooling method in the SIEC system would give cooling effect to the tube external surface by using a cold stagnant water inside the tube which is externally cooling by the secondary air in a cooling chamber. Instead of using a solid plate heat exchange as in indirect system which is separated primary air and secondary air exclusively, the SIEC use only the porous tube as the heat exchange medium, which allowing water capillarity transport to the tube external surface and this would simplify and shorten the evaporative cooling process. The most material used for the SIEC system including porous ceramic tube [14-18], combined porous ceramic tube and heat pipe [19], hollow bricks[20]. Regarding those papers reviewed, it seems that there has not been specific study about the use of nanopore porous material for semi indirect evaporative cooling yet. This really encourage to be studied even further to investigate the hygrothermal and surface morphology characteristics of nanopore skinless bamboo as a new porous material for semi indirect evaporative cooling.

2. Literature Review

Further discussion on indirect evaporative cooling (IEC) should be mentioned a requirement to improve the efficiency of the IEC, as in fact, the IEC has a lower efficiency that the direct evaporative cooling (DEC) system [21]. It then is introduced a semi-indirect evaporative cooling (SIEC) system that was a successful attempt to improve the efficiency of the IEC system. It should be clear that the terms of “semi-indirect” is used to describe this IEC system as it designed to operate either as a direct evaporative cooling or indirect evaporative cooling depending on the relative humidity of outside air and return air stream [22]. The SIEC is usually composed of porous material pipes, such as porous ceramic pipes, hollow brick and it has two air flow supplies, first air flow , supply air flow is used for cooling and the second one to be used to conduce heat and mass transfer process by forcing it against the downstream sprayed water, [23]. The whole process was occurred in the inside and outside of a single pipe from a bank porous pipes, in which the cooling effect was provide by two heat exchange processes, i.e. first heat exchange process between supply and return air, and the second one between supply air and pipe external surface. Several studied has been conducted relates to the semi-indirect evaporative cooling system. R.Herrero Martin et al [23] studied experimentally the semi-indirect evaporative cooling as a device used in energy recovery in air conditioning system, which is assessed in various air flow and relative humidity level. It employed three air flow levels of 140, 260, 380 m3/h and three relative humidity levels of less than 30%, between 30-60%, and more than 60%, then five temperature levels of 40, 36.5, 33, 29.5, 26oC. The results showed this system is better used in tropical climate region with high ambient air temperature and humidity, in which the high humidity of supply air or primary air would be decreased using the cooling effect of evaporative cooling the secondary air. E.Velasco Gomez et.al [24] investigated fundamental operation of two different configuration of the SIEC system which

described as, first, semi-indirect evaporative recuperator made with ceramic pipes (SIERCP) and second one, semi-indirect evaporative cooler made with hollow brick (SIECHB) and characterize those both system behavior based on different outside air condition. The tests would be performed in different air volume flow rate, dry bulb temperature and relative humidity for each of those two systems. The air volume flow rate was varied of 290, 410 and 515 m3/h for SIERCP and 180, 360 and 540 m3/h for SIECHB, the different air volume flow rate setting for SIERCP and SIECHB due to the different in pressure drop as the air handling unit was not possible to provide the same air volume flow rate. This setting could not be valid as the two system has been performed with different sets of air volume rate. In order to develop enough data for a comparative analysis, the same relative humidity levels for each of dry bulb temperature would be applied, in which for 20oC the relative humidity was set to 50%, then 25, 30, 35, and 40oC with 45, 35, 25, and 20% relative humidity. It concluded that the SIECHB system obtained a slightly higher cooling capacity, thermal conductance and wet bulb thermal effectiveness than SIERCP system, and it found as well that the performance of these system improve when the outdoor air temperature increase within a lower air relative humidity. E.Velasco Gomez et.al [25] studied a semi-indirect cooler used a porous ceramic as a heat exchange medium between outdoor air and conditioned return air which is directly force against the water sprayed. It found that this system is then would introduce as the semi-indirect evaporative cooling which recover energy between outdoor air and conditioned return air. As well, this introduced system had a ceramic structure that acts as a filter to eliminate outdoor air contamination, as it has not been in directly contact with sprayed water and avoid the product air from Legionnaire's disease spreading. Fenghao Wang et.al.[26] studied a novel indirect evaporative cooling system with made of a porous ceramic tube type, to improve surface hydrophilicity of wet channel and reduce pump energy consumption compared to the traditional IEC system. It resulted the increasing of secondary/primary air ratio to 0.9 and the decreasing of spray water rate would improve the wet bulb efficiency or cooling efficiency of IEC system. This novel IEC system enables to save 95% pump energy consumption compared to the traditional IEC, as well as this system work stable under the typical hot and dry condition within a wet bulb efficiency fluctuation of 40.3% to 42.2% and obtained the highest COP of 34.9. Previous study by F.J. Rey Martinez et.al [27] investigated the comparison between indirect evaporative cooling (IEC) using an aluminum plate as the interchanger and semi-indirect evaporative cooling (SIEC) made with solid porous ceramic. In this IEC system, it only heat transfer taking place on the primary air stream (air supply), while for SIEC, both heat and mass transfer are taking place, allowing sensible and latent cooling of the primary air stream. The primary air flow for IEC and SIEC are setting on 118.8 or 220.2 m3/h and 140 or 260 m3/h respectively, while different humidity range are applied for IEC on 20-40%, 40-60%, and more than 60%, while for the SIEC system on less than 30%, 30-60% and more than 60%. The results showed the SIEC system has a better performance as it allowed the sensible and latent heat transfer taking place, which not only lowering air supply temperature but also reduce air supply moisture content due to evaporative cooling process on the porous ceramic tube surface. X.Zhao et.al [28] investigated the selection of various material that suitable used as heat and mass transfer medium for IEC system, in which thermal conductivity (TC) and water retaining capacity (porosity) has a little influence in this material selection. The more important influenced factors would be the holding ability, durability, compatibility, contamination risk and cost. It concluded that the most suitable material for IEC system in terms of heat and mass transfer capability are included the wick attained copper or aluminum (metal type) , low porosity wooden or flax fiber (fiber type), low porosity ceramic, low porosity and high thermal conductance zeolite and carbon. S.B. Riffat and Jie Zhu [29] has been studied the mathematical model of SIEC using porous ceramic and heat pipe as cooling sources and heat transfer device respectively. It applied two air

passage distinctively, first air passage for indoor air and the second for outdoor air. It constructed with a porous ceramic which filled with water for the first air passage and a heat pipe is situated along the two air passage. The heat pipe would transfer the cold from porous ceramic passage to the interior of building and absorb the indoor air heat. It found that the high cooling capacity would be obtained in the dry and windy weather and to achieve a higher cooling efficiency, the indoor air velocity should be set at 0.6 m/s [30].

Most study has been investigated bamboo, in engineering aspect, as a building constructions material, or as a natural fiber from plants to reinforce composite material or even to replace polymeric fiber with plants fiber. The study in using skinless bamboo as a porous material in evaporative air-cooling application has not been done yet. Bamboo is an abundance plant that has significant low density, high strength and stiffness [31]. In choosing bamboo for evaporative cooling purposes, some physical and morphology characteristics of material should be considered including density, porosity, wall thickness. Bamboo tree has composed of inner most, culms and skin, as can be seen in Fig.2. Varied mechanical and physical properties of bamboo is depend on the structure of bamboo culms, density, average size, and also their vascular number [32,33]. The low density of bamboo would be useful for mass and heat transfer in evaporative cooling, as it has a higher porosity. The reduction of bamboo wall thickness as a result of diminution process would decrease the bamboo diameter from the bottom to the top portion [34]. A thinner material would provide a better heat and mass transfer for indirect and semi indirect evaporative cooling. In addition, the height of bamboo can be indicated by the length of its internodes [35]. Those bamboo properties have been appropriate to the working principle of the evaporative cooling proposed. The thermal engineered bamboo then would be test to study its hygrothermal and surface morphology characteristics before it employed to be a nanopore porous material for semi indirect evaporative cooling.

3. Future Development of Nanopore Skinless Bamboo Potency as An Evaporative Cooling New Porous Material

Based on the paper have been reviewed, although various porous material has been used in those evaporative cooling systems, the uses of the nanopore skinless bamboo as an evaporative cooling porous material has not yet been investigated. For the future development, it would be utilized the use of local bamboo, bamboo tali (gigantochloa apus), which would be thermal engineered to develop a nanopore porous material for semi indirect evaporative cooling. Thermal engineering process would be conducted by applying four pyrolysis stage including drying, pre-carbonization, carbonization and calcination, before its carbon activated. Once those thermal engineering processes was accomplished, the nanopore skinless bamboo porous material would be examined their surface morphology and several hygrothermal properties including sorption, water vapor transmission, drying, thermal conductivity test, and thermal analysis based on ISO and or ASTM standard.

4. Conclusions

By selecting the appropriate density, porosity, permeability of the skinless bamboo, it would be developed a novel indirect evaporative cooling system named Semi Indirect Evaporative Cooling made of Nanopores Skinless Bamboo (SIECNSB). In this novel system, the appropriate nanopores skinless bamboo would be utilized as a new porous material for semi indirect evaporative cooling system. It has a great potential to act as a better cooling medium in absorbing heat and mass

transferred during the cooling process. It expected to have a higher nanopore distribution that could enlarge heat and mass transfer area. This new nanopore material could then to be expected to improve cooling efficiency and cooling capacity for semi indirect evaporative cooling.

Acknowledgement

This article's publication is supported by The Indonesian Ministry of Research Technology and High Education for Doctor Dissertation Research Grant 2018/2019

References

[1] Duan, Zhiyin, Changhong Zhan, Xingxing Zhang, Mahmud Mustafa, Xudong Zhao, Behrang Alimohammadisagvand, and Ala Hasan. "Indirect evaporative cooling: Past, present and future potentials." Renewable and Sustainable Energy Reviews 16, no. 9 (2012): 6823-6850.

[2] Mariotti, Marco, and Lorenzo Moro. "Indirect evaporative cooling combined with dehumidification in a MVHR system for radiant cooling." Energy Procedia 101 (2016): 448-455.

[3] Kim, Min-Hwi, and Jae-Weon Jeong. "Cooling performance of a 100% outdoor air system integrated with indirect and direct evaporative coolers." Energy 52 (2013): 245-257.

[4] Bellemo, Lorenzo, Brian Elmegaard, Lars O. Reinholdt, and Martin Ryhl Kærn. "Modeling of a regenerative indirect evaporative cooler for a desiccant cooling system." In 4th IIR Conference on Thermophysical Properties and Transfer Processes of Refrigerants. 2013.

[5] Bruno, Frank. "On-site experimental testing of a novel dew point evaporative cooler." Energy and Buildings 43, no. 12 (2011): 3475-3483.

[6] Kiran, T. Ravi, and S. P. S. Rajput. "An effectiveness model for an indirect evaporative cooling (IEC) system: Comparison of artificial neural networks (ANN), adaptive neuro-fuzzy inference system (ANFIS) and fuzzy inference system (FIS) approach." Applied Soft Computing 11, no. 4 (2011): 3525-3533.

[7] Lee, Joohyun, BongSu Choi, and Dae-Young Lee. "Comparison of configurations for a compact regenerative evaporative cooler." International Journal of Heat and Mass Transfer 65 (2013): 192-198.

[8] Mathews, E. H., M. Kleingeld, and L. J. Grobler. "Integrated simulation of buildings and evaporative cooling systems." Building and Environment 29, no. 2 (1994): 197-206.

[9] Wani, Chandrakant, Satyashree Ghodke, and Chaitanya Shrivastava. "A review on potential of Maisotsenko cycle in energy saving applications using evaporative cooling." International journal of advance research in science, engineering and technology 1, no. 1 (2012): 15-20.

[10] Porumb, Bogdan, Paula Ungureşan, Lucian Fechete Tutunaru, Alexandru Şerban, and Mugur Bălan. "A review of indirect evaporative cooling technology." Energy Procedia 85 (2016): 461-471.

[11] Xu, Peng, Xiaoli Ma, Xudong Zhao, and Kevin S. Fancey. "Experimental investigation on performance of fabrics for indirect evaporative cooling applications." Building and Environment 110 (2016): 104-114.

[12] Gómez, E. Velasco, FJ Rey Martínez, and A. Tejero González. "Experimental characterisation of the operation and comparative study of two semi-indirect evaporative systems." Applied Thermal Engineering 30, no. 11-12 (2010): 1447-1454.

[13] Wang, S. K. "Incorporating evaporative cooling with other coolers, handbook of air-conditioning and refrigeration." (1994).

[14] Martín, R. Herrero. "Characterization of a semi-indirect evaporative cooler." Applied Thermal Engineering 29, no. 10 (2009): 2113-2117.

[15] Wang, Fenghao, Tiezhu Sun, Xiang Huang, Yi Chen, and Hongxing Yang. "Experimental research on a novel porous ceramic tube type indirect evaporative cooler." Applied Thermal Engineering 125 (2017): 1191-1199.

[16] Martınez, FJ Rey, E. Velasco Gómez, R. Herrero Martın, J. Martınez Gutiérrez, and F. Varela Diez. "Comparative study of two different evaporative systems: an indirect evaporative cooler and a semi-indirect ceramic evaporative cooler." Energy and Buildings 36, no. 7 (2004): 696-708.

[17] Zhao, X., Shuli Liu, and S. B. Riffat. "Comparative study of heat and mass exchanging materials for indirect evaporative cooling systems." Building and Environment 43, no. 11 (2008): 1902-1911.

[18] Gómez, E. Velasco, FJ Rey Martínez, F. Varela Diez, MJ Molina Leyva, and R. Herrero Martín. "Description and experimental results of a semi-indirect ceramic evaporative cooler." International journal of refrigeration 28, no. 5 (2005): 654-662.

[19] Riffat, S. B., and Jie Zhu. "Mathematical model of indirect evaporative cooler using porous ceramic and heat pipe." Applied Thermal Engineering 24, no. 4 (2004): 457-470.

[20] Gómez, E. Velasco, FJ Rey Martínez, and A. Tejero González. "Experimental characterisation of the operation and comparative study of two semi-indirect evaporative systems." Applied Thermal Engineering 30, no. 11-12 (2010): 1447-1454.
[21] Martín, R. Herrero, FJ Rey Martínez, and E. Velasco Gómez. "Thermal comfort analysis of a low temperature waste energy recovery system: SIECHP." Energy and Buildings 40, no. 4 (2008): 561-572.
[22] Gómez, E. Velasco, FJ Rey Martínez, and A. Tejero González. "Experimental characterisation of the operation and comparative study of two semi-indirect evaporative systems." Applied Thermal Engineering 30, no. 11-12 (2010): 1447-1454.
[23] Martín, R. Herrero, FJ Rey Martínez, and E. Velasco Gómez. "Thermal comfort analysis of a low temperature waste energy recovery system: SIECHP." Energy and Buildings 40, no. 4 (2008): 561-572.
[24] Gómez, E. Velasco, FJ Rey Martínez, and A. Tejero González. "Experimental characterisation of the operation and comparative study of two semi-indirect evaporative systems." Applied Thermal Engineering 30, no. 11-12 (2010): 1447-1454.
[25] Gómez, E. Velasco, FJ Rey Martínez, F. Varela Diez, MJ Molina Leyva, and R. Herrero Martín. "Description and experimental results of a semi-indirect ceramic evaporative cooler." International journal of refrigeration 28, no. 5 (2005): 654-662.
[26] Wang, Fenghao, Tiezhu Sun, Xiang Huang, Yi Chen, and Hongxing Yang. "Experimental research on a novel porous ceramic tube type indirect evaporative cooler." Applied Thermal Engineering 125 (2017): 1191-1199.
[27] Martınez, FJ Rey, E. Velasco Gómez, R. Herrero Martın, J. Martınez Gutiérrez, and F. Varela Diez. "Comparative study of two different evaporative systems: an indirect evaporative cooler and a semi-indirect ceramic evaporative cooler." Energy and Buildings 36, no. 7 (2004): 696-708.
[28] Zhao, X., Shuli Liu, and S. B. Riffat. "Comparative study of heat and mass exchanging materials for indirect evaporative cooling systems." Building and Environment 43, no. 11 (2008): 1902-1911.
[29] Riffat, S. B., and Jie Zhu. "Mathematical model of indirect evaporative cooler using porous ceramic and heat pipe." Applied Thermal Engineering 24, no. 4 (2004): 457-470.
[30] Osorio, Lina, E. Trujillo, Aart Willem Van Vuure, and Ignace Verpoest. "Morphological aspects and mechanical properties of single bamboo fibers and flexural characterization of bamboo/epoxy composites." Journal of reinforced plastics and composites 30, no. 5 (2011): 396-408.
[31] Londoño, Ximena, Gloria C. Camayo, Néstor M. Riaño, and Yamel López. "Characterization of the anatomy of Guadua angustifolia (Poaceae: Bambusoideae) culms." Bamboo Science and Culture: The Journal of the American Bamboo Society 16, no. 1 (2002): 18-31.
[32] Zakikhani, Parnia, R. Zahari, M. T. H. Sultan, and D. L. Majid. "Extraction and preparation of bamboo fibre-reinforced composites." Materials & Design 63 (2014): 820-828.
[33] Liese, W.et.al., 2003. Proceeding of International Workshop on Bamboo Industrial Utilization. International Network for Bamboo and Rattan, Xianning,Hubei, China
[34] Amada, Shigeyasu, and Sun Untao. "Fracture properties of bamboo." Composites Part B: Engineering 32, no. 5 (2001): 451-459.

Penerbit Akademia Baru

Engineering Science and Technology Conference Proceedings

Journal homepage: www.akademiabaru.com/EST.html

Evaluation on the Performance of Cross-Matrix Absorber Double-Pass Solar Air Heater (CMA-DPSAH) With and Without Thermal Energy Storage Material

Open Access

Ahmad Fadzil Sharol[1], Amir Abdul Razak[1*], Zafri Azran Abdul Majid[2], Muhammad Amirul Azwan Azmi[1], Muhammad Amir Syahiran Muhammad Tarminzi[1]

[1] Department of Energy and Environmental, Faculty of Engineering Technology, Universiti Malaysia Pahang, 26300 Gambang, Pahang, Malaysia
[2] Department of Radiography, Kuliyyah of Allied Health and Sciences, International Ismalic University of Malaysia, 25200 Kuantan, Pahang, Malaysia

ABSTRACT

Solar engineering technology was going through a great technological advancement in terms of the design of the solar collector in the past decades. However, due to the intermittent nature of solar energy, it is very difficult to achieve a better performance of the solar heater especially in the application of air as the heat transfer fluid. The utilization of thermal storage materials demonstrates an effective way in order to improve an overall performance of solar air heater. In the present study, the performance of cross-matrix absorber double-pass solar air heater (CMA-DPSAH) integrated with the phase change material (PCM) as thermal energy storage was conducted. The PCM material was inserted inside the rectangular aluminium tube used as the thermal absorber. The air mass flow rate of 0.007 kg/s was used during the entire experimental period. The experiment was conducted on several phase; Phase 1 (CMA-DPSAH with PCM) and Phase 2 (CMA-DPSAH without PCM) in order to compare and evaluate the effectiveness of the PCM utilization. Based on the result, CMA-DPSAH with PCM performed better than the CMA-DPSAH without PCM with maximum of heat gain and temperature output were 127 W and 53 ^{o}C, respectively. The instantaneous efficiency of CMA-DPSAH with PCM consistently higher than the CMA-DPSAH without PCM for about 17 – 19% with the maximum was 64 % during the low radiation flux. This feature offers a great potential of solar air heater application in the intermittent solar radiation condition, especially for drying of the agriculture products.

Keywords:
Cross-Matrix absorber (CMA); Double-pass solar air heater (DPSAH); Phase change material (PCM); Instantaneous efficiency

Copyright © 2019 PENERBIT AKADEMIA BARU - All rights reserved

1. Introduction

Solar engineering technology was going through a great technological advancement in terms of the design configuration of the solar collector in the past decades. In the application of solar air heater (SAH), there were a lot of innovative design of the solar energy harvesting devices have been highlighted in the literature in order to maximize the rate of heat transfer from the surface of thermal absorber to the flowing heat transfer fluid [1]. These advancement including the utilization of finned thermal absorber surfaces [2–4], insertion of porous structure [5–7] and the implementation of artificial roughness on the thermal absorber surface [8–10]. However with the

* *Corresponding author.*
E-mail address: amirrazak@ump.edu.my (Amir Abdul Razak)

intermittent nature of solar energy source [11,12], making the SAH difficult to achieve a better overall efficiency and limit their operating time. The incorporation of thermal energy storage material into the solar energy system has been seen as a suitable and practical solution in order to maximize the utilization of solar thermal devices in the situation of intermittent solar radiation and/or during off-sunshine period.

From literature, there have been increasing trends on the study related to the integrated SAH with the thermal energy storage system. Bouadilla et al. [13] has conducted an experimental investigation about the SAH integrated with packed-bed of spherical capsules of SN27 material as the thermal energy storage materials. The spherical capsules were built from a blend of polyolefin and was painted with flat black in order to act as the thermal absorber component of the SAH. Based on their study, it was concluded that the SAH system managed to supply an amount of useful heat of 200 W/m^2 for an extended period of time after the off-sunshine period. Double-pass solar air heater (DPSAH) integrated with rectangular capsules of paraffin wax was investigated by Salih et al. [14]. The experimental work was conducted to evaluate the DPSAH thermal efficiency with the variation of solar radiation and mass flow rate. The numerical study was also conducted with the result from the developed mathematical model agreed well with the experimental result. W. Baig and M.H. Ali [15] investigated the effect of using the aluminum foam embedded in the PCM duct located on the top of the thermal absorber of DPSAH. The configuration was compared with the DPSAH having a similar arrangement but with no aluminum foam insertion. They concluded that the insertion of aluminum foam material was increase the PCM conductivity but reduce its thermal storage capability with useful heat gain time was 30 minutes faster than the one without aluminum foam insertion.

Comparison between rectangular and cylindrical shape of PCM encapsulation was conducted experimentally by A.K. Raj et al. [16]. The PCM encapsulations were located on the top side of thermal absorber in order to investigate the thermal efficiency of both DPSAH configurations. According to the studies, they concluded that the rectangular encapsulation provides thermal storage efficiency of 67 % as compared to the cylindrical encapsulation of 47.2 %. This was due to the fact that during the rectangular encapsulation mode, the temperature different between the thermal absorber and the bottom plate is higher, which mean that the absorption of radiation flux was higher than the cylindrical encapsulation mode. The indoor experimental investigation of integrated zig-zag configuration of cross-matrix absorber in single-pass solar air heater (SPSAH) has been conducted by A.F. Sharol et al. [17] by varying the input parameters of mass flow rate and solar radiation. Based on the result, it is concluded that the output temperature and heat gain were directly and indirectly proportional to the mass flow rate, respectively. Based on author knowledge, there was no study conducted on the integration of thermal storage material into the rectangular aluminum tube of cross-matrix absorber with staging configuration in the DPSAH. In this study, the effect of incorporation of thermal storage material into cross-matrix absorber of DPSAH was investigated experimentally.

2. Description of CMA-DPSAH

The schematic diagram of the CMA-DPSAH as shown in Fig. 1 was constructed using the locally available materials. The device consists of a set of collector made of polypropylene having a dimension of 525 mm length, 400 mm width and 180 mm height. The CMA-DPSAH was built from polycarbonate transparent cover, intermediate polycarbonate transparent cover, and set of rectangular aluminium tubes act as an absorber. The rectangular aluminium tube comprises of two types of aluminium tube namely; type A (326 mm Length, 19.1 mm width, 19.1 height and 1 mm

thickness) which was positioned perpendicular to the air flow and type B (427 mm Length, 19.1 mm width, 19.1 height and 1 mm thickness) which was positioned parallel with the air flow. The spacers were located at the bottom absorber of each pass in order to avoid direct contact to the bottom wall of the absorber and surface of the intermediate glazing plate. The tubes were sprayed with flat black coating and arranged in a saging manner in order to increase the heat absorption and to optimize the aperture area of the tubes [18], respectively. The total aperture area of the thermal absorber was calculated to be 0.3786 m^2. The 6 mm thickness of insulation sheet was applied at the edge and bottom side of the collector in order to reduce the heat losses. Three units of brushless 24 V DC fan were installed at the outlet chamber of the collector in order to force the outdoor air into the air passage of the collector. The incoming air entered to the first pass of the collector through the three identical circle shape inlet duct before went to the second pass through 3.3 cm diameter flexible hose. Fig. 2 shows the experimental setup used in this work.

Additionally, paraffin wax in the form of granulated particle was inserted in the tube type B and was sealed with rubber cap to prevent from leaking. The thermophysical properties of the paraffin wax is shown in Table 1.

Table 1
Thermophysical properties of paraffin wax used in this study [19]

Properties	Value
Melting temperature, T_m (°C)	58 - 60
Specific heat (solid), $C_{P,s}$ (J/kg.K)	900
Enthalpy of fusion, H_f (kJ/kg)	214.4
Total weight (g)	624

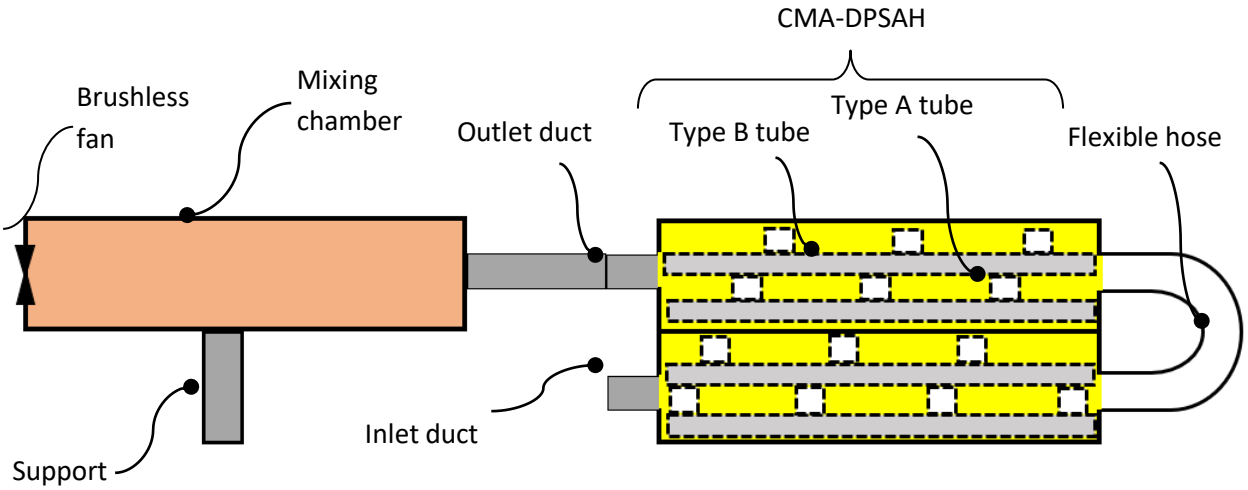


Fig. 1. Schematic diagram of the CMA-DPSAH system

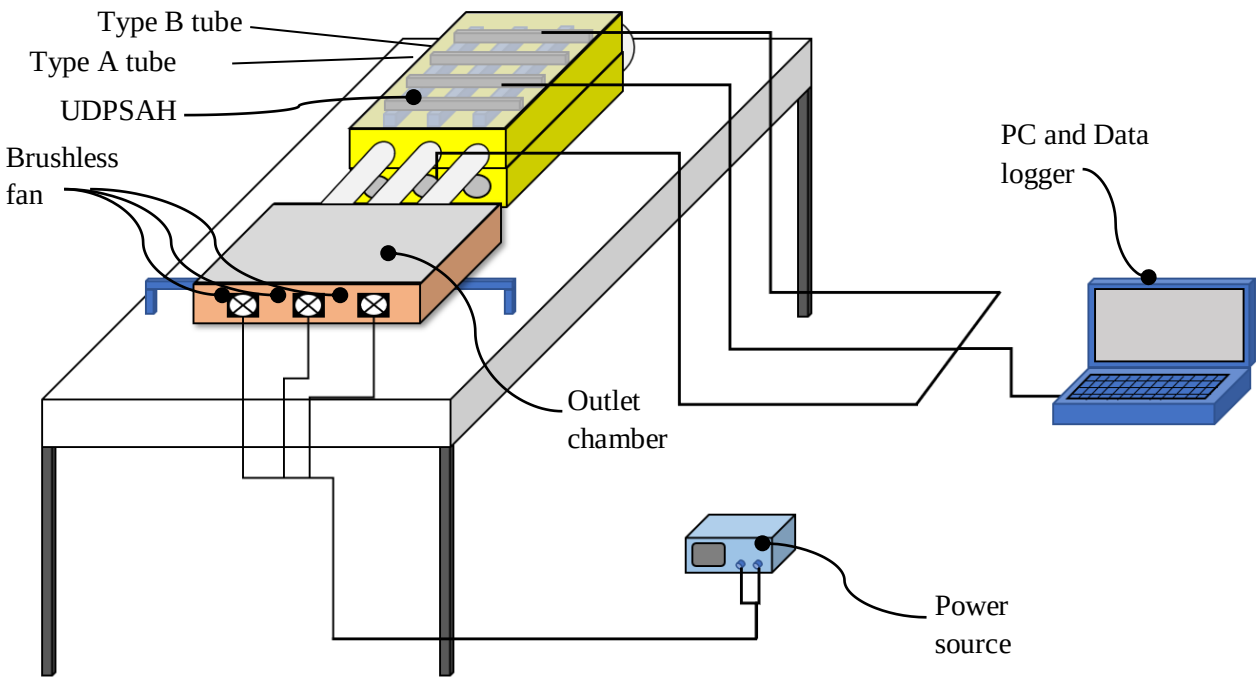


Fig. 2. Experimental setup used in this work

2.1 Description of experimental method and apparatus

The outdoor experiment was conducted at Islamic International University of Malaysia (IIUM) located in Kuantan, Pahang (latitude N 3°50'42.47'' (3.84513°) and longitude of E 103°18'11.76'' (103.30327°)). The temperature data was recorded by using Advantech ADAMview data logger system at every 1-minute time span from 9:00 a.m. until 7:00 p.m. The K-type thermocouple with reading tolerance of ± 1.5 °C used to measure the temperature data was installed at multiple location across the system as shown in the Fig. 3. The solar radiation and wind speed were measured using Apogee pyranometer (calibration uncertainty of 5 %) and hot wire anemometer, respectively. The air mass flowrate was set to be flowing through the collector at 0.007 kg/s for the entire experimental period. The thermal performance of CMA-DPSAH (Phase 1) was compared with the CMA-DPSAH without thermal energy storage (Phase 2) material inserted.

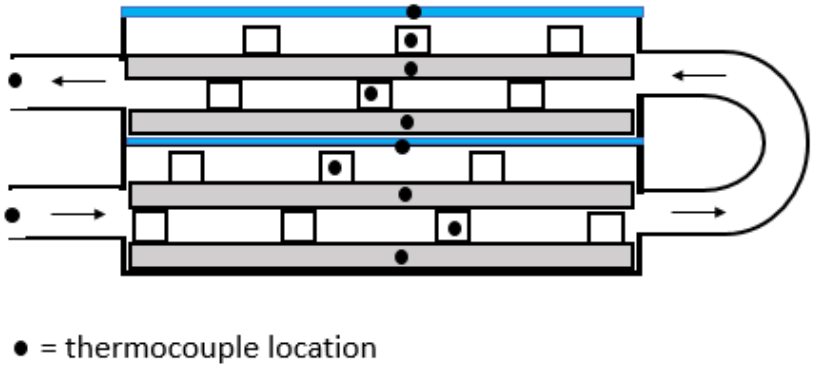


Fig. 3. Thermocouple positioning on respective tube and glazing

The thermal efficiency of the collector during charging and discharging process was calculated based on the equation (1) and (2), respectively [20]:

$$\eta_{Charging} = \frac{Q_U + Q_S}{A_T I} \tag{1}$$

$$\eta_{Discharging} = \frac{Q_U}{Q_S} \tag{2}$$

where Q_U and Q_S are useful heat gained and heat stored which were given by equation (3) and (4), as follows:

$$Q_U = \dot{m} c_p (T_{out} - T_{in}) \tag{3}$$

$$Q_s = \frac{m_{pcm}}{\Delta t} c_{p,s} \Delta T_{pcm} \qquad T_{avg,pcm} < T_m$$

$$Q_s = \left(\frac{m_{pcm} L_{pcm}}{\Delta t}\right) \qquad T_{avg,pcm} = T_m \tag{4}$$

$$Q_s = \frac{m_{pcm}}{\Delta t} c_{p,l} \Delta T_{pcm} \qquad T_{avg,pcm} > T_m$$

where T_{pcm}, $T_{avg,pcm}$, T_m, $c_{p,s}$, $c_{p,l}$ and m_{pcm} are PCM temperature rise, average PCM temperature, solid phase, liquid phase specific heat of PCM and PCM mass, respectively. As for latent heat calculation, in which for the case of stored heat by the PCM, the sensible heat mode will be take placed when the average PCM temperature, $T_{avg,pcm}$ is below or exceeding the melting temperature, T_m, otherwise the method will be latent heat [20,21].

2.2 Uncertainty analysis

It is imperative to ensure the measurement of the parameters taken using the correct tool in order to produce the reliable data and to avoid error. This error might come from a various source such as human, measurement apparatus and environment of an experimental work. In this work, uncertainty analysis was conducted using the method available in the literature [22,23] based on the following expression:

$$W_R = \left[\left(\frac{\partial R}{\partial x_1} w_1\right)^2 + \left(\frac{\partial R}{\partial x_2} w_2\right)^2 + \cdots + \left(\frac{\partial R}{\partial x_n} w_n\right)^2\right] \tag{5}$$

In which the average percentage value of an uncertainty of each measured and calculated parameter were 1.52 % and 7.85 %; respectively.

3. Results and Discussion

The experimental work was conducted in between the month of April and May 2019 under the cloudy sunny day condition. Fig. 4 show the solar radiation profile as a function of time starting from 9:00 a.m. until 7:00 p.m. for each phase of an experiment. As can be seen in the Fig., the solar radiation distribution for phase 1 having a stable profile with the weather slightly in better shape as

compared to the condition of phase 2. During the phase 2, the weather condition in the morning was slightly cloudy with the condition becomes better as the day passes by. As expected, the highest solar radiation was recorded during the middle of the day for both cases with maximum value of 1017 W/m^2 and 944 W/m^2 for phase 1 and phase 2, respectively. At the end of the experiment period which was at around 6:30 p.m., solar radiation for both phases approached zero.

In order to further enlighten this occasion, inlet and outlet temperature of each phase were plotted as a function of time as shown in Fig. 5. The output temperature profile was increased gradually with the increase of inlet temperature and also solar radiation as previously explained from the Fig. 4. It is expected that the inlet and outlet temperature of phase 1 experiment was higher than the one of phase 2 experiment due to the slightly higher solar radiation. During this period, the temperature increases due to the sensible heat of the absorber material for each CMA-DPSAH used in the experiment. In the middle of the day, which was around 12:30 p.m. to 1:30 p.m., the latent heat of fusion started to take over for the CMA-DPSAH used in phase 1 (with PCM). As can be seen in the purple dotted box region shown in Fig. 5, the output temperature profile slightly shows a flat profile even though the radiation flux already started to descend. This shows that albeit part of the PCM was melted, it gave the significant improvement in terms of maintaining the output temperature stability of the CMA-DPSAH. As compared to the one of without PCM from phase 2, the output temperature profile was fluctuated with the fluctuation of the solar radiation.

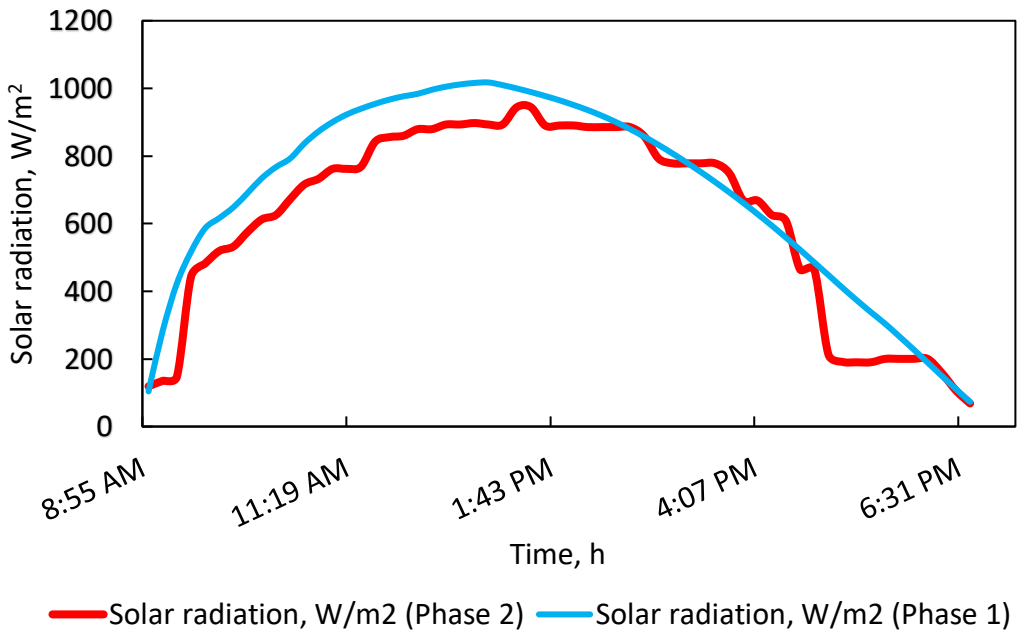


Fig. 4. Solar radiation distribution during phase 1 (CMA-DPSAH with PCM) and phase 2 (CMA-DPSAH without PCM) of the experiments

In order to evaluate the effectiveness of using PCM inside the absorber tube, the heat gain and temperature different for each phase was presented in Fig. 6. Heat gained by each collector was calculated using equation (3) and (4) with the latent heat effect was take into consideration for the phase 1 collector. The maximum energy gain by each collector was at a maximum value at the middle of the day as expected with CMA-DPSAH with PCM and CMA-DPSAH without PCM maximum heat gain is 127 W and 89 W, respectively at around 1:40 p.m. The temperature difference profile for each collector is in according to the heat gain profile, with the CMA-DPSAH with PCM achieved better performance as compare to the one of without PCM. This is expected, because the total heat

gained by the collector with PCM was not only in the form of sensible heat from the absorber tube material itself, but also from the sensible heat (before the melting of the paraffin wax) and latent heat (during the freezing of the melted paraffin wax due to the fluctuation of the radiation flux) of the paraffin wax.

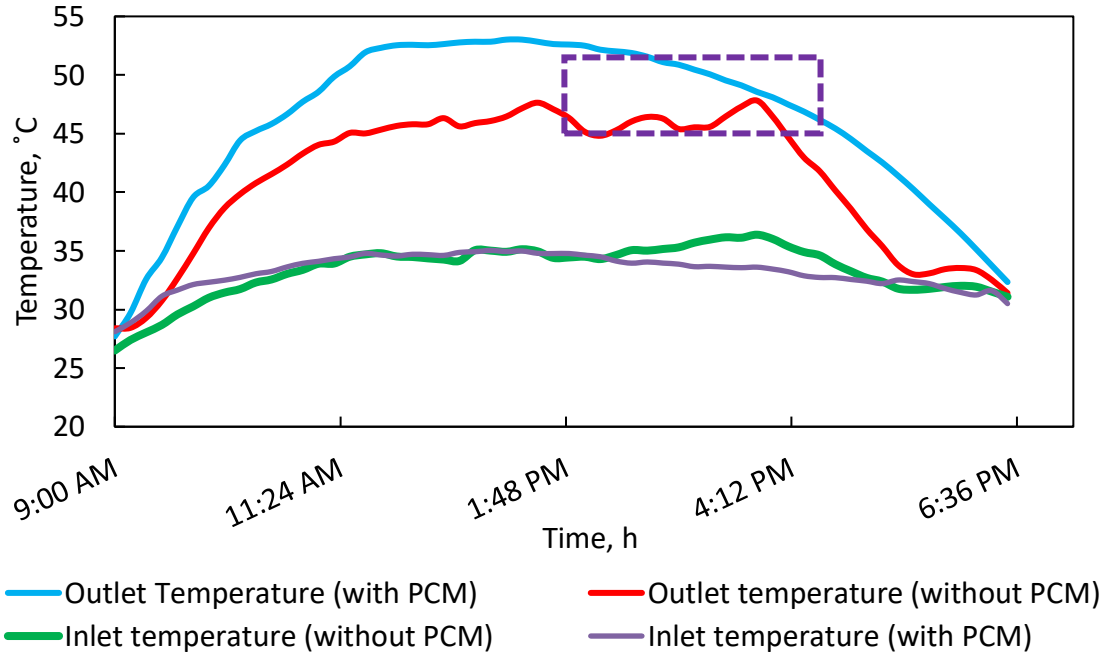


Fig. 5. Inlet and outlet temperature profile for configuration with PCM (Phase 1) and without PCM (Phase 2)

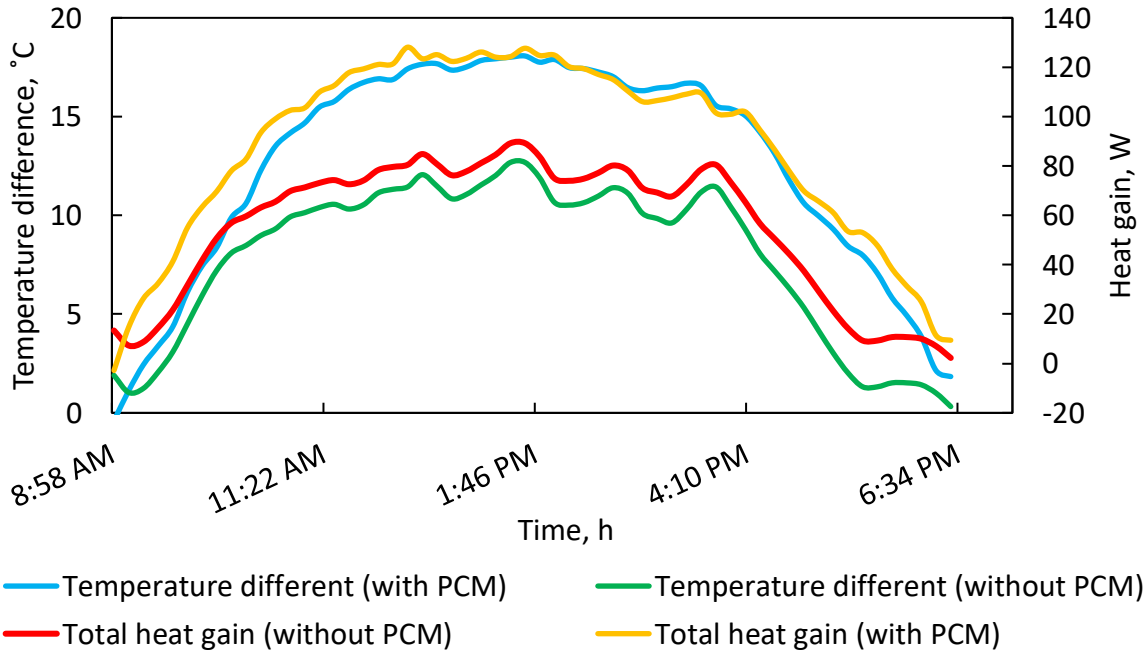


Fig. 6. Temperature difference and heat gain profile for each collector.

This is proven with the instantaneous efficiency value of CMA-DPSAH with PCM which is consistently higher than the one without PCM as presented by Fig. 7. From the Fig. 7, the

instantaneous efficiency of CMA-DPSAH with PCM varies with the maximum value was achieved during the condition of low radiation flux, which is about 64 %. This was due to the fact that during the low radiation flux, the air flowing through the collector still be heated by the heat that released from the paraffin wax during the freezing process. The instantaneous efficiency for CMA-DPSAH with PCM during the dropping of the radiation flux, which was significantly started at 3:00 p.m., was varied between 40 – 64 % whereas for CMA-DPSAH without PCM, the instantaneous efficiency was consistently lower by 17- 19 %. This result was due to the fact that the only heat source for the air going through the collector was a sensible heat of absorber tube material, which was aluminium. The higher value of thermal diffusivity of Aluminium making the temperature of the absorber tube drop much faster with the dropping of radiation flux [24,25].

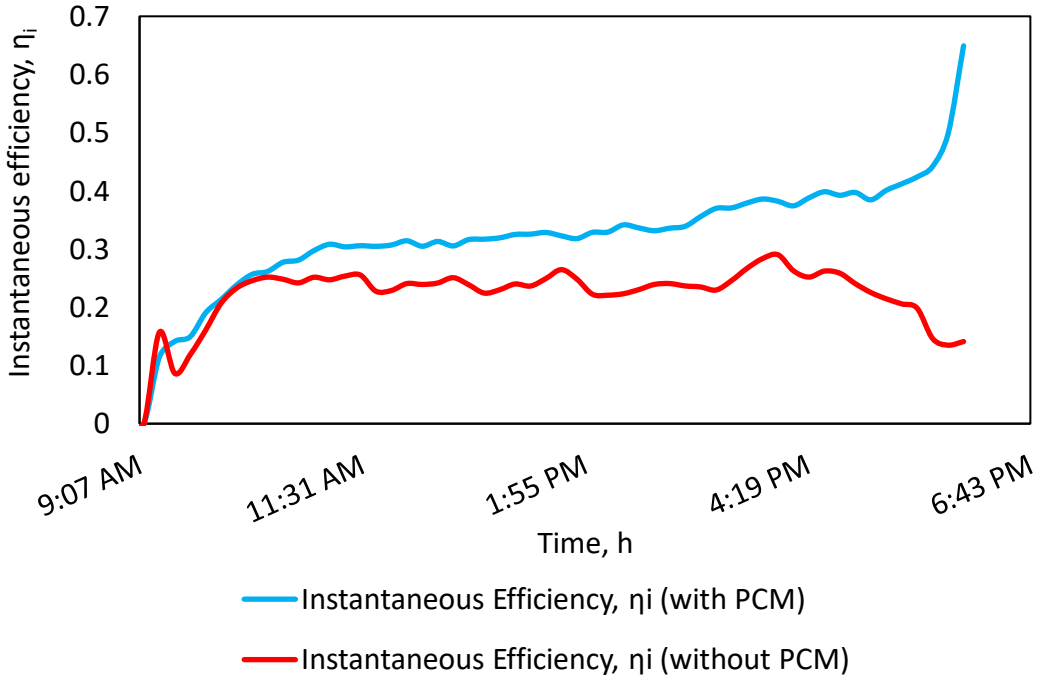


Fig. 7. Instantaneous efficiency of each collector as a function of time

4. Conclusions

The performance of DPSAH with PCM and without PCM were evaluated experimentally in the outdoor condition. Based on the result, several conclusions can be drawn as follows:

i) With the incorporation of PCM, the performance of CMA-DPAH can be improved significantly especially in the condition where there is a fluctuation of solar radiation or during the off-sunshine period.

ii) The ability of the PCM to store the energy is depend on the mass of the PCM used. The total weight of the PCM used in this study was 0.624 kg. With the value of latent heat of fusion, the energy can be stored by the PCM will be higher if the total weight of the PCM increased.

iii) The instantaneous efficiency of the CMA-DPSAH with the PCM was consistently higher than the one without PCM by 17- 19 % with the CMA-DPSAH with PCM gaining more energy that can be transferred to the flowing air. This condition was significant after the solar radiation flux started to drop (from 3:00 p.m. onwards).

iv) The features demonstrated by the CMA-DPSAH with PCM is suitable to be used in the drying application, especially for the agriculture products as that is the main focus by the Malaysian government in order to increase the production of drying products for Small and Medium-sized Industries.

.

Acknowledgement

The authors would like to thank University Malaysia Pahang (UMP) for the financial support under project grant RDU1703137 and International Islamic University of Malaysia (IIUM) for providing testing facilities.

References

[1] Kannan, Nadarajah, and Divagar Vakeesan. "Solar energy for future world:-A review." Renewable and Sustainable Energy Reviews 62 (2016): 1092-1105.
[2] Mahmood, A. J., L. B. Y. Aldabbagh, and F. Egelioglu. "Investigation of single and double pass solar air heater with transverse fins and a package wire mesh layer." Energy conversion and management 89 (2015): 599-607.
[3] Mahmood, A. J., and L. B. Y. Aldabbagh. "Double Pass Solar Air Heater with Transvers Fins and without Absorber Plate." World Academy of Science, Engineering and Technology, International Journal of Mechanical, Aerospace, Industrial, Mechatronic and Manufacturing Engineering 7, no. 6 (2013): 1293-1298.
[4] Wong, Rudy JD, Manar Al-Jethelah, Soroush Ebadi, Ashutosh Singh, and Shohel Mahmud. "Investigation of phase change materials integrated with fin-tube baseboard convector for space heating." Energy and Buildings 187 (2019): 241-256.
[5] Jamal-Abad, Milad Tajik, Seyfolah Saedodin, and Mohammad Aminy. "Heat transfer in concentrated solar air-heaters filled with a porous medium with radiation effects: A perturbation solution." Renewable Energy 91 (2016): 147-154.
[6] Zhou, Dan, and Chang-Ying Zhao. "Experimental investigations on heat transfer in phase change materials (PCMs) embedded in porous materials." Applied Thermal Engineering 31, no. 5 (2011): 970-977.
[7] Dehghan, Maziar, Yousef Rahmani, Davood Domiri Ganji, Seyfollah Saedodin, Mohammad Sadegh Valipour, and Saman Rashidi. "Convection–radiation heat transfer in solar heat exchangers filled with a porous medium: Homotopy perturbation method versus numerical analysis." Renewable Energy 74 (2015): 448-455.
[8] Hans, V. S., R. S. Gill, and Sukhmeet Singh. "Heat transfer and friction factor correlations for a solar air heater duct roughened artificially with broken arc ribs." Experimental Thermal and Fluid Science 80 (2017): 77-89.
[9] Ravi, Ravi Kant, and R. P. Saini. "Experimental investigation on performance of a double pass artificial roughened solar air heater duct having roughness elements of the combination of discrete multi V shaped and staggered ribs." Energy 116 (2016): 507-516.
[10] Ravi, Ravi Kant, and R. P. Saini. "Effect of roughness elements on thermal and thermohydraulic performance of double pass solar air heater duct having discrete multi V-shaped and staggered rib roughness on both sides of the absorber plate." Experimental Heat Transfer 31, no. 1 (2018): 47-67.
[11] Kalaiarasi, G., R. Velraj, and Muthusamy V. Swami. "Experimental energy and exergy analysis of a flat plate solar air heater with a new design of integrated sensible heat storage." Energy 111 (2016): 609-619.
[12] Singh, Sameer Kumar. "Performance Analysis of Solar Air Heater With Phase Change Material." *National Institute of Technology Jamshedpur,* Jharkhand, (2017).
[13] Bouadila, Salwa, Sami Kooli, Mariem Lazaar, Safa Skouri, and Abdelhamid Farhat. "Performance of a new solar air heater with packed-bed latent storage energy for nocturnal use." Applied Energy 110 (2013): 267-275.
[14] Salih, Salah M., Jalal M. Jalil, and Saleh E. Najim. "Experimental and numerical analysis of double-pass solar air heater utilizing multiple capsules PCM." Renewable Energy 143 (2019): 1053-1066.
[15] Baig, Wajahat, and Hafiz Muhammad Ali. "An experimental investigation of performance of a double pass solar air heater with foam aluminum thermal storage medium." Case Studies in Thermal Engineering 14 (2019): 100440.
[16] Raj, A. K., M. Srinivas, and S. Jayaraj. "A cost-effective method to improve the performance of solar air heaters using discrete macro-encapsulated PCM capsules for drying applications." Applied Thermal Engineering 146 (2019): 910-920.
[17] Sharol, A. F., A. A. Razak, Z. A. A. Majid, M. A. A. Azmi, and M. A. S. M. Tarminzi. "Performance of force circulation cross-matrix absorber solar heater integrated with latent heat energy storage material." In IOP Conference Series: Materials Science and Engineering, vol. 469, no. 1, p. 012107. IOP Publishing, 2019.

[18] Razak, A. A., Z. A. A. Majid, F. Basrawi, A. F. Sharol, Mohd Hafidz Ruslan, and Kamaruzzaman Sopian. "A performance and technoeconomic study of different geometrical designs of compact single-pass cross-matrix solar air collector with square-tube absorbers." Solar Energy 178 (2019): 314-330.
[19] Enibe, S. O. "Thermal analysis of a natural circulation solar air heater with phase change material energy storage." Renewable Energy 28, no. 14 (2003): 2269-2299.
[20] Kabeel, A. E., A. Khalil, S. M. Shalaby, and M. E. Zayed. "Improvement of thermal performance of the finned plate solar air heater by using latent heat thermal storage." Applied Thermal Engineering 123 (2017): 546-553.
[21] El-Sebaii, A. A., A. A. Al-Ghamdi, F. S. Al-Hazmi, and Adel S. Faidah. "Thermal performance of a single basin solar still with PCM as a storage medium." Applied Energy 86, no. 7-8 (2009): 1187-1195.
[22] Yahya, M., Ahmad Fudholi, and Kamaruzzaman Sopian. "Energy and exergy analyses of solar-assisted fluidized bed drying integrated with biomass furnace." Renewable energy 105 (2017): 22-29.
[23] Şevik, Seyfi. "Experimental investigation of a new design solar-heat pump dryer under the different climatic conditions and drying behavior of selected products." Solar Energy 105 (2014): 190-205.
[24] Majid, Z. A. A., A. A. Razak, Mohd Hafidz Ruslan, and Kamaruzzaman Sopian. "Characteristics of solar thermal absorber materials for cross absorber design in solar air collector." International Journal of Automotive and Mechanical Engineering 11 (2015): 2582.
[25] M.B. Y. Cengel. "Thermodynamics-An engineering approaches." *5th ed., Mc Graw-Hill*, 2010.

Penerbit Akademia Baru

Engineering Science and Technology
Conference Proceedings

Journal homepage: www.akademiabaru.com/EST.html

Plasma Temperature Profiles Modelling and Experimental Validation Using Graphene Electrode for Steel Wire Surface Cleaning

Open Access

M. F. Ikmal Misnal[1], N. Redzuan[1,*], M. N. Firdaus Zainal[1], N. Ahmad[1], R. K. Raja Ibrahim[2] , Agun L.[1]

[1] Department of Materials, Manufacturing and Industrial Engineering, School of Mechanical Engineering, Faculty of Engineering, Universiti Teknologi Malaysia, 81310 Skudai, Johor, Malaysia.
[2] Department of Physics, Faculty of Science, Faculty of Engineering, Universiti Teknologi Malaysia, 81310 Skudai, Johor, Malaysia.

ABSTRACT

Plasma temperature is one of the most important parameters to measure the plasma intensity. However, measuring temperature inside non-thermal plasma (NTP) reactor is a major challenge due to the lack of suitable techniques. For thermocouple, measurement error is the major issue while the usage of fiber Bragg grating (FBG) had to deal with its expensive and sensitive setup to environment. Therefore, mathematical model is essentially required to solve the problem. In this research, effect of axial plasma temperature profiles with respect to treatment time using graphene electrode and various applied voltages were investigated on rusted wire. Simulated temperature profiles were compared with experimental results using mean absolute percentage error (MAPE). From the model, it is found that most accurate plasma temperature profile model is recorded by the lowest applied voltage, 7 kV followed by 8 kV and 9 kV, at NTP reactor center point.

Keywords:
Plasma temperature; modeling;
experimental validation; graphene

Copyright © 2019 PENERBIT AKADEMIA BARU - All rights reserved

1. Introduction

Non-thermal plasma (NTP) has received much attention over the last ten years especially in metal surface treatment application [1-3]. On top of that, plasma temperature is one of the important NTP operating parameters in order to improve the quality of surface treatment via cleaning and coating. Recent findings in plasma temperature showed that higher temperature led to higher efficiency of metal surface cleaning [4-5].

Despite this interest, the plasma temperature measurement has become a challenge due to the NTP formation inside plasma reactor, especially for cylindrical dielectric barrier discharge (DBD) design. With this situation, it is difficult to measure the plasma temperature using thermocouple, as the measurement was only limited to the temperature of NTP external reactor wall which did not represent the actual plasma temperature [6-8]. In fact, few researchers have addressed the issue regarding the temperature measurement technique using thermocouple. The usage of thermocouple is often impractical due to many errors such as radiative exchange between the

* *Corresponding author.*
E-mail address: norizah@utm.my (Corresponding Author's name)

probe junction with the surrounding, thermal inertia, heat conduction along the wires and catalytic effects [9-10].

Alternatively, Fiber Bragg grating (FBG) might became as an option for plasma temperature sensor [11-12]. Although this approach is interesting, it appears to be a costly technique as equipment setup for FBG (single mode fiber) was more expensive than multi-mode fiber. Furthermore, optical connectors in FBG required critical mechanical tolerances in order to align with smaller optical connectors, as well as proper handling due to its sensitivity towards dust particles [13].

Another interesting part in this study is the involvement of graphene as an electrode. In addition, the thermal behavior of graphene has not been dealt with in depth as most of the researchers assumed that graphene electrode exhibited same thermal properties with graphite [14-15]. Despite its uncertainty in terms of thermal behavior, graphene is set to become an important component in electrical and optical devices especially as electrodes due to its mechanical strength, transparency, high charge mobility and flexibility [16-19].

Based on the current situation, the development of mathematical modelling and simulation is required in order to study, investigate and verify the thermal behavior of plasma with graphene as electrode. Several equivalent circuit models have been proposed to study the electrical characteristics in NTP [20-23]. Meanwhile, several heat transfer models have been introduced to study the thermal characteristics in NTP [24-27]. Despite the interests shown by a few researchers in mathematical modelling development, no one as far as we know has modelled the NTP by considering both electrical and thermal properties. Therefore, in this study, the plasma temperature profile for NTP discharge system is modelled and developed, with effects of different axial locations and magnitude of applied voltages. In order to validate the simulation results, the simulated plasma temperature profiles are compared with experimental plasma temperature profiles.

2. Methodology

2.1 Plasma Discharge Model

In this study, plasma discharge system for metal surface cleaning was modelled and represented by the equivalent discharge circuit, with the effect of electrical and material properties of graphene as the electrodes. The equivalent circuit as shown in Figure 1 has been modelled with integration of graphene equivalent circuit, glass tube equivalent circuit and air equivalent circuit. Simulink circuit modelling software was used to model the main discharge circuit. The modelling was done to provide further insight into the circuit characteristics before building the prototype system. The oscilloscope and current probe models in Simulink were connected to the model circuit during the simulation, to display the circuit result for discharge voltage and discharge current.

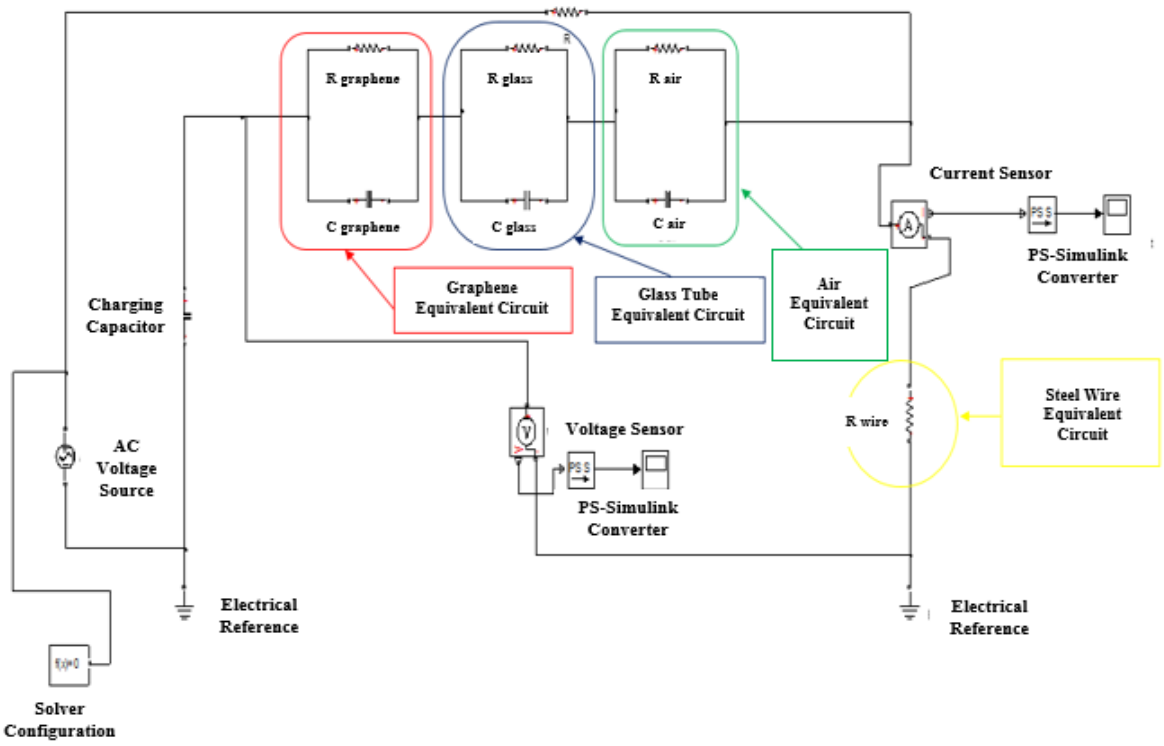


Fig. 1. Simulink equivalent circuit for plasma discharge system consists of electrode, dielectric and air modelling

From the simulated discharge current and discharge voltage, the thermal properties model was carried out using Ansys software version 15.0.7. Using transient thermal analyses, the temperatures and other thermal quantities that vary over time were determined. The temperature distribution over time has become an interest, as higher temperature distribution results in thermal stresses which lead to design or system failure. In this analysis, four major steps were done which were geometry set up (as shown in Figure 2), meshing analysis, and operational parameters input.

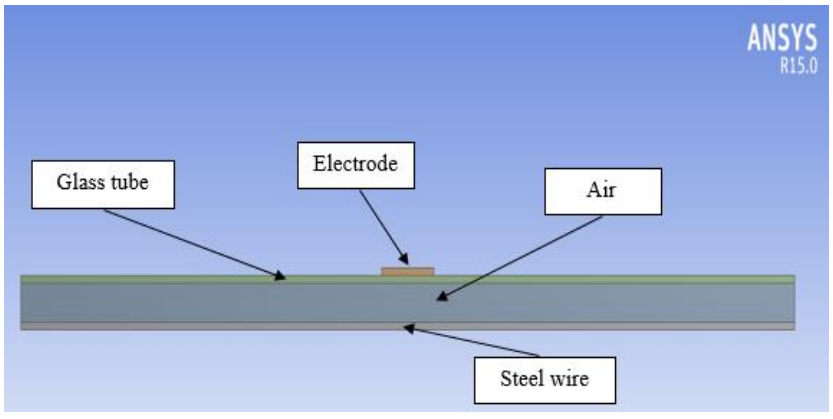


Fig. 2. Simplified two-dimensional plasma discharge model using Ansys

The thermal properties model considers the energy balance between heat transfer to the temperature probe and radiation losses from the temperature probe, in order to model the thermal and heat transfer properties for plasma discharge system. The energy balance can be represented as follows:

$$Q_c = h_c A(T_g - T_p) \quad (1)$$

$$Q_r = \varepsilon\sigma A(T_p^4 - T_{p,surr}^4) \quad (2)$$

Then, the conduction heat transfer, Q_c (Equation 1) and radiation heat transfer, Q_r (Equation 2) to be balanced, which yields

$$h_c A(T_g - T_p) = \varepsilon\sigma A(T_p^4 - T_{p,surr}^4) \quad (3)$$

Eventually, the radiation heat transfer from surrounding to the steel wire can be neglected, thus, Equation 3 becomes

$$h_c A(T_g - T_p) = \varepsilon\sigma A T_p^4 \quad (4)$$

From Equation 4, the difference of temperature, ΔT can be evaluated as

$$\Delta T = T_g - T_p = \frac{\varepsilon\sigma T_p^4}{h_c} \quad (5)$$

where

Q_c is the conduction heat transfer
Q_r is the radiation heat transfer
h_c is the convective heat transfer coefficient
A is the cross-sectional area of plasma discharge
T_g is the temperature of gas carrier (air)
T_p is the probe temperature
ε is the radiation emissivity
σ is the Stefan-Boltzmann constant (5.67×10^{-8} $\mathrm{W/m^2.K^4}$)
ΔT is the temperature difference between two ends

Table 1 summarizes the operational parameters of plasma discharge model. The operational parameters include electrical properties parameters, thermal properties parameters and physical properties parameters. Generally, the electrical properties parameters set up consists of the magnitude of applied voltage, capacitance and resistance values for materials involved. Whereas, the thermal properties parameters set up includes the thermal conductivity and specific heat values for corresponding materials, while the physical properties set up consists of the treatment time, density of materials, dielectric thickness and length of steel wire (treated specimen/cathode electrode).

Table 1
Operational parameters of plasma discharge model

Set Up/Materials	Electrical Properties Parameters	Thermal Properties Parameters	Physical Properties Parameters
Tested Applied Voltages	7 kV, 8 kV, 9 kV	-N/A-	-N/A-

Graphene sheet (anode electrode)	Resistivity: 2.5×10^{-6} Ω.m	Thermal conductivity: 15 W/m. K Specific heat: 700 J/kg.°C	Density: kg/m^3 Thickness: 0.025 mm
Glass tube (dielectric)	Resistivity: 2.0×10^{14} Ω. m	Thermal conductivity: 0.8 W/m. K Specific heat: 753 J/kg.°C	Density: 2210 kg/m^3 Thickness: 1 mm
Air (dielectric)	Resistivity: 1.3×10^{14} Ω. m	Thermal conductivity: 0.024 W/m. K Specific heat: 1005 J/kg.°C	Density: 1.225 kg/m^3 Thickness: 5 mm
Steel wire (treated specimen/cathode electrode)	Resistivity: 1.43×10^{-7} Ω. m	Thermal conductivity: 43 W/m. K Specific heat: 490 J/kg.°C	Density: 7820 kg/m^3 Length: 150 mm

2.2 Plasma Discharge Experimental Setup

The experimental works were carried out to validate the mathematical modelling and simulation results. The experimental work stage included the designing of plasma discharge system prototype and instrumentation set up, so that the modelling results can be compared with experimental results. Figure 3 shows the schematic and actual design of plasma discharge system. This system was able to function properly with the presence of high voltage power supply, electrodes (anode and cathode), dielectric materials and working gas. In this study, graphene sheet was used as anode electrode while untreated steel wire was used as cathode electrode. Air was used as the working gas for plasma to generate, whereas glass tube acts as dielectric barrier in our plasma discharge system.

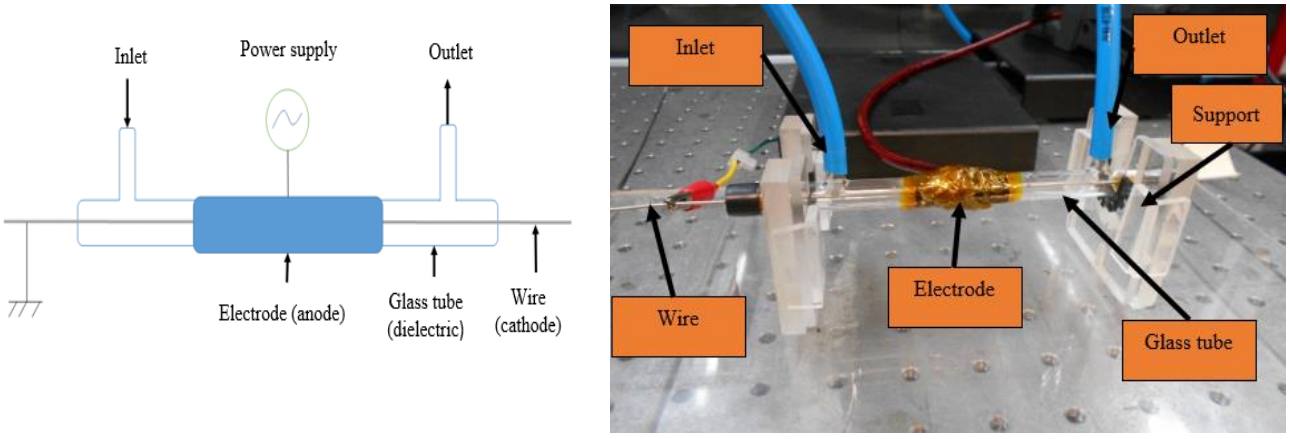


Fig. 3. Schematic (left hand side) and actual (right hand side) design of plasma discharge system

Air compressor (FD 1006 A, 1 HP) was used to supply air through the plasma discharge reactor. The air flowrate was controlled using flow meter (MKS Multi Gas Controller 647C) and was kept constant at 5 sccm. In this experiment, three different applied voltages were used (7 kV, 8 kV and 9 kV) with constant frequency of 70 kHz. The power supply (PVM500 Plasma Resonant and Dielectric Barrier Corona Driver) becomes the primary high voltage source, thus enable the electrical

discharge between two electrodes (anode and cathode). The desired discharge voltage and current were obtained with the aid of voltage probe (40 kV Testec high voltage probe) and current probe (Fluke 80i-400 AC Current Clamp). They were connected to picoscope (TDS2014, American Tektronix Co.), where voltage and current profiles can be displayed via a computer. The fiber Bragg grating (FBG) was placed on top of untreated steel wire surface, so that the temperature distribution of plasma discharge can be detected through computer display and data were recorded.

2.3 Plasma Temperature Measurement Technique

The results analysis consists of simulated and experimental axial plasma temperature profile with effect of applied voltages. The simulated axial plasma temperature profiles were obtained by locating three modelled temperature probes, Probe 1, Probe 2 and Probe 3 based on simulation setup in **Fig. 4 (b)**, while the experimental axial plasma temperature profile was obtained by locating three FBG's, FBG 1, FBG 2 and FBG 3 based on experimental setup in **Fig. 4 (a)**. For simulation, the temperature probes were modelled using transient thermal analyses in Ansys software version 15.0.7. For experiment, fiber Bragg grating inscribed in this single mode fiber is a uniform grating with operating wavelength at 1550 nm, reflectivity of 90%, and bandwidth of 0.5 nm. FBG temperature sensitivity was calculated from calibration curve at 10.8 pm/°C. The distance between modelled probes were set at 5 mm, so as the distance between FBG's for the sake of modelling validation.

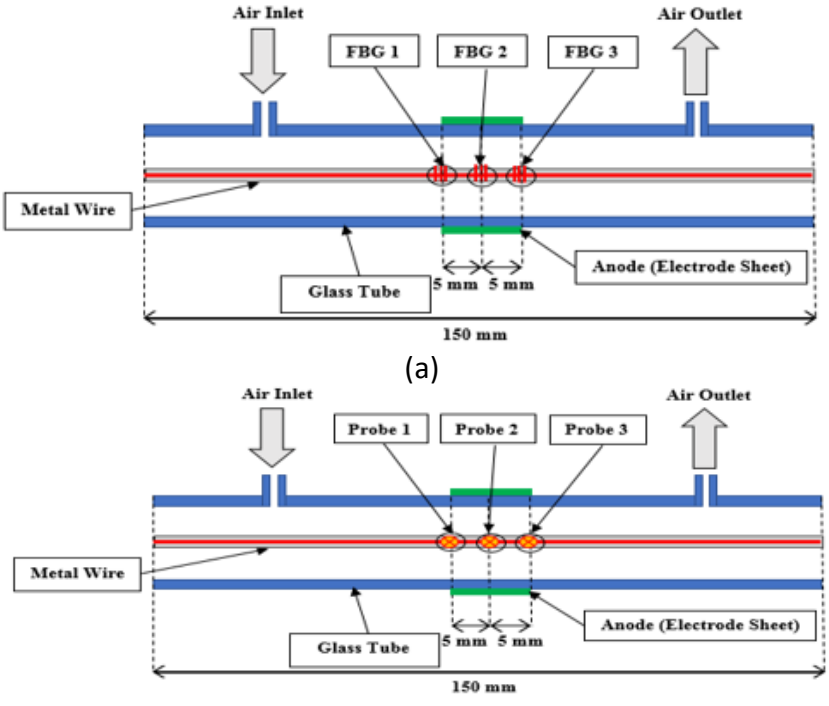


Fig. 4. Plasma temperature measurement technique using (a) FBG, (b) modelled temperature probes

2.4 Mathematical Model Validation

The simulated and experimental plasma temperature profile was plotted at the same axis, so that we can compare the closeness in terms of plasma temperature range between the simulation

and experimental work, which is being evaluated by using mean absolute percentage error (MAPE). MAPE can be defined by using the following formula

$$MAPE = \frac{100}{n} \sum_{t=1}^{n} \left| \frac{T_{exp(FBG)} - T_{sim\ (probe)}}{T_{exp(FBG)}} \right| \quad (6)$$

where $T_{exp(FBG)}$ is the experimental value of plasma temperature, $T_{sim\ (probe)}$ is the simulated value of plasma temperature and n is the number of plasma temperature points. From the formula, technically, it can be deduced that the closer the simulated plasma temperature towards the experimental plasma temperature, the lower the MAPE.

3. Results

3.1 Plasma Temperature Profiles Comparison

Figure 5 showed the simulation and experimental plasma temperature profiles comparison for 7 kV at 5 (a) Probe 1 and FBG 1, 5 (b) Probe 2 and FBG 2 and 5 (c) Probe 3 and FBG 3. Meanwhile, Figure 6 showed the simulation and experimental plasma temperature profiles comparison for 8 kV at 6 (a) Probe 1 and FBG 1, 6 (b) Probe 2 and FBG 2 and 6 (c) Probe 3 and FBG 3. Whereas, Figure 7 showed the simulation and experimental plasma temperature profiles comparison for 9 kV at 7 (a) Probe 1 and FBG 1, 7 (b) Probe 2 and FBG 2 and 7 (c) Probe 3 and FBG 3.

Theoretically, for all plasma temperature profiles, the trend showed typical Townsend discharge characteristics with a steady increment for the first 20 to 25 seconds, before it started to stabilize. The steady increment displayed the condition where glow discharge was formed while the stagnant stage of temperature exhibited the condition of initiation of filamentary discharge due to electrical charge and heat accumulation [12]. By comparison, our simulated plasma temperature profile behaved similarly with the plasma temperature profile recorded from the proposed lumped capacitance model by Sadat *et al*. (2010). In the proposed lumped capacitance model, it is assumed that the heat generated in plasma zone is flows radially to reach central electrode (cathode) through convection and radiation heat transfer [25]. Those assumptions also applied in our case, just we were more interested in axial plasma temperature distribution behaviour. Maximum plasma temperature was approximately recorded using simulated temperature probes in descending order from 29 to 30 °C, 28 to 29 °C and 23 to 24 °C for 9 kV, 8 kV and 7 kV applied voltages respectively. Therefore, our modelling itself showed that the axial plasma temperature profiles were non-uniformly distributed alongside the center of plasma reactor. According to Chen *et al*. (2015), modelled probe junction increased gradually and eventually stabilized approximately at gas temperature. The stabilized plasma temperature profiles might be due to the influence of thermal radiation with heat exchange between solid (modelled probe) and gas (modelled plasma). In simple understanding, the conduction heat transfer had been balanced with radiation heat transfer, eventually led to stable temperature profile [27].

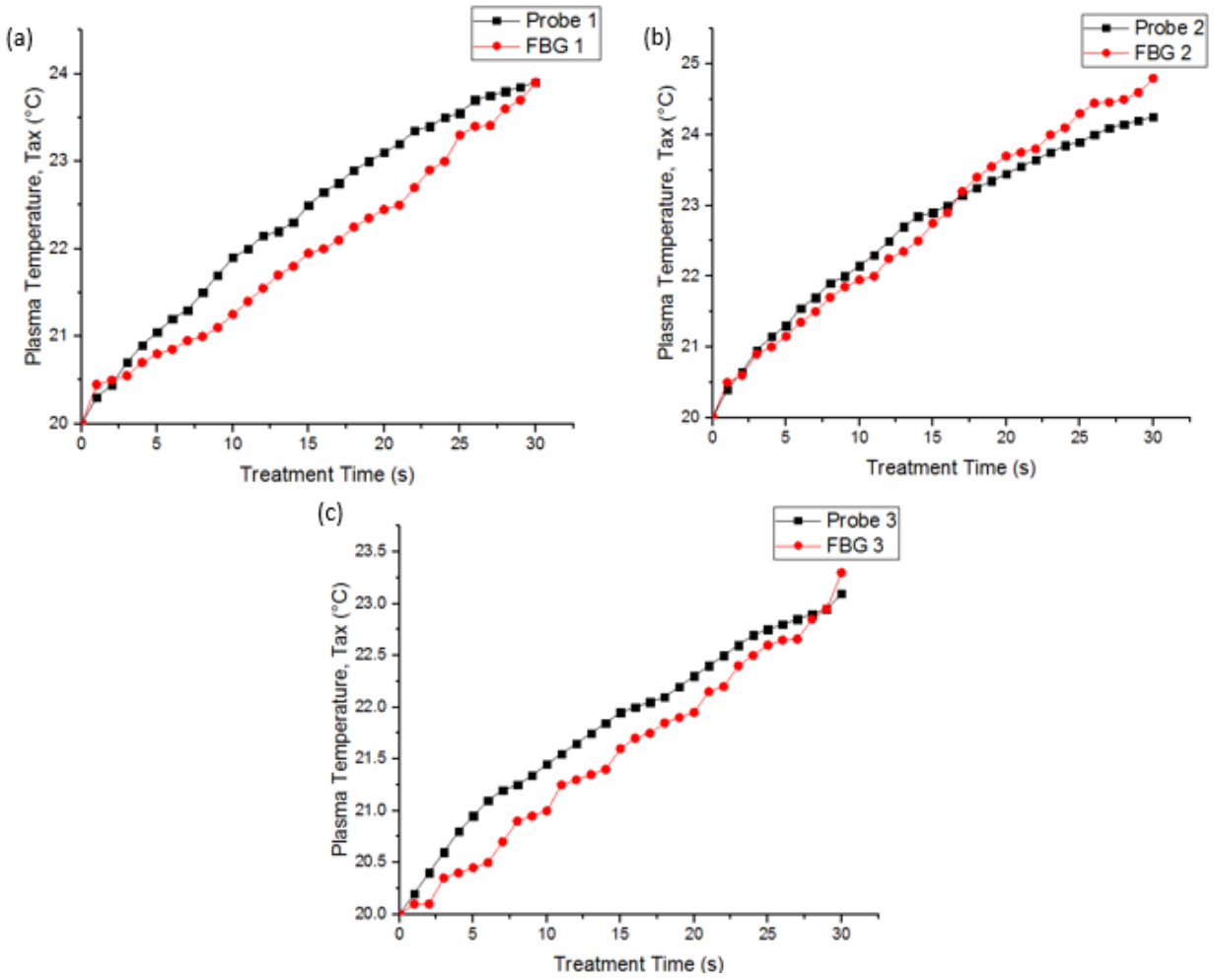


Fig. 5. Simulation and experimental plasma temperature profiles comparison for 7 kV at (a) Probe 1 and FBG 1, (b) Probe 2 and FBG 2 and (c) Probe 3 and FBG 3

Experimentally, it is almost a linear temperature increment for 7 kV and 8 kV, while for 9 kV, the plasma temperature profile showed temperature fluctuation. Linear temperature rises in all plasma temperature profiles reflected to Townsend discharge, which initiated by the impact ionization acceleration due to surface charge accumulation from high voltage induction (Huang *et al*., 2016). After approximately 25 seconds onwards, for higher applied voltages of 8 kV and 9 kV, the temperature profiles tend to stabilize. At this stage, there is higher possibility of arcing production due to filamentary discharge or microdischarge, as higher energy is required to break the diatomic molecules of oxygen atoms in air [12].

In descending order, maximum plasma temperature was approximately recorded using FBGs from 29 to 31 °C, 28 to 29 °C and 24 to 25 °C for 9 kV, 8 kV and 7 kV applied voltages respectively. Normally, for plasma reactor which has been designed based on cylindrical dielectric barrier discharge (DBD), it is expected for radial plasma temperature to displayed non-uniform temperature distribution, due to the difference radial distance between high voltage electrode (anode) and central electrode (cathode) [24]. However, for our case, plasma temperature profiles also showed non-uniform temperature distribution although the temperature measurement is recorded in axial direction. Based on this fact, we believe that the non-uniformity of plasma temperature is due to the dynamic characteristics of plasma itself [28-29].

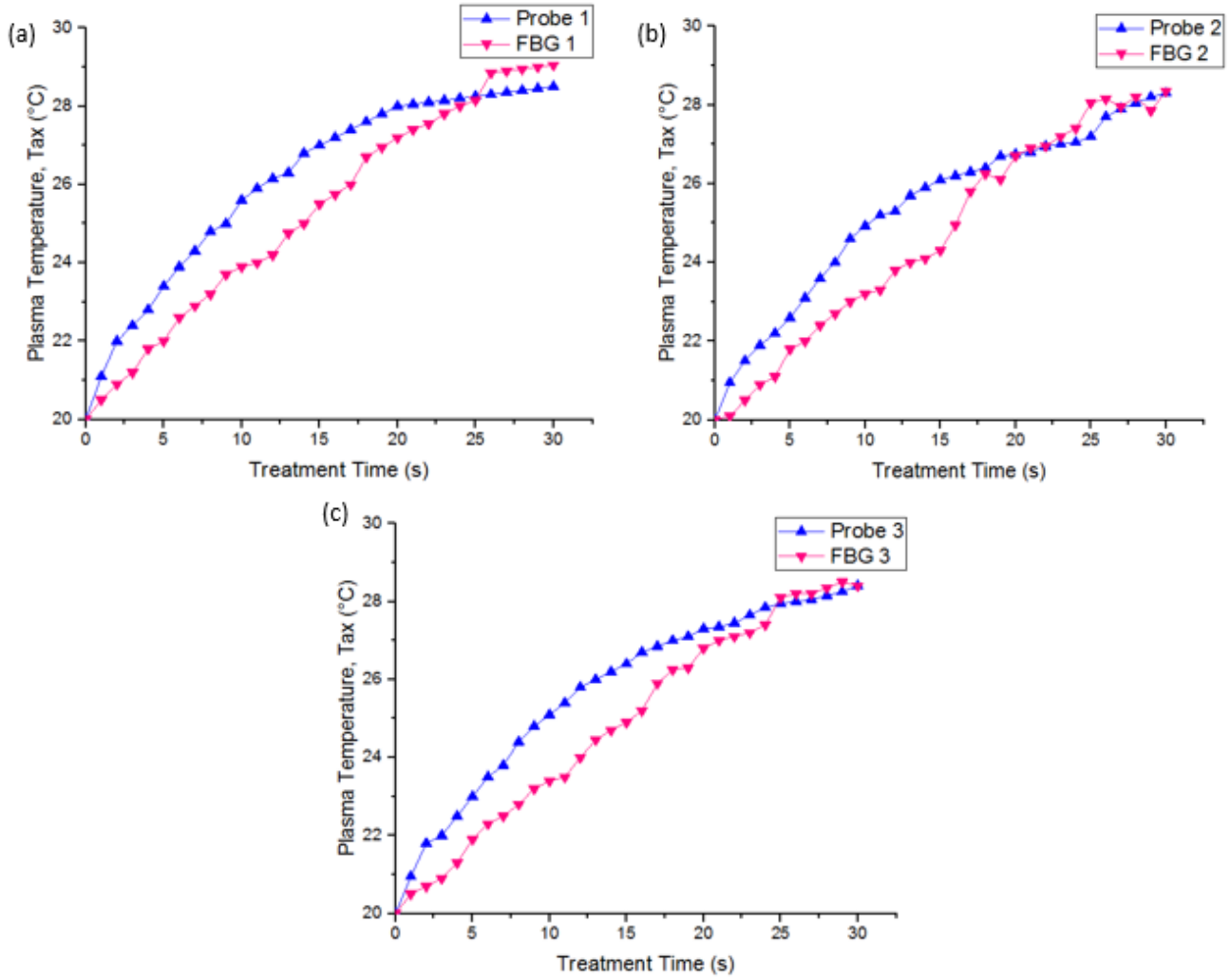


Fig. 6. Simulation and experimental plasma temperature profiles comparison for 8 kV at (a) Probe 1 and FBG 1, (b) Probe 2 and FBG 2 and (c) Probe 3 and FBG 3

Thermal behaviour shown by 9 kV was an instantaneous temperature rise due to further increment of applied voltage which spread the microdischarge filaments into surface discharge, eventually led to intensified discharge interactions and collisions. Intensified discharge interactions and collisions contributed to non-uniformity of charge distribution and electron instability which caused temperature fluctuation [28-29]. This is the cause of the plasma temperature instability in FBG 1, FBG 2 and FBG 3 especially for 9 kV case.

Plasma temperature increment was expected as it was greatly influenced by the electron emission in order to form plasma. When applied voltage increased, electron gained more energy, which caused the electron to move and vibrate vigorously. Vigorous vibration and movement of electron became excess energy (in heat form), eventually contributed plasma temperature rise. The excess energy then initiated more frequent electron collision, which later on produce plasma [11]. Acceleration of electrons was induced by the electrical current produced by higher applied voltage. According to Ohm's Law and Joule's First Law, higher induced current contributed more heat due to greater dissipated power. Therefore, excessive heat in plasma stream produced, eventually led to substantial temperature rise [12].

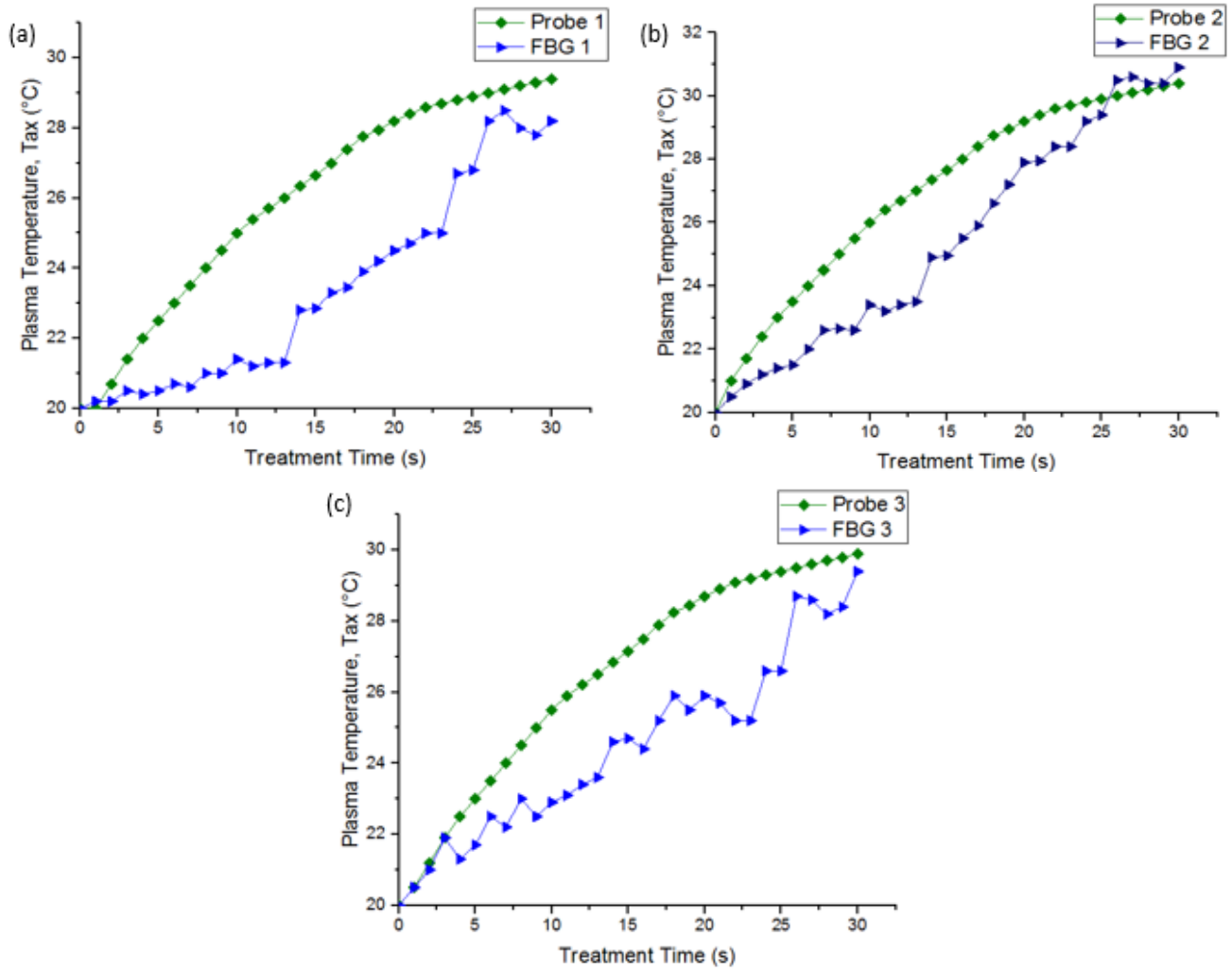


Fig. 7. Simulation and experimental plasma temperature profiles comparison for 9 kV at (a) Probe 1 and FBG 1, (b) Probe 2 and FBG 2 and (c) Probe 3 and FBG 3

Based on our electrode geometry design, positive current pulse is formed in plasma reactor. Positive current pulse is caused by electrons movement towards the glass tube (dielectric) from the steel wire (cathode) and ion streamer mobility from the glass tube (dielectric) to the steel wire (cathode). For this case, secondary emission effect is influenced by the steel wire, as the steel wire acts as cathode and the glass tube (dielectric) as anode. The electrons eventually experienced photo desorption from steel wire and move towards glass tube. The previous free electrons are not trapped by the steel wire surface and hence the secondary electron emission is from the steel wire surface. Higher energy is required to initiate secondary electron emission to reduce collective effect, thus led to low intensity of filamentary current [21]. Scientifically, this might be the reason of low range of plasma temperature recorded (24 to 31 °C).

3.2 Mathematical Model Validation

Table 2 shows the mean absolute percentage error (MAPE) calculated by 7 kV, 8 kV and 9 kV, as it compared both simulation and experimental data numerically. From section 2.4, as MAPE value decreased, the closeness between simulation and experimental temperature profiles increased. In general, the range of MAPE calculated in ascending order from 0.97 to 1.89, 3.53 to 4.13 and 6.65 to 11.33 for 7 kV, 8 kV and 9 kV respectively. We can see that MAPE calculated in Probe 2 /FBG 2

for all applied voltages recorded the lowest MAPE value, which means the lowest error. Therefore, we can deduce that the center position in steel wire (cathode electrode) is the most suitable location to measure the temperature in plasma reactor. The higher MAPE values calculated in Probe 1/FBG 1 (left hand side) and Probe 3/FBG 3 (right hand side) for all applied voltages might be reflected to air flow, as Probe 1/FBG 1 is located nearest to air inlet while Probe 3/FBG 3 is located nearest to air outlet, thus make Probe 2/FBG 2 as the most stable location with less air flow turbulence. Discharge uniformity is clearly influenced by the air flowrate, as the air flowrate is increased, more homogenous plasma discharge can be formed, but it is difficult to achieve stable or uniform discharge when the air flowrate is too high [30].

Table 2
Mean absolute percentage error (MAPE)

Applied Voltage (kV)	Mean absolute percentage error (MAPE) (%)			
	Probe 1/FBG 1	Probe 2/FBG 2	Probe 3/FBG 3	Average
7	1.89	0.97	1.28	1.38
8	4.13	3.53	3.94	3.87
9	11.33	6.65	7.97	8.65

4. Conclusions

In this study, we have successfully proposed the development of localized plasma temperature profile model for non-thermal discharge system for graphene electrode by considering both electrical and thermal properties using Simulink and Ansys. In general, the findings of this study indicate that

- Center point in NTP reactor where Probe 2 and FBG 2 was located recorded most accurate plasma temperature profile model due to its lowest MAPE.
- Most accurate plasma temperature profile model is recorded by the lowest applied voltage, 7 kV followed by 8 kV and 9 kV.
- By average, lower MAPE of less than 10% is approximately recorded at 1.38%, 3.87% and 8.65% for 7 kV, 8 kV and 9 kV respectively. Here, we have demonstrated satisfactory plasma temperature profile model especially for lower applied voltages of 7 kV and 8 kV.

The present findings are the beginning step towards enhancing our understanding in electrical and thermal characteristics for graphene electrode. Therefore, we believe that our results may improve knowledge about the real potential of graphene electrode for various applications especially in NTP.

Acknowledgement
This research was funded by a grant from Ministry of Education of Malaysia through Fundamental Research Grant Scheme (FRGS) 7843.4F808 and Research University Grant (GUP) Tier 1 2524.04H74. First author also wants to express very profound gratitude to UTM Zamalah Scholarship for his financial assistance.

References

[1] Rodríguez-Villanueva, C., N. Encinas, J. Abenojar, and M. A. Martínez. "Assessment of atmospheric plasma treatment cleaning effect on steel surfaces." *Surface and Coatings Technology* 236 (2013): 450-456.
[2] Cherenda, Nikolai Nikolaevich, A. A. Smilgin, Vladimir Vasilevich Uglov, V. M. Astashynski, A. M. Kuzmitski, and Gennady Efimovich Remnev. "Cleaning of steel surface from scale by compression plasma flows." *Surface and Coatings Technology* 255 (2014): 79-83.
[3] Zainal, Muhamad Nor Firdaus, Norizah Redzuan, and Mohd Fadthul Ikmal Misnal. "Brief review: Cold plasma." *Jurnal Teknologi* 74, no. 10 (2015).
[4] Muñoz, J., J. A. Bravo, and M. D. Calzada. "Aluminum metal surface cleaning and activation by atmospheric-pressure remote plasma." *Applied Surface Science* 407 (2017): 72-81.
[5] Juřík, P., P. Slepička, M. Nagyová, and V. Švorčík. "Wrinkle pattern on PLLA induced by stress of polymer-metal bilayer." *Surface and Coatings Technology* 311 (2017): 344-350.
[6] Harling, Alice M., Anna E. Wallis, and J. Christopher Whitehead. "The Effect of Temperature on the Removal of DCM using Non-Thermal, Atmospheric-Pressure Plasma-Assisted Catalysis." *Plasma Processes and Polymers* 4, no. 4 (2007): 463-470.
[7] Kim, D-H., Y. S. Mok, and S. B. Lee. "Effect of temperature on the decomposition of trifluoromethane in a dielectric barrier discharge reactor." *Thin Solid Films* 519, no. 20 (2011): 6960-6963.
[8] Young Sun, Mok, and Kim Dong-Hong. "Decomposition of sulfur hexafluoride by using a nonthermal plasma-assisted catalytic process." *Journal of Korean Physical Society* 59 (2011): 3437.
[9] Kim, J. S., and M. A. Cappelli. "Temperature measurements in low-pressure, diamond-forming, premixed flames." *Journal of applied Physics* 84, no. 8 (1998): 4595-4602.
[10] Brohez, Sylvain, Christian Delvosalle, and Guy Marlair. "A two-thermocouples probe for radiation corrections of measured temperatures in compartment fires." *Fire Safety Journal* 39, no. 5 (2004): 399-411.
[11] Musa, Siti Musliha Aishah, RK Raja Ibrahim, and Asrul Izam Azmi. "Development of Fiber Bragg Grating (FBG) as Temperature Sensor Inside Packed-bed Non-thermal Plasma Reactor." *Jurnal Teknologi* 68, no. 3 (2014).
[12] Nor Zazwani Rosdi, Ibrahim, RK Raja, S. M. A. Musa, Raheleh Hosseinian, Asrul Izam Azmi, and Norhayati Ahmad. "Reactor temperature profiles of non-thermal plasma reactor using fiber Bragg grating sensor." *Sensors and Actuators A: Physical* 244 (2016): 206-212.
[13] Pinet, Éric, Sébastien Ellyson, and Frédéric Borne. "Temperature fiber-optic point sensors: commercial technologies and industrial applications." In *Proc. 46th Int. Conf. Microelectron. Devices Mater.(MIDEM 2010)*, pp. 31-43. 2010.
[14] Nihira, Takeshi, and Tadao Iwata. "Temperature dependence of lattice vibrations and analysis of the specific heat of graphite." *Physical Review B* 68, no. 13 (2003): 134305.
[15] Tohei, Tetsuya, Akihide Kuwabara, Fumiyasu Oba, and Isao Tanaka. "Debye temperature and stiffness of carbon and boron nitride polymorphs from first principles calculations." *Physical Review B* 73, no. 6 (2006): 064304.
[16] Chen, Shanshan, Arden L. Moore, Weiwei Cai, Ji Won Suk, Jinho An, Columbia Mishra, Charles Amos et al. "Raman measurements of thermal transport in suspended monolayer graphene of variable sizes in vacuum and gaseous environments." *ACS nano* 5, no. 1 (2010): 321-328.
[17] Balandin, Alexander A. "Thermal properties of graphene and nanostructured carbon materials." *Nature materials* 10, no. 8 (2011): 569.
[18] Jo, Gunho, Minhyeok Choe, Sangchul Lee, Woojin Park, Yung Ho Kahng, and Takhee Lee. "The application of graphene as electrodes in electrical and optical devices." *Nanotechnology* 23, no. 11 (2012): 112001.
[19] Chen, Shanshan, Qingzhi Wu, Columbia Mishra, Junyong Kang, Hengji Zhang, Kyeongjae Cho, Weiwei Cai, Alexander A. Balandin, and Rodney S. Ruoff. "Thermal conductivity of isotopically modified graphene." *Nature materials* 11, no. 3 (2012): 203.
[20] Fang, Zhi, Shengchang Ji, Jun Pan, Tao Shao, and Cheng Zhang. "Electrical model and experimental analysis of the atmospheric-pressure homogeneous dielectric barrier discharge in He." *IEEE Transactions on Plasma Science* 40, no. 3 (2012): 883-891.
[21] Tay, W. H., S. L. Yap, and C. S. Wong. "Electrical characteristics and modeling of a filamentary dielectric barrier discharge in atmospheric air." *Sains Malaysiana* 43, no. 4 (2014): 583-594.
[22] López-Fernandez, J. A., R. Peña-Eguiluz, R. López-Callejas, A. Mercado-Cabrera, R. Valencia-Alvarado, A. Muñoz-Castro, and B. G. Rodríguez-Méndez. "Electrical model of dielectric barrier discharge homogenous and filamentary modes." In *Journal of Physics: Conference Series*, vol. 792, no. 1, p. 012067. IOP Publishing, 2017.
[23] Tschiersch, R., S. Nemschokmichal, M. Bogaczyk, and J. Meichsner. "Surface charge measurements on different dielectrics in diffuse and filamentary barrier discharges." *Journal of Physics D: Applied Physics* 50, no. 10 (2017): 105207.
[24] Sadat, Hamou, N. Dubus, Ludovic Pinard, Jean-Michel Tatibouet, and Joël Barrault. "Conduction heat transfer in a cylindrical dielectric barrier discharge reactor." *Applied Thermal Engineering* 29, no. 5-6 (2009): 1259-1263.

[25] Sadat, H., N. Dubus, V. Le Dez, J. M. Tatibouët, and J. Barrault. "A simple model for transient temperature rise and fall in a dielectric barrier discharge reactor after ignition and shut down." *Journal of Electrostatics* 68, no. 1 (2010): 27-30.
[26] Sadat, Hamou, Nicolas Dubus, and Jean Michel Tatibouët. "Temperature runaway in a pulsed dielectric barrier discharge reactor." *Applied Thermal Engineering* 37 (2012): 324-328.
[27] Chen, Xue, Xin-Lin Xia, Chuang Sun, and Yang Li. "Numerical analysis on the transient measurement of gas temperature in porous material using thermocouples at high temperatures." *International Journal of Heat and Mass Transfer* 91 (2015): 1060-1068.
[28] Huang, Zhiming, Lin Yang, Yanpeng Hao, and Licheng Li. "Dynamic Characteristics of Dielectric Barrier Columnar Discharge During Its Decay." *IEEE Transactions on Plasma Science* 44, no. 11 (2016): 2568-2575.
[29] Russ, Holger, Manfred Neiger, and Jurgen E. Lang. "Simulation of micro discharges for the optimization of energy requirements for removal of NO/sub x/from exhaust gases." *IEEE transactions on plasma science* 27, no. 1 (1999): 38-39.
[30] Zhang, Ying, Jie Li, Na Lu, Kefeng Shang, Akira Mizuno, and Yan Wu. "Evaluation of discharge uniformity and area in surface dielectric barrier discharge at atmospheric pressure." *Vacuum* 123 (2016): 49-53.

Penerbit Akademia Baru

Engineering Science and Technology
Conference Proceedings

Journal homepage: www.akademiabaru.com/EST.html

Stability Analysis on Stagnation-Point Flow and Heat Transfer Towards a Permeable Shrinking Sheet with Heat Source in a Casson Fluid

Open Access

Ubaidullah Yashkun[1], Fatinnabila Kamal[1], Khairy Zaimi[1,*], Nor Ashikin Abu Bakar[1], Norshaza Atika Saidin[1]

[1] Institute of Engineering Mathematics, Universiti Malaysia Perlis, Pauh Putra Campus, 02600 Arau, Perlis, Malaysia

ABSTRACT

The stagnation-point boundary layer flow and heat transfer of a Casson fluid towards a stretching/shrinking sheet in the presence of heat source and injection effect is studied. The governing nonlinear partial differential equations are transformed into a system of nonlinear ordinary differential equations by using similarity transformation, before being solved numerically using the boundary value problem solver bvp4c in Matlab. The numerical solutions for the skin friction coefficient and the local Nusselt number as well as the velocity and temperature profiles are presented in the forms of tables and graphs. Dual solutions are found to exist for the shrinking sheet case, whereas the solution is unique for the stretching case. The stability analysis verified that the first solution is stable and physically reliable while the second solution is not. With the decreasing of injection parameter, both the skin friction coefficient and the heat transfer rate at the surface increase for the stable solution. Meanwhile, the heat transfer rate at the surface decreases with the inclusion of heat source.

Keywords:
Stability analysis; stagnation point flow; heat transfer; heat source; injection effect; Casson fluid

Copyright © 2019 PENERBIT AKADEMIA BARU - All rights reserved

1. Introduction

Stagnation-point is a rest point in the moving fluid. The stagnation-point region encounters the highest pressure, the highest heat transfer and the highest rates of mass decomposition, exists on all solid bodies moving in a fluid [1]. Hiemenz was the first who examined the two-dimensional flow of a fluid near a stagnation-point. He was demonstrated that the governing flow equations of Navier-Stokes equations can be reduced to an ordinary differential equation of third order using similarity transformation. Stagnation-point flow is continuing to be an interesting area of research among scientists and investigators due to its importance in a wide variety applications both in industrial and engineering processes such as cooling of electronic devices by fans, cooling of nuclear reactors during emergency shutdown, polymer extrusion, wire drawing and drawing of plastic sheets (Makinde *et al.* [2]). Since then, many investigators have extended the idea to different aspect of the stagnation-point flow problems. Nandy and Pop [3] studied the effects of magnetic field and thermal radiation on the stagnation flow and heat transfer of a nanofluid over a shrinking

* *Corresponding author.*
E-mail address: khairy@unimap.edu.my (Khairy Zaimi)

surface. Later, Fauzi *et al.,* [4] investigated the effect of the slip parameter on the stagnation-point flow and heat transfer over a nonlinear shrinking sheet. Besides that, the problem of the stagnation-point flow of Maxwell fluid towards a permeable surface in the presence of nanoparticles has been considered by Ramesh *et al.,* [5]. Furthermore, Mahapatra and Gupta [6] studied the steady two-dimensional stagnation-point flow of an incompressible viscous fluid over a flat deformable sheet when the flow is started impulsively from rest and suddenly stretched in its own plane with a velocity proportional to the distance from the stagnation-point. Nazar *et al.,* [7] presented the unsteady two-dimensional stagnation-point flow of an incompressible viscous fluid over a flat deformable sheet when the flow is started impulsively from rest and suddenly stretched in its own plane with a velocity proportional to the distance from the stagnation-point. More studies on the stagnation-point flow include those by Othman *et al.,* [8], Rehman *et al.,* [9], Naganthran *et al.,* [10] and Sharma *et al.,* [11].

Problems involving fluid flow over stretching or shrinking surfaces can be found in many industrial manufacturing processes such as hot rolling, paper production, metal spinning, drawing plastic films, glass blowing, continuous casting of metals and spinning of fibers (Roşca and Pop [12]). Due to the numerous applications, the study of stretching/shrinking sheet was subsequently extended by many authors to explore various aspects of skin friction coefficient and heat transfer in a fluid. For example, Yasin *et al.,* [13] numerically examined the steady two-dimensional magnetohydrodynamic flow past a permeable stretching/shrinking sheet with radiation effects. Recently, Naganthran *et al.,* [14] investigated the unsteady stagnation-point flow and heat transfer of a special third grade fluid past a permeable stretching/shrinking sheet. Since then, many researchers have been working on the stretching or shrinking sheet with various physical conditions such as Alam *et al.,* [15], Jamaludin *et al.,* [16], Jusoh *et al.,* [17], Nasir *et al.,* [18], Seth *et al.,* [19], Hamid *et al.,* [20] and Soid *et al.,* [21].

Casson fluid is defined as a shear thinning liquid which is assumed to have an infinite viscosity when rate of shear is zero, a yield stress below which no flow occurs and a zero viscosity at an infinite rate of shear (Dash et al. [22]). Casson fluid is one of the non-Newtonian fluids, which has attracted much attention because of their extensive variety of applications in engineering and industry especially in extraction of crude oil from petroleum products, production of plastic materials and syrup drugs (Animasaun *et al.,* [23]). Hayat *et al.,* [24] investigated the mixed convection stagnaton-point flow of a Casson fluid with convective boundary conditions. On the other hand, Bhattacharyya [25] analyzed the steady boundary layer stagnation-point flow of a Casson fluid and heat transfer towards a stretching/shrinking sheet. This work has been extended by Kameswaran *et al.,* [26] with the inclusion of Soret and Dufour effects over a stretching sheet. Afterwards, the researcher explored the behaviour of the Casson fluid under various effect and circumstances (see Abd El-Aziz and Yahya [27], Hakeem *et al.,* [28], Khan *et al.,* [29], Maity *et al.,* [30], Medikare *et al.,* [31], Raju and Sandeep [32,33], Raju *et al.,* [34], Rehman *et al.,* [35] and Shateyi *et al.,* [36]).

In this paper, we analyze the behaviour of stagnation-point flow and heat transfer towards a stretching/shrinking sheet with heat source and injection effects in a Casson fluid. This study is different from that investigated by Bhattacharyya [25] where we consider a stretching/shrinking sheet with the heat source and injection effects are taken into consideration. The effects of stagnation-point flow, injection and heat source on the velocity profile, temperature profile, skin friction coefficient and local Nusselt number will be presented and discussed. The dual solutions are expected to exist for the shrinking case. A temporal stability analysis is conducted to verify which solution is stable and has real physical implication.

2. Methodology

Consider the steady two-dimensional stagnation-point flow of an incompressible Casson fluid located at $y=0$, with the flow being confined in $y>0$. It is assumed that the velocity of the stretching/shrinking sheet is $u_w(x)=ax$, where $a>0$ is for the stretching sheet and $a<0$ is for the shrinking sheet, while the free stream velocity is $u_e(x)=bx$ where b is a positive constant. We also assume that the surface temperature T_w is constant. The physical model and the coordinate system is shown in Figure 1, where the *x*-axis is taken along the direction of the stretching/shrinking sheet and the $y-$axis is measured normal to it. The rheological equations of the state for an isotropic and incompressible flow of the Casson fluid is given by (see Bhattacharyya [25,37])

$$\tau_{ij}=\begin{cases}2\left(\mu_B+p_y/\sqrt{2\pi}\right)e_{ij,} & \pi>\pi_c,\\ 2\left(\mu_B+p_y/\sqrt{2\pi_c}\right)e_{ij,} & \pi<\pi_c,\end{cases} \tag{1}$$

where μ_B is plastic dynamic viscosity of the non-Newtonian fluid, p_y is the yield stress of fluid, π is the product of the component of deformation rate with itself, namely $\pi=e_{ij}e_{ij}$, e_{ij} is the (i,j) - th component of deformation rate and π_c is a critical value of π based on non-Newtonian model.

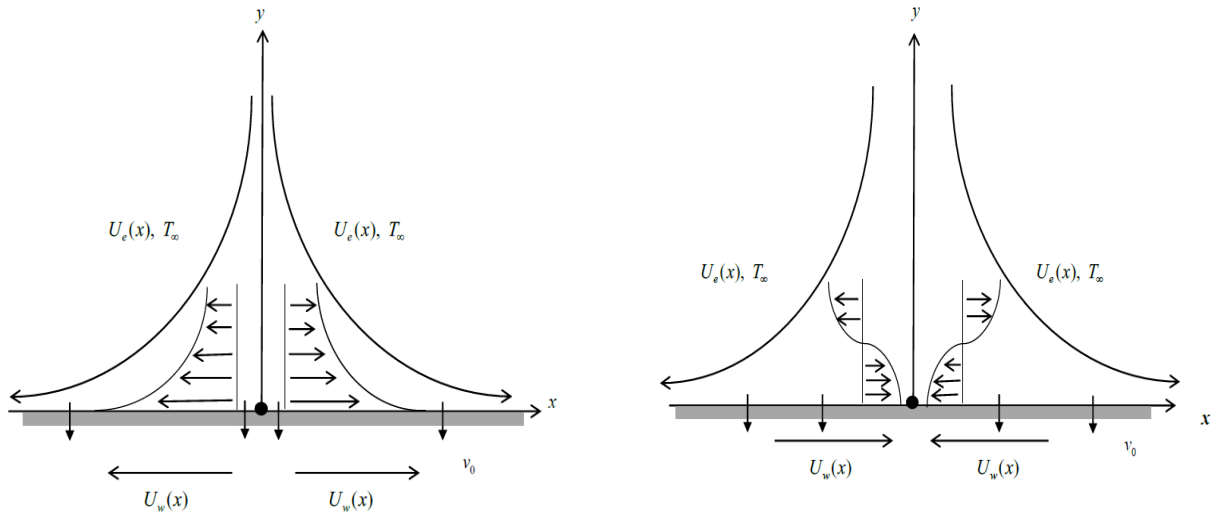


Fig. 1. Physical model and coordinate system: (a) Stretching sheet, (b) Shrinking sheet

Under above conditions, the boundary layer equations can be written as:

$$\frac{\partial u}{\partial x}+\frac{\partial v}{\partial y}=0, \tag{2}$$

$$u\frac{\partial u}{\partial x}+v\frac{\partial u}{\partial y}=u_e\frac{du_e}{dx}+\nu\left(1+\frac{1}{\beta}\right)\frac{\partial^2 u}{\partial y^2} \tag{3}$$

$$u\frac{\partial T}{\partial x}+v\frac{\partial T}{\partial y}=\frac{\kappa}{\rho C_p}\frac{\partial^2 T}{\partial y^2}+\frac{Q_0}{\rho C_p}\left(T-T_\infty\right) \tag{4}$$

where u and v are the velocity components in the x and x directions, respectively, ν is the kinematic viscosity, $\beta=\mu_B\sqrt{2\pi_c}/p_y$ is the Casson fluid parameter, κ is the thermal diffusivity, ρ is the density, C_p is the specific heat and Q_0 is the temperature dependent heat generation/absorption.

We assume that equations (2)-(4) are subjected to the boundary conditions

$$\begin{aligned} &u(x,0)=u_w(x),\quad v(x,0)=v_0,\quad T(x,0)=T_{w,}\\ &u(x,y)\to u_e(x),\quad T(x,y)\to T_{\infty,}\quad \text{as } y\to\infty. \end{aligned} \tag{5}$$

We look for a similarity solution of equations (2) - (4) of the following form

$$\psi=(\nu x u_e)^{\frac{1}{2}} f(\eta),\ \theta(\eta)=\frac{T-T_\infty}{T_w-T_\infty},\ \eta=\left(\frac{u_e}{\nu x}\right)^{\frac{1}{2}} y, \tag{6}$$

where $\psi(x,y)$ is the stream function defined as $u=\frac{\partial\psi}{\partial y}$ and $v=-\frac{\partial\psi}{\partial x}$, which identically satisfies Equation (2). By substituting equation (6) into equations (3) and (4), the following ordinary differential equations are obtained:

$$\left(1+\frac{1}{\beta}\right)f'''+ff''-f'^2+1=0 \tag{7}$$

$$\theta''+\Pr(f\theta'+Q\theta)=0 \tag{8}$$

and the boundary conditions (5) become

$$\begin{aligned} &f(0)=\gamma,\ f'(0)=\varepsilon,\ \theta(0)=1\\ &f'(\eta)\to 1,\ \theta(\eta)\to 0 \text{ as } \eta\to\infty \end{aligned} \tag{9}$$

where $\Pr=\frac{\mu C_p}{\kappa}$ is the Prandtl number, $Q=\frac{Q_0}{\rho C_p b}$ is the heat source parameter, $\gamma=-\frac{v_0}{\sqrt{b\nu}}<0$ is the injection parameter, $\varepsilon=a/b$ is the stretching $(\varepsilon>0)$ or shrinking $(\varepsilon<0)$ parameter and prime denotes differentiation with respect to η.

The physical quantities of interest are the skin friction coefficient, C_f and the local Nusselt number, Nu_x which are defined as

$$C_f = \frac{\tau_w}{\rho u_e^2(x)},\ Nu_x = \frac{xq_w}{k(T_w - T_\infty)}, \tag{10}$$

where τ_w is the skin friction or surface shear stress along the plate and q_w is the heat flux from the plate which are given by

$$\tau_w = \mu\left(\frac{\partial u}{\partial y}\right)_{y=0},\ q_w = -k\left(\frac{\partial T}{\partial y}\right)_{y=0}. \tag{11}$$

where k is the fluid thermal conductivity.
Substituting equation (6) into equation (11) and using equation (10), the following expression are obtained

$$\mathrm{Re}_x^{1/2} C_f = \left(1+\frac{1}{\beta}\right) f''(0),\ \mathrm{Re}_x^{-1/2} Nu_x = -\theta'(0), \tag{12}$$

where $\mathrm{Re}_x = \frac{u_e x}{\nu}$ is the local Reynolds number.

3. Stability of solutions

Following Weidman *et al.,* [38], to study the temporal stability of the solutions of equation (7)-(8) subject to boundary conditions (9), we consider the unsteady case for equations (3)-(4) which are replaced by

$$\frac{\partial u}{\partial t} + u\frac{\partial u}{\partial x} + v\frac{\partial u}{\partial y} = u_e\frac{du_e}{dx} + \nu\left(1+\frac{1}{\beta}\right)\frac{\partial^2 u}{\partial y^2} \tag{13}$$

$$\frac{\partial T}{\partial t} + u\frac{\partial T}{\partial x} + v\frac{\partial T}{\partial y} = \frac{\kappa}{\rho C_p}\frac{\partial^2 T}{\partial y^2} + \frac{Q_0}{\rho C_p}(T - T_\infty) \tag{14}$$

where t denotes the time. The new similarity transformation of the unsteady-state problem by considering dimensionless time variable τ is introduced as

$$\eta = y\sqrt{\frac{b}{\nu}},\ u = bx\frac{\partial f}{\partial \eta}(\eta,\tau),\ v = -\sqrt{b\nu}\, f(\eta,\tau)$$
$$T = T_\infty + (T_w - T_\infty)\theta(\eta,\tau),\ \tau = bt \tag{15}$$

By substituting equation (15) into equations (13) and (14), the following equations are obtained:

$$\left(1+\frac{1}{\beta}\right)\frac{\partial^3 f}{\partial \eta^3} + f\frac{\partial^2 f}{\partial \eta^2} - \left(\frac{\partial f}{\partial \eta}\right)^2 + 1 - \frac{\partial^2 f}{\partial \eta \partial \tau} = 0 \tag{16}$$

$$\frac{1}{\Pr}\frac{\partial^2\theta}{\partial\eta^2}+f\frac{\partial\theta}{\partial\eta}+Q\theta-\frac{\partial\theta}{\partial\tau}=0 \tag{17}$$

subject to boundary conditions

$$f(0,\tau)=\gamma,\ \frac{\partial f}{\partial\eta}(0,\tau)=\varepsilon,\ \theta(0,\tau)=1,$$
$$\frac{\partial f}{\partial\eta}(\eta,\tau)=1,\ \theta(\eta,\tau)=0,\ \text{as}\ \eta\to\infty. \tag{18}$$

To test the stability of the steady flow and heat transfer solution, $f(\eta)=f_0(\eta)$ and $\theta(\eta)=\theta_0(\eta)$ satisfying the boundary value problem (7)-(9), let us write (see Weidman *et al.,* [38])

$$f(\eta,\tau)=f_0(\eta)+e^{-\lambda\tau}F(\eta),$$
$$\theta(\eta,\tau)=\theta_0(\eta)+e^{-\lambda\tau}G(\eta), \tag{19}$$

where λ is an unknown eigenvalue, and $F(\eta)$ and $G(\eta)$ are small relative to $f_0(\eta)$ and $\theta_0(\eta)$. Solutions of the eigenvalue problem (16)-(18) give an infinite set of eigenvalues $\lambda_1<\lambda_2<\lambda_3$ …, if λ_1 is negative, there is an initial growth of disturbances and the flow is unstable but when λ_1 is positive, there in an initial decay and the flow is stable. By substituting equation (19) into equations (16) and (17), one obtains the following linearized problem:

$$\left(1+\frac{1}{\beta}\right)F'''+f_0F''+f_0''F-\left(2f_0'-\lambda\right)F'=0 \tag{20}$$

$$\frac{1}{\Pr}G''+f_0G'+F\theta_0'+(Q+\lambda)G=0 \tag{21}$$

along with the following boundary conditions:

$$F(0)=0,\ F'(0)=0,\ G(0)=0,$$
$$F'(\eta)=0, G(\eta)=0\ \text{as}\ \eta\to\infty. \tag{22}$$

It should be mentioned that for particular values of $\Pr$, Q, γ and ε, the stability of the corresponding steady flow solution $f_0(\eta)$ and $\theta_0(\eta)$ is determined by the smallest eigenvalue λ.

4. Results

The ordinary differential equations (7) and (8) subject to the boundary conditions (9), were solved numerically using the bvp4c function in Matlab software. The results from the numerical solution are presented in terms of the skin friction coefficient $\mathrm{Re}_x^{1/2}C_f$, the local Nusselt number

(represents the heat transfer rate) $\mathrm{Re}_x^{-1/2} Nu_x$ velocity profile, $f'(\eta)$ and temperature profile, $\theta(\eta)$ for different values of the non-dimensional parameters, namely the injection parameter γ, stretching/shrinking parameter ε and heat source parameter Q, while the Prandtl number Pr is fixed at $\mathrm{Pr}=1$ for the comparison.

For the validation purpose, we have compared the numerical results with those reported by Mahapatra and Gupta [6], and Bhattacharyya [25]. Table 1 shows the comparison values of $\theta'(0)$ with those of Mahapatra and Gupta [6] for the case of a stretching sheet without injection and heat source effects by setting $\beta \to \infty$ and $Q=0$ in equations (7) and (8), $f'(0)=1$ and $f(0)=0$ in the boundary conditions (9) and $a/c=1$ in Eqs. (12)-(13) of the paper by Mahapatra and Gupta [6]. The present results were also compared with those obtained by Bhattacharyya [25] for the case of Newtonian fluid case $(\beta \to \infty)$, without heat source $(Q=0)$ in equations (7) and (8), injection effect is absent, i.e. $f(0)=0$ in the boundary conditions (9) and $c/a=1$ in Eq. (10) of the paper by Bhattacharyya [25] for several values of ε as presented in Table 2. Both comparisons are found to be in a very good agreement, and thus we are confident that the present numerical results are correct and accurate.

Table 1
Comparison of the values $\theta'(0)$ with those of Mahapatra and Gupta [6] for the case of a stretching sheet in Newtonian fluid case without injection and heat source effects by setting $\beta \to \infty$ and $Q=0$ in equations (7) and (8), $f'(0)=1$ and $f(0)=0$ in the boundary conditions (9) and taking $a/c=1$ in Eqs. (12)-(13) of the paper by Mahapatra and Gupta [6]

Pr	Mahapatra and Gupta [6]	Present study
0.05	-0.178	-0.178413806
0.1		-0.252313245
0.5	-0.563	-0.564189588
1.0	-0.796	-0.797884572
1.5	-0.974	-0.977205026
2.0		-1.128379165
3.0		-1.381976604
4.0		-1.595769135
5.0		-1.784124125

Table 2
Comparison of the values $f''(0)$ with those of Bhattacharyya [25] for the case of Newtonian fluid case $(\beta \to \infty)$, without heat source effect $(Q=0)$ in equations (7) and (8), neglecting injection effect $(f(0)=0)$ in the boundary conditions (9) and taking $c/a=\varepsilon$ in Eq. (10) of the paper by Bhattacharyya [25] for both stretching/shrinking sheet

ε	Bhattacharyya [25]	Present study
0	1.2325878	1.232587653
0.1	1.1465608	1.146560998

0.2	1.0511299	1.051129992
0.3		0.946816117
0.4		0.834072086
0.5	0.7132951	0.713294954
0.8		0.306094758
1.0	0	0
-0.25	1.4022405	1.402240807
-0.5	1.4956697	1.495669765
-0.6		1.507024704
-0.7		1.500360770
-0.75	1.4892981	1.489298235
-0.8		1.472388354
-0.9		1.418077379
-1.0	1.3288169 (0)	1.328816865 (0)
-1.05		1.266227907 (0.012177915)
-1.1	1.1866806 (0.0492286)	1.186680255 (0.049228945)
-1.15	1.0822316 (0.1167023)	1.082231137 (0.116702101)
-1.2	0.9324728 (0.2336491)	0.932473321 (0.233649679)
-1.22		0.845110242 (0.308849262)
-1.24	0.7066020 (0.4356712)	0.706605223 (0.435672076)

( ) second solution

Figures 2-4 demonstrate the variation of the skin friction coefficient $\mathrm{Re}_x^{1/2} C_f$ and the local Nusselt number $\mathrm{Re}_x^{-1/2} Nu_x$ with ε for some values of γ and Q when β and Pr are fixed. For these Figures 2-4, the solid lines representing first (upper branch) solution while the dotted lines indicate the second (lower branch) solution. Based on Figures 2-4, the dual solutions exist for a certain range of the shrinking strength. Thus, there is a necessity to conduct the stability analysis to verify which solution could be utilized in the real-world phenomena. A stability analysis is carried out by solving eigenvalue problems (20)-(21) with boundary conditions (22). The stable solution is identified based on the positive smallest eigenvalues λ, whereas the unstable solution is recognized based on the negative smallest eigenvalues λ. Positive values of λ gives an initial decay of disturbance which results in a stable flow, whereas negative values of λ results in the growth of disturbance and causes an unstable flow. For the present problem, the smallest eigenvalues, λ_1 at several values of ε when $\beta = 5,\ \gamma = -0.2$ and $\mathrm{Pr} = Q = 1$ are tabulated in Table 3, which reports that the smallest eigenvalues are $\lambda_1 > 0$ for the first solution and $\lambda_1 < 0$ for the second solution. So, the first solution is stable and is physically reliable while the second solution is unstable.

Table 3
Smallest eigenvalue, λ_1 for some values of ε when $\beta = 5,\ \gamma = -0.2$ and $\mathrm{Pr} = Q = 1$

ε	First solution (Upper branch), λ_1	Second solution (Lower branch), λ_1

-1.1	0.6984	-
-1.13	0.5215	-
-1.16	0.2521	-0.2388
-1.163	0.2084	-0.1993
-1.166	0.1535	-0.1485
-1.169	0.0633	-0.0625
-1.1693	0.0457	-0.0453
-1.1696	0.0136	-0.0136

Figures 2 and 3 show the variations of the skin friction coefficient and the local Nusselt number, respectively, for different values of injection parameter γ. From Figures 2-3, it is found that it is possible to obtain dual solutions of the similarity equations (7) and (8) subject to the boundary conditions (9). These Figures 2-3 indicate that there are dual solutions for $\varepsilon_c \le \varepsilon < -1$, unique solutions for $\varepsilon \ge -1$ and no solutions obtained for $\varepsilon < \varepsilon_c < 0$, where ε_c is the critical values of ε for which equations (7) and (8) have no solutions and the full Navier–Stokes and energy equations should be solved. Based on our computation, the critical values ε_c obtained for $\gamma = 0, -0.2$ and -0.4 are $\varepsilon_{c1} = -1.24657$, $\varepsilon_{c2} = -1.16962$ and $\varepsilon_{c3} = -1.10580$, respectively as shown in Figures 2- 3.

Figure 2 reveals the skin friction coefficient $\mathrm{Re}_x^{1/2} C_f$ appears to decrease with increasing magnitude of injection parameter γ. This is because of injection effect that decreasing the surface shear stress, delay the fluid flow and thus, decrease the velocity gradient at the surface which is consistent with the graph in Figure 5. As it can be seen in Figures 2 and 3, the values of $|\varepsilon_c|$ increase with decreasing of magnitude γ suggests that reducing injection effect increases the range of existence of solutions to the similarity equations (7) and (8) subject to boundary conditions (9). Physically, decreasing γ appears to delay the boundary layer separation.

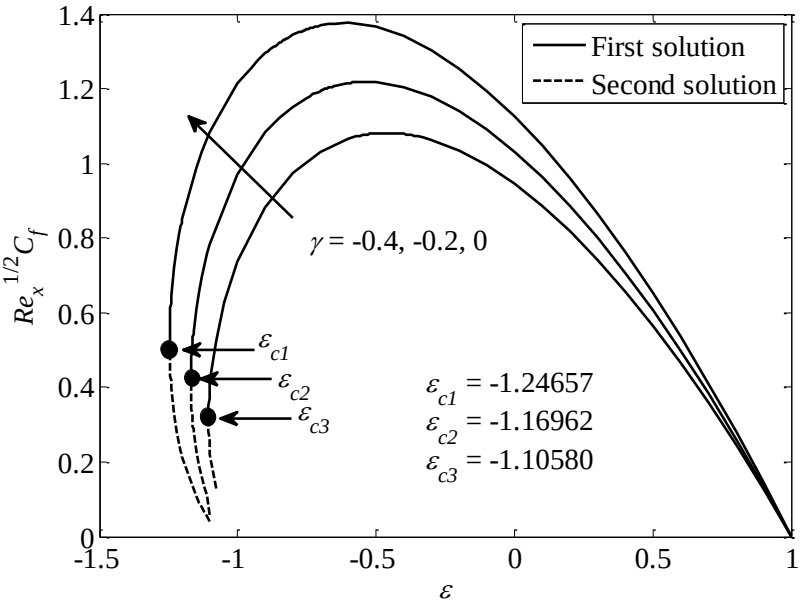


Fig. 2. Variation of the skin friction coefficient $\mathrm{Re}_x^{1/2} C_f$ with ε for different values of γ when $\mathrm{Pr} = 1, Q = 1$ and $\beta = 5$

Figure 3 displays the variation in the local Nusselt number as a function of the stretching/shrinking parameter ε with some values of the injection parameter γ. As the magnitude of γ increases, the temperature gradient at the surface decreases. As a result, the heat transfer rate at the surface decreases with the decreasing magnitude of injection parameter.

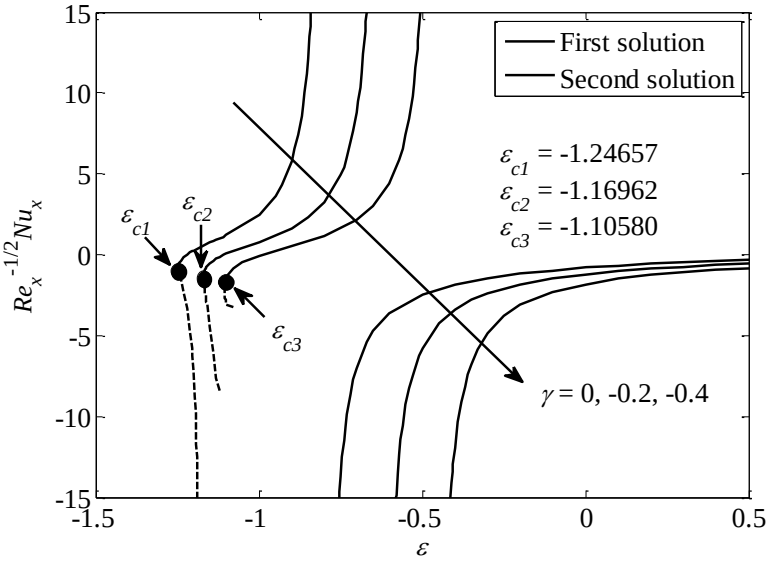


Fig. 3. Variation of the local Nusselt number $\mathrm{Re}_x^{-1/2} Nu_x$ with ε for different values of γ when $\mathrm{Pr} = 1, Q = 1$ and $\beta = 5$

Figure 4 shows the influence of the heat source parameter Q on the local Nusselt number. It is noticed that the values of $\mathrm{Re}_x^{-1/2} Nu_x$, which indicate the heat transfer rate at the surface decrease with an increase in Q.

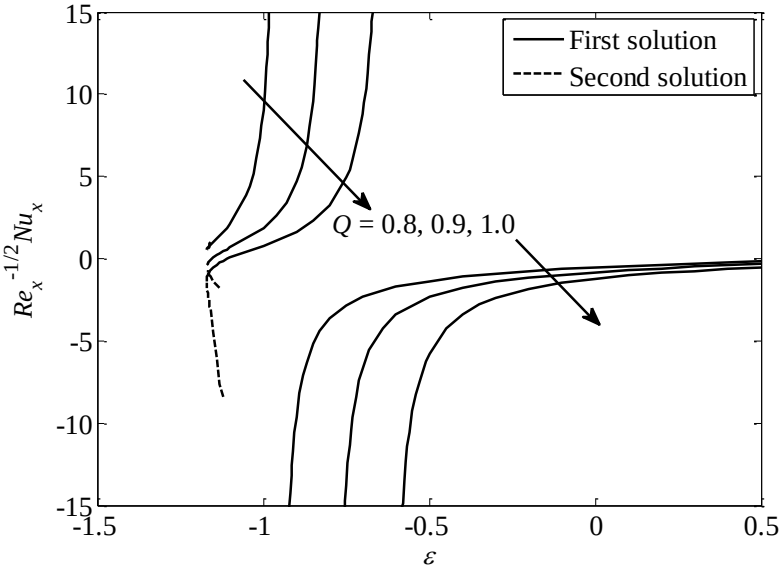


Fig. 4. Variation of the local Nusselt number $\mathrm{Re}_x^{-1/2} Nu_x$ with ε for different values of Q when $\mathrm{Pr}=1$, $\gamma=-0.2$ and $\beta=5$

Figures 5 and 6 show the effect of the injection parameter γ on the dimensionless velocity and temperature profiles, respectively. It is seen that the boundary layer thickness for the second solution is higher than that of the first solution, as depicted in Figures 5 and 6. Meanwhile, Figures 5 and 6 show that increasing magnitude of γ is to increase the momentum and thermal boundary layer thicknesses for the first solutions and thus decreasing the velocity and temperature gradients, in consequence decreases the skin friction coefficient and the heat transfer rate at the surface which are consistent with the graphs in Figures 2 and 3. In contrast, the second solution shows an opposite trends.

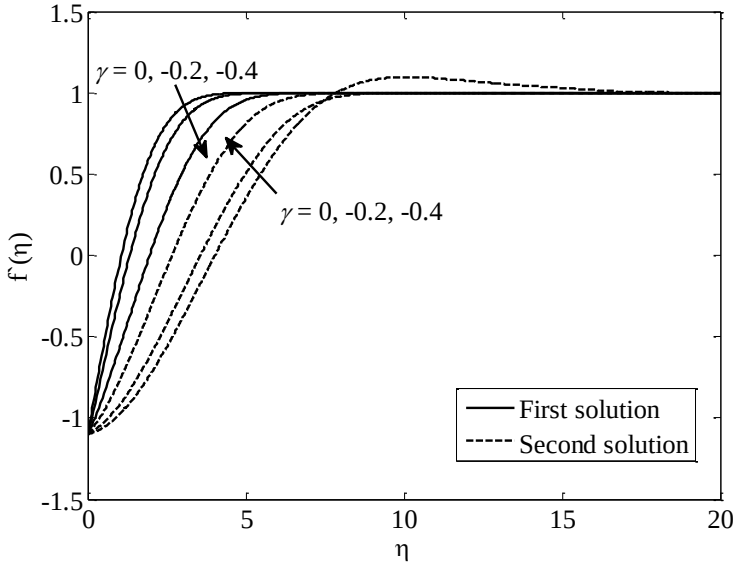


Fig. 5. The velocity profiles $f'(\eta)$ for different values of γ when $\mathrm{Pr}=1$, $Q=1, \beta=5$ and $\varepsilon=-1.1$ (shrinking case)

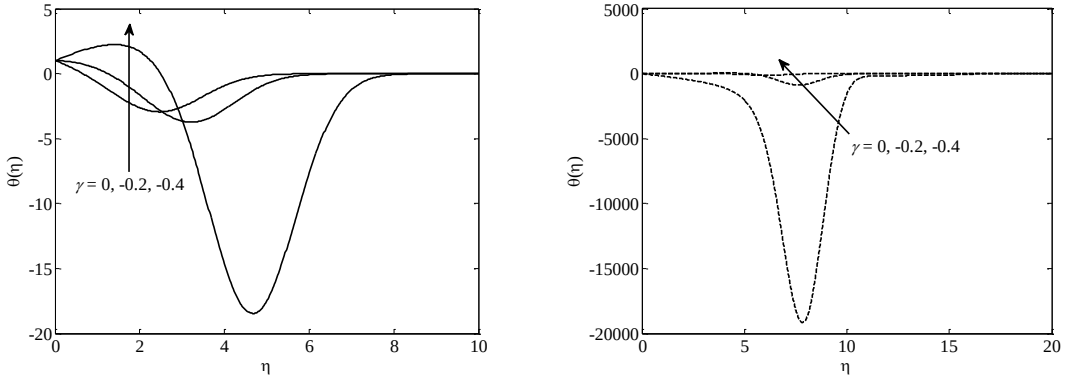


Fig. 6. The temperature profiles $\theta(\eta)$ for (a) first solution and (b) second solution for different values of γ when $\mathrm{Pr}=1$, $Q=1, \beta=5$ and $\varepsilon=-1.1$ (shrinking case)

It is clear that the temperature decreases as the value of heat source increases as plotted in Figure 7. This is due to the fact that additional energy is generated in the boundary layer in the presence of heat source. This additional energy increases the thickness of the thermal boundary layer, so that decreases the temperature gradient and in consequences the heat transfer rate at the surface is enhanced (reduce) which is consistent with the graph in Figure 4.

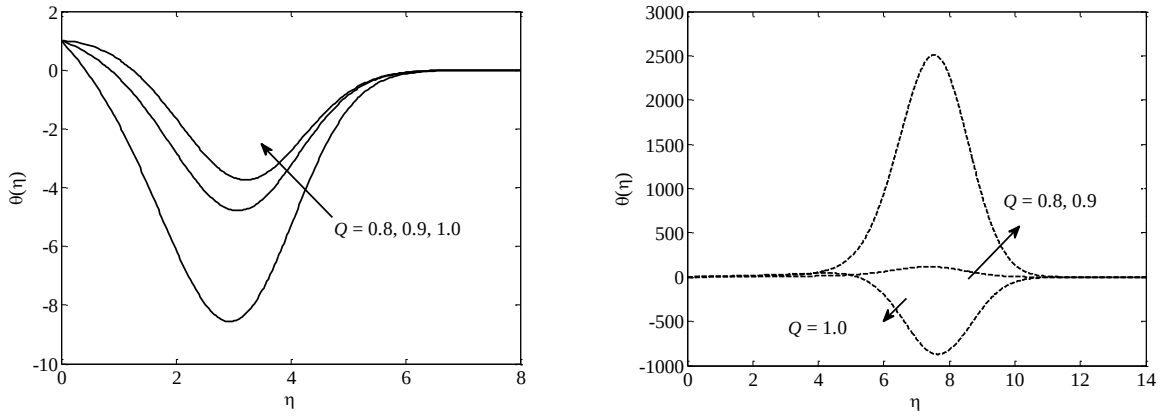


Fig. 7. The temperature profiles $\theta(\eta)$ for (a) first solution and (b) second solution for different values of Q when $\Pr = 1$, $\gamma = -0.2$, $\beta = 5$ and $\varepsilon = -1.1$ (shrinking case)

Furthermore, it is worth highlighting that in all Figures 5-7 presented here, the velocity and temperature profiles satisfy the far field boundary conditions (9) asymptotically. This helps to validate the numerical results of the boundary value problem (7)-(9) and the existence of the dual solutions presented in Figures 2-4.

5. Conclusions

In this paper, the problem of the stagnation-point flow and heat transfer over a stretching/shrinking sheet with heat source and injection effect in a Casson fluid was investigated and solved numerically using bvp4c in Matlab. The analysis shows that the skin friction coefficient and the local Nusselt number as well as the velocity and temperature were influenced by injection parameter, stretching/shrinking parameter and heat source parameter. However, the skin friction coefficient was not affected by heat source effect. The domain of solution increases as the injection decreases. Moreover, both the skin friction coefficient and the local Nusselt number are increasing when weak injection strength is applied into the system. We also found that the local Nusselt number decreases in the presence of heat source. Dual solutions were found to exist for the certain range of shrinking strength and the unique solution was exist for the stretching case. The stability analysis has been conducted to show that the first solution is stable, whereas the second solution is unstable.

Acknowledgement

The author would like to acknowledge the support from the Fundamental Research Grant Scheme (FRGS) under a grant number of FRGS/1/2018/STG06/UNIMAP/02/3 from the Ministry of Education Malaysia.

References

[1] Patel, M. and Timol, M. "Magneto hydrodynamic orthogonal stagnation point flow of a power-law fluid toward a stretching surface," *Am. J. Comput. Math*. 1 (2011): 129-133.
[2] Makinde, O.D., Khan, W.A. and Khan, Z.H. "Buoyancy effects on MHD stagnation point flow and heat transfer of a nanofluid past a convectively heated stretching / shrinking sheet." *Int. J. Heat Mass Transf*. 62 (2013): 526-533.
[3] Nandy, S.K. and Pop, I. "Effects of magnetic field and thermal radiation on stagnation flow and heat transfer of nano fluid over a shrinking surface." *Int. Commun. Heat Mass Transf*. 53 (2014): 50-55.
[4] Fauzi, N.F., Ahmad, S. and Pop, I. "Stagnation point flow and heat transfer over a nonlinear shrinking sheet with slip effects." *Alexandria Eng. J.* 54, no. 4 (2015): 929-934.
[5] Ramesh, G.K., Gireesha, B.J., Hayat, T. and Alsaedi, A. "Stagnation point flow of Maxwell fluid towards a permeable surface in the presence of nanoparticles." *Alexandria Eng. J.* 55, no. 2 (2016): 857-865.
[6] Mahapatra, T.R and Gupta, A.S. "Heat transfer in stagnation-point flow towards a stretching sheet." *Heat Mass Transf.* 38, no. 6 (2002): 517-521.
[7] Nazar, R., Amin, N., Filip, D. and Pop, I. "Unsteady boundary layer flow in the region of the stagnation point on a stretching sheet." *Int. J. Eng. Sci*. 42, no. 11–12 (2004): 1241-1253.
[8] Othman, N.A., Yacob, N.A., Bachok, N., Ishak, A. and Pop, I. "Mixed convection boundary-layer stagnation point flow past a vertical stretching / shrinking surface in a nanofluid." *Appl. Therm. Eng.* 115 (2017): 1412-1417.
[9] Rehman, F.U., Nadeem, S. and Haq, R.U. "Heat transfer analysis for three-dimensional stagnation-point flow over an exponentially stretching surface." *Chinese J. Phys.* 55, no. 4 (2017): 1552-1560.
[10] Naganthran, K., Nazar, R. and Pop, I. "Stability analysis of impinging oblique stagnation-point flow over a permeable shrinking surface in a viscoelastic fluid." *Int. J. Mech. Sci.* 131–132 (2017): 663-671.
[11] Sharma, P.R., Sinha, S., Yadav, R.S. and Filippov, A.N. "MHD mixed convective stagnation point flow along a vertical stretching sheet with heat source/sink." *Int. J. Heat Mass Transf.* 117 (2018): 780-786.
[12] Roşca, A.V. and Pop, I. "Flow and heat transfer over a vertical permeable stretching / shrinking sheet with a second order slip." *Int. J. Heat Mass Transf*. 60 (2013): 355-364.
[13] Yasin, M.H.M., Ishak, A. and Pop, I. "MHD heat and mass transfer flow over a permeable stretching / shrinking sheet with radiation effect." *J. Magn. Magn. Mater*. 407 (2016): 235-240.
[14] Naganthran, K., Nazar, R. and Pop, I. "Unsteady stagnation-point flow and heat transfer of a special third grade fluid past a permeable stretching / shrinking sheet." *Scientific Reports* 6, 24632 (2016).
[15] Alam, M.S., Khatun, M.A., Rahman, M.M. and Vajravelu, K. "Effects of variable fluid properties and thermophoresis on unsteady forced convective boundary layer flow along a permeable stretching/shrinking wedge with variable Prandtl and Schmidt numbers." *Int. J. Mech. Sci.* 105 (2016): 191-205.
[16] Jamaludin, A., Nazar, R. and Pop, I. "Three-dimensional mixed convection stagnation-point flow over a permeable vertical stretching/shrinking surface with a velocity slip." *Chinese J. Phys.* 55, no. 5 (2017): 1865-1882.
[17] Jusoh, R., Nazar, R. and Pop, I. "Flow and heat transfer of magnetohydrodynamic three-dimensional Maxwell nanofluid over a permeable stretching/shrinking surface with convective boundary conditions." *Int. J. Mech. Sci.* 124–125 (2017): 166-173.
[18] Nasir, N.A.A.M., Ishak, A. and Pop, I. "Stagnation-point flow and heat transfer past a permeable quadratically stretching/shrinking sheet." *Chinese J. Phys.* 55, no. 5 (2017): 2081-2091.
[19] Seth, G. S., Singha, A. K., Mandal, M.S. , Banerjee, A. and Bhattacharyya, K. "MHD stagnation-point flow and heat transfer past a non-isothermal shrinking / stretching sheet in porous medium with heat sink or source effect." *Int. J. Mech. Sci.* 134 (2017): 98-111.
[20] Hamid, R.A., Nazar, R. and Pop, I. "Boundary layer flow of a dusty fluid over a permeable shrinking surface." *Int. J. Numerical Methods for Heat & Fluid Flow* 27, no. 4 (2017): 758-772.
[21] Soid, S.K., Ishak, A. and Pop, I. "MHD flow and heat transfer over a radially stretching/shrinking disk." *Chinese J. Phys*. 56, no. 1 (2018): 58–66.
[22] Dash, R.K., Mehta, K.N. and Jayaraman, G. "Casson fluid flow in a pipe filled with a homogeneous porous medium." *Int. J. Engng. Sci.* 34, no. 10 (1996): 1145–1156.
[23] Animasaun, I.L., Adebile, E.A. and Fagbade, A.I. "Casson fluid flow with variable thermo-physical property along exponentially stretching sheet with suction and exponentially decaying internal heat generation using the homotopy analysis method." *J. Niger. Math. Soc.* 35 (2016): 1-17.
[24] Hayat, T., Shehzad, S.A., Alsaedi, A. and Alhothuali, M.S. "Mixed convection stagnation point flow of Casson fluid with convective boundary conditions." *Chinese Phys. Lett.* 29, no. 11 (2012): 114704.
[25] Bhattacharyya, K. "Boundary layer stagnation-point flow of casson fluid and heat transfer towards a shrinking/stretching sheet." *Front. Heat Mass Transf.* 4, 023003 (2013).
[26] Kameswaran, P. K., Shaw, S. and Sibanda, P. "Dual solutions of Casson fluid flow over a stretching or shrinking sheet." *Sadhana* 39, no. 6 (2014): 1573-1583.

[27] Abd El-Aziz, M. and Yahya, A.S. "Perturbation analysis of unsteady boundary layer slip flow and heat transfer of Casson fluid past a vertical permeable plate with Hall current." *Appl. Math. Comput.* 307 (2017): 146-164.
[28] Hakeem, A.K.A., Renuka, P., Ganesh N.V., Kalaivanan, R. and Ganga, B. "Influence of inclined Lorentz forces on boundary layer flow of Casson fluid over an impermeable stretching sheet with heat transfer." *J. Magn. Magn. Mater.,* 401 (2016): 354–361.
[29] Khan, M.I., Waqas, M., Hayat, T. and Alsaedi, A. "A comparative study of Casson fluid with homogeneous-heterogeneous reactions." *J. Colloid Interface Sci*. 498 (2017): 85–90.
[30] Maity, S., Singh, S.K. and Kumar, A.V. "Unsteady three-dimensional flow of Casson liquid film over a porous stretching sheet in the presence of uniform transverse magnetic field and suction/injection." *J. Magn. Magn. Mater.* 419 (2016): 292–300.
[31] Medikare, M., Joda, S. and Chidem, K. K, "MHD Stagnation Point Flow of a Casson Fluid over a Nonlinearly Stretching Sheet with Viscous Dissipation." *Am. J. Comput. Math.* 6 (2016): 37–48.
[32] Raju, C.S.K. and Sandeep, N. "Unsteady Casson nanofluid flow over a rotating cone in a rotating frame filled with ferrous nanoparticles: A numerical study." *J. Magn. Magn. Mater.* 421 (2017): 216-224.
[33] Raju, C.S.K. and Sandeep, N. "MHD slip flow of a dissipative Casson fluid over a moving geometry with heat source/sink: A numerical study." *Acta Astronaut* 133 (2017): 436–443.
[34] Raju, C.S.K., Hoque, M.M. and Sivasankar, T. "Radiative flow of Casson fluid over a moving wedge filled with gyrotactic microorganisms." *Adv. Powder Technol.* 28, no. 2 (2017): 575–583.
[35] Rehman, K.U., Qaiser, A., Malik, M.Y. and Ali, U. "Numerical communication for MHD thermally stratified dual convection flow of Casson fluid yields by stretching cylinder." *Chinese J. Phys*. 55, no. 4 (2017): 1605–1614.
[36] Shateyi, S., Mabood, F. and Lorenzini, G. "Casson fluid flow: Free convective heat and mass transfer over an unsteady permeable stretching surface considering viscous dissipation." *J. Eng. Thermophys*. 26, no. 1 (2017): 39-52.
[37] Bhattacharyya, K. "MHD stagnation-point flow of Casson fluid and heat transfer over a stretching sheet with thermal radiation." *J. Thermodyn.* 2013, 169674 (2013).
[38] Weidman, P. D., Kubitschek, D. G. and Davis, A.M.J. "The effect of transpiration on self- similar boundary layer flow over moving surfaces." *Int. J. Eng. Sci.* 44, no. 11-12 (2006): 730–737.

Penerbit Akademia Baru

Engineering Science and Technology Conference Proceedings

Journal homepage: www.akademiabaru.com/EST.html

Unsteady Three-Dimensional Free Convection Flow near the Stagnation Point over a General Curved Isothermal Surface in a Nanofluid

Open Access

Norshaza Atika Saidin[1], Mohd Ariff Admon[2], Khairy Zaimi[1,*]

[1] Institute of Engineering Mathematics, Universiti Malaysia Perlis, 02600 Arau, Perlis.
[2] Department of Mathematical Sciences, Faculty of Science, Universiti Teknologi Malaysia, 81310 Johor Bahru, Johor, Malaysia.

ABSTRACT

This study deals with the study of unsteady three-dimensional free convection flow near the stagnation point region over a general curved isothermal surface placed in a nanofluid The momentum equations in x- and y-directions, energy balance equation, and nanoparticle concentration equation are reduced to a set of four fully-coupled nonlinear differential equations under appropriate similarity transformations. The well-known technique Keller-box method is used numerically for different values of governing parameters entering these equations. Furthermore, the effects of the physical parameters, such as the Lewis number, the Brownian motion parameter, the thermophoresis parameter, and the buoyancy ratio on the profiles of velocities, temperature, and concentration, are studied and discussed.

Keywords:
Free convection; stagnation point, three-dimensional; nanofluid; numerical solution

Copyright © 2019 PENERBIT AKADEMIA BARU - All rights reserved

1. Introduction

Nowadays, problems that are related to boundary layer near stagnation point can be found in many high technology products. Various aspects of the flow and heat transfer problem for boundary layer flow near stagnation point have been explored in many investigations. Amin *et al.*, [1,] Seshadri *et al.*, [2] and Nazar *et al.*, [3] had been extensively investigating about the unsteady laminar free and mixed convection boundary layer flow in the neighborhood of a two-dimensional and axisymmetric stagnation point. In steady two-dimensional stagnation-point flow of an incompressible fluid over a stretching sheet [1-3], Pop *et al.,* [4] investigated theoretically by taking into account radiation effects using the Rosseland approximation to model the radiative heat transfer. This approximation leads to a considerable simplification in the radiation flux [4].

The steady laminar flow of an incompressible non-Newtonian micropolar fluid at a two-dimensional stagnation point with heat transfer has been studied by Attia [5]. This author focused on the effect of uniform suction or blowing directed normal to the wall [5]. Salleh *et al.*, [6] presented the free convection boundary layer flow on a solid sphere with Newtonian heating.

* *Corresponding author.*
E-mail address: khairy@unimap.edu.my (Khairy Zaimi)

Ahmad *et al.*, [7], Panigrahi *et al.*, [8], Yasin *et al*., [9], Shateyi *et al*., [10] and Dessie *et al*., [11] presented a problem of MHD near stagnation-point.

On the other hand, another work had been done by Raj *et al.*, [12]. They focused on the effects of thermal radiation and variable fluid viscosity on stagnation point flow past a porous stretching sheet embedded in a porous medium with partial slip condition. They solved the governing equation numerically using the same method by Dessie et al., [11] but along with the shooting technique and result, they are present in graphical form [11-12]. Non-axisymmetric stagnation point flow and heat transfer of a viscous fluid with variable viscosity on a cylinder in constant heat flux studied by Alizadeh *et al.*, [13]. Sharma *et al.*, [14] considered the unsteady two-dimensional stagnation point flow of a viscous and incompressible nanofluid over a permeable flat plat. They investigated the heat transfer characteristics caused by the stagnation-point flow of a nanofluid over a permeable flat plate using finite element method and it is stated that the result for this problem is new and very important for fluid mechanic and heat transfer field [14].

Nanofluids are of great scientific interest because these new thermal transport phenomena surpass the fundamental limits of conventional macroscopic theories of suspensions. These fluids are engineered colloidal suspensions of nanoparticles in a base fluid, which is the term proposed by Choi [15] to describe the new class of nanotechnology-based heat transfer fluids that exhibit thermal properties superior to those of their base fluids or conventional particle fluid suspensions. Hassani *et al.*, [16] studied an analytical research for boundary layer flow of a nanofluid past a stretching sheet by using Homotopy Analysis Method to solve the resulting equations. Next, laminar convective heat transfer of CuO/water nanofluid through an equilateral triangular duct at constant wall heat flux was investigated by Edalati *et al.*, [17]. Furthermore, in a paper by Hajipour *et al.*, [18] they carefully studied about transient two-dimensional mixed convection of nanofluids in the entrance region of a vertical channel.

A research by Farooq *et al*., [19] presented an analytical result on steady free convection flow near the stagnation point of a three-dimensional body over a general curved isothermal surfaced placed in a nanofluid [19]. The previous research about free convection flow near stagnation point in three-dimensional body was investigated by Admon *et al.*, [20] by using the Keller-box method [19-20]. Meanwhile, Hayat *et al.*, [21] dealt with the boundary layer flow of nanofluid over power-law stretched surface. Khan *et al.*, [22] investigated the three-dimensional flow of nanofluid over a bi-directional exponentially stretching sheet.

Motivated from the previous wonderful research in relation with viscous and incompressible fluid near stagnation point, the present study will adopt the concept of unsteady free convection boundary layer flow to focus on nanofluid near the stagnation point of three-dimensional. The governing system of partial differential equations is first transformed into a system of ordinary differential equations, and then they are solved numerically by a finite-difference scheme, namely the Keller-box method.

2. Problem Formulation

We consider the unsteady free convection flow near the stagnation point of a heated three-dimensional body located in a viscous and incompressible nanofluid with a uniform temperature T_∞. It is assumed that the constant wall temperature of the body is suddenly changed from T_w to T_∞, where $T_w > T_\infty$. A locally Cartesian orthogonal system(x, y, z) is chosen with the origin O at the nodal stagnation point, where the *x*- and *y*-coordinates were measured along the body surface, while the *z*-coordinates was measured normal to the body surface. Under these assumptions, the

governing equations for free convection nanofluid flow in the stagnation-point region of a three-dimensional body are [19]:

$$\frac{\partial u}{\partial x}+\frac{\partial v}{\partial y}+\frac{\partial w}{\partial z}=0 \tag{1}$$

$$\frac{\partial u}{\partial t}+u\frac{\partial u}{\partial x}+v\frac{\partial u}{\partial y}+w\frac{\partial u}{\partial z}=-\frac{1}{\rho_{f_\infty}}+\nu\left(\frac{\partial^2 u}{\partial x^2}+\frac{\partial^2 u}{\partial y^2}+\frac{\partial^2 u}{\partial z^2}\right) + \left[\left(1-C_\infty\right)\beta\left(T-T_\infty\right)-\frac{\rho_p-\rho_{f_\infty}}{\rho_{f_\infty}}\left(C-C_\infty\right)\right]gax, \tag{2}$$

$$\frac{\partial v}{\partial t}+u\frac{\partial v}{\partial x}+v\frac{\partial v}{\partial y}+w\frac{\partial v}{\partial z}=-\frac{1}{\rho_{f_\infty}}+\nu\left(\frac{\partial^2 v}{\partial x^2}+\frac{\partial^2 v}{\partial y^2}+\frac{\partial^2 v}{\partial z^2}\right) + \left[\left(1-C_\infty\right)\beta\left(T-T_\infty\right)-\frac{\rho_p-\rho_{f_\infty}}{\rho_{f_\infty}}\left(C-C_\infty\right)\right]gby. \tag{3}$$

$$\frac{\partial T}{\partial t}+u\frac{\partial T}{\partial x}+v\frac{\partial T}{\partial y}+w\frac{\partial T}{\partial z}=\alpha\left(\frac{\partial^2 T}{\partial x^2}+\frac{\partial^2 T}{\partial y^2}+\frac{\partial^2 T}{\partial z^2}\right) + \tau\left\{\begin{array}{l} D_B\left(\frac{\partial C}{\partial x}\frac{\partial T}{\partial x}+\frac{\partial C}{\partial y}\frac{\partial T}{\partial y}+\frac{\partial C}{\partial z}\frac{\partial T}{\partial z}\right) \\ +\left(\frac{D_T}{T_\infty}\right)\left[\left(\frac{\partial T}{\partial x}\right)^2+\left(\frac{\partial T}{\partial y}\right)^2+\left(\frac{\partial T}{\partial z}\right)^2\right] \end{array}\right\} \tag{4}$$

$$\frac{\partial C}{\partial t}+u\frac{\partial C}{\partial x}+v\frac{\partial C}{\partial y}+w\frac{\partial C}{\partial z}=D_B\left(\frac{\partial^2 C}{\partial x^2}+\frac{\partial^2 C}{\partial y^2}+\frac{\partial^2 C}{\partial z^2}\right) + \left(\frac{D_T}{T_\infty}\right)\left(\frac{\partial^2 T}{\partial x^2}+\frac{\partial^2 T}{\partial y^2}+\frac{\partial^2 T}{\partial z^2}\right) \tag{5}$$

Subject to initial and boundary conditions;

$$\begin{aligned} &t<0: \quad u=v=w,\ T=T_\infty,\ C=C_\infty \ \text{ for any } x, y, z \\ &t\geq 0: \quad u=v=0,\ T=T_w,\ C=C_w \ \text{ on } z=0,\ x\geq 0,\ y\geq 0 \\ &\qquad u=v=0,\ T=T_\infty,\ C=C_\infty \ \text{ on } x=0,\ y\geq 0,\ z>0 \\ &\qquad u=v=0,\ T=T_\infty,\ C=C_\infty \ \text{ on } y=0,\ x\geq 0,\ z>0 \\ &\qquad u=v=0,\ T=T_\infty,\ C=C_\infty \ \text{ on } z\to\infty,\ x\geq 0,\ y\geq 0 \end{aligned} \tag{6}$$

Here t is time, u, v, w stand for velocity component along the x-, y-, z-axis respectively, T for fluid temperature, g is the magnitude of the gravity acceleration, α denoted as the coefficient of thermal diffusivity, while ν and β are labelled as kinematic viscosity and volumetric coefficient of

thermal expansion. *C* are the nanoparticle volume fraction, the thermophoretic diffusion coefficient are considered as D_T and D_B stand for the Brownian diffusion coefficient and *a* and *b* are the parameter of the principal curvature at *O* of the body measured in the plane *x* and *y*, respectively. A little inspection shows that Eq.1 to 5 along with the boundary conditions (Eq.6) admit a semi-similar solution of the form [19-20]:

$$\eta = Gr^{1/4} a \xi^{-1/2} z, \qquad u = \nu a^2 x Gr^{1/2} f'(\xi,\eta)$$

$$v = \nu a^2 cy Gr^{1/2} h'(\xi,\eta), \qquad w = -\nu a Gr^{1/4} \xi^{1/2} (f + ch)$$

$$\theta(\xi,\eta) = \frac{(T - T_\infty)}{(T_w - T_\infty)}, \qquad \phi(\xi,\eta) = \frac{(C - C_\infty)}{(C_w - C_\infty)}$$

$$\xi = 1 - e^{-\tau}, \qquad \tau = \nu a^2 Gr^{1/2} t \tag{7}$$

where $Gr = (1 - C_\infty) g\beta (T_w - T_\infty) \Big/ (a^3 \nu^2)$ is the Grashof number, $Pr = \frac{\nu}{\alpha}$ is the Prandtl number, $c = \frac{b}{a}$, $\nu = \frac{\mu}{\rho}$, $N_b = \frac{\tau D_B (C_w - C_\infty)}{\alpha}$ is the Brownian motion parameter, $N_r = \frac{(\rho_p - \rho_{f_\infty})(C_w - C_\infty)}{a^3 \alpha \mu}$ is the buoyancy parameter, $N_t = \tau \frac{D_T}{T_\infty} \frac{(T_w - T_\infty)}{\alpha}$ is the thermophoresis parameter and primes denote partial differentiation with respect to η.

Substitution of Eq. 7 in Eq.2 to 5 gives:

$$f''' + (1 - \xi)\frac{\eta}{2\xi} f'' + \xi\left[(f + ch) f'' - (f')^2\right] + \xi\theta - \xi \frac{N_r}{Pr\, Gr}\phi = \xi(1 - \xi)\left(\frac{\partial f'}{\partial \xi}\right) \tag{8}$$

$$h''' + (1 - \xi)\frac{\eta}{2\xi} h'' + \xi\left[(f + ch) h'' - (ch')^2\right] + \xi\theta - \xi \frac{N_r}{Pr\, Gr}\phi = \xi(1 - \xi)\left(\frac{\partial h'}{\partial \xi}\right) \tag{9}$$

$$\theta'' + Pr(1 - \xi)\frac{\eta}{2}\theta' + \xi Pr(f + ch)\theta' + N_b \theta'\phi' + N_t(\theta')^2 = \xi Pr(1 - \xi)\frac{\partial \theta}{\partial \xi} \tag{10}$$

$$\phi'' + LePr(1 - \xi)\frac{\eta}{2}\phi' + \xi\, LePr(f + ch)\phi' + \frac{N_t}{N_b}\theta'' = \xi\, LePr(1 - \xi)\frac{\partial \phi}{\partial \xi} \tag{11}$$

While the boundary conditions Eq.6 become:

$$f(\xi,0) = f'(\xi,0) = 0, \quad h(\xi,0) = h'(\xi,0) = 0, \quad \theta(\xi,0) = \phi(\xi,0) = 1$$

$$f' \to 0, \quad h' \to 0, \quad \theta \to 0, \quad \phi \to 0 \ \ as \ \ \eta \to \infty \tag{12}$$

for $0 \le \xi < 1$. Here *Pr* is the Prandtl number and primes denote partial differentiation with respect to η.

The physical quantities of practical interest in this problem are the skin friction coefficient in the *x*- and *y*-directions, C_{fx} and C_{fy} and the Nusselt number, Nu, and Sherwood number, *Sh*, that are defined as

$$C_{fx} = \frac{\mu\left(\frac{\partial u}{\partial z}\right)_{z=0}}{\rho\nu^2 a^3 x}, \qquad C_{fy} = \frac{\mu\left(\frac{\partial v}{\partial z}\right)_{z=0}}{\rho\nu^2 a^3 cy},$$
$$Nu = \frac{a^{-1}\left(\frac{\partial T}{\partial z}\right)_{z=0}}{T_w - T_\infty}, \qquad Sh = \frac{a^{-1}\left(\frac{\partial C}{\partial z}\right)_{z=0}}{C_w - C_\infty} \tag{13}$$

where ρ and μ are the density and dynamic viscosity, respectively. In terms of the non-dimensional variables, we have

$$\frac{C_{fx}\,\xi^{1/2}}{Gr^{3/4}} = f''(\xi,0), \quad \frac{C_{fy}\,\xi^{1/2}}{Gr^{3/4}} = h''(\xi,0),$$
$$\frac{Nu\,\xi^{1/2}}{Gr^{1/4}} = -\theta'(\xi,\eta), \quad \frac{Sh\,\xi^{1/2}}{Gr^{1/4}} = -\phi'(\xi,\eta). \tag{14}$$

For the unsteady-initial flow case, where ξ is small that is $\xi \approx 0$, Eq. 8 to 11 become to the following form:

$$f''' + \frac{\eta}{2} f'' = 0, \qquad h''' + \frac{\eta}{2} h'' = 0$$
$$\theta'' + Pr\frac{\eta}{2}\theta' + N_b\,\theta'\phi' + N_t(\theta')^2 = 0, \tag{15}$$
$$\phi'' + LePr\frac{\eta}{2}\phi' + \frac{N_t}{N_b}\theta'' = 0$$

subject to the boundary conditions

$$f(0) = f'(0) = 0, \quad h(0) = h'(0) = 0, \quad \theta(0) = 1, \quad \phi(0) = 1$$
$$f'(\infty) = 0, \quad h'(\infty) = 0, \quad \theta(\infty) = 0, \quad \phi(\infty) = 0 \tag{16}$$

For final steady-state case, where $\xi = 1$, Eq. 8 to 11 become to the following form

$$f''' + (f + ch)f'' - (f')^2 + \theta - \frac{N_r}{Pr\,Gr}\phi = 0 \tag{17}$$

$$h''' + (f + ch)h'' - (ch')^2 + \theta - \frac{N_r}{Pr\,Gr}\phi = 0 \tag{18}$$

$$\theta'' + Pr(f + ch)\theta' + N_b\theta'\phi' + N_t(\theta')^2 = 0 \tag{19}$$

$$\phi'' + LePr(f + ch)\phi' + \frac{N_t}{N_b}\theta'' = 0 \tag{20}$$

Subject to the boundary conditions (Eq.16). These equations are identical with those first found by Poots [23].

3. Results

The two sets of Eq. 8 to 11 and 17 to 20 subjects to the boundary conditions (12) and (16) were solved numerically using Keller-box method described in book by Cebeci *et al.,* [24]. Result are obtained of Prandtl number, Pr $(Pr = 0.72, 1)$, Grashof number, $Gr(Gr = -1, 1)$, Lewis number, $Le(Le = 1, 5, 10)$, brownian motion parameter, $N_b(N_b = 0.00001, 0.1, 0.2)$, buoyancy parameter, $N_r(N_r = 0, 0.1, 0.2)$, thermophoresis parameter, $N_t(N_t = 0, 0.1, 0.2)$, c = 0 (plane stagnation point), 0.5 and 1 (axisymmetric stagnation point) and the values of $\eta = 10$ is enough to satisfied the boundary conditions. To access the exact of the solutions, the present results for the reduced skin friction coefficients $f''(0)$ and $h''(0)$, and heat transfer from the surface of the body, $-\theta'(0)$ are compared with Admon *et al.*, [20]. Table 1 is presented for $Pr = 0.72$ and c = 0 (plane stagnation point) and 1 (axisymmetric stagnation point). It can be concluded that agreement between the present results for the case $\xi = 1$ (final steady-state flow), and Admon *et al.*, [20] obtained using finite-difference method are excellent. It can be concluding that all these results are in very good agreement.

Table 1 Comparison of reduced skin frictions $f''(0)$, $h''(0)$ and heat flux rate $-\theta'(0)$ for $\xi = 1$ (final steady-state), *Pr* = 0.72 and various values of *c*.

	c = 0		*c* = 1	
	Admon *et al.*, [20]	**Present result**	**Admon *et al.*, [20]**	**Present result**
$f''(0)$	0.855909	0.856447	0.764685	0.764712
$h''(0)$	1.080763	1.077572	0.764685	0.764712
$-\theta'(0)$	0.374102	0.373870	0.462223	0.462259

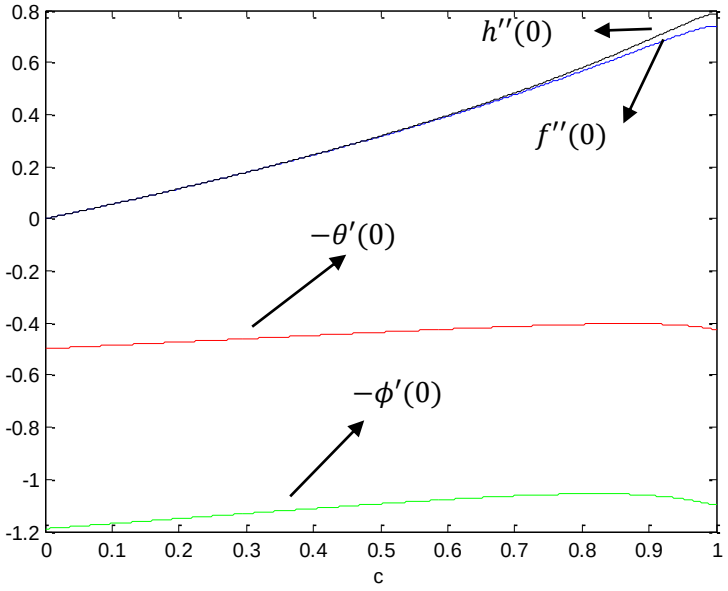


Fig. 1. Graph of skin friction coefficient, Nusselt and Sherwood number $N_b = N_t = N_r = 0.1$ and *Le* = 1.0.

Figure 1 illustrates the graph of the skin friction coefficients, local Nusselt and local Sherwood number for various values of *c* keeping the other parameters such as *Pr* = *Gr* = *Le* = 1.0 and $N_t = N_r = N_b = 0.1$. It can be seen in this figure that the skin friction coefficients reach their maximum values in the stagnation point under the boundary layer effects and the increase in the value of *c* raised the skin friction. Besides that, the analysis of the parameter *c* on the heat and mass transfer depicts the increase in the values of *c* will increases the Nusselt number and the Sherwood number but when values of *c* more than 0.9 and reaches to 1 (axisymmetric stagnation point) result shows the values of Nusselt and Sherwood number slowly decrease.

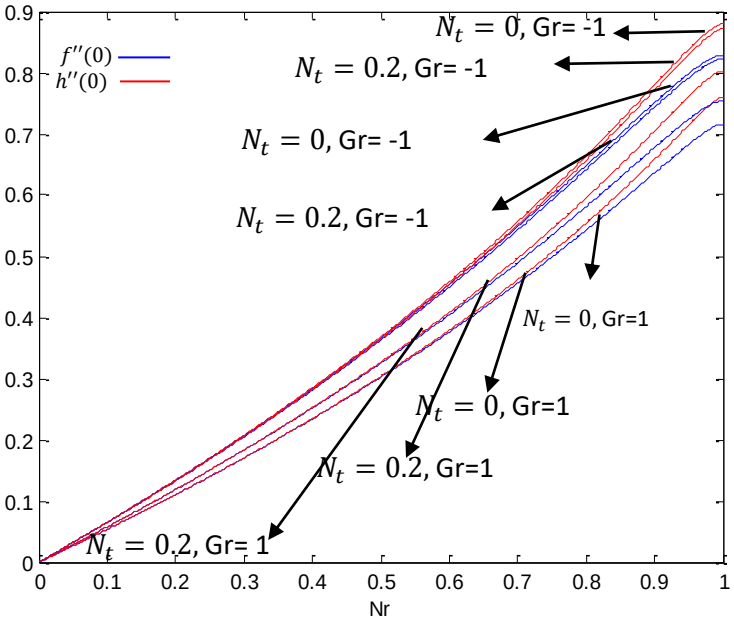


Fig. 2. Graph of skin friction coefficient for N_b, *Le* = *Pr* = 1.0 and *c* = 0.5 with varying N_t and *Gr.*

Graph of skin friction coefficient for varying N_r in Figure 2 reveals the effects of N_r and N_t on the skin friction for value *Gr* = -1.0 and 1.0. For *Gr* = 1.0, the temperature at the stagnation points T_w is greater than the ambient fluid temperature T_∞ that is $T_w > T_\infty$. When the values of N_r increase, the values of density and nanoparticles mass difference also increase. For *Gr* = -1.0, the ambient fluid temperature greater than temperature at stagnation point, $T_\infty > T_w$ the result also shows the values of density and nanoparticle mass difference increase.

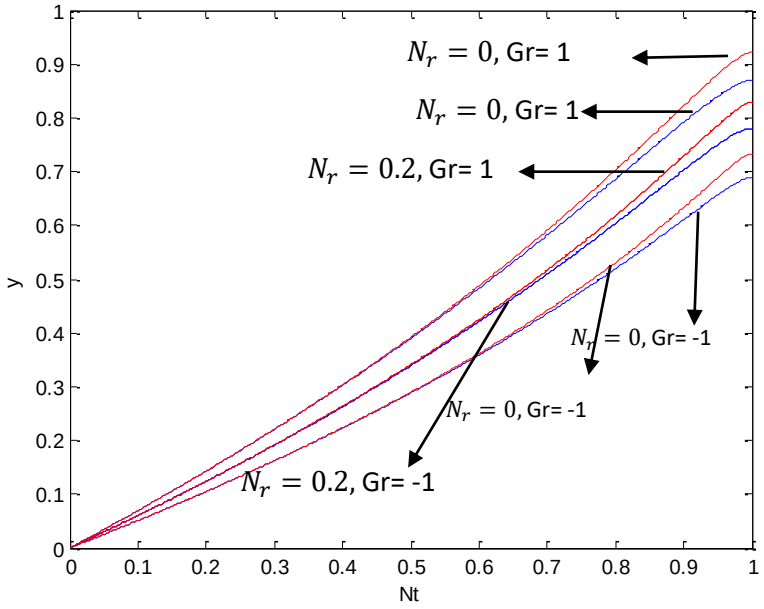


Fig. 3. Graph of skin friction coefficient for N_b = 0.2, *Le* = *Pr* = 1.0 and *c* = 0.5 with varying N_r and *Gr*.

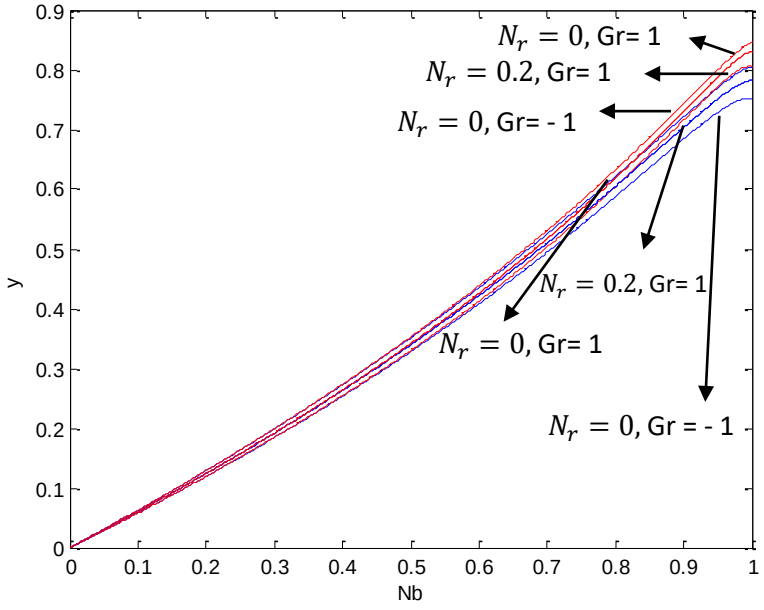


Fig. 4. Graph of skin friction coefficient for N_t =0.2, *Le* = *Pr* = 1.0 and *c* = 0.5 varying N_r and *Gr.*

Figure 3 describes the effect of N_t on skin friction coefficient. For *Gr* = 1.0, the increase in the values of N_r will increase the skin friction for both $f''(0)$ and $h''(0)$. For *Gr* = -1.0, the result also increases for both $f''(0)$ and $h''(0)$ same like *Gr* = 1.0. It can be summarizing that both values of *Gr* increase when N_r = 0 and 0.2 but the value of *Gr* = 1.0 higher than *Gr* = -1.0 in the graph. For Figure 4, the result demonstrates that *Gr* =1.0 increase for both skin friction $f''(0)$ and $h''(0)$ for values of N_r = 0 and 0.2. For *Gr* =-1.0, the result also shows raised the skin friction but it lower than *Gr* =1.0.

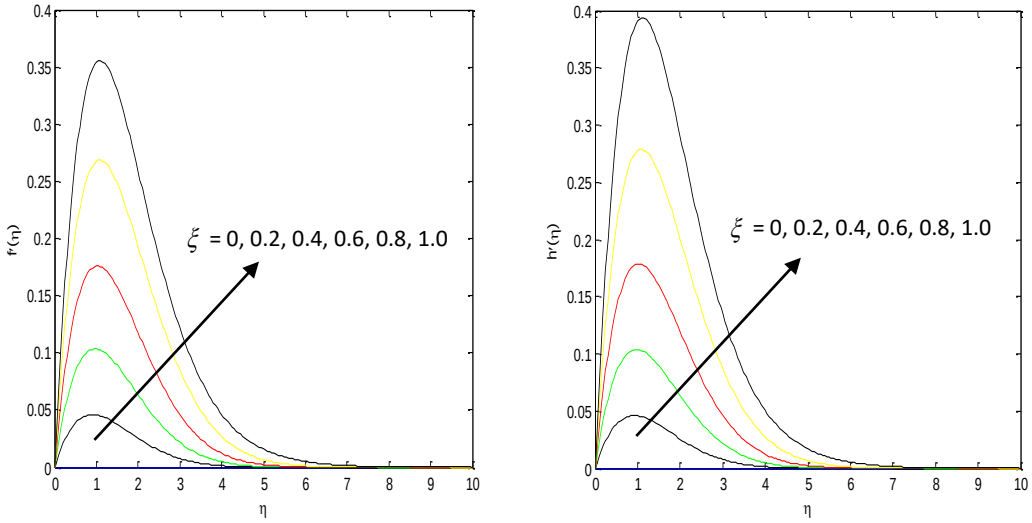


Fig. 5. Velocity profile in *x*- and *y*-direction for various ξ with N_r = N_t = 0, N_b= 0.001, *Gr* = *Pr* = 1.0, *c*= 0.5 and various values of *Le*

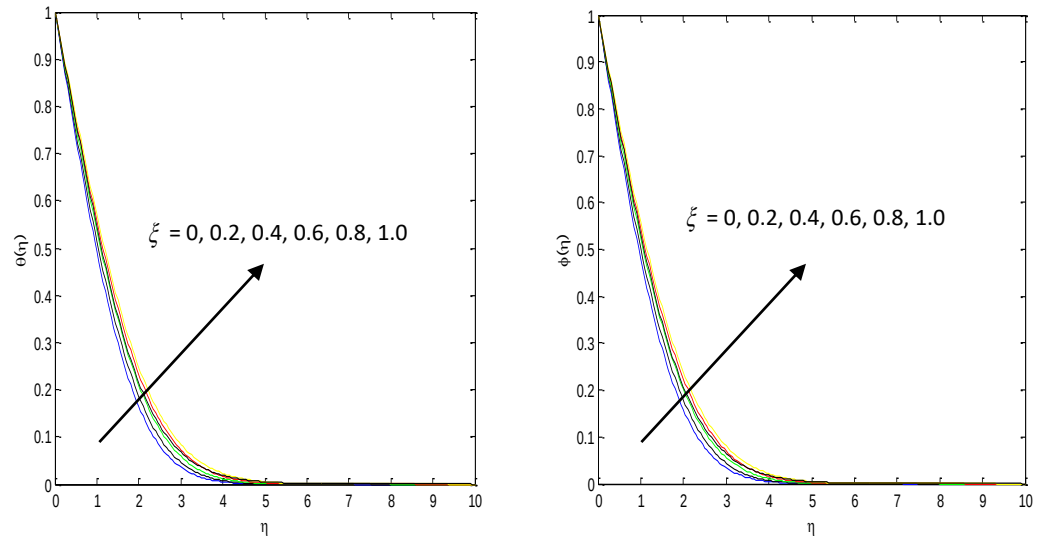


Fig. 6. Temperature and concentration profile $\theta(\eta)$ and $\phi(\eta)$ for various ξ with N_r = N_t = 0, N_b = 0.001, *Gr* = *Pr* = 1.0, *c* = 0.5 and various values *Le*

Figure 5 presented that general trend of velocity profile and the behaviour of increase in the values of *Le* on the velocity field. From this figure, it can be seen that at stagnation point the effect of velocity become zero and velocity tends to increase when particles is moving from cold to hot region. When values of *Le* increase, then the velocity and momentum boundary layer thickness will increase too. Besides that, thermal diffusivity in free convection increase when *Le* increase. Therefore, flow field become higher when higher in Lewis number. On the other hand, Figure 6

describes the effects of dimensionless temperature and concentration profile for various values of *Le*. Temperature is maximum at wall but notice that it reduces and approaches to the free stream temperature. It is detected that the temperature and concentration profiles become decrease throughout boundary layer when the value of *Le* is increase. It can be concluding that reduce the mass diffusivity because of higher value in Lewis number. Therefore, heat transfer and mass transfer slow down through fluid.

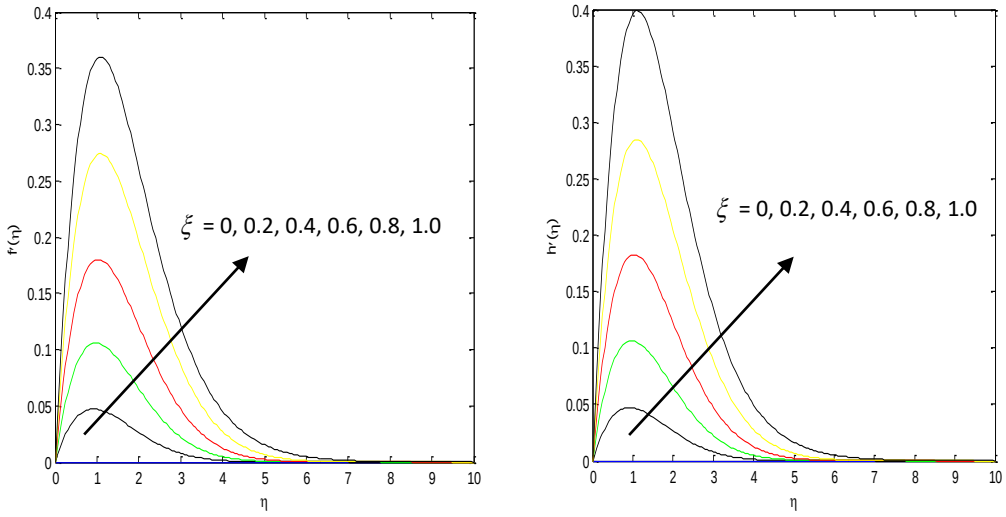


Fig. 7. Velocity profile in *x*- and *y*-direction for various ξ with $N_t = N_b = 0.1$, $Le = Gr = Pr = 1.0$, $c = 0.5$ and various values of N_r.

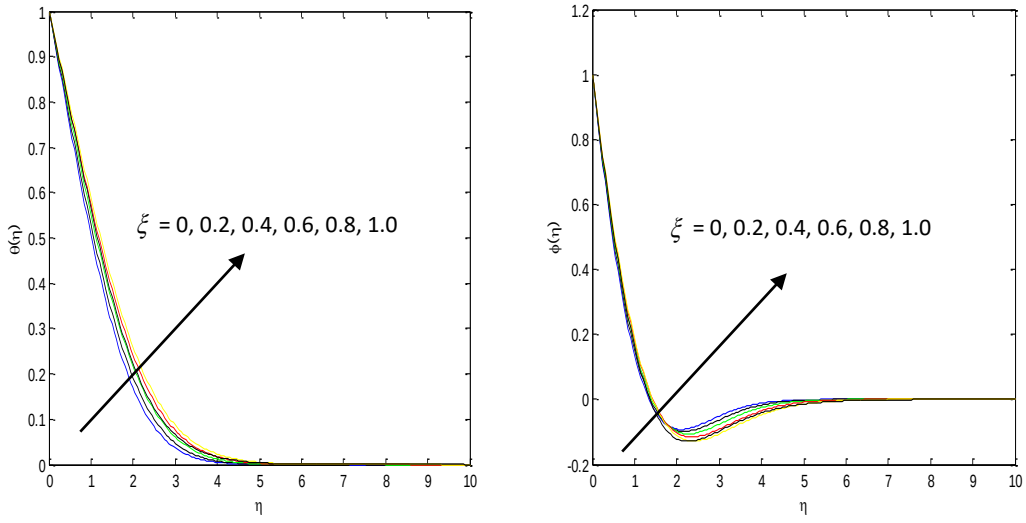


Fig. 8. Temperature and concentration profile $\theta(\eta)$ and $\phi(\eta)$for various ξ with $N_t = N_b = 0.1$, $Le = Gr = Pr = 1.0$, $c = 0.5$ and various value of N_r.

Further, Figure 7 shows the strong effect of buoyancy coefficient N_r on velocity, temperature and concentration profiles. In the absence of buoyancy parameter, the density difference is zero hence the flow is maximum as we increase the buoyancy parameter. The density difference increase will make fluid flow decrease. The increase in the buoyancy parameter will increase the density difference and mass concentration difference is shown in Figure 8. Hence, it improves the

temperature and concentration profiles. In free convection, Thermophoresis parameter acts as important parts in the flow, heat transfer, and mass transfer properties.

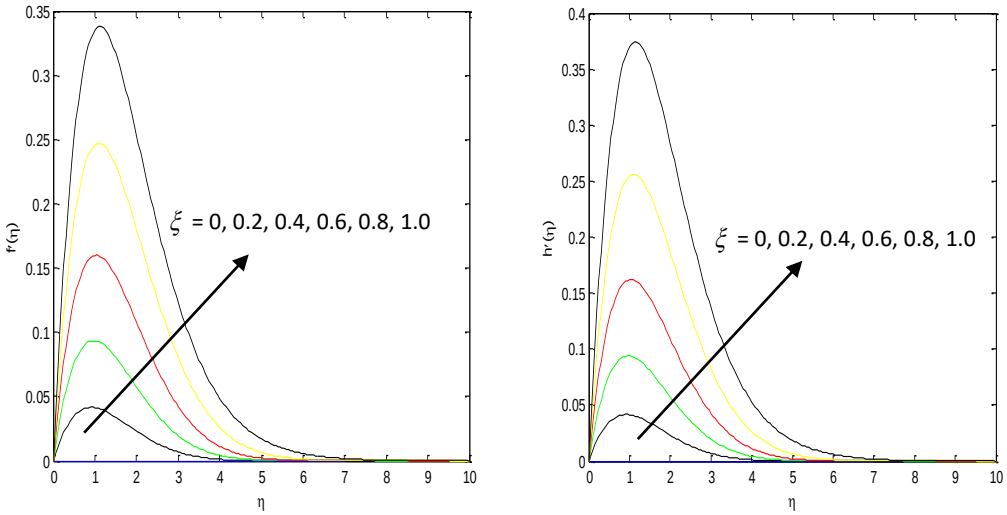


Fig. 9. Velocity profile in *x*- and *y*-direction for various ξ with $N_r = N_b = 0.1$, $Le = Gr = Pr = 1.0$, $c = 0.5$ and various values of N_t

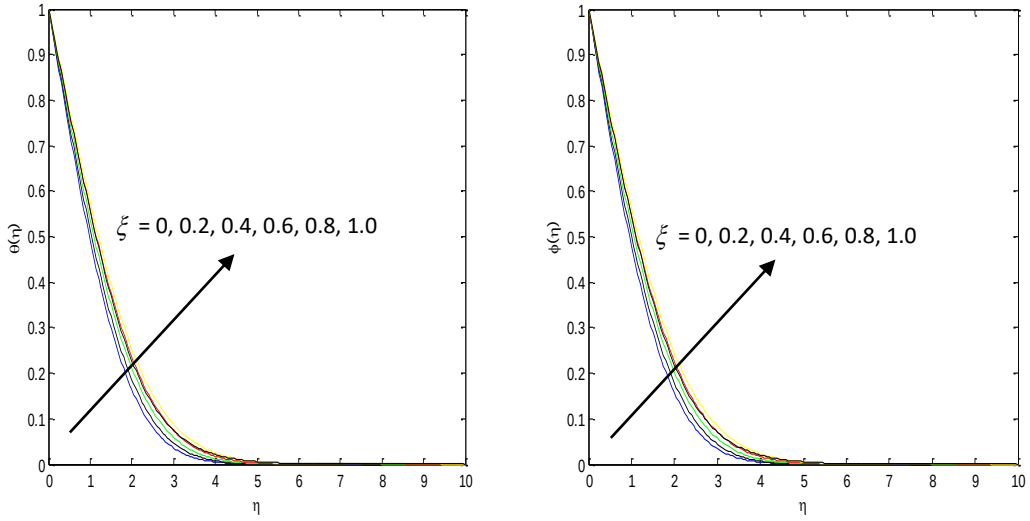


Fig. 10. Temperature and concentration profile $\theta(\eta)$ and $\phi(\eta)$ for various ξ with $N_r = N_b = 0.1$, $Le = Gr = Pr = 1.0$, $c = 0.5$ and various values of N_t

From Figure 9, the values of N_t is increase with the reduced in the fluid flow. It is clearly state that the increase in values of N_t will increase the temperature difference. Therefore, fluid flow will decrease. In Figure 10 depicts the effect of thermophoresis parameter on the fluid temperature and concentration profile. The increase in the values of N_t will affect the temperature and concentration profile also increase. Hence, the nanoparticle enhances heat and mass transfer.

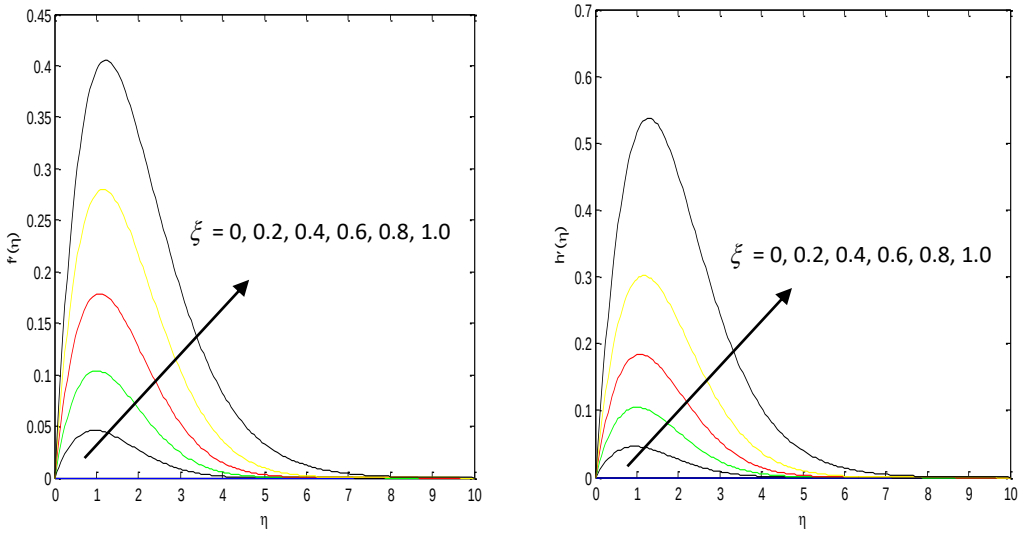


Fig. 11. Velocity profile in *x*- and *y*-direction for various ξ with $N_r = N_t = 0.1$, $Le = Gr = Pr = 1.0$, $c = 0.5$ and various values of N_b

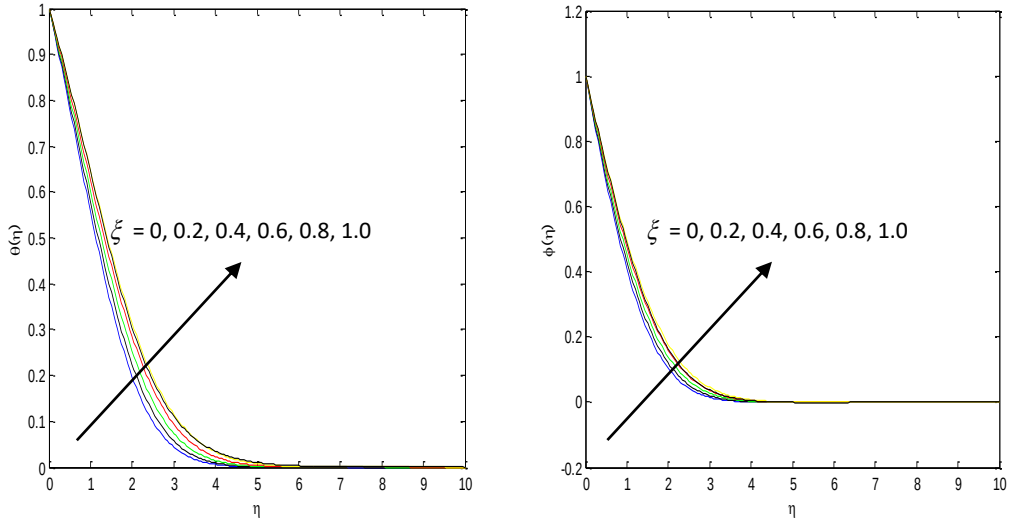


Fig. 12. Temperature and concentration profile $\theta(\eta)$ and $\phi(\eta)$for various ξ with $N_r = N_t = 0.1$, $Le = Gr = Pr = 1.0$, $c = 0.5$ and various values of N_b

Figure 11 shows Brownian motion parameter make the mass diffusivity increase and at the same time enhances the momentum transfer when the values of N_b increase. Finally, Figure 12 illustrates increase the values of Brownian motion will increase mass diffusivity and heat transfer process. So we can conclude that temperature profiles increase when value of N_b increase. In addition, increase values of N_b will reduce thermal diffusivity therefore decrease the mass transfer and concentration profiles.

4. Conclusions

The problem of unsteady flow and heat transfer of free convection boundary layer flow near the stagnation-point region in the presence of nanoparticles is studied numerically. The governing equations are nondimensionalized using proper nondimensional quantities. The resulting boundary value problem is solved by Keller-box method. The effects of the various values of the pertinent

parameters c, Nb, Nt, Nr, and Le on the fluid velocity, temperature profile, and concentration profile are illustrated through graphs. We may extract some important findings from our results:

- The increase in the values of curvature parameter, *c,* will increase the skin friction.
- The increase in the values of curvature parameter, *c* will increase the local Nusselt and Sherwood number therefore it enhances heat and mass transfer.
- The increase in the values of *Le* and N_b will enhance flow in both *x*- and *y*-directions.
- The effect of the increase in the values of N_r and N_t is to decelerate the flow.
- The increase in the values of N_r, N_t, and N_b increase the temperature while quite the opposite is true for *Le*.
- The increase in the values of N_r and N_t will increase the concentration profiles.
- The increase in the values of *Le* and N_b will decrease the concentration profiles.

We may conclude the flow and heat transfer properties of free convection boundary layer flow in the stagnation-point region in the presence of nanoparticles can be controlled by changing the quantity of the physical parameters. Hence Keller-box is very effective method to solve strongly nonlinear problems.

Acknowledgement
The author would like to acknowledge the support from Fundamental Research Grant Scheme (FRGS) under a grant number of FRGS/1/2018/STG06/UNIMAP/02/3 from the Ministry of Education Malaysia.

References

[1] AMIN, NORSARAHAIDA, and N. Riley. "Mixed convection at a stagnation point." The Quarterly Journal of Mechanics and Applied Mathematics 48, no. 1 (1995): 111-121.
[2] Seshadri, Rajeswari, Nalini Sreeshylan, and G. Nath. "Unsteady mixed convection flow in the stagnation region of a heated vertical plate due to impulsive motion." International Journal of Heat and Mass Transfer 45, no. 6 (2002): 1345-1352.
[3] Nazar, Roslinda Mohd, N. Amin, and I. Pop. "Unsteady mixed convection near the forward stagnation point of a two-dimensional symmetric body." International communications in heat and mass transfer 30, no. 5 (2003): 673-682.
[4] Pop, S. R., T. Grosan, and I. Pop. "Radiation effects on the flow near the stagnation point of a stretching sheet." Technische Mechanik 25, no. 2 (2004): 100-106.
[5] Attia, Hazem Ali. "Stagnation point flow and heat transfer of a micropolar fluid with uniform suction or blowing." Journal of the Brazilian Society of Mechanical Sciences and Engineering 30, no. 1 (2008): 51-55.
[6] Salleh, M. Z., R. Nazar, and I. Pop. "Modeling of free convection boundary layer flow on a solid sphere with Newtonian heating." Acta applicandae mathematicae 112, no. 3 (2010): 263-274.
[7] Ahmad, K., R. Nazar, A. Ishak, and I. Pop. "Unsteady three-dimensional boundary layer flow due to a stretching surface in a micropolar fluid." International Journal for Numerical Methods in Fluids 68, no. 12 (2012): 1561-1573.
[8] Panigrahi, Satyaban, and Motahar Reza. "Analytic Solution of MHD Stagnation Point Flow over a Stretching Permeable Surface with Effects of Viscous Dissipation and Joule Heating." Engineering 6, no. 12 (2014): 827.
[9] Yasin, Mohd Hafizi Mat, Anuar Ishak, and Ioan Pop. "MHD stagnation-point flow and heat transfer with effects of viscous dissipation, Joule heating and partial velocity slip." Scientific reports 5 (2015): 17848.
[10] Shen, Ming, Fei Wang, and Hui Chen. "MHD mixed convection slip flow near a stagnation-point on a nonlinearly vertical stretching sheet." Boundary value problems 2015, no. 1 (2015): 78.
[11] Dessie, Hunegnaw, and Kishan Naikoti. "Scaling group analysis on MHD effects on heat transfer near a stagnation point on a linearly stretching sheet with variable viscosity and thermal conductivity, viscous dissipation and heat source/sink." Theoretical and Applied Mechanics 42, no. 2 (2015): 111-133.

[12] Raj, M., Jha, A., and Sharma, A. "Effect of Thermal Radiation and Variable Fluid Viscosity on Stagnation Point Flow Past a Porous Streching Sheet Embedded in Porous Medium with Partial Slip Condition." International Journal of Mathematics and Its Application, 3 (2016): 139-148.
[13] Alizadeh, Rasool, Asghar B. Rahimi, Reza Arjmandzadeh, Mohammad Najafi, and Ahmad Alizadeh. "Unaxisymmetric stagnation-point flow and heat transfer of a viscous fluid with variable viscosity on a cylinder in constant heat flux." Alexandria Engineering Journal 55, no. 2 (2016): 1271-1283.
[14] Sharma, R., Ishak, A., and Pop, I. (2014). "Dual Solution of Unsteady Separated Stagnation-Point Flow in a Nanofluid with Suction: A Finite Element Analysis." Indian Journal of Pure & Applied Physics 55, (2015): 275-283.
[15] Choi, Stephen US, and Jeffrey A. Eastman. Enhancing thermal conductivity of fluids with nanoparticles. No. ANL/MSD/CP-84938; CONF-951135-29. Argonne National Lab., IL (United States), 1995.
[16] Hassani, M., M. Mohammad Tabar, H. Nemati, G. Domairry, and F. Noori. "An analytical solution for boundary layer flow of a nanofluid past a stretching sheet." International Journal of Thermal Sciences 50, no. 11 (2011): 2256-2263.
[17] Edalati, Z., Saeed Zeinali Heris, and S. H. Noie. "The study of laminar convective heat transfer of CuO/water nanofluid through an equilateral triangular duct at constant wall heat flux." Heat Transfer—Asian Research 41, no. 5 (2012): 418-429.
[18] Hajipour, Mastaneh, Asghar Molaei Dehkordi, and Saeid Jamshidi. "Numerical Investigation of Nanofluid Mixed-Convection Flow in the Entrance Region of a Vertical Channel Partially Filled with Porous Medium." Heat Transfer—Asian Research 43, no. 7 (2014): 607-627.
[19] Farooq, Umer, and Hang Xu. "Free convection nanofluid flow in the stagnation-point region of a three-dimensional body." The Scientific World Journal 2014 (2014).
[20] Admon, M. A., S. Shafie, and I. Pop. "Unsteady free convection flow near the stagnation point of a three-dimensional body." Journal of Applied Sciences 11, no. 8 (2011): 1441-1444.
[21] Hayat, Tasawar, Madiha Rashid, Maria Imtiaz, and Ahmed Alsaedi. "Magnetohydrodynamic (MHD) stretched flow of nanofluid with power-law velocity and chemical reaction." AIP Advances 5, no. 11 (2015): 117121.
[22] Khan, Junaid Ahmad, M. Mustafa, T. Hayat, M. Sheikholeslami, and A. Alsaedi. "Three-dimensional flow of nanofluid induced by an exponentially stretching sheet: An application to solar energy." PloS one 10, no. 3 (2015): e0116603.
[23] Poots, G. "Laminar free convection near the lower stagnation point on an isothermal curved surface." International Journal of Heat and Mass Transfer 7, no. 8 (1964): 863-874.
[24] Cebeci, Tuncer, and Peter Bradshaw. "Momentum transfer in boundary layers." Washington, DC, Hemisphere Publishing Corp.; New York, McGraw-Hill Book Co., 1977. 407 p. (1977).

Penerbit Akademia Baru

Engineering Science and Technology Conference Proceedings

Journal homepage: www.akademiabaru.com/EST.html

Application of Flywheel Energy Storage on Generator-set

Open Access

Fakhrizal Akbar Ilmiawan[1], Sheikh Ahmad Zaki[1,*]

[1] Department of Mechanical Precision Engineering, Malaysia-Japan International Institute of Technology, Universiti Teknologi Malaysia

ABSTRACT

The generator-sets have been widely used as a secondary or an emergency standby power by the society. Despite their several benefits such as their simplicity and reliability, they meet a stability and efficiency decrease when they produce the power. Referring to the above reason, this experimental study is aimed to investigate the potential benefits of the addition of the flywheel energy storage device to generator-set systems, in the term of output power stability concept. In this research, the generator-set system is simulated by using an electromotor as a prime mover coupled with a flywheel, to generate electricity from a generator or alternator. The flywheel basically acts as an energy storage device that stores energy in the form of the rotational kinetic energy. Therefore, the generator-set simulations are performed in loaded and unload conditions, with three different variations; (1) no flywheel, (2) connected to an 8.5 kg flywheel and (3) connected to a 16 kg flywheel. The result shows that the system which is connected to a 16 kg flywheel has a higher magnitude of the rotational kinetic energy than two other test variations, due to its bigger mass of flywheel. The variation (3) also has more stable and economic output when it is fully loaded by two sets of drilling machine in which indicated by the smallest drop rate of the alternator rotational speed and the less electromotor current usage among two others.

Keywords:
Flywheel energy storage; energy;
rotational kinetic energy; generator-set;
electromotor, generator

Copyright © 2019 PENERBIT AKADEMIA BARU - All rights reserved

1. Introduction

The global demand for secondary or emergency power supply continues to increase due to the population growth and the development of the industry [1]. There are many kinds of secondary power sources that have commonly been known such as the generator sets (gen-set) and the uninterruptible power supplies (UPS), or the latest developed ones like solar powers, fuel cells and the combination of certain models of power generations called the hybrid systems [2-4]. Due to the benefits such as their simplicity and reliability, generator set systems have been widely used by the society and industrial world. However, they meet an output stability and efficiency decrease when they are operated in a peak condition [5].

The generator sets basically consist of a diesel or electrical motor (the driver) that are connected to generators or alternators (the driven) by using the pulleys and the belts to generate electricity. In the term of the quality and the efficiency of gen-set systems, the load consideration factor, along

* *Corresponding author.*
E-mail address: fkhrzlakbr@gmail.com (Fakhrizal Akbar Ilmiawan)

with the fuel, the operating conditions and the capacity design, is one of the factors that affects them. The systems are ideally operated in the standard temperature and pressure (STP) condition around 80% of their total capacity, although it is designed to bear the 100% load. However, the gen-sets are sometimes maximumly operated to deliver the 100% of their capacity under the emergency usage resulting in the decrease of the rotational speed that causes an output drop [6,7].

Numerous researches have been conducted in order to study the possibility to enhance the quality and the efficiency of the generator from various aspects, such as the fuel combinations [8] and the frequency controls [9]. In a brief, this experimental study is designed to investigate the potential benefits from the mechanical point of view by adding the flywheel energy storage (FES) in the gen-set systems. The previous study shows that the FES has been applied in the small-scale microhydro turbine power plant and the result is that the FES can smoothen the output of the microhydro power plant when there is a sudden load change, because the flywheel acts as the reservoir that stores the energy in the form of the rotational kinetic energy and releases it when it is needed [10]. Due to the above reasons, this paper is aimed to study the advantage possibility of the application of FES in the term of the output stability concept.

2. Theoretical Review

The theoretical reviews on this research are emphasized on the theories that are used to analyze the application of the flywheel on the gen-set system. They are the flywheel energy storages and the rotational kinetic energy.

2.1 Flywheel Energy Storage (FES)

The energy storage has recently become a discussion topic in the context of the energy shifting and the transition from the fossil fuels to the renewable ones [11]. Among the existing energy storage technologies, the electrochemical batteries are the leading ones. However, they also have a number of environmental disadvantages such as the hazardous chemical substances and the “grey” energy. Therefore, an environmentally friendlier technology will be needed here [12,13].



(a) (b)

Fig. 1. (a) Steel flywheel [16], (b) Composite flywheel [22]

Basically, the flywheel energy storages (FES) are a rotating cylinder or wheel with a specific mass and diameter that stores energy in the form of the rotational kinetic energy. They are mostly manufactured from the iron or steel (as shown in Figure 1.a) for the commercial usage and the composite or the fiber (as shown in Figure 1.b) for the special application or the research. The FES acts as the energy reservoir during the period when the energy supply is more than the required

and release it when the energy required is more than the energy supply [14-17]. The FES models have also been developed for several years and they have been widely applied in various ways, whether for the commercial use such as the combustion engines, the reciprocating compressors and the pumps, or the specialized purpose like the uninterruptible power supply (UPS) systems, the automobile breaking systems, the hybrid cars and the grid stabilizations [18-21].

2.2 Rotational Kinetic Energy

The rotational kinetic energy theorem begins with a basic concept of the kinetic energy itself. The kinetic energy is the representation of the energy associated with the motion of the particle or object. Hence, the rotational kinetic energy is defined as the energy associated with the object that rotates in a circular path [23].

$$K = \frac{1}{2} m v^2 \tag{1}$$

The basic kinetic energy equation (K) expressed in the Eq. 1, where *m* (kg) and *v* (m/sec) are the mass and the tangential speed of the object respectively. Consider the object as the flywheel (Figure 1) and assume it rotates about a fixed axis with an angular speed ω (rad/sec), then the tangential speed can be written as

$$v = \omega r \tag{2}$$

where r represents the radius of the flywheel (m). From the Eq. 1 and Eq. 2, the rotational kinetic energy (K_R) can be expressed as

$$K_R = \frac{1}{2} m v^2 = \frac{1}{2} m r^2 \omega^2 \tag{3}$$

From the above equation, the bigger the magnitude of the rotational kinetic energy, the more the object tends to rotate about its axis and vice versa [16,23]. Therefore, the flywheel application on this research is expected to smoothen and to stabilize the output of the generator set when it comes to be fully loaded because of the rotational kinetic energy from the flywheel.

3. Methodology

This methodology will explain the system design and the specification, and the data compilation.

3.1 System Design

This experimental study is conducted by adopting the flywheel generator module that has been designed by Pratitis et al, 2013 [5] and by varying the flywheel in order to investigate the effect of the flywheel addition. The generator set module design, as shown in the Figure 2, is composed by the aluminum frame (1), the flywheel (2), the alternator or generator (3), the electromotor (4), the flywheel shaft (5) and the pulley transmissions (6-8).

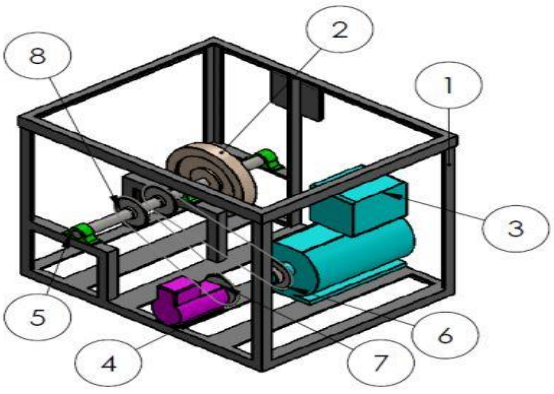


Fig. 2. Generator set module design [5]

The application of the flywheel in the generator set system is the main analysis point in this experimental study. Thus, two kinds of flywheel with different mass and geometry are used to study the effect of the rotational kinetic energy of the flywheel in the genset system.



(a) (b)

Fig. 2. (a) Flywheel type A, (b) Flywheel type B

Table 1
The specification of flywheel

	Flywheel A	Flywheel B
Mass	8.5 kg	16 kg
Diameter	34 cm	40 cm
Height	2.1 cm	3 cm

Besides the flywheel, the genset system also composed of the electromotor and alternator. The electromotor is used to convert the electrical energy into the mechanical energy. The mechanical energy is then transmitted by using the pulley transmission to rotate the alternator to generate the electricity. This experimental study uses a 1-phase, 1.1 kW electromotor with 1400-1435 nominal rpm and a 1-phase synchronous generator with 1440-1500 nominal rpm.

3.2 System Simulation and Data Compiling

The gen-set system is simulated in three conditions : (1) unloaded condition, (2) loaded with one set of drilling machine and (3) loaded with two sets of drilling machines, and by using three kind of variations : (1) no flywheel, (2) using type A flywheel and (3) using type B flywheel. Several data are compiled and then analyzed and correlated with the rotational kinetic energy theory in order to study the effect of the application of the flywheel in the genset system. The data include:

i. The electromotor current test when it is in unloaded and loaded condition, with (1) the non-flywheel variation, (2) the type A flywheel and (3) the type B flywheel.
ii. The electromotor rotation speed test (rpm test) when it is in unloaded and loaded, with (1) the non-flywheel variation, (2) the type A flywheel and (3) the type B flywheel.
iii. The generator rotation speed test when it is in unloaded and loaded with (1) the non-flywheel variation, (2) the type A flywheel and (3) the type B flywheel.
iv. The system stopping time test

4 Result and Discussion

The analysis of this experimental study is divided into 2 parts : the rotational kinetic energy analysis and the electromotor current test and the system time-to-stop test analysis.

4.1 Rotational Kinetic Energy Analysis

The results and analysis of rotational kinetic energy are based on the data from the electromotor rotation rotational speed test, the generator rotational speed test and flywheel rotational speed test by using the tachometer (as shown in Figure 3) when the generator is in unloaded and loaded conditions with the non-flywheel variation, with the type A flywheel (8.5 kg) and the type B flywheel (16 kg). The test results are then processed into the rotational kinetic energy data using the Equation 3.

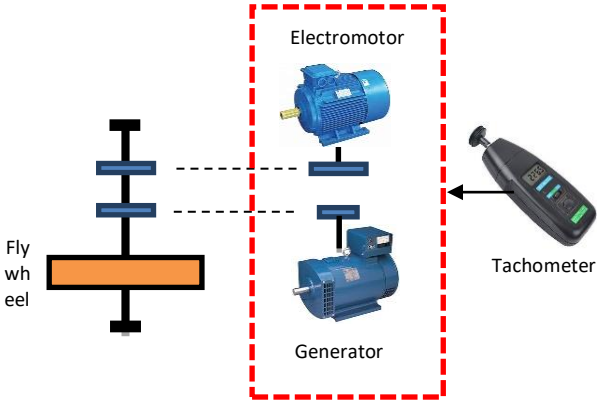


Fig. 3. The schematic of the electromotor and the generator rotational speed test

Based on the Figure 4, it can be observed that by adding the flywheel, the rotational kinetic energy of the system increases. It is shown by the increasing trend line when the flywheel is applied. The rotational kinetic energy increases when the flywheel with a bigger mass is used. This is indicated when type A flywheel with a mass of 8.5 kg is used, the rotational kinetic energy of the system is 3328.94 J, and it is increased to 7364.82 J when the type B flywheel with mass of 16 kg is applied.

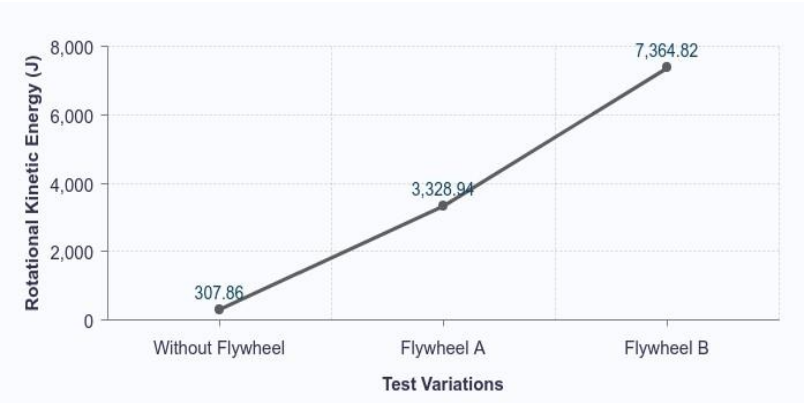


Fig. 4. The rotational kinetic energy of the system

The application of the flywheel also affects the rotational speed of electric motor and the generator when given a load. The results of the electromotor and the generator rotational speed test with the non-flywheel variation shows that the greater the load given to the generator, the more the rotational speed of the generator and the electric motor decreases. This is proven by the Figure 5 and Figure 6 when the load is getting closer to the nominal power of the electric motor, the rotational speed of the electric motor is only 530 rpm out of 1400 rpm and the generator decreased to 1123 rpm from the nominal rotation speed of 1440 rpm.

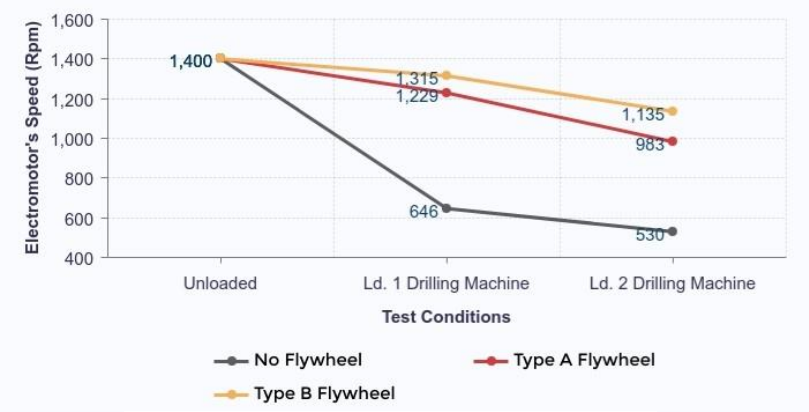


Fig. 5. The electromotor speed test result

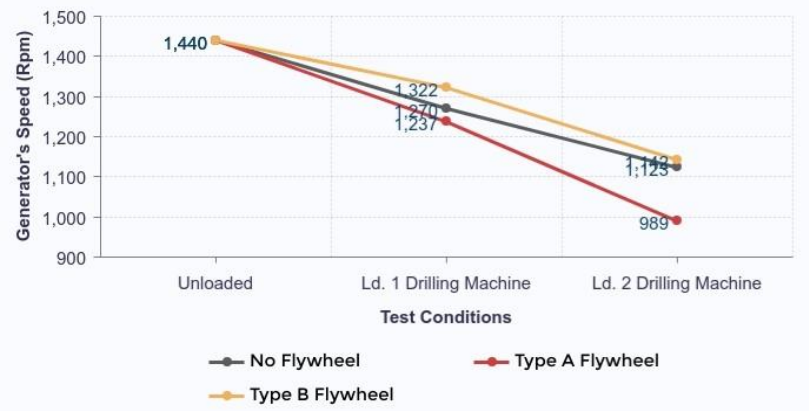


Fig. 6. The generator speed test result

In the type A and B flywheel variations, the rotational speed of the electromotor and the generator has better magnitude compared with the non-flywheel variation. From the three test variations, the type B flywheel has better electromotor and generator rotational speed which are closer to their nominal speed. This shows that the application of type B flywheel to the genset system causes a greater rotational kinetic energy, so that the fluctuation of the rotational speed of

the electromotor and the generator is decreasing and the genset system is getting more stable, because the electromotor and the generator are closer to their nominal speed.

4.2 Electromotor Current and System Stopping Time Analysis

Based on the rotational kinetic energy analysis, the kinetic energy that is typically stored in the system can be correlated to the electromotor current and the system stopping time. The results of the electromotor current test shows that the non-flywheel variation experiences a fair increase in its current, i.e. from 3.5 A under the unloaded condition and rises to 4.8 A when given a load of 1 kW of two sets of drilling machines which are close to the nominal power of the electromotor. When the gen-set system is connected to the variation of type A and B flywheels, there is a slight current increase compared with the non-flywheel variation when the generator is given a load close to the nominal power of the electric motor in which proven by the Figure 7. The fewest current increase occurs when the type B flywheel variation is used and when the generator is given a load close to the nominal power of the electric motor, there is only a slight current increase of 0.5 A from the initial value of 3.5 A to 4 A. The current increase of the electric motor indicates that the work of the electric motor is getting heavier because of the load given, especially when the load is getting closer to the nominal power of the electric motor. This impacts on the reduction of the rotational speed of the electric motor as well as the rotational speed of the generator.

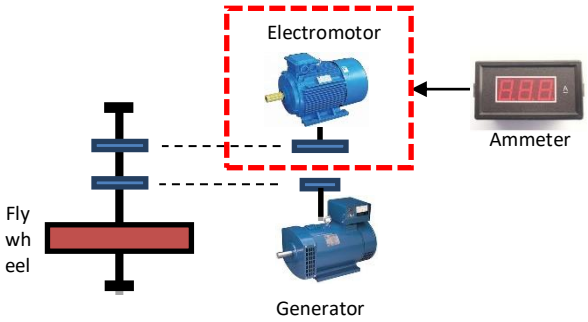


Fig. 7. The schematic of the electromotor current test

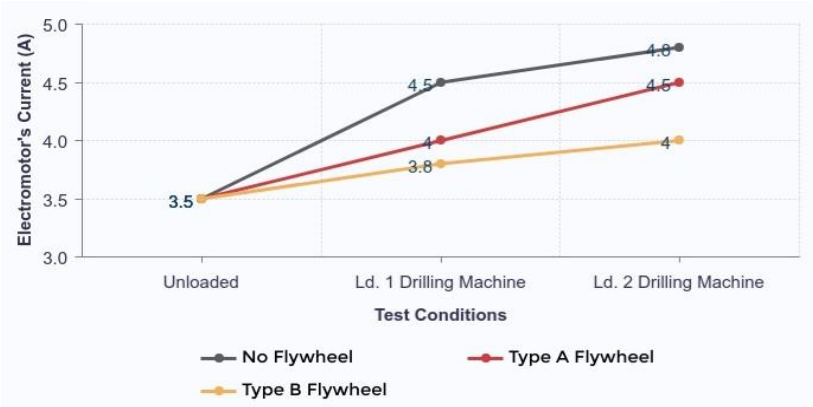


Fig. 8. The electromotor current test result

Based on the figure 8, The application of the flywheel to the gen-set system eases the workload of the electric motor. When the generator is given a load, which is closer the nominal power of the electromotor, the rotational speed of the electromotor decreases due to the heavy workload. The role of the flywheel, as shown by the results of the rotational speed test of the electromotor, helps the electromotor stabilize its speed which in return also stabilizes the rotational speed of the generator as well, as indicated in the results of the generator rotational speed test.

Furthermore, the electrical power that is used by the electromotor is also reduced when the electromotor has a lighter workload in which it is evidenced by the smaller magnitude of the electric current when the flywheel is applied. Therefore, the electromotor becomes more efficient when the electromotor uses less electrical power.

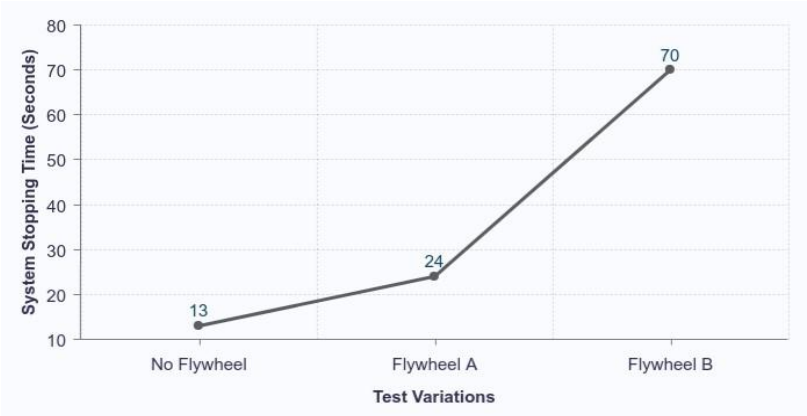


Fig. 9. The system stopping time test result

As shown in the Figure 9, the gen-set system in which the type B flywheel is applied has a longer stopping time when the electrical power supply is removed, about 70 seconds, than the type A flywheel variation which has 24 seconds and the non-flywheel variation with only 13 seconds of stopping time. This indicates that the application of the flywheel helps the gen-set system to maintain its rotational speed while it is operated or even when the power supply is removed for a certain time interval because of the rotational kinetic energy that is stored and released by the flywheel itself.

5. Conclusion

Referring to above explanation, it can be concluded that the application of the flywheel on the generator set helps the system stabilizes its output under a heavier load in which it is proven by the fewer reduction of the electromotor and the generator rotational speed as shown in the Figure 5 and 6. The addition of the flywheel also lightens the workload of the system as indicated by the smallest increase rate of the electromotor current usage under a loaded condition as proven in the Figure 7. The rotational kinetic energy that is stored inside the flywheel also helps the gen-set system to maintain its rotational speed while it is operated under a loaded condition or even when the power supply is removed as proven the system stopping time test and the Figure 8. Therefore, the expected research result is achieved and the flywheel can stabilize the gen-set system.

Acknowledgement

The authors would like to thank Assoc. Prof Sheikh Ahmad Zaki of the Department of Mechanical Precision Engineering of Malaysia-Japan International Institute of Technology, Universiti Teknologi Malaysia for his supervision and Drs. Sudarno, M.H from Indonesia as the personal English expert.

References

[1] Benton, Kelly, Xufei Yang, and Zhichao Wang. "Life cycle energy assessment of a standby diesel generator set." Journal of Cleaner Production 149 (2017): 265-274.

[2] Zhang, Z., K. Sato, Y. Nagasaki, M. Tsuda, D. Miyagi, T. Komagome, K. Tsukada, T. Hamajima, Y. Ishii, and D. Yonekura. "Continuous operation in an electric and hydrogen hybrid energy storage system for renewable power generation and autonomous emergency power supply." International Journal of Hydrogen Energy 44, no. 41 (2019): 23384-23395.

[3] Lyman, Dale. " Chapter 8 : Emergency power, supplies and electrical systems." *Ambulatory Surgery Center Safety Guidebook*, p 37-41. 2018.

[4] Zhang, Z., Y. Nagasaki, D. Miyagi, M. Tsuda, T. Komagome, K. Tsukada, T. Hamajima, H. Ayakawa, Y. Ishii, and D. Yonekura. "Stored energy control for long-term continuous operation of an electric and hydrogen hybrid energy storage system for emergency power supply and solar power fluctuation compensation." International Journal of Hydrogen Energy 44, no. 16 (2019): 8403-8414.

[5] Yuniarsih, Pratitis, F. Bahtiyar, R. Mufti and Trisakti Prabawanto. " Flywheel Generator. " *Institut Teknologi Sepuluh Nopemper Surabaya*. 2013.

[6] Shakti Foundation. "Diesel generators : Improving efficiency and emission performance in India." *Retrieved from* *www.shaktifoundation.in/wp-content/uploads/2017/06/ICF-2014-Diesel-Generators-Improving-Efficiency-and-Emission-Performance-in-India.pdf* (accessed in july 2018).

[7] Diesel service and Supply. "Factors affecting generator output rating." *Available at* *www.dieselserviceandsupply.com/Generator_Output_Rating.aspx* (accessed in july 2018).

[8] Lee, Seokhwan, Young Choi, and Kernyong Kang. "Application of blended fuel containing coffee ground pyrolysis oil in a diesel generator." Fuel 256 (2019): 115998.

[9] Semshchikov, Evgenii, James Hamilton, Liuer Wu, Michael Negnevitsky, Xiaolin Wang, and Sarah Lyden. "Frequency control within high renewable penetration hybrid systems adopting low load diesel methodologies." Energy Procedia 160 (2019): 483-490.

[10] Aminudin, Moh. Syaikhu, Sarwono and Ridho Hantoro. "Studi aplikasi flywheel energy storage untuk meningkatan dan menjaga kestabilan pembangkit listrik tenaga mikrohidro (PLMTH)." *Institute Teknologi Sepuluh Nopember Surabaya*. (2010).

[11] Akinyele, D. O., and R. K. Rayudu. "Review of energy storage technologies for sustainable power networks." Sustainable Energy Technologies and Assessments 8 (2014): 74-91.

[12] Köhler, Jonathan, Wolfgang Schade, Guillaume Leduc, Tobias Wiesenthal, Burkhard Schade, and Luis Tercero Espinoza. "Leaving fossil fuels behind? An innovation system analysis of low carbon cars." Journal of Cleaner Production 48 (2013): 176-186.

[13] Longo, Sonia, Vincenzo Antonucci, Maurizio Cellura, and Marco Ferraro. "Life cycle assessment of storage systems: the case study of a sodium/nickel chloride battery." Journal of cleaner production 85 (2014): 337-346.

[14] Wicki, Samuel, and Erik G. Hansen. "Clean energy storage technology in the making: An innovation systems perspective on flywheel energy storage." Journal of cleaner production 162 (2017): 1118-1134.

[15] Khurmi, R. S., and J. K. Gupta. "A text book of Machine Design. Eurasia Publishing house (PVT.) Ltd." First multi color edition (2005).

[16] Ilmiawan, Fakhrizal Akbar, Joke Pratilastiarso, and Prima Dewi Permatasari. "Studi Eksperimen Aplikasi Flywheel Pada Pembangkit Listrik Untuk Daerah Terpencil." In Prosiding Seminar Nasional Teknologi Elektro Terapan, vol. 1, no. 01, pp. 181-186. 2017.

[17] Han, Yongjie, Zhengyi Ren, and Yongxiang Tong. "General design method of flywheel rotor for energy storage system." Energy Procedia 16 (2012): 359-364.

[18] Hadjipaschalis, Ioannis, Andreas Poullikkas, and Venizelos Efthimiou. "Overview of current and future energy storage technologies for electric power applications." Renewable and sustainable energy reviews 13, no. 6-7 (2009): 1513-1522.

[19] Doucette, Reed T., and Malcolm D. McCulloch. "A comparison of high-speed flywheels, batteries, and ultracapacitors on the bases of cost and fuel economy as the energy storage system in a fuel cell-based hybrid electric vehicle." Journal of Power Sources 196, no. 3 (2011): 1163-1170.

[20] Boroojeni, Kianoosh G., M. Hadi Amini, and Sundararaja S. Iyengar. Smart grids: security and privacy issues. Springer International Publishing, 2017.

[21] Bergek, Anna, Marko Hekkert, Staffan Jacobsson, Jochen Markard, Björn Sandén, and Bernhard Truffer. "Technological innovation systems in contexts: Conceptualizing contextual structures and interaction dynamics." Environmental Innovation and Societal Transitions 16 (2015): 51-64.
[22] Bai, J. G., X. Z. Zhang, and L. M. Wang. "A flywheel energy storage system with active magnetic bearings." Energy Procedia 16 (2012): 1124-1128.
[23] Jewett, John W., and Raymond A. Serway. Physics for scientists and engineers with modern physics. Cengage Learning EMEA, 2008.

Penerbit Akademia Baru

Engineering Science and Technology
Conference Proceedings

Journal homepage: www.akademiabaru.com/EST.html

Comparative Assessment of Closed Loop Heat Pump Dryer and Direct Solar Dryer System for Banana Drying

Open Access

Azridjal Aziz[1,*], Joko Harianto[1], Afdhal Kurniawan Mainil[2], Rahmat Iman Mainil[1]

[1] Department of Mechanical Engineering, Faculty of Engineering, Universitas Riau Jl. Subrantas km 12, Pekanbaru 28293, Indonesia
[2] Department of Mechanical Engineering, Faculty of Engineering, Universitas Bengkulu Jl. WR. Supratman, Kandang Limun, Bengkulu 38371A, Indonesia

ABSTRACT

The comparative assessment of direct solar dryer system (DSDS) and closed loop heat pump dryer (CLHPD) for drying of banana has been investigated. This study was carried out with 3 drying methods including DSDS, CLHPD without preheating and CLHPD with preheating for 30 minutes to determine the performance and drying characteristics of banana dryer from the initial mass of 8 kg to evaporate of moisture content of 3.2 kg. The results showed that the drying time of banana using CLHPD with preheating (30 minutes), CLHPD without preheating and DSDS are 255 minutes, 305 minutes and 720 minutes, respectively. The higher value of Specific Moisture Extraction Rate (SMER) of banana using CLHPD with preheating (30 minutes), CLHPD without preheating and DSDS were 1.29 kg/kWh, 1.18 kg/kWh and 0.35 kg/kWh, respectively. The SMER of CLHPD with pre-heating was higher than that CLHPD without pre-heating and it was the highest compared to DSDS. The CLHPD with preheating showed a better performance in comparison with CLHPD without preheating and it was the best performance compared to DSDS. The CLHPD drying time with pre-heating was faster than CLHPD without pre-heating and it was the fastest compare to DSDS.

Keywords:
Direct solar dryer system; closed loop heat pump dryer; banana drying; heating, performance

Copyright © 2019 PENERBIT AKADEMIA BARU - All rights reserved

1. Introduction

Drying is a process of dehumidification in which moisture is removed from a solid using thermal energy [1]. The use of sunlight in open space for drying has been existed since ancient times. But, it has not been widely integrated in home or the industrial sector. In principle, the drying process involves the process of heat and mass transfer that occurs simultaneously, in most cases will change products properties. First, the heat must be transferred from the heating medium to the material. And then, after water evaporation occurs, the moisture content must be moved through the material structure to the surrounding medium. This process involves fluid flow where the water content must be transferred through the material structure during the drying process. The length of drying time process depends on the material being dried and the method of heating used [2-5]. Drying is one of the most common ways to extend the storage time of agricultural products including fisheries and other food products. The process of drying product after post-harvest is important so that the growth of bacteria or micro-organisms that because decay stops growth and the product can be stored in longer time before consumption [6].

* *Corresponding author.*
E-mail address: azridjal.aziz@lecturer.unri.ac.id (Azridjal Aziz)

The energy as heat for drying supplied in various sources (solar energy, natural gas, fossil fuel, biomass etc.). Although solar dryers are used for drying various commodities, it has not yet been widely commercialized because of high investment cost, time-consuming operation, human habit etc. [7]. The evaluation and review on the use of solar dryer for drying of various commodities have been presented by many researchers [2, 4, 8-12]. Kumar et al. [3] reported a review of solar dryer in various types namely, direct solar dryers, indirect solar dryers, hybrid solar dryers and their drying applications for various commodities. Hedge et al. [13] reported design and fabrication of solar dryer and performance evaluation of solar dryer for banana and reported their performance for banana drying. They found that the drying rate increase when wooden skewers were used instead of conventional trays. The total difference is found to be 3.1% for moisture content which is considerable knowing that the rate of drying drastically decreases with time at the end of the day.

Many dryer technologies have been developed over the past years such as freeze drying, vacuum drying, hot air drying, heat pump dryer etc. Many researchers found that the quality of the dried product is strongly dependent on the processes and methods of drying involved because drying is a complex operation and could be degraded during operation [14]. Heat pump technology has been used in residential, domestic and industrial sectors in most developed countries for cooling space using air conditioning. However, heat pump technology for drying of commodities like food, fruits and vegetables has been largely unexploited in Indonesia. Very little literature studies about heat pump technology conducted in Indonesia [15-17]. Fayose et al. [18] Reported that heat pump technology for drying of fruits and vegetables had been used in domestic and industrial sectors in Sub Sahara Africa including South Africa. Several studies of heat pump technology have been performed by many researchers, including applying heat recovery process [19, 20] and drying technology [21-23]. Liu et al. [24] conducted the design and thermal analysis of an air source heat pump dryer for food drying. Their results showed that the open and semi-open heat pump dryers were greatly affected by ambient temperature and humidity. The closed heat pump drying system was greatly affected by the bypass air rate. Heat pump dryer uses a closed loop and fully recovers energy. The amount of heat recovered in a heat pump dryer depends on heat transfer area, refrigerant properties and moist air recirculation.

In this study, closed loop heat pump dryer (CLHPD) compared to direct solar dryer system (DSDS) for banana drying was designed, constructed and tested. The experimental result was performed on the system to determine the optimum performance and drying characteristic between CLHPD and DSDS. This study was carried out with 3 drying methods namely DSDS, CLHPD without preheating and CLHPD with preheating for 30 minutes from the initial mass of 8 kg to evaporate of moisture content of around 3.2 kg.

2. Methodology

The experimental apparatus of closed loop heat pump dryer (CLHPD) and direct solar dryer system (DSDS) were designed, constructed and tested at the Thermal Engineering Laboratory (Faculty of Engineering, Universitas Riau) as shown in Figure 1 and Figure 2, respectively. CLHPD apparatus consists of heat pump system and dryer room. Table 1 shows the specifications of the heat pump used in this study that modified from a split type of residential air conditioning.

Closed loop heat pump dryer has dimension of dryer room with size 1500 mm x 750 mm x 1800 mm (length x width x height) and heat pump dryer package has dimension size 730 mm x 600 mm x 550 mm (length x width x height), where net volume of dryer volume is 1.78 m^3. DSDS has volume 1.5 m^3 and dimension size 970 mm x 1000 mm x 1030 mm (length x width x height) with slope angle 45^o and consist of V type corrugated black aluminum absorber plate with 0.4 mm thick and

1.344 m^2, glass cover 0.5 mm, isolator 17 mm plywood, fan for air circulation with power 4W from solar cell.

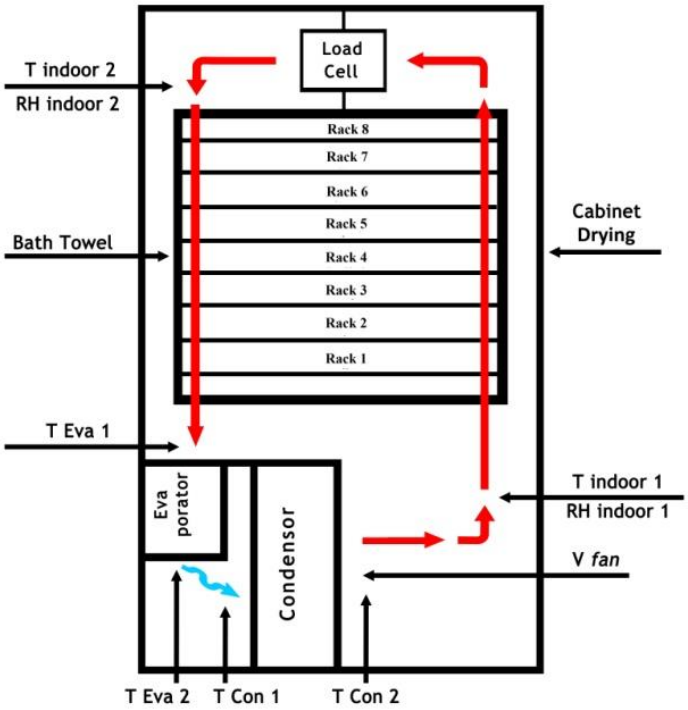


Fig. 1. The schematic of Closed Loop Heat Pump Dryer (CLHPD) apparatus

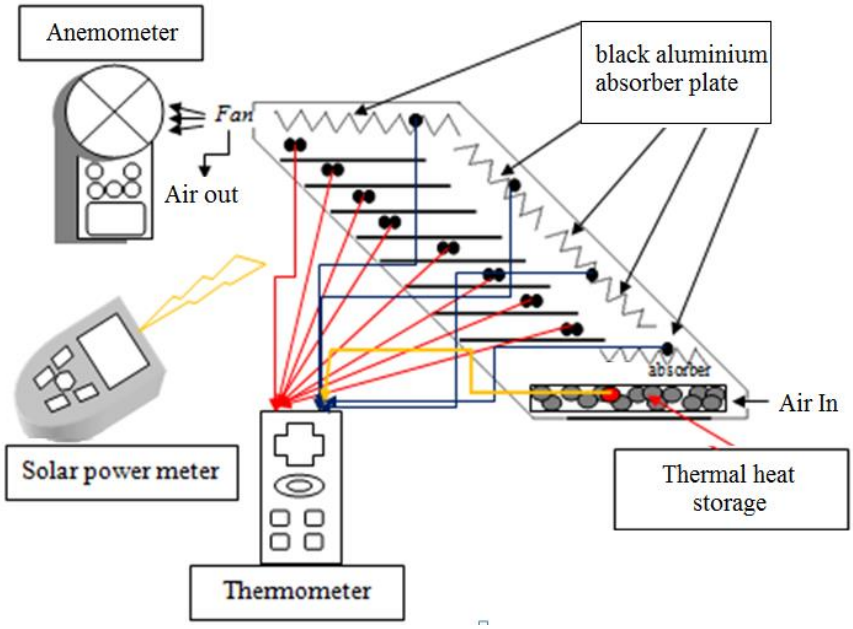


Fig. 2. The schematic of Direct Solar Dryer System (DSDS) apparatus

Table 1
Specification of Heat Pump

Characteristics	Technical Description
Type	Split Unit

Volt/Ph/Hz	220V/1/50 Hz
Power (averaged)	305 W
Nominal Ampere	1.3 A
Cooling Capacity	5000 Btu/h
Refrigerant/mass	R22/320 g
Pipe size, Liquid/Gas	⌀1/4 inch / ⌀3/8 inch
Dimension of indoor unit	770 mm x 260 mm x 320 mm
Dimension of outdoor unit	790 mm x 340 mm x 490 mm

K-type thermocouple with data acquisition was used for measurement of temperatures from apparatus with accuracy 0.2% (± 0.5°C) and resolution 0.1°C. The electric current input and voltage input were measured by ampere-meter (accuracy ± 2.0 percent and 3 digits) and voltmeter (accuracy ± 1.0 percent and 3 digits), respectively. The mass of banana was measured by digital weight scale with accuracy ±10 gram using type-S Load cell.

The experimental drying data of banana was analyzed using the moisture ratio, where the moisture ratio (MR) is the amount of water content remaining in the banana sample compare to the initial water content of banana [5, 17, 25]. Where *m*, *mo* and *me* are the mass of the banana dried at measured time, at initial time and at equilibrium, respectively. It was calculated using equation (1):

$$MR = \frac{m-me}{mo-me} \quad (1)$$

Specific moisture extraction rate (SMER) was used in this study as drying performance of CLHPD, which defined as number of water content removed from the banana dried per unit consumption of energy [5, 17, 25]. SMER is indicated as energy effectiveness use in drying banana. Thus, SMER [kg/kW h] is calculated using equation (2):

$$SMER = \frac{m}{\dot{m}airxCpx(Tin-Tout)+Win} \quad (2)$$

Where $\dot{m}\ air$, *Cp*, *Tin*, *Tout*, *Win* are mass of the air (kg/s), constant pressure specific heat of air (kJ/kgK), air temperature entering the evaporator (°C), air temperature leaving the evaporator (°C) and power consumption(kWh), respectively.

3. Results

Figure 3, figure 4 and figure 5 show the moisture ratio, average temperature of drying chamber (*Tin*) and surrounding temperature (*Tout*) during drying time (minutes) of banana at CLHPD without preheating, with preheating (30 minutes) and DSDS, respectively. During the drying process at CLHPD as shown in Figure 4 and Figure 5 the temperature of the drying chamber during drying process increase with the enhancement of drying time. This is because of the effect of the closed loop heat pump (CLHPD), so the air in the drying chamber increase with the increasing of enhancement drying time. Heat rejection from condenser was used for heating air in the drying chamber so that the water content of banana will reduced because of evaporation. The temperature distribution of the drying chamber with DSDS reaches the maximum temperature 57.1°C at 360 minutes then continues to decrease gradually following the daily solar radiation pattern in the form of a parabolic curve with time. The hot air was circulated back through the evaporator and condenser until the evaporation of water content evaporation achieved 3.2 kg.

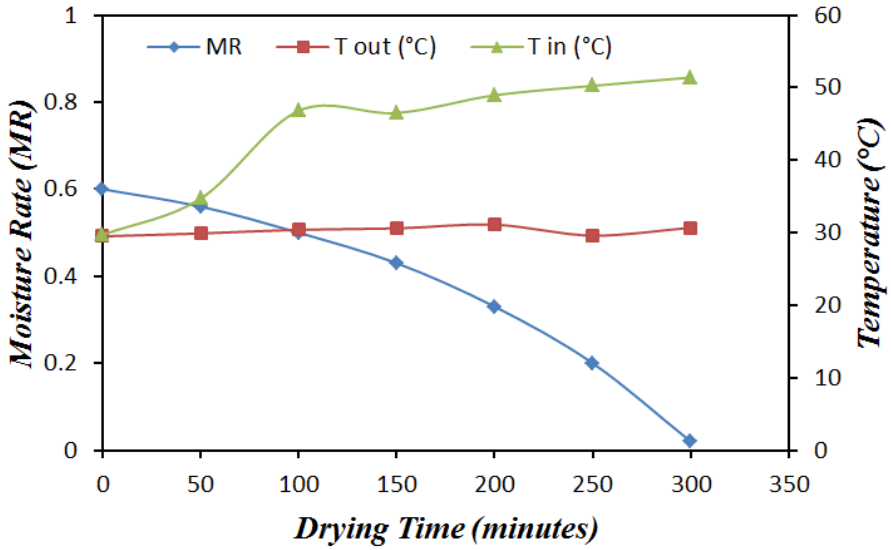


Fig. 3. Moisture Ratio, average temperature of drying chamber (*Tin*) and surrounding temperature (*Tout*) in drying time (minutes) of CLHPD without preheating.

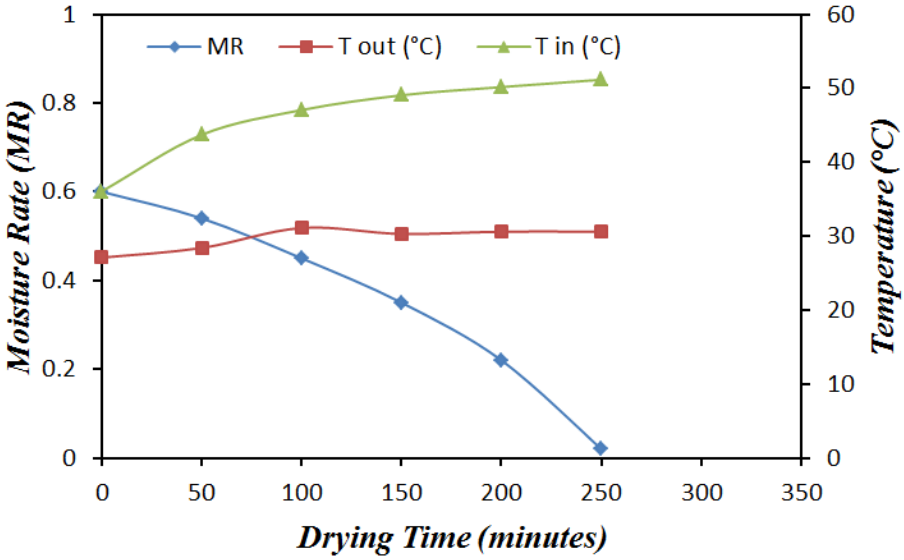


Fig. 4. Moisture Ratio, temperature average of drying chamber (*Tin*) and surrounding temperature (*Tout*) in drying time (minutes) of CLHPD with 30 minutes preheating.

Figure 3, figure 4 and figure 5 show that drying time at CLHPD with preheating 30 minutes is faster than CLHPD without preheating around 55 minutes, because average temperature of CLHPD with preheating higher than average temperature without preheating. The average drying temperature of CLHPD with preheating 30 minutes and without preheating is around 47°C and 44.5°C respectively, where average drying temperature of DSDS is around 43.8°C. The average temperature of CLHPD with preheating is higher than CLHPD without preheating and highest than DSDS.

In the drying process, moisture ratio (MR) decreases with increasing temperature of drying chamber, where the temperature drop using CLHPD with or without preheating, faster than using

DSDS. Banana drying using CLHPD with preheater 30 minutes requires 255 minutes while CLHPD without preheating requires 305 minutes then DSDS requires 720 minutes. The results show that banana drying when viewed on MR and drying time using CLHPD with 30 minutes preheater was better than using DSDS and CLHPD without preheater as shown in Figure 3, Figure 4 and Figure 5.

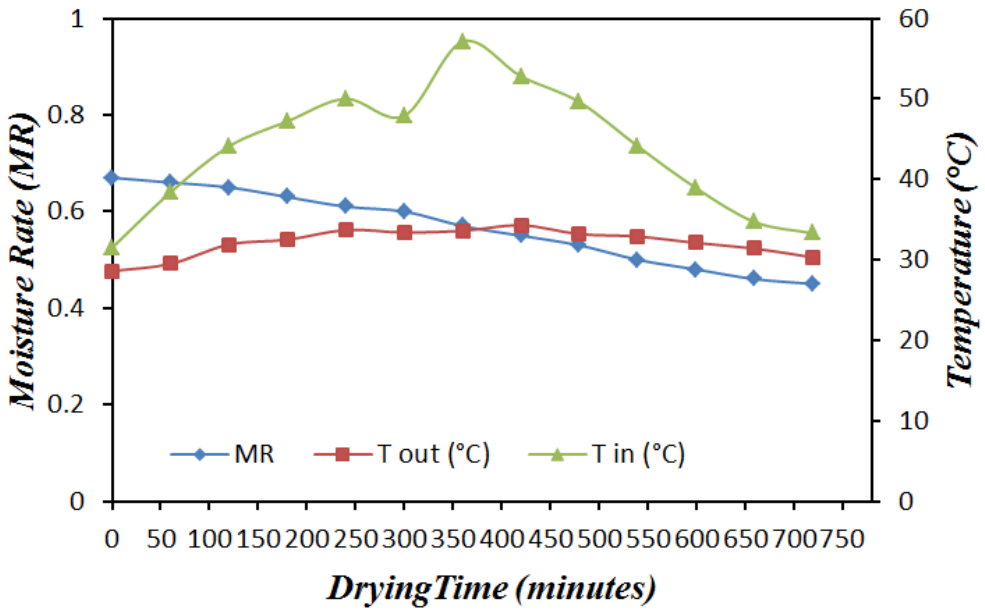


Fig. 5. Moisture Ratio, temperature average of drying chamber (*Tin*) and surrounding temperature (*Tout*) in drying time (minutes) of DSDS.

Figure 6 shows the mass reduction of banana drying versus drying time comparison using DSDS, CLHPD without preheating, with preheating 30 minutes. It can be seen in figure 5, that the mass of moisture content of banana that dried directly using CLHPD without preheating and with preheating of drying chamber 30 minutes decreases in mass due to the effect of drying chamber temperature increase. The result shows that banana drying using CLHPD without preheating of drying chamber for mass reduction of 3.2 kg requires 305 minutes, while using CLHPD with preheating the drying chamber for 30 minutes for mass reduction of 3.2 kg requires 255 minutes, and using DSDS requires 720 minutes. Drying time of banana using CLHPD with preheating 30 minutes is faster than the others (CLHPD without preheating and DSDS).

The variation of Specific moisture extraction rate (SMER) of banana with drying time comparison of CLHPD without preheating, with preheating 30 minutes and DSDS is shown in figure 7. As shown in Figure 7 the SMER value in this study using a heat pump (CLHPD) is higher than the test using a solar dryer (DSDS). The highest SMER value in the heat pump (CLHPD) without preheating is 1.18 kg / kWh and the lowest SMER is 0.83 kg / kWh, while the highest SMER value with preheating 30 minutes is 1.29 kg / kWh and the lowest SMER is 0.87 kg / kWh, where the highest SMER value in the solar dryer is 0.35 kg / kWh and the lowest SMER is 0.21 kg / kWh. This result was showed that time required for banana drying is faster using a heat pump (CLHPD with preheating 30 minutes) when compared to banana drying using a solar dryer (DSDS).

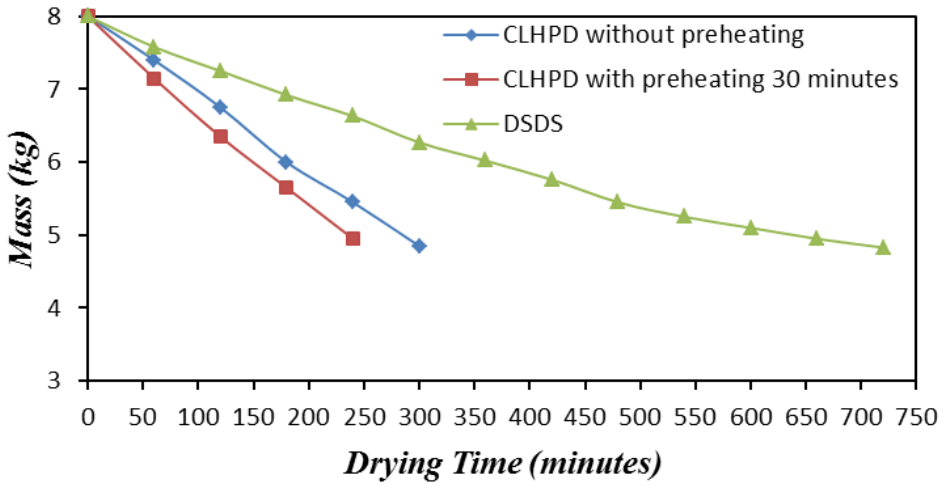


Fig. 6. Mass reduction of banana versus drying time comparison using CLHPD without preheating, with preheating 30 minutes and DSDS

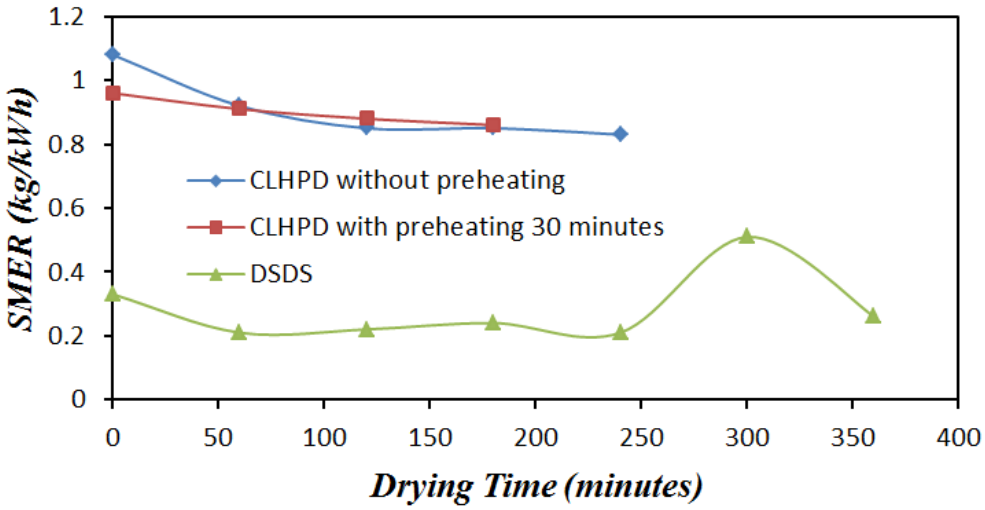


Fig. 7. SMER of banana versus drying time comparison of CLHPD without preheating, with preheating 30 minutes and DSDS

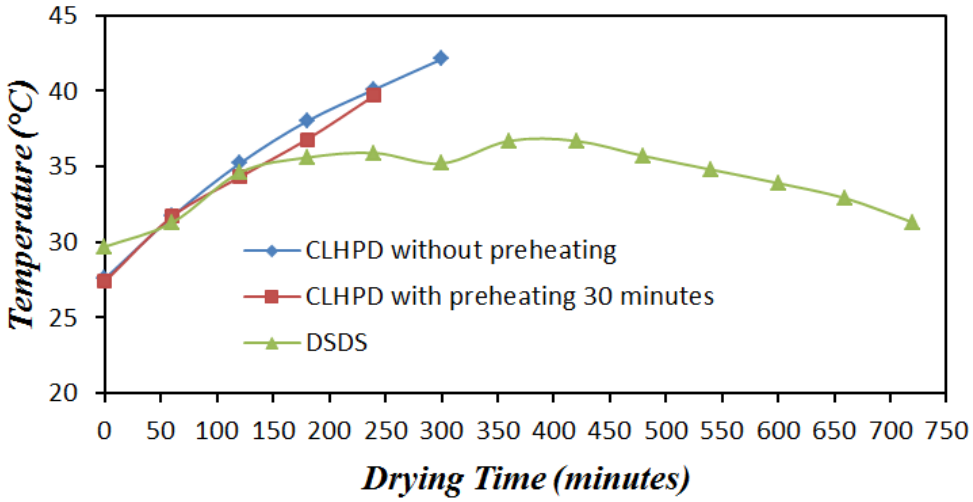


Fig. 8. Drying chamber temperature versus drying time comparison of CLHPD without preheating, with preheating 30 minutes and DSDS

Figure 8 shows the drying chamber temperature versus drying time comparison of heat pump (CLHPD) without preheating, with preheating 30 minutes and solar dryer (DSDS). It can be seen in Figure 8 that drying of banana in drying chamber with initial mass of 8 kg and the water content evaporated from around 3.2 kg in variation of drying time. During drying process using a heat pump (CLHPD) the drying time required to dry the banana was faster than the test using a solar dryer (DSDS), where CLHPD with preheating 30 minutes drying time was faster than CLHPD without preheating. During the test, drying temperature in the drying chamber with a heat pump (CLHPD) is higher than the drying temperature using a solar dryer (DSDS), where CLHPD with preheating 30 minutes drying temperature was higher than CLHPD without preheating.

4. Conclusions

The performance and drying characteristic of 3 drying methods including direct solar drying system (DSDS), closed loop heat pump dryer (CLHPD) without preheating and CLHPD with preheating for 30 minutes of banana dryer from the initial mass of 8 kg to evaporate of moisture content of 3.2 kg have been reported. The drying time of banana drying using CLHPD with preheater 30 minutes requires 255 minutes while CLHPD without preheating requires 305 minutes then DSDS requires 720 minutes. The results was showed that banana drying of MR and drying time using CLHPD with 30 minutes preheater was better than using DSDS and CLHPD without preheater. The highest SMER value in the heat pump (CLHPD) without preheating is 1.18 kg / kWh and the lowest SMER is 0.83 kg / kWh, while the highest SMER value with preheating 30 minutes is 1.29 kg / kWh and the lowest SMER is 0.87 kg / kWh, where the highest SMER value in the solar dryer is 0.35 kg / kWh and the lowest SMER is 0.21 kg / kWh. It was concluded that the time required for banana drying is faster using a heat pump (CLHPD with preheating 30 minutes) when compared to banana drying using a solar dryer (DSDS).

References

[1] Hawlader, MNA (2013). "Drying of food products under inert atmosphere using heat pump: Processing and drying of foods, vegetables and fruits " (2013): 69-82.
[2] Maia, Cristiana Brasil, André Guimarães Ferreira, Luben Cabezas-Gómez, Janaína de Oliveira Castro Silva, and Sérgio de Morais Hanriot. "Thermodynamic analysis of the drying process of bananas in a small-scale solar updraft tower in Brazil." Renewable energy 114 (2017): 1005-1012.
[3] Kumar, Mahesh, Sunil Kumar Sansaniwal, and Pankaj Khatak. "Progress in solar dryers for drying various commodities." Renewable and Sustainable Energy Reviews 55 (2016): 346-360.
[4] Fudholi, Ahmad, Kamaruzzaman Sopian, B. Bakhtyar, Mohamed Gabbasa, Mohd Yusof Othman, and Mohd Hafidz Ruslan. "Review of solar drying systems with air based solar collectors in Malaysia." Renewable and Sustainable Energy Reviews 51 (2015): 1191-1204.
[5] Islam, Md Raisul, and Arun S. Mujumdar. "Heat pump-assisted drying." Drying technologies in food processing (2008): 190-224.
[6] Norton, B. "Characteristics of Different Systems for the Solar Drying of Crops: Solar Drying Technology. Green Energy and Technology." (2017): 69-88.
[7] Lingayat A, Chandramohan VP, and Raju VRK. “Design, development and performance of indirect type solar dryer for banana drying.” *Energy Procedia* 109 (2017): 409-416.
[8] Chapchaimoh K, Poomsa-ad N, Wiset L, and Morris J. “ Thermal characteristics of heat pump dryer for ginger drying.“ *Applied Thermal Engineering 95 (*2016): 491-498.
[9] Tiwari S, Tiwari GN, and Al-Helal IM. “Development and recent trends in greenhouse dryer: A review.” *Renewable and Sustainable Energy Reviews* 65 (2016): 1048-1064.
[10] Singh P, Shrivastava V, and Kumar A. “Recent developments in greenhouse solar drying: A review.” *Renewable and Sustainable Energy Reviews* 82 (2018): 3250-3262.
[11] Mustayen AGMB, Mekhilef S, and Saidur R. “Performance study of different solar dryers:” *A review. Renewable and Sustainable Energy Reviews* 34 (2014): 463-470.

[12] Pirasteh G, Saidur R, Rahman SMA, and Rahim NA. "A review on development of solar drying applications." *Renewable and Sustainable Energy Reviews* 31 (2014): 133-148.
[13] Hegde VN, Hosur VS, Rathod SK, Harsoor PA, and Narayana KB. "Design, fabrication and performance evaluation of solar dryer for banana." *Energy, Sustainability and Society* 5, no. 23 (2015): 1-12.
[14] Suji P.V, Issac JM, Shidin K, and Abdul SCA. "Experimental Analysis through Heat Pump Assisted Dryer." *International Research Journal of Engineering and Technology* 5, no. 4 (2018): 167 -171.
[15] Aziz A, Mainil RI, Mainil AK, and Listiono H. "Effect of water temperature and air stream velocity on performance of direct evaporative air cooler for thermal comfort." *Proceeding of International Conference on Engineering, Science and Nanotechnology (ICESNANO 2016), AIP Conference Proceedings* 1788, 010001 (2016): 030024-1-030024-5.
[16] Ambarita H, Nasution DM, Gunawan S, and Nasution AH. "Performance and characteristics of heat pump clothes drier." Proceeding of Annual Applied Science and Engineering Conference, IOP Conference Series: Materials Science and Engineering 180, 012027 (2016): 1-8.
[17] Aziz A, Mainil RI, Mainil AK, and Saputra E. "Experimental evaluation on the use of capillary tube and thermostatic expansion valve with heat recovery hot spot water heater in air source refrigeration system." *Proceeding of International Conference on Engineering, Science and Nanotechnology (ICESNANO 2016), AIP Conference Proceedings* 1788, 010001 (2016): 030023-1- 030023-7.
[18] Fayose F and Huan Z. "Heat pump drying of fruits and vegetables: principles and potential for sub Sahara Africa." *ANNALS of Faculty Engineering Hunedoara-International Journal of Engineering* 14, no. 1 (2016): 207-214.
[19] Wessapan T and Borirak T. "An Experimental Study on Banana Drying using a Combined Rejected Heat from Split-type Air Conditioner and Solar Energy." *Applied Mechanics and Materials* 110-116 (2012): 2170-2176.
[20] Yamankaradeniz N, Sokmen KF, Coskun S, Kaynakli O, and Pastakkaya B. "Performance analysis of a re-circulating heat pump dryer." *Thermal Science* 20, no. 1 (2016): 267-277.
[21] Yang Z, Zhu Z, and Zhao F. "Simultaneous control of drying temperature and superheat for a closed-loop heat pump dryer." *Applied Thermal Engineering* 93 (2016): 571-579.
[22] Coşkun S, Doymaz I, Tunçkal C, and Erdoğan S. "Investigation of drying kinetics of tomato slices dried by using a closed loop heat pump dryer." *Heat Mass Transfer* 53, no. 6 (2017): 1863-1871.
[23] Zlatanovic I, Komatina M, and Antonijevic D. "Experimental investigation of the efficiency of heat pump drying system with full air recirculation." *Journal of Food Process Engineering* 40, n0. 1 (2017): 1-9.
[24] Liu H, Yousaf K, Chen K, Fan R, Jiaxin L, and Soomro, SA. "Design and Thermal Analysis of an Air Source Heat Pump Dryer for Food Drying." *Sustainability* 10, no. 9 (2018): 1-17.
[25] Mahlia TMI, Hor CG, Masjuki HH, Husnawan M, Farman M, and Mekhilef S. "Clothes drying from room air conditioning wasteheat: Thermodynamics Investigation." *The Arabian Journal for Science Engineering* 35, n0. 1B (2009): 339-351.

Penerbit Akademia Baru

Engineering Science and Technology
Conference Proceedings

Journal homepage: www.akademiabaru.com/EST.html

The Effect of Downcomer Depth Variation with Air Entrainment Process on Vertical Plunging Water Jet with a Height of 28 Cm on the Water Surface.

Open Access

Warjito[1], Rhesa Giovani [1,*]

1 Department of Mechanical Engineering, Faculty of Engineering, Universitas Indonesia, Kampus Baru UI, Depok, 16424, Indonesia

ABSTRACT

Advances in flotation and water treatment technology are increasing very fast. Micro-bubbles are this environment-friendly technology. Micro-bubbles are often used to distinguish useful materials from other materials in the separation process. As found in flotation, bubble characteristics determine the separation process so it is important to investigate the phenomenon of bubble production. One way to produce bubbles is to use the phenomenon of air entraiment. The purpose of this study is to determine the parameters that affect air entrainment events, namely the relationship between downcomer depth and jet air entrainment speed using a jet height of 28 cm. The experimental setup consisted of pump, nozzle, downcomer, flow meter and standing water. Videos and photos are obtained using a backlit camera and video represents data. A processing program analyzes information in the form of images to obtain qualitative and quantitative data to process quantitative data using the imageJ image processing program. The results showed that jet height and downcomer depth affected air train levels, bubble penetration depth and bubble size.

Keywords:

Air entrainment rate; bubble dispersion, bubble penetration depth; vertical plunging jets

Copyright © 2019 PENERBIT AKADEMIA BARU - All rights reserved

1. Introduction

Technological developments continue to occur along with the development of the times. This development was followed by the utilization of natural resources in producing certain energy. The resulting impact can damage the environment and disturb the balance of nature. This causes environmental damage a special concern for the world community. This special attention is realized by creating technologies that are environmentally friendly and save energy consumption. One such technology is microbubble whose research has long been carried out by many researchers. Microbubble has characteristics that are safe against environmental damage. In addition, microbubble also has a wide application field. Not only is it used to advance technology in an environmentally friendly manner, but it also improves the environment that has been damaged by the use of natural resources that were previously not environmentally friendly.

Microbubble is an air bubble with a diameter of less than 200 µm in water (Elisabeth, 2010). The unique characteristics of microbubble have led to the rise of the use of microbubble in the industrial world. Microbubble is most widely used in the field of gas exchange between two phases, namely, the gas and liquid phases. The high ratio of surface area to microbubble volume is one of

* Correspondent author.
E-mail address: rhesagiovani@yahoo.co.id (Rhesa Giovani)

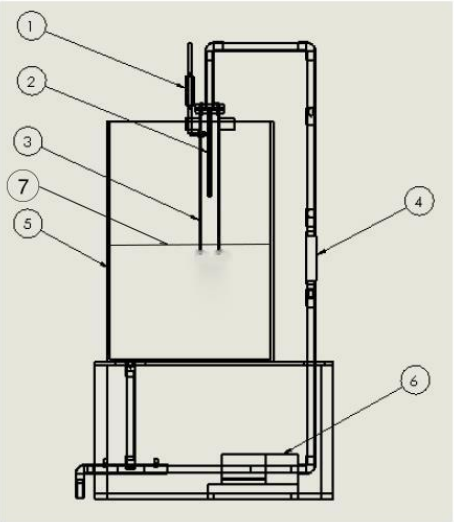
the characteristics of microbubble, which allows transportation phenomena so that it can be used to reduce energy requirements, especially in various forms of applications such as aeration of wastewater, separation of oil emulsions, and evaporation dynamics (Stuart dynamics) (Stuart) Brittle, Pratik Desai, Woon Choon Ng, Alan Dunbar, Robert Howell, Vaclav Tesar, William B. Zimmerman, 2015). In addition, microbubble is also widely applied in the biomechanical field such as utilizing oxygen contained in microbubble to create osteoblastic cell culture (Kosaku Kurata, Hiroyashu Taniguchi, Takanobu Fukunaga, Junpei Matsuda, Hidehiko Higaki, 2007).

Microbubble is an environmentally friendly technology. Microbubble is an air bubble with a diameter of 10-50µm (Agrawal, Ashutosh. Wun Jern Ng. Yu Liu, 2011). Microbubble can be said to be environmentally friendly technology, because microbubble can produce free radicals that are very reactive without having to use hazardous materials.

2. Methodology

In the Air Entrainment research conducted using a vertical plunging jets model. Where liquid will move down to the surface of the pond. The Air Entrainment Process involves air entering through a vertically mounted downcomer pipe. And air through the flowmeter in advance to find out the volumetric rate of the flow of air into the downcomer pipe.

This research was conducted to determine and document the effects of downcomer diameter with jet height and nozzle diameter. The nozzle is inside the downcomer, and the downcomer is immersed in a holding pond that will vary in depth starting from 3 cm, 8 cm and 13 cm. Water flowing in the pipe will go to the nozzle with different discharge. Water coming out of the nozzle will form a jet, and pass through the downcomer. The nozzle used in the study is 9 mm, 12 mm and 14 mm downcomers in settings according to the research needs, with diameters of 24 mm, 34 mm and 44 mm. In addition, the jet height is also set to 22 cm, 25 cm and 28 cm.



Information

1. Air Flowmeter
2. Nozzle
3. Downcomer
4. Water Flowmeter
5. Pond
6. Water Pump
7. Height of Water

Fig. 1. Schematic Design of Experimental Equipment

The pump will be used to pump the water fluid for and circulate it. This "SHIMIZU" brand pump is capable of issuing debits of 10-18 L / min, with engine pump speeds up to 2900 RPM. The pump used is a pump from the results of previous studies that are reused.

In the piping system, PVC pipes with a diameter of 1 "are used. In the suction section, the pipe is connected by a drain from the pool vertically along the 20 cm. This pipe is joined by a 'T' connection, where one side flows to the gate valve which is parallel to the outlet pipe and laboratory drainage. The other side is connected to a horizontal pipe of 70 cm in length, and that also includes the addition of a connection with an inlet at 1.5 ". In the discharge section, the 1.5

"pipe has decreased diameter to 1" pipe extended 70 cm before the gate valve is installed. Gate valve is used to regulate the discharge coming out of the pump, so researchers can observe the discharge from the flowmeter that is already installed.

After the water has passed through the flowmeter, the water will pass through a 1 "pipe along 30 cm and have a flange attached to the end. the nozzle is connected with a 1 "pipe, and the nozzle is also wrapped with a downcomer along 700 mm, so that air trapped in the downcomer so that the phenomenon of air entrainment can occur properly.

Flowmeter used is a flowmeter with rotameter type that can measure flow of 2 LPM to 28 LPM. Downcomers installed for data collection in this study have different diameters. The diameter of the downcomer is 24 mm, 34 mm and 44 mm. The length of the downcomer at each diameter is 400 mm, 450 mm and 500 mm. For nozzles, the length used is 100 mm, and has a diameter that varies. The nozzle diameter is 9 mm, 12 mm, 14 mm. The flange diameters for all sizes are the same, that is 110 mm with a thickness of 5 mm.

Anemometer can measure air flow and air velocity with range measurements for air flow around 0 - 999,900 m^3/min and range for air velocity around 0.8 - 12.00 m/s. The frame has a size of 1000 mm x 1400 mm x 1750 mm. Then this frame is held by a 3-inch caster wheel made of PVC.

To get the best picture results when shooting air Entrainment, minimum incoming light is needed. The light needed is only from the light of the firing light which is opposite to the camera in the pool (back light) so that the Air Entrainment image obtained is as sharp as possible and easier to observe.

To obtain data as accurate as possible, the authors use a data processing application (image processing) which is software 'ImageJ' which is an open source image processing software based on Java. This software can filter images with pixels of 2048 x 2048 in just 0.1 seconds, 8-32bit in RGB color in a wide format, ImageJ offers image improvement as a choice, because of the need to take pictures at high speed (high speed photo capturing).

3. Results

The phenomenon of Air Entrainment is obtained from visual data in the form of videos that have been taken which are then processed into quantitative data. Data needs to be changed from the form of video into a frame taken from the video.

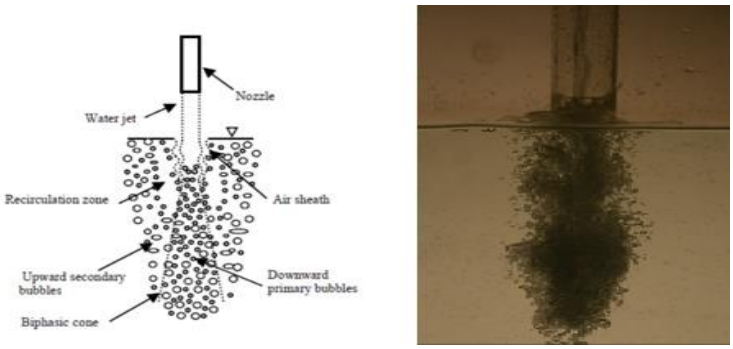


Fig. 2. Schematic Drawing of Bubble Formation

Water jets that hit the surface of a stationary water at a speed below the inception, a curve of the water-free meniscus is formed. When the jet velocity increases, the meniscus depression also increases. If the jet speed is more than the inception speed, air will be carried in the form of bubbles and the observed entrainment. Bubbles are small and follow the helicoidal path, which is around the centre line from the direction of the jet crash. The entrained bubble moves downward, slowly decelerating. When a certain point the speed becomes zero so that the bubbles rise to the surface of the water.

Based on the picture above, seen when the jet hits the surface of the pool water, the surface tension of the pool breaks, creating a vacuum in the form of cavity water. Water cavity in this study is how the surface tension breaks and the meniscus of water is carried by jets that jump from the nozzle to form a cavity. The energy that comes from the rupture of the meniscus at a certain depth, forms a torus bubble after reaching its maximum size at a certain depth. The trapped air continues to move down before it splits into smaller bubbles.

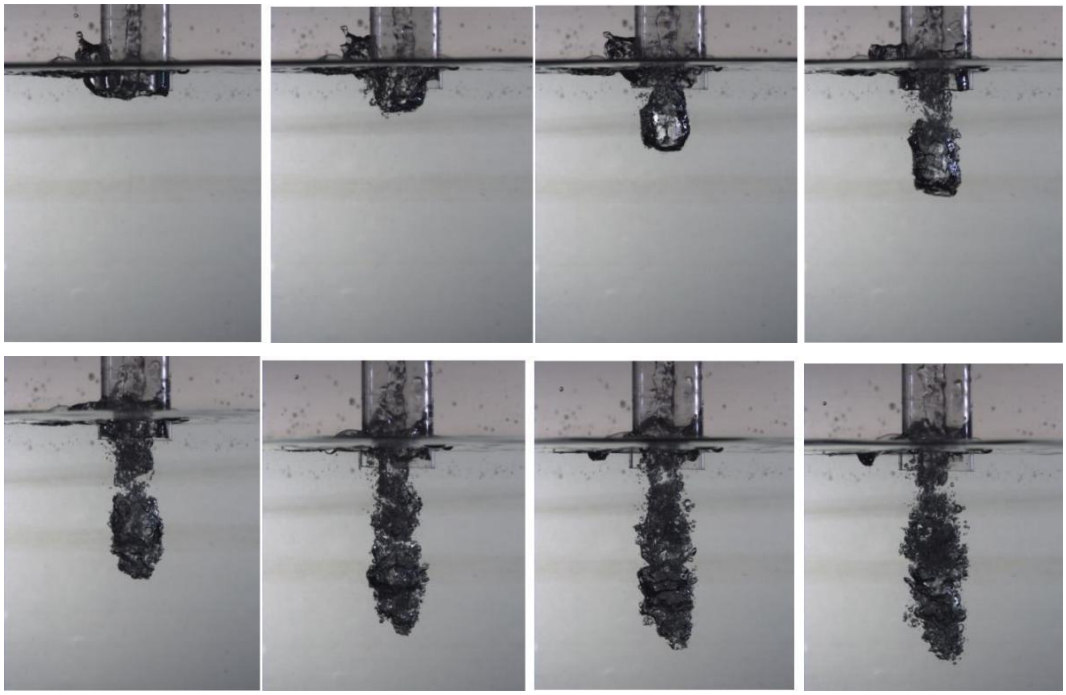


Fig. 3. Motion of Air Cavity Formation

Rupture of surface tension causes the meniscus to form a sac. The bag has a depth and width profile of depression depending on the design of the nozzle, and the function of the Reynolds number and Froude number

3.1 The Chart of Velocity Jet

From the graph the value of air entrainment rate at 9 mm nozzle diameter with a jet velocity range from 2.7 m/s to 4.6 m/s. The graph shows that the larger the diameter of the downcomer, the greater the rate of air entrainment. The value of the entrainment air rate is not always greater when the diameter of the downcomer is getting bigger.

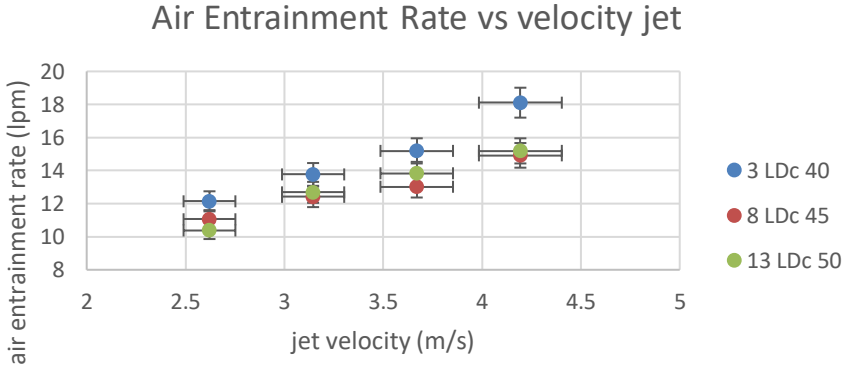


Fig. 4. Chart between Jet Velocity and Air Entrainment Rate

The graph is a comparison of jet velocity with depth of penetration at each downcomer diameter at the nozzle diameter of 9 mm. From the graph, you can see that the deepest penetration depth is at 24 mm downcomer diameter. So, when the diameter of the downcomer gets smaller, the resulting entrainment water gets smaller. So that when the jet of water crashes into the surface of the water the fewer bubbles it produces.

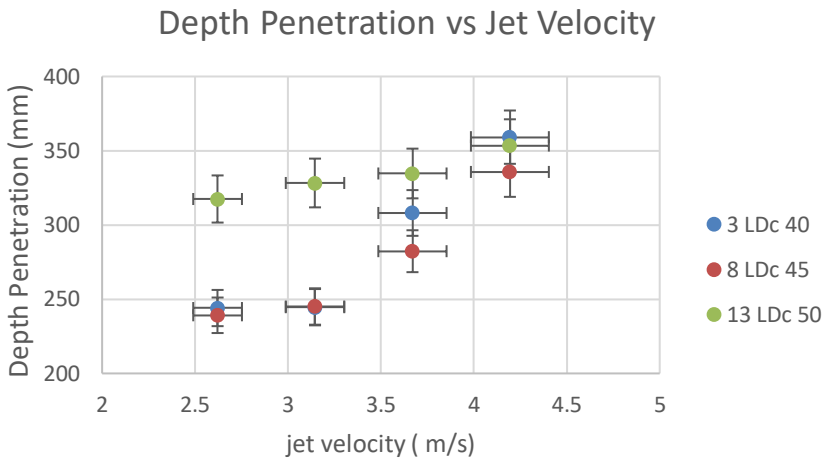


Fig. 5. Chart between Jet Velocity and Depth Penetration

The graph between the Nozzle Diameter and the Bubble disperse Area in the nozzle diameter of 9 mm with a downcomer length of 40 cm, 45 cm and 50 cm the value of the bubble dispersion area almost always increases every jet speed. The value of bubble dispersion area at 24 mm downcomer diameter is always the highest compared to other downcomer diameters. And the larger the diameter of the downcomer, the smaller the bubble dispersion area produced.

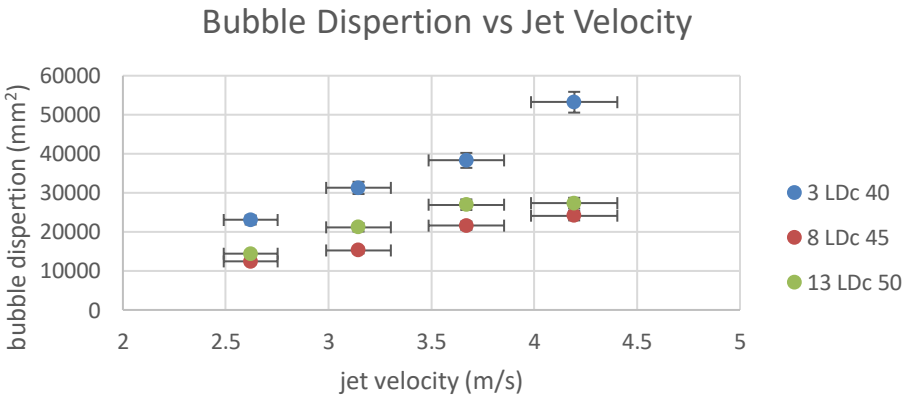


Fig. 6. Chart between Jet Velocity and bubble dispersion area

The graph shows the relationship between the water level in the downcomer and the downcomer diameter at 24 mm. with a nozzle diameter at 9 mm. Height of water enter downcomer tends to rise when the diameter of the downcomer is getting bigger, this is the greater pressure of the downcomer so that the more water entering the downcomer causes more liquid.

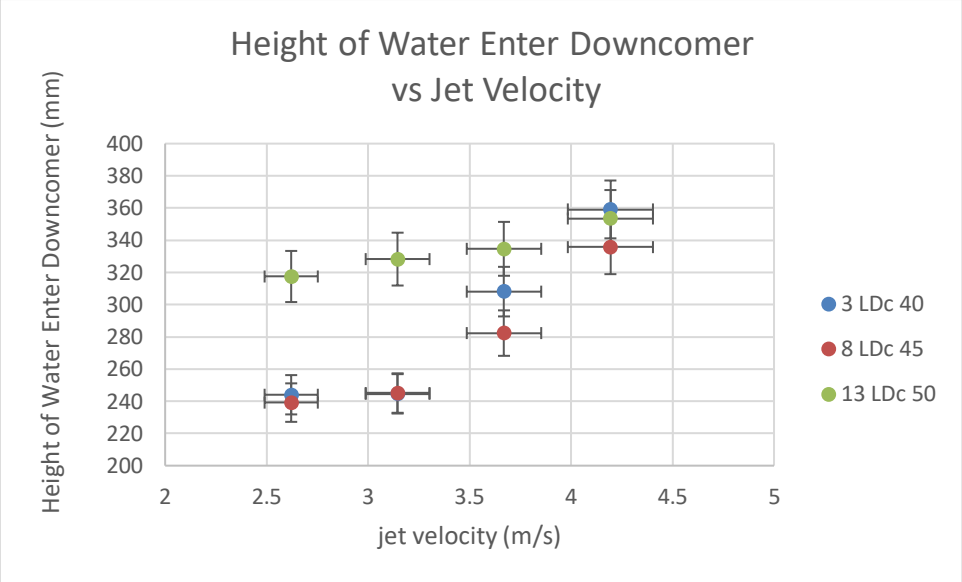


Fig. 7. Chart between jet velocity and height of water enter downcomer

Graph between the Webber Numbers with the Ratio of Water and Gas Flow Rate at the downcomer diameter of 24 mm. The points drawn on the graph are 9 mm diameter nozzles. The density value remains constant because water is used. The Qg / Qw ratio at the 9 mm nozzle affects the Webber value. The graphics depicted tend to be linear, Webber produced is not affected by the value of the ratio.

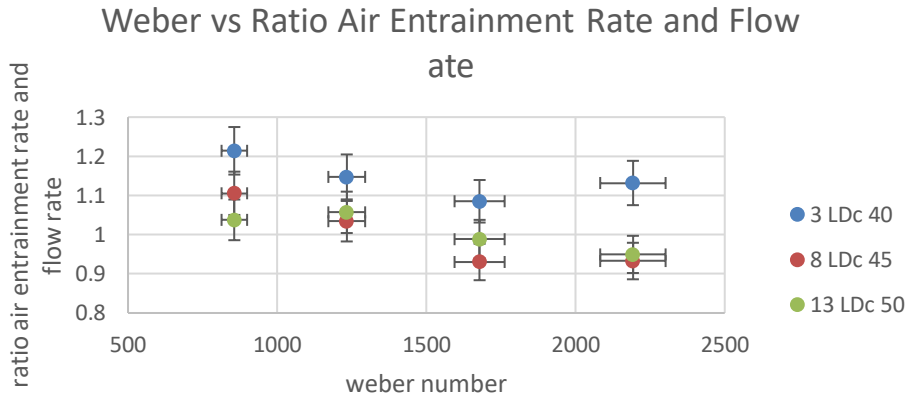


Fig. 8. Chart between weber number and ratio of water and gas flow rate

The fraud chart shows a graph between the number of fraud and the speed of the water when it hits the observation pool. The graph presented is in the diameter of a 24 mm. The graph shows linear results. From the nozzle diameter of 9 mm, 12 mm, up to 14 mm. Means the parameter velocity when striking water level is one of the parameters that affect the value of the Fraud number. The greater the value of discharge, the greater the value of velocity when striking water level. Because the speed of the mash in the observation pool is getting bigger

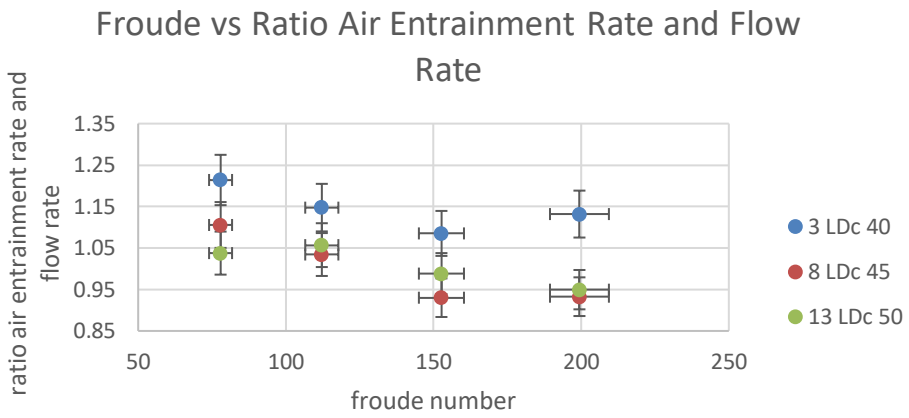


Fig. 9. Chart between fraud number and velocity when striking water level

4. Conclusions

The mechanism of the air entrainment process is when a jet hits the surface of a pond, causing surface tension to break and form an air cavity and then move down and form bubbles. The process is influenced by the diameter of the nozzle. The effect of the nozzle diameter and the immersed depth is the depth of bubble penetration and the area of bubble dispersion increasing with increasing nozzle diameter and downcomer depth but the rate of air entrainment and the height of liquid entering the downcomer decreases with increasing nozzle diameter. Non-dimensional figures (Fr and We,) increase when the nozzle diameter and the depth of the downcomer are immersed and the flow velocity increases.

References

[1] Harby, K., S. Chiva, and Jose-Luis Muñoz-Cobo. "An experimental study on bubble entrainment and flow characteristics of vertical plunging water jets." Experimental Thermal and Fluid Science 57 (2014): 207-220.
[2] Bińi, Andrzej K. "Gas entrainment by plunging liquid jets." Chemical Engineering Science 48, no. 21 (1993): 3585-3630.
[3] McKeogh, E. J., and D. A. Ervine. "Air entrainment rate and diffusion pattern of plunging liquid jets." Chemical Engineering Science 36, no. 7 (1981): 1161-1172.
[4] Smith, Amout. "March, Air entrainment with plunging jets." Delft University of Technology (2007).
[5] Setiadi, Setiadi, Hantizen Hantizen, and Dijan Supramono. "Studi Absorpsi Co2 Menggunakan Kolom Gelembung Berpancaran Jet (Jet Bubble Column)." MAKARA 12, no. 1 (2008): 31-37.
[6] Ide, Mitsuharu, Hiroki Uchiyama, and Toshifumi Ishikura. "Mass transfer characteristics in gas bubble dispersed phase generated by plunging jet containing small solute bubbles." Chemical engineering science 56, no. 21-22 (2001): 6225-6231.
[7] Lin, Tong Joe, and Harold G. Donnelly. "Gas bubble entrainment by plunging laminar liquid jets." AIChE Journal 12, no. 3 (1966): 563-571.
[8] Taşdemir, T., B. Öteyaka, and A. Taşdemir. "Air entrainment rate and holdup in the Jameson cell." Minerals Engineering 20, no. 8 (2007): 761-765.

Penerbit Akademia Baru

Engineering Science and Technology Conference Proceedings

Journal homepage: www.akademiabaru.com/EST.html

Open Access

Meshless Fluid Structural Interaction (FSI) Simulation of Deformation of Flexible Structure due to Water Dam Break

Khai Ching Ng[1,*], Lit Ken Tan[2], Wah Yen Tey[2,3]

[1] Department of Mechanical, Materials and Manufacturing Engineering, The University of Nottingham Malaysia Campus, Jalan Broga, 43500 Semenyih, Selangor Darul Ehsan, Malaysia
[2] Takasago i-Kohza, Malaysia-Japan International Institute of Technology, Universiti Teknologi Malaysia, Jalan Sultan Yahya Petra, Kampung Datuk Keramat, 54100 Kuala Lumpur, Malaysia
[3] Department of Mechanical Engineering, 1, Jalan Puncak Menara Gading, Taman Connaught, 56000 Kuala Lumpur, Malaysia

ABSTRACT

A new meshless-based solver has been used to study the deformation of flexible structure due to water dam break. This meshless Fluid Structural Interaction (FSI) solver couples the Smoothed Particle Hydrodynamics (SPH) and Lattice-Spring Model (LSM). SPH and LSM are used to model the motions of fluid and solid particles, respectively. As both are essentially particle-based methods, the force coupling at the interface is straightforward. The numerical results have been compared with the benchmark numerical solutions of dam break problem and good agreement has been found.

Keywords:
Meshless; Smoothed Particle Hydrodynamics (SPH); Lattice-Spring Model (LSM); Fluid Structural Interaction (FSI); particle method

Copyright © 2019 PENERBIT AKADEMIA BARU - All rights reserved

1. Introduction

The numerical method for simulating fluid flow can be broadly classified into two categories. The first category refers to those methods that require discretization of the entire flow domain using polygons (or meshes), or more-specifically known as the mesh-based methods. One of the common mesh-based methods is the Finite Volume Method [1-12], which is very popular amongst the CFD users. The second category does not require the use of polygons (mesh); however, computation is performed using zero-dimensional points (mesh-less method). Some examples are Moving Particle Semi-implicit (MPS) method [13-15], hybrid particle-mesh methods [16-18], Dissipative Particle Dynamics (DPD) [19, 20] and Smoothed Particle Hydrodynamics (SPH) [21, 22], to name a few. SPH is one of the oldest meshless methods that has been gaining popularity in CFD nowadays.

Likewise, the methods available in simulating solid mechanics can be broadly classified into mesh-based and mesh-less methods. Undoubtedly, Finite Element Method (FEM) can be regarded as the popular mesh-based method in studying solid deformation. Recently, the use of meshless

* *Corresponding author.*
E-mail address: ngkhaiching2000@yahoo.com (Khai-Ching Ng)

method such as Lattice Spring Model (LSM) has been gaining popularity as well [23]. The accuracy of LSM has been proven to be at par with that of FEM [24, 25].

In the current work, we intend to use the coupled SPH-LSM meshless method in simulating Fluid Structure Interaction (FSI) problem. Specifically, we intend to study the accuracy of SPH-LSM method in solving the dam-break flow involving a flexible gate.

2. Methodology

In the current work, the continuity and momentum equations are discretized using SPH:

$$\frac{d\rho_i}{dt} = \rho_i \sum_j V_j (\mathbf{v}_i - \mathbf{v}_j) \cdot \nabla_i W_{ij} \tag{1}$$

$$m_i \frac{d\mathbf{v}}{dt} = -\sum_j (V_i^2 + V_j^2) \frac{P_i\rho_j + P_j\rho_i}{\rho_i + \rho_j} \nabla_i W_{ij} + \sum_j (V_i^2 + V_j^2) \frac{2\mu_i\mu_j}{\mu_i + \mu_j} \frac{\mathbf{v}_i - \mathbf{v}_j}{\|\mathbf{r}_{ij}\|} \nabla_i W_{ij} \cdot \frac{\mathbf{r}_{ij}}{\|\mathbf{r}_{ij}\|} + m_i \mathbf{g} \tag{2}$$

Where V is the fluid volume, m is the fluid mass, $\mathbf{v}$ is the fluid velocity vector, ρ is the fluid density, P is the fluid pressure, $\boldsymbol{r}_{ij}$ denotes $\boldsymbol{r}_i$–$\boldsymbol{r}_j$, $\boldsymbol{g}$ is the gravitational vector and μ is the fluid viscosity. The quintic spline kernel function [26] was used to represent W.

In order to model the solid motion, each solid particle was connected with its neighbouring solid particles via springs as shown in Figure 1. Here, the spring stiffness for horizontal and vertical springs are denoted as k_L and the spring stiffness for diagonal spring is denoted as k_D. These particles would then serve as the dummy particles in SPH for enforcing no-slip and no-penetration boundary conditions. Details can be found in [27]. Following the LSM method [24] for 2D plane strain problem, the following spring stiffness values can be obtained.

$$k_L = \frac{2E}{1+\upsilon} \tag{3}$$

$$k_D = \frac{E}{1+\upsilon} \tag{4}$$

$$T = \frac{E(4\upsilon - 1)}{(1+\upsilon)(1-2\upsilon)(2+\sqrt{2})^2} \tag{5}$$

Here, the stiffness T was introduced to simulate the elastic behaviour at arbitrary Poisson ratio. These stiffness values are dependent on Young's modulus E and Poisson ratio v.

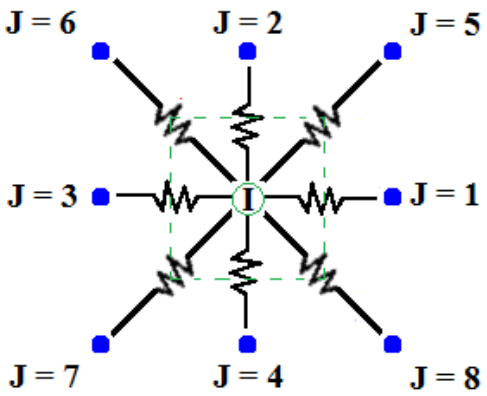


Fig. 1. Spring network in the solid body

3. Results and Discussion

The SPH-VCPM solver has been developed and it was applied to solve the dam break flow involving a flexible structure. This test case is attractive as the experimental data of the gate displacement is available [28]. Also, previous researchers [29] have done validations on their SPH-FEM FSI solver using this test case as well. Figure 2 shows the size of the water column before collapsing, whereby its width (W) and height (H) were fixed at 0.1 m and 0.14 m, respectively. The following fluid properties were employed: μ = 0.001 Pa.s and ρ = 1000 kgm^{-3}. There is a hinge at the top of the flexible gate. In order to model the hinge, the top elastic gate particles were connected with the neighbouring stationary dummy particles as shown in Figure 2. The thickness and the height of the flexible gate were fixed at 0.005 m and 0.079 m, respectively. The material properties of the flexible gate were fixed as: E = 12 MPa, ν = 0.40 and ρ = 1100 kgm^{-3}. A uniform particle spacing of 1.0 mm was used. A monitor point was placed at the free end of the flexible gate. Its displacement with respect to time was then monitored as time progresses. The flow computation was executed until t = 0.4 s.

Figure 3 compares the simulated displacement values against those obtained from the SPH-FEM solution [29]. Overall, the agreement is very encouraging. While the agreement between SPH-VCPM and experimental data is good at t < 0.08 s, our numerical results are somewhat lower than those measured at t > 0.08 s. This could be due to the 2D plane-strain assumption made in our current model. In addition, we anticipate that the model can be further improved if the flexible gate is modelled using the hyperelasticity model, as Yang and his co-workers [29] have shown that the hyperelasticity model could give better accuracy.

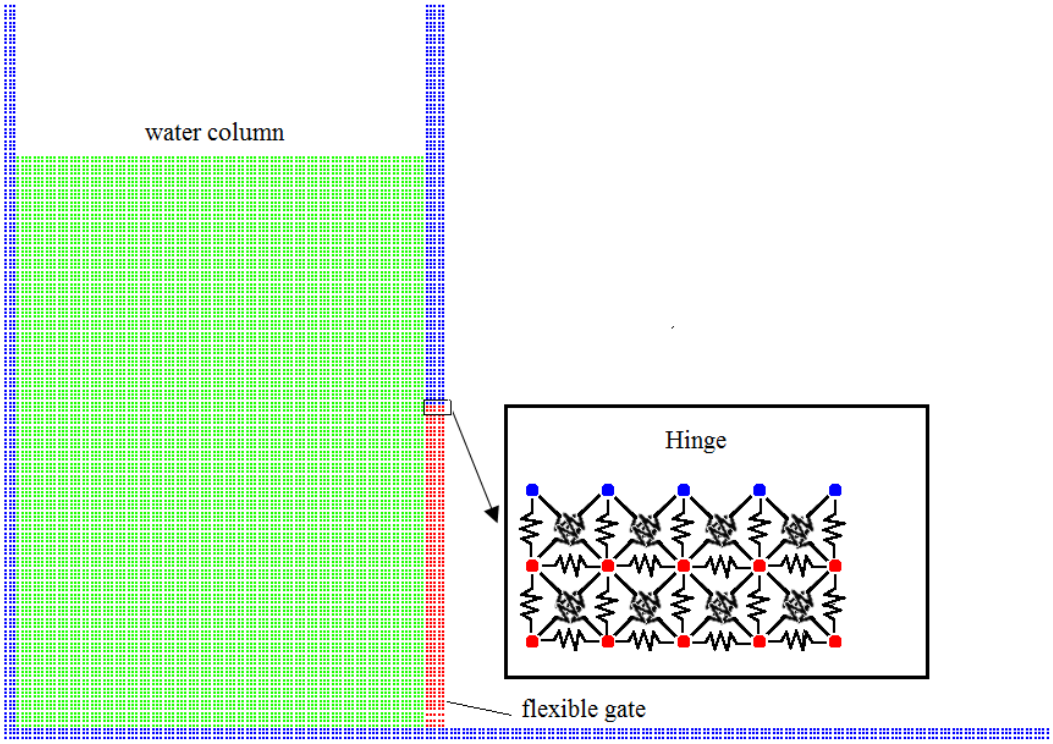
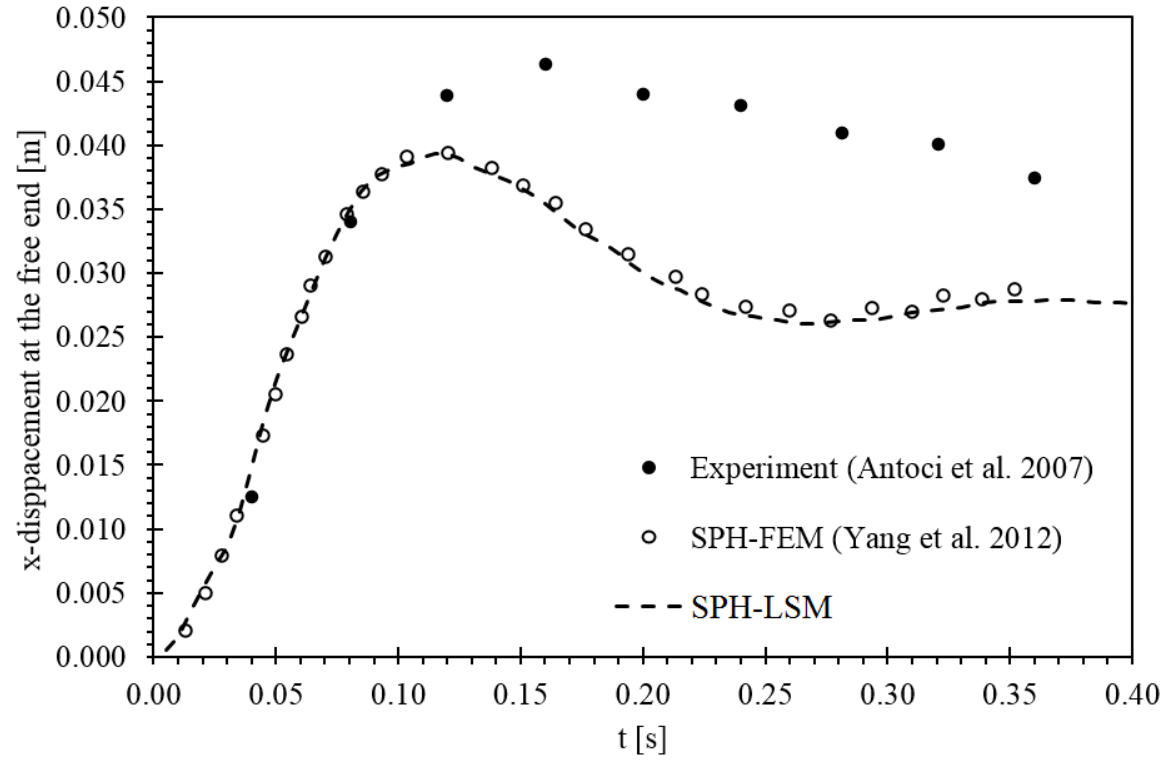
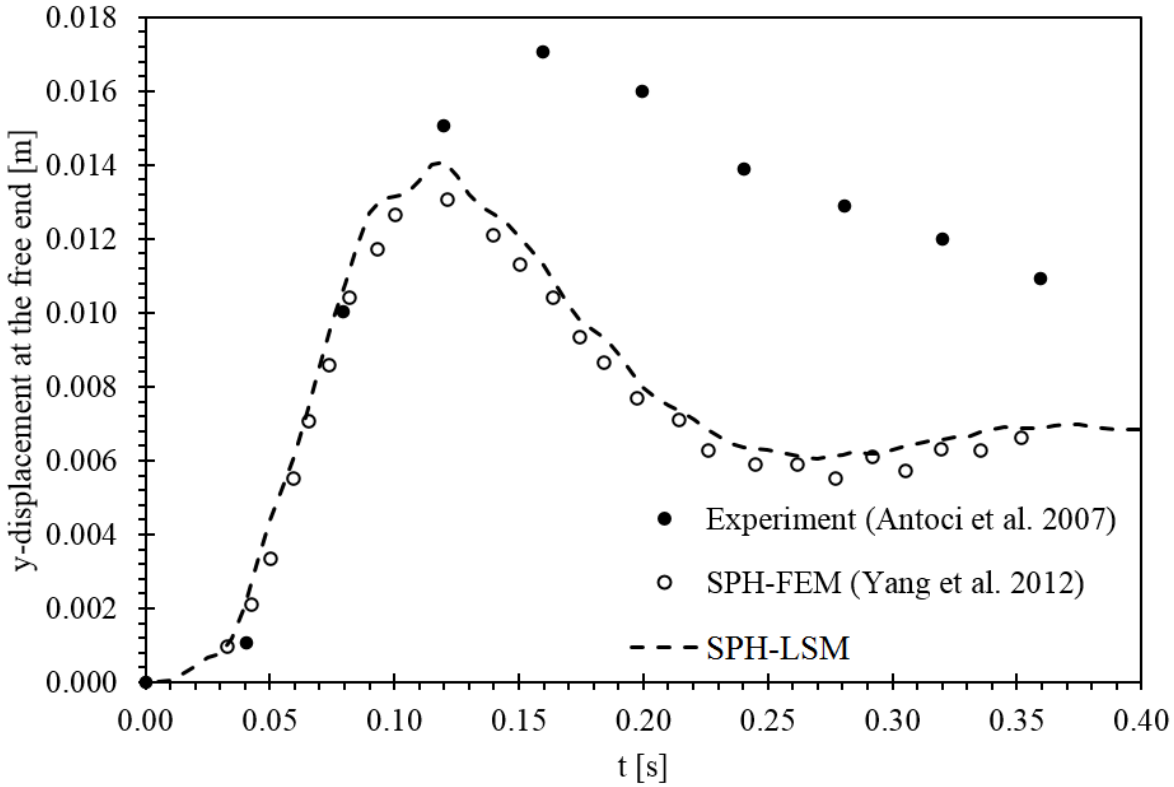


Fig. 2. Initial positions of particles (red: flexible gate; blue: fixed wall; green: water)



(a)



(b)

Fig. 3. x- (a) and y- (b) displacements at the free end of the flexible gate

Acknowledgment

The authors would like to thank Takasako i-Kohza research fund [Vote No: R.K130000.7343.4B365] and Universiti Tenaga Nasional (UNITEN) for providing the computational facility in performing the simulation work.

References

[1] W.Y. Tey, Y.W.H. Ryan, Y. Asako, H.S. Kang and K.C. Ng. "Analysis on computational efficiency of convection discretisation schemes in simple algorithm." *Journal of Advanced Research in Fluid Mechanics and Thermal Sciences* 58, no. 1 (2019): 100-117.

[2] Eymard, Robert, Thierry Gallouët, and Raphaèle Herbin. "Finite volume methods." *Handbook of Numerical Analysis* 7 (2000): 713-1018.

[3] K.C. Ng, E.Y.K. Ng, M.Z. Yusoff, and T.K. Lim. "Applications of high-resolution schemes based on normalized variable formulation for 3D indoor airflow simulations." *International Journal for Numerical Methods in Engineering* 73, no. 7 (2008): 948–981.

[4] Barth, Timothy, Raphaèle Herbin, and Mario Ohlberger. "Finite volume methods: foundation and analysis." *Encyclopedia of Computational Mechanics Second Edition* (2018): 1-60.

[5] A. Mukhtar, K. C. Ng, and M.Z.Yusoff. "Design optimization for ventilation shafts of naturally-ventilated underground shelters for improvement of ventilation rate and thermal comfort." *Renewable Energy* 115 (2018): 183-198.

[6] Droniou, Jerome. "Finite volume schemes for diffusion equations: introduction to and review of modern methods." *Mathematical Models and Methods in Applied Sciences* 24, no. 08 (2014): 1575-1619.

[7] K.C. Ng. "A collocated finite volume embedding method for simulation of flow past stationary and moving body." *Computers and Fluids* 38, no. 2 (2009): 347–357.

[8] Chris J. Greenshields and H. G. Weller. "A unified formulation for continuum mechanics applied to fluid-structure interaction in flexible tubes." *International Journal for Numerical Methods in Engineering* 64, no. 12 (2005): 1575–1593.

[9] A. Mukhtar, K. C. Ng, and M.Z. Yusoff. "Passive thermal performance prediction and multi-objective optimization of naturally-ventilated underground shelter in Malaysia." *Renewable Energy* 123 (2018): 342-352.

[10] Eymard, Robert, Tierry Gallouët, and Raphaele Herbin. "A cell-centred finite-volume approximation for anisotropic diffusion operators on unstructured meshes in any space dimension." *IMA Journal of Numerical Analysis* 26, no. 2 (2006): 326-353.

[11] K. C. Ng, Yusoff, M.Z. and E.Y.K. Ng. "Multigrid solution of Euler equations using high-resolution NVD differencing scheme for unstructured meshes." *Progress in Computational Fluid Dynamics, an International Journal* 6, no. 7 (2006): 389-401.

[12] K. C. Ng, MA Abdul Aziz, and E. Y. K. Ng. "On the effect of turbulent intensity towards the accuracy of the zero-equation turbulence model for indoor airflow application." *Building and Environment* 46, no. 1 (2011): 82-88.

[13] Hao Xiang and Bin Chen. "Simulating non-newtonian flows with the moving particle semi-implicit method with an SPH Kernel." *Fluid Dynamics Research* 47, (2015): 1-27.

[14] S. Koshizuka and Y. Oka. "Moving-particle semi-implicit method for fragmentation of incompressible fluid." *Nuclear Science and Engineering* 123, no. 3 (1996): 421–434.

[15] K.C. Ng, E.Y.K. Ng, and W.H. Lam. "Lagrangian simulation of steady and unsteady laminar mixing by plate impeller in a cylindrical vessel." *Industrial and Engineering Chemistry Research* 52, no. 29 (2013): 10004–10014.

[16] K. S. Liu, T.W.H. Sheu, Y. H. Hwang, and K. C. Ng. "High-order particle method for solving incompressible Navier–Stokes equations within a mixed Lagrangian–Eulerian framework." *Computer Methods in Applied Mechanics and* Engineering 325 (2017): 77-101.

[17] K.C. Ng, T.W.H. Sheu, and Y. H. Hwang. "Unstructured Moving Particle Pressure Mesh (UMPPM) method for incompressible isothermal and non-isothermal flow computation." *Computer Methods in Applied Mechanics and Engineering* 305 (2016): 703-738.

[18] K.C. Ng, Y.H. Hwang, T.W.H. Sheu and C. H. Yu. "Moving Particle Level-Set (MPLS) method for incompressible multiphase flow computation." *Computer Physics Communications* 196 (2015): 317–334.

[19] R. D. Groot and P. B. Warren. "Dissipative particle dynamics: bridging the gap between atomistic and mesoscopic simulation." *Journal of Chemical Physics* 107, no. 11 (1997): 4423–4435.

[20] K.C. Ng and T.W.H. Sheu. “Refined energy-conserving dissipative particle dynamics model with temperature-dependent properties and its application in solidification problem.” *Physical Review E* 96, no. 4 (2017): 043302.
[21] J.J. Monaghan. “Smoothed particle hydrodynamics.” *Annual Review of Astronomy and Astrophysics* 30 (1992): 543–574.
[22] K.C. Ng, Y.L. Ng, T.W.H. Sheu and A. Mukhtar. “Fluid-solid conjugate heat transfer modelling using weakly compressible smoothed particle hydrodynamics.” *International Journal of Mechanical Sciences* 151 (2019): 772–784.
[23] M. Xia, H. Zhou, H. Chen, Q. C. Zhang, and Q. Q. Li. “A rectangular-grid lattice spring model for modeling elastic waves in Poisson’s Solids.” *Geophysics* 83, no. 2 (2018): T69–T86.
[24] H. Chen, E. Lin, and Y. Liu. “A novel volume-compensated particle method for 2D elasticity and plasticity analysis.” *International Journal of Solids and Structures* 51, no. 9 (2014): 1819–1833.
[25] H. Chen, E. Lin, J. Yang and Y.Liu. “A generalized 2D non-local lattice spring model for fracture simulation.” computational mechanics 54, no. 6 (2014): 1541–1558.
[26] I. J. Schoenberg. “Contributions to the problem of approximation of equidistant data by analytic functions. Part A. On the problem of smoothing or graduation. A first class of analytic approximation formulae.” *Quarterly of Applied Mathematics* 4 (1946): 45.
[27] S. Adami, X. Y. Hu, and N. A. Adams. “A generalized wall boundary condition for smoothed particle hydrodynamics.” *Journal of Computational Physics* 231 (2012): 7057–7075.
[28] Antoci, Carla, Mario Gallati, and Stefano Sibilla. "Numerical simulation of fluid–structure interaction by SPH." *Computers & Structures* 85, no. 11-14 (2007): 879-890.
[29] Q. Yang, V.Jones, and L. McCue. “Free-surface flow interactions with deformable structures using an SPH-FEM model.” *Ocean Engineering* 55 (2012): 136–147.

Penerbit Akademia Baru

Engineering Science and Technology Conference Proceedings

Journal homepage: www.akademiabaru.com/EST.html

Experimental Investigation In Improving Thermal Performance Of Passive Heat Removal System Of VVERs Using Mist Assisted Evaporative Cooling

Open Access

Akram H. Abed[1,2,*], Sergey E. Shcheklein[1], Valery M. Pakhaluev[1]

[1] Department of Nuclear Power Plants and Renewable Energy Sources, Ural Power Engineering Institute, Ural Federal University named after the first President of Russia B. N. Yeltsin 19 Mira St., Yekaterinburg 620002, Russia
[2] Department of Electromechanical Engineering, University of Technology, Baghdad, Iraq

ABSTRACT

Demands to increase the safety and reliability of the modern nuclear reactors are constantly being made. Typical demands include the increases the thermal performance of the passive heat removal system PHRS by removing larger amounts of energy and applied a technique that leads to reduce size and weight of the PHRS unit. An experimental investigation on the natural convection has been conducted using an alternative cooling approach by water mist, which takes advantage of the substantial latent heat of water evaporation. The effect of water mist rate on the heat transfer enhancement has been investigated for (j=20.48 – 97.85 kg m^{-2} hr^{-1}) while the Rayleigh number varies from (Ra = $18 \cdot 10^2$ ~ $12 \cdot 10^3$). The results obtained from the related experimental work indicated that the heat transfer rate was enhanced over that for the airflow as a result of water mist evaporation on the tubes surface. The Nu number increases by about 148%, 144%, and 128% respectively for all tube rows compared with airflow under (j=97.85 kg m^{-2} hr^{-1}). The experimental results of the thermal performance factor values obtained by suspended water mist were correlated as functions of Rayleigh number (Ra) and Weber number (We). Subsequently, the predicted thermal performance factor from the correlation was plotted to compare with the experimental data. It was found that thermal performance factor was within ±11%.

Keywords:
PHRS; water mist; thermal performance factor

Copyright © 2019 PENERBIT AKADEMIA BARU - All rights reserved

1. Introduction

After Fukushima Daiichi disaster, the passive heat removal system PHRS become very important in nuclear power plants NPPs to improve the safety and reliability of the nuclear reactors. The PHRS is aimed to protect the primary circuit by removing the decay heat from the reactor core in an emergency shutdown or blackout conditions [1]. In the Water-Water Energetic Reactor-WWER or VVER design, the PHRS system comprises of four independent coolant circuits, each one involves heat exchange modules, air gates, steam pipelines and air ducts to supply the ambient air and bleed the heated air as shown in figure 1. In normal operation conditions of NPPs, the air gates are closed and PHRS circuits are in a standby mode. During NPPs blackout condition, the steam that is generated in the steam generator (SG) due to the released heat from the reactor core and subtracts its heat to the ambient air by PHRS system. The heat dissipation from the outer surface of the PHRS to surrounding air based on natural forces, such as gravity and buoyancy induced-natural

* *Corresponding author.*
E-mail address: akraaam82@yahoo.com (Akram H. Abed)

circulation without any external power. Unfavorable several ambient factors such as air temperature, solar radiation, crosswind, rain, and snow can indeed be affected on the PHRS operation mechanism [2]. In hot-arid or subtropical climates regions such as Iran, Bangladesh, Egypt, Saudi Arabia, etc, with high ambient temperature (Up to 45°C in summer) have an additional challenge when designing the PHRS modules. Accordingly, advanced cooling technologies are needed to meet the operating conditions and developing more compact and efficient PHRS that are still working at high ambient air temperature. In this study, a water droplet cooling technique or (water mist cooling technique) were developed by suspending fine water droplets into the working fluid. The water mist techniques, not a new cooling concept and has been successfully applied in many industrial applications [3–6]. However, the application of water mist techniques related to a PHRS not common, and limited numerical and experimental investigations [7–10] are found on the PHRS performance enhancement by applying various techniques including (grooves, ribs, and extended surfaces, etc.). Utilizing water mist as a cooling medium provides excellent cooling approaches to dissipate heat even larger than the single-phase air cooling approaches. To simulate the PHRS modules, a staggered horizontal tube bundle consists of three rows were designed and fabricated. In the experimentation, the influence of surface temperature and the water mist rate on free convection heat transfer characteristics were investigated.

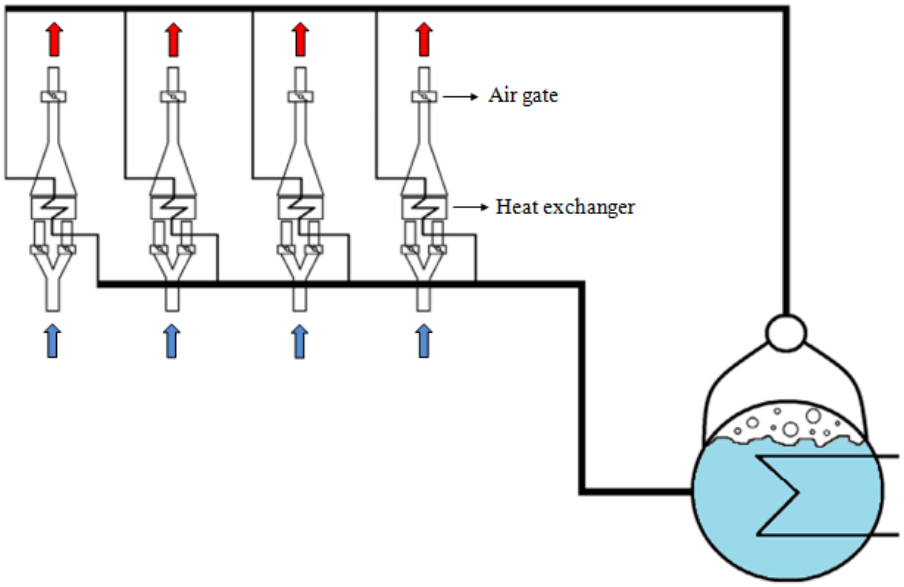


Fig. 1. The simplest diagram of PHRS.

2. Experimental apparatus and methodology

An experimental apparatus has been constructed to simulate the PHRS and investigate the water mist effect on natural convection heat transfer characteristics. The experimental apparatus mainly consists of an isolated channel having a rectangle cross-section of 117 x 55 mm is set vertically, tube bundle, heating element, data acquisition system and water mist system. The staggered tube bundle consists of three rows of tubes of 14mm outside diameter and 55 mm length. The test tube was constructed from a copper rod and each one was heated internally by using A.C. cartridge heater with 100W maximum power. The pitches of the tube bundle were chosen to be 2.14 and 2.85 of tube diameter in the transverse and longitudinal directions. To measure the surface temperature, Eight k-type thermocouples are implanted on the backside of the tubes with 180° from the forward stagnation point. All thermocouples are connected to a data acquisition system

that consists of a signal input module with a data logging system. Water mists with micro-sized (2–10µm) were suspending in the air by an ultrasonic mist generator comprises of a piezoelectric atomizing transducer that generates a high-frequency oscillation of 1.7MHz, and sprays the water away from the water surface to produce a natural floating water mist without any heating or mechanical agent. Due to the low energy needed and a very quiet operation condition compared to other mist and evaporative generators, this type of mist generator was selected. Based on the capillary wave theory, the increases of the ultrasonic wave's frequency lead to decreases the capillary wavelength; thus, the finer mist is generated at higher frequencies. Lang [11] proposed an equation to obtain the count median diameter (CMD) of the generated water mist depends on the ultrasonic frequency as formula (1):

$$d_p = 0.34\left(\frac{8\pi\sigma}{\rho f^2}\right)^{1/3} \quad (1)$$

Where σ - the surface tension coefficient, and *f*- the working frequency of the ultrasonic mist generator. When analyzing the interaction between the water mist flow and heated surface, it is usually considered an equation in the form of total heat carried by the mixture and water mist evaporation rate [12].

$$Q = \alpha_k \cdot S \cdot (T_s - T_i) + r \cdot \beta \cdot (x_s - x_{sat.}) \quad (2)$$

Where α_k - the water mist heat transfer coefficient, *S*- surface area, $T_s - T_i$ -surface temperature and input mixture temperature, *r* - the latent heat of evaporation, β- mass transfer coefficient, $X_s - X_{sat.}$-moisture content of saturated air by temperature Ts – Ti. According to Lewis number, equation (2) can be written as:

$$\frac{\alpha}{\beta} = C_p = 1,005 + 1,8 \cdot x_{sat.} \cdot 10^{-3}) \quad (3)$$

$$Q = \alpha_k \cdot S \cdot (T_s - T_i) + r/C_p \cdot n \cdot (x_s - x_{sat.}) \quad (4)$$

With a high water mist rate, the water droplets can partially settle on the tube surface without evaporation in the boundary layer. Taking into account the heating of the water mist settling in the form of separate droplets or a water film to the surface temperature, the resulting heat flux from the cooled surface can be defined as:

$$Q = \alpha_k (T_s - T_\infty) + j\left[r + C_{p,w}(T_s - T_\infty)\right] \cdot n \quad (5)$$

The corresponding heat transfer coefficient can be defined as:

$$\alpha = \frac{q}{(T_s - T_\infty)} = \alpha_k + \alpha_r \left[1 + \frac{C_{p,w}(T_s - T_\infty)}{r} \right].n \tag{6}$$

$$\alpha_r = \frac{j \cdot r}{(T_s - T_\infty)} \tag{7}$$

Where j – the water mist rate. The Rayleigh number (Ra) can be determined as follow:

$$Ra = Gr \cdot Pr \tag{8}$$

$$Ra = \frac{\Delta T \cdot \rho^2 \cdot g \cdot \beta \cdot d_{sp}^3}{\mu^2} \cdot \frac{\mu \cdot c_p}{k}; \beta = -\frac{1}{\rho_\infty}\left(\frac{\partial \rho}{\partial T}\right)_p \tag{9}$$

The Weber number is defined as (10):

$$We = \frac{1}{N}\sum_i^N \frac{j^2 d_p}{2\rho_w \sigma} \tag{10}$$

According to the Moffat and Kline [13-14], the uncertainty analyses of the experimental results are performed by computing the error associated with the measured variables and estimating its effect on the final uncertainty value. The maximum uncertainty in the parameters Nu, Ra are 5 % and 5.42% respectively.

$$\left(\frac{\Delta Nu}{Nu}\right)^2 = \frac{1}{Nu}\left[\left(\frac{\partial}{\partial \alpha}(Nu)\Delta\alpha\right)^2 + \left(\frac{\partial}{\partial d_s}(Nu)\Delta d_s\right)^2 + \left(\frac{\partial}{\partial k_s}(Nu)\Delta k_s\right)^2\right] \tag{11}$$

$$\left(\frac{\Delta Ra}{Ra}\right)^2 = \frac{1}{Ra}\left[\left(\frac{\partial}{\partial \Delta t}(Ra)\Delta t\right)^2 + \left(\frac{\partial}{\partial \rho}(Ra)\Delta\rho\right)^2 + \left(\frac{\partial}{\partial \mu}(Ra)\Delta\mu\right)^2 + \left(\frac{\partial}{\partial d}(Ra)\Delta d\right)^2\right] \tag{12}$$

3. Results and Discussion

An experimental investigation on natural convection from a staggered arranged tube bundle has been conducted in air as well as water mist. Initially, the tube bundle is at a uniform heat flux and the fluid is in steady-state motion due to natural convection. The effect of water mass rate on the heat transfer enhancement has been investigated for (j=20.48 – 97.85 kg m^{-2} hr^{-1}) while the Rayleigh number varies from (Ra = $18 \cdot 10^2$ ~ $12 \cdot 10^3$) to cover a wide range of the flow. Close to each tube, there is a thin boundary layer in which the fluid temperature changes from the maximum temperature at the surface of the tube (Ts) to the fluid temperature (T∞). The heat transfer rate between the tube and the fluid is defined by the steady-state natural convection and the physical properties of the fluid are assumed to be constant.

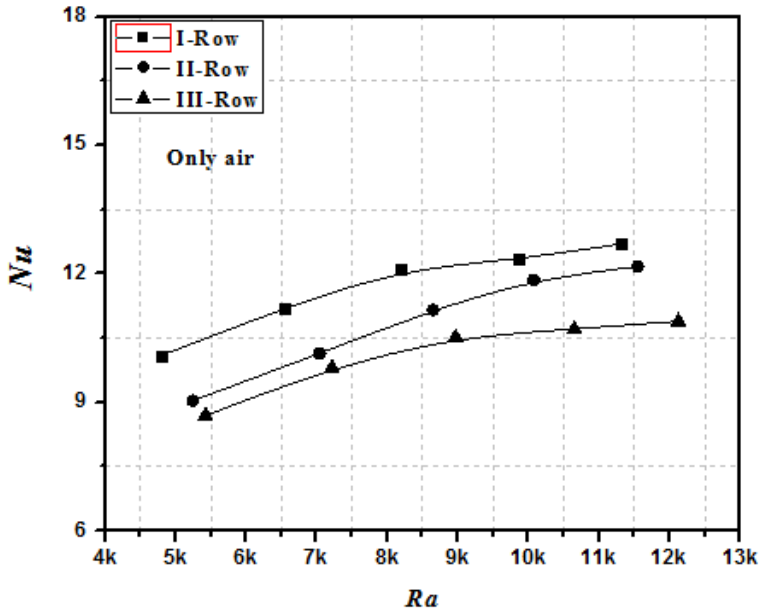


Fig. 2. Variations of Nusselt number with Rayleigh number for various tubes row.

Figure 2 depicts the Nusselt number averaged for each row of tubes bundle over natural airflow. The average Nusselt number significantly increases as the Ra number increases as expected. From this figure, it is observed that the Nusselt number of the first row is the highest among the second and third rows for all range of Ra number. This can be elucidated that the flow first touches the first row, and then the second and third rows in the upper direction, the cooling process of second and third rows can be achieved by the hot air bleed from the first one. When the tube bundle exposed to water mist flow, the effect of water mist evaporation on/near the surface of the tubes appeared and can be observed that the heat transfer rate in the terms of Nu number increases as water mist rate increases for constant heat flux as shown in figure 3. These indicated that the suspended water mist is an effective working fluid for thermal control and heat dissipation of heated surfaces. Also, it can be observed that the Nu number increases to a maximum value for all rows under a range of water mass rate and then decreases on increasing Ra number. These could be associated with the increase of the temperature difference due to water film formed on the large part of the tube's surface and posing an increased thermal resistance.

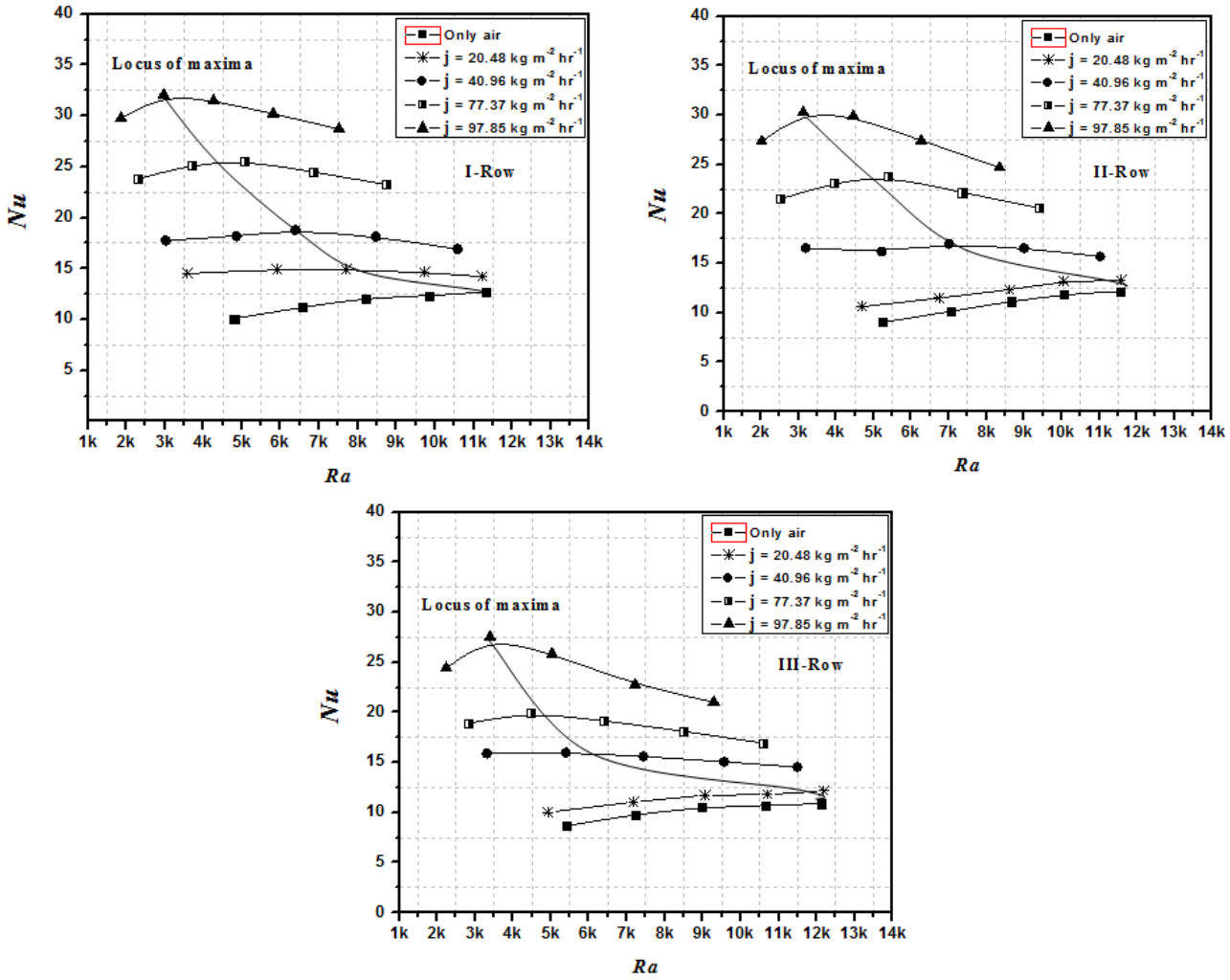


Fig. 3. Variations of Nusselt number with Rayleigh number for various water mist rate

Therefore, the maximum Nu number may occur at a certain ΔT. The Nu number increases by about 148%, 144%, and 128% respectively under (j= 97.85 kg m^{-2} hr^{-1}) for all tube rows compared with single-phase airflow. The heat transfer enhancement mechanism by water mist may include three leading physical process: water mist evaporation on the tubes surface (wet region), convective heat transfer (dry region), and reduce the air temperature from dry bulb to wet bulb temperature. The obtained experimental results provided a possibility to estimate the relative mass of water mist reaching to the surface of the tubes before they evaporate in the boundary layer.

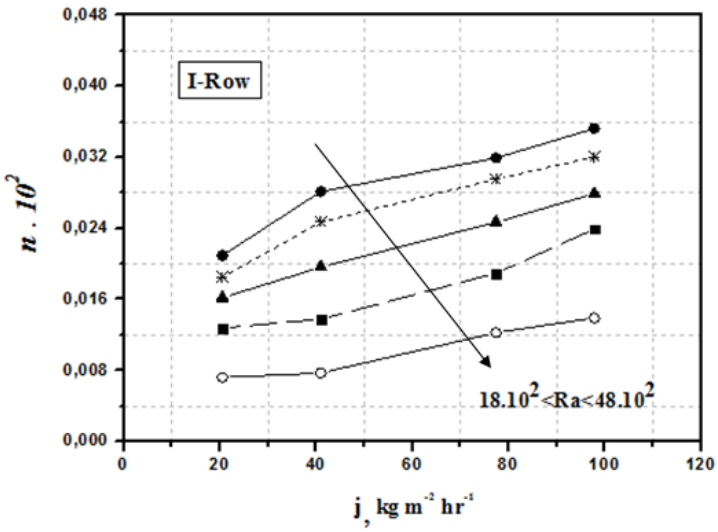


Fig. 4. Variations of the relative mass of water mist settling on the tubes surface with water mist rate

Figures 4 depicted the ratio of the effective wet area to the total heat transfer area of the tube as a function of water mist rate supply per unit area of the channel. It can be seen that the effective wet area increases as the water mist rate increases. Conversely, the effective wet area decreases as the temperature difference ΔT increases. At a low water mist rate (j= 20.48 kg m^{-2} hr^{-1}), the effective wet area is less than 2%, and the corresponding values of the Nu number were achieved as a result of water mist evaporating before reaching to the heated tubes as can be seen from figure. 3, a little differs from the corresponding values for flow without water mist. The main amount of water mist settled on the first row, which justifies the large Nu number values in comparison with the subsequent rows. The last third row almost cooled by the vapor-air flow with a minimum content of water mist as shown in figure 5.

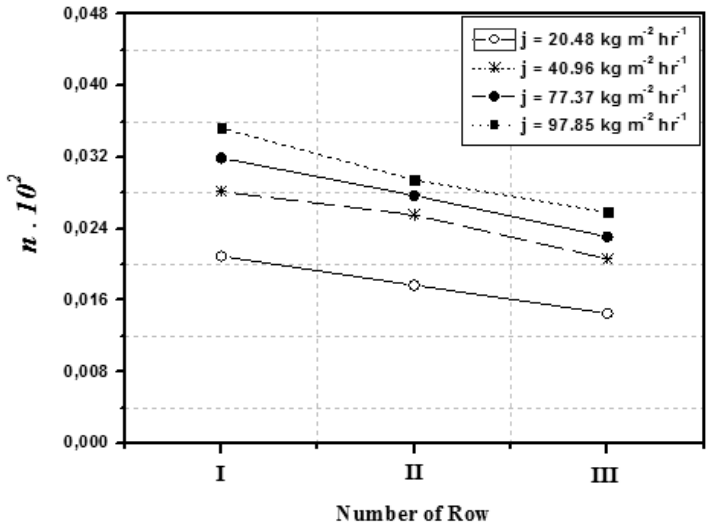


Fig. 5. Variations of the relative mass of water mist settling on the tubes surface as a function of tubes row number

The ratio of the Nu number measured of tubes exposed to water mist (Nu_m) to that when water mist was not suspended (Nu_0) at the same heat flux can be defined as the thermal performance factor. Figure 6 depicts the variation of thermal performance factor with Ra number for a range of water mist rate. It is seen that the thermal performance factor tends to increase with increasing water mist rate for all the rows depending on Ra values. The maximum performance factor of about 270% is achieved for the first row with under (j= 97.85 kg m^{-2} hr^{-1}) and is higher than the other water mist rate around 30–120%. Meanwhile, the maximum performance factor for the second and third rows about 260% and 245% is achieved with (j= 97.85 kg m^{-2} hr^{-1}). The experimental results of the performance factor values obtained by suspended water mist were correlated as functions of dimensionless Rayleigh number (Ra) and Weber number (We) as given in Eq. (13). Where the coefficient C = 1.95; 1.91 and $1.85 \cdot 10^7$ - for the first, second and third tubes bundle. These correlations of performance factor for all range of water mist rates are valid for ($Ra = 18 \cdot 10^2$ ~ $12 \cdot 10^3$) with absolute deviations between the experimental and predictions data are as shown in figure 7.

$$\frac{Nu_m}{Nu_0} = 1 + CRa^{-0.79}We^{0.67} \tag{13}$$

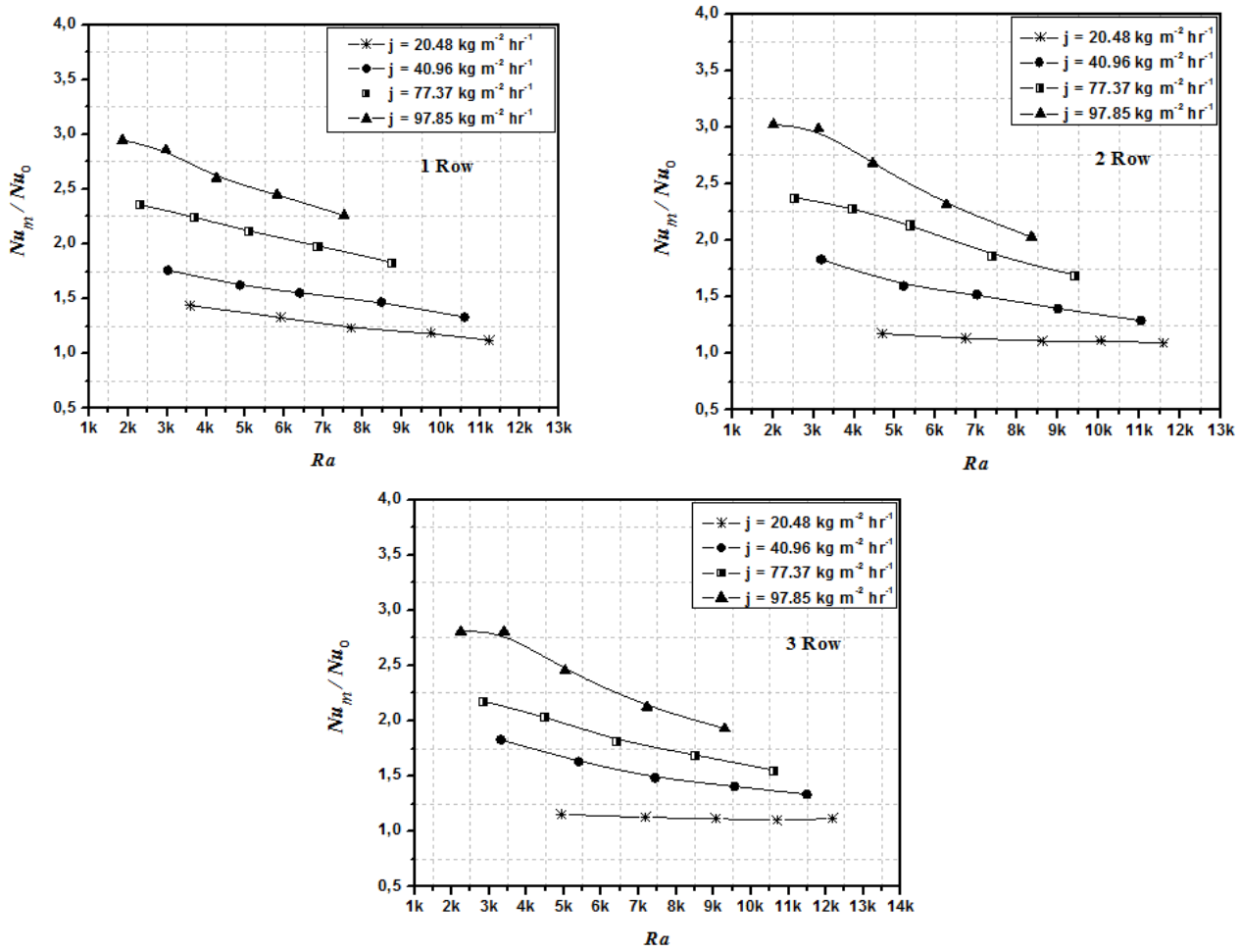


Fig. 6. Variations of thermal performance factor with Ra number for various water mist rate.

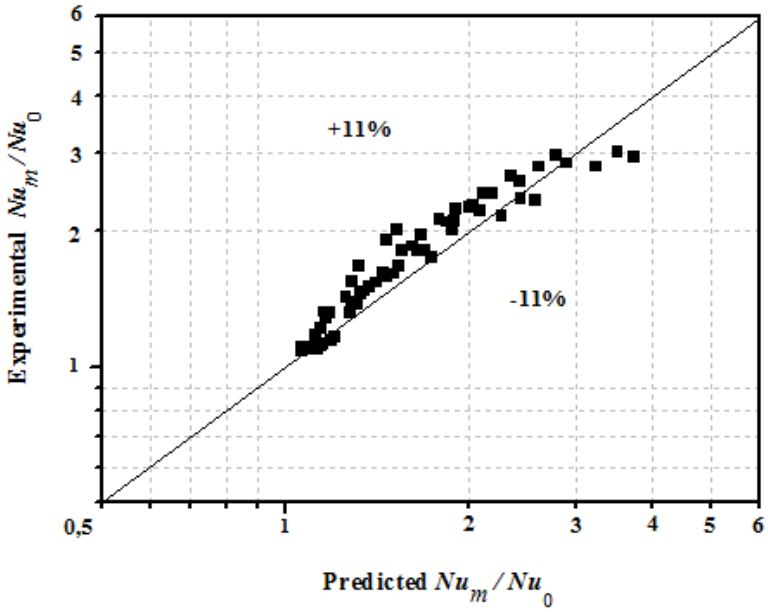


Fig.7. Comparison between predicted and experimental thermal performance factor.

The test configuration for this experiment is in Table 1. Nevertheless, for the experiment at Reynolds number of 2×10^6, the angle of attack was limited to $\alpha = 23°$ only.

4. Conclusions

In this study, the water mist was suspended into the airflow and their effect on the natural convection heat transfer performance of the tube bundle was investigated experimentally. The attention was focused on the micro-sized and low rates of water mist (j=20.48 – 97.85 kg m^{-2} hr^{-1}). The heat transfer rate of the tube bundle could be increased significantly by suspending water mist, the Nu number increases by about 148%, 144%, and 128% respectively for all tubes row compared with single-phase airflow under (j= 97.85 kg m^{-2} hr^{-1}). The heat transfer rate on each tube depends to a significant extent on the temperature difference ΔT. This demonstrates the importance of water film evaporation from the wetted part of the tubes surface in the heat transfer enhancement. The thermal performance increased significantly by suspending water mist, the present experimental results show up to 270% of thermal enhancement for all tubes row under a range of water mist rate. The empirical formula is derived, which correlates the performance factor as functions of dimensionless Rayleigh number (Ra) and Weber number (We).

References

[1] Bezlepkin, Vladimir, Sergey Semashko, Sergey Alekseev, Marina Ivanova, Teimuraz Vardanidze, and Yuriy Petrov. "Improvement of the System for Passive Heat Removal Through Steam Generators (SG PHRS) on NPP With VVER-1200 in the Light of "Fukushima" Accident." In 2014 22nd International Conference on Nuclear Engineering. American Society of Mechanical Engineers Digital Collection, 2014.

[2] IAEA (2012). "Natural Circulation Phenomena and Modelling for Advanced Water Cooled Reactors". IAEA-TECDOC-1677.

[3] Kumari N, Bahadur V, Hodes M, Salamon T, Kolodner P, Lyons A and Garimella S V. "Analysis of evaporating mist flow for enhanced convective heat transfer." Int. J. Heat Mass Transf. 53, no. 15-16 (2010): 3346–3356.

[4] Kim K. H., Ko H. J., Kim K., and Perez-Blanco H. "Analysis of water droplet evaporation in a gas turbine inlet fogging process." Appl. Therm. Eng. 33, no. 34 (2012): 62–69.

[5] Bian Q, Wang J, Chen Y, Wang Q and Zeng M. "Numerical investigation of mist/air impingement cooling on ribbed blade leading-edge surface." Journal of Environmental Management 203. (2017):1062–1071.
[6] Hayashi Y., Takimoto A., and Matsuda O. (1991). "Heat transfer from tubes in mist flows." Experimental Heat Transfer. 4, no. 4 (1991): 291-308.
[7] Liu Y., Wang X., Meng X. and Wang D. "A review on tube external heat transfer for passive residual heat removal heat exchanger in nuclear power plant." Applied Thermal Engineering 149 (2019): 1476–1491.
[8] Ayhan H., and Sökmen C. N. "Investigation of passive residual heat removal system for VVERs : Effects of finned type heat exchanger tubes." Applied Thermal Engineering. 108(2016): 466–474.
[9] Ayhan H., and Sökmen C. N. "Annals of Nuclear Energy Design and modeling of the passive residual heat removal system for VVERs." Annals of Nuclear Energy. 95 (2016): 109–115.
[10] Ayhan H., and Sökmen C. N. "Investigation of passive residual heat removal system for VVERs : Effects of finned type heat exchanger tubes." Applied Thermal Engineering. 108(2016): 466–474.
[11] Lang R. J. "Ultrasonic atomization of liquid." J. Acoust. Soc. Am. 34 (1962): 6–8.
[12] Abed A. H., and Shcheklein S. E. "Experimental investigation of hydrodynamics and heat transfer characteristics of two-phase gas/liquid mist flow in a tandem arrangement of heated spheres." Bulletin of South Ural State University. Series “Power Engineering”. 19, no.2 (2019): 14–21.
[13] Moffat, R. J. "Describing the Uncertainties in Experimental Results." Experimental Thermal and Fluid Science. 1(1988): 3-17.
[14] Kline, S. J., and McClintock. "Describing Uncertainties in Single-Sample Experiments." Mechanical Engineering Journal of ASME. 75, no.1 (1953): 3–8.

Penerbit Akademia Baru

Engineering Science and Technology Conference Proceedings

Journal homepage: www.akademiabaru.com/EST.html

Study on the Performance Analysis on Dual Fuel Diesel Main Engine of Passenger Ship 3200 DWT

Open Access

Muhammad Arif Budiyanto [1,*], Agus Sunjarianto Pamitran[1] , Hadi Tresno Wibowo [1], Fahd Naufal Murtado [1]

[1] Department of Mechanical Engineering, Universitas Indonesia, Kampus Baru UI Depok, Jawa Barat, Indonesia. 16424

ABSTRACT

The idea of converting a High-Speed Diesel (HSD) or dual fuel engine into a dual-fuel retrofit use Liquid Natural Gas (LNG) as secondary fuels, especially for passenger ships is a new idea. Ministry of Transportation Republic of Indonesia (MTRI) has considered the advantages and disadvantages in terms of material run this project but, there is no analysis of engine performance conducted by MRTI to be able to convince if the project is successful in terms of economics and engineering. The aim this paper is to analyse the change of dual fuel diesel performance needs to be done in order to know other aspect consideration in converting single diesel to diesel fuel dual diesel on ship owned by Ministry of Transportation. In conducting this analysis, data from one ship belonging to MTRI were collected and analysed, and also the author uses Ansys software and also validation journals that focus on dual fuel themes so that this research can minimize the amount of error that can happen. The results of the analysis show different performance characteristics of the dual fuel engine when the engine is operated in dual fuel mode with the best mixture at 60% LNG have better power, torque, Specific Fuel Consumption, and thermal efficiency performance than other mixture and diesel itself.

Keywords:

LNG; dual-fuel engine; passenger ship

Copyright © 2019 PENERBIT AKADEMIA BARU - All rights reserved

1. Introduction

Nowadays, marine diesel oil is widely used as major fuel in marine diesel engines for ship propulsion [1,2]. According to the Indonesian Central Bureau of Statistics, ship calls of port in Indonesia in 2017 reached 842,08 thousand unit or increased by 6,73 percent in 2017 [3]. This resulted in the need for fossil fuels in Indonesia will continue to increase and inversely proportional to the declining availability of fossil fuels. The use of gas fuel in modern transportation has been introduced in the world for a long time [4]. The use of natural gas as fuel is the main solution to reduce fossil fuel consumption due to the declining number of fossil fuels but increased gas fuel production from 1800 BCM (Billion Cubic Meter) to 2500 BCM in the Asia Pacific within 10 years and also consumption is increasing in the last 10 years [5].

The Ministry Transportation of Republic Indonesia (MTRI) aims to regulate national shipping that provides sea transportation services, including passenger transport services, and inter-island cargo. Currently, the company under the MTRI operates approximately 26 passenger ships, 46 pioneer ships, 6 sea freighter ships, and 1 livestock vessel [6]. The fuel used in all of the company's vessels is diesel oil with single fuel main engines ie engines that use one type of fuel. The use of

* *Corresponding author.*
E-mail address: arif@eng.ui.ac.id (Muhammad Arif Budiyanto)

main engine vessels that use DF engines (dual fuel) is one solution to reduce the use of fossil fuels [7,8]. Without having to change the main engine, single fuel engine conversion into dual fuel can be done with retrofit in the form of spark plug installation and gas injection on a used diesel engine [9–11].

The performance analysis of the single fuel dual-fuel engine conversion into dual-fuel was carried out on a 3200 DWT passenger vessel to determine the performance ratio on this ship's engine after retrofitting based on diesel fuel usage used by 3200 DWT passenger vessels with mixed use of diesel and gas. The main purpose of this research is to analyze the change in performance of dual fuel diesel engines in the percentage variation of LNG and diesel fuel consumption compared with 100% diesel usage on 3200 DWT passenger vessels as a parameter of consideration in academic terms.

2. Basic Theory

2.1 Dual-fuel Diesel Engine

The dual-fuel diesel engine is a diesel engine fueled by gas in the intake manifold or directly into the combustion chamber and ignition is done by a spray of diesel oil [12,13]. The addition of fuel to the combustion chamber to reduce the function of diesel in the combustion process. Apart from reducing the use of diesel fuel, folding fuel gas and reducing the negative emissions resulting from combustion. When the dual fuel diesel engine works in gas mode, it works by loading air and gas and also a bit of diesel fuel into the combustion chamber. At the time this engine works in diesel mode, diesel fuel alone is sprayed into the combustion chamber. The development of a dual-fuel diesel engine was started there in 1987 by Wartsila with the first concept of gas diesel engine, and the first dual-fuel engine was introduced in 1995 [14].

Dual fuel engine technology can be used as fuel and also diesel at the same time and also in rotation mode on this machine, which can be done without loss of power or speed on the machine [15]. One device used on this machine is a diesel pilot that aims to spray a little diesel on the surface of the room with the aim that it can occur in the compression process. The goal is that spraying diesel is not done in gas mode, incomplete combustion in the combustion chamber.

In Figure 1, the shift on dual diesel engine fuel engines in the same game as the diesel engine in general. However, in the intake phase, not only air enters the combustion chamber in this phase, natural gas has entered the combustion chamber.

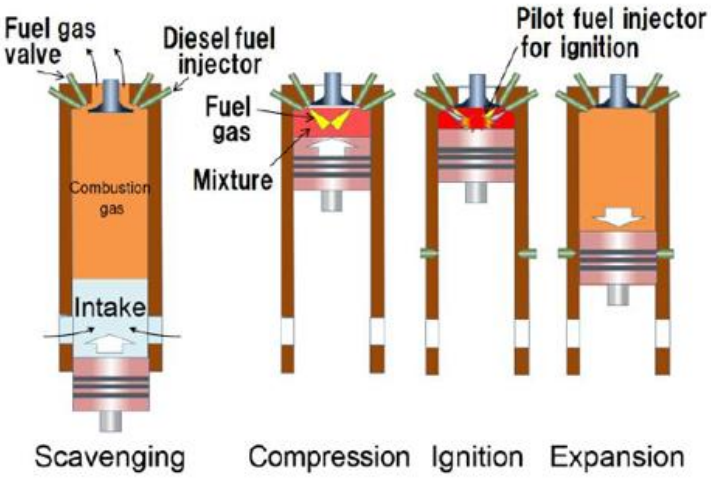


Fig. 1. Step work dual-fuel diesel engine [16]

2.2 Piston Profile Movement

Volume change on the piston based on rake angle change is a parameter required to know the piston pressure at the time of compression of the fuel to know the pressure on the piston. Changes in piston volume based on rake angle can be formulated in equation (1) [17]:

$$v(\varphi) = Vmin + \frac{Vpiston}{2.r}.\left[r.(1-cos\varphi) + l.\left(1-\sqrt{1-\left(\frac{r}{l}\right)^2.sin^2\varphi}\right)\right] \quad \text{.....(1)}$$

Where v min is the piston clearance volume and v piston is the piston volume, ϕ is the angle of the crank angle, and l is the length of the connecting rod.

To know the magnitude of the pressure that occurs in the cylinder based on each piston position when the incidence of combustion, obtained from equation (2) [18]:

$$p = p0\ x\ Cr^{\gamma} \quad \text{.....(2)}$$

Where p is the pressure in the cylinder prior to the combustion, the Cr value is a large value of the compression ratio and also γ is the value of the specific ratio of heat fluid. The amount of pressure that occurs on the piston after the fuel has been compressed is influenced by motor pressure characteristics, volume change, and also the type of fuel.

2.3 Engine Performance

One important paratemer of the reciprocating engine is the mean effective pressure (MEP) value which means that the pressure acting on the piston will produce the same net work value at the actual cycle. The value of MEP can be formulated with equation (3):

$$MEP = \frac{Wnet}{Vpiston} \quad \text{.....(3)}$$

By knowing the value of MEP, it can be seen also equations related to MEP in the form of equations (4) and (5):

$$MEP(kPa) = \frac{P(kW)nR\ x\ 10^3}{Vd(dm^3)N\left(\frac{rev}{s}\right)} \quad \text{.....(4)}$$

$$MEP(kPa) = \frac{(6.28.nR.T(N.m))}{Vd(dm^3)} \quad \text{.....(5)}$$

The Specific Fuel Consumption is the amount of fuel consumed in units of time to convert into a large power (kw) on the machine [19]. The Specific Fuel Consumption can be written in equation (6):

$$SSFC = \frac{\dot{m}(a)+\dot{m}(b)}{Power} \quad \text{.....(6)}$$

Where the values of a and b represent two different types of fuels used in the primary machine. In thermodynamics, thermal efficiency is a dimensionless measure that shows the performance of

thermal equipment such as internal combustion engines and so on. The incoming heat is energy derived from energy sources. The desired output can be either heat or work, or maybe both. Thus, thermal efficiency can be formulated by equation (7):

$$\eta th = \frac{Power\ x\ 100\%}{[\dot{m}(a)\ \ \text{Fuel Heating Value}(a)]+[\dot{m}(b)\ \ \text{Fuel Heating Value}(b)]} \quad \text{.....(7)}$$

3. Research Methods

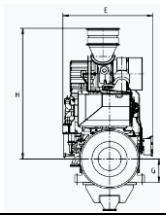
3.1 Engine Specification

The work of this paper will require some data before then the data can be processed and analysed, with the main data provided by the MTRI in the form of related vessel data which became the review of thesis work and also fuel consumption on the vessel during sailing. The vessel to be analyzed is an Inter-island Sailing Ship owned by the Ministry of Transportation, which is a 3200 DWT passenger vessel with specification in Table (1) and engine data in table (2).

Table 1. Ship particular dimension

LOA	: 146.5 meter
LBP	: 130 meter
B	: 23.4 meter
T	: 5.9 meter
Tmin	: 4.35 meter
DWT	: 3200 ton
Vs	: 17.6 knots

Table 2. Engine specification

Main Engine		
Type	Krupp-MaK 6M601C	
Power	6400kW/428rpm	
Bore	430 mm	
Stroke	610 mm	
Specific fuel consumption	177 g/kWh	

3.2 Simulation Process

Ansys Fluent software is chosen for use in completion with some considerations in the form of this software can model 3-dimensional flow, and also in completing the simulation of the combustion process in the piston chamber, this software can be used because it can provide accurate results [20]. To do the modelling on this software, there are several steps that must be done in the form of create geometry and mesh on the model, checking the mesh model, choosing the right formulation, select the basic equations to be used and analysed, determine the type of material on the model, determine the boundary condition, iterates [21,22]. Modeling is important in using Ansys software. In doing the modeling, the objects depicted in this software must have the same geometry with the original object. This results in prior to the drawing, it is necessary to review the data to reduce the form of errors that can occur later.

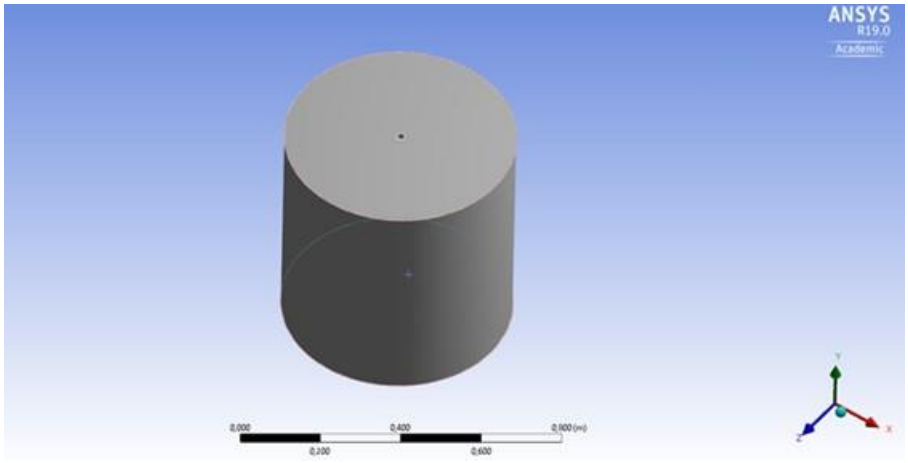


Fig. 2. Piston Model

In Figure (2) it is a modeling using DesignModeller that has one package in the fluent. In this case, the component to be analyzed is a diesel piston cylinder because it is related to combustion in a diesel engine. Therefore the depiction is done in three dimensional form with the geometry resembling the original.

3.3 Meshing and Set Up

Performing meshing on a model object aims to model divided into small parts in order to influence the accuracy of CFD analysis. The smaller the object is divided, then the accuracy of the analysis on this software will be more accurate [23,24]. In Figure (3) we can see the model already in mesh.

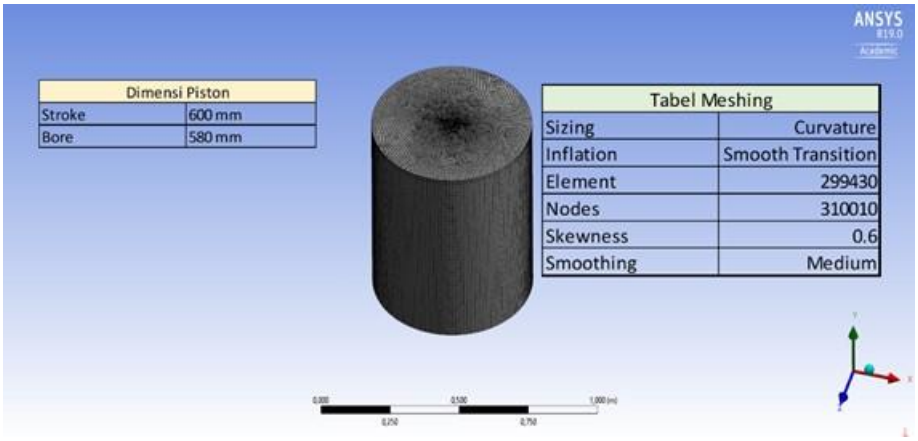


Fig. 3. Mesh set-up of piston model

Before performing simulations on Ansys software, setup on this software is essential for simulation to work on the conditions we want. In this process, we determine any formulation which is influential during the simulation process that runs in Fig.4. Changes in piston volume, type of fuel used, and pressure changes are formulations included in this process. Equation.1 and equation.2 are parameters included in this process with the aim of limiting the movement occurring in later simulations.

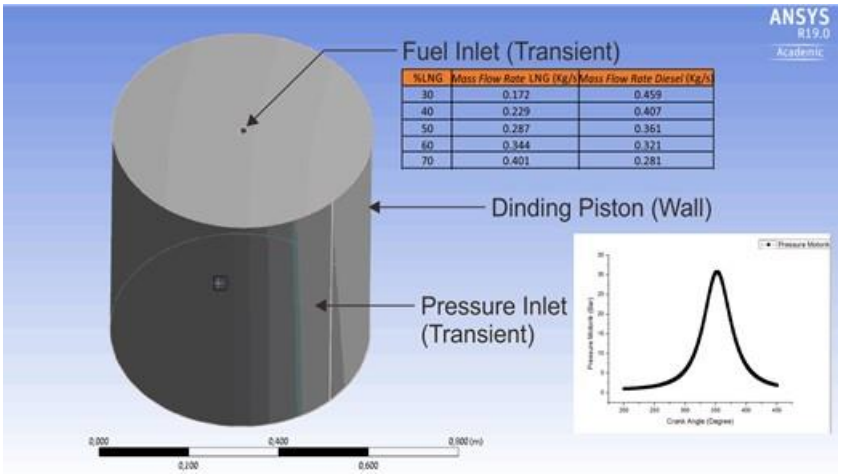


Fig. 4. Set up of boundary condition

4. Results and Discussion

Measuring the performance value of dual fuel diesel engines in this study was obtained by calculating using the formula that has been used in the research chapters. This study was conducted based on data provided by the company. The parameters used are to determine the value at the 30%, 40%, 50%, 60%, and 70% used LNG-diesel mass fraction used by the dual fuel engine of the 3200 DWT passenger vessel. The mass flow rate value is calculated and obtained based on data provided by the MTRI. From the data provided, the use of fuel based on the duration of the trip in one voyage, then processed to get fuel consumption every second.

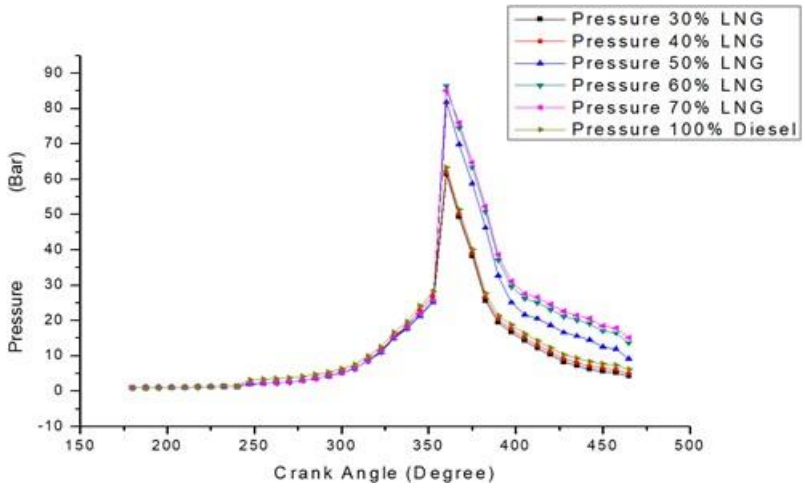


Fig. 5. Piston Pressure vs Crank Angle

At figure 5, the angle of the crank angle starts at 270 ° to 450 °. At an angle of 270 ° is the condition where the piston is undergoing a compression step that is the reduction of the volume of the piston chamber in order to increase the pressure. The compression step ends at a 360 ° angle because at this angle, the piston is at the top dead center and is unlikely to re-compress. After passing the 360 ° angle, the piston moves toward the bottom dead center to perform the working step until the angle reaches 540 °. At the angle of the crank angle is 270 °, the pressure on the piston begins to rise, but the rise of the pressure has a sloping trend. The increase continues to occur at an angle of 350 °. After passing through the 350 ° angle, the increase in pressure occurs

significantly. This is indicated if at the angle crank angle is going on the process of combustion. The pressure rise has a peak value at 360 ° angle. After passing the 360 ° angle, the piston pressure decreases this due to volume expansion resulting in the pressure inside the piston decreasing.

The pressure height values in each LNG-diesel variation vary. In a 30% LNG mixture, the maximum pressure generated at the combustion is 60,000 Pa, but with the addition of flow rate from LNG, the pressure on the cylinder increases up to 80,000 Pa in the 60% LNG mixture. Increased pressure on the cylinder in line with the addition of mass flow rate in LNG is due to the value of lower heating value in LNG greater than diesel which will result in LNG energy will be greater than diesel generated energy.

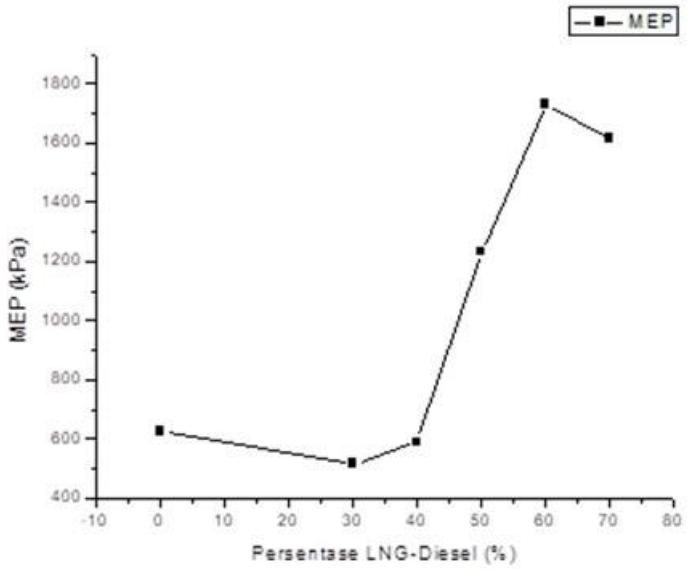


Fig. 6. MEP on Dual Fuel Condition

The value of the mean effective pressure obtained on each percentage of LNG-Diesel fuel consumption has different values. The value of the mean effective pressure is only influenced by the work net generated by each percentage of fuel due to the same combustion chamber at each percentage percentage of the fuel. The net work value obtained by each percentage of fuel has a relation to pressure in Figure 6. Because, the greater the pressure reached in a combustion cycle, the greater the value of the net work that can be generated. The percentage of 30% LNG-diesel fuel has a mean effective pressure value of 515.88 kPa. Then, as the LNG flow rate added into the combustion chamber, the mean effective pressure value increases until the 60% percentage of fuel has a mean effective pressure of 1730.63 kPa.

The relationship between the graph of the mean effective pressure also has an effect on the torque obtained. Percentage of fuel use condition with percentage 60% has torque of 23424.15 NM and at 30% usage condition having torque of 6982.52 NM. Can be seen from the trend of the graph when the addition of LNG flow mass into combustion chamber, at a certain point can add torque to the engine the big difference in torque obtained in the percentage of 30% LNG usage and 60% usage, the torque increases up to three times in figure 7.

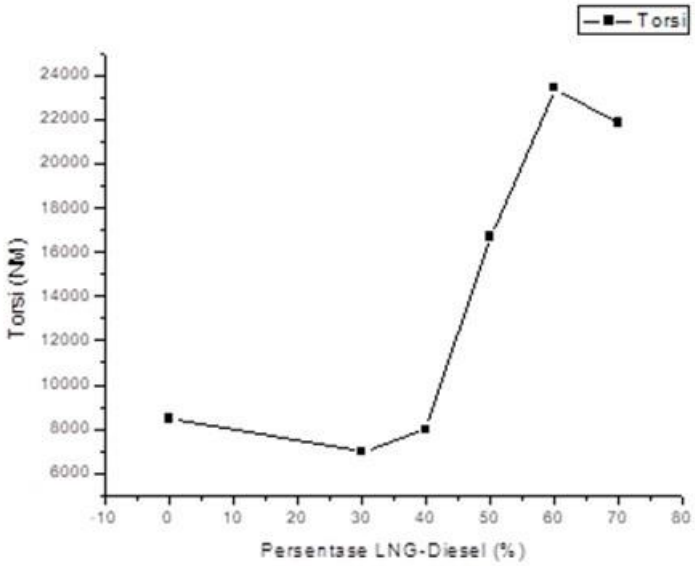


Fig. 7. Torsion on Dual Fuel Condition

Another relationship that has an effect on the value of mean effective pressure is between the amount of engine power obtained. Viewed from Figure 8, the addition of LNG flow mass also affects the power performance of the engine. At 30% LNG percentage, engine power obtained based on mean effective pressure is 295.98 Kw. And at 60% LNG percentage has power of 992.94 Kw. From the graphic form obtained can be seen if the addition of LNG into the combustion chamber can increase the value of power in the combustion engine. The power difference between the usage percentage of 30% and 60% triples.

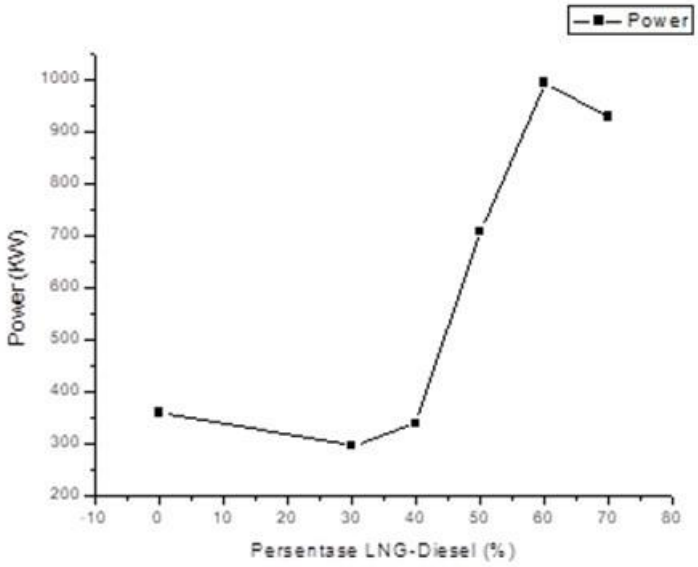


Fig. 8. Power on Dual Fuel Condition

From the three graphs obtained, the addition of LNG into the combustion chamber improves the performance of torque, power and also mean effective pressure on the combustion engine. The LNG-Diesel mass flow rate is calculated based on the data of fuel consumption given by the company and processed and then got the value, the mass flow rate of the LNG-Diesel mixture is

calculated based on the mass fraction on the mixture of both fuels and processed to obtain the specific fuel consumption graph for the percentage change of the LNG-Diesel mixture.

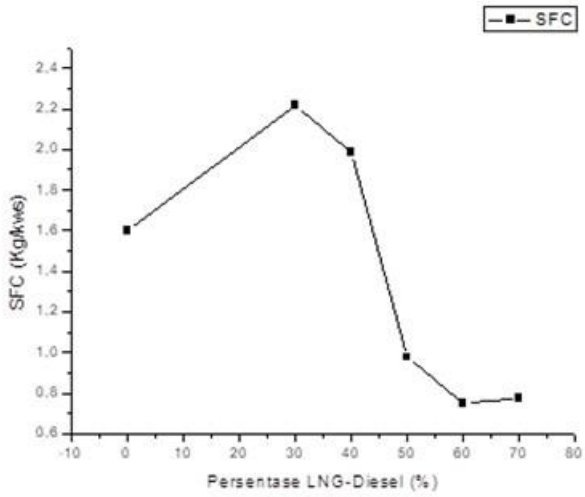


Fig. 9. SFC on Dual Fuel Condition

Lower heat value value determined by the property of the LNG fuel type and also the diesel. The amount of power in the calculation of specific fuel consumption is obtained from Figure 8. Viewed from figure 9, the specific fuel fuel value for each percentage of fuel has a different value from the range 0.74 kg / kws to 2.21 kg / kws. At the fuel consumption percentage of 30%, the specific fuel fuel consumption value is highest than the other fuel consumption percentage of 2.21 kg / kws. With the added use of LNG into the combustion chamber, the specificity fuel consumption value of the engine decreases to the smallest specificity fuel consumption value in the 60% LNG-diesel mixture of 0.74 kg / kws. In other words, the 60% LNG-diesel percentage mix is the most efficient mixture because it can get the least amount of fuel mass per second power even though this percentage has the greatest power value than any other LNG-diesel percentage.

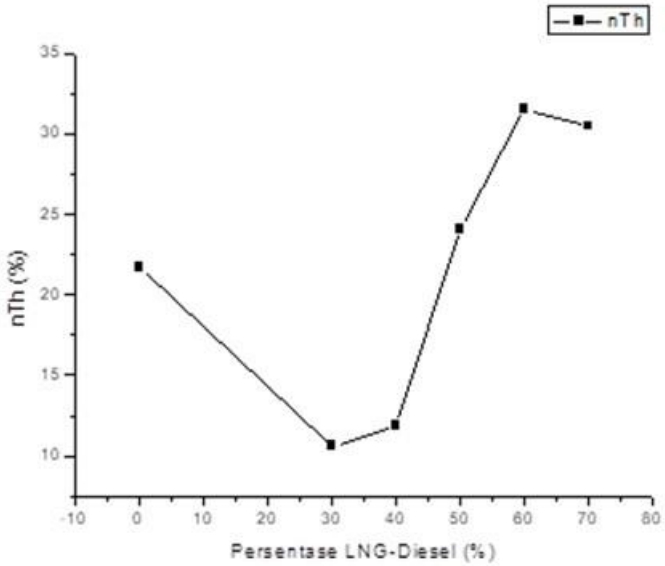


Fig. 10. Thermal efficiency on Dual Fuel Condition

The value of thermal efficiency is calculated on each percentage of LNG-diesel fuel to know how efficiently the usage is based on the amount of work performed on the given heat. In figure 10, the efficiency gained is between 10 and 31 percent. This efficiency value is calculated from the power obtained by the mean effective pressure. The smallest thermal efficiency value is obtained by the percentage of LNG-diesel fuel consumption in the 30% mixture. Then, the greatest thermal efficiency is obtained by a 60% mixture. It can be seen if the mixture of 30% and 40% has not big enough difference, but after the fuel consumption rate is increased, thermal efficiency increases and decreases at the percentage of 70% LNG-diesel usage. From the results obtained, the nett work affects the magnitude of MEP, power, torque, SFC and nTh where the increase in net work value is directly proportional to MEP, power, torque, and thermal efficiency. However, it is inversely related to the value of SFC.

5. Conclusion

The analysis of this study indicates that the characteristics of each percentage of LNG and diesel usage can be parameters in determining the performance of dual fuel diesel engines. The analysis determined based on the empirical equations of literature and simulation using software. The conclusions obtained based on simulation and analysis of this research as follows:

a) The given variation value determines 30%, 40%, 50%, 60%, 70% influence different performance changes in each variation because LNG and diesel have different fuel properties.

b) From the performance results by each variation of fuel consumption, the value of power, torque, and also the mean effective pressure is influenced by the maximum pressure that can be achieved by the LNG-diesel mixture at the time of the compression phase to the working step. In this case, the fuel that has more LNG percentage then has better performance than the fuel that has fewer LNG percentage

c) Based on the SFC graph and thermal efficiency, the addition of LNG content to this mixture results in reduced SFC values as well as increased thermal efficiency

d) The addition of LNG content to the LNG-diesel mixture largely improves engine performance because the lower heating value value of LNG is greater than the value of diesel's lower heating value.

Acknowledgement

The authors are thanks to the Directorate of Research and Community Engagement Universitas Indonesia (DPRM-UI) with grant PITTA B No: NKB-0761 / UN2.R3.1 / HKP.05.00 / 2019. Authors also grateful to Ministry Transportation of Republic Indonesia for supporting the ship data and also the Department of Mechanical Engineering Universitas Indonesia for supporting the software license.

References

[1] C.-Y. Lin, K.-H. Wang, Diesel engine performance and emission characteristics using three-phase emulsions as fuel, Fuel. 83 (2004) 537–545. doi:10.1016/J.FUEL.2003.08.012.

[2] Royal Academy of Engineering, Future Ship Powering Options Exploring alternative methods of ship propulsion, 2013. http://www.imo.org/en/OurWork/Environment/PollutionPrevention/AirPollution/Documents/Air pollution/Future_ship_powering_options_report.pdf (accessed November 27, 2019).

[3] Sea Transportation Statistic 2017, Jakarta, 2017. https://www.bps.go.id/publication/download.html?nrbvfeve=YWNlMzUyYTYyNDdlM2U5ZDQ4NTZiMzU3&xzmn=aHR0cHM6Ly93d3cuYnBzLmdvLmlkL3B1YmxpY2F0aW9uLzIwMTgvMTEvMjcvYWNlMzUyYTYyNDdlM2U5ZDQ4NTZiMzU3L3N0YXRpc3Rpay10cmFuc3BvcnRhc2ktbGF1dC0yMDE3Lmh0bWw%3D&twoadfnoarfea (accessed November 27, 2019).

[4] M.M. El-Gohary, The future of natural gas as a fuel in marine gas turbine for LNG carriers, Proc. Inst. Mech. Eng.

Part M J. Eng. Marit. Environ. 226 (2012) 371–377. doi:10.1177/1475090212441444.
[5] K. Ito, Asia / World Energy Outlook 2016, 2016. https://eneken.ieej.or.jp/data/7199.pdf (accessed November 27, 2019).
[6] PT. Pelni, Transformation Towards Higher Growth, 2016. https://admin.pelni.co.id/content/File/konten/AR_Pelni_2016.pdf (accessed November 27, 2019).
[7] J. Herdzik, LNG as a marine fuel - possibilities and problem, J. KONES. Vol. 18, No. 2 (2011) 169–176. http://yadda.icm.edu.pl/baztech/element/bwmeta1.element.baztech-article-BUJ5-0039-0022 (accessed November 27, 2019).
[8] F. Burel, R. Taccani, N. Zuliani, Improving sustainability of maritime transport through utilization of Liquefied Natural Gas (LNG) for propulsion, Energy. 57 (2013) 412–420. doi:10.1016/J.ENERGY.2013.05.002.
[9] K. Cheenkachorn, C. Poompipatpong, C.G. Ho, Performance and emissions of a heavy-duty diesel engine fuelled with diesel and LNG (liquid natural gas), Energy. 53 (2013) 52–57. doi:10.1016/J.ENERGY.2013.02.027.
[10] G.. Abd Alla, H.. Soliman, O.. Badr, M.. Abd Rabbo, Effect of injection timing on the performance of a dual fuel engine, Energy Convers. Manag. 43 (2002) 269–277. doi:10.1016/S0196-8904(00)00168-0.
[11] V. AEsoy, P. Magne Einang, D. Stenersen, E. Hennie, I. Valberg, LNG-Fuelled Engines and Fuel Systems for Medium-Speed Engines in Maritime Applications, in: 2011. doi:10.4271/2011-01-1998.
[12] A. Kumaraswamy, B.D. Prasad, Performance Analysis of a Dual Fuel Engine Using LPG and Diesel with EGR System, Procedia Eng. 38 (2012) 2784–2792. doi:10.1016/J.PROENG.2012.06.326.
[13] B. Ashok, S. Denis Ashok, C. Ramesh Kumar, LPG diesel dual fuel engine – A critical review, Alexandria Eng. J. 54 (2015) 105–126. doi:10.1016/J.AEJ.2015.03.002.
[14] WÄRTSILÄ, DUAL- FUEL ENGINES FROM WÄRTSILÄ, (n.d.). https://www.wartsila.com/encyclopedia/term/dual--fuel-engines-from-wärtsilä (accessed November 27, 2019).
[15] C.S. Weaver, S.H. Turner, Dual Fuel Natural Gas/Diesel Engines: Technology, Performance, and Emissions, in: 1994. doi:10.4271/940548.
[16] Yanmar, Dual-Fuel Marine Engine (Highly Reliable Environmentally Friendly Engine) | YANMAR Technical Review | Technology | YANMAR, (2015). https://www.yanmar.com/global/technology/technical_review/2015/0727_2.html (accessed November 27, 2019).
[17] Y. Nilsson, Cylinder volume function for SVC engines, n.d. https://www.fs.isy.liu.se/Publications/Reports/01_R_2408_YN.pdf (accessed November 27, 2019).
[18] M.J. TINDAL, O.A. UYEHARA, Diesel Engines, Intern. Combust. Engines. (1988) 101–155. doi:10.1016/B978-0-12-059790-1.50009-2.
[19] J.B. (Of the M.I. of T. Heywood, Internal combustion engine fundamentals, McGraw-Hill Education: New York, Chicago, San Francisco, Athens, London, Madrid, Mexico City, Milan, New Delhi, Singapore, Sydney, Toronto, 2018. https://www.accessengineeringlibrary.com/content/book/9781260116106?implicit-login=true (accessed November 27, 2019).
[20] ANSYS FLUENT, (2017). https://www.ansys.com/-/media/ansys/corporate/resourcelibrary/brochure/ansys-fluent-brochure-140.pdf (accessed November 27, 2019).
[21] T. Stolarski, Y. (Yuji) Nakasone, S. (Shigeka) Yoshimoto, Engineering analysis with ANSYS software, n.d. https://books.google.co.id/books?hl=id&lr=&id=50IyDwAAQBAJ&oi=fnd&pg=PP1&dq=ansys&ots=jLh1R5mZV3&sig=NFgwIiyt4ImdByrQGBX46eM9M_s&redir_esc=y#v=onepage&q=ansys&f=false (accessed November 27, 2019).
[22] A. Budiyanto, B. Sugiarto, B. Anang, Multidimensional CFD simulation of a diesel engine combustion: A comparison of combustion models, 2013. doi:10.1007/978-3-642-33750-5-5.
[23] T. Matsushima, An Automatic Mesh Generator Based CFD System to be used as a Design Tool, SAE Trans. 110 (2001) 90–98. doi:10.2307/44718310.
[24] K.-J. Bathe, H. Zhang, A mesh adaptivity procedure for CFD and fluid-structure interactions, Comput. Struct. 87 (2009) 604–617. doi:10.1016/J.COMPSTRUC.2009.01.017.

Penerbit Akademia Baru

Engineering Science and Technology Conference Proceedings

Journal homepage: www.akademiabaru.com/EST.html

Oil Reclamation of In-Service Power Transformer using Fuller's Earth: An Experience

Open Access

Sharin Ab Ghani[1], Imran Sutan Chairul[1,*], Norazhar Abu Bakar[1], Mohd Shahril Ahmad Khiar[1], Aminur Hazieq Zulkefli [1], and Asimi Ana Ahmad[2]

[1] High Voltage Engineering Research Laboratory, Centre for Robotics and Industrial Automation, Faculty of Electrical Engineering, Universiti Teknikal Malaysia Melaka, Malaysia.
[2] Chemical Engineering Technology, Universiti Kuala Lumpur - Malaysian Institute of Chemical and Bioengineering Technology, Melaka, Malaysia.

ABSTRACT

This paper described in-laboratory oil reclamation process of aged transformer oil using adsorbent; Fuller's earth. The niche of this paper is the usage of real aged transformer oil taken from an 11kV/433V in-service power transformer made by ACEC Transformer in 1986. The reclamation process is achieved by forcing a mixture of aged transformer oil and Fuller's earth through a filter paper with the aid of a vacuum pump, hence producing reclaimed transformer oil. This oil were then inserted in an amber glass bottle, blanketed with nitrogen, tightly sealed and labeled. To test the effectiveness of Fuller's earth as adsorbent, parameters of Dissolved Decay Product (DDP) were measured using UV-Visible Spectrophotometer (UV-Vis) by referring to ASTM D6802. In addition, Total Acid Number (TAN) and Breakdown Voltage (BdV) measurement were carried out complying the ASTM D974 and ASTM D1816 respectively. Results of UV-Vis indicated that Fuller's earth can adsorbed 25.24% of DDP in aged transformer oil. As the DDP decreased, TAN is 84.62% reduced while BdV increased 50%. These findings are parallel with the breakdown voltage mechanism due to acidity emergence. It is proved that Fuller's earth is effective adsorbent for oil reclamation process.

Keywords:
Aged Mineral Oil; reclamation; UV-Visible Spectrophotometer (UV-Vis); Total Acid Number (TAN); Breakdown Voltage (BdV)

Copyright © 2019 PENERBIT AKADEMIA BARU - All rights reserved

1. Introduction

Lifespan of a power transformer depends on its insulation; liquid (transformer oil) [1] and solid (cellulose-based paper/pressboard) [2]. Transformer oil such mineral oil and natural ester oil also acts as coolant for power transformer's winding due to oil ability to dissipate heat by convection [3]. Ageing of transformer oil usually cause by electrical and thermal stresses but can be speed up if humidity, high heat, oxidation and level of acidity are present in the oil [4]. Since mineral oil; a petroleum-based product is commonly used as transformer oil, ecosystem can be threatened if aged mineral oil are improperly disposed. The disposing problem can be overcome by recycling the aged mineral oil through reclamation process [5]–[7]. This process helps improving the quality of aged mineral oil by removing contaminants as well as sludge present in the aged mineral oil using various adsorbents such Fuller's earth [5], palm shell activated carbon [8] and activated bentonite

* *Corresponding author.*
E-mail address: imransc@utem.edu.my (Imran Sutan Chairul)

[7]. Although many studies have been conducted previously, the niche of this study is a reclamation process carry out on real aged transformer oil taken from an 11kV/433V in-service power transformer made by ACEC Transformer in 1986. An almost 30 year's aged mineral oil samples. The reclamation process is conducted in laboratory using Fuller's earth as adsorbent.

2. Methodology

Figure 1 shows a flowchart of research methods for this study. All works were done in a laboratory. The study starts with collecting few liters of aged mineral oil samples. This oil will be used in reclamation processes. The reclamation process is based on IEEE Guide for Reclamation of Insulating Oil [5] and [8] while works of detecting Dissolved Decay Product (DDP) using UV-Visible Spectrophotometer (UV-Vis), measuring Total Acid Number (TAN) as well as determining Breakdown Voltage (BdV) are referred to standards of ASTM D6802 [9], ASTM D974 [10] and ASTM D1816 [11] respectively. Aged mineral oil samples for this research were courtesy of Tenaga Nasional Berhad (TNB) taken from an in-serviced power transformer made by ACEC. The transformer is as shown in Figure 2(a) and 2(b). The transformer's rating is 500 kVA, 11kV/433V. Mineral oil in the transformer have undergoes ageing process for nearly 30 years because it never been filtered, replaced or reclaimed since manufactured in 1986.

Reclamation processes [5] used in this study is combination between contact process and filtration. Contact process is mixing an amount of adsorbent with aged mineral oil samples producing mixed oil. The mixing was done using digital hotplate magnetic stirrer as shown in Figure 3(a). The stirrer speed and temperature is maintained at 750 rpm and 60℃ for 4 hours so that the mixture can be homogenized. The mixed oil produced from contact process will be filtered through filtration process. Filtration is separating the mixed oil using filter paper to remove sludge (adsorbents and DDP formed during ageing of mineral oil) producing reclaimed oil. As the filter paper used (Whatman No 42) is a 2.5 μm in pore sizes, time taken for filtration process will take several days to complete. This delay can cause the mixed oil under filtration, exposed to moisture and oxidation. Therefore, the aid of a vacuum pump is used to speed up the process as well as preventing any moisture or oxidation. Figure 3(b) shows a filtration process. Mixed oil from contact process is poured directly to a fleaker. The oil is filtered through a filter paper initially put between the fleaker and a flask. A vacuum pump is connected to the flask using rubber hose to speed up the flow rate of the mixed oil as well removing air and moisture in the flask. With the aid of a vacuum pump, filtration can be completed within 2 hours.

Figure 4 shows a UV-Vis set used to determine a relative content of DDP. Initially, a cuvette is filled with 5 ml of oil sample using a syringe. Then, the cuvette is placed into the UV-Vis set. When light radiations interact with the oil sample, the passing lights are carried to the spectrophotometer through an output fiber. The fiber is connected to a screen that displaying an absorption spectrum curve. As for analysis, the absorption spectrum of oil samples are measured over a wavelength range between 360 to 600 nm in accordance with ASTM D6802 [9]. Chemical substances such Potassium Hydroxide (KOH), Isopropyl Alcohol (IPA) and Potassium Hydrogen Phthalate (KHP) are required to determine TAN in oil samples. Procedures for this test are referred as in [12]. Firstly, 5g oil samples are weighed into a titration vessel and 20 mL IPA solvent are added. The solution is then titrated using c(KOH in IPA) = 0.1 mol/L. TAN of oil samples are displayed and recorded. Figure 5 shows a TAN test set. Initially, BdV test electrodes are cleaned using acetone and dried. Next, the gap between electrodes is set to 1mm. After that, the electrodes were immersed into a beaker of 500 ml oil samples and placed into the BdV set as shown in Figure 6. The electrodes must fully

immerse into the oil and there should be no air bubbles present in the oil before BdV measurement can be done as per ASTM D1816 [11].

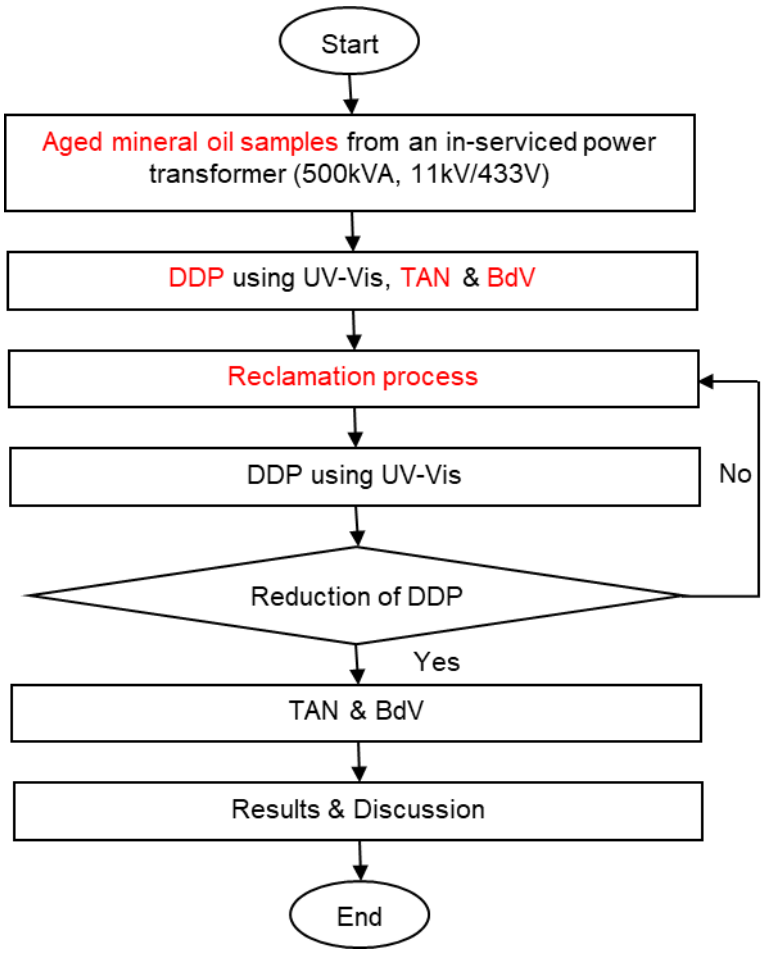
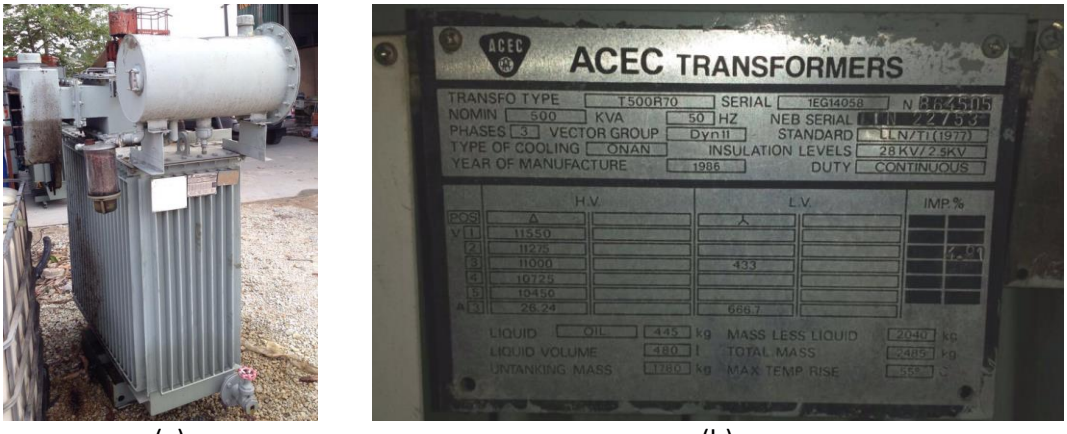
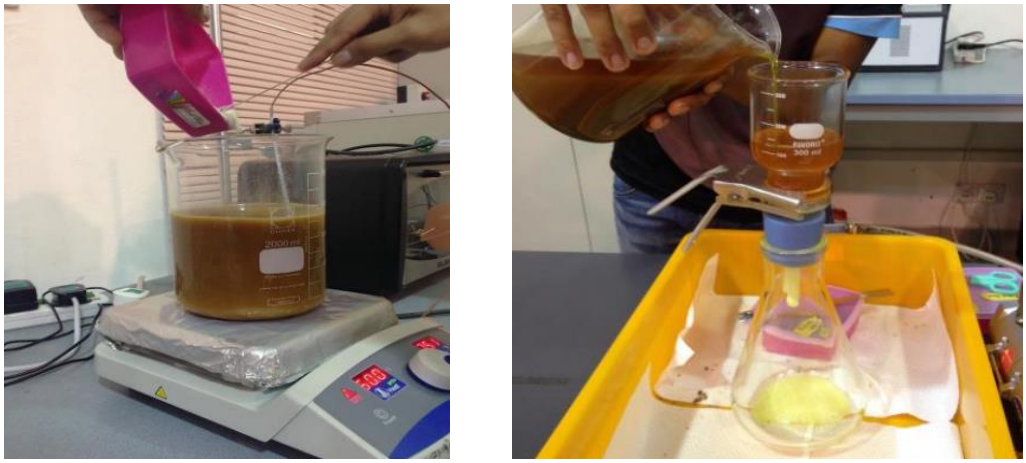


Figure 1 Flowchart of Research Methods



(a) (b)

Figure 2 (a) In-Serviced ACEC's Power Transformer (b) Nameplate of ACEC's Power Transformer



(a) (b)

Figure 3 (a) Contact Process (b) Filtration Process



Figure 4 UV-Visible Spectrophotometer (UV-Vis) Set



Figure 5 Total Acid Number (TAN) Test Set.



Figure 6 Breakdown Voltage (BdV) Set

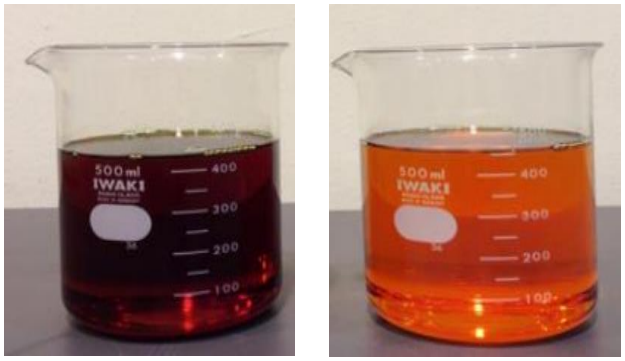
3. Results and Discussion

Parameters of Dissolved Decay Product (DDP) were measured using UV-Visible Spectrophotometer (UV-Vis) by referring to ASTM D6802[9]. In addition, Total Acid Number (TAN) and Breakdown Voltage (BdV) measurements were carried out complying the ASTM D974[10] and ASTM D1816[11] respectively. All tests were carried out on aged mineral oil samples and reclaimed oil for comparison. Regarding reclamation process, there are two (2) different oil samples were prepared namely Sample 1 and Sample 2. Sample 1 is a mixture between 100g adsorbent and 1000ml aged mineral oil while Sample 2 is a mixture of 5g adsorbent with 500ml aged mineral oil. Adsorbent used for this study is Fuller's earth from Sigma-Aldrich [13]. This adsorbent is in powder forms and harmful if exposed to skin or inhale. Thus, safety gears of mask, rubber gloves and safety goggles were worn. The weights of adsorbent were measured using digital analytical balance whereas the aged mineral oil volumes were measured using beaker. The summary on quantities of adsorbent and aged mineral oil to prepare Sample 1 and 2 are shown in Table 1. The different quantities are by referring to previous research in [7] and [14].

Table 1: Quantities of Adsorbent and Aged Mineral Oil

Oil Sample	Adsorbent (g)	Aged Mineral Oil (ml)
Sample 1	100	1000
Sample 2	5	500

Sample 1 is reclaimed once to produce reclaimed oil but Sample 2 will undergoes several cycles of reclamation process. The reclaimed oil from the first cycle of Sample 2 will be reused for the second cycle of reclamation process. During new cycle, new 5g of adsorbent is used. The process is repeated 5 times. Transformer oil is exposed to oxidation process due to present of dissolved oxygen in oil. Presence of oxidation by-product as well as deterioration of transformer oil can be indicated by colour changes of oil. Figure 7(a) shows colour of aged mineral oil (AMO) while Figure 7(b) shows colour of Sample's 1 reclaimed oil (S1RO). It shows that the colour of AMO will change from dark brown to light brown due to reclamation process. Same result is achieved for Sample's 2 reclaimed oils (S2RO) as shown in Figure 8(a)-(e). The colour is lighter after each cycle of reclamation process. This decolourized of aged mineral oil from dark to lighter brown is due magnesium and calcium ion contain in Fuller's earth.



(a) (b)

Figure 7 (a) Colour of Aged Mineral Oil (AMO). (b) Colour of Sample 1's Reclaimed Oil (S1RO).



(a) (b) (c) (d) (e)

Figure 8 (a) Colour of Sample 2's Reclaimed Oil After 1st Reclamation. (b) Colour of Sample 2's Reclaimed Oil After 2nd Reclamation. (c) Colour of Sample 2's Reclaimed Oil After 3rd Reclamation. (d) Colour of Sample 2's Reclaimed Oil After 4th Reclamation. (e) Colour of Sample 2's Reclaimed Oil After 5th Reclamation.

The wavelength range chosen for this study is between 360 nm and 600 nm as referred to ASTM D6802[9]. The absorbance unit is a value that indicates the amount of UV-light absorb by the DDP. High value of absorbance indicates high DDP. The DDP's relative content of oil samples is determined by integrating the area under an absorbance versus wavelength curves'. Figure 9 shows curves of absorbance (range of 0-4.5a.u) with respect to wavelength (range of 360-600nm) for aged mineral oil (red line), Sample's 1 reclaimed oil (green line) and Sample's 2 reclaimed oil-after 5 cycle of reclamation process (blue line).

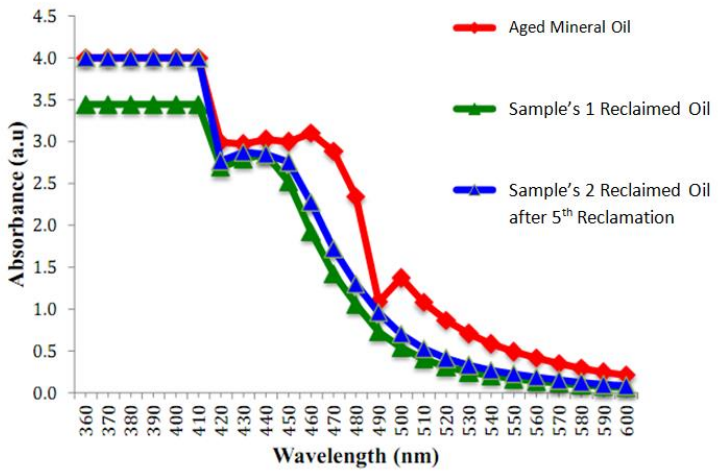


Figure 9 Curves of Absorbance (a.u) versus Wavelength (nm)

The wavelength at 420 nm is chosen as reference to analyze the reclamation process. As shown in Figure 9, at 420nm, absorbance unit of aged mineral oil, Sample's 1 reclaimed oil and Sample's 2 reclaimed oil-after 5 cycle of reclamation process is 2.9929a.u, 2.771a.u and 2.6919a.u respectively. These decrement value of absorbance unit indicate that DDP or oxidation by-products such low molecular weight acid decrease after reclamation process as found in [8]. Figure 10 shows graphs of DDP's of aged mineral oil (red), Sample's 2 reclaimed oil-after 5 cycles of reclamation process (blue) and Sample's 1 reclaimed oil (green). The DDP values are 498.34a.u, 422.8625a.u and 372.57a.u accordingly.

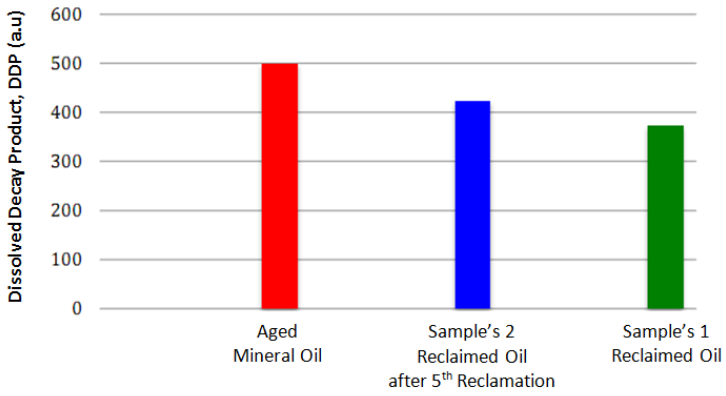


Figure 10 Dissolved Decay Product, DDP (a.u)

DDP values' signified that oil has undergone oxidation during service and by doing reclamation on the aged mineral oil such have been done on Sample 1 and Sample 2, decrement of DDP values' are shown. Yet, Sample 1 show 25.24% decrement compared to Sample 2 with only 15.15% DDP reduction. These results implying that using 100g of Fuller's earth for one cycle of reclamation (Method 1) is more effective compared to using 5g of Fuller's earth for 5 cycles of reclamation (Method 2). Additionally, the different amount of Fuller's earth used in Method 1 & 2 matching with results of reduction in DDP values of Sample 1 and Sample 2. This is because amount of adsorbent is directly proportional to the ability of adsorbents to absorb polar contaminants. Due to the effectiveness and lesser time required, Method 1 is chosen for the next two (2) study phases, Total Acid Number (TAN) and Breakdown Voltage (BdV). TAN measurements as per ASTM D974 were repeated three (3) times to find out the average value of acids in mineral oil. Figure 11 show results of average TAN for AMO and S1RO. The values are 0.13mgKOH/g and 0.02mgKOH/g respectively. As per reference, the suggested TAN limits for transformer is 0.10mgKOH/g [5]. High TAN values' proved that there is formation of acid in AMO accumulated during in-services due to oxidation process. The process can occurred between dissolved oxygen presence in oil with the mineral oil molecule or with cellulose-based insulation such as Kraft paper. Molecules of mineral oil that mainly consist of hydrogen and carbon can form carboxylic acids if interact with oxygen [1], while according to Bronsted-Lowry and Lewis Acids, the hydroxyl group (OH) in cellulose based paper can react with carboxylic acid and water to produce donating proton (H+). This donating proton (H+) can react with other molecule to form acid such as acetic and levulinic.

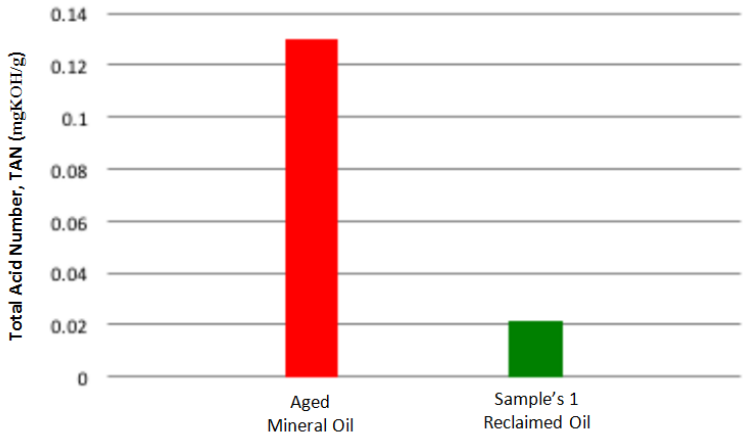


Figure 11 TAN of Aged Mineral Oil & Sample's 1 Reclaimed Oil

Subsequently, this decay product reaction will produce sludge, which can cause the dielectric strength decreases as the breakdown will occur at the sludge. Eventually, after the AMO undergone reclamation process, the S1RO average TAN values' decreased to 0.02mgKOH/g. This indicates the effectiveness of Fuller's earth as adsorbent for reclamation process thus also reducing acids in oil by 84.62%. This is due to chemical structure of Fuller's earth that containing internal and external polar active sites. It allowed the non-polar substances in the oil to flow but block or adsorb the polar contaminants dissolved in the oil. Acid is a polar molecule as they have opposing charge on their molecule [15]. 25 BdV measurements were recorded for each aged mineral oil AMO and Sample's 1 reclaimed oil S1RO. All measurements were done using Megger Oil Tester OTS60PB as per ASTM D1816. Figure 12 shows the average values for both oil samples. The values clearly indicate that the breakdown voltage for both AMO and S1RO are lower than the limit suggested by IEEE where a transformer that runs below 69kV, the BdV limit of oil insulation used should be 23 kV and above [5], Yet, BdV of S1RO is 4kV bigger than AMO's BdV or 50% improvement through reclamation process. As BdV of transformer oil is primarily depending on factors such moisture content, void or bubbles, sludge or suspended particles and acidity of oil[8], this improvement of BdV can be due to decrement of DDP, sludge and acids that have been absorbed by Fuller's earth during reclamation process. Hence, it is believed that if the reclamation process is done repeatedly for several cycles, more DDP, sludge and acids can be removed from the AMO thus increasing BdV steadily.

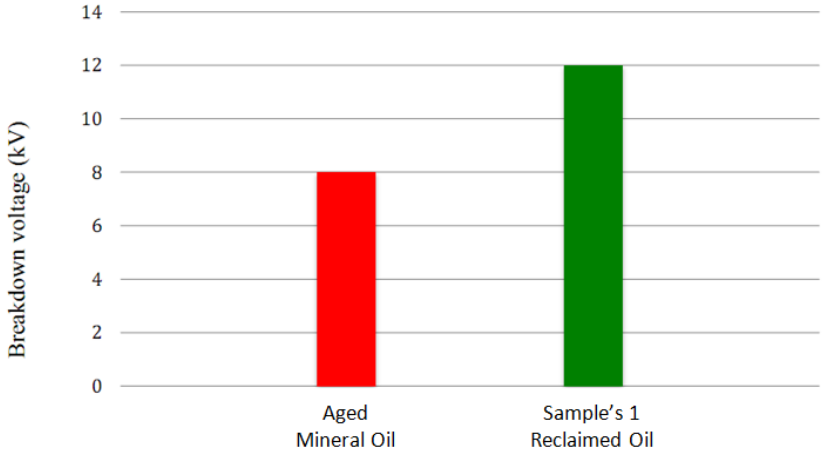


Figure 12 BdV of Aged Mineral Oil & Sample's 1 Reclaimed Oil

4. Conclusions

Parameter of DDP was measured using UV-Vis by referring to ASTM D6802. In addition, TAN and BdV measurements were carried out complying ASTM D974 and ASTM D1816 respectively. Through this study, it can be concluded that reclamation process using Fuller's earth can reduce 25.24% of DDP and 84.62% of acids present in aged mineral oil hence improving its' BdV by 50%. These findings are parallel with breakdown voltage mechanism due to acidity emergence. It is also proved that Fuller's earth is effective adsorbent for oil reclamation process and as Fuller's earth is harmless to environment, it can be disposed safely on landfill.

Acknowledgement

The authors gratefully acknowledge the financial support provided by the Universiti Teknikal Malaysia Melaka (UTeM) under the following grant: UTeM (PJP/2019/FKE(5A)/S01670).

References

[1] N. Lelekakis, J. Wijaya, D. Martin, and D. Susa, "The Effect of Acid Accumulation in Power-Transformer Oil on the Aging Rate of Paper Insulation," IEEE Electrical Insulation Magazine, vol. 30, no. 3, pp. 19–26, 2014.
[2] I. S. Chairul, S. A. Ghani, M. S. A. Khiar, Y. H. M. Thayoob, and Y. Z. Y. Ghazali, "Kraft Paper Insulation's Life Assessment and Effects of Oxygen and Moisture to Paper Insulation's Deterioration Rate," in IEEE International Conference on Power and Energy (PECon), 2012, pp. 728–731.
[3] M. S. Naidu and V. Kamaraju, High Voltage Engineering, 2nd ed. United States of America: McGraw-Hill, 1996.
[4] I. Liapis and M. G. Danikas, "A Study of Parameters Affecting the Ageing of Transformer Oil in Distribution Transformers," in IEEE International Conference on Dielectric Liquids, 2011, pp. 1–4.
[5] I. S. C57.637^{TM}-2015, "IEEE Guide for the Reclamation of Insulating Oil and Criteria for Its Use," IEEE Standards Association. 2015.
[6] J. S. N'cho, I. Fofana, A. Beroual, T. Aka-Ngnui, and J. Sabau, "Aged Oils Reclamation: Facts and Arguments Based on Laboratory Studies," IEEE Trans. Dielectr. Electr. Insul., vol. 19, no. 5, pp. 1583–1592, Oct. 2012.
[7] A. Raymon and R. Karthik, "Reclaiming Aged Transformer Oil with Activated Bentonite and Enhancing Reclaimed and Fresh Transformer Oils with Antioxidants," IEEE Trans. Dielectr. Electr. Insul., vol. 22, no. 1, pp. 548–555, Feb. 2015.
[8] S. A. Ghani, N. A. Muhamad, and H. Zainuddin, "Performance of Palm Shell Activated Carbon as An Alternative Adsorbent for Reclamation of Used Transformer Oil," ARPN J. Eng. Appl. Sci., vol. 10, no. 22, pp. 10752–10758, 2015.
[9] ASTMD6802−02(2010), "Test Method for Determination of the Relative Content Of Dissolved Decay Products in Mineral Insulating Oils by Spectrophotometry." pp. 1–6, 2010.
[10] ASTMD974-14, "Standard Test Method for Acid and Base Number by Color-Indicator Titration." pp. 1–7, 2014.
[11] ASTMD1816-12, "Standard Test Method for Dielectric Breakdown Voltage of Insulating Liquids Using VDE Electrodes." pp. 1–5, 2012.
[12] "Determination of The Total Acid Number in Petroleum Products," Metrohm. [Online]. Available: http://partners.metrohm.com/GetDocument?action=get_dms_document&docid=1360923. [Accessed: 05-Jan-2016].
[13] "Product Specification Fuller's Earth," Sigma Aldrich. [Online]. Available: http://www.sigmaaldrich.com/Graphics/COfAInfo/SigmaSAPQM/SPEC/F2/F200/F200-BULK_SIGALD_. pdf. [Accessed: 07-Jan-2016].
[14] H. M. Wilhelm, G. B. Stocco, and J. S. G. Batista, "Reclaiming of In-service Natural Ester-based Insulating Fluids," IEEE Trans. Dielectr. Electr. Insul., vol. 20, no. 1, pp. 128–134, 2013.
[15] R. Kurtus, "Polar and Non Polar Molecules (revised 19 September 2016)." [Accessed: 07-Jan-2016].

Penerbit Akademia Baru

Engineering Science and Technology Conference Proceedings

Journal homepage: www.akademiabaru.com/EST.html

Evaluation of The Prediction of Wave Pattern And Hull Performance of MTC 092 Hull Form Using Commercial Software

Open Access

Leow Jing Shuo[1], Nasrudin Haji Ismail[1], Arifah Ali[1*] and Ummu Saiyidah[1]

[1] Aeronautical, Automotive and Ocean Engineering, Faculty of Engineering, Universiti Teknologi Malaysia, 81310 Skudai, Johor, Malaysia

ABSTRACT

Ansys CFX is a powerful commercial CFD software that had been proven as having the ability to predict the resistance and generated wave pattern of a ship model in a free surface problem. However, recently due to the present of a competitive opensource software, OpenFoam, together with several CFD forum, it provided an alternative platform for people to choose, either to build the CFD model by coding on his own or pay to use a well establish commercial software. In this paper, the evaluation on the competitive of the commercial software over the opensource software in term of free surface problem on predicting a ship model resistance and wave pattern would be done. The reference result would be the experimental result from towing tank at MTC UTM. Planing hull type with model MTC 092 was used for the accuracy evaluation.

Keywords:
OpenFoam; Ansys CFX; CFD; free surface problem; ship resistance

Copyright © 2019 PENERBIT AKADEMIA BARU - All rights reserved

1. Introduction

The performance prediction of vehicles is a crucial procedure in the vehicle design process. Many attempts have been proposed to improve the quality of the prediction, including the application of Computational Fluid Dynamics (CFD) in Computer Aided Engineering (CAE). For instance in the maritime field, most of the towing test for boat and ship model have been partially replaced with the CFD simulation study to predict the resistance components and the drag properties of a particular ship model [1]. The results from CFD simulation show the CFD tool is very reliable as it have small error percentage when compared to the experimental one.

Currently, various software has been introduced in the world of CAE to simulate the ship resistance prediction and it can be categorized into commercial and non-commercial software. Commercial CFD software such as Ansys Fluent, CFX, Maxsurf and Shipflow are quite popular in the ocean engineering field not only the promising performance in obtaining the hydrodynamics result, but also it is user friendly and easy to use. It can be said that the commercial CFD are most preferred in well-established engineering companies. However, the commercial software has drawbacks such as the expensive license price and the limitation for the users to modify the CFD code structure CFD code structure according to user's will.

* *Corresponding author.*
E-mail address: arifahali@utm.my (Arifah Ali)

The solution to overcome the drawbacks, if CFD simulation method is favored, is to choose the non-commercial software, also known as Free and Open Source Software (FOSS). This alternative is available and free for everyone as it is license-free software and the users enable to build or modify the codes [2]. However, this type of software usually is not user friendly as the commercial ones and this drawback requires the user to have many stages of learning and exploring in order to understand the concept and solution. Therefore, training is still needed as a guide to use this software. However, users can get a hang on the software once they are familiarized with the codes.

Hence, this study is conducted as a guideline to consider either the free or commercial software in doing resistance prediction of a ship. The comparison between the result of commercial and uncommercial software can be referred as to improve the accuracy of FOSS as an open source Computational Fluid Dynamics (CFD) tool for ship resistance prediction. To date, the CFD simulation for ship resistance majorly use commercial software including Ref. [3] to [6]. However, these literatures did not address the FOSS usage. Work done by author [7] to [9] contain the comparison between the efficient of commercial and uncommercial software, but not for ship resistance and wave pattern prediction. In the other hand, author [10] to [15] have performed simulation on hull resistance prediction using open source software but they did not compare to commercial software.

In the work presented in this paper, the hull being studied is one of ship model constructed in Marine Technology Centre, Universiti Teknologi Malaysia named MTC 092. The ship is a planing hull and high speed vessel. The ship operates with Froude number (Fn) larger than 0.4. This paper is a further study in evaluating the hull form resistance and wave pattern prediction results that was performed by both opensource software and commercial software. In this paper, the possible reasons regarding the results' accuracy difference between the two software would be discussed. This paper will present the process flow of predicting the hull resistance and wave pattern of the models on commercial software, the evaluation flow as well as the observation throughout this study. OpenFOAM, which is an open source CFD software was used in the previous work to obtain MTC092 resistance and wave pattern. Resistance result was then obtained by commercial software, ANSYS CFX to evaluate the result. The experiment data from the towing tank would be set as the reference result.

The resistance of a ship at a given speed is the force that required to tow the ship at that speed in calm water which assuming there is no interference from the towing ship. The total resistance of the ship could be split into two components, which are frictional resistance and residuary resistance. It can be concluded that the total resistance can be separated into four components which is independent of each other. The total resistance components are as shown in Table 1. Therefore, the chosen CFD software is expected to be able in simulating the correct and sufficient forces to ensure the accuracy of ship resistance and power prediction.

2. Methodology

The CAD model of the ship hulls, MTC 092 was modelled by using Rhinoceros software. The surface of the hull would be built by using networksurf command from the software. Then, the CAD model would be export to Maxsurf for validating the hydrostatic data with the real ship model. After the model passed the hydrostatic checkup, it will be imported to Ansys Design Modeler for domain drawing. The domain size for MTC 092 is 2.5m depth, 4m width, 5 LBP length and 1 LBP length between the inlet and the bow. After that, the domain would be transfer to Ansys Mechanical for meshing. Majority of the meshing element is tetrahedral shape and inflation is only

set on the hull, bottom, top and the free surface. Then, the mesh file will be transferred to CFX-Pre for setup.

Table 1. Cause of Each Resistance Components

Main Components	Due to
Frictional resistance	The motion of the hull through a viscous fluid.
Wave-making resistance	The energy that must be supplied continuously by the ship to the wave system created on the free surface.
Eddy resistance	The energy carried away by eddies shed from the hull or appendages and it severe especially at stern part of the ship.
Air resistance	The motion of the ship through the air

The simulation used steady state analysis, multiphase homogeneous model, SST turbulence model and buoyant flow. The boundary condition for the domain is determined as in Table 2. The governing equations used in ANSYS is Navier-Stokes Equation to describe how the velocity, pressure, temperature, and density of a moving fluid are related. The turbulence model is K-ω SST which makes the model directly usable all the way down to the wall through the viscous sub-layer. Finite Volume Method divides the domain into a number of control volumes (cells or elements), by which the variable of interest is located at the centroid of the control volume [16].

Table 2. Boundary Condition for simulation in commercial and non-commercial software

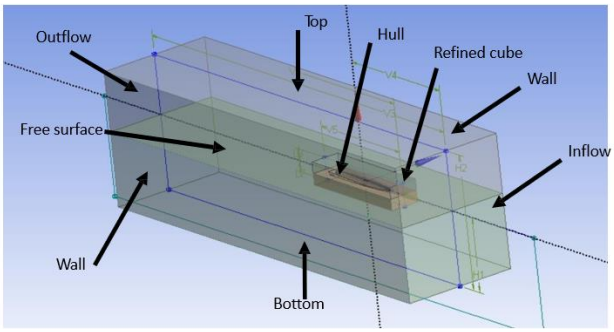
Location	Boundary Condition
Inlet	• Inlet • 1 % Turbulence Intensity • Cartesian Velocity Components
Outlet and Side	• Opening • Entrainment • Turbulence – Zero Gradient
Hull, Top and Bottom	• Wall

In modelling phase, FreeCAD is required to model the hull. However, due to the time-consuming and the complicated of the software, commercial CAD software such as AUTOCAD is used as the alternative. The nature of this software is curves are created by joining various discretized small line. This type of curves may cause difficulties in calculating the normal force and tangential force about the model surface in OpenFOAM and yielding an inaccurate result. Therefore, it is a good practice to import the geometries to Maxsurf Modeler which can produce better curves. The hydrostatic particular for the CAD model is checked by comparing with the real ship model that had been used for experiment. Table 3 shows the comparison between the hydrostatic particular of the model ship and the CAD model for MTL092.

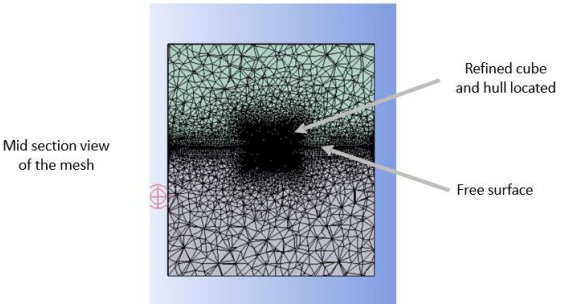
Table 3. CAD Hydrostatic Validation on MTC092 [14]

	Experiment Model	CAD model	Percentage Difference (%)
Displacement (tonne)	0.0948	0.0954	0.63
Block Coefficient	0.552	0.530	3.99
Prismatic Coefficient	0.72	0.723	0.42
Wetted Area (m^2)	1.481	1.492	0.74

For MTC 092 model, the domain length would be 5 times the ship hull LBP length with upstream boundary (inflow of water) be 1 LBP length from bow and downstream boundary (outflow of water) be 3 LBP length from stern. The overall width of the domain would be 4 m, while the water depth of the domain is 2.5m, both are same as the towing tank condition. Fig. 1 (a) and (b) shows the faces and meshing of computational domain.



(a) Domain with Predefined Faces for MTC 092



(b) Cross Sectional View of Meshed Domain for MTC 092

Fig 1. Computational domain and meshing of the water and ship

The International Towing Tank Conference (ITTC) [17] also provides standard recommendation on CFD simulation, majorly the scope would be narrowed to domain modelling guidelines, meshing Guidelines and simulation setup guideline. Three typical fixed boundaries would be used on ship viscous-flow computations, which are the ship surface, the symmetry plane and the (still) water surface. Three additional boundaries have to be defined in order to have a closed domain around the ship. Independent of the grid type used these will include an inlet, an outlet and an exterior boundary, where approximate boundary conditions have to be defined. These boundaries have to be placed sufficiently far from the ship to minimize the effect of the location of these boundaries on the solution. The upstream boundary (inflow of water) should be 1 LBP length from bow and downstream boundary (outflow of water) should be 3 LBP length from stern.

For estimating the distance to the wall for near wall boundary condition, suggest to use $Y+ \leq 1$ and the first required cell height, Y can be calculated by using the following formula.

$$Y = \frac{Y^+}{Re\sqrt{C_F/2}} * LPP$$

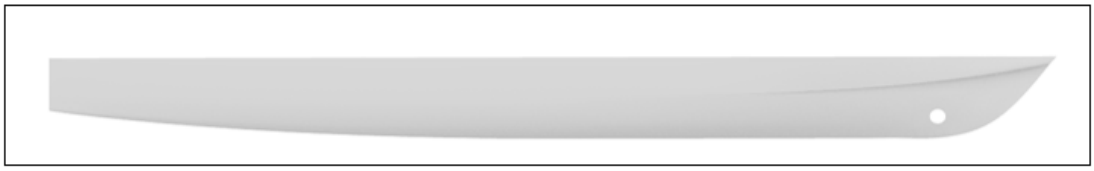
$$= 0.075/(log_{10}Re - 2)^2$$

3. Results

The simulation result for MTC 092 using OpenFOAM and ANSYS. The CFD result is compared between resistance of ship at position without trim from both software, as shown in Table 4. On order to improve the result, the trimming and heaving during experiment as shown in Fig. 2 and Table 5 is considered. Table 6 shows the comparison of simulation accuracy for model at even keel and trim condition with ANSYS result. The wave pattern generated at different speed and the detail look on the effect of ship's trimming condition on the simulation result for MTC 092 is discussed.

Table 4. Simulation Result Comparison between ANSYS and OpenFoam at Even Keel Condition for MTC092

Speed (m/s)	Experimental Result (With Trim) (N)	OpenFoam Result [5] (Without Trim)		ANSYS Result (Without Trim)	
		Resistance (N)	Relative Percentage error (%)	Resistance (N)	Relative Percentage error (%)
1.96	30.62	21.9	28.48	24.08	21.36
2.24	43.83	28.3	35.43	32.94	24.85
2.52	58.47	14.2	75.71	44.63	23.67
2.8	69.61	43.9	36.93	54.61	21.55
3.08	77.10	53.2	31.00	65.06	15.62



(a)



(b)

Fig. 2. Ship trim at the condition of hull at evenkeel (a) and trim condition (b)

Table 5. Trimming and Heaving Amplitude of MTC 092 recorded during the experiment

Speed (m/s)	Experimental Result	
	Trimming Angle (Degree)	Heave Amplitude (m)
1.96	0.239	0.0125
2.24	0.836	0.0154
2.52	1.718	0.0154
2.8	2.457	0.0159
3.08	3.010	0.0155

Table 6. Simulation Result Comparison between ANSYS at Even Keel and Trim Condition for MTC092

Speed (m/s)	Experimental Result (With Trim) (N)	ANSYS Result [5] (Without Trim)		ANSYS Result (With Trim and Opening)	
		Resistance (N)	Relative Percentage error (%)	Resistance (N)	Relative Percentage error (%)
1.96	30.62	24.08	21.36	29.09	5.00
2.24	43.83	32.94	24.85	43.07	1.73
2.52	58.47	44.63	23.67	53.27	8.89
2.8	69.61	54.61	21.55	64.06	7.97
3.08	77.10	65.06	15.62	81.17	5.28

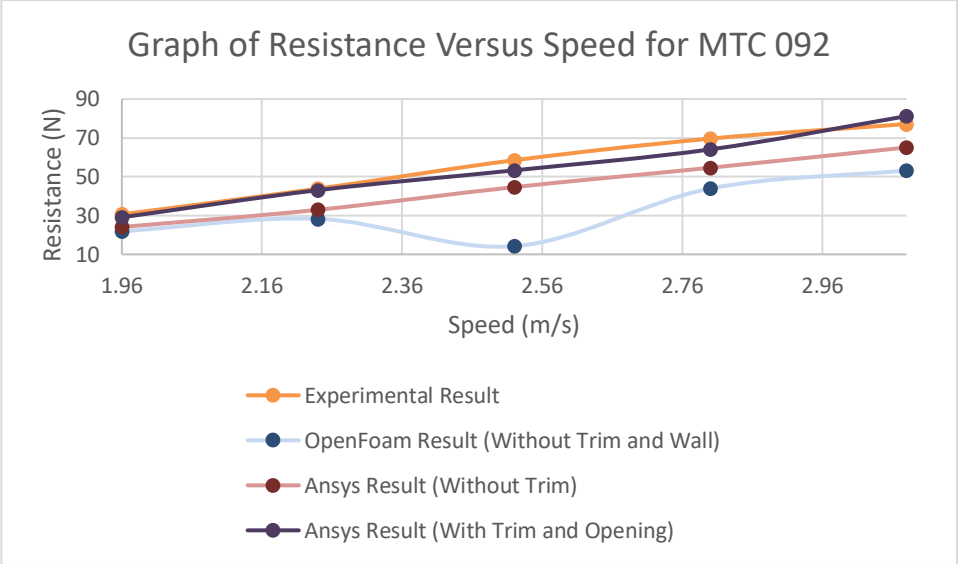


Fig. 5. Graph of Resistance Versus Speed for MTC 092 at Different Condition

The simulation result from the ANSYS at even keel condition have a relatively similar result with the OpenFoam's results, except there is a sharp drop of resistance at the speed of 2.52 m/s. For other speeds, a quite linear relationship between the ship resistance and speed is showed. It is indicated that the trim position effect is significant at that speed [18][19]. The speed at where the OpenFOAM result drop in resistance is actually the hump speed of the ship, it is a transitional stage for a planning hull to change its behavior from displacement hull to planning hull [20]. It can be claimed that the factor for inaccurate result from OpenFOAM simulation is the even keel condition. Result in Ref. [10] to [15] is acceptable might because the resistance of the ship is not strongly affected by trim and sinkage.

Generally, for the simulation result of ANSYS, the resistance of the ship hull increased as the speed increased. At hump speed, the result also shows a high percentage error for the ANSYS simulation. After the ship set in trimmed position in ANSYS, the simulation result actually produced a better result. The reason to use opening as side boundary condition but not wall for the simulation of ANSYS is because the wall would have interaction with the inlet flow and caused wave

form at the inlet region and caused the resistance of the ship to keep fluctuate and would not converge.

4. Conclusions

The evaluation of the prediction on wave pattern and hull performance of MTC 092 hull form using commercial software had been carried out successfully. The resistance of the ship models is being successfully predicted by using Ansys CFX with overall less than 10 % error, with maximum 8.89 % for MTC 092. For MTC 092 the main problem for the accuracy issue OpenFOAM would be the ship condition during the simulation is at even keel condition. The trim condition should be considered in performing the future work of resistance prediction using OpenFOAM. Also, one who choose rigid body solution should provide the mass moment of inertia value of the ship to the solver. From the result, it can be said that the commercial software can be replaced by free open source software for predicting the ship resistance, provided that the geometry and meshing of the hull is accurate. It is hoped that the obtained result can be a reference for hull resistance analysis using FOSS.

Acknowledgement

Appreciation is given to Center of Information and Communication Technology (CICT) and School of Mechanical Engineering, Universiti Teknologi Malaysia who provide licence and training for the software, and Marine Technology Center, Universiti Teknologi Malaysia for the resistance experiment in towing tank.

References

[1] Aksenov, A. A., A. V. Pechenyuk, and D. Vučinić. "Ship hull form design and optimization based on CFD." In Towards Green Marine Technology and Transport, pp. 215-223. CRC Press, 2015.
[2] Gaggero, S., Villa, D., and Viviani, M."The Kriso Container Ship (KCS) test case: an open source overview." In VI International Conference on Computational Methods in Marine Engineering–MARINE. 2015.
[3] Perez, G., M. Tan, and P. A. Wilson. "Validation and verification of hull resistance components using a commercial CFD code." (2008).
[4] Ahmed, Y. M. "Numerical Simulation For The Free Surface Flow Around A Complex Ship Hull Form At Different Froude Numbers". Alexandria Engineering Journal (2010): 229 - 235.
[5] Kadam, S. S. CFD Simulation and Analysis for Free Surface Computations around Fixed 'DTMB 5415' Model. International Journal of Current Engineering and Technology. (2014).
[6] Banks, J., A. B. Phillips, P. W. Bull, and S. R. Turnock. "RANS simulations of the multiphase flow around the KCS hullform." (2010).
[7] Medina, Humberto, Abhinivesh Beechook, Jonathan Saul, Sophie Porter, Svetlana Aleksandrova, and Steve Benjamin. "Open source computational fluid dynamics using OpenFOAM." In Royal Aeronautical Society, General Aviation Conference, London. (2015)
[8] Welahetti, Prasanna, and Knut Vågsæther. "Comparison of OpenFoam and ANSYS Fluent. Compitational Fluid Dynamic Simulation of Gas-Gas Single Phase Mixing with and without Static Mixer." (2016).
[9] Misirlis, Dimitrios, Zinon Vlahostergios, Christina Salpingidou, and Kyros Yakinthos. "Investigation of heat transfer and flow field development around a low-pressure turbine blade with the use of open source CFD tools." Chemical Engineering Transactions 70 (2018): 757-762.
[10] Shen, Zhirong, and Decheng Wan. "Computation of Steady Viscous Flows around Ship with Free Surface by Overset Grids Techniques in OpenFOAM." In The Twenty-fourth International Ocean and Polar Engineering Conference. International Society of Offshore and Polar Engineers, 2014.
[11] Inok, F. L. Analysis of the free surface turbulent flow around a forward moving Wigley hull with OpenFOAM. Developments in Maritime Transportation and Exploitation of Sea Resources. (2014). 33 - 40
[12] Axner, L., J. Gong, A. Chiarini, and L. Mascellaro. "SHAPE pilot Monotricat SRL: Hull resistance simulations for an innovative hull using OpenFOAM." PRACE Partnership for Advanced Computing in Europe (2014). 1-8.
[13] Shahzad, Muhammad Tufail. "Ship Resistance Computations using OpenFOAM." (2017).

[14] Ummu, S. N. Predictions of Wave Pattern And Hull Performance of Model MTC092 Hull Form Using OpenFOAM. Bachelor Degree Thesis. (2018)
[15] Nur, S. N. (2018). Predictions of Wave Pattern And Hull Performance of Model MTC098 Hull Form Using OpenFOAM. Bachelor Degree Thesis. (2018)
[16] CFX-Solver, A. N. S. Y. S. "Theory guide." Release ll (2006).
[17] International Towing Tank Conference (ITTC). ITTC Recommended Procedures and GuidelinesRecommended. Practical Guidelines for Ship CFD Application.(2011)
[18] Sherbaz, Salma, and Wenyang Duan. "Ship trim optimization: assessment of influence of trim on resistance of MOERI container ship." The Scientific World Journal 2014 (2014).
[19] Park, Hyun-Suk, Dae-Won Seo, Ki-Min Han, Dae-Heon Kim, and Tae-Bum Ha. "A study on resistance performance for various trim conditions and bulb shapes on a container ship under slow steaming." In ASME 2015 34th International Conference on Ocean, Offshore and Arctic Engineering, pp. V007T06A012-V007T06A012. American Society of Mechanical Engineers, 2015.
[20] De Marco, Agostino, Simone Mancini, Salvatore Miranda, Raffaele Scognamiglio, and Luigi Vitiello. "Experimental and numerical hydrodynamic analysis of a stepped planing hull." Applied Ocean Research 64 (2017): 135-154.

Penerbit Akademia Baru

Engineering Science and Technology Conference Proceedings

Journal homepage: www.akademiabaru.com/EST.html

Preliminary Study of Occupants' Thermal Sensation with Different Set-point temperature of Postgraduate Office with Cooling Mode in University Campus

Open Access

Noor Syazwanee Md Taib[1], Sheikh Ahmad Zaki Shaikh Salim[1,*], Aya Hagishima[2], Waqas Khalid[3], Fitri Yakub[1], Nurul Izzati Kamaruddin[1]

[1] Wind Engineering for (Urban, Artificial, Man-made) Environment Laboratory, Malaysia-Japan International Institute of Technology, Universiti Teknologi Malaysia Kuala Lumpur International Campus, Jalan Sultan Yahya Petra 54100 Kuala Lumpur
[2] Department of Energy and Environmental Engineering, Interdisciplinary Graduate School of Engineering Sciences, Kyushu University, 6-1 Kasuga Koen, Kasuga, Fukuoka 816-8580, Japan
[3] Department of Mechanical Engineering, School of Mechanical and Manufacturing Engineering, National University of Sciences and Technology (NUST), Islamabad, Pakistan

ABSTRACT

With rapid urbanization, massive amount of energy is required to compensate the electricity usage thus calls for a need to Malaysian government issuing standard MS1525:2014 for temperature settings in office buildings to meet energy efficiency goal. In co-sharing spaces, personal thermal comfort is often not met due to the different thermal sensation at different location inside office rooms. Therefore, in this study the field measurement is conducted at a postgraduate office space with cooling mode in university campus located at Kuala Lumpur to evaluate the occupant's thermal sensation. We used four different set-point temperature of air conditioning ranging from 20.1°C to 27.2°C. The indoor thermal variables such as air temperature, globe temperature, relative humidity, and air velocity are measured at each respondent's workspace. Thermal sensations are evaluated from the scale-basis survey. Occupants were found to felt neutral when air temperature were within 22.3°C to 25.0°C and feels warm when temperature reaches 26.0°C. Humidity was not significant as more than half quarter of votes feels neutral when relative humidity is within 56.7% and 74.4%. Finally, for air velocity of 0.09m/s to 0.34m/s, air movement sensations were mainly voted neither high nor low.

Keywords:
Thermal comfort; office rooms; set-point temperature

Copyright © 2019 PENERBIT AKADEMIA BARU - All rights reserved

1. Introduction

The steadily fast growth of urbanization has tempered the thermal properties of land causing alteration in urban environmental system and leads to Urban Heat Island (UHI) phenomenon [1,2]. The major energy consumer in buildings are the heating, ventilation and air conditioning (HVAC) system which accounted for approximately 40% of total energy [3]. With the increasing trend of global temperature, ambient temperature is one of the dominant factors that pushes high energy use as appliances such as air-conditioners are intensely utilized hence a competent cooling system in buildings are necessary [4].

In a context of indoor thermal environment, maintaining comfort is important for productivity and well-being of humans [5]. Predicted Mean Vote (PMV) is a widely adopted method to

* *Corresponding author.*
E-mail address: sheikh.kl@utm.my (Sheikh Ahmad Zaki)

mathematically estimate the comfortability of 80% occupants indoors [6]. However, more studies have found some discrepancies of PMV model then later introduce adaptive thermal comfort model [7] which includes psychological and behavioral factors that is commonly used in naturally ventilated spaces [8,9].

A review study shows that there is 0.5 - 8.5% increase in electricity demand for every one-degree temperature rise which is equivalent to 21 (±10.4) Watts per person [10]. A study in an office building in the Philippines shows 1.4% cooling energy saving cost-wise when raising the temperature setting from 22 °C to 24 °C [11] while another study estimates 29% of cooling energy savings from increasing set-point temperature by 2.8 °C [12]. While energy savings are very much desirable in this era, thermal perception to the temperature change is important be taken into account in thermal comfort context.

The main thermal comfort standards were originated from Europe and United States [6,13,14]. A report by State of the Tropics claimed that 50% of the world's population will live in the tropical region by the year 2050 [15] thus thermal comfort studies are important to compensate the growing number of populations. Although thermal comfort research has gained interest among researchers, compared to other parts of the world, research on indoor thermal comfort in the tropics are lacking [16]. This preliminary study aims to investigate thermal sensation of occupants at multiple set-point air temperatures of an office space in hot and humid city of Kuala Lumpur.

2. Methodology

2.1 Description of Study Area

This research takes place at a university campus in Kuala Lumpur (3°10'21.3168''N, 101°43'9.3036''E) located in the west peninsular of Malaysia near the equatorial region with tropical rainforest climate. In average, Kuala Lumpur is subjected to maximum temperature of 33°C and 23°C minimum with annual humidity at 80% on average [17]. A two-storey laboratory's office space equipped with air-conditioning units is selected for the preliminary study. The office space is located on the 2nd floor having floor area of $51.1\ \mathrm{m}^2$ with $4.0\ \mathrm{m}$ in height.



Fig. 1. Two-storey building of study location

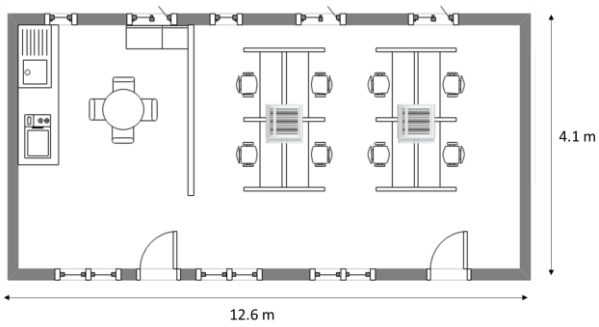


Fig. 2. Floor plan layout of office space.

2.2 Thermal Measurements

Thermal environmental parameters measured in this study are air velocity (v_a), air temperature (T_a), globe temperature (T_g) and relative humidity (RH), while the personal factors of clothing insulation (I_{cl}) and metabolic rate (M) are estimated from ASHRAE Standard 55 [6] via questionnaire survey. Air temperature, T_a was measured using HHA-3151 and TMC1-HD sensors, A 4 mm black sphere is fixed to another TMC1-HD sensor to measure globe temperature [9,18–23].

HOBO data logger internal sensor is used to measure RH while Kanomax 6501-0G with hot wire anemometer probe 6542-2G measures v_a.

Table 1
Specifications of instruments used in field measurement

Device	Sensor	Parameter Measured	Range	Accuracy
TnD TR-77Ui	HHA-3151	Air Temperature	-30 to 80°C	±0.3°C (10 to 40°C) ±0.5°C (at all other temperatures)
		Relative Humidity	0 to 99% RH	±2.5% RH (at 25°C and 10 to 85% RH) ±4% RH (at 25°C and 0 to 10% RH or 85 to 99% RH)
HOBO Data Logger	Internal sensor	Relative Humidity	5 to 95% RH	±2.5% (10 to 90% RH)
	TMC1-HD sensors	Air Temperature	-40° to 100°C	±0.25°C (0 to 50°C)
	TMC1-HD sensors + 40mm black sphere	Globe Temperature	-40° to 100°C	±0.25°C (0 to 50°C)
Kanomax 6501-0G	Needle Probe 6542-2G	Air Velocity	0.01 to 50 m/s	±2% or 0.015 m/s

2.3 Pre-test measurement

The studied postgraduate office space has two working areas, one near the west wall of the office and the other near the east wall as depicted in Fig.2. Pre-test measurement was done in order to test the health of AC operating cooling mode because the study involves conducting four thermal conditions from lowest to highest set-point AC air temperatures. Thus, the minimum ambient temperature of the working area at lowest AC settings were considered in the pre-test measurement to examine the maximum cooling capability of the AC. Two TnD TR-77ui sensors were placed at the centre of each working island to measure the air temperature, T_a and set to 10 seconds interval as shown in Fig. 3. Air conditioner (AC) are set to the lowest setting temperature, T_s at 16°C for 2 hours, from 10:10 AM to 12:10 PM during the day and T_a was recorded.

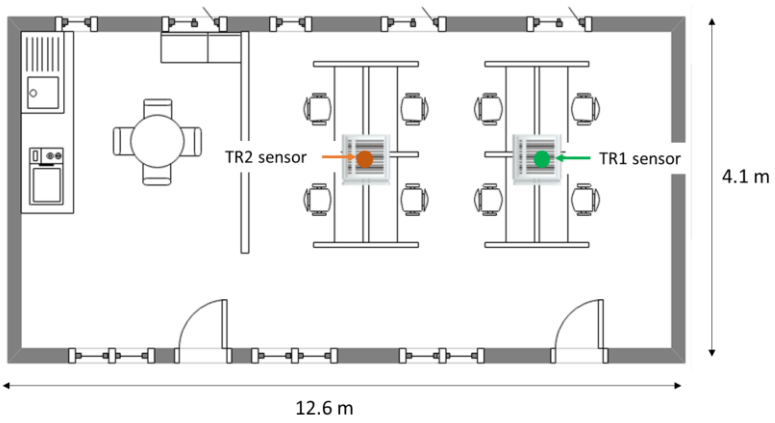


Fig. 3. Floor plan layout of pre-test measurement



Fig. 4. Thermo recorder (TR) sensors in office space

The minimum temperature of the office space at the lowest settings were found to be 16.8°C and 18.7°C for TR1 and TR2 respectively. The 1.9°C difference between the two sensors might be due to airflows on the smaller area around TR1 than TR2 which extends towards the east side of the room. In addition, the pre-test measurement was done during regular working hours in the office with two occupants near TR1 and only one occupant near TR2 hence the radiant heat from humans or objects like computers may contribute to higher ambient temperature near TR1. The disparity between measured air temperature and setting temperature could also cause by the outdoor temperature [24]. A study on energy consumption at varying temperature settings conducted in Durban, South Africa revealed that at 23°C set point temperature, the ambient temperature is 1.18°C warmer [25]. Based on the pre-test measurement, the office space is able to cool the room at approximately 16.8°C when set to lowest settings at 16°C.

2.4 Field measurement

60 samples were collected from 25th April until 27th August 2019 in the field measurement from four postgraduate students comprise of three female and one male aged 22 to 30 years old. Each subject was exposed to different set-point air temperature ranging from 20°C to 28°C resulting in measured T_a within 20.1°C to 27.2°C. The measured T_a were classified into four cases, Case 1, 2, 3 and 4 for T_a of 20°C to 21°C, 22°C to 23°C, 24°C to 25°C and 26°C to 27°C respectively as shown in Table 1. Although this study investigates the thermal sensations in varying air temperature, the environment cannot be fully control like a climate chamber experiment since this study uses field measurement method in real offices. Hence, the study location was exposed to other uncontrollable factors such as outdoor temperature and radiant heat from objects in the office space.

Equipment was placed on subject's work space as shown in Fig. 4 to measure the thermal exposure on a personal level. One set of equipment measured the thermal environment for each subject of study where the setup is as shown in Fig. 6. TMC1-HD sensors are installed inside an aluminium cup to simulate an aspirated setup as a mean to avoid radiation [26]. The thermo recorder (TR) sensors and probe are installed parallel to each other and is located at 1.1 meter from the floor based on ASHRAE guidelines [6]. Tewari et al. [27] conducted a field study in office buildings in India following the guidelines and the equipment is located next to occupants at similar heights. Similar setup was conducted in Malaysian offices for thermal comfort field studies by Damiati et al [18] and Mustapa et al [19].

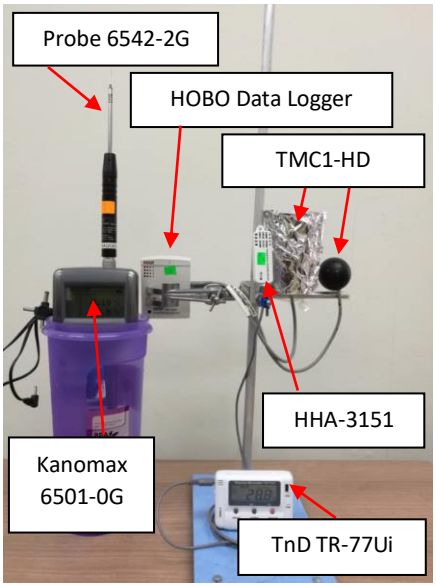


Fig. 6. Equipment setup

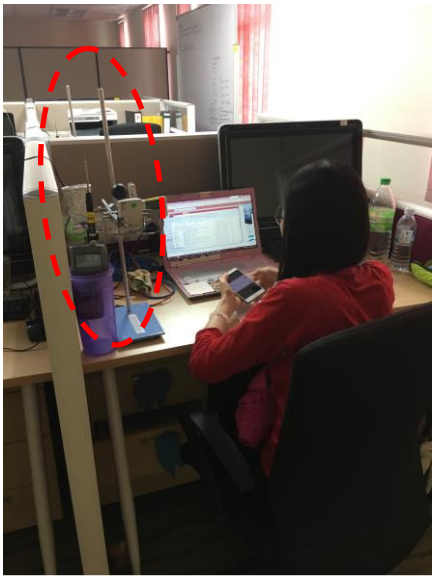


Fig. 7. Field measurement setup. Red dotted circle shows the equipment setup for measuring the thermal environment

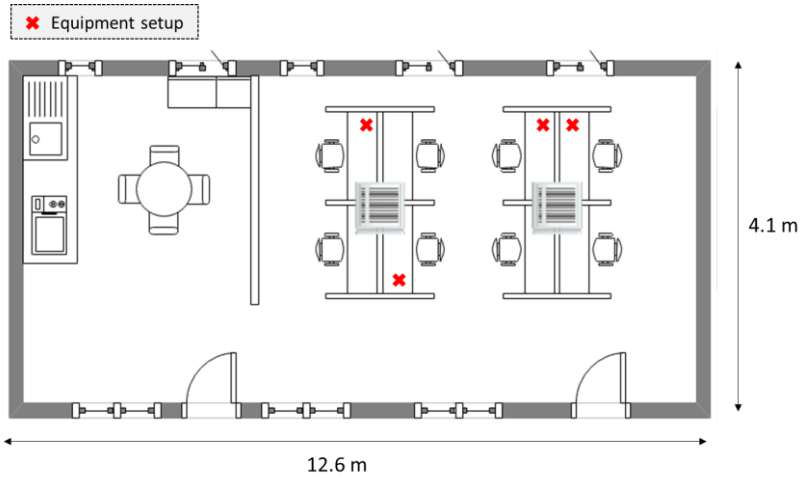


Fig. 8. Field measurement setup

Table 1
Period of Measurement

Date of Measurement	Number of Samples, *N*			
	Case 1 (20 – 21 °C)	**Case 2 (22 – 23 °C)**	**Case 3 (24 – 25 °C)**	**Case 4 (26 – 27 °C)**
25/4/2019 – 27/8/2019	11	20	13	16

Respondents participated in this study has signed a consent form in compliance to the Malaysian Personal Data Protection Act 2010. Prior to starting the measurement, equipment was placed in occupants' own work space. With limitation of only two sets of equipment, the measurement was done for two respondents at a time hence most data collections period was not simultaneous for all respondents in the room. However, since the study focuses on personal comfort, comparison of votes will be based on the four-case temperature. As presented in Fig. 9, 20

minutes were allocated for measurement setup and changing the setting temperature. The thermal conditions set in this study were specific hence the measured air temperature at each workspace should be within the desired case temperature and allowed to stabilize for a period of 10 minutes minimum. Questionnaire survey on thermal sensations were given to evaluate occupants' sensation towards the given case temperature.

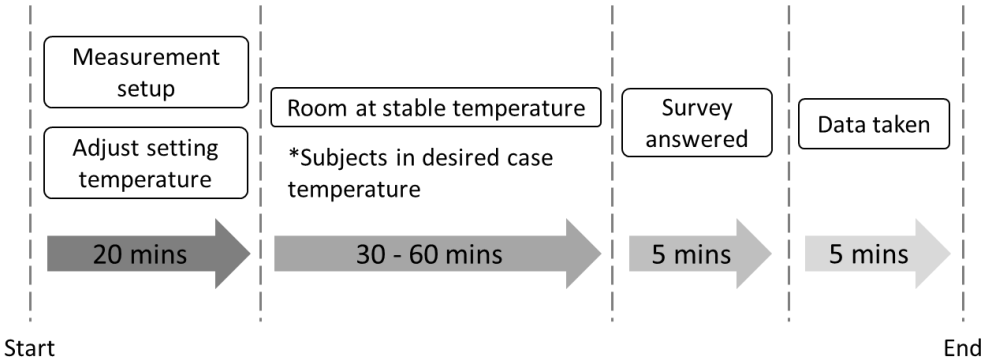


Fig. 9. Field measurement procedure

To assess the comfort level in a particular environment, scaled-surveys that rate occupants' thermal sensation, preference and among others are generally used in thermal comfort studies [6]. This study uses survey to show the distribution of votes among occupants in a postgraduate work space. The survey is paperless and done online via Google Form platform. Thermal Sensation Vote (TSV) is measured by modified ASHRAE 7-point scale [22] in this survey.

Table 3
Thermal Comfort Survey Scale

Scale	Thermal Sensation Vote (TSV)	Thermal Preference (TP)	Humidity Sensation (HS)	Humidity Preference (HP)	Air Movement Vote (AMV)	Overall Comfort (OC)
-3	Very cold		Very dry			
-2	Cold	Much cooler	Dry	Much drier		
-1	Slightly cold	A bit cooler	Slightly dry	A bit drier		
0	Neutral	No change	Neutral	No change		
1	Slightly hot	A bit warmer	Slightly humid	A bit humid	No movement	Very uncomfortable
2	Hot	Much warmer	Humid	More humid	Low	Moderately comfortable
3	Very hot		Very humid		Neither high nor low	Slightly uncomfortable
4					High	Slightly comfortable
5						Moderately comfortable
6						Very comfortable

3. Results

3.1 Correlation between measured and setting temperature

In field measurement, setting temperature of the ACs were manipulated from 20°C to 28°C for each occupant to see the pattern of thermal sensation in varying air temperature. The measured air temperatures were then found to be within 20.1°C o 27.2°C. Regression line correlating the T_a and T_s are shown in Fig. 10. Illustrating the linear correlation of setting temperature and air temperature in the office space. As the AC were positioned directly above each working islands, the ambient air temperature in the office space correlates with its setting temperature with r-square value of approximately 0.8583 and brings the correlation equation of air temperature and setting temperature in the office space as $T_a = 0.8218T_s + 3.4823$.

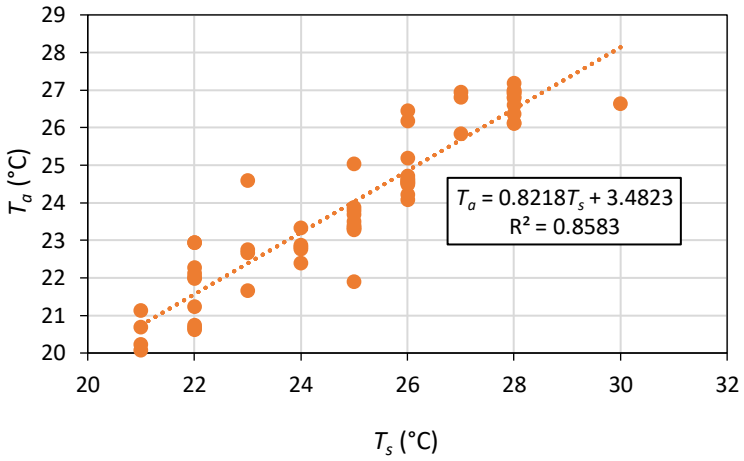


Fig. 10. T_a versus T_s in field measurement

3.2 Indoor conditions and subjective votes

Table 4
Average Thermal Conditions, N=60

Parameters	Case 1 (20 – 21 °C)	Case 2 (22 – 23 °C)	Case 3 (24 – 25 °C)	Case 4 (26 – 27 °C)
T_a	20.90°C	22.96°C	24.70°C	26.68°C
RH	62.47%	63.70%	64.26%	71.57%
v_a	0.23m/s	0.27m/s	0.17m/s	0.17m/s

Note: N; Number of Samples

During cooling operation of Heating, Ventilating, Air Conditioning (HVAC) system, moisture is drawn out of the air as cool air flows in a room. Hence, when air temperature is cooled at an average of 20.9°C, relative humidity is low compared to other case temperatures with higher T_a which can be seen on Table 4. Air velocity were low when T_a is higher in case 3 and 4 might be due to the auto fan mode was set during measurement.

Collectively, occupants start to feel warm (+1) when T_a is close to 26.0°C (25.8°C), up to 27.2°C while most neutral votes (0) falls within 22.3°C to 25.0°C air temperature. As temperature drops just below 22.0°C, occupants started to feel slightly cold (-1) thus further temperature drops

resulted in more negative votes, contrary to a study during summer time in a Brazilian's classrooms found that at 23°C set point temperature, students at the back of the classroom, near the wall has low values of votes (-1) [28]. A recent study mentions that neutral votes does not necessarily assure thermal comfort and later suggested that thermal preference may give more accurate representation of comfort [29]. However, in this study, occupants with neutral votes prefer no changes in their thermal environment but they were a few occasions that occupants prefer warmer conditions at 22.8°C to 23.9°C range, which was within the neutral zone for thermal sensations in this study.

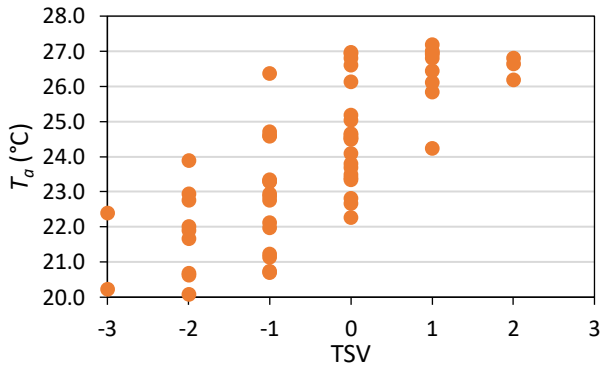


Fig. 6. T_a versus Thermal Sensation Votes

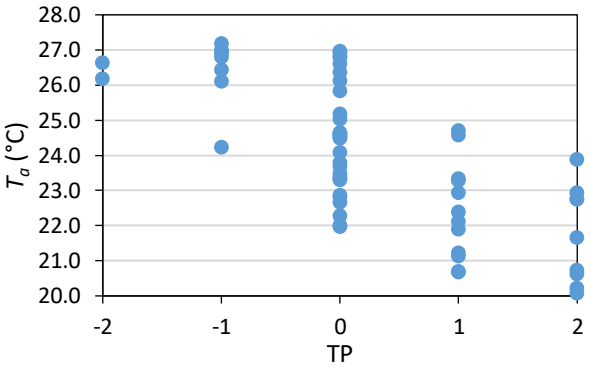


Fig. 7. T_a versus Thermal Preference

Referring to Fig. 8 and 9, humidity sensations were mainly neutral with 66.7% of votes at RH of 56.7% to 74.4%. Between dry and humid, there were higher votes on humid sensations (+1 and +2) compared to dry sensations which were 10% and 23.3% of votes respectively. This may be due to the small effect of humidity has on comfort temperature [22] with addition to residing in a generally humid country thus the occupants could have been adapted to the humid surroundings. Air velocity during the field measurement were between 0.09m/s to 0.34m/s which is unnoticed in sensations for v_a of less than 0.25m/s but for v_a of 0.25m/s to 0.50m/s might feel draughty at cool temperatures [30] which explains the 78.3% votes are on the scale of neither high nor low air movement sensations as shown in Fig. 10.

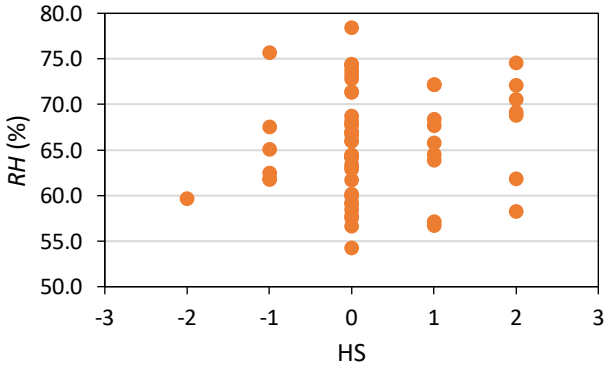


Fig. 8. RH versus Humidity Sensation

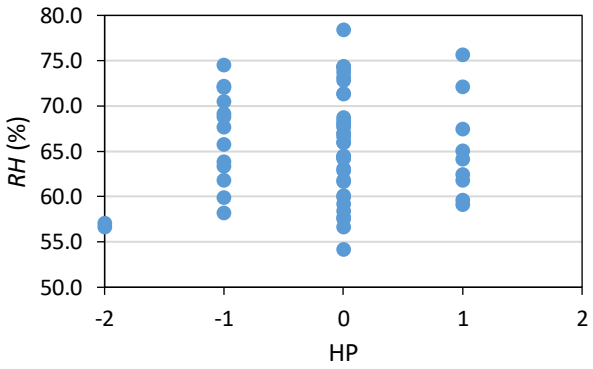


Fig. 9. RH versus Humidity Preference

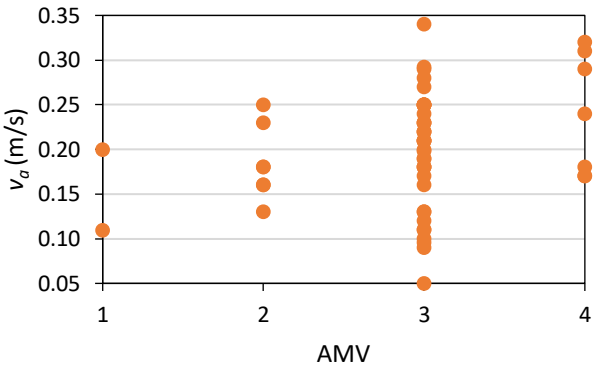


Fig. 10. v_a versus Air Movement Vote

4. Conclusions

This study presented the thermal sensation of occupants in postgraduate office space at different set-point air temperature ranging from 20.1°C o 27.2°C. Pre-test measurement was done to test the health of AC and minimum ambient temperature in the office space was taken prior to conducting the field measurement. The minimum temperature at 16°C settings were 16.8°C and 18.7°C for the two nearing locations.

Occupants started to feels warm (+1) when air temperature reaches 25.8°C. When air temperature is within 22.3°C to 25.0°C occupants mostly feel neutral (0) and generally prefer no changes of air temperature. Cool sensations were felt when air temperature drops just below 22.0°C with occupant prefers much warmer (+2) environment. Since relative humidity has small effect on comfort, occupants are not sensitive to the humidity changes so majority of the votes were neutral for relative humidity range of 56.7% to 74.4%. Throughout the measurement, air velocity were within 0.09m/s to 0.34m/s hence neither high nor low movement of air were felt. The preliminary study presented only shows measurement and survey results in one office room. More field measurements needed to be carried out to understand the thermal sensation perception of occupants at different seating positions.

Acknowledgement

This research was funded by a grant from Johnson Controls-Hitachi Air Conditioning vot 4B395

References

[1] Huang S, Taniguchi M, Yamano M, Wang C ho. Detecting urbanization effects on surface and subsurface thermal environment - A case study of Osaka. Science of the Total Environment 2009;407:3142–52. doi:10.1016/j.scitotenv.2008.04.019.

[2] Ichimura M. Urbanization, Urban Environment and Land Use: Challenges and Opportunities. Guilin, People's Republic of China: 2003.

[3] Pérez-Lombard L, Ortiz J, Pout C. A review on buildings energy consumption information. Energy and Buildings 2008;40:394–8. doi:10.1016/j.enbuild.2007.03.007.

[4] Li X, Zhou Y, Yu S, Jia G, Li H, Li W. Urban heat island impacts on building energy consumption: A review of approaches and findings. Energy 2019:407–19. doi:10.1016/j.energy.2019.02.183.

[5] Frontczak M, Wargocki P. Literature survey on how different factors influence human comfort in indoor environments. Building and Environment 2011;46:922–37. doi:10.1016/j.buildenv.2010.10.021.

[6] ASHRAE, ANSI/ASHRAE Standard 55-2017: Thermal Environmental Conditions for Human Occupancy. Atlanta (2017).

[7] Nicol F, Roaf S. Pioneering new indoor temperature standards: the Pakistan project. Energy and Buildings 1996;23:169–74.

[8] Indraganti M. Using the adaptive model of thermal comfort for obtaining indoor neutral temperature: Findings from a field study in Hyderabad, India. Building and Environment 2010;45:519–36. doi:10.1016/j.buildenv.2009.07.006.
[9] Lu S, Pang B, Qi Y, Fang K. Field study of thermal comfort in non-air-conditioned buildings in a tropical island climate. Applied Ergonomics 2018;66:89–97. doi:10.1016/j.apergo.2017.08.008.
[10] Santamouris M, Cartalis C, Synnefa A, Kolokotsa D. On the impact of urban heat island and global warming on the power demand and electricity consumption of buildings - A review. Energy and Buildings 2015;98:119–24. doi:10.1016/j.enbuild.2014.09.052.
[11] Andamon M. Thermal comfort standards and building energy use in philippine office environments. 40th Annual Conference of the Architectural Science Association ANZAScA, University of Adelaide; 2006, p. 66–72.
[12] Hoyt T, Arens E, Zhang H. Extending air temperature setpoints: Simulated energy savings and design considerations for new and retrofit buildings. Building and Environment 2014;88:89–96. doi:10.1016/j.buildenv.2014.09.010.
[13] CEN. Indoor environment input parameters for design and assessment of energy performance of buildings addressing indoor air quality, thermal environment, lighting and acoustics. 2012.
[14] ISO. ISO 7730: 2005: Ergonomics of the Thermal Environment. Analytical Determination and Interpretation of Thermal Comfort Using Calculation of the PMV and PPD Indices and Local Thermal Comfort Criteria 2005.
[15] Edelman A, Gelding A, Konovalov E, McComiskie R, Penny A, Roberts N, et al. State of the Tropics 2014 report 2014.
[16] Rodriguez CM, D'Alessandro M. Indoor thermal comfort review: The tropics as the next frontier. Urban Climate 2019;29:100488. doi:10.1016/j.uclim.2019.100488.
[17] Kottek M, Grieser J, Beck C, Rudolf B, Rubel F. World map of the Köppen-Geiger climate classification updated. Meteorologische Zeitschrift 2006;15:259–63.
[18] Damiati SA, Zaki SA, Rijal HB, Wonorahardjo S. Field study on adaptive thermal comfort in office buildings in Malaysia, Indonesia, Singapore, and Japan during hot and humid season. Building and Environment 2016;109:208–23. doi:10.1016/j.buildenv.2016.09.024.
[19] Mustapa MS, Zaki SA, Rijal HB, Hagishima A, Ali MSM. Thermal comfort and occupant adaptive behaviour in Japanese university buildings with free running and cooling mode offices during summer. Building and Environment 2016;105:332–42. doi:10.1016/j.buildenv.2016.06.014.
[20] Nematchoua MK, Tchinda R, Ricciardi P, Djongyang N. A field study on thermal comfort in naturally-ventilated buildings located in the equatorial climatic region of Cameroon. Renewable and Sustainable Energy Reviews 2014;39:381–93. doi:10.1016/j.rser.2014.07.010.
[21] García A, Olivieri F, Larrumbide E, Ávila P. Thermal comfort assessment in naturally ventilated offices located in a cold tropical climate, Bogotá. Building and Environment 2019;158:237–47. doi:10.1016/j.buildenv.2019.05.013.
[22] Rijal HB, Humphreys M, Nicol F. Adaptive thermal comfort in Japanese houses during the summer season: Behavioral Adaptation and the Effect of Humidity. Buildings 2015;5:1037–54. doi:10.3390/buildings5031037.
[23] Kong D, Liu H, Wu Y, Li B, Wei S, Yuan M. Effects of indoor humidity on building occupants' thermal comfort and evidence in terms of climate adaptation. Building and Environment 2019;155:298–307. doi:10.1016/j.buildenv.2019.02.039.
[24] Nguyen JL, Schwartz J, Dockery DW. The relationship between indoor and outdoor temperature, apparent temperature, relative humidity, and absolute humidity. Indoor Air 2014;24:103–12. doi:10.1111/ina.12052.
[25] Wang N, Zhang J, Xia X. Energy consumption of air conditioners at different temperature set points. IEEE AFRICON Conference 2011. doi:10.1109/AFRCON.2011.6072174.
[26] Tarara JM, Hoheisel GA. Low-cost shielding to minimize radiation errors of temperature sensors in the field. HortScience 2007;42:1372–9.
[27] Tewari P, Mathur S, Mathur J, Kumar S, Loftness V. Field study on indoor thermal comfort of office buildings using evaporative cooling in the composite climate of India. Energy and Buildings 2019;199:145–63. doi:10.1016/j.enbuild.2019.06.049.
[28] Anastácio da SJ, Kátia CM, Rogério V, Luiz PM, Nathan M. On the improvement of thermal comfort in indoor spaces conditioned by split-type systems. E3S Web of Conferences 2019;111:02052. doi:10.1051/e3sconf/201911102052.
[29] Shahzad S, Rijal HB. Preferred vs neutral temperatures and their implications on thermal comfort and energy use: Workplaces in Japan, Norway and the UK. Energy Procedia 2019;158:3113–8. doi:10.1016/j.egypro.2019.01.1007.
[30] Department of Standard Malaysia. MS 1525:2014: Energy efficiency and use of renewable energy for non-residential buildings - Code of practice 2014.

Penerbit Akademia Baru

Engineering Science and Technology Conference Proceedings

Journal homepage: www.akademiabaru.com/EST.html

Indirect Evaporative Cooler Using Solar Energy

Open Access

Dzullijah Ibrahim[1,*], Yusli Yaakob[1], Murni bt Alwi[1], Hamid Yusoff[1], Normariah Che Maideen[1], Hazim Moria[2].

[1] Faculty of Mechanical Engineering, Universiti Teknologi MARA, Cawangan P. Pinang, 13500 Permatang Pauh, P.Pinang, Malaysia
[2] Mechanical Engineering Department,Yanbu Industrial College, Yanbu Al-Sinaiyah, P.O.Box 30436, Post Code 41912, KSA

ABSTRACT

An indirect evaporative cooler (IEC) is an alternative method for a cooling system instead of using air conditioning. It was useful for energy saving and an environmentally friendly system. This research was to study the effect of the indirect evaporative cooler to the human comfort level at indoor. IEC used water evaporation technique to cool the supply air, solar energy was used as an energy source to run the cooling system as it can generate electricity naturally and water tubes were used for the water distribution system. The simulation of water flow in the tube was analyzed to obtain the minimum pressure of water flow. Aluminum tube heat exchanger (HE) was used to transfer the heat between two fluids (dry air and water) so that the supply air reached the indoor thermal comfort level (23℃ - 30.4℃). Heron's fountain technique was applied to circulate water in the cooler. The water pump was utilized to ensure the continuous flow of water. The results presented that IEC was able to reduce the air temperature of about 1℃ to 3℃. The lowest temperature reached from the experiment was 29℃ which was affected by the high ambient air temperature. The average of air humidity supplied was in the range of comfort zone (19.8% - 79.5%). The wet-bulb efficiency was 51.7%, which was in the range of recommended IEC efficiency (40% - 80%). The power consumption was 42.6W, lower than other cooling devices that consume electricity. Thus, the IEC has the potential to produce a good cooling effect for residential sectors in Malaysia as it could reach the indoor thermal comfort level.

Keywords:
Indirect evaporative cooler; heat exchanger; thermal comfort

Copyright © 2019 PENERBIT AKADEMIA BARU - All rights reserved

1. Introduction

Malaysia is one of the countries which is experiencing hot and humid climate throughout the year. The climate changes cause the residentials especially from urban areas to use air conditioning as a cooling system to bring down the temperature in their houses. These modern houses are constructed from bricks and concretes unlike traditional houses which are mostly made of wood with better air circulation.

A survey conducted in 2015 in residential areas of Putrajaya and Kajang, Malaysia [1] revealed that air conditioner consumes a huge amount of electricity either on weekdays or weekend even though the measured power for the air conditioner was a bit lower than an electric kettle, water heater, and electric iron. The data is shown in Table 1.

* *Corresponding author.*
E-mail address: dzullijah@uitm.edu.my (Dzullijah Ibrahim)

Table 1
Energy consumption by home appliances [1]

NO	Appliances	Measured Power in (kW)	Weekday Energy (kWh/day)	Weekend Energy (kWh/day)
1	Air conditioner	1.2	6.06	9.69
2	Water heater	2	0.32	3
3	Electric kettle (5L)	2-2.2	1.0560.742	0.968
4	Electric Iron	1.4	0.12	0.644
5	Hair dryer	1.2	0.198	0.06
6	Microwave	1-1.1	0.884	0.187
7	Washing machine (5kg)	0.85	0.576	0.884
8	Rice cooker	0.7-0.8	1.4775	0.584
9	Computer	0.75	2.5	1.365
10	Fridge	0.5	0.00424	4
11	Exhaust hood	0.212	0.0546	0.0212
12	Blender	0.205	0.287	0.03895
13	Laptop	0.1	1.155	0.382
14	Fan (ceiling)	0.1	0.456	1.8
15	Television	0.08	0.001	0.652
16	Printer	0.05	0.4	0.0045
17	Florescent light	0.04	0.4	0.52
18	TM system (receiver + phone + wireless)	0.03	0.57	0.72

An evaporative cooling system is an alternative to the conventional air conditioning system [2]. It is based on heat and mass transfer between air and cooling water [3]. There are two types of evaporative coolers which are direct evaporative cooler (DEC) and indirect evaporative cooler (IEC). DEC is based on mechanical and thermal contact between air and water, while IEC is based on heat and mass transfer between two streams of air, separated by a heat transfer surface with a dry side where only air is cooling and a wet side where both air and water are cooling.

However, this study is done for IEC as it is completely environmentally friendly [4]. The IEC use solar as an energy source to generate electricity. It is green energy and use for the purpose of reducing the global warming impact on the environment. Moreover, it is available in abundance in Malaysia. Heron's fountain technique is used to circulate water in the cooling system and a water pump is used to ensure the continuous flow of water. Heat exchanger helps to transfer heat in order to achieve a thermal comfort level at indoor. The heat exchangers were made up from aluminium as it has good thermal conductivity. Water is used as the cooling media.

2. Methodology

A schematic of an indirect evaporative cooling system is shown in Figure 1. The pump continuously circulated the water from the water tank to the water distribution system. Then, the water dripped on the tubes outer walls which caused the outer surface of the heat exchanger became wet and drop into the water tank [5]. The evaporation process occurred when the secondary air and water sprayed were in direct contact which exchanged both heat and moisture.

Hence, it cooled the tubes which were in contact with it. Thus, the cooled supply air was released to the room. Meanwhile, the primary air passed through the tubes with the aided of fans which mounted at the front side and at the back side of the cooler. A fan located at the top exhausted the secondary air.

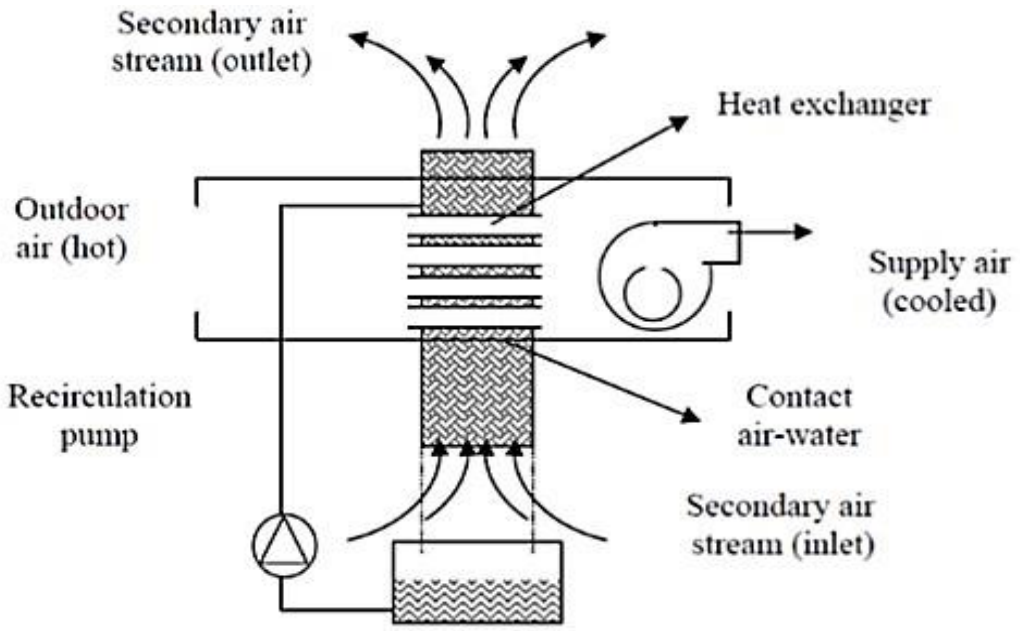


Fig.1. Schematic diagram of IEC [6]

The objective of this experiment was to observe the cooling performance of the IEC at a designated area. The experiment was conducted in a small bedroom of 90 square feet. Four Arduino sensors were used to determine and record the difference in the temperature and humidity of IEC.

The procedure to measure the temperature and humidity as followed:

1. The Arduino sensors were set up before started the experiment to measure the ambient temperature of the room.
2. The IEC was set up together with Heron's fountain.
3. The experiment was done about 100 minutes for each experiment in the morning, afternoon, evening, and at night.
4. The Arduino sensors were set up to measure the temperature and humidity of IEC every 5 minutes.

2.1 Design of cooler body

The design of IEC body consists of three units of container to form Heron's fountain and a round shape hole on the top cover to locate the fan as shown in Figure 2. Other holes were the way or space to allow the primary air and secondary air to pass through the IEC. Figure 3 showed the complete design of IEC in which it was assembled together with the fans, heat exchanger, Heron's fountain, battery, water pump, water distribution system and bottom container.

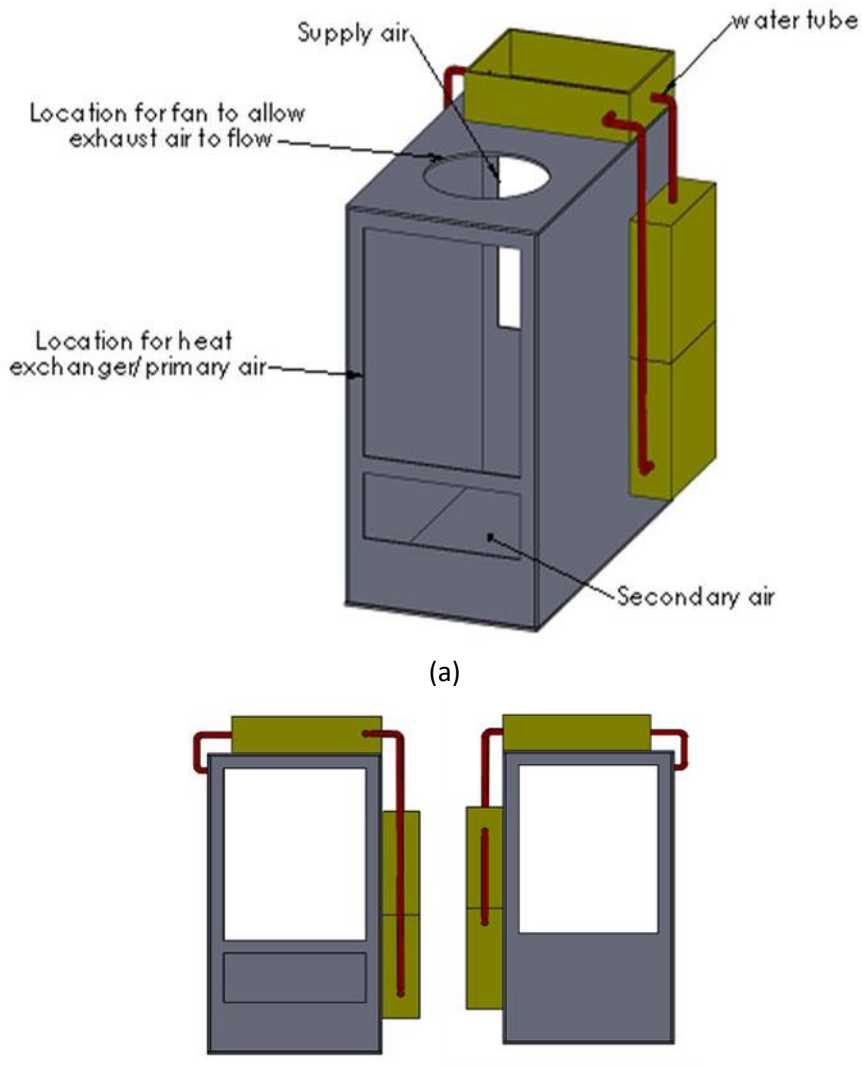


Fig. 2. Design of cooler body: a) Isometric view of cooler body; b) Back view of cooler body; c) Front view of the cooler body

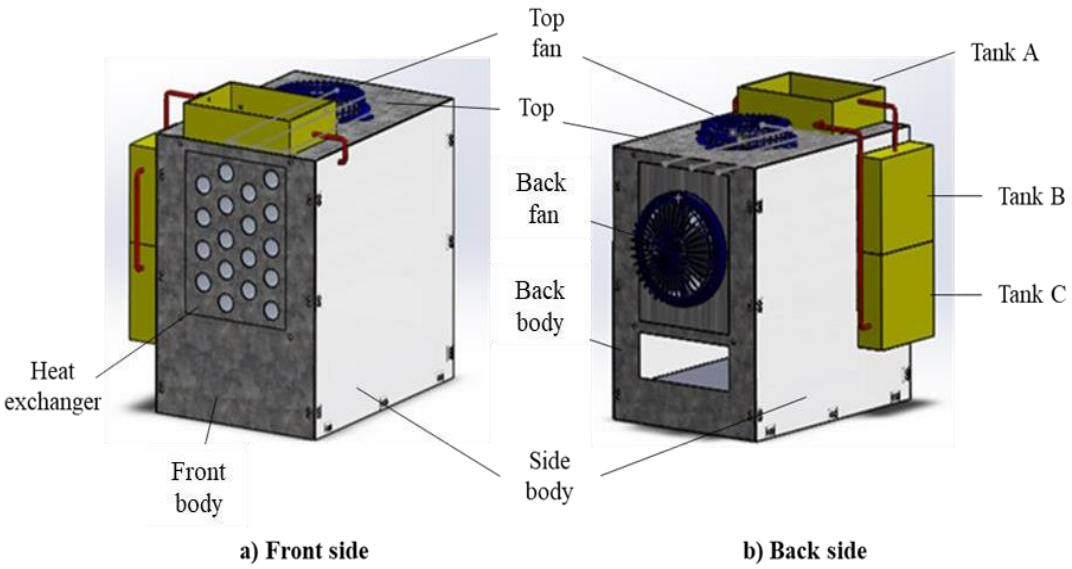


Fig. 3. Design of cooler with a complete system

Figure 4 showed the design of aluminium tube heat exchanger. It consists of eighteen tubes of aluminium and two sheets of galvanized steel. The size of the aluminium tube was 58.5 cm length and 4 cm diameter while the size of the galvanizing sheet was 40 cm height and 31.5 cm width. Many tubes were used to produce a large surface area for primary air to flow in and out of the cooler. According to the previous studies, a large surface area of the heat exchanger was required to increase the performance of the cooler.

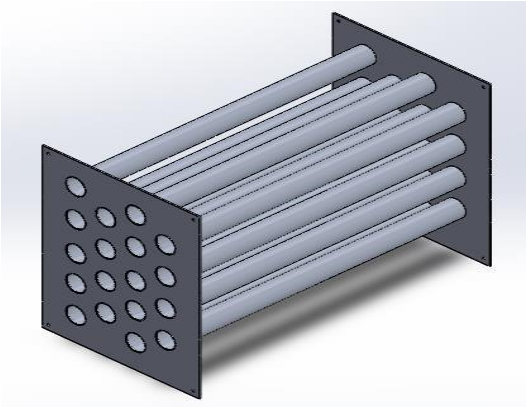


Fig. 4. The heat exchanger

2.2 Fabrication of cooler

A simple IEC was fabricated to produce a thermal comfort device. The size was not too big but enables to bring it anywhere. On the other hand, lightweight materials like perspex acrylic and galvanized sheet were used to fabricate the body of the cooler so that it would not too heavy. Thus, the selection of material was important to make sure the cooler has high strength and easy to fabricate.

An IEC model was fabricated and assembled together with the Heron's fountain. This model was used to test the cooling performance of IEC. Figure 5 showed the fabricated aluminium tubes and its stands for heat exchanger. Figure 6 presented the water sprayer used for the water distribution system of IEC.



a) Stand of heat sink b) Aluminium tube c) Assembled heat sink

Fig. 5. Model of the heat exchanger



Fig. 6. Model of the water distribution system

2.3 Heron's fountain with water pump

The earliest stage of this project was started by testing the Heron's fountain. After tested, this model produced positive feedback and it worked. Therefore, Heron's fountain is suitable for the water circulation system of IEC. However, the container must be airtight especially the bottom and middle containers. This was because to no leakage occur when the system operates. Any leakage of air would interrupt the water flow and will reduce the usability of the fountain will. Figure 7 indicated the model of Heron's fountain.



Fig. 7. Model of Heron's fountain

The pressure difference of hydrostatic pressure in container B and C can be calculated using Eq. 1 as followed:
Where, density of water, ρ = 1 g/cm^3 or 1000 kg/m^3
Acceleration of gravity, g = 9.81 m/s^2
$\Delta P = (1000)(9.81)(0.4) - (1000)(9.81)(0.23)$
ΔP = 1667.7 Pa (1)

The water velocity that spurt out of the fountain is calculated using the Eq. 2 as shown below:

$$\boldsymbol{v = \sqrt{\frac{2\Delta P}{\rho}} = \sqrt{\frac{2(1667.7)}{1000}} = 1.8263\ m/s}$$

(2)

The calculated velocity is used to calculate the water volume flow rate using Eq. 2 as below:

$$Q = AV \quad (2)$$

Where,

Q = Volume flow rate

A = Cross-section of the area of pipe = $\boldsymbol{\pi}$r^2 where r is the radius of the pipe

V = Velocity of water flow

Therefore,

$Q = (\pi\ X\ r^2) = (\pi\ X\ 0.005^2)(1.8263) = 1.4344\ X\ 10^{-4} m^3/s$

But then, the volume flow rate, Q is converted into litre per second as indicated below:

$Q = 0.14344\ l/s$

2.4 Power of water pump

The power consumed by a water pump was calculated using the Eq. 3 as followed:

P = (1.4344 X 10^{-4})(1000)(9.81)(0.43) = 0.6051 W (3)

The power of the water pump was calculated with the height of the head of the water pump at 43 cm. The maximum power of pump used for 3 m head was about 3.6 W and the voltage was 12 V. Meanwhile, the power of water pump for 43 cm was 0.6051 W. Thus, it can be concluded that the higher the head of the pump, more power will be consumed without including the other factors.

2.5 Power Consumption

Solar energy was used as the energy source for the IEC. Then, it was converted and stored into a rechargeable battery of 12 V. After that, the collected energy was used to supply energy to the fans and water pump. The following calculations showed the IEC operation time and time taken used to charge the battery:

To determine the total current of fans and water pump, the current of each component was calculated using Eq. 4 as followed:

Current for cooling fans (top and back):

$$I = \frac{P}{V} = \frac{21}{12} = 1.75\ A \quad (4)$$

$$2\ X\ 1.75 = 3.5\ A$$

Current for water pump:

$$I = \frac{P}{V} = \frac{0.6051}{12} = 0.05043\ A$$

Total current = 3.5 + 0.05043 = 3.55 A

By finding the total current used by the fans and water pump, the total operating hours of IEC are calculated using Eq. 5 as followed:

$$Operating\ hours = \frac{12}{3.55} = 3.380 \approx 4\ hours \quad (5)$$

Therefore, the IEC able to operate about 4 hours without stopping with 100% of battery capacity to 50% of battery capacity. This was because it was not encouraged to discharge battery lower than 50% for solar system, otherwise the battery would be damaged. However, in order to maximize the operating hours, using the separate batteries for water pump and fans. So, the new operating hours of IEC would be: $Operating\ hours = \frac{24}{3.55} = 6.761 \approx 7\ hours$

The total time taken to charge the battery is calculated using the Eq. 6 and Eq. 7 as followed:

$$Charge\ rate = \frac{50W}{12V} = 4.1667\ A$$

$$Charge\ time(hours) = \frac{12-0\ x\ 1.15}{4.1667} = 3.312\ hours$$

Therefore, the battery takes about 3.312 hours to fully charge. In this project, the battery was only used to provide the energy to the cooler instead of improving the performance of the battery.

The power consumption of IEC was calculated using Eq.8 as followed:

$$P = (12\ V)(3.55\ A) = 42.6\ W$$

3. Results

3.1 IEC performance test

The IEC was tested in a small bedroom of 90 square feet. Four experiments have been done at different times on a particular day to observe the performance of the cooler. The relative humidity and temperature at four different locations were recorded using Arduino sensors to capture the measurement of temperature and humidity for every ten minutes. In fact, the temperature of IEC could not be controlled as it would produce its own cooling effects. On the contrary, the

temperature of the air conditioner could be controlled depending on the user comfort as it was able to yield the cooling temperature in the range of 16℃ to 30℃.

The experiment was conducted in the morning, afternoon, evening and midnight. From the experiment, eight measurements of the IEC performance have been taken at four different locations which were at inlet primary air, outlet primary air (supply air), inlet secondary air and exhaust air.

3.1.1 The temperature profiles

Four experiments were conducted to observe the temperature produced by IEC in the morning, afternoon, evening and midnight. The dashed line in the graphs at 30.4℃was the acceptable thermal comfort level (ATCL) based on the previous research [7]. Another dotted line at 28℃was the maximum thermal comfort level (MTCL) recommended by ASHRAE [8].

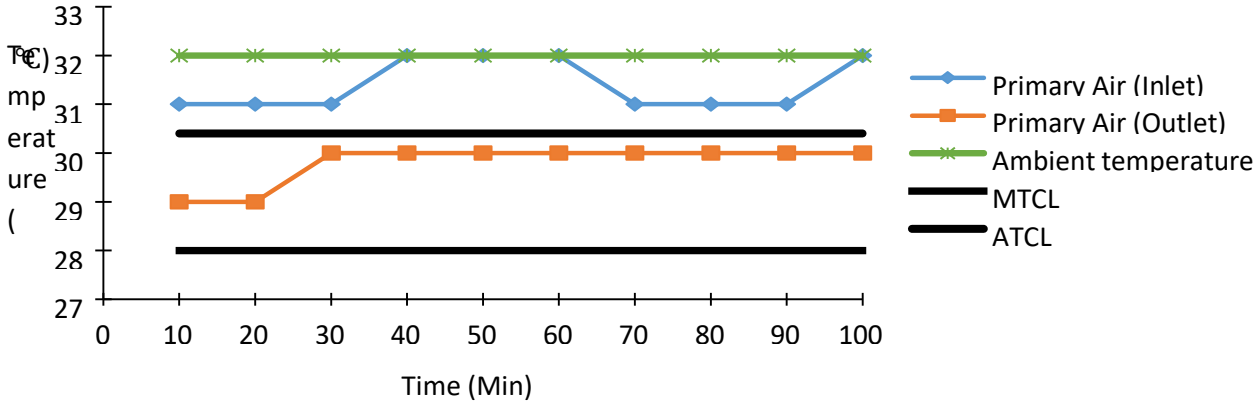


Fig. 8. Graph of indoor air temperature in the morning (8am to 9 am)

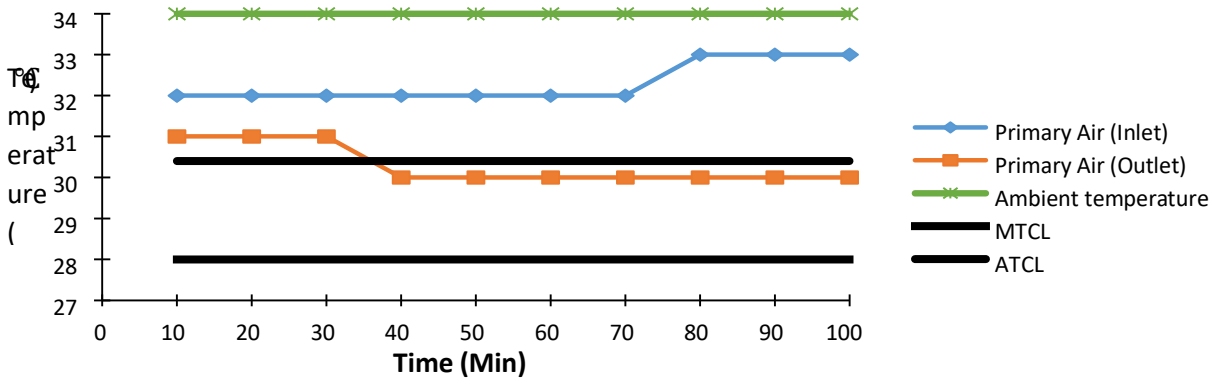


Fig. 9. Graph of indoor air temperature in the afternoon (12noon to 1.40pm)

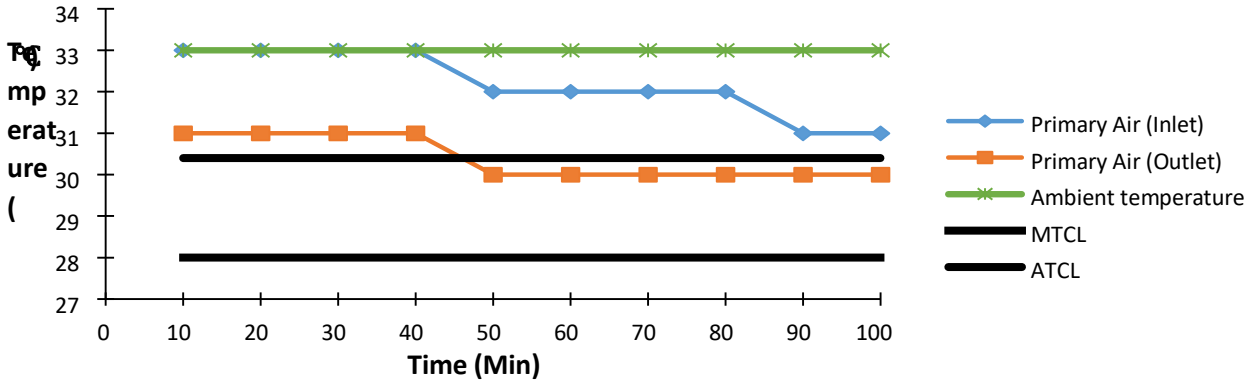


Fig. 10. Graph of indoor air temperature in the evening (3pm to 4.40pm)

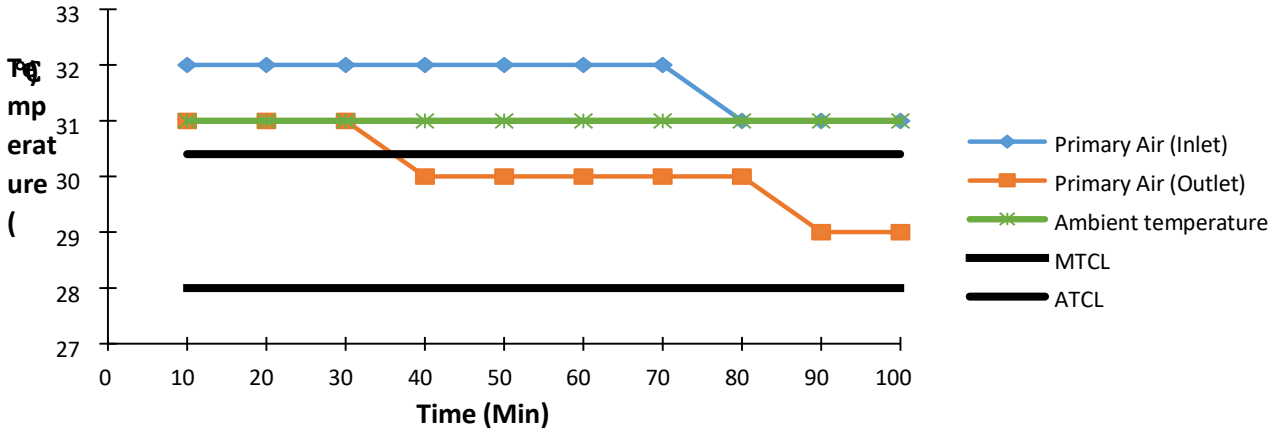


Fig. 11. Graph of indoor air temperature in the night

Figure 8 until Figure 11 showed that IEC was able to produce the indoor air temperature lower than the outdoor temperature. The temperature reduction was about 1℃, 2℃ or 3℃ from the surrounding temperature. The supply air did not differ much, ranging from 31℃ to 29℃, and close to the ambient temperature at a certain time. Thus, the average of supply air temperature in the morning, afternoon, evening and night were 29.8℃, 30.3℃, 30.4℃ and 30.1℃ respectively. However, the supply air produced was still within the range of thermal comfort level which was below the ATCL even though it was higher than MTCL.

From the experiment, almost the inlet dry bulb temperature was above the ATCL and MTCL and quite close to the ambient temperature. Thus, a higher temperature of ambient air may degrade the performance of the cooler in which the supply air produced would not achieve the thermal comfort level. This can be concluded that the temperature inside the room might be influenced by the outside temperature. Since Malaysia was in the equator area, it received the maximum sunlight throughout the year due to the equinox phenomenon [9]. This caused the ambient air temperature slightly increases especially during the daytime [10]. According to the World Weather Online website [11], the average outside temperature for that day in the morning was 32℃, in the afternoon was 34℃, in the evening was 33℃ and in the night was 31℃.

Initially, the supply air and the ambient air temperature were similar during at night. And the inlet dry air passed through the heat exchanger also higher than ambient temperature. This was because the trapped heat inside the room restricted the performance of the cooler that caused high in temperature inside the room. Heat is being trapped due to poor ventilation inside the room wherein the windows were closed. Moreover, the retaining heat inside the room during the daytime might influence the air temperature at night when the windows are closed. Besides, the heat produced by the lamps also could affect the air temperature produced by the cooler. Nevertheless, the supply air temperature became lower after several minutes because the outside air humidity controlled the inlet dry bulb temperature.

In addition, the evaporation process may take much time to cool the dry air inside the heat exchanger. This might be due to the temperature of water used to circulate them in the cooling system. And the speed of sprayed water. Therefore, the cooling process and the reduction of supply air temperature would be disrupted. Furthermore, the capability of the water pump to circulate the water to the water distribution system would impact the speed of sprayed water. This situation could cause the water would not be distributed to all external surface of the aluminium tubes.

3.1.2 The humidity profiles

The humidity of air was one of the factors that determined the thermal comfort level. Thus, it needed to take into consideration as it would influence the air temperature. That was why the humidity of air produced by the cooler is required to be recorded.

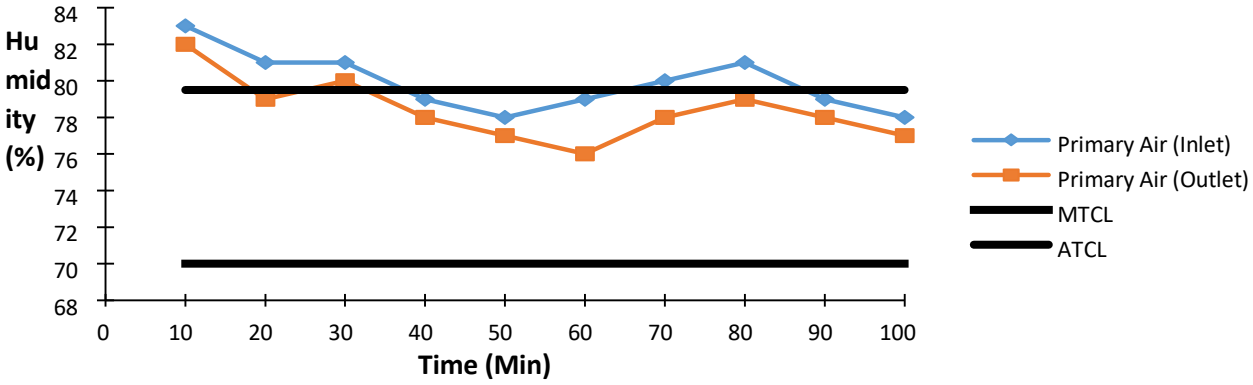


Fig. 12. Graph of relative humidity in the morning (8 to 9.40 am)

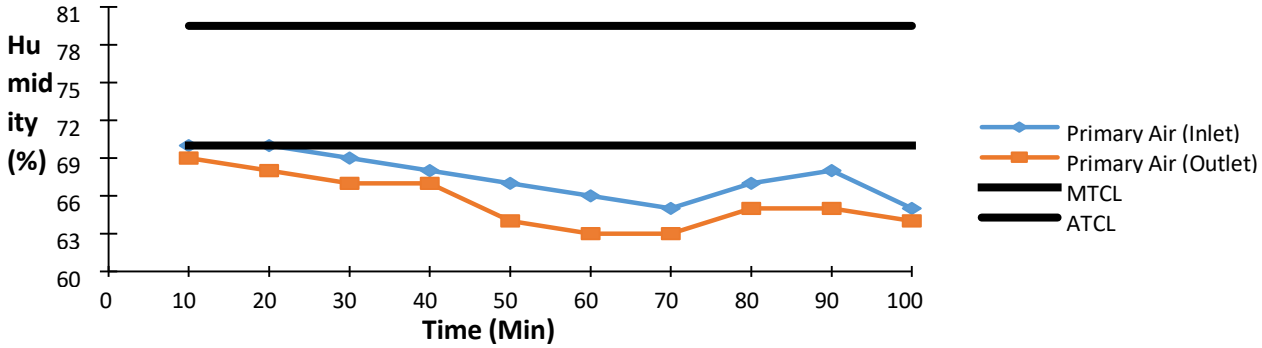


Fig.13. Graph of relative humidity in the afternoon (12 noon to 1.40 pm)

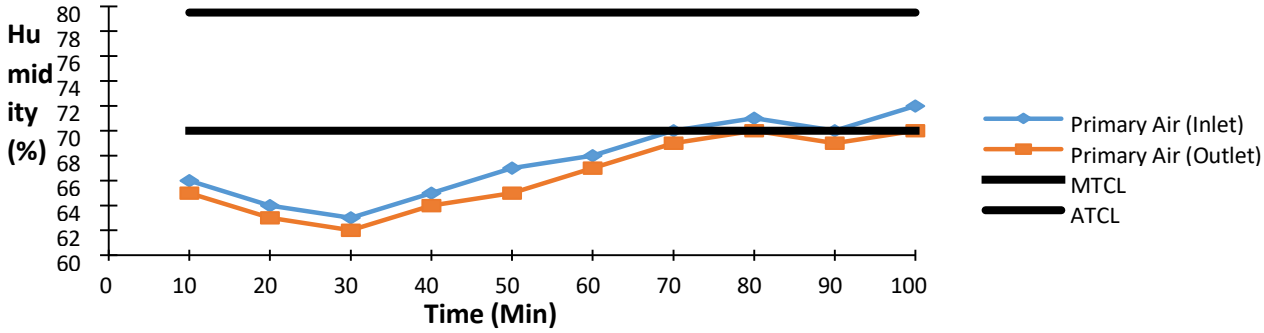


Fig.14. Graph of relative humidity in the evening (3pm to 4.40 pm)

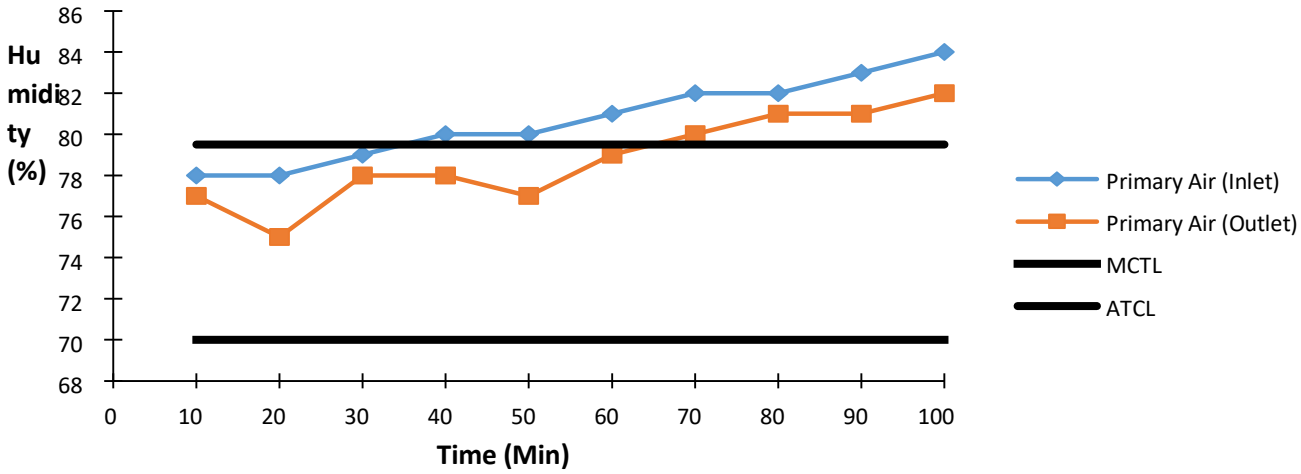


Fig. 15. Graph of relative humidity in the midnight (9 pm to 10.40 pm)

Figure 12 until Figure 15 indicated the humidity of air produced by the cooler at four different times. The results showed that the percentage of air humidity supplied into indoor was lower than the outdoor. So, the supply air produced related to the theory in which there was no moisture was added in the supply air when using IEC as discussed in the previous chapter.

In the morning and at night, the humidity level was slightly exceeded the ATCL at certain minutes because the relative humidity of inlet dry air was higher. When the moisture of inlet air enters indoor, the moist air will be trapped. This caused the rate of water evaporation process less efficient which resulted in a low cooling effect. In the afternoon and evening, the humidity level was below the MCTL as recommended in MS1525:2007 [12-13]. This was probably due to higher ambient air temperature that influenced the humidity level of air. During this moment, the air supplied will be less humid.

Previous researches concluded that the thermal comfort for humidity was about 55% until 70% [8, 12-14]. According to ASHRAE, a comfort zone for relative humidity is about 19.8% - 79.5% [15]. Mostly the humidity level of air produced from the experiment was below the ATCL. This was because the weather nowadays was very hot due to the uncertainty of weather changes and deficiency of rainfall when the experiment was conducted. According to the World Weather Online website [11], the average outside humidity for that day in the morning was about 78%, 69% in the afternoon, 68% in the evening and 77% at night.

3.2 Wet-bulb Efficiency

The performance of IEC in term of wet-bulb efficiency was calculated using the results of the experiment. The wet-bulb efficiency obtained was only 51.7%. When compared the performance of aluminium tubes IEC with other IEC, the wet-bulb efficiency of the porous ceramics IEC was lower than aluminium tubes IEC [16]. Based on the previous study researched by F. Wang et al [17], the wet-bulb efficiency of aluminium tubes IEC obtained was 65%. The difference in efficiency was due to the different length of the tubes used. However, according to ASHRAE, the efficiency of IEC was within the range of 40%-80% [18]. Therefore, the efficiency of the experimental IEC was still in the range of recommended wet-bulb efficiency

4. Conclusions

The results of the performance of experimental aluminium tubes IEC showed that IEC has good potential to become a thermal comfort cooling device. It was a cooling device that able to replace the usage of air conditioning, especially in an urban area. The occupants in the rural area can own the IEC because it was suitable to produce a cooling effect for indoor thermal comfort. This IEC was able to reduce the indoor temperature about 1℃ to 3℃ which is below ATCL for a small bedroom of 90 square feet. Besides, the humidity of IEC was within the range of humidity design as recommended for thermal comfort condition (19.8% - 79.5%) at certain period due to the outside temperature [19]. The wet-bulb efficiency of IEC performance was 51.7% which was within the range of 40% - 80% as recommended by ASHRAE [20].

Acknowledgement

The authors would like to thank the Faculty of Mechanical Engineering, Universiti Teknologi MARA Cawangan Pulau Pinang for their support and encouragement.

References

[1] M. S. Ahmed, A. Mohamed, R. Z. Homod, and H. Shareef, “Awareness on energy management in residential buildings: A case study in Kajang and Putrajaya,” no. 1 May, 2017.

[2] J. Hwi Kim,Min;Weon Jeong, “Cooling performance of a 100% outdoor air system integrated with indirect and direct evaporative coolers,” *Energy*, vol. 52, (2013): 245–257.

[3] B. Porumb, P. Ungureşan, L. F. Tutunaru, A. Şerban, and M. BĂlan, "A Review of Indirect Evaporative Cooling Technology," *Energy Procedia*, vol. 85, (2016): 461–471.
[4] Z. Duan *et al.*, "Indirect evaporative cooling: Past, present, and future potentials," *Renew. Sustain. Energy Rev.*, vol. 16, no.9, (2012): 6823–6850.
[5] V. S. K. Reddy, S. Praveen, and J. H. Arakeri, "Design and Performance Evaluation of an Indirect Evaporative Air Cooler," vol. 02, no. 01, 2012.
[6] "The Concept of Indirect Evaporative cooling," vol. 2, no. 5, (2013): 391–396.
[7] S. Mekhilef, A. Safari, W. E. S. Mustaffa, R. Saidur, R. Omar, and M. A. A. Younis, "Solar energy in Malaysia: Current state and prospects," *Renew. Sustain. Energy Rev.*, vol. 16, no. 1, (2012): 386–396.
[8] A. Jindal, "Thermal comfort study in naturally ventilated school classrooms in composite climate of India," *Build. Environ.*, vol. 142, (2018): 34–46.
[9] Y. Yong, "Equinox to have small impact on the country," *Staronline*, (2019). [Online]. Available: https://www.thestar.com.my/news/nation/2019/03/23/equinox-to-have-smallimpact-on-the-country. [Accessed: 06-May-2019].
[10] P. G. Bhwana, "Equinox Phenomenon;Temperature Slightly Increases," 2018. [Online]. Available: https://en.tempo.co/read/916936/equinox-phenomenontemperature-slightly-increases. [Accessed: 06-May-2019].
[11] "Permatang Pauh Weather Forecast." [Online]. Available: https://www.worldweatheronline.com/permatang-pauh-weather/pulaupinang/my.aspx. [Accessed: 20-Apr-2019].
[12] N. Jamaludin, N. I. Mohammed, M. F. Khamidi, and S. N. A. Wahab, "Thermal Comfort of Residential Building in Malaysia at Different Micro-climates," *Procedia - Soc. Behav. Sci.*, vol. 170, (2015): 613–623.
[13] Y. H. Yau, L. C. Ding, and B. T. Chew, "Thermal comfort and Indoor Air Quality at Green Building in Malaysia," *Int. J. Low Carbon Technol.*, vol. 1, no. 2, (2006): 167–176.
[14] N. A. Basri, A. T. Ramli, and A. S. Aliyu, "Malaysia energy strategy towards sustainability: A panoramic overview of the benefits and challenges," *Renew. Sustain. Energy Rev.*, vol. 42, (2015): 1094–1105.
[15] A. You, M. A. Y. Be, and I. In, "Effect of water temperature and air stream velocity on performance of direct evaporative air cooler for thermal comfort Effect of Water Temperature and Air Stream Velocity on Performance of Direct Evaporative Air Cooler for Thermal Comfort," vol. 030024, (2017): 1– 6.
[16] G. Heidarinejad and M. Bozorgmehr, "Modelling of Indirect Evaporative Air Coolers," vol. 1, no. September, (2007): 416–420.
[17] F. Wang, T. Sun, X. Huang, Y. Chen, and H. Yang, "Experimental research on a novel porous ceramic tube type indirect evaporative cooler," *Appl. Therm. Eng.*, vol. 125, (2017): 1191–1199.
[18] J. K. Jain, D. A. Hindoliya, and M. Pradesh, "Energy saving potential of the indirect evaporative cooler under Indian climates," no. October 2013, (2016): 193–198.
[19] C. Patil And K. Hirde, "The Concept of Indirect Evaporative cooling," *Int. J. Eng. Sci. Innov. Technol.*, vol. 2, no. 5, (2013): 391–396.
[20] B. Porumb, M. BĂlan, and R. Porumb, "Potential of Indirect Evaporative Cooling to Reduce the Energy Consumption in Fresh Air Conditioning Applications," *Energy Procedia*, vol. 85, (2016): 433–441.

Penerbit Akademia Baru

Engineering Science and Technology Conference Proceedings

Journal homepage: www.akademiabaru.com/EST.html

Evaluation of Atmospheric Boundary Layer in Open Loop Boundary Layer Wind Tunnel Experiment

Open Access

Vikneshvaran[1], Sheikh Ahmad Zaki[1,*], Nurizzatul Atikha Rahmat[2,*], Mohamed Sukri Mat Ali[1], Fitri Yakub[1]

[1] Wind Engineering for (Urban, Artificial, Man-Made) Environment Lab, Malaysia Japan International Institute of Technology, Universiti Teknologi Malaysia, Malaysia
[2] Faculty of Technology Mechanical and Automotive Engineering, Universiti Malaysia Pahang (UMP), Malaysia

ABSTRACT

Present work discusses in detail on the development of the quasi-atmospheric boundary layer in an open loop boundary layer wind tunnel over smooth surface. The wind tunnel has 1 m height and 9 m long working section which divided into three parts, 3 m long each. Constant temperature anemometer (CTA) hot wire was used to measure the air velocity inside the test section. The velocity of the wind tunnel is performed at 10 m/s. The measurement consists of three streamwise positions at three test sections, 162 vertical heights and 35 lateral points for each height. The vertical velocity distribution, standard deviation, and skewness are presented and it is observed that the boundary layer height is developing from windward to downward of the wind tunnel. The flow uniformity of the lateral velocity distribution and turbulence intensity of the inflow condition are confirmed to be 7.1 % and 6.4 % respectively.

Keywords:
Open loop wind tunnel; smooth surface; turbulence intensity

Copyright © 2019 PENERBIT AKADEMIA BARU - All rights reserved

1. Introduction

For decades, wind tunnel is widely used for studying the response of aircrafts and, vehicles [1]–[3]. Later, the utilization of wind tunnel was expanded to other areas, namely, the investigation of wind turbine efficiency for wind energy harvesting [4], [5], wind related researches in agriculture, forestry [6], [7] and also in sports [8], [9]. Nevertheless, wind tunnel is heavily employed over the last half century to examine the flow natures around various shapes of buildings and rigid bodies [10]–[13], to investigate wind pressure acting on building walls [14] which deeply related to the flow separation and vortex shedding [15], and to understand the strong wind effects on super tall buildings [16]. These factors are critical and have long been the main interest in the wind engineering field for robust structural design [17] to establish assessment and countermeasures of the safety of pedestrians [15].

However, in order to perform such experiments, deep wall boundary layer similar to the real atmosphere, namely quasi-atmospheric boundary layer is needed in the wind tunnel where in real condition, building is submerged in the lowest few hundred meters of the atmospheric boundary layer (hereafter, ABL), known as surface layer [18], [19]. Quasi-ABL generation is very important in wind tunnel study in order to understand the air flow around buildings [20] and examine the ventilation of an area inside the surface layer. The wind tunnel designed to simulate quasi-ABL is called the boundary layer wind tunnel (hereafter, BLWT) [19]. However, BLWT consists of a very

long test section varies from 15 m to 30 m length [21] hence rarely used nowadays due to its space and cost consuming. Therefore, a shorter test section wind tunnel is employed [15]. However, due to the limited fetch length of wind tunnel, the generation of deep boundary layer height (BLH) imitating the real atmospheric boundary layer (ABL) becomes difficult and methodologies to create quasi-ABL inside a wind tunnel with limited fetch length have been intensively developed [22]–[24]. Simulation of ABL in wind tunnel can be achieved by introducing man-made devices, in particular, the installation of passive devices (hereafter, PD) [25]–[30] and active devices (hereafter, AD) [31]–[33] at the wind ward position of the wind tunnel test section to generate acceptable mean and turbulent flow conditions. Once the quasi-ABL inside the wind tunnel is obtained, then the experimental study of wind flow natures around full or model scaled rigid bodies under controlled condition can be conducted [34]. During the test, the model was placed inside the test section and the effect of wind flow behind the model was measured and analyzed [35].

Previously, several experimental studies have been conducted to generate desired boundary layer in a limited fetch length wind tunnel [15], [36]–[38]. Although some research [39], [40]has been carried out using smaller building models with longer streamwise position, the evaluation of the development of the quasi-ABL is scarce to find. In addition, only few previous studies [41], [42] compared the obtained vertical velocity profiles with power law equation to verify its similarity. Therefore, present study aims to evaluate the development of the quasi-ABL over smooth surface in an empty open loop boundary layer wind tunnel with a longer fetch test section. Present experimental work is considered pre requisite task to investigate flow natures around buildings before the installation of building models inside the wind tunnel.

2. Past Studies on Boundary Layer Wind Tunnel (BLWT)

There are various wind tunnel experimental settings conducted by previous study to generate deeper BLH Table 1 lists literature that investigated the generation of the ABL under different method. The table allow to identify and compare the type of surface used, wind tunnel dimension and fetch length used by previous study and make comparison with current study. Mean wind velocity, turbulence intensity and power spectral density profile were among measured parameter analysed in the wind tunnel [31], [32]. In addition, surface shear stress [30], [36] also taken into account as an important parameter by some researcher.

Table 1
Previous study on ABL generation from year 1968 to 2018

Authors	Type of surface	Height	Width	Fetch length	Method to generate deeper BLH in the wind tunnel.	Remarks
Armitt et al., [22]	Rough	1.25 *S*	3.83 *S*	0.5 *S*, *S*, 1.5 *S* and 3.2 *S*	PD- Triangular spire	X-type hot wire Anemometer
Counihan, [23]	Smooth, Rough	1.22 *S*	4 *S*	3 *S* and 5 *S*	PD- Triangular plane-elliptic and quarter elliptic wedge spire	-
Shuyang [31]	Smooth	1.25 *S*	2.25 *S*	1.88 *S*	AD- multiple fan	Constant temperature hot wire anemometer
Cao et al., [32]	Smooth	2.25 *S*	3.25 *S*	6.25 *S*	AD- multiple fan	Hot wire anemometer
Hagishima et.al, [36]	Rough	1.25 *S*	1.88 *S*	3.83 *S*	PD- Roughness element	Split-film anemometer
Pires et al., [28]	Rough	1.33 *S*	1.50 *S*	5.20 *S*	PD- Triangular spire	Hot wire anemometers, Split- film anemometer

Hohman et al.,[29]	Rough	1.60 *S*	2.40 *S*	7.90 *S*	PD- Quarter elliptic wedge spire	Stereo particle Image Velocimetry (SPIV)
Rahmat et al., [38]	Smooth, Rough	1.25 *S*	1.88 *S*	2.70 *S*	PD- Quarter elliptic wedge spire	Split film anemometer
Hancock et al., [30]	Smooth, Rough	2.50 *S*	5.83 *S*	10.67 *S*, 17.83 *S*, 25 *S*	PD- Triangular spire	Laser-doppler anemometer (LDA)
Rahmat et al., [15]	Smooth	6 *S*	6 *S*	26 *S*	PD- Quarter elliptic wedge spire	Hot wire and CTA unit

Note: AD and PD refer to Active Device and Passive Device

3. Methodology

3.1 Wind Tunnel

The experiment was conducted in an open loop wind tunnel located at Malaysia-Japan International Institute of Technology (MJIIT) in Universiti Teknologi Malaysia Kuala Lumpur (UTMKL) campus. Figure 1 shows the schematic diagram of the wind tunnel which has a maximum length of 22.7 m. It consists of two centrifugal fans, wide angle diffuser, settling room front, contraction cone and a long test section divided into three section. The air sucked by the centrifugal fan will enter the wide-angle diffuser. The diffuser allows to obtain best quality of air before entering the test section. Meanwhile, the settling chamber which installed with honeycombs and mesh screen help to straighten the air flow and reduce turbulence effect. The contraction cone increases the speed of wind into the test section by providing a stable flow and reduces the pressure loss.

The test section designed in aluminum frame and composed with wide transparent windows made up of perspex to observe model placed in the test section. The test section roof and floor composed by wood panels and it is divided into three equal parts, 3 m long each. The vertical height of the test section is at 1 m from the bottom ground and width is at 1.35 m to have enough space for model setup. The wind speed in the test section ranged up to 30 m/s through fan rotation speed. Table 2 summarizes the specification of the BLWT tunnel.

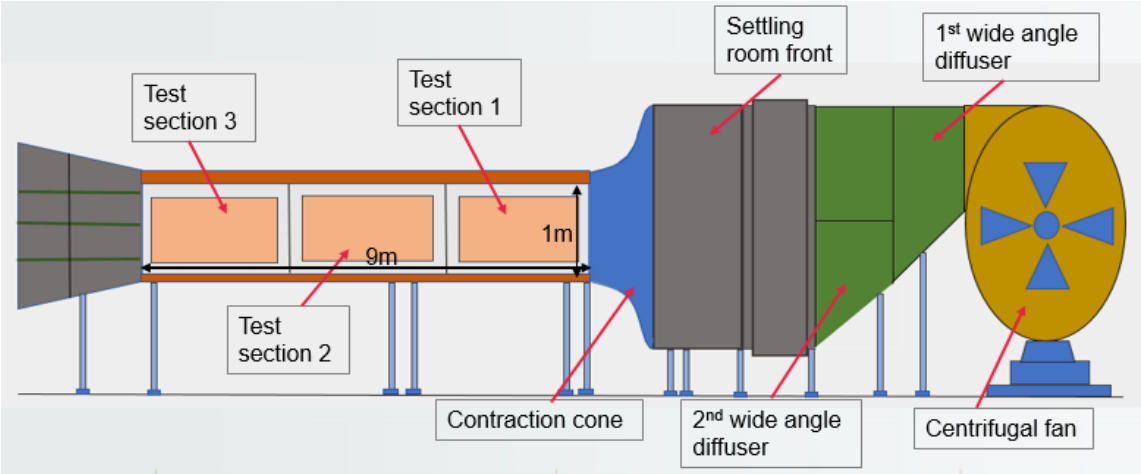


Fig. 1. Schematic side view diagram of an open-loop wind tunnel at MJIIT, Universiti Teknologi Malaysia Kuala Lumpur, (UTMKL)

Table 2
Basic specification of wind tunnel in this study

Item	Specification
Wind Tunnel	Open Loop
Maximum Dimension	22.7 m (*l*) x 3.4 m (*w*) x 3 m (*h*)
Test Section	9 m (*l*) x 1.35 m (*w*) x 1 m (*h*)
Velocity Range	0-30 m/s
Contraction Ratio	1: 5.6
Fan Power	50 000 Watt
Fan Voltage	380 V

Note: *l* is length, *w* is width and *h* is height

3.2 Measurement Positions

The vertical profile of the streamwise velocity was measured at 7 mm from the wind tunnel surface and was vertically increased at an interval of 1 mm, 5 mm, and 10 mm at 7 mm ≤ *z* ≤ 140 mm, 140 mm < *z* ≤ 160 mm, and 160 mm < *z* ≤ 400 mm, respectively, in a laterally centred points (*y* = 0) at all three leeward positions, *x* = 1.38 *S*, 5.13 *S* and 8.88 *S* (*S* refers to the height of spire, 800 mm [15]). Fig. 2 shows the schematic figure of test section of the wind tunnel. The total number of measurement points in the vertical line at each test section was 162. The streamwise velocity measurements and the reference velocity (hereafter, U_{400}), where subscript 400 refers to vertical height of 400 mm, were conducted with a stream velocity of 10 m/s, at *y* = 0, *z* = 0.5 *S*, respectively. Table 3 summarizes the vertical increments at all heights.

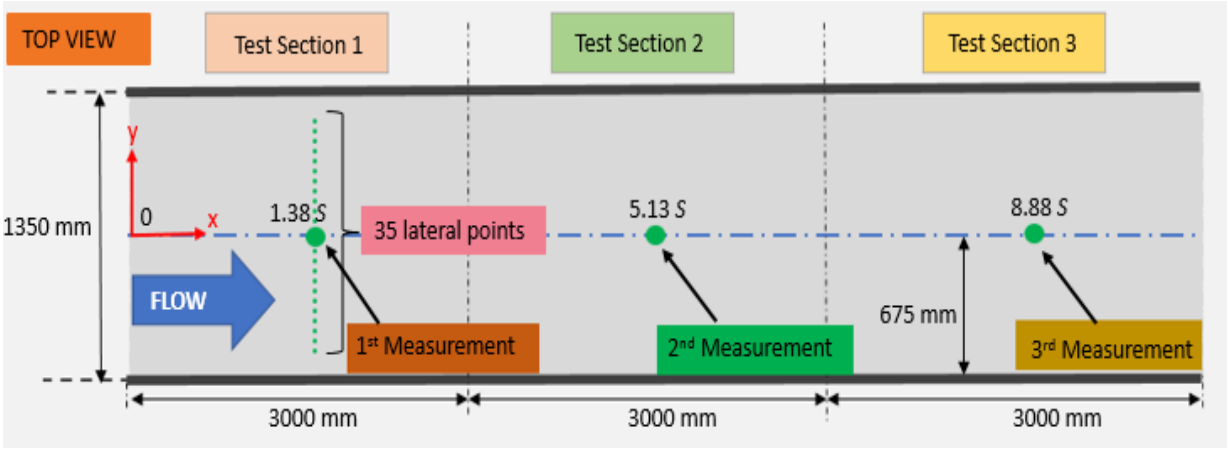


Fig. 2. Schematic figure of test section of wind tunnel with its streamwise measurement positions (*S* is 800 mm)

Table 3
Vertical measurement heights and its increments

Height, *z* (mm)	Δ *z* (mm)	Measured points
7 ≤ z ≤ 140	1	134
140 < z ≤ 160	5	4
160 < z ≤ 400	10	24
	Total	**162 points**

In addition, the distribution of the streamwise velocity in the lateral-vertical planes were measured at a leeward position, 1.38 *S*. At the lateral-vertical planes, measurements were conducted at three elevations based on acquired boundary layer height (hereafter, BLH = δ)

calculated from the negative peak of skewness of streamwise velocity profile, namely, within, at, and above BLHs. The measurement points are summarised in Table 4 below. The spatial resolution of the measurement in the spanwise direction was 30 mm (= 0.038 *S*) for the range of $-0.64\ S < y < 0.64\ S$. The total number of measurement points in a lateral line was 35 points.

Table 4
Determination height for streamwise velocity in the lateral-vertical planes

Position	Calculation
Below BLH	$0.5 \times \delta \times S$
At BLH	$1.0 \times \delta \times S$
Above BLH	$1.5 \times \delta \times S$

Note: (BLH = δ) is boundary layer height and *S* is spire height

3.3 Measurement Instrumentations and Experimental Setup

The streamwise velocity was measured using a single sensor hot-wire anemometer (straight, Dantec, 55P11) and a miniCTA unit (Dantec, Model 54T42). The hot wire supplies the sensor with a heating current that varies with the wind velocity. Two legs of hot wire connected with tungsten wire welded to the prongs. The hot wire is connected to the National Instrument device called Hi-Speed USB Carrier for data transmission and then connected to the LabView software for data collection. The measurement frequency and period were 1000 Hz and 10 s, and were recorded using LabView software. All measurements data were performed at a reference streamwise velocity of 10 ms^{-1} at vertical height of 0.5 *S*.

The hot wire was calibrated every time before measurement using a pitot tube (Dwyer, series 160-36). Both hot wire and pitot tube was brought into the wind tunnel test section using a three-dimensional traverse system. The pitot tube calculates the air speed by measuring the differential pressure inside the wind tunnel, given in eq.1,

$$V = 4.43\sqrt{\frac{P_D}{\rho_{air}}} \tag{1}$$

where P_D represent air density based on temperature and humidity inside the wind tunnel and ρ_{air} denotes differential pressure measured from the pitot tube. In present experimental work, P_D is kg/m^3 and ρ_{air} in the unit of mmH_2O.The pitot tube was connected with the pressure transducer located at pneumatic cabinet for pressure transmission using rubber hose. The pneumatic cabinet is directly connected to the control panel of the control room which allows the control of wind tunnel speed. Finally, the measurement was then recorded inside the wind tunnel, thus, can be directly taken from the control panel. Table 5 lists the specification of instruments used in the present study.

The hot sire was set to collect data at measurement frequency of 1 kHz for 10 seconds. A calibration curve for hot wire was obtained using polynomial curve fitting as in equation (2) where *E* is the corrected output voltage constant while *A*, *B* and *C* are calibration constant.

$$U = AE^4 + BE^2 + C \tag{2}$$

Once the calibration was completed, the pitot tube was removed and the hot wire was moved to the target position. The speed of wind was set remained 10 m/s inside the wind tunnel. Based on

the analysis conducted previously, wind tunnel fan was found to achieve stability at speed above 10 m/s. Thus, this experiment was carried out at minimum speed where the fan is stable.

Table 5
Specification of instruments used in present study

Item	Hot Wire	Hi-Speed USB Carrier	Pitot tube
Brand	Dantec	National Instrument	Dwyer
Model	55P11	NI USB-9162	Series 160-36
Type	Constant Temperature Anemometer (CTA)	CompactDAQ chassis	Pitot static tube
Material	Tungsten	-	Stainless Steel
Diameter	5 µm	-	8 mm
Output Channel	-	4	-
Current Consume	-	500 mA	-
Maximum sampling frequency	20 000 Hz	-	1000 Hz

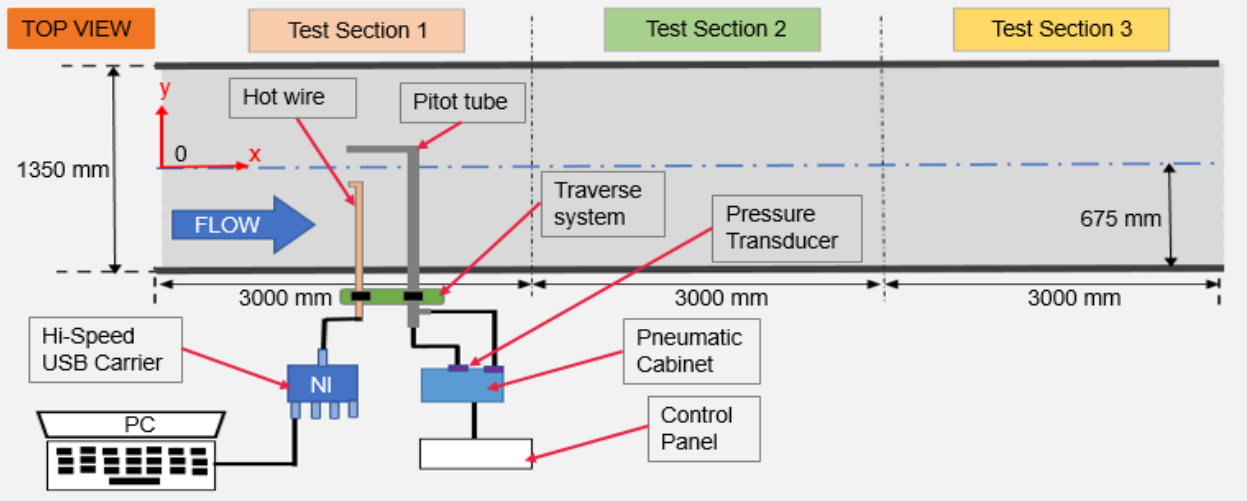


Fig. 3. Schematic figure of experimental setup for calibration of the wind tunnel

4. Results and Discussion

4.1 Vertical Velocity Profiles Over Smooth Surface

Fig. 4 depict the vertical velocity profiles of the mean, standard deviation, and skewness of the streamwise velocity at the lateral central point, $y = 0$ of streamwise positions, $x = 1.38\ S$, $5.13\ S$ and $8.88\ S$, respectively. The mean wind velocity and standard deviation were normalised by U_{400}, the mean velocity at $y = 0$ and $z = 0.5\ S$.

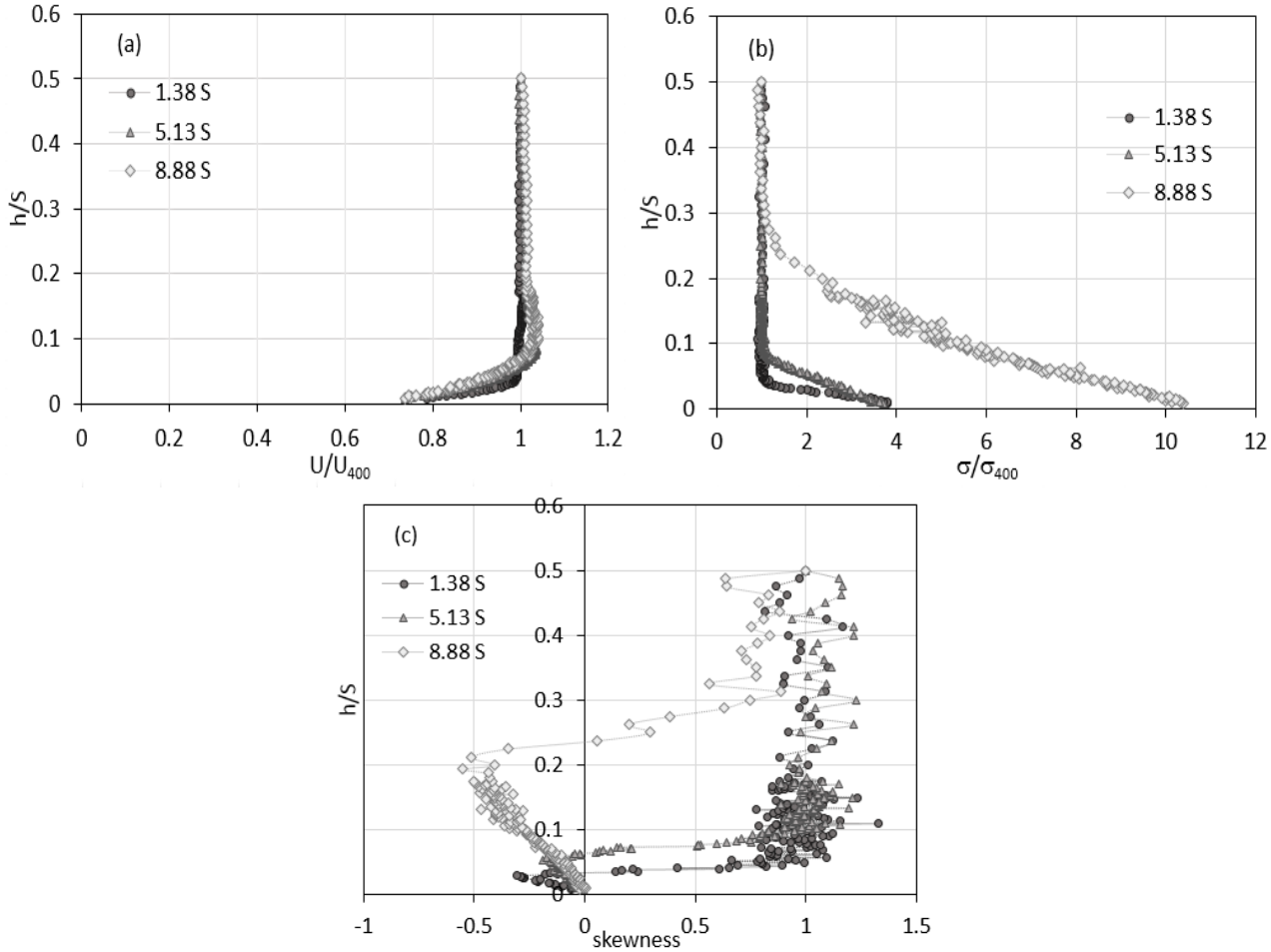


Fig. 4. Normalized vertical velocity profile of (a) mean, (b) standard deviation and (c) skewness of streamwise velocity at lateral centre point (y=0) of streamwise positions, *x* = 1.38 *S*, 5.13 *S* and 8.88 *S*

The mean wind velocity profile shown in Fig. 4(a) display an obvious change in the velocity gradient at heights around 0.009 *S* to 0.194 *S*. One can clearly observe the development of the boundary layer depth with the increased of the fetch length, from windward *x* = 1.38 *S* to leeward *x* = 8.88 *S* before it achieved a constant velocity at a particular height. For each streamwise positions *x* = 1.38 *S*, 5.13 *S*, and 8.88 *S* the velocity become gradually constant at vertical heights above *z* = 0.04 *S*, 0.054 *S*, and 0.2 *S*, respectively.

With regard to the standard deviation, the data for each point was calculated using below equation 3,

$$\sigma = \sqrt{\frac{\sum_{i=1}^{N}(x_i - \bar{x})^2}{N-1}} \tag{3}$$

where x_i represent value of sample while $\bar{x}$ refer mean value of sample and *N* is number of samples. The data of the standard deviation in Fig. 4(b) show the highest values at the lowest measurement height, and the value gradually decrease with the height. At each fetch distance the standard deviation become large near the surface because of strong shear and it shows monotonic decrease with the height.

In contrast, the skewness in Fig. 4(c) is drawn for all streamwise position. The skewness for each point was calculated by

$$skewness = \frac{[(N-1)(N-2)]}{N} \sum_{j=1}^{N} \frac{(x_j - \bar{\bar{x}})^3}{\sigma_x^3} \quad (4)$$

The skewness of the streamwise velocity decreases with the height near the surface, shows a sharp negative peak, and returns to around the value one at all streamwise condition. By comparing the skewness with mean wind profiles, it can be observed that the height of the negative peak in the skewness is almost consistent with the height at which the mean velocity becomes almost height independent. Considering the fact that the mean wind profile far above the wind tunnel floor shows a weak height dependency, it is hard to precisely determine the 99% boundary layer height. Consequently, we treated the height of the negative sharp peak of the skewness profile as the BLH δ for the following analysis. Table 6 summarise the BLH obtained and measured height of uniformity at each streamwise position.

Table 6
Table of BLH for all 3-test section and measured height of uniformity

Streamwise position	BLH	Height (below BLH) (mm)	Height (at BLH) (mm)	Height (above BLH) (mm)
1.38 *S*	0.03 *S*	12	24	36
5.13 *S*	0.054 *S*	22	43	65
8.88 *S*	0.194 *S*	78	155	233

Meanwhile, Fig. 5 shows the boundary layer height over smooth surfaces at each streamwise position observed by present study. The spatially averaged BLH was calculated based on the negative skewness peak at all spanwise position. The previous experimental data and theoretical derivation for a smooth wall based on eq.5 are also included in Fig. 5 for comparison.

$$\delta(x) = 0.38\left(\frac{U_\infty x}{\nu}\right)^{-1/5} x \quad (5)$$

The value U_∞, represent reference velocity (m/s) and ν denotes the kinematic viscosity of air (m^2/s). As been illustrated in the Fig. 5, the dashed line refers to equation of boundary layer depth over smooth wall. Theoretically, the depth of naturally-grown turbulent boundary layer over a smooth wall shows continuous and gradual increase as the dashed line behave. Fortunately, the present data for smooth surface indicates continuity of the BLH growth. As shown in Fig. 5, the BLH measured at the streamwise position given by present study and Rahmat et al. 2016 [38] is almost consistent with the theoretical equation curve and indicates continuity of the BLH growth. However the other two experiment of Hamoud et al. 2010 [27] and Rahmat et al. 2018 [15] shows discrepancies which were probably caused by the effect of the inflow condition.

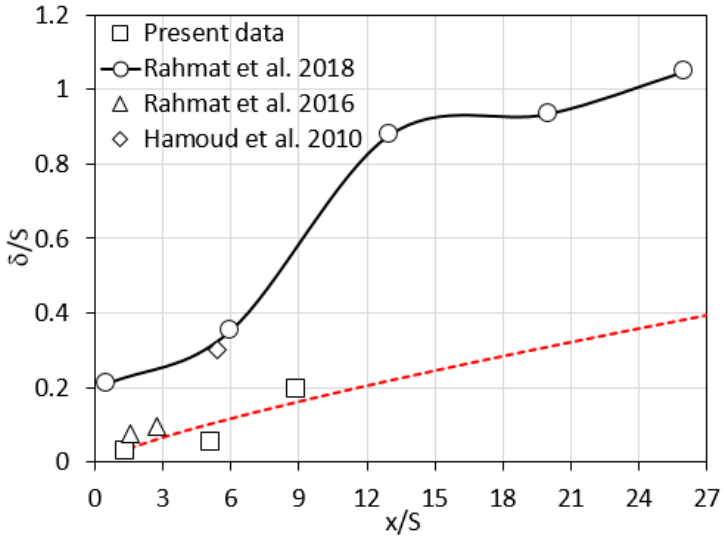
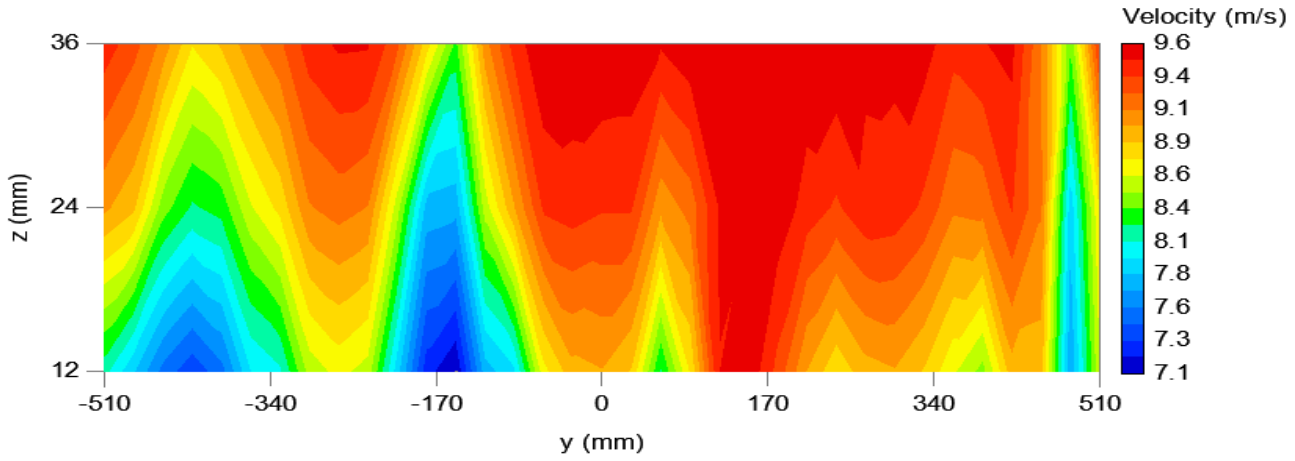


Fig. 5. Boundary layer height normalized by spire height against streamwise distance over smooth surface observed by various experiments including present study. Dashed line refers to equation of boundary layer over smooth wall. (depicted from Rahmat et al. 2018 [15])

4.2 Spanwise Uniformity and Turbulence Intensity

Contour colour drawn for velocity and turbulence intensity distributions measured at lateral position along 1.38 *S*. Fig 6 shows the contour colour of 35 lateral points measured for each height with three different heights. In total there were 105 points of measurement took place for the provided contour plot. The scaled measurement data construct the final output plots by providing the distribution of mean velocity and turbulence intensity level along the lateral position. Turbulence intensity of the flow quality in terms of the turbulence generated inside wind tunnel was computed as

$$Tu = \frac{rms\,(V)}{Vmean} \tag{6}$$



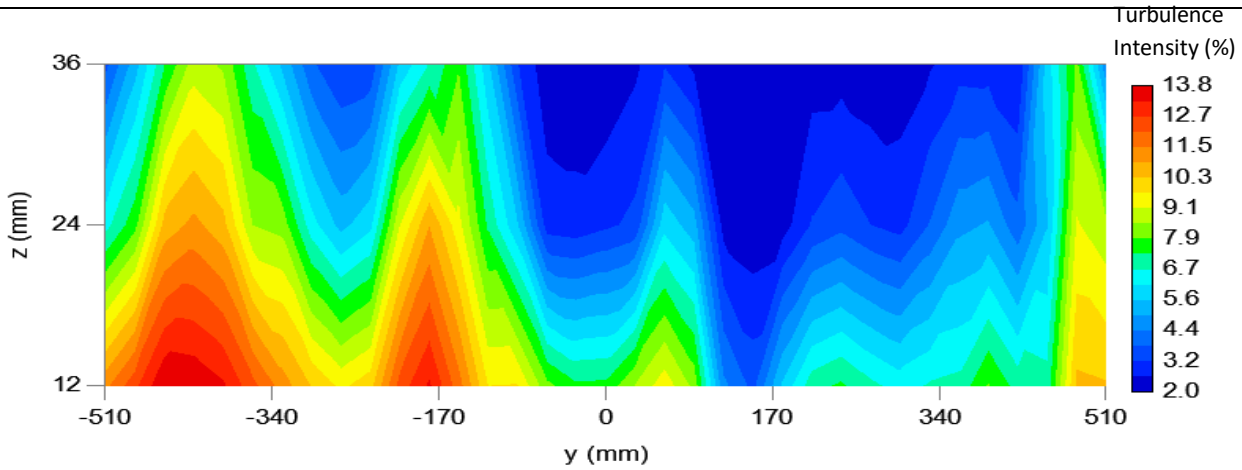


Fig. 6. Contour color of flow velocity and turbulence intensity

Mean velocity and turbulence intensity colour plots were obtained using Graph R software. The average velocity recorded was 8.91 m/s and velocity distribution show less uniformity along both the *y* and *z* direction. Velocity differences are contained in a bin of the order of 0.25 m/s. There were high number of turbulences found at the left side edge of the contour plot especially near to the ground surface of test section. The average flow uniformity and turbulence intensity obtained was 7.1 % and 6.4 % respectively. Table 7 provide percentage uniformity measured at each height.

Table 7
Uniformity and turbulence intensity at each height

Height	Flow uniformity (%)	Turbulence Intensity (%)
Below BL	7.55	9.21
At BL	5.66	5.91
Above BL	3.66	4.13

The definitions for the boundary layer depth δ is the height where the streamwise velocity is 99% of the free stream velocity, namely 99% thickness. However, it is difficult to quantify the exact height due to the slightly large spanwise non-uniformity of approaching flow in the wind tunnel. Therefore, the other way to determine the boundary layer depth is by using the spatially averaged vertical profiles of mean, standard deviation, and skewness.

4.3 Power Law

The power-law of mean wind often used as a substitute for the logarithmic wind velocity profile and adopted as target profiles to be reproduced inside the wind tunnel. The *U* denoted by the velocity at the height *Z* and U_R is known wind speed at reference height Z_R while the α is the power law exponent.

$$\frac{U}{U_R} = \left(\frac{Z}{Z_R}\right)^{\alpha} \quad (7)$$

For the case of turbulence boundary layer over smooth surfaces, the power index value should be around 0.142 [43] while for the case of boundary layer over rough surfaces, the range of power index is between 0.167 to 0.25. For this study, the power index found to be 0.147. Fig 7 below

provided with the comparison of power law equation with measured data at three streamwise position.

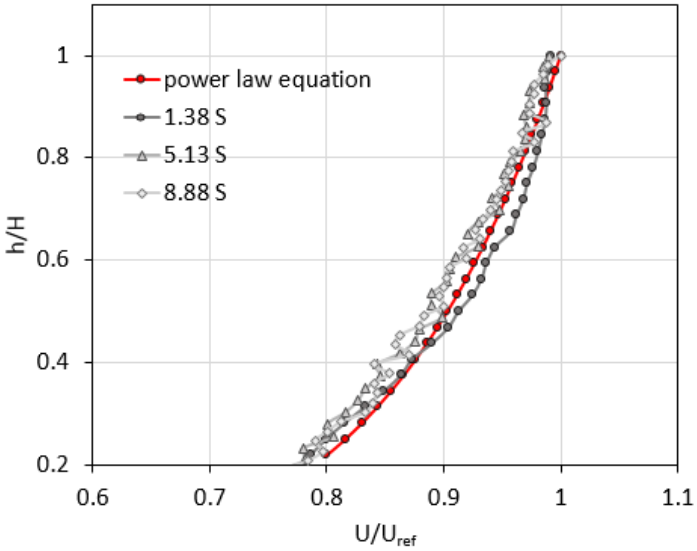


Fig. 7. Comparison of power law equation with measured data at streamwise 1.38 *S*, 5.13 *S* and 8.88 *S*

The comparison shows measured velocity profile graph lies almost similar with graph of equation of power law. The graph was normalised at height *H* where the air velocity become constant. The air velocity at height *H* denoted with U_{ref}. Few points can be seen intercept parallel with power law equation curve. The comparison allows understanding real data with the theoretical data.

5. Conclusions

The present study was designed to investigate the development of the quasi-atmospheric boundary layer in an open loop wind tunnel over smooth wall. The study was conducted at speed 10 m/s and measurement was done by using Constant Temperature Anemometer (CTA) hot wire. The experiment analysed the velocity profile of mean, standard deviation and skewness of streamwise velocity at lateral central point $y = 0$ of streamwise position x = 1.38 *S*, 5.13 *S* and 8,.88 *S*. The uniformity flow also been analysed along lateral position at streamwise position of 1.38 *S*. The obtained vertical velocity profiles were compared with power law equation to verify its similarity

In conclusion, the experimental results highlighted that boundary layer was found developing with the fetch length from 1.38 *S* to 8.88 *S*. The comparison of skewness with mean wind profile found that the negative peak height in the skewness is almost the same with the height of mean velocity where it become gradually constant. Thus, present study treated the height of the negative sharp peak of the skewness profile as the boundary layer height in the analysis. The flow uniformity and turbulence intensity were found 7.1 % and 6.4 % respectively. With these findings, the distribution of wind flow structure become a reference for smooth surface inflow condition of any scaled model tested inside the wind tunnel in the future. There is abundant room for further progress in generating deeper atmospheric boundary layer by applying passive device inside the wind tunnel.

Acknowledgement

This research was funded by a grant from Research University Grant (Vot 01M46) of Universiti Teknologi Malaysia).

References

[1] D. P. Witkowski, A. K. H. Lee, and J. P. Sullivan, "Aerodynamic interaction between propellers and wings," *J. Aircr.*, 1989.

[2] J. S. Flanagan, R. C. Strutzenberg, R. B. Myers, and J. E. Rodrian, "Development and flight testing of a morphing aircraft, the NextGen MFX-1," in *Collection of Technical Papers - AIAA/ASME/ASCE/AHS/ASC Structures, Structural Dynamics and Materials Conference*, 2007.

[3] F. Cheli, R. Corradi, D. Rocchi, G. Tomasini, and E. Maestrini, "Wind tunnel tests on train scale models to investigate the effect of infrastructure scenario," *J. Wind Eng. Ind. Aerodyn.*, 2010.

[4] I. Bayati, M. Belloli, L. Bernini, and A. Zasso, "Aerodynamic design methodology for wind tunnel tests of wind turbine rotors," *J. Wind Eng. Ind. Aerodyn.*, 2017.

[5] S. Roy and U. K. Saha, "Wind tunnel experiments of a newly developed two-bladed Savonius-style wind turbine," *Appl. Energy*, 2015.

[6] T. A. M. Van De Ven, D. W. Fryrear, and W. P. Spaan, "Vegetation characteristics and soil loss by wind," *J. Soil Water Conserv.*, 1989.

[7] K. Saxton, D. Chandler, L. Stetler, B. Lamb, C. Claiborn, and B. H. Lee, "Wind erosion and fugitive dust fluxes on agricultural lands in the Pacific Northwest," *Trans. Am. Soc. Agric. Eng.*, 2000.

[8] B. Blocken and Y. Toparlar, "A following car influences cyclist drag: CFD simulations and wind tunnel measurements," *J. Wind Eng. Ind. Aerodyn.*, 2015.

[9] L. Wang, Z. H. Shi, G. L. Wu, and N. F. Fang, "Freeze/thaw and soil moisture effects on wind erosion," *Geomorphology*, 2014.

[10] N. Lin, C. Letchford, Y. Tamura, B. Liang, and O. Nakamura, "Characteristics of wind forces acting on tall buildings," *J. Wind Eng. Ind. Aerodyn.*, 2005.

[11] Q. M. Zahid Iqbal and A. L. S. Chan, "Pedestrian level wind environment assessment around group of high-rise cross-shaped buildings: Effect of building shape, separation and orientation," *Build. Environ.*, 2016.

[12] E. Aristodemou *et al.*, "How tall buildings affect turbulent air flows and dispersion of pollution within a neighbourhood," *Environ. Pollut.*, 2018.

[13] Y. Liu, G. A. Kopp, and S. Chen, "Effects of plan dimensions on gust wind loads for high-rise buildings," *J. Wind Eng. Ind. Aerodyn.*, 2019.

[14] W. Lou, M. Huang, M. Zhang, and N. Lin, "Experimental and zonal modeling for wind pressures on double-skin facades of a tall building," *Energy Build.*, 2012.

[15] N. A. Rahmat, A. Hagishima, and N. Ikegaya, "Experimental Study on Effect of Spires on the Lateral Nonuniformity of Mean Flow in a Wind Tunnel," *Evergreen*, vol. 5, no. 1, pp. 1–15, 2018.

[16] Q. S. Li, X. Li, Y. He, and J. Yi, "Observation of wind fields over different terrains and wind effects on a super-tall building during a severe typhoon and verification of wind tunnel predictions," *J. Wind Eng. Ind. Aerodyn.*, 2017.

[17] J. C. R. Hunt, "The Effect of Single Buildings and Structures," *Philos. Trans. R. Soc. A Math. Phys. Eng. Sci.*, 1971.

[18] M. Li *et al.*, "CFD simulation of the wind field in Jinjiang City using a building data generalization method," *Atmosphere (Basel).*, 2019.

[19] R. Stull, "An Introduction to Boundary Layer Meteorology," *Book*, 1998.

[20] W. D. Lubitz and B. R. White, "Atmospheric Boundary Layer Wind Tunnel Applications in Wind Turbine Siting," *AIAA/ASME Wind Energy Symp. Reno, USA*, 2004.

[21] F. H. D. J.E. Cermak, A.G. Davenport, S. R. R. P.A. Irwin, N. Isyumov, J.A. Peterka, T. S. T.A. Reinhold R.H. Scanlan, and and P. J. V. A.C. Steckley, H. Tieleman, *Wind Tunnel Studies of Buildings and Structures*. ASCE Manuals and Reports on Engineering Practice No. 67, 1999.

[22] J. Armitt and J. Counihan, "The simulation of the atmospheric boundary layer in a wind tunnel," *Atmos. Environ.*, 1968.

[23] J. Counihan, "An improved method of simulating an atmospheric boundary layer in a wind tunnel," *Atmos. Environ.*, 1969.

[24] J. Counihan, "Further measurements in a simulated atmospheric boundary layer," *Atmos. Environ.*, 1970.

[25] N. J. Cook, "Wind-tunnel simulation of the adiabatic atmospheric boundary layer by roughness, barrier and mixing-device methods," *J. Wind Eng. Ind. Aerodyn.*, vol. 3, no. 2–3, pp. 157–176, 1978.

[26] I. P. Castro, "Relaxing wakes behind surface-mounted obstacles in rough wall boundary layers," *J. Fluid Mech.*, vol. 93, no. 4, pp. 631–659, 1979.

[27] H. A. Al-Nehari, A. K. Abdel-Rahman, A. El-Moneim Nassib, and H. M. Shafey, "Design and construction of a wind tunnel for environmental flow studies," *J. Eng. Sci. Assiut Univ.*, vol. 38, pp. 177–193, 2010.
[28] L. B. M. Pires, I. B. de Paula, G. Fisch, R. Gielow, and R. da M. Girardi, "Simulations of the atmospheric boundary layer in a wind tunnel with short test section," *J. Aerosp. Technol. Manag.*, 2013.
[29] T. C. Hohman, T. Van Buren, L. Martinelli, and A. J. Smits, "Generating an artificially thickened boundary layer to simulate the neutral atmospheric boundary layer," *J. Wind Eng. Ind. Aerodyn.*, 2015.
[30] P. Hancock and P. Hayden, "Wind-Tunnel Simulation of Weakly and Moderately Stable Atmospheric Boundary Layers," *Springer*, vol. 168, no. 1, pp. 29–57, 2018.
[31] C. Shuyang *et al.*, "An actively controlled wind tunnel and its application to the reproduction of the atmospheric boundary layer," *Boundary-Layer Meteorol.*, pp. 61–76, 2001.
[32] S. Cao, A. Nishi, H. Kikugawa, and Y. Matsuda, "Reproduction of wind velocity history in a multiple fan wind tunnel," *J. Wind Eng. Ind. Aerodyn.*, 2002.
[33] J. . Pang and Z. . Lin, "Development and experimental study on the active simulation device in boundary layer wind tunnel," *J. Exp. Fluid Mech.*, no. 22(03), pp. 80–85, 2008.
[34] J. K. Calautit, H. N. Chaudhry, B. R. Hughes, and L. F. Sim, "A validated design methodology for a closed-loop subsonic wind tunnel," *J. Wind Eng. Ind. Aerodyn.*, 2014.
[35] C. Stout *et al.*, "Efficiency Improvement of Vertical Axis Wind Turbines with an Upstream Deflector," in *Energy Procedia*, 2017.
[36] A. Hagishima, J. Tanimoto, K. Nagayama, and S. Meno, "Aerodynamic parameters of regular arrays of rectangular blocks with various geometries," *Boundary-Layer Meteorol.*, 2009.
[37] S. Ahmad Zaki, A. Hagishima, and J. Tanimoto, "Experimental study of wind-induced ventilation in urban building of cube arrays with various layouts," *J. Wind Eng. Ind. Aerodyn.*, 2012.
[38] N. A. Rahmat, A. Hagishima, N. Ikegaya, and J. Tanimoto, "An Experimental Study on Aerodynamic Interaction Between a Boundary Layer Generated by a Smooth and Rough Wall and a Wake Behind a Spire," pp. 19–26, 2016.
[39] S. Hassanli, K. Chauhan, M. Zhao, and K. C. S. Kwok, "Application of through-building openings for wind energy harvesting in built environment," *J. Wind Eng. Ind. Aerodyn.*, vol. 184, pp. 445–455, 2019.
[40] M. Shirzadi, Y. Tominaga, and P. A. Mirzaei, "Wind tunnel experiments on cross-ventilation flow of a generic sheltered building in urban areas," *Build. Environ.*, vol. 158, pp. 60–72, 2019.
[41] H. Kozmar and B. Laschka, "Wind-tunnel modeling of wind loads on structures using truncated vortex generators," *J. Fluids Struct.*, vol. 87, pp. 334–353, 2019.
[42] D. Hlevca and M. Degeratu, "Atmospheric boundary layer modeling in a short wind tunnel," *Eur. J. Mech. B/Fluids*, vol. 79, pp. 367–375, 2020.
[43] M. T. Schobeiri, *Fluid mechanics for engineers: A graduate textbook*. 2010.

Penerbit Akademia Baru

Engineering Science and Technology Conference Proceedings

Journal homepage: www.akademiabaru.com/EST.html

Characterization of Raw Materials and Manufactured Binderless Particleboard from Spent Mushroom Substrate and Open Rubberwood Sawdust

Open Access

Mohammad Aliff Shakir[1], Baharin Azahari[2], Yusri Yusup[1], Mohd Firdaus Yhaya[3] , Ali Salehabadi[1] and Mardiana Idayu Ahmad[1,*]

[1] Environmental Technology Division, School of Industrial Technology, Universiti Sains Malaysia, 11800 Gelugor, Pulau Pinang, Malaysia
[2] Bio-resource, Paper and Coatings Technology Division, School of Industrial Technology, Universiti Sains Malaysia, 11800 Gelugor, Pulau Pinang, Malaysia
[3] Biomaterial and 3D Imaging (BioM3D) Laboratory, School of Dental Sciences, Universiti Sains Malaysia, 16150 Kubang Kerian, Kelantan, Malaysia

ABSTRACT

This study aimed to examine the extractive, alpha-cellulose, hemicellulose, and lignin content in the spent mushroom substrate (SMS) and rubberwood sawdust (RWS) to evaluate its suitability in production of binderless particleboard. In this study, SMS fiber and RWS fiber were used to produce experimental binderless particleboard panels. Binderless particleboards were made with a target density of 0.80 g/cm^3 at temperature 130^{o}C and a pressure at 5 MPa during the hot press. The chemical composition of the SMS fiber was found slightly lower than RWS fiber. The degradation of the chemical composition has result reduction of particle size and discolouration of fiber. Binderless particleboard made from SMS fiber also has slightly lower mechanical strength compare to RWS fiber. The reaction profile and thermal stability thermogram did not show any substantial difference between SMS and RWS samples. Based on the finding of this study, spent mushroom substrate (SMS) does not have an extreme reduction in chemical, thermal and mechanical properties compare to rubberwood sawdust (RWS).

Keywords:
Cellulose; thermal; binderless; particleboard

Copyright © 2019 PENERBIT AKADEMIA BARU - All rights reserved

1. Introduction

The spent mushroom substrate (SMS) is a valuable by-product from the mushroom industries. It consists of partially degraded of lignocellulose material commonly rubberwood sawdust [1, 2]. Mushroom cultivation has consistently been increasing and producing a tremendous amount of mushroom waste [3, 4]. For one kilogram of mushroom required about five-kilogram substrate material to be turned into waste [5]. Rubberwood sawdust (RWS) degraded by during mushroom growth known as spent mushroom substrate (SMS) were selected as the materials for this study. Oyster mushroom known as white-rot fungi is the most common mushroom being grow in Malaysia [2, 3]. Substrate inoculated with white-rot fungi will have tendency discolour from brown to white due to degradation of lignin [2, 12].

* *Corresponding author.*
E-mail address: drmia707@gmail.com (Mardiana Idayu Ahmad)

The wood degraded by the mushroom is considered as waste material from mushroom cultivation process and product of natural lignocellulosic enzymatic systems [13, 14]. The previous study reports that the mechanical properties of wood fiber can be improved by exposed to enzymatic pre-treatment during mushroom cultivation. The studies also mentioned that the laccase enzyme during mushroom production will degraded the phenolic molecules in wood fiber. As the result, binderless particleboard made from the wood fiber will have an improvement in mechanical properties of the board [15].
Besides, Oyster mushroom species used in this study also able to secrete an enzyme that able to digest lignocellulosic component by breakdown the polysaccharides into low molecular weight monomer and oligomer sugar as energy uptake for the growing activity of mushroom [11, 16, 17]. The degradation of the chemical composition such as cellulose and hemicelluloses might give a negative or positive effect on the wood fiber during the production of binderless particleboard. Recent studies mentioned that the breakdown of hemicelluloses into small sugar monomer and degradation of lignin during pre-treatment might contribute to the self-bonding between fiber [18-20]. This also will lead to improve the mechanical properties of the particleboard.
Previous studies report that the chemical composition of wood fiber was important as it will affect the mechanical performance of the board [18, 21]. The determination amount of lignocelluloses component that undergoes degradation during mushroom growth activity is important. The purpose of this study was to compare with the current raw materials (RWS) with mushroom waste product (SMS) and examine its suitability for production binderless particleboard.
Hence, this study also analyzes the chemical, thermal and mechanical properties of the spent mushroom substrate (SMS) as it might be potentially be utilized to replace the current RWS as raw materials in binderless particleboard.

2. Methodology

2.1 Materials

The SMS fiber and RWS fiber used in this study was obtained from mushroom farm house in PPK Lahar Bubu, Pulau Pinang, Malaysia. SMS fiber is a waste from mushroom substrate made from rubberwood. The SMS fiber was used as substrate for mushroom production about 3 month. While the RWS fiber is unused raw material before preparation fresh new mushroom substrate.



Fig. 1 Spent mushroom substrate block

2.2 Fabrication of particleboard

The SMS fiber and RWS fiber was obtained and disintegrated homogenously. The fibers was placed and dispersed in steel mould with dimension 21 cm × 15 cm × 0.6 cm at target density 0.80 g/cm^3. Then, the fabrication process was continued by heating process using a hot pressed machine at temperature 130 ^oC with pressure of 5 MPa for 40 min. For flexural test, the particleboard was cut and tested according to Japanese Industrial Standard JIS A 5908:2003 [22]. While for tensile test, the board samples was prepare according to ASTM D3039 [23].

2.3 Chemical composition analysis

The chemical composition of SMS fiber and RWS fiber were determined. Both samples was dried and disintegrated into powder. Samples were extracted by a mixture of ethanol and toluene (2:1, v/v) for 6 hour of refluxing. Hollocellulose and lignin contents were determined by using Wise Methods and TAPPI standard 22 os 74, respectively [18, 24]. Alpha cellulose content was determined by extraction of hollocelulose with 17.5 % NaOH solution. Hemicellulose content was calculated by subtracting the alpha cellulose content from the hollocellulose content. All analyses were carried out in triplicate.

2.4 Particle size distribution analysis

The particle size distribution of micro-sawdust particles was measured by the dry sieving method using dry laser diffraction (Malvern Sciro2000 Mastersizer). The fiber samples were disintegrated and dry at 50 ^oC for 24 hours to ensure that the fiber will not agglomerate during analysis. The refractives index for the fiber was set at 1.53. The mean of particle size distribution of the both fiber sample were reported in the graph. 97

2.5 Fourier transforms infrared spectroscopy (FTIR)

The functional groups exist in fibers were analyzed using Fourier Transform Infrared Spectroscopy (FTIR) analyses using Perkin Elmer 1600 Infrared spectrometer. Approximately 5 mg of fibers of each type of sample with 95 mg of finely ground potassium bromide (KBr) were mixed together and pressed into pellets of about 1mm in thickness. The FTIR spectrum of each sample was then analyzed using the Nicole infrared spectrophotometer (Avatar 360 FTIR E.S.P) between

wave numbers of 4000 cm^{-1} and 470 cm^{-1} with a resolution 4 cm^{-1} . The functional groups of the compound of each sample were recorded. The significant transmittance peaks at particular wave numbers were measured using the "find peak tool" provided by Nicolet OMNIC 5.01 software

2.6 Thermogravimetric (TG)

The thermal stability of fiber samples was conducted using a Perkin Elmer 7 thermogravimetric thermograph. Scans were recorded from 30 °C to 800 °C for samples of 5-10 mg placed in an aluminum pan with a heating rate 20 °C min^{-1} under a nitrogen atmosphere.

2.7 Mechanical strength test

Five replicate specimens for flexural strength test and tensile strength test with the dimension of 5 cm × 15 cm and 2.5 cm × 25 cm respectively, were prepared from particleboard for the evaluation of mechanical properties. For the flexural strength, the test was followed according to Japanese Industrial Standard JIS A 5908:2003 [22]. While for tensile strength, the test was followed according to ASTM D3039 [23]. The tests were determined using an Instron Testing System Model UTM-5582 equipped with a load cell capacity of 1000kg.

3. Result

3.1 Chemical composition analysis

The chemical composition in the fiber such as extractives, cellulose, hemicelluloses and lignin of SMS and RWS is present in Figure 2. The result shows that, the chemical composition for SMS fiber and RWS fiber were almost similar. In production of particle board, the chemical composition in raw materials is one of the important factors as it might give negative or positive effect in the performance of the board [25].

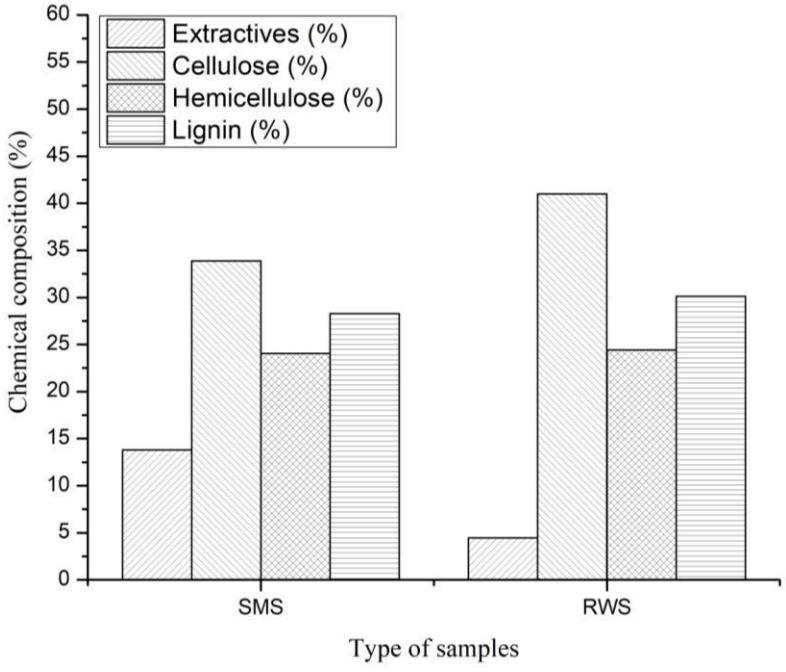


Fig. 2 Chemical composition of SMS fiber and RWS fiber 138

During the extraction process, a high amount of extractives about 13.81 % was able to be extracted from SMS fiber, while RWS fiber was only 4.46 %. The increasing amount of extractives can be assumed as increasing of sugar content in the fiber [21].This was due to breakdown of lignocellulose component in SMS fiber by enzymatic reaction during production of mushroom [26].
The enzymatic reaction during mushroom growth from SMS fiber has results the degradation of wood polysaccharides such as alpha cellulose and hemicellulose into sugar for energy uptake [19, 145 20]. By comparing the chemical composition between SMS fiber and RWS fiber, it can be clearly seen that there are reduction was occur from 41% to 33.87 % for alpha cellulose and 24.43% to 24.04% for hemicellulose. The particle size distribution analysis in Figure 3 also showed that, the degradation of lignocelluloses component has resulted reduction of the particle size of the fiber by 686.747 µm for SMS and 852.616 µm for RWS [21].The reduction of the particle size might influence the mechanical properties of the binderless particleboard [27]. The high amount of extractives remaining in SMS fiber about 13.81 % can be considered as inefficient of uptake of monomer and oligomer sugar during mushroom growth activity [21].

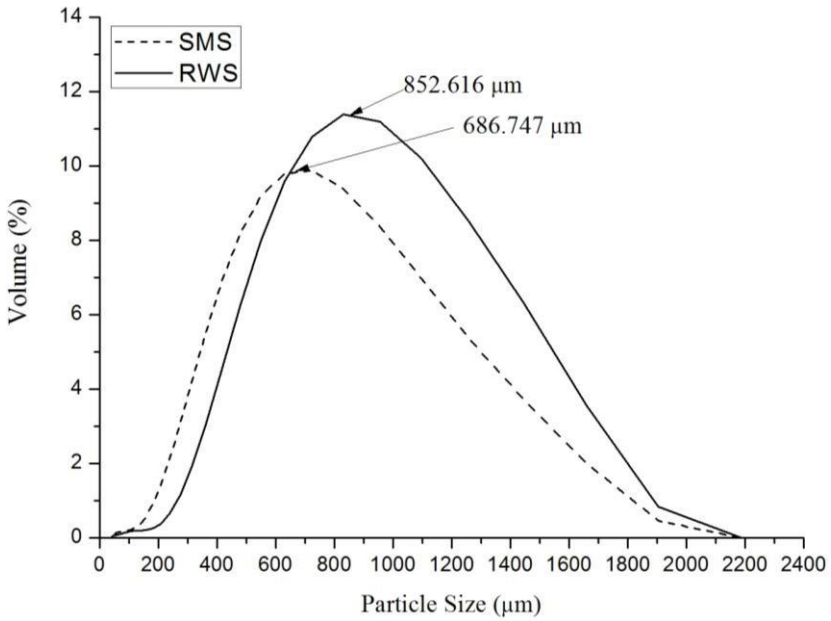


Fig. 3 Average particle size for SMS fiber and RWS fiber 164

Lignin has been report as natural self bonding binder and important part in production of particleboard [28]. In this study, the lignin content obtained was 28.28 % for SMS and 30.11% for RWS. Although the lignin was not a sugar for energy source, but the mushroom grow from SMS fiber is Oyster mushroom or also known as white rot fungi. The white rot fungi more likely tend to consume lignin as energy source during growth. It can easily metabolize carbon sources to degrade lignin from fiber substrates [2, 12]. As the result, the lignin content in the fiber was also reduced and causes discolouration on the fiber from brown to yellowish as shown in Figure 3. Based on the chemical composition results, the changes of lignocellulose component between SMS and RWS were not too extreme and seem to be acceptable for production of particleboard.

Fig. 4 SMS fiber and RWS fiber colour differences 182

3.2 Fourier Transform Infrared Spectroscopy (FTIR)

Fourier transform infrared (FTIR) spectroscopy was analysed to identify any differences between the FTIR spectra of SMS fiber and RWS fiber. The spectra for both sample were presented in Figure 5. From the result, the functional groups are generally almost similar between SMS and RWS samples. The peak at between 3200 cm^{-1} to 3600 cm^{-1} and 2800 cm^{-1} to 3000 cm^{-1} was corresponds to intermolecular hydrogen bonding and C-H stretching respectively [25]. The strong intensities were probably due to abundant of hydroxyl group contributed by presence of cellulose in SMS fiber and RWS fiber [29]. The small reduction on the cellulose peak can be assumed as cellulose degradation during mushroom growth. Next, the peak intensity of the absorption of C=O for both samples were observed at 1650 cm^{-1}. This peak was attributed to the stretching in the acetyl, carbonyls, and ester group of the hemicelluloses [30]. The presence of this peak in SMS fiber has shows that the there are inefficiency of energy uptake occur during growth activity of mushroom which does not fully breakdown the hemicelluloses into sugar monomers. As the result, the hemicelluloses are still presence in the SMS fiber. Last, the peak for both samples at 1037 cm^{-1} can be assigned to the presence of lignin in the fibers. Although, the type of mushroom use in this study was white-rot fungi, lignin are still remain before or after mushroom growth activity [31].

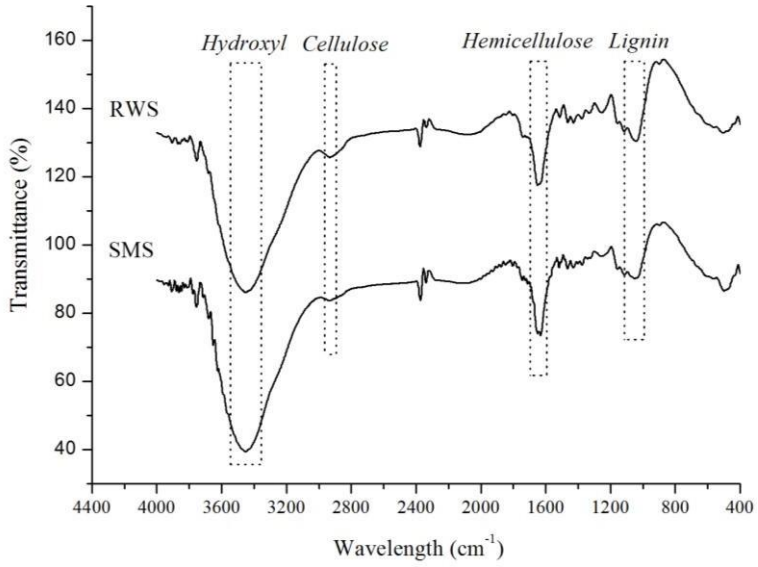


Fig. 5 FTIR spectra of SMS and RWS fiber

3.3 Thermal stability

Figure 6 represents the weight loss curve TG thermograms for SMS fiber and RWS fiber. The curves show that the weight loss for both sample starts to decrease at three stages. In each stages, the temperature increases between 30 °C to 100 °C, 250 °C to 390 °C, and 390 °C to 550 °C. This is because during this three stage the materials begin to absorb the heat energy. By comparing SMS fiber and RWS fiber, generally the thermograms for both sample was almost similar. However, the result in Figure 6 showed that the SMS fiber has a lower thermal stability compare to RWS fiber in stage 1, stage 2 and more clearly in stage 3.

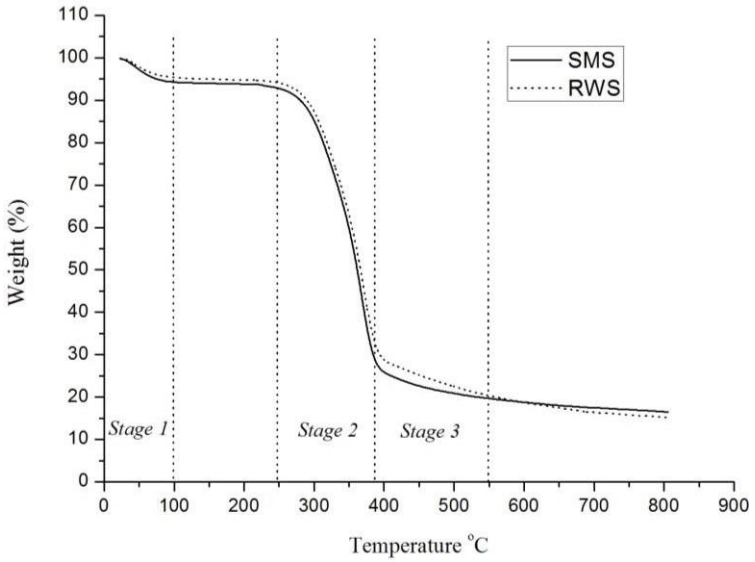


Fig. 6 TG thermogram of SMS fiber and RWS fiber

In stage 1, a small reduction of weight loss was occur at both samples was due to evaporation of moisture including water loss in the fibers [32]. The small reduction showed that the fibers does not have tendency to absorb huge amount moisture when expose in open air. For stage 2, the weight loss for both samples start at 250 °C due to degradation of lignocelluloses component which was hemicelluloses and followed by cellulose [33]. However, the weight residue was not fully degraded at this stage or below 350 °C due to the presence of lignin. Thus, compared to other lignocelluloses components, lignin required a more extended period of time and higher temperature to ensure the degradation was complete which is occur in stage 3 [34].

3.4 Mechanical properties

The average value of the flexural strength and the tensile strength of binderless particleboard from SMS fiber and RWS fiber is shown in Figure 7. From the figure, it can be observed that particleboard made from SMS fiber has slightly low mechanical strength.

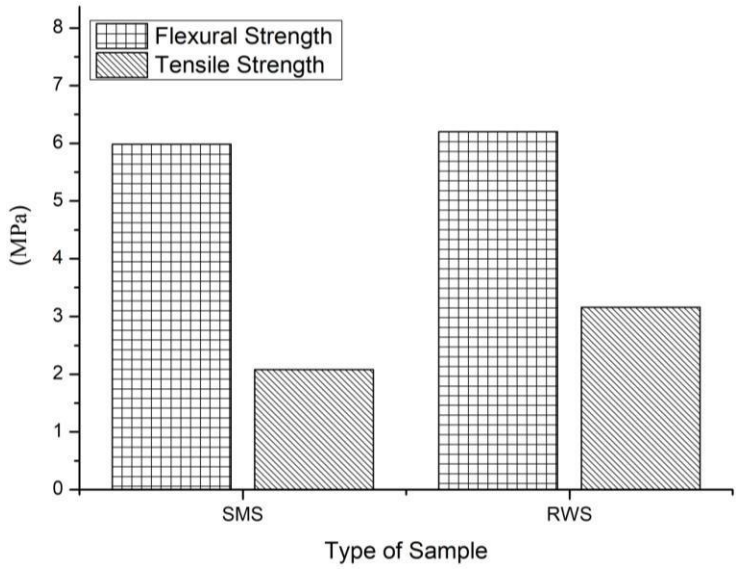


Fig. 7 Changes of flexural strength at different pressing time

The test result revealed that, the particleboard made from SMS fiber has slightly lower values. The SMS particleboard has 5.98 MPa flexural strength followed by 2.08 MPa tensile strength. While, the RWS particleboard has 6.2 MPa flexural strength followed by 3.16 MPa tensile strength. The flexural strength for both particleboards does not meet the requirement of the Japanese Industrial Standard. Both particleboards had low mechanical strength because the formation of both particleboard was attributed by self-hydrogen bonding between fiber particles only [34]. The total chemical composition in Figure 2 shows SMS fiber has lower content of lignocelluloses component compared to RWS fibers. The reduction of particle size also shows in Figure 3 was one of the factors that reduce the mechanical properties of the board [18, 27].

4. Conclusions

An investigation on the chemical composition, characterization and mechanical properties of binderless particleboard from SMS fiber and RWS fiber was determined. The result revealed that the SMS fiber which known as waste in mushroom industries has potential to replace RWS fiber as raw material for production of binderless particleboard. The chemical composition such as alpha cellulose, hemicelluloses and lignin does not cause an extreme degradation as it is responsible to the mechanical properties of the board. However, the degradation of lignocelluloses component has result reduction of the particle size and discolours of the wood fiber. Hence, the characterization analysis using FTIR and TG analysis report that the functional group and thermal stability properties of SMS fiber was generally almost the same with RWS fiber. This factor has increase the suitability and potential in utilization of SMS fiber to replace RWS fiber in production of binderless particleboard. Since, the mechanical properties test by flexural and tensile test also does not have any significant difference value .Thus, it revealed that, slightly reduction lignocelluloses component in SMS fiber do not give any significant effect in mechanical performance of the board. It can be concluded that, by replacing the RWS fiber with SMS fiber will reduce material purchasing cost and also preventing from environmental pollution cause by abundance of mushroom waste product. Thus, it is believed that the utilization of SMS fiber in production of binderless particleboard replacing RWS fiber is nearly possible.

Acknowledgement
This research was funded by the Universiti Sains Malaysia, under Graduate Research Assistant Scheme,

308/AIPS/415401.

References

[1] Tallapragada, P., et al., *Comparing the potential of spent mycelium substrate of Pleurotus florida with biofertilizers to enhance growth of Capsicum annuum.* Asian Journal of Plant Science and Research, 297 2011. **1**(4): p. 76-86.
[2] Phan, C.-W. and V. Sabaratnam, *Potential Uses of Spent Mushroom Substrate and Its Associate Lignocellulosic Enzymes.* Applied microbiology and biotechnology, 2012. **96**: p. 863-73.
[3] Singh, A., et al., *Enzymes from spent mushroom substrate of Pleurotus sajor-caju for the decolourisation and detoxification of textile dyes.* World Journal of Microbiology and Biotechnology, 302 2011. **27**: p. 535-545.
[4] Royse, D.J., *A global perspective on the high five: Agaricus, Pleurotus, Lentinula, Auricularia & Flammulina*. 2014, ICAR-Directorate of Mushroom Research: Solan. p. 1-6.
[5] Marín-Benito, J.M., M.J. Sánchez-Martín, and M.S. Rodríguez-Cruz, *Impact of Spent Mushroom Substrates on the Fate of Pesticides in Soil, and Their Use for Preventing and/or Controlling Soil and Water Contamination: A Review.* Toxics, 2016. **4**(3): p. 17.
[6] Beyer, D.M., *The impact of the mushroom Industry on the environment.* MUSHROOM NEWS- 309 KENNETT SQUARE-, 1996. **44**: p. 6-13.
[7] Magalhães, A.C., B.R.d.A. Moreira, and D.C. Zied, *AXENIC CULTIVATION OF Pleurotus ostreatus var. Florida IN SUPPLEMENTED SUGARCANE BAGASSE BRIQUETTES.* Engenharia Agrícola, 2018. **38**: p. 312 835-843.
[8] Higgins, C., et al., *Mushroom cultivation in the developing world: A comparison of cultivation technologies*. 2017. 1-7.
[9] Atila, F., *Effect of Different substrate Disinfection Methods on the Production of Pleurotus ostreatus.* 316 2016, 2016. **4**(4): p. 13.
[10] Ashrafi, R., et al., *Recycling of spent mushroom substrate for the production of oyster mushroom.* Research in Biotechnology, 2014. **5**(2).
[11] Rashid, M., et al., *Effect of different saw dust substrates on the growth and yield of Oyster Mushroom (Pleurotus florida).* Biores Comm, 2016: p. 193-199.
[12] Bellettini, M.B., et al., *Factors affecting mushroom Pleurotus spp.* Saudi Journal of Biological 322 Sciences, 2019. **26**(4): p. 633-646.
[13] Phan, C.-W. and V. Sabaratnam, *Potential uses of spent mushroom substrate and its associated lignocellulosic enzymes.* Applied Microbiology and Biotechnology, 2012. **96**(4): p. 863-873.
[14] Sasek, V. and T. Eggen, *Use of Edible and Medicinal Oyster Mushroom [Pleurotus ostreatus (Jacq.: Fr.) Kumm.] Spent Compost in Remediation of Chemically Polluted Soils.* 2002. **4**(3): p. 7.
[15] Zexun, Y., et al., *The Effect of Laccase Pretreatment Conditions on the Mechanical Properties of Binderless Fiberboards with Wheat Straw.* BioResources, 2017. **12**: p. 3707-3719.
[16] Islam, M.R., et al., *Morphology and mechanics of fungal mycelium.* Scientific Reports, 2017. **7**(1): p. 330 13070.
[17] Badu, M., S. Twumasi, and N. Boadi, *Effects of Lignocellulosic in Wood Used as Substrate on the Quality and Yield of Mushrooms.* Food and Nutrition Sciences, 2011. **2**: p. 780-784.
[18] Nonaka, S., K. Umemura, and S. Kawai, *Characterization of bagasse binderless particleboard manufactured in high-temperature range.* Journal of Wood Science, 2013. **59**(1): p. 50-56.

[19] Zhu, H., et al., *Extraction, purification and antibacterial activities of a polysaccharide from spent mushroom substrate.* International Journal of Biological Macromolecules, 2012. **50**(3): p. 840-843.
[20] Vane, C.H., T.C. Drage, and C.E. Snape, *Biodegradation of Oak (Quercus alba) Wood during Growth of the Shiitake Mushroom (Lentinula edodes): A Molecular Approach.* Journal of Agricultural and Food 339 Chemistry, 2003. **51**(4): p. 947-956.
[21] Lui, F.H.Y., et al., *The effects of chemical components and particle size on the mechanical properties of binderless boards made from oak (Quercus spp.) logs degraded by shiitake fungi (Lentinula edodes).* Journal of Wood Science, 2018. **64**(3): p. 246-255.
[22] JIS, A., *5908: Particleboards.* Japanese Industrial Standards. Tokyo, 2003.
[23] Sapuan, S.M., M. Harimi, and M.A. Maleque, *Mechanical properties of epoxy/coconut shell filler particle composites.* Arabian Journal for Science and Engineering Section B: Engineering, 2003. 346 **28**(2B): p. 171-181.
[24] Fengel, D. and G. Wegener, *Wood: chemistry, ultrastructure, reactions*. 2011: Walter de Gruyter.
[25] Hashim, R., et al., *Characterization of raw materials and manufactured binderless particleboard from oil palm biomass.* Materials & Design, 2011. **32**(1): p. 246-254.
[26] Lee, J.-W., et al., *Evaluation of waste mushroom logs as a potential biomass resource for the production of bioethanol.* Bioresource Technology, 2008. **99**(8): p. 2736-2741.
[27] Lamaming, J., et al., *Influence of Chemical Components of Oil Palm on Properties of Binderless Particleboard.* Bioresources, 2013. **8**: p. 3358-3371.
[28] Okuda, N., K. Hori, and M. Sato, *Chemical changes of kenaf core binderless boards during hot pressing (II): effects on the binderless board properties.* Journal of Wood Science, 2006. **52**(3): p. 249- 356 254.
[29] Chen, W., et al., *Individualization of cellulose nanofibers from wood using high-intensity ultrasonication combined with chemical pretreatments.* Carbohydrate Polymers, 2011. **83**(4): p. 359 1804-1811.
[30] Poddar, P., et al., *Isolation of Nano Cellulose from Rubber Wood Fibre and Fibrillation Effects on Nano Cellulose Reinforced Poly (Ethylene Oxide)*. 2016.
[31] Sun, R.C., et al., *Physico-Chemical and Structural Characterization of Alkali Lignins from Abaca Fibre.* Journal of Wood Chemistry and Technology, 1998. **18**(3): p. 313-331.
[32] Monteiro, S., et al., *Thermogravimetric behavior of natural fibers reinforced polymer composites—An overview.* Materials Science and Engineering: A, 2012. **557**: p. 17–28.
[33] Ghani, W.A.W.A.K., et al., *Biochar production from waste rubber-wood-sawdust and its potential use in C sequestration: chemical and physical characterization.* Industrial Crops and Products, 2013. **44**: 368 p. 18-24.
[34] Baskaran, M., et al., *Properties of binderless particleboard and particleboard with addition of urea formaldehyde made from oil palm trunk waste.* Journal of Physical Science, 2017. **28**(3): p. 151-159. 371

Penerbit Akademia Baru

Engineering Science and Technology Conference Proceedings

Journal homepage: www.akademiabaru.com/EST.html

Open Access

A Recent Review of Energy Recovery Ventilator on Low and High-Rise Buildings

Nor Amalin Keling[1], Yusri Yusup[1], Sheikh Ahmad Zaki[2], Mardiana Idayu Ahmad[1,*]

[1] Division of Environmental Technology, School of Industrial Technology, Universiti Sains Malaysia, 11800 Penang, Malaysia
[2] Environment Laboratory, Malaysia-Japan International Institute of Technology (MJIIT), Universiti Teknologi Malaysia, Kampus Kuala Lumpur, Jalan Sultan Yahya Petra, 54100, Kuala Lumpur

ABSTRACT

Due to the extreme heat events, there are a lots of energy consumption needed in the building. It hits much consumption in high-rise buildings compared to low-rise buildings, where, the energy used for space cooling growth years by years. One of the methods to recover the energy consumption demand is to install an aid mechanical ventilation in the building such as an energy recovery ventilator. To acknowledge this kind of application of energy recovery ventilator efficiency into low and high-rise building, a review has been done according to the previous research. This review includes type of simulation used to analyse the application of energy recovery ventilator, the performances of energy savings and indoor air quality on different climates. This paper also presents the integration system of energy recovery ventilator with other mechanical ventilation system. Future researches of the energy recovery ventilator in low and high-rise buildings is also discussed.

Keywords:
Energy recovery ventilator; high-rise building; indoor air quality; simulation; low-rise building

Copyright © 2019 PENERBIT AKADEMIA BARU - All rights reserved

1. Introduction

In this day and age, climate change is a global problem cause the heat events which increase the temperature of environment causes the heat condition. Building condition is also affected by this phenomenon. Regards of this issue leads to the energy consumption in the low to the high-rise buildings. The energy demand in the U.S. reached 39%, 69% of the electricity used and 38% of the national CO2 emissions [1]. Majority causes of the increasing on the energy consumption is from their space cooling.

Low rise building definition according to the British Standard (BS 8103) is a building that not more than three storeys above ground, intended for domestic occupation and within the limitation [2]. The high-rise buildings mean, a building that has more than seven storeys and above. However, it can be a linear height (feet or meters) rather than stories [3]. While ASHRAE terms the meaning of high-rise building as a tall building that has 91m or 300ft [4].

* *Corresponding author.*
E-mail address: mardianaidayu@usm.my (Mardiana Idayu Ahmad)

The factors that contribute to energy consumption in those building sectors is because of the used of the mechanical ventilation. They using the mechanical ventilation for the space cooling to provide the thermal comfort to the occupants. The words thermal comfort can be defined as '…that condition of mind which expresses satisfaction with the thermal environment.' [5]. For example, a person who is comfort with their ambient temperature whether in hot or cold. One of the methods to reduce the energy consumption in building is by using energy recovery ventilator.

Energy recovery ventilator known as a system that recover energy from the stale air in the buildings which then will be circulate and maintain the comfort ambient temperature whether during hot or cold condition. Variety of study has been conducted in this area as reviewed in few papers. According to the Mardiana and Riffat [6], there are two types of efficiency that must considerate in energy recovery ventilator which is sensible and total efficiency. The parameters of energy recovery ventilator have taken to measure the efficiency of the system. There are i) size, structure and material of the heat exchanger core, ii) size of ducts and fans, iii) configurations or flow management, iv) heat and mass transfer, v) flow and pressure drops in a duct, vi) temperature and humidity, vii) air flow rates [6]. In general, there a few types of ERV which are suitable with their building's conditions. There is fixed plate, heat pipe, rotary wheel, and run-around [7].

All these functions of energy recovery ventilator will used depends on the suitability to the buildings. For the fixed plate or air to air heat recovery ventilator, it involves the cross flow, counter flow and parallel flow where the typical effectiveness of sensible heat transfer is about 50-80% [8]. An experiment conducted by Lu et. Al [9] mention about how they have evolved the performance on the plastic film plate heat recovery ventilator and manage to get about 65% to 85% effectiveness with pressure drop less than 20Pa. Whilst, another research done 80% thermal efficiency was developed by Fernandez-Seara et. Al [10]. Therefore, to acknowledge this kind of application of energy recovery ventilator efficiency into low and high-rise building, a review has been done according to the previous research. This review includes type of simulation used to analyze the application of energy recovery ventilator, the performances of energy savings and indoor air quality on different climates. This paper also presents the integration system of energy recovery ventilator with other mechanical ventilation system. Future researches of the energy recovery ventilator in low and high-rise buildings is also discussed.

2.Type of simulation

Space cooling demand about 50% in energy of the building. It was estimated rose 15% within 2017 and 2018 globally [11]. There is enormous number of simulations applied on energy recover ventilator to show their efficiency. This is important to ensure the products of energy recovery ventilator was energy-efficient or behind it. The process of simulation was specifically included difference climates in order to differentiate in which climates the energy recovery ventilator really performed.

2.1 Excel-based analysis tool (Ebat)

Current simulation of the energy recovery software was built to show the efficiency and performance of the energy recover ventilator through an aided program. The purpose is to ease monitoring of the energy recovery ventilator with tools that can be controlled. Simple excel -based analysis tool is to measure quantitatively the feasibility of the HERV in a counter-flow arrangement. This tool is simple and user-friendly interface, thus, people that is not from technical background

also can used. The development of analysis tool has four division which are inputs, database, computations, and outputs. The program will automatically change the inputs into outputs by deploying the database and the computational functions that has build in it. Users just need to fill required inputs for example house envelope and others. This tool also differentiates between conventional HRV/ERV users and the combination of HERV to make the of this system in the between pros and cons side in different climate surrounding. The Fig. 1 shows how the four development of analysis tool were divided in one residential area.

J. Zhang et al. / Energy and Buildings 75 (2014) 430–438 [12]

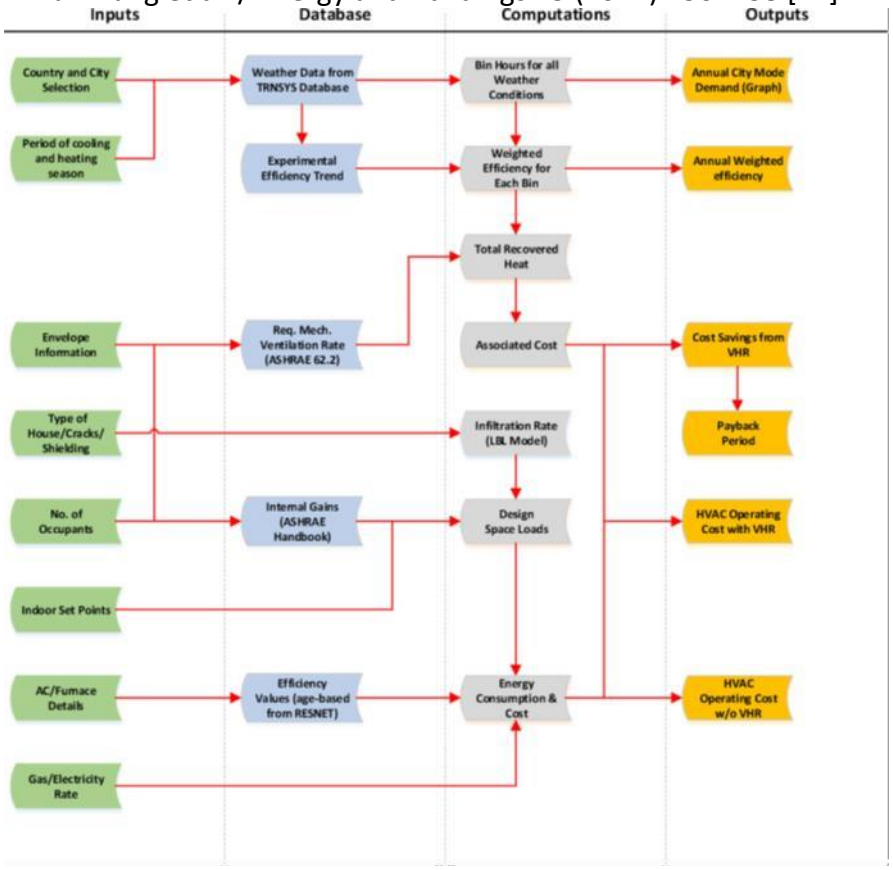


Fig. 1. Analysis tool

This system required performance with high efficiency under multiples operating condition. Regards to this, the design must be simple and compact enough on maintenance and operating [13]. According to the Liu et. Al [14], energy recovery ventilator efficiency and energy saving percentage found non-linearly related.

2.2 CFD Software

There is a lot of software to simulate the efficiency of the energy recovery ventilator define by their type of building and acceptance climate. CFD or known as computational fluid dynamic was used in numerous software engineering field. Regards to this software used in energy recovery ventilator is to achieved zero energy buildings. The performance can be reached 49% to 62% [15]. The numerical analysis of CFD conjoin the heat and mass transfer mechanism for laminar flow to study the thermal performance of the system [16]. Ones study at school using CFD as tools to

simulate found out that consumption of energy recovery ventilator can simultaneously motivate to reduction of classroom of energy demand for cooling and ventilation [17]. Therefore, this leads to less energy consumption on air conditioning system. The less of energy consumption can help to energy saving and cost. These two factors always be in concerned on mechanical ventilation system.

The numerical modelling in CFD were used to validate the results and monitor the flow of heat transfer inside the energy recovery ventilator. Interface that be used in the CFD includes air flow motion, thermal transport, and indoor CO2 transient dispersion. Whilst, the parameters comprise common thermal comfort including percentage dissatisfied, vertical temperature difference between human head to ankle as well as the normalized standard deviations of horizontal plane averaged
temperatures in the classroom. Effect of ventilation strategies on the classroom volume averaged temperature, vertical thermal gradient as well as classroom CO2 concentration reductions, will also be included [18]. The general numerical methods and modeling described by the set of differential equations, including momentum, energy, and species equation expressed as below:

$$\frac{\partial}{\partial \tau}(\rho\varphi) = \frac{\partial}{\partial x_j}\left(\Gamma_\varphi \frac{\partial \varphi}{\partial x_j} - \rho u_j \varphi\right) + S_\varphi \quad (1)$$

2.3 EnergyPlus

Another tools or software that can analyse the efficiency and performance of energy recovery ventilator is using EnergyPlus. There are a lot of series in EnergyPlus that been updated years by years. This software can get to far down on the activity that happened on the surface heat transfer coefficients and using advanced various selection of the convection models based on the space conditions defined in the model of EnergyPlus [19]. According to the AHSRAE design stated that EnergyPlus is used to study the hybrid heating, ventilation, and air-conditioning (HVAC) energy conservation measures that effectively achieve energy saving above requirement of ANSI/ASHRAE/IES standard 90.1-2010 [20].

Parameters by ASHRAE Standard 90.2-2010 mention about the design supply air flow, climate zone, and the outdoor air at the design supply air flow rate [20]. A study combining two or three HVAC system consist of few climates to differentiate the effect of efficiency and performance on heat transfer according to multitype of buildings [21]. From that study result show that combination ERV with Demand Control Ventilation (DCV) keep increasing the energy saving in Miami climate and this study also differentiated the type of buildings whether low-rise and high rise building which low rise building performed well in efficiency of energy recovery ventilator and performance.

3. Performance of energy saving and IAQ in different climate

Besides of the low and high-rise building, climate also play the main factors that will affect the efficiency and performance of energy saving. Decreasing of indoor air quality for hot and humid climate caused the interior moisture increasing risk of building failure, discomfort and poor indoor air quality [21]. However, with the aid of other mechanical ventilation that fulfil the requirement by AHSRAE such as energy recovery ventilator helps to reduce the moisture content from outdoor air.

With this reason also leads to the longer life span of the buildings. The advantages of ERV are able to filter, humidify, dehumidify, heat, or cool the incoming fresh air.

General study on ERV and different climate show, the warm and humid climate is the most energy savings because of low of energy consumption on low-rise buildings. It is because of outdoor air or fresh air that extract into the energy recovery ventilator does not require high energy consumption. On certain climate like in Miami which has hot and humid climate, the energy saving in primary school that have only one level show the increasing energy consumption, then, the increasing happened when it is on warm and humid climate in Memphis at two-levels building [22].

4. Conclusion

From the review, it can be concluded that a lot of research has been done but future research still can be carried out. An energy recovery ventilator can be paired with other mechanical ventilation system to improve the efficiency and energy saving performance. Low- and high-rise building were giving the same efficiency but it also depends on their climates. These few factors contribute more in energy recovery ventilator and building life span. It also shows that a new development of design of energy recovery ventilator can achieved the ASHRAE requirement.

Acknowledgement

This research is full financial assistance from the Ministry of Higher Education (MyPhD, MyBrain15).

References

[1] USEPA. (2010b). “Action memorandum (AM) fact sheet on selected engineering evaluation/cost analysis (EE/CA) alternative Kingston fossil fuel plant release site Harriman, Roane County, Tennessee.
[2] British Standard (2013). BS 8130(a) – Structural Design of Low-Rise Buildings Part 2: Code of practice for masonry walls for housing. The British Standard Institution.
[3] Hall Jr JR (2005). High-Rise Building Fires. Quincy, MA: National Fire Protection Association.
[4] Ellis, P.G.; Torcellini, P.A. (2008). Simulating tall buildings using EnergyPlus. In Proceedings of the 9th International IBPSA Conference on Building Simulation, Montreal, QC, Canada, pp. 279–286.
[5] BS EN ISO 7730. Ergonomics of the thermal environment. Analytical determination and interpretation of thermal comfort using calculation of the PMV and PPD indices and local thermal comfort criteria.
[6] A. Mardiana,; S.B. Riffat (2013). Review on physical and performance parameters of heat recovery systems for building applications.
[7] A. Mardiana,; S.B. Riffat (2011). Review on heat recovery technologies for building application. Renewable and sustainable energy reviews.
[8] ASHRAE (2005). ASHRAE handbook of fundamentals, American society of heating. Atlanta, GA: Refrigerating and air condition engineers.
[9] Lu. Y, Wang Y, Zhu L, Wang Q (2010). Enhanced performance of heat recovery ventilator by air-flow -induced film vibration (HRV performance enhanced by FIV) International Journal of Thermal Science.
[10] Fernandez- Seara J, Diz. R, Uhia FJ, Dopazo A, Ferro JM (2011). Experimental analysis of an air to air heat recovery unit for balanced ventilation system in residential buildings. Energy conservation and management.
[11] Gavin Haper (2015). Doing cold smarter. Univeristy of Birmingham.
[12] Junlong Zhang, Alan S. Fung, Sumeet Jhingan (2014). Analysis and feasibility study of residential integrated heat andenergy recovery ventilator with built-in economizer using an excel spreadsheet program. Energy and Buildings.
[13] Agustin Olt, Jun Zhang and Alan S. Fung (2014). Feasibility study of a compact residential HRV/ERV/Economizer based ventilation system. ASHRAE Transactions (Vol. 120, Issue 2.)

[14] Liu, J, Li, W, Liu, J & Wang, B 2010, "Efficiency of energy recovery ventilator with various weathers and its energy saving performance in a residential apartment". Energy and Buildings, vol. 42, pp 43-49.
[15] Javier Bermejo-Bustoa, César Martín-Gómeza, Amaia Zuazua-Rosa, Enrique Baquerob,Rafael Miranda (2016). Performance simulation of heat recovery ventilator cores in cascade connection. Energy and Buildings.
[16] Wahiba Yaïci, Mohamed Ghorab, Evgueniy Entchev (2013). Numerical analysis of heat and energy recovery ventilators performance based on CFD for detailed design. Applied Thermal Engineering.
[17] Wang Y, Zhao FY, Kuckelkorn J, Liu D, Liu LQ, Pan XC (2014). Cooling energy efficiency and classroom air environment of a school building operated by the heat recovery air conditioning unit. Chemical engineering and materials research information centre.
[18] Yang Wanga, Fu-Yun Zhao, Jens Kuckelkorn, Hartmut Spliethoff, Ernst Rank (2013). School building energy performance and classroom air environment implemented with the heat recovery heat pump and displacement ventilation system. Applied Energy.
[19] EnergyPlus (2015). Engineering Reference, Version 8.4.0 Documentation, U.S. Department of Energy.
[20] ASHRAE Standard 90-2010. Energy Standards for Buildings Except Low-Rise Residential Buildings.
[21] Moyer, Neil, D. Beal, D. Chasar, J. McIlvaine, C. Withers, S. Chandra (2001). Moisture Problems in Manufactured Housing: Probable Causes and Cures. ASHRAE Conference Proceedings IAQ2001. American Society of Heating, Refrigerating and Air-Conditioning Engineers, Inc. Atlanta, Georgia.
[22] Teshome Edae Jiru (2014). Combining HVAC energy conservation measures to achieve energysavings over standard requirements. Energy and Buildings.

Penerbit Akademia Baru

Engineering Science and Technology Conference Proceedings

Journal homepage: www.akademiabaru.com/EST.html

Characterisation of Calcium Carbonate and Its Polymorphs from Molluscan Shells of *Anadara Granosa* (Blood Cockle), Open *Paphia Undulata* (Surf Clam), *Dosinia Exesperata* (Venus Access Clam) and Marble

Open Access

Siti Norfazira Ramli[1], Mardiana Idayu Ahmad [1,*], Mohd Firdaus Yhaya[2]

[1] School of Industrial Technology, Universiti Sains Malaysia, 11800 Pulau Pinang, Malaysia
[2] School of Dental Sciences, Health Campus, Universiti Sains Malaysia, 16150 Kubang Kerian, Kelantan, Malaysia

ABSTRACT

Calcium carbonate and its polymorphs from cockle shells (*Anadara granosa*), surf clam shells (*Paphia undulata*), venus clam shells (*Dosinia exasperata*), marble and commercial calcium carbonate were characterised using a field emission scanning electron microscopes (FESEM), an energy dispersive X- ray analyser (EDX), X-ray diffraction (XRD) and Fourier transmission-infrared spectroscopy (FT-IR). Needle-like calcite crystals (orthomof commercial calcium carbonate and cube-like calcite crystal of marble; needle-like aragonite crystal of *Anadara granosa* shell and cube-like aragonite crystals of *Dosinia exasperata* and *Paphia undulata* shell powders were observed by FESEM. Cube-like crystal (rhombohedral) is more stable than the needle- like crystal (orthorhombic). The EDX results showed that the *Anadara granosa*, *Paphia undulata*, *Dosina exasperata* and marble contained more carbon and oxygen than the commercial calcium carbonate, whereas the commercial calcium carbonate contained more calcium than others. FT-IR analyses revealed the presence of carbonate groups in all molluscan shells, marble and the commercial calcium carbonate. FT-IR analyses also showed the presence of aragonite in *Anadara granosa*, *Dosinia exasperata*, *Paphia undulata*; and calcite in marble and commercial calcium carbonate. XRD analyses showed that Anadara granosa contain pure aragonite, while *Dosinia exasperata* and *Paphia undulata* shell powder contained mixed of calcite and aragonite. Whereas, marble and the commercial calcium carbonate composed of pure calcite.

Keywords:
Calcium carbonate; aragonite polymorphs, cockle shell; *Paphia undulata*

Copyright © 2019 PENERBIT AKADEMIA BARU - All rights reserved

1. Introduction

Calcium carbonate ($CaCO_3$) is a naturally occurring inorganic biomaterial, found all over the world and covers more than four percent (4%) of total earth's crust [1]. It has three crystal phases: calcite, aragonite and vaterite [2] and calcite are thermodynamically the most stable phase under the ambient temperature [3]. Although calcite is the most stable polymorphism of calcium carbonate, aragonite has higher density and hardness that make it suitable for material in plastic, paper, cosmetics, rubber and paint ink [4]. Its crystal shape is trigonal, and appears in a range of morphologies, commonly being rhombohedral and scalenohedral forms [5] while aragonite is a metastable polymorph, the most common is orthorhombic, and crystals are needle-like (acicular)

* *Corresponding author.*
E-mail address: mardianaidayu@usm.my (Mardiana Idayu Ahmad)

or spindle-like, cauliflower and flake-like crystals [6]. Aragonite is commonly occurring in aquatic environments and it can be found in shell structures [7]. Lastly, vaterite is the rarest polymorph and unstable, which hexagonal crystal shape and spherical morphology [8].

Calcium carbonate can be existed in the form of limestone, marble, chalk and seashells. The common natural sources of $CaCO_3$ that have been used by industry these days are such as limestone, dolomite and magnesite [9]. However, mining large quantities of these sources will contribute to great environmental damage such as extensive deforestation and top soil loss [10, 11]. Hence, seashells are currently taken into an interest as they can substitute the main sources of $CaCO_3$. Shell waste after consume were dumped on land and will produce unpleasant smell and creates pollution if it was not treated. Seashells contained about 95-99% by weight of $CaCO_3$ [12, 13] while limestone, dolomite and magnesite contain up to 50% [14]. Besides, previous finding by Li et al. has stated that the composition of calcium oxide in seashell is higher than limestone, making them one of the best alternative sources of CaCO3 [15]. In this paper, blood cockles (*Anadara granosa*), surf clams (*Paphia undulata*), venus clams (*Dosinia exasperata*), marble and commercial calcium carbonate were investigated and comparatively studied.

Cockle belonging to the species of *Anadara granosa* (*A. granosa*) is a type of sea molluscan widely consumed in South East Asian countries such as Malaysia, Singapore and Thailand. The shells represent a large portion of waste products after the mussels were consumed. The potential uses of the cockle shells based on calcium carbonate powder have been investigated by many researchers. Hemabarathy et al. [16], Zuki et al. [17] and Hazmi et al. [18] have studied the cockle shell powder as source of biomineral for bone tissue applications. Cockle can also be a potential partial coarse aggreagate replacement in concrete [19].

Paphia Undulata (*P.undulata*) also known as surf clams were commonly casted away on the restaurants, food and canneries industry in Malaysia without any eminent utilization for valuable products. The utilization of the heterogeneous catalyst such as *P. undulata* shell for biodiesel does not produce soap through free fatty acid neutralization and triglyceride saponification [17]. While for venus clam, *Dosinia exasperata* (*D. exasperate*) is still lack of research investigation. Previous study has taken an interest in producing calcium carbonate from cockle shell but studies on other molluscan shell are still few. Thus, this study paper aims to add data on polymorphs and characteristics of a few common molluscan shells to the existing data on cockles and marble.

2. Methodology

Approximately 500 g of molluscan shells were washed, scrubbed to remove dirt. The shells were then washed thoroughly with distilled water and dried in an oven (Memmert, Komita, Germany) for 2 h at 120 °C. About 500 g of marble chips and the cleaned seashells were crushed using pestle and mortar. They were then ground using grinder (Riken, Japan) to reduce the particle sizes. The powders were sieved using a stainless laboratory test sieve with an aperture size of 250 µm (Endecott Ltd., made in London, England). The powders were dried again in an oven for 24 h at 50 °C and packed in a polyethylene plastic bag. For comparison, commercial calcium carbonate was purchased from Hmbg with reagent pure of 99.9%. This calcium carbonate was dried in an oven at 90 °C for 24 h to remove any moisture.

Next, the characterisation analysis of $CaCO_3$ prepared from molluscan shell of *Anadara granosa*, *Paphia undulata* and *Dosinia exasperata* was conducted. Surface morphological changes on the samples were studied using a field emission scanning electron microscope (FESEM, Quanta FEG 650, Netherlands) after coating the powder with gold. The elemental analysis was carried out using an energy dispersive X-ray analyzer, which was directly connected with the FESEM. Its environmental mode was similar to SEM analysis as both high vacuum and low vacuum can be used to obtain high resolution image with better quality. The composition, purity and the crystal structure of the powder were investigated by an X-ray powder diffractometer (XRD, PANalytical X'Pert PRO, Netherlands). Chemical analyses were carried out using a Fourier transform -infrared (FT-IR) spectrophotometer (Model Nicolet, AVATAR 380) over a range of 4000 cm^{-1} to 400 cm^{-1}.

3. Results

3.1 The surface morphology and crystal structure of A. granosa, D. exasperata, P. undulata, marble and the commercial calcium carbonate powders

Figure 1 below illustrate the surface morphology of *A. granosa* shell, *D. exasperata* shell, *P. undulata* shell, marble and the commercial $CaCO_3$ powders as studied by FESEM. Calcite and aragonite possessed different crystal growth and crystal structure. Rod-like calcite crystals were observed in the commercial $CaCO_3$ (Fig. 1e), and cube- like calcite crystals were observed in marble (Fig. 1d) whereas rod-like aragonite crystals were found in the *A. granosa* (Fig. 1a). Cube – like aragonite crystals were found in *D. exasperata* (Fig. 1b) and *P. undulata* (Fig. 1c).

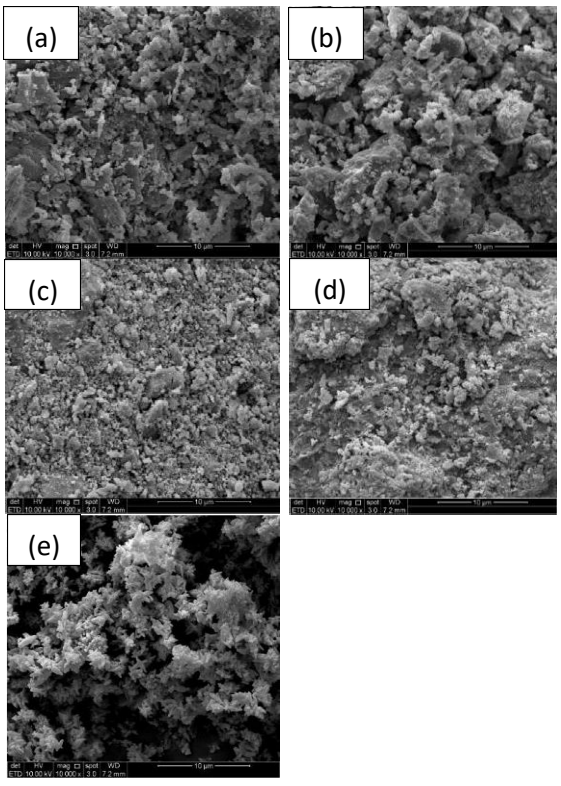


Fig.1. The surface morphology of (a) *A. granosa*, (b) *D. exasperata*, (c) *P. undulata*, (d) marble and (e) the commercial $CaCO_3$ powder were studied using FESEM.

3.2 Elemental analysis of A. granosa, D. exasperata, P. undulata, marble and the commercial calcium carbonate powders

The elemental compositions of *A. granosa*, *D. exasperata*, *P. undulata,* marble and commercial calcium carbonate are tabulated in Table 1. These findings showed that *A. granosa* contained more carbon and oxygen with (15.69 % C and 51.90 % O) than *D. exasperata* (11.03 % C and 45.58 % O), *P. undulata* (15.01 % C and 49.48 % O), marble (12.35 % C and 48.86 % O) and commercial $CaCO_3$ (11.16 % C and 42.90 % O); whereas commercial $CaCO_3$ contained higher in calcium (45.94 % Ca) than *P. undulata* (32.87 % Ca), *D. exasperata* (43.39 % Ca), *A. granosa* (31.56 % Ca) and marble (38.69 % Ca). The result obtained from EDX analysis showed that cockle shell contains 15.69 % C, 51.90 % O, 31.56 % C, 0.31 % Na and 0.54 % Al and almost the same with the previous findings on cockle shells. Meanwhile, P. undulata contains 15.01 % C, 49.48 % O, 32.87 % Ca and 2.64 % Mg. Therefore, it was concluded that Malaysian cockle shell normally have Carbon (C), Oxygen (O), Calcium (Ca), Copper (Cu), Iron (Fe), Magnesium (Mg), Potassium (K), Silica (Si), Boron (B), Zinc (Zn), Nickel (Ni) and Sodium (Na). Thus, it is reasonable for the molluscan shell to have Sodium (Na) and Aluminium (Al) and Magnesium (Mg).

Table 1
Percentages of the elemental contents in A. Granosa, P. Undulata, D.Exasperata, marble, and commercial $CaCO_3$ powders

Spectrum	*C*	*O*	*Ca*	*Na*	*Al*	*Mg*	*Total*
A. Granosa	*15.69*	*51.90*	*31.56*	*0.31*	*0.54*	*-*	*100*
P. Undulata	*15.01*	*49.48*	*32.87*	*-*	*-*	*2.64*	*100*
D. Exasperata	*11.03*	*45.58*	*43.39*	*-*	*-*	*-*	*100*
Marble	*12.35*	*48.96*	*38.69*	*-*	*-*	*-*	*100*
Commercial $CaCO_3$	*11.16*	*42. 90*	*45.94*	*-*	*-*	*-*	*100*

3.3 FT-IR patterns of A. granosa, D. exasperata, P. undulata, marble and the commercial calcium carbonate powders

The FT-IR spectra from the *A. granosa*, *D. exasperata*, *P. undulata*, the commercial $CaCO_3$ and marble powder were comparatively study in a stack diagram in Figure 2. These findings showed that all graph composed of an organic matrix and a mineral phase with numerous prominent absorption peak from 400 cm^{-1} to 4000 cm^{-1}. The peak of carbonate ions was observed at ~705 cm^{-1}, ~1455 cm^{-1} in *P. undulata*, *A. granosa*, *D. exasperata*, the commercial $CaCO_3$, and marble powder (Figure 2). The FT-IR results also showed the absorption peak of calcite at 875 cm^{-1} of CO_3^{-2} in marble and commercial $CaCO_3$ (Figure 2d and Figure 2e). The absorption peaks of aragonite were found at ~860 cm^{-1} of cockle shells (Figure 2a), *D. exasperata* (Figure 2b) and *P. undulata* (Figure 2c). This agrees well with the results reported by Choi et al. (2000) in which they observed the absorption peak of calcite at 875 cm^{-1} and the absorption peaks of aragonite at 857 cm^{-1} of CO_3^{-2}[20].

From the FT-IR graph, *A. granosa* shell powder in Figure 2 (a) showed a strong absorption peak of carbonyl group (CO_3^{-2}) at 709 cm^{-1} and at 1473 cm^{-1} as compared to others. This means that cockle contains more carbonate (CO_3^{-2}) content than others respectively. This was proven by the result from EDX analysis of cockle shell contains more carbon and oxygen than others. Besides, a sharp peak at 860 cm^{-1} showed that cockle contains pure aragonite as compare to others. The other functional groups, represented by the smaller absorption bands in both molluscan shell and commercial $CaCO_3$ powder, were amide (~1630cm^{-1} and ~1789 cm^{-1}). While the smaller absorption band in the range 2515 - 2526 cm^{-1} of *A. granosa*, *P. undulata* and commercial $CaCO_3$ which may be due to the OH groups of carboxylic acids.

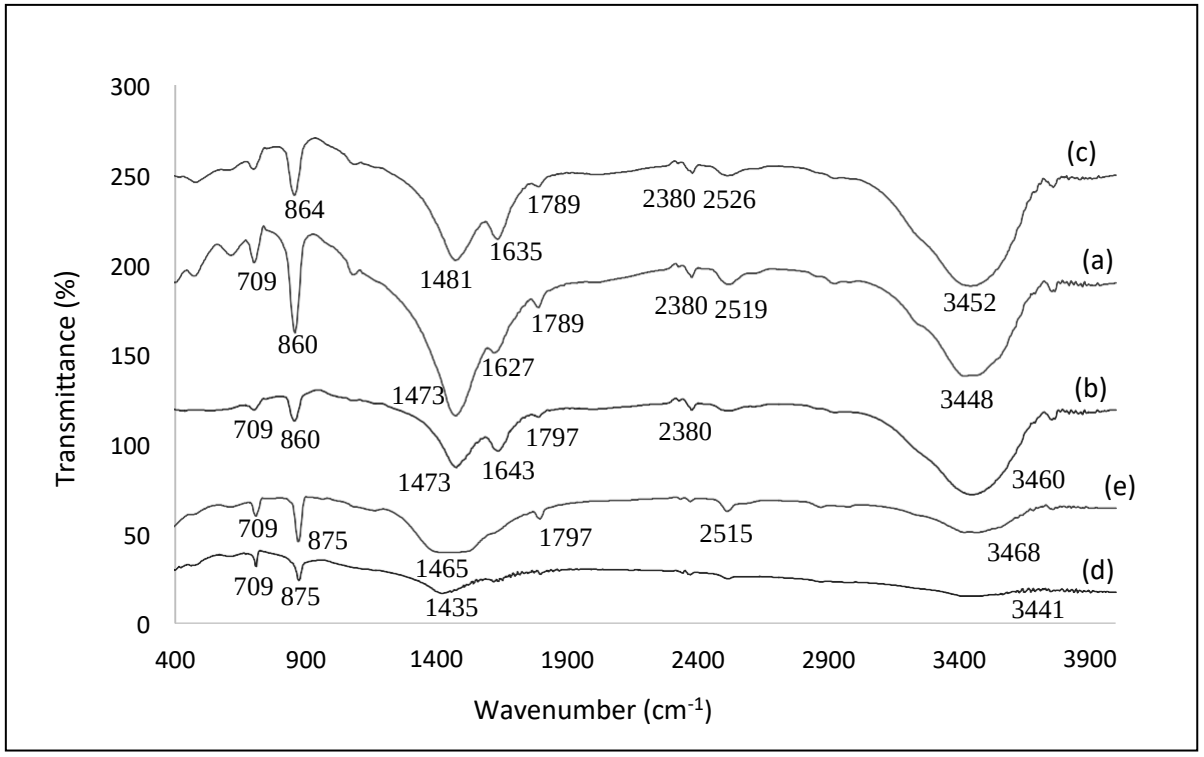


Fig.2. The surface morphology of (a) *A. granosa*, (b) *D. exasperata*, (c) *P. undulata*, (d) marble and (e) Commercial $CaCO_3$ powder were studied using FESEM

3.4 XRD patterns of A. granosa, D. exasperata, P. undulata, marble and the commercial calcium carbonate powders

The X-ray diffraction patterns of $CaCO_3$ powders obtained from *A. granosa*, *P. undulata*, *D. exasperata*, marble and commercial $CaCO_3$ powder were comparatively presented in Figure 3. All peaks in the commercial calcium carbonate and marble were matched with the calcite phase (Figure 3a, Figure 3b and Joined Committee on Powder diffraction society (JCPDS) file no. 01-072-1937). The XRD pattern at Figure 3 (b) of commercial $CaCO_3$ powder with peaks at 2θ of 23.0°, 29.4°, 30.9°, 36.0°, 39.4°, 43.2°, 43.3°, 47.5°, 48.5°, and 57.3°, which represent (43), (922), (378), (26), (46), (50), (18), (54), (66) and (16); and Figure 3 (a) of marble with peaks at 2θ of 23.0°, 29.4°, 35.9°, 39.3°, 43.1°, 47.5°, 48.4°, and 57.3°, which represent (55), (450), (66), (75), (75), (79), (77), (92) and (39); indicates that the composition of the $CaCO_3$ microspheres of pure calcite. The XRD also revealed that all peaks in *A. granosa*, *D. exasperata* and *P. undulata* shell powder were matched with the aragonite phase (Figure 3c, Figure 3d, Figure 3e and JCPDS file no.00-041-1475).

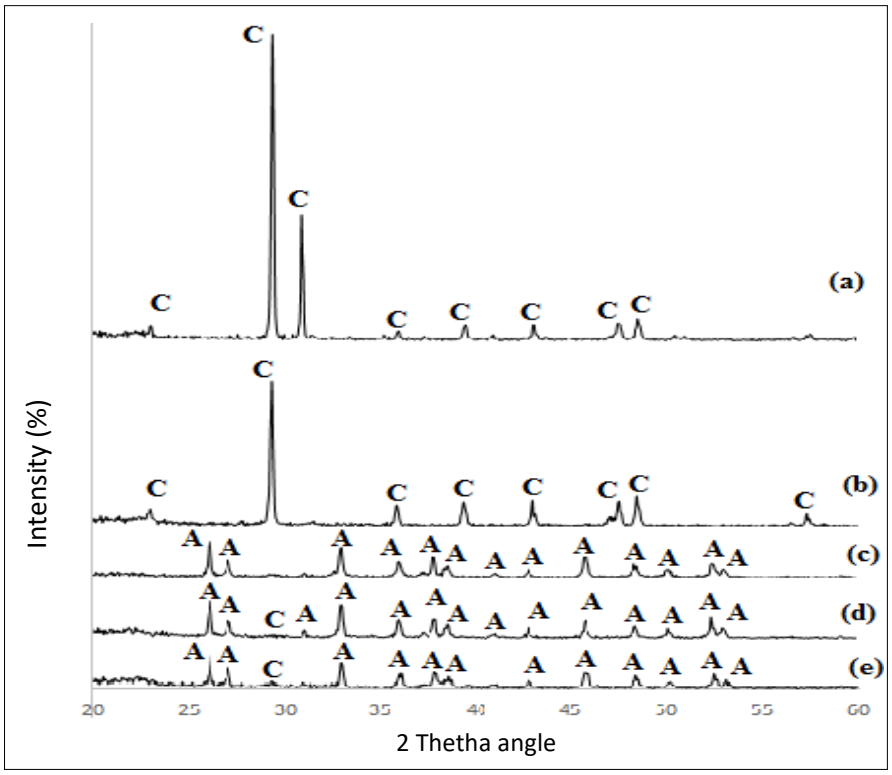


Fig. 3.The XRD pattern of (a) marble, (b) commercial $CaCO_3$, (c) *A. granosa*, (d) *D. exasperata* and (e) *P. undulata*

From the XRD graph, Figure 3 (d) and (e), aragonite and calcite crystals of $CaCO_3$ are coexisted, which the small peaks of calcite at 2θ is 29.6° (1), whereas peaks of aragonite at 2θ are 26.2° (100), 27.2° (45), 31.1° (17), 33.1° (93), 36.1° (51), 37.1° (14), 37.9° (45), 38.5° (33), 42.9° (27), 45.8° (50), 48.4° (26), 50.3° (14), 52.4° (58) and 53.0° (25) of *D. exasperata*. For *P.undulata* in Figure 3e, peak of calcite at 2θ is 29.5° (8), whereas peaks of aragonite at 2θ are 26.2° (100), 27.2° (51), 33.1° (82), 36.1° (29), 37.0° (13), 37.9° (42), 38.5° (23), 42.9° (17), 45.9° (40), 48.3° (38), 50.2° (17), 52.4° (37) and 52.9° (16). Besides, 2θ values of 26.2°, 27.2°, 31.1°, 33.3°, 36.1°, 37.9°, 38.6°, 42.9°, 45.9°, 48.4°, 50.2°, 52.4°, and 52.9°as shown in Figure 3 (c) of *A. granosa* are correspond to the basal planes of (100), (44), (11), (85), (43), (57), (28), (14), (60), (23), (21), (39) and (23) are assigned to pure aragonite crystalline form of $CaCO_3$ [21].

4. Conclusions

Natural mineral calcium carbonate and its polymorph (aragonite) from molluscan shell and (calcite) from marble and commercial calcium carbonate were characterised. Rod-like calcite crystals in the commercial calcium carbonate and cube like calcite crystals in marble powder were found. Whereas, rod-like aragonite crystals were in the *Anadara granosa* shells powder and cube-like aragonite crystals in *Paphia undulata* shell powder and *Dosinia exasperate* shell powder were observed by FESEM. The FT-IR and XRD data illustrate the presence of calcite in the commercial calcium carbonate and marble powder; and aragonite in all of the molluscan shell. The molluscan shell powder also contained a large amount of carbon and oxygen, which are essential for bone

mineralization. The absorption peak of calcite was observed in the commercial calcium carbonate and marble, whereas the absorption peaks of aragonite were found in all molluscan shell powder.

Acknowledgement
The author thanks Dr. Mohd Firdaus Bin Yhaya and Associate Professor Dr. Mardiana Idayu Ahmad for reviewing the manuscript. The author also thanks the staffs in the Division of Bioresource, Paper and Coatings, School of Industrial Technology, Universiti Sains Malaysia that helped with the preparation of calcium carbonate powder. Besides, the author also thanks the staff in the Global Archaeology Research Centre, Universiti Sains Malaysia that helped with FESEM and EDX. Not to forget, the employees of School of Physics, USM that greatly helped with XRD. This research was supported financially by the Malaysian Government under the Fundamental Research Grant Scheme (FRGS) 203/PTEKIND/6711574.

References

[1] Hoque, M.E., M. Shehryar, and K.N. Islam, *Processing and characterization of cockle shell calcium carbonate (CaCO3) bioceramic for potential application in bone tissue engineering.* J Mater Sci Eng, 2013. **2**(4): p. 132.
[2] Manoli, F. and E. Dalas, *Spontaneous precipitation of calcium carbonate in the presence of ethanol, isopropanol and diethylene glycol.* Journal of crystal growth, 2000. **218**(2-4): p. 359-364.
[3] Hayakawa, S., et al., *Characterization of calcium carbonate polymorphs with Ca K edge X-ray absorption fine structure spectroscopy.* Analytical Sciences, 2008. **24**(7): p. 835-837.
[4] Yasue, T. and Y. Arai, *Particle design for new development of calcium compound; Ryushi sekkei ni yoru calcium kagobutsu no shintenkai.* 1995.
[5] Vecht, A. and T. Ireland, *The role of vaterite and aragonite in the formation of pseudo-biogenic carbonate structures: implications for Martian exobiology.* Geochimica et Cosmochimica Acta, 2000. **64**(15): p. 2719-2725.
[6] Zhou, G.-T., et al., *Sonochemical synthesis of aragonite-type calcium carbonate with different morphologies.* New Journal of Chemistry, 2004. **28**(8): p. 1027-1031.
[7] Ryu, M., et al., *Comparison of dissolution and surface reactions between calcite and aragonite in L-glutamic and L-aspartic acid solutions.* Molecules, 2010. **15**(1): p. 258-269.
[8] Wang, L., I. Sondi, and E. Matijević, *Preparation of uniform needle-like aragonite particles by homogeneous precipitation.* Journal of colloid and interface science, 1999. **218**(2): p. 545-553.
[9] Rashidi, N.A., M. Mohamed, and S. Yusup, *A study of calcination and carbonation of cockle shell.* 2011.
[10] Mehta, K.P., *Reducing the environmental impact of concrete.* Concrete international, 2001. **23**(10): p. 61-66.
[11] Langer, W.H., *Potential environmental impacts of quarrying stone in karst: a literature review*. 2001: Citeseer.
[12] Barros, M., et al., *From waste to commodity: transforming shells into high purity calcium carbonate.* Journal of Cleaner Production, 2009. **17**(3): p. 400-407.
[13] Awang-Hazmi, A., et al., *Mineral Composition of the Cockle (Anadara granosa) Shells of West Coast of Peninsular Malaysia and It? s Potential as Biomaterial for Use in Bone Repair.* Journal of Animal and Veterinary Advances, 2007.
[14] Bliss, J.D., T.S. Hayes, and G.J. Orris, *Limestone, a Crucial and Versatile Industrial Mineral Commodity*. 2008: US Department of the Interior, US Geological Survey.
[15] Li, Y.J., et al., *CO2 capture behavior of shell during calcination/carbonation cycles.* Chemical Engineering & Technology: Industrial Chemistry-Plant Equipment-Process Engineering- Biotechnology, 2009. **32**(8): p. 1176-1182.

[16] Hemabarathy Bharatham, M. and E.K. PERIMAL, *Mineral and physiochemical evaluation of Cockle shell (Anadara granosa) and other selected Molluscan shell as potential biomaterials.* Sains Malaysiana, 2014. **43**(7): p. 1023-1029.
[17] Bakar, Z.A., B.F. Hussein, and N.M. Mustapha, *Cockle shell-based biocomposite scaffold for bone tissue engineering*, in *Regenerative Medicine and Tissue Engineering-Cells and Biomaterials*. 2011, InTech.
[18] Hazmi, A.A., et al., *Mineral composition of the cockle (Anadara granosa) shells of west coast of peninsular Malaysia and it's potential as biomaterial for use in bone repair.* Journal of Animal and Veterinary Advances, 2007. **6**(5): p. 591-594.
[19] Muthusamy, K. and N. Sabri, *Cockle shell: a potential partial coarse aggregate replacement in concrete.* International Journal of Science, Environment and Technology, 2012. **1**(4): p. 260-267.
[20] Choi, C.-S. and Y.-W. Kim, *A study of the correlation between organic matrices and nanocomposite materials in oyster shell formation.* Biomaterials, 2000. **21**(3): p. 213-222.
[21] Chong, K.-Y., C.-H. Chia, and S. Zakaria. *Polymorphs calcium carbonate on temperature reaction*. In *AIP Conference Proceedings*. 2014. AIP.

Penerbit Akademia Baru

Engineering Science and Technology Conference Proceedings

Journal homepage: www.akademiabaru.com/EST.html

Mechanical Properties of Palm Composites: Date, Bertam, Coconut and Oil Palm – A Review

Open Access

M.H. Norhidayah[1,2], A.Hambali[1], Y.Mohd Yuhazri[1], H.Y. Mujahideen[2]

[1] Faculty of Manufacturing Engineering, Universiti Teknikal Malaysia Melaka, Durian Tunggal, 76100 Melaka, Malaysia.
[2] Kolej Islam Antarabangsa Sultan Ismail Petra (KIAS), Kota Bharu, Kelantan, Malaysia

ABSTRACT

Nowadays, natural fiber is an interesting option and it is the most widely applied fiber in composite technology. This research paper aims to enlighten the existing properties in natural fiber composites especially the same species; palms. Finally, a summary of mechanical properties that have been identified for treated and untreated fibers.

Keywords:
Bertam; mechanical properties; date

Copyright © 2019 PENERBIT AKADEMIA BARU - All rights reserved

1. Introduction

The natural fiber can divide to three types which are vegetables, animals, and minerals. Several plants from which fibers can be sourced are Hemp (*Cannabis sativa*), Coconut (*Cocos nucifera*), Flax (*Linum usitatissimum*), Sisal (*Agave sisalana*), and Jute (*Corhorus capsularis*). Animal fibers are natural fibers that consist largely of particular proteins. Instances are silk, hair including wool, and feathers. The example of mineral fiber is asbestos which is used in insulating houses. However, in the automotive industry, the vegetable category is the most popular. This category can divide into three groups;

a) Fruit fibers are extracted from the fruits of the plant, they are light and hairy, and allow the wind to carry the seeds such as cotton and coir.
b) Bast fibers are found in the stems of the plants providing the plant its strength. Usually they run across the entire length of the stem and are therefore very long. Examples such as flax, kenaf and hemp.
c) Leaves fiber is rough and sturdy and form part of the plant's transportation system, they are also called leaf fibers [1]. Sisal and Bertam are the example of these groups.

The properties of natural fibers are affected by some factors such as type of fibers, moisture content and form of fibers. Additionally, natural fibers are affected regarding to growth species, crop cultivation, location and local ultimate, harvest, supply (transportation supply, age of fiber) and retting or extracting process [2,3].

Eugeissona tristis known as Bertam is one of the plant in the group which is have many benefits in medical and housings sector [4-7]. Usually, it has 6-10 m tall large ascending leaves with a green leaflet and spiny leafstalks. In Malaysia, the fronds of Bertam usually use as wall of chalets or resorts. Moreover, fruit eaten fresh can relieve from fever, the sap from the stem is used for insect sting. The leaves are used as thatch and the leafrachis for fish traps and fishing poles [6]. Others

example plants are in same species, which are oil, coconut and date palm. The date palm (Phoenix dactylifera L.) is a mono cotyledon of the family of the Palmate. It is a feather palm, characterized by compound leaves with a series of leaflets on each side of a common petiole, originating from growing point at the top of the trunk [18].

2. Methodology

The method section describes in detail how the study was conducted. Contents of articles published on the international journals discussing about the oil, coconut, date and Bertam composites were identified. The authors have designed a structured process for selection appropriate articles. The research of the articles was carried out using online databases and library services. This was done by reading the articles and reflecting upon their appropriateness for the topic studied. The information such as palm species, part of fiber, and properties were identified, and then discuss the findings and finally draw conclusions.



Fig. 1. Bertam plant(a),and Bertam Leaves (b)

3. Results

The analysis regarding to some papers related with the palms fibers. The table 1 shows the mechanical properties of bertam, oil palm, date, and coconut palm. Bertam have tensile, flexural and impact strength for untreated fiber composites with polyester. Bertam composites, coconut and oil palm have used the untreated fiber to examine the properties.

No	Composites	Part of fiber	Treated/ untreated	Mechanical properties			References
				Tensile Modulus (MPa)	Flexural Modulus (MPa)	Impact Strength (kJ/m^2)	
1	Bertam	Leaves	Untreated	204	1827	12.29	[5][6][7]
2	Date	Trunk	Treated	1500	1590		[8]
		Rachis	Treated	1090	1590		[8]
		Petiole	Treated	1050	1610		[8]
		Pits	Treated	319	398		[14]
3	Coconut	Coir	Treated	24.8			[3]
		Fruit (shell)				4.76	[15]
		Fruit	Untreated	250			[17]
4	Oil palm	fruit	treated			4.6	[15]
		bunch	untreated	1430	3300		[16]

Table 1: Tensile modulus, flexural modulus and impact strength for palms.

4. Conclusions

As conclusion, date fiber have tensile and flexural modulus highest than other palms. But, in this case, date fiber have done treatments. For untreated fiber, the oil palm bunch has the highest value of tensile modulus and bertam has the highest value of flexural modulus and impact strength. In spite of that, Coconut fibres have the highest toughness amongst natural fibres. They have potential to be used as reinforcement in low-cost concrete structures, especially in tropical earthquake regions[20].The fiber treatment has improved the mechanical properties of fiber composites.

Acknowledgement

The authors sincerely grateful to Kolej Islam Antarabangsa Sultan Ismail Petra(KIAS) which has given opportunity and financial support for this research. And also, a lot of thanks to Faculty of Manufacturing Engineering of Universiti Teknikal Malaysia Melaka (UTeM) for providing facilities for this research. Last but not least, the authors gratefully acknowledge the comments of an anonymous reviewer.

References

[1] Vilay, V., M. Mariatti, R. Mat Taib, and Mitsugu Todo. "Effect of fiber surface treatment and fiber loading on the properties of bagasse fiber–reinforced unsaturated polyester composites." *Composites Science and Technology* 68, no. 3-4 (2008): 631-638.

[2] Paridah, Md Tahir, Amel B. Basher, Syeed SaifulAzry, and Zakiah Ahmed. "Retting process of some bast plant fibres and its effect on fibre quality: A review." *BioResources* 6, no. 4 (2011): 5260-5281.

[3] Kabir, M. M., H. Wang, K. T. Lau, and F. Cardona. "Chemical treatments on plant-based natural fibre reinforced polymer composites: An overview." *Composites Part B: Engineering* 43, no. 7 (2012): 2883-2892.

[4] Syafinie, A. M., and A. N. Ainuddin. "Biomass and carbon estimation of Eugeissona tristis." *Sains Malaysiana* 42, no. 10 (2013): 1461-1466.

[5] Mansor, Asyraf, and Rahmad Zakaria. "The distribution of palms and pandans in Teluk Bahang permanent forest reserve, Penang." *Pertanika Journal of Tropical Agricultural Science* 35, no. 1 (2012).

[6] Jin, Chee Beng. "Medicinal properties and common usages of some palm species in the Kampung Peta community of Endau-Rompin National Park, Johor." *Journal of Tropical Medicinal Plants* 6, no. 1 (2005): 79.

[7] Rozman, H. D., M. J. Saad, and ZA Mohd Ishak. "Flexural and impact properties of oil palm empty fruit bunch (EFB)–polypropylene composites—the effect of maleic anhydride chemical modification of EFB." *Polymer Testing* 22, no. 3 (2003): 335-341.

[8] Zaman, Izzuddin, and Muhamad Khairudin Awang. "Influence of fiber volume fraction on the tensile properties and dynamic characteristics of coconut fiber reinforced composite." *Journal of Science and Technology* 1, no. 1 (2009).
[9] Norhidayah, M. H., Arep Ariff Hambali, Mohd Yuhazri bin Yaakob, M. Zolkarnain, and H. Y. Saifuddin. "A Review of Current Development in Natural Fiber Composites in Automotive Applications." In *Applied Mechanics and Materials*, vol. 564, pp. 3-7. Trans Tech Publications, 2014..
[10] Norhidayah, M. H., A. Hambali, and Y. Mohd Yuhazri. "Impact behaviour of the Bertam fibers reinforced with unsaturated polyester." *Advances in Environmental Biology* 8, no. 8 (2014): 2753-2755.
[11] Norhidayah, M.H., A. Hambali and Y. Mohd Yuhazri. "Study the effect of particle size on the water absorption behavior and density of Polyester/ Bertam fiber composites." Australian Journal of Basic and Applied Sciences, 8(15) Special 2014: 374-376
[12] Norhidayah, M. H., Arep Hambali, and M. Y. Yuhazri. "The Effect Of Fiber Size on The Mechanical Properties of Bertam/Unsaturated Polyester Composites." In *Applied Mechanics and Materials*, vol. 761, pp. 52-56. Trans Tech Publications, 2015.
[13] Elseify, Lobna A., Mohamad Midani, Lamia A. Shihata, and Hamed El-Mously. "Review on cellulosic fibers extracted from date palms (Phoenix Dactylifera L.) and their applications." *Cellulose* 26, no. 4 (2019): 2209-2232.
[14] Ghazanfari, A., S. Emami, S. Panigrahi, and L. G. Tabil. "Thermal and mechanical properties of blends and composites from HDPE and date pits particles." *Journal of composite materials* 42, no. 1 (2008): 77-89.
[15] Durowaye, S. I., G. I. Lawal, M. A. Akande, and V. O. Durowaye. "Mechanical properties of particulate coconut shell and palm fruit polyester composites." *Int J Mater Eng* 4, no. 4 (2014): 141-147.
[16] Yusoff, Mohd Zuhri Mohamed, Mohd Sapuan Salit, Napsiah Ismail, and Riza Wirawan. "Mechanical properties of short random oil palm fibre reinforced epoxy composites." *Sains Malaysiana* 39, no. 1 (2010): 87-92.
[17] Rassiah, Kannan, and Haeryip Sihombing. "Effect on mechanical properties of hybrid blended coconut coir/paraffin wax/ldpe." *International Journal of Integrated Engineering* 3, no. 2 (2011).
[18] Shamsi, M., and S. M. Mazloumzadeh. "Some physical and mechanical properties of date palm trees related to cultural operations industry mechanization." *Journal of Agricultural Technology* 5, no. 1 (2009): 17-31.
[19] Jacob, Maya, Sabu Thomas, and Konnanilkunnathal Thomas Varughese. "Mechanical properties of sisal/oil palm hybrid fiber reinforced natural rubber composites." *Composites science and Technology* 64, no. 7-8 (2004): 955-965.
[20] Ali, Majid, Anthony Liu, Hou Sou, and Nawawi Chouw. "Mechanical and dynamic properties of coconut fibre reinforced concrete." *Construction and Building Materials* 30 (2012): 814-825.

Penerbit Akademia Baru

Engineering Science and Technology Conference Proceedings

Journal homepage: www.akademiabaru.com/EST.html

Open Access

Hall Effect on Mixed Convection Casson Fluid Flow over an Exponentially Extending Sheet in Porous Media

Kartini Ahmad[1*], Siti Suzilliana Putri Mohamed Isa[2], Zahir Hanouf[3]

[1] Department of Science in Engineering, Kulliyyah of Engineering, International Islamic University Malaysia, 53100 Gombak, Selangor, Malaysia
[2] Institute for Mathematical Research, Universiti Putra Malaysia, 43400 UPM Serdang, Selangor, Malaysia
[3] Department of Mechanical Engineering, University of Bahrain, Sakheer, Kingdom of Bahrain

ABSTRACT

Imposition of viscous dissipation on the mixed convection Casson fluid flow over an exponentially stretching sheet embedded in porous media is studied. The flow is exposed to strong magnetic field applied perpendicularly to the sheet which causes the effect of Hall current. Equations of the fluid motion are reduced to nonlinear ordinary differential equations via similarity transformation which are later solved numerically using finite difference method for few values of embedded parameters. The effects of the non-dimensional governing parameters on the skin friction and heat transfer are tabulated and depicted for this purpose. Various velocity, transverse velocity and temperature profiles are graphically displayed.

Keywords:
Viscous dissipation; boundary layer; stretching sheet

Copyright © 2019 PENERBIT AKADEMIA BARU - All rights reserved

1. Introduction

The manifestation of fluid flow over a stretching sheet occurs enormously in industry. The fancy of the final products influence how the sheet should be stretched. Realistically, stretching the sheet may not necessarily be linear [1]. Sometime it is stretched linearly, exponentially, quadratically or etc. This includes the process of polymer sheet, filaments and wires. During the process, stirring sheet is assumed to extend on its own plane and elongated surface interacts with surrounding fluid naturally and thermally. Crane [2] was the first who investigate fluid flow over linearly stretched sheet whilst exponential stretching sheet was considered by Magyari and Keller [3]. Since then, lots of works have been done to determine the effects of exponential stretching sheet on Newtonian/non-Newtonian fluids with numerous physical parameters using various approaches [4- 11].

Another important factor that contributes to the result of the final product is the rate of cooling. This is controlled by drawing such strips or filaments in an MHD fluid. The magnetic field enhances Lorentz force even in a weak electric current and magnetization force. The existence of Hall current is very important in the presence of a strong magnetic field.

* *Corresponding author.*
E-mail address: kartini@iium.edu.my (Kartini Ahmad)

Nagalakshmi *et al*. [14] studied unsteady boundary layer flow of an incompressible, viscous electrically conducting fluid over an exponentially stretching sheet in the presence of viscous dissipation, thermal radiation, temperature dependent heat source with chemical reaction and Hall currents with slip effect, Mahaboobjan *et al*. [15] considered unsteady MHD mixed convection of radiative heat and mass transfer for viscous fluid over a permeable stretching exponentially stretching sheet with Hall currents in the presence of heat generation and first order chemical reaction and Srinivasacharya and Jagadeeshwar [16] investigate the effect of Hall current, chemical reaction and thermal radiation on the boundary layer flow of viscous incompressible fluid over an exponentially stretching sheet.

To our knowledge, the effect of Hall current on the mixed convection Casson fluid flow is considered by Ashraf *et al*. [13] for the case of linear stretching sheet with convective boundary condition, whilst mixed convection flow passing over an exponentially stretching sheet with Hall current was considered by El-Aziz and Nabil [12]. However the study in [12] is limited to Newtonian fluid with the absence of viscous dissipation over a smooth wall. As such, this study aims to investigate the effect of Hall current on mixed convection Casson fluid flow over an exponentially stretching sheet along with viscous dissipation effect in porous media. Viscous dissipation changes the temperature distributions by playing a role like an energy source, which leads to affecting heat transfer rates. The merit of the effect of viscous dissipation depends on whether the sheet is being cooled or heated [17].

2. Flow Analysis

Consider a steady mixed convection Casson fluid flow over a vertical wall in porous media with non-uniform permeability parameter κ_1. The sheet is stretched exponentially with velocity $u_w = u_0 \exp(Nx/L)$ and the distribution of the wall temperature is $T_w = T_\infty + T_0 \exp(2Nx/L)$, where N is the exponential parameter, L is the reference length, T_∞ is the temperature far away from the wall, u_o and T_o are the reference velocity and reference temperature, respectively. The x-axis is directed along the stretching sheet and the direction of the fluid motion, whilst y-axis is normal to it. The flow is subjected to a strong magnetic field B which causes the existence of Hall current. This in turn gives rise to force in the z-direction, which induces a crossflow in that direction and hence the flow becomes three-dimensional [12]. The governing mixed convection of Casson fluid flow can be expressed as [12, 13]

$$\frac{\partial u}{\partial x}+\frac{\partial v}{\partial y}+\frac{\partial w}{\partial z}=0, \tag{1}$$

$$u\frac{\partial u}{\partial x}+v\frac{\partial u}{\partial y}=\upsilon\left(1+\frac{1}{\beta}\right)\frac{\partial^2 u}{\partial y^2}+g\beta_T\left(T-T_\infty\right)-\frac{\upsilon}{\kappa_1}u-\frac{\sigma B^2}{(1+m^2)}(u+mw), \tag{2}$$

$$u\frac{\partial w}{\partial x}+v\frac{\partial w}{\partial y}=\left(1+\frac{1}{\beta}\right)\frac{\partial^2 w}{\partial y^2}-\frac{\upsilon}{\kappa_1}w+\frac{\sigma B^2}{(1+m^2)}(mu-w), \tag{3}$$

$$u\frac{\partial T}{\partial x}+v\frac{\partial T}{\partial y}=\frac{k}{\rho c_p}\frac{\partial^2 T}{\partial y^2}+\frac{\mu}{\rho c_p}\left(1+\frac{1}{\beta}\right)\left(\frac{\partial u}{\partial y}\right)^2 \quad (4)$$

where *u*, *v* and *w* are the velocity components in *x*-, *y* –and *z*-axis, respectively, υ is the kinematic viscosity, β is the Casson fluid parameter, *g* is the gravitational acceleration, β_T is the thermal expansion coefficient, σ is the electrical conductivity, ρ is the fluid density, *m* is the Hall parameter, *T* is the fluid temperature, *k* is the thermal conductivity, c_p is the specific heat at constant pressure and μ is the dynamic viscosity.

The boundary conditions for the problem under consideration are

$$u = , v = 0, w = 0, T = T_w \text{ at } y = 0$$

$$\to 0, \quad w \to 0, \quad T \to T_\infty \quad \text{as} \quad \to \infty. \quad (5)$$

For the sake of similarity solution, we assume that

$$= B_0 \exp\left(\frac{Nx}{2L}\right) \quad \text{and } \kappa_1 = \kappa_0 \exp\left(-\frac{Nx}{L}\right). \quad (6)$$

Equations (1) - (4) are reduced to ordinary differential equations by introducing the following similarity transformation [12]

$$\eta = \sqrt{\frac{u_0}{2\upsilon L}}\exp\left(\frac{Nx}{2L}\right) y, \qquad \psi(x,y) = \sqrt{2\upsilon L u_0}\exp\left(\frac{Nx}{2L}\right) f(\eta),$$

$$= u_0 \exp\left(\frac{Nx}{2L}\right) h(\eta), \qquad T = T_\infty + (T_w - T_\infty)\,\theta(\eta) \quad (7)$$

where *u* and *v* are defined in usual notation; i.e $u = \partial\psi/\partial y$ and $v = -\partial\psi/\partial x$. Using (7), (1) is automatically satisfied and (2) – (4) reduced to

$$\left(1+\frac{1}{\beta}\right) f''' - 2\kappa f' + 2\lambda\theta - 2\frac{M}{(1+m^2)}(f' + mh) - 2(f')^2 + Nff'' = 0 \quad (8)$$

$$\left(1+\frac{1}{\beta}\right) h'' - 2\kappa h + 2\frac{M}{(1+m^2)}(mf' - h) - 2Nf'h + Nfh' = 0 \quad (9)$$

$$\theta'' + PrEc\left(1+\frac{1}{\beta}\right)(f'')^2 + PrN(f\theta' - 4f'\theta) = 0 \quad (10)$$

where $\lambda = Gr_x/Re_x^2$ is the mixed convection parameter with $Gr_x = g\beta(T_w - T_\infty)L^3/\upsilon^2$ and $Re_x = u_w L/\upsilon$. $= \upsilon L/u_0\kappa_0$ is the porosity parameter, $M = \sigma B_0^2 L/\rho u_0$ is the magnetic parameter, $Pr = \mu c_p/k$ is the Prandtl number and $Ec = u_0^2/T_0 c_p$ is the Eckert number.

In similar fashion, the boundary conditions (5) can be written as

$$(0) = 0, f'(0) = 1, h(0) = 0, \theta(0) = 1$$

$$f'(\infty) \to 0, \quad h(\infty) \to 0, \quad \theta(\infty) \to 0. \tag{11}$$

3. Results and Discussion

Equations (8) - (11) have been solved numerically using finite-difference method for few values of porosity parameter κ, mixed convection parameter λ, magnetic parameter M, Hall parameter m, Prandtl number Pr, Eckert number Ec, when the exponential parameter N = 1 and 2, respectively in Newtonian fluid ($\beta \to \infty$) and Casson fluid (β = 1). The local skin friction coefficients and the local Nusselt number can be obtained once the numerical computation for $f''(0)$, $h'(0)$ and $\theta'(0)$ are generated which are of interest of this study. Table 1 and 2 are tabulated for this reason and for the sake of brevity, only few values of κ, Ec, N, M, m and λ are considered here. Nevertheless, to give better understanding of the flow characteristic at the boundary, the profiles of the velocity $f'(\eta)$, transverse velocity $h(\eta)$ and temperature $\theta(\eta)$ are also depicted.

Table 1 and 2 show the numerical values obtained for the local skin friction coefficient in the x-direction $-f''(0)$, the local skin friction coefficient in the z-direction $h'(0)$ and the local Nusselt number $-\theta'(0)$ taking into account N = 1, Pr = 0.72 and κ = Ec = 0 for various values of M , m and λ when the flow is dominated by Newtonian fluid ($\beta \to \infty$) and Casson fluid (β = 1), respectively. It is seen that the increment of Hall current given by m is found to decrease the magnitude of $f''(0)$ and opposite phenomenon occurred for both $h'(0)$ and $-\theta'(0)$. However, the increment of M increases the $f''(0)$ and $h'(0)$ but decreases the magnitude of $\theta'(0)$. Nevertheless, the imposition of non-Newtonian fluid (Casson fluid; i.e β = 1) is seen to decrease the magnitude of the $f''(0)$ and $h'(0)$ and contrary behaviour occur to the magnitude of $\theta'(0)$. On addition to the present results, Figures 1-6 are depicted to give clear and better understanding of the impact of those parameters onto $f''(0)$, $h'(0)$ and $\theta'(0)$ for the case of Newtonian fluid.

Table 1
Values of $f''(0)$, $h'(0)$ and $\theta'(0)$ when $\beta \to \infty$, N = 1, Pr = 0.72 and κ = Ec = 0

λ	M	m	$-f''(0)$	$h'(0)$	$-\theta'(0)$
0	0.1	0.1	1.358247	0.009183	1.458271
		0.5	1.344591	0.037665	1.462390
		1.2	1.338558	0.048272	1.653456
	1	0.1	1.908316	0.056756	1.287920
		0.5	1.822284	0.242571	1.311829
		1.2	1.615294	0.348189	1.337713
1	0.1	0.1	0.706792	0.010879	1.604393
		0.5	0.692571	0.044611	1.607315
		1.2	0.662284	0.056701	1.613689
	1	0.1	1.297360	0.068562	1.477938
		0.5	1.204147	0.294697	1.493342
		1.2	0.978687	0.427697	1.535998

Table 2
Values of $f''(0)$, $h'(0)$ and $\theta'(0)$ when $\beta = N = 1$, $Pr = 0.72$ and $\kappa = Ec = 0$

λ	M	m	$-f''(0)$	$h'(0)$	$-\theta'(0)$
0	0.1	0.1	0.960450	0.006473	1.562663
		0.5	0.950798	0.026622	1.565378
		1.2	0.930032	0.034093	1.571365
	1	0.1	1.349392	0.040132	1.445745
		0.5	1.288559	0.171522	1.461313
		1.2			
1	0.1	0.1	0.590377	0.007177	1.638622
		0.5	0.580640	0.029445	1.640876
		1.2	0.559860	0.037474	1.645773
	1	0.1	0.991526	0.045726	1.542029
		0.5	0.927708	0.195846	1.554826
		1.2	0.774305	0.281655	1.588695

Figures 1-3 show the variations of the local skin friction coefficient in the x-direction $-f''(0)$, the local skin friction coefficient in the z-direction $h'(0)$ and the local Nusselt number $-\theta'(0)$ when $N = M = \lambda = 1$, $Pr = 0.72$ for two values of Hall current m, and various values of porosity parameter κ and viscous dissipation parameter Ec for Newtonian fluid.

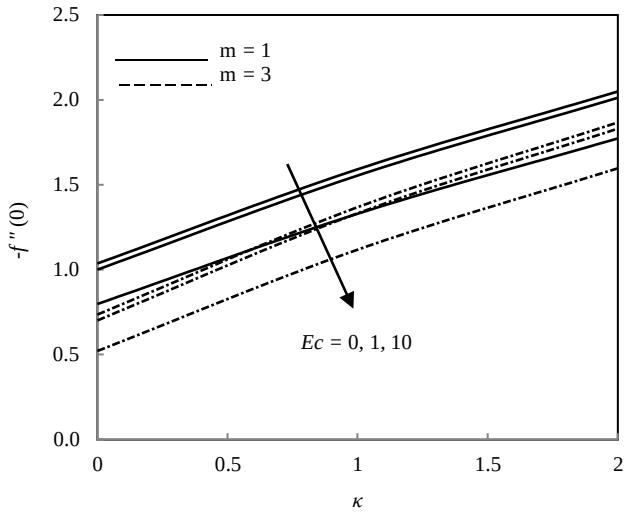


Fig. 1. The effects of porosity κ and viscous dissipation Ec onto $f''(0)$ when $N = M = \lambda = 1$ and $Pr = 0.72$

It is noticed that the skin friction in the x-direction $-f''(0)$ increases with the increment of porosity κ and decreases as the viscous dissipation Ec effect is more dominant. However, the Hall current m is seen to reduce the drag friction at the surface in the x-direction. These phenomenon however resulting to decrement of the local skin friction coefficient in the z-direction $h'(0)$ and the local Nusselt number $-\theta'(0)$ as κ increases. The impact of Hall current m gives rise to the $-\theta'(0)$ and this situation is

no longer valid for the $h'(0)$. Not much effect towards the $-\theta'(0)$ is seen when $Ec = 0$ as κ and m increase. This scenario is much pronounced for higher Ec number.

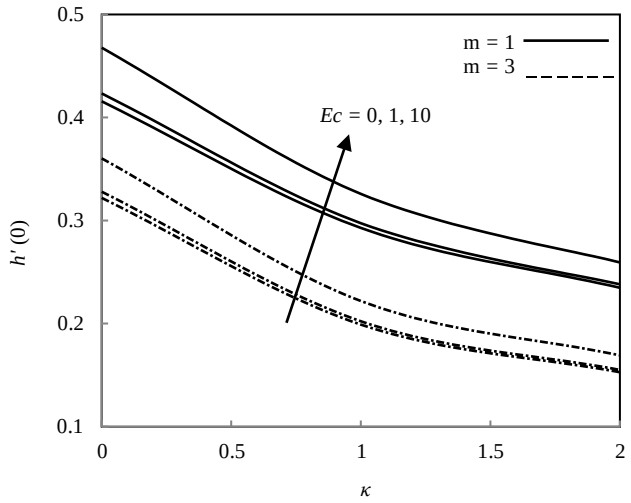


Fig. 2. The effects of porosity κ and viscous dissipation Ec onto $h'(0)$ when $N = M = \lambda = 1$ and $Pr = 0.72$

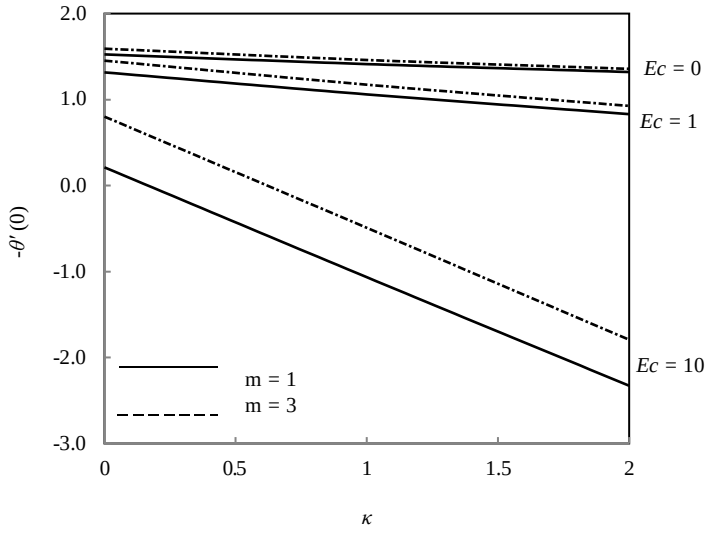


Fig. 3. The effects of porosity κ and viscous dissipation Ec onto $-\theta'(0)$ when $N = M = \lambda = 1$ and $Pr = 0.72$

The impact of the mixed convection λ for various values of Ec number and κ on the local skin friction coefficient in the x-direction $-f''(0)$, on the local skin friction coefficient in the z-direction $h'(0)$ and on the local Nusselt number $-\theta'(0)$ are depicted in Figures 4-6. It is seen that the increment of λ decreases the $-f''(0)$ and opposite phenomenon occurs for $h'(0)$ and $-\theta'(0)$. This is in line with the results obtained in Table 1. However, significant impact is seen on the $-\theta'(0)$ for low value of λ; i.e $\lambda << 1.3$ and higher Ec number ($Ec = 10$) in comparison with low Ec number. On top of that, the

increment of κ is found to increase the $-f''(0)$ and decrease both $h'(0)$ and $-\theta'(0)$, which in agreement with the results depicted in Figures 1-3.

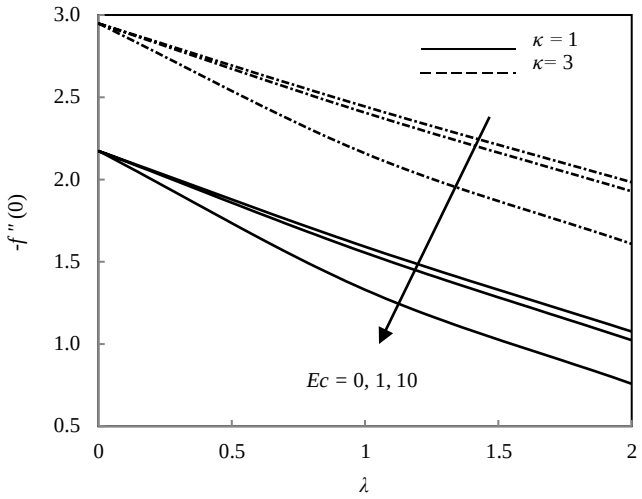


Fig. 4. The effects of mixed convection λ and Eckert number onto $-f''(0)$ when $N = M = m = 1$ and $Pr = 0.72$

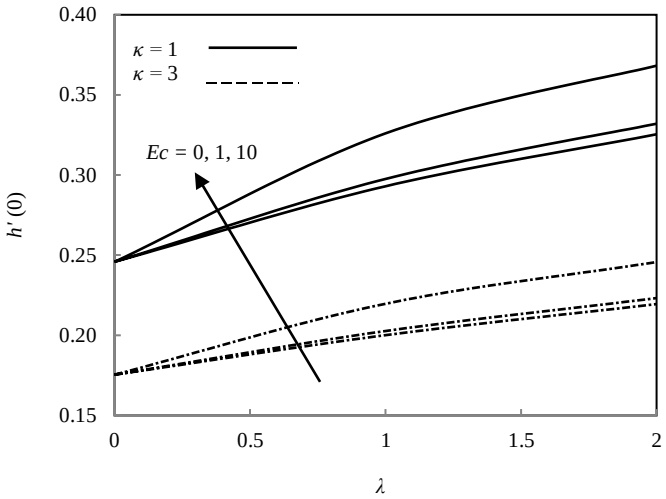


Fig. 5. The effects of mixed convection λ and Eckert number onto $h'(0)$ when $N = M = m = 1$ and $Pr = 0.72$

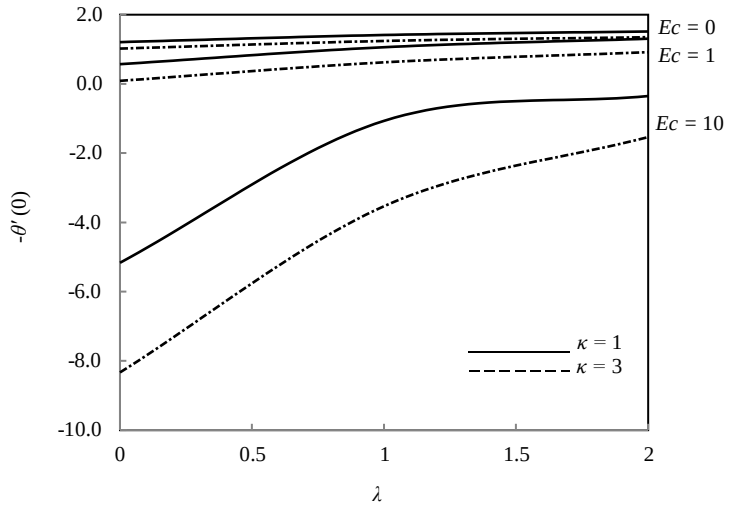


Fig. 6. The effects of mixed convection λ and Eckert number onto $-\theta'(0)$ when $N = M = m = 1$ and $Pr = 0.72$

Figures 7-9 depicted the tangential velocity $f'(\eta)$, transverse velocity $h(\eta)$ and temperature $\theta(\eta)$ profiles when $N = M = m = \lambda = 1$, $Pr = 0.72$ and for various values of κ and Ec numbers. The velocity f' and the temperature θ are maximize at the surface of the sheet ($\eta = 0$) and slowly deenergized as the boundary layer is completely formed. However, the transverse velocity $h(\eta)$ is drastically developed at the beginning of the motion and asymptotically reduces to zero after reaching a certain level of thickness. Besides giving ideas on the flow and temperature behaviour within the boundary layer, all the profiles obtained in Figures 7-9 satisfy the boundary conditions (11) which validates the numerical used in this study.

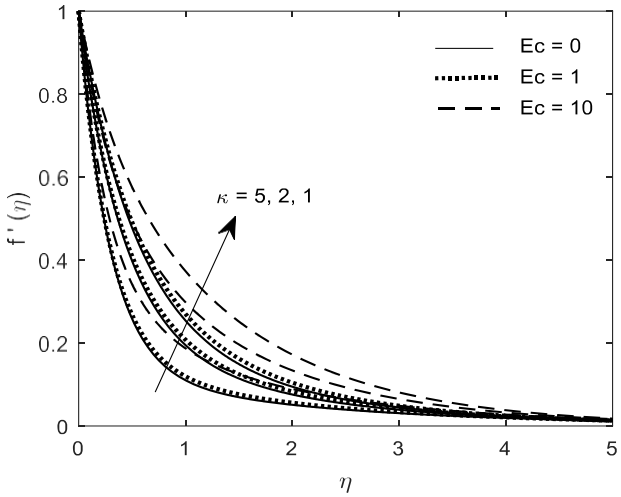


Fig. 7. Tangential velocity profiles $f'(\eta)$ for various values of Eckert number Ec and porosity parameter κ with $N = M = m = \lambda = 1$ and $Pr = 0.72$

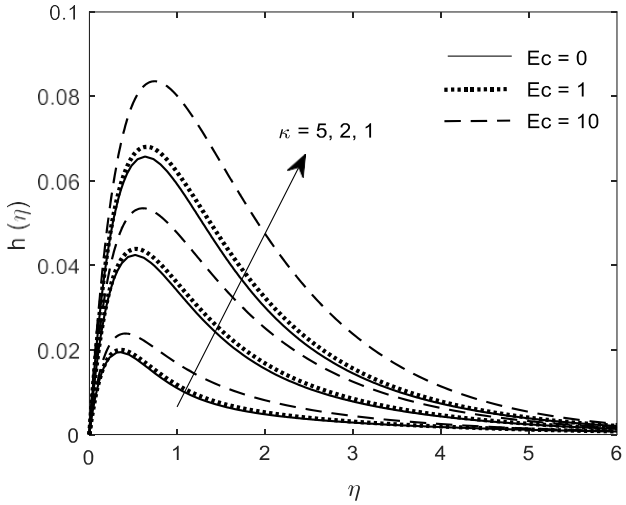


Fig. 8. Transverse velocity profiles $h(\eta)$ for various values of Eckert number *Ec* and porosity parameter κ with $N = M = m = \lambda = 1$ and $Pr = 0.72$

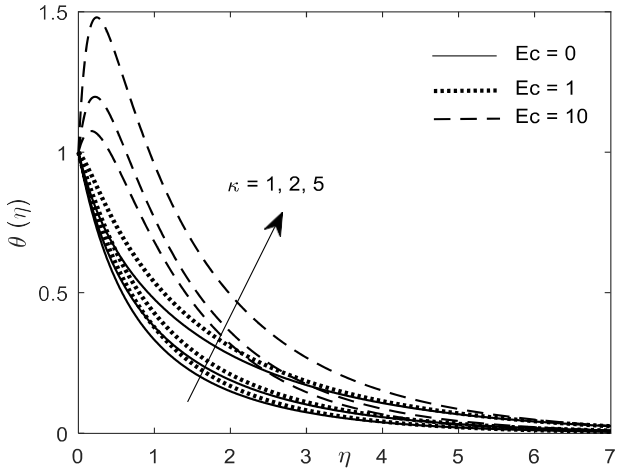


Fig. 9. Temperature profiles $\theta(\eta)$ for various values of Eckert number *Ec* and porosity parameter κ with $N = M = m = \lambda = 1$ and $Pr = 0.72$

4. Conclusions

The governing equations for a steady mixed convection Casson fluid flow over a vertical wall in porous media under the exposure of Hall current has been solved numerically for few arbitrary constants. It is found that the increment of Hall current decreases the magnitude of the $f''(0)$ and increases $h'(0)$ and $-\theta'(0)$. Same phenomenon occur for the increment of mixed convection.

Acknowledgement
The authors wish to thank the Putra Grant of Universiti Putra Malaysia (Project code: GP-IPM/2018/95969000) for the financial support received.

References

[1] Gupta, P.S. and Gupta, A.S. "Heat and mass transfer on a stretching sheet with suction or blowing." *Can . J. Chem. Eng.*55, (1977): 744-746.
[2] Crane, L.J. "Flow past a stretching plate." *Z. Ang. Math. Phys. ZAMP* 21, no. 4 (1970): 645-647.
[3] Magyari, E. and Keller, B. "Heat and mass transfer in the boundary layers on an exponentially stretching continuous surface." *J. of Phys. D: Appl. Phys*. 32, no. 5 (1999): 577.
[4] Khan, S.K. and Sanjayanand, E. "Viscoelastic boundary layer flow and heat transfer over an exponential stretching sheet." *Int. J. of Heat and Mass Transfer* 48, no. 8 (2005): 1534-1542.
[5] Abd El-Aziz, M. "Viscous dissipation effect on mixed convection flow of micropolar fluid over an exponentially stretching sheet." *Canadian J. of Phys*. 87, no. 4 (2009): 359-368.
[6] Wong, S.W., Awang, A.O. and Ishak, A. "Stagnation-point flow over an exponentially shrinking/stretching sheet." *Zeitschrift Fur Naturforschung A* 66, no. 12 (2011): 705-711.
[7] Oderinu, R.A. and Adepoja, O.A. "Approximate analytical solution to heat and mass transfer in the boundary layers on an exponentially stretching surface (Weighted residual approach)." *J. of Nigerian Assoc. of Math. Phys.* 21, no. 1 (2012): 101-104.
[8] Mebine, P. "On VIM-Pade method for boundary layer flow over an exponentially stretching surface." *Int. J. of Scientific and innovative Math. Research* 2, no. 3 (2014): 313-321.
[9] Sai, P.S., Ramakrishna, K., Puppala, N. and Reddy, K.J. "Chemical reaction and radiation effects on MHD flow over an exponentially stretching sheet with viscous dissipation and heat generation." *Int. J. Math. Comp. Appl. Res.* 5, no.3 (2015): 35-48.
[10] Ahmad, K., Hanouf, Z. and Ishak, A. "Mixed convection Jeffrey fluid flow over an exponentially stretching sheet with magnetohydrodynamic effect." *AIP Advances* 6, no.3 (2016), 035024-7. doi: 10.1063/1.4945401
[11] Ahmad, K. Wahid, Z. and Hanouf, Z. "Stagnation point flow of Casson fluid over an exponentially stretching sheet with thermal conductivity and Newtonian heating." *Int. J. of Advances in Mech. and Civil Eng*. 4, no. 2 (2017): 56-59.
[12] El-Aziz, M. and Nabil, T. "Homotopy analysis solution of hydromagnetic mixed convection flow past an exponentially stretching sheet with Hall current." *Mathematical Problems in Eng*. (2012): Article ID 454023, doi:10.1155/2012/454023
[13] Ashraf, M.B., Hayat, T. and Alsaedi, A. "Mixed convection flow of Casson fluid over a stretching sheet with convective boundary conditions and Hall effect." *Boundary Value Problems* (2017): doi 10.1186/s13661-017-0869-7.
[14] Nagalakshmi, Ch., Negendramma, V., Sreelakshmi, K. and Sarojamma, G. "Effects of Hall currents on the boundary layer flow induced by an exponentially stretching surface." *Procedia Eng.* 127 (2015): 440-446.
[15] Mahaboobjan, S., Sreelakshmi, K. and Sarojamma, G. "Unsteady MHD mixed convection flow, heat and mass transfer over an exponentially stretching sheet with suction, thermal radiation and Hall effect." *IQSR J. of Math*. 12, no. 4 (2016): 66-77.
[16] Srinivasacharya, D. and Jagadeeshwar, P. "Flow over an exponentially stretching sheet with Hall, thermal radiation and chemical radiation effects." *Frontiers in Heat and Mass Transfer* 9, no.37 (2017): 1-10, doi: 10.5098/hmt.9.37.
[17] Alinejad, J. and Samarbakhsh, S. "Viscous flow over nonlinearly stretching sheet with effects of viscous dissipation." *J. of Appl Math*. (2012), doi:10.1155/2012/587834.

Penerbit Akademia Baru

Engineering Science and Technology Conference Proceedings

Journal homepage: www.akademiabaru.com/EST.html

Enhancement of Tribological Behaviour and Thermal Properties of Hybrid Nanocellulose/Copper (II) Oxide Nanolubricant

Open Access

Sakinah Hisham[1],K.Kadirgama[1*], D.Ramasamy[2], R. Saidur[3]

[1] Faculty of Mechanical Engineering, Universiti Malaysia Pahang, 26600, Pekan, Pahang
[2] Research Centre for Nano-Materials and Energy Technology (RCNMET), School of Science and Technology, Sunway University, No 5, Bandar Sunway, 47500 Selangor Darul Ehsan

ABSTRACT

Many researchers tried to improve the tribological and thermal properties of the lubricating oil. The main advantages of using nanolubricants is they are relatively insensitive to temperature and that tribochemical reactions are limited, compared to the traditional additives. For this research, an attempt is made to enhance the tribological behaviour and thermal properties of lubricant (thermal conductivity and specific heat capacity) by adding hybrid nanocellulose/ copper (II) oxide (CNC-CuO) into the engine oil (SAE 40). CNC-CuO nanoparticle with an average size 80nm was dispersed into the SAE 40 at 0.1%, 0.5% and 0.9%wt concentration. Magnetic stirrer and ultrasonic bath was used to dispersed the nanoparticle in the SAE 40. Friction force and wear rate were measured using a tribometer based on ASTM G181. The results shows that frictional force when using the CNC-CuO nanolubricant at 0.1%was reduced by 54% and 22% comparing with the base oil respectively. The wear rate is also reduced when using the nanolubricants. Thermal Conductivity and specific heat capacity is also measured for the nanolubricants. The results showed that the thermal conductivity was increased about 4.2% while specific heat capacity was increase 2.1% when using CNC-CuO nanolubricant respectively. The results indicates that the hybrid CNC-CuO nanoparticles improve the tribological and thermal properties of the lubricant oil.

Keywords:
Nanocellulose; friction; wear; specific heat capacity; thermal conductivity

Copyright © 2019 PENERBIT AKADEMIA BARU - All rights reserved

1. Introduction

The major function of a lubricant is to protect two or more moving surfaces against friction and wear. Currently, developing nanolubricant as an alternative for current lubricant in the market has captured most of the researcher and academician's attention because it is proven that nanolubricants can reduce wear via "ball bearing" effect. Furthermore, using nanolubricant can improve engine efficiency in an internal combustion engine. All of these reasons can prove that using nanolubricant as an alternative lubricant can elongate the deterioration time for the engine component. The performance of nanolubricants is directly associated with the formulations, preparation and the nanoparticle characterization. Over several decades, researchers has developed several additives to diminish all of the tribological aspects challenges such as friction and

* *Corresponding author.*
E-mail address: sakinah.hisham0704@gmail.com (Sakinah Hisham)

wear (abrasion, adhesion, corrosion, and oxidation) on lubricant base stock. Furthermore, many attempts conducted to investigate the thermal behavior of the lubricant oil, their chemical composition and physical properties.

Thermal properties like thermal conductivity and specific heat capacity are the primary key parameters to study the nanolubricants properties. Material, size and the quantity of surfactant as a dispersant are all affected the thermal conductivity and specific heat capacity of nanolubricant. Despite the engine oil function serve as a lubricant to alleviate wear but it also acts as a cooling agent for the system. The two properties, thermal conductivity and specific heat capacity are crucial properties for heat transfer analysis. Higher specific heat capacity leads to a lower temperature increment as per amount of heat energy absorption. For example, uncooled low heat rejection (LHR) for diesel engines are not contain radiator and coolant thus only engine oil can reduce the amount of heat energy absorption from the engine. For that reason, the heat transfer properties of the lubricant for LHR diesel engines important to measure the heat transfer capability of lubricants . However, even though heat capacity is the crucial properties for thermal properties studies, research study for the specific heat capacity of lubricant are still inadequately. The aberration among the publishes values are up to 18% as the literature data uncertainty is very high. This paper discussed about the effecr tribological factor of nanolubricant (friction and wear) at different concentration together with the thermal properties of nanolubricant (thermal conductivity and specific heat capacity.

2. Methodology

2.1 Nanolubricants Preparation

Combination of Cellulose Nanocrystal (CNC) and Copper Oxide (CuO) has been considered in this research since they both exhibit better thermal conductivities, large surface area and chemically stable .CNC used in this research is extracted from the acetate grade dissolving pulp that is the Western Hemlock plant is to be in the white to slightly off-white cream form. CNC was procured from Blue Goose Biorefineries Inc with 7.4% weight/weight suspension. Two-step method suggested by Yu and Xie is used in the preparation of five diverse nano lubricant samples with volume concentrations from 0.1% to 0.5%. There are two processes in this method, which are (i) synthesis of the nanoparticles in the powder form (ii) dispersion of the nanoparticles into the base fluids to form a stable and homogeneous solution. Nanocellulose neither melts at high temperature nor dissolves in a universal aqueous solvent because of their hydrophilic nature is a significant challenge to properly dry CNC from an aqueous suspension. Amongst several methods of drying process for nanocellulose suspensions, spray drying was proposed as a technically appropriate process manufacturing. For the preparation of CNC in a powder form, the suspensions were spray dried with a mini blower . The moisture in these suspensions is quickly evaporated upon direct contact with the hot air flow through the orifice of the nozzle on the spray dryer resulting in drying–out and stable CNCs flake form. After that, the flakes were pulverized into powder form. The CNC then was dry mixing together with CuO. Nanolubricant samples with the solid volume fraction of 0.1%, 0.5% and 0.9% were prepared by adding CNC and CuO in SAE40 by using a magnetic stirrer and ultrasonic bath. Nanoparticles in suspension tend to agglomerate due to their high surface area and surface activity.

2.2 Tribological Testing

The test was conducted using custom-made friction and wear tester which also replicates regarding contact geometry relevant to the tribological phenomena occurring during the piston ring- cylinder liner contact in an engine. The schematic diagram of the friction pairs is shown in figure 1. The wear test conducted under lubricated sliding condition. Wear test involve making linear reciprocates movements similar to a cylinder-piston ring pair operating under real conditions. Wear morphology that caused at the surface of specimen and during the linear reciprocating sliding motion against the outer surface of aluminium 6061 for 30 minutes at boundary lubrication regime (low speed and high load) in the presence of SAE 40 and different concentration of nanoparticle (0.1,0.3 and 0.5) added in SAE 40 was also reported. The temperature was at 85˚C which is the regime temperature of the internal combustion engine and the operating time was 30 minutes per specimen. The coefficient of friction was recorded automatically using NI-DAQ via the ratio of friction force to normal load. The wear loss of the friction pairs was calculated by the weight of the samples before and after sliding, to an accuracy of 0.1 mg. Each sliding test was repeated three times to obtain a standard deviation.

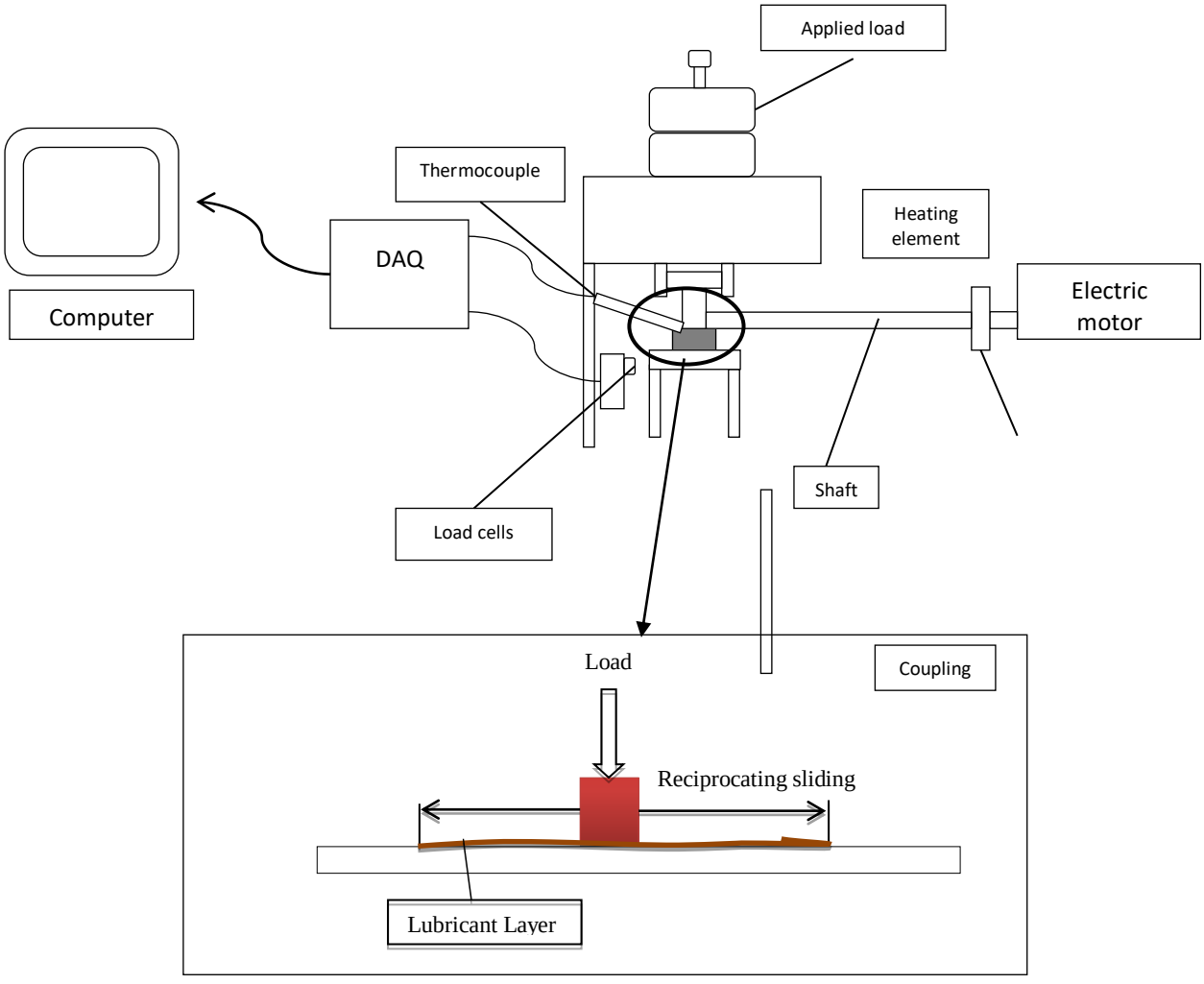


Figure 1: Tribology testing setup

2.3 Thermal Conductivity and Specific Heat Capacity Measurement

A KD2 Pro thermal property analyzer from Decagon Devices Inc., USA was used to measure thermal conductivity for nanofluid. Most researchers used KD2 Pro to measure thermal conductivity . The device works based on the transient hot-wire method and it has been calibrated by glycerin. The measured thermal conductivity value is supplied by the manufacturer which was 0.286 W/m K with an accuracy of ±0.35%. To keep a constant temperature of the samples uniformly, hot water bath temperature was used. The measurement of thermal conductivity was repeated five times and the average value of thermal conductivity from five sets of reading was considered. To minimize the error during the measurement of free convection, a minimum of 15-minute interval time was considered before the next reading for different concentrations and temperatures. The error can happen due to the variation along the sensor that had direct contact with the nanolubricant sample. Furthermore, the probe of the KD2 Pro device had to be kept vertically straight into the nanolubricant sample during the thermal conductivity measurement to minimize the errors resulted from the free convection,

In order to determine the specific heat capacity of nanolubricant, a differential scanning calorimeter (DSC), model DSC1000-/C from Linseis Messgeräte GmbH, Selb, Germany was employed. DSC is a thermal analysis technique that looks at how a material's heat capacity (Cp) is changed over temperature. Nanolubricant is heated or cooled and the changes in its heat capacity are tracked during changes in the heat flow. The samples were placed in aluminum crucibles and heated from 30℃ up to 90℃ at a heating rate of 5℃ min^{-1} under a dynamic atmosphere of nitrogen. The nanolubricant samples were heated from the room temperature at the heating rate of 5℃- 1 up to 30℃.

3. Results

3.1 Coefficient of Friction

Figure 2 present the coefficient of friction (COF) of samples lubricated by base oil (SAE 40) and nano lubricant at 0.1, 0.3 and 0.5 concentration at low speed and high load. At low speed and high load, usually COF is the highest and according to Wang et. al, at this state the index lubrication value is known as lambda value (λ) less than 1 which indicate the boundary lubrication regime at the Stribeck Curve. As shown in figure 2, SAE 40 clearly shows the highest friction compared to a lubricant that contents CNC-CuO nanoparticle. At the initial stage, 0.1, 0.5 and 0.9 show almost the same COF while SAE 40 shows the highest friction. At minutes 4 for 0.1 concentration, COF show a sudden increase of COF that almost the same as in SAE 40. This might be due to the slight vibration from the test rig base. From the figure curve as well, the graph indicates the same pattern, at minutes 2 until minutes 8, COF starts to increase and slowly become constant at from minutes 8 to 12 and start to drop at minutes 15 upwards. When the tribological tests are conducted at low speed and high load, the high friction makes temperature rise and the temperature of the friction region was taken during the experiment and it is approximately 40 °C, which results in a decrease in the viscosities of the SAE 40 and CNC-CuO nanolubricants. The average COF result as shown in figure 2 also shows that SAE 40 is the highest, while at different concentration of CNC-CuO did not shows many differences.

Figure 3 shows the weight loss of after the tribology testing. SAE 40 shows the highest COF while there is a drastic change when added with 0.1 CNC-CuO nanoparticle. In contrast, by adding different concentration, the weight loss value did show much different. This can be conclude that the concentration parameter did not affect the coefficient of friction and weight loss result.

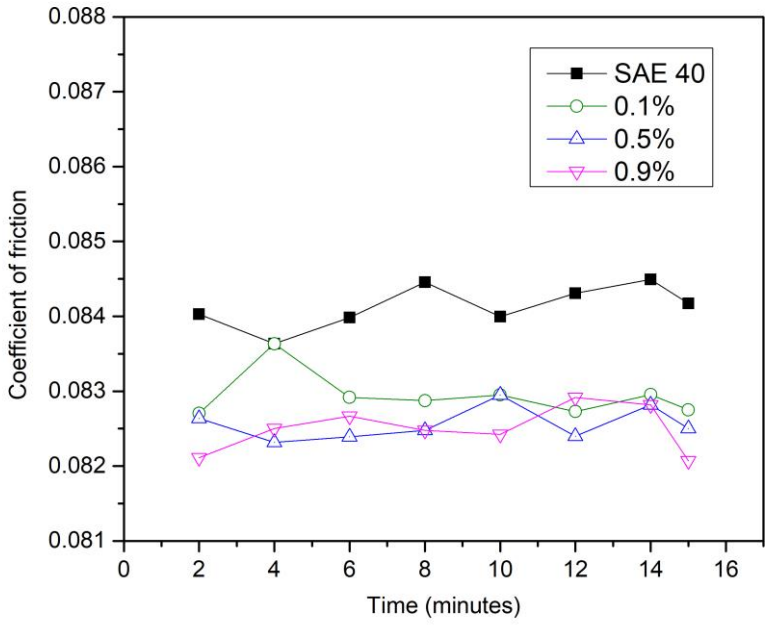


Figure 2: Coefficient of friction versus time for CNC-CuO

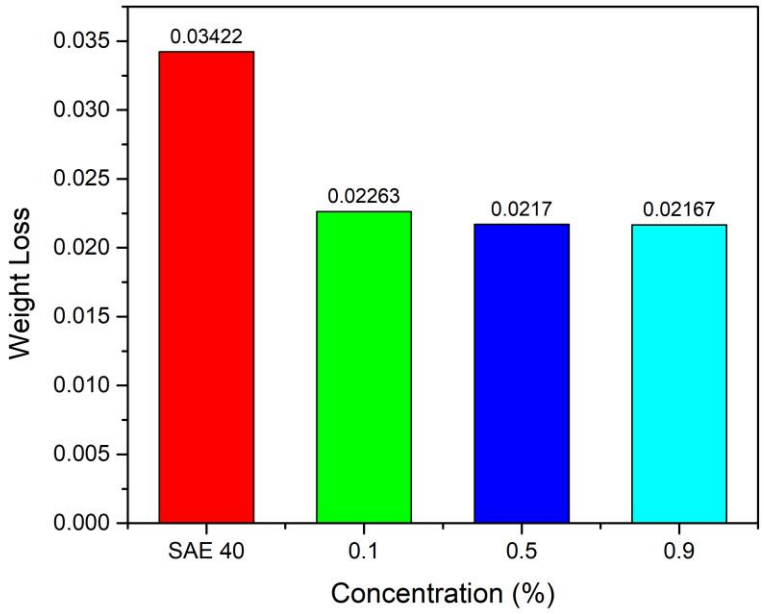


Figure 3: Wear loss after tribology testing

3.2 Thermal Conductivity and Specific Heat Capacity Evaluation

As shown in Figure 4, the thermal conductivity value shows the inconsistent result as the temperature increases. At 0.5, the value of thermal conductivity at 50℃ is increased first then it started to decrease gradually until 90℃. As for 0.9wt% the thermal conductivity value increases slightly until 90℃. This result might be due to the combination between organic nanoparticle (CNC) and inorganic nanoparticle (CuO) as the thermal conductivity value shows the consistent increasing

pattern for CNC nanolubricant as shown in Figure 5 while Mansor et al. shows the consistent decreasing pattern for CuO nanolubricant . Figure 6 shows the variation of experimental result for average specific heat capacity versus temperature of base fluid (SAE 40) with CNC-CuO nanolubricant at different concentration. Oil with a higher specific heat capacity value indicates lower temperature increment for an amount the absorption of heat energy thus the higher value of Cp exhibit the better lubricant in terms of heat transfer performance . In this circumstance, the specific heat capacity of the hydrodynamic lubricants is an important characteristic to improve the load carrying limit . The temperatures in the bearing gaps are smaller when the point where the specific heat capacity of engine oil is high, thus the heat capacity is high at the same operating condition .

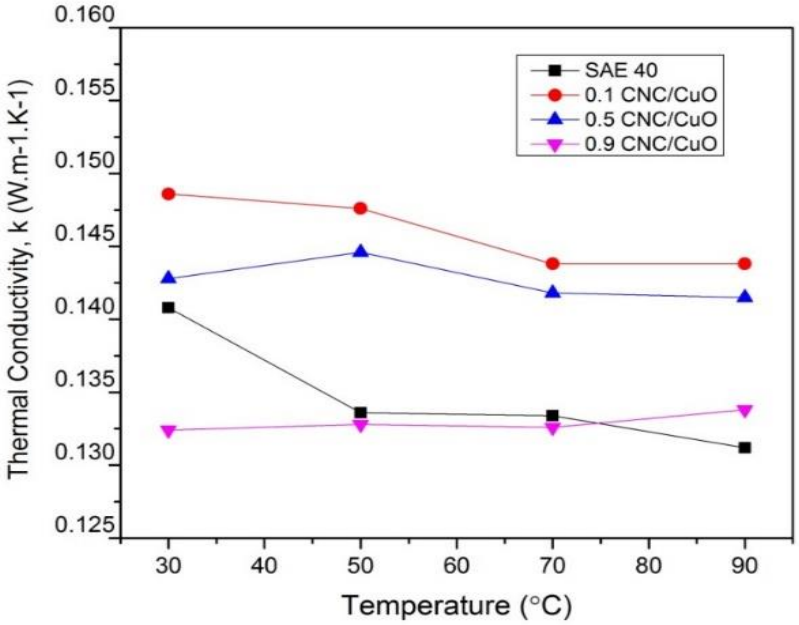


Figure 4: Thermal conductivity at increasing temperature

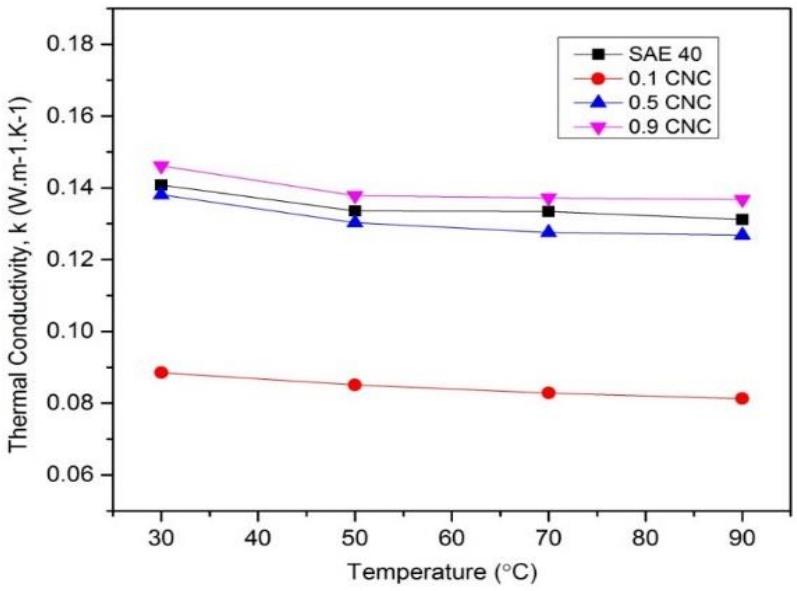


Figure 5: Thermal conductivity of CNC at different concentration

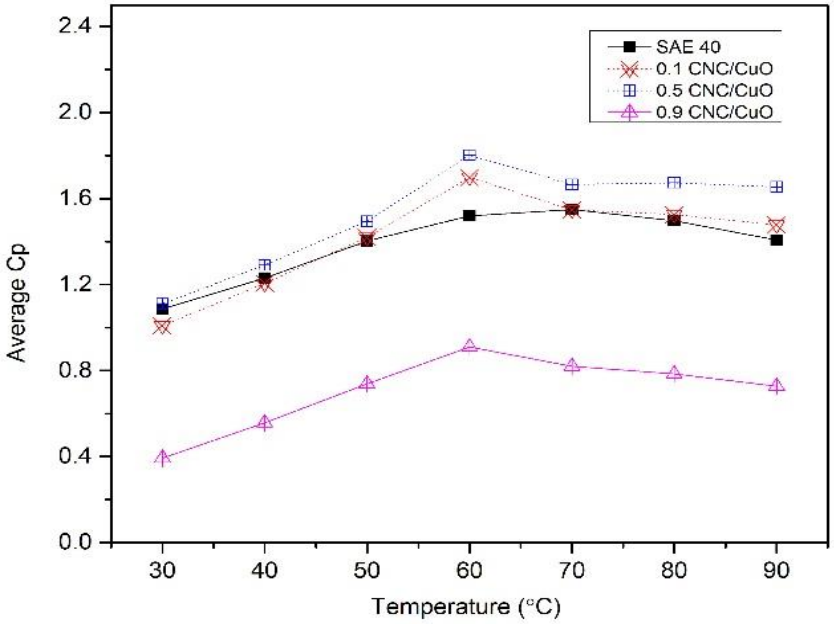


Figure 5: Specific heat capacity

4. Conclusions

The results shows that frictional force when using the CNC-CuO nanolubricant at 0.1%was reduced by 54% and 22% comparing with the base oil respectively. The wear rate is also reduced when using the nanolubricants. Thermal properties results showed that the thermal conductivity was increased

about 4.2% while specific heat capacity was increase 2.1% when using CNC-CuO nanolubricant respectively. The results indicates that the hybrid CNC-CuO nanoparticles improve the tribological and thermal properties of the lubricant oil.

Acknowledgement
The authors express their grateful appreciation to the University Malaysia Pahang for providing laboratory facilities and financial assistance under project no RDU1803136 and RDU190323.

References

[1] Abitbol, Tiffany, Amit Rivkin, Yifeng Cao, Yuval Nevo, Eldho Abraham, Tal Ben-Shalom, Shaul Lapidot, and Oded Shoseyov. "Nanocellulose, a Tiny Fiber with Huge Applications." *Current Opinion in Biotechnology* 39, no. Supplement C (2016/06/01/ 2016): 76-88.

[2] Almanassra, Ismail W., Abdallah D. Manasrah, Usamah A. Al-Mubaiyedh, Tareq Al-Ansari, Zuhair Omar Malaibari, and Muataz A. Atieh. "An Experimental Study on Stability and Thermal Conductivity of Water/Cnts Nanofluids Using Different Surfactants: A Comparison Study." *Journal of Molecular Liquids* (2019/05/22/ 2019): 111025.

[3] Asnida, M., S. Hisham, N. W. Awang, A. K. Amirruddin, M. M. Noor, K. Kadirgama, D. Ramasamy, G. Najafi, and F. Tarlochan. "Copper (Ii) Oxide Nanoparticles as Additve in Engine Oil to Increase the Durability of Piston-Liner Contact." *Fuel* 212, no. Supplement C (2018/01/15/ 2018): 656-67.

[4] Buongiorno, Jacopo, David C Venerus, Naveen Prabhat, Thomas McKrell, Jessica Townsend, Rebecca Christianson, Yuriy V Tolmachev*, et al.* "A Benchmark Study on the Thermal Conductivity of Nanofluids." *Journal of Applied Physics* 106, no. 9 (2009): 094312.

[5] Duangthongsuk, Weerapun, and Somchai Wongwises. "Comparison of the Effects of Measured and Computed Thermophysical Properties of Nanofluids on Heat Transfer Performance." *Experimental Thermal and Fluid Science* 34, no. 5 (2010): 616-24.

[6] Esfe, Mohammad Hemmat, Seyfolah Saedodin, Mohammad Akbari, Arash Karimipour, Masoud Afrand, Somchai Wongwises, Mohammad Reza Safaei, and Mahidzal Dahari. "Experimental Investigation and Development of New Correlations for Thermal Conductivity of Cuo/Eg–Water Nanofluid." *International Communications in Heat and Mass Transfer* 65 (2015): 47-51.

[7] Farbod, Mansoor, Razieh Kouhpeymani asl, and Amin Reza Noghreh abadi. "Morphology Dependence of Thermal and Rheological Properties of Oil-Based Nanofluids of Cuo Nanostructures." *Colloids and Surfaces A: Physicochemical and Engineering Aspects* 474 (2015/06/05/ 2015): 71-75.

[8] Gordon, JM, and Mahmoud Huleihil. "General Performance Characteristics of Real Heat Engines." *Journal of Applied Physics* 72, no. 3 (1992): 829-37.

[9] Hemmat Esfe, Mohammad, Ali Akbar Abbasian Arani, Saeed Esfandeh, and Masoud Afrand. "Proposing New Hybrid Nano-Engine Oil for Lubrication of Internal Combustion Engines: Preventing Cold Start Engine Damages and Saving energy." *Energy* 170 (2019/03/01/ 2019): 228-38.

[10] Laad, Meena, and Vijay Kumar S. Jatti. "Titanium Oxide Nanoparticles as Additives in Engine Oil." *Journal of King Saud University - Engineering Sciences* 30, no. 2 (2018/04/01/ 2018): 116-22.

[11] Li, Haoran, Li Wang, Yurong He, Yanwei Hu, Jiaqi Zhu, and Baocheng Jiang. "Experimental Investigation of Thermal Conductivity and Viscosity of Ethylene Glycol Based Zno Nanofluids." *Applied Thermal Engineering* 88 (2015): 363-68.

[12] Paul, Gayatri, Subhasis Shit, Harish Hirani, Tapas Kuila, and N. C. Murmu. "Tribological Behavior of Dodecylamine Functionalized Graphene Nanosheets Dispersed Engine Oil Nanolubricants." *Tribology International* 131 (2019/03/01/ 2019): 605-19.

[13] Rasheed, A. K., M. Khalid, A. Javeed, W. Rashmi, T. C. S. M. Gupta, and A. Chan. "Heat Transfer and Tribological Performance of Graphene Nanolubricant in an Internal Combustion Engine." *Tribology International* 103 (2016/11/01/ 2016): 504-15.

[14] Sajid, Muhammad Usman, and Hafiz Muhammad Ali. "Thermal Conductivity of Hybrid Nanofluids: A Critical Review." *International Journal of Heat and Mass Transfer* 126 (2018/11/01/ 2018): 211-34.

[15] Salgado, Josefa, Tamara Teijeira, Juan José Parajó, Josefa Fernández, and Jacobo Troncoso. "Isobaric Heat Capacity of Nanostructured Liquids with Potential Use as Lubricants." *The Journal of Chemical Thermodynamics* 123 (2018/08/01/ 2018): 107-16.

[16] Sanmamed, Yolanda A, Paloma Navia, Diego González-Salgado, Jacobo Troncoso, and Luis Romaní. "Pressure and Temperature Dependence of Isobaric Heat Capacity for [Emim][Bf4],[Bmim][Bf4],[Hmim][Bf4], and [Omim][Bf4]." *Journal of Chemical & Engineering Data* 55, no. 2 (2009): 600-04.

[17] Waliszewski, D, I Stępniak, H Piekarski, and A Lewandowski. "Heat Capacities of Ionic Liquids and Their Heats of Solution in Molecular Liquids." *Thermochimica acta* 433, no. 1-2 (2005): 149-52.

[18] Wang, Yongnan, Zhenping Wan, Longsheng Lu, Zhihui Zhang, and Yong Tang. "Friction and Wear Mechanisms of Castor Oil with Addition of Hexagonal Boron Nitride Nanoparticles." *Tribology International* 124 (2018/08/01/ 2018): 10-22.

[19] Yu, W, and SUS Choi. "The Role of Interfacial Layers in the Enhanced Thermal Conductivity of Nanofluids: A Renovated Maxwell Model." *Journal of nanoparticle research* 5, no. 1-2 (2003): 167-71.

[20] Yu, Wei, and Huaqing Xie. "A Review on Nanofluids: Preparation, Stability Mechanisms, and Applications." *Journal of nanomaterials* 2012 (2012): 1.

Penerbit Akademia Baru

Engineering Science and Technology Conference Proceedings

Journal homepage: www.akademiabaru.com/EST.html

Potential Augmentation of the Ampacity of a Medium Voltage Underground Cable in Power Distribution Networks by CHT Thermal Modelling

Open Access

Beriache M'hamed[1,*], Cherki Brahim Hicham[1], Mokhtar Saïdia Leila[1], Nor Azwadi Che Sidik[2], Wan Mohd Arif Aziz Japar[2], Ahmad Tajuddin Mohamad[2]

[1] Laboratory of Rheology and Mechanics, Department of Mechanical Engineering, Faculty of Technology, Hassiba Benbouali University of Chlef, Algeria

[2] Malaysia – Japan International Institute of Technology (MJIIT), University Teknologi Malaysia Kuala Lumpur, Jalan Sultan Yahya Petra (Jalan Semarak), 54100 Kuala Lumpur, Malaysia

ABSTRACT

This research aims at a deeper understanding of the steady-state thermal behavior of underground cables using Computational Heat Transfer (CHT) techniques modeling based Ansys Fluent software. The results concern the thermal study of 33 kV single and multiple copper conductors with a nominal conductor cross-section of 615 mm^2 buried in the ground for a single cable, two cables and for three cables in horizontal position. The most unfavorable summer conditions, the burial depth as well as the physical properties of the soil as a function of the moisture content, are studied. The operating current of the conductors is taken 940 A. The results show that the temperature of the cables decreases with the burial depth, a compromise temperature/cost of installation corresponds to 80 cm of burial depth. Further, the maximum temperature of a single cable buried in the ground is considerably lower than that allowed (363 K) for a good use, namely 313 K in summer conditions, so there is a considerable margin to increase its ampacity, also the temperature decrease with increase of water content of the soil surrounding the cable of approximately 2 to 5 degrees. The results obtained are in good agreement with those of the literature.

Keywords:
Underground cables; ampacity; thermal state; power distribution networks; CHT modeling

Copyright © 2019 PENERBIT AKADEMIA BARU - All rights reserved

1. Introduction

The use of underground power transmission and distribution has been steadily increasing in recent years due to the increased demand for electric power and the extensive expansion of populations into large cities, which the case of Algeria. This seems to be the best solution to reduce the environmental impact and diminish the electromagnetic pollution in highly populated zones [1]. However, it is extremely difficult to build new underground cable networks in urban areas because of the high cost, the difficulties posed by the various existing underground networks and the environmental demands of the population.

Therefore, it has become very important to try to increase the exploitation of the existing infrastructure of the power grids to overcome these challenges without additional investment to the extent possible. The problem of optimizing the electrical cables and their exploitation for good performance has become of great importance, especially with nowadays conditions, which require a high quality of service and the rationalization of the expenses. A good arrangement of the cable

configuration, thus the working parameters under different loads, climatic conditions and soil properties, can lead to improved cable performance. In 1957, Neher and McGrath presented an appropriate method for calculating the permissible current of underground cable systems [2]. As such, Benato et al. [3] presented a detailed study on different possibilities to increase the rated current of insulated cables. Proper thermal computation of a buried electrical cable system is essential to determine its permissible current. Commonly this calculation is based on IEC 60287-1-1 and IEC 60287-2-1. IEC 60287-1-1 [4] calculates the permissible current under a steady state, when at IEC 60287-2-1 [5], it estimates the thermal resistance between the cable system and the external environment. In this vision, computational heat transfer techniques can be used to predict numerically the thermal state of electrical buried cables in the ground under different configurations and working parameters. The numerical resolution of these problems for a precise estimate of the thermal state of the main components of the electricity distribution network will be the main and new contribution to academic and industrial knowledge in the field of very high voltage underground electric cables. Than can be used to assist specialists in performing the good cable configuration with the right parameters. The use of underground cables in Algeria has grown significantly over past two decades as a result of urban expansion and increased infrastructure activities. However, the weather conditions in Algeria are very severe especially in summer where the ambient temperature sometimes exceeds 50°C and the water content of the soil is very low. It adds to that the strong consumption of electrical energy by the population in this very hot period of the year. Under such conditions, current carrying capacity of the cable is highly influenced. The accuracy of methods for estimating the thermal state of underground conductors is crucial, especially in cases where the network is operating under high load conditions. The calculation of cable ampacity requires the evaluation of several parameters that can influence the operating characteristics of the underground cable. The ampacity depends not only on the structure and materials of the cable, but also on its installation method as well as the external environmental conditions such as the condition and properties of the backfill soil, configuration of the soil layers and its water content, the climatic conditions , and the depth of burial [6, 7, 8 and 9]. Chatzipanagiotou et al. 2017 [10] investigated experimentally the effect of soil moisture content and buried depth on the ampacity of underground power cables. A downscaled laboratory model for an underground cable has been investigated experimentally with respect to these parameters. The experimental results of their study indicate that the presence of soil humidity influences the cable temperature. They found from the measurements that the thermal resistance of the ground decreases with the humidity. Al-Saud et al. [11] presented an optimization model for underground power cable thermal circuit based on a generated gradient approach. The authors had demonstrated the use of nonlinear optimization in conjunction with finite element thermal field analysis. Sensitivity analysis of the cable temperatures on fluctuations in the cable circuit parameters was also included. The proposed finite element thermal analysis was implemented to evaluate cable temperature and its sensitivity concerning the optimized thermal parameters. Sellers et al. in [12] provide the brief overview of investigations of ampacity of underground cables starting with the first very simplified models for calculating the current carrying capacity of underground cables that were created more than 100 years ago. Their goals were to examine objectively several improvements to the Neher-McGrath model, to incorporate recent heat transfer correlations, and to remove several assumptions considered in [2]. The suggested changes resulted in a more complex ampacity model, which lead to an increase in ampacity in some cases and a decrease in others. De Lieto Volaro et al. [13] employed control-volume formulation of the finite difference method to determine the thermal resistance existing between an underground electrical power cable and the ground surface. Based on the numerical simulation, the authors had proposed

a semi-empirical correlating equation for the design of buried electrical power cables and compared the results with IEC 60287 standard. Andrea Vallati and Marcin Pilarczyk [14] presented a modified Jaya algorithm for optimizing the material costs and electric-thermal performance of an underground power cable system. A high voltage (HV) underground cable line with three 400 kV AC cables arranged in flat formation in an exemplary case study is considered. They found that the use of efficient thermal backfill materials allows the maximum cable conductor temperature to be lowered.

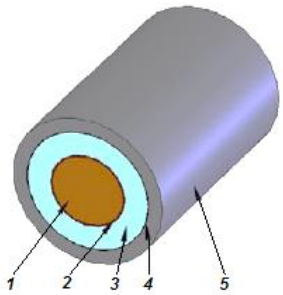
The effect of solar radiation on the thermal steady state of underground electric cables is not covered by IEC 60287 [4], IEC technical report TR 62095 [5] or 2017 edition of NFPA 70 [15]. This is why the effect of solar radiation is neglected by most researchers who deal with heating and charging problems with underground electric cables [16-17]. Among the researchers who considered this effect, there are those whose conclusions were consistent with the relevant IEC standards [18], those who found that solar radiation only affects the cables laid at low depths [19], as well as those who concluded that the effect of the sun can not be ignored in the case when the daily load peak coincides with the period of maximum solar activity [20, 21]. Existing commercial CFD software can be employed for the analysis of heat transfer in the conductors and surrounding domains. There are some publications on the application of CFD packages for underground cables; although a number of cases with similar geometries were investigated using the CFD software. For example, Ansys Fluent CFD, software based on the finite volume method, was presented by Makhkamova in [22] in order to investigate the thermal state for overhead line conductors or underground.

In this work, a new model based on the Computational Heat Transfer (CHT) technique of the electric cable taken in its real working environment is proposed. The main objective of the work is to predict numerically the thermal state of electrical cables buried in the ground under different configurations and working under a current of 940 amperes, taking into account the physical properties of the soil for a range of content values in moisture. Firstly, we need to have the correct laying configuration of the cables following which the operating temperature of the cable is the lowest, secondly, to do the same thing when the cables are housed in HDPE ducts for possible extensions of the cable network and reasons for maintenance especially. We are looking for the temperature and the limit current of the cables in order to better exploit the existing electricity network without any additional modifications with the support of the different factors of the problem, especially since most of these installations are oversized. The design engineer usually overdimensions the section of the conductor with respect to the correspondent air cable lines, to decrease the electrical resistivity [23].

2. Problem modeling

2.1. Geometry

The physical design of the conductor is presented in Fig. 2.2. The real geometry of the conductor is complex and contains the following components: the copper conductor core made of strands; the conductor screen (polyethylene); insulation (cross-linked polyethylene); the insulation screen (polyethylene); the copper screen; the binder tape (polyethylene) and oversheath (medium density polyethylene). For purpose of creating, the computational mesh the real geometry of the conductor was simplified (to reduce computational time) and presented as a combination of four co-axial cylinders. The outer diameter of the copper conductor and the oversheath is 28.3 and 60.4 mm, respectively.



1. Copper conductor; 2. Conductor screen; 3. Insulation;
4. Copper screen; 5. Oversheath

Fig. 2.1. Geometry model of the cable

The dimensions of the simplified model are as follows: the diameter of copper cable with nominal area of conductor of 630 mm² is 28.3 mm; the thickness of insulation is 8 mm; the thickness of the copper wire screen is 1 mm and the thickness of oversheath is 2.7 mm.

2.2. Computational Domain

Fig. 2.2 presents the computational domain used for the numerical modelling of the thermal state of a single copper cable buried in the soil. In this domain, the cable is placed at the centre of the soil the domain. These dimensions (in mm) of the domain are large enough to produce size independent solution [22].

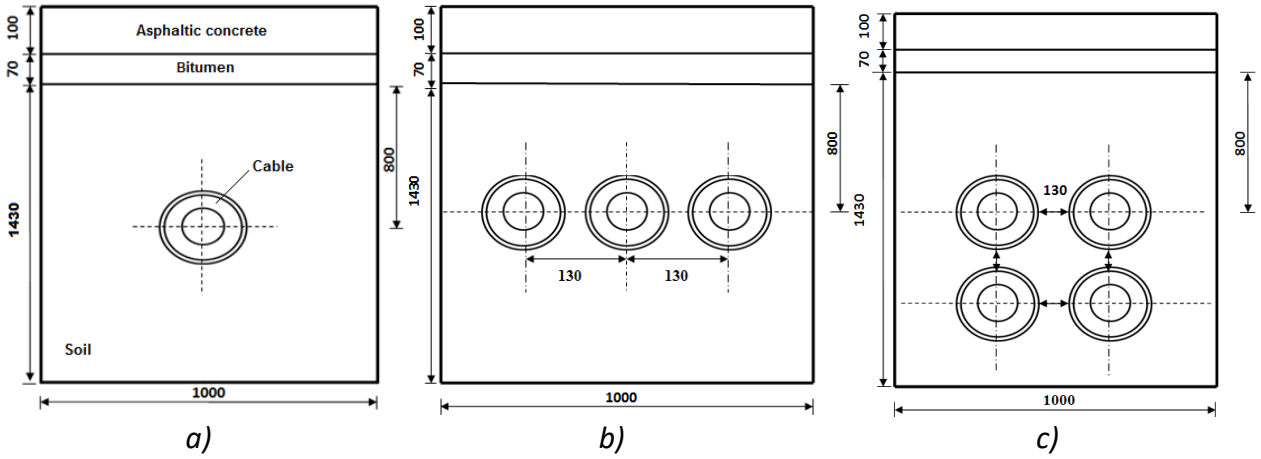


Fig. 2.2 Computational domain for numerical study

a) of single copper cable buried in soil, b) three buried cable, c) four buried cable

As previously, mesh refinement tests were conducted in order to ensure that the solutions are not mesh dependent.

2.3. Grid of Computational Domain

The choice of mesh is an essential point in the accuracy, we used the Tgrid-Map element that is triangular element and well suited for round shapes like cable case, (Fig.2.3).

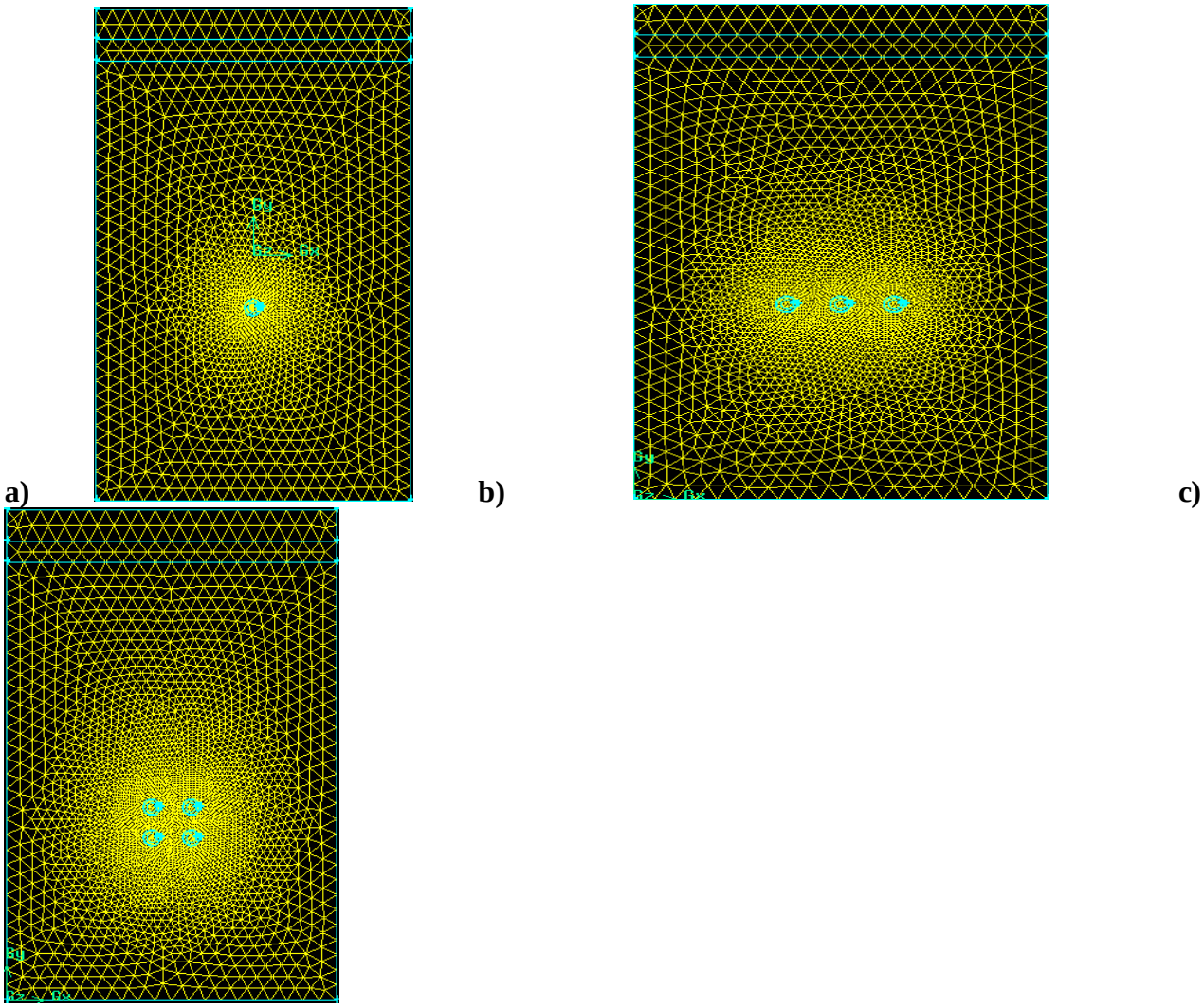


Fig. 2.3 Grid of computational domain
a) Single cable buried in soil, b) three buried cable, c) four buried cable

3. Data and assumptions for calculations

The thermo-physical properties of the cable (XPLE BS7078) [23] constituting our model are summarized in Table 3.1.

Table 3.1
Thermo-physical properties for components of the cable [23]

Components of the cable	Density kg/m^3	Heat capacity J/kg K	Thermal conductivity W/m.K
Copper conductor	8978	381	387.6
Conductor screen (PVC)	1300	1330	0.182
Insulation	950	2300 @ 293K 3750 @ 353K	0.333
Copper screen	8900	385	370.4
Oversheath	1600	1500	0.25

The cable backfills considered in the study are as follows: native soil, Bitumen and Asphaltic concrete. Constant thermal conductivities of the backfills in the dry state are assumed. Performance typically involves laying the cable in a sand bed, rather than in the soil of the same excavated area, to improve heat dissipation and allow for a more standard installation process. In our case, we used the same type of excavated soil for economic and simplification reasons. Soil is considered as a homogeneous medium and not as a porous substance. In summer conditions, the soil was assumed to dry soil. The thermo-physical properties of the backfills are gathered in Table 3.2.

Table 3.2
Thermo-physical properties for different types of physical domain [23]

Type of soil	Density, kg/m^3	Heat capacity, J/kg K	Thermal conductivity, W/m.K
Asphaltic concrete	2350	870	2.10
Bitumen	2350	870	1.90
Dry soil	1400	800	0.408

According to Electrical Standards P17 [24] for the summer conditions the soil and ambient temperatures are of 293 and 298 K, respectively [25]. The summer conditions are characterized by a low moisture content. The thermal rating for the 630 mm² cable in the flat formation in summer conditions is 940 A, which corresponds to a heat source, q, of 14200,7 W/m^3 [26], calculated as Joule losses by the following relation.

$$q = \frac{I^2 R}{A} \quad (1)$$

Where R is the AC resistance of the copper conductor (Ω/m); A is the cross sectional area of the conductor (mm²) and I is current in the cable (A). According to the BS 6622-1991 [26] the AC resistance of the copper is R = 0.0405 Ω/km at 363 K.

Accordingly, in all further simulations of the thermal state of underground cables the temperature at the top and at the bottom of the computational domain was set to be uniform and constant at the 298 K and 293 K level respectively in summer conditions. Additionally, a zero heat flux boundary condition was set on the left and right sides of the computational domain.

4. Results of numerical simulations

4.1. Grid independency test

The calculation time and the accuracy of the result are directly related to the quality of the mesh. In this study, we tested three meshes of increasing quality (1038, 3083, 241396 nodes). From the results obtained in the validation phase of the proposed numerical model (Fig. 4.1). We opted for the mesh of 3083 nodes. This mesh ensures a good compromise between the quality of the mesh and the computation time and the precision of the sought solution. The cable temperature is determined from the two-dimensional steady state heat conduction equation discretized using the CFD Ansys Fluent code.

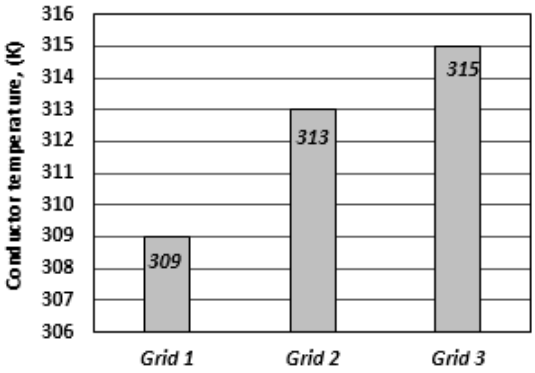


Fig. 4.1 Conductor temperature versus mesh

4.2. Effect of the burial depth

In aim to find the right depth of burial cable, several tests simulations were conducted. The results are presented in Fig.4.2. From the results, it can be seen that the conductor temperature decreases with depth. The choices of the height of the backfill are an optimization issue between the backfill cost and the current rating increase. Our choice was based on the 80 cm burial depth for which, it provides a satisfying compromise.

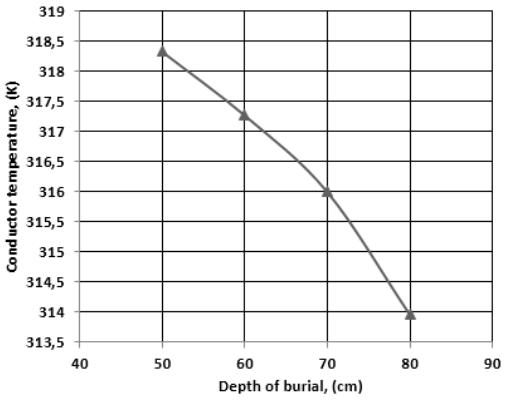


Fig. 4.2. Conductor temperature based on depth of burial

4.3. Effect of current on the temperature of the cable

Figure 4.3 presents the variation of temperature as a function of the current resulting from the simulation tests. It can be seen that the temperature of the cable increases proportionally with the operating current. This result is in the same trend as that obtained by Moya et al. [27].

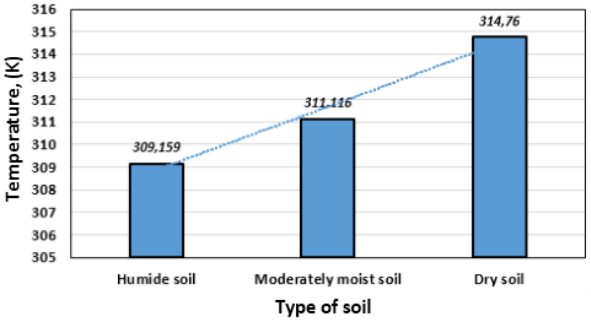


Fig. 4.3. Effect of current on cable temperature

4.4. Conductor temperature variation as a function of current

Figure 4.4 presents the variation of temperature as a function of the current resulting from the simulation tests. It can be seen that the temperature of the cable increases proportionally with the operating current. This result is in the same trend as that obtained by Moya et al. [28].

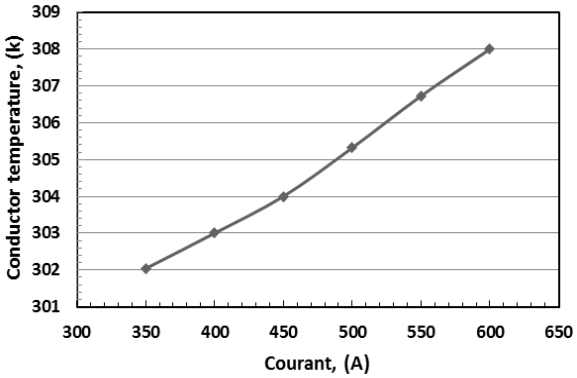


Fig. 4.4. Conductor temperature variation as a function of operating current

4.5. Temperature distribution in a single buried cable system

Figure 4.5. shows the temperature distribution at the cable as well as its vicinity for a working current of 940 A under summer conditions. As expected, the temperature distribution is symmetrical with reference to a vertical plane passing through the axis of the cable. In summer conditions, there is a low temperature gradient in the soil layers above the cable; this gradient is greater in the soil layer below the cable. This says that the temperature propagates from the cable to the roadway.

For summer conditions and a 940 A working current, the conductor's temperature rise is 313 K. This temperature is below the recommended limits [29]. Figure 4.6 shows the average temperature profile in the horizontal plane passing through the axis of the cable. There is a peak temperature at the cable level (place of the heat source) which is very normal, the temperature decreases as soon as we move away from the cable symmetrically. On the other hand, the temperature in the level of the pavement does not register a net change, this being said to the damping effect of soil on the propagation of the temperature.

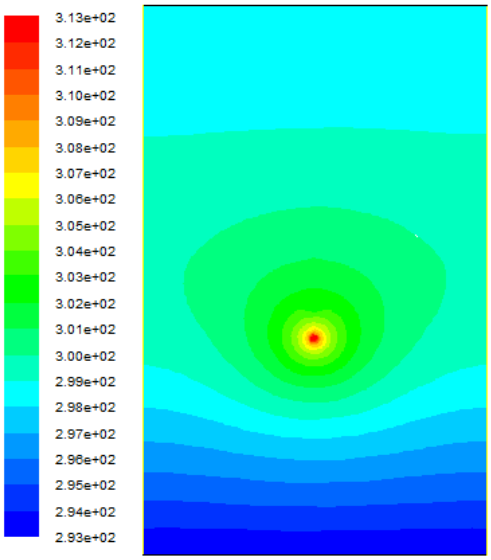


Fig. 4.5. Contours of temperature in a system of a single buried cable

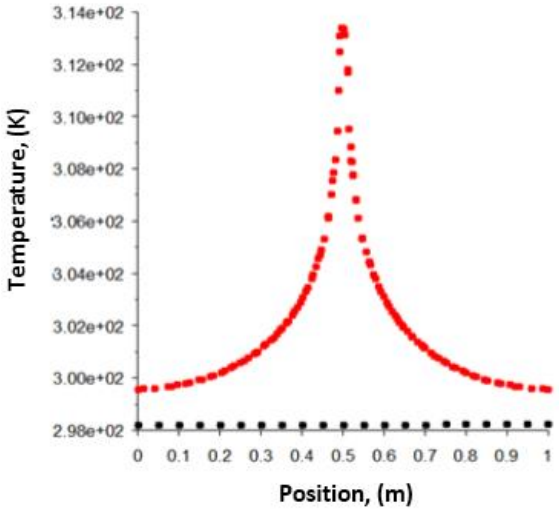


Fig. 4.6. Average temperature profile at the cable and the roadway

4.6. Distribution of temperature in a system of three buried cables

Figure 4.7 shows the distribution of temperature around a system of three buried cables in dry soil carrying 940 A in summer conditions. It is observed that the temperature of the central cable reaches 342.19 K (Fig.4.8), this temperature is higher than that recorded for the case of a single cable under the same functioning conditions. This increase is due to the accumulation of heat caused by the two cables located on either side of the central cable. Despite this rise in temperature, the cables remain operating in the recommended standards. This result is in the same trend as that obtained by Irina Makhkamova [22]. As a result, it is recommended to further space cables from each other to prevent heat build-up at the center cable. As such and without recourse to a new calculation, it is sufficient for this configuration to insert the cables twice as before that is to say 260 mm. Figure 4.8 shows the average temperature profile in the horizontal plane passing through the axis of the three cables.

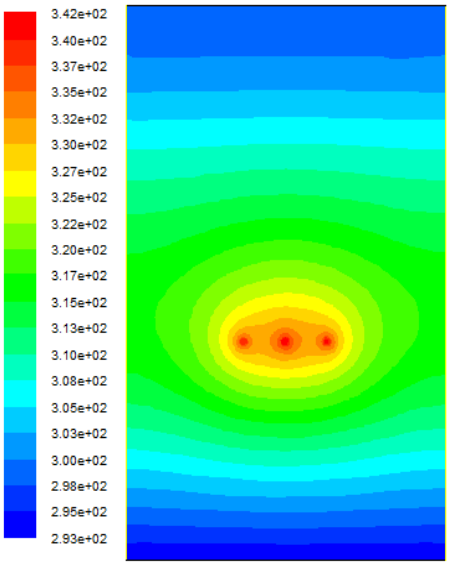


Fig. 4.7 Contours of temperature in a system of three buried cable

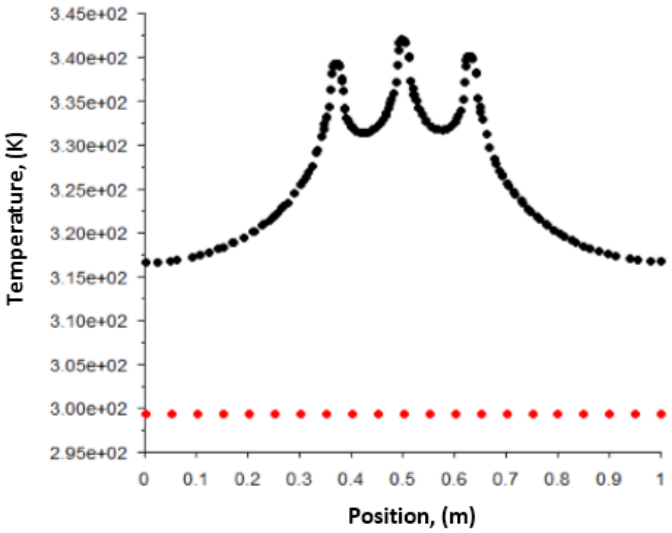


Fig. 4.8. Average temperature profile at the three cable and the roadway

There are three temperature peaks above the cables (heat source), the peak of the middle cable is higher than the others, and this is due to the extra heat gain caused by the neighboring cables. The temperature decreases as soon as one moves away from the cable symmetrically. On the other hand, the pavement temperature (≈ 300 K) shows a net increase compared to that recorded for a single cable.

4.7. Distribution of temperature in a system of four buried cables

In this system consisting of four cables, two cables are active; the other two are emergency cables. This type of system is used in long and high power lines. Two alternative cable placements may occur; two piled cables or two cables in line position. Fig. 4.9 (a) represents the distribution of the temperature in a system of two superimposed cables in operation carrying 940 A under severe climatic conditions. It is observed that the distribution of the temperature is non symmetric this is due to the barrier (resistance) represented by the two other spare cables. The maximum temperature recorded at the operational cable levels is 325 K. This temperature complies well with the recommended restrictions. It can be lowered further by increasing the inter-cable space to avoid the accumulation heat.

For the same system with four buried cables, Fig. 4.9 (b) presents the case of two operational cables in line position. In this configuration, the temperature distribution is symmetrical with respect to a vertical axis passing through the middle of the cables. It should be noted that this configuration has a lower cable temperature (325 K) than that of piled cable configuration (327 K). In conclusion, the configuration of two cables in line is thermally recommended than that of two superimposed cables, especially since its implementation is easier and consequently economical than the first one.

Figure 4.10 shows the average temperature profile in the horizontal plane passing through the axis of the two cables. There are two temperature peaks above the cables (heat source), these two peaks are interspersed by a temperature gradient decreasing symmetrically between the two peaks. This is due to the gap separating the two cables. On the other hand, the pavement temperature (299 K) shows a slight decrease compared to the one recorded for the three cables, which is very physically acceptable.

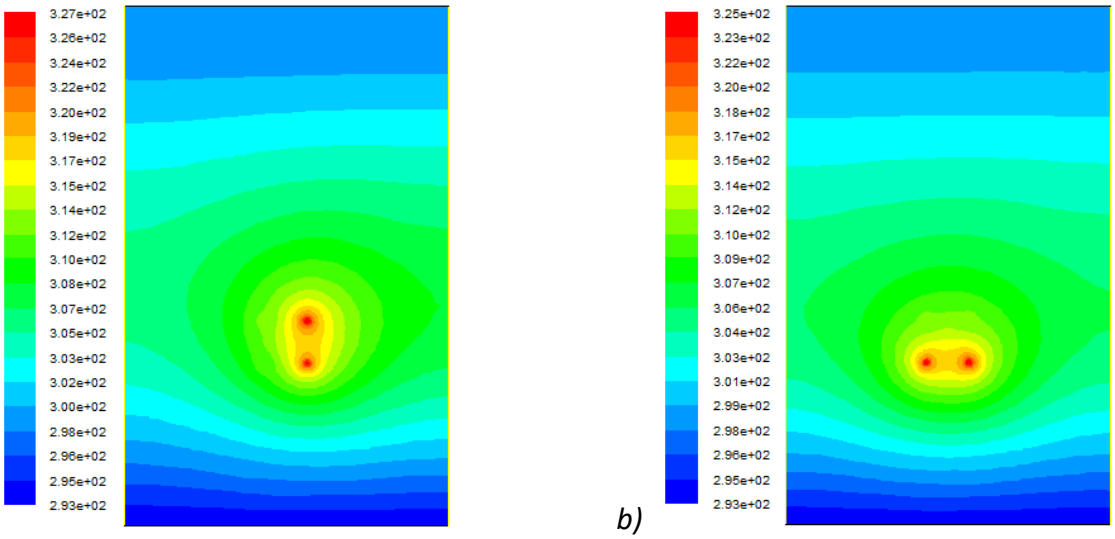


Fig. 4.9. Temperature contours in a system of four buried cables (a) two piled cables, (b) two cables in line

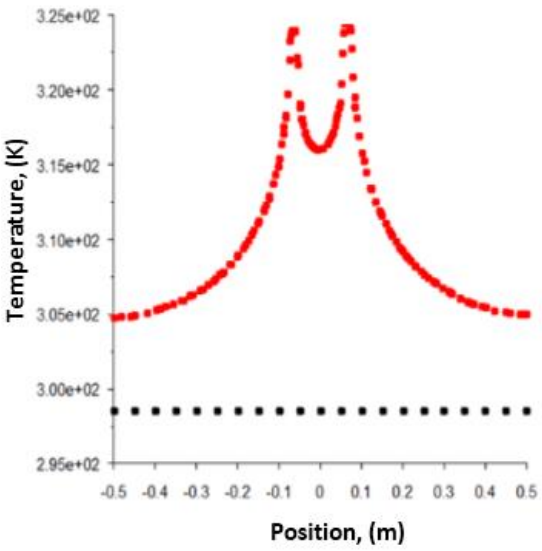


Fig. 4.10. Average temperature profile at the cables and the roadway

4.8. Effect of solar radiation

View the intensity of solar radiation in summer in our country. Examination of its possible effect on our model of electric cable buried in the ground is considered essential. Figure 4.11 shows the distribution of the temperature in the cable and its vicinity, for a working current of 940 A with summer condition with solar radiation support. As expected, the temperature distribution is symmetrical with reference to a vertical plane passing through the axis of the cable.

The results show that the temperature of the cable is 315 K and that of the roadway is 303 K. We conclude that the radiation effect on the cable is unimportant, although it significantly affects the ground surface. This conclusion is in good agreement with that obtained by Miller [30]. Figure 4.12 shows the average temperature profile in the horizontal plane passing through the axis of the cable.

There is a peak temperature at the cable (heat source) which is very normal. The temperature decreases as soon as you move away from the cable symmetrically. On the other hand, the temperature in the pavement level shows a net change compared to the case without radiation.

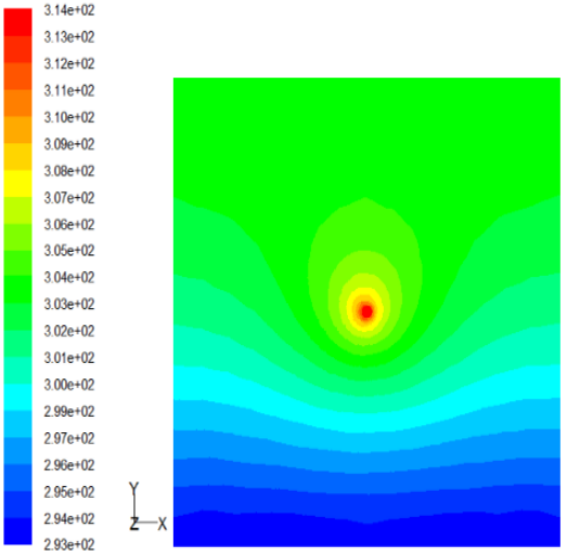


Fig. 4.11. Temperature contours of a cable under solar radiation

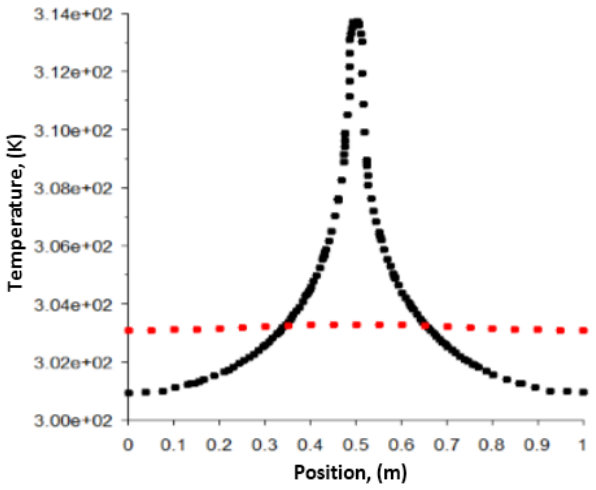


Fig. 4.12. Temperature profile of one buried cable and the roadway under solar radiation

5. Conclusions

The numerical results obtained in this work on the thermal exchanges around underground cables system in the most unfavorable working conditions make it possible to draw the following conclusions:

• The temperature of the conductor decreases with the cable depth, based on several numerical tests; it has been found that the best depth of burial is 80 cm.

• For a single buried cable operating under 940 A current in summer conditions, the maximum predicted conductor temperature is well below the recommended restrictions, so there is considerable potential for increasing its ability to carry more amperage.

• The thermal state of three underground cables laid horizontally under summer conditions is very close to the safety limit, so there is no possibility of increasing the ampacity of these cables unless the distance between the cables is increased interlocking between the cables.

• The maximum conductor temperature is approximately 327 and 325 K in summer conditions for two cables buried in vertical and horizontal forms respectively. Thermally, this means that the best landfill position is the horizontal form.

• The temperature of the cable working in full electric charge (940 A) placed in a cavity buried in the ground reaches 366 K. This exceeds the recommended restrictions. In this case, it is proposed to reduce the amperage up to 900 A so that the cable can operate within the safety limits.

• The temperature of cables buried in the ground is inversely proportional to the soil moisture. So adding water to a porous material drastically decreases its thermal resistance.

• The temperature of the cable increases proportionally with the increase of the operating current.

• The results also showed that the radiation effect on cable temperature is negligible, although it significantly affects the ground surface.

The analysis of the results of the CHT simulations shows that this numerical technique offers a good accuracy in the prediction of thermal transfer around a system of permanent high voltage underground cables and can be used in the analysis and the management of transports and distribution of electrical energy. Finally, the application of CHT techniques allows the calculation and analysis of heat transfer in underground electrical cable systems.

References

[1] CIGRE, Statistics of AC underground cables in Power networks. Working Group B1.07. ISBN 978-2-85873-026-1 Technical Brochure Ref. No.: 338 CE/SC: B1, 2007. Paris-France.

[2] Neher, J. H., & McGrath, M. H., The calculation or the temperature rise and load capability of cable systems. RATIO, 50 (2) (1994), 5.

[3] Roberto Benato, Luigi Colla, Sebastian Dambone Sessa, Marco Marelli, Review of high current rating insulated cable solutions, Electric Power Systems Research 133 (2016) 36–41.

[4] Calculation of the Current Rating – Part 1-1: Current Rating Equations (100% Load Factor) and Calculation of Losses – General, IEC 60287-1, 2006.

[5] Calculation of the Current Rating – Part 2-1: Thermal Resistance – Calculation of Thermal Resistance, IEC 60287-2, 2006.

[6] L. Exizidis, F. Vallee, Z. De Greve, J. Lobry, V. Chatziathanasiou, Thermal behavior of power cables in offshore wind sites considering wind speed uncertainty, Appl. Therm. Eng. 91 (2015) 471–478.

[7] H. Oh, J. Yao, J.M. Tinjum, W.J. Likos, Thermal resistivity dry-out curves for three sandy soils, 2014. Geotechnical Special Publication, (234 GSP), pp. 2795–2803.

[8] P. Oclon, D. Taler, P. Cisek, M. Pilarczyk, Fem-based thermal analysis of underground power cables located in backfills made of different materials, Strength Mater. 47 (2015) 770–780.

[9] P. Oclon, P. Cisek, M. Pilarczyk, D. Taler, Numerical simulation of heat dissipation processes in underground power cable system situated in thermal backfill and buried in a multilayered soil, Energy Convers. Manag. 95 (2015) 352–370.
[10] Panagiotis Chatzipanagiotou, Vasilis Chatziathanasiou, Gilbert De Mey, Boguslaw Wieçek (2017). Influence of soil humidity on the thermal impedance, time constant and structure function of underground cables: A laboratory experiment. Applied Thermal Engineering, 113, 1444–1451.
[11] Al-Saud, M.S., El-Kady, M.A., & Findlay, R.D. 2007. A new approach to underground cable performance assessment. Electrical Power Systems Research, DOI:10.1016/j.epsr.2007.06.010.
[12] Sellers, S.M. and Black, W. Z. 1996. Refinements to the Neher-McGrath Model for Calculating the Ampacity of Underground Cables. IEEE Transactions on Power Delivery 11:12-30.
[13] De Lieto Vollaro R, Fontana L, Vallati A. Thermal analysis of underground electrical power cables buried in non-homogeneous soils. Appl. Therm. Eng. 2011; 31(5):772e8.
[14] National Fire Protection Association, NFPA 70, National Electrical Code, 2017 ed., (2016) Quincy, MA, USA.
[15] Pawel Oclon, Piotr Cisek, Monika Rerak, Dawid Taler, R. Venkata Rao, Andrea Vallati, Marcin Pilarczyk, Thermal performance optimization of the underground power cable system by using a modified Jaya algorithm, International Journal of Thermal Sciences 123 (2018) 162e180
[16] G.M. Williams, P.L. Lewin, M. LeBlanc, Accurate determination of ambient temperature at burial depth for high voltage cable ratings, Conference Record of the 2004 IEEE International Symposium on Electrical Insulation, Indianapolis, IN USA, 19-22 September 2004, pp. 458–461.
[17] L. Lindström, Evaluating Impact on Ampacity According to IEC-60287 Regarding Thermally Unfavourable Placement of Power Cables, Masters' Degree Project Royal Institute of Technology (KTH), Stockholm, Sweden, November 2011 XR-EE-ETK 2011:009.
[18] J. Nahman, M. Tanaskovic, Evaluation of the loading capacity of a pair of threephase high voltage cable systems using the finite-element method, Elec. Power Syst. Res. 81 (2011) 1550–1555.
[19] J. Nahman, M. Tanaskovic, Calculation of the ampacity of high voltage cables by accounting for radiation and solar heating effects using FEM, Int. Trans. Elec. Energy Syst. 23 (3) (2013) 301–314.
[20] P. Ocłoń, P. Cisek, M. Rerak, D. Taler, R.V. Rao, A. Vallati, M. Pilarczyk, Thermal performance optimization of the underground power cable system by using a modified Jaya algorithm, Int. J. Therm. Sci. 123 (2018) 162–180.
[21] M. Rerak, P. Ocłoń, Thermal analysis of underground power cable system, J. Therm. Sci. 26 (5) (2017) 465–471.
[22] P. Ocłoń, M. Bittelli, P. Cisek, E. Kroener, M. Pilarczyk, D. Taler, R.V. Rao, A. Vallati, The performance analysis of a new thermal backfill material for underground power cable system, Appl. Therm. Eng. 108 (2016) 233–250.
[23] Makhkamova, Irina (2011). Numerical Investigations of the Thermal State of Overhead Lines and Underground Cables in Distribution Networks, Durham theses, Durham University.
[24] Ferdinando Salata, Fabio Nardecchia, Franco Gugliermetti, Andrea de Lieto Vollaro, How thermal conductivity of excavation materials affects the behavior of underground power cables, Applied Thermal Engineering 100 (2016) 528–537
[25] King, S.Y. and Halfter, M.A.1982. Underground power cables. London and New York, Longman, 185 pages.
[26] P17 Part3. Current Rating for distribution cables: Ratings for 11kV and 33 kV cables having extruded insulation. 2004. Issue 1.
[27] Energy Networks Association. Moore, G.F. (Editor), Electric Cables Handbook/ BICC Cables, 2004 Third Edition, Blackwell Science.
[28] Moya, R.E.S., Prata A.T. and Cunha Neto J. A.B.. Experimental analysis of unsteady heat and moisture transfer around a heated cylinder buried into a porous medium. International Journal of Heat and Mass Transfer 42 (1999), 2187-2198.
[29] Millar, R.J. and Lehtonen, M. 2005. Real-time transient temperature computation of power cables including moisture migration modelling. The 15th PSCC, Liege, 22-26 August 2005, 8 pages

Penerbit Akademia Baru

Engineering Science and Technology Conference Proceedings

Journal homepage: www.akademiabaru.com/EST.html

Aerodynamic Drag Study of Time-Trial Cycling Helmets Using CFD Analysis

Open Access

Mohd Salahuddin Mohd Basri[1,*], Khairul Manami Kamarudin[2], Nurul Ain Maidin[3], Mohd Hidayat Ab Rahman[3]

[1] Department of Process and Food Engineering, Faculty of Engineering, University Putra Malaysia, 43400 UPM Serdang, Selangor, Malaysia
[2] Department of Industrial Design, Faculty of Design and Architecture, University Putra Malaysia, 43400 UPM Serdang, Selangor, Malaysia
Faculty of Mechanical and Manufacturing Engineering Technology, Universiti Teknikal Malaysia Melaka, Hang Tuah Jaya, 76100 Durian Tunggal, Melaka, Malaysia

ABSTRACT

In cycling events, aerodynamic drag contributes most of the resistance experienced by a competitive cyclist. Accordingly, the majority of time-trial cycling helmets were designed to obtain low aerodynamic drag. The question arises what is the best position of cycling helmet and its tail flap that resulted in the lowest drag coefficient. This paper presents an aerodynamic drag analysis of helmet with different tail flap positions at a constant speed of 60 km per hour. The objective of this paper was to investigate the drag coefficient between the different designs of helmet and tail flips using CFD and thoroughly study the airflow near the surface of the cyclist helmet. The results are compared with the exceptional time trial cycling helmet in the market. Design of a 2D-model of cycling helmets is developed using GAMBIT software. Six helmet designs comprising varying tail flap positions were tested under ideal cycling position. The designs are the existing time trial cycling helmet available in the market (Helmet 1), the modified helmets with tail flap at 0, 3, 6 and 9 degrees to horizontal (Helmet 2 to 5) and the modified 10 degrees rotated helmet (Helmet 6). The computational fluid dynamics simulations are performed using ANSYS Fluent and the results in terms of the reduced drag coefficient and flow characteristics for optimal aerodynamic performance are analyzed. It is shown that the tail flap position of 6 and 9 degree to horizontal produce considerably low drag coefficient with 0.06 and 0.05, respectively, while the modified 10 degree rotated helmet recorded the highest drag coefficient due to large frontal area and flow separation. Evidently, closer tail flap to the back of the cyclist and smaller pressure difference resulted in the low drag coefficient.

Keywords:
Aerodynamic drag; time-trial; cycling helmet; CFD analysis; fluid flow

Copyright © 2019 PENERBIT AKADEMIA BARU - All rights reserved

1. Introduction

Time is the critical factor when cycling against the clock in a time trial or triathlon. Lower time taken leads to a better potential result. According to Bradford and Jenkins [1], a cyclist travelling at 20 mph on flat terrain experienced more than 80 percent resistance which is contributed by aerodynamic drag. When a cyclist or tri-athletes reaches speeds of more than 30 mph, low aerodynamic drag is a key quality of high-performance cycling. Barelle [2] studied drag resistance on three different positions; i.e., high, usual (normal) or low inclination of the head in the time trial. The result shows that the drag resistance for the usual inclination was the lowest indicating the best position with 37.2 N. The results for low and high inclinations were 37.8 N and 38.5 N, respectively. She concluded that helmet shape and inclination of the head can have different impacts on the projected frontal area of the athlete´s head and thus on aerodynamic drag.

* *Corresponding author.*
E-mail address: salahuddin@upm.edu.my (Mohd Salahuddin Mohd Basri)

Investigation on 14 time-trial helmets was conducted by Blair and Sidelko [3] to identify the effect of different yaw angles on the drag coefficient and performance. They found that the well-performing helmets were able to reduce the drag up to 10 percent as compared to that of the poorly performing helmets. Helmet with extreme high inclination angles produced an overall high drag. However, the relationship between helmet design and performance was not conducted.

Since the type of boundary layer and its thickness influence the surface friction drag and any flow separation, it is important to know that the layer is strongly influenced by how the pressure varies along the direction of flow. Other important factors are speed, density and viscosity of the air; also, for a given geometric shape, the size of the helmet is important. If the Reynolds number is increased by increasing the speed of the cyclist, the transition position moves forward, and the boundary layer becomes thinner [4]. It can, therefore, be seen that the value of the Reynolds number is important in determining the type of flow around the helmet.

When air flows over the top of a surface, the pressure then gradually rises again as the flow speed decreases. This means that the air has to travel from a low to a high pressure, which it can do by slowing down and losing some of its kinetic energy. The situation can be likened to that of a cyclist coasting up a hill, which is possible as long as it is travelling fast enough at the bottom [5]. If the increase in pressure is gradual, the process of turbulent mixing allows the outer layers to effectively pull the inner ones along. If the rate of increase of pressure is too great, however, the mixing process will be too slow to keep the lower part of the layer moving. When this happens, the boundary layer flow stops following the contours of the surface and separates away [6]. Air particles downstream of the separation position tend to move towards the lower pressure in the reverse direction to the main flow.

Besides empirical investigations, numerical modelling such as computational fluid dynamic (CFD) is an effective tool to simulate complex fluid flows [7]. Numerous studies have been conducted using CFD method to investigate the aerodynamic drag of cyclists [8, 9, 10] and improve the aerodynamic design of the bicycle helmet [1]. However, to our knowledge, limited numerical studies have been performed on the aerodynamic performance of a modified helmet with tail flip and discuss in detail the airflow within the boundary layer. Therefore, the objective of this paper was to investigate the drag coefficient between the different designs of helmet and tail flips using CFD and thoroughly study the airflow near the surface of the cyclist helmet.

2. Methodology

2.1 Geometry, Computational Domain and Boundary Conditions

To assess the effect of helmet shape on aerodynamic performance, a total of six different design of the time-trial cycling helmets were selected for this study. Helmet 1 is referred to as existing time-trial cycling helmet in the market. For the purpose of anonymity, the brand name and the manufacturer of the helmets we not identified in this study. Helmet 2, Helmet 3, Helmet 4 and Helmet 5 are referred to as a modified helmet with a tail flap of 0, 3, 6, 9 degrees to the horizontal, respectively as shown in Figure 1. Helmet 6 is referred to as a modified helmet rotated 10 degrees counter-clockwise with a tail flap placed closely to the back of the cyclist.

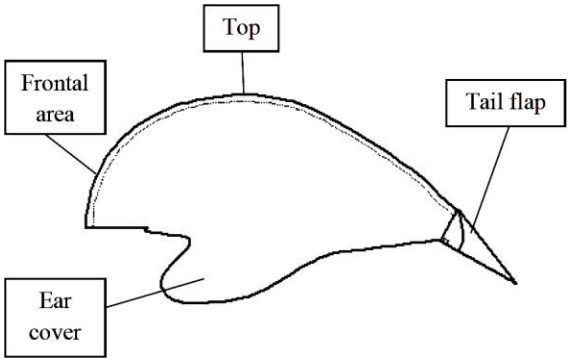


Fig. 1. Modified aerodynamic helmet with tail flap

The helmets were numbered as Helmet 1 to 6 as shown in Figure 2. All helmets were modelled in GAMBIT based on the ideal cycling position of the cyclist which the helmet tip was very close to the back of the cyclist.

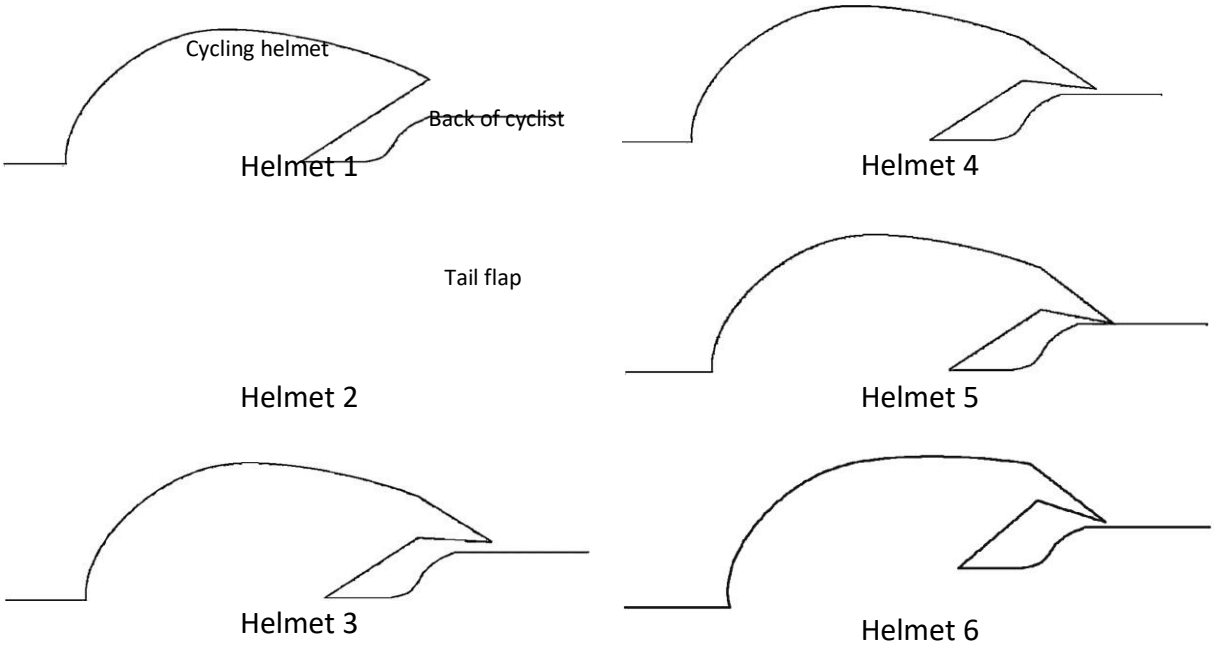


Fig. 2. 2-D models of different tip design and position of time-trial cycling helmets

For this computational fluid dynamics analysis, the geometry and the computational and fluid domain considered was 15 metres in length and 6 metres in height according to the best practice guidelines [11]. The helmet was positioned at 5 metres from the inlet of the domain. Only the upper part of the helmet and the back of the cyclist were modelled since the research is focusing on analyzing the airflow at these areas and the computation time will be minimized [8]. The finer mesh was constructed near the helmet surfaces and it was biased towards boundary walls. Quadrilateral elements were used to discretise the flow domain volume. Tetrahedral elements were built at the area under the tip of the helmet.

The model was imported to ANSYS Fluent where boundary conditions were applied. At the inlet velocity condition, a uniform constant horizontal velocity of 16.7 m/s was imposed. This condition is based on the time recorded in the time-trial competition for an elite cyclist which is between 50 to 60 km/h [12]. The speed of 57 to 60 km/h was mentioned to be the average speed for a winning time [13]. At the outlet, pressure conditions with ambient static pressure were applied.

2.2 Mesh

Three models with different mesh densities were created. Coarse, medium and fine mesh densities were compared. Referring to Ouakka and Fantuzzi [14], the mesh density for coarse mesh was decided to be reduced by half of the medium mesh and for fine mesh, the mesh density was doubled from the medium mesh. In order to determine which type of mesh was optimal for further simulation, the values of drag coefficient were compared and the percent difference calculated. Taking the medium mesh density as the benchmark, the difference in drag coefficient with fine mesh is relatively small which is 5.3 percent as compared to that of the difference with coarse mesh which is 26.3 percent. Medium-density mesh was considered optimal in providing sufficient resolution for drag coefficient analysis.

2.2 CFD Simulation

Simulations were performed using ANSYS Fluent 17. The turbulence model is used based on Reynold's Number calculated, which was 400141, and in accordance to other researches which yield reasonable results including in swimming and cycling studies [8, 15, 16]. The second-order discretization schemes were used to limit numerical dissipation. Standard wall functions were selected for the near-wall treatment of turbulence and the turbulence intensity at the entry of the field was set at one percent. During computations, the criterion of convergence of 10^{-5} was set in accordance with previous literature [17].

3. Results

3.1 Modelling Validation

The helmet used in previous literature reported by Alam *et al*., [18], with all the venting holes covered, was used as control. The numerical procedure was validated by comparing with experimental and computational data. The drag coefficient (C_D) reported for the helmet is 0.21. For validation purposes, the helmet was modelled in GAMBIT software and analyzed using ANSYS Fluent. The drag coefficient recorded after the CFD simulation is approximately 0.19. The difference compared to the literature was approximately 9 percent due mainly to dissimilarity in computational domain. Evidently, our results are close to the result deduced from Alam *et al*., [18] and the CFD simulation used is acceptable.

3.2 Analysis of Flow Patterns

In time-trial cycling competition, air flowing over the cycling helmet contributed to overall aerodynamics and has a huge impact on the overall performance of the cyclist. Formation of boundary layer around the helmet when it was exposed to the airflow can be changed by modifying

the shape or design of the helmet. The streamline patterns, coloured by velocity, for Helmet 1, 2 and 3 are shown in Figure 3(a-c) and analyzed in detail.

In Figure 3(a), laminar flow formed at the front part of the helmet (point A). As the flow travelled further, laminar separation bubbles occurred at point B due to a strong adverse pressure gradient (pressure changes along the surface), which forced the laminar boundary layer to separate from the curved helmet surface. At point C, the separation reattached to the helmet surface before the layer separated again and formed a vortex at point D. As the flow passed the tip of the helmet, turbulence formed with a large separation at point E. The vortex formed at this point slowly disappeared. High drag coefficient value was expected due to the large separation as mentioned by Bearman and Morel [19].

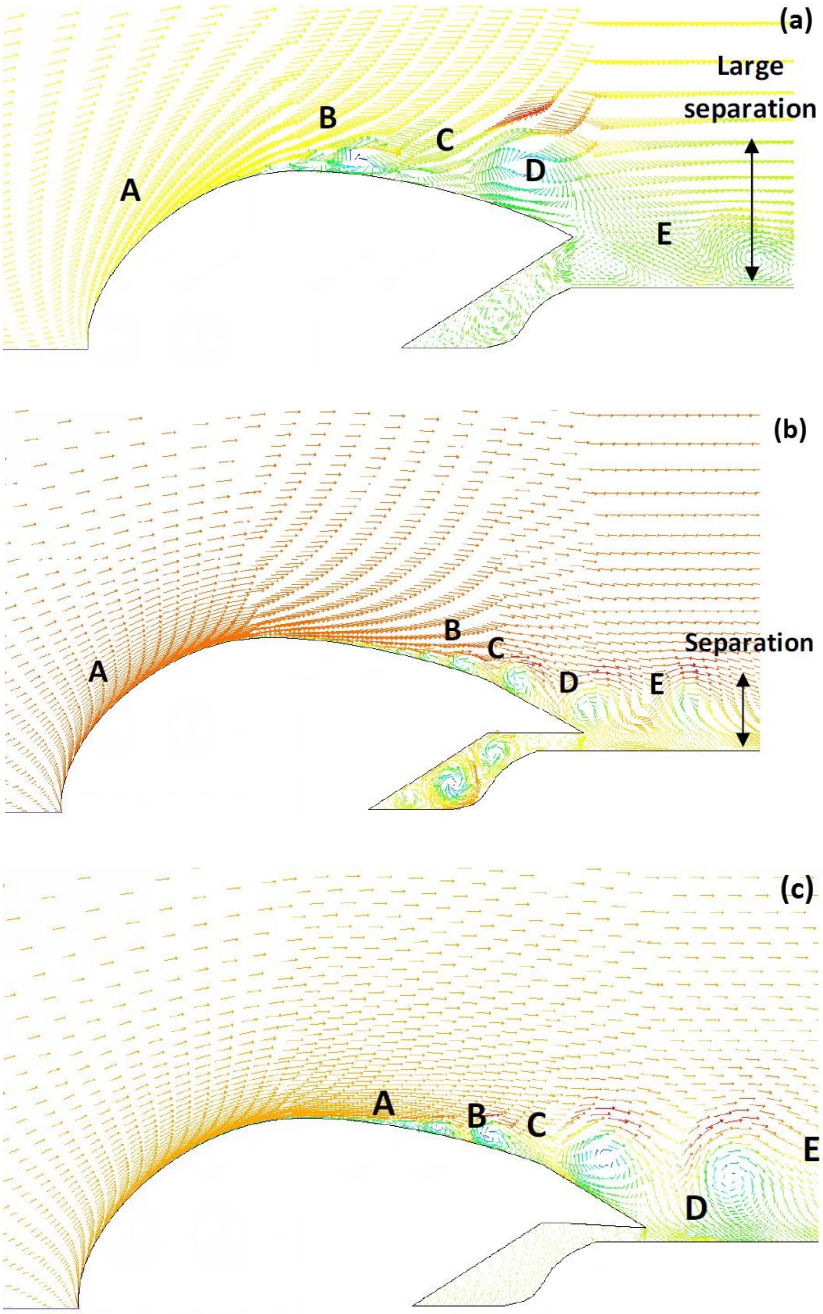
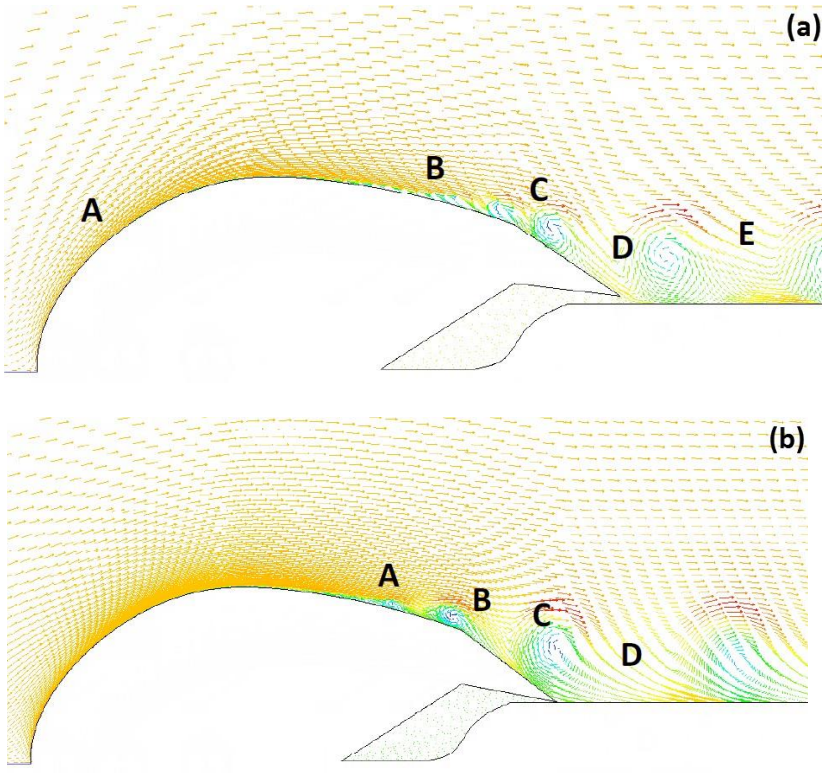


Fig. 3. Streamline patterns colored by velocity for (a) Helmet 1, (b) Helmet 2, and (c) Helmet 3.

In Figure 3(b), laminar flow occurred at the front part of the helmet (point A). Bubble separation at point B formed a little further from the frontal area as compared to Helmet 1. The separation was highly sensitive to disturbances. Thus, the flow reattached at point C and quickly formed a vortex at point D, very close to the surface, and producing more drag. As the flow travelled further, it reattached again and quickly forms more vortices with a considerable large separation at the tip of the helmet. Trailing vortex as well as high pressure formed at point E. The high drag coefficient obtained probably due to the high-pressure area.

At three degrees flap as shown in Figure 3(c), the separation occurred at point A further back from helmet face relative to that for Helmet 1 and 2. The flow however quickly reattached at point B and just as rapidly formed a vortex at point C. In this transition zone, the vortex attached closely to the surface and later reattached under low pressure at point D. Another low-pressure vortex formed beyond this (point E) but did not attach to the surface and was quickly shed. The total drag coefficient was lower compared to Helmet 2 because most of the low pressures were formed within the boundary layer in the transition and turbulent flow regions.

At point A in Figure 4(a), the laminar flow formed much earlier as in Helmet 1 and 2. As the flow travelled further to the back, it enters the transition region where a laminar separation bubble formed at point B. As the thickness of the bubble grew, a vortex appeared at point C. The flow reattached at point D and produced high pressure at the tip of the helmet. Immediately the flow to the rear formed a vortex not closely attached to the surface (point E) and where it quickly formed another vortex. The trailing vortices however quickly disappeared.



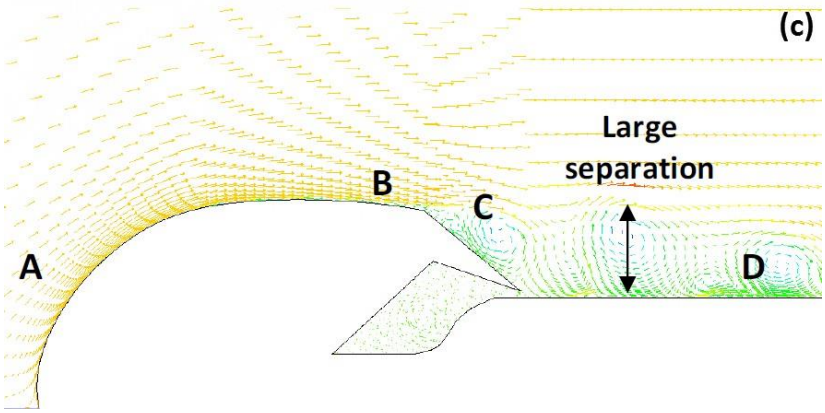


Fig. 4. Streamline patterns colored by velocity for (a) Helmet 4, (b) Helmet 5, and (c) Helmet 6.

In Figure 4(b), the tip of the helmet was placed exactly on the back of the cyclist. Laminar separation bubble appeared at point A. Inside the bubble, the flow was circular in the opposite direction to the outer flow at the surface. As the bubble thickened, it rapidly became turbulent generating a small vortex at point B. A low-pressure vortex than formed at point C but quickly reattached to the surface. The flow was quite similar to that in Helmet 4 except that the separation bubble formed was smaller and the vortices shed much quicker thus resulting in the lowest drag coefficient (0.05) of all the tested helmets.

During the competition, the cyclist cannot maintain his or her head at the optimal angle. When the cyclist rotated the helmet 10 degrees (yaw angle to the horizontal) counter-clockwise, the tail flap tended to move close to the cyclist´s back. At this position, a frontal area larger than usual would form resulting in higher drag coefficient as shown in Figure 4(c). This position also created higher total force (pressure and viscous force). Since total force is directly proportional to the drag coefficient, increase in total force will increase in drag coefficient. There was very small separation bubble formed at point B. However, as the flow entered point C, sudden changes in velocity and pressure created a turbulent flow with a trailing vortex at point D. Higher drag coefficients (0.16) obtained relative to other cases were most probably due to the larger frontal area and large flow separation. This result agrees with one reported by Zdravkovich *et al.*, [20]. Drag coefficients for all helmet are summarized in Table 1.

Table 1
The drag coefficient for six helmets

Helmet	1	2	3	4	5	6
Drag coefficient (C_D)	0.19	0.10	0.09	0.06	0.05	0.16

3.3 Analysis of the Pressure Field

According to Gibertini and Grassi [21], the largest proportion to the aerodynamic resistance is mainly from pressure drag. As air flows around the helmet, the local pressure and velocity were changed. The momentum of gas molecules changed was due to pressure, thus creating forces. The component of the aerodynamic force that was opposed to the airflow was called drag. Graph pressure versus position point on the helmet for each case was analyzed to show the relationship between pressures and drag as shown in Figure 5(a-f).

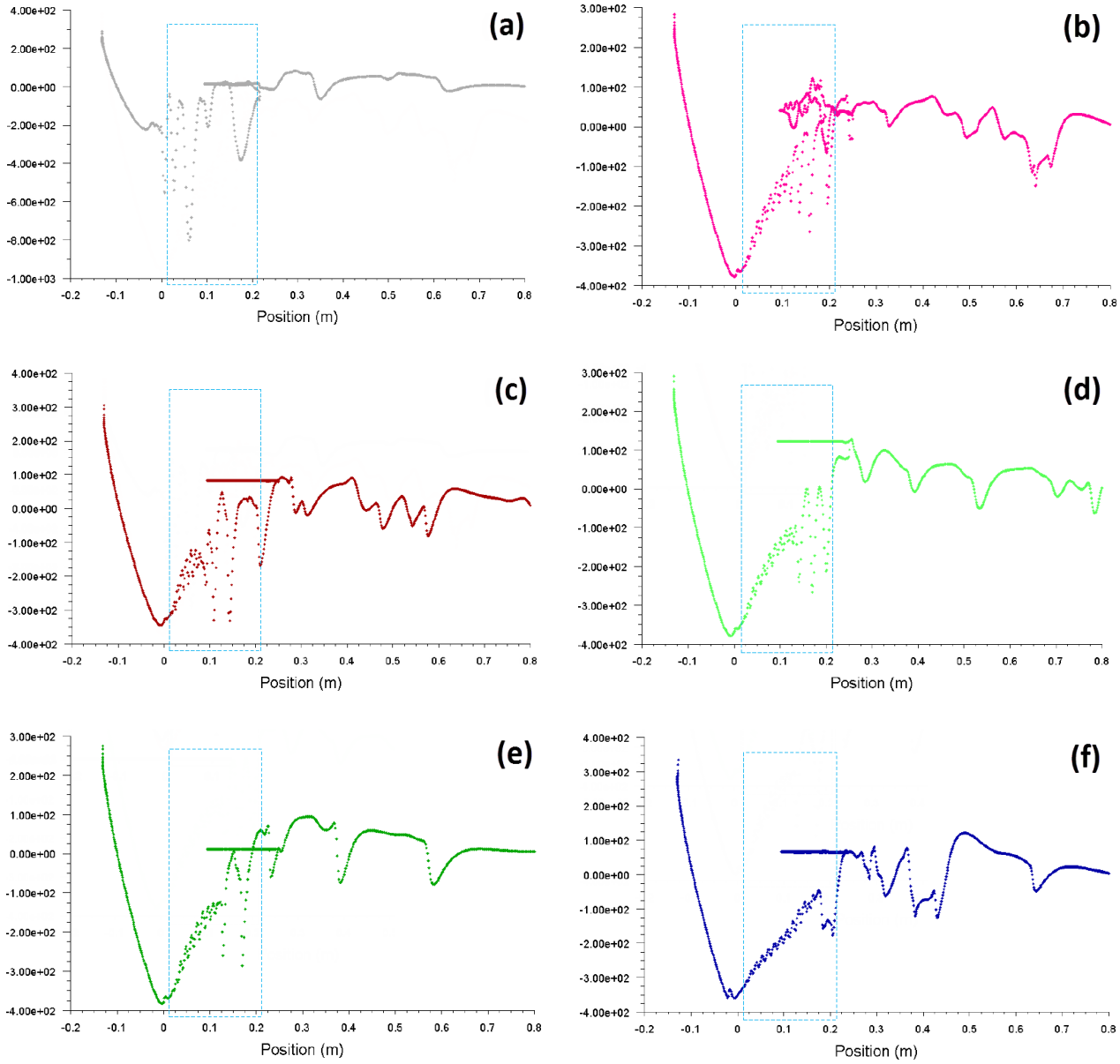


Fig. 5. Pressure on (a) Helmet 1, (b) Helmet 2, (c) Helmet 3, (d) Helmet 4, (e) Helmet 5, (f) Helmet 6

Rapid and persistent changes in pressure will easily form separation bubbles, vortices and turbulent flow. For Helmet 1 in Figure 5(a), pressure difference was larger, ranging between 0 m and 0.2 m compared to other helmets. This zone of pressure difference was located from middle to the tip of the helmet. For Helmet 2 to 5 in Figure 5(b-e), respectively, graph fluctuations within the 0 to 0.2 m zone were higher in Helmet 2, decreasing gradually until Helmet 5. Greater graph fluctuation indicates more pressure changes which bear influence on the value of drag coefficient. For Helmet 6 in Figure 5(f), pressure changes in similar zone range were the smallest. However, higher pressure formed at the frontal area of the helmet indicated higher drag occurrence. In this way, the frontal area can greatly affect the value of drag coefficient.

4. Conclusions

The primary objective of this study was to evaluate the effect of different designs of helmet and tail flips on the drag coefficient using CFD and thoroughly study the airflow near the surface of the

cyclist helmet. The cycling helmet with the tail flap position of 6 and 9 degree to horizontal, which is very close to the back of the cyclist, produce considerably low drag coefficient while the modified 10 degree rotated helmet recorded the highest drag coefficient (0.16) due to large frontal area and flow separation. Formation of vortices, trailing vortices, laminar separation bubbles, turbulent flow, and separation at the tip of the tail flap was recorded in all designs. However, the amount of pressure drags, size and position of the streamline flow significantly determine the value of the drag coefficient.

Acknowledgement
The authors would like to thank the Universiti Putra Malaysia for laboratory facilities.

References

[1] Sims, B. W.; Jenkins, P. E.;, "Aerodynamic bicycle helmet design using a truncated airfoil with trailing edge modifications," *In ASME 2011 International Mechanical Engineering Congress and Exposition,* pp. 453-462, 2011.
[2] Barelle, C.;, "Sport Aerodynamics: on the Relevance of Aerodynamic Force Modelling versus Wind Tunnel Testing," *Wind Tunnels and Experimental Fluid Dynamics Research,* pp. 349-368, 2011.
[3] Blair, K.B. and Sidelko, S., "Aerodynamic performance of cycling time trial helmets," in *The Engineering of Sport 7*, Paris, Springer, 2009, pp. 371-377.
[4] Barnard, R. H., "Mechanical, Aerospace and Automotive Engineering," in *Road vehicle aerodynamic design - An introduction*, Addison Wesley Longman Limited, 2001, pp. 20-50.
[5] Crouch, T.N., Burton, D., LaBry, Z.A. and Blair, K.B., "Riding against the wind: a review of competition cycling aerodynamics," *Sports Engineering,* vol. 20, no. 2, pp. 81-110, 2017.
[6] Stager, J.M. and Tanner, D.A., "The Mechanics of Swimming," in *Handbook of Sports Medicine and Science, Swimming*, John Wiley & Sons, 2008, p. 57.
[7] Gardan, N.; Schneider, A.; Polidori, G.; Trenchard, H.; Seigneur, Jean-Marc; Beaumont, F.; Fourchet, F.; Taiar, R.;, "Numerical investigation of the early flight phase in ski-jumping," *Journal of biomechanics,* vol. 59, pp. 29-34, 2017.
[8] Blocken, B.; Defraeye, T.; Koninckx, E.; Carmeliet, J.; Hespel, P., "CFD simulations of the aerodynamic drag of two drafting cyclists," *Computers & Fluids,* vol. 71, pp. 435-445, 2013.
[9] Defraeye, T.; Blocken, B.; Koninckx, E.; Hespel P.; Carmeliet, J.;, "Aerodynamic study of different cyclist positions: CFD analysis
and full-scale wind-tunnel tests," *Journal of biomechanics,* vol. 43, no. 7, pp. 1262-1268, 2010.
[10] Defraeye, T.; Blocken , B.; Koninckx, E.; Hespel, P.; Carmeliet, J.;, "Computational fluid dynamics analysis of drag and convective heat transfer of individual body segments for different cyclist positions," *Journal of biomechanics,* vol. 44, no. 9, pp. 1695-1701, 2011.
[11] Giappino, S.; Omarini, S.; Schito, P.; Somaschini, S.; Belloli, M.; Tenni, M.;, "Cyclist Aerodynamics: A Comparison Between Wind Tunnel Tests and CFD Simulations for Helmet Design," *In Conference of the Italian Association for Wind Engineering,* pp. 336- 349, 2018.
[12] Kyle C.R., and Bassett D.R. Jr., "The cycling world hour record," in *High-tech cycling: the science of riding faster*, Colorado, Human Kinetics, 2003, pp. 175-196.
[13] Broker, J.P., Kyle, C.R. and Burke, E.R., "Racing cyclist power requirements in the 4000-m individual and team pursuits," *Medicine and Science in Sports and Exercise,* vol. 31, no. 11, pp. 1677-1685, 1999.
[14] Ouakka, S. and Fantuzzi, N., "Trustworthiness in Modeling Unreinforced and Reinforced T-Joints with Finite Elements," *Mathematical and Computational Applications,* vol. 24, no. 1, p. 27, 2019.
[15] Zaidi, H.; Fohanno, S.; Taiar, R.; Polidori, G.;, "Turbulence model choice for the calculation of drag forces when using the CFD method," *Journal of biomechanics,* vol. 43, no. 3, pp. 405-411, 2010.
[16] Fintelman, D. M., Sterling, M., Hemida, H., Li, F. X., "The effect of crosswinds on cyclists: an experimental study," *Procedia Engineering,* vol. 72, pp. 720-725, 2014.
[17] Zaidi, H.; Taiar, R.; Fohanno, S.; Polidori, G.;, "Analysis of the effect of swimmer's head position on swimming performance using computational fluid dynamics," *Journal of biomechanics,* vol. 41, no. 6, pp. 1350-1358, 2008.
[18] Alam, F., Watkins, S., Subic, A., "Aerodynamic efficiency and thermal comfort of bicycle helmets," *Journal of Mechanical and Manufacturing Engineering,* vol. 1, pp. 1-6, 2005.
[19] Bearman, P.W. and Morel, T., "Effect of free stream turbulence on the flow around bluff bodies," *Progress I aerospace sciences,* vol. 20, no. 2-3, pp. 97-123, 1983.

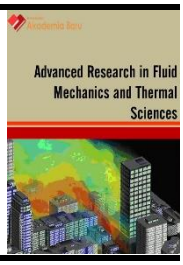
[20] Zdravkovich, M.M., Ashcroft, M.W., Chisholm, S.J. and Hicks, N., "Effect of cyclist's posture and vicinity of another cyclist on aerodynamic drag," *The engineering of sport,* vol. 1, pp. 21-28, 1996.

[21] Gibertini, G. and Grassi, D., "Cycling aerodynamics," in *Sport aerodynamics*, Vienna, Springer, 2008, pp. 23-47.

Penerbit Akademia Baru

Engineering Science and Technology Conference Proceedings

Journal homepage: www.akademiabaru.com/EST.html



Large-Eddy Simulation on Pedestrian Wind Environment in Urban Buildings of Random Staggered Arrays

Open Access

Saidatul Sharin Shuhaimi[1], Sheikh Ahmad Zaki[1*], Ahmad Faiz Mohammad[1], Mohamed Sukri Mat Ali[1]

[1] Malaysia-Japan International Institute of Technology, Universiti Teknologi Malaysia Kuala Lumpur, Jalan Sultan Yahya Petra, 54100 Kuala Lumpur, Malaysia

ABSTRACT

This study adopts the database of a large-eddy simulation (LES) of flows to investigate the effect of vertical random array in a staggered layout on the pedestrian wind environment. The vertical random arrays are configured with various buildings in the height range of 0.36*h* to 3.76*h* where *h* is defined as the standard building height of 0.025m. The LES data of the vertical random arrays in six plan area densities (ratio of building roof area to plan lot area, λ_p) ranging from 4.4% to 39.1% were utilized. The characteristics of the velocity inside the canopy for all arrays were firstly analysed using the spatially averaged profiles of the streamwise velocity. The results depicted a decrease in the mean streamwise velocity as λ_p increase. Moreover, the effect of height variability in the array causes the vertical velocity profiles to form a distinct change in the velocity gradient. Furthermore, the pedestrian mean velocity (V_p) around various building is correlated to the local frontal area density ($\lambda_{f(t)}$). The correlation showed that the greatest reduction of V_p is observed around tall-rise buildings.

Keywords:
Pedestrian wind environment; vertical random array; plan area density; large-eddy simulation

Copyright © 2019 PENERBIT AKADEMIA BARU - All rights reserved

1. Introduction

An urban area is typically highly populated and made up of various buildings. The common issues faced by those in the urban area include thermal comfort and air pollution. Optimal wind regulation in the urban canopy layer which is the region extending from ground to average building height [1] contributes to the pedestrians' safety and comfort. Wind environment in the urban canopy layer is generally affected by the geometric conditions of the urban area such as the urban layout, building shapes and packing density. Consequently, a poor wind environment has adverse effects on the pedestrian safety and comfort. The aim of this study is to assess the pedestrian wind environment due to effect of the urban geometry.

Over the years, various studies were conducted to reveal the relation of the urban geometry on the wind environment by using both numerical simulations [14-16] and wind-tunnel experiments [5,17]. Typically, the surface of urban area is disparate in the geometrical aspect as they are composed of obstacles such as buildings, streets, vegetation also known as the roughness element. Previous studies discussed the mean wind velocity inside a canopy is dependant on the roughness element [2,3]. Kubota [2] revealed in several residential areas in Japan, the mean wind

* *Corresponding author.*
E-mail address: sheikh.kl@utm.my

velocity decreases when the ratio of the roughness element is greater. In addition, roughness elements with height variability introduced by [2-5] has also been reported to affect the wind speed ratio. Likewise, the plan area density (ratio between building roof area and total ground area, λ_p) contributes to the vertical profile of mean wind velocity [5,6] as it shows a decreasing pattern as λ_p increases.

Nevertheless, to better assess the effects of urban geometries as mentioned above towards the pedestrian wind environment, vertical random array is focused as it is still lacking from existing findings. Vertical random array is described as a layout consisting of buildings with height variability. Hence, Razak [7] introduced a vertical random array which consists of two different building heights and compared them with the results of arrays with uniform height.

In summary, this study aims to investigate the effect of vertical random array where building height variability is adapted to unveil the effect of geometric conditions towards the pedestrian wind environment. To resemble the real urban condition, the highest building is positioned in the centre of the array and lower buildings surround the centre. The array is created to be asymmetric similar to the real urban cases as mentioned in several previous studies [5,8].

2. Methodology

All simulation results in this study are obtained from the database of vertical random arrays of Mohammad [8]. The large eddy simulation (LES) with a Smagorinsky model was performed on the configurations in this study using OpenFOAM software.

2.1 *Model Configuration of LES database*

To comprehensively estimate the wind environment in such urban area, vertical random staggered arrays were used in this study. Nine types of buildings with height variability (B_1 to B_9) were arranged in a staggered layout [8]. Figure 1 shows the arrangement of buildings within the staggered array for this case. Six cases with different plan area densities (λ_p) were selected for the simulations, as shown in Table 2. Further details on the model configuration and setup for the simulation can be obtained in Mohammad [8].

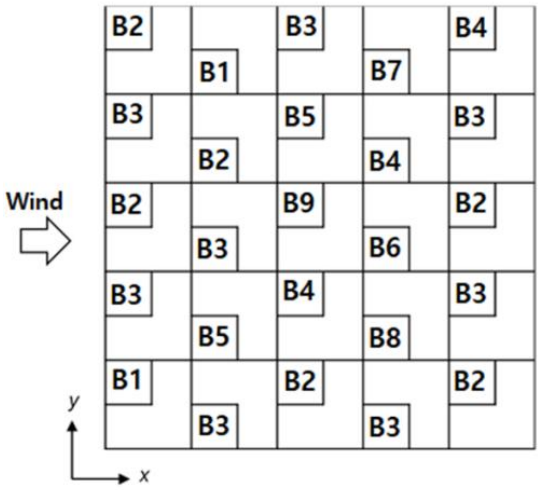


Fig 1. *Plan view of random staggered array with* wind flow in the x direction for for λ_p=25% [8]

Table1. Heights of building blocks where *h*=0.025*m*

Building	Height
B_1	$0.36h$
B_2	$0.84h$
B_3	$1.32h$
B_4	$1.50h$
B_5	$2.00h$
B_6	$2.64h$
B_7	$3.00h$
B_8	$3.32h$
B_9	$3.76h$

The computational domain vertical height (L_z) is $4h_{max}$ where h_{max} is the height of highest building i.e. $B_9(3.76h)$ for all arrays while the horizontal domain size (L_x and L_y) is adjusted to the condition of the arrays accordingly. Meanwhile, the boundary conditions are as follows: cyclic condition is applied in the streamwise direction to simulate continuous flow, symmetry condition in the lateral direction, free-slip on the top boundary followed by wall surfaces with no-slip condition. The minimum near wall grid size for all cases is kept at *h*/14 as this was considered adequate for the purpose of estimating the average wind flow inside the canopy [8].

Table 2. List of simulation cases

Case	λ_p (%)	Computational domain size
$R4A$	4.4	$24h \times 24h \times 15h$
$R8A$	8.2	$17.5h \times 17.5h \times 15h$
$R17A$	17.0	$12h \times 12h \times 15h$
$R25A$	25.0	$10h \times 10h \times 15h$
$R31A$	30.9	$9h \times 9h \times 15h$
$R39A$	39.1	$8h \times 8h \times 15h$

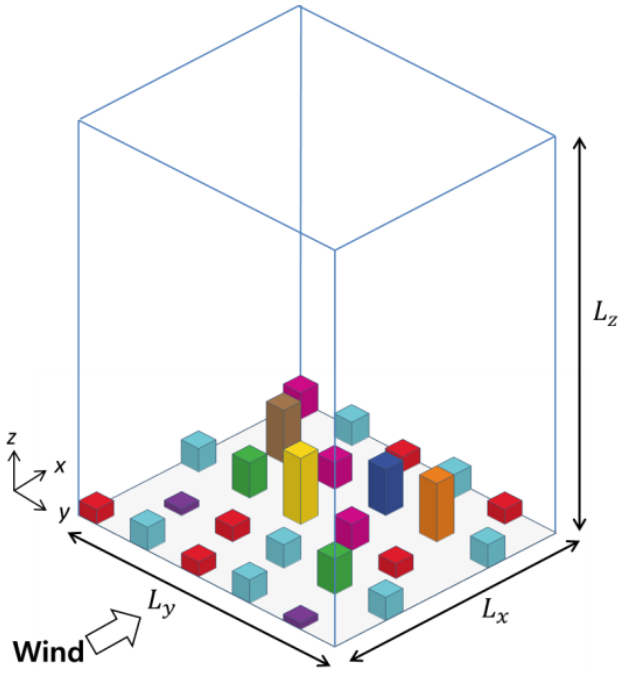


Fig 2. Schematic diagram of the computational domain for λ_p=25% [8]

3. Results

3.1 *Spatially averaged mean velocity profile*

In this section, the velocity profiles of the LES cases are compared with those of the wind tunnel experiment of Zaki [5] to substantiate the compatibility of both sets of data. Figure 3 compares the streamwise velocity profiles that are spatially averaged for all the random staggered

arrays in this study with the wind tunnel experiment of Zaki [5]. The velocities are normalized by the reference velocity (U_{ref}) taken at top of domain. The profiles of case *R17A* and *R31A* show good agreement with the wind tunnel results of Zaki [5] mainly in the region above $z/h = 4$. However, below this level which is the canopy region, the discrepancy of the profiles are slightly apparent. This is due to the effect of building height variability, leading to the deduction that the spatially averaged mean velocity is highly dependent on the vertical randomness of an array. Nevertheless, the boundary conditions for the numerical simulation are justified to be acceptable.

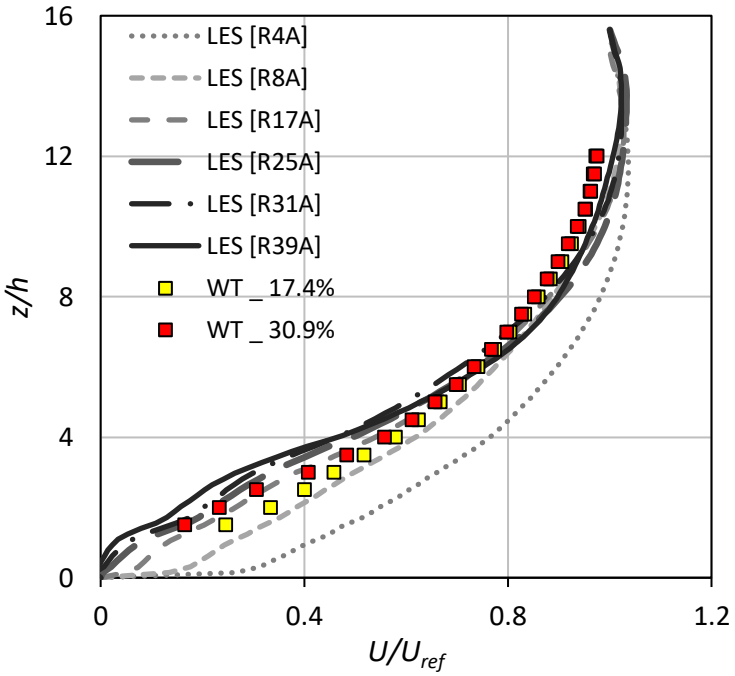


Fig 3. Streamwise mean velocity profile for all random staggered arrays. Squares are the wind tunnel results of Zaki [5] for λ_p =17.4% (yellow) and λ_p = 30.9% (red)

3.2 *Mean velocity under canopy*

The pedestrian wind environment is analysed by visualizing the mean wind velocity at the pedestrian level which is specified as the space on the street at height less than 2 m on real scale [2,7]. With the large height variability within the array, the analysis of pedestrian wind velocity are performed at $z = 0.16h$ which is below the height of the lowest building (B_1). Figures 4(a) and (b) illustrate the mean velocity field at pedestrian level for $\lambda_p = 4.4\%$ and $\lambda_p = 39.1\%$, respectively. Comparison between these plan area ratios indicates that the mean velocity greatly reduces as λ_p increases, which corresponds to the observations made in Figure 3. The mean velocity flows almost continuously within the array along the streamwise direction reaching the top velocity of 4 m/s (Figure 4(a)) as there is very little obstruction of flow. However, the flow velocity in most regions of $\lambda_p = 39.1\%$ (Figure 4(b)) is less than 1 m/s, which is relatively lower due to the high density of buildings. The gaps between buildings on the first two columns in the array experience an almost stagnant condition. This is due to the presence of taller buildings in the latter columns that produces a reverse flow towards their windward buildings. Meanwhile, the flow velocity downstream of building B_9 is much higher which is due to the effect of contraction flow. This

downstream flow is visualized in Figure 4(c) at a cross section $y = 0.12$ m, where skimming flow occurs above B_9 creating a large vortex behind the building at an approximate height of 0.06 m.

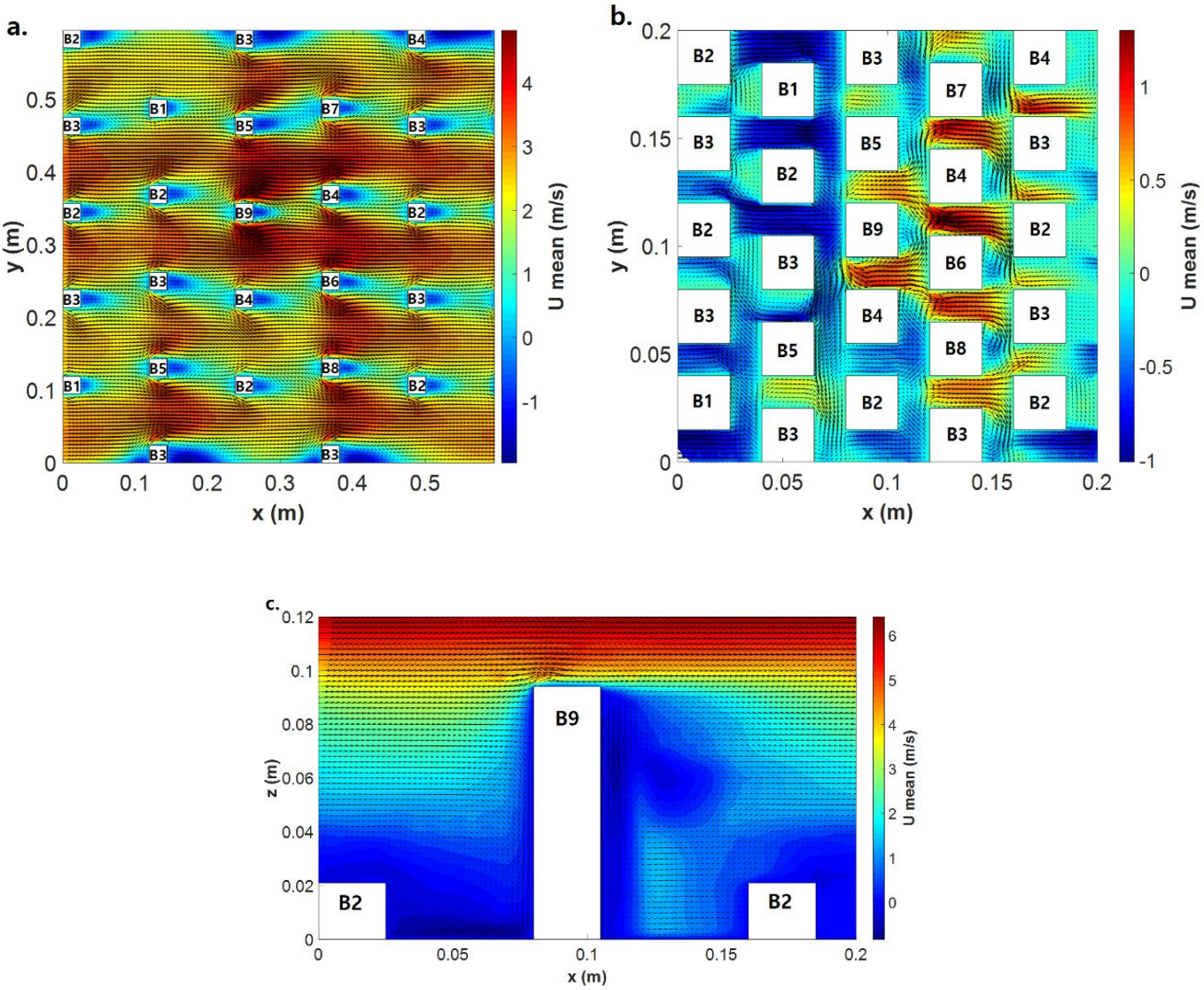


Fig 4. Vector and contour plot of streamwise mean wind velocity. (a) At pedestrian height *z*=0.16*h* for $\lambda_p = 4.4\%$, (b) At pedestrian height *z*=0.16*h* for $\lambda_p = 39.1\%$, (c) Cross section along x-axis at *y*=0.12m for $\lambda_p = 39.1\%$

In addition, Figure 5 shows the spatially averaged velocity in the streamwise direction within the canopy layer for various λ_p. The velocities are normalized with the values at the maximum building height of the canopy (h_c). The results from Razak [7] of random staggered arrays are also plotted in Figure 5 for comparison. Although the composition of the buildings in the prior study is different, however the average height of buildings used in the array is maintained as 1.5*h*. The effect of height variability causes the vertical profiles to form a distinct change in the velocity gradient. For smaller λ_p (4%, 8% and 17%), a large change in gradient occurs at ground surface due to high shear stress in the sparse area whereas, for larger λ_p (25%, 31% and 39%) the change in gradient is particularly apparent from $0.3h_c$ to $0.45h_c$. Also, a small deflection of gradient is observed near the ground surface and is depicted to be in relation with the reverse flow mentioned beforehand.

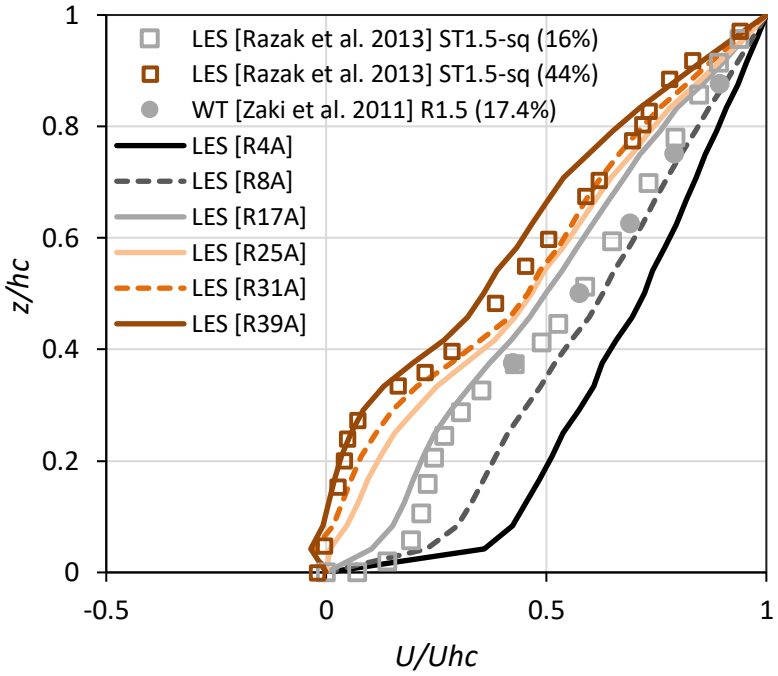


Fig 5. Normalized streamwise mean velocity profile inside canopy for random staggered arrays from LES database, LES results of Razak [7] and wind tunnel of Zaki [5]

3.3 *Pedestrian mean velocity around various buildings*

To evaluate the pedestrian wind environment in the vertical random array, Figures 6 and 7 show the relationship between the average surrounding velocity taken at pedestrian height around each building (V_p) and its local frontal area density ($\lambda_{f(t)}$) which is the product of the aspect ratio of local building and its plan area density. V_p is normalized with the values at two times the maximum block height.

The correlation is observed around every single building for various cases of λ_p as shown in Figure 6. The coefficient of determination R^2 obtained is 0.45, suggesting a low correlation between V_p and $\lambda_{f(t)}$ when all buildings are considered. Therefore to improve the correlation, these data are classified according to the height of buildings present in the array. Three categories are defined based on height ranges namely; low-rise buildings (0.36*h* to 0.84*h*), medium-rise buildings (1.32*h* to 2.00*h*) and tall-rise buildings (2.64*h* to 3.76*h*). Hence, the correlations are improved for these categories whereby the highest regression is obtained around tall buildings (R^2=0.80) compared to others (Figure 7(c)). This indicates that the pedestrian wind velocity is highly influenced by taller buildings than by lower buildings. Around low-rise and medium-rise buildings, the wind flow is less obstructed and the circulation is formed as the commonly known flow regimes which retains under the canopy. However, with the presence of taller buildings, the wind velocity becomes more complicated. As the velocity is relatively high on the upper part of the building hence due to less obstruction, more downward flow occurs towards the windward part of these buildings yielding a lower wind velocity at the pedestrian level. Due to this, pedestrians will experience less comfort around tall-rise buildings specifically in denser conditions.

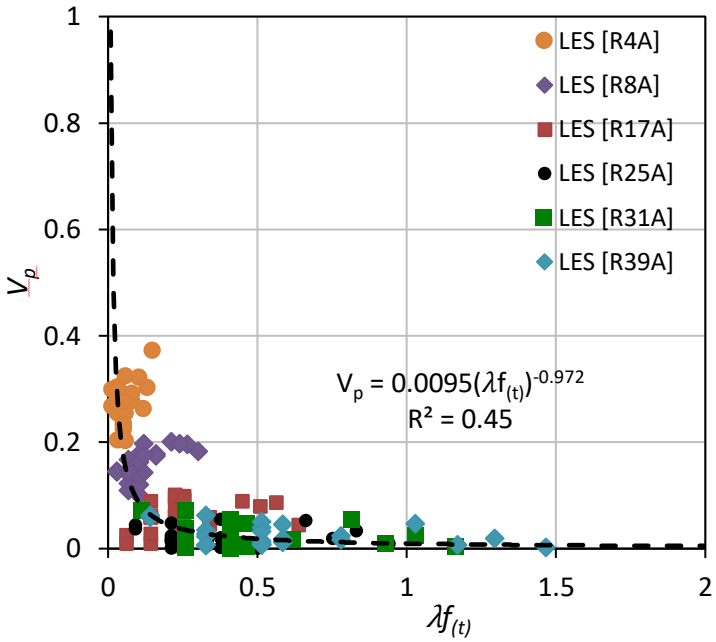
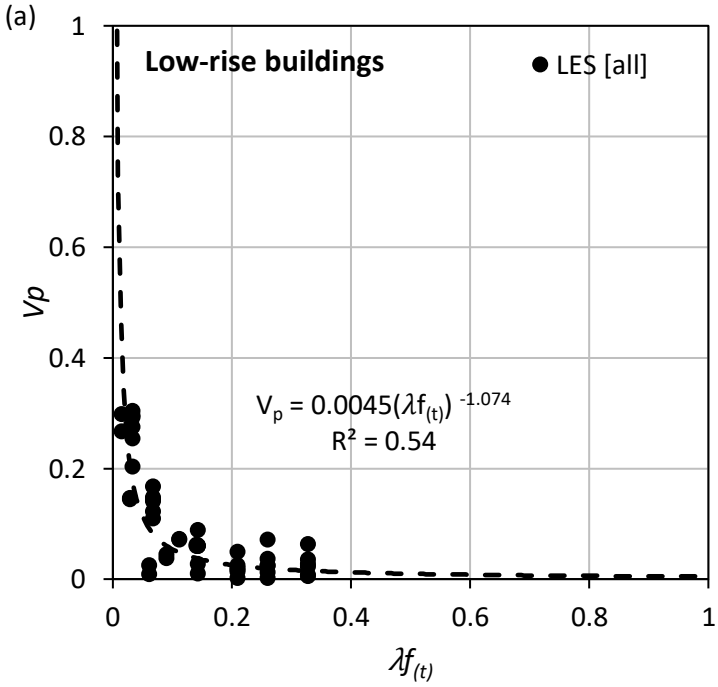


Fig 6. Relationship between V_p and $\lambda_{f(t)}$ of random staggered arrays results for all buildings



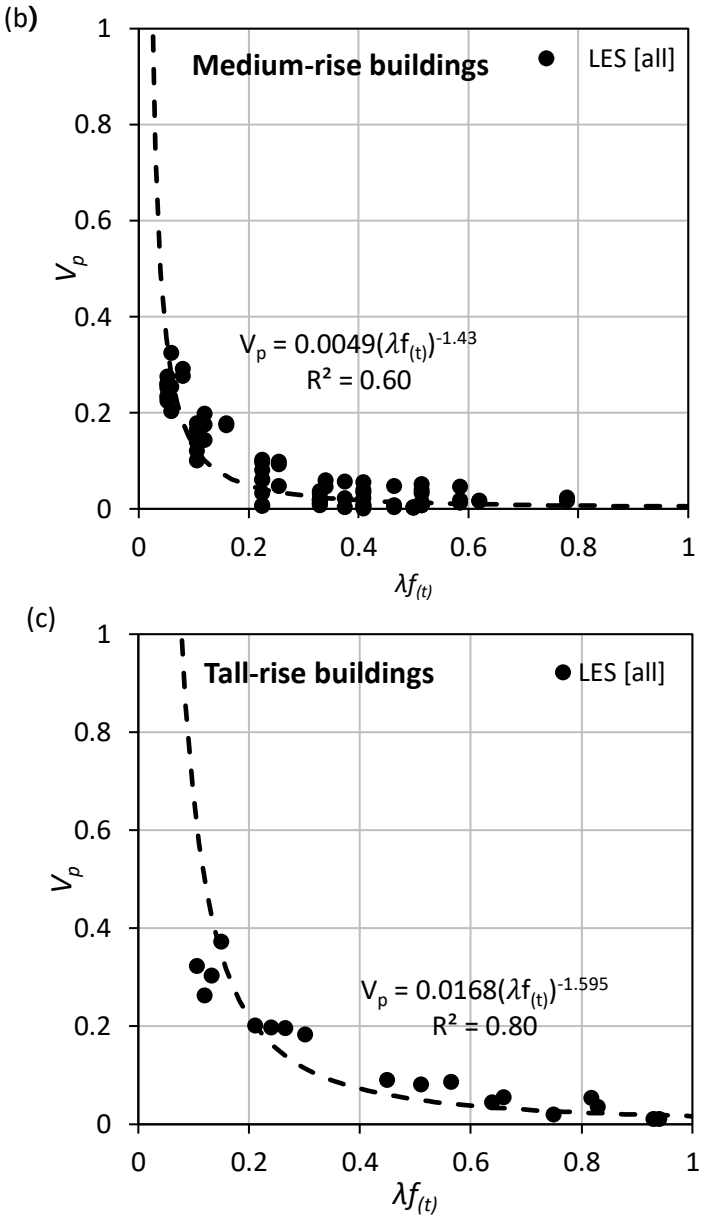


Fig 7. Relationship between V_p and $\lambda_{f(t)}$ of random staggered arrays categorized into (a) low-rise, (b) medium rise, and (c) tall rise buildings.

4. Conclusions

This study analysed the database of large eddy simulation over vertical random staggered arrays in various plan area densities. Based on the results, the velocity and contour plots observed at the pedestrian height are greatly altered according to the density of the area. Most importantly, the height variability of buildings in an array also results in the formation of flow within the canyons in between buildings. This can be further explained in terms of the pedestrian wind speed which is mainly influenced by plan area density and building aspect ratio (ratio of building's height with width, α_p). Hence from this study, the frontal area density was used to express these geometric parameters. Due to the vertical random array, the individual building's frontal area density is analysed because each building is surrounded by different buildings within their proximity. From the correlation with the pedestrian mean surrounding velocity, power law equations were formulated according to the aspect ratios of three building categories namely; low-rise buildings

(0.36 ≤α_p≤ 0.84), medium-rise buildings (1.32 ≤α_p≤ 2.00) and tall-rise buildings (2.64 ≤α_p≤ 3.76). The frontal area density sufficiently evaluates the correlation with pedestrian wind velocity highlighting that the greatest reduction of flow velocity is observed around tall-rise buildings. The results of this study are potentially beneficial for building design and urban planning.

Acknowledgement

This research was financially supported by the Research University Grant (17H94) project of Universiti Teknologi Malaysia.

References

[1] Hang, J., Sandberg, M., & Li, Y. (2008). Age of air and air exchange efficiency in idealized city models. *Building And Environment, 44(8),* 1714-1723.

[2] Kubota, T., Miura, M., Tominaga, Y., & Mochida, A. (2008). Wind tunnel tests on the relationship between building density and pedestrian-level wind velocity: Development of guidelines for realizing acceptable wind environment in residential neighborhoods. *Building And Environment, 43(10),* 1699-1708.

[3] Yoshie, R., Tanaka, H., Shirasawa, T., & Kobayashi, T. (2008). Experimental study on air ventilation in a built-up area with closely-packed high-rise buildings. *Journal Of Environmental Enginering (Transactions Of All), 73(627*), 661-667.

[4] Hagishima, A., Tanimoto, J., Nagayama, K., & Meno, S. (2009). Aerodynamic Parameters of Regular Arrays of Rectangular Blocks with Various Geometries. *Boundary-Layer Meteorology, 132(2),* 315-337.

[5] Zaki, S., Hagishima, A., Tanimoto, J., & Ikegaya, N. (2011). Aerodynamic Parameters of Urban Building Arrays with Random Geometries. *Boundary-Layer Meteorology, 138(1)*, 99-120.

[6] Coceal, O., Thomas, T., Castro, I., & Belcher, S. (2006). Mean Flow and Turbulence Statistics Over Groups of Urban-like Cubical Obstacles. *Boundary-Layer Meteorology, 121(3),* 491-51.

[7] Razak, A. A., Hagishima, A., Ikegaya, N., & Tanimoto, J. (2013). Analysis of airflow over building arrays for assessment of urban wind environment. *Building and Environment, 59*, 56-65.

[8] Mohammad, A.F., Zaki, S., Ikegaya, N., Hagishima, A., & Ali, M. (2018). A new semi-empirical model for estimating the drag coefficient of the vertical random staggered arrays using LES. *Journal Of Wind Engineering And Industrial Aerodynamics, 180*, 191-200.

[9] Mohammad, A. F., Zaki, S. A., Mat Ali, M. S., Abd Razak, A., & Hagishima, A. (2014). Large-Eddy Simulation of wind-induced ventilation in urban buildings of random staggered arrays. *6th International Symposium on Computational Wind Engineering,* University of Hamburg, Germany

[10] Cheng, H., & Castro, I. (2002). Near Wall Flow over Urban-like Roughness. *Boundary-Layer Meteorology, 104(2),* 229-259.

[11] Oke, T. (1988). Street design and urban canopy layer climate. *Energy And Buildings, 11(1-3),* 103-113.

[12] Kanda, M., Inagaki, A., Miyamoto, T., Gryschka, M., Raasch, S. (2013). A New Aerodynamic Parameterization for Real Urban Surfaces. Boundary-Layer Meteorology. 148, 357-377

[13] Ikegaya, N., Ikeda, Y., Hagishima, A., Razak, A., & Tanimoto, J. (2015). A prediction model for wind speed ratios at pedestrian level with simplified urban canopies. *Theoretical And Applied Climatology, 127(3-4),* 655-665.

[14] Kasim, N., Zaki, S., Ali, M., Ikegaya, N., & Razak, A. (2016). Computational Study on the Influence of Different Opening Position on Wind-induced Natural Ventilation in Urban Building of Cubical Array. *Procedia Engineering*, *169*, 256-263.

[15] Razali, M., Zaki, S., Ali, M., & Arai, N. (2016). A Numerical Analysis of Wind Flow within and above Idealised Modified Terraced House Canyon in Malaysia. *Procedia Engineering*, *169*, 289-296.

[16] Mohammad, A. F., Zaki, S., Hagishima, A., & Ali, M. (2014). Determination of aerodynamic parameters of urban surfaces: methods and results revisited. *Theoretical And Applied Climatology*, *122*(3-4), 635-649.

[17] Zaki, S. A., Hagishima, A., Tanimoto, J., Mohammad, A. F., & Razak, A. A. (2014). Estimation of aerodynamic parameters of urban building arrays using wind tunnel measurements. *Journal of Engineering Science and Technology, 9(2),* 176-190.

Penerbit Akademia Baru

Engineering Science and Technology Conference Proceedings

Journal homepage: www.akademiabaru.com/EST.html

CFD Investigation on The Jet-Engine Inspired Wind Turbine

Open

Nur Shamimi Amirah Md Sunhazim[1*], Fazila Mohd Zawawi[1], Ummikalsom Abidin[1], Syahrullail Samion[1]

[1] Department of Thermofluids, School of Mechanical Engineering, Faculty of Engineering, Universiti Teknologi Malaysia, 81310 Skudai Johor, Malaysia.
[2] Department of Applied Mechanics and Design, School of Mechanical Engineering, Faculty of Engineering, Universiti Teknologi Malaysia, 81310 Skudai Johor, Malaysia
[3] Department of Thermofluids, Faculty of Mechanical Engineering, Universiti Teknologi MARA, Johor Branch Pasir Gudang Campus, 81750 Bandar Seri Alam Johor, Malaysia

ABSTRACT

The potentiality of the Jet-Engine inspired Wind Turbine in augmenting the power generation and its corresponding performance by mean of Computational Fluid Dynamics (CFD) numerical approach were investigated in this study. The main objectives are to develop a reliable numerical model for accessing the capability of the Jet-Engine inspired Wind Turbine and to regulate its performance with influence of curly shroud on the induced flow. The conventional shrouded wind turbine has been modified which consisted a stator and a rotor blade covered by curly-shaped shroud adapting the concept of Jet-Engine. A constant wind speed of 5 m/s which is the average wind speed in Malaysia, and tip speed ratio (TSR) varies from 2 to 6 were specified in the simulation. The investigation discovered that the curly-shaped shroud gave an impact to the performance of the Wind Turbine as it can be reviewed from the comparison of the power coefficient on the Jet-Engine inspired Wind Turbine with shroud and without shroud. The effect of the curly shroud was also analysed by obtained the velocity and pressure contour from the ANSYS Fluent, where there is a swirl formation at the shroud as the air mixed at different angle, which causes the pressure drop and inlet velocity increased.

Keywords:
Jet-Engine inspired Wind Turbinel
Computational Fluid Dynamics (CFD);
curly-shaped shroud

Copyright © 2019 PENERBIT AKADEMIA BARU - All rights reserved

1. Introduction

Renewable energy is extensively commercialized in these recent days because of it can replenished naturally and does not have limited supplies compared to non-renewable energy. There are a few collective renewable energies used which are solar, wind, water (hydro), biomass, and geothermal. Comparing all these renewable energies, wind energy is the cleanest energy, as it does not produce any CO_2 emissions [1,2]. This means that wind energy does not contribute to the greenhouse effect and help to reduce global warming and devastating climate change unlike fossil fuels that need to be burned to generate significant amounts of energy [3]. The extraction of the wind energy can be done by the application of the wind turbine.

Numerous researches have been carried out in order to enhance the performance of the wind turbine and to obtain the optimum energy from the wind flow. The effect of applying shape memory alloys (SMA) wire in the prototype of the wind turbine were investigated [4]. The SMA wire gives a significant result as the blade that has higher volume fraction of SMA will help in the amplitude ratio reduction due to the increase of blade's stiffness properties and the damping

property. Based on the effect of geometrical parameters of an optimized wind turbine blade in turbulent flow shows the convincing performance results [7]. Power coefficient of optimized geometry 13.7% greater than based geometry. It is agreed that the performance wind turbine are depends on two main factors which are wind flow conditions and wind turbine design. Hence, wind turbine on the market show a variety of innovative concepts combined with proven technology for both generators and power electronics [8].

The performance of the wind turbine by designing the wind turbine with a shroud has been developed. By using an experimental and numerical method, it is showing a good agreement of the shrouded effect. The power output produced from the wind turbine with flange, called wind-lens wind turbine, produced more power compared to the conventional one for both approaches [5]. Shrouded brims around convention wind turbine gave significant power coefficient increased [9]. From the experimental study of shrouded micro wind turbine [10] obtained that the shrouding micro wind turbine not only improves performance but also points out how diffuser geometrical features Length diffuser and flange height can be used to design a turbine with performance curve to suit the location. From exploration [6] shows that the performance increased by 1.6 to 1.7 times than the conventional wind turbine. Furthermore, according to numerical study and design optimization of brimmed diffuser-wind lens around wind turbine [11], the present diffuser induces wake formation and significantly increase in mass flowrate available for the flow wind turbine.

Therefore, in this article the potentiality of the Jet-Engine inspired Wind Turbine in augmenting the power generation and its corresponding performance were investigated by using Computational Fluid Dynamics (CFD). The comparison of the power coefficient on the Jet-Engine inspired Wind Turbine with shroud and without shroud will be discussed. An average Malaysia's wind speed of 5 m/s and tip speed ratio (TSR) varies from 2 to 6 were used as detailed in the simulation.

2. Methodology

2.1 Jet-Engine inspired Wind Turbine Modelling

The jet-engine inspired wind turbine as per depicted in **Fig. 1.** is used as the baseline model for the analysis and is designed by using Computer Aided Design Commercial Software namely SolidWorks. The detailed dimension of the wind turbine is shown in **Table 1**. The design of the wind turbine consists of stator, rotor and two curly shrouds with different diameter. The curly shroud was designed in such a way that it has capability to enhance the performance of the wind turbine due to the vortex formation at the back of the wind turbine.

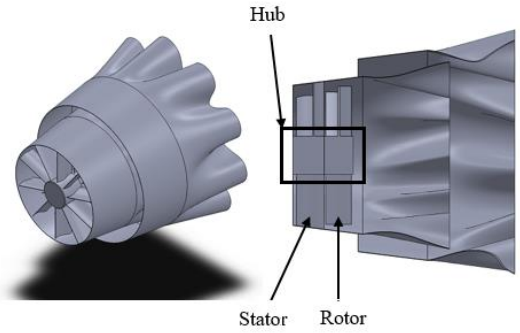


Fig. 1. Isometric and side view of the jet-engine inspired wind turbine concept

Table 1
Specifications on the jet-engine inspired wind turbine

Part	Specifications
Rotor	Length: 550 mm
Stator	Length: 605.09 mm
Hub	R220 mm
Curly Shroud (Large)	~ R1215 mm
Curly Shroud (Small)	~ R900 mm

The computational domain is designed using Design Modeller in ANSYS Fluent. Two cylindrical domains are created which are rotating and stationary domain, as illustrated in **Fig. 2**. The rotating domain is drawn around the rotor as it is the only part that is rotating, while the stationary domain acts as an enclosure for the fluid to flow. The boundary conditions are specified where the front part is set to be the inlet and the back part of stationary domain is that to be the outlet.

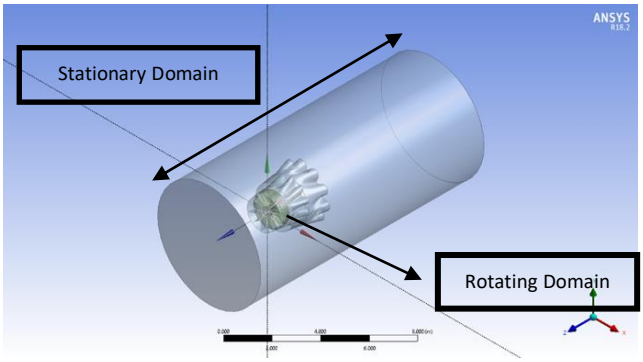


Fig. 2. Numerical domain on the jet-engine inspired wind turbine

2.2 Meshing Grid and Boundary Conditions

Meshing grid used in this study is tetrahedral mesh with sizing method. The sizing method was used to refine the mesh grid and reduce the skewness. This will help to reduce the number of elements and time taken for the simulation to be done. For this study, the number of elements is more than 4,000,000. Edge sizing method was used for every edge on the blades and shroud while body sizing method was used for the stationary domain as can be reviewed in **Fig. 3** and **Fig. 4.**

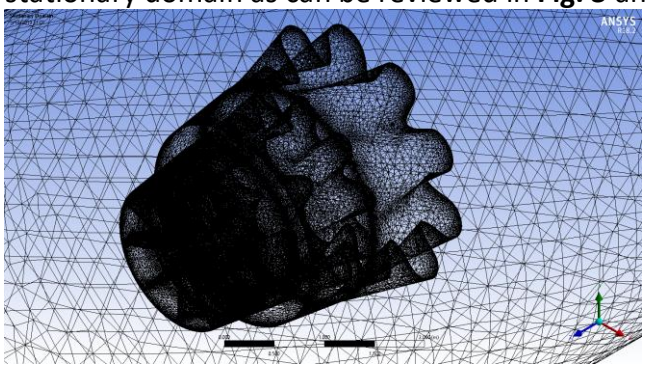


Fig. 1. Edge sizing on the blade and shroud of the jet-engine inspired wind turbine

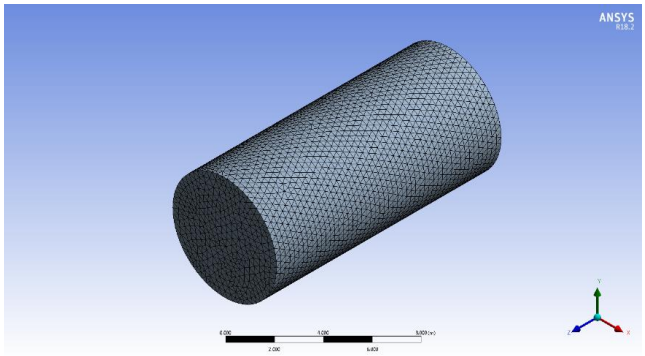


Fig. 4. Body sizing on the jet-engine inspired wind turbine

The wind velocity inlet is set constant which is 5 m/s meanwhile the value of tip speed ratio (TSR) is varied from 2 to 6. The value of the TSR is used to calculate the revolution per minute (RPM) of the wind turbine. These values of RPM were insert in the ANSYS Fluent to run the simulation.

2.3 Computational Fluid Dynamics

Computational Fluid Dynamics (CFD) were applied as a numerical study in this paper.

2.3.1 Turbulence Modelling

The k-omega Shear Stress Transport (k-ω SST) was used as turbulence model because of its commonly applied to signify a turbulence properties flow. With two additional equations, k-ω SST model was developed to overcome deficiencies of k-ω model. This model more accurate and reliable for wider class of flows than the standard k-ω model. Besides k-ω SST model can perform more precise formulation of the k-ω model in near-wall region [12].

2.3.2 Solution Methods

The pressure-velocity coupling setup was set to Semi-Implicit Method for Pressure Linked Equation SIMPLE with skewness correction of 0. This setup was used to convert the continuity equation into a discrete poison equation for pressure. or the spatial discretization setup, second order upwind was set for the Momentum, Turbulent Kinetic Energy and Specific Dissipation Rate. This is to deduce the link between pressure and velocity in calculating the domain by using a multidimensional linear reconstruction approach.

3. Results

3.1 Jet-Engine Inspired Wind Turbine Performance

The performance of the wind turbine is determined by calculating the mechanical power and power coefficient of the wind turbine. This can be done by obtaining the moment values from the ANSYS Fluent. Following are the equations involved in determining the wind turbine power coefficient and mechanical power.

$$TSR = \omega R/v \quad (1)$$

$$Pin = \tfrac{1}{2} AV^3\rho \quad (2)$$

$$Pout = T\omega \quad (3)$$

$$Cp = P_{out}/P_{in} \quad (4)$$

3.2 Comparison of the Performance

The performance of the wind turbine was validated by comparing the values of mechanical power and power coefficient between Jet-Engine inspired Wind Turbine with shroud and without shroud. Thus, the influence of the curly shroud towards the performance of the wind turbine can be studied. By using Equation (2) the value of wind power obtained are 150.1331W. From illustration in **Fig. 5.** and **Fig. 6.**, there is a minor increment between wind turbine with shroud and without shroud. As can be seen in both figures, there is no change of any values when TSR value of 2. Meanwhile, for TSR value of 6, mechanical power was increase from 52.03W to 56.96W and the value of power coefficient augmented from 0.35 to 0.38 respectively.

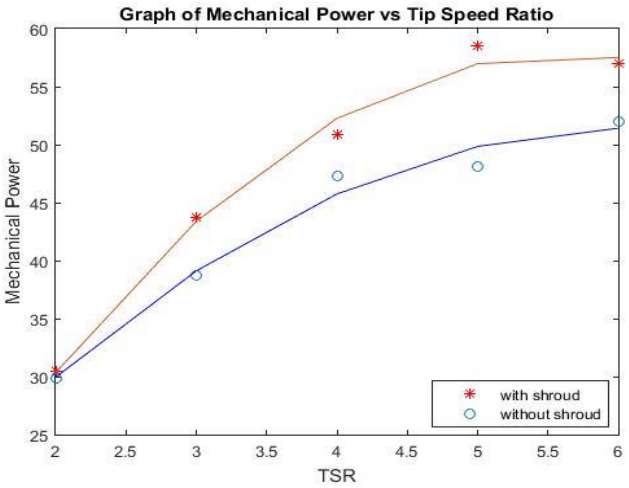


Fig. 5. Comparison on the mechanical power of the wind turbine with and without shroud

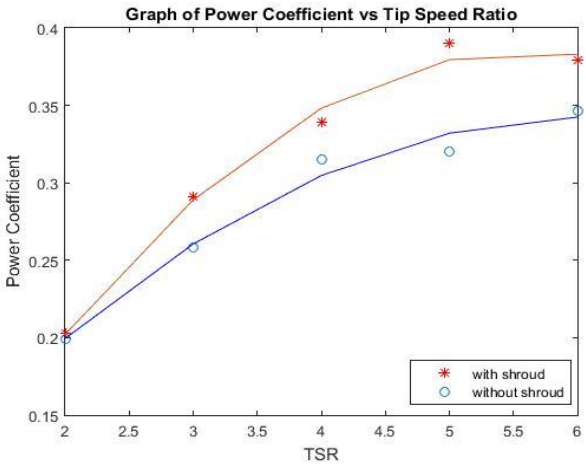


Fig. 6. Comparison on the power coefficient of the wind turbine with and without shroud

3.3 Effect of the Curly Shroud

The effect of the curly shroud on the performance of the wind turbine was also studied from the contour obtained in ANSYS Fluent. From **Fig. 7.**, swirl phenomena occurred at the of the shroud. This swirl happened as the air was mixing at different angle. There are two curly shrouds to dual the vortex formation.

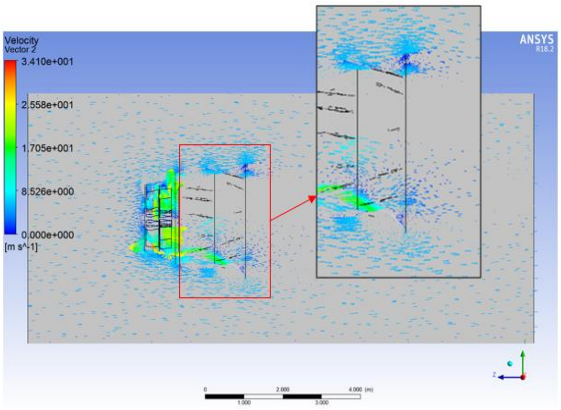


Fig. 7. Vector contour on the wind turbine to capture the swirl formation

Due to this vortex formation, it causes the pressure at the back of the wind turbine to drop. From the pressure contour in Figure 8, it is proven that the pressure was dropped from 0 Pa to -55 Pa. The pressure at the inlet is quite high which is around 50 Pa. This pressure difference will then cause a suction to happen where the high-pressure region will go to low pressure region. This will lead to the increment of the wind speed at the inlet to outlet as Figure 9. The velocity increased from 5 m/s to around 31 m/s. The increment of the velocity at the inlet means that the mass flow rate is increased. This helps to improve the performance of the Jet-Engine inspired Wind Turbine with shroud compared to without shroud.

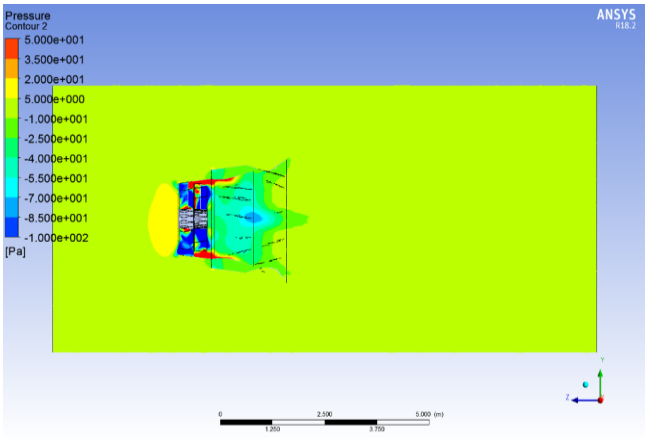


Fig. 8. Pressure contour

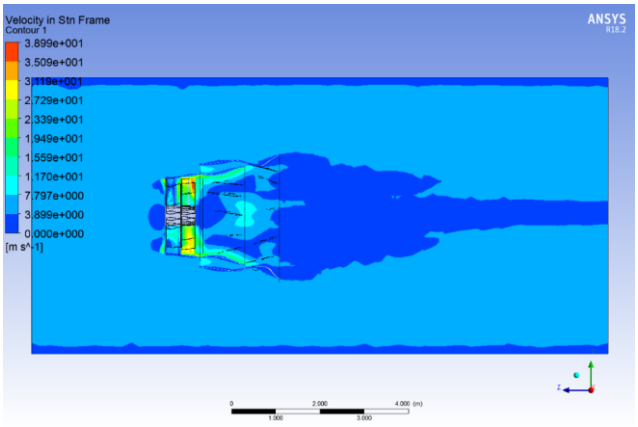


Fig. 9. Velocity contour

3.4 Comparison of the Contour for each TSR Values

For each TSR values, the velocity and pressure values were compared. From **Table 2**, the velocity at the inlet of the wind turbine is increasing from 13.5 m/s to 31 m/s while for the pressure at the outlet of the wind turbine is from -18 Pa to -80 Pa. This shows that the curly shroud attached on the Jet-Engine inspired Wind Turbine gave a significant increment in the performance of the wind turbine.

Table 2
Comparison of the velocity and pressure values for each TSR values

TSR	*Velocity at the Inlet (m/s)*	*Pressure at the outlet (Pa)*
2	*13.5*	*-18*
3	*17*	*-45*
4	*20*	*-60*
5	*26*	*-73*
6	*31*	*-80*

4. Conclusions

The research of Jet-Engine inspired Wind Turbine were successfully verified that this concept can generate power because it gave an enhancement to the performance of the wind turbine. The results obtained shows that the TSR value of 5 gives the highest mechanical power and power coefficient on the wind turbine. Increment of positive values of the mechanical power and power coefficient between wind turbine with and without shroud shows that the curly shroud influenced the fluid flow on the back of the wind turbine. Moreover, pressure drop at the back of the wind turbine due to the vortex formation causes the velocity on the inlet to increase.

Acknowledgement
The authors are grateful to the Universiti Teknologi Malaysia for providing the funding for this study under the Research University Grant (RUG) with a vot number 4G645. The financial support is managed by the Research Management Centre (RMC) Universiti Teknologi Malaysia

References

[1] Hansen, M. O. L. (2015). *Aerodynamics of Wind Turbines*: Taylor & Francis.3rd Edition.
[2] Peter J. Schubel, Richard J. Crossley. Wind Turbine Blade Design. Energie 2012, 5: 3425 - 3449
[3] Chiras, D. (2010). *Wind Power Basics: A Green Energy Guide*: New Society Publishers.
[4] V Jagadeesh, M Yuvaraja, A Chandhru, P Viswanathan, M Senthil kumar. Investigation on Vibration Characteristic of SMA Embedded Horizontal Axis Wind Turbine Blade. OP Conference Series: Materials Science and Engineering. 310 (2018) 012067.
[5] Yuji Ohya, Takashi Karasudani. A Shrouded Wind Turbine Generating High Output Power with Wind-lens Technology. Energies 2010, 3: 634–649
[6] Bilal Ahmed, Ateeque Ahmed, Ahmad Hussain. Modelling and Simulation of Diffuser augmented wind turbine (DAWT). 4th International Conference on Energy, Environment and Sustainable Development 2016 (EESD 2016).
[7] Tahani, M., Maeda, T., Babayan, N., Mehrnia, S., Shadmehri, M., Li, Q., Fahimi, R.,Masdari, M. Investigating the effect of geometrical parameters of an optimized WT blade in turbulent flow. Journal of Energy Conversion and Management. Volume 153(2017):71 -82.
[8] L. Chen, F.L.Ponta, L.I.Lago. Perspectives on innovative concepts in wind-power generation. Energy for Sustainable Development. Volume 15, Issue 4(2011): 398-410.
[9] AierkenDilimulati, TedStathopoulos, MariusParaschivoiua.Wind Turbine designs for urban applications: A case study of shrouded diffuser casing for turbines. Journal of Wind Engineering and Industrial Aerodynamics. Volume 175(2018): Pages 179-192
[10] Buyung Kosasih, Andrea Tondelli Experimental Study of Shrouded Micro Wind Turbine. Evolving Energy-IEF International Energy Congress (IEF-IEC2012). Procedia Engineering 49 (2012): 92 – 98
[11] Raju Govindharajan, K. M. Parammasivam, V. Vivek, R. Vishnu Priya. Numerical Investigation & Design Optimization of Brimmed diffuser-Wind lens around a Wind Turbine. Proceeding of the Eight Asia – Pacific Conference on Wind Engineering (2013).
[12] Carcangiu, C. E. (2008). CFD-RANS Study of Horizontal Axis Wind Turbines. University of Cagliari (DIMeCa), Italy, Cagliari.

Penerbit Akademia Baru

Engineering Science and Technology Conference Proceedings

Journal homepage: www.akademiabaru.com/EST.html

Feasibility Study of using Oil Palm Trunk Waste Fiber as Fluid Loss Control Agent and Lost Circulation Material in Drilling Mud

Open Access

A. Sauki[1,*], M. S. M. Azmi[1]; W. Z. W. Bakar[1]; H. H. Jarni[1]; T. A. T. Mohd[1]; P. N. F. M. Khamaruddin[1]; W. A. W. Ibrahim[2]

[1] Department of Oil and Gas, Faculty of Chemical Engineering, Universiti Teknologi MARA, 40450 Shah Alam, Malaysia
[2] Forest Research Institute Malaysia, Malaysia

ABSTRACT

An investigation was conducted on Oil Palm Trunk (OPT) fiber to be used as fluid loss control (FLC) agent and lost circulation material (LCM) in drilling fluid. API filtration test was performed to evaluate the performance of OPT fiber as FLC while sand bed test was performed to evaluate the performance of OPT fiber as LCM. For the API filtration test, the addition of OPT fiber has reduced the fluid loss while the filter cake thickness increases as higher amount of OPT fiber was added in the drilling mud. The use of smallest size of OPT fiber (<75µm) yielded the lowest fluid loss. For the sand bed test, mud invasion reduced as the concentration of OPT fiber increased. The findings also revealed that the OPT fiber with the size of 75-150µm performed best in reducing mud invasion with the value of merely 1 cm. Thus, it can be concluded that OPT fiber has a high potential to be used as FLC and LCM in drilling mud.

Keywords:
Drilled solid; Mud rheology; Spearman correlation

Copyright © 2019 PENERBIT AKADEMIA BARU - All rights reserved

1. Introduction

Fluid loss is the result of filtrate loss from drilling fluid into the formation. Invasion of filtrate into formation could reduce the permeability near the wellbore zone that can lead to lower production. If the filtrate invades the shale section, it can cause the clay swelling that can lead to pipe sticking [3]. In order to prevent or reduce the fluid loss, FLC additive need to be used in drilling fluid. According to [7], there were two basic mechanisms in which fluid loss control can be achieved. Firstly, fluid loss control can be achieved by increasing the overall viscosity of the drilling fluid using water-dispersible polymers such as Carboxymethyl cellulose (CMC), polyanionic cellulose (PAC), hyrdroxyethyl cellulose (HEC). The use of water dispersible polymers have direct impact to drilling mud bulk viscosity. Secondly, fluid loss control can be achieved by forming internal or external filter cake to plug the formation pore throats using insoluble material such as calcium carbonate and unmodified cellulosic fiber. According to [8], modification is necessary for natural cellulosic fiber to be used as FLC. This is because natural cellulose is insoluble in water. However, several researchers have proved that the use of unmodified cellulosic fiber could achieve the fluid loss control [4], [9], [10], [11], [12], [13], [14] but the result is minimal. According to [11], [12], [15],

small and fine particles of insoluble fibers are capable to fill the pore spaces between the filter cake. Therefore, fluid loss can be reduced. Thus, it can be concluded that the use of unmodified cellulosic fiber could also achieve the fluid loss control through the second mechanism. Since the control is achieved physically, it is expected the filter cake thickness will increase as more raw material is used to reduce the fluid loss. Study by [13], [14], [16] shows that as higher amount of raw material used to reduce the fluid loss, the thickness of filter cake was increased.

Loss circulation can be defined as total or partial loss of drilling fluid into the formation [4], [5]. Mud losses into formation does have economic impact and causing drilling problems. Mud is accountable for 25 to 40% of total drilling cost [6]. Non- productive time was spent to cure the lost circulation. Lost circulation also leads to poor hole cleaning, increase formation damage and pore plugging [6]. Severe mud losses will lead to well control problems. Total loss of drilling fluid occurred when there was no mud returning to the surface. Partial lost circulation is when volume of mud returned to the surface is less than the volume of mud pumped into the well [4]. In order to cure or prevent lost circulation or mud loss during drilling, lost circulation materials (LCM) can be used in the drilling fluids. There are four types of LCM, which is fibrous materials, flaky materials, granular materials and hydrated slurries [1]. LCM also can be divided into two types which is particulates LCMs and fibrous [6]. Particulates LCMs include granular and flaky materials. Amongst the example of fibrous materials is micronized cellulose, bagasse, sawdust, wood fibers, shredded tyres and paper pulp [1]. Fiber materials are the materials with less rigidity unlike granular materials. The working principle of LCM is simple. As the LCM has been transported to the fractures, the coarse LCM will bridge the fractures to provide the mechanical strength. In case of fiber, it will create the network structure across the fracture. Subsequent seal will be provided by deposition of small particles on top of the bridged or network created. Small particles are attributed to fine LCM or fine clay in the drilling fluid [6].

In this study, Oil Palm Trunk Fiber was used to investigate its potential as fluid loss control (FLC) additive and as loss circulation material (LCM). Oil palm biomass (OPB) can be classified as lignocellulosic wastes [17]. According to [18], OPB can be classified into six types which are oil palm fronds (OPF), oil palm trunks (OPT), empty fruit bunches (EFB), palm kernel shells (PKS), mesocarp fiber (MF) and palm oil mill effluent (POME). The first two types of OPB commonly been produced at the plantation site while the rest generated from the mill site. The main component of oil palm biomass (OPB) fiber is holocellulose and lignin accounting about (70%-80%) and (17%-25%) of the fiber respectively [19]. According to [20], oil palm-based plywood mills utilized 40% of OPT, the other 60% of OPT is discarded as waste or residue. The residue can be justified as Oil Palm Trunk Waste (OPTW). Free hydroxyl cellulose has strong attraction to solvents and solution and the moisture sorption process is achieved through hydrogen bond [21]. Thus, it is expected that OPT fiber can retain water in drilling mud through its lignocellulosic properties and reducing fluid loss. In addition, OPT fiber can be categorized as fibrous LCM.

2. Methodology

2.1 Preparation of Oil Palm Trunk Fiber

Oil Palm Trunk Waste Fiber was obtained from Forest Research Institute Malaysia (FRIM) located at Kepong. The OPT was originated from the core part of the Oil Palm Trunk. The OPT has been milled into a size of about 1 cm using milling machine owned by FRIM prior to collection. Then, the OPT was dried using oven at 70°C for 24 hours. The dried OPT fiber was ground into smaller sizes as shown in Table 1.

Table1
Classification of ground OPT fiber

Classification of sizes	Range of sizes
Fine	<75 µm
Medium	75 to 150 µm
Medium	150 to 250 µm
Intermediate	250 to 350 µm
Intermediate	350 to 500 µm

2.2 Preparation of mud samples

The materials used to formulate water base mud was formulated using materials obtained from Scomi Oil Tools Sdn Bhd located at Bukit Jelutong, Shah Alam. The materials were mixed using Hamilton Beach Mixer for 45 minutes. The base mud consists of water, soda ash, potassium chloride, starch, xanthan gum, NaOH and barite. The OPT fibers were added in the base mud at different sizes and concentrations as shown in Table 2.

Table 2
Mud samples composition

Sample	Sample's composition
Filtration Test	
A	Base Mud
B	Base Mud+ 4g <75 µm of OPT fiber
C	Base Mud+ 4g 75 to 150 µm of OPT fiber
C1	Base Mud+ 2g 75 to 150 µm of OPT fiber
C2	Base Mud+ 6g 75 to 150 µm of OPT fiber
D	Base Mud+ 4g 150 to 250 µm of OPT fiber
E	Base Mud+ 4g 250 to 350 µm of OPT fiber
F	Base Mud+ 4g 350 to 500 µm of OPT fiber
Sand Bed Test	
A	Base Mud
G	Base Mud+ 6% <75 µm of OPT fiber (≈ 6.49g)
G1	Base Mud+ 2% <75 µm of OPT fiber (≈ 2.17g)
G2	Base Mud+ 10% <75 µm of OPT fiber (≈ 10.83g)
H	Base Mud+ 6% 75 to 150 µm of OPT fiber (≈ 6.49g)
I	Base Mud+ 6% 150 to 250 µm of OPT fiber (≈ 6.49g)
J	Base Mud+ 6% 250 to 350 µm of OPT fiber (≈ 6.49g)
K	Base Mud+ 6% 350 to 500 µm of OPT fiber (≈ 6.49g)

2.3 API Filtration Test

Filtration test for mud samples A to F was conducted according to API Recommended Practice 13B-1 [22]. The filtration test was conducted at 100 psi for 30 minutes. After 30 minutes, filtrate volume was collected and measured using measuring cylinder. The filter cake thickness was also measured in mm unit using digital vernier caliper. The filtrate volume collected must be less than 15 ml [25] [24]. The good filter cake thickness should be less than 2/32 inch (≈ 1.6mm) or 2 mm [26] [3].

2.4 Sand Bed Test

Sand bed test was conducted for mud samples A, G1 to K. The procedure for conducting sand bed test was done based on [29] [30]. The sand bed test was conducted by using modified LPLT filter press with clear Plexiglas cylinder. The test was conducted at 100 psi for 30 minutes. After 30 minutes, depth of mud invasion into sand bed was measured. 20/40 frac sand was used as sand bed to simulate formation porosity and permeability. The mud invasion below 5 cm shows the good performance of LCM [11].

3. Results and Discussion

3.1 The effect of OPT fiber amount to filtration properties

Figure 1 shows the effect of increased amount of OPT fiber added in drilling mud to fluid loss. It could be observed that the filtrate loss was reduced as the higher amount of OPT fiber added to the drilling fluid. The addition of 2g, 4g and 6g of 75 to 150 µm of OPT fiber have reduced the API fluid loss from 6.5 ml to 5 ml. The results obtained were consistent with the findings from past researchers where the addition of cellulosic fiber into mud could reduce the fluid loss [10, 16]. Alsabagh et al. [10] have observed the reduction of fluid loss from 100 ml to 47ml, 38.8 ml and 29 ml by addition of 1.5%, 3% and 6% of coarse peanut hulls respectively. In addition, Okon et al. [16] observed the similar trend where the addition of 5g, 10g, 15g, and 20g of rice husk reduced the fluid loss from 47 ml to 42.5 ml, 35 ml and 24.5 ml respectively.

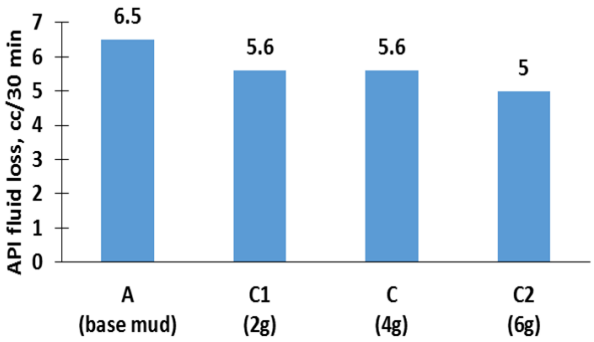


Fig. 1. Effect of increased amount of OPT fiber to filtration properties of drilling fluid

It can also be observed as the fluid loss reduced with increase amount of OPT fiber, the resultant filter cake's thickness was increased as shown in Figure 2. As the fluid loss reduced from 6.5 ml to 5 ml, the cake thickness increased from 0.5 mm to 0.79 mm. Several researchers have observed similar findings where Okon et al. [16] found that addition of 10g, 15g and 20g of rice husk to water based mud increased the cake thickness from 1mm to 1.5mm, 2.4 mm and 3.2 mm respectively. A study by Ramasamy & Amanullah [14] found that addition from 10 ppb to 30 ppb of deceased date tree waste have increased the cake thickness from 12.7mm, 14 mm, 13 mm and 12 mm to 29 mm, 21 mm, 19 mm and 21 mm respectively. The results showed that the thickness of filter cakes were within the acceptable limit. The cake thickness should be below than 2 mm [3], [26].

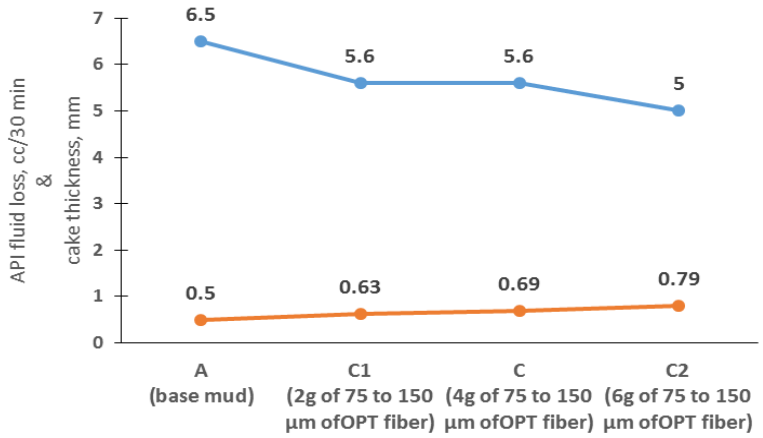


Fig. 2. Effect of increases amount of OPT fiber to filter cake thickness

3.2 The effect of different sizes of OPT fiber to filtration properties

Figure 3 shows the effect of different sizes of OPT fiber added in drilling mud to fluid loss. It can be observed that the use of smaller sizes of OPT fiber into drilling fluid reduced the fluid loss from 6.5 ml to 5.2 ml. Mud sample B formulated with smallest OPT fiber size (<75 micron) yield the lowest 5.2 ml of fluid loss. This is because a smaller particle size capable to fill the spaces between the filter cake better as compared to a coarser particles during filtration process [11], [12], [15].Therefore, fluid loss was reduced. Similar trends were also observed by several researchers. Ghazali et al. [9] observed that the addition of 150 micron, 250 micron and 500 micron of lemongrass to the water base mud resulting the fluid loss of 5 ml, 5.3 ml and 5.5 ml respectively. Majid et al. [12] found that the addition of fine durian rind powder yielded in 4.1 ml of fluid loss. While, the addition of coarse durian rind powder resulted in 11 ml of fluid loss.

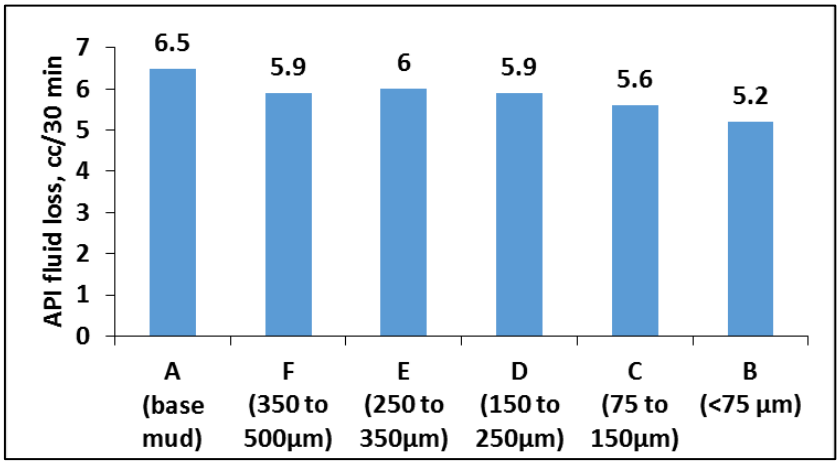


Fig. 3. Effect of different sizes of OPT fiber to filtration properties of drilling mud

Other than that, OPT fiber can act as FLC because it is comprised of cellulose and hemicellulose. Cellulose and hemicellulose could absorb the water in drilling fluid. Therefore, the base fluid can be retained and prevented from loss of fluid took places. Cellulose and hemicellulose are hydrophilic and contains large amount of hydroxyl group. Therefore, it is possible that the moisture sorption

process achieved through hydrogen bond [21]. Cellulose is classified as hygroscopic since it will absorb water and swell [31]. However, as we can observe from Figure 2 and 3, there was only small reduction of fluid loss took places. The addition of OPT fiber of 6g could only reduce the fluid loss approximately by 23%. This is maybe due to the presence of lignin in between cellulose and hemicellulose. The presence of lignin in between them cause disturbance for the absorption of water to take place. Lignin itself is hydrophobic therefore it does not absorb water [31]. It also interferes the swelling and refining of the fiber. Lignin will react as encrusting agent for the cellulose and hemicellulose loose matrix and commonly referred as plant cell wall adhesive [32]. Therefore, the surrounding and crosslinking of lignin between the polysaccharides- cellulose and hemicellulose in the cell wall provide an obstacle for effective water/ moisture absorption process to take place.

3.3 The effect of different sizes of OPT fiber to mud losses and mud invasion

Sand bed test was conducted with 6% of OPT fiber at different sizes. The purpose is to determine the suitable sizes of OPT fiber that can plug the pore spaces in between of 20/40 sand. Based on Figure 4, it can be observed that mud sample A, J and K have failed to prevent or reduce the mud losses. Other mud samples that are G, H, and I have successfully reduced the mud losses into formation. The mud invasion below 5 cm shows the good performance of LCM [11]. For sample A, mud losses occur due to the base mud contained no bridging particles thus pore spaces between sand or formation were not plugged. For samples E and F, failure in preventing or reducing mud losses was due to the size of the OPT fiber much larger than the pore sizes and the fiber was not placed in between the pore spaces. Formation of mechanical bridge did not take places; thus, no seal was created to prevent or reduced loss of mud. According to [33], the median particle size of the bridging additive needs to be equal to or slightly greater than one-third the median pore size of the formation. Therefore, the expected suitable fiber sizes, which is one-third of 20/40 sand frac range from 100 to 300µm. For the sample G, H and I, the use of suitable sizes of OPT fiber enable the fiber to travel into the pore spaces. Mechanical bridge was formed, and finer particles were able to deposit on top of it. Therefore, low permeability seal was formed. Low permeability seal is able to reduce or prevent the further mud loss and mud invasion into formation. Based on the results below, OPT fiber size of 75 to 100µm is the most suitable size since mud sample H has the lowest mud invasion of 1.0 cm.

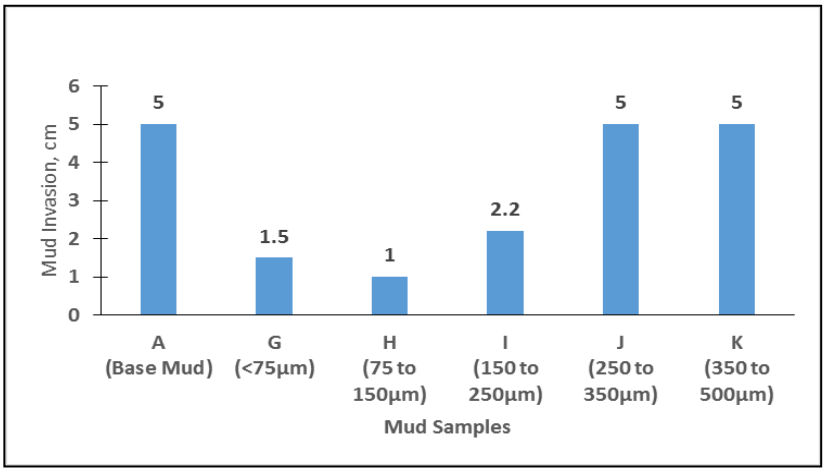


Fig. 4. Effect of different OPT fiber sizes to mud invasion

After sand bed test finished, the residual drilling fluid located on top of 20/40 sand bed was removed. Figure 5 shows a merely thin deposition of OPT fiber on top of sand bed for mud sample H. It showed that most of the OPT fiber added to drilling mud have travelled into the pore spaces between sand bed to form bridge and seal. Instead, from Figure 6, a thick deposition of OPT fiber was observed for mud sample K. This is because the size of OPT fiber used in mud sample K is too large and unsuitable for pore size of 20/40 sand bed. Therefore, most of the OPT fiber cannot invade and travelled into the pore spaces and deposited on top of the sand bed.

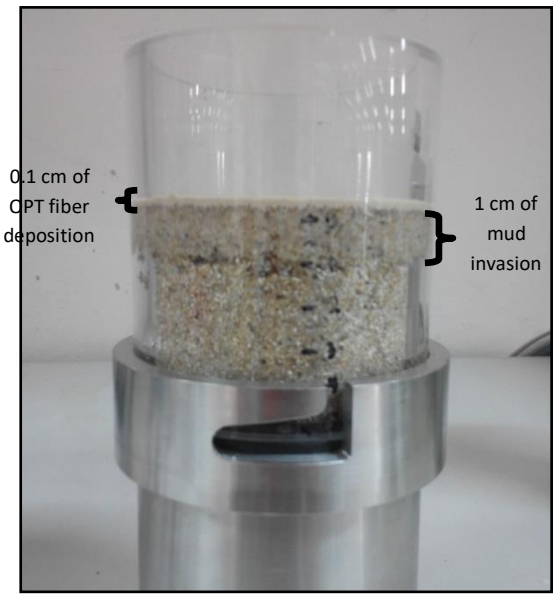


Fig. 5. Thin deposition of OPT fiber on top of sand bed for mud sample H

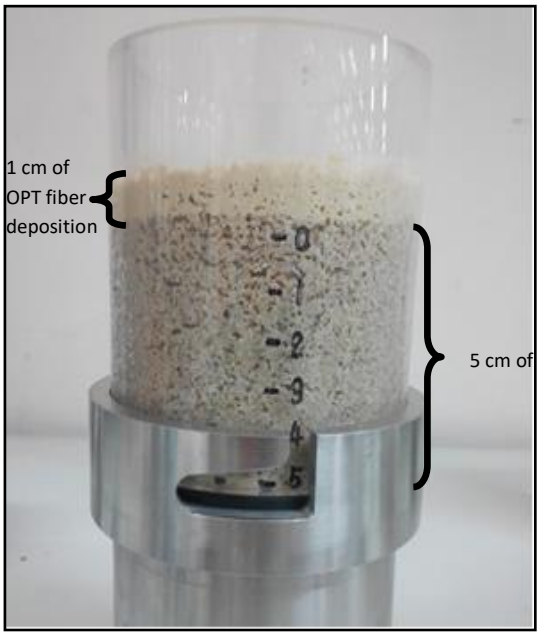


Fig. 6. Thick deposition of OPT fiber on top of sand bed for mud sample K

3.4 The effect of different amount of OPT fiber to mud losses and mud invasion

According to Abram's rule, the concentration of the bridging size solids must be at least 5 percent by volume of the solids in the final mud mix [33]. Figure 7 shows the result of the sand bed test conducted at increasing amount of <75µm OPT fiber. It can be observed that mud sample A and G1 having 5 cm mud invasion instantly at 0% and 2% of OPT. LCM performed poorly at this condition due to the concentration of OPT fiber used in the mud samples was less than 5%. Sufficient amount of OPT fiber is needed to create the bridge. Therefore, it can be concluded that 0% and 2% concentration of OPT fiber is insufficient to form a mechanical bridge and no permeability seal was created. On the other hand, it can be observed that mud sample G and G2 having 1.5 cm and 1.1 cm mud invasion respectively. It shows a good performance of LCM in combatting mud loss at 4% and 6% concentration of OPT fiber. Thus, it can be concluded for this experiment, 6% concentration of OPT fiber is the best concentration needed to form mechanical bridge and low permeability seal. The results obtained agreed to Abram's rule that stated the concentration of the bridging size solids must be at least 5% by volume of the solids in the final mud mix [33]. This can be seconded by the findings by Alsabagh et al. [10] who found the use of 6% cellulosic fiber produced the best performance in combatting lost circulation. They also observed that 6% of fine peanut hulls were able to reduce spurt loss from 120 ml to 24 ml. According to [34], mud invasion increased as the concentration of LCM depleted. As such, the concentration of LCM should be maintained properly in order to maintain the good seal. Several researchers have also observed similar trends. Increase concentration of sized durian rind used from 0 lb/bbl to 20 lb/bbl had reduced the mud losses from 3500 ml to 2600 ml [35]. The increase concentration of fiber used from 10 ppb to 30 ppb had reduced the spurt loss for four samples from 0 ml, 2 ml, 3 m, 2ml to 0 ml [14]. The increasing concentration of associative polymer NIF from 0 ppb to 10 ppb reduced the total mud invasion to 0.5 cm [29].

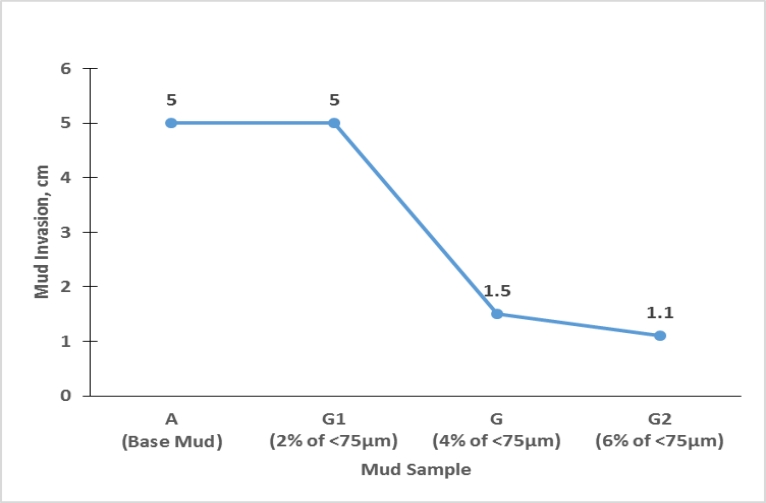


Fig. 7. Effect of different and increases concentration of OPT fiber to mud invasion

A conclusion could be drawn as concentration of OPT fiber used increased, mud losses into formation is reduced. It also shows OPT fiber yield a good performance as LCM concentration increased.

4. Conclusions

The conclusion that can be drawn from this study is the Oil Palm Trunk (OPT) fiber could be used as either FLC or LCM. However, the LCM performance is better than FLC. Further treatment is needed if it is to be used as FLC. The lowest fluid loss of 5.2 ml could be observed for the smallest sizes of OPT fiber (<75µm). As for the LCM, the OPT fiber range from 75 to 150 µm is the most suitable size for 20/40 sand bed. The addition of different concentration of OPT fiber shows that at least 6% concentration is needed to reduce mud invasion.

Acknowledgement

This work was supported by Faculty of Chemical Engineering- Universiti Teknologi MARA (UiTM) and FRGS research grant (RMI File No. 600-IRMI/FRGS 5/3 (104/2017). The authors would like to thank Forest Research Institute Malaysia (FRIM) and Scomi Oiltools Sdn Bhd for providing materials for this study. Special thanks to Mr. Ahmad Hafizan Muhammad Muhayyidin for the facilitation during mud testing conducted.

References

[1] R. Caenn, H. C. H. Darley†, and G. R. Gray†, "Drilling Fluid Components," in *Composition and Properties of Drilling and Completion Fluids*, 2017, pp. 537–595.
[2] X. Meng, Y. Zhang, F. Zhou, and P. K. Chu, "Effects of carbon ash on rheological properties of water-based drilling fluids," *J. Pet. Sci. Eng.*, vol. 100, pp. 1–8, Dec. 2012.
[3] N. A. Ghazali, N. H. Alias, T. A. T. Mohd, S. I. Adeib, and M. Y. Noorsuhana, "Potential of Corn Starch as Fluid Loss Control Agent in Drilling Mud," *Appl. Mech. Mater.*, vol. 754–755, no. September, pp. 682–687, 2015.
[4] A. Azizi *et al.*, "Agarwood Waste as A New Fluid Loss Control Agent in Water-based Drilling Fluid," *Internat. J. Sci. Eng. Int. J. Sci. Eng.*, vol. 552, no. 52, 2013.
[5] E. Fidan, T. Babadagli, and E. Kuru, "Use of cement as lost circulation material - Field case studies," *Proc. IADC/SPE Asia Pacific Drill. Technol. Conf. Exhib.*, pp. 303–312, 2004.
[6] A. Lavrov, *Lost circulation: Mechanisms and solutions*. 2016.
[7] R. C. Navarrete, K. Oil, F. Group, A. U. Monsanto, R. E. Himes, and J. M. Seheult, "SPE 59535 Applications of Xanthan Gum in Fluid-Loss Control and Related Formation Damage," 2000.
[8] R. Caenn, H. C. H. (Henry C. H. . Darley, and G. R. Gray, *Composition and properties of drilling and completion fluids*, Seventh ed. 2016.
[9] N. A. Ghazali, T. A. T. Mohd, N. H. Alias, A. Azizi, and A. A. Harun, "The Effect of Lemongrass as Lost Circulation Material (LCM) to the Filtrate and Filter Cake Formation," *Key Eng. Mater.*, vol. 594–595, no. February, pp. 68–72, 2013.
[10] A. M. Alsabagh, M. I. Abdou, H. E. S. Ahmed, A. A. S. Khalil, and A. A. Aboulrous, "Evaluation of some natural water-insoluble cellulosic material as lost circulation control additives in water-based drilling fluid," *Egypt. J. Pet.*, vol. 24, no. 4, pp. 461–468, 2015.
[11] A. Sauki, I. Hasan, F. Binti Md Naimi, and N. Hidayati Othman, "Development of environmental friendly lost circulation material from banana peel," *AIP Conf. Proc.*, 2017.
[12] N. F. A. Majid, I. Ismail, and M. F. Hamid, *Jurnal Teknologi Science and Engineering, Elektronische Ressource.*, vol. 78, no. 8. Penerbit UTM Press, 2016.
[13] N. A. Ghazali *et al.*, "Lost Circulation Material Characteristics of Apple Skin Powder in Drilling," *J. Adv. Mater. Res.*, vol. 1119, pp. 564–568, Jul. 2015.
[14] J. Ramasamy and M. Amanullah, "SPE-187989-MS Novel Fibrous Lost Circulation Materials Derived from Deceased Date Tree Waste," *SPE Kingdom Saudi Arab. Annu. Tech. Symp. Exhib.*, no. Economides 1998, Jun. 2017.
[15] A. Azizi, A. Sauki, N. A. Ghazali, N. H. Imam, S. K. Jamaludin, and T. A. T. Mohd, "Effective Bridging Agent Particle Sizes of Reservoir Drilling Mud," *Appl. Mech. Mater.*, vol. 548–549, pp. 1871–1875, Apr. 2014.
[16] A. N. Okon, F. D. Udoh, P. G. Bassey, and P. Engineering, "Evaluation of Rice Husk as Fluid Loss Control Additive in Water-Based," *Soc. Pet. Eng.*, no. March, 2014.
[17] M. Z. Alam, A. A. Mamun, I. Y. Qudsieh, S. A. Muyibi, H. M. Salleh, and N. M. Omar, "Solid state bioconversion of

oil palm empty fruit bunches for cellulase enzyme production using a rotary drum bioreactor," *Biochem. Eng. J.*, vol. 46, no. 1, pp. 61–64, 2009.
[18] A. H. R. Aljuboori, "Oil Palm Biomass Residue in Malaysia : Availability and Sustainability," *Int. J. Biomass Renewables*, vol. 2, no. January 2013, pp. 13–18, 2013.
[19] H. P. S. A. Khalil, M. S. Alwani, R. Ridzuan, H. Kamarudin, and A. Khairul, "Chemical composition, morphological characteristics, and cell wall structure of Malaysian oil palm fibers," *Polym. - Plast. Technol. Eng.*, vol. 47, no. 3, pp. 273–280, 2008.
[20] R. Dungani *et al.*, "A review on quality enhancement of oil palm trunk waste by resin impregnation: Future materials," *BioResources*, vol. 8, no. 2, pp. 3136–3156, 2013.
[21] H. Chen, *Biotechnology of lignocellulose: Theory and practice*. 2014.
[22] American Petroleum Institute, "Recommended Practice for Field Testing Water-based Drilling Fluids," no. August 2014, pp. 1–8, 2014.
[23] T. O. Salawudeen, A. O. Arinkoola, M. O. Jimoh, K. K. Salam, and E. O. Ogunmola, "Effect of inert fibre on performance of B. eurycoma as rheology and filtration control additive in water-based drilling fluid," *Int. J. Pet. Eng.*, vol. 2, no. 3, p. 191, 2016.
[24] O. C. Wilfred and A. E. Akinade, "Comparative Study of Basic Properties of Mud Prepared with Nigerian Local Clay and Mud Prepared with Foreign Clay: A Case Study of Abbi Clay Deposit," *Int. J. Eng. Technol.*, vol. 8, pp. 61–71, 2016.
[25] T. S. Mihalakis, P. G. Makri, V. C. Kelessidis, G. E. Christidis, A. E. Foscolos, and C. E. Papanikolaou, "Improving Rheological and Filtration Properties of Drilling Muds with Addition of Greek Lignite," *7th Natl. Congr. Mech.*, no. November 2015, pp. 1–6, 2004.
[26] I. OFI Testing Equipment, "140-30 - API Bench-Mount Filter Press, with CO2 Pressuring Assembly - Instruction Manual." 2014.
[27] W.-N. Wang and P. Wurm, "BET Standard Operating Procedure (SOP) Surface Area & Pore Size Distribution Analyses Preparations for Sample Analysis." 2010.
[28] P. Klobes, Klaus Meyer, and R. G. Munro, *Porosity and Specific Surface Area Measurements for Solid Materials*. 2006.
[29] P. Reid, H. Santos, F. Labenski, F. Sabins, and L. Watters, "Associative Polymers for Invasion Control in Water- and Oil-based Muds and in Cementing Spacers : Laboratory and Field Case Histories," *Am. Assoc. Drill. Eng.*, p. 15, 2004.
[30] T. F. Brookey, "Aphron-containing well drilling and servicing fluids," 2004.
[31] J. Asunción, *The complete book of papermaking*. 2003.
[32] R. M. Rowell, J. S. Han, and J. S. Rowell, "Characterization and Factors Effecting Fiber Properties," *Nat. Polym. an Agrofibers Compos.*, pp. 115–134, 2000.
[33] A. Abrams, "Mud Design To Minimize Rock Impairment Due To Particle Invasion," *J. Pet. Technol.*, vol. 5713, no. 05, pp. 586–592, May 1977.
[34] P. Reid and H. Santos, "Ultralow invasion drilling fluids: A practical route to reduced wellbore instability, reduced mud losses, wellbore strengthening, and improved well productivity," *SPE/IADC INDIAN Drill. Technol. Conf. Exhib. 2006 - Drill. India Challenges Oppor.*, vol. 2006, pp. 51–62, 2006.
[35] I. Ismail, A. B. M. Nor, M. F. Hamid, and A. R. Ismail, *Jurnal Teknologi Science and Engineering, Elektronische Ressource.*, vol. 74, no. 1. Penerbit UTM Press, 2015.

EST Conference Proceedings
Volume 1, (2019) XX-XX

Penerbit Akademia Baru

Engineering Science and Technology Conference Proceedings

Journal homepage: www.akademiabaru.com/EST.html

Open Access

Thermal Conductivity and Viscosity of TiO_2/CNTs-ethylene glycol based Nanofluids for Different Ratio of Nanoparticle

A.M. Zetty Akhtar [1], M.M Rahman [1*,2],K.Kadirgama [1,2]

[1] Automotive Engineering Research Group, Faculty of Mechanical Engineering, Universiti Malaysia Pahang, 26600 Pekan, Pahang, Malaysia
[2] Automotive Engineering Centre, Universiti Malaysia Pahang, 26600 Pekan, Pahang, Malaysia

ABSTRACT

Recently, there has been considerable interest in the use of nanofluids to enhance the thermal performance of conventional working liquids. This experimental study aim to measure and analyse the thermal conductivity, viscosity and stability of titanium dioxide (TiO_2)-carbon nanotubes (CNTs) nanofluid in presence of sodium dodecyl benzene sulfonate (SDBS) as surfactant. The enhancement of thermal physical properties of nanofluids in this study was investigated under different concentrations and ratios of nanoparticle. Ethylene glycol (base fluid), TiO_2 and CNTs nanoparticle were mixed together to produce hybrid nanofluid with concentration 0.02, 0.04, 0.06, 0.08 and 0.1wt.%. The mixing ratio of TiO_2: CNTs was 90:10 and 80:20, meanwhile the ratio of SDBS: CNTs was 10:1. The stability of nanofluid was checked using observation method and zeta potential analysis. To determine the relationship among concentration on nanofluid and thermal physical properties, thermal conductivity and viscosity of suspension were measured. Based on results obtained, zeta potential value for both nanofluid with different ratios range from -50 to -70mV indicates good stability of suspension. Thermal conductivity of nanofluid increase as nanofluid concentration increase and were also shows enhancement compared to base fluid. However, the increment in thermal conductivity for nanofluid with ratio 90:10 was more stable throughout the increasing temperature compared to nanofluid with ratio 80:20. Meanwhile, the viscosity of nanofluid shows decrement over increased temperature, remarks significant advantage in pumping power. In conclusion, the developed nanofluid with both ratios in this study was found to be stable, with enhanced thermal conductivity and decrease in viscosity.

Keywords:
Nanofluids; carbon nanotube; thermal conductivity; viscosity; stability

Copyright © 2019 PENERBIT AKADEMIA BARU - All rights reserved

1. Introduction

Nanofluids are new kind of heat transfer fluid containing small quantity of nanosized particles (usually 1 to 100nm) that uniformly and stably suspended in base fluids. Nanofluids were considered as the future of heat transfer fluid in various heat transfer applications. It expected to give better thermal performance than conventional fluids due to the presence of suspended nanoparticle which have higher thermal conductivity. Furthermore, nanofluids do not block flow channels and induces only a very small pressure drop during flow, which is beneficial for heat transfer applications [1]. There are few criteria to be considered in selecting nanomaterials, including chemical stability, suitability with base fluids, thermophysical properties, its toxicity and availability. Nanoparticle can be dispersed in conventional heat transfer fluids by two methods; single step technique and two steps technique. In single step method, the nanoparticles were simultaneously makes and dispersed into base fluids. Meanwhile in two steps methods the nanoparticles were made in separate process and then dispersed into base fluids.

Thermal conductivity is an important variable on enhancing the heat transfer performance of fluid. Nanoparticle, being an additive to nanofluids, plays an important role in changing the thermal transport properties of suspension [2]. Enhancement of thermal conductivity were affected by few factors such as temperature condition, shape of nanoparticles, size of nanoparticles, type of

nanoparticles and type of base fluids [3-5]. By mixing nanoparticles with base fluid, thermo-physical properties of the fluid may change as the nanoparticles have higher thermal conductivity compared to base fluid [6, 7]. Researchers [8-10] in their study have observed significant improvement in thermal behaviour of nanofluid as it enhanced the thermal conductivity as concentration of nanoparticles increased. Greater enhancement of thermal conductivity was recorded by Vajjha and Das [4], where Al_2O_3, CuO and ZnO nanofluid gave 69%, 60% and 48.5% increment respectively compared to base fluid (Ethylene glycol-water). However, the linearity of relationships still needs further research.

Besides enhancement of thermal conductivity, viscosity of nanofluids was also important factor to ensure overall effectiveness of nanofluids in heat transfer applications. Theoretically, viscosity is a measure of fluid's resistance to flow, or also describe as the internal friction of moving fluids. It is the ratio of the shear stress to shear rate. When the viscosity is constant at different shear rate, the liquid is known as Newtonian, while the viscosity that varies as a function of shear rate were known as non-Newtonian. Possible issue regarding the viscosity of nanofluids were addressed by Khairul, Shah [11] as they mentioned that addition of nanoparticle may enhanced the viscosity under certain conditions and give significant disadvantages due to rise in pumping power. This finding was supported by Prasher, Song [12], where they show that increment in viscosity ratio (nanofluid to base fluid) are more than four times compared to increment in thermal conductivity ratio (nanofluid to base fluid). However, another study conducted by other researchers [13-16], gave contradict results as the viscosity of nanofluids decrease with increased temperature and particle size of nanoparticle. It shows that the viscosity of nanofluids depends on many factors such as temperature, particle size and shape, surfactants used, dispersion technique, volume concentration etc. Thus, these criterions need to be considered in validating experimental results. Further works with different material is required to determined and understand the effect of nanoparticles on viscosity of nanofluids.

The current work focuses on investigating the stability of TiO_2-CNTs nanofluid with different concentration and ratio of nanoparticles in ethylene glycol as base fluid. Furthermore, the aim of this work is to evaluate the thermo physical properties of nanofluids in terms of thermal conductivity and viscosity. The stable and efficient nanofluid would lead to decrease in value of viscosity and enhanced thermal conductivity, thus enhanced the heat transfer performance.

2. Methodology

2.1 Materials and Nanofluid Preparation

Ethylene glycol as base fluid, titanium dioxide (TiO_2) nanoparticle, carbon nanotubes (CNTs) nanoparticle, and sodium dodecyl benzene sulfonate (SDBS) surfactants were used in preparing the TiO_2-CNTs nanofluid. TiO_2 nanoparticle were purchased from U.S Nanomaterial, obtained in powder form with average size 30-50nm. CNTs nanoparticle, also purchased from U.S Nanomaterial were doped with 10wt% of graphene with average size of particle 55nm. Ethylene glycol (with purity ≥99.75%) and SDBS surfactant were sourced from Sigma Aldrich. The properties of TiO_2 and CNTs nanoparticle used in this experiment are presented in Table 1.

The preparation of stable nanofluid in this study was based on two step method, direct mixing technique as shown in Figure 1. Nanofluids were prepared with different concentrations, ranging from 0.02 to 0.1wt% with 0.02 increments. Furthermore, there are two different ratio of TiO_2: CNTs used in this experiment which is 90:10 and 80:20 ratio. In this paper, solutions with ratio 90:10 were referred as Solution A, meanwhile solution with ratio 80:20 referred as Solution B. The required weight of nanoparticle to be dispersed in base fluid was calculated using Eq. 1 below, with pre-calculated density value using Eq. 2:

$$\emptyset = \frac{mnp/\rho np}{mnp/\rho np + mbf/\rho bf} \times 100 \quad (1)$$

$$\rho_{np} = \frac{\phi_1\rho_1 + \phi_2\rho_2}{\phi} \quad (2)$$

where 'np' indicate nanoparticle, 'bf' represent base fluid, Ø is volume concentration, ρ_1 is density for nanoparticle 1 and ρ_2 is density for nanoparticle 2. The suspension of TiO_2, CNTs, SDBS and ethylene glycol were first mixed using stirrer for 1 hour. Then, the high pressure ultrasonic homogenizer was used for another 3 hours to sonicate the suspension. Ultrasonic are most frequently used to overcome the strong cohesion forces between nanotubes, avoiding agglomeration.

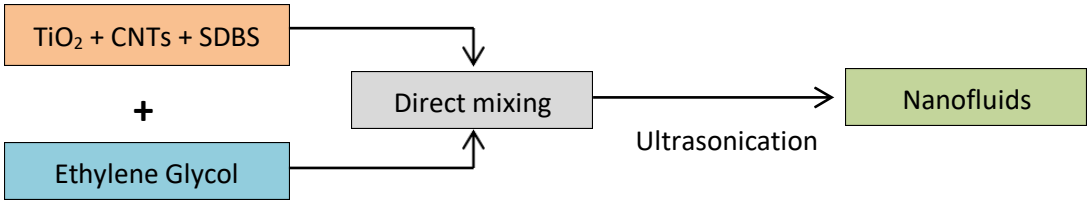


Fig. 1. Two step preparation process of nanofluids (direct mixing method)

2.2 Stability test

The stability of the nanofluids produced in this study were analyzed in two ways; using zeta potential analysis and observation methods. Particle analyzer (model Litesizer 500 from Anton Paar) were used to record the value of zeta potential. The desired nanofluid to be measured were first injected into the omega cuvette, that has inverted omega-shaped capilary tube with capacity 50µL. Then, it will placed in robust casing of Litesizer Paticle Analyzer before the zeta potential measured by electrophoretic light scattering (ELS) at targeted temperature 20˚C. In ELS, the speed of particle is measured in the presence of elctrical field. Thus, the faster the particle move, the higher the zeta potential value and indicates more stable suspensions. Typically accepted zeta-potential values were summarized in Table 1 below. Meanwhile, in observation method the photo of nanofluid were captured every day for two months duration. The height of sedimentation that occur at the bottom of nanofluid were also measured throughout the process.

Table 1
Zeta potential values and suspension stability

Zeta potential value, ±mV	Stability
0	Little or no stability
15	Some stability but settling lightly
30	Moderate stability
45	Good stability, possible settling
60	Very good stability, little settling likely

2.3 Thermal conductivity measurement

Thermal conductivity of nanofluid was measured by using KD2 Pro Thermal Analyzer. Hybrid nanofluid was placed in test tube before immersed in water bath at initial temperature 30˚C.

Needle (sensor) inserted all the way into test solution and adjusted to fits at the centre of test tube. Good thermal contact between the sensor and measured medium is critical for accurate measurement. The thermal conductivity reading value then can be collected at the main menu in SI unit; Watt per meter Celsius (W/m˚C). The error value of reading should be less than err = ±0.01. The temperatures of water bath were then gradually increased to 50 and 70˚C. Averages reading were taken 5 times for each solution concentration and temperature, with time gap 15 minutes respectively. The enhancements of thermal conductivity were calculated from measured thermal conductivity data using Eq. 3:

$$\frac{knf - kbf}{kbf} \text{ x } 100 \tag{3}$$

where '*knf*' and *'kbf'* refer to thermal conductivity of nanofluid and base fluid respectively.

2.4 Viscosity measurement

Viscosity of nanofluids suspension were measured using MCR 92 Anton Paar Rheometer. The condition during measuring viscosity includes temperature 25˚C, up to 100˚C and spindle speed 1000rpm. The measurement of viscosity appears in units of miliPascal per second (mPa/s) on the display. The shear stress reading also recorded in units of Pascal (Pa). Average readings were taken 50 times for each solution concentrations and temperature.

3. Results

3.1 Stability of Nanofluids

Stability is one of major concern in preparing nanofluids since nanoparticle have tendency to agglomerate due to van der Waals force and prone to sedimentation caused by density difference between nanoparticle and base fluids. Stability of nanofluids is crucial as it can alter the thermo physical properties such as thermal conductivity, viscosity, density, etc. with time. Thus, unstable nanofluid would results in depreciation of potential benefit of nanoparticle in heat transfer. There are several methods to evaluate nanofluid stability with time. The simplest method is sedimentation where the volume or mass of sediment is an indication of the stability of nanofluids [17, 18]. Nanofluids were left to observed in certain period of times to ensure there is no or minimal sedimentation settling at the bottom of solution. Minimal or no sedimentation observed indicates that nanoparticles are well dispersed and nanofluids are stable enough.

Figure 2 shows comparison of observation; as mixed and after two months for TiO_2-CNTs nanofluids with different ratios and concentration. There is no sedimentation spotted at the bottom of both Solution A and B for all concentrations. After two weeks, Solution B slightly turns into greyish colour especially for 0.08 and 0.1% wt.% concentration, with sedimentation less than 2mm. The other concentrations remain black in colour with no sedimentation. Similar results were observed for Solution A in all concentrations. However, after 2 months observation all Solution B turned into greyish colour with most particle sediment at the bottom of suspensions and separation between particles and base fluid can be seen. Solution A remained black in colour and no sedimentation occurred for 0.02, 0.04 and 0.06% wt.% concentration, while for 0.08 and 0.10% wt.% concentration, sediment occurred less than 1 mm. The visual observation findings were summarized in Table 2 below.

Table 2
Nanofluids stability (N: No sedimentation, MS: Minor sedimentation and S: Separation).

Duration (days)	Nanofluid stability									
	Solution A					Solution B				
	0.02	0.04	0.06	0.08	0.10	0.02	0.04	0.06	0.08	0.10
0	N	N	N	N	N	N	N	N	N	N
14	N	N	N	N	N	N	N	N	MS	MS
30	N	N	N	N	N	MS	MS	MS	S	S
60	N	N	N	MS	MS	S	S	S	S	S

Besides observation methods, stability of nanofluids also measured using zeta potential, which is qualitative observation of the nanofluids in static conditions. The relationship between nanofluids stability and zeta potential values arises from mutual repulsion that occurs between like charge particles. Particles with high surface charge tend not to agglomorate since contact is opposed, which then leads to good stability of the suspensions. Nanofluids with high zeta potential value (positive or negative charge within range 40-60mV), are considered as stabilized, while suspension with low zeta potential tend to agglomerate and sedimentation proned to occurred [19, 20].

Table 3 shows zeta potential value of Solution A and B for all concentrations. The zeta values for all hybrid nanofluid concentration were above 40mV (±), indicates that suspensions have good stability. Negative value of zeta potential were resulted from the use of surfactant in nanofluid. Surfactants were catogerized depending on the charge of the head group of surfactants. It can be anionic (negatively charge), cationic (positively charge), non-ionic (neutral) or amphotenic (both negative and positive charge). Sodium dodecylbenzene sulphonate (SDBS) that been used in this study fall into anionic group. Thus, addition of SDBS in suspension altered the surface charge of ananoparticles that high in positive charge initially to negative charge. The separation of SDBS in the suspension to produce phenyl sulfanic group which adsorbed on the nanoparticle, successively increasing the net negative charge on nanoparticle surface [11].

This findings also supported by [21, 22], were they concluded that pH value and used of SDBS as surfactant influenced the stability of water-based nanofluids. As mentioned before, nanoparticle tend to agglomerate which resulted in sedimentation and phase separation due to van der Waals force between particles. However, the surfactant are usually used to increase the stability by lowering the surface tension of base fluid and increase the wetting of nanoparticles. Surfactants tend to locate at the interface between nanoparticle and base fluid, thus creating continuity between nanoparticle and fluids.

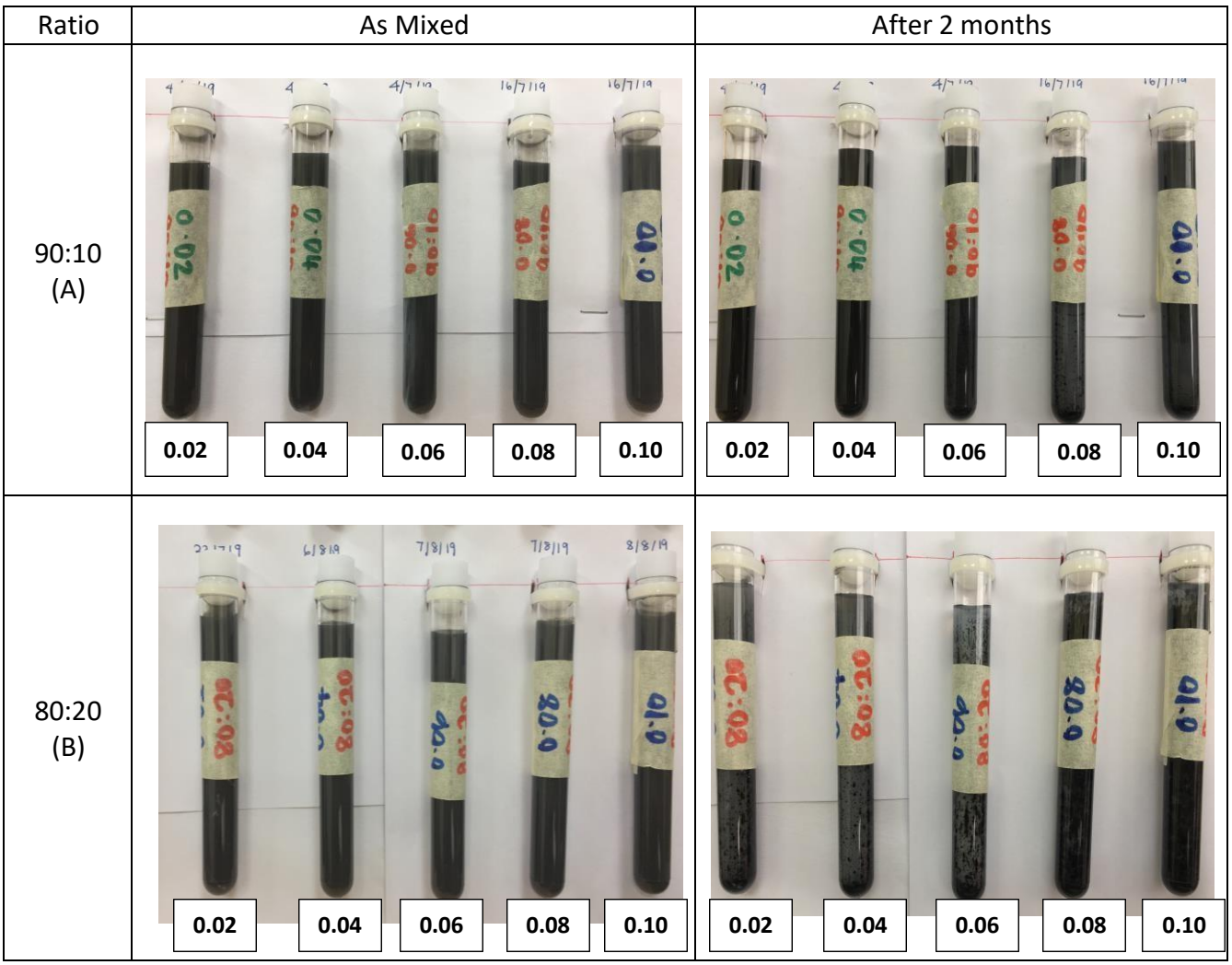


Fig. 2. As mixed and after 2 months observation of TiO_2-CNTs nanofluid for different ratios and concentrations.

Table 3
Zeta potential values for nanofluids

Concentration (%)	Zeta potential value (mV)	
	Solution A	Solution B
0.02	- 65.48	- 60.48
0.04	- 70.97	- 62.99
0.06	- 57.65	- 67.26
0.08	- 65.76	- 70.97
0.10	- 74.22	- 51.21

3.2 Thermal Conductivity Enhancement

The evaluation of thermo-physical properties of nanofluids are important, in order to implement nanofluid in practical applications. Moreover, the overall effectiveness of nanofluids in heat transfer system can be best evaluated if the enhancements of thermal conductivity and viscosity are considered at the same time. By adding the nanoparticles in base fluid, the thermal conductivity were expected to improve since nanoparticles have higher thermal properties compared to base fluid [6, 7].

Figure 3 and 4 shows the thermal conductivity (k) value of TiO_2-CNTs hybrid nanofluids as a function of temperature and volume concentrations for Solution A and Solution B

respectively. The graph shows increment in thermal conductivity value for all concentration as temperature and concentration increased, thus remarks the improvement of heat transfer system. However, thermal conductivity value for nanofluid with 0.08 and 0.1 wt.% concentration for both solution shows decreasing trend at 60˚C. After 60˚C, the decreasing trend of *k* value continued for all concentration in both solutions. The different in increase trend for some concentration for both solutions can be explained by Brownian motion of nanoparticles which increase the chaos in the fluid [23]. The increasing thermal conductivity with increasing temperature can be describe by kinetic energy of the particle. As temperature increase, the motion of particle also increase and contact between nanoparticle and fluid occuring in less time, so the heat transfer rate increase. This finding support the conclusions made by previous researchers that thermal conductivity increase with temperature rise due to more collusions between particle and increasing Brownian motions [24].

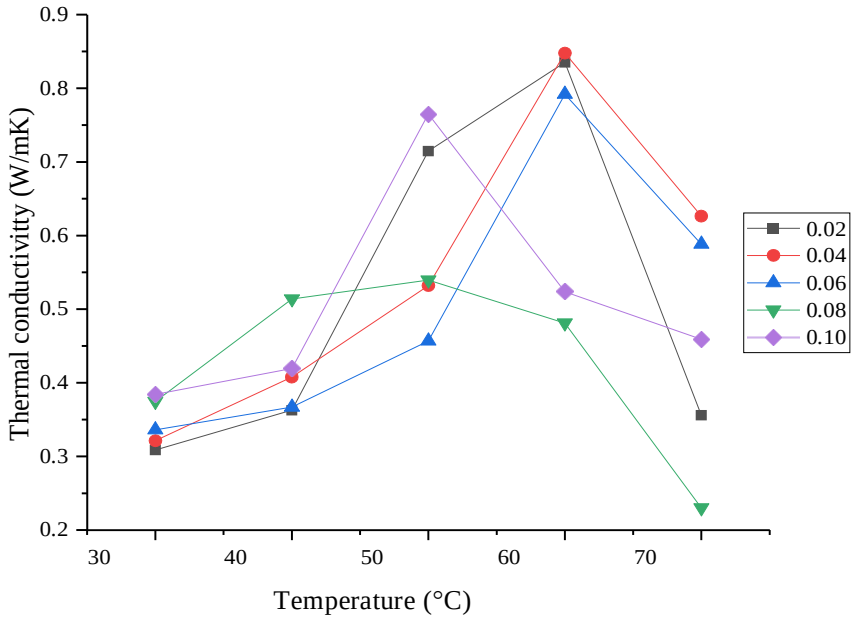


Fig. 3. Thermal conductivity of TiO_2-CNTs nanofluid (ratio 90:10) as a function of temperature.

Besides that, in base fluid-nanoparticles mixture, it is known that layer structured would be formed on particle surfaces by liquid molecules. This layer is important in heat transfer process from solid to adjacent liquid. Since the specific surface area (SSA) of nanoparticles is large compared to micron-sized particles, the effect of heat transfer across the interface were more significant. However, it is not dominating factor that led to increase in thermal conductivity.

Another mechanism that related to enhancement of thermal conductivity is clustering of nanoparticle. This phenomenon create paths of lower thermal resistance and eventually increase the *k* value significantly. When the larger cluster settle down in base fluid, physical volume of particles are much smaller compared to effective volume of cluster. Thus, the heat can move very rapidly within such cluster, and contribute to increase in thermal conductivity. However, as the concentration of nanoparticles increase, the effective volume of cluster decrease, thus resulting in decreased trend of *k* values. From the results obtained through this study, the increment of *k* value for nanofluid with lower concentration were found more higher throughout the increasing temperature compared to higher concentrations. It is understandable because the effective volume will be larger for loosely packed cluster than the closely packed cluster [25]. According to [26], the large

enhancement of thermal conductivity can occur in stable solution if aggregate are less dense and small enough to stay in solutions. Nevertheless, in some cases the clustering of nanoparticles were also results in decreased *k* value due to the settling particles in the base fluid. This settling particles would create larger regions of 'particle free' liquid with high thermal resistance and particle high arrangement at the bottom of fluid.

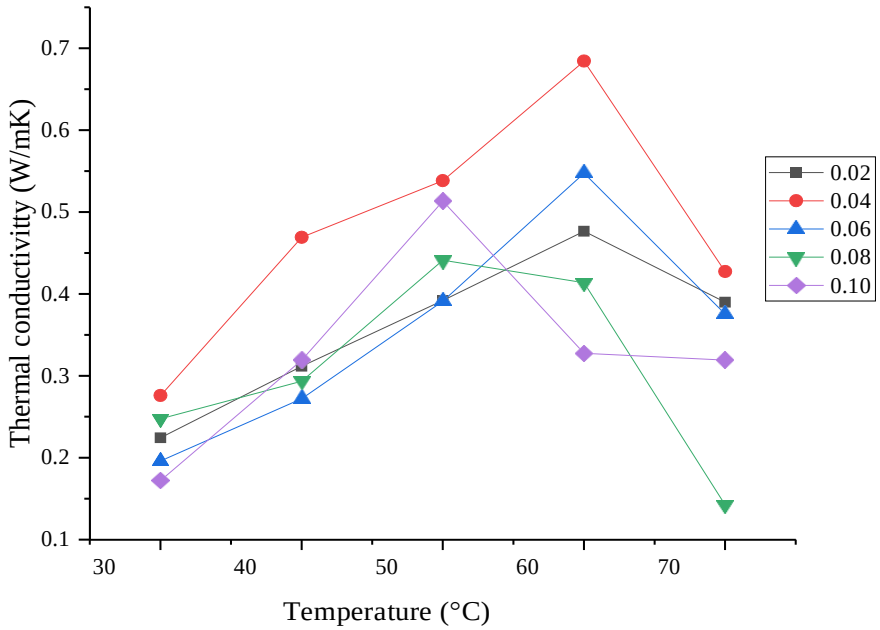


Fig. 4. Thermal conductivity of TiO_2-CNTs nanofluid (ratio 80:20) as a function of temperature.

3.3 Viscosity vs. Temperature

The study of viscosity and its measurement is a major concern in connection to lubrication of suspensions [27]. In machining process, the developed heat from the friction of tool-workpiece surfaces were reduced by the presence of a suitable film liquid created by cutting fluids between moving surface. Generally the least viscous lubricant which still forces the two moving surface apart to achieve 'fluid bearing' is desired. Lubricant that are too viscous will need larger energy to move and if it's too thin, the surface will come in contact and increase the friction. Thus, it is important to ensure that the addition of nanoparticles to base fluid did improve the viscosity properties of nanofluids, that lead to better heat transfer performance.

Figure 5 and 6 shows the viscosity of Solution A and B as a function of temperature and volume fractions respectively. The viscosity of Solution A decrease exponentially with increasing temperature for all concentrations, thus remarks almost dependent relationship between viscosity and temperature. The highest viscosity (17.998mPa/s) recorded at 25˚C by 0.02 wt.% concentration, while the lowest (16.307mPa/s) by 0.04wt.%. The viscosity keep reducing as temperature increasing, and at 70˚C, 0.04wt.% nanofluid still recorded lowest value of viscosity (4.148mPa/s) compared to other concentration. The viscosity value for Solution B also showed the same trend as Solution B, decreasing over increasing temperature. However, at 25˚C, the viscosity value of 0.10wt.% concentration recorded higher value compared to Solution A (19.095mPa/s). Nevertheless, the other difference of viscosity value prior to volume concentration were not obvious compared to Solution A.

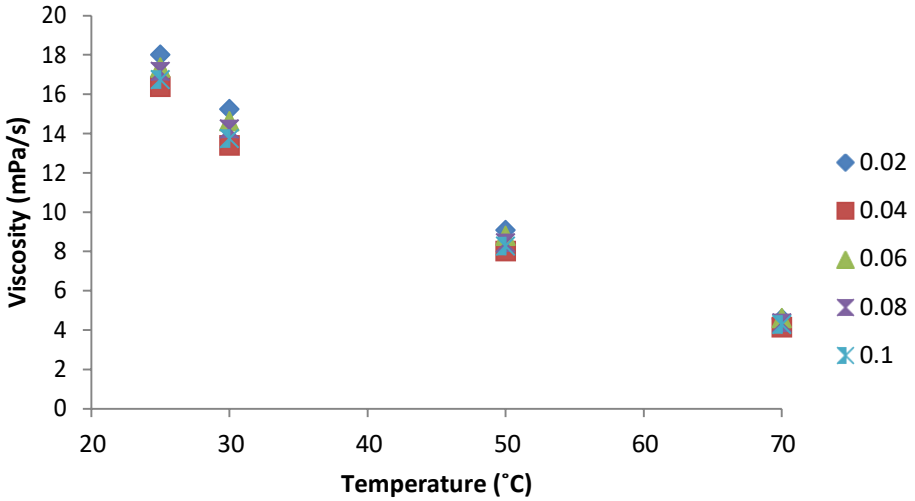


Fig. 5. Viscosity of TiO_2-CNTs nanofluid (ratio 90:10) as a function of temperature and concentrations.

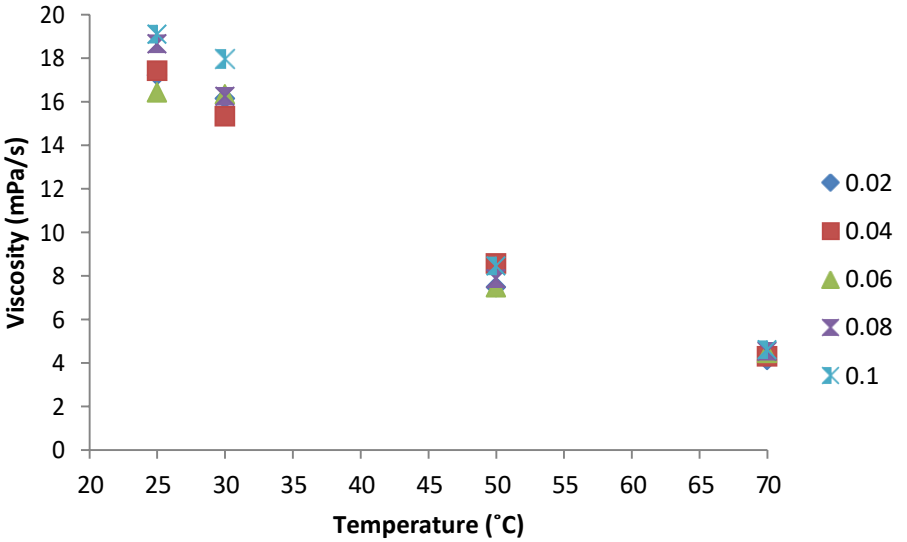


Fig. 6. Viscosity of TiO_2-CNTs nanofluid (ratio 80:20) as a function of temperature and concentrations.

This decreasing viscosity over increasing temperature can be explained with particle theory in liquid, where molecules are loosely packed and intermolecular attraction is strong. When the temperature increase, the energy level of liquid molecules increase and distance between molecule increase. The relative motion of molecules become easier, as the intermolecular attraction

between molecules decrease, resulting in reduced viscosity [28]. This findings were also supported by previous researchers [14, 29-32], where they found that addition of nanoparticle to base fluid improve the viscosity of suspension in the function of temperature. However, findings by Chen, Xie [33] slightly contradict to the data obtained, as they measured the temperature effect of multi-walled carbon nanotubes nanofluid for temperature 5˚C to 65˚C. The results indicated that the relative viscosity increase significantly with temperature after 55˚C. Thus, as the viscosity of nanofluid were influenced by many factors, the contradict value may have been caused by various variables.

Volume concentration of nanofluids were listed as one of few factors that gave significant effect on viscosity value. Eventhough no contradict results were spotted during literature review, data obtained from this study showed that viscosity of TiO_2-CNTs nanofluid were independent to the volume concentration. At 25˚C, the lowest concentration (0.02%) recorded a highest value of viscosity (17.998mPa/s), meanwhile highest concentration (0.1%) only valued 16.782mPa/s. However, the lowest viscosity value were given by 0.04% concentration, at 16.307mPa/s. The trend continue towards the tenperature increase, as 0.04% and 0.1% gave close value of viscosity with each other all the way to 100˚C. The viscosity value of nanofluid for all concentration however, shows a significant improvement compared to base fluid- ethylene glycol (19.83mPa/s) at 20˚C. The reduced value of viscosity than base fluid confirmed the effectiveness of adding nanoparticle to the suspension in improving its thermo-physical properties. Chen, Xie [33] in their study also reported that viscosity of MWCNTs nanofluid only increase after implying volume fraction more than 0.4 vol.%. Volume fraction less than 0.4 vol.% have lower viscosity compared to base fluid, due to lubricating effect of nanoparticles.

4. Conclusions

In this paper, hybrid nanofluid TiO_2-CNTs with addition of SDBS as surfactant was prepared by concentration ranging from 0.02% to 0.1% with ratio 90:10 and 80:20. The stability of nanofluids was observed using sedimentation photo capturing method and zeta potential analysis. Thermo-physical properties of nanofluids including thermal conductivity and viscosity were also measured for temperature between 30˚C-70˚C and 25˚C-70˚C respectively. Based on data obtained, there are few conclusion can be listed as below;

1) The nanofluids were stable enough for all concentration, with little sedimentation spotted after two weeks for 0.0.8% and 0.1% concentration. The best stabilization of nanofluid observed in 0.04% concentration, where the zeta potential analysis recorded at -70.97 mV and no sedimentation occurred for at least two month for Solution A. For Solution B, highest zeta potential recorded at 0.08wt% concentration (-70.97 mV).
2) Thermal conductivity of nanofluid increase as temperature increase, for all concentration. However, at 60˚C, the *k* value for nanofluid with 0.08 and 0.1 wt.% concentration decreased. The enhancement of thermal conductivity value calculated at 30˚C for 0.02wt.% concentration for Solution A and B were 52.67% and 11.04% respectively compared to base fluid.
3) Viscosity of nanofluid decrease linearly with increasing temperature, but independent to volume concentration. Addition of nanoparticle did reduce the viscosity of suspension compared to the base fluid, remarks good enhancement in terms of heat transfer system.

4) From the results obtained, a TiO_2-CNTs nanofluid (ratio 90:10) with 0.02 and 0.04 wt.% concentration shows the most effective enhancement in terms of stability, thermal conductivity and viscosity.

Acknowledgement
The authors would like to thank Universiti Malaysia Pahang for providing the laboratories facilities and the financial support under the University LEAP-3 FLAGSHIP Research Grants (Project number RDU172203) and University Research Grants No. RDU190367.

References

[1] Angayarkanni, S.A. and J. Philip, *Review on thermal properties of nanofluids: Recent developments.* Advances in Colloid and Interface Science, 2015. **225**: p. 146-176.
[2] Li, Y., et al., *A review on development of nanofluid preparation and characterization.* Powder Technology, 2009. **196**(2): p. 89-101.
[3] Elias, M.M., et al., *Experimental investigation on the thermo-physical properties of Al2O3 nanoparticles suspended in car radiator coolant.* International Communications in Heat and Mass Transfer, 2014. **54**: p. 48-53.
[4] Vajjha, R.S. and D.K. Das, *Experimental determination of thermal conductivity of three nanofluids and development of new correlations.* International Journal of Heat and Mass Transfer, 2009. **52**(21): p. 4675-4682.
[5] Azmi, W.H., et al., *The enhancement of effective thermal conductivity and effective dynamic viscosity of nanofluids – A review.* Renewable and Sustainable Energy Reviews, 2016. **53**: p. 1046-1058.
[6] Choi, S.U. and J.A. Eastman, *Enhancing thermal conductivity of fluids with nanoparticles*. 1995, Argonne National Lab., IL (United States).
[7] Wang, X.-Q. and A.S. Mujumdar, *Heat transfer characteristics of nanofluids: a review.* International Journal of Thermal Sciences, 2007. **46**(1): p. 1-19.
[8] Yu, W., et al., *Experimental investigation on the thermal transport properties of ethylene glycol based nanofluids containing low volume concentration diamond nanoparticles.* Colloids and Surfaces A: Physicochemical and Engineering Aspects, 2011. **380**(1): p. 1-5.
[9] Zeinali Heris, S., M. Nasr Esfahany, and S.G. Etemad, *Experimental investigation of convective heat transfer of Al2O3/water nanofluid in circular tube.* International Journal of Heat and Fluid Flow, 2007. **28**(2): p. 203-210.
[10] Pak, B.C. and Y.I. Cho, *HYDRODYNAMIC AND HEAT TRANSFER STUDY OF DISPERSED FLUIDS WITH SUBMICRON METALLIC OXIDE PARTICLES.* Experimental Heat Transfer, 1998. **11**(2): p. 151-170.
[11] Khairul, M.A., et al., *Effects of surfactant on stability and thermo-physical properties of metal oxide nanofluids.* International Journal of Heat and Mass Transfer, 2016. **98**: p. 778-787.
[12] Prasher, R., et al., *Measurements of nanofluid viscosity and its implications for thermal applications.* Applied Physics Letters, 2006. **89**(13): p. 133108.
[13] Nguyen, C.T., et al., *Temperature and particle-size dependent viscosity data for water-based nanofluids – Hysteresis phenomenon.* International Journal of Heat and Fluid Flow, 2007. **28**(6): p. 1492-1506.
[14] Kanjirakat, A., et al., *Rheological and flow characteristics of nanofluids: Influence of electroviscous effects and particle agglomeration*. Vol. 106. 2009. 034909-034909.
[15] Duangthongsuk, W. and S. Wongwises, *Measurement of temperature-dependent thermal conductivity and viscosity of TiO2-water nanofluids.* Experimental Thermal and Fluid Science, 2009. **33**(4): p. 706-714.
[16] Turgut, A., et al., *Thermal Conductivity and Viscosity Measurements of Water-Based TiO2 Nanofluids.* International Journal of Thermophysics, 2009. **30**(4): p. 1213-1226.

[17] Wei, X. and L. Wang, *Synthesis and thermal conductivity of microfluidic copper nanofluids.* Particuology, 2010. **8**(3): p. 262-271.
[18] Li, X., D. Zhu, and X. Wang, *Evaluation on dispersion behavior of the aqueous copper nano- suspensions.* Journal of Colloid and Interface Science, 2007. **310**(2): p. 456-463.
[19] Fedele, L., M. Concetti, and G. Mercuri, *Methodologies and techniques for advanced maintenance*. Methodologies and Techniques for Advanced Maintenance. 2011. 1-222.
[20] Pati, S.S., V. Mahendran, and J. Philip, *A Simple Approach to Produce Stable Ferrofluids Without Surfactants and With High Temperature Stability.* Journal of Nanofluids, 2013. **2**(2): p. 94-103.
[21] Zhu, D., et al., *Dispersion behavior and thermal conductivity characteristics of Al2O3–H2O nanofluids.* Current Applied Physics, 2009. **9**(1): p. 131-139.
[22] Wang, X.-j., X. Li, and S. Yang, *Influence of pH and SDBS on the Stability and Thermal Conductivity of Nanofluids.* Energy & Fuels, 2009. **23**(5): p. 2684-2689.
[23] Wong, K.V. and M.J. Castillo, *Heat Transfer Mechanisms and Clustering in Nanofluids.* Advances in Mechanical Engineering, 2010. **2**: p. 795478.
[24] Hemmat Esfe, M., et al., *Experimental study on thermal conductivity of ethylene glycol based nanofluids containing Al2O3 nanoparticles.* International Journal of Heat and Mass Transfer, 2015. **88**: p. 728-734.
[25] Keblinski, P., et al., *Mechanisms of heat flow in suspensions of nano-sized particles (nanofluids).* International Journal of Heat and Mass Transfer, 2002. **45**(4): p. 855-863.
[26] Ghadimi, A. and I.H. Metselaar, *The influence of surfactant and ultrasonic processing on improvement of stability, thermal conductivity and viscosity of titania nanofluid.* Experimental Thermal and Fluid Science, 2013. **51**: p. 1-9.
[27] Edwards, R.A., *CHAPTER 3 - Viscosity*, in *Physics for O.N.C. Courses*, R.A. Edwards, Editor. 1970, Pergamon. p. 41-52.
[28] Landau, L.D., A.I. Akhiezer, and E.M. Lifshitz, *CHAPTER XV - VISCOSITY*, in *General Physics*, L.D. Landau, A.I. Akhiezer, and E.M. Lifshitz, Editors. 1967, Pergamon: Oxford. p. 341-366.
[29] Namburu, P.K., et al., *Experimental investigation of viscosity and specific heat of silicon dioxide nanofluids.* Micro & Nano Letters, 2007. **2**(3): p. 67-71.
[30] Namburu, P.K., et al., *Viscosity of copper oxide nanoparticles dispersed in ethylene glycol and water mixture.* Experimental Thermal and Fluid Science, 2007. **32**(2): p. 397-402.
[31] Zhu, H., et al., *Preparation, characterization, viscosity and thermal conductivity of CaCO3 aqueous nanofluids.* Science China Technological Sciences, 2010. **53**(2): p. 360-368.
[32] Kole, M. and T.K. Dey, *Viscosity of alumina nanoparticles dispersed in car engine coolant.* Experimental Thermal and Fluid Science, 2010. **34**(6): p. 677-683.
[33] Chen, L., et al., *Nanofluids containing carbon nanotubes treated by mechanochemical reaction.* Thermochimica Acta, 2008. **477**(1): p. 21-24.

Penerbit Akademia Baru

Engineering Science and Technology Conference Proceedings

Journal homepage: www.akademiabaru.com/EST.html

Thermal Conductivity and Dynamic Viscosity of Nanofluids: A comprehensive review

Open Access

W.Safiei[1,*], M.M. Rahman[1], R.Kulkarni[2]

[1] Faculty of Mechanical Engineering, Universiti Malaysia Pahang, 26600, Pekan, Pahang, Malaysia
[2] Faculty of Engineering Technology, Universiti Malaysia Pahang, 26300, Gambang, Pahang, Malaysia

ABSTRACT

Thermal conductivity is one of the rheology properties that vital for engineering fluid that indispensable for heat transfer enhancement. For this reason, nanofluid is getting wider attention nowadays due to the presence of nanoparticles in the base fluid can further improve thermal conductivity and dynamic viscosity. These are two important properties for new engineering fluid in providing better cooling and lubricating, especially in mechanical and tribology applications. In this paper, specifically, nanofluid thermal conductivity and dynamic viscosity are discussed comprehensively. Both properties thermal conductivity and viscosity of nanofluids are improved over the base fluid. Furthermore, these two properties increase should more volume concentrations of nanomaterial are added. In addition, the thermal conductivity also improved with increasing the temperature. From the literature review, the maximum enhancement of thermal conductivity for single nanofluid is between 5.2% and 32.26%. On the other hand, the maximum enhancement of viscosity is between 17.62% and 294% over base fluid. The hybrid nanofluids that consist of more than one type of nanoparticles exhibit better thermal conductivity where the maximum enhancement is between 8.39% and 41%. For dynamic viscosity measurement, the maximum enhancement of hybrid nanofluids is between 33% and 115%. Therefore, to sum up, hybrid nanofluid is really promising to enhance heat transfer performance especially for heating and cooling in engineering applications.

Keywords:
Nanoparticle; nanofluid; hybrid nanofluid, thermal conductivity; viscosity; heat transfer; enhancement

Copyright © 2019 PENERBIT AKADEMIA BARU - All rights reserved

1. Introduction

Driven by green technology and long term manufacturing sustainability, nanofluids are introduced as an alternative to conventional fluid. Nanofluids are engineered colloidal suspension for minimizing environmental effects as well as for enhancing working fluid thermal and rheology properties. This is an innovative approach of new generation working fluid. Lubrication plays a vital role in any mechanical component's movement as it can reduce the friction and subsequently the operation common tasks are getting more convenience. It has been reported that lubrication was found 4000 years ago in Egypt based on a large statue of a man pouring a kind of liquid [1].Conventional liquids possess limited thermal conductivity, environmental pollution and worker's health issues that needs to resolve. Therefore, since 20 years ago the efforts have been devoted to come up with the solution. Since then, single nanofluid was introduced by the researchers and hybrid nanofluid also presented for the first time in 2015. The term "Nanofluid" was first introduced by Choi in 1995 [2]. Nanofluid by

* *Corresponding author.*
E-mail address: wahaizad.safiei@gmail.com (W.Safiei)

defination is referred to a working fluid that contains collaidal mixture of metallic or non-metallic nanomaterial with the particle size less than 100nm [3]. Research on nanoparticles has been increased rapidly by employing different type of nanosize materials with different volume concentrations particularly for various applications such as machining, heat exchanger, radiator, refrigerator, air-conditioner and electronics cooling. The thermal properties or convective heat transfer coefficient of base oil can further be enhanced using nanomaterials mainly due to thermal transport capability of each particle. The performance of nanofluid in carrying heat from the heat source depends on its thermal conductivity, specific heat, viscosity and density[4]. Besides, the nanoparticle's shape also significantly influences the thermal conductivity and dynamic viscosity of the fluid [5]. According to Pryazhnikov et al [6] there is direct proportional relationship between particle size and thermal conductivity. The thermal conductivity of nanofluid is improved remarkably if the thermal conductivity of the base fluid is lower. The solid heat transfer performance is much better compared with the liquid heat transfer performance. This is attributed to the mass molecule motion when nano coolant is circulating through the system. This is the reason why the presence of nanoparticles in a base fluid is indispensable for the thermal conductivity enhancement.

The volume percentage or weight percentage of nanoparticles dispersed in based-oil is between 0.25% and 5% for nanofluid preparation. It was reported that the presence of SWCNTs dispersed in the base coolant can increase the thermal conductivity up to 105% at 1 vol% of nanoparticles [7]. Thus, the heat is transferred more effectively from the cutting zone and thereafter the temperature would reduce outstandingly. S.Fotowat et al [8] mentioned that about 17% of thermal conductivity enhancement found of nanofluids over a base fluid. However there was a corrosion effect in Aluminium and Copper but it was neglible in Stainless Steel when all these materials were submerged in the Al_2O_3 nanofluid. Rashmi et al [9] also studied the effect of corrosion using carbon wall nanotube nanofluids and various of base fluids. On the other hand, nanofluid viscosity increases with increasing of nanoparticle diameter size and volume concentration but decreases drastically in increasing of temperature [10]. Murshed and Estelle [11] suggested that the study of nanofluid viscosity should also considers nanofluid pH value, nanoparticle size and shape as the published articles are very limited. According to Nabil et al [12], more research is needed to understand the behavior of nanofluid including its characteristics and suitability in engineering application.

2. Formulation Of Nanofluid

2.1 Base Fluid

Base fluid or single-phase liquid exhibits low thermal conductivity, thus in many problems related to heat transfer are found not suitable. This is the main reason why many researchers have attempted addressing this issue by introducing second-phase liquid either single nanofluid or hybrid nanofluid. The selection of base fluid is also crucial in preparing nanofluids prior to enhancing thermal properties of nanofluids. There are many types of base fluid which are commonly used nowadays such as water, deionized water, ethylene glycol (EG), vegetable oil, a mixture of water and ethylene etc. Each of these base fluids has its own advantages. For instance, Ethylene Glycol is commonly used as anti-freeze in heating and cooling applications. M.Nazari et al [13] revealed that 30% volume of Ethylene Glycol in the nanofluid has better cooling performance than 50% volume of Ethylene Glycol. It was recommended by Lim et al [14] to mix water and ethylene glycol of 60:40 ratio as the base fluid for cooling purposes. Vegetable oil-based fluid is one of many alternative lubricants that can be considered as base fluid due to

many reasons. Wang et al [15] revealed that palm oil has better lubrication properties compared to other vegetable oils. Commonly known for the biodegradability and low production cost, it also has good lubrication properties [16]. Furthermore, it has great potential as metal cutting liquid [17]. Despite good lubrication properties, synthetic or mineral oils possess lower thermal properties [16] which make them unsuitable for the manufacturing process that generates high temperature at the cutting zone especially for the high speed machining operation. According to Xuan et al [18], oil-based nanofluid is better than water-based nanofluid in terms of heat transfer characteristics. Duc et al [19] mentioned that based on comprehensive studies emulsion 5% coolant was more effective than soybean oil in enhancing hard milling performance in terms of surface roughness, cutting forces and the tool life span.

2.2 Nanomaterial

The characteristics of nanomaterials depend on their size, shape, physical properties and dispersibility. The nanoparticles can be divided into three groups which are based on its physical characteristics such as (i) Metallic particles like Fe, Al, Cu, Au, Ag, (ii) Non-metallic or metal carbide particles like Al_2O_3, CuO, SiC, TiO_2 and (iii) Carbon Nanotubes [20]. The size of the particle should be less than 100nm to be considered as a nanoparticle. The effectiveness of lubricating properties depends on the smaller size of nanoparticle which it can form a protective film layer and subsequently reduce friction between tool and workpiece during machining. Nanomaterials have a high ratio of surface area over its weight and possess anti-friction properties in base fluids [21]. According to Zhang et al [22], MoS_2 nanoparticles have good lubrication performance, while CNTs have higher heat transfer coefficient. By combining both nanomaterials, it would enhance the thermo-physical properties of nanofluid. Similarly findings by Wang et al [23] Al_2O_3, MoS_2, and SiO_2 have better lubricating properties when grinding Nickel Alloy GH4169. From the published research articles, Fe_3O_4 nanoparticles exhibited the maximum thermal conductivity enhancement of 200% in water [24]. From the literature review done by M. Vafaei et al [25], coincidently, the maximum enhancement of thermal conductivity of 48% associated with Fe_3O_4 nanoparticles. Similarly, the maximum enhancement of the nanofluid viscosity was found to be 294% when Fe_3O_4 nanoparticles dispersed in ethylene glycol-water mixture [26]. Li et al [27] evaluated the grinding performance of six different nanofluids (MoS_2, ZrO_2, CNT, polycrystalline diamond, Al_2O_3, and SiO_2) and found that CNT nano coolant yields excellent thermal properties compared with other nanofluids. According to Guo et al [28], carbon nanotubes have outstanding characteristics compared to other nanomaterials such as chemical stability, physical strength, high electrical and thermal conductivity, as well as mechanical resistance. Raju et al [29] mentioned that multiwall carbon nanotubes (MWCNT) nanoparticles have a maximum thermal conductivity of 3000 W/mK compared with other nanomaterials. This resulted in 36% improvement of thermal conductivity on nanofluid compared to conventional fluid. Moreover, this type of nanomaterial easily disperses in distilled water when sodium dodecyl sulfate (SDS) is added [30]. Copper metallic nanoparticles have 95% higher thermal conductivity at 400 W/mK compared to Copper Oxide (CuO) which was at 20 W/mK [31]. Al_2O_3 particles have better thermo-physical properties compared to SiO_2 and TiO_2 nanofluids for the same volume concentrations [32] whereas Al_2O_3 have lower lubrication properties [16]. Duc et al [19] claimed that Al_2O_3 nanoparticles have excellent tribological and anti-toxic properties. While Yu Su et al [33] mentioned that graphite nanoparticles have anti-friction characteristics where a physical deposition layer could form on the surface thereby

resulting in low friction forces. M. Sayuti et al [34] revealed that the Vickers hardness of silicon dioxide (SiO_2) nanoparticle is 1000kgfmm^{-2} which possess good mechanical properties of hard and brittle particles.

2.3 Single and Hybrid Nanofluid

Single nanofluid is referred to a one-type of nanoparticle with certain amount of volume fraction that disperse into the base fluid. Mono or single nanofluid has received great attention among researchers worldwide with the objective to enhance base fluid properties and improve cooling and lubricating characteristics. M.Yogeswaran et al [35] applied TiO_2 -Ethylene Glycol nanofluid for testing milling performance. M.H Esfe et al [36] evaluated MgO/water nanofluid thermal conductivity coefficient from 0.01 to 0.03 volume fractions. There is a long list of published research papers that employed single nanofluid as a main medium of liquid for various engineering applications. For the past few years, reseach of hybrid nanofluid attracted attention for further enhancing single nanofluid thermal and rheology properties. Hybrid nanofluid possess excellent thermal and rheology properties due to synergistic effect [37] and can be prepared by two methods : (i) suspending two or more different nanoparticles in base fluid, (ii) combining between two or more nanoparticles physically in the base fluid which is referred as hybrid material. For instance, MgO-MWCNTs in EG [25], Al_2O_3-SiC [38], MoS_2-CNT [22] in Synthetic Lipids and Al_2O_3-GNP in oil-water emulsion [16] were the hybrid nanofluids prepared by the researchers. This hybrid material exhibits better thermophysical properties due to synergistic effect which does not exist in the single or mono nanofluid. Many scholars mentioned that hybrid or composite nanoparticles that disseminate in the base fluid yield higher and produce better heat transfer enhancement, cooling effect and antifriction performance than single nanoparticles in the material cutting process [38][22][20]. The combination of two different nanoparticles for preparing the hybrid nanofluid attracts the attention of many researchers to solve heat transfer issue in many engineering applications. For example, application of hybrid nanofluids in heat exchanger [39], car radiator [40], rubbing process [41], electronics component cooling system [42], machining process[43] as well as in solar energy collector [44]. However, the research of hybrid nanofluids for improving machining performance especially in milling process is still unexplored by many researchers, therefore more experimental work needs to be conducted in order to explore its great potential [16][45]. The summary of hybrid nanofluids thermal conductivity, viscosity, and stability are shown in Table 3. Due to the advantages far outweigh the disadvantages, thus, the potential of hybrid nanofluid and its application in machining is very promising in the future.

3.0 Nanofluid Thermal And Rheological Properties

3.1 Nanofluid Thermal Conductivity

Heat can be transferred through conduction, convection and radiation. In these mode of heat transfer, the heat flows from high to low temperature. Thermal conductivity is defined as heat transfer rate within the temperature difference through a thickness material per unit area [46]. Thus, thermal conductivity can be described as the ability of a material to transfer the heat by conduction through it. This thermal property is very critical for nanofluid to carry and dissipitate the heat effectively. Subsequently, cooling rate could be more faster and operating system would be more reliable. It it essential that thermal conductivity measurement should be conducted for a new introduction of nanofluid. The related instruments for measuring both

thermal conductivity and viscosity shown in Table 1. Basically, the thermal conductivity can be measured by applying three different techniques;1) Transient hot-wire method, 2) Temperature oscillation method and 3)3-ω method. The main factor affecting the thermal conductivity of nanofluid is the volume concentration [47][48]. Besides, the nanoparticle size, shape, type of base fluid, temperature and preparation technique also will influence the thermal conductivity.

Table 1 Key instruments for measuring thermal conductivity and viscosity of nanofluid

Measurement	Objective	Instrumentation	Model / Manufacturer	References
Thermal Conductivity	To measure nanofluid thermal conductivity	Thermal Properties Analyzer	KD2 Pro (Decagon Devices, Inv., USA) TC3010L (Xi'an Xiatech, China)	[29],[49],[14],[50],[51] [52]
Nanofluid viscosity	To measure nanofluid dynamic viscosity	Viscometer	Rotating viscometer (NDJ-9S) Brookfield (USA)	[52] [49],[53],[54],[55]

Obviously, the enhancement of thermal conductivity depands on volume concentration and temperature. Higher thermal conductivity of nanofluid observed at higher volume concentration and temperature as reported by Alirazie et al [56]. However, the thermal conductivity decreased with the increase in percentage of Ethylene Glycol in the mixture of Ethylene Glycol/water as a base fluid [57]. Furthermore, thermal conductivity of oil-based nanofluid decreases at the temperature greater than 180°C due to vaporization of organic oil which regards to its flash point [58]. The summary of thermal conductivity and viscosity enhancement findings for single and hybrid nanofluid are shown in Table 2 and Table 3 respectively.

Table 2: Summary of single nanofluid thermal conductivity and viscosity findings

Author	Base Fluid	Nano-particles	Volume Fraction	Measure	Max. Enhancement %
L.Syam Sundar et al [59]	Ethylene Glycol (EG) : Water 20:80% 40:60% 80:20%	Al_2O_3	0.0%, 0.3%, 0.6%, 0.8%, 1.0%, 1.5%	Thermal Conductivity	32.26% of 1.5 vol% at 60C
				Dynamic Viscosity	1.37 times compared to base fluid
Wenjing Chen et al [60]	Natural Seawater	SiC	0.0% - 1.0%	Thermal Conductivity	5.2%
Gabriela Huminic et al [61]	Distilled Water	SiC	0.5 wt%, 1.0 wt%	Thermal conductivity	17.62% of 1.0 wt% at 50C
				Dynamic Viscosity	17.62%
A.H.A. Al-Waeli [62]	Deionized water	SiC	1% - 4%	Thermal Conductivity	8.2%

Wei Yu et al [63]	Ethylene Glycol (EG)	ZnO	0% - 5%	Thermal Conductivity	26.5% of 5 vol%
K.S Rajan et al [54]	Water	ZnO	0.25% - 2%	Dynamic Viscosity	28%
A.A. Nadooshan [64]	Ethylene Glycol (EG)	ZnO	0.125% - 4.0%	Thermal Conductivity	20% of 4 vol.%
S.K Lim et al [14]	Water-Ethylene glycol (EG)	Al_2O_3	0.2%, 0.4%, 0.6%, 0.8%, 1%	Thermal Conductivity	10% of 1 vol%
				Dynamic Viscosity	39% of 1 vol%
				Convective Heat Transfer Coefficient	25.4% of 1 vol%
R.A. Raju et al [29]	Distilled Water	MWCNTs	0.2%	Thermal Conductivity	36%
				Contact Angle	reduced by 33.3%
S.M.S. Murshed et al [65]	De-ionized Water	TiO_2	0.001% - 0.05%	Thermal Conductivity	17%
M.S. Najiha et al [66]	De-ionized Water	TiO_2	0.5%,2.5%,4.5%	Thermal Conductivity	11.4%
M.Nazari et al [13]	Water	Al_2O_3	0.1%, 0.25%, 0.5%	Heat Transfer Coefficient	6% of 0.5vol.%
		CNT		Heat Transfer Coefficient	13% of 0.25vol.%
X.Yimin et al [18]	Water	Cu	2wt% - 9wt%	Thermal Conductivity	1.78 times higher than base fluid
M.Baghbanzadeh et al [67]	Distilled Water	MWCNTs	0 wt.% - 1 wt.%	Thermal Conductivity	23.3%
S.U Ilyas et al [68]	Thermal Oil (THO)	MWCNTs	0 wt.% - 1 wt.%	Thermal Conductivity	28.7% of 1wt.%
W.Li et al [69]	Waste Cooking Oil	SiC	0.02% - 0.1%	Thermal Conductivity	23%
R.S. Khedkar et al [70]	Paraffin Oil	Fe_3O_4	0.01% - 0.1%	Thermal Conductivity	20%
M.Abareshi et al [71]	Deionized Water	Fe_3O_4	0% - 3%	Thermal Conductivity	11.5% of 3 vol.% at 40C

Table 3: Summary of hybrid nanofluid thermal conductivity and viscosity findings

Author	Base Fluid	Nanoparticles	Volume Fraction	Measure	Max. Enhancement (%)
S.Suresh et al [49]	De-ionized water	Al_2O_3 - Cu	0.1% - 2%	Thermal Conductivity	12.11% of 2 vol%
				Dynamic Viscosity	115% of 2 vol%
D.Toghraie et al [50]	Ethylene glycol (EG)	ZnO – TiO_2	0% - 3.5%	Thermal Conductivity	32% of 3.5 vol% when measured at 50C
M.Afrand et al [72]	Engine Oil (SAE40)	SiO_2 -MWCNTs	0.0625%, 0.125%, 0.25%, 0.5%, 0.75% 1.0%	Dynamic Viscosity	37.4%
S. Sarboolookzadeh Harandi et al [51]	Ethylene glycol (EG)	MWCNTs-Fe_3O_4	0.1%, 0.25%, 0.45%, 0.8%, 1.25%, 1.8%, 2.3%	Thermal Conductivity	30% of 2.3 vol% when measured at 50C
D. Madhesh et al[73]	De-ionized water	Cu – TiO_2	0.1% - 2.0%	Heat Transfer Coefficient	68%
S.K. Mechiri et al [74]	Vegetable Oils (Ground nut)	Cu - Zn	0.1%,0.3%, 0.5%	Thermal Conductivity	1.125-times
S. Akilu et al [75]	Ethylene glycol (EG)	TiO_2 - CuO/C	0.5% - 2.0%	Thermal Conductivity	16.7%
				Dynamic Viscosity	80%
M.H. Esfe et al[76]	Ethylene glycol (EG)	SWCNT- MgO	0.0% - 2.0%	Thermal Conductivity	32% of 2 vol.%
S.Aberoumand et al [77]	Transformer Oil	Ag - WO_3	1 wt.%, 2 wt.%, 4 wt.%	Thermal Conductivity	41%
S.Kannaiyan et al [78]	Water-Ethylene glycol (EG)	Al_2O_3 - CuO	0.05%, 0.1%, 0.2%	Thermal Conductivity	45%
M.Afrand [79]	Ethylene glycol (EG)	MgO - FMWCNTs	0% - 0.6%	Thermal Conductivity	21.3%
M.F. Nabil et al [80]	Water-Ethylene glycol (EG)	TiO_2 – SiO_2	0.5% - 3.0%	Thermal Conductivity	22.8%
				Dynamic Viscosity	62.5%
L.Syam Sundar et al [81]	Distilled Water	GO - Co_3O_4	0.05%, 0.1%, 0.15%, 0.2%	Thermal Conductivity	19.14%
				Dynamic Viscosity	1.70-times

	Ethylene glycol (EG)			Thermal Conductivity	11.85%
				Dynamic Viscosity	1.42-times
B.Wei et al [82]	Diathermic Oil	SiC – TiO_2	0.1% - 1.0%	Thermal Conductivity	8.39%
H.R. Allahyar et al [83]	Distilled Water	Ag – Al_2O_3	0.1% - 0.4%	Heat Transfer Rate	31.58% of 0.4 vol.%
S.M. Abbasi et al [84]	Gum Arabic (GA)	MWCNTs-γ-Al_2O_3	0% - 1%	Thermal Conductivity	20.68%
L.Syam Sundar et al [85]	Water-Ethylene glycol (EG)	ND - Co_3O_4	0% - 0.15%	Thermal Conductivity	16.0% at 60C
				Dynamic Viscosity	1.51-times at 60C
H.Yarmand et al [86]	Distilled Water	GNP - Pt	0.0% - 0.1%	Thermal Conductivity	17.77% of 0.1 vol.% at 40C
				Dynamic Viscosity	33% of 0,1% at 40C
O.Soltani et al [87]	Ethylene glycol (EG)	MgO -MWCNT	0.1% - 1.0%	Dynamic Viscosity	168%
L.Syam Sundar et al [88]	Water-Ethylene glycol (EG)	ND – Fe_3O_4	0.005%, 0.1%, 0.2%	Thermal Conductivity	17.8%
				Dynamic Viscosity	2.19-times

Table 2 and table 3 show important findings about nanofluids thermal conductivity and dynamic viscosity. It has summarized the maximum enhancement based on experimental studies. The maximum enhancement of thermal conductivity for single nanofluid is 32.26%. While, the enhancement range of viscosity for single nanofluid is between 17.62% and 294% over the base fluid. On the other hand, the hybrid nanofluids exhibit superior thermal conductivity over single nanofluid where the maximum enhancement is between 8.39% and 41%. Furthermore the enhancement percentage for hybrid nanofluid viscosity is between 33% and 115%.

3.2 Thermal Conductivity Model

The overall cost of experiments nowadays is getting more expensive and conducting the experiments may consume a lot of time. Hence, many researchers have developed the prediction correlation models of nanofluid thermal conductivity. However, the results that calculated using the correlation model should be verified with the actual experimental data.

Table 4 Thermal conductivity models developed by various scholars specifically for nanofluids.

Author	Thermal Conductivity Models	Description
Maxwell [89]	$\frac{k_{nf}}{k} = \frac{k_s + 2k + 2\varphi(k_s - k)}{ks_s + 2k - \varphi(k_s - k)}$	The first model and always referred when to define the effective thermal conductivity of combination liquid and solid suspensions.
Hamilton and Crosser [90]	$\frac{k_{nf}}{k} = \frac{k_s + (n-1)k + (n-1)\varphi(k_s - k)}{ks_s + (n-1)k - \varphi(k_s - k)}$	This model considers a non-sperical nanoparticles and a shape factor that affects the liquid-solid thermal conductivity. Where n is the empirical shape factor given by 3/ ϕ and ϕ is the particle sphericity where 1 for the spherical and 0.5 for the cylindrical shape respectively.
Yu and Choi [91],[116]	$k_{pe} = \frac{[2(1-\gamma) + (1+\beta)^3(1+2\gamma)]\gamma}{-(1-\gamma) + (1+\beta)^3 + (1+2\gamma)} k_p$ $\frac{k_{nf}}{k_f} = \frac{k_{pe} + 2k_b + 2(k_{pe} - k_p)(1+\beta)^3\phi}{k_{pe} + 2k_b - (k_{pe} - k_b)(1+\beta)^3\phi}$	The nanolayers at solid/liquid interface take into considerations when defining the equivalent thermal conductivity kpe. Where γ is the ratio of nanolayer thermal conductivity to particle thermal conductivity (γ = kpe/k). In extreme case, kpe = k, thus, γ is equivalent to 1. Where φ is the particle volume concentration and β is the ratio of thickness layer, *h* over particle radius, *r* (*β = h / r*).
Bruggeman [92]	$\frac{k_{nf}}{k_{bf}} = \frac{1}{4}(3\phi - 1)k_{np} + [(2 - 3\phi)k_{bf}] + \frac{k_{bf}}{4}\sqrt{\Delta}$ where $\Delta = [(3\phi - 1)^2(\frac{k_{np}}{k_{bf}})^2 + [(2 - 3\phi)^2 + 2(2 + 9\phi - 9\phi^2)]\frac{k_{np}}{k_{bf}}]$	Bruggeman has proposed better model than two models above to predict the thermal conductivity at any v/v% and valid for spherical shape nanoparticle.
Feng et al [117]	$\frac{k_s}{k_f} = \frac{k_p + 2k_f - 2\varphi(1 + \lambda_{nano})^3(k_f - k_p)}{k_p + 2k_f + \varphi(1 + \lambda_{nano})^3(k_f - k_p)}$	A model that considered of nanolayer, λ_{nano}which is referred to the ratio of nanoparticle thickness and radius $\left(\lambda_{nano} = \frac{t_p}{r_p}\right)$ in determining the nanofluid thermal conductivity.
Timofeeva et al [93]	$\frac{k_{eff}}{k_f} = (1 + 3\phi)$	The model considers geometry, agglomeration state and surface resistance of nanoparticles in determining the efficient of thermal conductivity.

M. Vafaei et al [25]	$\frac{k_{nf}}{k_{bf}} = 0.9787 + \exp(0.3081\phi^{0.3097} - 0.002T)$	The model is based on optimum condition using artificial neural network and can be used to predict hybrid nanofluids.

3.3 Dynamic Viscosity

Viscosity is a measure of the liquid tendency against the flow. It is very important rheology property of nanofluid that affecting the convective heat transfer coefficient [94]. When the liquid viscosity is constant over the shear rate, thus the liquid can be classified as Newtonian fluid as reported by Ghasemi et al [95]. On the other hand, if the fluid viscosity is changing over the shear rate, then the fluid is also known as Non-Newtonian fluid [96]. For nanofluids, volume concentration is the most important factor whether it can be classified as Newtonian or Non-Newtonian fluid. For instance, Hong et al [97] found that FeO_4/water nanofluid exhibited Newtonian at a low concentration but behave non-Newtonian at a higher volume concentration due to the viscosity is changing over shear rate. The viscosity level in nanofluid is crucial because it may lead to high-pressure drop and subsequently more energy is required for pumping power prior to supply the cutting fluid. Based on the experimental investigation done by Pak and Cho [98], there was no significant influence on fluid viscosity based on different pH values and there was additional 31% of the pumping penalty at a 3% of volume concentration where the fluid velocity remains constant.
However, nanofluid with higher viscosity has better performance for lubricating effect [52] due to it has better contact area between the cutting tool tip and the workpiece [99]. Moreover, higher viscosity prevents nanofluid from flowing freely out of machining zone. This relationship between cutting fluid viscosity and surface tension is associated with cutting fluid wetting and spray characteristics. L.S Sundar et al [20] reported out that the viscosity of nanofluids is directly proportional to mass or volume concentration. In contrast, the viscosity is inversely proportional to the temperature. Brownian motion effect where the molecules move freely and randomly could be attributed to the relationship between temperature and viscosity [100]. The viscometer is a key measurement instrument to measure the nanofluid viscosity.

3.4 Viscosity Model

Besides thermal conductivity model, the scholars since 1950s have also developed viscosity model for predicting nanofluid viscosity based on experimental works as can be seen in Table 4.

Table 5 Viscosity models developed by the scholars

Author	Viscosity Models	Description
Pak and Cho [98]	$\mu_{eff} = \mu_{eff}(1+39.11\phi+533.9\phi^2)$	This model is referred to two different metallic particles at room temperature
Einstein [101]	$\mu_{eff} = \mu(1+2.5\phi) \quad \phi <= 0.05$	Based on suspension of spherical particles
Roscoe [102]	$\mu_{eff} = \mu_f(1-\frac{\phi}{\phi_m})^{-2.5}$	A model for equal size rigid spheres and for all concentrations
Koo and Kleinstreuer [103]	$\mu_{Brownian} = 5x10^4 \beta\rho m\phi_p\sqrt{\frac{K_g T}{2\rho_p r_p}}[(-134.63+1722.3\phi_p)+(0.4705-6.04\phi_p)T]$	Small scale interaction may occur between hot and cold region. Thus, temperature, particle size and volume fraction also effect the viscosity.
Birkman [104]	$\frac{\mu_{eff}}{\mu_f} = \frac{1}{(1-\phi)^{2.5}}$	This model is extended from Einstein's model which dilute copper, gold, CNT suspension. The model includes base fluid, nanoparticle viscosity and volume fraction respectively.
Batchelor [105]	$\mu_{ef}\, f = 1+2.5\phi+6.5\phi^2$	The effect of Brownian motion take into

	consideration and it was extended from Einstein's model

The suitability of the models as shown in Table 4 and 5 is relied more on type of base fluid, type of nanoparticle, volume concentration and addition of surfactant. Moreover, the accuracy of these models had been tested which close to the experimental results. However, both properties thermal conductivity and viscosity can be predicted by referring to one of these models. However, the experimental works must be performed in a sense that a deviation of thermal conductivity and viscosity value can be avoided. Recently, many researchers have developed empirical correlation models using different methods like genetic algorithm and artificial neural network. The objective is to generate mathematical modelling that will be represented nanofluids prediction of thermal conductivity and dynamic viscosity.

4.0 Conclusion

The capability of nanofluid in enhancing thermal and rheology properties is really encouraging for the next generation of working fluid. Even though the pressure drop increases with higher nanofluid viscosity but the presence of single or more than one type of nanoparticle in nanofluid can further enhance the base fluid heat transfer capability. Due to the pressure drop, more energy is required for circulating the nanofluid. This circumstance might affect the pump specifically where the pump is over working in supplying the nanofluid consistently into the working zone. For that reason, the viscosity of hybrid nanofluid must be controlled wisely in getting a suitable range of viscosity level. Furthermore, appropriate selection of nanoparticle materials, base fluids, combination of different nanoparticle and combination with or without surfactant is very crucial to get the optimum condition of single and hybrid nanofluid physical, thermal and rheological properties. From the literature review, it can be concluded that hybrid nanofluids exhibit better performance than single nanofluid and base fluid. Thus, more experimental works must be carried out to further understand the behaviour of nanofluid in terms of the effect of nanoparticle shape, size and concentration to both thermal conductivity and dynamic viscosity as well as to explore its great potential. With the huge potential of hybrid nanofluid in terms of rheology properties, the elevation of overall engineering performance is realistic to be achieved.

Acknowledgement
The authors gratefully acknowledge the support of Universiti Malaysia Pahang for providing research grants RDU1703135 and UMP LEAP-3 flagship project number RDU172203 to conduct hybrid nanofluids related research for manufacturing application.

References

[1] H. J. Kim, K. J. Seo, K. H. Kang, and D. E. Kim, "Nano-lubrication: A review," *International Journal of Precision Engineering and Manufacturing*, 17, no. 6. 829–8412016, 2016.
[2] S. U. S. Choi and J. A. Eastman, "Enhancing thermal conductivity of fluids with nanoparticles," ASME International Mechanical Engineering Congress and Exposition, 66, no. March, 99–105(1995).
[3] A. K. Sharma, A. K. Tiwari, and A. R. Dixit, "Progress of Nanofluid Application in Machining: A Review," *Materials and Manufacturing Processes*, 30, no. 7. 813–8282015, 2015.

[4] M. H. Hamzah, N. A. C. Sidik, T. L. Ken, R. Mamat, and G. Najafi, "Factors affecting the performance of hybrid nanofluids: A comprehensive review," *International Journal of Heat and Mass Transfer*, 115. 630–6462017, 2017.
[5] O. A. Alawi, N. A. C. Sidik, H. W. Xian, T. H. Kean, and S. N. Kazi, "Thermal conductivity and viscosity models of metallic oxides nanofluids," International Journal of Heat and Mass Transfer, 116, 1314–1325(2018).
[6] M. I. Pryazhnikov, A. V. Minakov, V. Y. Rudyak, and D. V. Guzei, "Thermal conductivity measurements of nanofluids," International Journal of Heat and Mass Transfer, 104, 1275–1282(2017).
[7] S. U. S. Choi, Z. G. Zhang, W. Yu, F. E. Lockwood, and E. A. Grulke, "Anomalous thermal conductivity enhancement in nanotube suspensions," Applied Physics Letters, 79, no. 14, 2252–2254(2001).
[8] S. Fotowat, S. Askar, M. Ismail, and A. Fartaj, "A study on corrosion effects of a water based nanofluid for enhanced thermal energy applications," Sustainable Energy Technologies and Assessments, 24, 39–44(2017).
[9] W. Rashmi, A. F. Ismail, M. Khalid, A. Anuar, and T. Yusaf, "Investigating corrosion effects and heat transfer enhancement in smaller size radiators using CNT-nanofluids," Journal of Materials Science, 49, no. 13, 4544–4551(2014).
[10] E. B. Elcioglu, A. Guvenc Yazicioglu, A. Turgut, and A. S. Anagun, "Experimental study and Taguchi Analysis on alumina-water nanofluid viscosity," Applied Thermal Engineering, 128, 973–981(2018).
[11] S. M. S. Murshed and P. Estellé, "A state of the art review on viscosity of nanofluids," *Renewable and Sustainable Energy Reviews*, 76. 1134–11522017, 2017.
[12] M. F. Nabil, W. H. Azmi, K. A. Hamid, N. N. M. Zawawi, G. Priyandoko, and R. Mamat, "Thermo-physical properties of hybrid nanofluids and hybrid nanolubricants: A comprehensive review on performance," International Communications in Heat and Mass Transfer, 83, 30–39(2017).
[13] M. Nazari, M. Karami, and M. Ashouri, "Comparing the thermal performance of water, Ethylene Glycol, Alumina and CNT nanofluids in CPU cooling: Experimental study," Experimental Thermal and Fluid Science, 57, 371–377(2014).
[14] S. K. Lim, W. H. Azmi, and A. R. Yusoff, "Investigation of thermal conductivity and viscosity of Al2O3/water–ethylene glycol mixture nanocoolant for cooling channel of hot-press forming die application," International Communications in Heat and Mass Transfer, 78, no. November, 182–189(2016).
[15] Y. Wang *et al.*, "Comparative evaluation of the lubricating properties of vegetable-oil-based nanofluids between frictional test and grinding experiment," Journal of Manufacturing Processes, 26, 94–104(2017).
[16] R. K. Singh, A. K. Sharma, A. R. Dixit, A. K. Tiwari, A. Pramanik, and A. Mandal, "Performance evaluation of alumina-graphene hybrid nano-cutting fluid in hard turning," Journal of Cleaner Production, 162, 830–845(2017).
[17] M. N. S.Settu, "Experimental Investigation on Performance of Milling Operation Using Vegetable Oil Based Nano Cutting Fluid and Its Process Parameters Optimization Using Taguchi and Anova," 23, no. 78, 89–93(2014).
[18] Y. Xuan and Q. Li, "Heat transfer enhancement of nanofluids," International Journal of heat and fluid flow, 21, no. 1, 58–64(2000).
[19] D. T. Minh, L. T. The, and N. T. Bao, "Performance of Al2O3 nanofluids in minimum quantity lubrication in hard milling of 60Si2Mn steel using cemented carbide tools," Advances in Mechanical Engineering, 9, no. 7, 1687814017710618(2017).
[20] L. S. Sundar, K. V Sharma, M. K. Singh, and A. C. M. Sousa, "Hybrid nanofluids preparation, thermal properties, heat transfer and friction factor – A review," Renewable and Sustainable Energy Reviews, 68, 185–198(2017).
[21] P. V. Krishna, R. R. Srikant, R. Padmini, and J. Viswaditya, "Application of nanomaterials as coolants/ lubricants in machining," in *Proceedings of the International Conference on "Advanced Nanomaterials and Emerging Engineering Technologies", ICANMEET 2013*, 2013, 674–6822013.
[22] Y. Zhang, C. Li, D. Jia, D. Zhang, and X. Zhang, "Experimental evaluation of the lubrication performance of MoSinf2/inf/CNT nanofluid for minimal quantity lubrication in Ni-based alloy grinding," International Journal of Machine Tools and Manufacture, 99, 19–33(2015).
[23] Y. Wang *et al.*, "Experimental evaluation of the lubrication properties of the wheel/workpiece interface in MQL grinding with different nanofluids," Tribology International, 99, 198–210(2016).
[24] A. Gavili, F. Zabihi, T. D. Isfahani, and J. Sabbaghzadeh, "The thermal conductivity of water base ferrofluids under magnetic field," Experimental Thermal and Fluid Science, 41, 94–98(2012).
[25] M. Vafaei, M. Afrand, N. Sina, R. Kalbasi, F. Sourani, and H. Teimouri, "Evaluation of thermal conductivity of MgO-MWCNTs/EG hybrid nanofluids based on experimental data by selecting optimal artificial neural

networks," Physica E: Low-Dimensional Systems and Nanostructures, 85, 90–96(2017).
[26] L. Syam Sundar, E. Venkata Ramana, M. K. Singh, and A. C. M. De Sousa, "Viscosity of low volume concentrations of magnetic Fe 3O 4 nanoparticles dispersed in ethylene glycol and water mixture," Chemical Physics Letters, 554, 236–242(2012).
[27] B. Li *et al.*, "Heat transfer performance of MQL grinding with different nanofluids for Ni-based alloys using vegetable oil," Journal of Cleaner Production, 154, 1–11(2017).
[28] S. Guo, S. Dong, and E. Wang, "Gold/platinum hybrid nanoparticles supported on multiwalled carbon nanotube/silica coaxial nanocables: Preparation and application as electrocatalysts for oxygen reduction," Journal of Physical Chemistry C, 112, no. 7, 2389–2393(2008).
[29] R. A. Raju, A. Andhare, and N. K. Sahu, "Performance of multi-walled carbon nanotube-based nanofluid in turning operation," Materials and Manufacturing Processes, 6914, no. March, 1–7(2017).
[30] R. Sadri *et al.*, "An experimental study on thermal conductivity and viscosity of nanofluids containing carbon nanotubes.," Nanoscale research letters, 9, no. 1, 151–166(2014).
[31] K. Kwak and C. Kim, "Viscosity and thermal conductivity of copper oxide nanofluid dispersed in ethylene glycol," *Korea Australia Rheology Journal*, 17, no. 2. 35–402005, 2005.
[32] A. K. Sharma, A. K. Tiwari, and A. R. Dixit, "Characterization of TiO2, Al2O3 and SiO2 Nanoparticle based Cutting Fluids," in *Materials Today: Proceedings*, 2016, 3, no. 6, 1890–18982016.
[33] Y. Su, L. Gong, and D. Chen, "An Investigation on Tribological Properties and Lubrication Mechanism of Graphite Nanoparticles as Vegetable Based Oil Additive.," Journal of Nanomaterials, 2015, 1–7(2015).
[34] M. Sayuti, O. M. Erh, A. A. D. Sarhan, and M. Hamdi, "Investigation on the morphology of the machined surface in end milling of aerospace AL6061-T6 for novel uses of SiO2 nanolubrication system," Journal of Cleaner Production, 66, 655–663(2014).
[35] M. Yogeswaran, K. Kadirgama, M. M. Rahman, and R. Devarajan, "Temperature analysis when using ethylene-glycol-based TiOinf2/inf as a new coolant for milling," International Journal of Automotive and Mechanical Engineering, 11, no. 1, 2272–2281(2015).
[36] M. Hemmat Esfe, H. Rostamian, A. Shabani-samghabadi, and A. A. Abbasian Arani, "Application of three-level general factorial design approach for thermal conductivity of MgO/water nanofluids," Applied Thermal Engineering, 127, 1194–1199(2017).
[37] J. A. Ranga Babu, K. K. Kumar, and S. Srinivasa Rao, "State-of-art review on hybrid nanofluids," *Renewable and Sustainable Energy Reviews*, 77. 551–5652017, 2017.
[38] X. Zhang *et al.*, "Performances of Al2O3/SiC hybrid nanofluids in minimum-quantity lubrication grinding," International Journal of Advanced Manufacturing Technology, 86, no. 9–12, 3427–3441(2016).
[39] D. Huang, Z. Wu, and B. Sunden, "Effects of hybrid nanofluid mixture in plate heat exchangers," Experimental Thermal and Fluid Science, 72, 190–196(2016).
[40] R. R. Sahoo and J. Sarkar, "Heat transfer performance characteristics of hybrid nanofluids as coolant in louvered fin automotive radiator," Heat and Mass Transfer/Waerme- und Stoffuebertragung, 53, no. 6, 1923–1931(2017).
[41] H. Xie, B. Jiang, B. Liu, Q. Wang, J. Xu, and F. Pan, "An Investigation on the Tribological Performances of the SiO2/MoS2 Hybrid Nanofluids for Magnesium Alloy-Steel Contacts," Nanoscale Research Letters, 11, no. 1, 329(2016).
[42] P. Selvakumar and S. Suresh, "Thermal Performance of Ethylene Glycol Based Nanofluids in an Electronic Heat Sink," Journal of Nanoscience and Nanotechnology, 14, no. 3, 2325–2333(2014).
[43] F. Rabiei, A. R. Rahimi, and M. J. Hadad, "Performance improvement of eco-friendly MQL technique by using hybrid nanofluid and ultrasonic-assisted grinding," *International Journal of Advanced Manufacturing Technology*. 1–152017, 2017.
[44] T. K. Tullius and Y. Bayazitoglu, "Analysis of a hybrid nanofluid exposed to radiation," Numerical Heat Transfer, Part B: Fundamentals, 69, no. 4, 271–286(2016).
[45] J. Sarkar, P. Ghosh, and A. Adil, "A review on hybrid nanofluids: Recent research, development and applications," *Renewable and Sustainable Energy Reviews*, 43. 164–1772015, 2015.
[46] Y. A. Cengel, "Heat Transfer: A Practical Approach," Mc Graw-Hill, 785–841(2003).
[47] M. M. Tawfik, "Experimental studies of nanofluid thermal conductivity enhancement and applications: A review," *Renewable and Sustainable Energy Reviews*, 75. 1239–12532017, 2017.
[48] P. B. Maheshwary, C. C. Handa, and K. R. Nemade, "A comprehensive study of effect of concentration, particle size and particle shape on thermal conductivity of titania/water based nanofluid," Applied Thermal Engineering, 119, 79–88(2017).
[49] S. Suresh, K. P. Venkitaraj, P. Selvakumar, and M. Chandrasekar, "Synthesis of Al2O3-Cu/water hybrid

nanofluids using two step method and its thermo physical properties," Colloids and Surfaces A: Physicochemical and Engineering Aspects, 388, no. 1–3, 41–48(2011).
[50] D. Toghraie, V. A. Chaharsoghi, and M. Afrand, "Measurement of thermal conductivity of ZnO–TiO2/EG hybrid nanofluid," Journal of Thermal Analysis and Calorimetry, 125, no. 1, 527–535(2016).
[51] S. Sarboolookzadeh Harandi, A. Karimipour, M. Afrand, M. Akbari, and A. D'Orazio, "An experimental study on thermal conductivity of F-MWCNTs-Fe3O4/EG hybrid nanofluid: Effects of temperature and concentration," International Communications in Heat and Mass Transfer, (2016).
[52] Y. Su, L. Gong, B. Li, Z. Liu, and D. Chen, "Performance evaluation of nanofluid MQL with vegetable-based oil and ester oil as base fluids in turning," International Journal of Advanced Manufacturing Technology, 83, no. 9–12, 2083–2089(2016).
[53] M. Afrand, D. Toghraie, and B. Ruhani, "Effects of temperature and nanoparticles concentration on rheological behavior of Fe3O4-Ag/EG hybrid nanofluid: An experimental study," Experimental Thermal and Fluid Science, 77, 38–44(2016).
[54] K. S. Suganthi and K. S. Rajan, "Temperature induced changes in ZnO-water nanofluid: Zeta potential, size distribution and viscosity profiles," International Journal of Heat and Mass Transfer, 55, no. 25–26, 7969–7980(2012).
[55] M. Hemmat Esfe, A. A. Abbasian Arani, M. Rezaie, W. M. Yan, and A. Karimipour, "Experimental determination of thermal conductivity and dynamic viscosity of Ag-MgO/water hybrid nanofluid," International Communications in Heat and Mass Transfer, 66, 189–195(2015).
[56] A. Alirezaie, M. H. Hajmohammad, M. R. Hassani Ahangar, and M. Hemmat Esfe, "Price-performance evaluation of thermal conductivity enhancement of nanofluids with different particle sizes," Applied Thermal Engineering, 128, (2018).
[57] Y. Guo, T. Zhang, D. Zhang, and Q. Wang, "Experimental investigation of thermal and electrical conductivity of silicon oxide nanofluids in ethylene glycol/water mixture," International Journal of Heat and Mass Transfer, 117, 280–286(2018).
[58] Y. X. Zeng, X. W. Zhong, Z. Q. Liu, S. Chen, and N. Li, "Preparation and enhancement of thermal conductivity of heat transfer oil-based MoS2 nanofluids," Journal of Nanomaterials, (2013).
[59] L. Syam Sundar, E. Venkata Ramana, M. K. Singh, and A. C. M. Sousa, "Thermal conductivity and viscosity of stabilized ethylene glycol and water mixture Al2O3 nanofluids for heat transfer applications: An experimental study," International Communications in Heat and Mass Transfer, 56, 86–95(2014).
[60] W. Chen, C. Zou, X. Li, and L. Li, "Experimental investigation of SiC nanofluids for solar distillation system: Stability, optical properties and thermal conductivity with saline water-based fluid," International Journal of Heat and Mass Transfer, 107, 264–270(2017).
[61] "Thermo-physical properties of water based SiC nanofluids for heat transfer applications," International Communications in Heat and Mass Transfer, 84, 94–101(2017).
[62] A. H. A. Al-Waeli, K. Sopian, M. T. Chaichan, H. A. Kazem, H. A. Hasan, and A. N. Al-Shamani, "An experimental investigation of SiC nanofluid as a base-fluid for a photovoltaic thermal PV/T system," Energy Conversion and Management, 142, 547–558(2017).
[63] W. Yu, H. Xie, L. Chen, and Y. Li, "Investigation of thermal conductivity and viscosity of ethylene glycol based ZnO nanofluid," Thermochimica Acta, 491, no. 1–2, 92–96(2009).
[64] A. Ahmadi Nadooshan, "An experimental correlation approach for predicting thermal conductivity of water-EG based nanofluids of zinc oxide," Physica E: Low-Dimensional Systems and Nanostructures, 87, 15–19(2017).
[65] S. M. S. Murshed, K. C. Leong, and C. Yang, "Enhanced thermal conductivity of TiO2 - Water based nanofluids," International Journal of Thermal Sciences, 44, no. 4, 367–373(2005).
[66] M. S. Najiha, M. M. Rahman, and K. Kadirgama, "Performance of water-based TiO2 nanofluid during the minimum quantity lubrication machining of aluminium alloy, AA6061-T6," Journal of Cleaner Production, 135, 1623–1636(2016).
[67] M. Baghbanzadeh, A. Rashidi, D. Rashtchian, R. Lotfi, and A. Amrollahi, "Synthesis of spherical silica/multiwall carbon nanotubes hybrid nanostructures and investigation of thermal conductivity of related nanofluids," Thermochimica Acta, 549, 87–94(2012).
[68] S. U. Ilyas, R. Pendyala, and M. Narahari, "Stability and thermal analysis of MWCNT-thermal oil-based nanofluids," Colloids and Surfaces A: Physicochemical and Engineering Aspects, 527, 11–22(2017).
[69] W. Li, C. Zou, and X. Li, "Thermo-physical properties of waste cooking oil-based nanofluids," Applied Thermal Engineering, 112, 784–792(2017).
[70] R. S. Khedkar, K. A. Sai, S. S. Sonawane, K. Wasewar, and S. S. Umre, "Thermo physical characterization of

paraffin based Fe3O 4 nanofluids," in *Procedia Engineering*, 2013, 51, 342–3462013.
[71] M. Abareshi, E. K. Goharshadi, S. Mojtaba Zebarjad, H. Khandan Fadafan, and A. Youssefi, "Fabrication, characterization and measurement of thermal conductivity of Fe3O4 nanofluids," Journal of Magnetism and Magnetic Materials, 322, no. 24, 3895–3901(2010).
[72] M. Afrand, K. Nazari Najafabadi, and M. Akbari, "Effects of temperature and solid volume fraction on viscosity of SiO2-MWCNTs/SAE40 hybrid nanofluid as a coolant and lubricant in heat engines," Applied Thermal Engineering, 102, 45–54(2016).
[73] D. Madhesh, R. Parameshwaran, and S. Kalaiselvam, "Experimental investigation on convective heat transfer and rheological characteristics of Cu-TiO2 hybrid nanofluids," Experimental Thermal and Fluid Science, 52, 104–115(2014).
[74] S. K. Mechiri, V. Vasu, and A. Venu Gopal, "Investigation of thermal conductivity and rheological properties of vegetable oil based hybrid nanofluids containing Cu–Zn hybrid nanoparticles," Experimental Heat Transfer, 30, no. 3, 205–217(2017).
[75] S. Akilu, A. T. Baheta, and K. V Sharma, "Experimental measurements of thermal conductivity and viscosity of ethylene glycol-based hybrid nanofluid with TiO 2 -CuO/C inclusions," Journal of Molecular Liquids, 246, 396–405(2017).
[76] M. Hemmat Esfe, A. Alirezaie, and M. Rejvani, "An applicable study on the thermal conductivity of SWCNT-MgO hybrid nanofluid and price-performance analysis for energy management," Applied Thermal Engineering, 111, 1202–1210(2017).
[77] S. Aberoumand and A. Jafarimoghaddam, "Tungsten (III) oxide (WO3) - Silver/transformer oil hybrid nanofluid: Preparation, stability, thermal conductivity and dielectric strength," *Alexandria Engineering Journal*. 2016, 2016.
[78] S. Kannaiyan, C. Boobalan, A. Umasankaran, A. Ravirajan, S. Sathyan, and T. Thomas, "Comparison of experimental and calculated thermophysical properties of alumina/cupric oxide hybrid nanofluids," *Journal of Molecular Liquids*. 2017, 2017.
[79] M. Afrand, "Experimental study on thermal conductivity of ethylene glycol containing hybrid nano-additives and development of a new correlation," Applied Thermal Engineering, 110, 1111–1119(2017).
[80] M. F. Nabil, W. H. Azmi, K. Abdul Hamid, R. Mamat, and F. Y. Hagos, "An experimental study on the thermal conductivity and dynamic viscosity of TiO2-SiO2 nanofluids in water: Ethylene glycol mixture," International Communications in Heat and Mass Transfer, 86, 181–189(2017).
[81] L. Syam Sundar, M. K. Singh, M. C. Ferro, and A. C. M. Sousa, "Experimental investigation of the thermal transport properties of graphene oxide/Co3O4 hybrid nanofluids," International Communications in Heat and Mass Transfer, 84, 1–10(2017).
[82] B. Wei, C. Zou, X. Yuan, and X. Li, "Thermo-physical property evaluation of diathermic oil based hybrid nanofluids for heat transfer applications," International Journal of Heat and Mass Transfer, 107, 281–287(2017).
[83] H. R. Allahyar, F. Hormozi, and B. ZareNezhad, "Experimental investigation on the thermal performance of a coiled heat exchanger using a new hybrid nanofluid," Experimental Thermal and Fluid Science, 76, 324–329(2016).
[84] S. M. Abbasi, A. Rashidi, A. Nemati, and K. Arzani, "The effect of functionalisation method on the stability and the thermal conductivity of nanofluid hybrids of carbon nanotubes/gamma alumina," Ceramics International, 39, no. 4, 3885–3891(2013).
[85] L. S. Sundar, G. O. Irurueta, E. Venkata Ramana, M. K. Singh, and A. C. M. Sousa, "Thermal conductivity and viscosity of hybrid nanfluids prepared with magnetic nanodiamond-cobalt oxide (ND-Co3O4) nanocomposite," Case Studies in Thermal Engineering, 7, 66–77(2016).
[86] H. Yarmand *et al.*, "Study of synthesis, stability and thermo-physical properties of graphene nanoplatelet/platinum hybrid nanofluid," International Communications in Heat and Mass Transfer, 77, 15–21(2016).
[87] O. Soltani and M. Akbari, "Effects of temperature and particles concentration on the dynamic viscosity of MgO-MWCNT/ethylene glycol hybrid nanofluid: Experimental study," Physica E: Low-Dimensional Systems and Nanostructures, 84, 564–570(2016).
[88] L. S. Sundar, E. Venkata Ramana, M. P. F. Graça, M. K. Singh, and A. C. M. Sousa, "Nanodiamond-Fe3O4 nanofluids: Preparation and measurement of viscosity, electrical and thermal conductivities," International Communications in Heat and Mass Transfer, 73, 62–74(2016).
[89] J. C. Maxwell, "A treatise on electricity and magnetism," *Oxford: Clarendon Press*. 360–3661873, 1873.
[90] R. L. Hamilton and O. K. Crosser, "Thermal Conductivity of Heterogeneous Two-Component Systems,"

Industrial & Engineering Chemistry Fundamentals, 1, no. 3, 187–191(1962).
[91] W. Yu and S. U. S. Choi, "The role of interfacial layers in the enhanced thermal conductivity of nanofluids: A renovated Maxwell model," Journal of Nanoparticle Research, 5, no. 1–2, 167–171(2003).
[92] D. Bruggeman, "Calculation of various physics constants in heterogenous substances I Dielectricity constants and conductivity of mixed bodies from isotropic substances," Annalen der Physik, 24, no. 7, 636–664(1935).
[93] E. V Timofeeva *et al.*, "Thermal conductivity and particle agglomeration in alumina nanofluids: Experiment and theory," Physical Review E - Statistical, Nonlinear, and Soft Matter Physics, 76, no. 6, (2007).
[94] M. Jama *et al.*, "Critical Review on Nanofluids: Preparation, Characterization, and Applications," *Journal of Nanomaterials*, 2016. 2016, 2016.
[95] S. Ghasemi and A. Karimipour, "Experimental investigation of the effects of temperature and mass fraction on the dynamic viscosity of CuO-paraffin nanofluid," Applied Thermal Engineering, 128, (2018).
[96] D. K. Devendiran and V. A. Amirtham, "A review on preparation, characterization, properties and applications of nanofluids," *Renewable and Sustainable Energy Reviews*, 60. 21–402016, 2016.
[97] R. Y. Hong, Z. Q. Ren, Y. P. Han, H. Z. Li, Y. Zheng, and J. Ding, "Rheological properties of water-based ferrofluids," Chemical Engineering Science, 62, no. 21, 5912–5924(2007).
[98] B. C. Pak and Y. I. Cho, "Hydrodynamic and heat transfer study of dispersed fluids with submicron metallic oxide particles," Experimental Heat Transfer, 11, no. 2, 151–170(1998).
[99] Y. Zhang, C. Li, D. Jia, D. Zhang, and X. Zhang, "Experimental evaluation of MoS2 nanoparticles in jet MQL grinding with different types of vegetable oil as base oil," Journal of Cleaner Production, 87, no. 1, 930–940(2015).
[100] S. P. Jang and S. U. S. Choi, "Role of Brownian motion in the enhanced thermal conductivity of nanofluids," Applied Physics Letters, 84, no. 21, 4316–4318(2004).
[101] A. Einstein, "A New Determination of Molecular Dimensions," *Annalen der Physik*, 324, no. 2. 289–3061906, 1906.
[102] R. Roscoe, "The viscosity of suspensions of rigid spheres," British Journal of Applied Physics, 3, no. 8, 267–269(1952).
[103] J. Koo and C. Kleinstreuer, "A new thermal conductivity model for nanofluids," Journal of Nanoparticle Research, 6, no. 6, 577–588(2004).
[104] H. C. Birkman, "The viscosity of concentrated suspensions and solution," the Journal of Chemical Physics, 20, 571(1952).
[105] G. K. Batchelor, "The effect of Brownian motion on the bulk stress in a suspension of spherical particles," Journal of Fluid Mechanics, 83, no. 01, 97(1977).

Penerbit Akademia Baru

Engineering Science and Technology Conference Proceedings

Journal homepage: www.akademiabaru.com/EST.html

Experimental Assessment of a Novel Eutectic Binary Molten Salt-based Hexagonal Boron Nitride nanocomposite as a Promising PCM with Enhanced Specific Heat Capacity

Open Access

Navid Aslfattahi[1,*], R. Saidur[2, 3,*], Nor Azwadi Che Sidik[4,*], Mohd Faizul Mohd Sabri[1,*], Md. HasanZahir[5]

[1] Department of Mechanical Engineering, Faculty of Engineering, University of Malaya, 50603, Kuala Lumpur
[2] Research Center for Nano-Materials and Energy Technology (RCNMET), School of Science and Technology, Sunway University, Bandar Sunway, Petaling Jaya, 47500, Selangor Darul Ehsan, Malaysia
[3] Department of Engineering, Lancaster University, Lancaster, LA1 4YW, UK
[4] Malaysia _ Japan International Institute of Technology (MJIIT), University Teknology Malaysia, Jalan Sultan Yahya Petra, 54100 Kuala Lumpur, Malaysia
[5] Center of Research Excellence in Renewable Energy (CoRERE), King Fahd University of Petroleum & Minerals (KFUPM), Dhahran 31261, Saudi Arabia

ABSTRACT

In this study, novel nanocomposites containing the pre-defined mass ratio of binary molten salt ($NaNO_3$-KNO_3: 60-40 wt.%) dispersed with hexagonal boron nitride (hBN) nanoparticles with nominal size of 70 nm, were prepared through one-phase preparation method. Four different types of samples including pure binary molten salt and binary molten salt-based hBN nanocomposites with loading concentrations of 0.5, 1 and 1.5 wt.% were prepared. The proposed amount of sodium nitrate and potassium nitrate was added to certain amount of DI water, comprising with 0.5, 1 and 1.5 wt.% concentration of hBN nanoparticles. Scanning electronic microscopy (SEM) was conducted to evaluate the uniformity of the synthesized binary molten salt-based hBN nanocomposites. The SEM images revealed uniform dispersion of hexagonal boron nitride nanoparticles and fractal-like structures were observed clearly. Specific heat capacity (c_p) and melting temperature measurements were performed using a differential scanning calorimetry (DSC). The experimental achieved data for melting temperature proved that hexagonal boron nitride nanoparticles do not affect the melting temperature of the synthesized nanocomposites. The experimentally achieved data for the average c_p values of the binary molten salt in solid and liquid phases were 1.14 and 1.13 J/g K, respectively. While, the average c_p values for the binary molten salt-based hBN nanocomposite with the highest loading concentration of nanoparticles (1.5 wt.%) in solid and liquid phases were 2 and 3.17 J/g K, respectively. The measured average c_p value in the liquid phase for binary molten salt-based hBN nanocomposite with the highest loading concentration (1.5 wt.%) of nanoparticles revealed enhancement of ~180% in comparison with pure binary molten salt. Thermal stability measurements expressed enhancement of thermal stability in binary molten salt induced with hBN nanoparticles. Binary molten salt-based hBN nanocomposite with loading concentration of 1.5 wt.% represented ~16% enhancement in thermal stability over the binary molten salt.

Keywords:
Molten salt; hBN; TES; specific heat capacity; PCM

Copyright © 2019 PENERBIT AKADEMIA BARU - All rights reserved

1. Introduction

Over the past decades the world energy demand (fossil-based energy) has increased excessively due to the development of the globe economy and enhancement of 60% is anticipated in the

* Corresponding authors.
E-mail address: navid.fth87@yahoo.com (Navid Aslfattahi); saidur@sunway.edu.my (Saidur Rahman); azwadi@utm.my (Nor Azwadi Che Sidik); faizul@um.edu.my (Mohd Faizul Mohd Sabri)

energy demand by 2030 [1]. Renewable energy sources are promising replacements for petroleum resources. The significance of solar energy as a noticeable clean source of renewable energy is elucidated [2]. Solar energy is considered as eco-friendly abundant sorce of energy with expectation of suppling the 70% of the world energy demand by 2100 [3]. Capturing the solar radiation energy by using solar thermal systems depends on the efficient conversion of the thermal energy from sun. Accessibility to broad range of operation temperatures in solar thermal systems can be achieved by improvement of the efficent light-to-heat conversion process in high temperatures (above 300 °C). In solar thermal systems, thermal energy storage (TES) medium and heat transfer fluids (HTFs), play dominant role, since the thermal storage and transporting the thermal energy occurs through these critical components. Improvement in the efficiency of the solar thermal systems can be obtained by using nanofluids as promising HTFs as effective medium to absorb the solar radiation consequently [4]. Conventional HTFs such as water and industrial oils with addition of nanoparticles as practical nanofluids have been studied extensively in terms of thermal storage and thermal conductivity [5]. However, the conventional HTFs are not applicable for several industrial processes and concentrated solar thermal systems that require the application of the fluids at higher temperatures due to the limitation in operation temperatures. Lower thermal stability up to 400 °C is another drawback of conventional nanofluids. These issues have attracted scientists to study new class of nanofluids to overcome the operation temperature limitations with improved efficiency in TES. The enhancement of the theoretical thermodynamic efficiency (The Carnot efficiency) can be obtained from 50 to 65% by increasing the operation temperature from 300-400 °C to 560 °C [6]. Molten salts are capable candidates to be considered as working fluids at high temperatures (up to 600 °C) [7]. High temperature stability of the molten salts can significantly improve the thermodynamic efficiency of the systems that utilize these TES materials as working fluid, especially in concentrated solar power (CSP) system the cost of the generated electricity will be reduced drastically [6]. Molten salts are naturally abundant and environmentally safe with lower price compared with conventional TES materials. However, poor thermophysical properties of the molten salts, particularly specific heat capacity (c_p is less than 2 kJ/kg °C) is important challenge in terms of using molten salts as TES materials [7, 8]. Nanoparticles dispersion can enhance the specific heat capacity of the nanofluids when they are doped into a fluid mixture. Nelson et al. [9] reported 50% enhancement in the specific heat capacity of the polyalphaolefin (PAO)-based graphite nanofluids with loading concentration of 0.6 wt.%. In a research work conducted by Shin and Banerjee [10], they revealed 15% and 26% enhancement in the specific heat capacity of molten salt-based silica nanofluids with loading concentration of 1 wt.% of silica nanoparticles. Bridge et al. [11] represented enhancement of 30% in the specific heat capacity of the ionic liquid mixture-based Al_20_3 nanofluids with loading concentration of less than 2.5 wt.%. Chieruzzi et al. [12] investigated the effects of four different nanoparticles including Al_2O_3, TiO_2, SiO_2 and hybrid SiO_2-Al_2O_3 on the specific heat capacity of a binary molten salt ($NaNO_3$-KNO_3 60:40 wt.%) in the loading concentrations of 0.5, 1 and 1.5 wt.%. They reported enhancement of 15 to 57% in the specific heat capacity (solid phase) and enhancement of 1 to 22% in the specific heat capacity (liquid phase). Dudda et al. [13] evaluated the effects of the nanoparticles on the specific heat capacity of a binary nitrate salt eutectic. They prepared binary molten salt-based SiO_2 nanoparticles in the loading concentration of 1 wt.% and with variety of the nanoparticles size consisting of 5, 10, 30 and 60 nm. They reported enhancements of 8, 12, 19 and 27% in the specific heat capacity for the nanoparticle sizes of 5, 10, 30 and 60 nm, respectively. Enhancement of 13% in specific heat capacity of a ternary nitrate salt doped with SiO_2 nanoparticles (loading concentration of 1 wt.%) was reported by Seo et al. [14]. Influence of the MWCNT and Au nanoparticles on the specific heat capacity of the binary molten salt was investigated by Liu et al. [15] extensively. They proved that application of MWCNT

and Au nanoparticles to the binary molten salts can remarkably increase the specific heat capacity by a factor approaching 100%.

Hexagonal boron nitride (hBN) has attracted great attention of the scientists due to the high thermal conductivity, a large band gap (almost 5.9 eV) and low density with promising performance for the applications in thermal interface materials (TIMs) [16, 17]. Fang et al. [18] utilized hexagonal boron nitride as a filler in paraffin-based composite phase change materials. They proved that the inclusion of 10 wt.% hBN in the composite will cause enhancement in thermal conductivity by up to 60% and decrease in latent heat of fusion by less than 12%. Su et al. [19] introduced hexagonal boron nitride nanoparticles to the eutectic mixture of n-octadecane (ODE) and stearic acid (SA) as phase change materials to investigate the thermal properties of the composite PCM (CPCM). They reported that the thermal conductivity of the eutectic SA-ODE composite PCM with loading concentration of 10 wt.% of the hBN nanoparticles increased, whereas their latent heat of fusion decreased slightly.

The present study, investigates the effects of the hexagonal boron nitride nanoparticles in thermophysical properties of binary nitrate base molten salt. A conventional binary molten salt ($NaNO_3$-KNO_3: 60-40 wt.%) is utilized as a base fluid and the suspended nanoparticles are hBN nanoparticles in three different loading concentrations of 0.5, 1 and 1.5 wt.%. Investigation of the thermo-physical properties, including specific heat capacity (c_p) and thermal durability of the eutectic binary molten salt-based hBN nanocomposite as PCMs is the first study to the best of authors' knowledge. Well-dispersed binary molten salt-based hBN nanocomposite was synthesized in one-phase preparation method. The specific heat capacity (c_p) and melting temperature of alkali binary molten salt with/without nanoparticles were measured using DSC. Measured specific heat capacity (c_p) of the synthesized binary molten salt was compared with literature to verify the accuracy. The nanostructures of the synthesized binary molten salt with/without NPs were observed using SEM images.

2. Methodology

2.1 Materials and methods

Potassium nitrate (KNO_3) with molar mass of 101.1 g/mol was procured from Merck company. Sodium nitrate ($NaNO_3$) with molar mass of 84.99 was supplied by R&M Chemicals company. Hexagonal boron nitride (hBN) nano powder with average particle size of 70 nm and purity of 99% procurement was through Lower Friction company.

2.2 Preparation of eutectic alkali binary molten salt-based hBN nanocomposites

Purity and the average particle size (70 nm) of the hexagonal boron nitride (hBN) was confirmed with the supplier [20]. The method of synthesizing the eutectic alkali binary molten salt is similar to that adopted by Shin and Banerjee [10] consisting of some modifications in the method. Initially, 6 g of sodium nitrate ($NaNO_3$) was measured by using microbalance (TX323L, UNIBLOC) and added to a glass beaker (of 100 ml volume). Then 50 ml of deionized (DI) water was added to the beaker, followed by stirring the solution on the hot plate (RCT BASIC, IKA) at 600 rpm. The temperature of hot plate was maintained at 50 °C to assure the uniform dissolving of the sodium nitrate in DI water. Afterward, 4 g of potassium nitrate (KNO_3) was added to the beaker, followed by stirring for 15 minutes at 600 rpm. Finally, the resultant solution was sonicated by using probe sonicator (FS-1200N) for 60 minutes with on/off time of 7/3 seconds and power of 70%. Synthesizing the binary molten salt-based hBN nanocomposite with different loading concentrations of nanoparticles

consisting of 0.5, 1 and 1.5 wt.% was followed by adopting same protocol (one-phase preparation) for all samples to assure the uniform synthesis method. For synthesizing binary molten salt-based hBN nanocomposite with loading concentration of 0.5 wt.% of nanoparticles, 570 mg of $NaNO_3$ and 380 mg of KNO_3 were added to the beaker followed by addition of 50 mg of hBN. Then, 50 ml of DI water was added to the beaker, followed by stirring the solution on the hot plate at 600 rpm for 1 h in the maintained temperature of 50 °C. Probe sonication was conducted for 60 minutes with on/off time of 7/3 seconds and power of 70%. Same method was conducted for preparation of binary molten salt-based hBN nanocomposite with loading concentrations of 1 and 1.5 wt.%. The utilized amount of $NaNO_3$ and KNO_3 for the synthesis of binary molten salt-based hBN nanocomposite with loading concentration of 1 wt.% was 540 and 360 mg respectively including the addition of 100 mg of hBN nanoparticles. Addition of 150 mg of hBN nanoparticles was considered for the binary molten salt-based hBN nanocomposite with loading concentration of 1.5 wt.%. The utilized amount of $NaNO_3$ and KNO_3 for the preparation of the mixture with loading concentration of 1.5 wt.% was 510 and 340 mg, respectively.

2.3 Characterization method

2.3.1 Morphology and elemental analysis of the binary molten salt-based hBN nanocomposites

Morphology and homogeneity of the synthesized alkali binary molten salt-based hBN phase change materials were checked through scanning electronic microscopy (VEGA3, TESCAN) and energy-dispersive x-ray spectroscopy (EDX, OXFORD INSTRUMENT). Digital Ion coater (COXEM Co, SPT-20) was utilized for Pt coating of the samples in the fixed current of 3 mA for 300 seconds for the purpose of SEM imaging.

2.3.2 Specific heat capacity (c_p) and melting temperature measurements

In this study, the specific heat capacity (c_p) and melting temperature measurements of the pure binary molten salt and alkali binary molten salt-based hBN nanocomposites are performed using a differential scanning calorimetry (DSC). DSC-8000 (Perkin Elmer, USA) is a double-furnace, power compensation DSC with greater sensitivity and accuracy instrument. The colorimetric and temperature accuracy of the above-mentioned DSC is considered as <±0.2% and ±0.05 °C, respectively. The measurements are conducted using aluminum crucibles of 40 µl. The temperature range for measurements is between 25-500 °C with the heating rate of 10 °C/min. The c_p values and melting temperature analysis was through Pyris software.

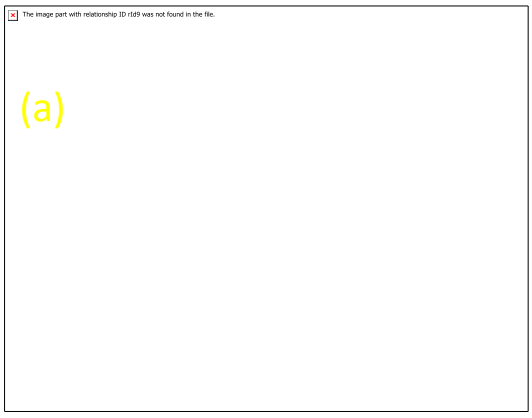
2.3.3 Thermal durability characterization

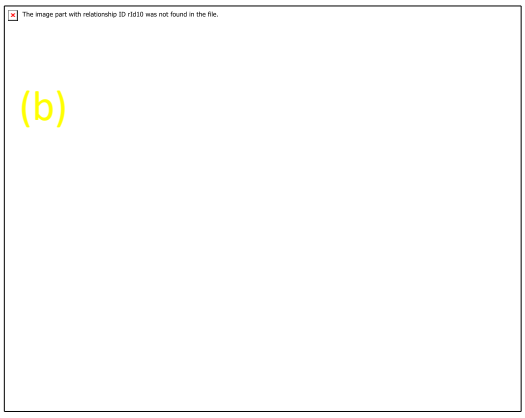
Thermogravimetric analysis (TGA) of the pure binary molten salt and alkali binary molten salt-based hBN nanocomposites are conducted using Perkin Elmer TGA 4000. A 180 µl alumina crucible (with temp. ~1750 ˚C) under an ultra-high pure nitrogen gas flow of 19.8 ml/min with the gas pressure of 2.6 bar is selected to examine the samples. The utilized heating rate is 10 ˚C/min for raising the temperature from 30 to 850 ˚C. About 12 mg of the synthesized samples is used for the decomposition temperature measurement. The obtained data is analyzed using Pyris Software.

3. Results

3.1 Morphological characterization of alkali binary molten salt-based hBN nanocomposites

Scanning electronic microscopy (SEM) and energy-dispersive x-ray spectroscopy (EDX) were performed to evaluate the homogeneity and dispersion of nanoparticles in the synthesized alkali binary molten salt-based hBN nanocomposites and elemental analysis, respectively. The flat surface area of the nitrate materials and existence of some holes in the surface area can be observed form figure 1. (a, b). Uniform structure of the synthesized binary molten salt and smooth corners can be observed from figure 1. b, which is in agreement with the morphology analysis performed by Huang et al. [21] for the same binary molten salt mixture. EDX spectroscopy analysis for the binary molten salt represented the existence of ~15.7, ~7.7, ~19.7 and ~57 weight% of sodium, potassium, nitrogen and oxygen, respectively. Atomic% value for sodium, potassium, nitrogen and oxygen was found ~11.7, ~3.3, ~24 and ~61, respectively. Energy-dispersive spectroscopy analysis for synthesized alkali binary molten salt-based hBN nanocomposite in three different loading concentrations of nanoparticles indicated good dispersion of nanoparticles in the matrix of molten salt. Figure1. (c, d) show SEM images of synthesized binary molten salt-based hBN nanocomposites. Chain-like structures due to the presence of hBN nanoparticles are evident in the achieved images. EDX results for nanocomposites with loading concentration of 0.5 wt.%, indicated the values of ~12.3, ~9.6, ~19.5, ~53.1 and ~5.3 weight% for sodium, potassium, nitrogen, oxygen and boron, respectively. The achieved weight% values of the components is in good agreement with the pre-defined mass fraction of utilized materials. The achieved atomic% values for sodium, potassium, nitrogen, oxygen and boron, were ~8.9, ~4.1, ~23.2, ~55.3 and ~8.52, respectively. The same trends of the weight% and atomic% was acquired for binary molten salt-based hBN nanocomposites, from figure1. (e, f) and figure 1. (g, h) which represents uniformity of the synthesized samples. The acquired atomic% for boron in the binary molten salt-based hBN nanocomposites with loading concentrations of 1 and 1.5 wt.% was ~11.1 and ~14.5, respectively that proved the accuracy of the synthesized samples. Fractal-like structures due to the presence of hBN nanoparticles are clear in the SEM images [22].





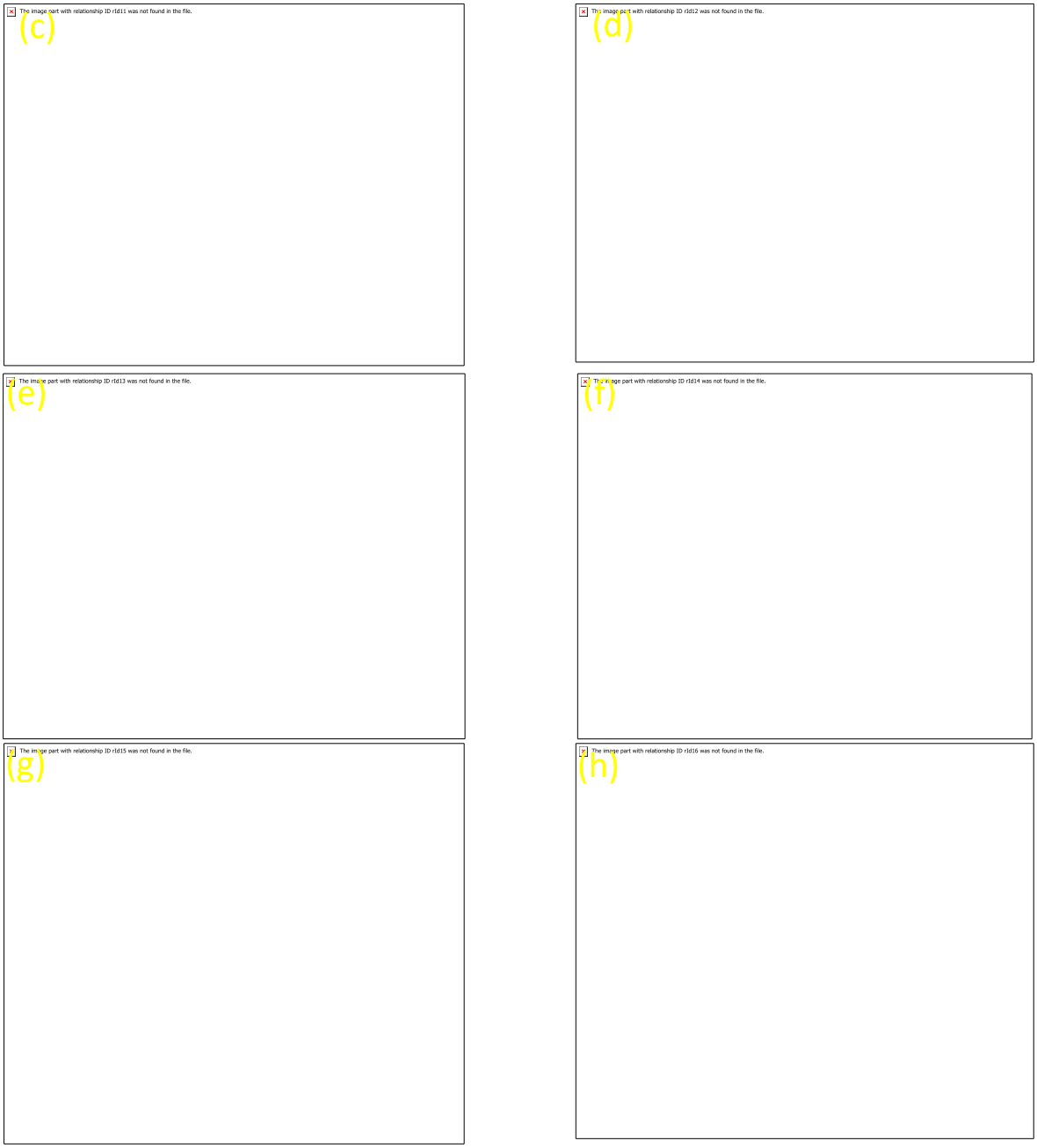


Figure 1. Scanning electronic microscopy (SEM) images for (a, b) pure binary molten salt (c,d) synthesized binary molten salt-based hBN nanocomposite with loading concentration of 0.5 wt.% (e,f) synthesized binary molten salt-based hBN nanocomposite with loading concentration of 1 wt.% (g,h) synthesized binary molten salt-based hBN nanocomposite with loading concentration of 1 wt.%

3.2 Specific heat capacity (c_p) characterization

Specific heat capacity (c_p) and melting temperature of the samples were measured using differential scanning calorimetry (DSC-8000, Perkin Elmer, USA). DSC curves for the binary molten salt and binary molten salt-based hBN nanocomposites are shown Figure 2. The results are represented as a function of temperature. To verify the accuracy of the measurement method, the melting temperature of the pure eutectic binary molten salt was measured and compared with literature data. The estimation of measurement uncertainty is 1.5%. The measured value for

melting temperature of binary molten salt was ~225.6 °C which is in good agreement with the reported value in literature (222 °C) [8]. The acquired melting temperature for the binary molten salt-based hBN nanocomposites with concentrations of 0.5, 1 and 1.5 wt.% was ~225 °C, which revealed that hBN nanoparticles do not affect the melting temperature of the synthesized samples. Figure 2. (a) demonstrates the obtained DSC curve for c_p measurement of the binary molten salt with the average value of 1.14 J/g K (solid phase) and 1.13 J/g K (liquid phase). The achieved c_p value for the binary molten salt is in agreement with the literature [21]. The experimentally achieved data for the average c_p value of the binary molten salt-based hBN nanocomposite with loading concentration of 0.5 wt.% proved ~42% (1.62 J/g K) and ~110% (2.38 J/g K) enhancements compared with the binary molten salt in the solid and liquid phases, respectively (Fig 2. b). In the present research work, enhancements of ~44% (1.64 J/g K) and ~75% (2 J/g K) were obtained for average c_p value in the solid phase of binary molten salt-based hBN nanocomposites with loading concentrations of 1 and 1.5 wt.% (Fig 2. (c, d)). The achieved average c_p value for the binary molten salt-based hBN nanocomposite with loading concentration of 1 wt.% in the liquid phase revealed ~118% enhancement over the binary molten salt without nanoparticles (Fig 2. c). The measured average c_p value of the binary molten salt-based hBN nanocomposite with loading concentration of 1.5 wt.% in the liquid phase represented promising enhancement of ~180% in comparison with pure binary molten salt (Fig 2. d).

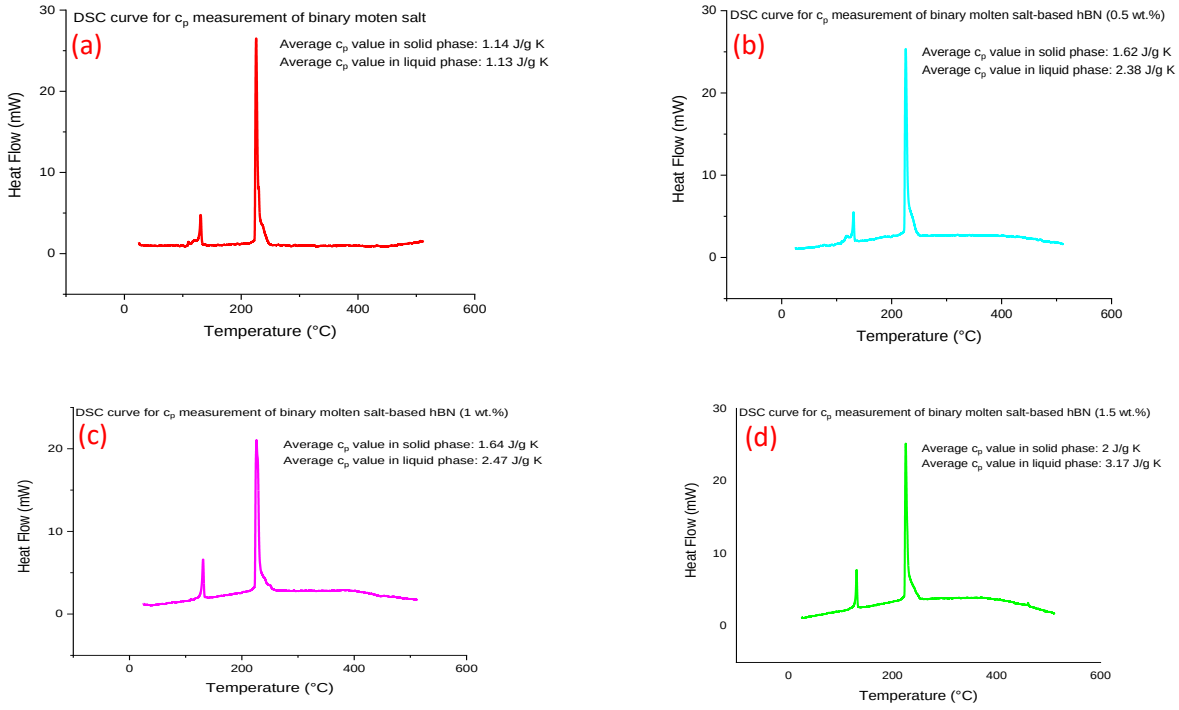


Figure 2. DSC curve for cp measurements of (a) binary molten salt (b) binary molten salt-based hBN nanocomposite (0.5 wt.%) (c) binary molten salt-based hBN nanocomposite (1 wt.%) (d) binary molten salt-based hBN nanocomposite (1.5 wt.%)

In this study, the addition of hexagonal boron nitride to the binary molten salt proved promising enhancements in the average value of specific heat capacity (c_p). The highest enhancement was obtained for the binary molten salt-based hBN nanocomposite with loading concentration of 1.5 wt.%. In a general model proposed by Shin, Tiznobaik and Banerjee [23], the enhancement in the c_p value is associated with fractal-like structures in MSBNFs which is composed of ions of the inorganic

salts. The fractal-like structures of the synthesized samples in this study are clear from SEM images in Figure 1. which represent the reasoning phenomenon in agreement with the proposed model by Shin et al. [23] for the specific heat capacity (c_p) enhancement mechanism.

3.3 Thermal stability characterization

Thermogravimetric analysis (TGA) was employed to measure mass loss and thermal stability. Heating rate was fixed at 10 °C/min and the measurements were performed at temperature range of 30-850 °C. The experimentally achieved results (Fig 3.) indicated increment of thermal stability for nanocomposites in compare with pure binary molten salt. Figure 3. revealed that the thermal decomposition in the binary molten salt starts from ~560°C, while the beginning of decomposition temperatures for binary molten salt-based hBN nanocomposites with loading concentrations of 0.5, 1 and 1.5 wt.% are ~639, ~642 and ~652°C. Smooth decomposition performance can be observed from figure 3. with introduction of more amount of hBN nanoparticles into the binary molten salt. Binary molten salt-based hBN nanocomposite with loading concentration of 1.5 wt.% represented ~16% enhancement in thermal stability over the binary molten salt. The chain-like structures (SEM images) due to presence of hBN nanoparticles and interfacial interacting between binary molten salt molecules and induced nanoparticles might be the consequent of enhancement in thermal stability.

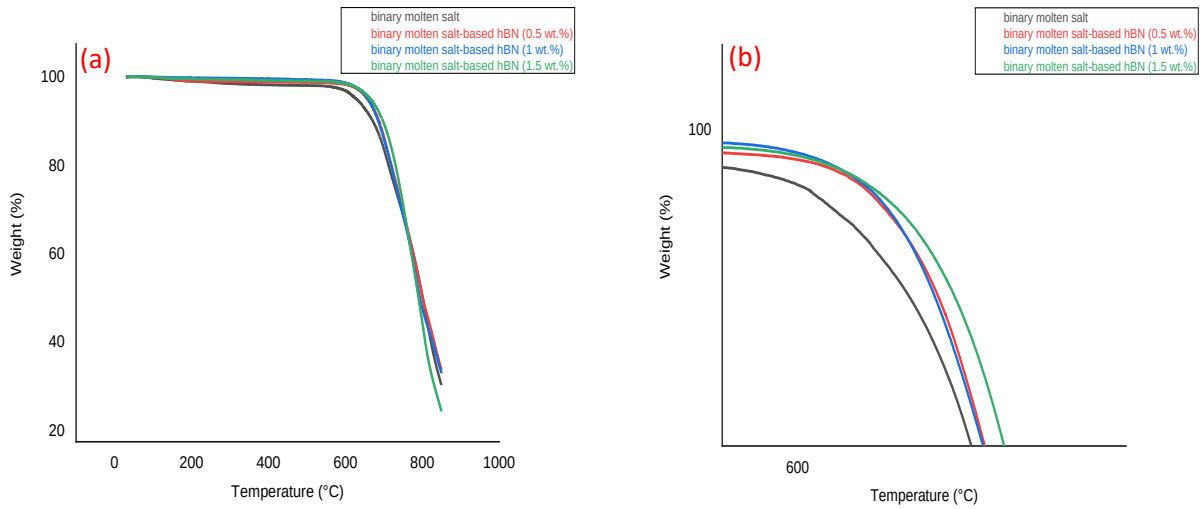


Figure 3. Thermal stability measurements of binary molten salt and binary molten salt-based hBN nanocomposites in three different concentrations (a) TGA curve for all samples (b) enlarged area of beginning of decomposition in TGA curve

4. Conclusions

In conclusion, the eutectic alkali binary molten salt-based hBN phase change materials with loading concentrations of 0.5, 1 and 1.5 wt.% and pure eutectic binary molten salt were synthesized using one-phase method. The alkali binary molten salt with/without nanoparticles were mixed physically (stirring), followed by mixing by using probe sonicator. The resultant samples were in well-dispersed circumstances. Scanning electronic microscopy (SEM) and energy-dispersive x-ray (EDX) indicated chain-like structures in the resultant nanofluid and elemental analysis using EDX proved good dispersion of hexagonal boron nitride nanoparticles. Specific heat capacity (c_p) and

melting temperature measurements were performed by using DSC. The experimentally achieved data for melting temperature of the pure binary molten salt and binary molten salt-based hBN nanocomposites with concentrations of 0.5, 1 and 1.5 wt.% was ~225 °C, which revealed that hBN nanoparticles do not affect the melting temperature of the synthesized samples. The average specific heat capacity (c_p) was measured for binary molten salt with/without nanoparticles in solid and liquid phases. The experimentally achieved data for average c_p values of the binary molten salt in solid and liquid phases were 1.14 and 1.13 J/g K, respectively. While, the average c_p values for the binary molten salt-based hBN nanocomposites with the highest loading concentration of nanoparticles (1.5 wt.%) in solid and liquid phases were 2 and 3.17 J/g K, respectively. The measured average c_p value of the binary molten salt-based hBN nanocomposite with loading concentration of 1.5 wt.% in the liquid phase represented promising enhancement of ~180% in comparison with pure binary molten salt. Thermal stability measurements expressed enhancement of thermal stability in binary molten salt induced with hBN nanoparticles. Binary molten salt-based hBN nanocomposite with loading concentration of 1.5 wt.% represented ~16% enhancement in thermal stability over the binary molten salt.

Acknowledgement
"R. Saidur would like to acknowledge the financial support provided by the Sunway University through the project no# STR-RCTR-RCNMET-001-2019".

References

1. Kuang, Y., et al., *A review of renewable energy utilization in islands.* Renewable and Sustainable Energy Reviews, 2016. **59**: p. 504-513.
2. Thirugnanasambandam, M., S. Iniyan, and R. Goic, *A review of solar thermal technologies.* Renewable and sustainable energy reviews, 2010. **14**(1): p. 312-322.
3. Quoilin, S., et al., *Techno-economic survey of Organic Rankine Cycle (ORC) systems.* Renewable and Sustainable Energy Reviews, 2013. **22**: p. 168-186.
4. Li, X., et al., *Improved transmission method for measuring the optical extinction coefficient of micro/nano particle suspensions.* Applied optics, 2016. **55**(29): p. 8171-8179.
5. Kalogirou, S.A., *Solar thermal collectors and applications.* Progress in energy and combustion science, 2004. **30**(3): p. 231-295.
6. Tiznobaik, H. and D. Shin, *Enhanced specific heat capacity of high-temperature molten salt-based nanofluids.* International Journal of Heat and Mass Transfer, 2013. **57**(2): p. 542-548.
7. Janz, G.J., *Physical properties data compilations relevant to energy storage...: data on additional single and multi-componant salt systems. Molten salts*. Vol. 4. 1981: US Dept. of Commerce, National Bureau of Standards: for sale by the Supt. of ….
8. Araki, N., et al., *Measurement of thermophysical properties of molten salts: mixtures of alkaline carbonate salts.* International journal of thermophysics, 1988. **9**(6): p. 1071-1080.
9. Nelson, I.C., D. Banerjee, and R. Ponnappan, *Flow loop experiments using polyalphaolefin nanofluids.* Journal of thermophysics and heat transfer, 2009. **23**(4): p. 752-761.
10. Shin, D. and D. Banerjee, *Enhancement of specific heat capacity of high-temperature silica-nanofluids synthesized in alkali chloride salt eutectics for solar thermal-energy storage applications.* International journal of heat and mass transfer, 2011. **54**(5-6): p. 1064-1070.
11. Bridges, N.J., A.E. Visser, and E.B. Fox, *Potential of nanoparticle-enhanced ionic liquids (NEILs) as advanced heat-transfer fluids.* Energy & Fuels, 2011. **25**(10): p. 4862-4864.
12. Chieruzzi, M., et al., *Effect of nanoparticles on heat capacity of nanofluids based on molten salts as PCM for thermal energy storage.* Nanoscale research letters, 2013. **8**(1): p. 448.
13. Dudda, B. and D. Shin, *Effect of nanoparticle dispersion on specific heat capacity of a binary nitrate salt eutectic for concentrated solar power applications.* International journal of thermal sciences, 2013. **69**: p. 37-42.

14. Seo, J. and D. Shin, *Enhancement of specific heat of ternary nitrate (LiNO3-NaNO3-KNO3) salt by doping with SiO2 nanoparticles for solar thermal energy storage.* Micro & Nano Letters, 2014. **9**(11): p. 817-820.
15. Liu, S., et al., *Development of a novel molten-salt filled with nanoparticles for concentration solar plants.* 2013.
16. Lin, Z., et al., *Exfoliated hexagonal boron nitride-based polymer nanocomposite with enhanced thermal conductivity for electronic encapsulation.* Composites Science and Technology, 2014. **90**: p. 123-128.
17. Song, W.L., et al., *Polymer/boron nitride nanocomposite materials for superior thermal transport performance.* Angewandte Chemie International Edition, 2012. **51**(26): p. 6498-6501.
18. Fang, X., et al., *Thermal energy storage performance of paraffin-based composite phase change materials filled with hexagonal boron nitride nanosheets.* Energy conversion and management, 2014. **80**: p. 103-109.
19. Su, D., et al., *Preparation and thermal properties of n–octadecane/stearic acid eutectic mixtures with hexagonal boron nitride as phase change materials for thermal energy storage.* Energy and Buildings, 2016. **131**: p. 35-41.
20. Friction, L., *Hexagonal Boron Nitride (hBN) Powder* 2008.
21. Huang, Y., et al., *Effect of in-situ synthesized nano-MgO on thermal properties of NaNO3-KNO3.* Solar Energy, 2018. **160**: p. 208-215.
22. Muñoz-Sánchez, B., et al., *Molten salt-based nanofluids as efficient heat transfer and storage materials at high temperatures. An overview of the literature.* Renewable and Sustainable Energy Reviews, 2018. **82**: p. 3924-3945.
23. Shin, D., H. Tiznobaik, and D. Banerjee, *Specific heat mechanism of molten salt nanofluids.* Applied Physics Letters, 2014. **104**(12): p. 121914.

Penerbit Akademia Baru

Engineering Science and Technology Conference Proceedings

Journal homepage: www.akademiabaru.com/EST.html

Investigation of Newtonian and Power-Law Blood Flow Models in a 180° Curved Pipe at Low to Medium Shear Rate

Open Access

Samar A. Mahrous[1,2,*], Nor Azwadi Che Sidik[1,3] and Khalid M. Saqr[2,4]

[1] Department of Thermo-fluid Universiti Teknologi Malaysia, 81310 UTM Skudai, MALAYSIA
[2] College of Engineering and Technology, Arab Academy for Science, Technology and Maritime Transport, P.O.BOX 1029 Alexandria, EGYPT
[3] Malaysia – Japan International Institute of Technology (MJIIT), University Teknologi Malaysia Kuala Lumpur, 54100 Kuala Lumpur, MALAYSIA
[4] Research Center for Computational Neurovascular Biomechanics (RCCNB), Alexandria University Hospital in Smouha, 21554 Alexandria, EGYPT

ABSTRACT

Numerical investigations of blood flow were conducted to obtain quantitative information on axial velocity distribution in ideal vasculature (i.e. straight and toroidal pipes) for a Newtonian and non-Newtonian fluid at low to medium shear rates. Validated CFD models of blood flow were established and parameterized to solve steady incompressible blood flow under Reynolds number of 50~200. The calculations of the Reynolds number and boundary conditions adopted the shear-thinning index of the power-law models to provide physically correct benchmark for the comparison presented herein. Shear rate values had a range of 20~200 s^{-1} which represents the physiological range found in cerebral vasculature. This study provides the means to estimate the effect of the non-Newtonian properties of the blood on the flow patterns. It is clearly shown that the difference between Newtonian and power-law blood flow models is not significantly affected by Reynolds number for the current range of shear rate. The differences identified in the pressure-drop per unit length and average wall-shear stress were found to be of significant values. The difference between the Newtonian and power-law model (case1) in the pressure drop per unit length for the straight pipe was 386 while for the curved pipe was 371. These differences increased to 538 at Re=200 for the straight pipe and reached 603 for the curved pipe. This research suggests that the non-Newtonian effects of cerebral blood flow should be considered in the respective CFD models.

Keywords:
non-Newtonian fluid; CFD; shear rate;
average wall shear stress; pressure drop

Copyright © 2019 PENERBIT AKADEMIA BARU - All rights reserved

1. Introduction

Blood shows non-Newtonian behaviour as a result of its complex mixture of proteins and of suspended cellular elements in plasma [1, 2]. However, several studies have considered blood as a Newtonian fluid under the justification that in large arteries the rheological properties of blood become linear when shear rate is greater than 100 s^{-1} [3-5]. The non-Newtonian flow effects could become significant when the shear rate is below 100 s^{-1} [6].

In reality blood exhibit non-Newtonian characteristics including shear-thinning and viscoelasticity, but in this study, we will focus on the shear-thinning behaviour. Several

* *Corresponding author.*
E-mail address: samar.mahrous@aast.edu (Samar A. Mahrous)

studies have presented that viscoelastic behaviour is only noticeable in pulsatile flow [7], and that viscoelasticity is only substantial at shear rates less than $10s^{-1}$ [8].

Studies revealed that WSS is an important hemodynamic factor in intracranial aneurysm genesis, growth and rupture [9-12]. The most important parameter that affect the WSS is the blood viscosity. Previous works proved that there is an overestimation of the WSS, when neglecting the effect of the shear-thinning in the simulation [13, 14]. On the contrary, some discovered that there is an underestimation of the WSS by neglecting the shear-thinning [15, 16].

The effect of four non-Newtonian models (Casson, generalized power law, and the two form of Carreau models) have been investigated by studying the WSS of cerebral aneurysms [17]. It was found that all the non-Newtonian models report a lower WSS than that obtained with a Newtonian model in the same geometry. Additionally, they found that the Carreau model is the most conservative predictor of aneurysm vulnerability as well. Johnston et al. [18] studied five non-Newtonian blood models (power-law, Carreau, walburn-schneck, casson and generalized power law), as well as the usual Newtonian model of blood viscosity to determine the wall shear stress in four different right coronary arteries at a particular point in the cardiac cycle. It was found that the Newtonian model of blood viscosity is a good approximation in regions of midrange to high shear greater than 100 s^{-1}, it is recommended to use the Generalised Power Law model (which tends to the Newtonian model in those shear ranges in any case) in order to reach better approximation of wall shear stress at low shear less than 100 s^{-1}.

Some authors concluded that the non-Newtonian behavior for flow in large arteries is crucial [19-21] while others found it is insignificant assumption [22, 23]. Gijsen et al. [21] highlighted several differences in the velocity profiles between Newtonian and non-Newtonian models when they investigated the blood flow through 90° curved tube. It is more accurate to include the shear-thinning non-Newtonian property of blood viscosity [24, 25]. Xiao Liu et al., investigated the effect of the non-Newtonian (Carreau model) pulsatile blood flow on the transports of oxygen and low-density lipoproteins (LDLs) in the human aorta and compared the results with those of the Newtonian steady blood flow [26]. Results showed that the shear thinning nature of blood has small effect on LDL and oxygen transport in most regions of the aorta, but in the atherogenic-prone areas where luminal surface LDL concentration is high and oxygen flux is low, its effect is significant. In addition, Durairaj et al. [27] reported that the non-Newtonian behavior of blood has a significant influence on the WSS value in human aorta. Thus, the non-Newtonian properties should be considered, when simulating the blood flow in aorta. The effect of the blood viscosity changes due to hematocrit (Hct) variations and for a wide range of shear rate on the oxygen transport in a stenosed artery after angioplasty has been studied [28]. Results revealed that the oxygen transport in this constricted artery is significantly influenced by the non-Newtonian shear-thinning (Carreau model) property of blood viscosity with different Hct concentrations. This study has significant implications for drug therapy related to blood-thinning medication. A numerical study has shown that the blood's nonlinear non-Newtonian (Carreau-Yasuda) properties resulted in more accurate predictions of wall shear stress than the Newtonian model within a stented artery [29]. Therefore, the blood's nonlinearity plays an important role, and that the Newtonian model is not appropriate to be used to model the blood flow.

The purpose of this paper is to elucidate the difference between Newtonian and power-law blood flow models at shear rate values corresponding to such found in cerebral

vasculature. The importance of this work is driven by the ongoing debate in literature regarding the viability of modelling the non-Newtonian effects in cerebral vessels.

2. Mathematical Model and Numerical Approach

2.1 Governing equation

The flow field is assumed to be incompressible, steady and three dimensional. The governing equations are the continuity equation (conservation of mass) and the momentum equation in the three dimensions (conservation of momentum).

$$\nabla.\mathbf{v} = 0 \tag{1}$$

$$\rho(\mathbf{v}.\boldsymbol{\nabla}\mathbf{v}) = -\boldsymbol{\nabla}p + \nabla.\boldsymbol{\tau} \tag{2}$$

Where,

$\rho = density\ of\ the\ blood\ equals\ to\ 1060\ kg/m^3$
$\mathbf{v} =$ velocity field
$p = pressure$
$\boldsymbol{\tau} = deviatoric\ stress\ tensor$

The stress tensor is related to the strain rate tensor ($\dot{\gamma}$) as follows,

$$\boldsymbol{\tau} = \boldsymbol{\mu}\,\dot{\gamma} \tag{3}$$

Where,

$$\dot{\gamma} = \left(\frac{\partial v_i}{\partial x_j} + \frac{\partial v_j}{\partial x_i}\right) \tag{4}$$

Newtonian flow model:

For the Newtonian flow model, the value of blood viscosity is constant (0.0035 Pa.s).

Power-law model:

In this study the Power-law model, has been used to account for the shear-thinning behavior of the blood.

$$\mu = k\,\dot{\gamma}^{n-1} \tag{5}$$

Where,

$\mu = dynamic\ viscosity$
$k = flow\ consistancy\ index$
$\dot{\gamma} = shear\ rate$
Case 1

Parameters for Power Law model put as consistency index (k = 0.035 Pa.s^n), Power law index (n = 0.6) and density of blood 1060 kg/m3 .

Case 2

Parameters for Power Law model put as consistency index (k = 0.01467 Pa.s^n), Power law index (n = 0.7755) and density of blood 1060 kg/m3 [2].

2.1.1 Reynolds number calculations

For the Newtonian model, the Reynolds number is calculated as

$$Re = \frac{\rho u_m \mathrm{d}}{\mu} \tag{6}$$

Table 1
The corresponding mean velocity at different Reynolds number for the Newtonian model

Reynolds number, Re	(m/s)u_m
50	0.033
100	0.066
200	0.132

For the non-Newtonian model, the Reynolds number is calculated as

$$Re = \frac{\rho {u_m}^{2-\mathrm{n}} \mathrm{d}^{\mathrm{n}}}{\mathrm{k}} \tag{7}$$

Table 2
The corresponding mean velocity at different Reynolds number for the non-Newtonian model (case 1 and case 2)

Reynolds number, Re	u_m (m/s) Case (1)	u_m (m/s) Case (2)
50	0.0997	0.0753
100	0.164	0.133
200	0.268	0.233

2.2 Models Geometry

The first stage concerning modelling flow in more realistic vessel shapes is to study simple geometries such as straight pipe (case 1) and curved pipe (case 2) in order to mimic the intracranial arteries. Both models were meshed using GAMBIT software (meshing generator).

2.2.1 Straight pipe

The geometry used in validation cases for Newtonian and Non-Newtonian models of flow of blood is a simple rigid straight pipe as that shown in figure (1) with length of 0.1m and a diameter of 0.005m.



Fig. 1. Ideal geometry used in straight pipe

Table 3
Summaries of geometries

Grid	Number of elements	Element shape	Turning angle	Dimension
Straight pipe	150000	Hexahedral	0	D=5mm
Curved pipe	300000	Hexahedral	180^0	D=5mm

2.2.2 Curved pipe

The curved pipe used to model the flow of is shown in figure 5 with a diameter of 0.005m. Several models with different grid sizes were tested and the result of the grid independence study was a grid with a total number of elements 300000 elements with 10 boundary layers have been attached to the walls of the curved pipe thus ensuring accurate computation, with interval size equal to 0.06 (mm). The wall of the pipe is assumed to be rigid. The velocity profiles of all models were plotted on five locations, as shown in figure 2. The velocity profiles are compared at different Reynolds number in figures 6-10. The pulsatility of the flow was not included in this study.

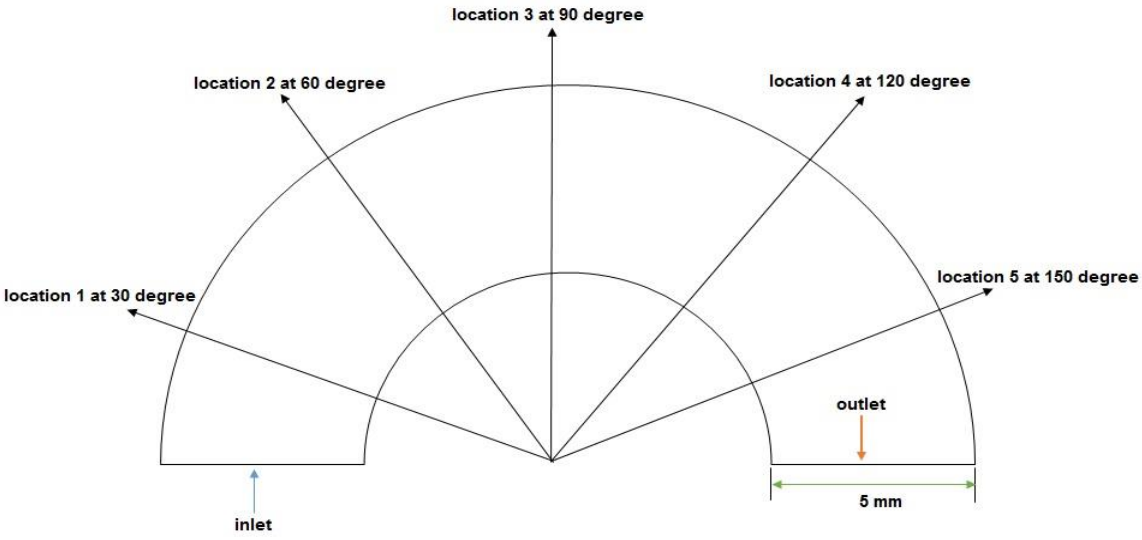


Fig. 2. Ideal geometry used in curved pipe

2.3 Mesh Sensitivity Analysis

An analysis of mesh sensitivity was firstly carried out with a steady flow condition. The mesh refinement was confirmed with several mesh systems with the element number increasing up to 200000 cells for the straight pipe and up to 0.5 million for the curved pipe based on the velocity profile. The velocity difference in-between 50000 ~ 200000 elements for the straight pipe and 100000 ~ 0.5 million elements for the curved pipe were less than 2%. This is made to make sure that the cells larger number do not affect the simulation results. For the straight pipe, the results are similar when used 200000 cells and 150000 cells as shown in figure 3. However, it was slightly different when used 100000 cells, so the 150000 hexahedral cells considered for simulation with a minimum element size of 0.06 mm and 0.3 ms. For the curved pipe, we considered the mesh system of 300000 hexahedral elements with a minimum element size of 0.06 mm and 0.2 ms.

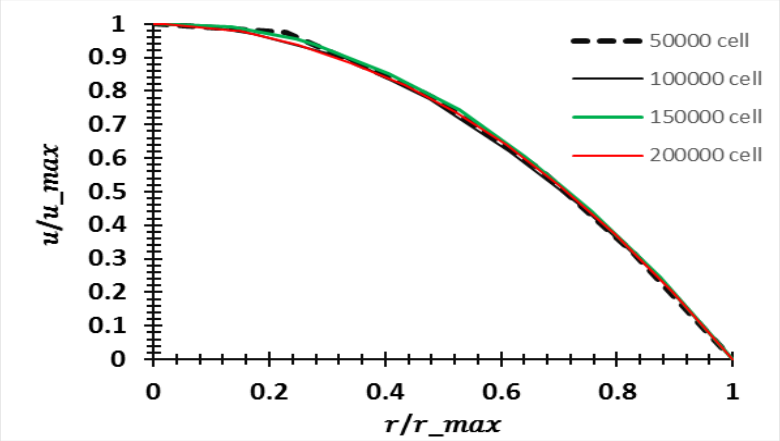


Fig. 3. Mesh Sensitivity Test (Re=100) of straight pipe

2.4 Boundary Condition

The model has one inlet (velocity inlet) and one outlet (pressure outlet, P = 0 pa) with no slip boundary condition and the wall of the pipe was assumed to be rigid.

2.4.1 The Newtonian case

For the Newtonian case, the inlet velocity profile is the fully developed Hagen-Poiseuille flow.

$$u(r) = u_m(1 - \frac{r^2}{R^2}) \tag{8}$$

2.4.2 The non- Newtonian case

For the non-Newtonian case, the inlet velocity profile is the fully developed Power-law pipe flow [30-35].

$$u(r) = \frac{\mathrm{n}}{\mathrm{n+1}}\left(\frac{\mathrm{dp}}{\mathrm{dz}}\ \frac{1}{2\mathrm{k}}\right)^{\frac{1}{\mathrm{n}}}\left[R^{\frac{n+1}{n}} - r^{\frac{n+1}{n}}\right] \tag{9}$$

$$u_m = \frac{n}{n+1}\left(\frac{dp}{dz}\frac{1}{2k}\right)^{\frac{1}{n}} R^{\frac{n+1}{n}} \quad (10)$$

$$\frac{u(r)}{u_m} = 1 - \left(\frac{r}{R}\right)^{\frac{n+1}{n}} \quad (11)$$

$$u(r) = u_m\left[1 - \left(\frac{r}{R}\right)^{\left(\frac{n+1}{n}\right)}\right] \quad (12)$$

2.5 CFD FLUENT Solver Implementation and Numerical Schemes

The models used in this study were 3D model, incompressible, laminar and steady. The governing equations described before were discretized by the finite volume method. The numerical simulation was carried out with the ANSYS package (FLUENT 16). No turbulence model was applied due to the relatively low Reynolds number in this study. Each model required approximately 4 days of CPU time on an HPC with a 4 Intel Xeon (2.6GHz); parallel computation with a cluster on 32 nodes was carried out with Platform Computing. The convergence criteria for iterative errors were set to be of 1×10^{-6}.

2.6 Validation with Exact Solution

The model has been validated for the steady Newtonian and non-Newtonian (Power-law) against the exact solution of the fully developed pipe flow (Hagen-Poiseuille solution) figure 4 and figure 5 respectively, at Reynolds number (Re) =100. The numerical results agree well with the exact solution with error less than 2%.

2.6.1 Validation of the Newtonian case

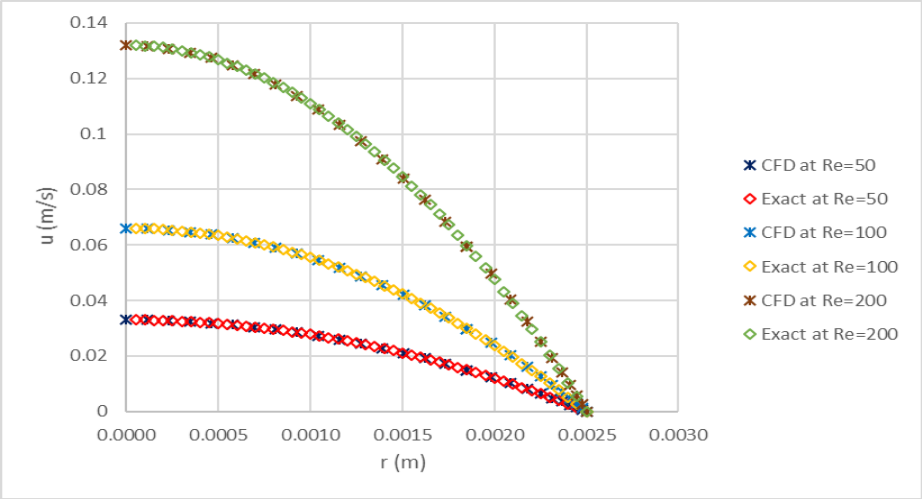
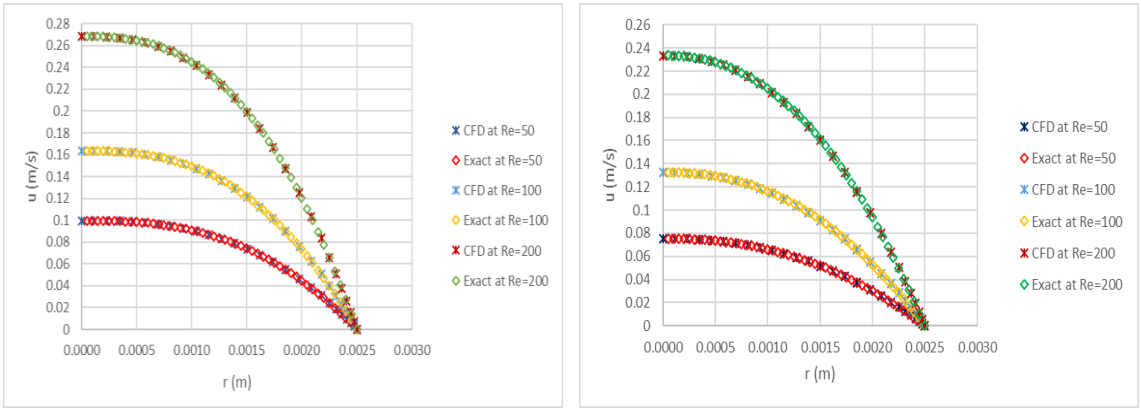


Fig. 4. velocity profile at different Reynolds number for Newtonian model in straight pipe (Density of blood 1060 kg/m^3 and viscosity 0.0035 Pa.s)

2.6.2 Validation of the non-Newtonian case



(a) (b)

Fig. 5. velocity profile at different Reynolds number for the power-law model in straight pipe A) case 1 and B) case 2

3. Results and Discussion

A Newtonian model and two groups of Power-law model with different parameters have been simulated on the curved pipe at five different locations. Each of the three models simulated at three different Reynolds number ranged from (50 to 200) to clarify the effect of the rheological models (Newtonian and Power-law) on hemodynamic factors like the velocity profiles, the wall shear stress (WSS) and pressure drop per unit length.

3.1 Flow structure and velocity profiles in Curved pipe

Figures 6-10 show the velocity profiles of the curved pipe with different rheological models at different locations. Differences between the measured velocity distribution of the Newtonian and non-Newtonian fluid are evident. It can be noticed that the velocity profiles of the Newtonian model at Reynolds number ranging from 50 to 200 showed usual parabolic profiles. In addition, the two groups of the non-Newtonian model have similar behavior. However, there are quantitative differences recorded.

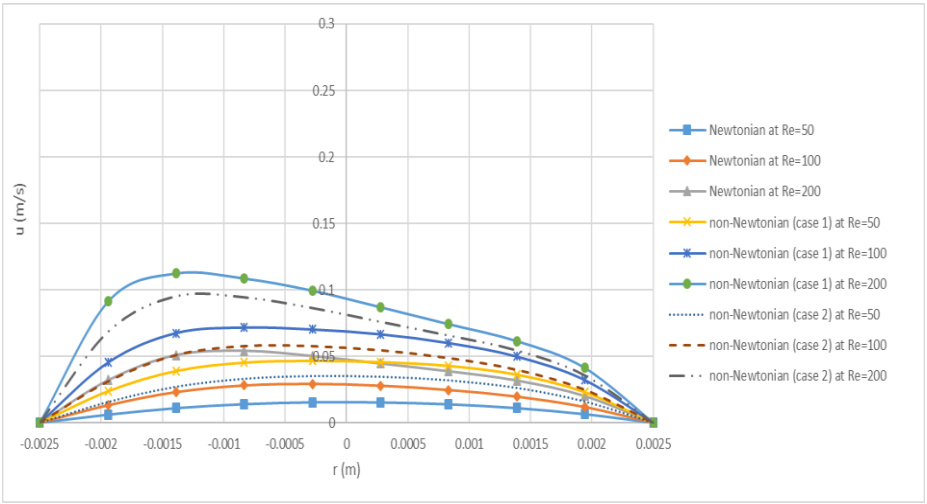


Fig. 6. Velocity profile at different Reynolds number for Newtonian and non-Newtonian models in curved pipe at location 1

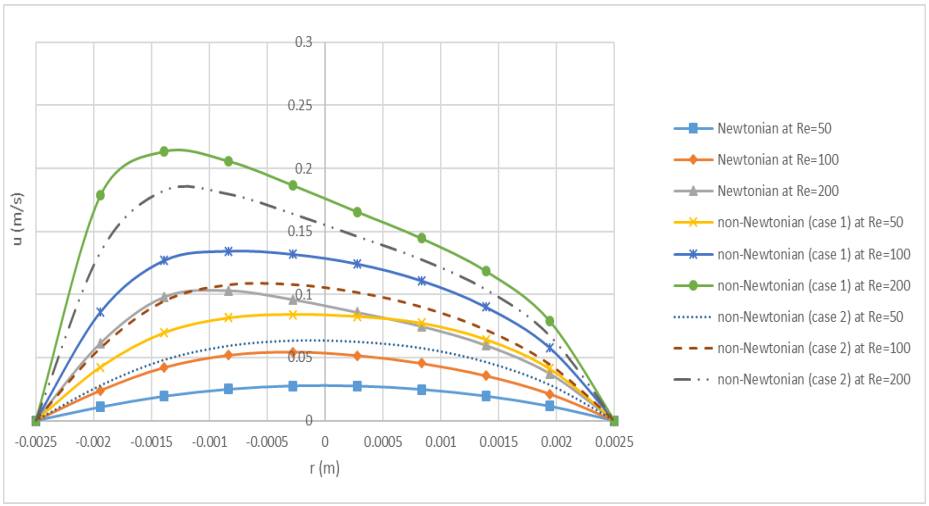


Fig. 7. Velocity profile at different Reynolds number for Newtonian and non-Newtonian models in curved pipe at location 2

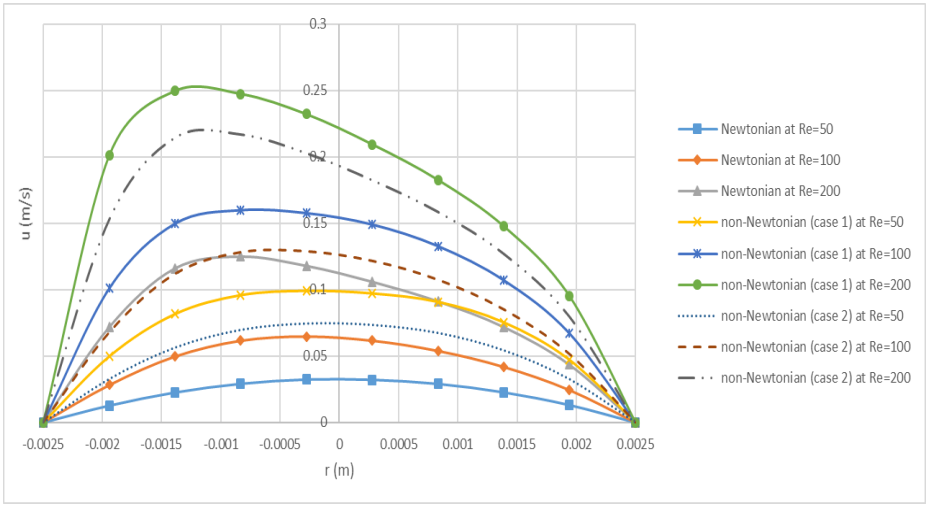


Fig. 8. Velocity profile at different Reynolds number for Newtonian and non-Newtonian models in curved pipe at location 3

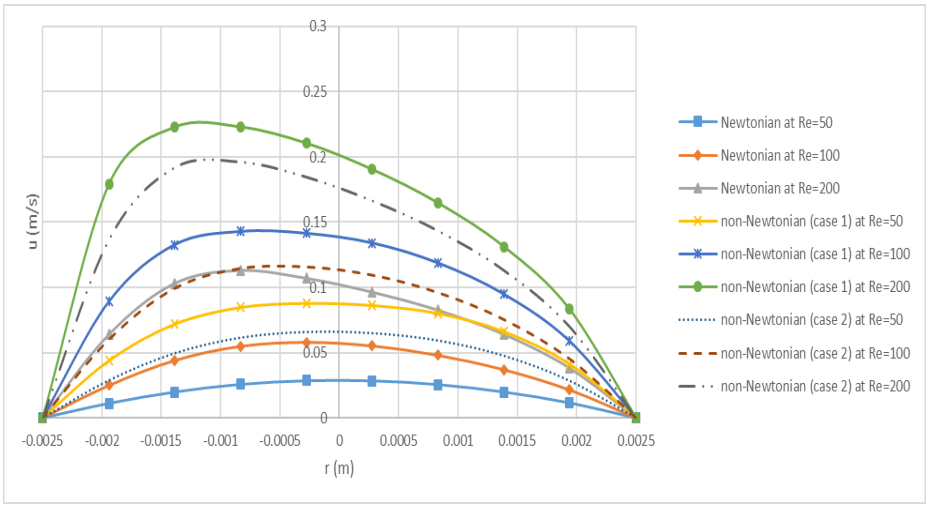


Fig. 9. Velocity profile at different Reynolds number for Newtonian and non-Newtonian models in curved pipe at location 4

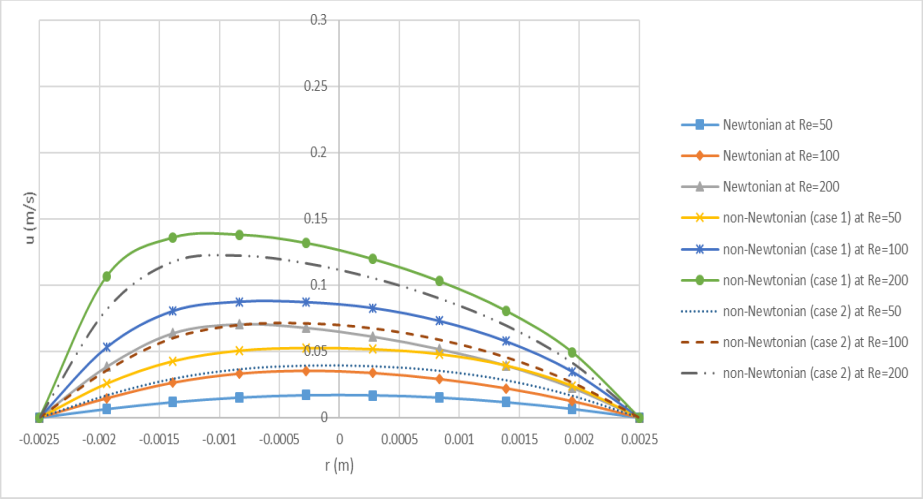


Fig. 10. Velocity profile at different Reynolds number for Newtonian and non-Newtonian models in curved pipe at location 5

The flow field for Re = 50 exhibits similar behaviour for all Newtonian and non-Newtonian solutions, which has axisymmetric profile in space. It is shown that the maximum velocity reached during the Newtonian solution is 0.033 m/s at station 3 ($90°$) while the minimum velocity reached is 0.015 m/s at the first station ($30°$). In addition, during the non-Newtonian solution such values increased. For case 1, the maximum velocity is 0.1 m/s at station 3 ($90°$), while the minimum velocity reached is 0.044 m/s at ($30°$). On the other hand, when increasing the power-law index in case 2 (n=0.7755), the velocity values decreased than case1(n=0.6) but still larger than the Newtonian solution. Starting from Re = 100, The flow field exhibits similar properties for Newtonian as such of Re = 50, however, this behaviour become axisymmetric pattern for both non-Newtonian cases. it is clear that the asymmetric behaviour of the instability region becomes more manifested at power-law index (n=0.6), as shown in figures 6-10.

3.2 Wall shear stress comparison between Newtonian and non-Newtonian
3.2.1 Straight pipe

It is evident that the magnitude of the average WSS of the non-Newtonian model for both cases are greater than the Newtonian model in straight pipe as shown in table 4. The deviation between them at Re =50 for case 1 is 84% while for case 2 is 75%. At Re=100, the deviation between the two rheological model is decreased for case 1 is 75% while at case 2 is 66%. At Re=200, the difference between the Newtonian and both cases of non-Newtonian are almost 3% for case 1, the deviation is 67% while for case 2, the deviation is 64%.

Table 4
The average wall shear stress of both Newtonian and non-Newtonian models in straight pipe

	Newtonian model	non-Newtonian model (case 1)	non-Newtonian model (case 2)	Deviation between Newtonian and non-Newtonian	Deviation between Newtonian and non-Newtonian
Re	**WSS (Pa)**	**WSS (Pa)**	**WSS (Pa)**	**(case 1)**	**(case 2)**
50	0.09238913	0.57531012	0.3908808	0.48292099	0.29849167
100	0.1847913	0.7743354	0.6063396	0.5895411	0.4215483
200	0.36961975	1.0422015	0.9405627	0.67258175	0.57094295

3.2.2 Curved pipe

Table 5 represents the average WSS of the Newtonian and both cases of the non-Newtonian models in the curved pipe. It is clear that the values are nearly similar to the straight pipe. The difference between the two geometries regarding the average WSS is 1%.

Table 5
The average wall shear stress of both Newtonian and non-Newtonian models in curved pipe

	Newtonian model	Non-Newtonian model (case 1)	Non-Newtonian model (case 2)	Deviation between Newtonian and non-Newtonian	Deviation between Newtonian and non-Newtonian
Re	**WSS (Pa)**	**WSS (Pa)**	**WSS (Pa)**	**(case 1)**	**(case 2)**
50	0.092516523	0.57935402	0.3924499	0.486837497	0.299933377
100	0.19052201	0.82062814	0.6347463	0.63010613	0.47295262
200	0.4256658	1.237555	1.1102546	0.8118892	0.6845888

It can be noted that the difference in WSS values between all cases is less prominent than for the velocity profiles. This difference is noticeable mostly in large Reynolds number.

3.3 Shear rate comparison between Newtonian and non-Newtonian in straight and curved pipes

The shear rate of both non-Newtonian cases is greater than the Newtonian model as shown in table 6. The high shear rate is present at the non-Newtonian model (case 1) which indicates that the flow is fast, while the Newtonian case is presented the low shear rate which means that the flow is slow at all values of Reynolds number and at a constant diameter for both geometry which is 5mm.

Table 6
The shear rate of both Newtonian and non-Newtonian models

	Shear rate Newtonian	Shear rate non-Newtonian (case 1)	Shear rate non-Newtonian (case 2)
Re	$\dot{\gamma}\ (1/s)$	$\dot{\gamma}\ (1/s)$	$\dot{\gamma}\ (1/s)$
50	26.4	79.76	60.24
100	52.8	131.2	106.4
200	105.6	214.4	186.4

3.4 Pressure drop comparison between Newtonian and non-Newtonian

As a final comparison, the effect of shear-thinning model with respect to Newtonian model has been integrated by computing the pressure drop per unit length for both geometries at different Reynolds number as shown in table 7 and 8. It is found that the pressure drop per unit length for the curved pipe is less than the straight pipe for both rheological models. However, it can be seen that the variation regarding the rheological models is greater than the variation regarding the geometry. It can be seen that the choice of blood rheology impacts the result of pressure drop. The pressure drop per unit length calculated from the non-Newtonian models was significantly greater than the obtained from the Newtonian case. This result reveals that the shear-thinning model have larger viscous

forces than the Newtonian model and hence the blood rheology can play a perceptible role in the resulting computed pressure drop.

3.4.1 Straight pipe

Table 7
The pressure drop per unit length of the Newtonian model and the non-Newtonian cases in straight pipe

	Newtonian model	Non-Newtonian model (case 1)	Non-Newtonian model (case 2)
Re	**(mPa/mm)Δp**	**(mPa/mm)Δp**	**(mPa/mm)Δp**
50	73.91963	460.30552	312.74418
100	147.86166	619.58694	485.17105
200	295.7867	833.98041	752.6723

3.4.2 Curved pipe

Table 8
The pressure drop per unit length of the Newtonian model and the two cases of the non-Newtonian model in curved pipe

	Newtonian model	Non-Newtonian model (case 1)	Non-Newtonian model (case 2)
Re	**(mPa/mm)Δp**	**(mPa/mm)Δp**	**(mPa/mm)Δp**
50	70.61956	442.0148	299.4461
100	144.4571	619.922	479.9669
200	316.1621	919.2894	822.4815

It was found that the effect of the rheology with respect to the pressure drop per unit length is more significant than the impact of the geometry. For the Newtonian model, the maximum deviation between the straight and curved pipe regarding the pressure drop per unit length at Re=200 was 6% while, for the non-Newtonian model (case 1) the maximum difference was 9% and that the difference between the straight and curved pipe for the non-Newtonian model (case 2) was 8%. Furthermore, it was shown that for the straight pipe the maximum deviation between the Newtonian and the power-law model (case 1) was 65% while between the Newtonian and power-law (case2) was 61%. For the curved pipe these values slightly increased by 1%. Thus, it was clearly shown that the non-Newtonian behaviour could not be neglected when simulating blood flow.

4. Conclusions

In most studies, the non-Newtonian behaviour is often neglected. This study was conducted for two simple flow geometries related to cerebral arteries in order to compare between Newtonian and non-Newtonian rheologies at low to medium shear rates. It was found that the geometry has a little impact on the rheological behaviour of blood. Neglecting the non-Newtonian effects causes significant change in the pressure drop per unit length. However, the deviation between the Newtonian and both cases of the power-law model with respect to the WSS in the two geometries was less prominent than the differences in the pressure drop per unit length. This work could be extended by simulating unsteady flow in curved pipe. Comparing unsteady flow simulations with the current study would provide a more complete insight into the influences of using the non-Newtonian model.

Acknowledgement

The authors would like to thank the Center for Information and Communication Technology (CICT) in Universiti Teknologi Malaysia for supporting and providing facilities and services of high-performance computing.

References

[1] Thurston, G. B. "Rheological Parameters for the Viscosity Viscoelasticity and Thixotropy of Blood." [In eng]. *Biorheology* 16, no. 3 (1979): 149-62.

[2] Campo-Deaño, Laura, Mónica S. N. Oliveira, and Fernando T. Pinho. "A Review of Computational Hemodynamics in Middle Cerebral Aneurysms and Rheological Models for Blood Flow." *Applied Mechanics Reviews* 67, no. 3 (2015): 0308011-16.

[3] Carlier, S. G., L. C. van Damme, C. P. Blommerde, J. J. Wentzel, G. van Langehove, S. Verheye, M. M. Kockx, M. W. Knaapen, C. Cheng, F. Gijsen, D. J. Duncker, N. Stergiopulos, C. J. Slager, P. W. Serruys, and R. Krams. "Augmentation of Wall Shear Stress Inhibits Neointimal Hyperplasia after Stent Implantation: Inhibition through Reduction of Inflammation?" [In eng]. *Circulation* 107, no. 21 (Jun 03 2003): 2741-6.

[4] Benard, N., D. Coisne, E. Donal, and R. Perrault. "Experimental Study of Laminar Blood Flow through an Artery Treated by a Stent Implantation: Characterisation of Intra-Stent Wall Shear Stress." [In eng]. *J Biomech* 36, no. 7 (Jul 2003): 991-8.

[5] Cho, Y. I., and K. R. Kensey. "Effects of the Non-Newtonian Viscosity of Blood on Flows in a Diseased Arterial Vessel. Part 1: Steady Flows." [In eng]. *Biorheology* 28, no. 3-4 (1991): 241-62.

[6] Pedley, T. J. *The Fluid Mechanics of Large Blood Vessels*. Cambridge Monographs on Mechanics. Cambridge: Cambridge University Press, 1980. doi:DOI: 10.1017/CBO9780511896996.

[7] Rojas, H. A. "Numerical Implementation of Viscoelastic Blood Flow in a Simplified Arterial Geometry." [In eng]. *Med Eng Phys* 29, no. 4 (May 2007): 491-6.

[8] Lerche, Dietmar, Georgios Vlastos, Brigitte Koch, Manfred Pohl, and Klaus Affeld. "Viscoelastic Behaviour of Human Blood and Polyacrylamide Model Fluids for Heart Valve Testing." 3 (1993): 1283-89.

[9] Burleson, A. C., and V. T. Turitto. "Identification of Quantifiable Hemodynamic Factors in the Assessment of Cerebral Aneurysm Behavior. On Behalf of the Subcommittee on Biorheology of the Scientific and Standardization Committee of the Isth." [In eng]. *Thrombosis and haemostasis* 76, no. 1 (1996/07// 1996): 118-23.

[10] Singh, P. K., A. Marzo, B. Howard, D. A. Rufenacht, P. Bijlenga, A. F. Frangi, P. V. Lawford, S. C. Coley, D. R. Hose, and U. J. Patel. "Effects of Smoking and Hypertension on Wall Shear Stress and Oscillatory Shear Index at the Site of Intracranial Aneurysm Formation." [In eng]. *Clin Neurol Neurosurg* 112, no. 4 (May 2010): 306-13.

[11] Shojima, M., S. Nemoto, A. Morita, M. Oshima, E. Watanabe, and N. Saito. "Role of Shear Stress in the Blister Formation of Cerebral Aneurysms." [In eng]. *Neurosurgery* 67, no. 5 (Nov 2010): 1268-74; discussion 74-5.

[12] Evju, O., K. Valen-Sendstad, and K. A. Mardal. "A Study of Wall Shear Stress in 12 Aneurysms with Respect to Different Viscosity Models and Flow Conditions." [In eng]. *J Biomech* 46, no. 16 (Nov 15 2013): 2802-8.

[13] Xiang, J., M. Tremmel, J. Kolega, E. I. Levy, S. K. Natarajan, and H. Meng. "Newtonian Viscosity Model Could Overestimate Wall Shear Stress in Intracranial Aneurysm Domes and Underestimate Rupture Risk." [In eng]. *J Neurointerv Surg* 4, no. 5 (Sep 2012): 351-7.

[14] Morales, H. G., I. Larrabide, A. J. Geers, M. L. Aguilar, and A. F. Frangi. "Newtonian and Non-Newtonian Blood Flow in Coiled Cerebral Aneurysms." *Journal of Biomechanics* 46, no. 13 (2013): 2158-64.

[15] Cavazzuti, Marco, Mark Atherton, Michael Collins, and Giovanni Barozzi. "Beyond the Virtual Intracranial Stenting Challenge 2007: Non-Newtonian and Flow Pulsatility Effects." *Journal of Biomechanics* 43, no. 13 (2010/09/17/ 2010): 2645-47.

[16] Cavazzuti, M., M. A. Atherton, M. W. Collins, and G. S. Barozzi. "Non-Newtonian and Flow Pulsatility Effects in Simulation Models of a Stented Intracranial Aneurysm." *Proceedings of the Institution of Mechanical Engineers, Part H: Journal of Engineering in Medicine* 225, no. 6 (2011/06/01 2011): 597-609.

[17] Fisher, C., and J. S. Rossmann. "Effect of Non-Newtonian Behavior on Hemodynamics of Cerebral Aneurysms." [In eng]. *J Biomech Eng* 131, no. 9 (Sep 2009): 0910041-9.

[18] Johnston, B. M., P. R. Johnston, S. Corney, and D. Kilpatrick. "Non-Newtonian Blood Flow in Human Right Coronary Arteries: Transient Simulations." [In eng]. *J Biomech* 39, no. 6 (2006): 1116-28.

[19] Rodkiewicz, C. M., P. Sinha, and J. S. Kennedy. "On the Application of a Constitutive Equation for Whole Human Blood." [In eng]. *J Biomech Eng* 112, no. 2 (May 1990): 198-206.
[20] Tu, C., and M. Deville. "Pulsatile Flow of Non-Newtonian Fluids through Arterial Stenoses." [In eng]. *J Biomech* 29, no. 7 (Jul 1996): 899-908.
[21] Gijsen, F. J., E. Allanic, F. N. van de Vosse, and J. D. Janssen. "The Influence of the Non-Newtonian Properties of Blood on the Flow in Large Arteries: Unsteady Flow in a 90 Degrees Curved Tube." [In eng]. *J Biomech* 32, no. 7 (Jul 1999): 705-13.
[22] Perktold, K., R. Peter, and M. Resch. "Pulsatile Non-Newtonian Blood Flow Simulation through a Bifurcation with an Aneurysm." [In eng]. *Biorheology* 26, no. 6 (1989): 1011-30.
[23] Ballyk, P. D., D. A. Steinman, and C. R. Ethier. "Simulation of Non-Newtonian Blood Flow in an End-to-Side Anastomosis." [In eng]. *Biorheology* 31, no. 5 (Sep-Oct 1994): 565-86.
[24] Marossy, A., P. Svorc, I. Kron, and S. Gresova. "Hemorheology and Circulation." [In eng]. *Clin Hemorheol Microcirc* 42, no. 4 (2009): 239-58.
[25] Pohl, M., M. O. Wendt, S. Werner, B. Koch, and D. Lerche. "In Vitro Testing of Artificial Heart Valves: Comparison between Newtonian and Non-Newtonian Fluids." [In eng]. *Artif Organs* 20, no. 1 (Jan 1996): 37-46.
[26] Liu, Xiao, Yubo Fan, Xiaoyan Deng, and Fan Zhan. "Effect of Non-Newtonian and Pulsatile Blood Flow on Mass Transport in the Human Aorta." *Journal of Biomechanics* 44, no. 6 (2011/04/07/ 2011): 1123-31.
[27] Durairaj, Kumar, R. Vinoth, A. Raviraj, and C. S. Vijay Shankar. "Non-Newtonian and Newtonian Blood Flow in Human Aorta: A Transient Analysis." 28 (2017): 3194-203.
[28] Kwon, O., M. Krishnamoorthy, Y. I. Cho, J. M. Sankovic, and R. K. Banerjee. "Effect of Blood Viscosity on Oxygen Transport in Residual Stenosed Artery Following Angioplasty." [In eng]. *J Biomech Eng* 130, no. 1 (Feb 2008): 0110031-11.
[29] Mejia, J., R. Mongrain, and O. F. Bertrand. "Accurate Prediction of Wall Shear Stress in a Stented Artery: Newtonian Versus Non-Newtonian Models." [In eng]. *J Biomech Eng* 133, no. 7 (Jul 2011): 0745011-8.
[30] Yamaguchi, H. "Fluid Mechanics and Its Applications ". *Engineering Fluid Mechanics-Springer Netherlands* (2008).
[31] Madlener, K., B. Frey, and H. K. Ciezki. "Generalized Reynolds Number for Non-Newtonian Fluids." *EDB Science* (2011): 237-50.
[32] Evju, Øyvind, and Kent-Andre Mardal. "On the Assumption of Laminar Flow in Physiological Flows: Cerebral Aneurysms as an Illustrative Example." In *Modeling the Heart and the Circulatory System*, edited by Alfio Quarteroni, 177-95. Cham: Springer International Publishing, 2015.
[33] Carty, Gregory, Surapong Chatpun, and Daniel M. Espino. "Modeling Blood Flow through Intracranial Aneurysms: A Comparison of Newtonian and Non-Newtonian Viscosity." *Journal of Medical and Biological Engineering* 36, no. 3 (June 01 2016): 396-409.
[34] Schirmer, C. M., and A. M. Malek. "Critical Influence of Framing Coil Orientation on Intra-Aneurysmal and Neck Region Hemodynamics in a Sidewall Aneurysm Model." *Neurosurgery* 67, no. 6 (2010): 1692-702.
[35] Campo-Deaño, Laura, Mónica S. N. Oliveira, and Fernando T. Pinho. "A Review of Computational Hemodynamics in Middle Cerebral Aneurysms and Rheological Models for Blood Flow." *Applied Mechanics Reviews* 67, no. 3 (2015): 030801.

Penerbit Akademia Baru

Engineering Science and Technology Conference Proceedings

Journal homepage: www.akademiabaru.com/EST.html

Open Access

Influence of Double Entry Volute on Incidence Angle Variation Under Steady Flow: Numerical Investigation

Balamurugan A Gurunathan[1], Uswah Khairuddin[2], Nazrun Nabill Azlan Shah[1], and Ricardo Martinez-Botas[3]

[1] Department of Mechanical Engineering, Universiti Pertahanan Nasional Malaysia
[2] Department of Mechanical Precision Engineering, MJIIT, Universiti Teknologi Malaysia
[3] Department of Mechanical Engineering, Imperial College London

ABSTRACT

EGR extraction from one side of the exhaust manifold creates imbalance of mass flow in a double entry turbine. To overcome this problem, the asymmetric double entry turbine was introduced. The performance maps of this turbine were obtained through extensive test configurations in both steady and unsteady flow conditions at Imperial College cold flow test rig. Two main configurations were investigated; nozzleless and nozzle vane setting. Nevertheless, no attempt has been made to compare the performance of asymmetric double entry turbine to that of the symmetric counterpart. One way to make comparison between these two double entry turbine volutes, is by using numerical simulation. This is achieved by using ANSYS CFX tool in this paper. A symmetric double entry volute CAD model is developed using the same A/R ratio as the asymmetric counterpart, adopting the same mixed flow rotor, inlet and exit ducts. The steady state numerical investigation was conducted at two turbine speeds, 30k RPM and 48k RPM, for the nozzleless configuration. Steady state experimental results of asymmetric double entry turbine is set as the boundary condition in the simulation. Validation of the simulation results with that of the experimental data, shows good agreements for both speed lines for the asymmetric double entry turbine. The symmetric double entry turbine recorded peak efficiencies; lower by 2.8% and 8%, at 30k RPM and 48k RPM respectively, compared to that of asymmetric double entry turbine. The results of steady state conditions of the asymmetric double entry turbine suggest that the distribution of the incidence angle is better than the symmetric double entry turbine as it is able to maintain the incidence angle at off-design and design point operating condition within the same range.

Keywords:
Turbochargers volute; symmetric volute; double entry volute; incidence angle

Copyright © 2019 PENERBIT AKADEMIA BARU - All rights reserved

1. Introduction

Diesel engines are widely in use worldwide as it provides high power with low fuel consumption and low CO2 emission. In diesel engines, the nitrogen oxides (NOx) emission which contributes towards the major hazardous pollutants remain high [1]. The formation of NO_X in diesel engines is such a complex mechanism as owing to heterogeneous and transient type of combustion nature in diesel engine [2]. One way of to reduce NO_X to up to 80% is by introducing EGR in which it recirculates part of exhaust gas to the combustion chamber [3,4]. However, EGR extraction from one side of the exhaust manifold creates imbalance of mass flow entering a turbocharger [5]. Twin and double entry turbine was introduced to overcome this problem and various study under steady and unsteady condition were conducted in this configuration [5, 6, 7-14].

Newton [10] experimented with a symmetric double entry turbine with a mixed flow turbine rotor 'A' which was designed in Imperial College London [15], and has shown that peak efficiency can be achieved up to 79.7% with nozzle setting in steady state condition. A year later, Ricardo Martinez Botas and M Sakai [16] designed an asymmetric double entry turbine which they claim can improve flow balance around turbine wheel during high EGR rate and subsequently improved

energy extraction capability. Gurunathan [17] then used this asymmetric turbine with the same mixed flow rotor 'A' with nozzleless setting and recorded 77% peak efficiency at 0.68 velocity ratio in both experiment and simulations. It is thought that with a nozzled setting, the performance might match or higher than achieved by Newton in [10]. However, a direct comparison between the volutes is not suitable due to different volute shape used in [17] and [10]. Therefore, a conclusion for which volute design is better- asymmetric or symmetric; cannot be made.

In this paper, the asymmetric volute design by [16] is modified to be symmetric while maintaining the shape and A/R ratio. The new symmetric design will be analyzed using CFD simulations and compared with the asymmetric CFD simulation results which has already been validated in experimental tests. Due to similar geometric specifications, a direct and fair comparison can be made and finally a decision on which design is more suitable for EGR exhaust gas characteristics, can be made.

2. Methodology

The design of the symmetric double entry turbine volute and the setup of simulation is the result of modification of asymmetric double entry turbine geometry from Gurunathan [17], considering Rotor 'A' specification designed by Abidat [18] in Imperial College London.

2.1 A/R ratio of turbine

The design will consider same A/R ratio of the turbine with different azimuth angle for each scroll. The corresponding value of A/R ratio of each of the scroll for the asymmetric turbine volute is stated in the equation below [17].

$$\left(\frac{A_2}{r_2}\right)_i = 13.33\ \text{mm} \quad \text{(Eq. 1)}$$

$$\left(\frac{A_2}{r_2}\right)_o = 16.67\ \text{mm} \quad \text{(Eq. 2)}$$

The relationship between A/R ratio with azimuth angle represented in the figure 1.

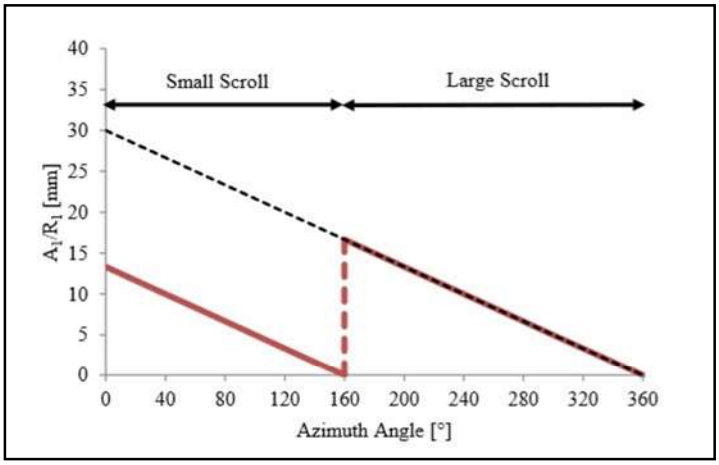


Fig. 1. Relationship between A/R ratio with azimuth angle of asymmetric double entry turbine [17]

2.2 Volute cross section shape

The flow of exhaust gas to the volute passage is influenced by the type of volute cross sectional shape. The right shape will contribute to the smooth flow of exhaust gas and there are a few volute shapes are used conventionally. Figure 2 shows the conventional volute design with different shapes. In this research, the volute shape (I) is used.

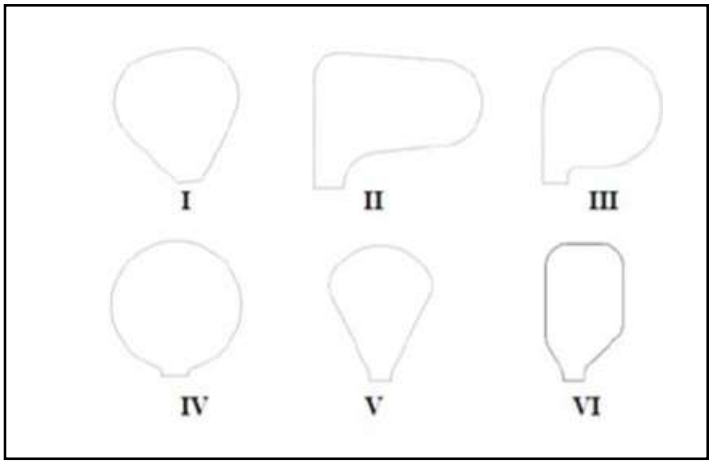


Fig. 2. Conventional volute design with different shapes [36]

The area of cross section from asymmetric volute is taken as this will calculate in the equations (1) and (2). In asymmetric turbine volute design, Sakai [19] used $rr_{\psi\psi=0} = 96.45$ mm and and $AA_{\psi\psi=0} = 1322.02$ mm^2 for small scroll. For the large scroll, the values are $rr_{\psi\psi=0} = 101.32$ mm and $AA_{\psi\psi=0} = 1749.27$ mm^2. The symmetric radius is determined by forecasting the value of A/R ratio with azimuth angle. Then, the values of radius are inserted back into the equation (1) and (2) and the area of volute cross section are calculated with the values of A/R which correspond to the new azimuth angle. The difference in A/R between asymmetric and symmetric turbine volute are shown in Figure 3. For the inner scroll, at ψ=0°, both scrolls show same value of A/R ratio of 13.33 mm. As

for the outer scroll, the value of A/R ratio are 16.67 mm at ψ=160° for asymmetric volute at ψ= 180° for symmetric volute.

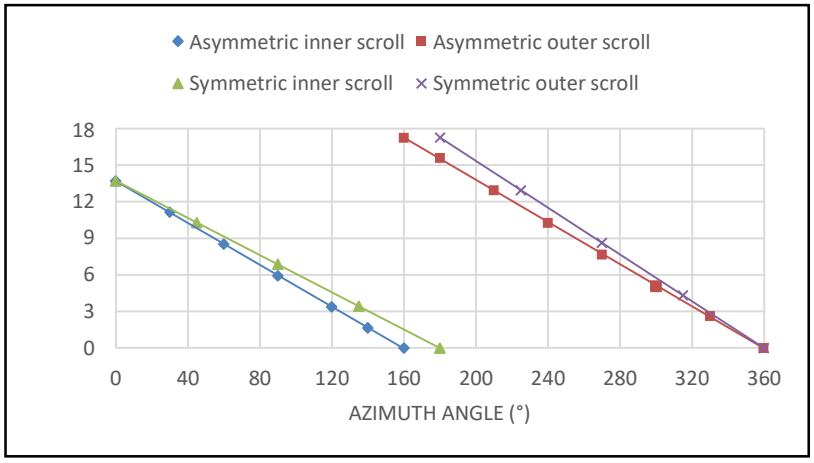


Fig. 3. Graph of A/R ratio versus azimuth angle of asymmetric and symmetric volute

2.3 3D volute model

A new 3D volute model is developed by using the new symmetric volute dimension in Solidworks. As shown in Figure 4, the sketch for the area and radius are divided with 9 sections from 0° to 360°. The difference of asymmetric and symmetric 3D model as shown in Figure 5.



Fig. 4. Sketch of symmetric volute in Solidworks

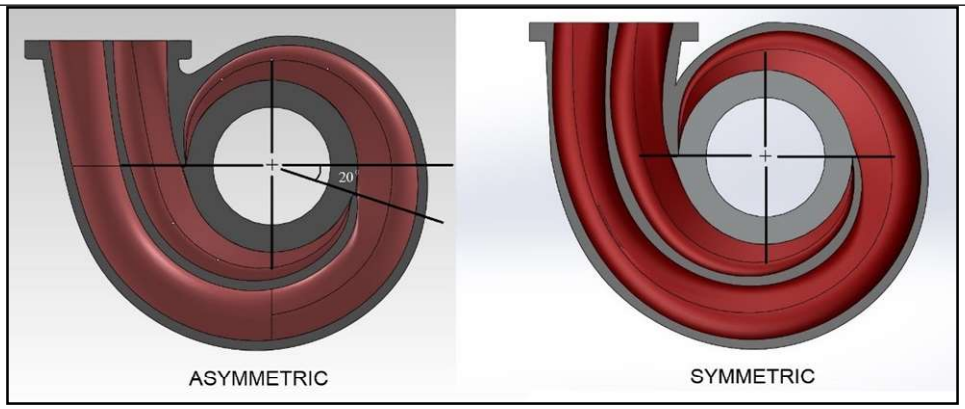


Fig. 5. Comparison of asymmetric and symmetric turbine

2.4 Computational Fluid Dynamics (CFD) simulation

The simulation software used in this project is ANSYS CFX. There are 4 stages in this simulation which consist of preparation of CFD domains, Pre Processing, Solver and Post Processing. The domains consist of conversion inlet, symmetric turbine housing, rotor and outlet and the assembly of these domains are set same as the real assembly on the experimental rig. Figure 6 below show the 3D CAD models of the simulation.

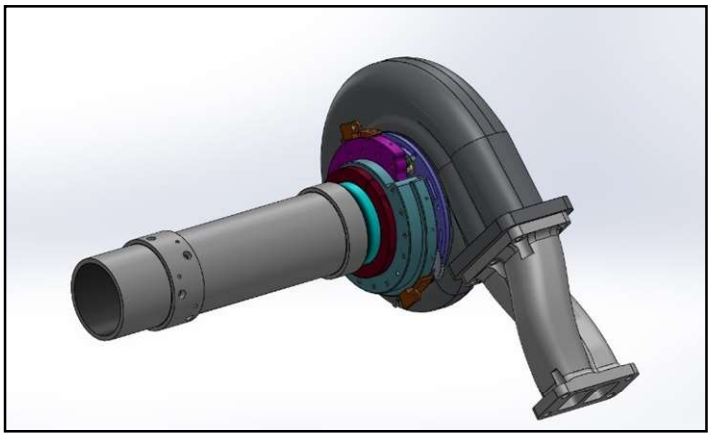


Fig. 6. Assembly of 3D models following the experiment arrangement

Every fluid domain is meshed using ANSYS Mesh Workbench except for the rotor. The rotor is meshed using the ANSYS Turbogrid in which the software is specific to mesh the rotor for turbomachinery case. The meshing and setup for the symmetric turbine is similar to that of asymmetric turbine. Table 1 shows the details of the meshing of the domains.

Table 1
Domain meshing parameters

Mesh preference	
Physics preference	CFD
Solver preference	CFX
Relevance center (mesh size)	Fine
Type of mesh	Hexahedral, prism and pyramid
Turbine mesh near wall spec.	Y+ and Reynolds No $1.0e^{6}$

Domain details		
Type of mesh	Unstructured	
Domain	Total nodes	Total elements
Conversion inlet	65135	190325
Symmetric volute	185367	500829
Vanesless	131192	30740
Outlet	25323	70489
Type of mesh	Structured	
Turbine A	3072708	2817336

The equation of k-epsilon (k-ε) turbulent model is used in this simulation. The prediction of turbulent flow to analyze turbocharger performance by using this turbulent model is accurate as mentioned by Palfreyman [20]. The data for inlet and outlet boundary condition are taken from the experimental data. The data are extracted as listed below.

1. Turbine inner scroll total inlet pressure
2. Turbine inner scroll total inlet temperature
3. Turbine outer scroll total inlet pressure
4. Turbine outer scroll total inlet temperature
5. Turbine outlet static pressure
6. Rotor rotational speed

The simulation is run with two different speeds; 30k RPM and 48k RPM. In this boundary condition setup, 30k RPM resembles of 50% of the turbine speed and 48k RPM speed resembles of 80% of the turbine speed.

3. Results

The simulation results of symmetric turbine volute are compared directly with simulation results of asymmetric turbine volute

3.1 Performance comparison at 30K RPM

Figure 7 shows overall mass flow parameter of asymmetric and symmetric volute at 30k RPM. At pressure ratio below 1.2, both volutes show negligible difference of mass flow parameter. As the pressure increases, the symmetric demonstrated lower trend of mass flow parameter. The highest mass flow parameter recorded is $5.78 \times 10^{-5}(\mathrm{kgs}^{-1}.\sqrt{\mathrm{K}})/\mathrm{Pa}$ of asymmetric volute. The overall percentage difference between both volutes is 8.21%. Table 17 shows the overall mass flow parameter between asymmetric and symmetric at 30k RPM. In overall, the asymmetric has higher

mass flow parameter compared symmetric with highest percentage difference of 18.09% at 1.33 pressure ratio.

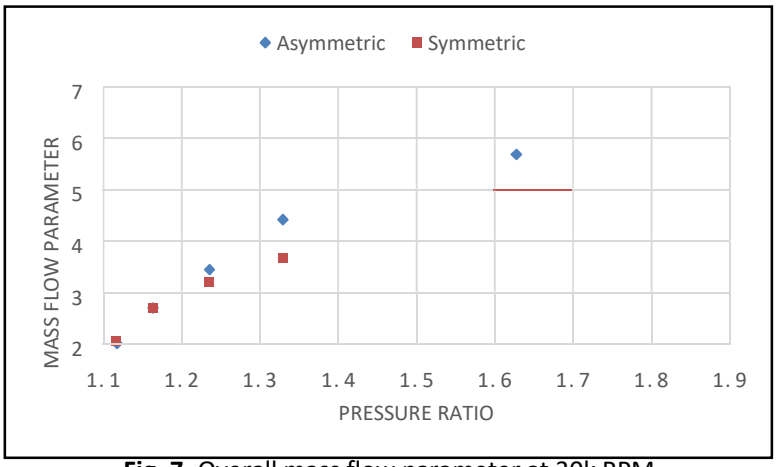


Fig. 7. Overall mass flow parameter at 30k RPM

The total to static efficiency of asymmetric and symmetric turbine volute are compared at this operating speed. Figure 8 shows the plot of total to static efficiency of asymmetric and symmetric volute at 30k RPM operating speed. The efficiencies are observed in the range of 0.2 to 0.45. Both volutes have demonstrated the increase in efficiency from 0.2 to 0.35 velocity and the efficiency decreases as the velocity ratio increases. From the figure, the symmetric curve shows same trend of asymmetric curve. Below 0.3 velocity ratio, significant difference in efficiency recorded. The peak efficiencies of asymmetric and symmetric volute are 73.2% and 71.2%. The symmetric volute shows higher efficiency at 0.37 velocity ratio with 65.6% compared to asymmetric volute with 64.5%. The lowest efficiency recorded is 53.6% for symmetric volute at 0.44 velocity ratio. The average percentage difference between volutes is 6%.

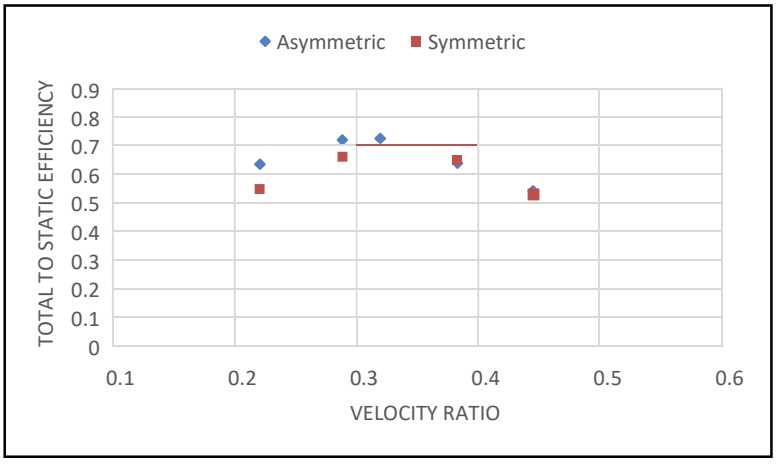


Fig. 8. Total to static efficiency at 30k RPM

3.2 Performance comparison at 48K RPM

Figure 9 presents the overall mass flow parameter at 48k RPM. It can be seen the symmetric curve has same trend of asymmetric. Based on observation, pressure ratio below 1.4 shows negligible difference of mass flow parameter between the volutes. At 1.43 pressure ratio, the symmetric mass flow parameter shows slightly higher than asymmetric. However, asymmetric volute overcomes symmetric at the pressure 1.59 pressure ratio value of mass flow parameter, $4.80 \times 10^{-5}(\mathrm{kgs}^{-1}.\sqrt{\mathrm{K}})/\mathrm{Pa}$. The average percentage difference of overall mass flow parameter between asymmetric and symmetric is 3.06%. The highest percentage difference is 6.45% at 1.59 pressure ratio.

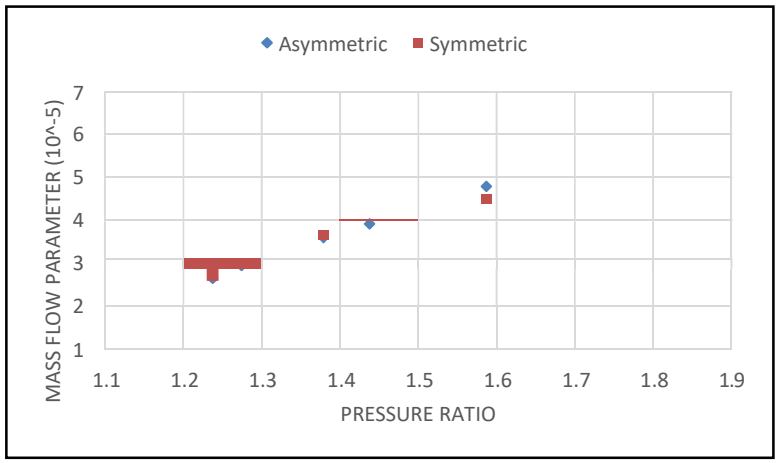


Fig. 9. Overall mass flow parameter at 30k RPM

Figure 10 shows the graph total to static efficiency of asymmetric and symmetric volute at 48k RPM. The velocity ratio observed in between 0.3 to 0.55. It can be observed both volutes have the same trend but consistent difference in efficiency. Based on observation, the efficiency decreases as the velocity ratio increases for both volutes. From the plot, it can be seen the asymmetric volute has higher total to static efficiency compared to symmetric volute. The peak efficiency recorded from both volutes at 0.34 velocity ratio with 73.3% for asymmetric and 67.7% for symmetric. At the highest velocity of 0.51, both volutes show similar decrease in efficiency. The average percentage different for both volutes is 8.43%. Table 20 shows the total to static efficiency of asymmetric and symmetric volutes. The highest percentage difference recorded is 12.01% at 0.48 velocity and the lowest percentage difference recorded is 5.86% at 0.40 velocity ratio.

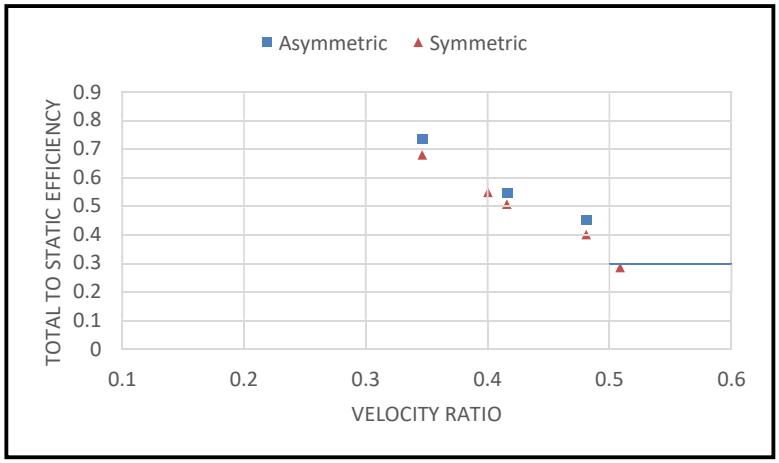


Fig. 10. Total to static efficiency at 30k RPM

3.3 Flow performance analysis

The flow performance was analyzed by comparing the incidence angle between the volutes. The incidence angle is referring to the difference between rotor inlet flow angle and blade angle at the rotor leading edge. As mentioned by Japikse and Baines [21], the optimum incidence angle for radial turbine in range of -20° to -40°. The closer the incidence angle of the flow approaching to the optimum incidence angle range, the higher the turbine efficiency.

Figure 11 shows the incidence angle of asymmetric and symmetric volute plotted on the azimuth angle. In asymmetric volute, the lowest magnitude of incidence angle approached to optimum incidence angle is -12.4°. It can be seen that in inner scroll asymmetric volute, the incidence angles are lower below ψ=40° and slightly increase and maintained until ψ=160°. The incidence angles are observed and recorded lower as approach to ψ=200° and remained in constant magnitude. It also observed that the incidence angle increases as approached to tongue area from ψ=320°. For symmetric volute, -11.4° is the lowest magnitude of incidence angle to approach the optimum angle. The inner scroll from ψ=0°, the incidence angles are constant and slightly decreases at ψ=150°. The outer scroll shows lower incidence angle recorded and the lowest incidence angle are observed at ψ=330°. From the Figure 11, the incidence angle of asymmetric volute approached closer to optimum incidence angle of -20° with difference of 7.6° compared to symmetric volute with difference of 8.6°.

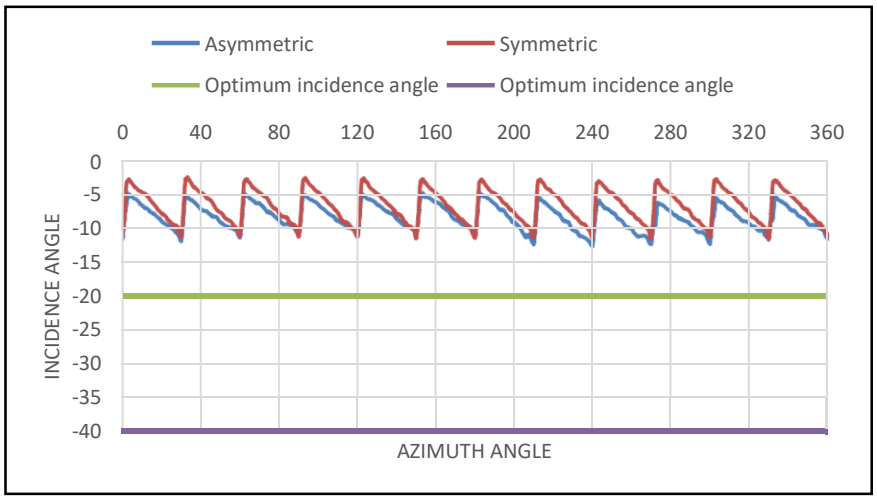


Fig. 11. Incidence angle comparison at 30k RPM

Figure 12 shows the incidence angle at 48k RPM. The lowest incidence angle recorded for asymmetric volute is -9.63°. As for the symmetric volute, the lowest incidence angle recorded is -8.62°. The asymmetric volute shows constant low incidence angle at inner scroll correspond to ψ=0° to ψ=160°. The incidence angle started to slightly lower as approached to ψ=180° and remained at the same magnitude in which refer to the flow in outer scroll. As for symmetric volute, the incidence angles are higher than asymmetric in overall. At ψ=180°, the difference of incidence angle recorded between asymmetric and symmetric is 1°. For outer scroll, the magnitude of incidence angles are same at ψ=300° and 330°. From observation, clearly asymmetric volute also has higher efficiency as the incidence angle approaches closer to the optimum incidence angle of -20° with difference angle of 10.37°. The symmetric volute shows lower efficiency with difference in angle of 11.38°.

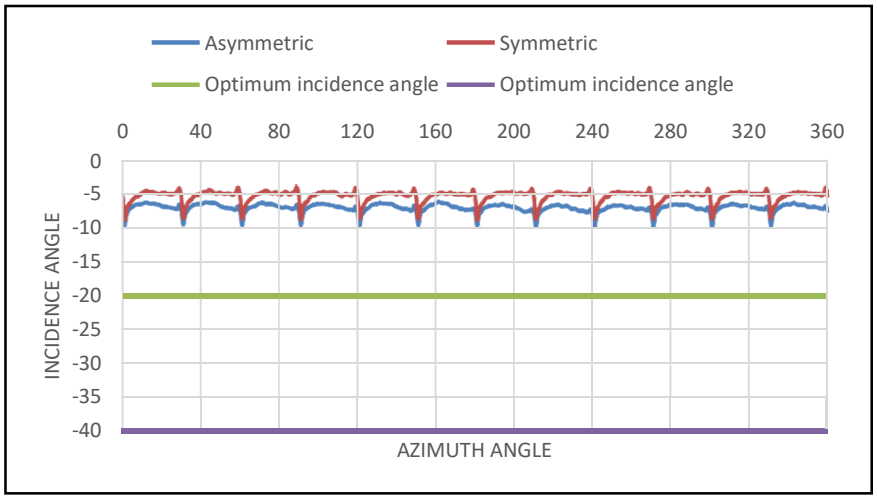


Fig. 12. Incidence angle comparison at 48k RPM

4. Conclusions

An asymmetric volute design is said to improve flow balance from high EGR rate around turbine wheel and improve overall turbine energy extraction capability. Both experimental tests and CFD simulations shows that a nozzleless asymmetric turbine (nozzleless) with mixed flow rotor 'A' designed in Imperial college London is able to reach 77% peak efficiency at 0.68 velocity ratio. A similar specification volute was designed but with symmetric configuration in order to compare the performance of turbines in asymmetric and symmetric configurations. The comparison was made using CFD simulations under steady conditions at 30K RPM and 48K RPM to reflect 50% and 80% turbine speed respectively.

Comparison of CFD simulations shows that the symmetric volute design achieved lower total to static efficiency compared to asymmetric volute with 2.77% and 8% lower efficiencies at peak efficiency for 30K RPM and 48K RPM respectively. Further analysis on incidence angles shows that magnitude of incidence angle for asymmetric volute is closer to the optimum incidence angle of -20° and the incidence angle for symmetric volute is closer to the positive range. Therefore, asymmetric volute design is more optimum for EGR exhaust gas operations.

This paper presents simulation results under steady condition. In a real engine application, the turbine will undergo unsteady flow condition of EGR exhaust gas. In future work, the comparison can be made for both asymmetric and symmetric turbines in unsteady conditions to match real applications.

Acknowledgement
Our appreciation goes to Dr Uswah Khairuddin of Universiti Teknologi Malaysia for her contribution through her project grant Reduction of damper-hunting to duct pulsation in high- speed VAV system (R.K130000.7343.4B370).

References

[1] Gurumoorthy S. Hebbar, Anant Krishna Bhat (2013). Investigations on Performance and Emissions of a Stationary DI Diesel Engine with Different Exhaust Gas Recirculation Temperatures, International Journal of Automotive Engineering and Technologies, Vol. 2.
[2] Levendis Y. A, Pavalatos I., Abrams R F (1994). Control of Diesel Soot Hydrocarbon and NO_X Emissions with a Particular Trap, SAE 940460.
[3] Srinath Pai, Amriya Tasneem H.R., Shivaraju N, Dr. Sreeprakash (2013). The study of EGR Effect on Diesel Engine Performance and Emission, International Conference, ICEITSW, Institute of Engineering and Technology.
[4] Mukesh Rameshbhai Zala (2012). Optimization of EGR Rate on Multi Cylinders 4-Stroke Diesel Engine, International Journal of Engineering Research & Technology (IJERT), ISSN: 2278-0181, Vol. 1 Issue 4.
[5] Pischinger, F. and Wunsche A. (1977). The Characteristic Behavior of Radial Turbines and its Influence on the Turbocharging Process, Proceedings 12th International Congress on Combustion Engines, Vol A, pp545-568.
[6] Muller, M. et al., (2011). The Asymmetric Twin Entry Scroll Turbine for Exhaust Gas Turbochargers, Proceedings of the ASME Turbo Expo, GT2008-50614.
[7] Mizumachi. N. et al (1979). A Study on Performance of Radial Turbine under Unsteady Flow Conditions, Report Institute of Industrial Science. University of Tokyo. Vol. 28.
[8] Benson, R.S. and Scrimshaw (1965). An Experimental Investigation of Non-Steady Flow In a Radial Turbine, Proceedings of the Institution of Mechanical Engineerd, Part 3J, Paper 23.
[9] Wallace, F.J and Blair, G.P.(1965). The Pulsating-Flow Performance of Inward Radial-Flow Turbines", 65-gtp-21, ASME.
[10] Newton P. (2013). An Experimental and Computational Study of Pulsating Flow within a Double Entry Turbine with Different Nozzle Settings. PhD thesis, Imperial College London.

[11] C. D. Copeland (2009). The Evaluation of Steady and Pulsating Flow Performance of a Double Entry Turbocharger Turbine, PhD Thesis, Imperial College of London.
[12] C. D. Copeland, M. Seiler and R. F. Martinez Botas (2012). Unsteady Performance of a Double Entry Turbocharger Turbine with a Comparison to Steady Flow Conditions, Journal of Turbomachinery, Vol. 134.
[13] C. D. Copeland, R. F. Martinez Botas and M. Seiler (2011). Comparison Between Steady and Unsteady Double-Entry Turbine Performance Using the Quasi-Steady Assumption," Journal of Turbomachinery, Vol. 133.
[14] C. D. Copeland, P. Newton, R. F. Martinez Botas, M. Seiler (2012). The Effect of Unequal Admission on the Performance and Loss Generation in a Double Entry Turbocharger Turbine, Journal of Turbomachinery, Vol. 134.
[15] N. Karamanis, R F Martinez Botas and C.C Su (1999). Detailed Flow Measurement at the Exit of a Mixed Flow Turbine Under Steady Flow Conditions, ASME, International Gas Turbine & Aeroengine Congress & Exhibition, Indiana.
[16] An asymmetric Double Entry Turbine for Better Exhaust Gas Recirculation, Reference number: 6132, 6833, www.imperialinnovations.co.uk.
[17] B.A Gurunathan (2016). Experimental Evaluation of Steady and Pulsating Flow Performance of an Asymmetric Double Entry Turbine for An Automotive Turbocharger, PhD Thesis, Imperial College London.
[18] Abidat M. (1991). Design and Testing of a Highly Loaded Mixed Flow Turbine. PhD Thesis, Imperial of London.
[19] M. Sakai, A. Romagnoli, R.F Martinez Botas (2014). 11th International Conference on Turbochargers and Turbocharging : 13-14 May, the British Museum, London.
[20] D. Palfreyman and R. F. Martinez Botas (2005). The Pulsating Flow Field in a Mixed Flow Turbine: An experimental and Computational Study, Transactions of the ASME, Journal of Turbomachinery, Vol. 127.
[21] D. Japikse, N. C. Baines (1997). Introduction to Turbomachinery Concepts, ETI.

Penerbit Akademia Baru

Engineering Science and Technology Conference Proceedings

Journal homepage: www.akademiabaru.com/EST.html

Experimental Investigation of the Effect of a Downstream Square Plate on Vortex-induced Vibration and Galloping of a Square Cylinder in Uniform Flow

Open Access

Azhar Mohamed[1], Sheikh Ahmad Zaki[1,*], Masataka Shirakashi[2], Mohamed Sukri Mat Ali[1], Muhammad Zulfahmi Samsudin[3], Ahmad Faiz Mohammad[1]

[1] Malaysia-Japan International Institute of Technology, Universiti Teknologi Malaysia, Jalan Sultan Yahya Petra, 54100 Kuala Lumpur, Malaysia
[2] Nagaoka University of Technology, Kamitomioka 1603-1, Nagaoka, Niigata, Japan.
[3] Mechanical Engineering Section, Science and Engineering Department, Malaysia Japan Higher Education Program (MJHEP), Lot 2333 Jalan Kajang Seremban, 43700 Beranang, Selangor, Malaysia

ABSTRACT

A square cylinder exposed to a fluid flow is regarded as the simplest model of the structures in sea water or air flow, and known to show the Karman vortex induced vibration (KVIV) and the galloping in separate or overlapping ranges of flow velocity. In this study, wind tunnel experiments were performed on the cross-flow vibration of a square cylinder, and effects of a downstream square plate on the vibration were investigated to develop a convenient passive technique for vibration control. The square plate has a side length w equal to the side length of the square cylinder D (= 26 mm) and set downstream with the gap ratio S/D in the range of 0.12 to 2.90 where S is the separation gap. The results show that the square plate has only little influence on KVIV and enhances the galloping, resulting in the lower critical reduced velocity of galloping U_g i.e. the onset velocity of galloping reduced to about half of the isolated counterpart at S/D = 0.98. Most remarkable effect of the downstream square plate is the enhancement of the vibration near the peak velocity of KVIV at S/D = 1.17, which is around five times larger as compared with the isolated counterpart. This may indicate occurrence of the wake-body-interference fluid elastic vibration.

Keywords:
Square cylinder; square plate;
vortex-induced vibration; galloping;
vibration control

Copyright © 2019 PENERBIT AKADEMIA BARU - All rights reserved

1. Introduction

The study of flow induced vibrations (FIVs) of a cylindrical body exposed to flow is important in many fields including aeronautical, offshore, civil and mechanical engineering. FIV has caused tremendous damage to structures such as the Tacoma Narrows bridge collapse in 1940, sodium leak and fire of the Monju fast breeder reactor in December 1996 and the oscillation observed for Storebaelt East Bridge in Denmark, May 1998 (Terres-Nicoli and Kopp [1]). Hence, numerous studies have been devoted to clarify their mechanisms and to predict and control FIVs of cylindrical bodies, mainly for a circular cylinder because it is most significant from the view point of fluid mechanics and commonly used in engineering application.

Among passive techniques proposed so far to suppress the vibration, the near-wake-body methods are advantageous since they require neither additional body touching the vibrating structure nor change of the supporting structure. In this method, other bodies are positioned downstream of the oscillating cylinder, e.g. splitter plates (Assi et al., [2]; Ali et al., [3]; Maruai et al., [4]), a circular cylinder (Shirakashi et al., [5]; Bae et al., [6]; Ngyuen et al., [7]) or a strip plate in

cruciform arrangement (Koide et al., [8]; Kato et al., [9]; Kawabata et al., [10]) and fairings (Assi et al., [11]; Yu et al., [12]; Wang et al., [13]; Lou et al., [14]).

Two different cross-flow vibrations, the Karman Vortex Induced Vibration (KVIV) and the galloping, are well known for cylindrical bodies with non-circular cross section. KVIV is a resonant like vibration excited by the alternating lift force due to the periodic shedding of Karman vortex (KV) which exists if the cylinder is at rest. Synchronization, often called "lock-in", of the vortex shedding with the oscillation gives a non-linear character to KVIV, making its prediction extremely difficult. The galloping is caused for cylinders with a non-circular cross section due to the instability of a fluid- structure system. The vibration is considered to be driven by the time-averaged fluid force which develops in a quasi-steady flow relative to the oscillating body.

A square cylinder is regarded as the simplest model of the non-circular cross section structures, and known to show KVIV and galloping in separate or overlapping ranges of flow velocity, depending on the condition of the system. Koide et al. [8] studied the influence of a long strip plate with a width w on the vibration of a square cylinder with a side length D, where the strip plate is set downstream in cruciform arrangement with a gap S. They reported that a strip plate with a width ratio w/D = 1 effectively suppresses KVIV at S/D < 2 and galloping at S/D < 3.8. However, a new vibration induced by periodic shedding of longitudinal vortices near the cross, known as the longitudinal vortex induced vibration (LVIV), was found to occur over a certain velocity range when S/D is around 1.4.

Recently, Kawabata et al. [10] conducted wind tunnel experiments to investigate the influence of the downstream strip plate length on the phenomena reported by Koide et al. [8]. The results are summarized as follows: KVIV is less suppressed when the plate length l_d is smaller and almost no-suppression occurs at l_d/D = 1 (square plate). The galloping is effectively suppressed by short strip plates by setting the gap ratio smaller when the strip plate is shorter, e.g. S/D < 2 for l_d/D = 1. Although the LVIV does not occur when ld/D < 4, a large amplitude vibration was found to be induced by short strip plates, i.e. l_d/D = 1.5 and 2 when S/D ≤ 1. Since this vibration is considered to be caused by the fluid elastic instability, they called it "wake body interference fluid elastic vibration (WBIFEV)".

The abovementioned findings by Kawabata et al. [10] for the influence of downstream square plate on the vibration of square cylinder can potentially lead to a novel technique to control FIVs of cylindrical body, which is not only to avoid structural damage but also to be utilized for beneficial purposes such as electricity generation. However, their experiment was carried out for limited conditions and the influences on KVIV and galloping were investigated by varying the gap at respective velocities of KVIV and galloping. Therefore, the objectives of this study are:

1. To investigate the influence of the downstream square plate on the cross-flow vibration of square cylinder by performing wind tunnel experiments under comprehensive conditions in which vibration response against varying flow velocity is measured for fixed values of S/D.
2. To identify the effect of gap conditions on vibration behaviour to develop a novel passive technique to induce or to suppress the vibration.

2. Experimental apparatus, instruments, procedure and parameters of vibrating system

Experiments were conducted in the test section connected to a blow-down type wind tunnel in the mechanical laboratory of the Malaysian Japan Higher Education Project (MJHEP), Beranang, Malaysia. The test section has a 0.36 m × 0.36 m cross section, being identical with the outlet nozzle section of the wind tunnel, and a 0.8 m length. The walls of the test section are made of transparent acrylic plates to record the cylinder oscillation using a camera. Fig. 1 shows the

outline of the experimental apparatus and setting of instruments, together with the coordinate system *O- x, y, z* used in this paper. Note that the origin '*O*' is set at the centre of the square cylinder. The rigid square cylinder models are made from acrylic resin plate with a side length D = 26 mm and a length L = 349 mm. The cylinder is fixed to a supporting rod passing through the slots on the side walls of the test section and supported by springs outside the test section. Circular disks made of acrylic plate with a thickness 1.2 mm are attached to the cylinder at both ends to prevent air flow through the slots. The length of the cylinder L is defined as the distance between the two end disks. The twin-plate springs ensure the oscillation in a purely cross-flow mode. The magnetic dampers are mounted on the frame structure at both sides of the cylinder to support the rod outside the measuring section. The damping factor is adjusted by moving the magnets mounted on the traversing device (Kawabata et al. [10], Marra et al. [15], Mannini et al. [16-17], etc). The downstream square plate is made of spring steel plate with a thickness of 5 mm and has a side length w equal to that of the cylinder, i.e. w = 26 mm. The gap S between the cylinder and the plate is adjusted in the range of S/d = 0.12 ~ 2.90.

The flow velocity U is measured by a Pitot tube (JIS type, Ø9 x (L) 0.5 m) connected to a pressure gauge (Manostar, Type W081, Range: 0-100Pa & 0-500Pa). A hot wire anemometer (Dantec Dynamics, Probe type 55 P11) is used to detect the x-component of velocity at a point in the near wake, i.e. $x = 2D$, $y = D$ and $z = 1.5D$. The vortex shedding frequency f_v is determined from the peak frequency in the spectrum of the velocity signal u detected by the hot wire anemometer. A laser displacement sensor (Omron ZX-LDA11) is used to measure the vertical displacement of cylinder Y. The oscillation amplitude is determined as the root mean square value of Y, and the oscillation frequency f_c is determined from the peak frequency in the spectrum of Y. The data processing for u and Y is carried out using the LabVIEW program after converting them into digital signals with NI USB-9215. The data acquisition system has four channels with a sampling rate of 100 kHz/ch and a resolution of 16 bit in analogue-to-digital converters (ADCs).

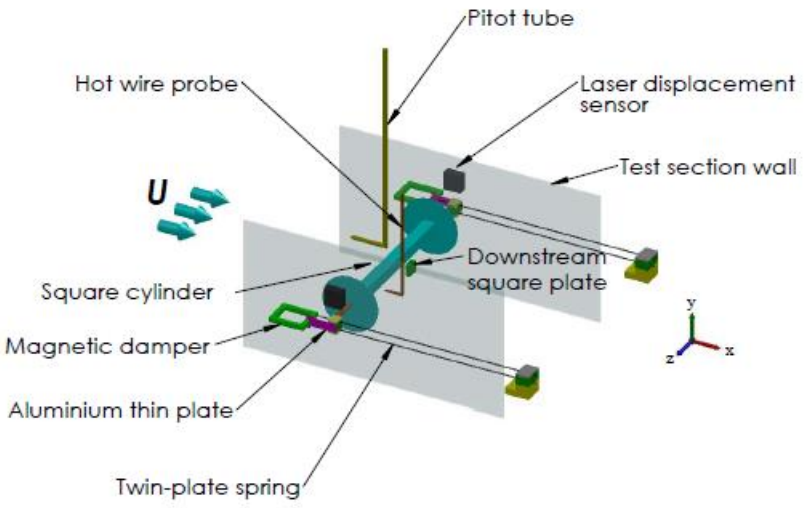


Figure 1. Schematic diagram of experimental apparatus and instruments, together with the coordinate system used in this paper. U is the flow velocity.

The natural frequency and the logarithmic damping factor are determined from the displacement signal Y of the free dumping oscillation at U = 0. That is, the time interval T_m for m-

cycles of Y is measured and f_n is determined as $f_n = m/T_m$, which is fixed at 16.5 Hz and equal to that of Kawabata et al. [10]. The logarithmic damping factor δ is determined by using Eq. (1):

$$\delta = (1/m)\ln(Y_1/Y_{(m+1)}), \quad (1)$$

where Y_1 is the peak amplitude in the first cycle and $Y_{(m+1)}$ is that of (m+1)-th cycle. The value of δ is also adjusted to make the value of critical reduced velocity of galloping U_g approximately equal to that of Kawabata et al. [10]. Then, the effective mass m_e is calculated by

$$m_e = k/(2\pi f_n)^2, \quad (2)$$

where k is the total spring constant of the supporting system measured separately. The mass ratio, i.e. the ratio of the effective mass to the mass of fluid displaced by the cylinder, is defined as $M_R = m_e/(\rho D^2 L)$. Scruton number, Sc defined by Eq. (3) represents the coupled effect of the mass and the damping and considered to be the dominating parameter for the oscillation response (see e.g. Kawabata et al., [10] or Kaneko et al., [18]).

$$Sc = 2M_R\delta \quad (3)$$

The conditions, specification of the cylinder system and the non-dimensional parameters obtained from the above procedure are shown in Table 1, together with those of other studies for comparison.

Firstly, the vibration amplitude Y_{rms}, the vibration frequency f_c and the vortex shedding frequency f_v against flow velocity U were measured for the isolated square cylinder. The velocity range was from the velocity lower than KVIV until the full galloping velocity. Then, the influence of the square plate on the relationships between Y_{rms}, f_c, f_v and U was measured for various values of S. The results of Y_{rms}, f_c, f_v are properly normalised and plotted against the reduced velocity U_R defined by Eq. (4).

$$U_R = U/(f_n D) \quad (4)$$

Table 1. Conditions and parameters of studies compared in Fig. 2. (Wind tunnel experiment: The present study, Ismail et al. [19] and Kawabata et al. [10]; Numerical simulation: Maruai et al. [4])

Parameter	Present	Maruai	Ismail	Kawabata
Square cylinder side length, D (mm)	26	26	26	26
Length of cylinder, L (mm)	349	315	315	315
Kinematic viscosity of air, ν (m^2/s)	1.55×10^{-5}	1.54×10^{-5}	1.54×10^{-5}	1.56×10^{-5}
Air density, ρ (kg/m^3)	1.134	1.201	1.204	1.157
Natural frequency, f_n (Hz)	16.5	14.3	14.3	16.5
Spring constant, k (N/m)	2495	1173	1173	1181
Logarithmic damping factor, δ	0.018	0.027	0.027	0.027
Effective mass, m_e (kg)	0.23	0.15	0.15	0.11
Mass ratio, M_R	867.58	566.74	565.22	446.30
Scruton number, Sc	31.75	31.17	31.09	24.10
Reynolds number, Re	$3.9 - 14.8 \times 10^3$	$4.2 - 10.7 \times 10^3$	$3.67 - 11.73 \times 10^3$	$3.8 - 16.2 \times 10^3$
Reduced velocity, U_R	5.5 - 20.6	5 - 20	5.7 - 18.2	5.3 - 19.5

3. Results and discussions

3.1 Vibration behaviour of isolated square cylinder

Fig. 2 shows the results of the present experiments for the isolated cylinder, comparing with the previous studies, i.e. the experiments by Kawabata et al. [10] and Ismail et al. [19], and the simulation study by Maruai et al. [4] as shown in Table 1. In Fig. 2 (a), the non-dimensional amplitude is multiplied by Sc and plotted against the reduced velocity U_R for fair comparison since the maximum KVIV amplitude would be inversely proportional with Sc if the vibration system were linear. The vortex shedding frequency f_v and the vibration frequency f_c are determined as the highest peak frequency of spectra S_u and S_Y respectively as shown in Fig. 3. They are normalized by the natural frequency f_n and plotted against U_R in Figs. 2 (b) and (c).

The tendency of the amplitude response of the present work agrees well with all the other studies as shown in Fig. 2 (a), and this can be described as follows: 1) The velocity ranges of KVIV and galloping are separated by essentially zero vibration range. 2) KVIV occurs in the velocity range around the velocity at which the natural vortex shedding frequency f_{v0} is equal to the natural frequency f_n, although the maximum KVIV amplitude peak A_{KVIV} is significantly scattered among the studies even when it is normalized by multiplying Sc. 3) The critical reduced velocity of galloping U_g, i.e. onset of vibration due to galloping, coincides well, but the increasing gradient after U_g is different among the studies. Ismail et al. [19] mentioned that the second peak value of around U_R = 10.5 in the result of Kawabata et al. [10] was due to the rolling motion of the cylinder due to un-symmetry of the cylinder structure. This vibration is properly erased in the present study.

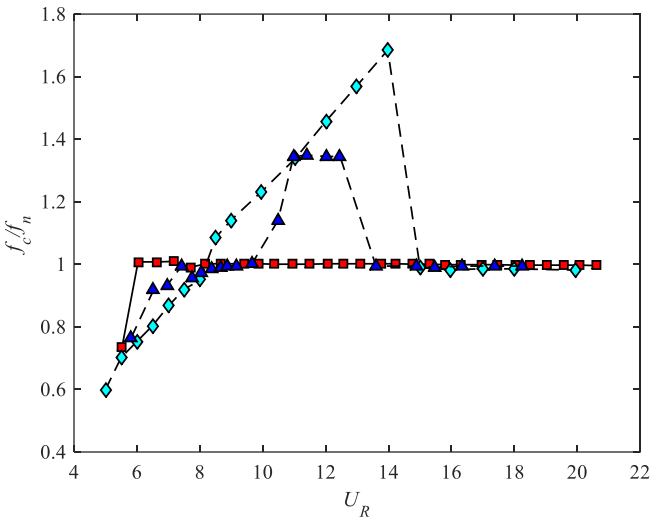
The vibration at velocities lower than the KVIV range is the forced vibration excited by the alternating lift of natural vortex shedding. That is, the amplitude remains small, and f_v increases linearly with U while $f_c = f_v < f_n$ as seen in Fig. 2. Similar to the cases of studies by Khalak and Williamson [20] and Feng [21] for a circular cylinder, the vibration amplitude starts increasing at U_R at which the natural vortex shedding frequency f_{v0} is lower than the natural frequency f_n. The KVIV regime is confirmed by seeing whether the Karman vortex synchronizes with the cylinder oscillation. When the synchronization occurs, the spectrum S_u has a sharp peak at the oscillation frequency f_c which is nearly equal to f_n as seen in Fig. 3 (a). The maximum KVIV amplitude A_{KVIV} appears at around the critical reduced velocity at which $f_{vo} = f_n$. The KVIV regime persists over a certain range of velocity until the desynchronization and the drop of vibration amplitude occur showing the end of KVIV. In many cases, this regime near the higher velocity end of KVIV is unstable in the sense that the KVIV and the small vibration-desynchronization regimes are irregularly alternating.

The vibration in the intermediate range is also the forced vibration excited by the natural vortex shedding. As a result, f_v increases linearly with U and $f_c = f_v$, being higher than f_n. However, the present study shows that $f_c/f_n = 1$ in the range of $8.5 \leq U_R \leq 15.3$ as shown in Fig. 2 (c). This paradoxical result is caused by the selective resonance explained as follows.

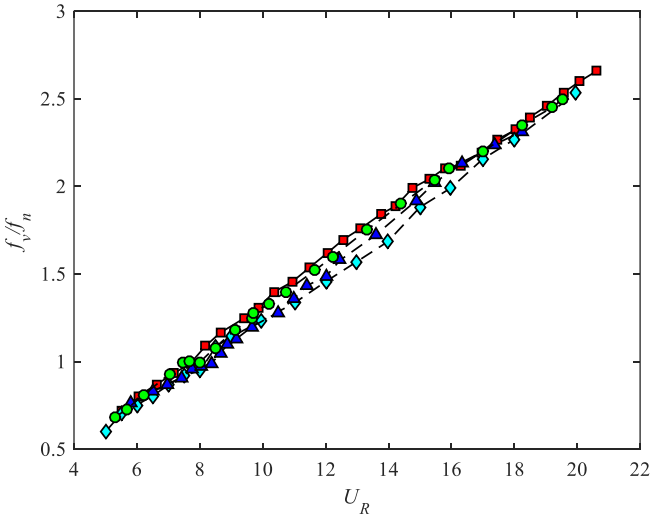
When the exciting force has a widely distributing spectrum, the vibration response will also have a wide spectrum in which every frequency component is amplified according to the theory of vibration. Therefore, when the damping factor is small, the component of the exciting force at the frequency equal to the natural frequency f_n causes very large vibration at $f = f_n$. This phenomenon is called “selective resonance”. As a result, the spectrum of displacement can have a peak at f_n higher than the peak at the exciting force frequency. In the present study, this occurs in the intermediate region, as clearly observed in Fig. 3 (b) for U_R = 10.93, making $f_c/f_n = 1$ since the oscillation frequency f_c is defined as the highest peak frequency in S_Y.

The amplitude abruptly starts increasing at U_R = 15.8 with the frequency $f_c = f_n$, while the vortex shedding frequency f_v remains equal to f_{v0} as shown in Fig. 2. Hence, this is identified as the critical reduced velocity of galloping U_g (Sun et al., 2016). In the full galloping regime, S_Y has a very high sharp peak at f_n, and the peak at f_v due to the selective resonance disappears as seen in Fig. 3 (c). The galloping regime persists up to the maximum U_R of measurement of the present experiment. The agreement of the value of U_g is excellent among the studies, but the increasing gradient of vibration amplitude is definitely different. Although the values of Scruton number *Sc* in Table 1 are nearly equal among the researches compared in Fig. 2, the amplitude normalized by *Sc* is significantly different each other. This result confirms that the mass ratio and the damping factor influence the amplitude response independently (Nguyen et al. [7]; Mannini et al. [16]; Sun et al. [22]).

c



b



a

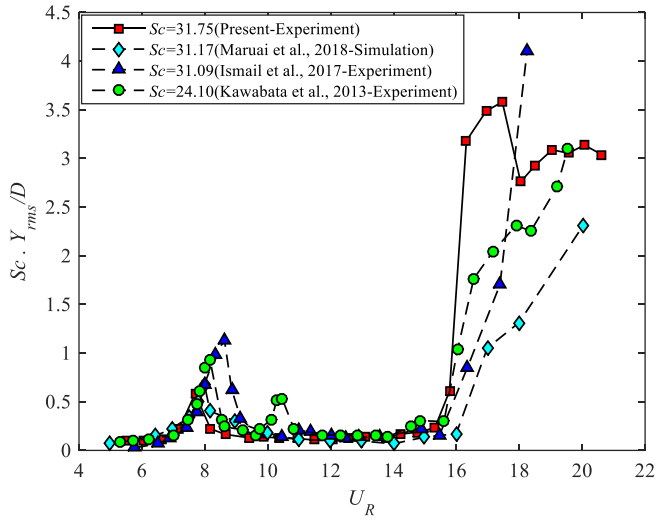
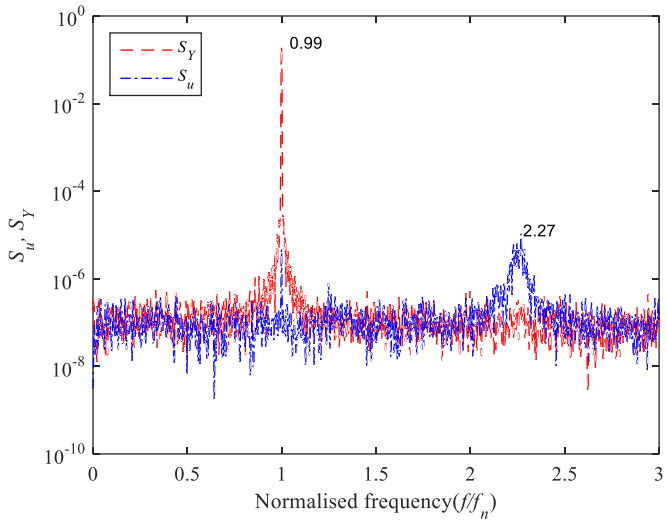
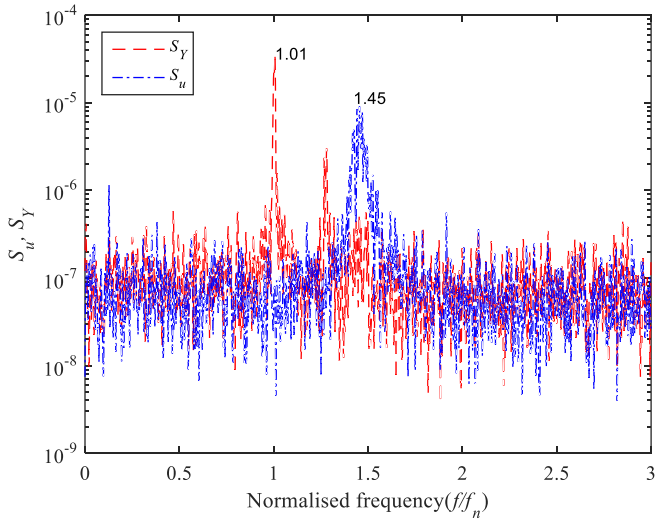


Fig. 2. Vibration and vortex shedding behaviours for the isolated cylinder, compared with previous studies i.e. the simulation study by Maruai et al. [4] and the experimental studies by Ismail et al. [19] and Kawabata et al. [10].

c



b



a

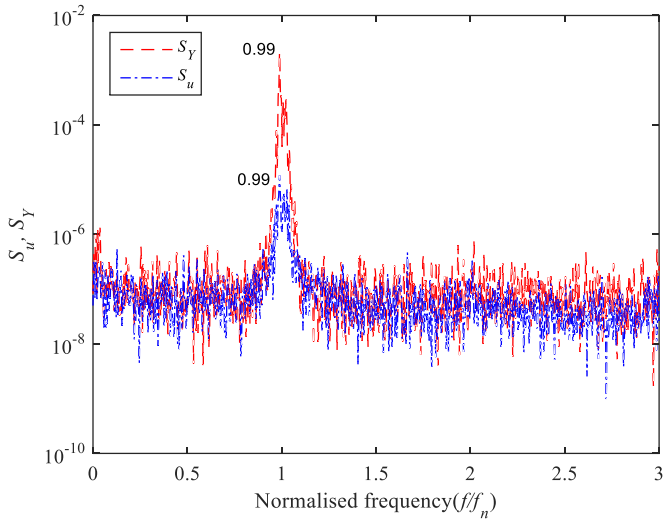


Fig. 3. Power Spectrum Density (PSD) of displacement Y and velocity u. (Isolated square cylinder, Sc = 31.75, S_y: red line, S_u: blue line): a: U_R = 7.69 (f_c/f_n = 0.99, f_v/f_n = 0.99); b: U_R = 10.93 (f_c/f_n = 1.00, f_v/f_n = 1.45); c: U_R = 17.46 (f_c/f_n = 0.99, f_v/f_n = 2.27)

3.2 Effect of the downstream square plate

In Fig. 4, the non-dimensional amplitude is plotted against U_R for various gap ratios S/D over a range from 0.12 to 2.90. To see the effect of the downstream plate on KVIV, the maximum amplitude A_{KVIV} and the reduced velocity U_A for A_{KVIV} are obtained from the results in Fig. 4. and plotted against S/D in Fig. 5. Fig. 5 shows that A_{KVIV}/D and U_A are only slightly affected in the range of gap ratio $S/D \leq 0.98$. At S/D = 1.17, A_{KVIV}/D reaches the largest value, around five times larger and U_A increases higher by 20%, as compared with the isolated counterpart. They decrease with S/D in the range of $1.17 \leq S/D \leq 2.33$ and return to their respective values of the isolated counterpart at S/D = 2.90. This result is consistent with that of Kawabata et al. [10] which reported that the influence of downstream square cylinder on KVIV is insignificant, except the large vibration observed at S/D = 1.17.

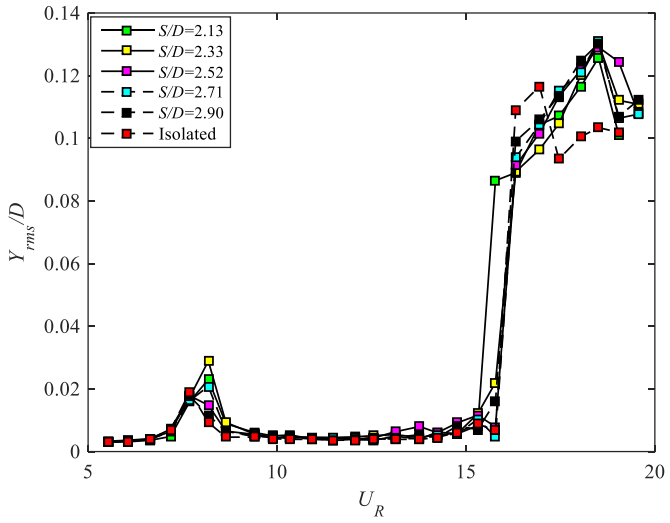
The influence of the downstream plate on the galloping observed in Fig. 4 can be summarized as follows: i) When $S/D \geqq 1.75$, the influence of the downstream plate is small, ii) When $1.37 \geqq S/D \geqq 1.17$, the increasing gradient of amplitude after U_g decreases with the decreasing gap ratio while U_g is not affected, iii) When $0.98 \geqq S/D \geqq 0.12$, U_g is much smaller than that of the isolated counterpart while the increasing gradient of amplitude after U_g is almost un-affected. In order to compare with Kawabata et al. [10], the vibration amplitude in the full galloping regime, i.e. at U_R = 18.4 indicated by the vertical red broken line in Fig. 4 (b), is obtained and normalized by that without the downstream plate, defined as $Y_{rms}/Y_{rms\infty}$. It is plotted against S/D in Fig. 6 (a) and compared with the results of Kawabata et al. [10] together with U_g vs. S/D as shown in Fig. 6 (b). Since in Fig. 4 (a) the data of the present study at U_R = 18.4 is not available for S/D < 1.17, the amplitude at the maximum U_R of measurement in the galloping regime is regarded to be equivalent, and this is also plotted in Fig. 6 (a).

In contrast to the findings of Kawabata et al. [10] the downstream square plate does not suppress, but rather enhances the galloping as seen in Fig. 6. That is, the critical reduced velocity

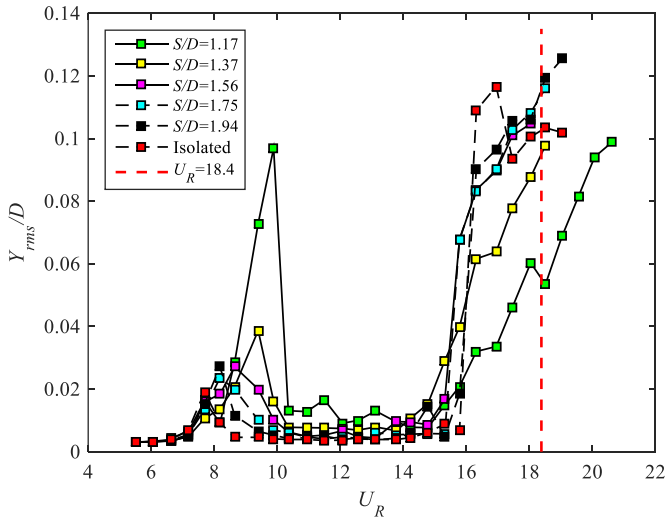
U_g is lower than that of the isolated counterpart when $S/D \leqq 2.13$, and, generally speaking, decreases with decreasing S/D. However, U_g is minimum, around half of the isolated counterpart, at $S/D = 0.98$. Although the galloping amplitude seems a little suppressed in the range of $1.17 \leq S/D \leq 1.94$, this suppression is considered to be brought by the slow gradient of galloping amplitude after U_g. At the present stage, the reason for this inconsistency is quite unclear and left for further investigation.

From the viewpoint of physics of fluid motion, it is questionable to identify the large amplitude vibration at $U_R = 9.88$ for $S/D = 1.17$ shown in Fig. 4 (b) as the KVIV is enhanced by the downstream plate, and because its maximum amplitude is around five times larger than that of KVIV of the isolated counterpart. It is not plausible that the small downstream plate can enhance the excitation force of KV so largely. The spectra of Y and u at this vibration are presented in Fig. 7. By comparing this figure with Fig. 3 (a), it seems that the synchronization of KV on the cylinder oscillation is not so firm. Hence, this phenomenon may be regarded as the "Wake body interference fluid elastic vibration (WBIFEV)" as found by Kawabata et al. [10].

c



b



a

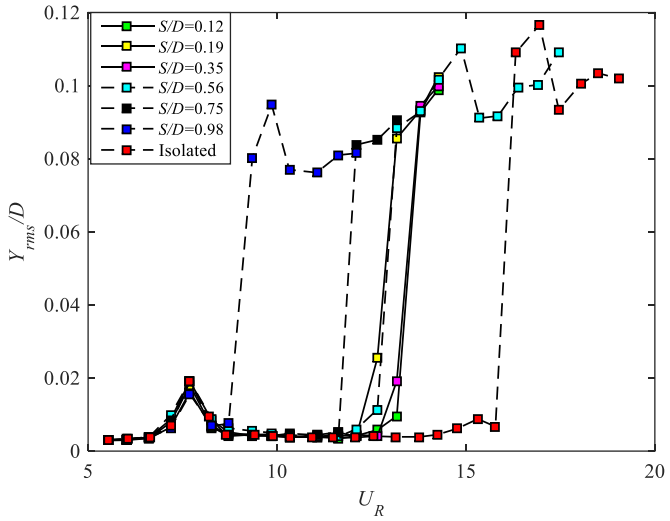
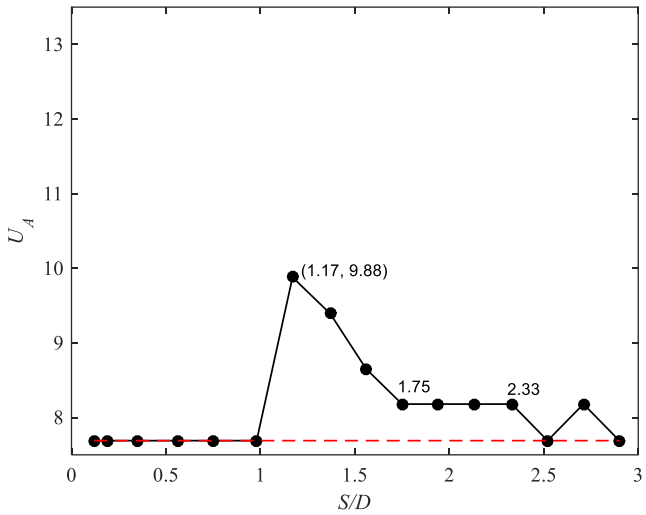


Fig. 4. Influence of square plate (*w/D* = 1) on relationship between vibration amplitude and flow velocity of the square cylinder. a: 0.12 ≤ *S/D* ≤ 0.98; b: 1.17 ≤ *S/D* ≤ 1.94; c: 2.13 ≤ *S/D* ≤ 2.90. The vertical red broken line in Fig. 4(b) at U_R = 18.38 indicates the reduced velocity in the experiment by Kawabata et al. [10] for varying *S/D*.

b



a

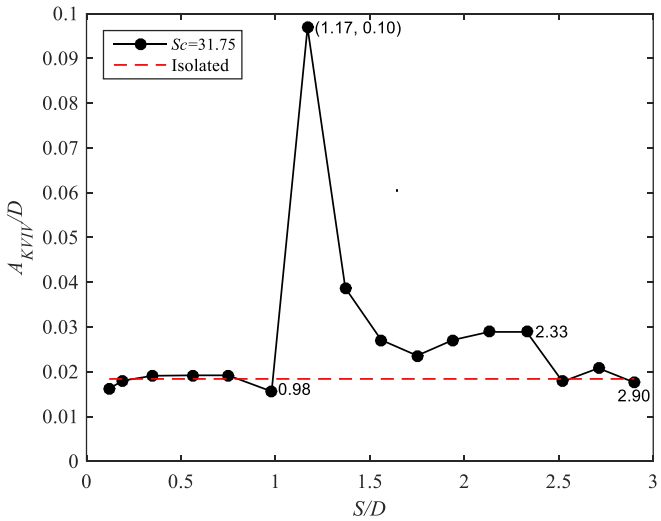
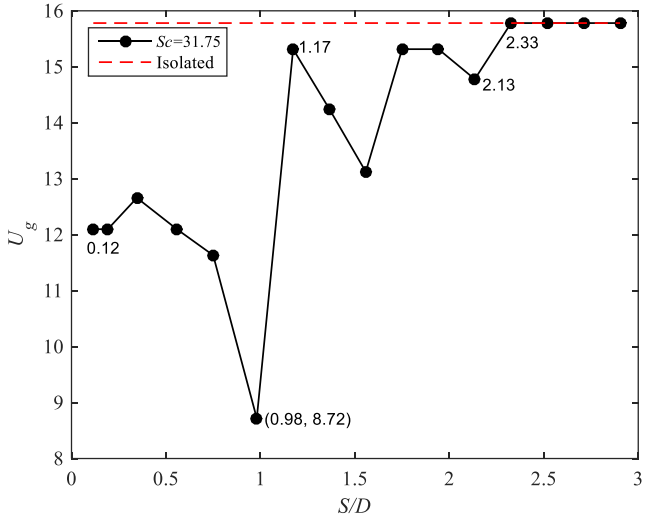


Fig. 5. The influence of square plate (l_d/D = w/D = 1) on KVIV of the square cylinder: a) Maximum amplitude of KVIV, b) Reduced velocity at maximum amplitude of KVIV. The horizontal red broken line represents the case of the isolated counterpart.

b



a

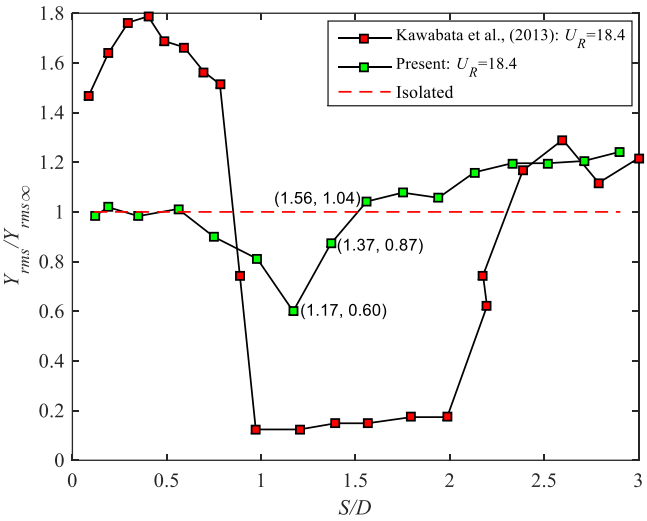


Fig. 6 The influence of square plate (w/D = 1) on galloping of the square cylinder compared with Kawabata et al. [10]: a) Galloping amplitude normalized by that without downstream plate at U_R = 18.4, b) Critical reduced velocity of galloping U_g. The horizontal red broken line represents the case of the isolated counterpart.

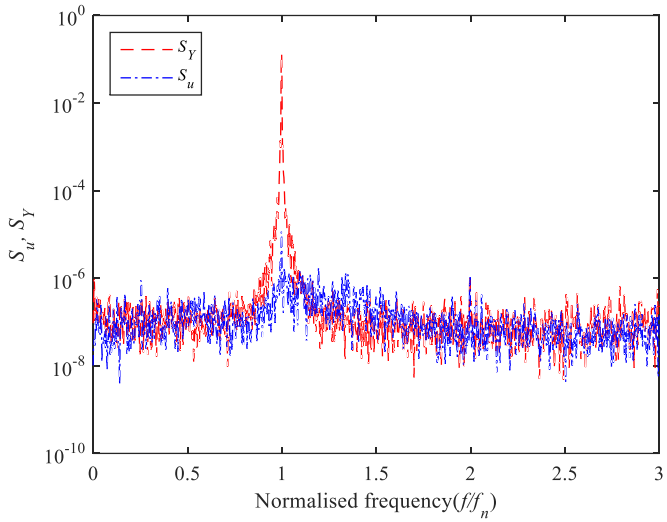


Fig. 7 Power Spectrum Density S_Y and S_u at U_R = 9.88 for the maximum KVIV peak with the downstream plate placed at S/D = 1.17.

4. Conclusions

The present study is aimed at the development of a passive technique to control cross-flow vibrations of a square cylinder utilizing the influence of a downstream square plate found by Kawabata et al. [10], since the square plate with a side length equal to that of the square cylinder is most simple and desirable as the downstream body from the practical point of view. The results of wind tunnel experiment for the isolated square cylinder are in good agreement with the previous experiments and simulations for the amplitude response against varying velocity, which validated the experimental facilities/techniques in the present study.

The downstream square plate is shown to only have a slight effect on KVIV as reported by Kawabata et al. [10]. In contrast, it enhances the galloping in the sense that the onset velocity of galloping reduces to about half of the isolated counterpart at S/D = 0.98. The most remarkable effect of the downstream square plate is the enhancement of the vibration near the peak velocity of KVIV at S/D = 1.17. This may indicate the occurrence of the wake-body-interference fluid elastic vibration reported by Kawabata et al. [10]. The effect of the downstream square plate on the square cylinder found in this study will lead to a novel technique for vibration control. However, more detailed and comprehensive experiments are expected to clarify the cause of difference with respect to the findings of Kawabata et al., [10].

Acknowledgement

This research was supported by a university grant (grant number 4B395) from the Universiti Teknologi Malaysia.

References

[1] Terres-Nicoli and J.M., Kopp, G.A. (2009). *Mechanisms of the Vertical Vortex Induced Vibration of the Storebaelt Bridge*. 11th Americas Conference on Wind Engineering – San Juan, Puerto Rico

[2] Assi, G.R.S., Bearman, P.W., Kitney, N. (2009). *Low drag solution for suppressing vortex-induced vibration of circular cylinder*. J. Fluids Struct. 25, 666-675

[3] Ali, M.S.M., Doolan, C.J., Wheatley, V. (2012). *Low Reynolds number flow over a square cylinder with a detached flat plate.* Int. J. Heat Fluid Flow 36, 133-141.

[4] Maruai, N.M., Ali, M.S.M., Ismail, M.H., Zaki, S.A. (2018). *Flow-induced vibration of a square cylinder and downstream flat plate associated with micro-scale energy harvester*. J. of Wind Engineering & Industrial Aerodynamics 175, 264-282.
[5] Shirakashi, M., Mizuguchi, K., Bae, H.M. (1989). *Flow induce excitation of an elastically-supported cylinder caused by another located downstream in cruciform arrangement*. Journal of fluids and structures 3, 595-607
[6] Bae, H.M., Baranyi, L., Takahashi, T., Shirakashi. (2001). *Suppression of Karman vortex excitation of a circular cylinder by a second cylinder set downstream in cruciform arrangement*. J. of Computational and Applied Mechanics, Vol. 2, No. 2, pp. 175-188
[7] Nguyen, T., Koide, M., Yamada, S., Takahashi, T., Shirakashi, M. (2012). *Influence of mass and damping ratios on VIVs of a cylinder with a downstream counterpart in cruciform arrangement*. J. of Fluids and Structures 28, 40-55
[8] Koide, M., Kato, N., Yamada, S., Kawabata, Y., Takahashi, T., Shirakashi, M. (2007). *Influence of a cruciform arrangement downstream strip plate on crossflow vibration of a square cylinder*. J. of Computational and Applied Mechanics, Vol. 8, No. 2, 135-148.
[9] Kato, N., Koide, M., Takahashi, T., Shirakashi, M. (2012). *VIVs of a circular cylinder with a downstream strip-plate in cruciform arrangement.* J. of Fluids and Structures 30, 97-114
[10] Kawabata, Y., Takahashi, T., Haginoya, T., Shirakashi, M. (2013). *Interference effect of downstream Strip-plate on the crossflow vibration of a square cylinder*. J. of Fluid Science and Technology, Vol.8, No.3., 348-363
[11] Assi, G.R.S., Peter, W.B., Micheal, A.T. (2014). *On the stability of a free-to-rotate short-tail fairing and splitter plate as suppressions of vortex-induced vibration*. Ocean Eng. 92, 234-244
[12] Yu, Y., Xie, F.F., Yan, H.M., Constantinides, Y., Oakley, O., Karniadakis, G.E. (2015). Suppression of vortex-induced vibrations by fairing: a numerical study. J. Fluids Struc. 54, 679-700
[13] Wang, J.S., Zheng, H.X., Tian, Z.X. (2015). Numerical simulation with a TVD-FVM method for circular cylinder wake control by a fairing. J. Fluids Struc. 57, 15-31
[14] Lou, M., Wu, W-g., Chen, P. (2017). *Experimental study on vortex induced vibration of risers with fairing considering wake interference*. J. of Naval Architecture and Ocean Engineering 9, 127-134.
[15] Marra, A.M., Mannini, C., Bartoli, G. (2015). Measurement and improved model of vortex-induced vibration for an elongated rectangular cylinder. J. Wind Eng. & Ind. Aerodyn, 147, 358-367
[16] Mannini, C., Marra, A.M., Bartoli, G. (2014). *VIV-Galloping instability of rectangular cylinders: Review and new experiments*. J. of Wind Eng. And Industrial Aerodynamics 132, 109-124
[17] Mannini, C., Marra, A.M., Massai, T., Bartoli, G. (2016). *Interference of vortex-induced vibration and transverse galloping for a rectangular cylinder*. J. of Fluids and Structures 66, 403-423
[18] Kaneko, S., Nakamura, T., Inada, F., Kato, M., Ishihara, K., Nishihara, T. (2014). *Flow- induced vibrations classification and lessons from practical experiences.* Second edition, Elsevier Ltd
[19] Ismail. M.H., Ali, M.S.M., Zaki, S.A., Shirakashi, M., Sallehuddin. M. (2017). *Flow induced vibration of a square cylinder with high Scruton number*. ARPN J. of Eng. and Applied Sciences, Vol.12, No.10
[20] Khalak, A., and Williamson, C.H.K. (1999). *Motions, Force and Mode Transitions in Vortex-Induced Vibrations at Low Mass-Damping.* J. of Fluids and Structures, 13, pp. 813-851.
[21] Feng, C.C., (1968). *The measurement of vortex-induced effects in flow past a stationary and oscillating circular and D-section cylinders.* Master's Thesis, University of British Columbia, Vancouver, B.C., Canada
[22] Sun, H., Kim, E.S., Nowakowski, G., Mauer, E., Bernitsas, M.M. (2016). *Effect of mass-ratio, damping and stiffness on optimal hydrokinetic energy conversion of a single rough cylinder in flow induced motions*. J. Renewable Energy 99, 936-959

Penerbit Akademia Baru

Engineering Science and Technology Conference Proceedings

Journal homepage: www.akademiabaru.com/EST.html

Experimental Investigation of Mixed Convection Heat Transfer Within a Cavity Containing a Rotating Cylinder

Open Access

Zinah Salman [1,*], Falah Aiss[2] , Mujtaba Almudhaffar [1]

[1] Department of Engineering Technical College, Southern Technical University, Basra, Iraq
[2] Department of Mechanical Engineering, Engineering College, University of Basrah, Iraq

ABSTRACT

Mixed convection in a semi-circle enclosure of radius 0.15 m and length 0.75 m is studied experimentally. An insulated rotation cylinder is fixed at the center of the cavity to improve the heat transfer coefficient, the bottom wall of the enclosure is subjected to constant heat flux while the external curved wall is exposed to the ambient temperature. The values of inclination angles used in this study are Ø=(0°,90°) and the angular velocities(62.8,83.73,125.6) rad/s. Results show an improvement of heat transfer coefficient with increasing angular velocity and with increasing the inclination angles from Ø =0° to 90°.

Keywords:
Heat transfer; turbulent flow; mixed convection; semi circle enclosure; rotating cylinder

Copyright © 2019 PENERBIT AKADEMIA BARU - All rights reserved

1. Introduction

Heat transfer is considered alone of the challenges in engineering. The adding of heat to a system or the removing of heat from a system occurs in different ways, for example, removing of heat from computer chips or optical devices, cooling of systems for power plants, Refrigerators, indoor temperature control devices. The above heat transfer applications impact people's daily lives and support on the carried out of new research in order to enhance their efficiency [1]. The mixed convection phenomena take place when natural and forced convection mechanisms to act together. The classic problems of mixed convection heat transfer in a cavity have received considerable interest due to powerful relation to many practical's engineering utilization. A cavity model uses to simplify for numerous heat transfer issues. Many researchers presented with experimental and numerical investigation on various gaps for convection problems involving a rotating or stationary cylinder. Ridouane et al.[2] studied heat transfer numerically in an isosceles triangular cavity. Rahman et al.[3] used a vented square enclosure to study mixed convection flow. Rahman et al.[4] performed a rectangular enclosure by a heat source that utilized on the right perpendicular wall . Costa and Raimundo [5] studied the square cavity with a rotary cylinder positioned at the center. Brito et al. [6] investigated numerical in a square enclosure with a localized heating source on the center of the horizontal bottom surface. Alshara et al. [7] used an equilateral triangular cavity full of with air to investigation for the impact of rotating horizontal

* *Corresponding author. Zinah Salman*
E-mail address: zenaselman0@gmail.com (Zinah Salman)

single and multi-cylinders on mixed convection heat transfer. Salem [8] Investigated an experimental for impact of inclination angle in a rectangular cavity by uses the heat fluxes ranges (4 - 108) w/m^2 , Rayleigh number(1.9 ×105-5×106), inclination angles(15 - 75) and mass flow rates(0 –0.062) kg/sec it can be shown that an improvement of Nussle number with increasing of the heat flux and the mass flow rate and also with increasing the inclination angle. Liao and Lin [9] studied mixed and free convection of a two-dimension square cavity that includes a stationary, or a rotating cylinder was .Yasin et al.[10]Investigated experimental heat transfer to air inside a cavity. Turbulent natural convection and laminar flow for solving the mixed convection of air flow in a room was a numerically by Safari et al.[11].The infinite volume method had been utilized to resolve governing differential equations for this flow. Karimi et al.[12].The investigation was carried out numerical in a two-dimensional square cavity two heated horizontal cylinders. Aithal et al.[13]Studied simulation of high Rayleigh number produced from a hot cylinder located in the center of in a cold square enclosure. Kareem and Gao [14] performed a differential treatment in three dimension cavity with a thermally insulated rotating circular cylinder Reynolds numbers were varied from (5000-30000). Sabbar et al. [15] studies fluid flows at cavity including of a flexible wall connected to the horizontally channel. These are different parameters effects investigated on the heat exchange, the channel height to cavity, height ratio, heat source length, heat source location, and Ri = 0.1 to 100.The results presented when source length decrease lead to a maximum raise Nusselt number.

2. Experimental Setup

An experimental study was carried out in a semi-circle enclosure (30x15x75 cm) at Figure (1) shows a schematically diagram of the cavity. The figure (2) illustrates the diagram of the practical device. Semi-circle container made of aluminum mounted on a rectangular wooden box. Teflon cylinder installed in the center of the gap and is rotated by an electric motor. Temperature and control measure .Heater is installed at the bottom surface of the test section for the provide constant heat flux. The bottom wall of the enclosure is undergone to constant heat flux, while the rotating cylinder located in the center of the cavity and external curved wall is exposed to the ambient temperature. The values of inclination angles used in this study are Ø (0°,90°) and the angular velocities (62.8,83.73, 125.6) rad/s.

2.1 Processing the experimental data

The measured value of net e.m.f by MultiMate between ice –bath and each thermocouple is substituted into Eq. 1 in order to determine the temperature measured by that thermocouple.

$$T_L=\frac{V(v)}{0.041}+T_\infty \quad (1)$$

Where local temperature along bottom wall, T_L, voltage reading from Multimater, V, environmental temperature, T_∞, 0.041: constant . The average temperature of the heated surface of the bottom wall can be computation as following in Eq. 2 where the value of hot wall temperature, T_s, and the number of thermocouples installed in the hot wall, n .The angular speed of the roller is calculated as follows in Eq. 3 where the revaluation per mint, N. The heat flux along the heated surface can be calculated as [16] and the experimental cases the average Nusselt number in Eq. 4 where mean temperature of fluid, T_f , the voltage,V, current, I, and heated surface area, A. The Rayleigh number can calculated as following in Eq. 5 where Gravitation acceleration, g, rate of

change in of density with respect to the change in temperature, ß, Hydraulic diameter, D_h, thermal conductivity, k, Thermal diffusivity of fluid, α, and the kinematic viscosity, υ.

$$\overline{Ts} = \frac{\sum Ts}{n} \tag{2}$$

$$\omega = \frac{2\pi N}{60} \tag{3}$$

$$Nu_{av} = \frac{q^{"}}{k(T_s - T_f)} \tag{4}$$

$$Ra = \frac{g\beta q^{"} D_h^4}{k\, v\alpha} \tag{5}$$

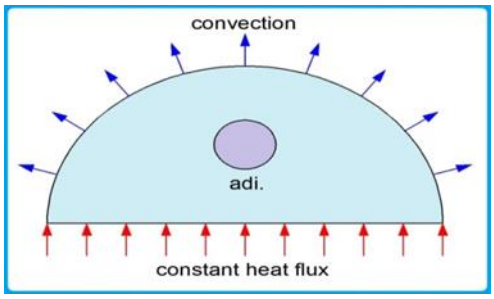
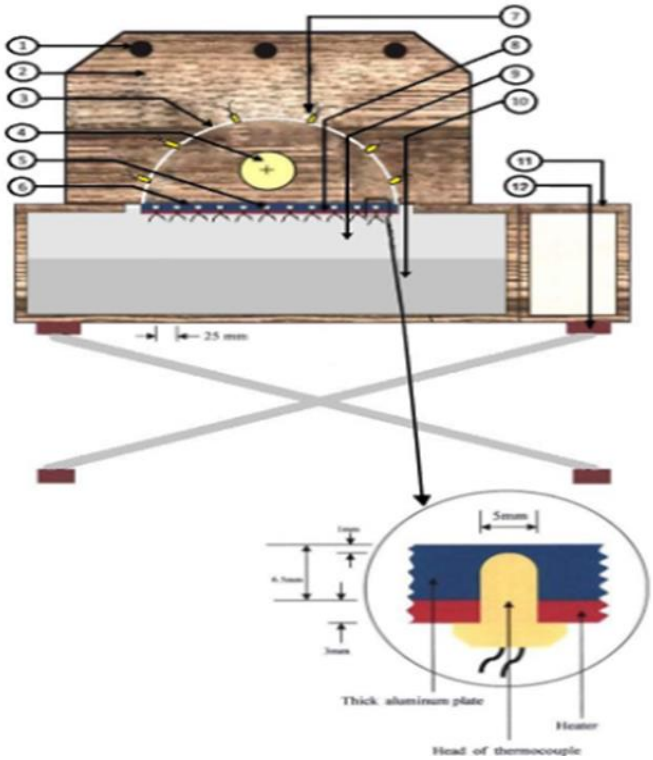


Fig. 1. Schematic diagram of cavity



1.Fixing rod 2.woodenportion 3. Aluminum enclosure 4.Teflon wall 5.Bottom wall 6. Thick plate 7.Thermocouple for curved walls 8.Heater 9.ceramic fiber insulation 10.Reinforced thermal cork 11.wooden chamber 12.wooden board for inclination

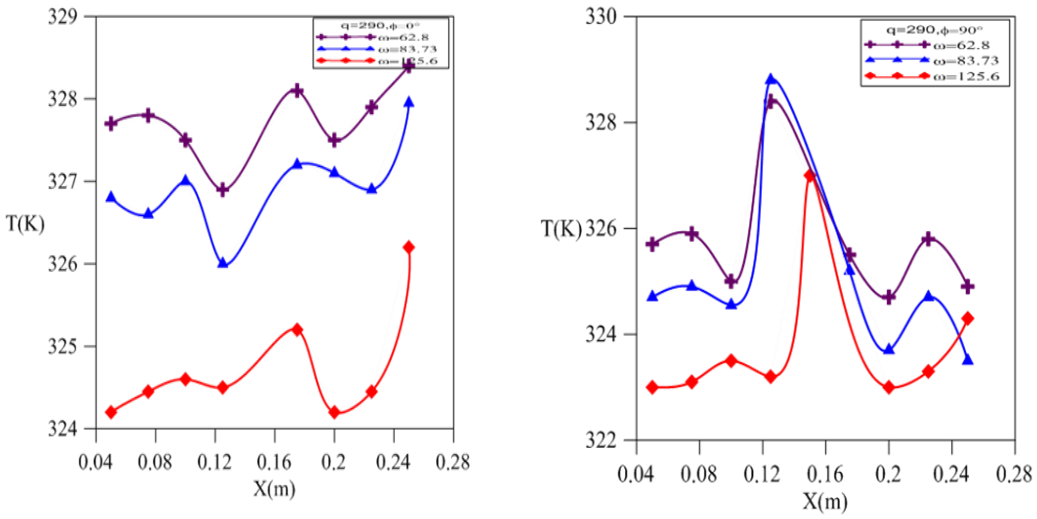
Fig. 2. Schematic of apparatus (transverse section)

3. Results and Discussion

The results were performed using a variation of local Nusselt number along with the heated surface cavity. Present work by using two values of heat flux. Show experimental results at the effect of inclination angle Ø and angular velocity ω.

3.1 The effect of angular velocity on local temperature

Figure. 3. illustrates effect of inclination angles and the angular velocity for the solid cylinder on the temperature variation along the bottom wall. For this figure the value of Rayleigh number of $2.9*10^8$which correspondingly heat flux q=290w/m^2 with constant inclination angles and different angular velocity ω= 62.8, 83.73, 125.6. It can be seen from this figure that for the inclination angle Ø=0° (Horizontal situation) The temperature of the surface is high and that the distribution of the temperature will along the cross-section of the hot surface where we observe a small rise in the temperature of the area under the rotary cylinder and the reason for increasing the resistance of heat transfer in the area narrow under the cylinder . At Ø=90° (vertical situation) it can be observed that the temperature of the surface is lower than in the horizontal situation cause of the impact of forced convection on the hot wall**.** Increasing heat flux q=540 w/$m^2$for Rayleigh number $Ra=5*10^8$with various angular velocity 62.8, 83.73,125.6 rad/s, at constant inclination angle Ø=0° it is important to observation the trend of temperature curves starts increasing then shown maximum peak at distance x=0.175m. At constants inclination angle Ø=90° it can be seen regular curves for temperature along the heated surface of the cavity.



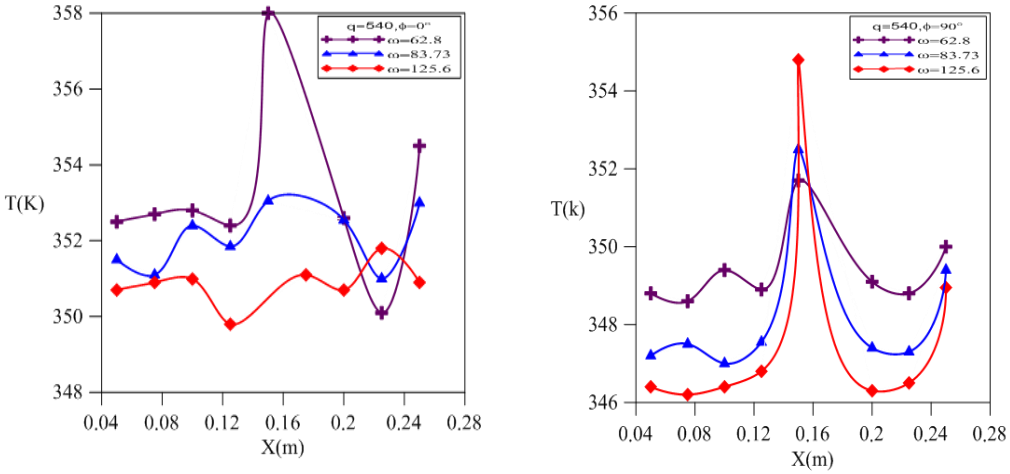


Fig3: Temperature distribution along bottom wall at heat flux q=290 w/m^2 and 540 w/m^2 with different ω and ø=0̂, 90̂

3.2 Nusselt Number

The variations of local Nusselt number are sketching along the heated bottom wall for various inclination angles with for various angular velocities. Figure .4 shows the variation of experimental local Nusselt number with various angular velocities ω= 62.8, 83.73, 125.6 rad/s at heat flux(q=290w/m^2) with constant inclination angles(0°,90°), it can observe that for inclination angle0° the increases angular velocity lead to increase Nu. This figure shows the values of Nusselt number at the left side of the below surface is higher than the values at right side this is because of the buoyancy effect at the left side it is opposing to the air rotation motion and vice versa at the right side. For Ø = 90 °, it can be seen that for higher angular velocity the Nusselt number is decreased at x=0.15 m cause of the decreasing the effect of forced convection in this region. At same figure represent the impact increasing heat flux to 540 w/m^2 with angular velocity 62.8,83.73,125.6 rad/s in Ø=90°, it can be found that a lower peak of the curves of Nu occurs in the middle point of the heated surface at a region under the rotating cylinder due to resistance to flow. For heat flux 540 w/m^2 with inclination angle Ø=0°, it can be seen increasing Nusselt number with increasing angular velocity due to dominant of forced convection**.** Figure . 5 shows that for q= 290 w/m ^{2} and ω= 62.8,83.73 rad/s presents variation of local Nusselt number at inclination angle for two cases Ø=90° the maximum summit for two curves local Nusselt number take place at two-point of distance (x=0.1,x=0.2)m. reducing the values of Nusselt in the near middle of the heated surface due to increasing the resistance of convection heat transfer in this region. with increasing angular velocity ω=125.6rad/s for Ø= 90° the values of Nusselt number decreasing the middle point due to the change the direction of buoyancy with the direction of the flow motion of the air. At heat flux q=540 w/m^2 and angular velocity =62.8,83.73 ,125.6 rad/s with inclination angles 0°,90°in Figure .5 illustrates the trend of the curves of local Nusselt number along the bottom wall decreasing at the middle surface because the increasing of convection heat transfer resistance at the ends of the heated surface. At heat flux 540 w/m^2 and angular velocity 125.6 rad/s , show the maximum peak takes place at distance of x=0.2 m the figure shows a difference in the distribution of Nusselt on both sides of the hot surface due to the difference in the direction of the buoyancy with the direction of air movement inside the cavity.

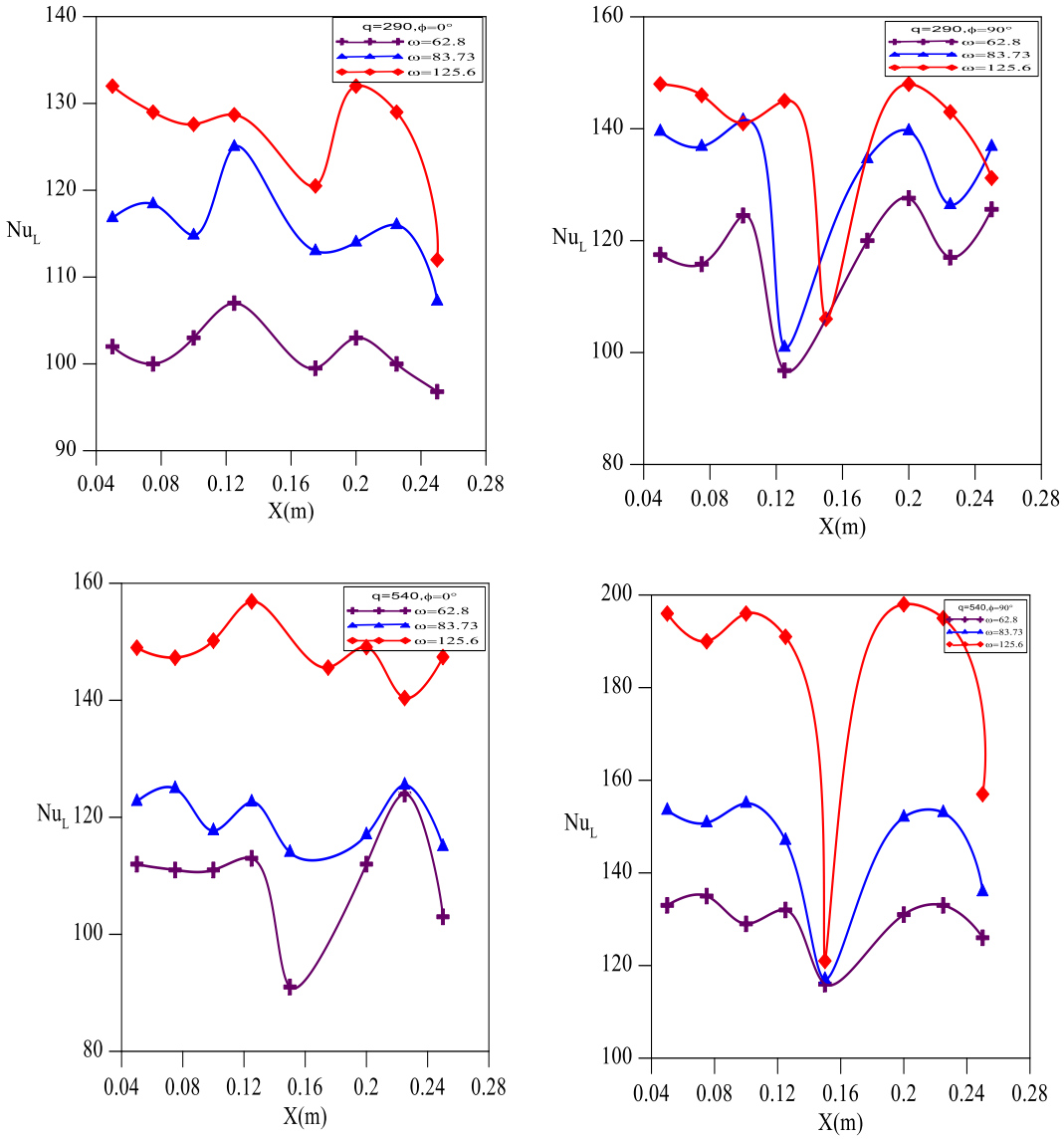


Fig.4. Variation local of Nusselt number along the bottom wall at heat flux q=290 w/m^2 and 540 w/m^2 with different ω and ø=0̊, 90̊.

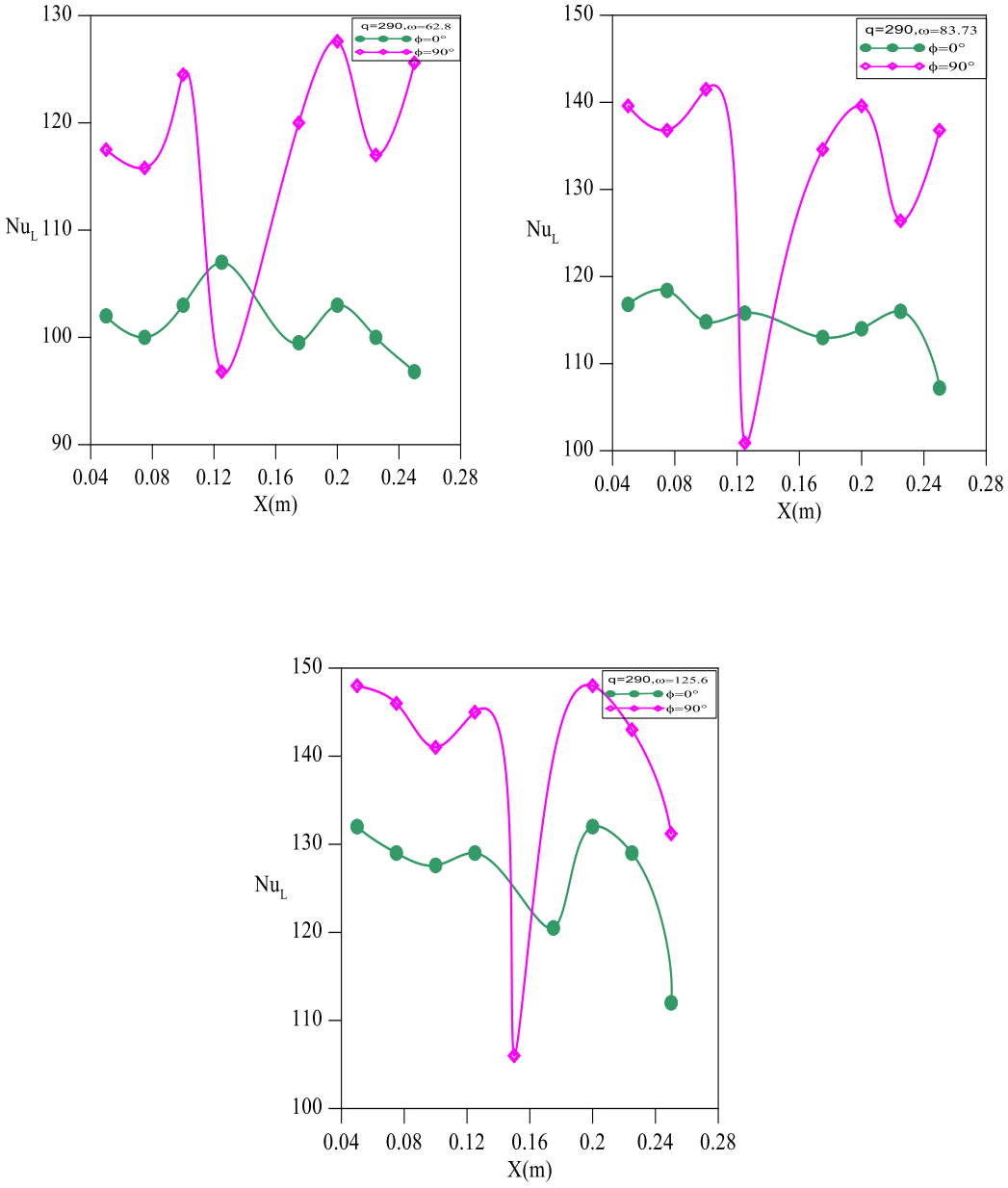
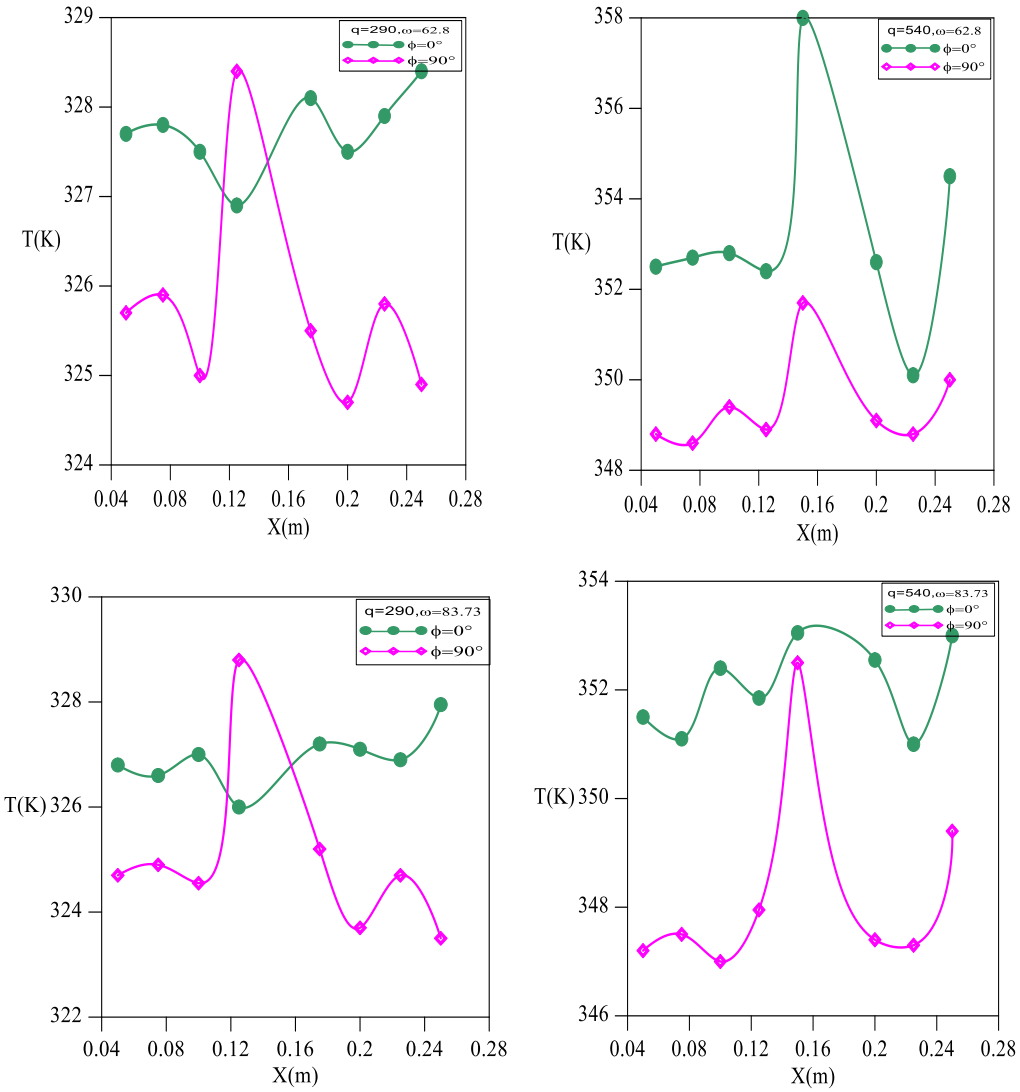


Fig.5. Variation of local Nusselt number along the bottom wall at heat flux q=290 w/m^2 with different ø and ω=62.8,83.73,125.

3.3. The influence of inclination angle on local temperature

Figure 6 Shows that the variation of local temperature distribution the below wall for two inclination angles at heat flux q=290 w/m^{2}and angular velocities 62.8,83.73,125.6 rad/s respectively. The results show it can be observed that for inclination angles 0° the minimum value of temperature has occurred at x=0.125m the perform of two angular velocity ω=62.8, 83.73 rad/s while it has occurred at the angular velocity 125.6 maximum value temperature at x= 0.18 for the inclination angle 0°.A maximum value of temperature occurs at midpoint while, its minimum value of temperature happens in the edge near the curved wall at angular velocity equal 62.8,83.73 rad/s

when Ø=90° . For the heat flux q=540 w/m^2 and ω = 62.8 rad/s as in figure 3 it can be observed the local temperature distributions for inclination angles 0 °, 90 °these curves will approach from each other, also shown the peak at a distance of x=0.15. With the angular velocity to the 125.6 rad/s, the values of local temperature for inclination angle 0° is higher than the inclination angle 90° and showed the maximum value of the temperature has occurred at a distance x=0.15 m because the influence of location of solid cylinder .



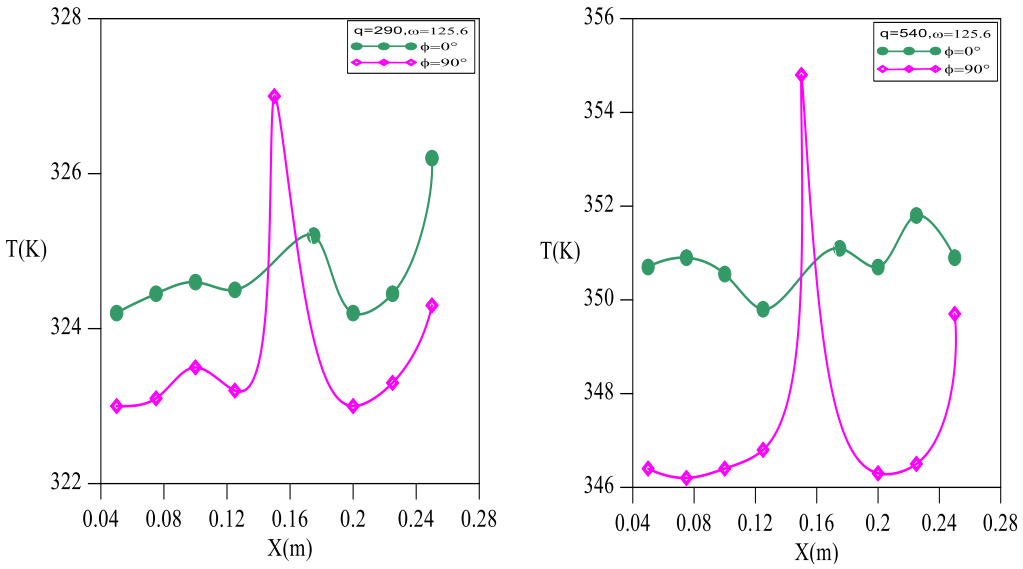


Fig.6. Temperature distribution along bottom wall at heat flux 290w/m^{2}and 540w/m^{2}with different Ø and ω=62.8,83.73,125.6 rad/s.

4. Conclusions

An experimental study of turbulent mixed convection heat Transfer of semi-circle cavity that contains a rotating cylinder has been completed at different rotational speeds, and inclination angle at horizontal and vertical The present outcomes have displayed heat transfer enhancement in the enclosure can be summarized in below:

- There are the effect on the heat transfer and fluid flow fields at using the rotating cylinder or raising the Reynolds number, especially at high rotational speeds .also, it leads to promote local Nusselt number at a high angular velocity.
- Also it is observed maximum heat rate of average Nusselt number at angle 90^o. Accordingly increasing the heat transfer rate occurs at increment the inclination angle

References

[1] Omranian, S.A. (2011) "The computation of turbulent natural convection flows" (Doctoral dissertation, University of Manchester).

[2] Ridouane, E.H., Campo,A., Hasnaoui, M. "Turbulent natural convection in an air-filled isosceles triangular enclosure,. *International Journal of Heat and Fluid Flow*, vol. 27.3, (2006); pp.476-489

[3] Rahman, M., Alim, A., Saha, S., Chowdhury, M.k "Mixed convection in a vented square cavity with a heat conducting horizontal solid circular cylinder". *Journal of naval architecture and marine engineering* , vol 5.2, (2008): pp. 37-46.

[4] Rahman, M., Alim, A., Mamun, M.A.H. "Finite element analysis of mixed convection in a rectangular cavity with a heat-conducting horizontal circular cylinder". *Nonlinear Analysis: Modelling and Control*, vol. 14.2, (2009): pp.217-247.

[5] Costa,V.A. and Raimundo, A.M. "Steady mixed convection in a differentially heated square enclosure with an active rotating circular cylinder". *International Journal of Heat and Mass Transfer*, vol. 53.(2010): pp.1208-1219.

[6] Brito, R.F., Menon, G.J., Pirani, M.J. " Turbulent natural convection in enclosures using large-eddy simulation with localized heating from horizontal bottom surface and cooling from vertical surfaces". *Journal of the Brazilian Society of Mechanical Sciences and Engineering* vol.31.3 (2009): pp. 199-209.

[7] Alshara, A.K."Effect Of Single Or Multi Rotating Horizontal Cylinders On The Mixed Convection Heat Transfer Inside A Triangular Enclosure". *Al-Qadisiyah Journal for Engineering Sciences,* vol. 5.1 (2012): pp. 95-110.

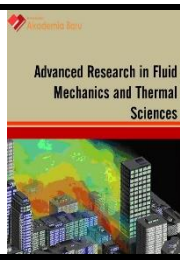
[8] T. K. Salem, T.K "The influence of inclination angle on natural convection in a rectangular enclosure". *Academic Research International*, vol. 4.2 (2013): pp. 111.

[9] Liao,C.C, Lin, C. A. " Mixed convection of a heated rotating cylinder in a square enclosure". *International Journal of Heat and Mass Transfer*, vol. 72 (2014) pp.9-22.
[10] Abdulla, A.S., Alwan, D.A.D.H., Yasin, N.J. "Experimental Study of Mixed Convection in an Enclosure with a Cold Movable Top Wall and Hot Bottom Wall". *Al-Khwarizmi Engineering Journal*, vol.10.1 (2014): pp. 32-46.
[11] Safaei, M., Goodarzi,M., Mohammadi,M. "Numerical modeling of turbulence mixed convection heat transfer in air filled enclosures by finite volume method". *The International Journal of Multiphysics*, vol.5.4, (2016).
[12] Karimi,F., Wang,Z., Yang,M. Zhang,Y., "Numerical simulation of steady mixed convection around two heated circular cylinders in a square enclosure". *Heat Transfer Engineering*,vol. 37.1 (2016): pp.64-75.
[13] Aithal, S.M. "Turbulent natural convection in a square cavity with a circular cylinder". *Journal of Thermophysics and Heat Transfer*, vol.30.4 (2016) pp. 843-853.
[14] Kareem, A.K., Gao,S., "Mixed convection heat transfer of turbulent flow in a three-dimensional lid-driven cavity with a rotating cylinder". *International Journal of Heat and Mass Transfer*, vol.112 (2017): pp.185-200.
[15] Walaa, A.S., Muneer, A.I., Al.Mujtaba," Numerical Investigation of Fluid-Structure Interaction with Mixed Convection in an Open Cavity of Flexible Wall: Effect of Geometrical Parameters" *International Journal of Engineering and Technology*, vol.8 (2019): pp.523-531.
[16] Theraja, B.L., Theraja,A.K, "Textbook of Electrical Technology Volume I IN System of units .S. Chand (2017).

Penerbit Akademia Baru

Engineering Science and Technology Conference Proceedings

Journal homepage: www.akademiabaru.com/EST.html



Magnetohydrodynamic Flow of Maxwell Nanofluid Over a Vertical Plate in a Porous Medium

Open Access

Sidra Aman[1], Zulkhibri Ismail[1,*], Mohd Zuki Salleh[1], Ilyas Khan[2]

[1] Applied and Industrial Mathematics Research group, Faculty of Industrial Science & Technology, Universiti Malaysia Pahang, 26300 UMP Kuantan, Pahang, Malaysia
[2] Basic Engineering Sciences Department, College of Engineering Majmaah University, Majmaah 11952, Saudi Arabia

ABSTRACT

This article analysis free convection flow of Maxwell nanofluid over a vertical plate in a porous medium. Magnetohydrodynamic effects are influencing the flow over the oscillating plate. The governing equations are in terms of Partial differential equations (PDE) with boundary conditions. Non-dimensionalization process is carried out and Laplace transform is applied to transform the governing equations into ordinary differential equations. The resulting equations are tackled via Inverse Laplace transform technique. Exact solutions are established for velocity, shear stress and temperature. These solutions are significantly controlled by the embedded parameters. The present outcomes are portrayed via graphs and briefly explained in the Results discussion section. The thermal conductivity and Nusselt number of nanofluid increases with increasing the amount of cobalt nanoparticles while velocity decreases with increasing magnetic number due to opposing forces..

Keywords:
Maxwell fluid; nanoparticles; free convection; Laplace transform technique

Copyright © 2019 PENERBIT AKADEMIA BARU - All rights reserved

1. Introduction

Non-Newtonian nanofluids has been studied by the researchers with a great interest due to its significance and applications in the theoretical and practical areas. Maxwell fluid model being the rate type fluid appealed researchers being the first and one of the least complex fluid models. It is as yet utilized generally exceptionally to depict the reaction of some polymeric fluids. Instead of its least complexity, Maxwell fluid model has few restrictions. For instance, this model does not legitimately portray the regular connection between shear rate and shear stress in a straightforward shear stream [1]. Mostly the investigation on Maxwell fluid especially on the diagnostic side are restricted to force exchange. The Maxwell fluid with different boundary conditions and under diverse effects is explored by Fetecau *et al.*, [2], Salah *et al.*, [3] and Vieru and Zafar [4].

Exact solutions for Maxwell fluid induced by oscillatory and accelerating plate was studied by Zheng *et al.*, [5]. Moreover, Giacomin *et al.*, [6] studied single relaxation time Maxwell fluid for Large amplitude oscillatory flow and obtained analytical solution. Recently, Han *et al.*, [7] studied the boundary layer flow of Maxwell fluids from a stretching sheet with the Cattaneo–Christov heat flux model. Nadeem *et al.*, [8] studied numerically the heat transfer in boundary layer flow of an Oldroyd-B nanofluid model toward a stretching sheet with a non-Fourier thermal flux model. They observed that the Brownian motion parameter enhances the Nusselt number and Sherwood

number. Mustafa [9] investigated analytically and numerically the non-Fourier convection in rotating Maxwell fluid flow. He presented both analytical and numerical solution and showed that both the results are in excellent agreement.

MHD free convection flow is also an important area in modern engineering sciences. Recent developments in materials synthesis, electromagnetic flow control, magnetic levitation in metallurgy and electro-conductive polymers have stimulated significant interest in magneto-convective flow simulations. The resurge in renewable energy devices employing electromagnetic pumps and hydro magnetic generators has also mobilized substantial efforts in MHD heat transfer analysis.

Hsiao [10] examined Maxwell fluid flow with viscous dissipation and MHD heat transfer via numerical finite difference method. A three dimensional flow of viscous fluid through an oscillatory disk and porous medium was inspected by Rauf *et al*., [11].

Relatively few studies of magneto hydrodynamic non-Newtonian nanofluids heat transfer have appeared utilizing Laplace transform technique. One of them is carried by Khan *et al*., [12], to acquire exact solution for MHD oscillatory flow of Maxwell fluid in a porous medium. Joule heating on MHD flow of Maxwell fluid with thermophoresis effect was investigated by Hayat and Qasim [13]. MHD flow for upper-convected Maxwell fluid over a stretching sheet was studied by Abel *et al*., [14]. They utilized shooting technique with fourth order Runge-Kutta method. Ali *et al*., [15] reported a study on MHD oscillating and rotating flow of Maxwell fluid in a porous plane. Maxwell nanofluid flow over a vertical plate for carbon nanotubes was examined for heat transfer enhancement by Aman *et al*., [16]. A very rare research has been reported on nanofluids in this domain due to the complexity of Maxwell fluid model when acquire for nanofluids. In this case the exact solution is hard to acquire for such problems which kept the research very limited in this specific domain. However, a quality research can be found such as a revise model of Maxwell nanofluid was studied over a stretching sheet with thermal effects [17]. They considered zero mass flux of nanoparticles on the surface. Some recent studies on MHD flow of Maxwell fluids or nanofluids are in [18-20] and the references therein.

All the above studies were investigated for Maxwell fluid and none of them considered nanofluid with heat generation and porous medium for problem. In the present research, the objective is therefore to study the MHD free convection heat transfer in boundary layer flow of a Maxwell nanofluid over an oscillating vertical plate with the Laplace transform technique. The problem will be tackled by taking heat generation and porous media into account.

The problem of Maxwell nanofluid with carboxymethyl cellulose (CMC) base fluid and copper nano size particles has not been reported yet for oscillating vertical plate. Analaytical solution is obtained via Laplace transform technique and Inverse Laplace transform for the present model.

2. Mathematical Formulation

Consider flow of a Maxwell nanofluid over a vertical plate and occupies the porous medium $y>0$. A constant magnetic field is effecting the fluid such that $\mathbf{B}=(0,B_0,0)$. Initially, both the plate and fluid were at rest with constant wall temperature T_w. After some time $t>0$, the temperature raised to T_∞ as shown in Figure 1. The governing equations are

$$\rho_{nf}\left(1+\lambda_1\frac{\partial}{\partial t}\right)\frac{\partial u}{\partial t}=\mu_{nf}\frac{\partial^2 u}{\partial y^2}-\sigma_{nf}B_0^2\left(1+\lambda_1\frac{\partial}{\partial t}\right)u(y,t) - \frac{\mu_{nf}\varphi}{k_1}u(y,t)+\left(1+\lambda_1\frac{\partial}{\partial t}\right)(\rho\beta)_{nf}\,g\left(T-T_\infty\right), \tag{1}$$

$$\left(1+\lambda_1\frac{\partial}{\partial t}\right)\tau\left(y,t\right)=\mu_{nf}\frac{\partial u\left(y,t\right)}{\partial y}. \tag{2}$$

$$(\rho c_p)_{nf}\frac{\partial T}{\partial t}=k_{nf}\frac{\partial^2 T}{\partial y^2}+Q_0(T-T_\infty), \tag{3}$$

with the initial and boundary conditions:

$$\begin{aligned} &u\left(y,0\right)=0,\ u(0,t)=U_0\cos\omega t,\ u\left(\infty,t\right)=0,\\ &T\left(y,0\right)=T_\infty,\ \ T\left(0,t\right)=T_w,\quad T\left(\infty,t\right)=T_\infty. \end{aligned} \tag{4}$$

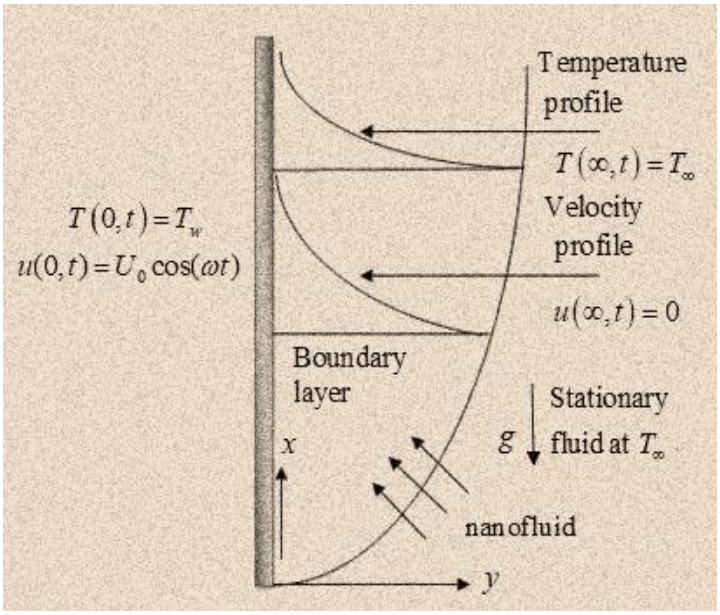


Figure 1. Flow geometry

where ω is the oscillating frequency, ρ_{nf} is density, μ_{nf} is the dynamic viscosity, σ_{nf} the electrical conductivity, $\tau\left(y,t\right)$ is the shear stress, $(\rho\beta)_{nf}$ the thermal expansion, $\left(\rho c_p\right)_{nf}$ is the specific heat capacity and k_{nf} is the thermal conductivity of nanofluid. In this analysis, the following non-dimensionless variables are introduced:

$$u^*=\frac{u}{U_0},\ \ y^*=\frac{yU_0}{\nu},\ \ t^*=\frac{tU_0^2}{\nu},\quad \tau^*=\frac{\nu\tau}{\mu U_0^2},\ \ \theta=\frac{T-T_\infty}{T_\infty}.$$

We get the non dimensional equations:

$$A_2\frac{\partial^2 u(y,t)}{\partial y^2}-A_1\left(1+\lambda\frac{\partial}{\partial t}\right)\frac{\partial u(y,t)}{\partial t}=A_3\left(1+\lambda\frac{\partial}{\partial t}\right)Mu(y,t) + A_2\gamma u(y,t)-A_4\left(1+\lambda\frac{\partial}{\partial t}\right)Gr\theta(y,t), \tag{5}$$

$$\left(1+\lambda\frac{\partial}{\partial t}\right)\tau(y,t)=A_2\frac{\partial u(y,t)}{\partial y}, \tag{6}$$

$$A_6\frac{\partial^2\theta(y,t)}{\partial y^2}-A_5 Pr\frac{\partial\theta(y,t)}{\partial t}+Q\theta(y,t)=0, \tag{7}$$

with initial and boundary conditions:

$$\begin{aligned} &u(y,0)=0,\ \theta(y,0)=0; y>0\\ &u(0,t)=U_0\cos\omega t,\ \theta(0,t)=1,\\ &u(\infty,t)=0,\quad \theta(\infty,t)=0, \end{aligned} \tag{8}$$

where

$$\lambda=\frac{\lambda_1 u^2{}_0}{\nu}, M=\frac{\sigma_f B_0^2\nu}{\rho_f U^2{}_0}, \gamma=\frac{\mu_f\varphi\nu}{\rho_f k_1 U^2{}_0}, Gr=\frac{\nu g\beta_f(T_w-T_\infty)}{U^3{}_0}, Pr=\frac{\mu_f c_p}{k_f},$$

are Maxwell parameter, magnetic parameter, porosity parameter, Grashof number and Prandtl number. While other constants introduced are

$$A_1=(1-\phi)+\phi\left(\frac{\rho_s}{\rho_f}\right),\ A_2=\frac{1}{(1-\phi)^{2.5}},\ A_3=\sigma_f\left(1+\frac{3(\sigma_f-1)\phi}{(\sigma_f+2)-(\sigma_f-1)}\right),$$

$$A_4=(1-\phi)+\phi\left(\frac{\rho_s\beta_s}{\rho_f\beta_f}\right),\ A_5=(1-\phi)+\phi\frac{(\rho c_p)_s}{(\rho c_p)_f},\ A_6=\frac{(k_s+2k_f)-2\phi(k_f-k_s)}{(k_s-2k_f)+\phi(k_f-k_s)},$$

Now we employ Laplace transform to equations (5)-(8), we obtain

$$\frac{\partial^2\bar{u}(y,q)}{\partial y^2}-\beta_0(1+\lambda q)q\bar{u}(y,q)=\beta_1(1+\lambda q)M\bar{u}(y,q) + \gamma\bar{u}(y,q)-\beta_2(1+\lambda q)Gr\bar{\theta}(y,q), \tag{9}$$

$$(1+\lambda q)\bar{\tau}(y,q)=A_2\frac{\partial\bar{u}(y,q)}{\partial y}, \tag{10}$$

$$A_6\frac{\partial^2\bar{\theta}(y,q)}{\partial y^2}-A_5\,\mathrm{Pr}\,q\bar{\theta}(y,q)+Q\bar{\theta}(y,q)=0, \tag{11}$$

with

$$\begin{aligned} &\bar{\theta}(0,q)=\frac{1}{q},\ \bar{\theta}(y,q)\to 0\ \ as\ \ y\to\infty.\\ &\bar{u}(0,q)=\frac{q}{q^2+\omega^2},\ \bar{u}(y,q)\to 0,\ as\ \ y\to\infty. \end{aligned} \tag{12}$$

The solution of Equations (9)-(11) subject to conditions, Equation (12) is given as

$$\bar{u}(y,q) = \bar{u}_1(y,q) + \bar{u}_2(y,q) - \bar{u}_3(y,q), \tag{13}$$

$$(1+\lambda q)\bar{\tau}(y,q) = A_2 \frac{\partial \bar{u}(y,q)}{\partial y}. \tag{14}$$

$$\bar{\theta}(y,q) = \frac{1}{q} exp\left(-y\sqrt{b_0}\sqrt{q-b_2}\right), \tag{15}$$

where

$$\begin{aligned}
&\bar{u}_1(y,q) = B(q),\ \bar{u}_2(y,q) = C(q)B(q),\\
&\bar{u}_3(y,q) = \frac{\beta_2(1+\lambda q)Gr\left(q-b_2\right)}{q\left[b_0(q-b_2)+\left\{(\lambda q+1)(\beta_0 q+\beta_1 M)+k\right\}\right]} D(q),\\
&B(q) = \frac{q}{q^2+\omega^2}\exp\left(-y\sqrt{\left\{(\lambda q+1)(\beta_0 q+\beta_1 M)+k\right\}}\right).\\
&C(q) = \frac{\beta_2(1+\lambda q)Gr}{q\left[b_0(q-b_2)+\left\{(\lambda q+1)(\beta_0 q+\beta_1 M)+k\right\}\right]}\frac{q^2+\omega^2}{q},\\
&D(q) = \frac{\exp\left(-y\sqrt{b_0}\sqrt{q-b_2}\right)}{\left(q-b_2\right)}
\end{aligned} \tag{16}$$

and

$$\beta_0 = \frac{A_1}{A_2},\ \beta_1 = \frac{A_3}{A_2},\ \beta_2 = \frac{A_4}{A_2},\ b_0 = \frac{A_5 Pr}{A_6},\ b_1^2 = \frac{QPr}{A_6},\ b_2 = \frac{b_1^2}{b_0}.$$

Taking the inverse Laplace transform and using Appendix (A1)-(A6):

$$u(y,t) = B(t) + \int_0^t B(y,s)C(t-s)ds - \int_0^t D(y,s)C(t-s)ds. \tag{17}$$

$$\tau(y,t) = \int_0^t G_1(t-s)H_1(y,t)ds + \int_0^t g_1(t-s)h_1(y,t)ds, \tag{18}$$

$$\theta(y,t) = \frac{1}{2}\left[e^{-y\sqrt{b_0 b_2}}erfc\left(\frac{y\sqrt{b_0}}{2\sqrt{t}} - \sqrt{b_2 t}\right) + e^{y\sqrt{b_0 b_2}}erfc\left(\frac{y\sqrt{b_0}}{2\sqrt{t}} + \sqrt{b_2 t}\right)\right], \tag{19}$$

where

$$B(t) = L^{-1}\left\{B(q)\right\} = e^{-mn}\cos\left(\omega(t-m)\right) + e^{-mn}\cos\left(\omega(t-m)\right) * \left(\frac{pme^{-nt}}{\sqrt{t^2+2mt}} I_n\left(p\sqrt{t^2+2mt}\right)\right),$$

$$C(t) = L^{-1}\left\{C(q)\right\},\ C(q) = \frac{E}{q} + \frac{F}{q^2} + \frac{Pq+R}{\lambda\beta_0\left(q-q_1\right)\left(q-q_2\right)},$$

$$D(t) = L^{-1}\left\{D(q)\right\} = erfc\left(\frac{y\sqrt{b_0}}{2\sqrt{t}}\right)e^{b_0 t}.$$

and

$$G_1(t) = a_5 \exp(-a_2 t) + a_6, \quad g_1(t) = a_7 \left[1 - \exp(-a_2 t)\right],$$

$$h_1(t) = \frac{e^{-y^2} \dfrac{b_1}{4t}}{\sqrt{\pi t}}, \qquad H_1(t) = \begin{cases} 0 & ;0 < t < yc \\ e^{-b_0 t} I_0\left(b_0 \sqrt{t^2 - (yc)^2}\right) & ;t > yc \end{cases} \tag{106}$$

Table 1
The values of CMC base fluid and nanoparticles

Thermophysical properties	CMC	Nanoparticles (Cu)
$\rho(Kgm^{-3})$	997.1	8933
$k(Wm^{-1}K^{-1})$	0.613	401
$\beta \times 10^5 (K^{-1})$	21	1.67

Table 2
Nusselt number Nu values for different values of ϕ

Nusselt number Nu	ϕ values	0	0.01	0.02	0.03
	$Q = 0.04$	8.888	9.187	9.316	9.622
	$Q = 0.2$	7.417	7.64	7.737	7.967

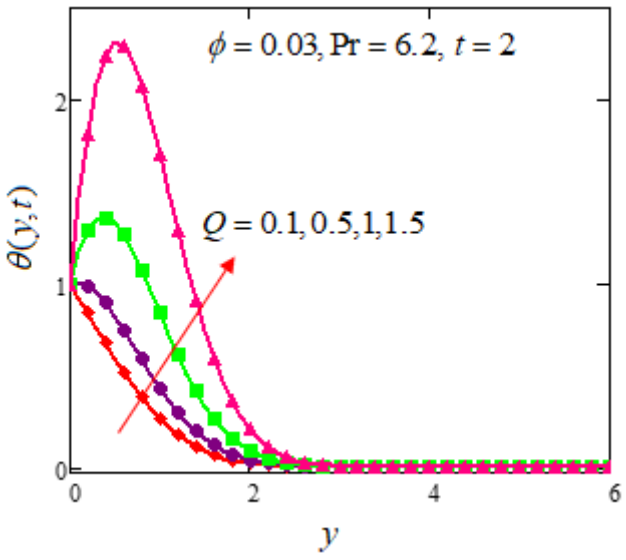


Figure 2. Temperature profile variation with heat generation parameter, Q.

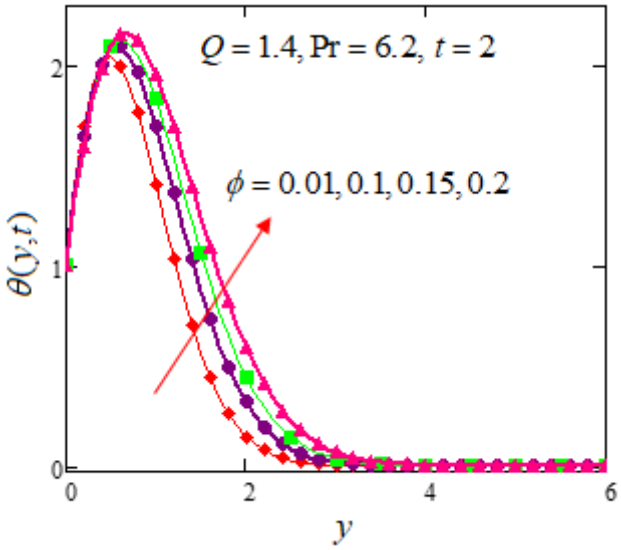


Figure 3. Temperature profile variation with volume fraction of nanoparticles, ϕ.

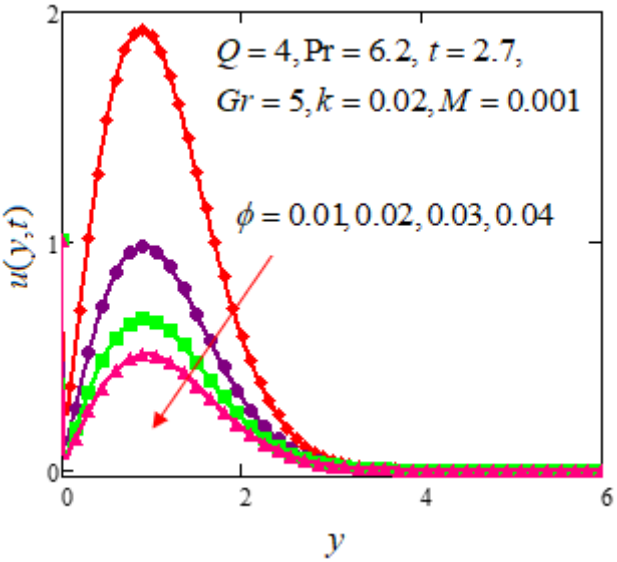


Figure 4. Velocity profile variation with volume fraction of nanoparticles, ϕ.

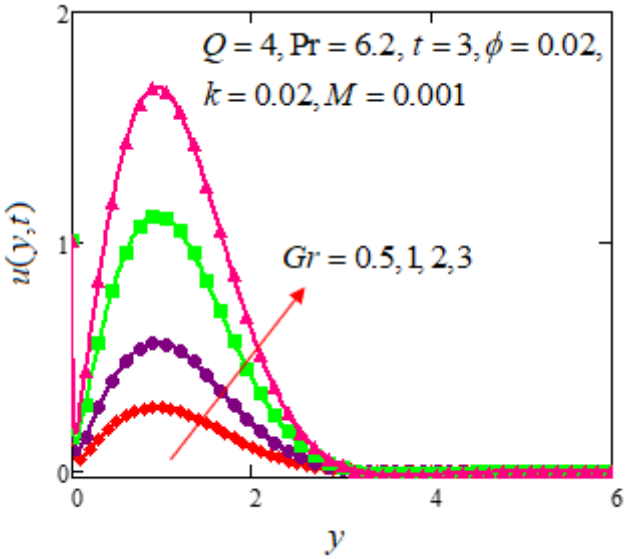


Figure 5. Velocity profile variation with Grashof number, Gr.

3. Results and Discussion

The problem of Maxwell nanofluid flow over a plate has been investigated for CMC base fluid and copper nanoparticles. The thermophysical properties of CMC and copper has been listed in the Table 1. All the results are plotted for constant value $\Pr = 6.2$ for CMC. Table 2 shows the values of Nusselt number variation with volume fraction and it is obvious that Nusselt number is increasing function of volume fraction ϕ. A parametric analysis has been made for the parameters effecting the flow.

Figure 2 shows the variation of temperature profile with heat generation parameter $Q = 0.1, 0.5, 1, 1.5$ for volume fraction and Prandtl number, $\phi = 0.03, \Pr = 6.2$ and time $t = 2$. Temperature is found to be an increasing function of Q. Physically, it is due to the increase in thermal conductivities of nanofluids due to absorption of heat by the nanofluid. Figure 3 presents the temperature profiles for different values of nanoparticles volume fraction ϕ and constant heat generation $Q = 1.4$ at time $t = 2$.The results are plotted for the range $\phi = 0.01, 0.1, 0.15, 0.2$. The fluid temperature is observed to exhibit a gradual increase with increasing number of cobalt nanoparticles which leads to an enhancement in the thermal conductivity.

Figure 4 depicts that increasing the volume fraction ϕ of cobalt nanoparticles, a gradual decrease is observed in the Maxwell nanofluid velocity. By adding more nanoparticles to the fluid, its viscosity increases by increasing its amount, thus a decrease in the velocity of nanofluid happens. These results are plotted for the range $0.01 \le \phi \le 0.04$ and constant parameters $Q = 4,\ k = 0.02, M = 0.01, Gr = 5, \Pr = 6.2$ at time $t = 2.7$.

We know that the convection flow is always effected by buoyancy forces thus the influence of Gr is very essential to consider in the flow and heat transfer problems. Figure 5 present the velocity profile for different values of Grashof number Gr for Maxwell nanofluid. It is observed that the fluid velocity increases by increasing the Grashof number Gr. The figure is portrayed for the range $Gr = 0.5, 1, 2, 3$ and the fluid velocity is lowest for $Gr = 0.5$. Physically, the buoyancy force are dominant for larger values of Gr which has a great impact on the flow of nanofluid. Other involved physical parameters are kept constant as $Q = 4,\ k = 0.02, M = 0.01, \phi = 0.02, \Pr = 6.2$. Near the plate the flow slowly increasing and at $0 < y < 2$ the flow has greater variation with Gr values. The

flow is greatly effected by the ingrained parameters influences, buoyancy forces, nanoparticles addition and heat generation.

4. Conclusion

The problem of Maxwell nanofluid with heat generation effects has been investigated using Laplace transform technique. It is concluded that Nusselt number has a significant enhancement due to increase in ϕ. From the plotted results it is found that temperature increases with increasing ϕ and Q. Velocity decreases with increasing ϕ because the fluid becomes more viscous whereas increases with Grashof number.

Acknowledgement
This research was funded by a grant from Universiti Malaysia Pahang (RDU190376).

References

[1] Takashima, M. (1970). “The effect of a magnetic field on thermal instability in a layer of Maxwell fluid”. Physics Letters A 33(6): 371-372.
[2] Fetecau, C., Jamil, M., Fetecau, C. and Siddique, I. (2009). “A note on the second problem of Stokes for Maxwell fluids”. International Journal of Non-Linear Mechanics. 44(10): 1085-1090.
[3] Faisal, S., Aziz, Z. A. and Dennis, L. C. C. (2011). “New exact solution for Rayleigh–Stokes problem of Maxwell fluid in a porous medium and rotating frame”. Results in Physics 1 (1): 9-12.
[4] Vieru, D. and Zafar, A. A. (2013). “Some Couette flows of a Maxwell fluid with wall slip condition." Appl Math Inf Sci 7: 209-219.
[5] Liancun, Z., Zhao, F. and Zhang, X. (2010). “Exact solutions for generalized Maxwell fluid flow due to oscillatory and constantly accelerating plate." Nonlinear Analysis: Real World Applications. 11(5): 3744-3751.
[6] Giacomin, A. J., Bird, R. B., Johnson, L. M. and Mix, A. W. (2011). “Large-amplitude oscillatory shear flow from the corotational Maxwell model”. Journal of Non-Newtonian Fluid Mechanics 166, no. 19-20: 1081-1099.
[7] Shihao, H., Zheng, L., Li, C. and Zhang, X. (2014) "Coupled flow and heat transfer in viscoelastic fluid with Cattaneo–Christov heat flux model." Applied Mathematics Letters 38: 87-93.
[8] Sohail, N., Ul-Haq, R. Akbar, N. S., Lee, C. and Zafar Hayat Khan. (2013) "Numerical study of boundary layer flow and heat transfer of Oldroyd-B nanofluid towards a stretching sheet." PloS one 8, no. 8: e69811.
[9] Mustafa, M. (2015). "Cattaneo-Christov heat flux model for rotating flow and heat transfer of upper-convected Maxwell fluid." AIP Advances 5, no. 4: 047109.
[10] Hsiao, K. L. (2017). "Combined electrical MHD heat transfer thermal extrusion system using Maxwell fluid with radiative and viscous dissipation effects." Applied Thermal Engineering 112: 1281-1288.
[11] Rauf, A., Abbas, Z. and Shehzad, S. A. (2019). "Utilization of Maxwell-Cattaneo law for MHD swirling flow through oscillatory disk subject to porous medium." Applied Mathematics and Mechanics: 1-14.
[12] Aman, S., Khan, I. Ismail, Z. Salleh, M. Z. and Al-Mdallal, Q. M. (2017). "Heat transfer enhancement in free convection flow of CNTs Maxwell nanofluids with four different types of molecular liquids." Scientific reports 7, no. 1: 2445.
[13] Hayat, T. and Qasim, M. (2010). "Influence of thermal radiation and Joule heating on MHD flow of a Maxwell fluid in the presence of thermophoresis." International Journal of Heat and Mass Transfer 53, no. 21-22: 4780-4788.
[14] Abel, M. S., Jagadish V. T. and Mahantesh M. N. (2012) "MHD flow and heat transfer for the upper-convected Maxwell fluid over a stretching sheet." Meccanica 47, no. 2: 385-393.
[15] Ali, A., Madeeha, T., Rabia, S., Aziz, U. A., Muhammad, I. and Maria Javaid. (2018) "Magnetohydrodynamic Oscillating and Rotating Flows of Maxwell Electrically Conducting Fluids in a Porous Plane." Punjab Univ. J. math 50: 61-71.
[16] Khan, S. U., Shehzad, S., Ali, N. and Bashir, M. (2018). “Some Generalized Results for Maxwell Fluid Flow over Porous Oscillatory Surface with Modified Fourier and Fick’s Theories”. Journal of the Brazilian Society of Mechanical Sciences and Engineering, 40(9), 474.
[17] Prabhakar, B. Shanker B. and Cherlacola S. R. (2019) "A revised model to analyze MHD flow of Maxwell nanofluid past a stretching sheet with nonlinear thermal radiation effect." International Journal of Fluid Mechanics Research 46, no. 2.

[18] Khan, M., Malik, M., Salahuddin, T., Saleem, S. and Hussain, A. (2019). "Change in Viscosity of Maxwell Fluid Flow Due to Thermal and Solutal Stratifications". Journal of Molecular Liquids, 288, 110970.
[19] Aman, S. and Almdallal, Q. (2019). "SA-copper based Maxwell nanofluid flow with second order slip effect using fractional derivatives". In AIP Conference Proceedings, 2116(1); 030021.
[20] Sadiq, M. A. and Hayat, T. (2019). "Darcy–Forchheimer Stretched Flow of MHD Maxwell Material with Heterogeneous and Homogeneous Reactions". Neural Computing and Applications, 31(2), 857-864.

Penerbit Akademia Baru

Engineering Science and Technology Conference Proceedings

Journal homepage: www.akademiabaru.com/EST.html

Intelligent Control Based Estimation of Heat Transfer Coefficient from Four Flat Tubes with Different Air Inlet Angles

Open Access

Muhammad Asmail Eleiwi [1,*], Tahseen Ahmad Tahseen [2,*], Ahmed Hasan Ghareeb[3]

[1] Department of Mechanical Engineering, College of Engineering, University of Tikrit, Tikrit, Iraq
[2] Department of Mechanical Engineering, College of Engineering, University of Kirkuk, Kirkuk, Iraq
[3] Department of Petroleum Engineering, College of Engineering, University of Kirkuk, Kirkuk, Iraq

ABSTRACT

The surface of heat exchanger in many cases for the direction of inlet air flow is not orthogonal. To study of the heat transfer performance with change of angles air inlet, the paper presents how to predict the heat transfer coefficient for four flat tubes in a crossflow using an artificial neural networks (ANNs). The experimental setup with inclined backward the air incoming flow direction, the heat transfer coefficient of three air inlet angles (90°, 45° and 30°) are studied separately for five inlet air velocity 0.2, 0.5, 0.6, 0.8, and 1.2 m/s in this study. The three cases of heat flux on the all tubes surface 13.2, 38.5, and 99.8 W/m^2. The predicted results for coefficient of heat transfer show a good agreement with experimental data. The accuracy between ANNs approach model and actual values (experimental) obtained with a mean relative error less than 2.2%, and the coefficient of determination (R^2) around 99.8%.

Keywords:
Flat tube; different inlet angle air; data driven; ANN modeling

Copyright © 2019 PENERBIT AKADEMIA BARU - All rights reserved

1. Introduction

The many industrial applications require the use of heat exchangers with configurations of tubes, finned or un-finned, represent as heat exchangers in refrigeration, air conditioning, heaters, radiators, etc. This equipment should be dimensioned in accordance to the availability of space in the plan (project) that are section usually having to be compact in size and lightweight to take these confined spaces. The air inlet flow direction is not orthogonal to the heat exchanger surface in many cases [1].

It has been of attentiveness to several researchers to investigate the heat transfer and fluid flow over objects with different shapes. Flat tubes have not been investigated to the same magnitude; therewith they play a significant role in several technical applications such as automobile radiators and trendy heat exchangers. The design of flat tubes has been recently inserted to be used in car air conditioning condensers and evaporators. The latest developments in automobile welded aluminum industrialization technology have made the cost of the heat exchanger with flat tube construction more convenient [2].

Heat exchangers with flat tube expected to have minimized pressure drop of air side and best air side coefficients of heat transfer compared to circular shape heat exchangers. It is expected

* *Corresponding author.*
E-mail address: muham76@tu.edu.iq (Muhammad Asmail Eleiwi)

the pressure drop less than that for circular shape due a smaller wake region. Also, the same reason noise and vibration is expected to be lower than in flat tube heat exchangers compared with heat exchangers circular shape. The tube heat exchangers are used in a great many chemical reaction systems and energy conversion for instance nuclear reactors to refinery condensers. More importantly design parameter of tube heat exchangers are the external coefficient of heat transfer of the tube and the pressure drop of the external fluid flow. According to previously published studies in the literature, the influence the shape of the tube and configuration have specific they can have a positive impact on heat transfer [3] [4].

Rocha et al. [5] expanded a mathematical model for hybrid configurations of circular and elliptical tubes finned conservation of energy and heat transfer coefficients acquired experimentally using the technique of sublimation of naphthalene and part of similarity with the transfer of heat and mass. Saboya et al. [6] and Saboya et al. [7] numerically obtained and the temperature distribution also the fin efficiency to the first and second rows of elliptical tubes in finned heat exchangers.

This paper focused on the capability of ANN for heat transfer analysis in laminar forced convection heat transfer across four flat tube bundles with different attack angles as well as change in the heat flux. The supervised data-driven ANN model is applied to predict the outcomes of new independent input data. Furthermore, to discover and learn patterns correlated between input data sets and the target values.

2. Experimental Setup

This work was carried out in the heat transfer laboratory in the Department of Mechanical Engineering-College of Engineering at the University of Kirkuk. The experimental setup consists of an open circuit wind tunnel, a variable electric power supply, cartridge heater, aluminum flat tubes, T-type of thermocouple, multi-channel temperature meter, hot wire anemometer, and volt and current measurement. The Figure 1 below shows the experimental setup.

The TecQuipment (TQ) cross flow heat exchanger is open circuit wind tunnel consists of four sections which are shown respectively: the stagnation, extended, test and end region. The extended region with length 1290 mm was placed before the test section to let the full developed of the flow before arriving the tube arrangement. At the entrance of the extended region, were arranged metal screen, that is intended to regulate the flow before entering the test section. The wind tunnel consists of an exhaust fan with direct drive by electric motor. The TQ wind tunnel operation range between 220 VAC to 240 VAC, with 5.25 A single phase, and 50 Hz frequency.

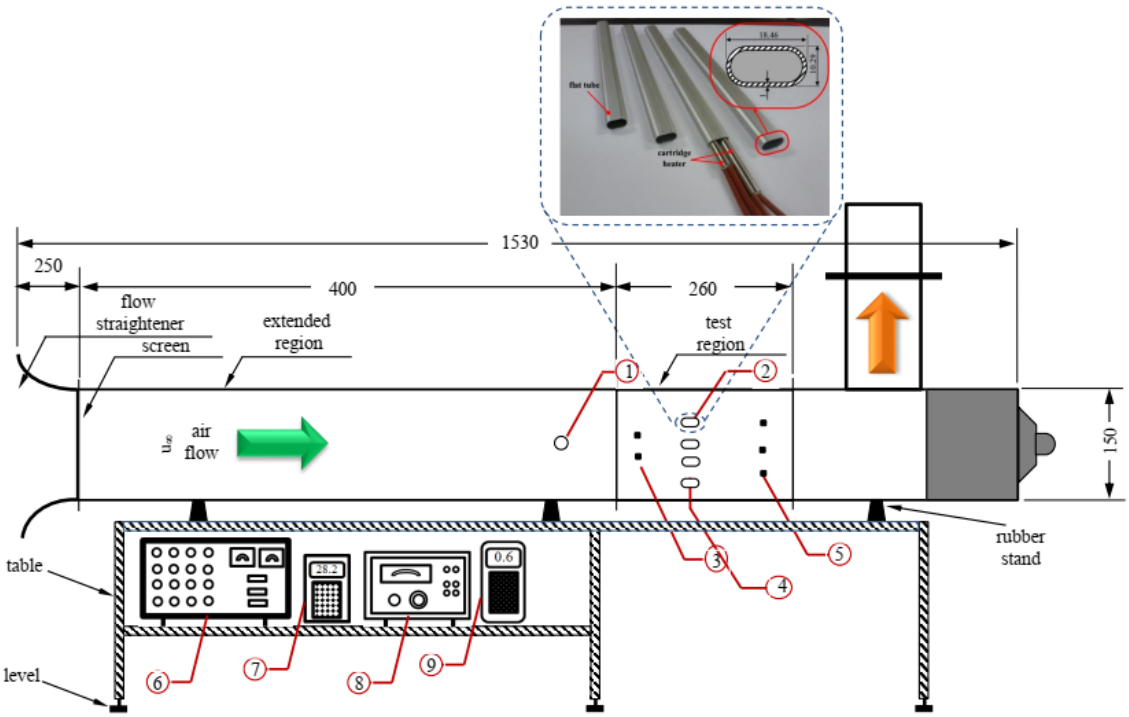


Figure 1: The TQ wind tunnel that is used in the experimental testing.

After finishing the installation of all materials and equipment show in Figure 2, measurements done on the essential parts of TQ (i.e. speed of air flow, pressure drop on the test rig and temperature for all points) respectively.

To measure the variation of temperature by forced convection at the test rig, fourteen thermocouples placed in each test rig. All of the thermocouples were placed in the middle between the side walls of the wind tunnel and on the midline of the elemental channels. Two thermocouples were placed at the arrangement inlet ($T_{in,1}$ -$T_{in,2}$), Three at surfaces of tubes ($T_{s,1}$ –$T_{s,3}$), and three at outlet air flow ($T_{out,1}$ -$T_{out,3}$) in one elemental channel. An additional thermocouple (T_{bef}) was placed on the extended region at 150 mm before the test module to measure the temperature of free stream as shown in Figure 2.

Thermocouples in the surfaces of tubes showed that the difference between the tubes in one element channel is negligible and the others are within ±0.53°C margin with respect to average of the four thermocouples. Finally, the thermocouples placed in the extended region for purpose of measuring the free stream temperatures within ±0.22°C margin with respect to the average temperature measured inlet arrangement, in all the tests carried out in this work.



1	Location of the anemometer	2	thermocouple at the surface of tube	3	Inlet thermocouple
4	Flat tube with heater	5	Outlet thermocouple	6	Power supply
7	Hot wire	8	Data logger	9	Hot wire anemometer

Figure 2: The schematic displayed of the experimental approach, all dimensions (mm).

Started each run by selecting the voltage and current for the cartridge heaters and air velocity of free stream, then we waited for (1.5-2.0) hour while monitor the changes in voltage, current, T_{bef}, $T_{in,1}$-$T_{in,2}$, $T_{s,1}$-$T_{s,3}$ and $T_{out,1}$-$T_{out,3}$. We had taken final readings when the relative changes in the voltage, current and temperature were less than (0.5-0.8), (0.03-0.09) and (0.044-0.075) %, respectively. These changes were estimated relative by repeating the same value Re_{Dh} value, between (4-6) hours. It should be noted that these relative changes are small when compared with the uncertainties in the relevant measurements.

3. Data Collection

This experiment involves laminar external airflow. The following relations for the relevant air properties are used in the following calculations. They are based on data and valid in the range temperature of $275\text{K} \leq 0.5(\overline{T_{in}} + \overline{T_{out}}) \leq 375\text{K}$ [8]:

$$\left.\begin{aligned}
\rho_a &= 2.209 - 3.414\times10^{-3}\left(\frac{\overline{T_{\text{in}}}+\overline{T_{\text{out}}}}{2}\right), && \text{kg/m}^3\\
c_{Pa} &= \left[9.848 + 6.76\times10^{-4}\left(\frac{\overline{T_{\text{in}}}+\overline{T_{\text{out}}}}{2}\right)\right]\times10^{2}, && \text{J/(kg K)}\\
k_a &= \left[3.479 + 7.58\times10^{-2}\left(\frac{\overline{T_{\text{in}}}+\overline{T_{\text{out}}}}{2}\right)\right]\times10^{-3}, && \text{W/(m K)}\\
\mu_a &= \left[4.475 + 4.564\times10^{-2}\left(\frac{\overline{T_{\text{in}}}+\overline{T_{\text{out}}}}{2}\right)\right]\times10^{-6}, && \text{kg/(m s)}
\end{aligned}\right\} \quad (1)$$

where $\overline{T_{\text{in}}} = \frac{1}{n}\sum_{i=1}^{n}(T_{\text{in}})_{\text{i}}, \quad n=2, \quad \overline{T_{\text{out}}} = \frac{1}{n}\sum_{i=1}^{n}(T_{\text{out}})_{\text{i}}, \quad n=3$

The electrical heat gain rate [voltage (E)×current (I)] and uniform heat flux (UHF) from the outer tube surface can be evaluated as:

$$q_{\text{in}} = E \times I \quad (2)$$

The steady state heat balance of the electrical heat test surface can be written as:

$$q_{\text{convection}} = q_{\text{in}} - q_{\text{conduction}} - q_{\text{radiation}} \quad (3)$$

Heat transfer from the system is;

- Conduction between laboratory and the wall of the tubes was neglected because of the extremely low thermal conductivity of air (0.23 W/m °C) and Teflon, negligible temperature difference between the laboratory and Teflon outer walls.
- Radiation heat transfer between the surfaces of the tubes and the surrounding were also neglected. Based on the measurement of $0.5(\overline{T_{in}}+\overline{T_{out}})$ and $\overline{Ts}$, the radiation heat transfer coefficient was estimated as [9]:

$$\overline{h_{\text{rad}}} = \varepsilon \times \sigma \times \left[\left\{\left(\frac{\overline{T_{\text{in}}}+\overline{T_{\text{out}}}}{2}\right)^2 + (\overline{T_{\text{s}}})^2\right\}\times\left\{\left(\frac{\overline{T_{\text{in}}}+\overline{T_{\text{out}}}}{2}\right)+\overline{T_{\text{s}}}\right\}\right] \quad (4)$$

where

$$\overline{T_{\text{s}}} = \frac{1}{n}\sum_{i=1}^{n}(T_{\text{s}})_{\text{i}}, \quad n=3$$

For a commercial aluminium tube with emissivity, $\varepsilon \cong 0.028$ (Collett, 1983), h_{rad} was found in a range of (0.174–0.205) W/(m^2 °C) with the convection heat transfer coefficient, h, approximately between 0.01% and 0.15%. Thus, the heat transfer between the air and the surface of the tubes was actually due to the convection, and the mechanism of the Eq. (3.4) was rewritten as (Naik et al., 1987):

$$q_{\text{convection}} \cong q_{\text{sup}} = \bar{h}\, A_{\text{s}} \left[\overline{T_{\text{s}}} - \left(\frac{\overline{T_{\text{in}}} + \overline{T_{\text{out}}}}{2} \right) \right] \quad (5)$$

where

$$A_{\text{s}} = n \times [\pi d + 2(D - d)] \times L$$

where $\overline{T_{in}}$ the inlet air temperature was the various between 17.1 °C to 24.8 °C and $\overline{T_s}$ the average temperature of tubes surface. For the steady state condition, the overall heat transfer rate, $q_{\text{convection}}$ was equal to the electrical heat supply, q_{in}. From Eq. (3.4), the overall heat transfer coefficient was determined as:

$$\bar{h} = \frac{q_{\text{sup}}}{A_{\text{s}} \left[\overline{T_{\text{s}}} - \left(\frac{\overline{T_{\text{in}}} + \overline{T_{\text{out}}}}{2} \right) \right]} \quad (6)$$

And it is usually used in the overall Nusselt number, which is defined as:

$$Nu = D_h \times \frac{h}{k_{\text{f}}} \quad (7)$$

where k_{f} , is the thermal conductivity of air.
It can be used with the hydraulic diameter of the flat tube:

$$D_{\text{h}} = 4 \times \frac{\left[\frac{\pi}{4} (d)^2 + (D - d)d \right]}{\pi d + 2(D - d)} \quad (8)$$

The Reynolds number based transverse diameter of flattened tube is defined as:

$$Re_d = u_{\max} \times d \times \frac{\rho_{\text{f}}}{\mu_{\text{f}}} \quad (9)$$

where $u_{\max} = S_T . u_\infty / (S_T - d)$

S_T is the distance between centre of two tubes.

u_∞ is the air free stream velocity.

The calculation of Colburn *j*–factor is presented by the following non–dimensional parameter:

$$j = \frac{Nu}{Re \times Pr^{1/3}} \quad (10)$$

4. Artificial neural network approach

Artificial Neural Networks (ANN) is a computational nonlinear model that is commonly used in machine learning. It is effectively implemented to a wide spectrum of fields, and highly strong modelling techniques, particularly when the mathematical relationship of the specified data is unknown or not readily discerned [10]. Analogous to the brain framework, ANNs consist of single processing units called neurons. The neurons are structured in layers in the network framework as shown in Figure 3. Each of the neurons in the input layer gets one of the variables in which the values to rely on in the process of creating the predictive model. A neuron also has a bias that is

regarded as an extra input to the neuron and a transfer function or activation defining the neuron type.

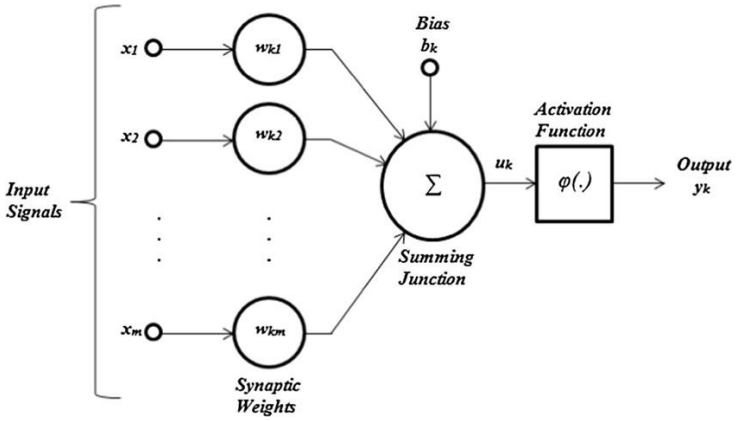


Figure 3: Block diagram of model of a neuron [11]

Typically, the purpose of changing the weights is to offer the same performance as seen in the training data when learning an ANN with a set of input and output data. After the training step, the weights comprise significant information, whereas they are random and have no significance before training [12]. Furthermore, the aim of finding optimal weights is to achieve close target values as output [13].

In feedforward networks, backpropagation algorithms are broadly used as ANN learning algorithms. In this paper, the Levenberg – Marquardt learning algorithm selected for adjusting the weights in the feedback systems. The fundamental concept of the Levenberg – Marquardt algorithm is to perform a combination training: it transfers to the steepest descent algorithm around the complicated curve region until the local curve is appropriate for a quadratic estimate.

Accordingly, the ANN was created in this paper to evaluate the Nusselt number in the four flat tube bundles. Four input variables are used to estimate the Nusselt amount (Nu): Reynold number (Re), Colburn j–factor (j), tube angle (θ), and the heat flux (q). The MATLAB software Neural Network toolbox was used for the ANN model implementation, the Figure 4 show the schematic representation of for the artificial neural network model. Neuron amount of hidden layer was determined by the trial and error.

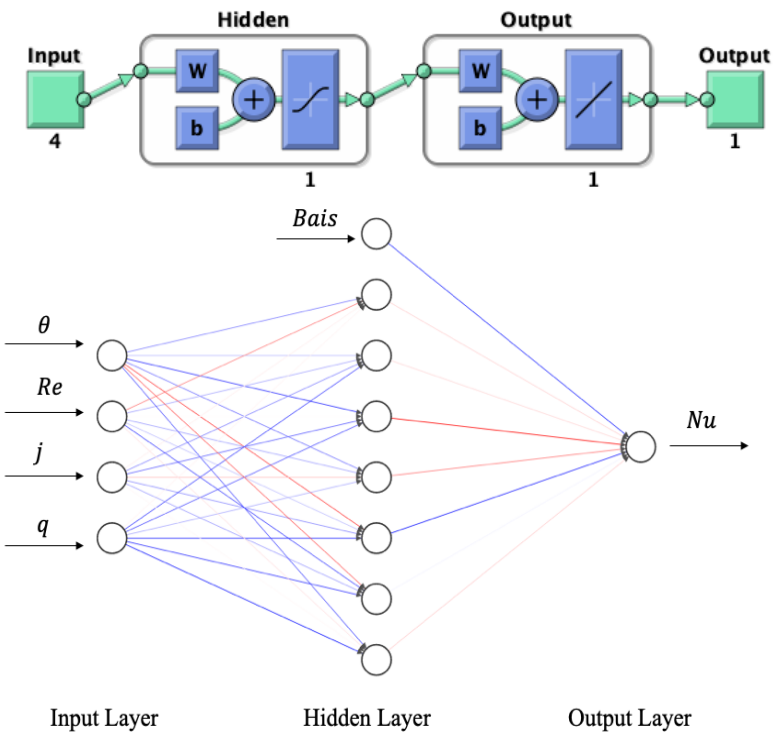


Figure 4: Neural network architecture trained via Levenberg-Marquardt algorithm for the estimation of the Nusselt number.

The data are randomly allocated to 70 percent, 15 percent and 15 percent respectively for training, testing and validation.

Results:

This section presents the experimental result of laminar forced convection heat transfer across four flat tube bundles with different attack angles. The main objective of the experimental part of this study is to conclude Reynolds number-Nusselt number relationship, Reynolds number-Coburn *j*-factor relationship and heat flux-Nusselt number Coburn *j*-factor and heat flux Colburn *j*-factor relationship.

Figure 5 shows the variations of mean Nusselt number (*Nu*) with Reynolds number (*Re*) for different heat flux supply and all air attack angles. It is clear that Nu number, increases with increase *Re* number. The heat flux except for the lowest value (q''= 13.2 W/m^2) as shown in Figure 4.1(a). On the other hand, the *Nu* number, increases with increase q'' for all cases. In addition, the *Nu* decreases with increase air angles attack.

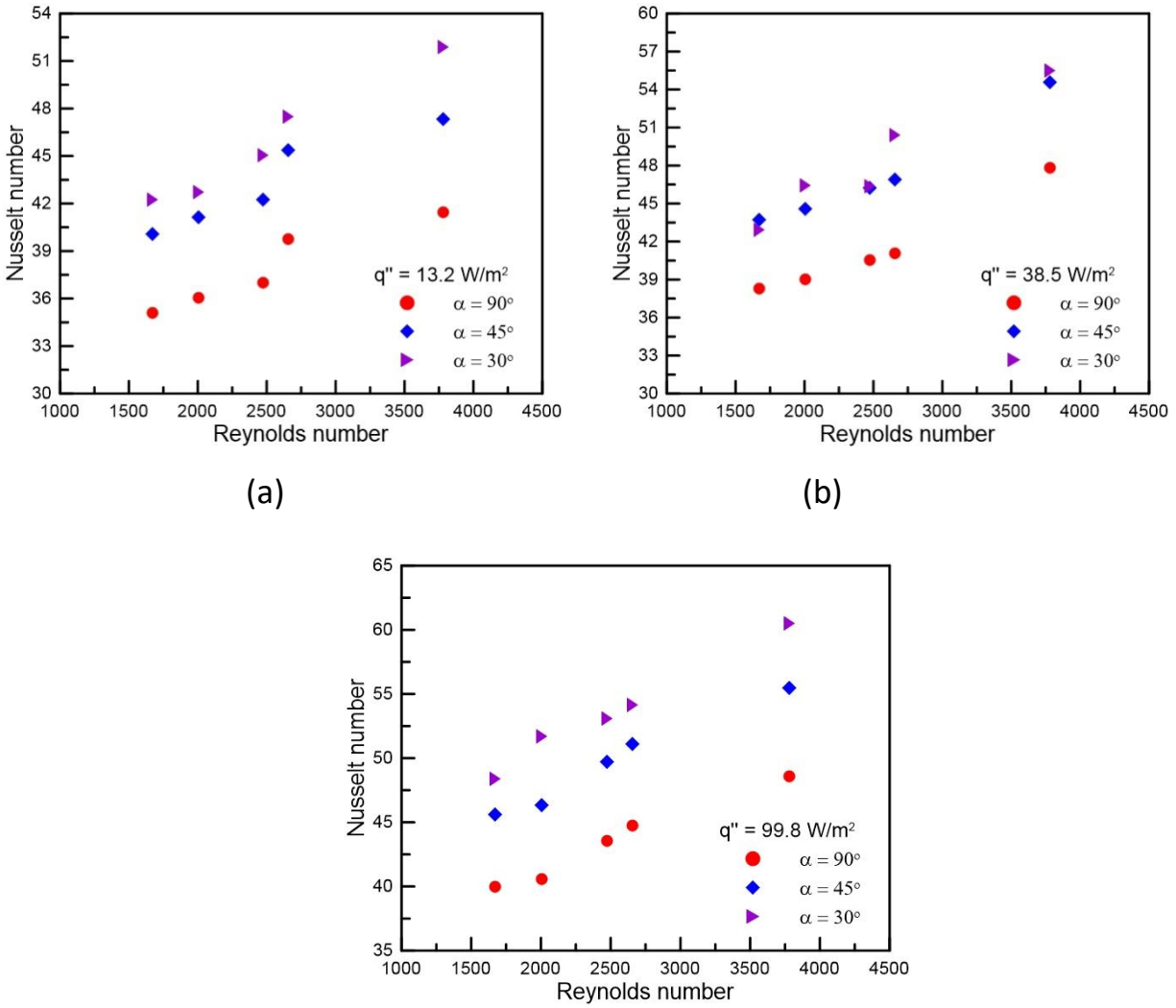


Figure 5: The relationship between Reynolds number with Nusselt number for different heat flux with three air attack angles.

The variation *Nu* with total heat flux supply at different *Re* number was plotted in Figure 4.2. The figure shows the Nu number decrease with increases angle attack. Figure clearly shows, increases *Nu* with increase q'' at all *Re* number, due to the temperature difference between the hot surface of the tube and air flow increases with *Re* increase also the time of contact of air flow and hot surface of tube, not enough and decrease with increase *Re*.

The variation of Colburn *j*–factor values with Reynolds number values for several inlet air attack angles for flat tube are presented in Figure 6. The resulting curve shows that *j*–factor decreases with an increase of Reynolds number for any heat flux supply or air attack angles. Colburn *j*–factor increases with the decrease of the air attack angles. This figure also presented the results of different heat flux supply. It could be noted that the heat transfer factor value is higher in low attack angles.

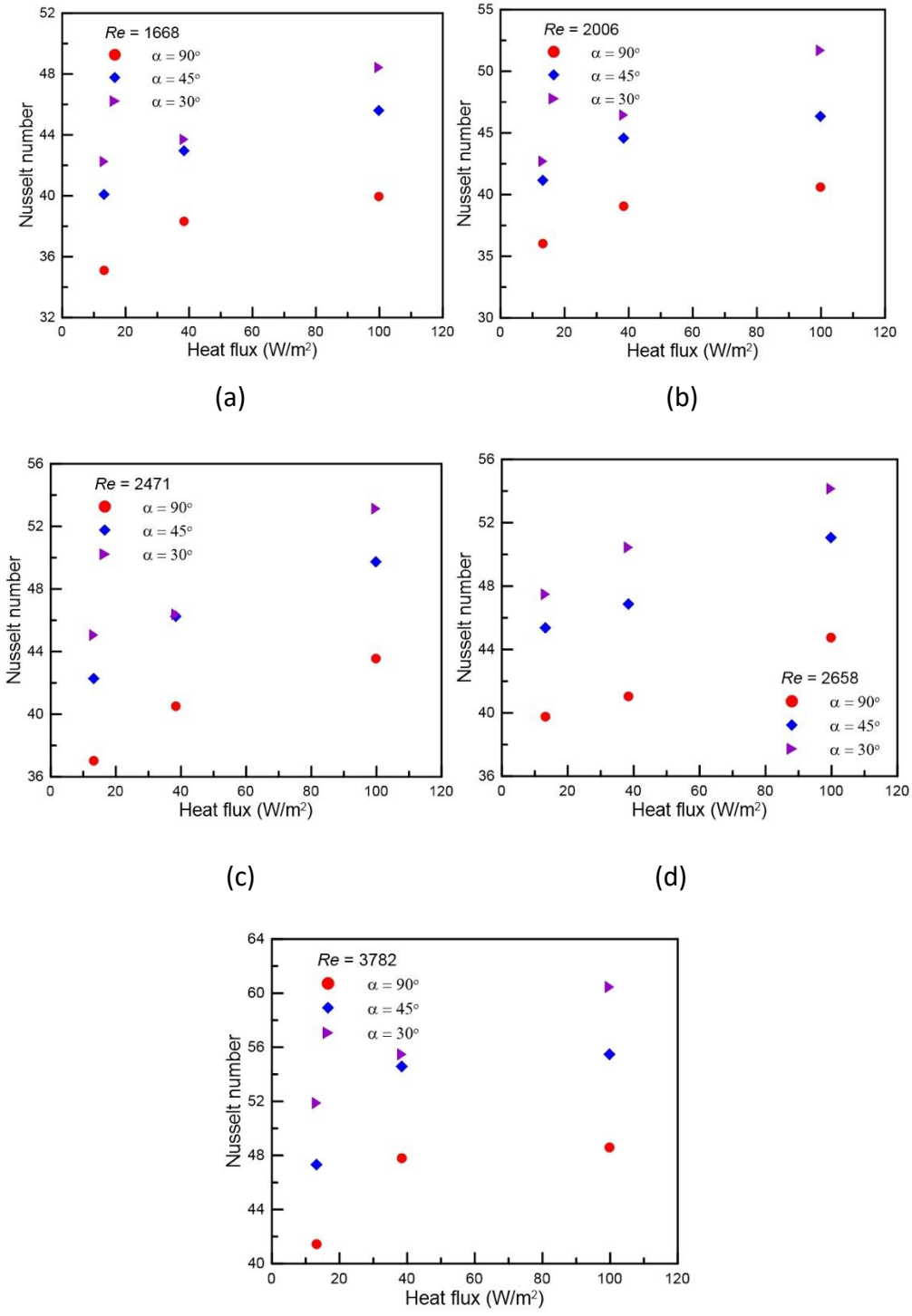


Figure 6: The effect of heat flux on Nusselt number for diffident Reynolds number with all experimental cases.

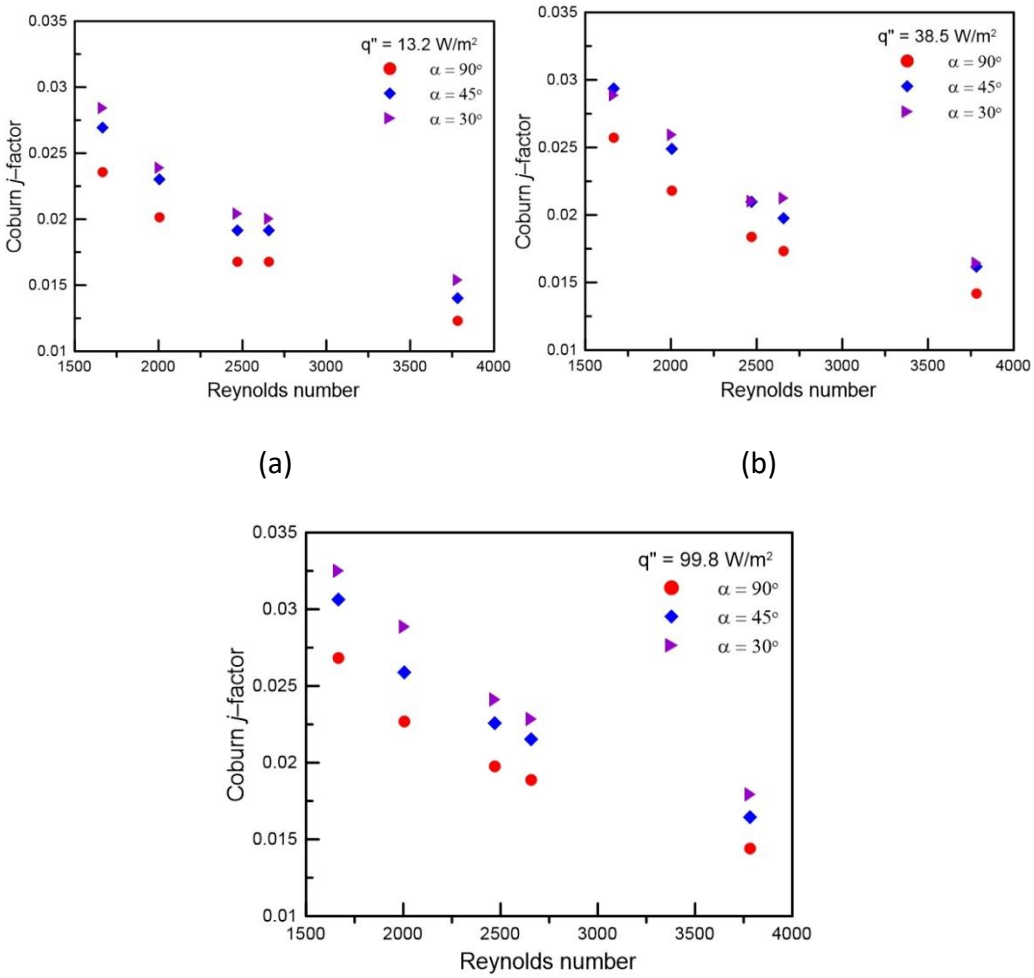


Figure 7: Effect of Reynolds number on Coburn *j*-factor for all experimental cases.

For the predicted output, the relative error and the average relative error were performed by:

$$RE\% = \frac{|X_{Num} - X_{Pre}|}{X_{Num}} \times 100 \qquad (11)$$

$$MRE\% = \frac{1}{N}\sum_{i=q}^{N}(RE\%)_i \qquad (12)$$

where Num, Pre, and N are referring to mean numerical values, expected values, and numeric data, respectively.

The determination ratio is used to quantify the degree of linear association between observed and predicted values. The general form for the coefficient of determination or (R2) equation is:

$$R^2 \equiv 1 - \frac{SS_{res}}{SS_{tot}} \qquad (13)$$

where SS_{res} is sum of squares of residuals, and SS_{tot} is the total sum of squares.
The ANNs model for training data and average Nusselt number shown in Figs. 8. Where Fig. 8 shows the compared between the experimental data with predicted date form ANNs model and Fig. 9 shows the relative error between the real data (experimental) and predicted data.

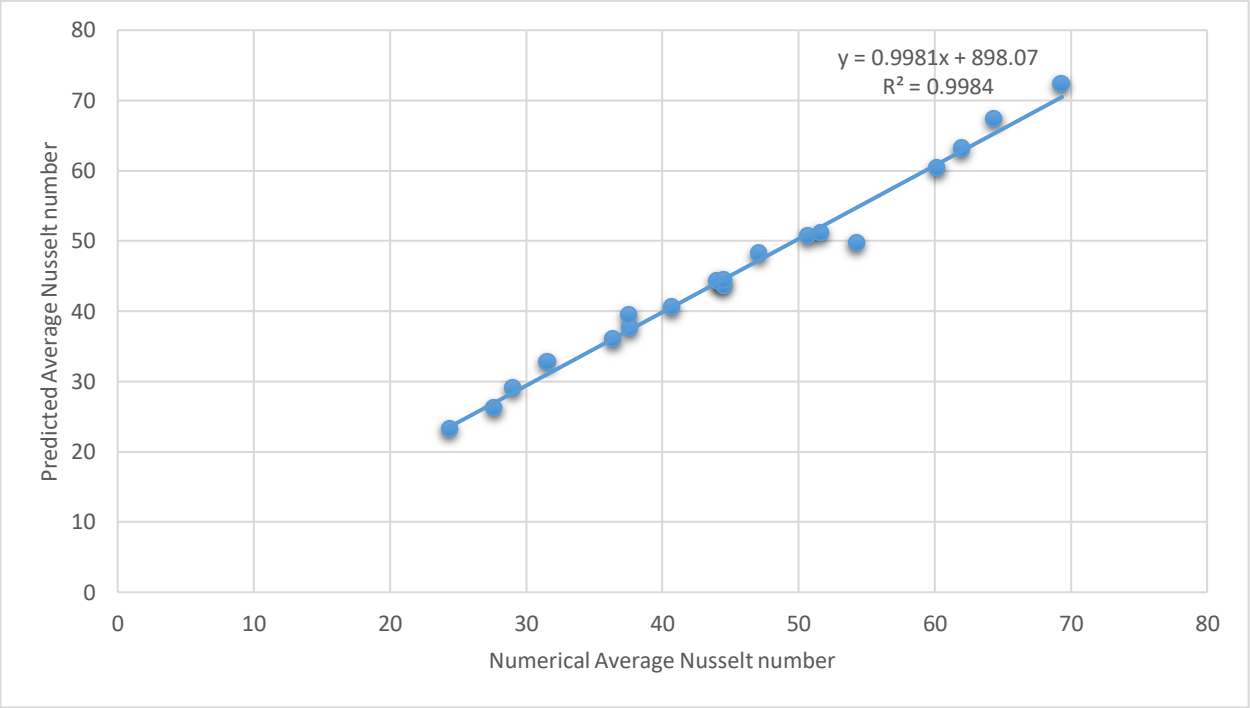


Figure .8 Average Nu predictions and experimental by ANNs with training data.

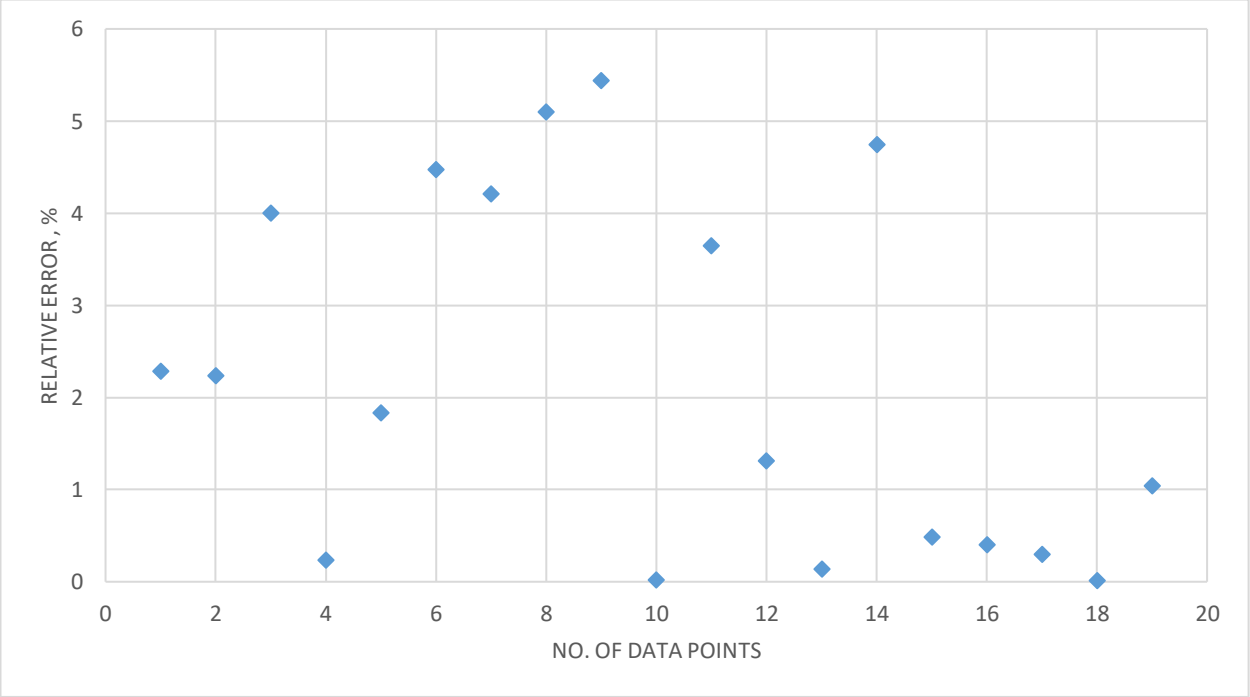


Figure 9: The ANNs model's relative error in training data.

5. Conclusions

This article involves the thorough experimental research experimental result of laminar forced convection heat transfer across four flat tube bundles. The second section created the ANN model using the estimation of the Nusselt number in this system. It has been shown that the ANN model is used efficiently to predict the heat transfer coefficient in airflow. The research findings for the training data: the mean relative error about 2.206% and the R2 is 99.8%. The ANN modeling can eventually be suggested to forecast the performance of heat transfer systems. Using ANN can prevent time-consuming and expensive experimental trials.

References

[1] A. Bejan, "Design with Constructal Law," vol. 22, no. 1, pp. 140–147, 2006.
[2] R. Webb, "Principles of enhanced heat transfer, 1994," *John Wiley&Sons, New York*, 1994.
[3] T. S. Wung, J. E. Niethammer, and C.-J. Chen, "MEASUREMENTS OF HEAT-MASS TRANSFER AND PRESSURE DROP FOR SOME NON-STANDARD ARRAYS OF TUBES IN CROSSFLOW," in *dl.begellhouse.com*, 2019, pp. 1041–1046.
[4] H. NISHIYAMA, T. OTA, and T. MATSUNO, "Heat Transfer and Flow Around Elliptic Cylinders in Tandem Arrangement," *JSME Int. journal. Ser. 2, Fluids Eng. heat Transf. power, Combust. Thermophys. Prop.*, vol. 31, no. 3, pp. 410–419, 2017.
[5] L. A. O. Rocha, F. E. M. Saboya, and J. V. C. Vargas, "A comparative study of elliptical and circular sections in one- and two-row tubes and plate fin heat exchangers," *Int. J. Heat Fluid Flow*, vol. 18, no. 2, pp. 247–252, 1997.
[6] F. E. M. Saboya and E. M. Sparrow, "Transfer characteristics of two-row plate fin and tube heat exchanger configurations," *Int. J. Heat Mass Transf.*, vol. 19, no. 1, pp. 41–49, 1976.
[7] S. M. Saboya and F. E. M. Saboya, "Experiments on elliptic sections in one-and two-row arrangements of plate fin and tube heat exchangers," *Exp. Therm. Fluid Sci.*, vol. 24, no. 1–2, pp. 67–75, 2001.
[8] G. F. C. Rogers and Y. R. Mayhew, *Thermodynamic and Transport Properties of Fluids*. B. Blackwell, 1995.
[9] S. Naik, S. Probert, M. S.-A. Energy, and U. 1987, "Forced-convective steady-state heat transfers from shrouded vertical fin arrays, aligned parallel to an undisturbed air-stream," *Appl. Energy*, vol. 26, no. 2, pp. 137–158, 1987.
[10] N. Nassif and J. Gooden, "Development and Validation of a Heat Pump System Model Using Artificial Neural Network," *Adv. Sci. Technol. Eng. Syst. J.*, vol. 2, no. 3, pp. 182–185, 2017.
[11] E. Tosun, K. Aydin, and M. Bilgili, "Comparison of linear regression and artificial neural network model of a diesel engine fueled with biodiesel-alcohol mixtures," *Alexandria Eng. J.*, vol. 55, no. 4, pp. 3081–3089, Dec. 2016.
[12] H. Yu and B. Wilamowski, "Levenberg–Marquardt Training, Auburn University," 2010.
[13] M. Bilgili and B. Sahin, "Comparative analysis of regression and artificial neural network models for wind speed prediction," *Meteorol. Atmos. Phys.*, vol. 109, no. 1–2, pp. 61–72, Nov. 2010.

Penerbit Akademia Baru

Engineering Science and Technology Conference Proceedings

Journal homepage: www.akademiabaru.com/EST.html

Open Access

Experimental Investigation on the Stability of 40% Ethylene Glycol Based TiO_2-Al_2O_3 Hybrid Nanofluids

Wajiha Tasnim Urmi[1], M.M. Rahman [1,*], W.A.W. Hamzah[1], K. Kadirgama[1], D. Ramasamy[1] and M.A. Maleque[2]

[1] Faculty of Mechanical and Automotive Engineering Technology, University Malaysia Pahang, 26600 Pekan, Pahang, Malaysia.
[2] Department of Manufacturing and Materials Engineering Faculty of Engineering, International Islamic University Malaysia, Jalan Gombak, 53100, Kuala Lumpur

ABSTRACT

This paper presents to investigate experimentally on the stability of 40% ethylene glycol-based TiO2-Al2O3 hybrid nanofluids. Recently, the research is more highlighted on the thermophysical-properties of nanofluids. Hence, the stability of the hybrid nanofluids derisively assessed in this research work. The study uses the two-step method for preparing 40% ethylene glycol-based TiO2-Al2O3 hybrid nanofluids. The experiment is carried out for the various combination of mixture ratios including 20:80, 40:60, 50:50, 60:40 and 80:20 of TiO2-Al2O3 nanoparticles with a volume concentration of 0.1%. The stability assessment of hybrid nanofluids is accomplished through visualisation effect, transmission electronic microscopic observation, UV-Vis spectrophotometry and zeta potential value from particle size analyser. The findings show the optimum mixing ratios of TiO2-Al2O3 nanoparticles in terms of stability which is further confirmed by Zeta potential and absorbency from UV-Vis spectrophotometry. The findings from the study reveals that 80:20 ratio of TIO2-Al2O3 nanoparticles possesses the best uniformity for over 21 days without any noticeable settlement of particles in the colloidal suspension. Moreover, 50:50 and 60:40 ratios show modest stability for almost two weeks while 20:80 and 40:60 ratios of TiO2-Al2O3 nanoparticles show minimum stability along with rapid sedimentation in the dispersion. However, it is also evident that the optimum mixing ratio of TiO2-Al2O3 hybrid nanofluids has excellent stability which will lead to further study on the thermal properties of nanofluids and finally motivate engineers to the real life application of nanofluids.

Keywords:
Hybrid nanofluids; TEM, sedimentation
Photograph; UV-vis spectral analysis;
zeta potential

Copyright © 2019 PENERBIT AKADEMIA BARU - All rights reserved

1. Introduction

The advancement with the thermal engineering, the emergence of improved heat transfer fluids is of keen interest of recent researches to enhance heat transfer in various industries such as manufacturing, biomedical, microelectronics, aerospace and others. The most important parameter which affects the heat transfer efficiency of fluids is the thermal conductivity of fluids. Thus, the low thermal conductivity of traditional fluids such as water, ethylene glycol, oils and others. is the initial shortcoming in the efficient heat transfer process. However, it is evident from numerous researches that the inclusion of nano-sized particles into the base fluid has superior thermal properties than traditional fluids [1, 2].

* *Corresponding author.*
E-mail address: mustafizur@ump.edu.my (Corresponding Author's name)

Thus, the development of nanofluids, which are composite materials or colloidal dispersion of nano-sized solid particles, tubes, rods or fibres into the base fluids [3], has attracted the attention of the recent scientists. The addition of solid particles also boosts up the load-carrying and anti-wear capacity of base fluids besides showing minimum friction [4-6]. Moreover, the heat transfer system can simplify through a size reduction of the system because of the application of ultrafine solid particles [7]. Despite having all these superior properties, the stability of nanofluids is still a challenge in the practical field of nanofluids because the nanoparticles tend to be agglomerated or sedimented causing pressure drops because of robust Van der Waals attraction among particles [8, 9]. It leads to the reduction of stability as well as thermal properties of nanofluids [10, 11] as stability directly correlated with the thermal properties [12, 13]. Hence, the stability of the nanofluids is an essential factor for sustaining the enhanced thermal features [12, 14]. So stability analysis is the prior most work in the field of nanofluids.

To achieve homogeneity or stability of nanofluids, the synthesis method of nanofluids can play an important role. There are two standard synthesis processes of nanofluids- one-step and two-step methods. The process of synthesization and suspension of nanoparticles into the base fluids occurs concurrently in the one-step process [15, 16]. On the other hand, in the two-step method, there are two processes for the preparation of nanoparticles using various synthesis techniques and then dispersion of particles into the fluid [15, 17]. Numerous researchers used a one-step method for preparation of multiple nanofluids such as Fe3O4- CNT/ distilled water [18], CuO/ distilled water [19], Cu/ diethylene glycol [20]. The one-step method is employed for achieving uniform dispersion of nanoparticles and for sustaining enhanced thermal properties [21], but this method is not preferred at the industries due to its higher production cost and limited application of this process for only fluids having low vapour pressure [22].

On the contrary, the two-step method is utilised mainly in various industries for the synthesis of nanofluids [9]. Additionally, most of the researchers use this method during the preparation of nanofluids [23-25]. Moreover, Choi and Eastman [3] especially suggested about two-step synthesis technique for oxide base nanoparticles rather than nanofluids based on metal particles. However, the agglomeration of nanoparticles is a critical challenge during employing this method [21]. Stability of nanofluids observed as the ability to resist sedimentation or agglomeration. Strong Van der Waals attraction force is responsible for the nanoclusters formation in the nanofluids [26-29]. Achieving stable nanofluids is a crucial need in the practical field of nanofluids. So in this research, the stability analysis of 40% ethylene glycol (EG) based TiO2-Al2O3 hybrid nanofluids is conducted for various ratios of nanoparticles. This study uses transmission electronic microscopic (TEM) photograph for showing the arrangement of the particles, UV-vis spectral analysis and zeta potential measurement for quantitatively characterise the uniformity of nanofluids.

As well, the visual observation correspondingly used by taking sedimentation photograph of dispersion. Hence, a combination of various methods reconfirms the results of the study. Some researchers use more than one ways to show the stability of nanofluids. For example, Li, Zhu and Wang [30] and Hamid, Azmi, Nabil, Mamat and Sharma [31] use UV-vis and visual observation for aqueous copper dispersion and water-EG based TiO2-SiO2 nanofluids. Asadi, Asadi, Rezaniakolaei, Rosendahl, Afrand and Wongwises [1] only uses zeta potential analysis to represent the stability period of nanofluids. Finally, the result of the present research compared with other literature. Thus, this research will contribute to achieving a clear view about the effect of solid particles and also stability of hybrid nanofluids which may finally direct to the practical application of nanofluids in different fields successfully.



a. Magnetic Stirring b. Ultrasonication

Fig.1. Preparation of 40% EG based TiO_2-Al_2O_3 hybrid nanofluids.

2. Methodology

2.1 Synthesis Method of Nanofluids

The most dominant two-step preparation method is employed to prepare 40% EG based TiO2-Al2O3 hybrid nanofluids. Fig. 1 presents the preparation of 40% EG based TiO2-Al2O3 hybrid nanofluids. In this study, six different mixing ratios of 20:80, 40:60, 50:50, 60:40, 80:20 of TiO2 and Al2O3 nanoparticles at 0.1% volume concentration used for synthesization of hybrid nanofluids without using any surfactant. All the nanoparticles are purchased from US Research Nanomaterials, Inc. The properties of nanoparticles given by manufacturer are presented in Table 1. Various metal oxides such as TiO2, SiO2, CuO, ZnO, Al2O3 have better dispersibility in working fluids [32]. For instance, improved stability of TiO2/water-EG [33], SiO2/water [34], Al2O3/water-EG (80:20) [35], TiO2-SiO2/ water-EG [36] are reported. Besides, A2O3 have greater thermal properties compared with the mentioned oxide solid particles [1]. So, it is expected that the composite of TiO2-Al2O3 nanoparticles will possess a good uniformity along with stimulating thermal properties. Eq. (1) is used to measure the nanoparticles volume concentration (ø) from weight concentration (ω) and Eq. (2) is used to achieve the required concentration through the dilution process . However, a specific amount of solid particles are dispersed into 40% of EG following six different mentioned mixing ratios. Firstly, the magnetic stirrer is used for 45 minutes to ix the nanoparticles into the base fluid uniformly. Again the dispersion is undergone to the sonication process to break down the agglomeration of particles and to achieve a homogenous solution with greater stability.

$$\phi = \frac{\omega\rho_{bf}}{\left(1-\frac{\omega}{100}\right)\rho_p + \frac{\omega}{100}\rho_{bf}} \quad (1)$$

$$\Delta V = (V_2 - V_1) = V_1(\phi_1/\phi_2 - 1) \quad (2)$$

Where, ρ_p, ρ_{bf} are the density of nanoparticles and base fluid respectively and V is the volume of colloidal suspension.

Table 1
Properties of TiO_2 and Al_2O_3 nanoparticles.

Characteristics	TiO_2	Al_2O_3
Purity (%)	>99	99.8
Color	White	White
Average particle diameter (nm)	30-50	13
Molecular Mass (g mol^{-1})	79.86	101.96
Density (Kg m^{-3})	4230	4000
Thermal conductivity (W m^{-1} K^{-1})	8.4	40
Specific heat (J Kg^{-1} K^{-1})	692	773

2.2 Stability of Nanofluids

Stability or the repulsive force to the settlement of nanoparticles in suspension have dominant effects on the attributes of nanofluids. This study conducts visual observation for 21 days for stability analysis of TIO2- Al2O3 hybrid nanofluids. Visual inspection is also followed in previous investigations [31, 36, 37]. Besides, absorbance value is found through Uv-vis spectral analysis for specifying the stability condition of nanofluids. The UV-vis spectrophotometer analysis method is also used by other researchers [38-40]. Moreover, particle size analyser (Malvern Zetasizer Ultra-DKSH) is employed to measure the zeta potential of nanofluids. For the size characterisation, the transmission electron microscopic images of TiO2-Al2O3 presents in Fig.2.

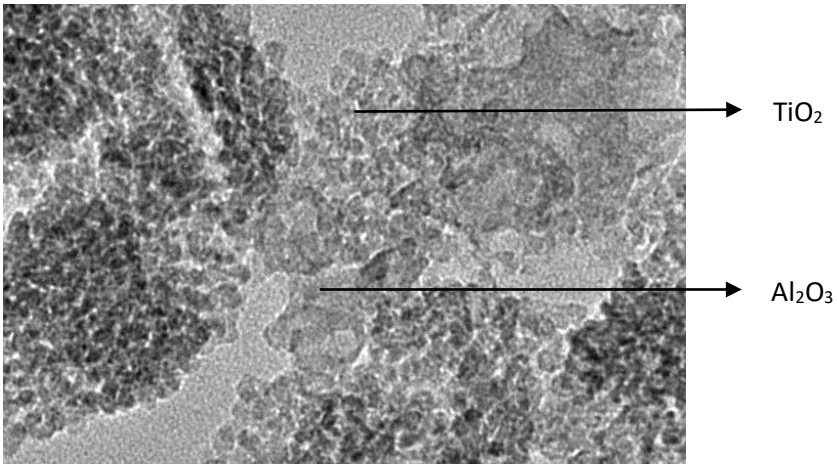


Fig. 2. TEM images of 40% EG based TiO_2-Al_2O_3 nanofluids at 0.1% concentration.

3. Results and Discussion

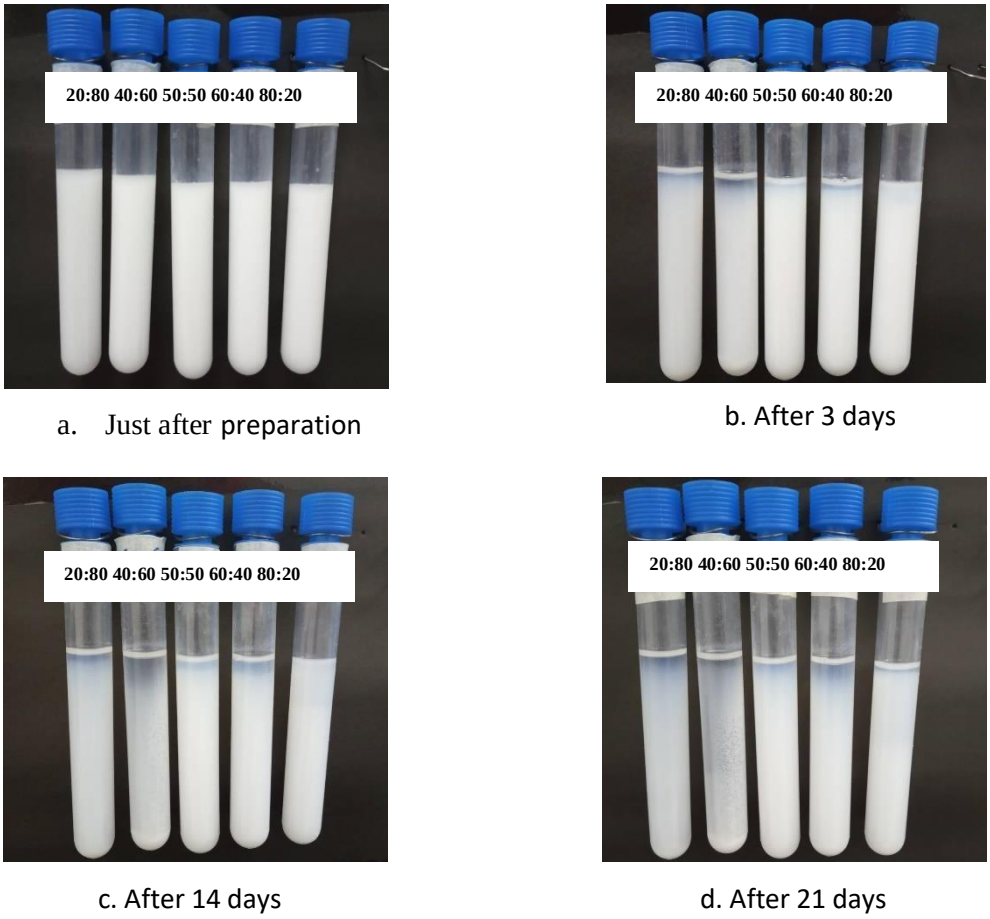
3.1 Sedimentation Photograph

The nanofluids are observed for one month, and images of the state of suspension are taken from time to time. From Fig. 3(a), no settlement of nanoparticles is found after the nanofluids are synthesised. After two days, 20:80, 40:60, 60:40 ratios of TiO2: Al2O3 containing samples start to settle down presented in Fig. 3(b). After seven days, a few settlements of nanoparticles is also observed for the ratio of 50:50 (Fig. 3(c)). Moreover, 80:20 ratio of TiO2: Al2O3 nanofluid is found as stable for two weeks without apparent sedimentation (Fig. 3(c)). Finally Fig. 3(d) represents the status of suspension after 21 days where 20:80, 40:60 ratios show a large amount of deposition followed by 60:40, 50:50 ratios of nanoparticles and 80:20 ratio shows very few amounts of deposition which may be due to gravitational force or the falling motion of nanoparticles [41].

3.2 UV-vis Spectral Analysis Method

The absorbance of the nanofluid is investigated in UV-vis spectrophotometer by comparing the light intensity between base fluid and nanofluid [42]. Yu and Xie [21] suggested about the wavelength range from 190 to1100nm for achieving the most authentic value. In this study, a constant wavelength of 903 nm selected through scanning the nanofluid in UV-vis spectrophotometer because the peak value of absorbance derived from this wavelength. The absorbance values of TiO2:Al2O3 for mixing ratios of 20:80, 40:60, 50:50, 60:40 and 80:20 at 0.1% concentration are presented in Fig.4. The absorbance value is increasing proportionately with increasing TiO2 particles and lowering Al2O3 nanoparticles. The trend of absorbance value aligned with Beer- Lambart Law [41, 43]. Because absorbance value is linearly increasing responding with

various mixing ratios of TiO_2-Al_2O_3. From Fig. 4, it is discovered that the more the ratio of TiO_2, the more the value of absorbance, which leads to more stability. On the other hand, the more the ratio of Al_2O_3, the less the value of absorbance of nanofluid which may be due to the strong van der Waals force among Al_2O_3 nanoparticles.



a. Just after preparation

b. After 3 days

c. After 14 days

d. After 21 days

Fig. 3. Sedimentation photograph of TiO2-Al2O3 hybrid nanofluids.

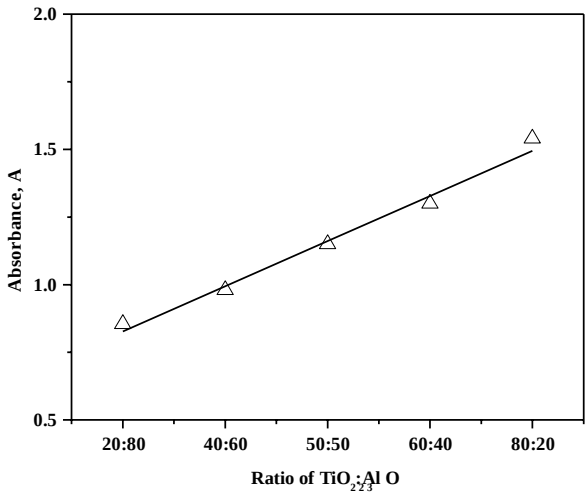


Fig.4. The absorbance value of 40% EG based TiO_2-Al_2O_3 hybrid nanofluids for various mixing ratios at 0.1% concentration.

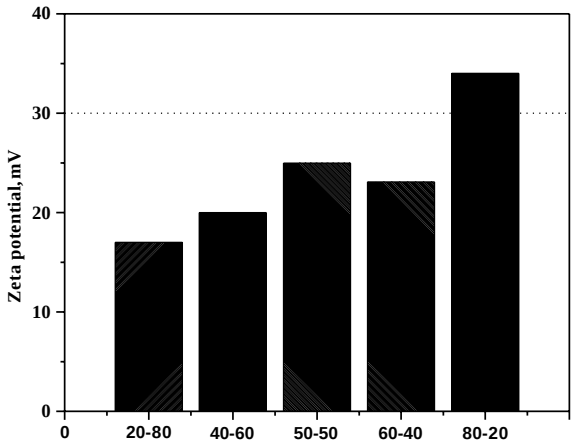
3.2 Zeta Potential

Zeta potential test is a critical method to assess the stability of nanofluid quantitatively. The electrostatic repulsive force between the suspension medium and static layer of fluid adhered to the particles [44]. The absolute value of zeta potential depicts the uniformity of colloidal suspension [21]. In general, the lower value of zeta potential expresses quick settlement of particles in the suspension [42]. However, zeta potential value with near to 30mV can be regarded as moderately stable [45]. Table 2 represents recognised zeta potential value with the stability state of colloidal suspension. However, this method has some limitation on the viscosity and concentration of fluid [9, 26].

Table 2
The state of stability of nanofluids against zeta potential value [45].

Stability state of Nanofluids	± Value of Zeta Potential (mV)
Excellent stability	60
Good stability	45
Moderate Stability	30
Lightly stable	15
No stability	0

In this study zeta potential value is employed to present the sedimentation of TiO_2-Al_2O_3 nanoparticles in 40% EG. The higher the value, the better the nanofluid in terms of the uniformity of suspension. Fig. 5 shows the absolute value of zeta potential for different mixing ratios of TiO-Al2O3 hybrid nanofluids. The maximum of the value of zeta potential is recorded up to 34mV for 80:20 ratio of TiO_2-Al_2O^3 while 50:50 and 60:40 ratios show the value of zeta potential near to 30mV (25mV and 23mV respectively). On the other hand, 20:80 and 40:60 ratios show little bit stability value of 17mV and 20mV, respectively. So it is evident that 80:20 ratio of TiO_2-Al_2O_3 nanofluid has good stability followed by 50:50 and 60:40 ratios are moderately stable.



Penerbit Akademia Baru

Mixing ratio of TiO_2:Al_2O_3

Fig.5. Zeta potential value 40% EG based TiO_2-Al_2O_3 hybrid nanofluids for various mixing ratios at 0.1% concentration.

Although there are numerous researches in the field of nanofluids, the use of nanofluid is still in the research and development stage, not in practical application broadly. Various factors like agglomeration, settlement of nanoparticles, corrosion and wear potential need to be characterised as detail according to the shape and size distribution in the research to make the findings more reliable and useful. However, the results from the previously published works of literature to date

are adequate to get an idea about some magnitude and also the trends in the enhancement of thermal properties of nanofluids, but still, some is lacking in the stability field of different types of nanofluids. So future research should be focused on the long term stability of nanofluids.

4. Conclusions

In this research, the stability analysis of 40% EG based TiO2-Al2O3 hybrid nanofluids shown after preparing using the most common two-step method. Ultrasonic vibration method employed in this study for stabilisation purpose of nanofluid without any surfactant and pH stabiliser. The time-dependent sedimentation observation method gives the qualitative idea of the stability of TiO2-Al2O3 hybrid nanofluids. Moreover, the peak value of absorbance of the nanofluid, linear relationship of absorbance and various mixing ratio of TiO2- Al2O3 hybrid nanofluids and also zeta potential value quantitatively confirms the stability analysis of studied nanofluids. This study reveals that the 80:20 ratio of TiO2-Al2O3 hybrid nanofluids has the highest stability for over 21days without any apparent settlement of particles and followed by 50:50, 60:40, 40:60 and 20:80 ratio of nanofluids. Moreover, among all ratios 50:50, 60:40 are also moderately stable for two weeks with very few sedimentations whereas 20:80, 40:60 ratios shows little stability with quick settle down of articles. Thus, 80:20, 50:50, 60:40 ratios are suitable to use in the practical field and stability period to enhanced with various treatment like surface modification, pH modification and if necessary additives addition. Future work will be carried out for improving the stability and sustaining the long term stability of different types of hybrid nanofluids which will contribute to practical and commercial application.

Acknowledgement
The authors would like to thank University Malaysia Pahang for providing the laboratory facilities and the financial support under the University LEAP-3 FLAGSHIP Research Grant No. RDU172203 and University Research Internal Grant No. RDU190367.

References:

[1] Asadi, A., Asadi, M., Rezaniakolaei, A., Rosendahl, L.A., Afrand, M., Wongwises, S. "Heat transfer efficiency of Al2O3-MWCNT/thermal oil hybrid nanofluid as a cooling fluid in thermal and energy management applications: An experimental and theoretical investigation." *International Journal of Heat and Mass Transfer* 117 (2018): 474-486.
[2] Ouikhalfan, M., Labihi, A., Belaqziz, M., Chehouani, H., Benhamou, B., Sarı, A., Belfkira, A. "Stability and thermal conductivity enhancement of aqueous nanofluid based on surfactant-modified TiO2." *Journal of Dispersion Science and Technology* (2019): 1-9.
[3] Choi, S.U., Eastman, J.A.: Enhancing thermal conductivity of fluids with nanoparticles. Argonne National Lab., IL (United States) (1995)
[4] Rahmati, B., Sarhan, A.A., Sayuti, M. "Investigating the optimum molybdenum disulfide (MoS 2) nanolubrication parameters in CNC milling of AL6061-T6 alloy." *The International Journal of Advanced Manufacturing Technology*

70, no. 5-8 (2014): 1143-1155.
[5] Saidur, R., Leong, K., Mohammed, H.A. "A review on applications and challenges of nanofluids."
[6] *Renewable and sustainable energy reviews* 15, no. 3 (2011): 1646-1668.
[7] Shen, B., Shih, A.J., Tung, S.C. "Application of nanofluids in minimum quantity lubrication grinding."
[8] *Tribology Transactions* 51, no. 6 (2008): 730-737.
[9] Li, Y., Tung, S., Schneider, E., Xi, S. "A review on development of nanofluid preparation and characterization." *Powder technology* 196, no. 2 (2009): 89-101.
[10] Chen, L., Xie, H. "Surfactant-free nanofluids containing double-and single-walled carbon nanotubes functionalized by a wet-mechanochemical reaction." *Thermochimica Acta* 497, no. 1-2 (2010): 67-71.
[11] Sajid, M.U., Ali, H.M. "Thermal conductivity of hybrid nanofluids: a critical review." *International Journal of Heat and Mass Transfer* 126 (2018): 211-234.
[12] Haghighi, E., Nikkam, N., Saleemi, M., Behi, M., Mirmohammadi, S.A., Poth, H., Khodabandeh, R., Toprak, M.S., Muhammed, M., Palm, B. "Shelf stability of nanofluids and its effect on thermal conductivity and viscosity." *Measurement Science and Technology* 24, no. 10 (2013): 105301.
[13] Srinivas, V., Moorthy, C.V., Dedeepya, V., Manikanta, P., Satish, V. "Nanofluids with CNTs for automotive applications." *Heat and Mass Transfer* 52, no. 4 (2016): 701-712.

1. Huminic, G., Huminic, A. "Hybrid nanofluids for heat transfer applications–a state-of-the-art review." *International Journal of Heat and Mass Transfer* 125 (2018): 82-103.
2. Sezer, N., Atieh, M.A., Koc, M. "A comprehensive review on synthesis, stability, thermophysical properties, and characterization of nanofluids." *Powder technology* (2018).
3. Nasiri, A., Shariaty-Niasar, M., Rashidi, A., Amrollahi, A., Khodafarin, R. "Effect of dispersion method on thermal conductivity and stability of nanofluid." *Experimental thermal and fluid science* 35, no. 4 (2011): 717-723.
4. Hatwar, A.S., Kriplani, V. "A review on heat transfer enhancement with nanofluid." *Int. J. Adv. Res. Sci. Eng* 3, no. 3 (2014): 175-183.
5. Zhu, H.-t., Lin, Y.-s., Yin, Y.-s. "A novel one-step chemical method for preparation of copper nanofluids." *Journal of colloid and interface science* 277, no. 1 (2004): 100-103.
6. Paul, G., Philip, J., Raj, B., Das, P.K., Manna, I. "Synthesis, characterization, and thermal property measurement of nano-Al95Zn05 dispersed nanofluid prepared by a two-step process." *International Journal of Heat and Mass Transfer* 54, no. 15-16 (2011): 3783-3788.
7. Shahsavar, A., Salimpour, M.R., Saghafian, M., Shafii, M. "Effect of magnetic field on thermal conductivity and viscosity of a magnetic nanofluid loaded with carbon nanotubes." *Journal of Mechanical Science and Technology* 30, no. 2 (2016): 809-815.
8. Manimaran, R., Palaniradja, K., Alagumurthi, N., Sendhilnathan, S., Hussain, J. "Preparation and characterization of copper oxide nanofluid for heat transfer applications." *Applied Nanoscience* 4, no. 2 (2014): 163-167.
9. Nikkam, N., Ghanbarpour, M., Saleemi, M., Haghighi, E.B., Khodabandeh, R., Muhammed, M., Palm, B., Toprak, M.S. "Experimental investigation on thermo-physical properties of copper/diethylene glycol nanofluids fabricated via microwave-assisted route." *Applied Thermal Engineering* 65, no. 1-2 (2014): 158-165.
10. Yu, W., Xie, H. "A review on nanofluids: preparation, stability mechanisms, and applications." *Journal of nanomaterials* 2012 (2012): 1.
11. Zhu, D., Li, X., Wang, N., Wang, X., Gao, J., Li, H. "Dispersion behavior and thermal conductivity characteristics of Al2O3–H2O nanofluids." *Current Applied Physics* 9, no. 1 (2009): 131-139.
12. Esfe, M.H., Afrand, M., Yan, W.-M., Akbari, M. "Applicability of artificial neural network and nonlinear regression to predict thermal conductivity modeling of Al2O3–water nanofluids using experimental data." *International Communications in Heat and Mass Transfer* 66 (2015): 246-249.
13. Geng, Y., Al-Rashed, A.A., Mahmoudi, B., Alsagri, A.S., Shahsavar, A., Talebizadehsardari, P. "Characterization of the nanoparticles, the stability analysis and the evaluation of a new hybrid nano-oil thermal conductivity." *Journal of Thermal Analysis and Calorimetry* (2019): 1-12.
14. Hamid, K.A., Azmi, W., Nabil, M., Mamat, R. "Experimental investigation of nanoparticle mixture ratios on TiO2–SiO2 nanofluids heat transfer performance under turbulent flow." *International Journal of Heat and Mass Transfer* 118 (2018): 617-627.
15. Hwang, Y.-j., Lee, J., Lee, C., Jung, Y., Cheong, S., Lee, C., Ku, B., Jang, S. "Stability and thermal conductivity characteristics of nanofluids." *Thermochimica Acta* 455, no. 1-2 (2007): 70-74.
16. Jiang, L., Gao, L., Sun, J. "Production of aqueous colloidal dispersions of carbon nanotubes." *Journal of colloid and interface science* 260, no. 1 (2003): 89-94.
17. Rao, Y. "Nanofluids: stability, phase diagram, rheology and applications." *Particuology* 8, no. 6 (2010): 549-555.
18. Xian-Ju, W., Xin-Fang, L. "Influence of pH on nanofluids' viscosity and thermal conductivity." *Chinese Physics Letters* 26, no. 5 (2009): 056601.
19. Li, X., Zhu, D., Wang, X. "Evaluation on dispersion behavior of the aqueous copper nano-suspensions." *Journal of colloid and interface science* 310, no. 2 (2007): 456-463.
20. Hamid, K.A., Azmi, W., Nabil, M., Mamat, R., Sharma, K. "Experimental investigation of thermal conductivity and dynamic viscosity on nanoparticle mixture ratios of TiO2-SiO2 nanofluids." *International Journal of Heat and Mass Transfer* 116 (2018): 1143-1152.
21. Afrand, M. "Experimental study on thermal conductivity of ethylene glycol containing hybrid nano-additives and development of a new correlation." *Applied Thermal Engineering* 110 (2017): 1111-1119.

22. Hamid, K.A., Azmi, W., Mamat, R., Sharma, K. "Experimental investigation on heat transfer performance of TiO2 nanofluids in water–ethylene glycol mixture." *International Communications in Heat and Mass Transfer* 73 (2016): 16-24.
23. Rahman, M., Kadirgama, K., Ab Aziz, A.S. "ARTIFICIAL NEURAL NETWORK MODELING OF GRINDING OF DUCTILE CAST IRON USING WATER BASED SiO 2 NANOCOOLANT." *International Journal of Automotive & Mechanical Engineering* 9 (2014).
24. Yiamsawas, T., Mahian, O., Dalkilic, A.S., Kaewnai, S., Wongwises, S. "Experimental studies on the viscosity of TiO2 and Al2O3 nanoparticles suspended in a mixture of ethylene glycol and water for high temperature applications." *Applied energy* 111 (2013): 40-45.
25. Nabil, M., Azmi, W., Hamid, K., Mamat, R. "Experimental investigation of heat transfer and friction factor of TiO2-SiO2 nanofluids in water: ethylene glycol mixture." *International Journal of Heat and Mass Transfer* 124 (2018): 1361-1369.
26. Nabil, M., Azmi, W., Hamid, K.A., Mamat, R., Hagos, F.Y. "An experimental study on the thermal conductivity and dynamic viscosity of TiO2-SiO2 nanofluids in water: ethylene glycol mixture." *International Communications in Heat and Mass Transfer* 86 (2017): 181-189.
27. Hajjar, Z., morad Rashidi, A., Ghozatloo, A. "Enhanced thermal conductivities of graphene oxide nanofluids." *International Communications in Heat and Mass Transfer* 57 (2014): 128-131.
28. Karami, M., Bahabadi, M.A., Delfani, S., Ghozatloo, A. "A new application of carbon nanotubes nanofluid as working fluid of low-temperature direct absorption solar collector." *Solar Energy Materials and Solar Cells* 121 (2014): 114-118.
29. Sharif, M., Azmi, W., Redhwan, A., Mamat, R., Yusof, T. "Performance analysis of SiO2/PAG nanolubricant in automotive air conditioning system." *international journal of refrigeration* 75 (2017): 204-216.
30. Ramadhan, A., Azmi, W., Mamat, R., Hamid, K., Norsakinah, S.: Investigation on stability of tri-hybrid nanofluids in water-ethylene glycol mixture. In: IOP Conference Series: Materials Science and Engineering, pp. 012068. IOP Publishing, (Year)
31. Ghadimi, A., Saidur, R., Metselaar, H. "A review of nanofluid stability properties and characterization in stationary conditions." *International journal of heat and mass transfer* 54, no. 17-18 (2011): 4051-4068.
32. Sharif, M., Azmi, W., Redhwan, A., Mamat, R., Najafi, G. "Energy saving in automotive air conditioning system performance using SiO 2/PAG nanolubricants." *Journal of Thermal Analysis and Calorimetry* 135, no. 2 (2019): 1285-1297.
33. Choudhary, R., Khurana, D., Kumar, A., Subudhi, S. "Stability analysis of Al2O3/water nanofluids." *Journal of Experimental Nanoscience* 12, no. 1 (2017): 140-151.
34. Vandsburger, L.: Synthesis and covalent surface modification of carbon nanotubes for preparation of stabilized nanofluid suspensions. McGill University (2009)

Penerbit Akademia Baru

Engineering Science and Technology Conference Proceedings

Journal homepage: www.akademiabaru.com/EST.html

Application Of Magneto Rheological Damper System In Warren Truss Bridge Structure

Open Access

Fatemeh Behbahani[1,*], Faranak Rabiei[2]

[1] Department of artificial intelligence and robotics (CAIRO), Malaysia-Japan International Institute of Technology (MJIIT), UTM, Kuala Lumpur, Malaysia

[2] Department of Applied mathematical, MONASH university Malaysia, Selangor Darul ehsan,47500.

ABSTRACT

This paper considers the application of magnetorheological (MR) damper, RD-8040-1, for attenuation vibration in flexible truss bridge deck structures. The modeling and identification of the damper property by using SAP2000 analysis software from an experimental data set generated by dynamic tests of the MR damper mounted in a testing machine where velocity and current are used as input, and the force as output. Theoretical investigations and in-site experiments are carried out in Chamran's laboratory, Ahvaz, Iran. Truss bridges are an innovative structure that shall be studied in their systems and connections to earn stability and damping in related to certain lateral loads such as seismic load's post-earthquake load. The issue of damping is the cooperation between elements in the truss bridge of deck systems. Significantly, MR damper among components based on their reaction can be defined in the form of a percentage of control of loads in the structure of deck in a bridge system. This article proposes the application of damper at interconnecting of bridge deck through minimizing vibration force by using the Bouc-wen model. In summary, this paper is understood the effect of damping application on overall formation nonlinear analysis Models at this major element.

Keywords:

Magnetorheological damper (nonlinear); Warren truss bridge; Seismic analysis; dynamic forces; modified Bouc-Wen model

Copyright © 2019 PENERBIT AKADEMIA BARU - All rights reserved

1. Introduction

Due to the inherent nonlinear nature of magnetorheological (MR) dampers, one of the challenging aspects for developing and utilizing these devices to achieve high performance is the development of models that can accurately describe their unique characteristics. For semi-active control of bridge suspension Magnetorheological (MR) dampers are usually used [1-2-3-4]. In this paper, the characteristics of MR dampers are summarized to the measured responses under different conditions. On these bases, the considerations, and method of the parametric dynamic modeling for MR damper is given, and the state-of-the-art parametric dynamic modeling, identification and validation technique for MR damper is explained. In the past, two decades, the models for MR dampers have been focused on how to improve modeling accuracy. Although the

force-displacement behavior is well represented by most of the proposed dynamic models for MR dampers, no simple parametric models with high accuracy for MR dampers can be found and the measured force–velocity data in the vicinity of zero velocity is still most of the researcher is working on that for describing more accurate in hysteresis behavior of MR damper, when the effect of hysteresis begins to take effect. Also, the parametric dynamic models for MR dampers with on-line updating ability and the inverse parametric models for MR dampers are scarcely explored. Moreover, whether one dynamic model for MR dampers can portray the force-displacement and force-velocity behavior is not only determined by the dynamic model itself but also determined by the identification method.

1.1 Magnetorheological fluids

Magnetorheological (MR) fluids are suspensions that exhibit a rapid, reversible and tunable transition from a free-flowing state to a semi-solid state on the application of an external magnetic field. These materials demonstrate dramatic changes in their rheological behavior with a magnetic field. MR fluids have attracted considerable interest recently because they can provide a simple and rapid response interface between electronic controls and mechanical systems [5]. The first discovery and development of MR fluids and devices can be credited to Rabinow at the US National Bureau of Standards in the late 1940s [6]. These fluids are suspensions of micron-sized, magnetizable particles in an appropriate carrier liquid. Normally, MR fluids are free-flowing liquids having a consistency similar to that of motor oil. However, in the presence of an applied magnetic field, the particles acquire a dipole moment aligned with the external field that causes particles to form linear chains parallel to the field. This phenomenon can solidify the suspension and restrict the fluid movement. Consequently, the yield stress is developed. The degree of change is related to the magnitude of the applied magnetic field and can occur in only a few milliseconds. The primary advantage of MR fluids stems from their large and controllable dynamic yield stress due to the high magnetic energy density that can be established in the fluids [7-12].

2. Experimental set up

From a practical application perspective, MR devices can be powered directly from common, low voltage sources. A higher dynamic yield stress would allow for a smaller device size and a higher dynamic range. Further, standard electrical connectors, wires and feedthroughs can be reliably used, even in mechanically aggressive and dirty environments, without fear of dielectric breakdown. These aspects are particularly promising for earthquake events and cost-sensitive applications.

In this paper, we will focus on the parametric dynamic model for MR dampers, and identification and validation which is used to characterize the MR damper model RD- 8040-1 by Lord Corporation as shown in Fig 1 And also, Table 1 is characterises of this type of damper The MR damper is exposed to different loading conditions by an damping force testing machine which provides the force and the displacement profiles induced to the damper. These data are processed and used to estimate the model parameters. Finally, the estimated model is compared with the experimental response showing the effectiveness of the parametric model to predict the MR behavior.



Fig. 1. MR damper model RD-8040-1 (short stroke) with current driver by Lord Corporation

Table 1
Specification data for the fluid damper RD8040-1

Lord MR damper RD-8040-1	
Parameter	Value
Extended length (mm)	208
stroke length (mm)	55
Body Diameter (mm) Shaft Diameter (mm)	42.1 max 10
Weight (g)	800
Operating temperature (°C)	Damper should be stored -40 to +100 (-40 to +212 °F)
Electrical characteristics: Maximum input current (A) Input voltage (VDC) Resistance (Ω)	 2 max 12 DC 5 Ω at ambient temperature 7 Ω at 71°C
Mechanical characteristics: Maximum extension force (N) maximum tensile strength Maximum operating temperature (deg) MR fluid (MRF132-DG) data	 2500 8896 71°C max
Response time (ms) (amplifier & power supply dependent)	<15 (time to reach 90% of max level during a 0 to 1 amp step input)

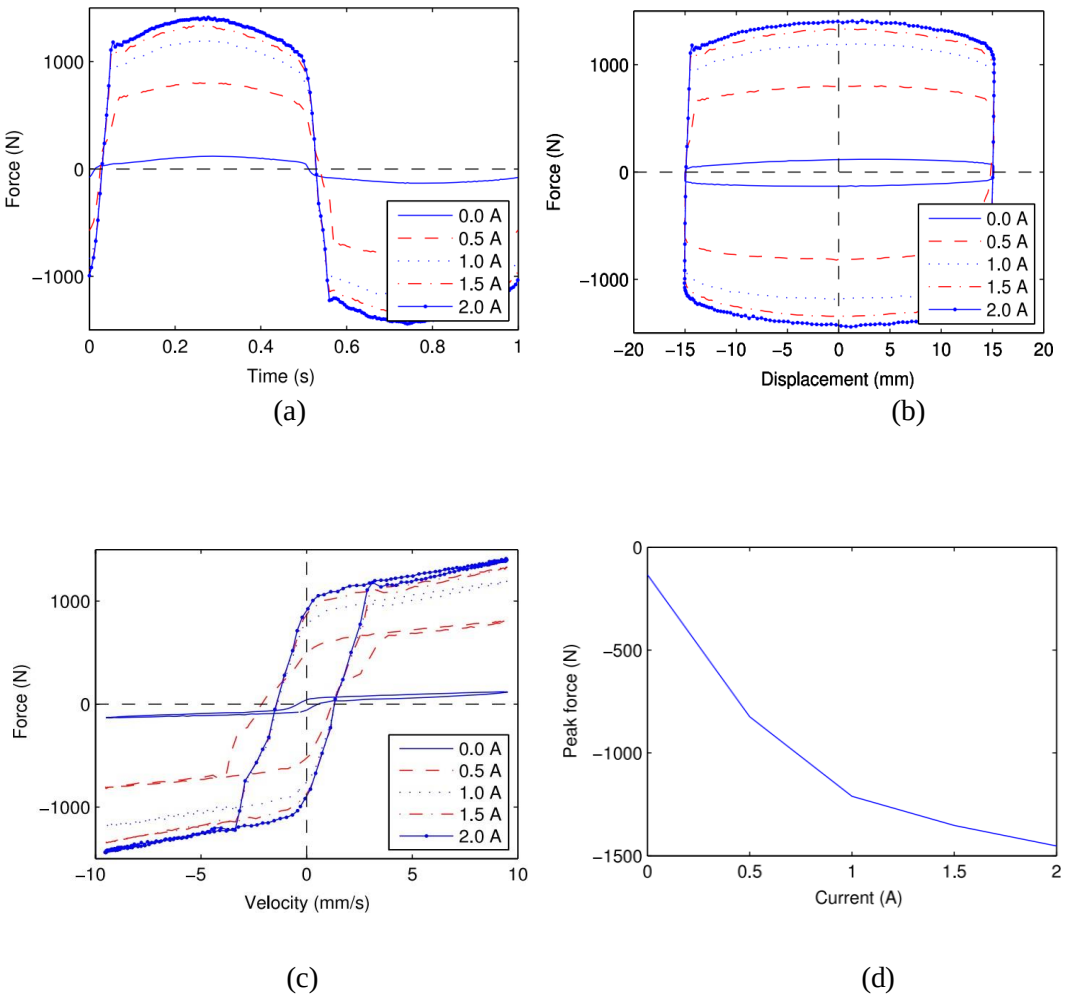


Fig. 2. Measured damping forces of the MR damper under a 1.00 Hz sinusoidal excitation with amplitude of 15.00 mm for five current levels: (a) the time histories, (b) the force versus displacement, (c) the force versus velocity and (d) the peak force versus current.

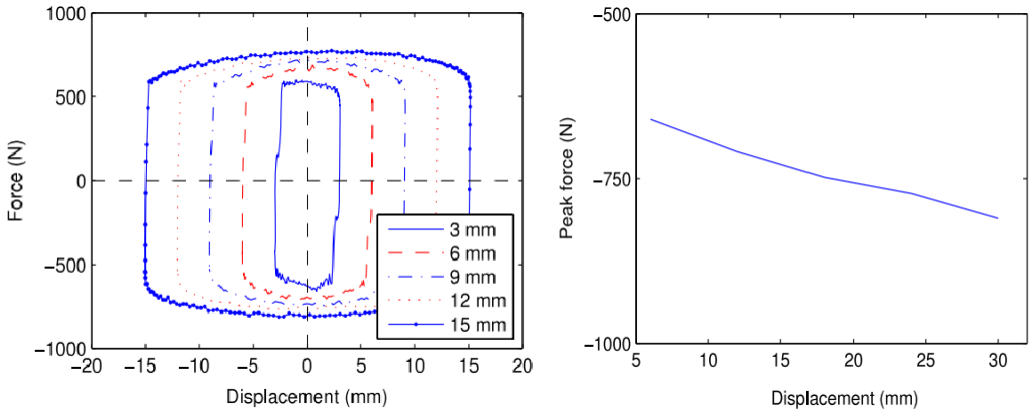


Fig. 3. Measured damping forces of the MR damper under a 1.00 Hz sinusoidal excitation with amplitudes of 3.00, 6.00, 9.00, 12.00 and 15.00 mm for current level 0.50 A: (a) the force versus displacement and (b) the

peak force versus displacement.

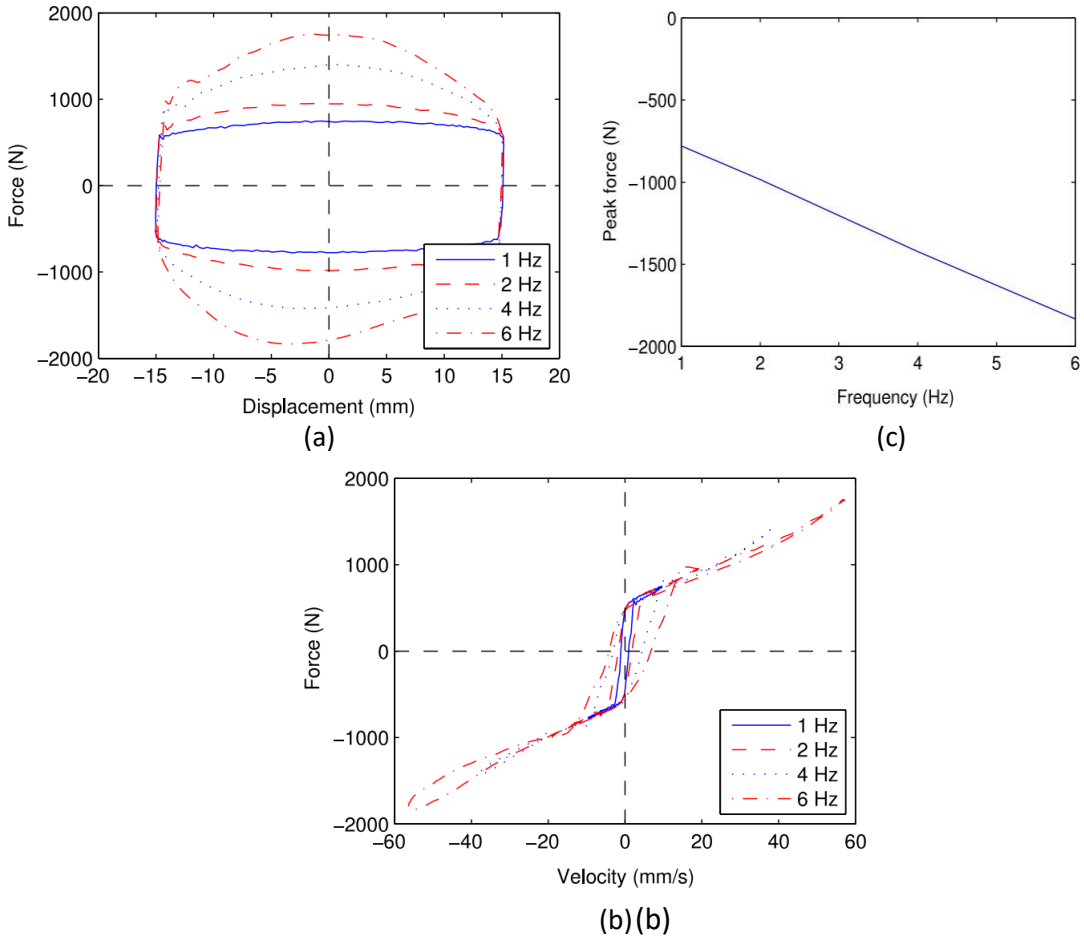


Fig. 4. Measured damping forces of the MR damper under a 1.00, 2.00, 4.00 and 6.00 Hz sinusoidal excitation with amplitude of 15.0 mm for current level of 0.50 A: (a) the force versus displacement, (b) the force versus velocity and (c) the peak force versus excitation frequency.

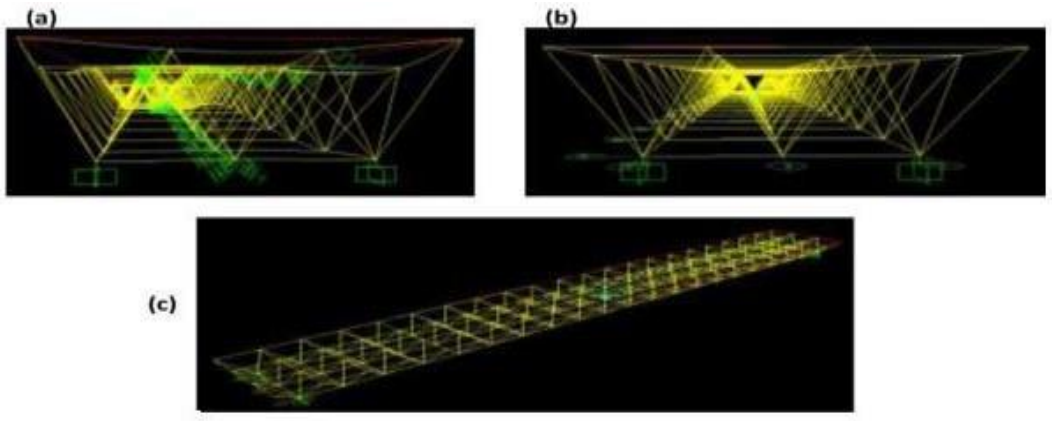


Fig. 5. Truss bridge structure (a) by using damper (b) without damper (c) full structure of bridge.

The proposed structure is truss bridge what has 100 m length and 10 m width. Type of truss is warren in two directions with divisions of 5m. Magnetic damper parameter has been defined in central perpendicular members in longitudinal way. Regular dynamic force has been loaded on it to check the function of damper in controlling of vibration cause of dynamic force which is verified by experimentation (See Fig 5).

2. Methodology

The parametric modeling technique characterizes the device as a collection of linear and/or nonlinear springs, dampers, and other physical elements. Various parametric dynamic models for MR dampers based on mechanical idealizations, including the Bingham-model-based dynamic models, biviscous models, viscoelastic–plastic models, stiffness–viscosity-elasto-slide models, Bouc–Wen hysteresis operator-based models, Dahl hysteresis operator-based models, LuGre hysteresis operator-based models, hyperbolic tangent function-based models, sigmoid function-based models, equivalent models and phase transition models, have been explored and validated. These parameterized models can model the dynamics of MR dampers in a limited range by identifying the parameters for the parametric dynamic models. However, parametric identification methods require assumptions of the structure of the mechanical model that simulates the behavior. Once a model is selected, the values of system parameters are determined in such a way that the error between the experimental data and the simulated responses is minimized. The approach could be divergent if the starting assumptions for the structure of the model are flawed, or if proper constraints are not applied to the parameters. Unrealistic parameters such as negative mass or stiffness may be obtained. In this work the modified Bouc-Wen model proposed by Spencer et al [8].

2.1 Modified Bouc-Wen Model

The mechanical idealization of an MR damper depicted in Fig 6 has been shown to accurately predict behaviour of the MR damper over a broad range of inputs. The phenomenological model proposed by Spencer et al [8] is governed by the following equations:

$$c_1\dot{y} = \alpha z + c_0(\dot{x}_d - \dot{y}) + k_0(x_d - y) \quad (1)$$

The total force generated by the system is given by

$$= \alpha z + c_0(\dot{x}_d - \dot{y}) + k_0(x_d - y) + k_1(x_d - x_0) \quad (2)$$

From Eq. 1, the total force can also be written as

$$= c_1\dot{y} + k_1(x_d - x_0) \quad (3)$$

Where the evolutionary variable z is governed by

$$\dot{z} = -\gamma|\dot{x}_d - \dot{y}|z|z|^{n-1} - \beta(\dot{x}_d - \dot{y})|z|^n + A\,(\dot{x} - \dot{y}) \quad (4)$$

And y is the internal displacement of the MR damper given by Solving Eq. 1 for $\dot{y}$ results in

$$\dot{y} = \frac{1}{c_0 - c_1}\{\alpha z + c_0\dot{x} + k_0(x_d - y)\} \quad (5)$$

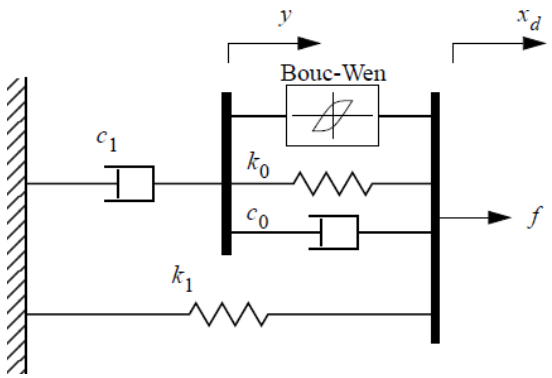


Fig. 6. Modified Bouc–Wen model for MR dampers [8].

In this model, the accumulator stiffness is represented by k_1 and the viscous damping observed at larger velocities is represented by c_0. A dashpot, represented by c_1, is included in the model to produce the roll-off that be observed in the experimental data at low velocities, k_0 is present to control the stiffness at large velocities, and x_0 is the initial displacement of spring k_1 associated with the nominal damper force due to the accumulator. Where x_d and f are the displacement of and the force generated by the MR damper respectively; y is the internal displacement of the MR damper. Where, A, β, γ and n are dimensionless quantities controlling the behavior of the model. For small values of the positive exponential parameter n the transition from elastic to post-elastic branch is smooth, whereas for large values the transition becomes abrupt, approaching that of a bilinear model. Parameters β and γ control the size and shape of the hysteretic loop. Parameter A was introduced in the original formulation of the model, but it became evident that it is redundant [9]. As in the simple Bouc-Wen model, the non-linear shape of the hysteretic curve can be adjusted by changing the values of the Bouc-Wen block parameters A, β, γ and n. Usually, these parameters are considered fixed while the parameters α, c_0, c_1 are assumed to be functions of the applied current.

In order to accurately characterize the behaviour of MR dampers using the modified Bouc–Wen model, a set of ten constant parameters that relate the characteristic shape parameters to current excitation should be identified, and the set of parameters is as follows:

$$\theta = [c_0, c_1, k_0, k_1, x_0, \alpha, \beta, \gamma, A, n] \quad (6)$$

To obtain a model which is valid for varying magnetic field strengths, the parameters are assumed to be dependent on the applied current (I), which is determined by the voltage (v) applied to the current driver. The proposed relationships between the parameters and the applied voltage are as follows:

Linear current relationship: Spencer et al [8] adopted a linear relationship between the parameters and the applied voltage, which is given by

$$= (u) = \alpha_a + \alpha_b u \quad (7)$$

$$c_1 = c_1(u) = c_{1a} + c_{1b} u \quad (8)$$

$$c_0 = c_0(u) = c_{0a} + c_{0b} u \quad (9)$$

where c_{0a} and α_a are the damping coefficient and Coulomb force of the MR damper at 0 V, respectively, and u is an intrinsic variable to determine the function dependence of the parameters on the applied voltage v. The relationship between u and v is modelled by the first order filter given by

$$\dot{u} = -(u - v) \quad (10)$$

Where η reflects the response time of the MR damper, namely, larger η means faster response time, and v is the command voltage sent to the current driver. In order to accurately characterize the behaviour of MR dampers using the current-dependent Bouc–Wen model given by Eq. 3 and Eq. 10, a set of 14 constant parameters that relate the characteristic shape parameters to current excitation should be identified, and the set of parameters is as follows:

$$\theta = (c_{0a}, c_{0b}, k_0, c_{1a}, c_{1b}, k_1, x_0, \alpha_a, \alpha_b, \gamma, \beta, n, \eta \text{ and } A) \quad (11)$$

2.2 Identification and validation

The parameters in the parametric dynamic models for MR dampers should be identified using experimental data to make the hysteresis loop agree with experimental data. A total of 14 model parameters which are given in Table 2, is obtained to characterize the MR fluid damper using experimental data and a constrained nonlinear optimization algorithm. The modified Bouc-Wen model is the most common model for studying the dynamic behavior of MR dampers theoretically. In order to calculate the output damping force easily, modified Bouc–Wen model is built in MATLAB/ Simulink. The relationship among Eq. 3 and Eq. 5 can be expressed by the integrators and summators, and the unknown parameters are replaced by the constant values in Simulink. The equations are compiled in embedded MATLAB functions. The velocity of the piston is calculated from displacement by differentiators. The modified Bouc–Wen model described in Simulink is shown in Fig 7.

Table 2
Parameters for the Model of MR Fluid Damper

variable	value	variable	value
c_{0a}	784 Nsm^{-1}	α_a	12441 Nm^{-1}
c_{0b}	1803 $NsV^{-1}\,m^{-1}$	α_b	38430
k_0	3610 Nm^{-1}	γ	136320 m^{-2}
c_{1a}	14649 Nsm^{-1}	β	2059020 m^{-2}
c_{1b}	34622 $NsV^{-1}\,m^{-1}$	n	2
k_1	840 Nm^{-1}	η	190 s^{-1}
x_0	0.0245 m	A	58

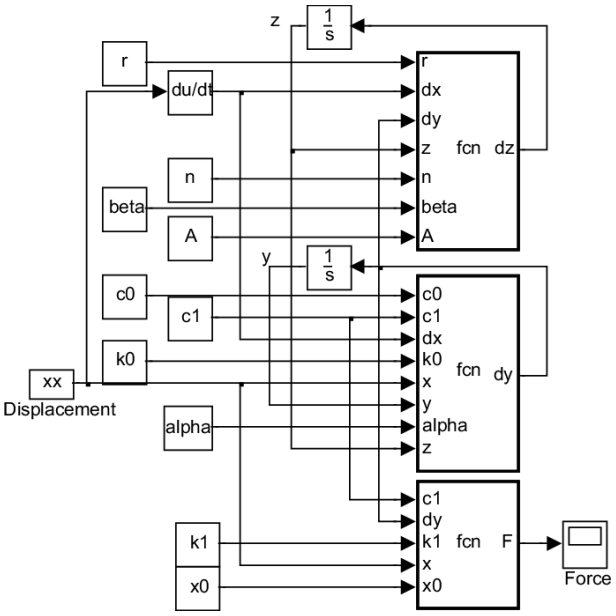


Fig. 7. The Bouc-Wen modified model described in Simulink [10].

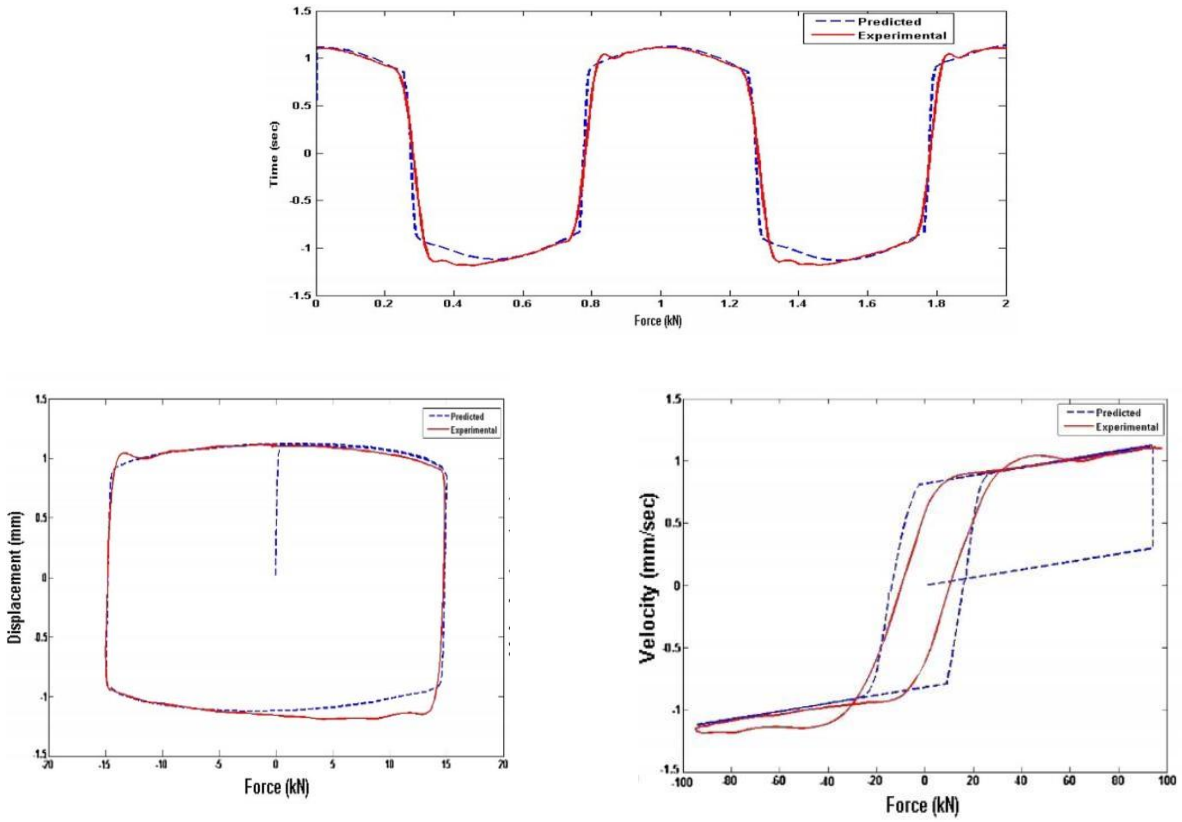


Fig. 8. Comparison of predicted and experimental results of RD 8040-1 short stroke MR damper with sinusoidal excitation of 15 mm amplitude 1 Hz frequency 1 A input current.

In [11] the model errors have been evaluated by means of an experimental setup with actuators, displacement and force transducers. In others Word, The quantitative study of the error between the predicted force and the measured force are calculated as a function of time,

displacement and velocity. The following expressions have been introduced and used as a reference for quantitative evaluation of normalized errors:

$$E_t = \sqrt{\frac{\int_0^T (f_{exp}-f_{model})^2 dt}{\int_0 (f_{exp}-\bar{f}_{exp})^2}} \quad (12)$$

$$E_x = \sqrt{\frac{\int_0^T (f_{exp}-f_{model})^2 \left|\frac{dx}{dt}\right| dt}{\int_0^T (f_{exp}-\bar{f}_{exp})^2 \left|\frac{dx}{dt}\right| dt}} \quad (13)$$

$$E_v = \sqrt{\frac{\int_0^T (f_{exp}-f_{model})^2 \left|\frac{d\dot{x}}{dt}\right| dt}{\int_0^T (f_{exp}-\bar{f}_{exp})^2 \left|\frac{d\dot{x}}{dt}\right| dt}} \quad (14)$$

f_{model} is the simulated or predicted force, f_{exp} represents the experimental or measured force, and $\bar{f}_{exp}$ is the measured force's average value along the T period. , E_x and E_v are normalized errors between model and experimental force in time, displacement and velocity domains respectively. Errors up to 15% for time, 4% for displacements and 13% for velocities have been reported for different current values.

3. Result and Conclusions

As the presented results show, it is possible to predict the non-linear hysteretic behavior of an MR damper by a proposed model. The model output damping forces are directly obtained through modified Bouc-Wen and compare between the model force and measured force. First, the dynamic responses were measured by doing experiments on a machine test with various sinusoidal displacement excitations whose different frequencies, applied currents and 15mm amplitude. Accordingly, the parametric dynamic modeling for MR damper was given and the identification and validation technique for MR dampers was presented. Generally speaking, in the past two decades, the models for MR dampers have been focused on how to improve the modeling accuracy. For the parametric dynamic modeling, identification and validation technique for MR dampers, the following conclusions can be drawn.

(i) The force-displacement behavior of MR dampers is well represented by the proposed dynamic model for MR damper.
(ii) No simple parametric model with high accuracy for MR damper can be found, although various kinds of models for MR dampers have been proposed and validated.
(iii) Whether one dynamic model for MR damper can portray the force-displacement, and force-velocity behavior is not only determined by the dynamic model itself but also determined by the identification method.

Figure 10 displays the modeling results of the modified Bouc-Wen model in a comparison with the real damping behavior for a 1Hz sinusoidal displacement excitation and 1A of the applied current to the better-estimated force of the truss bridge structure of MR fluid damper. The results show that the nonlinear characteristic of the MR fluid damper can be directly estimated with high accuracy for the force/time, force/displacement, and force/velocity relation in spite of the varying of applied

current for the damper. The proposed model shows a good predicting result, especially on the low current level. When the value of velocity is high, the proposed model describes well the MR fluid damper hysteresis. As a result, the proposed model can predict the damping force with higher accuracy.

Acknowledgement
We would like to express our appreciation for the support in a special way to university technology Malaysia and Chamran university, Ahvaz, Iran, their help to complete this article and patient encouragement aided the writing of this paper in innumerable ways.

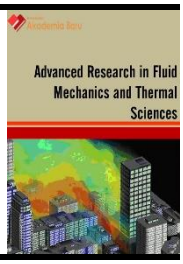
References

[1] Qiang Wang, Mehdi Ahmadian, and Zhaobo Chen1. 2014. "A Novel Double-Piston Magnetorheological Damper for Space Truss Structures Vibration Suppression." *Shock and Vibration* 11 pages.
[2] LS Minsili, T Zhong, H Xia, DE Manguelle. 2002. "Design and Vibration Control by Friction Dampers in Truss Bridges."
[3] Meng-Gang Yang, Zheng-Qing Chen and Xu-Gang Hua. 2011. "An experimental study on using MR damper to mitigate longitudinal seismic response of a suspension bridge." *Soil Dynamics and Earthquake Engineering 31 (2011) 1171–1181* 11.
[4] Haiping Du, James Lam and Nong Zhang. 2006. "Modelling of a magneto-rheological damper by evolving radial basis function networks." *Engineering Applications of Artificial Intelligence 19 (2006) 869–881* 13.
[5] W.I.Kordonsky. 1993. "Magnetorheological effect as a base of new devices and technologies." *Journal of Magnetism and Magnetic Materials* Volume 122 (Issues 1–3): Pages 395-398.
[6] T.M.Simon, F.Reitich, M.R.Jolly, K.Ito and H.T.Banks. 2001. "The effective magnetic properties of magnetorheological fluids." *Mathematical and Computer Modelling* 33 (1-3): Pages 273-284. doi:https://doi.org/10.1016/S0895-7177(00)00244-2.
[7] Billie F. Spencer, Jr.,Guangqiang Yang,J. David Carlson and Michael K. Sain. 1998. "Smart" Dampers for Seismic Protection of Structures: A Full-Scale Study." *the Second World Conference on Structural Control.* Kyoto, Japan. 10.
[8] B. F. Spencer Jr., S. J. Dyke,M. K. Sain and J. D. Carlson. 1997. "Phenomenological Model for Magnetorheological Dampers." *Journal of Engineering Mechanics* 123 (3). doi:https://doi.org/10.1061/(ASCE)0733-9399(1997)123:3(230).
[9] F. Ma, Fellow ASME , H. Zhang , A. Bockstedte , G. C. Foliente and P. Paevere. 2004. "Parameter Analysis of the Differential Model of Hysteresis." 71 (3): 8. doi:https://doi.org/10.1115/1.1668082.
[10] Yongqiang Liu and Shaopu Yang. 2011. "A Quantizing Method for Determination of Controlled Damping Parameters of Magnetorheological Damper Models." *Journal of Intelligent Material Systems and Structures* 11. doi:DOI: 10.1177/1045389X11425278.
[11] G. Yang, B. F. Spencer, J. D. Carlson, and M. K. Sain. 2002. "Large-scale MR fluid dampers: Modeling and dynamic performance considerations." 24 (3): 309–323.
[12] Radek Glaser, Vincent Caccese and Mohsen Shahinpoor. 2011. "Development of magneto- rheological fluid composites with rigidification characteristics." *Smart Materials and Structures* (IOP Publishing Ltd) 20 (4): 16. doi:doi:10.1088/0964-1726/20/4/045018.

Penerbit Akademia Baru

Engineering Science and Technology Conference Proceedings

Journal homepage: www.akademiabaru.com/EST.html



On-Design Operation and Performance Characteristic of Custom Engine

Open Access

Yazan S. M. Alterazi[1,3], Abd Rahim Abu Talib[1,2,*], Syamimi Saadon[1,2], Jianglong Yu[3], Ezanee Gires[1,2], Mohd Fahmi Abdul Ghafir[4], John Lucas[3]

[1] Aerodynamics, Heat Transfer & Propulsion Group, Department of Aerospace Engineering, Faculty of Engineering, Universiti Putra Malaysia, 43400 Serdang, Selangor, Malaysia
[2] Aerospace Malaysia Research Centre, Faculty of Engineering, Universiti Putra Malaysia, 43400 Serdang, Selangor, Malaysia
[3] Chemical Engineering, University of Newcastle, Callaghan, NSW 2308, Australia
[4] Department of Aeronautical Engineering, Faculty of Mechanical Manufacturing Engineering, Universiti Tun Hussein Onn Malaysia, 86400 Raja, Johor, Malaysia

ABSTRACT

The purpose of this study is to investigate the design point performance of a custom engine via GasTurb software. In this study, a turbojet engine model is simulated without afterburners and limited to design point (DP) simulation at a speed of 15,000 rpm. The input data were identified from previous studies as a reference point. Parameters such as pressure ratio (PR) for the main components, the mechanical and burner efficiency, isotropic PR for compressor and turbine were used. The results compared at different levels of the condition using GasTurb-13 and GSP-11 softwares. It was found that both softwares were able to provide similar results at various conditions tested. There are small differences in the values for the fuel flow and specific fuel consumption. In addition, similar results were obtained at the baseline point. Furthermore, the heating value has a primary effect on specific fuel consumption. It was also found that the optimal thrust value was at 34.2 kN, and the best value for optimal specific fuel consumption was 20.9 g/kN.s. For heating value, Methanol and Ethanol recorded the highest value of fuel consumption because they have the highest mass fuel flow than other types of fuel, while the mass fuel flow for green diesel was lower than other fuels, so its specific fuel consumption was lesser than other fuels.

Keywords:
Alternative fuel; optimization; gasturb; gsp; on-design; aero-engine

Copyright © 2019 PENERBIT AKADEMIA BARU - All rights reserved

1. Introduction

Simulation on cost and risk are the two most important activities in the engine development phase. Meanwhile, engine health monitoring is considered very important during the operation phase [1]. One of the aspects to develop the Engine Heath Management (EHM) system is an engine simulation model [2]. There are considerable advantages of simulating the models, such as (i) to understand the performance of the gas turbine engine running on different operation conditions, (ii) to generate required data for a gas turbine engine at an intermediate stage which cannot be acquired analogy [2].

GasTurb is one of a computer-aided system developed by Dr Joachim Kurzke that enables gas turbine engine on-design performance. It equips with some features to estimate (emission, dimensions, and weight) for the engine, real-time and flight simulation, and strength analysis for

* *Corresponding author.*
E-mail address: abdrahim@upm.edu.my (Abd Rahim Abu Talib)

the integrated components. On the other hand, National Aerospace Laboratory (NLR) has developed the CAE-system which is known as GSP. GSP software able to estimate the emission and it has all the parameters and settings for each module similar to GasTurb. Both of these programmes have a simple intuitive interface [3]. The cycle parameters determine which minimizes specific fuel consumption (SFC) subject to constraints series by optimization feature which provide into GasTurb 12.

Moreover, NASA computer program Chemical Equilibrium with Applications (CEA) generated a tabulated value of the gas properties which are used in GasTurb. Fuel-to air ratio injection, the inlet to the burner of pressure and temperature, and the fuel chemical composition are affected by increasing the temperature in the burner [4]. There are two types of cycle analysis which includes; (i) parametric cycle analysis (also known as design point DP or On-design) which determines engine performance at design choice values (as pressure ratio PR for compressor), fuel performance, and specific thrust with diverse flight conditions, and limits of design parameters (such as exit temperature of the combustor), (ii) engine performance analysis or as known off-design which determines specific engine performance at throttle settings and all flight conditions [5].

The traditional scaling method is compared between the data for the design point of the original maps with a new design point to derive the scale factors [1]. The off-design point map data scale then be multiplied with the original performance maps with scale factors to obtain the scale maps [1]. In GSP simulation program, the engine performance definition is fixed at DP (Design Point) condition which it has to run before off-design and accelerate or decelerate the engine cycles because the reference parameters generated from it [2]. GSP program also allows the user to perform cycle analysis from a number of compressor maps for the aero-engine [6]. The DP calculation in the GasTurb program for the isentropic efficiency, pressure ratio PR, and mass flow of the component be similar to the original map scaling reference point [1]. The demanded engine performance is achieved when selected PR, the efficiency of the components, and maximum temperature for the cycle at the DP for the gas turbine. The demanded power is given when the airflow rate and the thermal efficiency determine at DP [7].

For the data validity, Sankar *et al*., [2] validated the results for virtual engine model with engine testbed data (Twin Spool Turbo Jet Engine) at DP because the similar engine test data were not available. Leylek *et al*., [6] was repeated the tests and error analysis to validate the data. Leylek *et al*., [6] used different methods to predict the performance for the engine components such as computational fluid dynamics (CFD) analysis, standard empirical performance models, flow codes, and mean-line. They also used GasTurb software to predict dynamic and steady-state performance for a 12-pound thrust turbojet engine and compared it with test results at 15,556 rpm/s rate.

Anosike [8] compared the DP results for engine model with OEM's (Original Equipment Manufacturer's) and compared the data against a known commercial quality natural gas with associated gas. The results were found to have small variations between simulation and OEM test which may be due to difference in natural gas qualities. Kong *et al*., [1] compared the performance analysis between GAs map, scaled map, and experimental data. Nasir [7] used a GasTurb to carry out the GT of 40.7 MW SCTS (Simple Cycle Two Shaft), and found the performance for GT drops with reduces the mas flow when the ambient temperature increase. Krishnaraj and Wessley [5] used MATLAB and GSP to perform a parametric analysis of the micro turbofan engine at different bypass ratios. Abu Talib *et al*., [9] uses GasTurb-11 to perform a simulation of performance evaluation of a small scale turbojet engine running on palm oil biodiesel blends.

The purpose of this study is to investigate the design point performance of a custom engine via GasTurb software. In this study, a turbojet engine model is simulated without afterburners and limited to design point (DP) simulation at a speed of 15,000 rpm. The input data were identified

from previous studies as a reference point. Parameters such as pressure ratio (PR) for the main components, the mechanical and burner efficiency, isotropic PR for compressor and turbine were used. The output parameters such as thrust, fuel mass flow, and SFC for various levels were presented. Furthermore, the effect of changing the fuel type based on the heating value was also investigated.

2. Simulating the engine parameters

Both GSP-11 and GasTurb-13 programmes need to determine the input parameters and identify the design point DP before simulating the off-design point for any engines. The reference model into GSP is TJET, while GasTurb-13 is using Demo_jet.CYC. The DP is used in GSP and GasTurb simulation programmes as a reference point for further analysis. Moreover, the DP simulation was carried out by control in the parameters of the component for a custom engine. **Table 1** shows the input parameters for various components of the custom engine which included the specific heat constant pressure for the compressor and turbine (C_{pc}, C_{pt}), specific heat ratio for turbine and compressor (γ_t, γ_c), turbine temperature (T_{t4}), mass flow ($\dot{m}_0$), spool speed (N), turbine and burner efficiency (η_m, η_b), pressure ratio for inlet, compressor, burner, and nozzle (π_d, π_c, π_b, π_n), compressor and polytropic turbine efficiency (e_c, e_t), and the fuel heating value (h_{PR}) [10].

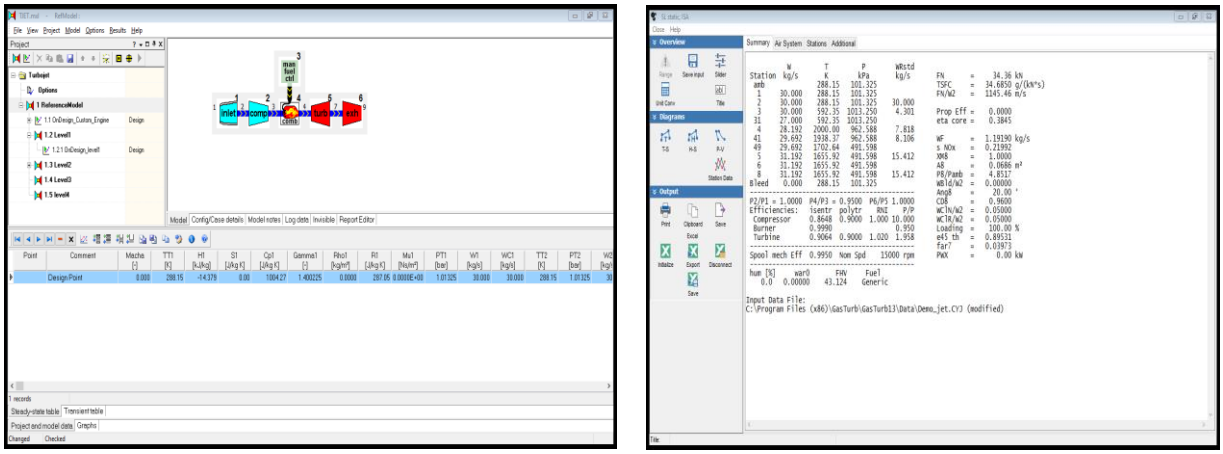
Table 1 The input data at the design point DP

Design Parameter	Units	Value	Design Parameter	Unit	Value
C_{pc}	kJ/kg.K	1.004	π_d	-	1
C_{pt}	kJ/kg.K	1.235	π_c	-	10
γ_t	-	1.4	π_b	-	0.95
γ_c	-	1.3	π_n	-	1
T_{t4}	K	1,800	P_0/P_9	-	1
$\dot{m}_0$	kg/s	30	e_c	-	0.9
N	rpm	15,000	e_t	-	0.9
η_m	-	0.99	h_{PR}	MJ/kg	42.0755
η_b	-	0.99			

The design point DP for the custom engine now can be established using different component parameters used to compare on-design performance, as shown in **Table 2**. The interfaces for each program are shown in **Fig.1**. The DP simulations at sea level static indicated that the Mach number and altitude are zero.

Table 2 The input data at the design point DP

Design Parameters	level1	level2	level3	level4
Burner Design Efficiency	0.880	0.940	0.990	0.999
Burner Pressure Ratio	0.900	0.920	0.940	0.950
Mechanical Efficiency	0.950	0.970	0.990	0.995
Burner Exit Temperature [K]	1110	1390	1780	2000
Polytr.Turbine Efficiency	0.880	0.850	0.890	0.900
Polytr.Compr.Efficiency	0.800	0.840	0.880	0.900



(a) (b)

Figure 1. (a) GSP-11 interface (b) GasTurb-13 output interface

3. Design point simulation

The same simple turbojet engine model has been simulated in both GasTurb-13 and GSP-11 software. The parameters used for the simulation using a normal JP-10 fuel for this engine are shown in **Table 2**. The results for different four levels and baseline for JP-10 fuel into GSP-11 and GasTurb-13 have been illustrated in **Table 3**, respectively. Simple turbojet engine performances at baseline were found to be similar in the two programmes with an only small variation.

Table 3. GSP-11 and GasTurb-13 software output data for JP-10 Fuel at different levels

Performance parameters	Net Thrust [kN]		Thrust Specific Fuel Consumption [g/kN.s]		Total Fuel Flow W_f_b [kg/s]	
	GSP	GasTurb	GSP	GasTurb	GSP	GasTurb
baseline	32.4965	31.3112	34.8333	32.5070	1.1323	1.0178
level1	13.3832	12.5522	32.9722	31.5075	0.4416	0.3954
level2	23.7375	22.0032	30.0000	29.0684	0.7123	0.6396
level3	31.8251	30.5857	34.6111	32.4047	1.1019	0.9911
level4	35.4383	34.2389	38.1111	35.5363	1.3513	1.2167

Fig. 2 shows that at a lower technology setting, GSP-11 calculates the impetus higher than GasTurb-13 by 6.2% for the first level. However, at high technology setting, GSP-11 calculates a 3.38% lower trend for the fourth level. This shows that the efficiency levels have a direct impact on the comparison between the calculations of ideal fuel.

Fig. 3 shows that the GSP-11 and GasTurb-13 are produced approximately fuel flow results. However, unlike thrust comparison, there are more distinct between GSP-11 and GasTurb-13. At level 1, the difference is 10.4%, but the difference in level 4 is 9.96%.

The fuel efficiency for the turbojet engine refers to the thrust specific fuel consumption which is a ratio between thrust and fuel flow rate. Therefore, the fuel consumption in the turbojet engine is higher than values calculated by GSP-11 for all levels of technology due to the high flow rate. **Fig. 4** shows that the GSP-11 has a higher SFC than the values calculated by GasTurb-13 due to the higher mass flow. The difference between GSP-11 and GasTurb-13 is 4.52% at level 1 while at level 4, the difference between them is 6.76%.

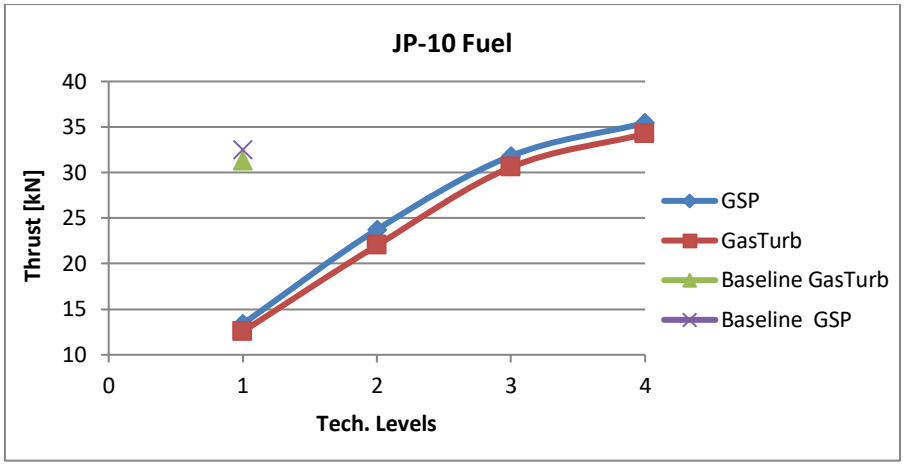


Figure 2. Thrust comparison at DP for JP-10

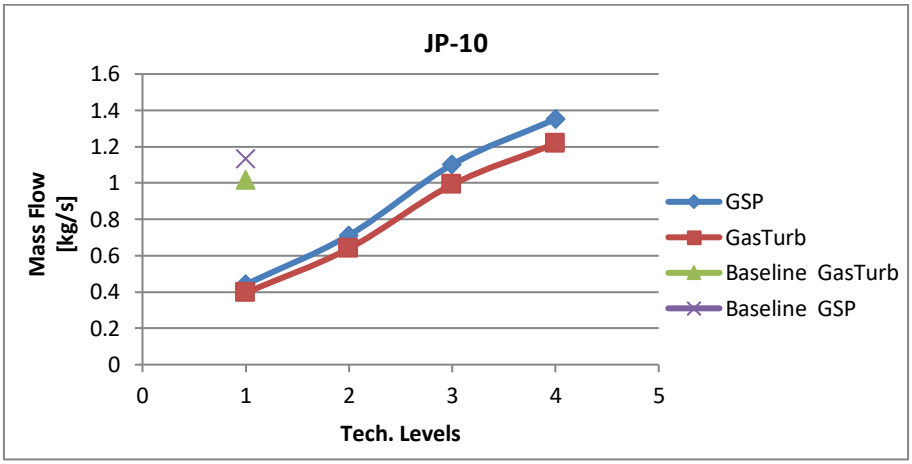


Figure 3. Mass flow comparison at DP for JP-10

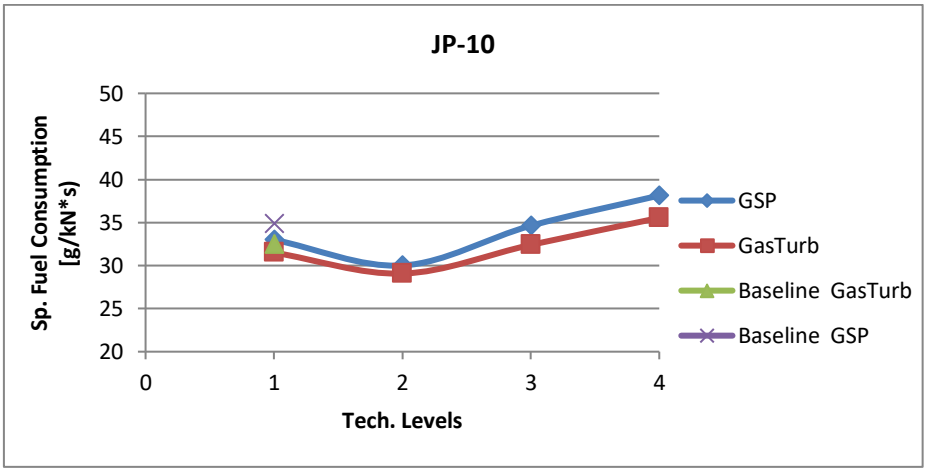


Figure 4. SFC comparison at DP for JP-10

Table 5 summarizes the design simulation results. The results between the GasTurb-13 and GSP-11 are noticeably close, indicating that the two programs on the performance of the turbojet engine with an affinity for real gas effects. The results from the GasTurb-13 shows the thrust and fuel flow rate slightly lower. As a result, GasTurb-13 produced lower fuel consumption in terms of thrust.

This is probably due to component maps that are not used for on-design analysis that resulted the differences outcome of variations in specific heat.

Table 4. Comparative DP performance of custom engine for JP-10 Fuel

Performance Parameters	GasTurb-13	GSP-11	Difference %
Thrust [KN]	31.31	32.49	3.65
Mass Flow [kg/s]	1.01	1.13	10.64
TSFC [g/KN*s]	32.50	34.84	6.71

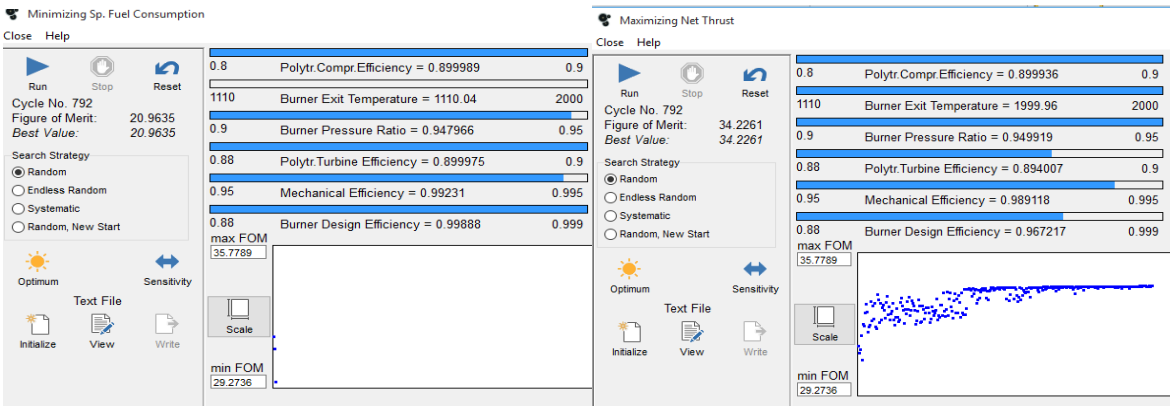
Based on the design simulations, it is clear that the two programmes follow the same trend. However, the performance of the turbojet engine is greatly amplified by the impact of different gas assumptions due to efficiency changes. It can be seen that the more significant this difference, the lower the efficiency.

4. Optimization variable

In this paper, there are four levels of technology setting used as shown in **Table 2**. This section illustrates how to optimize these four levels to get the best value for thrust and specific fuel consumption (SFC). Based on that, the GasTurb-13 was used to determine the optimum value for thrust and SFC based on the component variables in **Table 5**. Furthermore, the variables range as shown in **figure 5** as follows; Polytr. Compressor efficiency range (0.8-0.9), Polytr.Turbine efficiency (0.8-0.9), burner exist temperature (1,110-2,000K), mechanical efficiency (0.95-0.995), pressure ratio (0.9-0.95), and burner efficiency (0.88-0.999). However, the best value for SFC was 32.56 g/(kN.s) and 31.31 kN for the thrust as shown in **Table 4** before running the random strategy on the variables, but after the strategy applied on the variables, so the thrust is 34.22 kN at optimum input values as η_m, π_b, T_{t4} , e_c, and e_t are (0.9891, 0.9499, 1999.96 K, 0.8999, and 0.8940) as shown in **Column A**. As well as, the best value for SFC became 20.96 g/(kN.s) at optimum input values such as η_m is 0.9923, π_b is 0.9479, T_{t4} is 1110.03K, e_c is 0.899989 , and e_t is 0.899975 as illustrate in **Colum B**, respectively.

Table 5. The optimum values for the components

Design Parameters	A	B
Mechanical Efficiency	0.9891	0.9923
Burner Pressure Ratio	0.9499	0.9479
Burner Exit Temperature (K)	1999.96	1110.03
Polytr. Compr. Efficiency	0.8999	0.8999
Polytr. Turbine Efficiency	0.8940	0.8999
Performance parameters	**Best Thrust value**	**Best SFC value**
Net Thrust (kN)	34.2261	18.4428
Sp. Fuel Consumption g/(kN.s)	36.7158	20.9635
NOx Severity Index	0.2199	0.2199
Total Fuel Flow (kg/s)	1.2566	0.3866



(a) (b)

Figure 5. (a) Minimizing the Specific Fuel Consumption (b) Maximize Net Thurst

5. Fuel properties simulation

In order to study the mechanism of the effect of fuel property such as the calorific value of fuel on the engine performance, so the thrust, SFC, and flow of fuel are presented with the heating value of different fuels taken from previous studies. Furthermore, Kurzke [11] mentioned that most of the hydrocarbons (which have the chemical composition C_nH_n) such as Kerosen and JP-10 (chemical composition $C_{10}H_{16}$) and other fuels used to run the gas turbine. Fuel properties are essential for the design and operation of alternative fuel combustion, such as caloric value, humidity, and oxygen [12]. The heating value (HV) of biomass is one of the parameters to compare the difference between fuels [13]. Based on that, further simulation was conducted on the custom engine using GasTurb-13 with the same parameters in **Table 1,** but the heating value has been changed based on different types of fuels used, as shown in **Table 6**. The GasTurb-13 simulation was performed using the same fuel flow rate, and the design parameters under on-design condition, so the heat energy is emitted from various types of fuel due to varying the calorific value of different fuels can be evaluated.

Table 6. Heating value for different fuels

References	Fuel	Fuel Heating Value (MJ/kg)
[14]	Diesel fuel	41.59
	PO5	37.40
	PO10	38.72
[15]	Jet A-1	43.20
	HEFA R-8	44.10
	Green Diesel	43.70
[16]	kerosene	43.10
	Ethanol	26.81
	Methanol	19.92
[17]	Jatropha SPK	44.30
	Camelina SPK	44.00
[18]	WCO-based green diesel	40.80

Fig. 6 illustrated the effect of heating values for each fuel on thrust, SFC, and fuel flow. It can be seen that the waste cooking oil (WCO)-based green diesel has the lowest TSFC but having highest thrust compared to the other fuels because of the oxygen content is zero. In contrast, ethanol and methanol have the highest TSFC because the caloric value is lower than the other fuels. In contrast, the Jet-A1, HFFA R-8, Green Diesel, Kerosene, Jatropha SPK, and Camelina SPK have a similar thrust, SFC, and mass flow values.

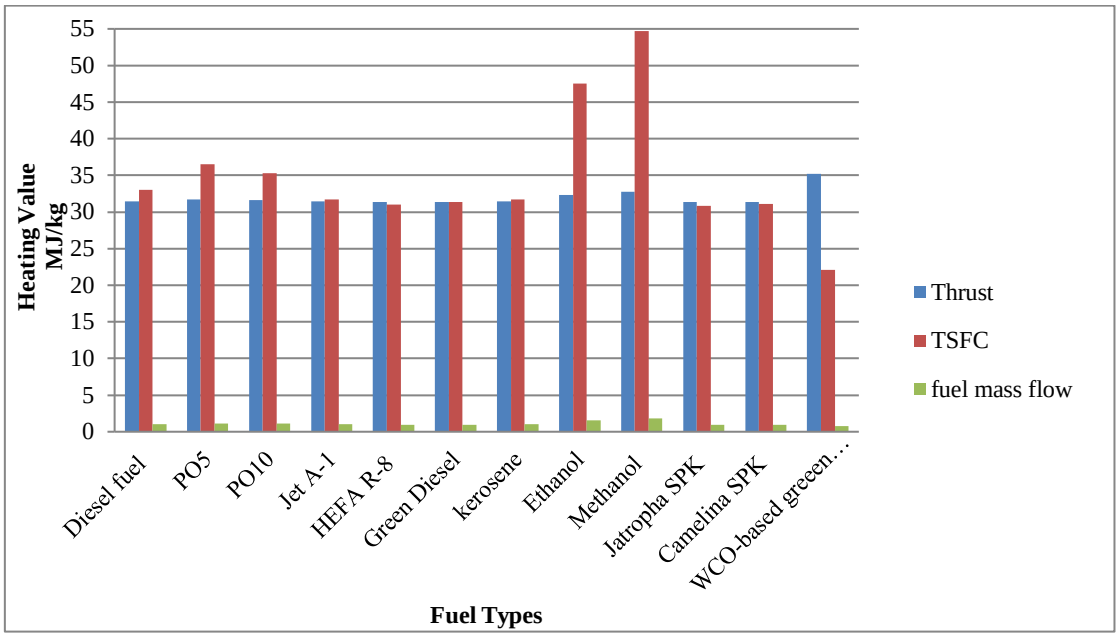


Figure 6. Effect type of fuel on the engine performance

Compared to previous studies, the results obtained in this study correspond well to the other researchers [14-17]. Zhou *et al*., [16] used GSP software to find the effect of heating value on the engine performance. It was found that the lower calorific value of methanol and ethanol compared to kerosene led to the reduction of engine thrust (FN), and therefore the specific fuel consumption (TSFC) is increased and to maintain the performance of the engine itself must increase the overall flow rate of fuel. However, Gaspar *et al*., [15] confirmed that specific fuel consumption was saved by 4% when alternative fuels were used to improve engine performance compared to conventional jet fuel. Besides, Tobib *et al*., [14] mentioned that palm oil blends led to increasing BSFC (Break Specific Fuel Consumption) on HCCI-DI engine compared to diesel fuel within the experimental data. Also, Yuons [17] found that the fuel consumption was reduced by 3% and the fuel flow rate was 2.7% compared with Jet-A; this is seen in **Fig. 6**. As for waste cooking oil based green diesel, there is no research on studying its impact on fuel engines.

6. Conclusions

GSP-11 and GasTurb-13 are the most popular software for engine performance on-design simulation. At on-design calculations, the thrust obtained were almost the same for both programmes at all levels. However, there are apparent differences in fuel mass flow and specific fuel consumption. The reasons for these differences due to the fuel properties in each program, for example, the JP-10 heating value is 42.10 MJ/kg in GSP, but it is 42.07 MJ/kg in GasTurb-13. Furthermore, the changed in fuel types did not show a big difference in the results.

Noticed at optimum values that the temperature has to increase with increasing on the other parameters to get the best value for thrust, but the best value for specific fuel consumption (SFC) needs to decrease the temperature with increasing of the other parameters. Moreover, when fixed the efficiency for mechanical and burner with decrease the temperature as shown in level 3, so the thrust and SFC were similar to baseline values.

The main factor affecting engine performance in general and fuel consumption, in particular, is the caloric value of fuel in the same line it affects the amount of fuel mass flow. Based on that, the best type of fuel which is studied in this paper was WCO-based green diesel.

As a future work, this paper did not use the off-design operation for this type of engine. Besides, comparing between GSP-11 and GasTurb-13 need more studies by applying different cases such as simulating turbojet or turbofan engines with afterburning or without and applying different conditions and study the differences between them.

Acknowledgment
The authors thanks to the Ministry of Education Malaysia for the financial support under the Fundamental Research Grant no. (FRGS No. TK07/UPM/02/2 No.5540072).

References

[1] C. Kong, S. Kho, and J. Ki, "Component map generation of a gas turbine using genetic algorithms," *Journal of Engineering for Gas Turbines and Power,* vol. 128, pp. 92-96, 2006.
[2] B. Sankar, T. Subramanian, B. Shah, V. Vanam, S. Jana, S. Ramamurthy*, et al.*, "Aero-thermodynamic modelling and gas path simulation for a twin spool turbo jet engine," in *ASME 2013 Gas Turbine India Conference*, 2013, pp. V001T06A008-V001T06A008.
[3] V. Kuz'michev, Y.A. Ostapyuk, A.Y. Tkachenko, I. Krupenich, and E. Filinov, "Comparative analysis of the computer-aided systems of gas turbine engine designing," *International Journal of Mechanical Engineering and Robotics Research,* vol. 6, pp. 28-35, 2017.
[4] A.R. Byerley, K.P. Rouser, and D. O. O'Dowd, "Exploring GasTurb 12 for Supplementary Use on an Introductory Propulsion Design Project," in *ASME Turbo Expo 2017: Turbomachinery Technical Conference and Exposition*, 2017.
[5] R. Krishnaraj and G.J. J. Wessley, "Performance Analysis of a Micro Turbofan Engine using Matlab and GSP Intended for the Propulsion of Male UAVs," *International Journal of Pure and Applied Mathematics,* vol. 118, pp. 157-163, 2018.
[6] Z. Leylek, W.S. Anderson, G. Rowlinson, and N. Smith, "An investigation into performance modeling of a small gas turbine engine," in *ASME Turbo Expo 2013: Turbine Technical Conference and Exposition*, 2013, pp. V05AT23A007-V05AT23A007.
[7] A. Nasir, "Design and Off-Design Operation and Performance Analysis of a Gas Turbine," *Proceedings of the World Congress on Engineering,* vol. II, 2018.
[8] N. Anosike, A. El-Suleiman, and P. Pilidis, "Associated Gas Utilization Using Gas Turbine Engine, Performance Implication—Nigerian Case Study," *Energy and Power Engineering,* vol. 8, p. 137, 2016.
[9] A.R Abu Talib, E. Gires, and M. Ahmad, "Performance evaluation of a small-scale turbojet engine running on palm oil biodiesel blends," *Journal of Fuels,* vol. 2014, 2014.
[10] J.D. Mattingly, *Elements of propulsion: gas turbines and rockets*: American Institute of Aeronautics and Astronautics, 2006.
[11] J. Kurzke, "GasTurb details 5," *An utility for GasTurb,* vol. 11, 2007.
[12] H. Maas, A. Schamel, C. Weber, and U. Kramer, "Review of combustion engine efficiency improvements and the role of e-fuels," in *Internationaler Motorenkongress 2016*, ed: Springer, 2016, pp. 463-483.
[13] A. Demirbas, "Relationships between heating value and lignin, moisture, ash and extractive contents of biomass fuels," *Energy exploration & exploitation,* vol. 20, pp. 105-111, 2002.
[14] H.M. Tobib, H. Rostam, M. A. Mossa, A. A. Hairuddin, and M. Noor, "The performance of an HCCI-DI engine fuelled with palm oil-based biodiesel," in *IOP Conference Series: Materials Science and Engineering*, 2019, p. 012079.

[15] R. Gaspar and J. Sousa, "Impact of alternative fuels on the operational and environmental performance of a small turbofan engine," *Energy conversion and management,* vol. 130, pp. 81-90, 2016.
[16] L. Zhou, Z.W. Liu, and Z.X. Wang, "Numerical study of influence of biofuels on the combustion characteristics and performance of aircraft engine system," *Applied Thermal Engineering,* vol. 91, pp. 399-407, 2015.
[17] S.M. Yunos, M.F. Abdul Ghafir, and A. Ab Wahab, "Evaluation on alternative jet fuels application and their impact on airportenvironmental charges," *ARPN Journal of Engineering and Applied Sciences,* vol. 27, p. 0, 2016.
[18] G.A. Alsultan, N. Asikin-Mijan, H. Lee, A.S. Albazzaz, and Y. Taufiq-Yap, "Deoxygenation of waste cooking to renewable diesel over walnut shell-derived nanorode activated carbon supported CaO-La_2O_3 catalyst," *Energy conversion and management,* vol. 151, pp. 311-323, 2017.

Penerbit Akademia Baru

Engineering Science and Technology Conference Proceedings

Journal homepage: www.akademiabaru.com/EST.html

Ferroconvection in an Anisotropic Porous Medium with Variable Gravity

Open Access

Nor Halawati Senin[1], Nor Fadzillah Mohd Mokhtar[1,2,*], Mohamad Hasan Abdul Sathar[1,2]

[1] Laboratory of Computational Sciences and Mathematical Physics, Institute for Mathematical Research (INSPEM), Universiti Putra Malaysia, Malaysia.
[2] Centre of Foundation Studies for Agricultural Science, Universiti Putra Malaysia, Malaysia.

ABSTRACT

A linear stability assessment was performed to study the impact of internal heating and variable gravity in an anisotropic porous medium of a ferrofluid layer system on the onset of Benard-Marangoni convection. The system is heated from below with both the lower and upper limits are considered as completely insulated to the disturbance of the temperature. The eigenvalue problem is solved by using regular perturbation technique to obtain the critical Marangoni number and also the critical thermal Rayleigh number. It is noted that the increase of value anisotropic permeability, Darcy number and also magnetic number will enhance the convection of the system while the increasing values of anisotropic thermal diffusivity will help to stabilize the system.

Keywords:
Ferrofluid; anisotropic; variable gravity

Copyright © 2019 PENERBIT AKADEMIA BARU - All rights reserved

1. Introduction

Ferrofluid or also known as magnetic fluid is a non-electric carrier fluid that includes small particles of strong ferromagnetic materials (Raju [1]). Kaiser and Miskolczy [2] state that ferrofluid has a special feature which is it can maintain it fluid properties in the existence of magnetic field but the magnetic properties of ferrofluid can be affected by the composition, distribution and also volume concentration. Previously ferrofluid is known in the rocket fuel by NASA and currently ferrofluid been used in a various field such as in electric devices, mechanical engineering, medical applications, optics, etc. There have been tremendous studies on the convection of ferrofluid. Stiles and Kagan [3] examined the instability of ferroconvection in a strong magnetic field. The impact of the vertical magnetic field in ferrofluid was researched by Hennenberg et al. [4]. Mokhtar and Arifin [5] had the impacts of feedback control in the ferrofluid layer system. Laroze et al. [6] employed chaos study in ferrofluid. Laroze et al. [7] explored the instability of viscoelastic ferrofluid. Recently, the impact of magnetic field dependent viscosity in a ferrofluid was proved by Prakash et al. [8].

Marangoni convection can be understood as convection that considered surface tension in the study. Nield [9] propose the idea of combination between surface tension forces and buoyancy forces study or usually name as Marangoni-Benard convection. The studied of Marangoni convection with a deformable surface had been done by McCaughan and Bedir [10]. In Marangoni-Benard convection, Hennenberg et al. [11] recorded a porous medium with Darcy law. Rudraiah

* *Corresponding author.*
E-mail address: norfadzillah.mokhtar@gmail.com (Nor Fadzillah Mohd Mokhtar)

and Prasad [12] had examined Brinkman's model in a porous medium. Saghir et al. [13] investigated dual-layer studies on the onset of Marangoni convection. Shivakumara et al. [14] employed Brinkman–Forchheimer–Lapwood extended Darcy model on the onset of Marangoni convection. Feedback control effect with a deformable surface in a variable viscosity fluid had been studied by Arifin and Abidin [15]. Marangoni convection of porous medium with a Biot number had been studied by Zhao et al. [16]. Dual-layer fluid with the impact of internal heating in an upper boundary that is set to be deformable on the Marangoni-Benard convection had been demonstrated by Mokhtar et al. [17].

The study of convection that involving porous medium had been done widely, all the porous medium studied previously taking into consideration isotropic porous medium since the assumptions that there is no preferred direction involve. Degan and Vasseurt [18] demonstrated the convection of an anisotropic medium that oblique to gravity. Sekar et al. [19] investigated the convection of ferrofluid in an anisotropic porous medium. Marangoni-Benard convection problem in the anisotropic porous medium had been examined by Shivakumara et al. [20]. The study of anisotropic with modified Brinkman Darcy flow model had been employed by Nanjundappa et al. [21] in a ferrofluid system. Shivakumara et al. [22] study the impact of internal heating in an anisotropic medium in Marangoni-Benard convection. Bhadauria [23] also study the anisotropic porous medium with the effect of internal heating on the onset of double-diffusive convection. Capone et al. [24] studied an anisotropic and non-homogeneous porous medium in a linear and non-linear stability study. Soret-driven convection in an anisotropic porous ferrofluid layer system had been studied by Sekar et al. [25]. Recently Sun et al. [26] studied the impacts of an external magnetic field in a ferrofluid while Zarifah et al. [27] examined the temperature profile in a binary fluid with anisotropic porous medium.

The ideas of gravity are well known in the theoretical investigation, a lot of studies related to variable gravity had been done before. S.Rionero and B.Straughan [28] investigated the combined effect of internal heating and variable gravity in convection of a porous medium. The effect variable gravity and internal heating with additionally inclined temperature gradient in a porous medium had been done by Alex et al. [29]. Chand [30] investigated rotating Maxwell of a visco-elastic porous medium with the additional effect of variable gravity. Bala and Chand [31] employed Brinkman porous medium with variable gravity of ferrofluid. Combination effect of rotating and variable gravity of porous nanofluid layer had been reported by Chand et al. [32]. Varshney [33] investigated on the stability on the convection of porous medium with the effect of gravity.

The aim of this paper is to investigate the impact of the variable gravity in Marangoni-Benard convection of an anisotropic porous medium. We assumed that the layer of ferrofluid is heated from below and that the conditions of the lower-upper boundary are considered to be a rigid-free boundary. Using a regular perturbation technique will solve the resulting eigenvalue problem.

2. Methodology

We considered a horizontal ferrofluid layer system is heated from below as shown in Fig. 1. The lower boundary is set to be rigid while the upper boundary is set to be free. Both of the boundaries are fixed to be constant but the temperature of the lower bound is higher compared to the upper bound. The ferrofluid layer scheme is applied by gravitational force $h(0,0,-h(z))$ where $h(z) = (1 + \lambda)h$ and λ are the parameter of variable gravity.

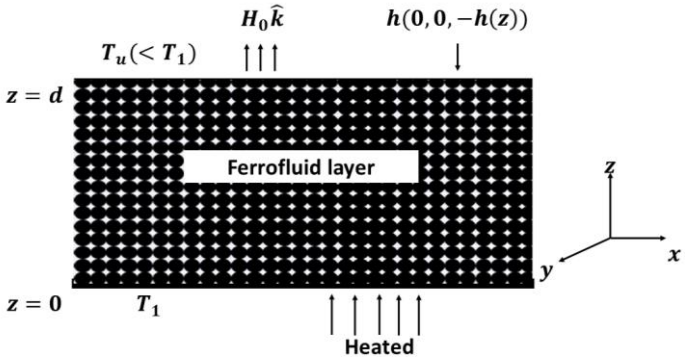


Fig. 1. Model of an anisotropic porous medium in ferrofluid layer system.

By referring to Nanjundappa and Vijay Kumar [34] and also Bala and Chand [31] the problem can be written in the following form after going through the process of non-dimensionalizing and normal mode

$$\left[(D^2 - a^2)^2 - Da^{-1}\left(\frac{1}{\xi}D^2 - a^2\right)\right]W - a^2Rm(1+\lambda)(D\phi - \theta) - a^2Rt(1+\lambda)\theta = 0, \quad (1)$$

$$D^2\theta - \eta a^2\theta - (1 - M_2)W = 0, \quad (2)$$

$$D^2\phi - a^2M_3\phi - D\theta = 0, \quad (3)$$

with the boundary condition

$$W = DW = D\theta = \phi = 0 \quad \text{at } z = 0, \quad (4)$$

$$W = D\theta = D\phi = D^2W + Ma\, a^2\theta = 0 \quad \text{at } z = 1, \quad (5)$$

where

$D = \frac{d}{dz}$,

λ is the gravity parameter,

a^2 is the wave number,

$Da = \frac{k_h}{d^2}$ is the Darcy number,

$\xi = \frac{k_h}{k_v}$ is an anisotropic permeability,

$Rm = Rt \cdot M_1 = \frac{\mu_0 K_1^2 \beta}{(1+\chi)\alpha_t \rho_0 g}$ is the magnetic Rayleigh number,

$Rt = \frac{\alpha_t g \beta d^4}{\nu\kappa A}$ is the thermal Rayleigh number,

$\eta = \frac{\kappa_h}{\kappa_v}$ is an anisotropic effective thermal diffusivity,

$M_2 = \frac{\mu_0 T_0 K_1^2}{1+\chi}$ is the magnetic parameter,

$M_3 = \frac{1+\frac{M_0}{H_0}}{1+\chi}$ is the nonlinearity of the ferrofluid,

$Ma = \frac{\sigma_T \Delta T d}{\mu\kappa}$ is the Marangoni number.

By referring to Finlayson [35], M_2 will not affect the Benard-Marangoni convection since the value of it will be approximated to zero because the value too small which is 10^{-6}. To solve (1) till (3) with the boundary conditions (4) and (5), regular perturbation method will be used. The variables are in following the form

$$(W, \theta, \phi) = (W_0, \theta_0, \phi_0) + a^2(W_1, \theta_1, \phi_1) + \cdots . \quad (6)$$

By substituting equation (6) into (1) till (5) we will get the zero*th* equation as follows

$$D^4 W_0 - \left(\frac{1}{Da\,\xi} D^2 W_0\right) = 0, \quad (7)$$

$$D^2\theta_0 - W_0 = 0, \quad (8)$$

$$D^2\phi_0 - D\theta_0 = 0, \quad (9)$$

with the boundary conditions

$$W_0 = DW_0 = \theta_0 = \phi_0 = 0 \qquad \text{at } z = 0, \quad (10)$$

$$W_0 = D^2 W_0 = D\phi_0 = D\theta_0 = 0 \qquad \text{at } z = 1. \quad (11)$$

The solution to the zero*th* order equation (7) till (9) by using boundary conditions (10) and (11) are as follow:

$$W_0 = 0, \theta_0 = 1, \phi_0 = 0. \quad (12)$$

By substituting (12) we will get the first order equations as follow

$$D^4 W_1 - \left(\frac{1}{Da\,\xi} D^2 W_1\right) + Rm\,(1+\lambda) - Rt(1+\lambda) = 0, \quad (13)$$

$$D^2\theta_1 - \eta - W_1 = 0, \quad (14)$$

$$D^2\phi_1 - D\theta_1 = 0, \quad (15)$$

with the boundary conditions

$$W_1 = DW_1 = D\theta_1 = \phi_1 = 0 \qquad \text{at } z = 0, \quad (16)$$

$$W_1 = \phi_1 = D\theta_1 = D^2 W_1 + Ma = 0 \qquad \text{at } z = 1. \quad (17)$$

The equation (13) to (17) will be solved by using MAPLE. The equation of Ma_c will be generate in term of $M_1, Rt, \eta, \lambda, \xi$ and Da.

3. Results

In this document, with the presence of variable gravity, the resulting eigenvalue problem of Marangoni-Benard convection in an anisotropic ferrofluid layer was analytically solved using regular perturbation technique. The boundaries are regarded rigid-free and insulating with a linear stability assessment. The selected values for the gravity parameter suggested by Bala and Chand [31]. The outcomes collected are described graphically in Figures (2)-(8) to show the effect of different parameters on the critical number of Marangoni, Ma_c and thermal Rayleigh, Rt_c. From the study, it revealed that M_3 has a no significant contribution toward the convection of the system and this finding coincides with a previous study from Nanjundappa et al. [36].

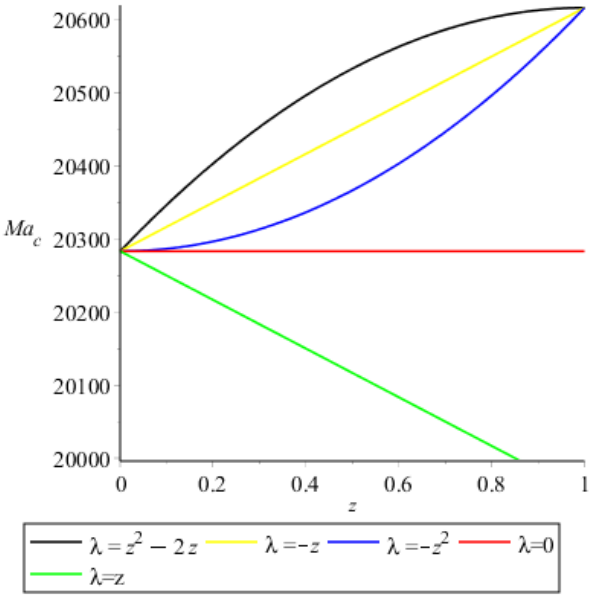


Fig. 2. Stability curve for different value of gravity

Fig. 2 demonstrated the impact of various gravity parameter on the onset of Benard-Marangoni convection with $Rt = 1000$, $M_1 = 1, \eta = 1, \xi = 0.1$ and $Da = 0.001$. The figure clearly shows that the decreasing gravity parameter which is $\lambda = z^2 - 2z$, $\lambda = -z$ and $\lambda = -z^2$ have stabilizing effect. It contrasts with increasing gravity parameter $\lambda = z$ that promotes the onset of Marangoni convection. The result obtained is in good agreement with the previous study from Bala and Chand [23].

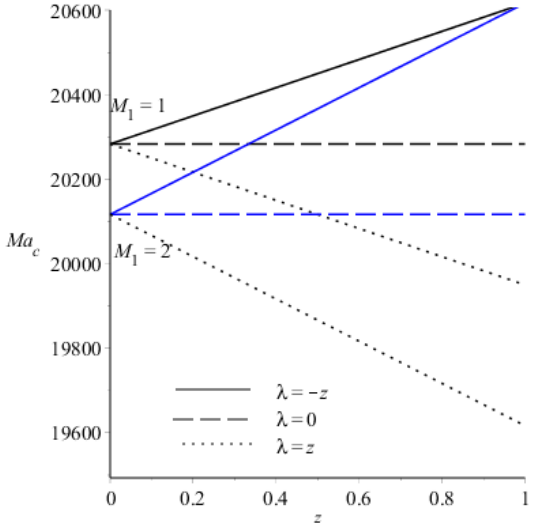


Fig. 3. Stability curve for different value of gravity and M_1

The impact of M_1 on variable gravity on the onset of Marangoni-Benard convection was noted in Fig. 3 The increment of M_1 will drop the values of Ma_c and destabilize the system. This situation happens because the increasing of M_1 will lead to increment of destabilize magnetic force in the system Nanjundappa et al. [36]. The combination of variable gravity parameter $\lambda = -z$ and M_1 is found to delay the convection while the combination of $\lambda = z$ and M_1 will enhance the onset of Marangoni-Benard convection.

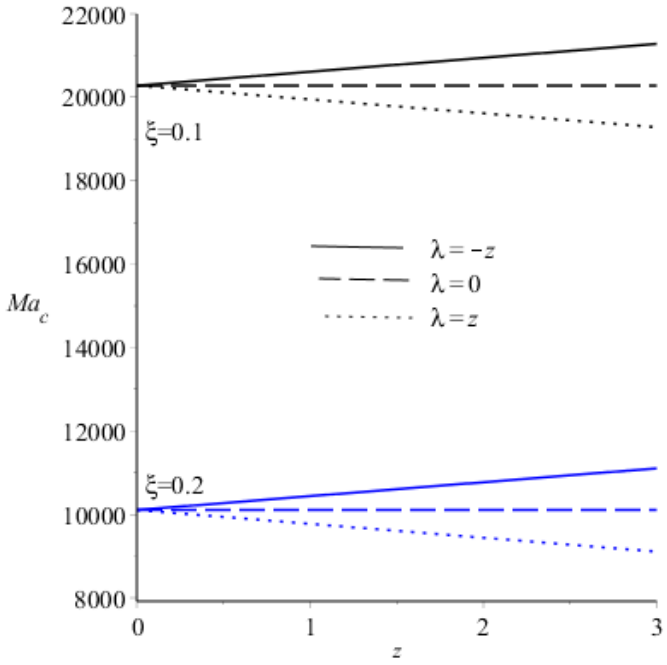


Fig. 4. Stability curve for different value of ξ.

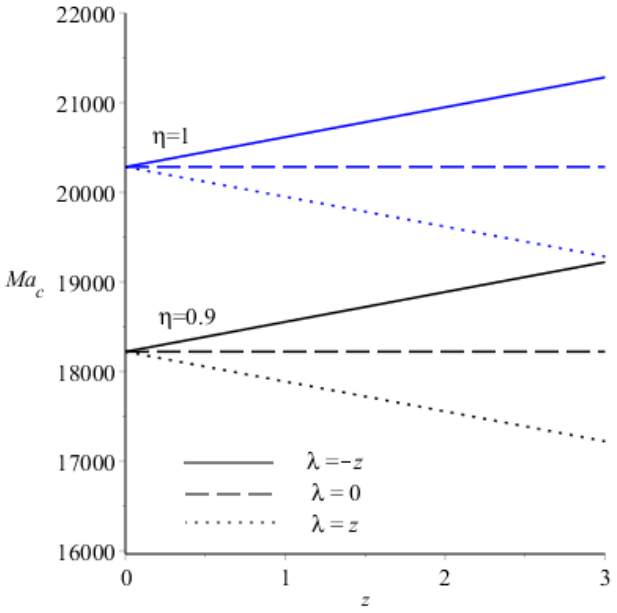


Fig. 5. Stability curve for different value of η.

The impact of two important parameters in anisotropic which is ξ and η are depicted in Figures 4 and 5 respectively. For both figures the value of other parameters are $Rt = 1000, M_1 = 1$ and $Da = 0.001$. In Fig. 4, the Ma_c values fall as the ξ parameter increases and thus encourages the convection rate in the ferrofluid layer system of an anisotropic porous medium. The reason behind this situation is the increasing of ξ will encouraged the fluid movement in the horizontal direction due to the large horizontal permeability. As an outcome the convection process in an anisotropic medium become unstable (Shivakumara et al. [20]). It is contrast with the effect of η in Fig. 5, the increasing of η lead to elevate the critical Marangoni number and delay the convection. This finding coincides with the previous study from Shivakumara et al. [22].

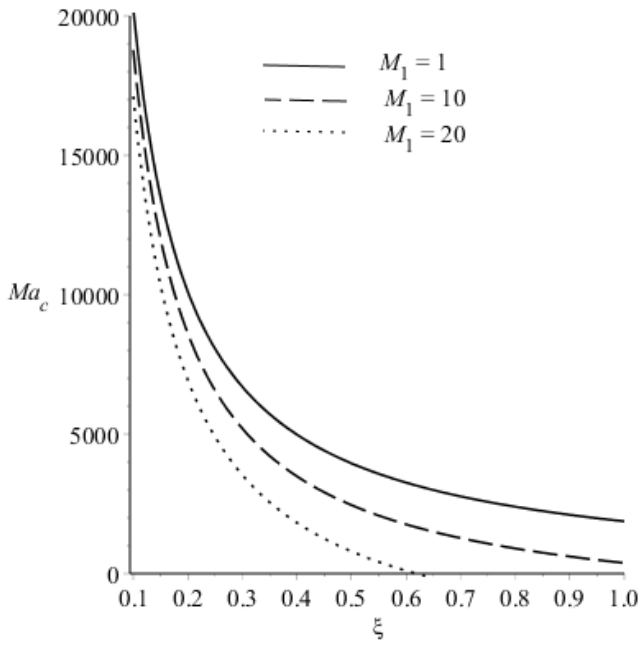


Fig. 6. Impact of M_1 on Ma_c against ξ.

The combination effects of M_1 and ξ are illustrated in Fig. 6 when $Rt = 1000, Da = 0.001, \lambda = 0$ and $\eta = 1$. From the graph, it can be seen that boost of both parameters M_1 and ξ cause a deterioration of the Ma_c values. This indicates the simultaneous effects of M_1 and ξ will promotes the convection of Marangoni-Benard in a ferrofluid layer system.

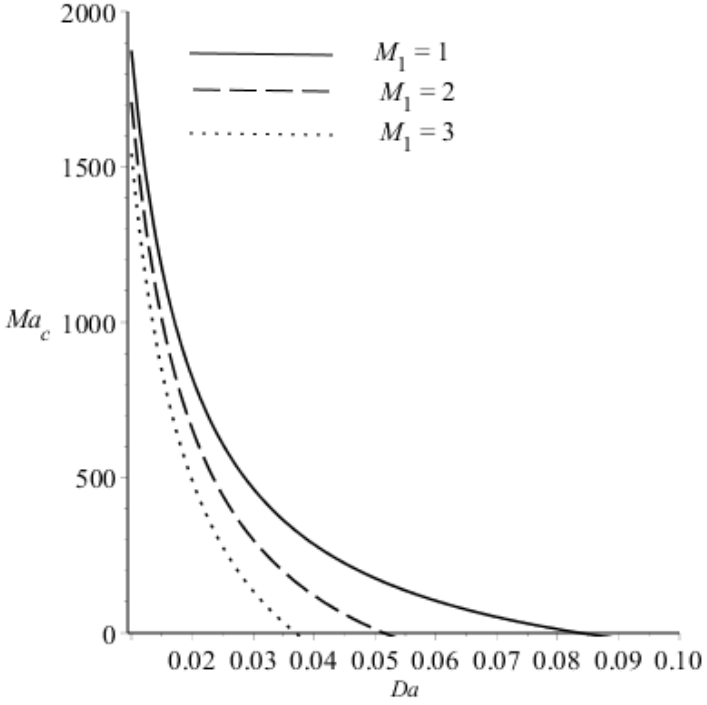


Fig. 7. Impact of M_1 on Ma_c against Da.

The impact of M_1 on Da is demonstrate in Fig. 7. Other parameters are set $Rt = 1000, \lambda = 0, \eta = 1$ and $\xi = 0.1$. As reported previously in Fig. 3, the escalation of M_1 will destabilize the system. This figure also shows the behaviour of Da on Ma_c. It can be seen clearly that the

increasing of Da cause the decline of Ma_c values. It indicates that the increasing of Da will promotes the convection. The same result also reported in Nanjundappa and Vijay Kumar [34].

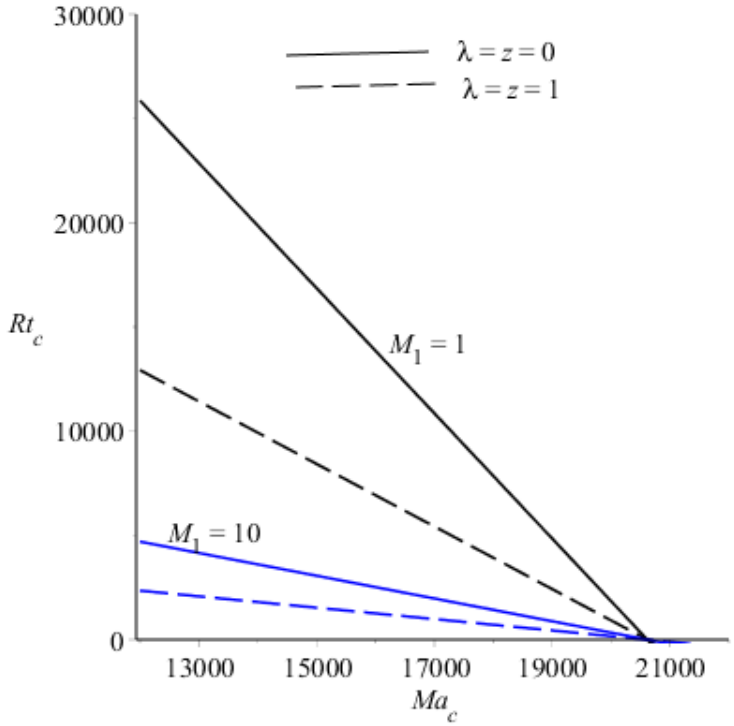


Fig. 8. Impact of M_1 on Rt_c against Ma_c.

Fig. 8 shows the response of M_1 on Rt_c against Ma_c for different value of λ at $M_1 = 1, \eta = 1, \xi = 0.1$ and $Da = 0.00\ 1$. From the graph, it can be seen clearly that the increasing of M_1 and Ma_c will lead to compress of Rt_c. M_1 value will be merged into a fixed value of Ma which is in this study the value is recorded at $Ma_c = 20606.3854$. This situation happens to all M_1 considered and when $Rt = 0$ shows that the Rt did not affect the convection process Nanjundappa et al. [36].

4. Conclusions

The theoretical investigation into the effects of variable gravity on the onset of Marangoni-Benard convection in an anisotropic ferrofluid layer system was conducted. We can conclude that the increasing values of M_1, Da and ξ will enhance the convection of a ferrofluid layer system while the increasing of η will help to stabilize the system. For the variable gravity, decreasing gravity parameter are found to help in delaying the convection contrast with increasing gravity parameter that promotes the convection.

Acknowledgement
We would like to thank Universiti Putra Malaysia for all the equipment and financial support. The present research was partially supported by the Putra Grant - Putra Graduate Initiative (IPS)-GP-IPS/2018/9642900.

References

[1] Raju, K. (2018). "Effect of temperature dependent viscosity on ferrothermohaline convection saturating an anisotropic porous medium with Soret effect using the Galerkin technique." *International Journal of Heat and Technology* 36(2): 439–446.

[2] Kaiser, R. and Miskolczy, G. (1970). "Some Applications of Ferrofluid Magnetic Colloids." *IEEE Transactions on Magnetics* 6(3): 694–698.

[3] Stiles, P.J. and Kagan, M. (1990). "Thermoconvective instability of a ferrofluid in a strong magnetic field." *Journal of Colloid And Interface Science* 134(2): 435–448.

[4] Hennenberg, M., Weyssow, B., Slavtchev, S., Alexandrov, V., and Desaive, T. (2005). "Rayleigh-Marangoni-Benard instability of a ferrofluid layer in a vertical magnetic field." *Journal of Magnetism and Magnetic Materials* 289: 268–271.

[5] Mokhtar, N.F.M. and Arifin, N.M. (2012). "Benard-Marangoni Ferroconvection With Feedback Control." *International Journal of Modern Physics: Conference Series* 9: 552–559.

[6] Laroze, D., Siddheshwar, P.G., and Pleiner, H. (2013). "Chaotic convection in a ferrofluid." *Commun Nonlinear Sci Numer Simulat* 18: 2436–2447.

[7] Laroze, D., Martinez-Mardones, J., and Pleiner, H. (2013). "Benard-Marangoni instability in a viscoelastic ferrofluid." *European Physical Journal: Special Topics* 219(1): 71–80.

[8] Prakash, J., Kumar, R., and Kumari, K. (2017). "Thermal Convection in a Ferromagnetic Fluid Layer with Magnetic Field Dependent Viscosity: A Correction Applied" *Studia Geotechnica et Mechanica* 39(3): 39–46.

[9] Nield, D.A. (1964). "Surface tension and buoyancy effects in cellular convection." *Journal of Fluid Mechanics* 19(3): 341–352.

[10] McCaughan, F. and Bedir, H. (1994). "Marangoni Convection With a Deformable Surface." *Journal of Applied Mechanics* 61: 681–688.

[11] Hennenberg, M., Saghir, M.Z., Rednikov, A., and Legros, J.C. (1997). "Porous Media and the Benard-Marangoni Problem" *Transport in Porous Media* 27(3): 327–355.

[12] Rudraiah, N. and Prasad, V. (1998). "Effect of Brinkman boundary layer on the onset of Marangoni convection in a fluid-saturated porous layer" *Acta Mechanica* 127(1-4): 235–246.

[13] Saghir, M.Z., Comi, P., and Mehrvar, M. (2002). "Effects of interaction between Rayleigh and Marangoni convection in superposed fluid and porous layers." *International Journal of Thermal Sciences* 41(3): 207–215.

[14] Shivakumara, I.S., Nanjundappa, C.E., and Chavaraddi, K.B. (2009). "Darcy-Benard-Marangoni convection in porous media." *International Journal of Heat and Mass Transfer* 52(11-12): 2815–2823.

[15] Arifin, N.M. and Abidin, N.H.Z. (2009). "Marangoni convection in a variable viscosity fluid layer with feedback control." *WSEAS Transactions on Mathematics* 8(8): 373–382.

[16] Zhao, S.C., Liu, Q.S., Liu, R., Nguyen-Thi, H., and Billia, B. (2010). "Thermal effects on Rayleigh-Marangoni-Benard instability in a system of superposed fluid and porous layers." *International Journal of Heat and Mass Transfer* 53(15-16): 2951–2954.

[17] Mokhtar, N., Arifin, N., Nazar, R., Ismail, F., and Suleiman, M. (2011). "Effect of internal heat generation on Marangoni convection in a superposed fluid-porous layer with deformable free surface." *International Journal of the Physical Sciences* 6(23): 5550–5563.

[18] Degan, G. and Vasseurt, P. (1995), "Convective Heat Transfer In A Vertical Anisotropic Porous Layer." *International Journal Heat Mass transfer* 38(11): 1975–1987.

[19] Sekar, R., Vaidyanathan, G., and Ramanathan, A. (1996). "Ferroconvection In An Anisotropic Porous Medium." *International Journal of Engineering Science* 34(4): 399–405.

[20] Shivakumara, I.S., Lee, J., and Chavaraddi, K.B. (2011). "Onset Of Surface Tension Driven Convection In A Fluid Layer Overlying A Layer Of An Anisotropic Porous Medium." *International Journal of Heat and Mass Transfer* 54(4): 994–1001.

[21] Nanjundappa, C.E., Shivakumara, I.S., Lee, J., and Ravisha, M. (2011). "The Onset Of Brinkman Ferroconvection In An Anisotropic Porous Medium." *International Journal of Engineering Science* 46(6): 497–508.

[22] Shivakumara, I.S., Suma, S.P., Indira, R., and Gangadharaiah, Y.H. (2012). "Effect of Internal Heat Generation on the Onset of Marangoni Convection in a Fluid Layer Overlying a Layer of an Anisotropic Porous Medium." *Transport in Porous Media* 92(3): 727–743.

[23] Bhadauria, B.S. (2012). "Double-Diffusive Convection in a Saturated Anisotropic Porous Layer with Internal Heat Source." *Transport in Porous Media* 92: 299–320.

[24] Capone, F., Gentile, M., and Hill, A.A. (2012). "Convection Problems in Anisotropic Porous Media with Nonhomogeneous Porosity and Thermal Diffusivity." *Acta Appl Math* 122: 85–91.

[25] Sekar, R., Raju, K., and Vasanthakumari, R. (2013). "A linear analytical study of Soret-driven ferrothermohaline convection in an anisotropic porous medium." *Journal of Magnetism and Magnetic Materials* 331: 122–128.
[26] Sun, X.h., Massoudi, M., Aubry, N., Chen, Z.h., and Wu, W.T. (2019). "Natural Convection and Anisotropic Heat Transfer in a Ferronanofluid Under Magnetic Field." *International Journal of Heat and Mass Transfer* 133: 581–595.
[27] Zarifah, N., Hamid, A., Fadzillah, N., Mokhtar, M., Arifin, N., and Hasan, M. (2019). "Effect of Nonlinear Temperature Profile on Thermal Convection in a Binary Fluid Saturated an Anisotropic Porous Medium." *Journal of Advanced Research in Fluid Mechanics and Thermal Sciences* 1: 43–58.
[28] S.Rionero and B.Straughan. (1990). "Convection In a Porous Medium with internal heat source and variable gravity." *Int. J. Engng Sci* 28(6): 497–503.
[29] Alex, S.M., Patil, P.R., and Venkatakrishnan, K.S. (2001). "Variable gravity effects on thermal instability in a porous medium with internal heat source and inclined temperature gradient." *Fluid Dynamics Research* 29: 1–6.
[30] Chand, R. (2013). "Thermal Instability Of Rotating Maxwell Visco-Elastic Fluid With Variable Gravity In Porous Medium." *Journal of the Indian Mathematical Society* 80(1): 30–38.
[31] Bala, A. and Chand, R. (2015) "Variable Gravity Effect on the Thermal Instability of Ferrofluid in a Brinkman Porous Medium." *International Journal of Astronomy, Astrophysics and Space Science*, 2(5): 39–44.
[32] Chand, R., Rana, G.C., and Kango, S.K. (2015). "Effect of variable gravity on thermal instability of rotating nanofluid in porous medium." *FME Transactions* 43(1): 62–69.
[33] Varshney, A.K. (2017). "Thermal Stability Of A Fluid Layer In A Variable Gravitational Field In Porous." *Journal of Advanced Computing and Communication Technologies* 5(3): 55–60.
[34] Nanjundappa, C.E., and B. Vijay Kumar. (2013). "Penetrative Ferroconvection Via Internal Heating In A Ferrofluid Anisotropic Porous Medium." *Magnetohydrodynamisc* 49 (3): 441–47.
[35] Finlayson, B.A. (1970). "Convective instability of ferromagnetic fluids." *Journal of Fluid Mechanics* 40(4): 753–767.
[36] Nanjundappa, C.E., Shivakumara, I.S., and Arunkumar, R. (2011). "Onset of benard-marangoni ferroconvection with internal heat generation." *Microgravity Science and Technology* 23(1): 29–39.

Penerbit Akademia Baru

Engineering Science and Technology
Conference Proceedings

Journal homepage: www.akademiabaru.com/EST.html

Unsteady MHD Mixed Convective Flow of Buongiorno's Nanofluid in a Lid-Driven Cavity with Heat Generation and Chemical Reaction Effects

Open Access

Nor Raihan Mohamad Asimoni[1], Nurul Farahain Mohammad[1,*], Abdul Rahman Mohd Kasim[2], Sharidan Shafie[3]

[1] Department of Computational and Theoretical Sciences, Kulliyyah of Science, International Islamic University Malaysia, 25200 Kuantan, Pahang, Malaysia
[2] Centre for Mathematical Sciences, College of Computing and Applied Sciences, Universiti Malaysia Pahang, 26300, Gambang, Pahang, Malaysia
[3] Department of Mathematical Sciences, Faculty of Science, Universiti Teknologi Malaysia, 81310 UTM Johor Bahru, Johor, Malaysia

ABSTRACT

The unsteady two-dimensional laminar mixed convective flow of a nanofluid in a lid-driven cavity with the presence of magnetic field, heat generation and chemical reaction effects is investigated. Buongiorno's nanofluid model, which comprises the effects of Brownian motion and thermophoresis, is considered in this study. The dimensional governing equations in vector form are transformed into dimensionless governing equations. Then, the dimensionless equations are solved numerically by finite element method (FEM) using automated solution technique which is FEniCS. The numerical solutions obtained are velocity, temperature, and nanoparticles volume fraction profiles. These profiles are presented and discussed to illustrate the effects of different physical parameters on the solution.

Keywords:
MHD; nanofluid; Buongiorno; cavity;
FEniCS

Copyright © 2019 PENERBIT AKADEMIA BARU - All rights reserved

1. Introduction

Nanofluid has been used to improve the efficiency of heat transfer performance in many applications [1]. Buongiorno's model [2] and Tiwari and Das' model [3] are the most popular mathematical models used to represent the behaviour of nanofluid. This research focuses on nanofluid using Buongiorno's model which encompasses Brownian motion and thermophoresis effects. There are several papers that investigated steady mixed convective flow in a lid-driven cavity filled with nanofluid using Buongiorno's model [4,5]. Sheremet et al. [4] stated that by increasing Brownian motion and thermophoresis effects, no significant changes on streamlines, isotherms and isoconcentrations However, Yu et al. [5] who studied nanofluid in incline cavity said that those effects give significant changes if extreme values of heat and mass transfer rate is applied.

The study of magnetohydrodynamics (MHD) has been considered recently in the problem of convective flow filled with nanofluid in cavity [6,7]. Elshehabey et al. [6] examined the MHD effect in lid-driven cavity with sinusoidal temperature distribution on both vertical walls while Alsabery et al.

* *Corresponding author.*
E-mail address: farahain@iium.edu.my (Nurul Farahain Mohammad)

[7] investigated nanofluid in a doubled lid-driven cavity. Both of them considered inclined magnetic field effect and found that velocity of fluid decrease as Hartmann number increases.

Besides, the effects of chemical reaction and heat generation or absorption effects in nanofluid is significant to study since there exist the interaction of nanoparticles and base fluid. There are existing studies heat generation/absorption effect in mixed convective flow of nanofluid using Tiwari and Das' model [8,9] and Buongiorno's model [10]. Based on the Tiwari and Das' model, Rashad et al [8] demonstrated MHD mixed convective flow in a porous lid-driven cavity filled with nanofluid and showed that increment in heat generation/absorption parameter increases the velocity and temperature distributions. Furthermore, Hussain et al. [9] focused on MHD mixed convective flow of nanofluid in double lid-driven cavity and discovered an enhancement of heat generation/absorption parameter can increase the heat transfer. Meanwhile, based on Buongiorno's model, Shekar et al. [10] found that local Nusselt number and skin friction decrease with the increasing of heat generation /absorption parameter in the case of natural convective flow of nanofluid filled in a porous square cavity.

Despite all of the previously mentioned research works, the effects of magnetic field, heat generation/absorption and chemical reaction on time dependent mixed convective flow of nanofluid using Buongiorno's mathematical model in a lid-driven cavity has not been considered yet. Thus, we solved this problem numerically by finite element method using automated solution technique.

In this paper, we discretized the problem using splitting scheme. This scheme is chosen as an effective way to compute time dependent incompressible fluid flow problems by solving velocity and pressure separately. There are a number of splitting schemes. Among them are Chorin's projection scheme [11], the incremental pressure correction scheme (IPCS) [12] and consistent splitting scheme (CSS)[13]. There are existing papers that successfully solved time dependent convective heat transfer using splitting scheme in cavity. Wong [14] solved mixed convection in lid driven cavity using CSS. Meanwhile, Górecki & Szumbarski [15] performed unconditionally stable splitting scheme to solve free convection in square cavity. Therefore, in this study, the problem is solved using automated solution technique which is FEniCS [16] by finite element method with Chorin's projection scheme.

2. Methodology

The unsteady two-dimensional MHD mixed convective flow of Buongiorno's nanofluid in a lid-driven cavity is studied by considering heat generation/absorption and chemical reaction effects. Let Ω be a bounded domain. The flow of configuration is shown through Fig. 1.

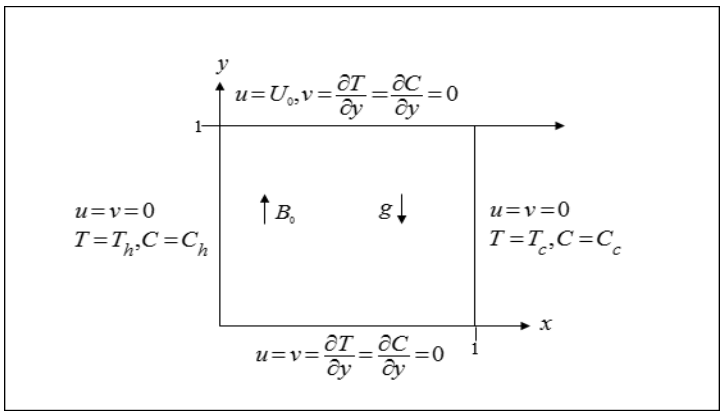


Fig. 1 Flow configuration with $\Omega=[0,1]\times[0,1]$

Following [2,17], the governing equations for this problem are:

Continuity Equation for Nanofluid:

$$\nabla \cdot \mathbf{u} = 0 \tag{1}$$

Continuity Equation for Nanoparticles:

$$\frac{\partial C}{\partial t} + \mathbf{u} \cdot \nabla C = D_B \nabla^2 C + \left(\frac{D_T}{T_\infty} \right) \nabla^2 T + \kappa_0 \left(C - C_\infty \right) \tag{2}$$

Momentum Equation:

$$\frac{\partial \mathbf{u}}{\partial t} + \rho_f \left(\mathbf{u} \cdot \nabla \right) \mathbf{u} = \mu \nabla^2 \mathbf{u} - \nabla p - \sigma B_0{}^2 \mathbf{u} + \left[\left(\rho_p - \rho_f \right) (C - C_\infty) + (1 - C_\infty) \rho_f \beta \left(T - T_\infty \right) \right] \mathbf{g} \tag{3}$$

Energy Equation:

$$\frac{\partial T}{\partial t} + \mathbf{u} \cdot \nabla T = \alpha \nabla^2 T + \tau \left[D_B \nabla C \cdot \nabla T + \left(\frac{D_T}{T_\infty} \right) \nabla T \cdot \nabla T \right] + \frac{Q_0}{\left(c\rho \right)_f} (T - T_\infty) \tag{4}$$

where $\mathbf{u} = (u, v)$ is the fluid velocity, C is the nanoparticle volume fraction, D_B is the Brownian diffusion coefficient, D_T is the thermophoretic diffusion coefficient, T is the fluid temperature, κ_0 is the chemical reaction rate, σ is the electrical conductivity of the fluid, B_0 is the magnetic field strength, ρ_f is the density of the base fluid, ρ_p is the density of the nanoparticles and $\mathbf{g} = \left(0, g_y \right)$ is gravity acceleration applied to the flow, $\alpha = \dfrac{k}{\left(c\rho \right)_f}$ with k is thermal conductivity of nanofluid and c_f is the heat capacitance of the base fluid, $\tau = \dfrac{\left(c\rho \right)_p}{\left(c\rho \right)_f}$ with c_p is the heat capacitance of the nanoparticles and Q_0 is the dimensional heat generation/absorption coefficient.

The governing equations are subjected to initial and boundary conditions:

$$\begin{aligned}
t = 0:&\ u = 0, \quad v = 0, \quad C = 0, \quad T = 0, && \text{for all } x, y \\
t > 0:&\ u = 0, \quad v = 0, \quad C = C_h, \quad T = T_h, && \text{for } x = 0,\ 0 \le y \le 1 \\
&\ u = 0, \quad v = 0, \quad C = C_c, \quad T = T_c, && \text{for } x = 1,\ 0 \le y \le 1 \\
&\ u = 0, \quad v = 0, \quad \frac{\partial C}{\partial y} = 0, \quad \frac{\partial T}{\partial y} = 0, && \text{for } y = 0,\ 0 \le x \le 1 \\
&\ u = U_0, \quad v = 0, \quad \frac{\partial C}{\partial y} = 0, \quad \frac{\partial T}{\partial y} = 0, && \text{for } y = 1,\ 0 \le x \le 1
\end{aligned}$$

Next, Equations (1) – (4) are transformed to non-dimensional form, using the following dimensionless parameters [2, 18]:

$$\mathbf{x}=\frac{\bar{\mathbf{x}}}{L},\ \mathbf{u}=\frac{\bar{\mathbf{u}}}{U},\ p=\frac{\bar{p}}{\rho U^2},\ \nabla=L\bar{\nabla},\ \theta=\frac{T-T_\infty}{T_w-T_\infty},\phi=\frac{C-C_\infty}{C_w-C_\infty},\ \ t=\frac{U}{L}\bar{t}$$

The dimensionless governing equations can be written as follows:

$$\nabla\cdot\mathbf{u}=0 \tag{5}$$

$$\frac{\partial\phi}{\partial t}+\mathbf{u}\cdot\nabla\phi=\frac{1}{\mathrm{Re}}\frac{1}{Sc}\left(\nabla^2\phi+\frac{Nt}{Nb}\nabla^2\theta\right)+\kappa\phi \tag{6}$$

$$\frac{\partial\mathbf{u}}{\partial t}+(\mathbf{u}\cdot\nabla)\mathbf{u}=\frac{1}{\mathrm{Re}}\nabla^2\mathbf{u}-\nabla p-M\mathbf{u}+Ri\left(Nr\phi+\theta\right) \tag{7}$$

$$\frac{\partial\theta}{\partial t}+\mathbf{u}\cdot\nabla\theta=\frac{1}{\mathrm{Re}}\frac{1}{\mathrm{Pr}}\nabla^2\theta+Nb\nabla\phi\cdot\nabla\theta+Nt\nabla\theta\cdot\nabla\theta+Q\theta \tag{8}$$

with corresponding dimensionless parameters defined as [18]:

$$\mathrm{Re}=\frac{\rho L^nU^{2-n}}{K},\mathrm{Pr}=\frac{K}{\rho\alpha U^{1-n}L^{n-1}},Sc=\frac{K}{\rho D_BU^{1-n}L^{n-1}},Nr=\frac{\left(\rho-\rho_{f\infty}\right)g\left(C_w-C_\infty\right)}{\rho\left(1-C_\infty\right)\beta g\left(T_w-T_\infty\right)},Nt=\frac{\tau D_T\left(T_w-T_\infty\right)}{T_\infty UL},$$
$$Nb=\frac{\tau D_B\left(C_w-C_\infty\right)}{UL},Ri=\frac{L}{U^2}\left(1-C_\infty\right)\beta g\left(T_w-T_\infty\right),M=\frac{\sigma B^2L}{\rho U},\kappa=\frac{L}{U}\kappa_0,Q=\frac{Q_0L}{c\rho U}, \tag{9}$$

where Re is Reynolds number, Pr is Prandtl number, Sc is Schmidt number where $Sc=Le\,\mathrm{Pr}$ with Le is Lewis number, Nr is buoyancy ratio, Nt is thermophoresis parameter, Nb is Brownian motion parameter, Ri is Richardson number, M is magnetic parameter, and κ is dimensionless chemical reaction parameter. It is called destructive reaction if $\kappa>0$ and generative reaction if $\kappa<0$. Chemical reaction involves endothermic and exothermic process where heat is generated or absorbed [19]. It is called heat generation if $Q>0$ and heat absorption if $Q<0$ where Q is dimensionless heat generation/absorption parameter. All dimensionless equations are subjected to dimensionless initial and boundary conditions:

$$\begin{aligned}
&t=0:\ u=0,\quad v=0,\quad \phi=0,\quad \theta=0,\quad && \text{for all } x,y\\
&t>0:\ u=0,\quad v=0,\quad \phi=1,\quad \theta=1,\quad && \text{for } x=0,\ 0\le y\le 1\\
&\qquad u=0,\quad v=0,\quad \phi=0,\quad \theta=0,\quad && \text{for } x=1,\ 0\le y\le 1\\
&\qquad u=0,\quad v=0,\quad \frac{\partial\phi}{\partial y}=0,\quad \frac{\partial\theta}{\partial y}=0,\quad && \text{for } y=0,\ 0\le x\le 1\\
&\qquad u=U_0,\ v=0,\quad \frac{\partial\phi}{\partial y}=0,\quad \frac{\partial\theta}{\partial y}=0,\quad && \text{for } y=1,\ 0\le x\le 1
\end{aligned}$$

To solve this time-dependent problem, we use Chorin's projection scheme due to smallest errors obtained for the problem of cavity using FEniCS [20]. Backward Euler scheme is used for the time derivatives. Following Kleanthous and Gorder [21], equations (5) – (8) can be written as following steps.

Step 1: We start by solving the intermediate velocity $\mathbf{u}$ by ignoring the pressure such that

$$\frac{\hat{\mathbf{u}}-\mathbf{u}^n}{\Delta t}+\left(\mathbf{u}^n\cdot\nabla\right)\mathbf{u}^n=\frac{1}{\mathrm{Re}}\nabla^2\hat{\mathbf{u}}-M\mathbf{u}^n+Ri\left(Nr\phi^n+\theta^n\right) \tag{10}$$

Step 2: Then, we compute p^{n+1} such that

$$\frac{\mathbf{u}^{n+1}-\hat{\mathbf{u}}}{\Delta t}=-\nabla p^{n+1} \tag{11}$$

Step 3: After that, applying $\nabla\cdot$ to equation (11) and $\nabla\cdot\mathbf{u}^{n+1}=0$, we have

$$\frac{1}{\Delta t}\nabla\cdot\hat{\mathbf{u}}=\nabla^2 p^{n+1} \tag{12}$$

Step 4: Now, we compute the corrected velocity $\mathbf{u}^{n+1}$ such that

$$\mathbf{u}^{n+1}=\hat{\mathbf{u}}-\Delta t\nabla p^{n+1} \tag{13}$$

Step 5: Since we obtain the velocity, thus we can compute temperature such that

$$\frac{\theta^{n+1}-\theta^n}{\Delta t}+\left(\mathbf{u}^{n+1}\cdot\nabla\right)\theta^{n+1}=\frac{1}{\mathrm{Re}}\frac{1}{\mathrm{Pr}}\nabla^2\theta^{n+1}+Nb\nabla\phi^n\cdot\nabla\theta^{n+1}+Nt\nabla\theta^n\cdot\nabla\theta^{n+1}+Q\theta^n \tag{14}$$

Step 6: Finally, we solve nanoparticle volume fraction such that

$$\frac{\phi^{n+1}-\phi^n}{\Delta t}+\left(\mathbf{u}^{n+1}\cdot\nabla\right)\phi^{n+1}=\frac{1}{\mathrm{Re}}\frac{1}{Sc}\left(\nabla^2\phi^{n+1}+\frac{Nt}{Nb}\nabla^2\theta^{n+1}\right)+\kappa\phi^n \tag{15}$$

Next, variational form is constructed to solve this problem using finite element method. We use Galerkin weighted residual approach for the discretization of governing equations. Taylor Hood element is considered to obtain the mesh of the domain for this problem where V is continuous quadratic polynomial function and Q is continuous linear polynomial function. Meanwhile, continuous linear polynomial function L is used for the continuity equation for nanoparticles and heat transfer equation. Equations (10) – (15) are multiplied by the test functions and integrated over the domain $\Omega=\left[0,1\right]\times\left[0,1\right]$. We have $\mathbf{u},p,\theta,\phi$ as functions and $\mathbf{v},q,s,r$ as test functions such that $\mathbf{u},\mathbf{v}\in V,\ p,q\in Q,\ \theta,s\in L$ and $\phi,r\in L$.

Step 1: First, we multiply (10) with test function $\mathbf{v}$. We apply integration by part and Gauss divergence theorem for second order derivatives $\nabla^2\mathbf{u}^{n+1}$.

$$\int_{\Omega} \frac{\hat{\mathbf{u}}-\mathbf{u}^n}{\Delta t}\cdot\mathbf{v}+\left(\mathbf{u}^n\cdot\nabla\right)\mathbf{u}^n\cdot\mathbf{v}=-\frac{1}{\mathrm{Re}}\nabla\hat{\mathbf{u}}\cdot\nabla\mathbf{v}-M\mathbf{u}^n\cdot\mathbf{v}+RiNr\phi^n\cdot\mathbf{v}+Ri\theta^n\cdot\mathbf{v} \tag{16}$$

Step 2: After that,we multiply (11) by a test function q.

$$\int_{\Omega}\left(\frac{\mathbf{u}^{n+1}-\hat{\mathbf{u}}}{\Delta t}\right)q=-\left(\nabla p^{n+1}\right)q \tag{17}$$

Step 3: Then, we multiply corrected velocity $\mathbf{u}^{n+1}$ in Equation (13) with test function $\mathbf{v}$.

$$\int_{\Omega}\mathbf{u}^{n+1}\cdot\mathbf{v}=\hat{\mathbf{u}}\cdot\mathbf{v}-\Delta t\nabla p^{n+1}\cdot\mathbf{v} \tag{18}$$

Step 4: Next, we multiply (14) with test function s. We apply integration by part and Gauss divergence theorem for second order derivatives $\nabla^2\theta^{n+1}$.

$$\int_{\Omega}\left(\frac{\theta^{n+1}-\theta^n}{\Delta t}\right)s+\left(\mathbf{u}^{n+1}\cdot\nabla\right)\theta^{n+1}s=-\frac{1}{\mathrm{Re}}\frac{1}{\mathrm{Pr}}\nabla\theta^{n+1}\cdot\nabla s+Nb\nabla\phi^n\cdot\nabla\theta^{n+1}s+Nt\nabla\theta^n\cdot\nabla\theta^{n+1}s+Q\theta^n s \tag{19}$$

Step 5: Lastly, we multiply (15) with test function r and integration by part and Gauss divergence theorem for second order derivatives $\nabla^2\phi^{n+1}$ is applied.

$$\int_{\Omega}\left(\frac{\phi^{n+1}-\phi^n}{\Delta t}\right)r+\left(\mathbf{u}^{n+1}\cdot\nabla\right)\phi^{n+1}r=-\frac{1}{\mathrm{Re}}\frac{1}{Sc}\nabla\phi^{n+1}\cdot\nabla r-\frac{1}{\mathrm{Re}}\frac{1}{Sc}\frac{Nt}{Nb}\nabla\theta^{n+1}\cdot\nabla r+\kappa\phi^n r \tag{20}$$

3. Results

In this section, we present mixed convective flow in a lid-driven cavity that is filled with nanofluid by considering magnetic field, chemical reaction and heat generation/absorption effects. Equations (16) – (20) are solved numerically using FEniCS and the post-processing of solutions obtained is interpreted using matplotlib in Python. The dimensionless parameters $\mathrm{Pr}=0.71, \mathrm{Re}=10, Ri=1, Le=1$ and $Nb=Nt=Nr=0.1$ are fixed throughout the computation. The time step $\Delta t=0.1$ is used with 100 steps and all the numerical results are completed at $t_f=10$. We demonstrate velocity, temperature and nanoparticle volume fraction profiles at four cases which are:

1) different magnetic parameters $(M=0,2,5)$
2) different heat generation/absorption parameters $(Q=-0.3,0.2,0.3)$
3) chemical reaction parameters $(\kappa=-1.0,-0.5,0.3)$

The present code is validated by the results obtained with [22] on the mixed convective flow of Newtonian fluid in a lid-driven cavity and considered isothermal top moving lid and isothermal bottom unmoving lid.

Table 1 Comparison of present velocity at the middle of the cavity for different Re ($Gr = 100, \mathrm{Pr} = 0.71, dt = 0.01$)

	Iwatsu et al. [21]	Present
	$\mathrm{Re} = 100$	
$u_{\min}$	-0.2037	-0.21014
$u_{\max}$	1.0000	1.00000
$v_{\min}$	-0.2448	-0.24855
$v_{\max}$	0.1699	0.17469
	$\mathrm{Re} = 400$	
$u_{\min}$	-0.3197	-0.31975
$u_{\max}$	1.0000	1.00000
$v_{\min}$	-0.4459	-0.44222
$v_{\max}$	0.2955	0.29445

The grid independence test has been conducted and the results are presented in Table 2. It is shown that grid size of 128×128 gives insignificant difference with grid size of 256×256. Hence, we use 128×128 grid size to execute all results.

Table 2 Grid Independence Test ($\mathrm{Re} = 100, Gr = 10000, \mathrm{Pr} = 0.71, M = 0, T = 40$)

	64×64	128×128	256×256
$u_{\min}$	-0.26273	-0.26458	-0.26499
s $u_{\max}$	1.00000	1.00000	1.00000
$v_{\min}$	-0.39840	-0.40129	-0.40214
$v_{\max}$	0.32302	0.32539	0.32620

Fig. 2 – 3 show the effects of magnetic parameter on the velocity, temperature and nanoparticle volume fraction profiles at constant $Q = 0.1$ and $\kappa = 0.1$. The circular pattern of velocity profiles in Fig. 2a shows the movement of the fluid clockwise and the longer vector arrow represents the faster fluid motion occurred. As M increases, the motion of upper wall fluid decreases as presented by the length of the vector arrow. This happens because magnetic parameter causes the Lorentz force to reduce the fluid motion. Besides, decreasing of the fluid movement could slightly enhance the temperature of the fluid and decline the nanoparticle volume fraction, as observed in Fig. 3(b)-(c).

Besides, Fig. 4 – 5 present the fluid velocity, temperature and nanoparticle volume fraction profiles in the presence of heat generation/absorption effects at constant $M = 5$ and $\kappa = 0.1$. Fig.

4b displays the pattern of temperature fluid and shows higher temperature on the left wall than right wall. By adding the heat generation/absorption parameter Q, kinetic energy of the fluid particles increases. This phenomenon lead to the movement of higher fluid temperature moves to the low temperature. Thus, it increases the temperature and velocity of the fluid. However, nanoparticle volume fraction shows different trend where it decreases as Q increases.

The influence of chemical reaction parameter on fluid velocity, temperature and nanoparticle volume fraction at $M = 5$ and $Q = 0.1$ is illustrated in Fig. 6 – 7 . Fig. 6c demonstrates the pattern of nanoparticle volume fraction and shows higher concentration on the left wall than right wall. The increment in chemical reaction parameter lead to enhancement in fluid concentration causes the movement of the nanoparticles from high concentration areas to low ones. Thus, velocity of the fluid slight increases as κ increases. Meanwhile, no essential effects occurred on temperature profile.

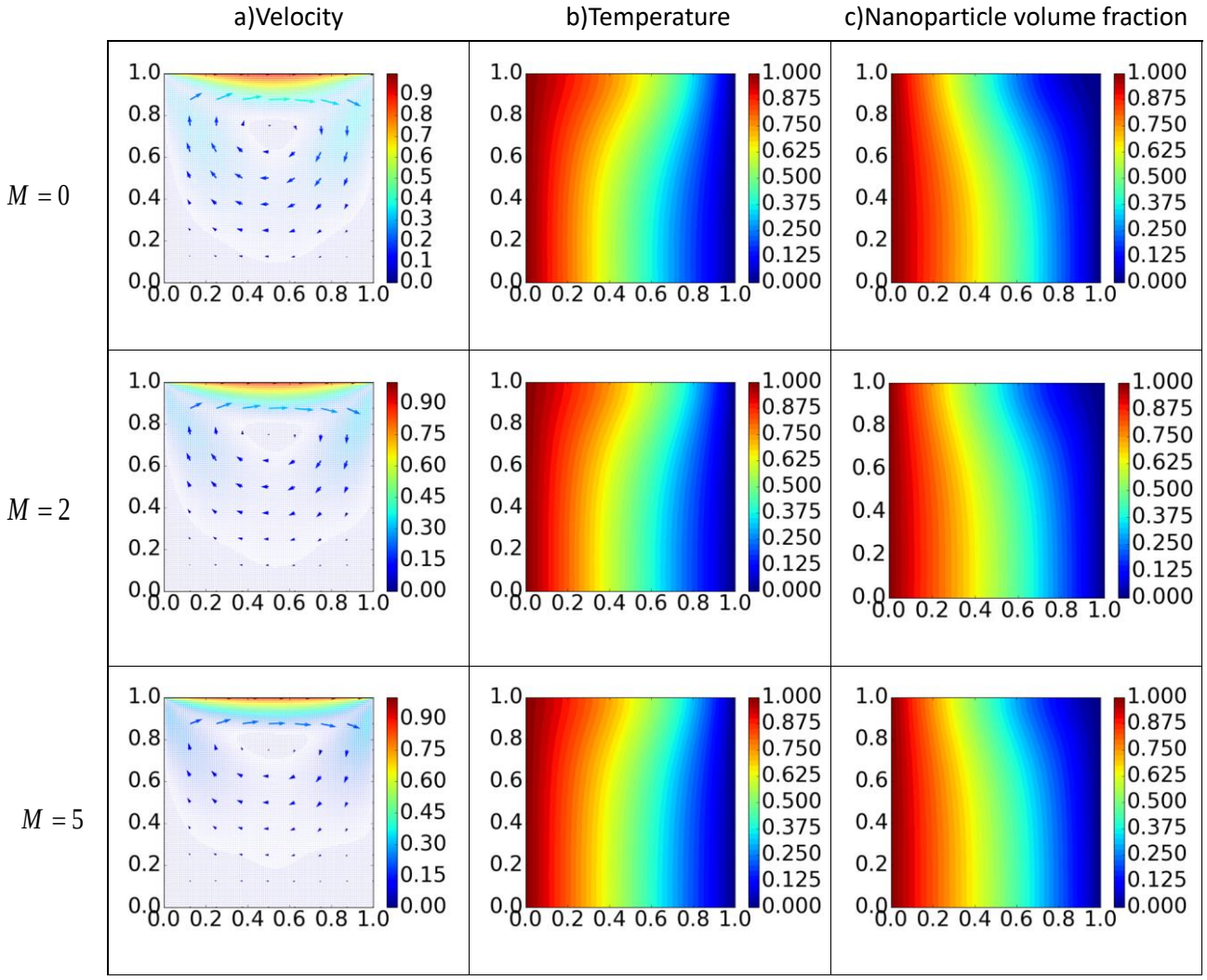
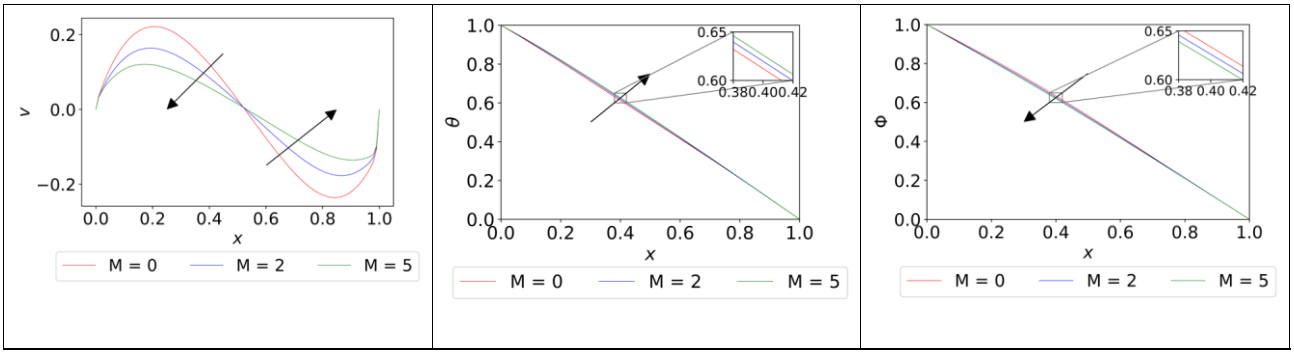


Fig. 2 Effect of magnetic parameter M on velocity, temperature and nanoparticle volume fraction profiles at $Ri = Le = 1, \Pr = 0.71, Nb = Nt = Nr = Q = \kappa = 0.1$



a)Velocity b)Temperature c)Nanoparticle volume fraction

Fig. 3 Effect of magnetic parameter M on velocity, temperature and nanoparticle volume fraction profiles in the middle of cavity $(y = 0.5)$ at $Ri = Le = 1, \Pr = 0.71, Nb = Nt = Nr = Q = \kappa = 0.1$

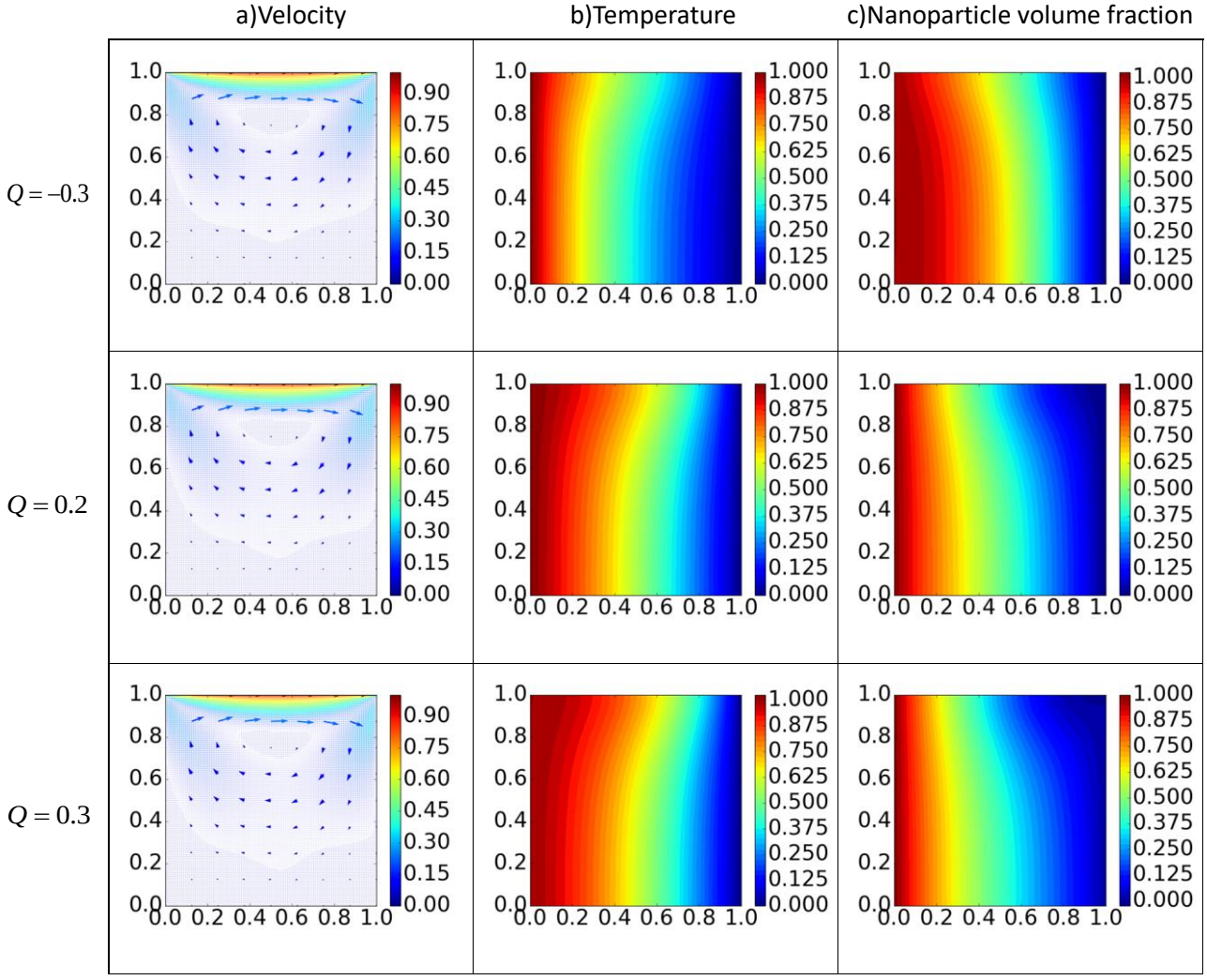
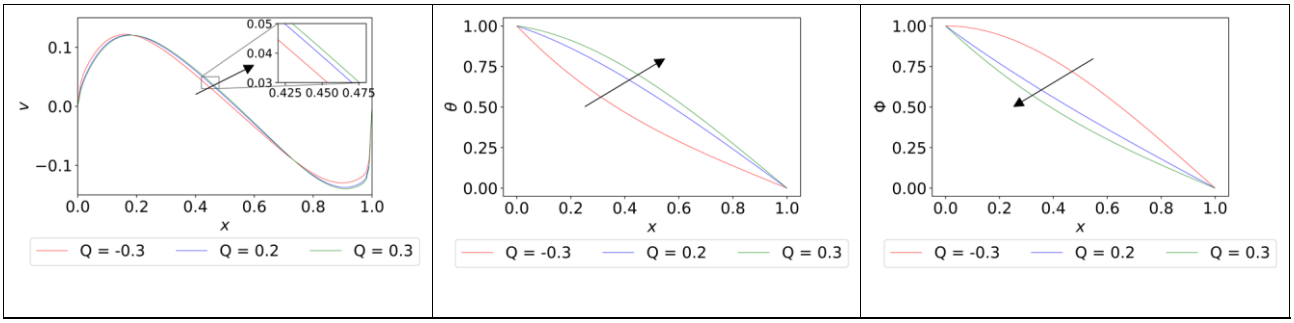


Fig. 4 Effect of heat generation/ absorption parameter Q on velocity, temperature and nanoparticle volume fraction profiles at $Ri = Le = 1, \Pr = 0.71, Nb = Nt = Nr = \kappa = 0.1, M = 5$



a)Velocity b)Temperature c)Nanoparticle volume fraction

Fig. 5 Effect of heat generation/ absorption parameter Q on velocity, temperature and nanoparticle volume fraction profiles in the middle of cavity $(y = 0.5)$ at $Ri = Le = 1, \Pr = 0.71, Nb = Nt = Nr = \kappa = 0.1, M = 5$

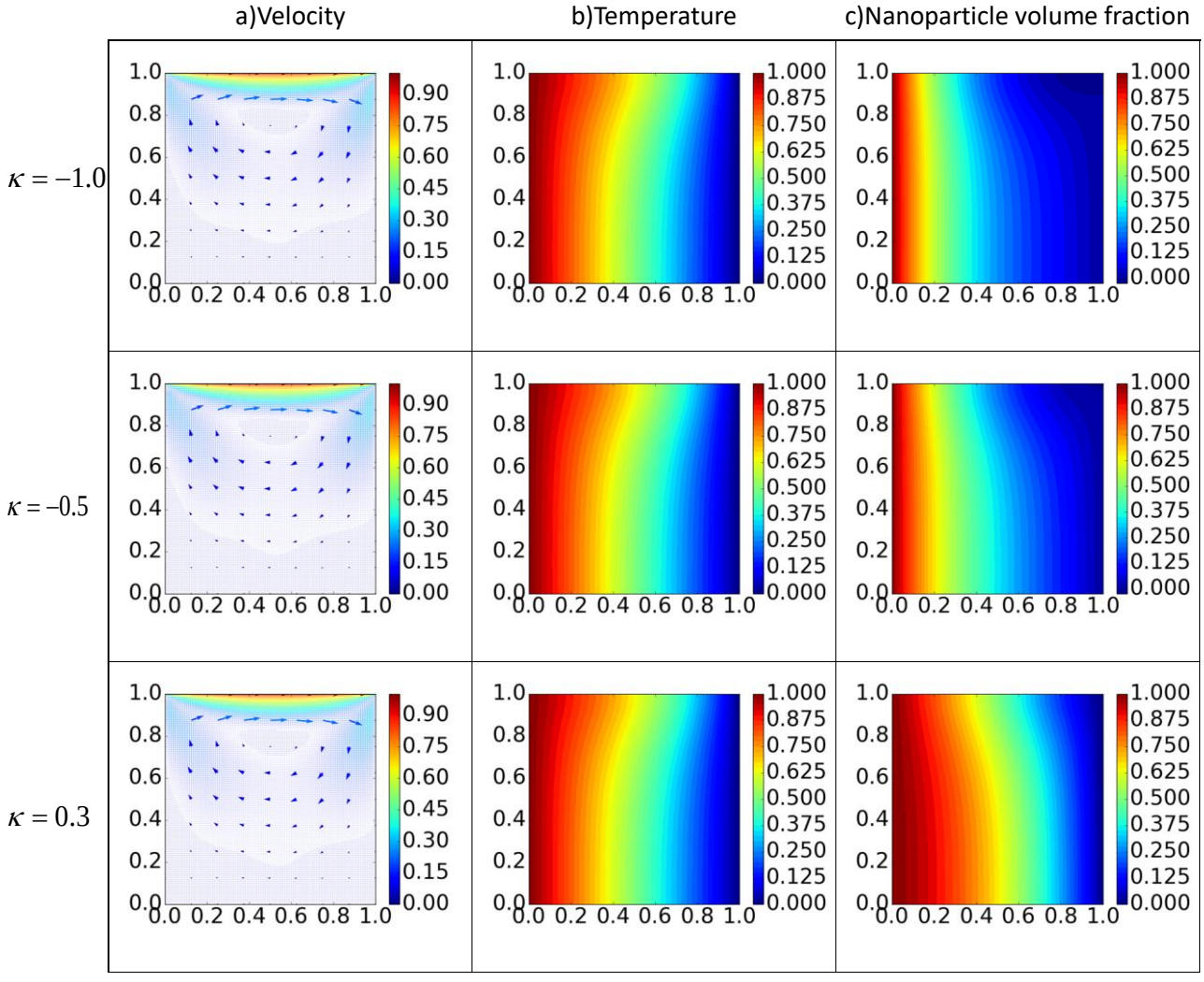
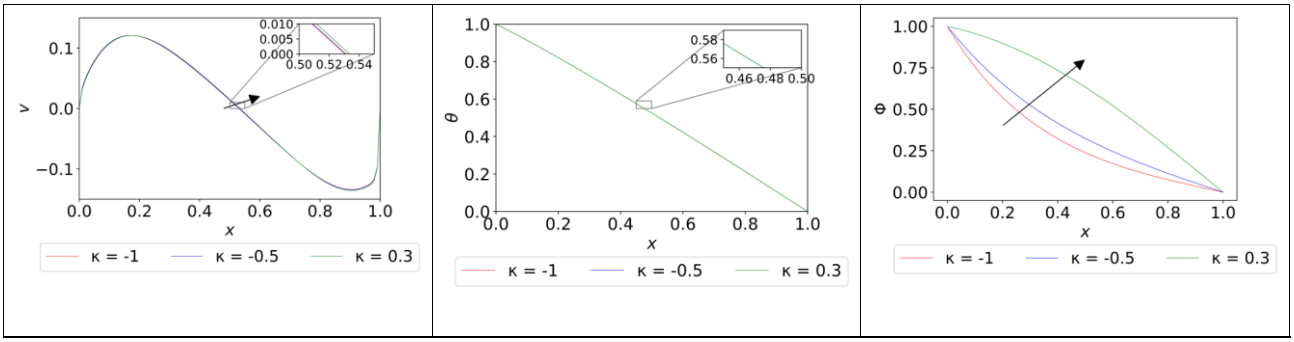


Fig. 6 Effect of chemical reaction parameter κ on velocity, temperature and nanoparticle volume fraction profiles in the middle of cavity $(y = 0.5)$ at $Ri = Le = 1, \Pr = 0.71, Nb = Nt = Nr = Q = 0.1, M = 5$



a)Velocity b)Temperature c)Nanoparticle volume fraction

Fig. 7 Effect of chemical reaction parameter κ on velocity, temperature and nanoparticle volume fraction profiles in the middle of cavity $(y = 0.5)$ at $Ri = Le = 1, \Pr = 0.71, Nb = Nt = Nr = Q = 0.1, M = 5$

4. Conclusions

In this paper, the unsteady two-dimensional mixed convective flow of nanofluid in lid-driven cavity with the presence of magnetic field, heat generation/absorption and chemical reaction effects was considered. The dimensionless governing equations were solved using finite element method in FEniCS. It was concluded that:

- Increasing magnetic parameter lead to decline the velocity and nanoparticle volume fraction profiles but enhance the temperature of a nanofluid.
- When heat generatin/absorption parameter increases, velocity and temperature of a nanofluid increases. Meanwhile, nanoparticle volume fraction profile shows the decreasing pattern.
- As chemical reaction parameter increases, velocity and nanoparticle volume fraction of a nanofluid increase.

Acknowledgement

This research was funded by the Ministry of Education (FRGS19-190-0799), Research Management Centre-IIUM (C-RIG18-004-0004) and Research Management Centre-UTM (vote numbers 07G70, 07G72, 07G76 and 07G77).

References

[1] Choi, S. U. (1995). “Enhancing thermal conductivity of fluids with nanoparticles”. *ASME-Publicatons-FED*, 231, 99-106.

[2] Buongiorno, J. (2006). “Convective transport in nanofluids”. *Journal of Heat Transfer,* 128(3), 240-250.

[3] Tiwari, R. K., & Das, M. K. (2007). “Heat transfer augmentation in a two-sided lid-driven differentially heated square cavity utilizing nanofluids”. *International Journal of Heat and Mass Transfer,* 50(9), 2002-2018.

[4] Sheremet, M. A., & Pop, I. (2015). “Mixed convection in a lid-driven square cavity filled by a nanofluid: Buongiorno's mathematical model”. *Applied Mathematics and Computation*, 266, 792-808.

[5] Yu, Q., Xu, H., & Liao, S. (2018). “Analysis of mixed convection flow in an inclined lid-driven enclosure with Buongiorno’s nanofluid model”. *International Journal of Heat and Mass Transfer*, 126, 221-236.

[6] Elshehabey, H. M., & Ahmed, S. E. (2015). “MHD mixed convection in a lid-driven cavity filled by a nanofluid with sinusoidal temperature distribution on the both vertical walls using Buongiorno’s nanofluid model”. *International Journal of Heat and Mass Transfer*, 88, 181-202.

[7] Alsabery, A. I., Armaghani, T., Chamkha, A. J., Sadiq, M. A., & Hashim, I. (2019). “Effects of two-phase nanofluid model on convection in a double lid-driven cavity in the presence of a magnetic field”. *International Journal of Numerical Methods for Heat & Fluid Flow*, *29*(4), 1272-1299.

[8] Rashad, A. M., Ahmed, S. E., Khan, W. A., & Mansour, M. A. (2017). "Inclined MHD mixed convection and partial slip of nanofluid in a porous lid-driven cavity with heat source-sink: effect of uniform and non-uniform bottom heating". *Journal of Nanofluids*, *6*(2), 368-378.
[9] Hussain, S., Öztop, H. F., Mehmood, K., & Abu-Hamdeh, N. (2018). "Effects of inclined magnetic field on mixed convection in a nanofluid filled double lid-driven cavity with volumetric heat generation or absorption using finite element method". *Chinese journal of physics*, *56*(2), 484-501.
[10] Shekar, C. B., Kishan, N., & Haritha, C. (2016). "Convection in nanofluid-filled porous cavity with heat absorption/generation and radiation". *Journal of Thermophysics and Heat Transfer*, *31*(3), 549-562.
[11] Chorin, A. J. (1968). Numerical solution of the Navier-Stokes equations. *Mathematics of computation*, *22*(104), 745-762
[12] Goda, K. (1979). "A multistep technique with implicit difference schemes for calculating two-or three-dimensional cavity flows". *Journal of computational physics*, *30*(1), 76-95.
[13] Guermond, J. L., Minev, P., & Shen, J. (2006). "An overview of projection methods for incompressible flows". *Computer methods in applied mechanics and engineering*, *195*(44-47), 6011-6045.
[14] Wong, J. C. F. (2007). "Numerical simulation of two-dimensional laminar mixed-convection in a lid-driven cavity using the mixed finite element consistent splitting scheme". *International Journal of Numerical Methods for Heat & Fluid Flow*, *17*(1), 46-93.
[15] Górecki, B., & Szumbarski, J. (2014). "Unconditionally stable numerical scheme for natural convection problems". International Journal of Numerical Methods for Heat & Fluid Flow, Vol.24, No.4, 907-919.
[16] Alnæs, M., Blechta, J., Hake, J., Johansson, A., Kehlet, B., Richardson, A. C., Ring, J., Rognes, M. E., & Wells. G. N. ()2015. The FEniCS Project Version 1.5. *Archive of Numerical Software*, Vol.3, No.100.
[17] Kuznetsov, A. V., & Nield, D. A. (2010). "Natural convective boundary-layer flow of a nanofluid past a vertical plate". *International Journal of Thermal Sciences*, 49(2), 243-247.
[18] Lin, Y., & Jiang, Y. (2018). "Effects of Brownian motion and thermophoresis on nanofluids in a rotating circular groove: A numerical simulation". *International Journal of Heat and Mass Transfer*, *123*, 569-582.
[19] Ibrahim, F. S., Elaiw, A. M., & Bakr, A. A. (2008). "Effect of the chemical reaction and radiation absorption on the unsteady MHD free convection flow past a semi-infinite vertical permeable moving plate with heat source and suction". *Communications in Nonlinear Science and Numerical Simulation*, 13(6), 1056-1066.
[20] Logg, A., Mardal, K. A., & Wells. G. (2012). "Automated solution of differential equations by the finite element method: The FEniCS Book", Vol. 84*, Springer Science & Business Media*.
[21] Kleanthous, A., & Van Gorder, R. A. (2017). Heat and mass transfer within a vertical pipe with a surface heating element of variable size. *International Communications in Heat and Mass Transfer*, *85*, 70-75.
[22] Iwatsu, R., Hyun, J. M., & Kuwahara, K. (1993). "Mixed convection in a driven cavity with a stable vertical temperature gradient". *International Journal of Heat and Mass Transfer*, 36(6), 1601-1608.

Penerbit Akademia Baru

Engineering Science and Technology Conference Proceedings

Journal homepage: www.akademiabaru.com/EST.html

Subsurface Vortex Control Parametric Study at Submersible Pump Intake Using Plate-Type Floor Splitters

Open Access

Zambri Harun[1,*], Tajul Arin Norizan[1], Shahrir Abdullah[1], Mazharul Islam[2]

[1] Faculty of Engineering and Built Environment, UKM Bangi, 43600, Malaysia
[2] Department of Mechanical and Production Engineering, Ahsanullah University of Science and Technology, 141 & 142, Love Road, Tejgaon Industrial Area, Dhaka-1208, Bangladesh

ABSTRACT

Vortex formation near the pump inlet in the sump during intake is a phenomenon that needs to be controlled to maximize the pump efficiency. In this study, five variants of an AVD type called the plate type floor splitter are installed in a single intake pump sump model to evaluate the effect of geometry of the floor splitter on the effectiveness of vortex control in the intake flow. The acceptance criteria according to ANSI HI 9.8 2012 standard are that the vortex formed in the sump must be eliminated and the swirl angle in the flow must not exceed 5°. The submergence of the inlet was varied to observe the swirl reduction effect at different water levels. All floor splitter variants employed in this study have successfully eliminated the vortex but most of them did not manage to reduce the swirl angle below 5° as required. The variants with different heights displayed significant differences in swirl angle values with higher variants produce greater swirl angle reduction. The highest floor splitter variant managed to produce a swirl angle reduction below 5°. With varying lengths, however, the swirl angle values did not differ much in each case with the installation of the floor splitter variants. The advantage of the long floor splitter is that the fluctuation of swirl angle values is minimum for all submergence depths greater than 0.9 times the minimum inlet submergence which implies that the swirl reduction effect is less affected by the change in water level. By combining the advantages of both floor splitter design variation, the optimal design of plate type floor splitter can be achieved.

Keywords:
Ankle foot orthosis, magnetorheological brake, ground reaction force, joint stiffness, prediction

Copyright © 2019 PENERBIT AKADEMIA BARU - All rights reserved

1. Introduction

The study of vortex formation in pump sump during intake for pumps with wet pit installation has been an ongoing effort by many researchers for the past decades. Although vortices may occur in dry pit installation as well, the effects are more detrimental for the wet pit installation due to the fact that the pump inlet is submerged in water and therefore the vortices can directly come in contact with the pump impeller and cause damages which will affect the pump performance [1]. This work will complement vortex-reduction effort in intake pipe which eventually affect impeller and pump performance [e.g. 2]. There are guidelines proposed by organizations related to pump

* *Corresponding author.*
E-mail address: zambri@ukm.edu.my

intake design such as ANSI [3], BSI [4] and JSME [5] which could help eliminate or at least control the formation of vortices in pump sump. These guidelines mainly focus on the geometry of the pump sump in the vicinity of the inlet where sharp edges or curvatures in the sump may alter the uniformity of the intake flow and thus create high vorticity regions which will be the source of vortex formation [6]. However, optimal design of pump sump may not be achieved in certain cases, for example limited space for the construction of pump sump, operational restriction that prevent adequate submergence of the pump and pump stations which are undergoing retrofitting works and modification of the existing pump sump structure. The limitations mentioned above are more common in urban areas because of the costs of relocating existing infrastructure. Therefore, the alternative remedial measures for these cases can be carried out by installing a control feature known as anti-vortex device (AVD). There are many types of AVD that can be used to control vortex formation, depending on the type of vortex that occurs in the sump. Generally, vortices in a pump sump can be divided into two main categories, namely free surface vortex and subsurface vortex. Free surface vortex may be eliminated by ensuring the submergence of the pump inlet as deep as possible. The detection of free surface vortex is also straight forward as it can be observed at the water surface. On the other hand, subsurface vortex is a more complex as it occurs under the surface level and could not be eliminated even with adequate submergence of the pump inlet. The occurrence of subsurface vortices is mainly due to small clearance under the suction inlet, high pump suction strength which results in high Froude Number and unsuitable sump geometry which causes non uniform approach flow to the inlet. This problem may be corrected by using a floor splitter. According to the study by Kang et al. [7], the cross-sectional feature of the floor splitter may influence the vortex elimination effect of the splitter. Kim et al. [8] also proposed that the height of floor splitter may change the profile of the intake flow and worsen the vorticity at the pump inlet if the height of the splitter exceeds 0.2 times the diameter of the inlet. In this study, five variants of plate type floor splitter are tested in a pump sump model to evaluate the effects of geometry on the effectiveness of vortex reduction.

2. Methodology

The experimental setup is shown in Figure 1. The rig consists of a single intake pump sump model with a closed loop piping system. The test section is made from acrylic to allow observation of any vortex formed at the suction inlet. The suction end is an acrylic pipe with bell shaped inlet resembling a real submersible pump. This is an extended experiment after an earlier ones which showed that the biggest reduction in swirl angle was displayed by biggest gap between the floor splitter and the inlet pipe [9].

A device called the swirl meter has been installed in the suction pipe at a distance about 4 times the inlet diameter from the suction inlet to measure the swirl angle in the intake flow. The design of the measurement device complies with ANSI HI 9.8-2012 standard [3] and the measurement procedures are performed according to the standard. When the pump is in operation, the swirl in the intake flow will rotate the swirl meter blade and the number of rotations along with its respective direction, either clockwise or anti-clockwise, are recorded for the period of 10 minutes. The number of rotations of the blade for every 30 seconds within the measurement period were also recorded to determine the short period swirl angles while the total number of rotations for the 10-minute period gives the average swirl angle. From the number of rotations of the swirl meter, the swirl angle θ can be calculated by the following equation [7]:

$$\theta = \tan^{-1}\frac{\pi dn}{u} \quad (1)$$

where, *d* is the inner diameter of the suction pipe, *u* is the average axial velocity at the position of the swirl meter, and *n* is the number of swirl meter rotations. The value for *u* is set to 0.094 mm in this experiment and *u* is controlled at a constant value of 1.44 m/s by using variable speed drive (VSD) to control the pump speed.

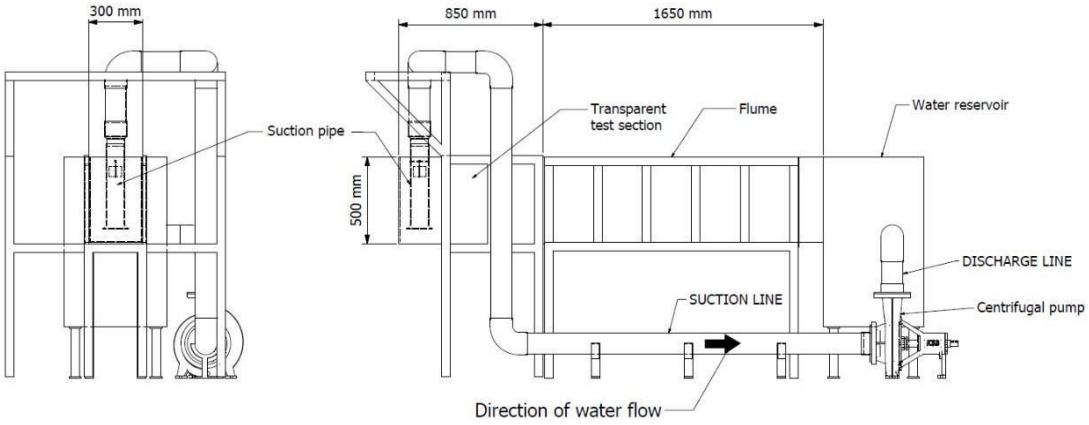


Fig. 1. Experimental rig of the study located at the Coastal and Water Resources Engineering Laboratory, Universiti Kebangsaan Malaysia.

The speed is monitored by calculating the flow rate from an ultrasonic flow meter. The rotation count is set to be the number of revolutions per second. According to ANSI HI 9.8-2012, the acceptable swirl angle value is below 5° and any value above that should be reduced by installing AVD. As the focus of this study is the reduction of subsurface vortices, therefore floor splitter has been considered as the best AVD type for the task. Floor splitter specimens are placed directly beneath the inlet and at the center of the inlet diameter. There are five variants tested in this study in which variant AVD1 is the base shape. Variant AVD2 and AVD3 represent variant 1 but with different heights, while variant AVD4 and AVD5 are designed based on variant 1 but with different lengths. The shapes of the floor splitter variants are shown in Figure 2.

In order to obtain comprehensive results, the inlet submergence has been varied between 0.8 to 1.2 times the value of minimum inlet submergence S_{min}, the submergence needed to prevent the formation of free surface vortices. S_{min} has been calculated by the following equation [3].

$$S_m = D(1.0 + 2.3Fr_{in}) \quad (2)$$

where, *D* is the inlet diameter (which is 150 mm), and Fr_{in} is the Froude Number at the inlet. Based on the above equation, the inlet Froude Number must be determined prior to the calculation of S_{min}. Fr_{in} can be calculated by using the following equation:

$$Fr_{in} = \frac{v_{in}}{\sqrt{gD}} \quad (3)$$

In the present study, v_{in} has been chosen as 0.58 m/s and therefore Fr_{in} equals to 0.48. From equation (2) the value for S_{min} is 316 mm. An inclined floor with 30 ° inclination angle is placed at a

distance about 5 times the inlet diameter from the suction inlet to create non uniform flow in the sump for the initiation of vortex at the inlet.

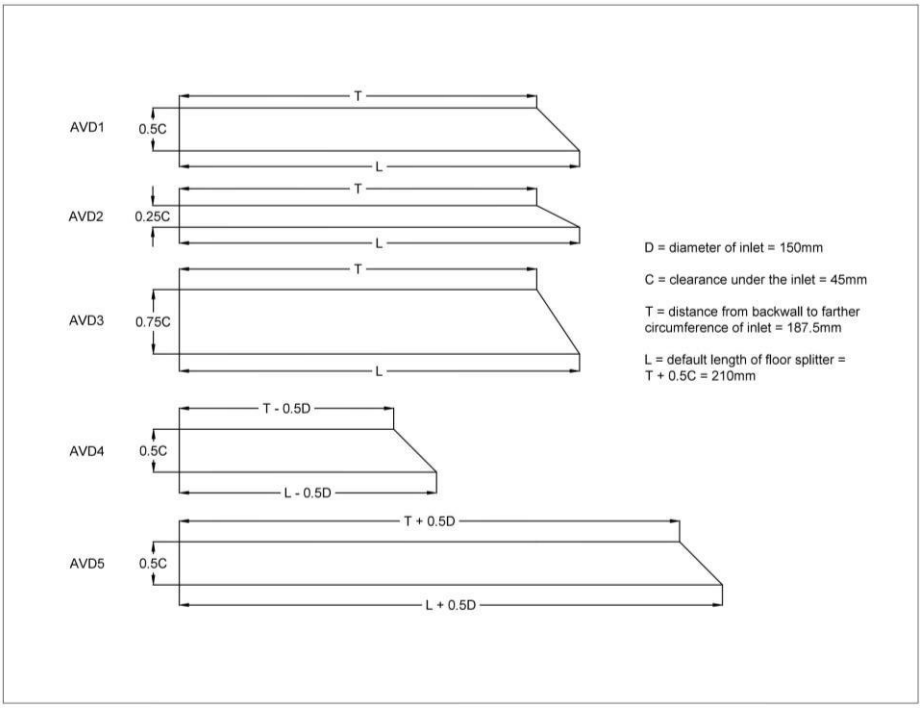


Fig. 2. Floor splitter variants tested in the experiment.

3. Results and Discussions

The swirl angle values for all cases with and without the installation of every floor splitter variant were recorded and evaluated. It has been observed that the subsurface vortex formed at the sump floor, as shown in Figure 3, has been successfully eliminated by the floor splitter installation. However, the swirl angle values remain high for certain floor splitter variants which propose that improvement must be carried out on the floor splitter design.

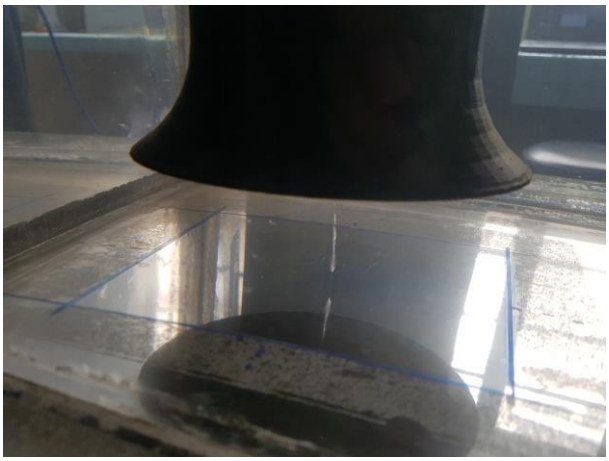


Fig. 3. Subsurface vortex formed at the sump floor.

The data is presented in two categories which are differentiated according to the floor splitter variant designs. Figure 4 shows the swirl angle values for the floor splitters with varying heights while Figure 5 represents the swirl angle values for the floor splitters with varying lengths. Generally, the swirl angle values are higher at lower S_{min} values and relatively constant when the value of S_{min} between 0.9 and 1.1 before increasing again for values of S_{min} greater than 1.1. This trend indicates that the swirl angle values are stable when the submergence is within $\pm$10% from S_{min} and increase in value when the submergence lies outside the stated range due to increase in velocity gradient near the suction inlet. The stationary trend of swirl angle values is also contributed due to the inception of free surface vortex near S_{min} which hinders the rotation of swirl meter blade and ultimately reduce the increment of swirl angle. For the case with floor splitter variants of different heights, it can be observed that the increase in floor splitter height reduces the swirl angle values significantly. The swirl reduction effect increases with increasing swirl angle as shown in Figure 4. For submergence ratio greater than 1.1, the swirl angle values are decreased further with the installation of AVD1, AVD2 and AVD3. AVD3 displays the smallest margin between the highest and the lowest swirl angles which is 1.65°. AVD1 has a margin of 3.37°, while the swirl angle margin for AVD 2 is the largest, which is at 4.87°.

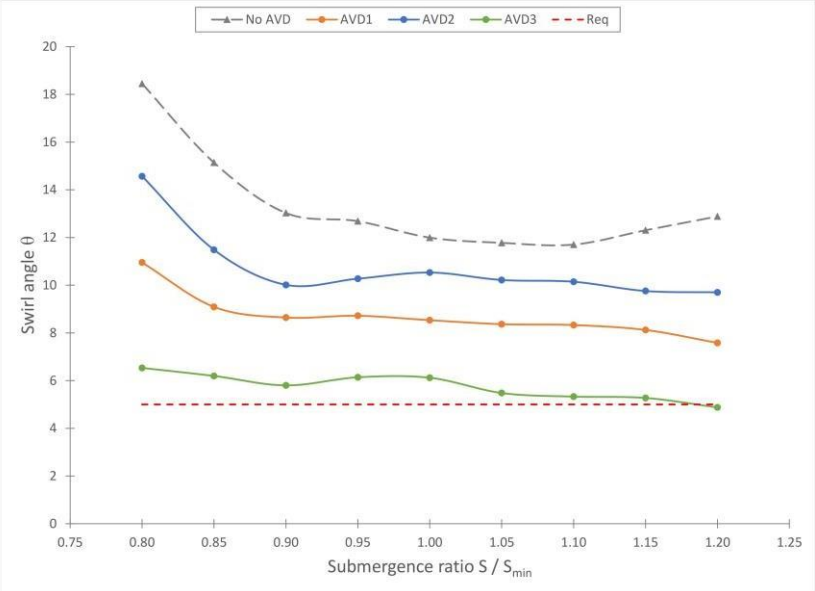


Fig. 4. Swirl angle values with di_erent floor splitter heights.

The trend of swirl angle values in Figure 5 indicates a different feature compared to the trend in Figure 6. For different floor splitter lengths, the swirl reduction effect is not apparent as it is in the case of height variation of floor splitter. The shorter floor splitter, which is AVD4, seems to be less effective than the base AVD, namely AVD1, which indicates that an exposure to a longer floor splitter is needed to improve the swirl reduction. As the length of the floor splitter increases, the trend of the swirl angle values shows only a slight reduction. This can be observed by the difference in the results for AVD1 and AVD5 which base length are L and $L + D$ respectively. This implies that longer floor splitters do not improve the swirl reduction effect significantly. However, the margin of swirl angle values is much smaller for submergence ratio greater than 0.9 when installed with AVD5 which indicates a more stable swirl angle fluctuations compared to AVD1. The plot also shows that for submergence ratio greater than 1.1, the swirl angle values are not reduced further with the installation of AVD4 and AVD5, unlike the case with different floor splitter heights. The lowest swirl angle values for AVD4 and AVD5 do not lies at the maximum submergence ratio, but rather at the values between 0.9 and 1.1. Margins of swirl angle values do not differ much between AVD1, AVD4

and AVD5. The flow with AVD4 produces a margin above the requirement (5.0°) of 3.52° and while flow with AVD5 produces 2.57°.

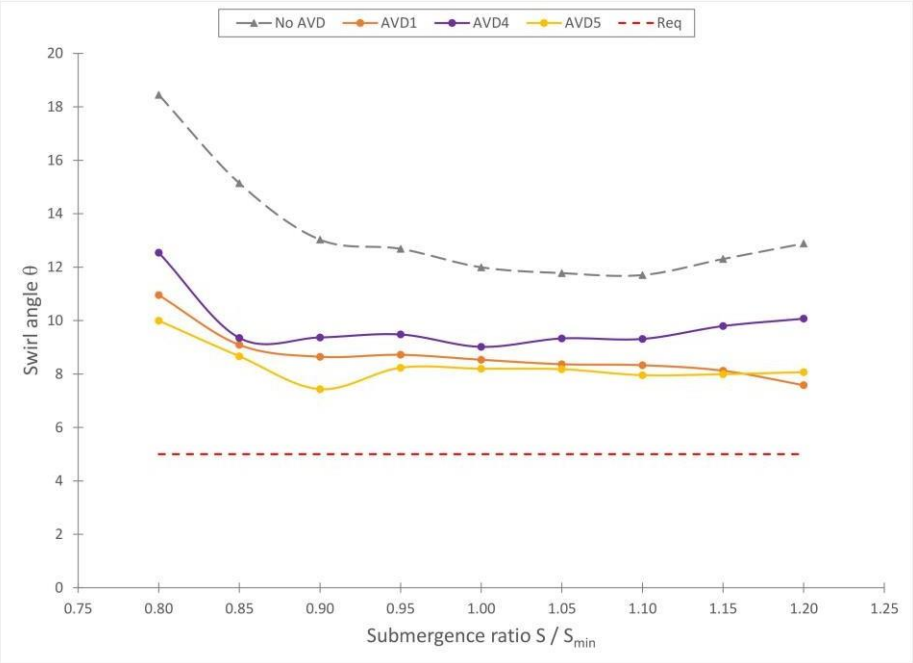


Fig. 5. Swirl angle values with different floor splitter lengths.

The lowest swirl angle values for AVD4 and AVD5 do not lies at the maximum submergence ratio, but rather at the values between 0.9 and 1.1. Margins of swirl angle values do not differ much between AVD1, AVD4 and AVD5. The flow with AVD4 produces a margin above the requirement (5.0°) of 3.52° and while flow with AVD5 produces 2.57°.

4. Conclusions

The effect of floor splitter installation on the vortex formation near the suction inlet of a pump in pump sump has been studied in this research. A single intake pump sump model has been constructed to measure the swirl angle in the pump intake flow with and without floor splitter installed according to ANSI HI 9.8 2012 standard. Five plate type floor splitter variants were designed and tested in the pump sump model and the results have been compared. A floor with an inclination angle of 30° is placed in the model to induce vortex formation at the suction inlet. The results show that the installation of floor splitter has successfully eliminated the vortex formed at the sump floor, however the swirl angle in the intake flow has not been reduced to the allowable value which is below 5° based on the requirement in ANSI HI 9.8 2012 standard for most of the floor splitter variants. Floor splitters with varying heights display significant change in swirl reduction effect with higher floor splitters produce lower swirl angle values. The margin of swirl angle values has also been smaller in higher floor splitters which indicate a more stable fluctuation of swirl angles. The swirl reduction effect for varying floor splitter lengths does not change much compared to varying floor splitter heights. Longer floor splitters, however, produce an almost constant swirl angle values for submergence ratio greater than 0.9. The advantages of each floor splitter dimension obtained from the results may be combined to get the best floor splitter shape.experimental data of UTM-LST VFE-2 model at high angle of attack is presented here. More experiments are needed to verify this complicated flow topology.

Acknowledgement

The research has been funded by Ministry of Science, Technology, Environment and Climate Change (MESTECC), Malaysia under Science Fund grant No. SF1326 and carried out in collaboration with the Department of Irrigation and Drainage (DID), Malaysia.

References

[1] Melville, B., Ettema, R. and Nakato, T. (1994) Review of Flow Problems in Water Intake Pump Sumps, EPRI Report, United States.
[2] Norizan, T.A., Reda, E. and Harun, Z. (2018) Enhancement of vorticity reduction by floor splitter in pump sump to improve pump effeciency, *Sustainable Energy Technologies and Assessments*, 26, pp. 28–36.
[3] ANSI (2012) ANSI/HI 9.8: Rotodynamic Pumps for Pump Intake Design, Hydraulic Institute, Parsippany.
[4] CEN (2009) PD CEN/TR 13930: Rotodynamic Pumps - Design of Pump Intakes Recommendations for Installation of Pumps, Comite Europeen de Normalisation, Brussels.
[5] TSJ (2005) S002: Standard Method for Model Testing the Performance of a Pump Sump, Turbomachinery Society of Japan, Tokyo.
[6] Tullis, J. (1978) Modelling in Design of Pumping Pits*, Journal of Hydraulic Division ASCE*, 105(9), pp.1053–1063.
[7] Kang, W., Shin, B. and Doh, D. (2014) An Effective Shape of Floor Splitter for Reducing Subsurface Vortices in Pump Sump, *Journal of Mechanical Science and Technology*, 28(1), pp. 175–182.
[8] Kim, H., Park, S. and Rhee, D. (2017) Numerical analysis of the effects of anti-vortex device height on hydraulic performance of pump sump, *KSCE Journal of Civil Engineering*, 21(4), pp. 1484–1492.
[9] Norizan, T.A., Harun, Z., Abdullah, A. and Wan Mohtar, W.H.M. (2019) Effects of floor splitter height on the effectiveness of swirl angle reduction in pump intake. *Journal of Advanced Research in Fluid Mechanics and Thermal Sciences,* 57(1), pp. 32-39.

Penerbit Akademia Baru

Engineering Science and Technology Conference Proceedings

Journal homepage: www.akademiabaru.com/EST.html

Application of Computational Fluid Dynamic Simulation for the Study of Heat Stress and Heat Strain- A Review

Open Access

Mohd Amin Mahd Asri[1,*], Ahmad Rasdan Ismail[1], Raemy Md Zein[2], Ismail Abdul Rahman[2]

[1] Fakulti Teknologi Kreatif dan Warisan, Universiti Malaysia Kelantan, 16300 Bachok, Kelantan, Malaysia
[2] National Institute of Occupational Safety and Health, Malaysia

ABSTRACT

The study on heat stress and heat strain has been conducted since early 20th century. However, in the current years, it attracts an increase of attention around the world mainly due to the global climate change issues. Traditionally, there are two main approaches in the study of heat stress and heat strain which are the climatic chamber studies and the field studies. But, with the recent development in the computational fluid dynamic (CFD) simulation, the researchers shift toward this approach as a new method for the study of heat stress and heat strain. Climatic chamber can be simulated with various environmental parameters such as air flow and heat transfer while a manikin is used to identify the effects of these parameters. In this article, recent developments of the CFD simulation for the study of heat stress and heat strain for indoor environment are reviewed while their methodology and results are compared. The discussions that will be presented in this work will focus on the various CFD techniques and its significance as a new method for the study of heat stress and heat strain.

Keywords:
Heat stress; thermal comfort; CFD

Copyright © 2019 PENERBIT AKADEMIA BARU - All rights reserved

1. Introduction

There are many factors that influence the level of heat exposure depends on whether the individual is indoors with or without air-cooling, outdoor in shade or in full sun. The duration of exposure, acclimatization, the level and type of activity and clothing also determine the effect of heat exposure [1]. To understand the influence of each of these factors, scientists have developed several heat stress/heat strain indexes based on two approaches; the climatic chamber studies and the field studies.

Climatic chamber studies aim to determine steady-state thermal comfort models which are the production of the desired environment conditions (radiant temperature, air temperature, relative humidity and air velocity) and at the same time, the unwanted variables can be controlled to avoid any influence on the results. This type of study is done in a climate simulation chamber which can fit human subjects for experimental purposes [2].

Field studies are used in order to study heat stress in the real world. Subjects can conduct their normal daily work without any attempt to control the environment factors [3]. Thus, this kind of study can be easily influenced by other indirect factors such as cultural and psychological factors [4].

* *Corresponding author.*
E-mail address: aminasri5455@gmail.com (Mohd Amin Mahd Asri)

As a consequence of the advancement in the computing technology, many researchers use the CFD technique for the study of thermal comfort or heat stress for more complex system. At the same time, the use of CFD is increasing widely in many fields of science and engineering. In the past two decades, CFD has shown a wide variety of applications in the field of aerospace and energy [5]. Computational Fluid Dynamics is a computer based simulation technique to analyze a system which involves fluid flow, heat transfer and associated phenomena. Most of the researchers use the abbreviation CFD and define it as a branch of fluid mechanics that solves and analyses fluid flow problems, using numerical methods and algorithms [6].

For the study of indoor thermal and airflow, CFD is used to numerically model physical processes occurring within a fluid by which mostly intend to solve Navier-Stokes equations. Navier-Stokes equations are the expression of the fundamental physical laws of a control volume of fluid which are the conservation of mass, momentum and thermal energy [7].

In most of the cases where CFD is used, there are previous validations for the modelling methodologies which usually taken from field studies and previous study or the data used to operate the system designed by CFD can be easily obtained. However, there is an increase of the usage of this technique because of the facility of knowledge transfer and the advancement of computational resources from academia, which include software and hardware developers [6].

2. Discussion

2.1 Environment Model

The indoor environment simulated varied from a simple closed chamber to a three level atrium which are usually designed to study the thermal condition of these environments. (Kamar *et al.,* [8] simulated a model of a double storey residential house with three rooms mainly, the hall, the upper hall and the kitchen. They simulated a solar chimney which is a natural-draft device for passive cooling as square-shaped openings on the roof at the middle and gable vents by introducing thin rectangular-shaped openings in the walls of the house.

A CFD model of an underground shelter was studied by *Mukhtar et al.,* [9]. In the study, they simulated a model of an underground shelter with passive ventilation by a supply duct and an exhaust duct which take the form of cylindrical tubes. Furthermore, a heating cable which replicates the heat release by the occupants is simulated by a flat rectangle. They claimed that the model suggested was validated by the data measured from previous study.

Jusoh *et al.,* [10] studied the thermal building in a non-uniform thermal environment. In their study, they simulated a workplace ergonomic simulator chamber which was a very small chamber with the size of 3.6 m x 2.4 m x 2.4 m. A small rectangular box was made on the top inside the chamber which replicated the air-condition unit of an office. However, no obstacles, such as furniture were introduced into the CFD chamber which simplifies the real situation in the office environment.

CFD simulation was also used for the study of hospital environment. In a heat related study, Kamsah *et al.,* [11] simulated a model of an operating room(OR) which incorporated with a vertical air supply system and four horizontal outlet grilles. The model consisted of an operating table, an air inlet diffuser, four air exhaust grilles, four medical staffs and two surgical lamps.

In a study of heat transfer and physiological responses of unclothed human body in hot environment, Yang *et al.,* [12] designed a simulation model of a simple 3D climate chamber with length, width and height of 5 m, 3 m, and 2.7 m, respectively. Another study simply used a 2D room 4m x 3m to investigate thermal sensation of occupants using a thermophysiological model [13]. The

air conditioner was included in the model with the air supply entrance on the top-left and the exit on the bottom-right.

Pérez *et al.,* [14] simulated an engine room of a ship which reproduces the real navigation conditions in tropical regions, with two main engines working, to predict indoor conditions. Tsai [15] developed a CFD model of an offshore platform by simulating a domain of boarding riser skid which has a dimension of 50ft x 50ft x 25ft. All the equipment and processing unit were modelled and incorporated with the model of boarding riser skid. Sugiono et al., [16] studied the thermal comfort of workers in the finished good warehouse. Thus, they proposed a model of a warehouse with an area of 2450 m^2 with the head of 7m which consists of 2 main sections. Section 1 with 1400 m^2 area, while section 2 with 1050 m^2 area.

There was another study which focuses on the effects of the double-glazed window with curtains on thermal condition. In the study, a simple bedroom chamber was simulated with length, width and height of 3 m, 3 m, and 3 m, respectively which oriented towards south. However, they put in place several obstacles such as desk, heat collector, light, person and bed which represent by 3D blocks with different size [17]. Abdullah and Wang [18] simulated the top-lit three-storey Malaysian atrium. They used a complex model with several doors, windows, and floor balcony and corridor areas as well. It was incorporated with fully glazed pitched roof top and void areas within the central atrium.

2.2 Heat Stress Index

Various heat stress index were used in the previous study to investigate the thermal environmental. Abdullah and Wang [18] used 'Predicted Mean Vote' (PMV) index to study the environment of an atrium. The software computed the air temperature, radiant temperature and air velocity, while the PMV index was computed by setting the individual parameter (Clo-value and metabolic rate) as well as the relative humidity which is an additional environmental parameter.

Jusoh *et al.* [10] used the combination of Predicted Mean Vote-Predicted Percentage of Dissatisfied (PMV-PPD) introduced by Fanger [19]. PPD can be derived from the PMV according ISO7730. The index which was presented used a fix activity level of 1 Met and a level of clothing insulation of 0.5 Clo. Zhang *et al.,* [17] and Sugiono *et al.,* [16] also used the same index to study the effect of double-glazed window with curtains on the thermal condition of a CFD model of a bedroom and to study the thermal comfort of warehouse respectively. This is supported by the fact that this index is also used by both the ASHRAE standards of USA and ISO standards for the evaluation of indoor thermal environment.

A multi-node thermal model was developed by Yang *et al.,* [12] to determine thermal responses of the human body with the inputs such as human activity intensity, clothing properties, and environmental conditions. The model has 20 segments of human body corresponding to the manikin Newton, which contain four layers: core, muscle, fat, and skin layer. There are three systems of the model; an active system, a passive system, and a clothing system. The active system simulated human thermoregulation while the passive system predicted the heat exchange within the human body and between human body and the environment.

Kamar *et al.,* [8] only measured the dry-bulb temperature, wet-bulb temperature and relative humidity in their CFD model for double-storey residential house. While Mukhtar *et al.,* [9] simply used dry temperature for their study on the underground shelter model. However, they mentioned about effective temperature when discussing the effect of heat from the occupant towards the thermal environment. Pérez *et al.,* [14] compared the globe temperature and operative temperature of a model of engine room in a ship. They found out that the operative

temperature obtained from the CFD can be used, instead of the globe temperature, without loss of precision. Angelova *et al.,* [13] took into account the skin temperature as an evaluation for heat stress for the study of the influence of clothing and activity on the occupants based on CFD simulation.

Tsai [15] proposed a CFD WBGT model using the incident radiation data, ambient temperature and wind speed from the CFD model. He claimed that the WBGT model developed could be used to analyse heat stress with high fidelity and accuracy for many applications in high temperature environments with complex equipment installations.

2.3 Manikin Model

Mukhtar *et al.,* [9] simulated the indoor occupants by a 3D model of heating cable which replicates the heat released by the occupants. However, this model was not very appropriate as it neglected the real distribution of heat release by the occupants. Kamsah *et al.,* [11] used standing 3D model of block manikin to simulate the medical staffs and laying 3D model of block manikin for the patient in their study. The model consisted of three parts. A block was for the legs and feet, another block was for the body and hand and a smaller block was for the head. Figure 1 shows the 2D representation of the manikin and Table 1 shows the dimensions of the manikin. The limitation of this manikin model was the effects of each human body parts could not be detected. However, this model could be used for simpler and less computational capacity. In their study, the distribution of heat of the manikin was not the focus; therefore it was not a compulsory to have a perfect manikin for the CFD simulation.



Fig.1. 2D representation of 3D Manikin proposed by Kamsah *et al.,* [11]

Table 1
Dimensions of the manikin [11]

Model	Dimensions (Length (m) × Width (m) × Height (m))
Medical staff	
-Body	0.3 × 0.2 × 0.6
-Head	0.16 × 0.16 × 0.30
-Hand	0.1 × 0.2 × 0.6
-Leg	0.3 × 0.2 × 0.7
Patient	
-Body	0.6 × 0.3 × 0.2
-Head	0.30 × 0.16 × 0.16
-Hand	0.6 × 0.1 × 0.2
-Leg	0.7 × 0.3 × 0.2

Angelova *et al.,* [13] placed a standing human body manikin in the middle of a 2D simulation room. The shape of the manikin was a simplified version of a previous study by Pichurov [20]. The height of the body was 1.65 m and its surface area was 1.7 m^2. Figure 2 shows the model of manikin used. The 2D model used can shorten the computational time for the simulation but with the cost of the real 3D representation of the thermal flow from the manikin. As in the real life condition, heat which is distributed from the front is not similar from behind the body. However, in a study which focused on the clothing of the manikin, the complex distribution of the bodily heat can be neglected to easily compare the part of the body which were covered and not covered by clothes.



Fig.2. 2D representation of 2D Manikin proposed by Angelova *et al.*, [13]

An advanced manikin was developed by Yang *et al.,* [12] by using a 3D laser scanning technique to obtain the geometrical details of an unclothed 20-zone manikin Newton in a standing position. Then, the surface of the numerical manikin was subdivided into 20 body segments (face, head, upper arms, forearms, hands, chest, shoulder, stomach, back, hips, thighs, calves, and feet) corresponding to the manikin Newton by the commercial software ANSYS 14.5. This manikin represented almost perfectly the real human body, but with less detail such as eyes and other smaller organs. In the study, they used the manikin to identify the physiological responses of the unclothed human body in hot environments. Thus, it is necessary to have a perfect manikin which can simulate a general distribution of heat throughout the body especially the skin.

Xu *et al.,* [21] studied the difference between different manikin models. They found out that 2D model can give the approximate air flow distribution in an indoor environment. However, the air flow predictions from 3D model were even closer to the real condition. The simplification of body structure also influenced the total heat transfer from the human body where they compared 'cylinder man' vs 'tin-man' model.

3. Conclusions

Computational Fluid Dynamic Simulation has a great potential in the research of heat stress or thermal environment. Many previous studies show that CFD could be used to support the findings from the field study or experimental study of heat stress such as the study of residential building, office environment, offshore and industry. Different heat stress indexes were used in the studies depends on the main focus of the study. Human model could be simulated by a manikin which differs for each study which influenced by the heat stress index used in the study. Therefore, to apply the CFD simulation in a heat stress study, these three factors should be decided beforehand; the environment design, heat stress index and manikin model.

Acknowledgement
This research was funded by a grant from National Institute of Occupational Safety and Health (NIOSH).

References

[1] Kjellstrom, Tord, David Briggs, Chris Freyberg, Bruno Lemke, Matthias Otto, and Olivia Hyatt. 2016. "Heat, Human Performance, and Occupational Health: A Key Issue for the Assessment of Global Climate Change Impacts." *Annual Review of Public Health* 37 (1): 97–112. https://doi.org/10.1146/annurev-publhealth-032315-021740.

[2] Ismail, Ahmad Rasdan, M.R.A. Rani, Baba Md. Deros, Z. K.M. Makhbul, and Mohd Yusri Mohd Yusof. 2012. "Response Surface Method in Modelling the Environmental Factors Toward Workers' Productivity." *Journal Occupational Safety & Health* 9: 83–90.

[3] A.R Ismail, M. R. A. Rani, Z. K. M. Makhbul, M.J.M. Nor, and M.N.A Rahman. 2009. "A Study of Relationship Betwwen WBGT and Relative Humidity to Worker Performance." In *World Academy Of Science, Engineering And Technology, Volume 39*, 216–21.

[4] Taleghani, Mohammad, Martin Tenpierik, Stanley Kurvers, and Andy Van Den Dobbelsteen. 2013. "A Review into Thermal Comfort in Buildings." *Renewable and Sustainable Energy Reviews* 26: 201–15. https://doi.org/10.1016/j.rser.2013.05.050.

[5] Khalil, Essam E. 2012. "CFD History and Applications" 4 (2): 43–46.

[6] Raman, Ram Kumar, Yogesh Dewang, and Jitendra Raghuwanshi. 2018. "A Review on Applications of Computational Fluid Dynamics." *International Journal of LNCT* 2 (6): 137–43.

[7] H.K. Versteeg and W. Malalasekera. 1995. *Introduction to Computational Fluid Dynamics: The Finite Volume Method*. *Harlow: Longman Scientific and Technical*.

[8] Kamar, Haslinda Mohamed, Nazri Kamsah, and Kam Jia Liq. 2017. "Indoor Air of a Double-Storey Residential House in Malaysia." *Journal of Advanced Research in Fluid Mechanics and Thermal Sciences* 31 (1): 11–18.

[9] Mukhtar, Azfarizal, Khai Ching Ng, Mohd Zamri Yusoff, Wah Yen Tey, and Lit Ken Tan. 2019. "Performance Assessment of Passive Heating and Cooling Techniques for Underground Shelter in Equatorial Climate." *Journal of Advanced Research in Fluid Mechanics and Thermal Sciences* 61 (1): 20–32.

[10] Jusoh, Norfadzilah, Rosli Abu Bakar, Ahmad Rasdan Ismail, and Tanti Zanariah Shamshir Ali. 2015. "Computational Analysis of Thermal Building in a No-Uniform Thermal Environment." *Energy Procedia* 68: 438–45. https://doi.org/10.1016/j.egypro.2015.03.275.

[11] Kamsah, Nazri, Haslinda Mohamed Kamar, Muhammad Idrus Alhamid, and Wong Keng Yinn. 2018. "Impacts of Temperature on Airborne Particles in A Hospital Operating Room." *Journal of Advanced Research in Fluid Mechanics and Thermal Sciences* 44 (1): 12–23.

[12] Yang, Jie, Shunjiang Ni, and Wenguo Weng. 2017. "Modelling Heat Transfer and Physiological Responses of Unclothed Human Body in Hot Environment by Coupling CFD Simulation with Thermal Model." *International Journal of Thermal Sciences* 120: 437–45. https://doi.org/10.1016/j.ijthermalsci.2017.06.028.

[13] Angelova, Radostina A., George Pichurov, Iskra Simova, Peter Stankov, and Iosu Rodrigo. 2015. "CFD Based Study of Thermal Sensation of Occupants Using Thermophysiological Model. Part II." *International Journal of Clothing Science and Technology* 27 (1): 60–74.

[14] Pérez, José Antonio, José Antonio Orosa, and Teresa Grueiro. 2015. "A Three Dimensional CFD Simulation Study to Reduce Heat Stress in Ships." *Applied Thermal Engineering*. https://doi.org/10.1016/j.applthermaleng.2015.11.001.

[15] Tsai, Kuochen. 2015. "CFD Modeling of WBGT For an Offshore Platform." In *SPE Annual Technical Conference and Exhibition*, 28–30. Houston, Texas, USA.

[16] Sugiono, Sugiono, Rio Prasetyo Lukodono, and Rizky Tiovana. 2019. "Improving Thermal Comfort Of Workers In The Finished Good Warehouse Based On Predicted Mean Vote (PMV) Using Computational Fluid Dynamics (CFD)." *IETI Transactions on Ergonomics and Safety* 3 (1): 12–24. https://doi.org/10.6722/TES.201907.

[17] Zhang, Yan, Lifei Huang, and Yuanyuan Zhou. 2015. "Analysis of Indoor Thermal Comfort of Test Model Building Installing Double-Glazed Window with Curtains Based on CFD." *Procedia Engineering* 121: 1990–97. https://doi.org/10.1016/j.proeng.2015.09.197.

[18] Abdullah, a H, and F Wang. 2011. "Modelling Thermal Environmental Performance In Top-Lit Malaysian Atrium Using Computational Fluid Dynamics (CFD)." *International Journal of Integrated Engineering* 1 (2): 27–42.

[19] Fanger, P.O. 1970. "Thermal Comfort: Analysis and Applications in Environmental Engineering." *Danish Technical Press*.

[20] Pichurov, G. 2008. "Gagge Model, Tanabe Model – Integration of CFD." In *EuroAcademy on Ventilation and Indoor Climate, Course 5 "CFD Based Design of Indoor Environment*, 47–51. Pamporovo, Bulgaria.

[21] Xu, J., A. Psikuta, S. Annaheim, R. M. Rossi, and J. Li. 2018. "2D and 3D Simulation on Thermal Flow Around the HumanBody." In *Comsol Conference*.

Penerbit Akademia Baru

Engineering Science and Technology Conference Proceedings

Journal homepage: www.akademiabaru.com/EST.html

Rheological Behaviour of Purified Acid-extracted Pectin from 'Saba' Banana [*Musa* BBB 'saba' (*Musa acuminata x Musa balbisiana*)] Peel Applied to Beverage

Open Access

Joel P. Rivadeneira[1,*], Tao Wu[2], Prince Joseph V. Gaban[1], Katherine Ann T. Castillo-Israel[1]

[1] Institute of Food Science and Technology, College of Agriculture and Food Science, University of the Philippines Los Baños, College, Laguna, 4031, Philippines
[2] Department of Food Science, The University of Tennessee, Knoxville, 2510, River Drive, Knoxville, Tennessee, 37996

ABSTRACT

Purity of a previously studied acid-extracted pectin from 'saba' banana peel was further improved (170% increase) through ultrasound-assisted dissolution in dilute acid, reprecipitation by ethanol, and freeze-drying to widen its potential use for food application. Purified banana peel pectin (BPP) was applied to two different beverages: protein solution and orange juice; and to soybean oil to test its thickening and emulsifying properties, respectively. The viscosity profile showed that the formed protein-pectin complex exhibits a shear-thinning property. The highest viscosity was also achieved at [WPI]/[BPP] = 5 and at pH 5 for both purified BPP and commercial pectin. For the effect of pectin on the *in vitro* digestion viscosity of orange juice, results showed that purified BPP increased the viscosity of the juice both in the gastric and intestinal levels, thus, potentially increasing the satiety value of the orange juice. For the emulsifying property, purified BPP and commercial pectin were most effective at 40% and 50% oil content, with the earlier producing a more stable emulsion.

Keywords:
Banana peel; pectin; emulsion; viscosity

Copyright © 2019 PENERBIT AKADEMIA BARU - All rights reserved

1. Introduction

Banana is one of the most important crops in the Philippines. It is a locally-grown fruit that is available in the market year-round. Aside from being utilized locally, banana fruits are exported to other countries. Food and Agriculture Organization of the United Nations (FAO) [1] reported that the Philippines is second largest exporter of banana fruits in the world accounting for a 13% share of the total global shipment. In 2018, the Philippines was able to produce around 9.35 million metric tons comprised the majority of Cavendish and 'saba' variety [2, 3, 4, 5]. Banana fruits are normally consumed fresh in its ripened state but are also processed to provide variety on the food product. Preliminary studies showed that the waste produced during the processing, which is mostly peel, is around two thirds of the fresh material in terms of weight. Considering the high volume of banana production and processing activities, it can be assumed that waste production is also high. These wastes, especially banana peel, contain high-value compounds with potential food applications. Utilizing them to produce high-value products could add value to the fruit itself and ultimately, help the banana industry in the country.

Pectin, a high-value food ingredient, is present in banana peel. It is a complex heteropolysaccharide consisting of a backbone of α-1,4-galacturonic acid residues which are partially esterified with methyl alcohol or acetic acid at the carboxylic acid. It comprises 8-14% of the cell wall [6] and like most of the polysaccharide in plants, it is considered to be both

polymolecular and polydiverse. In fruit peels, pectin is found in the middle lamellae and primary cell wall together with cellulose and hemicellulose. At least 300 galacturonic acid units linked by α-1,4 glycosidic linkages make up a pectin [7]. In some portions of the structure, presence of neutral sugars such as arabinose, galactose, glucose, xylose and rhamnose may be seen as side chains. Various groups of acidic polysaccharides, pectin included, that are linked together form a pectic network in plants.

Pectin is normally used in the food industry as gelling agent in fruit applications. It also acts as stabilizers for emulsions, sauces, juices, dairy and frozen products. The market for pectin in the global scale is estimated to to account for a value of USD 1.0 billion in 2019 and is expected to reach USD 1.9 billion by 2025 due to the increasing demand for natural and organic products [8]. In the Philippines, data from the Department of Trade and Industry showed that about 95,000 kilograms was imported in 2011 valued at around $52.4 million [9]. While there have been no recent data on pectin importation, the global projection on its demand can indicate that pectin production from different potential raw materials is a good direction for research

In this study, crude pectin extracted from 'saba' banana [*Musa BBB* '*saba*' (*Musa acuminata x Musa balbisiana*)] peel using the protocol described by Castillo-Israel [10] was further purified to widen its potential for food application. As a thickening agent, this study explored the potential of the purified BPP in enhancing the viscosity of some beverages. An improvement of this sensory attribute could increase consumer satisfaction translatable to increased sales and revenue. In addition, Zhu et al. [11] suggests that intake of a viscous food results in a slower eating rate and increases the level of fullness. Thus, viscous food products may also be catered to health-conscious individuals. The study also looked into the effectiveness of purified BPP as an emulsifier in soybean oil-water mixture. A stable emulsion, if achieved, would make it easier for a soybean oil to be incorporated in food products. Soybean oil is a good choice for study as it meets the human's requirement for essential fatty acid [12]. Overall, results of this study would promote the use of waste material as an alternative source of important food ingredients in product development and innovation.

2. Methodology

2.1. Materials

Banana peel was sourced out from a banana chips manufacturing plant in Lipa, Batangas. Chemicals used were analytical reagent-grade purchased from either Sigma Aldrich (USA) or Fisher Scientific (USA).

2.2. Purification and characterization

Acid-extracted BPP was produced following the protocol described by Castillo-Israel [13]. Ten percent (w/v) of acid-extracted BPP was dispersed in a hydrochloric acid solution (pH 3). The mixture was subjected to an ultrasonication (Sonics and Materials VC-750, USA, 0.5 in. probe) at a 60% pressure amplitude for two minutes in a cold-water bath. The mixture was subjected to centrifugation at 15,000 x g for 15 minutes followed by filtration using miracloth. An equal volume of 100% ethanol was added to the filtrate to precipitate the pectin. The resulting mixture was subjected to another round of centrifugation and filtration. The resulting purified BPP was then freeze-dried and stored at room temperature. It was later analyzed for methoxyl content and equivalent weight [14], and total pectic content [15].

2.3. Thickening property

Stock solutions of WPI (15% w/v) and purified BPP (4% w/v) were prepared. WPI was mixed with purified BPP such that the final ratios [WPI]/[BPP] were 5, 10 and 15. The final pH of the mixtures was adjusted to pH 5 using 0.1 M NaOH. Mixtures were homogenized with a dispenser (IKA T18 homogenizer, Germany) at 10,000 rpm for 2 minutes then stored at 10°C for 24 hours.

Another set of mixtures was prepared ([WPI/BPP] = 5). Mixtures were adjusted to pH 4, 5 and 6 using 0.1 M NaOH and then homogenized and stored following the same conditions as the previous set. Commercial pectin was also used as a reference. Viscosity profile of the mixtures was measured from 2 to 200 s^{-1} at 25°C.

2.4. In vitro digestion viscosity

Two percent (w/v) of purified BPP in a commercial orange juice was prepared. *In vitro* digestion of the solution was performed following the protocol described by Logan et al. [16]. Aside from the purified BPP, effect of commercial pectin was also evaluated.

2.5. Emulsifying property

A stock solution of 0.5% purified BPP in deionized water with a final pH of 6 was prepared. An appropriate volume of this solution was added to soybean oil such that the final mixture contained 30%, 40%, and 50% oil. Mixtures were homogenized at 10,000 rpm for two minutes, then sonicated at 40% amplitude (3s pulse) for one minute. Final emulsion was stored at 10°C for 24 hours. Viscosity profile of the emulsion at continuous ramp was measured from 2 to 200 s^{-1} at 25°C. Moreover, the appearance of each emulsion was observed under a microscope.

3. Results

3.1 Characteristics of the purified BPP.

Methoxyl content refers to the methyl ester group attached to the galacturonic acid chain. Depending on the degree of its presence, pectin may be classified as low-methoxy or high-methoxy pectin. In this study, the methoxyl content of both acid-extracted BPP and purified BPP are within the typical 0.5-7% values for low-methoxy pectin [17]. Pectin from other banana varieties, however, are high-methoxy in nature [18]. To further validate the observed property (data not shown), their gel formation was tested in an alkaline solution with calcium salt, a condition suitable for low-methoxy pectin [19]. Both pectins formed a gel, hence, a positive result.

Total pectic content is the number of galacturonic acid units in the material. It dictates the level of purity of the pectin, which in this study, has significantly increased by 170% upon innovation in the purification method.

Table 1. Characteristics of acid-extracted banana peel pectin (BPP).

	Crude BPP	Purified BPP
Methoxyl content, %	5.25 ± 0.0	0.10 + 0.0
Total pectic content, %	17.25 + 0.4	46.77 + 0.7
Equivalent Weight (approx.), g/eq	1,500	900

3.2 Viscosity of protein-pectin mixture

WPI solution exhibited a shear-thinning property or a decrease in viscosity in response to increased shear rates. The addition of pectin further increased the WPI solution's viscosity while maintaining the solution's shear thinning property. This rheological property is similar to that of other carbohydrates such as guar gum [20], carboxymethyl cellulose [21] and xanthar gum [22]. It was also observed that for both types of pectin, the most viscous mixture was the one with the highest pectin concentration (a=5). Between the purified BPP and commercial pectin, the latter resulted in a more viscous mixture as it has a higher purity than the earlier. The complex formed by the negatively-charged protein and slightly positive protein contributed to the increased viscosity of the mixtures.

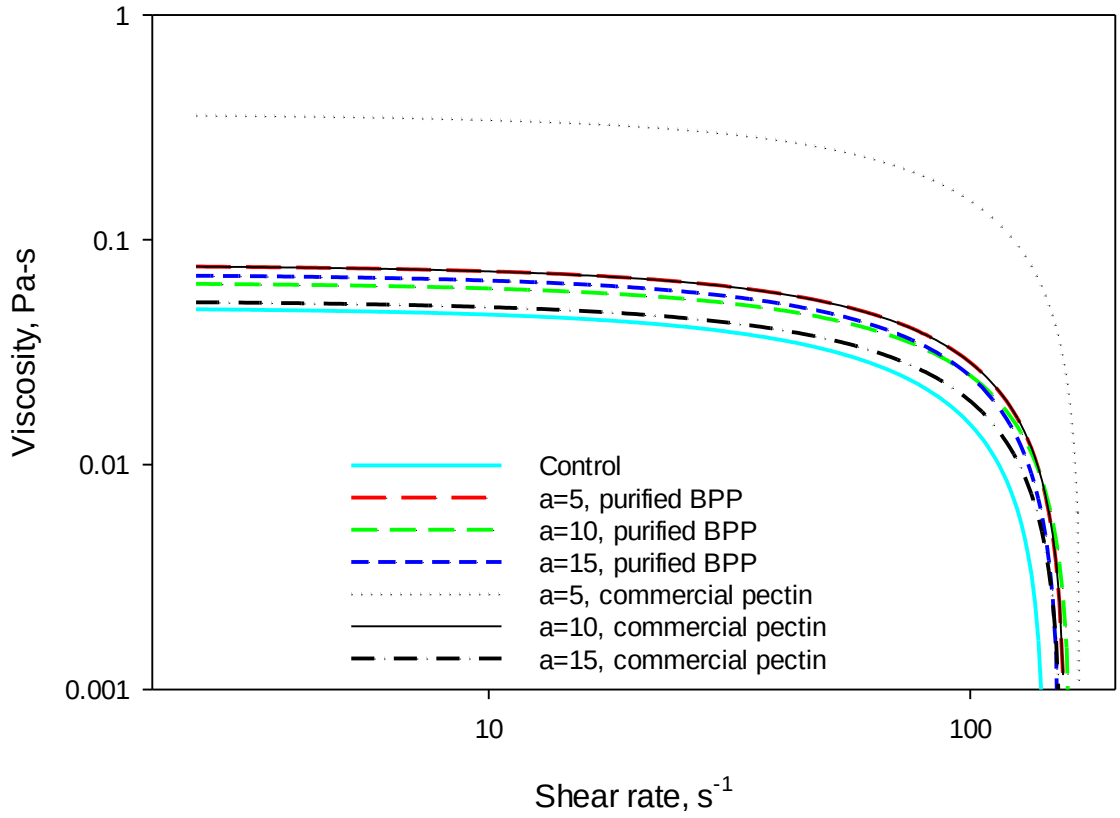


Figure 1. Effect of mixing ratio on the rheology of protein-pectin complex (pH 5).

At pH 4, aggregation of precipitates was observed and a suspension instead of a solution was formed. Electrostatic interaction between the positively charged protein and the negatively charged pectin was very high at this condition, hence the formation of precipitates [23]. The aggregation of precipitates may be attributed to the charge neutralization of the complex [24]. Viscosity was low at this pH because the aggregates formed a separate phase at the bottom part of mixture. At pH 5, interaction between the oppositely charged molecules was still present but this time, a colloidal complex was formed. This resulted in higher viscosity of the mixture. At pH 7, both protein and pectin were negatively charged. This incompatibility due to repulsion of charges prevented the assembly of a complex, resulting in two soluble co-solutes with low final viscosity [25]. The formation of complex at pH 4 and 5 suggests that purified BPP could be a potential

material for hierarchical structures and delivery systems. In food application, despite performing inferior relative to the commercial pectin, results suggest that purified BPP can improve the texture or viscosity of a protein beverage at an appropriate pH.

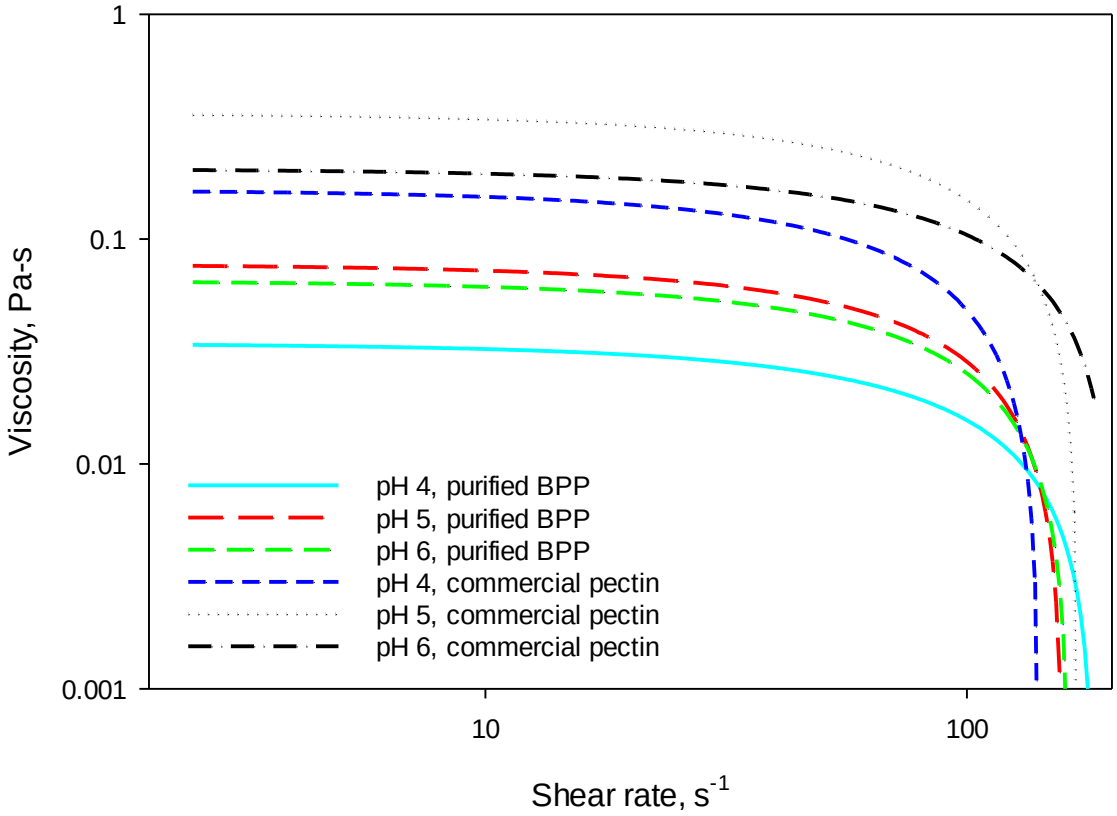


Figure 2. Effect of pH on the rheology of protein-pectin complex (a=5).

3.3 In vitro digestion viscosity of orange juice

Similar to the effect on WPI solution, BPP increased the initial apparent viscosity of orange juice. During the first hour of gastric digestion, both at $10s^{-1}$ and 50 s^{-1} shear rates, orange juice with pectin exhibited higher viscosity than the control. On the second hour, same trend was observed at $10s^{-1}$ shear rate. However, at 50 s^{-1} shear rate, orange juice with purified BPP exhibited similar viscosity as the control. Only the commercial pectin was able to maintain the viscous property at the high levels of shear rates. In the intestinal digestion, the viscosity was higher for orange juice with purified BPP and commercial pectin at $10s^{-1}$ shear rates. However, increasing the shear rate to $50s^{-1}$ produced fluids with significantly equivalent viscosities. In general, the whole digestion process reduced the viscosity of orange juice with and without pectin. This finding is in agreement with the results of a related study [26] wherein other commercial brands of pectin were used.

At some point in the *in vitro* digestion, addition of pectin increased the viscosity of the orange juice. A study correlating viscosity of food with satiety suggested that fullness during meal is higher for highly viscous food [27]. Hence, aside from the improvement of texture of the juice, addition of purified BPP or commercial pectin could possibly increase the level of fullness during meals. For health-conscious individuals, this could be a potential diet option in maintaining a healthy body weight.

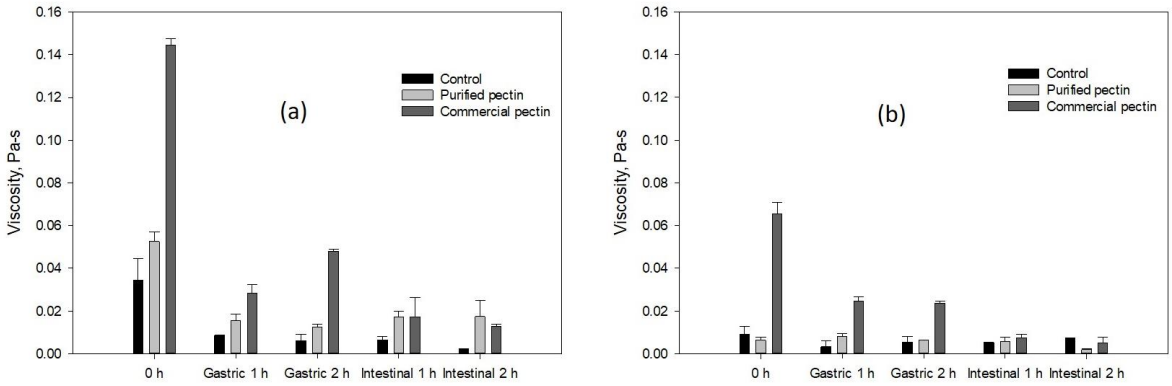


Figure 3. In vitro digestion viscosity of orange juice at 10 s^{-1} (a) and 50 s^{-1} (b) shear rate.

3.4 Emulsifying property of pectin

As seen in Figure 4, both pectins were able to form soybean oil-water emulsion. Visually, the difference in the phase separation of oil and water between the control and the samples confirms that an emulsion was formed. It is the white to cream layer between the two components. Emulsion index (Figure 5) of the emulsions showed that at 30% oil ratio, commercial pectin resulted in a higher volume of emulsion whereas, at 40% and 50% oil ratio, there was no significant difference in the cream indices. Thus, purified BPP is comparable with commercial pectin.

Microscopy (Figure 6) of the samples showed that purified BPP produced smaller droplets than commercial pectin, making the earlier a more stable emulsion [28]. In pharmaceutical research, these are used to encapsulate lipophilic drugs for increased bioavailability [29]. Similarly, for food application, a stable emulsion can be used to encapsulate lipophilic functional food [30]. Purified PBB, having produced a more stable emulsion in terms of the droplet size, can be a potential emulsifier for functional food research and development.

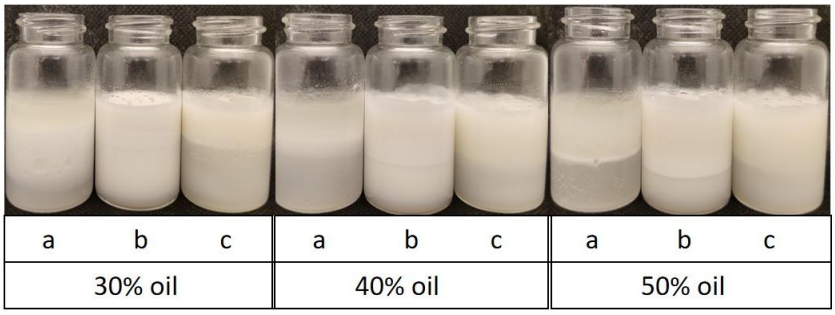


Figure 4. Phase separation of oil-water emulsion.
(a=0without pectin; b=2% purified BPP; c=2% commercial pectin)

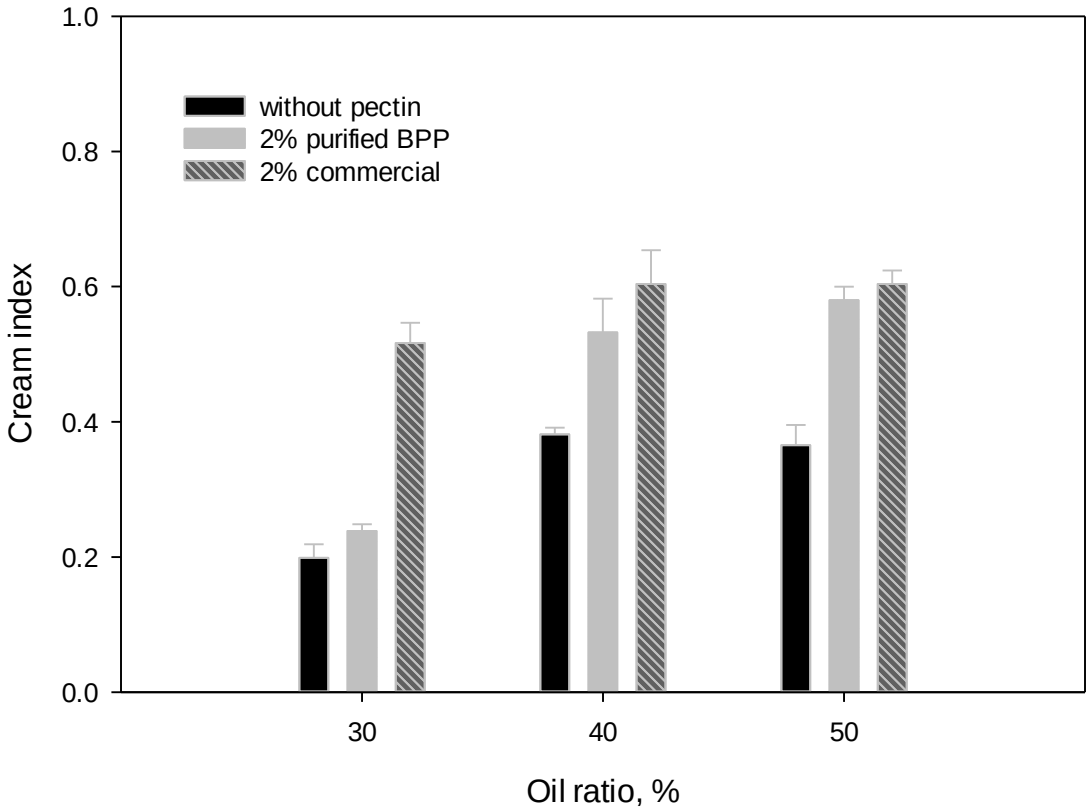


Figure 5. Cream index at various oil ratio.

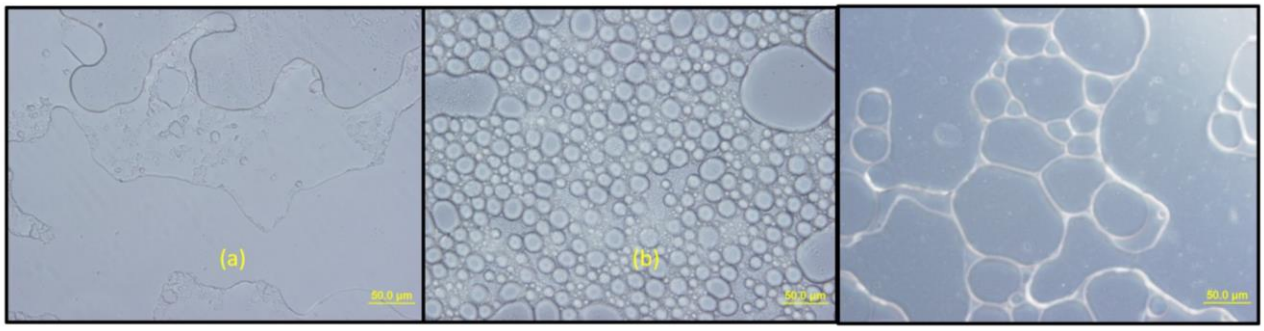


Figure 6. Microscopy of 30 %soybean oil-water emulsion (a=control; b=w/ purified BPP; c=w/ commercial pectin)

4. Conclusions

Protein-pectin mixture exhibited a shear thinning property. Increasing the ratio of pectin increases the mixture's apparent viscosity. In the *in vitro* digestion of orange juice with and without pectin, decreased viscosity relative to the initial apparent viscosity was observed. At certain points of digestion, especially in the gastric phase where the feeling of fullness during a meal occurs, the presence of pectin resulted in a higher viscosity of the orange juice. For the emulsifying effect, purified BPP and commercial pectin had no difference in the cream index at higher oil ratio but the earlier produced smaller droplets and thus, a more stable emulsion.

Acknowledgement

This research was funded by the Accelerated Science and Technology Human Resource Development Program of the Department of Science and Technology.

References

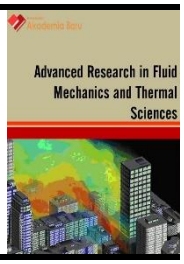
[1] Food and Agriculture Organization. (2018). Banana market review: preliminary results for 2018. Rome. 12pp. License: CC BY-NC-SA 3.0 IGO
[2] Philippine Statistics Authority. (2018). Major fruit crops quarterly bulletin. Volume 12. No. 1. https://psa.gov.ph/sites/default/files/Major%20Fruit%20Crops%20Quarterly%20Bulletin%2C%20January%20-%20March%202018.pdf
[3] Philippine Statistics Authority. (2018). Major fruit crops quarterly bulletin. Volume 12. No. 2. https://psa.gov.ph/sites/default/files/Major%20Fruit%20Crops%20Quarterly%20Bulletin%2C%20April-June%202018_0.pdf
[4] Philippine Statistics Authority. (2018). Major fruit crops quarterly bulletin. Volume 12. No. 3. https://psa.gov.ph/sites/default/files/Major%20Fruit%20Crops%20Quarterly%20Bulletin%2C%20July-September%202018_0.pdf
[5] Philippine Statistics Authority. (2018). Major fruit crops quarterly bulletin. Volume 12. No. 4. https://psa.gov.ph/sites/default/files/Major%20Fruit%20Crops%20Quarterly%20Bulletin%2C%20October-December%202018_0.pdf
[6] Walter, R. H. (2012). *The Chemistry and Technology of Pectin: 1st Edition*, Academic Press: New York, USA
[7] Akash, M. S. H., Rehman, K. & Chen, S. "Natural and Synthetic Polymers as Drug Carriers for Delivery of Therapeutic Proteins", *Polymer Reviews*, (2015). doi: 10.1080/15583724.2014.995806
[8] Markets and Markets. Pectin Market by Type (HM Pectin, LM Pectin), Raw Material (Citrus fruits, Apples, Sugar beet), Function, Application (Food & beverages, Pharmaceutical & Personal Care Products, Industrial Applications), and Region - Global Forecast to 2025, 2019. https://www.marketsandmarkets.com/Market-Reports/pectin-market-139129149.html
[9] "Pectin extraction process headed for commercialization," Department of Science and Technology-Philippine Council for Agriculture, Aquatic and Natural Resources Research and Development, accessed June 5, 2019, http://www.pcaarrd.dost.gov.ph/home/portal/index.php/quick-information-dispatch/2198-pectin-extraction-process-headed-for-commercialization
[10] Castillo-Israel, K. A. T., Baguio, S. F., Diasanta, M. D. B., Lizardo, Rona Camille M., Dizon, Erlinda I. and Mejico, M. I. F. "Extraction and characterization of pectin from Saba banana [Musa 'saba'(Musa acuminata x Musa balbisiana)] peel wastes: A preliminary study." *International Food Research Journal* 22, no.1 (2015):202–207
[11] Zhu, Y., Hsu, W.H. &Hollis, J.H. "The impact of food viscosity on eating rate, subjective appetite, glycemic response and gastric emptying rate." *PLoS One*. No. 8 (2013): e67482. doi: 10.1371/journal.pone.0067482
[12] Fan, L. & Eskin, M. "The use of antioxidants in the preservation of edible oils." *Handbook of Antioxidants for Food Preservation.* (2015): 373-388. doi: 10.1016/B978-1-78242-089-7.00015-4.
[13] Castillo-Israel, Baguio, Diasanta, Lizardo, Dizon, Mejico, "Extraction and characterization, 202-207
[14] Ibid
[15] Blumenkrantz, N., & Asboe-Hansen, G. "New method for quantitative determination of uronic acids". *Analytical Biochemistry.* no. 54 (1973): 484–489. doi: https://doi.org/10.1016/0003-2697(73)90377-1
[16] Logan K, Wright AJ, Goff HD. "Correlating the structure and in vitro digestion viscosities of different pectin fibers to in vivo human satiety". *Food Function*, no. 6 (2016): 62–70. doi: 10.1039/c4fo00543k
[17] Featherstone, S., *Jams, jellies, and related products, In Woodhead Publishing Series in Food Science, Technology and Nutrition, A Complete Course in Canning and Related Processes (Fourteenth Edition).* England: Woodhead Publishing.
[18] Khamsucharit P, Laohaphatanalert K, Gavinlertvatana P, Sriroth K, Sangseethong K "Characterization of pectin extracted from banana peels of different varieties". *Food Science and Biotechnology* no. 27 (2018):623–629. doi: 0.1007/s10068-017-0302-0
[19] Yuliarti, O., Hoon, A.L.S., Chong, S. Y. "Influence of pH, pectin and Ca concentration on gelation properties of low-methoxyl pectin extracted from Cyclea barbata Miers". *Food Structure*, no. 11 (2017): 16-23. doi: 10.1016/j.foostr.2016.10.005
[20] Hussain, M., Bakalis, S., Gouseti, O., Zahoor, T., Anjum, F. M. & Shahid, M. "Dynamic and shear stress rheological properties of guar galactomannans and its hydrolyzed derivatives". *International Journal of Biological Macromolecules*, no. 72 (2015): 687–691. doi: 10.1016/j.ijbiomac.2014.09.019.

[21] Benchabane, A., and Karim. B. ”Rheological properties of carboxymethyl cellulose (CMC) solutions”. *Colloid and Polymer Science*, no.286 (2008): 1173-1180. 10.1007/s00396-008-1882-2.
[22] Zhong, L., Oostrom, M., Truex, M.J., Vermeul, V.R., Szecsody, J.E. “Rheological behavior of xanthan gum solution related to shear thinning fluid delivery for subsurface remediation”. *Journal of Hazardous Materials,* no. 244-245 (2012): 160-170. doi: 10.1016/j.jhazmat.2012.11.028
[23] Bédié, G., Turgeon, S. & Makhlouf, J. “Formation of native whey protein isolate-low methoxy pectin complexes as a matrix for hydro-soluble food ingredient entrapment in acidic foods”. *Food Hydrocolloids*, no.22 (2008): 836-844. 10.1016/j.foodhyd.2007.03.010.
[24] Salminen, H. & Weiss, J. “Effect of pectin type on association and pH stability of whey protein—pectin complexes”. Food Biophysics, no.9 (2014): 29. doi: 10.1007/s11483-013-9314-3
[25] de Kruif, C.G., Weinbreck, F. & de Vries, R.. “Complex coacervation of proteins and anionic polysaccharides*”. Current Opinion in Colloid & Interface Science*, no. 9 (2004): 340–349. doi: 10.1016/j.cocis.2004.09.006
[26] Logan, K., Wright, A. & Goff, H. “Correlating the structure and in vitro digestion viscosities of different pectin fibers to in vivo human satiety*”. Food & Function*, no. 6 (2014): 63-71. doi: 10.1039/c4fo00543k
[27] Marciani, L., Gowland, P.A., Spiller, R. C., Manoj, P., Young, P. & Fillery-Travis, A.J. ”Effect of meal viscosity and nutrients on satiety, intragastric dilution, and emptying assessed by MRI.” *American Journal of Physiology. Gastrointestinal and Liver Physiology*. no. 280 (2001) 1227–G1233. doi: 10.1152/ajpgi.2001.280.6.G1227
[28] Fontenot, K. & Schork, F. J. “Sensitivities of droplet size and stability in monomeric emulsions.” *Industrial & Engineering Chemistry Research.* no. 32-2 (1993) 373-385. doi: 10.1021/ie00014a014
[29] Padalkar, A., Shahi, S. & Thube, M. “Micro particles: An approach for betterment of drug delivery system.” *International Journal of Pharma Research and Development* – Online. no. 3 (2011) March/012.
[30] McClements, D.J., Decker, E.A., & Weiss, J. “Emulsion-based delivery systems for lipophilic bioactive components”. *Journal of Food Science,* no. 27 (2007): R109–R124. doi: 10.1111/j.1750-3841.2007.00507.x.

Penerbit Akademia Baru

Engineering Science and Technology Conference Proceedings

Journal homepage: www.akademiabaru.com/EST.html



Waste Heat Recovery from Automotive Exhaust Using Thermoelectric Cell for Electrical Power Generation

Open Access

Y. Yaakob*[1], Ahmad Fahmi[1], D. Ibrahim[1], Baljit Singth[2], , H. Moria[3]

[1] Faculty of Mechanical Engineering, Universiti Teknologi MARA Cawangan Pulau Pinang, 13500 Permatang Pauh, Penang, Malaysia
[2] Mechanical Engineering Department,Yanbu Industrial College, Yanbu Al-Sinaiyah, P.O.Box 30436, Post Code 41912, KSA

ABSTRACT

Thermoelectric generator (TEG) is a device which can convert thermal energy into electrical energy. Theinternal combustion engine release waste heat into the environment in the form of exhaust gas. This contributes to global warming and air pollution. The main purpose of this study is to experimentally investigate the potential of TEG to convert waste heat from an automobile exhaust into electricity. Four TEGs (SP1848-27145) were attached to the top of the exhaust muffler in sequence. The tests were conducted using two different cooling mechanisms. One cooling mechanism was based on airflow from the standing fan and the other based on flowing cold water.The maximum voltage of 2.42 V was obtained when the temperature difference 83 °C. A LED bulb was used to show current flow in the system. The LED bulb illuminated when a minimum voltage of 1.60 V was achieved. The findings showed that the temperature difference between the two sides of the TEG is the dominant effect to determine TEG performance. The generated energy could be used in the car as a possible potential for powering automobile accessories like radio and others. This will result in better overall improved efficiency of the automobile engine.

Keywords:
Thermoelectric generator; exhaust waste heat; power generation

Copyright © 2019 PENERBIT AKADEMIA BARU - All rights reserved

1. Introduction

The continuous discussion on global warming is unanimous in that the change is caused primarily by many factors. The hazard of global warming is considered as one of the critical problems of the world. The increased global warming was resulted by numerous manmade activities, such as fossil fuel combustion, hazardous gasses release from industry, chemicals in fertilizers, agricultural deforestation, and transportation. With millions of cars on the road, emission of polluted air and hot exhaust gas into the environment further deteriorated the effect of global warming. The excess heat released from the combustion in automotive engine should be harvested for better efficiency and also a step toward mitigating global warming effects. Road vehicle has been identified as one of the potential to provide renewable energy from waste heat. According to a study by Demir and Dincer [1] and Kim et al. [2], the transport sector is responsible for 27% of the total greenhouse gas emissions. Approximately 40% of the energy used is lost as heat to exhaust gasses that are sure to be discarded to the environment [3]. It is therefore extremely important to

recover this waste heat and transform it into electricity for practical applications. Thermoelectric generator (TEG) is seen as the best solution to overcome the issue of the waste heat from internal combustion TEG is the best candidate to convert thermal energy into electrical energy. Thermoelectric generators are increasingly becoming popular because of many advantages as they offer. TEGs are environmentally friendly, and they can convert heat to electricity with a temperature difference between their top and bottom sides without contributing to the environmental issues [4]. TEG make use of the "Seebeck effect" where the electricity could be produced from two different conductors that form a thermal gradient. It has the advantage of working without any moving part, less space consumption, quiet and environmentally friendly. Orr et al. [7] have used eight cells on bench type, proof of concept model of power production by TEG using heat pipes and hot engine exhaust gases and managed to produce 6.03 W for charging the battery. Orr et al. [8] evaluated the TEG efficiency in another research by attaching the cells to the exhaust of the passenger carand managed to achieve 28.18 W when the surface temperature reached 250 ^{o}C and 4000 rpm. Cao et. al. [9] conducted a further research by adding the amount of TEGs to improve the efficiency of the TEG-HP mixture for automotive exhaust energy generation where it was possible to generate up to 81.09 V. The primary goal of the research is to explore the option of using TEG in stagnation condition to generate energy from waste heat in road vehicles. Restoring the energy to the engine alternator could be beneficial and contribute to reducing global warming and pollution problems.

2. Methodology

There are two ceramic substrates composed of a typical thermoelectric Cell Generator(TEG) module. Within the module, two types of thermoelectric materials are configured to be connected in series and thermally parallel. The thermoelectric module is a circuit containing thermoelectric materials which are packed between the hot side and the cold side that can produce electricity from heat directly. The temperature difference between two dissimilar materials will provide a direct electrical current to flow in a circuit [2]. Connecting two different thermoelectric materials in the form of a semiconductor n-type (negative charge) and a semiconductor p-type (positive charge). The type of the thermoelectric module used for this study is shown in Figure 1.

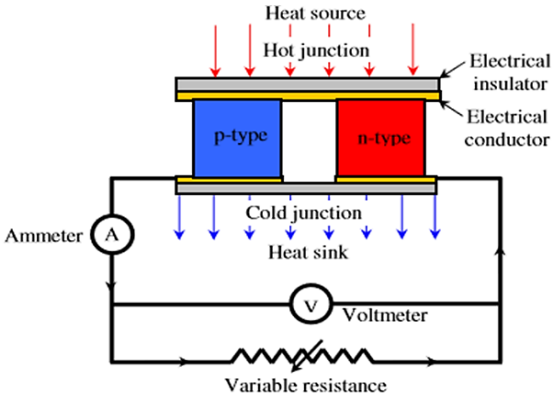


Fig. 1: Structural diagram of thermoelectric module [6]

The voltage generated by a TEG can be calculated from the following formula;

$$V=\alpha\Delta T \quad (1)$$

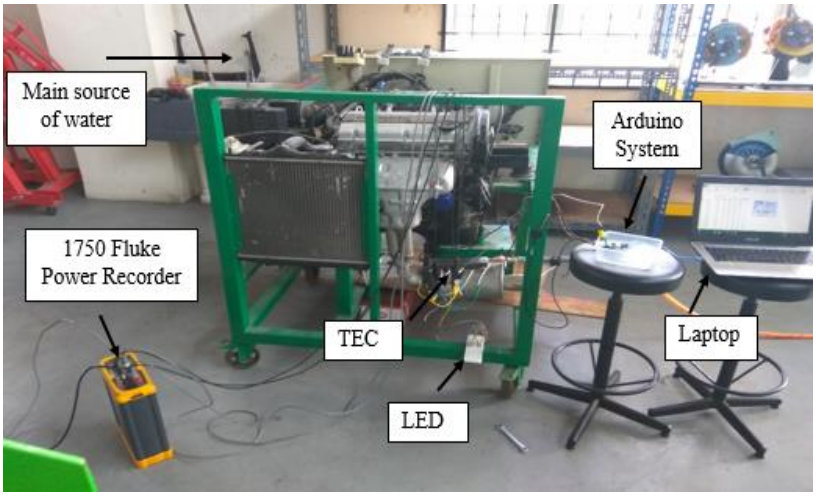
where the temperature difference, $\Delta T = T_h - T_c$, and α is the Seebeck coefficient, which is considered to be material coefficient and constant at all temperature [3].

If α is positive, then it is driving an electric current through the wire from hot to cold junction [5]. Increasing the voltage difference (ΔV) raises the temperature difference between two joints (ΔT). The Seebeck coefficients are a nonlinear function of temperature. The relatively low electrical power generation and has restricted their use to specific situations where reliability is a significant consideration [8].

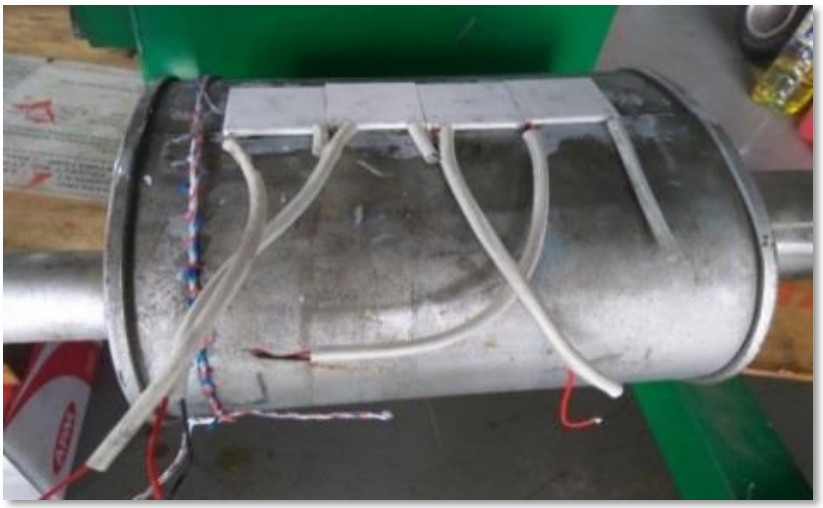
3. Experimental Set-up

3.1 Experimental Set-up

The Proton petrol engine-testing unit of 1500 CC DOHC (4G91) at Automotive Laboratory, UiTM Pulau Pinang was used for this study. Four units of TEG, Bismuth Telluride thermoelectric device (SP1848-27145) composed of ceramic substrates were used in this project. The four TEG units were arranged in sequence on top of the exhaust muffler surface as shown in Figure 2. The TEC was sandwiched as a heat sink between the warm surface of the engine muffler and a cold air from the standing plant. Another method of cooling is the use of cold water flowing through the manufactured channel on top of the TEC as shown in Figure 3. The programmed Arduino system is used as the data logger to monitor the temperature and the Fluke 1750 power recorder to measure the power generated.



(a)



(b)

Fig. 2: (a) Experimental setup using Proton petrol engine; and (b) the arrangement of TEG on the exhaust muffler

3.1.1 Experimental works

The tests were performed in two stages with regulated engine velocity at a maximum of 2500 rpm. This was designed to prevent exhaust surface temperature from becoming too hot, which could damage the TEG unit. The first stage of the work was based on using the cold air from a standing fan as a cooling medium while the engine was still running. The experiment lasted for 24 minutes, and the exhaust surface temperature, TEG's topside temperature, and the output voltage were recorded. In the second stage of the experiment, a tap water supply was channeled to flow in the hollow steel block on top of TEGs to cool the top of the TEGs as the engine was running. The average water flow rate was set at 0.11 kg / s,. The duration of this test was kept similar to the first stage test, All relevant data on hot surface temperature, cold side temperature, and output voltages were recorded in the data logger.

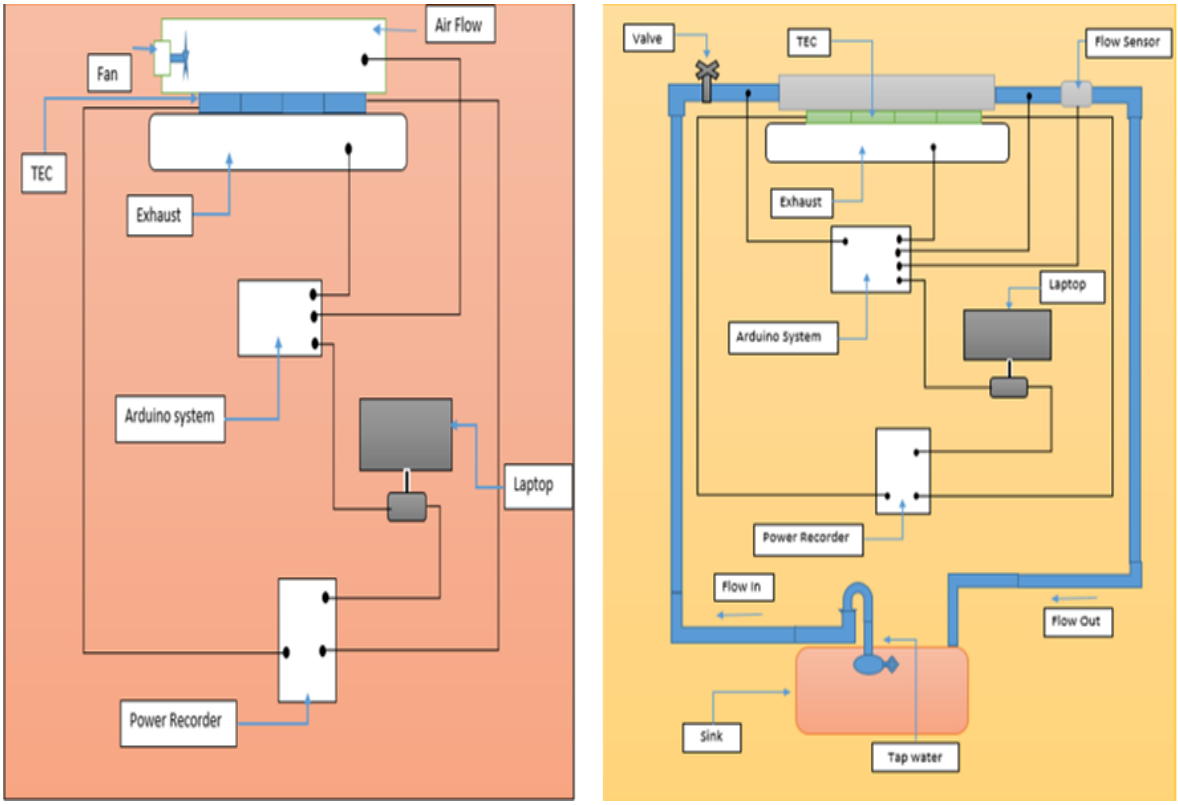


Fig. 3: Schematic diagram of the experimental setup for air cooling (left); and cold water cooling (right)

4. Results and Discussions

Figure 4 shows the hot surface temperature and cold side temperature of the TEGs. The hot surface for the air cooled demonstrates greater temperatures compared to the water cooled experiment. The maximum temperature reached 132 ^{o}C for air cooled and 114 ^{o}C for the water cooled setup. This is due to the inconsistency of the engine timing, which influenced the engine speed and affected combustion in the engine block. On the cold side, the water cooling provides a lower temperature of 30 ^{o}C, around 7 ^{o}C less compared to the air cooling temperature of 37 ^{o}C. The incoming water temperature could be kept constant. While for the air cooling, it was exposed to the effect of heat from the exhaust hot surface due to the convection phenomenon. The maximum temperature difference of 92 ^{o}C for air cooling and 86 ^{o}C for water cooling was obtained, as shown in Figure 5.

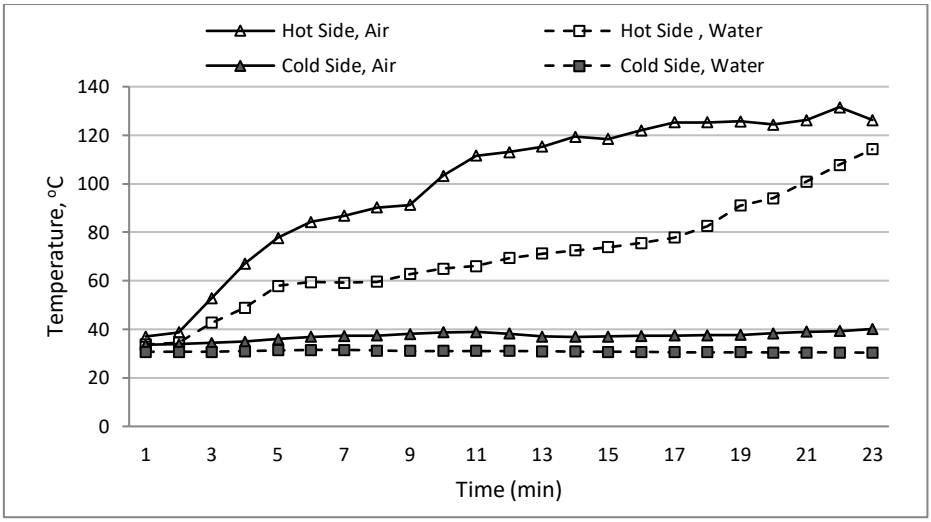


Fig. 4: Cold and hot temperature for both cooling method

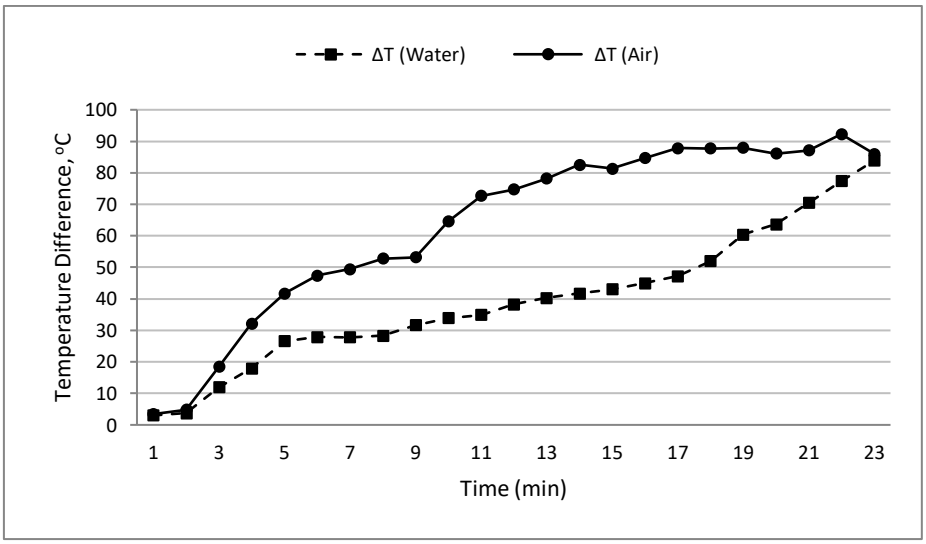


Fig. 5: Temperature difference between air and water cooling

The voltage obtained for both the f air and water cooled method is shown in Figure 6 and Figure 7. The voltage gradually increased to reach the maximum value of 1.6 V at 88 °C temperature difference for the air cooling method. While for cold water, a significant effect on producing voltage occurs after passing the temperature difference of 45 °C. It has shown a drastic increment from a consistently low voltage of 0.2 V to reach a maximum 2.26 V at 84 °C of temperature difference. At this point, one of the TEG units was burnt that directly affected the sudden drop in the voltage value. Nevertheless, the results have revealed a good agreement with the previous study conducted by Orr et al. [7].

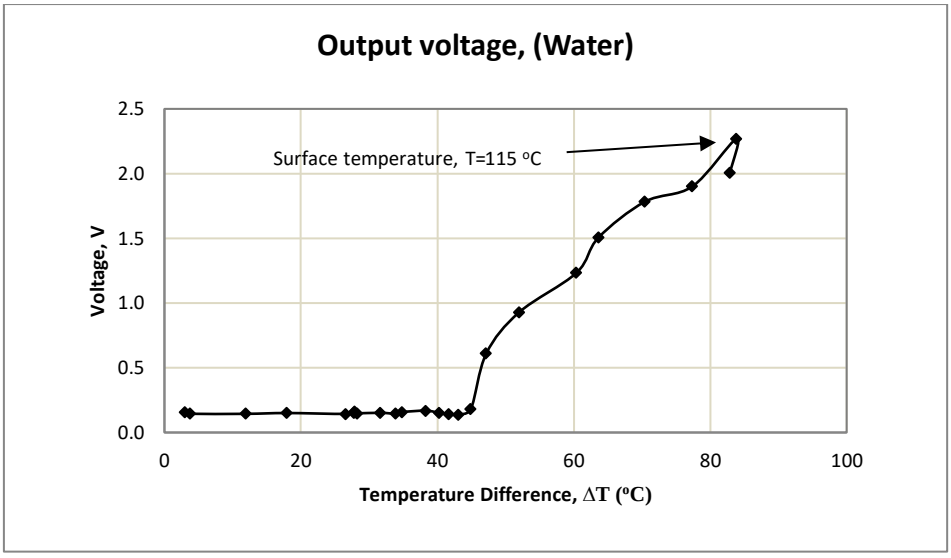


Fig. 6: Output voltage from water cooling

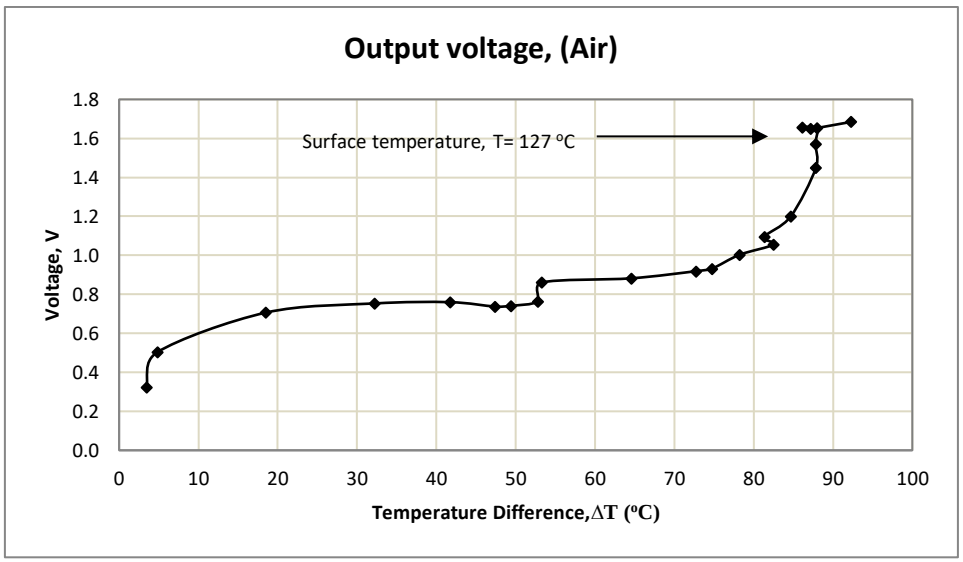


Fig. 7: Output voltage from air cooling

The heat transfer effect was calculated by

$$\dot{Q} = \dot{m}Cp\dot{(}T_{co}^{\cdot} - T_{ci}) \quad (2)$$

Where, $\dot{m}$ is the wáter mass flow rate in kg/s, C_p is the specific heat for wáter in KJ/kg.°C, T_{co} is the outgoing water temperature, and the T_{ci} is the incoming water temperature in °C. The $\dot{Q}$ shows the amount of heat extracted by the water. Figure 8 shows the maximum amount of heat that had been extracted is 68 W, which was occurred in the middle of the duration. Beyond this point, the amount of extracted heat is decreasing. One of the main reasons was the temperature difference of the water is decreased due to the effect of the surface temperature. This would directly affect the temperature of the incoming flow to increase further. To improve the situation, the better quality

of TEG that could stand high-temperature range is to be used. The design of the water channel also needs to be revisited so that the temperature of the water could remain constant.

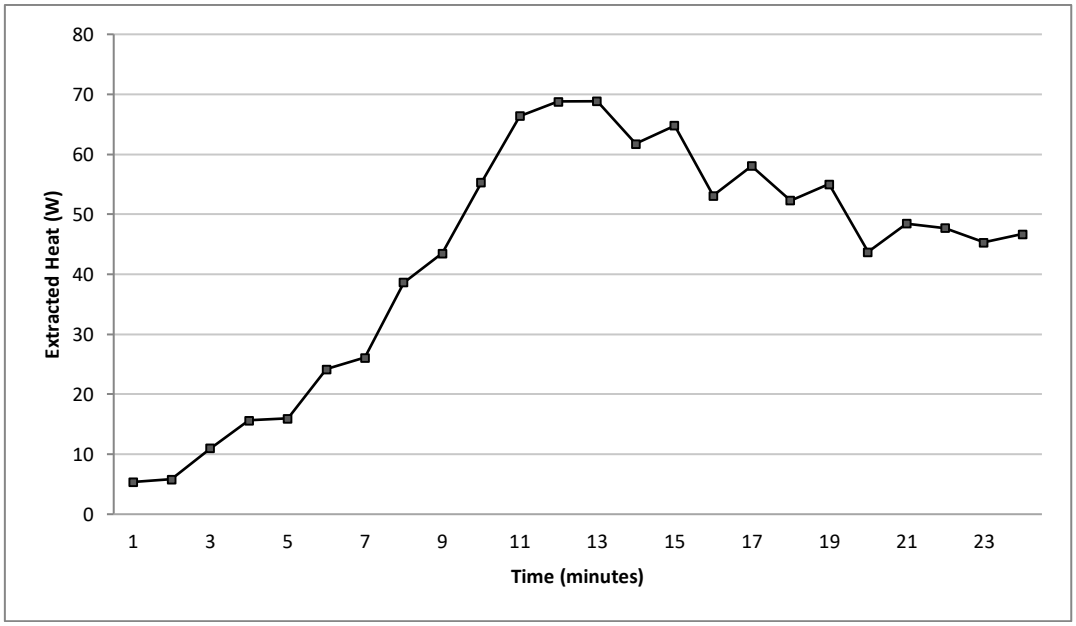


Fig. 8: The amount of heat extracted for water cooling method

4.1 Verification of the result

The aim of this investigation was to observe the generating current from the TEG effect of temperature difference. Due to limited output in terms of direct current from the experimental setup, three units of small LED light were connected to TEG in the experiment for justification purposes as shown in Figure 9. All the LEDs lighted up when the voltage reached 1.6 V. It shows that the TEG start to shows the effect of producing current when the temperature difference reached 70 °C for water cooling and 80 °C for air cooling. The light was on the whole period of experiment. The LEDs shows brighter light on the experiment with water cooling. This is obviously due to the higher voltage produced that directly contributed for higher current. It has proven that the use of TEG for waste heat recovery would produce energy directly for helpful applications.

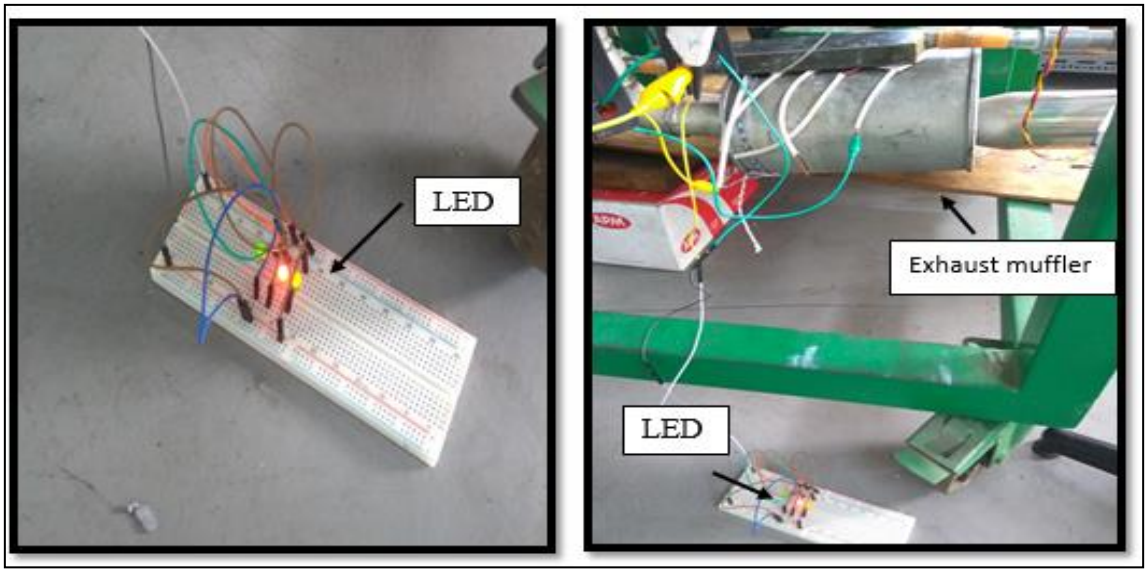


Fig. 9: The connected LED to TEGs

4. Conclusions

In this study, an exhaust heat recovery system has been proposed. The experimental set-up was tested to evaluate the efficiency of the TEG in two cooling modes using the air stream from the standing fan and by mounting the cold water channel block on top of the TEC. The difference in effect temperature between the two sides affecting TEG performance. The current experiment using four TEG units showed the ability to produce 2.42V output voltage when the temperature difference was 83 ° C, and the LED bulbs were illuminated. It shows from the experiments that water cooling provides better performance of TEG, but in the actual condition TEC would expose to air of the moving vehicle. By adding more TEG units, system efficiency could be enhanced, and the outcome has shown TEG's ability to regenerate energy from exhaust collector waste heat. The energy produced could be a channel to the running battery that could possibly boost its service life. The research also showed the system's capacity to extract a certain quantity of heat for power generation purposes and to reduce the impact on global warming.

Acknowledgement
The authors would like to express their appreciation to the Universiti Teknologi MARA, Penang Campus for providing financial support attending 4th IS-FMTS 2019.

References

[1] M.E Demir, I. Dincer.," Development and heat transfer analysis of a new heat recovery system with thermoelectric generator,"Heat and Mass Transfer, vol. 108, pp. 2002-2010, 2017.
[2] S. L. Kim, K. W. Choi, K. Lee, and K. Kim, "Evaluation of automotive waste heat recovery for various driving modes," Energy, vol. 106, pp. 579-589, 2016.
[3] S. Kim, S. Park, S.Kim, S.H. Rhi "A thermodynamics generetor using engine coolant for light-duty internal combustion engine-powered vehicles," J. Electron. Mater, , vol.40, pp. 812-816 2011.
[4] M.E Demir, I. Dincer.," Performance assessment of a thermoelectric generator applied to exhaust waste heat recovery," Applied Thermal Engineering, vol. 120, pp. 694-707, 2017.
[5] Z.G Shen, L.L Tian, X. Liu, "Automotive exhaust thermoelectric generators: Current status, challenges and future prospects," Energy Conversion and Management, vol. 195, pp. 1138-1173, 2019.
[6] S. a. Abdul-Wahab et al., "Thermoelectric Cooling for Low Temperature Space Environment," Applied Thermal Engineering, vol. 2, no. 2, pp. 1–9, 2013.
[7] B. Orr, B. Singh, L. Tan, A. Akbarzadeh, "Electricity generation from an exhaust heat recovery system utilising thermo electric cells and heat pipes", Applied Thermal Engineering, vol. 73, pp. 588-597, 2014.
[8] B. Orr, A. Akbarzadeh, P. Lappas,"An exhaust heat recovery system utilising thermoelectirc generator and heat pipes," Applied Thermal Engineering, vol. 126, pp. 1185-1190, 2017.
[9] Q. Cao, W. Luan, T. Wang, "Performance enhancement of heat pipes assisted thermoelectric generator for automobile exhaust heat recovery," Applied Thermal Engineering. Vol. 130, pp. 1472-1479, 2018.
[10] H. Fan, R. Singh, and A. Akbarzadeh, "Power Generation from Thermoelectric Cells by Using High Concentrated Solar Dish," 2010.
[11] Rowe, D.M., 1995. CRC Handbook of Thermoelectrics. CRC Press.

Penerbit Akademia Baru

Engineering Science and Technology
Conference Proceedings

Journal homepage: www.akademiabaru.com/EST.html

Preparation methods and challenges of hybrid nanofluids: A review

Open Access

N.S.M. Sahid[1], M.M. Rahman[1*], K . Kadirgama[1], D. Ramasamy[1] and M.A. Maleque[2]

[1] Faculty of Mechanical and Automotive Engineering Technology, University Malaysia Pahang, 26600 Pekan, Pahang, Malaysia.
[2] Department of Manufacturing and Materials Engineering, Faculty of Engineering, International Islamic University Malaysia, P.O. Box 10, Kuala Lumpur, 50728, Kuala Lumpur, WP Kuala Lumpur, Malaysia

ABSTRACT

This paper reviews the preparation methods and some challenging issues that need to be addressed during the preparation of hybrid nanofluids. The recent years have seen the rapid development of hybrid nanofluids in different aspects, where the researchers focused mainly on the enhancement of heat transfer. Hybrid nanofluids are potential fluids offer enhanced heat transfer performance and thermo-physical properties than conventional heat transfer fluids as well as single-faced nanofluids. However, hybrid nanofluids preparation deserves similar attention since the final properties of hybrid nanofluids are dependent on the stability of the dispersion. In this paper, the recent progress related to preparation methods of hybrid nanofluids, factors affecting their stability, methods of enhancing thermal properties and applications of hybrid nanofluids.

Keywords:
Nanoparticles, Hybrid nanofluids, thermal conductivity, density, heat transfer, pressure drop, viscosity.

Copyright © 2019 PENERBIT AKADEMIA BARU - All rights reserved

1. Introduction

Nanoparticles practically used in science and engineering fields. Associated to conventional cooling liquid, water, oil and ethylene glycol are usually used as working fluids for transfer of heat in many industrial types of equipment such as heat exchangers, cooling and heating device and chemical processes and microelectronics. Conversely, these fluids have relatively low thermal conductivity and thus cannot reach high heat exchange rates in thermal engineering devices. Since the thermal conductivity of these liquids is low, there has been interested in using suspended solid particles to enhance the thermal conductivity of the base-fluid [1-5]. Dispersion of micrometre or even millimetre particles in base-fluid was used earlier by researchers. However, these earlier attempts have faced obstacles such as increasing in pressure drop, sedimentation of particles and erosion of equipment [6]. Then the new researchers find the new method which uses hybrid nanofluids. Hybrid nanofluids have some unique structures which are quite different from dispersions of mm or μm sized particles. Further, hybrid nanofluids can diffuse quickly and induces only a minimal pressure drop during flow, which is beneficial for heat transfer application. Studies show that relatively small amounts of nanoparticles can enhance the thermal conductivity of base fluids in no small extent. Two features that are very important for heat transfer systems are extreme stability, and high thermal conductivity.

1.1 Hybrid Nanofluids

Hybrid nanofluids are a relatively new class of fluids which consist of a base fluid with nano-sized particles (1–100 nm) suspended within them [7, 8]. There has the advantage of using hybrid nanofluids which are the high specific surface area. Therefore, There has an extra heat transfer surface between the particles and fluids. It has extraordinary dispersion stability with predominant Brownian motion of particles. Then, it can reduced pumping power as compared to pure liquid to achieve equivalent heat transfer intensification and reduced particle clogging as compared to conventional slurries, thus promoting system miniaturisation. Lastly, it adjustable properties, including thermal conductivity and surface wettability, by varying particle concentrations to suit different applications [7, 9]. Nanoparticles can be considered as the potential lubricant additives and several significant advantages compared to organic molecules currently used as lubricant additives [10]. For example, their nanometer size allows them to enter the contact area easily. Then they are frequently active at ambient temperature. Thus there is no induction period is necessary to obtain interesting tribological properties. Nanoparticles can improve the tribilogical of coating itself, but it can also be released by the coating during wear and can thus lubricate in the same way as if they were in the oil [11]. Nanomaterials also offer applications to pollution prevention through improved catalytic processes that produce less waste, better sensors for process controls, enhanced separations, and increased understanding of the nanosized natural processes that are involved in industrial processes [12]. Hybrid nanofluids can be used for various industries including biotechnology, transportation to energy production, Micro-Electro-Mechanical Systems (MEMS), electronics systems. Recently, the number of companies that observe the potential of hybrid nanotechnology and their focus for specific industrial applications is increasing. In the transportation industry, nano cars, GM and Ford, among others, are focusing on nanofluids research projects [13]. Hybrid nanofluids can be used in following specific areas: which are heat-transfer hybrid nanofluids, tribological hybrid nanofluids, surfactant and coating hybrid nanofluids, chemical hybrid nanofluids, process/extraction hybrid nanofluids, environmental (pollution cleaning) hybrid nanofluids, bio- and pharmaceutical- hybrid nanofluids and medical hybrid nanofluids (drug delivery and functional tissue–cell [14].

1.2 Thermal Conductivity

An innovative way of cutting fluids synthesised by the mixing the carbon nanoparticles, ceramic, metallic, non-metallic and ceramics in a conventional flooded cutting fluid because as compared with suspended milli- or micro-sized particles. The hybrid nanofluids show better stability, rheological properties, excellent thermal conductivity, and no adverse effect on pressure drop [15]. Chen and Ding [16] reviewed the literature regarding the improvement in thermal conductivity of metallic, carbon, inorganic and carbide materials and concluded that thermal conductivity of hybrid nanofluids increases with an increase of nanoparticle concentration. The addition of nanoparticles in cutting fluids was investigated and improved their coolant properties [17]. They also estimated the optimum required nanoparticle concentration to be of 6 wt%. Many pieces of research reviewed the work and found that hybrid nanofluids may possess outstanding heat extraction capabilities (thermal conductivity) over conventional cutting fluids. They concluded that this enhanced thermal conductivity might be an essential factor for better performance in various applications. The inclusion of nanoparticles of metal oxides into any base fluid enhances its thermal conductivity. A few researchers reported a very significant improvement in thermal conductivity of hybrid nanofluids by adding multi-walled carbon nanofluids tube (MWCNT) up to

150% and 200%, respectively, as compared to the base fluid [18, 19]. Furthermore, many researchers reported an appreciable improvement in thermal conductivity of base fluid by the inclusion of metallic, non-metallic, carbon nanotubes (CNTs), and ceramic particles [20-27]. Most authors agreed that hybrid nanofluids provide higher thermal conductivity compared to base fluids. It is increased with the concentration of the particles. The stability, particle size, temperature, and dispersion are played an essential role in determining the thermal conductivity of hybrid nanofluids [28]. The thermal conductivity of common liquids, polymers and solids are analysed in [29]. The thermal conductivity of hybrid nanofluids at different temperatures are evaluated in [30]. The optimisation of hybrid nanofluids thermophysical properties requires successful synthesis procedures for creating stable suspensions of nanoparticles in liquids. Many combinations of particle materials and fluids are of potential interest depending on the requirements of a particular application. For example, nanoparticles of oxides, carbides, metals and nonmetals can be dispersed into the conventional fluids such as deionised (DI) water, ethylene glycol (EG), or engine oil [2, 31, 32].

Table 1. Summary of synthesis methods of hybrid nanofluids.

Method	Base fluids	Materials	Observation
One-step method	Transformer oil	Silver/silica	The viscosity of the oil could be crucial for the dispersion and stability
One-step method	water	Silver/silica	No surface contamination was observed
Two-step method	water	Cu/CuO_2	Exhibit excellent stability with high absorbance due to it possessing small size particles with poor cohesion among Cu_2O particles
Two-step method	Water	Al_2O_3/Cu	Thermal conductivity of water-based nanofluids containing both Cu and Cu_2O nanoparticles showed more (about 2%) thermal conductivity enhancement comparing nanofluids containing Cu nanoparticles of Cu_2O nanoparticles.

Hybrid nanofluids are prepared by one-step or two-step method. Table 1 is tabulated the synthesis methods of hybrid nanofluids. In the one-step method, the production of nanoparticles and their dispersion in a base fluid are done simultaneously. The drying, storage, transportation, and dispersion of nanoparticles are avoided. Thus the agglomeration of nanoparticles is minimised and the stability of the hybrid nanofluids is increased. However, it is impossible to scale it up for large scale industrial application, which limits the application of this method. [1, 5, 33, 34]. Two-step technique which dry nanoparticles are first by produced, and then they are dispersed in a suitable liquid host. Nevertheless, as nanoparticles have high surface energy, aggregation and clustering are unavoidable and will appear easily — afterwards, the particles clog and sediment at the bottom of the container. A few review papers have discussed the preparation methods for hybrid nanofluids [1, 5, 35, 36]. In the present paper, we attempt to review the preparation methods of hybrid nanofluids presented in previously published data with much more details. However, there is no comprehensive literature on the preparation and challenges of hybrid nanofluids to the best of authors' knowledge. There are three methods for stabilising the suspension: addition of surface activators (surfactants), changing the pH value, and using ultrasonic vibrations. Tables 2-4 summarised on the heat transfer and pressure drop; the density, heat capacity and viscosity; the thermal conductivity of hybrid nanofluids, respectively.

Table 2. Summary on the heat transfer and pressure drop of hybrid nanofluids.

References	Nanofluids	Observation
[37]	Al_2O_3 nanoparticles into the pure PCM	Laminar forced convection in the tube; heat transfer efficacy appears severely outweighed by pressure drop penalty
[38]	Ag (0.05%)+Al_2O_3(0.005%)	Flow in grooved heat pipe; hybrid nanofluids make the system deteriorate in terms of thermal resistance
[39]	Al_2O_3–Cu/water	Fully developed laminar convection in the uniformly heated circular tube; maximum enhancement of 13.56% in Nusselt number
[40]	Al_2O_3–Cu/water	Average turbulent heat transfer enhancement of 8%
[41-43]	Ag/(MWNT–HEG)–water and Ag/(MWNT–HEG)–EG	Laminar forced convective tube flow, Tremendous enhancement in heat transfer coefficient
[44]	CuO–HEG/water and CuO–HEG/EG	The enhancement in heat transfer is more for EG based nanofluids
[45, 46]	(CNT–graphene)–water and (CNT–graphene)–EG	Laminar forced convective tube flow, tremendous enhancement in heat transfer coefficient at a particle volume fraction of 0.01% and that is more for EG based
[47]	(CNTs+Al_2O_3)–water	Laminar forced convective tube flow; enhanced the convective heat transfer performance significantly.
[48]	MWCNT–Fe_3O_4/water	Fully developed turbulent flow in the constant heat-flux circular tube; a maximum of 31.1% enhancement in Nusselt number with a penalty of 1.18-times pumping power
[49]	Cu–TiO_2/water	Convective heat transfer coefficient, Nusselt number and overall heat transfer coefficient were increased by 52%, 49% and 68% respectively

Table 3. Summary on the density, heat capacity and viscosity of hybrid nanofluids.

References	Nanofluids	Observation
[50]	Al_2O_3–MEPCM/water	Density and heat capacity; independent temperature measurement, classical correlations are applicable
[50]	Al_2O_3–MEPCM/water	Viscosity; drastically increase of the effective dynamic viscosity of the hybrid suspension.
[51]	Al_2O_3–Cu/water	Viscosity; viscosity increase is substantially higher than the increase in thermal conductivity
[52]	Ag-Silica/oil	Viscosity; the nanofluid showed Newtonian behaviour at lower silica concentrations and followed the Bingham flow model at high concentrations
[53]	Silica/MWCNT–water	Density and viscosity; at high concentration, better influence compared to mono nanofluids

1.3 Ag–MgO hybrid Nanofluids

The Ag–MgO hybrid nanofluid was used, and distilled water was used as base fluid, and the average diameter of the Ag and MgO provided was 25 nm and 40 nm, respectively. XRD was used to determine the size of nanoparticles. For breaking down the agglomeration of nanoparticles in water, an ultrasonic vibrator was used about three hours. Cetyl Trimethyl Ammonium Bromide (CTAB) was used to ensure better stability and proper dispersion without affecting hybrid nanofluids' thermos physical properties since the surfactant concentrations used in the experiments were very low. After preparing the hybrid nanofluids with the different volume concentrations, pH was measured, and the value was 5.74. The suspensions were stable for several hours (days) [64].

Table 4. Summary of the thermal conductivity of hybrid nanofluids.

References	Nanofluids	Observation
[54]	sphere-CNT/poly-alpha-olefin	Thermal conductivity of hybrid nanofluids higher than that of simple spheres and even slightly higher than those for CNTs
[55]	CNT–AuNP/water and CNT–CuNP/water	Thermal conductivity for hybrid nanofluids was lower than CNT, AuNP and CuNP nanofluids
[50]	Al_2O_3–MEPCM/water	Significant enhancement of thermal conductivity of PCM suspension with Al_2O_3 nanoparticle dispersion relative to pure water
[56, 57]	Al_2O_3–Cu/water	A very significant enhancement in the effective thermal conductivity due to hybridisation of alumina nanoparticles using metallic copper particles
[58]	Ag–silica/oil	The theoretical increase in thermal conductivity is much lower than that observed. It does suggest there is some synergistic effect between the Ag nanoparticles and the silica support
[59]	Al–Zn/ethylene glycol	A maximum 16% thermal conductivity enhancement at 0.1 vol% particle concentration was achieved
[60]	Silica/MWCNT	Thermal conductivity in the case of hybrid nanofluids is between enhancement of MWCNTs and silica nanofluids
[61]	γ-Al_2O_3/MWCNT	Enhancement of the thermal conductivity of hybrid nanofluids can reach up to 14.75% at a volume fraction of 0.01
[62]	Al_2O_3–MWCNT/water	Thermal conductivity better with non-ground MWCNTs compared to ground MWCNTs
[63]	Ag–MWCNT/water	Improved dispersion of CNTs in the matrix, as well as the decoration of the MWCNTs with silver, maybe the reason for enhancement in thermal conductivity

1.4 Silicon dioxide-nanofluids

The dispersion of silicon dioxide nanopowders in the non-polar organic fluid was evaluated [65]. Benzalkonium chloride, benzethonium chloride, and cetyl trimethyl ammonium bromide were tested as surfactants for dispersing silica. Surfactants were dispersed into the base fluid first, followed by an introduction of the nanopowder. The mixture was homogenised by continuous stirring and sonicated ten times (~80W) for 5min each time. Suspensions with 1 vol.% of SiO_2 nanoparticles with no surfactant and excess of each surfactant (5 wt.% or ~ 0.12–0.14 M) were prepared using the adsorption model with 'laying flat' and compacted 'standing up' layers of the surfactant molecules The visual appearance of suspensions 24 h after the last sonication was the best stabilizer for SiO_2/TH66 [65]. Besides thermal conductivity, the friction between tool and workpiece may also be an important factor responsible for high-temperature generation at the cutting zone that affects the workpiece dimensional accuracy, surface quality, and, more importantly, the tool life during machining. Other researcher found that the addition of graphite nanoparticles improves the lubricating property of conventional lubricants due to the reduction in the friction coefficient [66]. Because of their low friction behaviour, the graphite and MoS_2 solid lubricants may contribute to the reduction of cutting force and reduce the surface roughness in machining [67]. Also, the addition of nanoparticles into base fluid can enhance their convective heat transfer coefficient, lubricating properties, and wettability. On the other hand, it can reduce

tool wear, surface roughness, cutting force, and chip thickness compared with dry machining and conventional fluid machining [68-71].

An investigation on the morphology of the machined surface during milling of aerospace AL6061-T6 for novel uses of SiO_2 nano lubrication system. In the present case, SiO_2 was used in place of MoS_2. A morphological analysis of AL6061-T6 after machining with SiO_2 nanofluids lubricant was done at different nanofluids lubricant concentrations using FESEM and XRD machines. FESEM was applied at different nanoparticle concentrations set at 0.0, 0.2, 0.5, and 1.0 wt% in nanofluid. It was noticed from the results that the increase of SiO_2 concentration at 0.2 wt% increased the growth of thin protective film on the tool–chip interfaces. These formations of the thin film on the machined surface enhanced the machining performance by improving the surface quality and lowering the cutting temperature and cutting forces [72]. The best G-ratio was achieved by 4% Al_2O_3 concentration using MQL, while the best surface finish could be achieved by flood cooling [73]. The lower grinding force, better G-ratio, and higher surface quality could be achieved due to the formation of a slurry layer at the tool-workpiece interface. Also, a significant reduction in the grinding temperature with MQL was observed as compared to dry grinding. However, the use of hybrid nanofluids did not affect grinding temperature significantly [73].

1.5 Titanium oxide hybrid nanofluids

The advantages of hybrid nanofluids are better stability compared to those fluids containing micro- or milli-sized particles and higher thermal conductive capability than the base fluids themselves. Hybrid nanofluids are proposed for various uses in important fields such as electronics, transportation, medical, and HVAC [74]. Hence, there is a necessity for a fundamental understanding of the heat transfer behaviour of hybrid nanofluids to exploit their potential benefits and applications. Nanoparticles have been investigated by several researchers who found significant enhancement of thermal conductivity (5–60%) over the volume fraction range of 0.1–5% [75-78]. A hybrid nanofluids do not mean a simple mixture of liquid and solid particles. To prepare hybrid nanofluids by suspending nanoparticles into base fluids, proper mixing and stabilisation of the particles are essential. Hybrid nanofluids dispersing copper, aluminium and their oxide nanoparticles widely investigated by many researchers [79]. However, titanium oxide, which has excellent chemical and physical stability, is not widely used, although it is an economy and commercially available mineral product. The reasons for choosing TiO_2 because TiO_2 is mostly regarded as safe material for human being and animals (they are mainly used in the cosmetic products, and water treatment), TiO_2 nanoparticles are easily obtained (they are produced in very large industrial scales), TiO_2 hybrid nanofluids have an excellent stability even without using any stabilizer and metal oxides such TiO_2 nanoparticles are chemically more stable than their metallic counterparts [74, 80]. The primary nanoparticles are approximately spherical with an average diameter of about 20 nm.

1.6 Graphene nanofluids

New research shows that graphene hybrid nanofluids could provide higher thermal conductivity enhancement in comparison to other tested hybrid nanofluids. Graphene particles have better thermal conductivity and also higher mechanical strength and electrical conductivity. Favourable thermo-physical properties of graphene have made it an excellent candidate for use in hybrid nanofluids [81]. Besides, synthesising graphene nano-particles is relatively easy and cost-effective. A small variation of properties of graphene has been reported due to different methods

used to manufacture one layer or multi-layer graphenes such as exfoliation of the graphene oxide layer, deposition with chemical vapour and mechanical cleavage. [81-83]. An experimental investigation has revealed that the thermal conductivity and heat transfer properties of one layer graphene are higher than CNT. Two-dimensional honeycomb lattice graphene with more than ten layers called Graphene nanoplatelets (GNP). Dispersion of graphene with good stability is one of the big issues must be solved. So by using functionalization method (acid treat and amino function), proper ultrasonic and solvent, it could be able to prepare stably dispersed graphene-based hybrid nanofluids [84, 85].

2. Inorganic and Organic Compounds

Inorganic and organic compounds were proposed as sensing materials, and have gained development increasingly, respectively, due to some particular advantages. Inorganic compounds usually perform high chemical and thermal stability that allows their application under different operating conditions, and cheap processes can obtain it and be quickly deposited in thin or thick film form by different techniques. Organic compounds are characterised by a synthetic versatility and reactivity, which makes it possible to modulate the molecular structure of the sensing materials to enhance the selectivity toward a target analyte [86]. Additionally, in the fields of sensors, the organic sensing materials such as conducting polymers (polyaniline (PANI), polypyrrole (PPy), and polythiophene (PTP), etc.) can show response to target analytes at room temperature or low temperature, which has a convenient operating and attractive prospect [87-91]. Nevertheless, the drawbacks for single inorganic or single organic sensing materials, namely, high operating temperature and low selectivity for inorganic sensing materials, and poor chemical stability and mechanical strength for organic sensing materials, could restrict their practical application.

The researches have proved that the mechanical strength and chemical stability can be enhanced by the addition of inorganic particles into the organic materials to form hybrids [92-94]. Following this idea, the most general approach has been the exploitation of the inorganic compound as a protective matrix where the organic moiety, which is the sensing component, is dispersed by different techniques [95, 96]. A different and more intriguing approach can be that in the hybrid materials, both components cooperate in the sensing mechanisms, resulting in enhanced performances. Therefore, in the past decades, the organic/inorganic hybrid materials with different combinations of the two components, expected to obtain new kind composite materials with synergetic or complementary behaviors, have received more and more attention worldwide and become attractive for many new electronic, optical, magnetic or catalytic applications since their properties or performances can be improved, considering the possibility to combine the advantages of organic and inorganic counterparts [97]. As far as sensor applications concerned, many reports have been published based on the organic/inorganic hybrid sensing materials for the applications in gas sensors, humidity sensors, ultraviolet sensors, strain sensors, and other sensors. However, the independent review of the recent development of inorganic/organic hybrid materials for sensors is still an absence.

3.0 Configuration and Preparation Methods

3.1 Organic-intercalated-inorganic nanohybrids

In the hybrid nanofluids, the organic guest components are embedded into the interlayers of inorganic host frameworks, and organic and inorganic layers stack alternately at a nanometer

scale [98-100]. Many organic components can be intercalated into the interlayers. Itoh and Matsubara et al. [101-104] reported layered organic-inorganic hybrid films composed of an inorganic semiconductive metal oxide molybdenum oxide (MoO_3) host and various organic guests (e.g. PANI, PPy, and poly(2,5-dimethylaniline) (PDMA)). The intercalated organic/inorganic hybrid thin films could be prepared by an ex-situ intercalation process, in which the host MoO_3 films were first deposited on $LaAlO_3$ (LAO) single-crystal substrates by using a CVD method followed by the intercalation of organic guests into the MoO_3 films. The depiction of the preparation for (PoANIS)xMoO_3 and (PANI)xMoO_3 hybrid thin films [102]. They also prepared (PANI)xMoO_3 and (PoANIS)xMoO_3 hybrid thin films on the $LaAlO_3/SiO_2/Si$ substrate by a modified process, i.e. [Na(H2O)$_2$]xMoO_3 thin films were immersed into carefully filtrated PANI and PoANIS solutions, respectively, for intercalation of organic components [102].

3.2 Core-shell hybrids

The synthesis of core-shell hybrids with metal oxide as core and polymer as shell requires the polymerisation of the monomer by various methods in the presence of metal oxide particles. The polymer shell could be produced by electropolymerization of monomers [105]. In the preparation process of the hybrid system, a novel series of terthiophene monomers 1, 2, 3, and 4 with a carboxylic acid functionality to modify the TiO_2 surface were adopted. Nanocrystalline TiO_2 films were deposited onto the surface of QCMs by spin-coating of TiO_2 paste, followed by drying at 120 ◦C, resulting in the formation of robust porous films onto the QCMs. The films were then immersed in a THF solution of terthiophene monomer to give the terthiophene-modified TiO_2 films. Frequency changes in the QCMs could monitor the adsorption amount of monomer. Electro polymerisation of thiophene monomers to produce polythiophene resulted in the covering of the TiO_2 surface with the polythiophene (PTP) layer. Ram et al. [106] fabricated the TiO_2 (or SnO_2)-conducting polymer hybrids by in situ self-assembly technique. PANI–TiO_2 films were fabricated on a polystyrene sulfonate treated substrates. The oxidative chemical polymerisation of aniline in the presence of colloidal TiO2 was carried out in HCl acid medium at pH = 2 and using 0.5 mol/L ammonium persulfate drop-by-drop addition as an oxidizing agent. PTP/SnO_2 core/shell hybrid materials and PPy/coated SnO_2 hollow spheres hybrid materials the synthesise through in-situ polymerisation of Py, TP monomers in the presence of prepared SnO2 nanoparticles or hollow spheres. [107].

4. Challenges of Hybrid Nanofluids

Preparation of homogeneous suspension remains a technical challenge since the nanoparticles always form aggregates due to powerful van der Waals interactions. The physical and chemical treatment have been conducted such as an addition of surfactant, surface modification of the suspended particles or applying strong force on the clusters of the suspended particles to get stable nanofluids. Dispersing agents, surface-active agents, have been used to disperse fine particles of hydrophobic materials in aqueous solution [108]. Generally, long term stability of nanoparticles dispersion is one of the basic requirements of hybrid nanofluids applications. Stability of hybrid nanofluids has a corresponding good relationship with the enhancement of thermal conductivity were the better dispersion behaviour, the higher thermal conductivity of hybrid nanofluids [28]. However, the dispersion behaviour of the nanoparticles could be influenced by a period of time as can be seen. As a result, the thermal conductivity of hybrid nanofluids is eventually affected. Other prove the thermal conductivity of ethylene glycol-based hybrid

nanofluids containing 0.3% copper nanoparticles is decreased with time [78]. In their study, the thermal conductivity of hybrid nanofluids was measured twice: first was within two days and the second was two months after the preparation. It was found that fresh hybrid nanofluids exhibited slightly higher thermal conductivities than hybrid nanofluids that were stored up to two months. It might occur due to the reduced dispersion stability of nanoparticles to time. Nanoparticles may tend to agglomerate when kept for long period of time. The research compared the Al_2O_3 hybrid nanofluids stability visually over some time. The hybrid nanofluids kept for 30 days exhibit some settlement and concentration gradient compared to fresh hybrid nanofluids. It indicated long term degradation in thermal performance of hybrid nanofluids could have happened. Particles settling must be scrutinized since it may lead to clogging of coolant passages [109].

5. Conclusions

The present paper presents a comprehensive review of the hybrid nanofluids preparation methods. Although many preparation methods were proposed, it is still a challenge to make a hybrid nanofluids homogeneous and long-term stable with negligible agglomeration, and without affecting the thermophysical properties. Since nanoparticles cannot be anticipated to be healthily dispersed in their base fluids, surfactants can play a useful role for proper dispersion of nanoparticles to ensure higher heat transfer performance of hybrid nanofluids. The addition of nanoparticles into the base fluid to enhance the thermal conduction and enhancement increases of thermal properties with increasing particle concentration and decreasing particle (agglomerate) size.

Acknowledgement
The authors would like to thank University Malaysia Pahang for providing the laboratory facilities and the financial support under the University LEAP-3 FLAGSHIP Research Grants (Project number RDU172203).

References:

[1] Li Y, Tung S, Schneider E, Xi S. A review on development of nanofluid preparation and characterization. Powder Technology. 2009;196:89-101.
[2] Mahian O, Kianifar A, Kalogirou SA, Pop I, Wongwises S. A review of the applications of nanofluids in solar energy. International Journal of Heat and Mass Transfer. 2013;57:582-94.
[3] Angayarkanni S, Philip J. Review on thermal properties of nanofluids: Recent developments. Advances in colloid and interface science. 2015;225:146-76.
[4] Lee J-H, Lee S-H, Choi C, Jang S, Choi S. A review of thermal conductivity data, mechanisms and models for nanofluids. International Journal of Micro-Nano Scale Transport. 2010;1:269-322.
[5] Ghadimi A, Saidur R, Metselaar H. A review of nanofluid stability properties and characterization in stationary conditions. International Journal of Heat and Mass Transfer. 2011;54:4051-68.
[6] Yarmand H, Gharehkhani S, Ahmadi G, Shirazi SFS, Baradaran S, Montazer E, et al. Graphene nanoplatelets–silver hybrid nanofluids for enhanced heat transfer. Energy Conversion and Management. 2015;100:419-28.
[7] Saidur R, Leong K, Mohammad H. A review on applications and challenges of nanofluids. Renewable and Sustainable Energy Reviews. 2011;15:1646-68.
[8] Saidur R, Kazi S, Hossain M, Rahman M, Mohammed H. A review on the performance of nanoparticles suspended with refrigerants and lubricating oils in refrigeration systems. Renewable and Sustainable Energy Reviews. 2011;15:310-23.
[9] Wen D, Lin G, Vafaei S, Zhang K. Review of nanofluids for heat transfer applications. Particuology. 2009;7:141-50.
[10] Martin JM, Ohmae N. Nanolubricants: John Wiley & Sons; 2008.
[11] Martin JM, Ohmae N. Colloidal lubrication: general principles. Nanolubricants.1-13.
[12] Masciangioli T, Zhang W-X. Peer reviewed: environmental technologies at the nanoscale. Environmental science & technology. 2003;37:102A-8A.

[13] Das SK. Nanofluids—the cooling medium of the future. 2006.
[14] Bhogare RA, Kotahwale B. A review on applications and challenges of nanofluids as coolant in automobile radiator. International journal of scientific and research publications. 2013;3.
[15] Daungthongsuk W, Wongwises S. A critical review of convective heat transfer of nanofluids. Renewable and Sustainable Energy Reviews. 2007;11:797-817.
[16] Chen H, Ding Y. Heat transfer and rheological behaviour of nanofluids–a review. Advances in transport phenomena: Springer; 2009. p. 135-77.
[17] Srikant R, Prasad M, Amrita M, Sitaramaraju A, Krishna PV. Nanofluids as potential solution for Minimum Quantity Lubrication: A review. Proceedings of the Institution of Mechanical Engineers, Part B: Journal of Engineering Manufacture. 2013:0954405413497939.
[18] Choi S, Zhang Z, Yu W, Lockwood F, Grulke E. Anomalous thermal conductivity enhancement in nanotube suspensions. Applied physics letters. 2001;79:2252-4.
[19] Yang Y. Carbon nanofluids for lubricant application: University of Kentucky; 2006.
[20] Murshed S, Leong K, Yang C. Investigations of thermal conductivity and viscosity of nanofluids. International Journal of Thermal Sciences. 2008;47:560-8.
[21] Turgut A, Tavman I, Chirtoc M, Schuchmann H, Sauter C, Tavman S. Thermal conductivity and viscosity measurements of water-based TiO2 nanofluids. International Journal of Thermophysics. 2009;30:1213-26.
[22] Pastoriza-Gallego MJ, Lugo L, Legido JL, Piñeiro MM. Thermal conductivity and viscosity measurements of ethylene glycol-based Al2O3 nanofluids. Nanoscale research letters. 2011;6:1-11.
[23] William JKM, Ponmani S, Samuel R, Nagarajan R, Sangwai JS. Effect of CuO and ZnO nanofluids in xanthan gum on thermal, electrical and high pressure rheology of water-based drilling fluids. Journal of Petroleum Science and Engineering. 2014;117:15-27.
[24] Yang Y, Grulke EA, Zhang ZG, Wu G. Thermal and rheological properties of carbon nanotube-in-oil dispersions. Journal of Applied Physics. 2006;99:114307.
[25] Phuoc TX, Massoudi M, Chen R-H. Viscosity and thermal conductivity of nanofluids containing multi-walled carbon nanotubes stabilized by chitosan. International Journal of Thermal Sciences. 2011;50:12-8.
[26] Meng Z, Han D, Wu D, Zhu H, Li Q. Thermal Conductivities, Rheological Behaviors and Photothermal Properties of Ethylene Glycol-based Nanofluids Containing Carbon Black Nanoparticles. Procedia Engineering. 2012;36:521-7.
[27] Rashidi A, Ahmadi H, Mohtasebi SS, Pourkhalil M. Thermal and rheological properties of oil-based nanofluids from different carbon nanostructures. International Communications in Heat and Mass Transfer. 2013;48:178-82.
[28] Sergis A, Hardalupas Y. Anomalous heat transfer modes of nanofluids: a review based on statistical analysis. Nanoscale research letters. 2011;6:1-37.
[29] Wen D, Ding Y. Effective thermal conductivity of aqueous suspensions of carbon nanotubes (carbon nanotube nanofluids). Journal of Thermophysics and Heat Transfer. 2004;18:481-5.
[30] Tawakoli T, Hadad M, Sadeghi MH, Daneshi A, Sadeghi B. Minimum quantity lubrication in grinding: effects of abrasive and coolant–lubricant types. Journal of Cleaner Production. 2011;19:2088-99.
[31] Keblinski P, Eastman JA, Cahill DG. Nanofluids for thermal transport. Materials today. 2005;8:36-44.
[32] Sarkar J. A critical review on convective heat transfer correlations of nanofluids. Renewable and Sustainable Energy Reviews. 2011;15:3271-7.
[33] Salehi J, Heyhat M, Rajabpour A. Enhancement of thermal conductivity of silver nanofluid synthesized by a one-step method with the effect of polyvinylpyrrolidone on thermal behavior. Applied Physics Letters. 2013;102:231907.
[34] Das SK, Choi SU, Yu W, Pradeep T. Nanofluids: science and technology: John Wiley & Sons; 2007.
[35] Yu W, Xie H. A review on nanofluids: preparation, stability mechanisms, and applications. Journal of Nanomaterials. 2012;2012:1.
[36] Wu D, Zhu H, Wang L, Liu L. Critical issues in nanofluids preparation, characterization and thermal conductivity. Current Nanoscience. 2009;5:103-12.
[37] Ho C, Huang J, Tsai P, Yang Y. On laminar convective cooling performance of hybrid water-based suspensions of Al 2 O 3 nanoparticles and MEPCM particles in a circular tube. International Journal of Heat and Mass Transfer. 2011;54:2397-407.
[38] Han W-S, Rhi S-H. Thermal characteristics of grooved heat pipe with hybrid nanofluids. Thermal Science. 2011;15:195-206.
[39] Suresh S, Venkitaraj K, Selvakumar P, Chandrasekar M. Effect of Al 2 O 3–Cu/water hybrid nanofluid in heat transfer. Experimental Thermal and Fluid Science. 2012;38:54-60.
[40] Suresh S, Venkitaraj K, Hameed MS, Sarangan J. Turbulent Heat Transfer and Pressure Drop Characteristics of Dilute Water Based Al2O3–Cu Hybrid Nanofluids. Journal of nanoscience and nanotechnology. 2014;14:2563-72.
[41] Baby TT, Ramaprabhu S. Synthesis and nanofluid application of silver nanoparticles decorated graphene. Journal of Materials Chemistry. 2011;21:9702-9.

[42] Baby TT, Ramaprabhu S. Experimental investigation of the thermal transport properties of a carbon nanohybrid dispersed nanofluid. Nanoscale. 2011;3:2208-14.
[43] Baby TT, Sundara R. Synthesis of silver nanoparticle decorated multiwalled carbon nanotubes-graphene mixture and its heat transfer studies in nanofluid. AIP Advances. 2013;3:012111.
[44] Baby TT, Sundara R. Synthesis and transport properties of metal oxide decorated graphene dispersed nanofluids. The Journal of Physical Chemistry C. 2011;115:8527-33.
[45] Chen L, Yu W, Xie H. Enhanced thermal conductivity of nanofluids containing Ag/MWNT composites. Powder technology. 2012;231:18-20.
[46] Aravind SJ, Ramaprabhu S. Graphene wrapped multiwalled carbon nanotubes dispersed nanofluids for heat transfer applications. Journal of Applied Physics. 2012;112:124304.
[47] Labib MN, Nine MJ, Afrianto H, Chung H, Jeong H. Numerical investigation on effect of base fluids and hybrid nanofluid in forced convective heat transfer. International Journal of Thermal Sciences. 2013;71:163-71.
[48] Sundar LS, Singh MK, Sousa AC. Enhanced heat transfer and friction factor of MWCNT–Fe 3 O 4/water hybrid nanofluids. International Communications in Heat and Mass Transfer. 2014;52:73-83.
[49] Madhesh D, Parameshwaran R, Kalaiselvam S. Experimental investigation on convective heat transfer and rheological characteristics of Cu–TiO 2 hybrid nanofluids. Experimental Thermal and Fluid Science. 2014;52:104-15.
[50] Ho CJ, Huang JB, Tsai PS, Yang YM. Preparation and properties of hybrid water-based suspension of Al2O3 nanoparticles and MEPCM particles as functional forced convection fluid. International Communications in Heat and Mass Transfer. 2010;37:490-4.
[51] Suresh S, Venkitaraj KP, Selvakumar P, Chandrasekar M. Synthesis of Al2O3–Cu/water hybrid nanofluids using two step method and its thermo physical properties. Colloids and Surfaces A: Physicochemical and Engineering Aspects. 2011;388:41-8.
[52] S.S. Botha PN, B.J. Bladergroen. Physicochemical properties of oil-based nanofluids containing hybrid structures of silver nanoparticles supported on silica. Industrial & Engineering Chemistry Research. 2011;50:3071-7.
[53] Baghbanzadeh M, Rashidi A, Soleimanisalim AH, Rashtchian D. Investigating the rheological properties of nanofluids of water/hybrid nanostructure of spherical silica/MWCNT. Thermochimica Acta. 2014;578:53-8.
[54] Z.H. Han BY, S.H. Kim, M.R. Zachariah Application of hybrid sphere/carbon nanotube particles in nanofluids. Nanotechnology. 2007;18:105701.
[55] Jana S, Salehi-Khojin A, Zhong W-H. Enhancement of fluid thermal conductivity by the addition of single and hybrid nano-additives. Thermochimica Acta. 2007;462:45-55.
[56] Suresh S, Venkitaraj K, Selvakumar P, Chandrasekar M. Synthesis of Al 2 O 3–Cu/water hybrid nanofluids using two step method and its thermo physical properties. Colloids and Surfaces A: Physicochemical and Engineering Aspects. 2011;388:41-8.
[57] Suresh S, Venkitaraj K, Selvakumar P. Synthesis, Characterisation of Al2O3-Cu Nano Composite Powder and Water Based Nanofluids. Advanced Materials Research: Trans Tech Publ; 2011. p. 1560-7.
[58] Botha SS, Ndungu P, Bladergroen BJ. Physicochemical properties of oil-based nanofluids containing hybrid structures of silver nanoparticles supported on silica. Industrial & Engineering Chemistry Research. 2011;50:3071-7.
[59] Paul G, Philip J, Raj B, Das PK, Manna I. Synthesis, characterization, and thermal property measurement of nano-Al 95 Zn 05 dispersed nanofluid prepared by a two-step process. International Journal of Heat and Mass Transfer. 2011;54:3783-8.
[60] Baghbanzadeh M, Rashidi A, Rashtchian D, Lotfi R, Amrollahi A. Synthesis of spherical silica/multiwall carbon nanotubes hybrid nanostructures and investigation of thermal conductivity of related nanofluids. Thermochimica acta. 2012;549:87-94.
[61] Abbasi SM, Rashidi A, Nemati A, Arzani K. The effect of functionalisation method on the stability and the thermal conductivity of nanofluid hybrids of carbon nanotubes/gamma alumina. Ceramics International. 2013;39:3885-91.
[62] Nine MJ, Batmunkh M, Kim J-H, Chung H-S, Jeong H-M. Investigation of Al2O3-MWCNTs hybrid dispersion in water and their thermal characterization. Journal of nanoscience and nanotechnology. 2012;12:4553-9.
[63] Munkhbayar B, Tanshen MR, Jeoun J, Chung H, Jeong H. Surfactant-free dispersion of silver nanoparticles into MWCNT-aqueous nanofluids prepared by one-step technique and their thermal characteristics. Ceramics International. 2013;39:6415-25.
[64] Esfe MH, Arani AAA, Rezaie M, Yan W-M, Karimipour A. Experimental determination of thermal conductivity and dynamic viscosity of Ag–MgO/water hybrid nanofluid. International Communications in Heat and Mass Transfer. 2015;66:189-95.
[65] Timofeeva EV, Moravek MR, Singh D. Improving the heat transfer efficiency of synthetic oil with silica nanoparticles. Journal of colloid and interface science. 2011;364:71-9.
[66] Lee CGH, Y.J. Choi, Y.M.; Lee, J.K.; Choi, C.; Oh, J.M. A Study on the Tribological characteristics of graphite nano lubricants. . International Journal of Precision Engineering and Manufacturing 2009;10:85-90.

[67] Reddy NSKR, P.V. Experimental investigation to study the effect of solid lubricants on cutting forces and surface quality in end milling. International Journal of Machine Tools and Manufacture 2006:189-98.
[68] Sarhan AADS, M.; Hamidi, M. Reduction of power and lubricant oil consumption in milling process using a new SiO2 nano lubrication system. International Journal of Advanced Manufacturing Technology 2012:505-12.
[69] Sayuti MS, A.A.D.; Tanaka, T.; Hamdi, M.; Saito,Yamamoto, K. Cutting force reduction and surface quality improvement in machining of aerospace duralumin AL-2017-T4 using carbon onion nanolubrication system. International Journal of Advanced Manufacturing Technology. 2013:1493–500.
[70] Rahmati BS, A.A.D.; Sayuti, M. . Morphology of surface generated by end milling AL6061-T6 using molybdenum disulfide (MoS2) nanolubrication in end milling machining. Journal of Cleaner Production. 2013:685-91.
[71] Sayuti MS, A.A.D.; Salem, F. Novel uses of SiO2 nano-lubrication system in hard turning process of hardened steel AISI4140 for less tool wear, surface roughness and oil consumption. Journal of Cleaner Production 2014:265-76.
[72] Sayuti ME, O.M.; Sarhan, A.A.D.; Hamdi, M. Investigation on the morphology of the machined surface in end milling of aerospace AL6061-T6 for novel uses of SiO2 nanolubrication system. Journal of Cleaner Production. 2013;66: 655-63.
[73] Shen BS, A.J.; Tung, S.C. Application of nanofluids in minimum quantity lubrication grinding. Tribology Transactions. 2008:730-7.
[74] Murshed S, Leong K, Yang C. Enhanced thermal conductivity of TiO 2—water based nanofluids. International Journal of Thermal Sciences. 2005;44:367-73.
[75] Eastman JA, Phillpot S, Choi S, Keblinski P. Thermal transport in nanofluids 1. Annu Rev Mater Res. 2004;34:219-46.
[76] Das SK, Putra N, Thiesen P, Roetzel W. Temperature dependence of thermal conductivity enhancement for nanofluids. Journal of Heat Transfer. 2003;125:567-74.
[77] Xuan Y, Li Q, Hu W. Aggregation structure and thermal conductivity of nanofluids. AIChE Journal. 2003;49:1038-43.
[78] Eastman J, Choi S, Li S, Yu W, Thompson L. Anomalously increased effective thermal conductivities of ethylene glycol-based nanofluids containing copper nanoparticles. Applied physics letters. 2001;78:718-20.
[79] Xuan Y, Li Q. Heat transfer enhancement of nanofluids. International Journal of heat and fluid flow. 2000;21:58-64.
[80] He Y, Jin Y, Chen H, Ding Y, Cang D, Lu H. Heat transfer and flow behaviour of aqueous suspensions of TiO 2 nanoparticles (nanofluids) flowing upward through a vertical pipe. International Journal of Heat and Mass Transfer. 2007;50:2272-81.
[81] Novoselov KS, Geim AK, Morozov S, Jiang D, Zhang Y, Dubonos Sa, et al. Electric field effect in atomically thin carbon films. science. 2004;306:666-9.
[82] Tung VC, Allen MJ, Yang Y, Kaner RB. High-throughput solution processing of large-scale graphene. Nature nanotechnology. 2009;4:25-9.
[83] Kaniyoor A, Baby TT, Ramaprabhu S. Graphene synthesis via hydrogen induced low temperature exfoliation of graphite oxide. Journal of Materials Chemistry. 2010;20:8467-9.
[84] Sridhar V, Jeon J-H, Oh I-K. Synthesis of graphene nano-sheets using eco-friendly chemicals and microwave radiation. Carbon. 2010;48:2953-7.
[85] Zhang W, He W, Jing X. Preparation of a stable graphene dispersion with high concentration by ultrasound. The Journal of Physical Chemistry B. 2010;114:10368-73.
[86] Geng L, Huang X, Zhao Y, Li P, Wang S, Zhang S, et al. H 2 S sensitivity study of polypyrrole/WO 3 materials. Solid-state electronics. 2006;50:723-6.
[87] Huang J, Kaner RB. A general chemical route to polyaniline nanofibers. Journal of the American Chemical Society. 2004;126:851-5.
[88] Zhang X, Goux WJ, Manohar SK. Synthesis of polyaniline nanofibers by “nanofiber seeding”. Journal of the American Chemical Society. 2004;126:4502-3.
[89] Nuraje N, Su K, Yang N-l, Matsui H. Liquid/liquid interfacial polymerization to grow single crystalline nanoneedles of various conducting polymers. ACS nano. 2008;2:502-6.
[90] Zotti G, Vercelli B, Berlin A. Monolayers and multilayers of conjugated polymers as nanosized electronic components. Accounts of chemical research. 2008;41:1098-109.
[91] Li B, Lambeth DN. Chemical sensing using nanostructured polythiophene transistors. Nano letters. 2008;8:3563-7.
[92] Gai L, Du G, Zuo Z, Wang Y, Liu D, Liu H. Controlled Synthesis of Hydrogen Titanate− Polyaniline Composite Nanowires and Their Resistance− Temperature Characteristics. The Journal of Physical Chemistry C. 2009;113:7610-5.
[93] Chuang F-Y, Yang S-M. Titanium oxide and polyaniline core-shell nanocomposites. Synthetic metals. 2005;152:361-4.
[94] Sadek A, Wlodarski W, Shin K, Kaner RB, Kalantar-Zadeh K. A layered surface acoustic wave gas sensor based on a polyaniline/In2O3 nanofibre composite. Nanotechnology. 2006;17:4488.
[95] Ulman A. An Introduction to Ultrathin Organic Films: From Langmuir--Blodgett to Self--Assembly: Academic press; 2013.
[96] Ulman A. Formation and structure of self-assembled monolayers. Chemical reviews. 1996;96:1533-54.

[97] Ansari MO, Khan MM, Ansari SA, Raju K, Lee J, Cho MH. Enhanced Thermal Stability under DC Electrical Conductivity Retention and Visible Light Activity of Ag/TiO2@ Polyaniline Nanocomposite Film. ACS applied materials & interfaces. 2014;6:8124-33.
[98] Yui T, Tsuchino T, Akatsuka K, Yamauchi A, Kobayashi Y, Hattori T, et al. Visible light-induced electron transfers in titania nanosheet and mesoporous silica integrated films. Bulletin of the Chemical Society of Japan. 2006;79:386-96.
[99] Okada A, Usuki A. Twenty Years of Polymer-Clay Nanocomposites. Macromolecular Materials and Engineering. 2006;291:1449-76.
[100] Takagi S, Eguchi M, Tryk DA, Inoue H. Porphyrin photochemistry in inorganic/organic hybrid materials: Clays, layered semiconductors, nanotubes, and mesoporous materials. Journal of Photochemistry and Photobiology C: Photochemistry Reviews. 2006;7:104-26.
[101] Itoh T, Matsubara I, Shin W, Izu N, Nishibori M. Analytical study of resistance drift phenomena on (PANI) xMoO3 hybrid thin films as gas sensors. Bulletin of the Chemical Society of Japan. 2008;81:1331-5.
[102] Itoh T, Matsubara I, Shin W, Izu N. Preparation and characterization of a layered molybdenum trioxide with poly (o-anisidine) hybrid thin film and its aldehydic gases sensing properties. Bulletin of the Chemical Society of Japan. 2007;80:1011-6.
[103] Itoh T, Matsubara I, Shin W, Izu N, Nishibori M. Preparation of layered organic–inorganic nanohybrid thin films of molybdenum trioxide with polyaniline derivatives for aldehyde gases sensors of several tens ppb level. Sensors and Actuators B: Chemical. 2008;128:512-20.
[104] Itoh T, Matsubara I, Shin W, Izu N, Nishibori M. Characterizations of interlayer organic–inorganic nanohybrid of molybdenum trioxide with polyaniline and poly (o-anisidine). Materials Chemistry and Physics. 2008;110:115-9.
[105] Kimura M, Sakai R, Sato S, Fukawa T, Ikehara T, Maeda R, et al. Sensing of vaporous organic compounds by TiO2 porous films covered with polythiophene layers. Advanced Functional Materials. 2012;22:469-76.
[106] Ram MK, Yavuz Ö, Lahsangah V, Aldissi M. CO gas sensing from ultrathin nano-composite conducting polymer film. Sensors and Actuators B: Chemical. 2005;106:750-7.
[107] Xu M, Zhang J, Wang S, Guo X, Xia H, Wang Y, et al. Gas sensing properties of SnO 2 hollow spheres/polythiophene inorganic–organic hybrids. Sensors and Actuators B: Chemical. 2010;146:8-13.
[108] Yu W, France DM, Routbort JL, Choi SU. Review and comparison of nanofluid thermal conductivity and heat transfer enhancements. Heat Transfer Engineering. 2008;29:432-60.
[109] Lee J M. Assessment of the effectiveness of nanofluids for singlephase and two-phase heat transfer in micro-channels. International Journal Heat Mass Transfer. 2007;50:63-452.

Penerbit Akademia Baru

Engineering Science and Technology
Conference Proceedings

Journal homepage: www.akademiabaru.com/EST.html

Drying Droplets : A Review on Its Numerical and Experimental Studies To Remove Coffee Ring Effect

Open Access

Eng Pei Ying[1], Zamani Bin Ngali[1], Mohd Omar Mukhtar Zainul Azmi[2], Wee Chang Ann[1]

[1] Department of Mechanics Engineering, University Tun Hussein Onn Malaysia, 86400 Parit Raja, Johor, Malaysia
[2] School of Mechanical Engineering Universiti Teknologi Malaysia, Sultan Ibrahim Chancellery Building, Jalan Iman, 81310 Skudai, Johor

ABSTRACT

It is widely known that significant rejection percentage of substrates in the hard disk manufacturing industry is due to the stain appeared during drying of cleaning solution after platting process. Comparison of the characteristics and the causes of these stains suggested that the study of coffee ring effect (CRE) and droplets analysis are needed before any further analysis is carried out. In this reviews on CRE and droplets, both numerical and experimental works were critically analyzed. Previous studies have highlighted that the drying process of the water droplets are affected by the properties of the water droplets, substrate and temperature. Manipulation of Constant Contact Angle, Constant Contact Radius, advanced contact angle and receding contact angle by varying the arrangement of the substrates and the position of the drying equipment is required to attain the optimum setup to eliminate CRE. Furthermore, manipulation of the temperature of the substrates can enhance the drying process of the droplets before the formation of CRE but the process must not changes the properties of the substrates. CRE formation also depends on the properties of the substrates and water droplets. Changing the chemical properties substrates are not advisable to eliminate CRE due to its complex design of the substrates for data storing. All the numerical tests have to be performed according to correct procedures to ensure accurate and acceptance by the industries. Verified and validated results from the evaluation will help to accurately predict the real consequences for further optimization. Knowing that the formation of CRE is caused by the evaporating of the water droplets, we need to find ways to eliminate the formation of water droplets before the heating process, in order to eliminate CRE.

Keywords:
Numerical evaluation analysis;
coffee ring effect; substrates; hard disk

Copyright © 2019 PENERBIT AKADEMIA BARU - All rights reserved

1. Introduction

In hard disk manufacturing industries, substrates need to undergo cleaning process for enhancement [1]. The cleaning process consists of sub processes such as rinsing, blowing and heating. The rinsing process, will wash away any non-volatile solute particles remaining on the substrates. The substrates then conveyed through the air blowing process to wipe away the cleaning solution before heating process to dry the substrate. For any data recording substrates or any high quality surface substrates, it is important for the surface of the substrate to remain clean and stainless [2]. However, stains appeared on the substrates after the heating process. The stains then become permanent. This paper discusses related questions with regards to this issue including what are these stains, what are the causes of the stains, what are the ways to suppress it and the simulation analysis used to evaluate the current cleaning process.

Often stains on substrates, are known as coffee-ring effect or CRE. However, we can never conclude anything before comparing the physical characteristics of these stains and the physical

characteristics of CRE. Deegan et al. [3, 20, 25, 26] reported that the CRE is attributable to a pinned contact line during evaporation and nonuniform evaporation flux on the droplet surface, which is considered as an evaporating sessile droplet with its edge pinned on the substrate. The liquid contains dispersed non-volatile solute particles move towards the drop edge and deposit the particles there. At the end of the evaporation process a ring-like residue of the particles is left on the substrate. According to this definition of CRE, Table 1 below shows the comparison of the stains and CRE.

Table 1 Comparison of the stains and CRE

Physical Characteristics	**Stain on the substrates**	**Coffee ring effects**
Pinned contact line	The actual view of stain on the substrate  The microscope view of stain on the substrate 	 Pratibha Mahale (2017). Suppression of the Coffee-Ring Effect and Evaporation-Driven Disorder to Order Transition in Colloidal Droplets [4].
Non-uniform evaporation flux	Yes	Yes
sessile droplet	Present before evaporation	Present before evaporation
Surface	Substrates with multiple coated surface	Can be various : polymer, glass and substrates [5]
Shape of the stains	ring-like residue	ring-like residue
Physical process	An evaporation of sessile droplet under a high heat	An evaporating sessile droplet with its edge pinned on the substrate
non-volatile solute particles on the substrates	Assume to be absent as the substrate go through rinsing process	Present
Outcome after evaporation or heating	The present of Permanent stains	Depend on the surface. Hardly clean or removed.

The difference on the comparison shown in Table 1 is relevant when we assume that the substrates have no non-volatile solute particles after going through the rinsing process. However during the production, the substrates were never examined under the microscope after the rinsing and blowing process. Other than the differences mentioned, the characteristics show that both CRE and stains are alike in nature. We might not able to draw a conclusion that these stains are CRE, but these similarities show that CRE can be a reference for elimination of these stains through eliminating the water droplets or manipulating the evaporation flux of the water droplets.

According to the hard disk manufacturer, the stains appeared when there exist remaining water droplets on the substrates before the heating process which is tally with what we conclude from Table 1. Hence, this paper covers the discussion on the physical properties of the substrate and the

physical properties of the droplets which is important in the aspect for both the stains and CRE. Through these findings, we able to come out with a better solution to eliminate the stains. This review article will focus on gathering literature on various aspects and knowledge of droplets on the substrate, ways to eliminate droplets and numerical model that used to evaluate droplets procedures which can later be used to develop the frame work of the numerical evaluation and optimization analysis for cleaning process of hard disk substrates. This paper filter off any methods and analysis available for removing CRE yet not suitable to be implement on the hard disk substrates. There are many previous works and studies made on hard disk substrate as well as droplets. However, this paper focus more on the physical process of the cleaning of hard disk substrates which contribute to the formation of the stains by relating it with the formation of droplets. Those methods to suppress the CRE, are not practical to be carried out in hard disk substrates that will be discussed in this paper as well. It is also obvious that, in hard disk substrates industries, we are not going to utilize the CRE for any positive outcome as some industries does. Utilizing the CRE meaning encouraging the formation of CRE. This paper is aimed to guide hard disk manufacturer whether to retain the current cleaning process system with optimized condition or to change the whole cleaning process system.

2. The study on droplets.

Controlling the process of solute deposition in the presence of droplets is important especially when it involves evaporation on surfaces. Drying of droplet is actually a complex, non-equilibrium and difficult-to-control process [5], the control of the deposition morphology of droplet has significant influence. Further studies on this non-uniform redistribution process indicate that inner flows, including capillary flow [6] and Marangoni flow [7], dynamics of the three-phase contact line [8], and particle-particle/particle-interface interaction [9] will influence the final particle distribution.

Other worthy suppressing methods that we can consider are electro-wetting, electro-osmotic flow, vibrations interactions at solid-liquid and liquid-gas interfaces, humidity cycling and porous substrates [10]. Before these methods are suggested, it is important to understand the cleaning process of the hard disk substrate and study the droplets on these substrates. This is what this paper is all about. Even though it is considered as fundamental, but it directs us straight in relating the theory and the solution to the actual problem in the industry. As the results, none of the suppressing methods mentioned above is suitable in contribute to the effectiveness of cleaning hard disk substrates.

2.1 Drying Droplets Phenomenon on the substrate

Droplet evaporation characteristics depend on surface wettability, contact angle hysteresis (CAH), [11] and surface roughness [12]. There are many ways to measure the surface wettability on substrates such as contact angle measurements, microscopic examination, glass slide method and nuclear magnetic resonance. However, to known the wettability of the hard disk substrates, we can simply just by using glass slide method. This draw the conclusion that the structured of the hard disk substrates are superhydrophilicity due to the water droplets hardly slip out of the substrates even with the tilting angle of 90 deg and under the blowing of a high pressure blowers.

On experiments of droplet evaporation on a structured superhydrophobic surface that displays very high contact angle (CA ~ 160 deg), and negligible CAH (<1 deg) [8]. The droplet evaporation is observed to occur in a constant-contact-angle mode, with contact radius shrinking for almost the

entire duration of evaporation [15]. Contact angle hysteresis cannot be measured directly but through the measurement of advancing and recending contact angles. Surface roughness is a component of surface texture [14]. According to the previous works, the structured of superhydrophobic surface, the experiments indicate that the time taken for complete evaporation of the droplet is greater than the predicted time, across all droplet volumes [16]. With this, it indicates that the hard disk substrates is superhydrophilicity as the rate of evaporation is high.

Picknett and Bexon [17] were among the first researchers to study the evaporation of a droplet placed on a substrate in still air. They identified two modes of evaporation of a droplet resting on a smooth homogeneous surface, namely, the constant contact angle (CCA) mode and the constant contact radius (CCR) mode. McHale et al. [18] concluded that the evaporation rate on a hydrophobic surface is proportional to the droplet height during evaporation and that the mode of evaporation is determined by the initial contact angle of the droplet. Yu et al. [19] also reported the droplet evaporation rate on a hydrophobic surface to be proportional to the droplet height. Popov [21] drew attention to the nonuniformity of evaporation flux along the droplet surface. In his report, reported a closed-form solution to describe the rate of evaporation valid over the entire range of contact angles [22].

The transient evaporation of a droplet is affected by the initial contact angle of the droplet as well as the contact angle hysteresis [23]. Most studies in the past have focused on droplet evaporation in a constant contact radius mode [21,22,23,24]. Another intermediate mode—Stick-Slide (SS) or mixed mode is also commonly observed. Therefore, Saptarshi Basu et al. [13] are able to provide a graphical representation to these modes, named as MOE plot. Thus, various substrates can now be compared based on mode of evaporation, which are governed by fluid property and surface characteristics.

CRE can be eliminated due to the increasing the hydrophobicity of surfaces which accompanied by decreasing CAH [40]. Lower CAH in essence means reduced contact line pinning which leads to suppression of CRE. It can be achieved by patterning of controllable surface wettability as reviewed previously by Tial et al [44]. However, the preparation of superhydrophobic surfaces is expensive. Comprehensive study the physical properties of the surface of the hard disk substrates is needed to eliminate the effect on other properties of the substrates. Thus, suppression of CRE in hard disk substrates using of hydrophobic surfaces is a challenge.

2.2 The effect of temperature on the drying phenomenon of droplets

Xu et al. [27] experimentally investigated internal flow in evaporating water droplets. The authors demonstrated the existence of Marangoni convection in evaporating deionized water droplets seeded with fluorescent particles on glass substrates. They have also shown the existence of a stagnation point on the interface where the surface flow, surface tension and interfacial temperature gradients change direction. The investigated droplets were at room temperature (28°C) and have a base radius of 2 mm and 10° of initial contact angle. In recent studies, the conductivity of the substrate has been reported to be of importance in determining the rate of evaporation of pinned sessile droplet. [28,29] The thermal Marangoni flow can be enhanced by elevating the temperature of the substrate [16] resulting in an increased solute concentration near the center of the droplet [18]. An increased temperature also increases the outwards capillary flow producing a ring as well. The result is a spot-inside-ring. The effect of buoyant motion of the liquid from the hot substrate to relatively cooler liquid-air interface is often negligible [28].

It is worth noting that Savino et al [30] have experimentally shown that in the case of pendent drops, the existence of Marangoni flows is observed in organic liquids (n-octane) but not in water.

Risten part et al [31], argued that, for organic liquids, non-uniform evaporation along the surface induces temperature variations along the droplet interface. These variations are found to generate a thermocapillary flow within the drop. The droplets were deposited on substrates and have typical initial volume of 2 µL. They were seeded with 1 µm solid particles to reveal Marangoni convection patterns after drying out. Moreover, the authors introduced a criterion to determine the occurrence and direction of Marangoni flow, with the latter being the ratio of thermal conductivities of the substrate and the liquid [32]. Hu et al. [33] studied both experimentally and theoretically the formation of particles deposits near the edge of a drying droplet on glass substrates. They demonstrated that surface Marangoni flow can redirect evaporation-driven deposition and assembly of suspensions. This will undoubtedly affect pattern formation, resulting from the dry out of droplets containing suspensions.

Hu et al. [34,35] also analysed the effect of Marangoni stresses on the flow in an evaporating droplet. The authors described the effect of Marangoni stress on the flow of an evaporating droplet using a numerical approach. The temperature field within the droplet was computed and the role of surfactant contamination was also addressed. The authors showed that small contamination tends to prevent Marangoni convection. Moreover, when the contact angle is below a critical value of approximately 14°, Marangoni flow disappears. Girard et al. [36] numerically investigated the evaporation dynamics of small sessile water droplets under microgravity conditions. The numerical analysis revealed temperature gradients on the free interface and as a result, Marangoni convection is generated within the droplet. The authors also found a slowdown in evaporation toward the end of the droplet lifetime.

At room temperature, the presence of coffee rings in lines and drops by utilizing Deegan's explanation. However, with a heated or cooled substrate, evaporating features are now subject to a heat flux from the surface, breaking the symmetry that permitted Deegan's exact solution. In evaporating drops and lines, heat is readily transferred from the substrate to the thin pinned edge of the drop, leading to enhanced evaporation near the drop's edge compared to that at the center.

In the case of cooling, decreased rim evaporation eliminates CRE formation altogether because the cooled substrate retards edge evaporation more than that in the center. Comparing the line and drop cross sections, the effect of temperature on CRE formation is enhanced in drops. Hence, the drop shows a greater transfer of solute to its edge when subjected to heating. The effect of temperature on CRE deposits does not require a consideration of the temperature dependence of surface tension. However, published research on the CRE warrants a discussion of surface tension-driven flow, known as the Marangoni effect. Previous work has shown that the coffee ring effect can be controlled or eliminated through engineering an appropriate Marangoni flow. Hu and Larson [34] show that Marangoni flows in an evaporating octane drop lead to a deposition of solute at its center rather than a coffee ring at its perimeter. However, in the same letter they found no such effect in an evaporating water droplet, even when avoiding surfactant contamination. Other work by Savino et al. [30] presented a similar conclusion, witnessing Marangoni flows in drops of evaporating organic solvent but not water. The weak influence of thermal Marangoni flow on the drying of a sessile droplet could be attributed to the following reasons. Firstly, the Marangoni flow is weak in an evaporating water droplet. Secondly, it is partially counteracted by the enhanced edge aggregation because of the accelerated evaporation due to the hot edge near the heated plate.

By controlling the substrate temperature beneath the drying feature, Dan Soltman and Vivek Subramanian [16] demonstrated control of its topology, reversing or enhancing the CRE of Inkjet-Printed. A heated substrate leads to greater evaporation at the bead's edge, which then yields an enhanced coffee ring, compared to room-temperature drying. Analogously, a cooled substrate suppresses edge evaporation and eliminates the coffee ring at the feature's edge. These effects

occur more strongly in a circular drop than in a straight line because of the greater ratio of edge length to center area in the drop. David et al. [37] experimentally investigated the effect of thermal properties of the substrate on the wetting and evaporation of sessile drops. The authors measured the temperature field inside millimeter sized evaporating water and organic liquid droplets using a miniature thermocouple. Substantial evaporative cooling was observed and a strong influence of the substrate thermal properties was demonstrated. It is clear from the available literature that the evaporation of liquid sessile droplets is accompanied by internal convection. Girard et al. [38] investigated water droplets evaporating on heated substrates. The role played by the substrate temperature as well as droplet radius was investigated.

However, the heating process is to enhance the properties of the hard disk substrates. It is not for drying purposes. Therefore, during blowing process, all droplets must be clear before going to the heating process. There is a discussion of reversing the process by going through heating process first, then only rinsing and blowing. In contrast to the expecting result the effect of suppressing the stain are very minor due to the waiting time of transferring the substrates from heating process to rinsing process and blowing process. The humidity of the rinsing process is very high and the effect of the heated substrates become negligible. Even though there might be a possibility of manipulating the waiting time to suppress the CRE. Nevertheless, changing the cleaning process will affect the other process. Other than this, manipulating the waiting time for mass production in industries is a difficult task. Theoretically, it might work. However, practically in industries is a challenge.

2.3 The physical properties of the droplet

Liquid properties such viscosity and pH and altering temperatures of substrate and droplet are studied to investigate CRE. Cui et al. [39] demonstrated when an added hydrosoluble polymer increased the solution viscosity, resulting in a large resistance to the radially outward flow and subsequently a small amount of spheres deposited at droplet edge. This result shows how the drying behaviour of the droplet will determine the pressure distribution within the water phase and this will, when combined with the mechanical properties of the other surfactant concerned, determine the dried shape of the drop. Whilst such drying behaviour is interesting scientifically, there are also numerous potential uses for such 3D structures that are created, merely through evaporation. Also, Bhardwaj et al. [41] demonstrated the effect of the pH of the solution on the deposit pattern, which is the results of force interactions between substrate and particles such as the electrostatic and van der Waals forces. Parsa et al. [42] reported that depending on the substrate temperature, three distinctive deposition patterns are observed: a nearly uniform coverage pattern, a “dual-ring” pattern, and multiple rings corresponding to “stick–slip” pattern. Hu et al. [33,34,35] utilized the temperature-dependent surface tension of liquid and reported a repulsive Marangoni force in the evaporating droplet by the latent evaporation heat. Meanwhile, Still et al. [43] visualized the surfactant-driven Marangoni effect using suspended microparticles. A small ionic surfactant (i.e., Sodium dodecyl sulfate, SDS) induced the Marangoni flow because of a surface tension gradient at a droplet’s air–water interface. The result of the evaporation induced outward flow and the inward Marangoni flow is the “Marangoni vortex (eddy)” phenomenon. This phenomenon induces a uniform deposition of the evaporating droplet by forming tree-like multiple rings.

Kajiya et al. [45,46] developed a method to determine the concentration profiles in the evaporating droplets of polymer solution by combining the fluorescence intensity measurement and the lateral thickness profile measurement of a droplet. This experimental protocol was exactly

adopted in the present study to determine polymer concentration profile in a droplet. Recently, Kim et al. [47] reported that multiple sequential Marangoni flows and particle-surface interactions are key parameters to achieve uniform particle coatings in a droplet and suggested a small concentration of surfactant and surface-adsorbed polymer via physisorption for a uniform deposit in a binary mixture. Zhiliang Zhang al [49] propose an effective and facile strategy to deposit silver nanoparticles in various patterns by utilizing the coffee-ring effect with an inkjet printing technique based on investigation of the influence of substrate wettability on the coffee-ring effect. The droplets of silver nanoparticle ink are inkjet-printed on the substrate; subsequently, capillary fluid flows are induced to replenish the evaporation loss at the edge owing to the CRE, originating from the differential evaporation rates across the droplets [49].

When a liquid droplet impacts a non-wetting surface, it generally spreads on the surface and then retracts back. Eventually, the droplet either stick to or rebound from the surface depending on the impact velocity, surface wettability and liquid viscosity. Kuan-Ming Huang [50], conducted a systematic study of droplet impact of pure water and various glycerol-water mixtures on the superamphiphobic surface. They found that droplets could only rebound from the surface above a critical impact velocity, below which droplet deposition was observed. However, further increase of the impact velocity led to the occurrences of partial rebound, sticking and splashing of droplets. Comparative investigation on the impact dynamics of various viscous droplets on superamphiphobic surfaces, found that the droplets with highviscosity spread and retract slower, take off the surface later and eventually rebound lower and less times than droplets with low viscosity. This phenomenon demonstrates that the viscous dissipation within droplet can strongly affect the impact process. Experiments also showed that the critical impact velocity for droplet rebound linearly increases with the liquid viscosity, which can be explained by a scaling argument. Furthermore, the maximum spreading factor of various viscous droplets on superamphiphobic surfaces cannot be described by the scaling analyses recently reported in the literatures [50].

Changdeok Seo [51], made an effort to deposit suspended particles more uniformly by adding polyethylene glycol (PEG). PEG is known as a non-toxic and non-immunogenic polymer widely used in food, cosmetic, and pharmaceutical research fields. It is worthy to note that PEG molecules in water, which are solution-like surfactants cause to decrease surface tension and to increase the solution viscosity in a concentration-dependent manner. Also, adding PEG would induce Marangoni flow, resulting in change of de-pinning characteristics of contact line. They added a biocompatible surfactant polymer in a droplet solution and expected to obtain a better homogenous coating of suspended microparticles because of the combined effects of surface tension and viscosity changes in the evaporation process. Therefore, different fluid have different existing mechanisms of the internal flow and coating pattern, concentration profile [52].

Addition of a surfactant introduced a Marangoni flow which counteracts the outward capillary flow. Altering the pH 18,19 can influence the DLVO interactions (the force between charged surfaces interacting through a liquid medium) and introduce an attraction between the nonvolatile component and the substrate, which dominates the capillary flow. Recently, it has been shown that through careful selection of an electric field, the coffee-ring can be suppressed. Electrowetting can be used to prevent pinning. Changing particle shape, such as using ellipsoids rather than spheres, can also prevent CRE formation. The transport in, and residual patterns left by, droplets has been an area of significant research interest since there are plethora of phenomena that could influence the dynamic behavior of the drying process.

There is a significant debate about the exact nature of the evaporative flux distribution across a droplet. For the final shape, knowing the droplets' internal flow profile is important and this depends on the evaporative flux distribution. A spatially uniform or edge enhanced evaporation

profile leads to an outward flow. If the evaporation is somehow enhanced at the center of the droplet, there is an inward flow. For large droplets with significant ventilation, one expects a uniform evaporation profile. For small droplets with stagnant surroundings, one expects larger evaporation toward the droplet edge. The drops coming out of the nozzle are measured with all kind of optical techniques. The drop formation with sized droplets at high repetition rates (up to 100 kHz) is measured with ultra-high speed cameras (up to 25 Mfps) or with a laser induced fluorescent stroboscopic recording.

Many authors argue that when the atmosphere is stagnant and the liquid side mass transfer resistance is negligible, evaporation is controlled by diffusion of vapour away from the droplet surface, while consider an appreciable liquid side mass transfer resistance [53]. The general situation is not straight forward and it has been shown experimentally that for ambient conditions, the evaporative profile differs significantly from vapour diffusion models. For all physically realizable situations, the magnitude of the capillary number is small and surface tension dominates viscous effects. If the magnitude of the viscosity, surface tension, and volatility of the liquid have little influence.

In spite of all that mentioned above, hard disk manufacturers had tried to manipulate the physical properties of the fluid by adding surfactant but the results are not very encouraging. As mentioned earlier, the hard disk substrates are superhydrophilicity and the humidity of the rinsing process are very high, these affect the outcome.

3. The numerical analysis of water droplet in cleaning process

The earliest significant work attempting to understand the mechanisms of drop generation was by Fromm [54]. He identified the Ohnesorge number, Oh. It is regarded as the appropriate grouping of physical constants to characterize drop formation. He used the parameter Z=1/Oh and proposed that Z > 2 for stable drop generation. This analysis was further refined by Reis & Derby [55], who used numerical simulation of drop formation to propose the following range, 10> Z > 1, for stable drop formation. At low values of Z, viscous dissipation prevents drop ejection, whereas at high values the primary drop is accompanied by a large number of satellite droplets. Numerical solution is invariably required to predict the final profile. Among the small number of investigations that considered asymmetric sessile droplets, Deegan Thesis [56] numerically examined the drying of (and the resulting flow field inside) two-dimensional colloidal droplets on inclined substrates. Also, S´aenz et al. [57] studied, both experimentally and numerically, the evaporation kinetics of non-axisymmetric drops placed on a flat surface and presented a general scaling law for the integrated evaporative flux.

In the cleaning process of hard disk substrates, it involves blower to dry the droplets. In the blowing process, the blower (gas phase), substrates (structure) and water droplets. In the case of a liquid discrete phase and a gas continuous phase, these stresses are the drag and turbulent stresses [58]. Many multiphase break-up models can be found in the literature. Coulaloglou & Tavlarides [59] proposed a break-up model for liquid-liquid dispersion systems in which the break-up frequency is defined by the fraction of particles breaking divided by a characteristic time scale. Luo & Svendsen [60] devised a kinetic theory-type model for bubbles break-up. In their model, the break-up frequency is calculated as a collision frequency between eddies and particles multiplied by a collision efficiency. Martinez et al. [61, 62] proposed a break-up model for bubbles based on kinematic ideas (energy balance).

There are also other modeling liquid droplets in gas systems such as spray systems. A mathematical model was devised by Hossam S. Aly et al [63] for predicting liquid droplets breakup

in spray systems without neglecting the contribution of the drag stresses [64]. This model is used to quantitatively compare the roles of turbulent and drag stresses in the break-up process. The model takes into account the effects of both drag and turbulence induced fragmentation stresses on droplet break-up. The model is coupled with an Eulerian-Eulerian CFD model that solves the governing Navier-Stokes equations for all the phases. A reasonable agreement has been reached with experimental data of SMD values. Likewise, the water droplets on the hard disk substrates under the blower, the same method can be applied.

Eq. (1) below takes into account momentum transfer due to mass transfer between the droplets phases. In this equation, the liquid phase is treated as one dispersed phase rather than multiple droplet phases, this term is set to zero in all the simulations. The drag contribution is calculated based on the Schiller-Naumann model [65-67] In order to track the droplets diameter in the Eulerian solver, a conservation equation for the droplet numbers that governs the distribution function of the droplets must be solved. Such equation is known as the population balance equation [68] and can be written in the following form:

$$\frac{\partial}{\partial t} n(d, U_i) + \frac{\partial}{\partial x}[U_i n(d, U_i)] + \frac{\partial}{\partial U_i}[F_i n(d, U_i)] = S\,(d, U_i) \quad (1)$$

S. Sharafatmandjoor [69] study the effect of surface tension and gravity on the kinematics of a droplet. The results of his study, can observe that the droplet's deformation phenomenon has a definite effect on the wake dynamics and the surrounding gas. On the other hand, the co-effect of different droplets strongly affects their acceleration, which is observable in the long time behavior of the system. When droplets are exposed to a gaseous high velocity flow, they show certain characteristics which have been extensively studied by experiments [70-75]. Simulations of such a process have been done in the past [75-82]. Jozsef Nagy [83] presents the computational simulation results of turbulent phenomena in a high velocity multiphase flow, where the predominantly turbulent phase is the gaseous phase. When liquid droplets are suddenly exposed to high speed gas flows, they shatter. However, in hard disk substrates, the water droplets cannot slip completely out substrates due to the superhydroplilicity surface. Proper speed gas should be applied, not to cause any damage to the substrates.

Alejandro Acevedo-Malavé [84] study the interaction between three unequal-size drops is studied. In his paper he modelled of the coalescence process using the Smoothed Particle Hydrodynamics method. This method is used to solve the equations of fluid dynamics using a set of particles that interacts between them depending on the value for the smoothing length, h. Which is very similar to the cleaning process of the hard disk substrates. The model reported in his paper is performed in 3D and it is used the cubic B-spline kernel Monaghan [85]. In his work water drops are considered. An adequate methodology has been proposed for the modeling of hydrodynamical collisions between liquid drops using the SPH formalism in three-dimensional space. Two scenarios for the collisions of liquid drops in three dimensions have been carried out in the simulations. A flat circular section arises as the initial stage in all SPH calculations reported in this work. This flat circular section appears due to the existence of surface tension forces acting on each droplet. Arrange of values for the collision velocity is chosen and the possible outcomes for the collision process are obtained: coalescence and flocculation of drops. The velocity vector fields were constructed by different calculations. It can be seen that the fluid inside the drops tends to accelerate the SPH particles at the zone of contact between the droplets. This behavior is due to the nonuniform pressure differential inside the drops. At the zone of the drops which have no interaction with any other drop, the fluid tends to diminish the internal velocity. This can be

explained by the behavior of the pressure field inside the drops, in fact, in that zone of the droplets, the inhomogeneous pressure field has a minimal value.

Mohd. Seraj [86] had designed a self-cleaning filter, whereby the liquid droplets collect on the filter and drain down onto some collecting device. The underlying need for all these applications is estimation of the velocity of a drop along the fiber axis. The different between his study and the the cleaning process of the substrates is the surface. He had dedicated to investigate the role of micro scale droplet motion in non-woven fibrous media and their effect on saturation and collection efficiency. Therefore, the hard disk substrates can be investigate under micro scale using numerical analysis as well.

3.1 Numerical analysis of CRE

Yunker et al [87] has demonstrated that the use of ellipsoidal particles suppresses the transport of particles to the edge - Three-dimensional Monte Carlo model of the CRE in evaporating colloidal droplets. The previous attempts to simulate the effect were commonly based on the numerical techniques, such as the finite-element method, applying the analytical equations to figure out the evolution of the average particle density profile. Another family of approaches, based on the Monte Carlo methods, uses randomly distributed particles on the discrete lattice and calculates the probabilities of the possible particle motion directions on each simulation step. One recent attempt to build a Monte Carlo model of the droplet evaporation, capillary flow and contact line deposition has been performed by Kim et al. [47] The model used a simple power-law assumption about the particle motion on the basis of the flow analysis of Deegan et al. [25,26] and reproduced the contact line deposition profile. However, the simulation has been limited to the simplified radial particle motion and has not considered the vertical velocity component and dependence on the vertical coordinate. In the work of Yunker et al.[87] , the CRE growth was modelled in two dimensions (2D) as the Poisson-like process of random particle deposition coupled with the surface diffusion. The model, focusing only on the vicinity of the contact line, has not considered the droplet evaporation and inward flow dynamics. The Monte Carlo approach based on the biased random walk (BRW) has been recently used to investigate the transition from the coffee-ring deposition towards the uniform coverage in 2D. We further develop the BRW method into the more realistic 3D domain and use the flow analysis of Hu and Larsson [88] to calculate the corresponding probabilities of the sampled particle moves on each Monte Carlo Step (MCS). This advancement allows achieving a full 3D structure of the coffee ring and analyzing the thickness profile of the structure. The evolution of the ring shape and dimensions is observed during the entire time period of the droplet drying.

To summarize, the CRE is simulated in the 3D domain, while including both particle diffusion and the capillary particle transport towards the three-phase contact line. The spatial domain of the model is the evaporating sessile droplet represented as a spherical cap. The time scale of the simulation is the full drying process, from the placement of the drop onto a substrate till the final dry-out of the remaining solvent. The simulation result provides a full 3D model of the CRE, and the vertical ring thickness profile is measured. The final shape of the simulated ring structure shows a reasonable dependence on the volumetric particle concentration and colloidal aggregation parameter.

Several models have been proposed to describe the evaporation process of a droplet. Popov [22] proposed an analytical diffusion model for quasi-steady natural evaporation of a droplet based on the solution to the Laplace equation describing the concentration field at the droplet surface in a toroidal coordinate system. The model accounts for the nonuniform vapor concentration field

around the droplet. The evaporation flux J(r) on the surface of a droplet in a toroidal coordinate system according to the diffusion-only model for evaporation is given as

$$J(r) = \frac{D(Cs-C\infty)}{Rc}\left[\frac{1}{2}\sin\theta + \sqrt{2}\,(\cosh\alpha + Cos\,\theta)1^{3/2}\int_0^{\infty}\frac{\cosh\theta\tau}{\cosh\pi\tau}\tanh\big((\pi-\theta)\tau\big)\,P_{-1/2+i\tau}(Cosh\propto)\tau d\tau\right] \quad (2)$$

where D is the coefficient of vapor diffusion, cs is the saturated vapor concentration on the droplet surface, c∞ is the concentration of water vapor at infinity, Rc is the contact radius of the droplet, θ is the contact angle of the droplet, and r is the radial coordinate at the baseline of the droplet such that r= Rc at the contact line. α and β are toroidal coordinates and are related to the height (h), contact radius Rc, and contact angle θ of the droplet as

$$\cosh\propto = \frac{\sin\theta}{\left(\frac{h}{Rc}\right)} - cos\theta \quad (3)$$

The expression for droplet evaporation rate, obtained by integration of evaporation flux over the droplet surface area, is based on the contact angle θ and contact radius Rc and is valid over the entire range of contact angles. It is noted that the contact-angle dependence of the evaporation rate as obtained by Picknett and Bexon converges to Popov's solution, although the final expressions are in different forms: The dependence of the evaporation rate on CA given by Picknett and Bexon is in the form of an approximate series solution, while Popov provided a closed-form expression. For any contact angle, the rate of mass loss as given by Popov is

$$\frac{d\theta}{dt} = -\frac{D(Cs-C\infty)}{\rho_L Rc1^2}\,(1+\cos\theta)1^2 f(\theta) \quad (4)$$

The model used in the present investigation is based on classical hydrodynamics. Two main approximations are made: droplets are supposed to be small with a spherical geometry and a fast relaxation of mass flows and temperature profiles inside and in the vicinity of the droplets interface is assumed. Based on mentioned assumptions, hydrostatic pressure gradients are neglected and quasi-stationary hypothesis is justified. Convection is neglected in the gas phase and assumed to be slow enough inside the droplets for viscous dissipation contributions to be negligible. The liquid phase is described using stationary Navier-Stokes and heat equations. Table 2 below shows the numerical analysis and the results.

Table 2 The numerical analysis and the results

Numerical analysis	Result/outcome
The 3D Monte Carlo model is developed in the spherical-cap-shaped droplet. [6]	the CRE is simulated in the 3D domain, while including both particle diffusion and the capillary particle transport towards the three-phase contact line. The spatial domain of the model is the evaporating sessile droplet represented as a spherical cap. The time scale of the simulation is the full drying process, from the placement of the drop onto a substrate till the final dry-out of the remaining solvent. The simulation result provides a full 3D model of the coffee ring, and the vertical ring thickness profile is measured. The final shape of the simulated ring structure shows a reasonable dependence on the volumetric particle concentration and colloidal aggregation parameter.
computational fluid dynamics and the finite element method (FEM) [7]	Study on the Effect of Marangoni Flow on Evaporation Rates of Heated Water Drops
commercial computational fluid dynamics software, Flow3D. [16]	Solve 3D Navier-Stokes and mass continuity equations for a predetermined mesh using a finite difference approximation with the volume-of-fluid method to study the Inkjet-Printed Line Morphologies and Temperature Control of the CRE
OpenFOAM 2.1 [29]	While this approach should not be considered trustworthy neither too close to the contact line nor in the center of the drop, nevertheless it gives quantitative results in the remaining portion of the interface. The droplet shape used is always adopted from the experiment. Quasi-stationarity is assumed at each moment during the droplet evaporation. Three different sets of interfacial conditions are examined for this analysis.
custom-programmed software based on MATLAB (version 2011a, Mathworks Inc., USA) which A Gaussian filter was applied [52]	The images and trajectories were calculated using the nearest-neighbour algorithm as the study on biosurfactants reverses the CRE in a bacterial system.
MAPLE (version 14, Maplesoft, Canada) which adaptations to the model developed by Hu and Larson [88]	Flow profiles and streamlines of the surfactant as the study on biosurfactants reverses the CRE in a bacterial system.
COMSOL Multiphysics (version 4.2, COMSOL Group, USA) which 1D diffusion equation was used, using parameters obtained from Stebe et al. [89]	Diffusion analysis of the biosurfactant concentration and surface tension evolution over time as the study on biosurfactants reverses the CRE in a bacterial system
MATLAB using a spherical-cap assumption, [90]	The droplet height and contact radius are also calculated and verified. Droplet mass, liquid density, the droplet volume, and the functional variation of CA evaluated as the study on droplet evaporation dynamics on a super hydrophobic surface with negligible Hysteresis
CFD modeling with the commercial codes Flow3D and Fluent [91]	Fluent include wall-flexibility, free surface flow, and two- phase flow with surface tension. Numerical simulations are done with the volume of fluid method on the continuum scale and with lattice Boltzmann and Cahn Hilliard on the meso-scale. Main challenge is to bridge the gap between continuum modeling and molecular dynamics to resolve the details of contact line dynamics, which are the driving mechanism behind the displacement of small drops.

4. Conclusions

The physics behind drying process of the water droplets during washing process are the game changing criteria to further understand the formation of CRE and ways to eliminate it. Previous studies have highlighted that the drying process of the water droplets are affected by the properties of the water droplets, substrate and temperature. In order to collaborate CCR, CCA, advancing contact angle and receding contact angle, the arrangement of the substrates, the position of the drying equipments can be manipulated to eliminate CRE. Furthermore, manipulation of the temperature of the substrates can enhance the drying process of the droplets before the formation of CRE. However, heating is an essential process for substrates enhancement. Therefore, manipulation of substrates temperature in eliminating CRE must not changes the properties of the substrates.

It actually create lot of concern to the industries once the temperature and chemical were manipulated as hard disk substrates are very sensitive part of the hard disk. Therefore, this paper suggested to optimize or replace the current cleaning physical process. As the substrates was blow under a humid environment, which prevent the elimination of water droplets, this paper suggest to increase the flow rate of the blower. According to the manufacturer, manipulating the flow rate do show improvement but not complete. Therefore, they replaced the current cleaning process with a new one which is more effective as the substrates are dried piece by piece.

To conclude, CRE can be studied using numerical analysis. The results can be verified using previous studies and validated by using the actual results provided by the industries. CRE formation also depends on the properties of the substrates and water droplets. Moreover, knowing the properties of the substrates and water by undergoing the wettability test and CAH testing as mentioned above are important. In this case, changing the chemical properties substrates are not advisable to eliminate CRE due to its complex design of the substrates for data storing. All the numerical tests have to be performed according to correct procedures to ensure accurate and acceptance results from the industries. Verified and validated results from the evaluation will help to predict the real consequences more accurately for further optimization. Knowing that the formation of CRE is caused by the evaporating of the water droplets, we need to find ways to eliminate the formation of water droplets before the heating process, in order to eliminate CRE.

Acknowledgement
The authors would like to thank University Tun Hussein Onn Malaysia (UTHM) for the financial support through Geran Penyelidikan Pascasiswazah (GPPS) with VOT no. H361 and also from Centre for graduate study.

References

[1] Martín Picón-Núñez, Jorge C. Melo-González and Jorge Luis García- Castillo. “Use of Heat Transfer Enhancement Techniques in the Design of Heat Exchangers” Web od science (2018).
[2] Rajat Chaudhary, Archika Kansal. “A Perspective On The Future Of The Magnetic Hard Disk Drive (Hdd) Technology” International Journal of Technical Research and Applications. No. 3 (2015) : 63-74.
[3] Deegan RD. “Pattern formation in drying drops.” Phys Rev (2000).
[4] Shyamashis Das, Atreya Dey, Govardhan Reddy, and D. D. Sarma, "Suppression of the Coffee-Ring Effect and Evaporation-Driven Disorder to Order Transition in Colloidal Droplets" *Journal of Physical Chemistry Letters* . No. 8 (2017) : 4704−4709.
[5] Susmita Dash and Suresh V. Garimella. "Droplet Evaporation Dynamics on a Superhydrophobic Surface with Negligible Hysteresis." *Langmuir* no. 29 (2013): 10785-10795.
[6] Yanan Li, QiangYang, Mingzhu Li & Yanlin Song. "Rate-dependent interface capture beyond the coffee-ring effect." *Scientific Reports* (2016).
[7] F. Girard, M. Antoni, and K. Sefiane. "On the Effect of Marangoni Flow on Evaporation Rates of Heated Water Drops.” Langmuir no. 24 (2008): 9207-9210.
[8] Mitch Timm (2018). “*Evaporation of a sessile droplet on a slope*.” Michigan Technological University. (Master’s theses and Master’s reports)
[9] J.Micromech.Microeng. “Statistical analysis of E-jet print parameter effects on Ag-nanoparticle ink droplet size.” Journal of Micromechanics and Microengineering. No. 27 (2017) : 095005
[10] Dileep Mampallil, Huseyin Burak Eralb, "A review on suppression and utilization of the coffee-ring effect." *Proceedings of the Institution of Mechanical Engineers, Part G: Journal of Aerospace Engineering* . No. 252 (2018) : 38-54.
[11] Wen-Kai Hsiao, Graham D. Martin, and Ian M. Hutchings. “Printing Stable Liquid Tracks on a Surface with Finite Receding Contact Angle.” Langmuir no. 30 (2014): 12447-12455.
[12] Binyu Zhao, Xiang Wang, Kai Zhang, Longquan Chen, Xu Deng,“Impact of Viscous Droplets on Superamphiphobic Surfaces.” Langmuir.
[13] Saptarshi Basu, Abhishek Tyagi, Saksham Sharma, Rishabh Hans, Lalit Bansal, “Universal representations of evaporation modes in sessile droplets” PLoS One no. 12 (2017): 9.
[14] Pengzhan Sun, Renzhi Ma, Kunlin Wang, Minlin Zhong, Jinquan Wei, Dehai Wu, Takayoshi Sasaki and Hongwei Zhu “Suppression of the coffee-ring effect by self-assembling graphene oxide and monolayer titania.” Nanotechnology no. 24 (2013): 075601.
[15] Pengzhan Sun, Renzhi Ma, Kunlin Wang, Minlin Zhong, Jinquan Wei, Dehai Wu, Takayoshi Sasaki and Hongwei Zhu “Three-dimensional Monte Carlo model of the coffee-ring effect in evaporating colloidal droplets.” Scientific Reports (2014).
[16] Dan Soltman and Vivek Subramanian. “Inkjet-Printed Line Morphologies and Temperature Control of the Coffee Ring Effect.” Langmuir no. 24 (2008): 2224-2231.
[17] R.G Picknett, R Bexon. “The evaporation of sessile or pendant drops in still air” Journal of Colloid and Interface Science61, no. 2 (1997): 336-350.
[18] Glen Mchale, Michael Ian Newton, S. M. Rowan, M. K. Banerjee. “The evaporation of sessile or pendant drops in still air” The Journal of Physical Chemistry B no. 102 (1998): 1964-1967.
[19] Yu-Chen Chuang, Che-Kang Chu, Shih-Yao Lin, Li-Jen Chen. “Evaporation of water droplets on soft patterned surfaces.” Soft Matter10 no. 19 (2014): 3394.
[20] Deegan, R. D.; Bakajin, O.; Dupont, T. F.; Huber, G.; Nagel, S.R.; Witten, T. A. “Contact line deposits in an evaporating drop.” Phys.Rev. E No. 62 (2000) : 756−765.
[21] Popov, Y. O., “Evaporative deposition patterns: spatial dimensions of the deposit,” Phys. Rev. E 71, no 3 (2005). 036313.
[22] Zheng R, Popov YO, Witten TA. “Deposit growth in the wetting of an angular region with uniform evaporation.” Physical Review. E, Statistical, Nonlinear, and Soft Matter Physics. No 72 (2005). 046303.
[23] Davis, S. H. “Moving Contact Lines and Rivulet Instabilities : The Static Rivulet”. J. Fluid Mech. No 98 (1980). 225−242.
[24] Schiaffino, S.; Sonin, A. A. “Formation and Stability of Liquid and Molten Beads on a Solid Surface”. J. Fluid Mech. No 343 (1997). 95−110.
[25] Deegan, R. D. et al. “Capillary flow as the cause of ring stains from dried liquids”. Nature no 389 (1997). 827–829
[26] Deegan, R. D. “Pattern formation in drying drops”. Phys. Rev. E 61. (2000). 475–485.
[27] Xu, C.; Feng, R.; Song, F.; Wu, J.; Luo, Y.; Wang, Xiu.; Wang, Y. “Continuous and controlled directional water transportation on a hydrophobic/superhydrophobic patterned surface”. Chem. Eng. J., no 352 (2018). 722-729.

[28] Jung-Hoon Kim, Sang-Byung Park, Jae Hyun Kim, and Wang-Cheol Zin, "Polymer Transports Inside Evaporating Water Droplets at Various Substrate Temperatures". Journal of Physical Chemistry, no 155 (2011). 15375-15383.
[29] Sam Dehaeck, Alexey Rednikov, and Pierre Colinet, "Vapor-Based Interferometric Measurement of Local Evaporation Rate and Interfacial Temperature of Evaporating Droplets". Langmuir no 30 (2014). 2002-2008.
[30] Raffaele Savino, N.Facaloro and Diego Paterna. "Buoyancy and Marangoni Effects in an Evaporating Drop". Journal of Thermophysics and Heat Transfer 16 no 4 (2002). 562-574.
[31] Ristenpart WD, Kim PG, Domingues C, Wan J, Stone HA. "Influence of substrate conductivity on circulation reversal in evaporating drops". Phys Rev Lett. No 99 (2007) 234502.
[32] Neil Graddage, Ta-Ya Chu, Heping Ding, Christophe Py, Afshin Dadvand and Ye Tao "Inkjet printed thin and uniform dielectrics for capacitors and organic thin film transistors enabled by the coffee ring effect" Organic Electronics no 29 (2016), 114-119
[33] Hu H, Larson RG. "Evaporation of a sessile droplet on a substrate". J Phys Chem B no 106 (2002), 1334–44.
[34] Hu H, Larson RG. "Analysis of the effects of Marangoni stresses on the microflow in an evaporating sessile droplet". Langmuir no 21 (2005). 3972–80.
[35] Hu H, Larson RG. "Marangoni effect reverses coffee-ring depositions". J Phys Chem B no 110 (2006), 7090–4.
[36] F.Girard, M. Antoni and K.Sefiane. "On the Effect of Marangoni Flow on Evaporation Rates of Heated Water Drops". Langmuir 24. No 17 (2008), 9207-9210
[37] David, S.; Sefiane, K.; Tadrist, L. "Experimental investigation of the effect of thermal properties of the substrate in the wetting and evaporation of sessile drops". Colloids Surf., A no 298 (2007), 108−114.
[38] F.Girard, M. Antoni and K.Sefiane. "Evaporation and Marangoni Driven Convection in Small Heated Water Droplets". Langmuir 22. No 26 (2006), 11085-11091
[39] Cui L, Li Y, Wang J, Tian E, Zhang X, Zhang Y. et al. Fabrication of large area patterned photonic crystals by ink-jet printing" . J Mater Chem no 19 (2009) 19 5499–502.
[40] Bonn D, Eggers J, Indekeu J, Meunier J, Rolley E. Wetting and spreading. Rev Modern Phys No 81 (2009): 739–804.
[41] Bhardwaj R, Fang X, Somasundaran P, Attinger D. "Self-assembly of colloidal particles from evaporating droplets: role of DLVO interactions and proposition of a phase diagram". Langmuir no 26 (2010), 7833–42.
[42] Parsa M, Harmand S, Sefiane K, Bigerelle M, Deltombe R. "Effect of substrate temperature on pattern formation of nanoparticles from volatile drops". Langmuir no 31 (2015) 3354–67.
[43] Still T, Yunker PJ, Yodh AG. "Surfactant-induced marazngoni eddies alter the coffee-rings of evaporating colloidal drops". Langmuir no 28 (2012). 4984–8.
[44] Tian D, Song Y, Jiang L. "Patterning of controllable surface wettability for printing techniques". Chem Soc Rev no. 42 (2013): 5184–209.
[45] Kajiya T, Kobayashi W, Okuzono T, Doi M. "Controlling the drying and film formation processes of polymer solution droplets with addition of small amount of surfactants". J Phys Chem B no 113 (2009) 15460–6.
[46] Kajiya T, Kobayashi W, Okuzono T, Doi M. "Controlling profiles of polymer dots by switching between evaporation and condensation". Langmuir no 26 (2010) 10429–32.
[47] Kim SJ, Kang KH, Lee JG, Kang IS, Yoon BJ. Control of particle-deposition pattern in a sessile droplet by using radial electroosmotic flow. Anal Chem no 78 (2006), 5192–7.
[48] Zhang Z, Zhu W. "Controllable fabrication of a flexible transparent metallic grid conductor based on the coffee ring effect". J Mater Chem C no 2 (2014) 9587–91.
[49] Zhiliang Zhang , Xingye Zhang , Zhiqing Xin , Mengmeng Deng , Yongqiang Wen , and Yanlin Song. " Controlled Inkjetting of a Conductive Pattern of Silver Nanoparticles Based on the Coffee-Ring Effect". No 23 (2013). 6714-6718
[50] Kuang M, Wang L, Song Y. "Controllable printing droplets for high-resolution patterns". Adv Mater no 26 (2014) 6950–8.
[51] Changdeok Seo, Daeho Jang, Jongjin Chae and Sehyun Shin. "Altering the coffee-ring effect by adding a surfactant like viscous polymer solution". Scientific reports no 500 (2017)
[52] Wouter Sempels, Raf De Dier2, Hideaki Mizuno, Johan Hofkens and Jan Vermant. "Auto-production of biosurfactants reverses the coffee ring effect in a bacterial system" Nature communication no 4 (2013) 1757
[53] Adam D. Eales, Alexander F. Routh, Nick Dartnell and Goddard Simon. "Evapoaration of pinned droplets containing polymer-an examination of the important groups controlling final shape". The Global Home of Chemical Engineers61, No.5 (2015) 14777.
[54] J.E.Fromm. "Numerical Calculation of the Fluid Dynamics of Drp-on-Demand Jets". IBM Journal of Research and Development28, no 3 (1984) 322-333.
[55] Brian Derby and Nuno Reis. "Inkjet Printing of Highly Loaded Particulate Suspensions". Injkjet Printing of Functional Materials28, no 11 (2003) 815-818.

[56] Deegan and Shane. "The molecular characterization of ER stress-induces autophagy and cell death". PHD thesis (2012)
[57] P. J. Sáenz, A. W. Wray, Z. Che, O. K. Matar, P. Valluri, J. Kim, and K. Sefiane. "Dynamics and universal scaling law in geometrically-controlled sessile drop evaporation" Nat Commun. No 8 (2017) 14783.
[58] Kolev, N.I. Multiphase Flow Dynamics 2 Thermal and Mechanical Interactions. Springer-Verlag, Berlin (2002).
[59] Coulaloglou, C.A. and L.L. Tavlarides, Description of interaction processes in agitated liquid-liquid dispersions. Chemical Engineering Science, 1977. 32(11): p. 1289-1297.
[60] Luo, H. and H.F. Svendsen, Theoretical Model for Drop and Bubble Breakup in Turbulent Dispersions. AIChE Journal, 1996. 42(5): p. 1225-1233.
[61] Martinez-Bazan, C., J.L. Montacs, and J.C. Lasheras, On the breakup of an air bubble injected into a fully developed turbulent flow. Part 1. Breakup frequency. Journal of Fluid Mechanics, 1999. 401: p. 157-182.
[62] Martinez-Bazan, C., J.L. Montacs, and J.C. Lasheras On the breakup of an air bubble injected into a fully developed turbulent flow. Part 2. Size PDF of the resulting daughter bubbles. Journal of Fluid Mechanics, 1999. 401: p. 183-207.
[63] Hossam.S.Aly, Yehia A. Eldrainy, Tholudin M.Lazim and Mohammad Nazri Mohd Jaafar, On the contribution of drag and turbulent stresses in the Fragmentation of Liquid Droplets : A Computational Study. CFD Letters, no 2 (2010). 2:97-105
[64] Aly, H.S., Eldrainy,Y.A., Saqr, K.M., Lazim, T. M. , Jaafar, M.N.M.., A mathematical model for predicting spray atomization characteristics in an Eulerian-Eulerian framework. International Communications in Heat and Mass Transfer, 2010, 37, (6), p. 618-623
[65] Choi, C.R., T.S. Kwon, and C.H. Song, Numerical analysis and visualization experiment on behavior of borated water during MSLB with RCP running mode in an advanced reactor. Nuclear Engineering and Design, 2007. 237(7): p. 778-790.
[66] Nieuwland, J.J., Van Sint Annaland M., Kuipers J.A.M, Van Swaaij W. P. M., Hydrodynamic Modeling of Gas/Particle Flows in Riser Reactors. AIChE Journal, 1996. 42(6): p. 1569-1582.
[67] Rundqvist, R., C. Ljus, and B. Van Wachem, Experimental and numerical investigation of particle transport in a horizontal pipe. AIChE Journal, 2005. 51(12): p. 3101-3108.
[68] Ramkrishna, D., The Framework of Population Balance, in Population Balances. 2000, Academic Press: San Diego.
[69] S. Sharafatmandjoor, C. S. Nor Azwadi, Numerical Simulation of the Dynamics of a Droplet in a Low-gravitational Field. Journal of Advanced Research Design. No.1 (2016) 16 p 15-20
[70] T.G. Theofanus and G.J. Li. On the physics of aerobreakup. Phys Fluids, 20:052103–01–052103–14, 2008.
[71] H. Zhao, H.-F. Liu, X.-K. Cao, W.-F. Li, and J.-L. Xu. Breakup characteristics of liquid drops in bag regime by a continuous and uniform air jet flow. Int J.Multiphase Flow, 2011.
[72] Ch.-L. Ng and T.G. Theofanous. Modes of aero-breakup with visco-elastic liquids. In Proceedings of XVth International Congress on Rheology, California, USA, August 2008.
[73] D.D. Joseph, J. Belanger, and G.S. Beavers. Breakup of a liquid drop suddenly exposed to a high-speed airstream. Int J.Multiphase Flow 25, 1999, p.1263–1303.
[74] T. Theofanous, G. Li, and T. Dinh. Aerobreakup in rarefied supersonic gas flows. J. Fluids Eng. 126, 2004, p.516–527.
[75] T.G. Theofanus, G.J. Li, T.N. Dingh, and C.-H. Chang. Aerobreakup in disturbed subsonic and supersonic flow field. J. Fluid Mech. 593, 2007, p.131–170.
[76] R.R. Nourgaliev, T.N. Dinh, and T.G. Theofanous. Adaptive characteristics-based matching for compressible multifluid dynamics. J. Comput. Phys. 213, 2006, p. 500–529.
[77] C.-H. Chang and M.-S. Liou. A robust and accurate approach to computing compressible multiphase flow: Stratified flow model and AUSM-up scheme. J. Comput. Phys. 225, 2077, p. 840–873.
[78] H. Terashima and G. Tryggvason. A front-tracking/ghost-fluid method for fluid interfaces in compressible flows. J. Comput. Phys. 228, 2009, 4012–4037.
[79] H. Terashima and G. Tryggvason. A front-tracking method with projected interface conditions for compressible multi-fluid flows. Computers & Fluids 39, 2010, p. 1804–1814.
[80] R.R. Nourgaliev, S.Y. Sushchikh, T.N. Dinh, and T.G. Theofanous. Shock wave refraction patterns at interfaces. J.Multiphase Flow 31, 2005, p. 969–995.
[81] M.-S. Liou, C.-H. Chang, H. Chen, and J.-J. Hu. Numerical study of shock-driven deformation of interfaces. Shock Waves XII, 2009, p. 919–924.
[82] T. Theofanous, R. Nourgaliev, G. Li, and N. Dinh. Compressible multi-hydrodynamics (cmh): Breakup, mixing, and dispersal, of liquids/solids in high speed flows. in Proceedings of the YUTAM Symposium on Computational Approaches to Disperse Multiphase Flow, 2006, p. 353–369, Dordrecht, Netherlands.

[83] Nagyc, J., Horvath, A., Jordan, C., Harasek, M. Turbulent phenomena in the aerobreakup of liquid droplets. 2012 CFD Letters4(3), pp. 112-126
[84] Acevedo-Malavé. Numerical modeling of unequal-size droplets collisions using a lagrangian mesh-free particle method. 2013 CFD Letters5(1-2), pp. 32-42
[85] Monaghan, JJ., Extrapolating B splines for interpolation. J. Comput. Phys., 1985. 60: p. 253-262.
[86] Mohd. Seraj, Syed Mohd. Yahya. Numerical Study of Droplet Motion inside Non-woven Fibrous Media. CFD Letters 11, Issue 5 (2019) 72-79
[87] Yunker PJ, Lohr MA, Still T, Borodin A, Durian DJ, Yodh AG. "Effects of particle shape on growth dynamics at edges of evaporating drops of colloidal suspensions". Phys Rev Lett no 110 (2013) 035501.
[88] Hu H, Larson RG. Marangoni effect reverses coffee-ring depositions. J Phys Chem B no 110 (2006) 7090–4.
[89] Stebe, K. J., Lin, S. & Maldarelli, C. "Remobilizing surfactant retarded fluid particle interfaces. I.Stress-free conditions at the interfaces of micellar solutions of surfactants with fast sorption kinetics". Phys. Fluids A no 3, (1991) 3–20.
[90] Jian H. Guan, Gary G. Wells, Ben Xu, Glen McHale, David Wood, James Martin and Simone Stuart-Cole. "Evapoaration of Sessile Droplets on Slippery Liquid-Infused Porous Surfaces (SLIPS)". Langmuir 31 no 43 (2015), 11781-11789.
[91] Herman Wijshoff. "Drop dynamics in the inkjet printing process". Elsevier Ltd. No 36 (2017), 20-27.

Penerbit Akademia Baru

Engineering Science and Technology Conference Proceedings

Journal homepage: www.akademiabaru.com/EST.html

Synthesis, Characterization and Modelling of Nickel Nanowires Synthesized Via Template-Assisted Electrodeposition

Open Access

A. G. N. Sofiah[1], M. Samykano[1,*], K. Kadirgama[2], M.M. Rahman[2]

[1] Department of Mechanical Engineering, College of Engineering, Universiti Malaysia Pahang, 26300 Gambang, Kuantan, Pahang, Malaysia
[2] Faculty of Mechanical and Automotive Engineering Technology, University Malaysia Pahang, 26600 Pekan, Pahang, Malaysia

ABSTRACT

Template-assisted electrochemical deposition is a straight forward approach for the synthesis of 1D nanostructures (eg: nanowire,nanorod, and nanobelt) with controllable morphology. This approach is suitable for mass production as it operates at ambient pressure and temperature with the properties of synthesized 1D nanostructures being influenced by synthesis condition during the electrochemical deposition process. The purpose of this research is to study the influence of stabilizing agent concentration and heating temperature to the physical behaviour of nickel (Ni) nanowires synthesized via template-assisted electrochemical deposition approach. In this research, electrolyte bath were prepared in three different concentration of stabilizing agent (6 g/L, 40 g/L and 70 g/L) and the deposition bath temperature were set at 30 °C, 70 °C, and 110 °C respectively. The elementary composition was determined using Energy Dispersive X-ray (EDX) analysis in order to investigate the percentage of pure Ni element in the synthesized nanowires. The diameter, surface texture and growth length of the synthesized Ni nanowires were characterized using Field Emission Scanning Electron Microscope (FESEM). X-ray diffractions (XRD) were used for crystal size and crystal orientation investigation. Additionally, the mechanical properties of different length modeled Ni nanowires were extracted via molecular dynamic simulation.

Keywords:
Template-assisted electro deposition; Ni nanowires; MD Simulation

Copyright © 2019 PENERBIT AKADEMIA BARU - All rights reserved

1. Introduction

Nanotechnology scientist have developed numerous techniques to fabricate the nanomaterials with different morphology which come out with interesting properties with different configuration [1, 2]. From the literature survey, template-based approach is one of the popular technique for synthesizing metallic nanostructures with controlled shape and size [3]. This method is known for its simplicity, high-throughput and cost-effectiveness which allow the duplication of complex topology present on the surface a template in a single step [4, 5]. The method typically operates at ambient temperatures and pressure as well as can be used to mass produce nanowires with controlled geometry and morphology [6-9]. For example, the diameters of nanowires can be well determined and maintained by controlling the diameter of pores, where else, the lengths can be controlled by controlling the thickness of template [10]. This techniques can be operated together

* *Corresponding author.*
E-mail address: mahendran@ump.edu.my (M.Samykano)

with the various type of templates capable to fabricate different shapes of 1D nanostructures for various materials.

Among the available templates, anodic alumina oxide (AAO) templates are the most widely as these template shown to be the most efficient medium for synthesis of metallic nanowires. These templates have the advantage to control the diameter of nanowires precisely, as the diameter dictated by the pore size of the nanochannels of AAO templates [6, 11-16]. Usually, the commercial template is used to avoid challenging template fabrication step and focus on the nanowire synthesis parameters [17]. Apart from the AAO templates, other available templates are polycarbonate [18, 19], nanochannel glass [20], porous silica [21], mica film[22], and block copolymers [23].

It is a well-established fact that the electrodeposition synthesis process in porous templates initiates at the bottom edge of the cathode (negative) surface of the pore. The high surface area and the presence of sites with low coordination number in the porous part of the alumina afford energetically favorable sites for initiating metal adsorption during electrodeposition [24]. The metal ion M^{n+} is transported from the electrolyte into the ionic metal lattice. Meanwhile, electrons are provided from the external electron source (power supply) to the electron gas of the metal M. This electrodeposition process illustrated in Figure 1a. Miguel García et al. [25] describes that during the electrodeposition process, the template pores are initially filled with a liquid precursor from the chemical reaction of the electrodeposition process. The solidification of the filled liquid precursor takes place to form nanowires as shown in Figure 1b. These are a very simple route, but it is critical to ensure that the pores are filled with the fluid. If the solution has an excellent wettability towards the template, it can diffuse through the membrane producing an enrichment of the solid component in the interior of the pores. Once the pores filled, the template is removed from the solution and dried. The mechanisms of the pore filling are different for various approach and template.

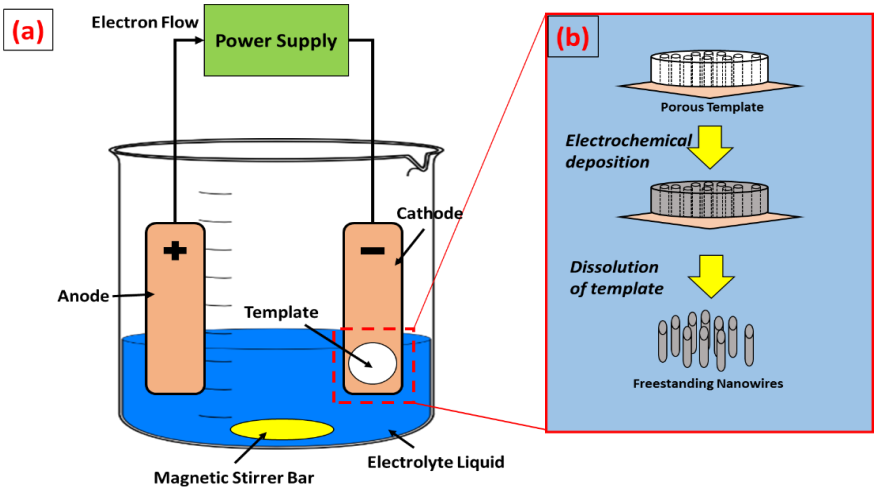


Fig. 1. Illustraion of template-assisted electrodeposition process

Blagg et al., synthesis niobium nanowires via template based electrodeposition techniques by using ionic liquid as electrolyte. The synthesized nanowires are polycrystalline in nature with grain size in the range of 14nm[26]. Zhang et al., successfully synthesized Cobalt nanowires with the diameter size of 25 nm to 75 nm by varying the voltages supply to the electrochemical cell setup. The study reveal that high voltage supply will increase the growth rate of nanowires inside the template pores[27]. Meier et al., used the same strategy for the fabrication of Copper nanowires and Nickel

nanowires. Freestanding Copper nanowires and nickel nanowires with diameter size of 300nm and length size of 10µm was successfully synthesized by using AAO as a template[28].

The mechanical properties of nanostructures can be expected to change when the dimensions of crystalline material decreased to nano size [29] due to the large surface-to-volume ratio thereby resulting in different surface effects [30, 31]. Additionally, the gradual change of engineering product dimensions to nano size have resulted into the complexion of micro testing procedure and the mechanical analysis procedure of individual nanostructures has become a big challenge [32]. These are due to the extremely small nanostructures, prohibiting the applications of the standard procedure of mechanical testing methods. As such, to overcome these challenges and to provide further insight on the mechanical deformation of nanostructures, numerical method such as molecular dynamics (MD) can be perform[33]. MD simulation is statistical mechanics approach that is used by the material scientist to observe the atom movement during the application of load (e.g.: bending, compression and tension) in order to extract these material behaviour [34].

2. Methodology

2.1 Materials

The chemicals including Nickel (II) chloride 6-hydrate (Bendosen,99.5%); Boric acid (Bendosen) and sodium hydroxide (Emsure ISO) were used without any further purification. Nickel plate with thickness of 1.0 mm (99.95%) was procured from Aldrich Chemistry. Deionised water was used thoughtout the entire study.

2.2 Experimental Methods

Main content of electrolyte bath for electrochemical deposition procedure may consist of metal salts and catalyst or stabilizer to accelerate the formation of nanowires. From the literature survey, we decide to follow Ertan et al. [19] experimental procedures due to the simple method with excellent outcomes. 175g/L of Ni sulfate hexahydrate ($NiSO_4.6H_2O$) metal salt solution was prepared and mixed with 37.5g/L of boric acid (H_3BO_3) solution. The solutions then stirred until both chemicals well mixed. Figure 2 show the apparatus arrangement for the electrochemical deposition process of Ni nanowires. Both Ni plate (anode) and 200 nm pore size Whatman anodic alumina oxide (AAO) (cathode) dipped into an electrolyte (refer Figure 2). Table 1 tabulated the parameter used for this experiment. Etching is the last procedure in the process of Ni nanowires synthesizing. Etching procedure involve dissolving of AAO templates by using 10g NaOH in 15ml distilled water in order to obtain free standing deposited nanowires. The obtained free-standing Ni nanowires are then ready for analysis.

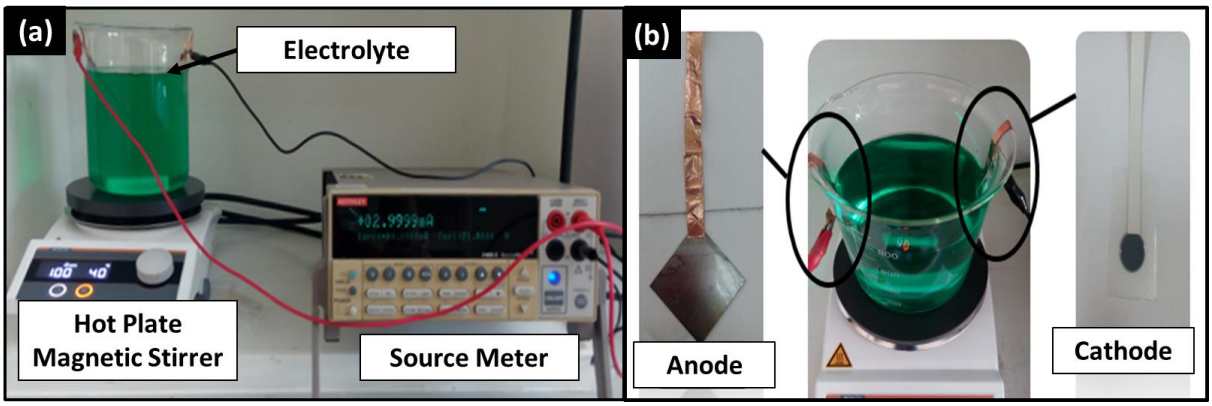


Fig. 2. (a) Apparatus and equipment arrangement for cell setup; (b) Nickel plate as anode and AAO template as cathode

Table 1
Synthesis parameter for electrochemical deposition

Electrolyte	Stabilizer Agent Concentration (g/L)	Deposition Period (min)	Applied Current (mA)	Deposition Bath Temperature (°C)
I	6	60	3.0	30 70 110
II	40	60	3.0	30 70 110
III	70	60	3.0	30 70 110

2.3 Characterization Techniques

We used BRUKER D8 Advance X-ray diffraction (XRD) with radiation source operated at 40 kV and 40 mA to study the crystallographic properties of Ni nanowires. The EDX analysis is performed using Oxford Instruments EDX attached to JOEL JSM-7800F FESEM at a beam source of 15kV to elementary composition analysis and FESEM to investigate nanowires morphology.

2.4 *Molecular Dynamic Simulation*

MD simulation was performed via Large-scale Atomic/Molecular Massively Parallel Simulator (LAMMPS) software. LAMMPS software was developed by Sandia National Laboratories and usually used to model particles in various state with different base material by generate coding in C++ language. This software have no numbers of atom limitation and able to perform simulation using different force fields and boundary conditions.

3. Results and Discussion

3.1 Elementary Composition

The EDX characterization proves that the Ni nanowires were composed of 96.99 % of Ni and 3.01 % of O_2 (Figure 3a and Figure 3b). The small percentage of O_2 observed indicates the possible absorption of O_2 from the air on the surface of Ni nanowires.

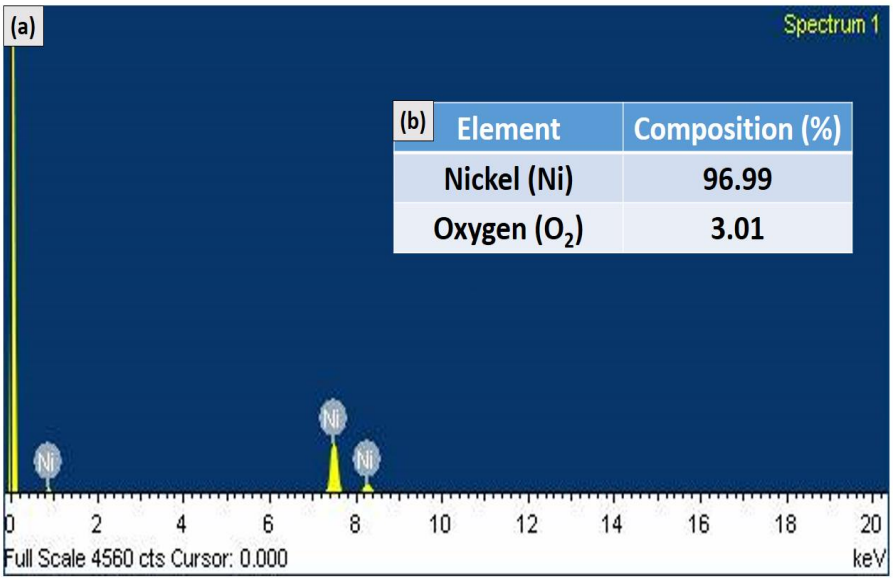


Fig. 3. EDX spectrum of synthesized Ni nanowires

3.2 FESEM Analysis

From the FESEM analysis, we can claimed that well-defined and excellent repeatability of Ni nanowires have been generated inside the pores of AAO templates on the AAO templates with uniform diameter (200 nm – 330 nm) as shown in Figure 4.

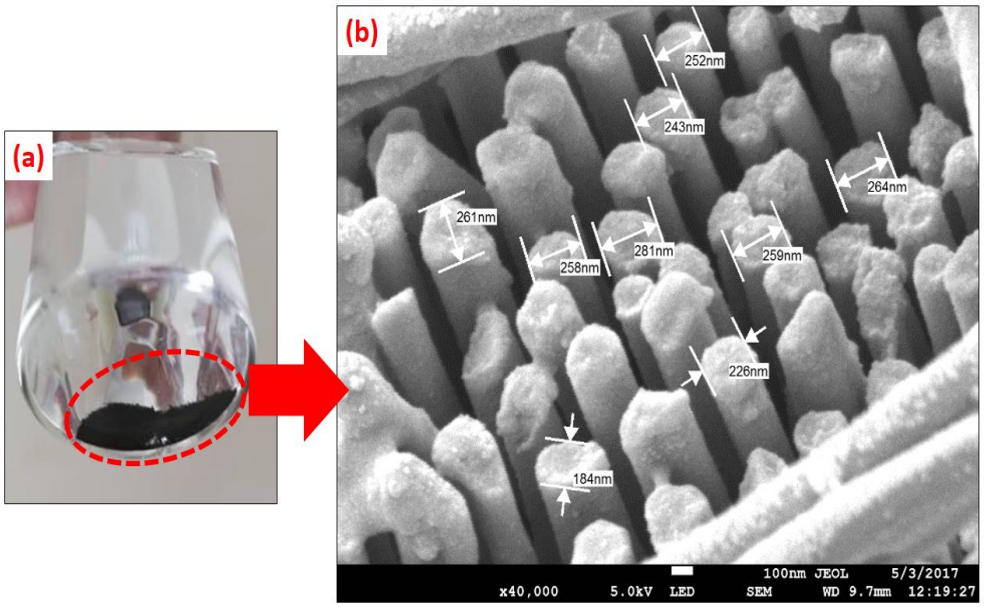


Fig. 4. (a) Obtained Ni nanowires; (b) Diameter measurement of synthesized Ni nanowires by FESEM analysis

3.2.1 Surface Texture

From the FESEM analysis, it is noticed that all the synthesized Ni nanowires have rough and flaky surface texture. Also, the observation found that there are significant differences when the parameter of the synthesis condition changed. All the surface texture become rougher with the increasing of stabilizer agent concentration. This is due to the increasing of internal stress which cause the cracks on the nanowires surface texture. This possible reason can be supported by Davolas et al., research findings; presence of boric acid in electrochemical deposition process cause the surface texture of deposited Ni to be smooth and glassy, instead of brittle and irregular surface appearance [35]. Boric acid serve as buffering agents for electrochemical deposition[36], and important for hasten the formation of nanowires. However, the present research findings found to be opposite with the literatures and the correlation of stabilizer agent concentration to the surface texture of Ni nanowires remains complex and ill-defined.

Additionally, the surface texture change to be very rough when the heating temperature increased to 110 °C. This is due to the formation of greater grain size at the high deposition temperature. The consequence from this phenomena, large Ni grains are obstructed to generate inside the templates pore during the formation of nanowires[37].

3.2.2 Growth Length

The average measured growth length of synthesized Ni nanowires for all synthesis condition is tabulated in Table 2. Figure 6 shows the average measured growth length of the synthesized Ni nanowires for all parameters. The length of Ni nanowires found to be longer when heating temperature set to be high. Higher temperature increase the rate of atomic diffusion[38], increase the speed of Ni nanowires formation and thus accelerates growth relative to the nucleation of new grains [39]. The influence of deposition temperature to the growth length of Ni nanowires also due to the lowered energy barriers [40]. However, the longer nanowire growth will creates a higher center of gravity which makes their position unbalanced [41].

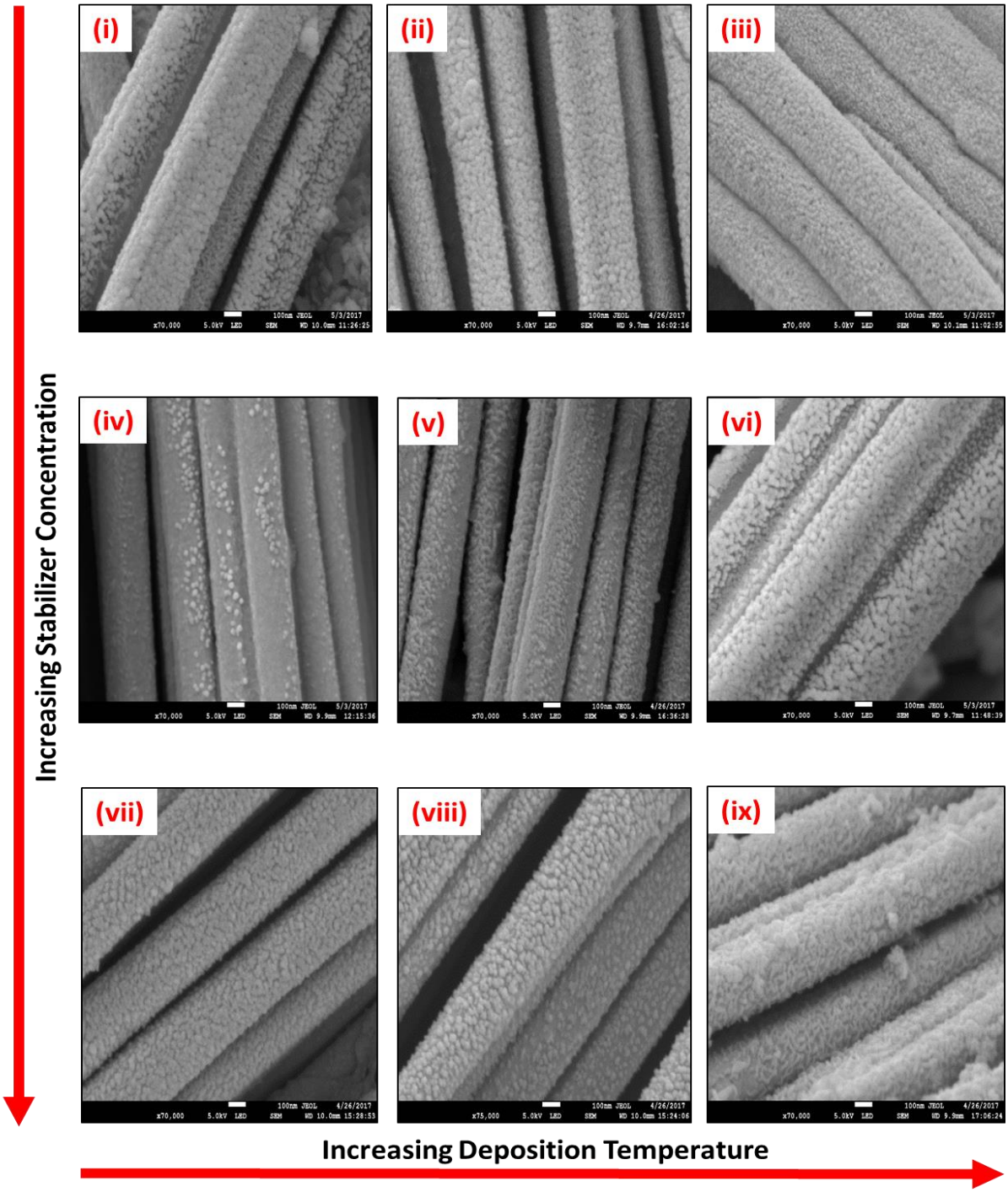


Fig. 5. FESEM analysis of synthesized Ni nanowires. (i-iii) stabilizer agents concentration of 6 g/L and deposition temperature of 30 °C, 70 °C and 110 °C respectively, (iv-vi) stabilizer agent concentration of 40 g/L and deposition temperature of 30 °C, 70 °C and 110 °C respectively, and (vii-ix) stabilizer agent concentration of 70 g/L and deposition temperature of 30 °C, 70 °C and 110 °C, respectively.

Table 2
Growth Length Measurement of Ni nanowire at different synthesis condition

Stabilizer agent concentration	Depostion Temperature (°C)	Growth Length (µm)
6g/L	30	26.888
	70	32.124
	110	33.617
40g/L	30	11.110
	70	14.859
	110	16.056
70g/L	30	10.320
	70	11.609
	110	15.801

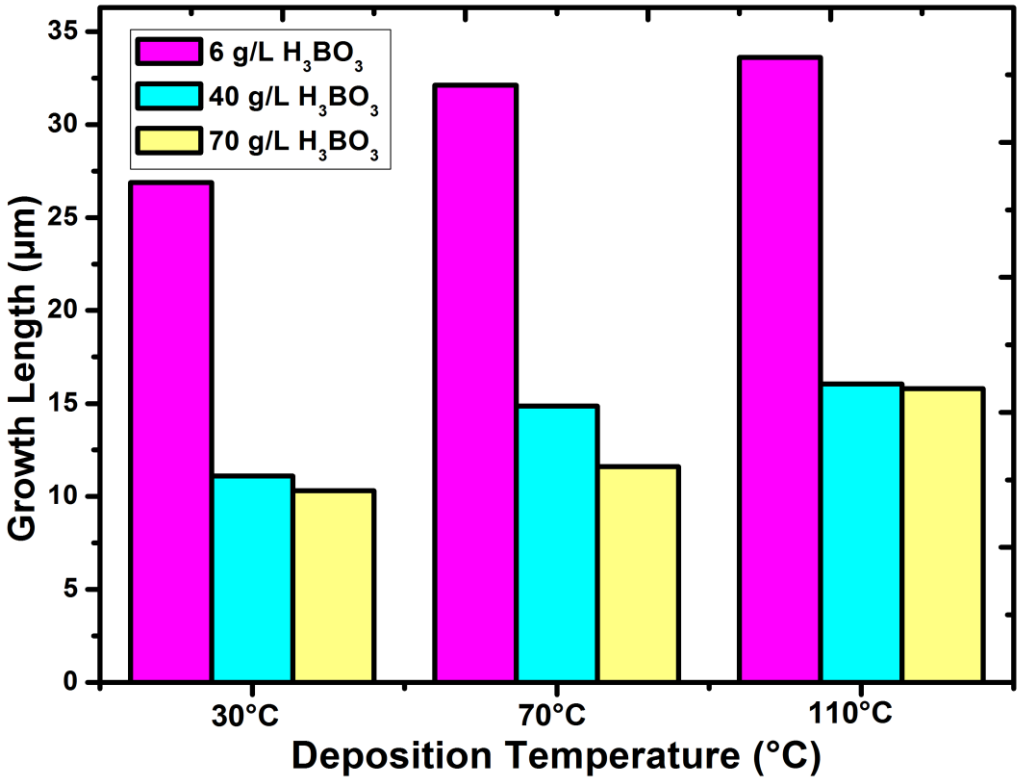


Fig. 6. Ni nanowire length for different synthesis condition

3.3 XRD Analysis
3.3.1 Crystal Orientation

Figure 7 show the XRD spectrum for the synthesized Ni nanowires at all synthesis condition. The diffraction patterns for all synthesis condition exhibited the synthesis Ni nanowires are polycrystalline as the crystalline planes with Miller indices of 111, 200, and 220. The relative intensity of Ni (111,200 and 220) peak increase as the deposition temperature increase showing that the quality of crystalline was increased with the higher deposition temperature [42].
In the aspect of boric acid concentration, it is observed that 40g/L of boric acid concentration with deposition temperature of 110 °C obtained the highest diffraction peak followed by 6g/L and 70g/L cases. These imply that 40g/L boric acid concentration give the best crystal quality to the synthesized Ni nanowires. It can be concluded that stabilizer agent concentration influence the

crystal quality of Ni nanowires with the ideal stabilizer agent concentration of 40 g/L with a heating temperature of 110 °C.

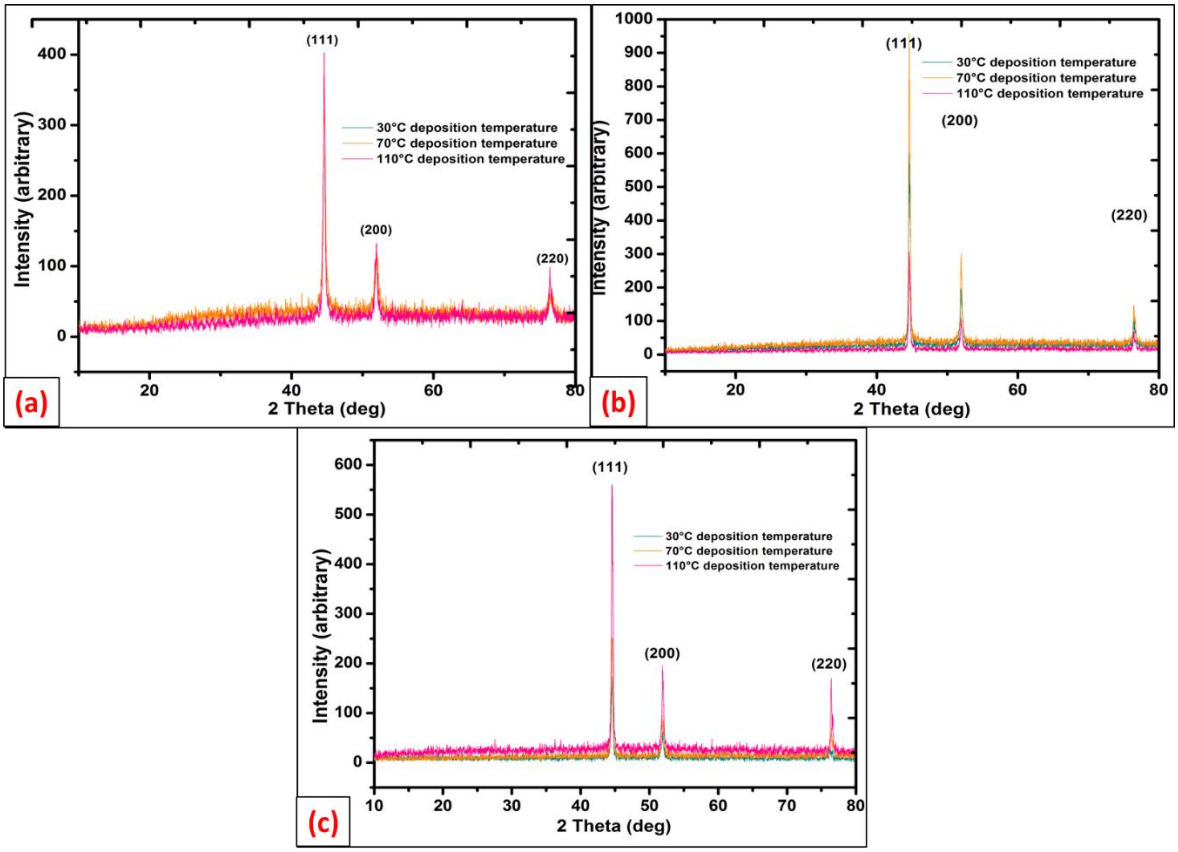


Fig. 7. XRD characterization. (a) 6 g/L stabilizer agent concentration with heating temperature of 30 °C, 70 °C and 110 °C respectively, (b) 40 g/L boric acid concentration with heating temperature of 30 °C, 70 °C and 110 °C respectively and (c) 70 g/L boric acid concentration with deposition temperature of 30 °C, 70 °C and 110 °C respectively.

3.3.2 Crystal Size

Figure 8 shows the calculated crystal size of Ni nanowires synthesized at all synthesis condition. The results strongly suggest that the crystal size improves as the heating temperature set to be higher. This indicates that higher temperature would exhibit the crystalline structure of the Ni nanowires due to the favouring growth of pre-existing nuclei during the initial stages of the electrochemical mechanism [38]. Discussing the influence of stabilizer agent concentration to the crystal size of nanowires, the crystal size of synthesized Ni nanowires found to be slightly decrease as the stabilizer agent become more concentrated. Further analysis needed to figure out the possible causes behind these hypothesis. Vicenzo and Cavallotti revealed that when boric acid added to the electrolyte at pH above 4, they extends the stability field of the crystallographic and improves its quality of crystals produced [43]. Another literature claimed that the reducing of boric acid concentration cause the increase in pH value, thus decrease the current efficiency (100% to 63%)[44].

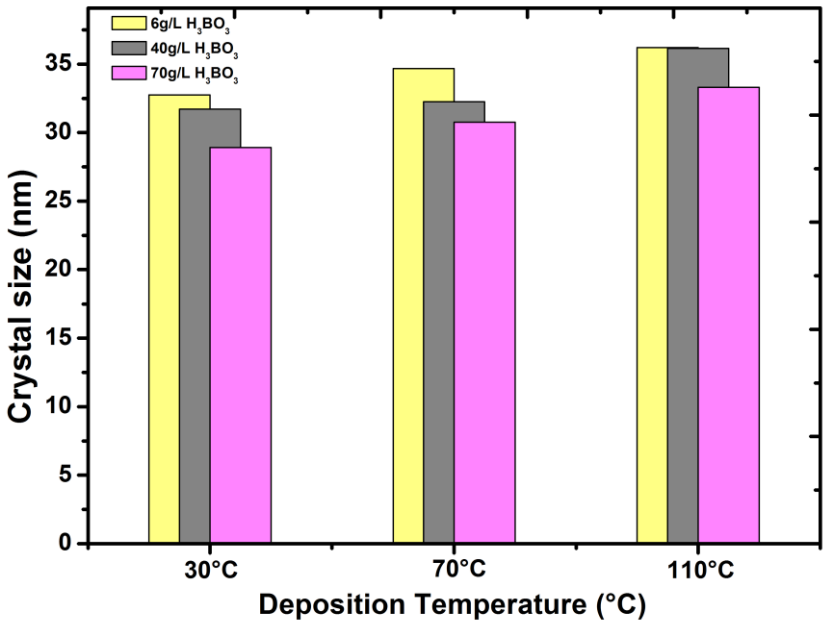


Fig.8. Crystal size of Ni nanowires synthesized at different stabilizer agent concentration and heating temperature

3.4 Mechanical Properties of Ni Nanowires by MD Simulation

The parameter used in modelling Ni nanowires via MD simulation can be summarize as follow:-

(a) Force field : Embedded-atom method potential for Ni-Al alloys by Mishin
(b) Temperature : 300 K
(c) Timestep : 0.001
(d) Relaxation period : 5000 steps
(e) Deformation : Tensile at X-direction at 0.0001 ps^{-1}

Table 3
Nickel Nanowire Model Dimension

Model	Diameter (nm)	Length (nm)	Number of atoms
A	8.05	18.5	62,828
B	8.05	22.11	75,398
C	8.05	24.63	87,964
D	8.05	29.15	100,528
E	8.05	32.67	113, 096
F	8.05	36.1	125,660
G	8.05	53.7	188,492
H	8.05	71.3	251,328

Figure 9 demonstrates the deformation process of a model H. During the relaxation state, some of the Ni atoms start to re rearranged themselves and the local lattice start to defect [45]. After 5000 steps of relaxation period, during the deformation stage, the surface of the nanowire is cracked abruptly and some lattices slide on the cracking area resulting in the necking shape until it deforms into the final rupture. With application of strain, the cyclical plastic deformation led to necking in the system, which culminate with failure of the nanowire [46].

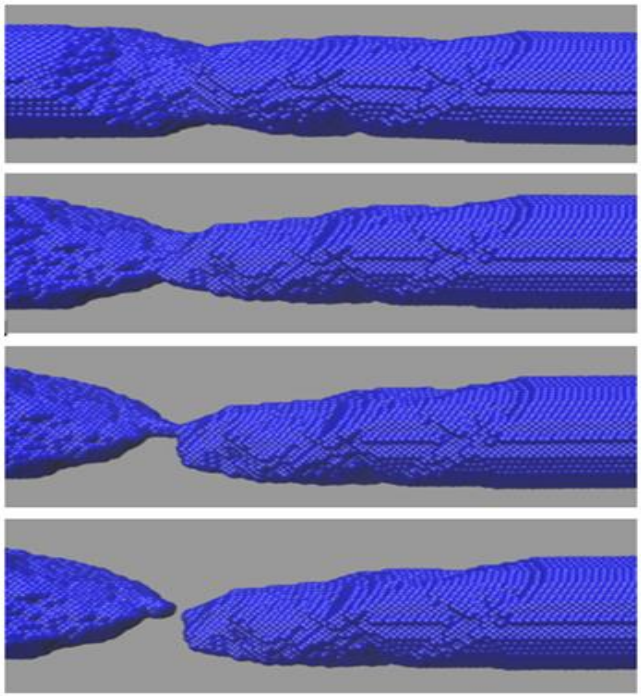


Fig. 9. Failure under tensile deformation process of Ni nanowire

Analyse from Table 4, all the mechanical properties of modelled Ni nanowires found to have quite similar trends. However, there were slight differences between the highest and lowest value of tensile modulus obtained. Also, it is clearly found that the value for yielding stress for all models is approximately in the range of 16 GPa with ductile failure mode.

Table 4
Simulated Mechanical Properties of Nickel Nanowires

Model	Young Modulus (GPa)	Yielding Stress (GPa)	Yielding Strain (GPa)	Failure mode
A	140.03	16.520	0.1181	Ductile
B	140.43	16.742	0.1208	Ductile
C	142.40	16.578	0.1189	Ductile
D	142.60	16.537	0.1181	Ductile
E	140.44	16.481	0.1186	Ductile
F	140.69	16.494	0.1180	Ductile
G	140.60	16.475	0.1184	Ductile
H	140.54	16.476	0.1184	Ductile

Figure 10 shows the stress-strain curve of all the modeled Ni nanowires. The stress-strain curve for all Ni nanowires models are entirely overlapped with the stress values are increasing up to approximately16.4 GPa strain showing that the length size have no significant influence to the mechanical properties of Ni nanowires. The yielding stress obtained in this study found to agrees with the finding from Wang et. al. and Mohan et. al. reported the yielding stress of 14.8 GPa and 15-17 GPa, respectively.

The obtained tensile modulus from this simulations is in the range of 140.03-142.60 GPa which is about 70% of its bulk value. Where else, Wang et. al. reported the tensile modulus in the range of 271 GPa – 324 GPa from the MD simulation of different sizes of Ni nanowires, while Dupont et. al. reported the slightly similar finding which is equal to 291 GPa. Additionally, Huang et. al.[47] in counterpart reported a higher value of tensile modulus which is in the range of 366-611 GPa. However, Wang et. al. and Mohan et. al. reported lower value modulus which is about 134 GPa and

182.71 GPa respectively. The variance in the obtained result can ascribed to the periodic boundary condition and force field used for the modeling.

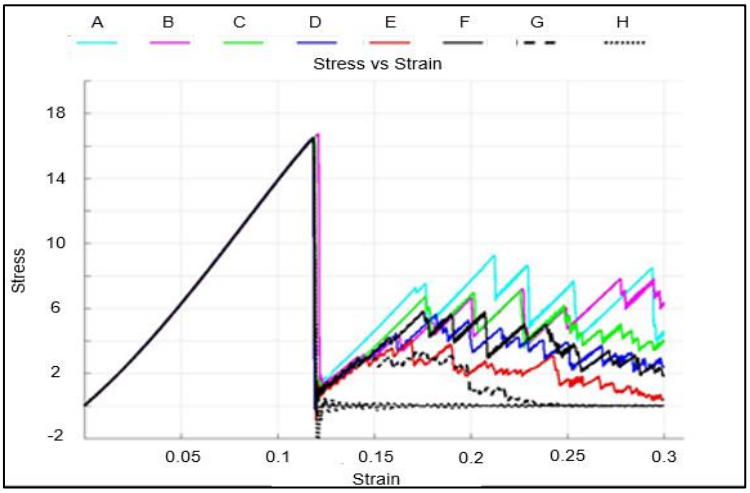


Fig. 10. Stress-strain curve of modeled Ni nanowire

4. Conclusions

Well-defined and excellent repeatability of Ni nanowires have been successfully deposited on the AAO templates with uniform diameter in the range of 200 nm – 330 nm via template-assisted electrochemical deposition approach. The obtained Ni nanowires with high purity (97.97% of nickel based on the EDX result) have rough and flaky surface texture for all the synthesis condition cases. Observation from FESEM analysis also claim that the surface texture roughness increased as the heating temperature increased. There are significant differences in the surface texture observed when stabilizer agent concentration increased. Overall growth length found to be greatly improved as the heating temperature increase but decrease when stabilizer agent concentration is high. The diffraction patterns for all synthesis condition exhibited the synthesis Ni nanowires are polycrystalline as the crystalline planes with Miller indices of 111, 200, and 220. The relative intensity of Ni (111,200 and 220) peak increase as the deposition temperature increase showing that the quality of crystalline was increased with the higher deposition temperature. It is also noted that the average of crystal size increase when stabilizer agent concentration decrease. Where else, the crystal size increased when the heating temperature increased. Further investigation needed to understand the rational reason for the characterization of obtained Ni nanowires influence by stabilizer agent concentration and heating temperature.

Eight Ni nanowires models successfully developed and modelled by using LAMMPS simulation software. The finding showed modelled Ni nanowires have a tensile modulus between 140.03-142.60 GPa, yielding stress between 16.475 to 16.742 GPa and yielding strain between 0.1180 to 0.1208. All the investigated nanowires showed ductile failure behavior, a typical behavior at larger length scales of Ni.

Acknowledgement
This research was funded by a grant from Universiti Malaysia Pahang, Malaysia (RDU1803176 and PGRS 190339).

References

[1] Weber, J., et al., *One-dimensional nanostructures: fabrication, characterisation and applications.* International Materials Reviews, 2008. **53**(4): p. 235-255.
[2] Gambhire, A.B., et al., *Synthesis and characterization of high surface area CeO2-doped SnO2 nanomaterial.* Materials Chemistry and Physics, 2008. **112**(3): p. 719-722.
[3] Bera, D., S.C. Kuiry, and S. Seal, *Synthesis of nanostructured materials using template-assisted electrodeposition.* JOM, 2004. **56**(1): p. 49-53.
[4] Xia, Y., et al., *One-Dimensional Nanostructures: Synthesis, Characterization, and Applications.* Advanced Materials, 2003. **15**(5): p. 353-389.
[5] Ghahremaninezhad, A. and A. Dolati, *A study on electrochemical growth behavior of the Co–Ni alloy nanowires in anodic aluminum oxide template.* Journal of Alloys and Compounds, 2009. **480**(2): p. 275-278.
[6] Irshad, M., et al., *Preparation and structural characterization of template assisted electrodeposited copper nanowires.* Int. J. Electrochem. Sci, 2014. **9**: p. 2548-2555.
[7] Şişman, İ., *Template-assisted electrochemical synthesis of semiconductor nanowires*, in *Nanowires–Implementations and Applications*. 2011, InTech. p. 41-58.
[8] Zheng, M., et al., *Fabrication and optical properties of large-scale uniform zinc oxide nanowire arrays by one-step electrochemical deposition technique.* Chemical Physics Letters, 2002. **363**(1): p. 123-128.
[9] Al-Salman, R., et al., *Template-Free Electrochemical Synthesis of High Aspect Ratio Sn Nanowires in Ionic Liquids: A General Route to Large-Area Metal and Semimetal Nanowire Arrays?* Chemistry of Materials, 2015. **27**(11): p. 3830-3837.
[10] Wang, Z.-L., et al., *Controllable Template-Assisted Electrodeposition of Single- and Multi-Walled Nanotube Arrays for Electrochemical Energy Storage.* Scientific Reports, 2013. **3**: p. 1204.
[11] Guo, Y.Y., et al., *Growth Mechanism for Controlled Synthesis of Metal Nanotube and Nanowire Arrays Using Anodic Aluminum Oxide Templates.* Acta Physico-Chimica Sinica, 2010. **26**(7): p. 2037-2043.
[12] Mu, C. and J.H. He, *Synthesis of Single Crystal Metal Sulfide Nanowires and Nanowire Arrays by Chemical Precipitation in Templates.* Journal of Nanoscience and Nanotechnology, 2010. **10**(12): p. 8191-8198.
[13] Bograchev, D.A., V.M. Volgin, and A.D. Davydov, *Simple model of mass transfer in template synthesis of metal ordered nanowire arrays.* Electrochimica Acta, 2013. **96**: p. 1-7.
[14] Choi, J.S., et al., *Monodisperse metal nanowire arrays on Si by integration of template synthesis with silicon technology.* Journal of Materials Chemistry, 2003. **13**(5): p. 1100-1103.
[15] Li, X.D., et al., *Nanochannel-Directed Growth of Multi-Segment Nanowire Heterojunctions of Metallic Au1-xGex and Semiconducting Ge.* Acs Nano, 2012. **6**(1): p. 831-836.
[16] Sharma, G., M.V. Pishko, and C.A. Grimes, *Fabrication of metallic nanowire arrays by electrodeposition into nanoporous alumina membranes: effect of barrier layer.* Journal of Materials Science, 2007. **42**(13): p. 4738-4744.
[17] Kline, T.R., et al., *Template-grown metal nanowires.* Inorganic chemistry, 2006. **45**(19): p. 7555-7565.
[18] Martin, C.R., *Membrane-based synthesis of nanomaterials.* Chemistry of Materials, 1996. **8**(8): p. 1739-1746.
[19] Ertan, A., S.N. Tewari, and O. Talu, *Electrodeposition of nickel nanowires and nanotubes using various templates.* Journal of Experimental Nanoscience, 2008. **3**(4): p. 287-295.
[20] Pearson, D. and R. Tonucci, *Nanochannel glass replica membranes.* Science, 1995. **270**(5233): p. 68.
[21] Wang, D.H., et al., *Electrodeposition of metallic nanowire thin films using mesoporous silica templates.* Advanced Materials, 2003. **15**(2): p. 130-+.
22] Chakravorty, D., et al., *Synthesis of nanocomposites using glasses and mica as templates.* Bulletin of Materials Science, 2008. **31**(3): p. 263-276.
[23] de AA Soler-Illia, G.J., et al., *Block copolymer-templated mesoporous oxides.* Current Opinion in Colloid & Interface Science, 2003. **8**(1): p. 109-126.
[24] Narayanan, T.N., et al., *On the growth mechanism of nickel and cobalt nanowires and comparison of their magnetic properties.* Nano Research, 2008. **1**(6): p. 465-473.
[25] García, M., P. Batalla, and A. Escarpa, *Metallic and polymeric nanowires for electrochemical sensing and biosensing.* TrAC Trends in Analytical Chemistry, 2014. **57**: p. 6-22.
26] Blagg, K., et al., *Template-based electrodeposition and characterization of niobium nanowires.* Electrochemistry Communications, 2019. **101**: p. 39-42.
[27] Zhang, H., et al., *Growth mechanism and magnetic properties of Co nanowire arrays by AC electrodeposition.* Journal of Magnetism and Magnetic Materials, 2018. **468**: p. 188-192.
[28] Meier, L.A., et al., *Formation of Cu and Ni Nanowires by Electrodeposition.* Procedia Materials Science, 2015. **8**: p. 617-622.

[29] Zhang, Q., Q.-K. Li, and M. Li, *Internal stress and its effect on mechanical strength of metallic glass nanowires.* Acta Materialia, 2015. **91**: p. 174-182.
[30] Wu, H.A., et al., *Progress in mechanical behavior of metal nanowire.* Acta Metallurgica Sinica, 2002. **38**(9): p. 903-907.
[31] Yao, Y. and S. Chen, *Surface effect in the bending of nanowires.* Mechanics of Materials, 2016. **100**: p. 12-21.
[32] Weber, F., et al., *Texture evolution during bending of a single crystal copper nanowire studied by EBSD and crystal plasticity finite element simulations.* Advanced Engineering Materials, 2008. **10**(8): p. 737-741.
[33] Setoodeh, A., H. Attariani, and M. Khosrownejad, *Nickel nanowires under uniaxial loads: A molecular dynamics simulation study.* Computational Materials Science, 2008. **44**(2): p. 378-384.
[34] Zhan, H., et al., *Tensile properties of Si nanowires with faulted stacking layers.* Science of Advanced Materials, 2014. **6**(7): p. 1489-1492.
[35] Davalos, C., et al., *Study of the role of boric acid during the electrochemical deposition of Ni in a sulfamate bath.* Int J Electrochem Sci, 2013. **8**: p. 9785.
[36] Ji, J., et al., *Surface pH measurements during nickel electrodeposition.* Journal of Applied electrochemistry, 1995. **25**(7): p. 642-650.
[37] Toimil-Molares, M.E., *Characterization and properties of micro- and nanowires of controlled size, composition, and geometry fabricated by electrodeposition and ion-track technology.* Beilstein Journal of Nanotechnology, 2012. **3**: p. 860-883.
[38] Cortés, A., et al., *Single-crystal growth of nickel nanowires: influence of deposition conditions on structural and magnetic properties.* Journal of nanoscience and nanotechnology, 2009. **9**(3): p. 1992-2000.
[39] Wang, J.-G., et al., *Controllable template synthesis of superconducting Zn nanowires with different microstructures by electrochemical deposition.* Nano letters, 2005. **5**(7): p. 1247-1253.
[40] Dayeh, S.A., E.T. Yu, and D. Wang, *III− V nanowire growth mechanism: V/III ratio and temperature effects.* Nano letters, 2007. **7**(8): p. 2486-2490.
[41] Li, Z., et al., *Effects of nanowire length and surface roughness on the electrochemical sensor properties of Nafion-free, vertically aligned Pt nanowire array electrodes.* Sensors, 2015. **15**(9): p. 22473-22489.
[42] Šupicová, M., et al., *Influence of boric acid on the electrochemical deposition of Ni.* Journal of Solid State Electrochemistry, 2006. **10**(2): p. 61-68.
[43] Vicenzo, A. and P. Cavallotti, *Structure and electrokinetic study of nickel electrodeposition.* Russian Journal of Electrochemistry, 2008. **44**(6): p. 716-727.
[44] Tsuru, Y., M. Nomura, and F. Foulkes, *Effects of boric acid on hydrogen evolution and internal stress in films deposited from a nickel sulfamate bath.* Journal of Applied Electrochemistry, 2002. **32**(6): p. 629-634.
[45] Hertzberg, R.W., *Deformation and fracture mechanics of engineering materials.* 1989.
[46] Branício, P.S. and J.-P. Rino, *Large deformation and amorphization of Ni nanowires under uniaxial strain: a molecular dynamics study.* Physical Review B, 2000. **62**(24): p. 16950.
[47] Huang, D., Q. Zhang, and P. Qiao, *Molecular dynamics evaluation of strain rate and size effects on mechanical properties of FCC nickel nanowires.* Computational Materials Science, 2011. **50**(3): p. 903-910.

Penerbit Akademia Baru

Engineering Science and Technology Conference Proceedings

Journal homepage: www.akademiabaru.com/EST.html

Numerical Simulation of Fluid Flow and Heat transfer Through Porous Media

Open Access

Farhan Lafta Rashid[1] , Hayder M. Abbood[2] , Salem Jawad Kadum[3]

[1] University of Kerbala/ College of Engineering

ABSTRACT

The flow pattern and heat and mass transfer in the porous media and fluid mixing area are widely found in the production and engineering, such as heat pipe, building envelope and insulation materials. Especially the slip effect at the at the interface between the fluid and the porous media has a great impact on the flow and heat and mass transfer. In this paper, the fluid flow and heat transfer through and porous media is studied by means of numerical simulation. Results were obtained for different flow velocity (Reynolds number) of steam ranged of (37374, 42315, 47275, and 52070) with inlet temperature of 400 K. The increase in Reynolds number (flow velocity) increases the pressure distribution along the porous zone segment. Velocity of steam is higher at inlet and outlet and be lower at the porous zone, so the increase in steam flow velocity increases velocity distribution. Steam temperature enter at high value at the inlet (400 K) and reduces along the segment distance (Z/L). The increase in steam flow velocity increases temperature along the section.

Keywords:

Fluid flow; heat transfer; porous media; numerical simulation

Copyright © 2019 PENERBIT AKADEMIA BARU - All rights reserved

1. Introduction

Flow through the porous media has been studied in terms of its various applicability such to civil engineering, biology, mechanical engineering, etc. For the mechanical engineering, porous media is utilized for the catalytic reactors, pneumatic silencers, micro heat exchangers, etc. As for the heat exchangers, while the working fluid flows through the porous media, it is heated or cooled by the interaction of the porous walls. The advantage of the porous media as the heat exchanger is its wide contact area to the working fluid. Furthermore, due to its tortuous shape, fluid flow is mixed and thus the heat transfer is enhanced. In terms of its merits, the heat and mass transfer through the porous media has been extensively studied. Vafai and Tien [1] employed the volume averaging technique to simulate the heat transfer and they discussed the effects of the inertia and boundary. Masuoka and Takatsu [2] investigated the turbulence inside the porous media and they evaluated 0- equation model for flow and heat transfer. Lu et al. [3] presumed the open-celled metallic porous media as the perpendicularly-structured cells, and overall heat transfer coefficient and the pressure drop depending on the porosity are numerically discussed. Calmidi and Mahajan [4-5] experimentally and numerically studied for the thermal conductivity and heat transfer for high-porosity open-celled porous heat exchanger. Angirasa [6] numerically investigated by using the volume-averaged vortex transport equations. Boomsma and Poulikakos [7] and Boomsma et al. [8] intensively studied the characterization of the porous media and the performance of the porous heat exchangers both by experiment. However, the aforementioned numerical computations for heat and fluid flow are based on the averaged governing equation, by which the detailed flow

inside the porous media is unavailable. To simulate the flow in the microscopic view, Krishnan et al. [9] constructed the open-cell structures and discussed effects of the porosity and the permeability on the friction factor and Nusselt number. Their computation is carried out by commercial software based on the finite volume method.

Ochoa-Tapia and Whitaker [10] pointed out that when solving the volume integral transfer equation, due to the differences of the integration program for the fluid variable between the two regions, and considering the effect of fluid effective viscosity in the porous medium (Effective Viscosity), it is recommended to using the Shear Stress Jump Condition at the interface. The problem in the application of shear jumps conditions is similar to that of Darcy's law. Estimating the jump degree of the shear force at the interface are the empirical coefficients, and different coefficients will lead to different calculation results. Kuznetsov [11] has studied the effects of shear jump conditions on the velocity of the free-flow region. And it is found that the shear lag and the effective viscous dynamic coefficient can affect the flow velocity distribution. Chandesris and Jamet [12] have found that the shear boundary condition is related to the pressure gradient and presented the corresponding method to deriving the interface boundary condition. Silva and de Lemos [13] applied the mathematics model established by the shear jump condition to analyze the influence of the physical properties of the porous media to the flow velocity distribution in the flow of the mixed region. Many researchers assume that the effective viscous power coefficient is equal to the external fluid viscous power coefficient, and then derived another way to deal with boundary conditions. That is when the dynamic viscosity coefficient is consistent, considering the fluid inside and outside the porous media as two kinds of fluid which have same characters (Single-Domain method) without special handling of interface boundary conditions. When using a single-domain method to solve a mixed-area flow problem, the value automatically satisfies the continuous conditions of velocity, pressure, shear, temperature and flux at the boundary. Vafai and Kim [14] found that the single-region method performed well in verifying the boundary conditions of the interface, and it was possible to predict the change of the gradient of fluid properties at the interface more precisely. Later Chandesris, Goyeau, Ochoa-Tapia [15,16]and some other scientists applied further tests on the single-region method generally, and developed a general-purpose model which includes the single-region method to calculate the change of the flow rate profile in the mixed area.

The present work involves simulation of fluid flow and heat transfer through vertical segment of porous media using CFD.

2. Fluid Properties

The physical and thermal properties of the steam (at 400 K) used in the present work are listed in table (1). These properties were entered as inlet boundary conditions in the set up process stage.

Table (1): Fluid properties

Property	Value	Units
Density	0.554	Kg/m^3
Thermal conductivity	0.0261	w/m.k
Dynamic viscosity	$1.34x10^{-5}$	Kg/m.s
Specific heat	2014	j/kg.k
Molecular weight	18.015	Kg/kgmol.

3. Fluid Flow Modelling

3.1 Navier-Stokes equation

The Navier-Stokes equation is the equation of motion for a Newtonian fluid with constant viscosity and density. The equation is greatly simplified when applied to 2D flow with the assumption that velocity is only in the axial direction [17, 18, 19].

3.2Standard k- ε Turbulence Model

At high Reynolds numbers, the viscous dissipation of kinetic energy (ε) will rise because of high inertial forces, multiplied by the fluctuating vorticity and from Navier-Stokes equation it can be derived the viscous dissipation at the exact transport fluctuating vorticity equation [20, 18, 19].

3.3CFD) model using ANSYS- FLUENT

The method of (CFD) used to simulate steam flow in porous media using the ANSYS-FLUENT, the pre-processor, solver and post-processor are the basic parts of the ANSYS-FLUENT software to analyze the process. The pre-processor step is usually carried out through a graphical interface. The velocity of steam, and the data of the porous cell condition, density of the gas and all coefficient values are entered to the solver software (user input values), to solve the numerical equations based on the entered values and the results are obtained to provide the post-processor step software [21]. In this work, the steam passes through the segment from the bottom. Flow Analysis by FLUENT is solved in steady state turbulent flow simulation. The boundary condition for turbulent model flow will range from 22.6 to 31.6 as inlet velocity and is used for inlet temperature equals 400 k (isothermal boundary condition). After the simulation is iterated, the final steps are post-processing and displaying the output in contours or in vectors, the data that is obtained by the solver can be visualized and displayed such as pressure, velocity, temperature, and streamlines.

4.Model Description and Meshing

The first step in CFD simulation of porous media is Pre-processing, which has been done by ANSYS Workbench 16.0. The geometrical model with (hexahedral grids) of 14661 nodes and 13079 quadrilateral cells as shown in Fig.(1).The geometric model was designed with 0.040 m in a diameter for inlet and outlet section, and 0.100 m in a diameter of porous zone, length of inlet and outlet section is 0.030 m, and length of porous zone is 0.400 m.

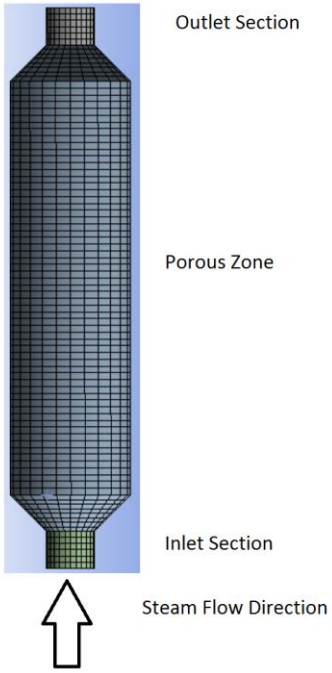


Fig.(1): Meshing the test section

5.Results and Discussion

For different flow velocity of gas (steam) through vertical porous media segment gives different pressure distribution, the pressure drop can be calculated by the difference between the pressure value at bottom and top of the segment, the pressure distribution contours have been simulated using Ansys Fluent 16.0 over the Reynolds numbers range of (37374, 42315, 47275, and 52070) as shown in Fig. (1). Pressure decrease along the porous zone because of the strong inertial forces of the porous media material, the increase in Reynolds number (flow velocity) increases the pressure distribution along the porous zone segment, this behavior shown clearly in fig.(6).

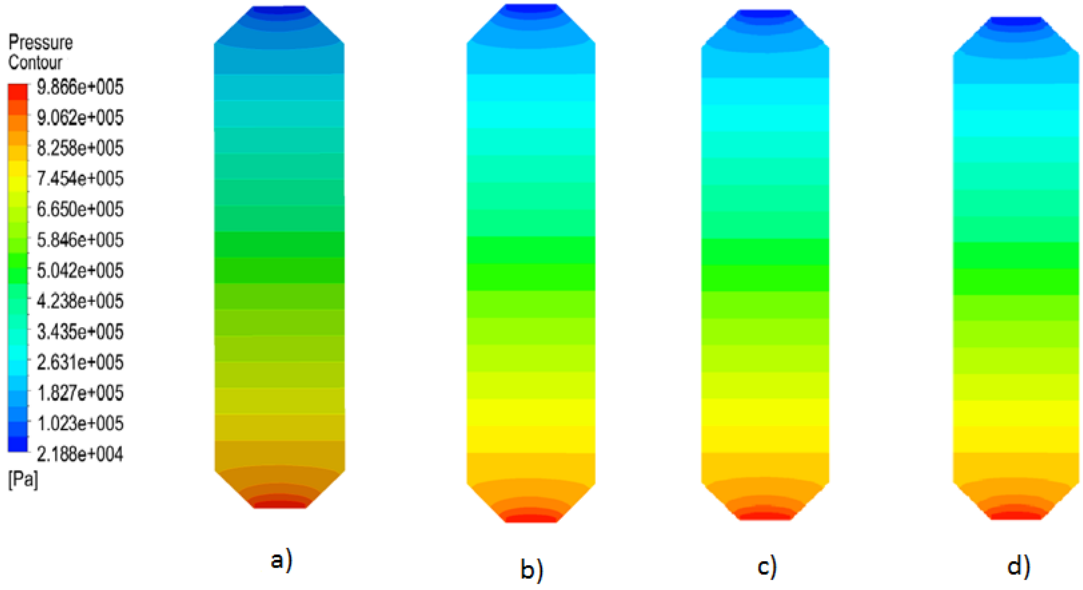


Fig.(1): Pressure contour through porous zone for different inlet velocity (a:22.6, b: 25.6, c:28.6, d:31.6 m/s)

Fig.(2) illustrates the contours of velocity distribution along the porous zone segment for different flow velocity (Reynolds number), velocity of steam is higher at inlet and outlet and be lower at the porous zone, so the increase in steam flow velocity increases velocity distribution as shown in fig.(7).

Fig.(3) reveals the velocity stream line of flowing the steam through the segment for different flow velocity, different flow velocities give different steam flow behavior.

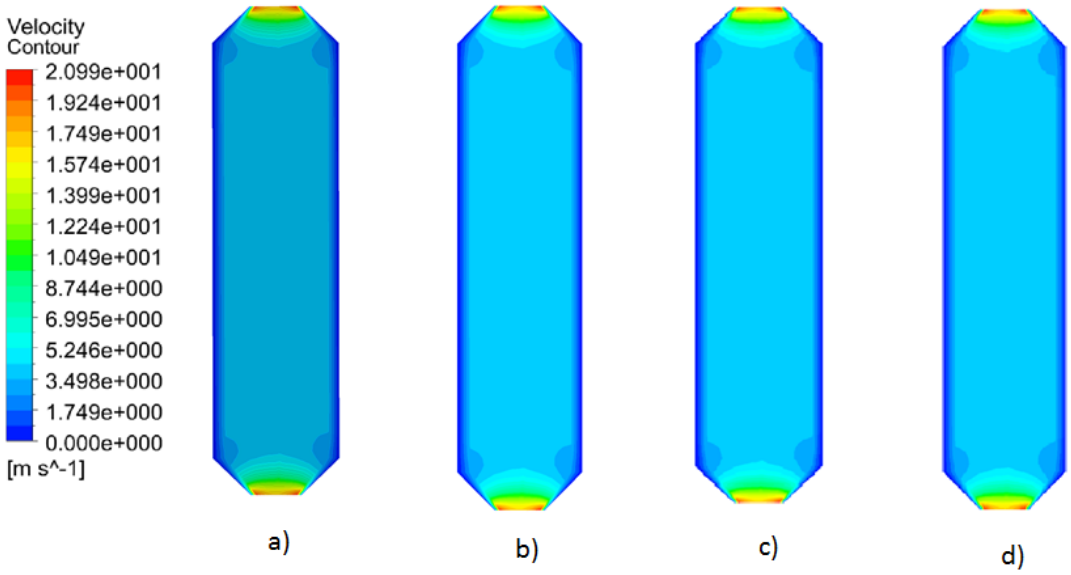


Fig.(2): Velocity contour through porous zone for different inlet velocity (a:22.6, b: 25.6, c:28.6, d:31.6 m/s)

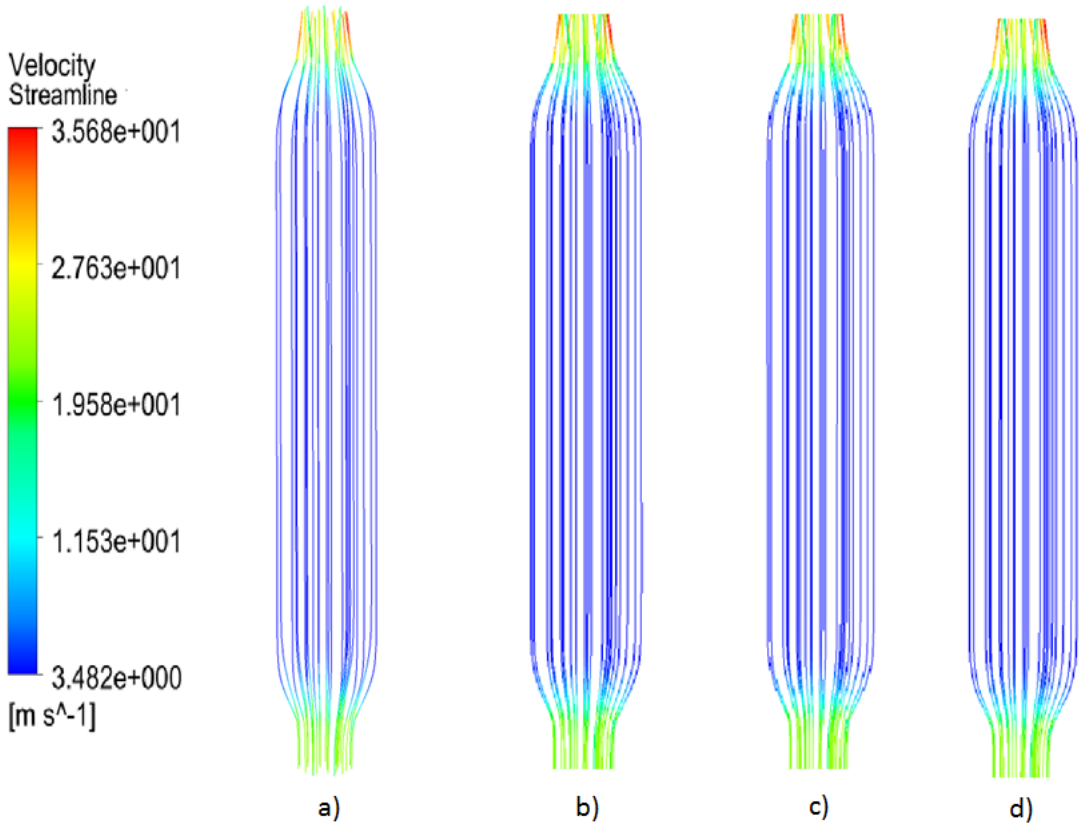


Fig.(3): Velocity streamline contour through porous zone for different inlet velocity (a:22.6, b: 25.6, c:28.6, d:31.6 m/s)

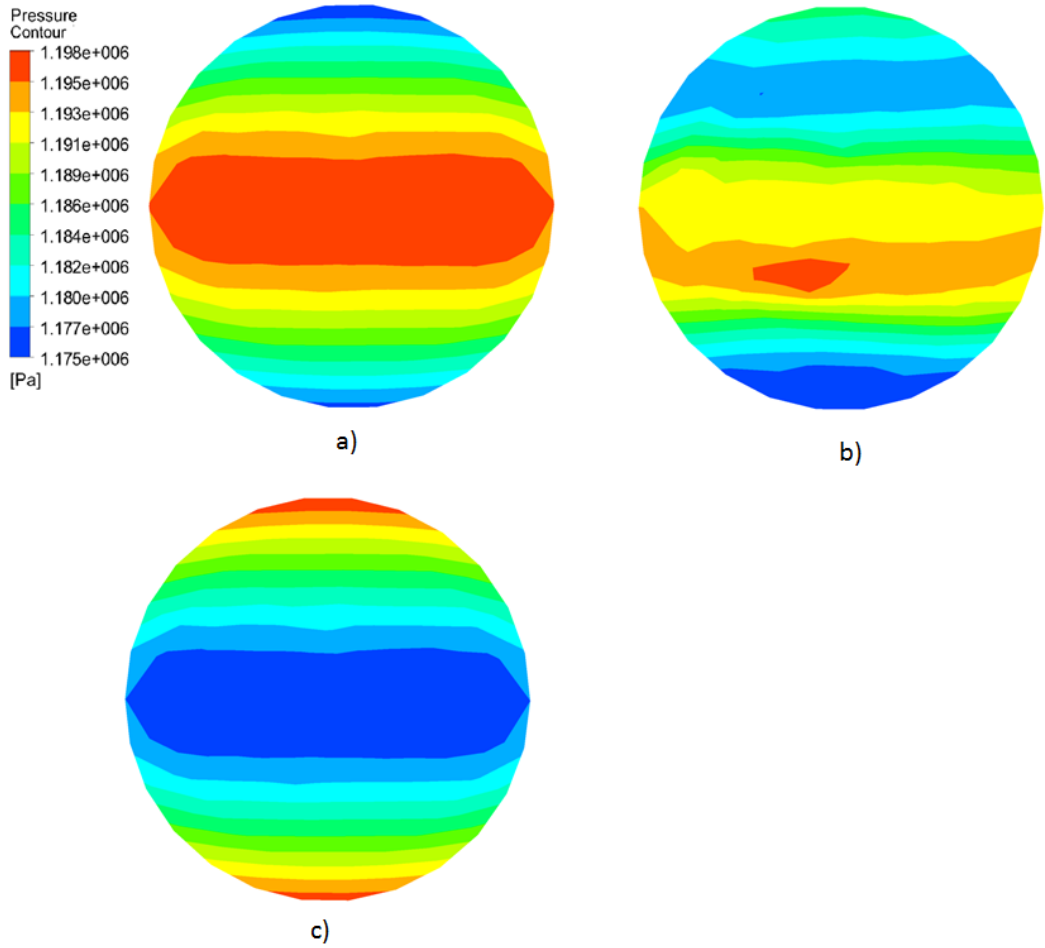


Fig.(4): Pressure contour through porous zone at different location (a: inlet , b: mid, c: exit,)

Fig.(4) present pressure contour at different location (Z/L) of porous zone, pressure be at high value at the inlet and decreases gradually to the end.

Fig.(5) shows pressure contour at different location (Z/L) of porous zone, it can be seen that flow velocity be at high value at the inlet and decreases gradually to the end.

Fig.(8) reveals temperature distribution along the porous zone segment, steam temperature enter at high value at the inlet (400 K) and reduces along the segment distance (Z/L), because of heat loss through porous body. The increase in steam flow velocity increases temperature along the section.

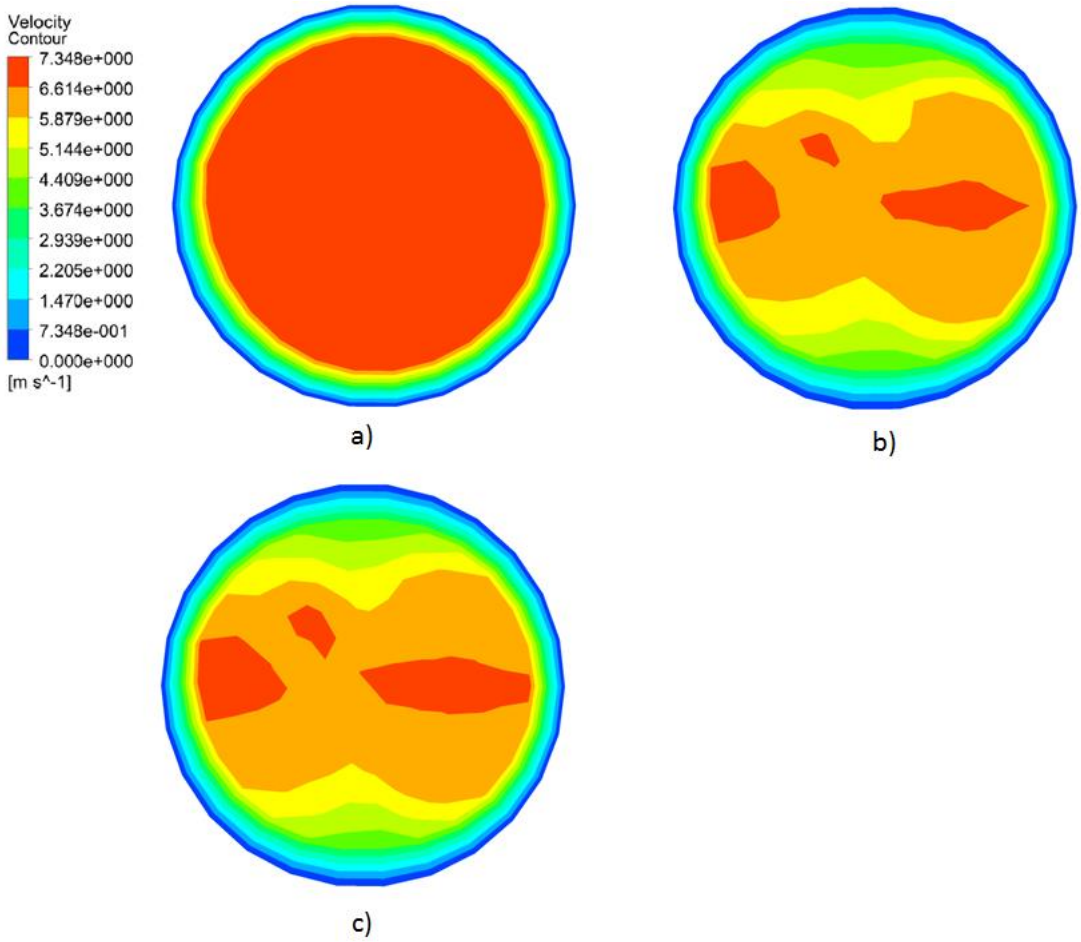


Fig.(5): Velocity contour through porous zone at different location (a: inlet , b: mid, c: exit,)

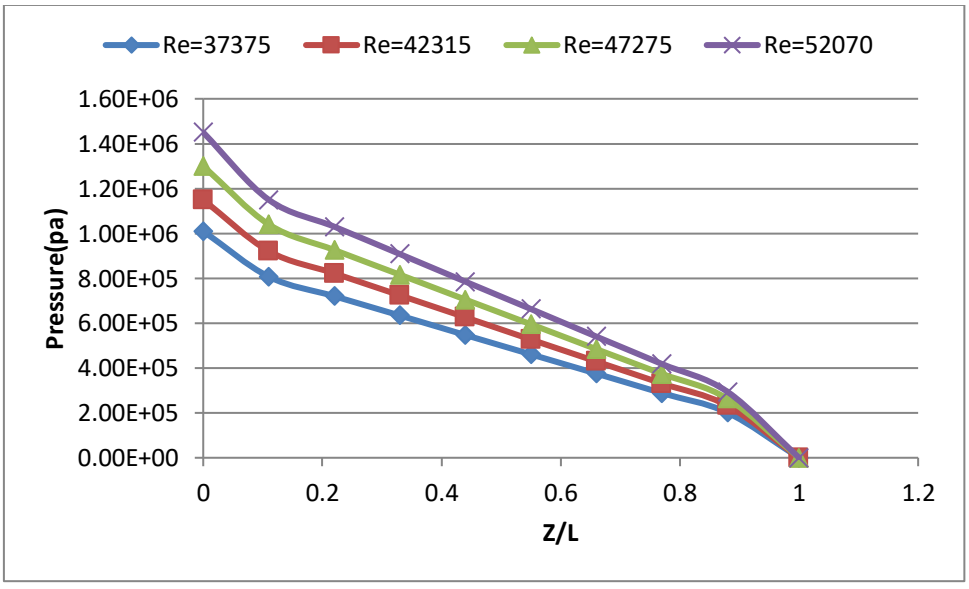


Fig.(6): Pressure distribution through porous zone for different Reynolds number

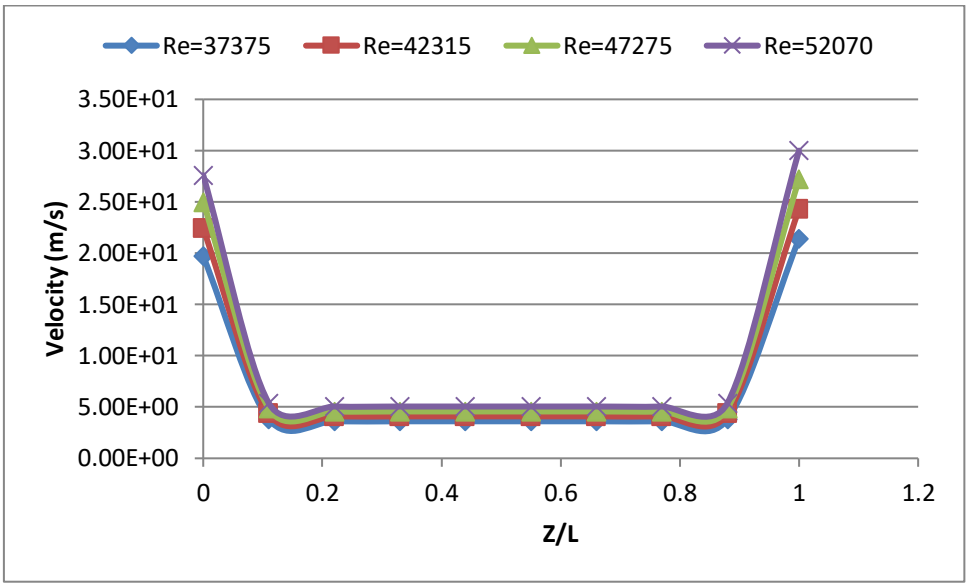


Fig.(7): Velocity distribution through porous zone for different Reynolds number

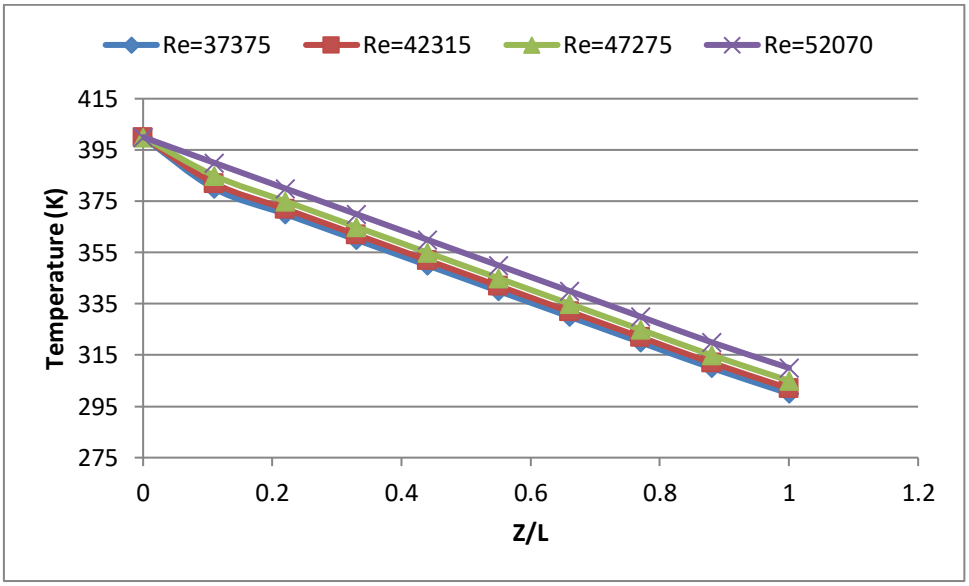


Fig.(8): Temperature distribution through porous zone for different Reynolds number

6.Conclusions

The present work studied the effect of varying steam flow velocity on some parameters for flow of steam vertically through porous zone, the following conclusion can be obtained:

1. The increase in Reynolds number (flow velocity) increases the pressure distribution along the porous zone segment.
2. Velocity of steam is higher at inlet and outlet and be lower at the porous zone, so the increase in steam flow velocity increases velocity distribution.
3. Steam temperature enter at high value at the inlet (400 K) and reduces along the segment distance (Z/L). The increase in steam flow velocity increases temperature along the section.

References

[1] Vafai, K. and Tien, C.L., 1981. “Boundary and Inertia Effects on Flow and Heat Transfer in Porous Media”, Int. J. Heat Mass Transfer, 24, pp. 195-203.
[2] Masuoka, T. and Takatsu, Y., 1996. “Turbulence Model for Flow Through Porous Media”, Int. J. Heat Mass Transfer, 39, pp. 2803-2809.
[3] Lu, T.J., Stone, H.A. and Ashby, M.F., 1998. “Heat Transfer in Open-cell Metal Foams”, Acta Mater., 46, pp. 3619-3635.
[4] Calmidi, V.V. and Mahajan, R.L., 1999. “The Effective Thermal Conductivity of High Porosity Fibrous Metal Foams”, J. Heat Transfer, 121, pp. 466-471.
[5] Calmidi, V.V. and Mahajan, R.L., 2000. “Forced Convection in High Porosity Metal Foams”, J. Heat Transfer, 122, pp. 557-565.
[6] Angirasa, D., 2002. “Forced Convective Heat Transfer in Metallic Fibrous Materials”, J. Heat Transfer, 124, pp. 739-745.
[7] Boomsma, K., Poulikakos, D., 2002, “The Effects of Compression and Pore Size Variations on the Liquid Flow Characteristics in Metal Foams”, J. Fluids Eng., 124, pp. 263-272.
[8] Boomsma, K., Poulikakos, D. and Zwick, F., 2003. “Metal Foams as Compact High Performance Heat Exchangers”, Mechanics of Materials, 35, pp. 1161-1176.
[9] Krishnan, S., Murthy, J. and Garimella, S.V., 2006. “Direct Simulation of Transport in Open-cell Metal Foam”, J. Heat Transfer, 128, pp. 793-799.
[10]Ochoa-Tapia J A, Whitaker S. Momentum transfer at the boundary between a porous medium and a homogeneous fluid—II. Comparison with experiment. International Journal of Heat & Mass Transfer, 1995, 38(14):2647-2655.
[11]Kuznetsov A V. Influence of the stress jump condition at the porous-medium/clear-fluid interface on a flow at a porous wall. International Communications in Heat & Mass Transfer, 1997, 24(3):401-410.
[12]Chandesris M, Jamet D. Boundary conditions at a planar fluid–porous interface for a Poiseuilleflow. International Journal of Heat & Mass Transfer, 2006, 49(13-14):2137-2150.
[13]Renato A. Silva, Marcelo J. S. de Lemos. NUMERICAL ANALYSIS OF THE STRESS JUMP INTERFACE CONDITION FOR LAMINAR FLOW OVER A POROUS LAYER. Numerical Heat Transfer Part A Applications, 2003, volume 43(6):603-617.
[14]Vafai K, Kim S. J. Analysis of surface enhancement by a porous substrate.ASME J. Heat Transfer, 1990,112:700-706.
[15]D’Hueppe A, Chandesris M, Jamet D, et al. Coupling a two-temperature model and a one-temperature model at a fluid-porous interface. International Journal of Heat & Mass Transfer, 2012, 55(s 9–10):2510-2523.
[16]Valdés-Parada F J, Aguilar-Madera C G, Ochoa-Tapia J A, et al. Velocity and stress jump conditions between a porous medium and a fluid[J]. Advances in Water Resources, 2013, 62(12):327-339.
[17] ANSYS Fluent Documentation ANSYS Inc. 2010 ANSYS Fluent 12.0/12.1 Documentation.
[18] Launder B E and Spalding D 1972 Lectures in Mathematical Models of Turbulence (London: Academic Press) edition 1 pp. 24
[19] Festuccia A and Bella G 2018 Journal of Porous Media 21(5).
[20] Hlushkou D and Tallarek U 2006 Journal of Chromatography 1126 (70).
[21] ANSYS Fluent Documentation ANSYS Inc. 2015 Release 16.0.

Penerbit Akademia Baru

Engineering Science and Technology Conference Proceedings

Journal homepage: www.akademiabaru.com/EST.html

Aerodynamic Performances of Paper Planes

Open Access

N.I. Ismail[1], Z.M. Ali[2, *], I.S. Ishak[3], R.M. Noor[1] & R. Rabilah[1]

[1] Faculty of Mechanical Engineering, Universiti Teknologi MARA, Cawangan Pulau Pinang, 13500 Permatang Pauh, Penang, Malaysia
[2] Faculty of Mechanical Engineering, Universiti Teknologi MARA, Cawangan Johor, Kampus Pasir Gudang, 81750 Masai, Johor, Malaysia
[2] School of Mechanical Engineering, Faculty of Engineering, Universiti Teknologi Malaysia, 81310 Skudai, Johor, Malaysia

ABSTRACT

Paper plane has a high potential to be upgraded as a Micro Air Vehicle (MAV). Due to its simplicity, paper plane offers easier design option compared to the biological inspired designs as shown in recent MAV development. However, researchers have underestimate and overlook the basic aerodynamic performance induced by these paper planes. This is due to its common usage as toys and wide range of paper plane design. Thus, the objective for current work is to analyse and compare the aerodynamics forces and its performance for selected paper plane design known as Glider, Wide Stunt Glider Plane and Stunt plane. A series of CFD simulations on each paper plane was executed by using ANSYS-CFX module. A steady state, incompressible flow Navier-Stokes equation (RANS) combined with Shear Stress Turbulence (SST) model were used in this works to solve flow problem over the paper planes. The analysis is mainly conducted to study and compare the lift coefficient (C_L), drag coefficient (C_D)and aerodynamic efficiency (C_L/C_D) performances for each paper planes. The C_L results show that the Glider paper plane has managed to produce better C_L performances in terms overall C_L magnitude, stall angle, wider angle of attack (α) envelope and higher maximum lift coefficient magnitude compared to the other paper plane design. However, Glider paper plane has the least C_D distributions by producing at least 14.3% larger C_D magnitude compared to the other plane design at certain α region. Instead, The Wide Stunt has promisingly produced better C_D distribution by producing lower C_D value compared to the other plane design. Based on C_L/C_D performance, the Wide Stunt paper plane has produced better C_L/C_D and maximum aerodynamic efficiency ($C_L/C_{D\,max}$) magnitudes compared to the other design. Wide Stunt paper plane induced at least 6.4% better $C_L/C_{D\,max}$ magnitude compared to the other paper plane design. Based on these results, it can be concluded that Wide Stunt paper plane has promising advantages which are very crucial for the paper plane especially during hovering operation, take-off and landing manoeuvre.

Keywords:
aerodynamics performances, paper plane, MAV

Copyright © 2019 PENERBIT AKADEMIA BARU - All rights reserved

1. Introduction

Paper planes is seen as a toy figures that gives inspiration in the aeronautical engineering studies which led to a variety of plane design. Indeed, paper plane offer less weight and cost which can be fold based on standard origami technique for any desire shape[1]. The less weight concept parallel with the MAV wing objective which is very crucial to be achieve. Unlike larger systems, MAVs are usually built based of lightweight material stock such as balsa wood[2], injection moulded plastics[3] or even aluminium sheet[4]. However, such materials require substantial processing to fabricate aerodynamic structures[5].

* *Corresponding author.*
E-mail address: zurrie_adik@yahoo.com (Zurriati M. Ali)

Paper is a biodegradable cellulose fibre sheet which is disposable[6], sturdy and low-cost[5]. Paper consists of a matrix of interlinked cellulose fibers which is a knit structure. The knit structure gives paper good tensile performance and formability with low bulk weight. A low-stiffness hinge can be formed when paper is bent[7]. Even simple bending and forging operations are sufficient to make permanent deformations to the shape of a paper structure, greatly reducing processing cost. At low production input, paper offer an exceptional strength to weight ratio with additional desirable aeroelastic properties [4]. The origami paper plane has been long regarded as flying toys and it can be easily fabricated from paper. Thus, the cellulose material has a bright future to be explored as potential material for disposable MAV option[5].

Paper planes flying in the same Reynolds-number regime as MAV, thus paper plane has a high potential to be upgraded as MAV. Due to its simplicity, paper plane offer easier design option compared to the biological inspired designs as shown in recent MAV development[8], [9]. Despite its huge potential through a wide range of origami design[10] and experimental test cycles, researchers have underestimate and overlook the basic performance of lift and drag induced by these paper planes. This is due to its common usage as toys and wide range of paper plane design. Thus, the objective for current work is to analyze the lift and drag performance for the selected paper plane designs. In this work, three different design of paper planes were selected as a basic paper plane design. The design selection was made based on its common usage as paper plane toys and recommendation to be used with PowerUp 3.0 device[11]. Each of paper planes will be analyzed through CFD simulation before the comparison study on lift and drag performance among the plane executed.

2. Methodology

2.1 Paper Plane Design Selection

There are three different paper plane design have been selected for current works. The selection is made based on its popular usage as paper plane toys and recommendation to be used with PowerUp 3.0 device. PowerUp 3.0[11] is a device that can remotely control a paper airplane through a Bluetooth® connected smartphone. This device has huge potential to convert the paper plane into MAV class. The three selected paper plane designs are known as The Glider, Stunt Plane and Wide Stunt Glider paper plane. The CAD drawing of each paper plane design is shown in Figure 1 to Figure 3. The overall wing dimension, aspect ratio and calculated velocity for each paper plane is given in Table 1. The velocity of each paper plane is determined based on equivalent Reynolds Number at chord, Re =100,000

2.2 CFD Simulation

The CFD simulation on each paper plane was executed by using ANSYS-CFX module. The computational air domain was built around the morphing MAV wing, in which the symmetrical condition is exploited by modelling only half of the computational domain. The air domain is built surrounding the symmetrical paper plane and sized based on the root chord as shown in Figure 4. The boundary conditions imposed on the air domain are also shown in Figure 4. The grid independent test results show that the optimized grid for each paper plane achieved around 300,000 tetrahedrons mesh elements as shown in Figure 5. The symmetrical wall and side wall are assigned as symmetrical boundary condition and slip surface boundary condition respectively.

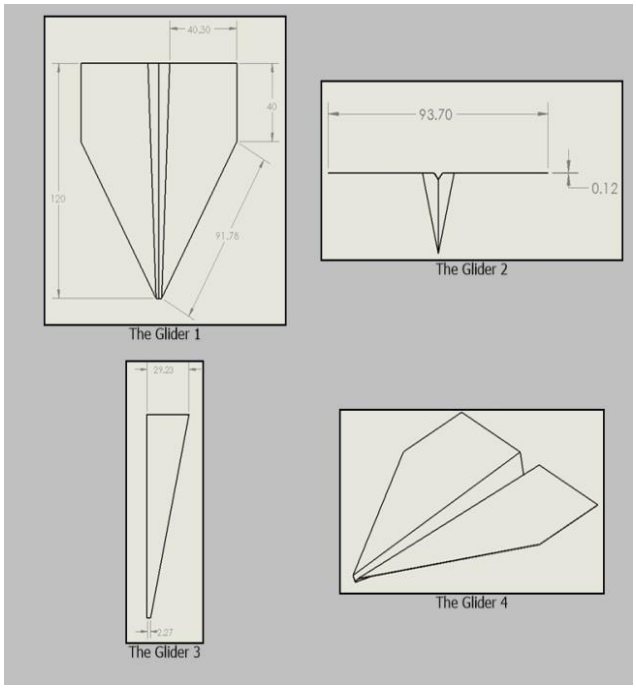


Fig. 1. The Glider paper plane

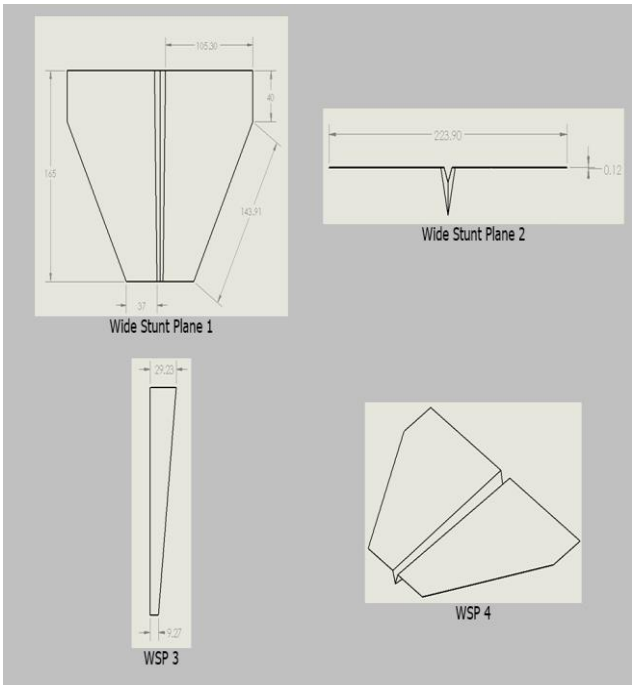


Fig. 2. The Wide Stunt Glider paper plane.

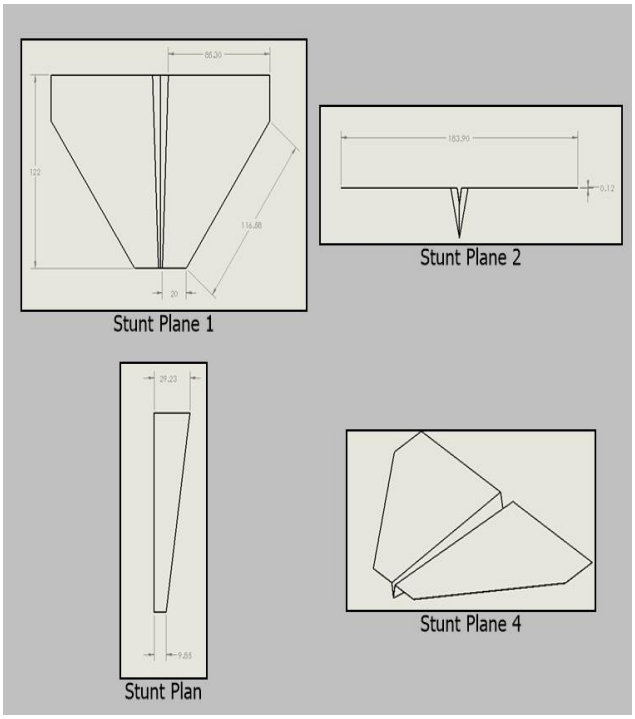


Fig. 3. Stunt paper plane.

Table 1
The basic dimension of the paper plane designs

Paper plane	The Glider	Wide Stunt Glider	Stunt Plane
Cord length (c)	120mm	165mm	122mm
Wing area (S)	3122.7mm	13166mm	7442.7mm
Aspect ratio (AR)	2.81	3.81	3.61
Velocity (U)	12.61 m/s	8.62 m/s	11.65 m/s

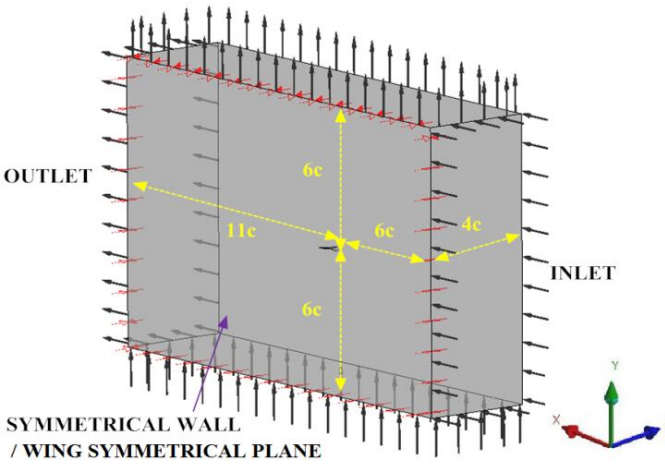


Fig. 4. Air domain sizing and boundary condition imposed on air domain

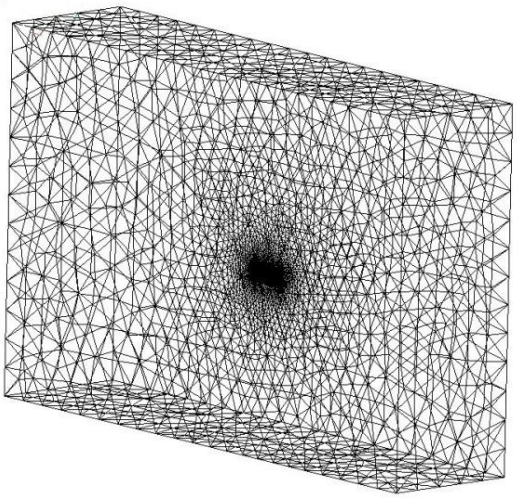


Fig. 5. The optimized grid for each paper plane study

Velocity magnitude (equivalent to Re=100,000 at chord) is specified at the inlet with zero pressure boundary condition is enforced at the outlet. The angle of attack (α) for all paper plane is varied between -5° to 40° with 2° interval. The wing surface itself is modelled as a non-slip surface. The turbulence intensity is set at 5% with the automatic wall function was fully employed to solve the viscous effect. A steady state, incompressible flow Navier-Stokes equation (RANS) combined with Shear Stress Turbulence (SST) model were used to solve the turbulence viscosity problems over each paper plane design. The simulation convergence was control based on the magnitude of momentum residual (below 1.0×10^{-5})) and monitoring the value of lift (C_L) and drag (C_D) coefficients.

3. Results

3.1 Lift coefficient (C_L) results

Figure 6 presents the lift coefficient (C_L) results for Glider, Stunt Plane and Wide Stunt Glider paper plane. The results exhibit that each paper plane produce almost similar C_L distribution with the increment of α. At pre-stall angle (starts from zero lift angle to stall angle), each plane induces almost linear C_L distribution up to the maximum lift coefficient magnitude (C_{Lmax}) at stall angle. However, C_L magnitude begins to deteriorate with the increment of α after the stall angle (α_{stall}).

Based on the C_L magnitude, the results show that Stunt Plane shows better C_L magnitude compared to the other plane design at α cases between 0° to 15°. At this α range, the Stunt plane managed to produce at least 4.4% better C_L magnitude compared to the other plane design. However, as the α magnitude increase over 15°, the Stunt plane has lower C_L magnitude than the Glider and Wide Stunt Plane. The Glider has produced almost 12% better C_L magnitude than Stunt plane produced. Even, the Wide Stunt plane also managed to produce averagely 4% better C_L magnitude than Stunt plane at α cases over 15°. Analysis on the magnitude of zero lift angle ($\alpha_{L=0}$) shows that the Glider paper plane produce the lowest $\alpha_{L=0}$ nearly at -2°. This is followed by the Wide Stunt and Stunt Plane at nearly $\alpha_{L=0}$=-1° and $\alpha_{L=0}$=-0.5°, respectively. In terms of α_{stall} magnitude, the Glider paper plane also induced better stall angle compared to Wide Stunt Plane and Stunt Plane. The Glider paper plane delayed stall at α_{stall} = 32° which is about 2° to 7° higher than the Wide Stunt Plane (α_{stall} = 30°) and Stunt Plane (α_{stall} =25°). Based on these $\alpha_{L=0}$ and α_{stall} performances, the α envelope is determine based on the α range started from the magnitude

of $\alpha_{L=0}$ towards α_{stall}. The results clearly exhibited that the Glider paper plane produced better α envelop compared to Stunt Plane and Wide Stunt Glider plane. The α envelop for Glider paper plane is 34° which is about 9.67% to 33.3% better than the α envelop produced by Stunt Plane and Wide Stunt Glider Plane, respectively. The investigation of C_L performance continues by evaluating the C_{Lmax} performances for each paper plane design. The results show that the Glider paper plane has the highest C_{Lmax} magnitude at C_{Lmax} =1.246. This is followed by the Wide Stunt Glider and Stunt paper plane at C_{Lmax}= 1.136 and 1.067, respectively. Thus, the Glider paper plane has at least 9.68% better C_{Lmax} magnitude compared to the other paper plane designs considered in this works. Based on these C_L results, one can presumed that the Glider paper plane has the best C_L performances among the paper plane designs. Despite of low aspect ratio magnitude (Glider's AR= 2.81), the Glider paper plane managed to produce better C_L (at α cases over 15°), α_{stall}, wider α envelope and higher C_{Lmax} magnitude.

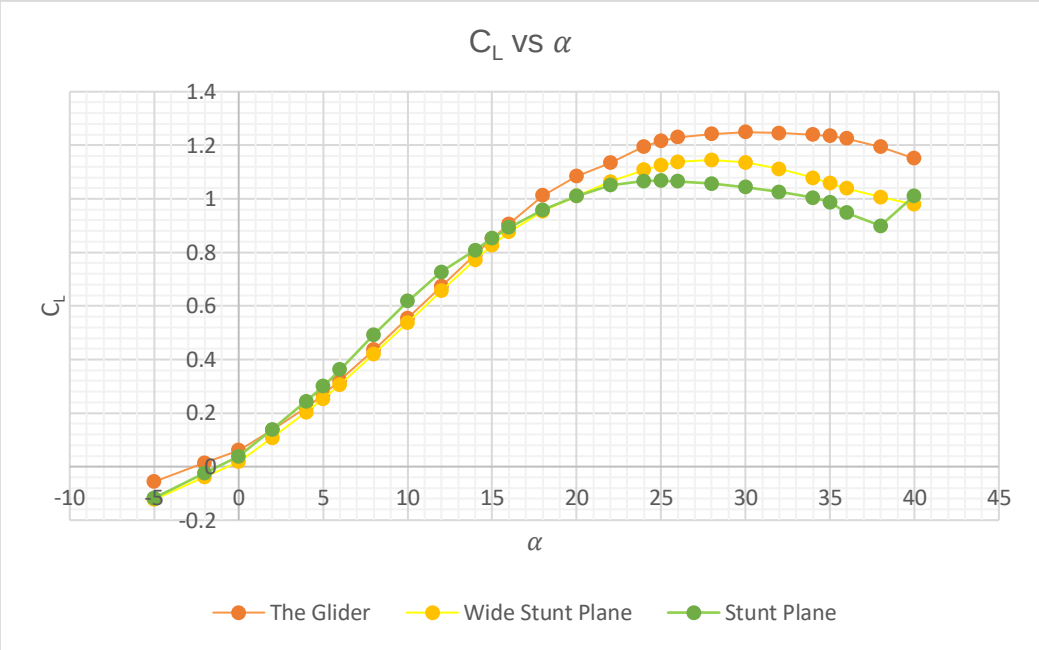


Fig. 6. Lift coefficient (C_L) results for Glider, Stunt Plane and Wide Stunt Glider paper plane

3.2 Drag coefficient (C_D) results

The Figure 7 presents the drag coefficient (C_D) results for Glider, Stunt Plane and Wide Stunt Glider paper plane. In overall, the results exhibit that each paper plane produce almost similar C_D trend towards the increment of α. C_D magnitude for all paper plane increase with the α increment. At low α region (between 0° to 15°), the results show that there is no clear difference in C_D magnitude among the paper plane. However, The Wide Stunt paper plane managed to produce averagely 5% lower C_D magnitude among the wing at this α region. As the α increase beyond 15°, the difference in C_D magnitude is more obvious. The Glider paper plane has at least 14.3% larger C_D magnitude compared to the other plane design at this α region. The Stunt paper plane

The investigation on minimum drag (C_{Dmin}) performances reveal that the Wide Stunt Glider paper plane has surprisingly produced the lowest drag magnitude at C_{Dmin}=0.0133 (at α =0°). This is followed by the Glider and Stunt paper plane which produced C_{Dmin}= 0.0246 (at α =-2°) and 0.0185(at α =0°), respectively.

Analysis of C_D increment between the paper planes was conducted to elucidate the drag performance among the paper planes. The analysis is divided into 2 α regions: low α region (α=0°-15°) and high α region (α =15°- α_{stall}). At low α region, the result shows that the C_D magintude for Glider paper plane increse about 31% for every 2° α changes. Wide Stunt Glider and Stunt plane produce about 41% and 36.7% increment at similar α changes. However, this C_D increments were reduced significantly to 12% (for Glider and Wide Stunt Glider) and 11% (Stunt) as the angle enter the high α region. Based on these C_D results, one can presumed that the Wide Stunt paper plane has more promising C_D performances among paper planes. Despite of large C_D increments, Wide Stunt has promisingly produced lower C_D value (at α region below 15°) and lower C_{Dmin} magnitude compared to the other plane design.

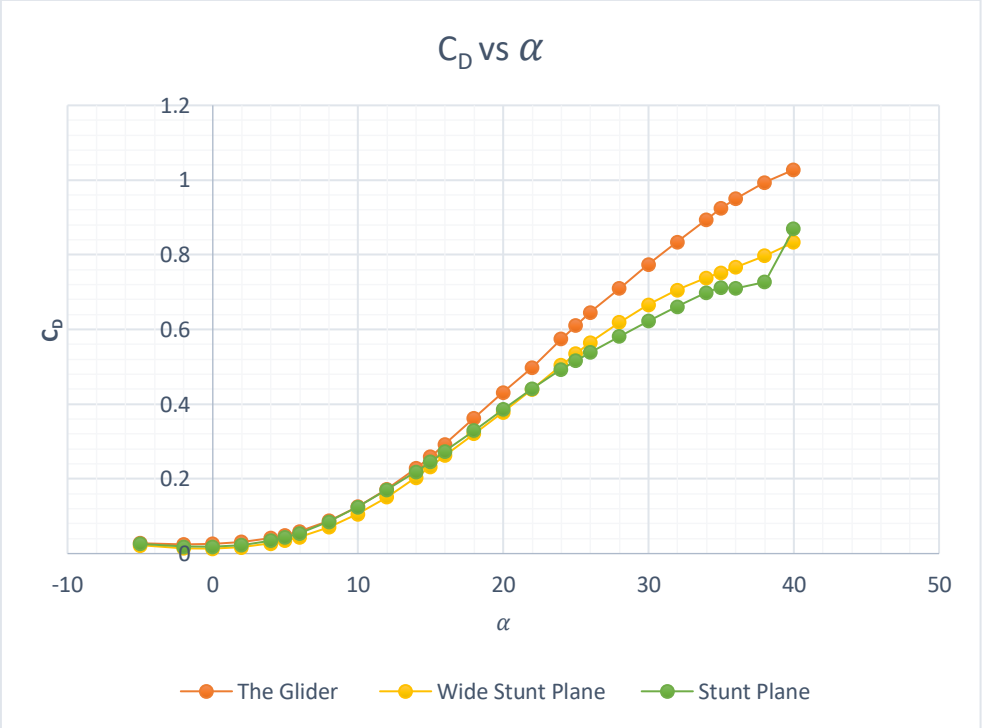


Fig. 7. Drag coefficient (C_D) results for Glider, Stunt Plane and Wide Stunt Glider paper plane.

3.2 Aerodynamic efficiencies (C_L/C_D) results.

Figure 8 presents the performance of aerodynamic efficiencies (C_L/C_D) for each paper plane design considered here. In overall, all paper plane induced almost similar trend of C_L/C_D curve with the increment of C_L magnitude. The magnitude of C_L/C_D increase almost linearly at early C_L increment which is between C_L=-0.056 to 0.269 which equivalently at α between -5° to 5°. The C_L/C_D magnitude reach its maximum value (known as C_L/C_{Dmax}) at C_L=-0.056 to 0.222 or which α between 2° to 5°. However, as the C_L increase further (or α > 5°), the C_L/C_D performances for each design is gradually drop towards the stall condition at C_L between 1.067 to 1.246 (or α between 25° to 32°). Based on the overall C_L/C_D performance, the result clearly shows that the Glider paper has the lowest C_L/C_D magnitude in almost every C_L cases. The design averagely produced at least 5.69% lower C_L/C_D magnitude compared to the other design. On the other hand, Wide Stunt paper plane has averagely produced at least 1.82% better C_L/C_D magnitude compared to the other design.

Comparative analysis was also conducted by focusing on the difference in C_L/C_{Dmax} magnitude among the paper plane. The result clearly shows that Wide Stunt paper plane induced the best C_L/C_{Dmax} magnitude among the paper plane at C_L/C_{Dmax}=6.32. This condition happens at C_L=0.108 and relatively at α=2°. This is followed by Stunt paper plane at C_L/C_{Dmax}=5.94 which relatively occurred at C_L=0.138 and α =2°. The Glider paper plane induced the lowest C_L/C_{Dmax} magnitude among the paper plane at C_L/C_{Dmax}=5.45. This is happening at C_L=0.269 and α =5°. Based on these results, it clearly shows that Wide Stunt paper plane induced at least 6.4% better C_L/C_{Dmax} magnitude compared to the other paper plane design. In fact, the C_L/C_{Dmax} magnitude for Wide Stunt paper plane is also produced at 3° earlier than the Glider paper plane. This means that optimal aerodynamic condition for Wide Stunt paper can be easily achieved with very minimal tilting α angle. These promising results is due to better C_D performance found on the Wide Stunt paper. Lower C_D value (at α region below 15°) and better C_{Dmin} magnitude has benevolently delayed the drag to overwhelm the lift distribution on the Wide Stunt paper plane design. On the other hand, despite of huge advantage in lift distributions, the the significant drag generation on the Glider plane design has overwhelm its lift performances which leads into lower C_L/C_D performances.

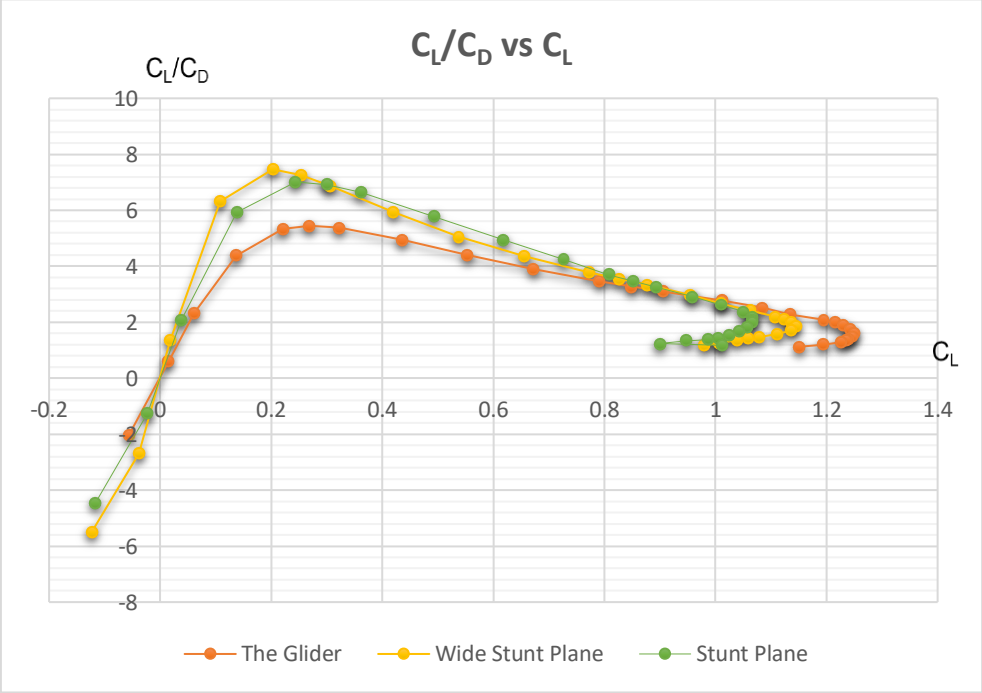


Fig. 8. C_L/C_D performance for Glider, Stunt Plane and Wide Stunt Glider paper plane

4. Conclusions

In this work the aerodynamic analysis on selected paper plane designs known as Glider, Wide Stunt Glider and Stunt plane was carried out. Based on CFD methods the results show that the Glider paper plane has surprisingly produces promising performances in C_L. Even at low aspect ratio magnitude (AR= 2.81), the Glider paper plane managed to produce better performances in the Glider paper plane managed to produce better C_L (at α cases over 15°), α_{stall}, wider α envelope and higher C_{Lmax} magnitude compared to the other paper plane design. Surprisingly, its promising advantages does not continue in C_D performances in which the Glider paper plane has at least

14.3% larger C_D magnitude compared to the other plane design at certain α region. Instead, The Wide Stunt has promisingly produced better C_D distribution based on its lower C_D value (at α region below 15°) and lower C_{Dmin} magnitude compared to the other plane design. Based on C_L/C_D performance, Wide Stunt paper plane has clearly produced better C_L/C_D and C_L/C_{Dmax} magnitudes compared to the other design. Wide Stunt paper plane induced at least 6.4% better C_L/C_{Dmax} magnitude compared to the other paper plane design. In fact, the C_L/C_{Dmax} magnitude for Wide Stunt paper plane is produced at 3° earlier than the Glider paper plane. Based on these results, one can conclude that Wide Stunt paper plane shows promising advantages in producing better aerodynamic efficiency at lower α angle. Such advantages are very crucial for the paper plane especially during hovering operation, take-off and landing manoeuvre.

Acknowledgement
The authors acknowledge technical and financial support from Universiti Teknologi MARA and the Government of Malaysia via the sponsorship by the Malaysia Ministry of Higher Education's Fundamental Research Grant Scheme (FRGS) (600-RMI/FRGS 5/3 (173/2019)).

References

[1] Adams, Christina. "Paper Plane." Education 92, no. 8 (2011): 20.
[2] Klaptocz, Adam, and Jean-daniel Nicoud. "Technology and Fabrication of Ultralight Micro-Aerial Vehicles." In Flying Insects and Robots, edited by Dario Floreano, Jean-Christophe Zufferey, Mandyam V. Srinivasan, and Charlie Ellington, 299–316. Berlin, Heidelberg: Springer Berlin.
[3] Witushynsky, Timothy Craig. "Experimental Investigation Into The Aerodynamics Of Small Air Vehicles With Thin Flexible Wings." MSc Dissertation,School Of Graduate Studies, Case Western Reserve University, 2008.
[4] Gresham, Nicholas T, and Æ Zhijin Wang. "Low Reynolds Number Aerodynamics of Free-to-Roll Low Aspect Ratio Wings." Experiments in Fluids 49, no. 1 (2009): 11–25.
[5] Pounds, Paul E I. "Paper Plane : Towards Disposable Low-Cost Folded Cellulose-Substrate UAVs." In Australasian Conference on Robotics and Automation, 3–5. Victoria University of Wellington, New Zealand, 2012
[6] Pounds, Paul E.I., and Surya P.N. Singh. "Integrated Electro-Aeromechanical Structures for Low-Cost, Self-Deploying Environment Sensors and Disposable UAVs." In Proceedings - IEEE International Conference on Robotics and Automation, 2013.
[7] Chamberlain, Daven Christopher. "Paper." In The Oxford Companion to the Book, 79–88, 2010.
[8] Suhaimi, S, H Yusoff, N Iswadi, Sh Mohd Firdaus, S Shuib, M K Abdullah, and A A Rashid. "Natural Rubber Latex Fabrication for Bio-Inspired Flapping Wing Skin Based on Bat Wings." Journal of Mechanical Engineering and Automation 6, no. 6 (2016): 151–55.
[9] Ismail, N.I., A.H. Zulkifl, M.Z. Abdullah, M. Hisyam Basri, and Norazharuddin Shah Abdullah. "Computational Aerodynamic Analysis on Perimeter Reinforced (PR)-Compliant Wing." Chinese Journal of Aeronautics 26, no. 5 (2013): 1093–1105.
[10] Turner, Nicholas, Bill Goodwine, and Mihir Sen. "A Review of Origami Applications in Mechanical Engineering." In Proceedings of the Institution of Mechanical Engineers, Part C: Journal of Mechanical Engineering Science, 2345–62, 2016.
[11] Toys, Tailor. "PowerUp 3.0 Smartphone Controlled Paper Airplane :User Guide," 2014

Penerbit Akademia Baru

Engineering Science and Technology Conference Proceedings

Journal homepage: www.akademiabaru.com/EST.html

Experimental Study on Two-Phase Flow of Gas-Liquid with High Viscosity in Capillary with The Slope of 5° Against Horizontal Position

Open Access

Sukamta[1,*] , Endradi Roziantho[1], Sudarja[1]

[1] Department of Mechanical Engineering, Faculty of Engineering, Universitas Muhammadiyah Yogyakarta, Jl. Brawijaya, Tamantirto, Kasihan, Bantul, Yogyakarta, 55183, Indonesia

ABSTRACT

Two-phase flow is part of the multi-phase flow. It can occur in large, small, or mini pipes. Mini pipe two-phase flow can be applied to high-density multi-chip modules on supercomputers, X-ray equipment, high-flux heat exchangers in aerospace systems, cryogenic cooling systems on satellites, and other high-power diagnostic equipment. The more widespread application of the two-phase flow on mini pipes, so it is very needed to study its problem there. One crucial issue is increasing pressure suddenly caused by a certain flow pattern. The research was carried out using experimental methods, with an inner glass pipe diameter of 1.6 mm and a length of 130 mm. The test section with a slope of 5 degrees against the horizontal position. The visualization method used a high-speed camera. The working fluid being used were air and water mixed with Glycerine with concentrations of 40%, 50%, 60%, and 70% for each blend, and varying the superficial gas and water velocity in the range J_G = 0 m/s–66.3 m/s; J_L = 0.033 m/s–4.935 m/s. The results of the videos obtained were then analyzed based on the values of J_G and J_L. Furthermore, they were plotted in the flow pattern maps. This research was divided into five new flow patterns: i.e., mini bubble, long plug, slug, slug-annular, and churn. The flow patterns were then compared to the previous research and indicated conformity but there was a shift in the transition line. This research also found a new invention that the slug flow pattern affected the increasing pressure difference significantly.

Keywords:
High viscosity; glycerine; mini pipe; transition line; two-phase

Copyright © 2019 PENERBIT AKADEMIA BARU - All rights reserved

1. Introduction

Two-phase flow is the fluid flow that has a preliminary condition or shape or form of a different substance in a stream. It can be categorized based on its channel size, i.e., large channel, normal channel, mini-channel, microchannel, and nanochannel. Based on the channel shape (square, triangle, and circle), the channel position (vertical, horizontal, and tilt), the flow direction (concurrent horizontal, counter-current horizontal, concurrent downward, concurrent upward, and counter-current), and the formation phase (liquid-solid, solid-gas, and liquid-gas). The application of two-phase flow in mini-pipe can be implemented in condensers, steam boilers, nuclear reactors, pipelines, heat exchangers, geothermal measuring devices, and natural gas searches.

Two-phase flow is the simplest phenomenon of multiphase flow. In this flow, the distribution of each phase (gas and liquid) in the channel is essential. The distribution is affected by the characteristic of flow, i.e., two-phase flow pattern and two-phase flow pattern map in the mini-

* *Corresponding author.*
E-mail address: sukamta@umy.ac.id (Sukamta)

channel and microchannel. The fluid has a unique characteristic, i.e., its surface tension is so dominant that Newton's laws cannot be implemented. The small channel diameter causes the occurrences of this phenomenon. As a consequence, the flow pattern formed is only influenced by the surface tension and the viscosity of the liquid fluid, and the value of the superficial velocity of the gas and the liquid fluid.

Triplett *et al.,* [1] conducted research by using air and water in circular microchannel pipes with a diameter of 1.1 and 1.45 mm, and also in semi-triangular microchannel pipes of 1.09 and 1.49 mm in diameter. The variation of superficial gas velocity (J_G) started from 0.02–80 m/s, and the superficial liquid velocity (J_L) was from 0.02–8 m/s. The occurred flow patterns were bubbly, slug, slug-annular, annular, and churn. A flow pattern of stratified was found in the study because of the influence of massive surface tension. Chung and Kawaji [2] studied the effect of channel diameter on the characteristic of adiabatic two-phase flow in a microchannel. In their study, the used fluids were nitrogen gas and water in the channel with a diameter of 530, 250, 100, and 50 µm. The used superficial liquid velocity ranged from 0.01–5.77 m/s while the superficial gas velocity reached 0.02–72.98 m/s. The used visualization method was a photographic image. The results of visualization showed the difference between the flow pattern in the 530 and 250 µm diameter pipes with 100 and 50 µm diameter pipes. The flow patterns observed in this study, with a diameter of 530 and 250 µm, were bubbly, slug, churn, slug-annular, and annular. Whereas in the 100 and 50 µm diameter pipes, the observed flow pattern was a slug. Liu D. and Sur A. [3] studied the water-air two-phase flow in circular flow with a diameter of 100, 180, and 324 µm. In the study, four flow patterns were formed, i.e., bubbly, slug, ring, and annular. The bubbly flow has a characteristic of the dispersed bubble single-flow pattern with a smaller size of diameter compared to the channel size. The slug flow has a characteristic as the circuit from Taylor Bubble, which is elongated and separated by a lump of water. Annular flow has a characteristic of a flow of gas that flows continuously at the center of the channel, forming a gas core surrounded by a film layer with a form of the ring like a neck around it. Annular flow is a continuous flow of gas at the center of the channel, forming a gas core surrounded by a stable layer of water.

Sudarja *et. al.,* [4] conducted research on the effect of viscosity in gas-liquid two-phase flow in the horizontal mini–channel. The used test section was a glass pipe with a diameter of 1.6 mm with a superficial gas velocity of 0.025–66.3 m/s, and superficial velocity of the fluid of 0.033–4.935 m/s. The used liquid was air and a mixture of distilled water—glycerine with a percentage of 0%, 20%, 40%, and 60%, and indices of W, G20, G40, and G60. The flow pattern data were obtained by analyzing video images and captured by using a high-speed camera. The results revealed that the flow patterns were bubbly, plug, slug-annular, annular, and churn, while a stratified flow was not found. Two-phase flow in mini–pipes and micropipes have been applied and continued to be developed rapidly in two fields, namely Micro-Electro-Mechanical System (MEMS, miniaturization of mechanical and electromechanical elements) and also in the flow in the structure of the human body. Two-phase flow in the mini–pipe can be applied in high-density multi-chip modules on supercomputers, X-ray equipment and other high-power diagnostic equipment, and high-flux heat exchangers in aerospace systems, as well as cryogenic cooling systems on satellites [5].

Korawan [6] studied a two-phase flow pattern (water and air) in a horizontal pipe with the superficial water velocity variations (U_{SL}) of 0.4, 0.55, 0.7, 0.85, and 1.0 m/s. The research was conducted by using a test module made of acrylic pipe with an inner diameter of 36 mm and a length of 2000 mm. The liquid fluid was in the form of water, whereas the gas fluid was in the form of air. The used method was by flowing water pumped from the tank to the flow meter and then to the injector. The air was supplied from the compressor and flowed through rota-meter to the injector. The water-air mixed in the injector flowed through the test module to the separator. In the

separator, the air was released into the atmosphere, and the water would flow into the tank to be circulated again. A digital camera was used to obtain pictures of the flow patterns. The results showed that the flow patterns were bubbly, slug, and stratified flow. The higher the value of U_{SL}, the longer the bubble region that occurred. Also, the higher the U_{SL} value led to the shift in changes in flow patterns. When the USL is low, bubble flow changed to be stratified flow, whereas when the USL was high, bubble flow changed to slug flow. The determination of sub-stratified water-air flow patterns in horizontal pipes using pressure measurements has been studied [7]. The purpose was to classify the sub-stratified water-air flow patterns in horizontal pipes based on the result of measuring the pressure sensor output signal. The method used in the study was the experimental study, visualization, and measurement of pressure difference fluctuations. The tool was a transparent acrylic pipe with a diameter of 26 mm and a length of 10 m. A high-speed camera was used to obtain visualization of sub-stratified flow patterns. The study utilized a test section with 180 and 210D tap positions to measure pressure difference fluctuations. The study revealed that the stratified flow pattern that could be visually observed was divided into sub-regions which included stratified smooth (J_L = 0.025 m/s and J_G = 1.88 m/s), two dimensional wave (J_L = 0.025 m/s and J_G = 3.77 m/s), roll wave (J_L = 0.05 m/s and J_G = 3.77 m/s), and atomization (J_L = 0.075 m/s and J_G = 3.77 m/s). Sudarja *et. al.,* [8] also conducted an experimental study on two-phase flow patterns in the mini-channel superficial velocity of gases and liquids respectively in the range of 0.025-66,300 m / s and 0.033-4,935 m / s. This study found a flow pattern of bubbly, plug, slug-annular, annular, and churn flow. These results are consistent with the results of the study of Triplett *et al.,* [9] and Chung and Kawaji [2]. Previous studies were carried out on two-phase gas-liquid flow in a micro-channel width of 5-20 µm using the Boltzmann method. This research looks at the dynamic behavior that continuously from bubbles and droplets. This study found that the wetting of solid walls determines the shape of bubbles in the slug flow. Also, the shape and number of bubbles under steady-state is influenced by surface tension, viscous force, and inertia. Meanwhile, the simulation results show that the steady-state flow regime is very dependent on the viscous force, surface tension, inertia force, channel width, and solid surface wetting [10]. Meanwhile, the previous study also observes the two-phase gas-liquid flow pattern accompanied by chemical reactions in 400 µm square microchannel using a high-speed camera and pressure sensor. This study found slug-bubbly flow, slug flow, and slug-annular flow [11].

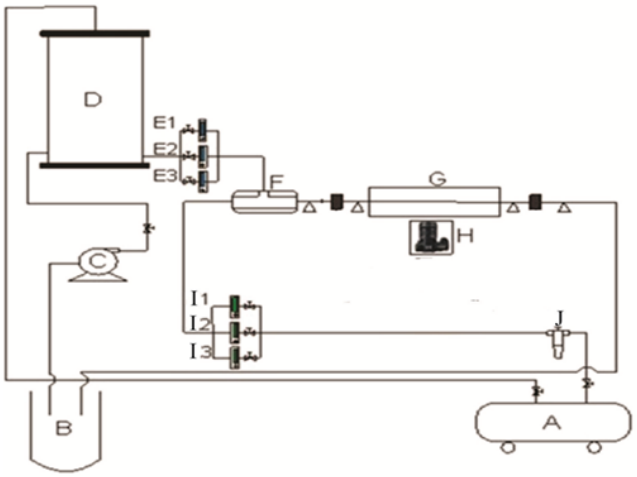
An experimental study to characterize air-water flow in pipes with a diameter of 3.81 cm has been carried out. This study uses a high-speed camera to verify the map of the previous flow regime. The two-phase flow is classified into bubbly, plug, slug, stratified, stratified-wavy, and annular flow regimes. While the transition boundaries identified in this study compared to previous studies include Mandhane et al., 1974 and Talley et al. 2015. The effects of increasing the gas flow rate on the void fraction, the average diameter of the bubble, and the speed of the bubble are discussed. Bubbles start to coalesce near the gas-liquid layer instead of in very dense areas because of the gas flow rate increases [12]. Previous research has also studied the behavior of two-phase flow in rectangular channels with varying air/water flow rates. Experimental data were recorded using pressure transducers and water-air flow behavior was visualized with a camcorder for airflow rates of 8.3, 16.6, and 25 L / min and water flow rates that differed from 5, 10, 15 and 20 L / min. The results showed that by increasing the value of water or airflow rates, the shape, size, and number of air bubbles in the water changed accordingly. Higher water flow rates cause the flow to be very turbulent and foamy [13]. The phenomenon of liquid carryover at the T-junction has been analyzed using Volume Faction together with the k-ε turbulence model. The efficiency of T-junction separation is measured through the fraction of air and water mass flow rates between branches and main arms at a diameter ratio of 0.6-1.0, surface water velocity of 0.186-0.558 m/s and air-

surface velocity of 4-8 m / s. The results show that the simulation model has been successfully validated with an average deviation of less than 5% and can be used to predict the phase separation of the snail flow at the T-junction. In the slug flow regime, the performance of the T-junction can be improved by reducing airspeed or increasing water speed [14].

The information and data on the study of two-phase flow pattern and flow pattern map in the mini pipe with the variation of the slope, surface tension, and liquid viscosity are minimal. Therefore, an experimental and numeric study needs to be carried out to complete the previous studies. This study tests the variation of liquid fluid viscosity with a mixture of water and glycerine. This study aims to compare the flow pattern and flow pattern map toward the variety of slope and the superficial gas velocity.

2. Methods

The installation of equipment used in the research is shown in Figure 1. The equipment consists of the main components, namely water tank, water pump, air compressor, pressure vessel, test section, water trap, mixer, and connector. Supporting equipment used in research includes amplifiers, optical correction boxes, cameras, computers, video processing systems, and acquisition systems. The working fluid was used air-water mixed by glycerine with a concentration of 40% (GL40), 50%(GL50), 60%(GL60), 70%(GL70). The used measuring instruments include a water flow meter, airflow meter, temperature indicator, thermocouple, pressure indicator, and pressure transducer. For streaming video shooting, a high-speed camera Nikon type J4 was used, with a speed of 1200 fps and a resolution of 640 x 480 pixels. Data acquisition from "National Instrument" was used to convert data from analog to digital so that it could be recorded, stored, processed, and analyzed on a computer. The condition of the study was adiabatic. Experiments were carried out at superficial gas velocity (JG) at intervals of 0.025–66.3 m/s, and superficial liquid velocity (JL) at intervals of 0.033–4,935 m/s.



Information:

A. Compressors
B. A container of a mixture of water and glycerine
C. Water pump
D. Pressurized vessel
E. Liquid fluid flowmeter
F. Mixer
G. Test section
H. Camera
I. Air flowmeter
J. Water trap

Fig. 1. Research installation scheme

3. Results And Discussion

These results document several key contributions made to the fields of two-phase flow in a mini channel. Bubbly flow pattern was formed at low J_G and high J_L as shown in Figure 2. In this case, solution discharge would flow to meet the mixing chamber while the low airflow would break through the dominating volume of solution in the mixing chamber. As the air volume increased and reduced the mixing chamber's surface area to the 1.6 mm diameter pipe, the air would try to push the solution and cause a two-phase flow to form on the mini channel. The value of the surface tension of the solution affected the airflow as if it was cut into small bubbles.

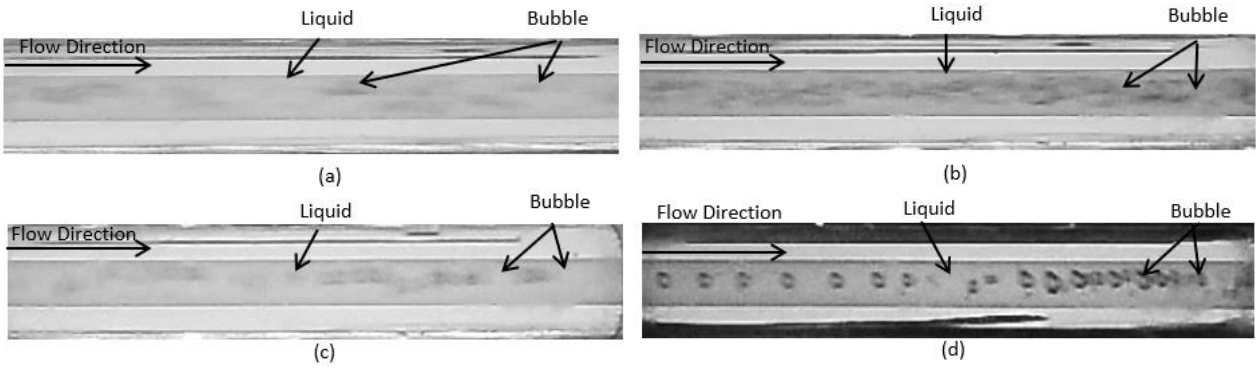


Fig. 2. The bubbly flow pattern formed on J_G = 0.871 m/s and J_L = 2,297 m/s (a) GL40, (b) GL50, (c) GL60, (d) GL70

Plug flow pattern was formed at low J_G and J_L as shown in Figure 3. This pattern was an elongated bubbly flow pattern with a more significant length than the diameter of the pipe. The bubble extension was due to the increase in air intensity in the flow. The shape of the plug flow pattern was like a capsule or bullet of varying lengths. The plug flow pattern occurred regularly and consistently at the beginning of J_G and J_L, but as the superficial velocity increased, the shape of the plug flow pattern would change. This flow pattern was a substitute for the stratified flow pattern formed in conventional pipes. In mini-pipes, the effect of capillary forces caused no stratified flow pattern to emerge. When the solution level in the mixing chamber began to increase and prepared to enter the channel along with the airflow, the capillary force of the liquid would form a liquid bridge, which was the initial formation of the plug flow pattern.

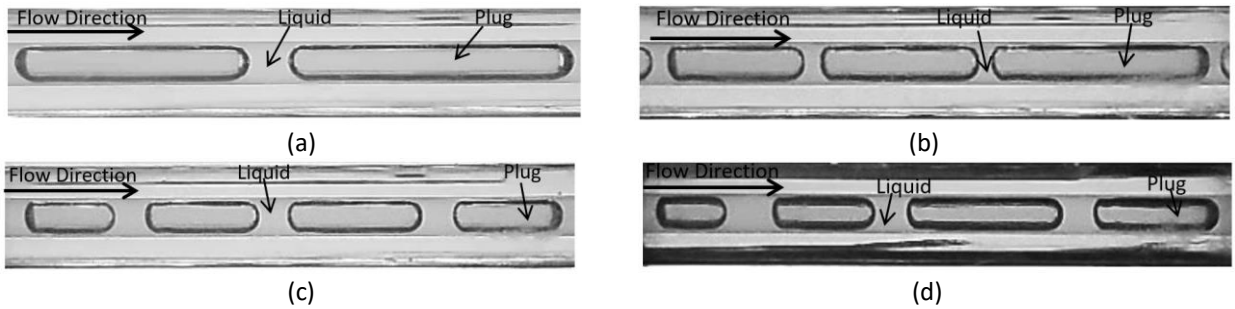


Fig. 3. Comparison of the length of plug flow patterns for each condition of the glycerinee concentration solution at J_G = 0.207 m/s and J_L = 0.149 m/s (a). GL40, (b). GL50, (c). GL60, (d). GL70

The slug-annular flow pattern was the flow pattern transition from a plug flow pattern to an annular flow pattern. The slug-annular flow pattern occurred when the airflow had flowed

continuously. Meanwhile, the flow of liquid fluid tried to penetrate the airflow that appeared around it. Also, in a liquid, the layer at the bottom was thicker than that at the top.

Furthermore, under certain conditions, the liquid fluid layer at the bottom increasingly thickened and formed waves. The slug-annular flow pattern was formed because the layer of water at the bottom was thicker compared to that at the top. Frothy bubbly was often obtained in this flow pattern, and it could break at any time. This result led to the formation of waves in the solution or made the airbag cut and formed a plug flow pattern. The increase of the viscosity of the liquid caused the thickening of the water layer around the air stream. The layer was moving continuously and occasionally experienced interference in the form of water waves that wanted to break the airflow rate. A comparison of slug-annular flow patterns with the same J_G and J_L values and the varied glycerine concentration can be seen in Figure 4.

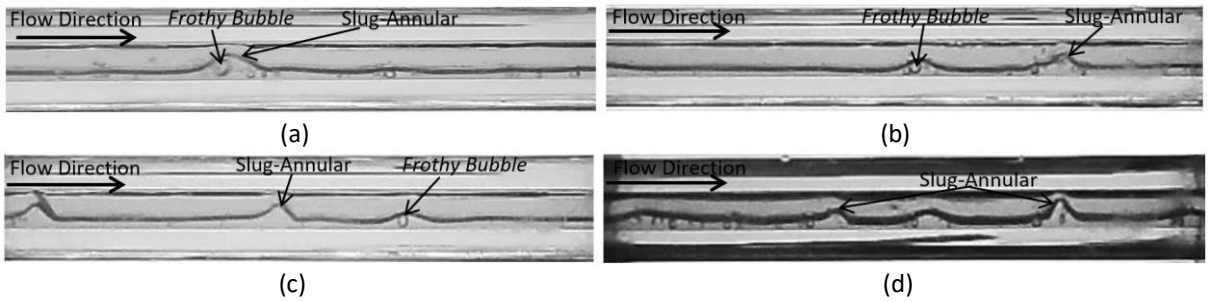


Fig. 4. Comparison of slug-annular flow patterns in various conditions of glycerine concentration with J_G = 4.238 m/s and J_L = 0.149 m/s (a). GL40, (b). GL50, (c). GL60, (d). GL70

The annular flow pattern (Figure 5) was a continuation of the slug-annular flow pattern of which the superficial velocity of the gas continuously increased to the maximum extent. It caused the waves that tried to pass the airflow. As a consequence, a flow pattern was formed, i.e., an airflow that flowed continuously with a liquid layer and little ripples stream alongside. The thickness of the top layer and the bottom layer had no significant differences. Therefore, this flow was usually called a 'ring' flow. When it was viewed from the front, a solution would appear. It seemed to encircle the core of the air as if it was forming a ring.

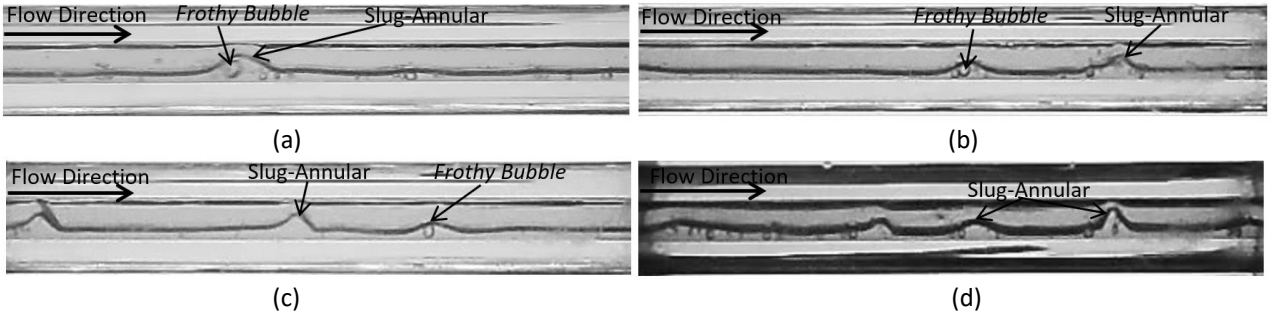


Fig. 5. Comparison of annular flow patterns in various conditions of glycerine and the concentration of J_G = 66.3 m/s and J_L = 0.539 m/s (a). GL40, (b). GL50, (c). GL60, (d). GL70

Churn flow pattern (Figure 6) occurred at a high superficial velocity of air and liquid, then the core of air and liquid became disordered. The increase of air and liquid volume in slug-annular and annular flow patterns caused the liquid layer on the pipe wall growing thicker. The previous airflow pattern which streamed continuously was interrupted by huge liquid volume. The amount of the volume of the flow solution should be able to form a slug flow pattern, but the large air velocity made the solution dispersed into a tiny size and flowed at high speed. As a consequence, in the

observation, only black shadows were visible in the air core flow, which was enveloped by the flow of liquid fluid that flowed quickly.

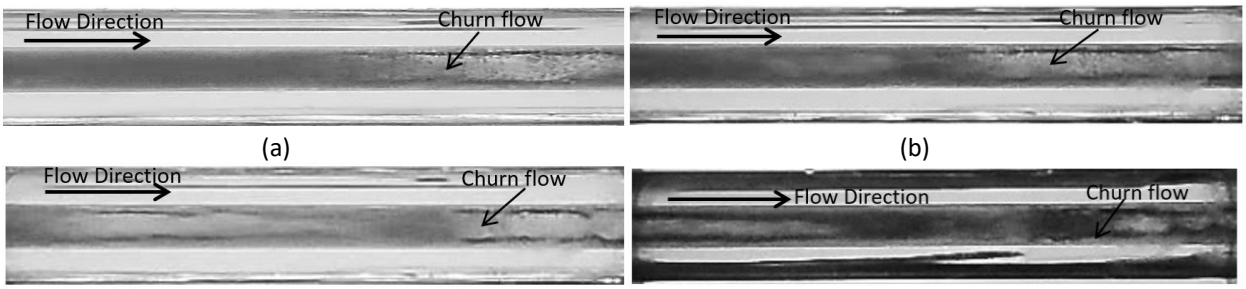


Fig. 6. Comparison of churn flow patterns in various conditions of glycerine concentration with J_G = 22.6 m/s and J_L = 2.297 m/s (a). GL40, (b). GL50, (c). GL60, (d). GL70

A comparison between the results of this study and previous research is needed to determine the consistency of the results obtained, and changes in results in the transition line caused by changes in the specific parameters tested. A comparison of flow pattern maps with changes in viscosity and slope angle is done using the results of the study of Triplett *et al.,* [9]. Figure 7 shows some differences in the transition lines. The transition lines between churn, slug-annular, and annular flow patterns are shifting. This phenomenon is caused by differences in the viscosity of the liquid fluid and the pipe diameter. The liquid in this study is a mixture of water and glycerin with concentrations of 40, 50, 60, and 70% and a diameter of 1.6 mm pipe. Meanwhile, in the study of Triplett *et al.,* [9], the liquid used is water with a pipe diameter of 1,097 mm. A review of the analysis of the factors affecting the regime boundaries of the two phases of the bubble, slug, and annular flow in different cross-sections of the mini channel has been carried out. The analysis involves the main parameters that affect the structure of the two-phase flow, namely the superficial velocity of the gas and liquid flow, the dimensions of the channel, the wetness of the inner surface of the channel, the liquid nature, and the gravitational force. It can be concluded that the development of two-phase flow instability has a significant impact on the formation, evolution, and change of flow regimes [15]. Previously, an experimental study of two-phase gas-liquid adiabatic flow patterns in a horizontal mini channel has also been conducted. This research uses a 1.6 mm inner diameter pipe. Working fluid uses air and water mixed with glycerol 0%, 20%, 40%, and 60%. It was found that changes in fluid viscosity affect the shifting of transition lines between flow patterns, especially slug-annular to annular and slug-annular and annular to churn flow [16].

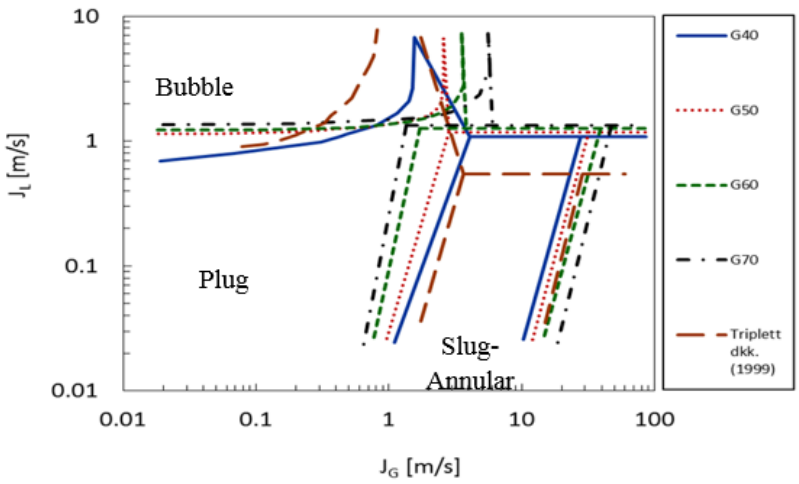


Fig. 7. Comparison between the transition patterns of flow pattern maps in this study and those in Triplet et al. (1999)

Previous papers have clearly demonstrated that there is a good fit between simulation and experimental data for slug-annular, annular and churn flow patterns. This research also clearly explains that fluid viscosity also has a significant impact on the pressure gradient, where the pressure gradient affects the flow pattern. So, the previous paper supports the new findings in this research [17]. On the other hand, The characteristics of two-phase water-air flow patterns in mini-square channels were investigated experimentally using channels made of permeable porous media. The flow patterns of this particular two-phase gas-liquid flow have been cataloged, and the effects of gas flow rates and liquid infiltration rates on flow patterns are also analyzed. The results show that the differential pressure is affected by the amount of liquid infiltration and the gas flow rate which increases significantly [18].

Meanwhile, An experimental two-phase flow study on the microchannel using propane working fluid on a microchannel with a diameter of 500 µm and a length of 0.5 m has also been carried out. The research variables are mass flux 360 to 915 kg/m^{2}s and vapor quality from 0 to unity. Homogeneous and separate models are used to determine the decrease in friction pressure in two-phase flow. Several correlations exist of the two-phase flow viscosity and density used to predict the decrease in friction pressure [19]. Previous studies present analytic models for the calculation of two-phase pressure drops for homogeneous separate flows. This study uses four different refrigerant variables, vapor quality, inner tube diameter, and mass flux at saturated temperature, to test the pressure drop model [20]. The results showed good appropriate with previous studies on the behavior of two-phase pressure gradient. These findings contribute to the design of heat exchangers, especially in small diameters.

4. Conclusion

This research resulted in new findings related to five types of the bubble, plug, slug-annular, annular, and churn flow patterns. The plug-annular flow pattern is formed due to an increase in the superficial velocity of the gas in the plug flow. With the increase in gas velocity, the liquid waves that occur in the lower layer will decrease and spread around the airflow to form an annular flow pattern. Churn flow patterns are formed when the velocity of gas and liquid is very high. Increased viscosity has a significant effect on flow patterns especially for bubbly and plugs flow patterns. The higher the viscosity value, the more regular the bubble flow patterns are formed, and the dispersed

bubbles will decrease. Meanwhile, in the plug flow pattern, the effect of increasing the viscosity value causes the plug to be shorter. The results of the comparison of flow pattern maps with previous studies show good suitability.

Acknowledgment
Thanks to the Ministry of Higher Education, Research and Technology of Republic Indonesia supported this research with contract no. 111/SP2H/LT/DRPM/2019.

References

[1] K. Triplett, S. Ghiaasiaan, … S. A.-K.-I. J. of, and undefined 1999, "Gas–liquid two-phase flow in microchannels: part II: void fraction and pressure drop," *Elsevier*.
[2] P. M. Y. Chung and M. Kawaji, "The effect of channel diameter on adiabatic two-phase flow characteristics in microchannels," *Int. J. Multiph. Flow*, vol. 30, no. 7-8 SPEC. ISS., pp. 735–761, Jul. 2004.
[3] A. Sur and D. Liu, "International Journal of Thermal Sciences Adiabatic air e water two-phase fl ow in circular microchannels," *Int. J. Therm. Sci.*, vol. 53, pp. 18–34, 2012.
[4] J. Sudarja, … D. I.-A. I. of, and undefined 2018, "The effect of liquid viscosity on the gas-liquid two-phase flow pattern in horizontal mini-channel," *adsabs.harvard.edu*.
[5] Q. C. Bi and T. S. Zhao, "Taylor bubbles in miniaturized circular and noncircular channels," *Int. J. Multiph. Flow*, vol. 27, no. 3, pp. 561–570, 2001.
[6] S. Pengajar, J. Teknik, M.-S. Tinggi, and T. R. Cepu, "Agus Dwi Korawan," 2015.
[7] *Proceeding Seminar Nasional Tahunan Teknik Mesin XIV (SNTTM XIV)*. 2015.
[8] Sudarja, A. Haq, Deendarlianto, Indarto, and A. Widyaparaga, "Experimental study on the flow pattern and pressure gradient of air-water two-phase flow in a horizontal circular mini-channel," *J. Hydrodyn.*, vol. 31, no. 1, pp. 102–116, Feb. 2019.
[9] K. Triplett, S. Ghiaasiaan, … S. A.-K.-I. J. of, and undefined 1999, "Gas-liquid two-phase flow in microchannels Part I: two-phase flow patterns," *Elsevier*.
[10] Q. Lou, M. Yang, and H. Xu, "Numerical investigations of gas-liquid two-phase flows in microchannels," *Proc. Inst. Mech. Eng. Part C J. Mech. Eng. Sci.*, vol. 232, no. 3, pp. 466–476, Feb. 2018.
[11] Y. Yin, C. Zhu, R. Guo, T. Fu, and Y. Ma, "Gas-liquid two-phase flow in a square microchannel with chemical mass transfer: Flow pattern, void fraction and frictional pressure drop," *Int. J. Heat Mass Transf.*, vol. 127, pp. 484–496, Dec. 2018.
[12] R. Kong and S. Kim, "Characterization of horizontal air–water two-phase flow," *Nucl. Eng. Des.*, vol. 312, pp. 266–276, Feb. 2017.
[13] D. Radhi, A. M. H. Mohsen, and A. Abdulkadhim, "Experimental investigation of two-phase fluid flow over a rectangular obstruction located inside an enlarged rectangular channel," *Math. Model. Eng. Probl.*, vol. 6, no. 2, pp. 183–187, Jun. 2019.
[14] M. Tran, Z. Memon, A. Saieed, W. Pao, and F. Hashim, "Numerical simulation of two-phase separation in T-junction with experimental validation," *J. Mech. Eng. Sci.*, vol. 12, pp. 4216–4230, Dec. 2018.
[15] E. A. Chinnov, F. V. Ron'shin, and O. A. Kabov, "Regimes of two-phase flow in micro- and mini channels (review)," *Thermophysics and Aeromechanics*, vol. 22, no. 3. Maik Nauka-Interperiodica Publishing, pp. 265–284, 27-May-2015.
[16] "The effect of liquid viscosity on the gas-liquid two-phase flow pattern in horizontal mini-channel."
[17] S. Sukamta, "Computational Fluid Dynamics (CFD) and Experimental study of Two-Phase Flow Patterns Gas-Liquid with Low Viscosity in a Horizontal Capillary Pipe," vol. 8, no. 8, pp. 16–23, 2019.
[18] J. Li, J. Zhao, and S. Wang, "Gas-liquid two-phase flow in a mini-channel with water infiltration continuously along the flow direction," *Int. J. Green Energy*, vol. 12, no. 3, pp. 207–214, Mar. 2015.
[19] S. Novianto, A. S. Pamitran, R. Koestoer, and K. Saito, "Two-phase Frictional Pressure Drop of Propane with Prediction Methods of Viscosity and Density in 500 µm Diameter Tube," in *IOP Conference Series: Materials Science and Engineering*, 2018, vol. 316, no. 1.
[20] A. Mohammed and A. Morad, "A Two-Phase Pressure Drop Model for Homogenous Separated Flow for Circular Tube Condenser, Examined with Four Modern Refrigerants Akademia Baru," vol. 2, no. 2, pp. 274–287, 2018.

Penerbit Akademia Baru

Engineering Science and Technology Conference Proceedings

Journal homepage: www.akademiabaru.com/EST.html

Investigation Of Thermal Hydraulic Performance Of Microchannel Heat Sink With Hourglass Profile

Open Access

Kok-Cheong Wong[1,*], Yih Loong Chan[1], Boon Hoe Goh[2]

[1] Department of Mechanical, Materials and Manufacturing Engineering, Faculty of Engineering and Science, University of Nottingham Malaysia, 43500 Semenyih, Selangor, Malaysia
[2] Department of Civil Engineering, Faculty of Engineering and Science, University of Nottingham Malaysia, 43500 Semenyih, Selangor, Malaysia

ABSTRACT

The present study investigates thermal and hydraulic performance of microchannel heat sink with hourglass profile (MCHS-HG) numerically. A 3-D conjugate heat transfer model is used to solve the problem with water as coolant and silicon as material of the heat sink. Performance of MCHS-HG are evaluated with 5 different contraction ratios, Rc (0.2, 0.4, 0.6, 0.8 and 1.0) and 3 different aspect ratios from 4, 5 and 6 with Reynolds number in the range of 300-1800. Thermal performance of MCHS-HG is compared with microchannel heat sink with straight rectangular channel (MCHS-R). Results showed that thermal performance of MCHS-HG is better than MCHS-R for any given aspect ratio. The study on the effect of contraction ratio show that the optimum thermal performance is given by the contraction ratio of 0.4. Microchannel with narrower throat of hourglass profile gives higher pumping power. The assessment on thermal- hydraulic performance of MCHS-HG shows that the MCHS-HG is less economical to be applied as compare to MCHS-R

Keywords:
Microchannel heat sink; hydraulic performance; thermal performance; hourglass profile; contraction ratio

Copyright © 2019 PENERBIT AKADEMIA BARU - All rights reserved

1. Introduction

Electronic devices are getting smaller in size in this few decades and it is expected to become even smaller in the future. One of the challenges in miniaturized electronic device is heat dissipation of the device as it operates under higher power density. The miniaturized microchannel heat sink, MCHS was first introduced by Tuckerman and Pease [1] in 1981 with microchannels etched to the upper surface of a silicon chip with water as coolant. The idea of using microscopic heat sink was suggested by them and experiments were performed to evaluate its performance. They stated that the best way to significantly increase the heat transfer coefficient is to reduce the characteristic length of the heat. In their experiments, lowest thermal resistance was recorded at 0.09 °C/W with heat flux of 790 $W/cm2$. They also predicted that MCHS is capable to dissipate 1300 $W/cm2$ heat flux with temperature difference of 50°C. Qu and Mudawar [2] conducted both experimental and numerical study on pressure drop and heat transfer of a MCHS made of copper. They obtained good agreement between experimental and numerical results and concluded that

* *Corresponding author.*
E-mail address: wongkc6@gmail.com (Kok-Cheong Wong)

conventional Navier–Stokes and energy equations can adequately predict the fluid flow and heat transfer characteristics of microchannel heat sinks.

Zhai *et al.,* [3] performed numerical and experimental work to validate previous analytical model used for predicting performance of microchannel heat sink with straight rectangular channel. An accuracy within 10% difference between analytical and empirical results was reported by them. Their results also showed that convective thermal resistance has a large effect on thermal performance of microchannel heat sink compared with other thermal resistances. They also stated that vicious dissipation can be neglected if water is used as coolant.

Raghuraman *et al.,* [4] studied numerically the thermal performance of different channel aspect ratio of a MCHS-R. Aspect ratios of 20, 30 and 46.66 over a range of Reynolds number were investigated. They found that pressure drop is the highest with AR 20. On the other hand, pumping power is highest with AR 46.66 due to high flowrate. AR 20 also have a higher Nusselt number as compared with ARs of 30 and 46.66. MCHS with AR 30 was found to be ideal among those investigated as it offers highest heat transfer rate with pumping power maintained at optimum level.

There were many interests in investigating thermal performance of MCHS with channel geometries other than rectangular shape. Wang *et al.,* [5] reported MCHS-R has lowest thermal resistance, followed by trapezoidal and triangular MCHS when number of channels, cross section area and hydraulic diameter are the same. MCHS-R gives the best performance when AR is in the range of 8.9-11.4. On the other hand, Tran *et al.,* [6] investigated numerically the thermal performance of MCHS with 5 different channel geometries i.e. circle, square, trapezium, concave, convex, with hydraulic diameter of 200 microns, in the range of Reynolds number 700–2200. They reported that the best thermal performance was achieved by circular channel which able to dissipate up to 1500 $W/cm2$ at Reynolds number of 2200 while square channel is the poorest among the 5 different geometries investigated.

Attempts were made to enhance the heat transfer with different structures of MCHS. Examples are double layer MCHS by Vafai and Zhu [7] and MCHS with interrupted microchannels and triangular ribs by Wong and Lee [8]. Both studies showed positive results as compared to MCHS-R. The former has an increase in heat transfer surface area and the latter has a better mixing of flow and increase in heat transfer area that promote heat transfer rate. Both Zhou *et al.,* [9] and Sakanova *et al.,* [10] studied the thermal hydraulic performance of MCHS with wavy channel. Results in both studies showed an increase in heat transfer rate with as high as 2.8 times as compared to straight microchannel. In addition, Sakanova *et al.,* [10] also studied the effect of nanofluid in MCHS. Positive results were obtained in their study. They concluded that diamond-water nanofluid exhibits the best thermal performance with lowest thermal resistance.

Ghani *et al.,* [11] investigated numerically MCHS with rectangular ribs, sinusoidal cavity and combined features of both in the range of Reynolds number 100-800. They obtained results that shows the MCHS with combined features is superior over individual feature as the combined features able to eliminate stagnation and promote flow mixing. The combination effectively reducing the pressure drop through providing larger flow area compare with microchannel with rectangular ribs.

Yang *et al.,* [12] and Yu *et al.,* [13] had focused their study in pin fin microchannel heat sink. The former studied five different pin fin configurations while latter focused in microchannel with piranha pin fin (PPF). Both did experiment and numerical simulation based on their proposed design. Yang *et al.,* [12] showed triangular pin fin has a greatest resistance to fluid flow while circular pin fin has the least resistance. They showed that hexagonal and circular pin fin has flow guided structure that proved to be vital in improving the cooling performance. Yu *et al.,* [13] stated

the friction factor of PPF is comparable with straight channel and much lower than other micro pin fin heat sinks. In their study, they concluded fluid extraction effect of PPF leads to the enhancement of heat transfer while reducing pressure drop.

Huang *et al.,* [14] conducted numerical simulation for microchannel heat sink with slotted flow passages. MCHS with different configurations i.e. parallel, staggered-slots and trapezoidal staggered channels were investigated. These configurations showed a better thermal-hydraulic performance than traditional straight rectangular channel. Larger slot width result in higher Nusselt number with pressure drop across heat sink almost identical. They concluded that staggered-slot channel provides better thermal performance than parallel-slot channel, but trapezoidal staggered channel shows lower pressure drop.

Riera *et al.,* [15] numerically and experimentally studied the performance of the stepwise varying width microchannel cooling device. They demonstrated that the thermal resistance coefficient of the tested device was 2.35×105 m2 K/W for a flow rate of 1.60 mL/s, enhancing near three-fold the performance at the millimetre scale for the same flow rate and showing high temperature uniformity.

Xia *et al.,* [16] experimentally and numerically investigated the heat transfer and fluid flow characteristics in MCHS with complex corrugated profile. Comparisons were made against MCHS with rectangular profile. The results show that the corrugated profile developes a higher pressure drop but a better heat transfer performance as the corrugated profile causes interruption and redevelopment of boundary layer.

Betz and Attinger [17] studied the use of segmented flow in enhancing heat transfer of MCHS. Segmented flow is created by injecting air bubbles periodically into water filled channels of MCHS. Results show that segmented flow is capable of enhancing the Nusselt number by more than 100% provided mass velocity is in range of 330−2000 $kg/m2s$.

Luo *et al.,* [18] was inspired by leaf vein structure that transports water in leaf to investigate thermal performance of leaf-vein-inspired microchannel. Three different channel structures based on the mid rib leaf structures of 3 selected plants were investigated. Numerical results show that pitted wall thickening patterns of one of the leaf structure had the best heat and mass transfer characteristics. These structures were applied and modeled into microchannel heat sink and results demonstrated that they provide excellent heat transfer characteristic.

Recently, several studies [19,20] related to wavy microchannel heat sink have been conducted. Study by Lin *et al.,* [19] found that a novel design heat sink with wavy microchannel is capable of enhancing the heat transfer. In the work done by Zhu *et al.,* [20], they employed a three-dimensional fluid-solid conjugate model to investigate the heat transfer performance of the left-right and up-down wavy microchannel heat sinks for various wavy amplitudes, wavelengths, channel aspect ratios, and width ratios of channel to pitch. The up-down wavy design if found to give better performance for small wavelengths.

Thermal and hydraulic performance of micro-channel heat sink with hourglass profile (MCHS-HG) are investigated in the present study numerically. To the knowledge of the authors, research studies related to thermal performance of hourglass profile in MCHS can hardly be found. The performance is investigated numerically with Reynolds number in the range of 300-1800 and aspect ratio in the range of 4-6. MCHS-HGs have different solid-fluid interface area as compared to MCHS-R and affect the heat exchange. The hourglass profile is expected to affect the flow resistance. Therefore, it is interesting to understand the effect of the hourglass profile on thermal performance by varying its throat size with various contraction ratio defined hereafter. In addition, the pumping power and performance enhancement factor will be evaluated.

2. Numerical Methodology

MCHS with overall dimensions of 10 mm × 10 mm × 480μm is employed for this numerical study. The dimensions correspond to the overall length L, overall width w and overall height H of the heat sink as illustrated in the physical model in Figure (1a). The overall dimensions used are referenced to the dimensions used by Pease and Tuckerman [1]. The heat sink consists of repeated sections, and only a single section will be used as computational domain. Figure (1b) illustrates cross-section of the repeated section, showing hourglass channel profile that is used for investigation with w_w, w_c, H_c, H_w and r equal to 50, 50, 50, 80 and 25 μm, respectively.

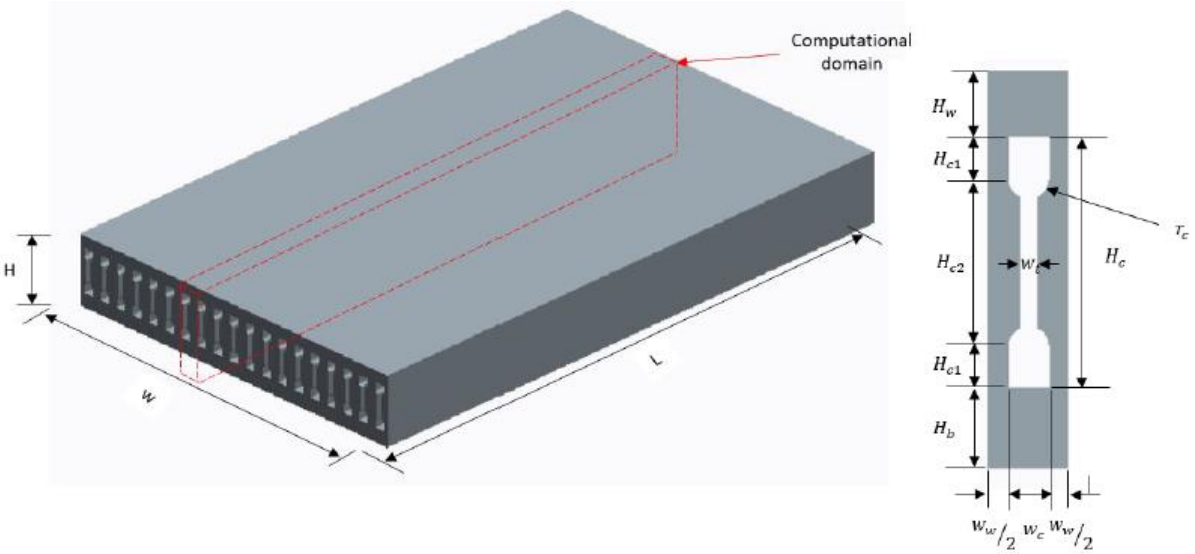


Fig. 1. (a) Schematic view of microchannel heat sink for study with computation domain clearly shown (b) Cross section of single channel used for simulation

In the present study, thermal and hydraulic performances of MCHS-HG are investigated. The hourglass geometry is constructed based on a rectangular channel with the center pinched to form a uniform throat with curves connecting the throat and upper and lower parts of channel. For a given AR, the channel height H_c and channel width w_c are fixed, and the hourglass profile is varied by contraction ratio, R_c which is defined as:

$$R_c = \frac{w_t}{w_c} \tag{1}$$

where w_t is the width of throat. Higher value of R_c means wider throat size and it becomes a rectangular channel when R_c=1. The aspect ratio AR is given as follows:

$$AR = \frac{H_c}{w_c} \tag{2}$$

The effect of AR is investigated with values 4, 5 and 6. For each value of AR, the thermal performance of the MCHS with hourglass profiles are investigated with Rc = 0.2, 0.4, 0.6, 0.8, 1.0. Silicon is used as the material of heat sink and water is used as coolant for the heat sink. Uniform heat flux of 790 $W/cm2$ [1] is applied at base of MCHS with inlet temperature of 296K. The front and back solid surfaces, as well as the top surface are assumed to be adiabatic. The side walls are

set to be symmetrical. The inlet velocity uin is set at the channel inlet, and pressure outlet is set at the channel outlet. The heat flux and temperature are conserved at the fluid-solid interface.

Few assumptions were made to simplify the simulations:

1. Fluid is steady, incompressible and laminar over the whole length of MCHS.
2. Properties for water and heat sink remain constant.
3. Heat transfer to surrounding is negligible.

With these boundary conditions and assumptions, the problem is solved using the following governing equations:

Continuity equation:

$$\nabla \cdot V = 0 \tag{3}$$

where V is velocity vector.

Momentum equation for fluid:

$$\rho(\mathrm{V} \cdot \nabla)V = -\nabla p + \mu_f \nabla^2 V \tag{4}$$

where ρ_f and μ_f is the density and dynamic viscosity of fluid respectively, and p is the pressure of the fluid.

Energy equation for fluid:

$$\rho_f c_{c,}(V \cdot \nabla T_f) = kf(\nabla^2 T_f) \tag{5}$$

where $c_{c,f}$, T_f and k_f is the specific heat capacity, temperature and thermal conductivity of fluid, respectively.

Energy equation for solid:

$$ks(\nabla^2 T_s) = 0 \tag{6}$$

where k_s and T_s is the thermal conductivity and temperature of solid, respectively.

SIMPLEC algorithm is used to for pressure velocity coupling with pressure using PRESTO! scheme, momentum and energy using power law scheme. The convergence residual criteria are set to below 10^{-5} for continuity and velocity while for energy is set to below 10^{-8}. Performance of MCHS is will be evaluated over a range of Reynolds number from 300-1800 for each case. Reynolds number is defined as:

$$Re = \frac{\rho_f u_{in} D_h}{\mu_f} \tag{7}$$

where u_{in} and D_h is the inlet velocity and hydraulic diameter of the MCHS respectively.

Hydraulic diameter, D_h is defined as:

$$D_h = \frac{4A}{P} \tag{8}$$

where A and P are the area and perimeter of cross section of channel, respectively. Pressure drop is defined as:

$$\Delta p = \overline{p_{in}} - \overline{p_{out}} \tag{9}$$

Where $\overline{p_{in}}$ and $\overline{p_{out}}$ is the average pressure of inlet and outlet, respective.

The average heat transfer coefficient, h is defined as follow:

$$\bar{h} = \frac{q''}{\bar{T}_w - \bar{T}_f} \tag{10}$$

where T_w and T_f is the average temperature of the heated base and average bulk fluid temperature, respectively. q'' is the heat flux at base of MCHS. T_w, T_f is calculated with formula below:

$$\bar{T}_f = \frac{\int \rho_f T_f \, dV}{\int \rho_f \, dV} \tag{11a}$$

$$\bar{T}_w = \frac{\int T_w \, dA}{\int dA} \tag{11b}$$

Pumping power for the fluid flow through the MCHS is defined as,

$$\Omega = V \, \Delta p \tag{12}$$

where V is the volumetric flow rate of coolant.

Table 1
Validation with Pease and Tuckerman [1] experimental results for numerical method used

				Results (K/W)		
wc (μm)	ww (μm)	Hc(μm)	Heat flux (W/cm^2)	Experiment [1]	Present study	Deviation (%)
56	44	320	181	0.110	0.1076	2.182
55	45	287	277	0.113	0.1131	0.088
50	50	302	790	0.090	0.0905	0.556

Table 2
Results of grid independence test

No. of elements	$\bar{h}(W/m^2K)$	Deviation (%)
330 thousand	23.25	3.165
629 thousand	23.67	1.416
1.3 million	23.86	0.6247
2.45 million	23.94	0.2915
3.4 million	24.01	-

3. Results

Present study is validated against experimental results obtained by Pease and Tuckerman [1]. Comparison presented in Table 1 shows a maximum deviation of 2.182%, which shows that the numerical model is in good agreement with the experiment results [1].

Grid independence test has been carried out and the results is showed in Table 2. Mesh with 1.3 million elements showed a different of 0.6247% with 3.4 million elements which is negligible. Therefore, mesh size of about 1.3 million is applied throughout all the simulations.

The thermal performance of the MCHS with hourglass profiles has been investigated with Rc = 0.2, 0.4, 0.6, 0.8, 1.0, and the results of average heat transfer coefficient □ against Reynolds number are presented in Figure 2a, 2b and 2c for aspect ratio 4, 5 and 6, respectively. Generally Figure 2 shows that, the value of $\bar{h}$ increases with Re regardless of the value of AR. For a given Reynolds number and R_c, increasing AR results in higher value of $\bar{h}$ [4]. For the effect of varying Rc, it can be observed in Figure 2a, 2b, and 2c that, Rc = 0.4 provides highest value of $\bar{h}$ except the case of Re=300 at which R_c = 0.6 is slightly higher in $\bar{h}$. For the range of Reynolds number investigated, the highest enhancement in $\bar{h}$ of about 28% can be achieved at the conditions of R_c = 0.4 at Re = 1800 as compared to MCHS-R.

Among the values of R_c investigated, the lowest value, R_c = 0.2 do not give highest value of $\bar{h}$ but mediocre despite having largest solid-fluid interface area. The value of $\bar{h}$ decreases as R_c increases from 0.6 to 1.0. This means there could be other factors that govern the heat transfer other than the solid-fluid interface area.

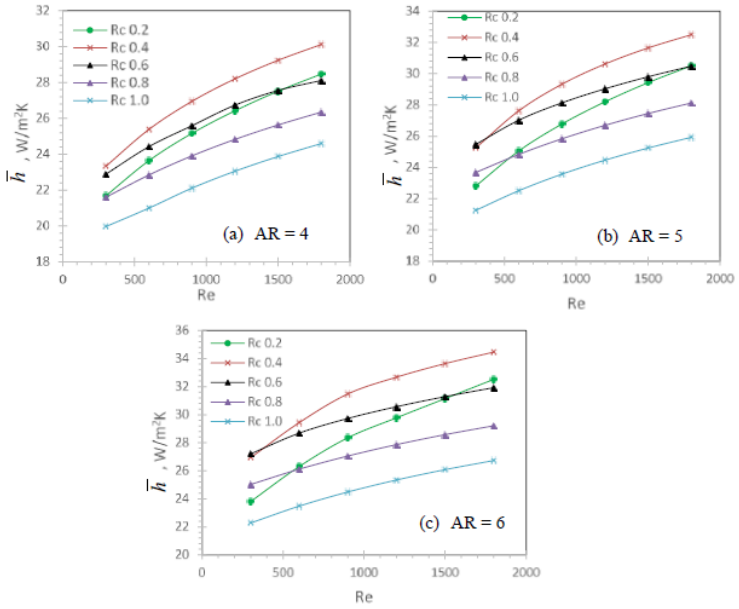


Fig. 2. Variation of $\bar{h}$ with Re for (a) AR = 4, (b) AR = 5 and (c) AR = 6

To further analyse the effect of contraction ratio on thermal performance, the temperature distribution of MCHS for the 5 values of Rc at Re = 1800 and AR = 5 are presented in Figure 3. Note that the temperature distribution is presented at the middle section between inlet and outlet. In Figure 3a (Rc = 0.2), it is clearly shown that, near the throat region, the fluid temperature is similar the solid temperature. In this case which the throat size is the smallest, most of the fluid that flows through has close proximity to the solid surface, and therefore most of the fluid absorbs large

amount of heat from solid, resulting in small difference in temperature between the solid and fluid. Since it is the narrowest throat, the volume flow rate is also the least among all which limit the amount of heat being carried away. This could be the reason why Rc = 0.2 do not give highest heat transfer coefficient despite having highest fluid-solid interface area and close proximity of fluid to the solid.

For the case of R_c 0.4, it can be observed Figure 3b at the fluid-solid interface region that, the fluid temperature is highest near the solid wall, but develop a significant temperature gradient towards the center of the throat. In Figure 3b, it also shows that, the fluid at the center has the lowest temperature as it is considered far for the heat from the solid to reach. Considering larger amount of fluid flowing through the throat as compared to the case of Rc = 0.2, the case Rc = 0.4 should have a higher capacity to transfer the heat away but not expected to be very much different as effective heat transfer is only occurring through the fluid near the interface. Further observation for other cases of MCHS-HG (R_c = 0.6, 0.8) in Figure 3c and Figure 3d reveals similar characteristics that heat is only transferred effectively to the fluid near the interface. Large fraction of liquid near the center of the fluid remains at low temperature. This means increasing the volume of fluid flow by having larger size of throat (higher value of R_c) enhances the heat transfer but not significantly. On the other hand, based on the hourglass profile, larger size of throat gives smaller solid-fluid interface area which is not favourable to the heat transfer. From the above, it implies that, the MCHS-HG with R_c = 0.4 gives highest heat transfer coefficient simply due to the compromise between the interfacial heat transfer area and the amount of fluid flow that subject to the size of the throat (hourglass profile).

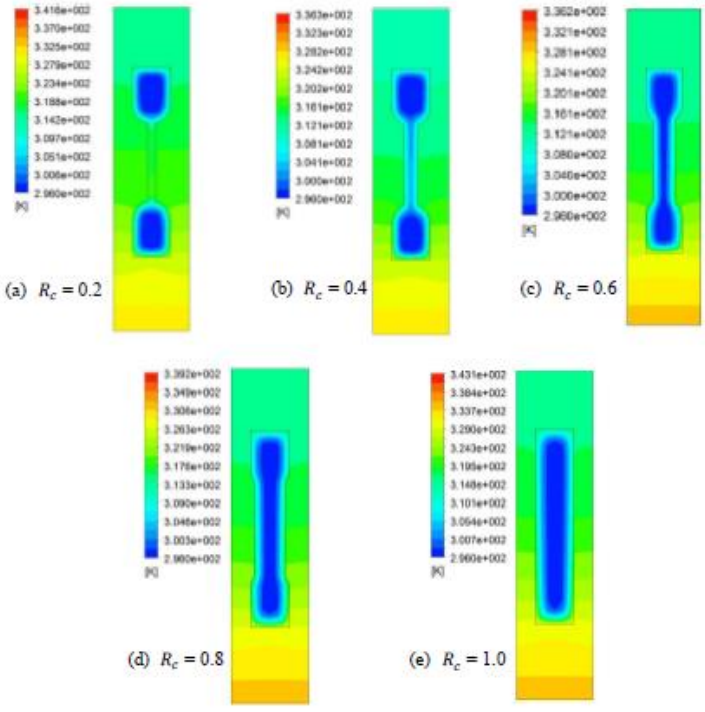


Fig. 3. Temperature distribution of MCHS midway between inlet and outlet for AR=5 and Re=1800

Despite the better thermal performance of MCHS-HG, increase in pumping power need to be considered for the practicability of MCHS-HG for future applications. To understand the hydraulic performance, the results of pumping power for different Reynolds numbers and different values of

R_c have been obtained. The results are presented in Figure 4a, 4b, 4c for AR = 4,5 and 6, respectively. The results show that, for any given value of Rc, Ω increases with AR or Re. This could be due to higher flow resistance as a results of higher aspect ratio [4]. Figure 4 also shows that, for any given values of Reynolds number, Ω increases with decrease in R_c. Literally this means narrower throat results in higher the pumping power. This is attributed to the increase in pressure drop when the throat is getting narrower. The large pressure drop could be due to the flow constriction at narrower throat and larger fluid-solid interface area.

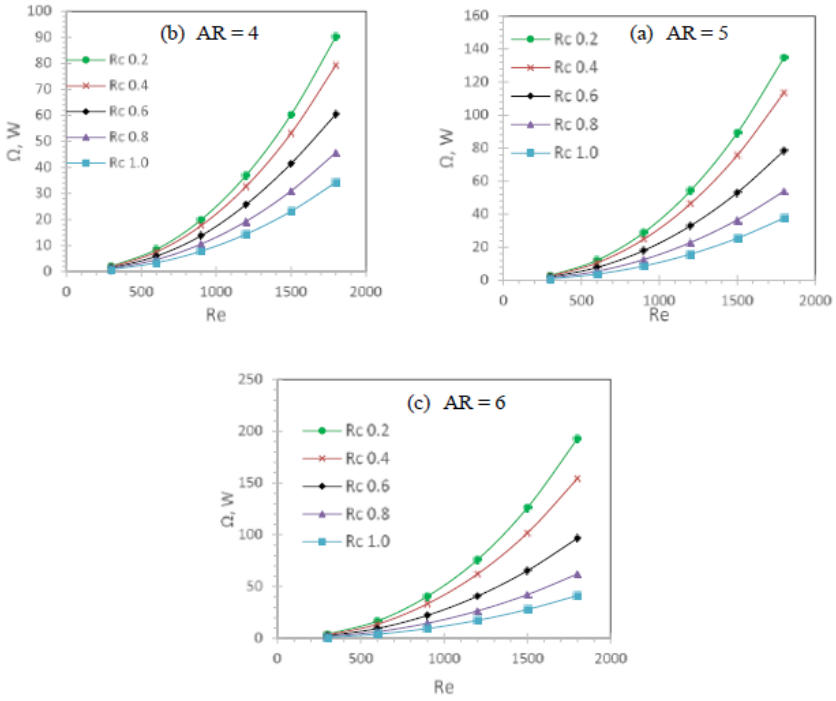


Fig. 4. Variation of pumping power with Re

The results discussed above reveal that the MCHS-HG offer better thermal performance at the expense of the pumping power. Performance enhancement factor, η is used to evaluate the thermal hydraulic performance to assess whether it is economical to be implemented. η is defined as follow:

$$\eta = \frac{\bar{h} / \bar{h}_o}{\Omega / \Omega_o} \tag{13}$$

in which subscript 'o' denotes MCHS-R.

Performance enhancement factor, η is the ratio of dimensionless heat transfer coefficient to dimensionless pumping power with reference to the rectangular channel. If it is larger than unity, enhancement in heat transfer is considered greater than the increase in pumping power, and therefore achieving a better thermal hydraulic performance than MCHS-R. Figure 5 showed all MCHS-HG has values of η lower than 1 with R_c of 0.2 being the poorest at high Reynolds number. Increase in $\bar{h}$ of MCHS-HG is at relatively higher expense of pumping power, and therefore MCHS-HG is not economical to be implemented. Figure 5 also shows that the most economical MCHS-HG are those design with lower value of AR and high value of R_c.

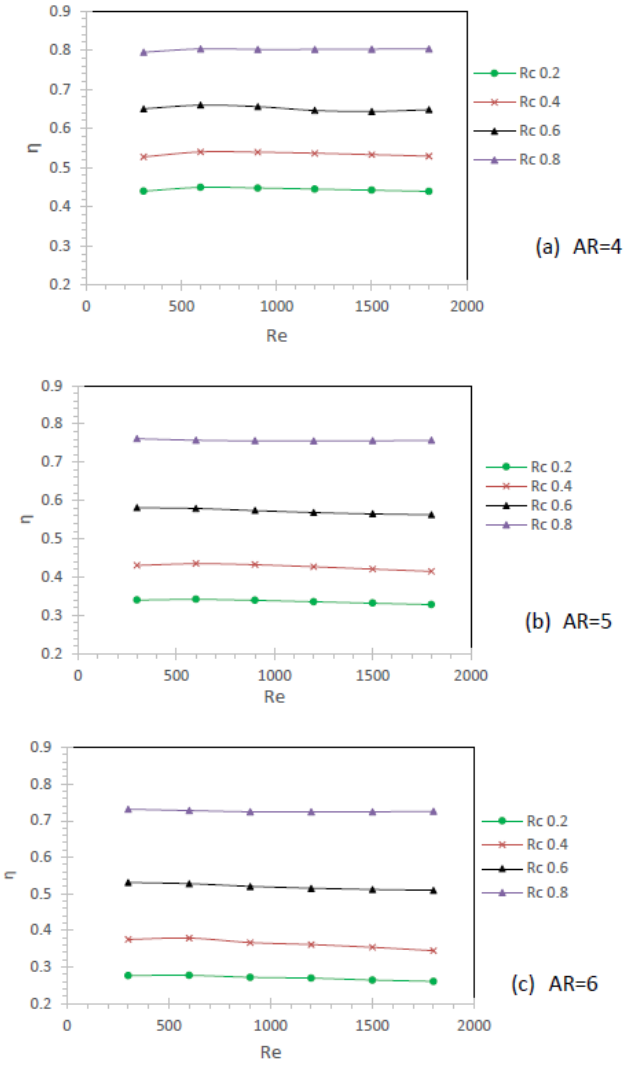


Fig. 5. Variation of η with Re for different AR

4. Conclusions

A numerical investigation has been carried out to study the thermal and hydraulic performance of microchannel heat sink with hourglass channel (MCHS-HG) and compared to microchannel heat sink with straight rectangular channel (MCHS-R). A 3-D conjugate heat transfer model was used to solve the problem. The numerical method used has been validated against the experimental work of a literature. MCHS-HG with 5 different values of contraction ratio and 3 different values of aspect ratio were investigated over a range of Reynolds number of 300-1800. The effect of these two parameters on the thermal and hydraulic performance has been investigated and the results can be concluded as follow:

1. The value of contraction ratio of 0.4 gives optimum heat transfer coefficient, capable of achieving 28% enhancement as compared to the MCHS-R.
2. Lower values of contraction ratio require higher pumping power.
3. Increase in aspect ratio of the MCHS-HG results in higher heat transfer coefficient but requires higher pumping power for MCHS-HG has much lower thermal-hydraulic performance than the MCHS-R and therefore not economical to be

implemented.

References

[1] Tuckerman, D.B., Pease, R.F.W., High-performance heat sink for VLSI, IEEE Electron Device Letters. EDL-2 (1981) 126-129.
[2] Qu, W., and Mudawar, I., Experimental and numerical study of pressure drop and heat transfer in a single-phase micro-channel heat sink, Int. J. Heat Mass Transfer 45 (2002) 2549-2565
[3] Zhai, Y., Xia, G., Li, Z., and Wang, H., Experimental investigation and empirical correlations of single and laminar convective heat transfer in microchannel heat sinks, Exp. Thermal Fluid Science 83 (2017) 207–214
[4] Raghuraman, D., Raj, R. T. K., Nagarajan, P., and Rao, B., Influence of aspect ratio on the thermal performance of rectangular shaped micro channel heat sink using CFD code, Alexandria Eng. J. 56 (2017) 43–54
[5] Wang, H., Chen, Z., and Gao, J., Influence of geometric parameters on flow and heat transfer performance of micro-channel heat sinks, Applied Thermal Eng. 107 (2016) 870–879.
[6] Tran, N., Chang, Y.-J., Teng, J.-T., Greif, R., A study on five different channel shapes using a novel scheme for meshing and a structure of a multi-nozzle microchannel heat sink, Int. J. Heat Mass Transfer 105 (2017) 429–442.
[7] Vafai, K. and Zhu, L., Analysis of two-layered micro-channel heat sink concept in electronic cooling, Int. J. Heat Mass Transfer 42 (1999) 2287–2297
[8] Wong, K.-C. and Lee, J.-H., Investigation of thermal performance of microchannel heat sink with triangular ribs in the transverse microchambers, Int. Com. Heat Mass Transfer 65 (2015) 103–110
[9] Zhou, J., Hatami, M., Song, D., and Jing, D., Design of microchannel heat sink with wavy channel and its time-efficient optimization with combined RSM and FVM methods, Int. J. Heat Mass Transfer 103 (2016) 715–724.
[10] Sakanova, A., Keian, C. C., and Zhao, J., Performance improvements of microchannel heat sink using wavy channel and nanofluids, Int. J. Heat Mass Transfer 89 (2015) 59–74.
[11] Ghani, I. A., Kamaruzaman, N., and Sidik, N. A. C., Heat transfer augmentation in a microchannel heat sink with sinusoidal cavities and rectangular ribs, Int. J. Heat Mass Transfer 08 (2017) 1969–1981.
[12] Yang, D., Wang, Y., Ding, G., Jin, Z., Zhao, J., and Wang, G., Numerical and experimental analysis of cooling performance of single-phase array microchannel heat sinks with different pin-fin configurations, Applied Thermal Engineering 112 (2017) 1547–1556
[13] Yu, X., Woodcock, C., Plawsky, J., and Peles, Y., An investigation of convective heat transfers in microchannel with Piranha Pin Fin, Int. J. Heat Mass Transfer 103 (2016) 1125–1132
[14] Huang, S., Zhao, J., Gong, L., and Duan, X., Thermal performance and structure optimization for slotted microchannel heat sink, Applied Thermal Engineering 115 (2017) 1266–1276
[15] Riera, S., Barrau, J., Omri, M., Fréchette, L.G., Rosell, J.I., Stepwise varying width microchannel cooling device for uniform wall temperature: Experimental and numerical study, Applied Thermal Engineering 78 (2015) 30–38
[16] Xia, G., Ma, D., Zhai, Y., Li, Y., Liu, R., Du, M., Experimental and numerical study of fluid flow and heat transfer characteristics in microchannel heat sink with complex structure, Energy Conversion Management 105 (2015) 848– 857
[17] Betz, A. R., and Attinger, D., Can segmented flow enhance heat transfer in microchannel heat sinks? Int J. Heat Mass Transfer 53 (2010) 3683–3691
[18] Luo, Y., Liu, W., Wang, L., and Xie, W., Heat and mass transfer characteristics of leaf-vein-inspired microchannels Zhu, J.F., with wall thickening patterns, Int. J. Heat Mass Transfer 101 (2016) 1273–1282
[19] Lin, L., Zhao, J., Lu, G., Wang, X.-D., Yan, W.-M., Heat transfer enhancement in microchannel heat sink by wavy channel with changing wavelength/amplitude, Int. J. Thermal Sciences 118 (2017) 423-434
[20] Zhu, J.-F., Li, X.-Y., Wang, S.-L., Yang, Y.-R., Wang, X.-D., Performance comparison of wavy microchannel heat sinks with wavy bottom rib and side rib designs, Int. J. Thermal Sciences 146 (2019) 106068

Penerbit Akademia Baru

Engineering Science and Technology Conference Proceedings

Journal homepage: www.akademiabaru.com/EST.html

Visualization of Heat Transfer via Heatlines and Entropy Generation for Marangoni Convection in an Open Top Rectangular Cavity

Open Access

Norazam Arbin[1,*], Shafaruniza Mahadi[1], Farah Suraya Md Nasrudin[1], Noor Syazana Ngarisan[1]

[1] Faculty of Computer and Mathematical Sciences, Universiti Teknologi MARA, Johor Branch, Segamat Campus, 85000 Segamat, Johor, Malaysia

ABSTRACT

The Marangoni effect towards entropy generation in natural convection is analyzed in open top rectangular cavity. The heatline approach is used to visualize the heat path across the cavity. The finite difference method is applied where the parameters taken into consideration are the Marangoni (Ma), Grashof (Gr) and Prandtl (Pr) numbers. The results are portrayed as the contours of streamlines, isotherms, heatlines and isocontours of entropy generations. The average Nusselt number, dimensionless entropies generation together with Bejan number are then been analyzed. The result shows that all considered values displays an increasing pattern except for Bejan number that illustrates a decreasing pattern for all Marangoni values. Also, it appears that the fluid thermal irreversibility dominates the convection.

Keywords:
Marangoni; Entropy; heat transfer

Copyright © 2019 PENERBIT AKADEMIA BARU - All rights reserved

1. Introduction

Natural convection in cavities induced by the difference in temperature between vertical or horizontal walls is widely studied [1-8]. These authors analyzed the influence of the temperature difference, aspect ratio, openings and inclinations of the cavity on convection. When there is an open surface between fluids, the surface tension effects will play an important role in micro-sized fluid dynamics such as thermal management of electronic devices and food processing [9]. The surface tension effect also known as Marangoni effect especially in a convection problem. Alexander *et al.,* [10] investigated Marangoni convection and heat transfer in thin liquid films with gas-liquid interface. They found that the substrate structure on the upper surface changes the flow patterns and affects the heat transfer rates. Another study of liquid films done by Roisman [11] reported that along the liquid-gas interface, the temperature gradients will lead to emergence of themocapillary stresses, to the development of vortices and to the interface deformation. Duan [12] investigates the Marangoni convection in rectangular cavity and comes to conclusion that the surface tension effect is the main factor in driven the convection for thin layer while the buoyancy effect takes place as major role for thick layer. Li *et al.,* [13] found a sudden increment of Nusselt number occurs when a fluid flow transits from a stable to violent state for a cylindrical cavity that is heated from below. A numerical study done by Li *et al.,* [14] on the thermal Marangoni effect on

* *Corresponding author.*
E-mail address: noraz574@johor.uitm.edu.my (Norazam Arbin)

wafer drying process concluded that evaporation is one of the factor that weakens the Marangoni effect. The heatline concept is a useful tool to visualize the heat flow in a cavity. It was proposed by Kimura and Bejan [15] and many authors have applied this in their research and experiment [16-19].

The entropy generation is a next interesting field to study. The presence of entropy generation in heat transfer which associated by thermodynamic irreversibility destroys the available work of a system. Morsli *et al.,* [20] showed that increasing the aspect ratio will increase the total entropy generation for natural convection in an enclosure. Al-Rashed *et al.,* [21] reported that the arrangements of heating and cooling regions are major factors that affected the fluid flow, heat transfer and entropy generation. Liquid-metal fluid is used in a study conducted by Das *et al.,* [22] and they found that high heat transfer rates and low entropy generation occurs when two heaters are located at central and lower halves of the square and triangular enclosures. Kolsi *et al.,* [23] studied the entropy generation in 3D enclosure and found that the total entropy generation and heat transfer increased as Marangoni number is taken higher. Oztop *et al.,* [24] observed that for a natural convection in a partially open enclosure, the highest heat transfer and entropy generation were found when the enclosure is fully opened.

This study is focusing on simulation of natural Marangoni convection in an open top cavity which exhibit surface tension effect and how it will affect the entropy generation.

2. Methodology

Figure 1 illustrates a diagram of a rectangular cavity filled with liquid-metal fluid which Prandtl number, Pr is 0.015. The open top free-surface and the fluid considered here is an incompressible Newtonian fluid. In this study, the free-surface is also assumed to obey the Newton's law of cooling, flat and non-deformable while the bottom wall is kept adiabatic. The right wall always has higher uniform temperature, T_h compared to the left wall, T_c.

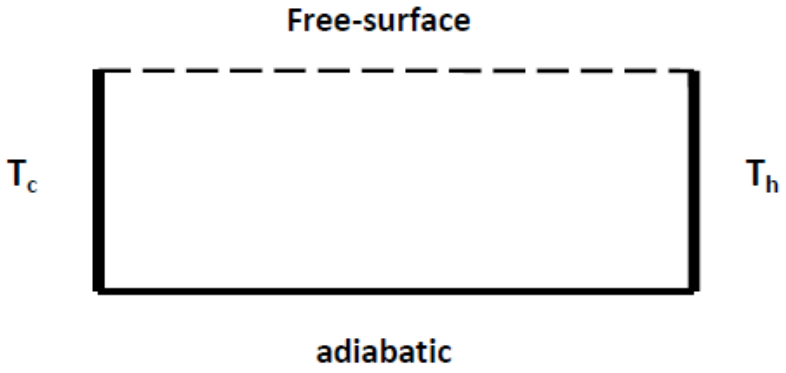


Fig. 1. Schematic diagram of problem considered

Converting the primitive variables of stream function, vorticity and temperature to non-dimensional equations, we have a set of equations as follows:

$$\frac{\partial^2\Psi}{\partial X^2}+\frac{\partial^2\Psi}{\partial Y^2}=-\Omega \tag{1}$$

$$\frac{\partial^2\Omega}{\partial X^2}+\frac{\partial^2\Omega}{\partial Y^2}=\frac{1}{Pr}\left(\frac{\partial\Psi}{\partial Y}\frac{\partial\Omega}{\partial X}-\frac{\partial\Psi}{\partial X}\frac{\partial\Omega}{\partial Y}\right)+GrPr\left(\frac{\partial\Theta}{\partial X}\right) \tag{2}$$

$$\frac{\partial^2\Theta}{\partial X^2}+\frac{\partial^2\Theta}{\partial Y^2}=\frac{\partial\Psi}{\partial Y}\frac{\partial\Theta}{\partial X}-\frac{\partial\Psi}{\partial X}\frac{\partial\Theta}{\partial Y} \tag{3}$$

where they subjected to dimensionless boundary conditions:

$$\Psi=0,\ \Omega=-\frac{\partial^2\Psi}{\partial X^2},\ \Theta=0,\ at\ \ X=0 \tag{4}$$

$$\Psi=0,\ \Omega=-\frac{\partial^2\Psi}{\partial X^2},\ \Theta=1,\ at\ \ X=1 \tag{5}$$

$$\Psi=0,\ \Omega=-\frac{\partial^2\Psi}{\partial Y^2},\ \frac{\partial\Theta}{\partial Y}=0,\ at\ \ Y=0 \tag{6}$$

$$\frac{\partial^2\Psi}{\partial Y^2}=-\Omega,\ \Omega=-Ma\frac{\partial\Theta}{\partial X},\ \frac{\partial\Theta}{\partial Y}=-Bi\Theta,\ at\ \ Y=1 \tag{7}$$

The average Nusselt number is given as:

$$\overline{Nu}=\int_0^1\left[\frac{\partial\Theta}{\partial X}\right]dY \tag{8}$$

and the boundary conditions for the dimensionless heat function are:

$$H(X,Y)=H(X,Y_0)+\int_{Y_0}^{Y}-\frac{\partial\Theta}{\partial X}\,dY \tag{9}$$

The dimensionless total entropy generation, S_{tot}, in the cavity is given by the summation of the integration over the region R of local entropy generation due to heat transfer, S'_{th}, and fluid friction, S'_{fric} which are given as follows:

$$S_{tot}=\int_R\left(S'_{th}+S'_{fric}\right)dR=S_{th}+S_{fric} \tag{10}$$

The Bejan number, Be, which plays as indicator to show whether the convection in the entire region is dominated by thermal or the fluid friction irreversibility is given as:

$$Be=\frac{S_{th}}{S_{tot}} \tag{11}$$

The convection is dominated by thermal if Be > 0.5 while it will be dominated by friction if Be < 0.5. The finite difference method is applied to solve Eqs. (1)-(3) based on the boundary conditions (4)-(7). Then the equations are discretized using central difference while the backward and forward difference schemes are used to solve the boundary conditions.

Next, the vorticity equation at the bottom wall is given by:

$$\Omega = -\frac{(8\Psi_{1,j} - \Psi_{2,j})}{2(\Delta Y)^2} \tag{12}$$

and similar equation is applied to the other walls except at the free-surface. The Gaussian self-over relaxation (GSOR) iteration is applied where the unknowns Ψ, Ω and Θ are evaluated as follows:

$$\frac{\sum_{i,j}\left|\varsigma_{i,j}^{k+1} - \varsigma_{i,j}^{k}\right|}{\sum_{i,j}\left|\varsigma_{i,j}^{k+1}\right|} \leq 10^{-5} \tag{13}$$

where ς is either Ψ, Ω or Θ and k is the iteration number. Finally, the simulation is run by MATLAB for 100x100 grid distribution.

3. Results

In this study, the effect of Marangoni, Ma towards the contours of fluid flow, temperature, heat flow and entropy generation (thermal, friction and total entropy) is observed and analysed. The value of parameters considered are Pr=0.015 and Gr=10^4 whereby 0<Ma<200.

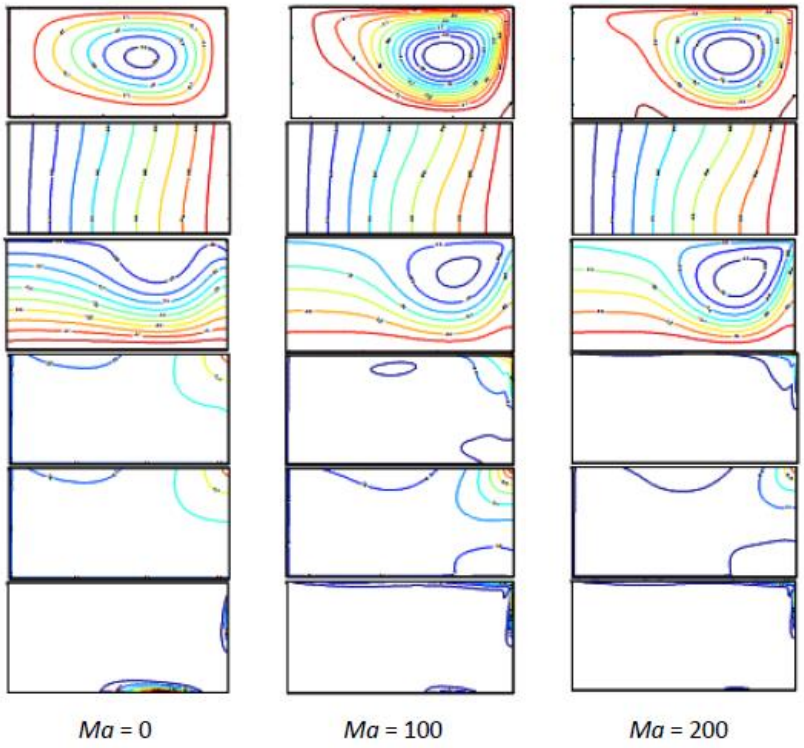


Fig. 2. From top to bottom: Streamlines, isotherms, heatlines, total entropy, heat entropy, friction entropy

The changes of contours of streamlines, isotherms, heatlines and entropy generation (total, thermal and friction) are depicted in Figure 2 as Marangoni number varies. A big circular-like anti-clockwise flow is dominating the convection without the effect of surface tension, (Ma = 0). Taking the Marangoni number higher, the shear stress at the free-surface start to increase and this made the streamlines are more focused at the upper-right region of the cavity. It is clearly observed that at Ma = 200, the fluid flow is more active at the free-surface which relates that stronger cohesion force binds the fluid molecules. The temperature contours become more skewed at the bottom region as Ma increase. This relates to the fact that hot molecules start to rise due to the surface tension effect. The distribution of heat can be visualized by the contours of heatline. At first, the heat is uniformly distributed at both walls where a circular vortex emerges when Ma ? 100, and suppress the heat path downward. The existence of this vortex is mainly cause by conduction of heat is greater at the free-surface.

The contours of total entropy generation, Stot, and entropy generation due to thermal, S_{th}, looks similar while the entropy generation due to friction, S_{fric}, occurs more to the right region and the vicinity of the left and bottom wall of the cavity when Ma = 0. As Marangoni number increased, the contours start to change where the entropies are more focusing at the free-surface, as happens like the heatline contours. This behaviour shows that the heat path has good relation with the entropies generation throughout the cavity. The isocontours of Stot tends to behave like S_{fric} while Sth displays similar patterns as Ma > 0. This behaviour indicates the thermocapillary effect makes the fluid molecules to have the capability to restrain energy and drive them to the upper free-surface.

Figure 3 illustrates the effect of various Ma towards Nusselt number, Bejan number, total entropy generation together with entropy generation due to thermal and friction. It is clearly seen that all dimensionless value exhibits an increasing pattern except for Bejan number. The Nusselt number which represents the heat transfer efficiency shows a little increment that is relates to the fact that the heat transfer rates are quite stable throughout the cavity. This behaviour is parallel to the visualization contours of heatlines where the distribution of heat is still uniform for high Ma as shown in Figure 2. The entropy generation due to thermal and total entropy generation also have similar values as Nusselt number while the friction entropy has lower values which indicates the fluid particles itself has less friction behaviour (Ma = 0).

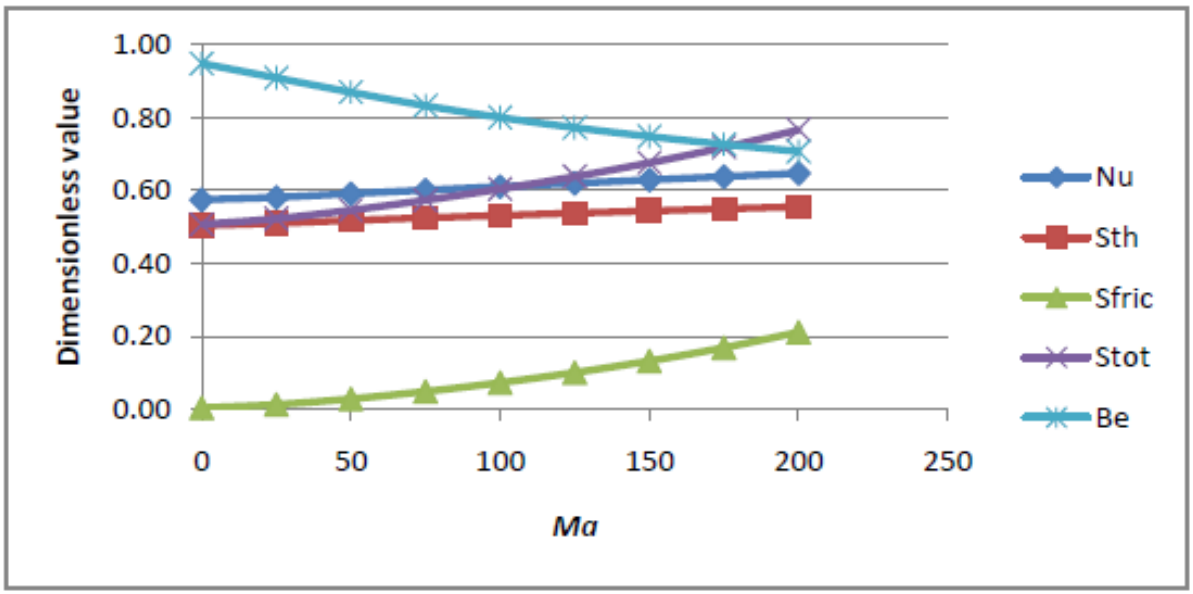


Fig. 3. Marangoni number vs dimensionless value

The Bejan number act as an indicator of irreversibilities domination for the convection. It shows here that Be > 0.5 which the convection is dominated by thermal entropy but as Ma increased the value of Bejan number is decreasing. This is an interesting finding because the Marangoni effect may change the irreversibility of the convection from thermal to friction. It is probably because the increment of cohesion force among the molecules due to shear stress will increase the friction effect.

4. Conclusion

This study involved the entropy generation in natural convection revealed the following:

1. The Marangoni effect has significant impact on every parameter considered.
2. The Bejan number and friction entropy have good correlation regarding the irreversibility domination as Marangoni number increased.
3. The heatline simulation helps to establish better understanding of entropy generation due to the relation to entropies distribution.

Acknowledgement

This research was funded by a grant from Universiti Teknologi MARA Johor Branch, Malaysia (GBEST/1/2019).

References

[1] Pesso, T. and Piva, S. “Laminar natural convection in a square cavity: low Prandtl numbers and large density differences.” *Int. J. Heat Mass Transfer* 52, (2009): 1036-1043.
[2] Barakos, G., Mitsoulis, E. and Assimacopoulos, D. “Natural convection flow in a square cavity revisited: laminar and turbulent models with wall functions.” *Int. J. Numerical Methods Fluids* 18, (2005): 695-719.
[3] Bilgen, E. and Oztop, H. “Natural convection heat transfer in partially open inclined square cavities.” *Int. J. Heat Mass Transfer* 48, (2005): 1470-1479.
[4] Costa, V. A. F. “Thermodynamics of natural convection in enclosures with viscous dissipation.” *Int. J. Heat Mass Transfer* 48, (2005): 2333-2341.
[5] Kuznik, F., Vareilles, J., Rusaouen, G. and Krauss, G. “A double-population lattice Boltzman method with non-uniform mesh for the simulation of natural convection in a square cavity.” *Int. J. Heat Fluid Flow* 28, (2007): 862-870.
[6] Nithyadevi, N., Kandaswamy, N. P. and Lee, J. “Natural convection in a rectangular cavity with partially active side walls.” *Int. J. Heat Mass Transfer* 50, (2007): 4688-4697.
[7] Mezrhab, A., Jami, M., Abid, C., Bouzidi, M. and Lallemand, P. “Lattice-Boltzman modelling of natural convection in an inclined square enclosure with partitions attached to its cold wall.” *Int. J. Heat Fluid Flow* 27, (2006): 456-465.
[8] Fontana, E., Capeletto, C. A., Silva, A. and Mariani, V. C. “Three-dimensional analysis of natural convection in a partially-open cavity with internal heat source.” *Int. J. Heat Mass Transfer* 61, (2013): 525-542.
[9] Tang, Z. M., Li, K. and Hu, W. R. “Influence of free surface curvature of a liquid layer on the critical Marangoni convection.” *Int. J. Heat Mass Transfer* 51, (2008): 5102-5107.
[10] Alexander, A., Tatiana, G. R. and Perter, S. “Marangoni convection and heat transfer in thin liquid films on heated walls with topography: experiments and numerical study.” *Physics of Fluids* 17, (2005): 0621061-06210613.
[11] Roisman, T. G. “Modulation of Marangoni convection in liquid film.” Advances in Colloid and Interface Science 222, (2015): 319-331.
[12] Duan, L., Kang, Q. and Hu, W. R. “Experimental study on liquid free surface in buoyant-thermocapillary convection.” *China Physics Letters* 25, (2008): 1347-1350.
[13] Li, Y.R., Jia, L., Zhang, L., Hu, Y.P. and Yu, J.J. “Direct numerical simulation of Rayleigh-Bénard-Marangoni convection of cold water near its density maximum in a cylindrical pool.” *Int. J. Thermal Sciences* 124, (2018): 327- 337.

[14] Li, C., Zhao, D., Wen, J. and Lu, X. "Numerical investigation of wafer drying induced by the thermal Marangoni effect." *Int. J. Heat Mass Transfer* 132, (2019): 689-698.
[15] Kimura, S. and Bejan, A. "The heatline visualization of convective heat transfer." *J. Heat Transfer* 105, (1983): 916- 919.
[16] Costa, V. A. F. "Unified streamline, heatline and massline methods for the visualization of two-dimensional heat and mass transfer in anisotropic media." *Int. J. Heat Mass Transfer* 46, (2003): 1309-1320.
[17] Basak, T., Aravind, G. and Roy, S. "Visualization of heat flow due to natural convection within triangular cavities using Bejan's heatline concept." *Int. J. Heat Mass Transfer* 52, (2009): 2824-2833.
[18] Varol, Y., Oztop, H. F., Mobedi, M. and Pop, I. "Visualization of heat flow using Bejan's heatline due to natural convection of water near 4^0C in thick walled porous cavity." *Int. J. Heat Mass Transfer* 53, (2010): 1691-1698.
[19] Saleh, H., Arbin, N. and Hashim, I. "Visualization and analysis of surface tension and cooling effects on differentially heated cavity using heatline concept." *Int. J. Heat Mass Transfer* 55, (2012):6000-6009.
[20] Morsli, S., Sabeur and Ganaoui, M.E. "Influence of aspect ratio on the natural convection and entropy generation in rectangular cavities with wavy-wall." *Energy Procedia* 139, (2017): 29-36.
[21] Al-Rashed, A.A.A.A, Kolsi, L., Hussein, A.K., Hassen, W., Aichouni, M. and Borjini, M.N. "Numerical study of dimensional natural convection and entropy generation in a cubical cavity with partially active vertical walls." *Case Studies Thermal Eng.* 10, (2017): 100-110.
[22] Das, D., Lukose, L. and Basak, T. "Role of multiple discrete heaters to minimize entropy generation during natural convection in fluid filled square and triangular enclosures." *Int. J. Heat Mass Transfer* 127, (2018): 1290-1312.
[23] Kolsi, L., Lajnef, E., Aich, W., Alghamdi, A., Aichouni, M.A., Borjini, M.N. and Aissia, H.B. "Numerical investigation of combined buoyancy-thermocapillary convection and entropy generation in 3D cavity filled with Al_2O_3 nanofluid." *Alexandria Eng. J.* 56, (2017): 71-79.
[24] Oztop, H., Kolsi, L., Alghamdi, A., Abu-Hamdeh, N., Borjini, M.N. and Aissia, H.B. "Numerical analysis of entropy generation due to natural convection in three-dimensional partially open enclosures." *J. Taiwan Ins. Checmical Eng.* 75, (2017): 131-140.

Penerbit Akademia Baru

Engineering Science and Technology Conference Proceedings

Journal homepage: www.akademiabaru.com/EST.html

Flow and Heat Transfer Characteristics of Impinging Bubbly Jet

Open Access

C. Aroonrujipjan[1], C. Nuntadusit[1,*]

[1] Department of Mechanical Engineering, Faculty of Mechanical Engineering, Prince of Songkla University, Hatyai, Songkla 90110, Thailand

ABSTRACT

This article presents the effect of air bubble on heat transfer enhancement for jet impingement. In this study, the Reynolds number of waters was fixed at 2.4×10^4 and the volumetric fraction was varied from 0.0 to 0.7. For heat transfer measurement, the bubbly jet impinged on the surface with constant heat flux. The temperature on the impingement surface was measured with an infrared camera. The flow behaviour was also recorded with a high-speed camera. The result shows that the bubbly jet at the condition the distance between nozzle and impingement surface at L=2D and the volumetric fraction at =0.2 give the highest of Nusselt number at 1.4 times of pure water jet at=0.0.

Keywords:
Water impinging jet, air bubble, heat transfer enhancement

Copyright © 2019 PENERBIT AKADEMIA BARU - All rights reserved

1. Introduction

In the present, the thermal management of equipment is important, whether it be gas turbine engine, electronic devices, and metal industrial, etc. These are operated at high temperature, which lead to destroyed. For example, the turbine blade in gas turbine engine and electronic component are over operated temperature range [1-6], and inappropriate temperature control of metal in manufacturing process lead to failure [7-9]. It has to cooling system and appropriate temperature control for long life and reduce to expense of service.

Jet impingement system is widely used in cooling about equipment that operate high temperature because it has high cooling rate in impingement region and rapid cooling system. Jet impingement are commonly divided into 3 regions (i) the free jet region, (ii) the stagnation region and (iii) the wall jet region, as illustrate in Figure 1. At the present, the study parameters effect of heat transfer characteristics of jet impingement is many investigated for improving performance cooling. The parameters are considered include heat transfer process, such as nozzle spacing plate (L), diameter of jet (D), Reynolds number (Re), and type of jet fluid, etc. Lv *et al.,* [11] studied heat transfer of jet impingement that the effect on nozzle spacing plate to jet diameter (L/D) from 2 to 5 and Reynolds number from 8000 to 13,000. The result showed that the maximum heat transfer coefficient at L/D=4 by different nozzle spacing plate. Nakharintr *et al.,* [12] studied different diameter of jet on heat transfer of jet impingement. They showed that the average Nusselt number decrease as the jet diameter decreases because small jet diameter had an effect on small

* *Corresponding author.*
E-mail address: chayut.n@psu.ac.th (C.Nuntadusit)

stagnation point, which is important point at high cooling rate on impingement plate. The different of jet fluid have result in different conductivity of fluid, so the researchers investigate heat transfer enhancement of two-phase fluid that use nanofluids for increasing conductivity value of fluid [13-17]. But, the problem of nanofluid for jet impingement occur deposit on impingement plate, which lead to decrease heat transfer rate [15].

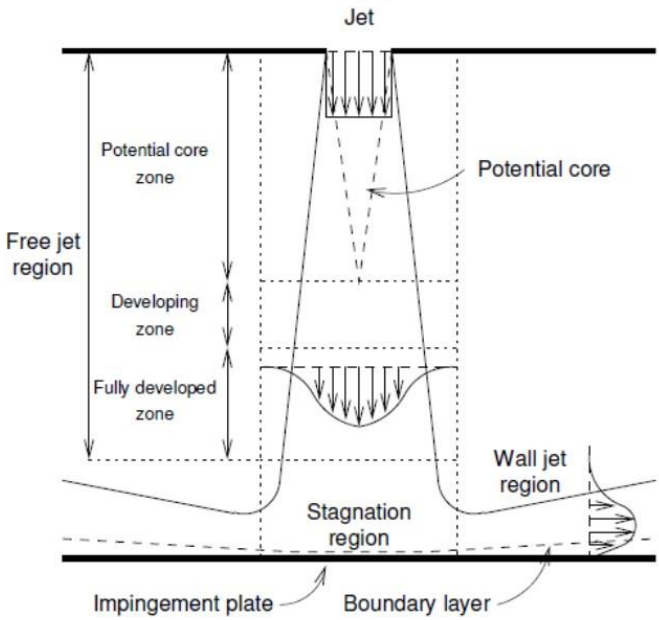


Fig. 1. Flow structure of jet impingement region [10]

The bubble jet impingement is investigated for application to the heat transfer enhancement because the jet flow is disturbed by the bubbles that lead to increase turbulence intensity on impinging jet. Choo and Kim [18] experimentally studied the heat transfer and flow characteristics of two-phase free surface jet impingement for fixed pumping power condition from $1.4x10^{11}$ to $2.8x10^{12}$ and volumetric fraction from $0 \leq \beta \leq 0.9$. The results showed that the maximum value of Nusselt number was found volumetric fraction at around $0.2 \leq \beta \leq 0.3$ that the flow in pipe showed bubbly flow region. Trainer *et al.*, [19] studied the heat transfer characteristic of air assistant water free surface jet impingement for Reynolds number of waters between $7500 \leq Re_L \leq 15000$ and Reynolds number of airs between $0 \leq Re_G \leq 5900$. The results showed that the local Nusselt number at stagnation point increased 2.6 times the liquid only. Friedrich *et al.*, [20] studied the effect of volumetric fraction increment for heat transfer characteristics of air assistant water jet impingement. The results showed that volumetric fraction between $0.1 \leq \beta \leq 0.8$ affected the increased stagnation Nusselt number. But the stagnation Nusselt number is rapidly decreased at around $0.8 \leq \beta \leq 0.9$ due to the jet flow is largely covered the quantity of air.

The purpose on this paper of study is determine flow and heat transfer characteristics of bubbly jet impingement under fixed Reynolds number of water (Re_L) at 2.4×10^4 and volumetric fraction is varied from $0.0 \leq \beta \leq 0.7$ that the distance between nozzle and impingement surface at L=2D. The effect of increase for volumetric fraction on the enhanced heat transfer and flow characteristics are shown that local Nusselt number on impinging jet surface from infrared camera and image from high-speed camera, respectively.

2. Methodology

2.1 The Model and Parameters of Experiment

This experiment for impinging jet system was selected a submerged jet impingement in Figure 2. the heat transfer of submerged impinging jet was investigated by many researchers. Kneer *et al.* [21] studied the heat transfer for submerged and free surface impinging jets, in resulting the heat transfer coefficient for submerged jet had higher than a free surface jet. Therefore, it was studied on this experiment in order to improve an air assisted water jet impingement system.

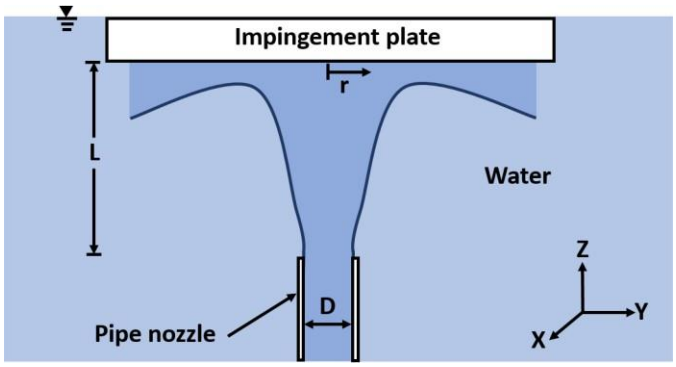


Fig. 2. Impinging jet model for experiment

The test section for experiment was a submerged jet impingement that was shown in Figure 3. the impingement plate was a stainless-steel plate (100 mm in width, 100 mm in length and 0.03 mm in thickness) that was contacted the jet flow.

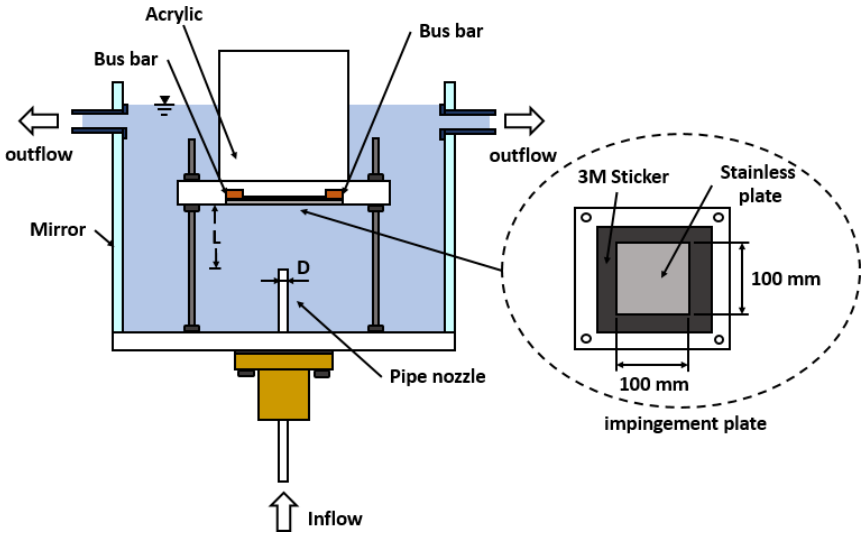


Fig. 3. Test section

The experiment is shown that the parameters in Table 1. The temperature of water flow rate was controlled around 28 ± 0.1 ℃, before it was mixed with the air flow rate. The room temperature was also controlled around 25 ± 0.5 ℃. The temperature of air flow rate was not controlled because the properties of air were kinematic viscosity and specific heat capacity, these were not concerned heat transfer coefficient for two phase impinging jet [19].

Table 1
The parameters for this experiment

Parameters and symbol	Values
Reynolds number of waters, ReL	2.4×10^4
Volumetric fraction, β	$0.0 \leq \beta \geq 0.7$
Diameter of jet, D	9.5 mm
Nozzle to impingement plate distance, L	2D

The Reynolds number of waters was fixed at 2.4×10^4 that corresponding to 9 LPM for water flow rate measurement, calculated from Eq. (1) and summarize in Table 1.

$$Re = \frac{\rho LVD}{\mu L} \tag{1}$$

Where the dynamic viscosity of water, μL, density of water, ρL, before mixing between water and air at 28 ℃, Velocity of pure water, V, Diameter of jet, D.

The volumetric fraction was varied from 0.0 to 0.7 by increments of 0.1. This parameter was important for two phase flow that showed that the ratio of quantity of air to total quantity, calculated from Eq. (2) and summarize in Table 2.

$$\beta = \frac{QG}{QL + QG} \tag{2}$$

Where the water flow rate, Q_L was taken as 9 LPM and the air flow rate, Q_G were taken as 0 to 21 LPM.

Table 2
The volumetric fraction values

β	Q_L (LPM)	Q_G (LPM)
0.0	9	0
0.1	9	1
0.2	9	2.25
0.3	9	3.86
0.4	9	6
0.5	9	9
0.6	9	13.5
0.7	9	21

The experiment of heat transfer for impinging jet used the infrared thermal imaging camera that captured the photos on painting flat black colour stainless surface, which was heated under constant heat flux. After, the photos were calculated through MATLAB® R2013a programming process. The equation was used in program process in order to get result of heat transfer variables for comparison of each case.

The constant heat flux on stainless surface, $\dot{q}input$, the loss of radiation to surrounding on stainless surface, $\dot{q}rad$, the loss of natural convection to surrounding on stainless surface, $\dot{q}conv$, and the net heat flux, $\dot{q}net$, The heat transfer coefficient, h, these were shown in Eq. (3) to Eq. (7).

$$q_{input} = \frac{IV}{A} \tag{3}$$

$$\dot{q}_{rad} = \sigma\varepsilon(\overline{T}_{heat} - \overline{T}_{sur}) \tag{4}$$

$$\dot{q}_{conv} = h_c(\overline{T}_{heat} - \overline{T}_{sur}) \tag{5}$$

$$\dot{q}_{net} = \dot{q}_{input} - \dot{q}_{rad} - \dot{q}_{conv} \tag{6}$$

$$h = \frac{\dot{q}_{net}}{(T_{heat} - T_{no\ heat})} \tag{7}$$

Where I, V and A were direct current, direct voltage of electric power and area of stainless surface, from Eq. (3). σ was the Stefan-Boltzmann constant, ε was the emissivity of flat black surface, these were taken as 5.67 $\times 10^{-8}$ W/m^{2}K^2 and 0.95, respectively, T_{heat} was the surface temperature with heat flux when was cooled by jet impingement, T_{surr} was the room temperature for experiment, $T_{no\ heat}$ was the surface temperature without heat flux Eqs. (4), (5) and (7). h was the natural heat transfer coefficient that was arranged a horizontal plate by upper surface of a hot plate.

Finally, the Nusselt number was calculated from Eq. (8).

$$Nu = \frac{hD}{k} \tag{8}$$

Where h was a heat transfer coefficient from Eq. (7), D was the diameter of exit jet, and k was the conductivity of water jet.

2.2 Experimental Setup

Experiment apparatus is shown in Figure 2. The water was pumped from reservoir tank by centrifugal pump. And then the water flowed through heater tank for control the constant working fluid temperature. In the meantime, the air was pumped by air compressor for mixing between water (for case, volumetric fraction from $0.1 \leq \beta \leq 0.7$). Both of working fluids was controlled mass flow rate by flow rotameter. The two-phase mixer was venturi pipe for mixing liquid phase and gas phase that cause two-phase flow. The temperature of air flow and water flow were measured by thermocouple type PT-100 before mixing at venturi pipe, and it still was measured in environment of test section that was monitored through data logger.

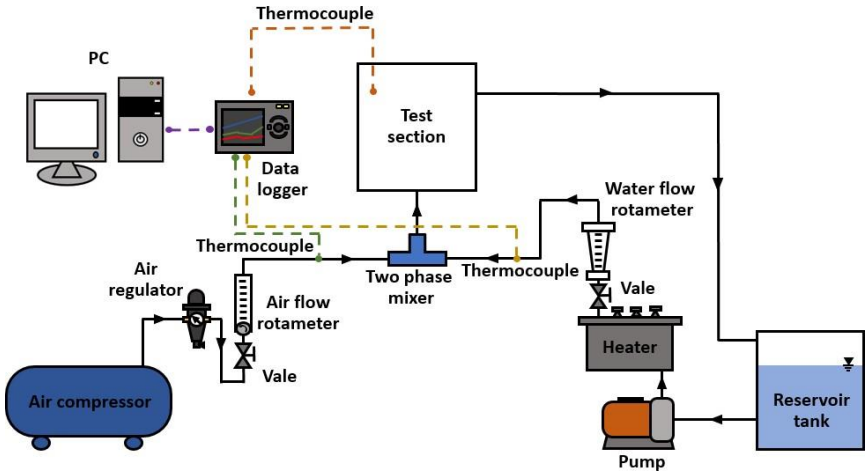


Fig. 4. Schematic diagram of experiment apparatus

2.3 The Flow Visualization

The experimental setup for study of flow visualization are shown that in Figure (5). The high-speed camera took a photograph on impinging jet at nozzle to impingement plate distances was 2 times of diameter jet (L = 2D) and flow in pipe nozzle for volumetric fraction from 0.1 to 0.7, the Reynolds of water was fixed 2.4×10^4. The test section was filled water through a pipe nozzle for using experimental jet impingement system. The pipe nozzle of diameter was used 9.5 mm for a diameter of jet and 1000 mm for a length tube that was selected in order to ensured fully developed flow at nozzle exit.

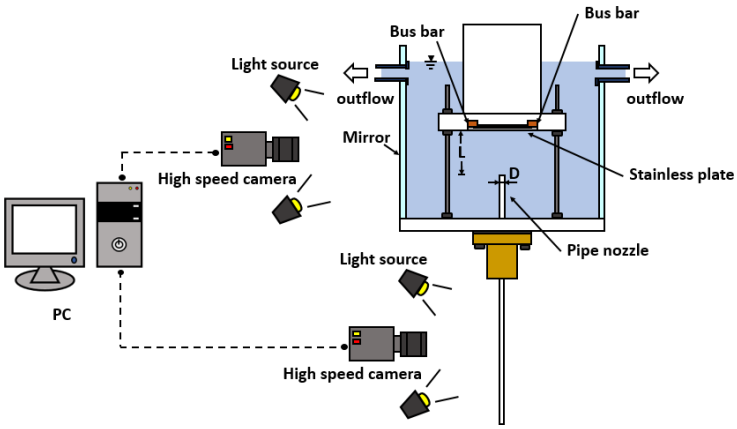


Fig. 5. Experimental setup for flow visualization

2.4 The Heat Transfer Measurement

The experimental setup for study of heat transfer measurement are shown in Figure 6. The infrared thermal imaging camera was used for taking a picture on the stainless surface that was painted with flat black colour by the emissivity value was estimated around 0.95. the stainless surface was stretched between copper bus bar both sides that was heated by DC power, but it must be considered for the loss of electric resistance in wires. The digital multimeter measured between a both sides of copper bus bar for getting the voltage drop and current drop values. The stainless surface was heated by DC supply power, when cooled a jet flow for volumetric fraction from 0.0 to

0.7, the nozzle to impingement plate distances was 2D and Reynolds number was also fixed 2.4×10^4 in order to compare the heat transfer in each case.

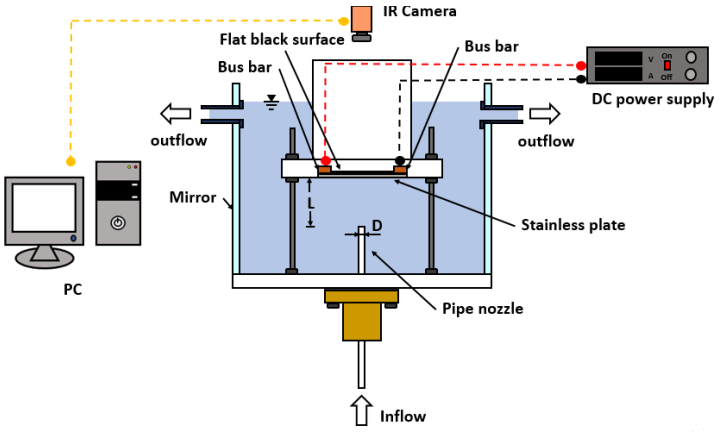


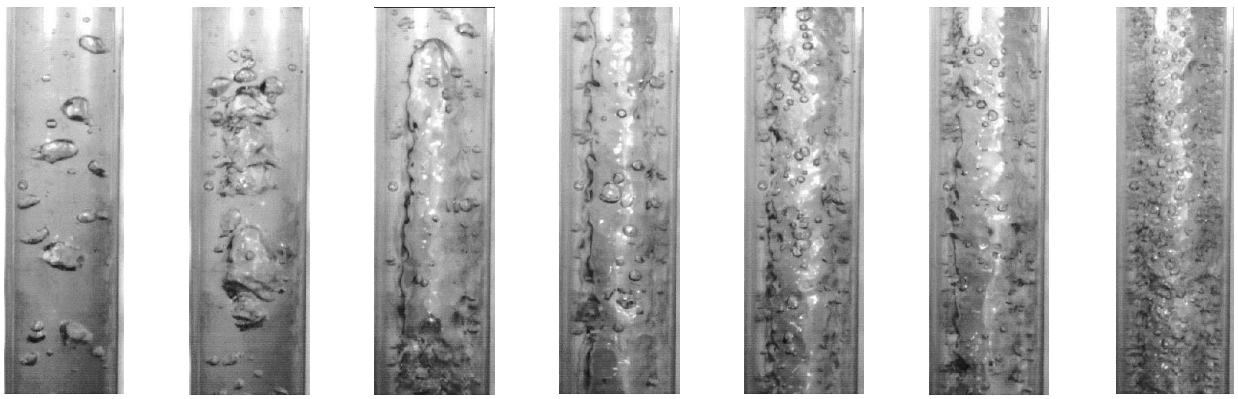
Fig. 6. Experimental setup for study of heat transfer measurement

3. Results

3.1 The flow visualization for in pipe nozzle and impinging jet

The experiment studied the two-phase flow visualization that were explained to bubbles behaviour at flow in pipe and nozzle exit to impingement region. The high-speed camera was used to capture the photos for back up observation at 6400 fps, it had to test in a dark room for using took a photo and the light sources (LED) by working together.

The results of flow patterns in pipe were divided into 3 regions, as illustrate in Figure 7, (i) β = 0.1, it was bubbly flow region that founded over distribution of small bubbles size in flow pipe, (ii) $0.2 \leq \beta \leq 0.3$, it was slug flow region that explained combination of bubbles for a bubbly flow region, the bubbles in this case was similar to the bullet shape, and (iii) $0.4 \leq \beta \leq 0.7$, it was annular flow region that explained the combination of the slug bubbles, resulting in bubbly continuous flow, the flow in pipe on this case was around covered by liquid phase and the most centerline of pipe was covered by gas phase.

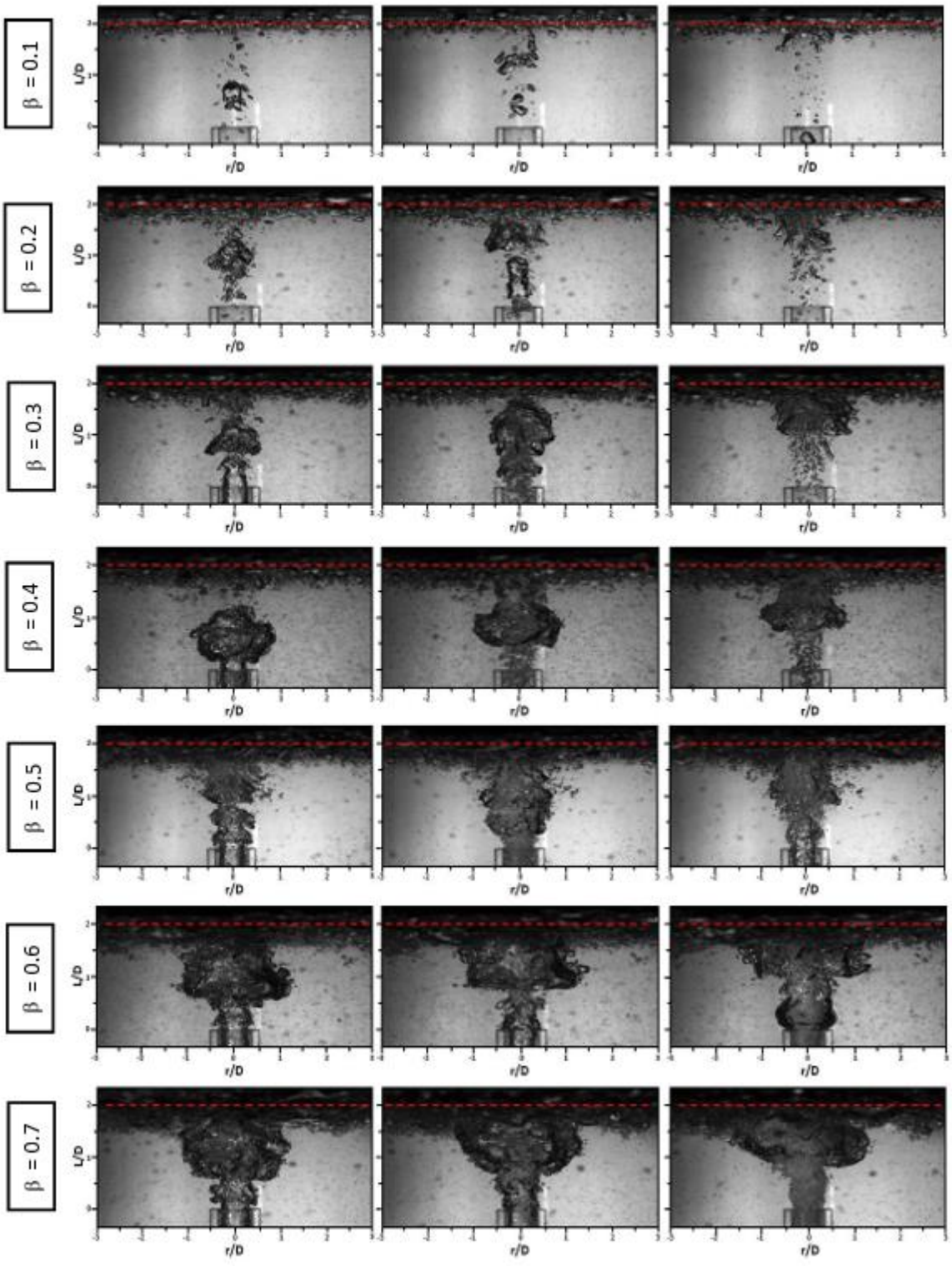


β = 0.1 β = 0.2 β = 0.3 β = 0.4 β = 0.5 β = 0.6 β = 0.7

Fig. 7. Flow visualization for in pipe nozzle

The results of flow patterns of impinging jet at 0 to 150 ms were divided into 4 patterns, as illustrate in Figure 8, (i) β = 0.1, the bubble of exit nozzle to impinge region was similar to bubble shape in pipe flow that was almost flat shape when it impinged to surface, (ii) β = 0.2 and 0.3, the

bubble of exit nozzle was similar to a bullet shape, and then it was sheared with the surrounding of fluid that was lead to a mushroom shape but the movement for each of bubbles did not impinged for this case, (iii) β = 0.4 and 0.5, the first, when the bubble moved from an exit nozzle, it occurred agglomerate of bubble that located between an exit nozzle and impinge plate, and then the bubbles that followed the agglomerate bubble in the first impinged, it occurred the large bubble that impinged a surface plate, and (iv) β = 0.6 and 0.7, this flow pattern was continuous bubble from the exit nozzle to impingement surface, in resulting the impinging surface was mostly covered by gas phase.



$t = 0$ ms $t = 75$ ms $t = 150$ ms

Fig. 8. Flow visualization of impinging jet for L=2D and Re_L=24,000

3.2 The Heat Transfer on Impinging Jet

The conditions for heat transfer measurement varied a volumetric fraction from 0.0 to 0.7 under fixed the nozzle to impingement plate distances, L = 2D and Reynolds number of waters, Re_L = 2.4×10^4. The contour of Nusselt number was shown in Figure 9 for all case. At β = 0.0 (pure water) gave the minimum Nusselt number distribution when compared each of case, and it founded the maximum heat transfer in $-1 \leq X/D \leq 1$ and $-1 \leq Y/D \leq 1$ that evaluated a diameter of jet, it still continuously decreased along X/D-axis and Y/D-axis distances from center point. For mixing water air assistance of impinging jets, it contributed to increase the Nusselt number distribution of radial on surface, when compared to pure water jet.

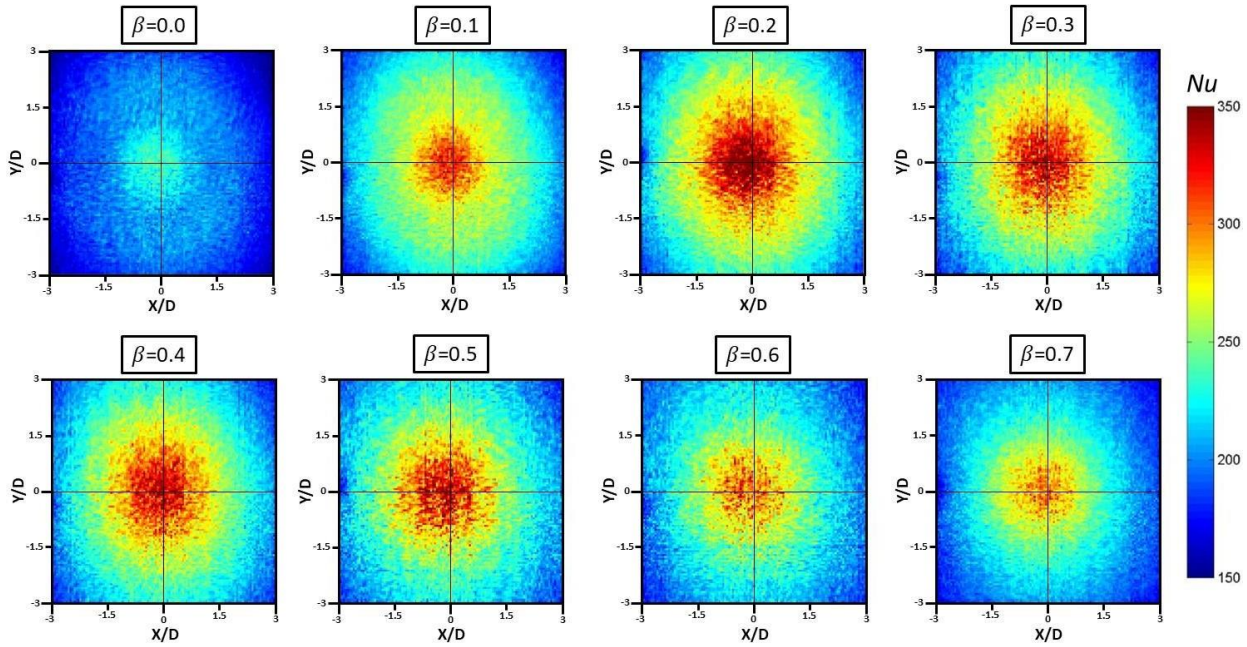


Fig. 9. Drag coefficient (C_D) results for Glider, Stunt Plane and Wide Stunt Glider paper plane

The Local Nusselt number for along X-axis passing centerline of middle jet was shown in Figure 10. For jet impingement of two-phase flow, it founded a many peak on the local Nusselt number because the bubble impacted on impinging plate, it will be dispersed around the radial direction on surface plate that had annular bubble shape. This phenomenon was led to all over turbulent flow on surface, therefore, it increased the local Nusselt number for mixing water air assistance jet case when compared to pure water jet case.

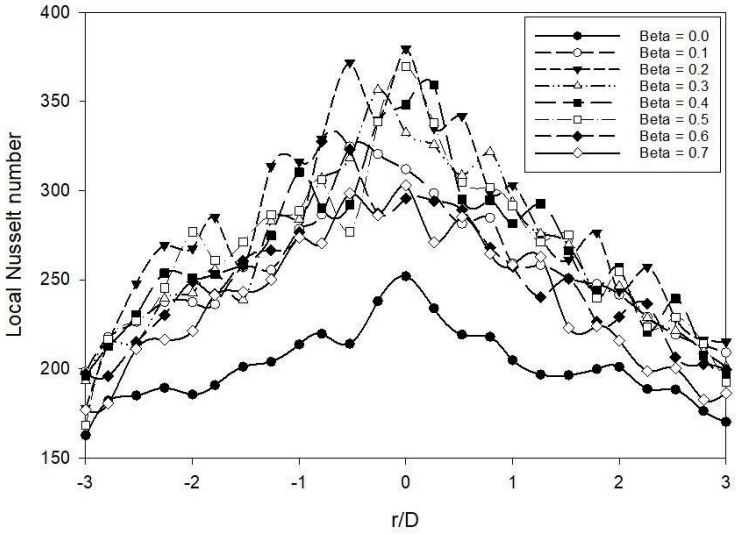


Fig.10. The Local Nusselt number distribution along X-axis passing centerline of middle jet

Table 3
The Nusselt number ratio between bubbly jet and water jet

β	Nu/Nu_0
0.1	1.273
0.2	1.400
0.3	1.331
0.4	1.327
0.5	1.324
0.6	1.234
0.7	1.188

The local Nusselt number for pure water jet (Nu_0) and the local Nusselt number for bubbly jet (Nu) were compared to the Nusselt number ratio that is shown in Table 2. At β = 0.2, it had a maximum Nusselt number ratio because the bubbles contributed to disturb on jet flow and impinging surface. For the Nusselt number ratio of volumetric fraction from 0.3 to 0.7 were continuously decreased cause impinging region was covered by gas phase that decrease heat transfer enhancement, but it had the Nusselt number ratio values more than pure water jet case.

4. Conclusions

In the present, this experiment for the heat transfer enhancement and flow visualization of bubbly jet impingement were investigated under fixed Reynolds number of water ($Re_L = 2.4\times10^4$) and nozzle to impingement plate distance (L = 2D), the volumetric fraction was varied from 0.0 to 0.7. Therefore, this paper was summarized main issue on experimentally investigation

i. Flow visualization for in pipe nozzle was divided into 3 regions, (i) bubble flow region, for β = 0.1, (ii) slug flow region, for β = 0.2 and 0.3, and (iii) annular flow region, for β = 0.4 to 0.7. And then flow visualization for impinging jet that was the exit nozzle to impinging plate was divided into 4 patterns (i) the bubble was flat shape, for β = 0.1, (ii) the bubble was bullet shape at near exit nozzle, after that was similar to mushroom shape at impinge region , for β = 0.2 to 0.3, (iii) the bubble was a long broken bullet, cause the each of slug flow was crashed, and then it impact on the impinge region, for β = 0.4 to 0.5, (vi) at the exit nozzle to impinging plate had continuous bubble, for β = 0.6 to 0.7.
ii. Heat transfer measurement on jet impingement was divided into 2 parts, (i) at β = 0.1 to 0.2,

it founded the Nusselt number ratio (Nu/Nu_0) increased because this region had the small bubble that contributed to turbulent on impingement plate, and (ii) at β = 0.2 to 0.7, it founded the Nusselt number ratio continuously decreased because the increase in volumetric fraction effected on most gas phase for jet flow, the impinge region was covered by the gas phase that decreased the heat transfer.

Acknowledgement
This research was funded by a grant from Department of Mechanical Engineering, Faculty of Engineering, Prince of Songkla University, Thailand.

References

[1] Zhang, H. Y., D. Pinjala, and Poi-Siong Teo. "Thermal management of high power dissipation electronic packages: From air cooling to liquid cooling." In *Proceedings of the 5th Electronics Packaging Technology Conference (EPTC 2003)*, pp. 620-625. IEEE, 2003.

[2] Saini, Manish, and Ralph L. Webb. "Validation of models for air cooled plane fin heat sinks used in computer cooling." In *ITherm 2002. Eighth Intersociety Conference on Thermal and Thermomechanical Phenomena in Electronic Systems (Cat. No. 02CH37258)*, pp. 243-250. IEEE, 2002.

[3] Cai, Yang, Yu Wang, Di Liu, and Fu-Yun Zhao. "Thermoelectric cooling technology applied in the field of electronic devices: Updated review on the parametric investigations and model developments." *Applied Thermal Engineering* 148 (2019): 238-255.

[4] Frąckowiak, Andrzej, Michał Ciałkowski, and Agnieszka Wroblewska. "Application of iterative algorithms for gas-turbine blades cooling optimization." *International Journal of Thermal Sciences* 118 (2017): 198-206.

[5] Frąckowiak, A., J. V. Wolfersdorf, and M. Ciałkowski. "Optimization of cooling of gas turbine blades with channels filled with porous material." *International Journal of Thermal Sciences* 136 (2019): 370-378.

[6] Moskalenko, A. B., and A. I. Kozhevnikov. "Estimation of gas turbine blades cooling efficiency." *Procedia Engineering* 150 (2016): 61-67.

[7] Cebo-Rudnicka, Agnieszka, and Zbigniew Malinowski. "Identification of heat flux and heat transfer coefficient during water spray cooling of horizontal copper plate." *International Journal of Thermal Sciences* 145 (2019): 106038.

[8] Waldeck, Steffen, Hermann Woche, Eckehard Specht, and Udo Fritsching. "Evaluation of heat transfer in quenching processes with impinging liquid jets." *International Journal of Thermal Sciences* 134 (2018): 160-167.

[9] Puschmann, Frank, and Eckehard Specht. "Transient measurement of heat transfer in metal quenching with atomized sprays." *Experimental Thermal and Fluid Science* 28, no. 6 (2004): 607-615.

[10] Réti, Ferenc. "Liquid Cooling of Electronic Devices by Single-phase Convection (Wiley—Interscience Publication, 1999, New York—Chichester—Weinheim—Brisbane—Singapore—Toronto) Frank P. Incropera." *Journal of Thermal Analysis and Calorimetry* 58, no. 3 (1999): 749-749.

[11] Lv, Jizu, Chengzhi Hu, Minli Bai, Ke Zeng, Shengnan Chang, and Dongdong Gao. "Experimental investigation of free single jet impingement using SiO2-water nanofluid." *Experimental Thermal and Fluid Science* 84 (2017): 39-46.

[12] Nakharintr, Lursukd, Paisarn Naphon, and Songkran Wiriyasart. "Effect of jet-plate spacing to jet diameter ratios on nanofluids heat transfer in a mini-channel heat sink." *International Journal of Heat and Mass Transfer* 116 (2018): 352-361.

[13] Naphon, Paisarn, and Somchai Wongwises. "Experimental study of jet nanofluids impingement system for cooling computer procfigureessing unit." *Journal of Electronics Cooling and Thermal Control* 1, no. 03 (2011): 38-44.

[14] Naphon, P., L. Nakharintr, and S. Wiriyasart. "Continuous nanofluids jet impingement heat transfer and flow in a micro-channel heat sink." *International Journal of Heat and Mass Transfer* 126 (2018): 924-932.

[15] Barewar, Surendra D., Shravan Tawri, and Sandesh S. Chougule. "Heat transfer characteristics of free nanofluid impinging jet on flat surface with different jet to plate distance: An experimental investigation." *Chemical Engineering and Processing-Process Intensification* 136 (2019): 1-10.

[16] Sun, Bin, Yi Qu, and Di Yang. "Heat transfer of single impinging jet with Cu nanofluids." *Applied Thermal Engineering* 102 (2016): 701-707.

[17] Lv, Jizu, Shengnan Chang, Chengzhi Hu, Minli Bai, Peng Wang, and Ke Zeng. "Experimental investigation of free single jet impingement using Al2O3-water nanofluid." *International Communications in Heat and Mass Transfer* 88 (2017): 126-135.

[18] Choo, Kyosung, and Sung Jin Kim. "Heat transfer and fluid flow characteristics of two-phase impinging

jets." *International Journal of Heat and Mass Transfer* 53, no. 25-26 (2010): 5692-5699.
[19] Trainer, Daniel, Jungho Kim, and Sung Jin Kim. "Heat transfer and flow characteristics of air-assisted impinging water jets." *International Journal of Heat and Mass Transfer* 64 (2013): 501-513.
[20] Friedrich, Brian K., Tamira D. Ford, Aspen W. Glaspell, and Kyosung Choo. "Experimental study of the hydrodynamic and heat transfer of air-assistant circular water jet impinging a flat circular disk." *International Journal of Heat and Mass Transfer* 106 (2017): 804-809.
[21] Rohlfs, Wilko, Johannes Jorg, Claas Ehrenpreis, Manuel Rietz, Herman Haustein, and Reinhold Kneer. "Flow Structures and Heat Transfer in Submerged Laminar Jet Impingement." In *ASTFE Digital Library*. Begel House Inc., 2015.

Penerbit Akademia Baru

Engineering Science and Technology Conference Proceedings

Journal homepage: www.akademiabaru.com/EST.html

CFD Investigation of The Effect of Heave Plate on Vertical Motion Responses of A Floating Jetty

Open Access

Ahmad Fitriadhy[1]*, Nur Amira Adam[2], Aqilah Mansor[2], Mohammad Fadhli Ahmad[1], Ahmad Jusoh[3], Noraieni Hj. Mokhtar[4] and Mohd Sofiyan Sulaiman[3]

[1] Programme of Maritime Technology, Faculty of Ocean Engineering Technology and Informatics, Universiti Malaysia Terengganu, Kuala Terengganu, Terengganu, Malaysia
[2] Postgraduate Student, Programme of Maritime Technology, Faculty of Ocean Engineering Technology and Informatics, Universiti Malaysia Terengganu, Kuala Terengganu, Malaysia
[3] Programme of Environmental Technology, Faculty of Ocean Engineering Technology and Informatics, Universiti Malaysia Terengganu, Kuala Terengganu, Terengganu, Malaysia
[4] Programme of Electronic and Instrumentation, Faculty of Ocean Engineering Technology and Informatics, Universiti Malaysia Terengganu, Kuala Terengganu, Terengganu, Malaysia

ABSTRACT

This paper aims to investigate effect of heave plate on vertical motion of a floating jetty. To achieve the objective, a Computational Fluid Dynamics (CFD) simulation approach has been conducted to analyse dynamic vertical motion responses (heave motion) of a floating jetty. Several effects of different drafts of the floating jetty have been taken into account at various wave periods (T) from 3 seconds up to 10 seconds. In addition, the heave motion of the floating jetty is then quantified through a Response of Amplitude Operators (RAO). Furthermore, the heave motion response of the floating jetty with and without heave plate structures has been comprehensively compared in the computational simulation. The CFD simulation results revealed that the floating jetty incorporated with the heave plate has generally reduced the heave motion of the floating jetty. Here, the RAO of her motion has sufficiently decreased by 20 percent as compared with the case without the heave plate ones particularly within the range of 3<T<10 seconds. Regardless of the wave periods, meanwhile, the subsequent increase of the floating jetty draft from 0.4 m to 0.8 m showed insignificant effect to decrease the RAO magnitude of her heave motion response. It was merely concluded that the attached structural heave plate on the floating jetty is deemed necessary to reduce her dynamic heave motion responses.

Keywords:
Floating jetty, heave plate, heave motion, draft, wave periods

Copyright © 2019 PENERBIT AKADEMIA BARU - All rights reserved

1. Introduction

Nowadays, the application of floating jetty has found more popular compared to fixed jetty. According to Niaounakis [1], the floating structure most commonly used due to the advantages offer, such as have a practical design with lightweight, durable, corrosion resistance and easy installations process. The floating jetty structure also was compatible with all types of seabed, not cause damage to marine environment and plants growing on the seabed. However, the interaction between the movement of fluid in wave and the floating jetty has a critical hydrodynamics responses due to effectiveness of wave energy absorption [2]. This condition may lead to a decrease in dock stability and occurred a serious accident during its operation.

In the recent studies, an additional heave plate attached at the bottom of free bodies to reduce the vertical motion responses caused by wave action have been successfully conducted by Holmes

et al., [3], Brown, A., J. Thomson, and C. Rusch [4] and Liang *et al.,* [5]. Tao and Cai [6], Koh and Cho [7], Panneer [8] and Yu, Hu [9] and Mecrow and Garvey [10] have studied the effect of the heave plate to the offshore structure. They found that the vertical response at offshore floating structure with heave plate will reduce significantly due to increase of added mass and damping coefficient of the structure. In additional, this structural heave plate also has been applied to a floating breakwater and floating offshore wind turbine. Ishihara, Waris [11], reported that the heave motion reduction was up to 50% at the extreme wave conditions; while increased the stability of the floating structure.

In the present study, a Computational Fluid Dynamics (CFD) investigation has been conducted to analyse the vertical motions performance of the floating jetty in waves. To achieve this research objective, several effect of various wave periods from 3 up to 10 seconds associated with different drafts of the floating jetty i.e., 0.4 m and 0.8 m, have been primarily taken into account in the current computational simulation. It should be noted here that a magnitude of the dynamic vertical motion (heave motion) responses presented in the form of Response of Amplitude Operators (RAO) of the floating jetty has been comprehensively quantified to predict her heave motion reduction. For conforming the computational prediction, the comparison of the RAO of the heave motion has been presented between the floating jetty with and without equipped by the structural heave plate. Here, a CFD software namely Flow-3D is employed through applying unsteady Reynolds-Averaged Navier-Stokes Equation (RANSE); which includes several techniques (TruVOF) to capture the free surface effect. The Response Amplitude Operator (RAO) of heave and pitch motion performances are then accordingly discussed.

2. Governing Equation

Basically, two equations in accordance to the law conservation of mass and momentum as clearly expressed in Eqs. (1)-(4). The current CFD simulation is based on the incompressible unsteady RANSE, which employs the volume of fluid (VOF).

2.1 Continuity and Momentum Equation

The general mass continuity equation presented in Eq. (1), for a moving object and the comparative VOF function transport equation; where the V_F is the fractional volume open to flow, ρ is the fluid density, R_{DIF} is a turbulent diffusion term, R_{SOR} is a mass source and A_x, A_y and A_z is the fractional area open to flow in x, y and z-direction, respectively [12].

$$V_F \frac{\partial \rho}{\partial t} + \frac{\partial}{\partial x}(\rho u A_x) + R\frac{\partial}{\partial y}(\rho v A_y) + \frac{\partial}{\partial z}(\rho \omega A_z) + \xi \frac{\rho u A_x}{x} = R_{DIF} + R_{SOR} \quad (1)$$

The momentum theory also applies in three coordinates direction (*u, v, w*) that has been used in the motion equation as displayed in Eqs. (2)-(4).

$$\frac{\partial u}{\partial t} + \frac{1}{V_F}\left\{uA_x\frac{\partial u}{\partial x} + vA_yR\frac{\partial u}{\partial y} + uA_z\frac{\partial u}{\partial z}\right\} - \xi\frac{A_y v^2}{xV_F} = -\frac{1}{\rho}\frac{\partial p}{\partial x} + G_x + f_x - b_x - \frac{R_{SOR}}{\rho V_F}(u - u_w - \delta u_s) \quad (2)$$

$$\frac{\partial v}{\partial t} + \frac{1}{V_F}\left\{uA_x\frac{\partial v}{\partial x} + vA_yR\frac{\partial v}{\partial y} + uA_z\frac{\partial v}{\partial z}\right\} + \xi\frac{A_y uv}{xV_F} = -\frac{1}{\rho}(R)\frac{\partial p}{\partial y} + G_y + f_y - b_y - \frac{R_{SOR}}{\rho V_F}(v - v_w - \delta v_s) \quad (3)$$

$$\frac{\partial w}{\partial t}+\frac{1}{V_F}\left\{uA_x\frac{\partial w}{\partial x}+vA_yR\frac{\partial w}{\partial y}+uA_z\frac{\partial w}{\partial z}\right\}=-\frac{1}{\rho}\frac{\partial p}{\partial z}+G_z+f_z-b_z-\frac{R_{SOR}}{\rho V_F}(w-w_w-\delta w_s) \quad (4)$$

where (G_x, G_y, G_z) are body accelerations, (f_x, f_y, f_z) are viscous accelerations and (b_x, b_y, b_z) are flow losses in porous media or across porous baffle plates, and the final condition account for the injection of mass at a source represented by a geometry element [12].

2.2 Turbulence Model

In the current CFD simulation, Renormalization-group (RNG) turbulence model has been chosen considering for low Reynolds number effects [13-15]. Through applying the double averaging strategy to the transport equations for Turbulent Kinetic Energy (TKE) and its dissipation rate produces the turbulence model for the flow as displayed in Eqs. (5)-(8).

$$\frac{\delta k}{\delta t}+U_j\frac{\delta k}{\delta x_j}=\frac{\delta}{\delta x_j}\left[\left(\nu+\frac{\nu_t}{\sigma_k}\right)\frac{\delta k}{\delta x_j}\right]+P_k+B_k+W_k \quad (5)$$

$$\frac{\delta \varepsilon}{\delta t}+U_j\frac{\delta \varepsilon}{\delta x_j}=\frac{\delta}{\delta x_j}\left[\left(\nu+\frac{\nu_t}{\sigma_\varepsilon}\right)\frac{\delta \varepsilon}{\delta x_j}\right]+C_{1\varepsilon}\frac{\varepsilon}{k}(P_k+B_k)(1+\quad C_{3\varepsilon}R_f)+W_\varepsilon-C_{2\varepsilon}^{*}\frac{\varepsilon^2}{k} \quad (6)$$

$$P_k=\nu_t S^2=\nu_t\left(\frac{\delta U_i}{\delta x_j}+\frac{\delta U_j}{\delta x_i}\right)\frac{\delta U_i}{\delta x_j} \quad (7)$$

$$B_k=\beta g_i\frac{\nu_t}{\sigma_s}\frac{\delta s}{\delta x_i} \quad (8)$$

where P_k is the shear production term of TKE, $S=\sqrt{2S_{ij}S_{ji}}$ is the average of strain tensor and $S_{ij}=\frac{1}{2}\left(\frac{\delta U_i}{\delta x_j}+\frac{\delta U_j}{\delta x_i}\right)$, B_k and W_k is the buoyant and wake production term of TKE, respectively. In addition, W_ε is the wake production term in ε, σ_k and σ_ε are the turbulent Prandtl numbers for k and ε, and $C_{i\varepsilon}$, $C_{3\varepsilon}$ and $C_{2\varepsilon}^{*}$ are model coefficients.

2.3 Body Motion Equation

Referring to the geometrical floating jetty, the body motion of the floating jetty is analysed in the global coordinate system, where the motion equations of the rigid floating jetty is expressed in Eqs. (9)-(10):

$$\frac{d}{dt}(m\vec{v}_c)=\vec{f} \quad (9)$$

$$\frac{d}{dt}(M_c.\vec{w}_c)=\vec{m}_c \quad (10)$$

The index C shows the center of mass of the body. *M* and M_c are the body mass and the tensor of the moments of inertia, respectively. The notations of $\vec{\omega}_c$ and $\vec{v}_c$ are the angular velocity and the velocity vectors, respectively. Meanwhile, $\vec{m}_c$ represents the resultant moment vector acting on the body [16]. In addition, $\vec{f}$ is the resultant force which is expressed in Eq. (11).

$$\vec{f} = \int_S (T - \rho I).\vec{n}dS + \int_V \rho_b \vec{b}dV + \vec{f}E \quad (11)$$

Here, ρ_b and $f\vec{E}$ are the density of the body and the external forces acting in the body, respectively [17]

2.4 Wave

The Stokes wave theory is the nonlinear theory for limited amplitude progressive surface wave, which can be generated through the mesh boundary. The wave theory implies that the fluid flow is incompressible and irrotational. The stream function ψ occurs and satisfies the Laplace equation (see Eq. 12) [18]:

$$\nabla^2\psi = 0 \quad (12)$$

Fluid velocity components in x and z are specified by Eqs. (13)-(14):

$$u = \frac{\partial\psi}{\partial x} \quad (13)$$

$$w = -\frac{\partial\psi}{\partial z} \quad (14)$$

Furthermore, the wave crest is assumed exist at x=0 and t=0. Here, the Laplace equation for ψ was applied along the free surface and the bottom of boundary conditions to solve the computation via the perturbation method. Then, it was considered the dimensionless wave amplitude, $\varepsilon = kH/2$, to compute the water velocity and elevation using Eqs. (15)-(17):

$$\eta(x,t) = d + \frac{\varepsilon}{k}\cos kX + \frac{\varepsilon^2}{k}B_{22}\cos 2kX + \frac{\varepsilon^3}{k}B_{31}(\cos kX - \cos 3kX) + \frac{\varepsilon^4}{k}B_{42}(\cos 2kX + B_{44}\cos 4kX) + \frac{\varepsilon^5}{k}[-(B_{53} + B_{55})\cos kX + B_{53}\cos 3kX + B_{55}\cos 5kX] \quad (15)$$

$$u(x,z,t) = U + C_0\left(\frac{g}{k^3}\right)^{V2}\sum_{i=1}^{5}\varepsilon^i\sum_{j=1}^{i}A_{ij}jk\cosh jkz\ \cos jkX \quad (16)$$

$$w(x,z,t) = C_0\left(\frac{g}{k^3}\right)^{V2}\sum_{i=1}^{5}\varepsilon^i\sum_{j=1}^{i}A_{ij}jk\sinh jkz\ \sin jkX \quad (17)$$

where $X = x - ct$,or $kX = kx - \omega t$. The coefficient A_{ij}, B_{ij} and C_0 are nonlinear functions of kd and are described in Fenton [19]. The wave number and frequency are not independent parameter but satisfy the nonlinear equation as shown in Eq. (18):

$$\left(\frac{k}{g}\right)^{V2}U - \frac{\omega}{(gk)^{\frac{1}{2}}} + C_0 + \left(\frac{kH}{2}\right)^2 C_2 + \left(\frac{kH}{2}\right)^4 C_4 = 0 \quad (18)$$

where C_0, C_2 and C_4 are nonlinear functions of kd [19].

3. Simulation Condition

3.1 Principle Data of Floating Jetty

The geometry of the floating jetty is clearly shown in Figure 1, which is basically composed of three main components i.e., floater incorporated with structural heave plate, struts and deck structure. The details particular of the floating is completely summarized in Table 1.

Table 1
Principle dimensions of floating jetty

Descriptions	Dimensions
Deck	9.0 x 16.0 x 0.2 m
Structural Deck Support	0.5 x 0.5 x 0.4 m (9 units)
Pontoon	9.0 x 16.0 x 1.2 m
Strut	0.2 x 0.2 x 2.5 m (6 units)
Heave Plate	2.25 x 2.25 x 0.1 m (6 units)

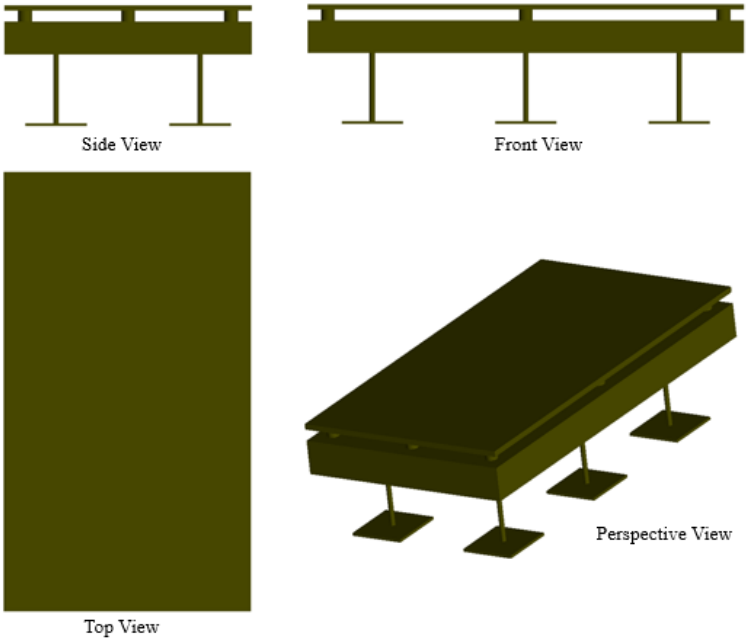


Fig. 1. Geometry of floating jetty

Table 2
Properties of floating jetty with and without heave plate

Descriptions	Heave plate	
	without	with
Vol. of Displacement (m^3)	$1.80\ x\ 10^{2}$	$2.06\ x\ 10^{2}$
LCG	$-1.39\ x\ 10^{-16}$	$-9.71\ x\ 10^{-10}$
TCG	0	0
VCG	$3.99\ x\ 10^{-1}$	$5.57\ x\ 10^{-2}$
LCB	$-1.39\ x\ 10^{-16}$	$-9.71\ x\ 10^{-10}$
TCB	0	0
VCB	$3.99\ x\ 10^{-1}$	$4.81\ x\ 10^{-1}$
I_{xx}	$2.47\ x\ 10^{6}$	$2.98\ x\ 10^{6}$
I_{xz}	$1.22\ x\ 10^{-11}$	$1.63\ x\ 10^{-4}$
I_{yy}	$6.97\ x\ 10^{5}$	$1.13\ x\ 10^{6}$
I_{zz}	$3.07\ x\ 10^{6}$	$3.72\ x\ 10^{6}$

3.2 Parametric Studies

In the current CFD simulation, the effect of the various wave periods (T) from 3 seconds up to 10 seconds have been employed as obviously summarised in Table 3. Here, the wave amplitude (A) of 0.25 m is set to be constant.

Table 3
Matrix of computational simulations

Structure of Floating Jetty	Draft (m)	Wave period (s) 3	4	5	6	7	8	9	10
Without Heave plate	0.8	√	√	√	√	√	√	√	√
With Heave Plate	0.4	√	√	√	√	√	√	√	√
	0.8	√	√	√	√	√	√	√	√

Table 4
Boundary conditions

Boundary	Mesh block 1	Mesh block 2
X_{min}	Wave	Symmetry
X_{max}	Outflow	Symmetry
Y_{min}	Symmetry	Symmetry
Y_{max}	Symmetry	Symmetry
Z_{min}	Symmetry	Symmetry
Z_{max}	Specified pressure	Symmetry

3.3 Computational Domain and Boundary Conditions

The computational domain is presented as the structured mesh. Each of the boundary conditions is shown in the mesh block 1 and mesh block 2, which is displayed in Figure 3 (left). Referring to the mesh block 1, the boundary condition at X_{min} is assigned as wave; while X_{max} is defined as outflow boundary, which is purposed to absorb the wave motion and reduce the reflection from the boundary. Y_{min}, Y_{max} and Z_{min} are assigned as the symmetry boundaries, which apply zero-gradient conditions; meanwhile Z_{max} is the specified pressure to create a uniform pressure in the boundary. All mesh boundaries for the mesh block 2 are defined as the symmetries. The detailed boundary conditions are completely presented in Table 4.

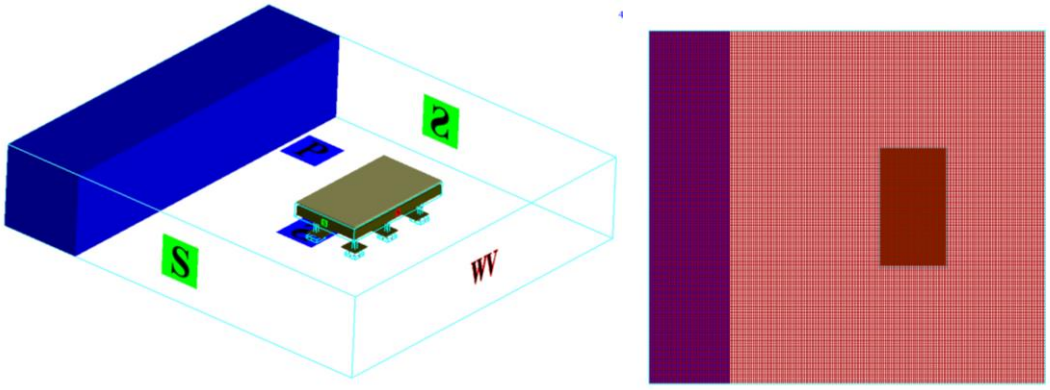


Fig. 2. Boundary condition (left) and mesh generation (right)

The meshing generation is created in Flow-3D as clearly displayed in Figure 2 (right). An extra refinement of the mesh called nested block is then added to increase meshing quality. It should be noted here that the floating jetty was assigned as the full-scale dimension model incorporated with two degrees of freedom (heave and pitch motions). Here, the convergence computational result has been assessed through monitoring the residuals of continuity values for heave motion response. A package software in Flow Sight is utilised to visualise the 3D-floating jetty model in waves as displayed in Figure 3.

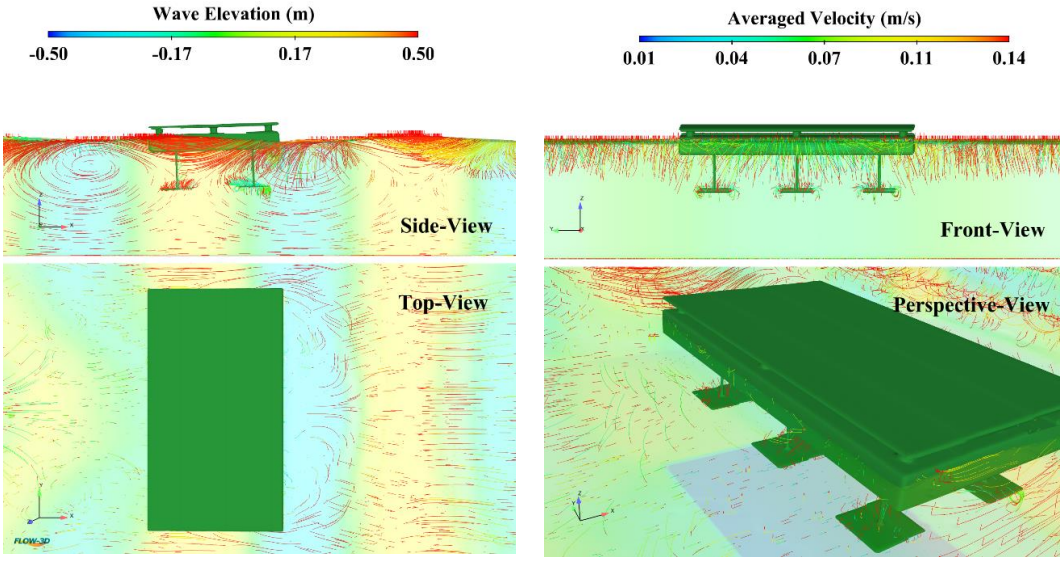


Fig. 3. Example visualisation of floating jetty performances at wave period of 3 seconds

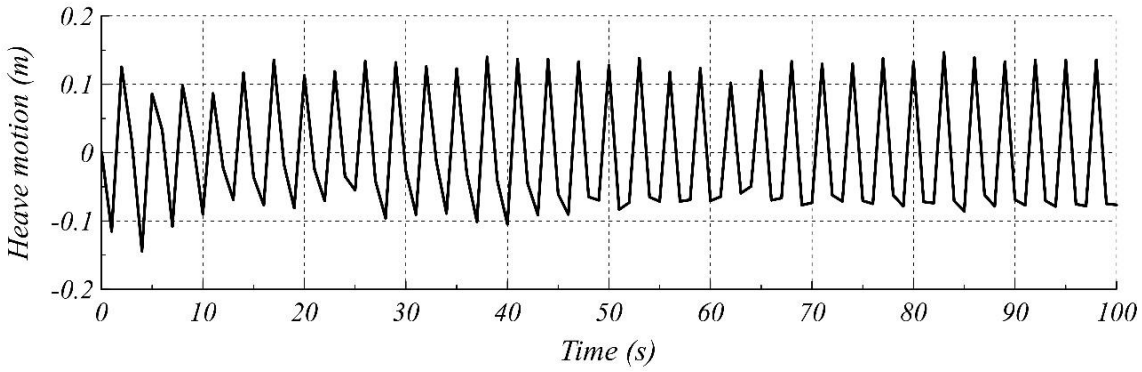


Fig. 4. Time history for heave motions of floating jetty at wave period of 3 seconds

4. Results and Discussion

The effect of the heave plate on the heave motion response of the floating jetty with draft of 0.8 m has been displayed in Figure 5. In general, the increase of wave periods from T=3 seconds up to 7 seconds has been proportional with the increase of the heave motions of the floating jetty, which inversely decreased as the wave periods further increased up to 10 seconds. When the floating jetty is equipped with the heave plate, the amplitude of the heave motion responses gradually decreased as compared to the floating jetty without the heave plate. Referring to Table 5, it should be noted that the maximum percentage of the heave motion reduction of the floating jetty incorporated with the heave plate is about 20.2%, which occurred at T=9 seconds. This can be explained by the fact that the heave plate has increased her damping coefficient [2] [20]. The

visualisation of the floating performances at various wave periods have been displayed in Figure 6. Based on CFD simulation results, it is merely concluded that the heave plate has sufficiently suppressed the heave motions of the floating jetty especially in less wave periods conditions.

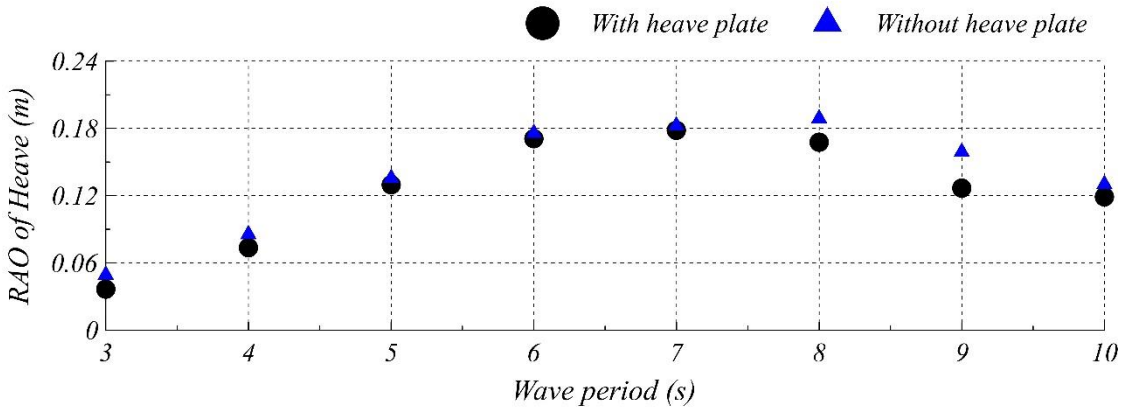
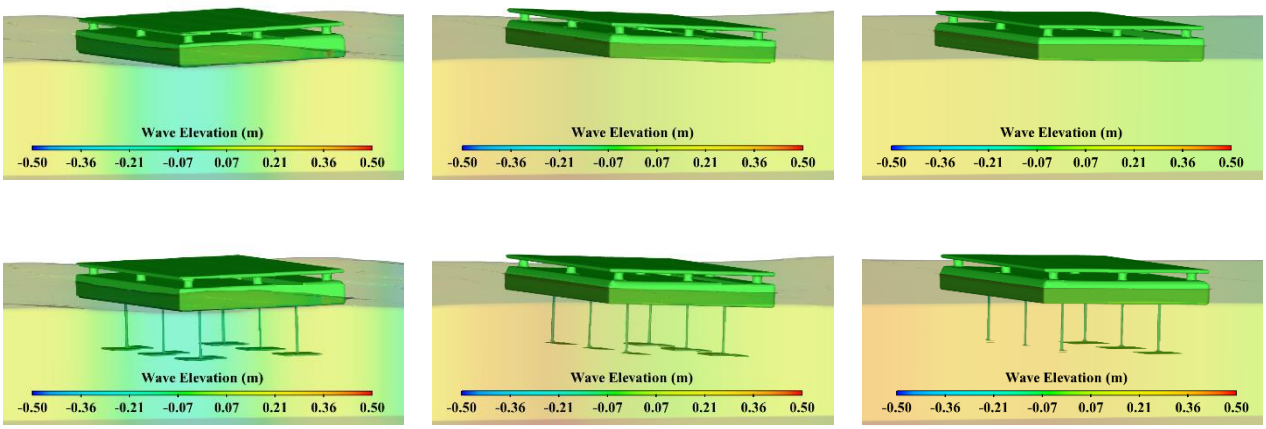


Fig. 5. Heave motion characteristics with and without heave plate at various wave periods

Table 5
Heave motions of floating jetty with and without heave plate at various wave periods

Wave period (s)	Amplitude of Heave Motion, (m)	
	Without heave plate	With heave plate
3	0.0492	0.0366
4	0.0854	0.0735
5	0.1356	0.1297
6	0.1757	0.1707
7	0.1825	0.1783
8	0.1888	0.1677
9	0.1589	0.1268
10	0.1301	0.1189



(a) (b) (c)

Fig. 6. Wave elevation characteristics of floating jetty with (below) and without (above) heave plates at various wave periods for (a) T=3s, (b) T=6s and (c) T=9s

The heave motion responses of the floating jetty incorporated with heave plate at various draft have been displayed in Figure 7. Basically, the increase of the draft from 0.4 m to 0.8 resulted in the reduction of the heave motion amplitude up to 8.9% at wave period of T=7 seconds as the heave motion amplitude decreased from 0.1958 m and 0.1783 m. This can be explained by the reasons that the added mass and damping coefficient of the floating jetty have increased as well-reported by Koh and Cho [7]. Similar to what was reported by [21], the increase of draft has decreased the heave motion of floating jetty associated with more stable platform. The visualization of the floating jetty performances with respect to the wave elevation characteristics have been displayed clearly in Figure 8. In general, the increase of the floating jetty draft has been still insignificant to reduce of the magnitude of the heave motion as summarised completely in Table 6.

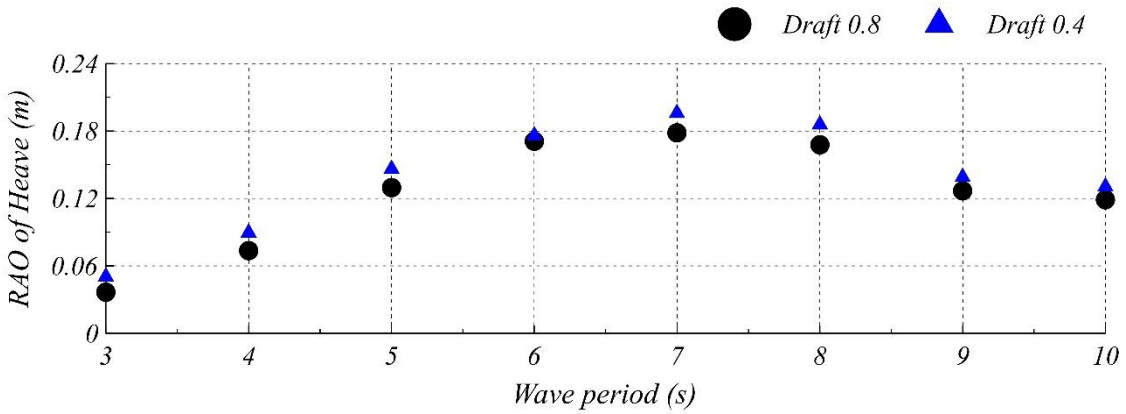
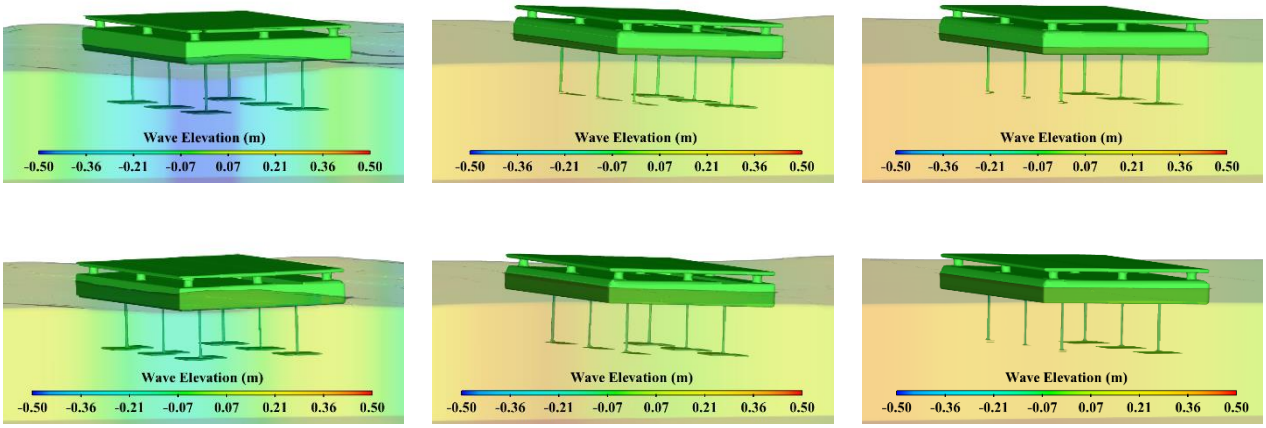


Fig. 7. Heave motion characteristics of floating jetty incorporated with heave plate at various drafts

Table 6
Heave motion responses of floating jetty incorporated with heave plate at various drafts

Wave period (s)	Amplitude of Heave Motion, (m)	
	D=0.4 m	D=0.8 m
3	0.0505	0.0366
4	0.0893	0.0735
5	0.1460	0.1297
6	0.1759	0.1707
7	0.1958	0.1783
8	0.1857	0.1677
9	0.1389	0.1268
10	0.1304	0.1189



(a) (b) (c)

Fig. 8. Wave elevation characteristics of floating jetty incorporated with heave plate in different drafts; 0.4 m (above) and 0.8 m (below) at various wave periods for (a) T=3s, (b) T=6s and (c) T=9s

5. Conclusion

The CFD investigation on predicting the heave response of the floating jetty in various wave periods was successfully performed. The simulation results are then presented in the form of amplitude motion responses. The effect of the heave plate on the heave motion of the floating jetty in various drafts and wave periods have been taken into account. The computation simulation results can be drawn as follows:

i. The floating jetty with heave plate produces insignificance reduction of heave motion where the maximum reduction percentage is about by 20.2% at wave period of T=7 seconds.
ii. The increase of the floating jetty draft from 0.4 m to 0.8 m results in the reduction of the heave motion amplitude by 8.9%.
iii. In general, the results tend to indicate that attaching the heave plate on the floating jetty is able to suppress the magnitude of the heave motion.

Acknowledgement

The authors wish to greatly thank to Translational Research Grant Scheme (TRGS) for providing founding to this project.

References

[1] Niaounakis, Michael. *Management of Marine Plastic Debris*. William Andrew, 2017.
[2] Chakrabarti, Subrata. *Handbook of Offshore Engineering (2-volume set)*. Elsevier, 2005.
[3] Holmes, Samuel, Shankar Bhat, Pierre Beynet, Anil Sablok, and Igor Prislin. "Heave plate design with computational fluid dynamics." *J. Offshore Mech. Arct. Eng.* 123, no. 1 (2000): 22-28.
[4] Brown, Adam, Jim Thomson, and Curtis Rusch. "Hydrodynamic Coefficients of Heave Plates, With Application to Wave Energy Conversion." *IEEE Journal of Oceanic Engineering* 43, no. 4 (2017): 983-996.
[5] Liang, Hai-zhi, Kun Liu, Lu-yu Li, and Jin-ping Ou. "Dynamic Performance Analysis of the Tuned Heave Plate System for Semi-Submersible Platform." *China Ocean Engineering* 32, no. 4 (2018): 422-430.
[6] Tao, Longbin, and Shunqing Cai. "Heave motion suppression of a Spar with a heave plate." *Ocean Engineering* 31, no. 5-6 (2004): 669-692.
[7] Koh, Hyeok-Jun, and I. H. Cho. "Motion response of a circular cylinder with a heave plate in waves." In *The Twenty-first International Offshore and Polar Engineering Conference*. International Society of Offshore and Polar Engineers, 2011.

[8] Panneer, R. "Effect of Viscous Damping on Hydrodynamic Response of Spar with Heave Plate." *Aquatic Procedia* (2015).
[9] Yu, Chenfang, Zhiqiang Hu, and Shisheng Wang. "Investigation of heave response of the deepwater octagonal FDPSO using various heave plate configurations." *Journal of Marine Science and Application* 16, no. 4 (2017): 446-457.
[10] Mecrow, Robert, and Seamus Garvey. "Hydrodynamic Performance of Conical Shaped Heave Plates." In *2019 Offshore Energy and Storage Summit (OSES)* IEEE, (2019): 1-9
[11] Ishihara, Takeshi, M. Waris, and Hiroyuki Sukegawa. "A study on influence of heave plate on dynamic response of floating offshore wind turbine system." In *Proceedings of the 3rd European Offshore Wind Conference and Exhibition, Stockholm, Sweden*, (2009): 14-16.
[12] Manual, Flow3D User. "Flow3D User Manual, v9. 4.2, Flow Science." *Inc., Santa Fe, NM* (2011).
[13] Yakhot, Victor, and Steven A. Orszag. "Renormalization group analysis of turbulence. I. Basic theory." *Journal of scientific computing* 1, no. 1 (1986): 3-51.
[14] Yakhot, A., S. Rakib, and W. S. Flannery. "Low-Reynolds number approximation for turbulent eddy viscosity." *Journal of Scientific Computing* 9, no. 3 (1994): 283-292.
[15] Koutsourakis, Nektarios, John G. Bartzis, and Nicolas C. Markatos. "Evaluation of Reynolds stress, k-ε and RNG k-ε turbulence models in street canyon flows using various experimental datasets." *Environmental fluid mechanics* 12, no. 4 (2012): 379-403.
[16] Maki, Kevin J., Riccardo Broglia, Lawrence J. Doctors, and Andrea Di Mascio. "Numerical investigation of the components of calm-water resistance of a surface-effect ship." *Ocean Engineering* 72 (2013): 375-385.
[17] Sisong, Yen, and Huang Genyu. "Dynamic performance of towing system-simulation and model experiment." In *OCEANS 96 MTS/IEEE Conference Proceedings. The Coastal Ocean-Prospects for the 21st Century*, vol. 1, pp. 216-230. IEEE, 1996. [18] *Flow3D 10.1.1 User Manual*. 2013: Flow Science Inc.
[19] Fenton, John D. "A fifth-order Stokes theory for steady waves." *Journal of waterway, port, coastal, and ocean engineering* 111, no. 2 (1985): 216-234.
[20] Li, Binbin, Zhenhua Huang, Ying Min Low, and Jinping Ou. "Experimental and numerical study of the effects of heave plate on the motion of a new deep draft multi-spar platform." *Journal of marine science and technology* 18, no. 2 (2013): 229-246.
[21] Liu, Xianqing, Puyang Zhang, Mingjie Zhao, Hongyan Ding, and Conghuan Le. "Influencing Factors of Motion Responses for Large-Diameter Tripod Bucket Foundation." *Applied Sciences* 9, no. 22 (2019): 4957.

Penerbit Akademia Baru

Engineering Science and Technology Conference Proceedings

Journal homepage: www.akademiabaru.com/EST.html

Flame Structure and Heat Transfer Characteristic of Premixed Flame Jet with pulsating effect

Open Access

W. Boonyopas[1], N. Upptam[1], C. Nuntadusit[1,*]

[1] Department of Mechanical Engineering, Faculty of Engineering, Prince of Songkla University, Hatyai, Songkla 90110, Thailand

ABSTRACT

This research presents the effect of pulsating of a flame jet on heat transfer rate on the surface with flame jet impingement. In the experiment, we used LPG as gas fuel and air as an oxidizer and mixed at equivalent ratio 0.8, 1.0 and 1.2. And nozzle to plate distance was varied at H/D = 2, 4, 6, 8 and 10 by D is a diameter of pipe nozzle at 12 mm. A solenoid valve was applied to generate a pulsating flow of mixed LPG and air. The frequency of pulsating was investigated in the range of 0, 5, 7 and 10 Hz. The flame jet structure was recorded using a digital camera. The average heat flux of the flame impinging jet was measured with different water temperature.

Keywords:
Premixed flame jet, Pulsating flame jet,
Heat transfer, lame structure

Copyright © 2019 PENERBIT AKADEMIA BARU - All rights reserved

1. Introduction

Current, the use of fast heating technology on surfaces by using jet flame directly to the surface is a method of heating the surfaces that are commonly used in various industrial sectors such as metal production, glass processing and melting of metal [12-15]. Because the use of flame directly to the surface is a forced convection method resulting in a high rate of heat transfer on the surface, especially where the flame hit directly. Impinging air jets, due to their high rate of cooling, are extensively used in industrial applications such as drying of food products, processing of some metals and glass. Have reviews on impinging air jets are also reported [16-19]. By this method, can exchange the heat energy quickly as a result, it can shorten the heating time and save energy compared to the conventional method using heat radiation mechanisms.

Flame heating techniques are popular and are widely used in the industry such as heating the metal and making glass by which has 4 types of heat transfer that occur in the impinging jet is convection, radiation, thermochemical heat release and condensation, by 80 % of the heat transfer comes from the convection of the flame [1]. So, using impinging flame jet to the surface has received a lot of attention and has been researched extensively because is the development of heat transfer. The advantages of using impinging flame jet to the surface, in addition to increasing the ability to heat transfer, also reduce fuel and production time. Van der Meer [2] said that using impinging flame jet with a burner that produces fast heat can save energy and time. For the rate heat exchange by using direct flame to the surface it depends on the flame flow structure such as

* *Corresponding author.*
E-mail address: chayut@me.psu.ac.th (C. Nuntadusit)

premixed flame or diffusion flame, distance between burner and heating surface, fuel type and oxidizer, equivalent ratio and Reynold number. By variables effect the characteristics and rate of heat transfer on the surface. From past to present, there are many studies on the heat transfer of impinging flame jet to flat surface, study structure of flame [3-5], heat transfer of flame jet both spot and average [6-9] and the release of pollution from the combustion of flames [10-11].

Nowadays, due to rising fuel costs Therefore, technology must be developed to increase the heat transfer capability of flame jets in order to save energy and reduce costs in industries that use high heat energy. However, most of the research is to study the flame jet from nozzles or orifice nozzles. Which can only provide a high rate of heat transfer in the area where the jet directly flows. In addition, the flame is low stable at certain fuel flow rates. It is the origin of this research that wants to study the effect of flame created from the nozzle that are equipped with pulsating flow generators Which can control the duration of the heating to prevent the device from overheating until damage. And provides a high rate of heat transfer [20].

The purpose of this research Want to study the effect of flame flaking frequency on the structure of free flame jet, impinging flame jet and rate of heat transfer at various crashing condition.

2. Methodology

2.1 The Model and Parameters of Experiment

This experiment was divided into two-part (i) study structure of free flame and impinging flame and (ii) study characteristic of heat transfer. The flame in this experiment was mixed between LPG (Propane 70%, Butane 30%) and air before flowed to solenoids valve after that continue into pipe nozzle. By the flame that came out from nozzle look like to a pulsating flame. The pulsating flame has the advantage of be able to control the temperature of material.

The nozzle made by steel pipe having diameter (D) 12 mm and length (L) 150 mm. The flame impinging to impingement plate. By impingement plate made from steel.

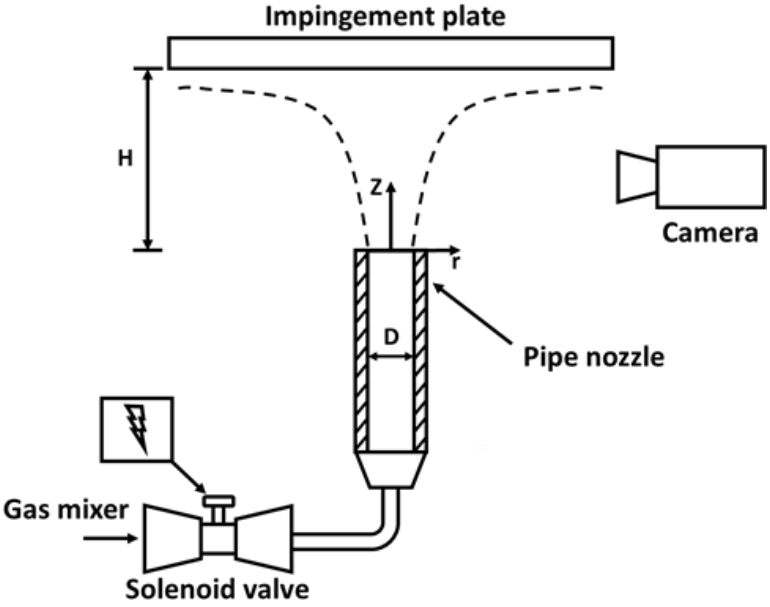


Fig. 1. Schematic of experiment setup for impinging flame jet

Table 1
The parameter for this experiment

Parameter and symbol	Values
Reynolds number of gas mixture, Re	500
Equivalent ratio, ⍰	0.8, 1.0 and 1.2
Diameter of pipe nozzle, D	12 mm
Distance nozzle to impingement plate, L	2, 4, 6, 8 and 10
Frequency of pulsating, f	0, 5, 7 and 10 Hz

The Reynolds number of gas mixture was fixed at 500 with lean-fuel, stochiometric and rich-fuel, can be calculated the viscosity and density of gas mixture from Eq. (1) and Eq. (2), can be calculated the Reynolds number of gas mixture from Eq. (3) and summarize in Table 1.

$$\mu_m = \frac{\sum \mu_j X_j \sqrt{M_j}}{\sum X_j \sqrt{M_j}} \tag{1}$$

$$\rho_m = \sum y_m \rho_m \tag{2}$$

$$\mathrm{Re}_m = \frac{\rho_m V_m D}{\mu_m} \tag{3}$$

Here *D* was diameter of pipe nozzle, V_m was velocity of gas mixture before flowed into the nozzle, ρ_m was density of gas mixture and μ_m viscosity of gas mixture.

2.2 Experiment Apparatus

Figure 2 show schematic in the experiment set up to studied the structure of free flame and impinging flame on impingement plate. The gas mixture is mixed between air and LPG. LPG was supplied from an LPG cylinder as the fuel for the experiment. The quantity of LPG was regulated by a control valve and measured by a calibrated LPG rotameter. The air required was supplied from a compressor. The air was dried by passing it through an air dryer and a pressure regulator. The amount of air required was controlled by a control valve and measured by a calibrated air rotameter. The LPG and air flowed into the mixed chamber, the inside will contain steel ball to ensure a uniform flow and avoid flashing back of the flame before flowed to solenoid valve for create pulsation flow .The frequency of pulsating is regulated by the speed control regulator at 0, 5, 7 and 10 Hz respectively. Have installed x-y table for separated distance nozzle to impingement plate is H/D = 2, 4, 6, 8 and 10. And x-y table to controlled by computer. The structure of pulsating flame and impinging flame in different operating condition photographs are taken with digital camera (cannon EOS 1200D).

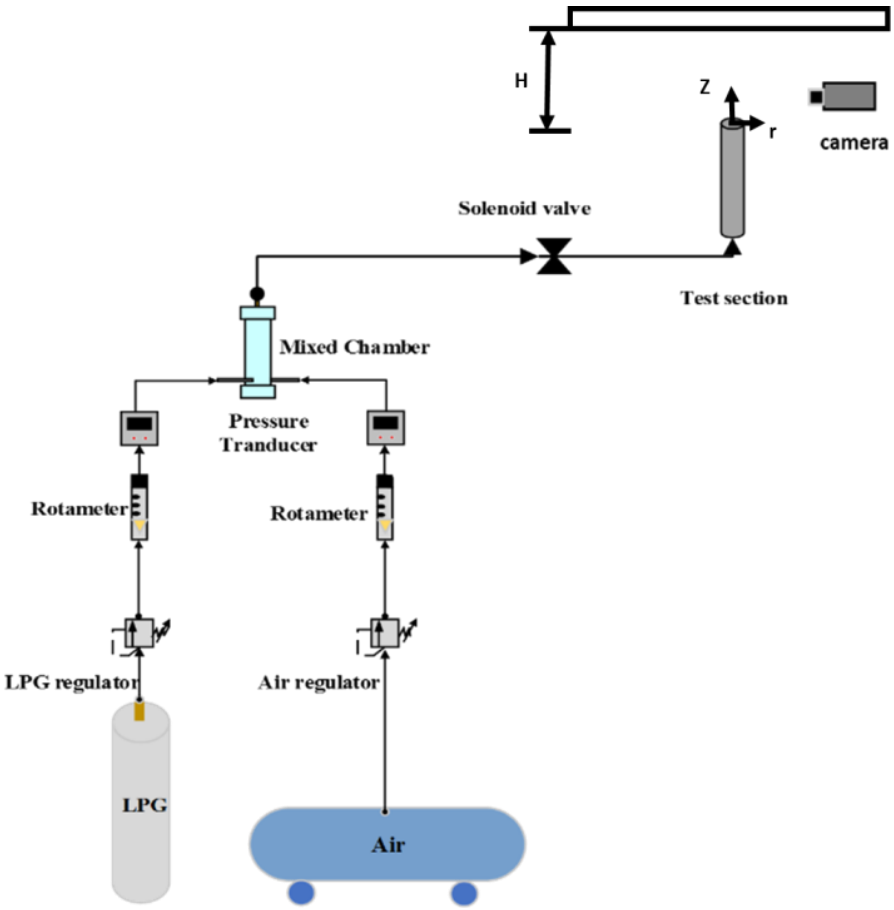


Fig. 2. Schematic in the experiment set up to studied the structure of free flame and impinging flame on impingement plate

2.3 Average Heat Flux

Figure 3 show schematic the experiment set up to studied the characteristic of heat transfer. The impingement plate made from stainless has circular having diameter 150 mm, thickness 5 mm and high 25 mm. The back of the impingement surface was uniformly cooled by water cooling. The inlet water come for cooling tank and will be controlled have temperature stable by through the heater before into impingement plate. The outlet water flowed into cooling tank to using again. The thermocouples installed to measure the inlet and outlet temperatures of the water impingement plate recording with data logger (midi GL840), for calculated average heat flux with different temperature water inlet and water outlet. Due to the different temperature, it can be calculated average heat flux from Eq. (4).

$$\dot{q} = mC_p\Delta T \tag{4}$$

Where the mass flow rate of water inlet to plate (m), specific heat of water depending on temperature of water inlet (C_p), different temperature between water inlet and water outlet (ΔT).

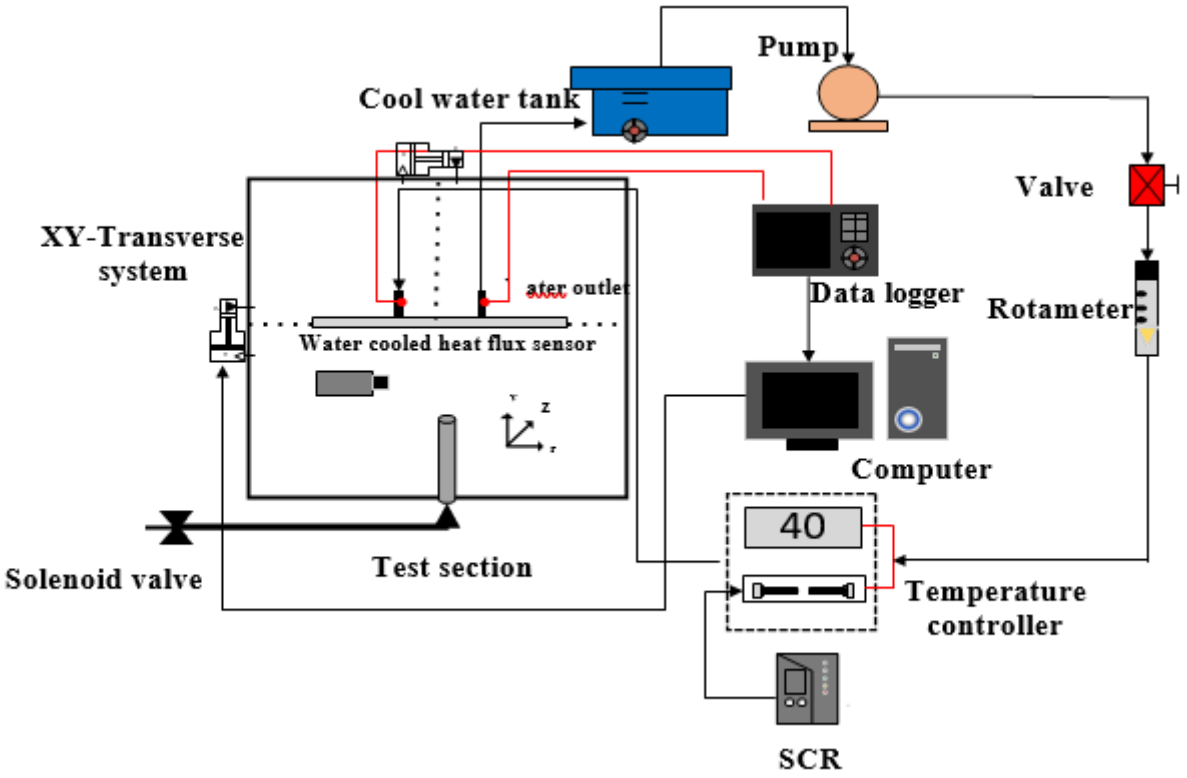


Fig. 3. Schematic the experiment set up to studied the characteristic of heat transfer

3. Results

3.1 Structure of Pulsating Free Flame

Figure 4 show Images structure of pulsating free flame Re = 500, f = 0 Hz at (a) equivalent ratio 0.8, (b) equivalent ratio 1.0 and (c) equivalent ratio 1.2, will see that at equivalent ratio 0.8 the flame has blue color a lot and has less orange color. At equivalent ratio 1.0 the flame has blue color decreased and orange color increased. And equivalent ratio 1.2 the flame has mostly orange color and has blue color little. In all three equivalent ratio when time passed the flame structure was not change and equivalent ratio 1.2 the flame has longest.

Figure 5 show Images structure of pulsating free flame Re = 500, f = 5 Hz at (a) equivalent ratio 0.8, (b) equivalent ratio 1.0 and (c) equivalent ratio 1.2, when time passed at equivalent ratio 0.8 the length of flame has longest and the flame has shortest at equivalent ratio 1.2. And at three equivalent ratio has length of flame was increase when time passed.

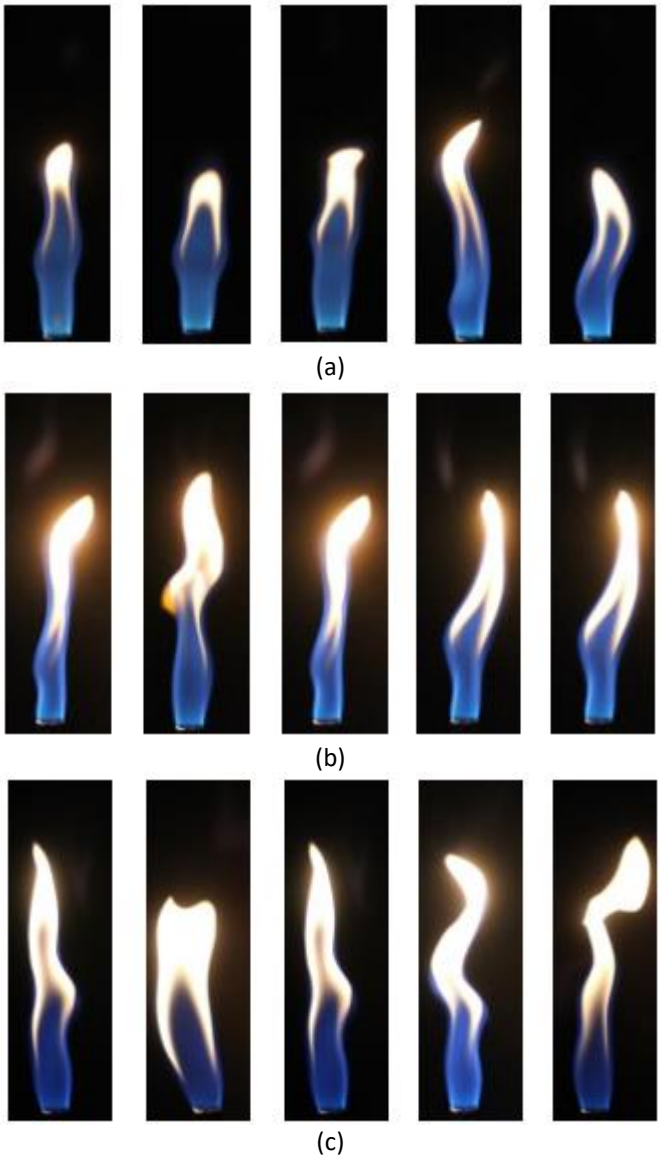


Fig. 4. Images structure of pulsating free flame Re = 500, f = 0 Hz at (a) equivalent ratio 0.8, (b) equivalent ratio 1.0 and (c) equivalent ratio 1.2

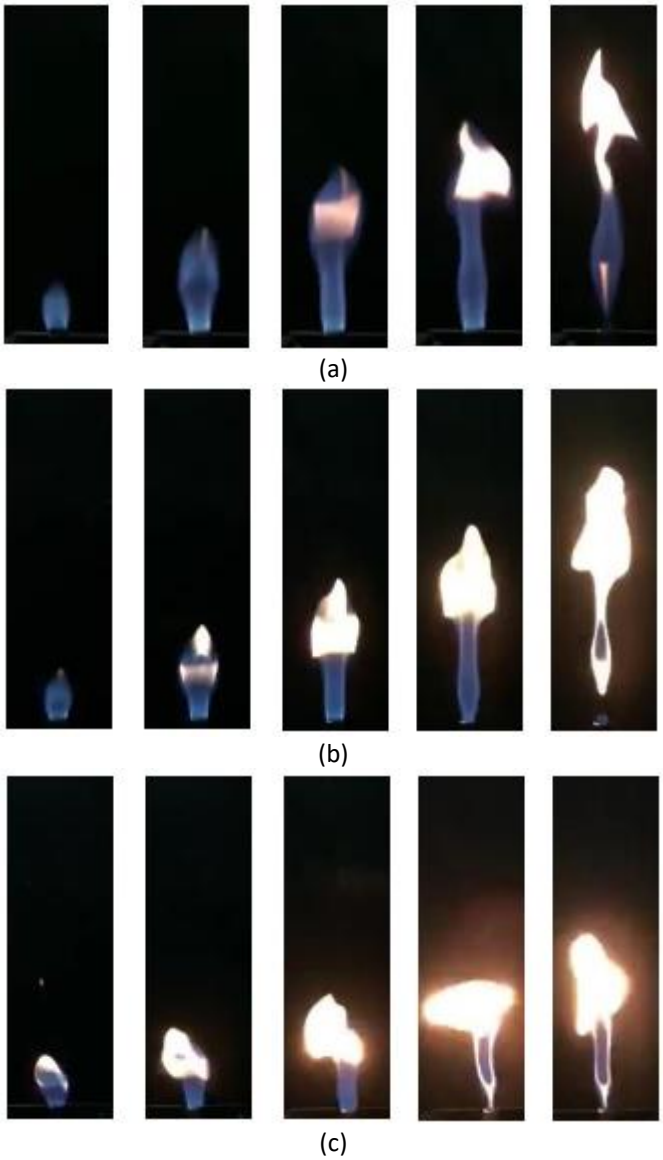


Fig. 5. Images structure of pulsating free flame Re = 500, f = 5 Hz at (a) equivalent ratio 0.8, (b) equivalent ratio 1.0 and (c) equivalent ratio 1.2

Figure 6 show Images structure of pulsating free flame Re = 500, f = 5 Hz at (a) equivalent ratio 0.8, (b) equivalent ratio 1.0 and (c) equivalent ratio 1.2. It can be seen that at three equivalent ratio the flame will change color from blue color to orange color increase when time passed. And can see separated the flame from this image.

Figure 7 show Images structure of pulsating free flame Re = 500, f = 10 Hz at (a) equivalent ratio 0.8, (b) equivalent ratio 1.0 and (c) equivalent ratio 1.2, from the images can see that at three equivalent ratio length of flame has longer when time passed. The flame at equivalent ratio 0.8 mostly had blue color and a bit orange color on the flame tip and at equivalent ratio 1.0 and 1.2 the flame mostly had orange color, a bit orange color on the flame tip when time passed.

From Figure 4 to Figure 7 will can see that at frequency of pulsating, f = 0 Hz the structure of flame was nothing change in three equivalent ratio but add frequency of pulsating, f will made the structure of flame was change by when time passed the length and color of flame also changed.

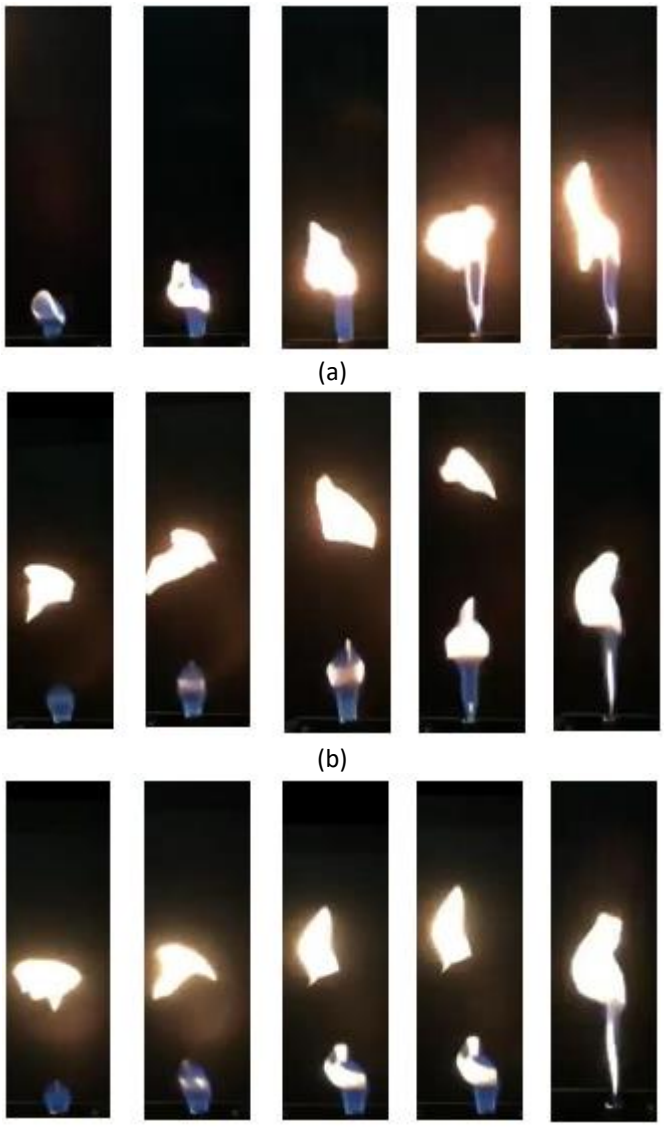


Fig. 6. Images structure of pulsating free flame Re = 500, f = 7 Hz at (a) equivalent ratio 0.8, (b) equivalent ratio 1.0 and (c) equivalent ratio 1.2

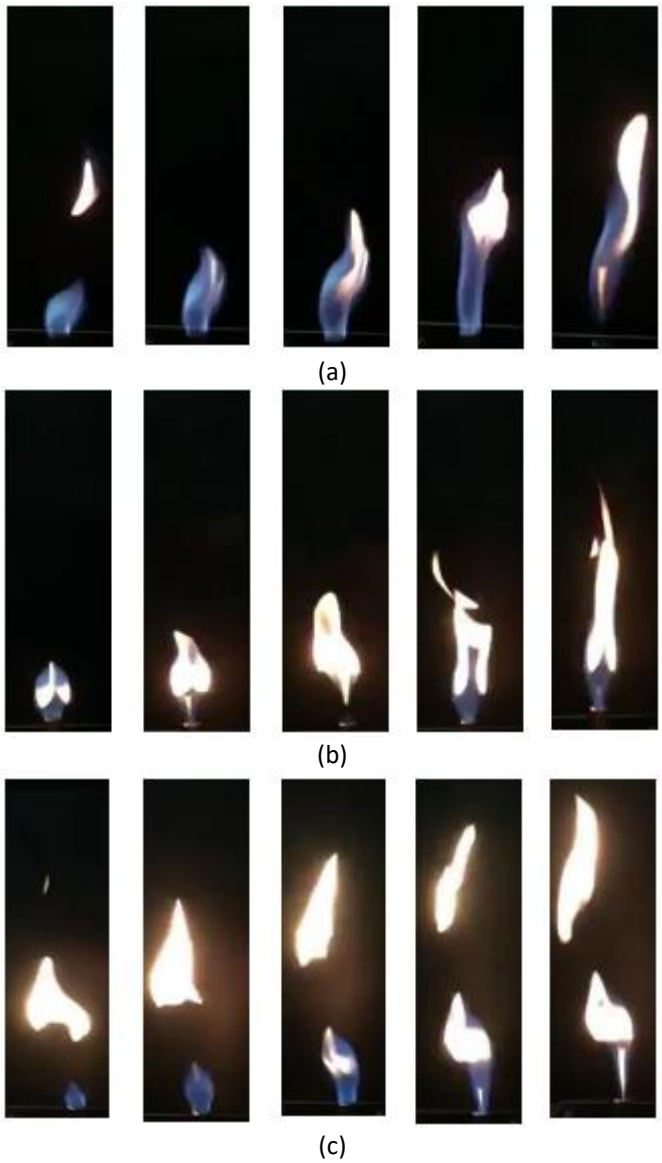


Fig. 7. Images structure of pulsating free flame Re = 500, f = 10 Hz at (a) equivalent ratio 0.8,(b) equivalent ratio 1.0 and (c) equivalent ratio 1.2

3.2 Structure f Pulsating Impinging Flame

The images structure of pulsating flame Re = 500, at equivalent ratio 0.8, 1.0 and 1.2 shown in Figure 8 to Figure 10. From images at H/D = 2 the flame had blue color and had orange color on the flame tip in every frequency of pulsating at equivalent ratio 0.8, 1.0 and 1.2. When distance H/D increase, at f = 0 Hz the flame mostly had blue color and orange color on the flame tip at equivalent ratio 0.8, 1.0 and 1.2. When frequency of pulsating increases the flame will had orange color increases and blue color decreases at equivalent ratio 0.8, 1.0 and 1.2. Can see that when distance H/D increases length of flame higher and increase separate also.

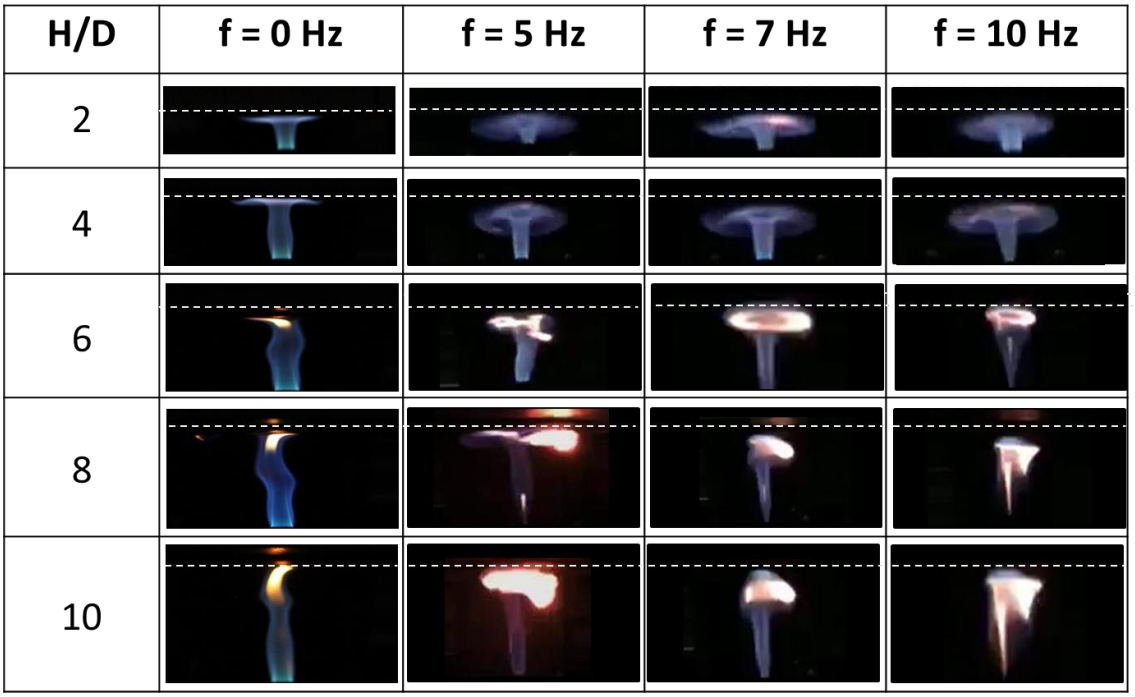


Fig. 8. Images structure of pulsating impinging flame Re = 500, equivalent ratio 0.8

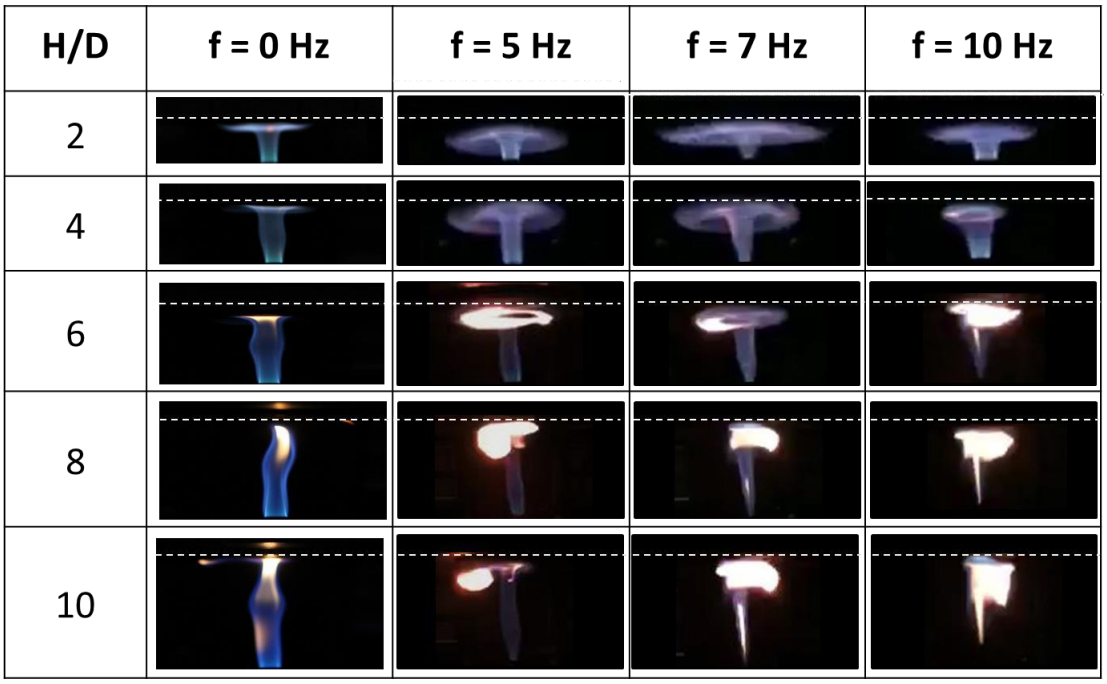


Fig. 9. Images structure of pulsating impinging flame Re = 500, equivalent ratio 1.0

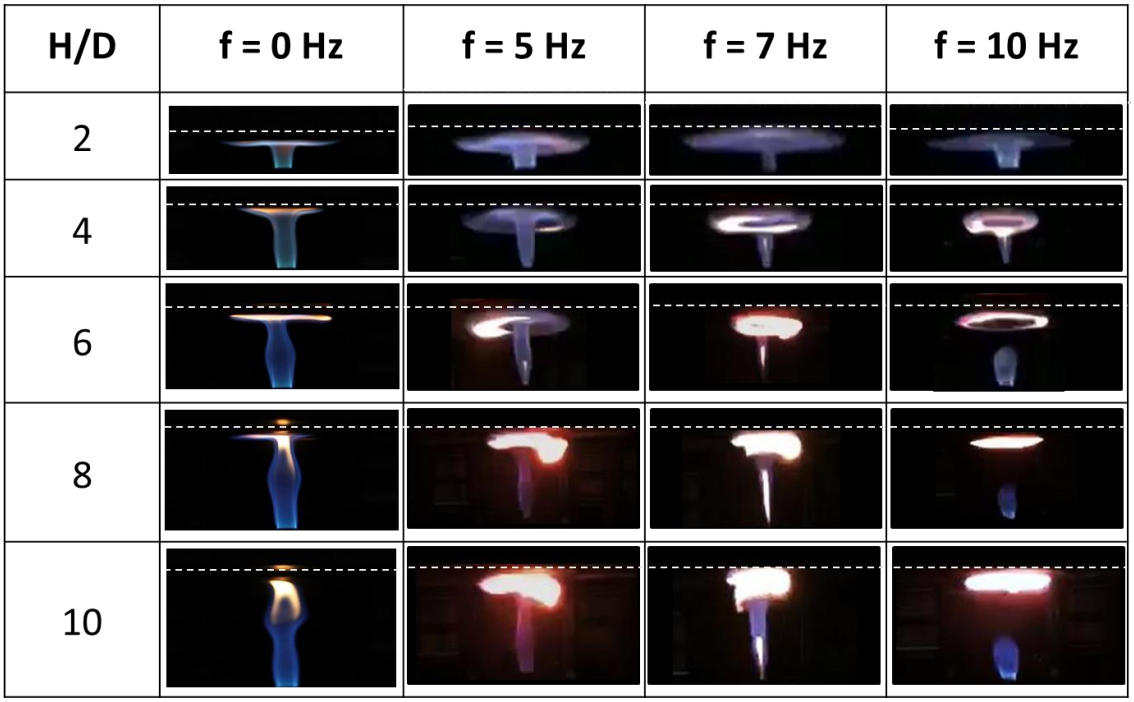


Fig. 10. Images structure of pulsating impinging flame Re = 500, equivalent ratio 1.2

3.3 Average Heat Flux

Figure 11 show graph the average heat flux of impinging flame at frequency (f) = 0, 5, 7 and 10 Hz, at (a) equivalent ratio 0.8, (b) equivalent ratio 1.0 and (c) equivalent ratio 1.2. From graph found that, when distance between nozzle to impingement increased the average heat flux will decreased accordingly. Because at H/D = 2 impinging flame was potential core region that was the maximum heat transfer. The heat transfer was decreased by distance between nozzle to impingement plate increment because impinge region was far from potential core region. From Figure 10, it explained at equivalent ratio 1.2 had maximum average heat flux when compared to equivalent ratio 0.8 and 1.0 at similar frequency. When changed frequency from 0 Hz to 5 Hz the average heat flux will decrease. And when the increase frequency, average heat flux will increase also.

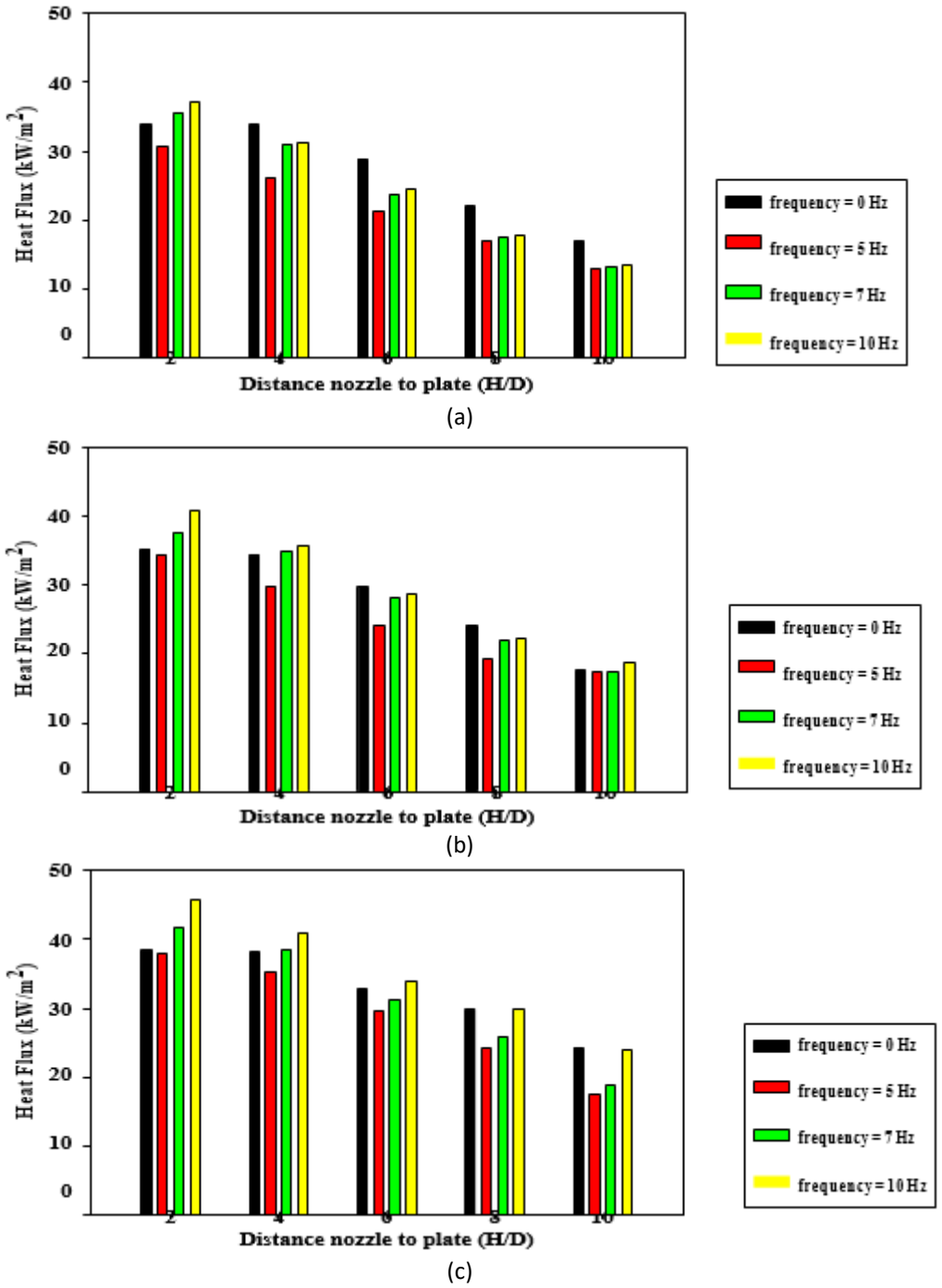


Fig. 11. Graph the average heat flux of impinging flame at frequency (f) = 0, 5, 7 and 10 Hz, at (a) equivalent ratio 0.8, (b) equivalent ratio 1.0 and (c) equivalent ratio 1.2

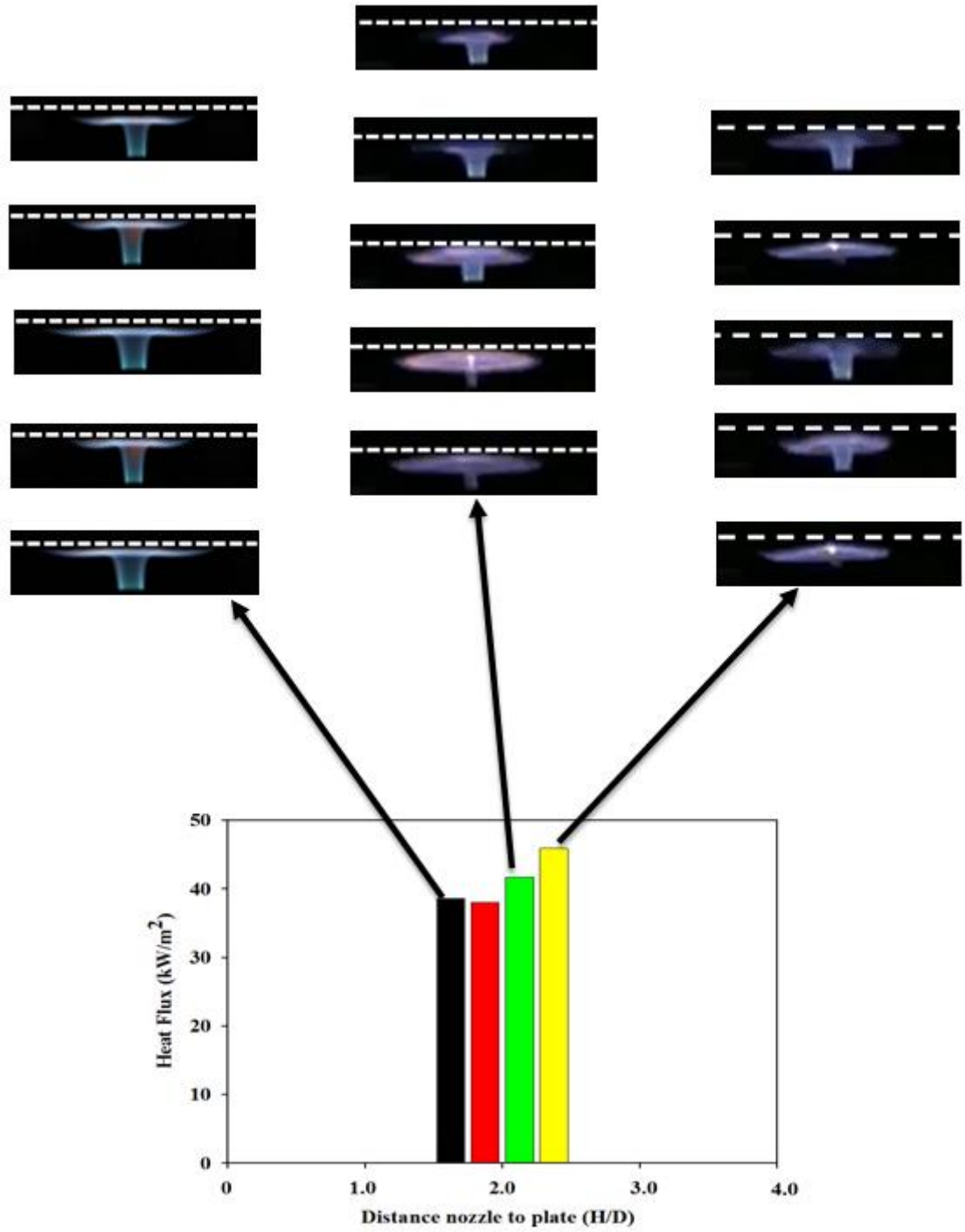


Fig. 12. Images impinging flame used compare average heat flux f = 0, 7 and 10 Hz, equivalent ratio 1.2, at H = 2D

4. Conclusions

This experiment to studied the characteristic of pulsating free flame and impinging flame, studied average heat flux under fixed Reynolds number of gas mixture (Rem = 500), distance between nozzle to impingement plate (H) = 2D, 4D, 6D, 8D and 10D, and frequency of pulsating (f) = 0, 5, 7 and 10 Hz. Therefore, this research was conclouded main issue on experimentally investigation.

i. At f = 0 Hz the structure of pulsating free flame was not change at all three equivalent ratio. At equivalent ratio 0.8 the flame mostly had blue color and less orange color on the flame tip. But when equivalent ratio increased to 1.2 the flame mostly had orange color. When add frequency of pulsating can see separated the structure of pulsating free flame clearly at f = 5 and 7 Hz and at f = 10 Hz will seen separate of flame decrease. And when the frequency of pulsating increased result in length of flame and the flame had orange color increase.

ii. At H/D = 2 the flame had blue color and had orange color on the flame tip in every frequency of pulsating at equivalent ratio 0.8, 1.0 and 1.2. When distance H/D increase, at f = 0 Hz the flame mostly had blue color and orange color on the flame tip at equivalent ratio 0.8, 1.0 and 1.2. When frequency of pulsating increase the flame will had orange color increases and blue color decreases at all three equivalent ratio because the air outside come into mixed with the gas mixture, causing the mixture to change which affects the flame color. Can see that when distance H/D increases length of flame higher and increase separate also.

iii. At equivalent ratio 0.8, f = 5 Hz will had minimum average heat flux in the same impinging distance and at equivalent ratio 1.2, f = 10 Hz will had maximum average heat flux in the same impinging distance. Because at H/D = 2 impinging flame was potential core region that was the maximum heat transfer. The heat transfer was decreased by distance between nozzle to impingement plate increment because impinge region was far from potential core region. When changed frequency from 0 Hz to 5 Hz the average heat flux will decrease. And when the increase frequency, average heat flux will increase also. When the frequency of pulsating increase will cause more kinetic energy resulting heat transfer increases.

Acknowledgement

This research was funded by a grant from Department of Mechanical Engineering, Faculty of Engineering, Prince of Songkla University, Thailand.

References

[1] Long, V. D. "SOME ASPECTS OF FUEL TECHNOLOGY OF GLASSWORKING." *GLASS TECHNOLOGY* 6, no. 4 (1965): 124.

[2] [2]Viskanta, R. "Enhancement of heat transfer in industrial combustion systems: problems and future challenges." *ASME/JSME Thermal Engineering Proceedings* 5, (1991): 161-173.

[3] Mohr, J. W., J. Seyed-Yagoobi, and R. H. Page. "Heat transfer characteristics of a radial jet reattachment flame." *Journal of heat transfer* 119, no. 2 (1997): 258-264.

[4] Zhang, Y., and Bray, K. N. C. "Characterization of impinging jet flame." *J. Combustion and flame*, 116, (1999): 671-674.

[5] Foat, T., K. P. Yap, and Y. Zhang. "The visualization and mapping of turbulent premixed impinging flames." *Combustion and flame* 125, no. 1-2 (2001): 839-851.

[6] Baukal, Charles E., and B. Gebhart. "Surface condition effects on flame impingement heat transfer." *Experimental thermal and fluid science* 15, no. 4 (1997): 323-335..

[7] Baukal, C. E., and B. Gebhart. "Heat transfer from oxygen-enhanced/natural gas flames impinging normal to a plane surface." *Experimental thermal and fluid science* 16, no. 3 (1998): 247-259.

[8] Mishra, D. P. "Experimental Studies of LPG-air Premixed Flame Impingement Heat Transfer." *Proceedings of Internation Symposium on Recent Trends in Heat and Mass Transfer*, (2002): 45-66.

[9] Tuttle, S. G., B. W. Webb, and M. Q. McQuay. "Convective heat transfer from a partially premixed impinging flame jet. Part I: Time-averaged results." *International Journal of Heat and Mass Transfer* 48, no. 7 (2005): 1236-1251.

[10] Mohr, J. W., J. Seyed-Yagoobi, and R. H. Page. "Combustion measurements from an impinging radial jet reattachment flame." *Combustion and flame* 106, no. 1-2 (1996): 69-80.

[11] Mishra, D. P. "Emission studies of impinging premixed flames." *Fuel* 83, no. 13 (2004): 1743-1748.

[12] Chander, Subhash, and Anjan Ray. "Flame impingement heat transfer: a review." *Energy conversion and*

Management 46, no. 18-19 (2005): 2803-2837.
[13] Viskanta, R. "Heat transfer to impinging isothermal gas and flame jets." *Experimental thermal and fluid science* 6, no. 2 (1993): 111-134.
[14] Baukal Jr, C. E., and B. Gebhart. "A review of empirical flame impingement heat transfer correlations." *International Journal of Heat and Fluid Flow* 17, no. 4 (1996): 386-396.
[15] Baukal, Charles E., and Benjamin Gebhart. "A review of semi-analytical solutions for flame impingement heat transfer." *International journal of heat and mass transfer* 39, no. 14 (1996): 2989-3002.
[16] J.N.B. Livingood, P. Hrycak, Impingement heat transfer from turbulent air jets to flat plates – a literature survey, NASA Technical Memorandum (NASA TM X-2778) (1970).
[17] Martin, Holger. "Heat and mass transfer between impinging gas jets and solid surfaces." In *Advances in heat transfer*, vol. 13, pp. 1-60. Elsevier, 1977.
[18] Jambunathan, K., E. Lai, M. A. Moss, and B. L. Button. "A review of heat transfer data for single circular jet impingement." *International journal of heat and fluid flow* 13, no. 2 (1992): 106-115.
[19] Meer, Theodorus Hendrikus van der. "Heat transfer from impinging flame jets." (1987).
[20] Hermanson, J. C., Hamid Johari, D. P. Stocker, and U. G. Hegde. "Buoyancy effects in strongly pulsed turbulent diffusion flames." *Combustion and flame* 139, no. 1-2 (2004): 61-76.

Penerbit Akademia Baru

Engineering Science and Technology Conference Proceedings

Journal homepage: www.akademiabaru.com/EST.html

Effect of Channel Rotation Speed on Heat Transfer Characteristics of Impinging Jets

Open Access

T. Nontula[1], N. Kaewchoothong[1], C. Nuntadusit[1, *]

[1] Department of Mechanical Engineering, Faculty of Engineering, Prince of Songkla University, Hatyai, Songkhla 90110, Thailand

ABSTRACT

Jet impingement has been applied for internal cooling in a gas turbine blade. In this study, heat transfer characteristics of impinging jets from a row of circular orifices were investigated in flow channel with rotation. The study condition consisted of jet impingement distance at L=2d and Rotation number at 0, 0.0033 and 0.0066 rpm at a same flow rate of air jets. The heat transfer on the jet impingement surface was measured by using a steady Thermo-chromic Liquid Crystal technique. The heat transfer on the pressure side and suction side have been also investigated. The results show that the heat transfer of impinging jets reduces gradually when increasing the rotation speed. This may due to the Coriolis and centrifugal acceleration from rotation.

Keywords:
Impinging jets, Rotation number, Heat transfer, Thermo-chromic liquid crystal

Copyright © 2019 PENERBIT AKADEMIA BARU - All rights reserved

1. Introduction

Currently, Trend in the gas turbine industry want to increase the efficiency of the gas turbine engine to decrease fuel consumption and environmental impact, One of the methods used to increase the efficiency of the gas turbine engine is Turbine Inlet Temperature (TIT).However, the evolution of TIT has a tendency to continuously high but is limited by the melting point temperature of the metal. The turbine blade essential use to the cooling technology. Which is divided into external cooling using Film cooling and internal cooling using impinging jet, rib turbulators in serpentine channel and pin-fin cooling at trailing edge [1-7] as shown in Fig. 1. to extend the service life and allow internal components to operate safely at high temperatures.

Jet impingement cooling is already used in many industrial applications because it has high cooling rate in impingement region and rapid cooling system. There are numerous studies on jet impingement systems. In case of the heat exchanger surface is large, a jet will be used instead of a single jet. But in the case of array jet into the flow visualization and heat transfer on the surface is complex more than in the case of a single jet due to the jet impingement on the surface, there would be a mixture of near jet [9]. Jet impingement on the surface then combine into a flow within the channel between the jet plate and the impingement surface. Resulting in a crossflow effect near the exit of flow, cause in heat transfer uncertain on the surface [10-11].

* *Corresponding author.*
E-mail address: zurrie_adik@yahoo.com (Zurriati M. Ali)

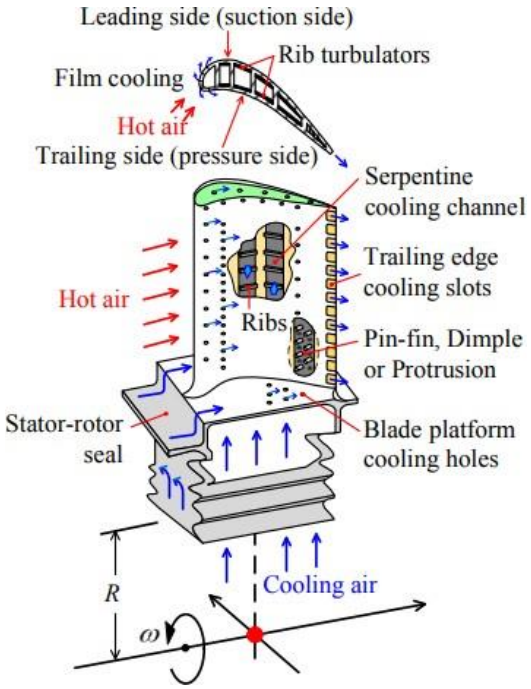


Fig. 1. Modern gas turbine rotor blade with cooling passage network [8]

There is a research that studies heat transfer of a impinging jet region with the leading edge of turbine blade [12-13] studied the heat transfer single row jet in semicircle and trapezoidal channel to imitate region leading edge of turbine blade. Under the rotation conditions the heat transfer is reduced a lot and asymmetric, Due to the Coriolis force. Yang et al. [14] studied heat transfer in a two-pass flow channel using impinging jet under the conditions of the Reynolds number from 25,000 to 100,000, the rotation number from 0 to 0.14, used to conducted Transient Liquid Crystal measurements. Rotation decreases the heat transfer on the impingement plate and enhances the heat transfer near the impingement channel exit. However, there is very few studies about rotation effect on midchord impingement cooling. Parsons et al. [15] studied the heat transfer of double row jet under the conditions of the Reynolds number from 5,000 to 10,000, the rotation number from 0 to 0.0028 and jet impingement distance constant at 6D. Results show that under rotation, a both of the leading side case and trailing side case heat transfer results are less than the stationary case. This is contrary to results from rib turbulators in serpentine channels, where heat transfer can be augmented greatly if the Coriolis force is favorable [16–19]. Lamont et al. [20] experimentally studied the heat transfer of single row jet rotating channel for Rotation number was varied from 0 to 0.0022 and impingement distance was also varied 1D,2D and 3D but the Reynolds number was investigated at 9,000, the result showed that heat transfer of leading side case was lower than stationary case but the trailing side case had a maximum heat transfer when compared to leading side case and stationary case. For experiment about the heat transfer on rotating channel had effect on Coriolis acceleration and centrifugal acceleration. The Coriolis acceleration is defined as $2\vec{\Omega}\times\vec{V}$ and the centrifugal acceleration is $\vec{\Omega}\times\vec{\Omega}\times\vec{r}$, where $\vec{\Omega}$ is the rotational speed, $\vec{V}$ is the mainstream velocity and $\vec{r}$ is the radius of the rotation.

In the present, this research was study models a single radially outward coolant channel with jet impingement. Instead of rib turbulators in serpentine channel. A single row of constant pitch jet

holes is used to demonstrate the rotational effects on impingement and using Thermo-chromic liquid crystal technique for rotating channels. The purpose of this study was to explore in more detail the heat transfer characteristics during the rotations inside a single row jet with rotation speed and Reynolds number affected to heat transfer distribution on impingement plate.

2. Methodology

2.1 The Model and Parameters of Experiment

This experiment for impinging jet by single row.The air from rotary seal enter the rotating arms at the base of the drive shaft into the single row drill on the aluminium plate in Figure 2. having length (L) 270 mm side wall thickness 3 mm, the diameter from single row (D) having 5 mm with pitch to jet (P) at 4D. The impingment chanel has a wide at 4D, the measurement effect of chanel rotating speed on heat transfer impinging plate fixed jet impinging distance at 2D.

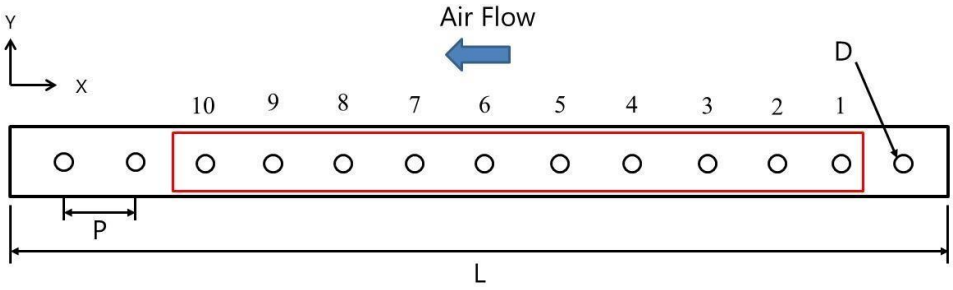


Fig. 2. Schematic single row

The impingement channel show on Fig.3 has one outlet in the channel, which creates the required crossflow effect. The thermo-chromic liquid crystals applied on the target surface from impingement channel. From the study heat transfer on surface condition at stationary with non- rotating, from leading side and trailing side, the motor rotates the test section on rotating arm in opposite direction. For experiment was determined the temperature of air inlet controlled at 26 ± 0.1 °C and the room temperature was also controlled around 25 ± 0.5 °C .

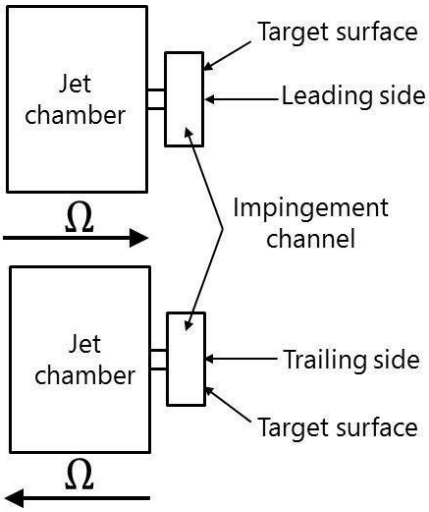


Fig. 3. Direction of rotation for leading side case and trailing side case

In addition, all of the experimental tests were performed at the parameter show on Table 1. The heat transfer measurement on rotating channel was varied Rotation number (R_o) under fixed jet number pitch to jet fixed at 4D and jet impingement distance (L) at 2D

Table 1
The parameters for this experiment

Parameters and symbol	Values
Reynolds number of jet, Re	10,000
Rotation number, R_o	0, 0.0033 and 0.0066
Jet number	13
Diameter of jet, D	5 mm
Jet impingement distance, L	2D
Pitch to jet, P	4D

The Reynolds number of air was fixed at 10,000, which was average velocity exit (V) above the jet exit, diameter of jet (D) and kinematic viscosity of air ( ) is can be calculated from Eq. (1) and summarize in Table 1.

$$Re = \frac{VD}{\upsilon} \tag{1}$$

$$R_o = \frac{\Omega D}{V} \tag{2}$$

where Ω is the rotating speed of the test section. The flow channel is operated at the rotational speed of 0, 200 and 400 rpm at Re = 10,000.

The constant heat flux on stainless surface, ($\dot{q}input$), the loss of radiation to surrounding on stainless surface, ($\dot{q}rad$), the loss of natural convection to surrounding on stainless surface, ($\dot{q}conv$), and the net heat flux, ($\dot{q}net$) , The heat transfer coefficient, (h), and the average temperature of the air flowing test section (T_m) these were shown in Eq. (3) to Eq. (8).

$$q_{input} = \frac{IV}{A} \tag{3}$$

$$\dot{q}_{rad} = \sigma\varepsilon(\overline{T}_{heat} - \overline{T}_{sur}) \tag{4}$$

$$\dot{q}_{conv} = h_c(\overline{T}_{heat} - \overline{T}_{sur}) \tag{5}$$

$$\dot{q}_{net} = \dot{q}_{input} - \dot{q}_{rad} - \dot{q}_{conv} \tag{6}$$

$$h = \frac{\dot{q}_{net}}{(T_{heat} - T_{no\ heat})} \tag{7}$$

$$T_m = \frac{T_i + T_{surr}}{2} \tag{8}$$

Where I, V and A were direct current, direct voltage of electric power and area of stainless

surface, from Eq. (3). σ was the Stefan-Boltzmann constant, ε_{TLC} was the emissivity for the TLC sheet which was 0.9 [21], T_w was the average temperature of the wall, T_i was the temperature of air inlet, T_{surr} was the room temperature for experiment, h_c was the natural heat transfer coefficient that was arranged a vertical plate.

Finally, the Nusselt number was calculated from Eq. (9).

$$Nu = \frac{hD}{k} \tag{9}$$

Where was a heat transfer coefficient from Eq. (7), D was the diameter of exit jet, and k was the thermal conductivity at the mean temperature of the air.

2.2 Experimental Setup

The experiment setup is supported by a 1.5 m x 1.5 m x 1.65 m steel frame, as shown in Figure 4. For the rotating part, the rotating arm was installed with a hollow drive shaft that had an outside diameter of 80 mm and an inner diameter of 65 mm. The hollow drive shaft was held by two bearing supports and one rotary seal. The rotary seal was connected under drive shaft for air coolant inlet. A 7.46 kW (10 hp) electric motor was used to drive the rotating arm by controlled inverter, measure the rotational speed by encoder. For the generated uniform heat flux part, there was a slip ring that was installed on a hollow drive shaft. Slip ring connect with power supply for the current source for heating the test section, both stationary and rotating. For the coolant part, a 2.24 kW (3 hp) blower that was blower mode to provide air in the test section and controlled by inverter. The coolant air inlet controlled by heater at 26 and measure with T-type thermocouples. In addition, measure room temperature with T-type thermocouples around the rotating test rig.

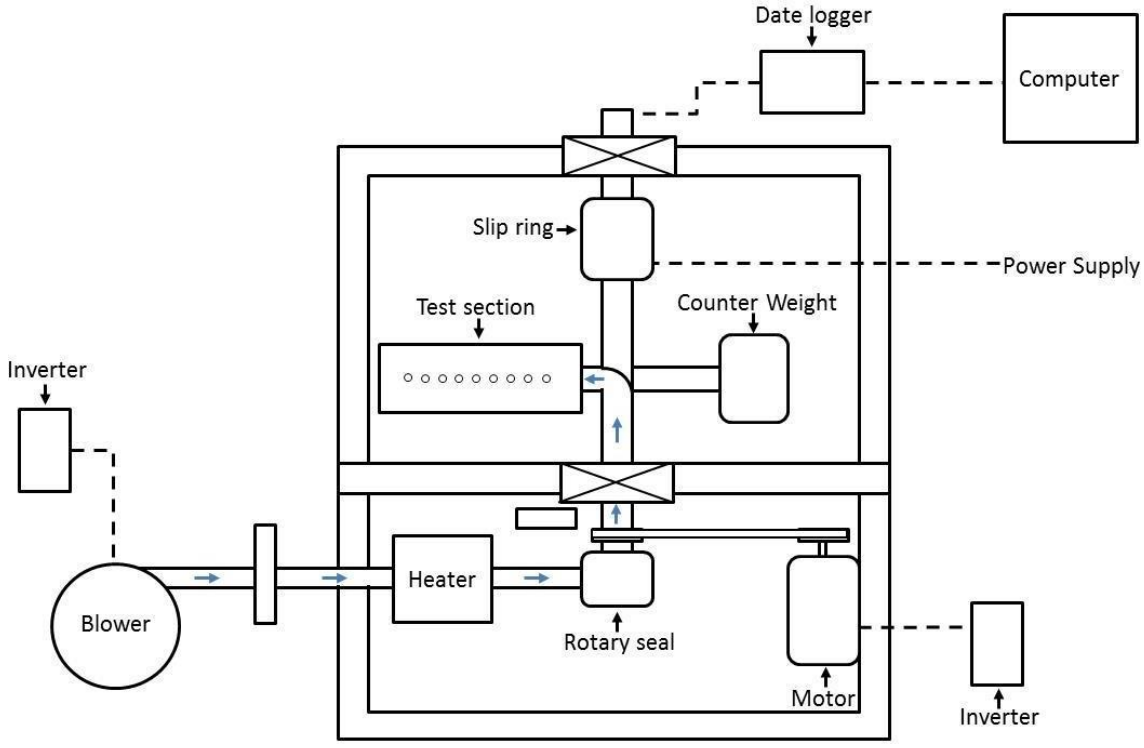


Fig. 4. Schematic diagram for experiment setup

2.3 *The Heat Transfer Measurement*

The experimental setup for study of heat transfer measurement are shown in Fig.6. The air from rotor seal enter the rotating arms at the base of the drive shaft into the single row drill on the aluminium plate impingement target surface and one direction (radially outward) as the exit condition. The target surface was used to study the heat transfer measurement, that was made of stainless-steel plate was 90 mm in width, 280 mm in length, and 0.03 mm in thickness. To obtain a constant uniform heat flux of about 750 W/m^2 on the target surface, electric current from a DC power supply was delivered to the stainless-steel plate through a slip ring and two copper bus bars that were positioned on both ends of the stainless-steel plate and acrylic plate. The thermo- chromic liquid crystals (TLC) sheet that was attached on the target surface measured distribution of temperature near wall. The colors of TLC sheet will change as the temperature changes. The TLC sheet was calibrated with T-type thermocouple in order to show the relation between hue and temperature of the target surface in Fig.7. it was shown distribution of temperature by capture a picture on TLC sheet which had controlled light by LED strip light. The pictures that were captured in experiment were converted image processing technique by MATLAB 2018a.

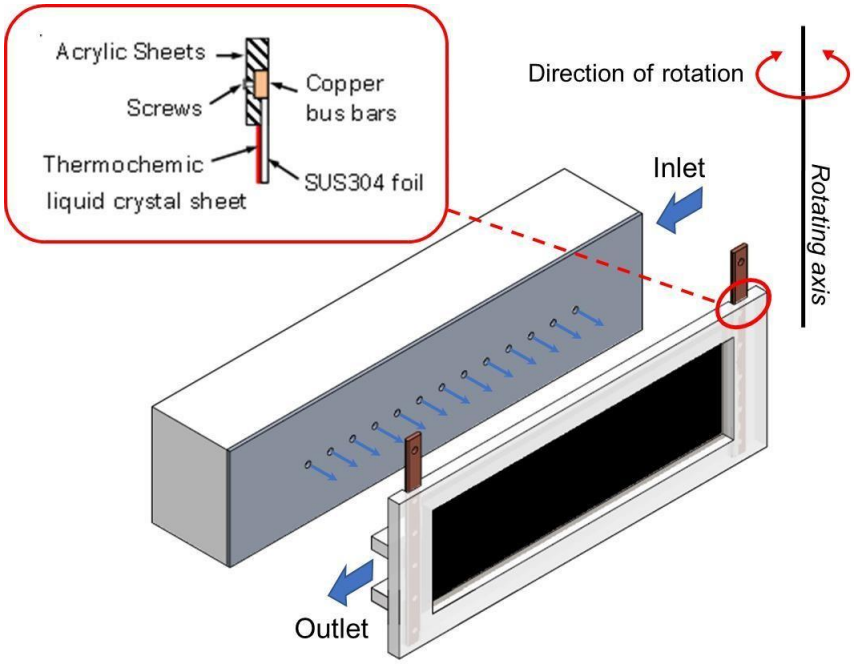


Fig. 6. Experimental setup for study of heat transfer measurement

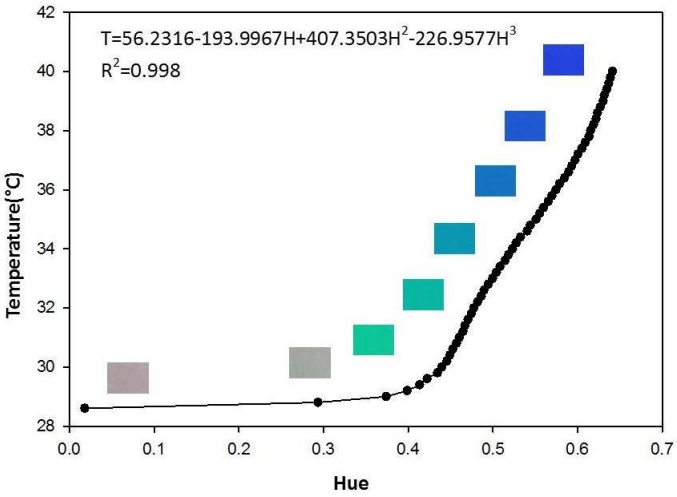


Fig. 7. The relation between hue and temperature of the target surface

3. Results

3.1The heat transfer measurement on rotating channel

The heat transfer from single row jet can be shown Nusselt number distribution on target surface jet impingement distance at L=2D fixed Reynolds number at 10,000, from the Reynolds number calculated with impinging jet having diameter at 5mm.In addition from the measurement varied rotational speed at 0, 200 and 400 rpm become to Rotation number (R_o) at 0, 0.0033 and 0.0066 respectively, from the direction leading side and trailing side.The result in Fig.9. it has been observed that Nusselt number distribution from jet near the impingement channel exit can be show crossflow in all condition. The position of jet 1 gave highest Nusselt number and decrease to position jet 10 also rotating channel decrease Nusselt number was effacted to heat transfer from leading side case and trailing side case compared non-rotating with stationary case.

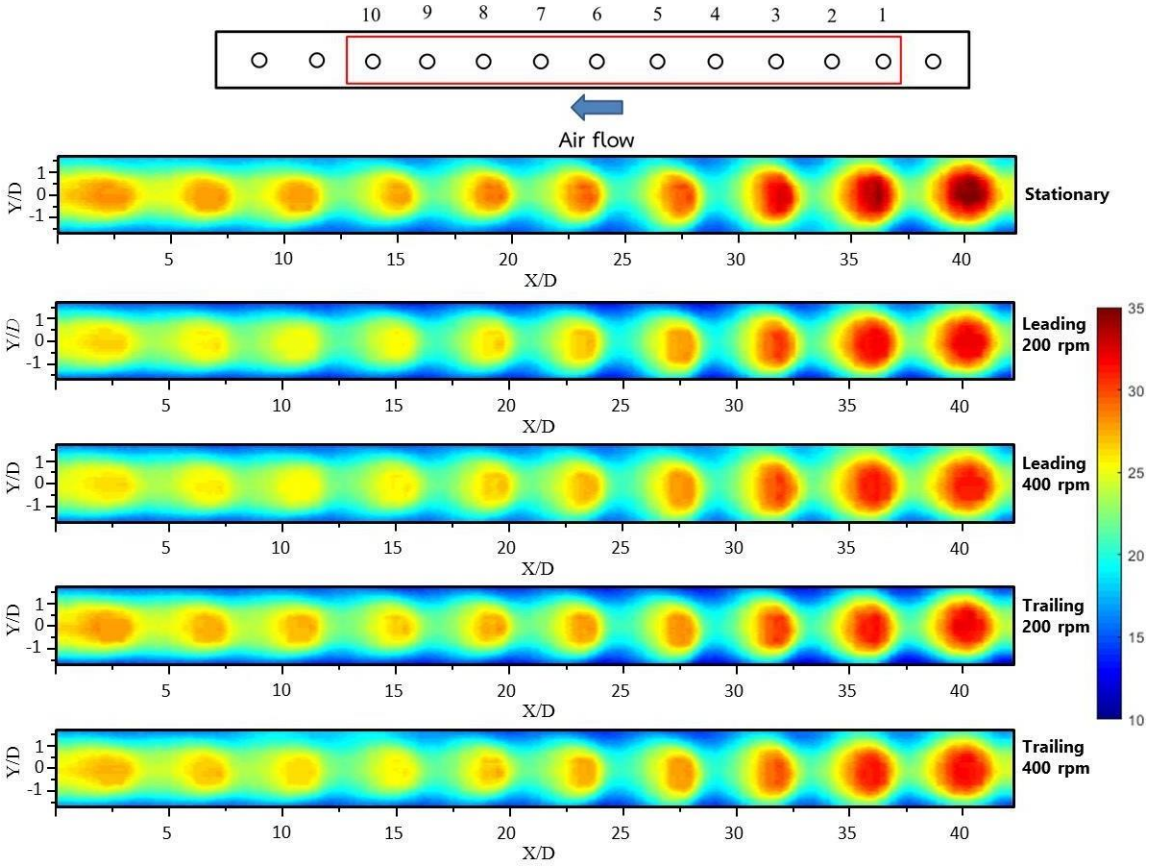


Fig.9. Contour of Nusselt number on impinging jet for L = 2D and Re = 10,000

The local Nusselt number at Y/D=0 in Figure 10, that position gave highest heat transfer, from the jet 1,2 and 3 with rotating leading side and trailing side to gave Nusselt number similar with rotation speed varied from the measurement and lowest then non-rotating with stationary. From near exit impingement channel with leading side at rotation speed 200 rpm, 400 rpm gave similar local Nusselt number, with trailing side gave different local Nusselt number clearly and from the rotation speed at 200 rpm gave high Nusselt number more than 400 rpm, However from the measurement local Nusselt number the result can be show with non-rotating at stationary gave highest Nusselt number in different operating condition.

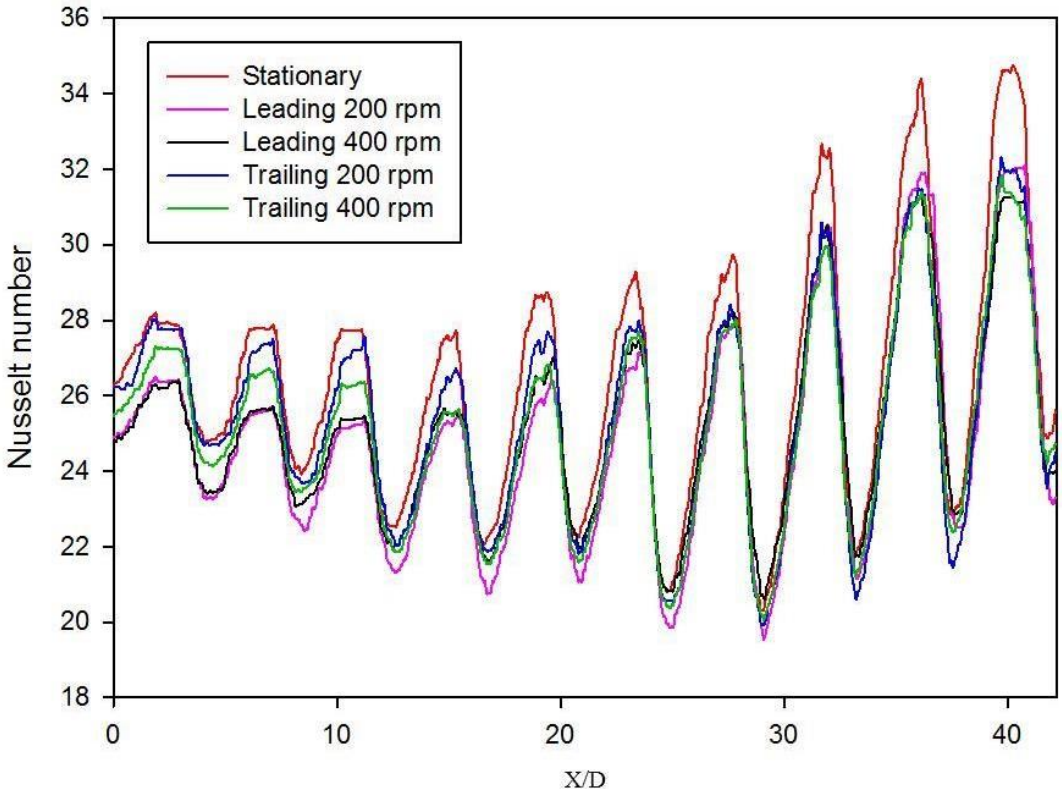


Fig.10. The Local Nusselt number distribution along X-axis passing at Y/D=0

4. Conclusions

The heat transfer on the jet impingement surface was measured by using a steady Thermo-chromic Liquid Crystal technique. The experimental parameter was single row jet, jet impingement distance at L=2D fixed Reynolds number at 10,000, jet diameter had 5mm.In addition from the measurement varied rotational speed at 0, 200 and 400 rpm become to Rotation number (R_o) at 0, 0.0033 and 0.0066 respectively. The result for study show that rotation effect on Nusselt number of leading side and trailing side that were lower than non-rotation with stationary because from Coriolis and centrifugal acceleration had the result decrease heat transfer. Jet number position at 1, 2 and 3 all rotation case approximately had the local Nusselt number and clearly less than in stationary case. For near the impingement channel exit, the local Nusselt number of leading side at 200 rpm, 400 rpm had similar values and minimum values when compare with all case. At trailing side 200 rpm more than 400 rpm had local Nusselt number.

Acknowledgement

This research was funded by a grant from Department of Mechanical Engineering, Faculty of Engineering, Prince of Songkla University, Thailand.

References

[1] Ligrani,P.M., Mahmood,G.I.,"Variable property Nusselt numbers in a channel with pin fins", *Journal of Thermophysics and Heat Transfer*, no.17(2003):pp. 103–111.

[2] Siddique,W., Khan,N.A., Haq,I.,"Analysis of numerical results for two-pass trapezoidal channel with different cooling configurations of trailing edge: the effect of dimples", *Applied Thermal Engineering*, no. 89(2015):pp. 763–771.

[3] Chen,Y., Chew,Y.T., Khoo,B.C.,"Heat transfer and flow structure in turbulent channel flow over

protrusions",*International Journal of Heat and Mass Transfer*, no. 66(2013):pp. 177–191.
[4] Wang,C., Liu,Z.L., Zhang,G.M., Zhang,M.,"Experimental investigations of flat plate heat pipes with interlaced narrow grooves or channels as capillary structure", *Experimental Thermal and Fluid Science*, no. 48(2013):pp. 222–229.
[5] Kreith,F., Margolis,D.,"Heat transfer and friction in turbulent vortex flow", *Applied Scientific Research*, no.8(1959):pp. 457–473.
[6] Han,J.C., Chen,H.C.,"Turbine blade internal cooling passages with rib turbulators", *Journal of Propulsion and Power*, no. 22:pp(2006). 226–248.
[7] Chupp,R.E., Helms,H.E., McFadden,P.,W., Brown,T.R.," Evaluation of Internal Heat-Transfer Coefficients for Impingement-Cooled Turbine Airfoils", *Journal of Aircraft,* no.6(1969):pp. 203–208.
[8] Kaewchoothong,N., Maliwan,K., Takeishi,K., Nuntadusit,C.," Effect of rotation number on flow and heat transfer characteristics in serpentine passage with ribbed walls", *Journal of Mechanical Science and Technology*, no.32(2018):pp. 4461–4471.
[9] San,J.Y., Lai,M.D.,"Optimum jet-to-jet spacing of heat transfer for staggered arrays of impinging air jets", *International Journal of Heat and Mass Transfer*, no.44(2001):pp. 3997-4007.
[10] Esposito,E.I.,"Jet impingement cooling configurations for gas turbine combustion", Thesis of Master in Mechanical Engineering, Louisiana State University(2006).
[11] Geers,L.F.G., Tummers,M.J., Bueninck,T.J., Hanjalic,K.,"Heat transfer correlation for hexagonal and in-line arrays of impinging jets", *International Journal of Heat and Mass Transfer*, no. 51(2008):pp. 5389-5399
[12] Elston,C.M., Wright, L.M., "Leading Edge Jet Impingement Under High Rotation Numbers." *Journal of Thermal Science and Engineering Applications*, no.120(2015):pp. 368-375.
[13] Chang,W.S., Yu, K.,"Thermal performance of radially rotating trapezoidal channel with impinging jet-row" *International Journal of Heat and Mass Transfer*, no.136(2019):pp. 246-264.
[14] Yang,L., Tyag,K., Ekkad,S., Ren,J., "Influence of Rotation on Heat Transfer in A Two-pass Channel with Impingement Under High Reynolds Number" Turbine Technical Conference and Exposition, June 15-19, Canada(2015).
[15] Pason,J.A., Han,J.C. Lee,C.P.,"Rotation Effect on Jet Impingement Heat Transfer in Smooth Rectangular Channels With Four Heated Walls and Radially Outward Crossflow" *Journal of Turbomachinery*,no.120(1998):pp. 79-85.
[16] Wagner,J.H., Johnson,B.V., Kopper,F.C.,"Heat Transfer in Rotating Serpentine Passages With Smooth Walls," *ASME J. Turbomach*., no.113(1991):pp. 321–330.
[17] Parsons,J.A., Han,J.C., Zhang,Y.,"Wall Heating Effect on Local Heat Transfer in a Rotating Two-Pass Square Channel With 90° Rib Turbulators," *International Journal of Heat and Mass Transfer*, no.37(1994):pp. 1411– 1420.
[18] Liou,T.M., Chen,C.C., Chen,M.Y.,"TLCT and LDV Measurements of Heat Transfer and Fluid Flow in a Rotating Sharp Turning Duct," *International Journal of Heat and Mass Transfer*, no.44(2001):pp. 1777–1787.
[19] Taslim,M.E., Rahman,A., Spring,S.D.,"An Experimental Investigation of Heat Transfer Coefficients in a Spanwise Rotating Channel With Two Opposite Rib-Roughened Walls," *ASME J. Turbomach*., no.113(1991):pp. 75–82.
[20] Lamont,J.A., Ekkad,S.V., Alvin,M.A.,"Effects of Rotation on Heat Transfer for a Single Row Jet Impingement Array With Crossflow" *Journal of Heat Transfer*, no.134(2012):pp. 082202.
[21] Kaewchoothong,N., Maliwan,K., Takeishi,K., Nuntadusit,C., "Effect of inclined ribs on heat transfer coefficient in stationary square channel", *Theor. Appl. Mech*. no. 7(2017):pp. 344–350.

Penerbit Akademia Baru

Engineering Science and Technology Conference Proceedings

Journal homepage: www.akademiabaru.com/EST.html

Temperature Profile Assessment of Sub-Bituminous Coal using a Single Burner Combustion Test Facility

Open Access

M.S.H. Mohd Samsuri[1,*], H. Hasini[2] , N.A.W. Mohd Noor[1], M.M.F. Meor Zulkifli[1]

[1] Fuels & Combustion Group, Generation & Environment Unit, TNB Research Sdn. Bhd., 43000 Kajang, Selangor, Malaysia
[2] Fluid Dynamics & Risk Reduction Research Group, Department of Mechanical Engineering, Faculty of Engineering, University Tenaga Nasional, 43000, Kajang, Selangor, Malaysia

ABSTRACT

This paper presents a thermogravimetric analysis and combustion test for different coals used in a coal-fired power plant in Malaysia. The main objective is to investigate the suitability of adopting a newly-introduced sub-bituminuous coal in an existing boiler furnace commonly firing standard design coals. In order to ensure that the new coal will not give an adverse effect to the boiler, detail analytical and thermal performance of the new coal is investigated, together with design and other limiting coals. The combustion test was performed in a scaled down, 150kW, single swirl burner combustion test facility available in TNB Research Sdn. Bhd. In the study, combustion gas temperature at different sectors downstream of burner region is measured to determine the peak temperature for all tested coals. Based on the investigation, it was noted that coal with the highest fixed carbon content gives the highest temperature measure at all sectors. Similarly, coal with the lowest fixed carbon gives the lowest temperature. The temperature profile for the newly tested coal was found to be comparable to the design and limiting value coals. Even though it was observed that the temperature given by the new coal is the highest slightly downstream of the burner, the temperature was observed to be decreases as combustion gas flow downstream of the combustor rig. Based on the observation it can be said that the new coal is suitable to be used by the existing boiler furnace.

Keywords:
Combustion test, Temperature profile, Coal

Copyright © 2019 PENERBIT AKADEMIA BARU - All rights reserved

1. Introduction

Coal has been widely used in the work until today for various purposes and one of the significant users of coal is power generation industry. It is known that pollution generated from coal combustion is harmful to human and environment, it cannot be denied that the dependence on coal as the main source for energy is still significant. In recent years, coal quality degradation gives a negative impact on coal-fired power plants. The current practice relies on coal certificate of analysis for assessment of newly-introduced coal before firing at power plant, however it is insufficient to illustrate the combustion behaviour of the coal sample. In Malaysia, research on the coal qualification to achieve the requirements of coal-fired power plant has not been widely explored, hence, offers the opportunity for study of assessment through analytical and combustion tests.

The introduction of coal blending method is one of the solutions to the aforementioned problem by blending low with higher-grade coals [1]. This method was done by past researchers with their own blending ingredients. Coal blending also can be a useful tool to reduce the

* *Corresponding author.*
E-mail address: ()

concentration of sulphur, mercury and other pollutants [2-5]. Generally, there are two approaches in determining blended ratio i.e. computational analysis and analytical fuel tests. Jin et al. [6] used multi-objective decision-making method based on fuzzy mathematics to determine the optimum blending ratio. Xi et al. [7] came up with different approach to optimize the coal blending properties by using Adaptive Simulated Annealing Genetic Algorithm (ASAGA). In addition of having a powerful optimizing ability, genetic algorithm also provides an impressive computing speed [8]. However, due to its limitation, this basic algorithm always produced insufficient information, also known as "premature" outcome [9]. These methods however might not be sufficient to illustrate the complexity of combustion behavior during coal firing. As mentioned by Biswas et al. [10], furnaces are designed for the use of specific fuels, and the substitution of the designed coal as well as the unpredictability of blended coal behaviour have become a great challenge for the plant operation. Prediction of the combustion behaviour inside the furnace cannot be made on the basis of these conventional analysis alone [11]. The blended coal composition may resemble the design coal, but the blend behaviour during the combustion may not be the same as expected [11]. The complexity of co-fired reaction of different ranks blended coal at the burner zone triggers the need of combustion test to simulate the combustion behaviour in pilot-scale [12].

Thus, the need of combustion test is crucial in illustrating the coal combustion behaviour. The complexity of several analytical properties could be summarised into one temperature profile which gives an overview of the combustion behaviour. The scaled down combustor might not be similar to the power plant, however the comparison of combustion tests between different coals could be made. It is important to have consistent parameters (e.g. excess air, coal flow, secondary air temperature, etc.) to prevent biasness between the combustion tests. This was proved by Toshiyuki et al. who studied the characterization and behaviour of pulverized coal combustion, and highlighted that less excess air leads to oxygen deficiency which results in increasing of unburned coal while reducing the NO_x emissions [13-17]. However, Debo et al. concluded that the increasing of air fuel ratio will reduce the CO formation; reacts with the excess oxygen to produce carbon dioxide however the emission of NO_x pollutant may also increases [18]. Thus, the optimal amount of 10-15% excess air is required for a common boiler combustion process [19]. Therefore, a properly controlling sets of parameters will be the key factor in enhancing the combustion efficiency.

2. Methodology

2.1 Analytical Test

2.1.1 Thermogravimetry analyser (TGA)

The TGA measures four basic properties of the coal sample namely inherent moisture, volatile matter, fixed carbon and ash content based on sample weight loss for a specific heating program. Other important parameters that could be deduced from the TGA plot are ignition and burnout temperatures, where the former indicates the minimum temperature at which the fuel ignites spontaneously, while the later indicates the temperature at which the fuel conversion reaches 99% as shown in Figure 1 (Note that a random coal sample is used in the figure for explanation purpose).

From this figure, the ignition temperature can be determined by identifying the initial point where coal mass starts to drop significantly, due to combustion. These values are then used to measure the overall combustibility index of the samples using Eq. (1).

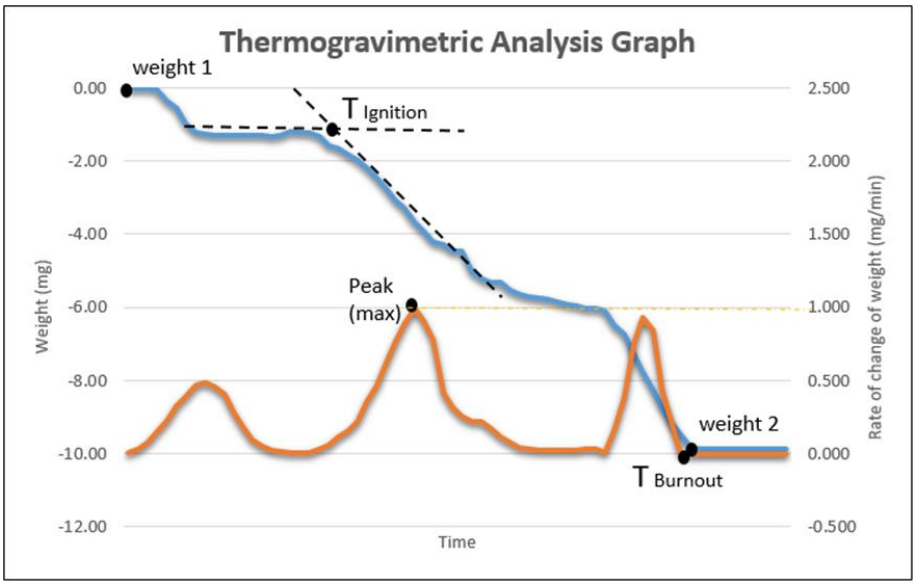


Fig. 1. Thermogravimetric data analysis (the blue and orange lines indicate the weight and rate of change of weight respectively)

Theoretically, the higher the index, the better the combustibility. However, if the 'designed coal' of a specific boiler is to be replaced, a new coal with the closest combustibility index value is always preferred. Maintaining this value would ensure the hotspot region or the flame profile of the new coal to mimic the 'designed coal'. In addition to this, several other factors such as combustion stability, coal particle trajectory trend etc. have to be assessed as well. Please note that for coal-fired boiler applications, coal that has a higher combustibility index (as compared to the designed coal) would potentially generate flame hotspots near the burner, while coal with a lower combustibility index would stretch the flame further downstream. The former usually leads to slag build-up at the radiation zone while the latter would increase the risk of secondary flame and related issues.

$$\text{Combustibility Index, Si} = \frac{{}^{dW}/_{dt}(max) \;\; x \;\; {}^{dW}/_{dt}(mean)}{Ti^2 \;\; x \;\; Tb} \quad (1)$$

$\frac{dW}{dt}(max)$ = rate of change of weight (max)
$\frac{dW}{dt}(mean)$ = rate of change of weight (mean)
Ti = Ignition temperature
Tb = Burnout temperature

2.1.2 CHNSO analyser

The main elemental components of the coal under investigation are determined using a CHNSO analyser. This information is important in determining the stoichiometry ratio of air and fuel, $AFR_{Stoichiometry}$ to achieve complete combustion using Eq. (2).

$$AFR_{Stoichiometry} = \frac{\dot{m}_{s,air}}{\dot{m}_{s,fuel}} \quad (2)$$

The ratio is then used to determine both mass flow rates of air and fuel for the combustion testing activity. Note that the excess air of 10% (ER = 1.1) is used for all combustion tests reported in this study. The equivalence ratio is then determined and read as:

$$\text{Equivalent Ratio (ER)} = \frac{AFR_{Actual}}{AFR_{Stoichiometry}} \quad (3)$$

To ensure a reasonable comparison between one sample to another, the mass flowrate of coal ($\dot{m}_{a,fuel}$) is fixed at 10kg/hr. The air-to-fuel ratio and air mass flowrate are determined using Eqs. (4) and (5) respectively:

$$AFR_{Actual} = \frac{\dot{m}_{a,air}}{\dot{m}_{a,fuel}} \quad (4)$$

$$\dot{m}_{a,air} = ER \times AFR_{Stoichiometry} \times \dot{m}_{a,fuel} \quad (5)$$

2.2 Combustion Test

Figure 2 shows the schematic diagram of the 150 kW combustion test rig used for the combustion analysis. The combustion test rig is equipped with a single swirl burner that has a fuel feed capacity of 10 – 40 kg/ hour, slagging and fouling probes, thermocouples as well as a flue gas analyser. The combustor main sections consist of the air and fuel inlet, main combustion section, heat exchanger and cyclone. The facility is capable of carrying out complete combustion tests that enable temperature profiles/ flame structure, ash deposition formation and flue gas emission analyses to be measured. The combustor is arranged in an L-shape configuration to mimic a real boiler configuration, whereby the radiation (high temperature furnace/ flame zone) and convection zones could be differentiated.

Primary air is used as a medium to transport the solid fuel sample while the secondary air acts as an oxidising agent for the combustion process. Based on this analysis, prediction of flame behaviour such as combustion delay can be determined and the thermal properties from thermogravimetric analysis can be justified.

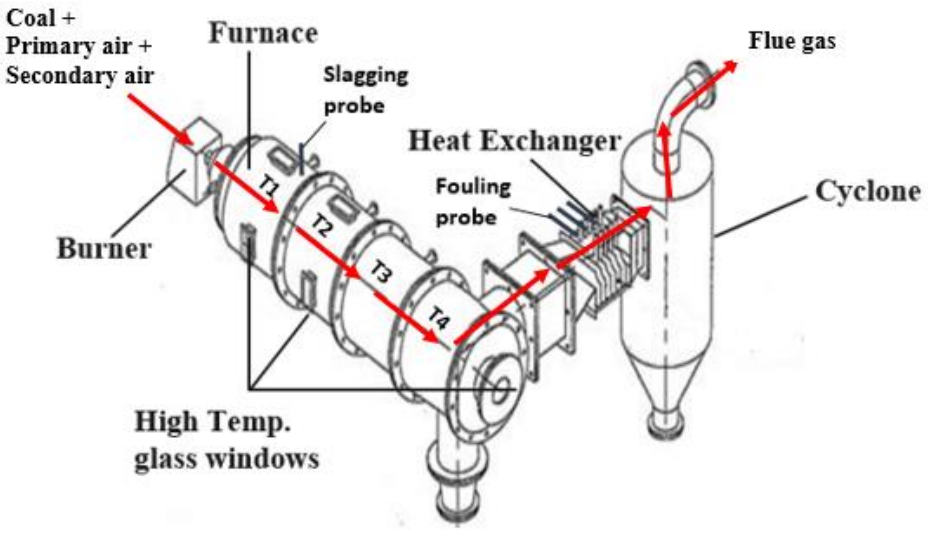


Fig. 2. Schematic diagram of a combustion test rig [20]

To ensure the combustion testing results are meaningful and comparable, the fuel feed rate and air to fuel ratio (A/F) for each test were maintained at 10 kg/hr and 10% excess air respectively. Details of the combustion test parameters for this work is shown in Table 1.

Table 1.
Parameters for combustion test

Parameters	X	A	B	C
Fuel				
Flowrate (kg/hr)	10	10	10	10
Primary Air				
Temperature (°C)	27	27	27	27
Flowrate (m3/hr)	5.5	5.5	5.5	5.5
Secondary Air				
Temperature (°C)	250	250	250	250
Flowrate (m3/hr)	82.2	77.8	95.3	77.0
Air to fuel ratio				
Equivalent Ratio	1.1	1.1	1.1	1.1

2.2.1 Coal samples

In this study, coal gravimetric analysis and combustion test is carried out on 4 different coal types, namely Coal A, Coal B, Coal C and Coal X. Coal A is used as a designed coal while Coal B and Coal C (used as limiting values) are considered as the bad coals due to extreme high and low temperature generated at power plant. Coal X is a newly introduced, sub-bituminuous coal, yet to be fired in the same power plant boiler furnace. However, due to unknown effect and boiler response to this coal, detail analysis and combustion test needs to be carried out to ensure that it does not have a negative implication to the existing boiler.

The results of analytical tests (i.e. proximate and ultimate analyses) are used to prepare and illustrate the combustion behaviour of four different coal samples, while the temperature profiles obtained from the combustion tests are used to further analysed the actual combustion behaviour of the samples. The global stoichiometry of each fuel and the amount of air needed in terms of volume flow rate is calculated using the ultimate analysis result (as-determined) as presented in Table 2 latter. The secondary air flow rate for each coal are different to maintain the approximately 15-20% excess air in all coal combustion cases.

3. Results and Discussions

3.1 Analytical Test Results

Results from the analytical tests are tabulated in Table 2. Comparing between different coals, it was noted that the properties are in closed range except for a few significant differences for some parameters. Based on the results obtained, Coal X is suspected to give combustion delay due to lower volatile matter and higher ignition temperature as compared to Coal A. Besides, higher fixed carbon is found for Coal X as compared to the designed coal i.e. Coal A might indicate a higher energy released and higher temperature generated during combustion process. However, these assumptions are insufficient without supporting information, hence combustion test analysis is required to justify the assumptions mentioned.

Table 2
Analytical test results

Properties (Air dried basic)			Sample Type			
			X	A	B	C
Proximate analysis	Moisture (Inherent)	%	9.63	13.30	6.55	13.45
	Volatile Matter	%	39.41	43.80	40.98	42.30
	Fixed Carbon	%	44.14	41.25	45.32	40.50
	Ash Content	%	6.83	1.65	7.16	3.75
	$T_{ignition}$	%	379.33	343.10	384.80	340.10
	$T_{ignition}$	%	938.93	938.80	940.05	939.70
	Combustibility index, Si (10^{-9})	%	1.63	1.69	1.70	1.55
Ultimate analysis	Carbon (C)	%	63.00	61.80	73.45	60.80
	Hydrogen (H)	%	6.00	5.63	5.76	5.62
	Nitrogen (N)	%	1.74	1.09	1.46	0.95
	Oxygen (O)	%	11.97	16.26	5.10	15.31
	Sulphur (S)	%	0.83	0.27	0.53	0.11

3.2 Temperature Profiles and Flame Behaviour of Different Coals

Comparison of temperature measurement at four different combustor sections (refer Figure 2) for the different coal samples are shown in Figure 3. All coals under test show almost the same temperature profiles as temperature is measured from sector 1 just downstream of the burner to sector 4, just before the 90° turns towards the heat exchanger. Coal B gives the highest temperature consistently throughout the sectors and this could be attributes to the fact that this coal possesses the highest fixed carbon as compared to other coal samples. On the other hand, Coal C was found to give the lowest temperature throughout combustor sectors due to its lowest fixed carbon content. In addition, the inherent moisture for this coal is the highest and this could also yield lowest temperature as energy produced were given up to overcome the enthalpy of vaporization of the moisture. A low temperature at T4 for all coals indicate that most of the combustible elements within the coal particle are consumed at the upstream sections.

When a new coal (Coal X) is introduced to be used together with other design coal, it was found the thermal performance is comparable. It was noted, however that the temperature recorded at sector 1 for Coal X is the highest. Also, the temperature profile is also found to be consistent as combustion gas travels downstream towards the combustor exit. This behaviour is also in comparison to other design coals. Higher temperature generated by Coal X at Sector 1 was found not to be an issue as the value decreases downstream of the flow. The high temperature recorded closed to burner region demonstrates one of its thermal properties, i.e. higher ignition temperature and this does not affect the flame structure in terms of combustion delay/ stability near the burner proximity. The surrounding temperature near the burner is high enough to 'self-ignite'

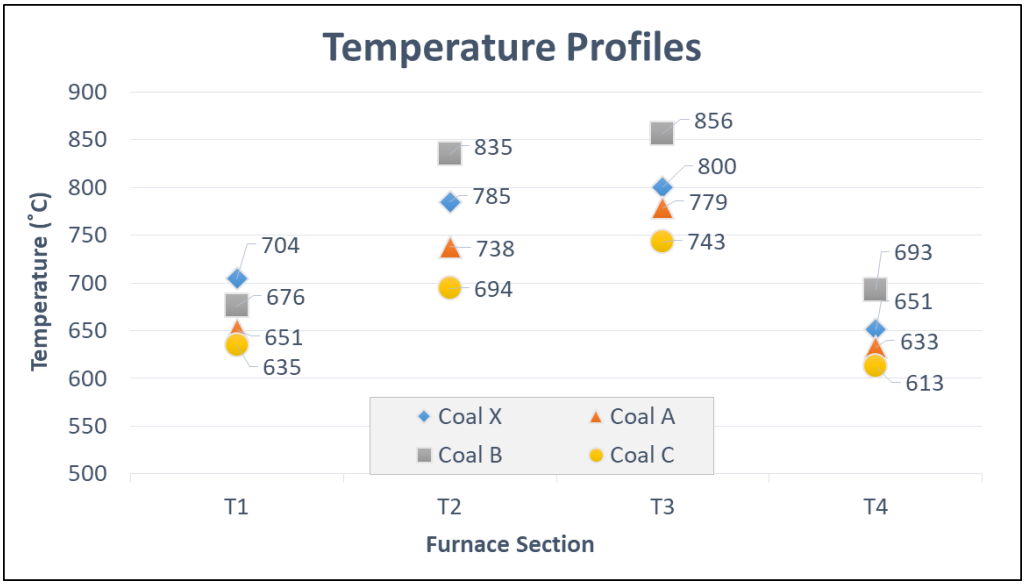


Fig. 3. Comparison of temperature profiles for different coal samples

4. Conclusions

Thermogravimetric analysis and combustion test of four different coals have been performed with the objective to determine suitability of a newly introduced coal to be fired in an existing boiler furnace firing only manufacturer's recommended coals. The combustion test was carried out in a scaled down combustor test facility available at TNB Research Sdn. Bhd. Based on the investigation, the following conclusions can be withdrawn:

i. Analytical test result shows comparable properties of the new coal (Coal X) as compared to other design coals (Coals A, B and C), except for the percentage of volatile matter, which was the lowest for this coal.
ii. The general temperature profiles for all tested coals show an identical profile with maximum temperature recorded at Sector 3 and minimum at Sector 4.
iii. Design Coal B gives the highest temperature in all sectors measured due to the highest fixed carbon content.
iv. Design Coal C gives the lowest temperature in all sectors measured due to its lowest fixed carbon content. In addition, the low temperature can also be attributed to the highest amount of inherent moisture possessed by this coal. Heat released is expected to be used to overcome the enthalpy of evaporation of the moisture.
v. Combustion performance of Coal X is also found to be comparable to other design coals even though it was noted that it gives higher peak temperature just downstream of the burner region. Further downstream, the temperature was reduced and within the range of other design coal temperature, thus it can be said Coal X is safe to be fired in the boiler.

Acknowledgement
This research was funded by a service project from Fuels & Combustion Group, TNB Research Sdn. Bhd. The second author would also like to acknowledge the financial support received from the Ministry of Education Malaysia under the FRGS scheme (20180110FRGS). The financial assistance from UNITEN BOLD Talent Scholarship programme is also acknowledged.

References

[1] Central Electricity Authority, Ministry of Power, Government of India, New Delhi. Report of the Group for Studying Range of Blending of Imported Coal with Domestic Coal, April 2012, p. 3. <www.cea.nic.in/reports/others/thermal/tetd/blending_coal.pdf>

[2] Wang, Qunying, Lian Zhang, Atsushi Sato, Yoshihiko Ninomiya, and Toru Yamashita. "Effects of coal blending on the reduction of PM10 during high-temperature combustion 1. Mineral transformations." *Fuel* 87, no. 13-14 (2008): 2997-3005.

[3] Wang, Q., L. Zhang, A. Sato, Y. Ninomiya, and T. Yamashita. "Reduction of PM10 by combustion of coal blends." In *6th Asia-Pacific conference on combustion program of ASPACC007, Nagoya, Japan*. 2007.

[4] Wang, Qunying, Lian Zhang, Atsushi Sato, Yoshihiko Ninomiya, and Toru Yamashita. "Effects of coal blending on the reduction of PM10 during high-temperature combustion 2. A coalescence-fragmentation model." *Fuel* 88, no. 1 (2009): 150-157.

[5] Sloss, Lesley. *Legislation, standards and methods for mercury emissions control*. IEA Clean Coal Centre, 2012.

[6] Jin, Y. A., J. W. Cheng, Q. Bai, and W. B. Li. "Study on the coal mixing ratio optimization for a power plant." In *IOP Conference Series: Materials Science and Engineering*, vol. 283, no. 1, p. 012019. IOP Publishing, 2017.

[7] Xi-jin, Guo, Chen Ming, and Wu Jia-wei. "Coal blending optimization of coal preparation production process based on improved GA." *Procedia Earth and Planetary Science* 1, no. 1 (2009): 654-660.

[8] Zhuang, X. C., Y. H. Lu, and Congxin LI. "Solving Job Shop Scheduling Problem by Genetic Algorithm." *Computer Engineering* 1 (2006): 193-195.

[9] Hwang, Shun-Fa, and Rong-Song He. "Improving real-parameter genetic algorithm with simulated annealing for engineering problems." *Advances in Engineering Software* 37, no. 6 (2006): 406-418.

[10] Biswas, Subhasis, Nandita Choudhury, P. Sarkar, A. Mukherjee, S. G. Sahu, P. Boral, and A. Choudhury. "Studies on the combustion behaviour of blends of Indian coals by TGA and drop tube furnace." *Fuel Processing Technology* 87, no. 3 (2006): 191-199.

[11] Raaj, S. Santhosh, S. Arumugam, M. Muthukrishnan, S. Krishnamoorthy, and N. Anantharaman. "Characterization of coal blends for effective utilization in thermal power plants." *Applied Thermal Engineering* 102 (2016): 9-16.

[12] Ulloa, C., A. G. Borrego, S. Helle, A. L. Gordon, and X. García. "Char characterization and DTF assays as tools to predict burnout of coal blends in power plants." *Fuel* 84, no. 2-3 (2005): 247-257.

[13] Suda, Toshiyuki, Makoto Takafuji, Tetsuya Hirata, Motoki Yoshino, and Junichi Sato. "A study of combustion behavior of pulverized coal in high-temperature air." *Proceedings of the combustion Institute* 29, no. 1 (2002): 503-509.

[14] Katsuki, Masashi, and Toshiaki Hasegawa. "The science and technology of combustion in highly preheated air." In *Symposium (International) on combustion*, vol. 27, no. 2, pp. 3135-3146. Elsevier, 1998.

[15] Flamme M., and Kremmer H. "NOx Emission and reduction potential from industrial gas burners with air preheat temperatures of up to 1,000^{oC}." *Proceedings of European Conference on Natural Gas Policies and Technologies, Athens, Greece*, (1992):136-144.

[16] Yuan J., and Naruse I. "Effects of air dilution on highly preheated air combustion in a regenerative furnace." *Energy Fuels*, 13 (1999): 99.

[17] C.E. Baukal, Oxygen-Enhanced Combustion, second ed., CRC Press, 2013.

[18] D. Li, Q. Lv, Y. Feng, C. Wang, X. Liu, K. Chen, K. Xu, J. Zhong, D. Che. Effects of Coal Blending and Operating Conditions on Combustion and NO_X, Emission Characteristics in a Tangentially-fired Utility Boiler. Energy Procedia 105 (2017) 4015-4020.

[19] Molina A., Shaddix C. R. Ignition and devolatilization of pulverized bituminous coal particles during oxygen/carbon dioxide coal combustion. Proceedings of the Combustion Institute 31 (2007) 1905-1912.

[20] H. Hassan, M. T. Lim, A. Ahmad, H. A. Hamid, N. M. Noor. Development of a Solid Fuel Testing Rig Facility for Research in Coal Combustion Performance. Journal of Mechanical Engineering and Automation 2015, 5(3A): 6-11.

Penerbit Akademia Baru

Engineering Science and Technology Conference Proceedings

Journal homepage: www.akademiabaru.com/EST.html

The Effect of Liquid Viscosity on The Gas-Liquid Two-Phase Flow Pattern In 45° Inclined Capillary Pipe

Open Access

Sudarja[1,*], Sukamta[1], Deendarlianto[2], Indarto[2]

[1] Department of Mechanical Engineering, Universitas Muhammadiyah Yogyakarta, Yogyakarta 55183, Indonesia
[2] Department of Mechanical and Industrial Engineering, Gadjah Mada University, Yogyakarta 55281, Indonesia
[2] School of Mechanical Engineering, Faculty of Engineering, Universiti Teknologi Malaysia, 81310 Skudai, Johor, Malaysia

ABSTRACT

The experiment on flow pattern of gas-liquid two-phase flow in 45° inclined capillary channel were carried-out. The research was conducted in 1.6 mm inner diameter glass pipe. The range of gas superficial velocity was 0.025 - 66.3 m/s, while that of liquid was 0.033 - 4.935 m/s. The gas fluid was represented by dry air, while that of liquid was glycerol-aqua solution in various percentage, i.e. 0%, 10%, 20%, and 30% indexed by W, GL10, GL20, and GL30, respectively. The addition of glycerin to the liquid phase was intended to vary the liquid viscosities. The high-speed camera was used to capture the two-phase flow. The captured video images were then analyzed to obtain the flow pattern. As a result, it was found that both gas and liquid superficial velocities affect significantly to the two-phase flow pattern observed. Five flow patterns, namely: plug, slug-annular, churn, bubbly, and annular were observed, while the stratified flow was not obtained. On the other hand, the change of liquid viscosity affects to the shift of the transition line between flow patterns in the flow pattern map.

Keywords:
Gas-liquid two-phase flow, inclined capillary pipe, glycerol aqueous solution, liquid viscosity, flow pattern

Copyright © 2019 PENERBIT AKADEMIA BARU - All rights reserved

1. Introduction

Zhao and Bi [1] expressed that the application of the two-phase flow in the mini pipe is very wide, such as in the field of the cooling of high-density multi-chip modules in supercomputers, high-flux heat exchangers in aerospace systems, cryogenic cooling systems in satellites, and high-powered X-ray and other diagnostic devices. Furthermore, Kawahara *et al.,* [2] stated that the uses of those channels are in microelectronic circuits, aerospace and micro heat pipes, bioengineering applications. Other authors reported the study results on the two-phase flow in small size channel among others Tsaoulidis *et al.,* [3], Hassan *et al.,* [4], Lee and Lee [5], Saidi *et al.,* [6], Chung and Kawaji [7], and Zhao *et al.,* [8].

The basic parameters in two-phase flow are flow pattern, void fraction, and pressure gradient. The variables which influence to the basic parameters are gas superficial velocity, liquid superficial velocity, viscosity and surface tension of working fluids. Some researchers have been investigated the effects of liquid viscosity to two-phase flow parameters. They are among others Fukano and Furukawa [9], Furukawa and Fukano [10], Sowinski and Dziubinski [11], Matsubara and Naito [12], Mc Neil and Stuart [13], Zhao *et al.,* [14], Sadatomi *et al.,* [15], and Sudarja *et al.,* [16].

* *Corresponding author.*
E-mail address: Sudarja_msn@yahoo.com (Sudarja)

Fukano and Furukawa [9] carried-out a research on two-phase flow, which used water and glycerol solution for annular flow in vertical pipe with inner diameter of 26 mm. They concluded that the increase of liquid viscosity affected to the increase of interface friction factor for the same gas phase Reynolds number. Furthermore, Furukawa and Fukano [10] also concluded that the liquid viscosity has a significant effect to the liquid film structure around big bubble in slug flow. In line with Fukano and Furukawa [9] and Furukawa & Fukano [10], Mc Neil and Stuart [13] also reported that, in the high viscosity liquid, the interface friction factor were significantly different to that in the low viscosity liquid

From the above mentioned explanation, it can be concluded that no researcher carried-out the experiment and discussed about the effect of liquid viscosity to the characteristics of two-phase flow in mini or micro channel in incline position. Therefore, study on the effect of liquid viscosity on the gas-liquid two-phase flow pattern in 45° inclined capillary pipe was very important to be carried-out experimentally.

2. Methodology

Gas and liquids were used as working fluid in the present experiment. The dry air provided by air compressor which was equipped by water trap and dryer was used as gas phase fluid. While the liquid phase fluid were the mixture solution of water and glycerol in various percentage (10%, 20%, and 30%). The physical properties of air used in the present study (at 25°C and 1 atmosphere) were density (ρ) of 1.163 kg/m^3, dynamic Viscosity (μ) of 1,8573 x 10^{-5} kg/(m.s), and kinematic Viscosity (ν) of 1.597 x 10^{-5} m^2/s. Meanwhile, those of liquid shown in Table 1. The experimental apparatus used in the research is shown schematically in Figure 1, as also previously used and reported by Sudarja *et al.,* [16-17]. As depicted in that figure, the liquid was pressed by the compressed air in the pressure vessel and then fed to the mixer and test section. The test section was a 1.6 mm inner diameter and 130 mm length circular glass pipe. The curve effect of pipe surface was eliminated by an optical correction box. Two perpendicular entrance type mixer was used to mix both gas and liquid phase working fluid prior to test section.

Table 1
Physical properties of liquid

Fluids	Specific gravity	Kinematic viscosity [mm^2/s]	Surface tension [mN/m]	Index
Water	1	0.84	71.03	W
Water+10% glycerin	1.036	1.33	67.97	GL10
Water+20% glycerin	1.062	2.32	60.93	GL20
Water+30% glycerin	1.084	2.36	60.87	GL30

Two kinds of liquid flow meter from Omega and TOKYO KEISO, with accuracy of $\pm$ 5 % and $\pm$ 3 %, respectively, were used to measure the liquid flow rate. Nikon J4 high-speed video camera with speed of 1200 fps and resolution of 640 x 480 pixel was employed to capture the flow images. The ranges of gas and liquid superficial velocity (J_G and J_L) were 0,025 – 66,3 m/s, and 0,033 – 4,935 m/s, respectively. The condition of the experiment was adiabatic.

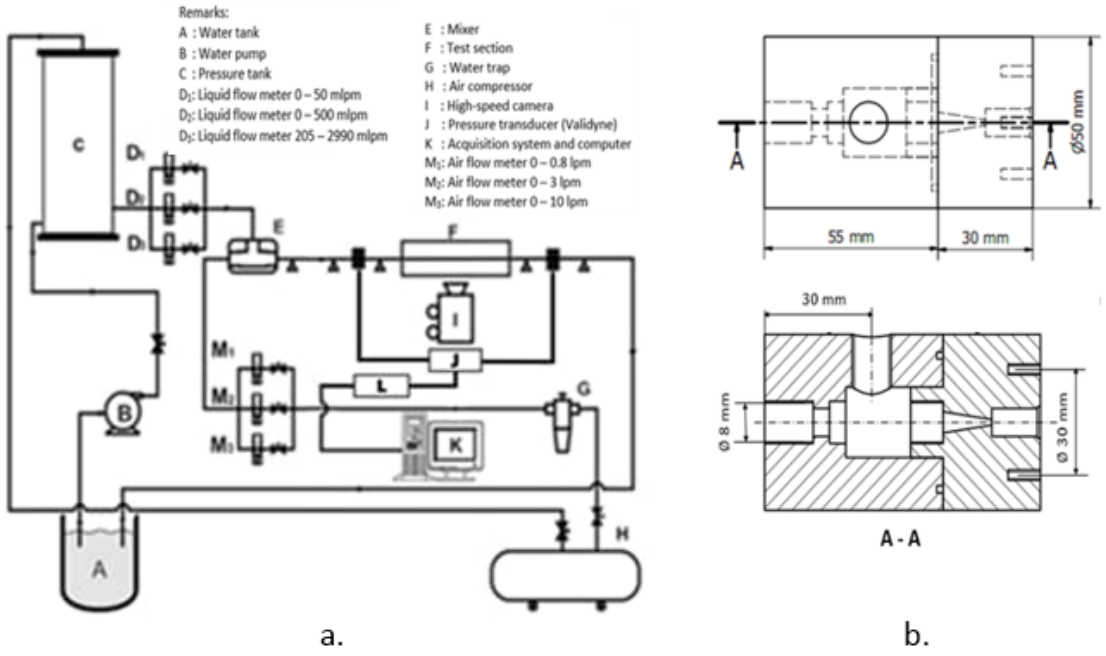


Fig. 1. (a). Schematic diagram of experimental apparatus, (b) mixer

3. Results

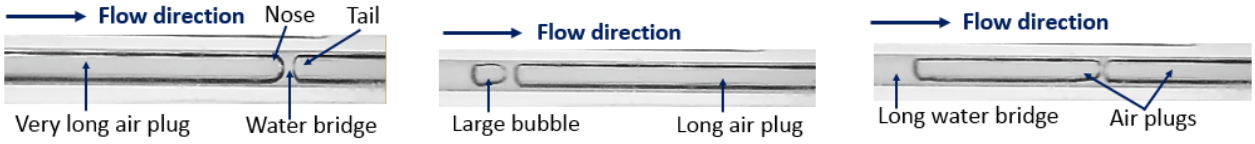
3.1 Flow Pattern

Five distinctive flow patterns was observed, namely plug, slug-annular, churn, annular, and bubbly were observed, while the stratified flow was not obtained. The absence of stratified or separated flow is caused by the dominance of surface tension effect against the gravitation one, as expressed by the previous researcher, such as Chung and Kawaji [7].

3.1.1 Plug flow

The slugs observed in the present study are in form of plugs, so that the flow is called as plug flow. Plug flow consists of gas plug (elongated bubble) and water bridge, which intermittently flow. Plug flow is occurred at low of both J_G and J_L, and at moderate J_G with low to moderate J_L. Fukano and Kariyasaki [18], and Saisorn & Wongwises [19] have ever reported that the plug length depended on J_G. Figures 2 and 3 illustrate the influences of J_G and J_L to the plug flow regime configuration. From those figure, it is clearly seem that parameter changes (increasing J_G or decreasing J_L) caused to form longer plug and shorter liquid bridge. This condition is an effect of the increasing void fraction, as ever been explained by Triplett *et al.,* [20].

The effect of liquid viscosity to the configuration of plug flow at the same J_G and J_L is illustrated in Figure 4. It is seen that, the plug length being shorter and the frequency being higher when the liquid viscosity is increased. Besides, the plug diameter is smaller when the liquid viscosity is increased, it means that the plug is surrounded by thin liquid film. This phenomenon has been reported previously by Sudarja *et al.,* [16].



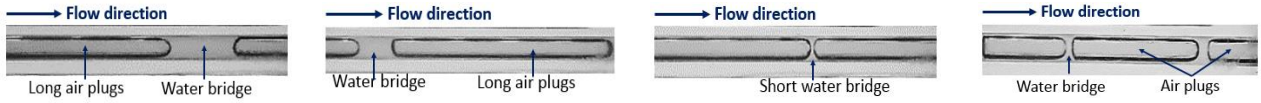
a. J_L = 0.232 m/s b. J_L = 0.539 m/s c. J_L = 0.89 m/s

Fig. 2. Plug flow at J_G = 0.207 m/s and various J_L for GL10, 45° inclined orientation



a. J_G = 0.116 m/s b. J_G = 0.207 m/s c. J_G = 0.423 m/s

Fig. 3. Plug flow at J_L = 0.539 m/s and various J_G for GL10, 45° inclined orientation



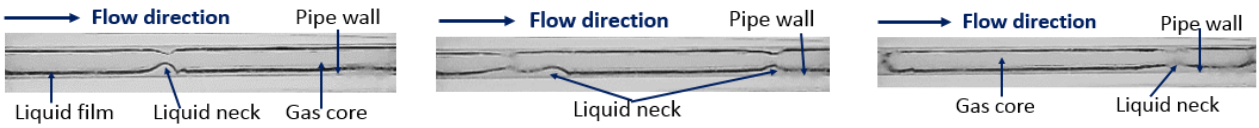
a. W b. GL 10 c. GL 20 d. GL 30

Fig. 4. Plug flow at J_G = 0.116 m/s and J_L = 0.033 m/s, for two-phase flow with various liquid viscosity, in 45° inclined orientation

3.1.2 Slug-Annular flow

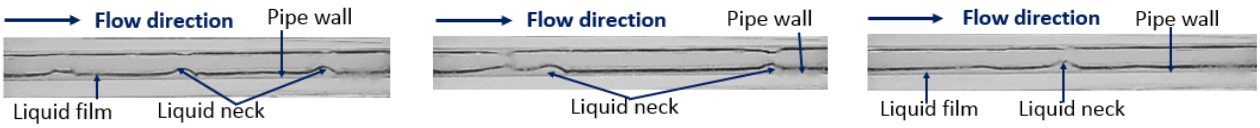
Slug-annular flow is formed from plug flow when the gas superficial velocity is increased up to a certain value, where the flow of air is able to push and pierce the water bridge. The gas flows in the centre of channel, and the liquid flows at the pipe wall, and both fluids form a ring flow. The liquid neck are formed at certain points, which the liquid rings are thicker than those at the other points. Therefore, it is then called as slug-annular flow.

Figure 5 shows the effects of the increase of J_L, where it is seen that liquid neck frequency is higher and those size is longer. Besides, liquid film becomes thicker. On the contrary, higher J_G caused decreasing of frequency of the liquid neck is and the size is shorter (Figure 6). In Figure 7, it can be concluded that the increased of liquid viscosity affects to the fewer and smoother liquid neck, also the thicker of liquid film.



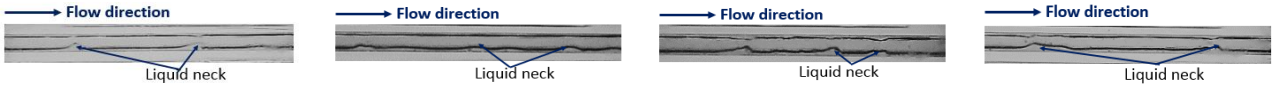
a. J_L = 0.091 m/s b. J_L = 0.149 m/s c. J_L = 0.232 m/s

Fig. 5. Slug-annular flow at J_G = 7 m/s and various J_L for GL10, 45° inclined orientation



a. J_G = 4.238 m/s b. J_G = 7 m/s c. J_G = 9.62 m/s

Fig. 6. Slug-annular flow at J_L = 0.232 m/s and various J_G for GL10, 45° inclined orientation

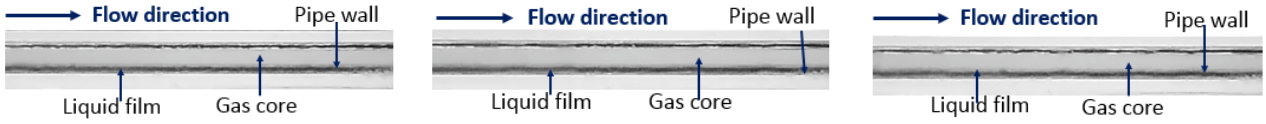


a. W b. GL 10 c. GL 20 d. GL 30

Fig. 7. Slug-annular flow at J_G = 4,238 m/s and J_L = J_L 0,091 m/s, for two-phase flow with various liquid viscosity, in 45° inclined orientation

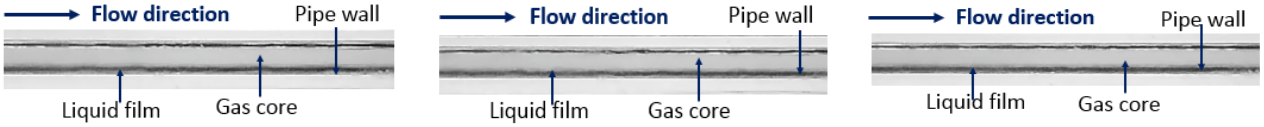
3.1.3 Annular flow

Annular flow or some authors called it ring flow, occurred at high J_G and low J_L. As shown in Figure 8, the increase of JG caused the thicker liquid film, conversely, the higher JG, the liquid film tends to thinner (Figure 9). The effect of the liquid viscosity to the annular flow pattern is exhibited in Figure 10. From that figure, it can be seen that the increase liquid viscosity led to the thicker liquid film and lower ripples. This condition is cause by the high viscous force which almost be able to overcome the shear force at the flow interface.



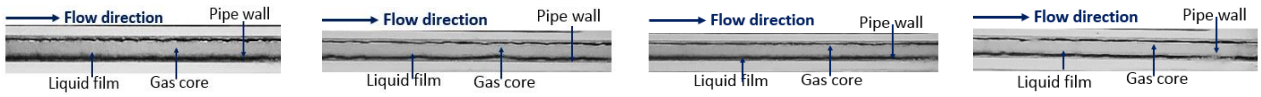
a. J_L = 0.091 m/s b. J_L = 0.149 m/s c. J_L = 0.232 m/s

Fig. 8. Annular flow at J_G = 50 m/s and various J_L for GL 20, 45° inclined orientation



a. J_G = 50 m/s b. J_G = 58.05 m/s c. J_G = 66.3 m/s

Fig. 9. Annular flow at J_L = 0,149 m/s and various J_G for GL 20, 45° inclined orientation

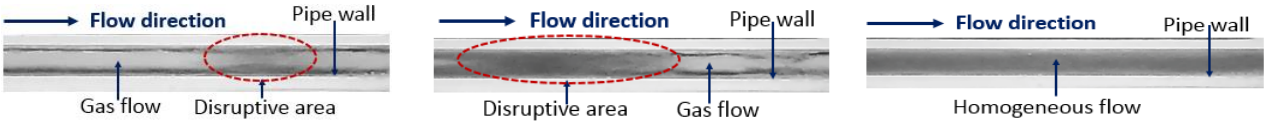


a. W b. GL 10 c. GL 20 d. GL 30

Fig. 10. Annular flow at J_G = 50 m/s and J_L = 0,149 m/s, for two-phase flow with various liquid viscosity, in 45° inclined orientation

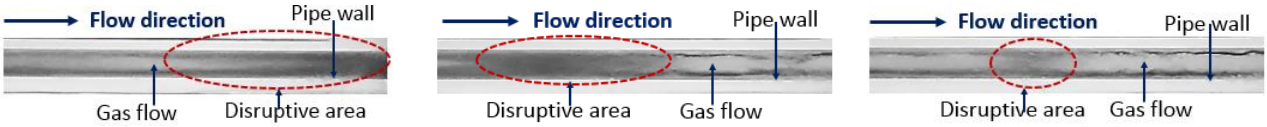
3.1.4 Churn flow

The characteristic of the churn flow is the appearance of disruption area or an irregular form in some point or sometimes along the flow. This flow is occurred at high both J_G and J_L. The increase of J_L in constant J_G tends to more disruptive area and the flow looked darker, as indicated in Figure 11. In contrary, the higher J_G in constant J_L caused the increase of void fraction and the flow is brighter (Figure 12). The liquid viscosity effect to the annular flow pattern is revealed in Figure 13. It can be seen clearly that at higher liquid viscosity the flow is not too disrupted. It is because of lower Reynolds number, so that the turbulence is also low.



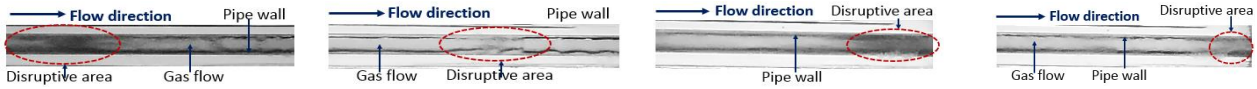
d. J_L = 0.7 m/s e. J_L = 2.297 m/s f. J_L = 4.935 m/s

Fig. 11. Churn flow at J_G = 50 m/s and various J_L for GL 20, 45° inclined orientation



d. J_G = 22.6 m/s e. J_G = 50.05 m/s f. J_G = 58.85 m/s

Fig. 12. Churn flow at J_L = 2.297 m/s and various J_G for GL 20, 45° inclined orientation

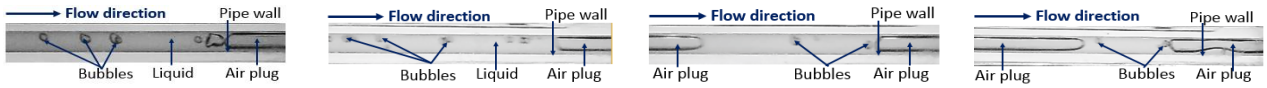


a. W b. GL 10 c. GL 20 d. GL 30

Fig. 13. Churn flow at J_G = 50 m/s and J_L = 2.297 m/s, for two-phase flow with various liquid viscosity, in 45° inclined orientation

3.1.5 Bubbly flow

Bubbly flow is characterized by the appearance of gas bubbles with the diameter are same as or smaller than inner pipe diameter. This flow pattern is occurred at very low J_G and moderate to high J_L. In current study, the observed bubbles are in small diameter and appeared behind the long plug. It may be the effect of the incline orientation of the flow (45°). The effect of liquid viscosity to the configuration of bubbly flow is shown in Figure 14, where for higher liquid viscosity, the bubbles size are smaller and the distance of the plugs being closer. Therefore, in the current experiment, the bubbly flow is not single flow, but mixed flow.



a. W b. GL 10 c. GL 20 d. GL 30

Fig. 14. Bubbly flow at J_G = 0.423 m/s and J_L = 0.89 m/s, for two-phase flow with various liquid viscosity, in 45° inclined orientation

3.2 Flow Pattern Map

The flow pattern map is plotted based on the flow pattern observed in each pair of J_G and J_L. The horizontal and vertical axis of the map are gas and liquid superficial velocities, respectively. Both axis are stated in logarithmic scale in order to accommodate the wide range of J_G and J_L, 0.025 – 66.3 m/s and 0.033 – 4.935 m/s, respectively (Figure 15). The effects of the liquid viscosity (W, GL 10, GL 20, and GL 30) to the transition lines is depicted in Figure 16. The transition lines are also compared to the previous study [17], which use dry air and water for gas and as liquid working fluid. It is shown that flow patterns obtained in this research (W, GL 10, GL 20, and GL 30) look similar, besides, the transition lines between corresponding flow patterns are also in similarity. However, there are some discrepancy of the transition lines when they are compared to the

previous results, especially the transition line between bubbly flow and plug flow, and between slug-annular flow and churn flow.

The transition boundary line between slug-annular and churn flow is shifted to upper side or toward higher J_L when the liquid viscosity is increased. It means that the churn flow area is narrower or in the other words, the churn flow is more difficult to formed when the liquid viscosity is higher. This condition is caused by the very low turbulence, the viscous force more dominant than the inertia force.

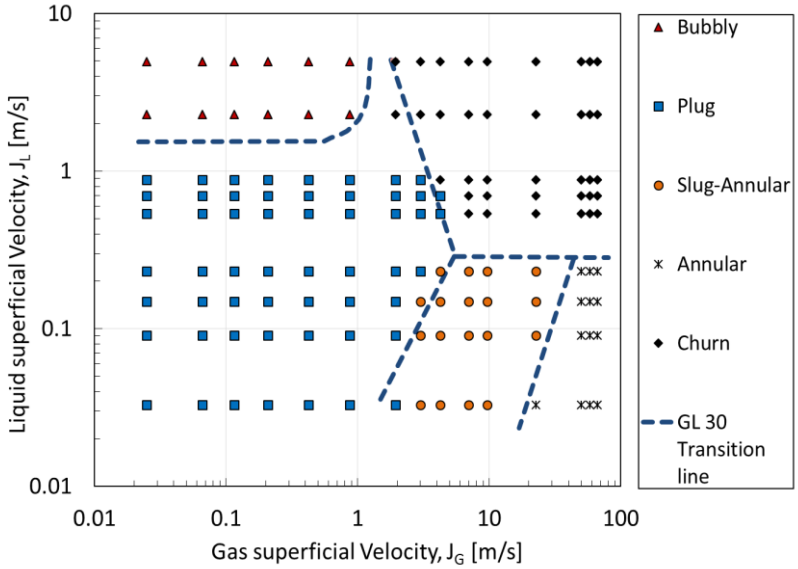


Fig. 15. Flow pattern map of G 30 gas-liquid two-phase flow

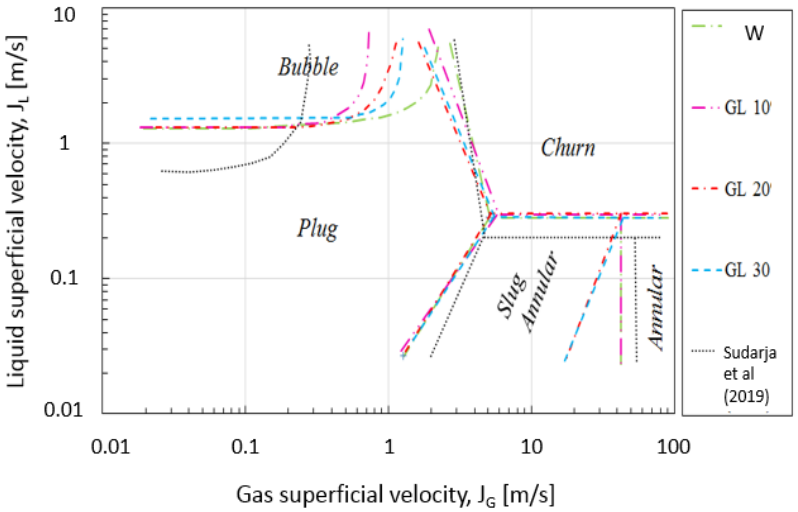


Fig. 16. Flow pattern map comparison for various liquid viscosity and against the previous study

4. Conclusions

The experimental study on the gas-liquid two-phase flow pattern in mini channel was done in adiabatic condition. The range of gas and liquid superficial velocities were 0.025 - 66.3 m/s and 0.033 - 4.935 m/s, respectively. The working fluids employed in the study were air (as

gas fluid) and solution of water and Glycerine in various percentage (as liquid fluid). The result of the research can be summarized as follows:

1. Plug, slug-annular, churn, annular, and bubbly flow patterns were observed, while the stratified flow was not appeared.
2. The orientation of channel slightly affects to the configuration of bubbly flow.
3. Liquid viscosity influenced the flow configuration, especially in the liquid film thickness for annular flow.
4. In term of flow pattern map, the transition lines configuration and the flow pattern area in maps are similar, even though for different liquid viscosity, except slightly shifting of some transition lines.

Acknowledgement

The authors would like to express their appreciation to The Ministry of Research and Higher Education of Indonesia for funding this research, and also to Mr. Windy Prasetyo for his contribution in preparing the experiment rig and collecting data of this study.

References

[1] T.S. Zhao, Q.C. Bi, 2001, Co-current air-water two-phase flow patterns in vertical triangular microchannel, *Int. J. Multiphase Flow*, Vol. 27, pp. 765-782.

[2] A. Kawahara, P.M. Chung, M. Kawaji, 2002, Investigation of two-phase flow pattern, void fraction and pressure drop in a microchannel, *Int. J. Multiphase Flow*, Vol. 28, pp. 1411-1435.

[3] D. Tsaoulidis, V. Dore, P. Angeli, N. V. Plechkova, K. R. Seddon, Flow patterns and pressure drop of ionic liquid–water two-phase flows in microchannels, *Int. J. Multiphase flow*, 2013, 54: 1–10.

[4] I. Hassan, M. Vaillancourt, K. Pehlivan, 2005, Two-phase flow regime transitions in microchannels: a comparative experimental study, *Microscale Thermophysical Engineering*, Vol. 9, pp. 165-182.

[5] C.Y. Lee, S.Y. Lee, 2008, Influence of surface wettability on transition of two-phase flow pattern in round minichannels, *Int. J. Multiphase Flow*, Vol.34, pp.706-711.

[6] M.H. Saidi, P. Hanafizadeh, A. Nouri Gheimasi, S. Ghanbarzadeh, 2011, Experimental investigation of air–water, two-phase flow regimes in vertical mini pipe, *Scientia Iranica B*, Vol. 18 (4), pp. 923–929.

[7] P.M.-Y. Chung, M. Kawaji, 2004. The effect of channel diameter on adiabatic two-phase flow characteristics in microchannel. *Int. J. Multiphase flow*, Vol. 30, pp. 735-761.

[8] Y. Zhao, H. Yeuang, E.E. Zorgani, A.E. Archibong, L. Lao, 2013, High Viscosity Effects on Characteristics of Oil and Gas Two-Phase Flow in Horizontal Pipes, *Chemical Engineering Science*, Vol 95, pp. 343-352.

[9] T. Fukano and T. Furukawa, 1998, Prediction of The Effects of Liquid Viscosity on Interfacial Shear Stress and Frictional Pressure Drop in Vertical Upward Gas-Liquid Annular Flow, Int. J. Multiphase Flow, Vol 24, No 4, pp. 587-603.

[10] T. Furukawa, T. Fukano, 2001, Effects of Liquid Viscosity on Flow Patterns in Vertical Upward Gas- Liquid Two-Phase Flow, *Int. J. Multiphase Flow*, Vol. 27, pp. 1109-1126.

[11] J. Sowinski, and Dziubinski, 2007, The effect of liquid viscosity on the void friction in a two-phase gas-liquid flow in narrow mini-channels, *Proceedings of European Congress of Chemical Engineering (ECCE-6),* Copenhagen, 16-20 September 2007

[12] H. Matsubara, and K. Naito, 2011, Effect of Liquid Viscosity on Flow Pattern of Gas-Liquid Two-Phase Flow in a Horizontal Pipe, *Int. J. Multiphase Flow*, Vol 37, pp. 1277-1281.

[13] DA. Mc Neil, and AD. Stuart, 2003, The Effects of a Highly Viscous Liquid Phase on Vertically Upward TwoPhase Flow in Pipe, *Int. J. Multiphase Flow*, Vol 29, pp. 1523-1549

[14] Y. Zhao, H. Yeuang, E.E. Zorgani, A.E. Archibong, L. Lao, 2013, High Viscosity Effects on Characteristics of Oil and Gas Two-Phase Flow in Horizontal Pipes, *Chemical Engineering Science*, Vol 95, pp. 343-352.

[15] M. Sadatomi, A. Kawahara, M. Matsuo, K. Ishimura, 2010, Effects of Surface Tension on Two-Phase GasLiquid Flows in Horizontal Small Diameter Pipes, *J. Power and Energy Systems*, Vol 4 No 2, pp. 290-300.

[16] Sudarja, Farid Jayadi, Indarto, Deendarlianto, Adhika Widyaparaga, 2018, The effect of liquid viscosity on the gas-liquid two-phase flow pattern in horizontal mini-channel, *AIP Conference Proceedings*, 2001, 030010 (2018); doi: 10.1063/1.5049982., pp. 030010-1 – 030010-10.

[17] Sudarja, Aqli Haq, Deendarlianto, Indarto, Adhika Widyaparaga, 2019, Experimental study on the flow pattern and pressure gradient of air-water two-phase flow in a horizontal circular mini-channel, *J. Hydrodynamics*, 2019, Vol. 31 No. 1, pp. 102-116

[18] T. Fukano, A. Kariyasaki, 1993, Characteristics of gaseliquid two-phase flow in a capillary tube, *Nuclear Engineering and Design*, Vol. 141, pp. 59-68.

[19] S. Saisorn, S. Wongwises, 2008, Flow pattern, void fraction and pressure drop of two-phase air-water flow in horizontal circular micro-channel, *Exp. Thermal and Fluid Science*, Vol. 32, pp. 748-760.

[20] K. A. Triplett, S. M. Ghiaasiaan, S.I., Abdel-khalik, and D. L. Sadowski, 1999a, Gas-Liquid two-phase flow in microchannels. Part I: Two-phase flow pattern. *Int. J. Multiphase flow*, Vol. 25, pp. 377-394**.**

Penerbit Akademia Baru

Engineering Science and Technology Conference Proceedings

Journal homepage: www.akademiabaru.com/EST.html

Nanofluid as an alternative coolant in machining: A review

Open Access

K. Kadirgama[1*]

[1] Faculty of Mechanical & Automotive Engineering Technology, Universiti Malaysia Pahang

ABSTRACT

This review paper is discussed on the important of nanofluid in machining. It is discussed in several parts such as cutting force, surface roughness, tool life and tool wear. Various type of nanofluid are discussed in this paper with effect on the surface roughness, force, tool life and wear. Nanofluid plays major role in increment of tool life and reducing of tool wear. Nanofluid creates an artificial layer on top of the workpiece and this reduces wear at the cutting tool It seems that nanofluid can be the next alternative coolant in machining.

Keywords:
Nanofluid, machining, wear, tool life

Copyright © 2019 PENERBIT AKADEMIA BARU - All rights reserved

1. Introduction

Machining plays major role in the manufacturing industry because machining is used to produce desired shape, size and surface finish through the removal of excess materials in the form of small chips. In machining operations, cutting tools are used to remove the excess material to produce the desired product. The machine tool gives necessary relative motion during the machining process. The temperature rises due to the direct mechanical contact between the workpiece and cutting tool during machining will reduce the tool strength. Hence it will lead to a faster tool failure and wear [1]. To produce at higher rate, high cutting speed is needed but it also will lead to a faster tool wear. To prevent the tool wear take place in a faster rate, the temperature should be controlled during machining. It is also important to reduce the heat produced during machining to avoid the cutting tool lose its sharpness and cause poor surface finish. The tool life also will be shortened if the excessive heat is not controlled. Thus, the usage of cutting fluid is essential to reduce the heat produced at the tool and work piece interface for a better surface finish, enhance the tool life and reduce the tool wear with a reduction in cutting force.

The cutting fluid plays important role in removing the heat generated from friction between cutting tool and workpiece which will eventually reduce temperature rise in cutting tool. Cutting tool's life span will be prolonged by lowering the heat generated at tool-workpiece interface during machining. The cutting fluid will dissipate the heat produced at the interface surface area and lower the friction force between the tool and workpiece. Chis deformation and high thermal load which cause tool wear to occur mainly developed by the friction force. To reduce the friction force the cutting force should be reduced during machining process and it will prolong the life span of the

* *Corresponding author.*
E-mail address: kumaran@ump.edu.my

cutting tool [2]. During cutting process, the tool wear occur especially at the edge of cutting tool [3]. The wear formation at the cutting tool results in poor surface finish and product with less dimensional accuracy. Cutting fluid also helps to prevent the formation of Build-up edge (BUE) and Build-up layer (BUL) defects which causes bad appearance on the workpiece. Other than that, cutting fluid also used to wash away chips during machining.

Many researchers have conducted various researches on alternating the cutting fluid as coolant. Most of the investigation of alternating the cutting fluid is mainly focused on minimum quantity lubricant technique and there are very few research and publication about using nanofluid as coolant [4] . On the other hand, it is reported that the dispersed nanoparticle additives (TiO_2, ZnO, SiC, etc) in the based liquid exhibits higher load carrying capacity, anti-wear and friction reduction properties [5] Therefore, these features can make the nanofluid very attractive in usage of machining coolant.

The concept of nanocoolant or nanofluid is referred to dispersions of nano particle into the based liquid which is water or ethylene glycol. Nanofluids are the next generation heat transfer fluid due to their higher thermal conductivity than those of based liquid [6]. From the viewpoints hybrid nanofluid show better performance in term of heat transfer rate, compare to conventional coolant for machining. Besides that, the cutting temperature could also be reduced in both work-piece and cutting tools due to its high heat transfer rate. Therefore, the tool life and the surface integrity considered to be much improved compared with normal commercial coolant [7].

2. Cutting force

The main objective of machining process is to obtain a good quality and cheap parts. The power consumption will rise when the cutting forces rise thus the machining costs also increase. Various researches reported that by adding the nanoparticles into coolant the cutting force reduced dramatically. Table 1 shows the percentage of reduction in cutting force when using nanofluids as cutting fluid. Through many literature reviews, it found out that the nanofluids tends to reduce the cutting force by reducing the friction between the surfaces in contact [8].

According to Padmini, Krishna, and Rao [9] and Singh *et al.,* [10] viscosity also plays some role which influences the reduction in cutting force. The authors stated that the dissipation capacity of nanofluid tends to increase when the viscosity is low. If the viscosity is high, the nanofluid is able to form a consistent barrier which will separate both the surfaces in contact during machining [8]. Jamil *et al.,* [11] also agree that there will be a layer formed which act as a barrier that reducing the cutting force. Due to the barrier, the friction between the surfaces in contact and the cutting forces reduce simultaneously [9]. Reddy and Rao [12] mentioned that the specific energy of the nanoparticles is effective in reducing the frictional forces between the tool and workpiece which leads to reduction in cutting force.

Raju, Andhare, and Sahu [13] and Sahu, Andhare, and Raju [14] reported that the nanofluid improved lubricant properties leads to a high wettability and enables to lubricate the cutting zone much better while resulting in lesser frictional force. According to Lee *et al.,* [15] and Zhou *et al.,* [16] nanofluids tends to reduce the cutting force due to its friction coefficient which evaluate the characteristics of a lubricant. Khandekar *et al.,* [17] stated that nanofluid reduce the cutting force magnitude better than conventional cutting fluid due to the enhanced cooling characterization.

According to Khrisna [18] nanofluid act as a film that reduce the coefficient friction between tool-workpiece interface which lead to reduction in cutting force. Yuan *et al.,* [19] stated that the larger surface area of diamond made the surface contact area flatter and lower the cutting force

generated. They also mentioned that the larger the surface area of a nanoparticle the more effective it will be in reducing the cutting force.

Table 1

Reduction in cutting force when using different nanofluids

Authors	Cutting Fluid	Reduction in Cutting Force
Padmini *et al.,* [9]	Coconut oil (CC) + nano molybdenum disulphide ($nMoS_2$)	37 percentage of reduction
Singh *et al.,* [10]	Alumina based fluid with graphene nano plates	9.94% reduction in cutting force
Redyy and Rao [12]	Graphite, Molybdenum disulphide (MoS_2)	20% of reduction for graphite powder and 28% reduction for MoS_2 powder.
Raju *et al.,* [13]	Multi wall carbon nanotubes and distilled water with sodium dodecyl sulphate as surfactant	5 to 8 percentage reduction
Lee *et al.,* [15]	Mineral oil with graphite nanoparticle	24% of reduction
Khandekar *et al.,* [17]	Aluminum Oxide added to the conventional cutting fluid	50% of reduction
Zhou *et al.,* [16]	Fe_3O_4 with conventional coolant	38.4% reduction
Khrisna [18]	Nano boric Acid with coconut oil	14.5% reduction than dry machining
Jamil *et al.,* [11]	Al_2O_3 with carbon nanotube (CNT) in vegetable oil	11.8% reduction
Sahu *et al.,* [14]	MWCNT nanofluid with distilled water	28% drop of cutting force
Yuan *et al.,* [19]	Natural777 oil-based diamond nanoparticle	10.71%

3. Surface roughness

In machining process achieving a desired surface quality is very important. The desired surface index of product quality basically called surface roughness which is a technical requirement for most of the mechanical products [20]. To achieve a fine surface roughness the friction and heat generated between the surface contacts reduced by using cutting fluids. By using nanofluid as a replacement for conventional cutting fluid, the quality of product increased by reducing the surface roughness of the product. Table 2 shows the surface roughness reduction when using different nanofluids.

Vasu and Kumar [21] stated that the generated intensive temperature at the workpiece surface will increase the residual stress and lead to micro cracking of the work piece. By adding Al_2O_3 nanoparticles the stress at workpiece surface area decreases and produces a fine surface roughness. Sharma *et al.,* [22] stated that nano fluid produce lowest surface roughness because the nanoparticles within the nanofluid enhance the heat dissipation and improve the properties of the tool's rake face. Hence it will lead to a smoother machining process and retain the tool's hardness and sharpness. Sharma *et al.,* [23] mentioned that Multi wall carbon nanotube (MWCNT) nanoparticles act as a layer which reduces the heat generated at the cutting zone. They also stated that other than providing a good surface roughness MWCNT also reduce tool wears.

Roy and Ghosh [24] reported that the high temperature caused by the high velocities is reduced greatly by adding nanoparticles into cutting fluid due to the thermal properties of the nanoparticles. According to nanofluid is considered as higher heat transfer fluid due to their improved thermal conductivity. Zhou *et al.,* [16] also share same opinion that the thermal conductivity enhancement helps to reduce the heat generated and also, act as a heat transfer medium and dissipate the heat generated at the cutting tool interphase. Therefore, less burning occurs at the cutting zone and enhance the surface quality of the workpiece.

Sharma *et al.,* [26] mentioned that the TiO_2 nanofluid enhances the wetting and lubricating properties of the rake face which retain the sharpness and hardness of the cutting tool for a longer period. Gupta *et al.,* [27] stated that graphite nanofluid produce better surface roughness than aluminum oxide nanofluid due to the better thermal conductivity properties of graphite than aluminum oxide. According to them, by achieving a fine surface quality the tool wears can be reduced drastically. Jamil *et al.,* [11] mentioned that the reduction in surface roughness is due to the better wetting properties of nanofluid at the workpiece and tool intact surface area.

According to Kulkani *et al.,* [28] and Mahadi *et al.,* [29] the temperature reduce at the tool interface is reduce due to the rolling action of the billions of nanoparticles that contributes to the heat dissipation. They also mentioned that thermal conductivity enhancement helps the nanofluid to perform better as heat transfer medium. Khrisna [18] stated that the nanofluid provide a better surface roughness by reducing the coefficient friction which lead to reduction in cutting temperature.

Table 2
Reduction in surface roughness when using different nanofluids

Authors	Cutting Fluid	Reduction in Surface roughness
Vasu and Kumar [21]	Al_2O_3 nanoparticles	20-30% surface roughness reduction
Sharma *et al.,* [22]	Aluminum oxide (Al_2O_3) with vegetable oil	47.8% reduction
Sharma *et al.,* [23]	MWCNT with SAE oil	Better surface reduction than conventional coolant
Roy dan Ghosh [24]	Multi wall carbon nanotube (MWCNT) with deionized water	30-35% reduction
Kadirgama *et al.,* [25]	Ethylene glycol (EG) with nanocellulose	0.251 – 0.984 µm
Sharma *et al.,* [26]	Titanium dioxide (TiO_2) with vegetable oil	34.7% reduction
Gupta *et al.,* [27]	Aluminum oxide/vegetable oil and graphite/vegetable oil	Graphite/vegetable oil give much better surface roughness than aluminum oxide/vegetable oil
Jamil *et al.,* [11]	Al_2O_3 with carbon nanotube (CNT) in vegetable oil	8.72% reduction
Zhou *et al.,* [16]	Fe_3O_4 with conventional coolant	27.75% reduction
Kulkarni *et al.,* [28]	Copper coated Al_2O_3 with distilled water	Surface roughness improved better than conventional coolant
Mahadi *et al.,* [29]	Boric acid with vegetable oil	7.21% surface roughness enhancement
Khrisna [18]	Nano boric Acid with coconut oil	24.74% enhancement than dry machining

4. Tool life

Tool life is usually depending on tool wear [30]. The longer the tool can withstand the wear the longer the tool life span will be Yıldırım *et al.,* [31]. Tool life also can be increased by reducing the coefficient friction occurs between tool-workpiece interface area Watmon & Ijeh [32]. Even tough conventional coolant helps to reduce the heat generated at intact surface area, many researches has been done to improve the thermal properties of the conventional coolant. Table 3 shows the tool life enhancement when using different nanofluids.

Vázquez *et al.,* [33] mentioned that by adding the nanoparticles into the conventional cutting fluid, their thermal properties enhanced and increase the tool life. Minh *et al.,* [34] stated that the main reason for the tool life prolonged is due to the oil mist and the number of nanoparticles

formed on flank face. The formed oil mist and nanoparticles in the cutting zone increases to create "roller effect" which eventually reduce the cutting force and tool wear. According to Sharma *et al.,* [35] the hybrid nanofluid able to maintain the hardness of the tool longer due to their wettability while extracting heat from the tool at high rate.

Lü *et al.,* [36] reported that due to the better wettability, better lubrication, higher stability, and higher heat dissipation characterization of TiO_2 nanofluid, increases the tool life 70% more than water. Jamil *et al.,* [11] stated that the reduction in cutting temperature at tool-workpiece surface will increase the tool life. Due to the enhanced heat transfer properties of nanofluid the cutting temperature reduced drastically and prolong the tool life. Eltaggaz *et al.,* [37] mentioned that the nanofluid penetrate in between the tool-workpiece surface area to form as a film that reduce the coefficient friction. They also stated that the higher the thickness of the film the more it will reduce the heat generated and prolong the tool life.

According to Singh *et al.,* [38] the reduction in cutting force and cutting temperature leads to tool life enhancement. They stated that when the heat generated at tool-workpiece interface is reduced the tool will be preserved from damaged. Muthusamy *et al.,* [39] found significant improvement in tool life in their research when using nanofluid. They stated that the improvement is due to the excellent performance of nanofluid as heat transfer medium at tool-workpiece interface.

Table 3
Tool life enhancement when using different nanofluids

Authors	Cutting Fluid	Tool life enhancement
Vázquez *et al.,* [33]	CuO nanoparticles with mineral oil	Increase the service life of the cutting tool up to 604%
Minh *et al.,* [34]	Al_2O_3 with soybean oil	Increase almost 177% of the tool life than base fluid
Sharma *et al.,* [35]	Al_2O_3/MWCNT hybrid nano fluid with vegetable oil	Improved the tool life much more better than base fluid and single nanofluid (Al_2O_3)
Lü *et al.,* [36]	TiO_2 with deionized water	70% more tool life than water
Jamil *et al.,* [11]	Al_2O_3 with carbon nanotube (CNT) in vegetable oil	23% enhancement
Eltaggaz *et al.,* [37]	Al_2O_3 with vegetable oil	23.5% enhancement in tool life
Singh *et al.,* [38]	Graphene with vegetable oil	178-190% of tool life enhancement
Muthusamy *et al.,* [39]	Ethylene glycol based TiO_2	Tool life is 54.9 minutes.

5. Tool wear

Tool wear is mainly dependent on cutting conditions Xavior & Adithan [40]. When there is much heat generated at tool-workpiece interface area the tool tends to lose its hardness and leading to wear at faster rate Shao *et al.,* [41]. The wear criteria normally set at 0.3 mm as worn tool Muthusamy *et al.,* [39]. There are a lot of wear types that occurs during machining for example notch wear, comb crack, crater wear and chipping wear [42-44]. But the major wear frequently occur is the flank wear Sharma *et al.,* [45]. To minimize the tool wear, many researches has been conducted on nanofluid to enhance the thermal properties. Table 4 shows the tool wears reduction when using nanofluid.

Zhou *et al.,* [16] mentioned that the nanofluid act as a lubricant that smooth the surface of the rake face during machining process. The author also reported that less adhesion occurs when using nanofluid which leads to a high resistance towards the tool wear. Jamil *et al.,* [11] reported that the nanofluid reduce the heat from the primary shearing zone at faster rate and preventing the

workpiece hardening. Therefore the cutting tool can sustain longer the hardness of the workpiece and prevent the tool wear occurs at faster rate.

Sahu *et al.,* [14] mentioned that high surface area of the MWCNT; results in high heat transfer rate that helps to tool wear reduction. The author also stated that even at low particle concentration the nanofluids are better as heat transfer fluid. Eltaggaz *et al.,* [37] stated that a mist composed nanoparticle and base fluid mist is created into tool-workpiece interface zone and forms a tribofilm. The heat generated reduced significantly by the tribofilm as well as minimizing the coefficient friction that occurs at interface zone. Thus, the tool hardness able to withstand for a longer period and prevent tool wear to occur faster.

Das *et al.,* [46] in their research work; they compared ZnO, CuO, Fe_2O_3 and Al_2O_3, nanofluids to measure the reduction in tool wear. They found out that the crater wear occur more in Al_2O_3 nanofluid than CuO nanofluid due to the high percentage of oxygen presence in Al_2O_3. The presence of high percentage of oxygen in Al_2O_3 caused significant weight percentage found during machining process and leads to improper cooling thus, crater wear and flank wear take place faster. According Das *et al.,* [46] CuO nanofluid has superior behavior compared to the other nanofluids while Al2O3 nanofluid was last in the row.

Table 4
Tool wears reduction when using different nanofluids

Authors	Cutting Fluid	Tool wear type/reduction
Zhou *et al.,* [16]	Fe_3O_4 with conventional coolant	Crack wear on rake face, wear resistance up to 63.3%
Jamil *et al.,* [11]	Al_2O_3 with carbon nanotube (CNT) in vegetable oil	Flank wear occurs after 292 seconds of machining
Sahu *et al.,* [14]	MWCNT nanofluid with distilled water	Average flank wear occurs at cutting length of 960 mm
Eltaggaz *et al.,* [37]	Al_2O_3 with vegetable oil	Up to 26.5% of flank wear reduced
Das *et al.,* [46]	ZnO, CuO, Fe_2O_3 and Al_2O_3, with distilled water	Crater wear and flank wear reduced
Muthusamy *et al.,* [39]	Ethylene glycol based TiO_2	Flank wear occurs after 940 mm cut length

6. Morphology analysis

Figure 1 shows the nanofluid forming a thermal barrier between chip and cutting tool. According to Kadirgama *et al.,* [25] the small chip shows the presence of less aluminum percentage proves that the nanofluid is capable to carry away the heat generated due to the superior thermal conductivity properties. They also mentioned that carbon element presence in the nanofluid embedded the chip surfaces and act as a thermal barrier which reduce thermal expansion greatly.

Figure 2 shows the flank wear occurs at faster rate when using the conventional cutting coolant. Muthusamy *et al.,* [39] found that at the 720 mm cut length the cutting tool using nanofluid still with stand the heat generated while conventional cutting fluid couldn't withstand the heat and lead to tool wear. Thamizhmanii and Hasan [46] also mentioned in their research work that flank wear is highly affected by the high heat generated on the flank wear. Khandekar *et al.,* [17] mentioned that the nanofluid has improved conduction, convection and wettability compare to the conventional cutting fluid. The superior properties of the nanofluid make them to withstand the high temperature at a longer period of time Lee *et al.,* [15].

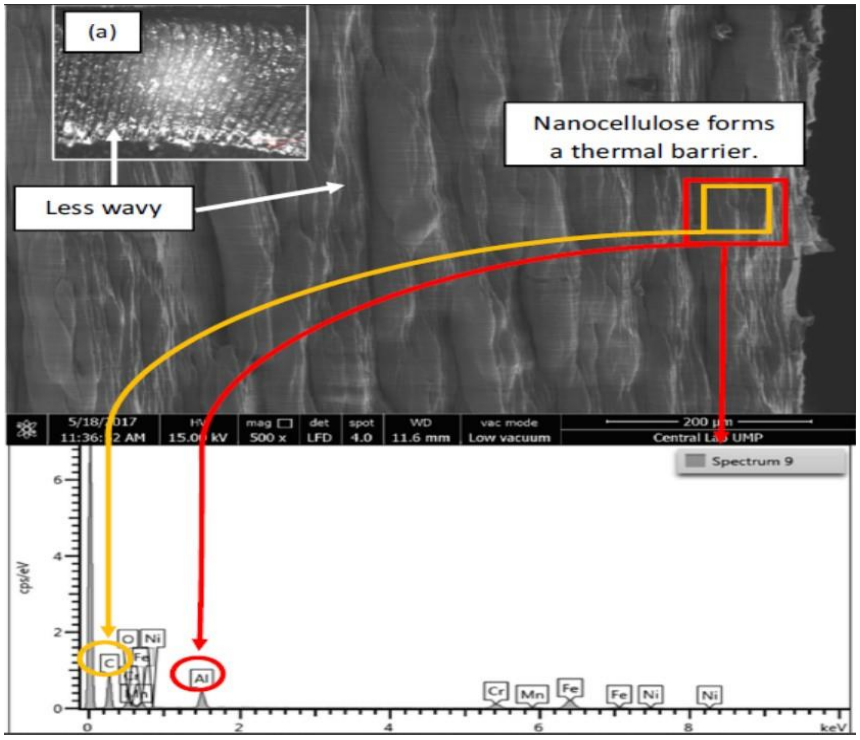


Fig. 1. Thermal barrier formed by nanofluid Kadirgama *et al.,* [25]

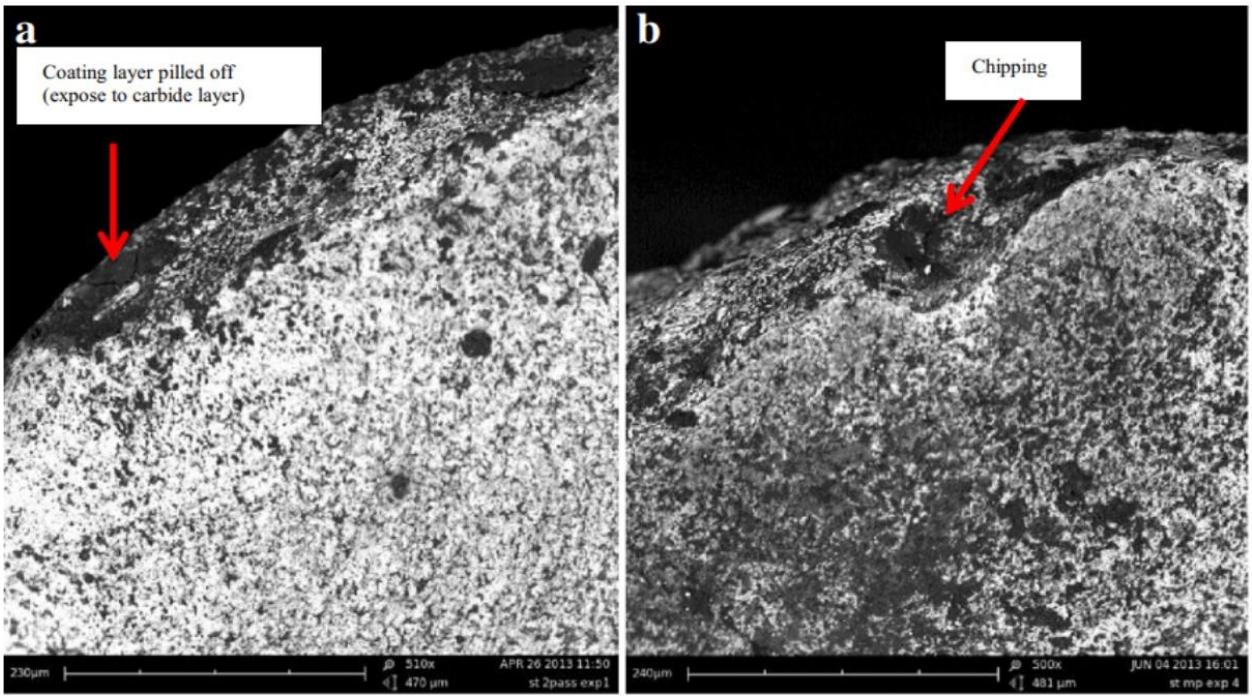


Fig. 2. SEM images after cut length of 720 mm with a) nanofluid and b) conventional cutting coolant Muthusamy *et al.,* [39]

7. Conclusions

From the reviews, the following conclusions can be summarized:

I. Nanofluid improved lubricant properties leads to a high wettability and enables to lubricate the cutting zone much better while resulting in lesser frictional force. Reduced frictional force resulting in reduction of cutting force.
II. Nanofluid produces lowest surface roughness because the nanoparticles within the nanofluid enhance the heat transfer and improve the properties of the tool's rake face. Hence it will lead to a smoother machining process and retain the tool's hardness and sharpness.
III. Nanofluid prolongs the tool life due to the oil mist and the number of nanoparticles formed on flank face. The formed oil mist and nanoparticles in the cutting zone increases to create a film of barrier which eventually reduce the cutting force and tool wear.
IV. Nanofluid reduces tool wear by reducing the heat from the primary shearing zone at faster rate and preventing the workpiece hardening. Thus, the cutting tool can sustain longer the hardness of the workpiece and prevent the tool wear occurs at faster rate.

Acknowledgement

The authors express their grateful appreciation to the University Malaysia Pahang for providing laboratory facilities and financial assistance under project no RDU1803136 and RDU190351.

References

[1] Bruni, C., Forcellese, A., Gabrielli, F., & Simoncini, M. (2006). Effect of the lubrication-cooling technique, insert technology and machine bed material on the workpart surface finish and tool wear in finish turning of AISI 420B. *International journal of machine tools and manufacture, 46*(12-13), 1547-1554.
[2] Samylingam, L., Anamalai, K., Kadirgama, K., Samykano, M., Ramasamy, D., Noor, M., . . . Sidik, N. A. C. (2018). Thermal analysis of cellulose nanocrystal-ethylene glycol nanofluid coolant. International Journal of Heat and Mass Transfer, 127, 173-181.
[3] Schuldt, S., Arnold, G., Kowalewski, J., Schneider, Y., & Rohm, H. (2016). Analysis of the sharpness of blades for food cutting. Journal of food engineering, 188, 13-20.
[4] Yazid, M., CheHaron, C., Ghani, J., Ibrahim, G., & Said, A. (2011). Surface integrity of Inconel 718 when finish turning with PVD coated carbide tool under MQL. Procedia Engineering, 19, 396-401.
[5] Murshed, S., Leong, K., & Yang, C. (2008). Investigations of thermal conductivity and viscosity of nanofluids. International Journal of Thermal Sciences, 47(5), 560-568.
[6] Lee, S., Choi, S.-S., Li, S., and, & Eastman, J. (1999). Measuring thermal conductivity of fluids containing oxide nanoparticles. Journal of Heat transfer, 121(2), 280-289.
[7] Sarkar, J., Ghosh, P., & Adil, A. (2015). A review on hybrid nanofluids: recent research, development and applications. Renewable and Sustainable Energy Reviews, 43, 164-177.
[8] Sivashanmugam, P. (2012). Application of nanofluids in heat transfer. An overview of heat transfer phenomena, 16.
[9] Padmini, R., Krishna, P. V., & Rao, G. K. M. (2016). Effectiveness of vegetable oil based nanofluids as potential cutting fluids in turning AISI 1040 steel. Tribology international, 94, 490-501.
[10] Singh, R. K., Sharma, A. K., Dixit, A. R., Tiwari, A. K., Pramanik, A., & Mandal, A. (2017). Performance evaluation of alumina-graphene hybrid nano-cutting fluid in hard turning. Journal of Cleaner Production, 162, 830-845.
[11] Jamil, M., Khan, A. M., Hegab, H., Gong, L., Mia, M., Gupta, M. K., & He, N. (2019). Effects of hybrid Al 2 O 3-CNT nanofluids and cryogenic cooling on machining of Ti–6Al–4V. The International Journal of Advanced Manufacturing Technology, 102(9-12), 3895-3909.
[12] Reddy, N. S. K., & Rao, P. V. (2006). Experimental investigation to study the effect of solid lubricants on cutting forces and surface quality in end milling. International journal of machine tools and manufacture, 46(2), 189-198.
[13] Raju, R. A., Andhare, A., & Sahu, N. K. (2017). Performance of multi-walled carbon nanotube-based nanofluid in turning operation. Materials and Manufacturing Processes, 32(13), 1490-1496.
[14] Sahu, N. K., Andhare, A. B., & Raju, R. A. (2018). Evaluation of performance of nanofluid using multiwalled carbon nanotubes for machining of Ti–6AL–4V. Machining Science and Technology, 22(3), 476-492.

[15] Lee, C.-G., Hwang, Y.-J., Choi, Y.-M., Lee, J.-K., Choi, C., & Oh, J.-M. (2009). A study on the tribological characteristics of graphite nano lubricants. International Journal of Precision Engineering and Manufacturing, 10(1), 85-90.
[16] Zhou, C., Guo, X., Zhang, K., Cheng, L., & Wu, Y. (2019). The coupling effect of micro-groove textures and nanofluids on cutting performance of uncoated cemented carbide tools in milling Ti-6Al-4V. Journal of materials processing technology, 271, 36-45.
[17] Khandekar, S., Sankar, M. R., Agnihotri, V., & Ramkumar, J. (2012). Nano-cutting fluid for enhancement of metal cutting performance. Materials and Manufacturing Processes, 27(9), 963-967.
[18] Khrisna, P. V. (2019). Effectiveness of Vegetable Oil based Nanofluids in Machining of Steel. Asian Journal of Multidisciplinary Studies, 2(1).
[19] Yuan, S., Hou, X., Wang, L., & Chen, B. (2018). Experimental Investigation on the Compatibility of Nanoparticles with Vegetable Oils for Nanofluid Minimum Quantity Lubrication Machining. Tribology Letters, 66(3), 106.
[20] Benardos, P., & Vosniakos, G.-C. (2003). Predicting surface roughness in machining: a review. *International journal of machine tools and manufacture, 43*(8), 833-844.
[21] Vasu, V., & Kumar, K. M. (2011). Analysis of nanofluids as cutting fluid in grinding EN-31 steel. *Nano-Micro Letters, 3*(4), 209-214.
[22] Sharma, A. K., Singh, R. K., Dixit, A. R., & Tiwari, A. K. (2016). Characterization and experimental investigation of Al2O3 nanoparticle based cutting fluid in turning of AISI 1040 steel under minimum quantity lubrication (MQL). *Materials Today: Proceedings, 3*(6), 1899-1906.
[23] Sharma, P., Sidhu, B. S., & Sharma, J. (2015). Investigation of effects of nanofluids on turning of AISI D2 steel using minimum quantity lubrication. *Journal of Cleaner Production, 108*, 72-79.
[24] Roy, S., & Ghosh, A. (2013). *High speed turning of AISI 4140 steel using nanofluid through twin jet SQL system.* Paper presented at the ASME 2013 International Manufacturing Science and Engineering Conference collocated with the 41st North American Manufacturing Research Conference.
[25] Kadirgama, K., Anamalai, K., Ramachandran, K., Ramasamy, D., Samykano, M., Kottasamy, A., & Rahman, M. (2018). Thermal analysis of SUS 304 stainless steel using ethylene glycol/nanocellulose-based nanofluid coolant. *The International Journal of Advanced Manufacturing Technology, 97*(5-8), 2061-2076.
[26] Sharma, A. K., Tiwari, A. K., Singh, R. K., & Dixit, A. R. (2016). Tribological investigation of TiO2 nanoparticle based cutting fluid in machining under minimum quantity lubrication (MQL). *Materials Today: Proceedings, 3*(6), 2155-2162.
[27] Gupta, M. K., Sood, P., & Sharma, V. S. (2016). Optimization of machining parameters and cutting fluids during nano-fluid based minimum quantity lubrication turning of titanium alloy by using evolutionary techniques. *Journal of Cleaner Production, 135*, 1276-1288.
[28] Kulkarni, H. B., Nadakatti, M. M., Kulkarni, S. C., & Kulkarni, R. M. (2019). Investigations on effect of nanofluid based minimum quantity lubrication technique for surface milling of Al7075-T6 aerospace alloy. *Materials Today: Proceedings*.
[29] Mahadi, M., Choudhury, I., Azuddin, M., & Nukman, Y. (2017). Use of boric acid powder aided vegetable oil lubricant in turning AISI 431 steel. *Procedia Engineering, 184*, 128-136.
[30] Karandikar, J. (2019). Machine learning classification for tool life modeling using production shop-floor tool wear data. *Procedia Manufacturing, 34*, 446-454.
[31] Yıldırım, Ç. V., Sarıkaya, M., Kıvak, T., & Şirin, Ş. (2019). The effect of addition of hBN nanoparticles to nanofluid-MQL on tool wear patterns, tool life, roughness and temperature in turning of Ni-based Inconel 625. *Tribology international, 134*, 443-456.
[32] Watmon, T. B., & Ijeh, A. C. (2010). *Coating Cutting Tools with Hard Substance Lowers Friction Co-efficient and Improves Tool Life- A Review.* Paper presented at the World Congress on Engineering 2012. July 4-6, 2012. London, UK.
[33] Vázquez, K., Cantú, D., Segura, A., Araiz, F., Peña-Parás, L., & Maldonado, D. (2014). Application of Nanofluids to improve tool life in machining processes. *Proceedings of the LUBMAT*, 1-8.
[34] Minh, D. T., The, L. T., & Bao, N. T. (2017). Performance of Al2O3 nanofluids in minimum quantity lubrication in hard milling of 60Si2Mn steel using cemented carbide tools. *Advances in Mechanical Engineering, 9*(7), 1687814017710618.
[35] Sharma, A. K., Singh, R. K., Dixit, A. R., Tiwari, A. K., & Singh, M. (2019). An Investigation on Tool Flank Wear Using Alumina/MoS 2 Hybrid Nanofluid in Turning Operation. In *Advances in Manufacturing Engineering and Materials* (pp. 213-219): Springer.
[36] Lü, Z., Deng, L., Tian, Q., & Zhao, X. (2018). Cutting performance of Si 3 N 4/TiC micro-nanocomposite ceramic tool in dry machining of hardened steel. *The International Journal of Advanced Manufacturing Technology, 95*(9-12), 3301-3307.

[37] Eltaggaz, A., Hegab, H., Deiab, I., & Kishawy, H. (2018). Hybrid nano-fluid-minimum quantity lubrication strategy for machining austempered ductile iron (ADI). *International Journal on Interactive Design and Manufacturing (IJIDeM), 12*(4), 1273-1281.

[38] Singh, R., Dureja, J., Dogra, M., Gupta, M. K., & Mia, M. (2019). Influence of graphene-enriched nanofluids and textured tool on machining behavior of Ti-6Al-4V alloy. *The International Journal of Advanced Manufacturing Technology*, 1-13.

[39] Muthusamy, Y., Kadirgama, K., Rahman, M., Ramasamy, D., & Sharma, K. (2016). Wear analysis when machining AISI 304 with ethylene glycol/TiO 2 nanoparticle-based coolant. *The International Journal of Advanced Manufacturing Technology, 82*(1-4), 327-340.

[40] Xavior, M. A., & Adithan, M. (2009). Determining the influence of cutting fluids on tool wear and surface roughness during turning of AISI 304 austenitic stainless steel. *Journal of materials processing technology, 209*(2), 900-909.

[41] Shao, H., Liu, L., & Qu, H. (2007). Machinability study on 3% Co–12% Cr stainless steel in milling. *Wear, 263*(1-6), 736-744.

[42] Ganesh Kumar, S., Thirunavukkarasu, V., Sureshkumar, R., Venkatesh, S., & Ramakrishnan, T. (2019). Investigation of wear behaviour of silicon carbide tool inserts and titanium nitride coated tool inserts in machining of en8 steel. *International Journal of Mechanical Engineering and Technology, 10*(01), 1862-1873.

[43] Sahoo, R. R., Bhattacharjee, S., & Das, T. (2013). *Development of nanofluids as lubricant to study friction and wear behavior of stainless steels.* Paper presented at the International Journal of Modern Physics: Conference Series

[44] Altin, A., Nalbant, M., & Taskesen, A. (2007). The effects of cutting speed on tool wear and tool life when machining Inconel 718 with ceramic tools. *Materials & design, 28*(9), 2518-2522

[45] Sharma, A. K., Katiyar, J. K., Bhaumik, S., & Roy, S. (2019). Influence of alumina/MWCNT hybrid nanoparticle additives on tribological properties of lubricants in turning operations. *Friction, 7*(2), 153-168.

[46] Das, A., Pradhan, O., Patel, S. K., Das, S. R., & Biswal, B. B. (2019). Performance appraisal of various nanofluids during hard machining of AISI 4340 steel. *Journal of Manufacturing Processes, 46*, 248-270.

[47] Thamizhmanii, S., & Hasan, S. (2006). Analyses of roughness, forces and wear in turning gray cast iron. *Journal of achievements in materials and manufacturing engineering, 17*(1-2), 401-404.

[48] Li, G., Yi, S., Li, N., Pan, W., Wen, C., & Ding, S. (2019). Quantitative analysis of cooling and lubricating effects of graphene oxide nanofluids in machining titanium alloy Ti6Al4V. *Journal of materials processing technology, 271*, 584-598.

[49] Abitbol, Tiffany, Amit Rivkin, Yifeng Cao, Yuval Nevo, Eldho Abraham, Tal Ben-Shalom, Shaul Lapidot, and Oded Shoseyov. "Nanocellulose, a Tiny Fiber with Huge Applications." *Current Opinion in Biotechn*

Penerbit Akademia Baru

Engineering Science and Technology Conference Proceedings

Journal homepage: www.akademiabaru.com/EST.html

Groundwater Analysis for Unconfined and Clayey Layer by using Response Surface Methodology

Open Access

Sabariah Musa[1,*], Ng Lee Bin[1], Adel Ali Saeed Abduh Algheethi[1]

[1] Faculty of Civil and Environmental Engineering, Universiti Tun Hussein Onn Malaysia, 86400 Parit Raja, Batu Pahat, Johor, Malaysia

ABSTRACT

Groundwater as a source of water stored in aquifers plays an important role in domestic use. However, excessive and uncontrolled water pump activities have side effects such as soil deposition and groundwater reduction. Therefore, Response Surface Methodology (RSM) is an alternative method to optimize the time and quantity of groundwater pumps based on other wells water level changes. The analysis using Design Expert version 10 involves changing the water level at the main wells R_1 dan R_5 with the monitoring of other wells at $R_2, R_3,$ and R_4 within 245 minutes with 48 samples. Based on 4 hours of pump test in different wells, it shows that groundwater production rates indirectly affect pump power factor, water level change, wells location, pump time, and infiltration of soil. R_1 (1 hp) has a groundwater rate of 28.65 m^3/day, while R_5 (2 hp) with 103.63 m^3/day. The selection of ANOVA Design-Expert model suitable for $R_1 R_2, R_3, R_4$ and R_5 has been evaluated and shows that optimum time is 116.24 minutes (1 hour 55 minutes) for case 1 and 117.48 minutes (1-hour 57 minute) for case 2. In conclusion, this study provides best and suitable pumping time towards the water balance of groundwater. Hence, the reaction from environment and the influences of other factors play an important role in ensuring the continuous water supplement of groundwater.

Keywords:
Water quantity, response surface methodology and groundwater levels

Copyright © 2019 PENERBIT AKADEMIA BARU - All rights reserved

1. Introduction

According to investigation's statistic, the average water consumption per day of Malaysians in 2013 was 210 litres. However, the average consumption has risen by 2 litres which means 212 litres or about 141 bottles of 1.5 litres per person daily in 2014 [1]. This statistic above shows that the consumption of water is still far beyond the water usage that recommended by the World Health Organization (WHO), which is 165 litres per day. It was expected that the population growth of human to be increased to two thirds, where 1.8 million of people live in countries or regions with absolute water scarcity and living under water stress condition on 2025 [2].

The excessive usage of water has increased the stress upon both our land and water resources of earth and resulting water scarcity and water quality risks. Besides, climate change that cause to the trapped heat within the atmosphere, which causing rising sea levels, severe weather events, and droughts that render landscapes more susceptible to wildfires is also a factor to threaten the fresh water on earth[3]. Besides, there are many countries that facing the high stresses in water capacity availability such as water irrigation, water shortage, droughts, land subsidence etc. For

[*] *Corresponding author.*
E-mail address: sabariah@uthm.edu.my (Sabariah Musa)

example, Mekong Delta which located in Vietnam that underwent excessive groundwater extraction has gradually increased the happening of subsidence [4]. In addition, the failure of unlimited groundwater extraction had made the falling of water tables in China, India, and the United States and influence the harvest production [5].

Therefore, groundwater as a water source that can be taken from underground of earth are greatly in concerning to avoid the depletion of water. With the help of gravity, water moves down into the soils and rocks, passing between particles of sand, gravel, or large particle until it reaches an empty space which called aquifer [7]. Besides, there are more than half of the groundwater withdrawn is for domestic water supplies and globally it provides 25% to 40% of the world's drinking water in other nation[6]. However, suitable water treatment such as filtration, biological, chemical, and physical treatment technologies are needed after extraction. The study of groundwater extraction was conducted at the main campus of Universiti Tun Hussein Onn Malaysia (UTHM) which is at Research Centre for Soft Soil Malaysia (RECESS) that established in order to carry out field experiments and adopt this center as a national center for soft soil research in Malaysia. The objectives of the study were to determine groundwater extraction capability (m^3/day) after 4 hours of pumping test in RECESS, UTHM and analyze the results from groundwater extraction by using Response Surface Methodology (RSM) from effect of time and volume of groundwater to the water level of existed wells in RECESS, UTHM.

1.1 Aquifer in RECESS

Well was installed vertically to extract the groundwater from underground. There are basically three types of aquifer such as unconfined aquifer, perched aquifer and confined aquifer[8]. In RECESS, an unconfined aquifer was located below the top soil and under a layer of more than 45 meters of fine, sandy, and turf clay as shown in Figure 1.

In Pumped Well (PW), 1 horsepower of submersible pump is installed in well. From a constant rate of 4 hours pumping continuously tests, the capacity of water withdrawal is 40 m^3 /day by using only 1horsepower of pump and the area in RECESS has low hydraulic conductivity below than 9.6 mm/hr[9]. Infiltration rate of top soil is in between of 0.004 to 0.007 mm/s and the soil classification based on particle size is between silt to fine sand [10].

1.2 Well System in RECESS

There are different types of well that used for extraction and functioning on their own purposes. The diverse sizes and depth of the wells are influenced by the water table fluctuations, alongside the groundwater capacity and water storage in the wells [11]. Several matter such as surface and subsurface geologic conditions, site conditions, properties of monitored aquifers, purpose of the well, and duration of monitoring need to be concerned when installation carry out before the groundwater extraction[12].

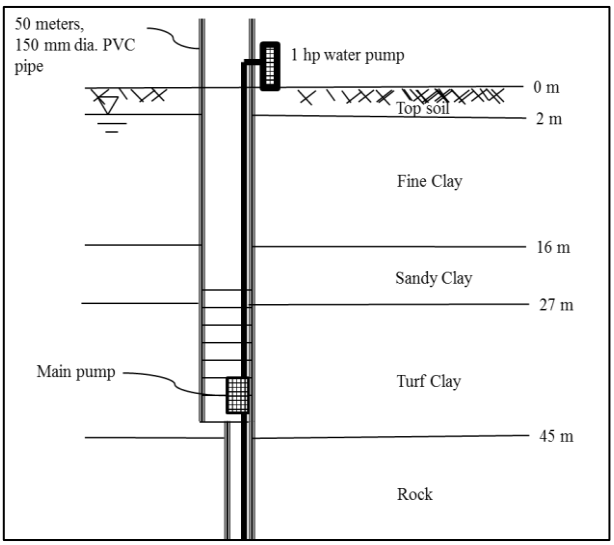


Fig.1. Soil profile of RECESS [11]

The well system that existed at RECESS, UTHM consists of 4 monitoring well and a pumped well as shown in Figure 2. The construction of wells was designed and constructed by drilling machines and installed with PVC pipe into the ground. The wells are constructed with PVC pipe of diameter 50mm, 100mm, and 150mm. The depths of wells are 50 meters for pumped well and monitoring well 1, 42 meters for extracted well and 30 meters for monitoring well 2. Pumped well (also known as recharge well) are the only well that installed with 1 horsepower of submersible pump.

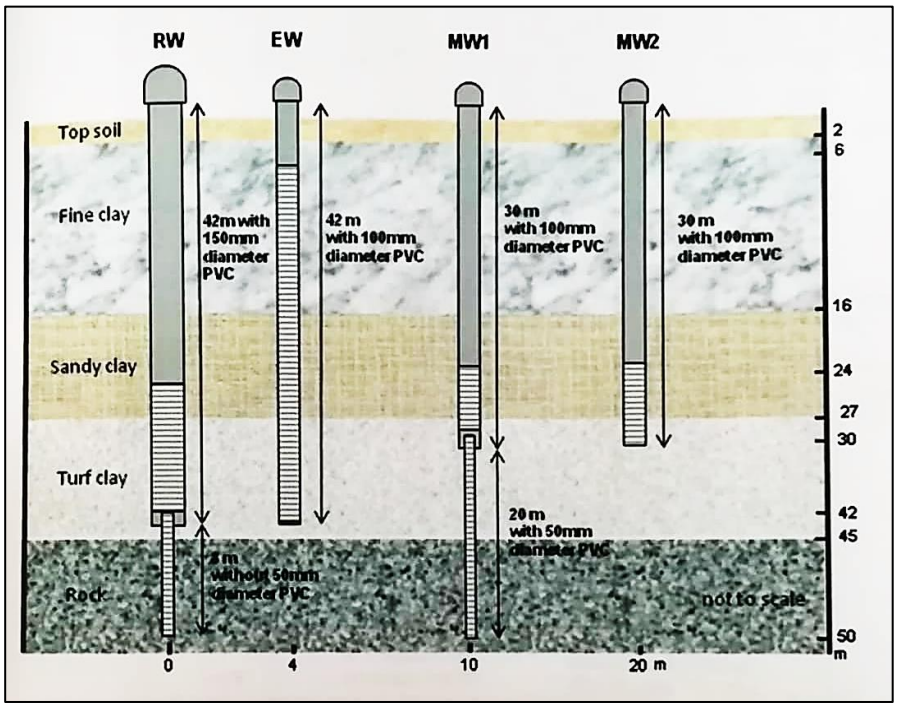


Fig.2. Well in RECESS, UTHM [11]

The wells' length is in 30 meters to 50 meters from top soil until rock layer. There is 60% above of clay soil in RECESS such as fine clay, sandy clay, and turf clay. It was summarized that the layer of clay was varied in thickness from 2 m to 27 m approximately and the layer of Tuff clay was covered up to 18 m of the sub surface to 5 m of hard rock at the bottom.

1.3 Drawdown and Recovery in RECESS

From previous pumping analysis showed that the radial flows within 4 hours were achieved around 0.135m with rapid recovery time compared to pumping time. Meanwhile, the water table in this area remains high while the pumping was discharge more than 4 hours continuously[9].

The recharge that occurs at RECESS UTHM is natural discharge. Different from artificial recharge, the natural recharge occurs through the process of infiltration where the water percolates from the surface to the bed of the aquifer[13]. After the water from precipitation had reached the ground surface, part of the water will carry out infiltration process and diffuse into the ground. However, the speed of water infiltration is depending on soil moisture and ground's hydraulic characteristics.

However, it is proved that the perforated pipe can act as a well that connected to aquifer and help to reduce the surface runoff of the excess stormwater as well as a flood prevention at the same time can increase the potential of groundwater capacity for water supply and reduce the contribution to channel of drainage system [10]. In this case, excess stormwater is stored in confined layer in subsurface. According this well test that carried out by[14], half of pumping yield was loss by recovery in range 25-26 m in 50 minutes.

2. Methods

The study was carried out at RECESS, UTHM within 245 minutes with the aims of data collection for the analysis of drawdown and the influences of pumping activities to the study area. In this study, two 4 hours pumping tests were carried out at different well which are Pumped well, R_1 and monitoring well 4, R_5. The test was carried out at two different day with same duration. The invert level of pumped well, R_1 and four monitoring wells, R_2, R_3, R_4, R_5 onsite were measured and recorded. There are four monitoring wells and one pumped well existed on the study area as shown in Figure 4. Water levels of wells were recorded from well head of the top soil, before and during pumping test.

2.1 Analyzation of Response Surface Methodology (RSM)

In this experiment, Response Surface Methodology (RSM) was carried out with the assist of Design-Expert 10. Design–Expert is statistical software which helps in design of experiments (DOE). Design-Expert 10 is software that consists of two-level factorial screening designs. It can help to control and improve water drawdown by identifying unrecognized drops of level, as a process to make breakthrough improvements[15]. A procedure of RSM was as shown in Figure 5. Before starts the methodology, appropriate knowledge must be studied and identified so that the design of experiments is correct. When factors undergo process, there is the existing of responses. Followed by Empirical Models and ANOVA, contour plots of the experiment can we obtained. Optimization of the experiment will be carried out as last step of RSM to find out the best result and performance among all the trials. Optimization process will be carried in last to obtain the desirable expectations results from this study.

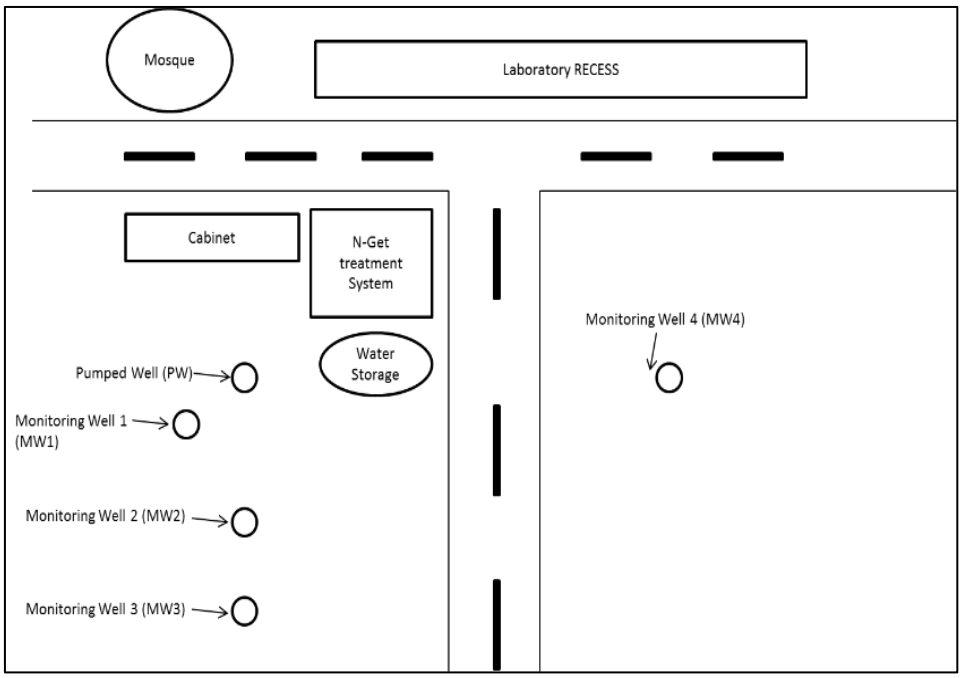


Fig.4. Plan view of well

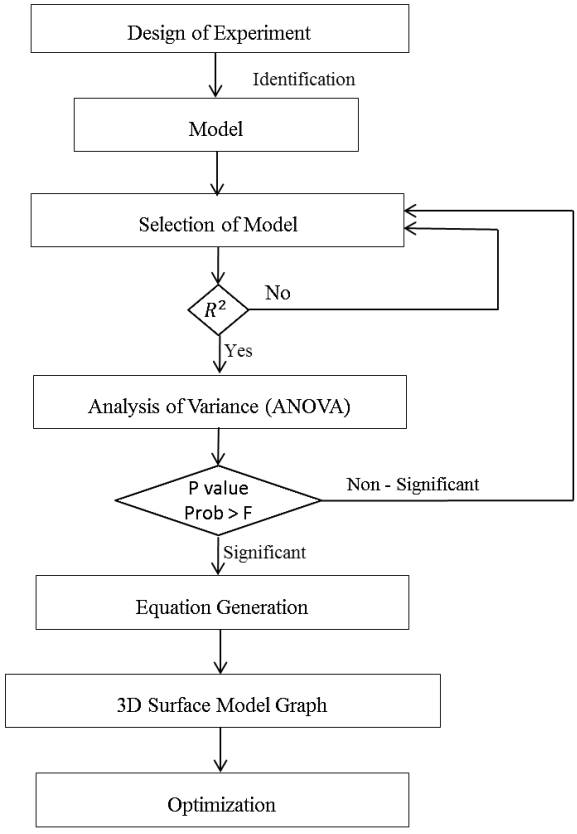


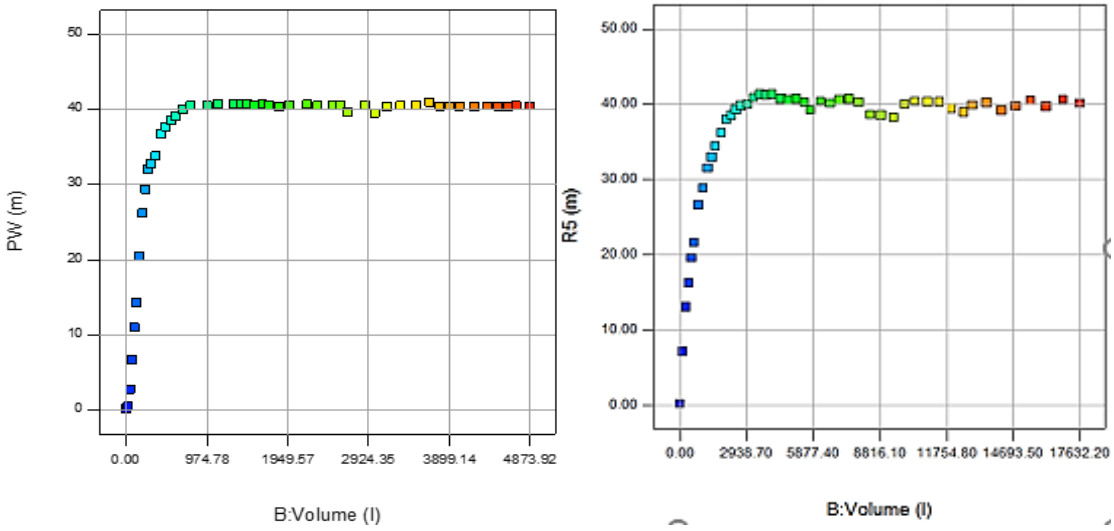
Fig. 5. Model analysis for R_1, R_2, R_3, R_4 *and* R_5

3. Results

Based on the analysis and results between parameters such as time, volume, and water level of responses, several conclusions were made accordingly to the relationships between Factor A,

Factor B and output from optimized value. After carried out the test, data were recorded and re-calculated accordingly to the experiment time. When the time taken for groundwater extraction was longer, the quantity of groundwater was also increasing at the same moment as shown in Figure 6(a) & (b).

The maximum reading for Factor A (time) is 245 minutes while Factor B (volume) is 4873.92 litres and 17632 litres each. It was concluded that the relationship between R and Factor B (volume) was moderately positive correlation as the correlation reading is positive and both $R_1 \& R_5$with Factor B are associable and in linear relationship by increasing together. It indicated that graph shows a huge climb and remained steady with range of 39.50m to 40.95m even Factor B was constantly increasing. It was explained that the location of pump is located at level of 41m, therefore the level inside the well maintained at 39.50 m to 40.95m.



(a) *R1* case (b) *R2* case

Fig. 6. Evaluation R to factor B

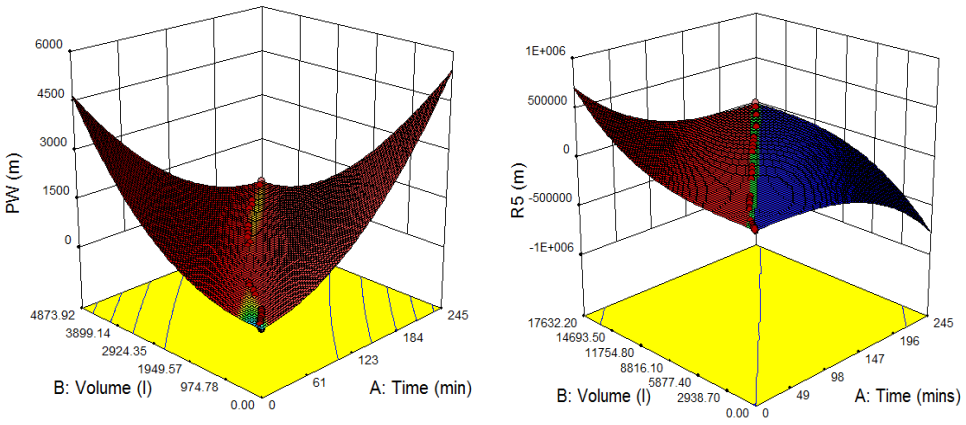
It was summarized that groundwater for case 1 was discharged at a constant rate of $28.65\mathrm{m}^3/$ day and increased by time. However, it was too low compared to case 2 with $103.63\mathrm{m}^3/\mathrm{day}$ of discharge. The lower value in case 1 might happen due to the 1 horsepower of pump that located at level of 40 m inside the well. Besides, it was explained that the location of pump is located at level of 41m, had directly affected to R_1 during 34 minutes to 245 minutes where the water maintained at 39.50 m to 40.95m. Besides, the reason that cause to the insignificant changing of water level was including low infiltration of clay soil between 0.004 – 0.007 mm/s[10]. In addition, the noticeable changing might happened due to the pumping area when pumping had changed the regular course and amount of groundwater flow inside the zone of depression[16]. When two cones of depression overlap, the interference reduces the water available to each well.

During pumping test in case 2, it was observed that $R_3 \mathrm{and} R_4$ that located 36m and 40m from R_5 had not changing during the pumping test. The water level remained 0.05m within 245 minutes and pumping test at R_5 had great influences towards the changing of R_1 only. It was explained that the distance is near (35m) and R_1 was located within the cone of depression, and distance of more than 36m was unaffected to pumping activities in RECESS, UTHM. It indicated that the extraction quantity of groundwater does not affect water level of another well in a far distance.

Pumping activities was directly and indirectly affecting the water level of nearby well. For the 48 samples run of pumping experiment within 245 minutes at RECESS UTHM, the changing of invert level by minutes was identified with the optimal value of Factor A and Factor B. Models are used for prediction in order to generate response surface graphs and contour plots. There are significant interactions between volume and time factors, the response surface graphs and contour plots as variation of the process conditions are shown in Figure 7.

When Factor A and Factor B are performing together, R_1 seems unaffected and maintained at the lowest point which formed 'U' shape as shown in Figure 7(a). However, when there was only one Factor performing in test, R_1 was able to reach to the highest point. It shows that the interaction between Factor A and Factor B will give the least expectation on the experiment.

R_5 in Figure 7 (b) shows that Factor B (volume) had achieved the biggest increment in graph as the as the point reached highest point on Factor B only. However, Factor A (time) do not affect much on the changing of the water level of R_5. It indicated that R_5 had more influences for itself water level changing from the amount extraction of groundwater. The much and less of extracted volume manipulated on water level of R_5.



(b) *R1* case (b) *R2* case

Fig. 7. 3D surface model of *R1* and *R2*

The numerical optimization finds a point that maximizes the desirability function as shown in Table 1. In fact, the goal of the test was to obtain maximize volume extraction with minimum time with the optimal water changing in $R_1, R_2, R_3, R_4 \text{and} R_5$.

Table 1
Desirability specifications of numerical optimization for crossed design

Name	Goal	Lower Limit	Upper Limit	Lower Weight	Upper Weight	Importance
A	minimize	0	Time	1	1	3
B	maximize	0	Volume	1	1	3

Table 2 and Table 3 show that all goals are joined into one desirability function which are based on various responses and factors. The suitable optimum formulation with high desirability of 0.541 and 0.513 were selected.

Table 2
Optimization conditions, prediction and desirability of model for R_1

Time	Volume	R1	R2	R3	R4	R5	Desirability
116.243	2719.049	40.950	0.195	0.136	0.024	0.275	0.541
115.280	2698.681	40.950	0.195	0.136	0.023	0.274	0.541
117.813	2752.084	40.950	0.194	0.136	0.026	0.277	0.541

Table 3
Optimization conditions, prediction and desirability of model for R_5

Time	Volume	R1	R2	R5	Desirability
117.484	8898.361	2.382	0.040	40.778	0.513
118.464	8966.769	2.388	0.040	40.719	0.512
116.419	8824.063	2.375	0.040	40.842	0.512

From the optimization test, it was analyzed that 116.243 minutes (1 Hour 55 minutes) to 117.484 minutes (1 Hour 57 minutes) of pumping can performed best in pumping activities to obtain maximize volume extraction with minimum time with the optimal water level changing in other well.

4. Conclusions

Groundwater extraction capability after 4 hours of pumping test in RECESS, UTHM had calculated and identified. In pumped well, R_1, the quantity discharged at $28.65\mathrm{m}^3/\mathrm{day}$. However, R_5 had been extracted at rate of $103.63\mathrm{m}^3/\mathrm{day}$ which is 3.62 times higher than R_1. The analysis from groundwater extraction by using Response Surface Methodology (RSM) with the assist of Design Expert software was performed. The model formulated from Design-Expert can generate the ideal performance towards each well by formulating the exact changing process of responses based on historical data with the aid of 2D contour and 3D surface graphs during optimization process. It was indicated that in 116.243 minutes (1 Hour 55 minutes) to 117.484 minutes (1 Hour 57 minutes) of pumping activity can performed best in pumping activities to obtain maximize volume extraction with minimum time with the optimal water changing.

Acknowledgement
The authors also wish to thank and gratefully acknowledge Ministry of Higher Education of Malaysia for the research project financial support under Exploratory Research Grant Scheme (ERGS) vot no E039.

References
[1] Abdullah, N. I. *Malaysians need to reduce water consumption*. *Malaysiakini*, pp. 1–2, 2014.
[2] Gleick, P. H. "Making Every Drop Count," *Sci. Am.*, vol. 248, (2007):, pp. 40–45.
[3] Pıelke, R. "What Is Climate Change?," 2004.
[4] Minderhoud, P., Erkens, G., Pham, V. H., Vuong, B. T. and Stouthamer, E. "To drink or to drown? Impact of groundwater extraction on subsidence in the Mekong Delta, Vietnam," vol. 9, no. 2014, p. 2015, 2016.
[5] Brown, L. "As countries over-pump aquifers , falling water tables mean falling harvests,"(2008).
[6] Siebert, S., Burke, J., Faures, J. M., Frenken K., Hoogeveen J., Doll, P. and Portmann, F. T. "Groundwater use for irrigation - A global inventory," *Hydrol. Earth Syst. Sci.*, vol. 14, no. 10, (2010): pp. 1863–1880,
[7] De Conceicao, P. "Differences between a confined aquifer and an unconfined aquifer," 2018.
[8] Perlman, H. "Water science for schools: aquifers," 2014.

[9] Musa,S., Zakaria, N. A., Lau, T. L., Ahmad Nazri, M. A. and Buhari, R. "Groundwater responses on pumping analysis for clayey aquifer," *Journal of Physics Conference Series, 1049* (2018): p 1-11.
[10] Ridzuan,M. B., Tjahjanto, D. and Musa, S. "A study on artificial recharge well as a part of drainage system and water supply in UTHM," pp. 106–111, 2008.
[11] Musa, S., Zakaria, N. A., Lau, T. L. and Tjahjanto, D. "Subsurface conditions with geo-hydraulic properties : empirical evidence from Parit Raja , Johor," Proceeding of International Conference Civil Engineering and Environemntal Sustainability (IconCEES), 2012.
[12] Brian S. "Designing and installing permanent and temporary groundwater monitoring wells," 2013.
[13] Kavuri, M., Boddu,M., Gopal, V. and Annamdas, M. "New methods of artificial recharge of aquifers : a review," pp. 1–9, 2011.
[14] Musa, S., Zakaria, N. A. and Tjahjanto, D. "The potential of recharge well system in flat area with low infiltration rate " *Proceeding of International Conference of Civil Engineering and Water Research (ICEWR),* 2015: p 1-10.
[15] Kolthoff, I. M. "V10 of Design-Expert ® Software : Top tool for Design of Experiments (DOE) rave reviews from the expert evaluators what ' s in it for you what ' s New," 2016.
[16] Victor P. M., "Groundwater utilization and sustainability," *Proceedings of 20th IASTEM International Conference*, pp. 1–12, 2006.

Penerbit Akademia Baru

Engineering Science and Technology Conference Proceedings

Journal homepage: www.akademiabaru.com/EST.html

Engineering Science and Technology Conference Proceedings

Open Access

Badrul Amin Hanafi[1], Nur Shamimi Amirah Md Sunhazim[1], Natrah Kamaruzaman[1], Ummikalsom Abidin[1*1]

[1] School of Mechanical Engineering, Faculty of Engineering, Universiti Teknologi Malaysia, 81310 Skudai, Johor, Malaysia

ABSTRACT

Microfluidics channel had been widely used in many applications, such as chemical, medical and biological applications. One of the microfluidics applications is in cell separation. In this study, investigation on the capability of 4.5 micrometer magnetic microbeads separation in continuous microfluidics flow using microchannel with trapping chamber design and magnet wire is conducted. The PDMS microchannel is fabricated using standard soft lithography technique from SU-8 mold. The planar spiral magnet wire is fabricated using 0.3 mm enamel copper wire. The planar spiral magnet wire with 20 turns is used in this study. At current supply 2 A or with 4.5 mT magnetic field generated, the maximum trapping efficiency is 91.43 % as flow rate of 5 µl/min. On the other hand, trapping efficiency of 82.86 % is demonstrated for 1 A current supply as the same flow rate. A decreasing trend of trapping efficiency is observed with increasing microchannel flow rate. In conclusion, the comparison between these two current supplies were made and it shows some significant change of trapping efficiency with increasing of the flowrate in microchannel

Keywords:
Microfluidics channel, Polydimethylsiloxane (PDMS), magnetic microbeads, magnet wire, trapping efficiency

Copyright © 2019 PENERBIT AKADEMIA BARU - All rights reserved

1. Introduction

Cell separation is a key application area for Lab-on-Chip (LOC) devices. Among the various methods, LOC with magnetic separation technique has promising potential in biological cell separation [1]. Cell sorting method using magnetic field is called magnetophoresis (MAP) and is categorized as active method due to external force field is required. To date, the magnet system used is either permanent magnet or electromagnet to capture targeted biological cells using labelled magnetic microbeads. Microbeads is also used as a carrier in medical applications such as magnetic resonance imaging, hyperthermia and medicine delivery [2]. LOC magnetic separation has the advantages of easy and simple to setup.

Furthermore, LOC as integrated chemical and biological processing device is preferred as Point of Care (POC) due to several merits such as small size, low cost, low sample and reagent consumption, biocompatibility, efficiency, simplicity portability, as well as fast analysis time [3]. Micro-scaled electromagnet system is commonly integrated with microfluidic channel as complete

* *Corresponding author.*
E-mail address: ummi@utm.my (Ummikalsom Abidin)

MAP. The microchannel function is for magnetic microbeads flowing in microfluidic flows. Polydimethylsiloxane (PDMS) microchannel fabricated using replica molding or soft lithography is commonly used in microfluidics and LOC purposes [4]. PDMS microchannel fabrication using replica molding is generally preferred due to its process simplicity with casting and curing [5]. In addition to its biocompatibility, PDMS transparency and permeable to gases are some of its advantages. Factors that need to consider in the design of an electromagnetic system for magnetic microbeads capturing are its direction, strength and gradient [6]. This is as the magnetic force, $\vec{F}_m$ on the magnetic microbeads of volume, $V = \left(\frac{4}{3}\right)\pi R^3$, is described in the Eq. (1)

$$\vec{F}_m = \frac{V\Delta\chi}{2\mu_o}\vec{\nabla}\left(\vec{B}\cdot\vec{B}\right) \quad (1)$$

where, $\Delta\chi$, is the difference in magnetic susceptibility ($\chi_p$for particle and χ_{pm} for the fluid buffer medium), μ_o , is magnetic constant of $4\pi \times 10^{-7}$, B and ∇B, is strength and gradient of the magnetic flux density respectively.

Comprehensive review on microelectromagnet in generating magnetic field and for magnetic microbeads separation has been discussed Basore & Baker. In the review, microelectromagnet geometrical aspect and its applications was compared [7]. Planar square or spiral-shaped coil is commonly used as microelectromagnet due to its capability in producing high gradient magnetic field at its center. Electric current is supply to the coil to produce the magnetic field. Planar square coil by Fulcrand *et al.,* successfully guide and separating magnetic microbeads to the microchannel outlet [8]. The same concept as Fulcrand *et al.,* but with meander-shaped microelectromagnet design was conducted by Kong *et al.,* [9]. In order to achieve high magnetic force, high gradient magnet system (HGMS) was proposed. Works by Ramadan *et al.,* [10] and Deng *et al.,* [11] integrated soft-magnetic core for its microelectromagnet system in producing HGMS to capture magnetic microbeads. The major disadvantages of the microelectromagnet system either low or high magnetic gradient is the microfabrication complexity and its high in cost. In addition, only low range of current can be applied to prevent the microcoil from laminating from its based substrate. In this work, a magnetic system of external planar spiral-shaped electromagnet from magnet wire is used for trapping magnetic microbeads in microfluidics flow. The magnet wire is effortlessly available, low in cost, simple to set-up, reliable and possible for high electric current injection. The trapping efficiency is the aim for quantitatively describe the magnetic system with different flow of magnetic microbeads.

2. Methodology

2.1 Replica molding of PDMS Microchannel

PDMS replica molding is one of the process of creating the microchannel pattern from SU-8 by applying the technique of soft lithography to create a channel pattern [12]. In this work, the design of the microfluidic channel or microchannel was based on previous work by Abidin *et al.,* [13]. The microchannel has one inlet and one outlet, 300 µm in width and 100 µm in thickness. The total length of the microchannel is 14.0 mm. A chamber of 750 µm was designed at the middle of the straight channel. The microchannel SU-8 mold was fabricated by Australian National Fabrication Facility (ANFF) using photolithography technique.

The Sylgard 184 Silicone Kit contained PDMS oligomer and crosslinking pre-polymer agent were used for fabrication of microchannel. The procedure of PDMS replica molding can be summarize as the Figure 1.

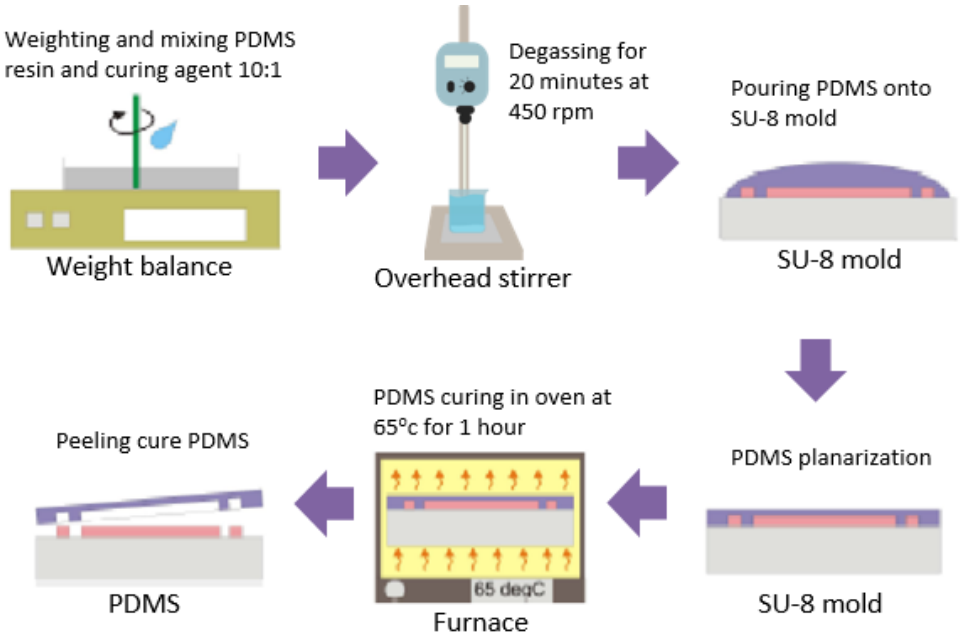


Fig. 1. Replica Molding of PDMS

2.2 PDMS bonding

PDMS microchannel undergoes bonding process with thin layer first layer of PDMS. The bonding conducted by the process of the oxygen plasma treatment [14]. The bonding is primarily to stick the PDMS layers together. The oxygen plasma process was performed for 12 seconds at 150 W The oxygen plasma treatment activated PDMS surface and facilitate the bonding. Furthermore, the hydrophobic PDMS surface is converted to hydrophilic surface by oxygen plasma treatment. This hydrophilic surface is need to make the liquid flow smoothly through the microchannel. The PDMS was tested to ensure there was no leakage in the microchannel before the trapping efficiency experiment is carry out.

2.3 Fabrication of the Spiral Planar Coil

The fabrication of the planar spiral-shaped coil being made by hand by using 0.3 mm enamel copper wire with number of turn, *N* of 20. Planar spiral coil is selected for the magnet wire due to the high gradient of the magnetic field at the center of the coil [15]. Some of the criteria for the coil planar spiral-shaped are the coil cannot be overlap with each other and the gap between the wire in being minimize. This is to maintain the closest distance between the magnet wire and the microchannel. A closest distance is necessary to prevent loss on magnetic field. Furthermore, the coil center is to minimize as small as possible. Figure 2 shows the accepted planar spiral-shaped coil fabricated using magnet wire

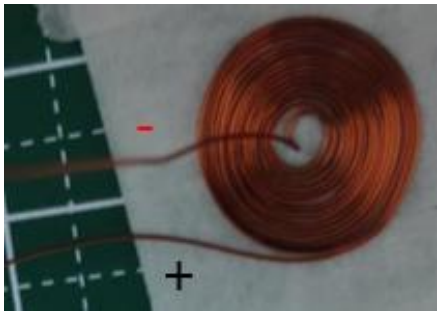


Fig. 2. planar spiral-shaped coil being made by hand by using 0.3 mm enamel copper wire with number of turn, *N* of 20

2.3 Measuring Magnetic strength using Digital Gaussmeter

The spiral planar coil produces magnetic field when being supply with current. The magnetic field was measured using the digital gaussmeter. The digital gaussmeter work base on the principle of hall-effect. The digital Gaussmeter and its specification are shown in Figure 3.



Digital Gaussmeter, Model DGM-102	
Range	0-2 K gauss & 0-20 K Gauss
Resolution	1 gauss at 0-20 gauss range
Accuracy	± 0.5 %
Temperature	Up to 50°c
Display	3½ digit, 7 segment LED DPM
Detector	Hall probe with an Imported Hall Element
Power	220 V, 50 Hz
Special	Indicates the direction of the magnetic field
Weight	3 Kg
Dimensions	280 mm × 255 mm × 120mm

Fig. 3. (a) Digital gaussmeter Model DGM-102 (b) Model DGM-102 specifications

The measurement of magnet wire for the experiment set up had being measured to check the magnetic field. Figure 4 shows the schematic for the probe location of the measurement.

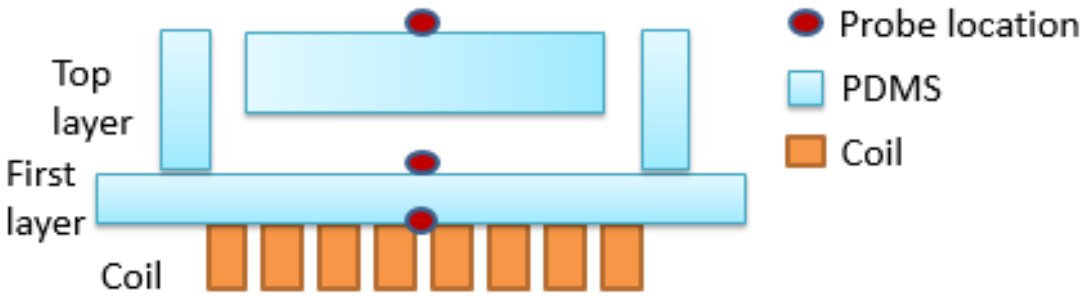
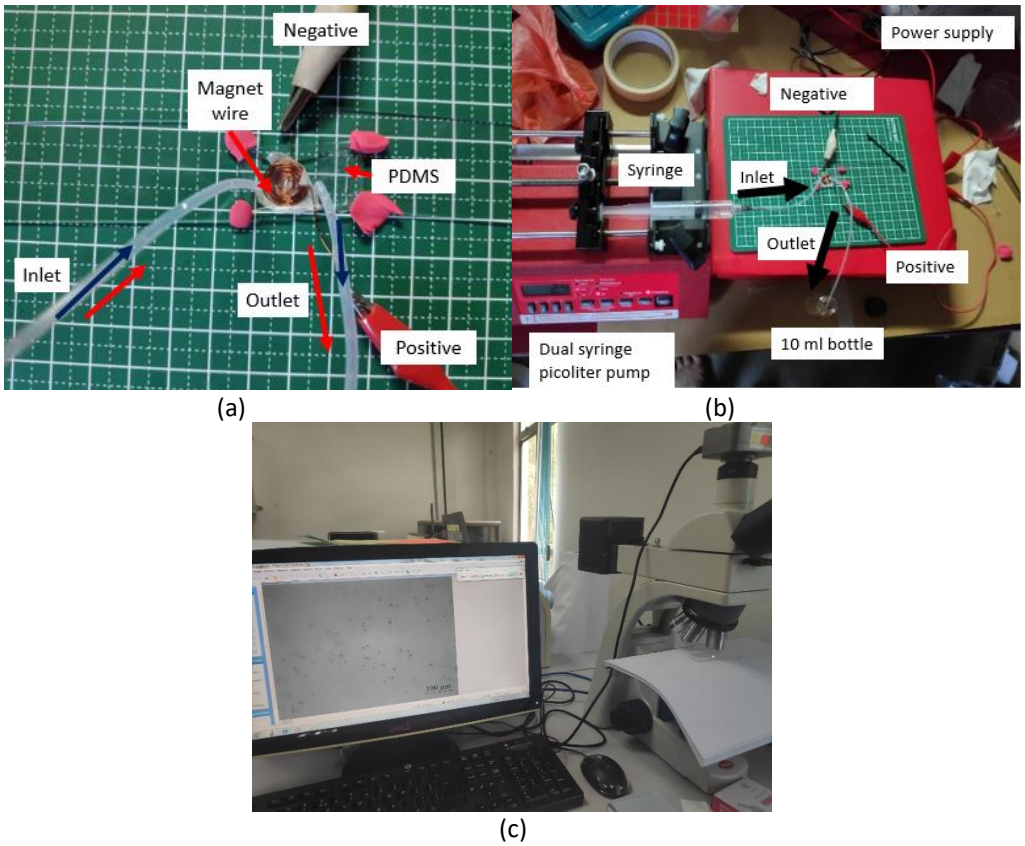


Fig. 4. Schematic Set Up for probe checking

2.4 Experimental Set Up and Testing

The experiment using the fabricated PDMS microchannel and magnet wire was conducted to determine the magnetic microbeads trapping efficiency. Prior to the experiment, DI water and microbeads were mixed and then injected into the microchannel. 2 µl of polystyrene magnetic particles were mixed with 5 ml of DI water. The dilution factor after mixing microbeads and DI water was 2501. The size of microbeads used in this project were average 4.5 µm with catalogue number of PMS-40-10. The concentration of the solution was 2.5% w/v with volume of 10 ml. These microbeads were manufactured by Spherotech Inc. USA. The estimation from the calculation of microbeads in that solution was for every 1 ml, the amount of microbeads was $4.99x10^8$ particles.

A dual syringe pump with model of NE 4000 (KdScientific) was used to control the flow rate. The flowrates used were 5, 10, 15, 20, 40 and 60 µl/min. A 10 ml B-D syringe was attached to the pump and the syringe tip was connected to the 2 mm tube at the inlet of microchannel. An the end of 2 mm outlet tube, 10 ml bottle was placed for collecting the samples for each of the flow rates. The collected DI water which content microbeads was checked under the optical microscope and its image at outlet was captured. The images were processed by using ImageJ software in counting the number of microbeads automatically. The processes were repeated with different flowrate and different electrical current supplied which are 1 Ampere and 2 Ampere. The actual experimental set up is shown in Figure 5.



(a) (b)

(c)

Fig. 5. (a) Magnetic wire set up (b) experimental set up (c) checking the outlet microbeads using optical microscope

3. Results

3.1 Magnetic Strength of the Magnet Wire

The configuration of the magnet wire coil and the PDMS microchannel layer together with the magnetic field measurement results were shown in Figure 6. As the PDMS height increases, the magnetic strength experience for the PDMS decreased. The highest magnetic field is achieved at the closest distance of the magnet wire with the PDMS layer which are 2.35 mT and 4.50 mT for 1A and 2 A electric current supplied respectively. At higher current of 2 A, the value of the generated magnetic field is almost double. The lowest magnetic field achieved were 1.80 mT and 3.48 mT at 1 A and 2 A respectively, which is at the greatest height from the magnet wire. The thickness of the PDMS plays a major role in the magnetic field which will be experienced by the magnetic microbeads. Therefore, the closest distance between the magnetic field source and the microfluidics channel must be maintain at all times.

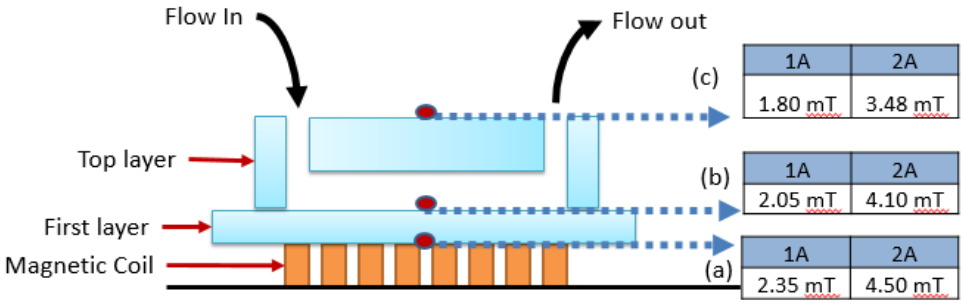


Fig. 6. Magnetic strength measurement for PDMS

3.2 Trapping Efficiency of Microbeads

Trapping efficiency is conducted to determine the magnet wire capability in trapping magnetic microbeads in the trapping chamber. Trapping efficiency is calculated automatically using ImageJ image processing software. For further analysis of trapping efficiency, this software is responsible for quantifying the number of microbeads at the outlet. Table 1 compared qualitatively ImageJ images at different current supplied of 1 A and 2 A and at 5 µl/min and 60 µl/min respectively. At 5 µl/min the lowest microbeads were captured, while at 60 µl/min shows the highest. This indicated that at lower flow rate is where the magnetic microbeads trapping in the trapping chamber is more efficient.

Table 1
Result of outlet microbeads from ImageJ at different flowrate and current

	5 µl/min	60 µl/min
1A		
2A		

In order to determine the trapping efficiency quantitatively, the trapping efficiency of the magnetic microbeads was calculated using Eq. (2) [9]:

$$\text{Trapping Rate} = \frac{(\text{input} - \text{outlet}) \text{of microbeads}}{\text{input of microbeads}} \times 100 \quad (2)$$

The Figure 7 shows the graph of the trapping efficiency versus flowrate at 1 A and 2 A electric current supplied to the magnet wire. At the lowest flow rate of 5 µl/min, the highest trapping efficiency of 82.86 % and 91.43 % were achieved at 1 A and 2 A current respectively. The trapping efficiency decreases significantly at 10 µl/min flow rate for both 1 A and 2 A current. The lowest trapping efficiency were at 60 µl/min of only 12.14 % and 15.71 % at 1 A and 2 A current respectively. At higher flow rate the drag force on the magnetic microbeads is expected to increase and the constant magnetic force generated by the magnet wire is not be able to capture or trap the magnetic field.

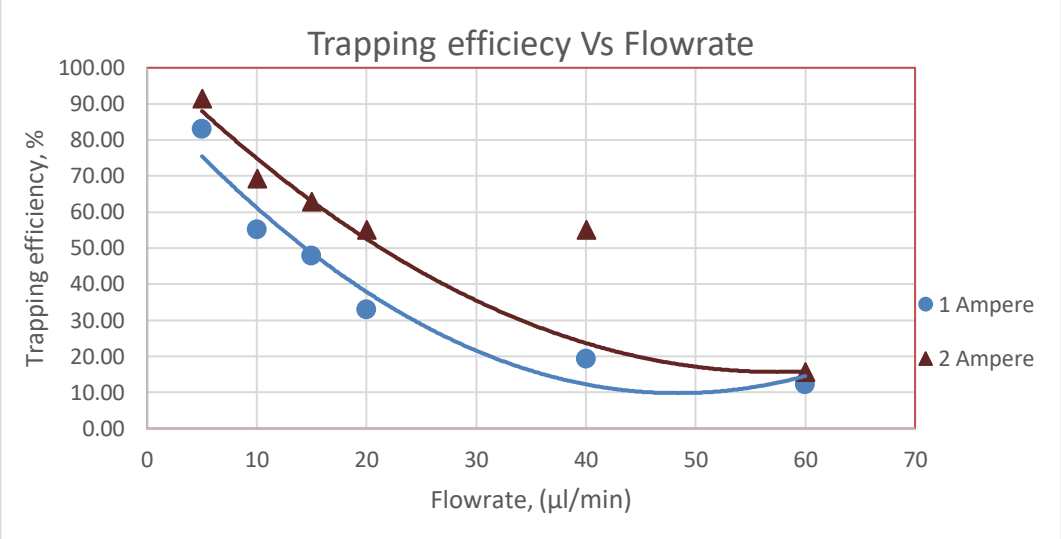


Fig. 7. Graph Trapping efficiency vs flowrate

The calculation of the magnetic force is as shown in Figure 8, revealed the effect of increasing drag force at increasing flow rate. The lowest drag force of ~ 20 pN is at flow rate of 5 µl/min while at 60 µl/min the drag force is 250 pN.

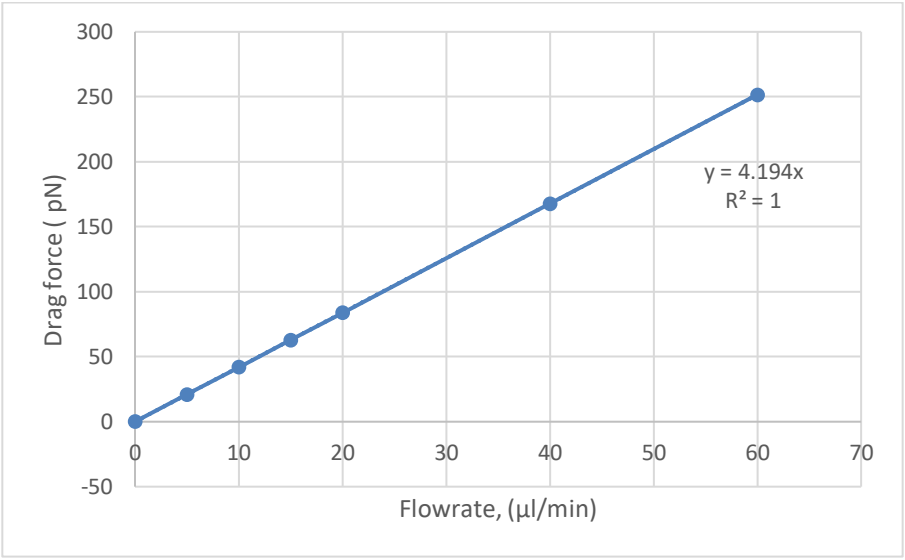


Fig. 8. Graph drag force vs flowrate

Therefore, it can be concluded from the experiment that the trapping efficiency decreases with the increase of the volumetric flow rate. The same trend was observed in the previous studies by Abidin *et al.,* [17], Ramadan *et al.,* [15] and Fulcrand *et al.,* [8].

For the future study, heat generation from the magnet wire system is proposed to be conducted. This is to ensure no Joule heating effect from the magnet wire could be generated. This is to ensure that the water inside the microchannel will not evaporate and the biological cells that bonded to the magnetic beads will survive. It is expected that temperature higher that 45 °C, denaturation effect starts to occur to the cells' protein [20]. Moreover, degenerated of Mesenchymal Stem Cell (MSC) is happened at temperature of 48 °C [21]. In proposed LOC cell separation application for biological cell studies, the live of the biological cells is at the utmost.

4. Conclusions

The PDMS fabrication was carried out successfully. The fabrication was performed using soft-lithography method for obtaining the perfect microchannel PDMS. The magnetic coil was then fabricated successfully and the magnetic strength was measured to validate the functionality. The microbeads trapping efficiency was performed, recorded and quantified. The optical microscope was used and the image for the microbeads was captured and processed successfully by the ImageJ software ImageJ. At 1 A supplied electric current to the magnet wire and flow rate of 5 µl/min the highest efficiency is 82.86 % and the lowest is 12.14 %. For 2 A current and flow rate of 5 µl/min, the highest efficiency is 91.43 % and the lowest is 15.71 %. A decreasing trend of trapping efficiency is observed with increasing microchannel flow rate. In conclusion, the comparison between these two current supply were made and it shows some significant change of trapping efficiency with increasing of the flowrate in microchannel

Acknowledgement

I would like to thank Ministry of Education Malaysia for the Fundamental Research Grant Scheme (FRGS) of R.J130000.7851.5F240 in supporting this research.

References

[1] Cao, Q., Han, X., & Li, L. "Configurations and control of magnetic fields for manipulating magnetic particles in microfluidic applications: Magnet systems and manipulation mechanisms." *Lab on a Chip*, 14(15), (2014): 2762–2777.

[2] Majid Hejazian, W. L.-T. "Lab on a chip for continuous-flow magnetic cell separation." *RSCPublishing* , (2012): 1-12.

[3] Shoshi, A., Schotter, J., Schroeder, P., Milnera, M., Ertl, P., Charwat, V., … Brueckl, H. "Magnetoresistive-based real-time cell phagocytosis monitoring." *Biosensors and Bioelectronics*, 36(1), (2012): 116–122.

[4] Whitesides, G. M. "The origins and the future of microfluidics." *Nature*, 442(7101), (2006): 368–373

[5] Abidin, U., Yunas, J., & Majlis, B. Y. "Fabrication and testing of polydimethylsiloxane (PDMS) microchannel for lab-on-chip (LOC) magnetically-labelled biological cells separation" *Jurnal Teknologi*, 78(8–4), (2016): 73–80.

[6] Cao, Q., Han, X. & Li, L. 2014. Configurations and control of magnetic fields for manipulating magnetic particles in microfluidic applications: magnet systems and manipulation mechanisms. *Lab on a chip*, 14(15), 2762–77.

[7] Basore, B. J. R., Lavrik, N. V & Baker, L. A. 2010. Single-Pore Membranes Gated by Microelectromagnetic Traps 37831, 2759–2763.

[8] Fulcrand, Rémy, Aurélien Bancaud, Christophe Escriba, Qihao He, Samuel Charlot, Ali Boukabache, and Anne-Marie Gué. 2011. "On Chip Magnetic Actuator for Batch-Mode Dynamic Manipulation of Magnetic Particles in Compact Lab-on-Chip." *Sensors and Actuators B: Chemical* 160 (1). Elsevier B.V.: 1520–28.

[9] Kong, T. F., E, H. S., Sugiarto, H. S., Liew, H. F., Wang, X., Lew, W. S., Nguyen, N.-T. *et al.,* 2010. An efficient microfluidic sorter: implementation of double meandering micro striplines for magnetic particles switching. *Microfluidics and Nanofluidics*, 10(5), 1069–1078.

[10] Ramadan, Qasem, Daniel P. Poenar, and Chen Yu. 2008. "Customized Trapping of Magnetic Particles." *Microfluidics and Nanofluidics* 6 (1): 53–62.

[11] Deng, T., Prentiss, M. & Whitesides, G. M. 2002. Fabrication of magnetic microfiltration systems using soft lithography. *Applied Physics Letters*, 80(3), 461.

[12] Elveflow (2018,November 22). HOW TO DO PDMS LITHOGRAPHY REPLICATION FROM A SU-8 MOLD. retrieved from: https://www.elveflow.com/microfluidic-tutorials/soft-lithography-reviews-and-tutorials/introduction-in-soft-lithography/pdms-softlithography-replication/

[13] U. Abidin, N. A. S. Mat Daud, and V. Le Brun, "Replication and leakage test of polydimethylsiloxane (PDMS) microfluidics channel," *AIP Conference Proceedings* **2062** 020064 (2019)

[14] Tan, Say Hwa, Nam-trung Nguyen, Yong Chin Chua, Tae Goo Kang, Say Hwa Tan, Nam-trung Nguyen, and Chin Chua. 2010. "Oxygen Plasma Treatment for Reducing Hydrophobicity of a Sealed Polydimethylsiloxane

Microchannel Oxygen Plasma Treatment for Reducing Hydrophobicity of a Sealed Polydimethylsiloxane Microchannel." 032204.

[15] Ramadan, Q., Poenar, D. P., & Yu, C. "Customized trapping of magnetic particles." *Microfluidics and Nanofluidics*, 6(1), (2009): 53–62.

[16] Ramadan, Q., Samper, V. D., Puiu, D. P., & Yu, C. "Fabrication of three-dimensional magnetic microdevices with embedded microcoils for magnetic potential concentration" *Journal of Microelectromechanical Systems*, 15(3), (2006): 624–638.

[17] U. Abidin, B. Yeop Majlis, and J. Yunas "Efficient Magnetic Microbeads Trapping using Lab-on-Chip Magnetic Separator," *J. of Advanced Research in Fluid Mechanics and Thermal Sciences* **57**(1) 1-11 (2019)

[18] Wiklund, M. "Acoustofluidics 12: Biocompability and cell viability in microfluidic acoustic resonators." *Lab on a chip,* 12(11), (2012).

[19] Reissis, Y., Garcia-Gareta, E., Korda, M., Blunn, G.W. & Hua, J. "The Effect of temperature on the viability of human mesenchymal stem cells." *Stem cell research & therapy*, 4(6), (2013): 139.

Penerbit Akademia Baru

Engineering Science and Technology
Conference Proceedings

Journal homepage: www.akademiabaru.com/EST.html

Analysis of Absorber Material Effect on Optimization of Heat Absorption in solar collectors

Open Access

Muhammad Ilham Maulana[1,*], Ahmad Syuhada[1]

[1] Department of Mechanical Engineering of Syiah Kuala University, Darussalam–Banda Aceh 23111, Indonesia

ABSTRACT

Drying technology using solar collectors can increase the temperature of the air-drying faster than direct drying. One factor that causes an increase in air temperature in the collector is the high absorber temperature that can achieve. Absorber serves to absorb heat from the intensity of the sun after that heats the air that flows in the airways above the absorber. An experimental study was carried out to clarify the effect of the solar collector absorber material on the characteristics of heat absorption with a rectangular sharp turn channel passage of the stationary conditions. To find out that, the ability of heat absorption by the solar collector absorber will be studied. Thus the characteristics of the heat absorption field can be predicted. The solar collector specification that is test had a 130-degree sharp turning channel and measuring 300 cm x 80 cm, with a variety of solar collector absorber material in the form of iron sand, iron waste mixed iron sand, hot mix asphalt, and iron sand mixed asphalt. The highest heat absorption value produce by iron sand absorber mixed with iron gram waste with a temperature of 96 °C with 967 W/m^2 sunlight intensity at 1 pm. The results showed that using absorber types of iron-grained sand could produce optimal air temperatures.

Keywords:
Solar collector, heat absorption, absorber, optimization, drying.

Copyright © 2019 PENERBIT AKADEMIA BARU - All rights reserved

1. Introduction

Drying using a solar collector can increase the drying temperature when compared to drying in the sun directly so that it can accelerate the decrease in water content of the dried material [1]. In a dryer with a solar collector, the temperature of the drying air produced can reach 45-60 degrees Celsius [2-3]. A fruit dryer with a maximum temperature of 57 degrees Celsius takes 24 hours in a series of processes. While the dryer with a drying temperature of 50 degrees Celsius, to reduce water content from 80% to 90%, takes 56 hours of drying [4-5]

To increase the drying rate and obtain high collector temperatures, research has been carried out on the use of solar collector techniques with sharp turn multi-channel technology. As a result, the temperature of the air obtained at the solar collector can reach above 80 degrees Celsius [6-8]. That is why research on the characteristics of heat transfer systems using multi-channel sharp turns for the solar collector case becomes very interesting to study.

The characteristics of heat transfer in sharp turn channels influence by several fluid flow characteristics that flow within the channel. Fluid flow in a rectangular cross-section with sharp turns has its characteristics, namely changes in flow patterns caused by changes in flow direction when going through sharp turns. The flow pattern in the channel has a complex three-dimensional

* *Corresponding author.*
E-mail address:

structure caused by centrifugal force. The rate of local convection heat transfer for the surface of small areas is expected to experience a significant level of change.

In forced convection heat transfer, the problem studied is the Reynold number (Re) for determining heat transfer characteristics. The assessment of the characteristics of forced convection heat transfer through sharp turn channels has been carried out for the internal cooling system [7,8]. However, the application of the sharp turn channels on medium technology such as in the process of cooling and heating using fuel-burning and solar energy is still very minimal.

In addition to flow patterns, the use of absorbers in the solar collector important role in influencing the characteristics of heat transfer in sharp turn solar collectors. One of the factors that can increase the output temperature of the collector is the high temperature that can be reached by the absorber. Absorber serves to absorb heat from the sun's intensity and then heats the air that flows above the absorber in the air duct.

The use of absorber tubes with a vacuum is proven to significantly reduce heat loss compared to broken tubes or tubes without vacuum. During operation poor electrical insulation or failure of the tube must be avoided for each solar power plant [9]. Experimental studies have also been carried out to clarify the effect of the thickness of the solar collector absorber on local heat absorption characteristics (masses) on rectangular channels with sharp turns under stationary conditions [10].

To analyze the effects of artificial roughness and friction characteristics on heat transfer in solar air heating ducts, experimental investigations have been carried out for various systems and operating parameters. In this case, the duct has dimpled elements arranged in angular mode (arc) as the roughness of elements on the absorbent plate. The duct has been tested for aspect ratio (W/H) of 11, the range of relative roughness (p/e) of the range 10-20, the height of the relative roughness (e / D) ranges from 0.021 to 0.036, the angle of the arc (a) the range of 45 -75 and the number Reynolds (Re) ranges from 3600 to 18,000 [11].

An experimental investigation was also carried out to see the performance, efficiency, and reliability of five types of solar collectors from various materials. The collectors tested were copper, copper, and aluminum selective blue and black coating collector in addition to the evacuated tube collector. The experiments were carried out during April under the same conditions for all collectors. Taking into account the size, cost of equipment, quality, and maintenance, the results show that evacuation tubes, blue and black selective copper collectors recommended for medium and large scale applications because of their long life and ease of efficiency in maintenance. Aluminum collectors are recommended for small applications such as homes [12].

Research on the effects of micro channel geometry on the thermal and hydraulic performance of absorber plates for compact (thin and light) solar heat collectors, shows that the Reynolds number depends on the Nusselt number, due to axial thermal conduction. Nusselt's number increases when the aspect ratio approaches unity. The measured friction factor has a tendency similar to rectangular channel predictions, although an increase in overall fluid temperature results in a slightly lower friction factor. The results show that thermal improvements can achieve by increasing fluid velocity. This result is useful for the design of micro channel absorbent plates. [14].

The ability of heat absorption by each solar collector absorber will investigate so that the characteristics of the heat absorption field can predict. The specifications of the solar collector tested based on previous research [16] with a sharp turn angle of 130 degrees with a variation of solar collector absorber material for iron sand, iron gram waste mixed iron sand, hot mix asphalt, and asphalt mixed iron sand.

The expected outcome of this research is to optimize the heat absorption of the solar collector absorber with a sharp multi-channel channel technique with an additional absorber. So the

absorber is used able to optimize the high temperature of the solar collector air output to the drying chamber needed by the dryer object.

2. Methodology

In this study, the equipment used as a heat-absorbing medium is solar collectors by utilizing solar energy made from wooden frames with insulation from rubber materials, as in Figure 1. The main dimensions of the collector are 305 cm x 80 cm with a thickness of 15 mm, using a transparent glass cover as thick as 5 mm. On each side box of the absorber, is coated with a thermal insulator in the form of a 10 mm thick black rubber. The position of the solar air-heating collector is tilted 15 degrees towards the earth with the aim that the airflow process can take place because of the difference in elevation between input and output. Modifications were made by adding buffers with a laying angle of 130 degrees in the channel to increase flow turbulence.

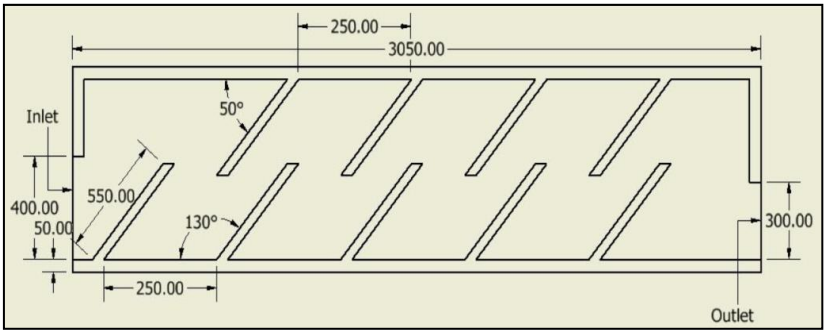


Fig. 1. Solar collector with a 130-degree obstacle

Experiments carried out in open space using solar energy as heating energy and temperature measurements made at many points along the flow path in the channel. For temperature measurements with sharp turns with a resistance angle of 130 degrees, nine obstacles and 10-point thermometer sensors also used. The scheme for placing obstacles and measuring points can see in Figure 2.

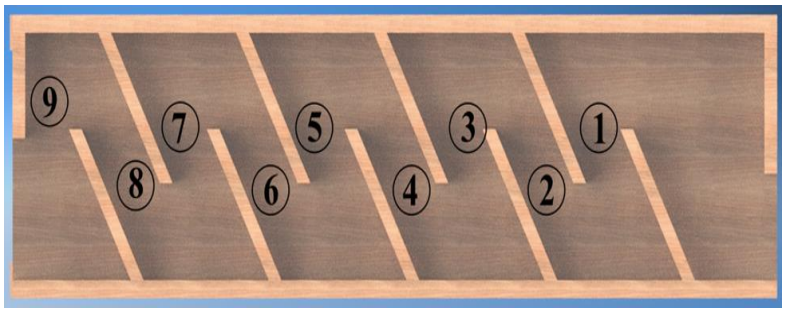


Fig. 2. Measurement location temperature of solar collector

Temperature measurements using digital thermometers and mercury thermometers that have a temperature range of 0 - 110 °C. As shown in Figure 2, the position of the thermometer sensor or temperature measurement point placed according to the measurement conditions on the collector heating line.

Temperature measurement on a heat absorber by utilizing solar energy is done every half-hour intervals, from 10 am to 4 pm. The intensity of the sun at the time of the experiment ranged from 700 to 967 W/m^2. At 12 o'clock the solar intensity is 900 w/m^2, at 1 pm the intensity is 967W/m^2,

and at 2 pm. The intensity is 930 W/m^2. Absorber for absorbing solar radiation in this test applied iron sand, hot mix asphalt, iron gram waste mixed sand, and asphalt mixed iron sand.

To get a temperature distribution that represents the flow of air, nine measurement points placed in the inlet, at the center, and the area around the outlet of the channel. After the temperature data taken, data processing or analysis is the final stage of a series of research methodologies. The data obtained from the measurements are then plotted in the form of temperature distribution graphically. Then a discussion and comparison between each material absorber collector is carried out.

3. Results and Discussion

3.1 Experimental Results

In addition to the intensity effect of the sun, air heating in the passageway solar collector influenced by the temperature of the absorber collector in which air passed. Therefore the study of the use of variations of the absorber in the solar collector becomes very important. The study investigated the effect of the application of iron sand, iron gram waste mixed iron sand, hot-mix asphalt, and iron sand asphalt as absorber, on the increase in air heat in the absorber channel.

3.1.1 Collector with iron sand absorber

Temperature distribution in solar collectors with iron sand adsorbent can see in Figure 3. This graph shows the value of the average temperature distribution along the solar collector pass from 12 am - 2 pm taken in one week. Figure 3 shows the difference in temperature distribution along the route, where the average temperature of point 1 to point 7 rises significantly.

Instead, the temperature rate decreases from point 7 to point 9, when the flow approaches the solar collector outlet. The highest temperature that can reach at 1 pm is 90 °C at measurement point 7.

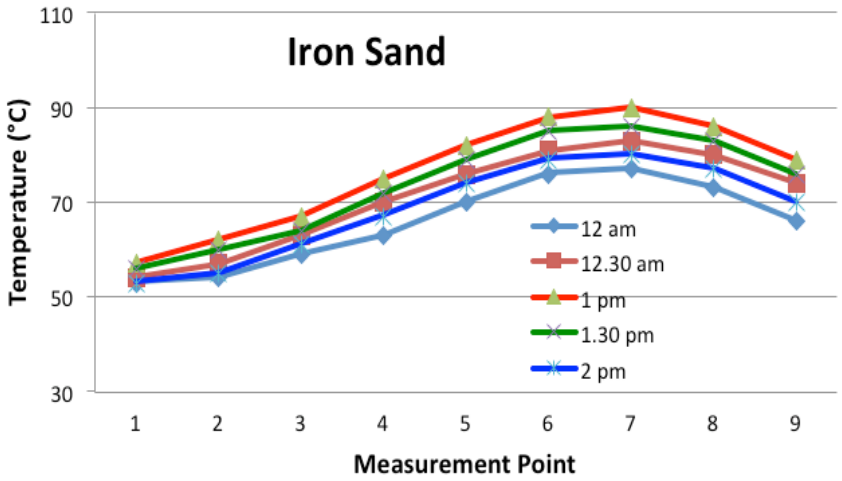


Fig. 3. Temperature distribution with iron sand absorber

3.1.2 Collector with hotmix asphalt absorber

Temperature distribution on the solar collector with hot-mix asphalt absorber can see in Figure 4. This figure shows the temperature distribution along the solar c ollector pass from 12 pm to 2 pm.

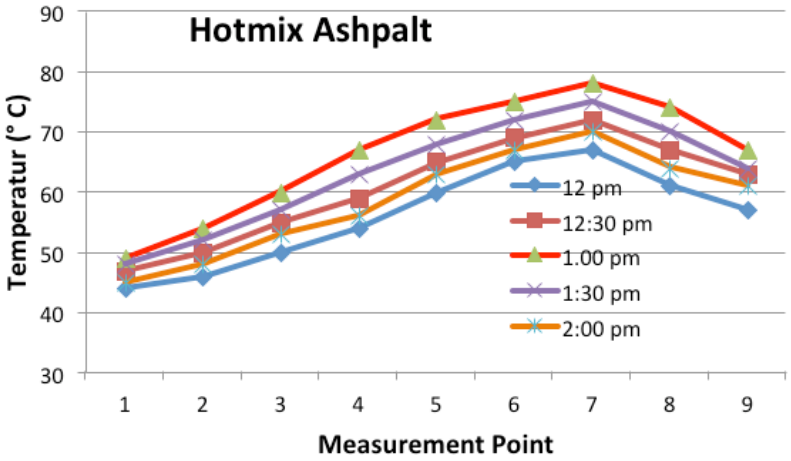


Fig. 4. Temperature distribution of hotmix asphalt absorber

Figure 4 show the pattern of temperature distribution along the path of the solar collector with the Hot Asphalt Absorber has the same temperature distribution pattern. The temperature rise that occurred at point 1 to point 6 raised rather significant. In point 6 is the highest temperature that can reach 77 °C at 1 pm. But from after point 6, the temperature starts dropping until to 9, because of the airflow to the solar collector outlet.

3.1.3 Collector with iron sand and iron gram waste absorber

The temperature distribution in the solar collector with iron sand and iron gram waste adsorbent can see in Figure 3. This graph shows the temperature distribution along the solar collector pass from 12 pm - 2 pm. The figure shows the difference in temperature distribution along the route, where the temperature point 1 to point 6 rises very significantly. The highest temperature reaches 96 °C at point 6 of 01.00 pm, while from point 7 to point 9 the temperature tends to decrease.

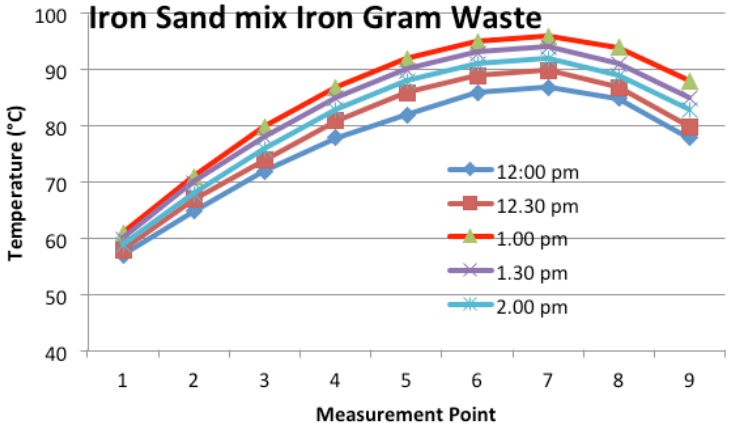


Fig. 5. Temperature distribution with adsorbents of iron sand mix iron gram waste

3.1.4 Collector with hotmix asphalt and iron sand absorber

Figure 6 shows the temperature distribution along the path of the solar collector with asphalt mix and iron sand absorber. We can see the distribution of the temperature difference along the

route from Figure 6, where a high increase in temperature occurs between points 1 and point 6. Point 6 gets the highest temperature rise at 1 pm reach to 80 °C. But from point 7 to point 9 the air temperature through the channel begins to decrease again.

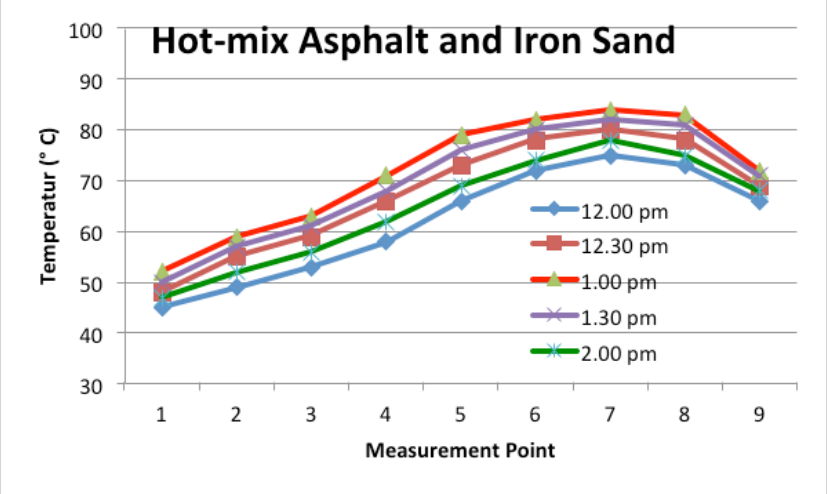


Fig. 6. Temperature distribution with adsorbents of Hot-mix Asphalt and Iron Sand

3.2 Discussion

The analysis results of the measurement data to the four absorber variations studied, namely iron sand, hot mix asphalt, iron gram waste mixed sand, and asphalt mixed iron sand have explained in Figures 3, 4, 5, and 6. The optimum conditions of all absorbers compare for evaluate, as shown in Figure 7.

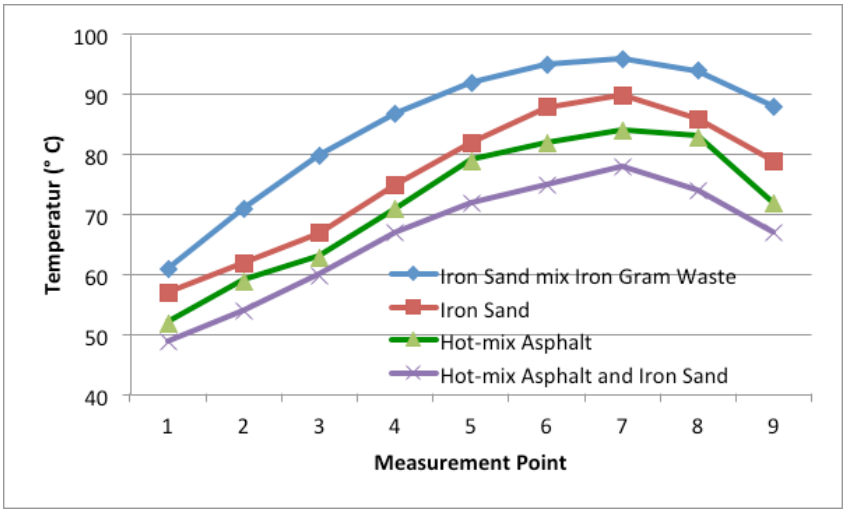


Fig. 7. Comparison of temperature distribution achieved for each Absorber

Based on the graph in Figure 7 above the highest temperature in the air inside the collector absorber channel consisting of hot mix asphalt, iron gram waste mixed sand, and asphalt mixed iron sand, occurs at 1 pm i.e. at point 6. Whereas in the iron sand absorber the highest air temperature

occurs at point 7. At 1 pm, the whole absorber receives high light intensity with an average of 967 W/m^2.

Figure 7 shows the difference in temperature distribution gradients between points along the path of the four absorbers. Thus the ratio of temperature obtained for each variation of the absorber as an evaluation material. Solar collector absorber of iron sand mixed with iron gram waste obtains the highest temperature reaching 96 °C and is the biggest absorber of heat absorption in the solar intensity. The highest air temperature entering the drying chamber occurs at points 6 and 8, which is 90 °C. Furthermore, iron sand absorber obtains a slightly lower temperature which is 85 °C. Whereas in hot mix asphalt absorber mixed with iron sand, the temperature reaches 80 0C, and for hot mix asphalt absorber, the maximum temperature is 77 °C.

In the iron sand absorber, the elemental content of iron reaches 50-60%, while in absorber iron sand mixed iron gram waste, the iron element content reaches 70-75%. This fact proves that the heat type of iron element is dominant and affects the heat absorption value. The higher the heat value of a material result the higher the heat absorption ability of the material.

4. Conclusions

Based on the analysis and discussion of the results of temperature distribution measurements for the four types of absorbers can be concluded as follows:

I. Optimal temperature distribution can achieve on the use of a type of iron gram waste and sand absorber, with a maximum air temperature of 96 °C at a sun intensity of 967 W / m^2.
II. The second-highest temperature distribution achieved by an iron sand absorber with a temperature of 90 °C.
III. Iron growers absorbers have a maximum temperature distribution of 85 °C, followed by asphalt and iron sand absorbers with a maximum temperature of 80 °C, and hot mix asphalt absorbers with a maximum temperature of 77 °C.

Acknowledgement

This research was funded by a grant from Syiah Kuala University. The author would like to thank the assistants and students of the Unsyiah Thermal Engineering Laboratory which helped in performing this research

References

[1] Stiling, James, Simon Li, Pieter Stroeve, Jim Thompson, Bertha Mjawa, Kurt Kornbluth, and Diane M. Barrett (2012). *Performance evaluation of an enhanced fruit solar dryer using concentrating panels*. Energy for sustainable development 16, no. 2, 224-230.

[2] Gutti, Babagana, Silas Kiman, and Ahmed M. Murtala. (2012). *Solar Dryer-An Effective Tool For Agricultural Products Preservation*. Journal of Applied Technology in Environmental Sanitation 2, no. 1.

[3] Hussain, Muhammad Ibrar, Esmail MA Mokheimer, and Shakeel Ahmed (2017). *Optimal Design of a Solar Collector for Required Flux Distribution on a Tubular Receiver*. Journal of Energy Resources Technology 139, no. 1, 012006.

[4] Alleyne, Fatima S., and Rebecca R. Milezarek (2015). *Design of solar thermal dryers for 24 hour food drying*. United State Department of Agriculture, Heating Processed Food Research Unit.

[5] Prakash, T. B., and S. Satyanayarana (2014). *Performance analysis of solar drying system for Guntur Chili*. Int J Latest Trends Eng Technol 4, 283-298.

[6] Ahmad Syuhada and Muhammad Ilham , (2018), *Characteristics of heat transfer on solar collector channel by using a sharp turn*, AIP Conference Proceedings vol. 1983.

[7] Ahmad Syuhada and Muhammad Ilham Maulana, (2018), *Study of heat transfer characteristics on sharp turn channels for solar collectors*, Journal of Advanced Research in Fluid Mechanics and Thermal Sciences vol. 45.

[8] Teja, Ravi, F. Z. Pathan, and Mandar Vahadne (2015). *Optimization of Heat Transfer through Rectangular Duct*. International Research Journal of Engineering and Technology (IRJET) 2, no. 4: 1906-1910.

[9] M. Yaghoubi, F. Ahmadi, and M. Bandehee, (2013), *Analysis of Heat Losses of Absorber Tubes of Parabolicthrough Collector of Shiraz (Iran) Solar Power Plant,* Journal of Clean Energy Technologies, Vol. 1, No. 1, January 2013.

[10] Ahmad Syuhada and Muhammad Ilham Maulana, (2018)*, Absorber Thickness Effect on The Effectiveness of Solar Collectors to Production Hot Air For Drying, 3rd i-TREC 2018,* E3S Web of Conferences 67, 04028.

[11] Muneesh Sethi, Varun, N.S. Thakur, (2012), *Correlations for solar air heater duct with dimpled shape roughness elements on absorber plate*, Solar Energy 86.

[12] A. Sakhrieh, A. Al-Ghandoor, (2013), *Experimental investigation of the performance of five types of solar collectors*, Energy Conversion and Management 65, 715–720.

[13] M.A. Oyinlola, G.S.F. Shire, R.W. Moss. (2015), *Investigating the effects of geometry in solar thermal absorber plates with micro-channels*, International Journal of Heat and Mass Transfer 90, 552–560.

[14] Rajendra Karwa & Girish Chitoshiya, (2013), *Performance study of solar air heater having v-down discrete ribs on absorber plate*, Energy 55, 939-955.

[15] Dara, J. E., K. O. Ikebudu, N. O. Ubani, C. E. Chinwuko, and O. A, (2013). Ubachukwu. *Evaluation of a passive flat-plate solar collector*. Int. J. of Advancements in Res. & Tech 2, no. 1.

[16] Syuhada, A., M. Hirota, H. Fujita, S. Araki, M. Yanagida, and T. Tanaka, (2001), *Heat (mass) transfer in serpentine flow passage with rectangular cross-section*, Energy conversion and management 42, no. 15-17: 1867-1885.

[17] Hirota, M., H. Fujita, A. Syuhada, S. Araki, T. Yoshida, and T. Tanaka, (1999). *Heat/mass transfer characteristics in two-pass smooth channels with a sharp 180-deg turn*, International Journal of Heat and Mass Transfer 42, no. 20: 3757-3770.

[18] Hirota, Masafumi, Hideomi Fujita, Hiroshi Nakayama, and Ahmad Syuhada, (2000). *Heat (mass) transfer characteristics in serpentine flow passages with a sharp turn*. Nagoya University, School of Engineering, Memoirs 52, no. 1, 1-52.

[19] Rosario, Ariane. "Calculating the Solar Energy of a Flat Plate Collector." *Undergraduate Journal of Mathematical Modeling: One+ Two* 6, no. 1 (2014): 1.

[20] Chabane, Foued, Noureddine Moummi, and Said Benramache, (2014). *Experimental study of heat transfer and thermal performance with longitudinal fins of solar air heater*, Journal of advanced research 5, no. 2: 183-192.

[23] Mozumder, Atish, Anjani K. Singh, and Pragati Sharma. "Study of cylindrical honeycomb solar collector." *Journal of Solar Energy* 2014 (2014).

[24] Mohammadkarim, Ahmadreza, Alibakhsh Kasaeian, and Abdolrazagh Kaabinejadian. "Performance investigation of solar evacuated tube collector using TRNSYS in Tehran." *International Journal of Renewable Energy Research (IJRER)*4, no. 2 (2014): 497-503.

[25] Mishra, Dilip. "Experimental Analysis of Thermal Performance of Evacuated U-Tube Solar Collector." *Advance Physics Letters* 2, no. 3 (2015).

[26] Ihaddadene, Nabila, Razika Ihaddadene, and Abdelwahaab Betka. "Experimental investigation of Using a Novel insulation Material on the Functioning of a Solar Thermal Collector." *Journal of Solar Energy Engineering* 140, no. 6 (2018): 061001.

Penerbit Akademia Baru

Engineering Science and Technology Conference Proceedings

Journal homepage: www.akademiabaru.com/EST.html

Study of Ability Level of the Sun Absorption Intensity by Building Yard Materials on Environmental Thermal Comfort

Open Access

Ahmad Syuhada[1], Muhammad Ilham Maulana[1,*], Murtadahadi[2]

[1] Department of Mechanical Engineering of Syiah Kuala University, Darussalam–Banda Aceh 23111, Indonesia
Lhokseumawe state, Indonesia

ABSTRACT

The environment temperature affects the thermal comfort in an environment. Material contained in a residential yard or office environment affects the level of absorption ability of the sun's radiation, thus affecting the temperature of the environment. The temperature of hot air in an environment is one of the causes of uncomfortable activities in the environment. This is the background, so the level of absorption ability of the sun's heat by the material on the home yard examined. The material tested is a material that is often used by the Indonesian people in the yard, namely asphalt, cement, paving blocks, soil, and lawns. The testing room is rectangular made of wooden blocks for the framework and clear plastic as a wall, with a width of 1.35 m, length 1.35 m and height 2.2 m. This testing room serves as isolation from the influence of the wind and to avoid heat loss from the testing room. Furthermore, the test room is placed on a yard with various materials tested. From the measurement results obtained by the fact how far the influence of the rate of heat absorption in each material. Asphalt, cement and paving blocks are included in the category of materials that are high in radiation heat absorption properties, while soil and grass are low in heat absorption properties and good for thermal comfort environments.

Keywords:
Yard material, heat absorption, solar radiation, temperature and thermal comfort.

Copyright © 2019 PENERBIT AKADEMIA BARU - All rights reserved

1. Introduction

Over the past several decades, there has been a significant increase in average temperatures throughout the world. Global warming has now been recognized as one of the main problems facing the world and very influential on thermal comfort in the environment. Global warming caused by the ever-increasing greenhouse effect caused by rising concentrations of greenhouse gases in the atmosphere. The increase in the number of vehicles and factories, as well as the increase in the population, is the cause of rising concentrations of greenhouse gases in the air as a result of the combustion and breathing process [1].

Also, the lack of plants as a result of the construction of people's homes is one of the main causes of global warming. The building absorbs the sun's radiant heat and then re-radiates the radiation around it that causes the temperature around it to rise [2]. An important part that is directly affected by solar radiation is the yard of the house, so the yard is a very important part of the thermal comfort of a housing.

* *Corresponding author.*
E-mail address

Recently, Hakki Gülşen at al is studying greenhouse gas (GHG) emissions. One source of greenhouse gas emissions is the anaerobic wastewater treatment process in the upper flow anaerobic sludge bed (UASB) reactor which is an anaerobic treatment unit located in a wastewater treatment plant (WWTP) in Turkey. Greenhouse gas (GHG) emissions emitted from anaerobic reactors due to biogas generation [3].

A study aimed at analyzing the characterization of national GHG emissions in Korea for the 12th period years (1990-2002), carried out in accordance with the 2006 IPCC guidelines. The results show that the Korea contributed 0.5% of the world's GHG emissions in 1990, but only 0.2% of emissions in 2002 [4].

The greenhouse effect related to global warming studied using artificial intelligence (AI) based neural network models. The stochastic impact of regression on population, prosperity, and technology (STIRPAT) models is applied to the greenhouse effect based on carbon dioxide gas. This is shown from the energy factor where four sources such as oil, coal, nuclear, and renewable are connected where the value is cumulative for comparison with nuclear energy [5].

Other research shows domestic animals raised in developing countries also produce greenhouse gases (GHGs). Local animals are animals that are not well characterized and are rarely subject to structured breeding programs but adapt well to local environmental conditions [6].

While research aimed at becoming a pioneer in the spread of carbon intensity approaches varies the time for carbon footprint calculation has been carried out in Turkey. The main objective of this research is to determine electricity utilization based on the distribution of CO2 emissions every hour. Turkey was chosen for this case study because of the intensive characteristics of the CO2 power plant [7].

Other researches discuss how much and what type of thermal mass is needed to reduce energy consumption following future climate change. The summer energy performance of the brick house in Konya, Turkey, was studied in terms of thermal mass characteristics using dynamic simulation software. Microclimate data measured and predicted for 2017 and 2050s are used to compare the passive impact of the choice of wall material, e.g. Adobe, limestone, vertical hollow brick, and volume of walls without night ventilation [8].

Thermodynamic analysis of the Rankine Cycle through energy and exergy approaches to environmental impacts for lignite, hard coal, biomass, fuel oil, and hydrogen also carried out. For this purpose, emission values of sulfur oxide, nitrogen oxides, carbon dioxide, and carbon monoxide calculated for different fuels. Emission values are calculated using the emission factor method. The use of biomass and hydrogen significantly reduces emissions [9].

The environmental product declaration (EPD) is a report on the use of resources and potential environmental impacts based on an environmental life cycle assessment (LCA) method. Asphalt paving and some other industries have some features that might not be easily captured in EPD if the impact is only put on the gate. This includes stored energy (raw material energy), stored carbon, high-recycled content, and high recycling. Research using the optional reporting module in EPD has been carried out based on international standards to capture stored energy and carbon, and recycling aspects [10].

An evaluation was also carried out to detect heat waves (HWs) using six methods and estimation of HW characteristics (duration, frequency, and intensity) from the observational (CarpatClim database) and modeling (RegCM simulation with the representative concentration pathway (RCP concentrations) 4.5 and 8.5). It can consider as a climatic hazard for people and the environment [11].

In addition to natural processes, urbanization, industrialization, consumption of fossil fuels, deforestation, and other human activities also contribute to high levels of greenhouse gases in the

atmosphere, which results in drastic climate change. Recently Belkacem Berghout also conducted a study to investigate the relationship between vehicle weight and CO2 emissions in light-duty passenger cars. This study also analyzes fuel consumption in various cases. The evaluation of emissions is based on the CO2 composition of the total emission [12].

Another article introduces the possibility of combining vernacular device strategies to reduce energy consumption and thus to more realistically assess opportunities to adapt this strategy in arid regions. The aim is to develop an overall process that focuses on the integration of vernacular devices and to realize effective returns for users and developers by increasing energy efficiency [13].

However, resolve and reducing the global warming cannot solve only by some groups, but the whole community has a role. The simplest way to do it is environmentally friendly behavior, one of which is by making a yard material that has the ability to absorb heat from the results of solar radiation and has a number of plants that make a cool impression. In general, yards in Indonesia from grass, paving blocks, asphalt or cement yard. Sometimes the surface of the yard is only filled with land, ordinary people choose the type of yard only in terms of the aesthetics of the park without thinking about the environmental effects.

In its development, parks and yards become an inseparable part of the comfort and beauty of the residence. Parks and yard materials, aside from supporting aesthetics, also function as heat absorbers of the sun's intensity. To select the yard material to be used, an understanding of the type and function of various yard materials is required for the thermal comfort of the environment, such as asphalt, cement, paving blocks, without materials and lawns.

This study aims to determine the ability of various types of yard material in absorbing the sun's heat. It is also expected to provide information to the public about the ability of each yard material to absorb heat for thermal comfort in the yard of a house, especially in Nanggroe Aceh Darussalam after the tsunami.

2. Methodology

This research was conducted at the Faculty of Engineering, Syiah Kuala University, Banda Aceh in December 2018. In the experimental system, the incoming sunlight was partially absorbed, partly continued and partly reflected into the free air. In the test room, the material absorbs the heat from solar radiation, and the heat value absorbed by the material will be directly proportional to the temperature of the air around the isolation area. For comparison two test chambers are used, namely room A where the heat from the sun is only absorbed by air and room B where the sun's heat is absorbed by the yard material being tested. A sketch of the test room is shown in Figure 1.

Temperature measuring instruments used are digital thermometer and mercury thermometer to measure the temperature of the air inside and outside the testing room. The material used in this study is asphalt mixed with sand, cement, paving blocks, grass and soil and without material (only white paper which does not absorb radiant heat).

The test room measuring 1.35 m x 1.35 m x 2.20 m, all parts covered with plastic with a thickness of 0.25 mm with the aim of conditioning the room, so that there is no influence of wind on the air conditions in the test room. The framework of the test chamber is made of wood, without a layer on the bottom to facilitate the fitting of the yard material in the test chamber as shown in Figure 2.

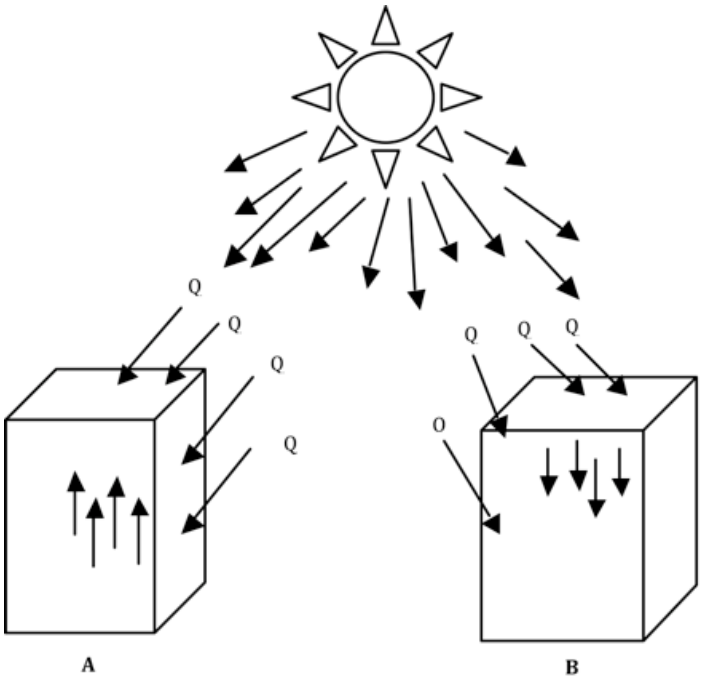


Fig. 1. Testing method; A. space without material, B. space filled with yard material

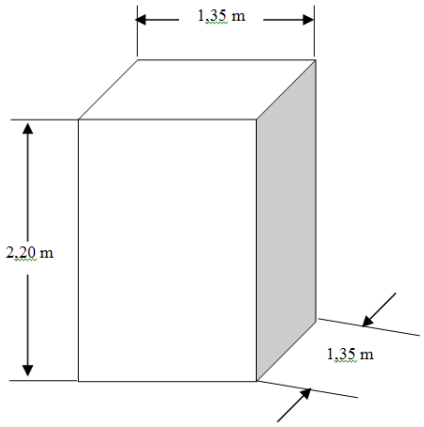


Fig. 2. Testing Room

This testing room is rectangular in shape. There are five testing rooms placed directly on asphalt-coated material, cement-coated yard, paving-block-coated yard, non-material room (only white paper that does not absorb radiation heat) and grass-coated material. Measurements are taken from 9 am - 4 pm, with an interval of measurement every hour for three days. The parameters measured are the temperature inside and outside the test room.

3. Results and Discussion

3.1 Experimental Results

Data was taken in December 2018 under sunny conditions with an average solar intensity of 600-620 W/m^2 at 9 am, amounting to 910-920 W/m^2 at 1 pm, and 720-750 W/m^2 at 4 pm. The results of measurements of temperature distribution carried out in isolation rooms are displayed graphically in Figure 3.

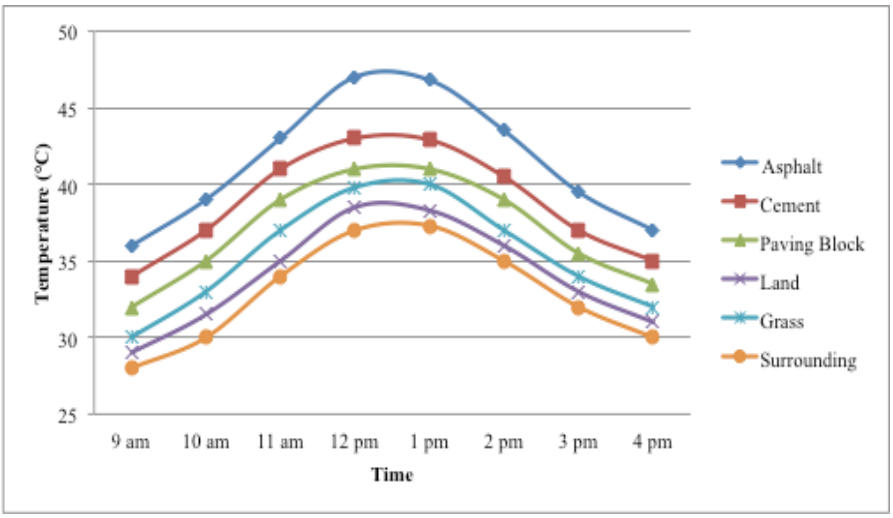


Fig. 3. Temperature Distribution in test room

Figure 3 shows the temperature of the yard material at every hour, from 9 am to 4 pm. It can be seen that the highest yard material temperature on asphalt occurs at 12 noon which is equal to 47 °C, and the lowest temperature occurs at 9 pm which is at 36 °C and at 4 pm is 37°C. In cement yard material, the highest temperature is reached at 12 pm, which is 43 °C. The lowest temperature occurs at 9 am at 34 °C and at 4 pm at 35 °C.

The highest temperature in the paving block yard material also occurs at 12 pm, which is 41°C and the lowest temperature occurs at 9 am at 32 °C and 33.5 °C at 4 pm. In the test chamber with soil material, the highest temperature that occurred at 12 pm was 38.5 °C while the lowest temperature occurred 9 am at 32 °C and 4 pm at 31 °C. On the lawn material, the highest temperature that occurs at 12 pm is 39.8 °C. The lowest temperature occurs at 9 am, which is 30 °C and 32 °C at 4 pm. The highest temperature in the environment occurs at 1 pm that is 37.3 °C. The lowest temperature in the environment occurs at 9 am at 28 °C and 4 pm at 30 °C.

From the measurement results, there was a gradual increase in temperature from 9 am to 12 pm and then gradually decreased after 12 pm to 4 pm for all yard materials. All graphs have the same tendency and greatly influenced by the magnitude of the sun's intensity.

3.2 Discussion

Based on the measurement results as shown in Figure 3 above, it is clearly seen that the highest absorption of heat in the sun's intensity by all six types of yard material occurs at 12 pm. The page material that has the highest heat absorption is asphalt. Asphalt temperature at that time reached 47 °C. Furthermore, slightly lower than asphalt, the cement floor test chamber experienced a temperature of 43 °C and a paving block material of 41 °C.

The material that absorbs the least heat is the soil. This material test chamber temperature is 38.5 °C at 12 pm. The lawn turned out to be slightly higher in temperature, which was 38.9 °C at 12 pm. All data are taken in the test chamber at the same ambient air temperature of 37°C.

From the results of the research conducted, then the average heat absorption rate will be obtained value each yard material being tested. The calculation is done using average air temperature data in each test room at maximum temperature conditions. The result is the absorption value of the solar radiation heat of each page material as shown in Figure 4.

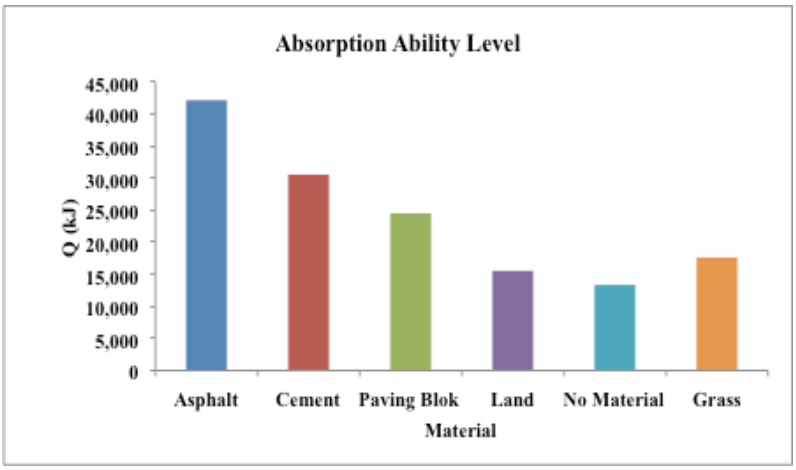


Fig. 4. Level of Absorption Ability

From Figure 4 it appears that the ability of the material to absorb heat is directly proportional to the temperature of each measured material test chamber as also seen in Figure 3. The ability of the material in terms of heat absorption is highly dependent on the specific heat possessed by each page material being tested.

The results showed that the asphalt test chamber had the highest air temperature, which showed, that the material absorbs more heat than the others. Cement and paving block material is included in the material category, which is quite high in heat absorption properties compared to other materials. If the material that is high in heat absorption properties of solar radiation is used in the yard, it will cause the ambient temperature to rise too and result in thermal discomfort.

As for soil and grass material, it is a material that has the ability to absorb heat radiation from the sun's eyes lower than the others. And it is the best material to use on the yard for thermal comfort, based on this study.

4. Conclusions

Based on the analysis and discussion of the results of temperature distribution measurements for the four types of absorbers can be concluded as follows:

I. Optimal temperature distribution can achieve on the use of a type of iron gram sand absorber, with a maximum air temperature of 96 °C at a sun intensity of 967 W / m^2.
II. The second-highest temperature distribution achieved by an iron sand absorber with a temperature of 90 °C.
III. Iron growers absorbers have a maximum temperature distribution of 85 °C, followed by asphalt and iron sand absorbers with a maximum temperature of 80 °C, and hot mix asphalt absorbers with a maximum temperature of 77 °C.

Acknowledgement

This research was funded by a grant from Syiah Kuala University. The author would like to thank the assistants and students of the Unsyiah Thermal Engineering Laboratory which helped in performing this research

References

[1] Stiling, James, Simon Li, Pieter Stroeve, Jim Thompson, Bertha Mjawa, Kurt Kornbluth, and Diane M. Barrett (2012). *Performance evaluation of an enhanced fruit solar dryer using concentrating panels*. Energy for sustainable development 16, no. 2, 224-230.

[2] Gutti, Babagana, Silas Kiman, and Ahmed M. Murtala. (2012). *Solar Dryer-An Effective Tool For Agricultural Products Preservation*. Journal of Applied Technology in Environmental Sanitation 2, no. 1.

[3] Hussain, Muhammad Ibrar, Esmail MA Mokheimer, and Shakeel Ahmed (2017). *Optimal Design of a Solar Collector for Required Flux Distribution on a Tubular Receiver*. Journal of Energy Resources Technology 139, no. 1, 012006.

[4] Alleyne, Fatima S., and Rebecca R. Milezarek (2015). *Design of solar thermal dryers for 24 hour food drying*. United State Department of Agriculture, Heating Processed Food Research Unit.

[5] Prakash, T. B., and S. Satyanayarana (2014). *Performance analysis of solar drying system for Guntur Chili*. Int J Latest Trends Eng Technol 4, 283-298.

[6] Ahmad Syuhada and Muhammad Ilham , (2018), *Characteristics of heat transfer on solar collector channel by using a sharp turn*, AIP Conference Proceedings vol. 1983.

[7] Ahmad Syuhada and Muhammad Ilham Maulana, (2018), *Study of heat transfer characteristics on sharp turn channels for solar collectors*, Journal of Advanced Research in Fluid Mechanics and Thermal Sciences vol. 45.

[8] Teja, Ravi, F. Z. Pathan, and Mandar Vahadne (2015). *Optimization of Heat Transfer through Rectangular Duct*. International Research Journal of Engineering and Technology (IRJET) 2, no. 4: 1906-1910.

[9] M. Yaghoubi, F. Ahmadi, and M. Bandehee, (2013), *Analysis of Heat Losses of Absorber Tubes of Parabolicthrough Collector of Shiraz (Iran) Solar Power Plant,* Journal of Clean Energy Technologies, Vol. 1, No. 1, January 2013.

[10] Ahmad Syuhada and Muhammad Ilham Maulana, (2018), *Absorber Thickness Effect on The Effectiveness of Solar Collectors to Production Hot Air For Drying, 3rd i-TREC 2018,* E3S Web of Conferences 67, 04028.

[11] Muneesh Sethi, Varun, N.S. Thakur, (2012), *Correlations for solar air heater duct with dimpled shape roughness elements on absorber plate*, Solar Energy 86.

[12] A. Sakhrieh, A. Al-Ghandoor, (2013), *Experimental investigation of the performance of five types of solar collectors*, Energy Conversion and Management 65, 715–720.

[13] M.A. Oyinlola, G.S.F. Shire, R.W. Moss. (2015), *Investigating the effects of geometry in solar thermal absorber plates with micro-channels*, International Journal of Heat and Mass Transfer 90, 552–560.

[14] Rajendra Karwa & Girish Chitoshiya, (2013), *Performance study of solar air heater having v-down discrete ribs on absorber plate*, Energy 55, 939-955.

[15] Dara, J. E., K. O. Ikebudu, N. O. Ubani, C. E. Chinwuko, and O. A, (2013). Ubachukwu. *Evaluation of a passive flat-plate solar collector*. Int. J. of Advancements in Res. & Tech 2, no. 1.

[16] Syuhada, A., M. Hirota, H. Fujita, S. Araki, M. Yanagida, and T. Tanaka, (2001), *Heat (mass) transfer in serpentine flow passage with rectangular cross-section*, Energy conversion and management 42, no. 15-17: 1867-1885.

[17] Hirota, M., H. Fujita, A. Syuhada, S. Araki, T. Yoshida, and T. Tanaka, (1999). *Heat/mass transfer characteristics in two-pass smooth channels with a sharp 180-deg turn*, International Journal of Heat and Mass Transfer 42, no. 20: 3757-3770.

[18] Hirota, Masafumi, Hideomi Fujita, Hiroshi Nakayama, and Ahmad Syuhada, (2000). *Heat (mass) transfer characteristics in serpentine flow passages with a sharp turn*. Nagoya University, School of Engineering, Memoirs 52, no. 1, 1-52.

[19] Rosario, Ariane. "Calculating the Solar Energy of a Flat Plate Collector." *Undergraduate Journal of Mathematical Modeling: One+ Two* 6, no. 1 (2014): 1.

[20] Chabane, Foued, Noureddine Moummi, and Said Benramache, (2014). *Experimental study of heat transfer and thermal performance with longitudinal fins of solar air heater*, Journal of advanced research 5, no. 2: 183-192.

[23] Mozumder, Atish, Anjani K. Singh, and Pragati Sharma. "Study of cylindrical honeycomb solar collector." *Journal of Solar Energy* 2014 (2014).

[24] Mohammadkarim, Ahmadreza, Alibakhsh Kasaeian, and Abdolrazagh Kaabinejadian. "Performance investigation of solar evacuated tube collector using TRNSYS in Tehran." *International Journal of Renewable Energy Research (IJRER)*4, no. 2 (2014): 497-503.

[25] Mishra, Dilip. "Experimental Analysis of Thermal Performance of Evacuated U-Tube Solar Collector." *Advance Physics Letters* 2, no. 3 (2015).

[26] Ihaddadene, Nabila, Razika Ihaddadene, and Abdelwahaab Betka. "Experimental investigation of Using a Novel insulation Material on the Functioning of a Solar Thermal Collector." *Journal of Solar Energy Engineering* 140, no. 6 (2018): 061001.

INDEX

A

Absorber 1-3, 6, 8, 109, 449-451, 454-456, 511, 1082-1088, 1092, 1095
Aerodynamic drag 667-668
Aerodynamics Performances 953
Aero-engine 836-837
Aged Mineral Oil 553-554, 557-561
Air bubble 519-520, 555, 963, 972, 988
Air entrainment rate 519, 522, 524
Alternative fuel 287, 302, 836, 842, 843
Aluminium Oxide (Al2O3) 326-328
Ampacity 654-665
Anisotropic 846-849, 851, 853
Ankle foot orthosis 868
ANN modeling 802, 814
Ansys CFX 224, 562-563, 568, 757, 761, 953-954
ANSYS fluent 11-12, 78, 112, 117-119, 163-165, 169, 223, 236-237, 413, 415, 545, 562, 654, 656, 659, 667, 670, 686, 688-689, 691, 945-946
Aragonite 623- 629
Arduino 85-88, 90, 92, 582, 587, 892
Assisting flow 130-131, 133, 139
Average wall shear stress 743, 752-753

B

Banana drying 510-511, 515, 517
Banana peel 881-883
BBDB 208-210, 212- 214, 216, 217
Bertam 631-633
Binderless 287, 289, 292, 294, 607-608, 611, 613-614
Biodiesel 11-15, 17-18, 21-23, 624, 837
Biopolymers 103
Blowout limit 227-228, 230-231, 233
Boiler 247, 380-381, 418, 961, 1036-1040, 1042
Boundary layer 130-131, 133-134, 141, 144-146, 154, 166-167, 191, 193-194, 196, 198, 371-373, 413, 424, 472-474, 480, 482-483, 486-487, 492, 494-495, 497-498, 534-535, 537, 594-595, 597-598, 600-601, 603-604, 635, 642, 668, 670-672, 747, 792-793, 972
Breakdown Voltage (BdV) 553-554, 557, 559
Briquette 257, 259, 287-297
Bubble dispersion 519, 523, 525
Bubble penetration 519, 525
Buongiorno 190-192, 856-857
Buoyancy ratio 130,131, 133-134, 139, 144, 156, 486, 859

C

Calcium carbonate 623-629, 694
Calibration 4, 85-86, 88, 90-92, 452, 464, 598-599
Capillary effect 58-60, 64, 71-72
Carbon nanotube 704-705, 713, 718, 793, 901, 1055-1058
Carbonyl Index (CI) 103-104, 106-107
Casson fluid 26, 130-131, 139, 153-154, 160, 191, 193, 196, 205, 472-475, 483, 635, 637, 638, 643
Casson nanofluid 190, 192-193, 205
Cavity 130, 522, 525, 665, 782-783, 784-786, 790, 856-857, 860- 862, 866, 971, 981-983, 985
Cellulose 26, 182, 288, 553, 559, 607- 614, 645-646, 694-695, 698-699, 793, 882, 884, 954
CFD 11-12, 50, 75, 78, 80-83, 110, 115, 117-118, 120, 162-163, 165, 168, 219-220, 222-224, 228, 236-238, 327, 331, 380-381, 405, 411-413, 526, 546, 562-563, 565-566, 619-620, 656, 659, 667-668, 670, 674, 686-687, 689, 743, 749, 758, 761, 767, 837, 875-879, 920, 923, 944-945, 953-954, 959, 1000-1002, 1005, 1007, 1009,
CFD analysis 117, 178, 546, 667, 837
CFD simulation 78, 80-81, 83, 162, 219-220, 222-223, 331, 381, 562-563, 565, 670, 758, 761, 767, 875-876, 878-879, 945, 953-954, 1000-1002, 1005, 1007
Char 259, 288-289, 301-302, 304-305
Chemical reaction 12, 104, 142, 190, 192-193, 195-196, 203, 205, 327, 360, 384, 645, 803, 856-859, 861, 863, 865-866, 930, 963
CHT modeling 654
Closed loop heat pump dryer 510-511, 517
Co- gasification 256-261, 264-265
Coal 247, 257, 260, 287-288, 301, 380-387, 1036-1042, 1091
Coal blending 380, 1036-1037
Coaxial jet 428-435, 439

INDEX

cockle shell 623-624, 626
coffee ring effect 912-913, 916
Coherent vortices 428-439
Combustion 11, 12, 13, 14, 15, 17, 18, 19, 21, 22, 23, 227, 228, 229, 230, 231, 233, 257, 262, 263, 287, 288, 289, 291, 293, 295, 296, 297, 301, 305, 338, 339, 342, 346, 348, 380, 381, 384, 385, 386, 387, 390, 391, 392, 397, 398, 400, 401, 402, 428, 437, 502, 543, 544, 545, 546, 548, 549, 550, 645, 647, 757, 842, 890, 891, 894, 1012, 1036, 1037, 1038, 1039, 1040, 1041, 1042, 1090
Combustion test 1036, 1037, 1039, 1040, 1042
Composite 97, 179, 180, 388, 389, 390, 391, 395, 397, 398, 399, 400, 401, 402, 409, 446, 501, 631, 632, 633, 719, 733, 735, 736, 737, 738, 739, 740, 741, 816, 817, 905
Computational Fluid Dynamics 11, 110, 112, 117, 163, 224, 228, 236, 237, 331, 380, 381, 404, 405, 411, 562, 563, 667, 669, 686, 687, 689, 761, 837, 876, 923, 1000, 1001
Concentration polarization 94, 95, 98, 99, 100, 101
Constant heat flux 268, 326, 329, 371, 418, 487, 536, 782, 783, 988, 991, 1029
Contraction ratio 597
Convective heat transfer 222, 229, 267, 268, 273, 308, 336, 375, 462, 487, 537, 717, 721, 725, 857, 902, 903
Cross-Matrix absorber (CMA) 1
Curly-shaped shroud 686
Cycling helmet 667, 668, 669, 670, 675

D

Data driven 802
Date 88, 360, 563, 574, 631, 632, 633, 697, 813, 821
Degradation 103-104, 107-108, 222, 288, 292, 296, 305, 327, 351, 352, 357, 358, 401, 607-608, 611-613, 614, 907, 1036
Density 12, 13, 14, 15, 21, 29, 36, 38, 40-44, 47, 62, 76, 103, 104, 105, 119, 132, 143, 154, 163, 164, 165, 182, 191, 193, 229, 238, 257, 259, 260, 262, 265, 276, 277, 279, 282, 283, 287, 288, 289, 291, 293, 295-297, 314, 315, 328, 330, 340, 374, 393, 399, 406, 414, 415, 429, 438, 446, 462, 463, 475, 490, 493, 495, 524, 527, 564, 586, 595, 598, 607, 609, 623, 637, 656, 658, 659, 668, 670, 677, 678, 680, 682, 684, 685, 705, 706, 707, 717, 735, 744, 745, 746, 749, 772, 776, 780, 784
Diesel combustion 11, 21-22
Different inlet angle air 22
Direct solar dryer system 510-512
Double entry volute 757
Double heat sources 307-308
Double-pass solar air heater (DPSAH) 450
Draft 113, 209, 876, 1000, 1001, 1005, 1006, 1008-1009
Drag reduction 351, 352, 353, 354, 356-358
Drilled solid 36, 37, 38, 40-47, 694
Drying 1, 8, 58, 59, 141, 246, 247, 248, 249, 251, 262, 294, 338, 446, 449, 457, 510, 511, 513, 514, 515, 516, 517, 646, 881, 901, 906, 912, 914, 915, 916, 917, 918, 919, 921, 923, 924, 982, 1011, 1082, 1084, 1088
Dual solutions 145, 153-154, 472-473, 479, 480, 483
Dual-fuel engine 542-543
Dufour number 133, 141-142, 144, 146-148, 150, 156
Dynamic forces 407, 825

E

Electromotor 500, 502-507
Emulsion 520, 718, 719, 881-883, 886-887
Energy 1-2, 4, 6, 8, 24, 50-52, 54, 56, 58, 61, 63, 75, 79, 81-83, 101-102
Energy efficiency 1, 793, 515, 701, 1092
Energy recovery ventilator 617, 621
Enhancement 198, 203, 222, 256, 332, 333-334, 336, 371-372, 375, 418, 513, 532, 533, 540, 645, 692, 704-705, 707
Entropy 223, 981, 982-987
Exhaust waste heat 890
Experimental validation 459
Extending/compressing sheet 153

F

FEM: Abaqus 388
FEniCS 856-857, 860-861, 866
Ferrofluid 846-849, 851-853

INDEX

Film condensation 58-61, 67-68, 70-72
Flame structure 338-339, 341, 343, 346, 348, 1011, 1015
Flat tube 802-803, 805, 807-810, 814
Floating jetty 1000-1009
Floating OWC 208
Flow pattern 77, 117-118, 120-124, 129, 237, 311, 411, 670, 743, 943, 961-969, 981, 994, 1044-1049
Flow rate effect 287
Fluid Flow 39, 59, 72, 119, 130-131, 141-142, 150, 153-160, 191-194, 197-2000
Fluid Structural Interaction (FSI) 526
Flywheel energy storage 500-501
Focused-SAW 359, 360
Forced convection 310, 328, 417, 418, 781, 784, 785, 802, 803, 808, 813, 901, 1010, 1082
Fourier transformation infrared spectroscopy 103
Free convection 327, 374, 418, 485- 487, 493, 495, 496, 497, 532, 647, 782, 791, 792, 856
Free surface problem 561
Friction 43, 45, 47, 110, 129, 130, 132, 133, 134, 137, 138, 140, 141, 143, 144, 147, 149, 156, 157, 189, 194, 195, 204, 222, 310, 350-353, 355, 356, 362, 371, 406, 471, 472, 474-476, 478, 479, 481, 482, 489-493, 497, 562, 563, 634, 637, 638, 639, 644-648, 650, 667, 704, 710, 715, 717, 718, 734, 815, 856, 902, 943, 967, 971, 982, 983, 984, 985, 1044, 1052-1057, 1059, 1082
Furnace exit gas temperature 379, 380, 382
Fuzzy c-mean clustering 275
Fuzzy logic 275-277, 279

G

Galloping 768, 769, 771, 772, 773, 775, 776, 778, 779
Gas flow 229, 266, 267, 269, 272, 385, 523, 735, 919, 962, 967, 1035, 1046
Gas-liquid two-phase flow 961, 1043, 1044, 1049
Gasturb 835-843
Generator 51, 78, 161, 208, 256, 362, 371, 373, 403, 499-506, 531, 533, 686, 745, 792, 889, 890, 1011
Generator-set 499
Glycerine 960, 961, 963-966, 105
Glycerol aqueous solution 1043
Governing equations 27, 61, 76, 79, 140-142, 154, 155, 162, 163, 191-193, 204, 327, 403, 410, 412, 413, 428, 487, 496, 563, 642, 744, 748, 791, 792, 855, 857, 858, 859, 865, 973
Graphene 458, 459, 462, 468, 704, 901, 903, 904, 1054, 1056
ground reaction force 867
Groundwater levels 1062
Gsp 835-840, 842, 843

H

Hard disk 911-914, 916, 918-920, 923
HBN 732, 734-740
Heat absorption 3, 201, 204, 450, 858, 1081, 1082, 1087, 1089, 1093, 1094
heat exchanger 58, 59, 140, 266, 417, 440, 579-581, 583, 589, 617, 716, 718, 801, 802, 898, 942, 960, 961, 967, 1025, 1038, 1040, 1043
Heat generation/absorption 189, 191, 194, 204, 474, 856-858, 860-865
Heat pipe 58, 59, 72, 306, 307, 310, 311, 443-445, 617, 890, 901, 942, 1043
Heat pump 245-247, 509-512, 514, 516
Heat recirculation 226, 227, 229
Heat source 8, 76, 201, 306, 307, 308, 455, 471, 472, 474, 477, 480, 482, 658, 660, 662, 663, 716, 781, 782
Heat stress 874-878
Heat transfer 1, 22, 27, 33, 58-61, 63, 66-72, 86, 130, 140, 147, 178-181, 183-187, 189-191, 201, 220-223, 227, 228, 250, 266, 267, 269-272, 302-304, 306-308, 310, 325-327, 329, 331, 332, 334, 335, 337-339, 341, 346, 347, 370-377, 388, 392, 394, 397, 417, 418, 444, 445, 448, 459-461, 464, 471, 472, 476, 477, 480-482, 485, 486, 490, 494-497, 510, 531-537, 539, 580, 617, 619, 634, 645, 649, 653-655, 664, 703, 704, 706, 708-710, 712, 715-718, 720-722, 724, 726, 733, 781, 782, 784, 785, 789, 791, 792, 798, 801, 802, 805, 806, 808, 809, 813-815, 855, 856, 859, 874, 875, 878, 895, 898-904, 906, 942, 943, 969-971, 973-978, 980-982, 984, 987-993, 995-997, 1010, 1011, 1013, 1014, 1020, 1023, 1025-1033, 1053-1057, 1059, 1081, 1082

INDEX

Heat transfer enhancement 370, 371, 374, 531, 534, 536, 539, 715, 718, 789, 792, 901, 987, 988, 996
Heat transfer rate 67, 68, 69, 70, 71, 72, 178, 185, 186, 187, 266, 267, 269, 271, 272, 308, 337, 338, 370, 371, 374, 375, 377, 471, 477, 480, 481, 482, 531, 534, 535, 539, 709, 718, 722, 789, 806, 970, 980, 981, 984, 988, 1010, 1053, 1057
Heating 51, 76, 77, 227, 245, 246, 255, 258-260, 262-264, 286-290, 293, 294, 296, 300-304, 308, 326, 337, 338, 343, 347, 373, 391, 394, 417, 485, 509, 510, 512-516, 532, 533, 544, 547, 550, 569, 575, 597, 608, 609, 619, 646, 647, 655, 715, 716, 735, 739, 781, 792, 835, 837, 841, 842, 845, 846, 875, 877, 898, 911, 912, 915, 916, 923, 928, 933, 936, 937, 939, 981, 1010, 1011, 1029, 1036, 1078, 1082-1084
Heave motion 999, 1000, 1005-1008
Heave plate 999, 1000, 1003-1008
High density polyethylene 103-105
High viscosity 960, 1044
High-rise building 616, 617, 619, 620
Hourglass profile 969, 971, 972, 975, 976
Hybrid nanofluid 703, 705, 707, 708, 712, 715, 716, 718, 719, 721, 722, 724, 726, 814-820, 898-906, 1053, 1056
Hydraulic Performance 969-972, 976-978, 1082
Hydrofoil 110, 112

I

Impinging flame jet 337, 338, 341, 1010, 1011
Impinging jets 989, 995, 1025
Incidence angle 756, 764-766
Inclined capillary pipe 1043, 1044
Indirect evaporative cooler 444, 579, 580
Indirect Evaporative Cooling System 440, 443-445, 580
Indoor air quality 616, 617, 619
Injection effect 33, 471, 472, 477, 479, 482
Instantaneous efficiency 1, 7, 8, 448, 454, 455
Internal undular bore of depression 312, 314,316, 318, 323
Irrigation 50, 51, 54, 56

J

Jet-Engine inspired Wind Turbine 685-691
Joint stiffness 687

K

K-type thermocouple 4, 85-92, 289, 451, 512, 532

L

Lame structure 1010
Laplace transform technique 26, 27, 33, 791, 792, 799
Large-eddy simulation 676
Laser-induced fluorescent 370, 373
Lattice-Spring Model (LSM) 75, 525
Liquid viscosity 724, 910, 963, 1043-1050
LNG 541, 542, 546-550
Low-cost data acquisition 85
Low-rise building 616, 620, 681-683

M

Machining 710, 716-718, 724, 902, 903, 1052-1057, 1059
Magnet wire 1071-1079
Magnetic microbeads 1071, 1072, 1075-1076
Magneto-hydrodynamics 140, 141
Magnetorheological brake 867
Magnetorheological damper (nonlinear) 824
Marangoni 845-852, 913-917, 922, 980-985
MAV 952, 953
MAX6675 85-92
Maxwell fluid 26, 130, 472, 791, 792
MD Simulation 928, 930, 931, 937, 938
Mechanical properties 107, 108, 181, 387, 393, 606-613, 630-632, 718, 916, 928, 930, 937, 938
Meshless 75, 525, 526
Method of lines 312, 315
MHD 27, 189-191, 204, 359, 360, 486, 634, 792, 855, 856
Micro combustion 226, 227
Microchannel Heat Sink 969-972, 978
Microfluidics channel 1071, 1076
Micromixing 359, 360, 362
Microtube 26, 267, 269, 270

INDEX

Mini pipe 960, 961, 963, 964, 1043
Mixed convection 129-131, 133, 138, 141, 143, 152-154, 159, 418, 472, 485, 486, 634, 636, 637, 639-642, 781, 782, 789, 865
Mixing process 116, 183, 360, 365, 368, 427, 428, 438, 667
Modelling 14, 15, 37, 77, 117, 129, 222, 223, 236, 237, 380, 387, 394-398, 404, 410, 411, 414, 415, 458-460, 462-464, 544, 563, 564, 619, 653, 656, 667, 669, 686, 688, 726, 744, 745, 806, 875, 928, 937, 944, 953
Modified Bouc-Wen model 824, 829, 830, 831, 833
Molten salt 732-740
Mud rheology 36-38, 40, 41, 43, 44, 47
Mud rheology 36-38, 40, 41, 43, 44, 47
Multi-phase behaviour 312, 322
Multiple reference frame 116, 117

N

Nanocellulose 644, 645, 1055
Nanofluid 26, 27, 33, 34, 130, 189-192, 201, 204, 221, 327, 331, 334, 471, 718, 719, 721, 723, 724, 726, 739, 791-793, 798, 799, 817-820, 846, 855-857, 860, 865, 970, 988, 1052-1059
Nanofluids 27, 33, 189, 221, 325-327, 329, 331-334, 486, 703-708, 710, 712, 715-718, 722-724, 726, 733, 791, 792, 798, 814-820, 898-906, 988, 1053-1057
Nanoparticle 221, 327, 485, 488, 492, 495, 644, 646-648, 703-707, 709, 712, 715-719, 723, 725, 726, 733, 857, 859-865, 899, 902, 903, 917, 1053, 1054, 1057
Nanoparticles 26-29, 32-34, 189-193, 195-197, 199-204, 221, 327, 351, 472, 486, 492, 496, 497, 644, 645, 651, 703, 704, 706-710, 712, 715-718, 721, 723, 732-736, 738-740, 791, 792, 796-799, 814-820, 855-857, 859, 862, 898-903, 905, 906, 917, 1053-1056, 1059
Nanopore Skinless Bamboo Potency 440, 445
Nata de coco fiber 350-357
Ni nanowires 928, 930-939
Non-Newtonian fluid 26, 40, 129, 152, 190, 191, 352, 353, 472, 473, 634, 637, 724, 742, 749
Nozzle 12, 13, 75, 78, 105, 161, 162, 165-169, 171, 172, 175, 176, 215, 216, 372, 434, 518-524, 645, 756, 757, 766, 769, 837, 918, 987, 988, 990, 992-996, 1010-1012, 1020, 1022, 1023
Numerical evaluation analysis 911
Numerical Solution 26, 58-60, 129, 132, 143, 144, 152, 153, 159, 168, 191, 204, 413, 471, 476, 485, 525, 792, 855, 918

O

Office rooms 569
Offshore structures 403, 406, 407
On-design 835-837, 840-842
Open loop wind tunnel 593, 595, 603
OpenFoam 411, 561-563, 565-567, 677, 922
Open-top downdraft gasifier 255
Optimization 207, 218, 222, 223, 301, 371, 654, 659, 686, 831, 835, 836, 840, 911, 913, 923, 1065, 1068, 1069, 1081
Organic solvent nanofiltration 94, 95
Orifice jet 370, 373
Ortex generating jet 370

P

Palm kernel shell 286, 287, 694
Paper Plane 952-959, 995
Paphia undulata 622-624, 627
Parameter estimation 94, 96, 100
Particle method 75, 525
Particleboard 606-610, 612, 613
Passenger ship 541
Patrol Boat 110, 111
PCM 1, 2, 5-8, 448, 449, 452-456, 732, 734, 902
Pectin 880-886, 916
Pedestrian wind environment 676, 677, 679, 681
PEMFC 325, 326, 335
Performance 1, 4, 6, 8, 44, 75, 77, 79, 83, 94-96, 100, 165, 175, 181, 189, 207, 208, 212, 216, 218, 219, 221, 237, 246-248, 253, 255, 256, 287, 288, 293, 306-309, 311, 325, 326, 335, 338, 359, 361, 364, 371, 379, 388, 393, 440-442, 444, 448, 451, 453, 455, 509, 510, 512, 516, 531, 532, 538, 539, 541-543, 546, 548, 550, 561, 567, 581, 583,

INDEX

586-589, 591, 607, 609, 613, 617-619, 644, 649, 653, 655, 658, 666, 667, 669, 685, 686, 688-691, 693, 696, 698, 700, 701, 703, 715-718, 724, 726, 727, 734, 739, 754, 756, 757, 761, 762, 764, 766, 801, 807, 813, 824, 835, 836, 838-840, 842, 843, 855, 867, 897-899, 901, 903, 906, 942, 952, 953, 956-958, 963, 969-973, 975-978, 987, 1000, 1035, 1040, 1041, 1053, 1056, 1065, 1069, 1082, 1090
Phase change material (PCM) 1, 448, 734, 735, 739
Photograph 341-345, 347, 814, 815, 817, 818, 961, 992, 1012
PHRS 531, 532
Plan area density 676, 677, 681, 683
Plasma temperature 458, 459, 463-468
Plaster 178, 181, 187
Polydimethylsiloxane (PDMS) 1071, 1072
Polymer 45, 94, 97, 100, 103-108, 117, 130, 152, 178, 179, 181, 183, 190, 350, 351, 445, 471, 634, 693, 700, 791, 792, 900, 904, 905, 912, 916, 917, 929, 1073
Polymorphs 622, 623, 627
Porous media 58-60, 67-71, 634, 635, 642, 792, 942-945, 657, 1001
Porous medium 58-61, 63, 71, 72, 189-192, 204, 486, 791, 792, 845-857, 850, 943
Power distribution networks 653
Power generation 54, 226, 301, 325, 326, 379, 380, 499, 685, 685, 889, 891, 897, 1035
Prediction 12, 15, 45, 68, 95, 96, 98, 236, 267, 275, 276, 278, 279, 284, 379, 380, 407, 427, 538, 561, 562, 567, 664, 722, 726, 743, 761, 769, 812, 867, 878, 1000, 1036, 1038, 1068, 1069, 1082
Premixed flame jet 337, 338, 340, 1010
Pressure drop 97, 119, 161, 162, 214, 236, 268, 325, 326, 329, 332, 333, 335, 350-355, 370, 444, 617, 685, 691, 703, 724, 726, 742, 749, 752, 753, 801-803, 815, 898-901, 907, 941, 945, 867, 969-971, 973, 977,
Primary conversion efficiency 207, 208, 211, 212, 215, 216
Pulsating flame jet 1010
Pump sump 235-238, 240-244, 867, 868, 872
PV panel 50, 52-54, 56

Q -

R
Reclamation 552, 553, 556-560
Refrigeration 245, 247-29, 253, 264, 801
Relative humidity 51, 245, 246, 248, 307, 308, 442-444, 569-571, 575, 577, 586, 589-591, 874, 876
Renewable densified fuels 255, 257, 259
Response Surface Methodology 1062, 1063, 1065, 1069
Rheological Model 36-40, 44-46, 352, 749, 751, 752
Rotating cylinder 500, 781, 782, 785, 789
Rotation number 1025-1028, 1031, 1033
Rotational kinetic energy 499-506

S
Second grade fluid 26-28, 33, 141
Sedimentation 36, 235, 236, 327, 351, 705-707, 712, 814, 815, 817-820, 898
Seismic analysis 825
Semi circle enclosure 782, 783
Semi-Indirect Evaporative Cooling System 441, 444
Serpentine 326, 327, 331, 334, 336, 1026, 1027
Set-point temperature 570, 571
Shape optimization 208
Shear rate 26, 39,40, 44-46, 353-355, 705, 725, 743, 744, 753, 754, 792, 884-886
Ship resistance 110, 113, 562, 563, 567, 568
Silicon Dioxide (SiO2) 326-328, 719
Simulation 12, 15, 27, 75, 77-83, 110, 111-113, 115, 117, 118, 120, 123, 124, 129, 162, 163,165, 167, 168, 176, 177, 219, 220, 222-224, 227-231, 233, 236-239, 313, 324, 328, 329, 331, 335, 372, 380, 381, 386, 387, 389, 405, 409, 411-413, 416, 428, 430, 433, 434, 439, 460, 463, 464, 466-468, 500, 503, 526, 530, 545, 546, 551, 562-568, 580, 595, 617, 618, 655, 659-661, 665, 667, 670, 677-680, 684, 686-689, 744, 748, 749, 754, 757, 758, 761, 762, 767, 772, 773, 775, 780, 783, 793, 836-840, 842, 843, 875, 876, 878, 879,

912, 919-921, 923, 929, 931, 932, 938-940, 943-945, 953, 954, 956, 963, 968, 971, 973, 976, 982, 984, 986, 1000-1003, 1005, 1007, 1009, 1091
Sludge 301, 553, 554, 560, 1091
Smooth surface 372, 594, 595, 599, 601-604
Smoothed Particle Hydrodynamics (SPH) 75, 526
Solar collector 1, 418, 449, 1082-1086, 1088
Solar radiation 1, 2, 4-6, 8, 50-54, 219, 223, 449, 450, 452-454, 456, 533, 656, 664, 734, 1085, 1090, 1092, 1094, 1095
Solar still 219-224
Solar System 50, 51, 56, 587
Solitary wavetrain 313, 319, 322-324
Soot emission 11, 12, 15, 22, 23
Soret number 133, 141, 144, 146, 148, 150, 156
Spearman correlation 37-39, 41, 42
Specific energy consumption 246, 248-250, 252, 253
Specific heat capacity 29, 86, 645, 646, 648, 649, 651, 652, 733-736, 738-741, 794, 974, 990
Spiral pipe 351-353, 355-358
Square cylinder 769-773, 776, 778-780
Square plate 769-772, 776, 778-780
Squeezing flow 190-192
Stability 6, 95, 103, 109, 133, 145, 153, 154, 156, 157, 227, 228, 256, 263, 290, 291, 357, 358, 363, 433, 434, 454, 467, 472, 473, 476, 477, 479, 483, 500, 501, 599, 607, 610, 613, 614, 704-708, 713, 718, 719, 733, 734, 740, 741, 752, 770, 815-821, 825, 846, 847, 849-851, 899-902, 904-907, 937, 967, 1000, 1001, 1038, 1041, 1057
Stability analysis 133, 145, 153, 154, 156, 157, 433, 472, 473, 479, 483, 816, 818, 821
Stagnation Point 339, 346, 472-474, 483, 486-488, 491-494, 497, 498, 533, 915, 989
Stagnation point flow 472-474, 483, 486, 487, 498
Starch binder 287, 289-292, 294, 297
Stern foil 110-116
Stretching sheet 130, 131, 134, 145, 146, 150, 154, 160, 473, 474, 478, 486, 487, 635, 792, 793
Stretching surface 131, 141
Structural damage capacity 388
Substrates 361, 611, 891, 892, 906, 912-917, 919-921, 924
Suction 26, 31, 33, 34, 132, 141, 143, 144, 155, 156, 240-245, 486, 520, 619, 869-873, 1026
Surface tension 15, 18, 21, 58-60, 68, 72, 165, 277, 307, 310, 311, 522, 525, 534, 708, 725, 846, 915-920, 923, 962-965, 981, 982, 985, 1044-1046
Swirling flame jet 338, 339, 342
Symmetric volute 757-760, 762-767
Syngas production 256, 265

T

TEM 815, 816, 818
Temperature 1-8, 13, 14, 17, 21, 22, 24, 31, 33, 34, 51, 52, 59-61, 67-69, 72, 75, 76-83, 85-92, 94, 103-105, 130-132, 134, 136-139, 141-150, 153-155, 157-160, 162, 165, 168, 169, 171, 172, 176, 180-182, 184-187, 190-194, 196-203, 205, 222-224, 228-231, 246-249, 251-254, 256-259, 261-265, 267-273, 276, 287-297, 302-305, 307-309, 314, 327, 329-332, 335, 339, 341, 342, 346-348, 353, 354, 371, 373, 374, 375, 380-383, 386, 388-395, 397, 399, 401, 402, 406, 414, 418-423, 425, 426, 441-445, 449-456, 459-462, 464-469, 472-475, 478, 481-483, 486-488, 493-498, 501, 511, 513-517, 533-538, 540, 554, 564, 570-578, 580, 582, 587-590, 592, 594, 595, 598, 599, 604, 607, 609, 613, 617, 618, 620, 623, 635, 636-638, 642, 643, 645-650, 653-656, 659-665, 704-707, 709-713, 716-720, 725, 726, 733-736, 738-741, 762, 782-786, 788-790, 792, 793-800, 803-807, 810, 827, 837, 838, 841, 844, 846, 847, 856-858, 860-866, 875, 877, 878, 882, 890-898, 900-905, 912, 915-917, 922-924, 929, 932, 934, 936-938, 940, 943-945, 949, 951, 964, 968, 970, 972-977, 981, 982, 984, 985, 988, 990, 992, 1011, 1012, 1014, 1026, 1028-1032, 1036-1042, 1053-1058, 1075, 1079, 1082-1088, 1090, 1092-1095
Temperature effect 287, 713
Temperature profile 5-7, 59, 72, 134, 136-138, 145-148, 157, 159, 197, 198, 200, 202, 261, 454, 455, 459, 460, 464-469, 472, 473, 478, 482,

INDEX

483, 486-488, 493, 497, 498, 588, 635, 662-664, 797-799, 847, 863, 922, 1036, 1037, 1039, 1040-1042
Template-assisted electro deposition 929
TES 733, 734
Thermal 1-4, 8, 15, 17, 27, 29, 33, 59, 67, 103, 104, 132, 134, 142, 143, 145, 148, 154, 179, 180-183, 188, 190-193, 198, 202, 205, 223, 227-230, 233, 248, 249, 268, 270-273, 302-305, 307-312, 326-330, 332, 335, 339, 347, 372, 338, 391-394, 398, 441, 445, 446, 449-453, 456, 459-465, 467, 469, 472, 475, 476, 482, 483, 487-489, 494, 497, 510, 511, 532, 536, 539, 540, 542, 544, 545, 550, 551, 553, 570, 571-578, 580, 581, 584, 588-590, 592, 607, 608, 610, 613, 614, 618-620, 637, 645, 646, 648-652, 654-659, 665, 667, 704-707, 709-711, 713, 714, 716-725, 727, 733, 735, 736, 740, 741, 784, 792-794, 799, 806, 807, 815-817, 821, 837, 846, 848, 849, 858, 875-877, 879, 890, 891, 899-907, 915-917, 943, 944, 970-974, 976-979, 981, 983-986, 988, 991, 993, 1030, 1036, 1039, 1041, 1053-1059, 1083, 1084, 1088, 1090-1092, 1095
Thermal comfort 179, 570, 571, 573, 575, 577, 580, 581, 584, 588-590, 592, 618, 620, 667, 875-877, 1090, 1092, 1095
Thermal conductivity 15, 29, 59, 180-183, 188, 190, 191, 193, 202, 228, 233, 310, 327, 328, 330, 332, 335, 392, 393, 441, 445, 446, 462, 463, 476, 581, 637, 645, 646, 648-651, 658, 659, 704-708, 709-711, 713, 714, 716-725, 727, 734, 735, 784, 792, 794, 799, 806, 807, 815, 817, 858, 899-907, 916, 943, 944, 974, 1030, 1054-1056, 1058,
Thermal conductivity viscosity 704, 705, 707, 716, 719
Thermal degradation 103, 104, 305,
Thermal expansion 132, 143, 154, 338, 391, 392, 394, 398, 424, 489, 637, 794, 1058,
Thermal performance 4, 182, 248, 307-310, 312, 327, 339, 372, 452, 532, 539, 540, 619, 656, 704, 907, 970-973, 976-978, 1036, 1041
Thermal performance factor 531,538-539,
Thermal radiation 27, 34, 138, 141, 150, 159-160, 181, 187, 189-191, 204-206, 464, 471, 483-484, 486, 498, 635, 643, 799
Thermal state 653-656, 658, 664-665
Thermo-chromic liquid crystal 1025, 1027, 1030, 1033
Thermoelectric generator 889-890, 897
Thermogravimetric Analysis 300, 735, 739, 1035, 1038
Three-dimensional 138, 141, 150, 159-160, 226-227, 232, 236, 386, 411, 483-486, 498, 635, 790, 866, 919-920, 924, 985-986, 1080-1081
Time-trial 666-669
Tool life717, 902, 1052-1053, 1055-1056, 1059-1061,
Torrefaction 256, 286-299,
Total Acid Number (TAN) 552-553, 555-556, 558
Total enthalpy and 266, 269-271
Transition line 960, 966, 1043, 1049,
Transport model 94-97, 100-101, 236,
Trapping efficiency 1071-1073, 1075-1079
Tubes 2-3, 84, 233, 267, 269, 273, 307, 357, 417, 423-424, 449, 450, 529, 531-532, 535-540, 579-581, 583, 589, 591, 801-803, 805-806, 875, 1082, 1088, 1095
Turbochargers volute 756
Turbulence intensity 372, 563, 593-594, 601-603, 669, 955, 988
Turbulence model 12, 77, 116, 161, 164-168, 177, 236-237, 413, 428-429, 529, 563, 669, 674, 688, 748, 944, 951, 962, 1001, 1009
Turbulent flow 117, 164, 219, 224, 270, 351, 354-358, 567, 594, 671-674, 686, 692, 761, 781, 790, 822, 901, 926, 944, 995
Turbulent mixing 12, 116, 434, 439, 667
Two-layer fluid system 312-313, 323
Two-phase 58-74, 116-117, 128, 176-177, 223, 540, 865, 910, 922, 960-964, 966-968, 988, 991, 993, 995, 997, 1043-1044, 1046-1051
Two-phase mixing 116
Two-phase region 58-61, 63, 67-70, 72

U

Ultra-violet irradiation 103-106
Underground cables 653-655, 658, 664-665
UV-vis spectral analysis 814-815, 817
UV-Visible Spectrophotometer (UV-Vis) 552-553, 555-556

INDEX

V

Variable gravity 845-846, 848-849, 952-854
Varying diameter 417
Vertical closed- loop oscillating heat pipe 306-307
Vertical plunging jets 518-519
Vertical random array 676-677, 681, 683
Vibration control 768, 779, 834
Viscosity 12-13, 36, 38-40, 43, 47, 77, 105, 118, 131, 142, 150, 153, 165, 177, 190, 192, 197, 268, 309, 327, 329, 334, 339, 352-353, 355, 413-414, 429, 472-474, 486-487, 489, 497-498, 526, 600, 636, 651, 667, 693, 703-704, 706-708, 710-722, 724-731, 743-748, 754-755, 783, 793, 798, 800, 819, 821-823, 845-846, 853, 880-901, 907-908, 916-918, 943-944, 955, 960-961, 963, 965-968, 973, 989, 990, 1009, 1012, 1028, 1043-1050, 1053, 1059
Viscous dissipation 138, 150, 160, 190-191, 199, 268, 327, 425, 484, 497, 634-635, 638-639, 643, 792, 799, 917-918, 921, 944, 985
Volatile 246, 257, 289-290, 293-294, 296, 298, 300-304, 381, 911-912, 925, 1036, 1039-1041
Volume flow rate 34, 50, 52, 54-56, 340,444, 585, 976, 1039
Vortex-induced vibration 768, 779-780

W

Warren truss bridge 824
Waste Material 178, 181-182, 301, 607, 881
Water impinging jet 987
Water mist 531-539
Water quantity 222, 1062
Water saturation 275-279, 284-285
Wave current interactions 403
Wave energy converter 207-208, 217
Wave periods 999-1000, 1004-1006, 1008
Wear 24, 644-646, 648, 650, 652, 815, 820, 899, 903, 909, 1052-1057, 1059-1061
Well depth 50, 52-56
Wet steam 161-163, 165, 167-170, 172, 175-177

X -

Y

Yard material 1089-1093

Z

Zeta potential 703, 705, 707-708, 712, 729, 814-815, 817, 819-820